

**NIST Special Publication 1069**

Advanced Technology for

# **Fire Suppression in Aircraft**

**The Final Report of the Next Generation  
Fire Suppression Technology Program**

Richard G. Gann, Editor  
Building and Fire Research Laboratory

June 2007



U.S. Department of Commerce  
Carlos M. Gutierrez, Secretary

Technology Administration  
Robert C. Cresanti, Under Secretary for Technology

National Institute of Standards and Technology  
William A. Jeffrey, Director



Page intentionally left blank

Certain commercial entities, equipment, or materials are identified in this document in order to describe an experimental procedure or concept adequately. Such identification is not intended to imply recommendation or endorsement by the National Institute of Standards and Technology or the Strategic Environmental Research and Development Program, nor is it intended to imply that the entities, materials, or equipment are necessarily the best available for the purpose.

The policy of NIST is to use metric units of measurement in all its publications, and to provide statements of uncertainty for all original measurements. In this document, however, data from organizations outside NIST are shown. These data may include measurements in non-metric units or measurements without uncertainty statements.

**National Institute of Standards and Technology Special Publication 1069**  
**Natl. Inst. Stand. Special Publication 1069, 1240 pages (June 2007)**  
**CODEN: NSPUE2**

U.S. GOVERNMENT PRINTING OFFICE  
WASHINGTON: 2007

---

For sale by the Superintendent of Documents, U.S. Government Printing Office  
Internet: [bookstore.gpo.gov](http://bookstore.gpo.gov) — Phone: (202) 512-1800 — Fax: (202) 512-2250  
Mail: Stop SSOP, Washington, DC 20402-0001

## ABSTRACT

---

Fires and explosions were, and continue to be, among the greatest threats to the safety of personnel and the survivability of military aircraft both in peacetime and during combat operations. Production of halon 1301 (CF<sub>3</sub>Br), long the fire suppressant of choice, ceased as of January 1, 1994 due to its high ozone depleting potential (ODP). By 1997, the U.S. Department of Defense (DoD) had identified the best available replacement for halon 1301 in aircraft, HFC-125 (C<sub>2</sub>H<sub>5</sub>F), but it requires two to three times the mass and storage volume and contributes to global warming. Meanwhile, new aircraft were in various stages of design, and the international community was questioning the necessity of maintaining the large reserves of halon 1301.

A new undertaking, the Next Generation Fire Suppression Technology Program (NGP), was created to identify, through research, fire suppression technologies with reduced compromises. Supported primarily by the DoD Strategic Environmental Research and Development Program (SERDP) as Project WP-1059, the NGP goal was to “Develop and demonstrate technology for economically feasible, environmentally acceptable and user-safe processes, techniques, and fluids that meet the operational requirements currently satisfied by halon 1301 systems in aircraft.” The multiple demands on the new technologies were daunting.

In its decade of systematic research (1997-2006), the NGP revitalized the field of fire suppression science. This book tells the story of how the NGP came about, what research was performed, how it modernized the thinking in the field, and the technical findings that emerged related to fire suppression in aircraft. The enclosed CD compiles the collected publications from the program.

Keywords: flame inhibition, fire research, fire suppression, halon, aircraft

Page intentionally left blank

# TABLE OF CONTENTS

---

<b>Abstract</b> .....	<b>i</b>
<b>Table of Contents</b> .....	<b>v</b>
<b>List of Figures</b> .....	<b>xvii</b>
<b>List of Tables</b> .....	<b>xlv</b>
<b>Chapter 1: Introduction</b> .....	<b>1</b>
1.1 Background.....	1
1.2 The Evolution of Fire Suppression .....	1
1.3 The Rise of Halons.....	3
1.4 The Atmospheric Threat .....	5
1.5 History of the NGP .....	9
1.6 This Book.....	15
1.7 References.....	16
<b>Chapter 2: History of Fire Suppression in Aircraft</b> .....	<b>19</b>
2.1 Fire Threats to Military Aircraft .....	20
2.2 Protected Compartments on Aircraft .....	24
2.2.1 Engine Nacelles .....	24
2.2.2 Other Powerplant-type Compartments .....	28
2.2.3 Dry Bay Compartments .....	31
2.2.4 Cargo Compartments .....	34
2.2.5 Other Compartments.....	36
2.2.6 Fuel Tank Ullage.....	37
2.3 Types of Fires Experienced .....	41
2.3.1 Safety-related Fires .....	43
2.3.2 Ballistically-induced Fires .....	45

2.3.3	Spray Fires .....	47
2.3.4	Pool Fires .....	49
2.3.5	Fire Characteristics .....	50
2.3.6	Aircraft Operational Temperature Environment.....	54
2.3.7	Reignition.....	79
2.4	Fire Suppressants Used on Aircraft .....	80
2.4.1	Powerplant Compartments.....	81
2.4.2	Dry Bay Compartments .....	86
2.4.3	Certification .....	86
2.5	Halon Alternative Technology Development Program (TDP).....	92
2.5.1	Phase 1 – Operational Parameters Study .....	93
2.5.2	Phase 2 – Operational Comparison of Selected Extinguishants .....	94
2.5.3	Phase 3 – Establishment of Design Criteria Methodologies.....	94
2.5.4	Impact of Halon Alternative Fire Suppression to the Aircraft.....	96
2.6	References.....	109
<b>Chapter 3: Flame Suppression Chemistry .....</b>		<b>119</b>
3.1	Introduction.....	120
3.2	Halogen-containing Compounds .....	121
3.2.1	Previous Understanding of the Inhibition Mechanism of CF <sub>3</sub> Br.....	121
3.2.2	Suppression of Nonpremixed Flames by Fluorinated Ethanes and Propanes.....	124
3.3	Metal-containing Compounds.....	142
3.3.1	Background.....	142
3.3.2	Metals with Demonstrated Flame Inhibition Potential .....	155
3.3.3	Flame Inhibition by Iron-containing Compounds.....	156
3.3.4	Flame Inhibition by Tin and Manganese .....	178
3.3.5	Complexation/Matrix Absorption of Super-effective Agents.....	199
3.3.6	Potential for Loss of Effectiveness of Other Metals.....	224
3.3.7	Flame Inhibition and Loss-of-effectiveness Summary.....	232
3.3.8	Conclusions.....	235

3.4	Phosphorus.....	236
3.4.1	Introduction.....	236
3.4.2	Inhibition of Non-premixed Flames by Phosphorus-containing Compounds.....	238
3.4.3	Effects of Dimethyl Methylphosphonate on Premixed Methane Flames.....	267
3.4.4	Summary: Phosphorus-containing Compounds in Flames.....	281
3.5	Comparative Flame Inhibition Mechanisms of Candidate Moieties.....	282
3.5.1	Introduction.....	282
3.5.2	Spectroscopic Studies of Inhibited Opposed Flow Propane/Air Flames.....	282
3.5.3	CF <sub>3</sub> Br and Other Suppressants: Differences in Effects on Flame Structure.....	291
3.5.4	Influence of Bond Energies on Catalytic Flame Inhibition.....	299
3.5.5	Temperature Regions of Optimal Chemical Inhibition of Premixed Flames.....	307
3.6	Insights on Flame Inhibition.....	316
3.7	References.....	318
<b>Chapter 4: Aerosol Properties.....</b>		<b>339</b>
4.1	Introduction.....	340
4.2	Previous Knowledge.....	341
4.2.1	Water.....	341
4.2.2	Powders.....	341
4.2.3	Combined Agents - Water Additives.....	342
4.2.4	Burning Surfaces.....	344
4.2.5	Large-scale Studies.....	345
4.2.6	Modeling.....	348
4.3	The Nature of Aerosols.....	348
4.3.1	Quantitative Descriptors.....	348
4.3.2	Generation Techniques.....	350
4.3.3	Quantification of Aerosols.....	351
4.3.4	Aerosol Size and Velocity Characterization.....	351

---

4.3.5	Aerosol Properties Affecting Behavior.....	355
4.4	The Nature of Flames.....	358
4.4.1	Flame Characteristics.....	358
4.4.2	Premixed Bunsen Type Flames .....	359
4.4.3	Non-premixed Flames.....	360
4.5	Aerosol Flame Suppression Studies.....	363
4.5.1	Water, a Physical Suppression Agent.....	363
4.5.2	Alkali Metal Bicarbonates, Chemically Active Fire Suppressants.....	397
4.5.3	Aqueous Metal Salt Solutions, Combined Chemical and Physical Suppression.....	412
4.5.4	Dendrimers, Combined Chemical and Physical Flame Suppression.....	430
4.6	Surface Cooling .....	438
4.6.1	Introduction.....	438
4.6.2	Evaporation of Liquid Droplets .....	440
4.6.3	Spray Cooling .....	443
4.6.4	Convective Regime.....	444
4.6.5	Nucleate Boiling Regime.....	445
4.6.6	Critical Heat Flux.....	446
4.6.7	Transition and Film Boiling Regimes.....	446
4.6.8	Summary .....	448
4.7	Aerosols and Burning Surfaces.....	448
4.7.1	Flame Spread Studies.....	449
4.7.2	Droplet Interaction with a Hot Surface.....	458
4.7.3	Summary and Conclusions .....	466
4.8	The New State of Knowledge of Flame Extinguishment by Aerosols.....	467
4.9	Relation of Findings to Practical Fires.....	468
4.10	References.....	469
	<b>Chapter 5: Instrumentation for Bench- and Large-scale Test Fixtures.....</b>	<b>481</b>
5.1	Introduction.....	482
5.2	Laser Induced Breakdown Spectroscopy for Measurement of Fire Suppressants.....	483

5.3	Tunable Diode Laser Absorption Spectroscopy (TDLAS) for Measurement of Combustion Products, Fuels, and Oxygen.....	485
5.3.1	General.....	485
5.3.2	HF.....	486
5.3.3	Oxygen.....	490
5.3.4	Fuels.....	490
5.3.5	Observations.....	501
5.4	Measurement of Fire Suppressant Concentration Using a Differential Infrared Rapid Agent Concentration Sensor (DIRRACS).....	502
5.4.1	Introduction.....	502
5.4.2	Original Instrument Design – DIRRACS I.....	502
5.4.3	Improved Hardware Design – DIRRACS II.....	505
5.4.4	Data Acquisition and Analysis.....	507
5.4.5	Calibration Experiments.....	507
5.4.6	Release Tests of HFC-125 in the TARPF Facility.....	508
5.4.7	HFC-125 Release Tests in a Bradley Vehicle.....	509
5.4.8	Assessment.....	513
5.5	Conclusion.....	513
5.6	References.....	514
<b>Chapter 6: Screening Tests for Candidate Fire Suppressants .....</b>		<b>517</b>
6.1	The Need for Screening Tests.....	518
6.2	General Approach.....	519
6.3	Agent Properties to be Screened.....	519
6.4	Fire Suppression Efficiency Screening.....	521
6.4.1	Estimation of Values.....	521
6.4.2	Cup Burner.....	522
6.4.3	Dispersed Liquid Agent Fire Suppression Screen (DLAFSS).....	525
6.4.4	Transient Application, Recirculating Pool Fire Apparatus (TARPF).....	535
6.4.5	Summation.....	557
6.5	Atmospheric Lifetime Screen.....	557
6.5.1	Factors Affecting Atmospheric Harm.....	557

6.5.2	Prior Estimation Methods .....	558
6.5.3	The Screening Protocol.....	561
6.5.4	Removal by Hydroxyl Radical Reaction .....	561
6.5.5	Measurement of Photolysis Rates.....	565
6.5.6	Estimation of Reactivity .....	568
6.5.7	Solution of Fluoroalkylamines.....	571
6.5.8	Reactivity of Alkyl Phosphates towards Radicals in Water .....	571
6.6	Volatility Screen .....	572
6.6.1	Extinguishant Volatility .....	572
6.6.2	Extinguishant Evaporation Equilibrium .....	572
6.6.3	Extinguishant Evaporation Rate .....	574
6.6.4	Boiling Temperature .....	576
6.7	Toxicity Screen .....	577
6.7.1	Hazards and Regulation .....	577
6.7.2	Screening Process .....	578
6.7.3	Literature Values.....	579
6.7.4	Quantitative Structure Activity Relationships .....	581
6.7.5	Non-animal Laboratory Testing.....	584
6.7.6	In vitro Tests .....	589
6.7.7	PBPK Modeling of Cardiotoxic Effects .....	590
6.7.8	Limit Tests .....	596
6.8	Application of Screen Tests.....	597
6.9	References.....	598
<b>Chapter 7: Search for New Fire Suppressant Chemicals .....</b>		<b>611</b>
7.1	Fire Suppressant Replacement Knowledge prior to the NGP.....	612
7.1.1	Overview of Early Halon Replacement Efforts .....	612
7.1.2	Fire Suppressant Research - 1974 through 1993 .....	613
7.1.3	DoD Technology Development Plan (1993 through 1997).....	615
7.1.4	Advanced Agent Working Group (AAWG).....	616
7.1.5	Summary: Alternative Agents and Selection Criteria prior to the NGP.....	622

7.2	The NGP Approach to New Chemicals Screening.....	623
7.3	NGP Surveys of Inorganic Chemical Families.....	626
7.3.1	Main Group Elements - Group I.....	626
7.3.2	Main Group Elements - Group II.....	627
7.3.3	Main Group Elements - Group III.....	627
7.3.4	Main Group Elements - Group IV.....	628
7.3.5	Main Group Elements - Group V.....	634
7.3.6	Main Group Elements - Group VI.....	645
7.3.7	Main Group Elements - Group VIII.....	646
7.3.8	Transition Metal-based Compounds.....	646
7.3.9	Inorganic Chemicals - Conclusions.....	647
7.4	NGP Surveys of Organic Compounds.....	647
7.4.1	Highly Efficient Thermal Agents.....	647
7.4.2	Tropodegradable Candidate Compounds.....	658
7.4.3	Bromofluoroalkenes.....	662
7.4.4	Fluoroalkoxide and Fluoroalkyl Phosphorus Compounds.....	665
7.4.5	Fluoroalkyl Nitrogen-based Candidates.....	680
7.4.6	Bromofluoroalkyl Nitrogen-based Candidates.....	685
7.4.7	Fluorinated Ethers.....	687
7.4.8	Bromofluoroethers.....	691
7.4.9	Bromofluorooxiranes.....	694
7.4.10	Bromofluoro/Fluorinated Aldehydes and Ketones.....	695
7.4.11	Bromofluoro Alcohols.....	695
7.4.12	Iodinated Hydrocarbons.....	696
7.5	Chemical Family Options and Replacement Issues.....	700
7.5.1	Suppressant Criteria and Selection Constraints.....	700
7.5.2	General Conclusions.....	701
7.6	References.....	702
<b>Chapter 8: Fluid Dispensing and Dispersion.....</b>		<b>721</b>
8.1	Introduction.....	722
8.1.1	Characteristics of Aircraft Engine Nacelle Fires.....	722

---

8.1.2	Summary of Suppressant Fluid Dynamics.....	723
8.1.3	Scope.....	724
8.2	Fluid Storage.....	725
8.3	Fluid Transport through Piping.....	726
8.3.1	Introduction.....	726
8.3.2	Previous Work .....	728
8.3.3	Base Code Selection .....	730
8.3.4	Code Development Work .....	732
8.3.5	Code Theory.....	733
8.3.6	Supporting Laboratory Data .....	753
8.3.7	Comparison of Code Predictions to Experimental Data .....	786
8.3.8	Assessment of Fluid Transport Model.....	804
8.4	Dynamics of Fluid Transport in Cluttered Spaces.....	805
8.4.1	Spray Transport past Generic Clutter Elements.....	805
8.4.2	Spray Interaction with Unheated and Heated Clutter Elements .....	809
8.4.3	Transport around Clutter and Recirculation Zones.....	821
8.4.4	Low Temperature Effects on Agent Dispersion .....	829
8.5	Modeling of Fluid Dispersion in a Nacelle.....	839
8.5.1	Background.....	839
8.5.2	CFD Models.....	839
8.5.3	Code Assessment Using Quarter-Scale Nacelle Tests and Simulations .....	847
8.5.4	Assessment of VULCAN Fire Suppression Sub-model .....	854
8.5.5	Assessment of VULCAN in Suppressant Distribution in a Full-scale Nacelle .....	863
8.5.6	Assessment of VULCAN in Pool Fire Suppression in a Full-scale Nacelle .....	868
8.6	Full-scale Nacelle Fire Suppression Tests .....	871
8.6.1	Experimental Design.....	871
8.6.2	Test Facility .....	872
8.6.3	Test Matrices and Decision Tree .....	876
8.6.4	Actual Test Program .....	878
8.6.5	Instrumentation .....	879

---

8.6.6	Test Procedure .....	879
8.6.7	Test Results and Comparisons to Simulations.....	882
8.7	Improved Transport of Water to Fires .....	889
8.7.1	Background.....	889
8.7.2	Electrically Charged Water Mist .....	889
8.7.3	A Self-atomizing Form of Water .....	909
8.8	Summary of Lessons Learned.....	916
8.9	References.....	918
<b>Chapter 9: Powder Panel and Propellant Discharge Technologies .....</b>		<b>927</b>
9.1	Introduction.....	927
9.2	Enhanced Powder Panels .....	929
9.2.1	NGP Objectives .....	929
9.2.2	Background on Powder Panel Technology.....	930
9.2.3	Operating Principle .....	931
9.2.4	Technical Issues .....	933
9.2.5	Survey of Powder Panel Applications .....	934
9.2.6	Powder Dispersion Screening Experiments.....	937
9.2.7	Live-fire Proof-of-concept Demonstrations.....	947
9.2.8	Optimization Program.....	951
9.2.9	Live-fire Demonstration Testing of Optimized Enhanced Powder Panels .....	957
9.2.10	Mass-trade Comparison Analysis .....	970
9.2.11	Summary of Powder Panel Research Program .....	974
9.3	Solid Propellant Gas Generators.....	976
9.3.1	Brief History .....	976
9.3.2	Operating Principles.....	977
9.3.3	Experimental Techniques.....	978
9.3.4	Results: General Behavior of Propellants .....	990
9.3.5	Results: Cooled Propellant Formulations .....	994
9.3.6	Results: Chemically Active Fire Suppressants .....	1003
9.3.7	Results: Hybrid Fire Extinguishers.....	1013

9.3.8	Summary of Solid Propellant Gas Generator Research .....	1020
9.4	References.....	1023
<b>Chapter 10: Life Cycle Costing of Fire Suppression Systems.....</b>		<b>1025</b>
10.1	Background.....	1025
10.1.1	Technical Concept .....	1025
10.1.2	NGP Tasks .....	1026
10.1.3	General Methodology .....	1027
10.2	Agent Properties.....	1027
10.3	Current System Description (Halon 1301) for Legacy Aircraft .....	1028
10.3.1	Cargo Aircraft .....	1028
10.3.2	Fighter Aircraft .....	1034
10.3.3	Rotary-wing Aircraft.....	1038
10.4	Proposed System Description (HFC-125) for Future Aircraft.....	1042
10.4.1	Design Guide .....	1042
10.4.2	Cargo Aircraft .....	1045
10.4.3	Fighter Aircraft .....	1048
10.4.4	Rotary-wing Aircraft.....	1052
10.5	Costs of Current and Replacement Systems .....	1054
10.5.1	Life-Cycle Cost Estimate (LCCE) Summary for Legacy Aircraft .....	1056
10.5.2	Life-Cycle Cost Estimate (LCCE) Summary for Future Aircraft.....	1058
10.5.3	Detailed Cost Element Structure (CES).....	1061
10.5.4	Cost Element Structure Data Development .....	1061
10.6	Cost Savings.....	1066
10.7	Cost Analysis Using Altered Fire Suppression Performance .....	1068
10.7.1	Factor of Safety Testing.....	1068
10.7.2	System Description .....	1069
10.7.3	Altered Fire Suppression Performance .....	1070
10.7.4	Cost Analysis .....	1073
10.8	Conclusions.....	1082
10.9	References.....	1083

<b>Chapter 11: Verification of Fire Suppression Principles .....</b>	<b>1087</b>
11.1 Context.....	1088
11.2 Complexity of In-flight Fires and Their Suppression.....	1088
11.3 New Understanding of the Fire Suppression Process.....	1090
11.3.1 Overview of Fire Suppression .....	1090
11.3.2 Control of the Air Supply to the Fire.....	1090
11.3.3 Delivery of the Fire Suppressant to the Fire.....	1090
11.3.4 Effectiveness of a Fire Suppressant at Quenching Flames.....	1094
11.4 Evaluation of Candidate Fire Suppressant Technologies .....	1098
11.4.1 Screening Measures .....	1098
11.4.2 Measurements during Fire Tests.....	1100
11.4.3 Life-cycle Cost Assessment.....	1101
11.5 Potential for New, Viable Suppressants.....	1101
11.6 Fire Suppression Principles to be Tested.....	1103
11.7 Methodology for Real-scale Testing and Validation.....	1106
11.7.1 Aircraft Engine Nacelle Test Facility Features and Capabilities.....	1106
11.7.2 Design of Experiments Methodology.....	1112
11.7.3 “Bracketing” Procedure for Testing.....	1115
11.7.4 Experimental Approach, Configuration and Procedure.....	1115
11.8 Results and Analysis.....	1125
11.8.1 Summary of General Data Collected .....	1125
11.8.2 Principle 1 .....	1126
11.8.3 Principle 3 .....	1127
11.8.4 Principle 5 .....	1128
11.8.5 Principle 6.....	1128
11.8.6 Principle 7.....	1129
11.8.7 Extinguishing Mixing Models .....	1130
11.8.8 Principle 4.....	1134
11.8.9 Principle 2.....	1137
11.8.10 Phase III Results.....	1141
11.9 Summary.....	1141

---

11.10	References.....	1143
<b>Chapter 12:</b>	<b>Afterword.....</b>	<b>1145</b>
12.1	A View Ahead.....	1145
12.2	References.....	1148
<b>Appendix A:</b>	<b>Acknowledgements.....</b>	<b>1149</b>
<b>Appendix B:</b>	<b>NGP Projects.....</b>	<b>1151</b>
<b>Appendix C:</b>	<b>NGP Publications.....</b>	<b>1155</b>
<b>Index</b>	<b>.....</b>	<b>1175</b>

## LIST OF FIGURES

---

Figure 1–1. Interior of an Aircraft Engine Nacelle.....	11
Figure 1–2. Projects Contributing to Deliverable 1: Best Alternative Suppressant Chemicals.....	13
Figure 1–3. Projects Contributing to Deliverable 2: Guidelines for Optimal Application of Extinguishants.....	14
Figure 1–4. Projects Contributing to Deliverable 3: Alternative Extinguishment Technologies.....	14
Figure 1–5. Projects Contributing to Deliverable 4: Technology Options Assessment Protocol.....	15
Figure 2–1. Significant Non-combat Fire Locations on U.S. Navy Aircraft 1977-1993.....	21
Figure 2–2. Combustion Threats in and around an Aircraft Fuel Tank.....	21
Figure 2–3. Illustration of Notional Reduction in Overall Rotorcraft Vulnerable Area.....	22
Figure 2–4. Known Ejection Locations of Navy Aircrewmembers Who Became POWs during the Southeast Asia Conflict.....	23
Figure 2–5. Locations of Navy Rescues of Navy Aircrewmembers during the Southeast Asia Conflict.....	23
Figure 2–6. Example Turboshaft Engine.....	25
Figure 2–7. A Fighter Aircraft Engine Nacelle.....	26
Figure 2–8. Diagram of an Aircraft Fire Suppression System Installation.....	26
Figure 2–9. An Aircraft Engine Nacelle Fire Suppression System Installation, Suppressant Bottle External to the Nacelle.....	27
Figure 2–10. An Aircraft Engine Nacelle Fire Suppression System Installation, Suppressant Bottle Within the Nacelle.....	28
Figure 2–11. A Transport Aircraft Auxiliary Power Unit Installation.....	29
Figure 2–12. A Fighter Aircraft Accessory Compartment With Fire Suppression System Installation.....	30
Figure 2–13. An Aircraft Gearbox Compartment with APU.....	30
Figure 2–14. A Secondary Power System (SPS) Installation.....	31
Figure 2–15. Typical Dry Bay Locations in a Fighter Aircraft.....	32
Figure 2–16. A Dry Bay Compartment Adjacent to a Fuel Tank; Fire Detector and Fire Suppressor Installed within the Dry Bay Compartment.....	32
Figure 2–17. Top View of a Wing Dry Bay Containing Drive, Hydraulic, and Electrical Systems Components.....	33
Figure 2–18. A Wing Leading Edge Dry Bay Containing Hydraulic and Electrical Systems Components, Leading Edge Structure Removed.....	33

Figure 2–19. Non-DoD Aircraft Halon 1301 Dry Bay Fire Protection System.....	35
Figure 2–20. Diagram of a Cargo Fire Suppression System Installation on a Transport Aircraft.....	36
Figure 2–21. Illustration of Ullage Fire/Explosion Protection Devices.....	38
Figure 2–22. F-16 Aircraft Inerting System Diagram.....	40
Figure 2–23. Imperial Japanese Navy Dry Bay and Ullage Fire Suppression System Concept, Late World War II.....	46
Figure 2–24. Ignition and growth of a flame in 7 % H <sub>2</sub> , 1.4 % C <sub>3</sub> H <sub>8</sub> Jet A Simulant Mixture at 295 K and 84.1 kPa.....	47
Figure 2–25. Spark-Initiated Ullage Combustion Process.....	48
Figure 2–26. Stabilized Pool Fire Formation within an Aircraft Dry Bay Compartment.....	49
Figure 2–27. Flame Temperature vs. Equivalence Ratio.....	50
Figure 2–28. Hydrocarbon Flame Emission Spectra. ....	52
Figure 2–29. Turbulent Fire within Aircraft Dry Bay Compartments. ....	53
Figure 2–30. Variation in Halon 1301 Peak Flammability Limits for Isobutane with Temperature.....	54
Figure 2–31 Variation in Halon 1301 and Three Halon Alternative Mass Fractions (Beta) Required to Suppress JP-8 Spray Flames with Temperature.....	55
Figure 2–32. Commercial Aviation Standard Climates vs. DoD WWAE Design Guidance. ....	56
Figure 2–33. DoD Land Environment Design Guidance.....	57
Figure 2–34 Variation of Ambient Pressure vs. Pressure and Geopotential Altitudes on Standard-day and Non-standard-day Temperature Conditions.....	61
Figure 2–35. Flammability Limits of Jet-A and Jet-B Fuels vs. Altitude and Standard Atmospheres. ....	62
Figure 2–36. Plot of Standard Climate Profiles and WWAEs vs. All DoD Aircraft Fire Events and Suppressant Releases where Both Altitude and OAT Were Provided.....	63
Figure 2–37. Plot of 1988-2000 Commercial Aircraft Fire Events vs. Altitude and OAT, Events for which NTSB Database Provided Both Altitude and OAT.....	64
Figure 2–38. Rotary Aircraft Nacelle/APU Compartment Fire Suppressant Releases by Altitude.....	64
Figure 2–39. Rotary Aircraft Nacelle/APU Compartment Fire Suppressant Releases by OAT.....	65
Figure 2–40. Fixed-wing Aircraft Nacelle/APU Compartment Fire Suppressant Releases by Altitude.....	65
Figure 2–41. Fixed-wing Aircraft Nacelle/APU Compartment Fire Suppressant Releases by OAT.....	65
Figure 2–42. Peak Nacelle Temperature at 50 knots Airspeed vs. Altitude.....	67
Figure 2–43. Peak Nacelle Temperature at 400 knots Airspeed vs. Altitude.....	67
Figure 2–44. Initial OAT per JAR-1 Arctic Standard Climate.....	71

Figure 2–45. OAT at Takeoff is -40 °C (-40 °F) with Bias Applied to OAT. ....	71
Figure 2–46. Fixed-Wing Aircraft Fire Mishaps and Incidents by Phase of Operation. ....	74
Figure 2–47. Distribution of DoD Rotary Aircraft Ground Fire Locations. ....	75
Figure 2–48. Distribution of DoD Fixed-Wing Aircraft Ground Fire Locations. ....	75
Figure 2–49. Distribution of DoD In-Flight Rotary Aircraft Fire Locations. ....	76
Figure 2–50. Distribution of DoD In-Flight Fixed-Wing Aircraft Fire Locations. ....	76
Figure 2–51. DoD Rotary Aircraft Fire Data vs. Atmospheric Profiles, Flammability Limit Profiles, Operational Ceiling, and Suppressant Release. ....	77
Figure 2–52 DoD Fixed-Wing Aircraft Fire Data vs. Atmospheric Profiles, Flammability Limit Profiles, Potential Stall Condition and Suppressant Release. ....	78
Figure 2–53. Example Conventional Halon 1001 Powerplant Fire Suppression System Distribution Installation, USN Turboprop Powerplant. ....	82
Figure 2–54. Example Conventional Halon 1011 Fire Extinguishing System Distribution Installation, Turboprop Powerplant. ....	83
Figure 2–55. Example Conventional Halon 1011 Fire Extinguishing System Distribution Installation, USAF Turbojet Powerplant. ....	84
Figure 2–56. Minimum Discharge Duration from an HRD System Using Halon 1011. ....	85
Figure 2–57. Zones Protected by the Nitrogen Fire Suppression System on C-5 Aircraft. ....	89
Figure 2–58. Fire Suppressant Concentration Analyzer Sampling Probe Installation. ....	90
Figure 2–59. Example Fire Suppression System Suppressant Concentration Measurement. ....	90
Figure 2–60. MIL-HDBK-221 Design Guidance for Explosion Suppression. ....	91
Figure 2–61. Typical Legacy OBIGGS Qualification Test Oxygen Concentration Measurement Location. ....	92
Figure 2–62. Comparison of Halon 1301 Certification Requirement and HFC-125 Design Equation Limits vs. Published Flammability Limits. ....	97
Figure 2–63. Example of Non-optimized Halon 1301 Nacelle Concentration Distribution. ....	98
Figure 2–64. Example of Non-optimized HFC-125 Nacelle Concentration Distribution. ....	98
Figure 2–65. Examples of HFC-125 Nacelle Concentrations. ....	100
Figure 2–66. Summary of HFC-125 and SPGG Fire Suppression Results from C-130J Live Fire Testing. ....	103
Figure 2–67. Time Sequence of Dry Bay Compartment Fire Suppression by Inert Gas Generators. ....	104
Figure 2–68. V-22 Inert Gas Generator Fire Suppression System. ....	104
Figure 2–69 NGP Testing Results Comparing Solid Propellant Inert Gas Generator Propellant Mass vs. Chemically Active Gas Generator Propellant Mass. ....	105
Figure 2–70. Effect of Suppressant Concentration and Mass Fraction on Peak Explosive Pressure for LFEs Pressurized to 1,000 psi, 12.7 mm API Threat and 3 % JP-4S. ....	107

Figure 3–1. Comparison of Local Strain Rates Measured by Laser Doppler Velocimetry in Non-premixed Counterflow Flames and Calculated Global Strain Rates.....	129
Figure 3–2. Extinction Strain Rate vs. Agent Molar Concentration for Non-premixed Methane-air Flames Suppressed by: a) Fluorinated Ethanes, SF <sub>6</sub> , and N <sub>2</sub> ; and b) Fluorinated Propanes. ....	130
Figure 3–3. Extinction Strain Rate vs. Agent Molar Concentration for Non-premixed Propane-air Flames Suppressed by: a) Fluorinated Ethanes, SF <sub>6</sub> , and N <sub>2</sub> ; b) Fluorinated Propanes; and c) Bromine- or Iodine-containing Methanes. ....	131
Figure 3–4. Reaction Pathways for Premixed Methane/air Flames Doped with 3.81 Volume % of: (a) HFC-134 and (b) HFC-134a.....	136
Figure 3–5. Extinction Concentrations for Agents Suppressing: (a) n-heptane/air Cup Burner Flames; (b) Methanol/air Cup Burner Flames; (c) Methane/air Counterflow Flames at a Strain Rate of 80 s <sup>-1</sup> ; (d) Propane/air Counterflow Flames at a Strain Rate of 80 s <sup>-1</sup> .....	139
Figure 3–6. Effect of Fuel Type on Agent Extinction Concentration.....	141
Figure 3–7. Mole Merit Number of Metal-containing Compounds for the Oxidizer Velocities in the Range of 50 cm/s to 60 cm/s.....	147
Figure 3–8. Main Catalytic Radical Recombination Cycle of Iron Found to be Important for Methane-air Flames. ....	156
Figure 3–9. Radical Recombination Reaction Pathways Found to be Important for CO-H <sub>2</sub> -O <sub>2</sub> -N <sub>2</sub> Flames.....	157
Figure 3–10. Different Classes of Reactions Which May Contribute to Iron's Super-efficient Flame Suppression Ability through the Catalytic Recombination of Radical Species.....	158
Figure 3–11. Calculated H-atom Super-equilibrium Ratio and Peak Temperature in a Counterflow Diffusion Flame as a Function of Strain Rate.....	158
Figure 3–12. Schematic Diagram of the Low Pressure Burner and Optical Measurement Arrangement. ....	160
Figure 3–13. Emission Image Collected from the Centerline of the Low Pressure, Opposed Flow, CH <sub>4</sub> -air flame with 10 % of the Fe(CO) <sub>5</sub> Concentration Required to Extinguish the Flame.....	163
Figure 3–14 LIF [OH] Profiles Collected from Inhibited CH <sub>4</sub> -air Flames Containing Nominally Half of the Concentration Required for Extinguishment. ....	163
Figure 3–15. Dependence of Normalized Maximum OH LIF Intensity on Inhibitor Concentration.....	165
Figure 3–16. Calculated and Measured Normalized Burning Velocity of Premixed CH <sub>4</sub> /O <sub>2</sub> /N <sub>2</sub> Flames.....	167
Figure 3–17. Normalized Burning Velocity and Maximum Measured Scattering Signal Q <sub>w</sub> for φ=1.0 CH <sub>4</sub> Flame with X <sub>O<sub>2</sub>,ox</sub> = 0.21 and 0.24.....	168
Figure 3–18. Maximum Scattering Signal and Normalized Burning Velocity for CO-H <sub>2</sub> Flames as Fe(CO) <sub>5</sub> Concentration Varies. ....	168
Figure 3–19. Maximum Q <sub>w</sub> for Flames of CH <sub>4</sub> and CO as a Function of Burning Velocity. ....	169

Figure 3–20. Calculated Normalized Burning Velocity for Several Diameters of Ideal Heterogeneous Inhibitor, $\text{Fe}(\text{CO})_5$ data, and Calculated Normalized Burning Velocity using the Perfect Gas Phase Inhibitor Mechanism.....	169
Figure 3–21. Normalized Extinction Strain Rate for Counterflow Diffusion Flames. ....	170
Figure 3–22. Correlation between Inhibition Effect in Counterflow Diffusion Flames and Maximum Measured Scattering Signal $Q_{vv}$ . ....	171
Figure 3–23. Volume Fraction of $\text{CO}_2$ Required for Extinction ( $X_{\text{CO}_2,\text{ext}}$ ) of Methane-air Cup Burner Flames as a Function of the Volume Fraction of Catalytic Inhibitor Added to the Air Stream. ....	172
Figure 3–24. Particle Light Scattering as a Function of Radial Position and Height above Cup Burner for Four Loadings of $\text{Fe}(\text{CO})_5$ .....	173
Figure 3–25. Calculated Temperature and Velocity Vectors for Methane-air Cup Burner Flame with an Oxidizer Stream $\text{CO}_2$ Volume Fraction of 0.1, with and without an Added $\text{Fe}(\text{CO})_5$ Volume Fraction of 100 $\mu\text{L/L}$ . ....	174
Figure 3–26. Map of Calculated Temperatures in Cup Burner Methane-air Flames with 10 % $\text{CO}_2$ in the Oxidizer Stream and (a) 0.011 and (b) 0.012 $\text{Fe}(\text{CO})_5$ Volume Fraction in the Air Stream, Illustrating the Blowoff Phenomenon. ....	174
Figure 3–27. Experimental and Calculated Extinction Volume Fraction of $\text{CO}_2$ and Peak Measured Scattering Cross Section as a Function of the Volume Fraction of $\text{Fe}(\text{CO})_5$ in the Air Stream. ....	175
Figure 3–28. (a) Calculated Volume Fractions, $X_i$ , of Iron-containing and Other Major Species as a Function of Radial Position at 4.8 mm above the burner (corresponding to the location of the reaction kernel in the flame base); and (b) the Supersaturation Ratio, $S_i$ , for Fe, FeO, and $\text{Fe}(\text{OH})_2$ .....	176
Figure 3–29. Calculated Particle Trajectories for Free Molecular Regime Particles in a $\text{CH}_4$ -air Flame with 10 % $\text{CO}_2$ in the Oxidizer Stream.....	177
Figure 3–30. Visible Images of Methane-air Premixed Flames. ....	186
Figure 3–31. Normalized Burning Velocity of Premixed $\text{CH}_4/\text{O}_2/\text{N}_2$ Flames Inhibited by TMT for $X_{\text{O}_2,\text{ox}}=0.21$ and $\phi=0.9, 1.0,$ and $1.1$ .....	187
Figure 3–32 – Normalized Burning Velocity of Premixed $\text{CH}_4/\text{O}_2/\text{N}_2$ flames Inhibited by TMT for $\phi=1.0$ and $X_{\text{O}_2,\text{ox}}=0.20, 0.21,$ and $0.244$ .....	188
Figure 3–33. Normalized Burning Velocity of Premixed $\text{CH}_4/\text{O}_2/\text{N}_2$ Flames Inhibited by MMT with $X_{\text{O}_2,\text{ox}}=0.21$ and $\phi=0.9, 1.0,$ and $1.1$ . ....	189
Figure 3–34. Normalized Burning Velocity of Premixed $\text{CH}_4/\text{O}_2/\text{N}_2$ Flames Inhibited by MMT, with $\phi=1.0$ and $X_{\text{O}_2,\text{ox}}=0.19, 0.20, 0.21,$ and $0.244$ . ....	189
Figure 3–35. Normalized Burning Velocity of Premixed $\text{CH}_4/\text{O}_2/\text{N}_2$ Flames Inhibited by $\text{CO}_2$ , $\text{CF}_3\text{Br}$ , $\text{Sn}(\text{CH}_3)_4$ , $\text{SnCl}_4$ , MMT, and $\text{Fe}(\text{CO})_5$ . $T_{\text{in}} = 353$ K for all data except $\text{Sn}(\text{CH}_3)_4$ and $\text{SnCl}_4$ which are at 298 K. ....	190
Figure 3–36. Normalized Burning Velocity of Premixed $\text{CH}_4/\text{O}_2/\text{N}_2$ Flames Inhibited by Pure MMT and $\text{Fe}(\text{CO})_5$ , and by a Blend of the Two. ....	191
Figure 3–37. Reaction Pathways for Sn, Mn, and Fe in a Premixed Methane-air Flame ( $\phi=1.0, X_{\text{O}_2,\text{ox}}=0.21, T_{\text{in}}=353$ K).....	192

Figure 3–38. First-order Sensitivity Coefficient of the Burning Velocity to the Specific Reaction Rate Constant for Reactions with Tin-containing Species (1963 $\mu\text{L/L}$ of TMT).....	194
Figure 3–39. First-order Sensitivity Coefficient of the Burning Velocity to the Specific Reaction Rate Constant for Reactions with Manganese-containing Species (150 $\mu\text{L/L}$ of MMT).....	195
Figure 3–40. Volume Fractions of O, and OH Radicals and Metal Species Intermediates as a Function of Temperature in Flame for $\text{Fe}(\text{CO})_5$ , MMT, and TMT	197
Figure 3–41 Fractions of Sn-, Mn-, and Fe-species at Equilibrium in Methane-air Flames as a Function of Temperature.....	198
Figure 3–42. Schematic of the Experimental Setup for $\text{Fe}(\text{CO})_5$ Absorption.....	201
Figure 3–43. High Resolution Transmission Electron Micrograph Images of Zeolite-NaX Particles.....	204
Figure 3–44. Schematic Diagram of Counterflow Diffusion Flame Burner with Provision for Addition of Particles to the Air Stream.....	206
Figure 3–45. Calculated and LDV-measured Velocity Profiles at Exit of Premixed Burner Nozzle for Total Flows of 7.4 and 9 L/min.....	207
Figure 3–46. Methane-air Counterflow Diffusion Flames: Pure and with $\text{NaHCO}_3$ Particles .....	208
Figure 3–47. $\text{NaHCO}_3$ and Silica Mass Fraction vs. Methane-air Nonpremixed Extinction Strain Rate.....	208
Figure 3–48 – Laser Scattering of $\text{NaHCO}_3$ Particles in a Counterflow Diffusion Flame of Methane and Air, Showing that the Particles Pass Through the Flame. ....	209
Figure 3–49. Premixed Methane-air Nozzle Burner Flames: Pure and with $\text{NaHCO}_3$ Particles .....	210
Figure 3–50. Comparison of Normalized Burning Velocities with Added Particles.....	210
Figure 3–51. Normalized Flame Strength as a Function of Added $\text{NaHCO}_3$ Mass Fraction for Premixed and Counterflow Diffusion Flames. ....	211
Figure 3–52. Normalized Flame Speed for a Methane-air Flame with Added Silica Gel Particles (14 to 40) $\mu\text{m}$ , with and without $\text{I}_2$ Impregnated in the Particles. ....	212
Figure 3–53. Normalized Burning Velocity of Premixed $\text{CH}_4/\text{O}_2/\text{N}_2$ Flames Inhibited by Ferrocene and $\text{Fe}(\text{CO})_5$ , Together with Modeling Predictions (dotted lines). ....	216
Figure 3–54. Normalized Burning Velocity of Stoichiometric $\text{CH}_4\text{-O}_2\text{-N}_2$ Flames at 400 $\mu\text{L/L}$ of Ferrocene as a Function of the Activation Energy of the One-step Ferrocene Decomposition Reaction.....	217
Figure 3–55. Normalized Burning Velocity of $\text{CH}_4/\text{O}_2/\text{N}_2$ Flames, a) $X_{\text{O}_2,\text{ox}} = 0.21$ , b) $X_{\text{O}_2,\text{ox}} = 0.244$ , Inhibited by $\text{CO}_2$ , by $\text{CO}_2$ -ferrocene Blends, and by $\text{CF}_3\text{Br}$ .....	219
Figure 3–56. Normalized Burning Velocity of $\text{CH}_4/\text{N}_2/\text{O}_2$ Flames, a.) $X_{\text{O}_2,\text{ox}} = 0.21$ , b.) $X_{\text{O}_2,\text{ox}} = 0.244$ , with 0, 2, and 6, or 0, 6, and 12 Volume Percent of $\text{CO}_2$ , Respectively, Added to the Reactant Stream, as a Function of Added Ferrocene.....	220
Figure 3–57. Normalized Burning Velocity of Premixed $\text{CH}_4/\text{O}_2/\text{N}_2$ Flames Inhibited by Pure $\text{CF}_3\text{H}$ and by $\text{CF}_3\text{H}$ with 0.35 % Ferrocene, Together with Data for $\text{CF}_3\text{Br}$ .....	221

Figure 3–58. Equilibrium Mole Fraction of Active Inhibiting Species (Fe, FeO, FeOH, Fe(OH) <sub>2</sub> ) and Iron-fluorine Species with 1 % to 4 % CF <sub>3</sub> H (Containing 0.35 % Ferrocene) Added to a Stoichiometric Methane-air Reaction Mixture.....	222
Figure 3–59. Linear Contribution of Burning Velocity from Each Component of a two-Component Blend of Inhibitors, Together with the Actual Reduction from the Blend. ....	223
Figure 3–60. Ratio of the Actual Reduction in SL from the Two-component Mix to the Predicted Reduction Based on Linear Combination of the Effect from Each Component.....	224
Figure 3–61. Volume Fraction of Cr-containing Species. Cr, CrO, CrO <sub>2</sub> , and CrO <sub>3</sub> above Cr <sub>2</sub> O <sub>3</sub> at 10.133 kPa under Neutral and Oxidizing Conditions above Cr <sub>2</sub> O <sub>3</sub> and Cr above itself .....	225
Figure 3–62. Pb Species Gas Phase Volume Fractions at Equilibrium over the Condensed Phase (at 101.3 kPa).....	226
Figure 3–63. Normalized Burning Velocity of Premixed CH <sub>4</sub> /O <sub>2</sub> /N <sub>2</sub> Flames Inhibited by MMT with X <sub>O<sub>2,ox</sub></sub> = 0.21 and φ = 0.9, 1.0, and 1.1.....	227
Figure 3–64. Mn Species Gas Phase Volume Fraction at Equilibrium over the Condensed Phase at 101.3 kPa .....	227
Figure 3–65. Tungsten-containing Species Gas Phase Volume Fraction at Equilibrium over the Condensed Phase at 101.3 kPa.....	228
Figure 3–66. Mo-containing Species Gas Phase Volume Fraction at Equilibrium over the Condensed Phase at 101.3 kPa.....	229
Figure 3–67. Normalized Burning Velocity of Premixed CH <sub>4</sub> /O <sub>2</sub> /N <sub>2</sub> Flames Inhibited by TMT with X <sub>O<sub>2,ox</sub></sub> = 0.21 and φ = 0.9, 1.0, and 1.1.....	229
Figure 3–68. Sn-containing Species Gas Phase Volume Fractions at Equilibrium over the Condensed Phase at 101.3 kPa.....	230
Figure 3–69 Co-containing Species Gas Phase Volume Fraction at Equilibrium over the Condensed Phase at 101.3 kPa.....	230
Figure 3–70. Cu-containing Species Gas Phase Volume Fractions at Equilibrium over the Condensed Phase at 101.3 kPa.....	231
Figure 3–71. Equivalent N <sub>2</sub> /O <sub>2</sub> Limiting Oxygen Index for Extinction of Polyethylene (PE)-halogen- Sb <sub>2</sub> O <sub>3</sub> Blends and Methane-air Cup Burner Flames with MMT, Fe(CO) <sub>5</sub> , and Sn(CH <sub>3</sub> ) <sub>4</sub> .....	232
Figure 3–72. Schematic of Opposed-jet Burner.....	239
Figure 3–73. Schematic of LIF Apparatus.....	241
Figure 3–74. Variation of Global Extinction Strain with Observed Flame Position at Extinction.....	246
Figure 3–75. Variation of Global Extinction Strain with Observed Flame Position at Extinction for Non-premixed CH <sub>4</sub> /N <sub>2</sub> -O <sub>2</sub> /N <sub>2</sub> Flames, with Z <sub>st</sub> = 0.50. ....	247
Figure 3–76. Observed Flame Positions as a Function of Predicted Distance to the Stagnation Plane for Non-premixed Flames of CH <sub>4</sub> -air (Z <sub>st</sub> = 0.054), and CH <sub>4</sub> /N <sub>2</sub> -O <sub>2</sub> /N <sub>2</sub> Flames, (Z <sub>st</sub> = 0.50) Near Extinction. ....	248

Figure 3–77. Inhibition of Non-premixed Methane-air Flames, Based on Reduction in the Global Extinction Strain Rate by Oxidizer-side Addition of Nitrogen, with and without Preheated Reactants. ....	249
Figure 3–78. Inhibition of Non-premixed Methane-air flames, Based on Reduction in the Global Extinction Strain Rate, by Oxidizer-side Addition of Trimethyl Phosphate (TMP), and Dimethyl Methylphosphonate (DMMP). ....	250
Figure 3–79. Adiabatic Flame Temperature vs. Stoichiometric Mixture Fraction for a Methane-nitrogen-oxygen-nitrogen Flame with the Extinction Strain Rate Held Constant at $350 \pm 10 \text{ s}^{-1}$ . ....	252
Figure 3–80. Flame Suppression Effectiveness of 25,000 $\mu\text{L/L}$ Argon as an Oxidant-side or Fuel-side Additive vs. Stoichiometric Mixture Fraction. ....	253
Figure 3–81. Normalized Flame Suppression Effectiveness of Argon-doped Flames vs. Stoichiometric Mixture Fraction at Fixed. ....	253
Figure 3–82. Flame Suppression Effectiveness of 500 $\mu\text{L/L}$ DMMP as an Oxidant-side or Fuel-side Additive vs. Stoichiometric Mixture Fraction. ....	254
Figure 3–83. Normalized Flame Suppression Effectiveness of DMMP-doped Flames vs. Stoichiometric Mixture Fraction. ....	255
Figure 3–84. Normalized effectiveness of DMMP-doped Flames as a Function of Adiabatic Flame Temperature. ....	256
Figure 3–85. Calculated Major Species and Temperature Profiles for Flame 1 and Flame 4, both undoped. ....	258
Figure 3–86. Calculated and Measured OH Concentration Profiles for Flames 1 and 4. ....	258
Figure 3–87. [OH] Profile Widths (FWHM). ....	259
Figure 3–88. Effect of 572 $\mu\text{L/L}$ of DMMP on [OH] in Flame 1. 260	
Figure 3–89. Effect of DMMP Loading for All Flames. ....	261
Figure 3–90. Temperature Dependence of Effectiveness. ....	262
Figure 3–91. Effect of 572 $\mu\text{L/L}$ of DMMP on Calculated OH, H, and O Concentration Profiles in Flame 1 ( $\text{CH}_4/\text{O}_2/\text{N}_2$ ). ....	263
Figure 3–92. Temperature Dependence of Effectiveness Defined as in Terms of Reduction in total [OH]. ....	264
Figure 3–93. OH, H, and O Production Rates in Flame 1 and Flame 4, Summed over All Reactions Involving Phosphorus. ....	264
Figure 3–94. Total OH Production Rates in Flame 1 by Reactions Not Involving Phosphorus. ....	265
Figure 3–95. Influence of the Addition of 572 $\mu\text{L/L}$ of DMMP on OH Production Rates in Flame 1. ....	266
Figure 3–96. H and O Production Rates by All Reactions Involving Phosphorus and by Individual Reactions in Flame 1. ....	267
Figure 3–97. Temperature Profiles Measured in (a) Rich and (b) Near-stoichiometric Flames. ....	274
Figure 3–98. $\text{CH}_4$ in Doped and Undoped (a) Rich and (b) Near-stoichiometric Flames, with GRI and Babushok and Glaude Predictions. ....	275

Figure 3–99. CO <sub>2</sub> in Doped and Undoped (a) Rich and (b) Near-stoichiometric Flames, with GRI and Babushok and Glaude Predictions.....	275
Figure 3–100. CO in Doped and Undoped (a) Rich and (b) Near-stoichiometric Flames, with GRI and Babushok and Glaude Predictions.....	276
Figure 3–101. CH <sub>2</sub> O in Doped and Undoped (a) Rich and (b) Near-stoichiometric Flames, with GRI and Babushok and Glaude Predictions.....	276
Figure 3–102. C <sub>2</sub> H <sub>2</sub> in Doped and Undoped (a) Rich and (b) Near-stoichiometric Flames, with GRI and Babushok and Glaude Predictions.....	277
Figure 3–103. C <sub>2</sub> H <sub>4</sub> in Doped and Undoped (a) Rich and (b) Near-stoichiometric Flames, with GRI and Babushok and Glaude Predictions.....	277
Figure 3–104. C <sub>2</sub> H <sub>6</sub> in Doped and Undoped (a) Rich and (b) Near-stoichiometric Flames, with GRI and Babushok and Glaude Predictions.....	278
Figure 3–105. CH <sub>3</sub> OH in Doped and Undoped (a) Rich and (b) Near-stoichiometric Flames, with GRI and Babushok and Glaude Predictions.....	278
Figure 3–106. Schematic Diagram of the Experimental Apparatus. ....	283
Figure 3–107. Representative PLIF Images and the Corresponding OH Intensity Profiles from an Opposed Flow Propane-air Flame Seeded with 0 % (by volume) CF <sub>3</sub> Br and 1.5 % (by volume) CF <sub>3</sub> Br.....	284
Figure 3–108. Normalized OH LIF Profile Areas vs. Inhibitor Agent Delivery Concentrations. □: N <sub>2</sub> , O: HFC-227ea, Δ: HFC-236, : PN, ◇: CF <sub>3</sub> Br, ■: DMMP, and ●: Fe(CO) <sub>5</sub> . Insert: Expanded data for PN, CF <sub>3</sub> Br, DMMP, and Fe(CO) <sub>5</sub> Concentrations up to 0.75 % by Volume. ....	286
Figure 3–109. Peak LIF Measured Temperatures vs. Inhibitor Delivery Concentrations.....	288
Figure 3–110. Calculated Burning Velocities vs. Delivered Inhibitor Concentration for a Numerical, Stoichiometric, Premixed, Propane-air Flame. ....	289
Figure 3–111. Normalized OH Concentrations vs. Delivered Inhibitor Concentrations. ....	290
Figure 3–112. Burning Velocity, Final Flame Temperature, Inhibition Parameter, and Superequilibrium Concentrations of Flame Radicals Computed for Atmospheric Pressure Stoichiometric Methane-air Mixtures Inhibited by NaOH.....	293
Figure 3–113. Burning Velocity, Final Flame Temperature, Inhibition Parameter, and Superequilibrium Concentrations of Flame Radicals Computed for Atmospheric Pressure Stoichiometric Methane-air Mixtures Inhibited by CF <sub>3</sub> Br. ....	293
Figure 3–114. Burning Velocity and Differential Inhibition Parameter computed for Atmospheric Pressure Stoichiometric Methane-air Mixtures Inhibited by N <sub>2</sub> and FeO <sub>2</sub> in Combination. ....	295
Figure 3–115. Relationship between Burning Velocity and Peak Concentration of Atomic Hydrogen for Methane-air Flames Inhibited by Various Compounds.....	296
Figure 3–116. Mole Fraction of Atomic Hydrogen as a Function of Local Flame Temperature for an Uninhibited and Uninhibited Atmospheric Pressure Methane-air Flame.....	298
Figure 3–117. Calculated Flame Velocity as a Function of Hypothetical Variation of the H-Br Bond Energy for Premixed Methane-air Flames Inhibited by 0.5 % HBr Using the H + H and H + OH Scavenging Cycles of Table 3. ....	304

Figure 3–118. Calculated Flame Velocity as a Function of Hypothetical Variation of the Na-OH Bond Energy for Premixed Methane-air Flames Inhibited by 0.1 % (NaOH) <sub>2</sub> using the H + OH scavenging cycle of Table 3 .....	305
Figure 3–119. Calculated Flame Velocity as a Function of Hypothetically Variation of Fe-O Bond Energy for Premixed Methane-air Flames Inhibited by 500 μL/L FeO <sub>2</sub> Using the Three-step O + O Scavenging Cycle of Table 3 .....	306
Figure 3–120. Shapes of the Reaction Rate Profile Bi Used to Describe: a) Perturbation of Chain Branching and Heat Release Rates, b) Addition of Perfect Inhibitor or CF <sub>3</sub> Br , c) Rapid Inhibitor Activation, and d) Rapid Inhibitor Deactivation. ....	308
Figure 3–121. Variation of Flame Speed for Four Types of Perturbation. ....	311
Figure 3–122. Net H-atom Reaction Rate for Three Important Reactions in Stoichiometric Methane-air Flames. ....	312
Figure 3–123 Effect of damping the rate of the H+O <sub>2</sub> reaction on normalized flame speed for φ=0.7, 1.0, and 1.3. ....	313
Figure 3–124. Calculated Volume Fraction Profiles for H, OH and O in Uninhibited Methane-air Flames for Three Stoichiometric Ratios.....	313
Figure 3–125. Effect of the Location of Perfect Inhibition on Normalized Flame Speed for φ=0.7, 1.0, and 1.3.....	314
Figure 3–126. Variation of Flame Speed for Stepwise Inhibitor Activation or Deactivation for a Stoichiometric Methane-air Mixture.....	315
Figure 4–1. Water Mist Size Histogram and Values of Several Mean Diameters.....	349
Figure 4–2. Lognormal and Rosin-Rammler Expressions Fit to the Water Mist Histogram Presented in Figure 4–1. ....	350
Figure 4–3. Schematic Diagram for Diffraction-based Particle Sizing. ....	352
Figure 4–4. Diagram for 1-D Phase Doppler Interferometry System for Obtaining Size and Velocity of “Spherical” Aerosol Particles. ....	353
Figure 4–5. Schematic Diagram for Imaging-based Particle Sizing.....	354
Figure 4–6. Predicted Evaporation Times for Water Droplets in Air at the Indicated Temperature as a Function of Initial Droplet Diameter.....	357
Figure 4–7 Predicted Terminal Settling Velocity for Water Droplets and Sodium Bicarbonate Particles in Air at 20 °C.....	357
Figure 4–8. Relationship of Flame Dimensionality and Modeling Complexity. ....	359
Figure 4–9. Representations of Aerosol Suppressed Premixed Flames.....	359
Figure 4–10. Experimental Schematic for Studying the Effects of Aerosols on the Extinction Strain Rate of Counterflow Non-Premixed Flames. ....	361
Figure 4–11. Schematic of Tsuji Burner and Flame Configuration.....	362
Figure 4–12. Cup Burner Apparatus Modified for Water Mist Suppression Studies. ....	363
Figure 4–13. Schematic of Water Aerosol Generation Methods.....	364

Figure 4–14. PDPA-determined Droplet Diameter Histogram 2 mm above the Air Tube Exit for Three Water Mists.....	364
Figure 4–15. Schematic for Liquid Aerosol Inhibited Burning Velocity Determination in Premixed Flames.....	365
Figure 4–16. Predicted Burning Velocity for a Stoichiometric, Premixed, Methane-air Flame as a Function of Initial Droplet Diameter and Water Mass Loading.....	367
Figure 4–17. (a) Image of Premixed Methane-air Flame Stabilized on Burner; (b) Image of Water Mist (no flame) as it Exits the Burner; (c) Image of Laser-illuminated Water Mist and Methane-air Flame Showing Disappearance of the Mist at the Flame Boundary.....	367
Figure 4–18. Normalized Burning Velocity Reduction vs. Mass of Added Inhibitor for an Inhibited Methane-Air Premixed Flame. ....	368
Figure 4–19. Premixed Methane-air Burning Velocity as a Function of Agent Mass Fraction, Normalized by the Uninhibited Burning Velocity.....	369
Figure 4–20. Measurements of Water Droplet Diameter and Number Density in a Stoichiometric Premixed Methane-air Flame as a Function of Height above the Burner Exit.....	370
Figure 4–21. Multi-phase Predictions of Water Mist Droplet Diameter and Number Density in a Stoichiometric Premixed Methane-air Flame. ....	370
Figure 4–22. Predicted Comparison of the Maximum Flame Temperature, $T_{\max}$ , vs. Flow Strain Rate, $a$ , for a Dry Flame and for Four Flames with Different Inflow Water Vapor Partial Pressures. ....	373
Figure 4–23. Calculated Gas Velocity, Velocities for Varied Water Droplet Diameters, and Gas Temperature (thick solid line) in a $130 \text{ s}^{-1}$ Methane/air Flame with Droplet Source Terms turned “off”.....	375
Figure 4–24. Comparison of $U$ of Gas and $U_d$ of Different Droplet Diameters, with Droplet Source Terms Turned “off”. ....	376
Figure 4–25. Comparison of Droplet Temperature, $T_d$ , of Different Droplet Diameters, with Droplet Source Terms Turned “off”. ....	377
Figure 4–26. Comparison of Flux Fraction Function, $F$ , of Different Droplet Diameters, with Droplet Source Terms Turned “off”. ....	377
Figure 4–27. Typical $S_m$ Profiles of Different Droplet Diameters, with $Y_0 = 0.02$ and Droplet Source Terms Turned “off”.....	378
Figure 4–28. Typical $S_U - U_{S_m}$ Profiles of Different Droplet Diameters, with $Y_0 = 0.02$ and Droplet Source Terms Turned “off”.....	379
Figure 4–29. Typical $S_h - h_i S_m$ Profiles of Different Droplet Diameters, with $Y_0 = 0.02$ and Droplet Source Terms Turned “off”.....	379
Figure 4–30. Comparison of $T_{\max}$ vs. Strain Rate for Different Droplet Diameters, with Water Mass Fraction = 0.01.....	379
Figure 4–31. Comparison of $T_{\max}$ vs. Strain Rate for Different Droplet Diameters, with Water Mass Fraction = 0.02. ....	380

Figure 4–32. Comparison of $T_{\max}$ vs. strain rate for Different Droplet Diameters, with Water Mass Fraction = 0.03. ....	380
Figure 4–33. Comparison of $a_{\text{ext}}$ vs. Droplet Diameter for Different Droplet Mass Fractions in the Condensed Phase at Inflow. ....	381
Figure 4–34. Comparison of $(\chi s)_{\text{ext}}$ vs. Droplet Diameter for Different Droplet Mass Fractions in Condensed Phase at Inflow. ....	382
Figure 4–35. Calculated Droplet Trajectory as a Function of Time, for $d = 50 \mu\text{m}$ and $Y_0 = 0.03$ . ....	383
Figure 4–36. Apparatus for Aerosol-inhibited, Non-premixed Counterflow Flames. ....	384
Figure 4–37. Droplet Diameter Distribution Evolution of a $30 \mu\text{m}$ Mist in a $170 \text{ s}^{-1}$ Strain Rate Flame ....	387
Figure 4–38 Droplet Diameter Distribution Evolution of an $18 \mu\text{m}$ Mist in a $170 \text{ s}^{-1}$ Strain Rate Propane/air Counterflow Flame. ....	388
Figure 4–39. Profiles of Number Density and Velocity of $30\mu\text{m}$ Droplets vs. Location in a $170 \text{ s}^{-1}$ Strain Rate Propane/air/ $30\mu\text{m}$ Mist Counterflow Flame. ....	389
Figure 4–40. Profiles of Number Density) and Velocity of $18 \mu\text{m}$ Droplets vs. Location in a Propane/air/water mist Counterflow Flame. ....	389
Figure 4–41. Droplet Flux Profile for a $30\mu\text{m}$ Mist in a $170 \text{ s}^{-1}$ Strain Rate Propane/air Flame. ....	390
Figure 4–42. Water Mist Effects on the Extinction of Non-premixed, Counterflow Propane/air Flames: (a) Flame Extinction Strain Rate as a Function of Mass of Water or Halon 1301 in the Air Flow; (b) Mass Fraction of Water Needed to Extinguish the Flames as a Function of Droplet Diameter, Compared to Mass of Gas-phase Halon 1301. ....	391
Figure 4–43. Variation of the Predicted Flame Temperature as a Function of the Flow Strain Rate for Propane-air, Non-premixed Counterflow Flames for Dry Air, Air Saturated with Water Vapor, and Saturated Air with Monodisperse Water Droplets. ....	393
Figure 4–44. Measured Extinction Strain Rate for Water Mist Suppressed Propane-air, Non-premixed Counterflow Flames vs. % Mass of Condensed-phase Water in the Air and Calculated Results for $14 \mu\text{m}$ , $30 \mu\text{m}$ , and $42 \mu\text{m}$ Diameter Monodisperse Water Mists in Saturated Air at 300 K. ....	394
Figure 4–45 Calculated Humidification Levels of a 296 K Air Stream Containing $14 \mu\text{m}$ , $30 \mu\text{m}$ , or $42 \mu\text{m}$ droplets, Following a Residence Time of 750 ms Starting in Dry Air, as a Function of the Mass Fraction of Liquid Water Remaining after Droplet Evaporation. ....	395
Figure 4–46. Schematic of the Non-premixed Counterflow Burner and Calculated Temperature, O, H, and OH Profiles for the Low Strain Flame. ....	398
Figure 4–47. Powder Delivery System. ....	399
Figure 4–48. Typical Micrographs of $\text{NaHCO}_3$ Powder Samples. ....	400
Figure 4–49. Typical Micrographs of $\text{KHCO}_3$ Powder. ....	400
Figure 4–50. Extinction Mass Concentration as a Function of Strain Rate for Various Particle Sizes Ranges of $\text{NaHCO}_3$ and $\text{KHCO}_3$ Powders in a Propane/air, Counterflow, Non-premixed Flame. ....	401

Figure 4–51. Data from Figure 4–50 Plotted to Show Extinction Mass Concentration as a Function of Particle Size Range for Each Flame Strain Rate and Added Powder.....	402
Figure 4–52. Extinction Mass Concentration as a Function of (a) Average Particle Diameter and Average Particle Surface Area for $\text{NaHCO}_3$ and $\text{KHCO}_3$ Powders in a Medium Strain Rate ( $310 \text{ s}^{-1}$ ) Propane/air Counterflow Non-premixed Flame.....	403
Figure 4–53. Calculated Particle Asymptotic Location as a Function of Particle Diameter for the Flow Conditions of the Low Strain Propane/air Flame.....	405
Figure 4–54. Schematic of the Counterflow Flame Apparatus with the Particle Seeder.....	407
Figure 4–55. % $\text{NaHCO}_3$ by Mass in air as a Function of Extinction Strain Rate for Different Size Groups of Particles.....	409
Figure 4–56. Numerical Prediction of $\text{NaHCO}_3$ Mass Fraction as a Function of Extinction Strain Rate, for Selected Particle Sizes.....	411
Figure 4–57. Schematic of the Counterflow Burner Configuration with the Water Droplet Atomizer.....	413
Figure 4–58. (a) Normalized Droplet Diameter Distribution of the Ultrasonic Atomizer as Reported by the Manufacturer; (b) and (c) Normalized Water Droplet Diameter Distributions Measured Using a PDPA at the Exit of the Air Nozzle for an Air Flow Corresponding to Counterflow Strain Rates of $285 \text{ s}^{-1}$ and $160 \text{ s}^{-1}$ , Respectively.....	415
Figure 4–59. Variation of Water Droplet Mass Fraction in the Condensed Phase as a Function of Flame Extinction Strain Rate.....	417
Figure 4–60. Droplet Mass Fraction in the Condensed Phase as a Function of Flame Extinction Strain Rate for Different Mass Loadings of $\text{NaOH}$ in Water.....	418
Figure 4–61. Variation of the Maximum Flame Temperature as a Function of Local Flow Strain Rate for Constant Droplet Mass Fractions and Constant Water Mass Flux Rates.....	419
Figure 4–62. Droplet Mass Fraction as a Function of Extinction Strain Rate of a Methane/air Non-premixed Flame for Several $\text{NaOH}$ Mass Fractions in Water.....	422
Figure 4–63. $Y_0$ and Mole Fraction of $\text{NaOH}$ in Air as a Function of $y_{\text{NaOH}}$ for the Extinction Strain of $125 \text{ s}^{-1}$ in Figure 4–62.....	423
Figure 4–64. Droplet Mass Fraction as a Function of Extinction Strain Rate of a Methane/air Non-premixed Flame for Several $\text{KOH}$ Mass Fractions in Water.....	424
Figure 4–65. Droplet Mass Fraction as a Function of Extinction Strain Rate of a Methane/air Non-premixed Flame for $\text{NaCl}$ and $\text{FeCl}_2$ in Water.....	425
Figure 4–66. Upper panel: Mole Fraction of Alkali Metal Atoms in Air as a Function of Non-premixed Methane/air Flame Extinction Strain Rate for $\text{NaOH}$ and $\text{KOH}$ Mass Fractions of 0.055 shown in Figure 4. Lower panel: Mole Fraction of $\text{Am}$ in Air as a Function of Non-premixed Methane/air Flame Extinction Strain Rate for $\text{NaOH}$ and $\text{NaCl}$ Mass Fractions of 0.03 Shown in Figure 4–63 and Figure 4–66 (upper panel).....	425
Figure 4–67. Square of the Normalized Burning Velocity of a Premixed Flame Inhibited with Fine Droplets of Water Solution for Several $\text{NaOH}$ Mass Fractions in Water.....	427
Figure 4–68. Normalized Flame Strength of Non-premixed and Premixed Methane/air Flames Inhibited with Droplets of Water with a Median Diameter of $20 \mu\text{m}$ .....	428

Figure 4–69. Non-premixed and Premixed Flame Structures Corresponding to Inhibited Conditions of Water Droplet Mass Fraction of $Y_0 = 0.01$ .	429
Figure 4–70. Setup for JP-8 Fire Suppression Experiments.	432
Figure 4–71. Blow-off Velocity Ratios for Various Candidate Agents to Air, and Reference Ratios for Water to Air Measured under the Same Conditions.	434
Figure 4–72. Blow-off Velocity Ratios for Various Candidate Agents to Air, and Reference Ratios for Water to Air Measured under the Same Conditions	434
Figure 4–73. Times for Various Experimental Fire Suppressants to Extinguish a 200 mL JP-8 Pan Fire.	436
Figure 4–74. Mass of Various Experimental Fire Suppressants to Extinguish a 200 mL JP-8 Pan Fire.	437
Figure 4–75. Mass flows for Various Fire Suppressants Deployed during JP-8 Screening Experiments.	437
Figure 4–76. Droplet Evaporation Time as a Function of Initial Droplet Diameter for Five Fluids.	442
Figure 4–77. Typical Boiling Curve Associated with Quenching of a Hot Surface by Liquid Droplets.	443
Figure 4–78. Calculated Boiling Curves in the Convective Regime for Five Liquids.	445
Figure 4–79. Calculated Boiling Curves for Five Liquids for the Transition and Film Boiling Regimes.	447
Figure 4–80. Wind Tunnel Used for Fire Spread Studies.	449
Figure 4–81. Flame Spread Experiment with Water Mist.	450
Figure 4–82. Schematic of the Two-color Planar Pyrometer.	451
Figure 4–83. Typical Flame Spread Time Trace Obtained using Focal Plane Array Imaging.	452
Figure 4–84. Flame Spread Rates without Water Mist.	452
Figure 4–85. Flame Spread Rate as a Function of Surface Loading for 3.2 mm Thick PMMA.	454
Figure 4–86. Flame Spread Rate as a Function of Surface Loading for 0.64 cm Thick PMMA.	455
Figure 4–87. Mean Droplet Size and Velocity as a Function of Spray Nozzle Discharge Rate.	456
Figure 4–88. Variation in Normalized Flame Spread with Liquid Loading.	457
Figure 4–89. Mean Flame Temperature Obtained Using the TCPP.	457
Figure 4–90. Experimental Arrangement for the Measurements.	458
Figure 4–91. Configuration of the Piezoelectric Atomizer.	459
Figure 4–92. Schematic Diagram of the Heater Assembly.	460
Figure 4–93. Temperature Measurement Locations on the Heater.	460
Figure 4–94. Steady State Temperature Field above the Hot Plate.	463
Figure 4–95. Change in Sauter Mean Diameter of the Water Droplets with Axial Distance.	464
Figure 4–96. Change in Sauter Mean Diameter of the Droplets with Axial Distance for Fluid 510.	464

Figure 4–97. Variation in Velocity with Axial Distance for Water Spray.....	465
Figure 4–98. Variation in Velocity with Axial Distance for Fluid 510. ....	465
Figure 5–1. Schematic of Laser Induced Breakdown Spectroscopy (LIBS) Measurement Apparatus. ....	484
Figure 5–2. Measured Concentrations of Fluorinated Fire Suppressants using LIBS. ....	484
Figure 5–3. Successive Signal Improvements in the Detection of HF using TDLAS. ....	487
Figure 5–4. Schematic of TDLAS Apparatus for Measurement of Gases Produced during Fire Suppression in Ground Vehicles. ....	487
Figure 5–5. HF Gas Produced during Suppression of Heptane Pan Fires by HFC-236 with and without the Addition of Ammonium Polyphosphate). ....	489
Figure 5–6. Oxygen Concentration Measured Within the Crew Compartment of a Bradley Fighting Vehicle During Suppression by $C_3F_8$ of a Spark-Initiated JP-8 Spray Fire.....	491
Figure 5–7. FT-IR Spectra of Dry Air Saturated at 294 K with Vapor from Unleaded gasoline, JP-8, and DF-2. ....	492
Figure 5–8. Schematic Diagram of the Laser Mixing Apparatus Used to Measure Fuel Vapor Concentrations. ....	495
Figure 5–9. Absorption Spectrum of Air Saturated with JP-8, DF-2, or Gasoline Vapor at 294 K Superimposed upon the Emission from the Optical Fiber Carrying the Mixed Wavelength Laser Beam. ....	496
Figure 5–10. Concentrations of Gasoline Vapor and Oxygen, Measured as Dry Air Saturated with JP-8 Vapor Displaces the Dry Air in a 13.7 L Optical Cell. ....	497
Figure 5–11. Loss of Lighter Hydrocarbons from JP-8 Caused by Repeated Fills of the Optical Cell Used for Testing the Mixed Laser Fuel Vapor Sensor. ....	497
Figure 5–12. Two Laser Interferogram Measured at the Detector for the Second Generation Fuel Vapor Sensor. ....	498
Figure 5–13. Experimental Apparatus Used for Fourier Transform Laser Spectroscopy. ....	500
Figure 5–14. Absorption of 1.71 $\mu\text{m}$ Laser Radiation as Air is Displaced by Air Saturated with Gasoline Vapor in a 2 m Cell. ....	500
Figure 5–15. Schematic of a 10-laser FT-LS Source in the Near Infrared. ....	501
Figure 5–16. Schematic of the DIRRACS I. ....	503
Figure 5–17. Schematic of the Optical Design Used in DIRRACS I. ....	503
Figure 5–18. Absorption Spectrum of HFC-125 Superimposed with the Transmittance Spectrum for the Bandpass Filter. ....	504
Figure 5–19. Schematic of DIRRACS II. ....	506
Figure 5–20. Photograph of the DIRRACS II with the Periscope Mounted within the Flow Channel of the TARP Facility. ....	506
Figure 5–21. Calibration Plot of Average Normalized Peak-to-valley Signals vs. Volume Fraction of HFC-125. ....	508

Figure 5–22. Normalized Peak-to-valley Signals Resulting from Processing the Raw Signal from the DIRRACS II for Two Releases of HFC125.....	510
Figure 5–23. HFC-125 Volume Fraction vs. Time for Two Releases of HFC-125 in the TARPF Facility.....	510
Figure 5–24. Bradley Armored Personnel Carrier Modified for Performing Agent Release and Fire Suppression Studies.....	511
Figure 5–25. Interior of the Bradley Vehicle Showing the Periscope of the DIRRACS II in the “High” Location.....	511
Figure 5–26. HFC-125 Volume Fraction and Cylinder Pressure vs. Time at the Upper Measurement Position.....	512
Figure 5–27. HFC-125 Volume Fractions vs. Time at the High and Low Positions During Two Different Releases.....	512
Figure 6–1. Schematic of the Cup Burner Apparatus.....	523
Figure 6–2. Photographs of a Standard Cup Burner.....	523
Figure 6–3. Schematic of Sample Nebulizer.....	524
Figure 6–4. Heated Cup Burner for Appraising High-boiling Flame Suppressants.....	525
Figure 6–5. Schematic of the DLAFSS Wind Tunnel.....	526
Figure 6–6. Photograph of the DLAFSS Wind Tunnel.....	527
Figure 6–7. Cut-away View of the DLAFSS Burner Insert.....	528
Figure 6–8. Photograph of the DLAFSS Burner Assembly.....	528
Figure 6–9. An Enveloped Flame and a Wake Flame.....	529
Figure 6–10. Schematic of the DLAFSS Nebulizer.....	531
Figure 6–11. Screening Results for Various Aqueous Fluids.....	533
Figure 6–12. Schematic of Step-stabilized Pool Fire Apparatus.....	537
Figure 6–13. Photograph of the TARPF.....	538
Figure 6–14. Photograph of a Baffle-stabilized Propane Flame in the TARPF.....	538
Figure 6–15. Liquid Aerosol Agent Injection System.....	540
Figure 6–16. Schematic Diagram of the SPGG Injection System.....	541
Figure 6–17. Photograph of TARPF Injection System with Housing Cover Removed.....	541
Figure 6–18. Disruption of a Stabilized Flame by the Injection of Nitrogen Upstream of 25 mm High Obstacle.....	543
Figure 6–19. Impact of Air Speed on Extinction of a 25 mm Baffle-stabilized Flame.....	545
Figure 6–20. Mass and Rate of Nitrogen Addition to Extinguish a 45 mL/s Propane Flame in 3.9 m/s Air Flow.....	545
Figure 6–21. Mass and Rate of Nitrogen Addition Required to Extinguish High Flow and Low Flow Propane/Air Flames Stabilized Behind a 25 mm Step.....	546

Figure 6–22. Mass and Rate of Nitrogen Addition Required to Extinguish High Flow and Low Flow Propane/Air Flames Stabilized Behind a 10 mm Baffle.....	547
Figure 6–23. Mass and Rate of Nitrogen Addition Required to Extinguish High Flow and Low Flow Propane/Air Flames Stabilized Behind a 55 mm Baffle.....	547
Figure 6–24. Impact of Obstacle Height on the Total Mass and Rate of Addition of Nitrogen Required to Suppress an Obstacle-stabilized Pool Fire. ....	548
Figure 6–25. Mole Fraction of Suppressants (N <sub>2</sub> and CF <sub>3</sub> Br) Added to Air at Extinction Boundary for High and Low Flow Conditions, as a Function of Injection Time Interval and Obstacle Geometry. ....	549
Figure 6–26. Injection interval and Calculated Mass Delivered to Flame as a Function of Area Ratio Times Total Mass of Gas Generated .....	551
Figure 6–27. Percentage of Flames Extinguished as a Function of Mass Delivered to Flame by an SPGG .....	552
Figure 6–28. Impact of Injection Time Interval on the Mass of Agent Required to Suppress a Step-stabilized Propane Pool Fire.....	553
Figure 6–29. Percentage of Flames Extinguished as a Function of Estimated Mass Fraction of Agent.....	553
Figure 6–30. Normalized Volume Fraction as a Function of Non-dimensional Injection Interval, Comparing N <sub>2</sub> , CF <sub>3</sub> Br, and SPGG.....	555
Figure 6–31. Suppression Volume Fraction of Agent (N <sub>2</sub> or CF <sub>3</sub> Br) Normalized by Cup Burner Values as a Function of Injection Time Interval Normalized by Characteristic Residence Time.....	556
Figure 6–32. Schematic of Flash Photolysis Resonance Fluorescence Apparatus for Measuring Reactivity of Compound with OH Radicals. ....	563
Figure 6–33. Apparatus for Measuring the Absorption Cross Section of Candidate Fire Suppressants.....	567
Figure 6–34. Estimated Maximum Boiling Points That Can Achieve Selected Values of Volume % in Air as a Function of Ambient Temperature.....	573
Figure 6–35. Comparison of Two Difluorobromopropene Log(K <sub>OW</sub> ) Calculation Methods.....	587
Figure 6–36. Comparison of Two Trifluorobromopropene Log(K <sub>OW</sub> ) Calculation Methods.....	588
Figure 6–37. Hypothetical Time Dependence of a Toxic Response to Exposure to a Fire Suppressant .....	590
Figure 6–38. Monte Carlo Simulations of Humans Exposed to Halon 1301.....	593
Figure 6–39. Monte Carlo Simulations of Humans Exposed to HFC-125. ....	593
Figure 7–1. Groups and Elements Studied.....	626
Figure 7–2. Resorcinol.....	635
Figure 7–3. Vinyl Phosphonates. ....	636
Figure 7–4. Example of a Fluoro-substituted Bis(dimethylamino) Cyclotriphosphonitrile. ....	637
Figure 7–5. Tris(hydroxymethyl)propane Bicyclic Phosphite.....	644

Figure 7–6. Relative Contributions of Liquid Heating, Vaporization, and Gas Heating to 1400 K to the Total Heat Absorbed by Various Thermal Agents.....	652
Figure 7–7. Air Velocities at Extinguishment of the DLAFFS Flame as a Function of Liquid Application Rate for Lactic Acid/water Mixtures.....	653
Figure 7–8. Air Velocities at Extinguishment of the DLAFFS Flame as a Function of Liquid Application Rate for HFE-7100.....	654
Figure 7–9. Maximum Flame Temperatures as a Function of the Equal Fuel and Air Velocity Magnitudes for a Methane/Air Opposed-Flow Diffusion Flame for Three Versions of the GRI-Mech Mechanism.....	656
Figure 7–10. Groups Required for Significant Tropospheric Photodissociation.....	662
Figure 7–11. Formation of a Six-membered Ring Transition State.....	670
Figure 7–12. Structural and Optical Isomerism of Bromopentafluoropropene Oxide.....	694
Figure 7–13. Vertical Profiles of CF <sub>3</sub> I Emissions for Fuel Tank Inerting in Military Aircraft .....	699
Figure 8–1. Schematic of Storage and Distribution System for Fire Suppression.....	723
Figure 8–2. Staggered Mesh Numerical Method.....	737
Figure 8–3. Curve Fit for Henry’s Constant.....	746
Figure 8–4. Effect of Release Coefficient on Calculated Pressure Response.....	746
Figure 8–5. Comparison of Calculated and Measured Bottle Pressure for Test.....	748
Figure 8–6. Void Fraction Responses in Lower Portion of Bottle.....	749
Figure 8–7. 90° Tee Model with Crossflow Junction.....	751
Figure 8–8. Tee Model with Normal Junctions.....	752
Figure 8–9. Schematic of Test Facility: Source Vessel, Discharge Piping, and Collection Vessel.....	754
Figure 8–10. Schematic of Source Vessel Showing Mass Inventory Measurement.....	755
Figure 8–11. Pressure vs. Temperature Saturation Curve for HFC-227ea and HFC-125.....	756
Figure 8–12. Schematic of a Marotta valve.....	757
Figure 8–13. Top View of Test Facility; Schematic of Discharge Piping System.....	757
Figure 8–14. Schematic of Pressure Fittings for Temperature and Pressure Ports.....	758
Figure 8–15. Schematic of Rack Used to Hold the Source Vessel.....	759
Figure 8–16. Picture of Test Facility: Source Vessel, Discharge Piping, Collection Vessel, Support Structure and Instrumentation .....	760
Figure 8–17. Pressure Traces for Experimental Run #5.....	761
Figure 8–18. Repeatability of the Source Vessel Pressure Traces.....	762
Figure 8–19. Schematic of Alternate Piping Configuration #1.....	763
Figure 8–20. Schematic of Alternate Piping Configuration #2.....	763

Figure 8–21. Transient Pressure Drop across a 90° Elbow from Run #9.....	764
Figure 8–22. Diagram of Transducer Setup for Mass Inventory Measurement.....	765
Figure 8–23. Transient Mass Inventory of Run #5.....	766
Figure 8–24. Schematic of Thermocouple Construction.....	767
Figure 8–25. Transient Temperature Trace from Film Thermocouples of Run #5.....	768
Figure 8–26. Transient Temperature Trace from Shielded Thermocouples of Run #5.....	769
Figure 8–27. Schematic of Capacitance Probe for Bench Setup.....	770
Figure 8–28. Bench Setup to Test Capacitance Sensor.....	771
Figure 8–29. Void Fraction from Bench Tests of Capacitance Sensor.....	771
Figure 8–30. Schematic of Capacitance Probe for Test Facility.....	772
Figure 8–31. Cross-section of Capacitance Setup Showing Electrical Field.....	772
Figure 8–32. Transient Void Fraction of Run #5.....	773
Figure 8–33. Cumulative Mass as a Function of Time for Runs #1 and #8.....	779
Figure 8–34. Pressure Drops across Top and Bottom Branch Tees from Run #13.....	781
Figure 8–35. Comparison of Temperature Traces in the Collection Vessel from Runs #5 and #16.....	782
Figure 8–36. Void Fraction Measurements from Run #5.....	782
Figure 8–37. Void Fraction Measurements from Run #16.....	783
Figure 8–38. Pressure Traces from Run #5.....	784
Figure 8–39. Pressure Traces from Run #16.....	784
Figure 8–40. Mass Inventory in the Source Vessel from Run #18.....	785
Figure 8–41. Temperature Traces at Various Positions from Run #18.....	785
Figure 8–42. Void Fraction Measurements from Run #19.....	786
Figure 8–43. NIST Test Apparatus.....	787
Figure 8–44. Piping Configurations for NIST Experiments.....	788
Figure 8–45. FSP Input Model.....	789
Figure 8–46. Comparison of Calculated and Measured Bottle Pressure for B-59.....	790
Figure 8–47. Comparison of Calculated and Measured Bottle Pressure for B-68.....	790
Figure 8–48. Comparison of Calculated and Measured Bottle Pressure for B-61.....	791
Figure 8–49. Comparison of Calculated and Measured Bottle Pressure for B-60.....	791
Figure 8–50. Comparison of Experimental and Predictive Source Vessel Pressure Data in Sensitivity Study on Critical Radius Value for Conditions of Run #4.....	793
Figure 8–51. Comparison of Experimental and Predictive Source Vessel Pressure Data in Sensitivity Study on Gas Release Rate Value for Conditions of Run #4.....	793

Figure 8–52. Comparison of Experimental and Predictive Void Fraction Data in Sensitivity Study on Gas Release Rate Value for Conditions of Run #4.....	794
Figure 8–53. Comparison of Experimental (in black) and Predictive Pressure Data Using Final Values for Code Operating Parameters for Conditions of Run #4. ....	795
Figure 8–54. Comparison of Experimental (in black) and Predictive Void Fraction Data Using Final Values for Code Operating Parameters for Conditions of Run #4.....	793
Figure 8–55. Comparison of Cumulative Mass for Experimental Run #5 and Predictive Computer Code Data.....	796
Figure 8–56. Comparison of Void Fraction for Experimental Run #5 and Predictive Computer Code Data .....	797
Figure 8–57. Comparison of Source Vessel Pressure for Experimental Run #5 and Predictive Computer Code Data.....	798
Figure 8–58. Comparison of Pipe Position #1 Pressure for Experimental Run #5 and Predictive Computer Code Data .....	798
Figure 8–59. Comparison of Pipe Position #2 Pressure for Experimental Run #5 and Predictive Computer Code Data .....	799
Figure 8–60. Comparison of Pipe Position #3 Pressure for Experimental Run #5 and Predictive Computer Code Data .....	799
Figure 8–61. Comparison of Collection Vessel Pressure for Experimental Run #5 and Predictive Computer Code Data .....	800
Figure 8–62. Comparison of Pressure Drop across a Capped Tee for Experimental Run #9 and Predictive Computer Code Data.....	801
Figure 8–63. Comparison of Pressure Drop across a 90° Elbow for Experimental Run #9 and Predictive Computer Code Data .....	801
Figure 8–64. Comparison of Pressure Drop across a Union for Experimental Run #9 and Predictive Computer Code Data .....	802
Figure 8–65. Comparison of Source Vessel Fluid Temperature for Experimental Run #16 and Predictive Computer Code Data. ....	803
Figure 8–66. Comparison of Pipe Position #1 Fluid Temperature for Experimental Run #16 and Predictive Computer Code Data.....	803
Figure 8–67. Comparison of Collection Vessel Gas Temperature for Experimental Run #16 and Predictive Computer Code Data.....	804
Figure 8–68. Zone A of the Test Section. ....	806
Figure 8–69. Clutter Recovery vs. Airspeed.....	808
Figure 8–70. Plenum Recovery vs. Airspeed.....	808
Figure 8–71. Heated Cylinder Test Section.....	809
Figure 8–72. Heated Cylinder. (A) Schematic and (B) Front View. ....	810
Figure 8–73. Body-centered Cube of Spheres. ....	811
Figure 8–74. Photographs of Seed/droplet-laden Flow Fields around Obstacles. ....	812

Figure 8–75. Variation of the Mean Streamwise and Cross-stream Velocities with Downstream Distance for the Unheated Cylinder. ....	813
Figure 8–76. Variation of the Mean Streamwise and Cross-stream Velocities with Downstream Distance for the Body-centered Cube of Spheres. ....	814
Figure 8–77. View and Schematic of the Experimental Arrangement with the Laser from the Phase Doppler Interferometry System. ....	816
Figure 8–78. Schematic of the Measurement Grid around the Cylinder. ....	816
Figure 8–79. Variation of Water Droplet (A) Sauter Mean Diameter and (B) Mean Streamwise Velocity with Streamwise Position at Different Cross-stream Positions for the Unheated Cylinder. ....	818
Figure 8–80. Variation of the Streamwise Velocity with Time upstream of the Unheated Cylinder at $Z = -15$ mm and along the Centerline. ....	818
Figure 8–81. Variation of the Streamwise Velocity with Time at Two Streamwise Positions of (A) $Z = 25$ mm and (B) $Z = 76$ mm along the Centerline, downstream of the Unheated Cylinder within the Recirculation Region. ....	819
Figure 8–82. Variation of Water Droplet (A) Sauter Mean Diameter and (B) Mean Streamwise Velocity for the Unheated (22 °C) and Heated (150 °C) Cylinders. ....	820
Figure 8–83. Comparison of the Droplet Mean Size and Streamwise Velocity for the Three Agents. ....	820
Figure 8–84. USNA Wind Tunnel Schematic. ....	822
Figure 8–85. Low-speed, High-turbulence, Open Jet USNA Wind Tunnel. ....	822
Figure 8–86. Photograph of the Wire Bundle Model. ....	824
Figure 8–87. Photograph of the Tandem Medium Cylinder Model. ....	824
Figure 8–88. Photograph of the Cube Model. ....	825
Figure 8–89. Strouhal Number vs. Reynolds Number for the Various Tested Configurations. ....	828
Figure 8–90. Schematic of the Test Fixture (ELEFANT). ....	830
Figure 8–91. Absorption Spectrum of $CF_3I$ . ....	833
Figure 8–92. Calibration Curve at 300 nm. ....	834
Figure 8–93. Variation of Bottle Pressure during Discharge at Room and Cold Temperatures. ....	834
Figure 8–94. $CF_3I$ Concentration Profiles at the Forward Port. ....	836
Figure 8–95. $CF_3I$ Concentration Profiles at the Aft Port. ....	836
Figure 8–96. Calculated Liquid Fraction as a Function of Bottle Temperature. ....	838
Figure 8–97. Photograph of the Quarter-Scale Nacelle Test Facility with LDV apparatus. ....	848
Figure 8–98. Measurement Stations in the Quarter-Scale Nacelle. ....	848
Figure 8–99. VULCAN Gridding for the Quarter-Scale Nacelle. ....	850
Figure 8–100. Section of the CFD-ACE Grid Used in the Simulation. ....	851
Figure 8–101. Inlet Velocity Profile. ....	851
Figure 8–102. Inlet Turbulence Intensity Profile. ....	852

Figure 8–103. Velocity and Turbulence Intensity Profiles at Measurement Station 4. ....	852
Figure 8–104. Velocity and Turbulence Intensity Profiles at Mid-nacelle. ....	853
Figure 8–105. Comparison of Simulation and Experimental Data at the Exit Cone. ....	853
Figure 8–106. Velocity and Turbulence Intensity Profiles Flow in the Exit Pipe. ....	854
Figure 8–107. Ray Tracing Image of Case A1 before Agent Injection and 0.2 s after Injection of 10% HFC-125 Images of Case A3 and A5 before Agent Injection.....	856
Figure 8–108. Centerline Contour Plots Showing (from top to bottom) the Temperature, Oxygen Mass Fraction, Fuel Mass Fraction and the Computational Grid for Case A1. ....	857
Figure 8–109. (a) Evolution of the Maximum Fluid Cell Temperature in the Domain for Case A1 for Various HFC-125 Mole Fractions. (b) Suppression Times as a Function of Added HFC-125 for Cases A1, A3 and A5. (c) Mass Fraction and Temperature Evolution in the Recirculation Zone (8 mm above pool and 8 mm behind step) for Case A1 with 10 % HFC-125 by Volume Injected at 5 s. ....	858
Figure 8–110. Centerline Contour Plots of Temperature and HFC-125 Mass Fraction at 0.1 s and 0.2 s after Suppressant Injection for Case A1 with 0.1 HFC-125 Mole Fraction Injected.....	859
Figure 8–111. Centerline Pressure Contours and Velocity Vectors for Cases A1, A3 and A5 prior to Suppressant Injection.....	860
Figure 8–112. Raytracing images of Cases B1 and B2.....	862
Figure 8–113. (a) Temporal Evolution of HFC-125 Mass Fraction in the Recirculation Zone at a Point 0.012 m above the Lower Surface and 0.05 m behind the Rib along the Centerline. (b) Suppression Times as a Function of HFC-125 Mole Fraction for Cases B1, B2, C1, and C2. ....	862
Figure 8–114. Locations of the Suppressant Nozzles and the Pools in the Nacelle Simulator.....	863
Figure 8–115. Contour Plots of $C_2HF_5$ at 3.0 s after Start of Suppressant Injection in Vertical Planes near Starboard Side near Nacelle Centerline and near Port Side.....	864
Figure 8–116. Simulation Results of Various Injection Periods.....	866
Figure 8–117. Simulation Results Showing the Effect of Nozzles on Agent Distribution.....	867
Figure 8–118. Simulated Agent Distribution along the Nacelle Centerline. ....	867
Figure 8–119. Ground Test Nacelle ‘Iron Bird’ Simulator.....	873
Figure 8–120. Drawing of Front Face of Ground Test Nacelle. ....	874
Figure 8–121. Transient Bottle Pressure during Discharge for Various Initial Pressures with Nozzles Discharging a Total of 3.2 kg of HFC-125. ....	880
Figure 8–122. Nacelle Configuration Used in FDS Simulations.....	883
Figure 8–123. Nacelle Configuration Used in FPM Simulations. ....	883
Figure 8–124. Results of Tests with All Nozzles Used. ....	887
Figure 8–125. Results of Tests with One Nozzle Capped. ....	888
Figure 8–126. Extinguishment of Heptane Pool Fires by Uncharged Water Mist. ....	892
Figure 8–127. Schematic Sketch of Fire Test Chamber .....	895

Figure 8–128. Electron Induction Electrode.....	895
Figure 8–129. Attraction of Charged Droplets to Grounded Metal Screen.....	896
Figure 8–130. Motion of Charged Droplets near Fires.....	898
Figure 8–131. 7N Seven Hollow Cone Nozzle Setup.....	899
Figure 8–132. Spray Charging Set-up.....	900
Figure 8–133. Effect of Center Nozzle Size on 7N Nozzles Water Flux.....	901
Figure 8–134. Effect of Electrical Charging on Water Flux Distribution of the 7N Nozzles with the 0.063 L/min Center Nozzle.....	902
Figure 8–135. Initial Data on Effect of Electrical Charging for a 10 cm Diameter Heptane Pool Fire.....	903
Figure 8–136. All Electrical Charging Data for a 10 cm Diameter Heptane Pool Fire.....	904
Figure 8–137. Schematic of Single Nozzle Electron Emission Electrode.....	905
Figure 8–138. Effect of Electrical Charging on Extinguishment for a 5 cm Diameter Heptane Pool Fire.....	906
Figure 8–139. AeroChem 5 cm and 10 cm and NMERI 5 cm Heptane Extinguishment Data.....	907
Figure 8–140. Experimental Setup for Testing the Relative Effectiveness of Fire Extinguishing Agents.....	911
Figure 8–141. Experimental Setup for Testing Agents Against an Obstructed Flame.....	912
Figure 8–142. Extinction of a Candle Flame by CO <sub>2</sub> .....	914
Figure 8–143. Extinction of a Candle Flame by Halon 1211.....	914
Figure 9–1. Typical Powder Panel Arrangements.....	928
Figure 9–2. Experimental Test Device and Powder Collection Methods.....	935
Figure 9–3. AVSF Range A Light-gas Gun.....	936
Figure 9–4. Test Example of Significant Panel Fracture and Material Loss.....	941
Figure 9–5. Test Example of Effective Powder Release and Dispersion.....	941
Figure 9–6. Effect on Powder Panel Fracture Area of Standard Design Features and Enhanced Designs.....	942
Figure 9–7. Effect on Powder Delivery of Standard Design Features and Enhanced Designs.....	943
Figure 9–8. Effect on Powder Dispersion of Standard Design Features and Enhanced Designs.....	943
Figure 9–9. JTCG/AS Test Article.....	946
Figure 9–10. Schematic of the FAA Test Article.....	946
Figure 9–11. Enhanced Powder Panel Fire Mitigation Capability.....	947
Figure 9–12. Comparison of Commercial and Enhanced Powder Panel Agent Release in JTCG/AS Dry Bay Fire Extinguishing Testing.....	948

Figure 9–13. Entire Contents of Enhanced Powder Panel Released During FAA Test in Which the Fire Was Prevented. ....	948
Figure 9–14. Enhanced Powder Panel Mass Reduction.....	952
Figure 9–15. Enhanced Powder Panel Thickness Reduction.....	953
Figure 9–16. Comparison of Enhanced and Commercial Panel Powder Released.....	953
Figure 9–17. Comparison of Enhanced and Commercial Panel Percent Powder Released.....	954
Figure 9–18. Comparison of Enhanced and Commercial Panel Front Face Area Removal.....	954
Figure 9–19. Range 2 at the WPAFB Aerospace Vehicle Survivability Facility.....	956
Figure 9–20. Test Article.....	956
Figure 9–21. Schematic of Test Article.....	957
Figure 9–22. Test Article Setup in Range 2.....	958
Figure 9–23. 12.7 mm API Type B-32 Projectile Description.....	959
Figure 9–24. Post-Test Damage Image of EPP-03 Commercial Powder Panel.....	961
Figure 9–25. Post-Test Damage Image of EPP-04 Enhanced Powder Panel.....	962
Figure 9–26. Post-Test Damage Image of EPP-05 Enhanced Powder Panel.....	963
Figure 9–27. Powder Suspension in the Dry Bay Well After the Test.....	964
Figure 9–28. Powder Dispersion on Striker Plate and Side Lexan Panel.....	964
Figure 9–29. Post-Test Damage Image of EPP-06 Enhanced Powder Panel.....	965
Figure 9–30. Post-Test Damage Image of EPP-07 Enhanced Powder Panel.....	965
Figure 9–31. Post-Test Damage Image of EPP-08 Enhanced Powder Panel.....	963
Figure 9–32. Powder Evident in Dry Bay More Than 5 min after EPP-09 Test.....	967
Figure 9–33. Post-Test Damage Image of EPP-09 Enhanced Powder Panel.....	967
Figure 9–34. NAWS-China Lake Propellant Burn Rate Apparatus.....	978
Figure 9–35. Aerojet Fire Test Fixture (FTF).....	979
Figure 9–36. Photograph of Fire Test Fixture.....	979
Figure 9–37. FTF Test Facility Schematic.....	980
Figure 9–38. Fire Test Fixture Operational Configurations.....	981
Figure 9–39. Aerojet Slow Discharge Solid Propellant Gas Generator Test Unit.....	983
Figure 9–40. Cutaway of Aerojet Slow Discharge Solid Propellant Gas Generator Test Unit.....	984
Figure 9–41. Aerojet Reusable Rapid Discharge Solid Propellant Fire Extinguisher Unit.....	985
Figure 9–42. Arrangement of a Typical Hybrid Fire Extinguisher.....	985
Figure 9–43. Consecutive Frames during SPGG Suppression of a Fire in the FTF.....	986
Figure 9–44. SPGG Installed in Sponson Test Article for Live-fire Demonstration.....	987
Figure 9–45. SPGGs Installed in Mid-wing Test Article for Live-fire Demonstration.....	987
Figure 9–46. Typical Setup of Preliminary Vise Shot for Hybrid Extinguisher.....	988

Figure 9–47. Chamber Pressure for Different Propellant Surface Areas (CA-04). .....	990
Figure 9–48. Housing Temperatures for Different Propellant Surface Areas (CA-04). .....	990
Figure 9–49. High-nitrogen Fuels Used in China Lake/Aerojet Propellant Development. ....	993
Figure 9–50. Synthetic Route to BTATZ.....	995
Figure 9–51. Temperature Dependence of Propellant Burn Rates for Different FS01-40/additive Combinations. ....	998
Figure 9–52. Effect of Coolant Percentage on Burning Rate (in./s) and Adiabatic Temperature of High Nitrogen Propellants Listed in Table 9–18.....	999
Figure 9–53. Representative SPGG Pressure-time Curve Obtained during Delivery of Candidate Chemically Active Agents.....	1004
Figure 9–54. Representative P-t Curve for SPGG Chamber Pressure. ....	1009
Figure 9–55. Representative P-t Curve for Fire Test Fixture Pressure before, during, and after SPGG discharge. ....	1009
Figure 9–56. Threshold Mass of Inert Propellant Plus Potassium Compound for Suppression in the FTF.....	1010
Figure 9–57. Schematic of Hybrid Extinguisher Workhorse Hardware Configuration.....	1012
Figure 9–58. Mounting Configuration of Multiple Hybrid Extinguishers Used to Bracket Threshold Levels.....	1012
Figure 9–59. Effectiveness of Various Hybrid Extinguisher Propellant/fluid Combinations.....	1017
Figure 9–60. Relative Effectiveness of Various SPGG Fire Extinguishers over the Span of the NGP Research.....	1020
Figure 9–61. Evolution of SPGG Fire Suppression Application Technologies.....	1020
Figure 10–1. Typical Cargo Aircraft Engine Nacelle Fire Protection System Location (Wing Leading Edge).....	1030
Figure 10–2. Close-up of Typical Engine Nacelle Fire Protection System Bottle. ....	1030
Figure 10–3. Typical Cargo Aircraft Engine Nacelle Fire Suppressant Storage and Distribution System (Wing Leading Edge).....	1031
Figure 10–4. Typical Auxiliary Power Unit Fire Protection System Location.....	1034
Figure 10–5. Typical General Location of Fighter Aircraft Fire Extinguisher Bottle. ....	1034
Figure 10–6. Schematic of Typical Fighter Aircraft Engine Bay. ....	1035
Figure 10–7. Typical Fighter Aircraft Fire Suppression System Installation. ....	1035
Figure 10–8. Typical General Location of Rotary-Wing Aircraft Fire Extinguisher Bottles. ....	1039
Figure 10–9. Typical Future Fighter Aircraft Agent Distribution System.....	1049
Figure 10–10. F-22 Factor of Safety Data. ....	1070
Figure 10–11. Legacy and Future Cargo Aircraft Net Costs vs. System Effectiveness for Halon 1301.....	1074

Figure 10–12. Legacy Cargo Aircraft Net Costs vs. System Effectiveness for HFC-125. ....	1074
Figure 10–13. Future Cargo Aircraft Net Costs vs. System Effectiveness for HFC-125. ....	1075
Figure 10–14. Legacy and Future Cargo Aircraft Cost Savings vs. System Effectiveness. ....	1075
Figure 10–15. Legacy Fighter Aircraft Net Costs vs. System Effectiveness. ....	1077
Figure 10–16. Future Fighter Aircraft Net Costs vs. System Effectiveness. ....	1077
Figure 10–17. Legacy and Future Fighter Aircraft Cost Savings vs. System Effectiveness. ....	1078
Figure 10–18. Legacy Rotary-wing Aircraft Net Costs vs. System Effectiveness for Halon 1301. ....	1079
Figure 10–19. Legacy Rotary-Wing Aircraft Net Costs vs. System Effectiveness for HFC-125. ....	1080
Figure 10–20. Future Rotary-Wing Aircraft Net Costs vs. System Effectiveness for Halon 1301. ....	1080
Figure 10–21. Future Rotary-Wing Aircraft Net Costs vs. System Effectiveness for HFC-125. ....	1081
Figure 10–22. Legacy and Future Rotary-Wing Aircraft Cost Savings vs. System Effectiveness. ....	1081
Figure 11–1. AENTF Primary Mechanical Components. ....	1107
Figure 11–2. Photograph of Universal Test Fixture. ....	1107
Figure 11–3. Cutaway View of the Engine Core inside the Nacelle Fixture. ....	1108
Figure 11–4. Vertical Extinguisher Unit Attached to the Nacelle Fixture. ....	1108
Figure 11–5. AENTF Control Room. ....	1109
Figure 11–6. Semi-Transparent View of Components in Fire Section of the Test Fixture. ....	1110
Figure 11–7. Pool Fire Pan in Nacelle. ....	1110
Figure 11–8. Schematic of Spray Fire Vicinity. ....	1111
Figure 11–9. 7.6 cm Ribs Mounted on the Underside of the Nacelle and the Engine Core. ....	1111
Figure 11–10. Discharge “T” and with Nozzles Added for Phase II. ....	1119
Figure 11–11. Halonyzer Probe Mounting in Flame Region. ....	1120
Figure 11–12. Halonyzer Probes in Nacelle Fixture. ....	1120
Figure 11–13. Phase II Nacelle Concentration Measurement Quadrants. ....	1123
Figure 11–14. Layout for Multi-Port Discharge. ....	1123
Figure 11–15. Variation of Moles of Injected Chemical per Fire Zone Volume Percent with Relative Air Temperature. ....	1127
Figure 11–16. Variation of Concentration Standard Deviation with Number of Discharge Sites. ....	1127
Figure 11–17. Variation of Concentration Standard Deviation with Rib Height. ....	1128

---

Figure 11–18. Reduction in Moles/Concentration with Increasing $\tau$ , Residence Time.....	1129
Figure 11–19. Effect of Agent Type and Relative Temperature on Extinguishing Concentration.....	1130
Figure 11–20. Notional Graphs of Concentration in the Free Stream and Recirculation Zone.....	1133
Figure 11–21. Sample Halonyzer Traces.....	1134
Figure 11–22. Influence of Flame Stabilizing Rib Height on Value of $\tau$ .....	1136
Figure 11–23. Influence of Fire Type on Value of $\tau$ .....	1136
Figure 11–24. Influence of Agent and Air Temperature on Value of $\tau$ .....	1137
Figure 11–25. Variability in Peak Concentration Required Due to Extinguisher Flow.....	1140
Figure 11–26. Variability in Peak Concentration Required Due to Rib Height.....	1141

Page intentionally left blank

## LIST OF TABLES

---

Table 1–1. Flame Suppression by Halon 1301 and Other Chemicals .....	5
Table 1–2. Use of Halon 1301 in Fielded Weapons Systems.....	7
Table 2–1. Evolution of Aircraft Vulnerability Based on Live Fire Test Vulnerability Assessments (API Threats).....	22
Table 2–2. Tabulation of Aircraft Fire Types.....	42
Table 2–3. Number of Mishaps and Incidents.....	60
Table 2–4. Percentage of Fire Mishaps and Incidents Occurring in Geographic Cold or Severe-Cold Environments.....	60
Table 2–5. Comparison of Modeled vs. Measured Nacelle Air Temperatures .....	68
Table 2–6. Estimate of Rate of Occurrence of Aircraft Lost Due to Failure to Extinguish a Nacelle Fire, Any Time .....	72
Table 2–7. Estimate of Rate of Occurrence of Aircraft Lost Due to Failure to Extinguish a Nacelle Fire, Any Time .....	72
Table 2–8. Estimate of Rate of Occurrence of Aircraft Lost Due to Failure to Extinguish a Nacelle Fire in a Climatic Extreme.....	73
Table 2–9. Estimate of Rate of Occurrence of Aircraft Lost Due to Failure to Extinguish a Nacelle Fire in a Climatic Extreme.....	73
Table 2–10. Fire Suppressants on DoD Aircraft.....	87
Table 2–11. Most Significant Fire Suppression Parameters Identified During Phase 1.....	93
Table 2–12. Halon Alternative Fire Suppressants Identified for Phase 2 Evaluation. ....	94
Table 2–13. Most Significant Fire Suppression Parameters Identified During Phase 2.....	94
Table 2–14. Fire Suppression Parameters in Design Guidance Developed from Phase 3. ....	95
Table 2–15. Minimum Fire Suppressant Quantities from F-22 Main Landing Gear Dry Bay Live Fire Testing, 150-grain Fragment Threat and Jet Fuel Except Where Noted. ....	103
Table 3–1. Agents Tested. ....	125
Table 3–2. Cup Burner Extinction Concentrations.....	137
Table 3–3. Catalytic Efficiency of Different Metals in Promoting Radical Recombination. ....	149
Table 3–4. Metals Which Have Shown Flame Inhibiting Properties. ....	155

Table 3–5. Inhibitor Concentrations ( $\mu\text{L/L}$ ) and Uncertainty ( $\pm \mu\text{L/L}$ ) at Flame Extinction.....	161
Table 3–6. Uninhibited Laminar Burning Velocities SL and Adiabatic Flame Temperatures TAFT from 1-D Planar Numerical Calculations, Together with the Average Burning Velocity Measured in the Bunsen-type Flames.....	180
Table 3–7. Reaction Rate Data for Tin Inhibition of Premixed Methane-air Flames.....	182
Table 3–8. Thermodynamic Properties of Tin- and Manganese-containing Species (298 K).....	183
Table 3–9. Reaction Rate Data for Manganese Inhibition of Premixed Methane-air Flames.....	184
Table 3–10. Summary of the Fe and Na Mass Loadings in Unheated and Heated Particles.....	203
Table 3–11. Components of Metallic Complexes.....	213
Table 3–12. Current State of Knowledge Relevant to Inhibition Potential of Metals, and Loss of Effectiveness due to Condensation.....	233
Table 3–13. Flame Conditions.....	256
Table 3–14. Probe Orifice Diameters Used in Specific Experiments.....	269
Table 3–15. FTIR Detection Limits and Wavenumber Ranges.....	270
Table 3–16. Operating Conditions.....	272
Table 3–17. Inhibitor Concentrations and Uncertainty at Flame Extinction.....	285
Table 3–18. Measured OH Profile Widths for the Uninhibited Flame and Inhibited Flames at 50 % of the Inhibitor Extinction Concentrations.....	287
Table 3–19. Comparison of Calculated Burning Velocities.....	297
Table 3–20. Kinetic Mechanisms for Suppressants.....	302
Table 3–21. Efficiencies and Sensitivities to Bond Energies of Catalytic Cycles.....	306
Table 3–22. Input Parameters and Calculated Temperatures and Flame Speeds.....	310
Table 4–1. Mean Diameter Definitions, Symbols, and Notations used to Describe Aerosol Size Distributions.....	348
Table 4–2. Thermodynamic Quantities for Physical Suppressants Compared to $\text{CF}_3\text{Br}$ .....	368
Table 4–3. Number Density and Droplet Separation Lengths for Some Selected Water Mass Fractions.....	374
Table 4–4. Stokes Number ( $S_t$ ) for Different Droplet Sizes for $a = 130 \text{ s}^{-1}$ .....	376
Table 4–5. PDPA Derived Diameter Information for the Experimental Mists Studied Measured at 2 mm from the Air Tube Exit.....	386

Table 4–6. Flow and Strain Rate Conditions for Extinction Experiments. ....	398
Table 4–7. Propane-air Counterflow Non-premixed Flame Extinction Mass Concentrations for Powders and Halon 1301. ....	401
Table 4–8. Experimental and Predicted Global Flame Extinction Strain Rates ( $s^{-1}$ ) for Different Droplet Size Distributions and Water Droplet Mass Fraction of 0.01. ....	420
Table 4–9. Elemental Composition of Pure Dendrimers and Dendrimer Salt Complexes. ....	431
Table 4–10. Average Blow-off Velocities for of Various Candidate Agents. ....	433
Table 5–1. Optical Diagnostics for Fire Species. ....	483
Table 6–1. Calculated Nominal Agent Mass Fractions at Reference Blow-off Air Velocity of 30 cm/s. ....	534
Table 6–2. Estimated and Reported ODP Values (Relative to CFC-11) for Selected Halocarbons. ....	559
Table 6–3. Atmospheric Lifetimes (years), from Theory and from OH Reactivity Measurements, for Selected Molecules. ....	570
Table 6–4. Reactions of Phosphates. ....	571
Table 6–5. Estimated Equilibrium Vapor Pressure as a Function of Boiling Point and Ambient Temperature. ....	573
Table 6–6. Estimated Maximum Boiling Point That Can Achieve a Given Volume Percent of Chemical in Air. ....	573
Table 6–7. Cardiac Sensitization Values for Fluorocarbons and Hydrofluorocarbons. ....	580
Table 6–8. Cardiac Sensitization Values for Br-, Cl-, and I-containing Alkanes. ....	581
Table 6–9. Cardiac Sensitization Values for CFCs and HFCs. ....	581
Table 6–10. Availability of QSARs for Various Chemical Classes and Toxic Endpoints. ....	583
Table 6–11. Air Concentration Inducing Cardiac Sensitization in 50 % of Animals. ....	585
Table 6–12. Partitioning ( $K_{OW}$ ) and Arrhythmia Properties of Selected Anesthetics. ....	586
Table 6–13. Comparison of Calculated and Measured Values of Log $K_{OW}$ of Selected Halocarbons. ....	588
Table 6–14. In vitro Cardiac Cell Systems. ....	589
Table 6–15. Time for Safe Human Exposure at Stated Concentrations for Halon 1301 and HFC-125. ....	592
Table 6–16. Nominal Quantities of Chemicals Needed for Screening Tests. ....	597

Table 7-1. Tropospheric Removal Mechanisms. ....	612
Table 7-2. NIST List of Recommended Chemical Families (1990). ....	615
Table 7-3. AAWG Preliminary List of Compounds. ....	617
Table 7-4. TOPKAT Toxicity Predictions. ....	618
Table 7-5. DEREK Toxicity Predictions. ....	619
Table 7-6. Acute Inhalation Toxicity Tropodegradable Bromofluoroalkenes. ....	621
Table 7-7. Ames Mutagenicity Test Results. ....	621
Table 7-8. Chromosomal Aberration Test Results. ....	621
Table 7-9. Cardiac Sensitization Testing of Bromofluoropropenes. ....	621
Table 7-10. Anesthesiology Testing of Fluoroalkenes. ....	622
Table 7-11. Chemical Families Selected for Further Study. ....	625
Table 7-12. Chemical Families Not Pursued Further. ....	625
Table 7-13. Silicon-containing Compounds. ....	628
Table 7-14. •OH Rate Constants for Silicon Compounds. ....	631
Table 7-15. Tetra(fluoroalkoxy)silanes. ....	633
Table 7-16. Phosphonitrile Flame Extinguishment. ....	637
Table 7-17. Phosphorus Halide Flame Extinguishment. ....	638
Table 7-18. Rate Constants •OH Reactions With Phosphorus Compounds. ....	640
Table 7-19. Toxicity Studies of Chlorophosphazenes. ....	642
Table 7-20. Perfluoroalkyl Sulfur Compounds. ....	646
Table 7-21. Family Types in the DIPPR Database. ....	648
Table 7-22. Compounds with High $\Delta H_{\text{Total}}$ (Molar Basis). ....	649
Table 7-23. Compounds with High $\Delta H_{\text{Total}}$ (Mass Basis). ....	650
Table 7-24. Extinguishing Volume Fractions of Inert Gases for CH <sub>4</sub> /Air Diffusion Flames. ....	657
Table 7-25. Extinguishing Volume Fractions of Inert Gases for C <sub>3</sub> H <sub>8</sub> /Air Diffusion Flames. ....	657
Table 7-26. Tropodegradable Brominated Candidates. ....	659
Table 7-27 Bromofluoropropenes. ....	663
Table 7-28 Bromofluoropropene Cup Burner Flame Extinguishment Data. ....	664
Table 7-29 Low Boiling Bromofluoroalkene Cup Burner Values. ....	664
Table 7-30 Phosphorus Compound Toxicity (Safety) Information. ....	665
Table 7-31. FID Extinguishment Estimates of Phosphorus Acids and Esters. ....	670

Table 7–32. Properties of Phosphorus-Containing Compounds.....	671
Table 7–33. Flame Extinguishment Values for Trimethylphosphite Blends with HFCs.....	672
Table 7–34. Enthalpy of Reaction for $\text{PF}_3 + 3 \text{O}=\text{CF}_2 \rightarrow \text{P}(\text{OCF}_3)_3$ .....	674
Table 7–35. Perfluoroalkyl Phosphines.....	675
Table 7–36. Amino Fluoroalkylphosphines.....	677
Table 7–37. Phosphorus-containing Compound Performance.....	679
Table 7–38. $\bullet\text{OH}$ Rate Constants for Nitrogen-containing Compounds.....	681
Table 7–39. Rate Constants for Reactions of $\text{O}_3$ with Amines.....	681
Table 7–40. Acute Inhalation Toxicity of Hydrofluoroamines.....	683
Table 7–41. Toxicity and Safety Information for Selected N, F Compounds.....	683
Table 7–42. Fluoroalkylamine Boiling Points.....	684
Table 7–43. Bromofluoroamine Candidate Compounds.....	685
Table 7–44. Bromofluoroamine Boiling Points and Flame Suppression Results.....	687
Table 7–45. Rate Constants for Hydrofluoroether Reactions with $\bullet\text{OH}$ .....	688
Table 7–46. Atmospheric Lifetimes for Fluorine-containing Ethers.....	688
Table 7–47. Fluoroether Cup Burner Extinguishment Data.....	691
Table 7–48. Bromofluoroether Cup Burner Testing Summary.....	693
Table 7–49. Bromofluoropropene Oxide Cup Burner Testing Summary.....	695
Table 7–50. Bromofluoro Alcohol Boiling Points.....	696
Table 7–51. Iodoalkane Boiling Points.....	697
Table 7–52. Compilation of Historic Firefighting Emissions of $\text{CF}_3\text{Br}$ .....	698
Table 7–53. Estimated Ozone Depletion Effects of $\text{CF}_3\text{I}$ for Two Emission Profiles.....	699
Table 8–1. PROFISSY Results for Henry’s Constants.....	745
Table 8–2. Operating Condition for Repeatability Tests.....	761
Table 8–3. Matrix of Experimental Runs Conducted.....	775
Table 8–4. Comparison of Experimental Pressure Drop Values to Literature Values.....	780
Table 8–5. Test Matrix from NIST Experiments.....	789
Table 8–6. Model Geometry and Test Conditions.....	823
Table 8–7. Summary of Drag Coefficients.....	826
Table 8–8. Frequency and Strouhal Number Resolution.....	827
Table 8–9. Selected Thermophysical Properties of $\text{CF}_3\text{I}$ and $\text{CF}_3\text{Br}$ .....	829

Table 8–10. Experimental Matrix.....	832
Table 8–11. Liquid Fraction of CF <sub>3</sub> I/N <sub>2</sub> Mixture after Isentropic Expansion to 0.101 MPa.....	835
Table 8–12. Description of Simulations of Pool Fires Stabilized behind a Backwards-facing Step.....	855
Table 8–13. Pool Characteristics.....	868
Table 8–14. Summary of Test Results with Four Nozzles.....	869
Table 8–15. Summary of Test Results with Individual Nozzles Capped.....	870
Table 8–16. Comparison of Predicted vs. Measured Pressures and Flows.....	876
Table 8–17. Summary of Full-Scale Tests Conducted.....	881
Table 8–18. Comparison of Fire Test Results and Pretest Simulations.....	882
Table 8–19. Effectiveness of Charged Water Mist Expressed as Percent of Successful Pool Fire Extinguishments.....	893
Table 8–20. Hollow Cone Nozzle Characteristics.....	894
Table 8–21. High Flow Capacity Seven Nozzle Assembly.....	899
Table 8–22. Low Flow Capacity Seven Nozzle Assembly.....	899
Table 8–23. Solid Cone Nozzle Characteristics.....	905
Table 9–1. Examples of Previously Tested Powder Panel Materials.....	933
Table 9–2. Phase I Powder Panel Configurations Tested.....	937
Table 9–3. More Effective Powder Panel Designs in Experimental Testing.....	939
Table 9–4. Less Effective Powder Panel Designs in Experimental Testing.....	940
Table 9–5. Phase II Optimization Tests.....	950
Table 9–6. Phase II Enhanced Powder Panel Live Fire Demonstration Tests.....	960
Table 9–7. C-130 Wing Leading Edge Dry Bay Fire Extinguishing System Component Mass Estimates.....	970
Table 9–8. C-130 Wing Leading Edge Dry Bay Total Fire Extinguishing System Mass Estimates.....	970
Table 9–9. V-22 Outboard Tip Rib Dry Bay Fire Extinguishing System Component Mass Estimates.....	971
Table 9–10. V-22 Outboard Tip Rib Dry Bay Total Fire Extinguishing System Mass Estimates.....	971
Table 9–11. Fire Test Fixture Operating Conditions.....	982
Table 9–12. Comparison of Aerojet FTF to Other Fire Test Fixtures.....	982
Table 9–13. Temperature Dependence of Burn Rate for Baseline Propellant, FS-0140.....	991

Table 9–14. Adiabatic Temperatures of High Nitrogen Propellant Fuels in Stoichiometric Mixtures with $\text{Sr}(\text{NO}_3)_2$ Oxidizer.....	994
Table 9–15. Adiabatic Temperatures of Oxidizers in Stoichiometric Mixtures with.....	996
Table 9–16. Development Propellant Compositions and Burning Parameters.....	997
Table 9–17. Effect of Different Coolants on Adiabatic Flame Temperature of 5AT- $\text{Sr}(\text{NO}_3)_2$ Propellant Mixture.....	999
Table 9–18. High Nitrogen Content Developmental Propellants with $\text{MgCO}_3$ Coolant: Compositions and Burning Parameters.....	1000
Table 9–19. Candidate Chemically Active Agents.....	1002
Table 9–20. Summary of SPGG Fire Suppression Testing with Chemically Active Agents.....	1004
Table 9–21. Chemically Active Developmental Propellants.....	1006
Table 9–22. Threshold Mass of Propellant and Potassium-based Additive for Fire Suppression in the FTF.....	1011
Table 9–23. Properties of Hybrid Fluid Candidates.....	1013
Table 9–24. Hybrid Extinguisher Fluorocarbon System Data Summary.....	1014
Table 9–25. Hybrid Extinguisher Aqueous System Data Summary.....	1015
Table 10–1. Properties of Halon 1301 and HFC-125 Used in Life-cycle Costing.....	1029
Table 10–2. Additional Legacy Cargo Aircraft Fire Protection System Information.....	1031
Table 10–3. Additional Legacy Fighter Aircraft Fire Suppression System Information.....	1036
Table 10–4. Legacy Rotary-wing Aircraft Specific Parameters.....	1040
Table 10–5. Additional Legacy Rotary-wing Aircraft Fire Suppression System Information.....	1041
Table 10–6. Design Guide Estimates of HFC-125 Concentration and Mass for Future Cargo Aircraft Engine Nacelles.....	1045
Table 10–7. Design Guide Estimates of HFC-125 Concentration and Mass for Future Cargo Aircraft Auxiliary Power Units.....	1046
Table 10–8. Future Cargo Aircraft Proposed System Estimates.....	1046
Table 10–9. Future Cargo Aircraft Extinguisher Container and Agent Mass.....	1047
Table 10–10. Future Fighter Aircraft Engine Nacelle Fire Protection System Components.....	1050
Table 10–11. Fighter Aircraft Fire Suppression System Mass Comparison.....	1050
Table 10–12. Future Fighter Aircraft Specific Parameters.....	1051
Table 10–13. Estimates of System Parameters for Proposed Future Fighter Aircraft System Description.....	1051

Table 10–14. Future Fighter Aircraft Extinguisher Container and Agent Mass.....	1052
Table 10–15. Future Rotary-wing Aircraft Specific Parameters. ....	1053
Table 10–16. Future Rotary-wing Aircraft Analysis of Increase in Total Mass. ....	1053
Table 10–17. Comparison of Halon 1301 and HFC-125 System Life-cycle (FY00 to FY22) Cost Estimates for Legacy Cargo Aircraft. ....	1056
Table 10–18. Comparison of Halon 1301 and HFC-125 System Life-cycle (FY00 to FY28) Cost Estimates for Legacy Fighter Aircraft.....	1057
Table 10–19. Comparison of Halon 1301 and HFC-125 System Life-cycle (FY03 to FY35) Cost Estimates for Legacy Rotary-wing Aircraft.....	1058
Table 10–20. Comparison of Halon 1301 and HFC-125 System Life-cycle (FY00 to FY31) Cost Estimates for Future Cargo Aircraft.....	1059
Table 10–21. Comparison of Halon 1301 and HFC-125 System Life-cycle (FY00 to FY32) Cost Estimates for Fighter Cargo Aircraft.....	1060
Table 10–22. Comparison of Halon 1301 and HFC-125 System Life-cycle (FY03 to FY41) Cost Estimates for Future Rotary-wing Aircraft.....	1061
Table 10–23. Detailed Cost Element Structure.....	1062
Table 10–24. Cargo Aircraft Cost Savings Estimation.....	1067
Table 10–25. Fighter Aircraft Cost Savings Estimation. ....	1067
Table 10–26. Rotary-wing Aircraft Costs Savings Estimation.....	1067
Table 10–27. Estimated Cargo Aircraft System Description.....	1069
Table 10–28. Estimated Fighter Aircraft System Description.....	1069
Table 10–29. Estimated Rotary-wing Aircraft System Description. ....	1070
Table 10–30. Cargo Aircraft Altered System Description.....	1071
Table 10–31. Fighter Aircraft Altered System Description.....	1072
Table 10–32. Rotary-wing Aircraft Altered System Description. ....	1072
Table 10–33. Legacy Cargo Aircraft Net Costs.....	1073
Table 10–34. Future Cargo Aircraft Net Costs.....	1073
Table 10–35. Legacy Fighter Aircraft Net Costs.....	1076
Table 10–36. Future Fighter Aircraft Net Costs.....	1076
Table 10–37. Legacy Rotary-wing Aircraft Net Costs.....	1078
Table 10–38. Future Rotary-wing Aircraft Net Costs.....	1079
Table 11–1. Local Conditions Fire Test (Phase I) Matrix. ....	1121
Table 11–2. Factors and Values for Phase I Fire Test Matrix. ....	1121
Table 11–3. Extinguishant Dispersion Optimization (Phase II) Test Matrix. ....	1124

---

Table 11–4. Factors and Values for Phase II Agent Distribution Test Matrix. ....	1124
Table 11–5. Phase I Summary Data.....	1126
Table 11–6. Phase II Summary Data. ....	1126
Table 11–7. Values of $X_{\text{F}}$ and $\tau$ from Prior Experimentation. ....	1131
Table 11–8. Rank Order of $\tau$ Values in All Test Run Conditions for Both Mixing Models.....	1135
Table 11–9. Flame Extinguishment Concentrations. (% by Volume).....	1137
Table 11–10. Calculated Peak Concentrations under Fire Extinguishment Conditions. ....	1139
Table 11–11. Results of Fire Experiments with HFC-227ea and 2-bromo-3,3,3- trifluoropropene. ....	1141

Page intentionally left blank

---

---

## Chapter 1: INTRODUCTION

Richard G. Gann, Ph.D.  
National Institute of Standards and  
Technology

---

---

### TABLE OF CONTENTS

1.1 Background.....	1
1.2 The Evolution of Fire Suppression.....	1
1.3 The Rise of the Halons.....	3
1.4 The Atmospheric Threat.....	5
1.5 History of the NGP.....	9
1.6 This Book.....	15
1.7 References.....	16

### 1.1 BACKGROUND

In its decade of research (1997-2006), the United States Department of Defense’s Next Generation Fire Suppression Technology Program (NGP) revitalized the field of fire suppression science. The NGP arose as a result of a discovery that garnered the Nobel Prize for two accomplished chemists and legislation that turned science into public policy. This book tells the story of how the NGP came about, what research was performed, how it modernized the thinking in the field, and the technical findings that emerged related to fire suppression in aircraft.

### 1.2 THE EVOLUTION OF FIRE SUPPRESSION

The ability to control fire is universally and exclusively human. The history of that controlled use is also the history of civilization.<sup>1</sup> While individuals likely recognized the first principles of fire control, it was the rise of organized societies that led to structured activities and, later, products to mitigate the unwanted outcomes of fires. Now, the application of chemicals, manually and by mechanical devices, to control fires has become a mainstay of modern society. In particular, the development of the use of fire suppressant chemicals has a rich history.<sup>2</sup>

There is geologic evidence of fires as far back as there is evidence of vegetation on this planet, about 350 million years ago. The fires were started by frequent natural events, lightning strikes and volcanoes, and this was still the case when the first hominids appeared, some 3 million to 5 million years ago.

In the earliest years, small nomadic groups of these pre-humans observed the nature of fire. While they could see its destructive power, they soon recognized its benefits as well. They saw that animals ran from it, and thus it became a tool for trapping food. They found that animals and nuts that had been exposed to the flames were easier to eat. They enjoyed the radiant warmth from the fire on cold nights. They no doubt observed that rain made the fires stop, and some might have even noticed that there were few fires

following a rainstorm. By about 400,000 years ago, the sparse nomadic clusters of homo erectus had learned how to “capture” fire and use it for their own purposes, both domestic and martial. Since the initial source of this benefactor occurred only episodically, they spent considerable effort to keep the fire from going out. A few burns and the occasional loss of a temporary dwelling was a small price to pay for its continuous availability.

The number of humans and their standards of living accelerated about 20,000 to 30,000 years ago, toward the end of the last glacial age. Over the next 10,000 years, the ability to use fire for clearing land for agriculture and capturing livestock engendered the rise of towns. Further amenities became available as fire was used to bake clay pots (about 20,000 years ago) and later (about 7000 years ago) to work with metal. It would be time for the appearance of codes to preserve these more permanent communities.

The first written records, about 5,000 years ago in Mesopotamia, made little mention of fire.<sup>1</sup> It is thus presumed that there was little concern for its use or misuse. Perhaps this was because all members of a family were well versed in the art of using fire, preserving it, and regenerating it when needed. It is noteworthy that there were two types of words for fire: one for intentional fires, another for dangerous ones. However, the hazard of a house fire was not regarded as paramount. Buildings were small and generally constructed of stone or mud brick, since these materials were readily available. With the small number of people and the ready availability of land, the dwellings were not tightly spaced. If a fire started, the interior wood framing (if any), the thatched roof, and the contents were lost, since there was little water available to quench the flames. Attempts to protect neighboring houses depended on wet cloths and a limited number of buckets of water. People had long since learned the use of firebreaks for clearing land intentionally, and these were used to contain fire spread in the residential clusters. The Code of Hammurabi (about 1780 BC), a collection of rules for everyday life that also reflected the serious crimes of the era, had no mention of fire prevention or arson. However, theft of goods during a fire was punishable by death in that fire. The first mention of an arson penalty (full reparation) appears in the laws of the Hittites, some 100 years to 600 years later, but there was still no text on controlling fires. In short, destruction by fire was not the most severe threat facing these early communities, and their only weapon against it, water, was not plentiful on short notice.

The citizens of Rome appear to have had the first formal building code for fire safety, and the Roman penchant for engineering provided a supply of water to attack fires.<sup>1</sup> The code required that houses could not be built too high, separations of at least 2½ feet, and means of escape. Tenants were often required to have a bucket of water in their flats, and intentional fires within those flats were often forbidden. Nonetheless, over 40 large conflagrations were recorded between 31 BC and 410 AD, including the famous fire in 64 AD during which the emperor Nero supposedly fiddled while one third of the city was destroyed. The city of Rome also had an official fire brigade and, because it was unable to cope with its charge, several private brigades arose as well. These featured intensive patrols to catch fires early and bucket brigades with access to the city’s superb aqueduct system. Of course, virtually none of this existed in the Empire outside of the capital city.

Pre-industrial Europe continued to have numerous major urban conflagrations even past the Middle Ages (e.g., London, 1212; Venice, 1514; London, again, 1666; Rennes, 1720).<sup>1</sup> Most urban construction was now of wood and clay, which were cheaper than stone and brick. This was the era when the latter began to connote wealth, in large part due to the ability of the rich to afford fire safety. Buckets of water were still the only major means for stopping fire spread. In urban areas, legal measures were often instituted to

bolster this limited capability. In the event of a fire, people were to leave the building and sound the alarm immediately; there were severe fines for removing their possessions first.

In the rural areas, fire control reflected an earlier time. The crime of arson, resulting from a grudge or as a threat to extort money, was considered second only to murder in severity and was punished accordingly.

An enabling breakthrough in fire suppression came in the late 17<sup>th</sup> century, with the invention by Jan van der Heyden of Holland of the rollable fire hose. In 1725, Richard Newsham of London patented an improved pump design that could take advantage of van der Heyden's hoses. Soon a variety of hand pumps were devised to move water (still the suppressant of choice) efficiently from a city reservoir to the fire. During the Industrial Revolution in the mid-nineteenth century, these pumps became combustion-powered.

Nonetheless, for the remainder of that century, large city fires continued to be a problem (e.g., Hamburg, 1842; Newcastle, 1854; Chicago, 1871; Boston, 1872). Life loss was significant, as city population densities rose and the buildings became taller, wider, and more densely situated. The San Francisco fire of 1906 was the "last" of the major urban conflagrations. This diminution is attributed to the rise of brick, concrete and steel for urban construction, the spreading of residences (e.g., detached houses with yards), and general adoption of improved fire fighting technology and procedures. Water continued to be the only suppressant.

The scientific and technologic revelations of the 18<sup>th</sup> and 19<sup>th</sup> centuries led to new capabilities for the control of fires. In particular, James Watt's invention of the steam engine in 1769 led to two major innovations. In 1812, William Congreve received a patent for a steam-driven, perforated pipe water distribution system. In the middle of the century, the fusible link and self-opening valve were added, making the system fully automatic. In 1852, Moses Latta produced the first steam-powered, self-propelled fire engine, and the first commercially successful ones followed in 1867. Now there were ways to bring water, still the predominant suppressant, to the fire. It thus became possible to react in time to save a complex commercial or residential structure and many of the people within. The installation of the first automatic sprinklers in the U.S. and England in the late 19<sup>th</sup> century began bringing the water directly into the building.<sup>3</sup> This provided faster response and further containment of the fire damage. What remained was the development of technology to assure the safety of the contents.

### 1.3 THE RISE OF THE HALONS

Just after the turn of the 20<sup>th</sup> century, another scientific advance stimulated just this capability. The prior years had produced breakthroughs in the understanding of the electrical behavior of solutions. Now, a process for the electrolysis of salt water enabled a large supply of inexpensive chlorine. This was used to make carbon tetrachloride (CCl<sub>4</sub>), which soon came into use as a fire suppressant.

CCl<sub>4</sub> was the first clean agent; that is, unlike water, it caused no damage to a building or its contents and left no residue itself. It was also the first halon, halon 104 (see below). Like water, it was what is now called a streaming agent, i.e., it was squirted at the fire or was thrown at the fire in frangible containers, called grenades. However, concerns soon arose about its toxic effects on firefighters and others at the fire scene. The chemical had briefly seen use as an anesthetic, a practice that stopped when it was found that the difference between the amount which produced unconsciousness and that which produced death was small.<sup>4</sup> There was also an awareness of interaction with the large amounts of alcohol that firefighters

consumed often before, during, and after their efforts at the fire scene. Nonetheless, the use of carbon tetrachloride continued through World War II, in which it was used extensively.<sup>5</sup>

By this time, the chemical similarities of the elements within a column in the periodic table were well known, and soon the neighboring halogen, bromine, was also considered as a possible component of fire suppressant compounds. Methyl bromide (halon 1001) appeared in the 1930s in the U.S., but did not find much acceptance, since it was found to be more toxic than  $\text{CCl}_4$ . The Germans developed and used chlorobromomethane (halon 1011) as their clean suppressant of choice during World War II. It was more efficient than halon 104, and after the war it found broad use elsewhere.<sup>5</sup>

Recognition of the need to consider agent toxicity was another milestone in the evolution of fire suppression technology. The drawbacks of water had been operational in nature, e.g., mechanical hurdles to overcome in its bulk transport to the fire, damage to building contents. Now the suppressant itself would need to be examined for its possible effects on fire fighters and building occupants. Clearly, the value system of this era appreciated the benefits of these new halogenated agents in protecting property and people. Some selection from among the effective halocarbons was in order, and toxicity was the new criterion on the list.

In 1948, the U.S. Army commissioned the Purdue Research Foundation to search for a suppressant of high fire suppression efficiency but low toxicity.<sup>6</sup> The Army coined the term "halon," short for halogenated hydrocarbon, and devised the naming system that shows the numbers of the types of atoms in the molecule in the order: carbon, fluorine, chlorine, bromine, iodine (terminal zeroes dropped). During the 1960s and 1970s, two of the compounds tested emerged as commercial successes. Halon 1301 ( $\text{CF}_3\text{Br}$ ) found widespread use as a total flooding agent; i.e., it dispersed throughout a space, quenching flames regardless of location. (To a lesser extent, halon 2402 ( $\text{C}_2\text{F}_4\text{Br}_2$ ) was used in this capacity, mainly in the Soviet Union and Italy.) Halon 1211 ( $\text{CF}_2\text{ClBr}$ ) became the predominant streaming agent.

As the use of these chemicals increased, there were additional research, testing, and assessments performed, for example:

- In the 1960s and 1970s, extensive engineering studies developed information needed to design systems for implementation of the halons.<sup>5</sup>
- In 1966, the National Fire Protection Association established the Halogenated Fire Extinguishing Agent Systems Committee. In 1973, NFPA issued Standard 12A for halon 1301 systems and Standard 12B for halon 1211 systems. Much of the data to support these standards came from research and testing conducted at industrial laboratories, such as Factory Mutual, ICI, and DuPont.<sup>5,7</sup>
- In the 1970s, research at the U.S. Bureau of Mines<sup>8</sup> was directed at obtaining a better understanding of the mechanisms of halon 1301 that could guide its use as a suppressant for methane explosions in mines. At the U.S. Naval Research Laboratory<sup>9</sup>, related fundamental research on halon 1301 was sponsored by the Naval Air Systems Command as part of a search for a more efficient extinguishing agent for in-flight fires.
- In 1972, the U.S. National Academy of Sciences held a Symposium to examine the state of knowledge on the toxicity and engineering applications of the halons.<sup>10</sup> The purpose was to provide "an up-to-date basis for intelligent selection of which, if any, of the halogenated agents should be used in a given set of circumstances." A summary of that symposium indicated that the halons were effective fire extinguishment agents, with the degree of

effectiveness depending greatly on the application. There was an awareness of toxicological risks from exposure to both the halons themselves and their decomposition products that were formed during the application of the chemical to the fire.

- In 1975, a symposium was held to examine the basic processes occurring in flames inhibited by the halons, leading to the inference of the mechanisms of flame suppression.<sup>11</sup>

Halon 1301 had turned out to be very efficient at quenching fires, as shown in Table 1–1. Because of the small amount needed, because it did no harm if deployed accidentally, and because it could put fires out before any significant damage occurred, halon 1301 systems were increasingly installed to protect contents of special value and spaces in which storage weight and volume were at a premium. By the 1980s, most computer rooms, nearly all commercial and military aircraft, and numerous museums were protected by these halon systems. As a footnote, their acceptance signaled the end of the use of CCl<sub>4</sub> as a fire suppressant, a prophetic result, as it was later determined that carbon tetrachloride was a carcinogen.

**Table 1–1. Flame Suppression by Halon 1301 and Other Chemicals (volume %).**

Flame/Fire	Halon 1301	HFC-227 ea	Carbon Dioxide
Small diffusion flame	3.1 <sup>12</sup>	6.6 <sup>12</sup>	21 <sup>13</sup>
Pool Fire (10 s extinguishment)	4 <sup>12</sup>	8 <sup>12</sup>	--
Wood	3.0 <sup>5</sup>	5.8 <sup>14</sup>	--
Fiberglass/polyester resin	3.5 <sup>5</sup>	--	--

## 1.4 THE ATMOSPHERIC THREAT

In 1974, F. Sherwood Rowland and Mario Molina published a paper showing that certain chlorinated compounds (chlorofluorocarbons, or CFCs), while playing beneficial roles as, e.g., coolants and solvents, posed a threat to the global environment. These compounds had long lifetimes in the earth's lower atmosphere, or troposphere. Eventually, they would rise to the stratosphere, where they were readily photodissociated by short wavelength ultraviolet (UV) light. There, the chlorine atoms aggressively catalyzed the conversion of ozone, which absorbed solar UV light and protected the earth's flora and fauna from excessive UV radiation, to ordinary oxygen, which provided no such protection. Unchecked, this could result in major changes in life on the planet.<sup>15</sup> Subsequent atmospheric measurements and modeling showed that the threat was real. Rowland and Molina were awarded the Nobel Prize in Chemistry in 1995.

The nations of the world moved toward an international agreement to protect the environment, the Montreal Protocol on Substances That Deplete the Ozone Layer.<sup>16</sup> As the agreement was being forged, it was realized that some brominated compounds were potentially even more dangerous than their chlorinated cousins,<sup>17</sup> and the halons (with the name mistakenly used to mean only brominated and chlorinated perhalocarbons) were named explicitly. Their production was curtailed sharply in amendments to the U.S. Clean Air Act of 1990. As of January 1, 1994, under the 1992 Copenhagen Amendments to the Montreal Protocol, halon 1301 was banned from production, except in certain developing countries and countries whose economies were in transition.

The dense and growing population had been informed of a threat on a global scale, and the nations of the world had clearly decided that fire safety must be weighed against other cultural values. For the fire safety community, this was a new paradigm. The prior bounds on saving lives, property and the

community had generally been local: budgets limitations, interferences with other social amenities, etc. Now, the protection of the planet as a whole took priority over local safety, which presumably could be provided in some other manner.

Even as the search for alternative fire suppressants was underway, usage was declining markedly. Major releases of the halons were from firefighting training, fire extinguishment system testing, and leakage from the storage containers. By the early 1990s, alternatives for training and testing had been identified. There were also approaches to fire protection that did not rely on clean agents, e.g., a number of facilities converted to automatic sprinklers. In some cases, fire suppression became unnecessary. For instance, with small and inexpensive computers able to do much of the work previously done by large mainframe units, it was less costly to back up the computer than to provide fire protection.

Halon 1301's exceptional performance and success over the years had resulted in minimal research into alternatives for fire suppression. After a period of bewilderment, denial, and indecision following the 1987 Montreal Protocol, manufacturers and users of the halons began searching for safe replacements and alternatives. The early solutions were identified during the quest for replacement refrigerants, a far larger commercial market. Some of these, such as the hydrochlorofluorocarbons (HCFCs) were ozone depleters themselves and were soon generally disregarded as fire suppressants. An early brominated compound, CHF<sub>2</sub>Br (halon 1201), was found to have a fire suppression efficiency comparable to halon 1301, but even though its ODP value was far lower than that of halon 1301, it was above that permitted by the U.S. Clean Air Act. For a variety of applications, chemical manufacturers began increased production of hydrofluorocarbons, or HFCs, which had no bromine or chlorine atoms and thus zero ozone depletion potential (ODP) values.<sup>i,18</sup> These were far less effective fire suppressants, but appeared to have no harmful atmospheric effects. Other commercial products included mixtures of inert gases, also less efficient suppressants, and blends of halocarbons.

The U.S. Department of Defense (DoD) had come to rely heavily on halon 1301 systems, in particular, for fire protection in its numerous ground, sea, and air systems, as shown in Table 1–2.<sup>19</sup>

These uses encompass a wide range of fire conditions. The locations vary in size, shape, function, and whether or not they are populated. The fuels are solids, vapors, and liquids; the latter burning as pool fires or sprays. The required time for suppression ranges from hundredths of a second to tens of seconds. In some cases, the agent must be "clean" and in others, not. The hazards to be avoided include harm to people, thermal damage to equipment, post-fire corrosion, loss of visibility, and overpressure. Finding a "one-size-fits-all" fire suppression approach to replace halon 1301 was highly improbable.

---

<sup>i</sup> The ozone depletion potential of a gas is defined as the change in total ozone per unit mass emission of the gas, relative to the change in total ozone per unit emission of CFC-11 (CFCl<sub>3</sub>).

**Table 1–2. Use of Halon 1301 in Fielded Weapons Systems.**

	Army	Navy	Air Force
Ground Armored Vehicles	Crew compartments Engine compartments	Crew compartments Engine compartments	
Shipboard	Maritime craft	Propulsion machinery Flammable liquid storerooms Fuel pump rooms Emergency generator rooms	
Aircraft	Engine nacelles APU compartments	Engine nacelles Dry bays Fuel tanks Crew compartments	Engine nacelles Dry bays Fuel tanks Weapon bays Cargo bays
Facilities	Communications shelters	General facilities	General facilities
Hand-held Extinguishers	Air/ground/maritime		Multiple uses

The U.S. Department of Defense was, and continues to be, committed to reducing its dependence on halon 1301 and made great strides in this direction by eliminating non-essential uses, totally revamping its fire suppression system testing, certification, and recycling procedures, and replacing halon systems with alternative technologies where possible. Nonetheless, there remained some applications where no substitute chemical or system was judged satisfactory, and several others where the identified alternatives were saddled with serious deficiencies. One of these applications was for military aircraft, which were particularly vulnerable to fire during combat and also needed in-flight fire protection during routine missions, a need shared by the commercial fleet. Further research would be needed to identify effective alternate fire suppression technologies.

The DoD delineated its policy on halon replacement research early in 1989.<sup>20</sup> The Directive stated that:

- DoD Components "... shall conduct R&D to identify or develop alternate processes, chemicals, or techniques for functions currently being met by CFCs and halons;"
- The Director, Defense Research and Engineering (DDR&E) "... shall coordinate R&D programs, as appropriate, on alternative chemicals or technologies for fire and explosion suppression and, if necessary, other CFCs;" and
- The Military Departments and Defense Agencies "... shall conduct R&D programs, as needed, to support mission requirements, with emphasis on substitutes for halons."

From 1993 to 1998, the DoD conducted a major program on ozone-depleting substances (ODSs), the Technology Development Program (TDP). It focused on the identification of near-term, environmentally friendly, and user-safe alternative fluids, developed by industry, that were either readily available or could enter commercial production in the near future. The TDP research was successful in identifying replacements for the non-firefighting ODSs.

However, despite the examination of a wide range of chemicals in the laboratory and at real scale, none of the available alternatives offered all the needed properties of halon 1301. The best available replacement

chemicals were two HFCs: C<sub>2</sub>F<sub>5</sub>H (HFC-125) onboard aircraft and C<sub>3</sub>F<sub>7</sub>H (HFC-227ea) for shipboard use.<sup>21</sup> These were substantially less efficient fire suppressants and thus required two to three times the mass and storage volume relative to halon 1301. This would severely compromise their implementation, given the tight weight and space limitations. In addition, their use would result in a post-deployment atmosphere containing appreciable concentrations of acid gases, that was not suitable for human occupancy, and that could chemically attack metals, synthetic materials, and electronics. Nonetheless, some engineering was conducted to adapt the use of these chemicals for some platforms. One alternative approach that showed some promise was the use of solid propellant fire extinguishers. Similar to the units developed for automobile airbags, these systems rapidly generated large quantities of inert gases. They were considered for use in aircraft dry bays, where people would not be exposed to the resulting sub-habitable oxygen levels.

At the then-current state of the technology, the DoD was faced with three options, each with significant and undesirable trade-off considerations. The use of dissimilar fluids required costly re-engineering of both the fire suppression system and the host weapon system. The vintaging of fielded weapon systems required indefinite dependence on a substance that was no longer in production and which was subject to future environmental regulations. The abandonment of fire protection altogether was not feasible, since personnel safety and weapon systems survivability are high DoD priorities. Recognition of these limitations led to a decision to formulate a successive research program focused on improved options for fire suppression in fielded weapons systems.

However, even before replacements for the CFCs and halons could be implemented, an additional threat to the global environment was identified. Since the middle of the 20<sup>th</sup> century, there had been concern that anthropogenic carbon dioxide was increasing in the lower atmosphere. Its increasing absorption of infrared radiation from the planet surface and re-radiation back to that surface would lead to warming of the earth. The term "greenhouse gas" was created, and it was soon realized that most of the replacements for clean fire suppressants fell into this category.<sup>22</sup> This added yet another constraint to the search for the successors to the halons.

As an interim measure, the DoD (among other organizations and governments in about 20 countries<sup>23</sup>) had created "banks" of halons 1301 and 1211 as a means of continuing protection during the search for alternatives. In 2000, the systems and banks were estimated to contain about 90 million pounds of halon 1301 and about 300 million pounds of halon 1211. It was estimated that the emission rate from fixed systems was about 2 % of the banks' capacity per year, and the rate from portable extinguishers was about 4 % of the banks' capacity per year.<sup>24</sup> It is these banks from which supplies are still drawn as the halons are deployed in theaters of conflict.

The security of such banks, however, is not assured. The few essential uses for ODSs allowed by international agreement were conditional on continued efforts to find environmentally benign alternatives. Furthermore, in 1994, the United Nations Environmental Program (UNEP) announced that just after the turn of the century, the mass of chlorine and bromine (and the accompanying ozone depletion) in the stratosphere would have peaked and would begin to diminish.<sup>25</sup> Their report also identified four principal actions that would speed this decrease. The second most effective of these was the non-release of all halons currently in existing equipment. This was a clear signal to the fire protection community that the world was watching the effort to identify and implement alternatives to the halons and that an accelerated phase-out was a clear possibility. In related activity, research was underway to develop processes for the economical conversion of the halogenated hydrocarbons into other useful chemicals.

At the time of publication of this book, the global average ozone depletion has stabilized. The ozone layer is now expected to begin to recover in the coming decades.<sup>24</sup>

## 1.5 HISTORY OF THE NGP

To ensure the safety and mission capability of U.S. forces and to preclude any long-term halon *use restriction* impacts, a new DoD technology program was formulated.<sup>26</sup> The Next Generation Fire Suppression Technology Strategy Program (NGP) had as its goal:

"to develop and demonstrate, by 2004, retrofitable, economically feasible, environmentally acceptable, and user-safe processes, techniques, and fluids that meet the operational requirements currently satisfied by halon 1301 systems in existing weapons systems."

The emphasis was on *retrofit*, i.e., developing technologies that could readily be installed on existing weapons systems.<sup>ii</sup> This led to an oversimplification of the task, by some observers, as a search for a "drop-in" replacement chemical. In fact, the NGP included examination of technologies that could improve the performance of a chemical whose inherent fire suppression efficiency was only mediocre relative to that of halon 1301, approaches that used granular materials, rather than compressed fluids, and even technologies that used no active suppressant at all. The Program would be complete when the generic know-how existed to design cost-effective alternates to halon 1301 systems.

The concept of the NGP was created by Dr. Donald Dix and Mr. Paul Piscopo of the Office of the Secretary of Defense. Planning began in 1994, and the Program was initiated in fiscal year 1997. Oversight and guidance of the Program was provided by a DoD Halon Alternatives Research and Development Steering Group (HASG). The HASG was chaired, in turn, by Dr. Dix and Mr. Piscopo. The membership consisted of representatives from the DoD agencies with responsibility for fire suppression research and development, testing, and implementation of new technology. The U. S. Environmental Protection Agency (EPA), which approved suppressants based on their environmental impact and safety during exposure, provided a liaison to monitor DoD development of alternatives to halon 1301.

The principal sponsor of the NGP was the DoD Strategic Environmental Research and Development Program (SERDP), directed initially by Dr. John Harrison and subsequently by Mr. Bradley Smith. The SERDP Pollution Prevention (later Weapons Systems and Platforms) Program Managers were Dr. Carl Adema, Dr. Robert Holst, and Mr. Charles Pellerin. The NGP was Project WP-1059.

The author of this chapter had the privilege of serving as the Technical Program Manager for the duration of the NGP. Providing additional scientific and pragmatic expertise was a Technical Coordinating Committee, whose membership evolved over the life of the Program: Mr. Lawrence Ash and then Mr. Donald Bein of the Naval Air Systems Command, Dr. Michael Bennett of the Air Force Research

---

<sup>ii</sup> Although not explicit in the goal statement, the presumption was that the new science and improved approaches to fire suppression would also be adaptable to the design of future weapons systems. The economics of adapting the new knowledge would likely be more restrictive for an existing aircraft, ship, or ground vehicle; and it was recognized that some expensive-to-retrofit technologies might not be pursued within the NGP, although they might be more viable economically for new weapons systems.

Laboratory and then Mr. Martin Lentz of the Air Force's 46<sup>th</sup> Test Wing, Dr. William Grosshandler of the National Institute of Standards and Technology, Dr. Andrzej Miziolek of the Army Research Laboratory, and Dr. Ronald Sheinson of the Naval Research Laboratory. Administrative support for the NGP was provided by Gamboa International Corporation.

The NGP was a closely integrated research program whose potential for success was maximized by bringing together the nation's best scientists and researchers in fire suppression and associated technologies, with extensive interactions between the technical disciplines and the project principal investigators. The research was organized into six technical thrusts:

1. Risk Assessment and Selection Methodology: development of a process for program managers to choose among alternative technologies for each application.
2. Fire Suppression Principles: establishment of the mechanisms of flame extinguishment, leading to new approaches for fire control.
3. Technology Testing Methodologies: development of test methods and instrumentation to obtain data on the effectiveness, toxicity, environmental impact, and materials compatibility of new suppressants and their principal degradation products during fire extinguishment.
4. New Suppression Concepts: definition of new ideas in processes, techniques, and fluids for fire suppression based on chemical and physical principles.
5. Emerging Technology Advancement: acceleration to maturity a variety of processes, techniques, and fluids that are currently under development.
6. Suppression Optimization: development of the knowledge to obtain the highest efficiency of each candidate technology.

While the early NGP research was underway, the military services were pursuing solutions, based on TDP technology, for some of the DoD platforms. The Army had identified fire suppression technologies for both current and planned ground vehicles that needed only engineering for implementation. The Navy had no plans to retrofit current ships and had initiated a research program on water mist technology for forward fit.

However, the aircraft safety and survivability engineering teams from all three Military Services had fire suppression needs for engine nacelles and dry bays that were not being addressed by Science and Technology (S&T) efforts outside the NGP. Thus, in 1999, the goal for the NGP was refined:

"to develop and demonstrate technology for economically feasible, environmentally acceptable and user-safe processes, techniques, and fluids that meet the operational requirements currently satisfied by halon 1301 systems in aircraft." <sup>27</sup>

In this revised statement, there was recognition that the NGP, as the only DoD S&T program in this field, should develop the technology base for both existing and planned aircraft. The deliverables, in addition to a well-documented science basis, were to be:

1. Identification of the best chemicals to consider as alternatives to halon 1301 for extinguishing in-flight fires in engine nacelles and dry bays;

2. Guidance for engineering the fire suppression system to obtain the most efficient use of the suppressant chemicals;
3. Development of practicable non-fluid-based suppression technologies; and
4. Creation of means for deciding among candidate solutions for a given application.

The documentation was to include not only those tests, models, and computations that led to improved firefighting capability, but also those that were not promising. This documentation would then serve as a resource for those who entered the field in future times.

Realization of the difficulty in searching for an effective fire suppressant system comes from viewing an aircraft engine nacelle (Figure 1–1).<sup>iii</sup> A dry bay is no less complex.

### Storage Bottles



// → Agent Discharge  
↓ ↓

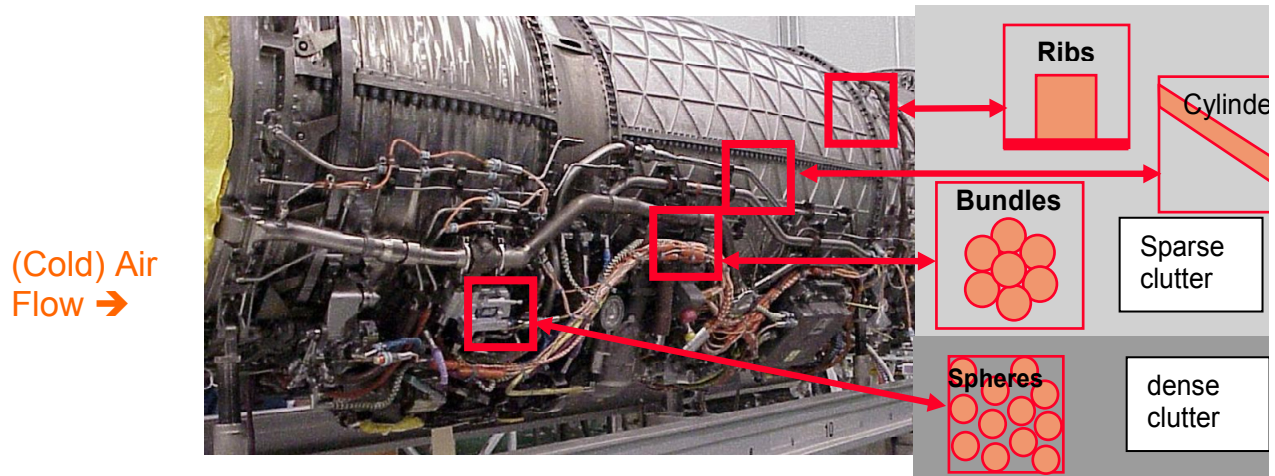


**Figure 1–1. Interior of an Aircraft Engine Nacelle.**

The suppressant is injected, at a small number of points, into this annular space between the pictured engine exterior and the outer, cylindrical housing (not shown in the figure). The agent must fill the annulus, reach all the nooks and crannies, and put out the flames from a fire in any location, all before the cold air flow flushes the chemical from the nacelle.

Scientists and engineers were thus looking for compounds that had:

- High fire suppression efficiency
- Effective quenching of flame re-ignition
- Low ozone depletion potential (ODP)

<sup>iii</sup> An engine nacelle is the housing of an aircraft jet engine. The exterior is aerodynamically smooth, while the interior has ribbing that provides the structural strength for the nacelle.

- Low global warming potential (GWP)<sup>iv</sup>
- Short atmospheric lifetime<sup>v</sup>
- Low suppressant residue
- Low electrical conductivity
- Low corrosivity to metals
- High compatibility with polymeric materials
- Stability under long-term storage
- Low toxicity of the chemical and its combustion and decomposition products
- High speed of dispersion

The research on advanced fire suppression processes, technologies, and fluids encompassed 42 interrelated projects. Many of these were outlined in the original NGP Strategy Document and were structured by successful proposals in an open competition. These were complemented by solicitations for proposals of new ideas. The remaining projects were commissioned by the Technical Coordinating Committee, with approval of the HASG and the sponsor, based on the outcome of the prior projects and newly acquired understanding of the additional research needed to meet the NGP goal.

Figures 1–2 through 1–5 depict the relationships between the projects and their relationships to the NGP deliverables. Cyan boxes are projects that were performed, red boxes indicate projects that were planned but not performed, the yellow box represents work in progress elsewhere at the time of this book, and orange boxes depict the deliverables. An asterisk (\*) notes projects that appear more than once.

As the research progressed, the findings were published in archival journals, issued as DoD reports, and presented at technical meetings. Prominent among these meetings were the annual Halon Options Technical Working Conferences (HOTWC), founded by Dr. Robert Tapscott of the New Mexico Engineering Research Institute. Attendance at these meetings included domestic and international representatives of weapons platforms manufacturers, the military services' safety and survivability teams, civilian customer for fire suppression systems, fire suppression systems manufacturers, and members of the national and international fire research and engineering communities. Eventually, when this key meeting lost its original host, the NGP assumed the responsibility for the organization and conduct of the meetings and for the publication of the cumulative papers.<sup>28</sup>

---

<sup>iv</sup> The global warming potential of a gas is defined as the change in irradiance at the tropopause (the boundary between the stratosphere and the troposphere) per mass of the gas emitted relative to the change in irradiance per mass of carbon dioxide.

<sup>v</sup> Faced with two chemically different effects of compounds on the environment, it was recognized that a broad approach to minimizing atmospheric perturbations was advisable. Atmospheric lifetime is an indicator of the potential for released chemicals to be degraded or removed from the environment before they could effect harm. It is the time, after its initial emission into the atmosphere, it takes for the compound to decay to  $1/e$  (37 %) of its original concentration.

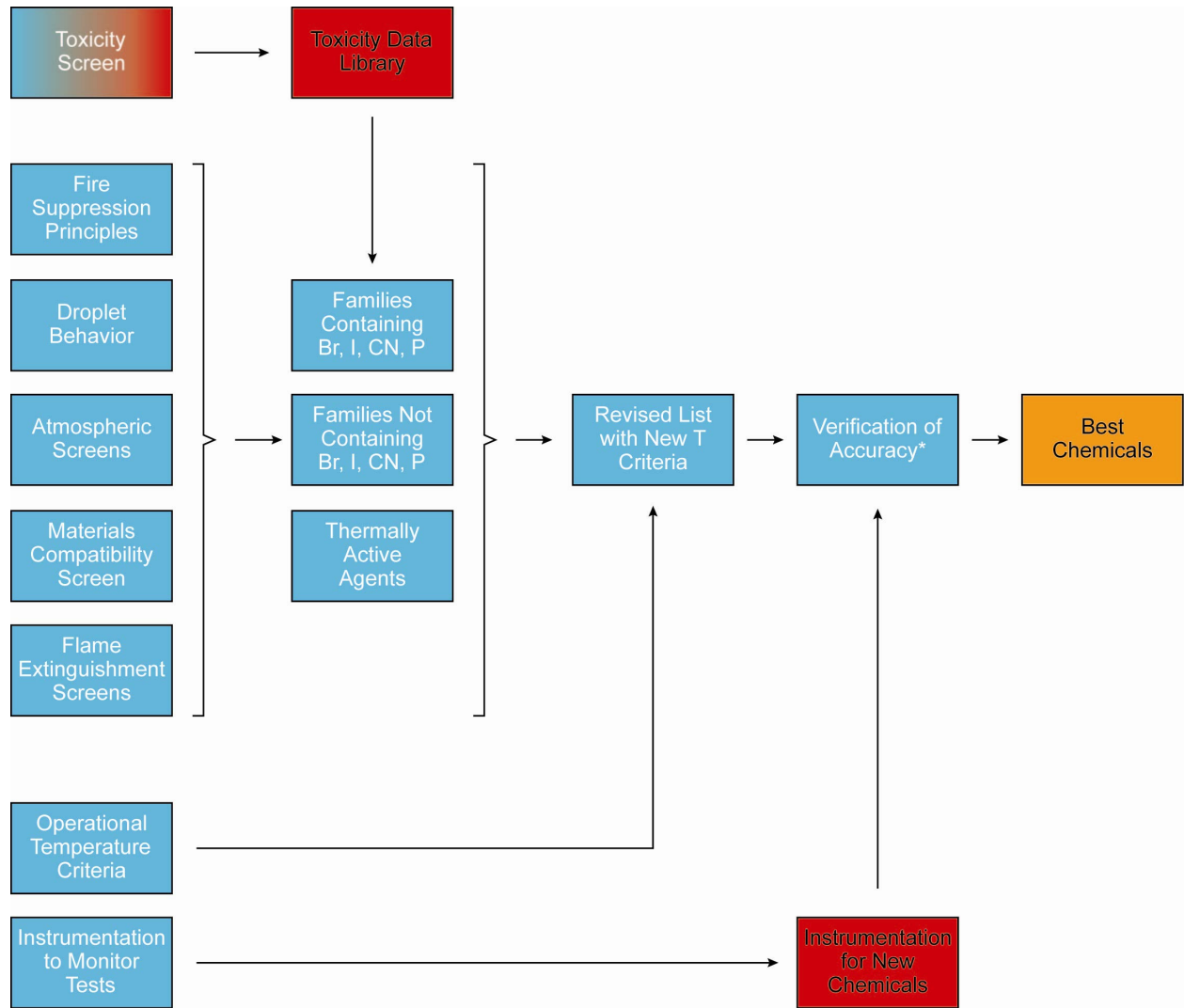


**Figure 1–2. Projects Contributing to Deliverable 1: Best Alternative Suppressant Chemicals.**

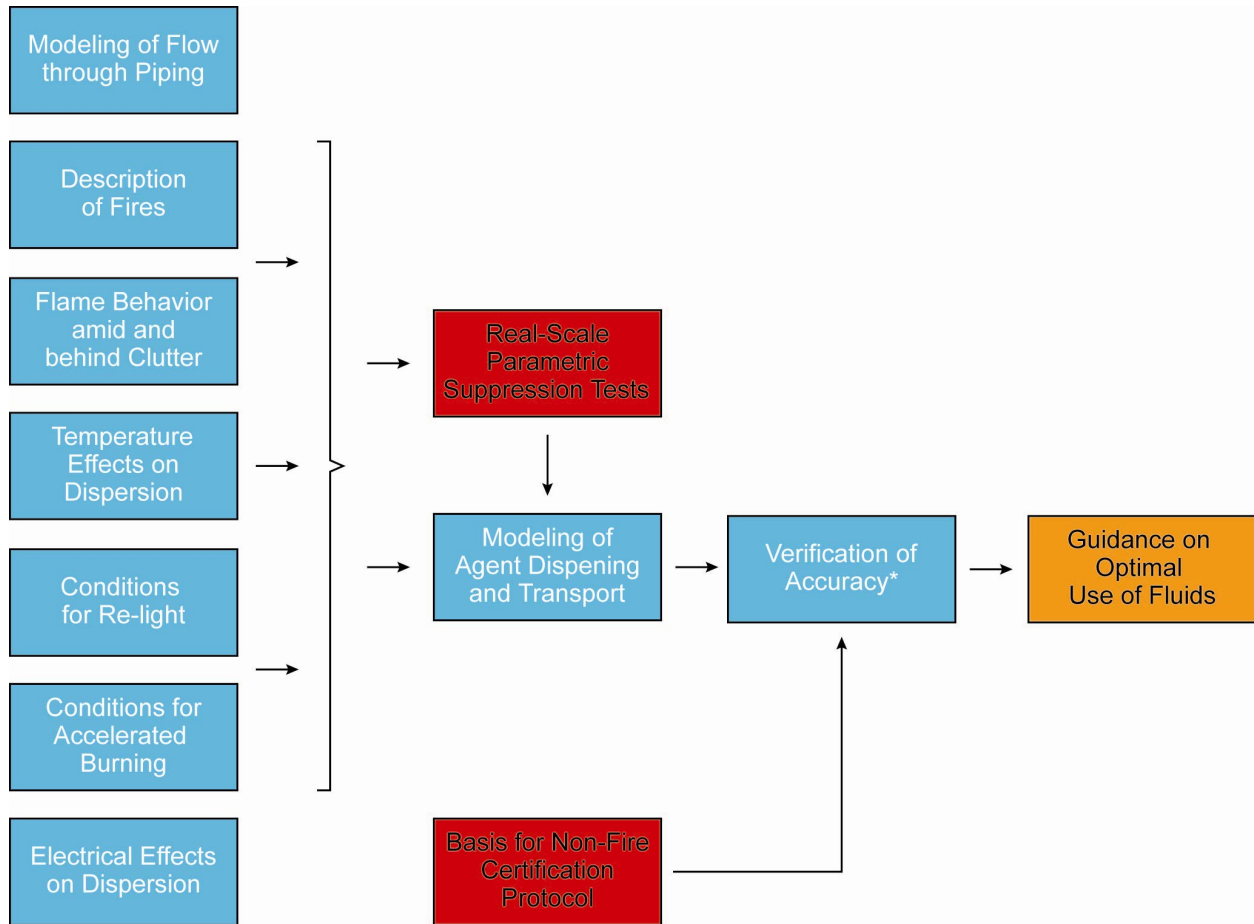


**Figure 1–3. Projects Contributing to Deliverable 2: Guidelines for Optimal Application of Extinguishants.**

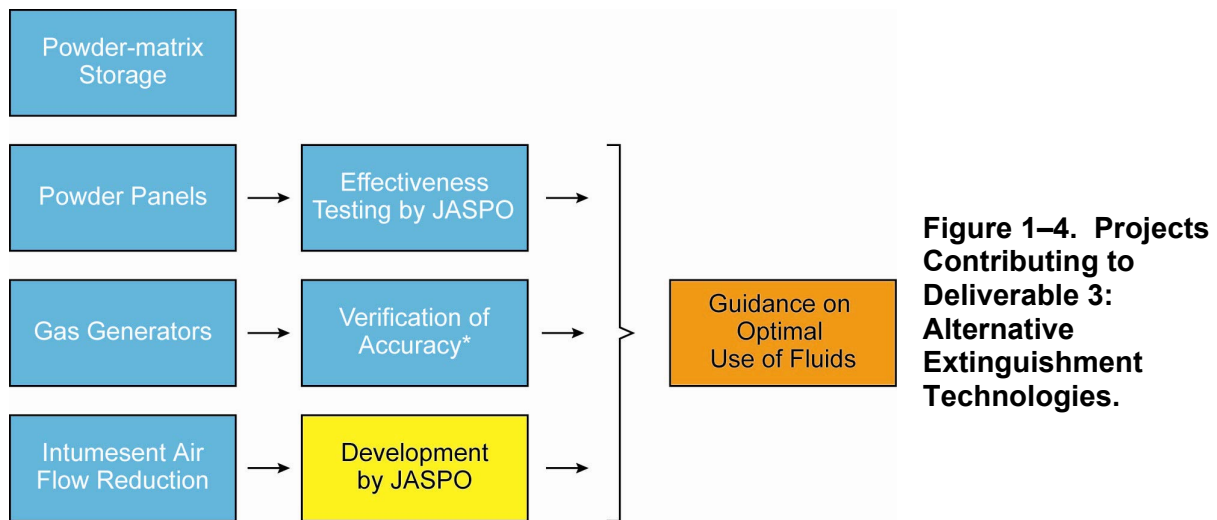


**Figure 1–4. Projects Contributing to Deliverable 3: Alternative Extinguishment Technologies.**

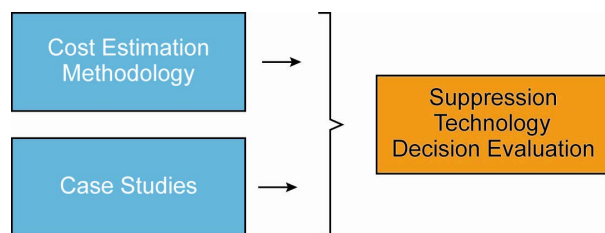


**Figure 1–5. Projects Contributing to Deliverable 4: Technology Options Assessment Protocol.**

## 1.6 THIS BOOK

There are multiple reasons behind the preparation of this book. First, as the search for alternative technologies began, reports of much of the prior work were not readily available. Some were out of print, some had only been issued for limited distribution, and other studies had not been fully documented. Second, building on increased knowledge of the fundamentals of fire, the NGP and contemporary studies re-defined the field. However, many of these reports were interim reports or were, for other reasons, not documented in the archival technical literature. Third, the large number of NGP reports makes it difficult to understand how the many projects combined to advance the science and engineering of fire suppression. Finally, it is the intent of the authors and sponsors to document this national research effort such that future researchers and engineers who work in this field (and we firmly believe this will arise again) will have an organized archive from which to begin their work. To this end, the authors of the chapters of this book have compiled, edited, and enhanced the contents of the numerous documents generated under the NGP. As appropriate, they have added information that puts this material in context.

The structure of this book is as follows. Chapter 2 presents an overview of how aircraft have been (and are) protected from the consequences of in-flight fires. Chapter 3 presents what NGP scientists have learned about the chemical suppression of flames. Chapter 4 discusses the properties of suppressant aerosols that contribute to (and detract from) efficient flame quenching. Chapter 5 summarizes the instrumentation the NGP developed for learning about and monitoring fire suppression processes, especially in real-scale tests. Chapter 6 describes the NGP approach to screening chemicals for their potential as alternatives to halon 1301. Chapter 7 describes the process and results of examining numerous chemicals. The amount of a chemical required to extinguish fires in full-scale engine nacelles and dry bays also depends on the geometry of the test fixture, the air flow field within the nacelle, the effectiveness of the mixing of the suppressant into this air flow, and the manner in which the flame is stabilized. These factors are separate from the properties of the suppressant itself. They are discussed in Chapter 8 for suppressants that are stored as compressed fluids and in Chapter 9 for agents that are powders or are delivered by chemically generated impulses. Chapter 10 presents a formalism for considering the life-cycle costs of alternative installed fire suppression systems, to be used in the implementation decision process by aircraft platform managers. Chapter 11 summarizes the key lessons learned during the conduct of the NGP and how they were verified with real-scale experiments. Readers might find the first part of this chapter useful to read first, providing an overview of the results of the technology presented in the rest of the volume. Chapter 12 establishes where the NGP has brought the field of fire suppression science and engineering and identifies the challenges that remain. Three appendices provide lists of the NGP projects and publications and acknowledge those who assisted with the preparation of this volume.

## 1.7 REFERENCES

1. Goudsblom, J., *Fire and Civilization*, The Penguin Press, London, 1992.
2. Gann, R.G., "A Millennial View of Fire Suppression," 2001, in Gann, R.G., Burgess, S.R., Whisner, K.C., and Reneke, P.A., eds., *Papers from 1991-2006 Halon Options Technical Working Conferences (HOTWC)*, CD-ROM, NIST SP 984-4, National Institute of Standards and Technology, Gaithersburg, MD, (2006).
3. Nash, P., and Young, R.A., *Automatic Sprinkler Systems for Fire Protection*, Victor Green Publications, Ltd., London, 1978. (2<sup>nd</sup> edition, Paramount Publishing, Ltd., Borehamwood, 1991.)
4. Auck, S.E., "Short History of Halogenated Fire Extinguishing Agents," in *An Appraisal of Halogenated Fire Extinguishing Agents*, National Academy of Sciences, Washington, 1972.
5. Ford, C.L., "An Overview of Halon 1301 Systems," in Gann, R.G., ed., *Halogenated Fire Suppressants*, ACS Symposium Series 16, American Chemical Society, Washington, DC, 1975.
6. *Final Report on Fire Extinguishing Agents for the Period September 1, 1947 to June 30, 1950*, Purdue Research Foundation, Lafayette, IN, 1950.
7. Miller, M.J., "The Relevance of Fundamental Studies of Flame Inhibition to the Development of Standards for the Halogenated Extinguishing Agent Systems," in Gann, R.G., ed., *Halogenated Fire Suppressants*, ACS Symposium Series 16, American Chemical Society, Washington, DC, 1975.
8. Biordi, J.C., Lazzara, C.P., and Papp, J.F., "The Effect of CF<sub>3</sub>Br on Radical Concentration Profiles in Methane Flames," in Gann, R.G., ed., *Halogenated Fire Suppressants*, ACS Symposium Series 16, American Chemical Society, Washington, DC, 1975.
9. Gann, R.G., "Initial Reactions in Flame Inhibition by Halogenated Hydrocarbons," in Gann, R.G., ed., *Halogenated Fire Suppressants*, ACS Symposium Series 16, American Chemical Society, Washington, DC, 1975.
10. *An Appraisal of Halogenated Fire Extinguishing Agents*, National Academy of Sciences, Washington, DC, 1972.
11. Gann, R.G., ed., *Halogenated Fire Suppressants*, ACS Symposium Series 16, American Chemical Society, Washington, DC, 1975.
12. Sheinson, R.S., Eaton, H.G., Black, B.H., Brown, R., Burchell, H., Maranghides, A., Mitchell, C., Salmon, G. and Smith, W.D., "Halon 1301 Replacement Total Flooding Fire Testing, Intermediate Scale," in Gann, R.G., Burgess, S.R., Whisner, K.C., and Reneke, P.A., eds., *Papers from 1991-2006 Halon Options Technical Working Conferences (HOTWC)*, CD-ROM, NIST SP 984-4, National Institute of Standards and Technology, Gaithersburg, MD, (2006).
13. Ewing, C.T., Hughes, J.T., and Carhart, H.W., "The Extinction of Hydrocarbon Flames Based on the Heat-absorption Processes Which Occur in Them," *Fire and Materials* **8**, 148-156 (1984).
14. Robin, M.L., Rowland, T.F., and Cisneros, M.D., "Fire Suppression Testing: Extinguishment of Class A Fires With Clean Agents," in Gann, R.G., Burgess, S.R., Whisner, K.C., and Reneke, P.A., eds., *Papers from 1991-2006 Halon Options Technical Working Conferences (HOTWC)*, CD-ROM, NIST SP 984-4, National Institute of Standards and Technology, Gaithersburg, MD, (2006).

15. Molina, M.J., and Rowland, F.S., "Stratospheric Sink for Chlorofluoromethanes: Chlorine Atom Catalyzed Destruction of Ozone," *Nature* **249**, 810-812, 1974.
16. *The Montreal Protocol on Substances that Deplete the Ozone Layer as Adjusted and/or Amended in London 1990, Copenhagen 1992, Vienna 1995, Montreal 1997, Beijing 1999*, United Nations Environment Programme, <http://hq.unep.org/ozone/Montreal-Protocol/Montreal-Protocol2000.shtml>
17. Wofsy, S.C., McElroy, M.B., and Yung, Y.L., "The Chemistry of Atmospheric Bromine," *Geophysical Research Letters* **2**, 215-218 (1975).
18. Wuebbles, D.J., "Chlorocarbon Production Scenarios: Potential Impact on Stratospheric Ozone," *Journal of Geophysical Research* **88**, 1433-1443 (1983).
19. *Technology Development Plan for Alternatives to Ozone-depleting Substances for Weapons Systems Use, Final Report*, Office of the Deputy Under Secretary of Defense (Science and Technology)/Weapons Systems, September 1998.
20. *Directive 6050.9, Subject: Chlorofluorocarbons (CFCs) and Halons*, Department of Defense, February 13, 1989.
21. *Technology Development Plan for Alternatives to Ozone-Depleting Substances for Weapons Systems Use, Final Report*, ODUSD (S&T) Weapons Systems, 1998.
22. Finlayson-Pitts, B.J., and Pitts, Jr., J.N., *Chemistry of the Upper and Lower Atmosphere*, Chapter 14, Academic Press, New York, 2000.
23. "Halon Banks," *FS World*, 63-65, Summer 2001, [www.fs-world.com](http://www.fs-world.com).
24. *Safeguarding the Ozone Layer and the Global Climate System*, Intergovernmental Panel on Climate Change and Technology and Economic Assessment Panel, United Nations Environmental Panel, New York, 2005.
25. *Scientific Assessment of Ozone Depletion: 1994, Executive Summary*, World Meteorological Organization, Geneva, 1994.
26. *Next-Generation Fire Suppression Technology: Strategy for a National Program*, Office of the Director, Defense Research and Engineering, 1996, available on the NGP web site: [www.bfrl.nist.gov/866/NGP](http://www.bfrl.nist.gov/866/NGP).
27. *Next Generation Fire Suppression Technology Program Strategy (Update)*, Office of the Deputy Undersecretary of Defense (Science and Technology), 2000, available on the NGP web site: [www.bfrl.nist.gov/866/NGP](http://www.bfrl.nist.gov/866/NGP).
28. Gann, R.G., Burgess, S.R., Whisner, K.C., and Reneke, P.A., eds., *Papers from 1991-2006 Halon Options Technical Working Conferences (HOTWC)*, CD-ROM, NIST SP 984-4, National Institute of Standards and Technology, Gaithersburg, MD, (2006).



---

---

## Chapter 2: HISTORY OF FIRE SUPPRESSION IN AIRCRAFT<sup>i</sup>

---

---

Donald P. Bein  
Naval Air Systems Command

---

---

### TABLE OF CONTENTS

2.1	Fire Threats to Military Aircraft .....	20
2.2	Protected Compartments on Aircraft .....	24
2.2.1	Engine Nacelles .....	24
2.2.2	Other Powerplant-type Compartments .....	28
2.2.3	Dry Bay Compartments .....	31
2.2.4	Cargo Compartments .....	34
2.2.5	Other Compartments .....	36
2.2.6	Fuel Tank Ullage .....	37
2.3	Types of Fires Experienced .....	41
2.3.1	Safety-related Fires .....	43
2.3.2	Ballistically-induced Fires .....	45
2.3.3	Spray Fires .....	47
2.3.4	Pool Fires .....	49
2.3.5	Fire Characteristics .....	50
2.3.6	Aircraft Operational Temperature Environment <sup>44</sup> .....	54
2.3.7	Reignition .....	79
2.4	Fire Suppressants Used on Aircraft .....	80
2.4.1	Powerplant Compartments .....	81
2.4.2	Dry Bay Compartments .....	86
2.4.3	Certification .....	86
2.5	Halon Alternative Technology Development Program (TDP) .....	92
2.5.1	Phase 1 – Operational Parameters Study .....	93
2.5.2	Phase 2 – Operational Comparison of Selected Extinguishants .....	94
2.5.3	Phase 3 – Establishment of Design Criteria Methodologies .....	94
2.5.4	Impact of Halon Alternative Fire Suppression to the Aircraft .....	96
2.6	References .....	109

---

<sup>i</sup> The content of this chapter has been approved for public release by the Naval Air System Command (NAVAIR), per NAVAIR public release authorization control numbers 063-06, SPR07-005B, and SPR07-005D.

## 2.1 FIRE THREATS TO MILITARY AIRCRAFT

Safety and survivability drive the requirements for fire suppression in aircraft. Whereas safety is concerned with mitigation of hazards associated with system or component failures or human error, survivability relates to susceptibility and vulnerability to threats directed at the aircraft. A fire is deemed a safety-related fire when it results from component failures, which may be due to inadequate design, a mechanical failure mechanism such as fatigue, or maintenance error, and results in either a flammable fluid contacting an always-present ignition source, or the failures themselves provide both the flammable fluid and the ignition source. Fires that relate to aircraft survivability are those that are ballistically induced in areas on an aircraft that, if not protected by some means, are vulnerable to fire or even explosion. Extensive literature compilations by the National Advisory Committee on Aeronautics (NACA) summarize investigations since 1922 of aircraft fire problems, fire prevention measures, fire detection, fire suppression, fuel tank explosion hazards, and inerting. These indicate that what was then the War Department had been addressing the field of aircraft fire protection at least as early as 1927.<sup>1,2</sup> In 1938, just prior to World War II, the issue of in-flight power-plant (engine compartment) fires led to the Civil Aeronautics Administration (CAA) expanding its fire test program to include fire extinguishing to mitigate the hazards associated with these fires.<sup>3</sup> Review of the combat data from World War II indicated that, in order, damage to engines, cooling and lubrication subsystems, fuel system, and flight control systems were to likely lead to aircraft loss, and that the majority of aircraft lost were on fire.<sup>4</sup>

Surveys conducted after World War II documented the obvious need for lower volatility fuels and separation of flammable fluid-carrying components from ignition sources with the engine emphasized as the principal ignition source.<sup>5</sup> It was also then recognized that during flight the fuel-air mixture within fuel tanks could be alternately combustible and noncombustible, depending upon flight conditions. However, engine failures were still found to be the most frequent cause of flammable fluid ignition by an ignition source in flight.<sup>6</sup> It is no surprise that years later, analysis conducted by the United States Navy (USN) indicated a similar outcome: non-combat in-flight fires, i.e., safety-related fires, occurred predominately in engine compartments, as illustrated in Figure 2-1.

The combat environment exposes military aircraft to ballistic and higher-level threats that, until recent years, have not been experienced in U.S. commercial aviation.<sup>7</sup> These threats can be incendiary or non-incendiary. The military conflicts in Korea and Southeast Asia and analysis of aircraft combat loss data from those conflicts indicated that the fires due to fuel-system-related damage were becoming the predominant fire vulnerability, as aircraft were lost mainly due to hits on the fuel system.<sup>4</sup> Analysis of aircraft losses suffered during the Vietnam conflict indicated generally that half were due to fuel fires and explosions, and that half of those were attributable to fuel explosions in dry bay areas on aircraft.<sup>8</sup>

As illustrated in Figure 2-2, dry bay areas along with the fuel tank ullage, which can itself contain a flammable fuel-air mixture, are vulnerable to ballistic threats.<sup>ii</sup> From the aircraft survivability design perspective, the fuel tank ullage and dry bay compartments contribute to an aircraft's ballistic vulnerable area. Incendiaries released from a ballistic round that penetrate the ullage can result in ignition of fuel vapor. A ballistic round entering into a dry bay adjacent to a fuel tank, and that also penetrates a fuel tank or other flammable fluid component, can cause fuel to leak and be ignited within the dry bay when incendiaries are released.

---

<sup>ii</sup> Dry bays are void areas on aircraft adjacent to fuel tanks or can be areas containing flammable fluid-carrying components.

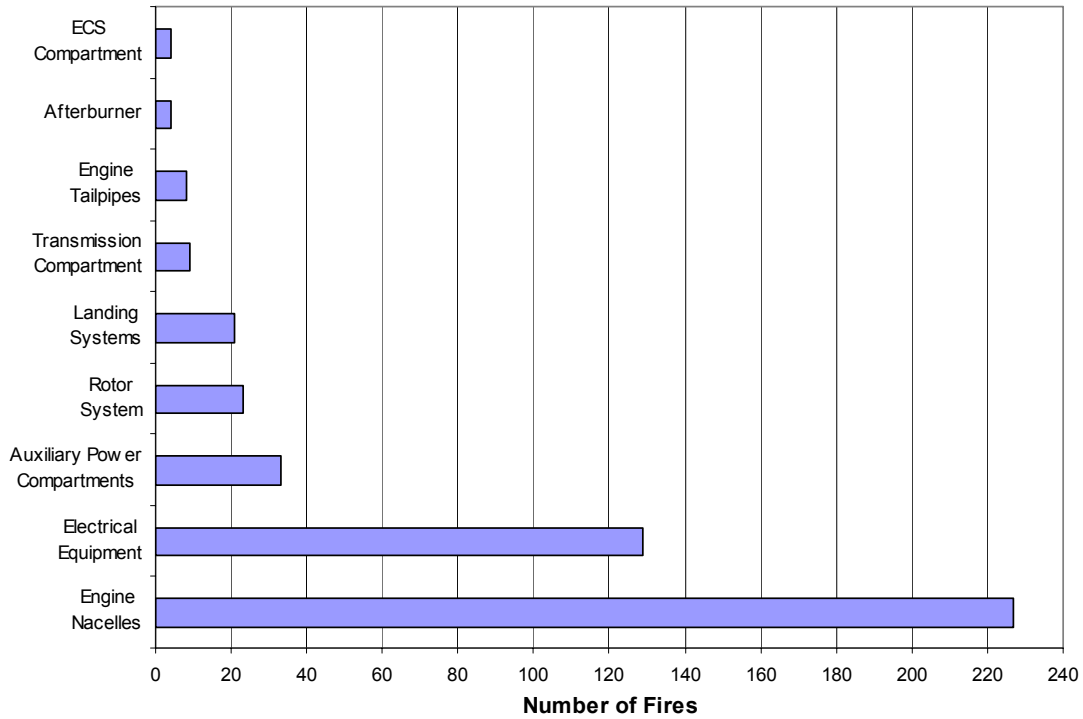


Figure 2-1. Significant Non-combat Fire Locations on U.S. Navy Aircraft 1977-1993.<sup>9, iii</sup>

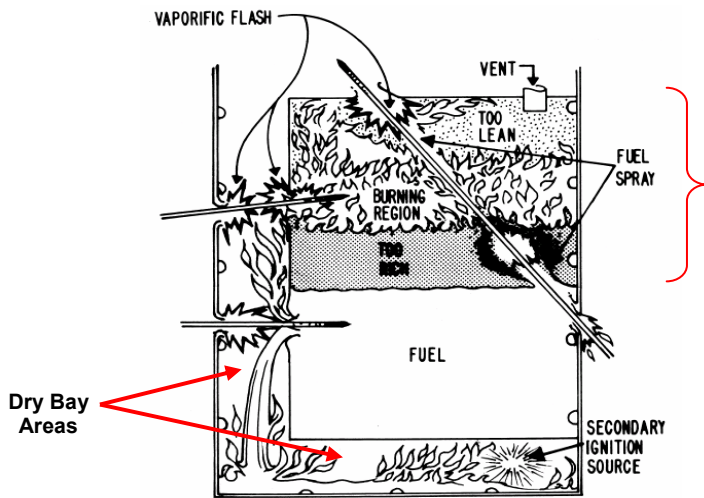


Figure 2-2. Combustion Threats in and Around an Aircraft Fuel Tank.<sup>4</sup>  
 (Reprinted by permission of the American Institute of Aeronautics and Astronautics, Inc.)

<sup>iii</sup> Forty-nine percent (49 %) of the fires represented in the electrical equipment bar in Figure 2-1 occurred on one aircraft platform type within the aircraft cabin and were readily extinguished by either securing electrical power to that equipment or by use of on-board portable fire extinguishers. Also in Figure 2-1, ECS is an acronym for Environmental Control System.

Table 2–1 provides a generalized evolution of tactical and rotary aircraft vulnerability based on live fire testing (LFT) vulnerability assessments for armor-piercing incendiary (API) threats.<sup>iv</sup> Though aircraft vulnerable areas have decreased over the years, as depicted notionally in Figure 2-3, fuel systems remain a significant vulnerability issue and drive the need for vulnerability-reduction measures such as fire suppression for aircraft dry bay compartments as well as for engine compartments.

**Table 2–1. Evolution of Aircraft Vulnerability Based on Live Fire Test Vulnerability Assessments (API Threats).<sup>iv</sup>**

Aircraft Category, System	Vulnerable Area Percentage	Vulnerable Area Percentage
<b>Tactical Aircraft</b>	<b>1960s through 1970s</b>	<b>Current</b>
Crew	8 %	10 %
Propulsion	54 %	5 %
Flight Controls	11 %	5 %
Fuel System	25 %	75 %
Structure	1 %	2 %
Other	1 %	3 %
<b>Rotorcraft</b>	<b>1980s</b>	<b>Current</b>
Crew	1 %	3 %
Propulsion	< 1 %	2 %
Drive System	15 %	20 %
Flight Controls	38 %	33 %
Fuel System	30 %	42 %
Structure	16 %	-
Other	-	< 1 %

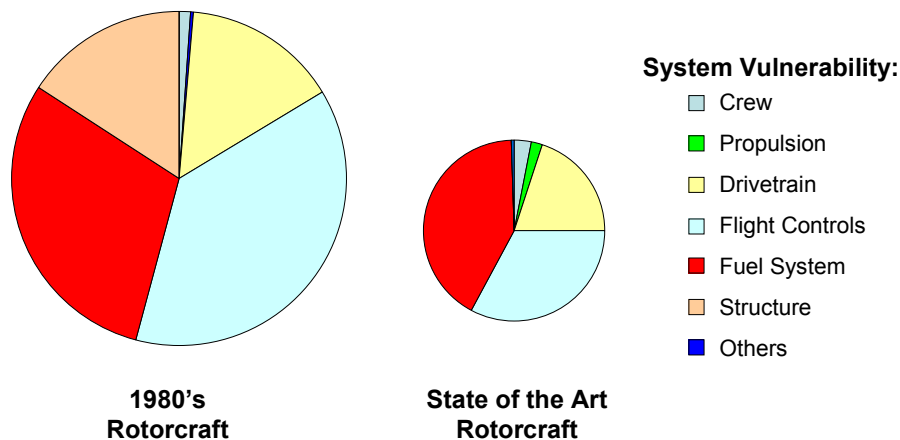


**Figure 2-3. Illustration of Notional Reduction in Overall Rotorcraft Vulnerable Area.**

<sup>iv</sup> Figure 2-3 and the percentages in Table 2-1 were provided by the Naval Air Warfare Center Weapons Division, Aircraft Survivability, and are printed with permission of the Naval Air Systems Command.

The susceptibility of aircraft to engine fires combined with the combat vulnerability to fuel-system-related fires cannot be overstated. Based on United States Air Force (USAF) experience, the combined historical cost from 1966 through projected cost through 2025 of aircraft loss due to fire from both operational and combat losses has been estimated as over \$30 billion. The cost to provide fire suppression for that same period has been estimated at less than \$1 billion.<sup>11</sup> Chapter 10 provides further discussion of life cycle cost of aircraft fire protection.

In terms of personnel safety, the fire risk is obvious. However, in terms of crew survivability in combat, the need for fire suppression takes on an added dimension. Figure 2-4 shows known ejection locations of U.S. Navy aircrewmembers who subsequently became prisoners of war (POW) during the Vietnam conflict, and Figure 2-5 shows locations of Navy rescues of Navy aircrewmembers during that conflict.<sup>12</sup> It had been estimated that the difference in terms of time was typically 5 min flight time between ejection locations and rescue locations. Thus the ability to provide fire suppression capability to address both predominant operational failure threats as well as combat threats is likely to increase aircrew survival and recovery.

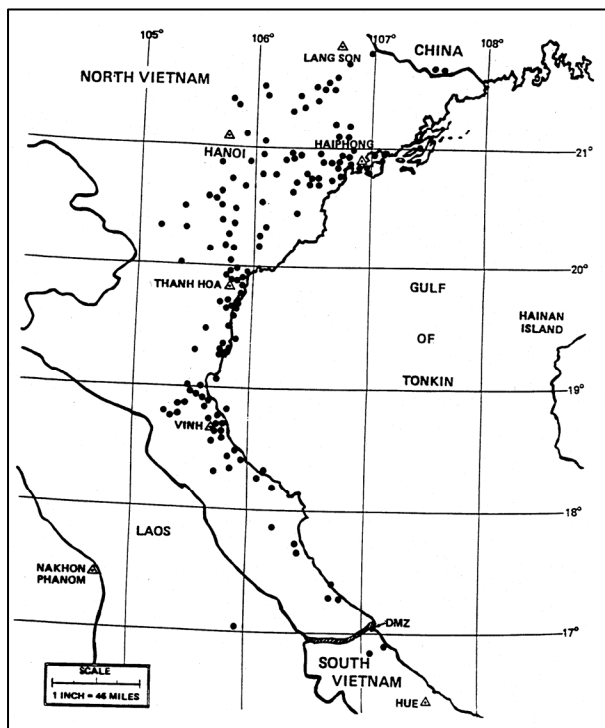


**Figure 2-4. Known Ejection Locations of Navy Aircrewmembers Who Became POWs During the Southeast Asia Conflict.**<sup>12</sup>

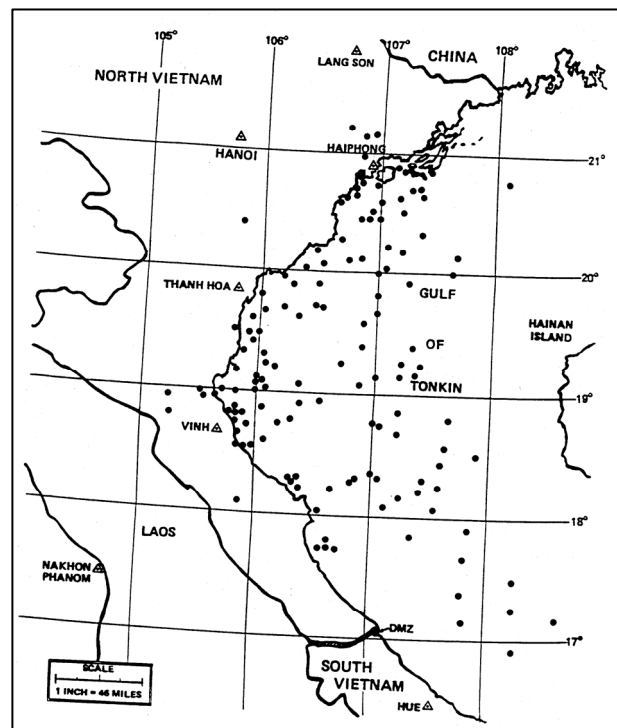


**Figure 2-5. Locations of Navy Rescues of Navy Aircrewmembers During the Southeast Asia Conflict.**<sup>12</sup>

The remainder of this chapter describes not only the aircraft compartments that were the primary focus of the United States Department of Defense's Next Generation Fire Suppression Technology Program (NGP), but also provides general summaries of all the various types of compartments on aircraft for which halon fire suppression has been implemented. This has been done so that the reader is reminded that, although the focus of the NGP addressed those compartments for which, statistically, the fire threat

has been the greatest, the work of the NGP is likely to influence in the future how fire suppression is applied for other aircraft compartments that may require protection.

The next section includes a brief discussion on various techniques for fuel tank ullage fire suppression, which was the subject of an exploratory effort during the NGP. This is followed by a summary of the NGP's investigation into the types of fires experienced in the compartments that were the focus of the NGP: engine nacelles, auxiliary power unit (APU) compartments, and dry bays. In particular, this section provides expanded discussion on the topic of temperature and historical experience related to fire suppressant releases relative to outside air temperature (OAT) and the nacelle temperature environment. Next, brief descriptions are provided for the fire suppressants that have been used on aircraft prior to the efforts to identify halon alternatives that commenced after production curtailments driven by the U.S. Clean Air Act of 1990 and amendments to the Montreal Protocol. Throughout this entire section, the word "halon" is used to denote any of the halogenated fire suppressants that have been used in aircraft fire suppression, except where the particular halon type is noted specifically. Finally, a brief overview of the Halon Alternative Technology Development Program (TDP) is provided to familiarize the reader with the "near-term" halon alternatives identified for use in aircraft fire suppression applications, their benefits, and their limitations, which led to the need for the NGP.

## **2.2 PROTECTED COMPARTMENTS ON AIRCRAFT**

The predominant implementation of halon-1301-based fire suppression on aircraft has been for fire protection of powerplant-type compartments. These compartments are those that contain engine-type equipment that require flammable fluids (aviation fuel, hydraulic fluid, and lubrication oil) to generate propulsion power, such as a turbojet engine that generates thrust power for a fighter jet or a turboshaft engine that generates shaft power to turn a propeller on a turboprop aircraft or turn rotors on a helicopter. Powerplant compartments include engine compartments, which are referred to as nacelles, but depending on the type of aircraft, e.g., transport, cargo, fighter, or helicopter, may also include additional types of powerplant-type compartments such as APU compartments. Also, depending on the type of aircraft, halon 1301 has been utilized to provide fire suppression for other compartments, such as dry bays, cargo compartments, avionics compartments, weapons bays, and fuel tanks. Although the final focus of the NGP was to address halon alternative fire suppression for engine nacelles, APU compartments and dry bay compartments, the intent of this section is to familiarize the reader with these compartments as well as other types of compartments for which fire suppression has been provided on military aircraft.

From the aircraft designer's perspective, "fire extinguishing" implies that a system is to be designed to extinguish a fire without subsequent reignition, whereas "fire suppression" implies that reignition can occur but that the system will suppress the fire until a safe landing can be achieved. However, the phrase "fire suppression" is used widely throughout aviation as well as in the NGP and its publications to mean fire extinguishment, except where specifically explained otherwise. The latter convention is followed in this chapter as well, except where noted otherwise.

### **2.2.1 Engine Nacelles**

Engine nacelles are the physical compartments on aircraft that house the engines. These compartments may be integral with the fuselage or mounted externally to the aircraft's wings. An example of a turboshaft engine is illustrated in Figure 2-6. The engine itself is physically complex, containing ribs,

tubing for fuel and bleed air, electrical harnesses, and externally-mounted accessory components (e.g., oil pump). Integration of an engine into an aircraft nacelle increases greatly the geometric complexity about an engine, as components and systems that must interface directly with the engine will also reside within the nacelle. Adding to the complexity of the installation are the dynamic conditions that exist within the nacelle during aircraft operation. Engine surface temperatures can exceed 538 °C. Ventilation airflow is required through the nacelle to ensure engine and accessory component performance is not degraded and is effected by incorporation of air inlets and outlets on the nacelle structure. Depending on the type of aircraft and flight conditions, nacelle mass airflow rates for DoD aircraft that have been fielded have ranged from under 0.23 kg/s (0.5 lbs/s) to in excess of 14 kg/s (30 lbs/s) for a fighter aircraft dash operation.<sup>13,14</sup> When the combined integration is considered, the nacelle becomes a geometrically-complex, turbulent compartment capable of sustaining fire. Additionally, components within the nacelle and the engine components themselves provide for potential flame holders, recirculation zones, and for potential areas of stagnation.

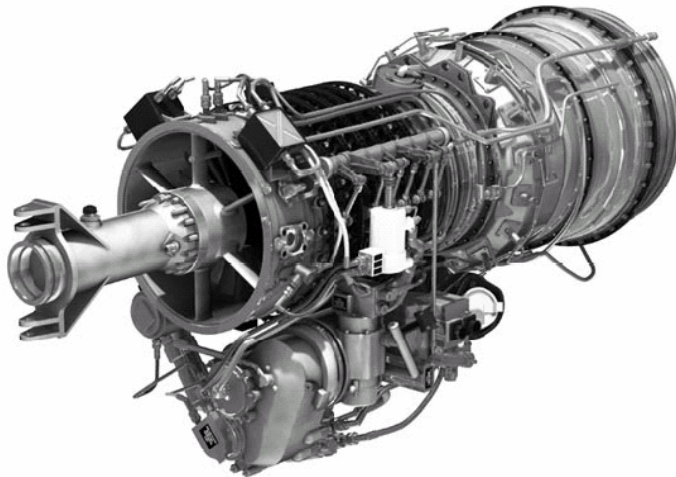


**Figure 2-6. Example Turboshaft Engine.**

(Reprinted with permission from Rolls-Royce Corporation.)

Figure 2-7 is an example of a military aircraft engine nacelle. As shown in Figure 2-8, the typical nacelle fire suppression system installation consists of one or more fire suppressant bottles, located external to the nacelles, connected to a directional control device that interfaces to distribution plumbing that routes discharged suppressant to the nacelles. This system may also be designed to deliver suppressant to an APU compartment. Discharge is effected by the pilot in the cockpit: an electrical signal causes activation of a pyrotechnic cartridge actuated device (CAD) to rupture a burst disk on the bottle to effect suppressant release. These systems are typically designed to provide a specified suppressant concentration level (6 % for halon 1301)<sup>v</sup> throughout each protected compartment for a minimum of 0.5 s. Figure 2-9 shows a fire suppression system installation for an engine nacelle in which the suppressant bottle is located in a compartment adjacent (and external) to the nacelle. Though not typical in currently fielded DoD aircraft, the fire suppression system bottle may also be located within the nacelle, as shown in Figure 2-10, increasing nacelle complexity.

---

<sup>v</sup> Throughout this chapter, where percentages are indicated in discussions related to suppressant concentrations, they are always referring to concentration by volume.



**Figure 2-7. A Fighter Aircraft Engine Nacelle.**  
(Printed with permission of the Naval Air Systems Command.)

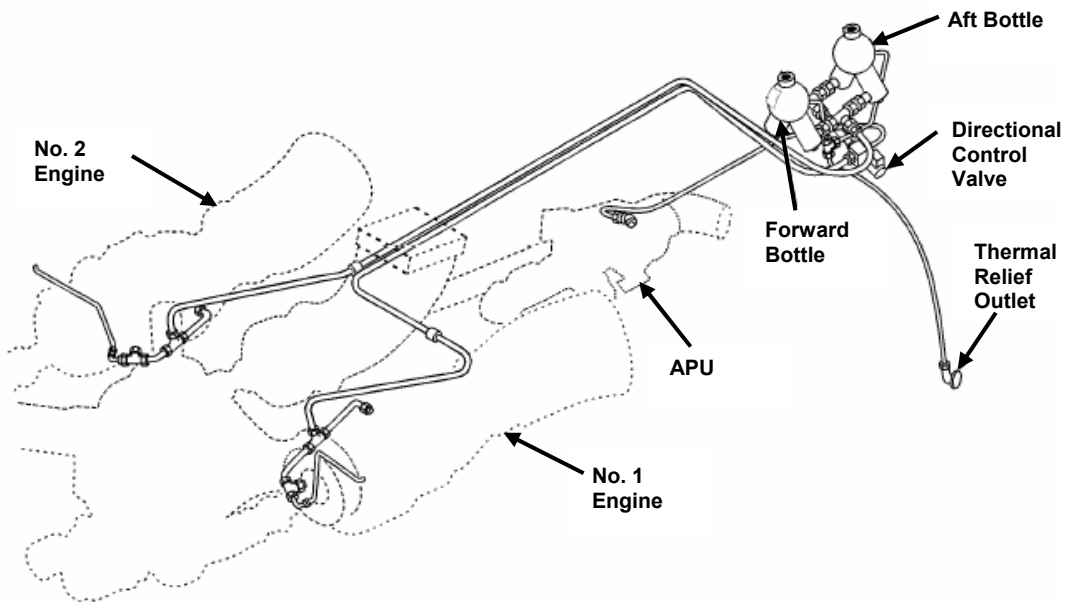


**Figure 2-8. Diagram of an Aircraft Fire Suppression System Installation.<sup>8</sup>**



- CAD
- Fire Suppressant Bottle (Mounted in Compartment External to the Nacelle)
- Discharge Line from the Bottle
- Nacelle Air Inlet Structure
- Distribution Line within Nacelle
- Distribution Line Outlet

**Figure 2-9. An Aircraft Engine Nacelle Fire Suppression System Installation, Suppressant Bottle External to the Nacelle.**

(Printed with permission of the Naval Air Systems Command.)

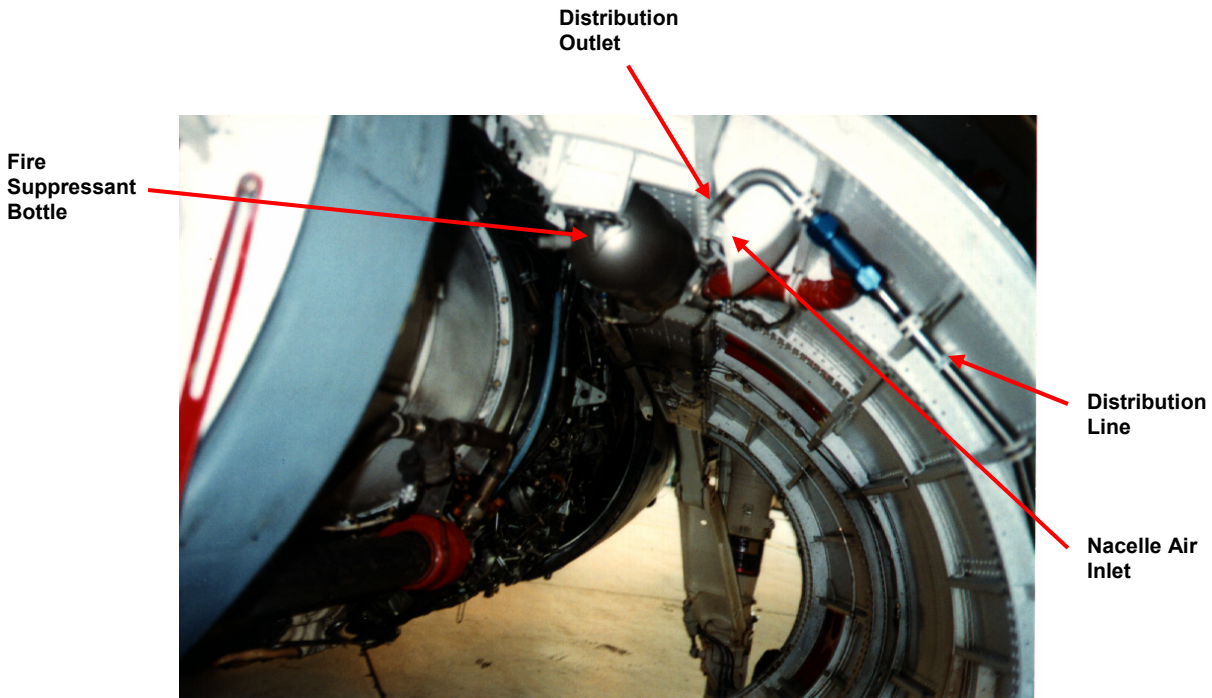


**Figure 2-10. An Aircraft Engine Nacelle Fire Suppression System Installation, Suppressant Bottle Within the Nacelle.**

(Printed with permission of the Naval Air Systems Command.)

### 2.2.2 Other Powerplant-type Compartments

In addition to engine compartments, DoD military aircraft may contain other types of powerplant compartments for which a fire suppression capability is provided, either dedicated or shared with another fire suppression system on the aircraft. The most common compartment that falls into this category is that containing the auxiliary power unit (APU). On some aircraft this compartment may also be referred to as the auxiliary powerplant (APP) or the gas turbine compressor (GTC) compartment. These units may be miniature turbines or other power generating equipment, but are typically smaller than the normal jet engine propulsion systems. These units furnish electrical power when engine-driven generators are not operating or when external power is not available, and they may be used to provide emergency power to all or some of the aircraft subsystems in the event of an in-flight engine shutdown.<sup>vi</sup> These units function and generate power independently from the normal aircraft engine systems. On the ground, the power output from the APU is used to generate power to drive a starter unit for engine starting.

<sup>vi</sup> Because aircraft power for the fire suppression system may not be available during startup, one fielded rotorcraft model actually employs a manually activated fire bottle for its APP compartment. A cable is run from the cockpit fire bottle actuation mechanism, referred to as the T-handle, through overhead cabin compartments, around a two-pulley system, and into the discharge port of the bottle.

In addition to or instead of a dedicated APU compartment, there are fielded DoD aircraft that contain an accessory compartment or secondary power system (SPS), or in the case of a rotary aircraft, a gearbox compartment. These compartments may contain the APU or other equipment utilized during ground engine starting and aircraft operation such as a Jet Fuel Starter (JFS) or an Airframe Mounted Accessory Drive (AMAD). Like engine nacelles, each of these compartments is likely to have ventilation airflow to ensure proper component performance and, like the main aircraft engines, components like the APU are potential ignition sources and their integration into the aircraft can present geometric complexities with respect to fire suppressant distribution. Figure 2-11 is an example of an APU installation on a transport aircraft. Figure 2-12 is an example of a fighter aircraft accessory compartment. Figure 2-13 is an example of an aircraft gearbox compartment that also contains an APU. Figure 2-14 is an example SPS installation on a fighter aircraft. Integration of an APU or similar component into an aircraft accessory, gearbox, or other powerplant-type compartment results in a complex compartment in which fire may be sustained, due to either a component failure or, in the case for some aircraft as will be described later, because the compartment is vulnerable to ballistically induced fires.

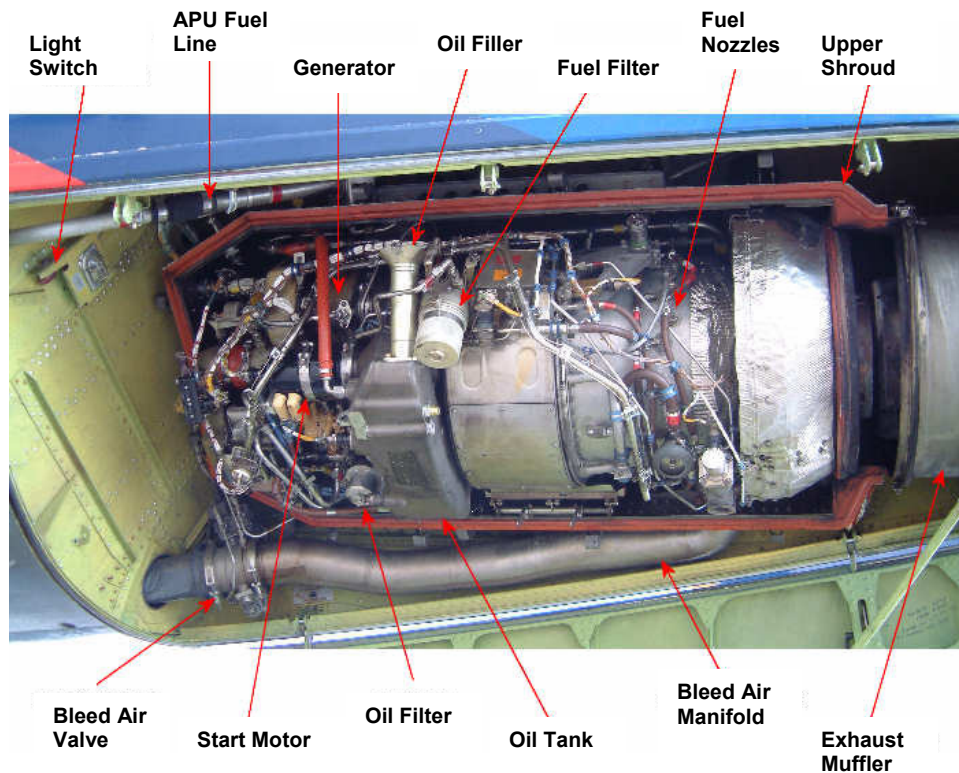


**Figure 2-11. A Transport Aircraft Auxiliary Power Unit Installation.**<sup>15, vii</sup>  
(Reprinted with permission of the author.)

<sup>vii</sup> Several DoD aircraft models are variants of commercial transport aircraft. Such aircraft are referred to within the DoD as commercial-derivative aircraft.

Fire Suppressant  
Bottle

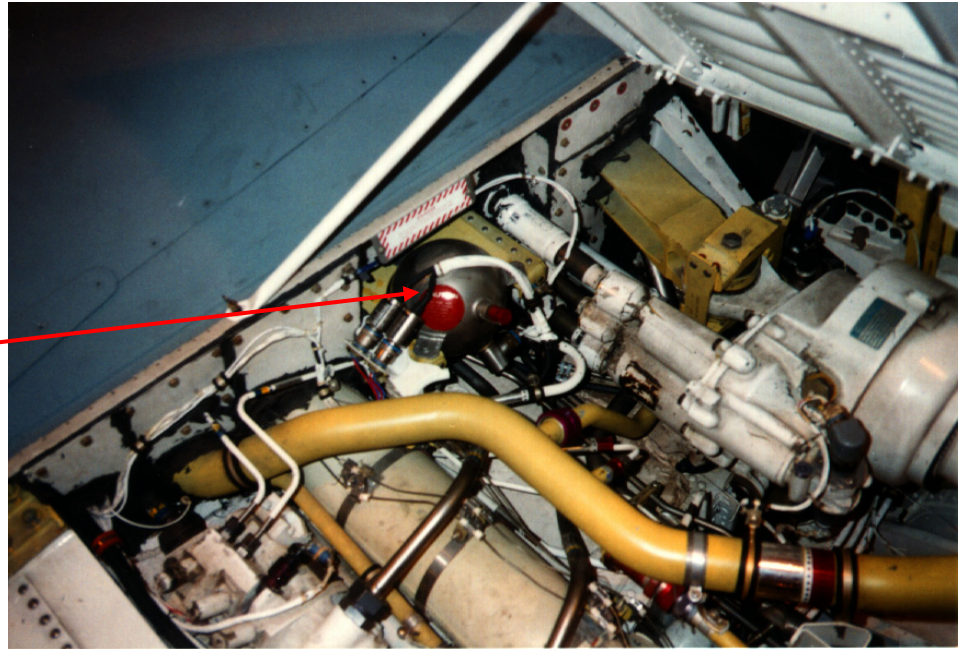


**Figure 2-12. A Fighter Aircraft Accessory Compartment With Fire Suppression System Installation.**  
(Printed with permission of the Naval Air Systems Command.)

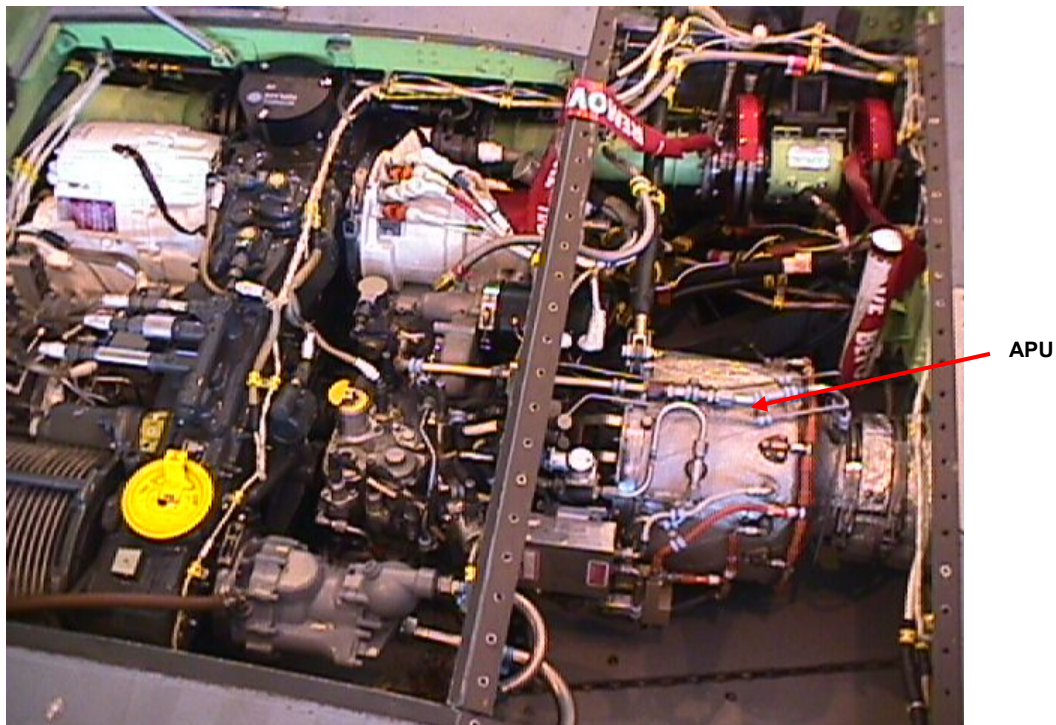


**Figure 2-13. An Aircraft Gearbox Compartment with APU.**  
(Printed with permission of the Naval Air Systems Command.)

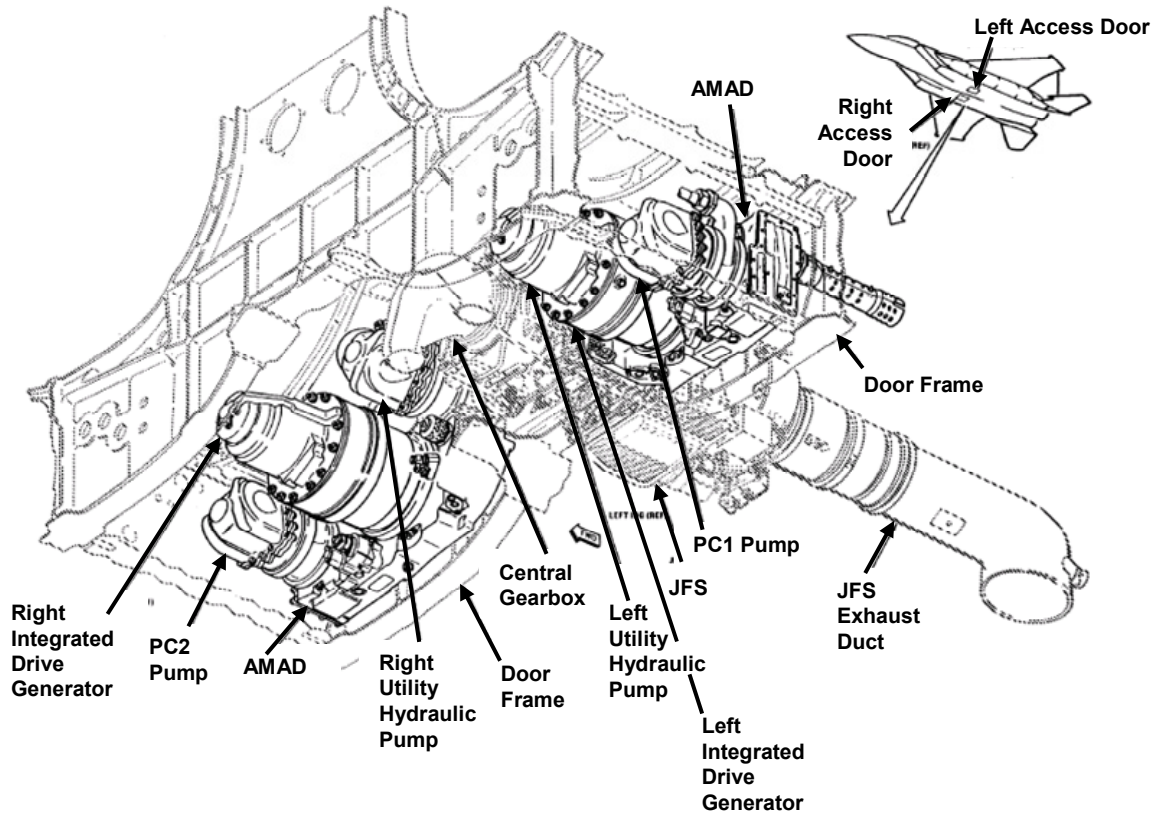


**Figure 2-14. A Secondary Power System (SPS) Installation.**<sup>16</sup>  
(Component callouts spelled out or simplified for clarity.)

### 2.2.3 Dry Bay Compartments

Dry bay compartments, or simply dry bays, are compartments on aircraft adjacent to fuel tanks or are compartments in which flammable-fluid-carrying components are located. The compartments adjacent to fuel tanks may contain other equipment, such as avionics equipment, or may be, for the most part, empty. There may or may not be ventilation airflow. If not empty, a dry bay can be geometrically complex, and if there is some ventilation airflow, the compartment may be turbulent. One study identified generally four types of dry bays: wing leading/trailing edge, wing midchord, fuselage fuel cell boundary, and fuselage forward and aft equipment bays.<sup>17</sup> Ballistic threats such as armor-piercing incendiary (API) rounds or high-explosive incendiary (HEI) rounds can penetrate a fuel tank or fuel-carrying component, effecting release of flammable fluid into a dry bay. The incendiary released by the round from the penetration can then ignite the fluid-air mixture. The damage inflicted by a ballistic round may also result in damage to an aircraft system that can result in a secondary ignition source, such as heated metallic fragments or arcing from a damaged electrical harness. Figure 2-15 illustrates that dry bay compartments may be located within the fuselage as well as in wing areas that surround a fuel tank. Figures 2-16 through 2-18 provide examples of actual aircraft dry bay compartments. Figure 2-16 illustrates a dry bay compartment adjacent to a fuel tank whereas Figures 2-17 and 2-18 show dry bay compartments that also contain flammable-fluid carrying components.

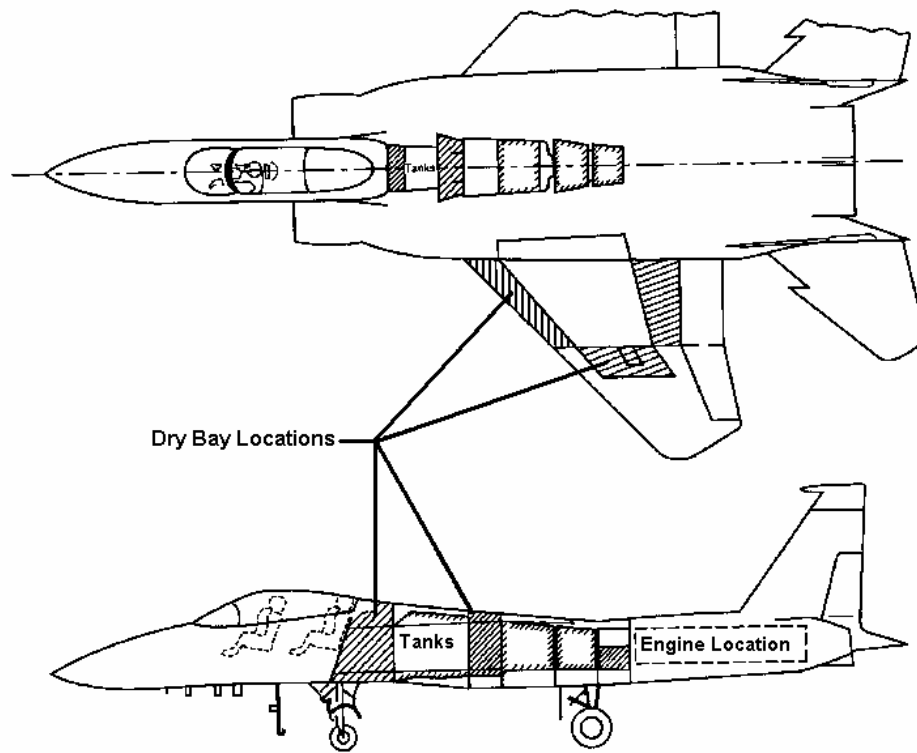


Figure 2-15. Typical Dry Bay Locations in a Fighter Aircraft.<sup>18</sup>

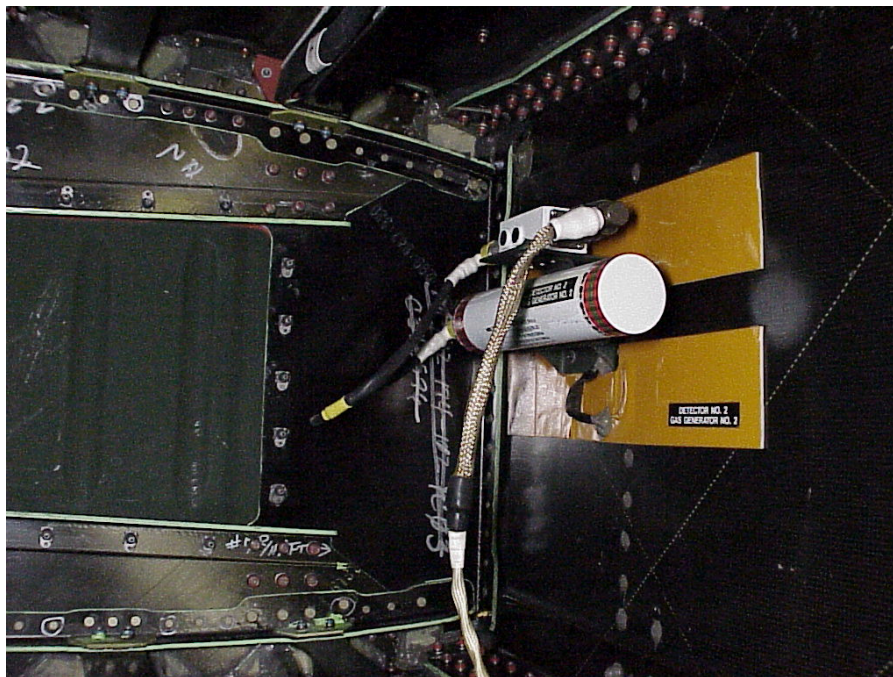
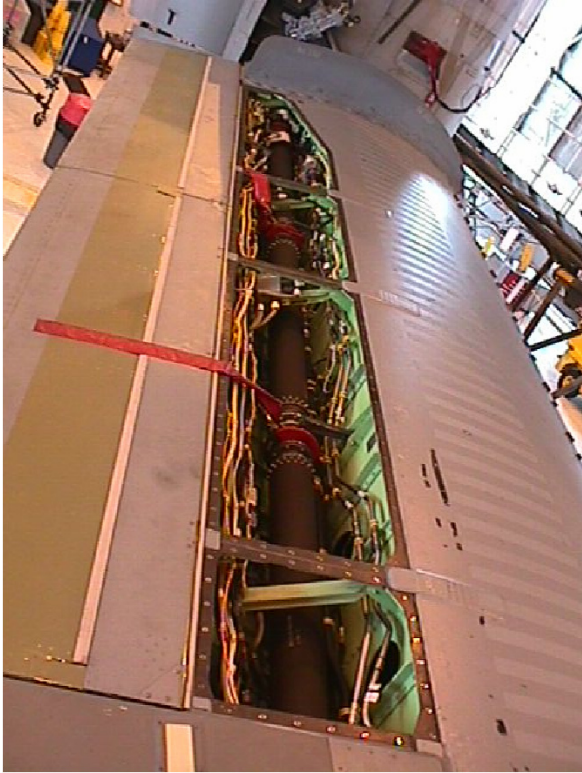


Figure 2-16. A Dry Bay Compartment Adjacent to a Fuel Tank; Fire Detector and Fire Suppressor Installed within the Dry Bay Compartment.

(Printed with permission of the Naval Air Systems Command.)



**Figure 2-17. Top View of a Wing Dry Bay Containing Drive, Hydraulic, and Electrical Systems Components.**

(Printed with permission of the Naval Air Systems Command.)

Powder Panel

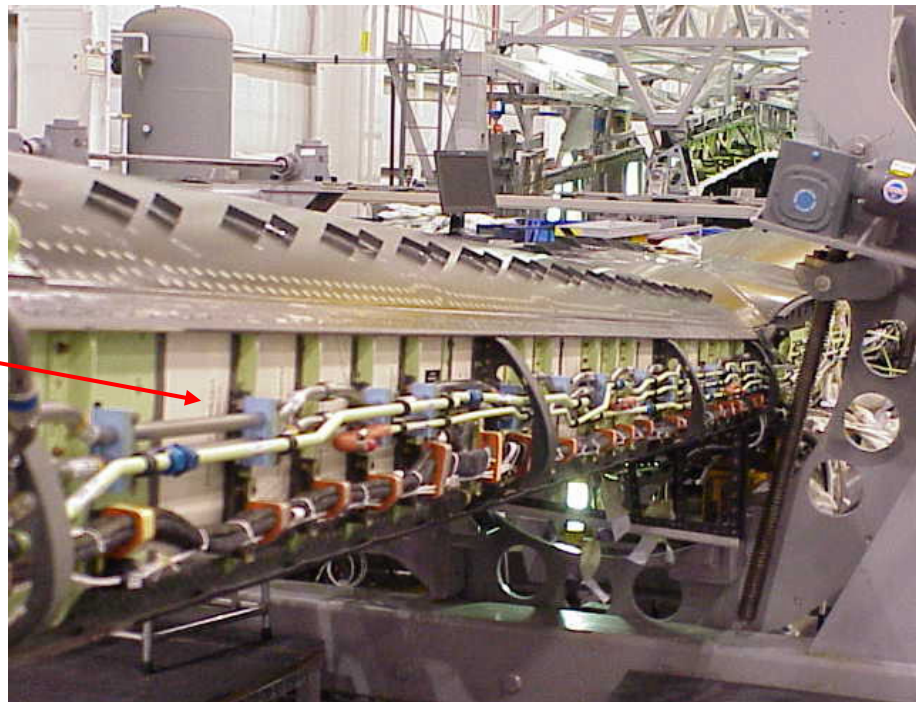


**Figure 2-18. A Wing Leading Edge Dry Bay Containing Hydraulic and Electrical Systems Components, Leading Edge Structure Removed.**

(Printed with permission of the Naval Air Systems Command.)

There are active and passive approaches for suppressing dry bay fires. An active dry bay fire protection system must be capable of detecting a fire on a time scale of less than 10 ms and suppressing the fire within a few hundred milliseconds. In the truest sense, fielding of halon 1301 fire suppression systems for protection against ballistic threats in dry bay compartments on military aircraft has been limited: no DoD aircraft have such dry bay fire protection systems, but halon 1301 dry bay fire suppression is known to be installed on United Kingdom CH-47 Chinook helicopters.<sup>19, viii</sup> Like halon systems designed to protect engine nacelles, the fire bottles used for dry bay fire suppression on the CH-47D helicopters also utilize a pyrotechnic device to rupture a burst disk on the bottle to effect suppressant release, but the bottles are automatically activated upon receipt of a signal from a pressure transducer – an initiator on the bottle also effects discharge.<sup>20</sup> Figure 2-19 depicts the components of this type of system, which is referred to as the COBRA system.<sup>ix</sup> The bottles are much smaller than those fielded for nacelle fire suppression systems, and the time to discharge agent is on the order of 10 ms, compared to typically 1 s for a nacelle fire bottle.<sup>21</sup> There are, however, DoD aircraft platforms for which halon 1301 is utilized to protect a powerplant or other type of compartment but in reality the protected compartment is a *quasi* dry bay compartment that is vulnerable to a ballistically induced fire; i.e., these compartments are either located adjacent to a fuel tank or they contain flammable-fluid-carrying components. For a few DoD platforms, those halon 1301 fire suppression systems are also intended to provide protection against dry bay fires.<sup>17</sup>

Passive techniques have been the predominant fire protection approach for aircraft dry bays on DoD aircraft, which have been implemented either by installation of a physical material to defeat the flame front, such as reticulated polyether foams and rigid foams, or by installation of panels adjacent to the compartment that, if ruptured by a ballistic projectile, release a powder suppressant to quench incendiaries released by the projectile. (In Figure 2-18, powder panels can be seen installed on the wing spar.) Performance limitations of this latter method were investigated under the NGP and resulted in development of new design techniques that dramatically improve powder panel protection capability.<sup>22</sup> This is described further in Chapter 9.

#### 2.2.4 Cargo Compartments

Cargo compartment fire suppression systems are typically installed on commercial transport aircraft, though there is at least one DoD aircraft equipped with this type of system, the C-5, an Air Force cargo transport aircraft.<sup>23</sup> Such systems are designed to provide a minimum knock-down concentration followed by a sustained minimum flooding concentration to suppress a fire that continues to burn until a safe landing is made. Such systems typically provide for 60 min of suppression capability. Thus unlike a fire suppression system designed to extinguish a nacelle, other powerplant, or dry bay fire, the protection philosophy for a cargo compartment is true fire suppression.

---

<sup>viii</sup> In Reference 32 it is stated "...the F22 dry-bay protection scheme...incorporates multiple 'bottles', using halon 1301, to provide appropriate coverage." This statement infers that DoD USAF F-22 aircraft use halon 1301 for dry bay fire suppression. Space and electrical wiring provisions are installed on delivered F-22 aircraft in the event it is decided in the future to install dry bay fire suppression system components. Though the system was designed for use of halon 1301, research conducted for this Chapter confirmed (Reference 19) that, as of the writing of this book, no F-22 aircraft are fielded at this time with halon 1301, i.e., no dry bay fire suppression system components are installed.

<sup>ix</sup> During research conducted for this book, it could not be confirmed if "COBRA" is an acronym, nor could it be confirmed why the system was assigned such a name. Literature provided by the system supplier indicates that it simply refers to the snake.

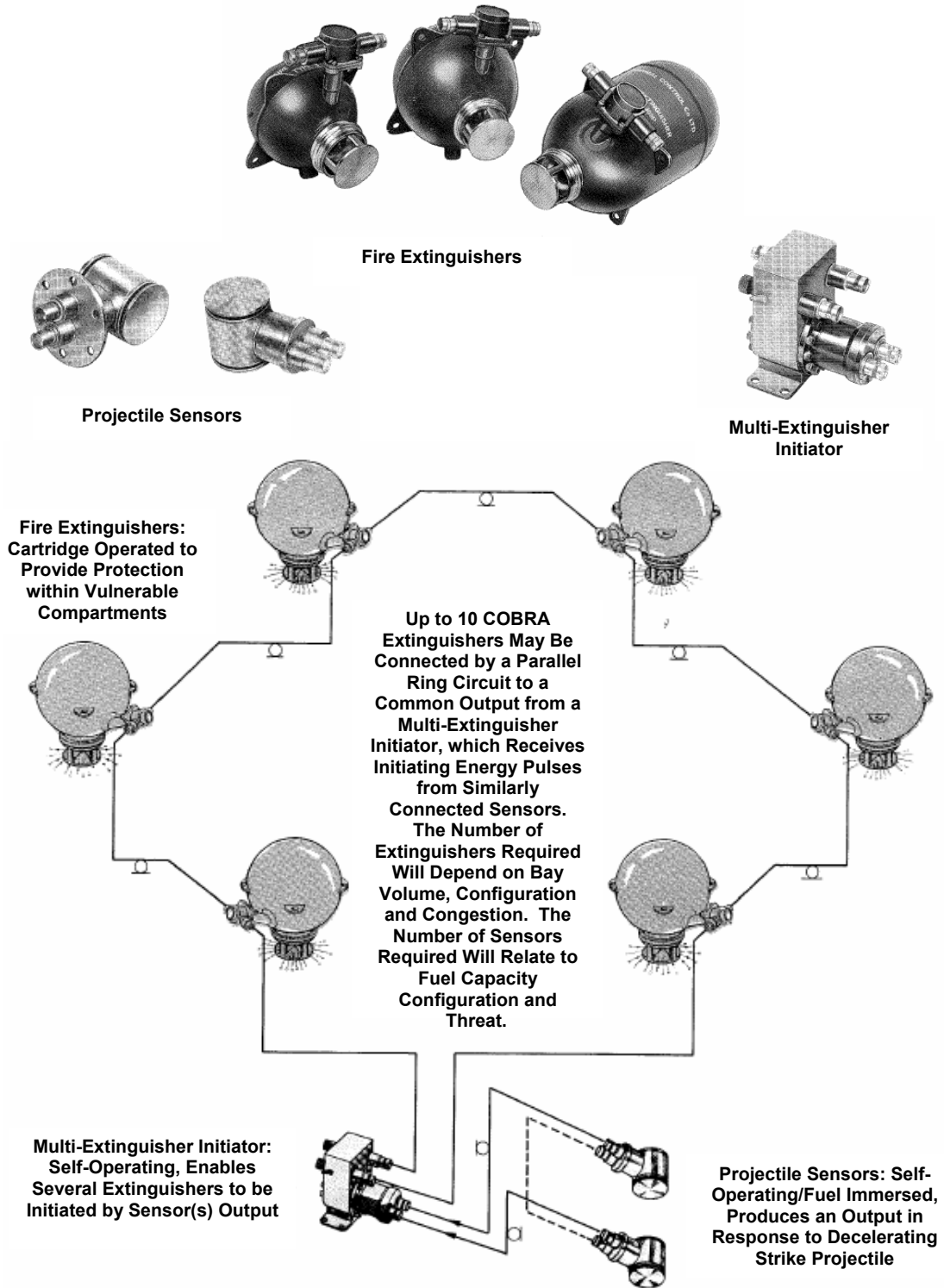


**Figure 2-19. Non-DoD Aircraft Halon 1301 Dry Bay Fire Protection System.**<sup>24,25</sup>  
 (Reprinted with permission of Aircrew Limited, U.K.)

The diagram in Figure 2-20 is an example of a cargo fire suppression system installation on a transport aircraft. Such systems today utilize halon 1301 for fire suppression. In the case of an engine nacelle or APU compartment fire, the fuel source is shut off from either of those compartments prior to effecting agent discharge; whereas in a cargo compartment, the fire may be deep-seated and not removed from its flammable material source. The amount of agent installed to provide extinguishing capability to protect engine nacelles may be relatively small compared to that required for the cargo compartment. For example, on C-5 aircraft, there are four halon 1202 bottles (6.8 kg agent each) for engine fire suppression, whereas 17 halon 1301 bottles (31.75 kg each) are installed for cargo compartment fire suppression. Though the focus of the NGP did not include cargo compartment fire suppression, extensive research and testing into application of halon alternatives for these compartments has been conducted by the FAA's Fire Safety Branch at the Hughes Technical Center.

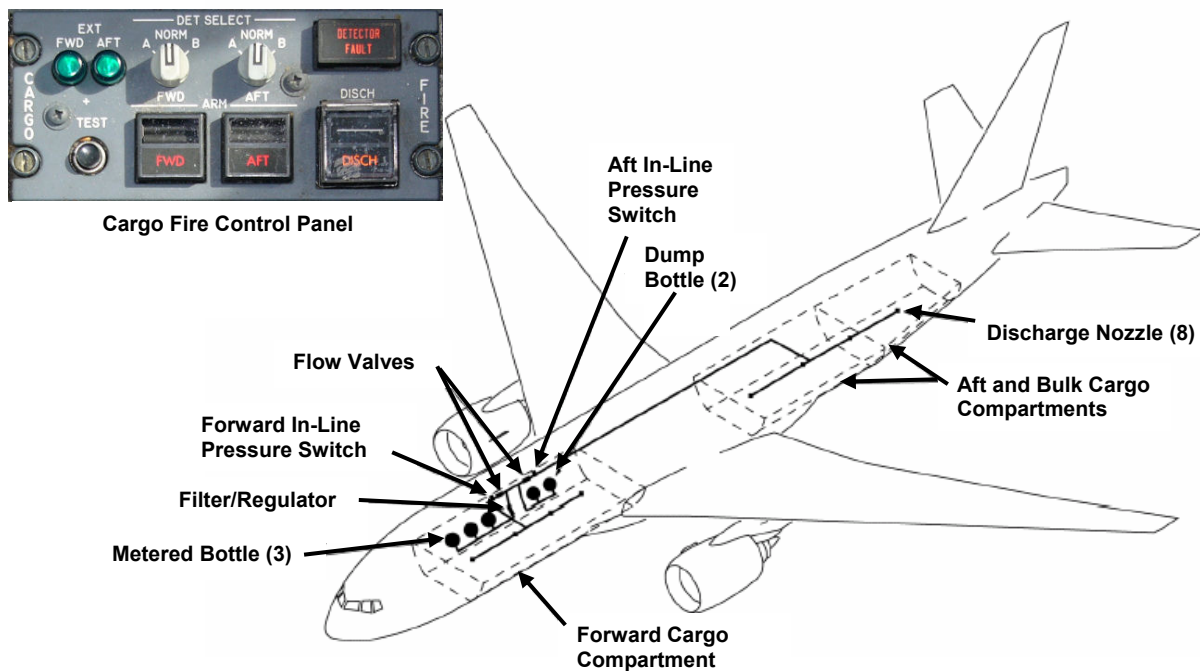


**Figure 2-20. Diagram of a Cargo Fire Suppression System Installation on a Transport Aircraft.**<sup>26,27</sup>

(Photograph of panel reprinted with permission of the author.<sup>15</sup>)

### 2.2.5 Other Compartments

During the development of an aircraft design, safety hazard and vulnerability analyses will identify potential fire threats aboard the aircraft in compartments other than powerplant-type, dry bay and, if applicable, cargo compartments. (The vapor space within fuel tanks is a separate case that is described in the next section.) Design solutions are then pursued to mitigate the likelihood of a catastrophic fire and implement ballistic vulnerability reduction measures if needed, which typically considers isolating potential ignition sources from flammable fluid or other flammable sources. If the risk for fire cannot be mitigated to an acceptable level, a dedicated fire suppression system will be installed to protect the compartment (or if not, the risk is accepted). Examples of such compartments on DoD aircraft are, or

were, the fuselage fire protection system installed on F-111 aircraft to protect the cheek and stabilization areas and weapons bay, the C-5 avionics compartment fire suppression system, and the A-6E/EA-6B aft equipment bay fire protection system. All are, or in the case of retired aircraft were, halon 1301 systems. The certification requirement for engine nacelle halon 1301 fire suppression systems was applied to certify the A-6E/EA-6B aft equipment bay system, and that requirement was likely applied to certify the other systems on the C-5 and F-111. Thus it follows that certification requirements developed for any agent or technology developed by the NGP for engine nacelle fire suppression would likely become certification benchmarks, or likely starting points for such benchmarks at minimum, for systems installed to protect most compartments on aircraft except for dry bays and cargo compartments. The exception for dry bay compartments is that although viable technologies for dry bay protection were developed under the NGP, certification for those systems will likely still be accomplished through live fire ballistic testing, as is done currently in accordance with live fire testing legislation. The exception for cargo compartments is the unique knock down and flooding suppression requirement, which was not addressed by the NGP.

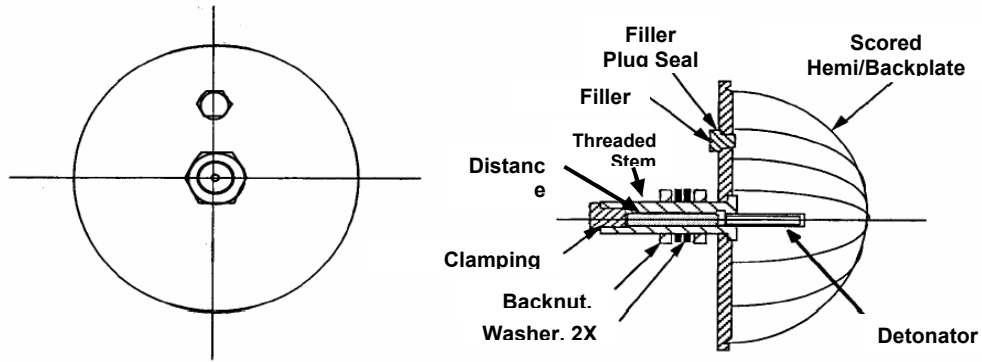
### 2.2.6 Fuel Tank Ullage

In contrast to dry bay compartments, fuel tanks are sometimes referred to as wet bays. The fuel tank ullage is that portion of the fuel tank volume not occupied by liquid fuel but contains an air and fuel-vapor mixture. From an operational safety perspective, though the potential for a fuel tank fire/explosion hazard exists on every aircraft due to a system or component malfunction or failure, safety has not been the requirements impetus for implementing ullage protection on DoD military aircraft. (Relatively recent activity has been conducted to reassess and develop such protection for commercial aircraft.<sup>28,29,30</sup>) The case for military aircraft is primarily, like dry bay fire protection, one of vulnerability reduction for combat survivability. Though there are several military platforms that incorporate some type of active ullage protection system, only three DoD aircraft have utilized halon 1301 to provide fuel tank inertion, the USAF F-16 and F-117 aircraft and the United States Navy (USN) A-6E, which is no longer in service.

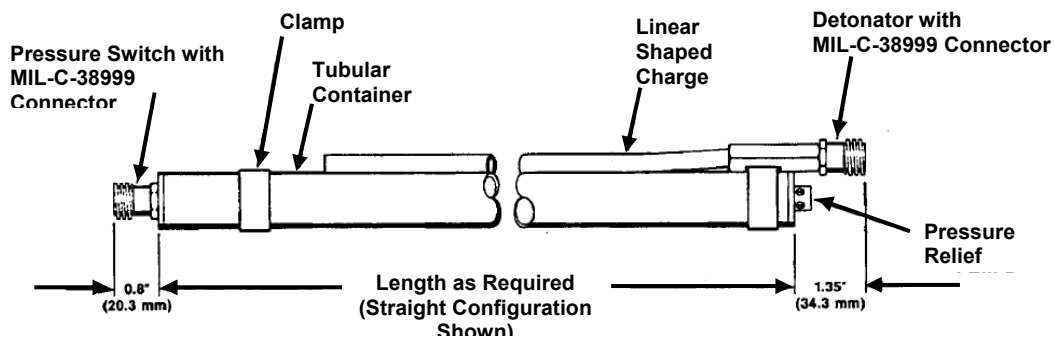
No research was performed under the NGP to identify or develop potential alternatives to halon 1301 for fuel tank inerting. However, the NGP did compile and appraise techniques for fuel-tank ullage suppression of fire and explosion, which had been previously developed and fielded.<sup>31</sup> That work identified the following technologies that can be installed within the ullage itself to discharge a suppressant upon detection of the fire/explosion flame front: scored canister system (SCS), linear fire extinguisher (LFE), and the Parker Reactive Explosion Suppression System (PRESS). Existing design guidance on fuel system fire and explosion suppression also identifies an additional technology, the Fenwal cylindrical suppressor.<sup>20</sup> Of these, only the cylindrical suppressors utilized a halon fire suppressant (halon 1011) and were fielded on several aircraft, one of which was the USAF F-105. These suppressors were also utilized on some commercial transport aircraft (Boeing 707 and 747-100 models) in surge tanks to prevent ground fires entering the wing. These systems were designed to provide fire protection, not explosion protection.<sup>32, x</sup> The SCS utilized pentane to create a fuel-rich environment and was also fielded on several platforms. The PRESS technology used water plus a brine additive to reduce the water's freezing temperature below -54 °C (-65 °F) and has not been fielded. Figure 2-21 illustrates the SCS, LFE, and cylindrical suppressor devices.

---

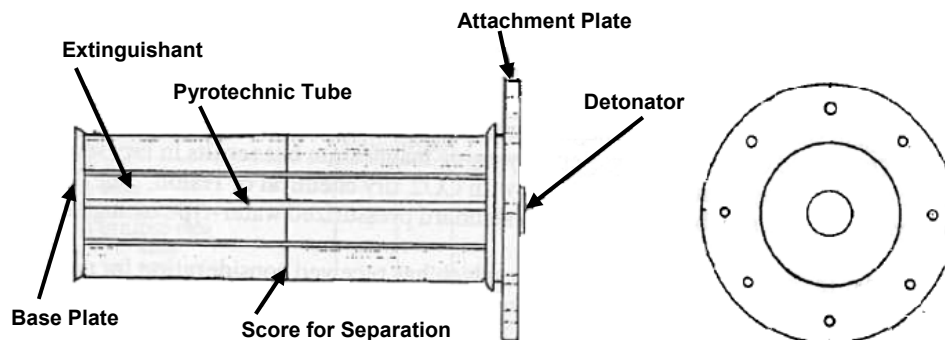
<sup>x</sup> Reference 32 suggests that this type of fire suppression was installed to protect against fires initiated by lightning strike.



(a) Scored Canister<sup>31</sup>  
(Reprinted with Permission of Kidde Aerospace.)



(b) Linear Fire Extinguisher<sup>33</sup>  
(Reprinted with Permission of Meggitt Safety Systems, Inc.)



(c) Cylindrical Suppressor<sup>20</sup>  
(Reprinted with Permission of Kidde Aerospace.)

Figure 2-21. Illustration of Ullage Fire/Explosion Protection Devices.

An additional technique identified during the NGP investigation was the nitrogen-gas-inflated ballistic bladder (NIBB) system, a double-walled fuel cell that is filled with nitrogen. Interestingly, this technique requires an on-board inert gas generation system (OBIGGS) to provide the nitrogen gas. The NIBB system has not been fielded on any DoD aircraft, whereas OBIGGS itself is fielded on several aircraft (C-17, MV/CV-22, F-22, UH-1Y, AH-1Z, and AH-64) to provide nitrogen-enriched air to inert the fuel tank ullage. OBIGGS is being considered for the USN's multi-mission maritime aircraft, to be designated as the P-8 aircraft.<sup>34</sup> The C-5 and the SR-71 had implemented liquid nitrogen inerting systems for ullage protection. In the SR-71 aircraft, a supersonic aircraft, the inerting system was implemented because of the high skin and fuel tank wall temperatures generated during supersonic flight, i.e., aerodynamic heating effected by supersonic flight could cause walls to become an ignition source for fuel vapor in the ullage.<sup>35</sup> The use of nitrogen as an inerting and fire suppression agent is described later in this chapter.

The NGP investigation classified the various ullage protection techniques into three categories: active (system is always providing a required level of protection), reactive, and passive. Active techniques fielded currently are halon-based inerting and OBIGGS. Engine exhaust has also been used as an ullage inerting agent - the Russian-built Ilyushin IL-2 Sturmovik cooled and piped engine exhaust gases into its fuel tank ullage spaces.<sup>4</sup> Some earlier DoD aircraft also incorporated ullage inerting using exhaust gas (B-50 aircraft) as well as CO<sub>2</sub> and dry ice (B-47 and B-36 aircraft), but these techniques were discontinued because of technical problems.<sup>36</sup> Reactive techniques would integrate a detection system and a suppression system utilizing the LFE, SCS, PRESS, or cylindrical suppressor technologies. Passive techniques involve installing material within the fuel tank itself to prevent an overpressure by extracting heat from a flame front. There are primarily two materials that have either been fielded or at least have been demonstrated by the DoD as viable for providing passive fuel tank ullage fire protection: reticulated (porous) polyurethane foam and aluminum mesh. Polyurethane foam has been used in numerous DoD platforms for years (A-7, A-10, F-15, F/A-18, C-130, and P-3), whereas aluminum mesh has not been implemented on DoD aircraft.

During the NGP, non-NGP investigations were performed into the use of trifluoroiodomethane (CF<sub>3</sub>I) as a replacement for halon 1301 in the F-16 fuel tank inerting system. A diagram of the F-16 inerting system is shown in Figure 2-22 and is a typical halon 1301 inerting system design implementation. The system also includes a 400-watt heater to maintain a constant halon reservoir pressure over the entire operating temperature envelope for the aircraft, as the reservoir was located in a wheel well area. A heater had also been part of the inerting system installed on A-6E aircraft.

Preliminary analysis and testing indicated CF<sub>3</sub>I was a promising alternative to halon 1301, as it was initially concluded that only minor airframe system modifications would be required.<sup>37,38</sup> However, CF<sub>3</sub>I had been previously removed from consideration for use in engine nacelle, APU, and dry bay applications on DoD aircraft due to toxicity and materials compatibility concerns, as well as due to its relatively high boiling point.<sup>xi</sup> Subsequent review later concluded that CF<sub>3</sub>I was inadequate as a replacement for halon 1301 in the existing F-16 system due to its higher boiling point and resultant reduced delivery pressure at low temperatures.<sup>39</sup> Additional conclusions were that:

---

<sup>xi</sup> CF<sub>3</sub>I is listed as one of many acceptable halon alternatives for use in unoccupied spaces on the Environmental Protection Agency's (EPA) Significant New Alternatives Program (SNAP) list, and a minimum performance standard of 7.1 % volumetric concentration is being developed for its use for nacelle fire suppression in commercial aircraft, as determined under the Engine Nacelle Halon Replacement Program conducted by the FAA. That program also developed minimum performance standards for use of HFC-125 (17.6 % volumetric concentration) and FK-5-1-12 (6.1 % volumetric concentration). Boiling points for HFC-125 and FK-5-1-12 are -48 °C and 49 °C, respectively.

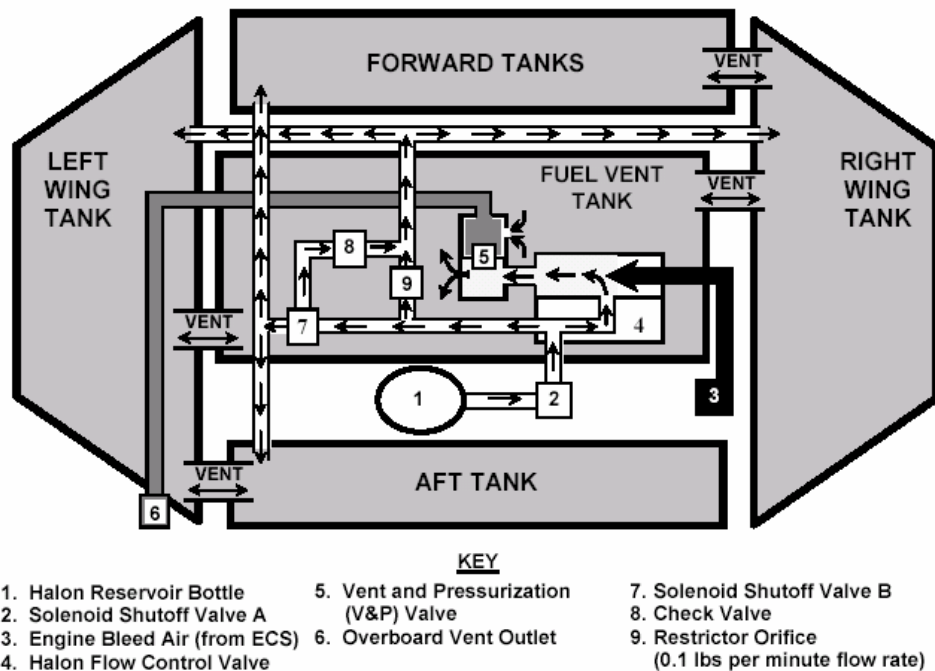


**Figure 2-22. F-16 Aircraft Inerting System Diagram.<sup>40</sup>**

- More flight qualification testing would be required on the materials compatibility of CF<sub>3</sub>I before it could be recommended as a replacement for halon 1301. CF<sub>3</sub>I is more chemically reactive than halon 1301, which could lead to metal corrosion or elastomer failure. It was indicated that it may be possible to specify materials that could be used in service with CF<sub>3</sub>I after such testing.<sup>xii</sup>
- CF<sub>3</sub>I is more toxic than halon 1301. It was indicated that under equivalent operational conditions, it would be considered unwise to replace a chemical with one that is 20 times more toxic, and that more rigorous toxicity testing of CF<sub>3</sub>I would provide a more quantitative estimate of its toxicity in realistic exposure scenarios.<sup>xiii, xiv</sup>

<sup>xii</sup> During design evolution of an aircraft and its systems and subsystems, assessment of materials compatibility is typically completed well prior to conduct of flight qualification testing. The rationale for recommending materials compatibility evaluation for CF<sub>3</sub>I as part of flight qualification testing was that it could degrade the fit, form, or function of any of the components that it contacts, and that it could introduce a contaminant or a degradation product into the fuel tank and fuel that produces damage. Due to the number of components involved, the extent of attack required to interfere with the operation of different components could vary. Thus it was assessed that it is virtually impossible to account for all possibilities in a laboratory and that engineering testing and evaluation would be required before CF<sub>3</sub>I could be fully qualified for use.

<sup>xiii</sup> An aircraft fuel tank as well as an engine nacelle or an APU-type compartment is a normally unoccupied space. For such spaces, this means it is permissible to use fire suppressants whose design or certification concentrations that are in excess of the Lowest Observed Adverse Effect Level (LOAEL).

<sup>xiv</sup> The LOAEL, which represents the volumetric concentration of a substance that can induce cardiac sensitization in testing using beagle dogs, is reported for halon 1301 and CF<sub>3</sub>I as 7.5 % and 0.4 %, respectively. The 20 factor was derived by the ratio of the halon 1301 LOAEL to the CF<sub>3</sub>I LOAEL (i.e., 7.5/0.4). Though cardiac sensitization LOAEL was one of several CF<sub>3</sub>I issues reviewed, the fielding of a suppressant whose LOAEL is significantly below a system certification concentration is not without precedent in the DoD. USAF C-130J and USN KC-130J aircraft, which are still being procured as of the

- The ODP of CF<sub>3</sub>I is highly dependent upon the altitude and latitude at which it is released. It was calculated that CF<sub>3</sub>I usage onboard an F-16 aircraft could be between 13 % and 167 % as damaging to the ozone layer than use of halon 1301, or, in other words, ozone depletion from F-16 application of CF<sub>3</sub>I could be as small as one-eighth that of halon 1301 (at lower altitudes) or as large as one and two-thirds times as damaging as halon 1301 (at higher altitudes). However, even for conservative choices, CF<sub>3</sub>I use onboard an F-16 would be a Class I ozone-depleting substance if significant amounts are released above 6.1 km (20,000 ft), and the US Clean Air Act bans use of Class I substances.

Subsequent NGP modeling of ODP associated with the use of CF<sub>3</sub>I in engine nacelle and APU-type applications is described in Chapter 7. This study was conducted using the same chemical transport model, but updated with the latest representation of atmospheric chemistry and dynamics. The results of the modeling indicated the ozone depletion effects would not be significant for CF<sub>3</sub>I use in engine nacelle and APU-type applications.<sup>41</sup>

## 2.3 TYPES OF FIRES EXPERIENCED

Both occurrence and suppression of fire on board an aircraft are probabilistic. Although obvious, assessment of such probabilities plays a role in determining whether a fire suppression system is implemented, or if implemented, the type of system, active or passive, and if implemented whether that system will provide protection under all flight and mission conditions. The level of protection implemented then becomes a risk trade for the program manager(s) responsible for the development, production, and fielding of a military aircraft.

Such trades receive additional attention from program managers, since they are most often applied when considering the need to implement fire suppression systems beyond those normally required by an aircraft specification for safety (i.e., engine nacelle and APU compartment) or those necessary to achieve desired vulnerability reduction (i.e., dry bay compartments). In short, such trade efforts are difficult to sell to a program manager, since they increase aircraft weight, cost, and complexity. It is no surprise that this would be case, since during the formulation of the NGP strategy it was found that majority of the types of fires experienced in DoD military aviation, as listed in Table 2-2, were types related to engine nacelle and dry bay compartment fires. This provided the NGP with an overarching view from which to investigate further the characteristics of fires within engine nacelles and dry bay compartments.

The primary aircraft design considerations are weight, performance, and cost. Key aircraft performance parameters (KPPs) include range, speed, and drag, all of which are impacted by weight. The aircraft program manager(s) and aircraft design engineers are always seeking the lowest weight possible for any system on the aircraft. For example, established fire suppression system specifications may require a redundant nacelle fire suppression capability. The reality may be that the aircraft just cannot physically accommodate the installation of an additional fire suppression agent container, or a risk trade analysis may be performed to assess the risk of not implementing the additional bottle, which will include a probabilistic analysis for failure to suppress the fire leading to loss of the aircraft and fatalities (in other words, what is the risk of not implementing redundancy to save weight). If it is decided to accept that

---

writing of this book, utilize halon 1211 for engine nacelle and APU fire suppression. The LOAEL for halon 1211 is 1.0 %, or 7.5 times higher than the value for halon 1301. Chapter 6 provides additional information regarding the cardiac sensitization protocol and the development of physiologically-based pharmacokinetic (PBPK) modeling of potential human exposure to halon alternative suppressants. Halon 1211 is also a Class I Ozone Depleting Substance (ODS).

risk, the requirement to provide the redundant capability will be removed or waived. Vulnerability analyses that effect whether or not dry bay and ullage fire protection are implemented is also probabilistic – analysis will assess probability of kill (aircraft loss) given a hit. Vulnerability reduction techniques are assessed for weight and performance, with performance assessed both from the vulnerability reduction perspective and aircraft performance perspective (for example, is it necessary to design a fuel cell so that all sides are completely self-sealing, or can weight be reduced by electing to employ self-sealing only on those sides or a portion of those sides having the greatest vulnerability).

**Table 2-2 Tabulation of Aircraft Fire Types.**<sup>42</sup>

Service	Fire Type	Location	Fuels	Suppression Time	Fixed System (F) or Hand-Held (H)	Occupied Compartment at Discharge (Y or N)
US Army	Fuel spray	Engine nacelle	JP-4 or JP-5	seconds	F	N
US Army	Stack fire	APU exhaust	JP-4 or JP-5	seconds	F	N
US Army	Turbine jet fire	Helicopter engine nacelle	JP-4 or JP-5	≈ 5 s	F, H	N
Tri-Service	Explosion	Dry bay	JP-8, hydraulic fluid	≈ 10 ms	F	N
Tri-Service	Turbine jet fire	Engine nacelle	JP-4, JP-8	≈ 5 s	F	N
USAF	Electrical	Compartment	Plastics	< 30 s	H	Y
USAF	Wall fire	Cargo bay	Paper, plastics, chemicals	≈ 5 min	F (H)	Y
USN	Fuel spray	Engine	JP-4, JP-5, JP-8, hydraulic fluid	seconds	F	N
USN	Fuel spray	Crew compartment	JP-4, JP-5, JP-8, hydraulic fluid	< 30 s	H	Y
USN	Electrical	Crew compartment	Insulation, plastics	< 30 s	H	Y
USN	Turbine jet Fire	Engine nacelle	JP-4, JP-5, JP-8, hydraulic fluid	10 s to 20 s	F	N
USN	Rapid growth	Dry bay	JP-4, JP-5, JP-8, hydraulic fluid	≈ 50 ms	F	N

The relevance of trade analyses that evaluate requirements, weight, and performance relates directly to the residual fire threat for the aircraft after all design considerations have been addressed to the extent possible or practicable, e.g., drainage provisions for leaked flammable fluid, separation of fuel sources from potential ignition sources, tolerance of components to fire or hardening, and fire containment, which themselves are subject to weight trades prior to or in consideration with implementing fire suppression. As a precursor to its research activities, the NGP conducted a review to characterize the nature, frequency, consequences, and severity of fires for which halon-based fire suppression systems have been fielded on DoD aircraft.<sup>43</sup> With the knowledge acquired from this review as well as from various studies conducted during the TDP, studies performed coincident with the NGP and presented at Halon Options

Technical Working Conferences (HOTWC), and continuing work by the FAA's Fire Safety Branch and the International Halon Replacement Working Group (IHRWG), the characteristics of all types of aircraft fires have been described.<sup>xv</sup> The remainder of this chapter discusses fire characteristics for areas specifically addressed by the NGP, engine nacelles, APUs and dry bay compartments, plus it includes a similar discussion on ullage fire/explosion characteristics.

### 2.3.1 Safety-related Fires

As described in the beginning of the chapter, an aircraft fire is deemed a safety-related fire when it results from component failures, which may be due to inadequate design, a mechanical failure mechanism such as fatigue, or maintenance error, and results in either a flammable fluid contacting an always-present ignition source, e.g., a hot engine case, or the failures themselves provide both the flammable fluid and the ignition source. These types of fires occur in flight or on the ground. The two most common types of fire hazard in the engine nacelle are a direct consequence of the means of fuel delivery and the failure mode that permits fuel to leak, i.e., either a spray fire or a pool fire.<sup>11</sup> A mechanical failure in the component path within the nacelle that provides fuel to the engine can either result in a fuel spray or the pooling of fuel. Examples of these types of failures are a cracked fuel line, or a fuel line or system component that was improperly installed and allows fuel to leak. An additional fire hazard associated with the aircraft engine nacelle is that even after extinguishment is achieved, a strong potential exists for reignition of the fire from hot surfaces on the engine. Hot surface reignition remains a threat as long as fuel vapor and air can come in contact with sufficiently hot surfaces. This concern prevails in flight as well as on the ground during or after engine shutdown. After engine shutdown, for a brief period, the engine case temperature and nacelle free volume temperature can actually increase due to engine temperature soak-back effected by removal of ventilation airflow that would occur with the engine operating. It is possible then that a small leak, which does not result in an in-flight fire, could result in a nacelle fire on the ground during engine shutdown. If the compartment is wetted with the flammable fluid, or if the fluid has pooled, the resulting ground fire event can impart extensive damage.

Given that dry bays may contain flammable fluid carrying components, such as fuel and hydraulic lines and hydraulic fluid reservoirs, and potential ignition sources such as bleed air ducts, safety-related fire events may also occur in these compartments. Even though the probable majority of dry bay fires over the lifetime of a particular military aircraft will result from ballistic threats, other events can result in a dry bay fire, such as an overheated electrical generator, arcing generated by failed electrical circuits or wiring, or damage induced by some other form of impact such as a bird strike.

### In-flight Fires

In-flight engine fires can result in catastrophic loss of an aircraft and fatalities if the aircraft has only a single engine, or if there are multiple engines and the fire goes undetected and suppression is not attempted until the fire has effected damage to the aircraft that results in loss of lift or thrust or the aircraft fails to execute a safe landing, or if the nacelle fire suppression system cannot suppress the fire even if activated immediately after a fire warning is provided to the pilot and there is subsequent catastrophic damage or failure to execute a safe landing. A qualitative assessment of pilot reaction was conducted by

---

<sup>xv</sup> As of the writing of this book, information related to work conducted by the FAA Fire Safety Branch and the IHRWG can be found at <http://www.fire.tc.faa.gov>.

the NGP and estimated that 95 % of the time pilot reaction was characterized as *normal*, meaning that the pilot response followed typical emergency procedures for effecting agent release without delay. After receipt of a fire warning, the pilot isolated the affected compartment to remove fuel flow to that compartment, armed the fire suppression system, confirmed that the fire warning persisted and had some secondary indications of the fire condition, and then discharged the suppressant into the compartment.<sup>44</sup> During the TDP, extensive review of fire incident and mishap data was conducted to evaluate effectivity of currently fielded halon 1301 fire suppression systems aboard USN aircraft.<sup>45,46</sup> That review revealed that 55 % of fixed-wing fire events occurred in flight, yet for rotorcraft only 35 % had occurred in flight. An additional significant finding was that in-flight effectivity of the nacelle halon fire suppression systems was 76 % for fixed-wing aircraft, yet just 47 % for rotorcraft. It is important to bear in mind that these percentages are overall numbers for each of the aircraft types. However, they infer that the different nature of fixed-wing and rotorcraft designs and the missions these aircraft are required to fly influence different fire threats from an operational safety perspective.

The most surprising finding in these studies was that related to the redundant fire suppression capability on most rotorcraft and several fixed-wing aircraft. For rotorcraft, it was found that this capability was not utilized frequently, and when utilized it was successful in suppressing fire less than 10 % of the time. Usage on fixed-wing aircraft was also infrequent, except on P-3 aircraft.<sup>47</sup> In those cases, the reserve capability was successful 67 % percent of the time. The rationale derived from the rotorcraft events was that as a fuel-fed fire continues to grow after the first discharge, it is not likely that there would be successful suppression by the time the pilot effects the second discharge, which is delayed since the pilot has spent time coping with the emergency.<sup>47</sup> This rationale has been applied to support implementation of non-redundant halon-alternative nacelle fire suppression capability on the USN UH-1HY and AH-1Z rotary aircraft models. (However, no rationale is provided in the USN fixed-wing analysis that describes the 67 % success rate of the redundant capability on P-3 aircraft.) Contrasting the USN effectivity analysis was analysis performed by the U.S. Army, where frequency of use and effectivity of the redundant fire suppression capability on their rotorcraft between 1985 and 1995 indicated an overall higher percentage of in-flight nacelle fires on aircraft with nacelle fire suppression systems and a much higher effectivity of the redundant fire suppression capability.<sup>48,49</sup> Given that Army and Navy analyses included similar model rotorcraft, these outcomes suggest that service-specific missions may have an impact on nacelle fire occurrence and the ability to suppress nacelle fires for similar aircraft models. As of the writing of this book, it is planned to revisit and update the U.S. Army and USN data in support of halon alternative nacelle fire suppression efforts under a joint U.S. Army-USN program for H-60 model helicopters (i.e., U.S. Army Blackhawk and USN Seahawk helicopters).<sup>50</sup>

## Ground Fires

Aviation mishap data from the DoD safety centers typically classify mishaps by whether the mishap occurred in flight; if not in flight then whether intent for flight existed; or whether the mishap occurred on the ground and there was no intent for flight, such as during a ground maintenance engine turn operation. Fire mishaps that fall into the intent-for-flight-existed category typically occur on the ground (e.g., a rotorcraft engine nacelle fire that occurs during rotor turns prior to takeoff). Also, fires that occurred on aircraft while on a ship's deck were also considered as ground fires. Both nacelle fires as well as internal engine fires have been experienced within the DoD. An internal engine fire can occur during startup or shutdown and may be a result of improper procedures, a component failure, or severe ambient conditions such as high winds while at sea. In the case of improper starting procedures or severe ambient conditions,

the engine does not ignite properly during startup and excess fuel is dumped into the engine combustor. The fuel can be blown into the turbine and tailpipe, subsequently igniting. In the case of a mechanical failure, a fuel line may rupture, a pressure and drain valve may fail, or the engine bearings may fail. Fuel can accumulate in the combustor, turbine, or tailpipe and may subsequently ignite. These internal fires are colloquially referred to as tailpipe fires.<sup>51</sup>

The reviews described in the previous paragraph revealed that 65 % of rotorcraft fires occurred on the ground, whereas for fixed-wing aircraft this number was 45 %, and the aggregate effectivity of the nacelle halon fire suppression systems was similar for each aircraft category: 65 % for fixed-wing aircraft and 64 % for rotary aircraft. APU fires occurred primarily on the ground, and their frequency of occurrence was noted to be far less than that for nacelle fires. Effectivity of halon fire suppression in APU compartments was even higher, though fire events were indicated for two aircraft platforms only – 100 % effectivity was found for P-3 APU fire suppression, and 75 % for H-53 APU fire suppression. Similar to ground nacelle fire suppression events, there is reduced or minimal airflow within an APU compartment during a fire suppression event.

### **Effectivity vs. Optimization vs. Over-design**

The extension of the preceding to the NGP relates to its efforts in the development and validation computational fluid dynamics (CFD) models for nacelle fires and nacelle fire suppression. Those efforts considered the complex physics of fire, suppressant discharge and transport, the effects of compartment clutter on transport and distribution, and the effects of ventilation airflow on the behavior of fire and suppressant distribution. That effectivity of current nacelle halon fire suppression systems would be lower for in-flight events correlates with the NGP focus to develop CFD modeling capabilities to optimize nacelle fire suppression system designs for the dynamics of in-flight conditions. The need for a design optimization capability cannot be overstated when considering that even with halon 1301 as the suppressant and *normal* pilot reaction to effect agent discharge, the overall effectivity of halon 1301 nacelle fire suppression systems was still less than 80 %. It is this dichotomy that challenges an overarching assertion formulated during the TDP and that has prevailed during the NGP that halon 1301 nacelle fire suppression systems are over-designed. Rather, whether a system is either over-designed or not optimized is more appropriately assessed on an aircraft-by-aircraft basis. In any event, the CFD capability developed under the NGP provides a tool for use in conducting such assessments.

### **2.3.2 Ballistically-induced Fires**

Fires that relate to aircraft survivability are those that are ballistically induced, usually during enemy combat. That combat projectiles could induce fire within an aircraft dry bay or fuel tank ullage with catastrophic results has never been unique to U.S. military aircraft. Imperial Japanese Navy design policies during the later part of World War II not only required carbon dioxide (CO<sub>2</sub>) for nacelle fire suppression, but also for protection of fuel cells and alcohol tanks on aircraft; and structural spaces surrounding fuel cells were to be air tight, structural and weight limitations permitting. The CO<sub>2</sub> systems protecting fuel cells were to be automatic, and because of combat experience in which hits on aircraft with alcohol tanks resulted in fires, an automatic CO<sub>2</sub> system was to be implemented for the spaces surrounding the alcohol tank, i.e., a reactive dry bay fire protection system; a pilot-activated system was to be implemented for discharge into the tank itself.<sup>52</sup> There is evidence that a concept for implementing active dry bay fire protection was being pursued by the Imperial Japanese Navy at the latter stage of

World War II (Figure 2-23) and was planned to be an automatic system utilizing CO<sub>2</sub> as the fire suppression agent. What was being investigated then still applies today, in that aircraft remain vulnerable to ballistically-induced fires in dry bays and in the fuel tank ullage. These types of fires are summarized below without the intent of describing all of the damage effects that could be effected by a ballistic projectile or without describing the functioning characteristics of various projectiles. Though it is possible for a ballistic projectile strike into another compartment to effect a fire, e.g., within an engine nacelle, dry bays and the fuel tank ullage remain the most vulnerable to ballistically-induced fires. Taking into consideration that a delay of only several hundred microseconds may occur before an HEI projectile functions after impact, the response time of any reactive ullage or dry bay protection system to detect the combustion event is typically on the order of microseconds. Whether this delay is longer is a function of several variables, including the thickness of the aircraft material that the projectile must penetrate and impact obliquity angles.<sup>43</sup>

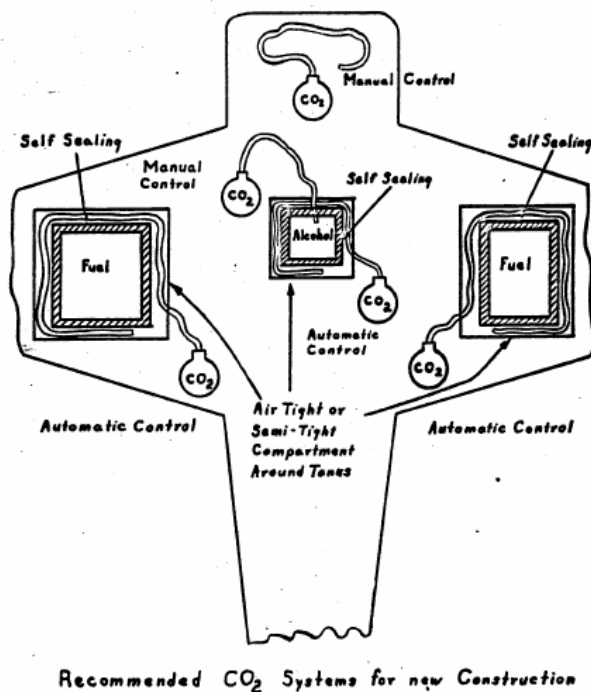


Figure 2-23. Imperial Japanese Navy Dry Bay and Ullage Fire Suppression System Concept, Late World War II.<sup>52</sup>

## Dry Bays

During aircraft dry bay live fire testing, the effects of wet-to-dry and dry-to-wet penetrations into the aircraft are characterized as follows. The wet-to-dry penetration is one in which the projectile first penetrates a fuel cell, travels through the fuel, and exits into dry bay. As the ballistic projectile travels through the fuel it creates an overpressure in the fuel cell. During exit, fuel may either leak or mist and can be ignited by hot spall; by pyrophoric, incendiary or tracer components of the projectile; or by an on-board ignition source, such as hot gases from penetrated bleed air lines, hot metallic surfaces (e.g., surfaces of bleed air or other hot gas ducts), or arcing electrical lines. The dry-to-wet penetration is one in which the projectile first enters into the dry bay and then penetrates either a fuel cell or a flammable fluid carrying component resulting in either leaking or misting fluid, or spall from the projectile will

damage such components sufficiently to effect a leak or mist, particularly if the damage to a system or component is one that operates at high pressures. In either case, fluid entering the dry bay can be ignited.

## Ullage

Various ideas to describe the ullage combustion by an electrical discharge are all based on the notion of a critical flame kernel or bubble. Experiments reveal that the initial disturbance created by the electrical discharge must exceed a minimum volume in order for the flame to become self-sustaining. Experimental observations show that this volume is often toroidal in shape for a spark generated between bare electrodes. Ullage ballistic testing performed by the USN described the ullage combustion process as two-stage, free-radical, branched-chain reactions, depending upon the ignition source. For a spark ignition source that is produced by a component failure within the ullage, it was described that in the first stage a *seed* of free radicals is produced, which in turn produces a blue flame front throughout the ullage fuel vapor/air mixture. That mixture then transitions rapidly to the second stage in which free radicals react with one another and produce a stable though accelerating set of molecules that are the products of combustion and can lead to explosion. This process can take place within a few hundred milliseconds, as depicted in Figures 2-24 and 2-25.<sup>xvi</sup> The functioning of an HEI ballistic projectile within the ullage will cause a violent reaction that, instead of a two-stage reaction, directly produces the products of combustion.<sup>53</sup>

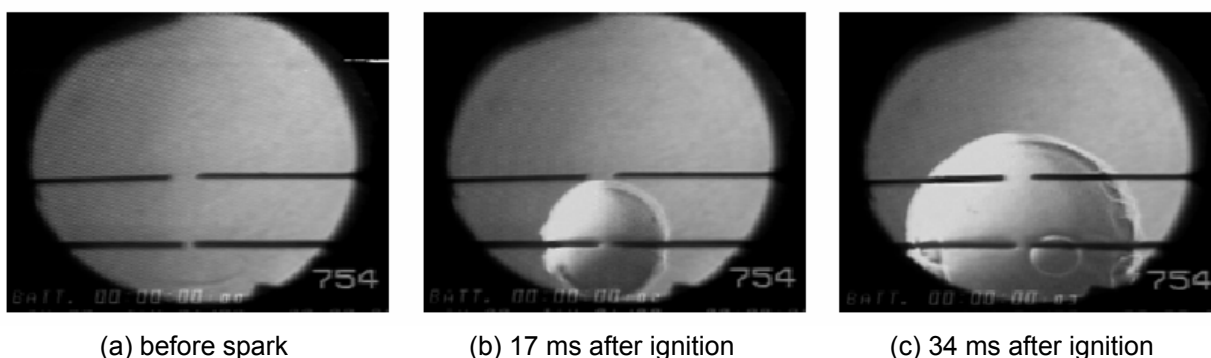


**Figure 2-24. Ignition and growth of a flame in 7 % H<sub>2</sub>, 1.4 % C<sub>3</sub>H<sub>8</sub> Jet A Simulant Mixture at 295 K (22 °C) and 84.1 kPa (0.83 atm).<sup>54</sup>**

### 2.3.3 Spray Fires

A cracked high pressure fuel, lubricant or hydraulic fluid line, or a cracked flammable fluid system component, such as a motor housing, can supply a steady spray of fuel for a fire stabilized behind obstacles in an engine nacelle. Small droplets quickly evaporate, and the momentum from the spray efficiently entrains the air necessary for combustion. The fuel-air mixture is ignited when it contacts a hot surface, or the mechanism that effected the failure mode can provide the ignition source, such as arcing onto a flammable fluid line as can occur when an electrical harness chafes against the line.

<sup>xvi</sup> For the process depicted in Figure 2-25, the spark source was a J-57 engine igniter that produced a spark from a capacitance discharge of 19 J of energy. The photographs in Figure 2-25 were provided by the Naval Air Warfare Center Weapons Division, Aircraft Survivability, and are reprinted with permission of the Naval Air Systems Command.

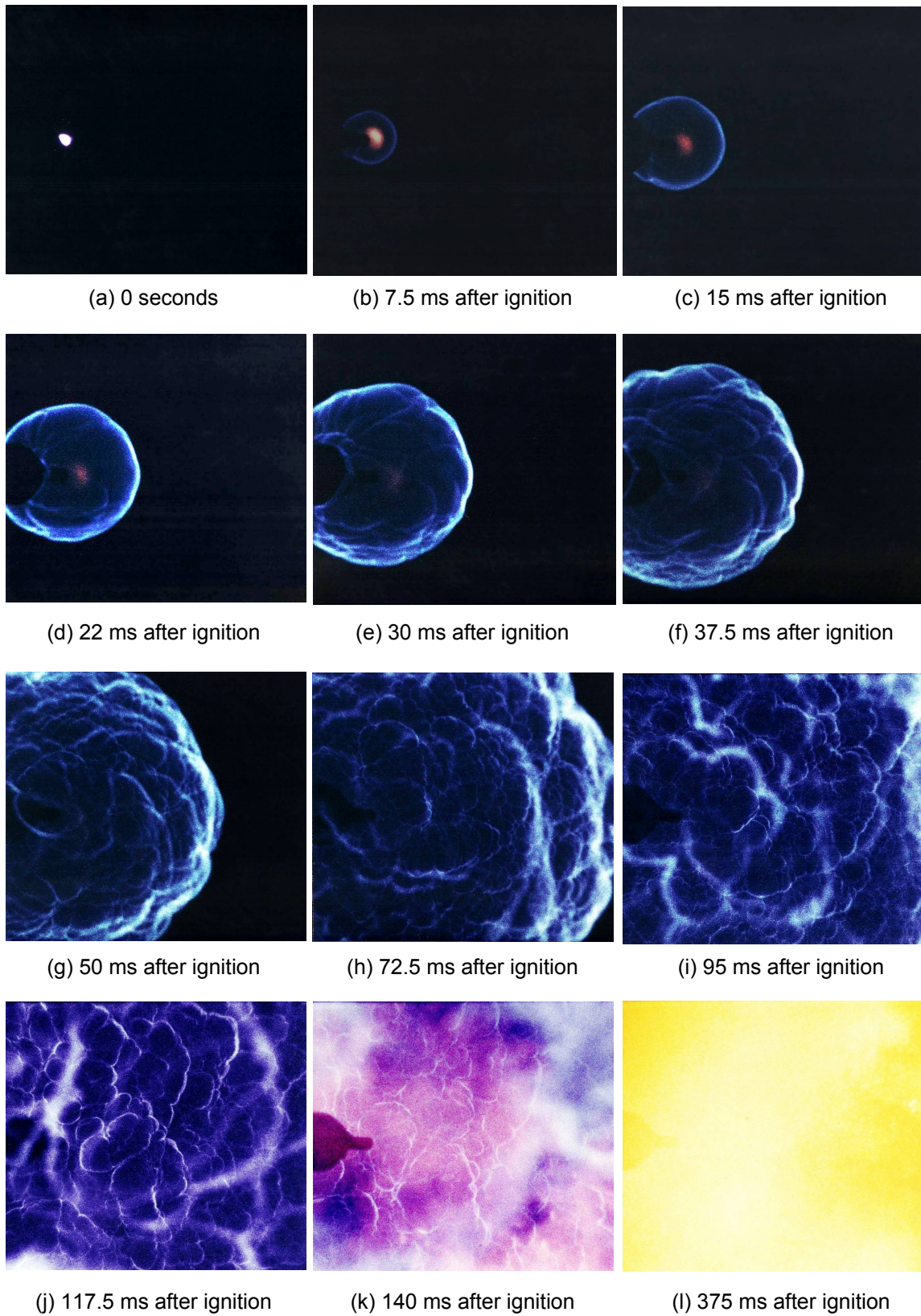


**Figure 2-25. Spark-Initiated Ullage Combustion Process.**

Extinguishment of the burning spray can occur if a critical amount of suppressant entrains into the combustion zone, or if the flammable fluid flow is cut off, thereby reducing the pressure effecting the spray, and the combustion is allowed to starve, or the combination of reduced flammable fluid flow and ventilation airflow provides sufficient strain. In addition to the flammable fluid system pressure and ventilation airflow, spray fire flame stability may also be influenced by ventilation airflow temperature, the type of flammable fluid, and the fire suppressant type.

### 2.3.4 Pool Fires

A pool fire can occur if failure of a flammable fluid line or component releases sufficient quantity of flammable fluid, which cannot drain away from the compartment and thus collects to form a pool. Ignition may occur by contact with a hot surface or by the mechanism that effected the failure mode, which could include a ballistic projectile. If there is ventilation airflow, such as within an engine nacelle, the stability of a pool fire can be greatly enhanced if an obstacle at the leading edge of the pool is present. In some nacelle configurations, obstacles in the form of structural ribs or other bluff bodies are present at locations where combustible liquids may puddle and fail to drain in a timely manner. Pool fire flames are believed to have a premixed structure and are more stable than the diffusion structure of spray flames, and both types of flame are believed to be less stable (more easily extinguished) at high airspeeds. Figure 2-26 depicts the sequence of events leading to a stabilized pool fire within a dry bay compartment having relatively low ventilation airflow.

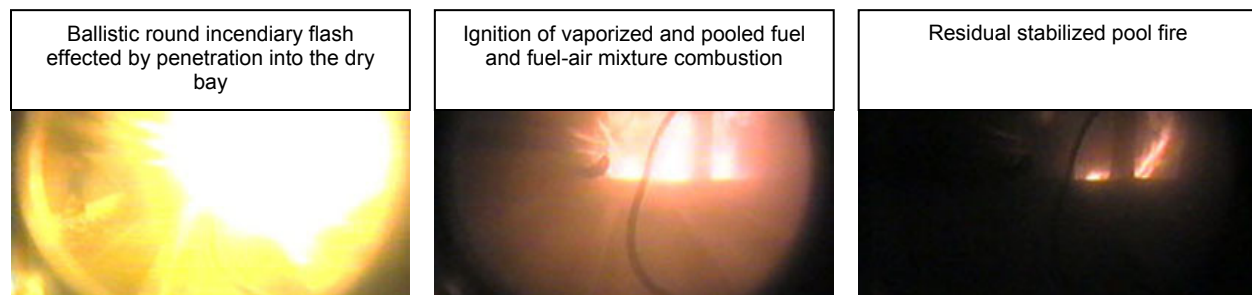


**Figure 2-26. Stabilized Pool Fire Formation within an Aircraft Dry Bay Compartment.**

Lab-scale fire suppression tests have shown that the stabilizing effect of a baffle in front of a pool fire can be very significant. Test results show that under similar airflow and baffle height conditions, a baffle-stabilized pool fire is dramatically more difficult to extinguish than a baffle-stabilized spray fire where the baffle is located in the middle of the flow field. Nacelle fire testing performed by the CAA and then later during the TDP has shown that occluded pool fires are more difficult to suppress than spray fires. The CAA reported that suppression mass quantity greatly increased with the presence of transverse structural ribs situated in the lower part of nacelles tested. This was attributed to difficulties in extinguishing pool fires between structural ribs. Later testing of three nacelle fire scenarios, fuel spray fire, burning of fuel as it flows as a thin film over a hot surface, and a burning pool of fuel, showed that greater suppressant concentrations were required for the hot surface and pool fire conditions than for spray fires.<sup>55</sup> That greater suppressant concentrations were required to suppress pool fires was again reconfirmed during the TDP in which it was found that stability of pool fires required larger suppressant concentrations and longer characteristic suppressant mixing times to achieve suppression due to recirculation zones. Pool fires were again found more difficult to suppress than spray fires during a nacelle fire test program for the USAF F-22 aircraft.<sup>56</sup>

### 2.3.5 Fire Characteristics

#### Flame Temperature

The fire triangle and fire pyramid are often used to describe the basic components of fire. In the fire triangle, the three sides are typically indicated as fuel (or substance that will burn), oxygen, and temperature (i.e., sufficient heat to initiate and sustain combustion). The four surfaces of the pyramid indicate a fourth component: chemical chain reactions involving free radicals, which are necessary for the reaction (hence combustion) to be sustained. For hydrocarbon fuels (which include aviation fuels), the reaction is usually written as  $\text{Fuel} + \text{O}_2 \rightarrow \text{H}_2\text{O} + \text{CO}_2$ . The net heat release for the reaction is referred to as the heat of combustion, and this can be used to estimate the maximum possible flame temperature, or the adiabatic flame temperature.<sup>57</sup> The net heats of combustion for JP-4, JP-5 and JP-8 aviation fuels used on DoD aircraft are within the range of 40 kJ/g to 45 kJ/g. As illustrated in Figure 2-27, the maximum flame temperature occurs when the equivalence ratio is one. The equivalence ratio is the actual fuel-air ratio divided by the stoichiometric fuel-air ratio. The fuel-air ratio is simply the ratio of the mass of fuel supplied to the mass of air supplied. In stoichiometric combustion, there is complete conversion of carbon and hydrogen to  $\text{CO}_2$  and  $\text{H}_2\text{O}$ , with no leftover oxygen. Thus, the stoichiometric fuel-air ratio is the ratio of the mass of fuel supplied to the mass of air supplied for which the stoichiometric condition is satisfied.

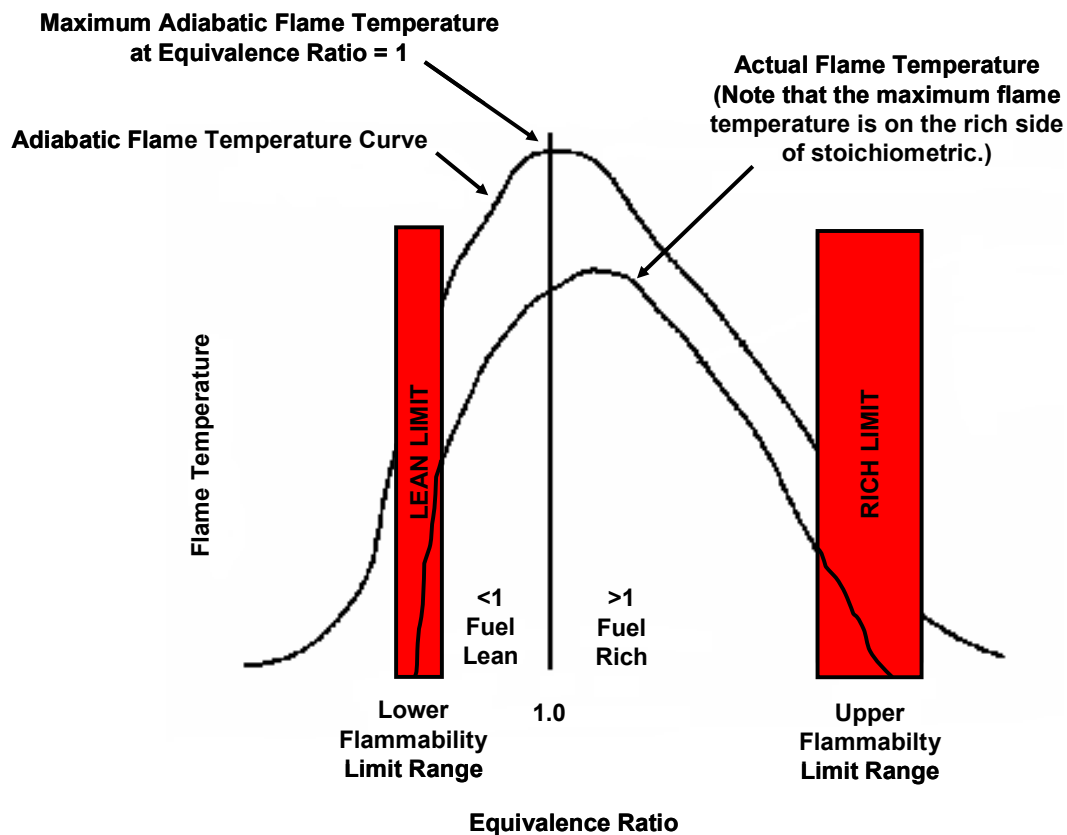


Figure 2-27. Flame Temperature vs. Equivalence Ratio.<sup>58</sup>

(Reprinted with permission by AFP Associates, Inc.)

In reality, the adiabatic flame temperature is not attained, particularly for highly-ventilated compartments such as engine nacelles as well as for dry bay compartments, as they may also be ventilated and have leakage (i.e., they are not completely sealed – openings such as drain holes may be present). Also, complete combustion of leaking fuel is not assured in the event a fire occurs in nacelle or dry bay compartments. It is not uncommon to find residual fuel or hydraulic fluid in these areas after a fire event. Thus, as illustrated in Figure 2-27, the actual flame temperature will be less than the adiabatic flame temperature, but the maximum flame temperature occurs on the fuel-rich side of an equivalence ratio of unity, as greater fuel mass available results in greater energy and heat release.

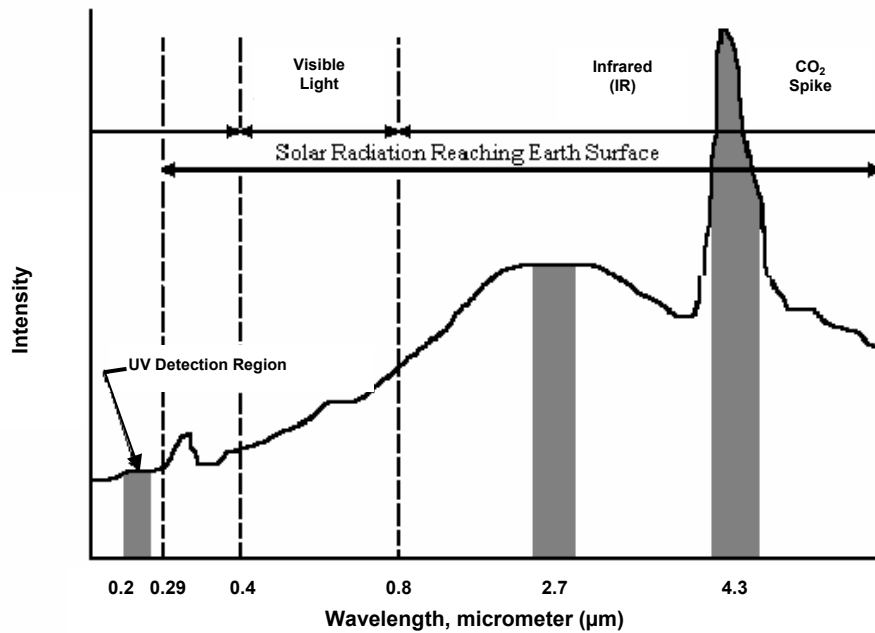
In work to determine the spectral characteristics for fire detection by optical fire detectors, it was shown that ultraviolet emissions from JP-4 flames increased with increasing altitude and that the ultraviolet (UV) power emitted at 10.7 km (35,000 ft) by the burning fuel was nearly double that emitted at sea level. Thus UV detection must be sensitive for the sea level condition. The power emitted at visible and near-infrared wavelengths decreased at higher altitude. Thus visible/near infrared detection must be sensitive at high altitude. The visible/near-infrared emission spectra are due to hot carbon particles in the diffusion flame, while the energy emitted at ultraviolet wavelengths is associated with the electronic transitions of free radicals in the flame. It is believed that as altitude is increased (and pressure decreases) the reduction in the available oxygen to sustain the combustion process may result in an increase in the density of these radicals, and thus stronger emissions of the ultraviolet radiation. In contrast, the reduction in oxygen pressure, as occurs with increasing altitude, may reduce the flame temperature and thus the intensity of the visible/near-infrared radiation emitted by the carbon particles.<sup>59</sup> Typical hydrocarbon flame and burning JP-4 fuel emission spectra are shown in Figure 2-28.

The relevance of the preceding discussion is that requirements for fire tolerance, thermal fire detection, optical fire detection, and ultimately fire suppression are related to temperature (and exposure at that temperature). Fire zone components are required to withstand exposure to a minimum flame temperature of 1093 °C (2000 °F) and minimum heat input (heat flux density) of 9.3 Btu/ft<sup>2</sup>-s (10.6 W/cm<sup>2</sup>) for 15 min. This temperature is also the DoD fire warning requirement threshold for continuous-loop thermal fire detectors used in many engine nacelles and APU compartments for fire detection, whereas optical fire detection for dry bay compartment fires are typically sensitive to the 4.3 μm wavelength (i.e., the CO<sub>2</sub> spike) associated with JP-type aviation fuel fires.

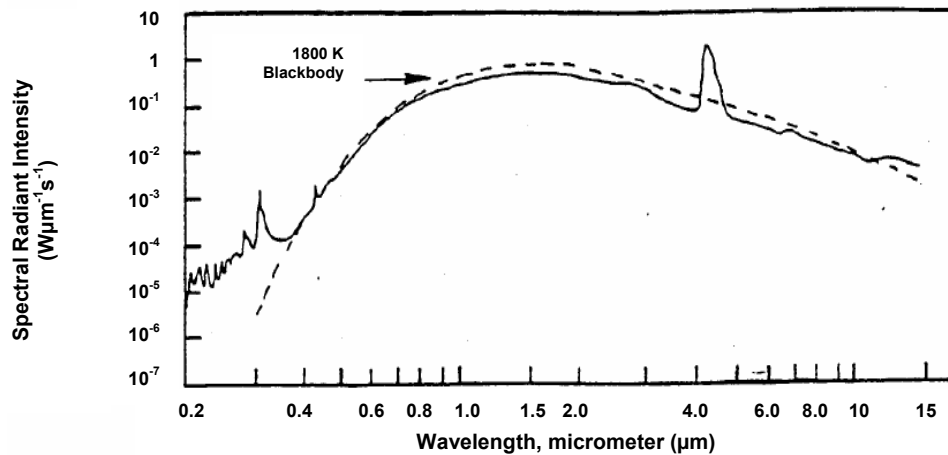
### **Deflagration vs. Detonation**

Deflagrations and detonations are distinguished by flame front velocity. Detonations involve supersonic burning velocities and are more likely to occur in oxygen than in air, whereas deflagrations are characterized by subsonic burning velocities.<sup>60</sup> Research and testing has clearly proven that nacelle, dry bay, and ullage fire events are deflagrations. Detonations and deflagrations may or may not lead to a (sustained) fire. When the combustion rate of energy release is rapid and there is a large increase in pressure, referred to as overpressure, it may be sufficiently large enough to damage or destroy portions of the aircraft structure and is referred to as an explosion. Aviation fuels typically deflagrate with overpressures normally less than 1380 kPa (200 psi).<sup>4</sup> In one series of ullage fire testing conducted at a simulated high altitude, with a pressure of 58 kPa (8.4 psia) and 21 % oxygen, an initial flame velocity measure from film was observed to be 3.35 m/s (11 ft/s).<sup>53</sup> If a combustion wave propagates throughout the ullage with near stoichiometric fuel/air mixture, a pressure increase of over 790 kPa (100 psig) or

eight times atmospheric pressure is theoretically possible.<sup>43</sup> Photographic evidence from full-scale dry bay testing indicates that turbulent flame speeds are below 300 m/s (984 ft/s).<sup>xvii</sup>



(a) Typical Hydrocarbon Fire Emission Spectrum<sup>61</sup>



(b) Emission Spectrum of Burning JP-4 Fuel above 35,000 ft<sup>59</sup>

**Figure 2-28. Hydrocarbon Flame Emission Spectra.**  
(1800 K = 1527 °C = 2780 °F)

<sup>xvii</sup> The speed of sound is 340.29 m/s at sea level.

## Turbulence

Turbulence within an aircraft engine nacelle or dry bay compartment is influenced by a variety of factors. The obvious is ventilation airflow through the compartment. The geometry of the compartment will also influence whether there are localized regions of higher ventilation airflow velocity, recirculation, or stagnation. Structural members (ribs, frames, longerons), subsystems equipment (engine and accessory components, bleed air ducts, flammable fluid components and lines, electrical components and harnesses), and mounting hardware (clamps, brackets), collectively referred to as bluff bodies or clutter, will effect complex flow fields within nacelle or dry bay compartments and also provide locations for flame holders or pooled fuel. Estimation of the increase of the Reynolds Number as change occurs in a recirculation zone of premixed gases burning in the wake a bluff body was known previously to support turbulence conditions.<sup>55</sup> (The Reynolds Number is used for determining whether flow is laminar or turbulent.) Estimation of the Reynolds Number at the air inlet of an engine nacelle indicates this area to be highly turbulent even prior to consideration of clutter-enhanced mixing.<sup>62</sup> Though ventilation airflow through an engine nacelle may be assumed to be longitudinal throughout the annular volume, it is also possible that ventilation airflow will in some places be found to be circumferential about the engine and even contain areas of reversed flow. An engine nacelle fire is typically a turbulent diffusion flame stabilized behind an obstruction in a moderately high-speed airflow that was typically found to range from 0.57 kg/s (1.25 lb/s) to 1.25 kg/s (2.75 lb/s).<sup>43</sup>

The primary design purpose of ventilation airflow through a nacelle is to provide cooling for the engine to ensure desired engine performance and not degrade operation of other subsystem components located in the nacelle, though in the case of the F-111 aircraft the nacelle design imparted unidirectional ventilation airflow to also prevent flame propagation as well as remove flammable vapors.<sup>63</sup> The number of air exchanges per unit time (volumetric air flow divided by net volume) depends on the aircraft design and may be as high as one per second.<sup>43</sup> Though nacelles are unique for each aircraft, the intended forward-to-aft nacelle ventilation airflow characteristic is typical. Dry bay compartment sizes, ventilation requirements, and geometries differ greatly from aircraft to aircraft, and thus turbulence within a dry bay compartment may or may not be more complex than within an engine nacelle. Figure 2-29 provides a contrasting example of this when compared to Figure 2-26. Both depict fires within a dry bay compartment. Whereas Figure 2-26 suggests a relatively benign turbulent environment, Figure 2-29 provides an example of a highly turbulent environment.

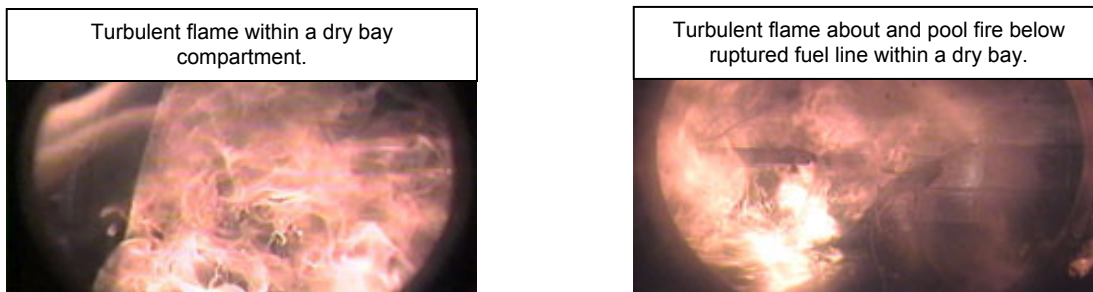


**Figure 2-29. Turbulent Fire within Aircraft Dry Bay Compartments.**

The same physical and environmental characteristics that contribute to turbulence will also influence flame strain, suppressant distribution, and suppressant effectiveness (and dilution), as the time required for an agent to entrain into the recirculation zone is a key parameter in the effectiveness of suppression with respect to baffle-stabilized flames. In computational fluids dynamics (CFD) modeling and model validation testing performed by the NGP, success or failure in extinguishing nacelle fires was largely correlated with the ratio of the rate of injection of suppressant to the total inflow rate into the nacelle (that is, ventilation airflow plus suppressant flow). For a suppression system that is not an optimized design (it is possible for an un-optimized system to pass a certification test), turbulence can effect inhomogeneities and failure to suppress a fire. If regions of the flow field exist where the suppressant concentration is locally below the value that leads to suppression, there can be failure to completely suppress a fire, since small pockets of fire can quickly propagate through the remaining premixed gases in the nacelle leading to accelerated burning under certain conditions and catastrophic results.<sup>64</sup>

### 2.3.6 Aircraft Operational Temperature Environment<sup>44</sup>

As discussed previously, temperature is the primary basis of current aviation requirements for fire detection and component tolerance to fire. Temperature is also a variable with regard to the potential for ignition of a fuel-air mixture, the amount of energy to ignite a flammable mixture, suppressant performance capability, and, in the case of hot surfaces within an engine nacelle, reignition, which is discussed separately in this chapter. Given a constant initial pressure, it has been established previously that a non-flammable fuel-air mixture may become flammable for some period of time if its temperature is elevated sufficiently.<sup>65</sup> Additionally, as shown in Figure 2-30, it had been established previously for halon 1301 that the peak flammability limit, the suppressant inerting concentration in air at which no mixture of fuel and air is flammable, can increase with temperature.<sup>66, xviii</sup> Lab-scale testing during the TDP with halon 1301 and several halon alternative suppressants also indicated similar trending as shown in Figure 2-31.<sup>13</sup>

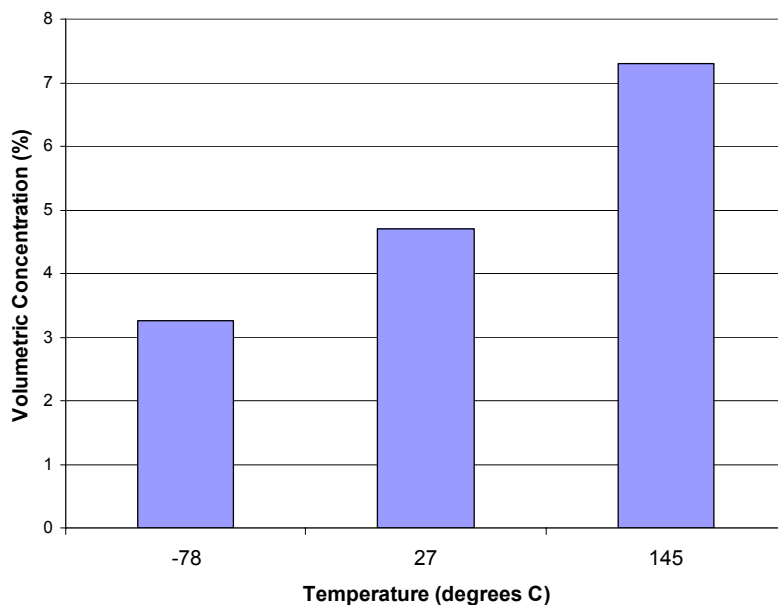


**Figure 2-30. Variation in Halon 1301 Peak Flammability Limits for Isobutane with Temperature.**

<sup>xviii</sup> The certification requirement for halon-1301-based nacelle fire suppression systems is suggested to be founded, per Reference 132, on the 6 % inerting concentration determined by the Purdue Research Foundation, whereas halon-1301-based fuel tank inerting systems have been designed to maintain even higher concentrations (e.g., 20 %).

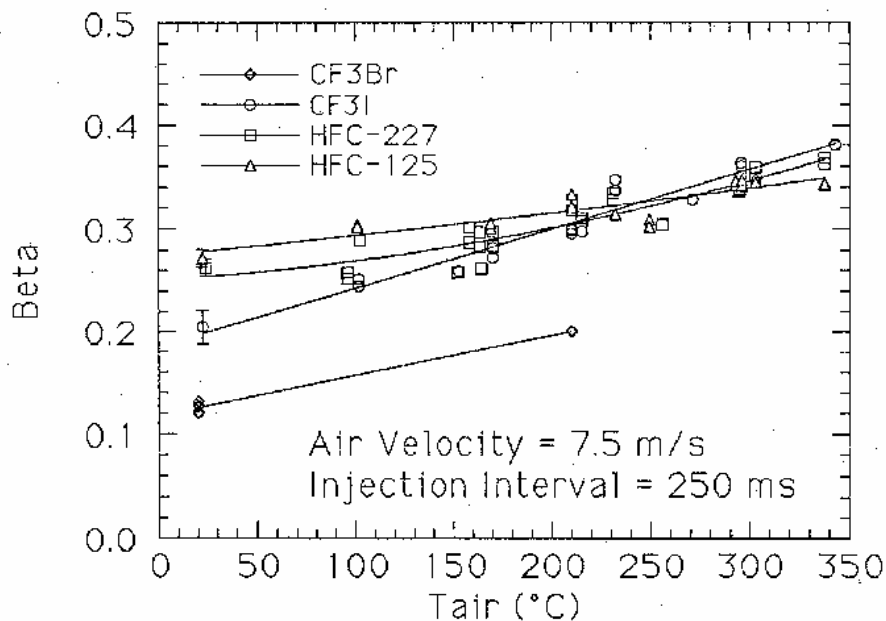


**Figure 2-31 Variation in Halon 1301 and Three Halon Alternative Mass Fractions (Beta) Required to Suppress JP-8 Spray Flames with Temperature.**<sup>13</sup>

(Beta is the ratio of the mass flow of the suppressant to the total flow of suppressant and air.)

What were not established until the NGP was the correlation of historical fire experience with outside air temperature (OAT) and altitude and how that correlates with suppressant low-temperature requirements. The temperature data that was previously indicated as design requirements but is currently promulgated as design guidance to define the low and high temperature extremes for DoD aircraft systems are worldwide air environments (WWAE), which represent conditions having a 1 %, 5 %, 10 % and 20 % frequency of occurrence.<sup>67</sup> In commercial aviation, standard climate profiles from the Joint Aviation Regulation (JAR) define temperatures based on arctic, temperate, tropical, intercontinental, and standard-day conditions.<sup>68</sup> (Note: there is no design guidance or DoD/JAR climate profile for altitude environments below 60 degrees south latitude, the Antarctic.) Figure 2-32 plots these climates vs. the WWAEs used for DoD acquisition programs. Figure 2-33 depicts the worldwide land environments provided as design guidance for DoD aircraft systems, which categorizes four land environment types: basic, hot, cold, and severe cold.<sup>67</sup>

The relevance of the aircraft temperature envelope requirement to on-board fire suppression systems that utilize a chemical suppressant, i.e., the engine nacelle and APU fire suppression systems on DoD aircraft, is that the low temperature extreme defined for the envelope has historically been applied to substantiate the boiling point requirement for the fire suppressant, which is predominantly halon 1301. Thus in the context of the WWAEs, a boiling point requirement based on halon 1301 would provide for in-flight fire suppression under atmospheric conditions down to temperatures consistent with arctic-like temperature conditions.

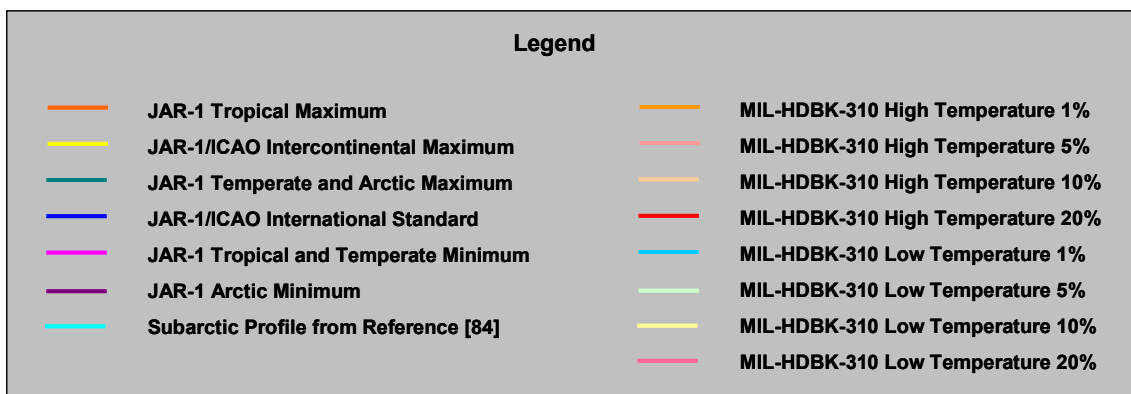
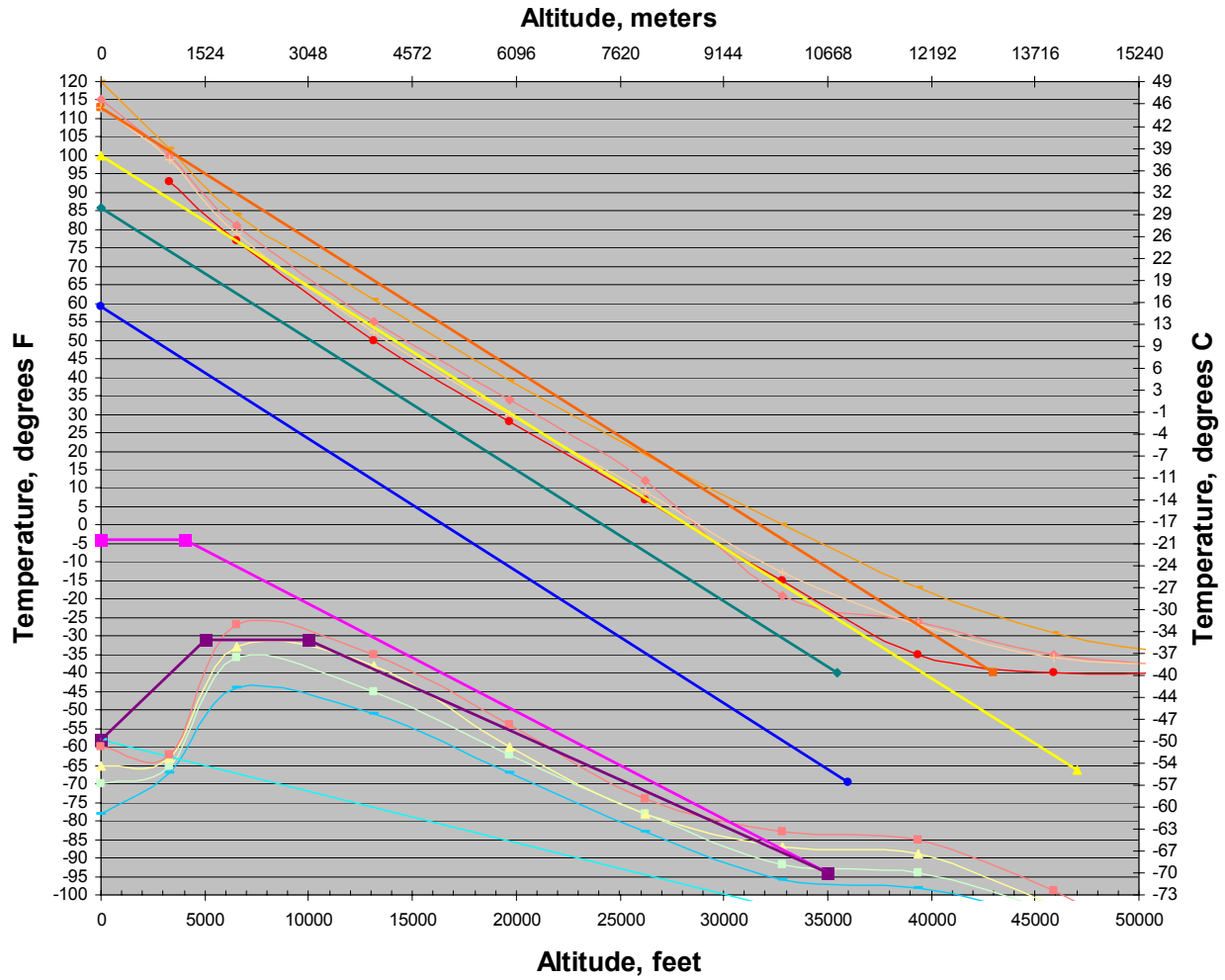
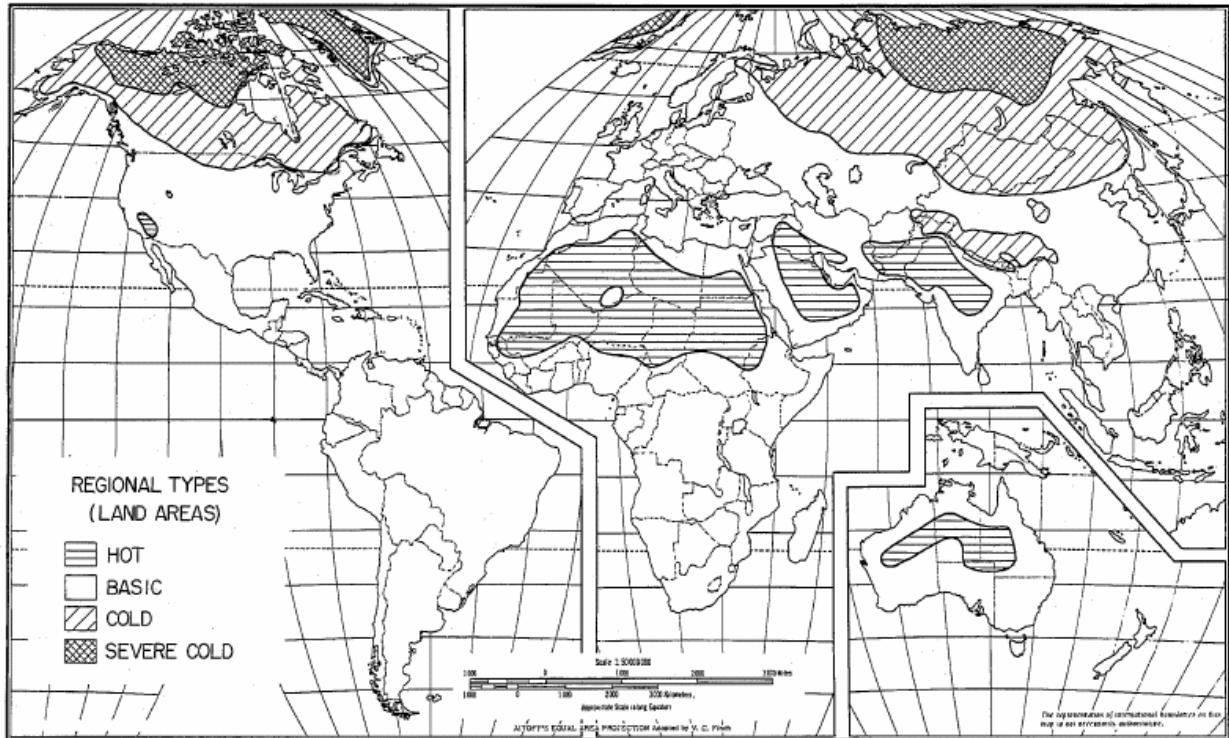


Figure 2-32. Commercial Aviation Standard Climates vs. DoD WWAE Design Guidance.



**Figure 2-33. DoD Land Environment Design Guidance.**<sup>67</sup>

With regard to ground fire suppression, land environments indicated as cold or severe-cold climates are the likely environments in which cold-soak conditions prior to aircraft startup would exist. The DoD design guidance indicates a low-temperature 1 % frequency of occurrence of  $-46\text{ }^{\circ}\text{C}$  ( $-50\text{ }^{\circ}\text{F}$ ) for cold land environments and a low-temperature 20 % frequency of occurrence of  $-51\text{ }^{\circ}\text{C}$  ( $-60\text{ }^{\circ}\text{F}$ ) for severe-cold land environments. Designers of legacy aircraft would develop fire suppression systems whose requirements were tailored to halon 1301 properties to likely assure fire suppression performance at such temperature conditions.

Boiling point (or  $T_b$ ) of a fire suppression agent has been used as one of the criteria to guide the search for new halon alternative chemical fire suppressants during the NGP.<sup>69</sup> Currently, this criterion is  $-40\text{ }^{\circ}\text{C}$  ( $-40\text{ }^{\circ}\text{F}$ ). It was also one of the parameters considered during the TDP, which identified HFC-125 as the best near-term alternative to halon 1301 for use in aircraft nacelle fire suppression system applications. However, even during the TDP it was recognized that, when operational contexts were considered such as the likely temperature environment within an operational engine nacelle at the time of suppressant discharge, the typical low temperature performance requirement could be a candidate for a performance trade. Minimum nacelle operating temperatures were indicated to range from below  $-18\text{ }^{\circ}\text{C}$  ( $0\text{ }^{\circ}\text{F}$ ) in commercial aviation to  $38\text{ }^{\circ}\text{C}$  ( $100\text{ }^{\circ}\text{F}$ ) in DoD aviation.<sup>70</sup> A subsequent review of nacelle compartment airflow temperature data for a variety of aircraft platforms, including a commercial transport aircraft, indicated temperatures ranging from  $-18.5\text{ }^{\circ}\text{C}$  ( $-1.3\text{ }^{\circ}\text{F}$ ) to  $274\text{ }^{\circ}\text{C}$  ( $525\text{ }^{\circ}\text{F}$ ).<sup>71,72,73,74,75</sup> Though this data may not address every operating environment, they suggest that even at low outside air temperatures (OAT) it is probable that the typical operational engine nacelle compartment temperature will be greater than  $-40\text{ }^{\circ}\text{C}$  ( $-40\text{ }^{\circ}\text{F}$ ).

For decades, high  $T_b$  suppressants have been used in military aircraft nacelle fire suppression systems. In addition to halon 1011 on C-130 aircraft, this also includes halon 1202 on C-5 and previously on F-111 aircraft, which are now retired.<sup>76</sup> Since the signing of the Montreal Protocol, at least two high  $T_b$  halon alternative agents have been fielded outside the DoD.<sup>xix,77,78</sup> Successful implementation and history of high  $T_b$  suppressants is likely attributable to several factors such as (1) the fact they are brominated halogens, (2) elevated nacelle operating temperatures, (3) applications that may benefit from the high  $T_b$  characteristic, e.g., single-phase flow in long distribution runs, (4) freezing points well below temperatures likely to be experienced on ground and at altitude, and (5) distribution system design that ensures adequate distribution throughout the nacelle. This last factor was also emphasized and applied in the development of the F/A-18E/F HFC-125 nacelle fire suppression system.<sup>79</sup> HFC-125 is a low boiling point fire suppressant. The obvious conclusion is that both low- and high-boiling-point suppressants are likely to realize higher probability of success when distribution is optimized. Chapter 8 discusses additional factors identified during NGP CFD experiments and modeling that need to be considered relating to suppressant delivery and evaporation.

Analysis of military aircraft experience regarding release of nacelle fire suppressants was conducted during the TDP, the purpose of which was to quantify halon discharges at altitude and for evaluating discharge frequency and quantity of agent discharged below and within the ozone layer.<sup>80</sup> Combining both fixed-wing and rotary aircraft discharges that analysis indicates:

- Approximately 77 % occurred between 0 km and 3 km (0 ft and 10,000 ft), and about 92 % occurred between 0 km and 6 km (0 ft and 20,000 ft).
- Over 60 % of all discharged suppressant was accounted for by only three of the 30 military aircraft platforms covered by the study. These three platforms (C-130, F-15, and P-3) have altitude ceilings that extend above 6 km (20,000 ft) but were contributors to the frequency of discharges below 3 km (10,000 ft).<sup>xx</sup>
- Over 25 % of all suppressant discharged was high-boiling point suppressant (i.e., halons 1011 and 1202).

Prior to the NGP, an operational context that had not been investigated was whether temperature conditions at the time of agent release correlated with the typical boiling point temperature requirement. These include OATs, nacelle operating temperatures, cold-soak temperature conditions and cold climatic extremes. Based on review of nacelle compartment airflow temperature data for a variety of aircraft platforms, it was reasonable to assume that nacelle compartment temperatures are well above boiling points of fielded nacelle fire suppression agents. When considering that historic release of nacelle fire suppression agents has typically occurred below 6 km (20,000 ft), with over 75 % occurring below 3 km

<sup>xix</sup> These agents are phosphorous tribromide ( $PBr_3$ ), which has a  $T_b$  of 173 °C, and trifluoroiodomethane ( $CF_3I$ ), which has a  $T_b$  of -22.5 °C.  $PBr_3$  is installed for nacelle fire protection on Eclipse 500 commercial aircraft, which are small commercial jet transport aircraft, and  $CF_3I$  is installed for nacelle and APU fire protection on Royal Australian Navy SH-2G rotary aircraft. The  $CF_3I$  system is similar to a halon 1301 system in its implementation in that the suppressant is distributed throughout the nacelle by means of remotely-contained storage bottles and plumbing. The  $PBr_3$  system implementation is different: suppressant discharge is targeted to the flame holding regions within the nacelle, which were identified through analysis and test, per Reference 77. Considering nacelle operating temperature environments, which are described later, and boiling points of each suppressant,  $CF_3I$  will likely be vaporized where as for  $PBr_3$  the heat from a fire will effect vaporization.

<sup>xx</sup> The aircraft platforms in the TDP study, Reference 80, that each accounted for at least 5 % of discharged suppressant were the P-3, C-130, F-15, F-111, C-5, C-141, and A-10 platforms, all fixed-wing aircraft. Review of the data utilized for the reference [44] study found similarly that the aircraft platforms each accounting for at least 5 % of discharged suppressant were the P-3, C-130, C-5, A-10, F-15, F/A-18, and F-111, and in general that fixed-wing aircraft accounted for 85% of all suppressant discharged.

(10,000 ft), and that the likely occurrence of fire while either cold soaked or while in cold climatic extremes is likely a low probability event, the likelihood of not extinguishing a nacelle fire after suppressant release and realizing a catastrophic event under such conditions suggests strongly that the combination of these events has a low probability. The implication of the preceding is that selection of a fire suppressant whose boiling point is compatible with cold soaking or a cold climatic extreme results in a protection capability against events whose likelihood of occurrence has a very low probability, and that halon alternative suppressants with higher boiling points are not likely to appreciably increase risk under such conditions. These preceding assertions provided the NGP with the impetus to perform the following efforts:

- Obtain and review aviation Safety Center fire incident data to extract, if possible, altitude and/or outside air temperature (OAT) information that would permit characterization of OAT conditions during which suppressant release has historically taken place. Based on this data, it may be possible to assess probability of suppressant release under conditions that are likely to be well above a suppressant's boiling point.
- Construct and validate an in-flight nacelle air temperature model to estimate likely nacelle compartment air temperature for given altitude, outside air temperature, general engine surface temperatures, and aircraft airspeed conditions. Such a model would be useful in allowing system designers to assess compartment temperatures at altitude relative to a suppressant's boiling point.
- Evaluate implications of aircraft cold-soak conditions, particularly during aircraft takeoff.
- Assess safety risk, considering the findings in the preceding elements, of utilizing a fire suppressant whose boiling point is much higher than of those agents commonly fielded today in military aircraft (i.e., halon 1301).

### DoD Safety Centers Fire Incident/Mishap Data

A review conducted within U.S. Army aviation of rotary aircraft fires between 1985 and 1995 had found that the lowest outside air temperature (OAT) reported was 0 °C (32 °F) and the highest reported was 35 °C (95 °F).<sup>81</sup> This review concluded that the only time a -50 degree temperature would remotely be encountered is at extremely high altitude or in extremely remote northern/southern areas of the earth.<sup>xxi</sup> The use of the term "remotely" has significance in that within DoD it relates to the rate of hazard occurrence. During the time period of the U.S. Army study, the aggregate rate of occurrence of in-flight rotary aircraft fires was 4.9 per million flight hours, a remote rate of occurrence. Thus the likelihood of a nacelle fire occurring at lower outside air temperatures or in an extremely cold environment and resulting in loss of aircraft would likely be even lower (improbable).<sup>xxii</sup>

Aviation fire incident data was obtained for the years 1980 through 2002 from the U.S. Army, Navy and Air Force Safety Centers. Table 2-3 summarizes the number of mishaps and incidents provided by the Safety Centers. (Note: the counts in Table 2-3 reflect incidents categorized by the DoD services as mishaps as well as lesser severity events or incidents.) The data was reviewed to determine whether

---

<sup>xxi</sup> The final memorandum did not indicate whether the temperature threshold considered was -50 °C or -50 °F.

<sup>xxii</sup> The terms remote and improbable are categories of hazard probability as described in DoD specification MIL-STD-882D, Standard Practice for System Safety. These terms may be described either qualitatively or quantitatively. Assigning a hazard probability category based on aircraft flight hours is one method per MIL-STD-882D of describing a probability quantitatively.

suppressant release occurred and to identify the altitude and OAT associated with each release. Only suppressant releases associated with discharge of systems protecting nacelle and APU compartments were considered. Combat-related events, or direct-enemy action events, are typically not provided by the DoD Safety Centers, and if they are provided they only contain limited information. For mishaps and incidents that provided altitude data but did not include temperature data, the International Civil Aviation Organization (ICAO) standard atmosphere model was applied to estimate OAT. For mishaps and incidents without altitude and temperature information, the methodology applied was that used during the TDP for assuming flight altitude based on aircraft flight phase from the previously-described discharge-at-altitude analysis.

**Table 2-3. Number of Mishaps and Incidents.**

Aircraft Type	Service		
	Army	Navy	Air Force
Fixed Wing	88	1,212	3,932
Rotary	465	834	98

Mishap and incident data was first reviewed for the geographic locations where fires and suppressant releases occurred. Table 2-4 summarizes the results of this review, which was performed to assess occurrence of fire in the cold or severe-cold land environments of Figure 2-33, for incidents occurring on the ground, and to assess occurrence of fire for incidents occurring in flight or characterized as in-flight for aircraft operating nearest to locations in those cold or severe-cold environments.

**Table 2-4. Percentage of Fire Mishaps and Incidents Occurring in Geographic Cold or Severe-Cold Environments.**

Event Phase	Service		
	Army	Navy	Air Force
Ground	0	1.5 %	1.1 % (a)
In-Flight	< 1 %	< 1 %	2.7 % (b)

- (a) From data categorized as ground fire mishaps and incidents only.
- (b) From data categorized as in-flight fires only but also includes mishaps and incidents on the ground characterized as flight fire mishaps and incidents (i.e., intent for flight existed).

Generally, the fire mishap and incident data provided by the Safety Centers included altitude information in terms of mean sea level (MSL), above ground level (AGL), or flight level (FL). Altitude expressed in these terms in the Safety Center data is typically in terms of pressure altitude, while the Standard Atmosphere is based on geopotential altitude. Figure 2-34 illustrates the variation of ambient pressure vs. pressure altitude and geopotential altitude on standard-day and non-standard-day temperature conditions. The implication with regards to estimating OAT using the ICAO Standard Atmosphere Model is that cold temperature conditions may be lower than estimated on non-standard-days or if altitude is based on pressure altitude. However, the percentages indicated previously in Table 2-4 suggested strongly that applying the MIL-HDBK-310 cold WWAEs or the JAR-1 Arctic Climate profile as the basis for estimating temperature conditions would not reflect operational experience.

An additional consideration for using the ICAO Standard Atmosphere Model for estimating OATs during suppressant release is fuel flammability limits. Figure 2-35 depicts flammability limits of Jet-A and Jet-B aviation fuels vs. altitude and standard atmospheres, including a subarctic profile (JP-8 limits are similar to limits for Jet A, and JP-5 limits are slightly higher than those depicted for Jet-A.). Though ignition depends on many variables, Figure 2-35 suggests that for military aircraft using JP-8 and JP-5 fuels, attaining the flammability limits is more likely at atmospheres above the Standard Atmosphere.

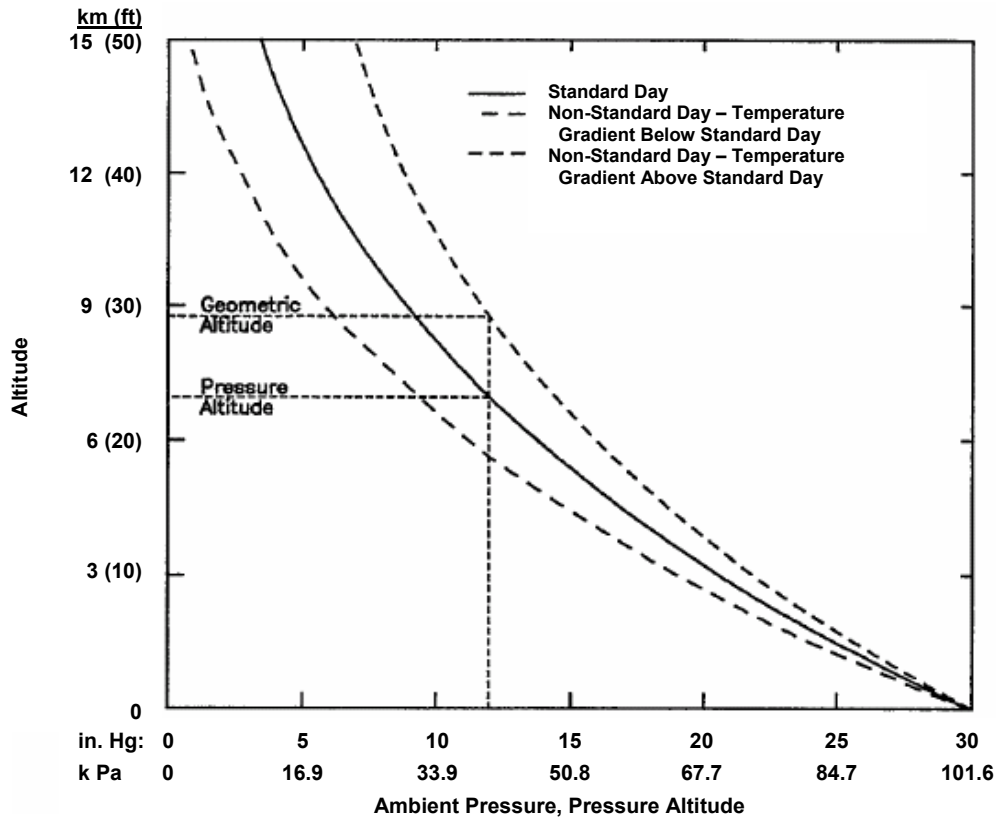


**Figure 2-34 Variation of Ambient Pressure vs. Pressure and Geopotential Altitudes on Standard-Day and Non-Standard-Day Temperature Conditions.**<sup>82</sup>

Figure 2-36 plots the safety center data for nacelle and APU fires in which suppressant release occurred and for which suppressant release did not occur. In addition, the figure also plots fire events that were not nacelle or APU fires. *This is done to plot all aircraft fire mishaps and incidents for which Safety Center data included both altitude and OAT.* It is interesting to note in Figure 2-36 that there are just two data points indicating a fire occurrence above 10.7 km (35,000 ft), three data points indicating fire above 9 km (30,000 ft), and only four data points indicating fire above 7.6 km (25,000 ft). In combustion experiments that established the spectral criteria for optical fire detection, it was established that flames could be maintained up to 10.7 km (35,000 ft); however, at higher altitudes, the flames would self extinguish.<sup>59</sup> Distribution of Safety Center data that included both altitude and OAT for which suppressant release occurred indicated that suppressant releases occurred generally about or above the Standard Atmosphere profile. The lowest OAT below the profile for which suppressant release occurred on the ground was indicated as -3.3 °C (26 °F). The highest altitude below the profile for which suppressant release was indicated to have occurred was 1.65 km (5,400 ft), and the lowest OAT was indicated as 2 °C (36 °F).

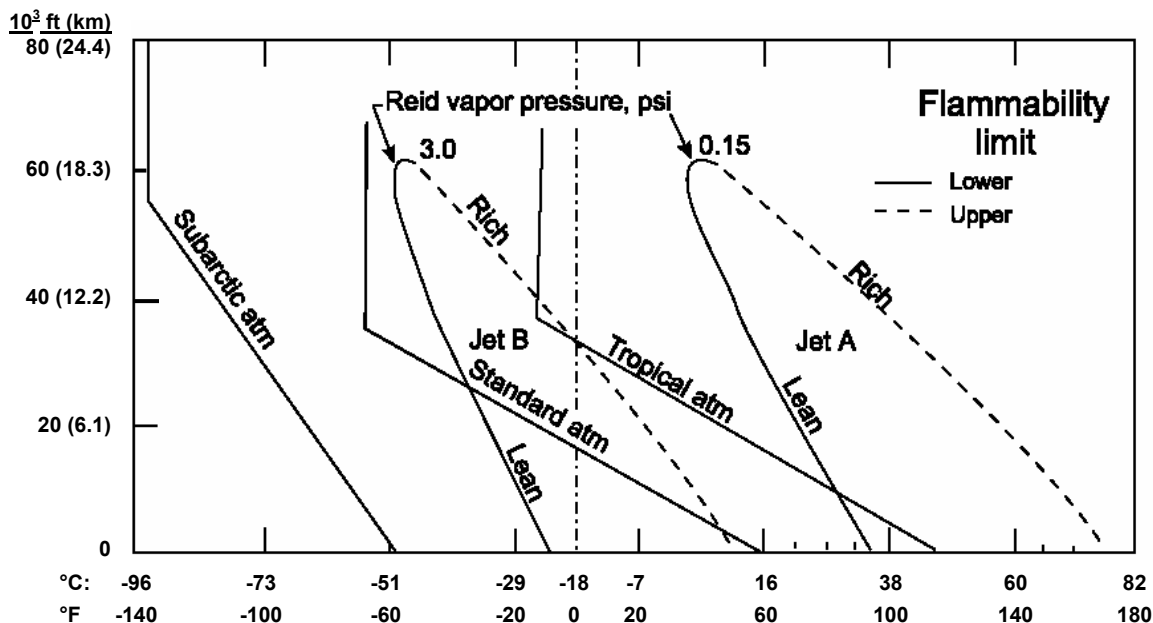


**Figure 2-35. Flammability Limits of Jet-A and Jet-B Fuels vs. Altitude and Standard Atmospheres.**<sup>76, 83, 84, xxiii</sup>

(JP-8 limits are similar to limits for Jet A; JP-5 limits are slightly higher than limits for Jet-A.)

For other fire incidents for which Safety Center data included both altitude and OAT but in which there may have been no engine or APU fire, or for which there was an engine or APU fire but *no* agent release, the majority of the incidents at altitude occurred above the Standard Atmosphere profile and below 6 km (20,000 ft). Only one incident is indicated that is beyond the profile at altitude and below -18 °C (0 °F), which occurred at 12 km (40,000 ft), -61 °C (-78 °F). This was the only incident for which *both altitude and OAT* were provided and that occurred below -40 °C (-40 °F). The highest altitude below the profile and above -18 °C (0 °F) occurred at 1.95 km (6,400 ft) with an OAT indicated as -10 °C (14 °F). There are three incidents indicated at zero altitude (on the ground) and below -18 °C (0 °F). These occurred with OATs at -25 °C (-13 °F), -28 °C (-18 °F), and -33 °C (-27 °F).

Commercial aircraft data was also reviewed from the National Transportation Safety Board (NTSB) aviation accident database for occurrence of fire at altitude vs. temperature. Data then obtained spanned the years 1988 through 2000. The distribution of fire events in which both altitude and OAT were provided is shown in Figure 2-37. The lowest temperature indicated in the Figure is -28 °C at zero altitude. There were several events at this condition. (Whether any were nacelle or APU fires was not further researched.) One event was identified in the data at -32 °C, but no corresponding altitude was provided so it is not shown in the figure. Additional fire occurrences at low temperature that were identified with no corresponding altitude and are not indicated in the figure occurred at -27 °C and -26 °C (one each) and at -22 °C (two events).

<sup>xxiii</sup> Reid vapor pressure (RVP) is a measure of fuel volatility. The higher the RVP, the more volatile the fuel is and the more readily it evaporates. RVP is measured at 37.8 °C (100 °F).

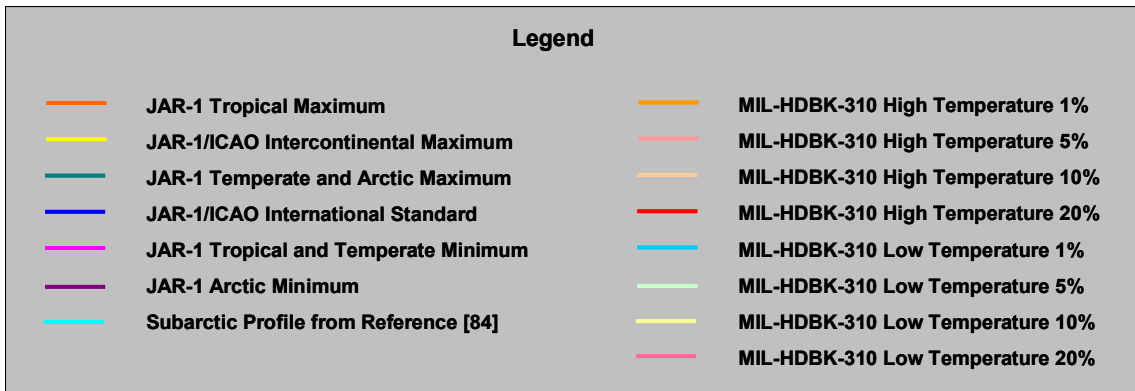
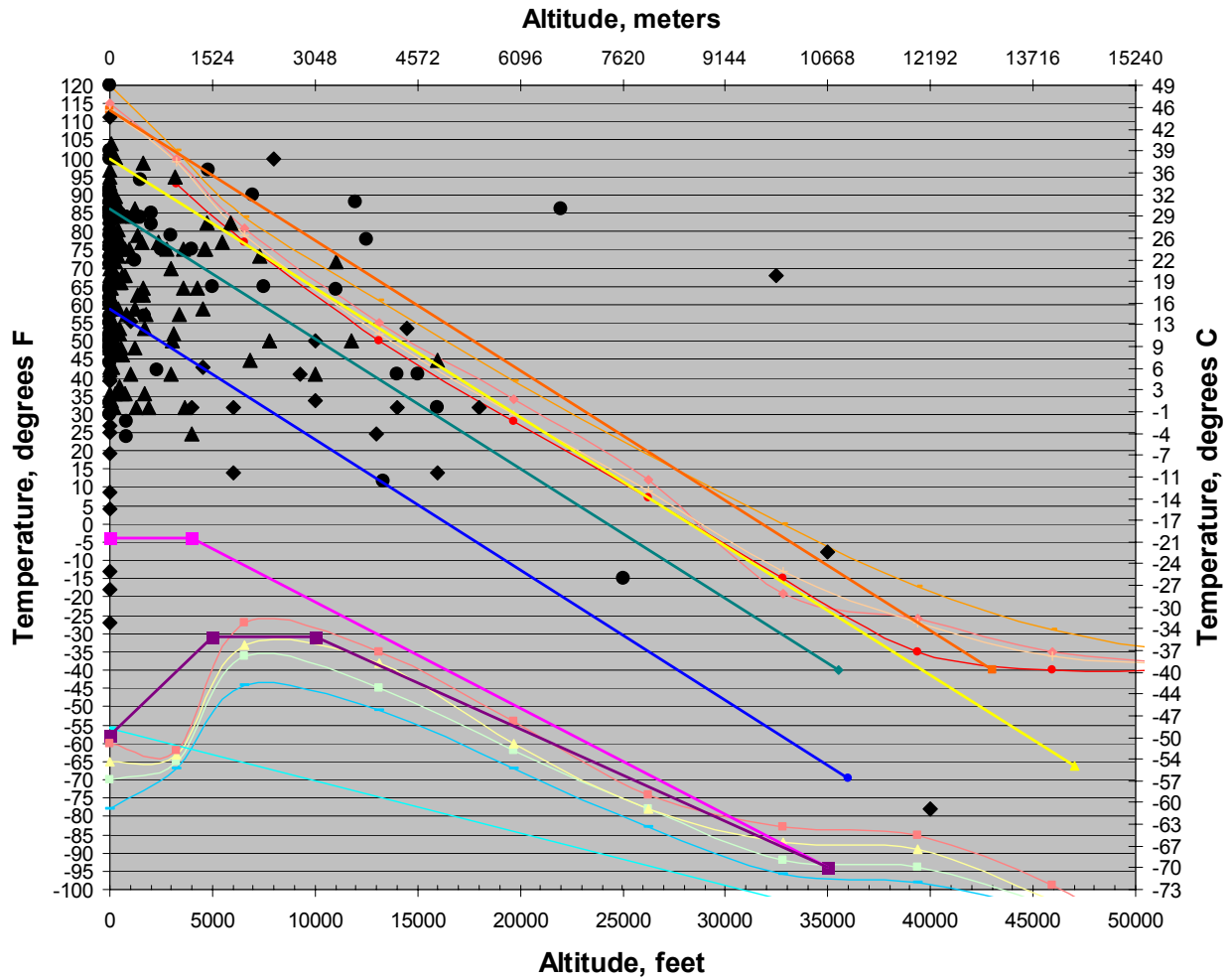
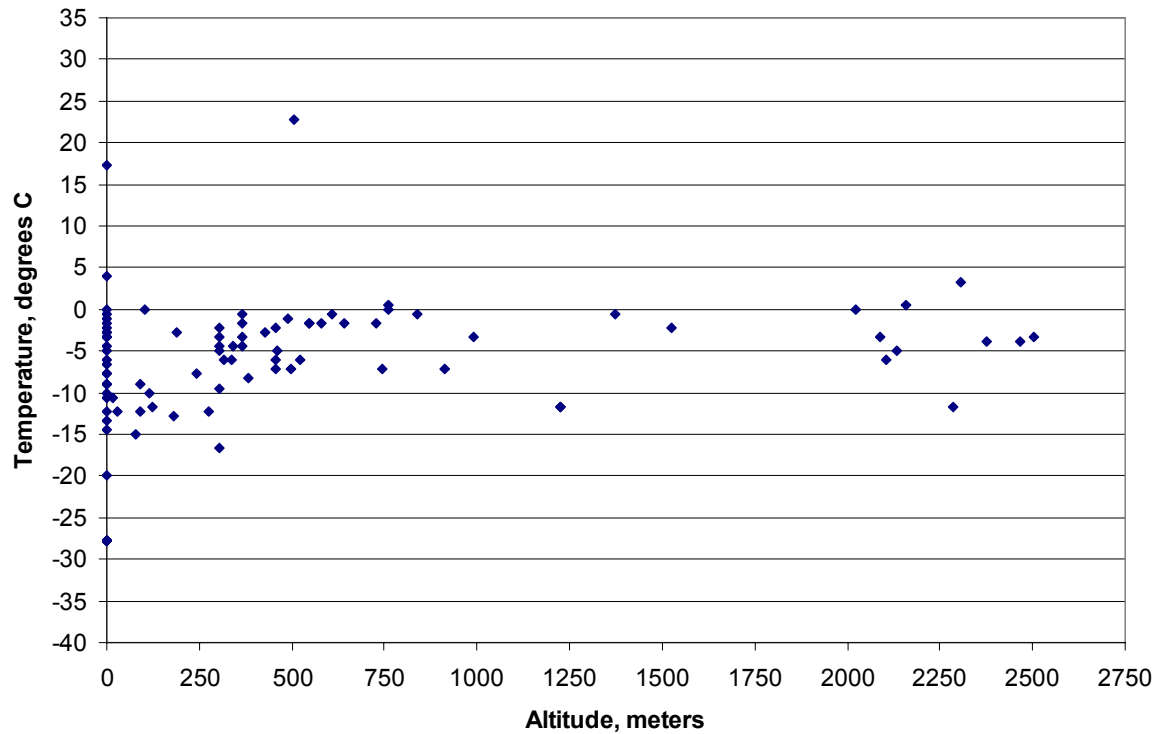
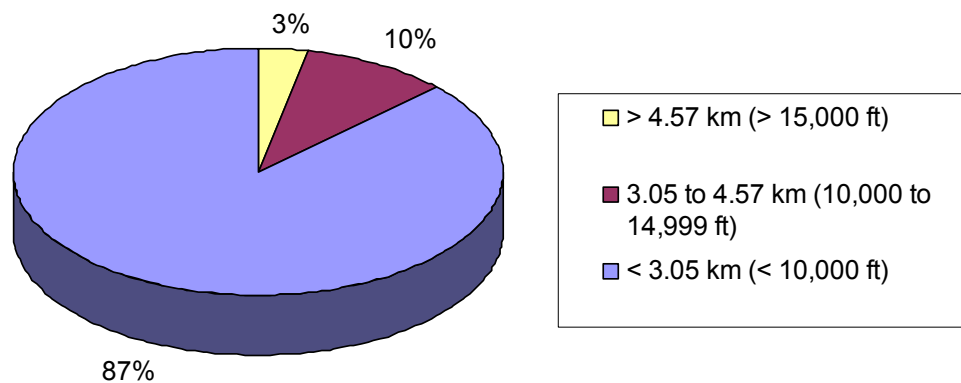


Figure 2-36. Plot of Standard Climate Profiles and WWAEs vs. All DoD Aircraft Fire Events and Suppressant Releases where Both Altitude and OAT Were Provided.

Given the preceding, it was concluded that the Standard Atmosphere Model could be used to provide a reasonable estimate for OATs at which suppressant releases at altitude have occurred. This model was applied to fire incidents for which there were no OAT data, which were then combined with incidents that had included OAT data. The results are summarized in Figures 2-38 through 2-41, with the data from Reference 44.



**Figure 2-37. Plot of 1988-2000 Commercial Aircraft Fire Events vs. Altitude and OAT, Events for which NTSB Database Provided Both Altitude and OAT.**



**Figure 2-38. Rotary Aircraft Nacelle/APU Compartment Fire Suppressant Releases by Altitude.**

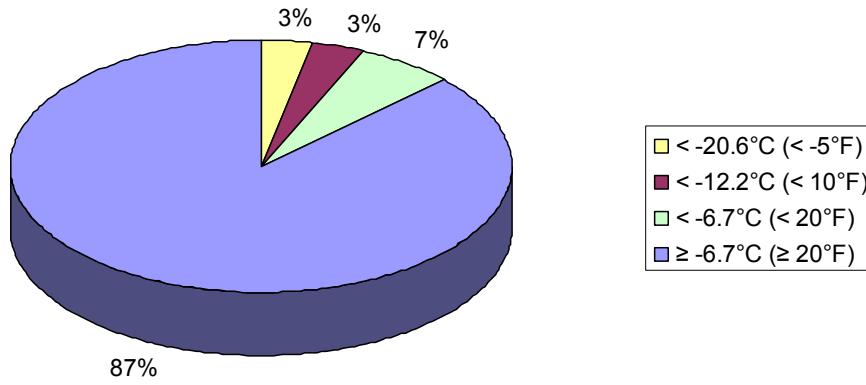


**Figure 2-39. Rotary Aircraft Nacelle/APU Compartment Fire Suppressant Releases by OAT.**

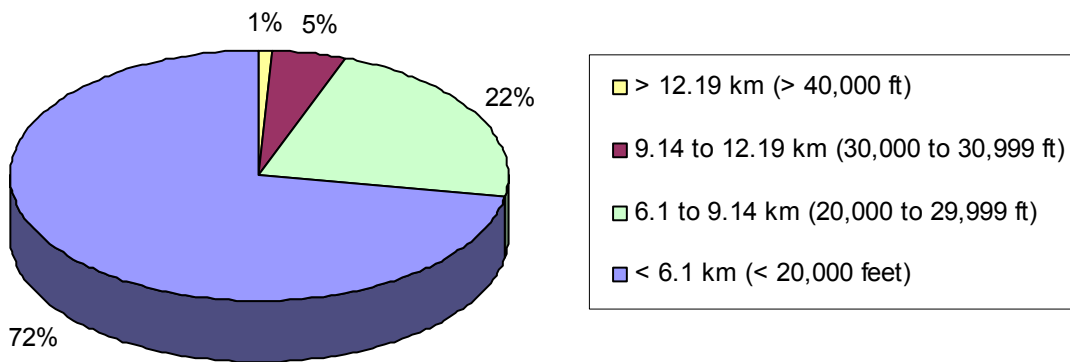


**Figure 2-40. Fixed-wing Aircraft Nacelle/APU Compartment Fire Suppressant Releases by Altitude.**

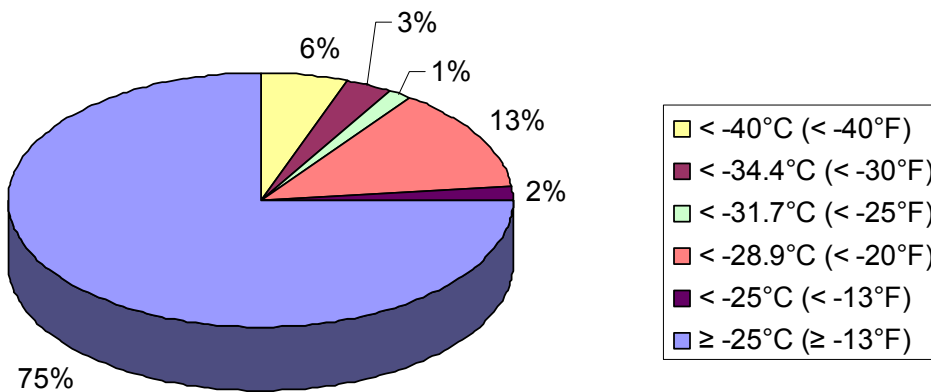


**Figure 2-41. Fixed-wing Aircraft Nacelle/APU Compartment Fire Suppressant Releases by OAT.**

## Nacelle Air Temperature Modeling

An in-flight nacelle air temperature model was constructed to estimate nacelle air temperature during flight conditions. The model uses the U.S. Standard Atmosphere 1976 data on pressure-altitude, temperature, and viscosity.<sup>85</sup> The model treats the nacelle as an air heat exchanger, and it computes the terminal temperature difference based on average, bulk values. The inlet conditions at the ram scoop are computed to be the stagnation properties for the given flight conditions, and these are taken to be the same as those inside the nacelle, close to the inlet. The effect of conduction and radiation heat transfer is assumed negligible; i.e., heat losses from air through the nacelle wall to the ambient outside by convection and conduction. The model is described in detail in Reference 44.

To evaluate in-flight conditions generally representative of likely flight and nacelle operating conditions, the model was evaluated for over 1,000 cases against the high and low operational parameter settings utilized during the TDP for nacelle configuration (length), clearance (net volume), nacelle mass airflow, and engine hot surface temperature. Conditions were evaluated for altitudes up to 9 km (30,000 ft). Model runs were limited to this altitude for two reasons: (1) only 6 % of all fixed-wing aircraft fire suppressant releases (Figure 2-40) were indicated to have occurred above 9 km (30,000 ft), and (2) though the Standard Atmosphere Model for the tropopause has a ceiling of 11 km (36,152 ft), only 1.7 % of all fixed-wing aircraft fire suppressant releases were indicated to have occurred above this ceiling. The OAT ranged from -45 °C (-48 °F) to 15 °C (58.7 °F) based on the model. The results are indicated in Figures 2-42 and 2-43, which depict peak nacelle temperature vs. altitude for the two airspeed conditions modeled: 50 knots and 400 knots.

Review of the model output showed that 88 % of the cases indicated nacelle air temperatures greater than -18 °C (0 °F). The remaining 12 % of the cases (those less than -18 °C) were for input conditions at 6 km (20,000 ft) or greater, and 89 % of these cases (89 % of the 12 %) were noted for airspeeds of 50 knots.

This group of calculated cases was considered to be artificial since military rotorcraft typically have operational ceilings less than 6 km, and 50 knots is below the stall speed for typical military fixed-wing aircraft that have nacelle fire suppression capability (e.g., fighter/attack aircraft, cargo transports, maritime patrol aircraft). The remaining 11 % (i.e., 11 % of the 12 %), or 1.5 % of all the cases modeled, were for input conditions at 9 km (30,000 ft) and 400 knots and indicated nacelle air temperatures ranging between -23 °C (-10 °F) and -24 °C (-12 °F). If the artificial cases were removed from consideration, the actual percentage of total cases indicating nacelle air temperatures greater than -18 °C became greater than 88 %. So modeling additional cases up to the ceiling of the Standard Atmosphere Model for the tropopause was likely to result in additional nacelle air temperatures less than -18 °C, but it was not likely to dramatically impact the percentages described.

The results of the modeling appeared counterintuitive, in that at higher airspeed the results would be expected to indicate lower compartment air temperature. This is due to the assumption in the model that the temperature at the nacelle inlet is based on the stagnation properties for the airspeeds chosen. This is an assumption that had been applied in previous work, with the rationale that the ventilation airflow temperature through the nacelle is influenced by the stagnation temperature at the nacelle air inlets as well as by heat rejected by the engine.<sup>63</sup> Thus, at the higher airspeed, the inlet temperature is greater. To investigate this further, results from the model were compared to data obtained previously during in-flight measurement of nacelle air temperatures for several different aircraft platforms.

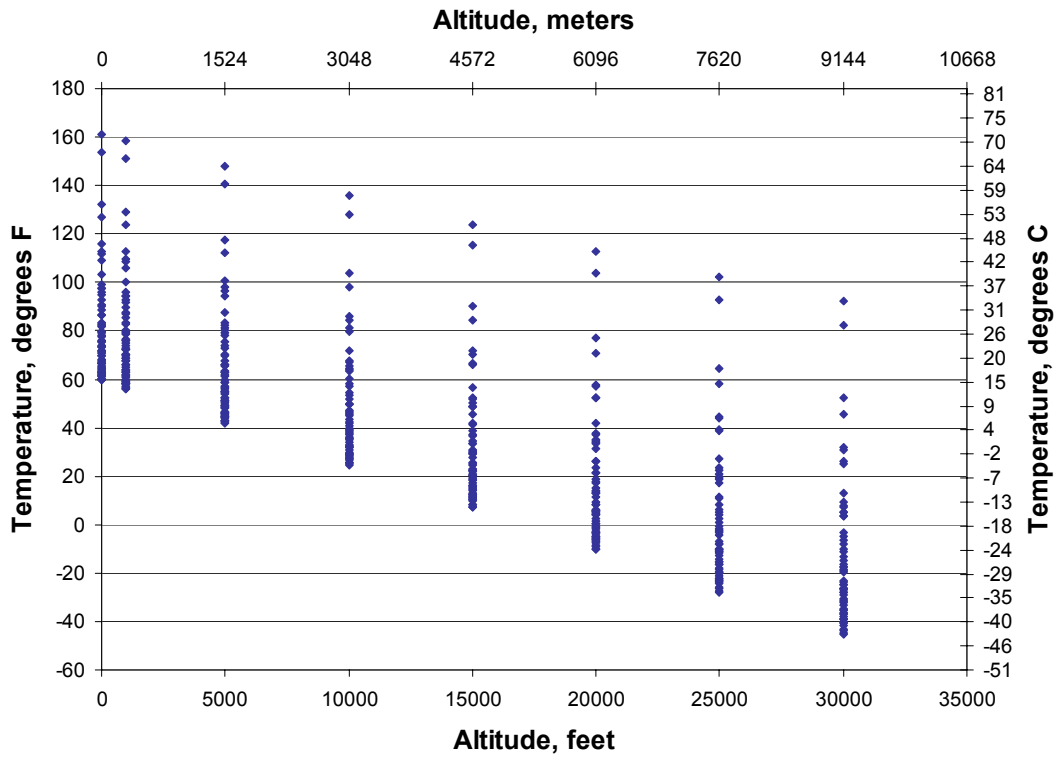


Figure 2-42. Peak Nacelle Temperature at 50 knots Airspeed vs. Altitude.

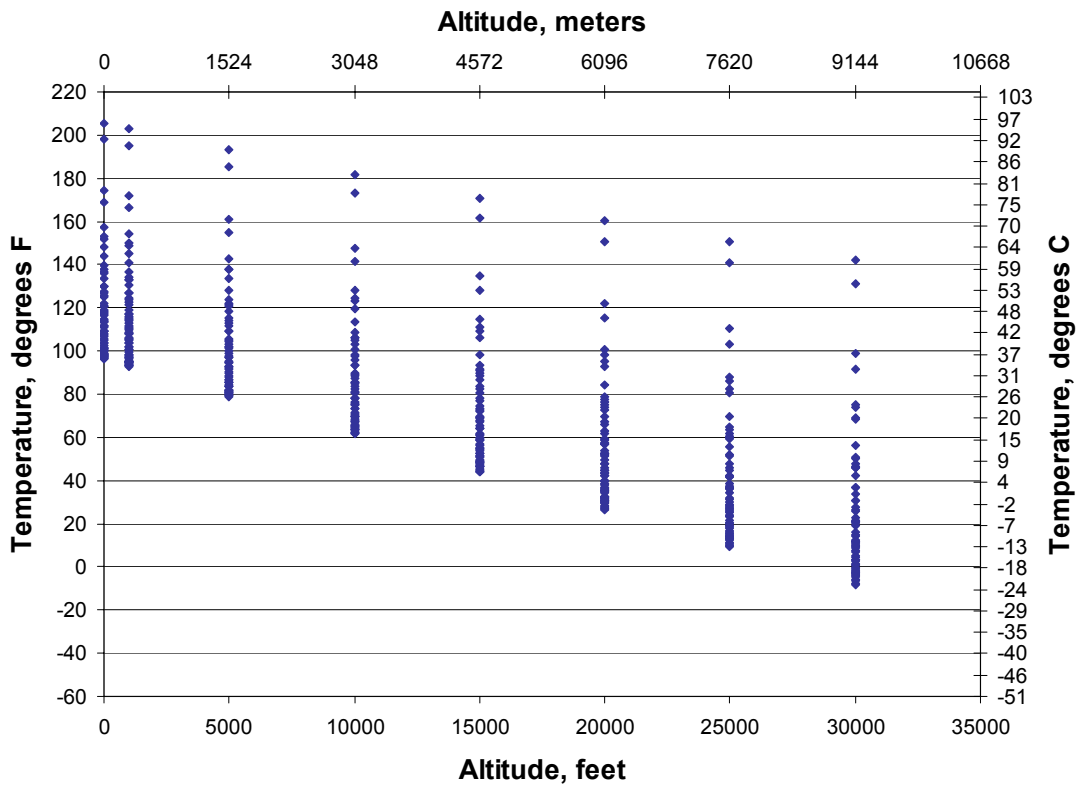


Figure 2-43. Peak Nacelle Temperature at 400 knots Airspeed vs. Altitude.

Additionally, nacelle air temperature data were obtained from current in-flight rotary aircraft propulsion temperature survey testing. The results of the comparison are summarized in Table 2-5. When the model was applied for the purposes of making comparisons, several of the inputs were varied to accommodate differing nacelle characteristics. For example, the clearance between the engine and the nacelle structure is not uniform, thus for each case this parameter was varied between the low and high values that had been utilized during the TDP, unless specific nacelle clearance information was obtained. In general, the model tended to predict (conservatively) lower temperature ranges as compared to measured temperature ranges.

**Table 2-5. Comparison of Modeled vs. Measured Nacelle Air Temperatures.**

Altitude (km)	OAT (°C)	Engine Surface Temperature Range (°C)	Measured Nacelle Air Temperature Range (°C)	Predicted Nacelle Air Temperature Range (°C)
Sea level	29	Not indicated	33 to 83	Not modeled since engine surface temperature range not indicated
>5	-21	Not indicated	-18 to 30	
0.4	28	102 to 392	33 to 82	23 to 33
0.6	Not indicated	176 to <260	≈ 90 to 160	20 to 115
0.6 to 14	Not indicated	Not indicated	≈ 100 at 0.6 km to ≈ 10 at 14 km	Not modeled since engine surface temperature range not indicated
3	-3	74 to 588	22 to 93	-3 to 28
Sea level	-3	60 to 467	19 to 55	16 to 39
3	1	81 to 587	27 to 94	-3 to 28
3	Not indicated	Up to 260	10 to 93	6 to 12
3	Not indicated	Up to 750	< 110 to < 275	7 to 23
Sea Level	Not indicated	Not indicated	210 <sup>xxiv</sup>	Not modeled since engine surface temperature range not indicated

### Cold Soak Conditions

The NGP also examined the effect of fire suppression effectiveness under cold-soak conditions, i.e., cases in which the aircraft had been on the ground in a cold climate. Of issue was the relationship between the OAT, the boiling point of a fire suppressant, and suppressant discharge under such conditions, especially during takeoff. Such conditions have been used to support the need for a suppressant with a boiling point of -40 °C (-40 °F) or lower.

Bein performed a literature review to identify existing work related to evaluation of aircraft cold soak conditions.<sup>44</sup> Work performed by Transport Canada was identified that characterized aircraft wing

<sup>xxiv</sup> Though the engine surface temperature data was not available for use in during modeling, this temperature data point from Reference 13 is listed as it was the highest nacelle airflow temperature found in the literature during the nacelle air temperature modeling effort.

surface temperatures during ground operations during Canadian winter and aircraft cold soak conditions after flights at altitude.<sup>86,87</sup> For flights in Canada and Alaska, a general conclusion was that wing temperature surveys of aircraft returning from flights at altitude failed to find evidence of significantly cold-soaked wing conditions. Their surveys generated data that indicate the following relative to non-deiced spot wing temperatures for aircraft on the ground:

- Below 0 °C (32 °F) OAT, wing temperatures were generally higher than OAT. The temperature difference generally ranged from 2 °C at 0 °C OAT to slightly greater than 6 °C at -25 °C OAT.
- Above 0 °C (32 °F) OAT, wing temperatures were generally lower than OAT.
- Radiative cooling on the ground (i.e., aircraft parked overnight in cold weather) is more likely than in-flight conditions to result in cold-soak conditions. Possible wing-to-OAT differential due to radiative cooling may range from -6 °C at 0 °C OAT and reducing to -2 °C at -25 °C OAT.<sup>88</sup>
- The lowest OAT for which cold-soak data was recorded was -13 °F (-25 °C), suggesting that aircraft operations on the ground in cold or extreme cold climates is infrequent. (Note that this correlates well with the operational fire experience indicated in Figures 2-36 and 2-37.)

The data generated during the Transport Canada surveys includes a flight profile for a flight at altitude in Alaska during which wing surface temperatures were recorded. The cruise altitude is not specified but is likely to be approximately 9 km (30,000 ft) based on the aircraft type that was instrumented and flown. At the time liftoff from the ground occurred, measured wing temperatures were higher than both OAT and the initial wing temperatures. During takeoff climb, there was a test point indication of a temperature increase of approximately 3 °C over the first 5 min before that test location temperature began to decrease, whereas all other measurement locations were noted to begin to decrease immediately. At 15 min after takeoff, wing temperatures were generally -20 °C (-5 °F). At 60 min after takeoff, wing temperatures were generally -23 °C (-10 °F). Wing temperatures were found to warm to approximately 7 °C (20 °F) in 15 min during descent to final landing. Except for the radiative cooling condition, these data indicated that temperature conditions of an operational aircraft are likely to be higher than the cold soak temperature conditions, suggesting that aircraft component temperatures are also likely to be higher. To analyze the concern of over too low fire suppressant and system component temperatures under cold or extreme cold temperature conditions during takeoff, a model was constructed to estimate stagnation temperature conditions during takeoff. The premise was that for suppressant bottle(s), distribution lines and components not located near/within heated compartments but adjacent to exterior surfaces, the stagnation temperature should provide a reasonable estimate of likely temperature conditions of components adjacent to the exterior surfaces. Figures 2-44 and 2-45 depict graphically the results of the minimum and maximum temperature profiles for cases modeled for a jet transport aircraft, fighter aircraft, and a turboprop transport aircraft.

- In Figure 2-44, an initial OAT for cold/severe-cold environments was based on the JAR-1 Arctic Standard Climate profile, and then the profile was applied during takeoff climb. This scenario was assumed to estimate a lower bound profile. The modeling estimated that during takeoff climb within a standard arctic profile that the stagnation temperatures can increase to greater than -25 °C (-13 °F) for a period of time, taking into consideration the likelihood that aircraft surface temperature will be greater than OAT at takeoff. The relevance of this is that fire suppression system components adjacent to these surfaces are likely to be similar in temperature. (The resultant temperature profiles indicate a period above -32 °C (-25 °F) for

as few as 3.7 min and as long as 14.2 min. The time to reach this threshold was estimated to occur approximately within 1.25 min or within 3.8 min.)

- In Figure 2-45, an initial OAT of -40 °C (-40 °F) was assumed but also applies a temperature bias condition based on difference of wing skin temperature to OAT described in the Transport Canada work. The JAR-1 Arctic Standard Climate profile is then applied during takeoff climb with the bias condition continuously applied to estimate a potential upper bound profile. The resultant temperature profiles indicated a period above -26 °C (-15 °F), for as few as 3 min and as long as 14.8 min. The time to reach this threshold was indicated to occur approximately within 1.25 min or within 3.6 min. Because of the duration of the climb for the jet transport aircraft, temperature was indicated to increase for a period of time to approximately -15 °C (4.5 °F) before beginning to decrease.

In each of the scenarios modeled it was clear that fire suppressant and system component temperatures could increase above -40 °C (-40 °F) during takeoff profiles for some period of time but continued ascent through the JAR-1 Arctic Standard Climate profile would effect temperature decrease. Thus it became necessary to review the DoD Safety Center data and the studies conducted during the TDP for establishing halon 1301 system effectivity to gage the DoD's historical engine nacelle fire risk during takeoff.

## Risk

Within DoD System Safety, organizations assess risk associated with hazards identified during development as well as during fielded operations of weapon systems, including aircraft systems and subsystems. Analytical processes are applied to assess worst-credible and most-probable severity and likely occurrence of identified hazards. Likely occurrence may be expressed as a rate of occurrence, typically per flight hour, or as a probability. The resulting assessment of severity and probability is then categorized as to the level of risk it presents (e.g., high, medium, low, unacceptable, etc.). Generally, assessment of fire hazards results in an assignment of a "Catastrophic" severity.<sup>xxv</sup> The issue becomes whether the rate of occurrence or probability of a fire hazard results in a risk that is deemed not low.

For example, when the total number of engine nacelle fires evaluated during the TDP for establishing halon 1301 system effectivity are considered, the aggregate rate of occurrence for a nacelle fire event during the period evaluated is approximately 8 per 10<sup>6</sup> flight hours. Those same data were reviewed during the NGP to estimate the potential hazard frequency of a catastrophic event due an unsuppressed engine nacelle fire hazard, as summarized in Tables 2-6 and 2-7. Note that in each case, the hazard frequency would be assessed as improbable. A catastrophic-improbable hazard is categorized as low risk, which is typically accepted by military aviation program managers. If the same rate of occurrence is considered in conjunction with operating in a low (or high) temperature climatic extreme, the hazard frequency would also be assessed as improbable as indicated in Tables 2-8 and 2-9.

---

<sup>xxv</sup> A Catastrophic hazard severity is defined in DoD specification MIL-STD-882D, Standard Practice for System Safety, as a hazard that can result in death, permanent total disability, loss exceeding \$1M, or irreversible severe environmental damage that violates law or regulation. The risk from fire in an aircraft would be presented to an aircraft program manager as the potential consequences of the different categories of possible fires and the likelihood of fire occurring for each category.

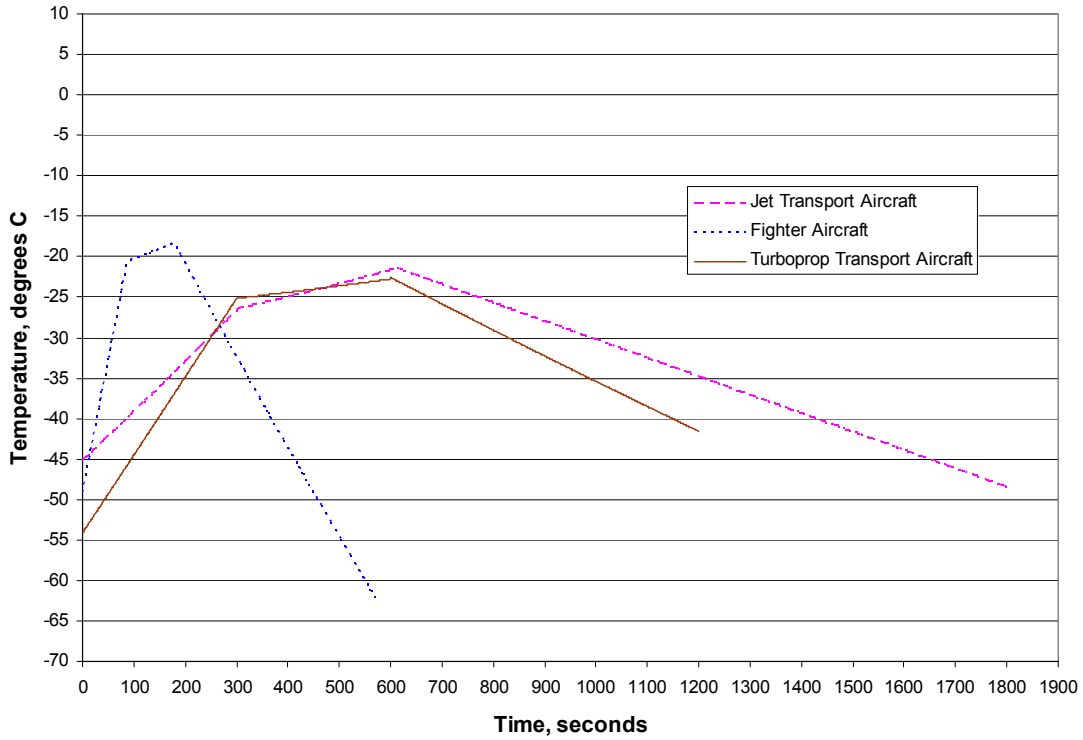


**Figure 2-44. Initial OAT per JAR-1 Arctic Standard Climate.**  
(OAT at Takeoff is -50 °C (-58 °F).)

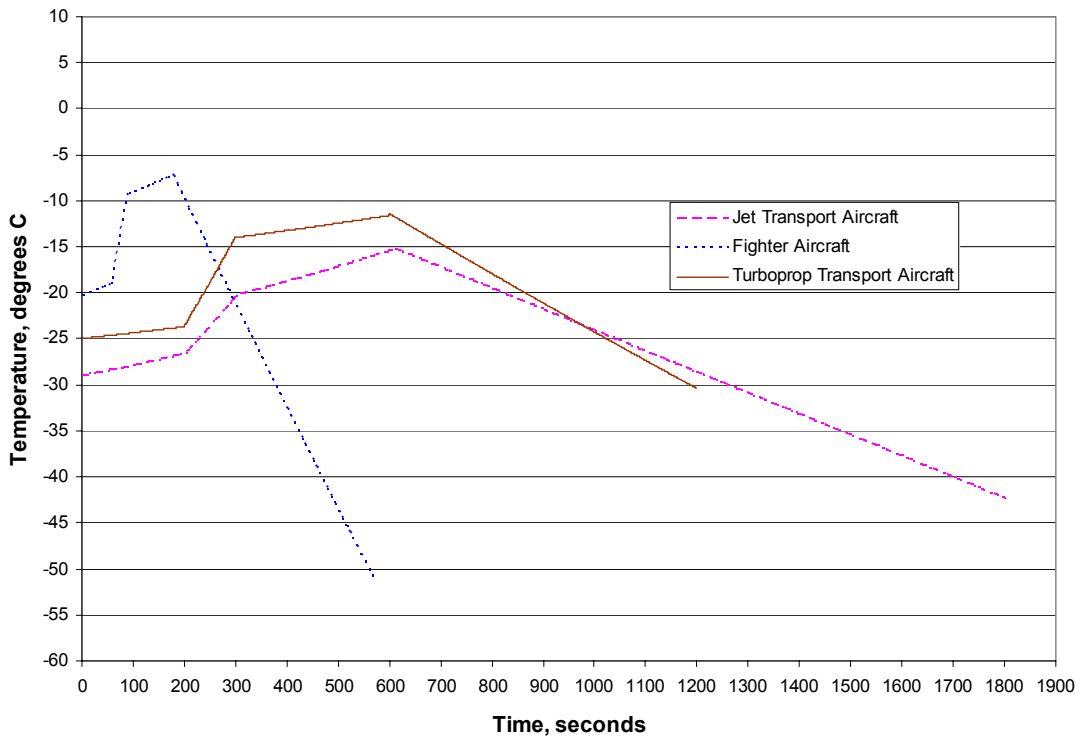


**Figure 2-45. OAT at Takeoff is -40 °C (-40 °F) with Bias Applied to OAT.**

**Table 2-6. Estimate of Rate of Occurrence of Aircraft Lost Due to Failure to Extinguish a Nacelle Fire, Any Time (Does not Consider Multiple Engines).<sup>xxvi</sup>**

Aircraft Category	Probability Occurrence In Flight	Probability Occurrence At Any Given Time	Probability Occurrence Fire Not Extinguished	Probability Occurrence Aircraft Lost	End Event Rate of Occurrence Per Flight Hour	MIL-STD-882 Hazard Frequency
Fixed-wing	0.55	1	0.24	0.09	9.84E-08	Improbable (E)
Rotary	0.35	1	0.53	0.27	4.15E-07	Improbable (E)
Aircraft Category	Probability Occurrence On Ground	Probability Occurrence At Any Given Time	Probability Occurrence Fire Not Extinguished	Probability Occurrence Aircraft Lost	End Event Rate of Occurrence Per Flight Hour	MIL-STD-882 Hazard Frequency
Fixed-wing	0.45	1	0.38	0.03	4.25E-08	Improbable (E)
Rotary	0.65	1	0.36	0.01	1.94E-08	Improbable (E)

**Table 2-7. Estimate of Rate of Occurrence of Aircraft Lost Due to Failure to Extinguish a Nacelle Fire, Any Time (Assumes Two Engines per Aircraft).<sup>xxvi</sup>**

Aircraft Category	Probability Occurrence In Flight	Probability Occurrence At Any Given Time	Probability Occurrence Fire Not Extinguished	Probability Occurrence Aircraft Lost	End Event Rate of Occurrence Per Flight Hour	MIL-STD-882 Hazard Frequency
Fixed-wing	0.55	1	0.24	0.09	4.92E-08	Improbable (E)
Rotary	0.35	1	0.53	0.27	2.08E-07	Improbable (E)
Aircraft Category	Probability Occurrence On Ground	Probability Occurrence At Any Given Time	Probability Occurrence Fire Not Extinguished	Probability Occurrence Aircraft Lost	End Event Rate of Occurrence Per Flight Hour	MIL-STD-882 Hazard Frequency
Fixed-wing	0.45	1	0.38	0.03	2.13E-08	Improbable (E)
Rotary	0.65	1	0.36	0.01	9.70E-09	Improbable (E)

<sup>xxvi</sup> Probabilities in Tables 2-6 and 2-7 are derived from References 45 and 46. End event rate of occurrences determined by multiplying  $8/10^6$  flight hours by probabilities indicated. This frequency is based on the aggregate number of nacelle fires over all flight hours for the period and aircraft evaluated in those references and is higher than the rate of  $4.9/10^6$  flight hours indicated in an evaluation of Army rotary aircraft fires per Reference 81. No rotary aircraft were indicated lost in ground fire events in Reference 46, but a 1 % probability is assumed for discussion purposes.

**Table 2-8. Estimate of Rate of Occurrence of Aircraft Lost Due to Failure to Extinguish a Nacelle Fire in a Climatic Extreme (Does not Consider Multiple Engines).**<sup>xxvii</sup>

Aircraft Category	Probability Occurrence In Flight	Probability Occurrence In Climatic Extreme	Probability Occurrence Fire Not Extinguished	Probability Occurrence Aircraft Lost	End Event Rate of Occurrence Per Flight Hour	MIL-STD-882 Hazard Frequency
Fixed-wing	0.55	0.2	0.24	0.09	1.97E-08	Improbable (E)
Rotary	0.35	0.2	0.53	0.27	8.30E-08	Improbable (E)
Aircraft Category	Probability Occurrence On Ground	Probability Occurrence In Climatic Extreme	Probability Occurrence Fire Not Extinguished	Probability Occurrence Aircraft Lost	End Event Rate of Occurrence Per Flight Hour	MIL-STD-882 Hazard Frequency
Fixed-wing	0.45	0.2	0.38	0.03	8.50E-09	Improbable (E)
Rotary	0.65	0.2	0.36	0.01	3.88E-09	Improbable (E)

**Table 2-9. Estimate of Rate of Occurrence of Aircraft Lost Due to Failure to Extinguish a Nacelle Fire in a Climatic Extreme (Assumes 2 Engines per Aircraft).**<sup>xxvii</sup>

Aircraft Category	Probability Occurrence In Flight	Probability Occurrence In Climatic Extreme	Probability Occurrence Fire Not Extinguished	Probability Occurrence Aircraft Lost	End Event Rate of Occurrence Per Flight Hour	MIL-STD-882 Hazard Frequency
Fixed-wing	0.55	0.2	0.24	0.09	9.84E-09	Improbable (E)
Rotary	0.35	0.2	0.53	0.27	4.15E-08	Improbable (E)
Aircraft Category	Probability Occurrence On Ground	Probability Occurrence In Climatic Extreme	Probability Occurrence Fire Not Extinguished	Probability Occurrence Aircraft Lost	End Event Rate of Occurrence Per Flight Hour	MIL-STD-882 Hazard Frequency
Fixed-wing	0.45	0.2	0.38	0.03	4.25E-09	Improbable (E)
Rotary	0.65	0.2	0.36	0.01	1.94E-09	Improbable (E)

The implication of the preceding is that when considering the risk of a catastrophic end event, the likelihood is driven primarily by whether fire occurs, and this likelihood is reduced by the likelihood of operating in a climatic extreme (e.g., cold temperature conditions). For example, Figure 2-46 summarizes fixed-wing fire mishaps and incidents by phase of operation. The takeoff-related categories total to 18.7 % of all events, and approximately 16 % of suppressant releases occurred during the takeoff phases. However, only 4 % of the takeoff-related releases (and thus fewer than 1 % of all releases) occurred in land environments categorized as cold or severe cold. This strongly suggests that risk is low (i.e., an

<sup>xxvii</sup> Probabilities in Tables 2-8 and 2-9 derived from References 45 and 46. End event rate of occurrences determined by multiplying  $8/10^6$  flight hours by probabilities indicated. This frequency is based on the aggregate number of nacelle fires over all flight hours for the period and aircraft evaluated in those references and is higher than the rate of  $4.9/10^6$  flight hours indicated in an evaluation of Army rotary aircraft fires per Reference 81. No rotary aircraft were indicated lost in ground fire events in Reference 46 but a 1 % probability is assumed for discussion purposes. Probability of operation in climatic extreme assumes exposure to either MIL-HDBK-310 20% low or high temperature WWAE.

improbable hazard frequency) for an engine nacelle fire during takeoff on a cold-soaked aircraft and in which the fire suppression system fails to extinguish the fire and a catastrophic event occurs.

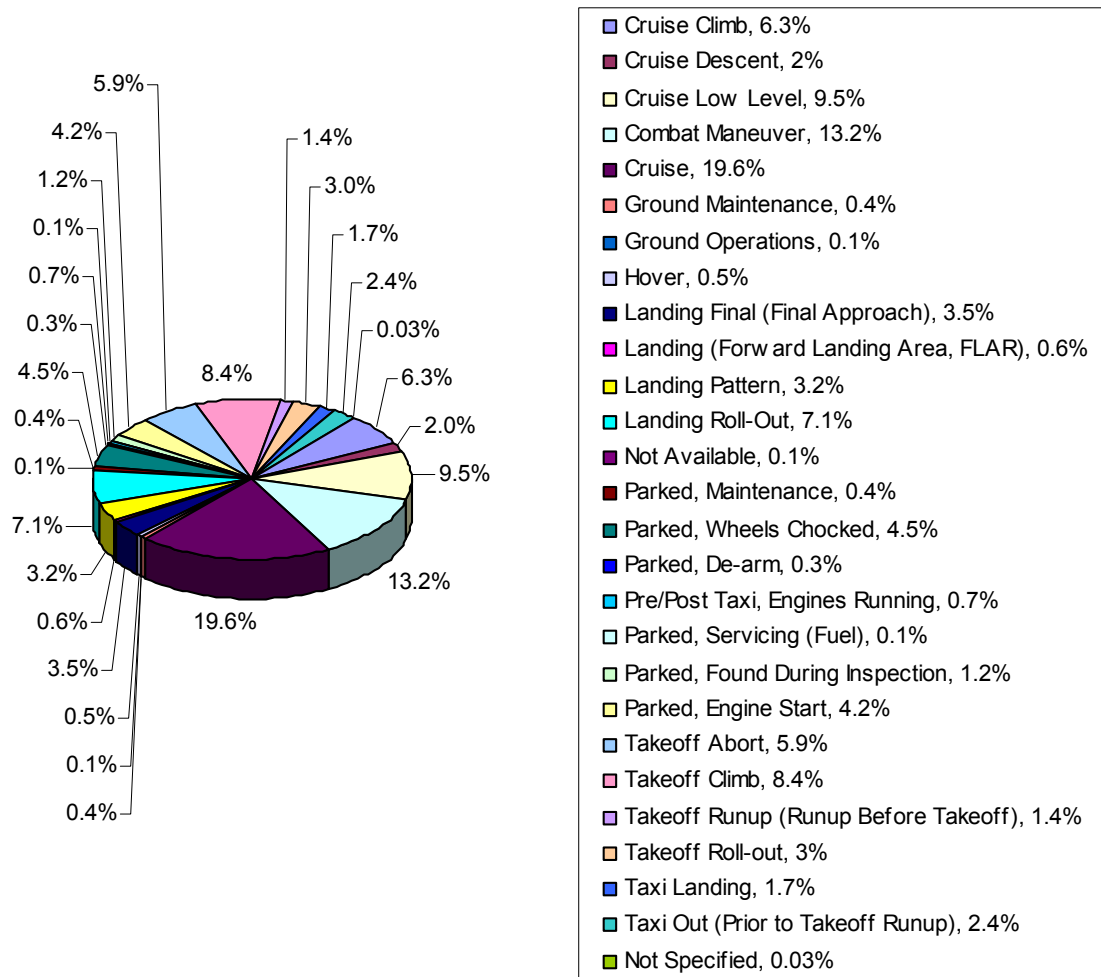


**Figure 2-46. Fixed-Wing Aircraft Fire Mishaps and Incidents by Phase of Operation.**

### Summary – Severity of Aircraft Temperature Environment Criterion

The conservatism of the  $-40\text{ }^{\circ}\text{C}$  criterion can be seen when the historical data is plotted against the DoD climatic land environment design guidance and previously published aviation fuel flammability limit profiles in conjunction with various atmospheric profiles. Figures 2-47 and 2-48 plot the geographic locations of ground fire events for rotary aircraft and fixed-wing aircraft, respectively, vs. the DoD climatic land environment design guidance. In these figures, it can be seen that the clear majority of ground fire events occurred in geographic locations associated with the basic land environment category. Figures 2-49 and 2-50 plot the nearest-to geographic locations of in-flight fire events for rotary aircraft and fixed-wing aircraft, respectively, to depict where these events occurred relative to the climatic land environments.

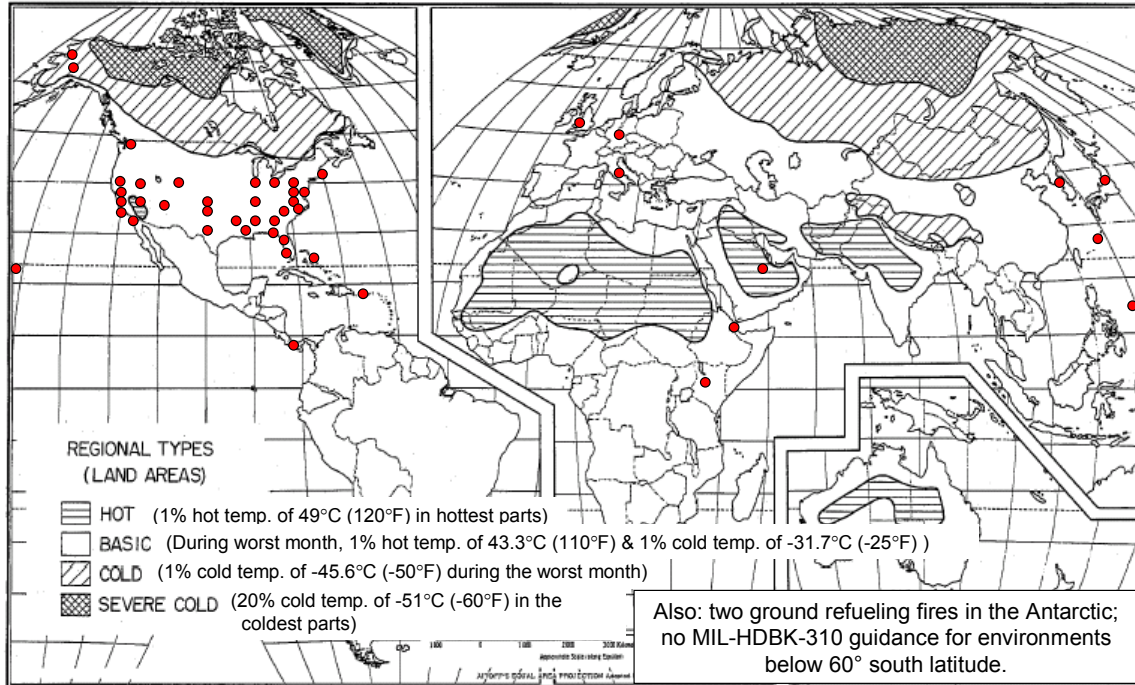


Figure 2-47. Distribution of DoD Rotary Aircraft Ground Fire Locations.<sup>89</sup>

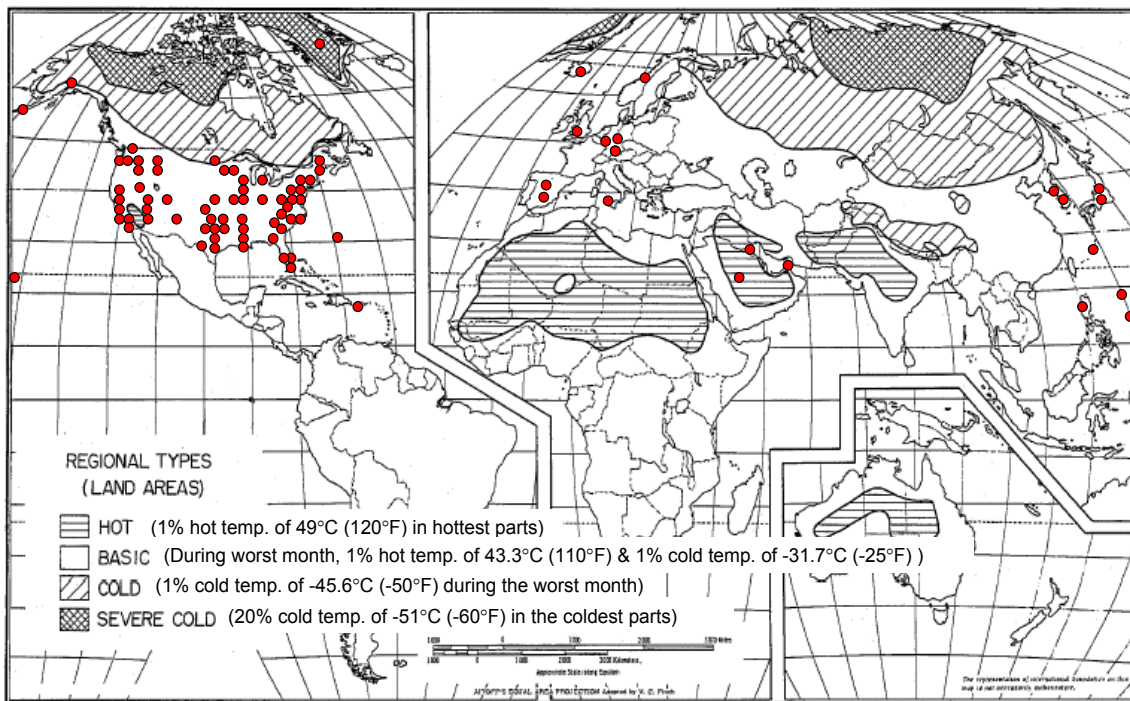
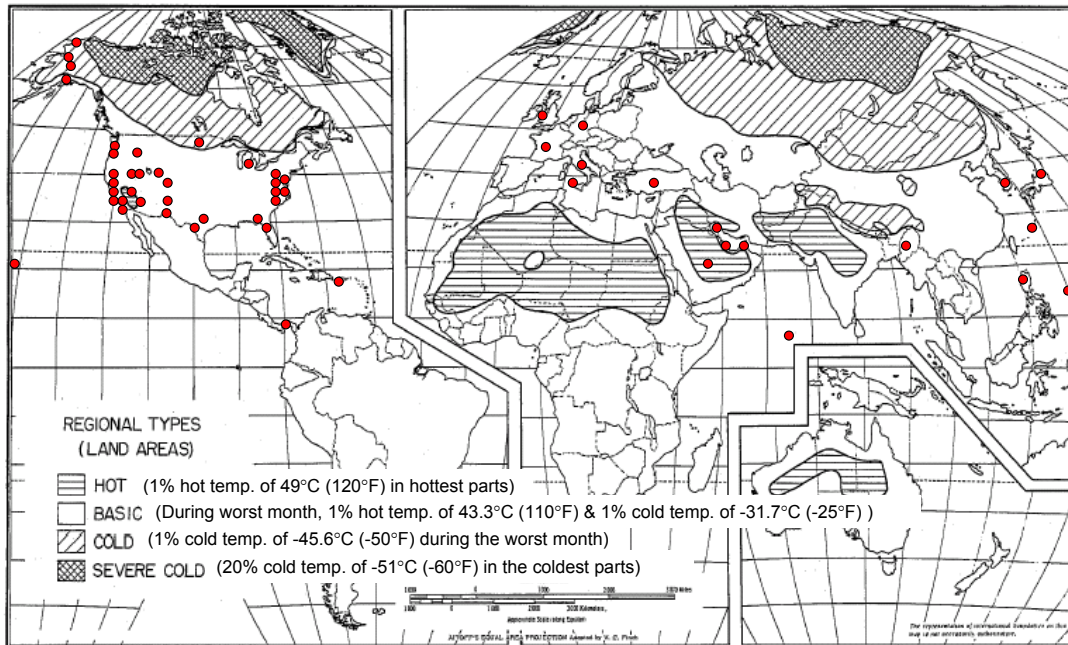
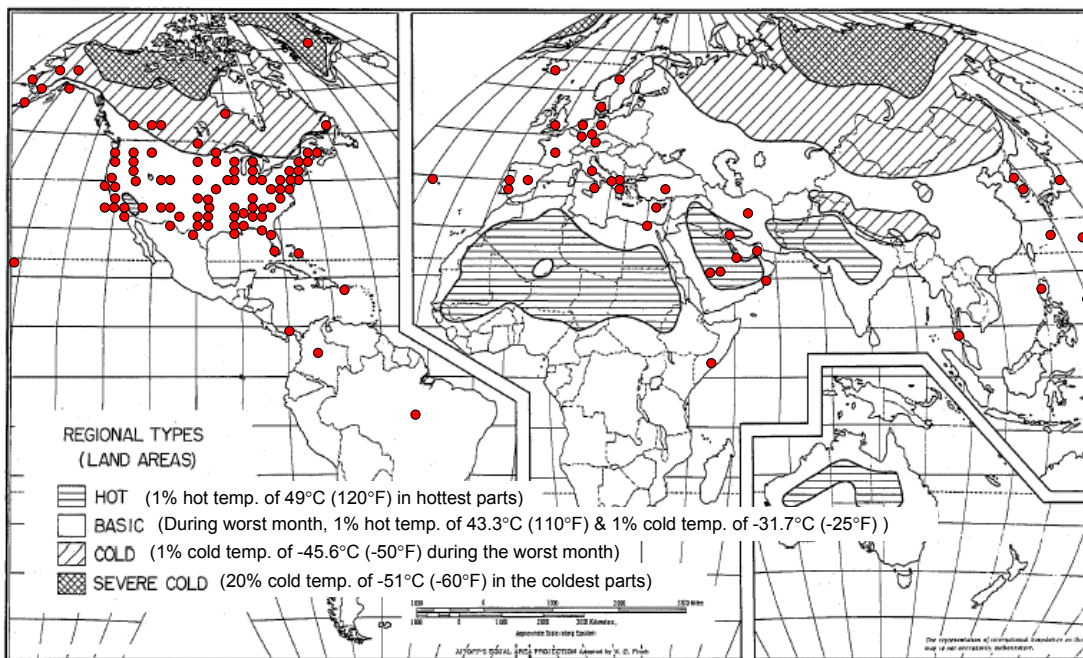


Figure 2-48. Distribution of DoD Fixed-Wing Aircraft Ground Fire Locations.<sup>89</sup>



**Figure 2-49. Distribution of DoD In-Flight Rotary Aircraft Fire Locations (Nearest-to Locations).<sup>89</sup>**



**Figure 2-50. Distribution of DoD In-Flight Fixed-Wing Aircraft Fire Locations (Nearest-to Locations).<sup>89</sup>**

In Figure 2-51, the DoD rotary aircraft fire data are plotted vs. the standard atmosphere (blue line) and tropical atmosphere profiles (orange line) and Jet A (right) and Jet B (left) flammability limit profiles. Also indicated is the typical rotorcraft operational ceiling and the majority (97 %) suppressant release envelope derived from Figures 2-38 and 2-39. Also shown for reference purposes is an artifact from previous fire testing, described previously in Section 2.3.5, to determine the flame spectral characteristics for optical fire detection at altitude: that testing at pressure conditions representative of altitude of 11.5 km (35,000 ft) resulted in inability to maintain sustained combustion. The preponderance of fire events and suppressant releases on rotorcraft is shown to occur well below the typical operational ceiling for rotorcraft and well above the  $-40\text{ }^{\circ}\text{C}$  ( $-40\text{ }^{\circ}\text{F}$ ) NGP boiling point criterion, with 97 % of all rotorcraft suppressant releases occurring above  $-12.2\text{ }^{\circ}\text{C}$  ( $10\text{ }^{\circ}\text{F}$ ).

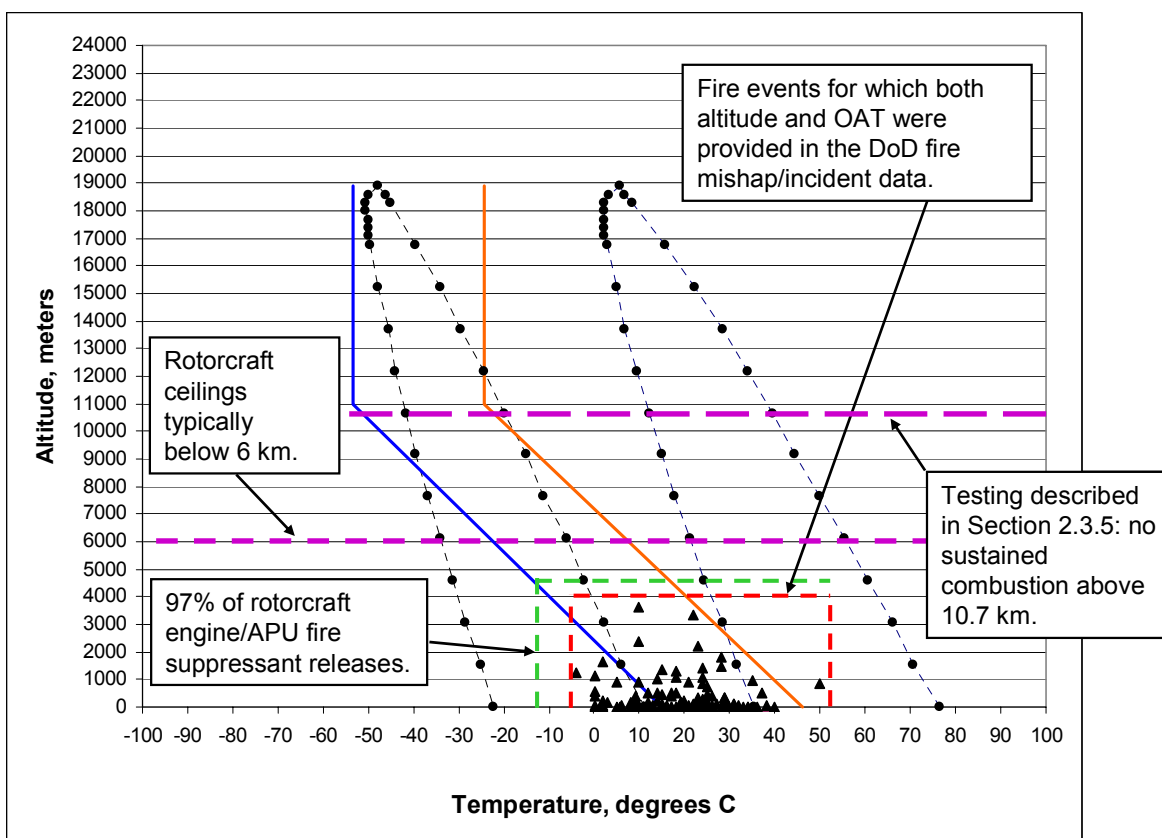


**Figure 2-51. DoD Rotary Aircraft Fire Data vs. Atmospheric Profiles, Flammability Limit Profiles, Operational Ceiling, and Suppressant Release.**<sup>89</sup>

Figure 2-52 plots the fixed-wing aircraft fire data in similar fashion. The overwhelming majority of fire events from the data is indicated below 7 km (23,000 ft), with 94 % of all suppressant releases occurring at an altitude just above 9 km (29,500 ft). Qualitatively, this latter altitude as a ceiling correlates well with the results of the conclusions drawn from previously described nacelle air temperature modeling and the testing described previously in Section 2.3.5. Additionally, the overwhelming majority of relevant nacelle air temperature modeling cases occurred for OAT conditions at or above  $-25\text{ }^{\circ}\text{C}$  ( $-13\text{ }^{\circ}\text{F}$ ), which also correlates well with that very few fire events are indicated below this OAT as well as with the distribution of fire events depicted previously in Figures 2-48 and 2-50. In the basic land environment depicted in those figures, the worst cold temperature exposure is 1% at  $-31.7\text{ }^{\circ}\text{C}$  ( $-25\text{ }^{\circ}\text{F}$ ), which also correlates well with the temperature boundary for 94 % all suppressant releases in Figure 2-52.

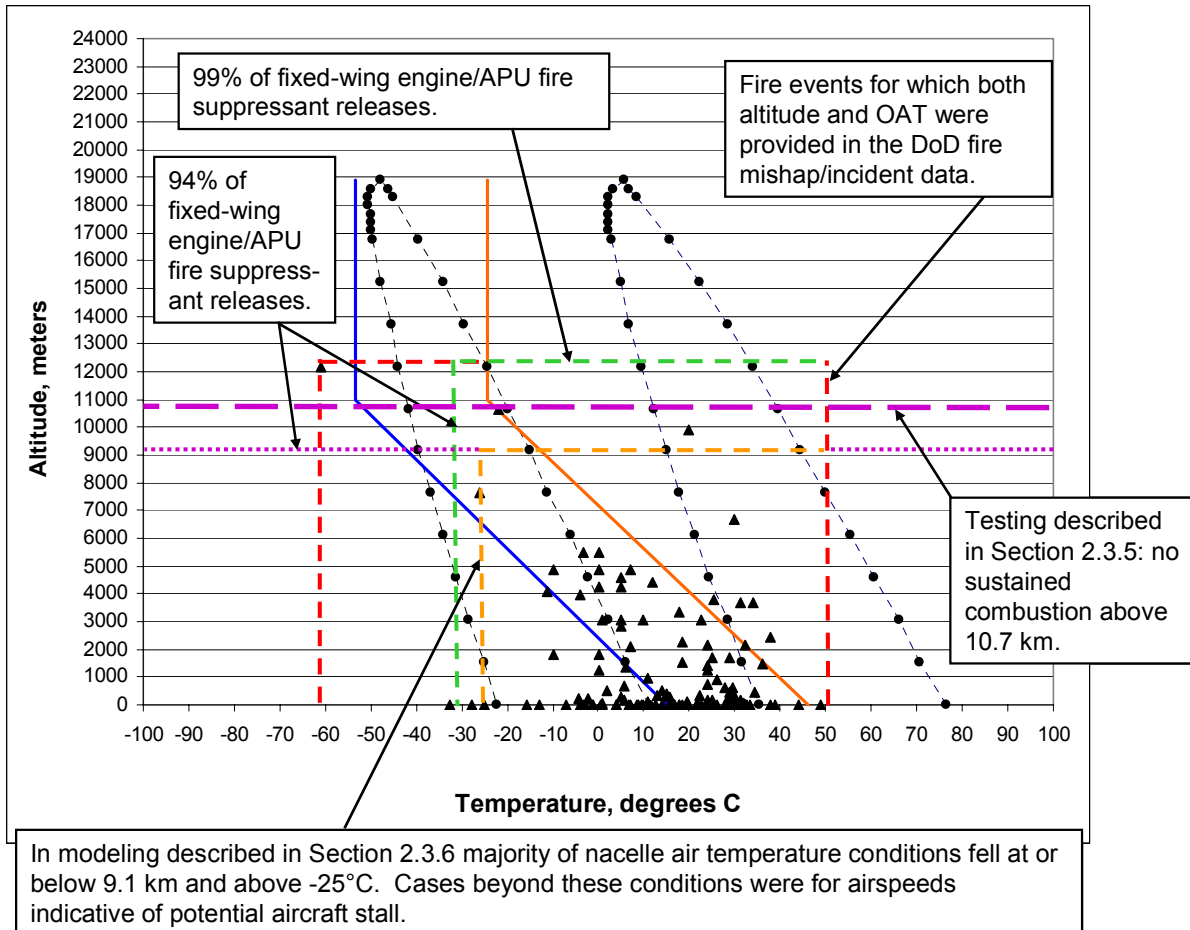


**Figure 2-52 DoD Fixed-Wing Aircraft Fire Data vs. Atmospheric Profiles, Flammability Limit Profiles, Potential Stall Condition and Suppressant Release.<sup>89</sup>**

In summary, the preceding figures indicate:

- As altitude increases, the number of fire events decreases.
- As altitude increases, occurrence of fire events trends above the standard atmosphere profile.
- Rotorcraft fire events occurred below 4 km (13,000 ft), below the typical operational ceiling for those aircraft, with 97 % of all suppressant releases occurring for OAT above  $-12.2^{\circ}\text{C}$  ( $10^{\circ}\text{F}$ ).
- A clear majority of fixed-wing aircraft fire events occurred below 6.1 km (20,000 ft).
- Similar to publicly-available data for commercial aviation shown in Figure 2-37, the vast majority of fixed-wing aircraft fire events, ground and in flight, occurred with OAT above  $-20^{\circ}\text{C}$  ( $-4^{\circ}\text{F}$ ).
- In-flight rotary and fixed-wing aircraft fire events occurred predominantly near geographic locations associated with the basic land environments, for which DoD design guidance indicates the worst cold temperature exposure as 1 % at  $-31.7^{\circ}\text{C}$  ( $-25^{\circ}\text{F}$ ).

The  $-40^{\circ}\text{C}$  criterion used by the NGP is likely conservative. The plots of the DoD fire mishap and incident data in the preceding figures suggest that qualification of nacelle fire suppression systems at an

OAT of 0 °C (32 °F) would respond to over 90 % of the expected fires, based on past experience. The qualification requirements are generally a DoD safety policy matter that rests ultimately with the DoD aircraft programs. This means that the safety and survivability risks associated with qualifying a system with a suppressant that has a boiling point greater than criterion of -40 °C would need to be assessed to determine whether the risk level is acceptable by the aircraft program manager, and the specific performance requirements for the fire suppression system would be reflected in the aircraft specification.

### 2.3.7 Reignition

Reignition within an engine nacelle or dry bay compartment is always a threat so long as fuel vapor and air can come in contact with sufficiently hot surfaces or if there is some other type of ignition source present, such as arcing from an electrical harness or sparks generated from a rotating component unintentionally in contact with another component. Within an engine nacelle, hot surfaces are the primary ignition threat, as engine case temperatures can easily exceed 538 °C (1000 °F). After suppressant discharge within a nacelle or APU compartment, hot fuel vapor may exist at levels which are flammable, leading to the possibility of reignition. A puddle of hydraulic fluid or jet fuel leaking from a cracked or failed line can vaporize as heat is transferred from a nearby hot metal surface. In addition, hot metal surfaces may occur due to heating by the fire itself, which could occur within a nacelle or APU compartment or even a dry bay compartment. Reignition may then arise from contact of the reactive fuel/air mixture with the hot metal surface.<sup>43</sup> In full-scale nacelle fire suppression testing during the TDP, it was observed that when hot operating engine case temperatures were simulated, reignition could occur due to residual fuel adhering to the surface or fuel continuing to be sprayed before being shut off. This was seen typically at surface temperatures at or above 538 °C.<sup>90</sup> That testing also indicated that when a hot metal surface at 704 °C (1300 °F) was present, greater quantities of fire suppressant were required when compared to no hot surface reignition condition. The NGP has also investigated how induction and convection may control the reignition process. This investigation found that reignition is controlled by cooling and mass transport towards the hot surface. A “worst-case” scenario for reignition was characterized by maximizing the fuel mass transfer while keeping the characteristic time for cooling of the surface shorter than the time to attain a flammable mixture.<sup>91</sup>

Reignition suppression requirements within a dynamic environment on an aircraft are very dependent on the specific scenario. Currently, there is no reliable method to predict the optimal agent requirements to prevent it, other than conduct of full-scale testing for the unique aircraft configuration for *all* possible reignition conditions. Strategies to prevent reignition include removing fuel vapor, reducing surface temperatures, either through design or active cooling, and inerting the fuel/air mixture with a suppressant. Fuel vapors can be removed intentionally by design or unintentionally as an affect of the ventilation airflow required by a compartment for cooling. Leaking flammable fluids can be removed by drain holes and systems or sump ejectors. Typically, before activation of the engine nacelle fire suppression system, the jet fuel to the particular engine and hydraulic fluid flow to engine compartment accessories is shut down. This limits the amount of fuel in the nacelle, but it could take a relatively long time to remove the combustibles from the nacelle, especially low vapor pressure liquids.

In considering the issue of reignition, it is important to distinguish between the temperature at which autoignition occurs vs. hot surface ignition. The autoignition temperature (AIT) is also referred to as the spontaneous ignition temperature, self-ignition temperature or autogenous ignition temperature. It is the lowest temperature at which the substance will produce a hot-flame ignition in air without the aid of an

external spark or flame.<sup>92</sup> This temperature is determined by heating a sample of a fluid in air in a laboratory flask. The AITs for JP-type military aviation fuels range between 204 °C (400 °F) and 232 °C (450 °F). For MIL-H-83282-type hydraulic fluid, the AIT is approximately 354 °C (670 °F). Aircraft manufacturers will typically self-impose a safe design temperature (SDT) practice that is usually 10 °C (50 °F) lower than the AIT of a fluid that may come in contact with a hot surface. This cannot be accomplished for engine nacelles or APU compartments due to their case temperatures.

Reignition on a hot surface within a dynamic environment such as within an aircraft engine nacelle is distinct from autoignition. Extensive lab-scale and full-scale testing has been conducted over the past several decades that demonstrates, generally, hot surface ignition of aviation JP-type fuels and hydraulic fluids used in military aircraft occurs at surface temperatures greater than the AIT for those fuels and fluids. Minimum hot metal surface ignition temperatures for JP-8 (or kerosene) for ambient temperatures and pressures and low air flows have been found to vary from 360 °C to 650 °C, depending on test conditions. Hot surface ignition temperatures will generally decrease as the size or surface area increases or as fuel contact time increases, and they will generally increase with increasing air velocity.<sup>93</sup> An exception is MIL-H-83282 hydraulic fluid, which during testing conducted in a nacelle simulator with a portion of a simulated F-16 engine was found to have the potential to ignite when exposed to a hot surface below the fluid's AIT and when ambient air temperature was heated to at least 150 °C (300 °F). At a ventilation air temperature of 316 °C (600 °F) the fluid would ignite without the hot surface.<sup>94,xxviii</sup>

From work conducted during the TDP it was asserted that a reasonable target concentration for suppressant in the fire zone (not the free stream) is the concentration which ensures that the most flammable fuel/air ratio cannot occur. Such a suppressant concentration should ensure both flame suppression and prevention of re-ignition for a period of time on the order of the suppressant injection (discharge) duration. After this period, however, it is likely that re-ignition would still be possible.<sup>13</sup>

## 2.4 FIRE SUPPRESSANTS USED ON AIRCRAFT

As early as 1922, there is reference to implementation of engine compartment fire suppression, which consisted of a fire extinguisher within that compartment that was controlled from the pilot's seat. Additionally, shutters were installed to eliminate external airflow into the compartment.<sup>95</sup> No specific reference is provided as to the fire suppressant in this case, but one could speculate. The Naval Studies Board reported that in the 1920s, non-fluorinated halon agents were tried experimentally in engine nacelle extinguishers, but their use was abandoned by the U.S. military in favor of the non-corrosive CO<sub>2</sub>.<sup>8</sup> Even as aircraft fire suppression matured, there are instances in which researchers and aircraft designers ponder the rationale for a specific requirement. An example of this is the unpublished technical data and various published statements supporting the certification requirement for engine nacelle halon 1301 fire suppression systems. Regardless, since the identification of stratospheric ozone depletion and subsequent efforts to identify alternatives to the halons for aircraft fire suppression, there have been numerous compilations of the history of fire suppressants used on aircraft.

---

<sup>xxviii</sup> Previous research indicated in Reference 149 also indicated for MIL-H-83282 an AIT of 354°C and a stream hot manifold ignition temperature of 322°C. The later was determined by Federal Test Method Standard (FTMS) 7916, Method 6053. In hot surface ignition studies surveyed in Reference 150, some of the studies showed MIL-H-5606 was more ignitable than MIL-H-83282, whereas other studies surveyed, which used different test configurations, indicated diametrically opposite results.

Perhaps the most comprehensive compilations are those in reports generated by the National Institute of Standards and Technology (NIST) under the TDP, by the Federal Aviation Administration (FAA) as part of work it has been performing related to development of minimum performance standards for halon alternative nacelle fire suppression systems, and by Kidde Aerospace and Defense, PLC, one of the primary suppliers of aircraft fire suppression system components today.<sup>13,96,97</sup> Additional historical references are contained within the investigation performed by the NGP to document active suppression technologies for ullage fire/explosion protection and work done by Boeing to document options for dry bay fire protection.<sup>31,98</sup>

The following provides a brief summary of fire suppressants that have been used on DoD aircraft for powerplant and dry bay fire protection, excluding halon alternative suppressants identified during the TDP or developed under the NGP. The reader is referred back to Section 2.2.6 for discussion of suppressants that have been utilized for ullage fire suppression. Fielding of halon alternative suppressants subsequent to the TDP is discussed briefly in the next section. Throughout this section, the phrase “powerplant” may refer to an engine or APU compartment or other type of powerplant described earlier in this chapter.

#### 2.4.1 Powerplant Compartments

The requirements for and implementation of aircraft fire suppression for powerplant compartments have evolved for a variety of reasons, primary among them being powerplant design and the fire suppressant. For example, powerplant fire suppression system design guidance published by the CAA in 1943 for use of methyl bromide (halon 1001) and CO<sub>2</sub> was relative to mass airflow in the compartment and the number of cylinders in a radial cylinder engine installation. For potential fire zones with high airflow, agent quantity was to be based on 20 % of the mass airflow through the zone in two seconds.<sup>99, xxix</sup> Agent distribution was to be accomplished using spray nozzles or perforated tubes providing approximate equal distribution and a “sheet of agent spray” across the cross section of the protected zone orthogonal to the airflow. These systems were to become known as conventional distribution systems. Figure 2-53 illustrates an example of this type of installation. The aircraft engine compartment fire suppression systems for the B-36 and XR60-1 aircraft employed halon 1001. Some of the first aircraft to deploy fixed CO<sub>2</sub> fire suppression systems for engine compartment protection included the C-46, C-47, B-17, B-26, and the B-45 aircraft.

During World War II the German Navy sponsored efforts by I.G. Farbonindustrie to develop an alternative to halon 1001 due to its toxicity, which resulted in the development of chlorobromomethane (CB or halon 1011) in the 1939 to 1940 time period. Halon 1011 was determined to be as effective as halon 1001 and less toxic. Testing in 1942 by then Junkers/Dessau for the German Luftwaffe focused on developing a powerplant fire suppression system using Dachlaurin (D-L), a mixture of 65 % halon 1011 and 35 % CO<sub>2</sub>. In early 1945 the Luftwaffe approved the principle of the D-L system and ordered its installation on all German military aircraft, subject to then not-yet-established priorities. It was planned that the D-L system was to be installed on the Messerschmitt ME 262, the first operational jet-powered fighter.<sup>100</sup> Given the time the directive was issued, it is likely D-L did not come into widespread use before the end of the war. After the war extensive evaluation of halon 1011 was conducted within the U.S. and by 1950, the USAF required use of halon 1011 systems instead of CO<sub>2</sub> systems in new aircraft

<sup>xxix</sup> As of the writing of this book, CAA reports are available from the Department of Transportation’s Online Digital Special Collections at <http://dotlibrary.specialcollection.net/>.

and subsequently issued a specification for such systems.<sup>101,102,103</sup> Design guidance for use of halon 1011 in powerplant fire suppression system evolved as jet propulsion became more widespread and was provided relative to compartment airflow and free volume. However, the conventional distribution system approach was still employed for halon-1011-based fire suppression systems. Examples of these arrangements are shown in Figures 2-54 and 2-55. Some aircraft known to have utilized halon 1011 for powerplant fire suppression include the C-97, C-119F, C-123, C-130 and B-57 aircraft.

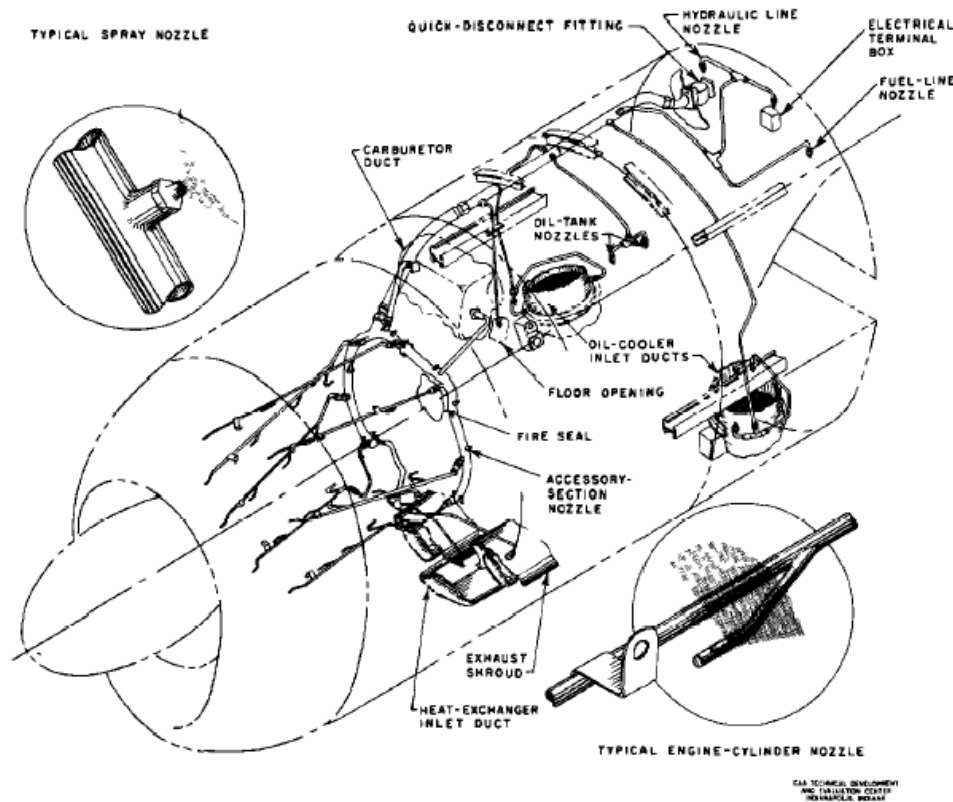


**Figure 2-53. Example Conventional Halon 1001 Powerplant Fire Suppression System Distribution Installation, USN Turboprop Powerplant.**<sup>104</sup>

Techniques for assessing adequate distribution, which are described later in this section, changed along with the evolution to jet propulsion powerplants. During testing conducted by the CAA, it was observed during filming and time recording of discharge duration from a conventional distribution system that the apparent full-strength discharge time was 1 s.<sup>104</sup> (The certification requirement that had been established for the conventional fire suppression systems was, and still is, a required concentration level maintained at all measured locations throughout the compartment for a minimum of 2 s.) During these same tests, comparisons were made of fire suppression performance of conventional systems vs. open-ended systems, which later became known as high-rate-discharge (HRD) systems. The HRD systems presented a simplified distribution approach in that perforated distribution lines were replaced with few open tubes out of which the fire suppressant would discharge at a much higher rate. Rather than relying on plumbing to disperse the suppressant, dispersion would be effected by the turbulent mixing of the suppressant discharge jet and the nacelle mass air flow. Further testing by the CAA demonstrated that the HRD design required less halogenated fire suppression agent to suppress nacelle fires and simplified

distribution system design. Testing conducted later by the Wright Air Development Center (WADC) promoted the conclusion that the efficiency of a fire suppression system would be improved with increasing suppressant discharge velocity, and that a “critical saturation value,” in percent by volume, occurred between 15 m/s (50 ft/s) and 30 m/s (100 ft/s) for the suppressants evaluated (halon 1011, halon 1301, and dibromodifluoromethane or halon 1202).<sup>105</sup> The example fire suppression system installation shown earlier in Figure 2-8 is a representative halon 1301 HRD system installation.

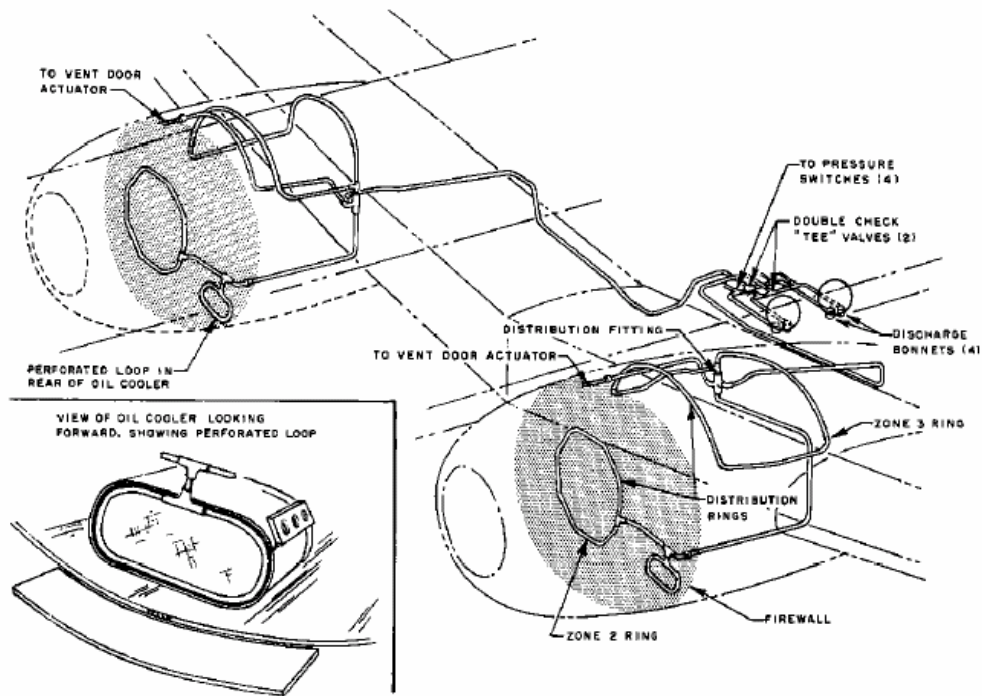


**Figure 2-54. Example Conventional Halon 1011 Fire Extinguishing System Distribution Installation, Turboprop Powerplant.**<sup>106</sup>

Halon 1301, which had been determined to be superior to halons 104 and 1001 in hand portable extinguishers during testing conducted by the Purdue Research Foundation (PRF),<sup>107</sup> was also found to be well-suited for use in powerplant HRD systems. During CAA tests that were performed that resulted in the design guidance for halon 1301, in which a minimum discharge duration of 0.5 s is required, discharge durations varied between 0.5 s and 0.9 s.<sup>108,109,110</sup> It is interesting to note that technical intelligence gathered after the end of World War II suggested that design policy for engine compartment CO<sub>2</sub> fire suppression systems followed by the Imperial Japanese Navy required discharge within 1 s.<sup>52</sup> A timeline of the evolution of the 0.5 s duration requirement for HRD systems can be hypothesized based on year of publication of the reports and specifications as follows:

- 1948: As mentioned previously in Chapter 1, the U.S. Army commissioned the PRF to search for a suppressant of high fire suppression efficiency but low toxicity. During flammability limit testing a halon 1301 inerting concentration was determined as 6 % volumetric concentration. This testing was not related to engine nacelle fire suppression.

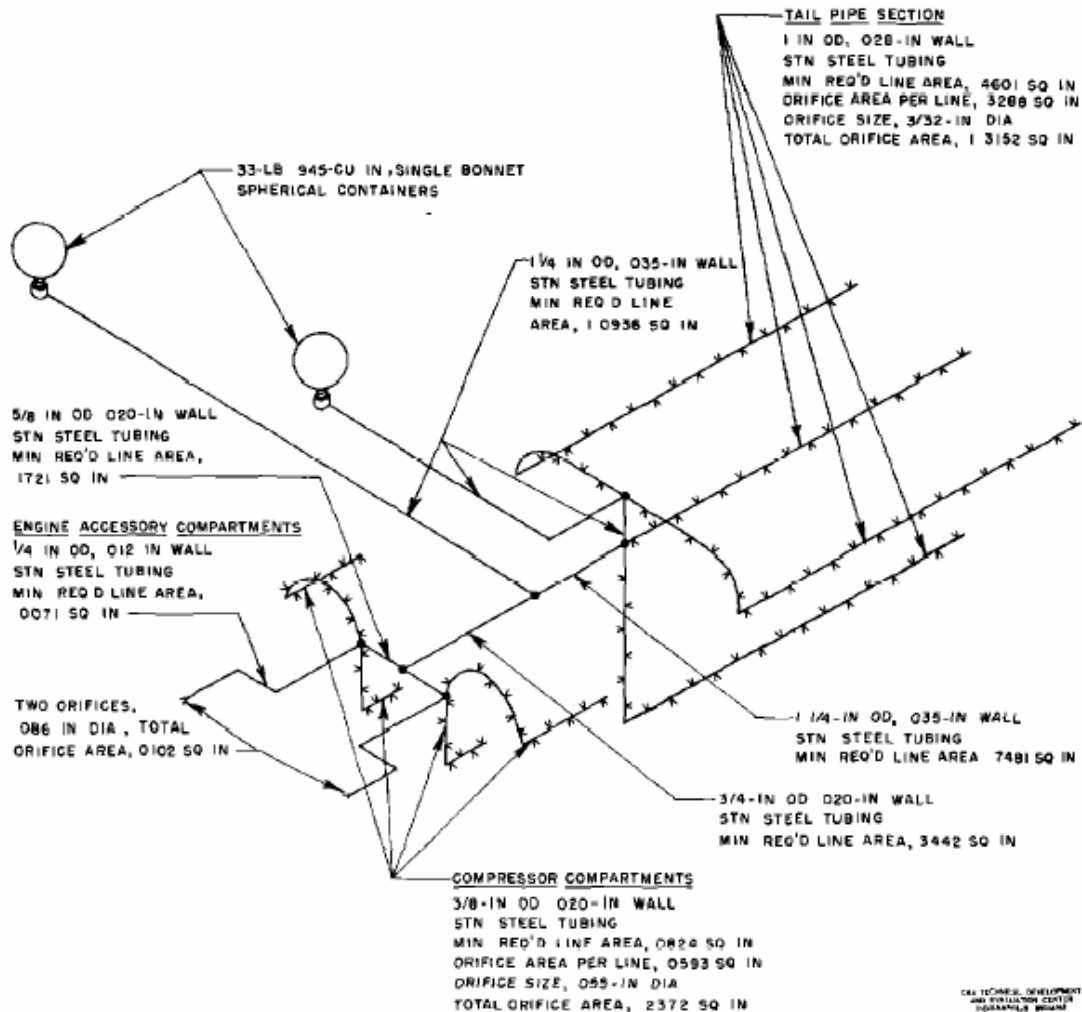


**Figure 2-55. Example Conventional Halon 1011 Fire Extinguishing System Distribution Installation, USAF Turbojet Powerplant.<sup>111</sup>**

- 1953: Fire testing is conducted by the CAA to determine the minimum amounts of suppressant required for varying airflows using CO<sub>2</sub> and halons 1001, 1011, and 1202.<sup>112</sup> Statham Laboratories began manufacturing the Model GA-1 Gas Analyzer for the USAF for use in measuring suppressant concentrations based on an experimental gas analyzer developed by the USAF.<sup>113</sup> This device is to later become known throughout the aviation fire suppression field as the Statham Analyzer.
- 1955: Fire and suppressant concentration testing was conducted by the CAA using halon 1011. A recommendation was developed that halon 1011 systems provide a minimum 15 % volumetric concentration for 1 s.<sup>106</sup>
- 1956: Fire testing of HRD systems was conducted by the CAA using CO<sub>2</sub> and halons 1001, 1011, 1202, and 1301, and design formulae for suppressant quantity are published. In successful fire extinguishment tests using the halons, discharge durations are indicated to have varied between 0.5 s and 0.9 s.<sup>108</sup> For CO<sub>2</sub> the duration was indicated to have varied between 1.25 s and 1.35 s.

- 1958: Fire testing of conventional and HRD systems was conducted by the CAA for the Northrop F-89 Scorpion using halons 1011, 1202 and, to a lesser extent, halon 1301.<sup>114</sup> This effort included specific tests to evaluate discharge duration and distribution using halon 1011. An overlapping time period of 0.44 s was noted for the two compartment sections evaluated, as indicated in Figure 2-56. (In Figure 2-56 the time axis is in 0.125 increments, thus 0.44 occurs between three and four increments.) Though the report indicates that by the time halon 1301 had been evaluated in the HRD system for fire testing some degradation in the test article had occurred, there is no indication in the report that this was a factor in the halon 1011 discharge duration and distribution tests (i.e., they may have been completed prior to conduct of halon 1301 fire testing).
- 1959: Fire and concentration measurement testing (using a then Statham Laboratories concentration analyzer) at WADC concluded for halon 1301 that roughly a 5.8 % “critical saturation value,” in percent concentration by volume, is required for fire extinguishment.<sup>105</sup> Later during the year, the required minimum relative concentration for halon 1301 was published as 15 %, which was specified to be maintained in all parts of the affected zone and persist in each part of the zone for at least 0.5 s at normal cruising condition. The relative value is that indicated by the Statham measurement device corresponding to a halon 1301 6 % volumetric concentration. At the end of the year, the military specification for installation and test of HRD aircraft fire suppression systems, MIL-E-22285, was issued.<sup>109</sup> The specification includes the previously published halon 1301 design formulae for suppressant quantity.
- 1960: The military specification for installation and test of HRD aircraft fire suppression systems was reissued, revising the concentration requirement from 15 % relative to 6 % volumetric.

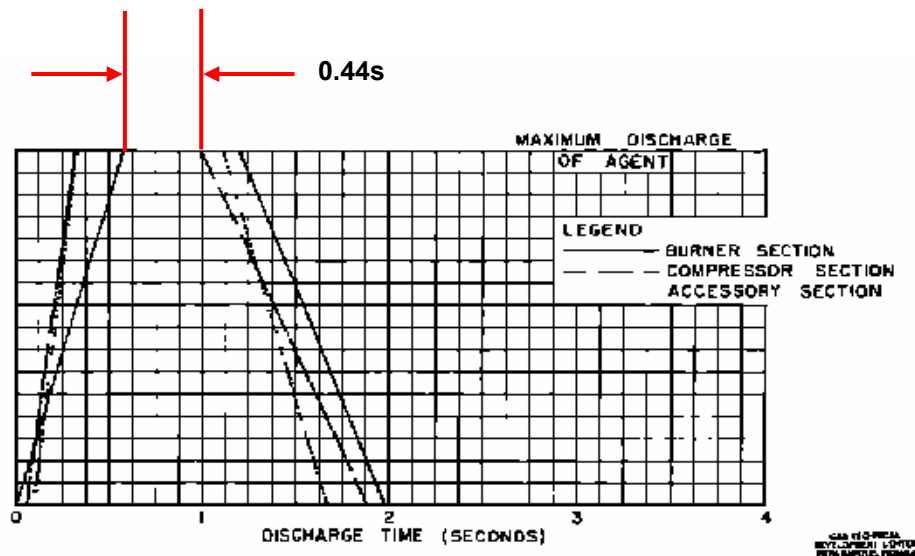


Figure 2-56. Minimum Discharge Duration from an HRD System Using Halon 1011.<sup>114</sup>

The HRD design formulae that have since been applied for sizing halon-1301-based systems in DoD aircraft applications have essentially remained unchanged since they were first published and were based on testing conducted on a single piston-engine powerplant and one jet power plant. Like the design

guidance for conventional halon 1011 systems, HRD system design guidance is also relative to compartment airflow and free volume. Additionally, a review of the CAA reports indicates that the number of tests conducted using halon 1301 preceding the issuance of MIL-E-22285 was limited. The CAA report that issued the design formulae indicates very few data had been obtained for halon 1301 but that it appeared equal to halons 1001 and 1202 on a weight basis. Given that the HRD design formulae published by the CAA were identical for halons 1001, 1202, and 1301, it is possible that in the case of halon 1301 the design guidance for it was asserted *qualitatively* at that time. It is also possible that this is the case for the 0.5 s discharge duration requirement, as discharge duration testing conducted by the CAA prior to the issuance of MIL-E-22285 was conducted using halons 1011 and 1202.

As indicated in Table 2-10, halon 1301 is today by far the most widely implemented of the halon suppressants for powerplant fire protection (nacelles and APU compartments) on DoD aircraft. Although Table 2-10 is not necessarily meant to be totally comprehensive, it depicts the magnitude of halon 1301 implementation across the DoD. The distribution systems are predominantly HRD designs. For reference, the table also lists other fire suppressants used today excluding halon-alternative fire suppressants installed on DoD aircraft since the Montreal Protocol. These are various forms of nitrogen-based fire protection and aluminum oxide, which is used on some aircraft in powder panels for passive dry bay protection.

#### **2.4.2 Dry Bay Compartments**

As discussed earlier in this chapter there are no active halon fire suppression systems installed currently on DoD aircraft for the specific purpose of ballistic dry bay fire protection, though there are compartments for which halon fire suppression is provided to protect against safety fire threats and for which such compartments are also vulnerable to ballistically-induced fire. The C-5 nitrogen fire suppression system provides protection for various dry bay compartments as indicated in Figure 2-57. System discharge is automatic for fires detected in the wing and pylon leading edge dry bays. Aluminum oxide powder ( $\text{Al}_2\text{O}_3$ ) has also been fielded on several DoD aircraft. The powder is contained within a parasitic honeycomb panel to prevent ballistically-induced fires in dry bays adjacent to fuel cells and was first developed by the Royal Aircraft Establishment in England.<sup>115</sup> If ruptured by a ballistic projectile, the panel releases a powder suppressant to quench incendiaries released by the projectile. The powder panel indicated in the example wing leading edge dry bay shown earlier in Figure 2-18 is an example of a parasitic powder panel installation. Chapter 9 describes NGP work to develop advanced powder panel design techniques.

#### **2.4.3 Certification**

The current requirement to certify other than dry-bay fire-suppression systems on aircraft that use halon 1301 requires demonstrating a minimum suppressant concentration for at least 0.5 s at all measurement locations simultaneously. Minimum suppressant concentration requirements for  $\text{CO}_2$ , and halons 1001, 1011, 1202, and 1301 are indicated in FAA Advisory Circular 20-100.<sup>116</sup> (Military specification MIL-E-22285 provides these requirements for halon 1301 only.) By today's method for certifying halon 1301 powerplant fire suppression systems, previous methods would seem somewhat subjective. One previous method was to discharge water through the distribution system, capture the discharge by large aerology balloons, and determine the quantity discharged as being equal to the difference between the total quantity and quantity captured, assuming a 10 % system loss.

**Table 2–10. Fire Suppressants on DoD Aircraft.**<sup>xxx</sup>

<b>Halon 1011 (CH<sub>2</sub>ClBr)</b>	<b>Halon 1202 (CF<sub>2</sub>Br<sub>2</sub>)</b>	<b>Halon 1211 (CF<sub>2</sub>ClBr)</b>	<b>Halon 1301 (CF<sub>3</sub>Br)</b>	<b>Nitrogen (N<sub>2</sub>)</b>	<b>Aluminum Oxide (Al<sub>2</sub>O<sub>3</sub>)</b>
<b>USAF:</b> C-130  <b>USN:</b> DC-130A LC-130F/R TC-130G	<b>USAF:</b> C-5, C-141  Note: halon 1202 is an alternate for halon 1011 on USAF and USN C-130 aircraft, except for C/KC-130J aircraft.	<b>USAF:</b> C-130J  <b>USN:</b> KC-130J	<b>USAF:</b> MH-53, HH-60 A/OA-10, B-2 B-1B (overwing fairing) C-5 (cargo, avionics, and center wing) C-9, KC-10, C-12 C-17, C-20, C-22B C-32A, C-40 C-135, VC-25A C-141, E-3A E-4A, E-8C F-16 (ullage) F-15, F-117 T-34A, T-39, T-43  <b>USN:</b> AH/UH-1, SH-2 HH/SH/UH-3 CH/HH-46 CH/MH-53 HH/SH-60 C-2A, C-9 C-12, C-20 E-2C, E-6A EA-6B, F-14 F/A-18C/D P-3, S-3 T-39, T-44A C-130 (excluding C-130s with halon 1011, 1202 or 1211)  <b>US Army:</b> AH-64, CH/MH-47 EH/MH/UH-60 C-7, C/RC-12, C-20	<b>USAF - LN<sub>2</sub> (ullage and dry bay):</b> C-5  <b>USAF – OBIGGS NEA (ullage):</b> F-22 C-17  <b>USN - OBIGGS NEA (ullage):</b> V-22 AH-1Z UH-1Y  <b>US Army – OBIGGS NEA (ullage):</b> AH-64 MH-47E MH-60	<b>USAF (dry bay):</b> CV-22  <b>USN (dry bay):</b> MV-22 AH-1W/Z UH-1N/Y

<sup>xxx</sup> Table 2-10 excludes halon alternative fire suppressants installed on DoD aircraft since the Montreal Protocol. These aircraft are the MV/CV-22, F-22, and AH-1Z/UH-1Y, each of which utilizes HFC-125 for nacelle fire suppression and OBIGGS NEA for fuel tank inerting. Also, the F/A-18E/F utilizes HFC-125 for nacelle fire suppression, except for EMD and LRIP 1 aircraft, which utilize halon 1301. The F/A-18E/F and MV/CV-22 use inert gas generators for dry bay fire suppression. The gas discharge is a gaseous mixture of carbon dioxide, nitrogen, and water vapor. Gas generator technology is also being evaluated for dry bay fire suppression on the Joint Strike Fighter (JSF) aircraft.

Distribution ratios were determined for each zone protected by the system, thus the required quantity of suppressant for each zone could be determined prior to testing. Another previous method was to measure discharge duration by means of motion pictures taken at the rate of 32 frames per second. Neither of these previous methods could be accomplished in flight.

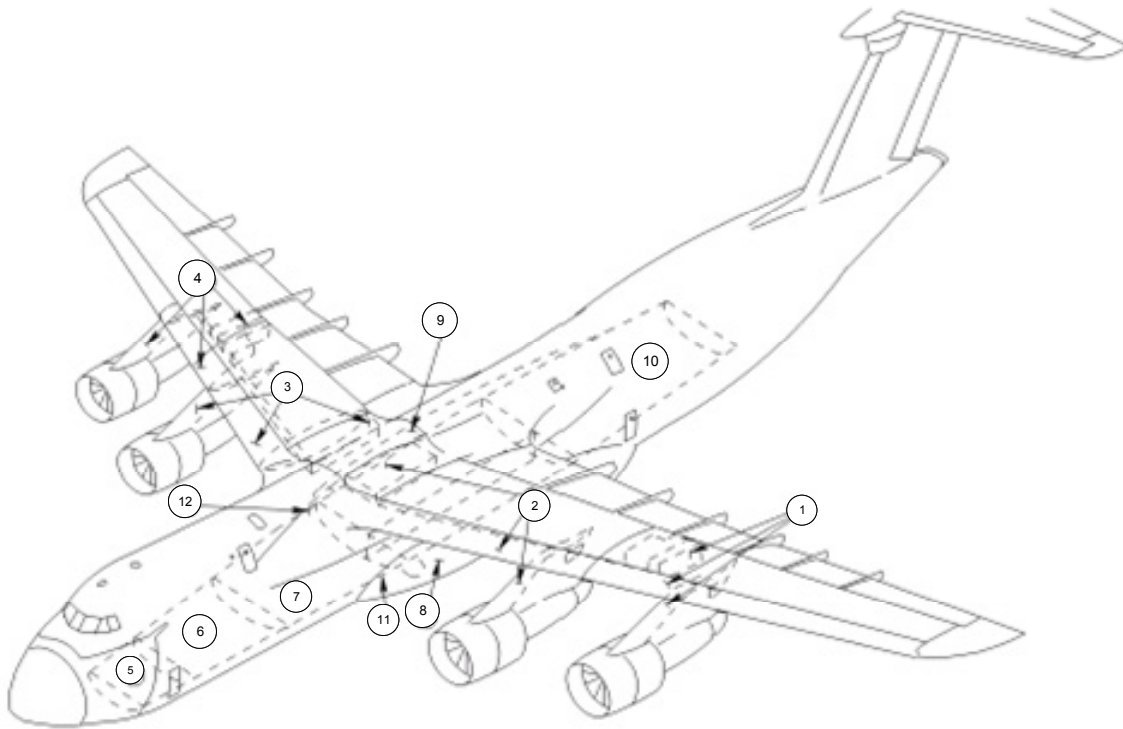
The Statham-type suppressant concentration analyzer device mentioned in the previous section permits in-flight measurement of fire suppressant concentration.<sup>xxxii,117</sup> This type of analyzer operates based on a linearized viscosity mixing theory using the weighted viscosities of a binary gas mixture, i.e., air and the fire suppressant. Since the viscosity of pure air differs from that of pure fire suppressants, readings will show that a mixture of gases is present and the “relative” concentration of the suppressant will be indicated by the differential pressure reading obtained. An algorithm converts relative concentration values to volumetric concentration values based on the unique calibration of the analyzer and the fire suppressant. A vacuum pump draws the gas mixture samples through twelve sampling probes (copper tubes) into sensor assemblies. Sampling probe ends are oriented perpendicular to compartment airflow and are located throughout the compartment (Figure 2-58). In each sensor assembly, the gas passes through filter screens, a heat exchanger, a capillary tube differential pressure sensor section, and finally through a sonic flow orifice. The heat exchanger section ensures uniformity of monitoring conditions, and tests are performed only after thermal equilibrium is achieved. The sonic flow orifice ensures a constant flow while the capillary tubes create the pressure drop measured by a transducer. The transducer transmits the pressure signal to a processor unit which performs the necessary calculations and then records and displays relative concentrations.<sup>118</sup> The relative concentrations are then converted to volumetric concentrations for evaluation as to whether the fire suppression system meets a certification requirement (Figure 2-59).

Until recently, non-dry-bay fire suppression systems qualification has been normally accomplished by concentration measurement. There are unique cases where a system such as a nacelle fire suppression system will be qualified by fire testing. In this case, performance requirements will be specified and agreed to by the acquisition or certifying agency and the aircraft manufacturer. Nacelle fire suppression systems that have been qualified through fire testing are those on the USN F/A-18E/F, which uses HFC-125 as the fire suppressant, and the commercial Eclipse 500 aircraft, which uses PBr<sub>3</sub>.

The certification requirement to demonstrate compliance with survivability and vulnerability requirements is Congressionally legislated in Title X, Section 2366 of the United States Code of Federal Regulations, which was passed in 1987. This live fire test legislation requires that realistic testing be done on new systems before they reach the field. The vast majority of DoD aircraft fielded today had initial operating capability prior to enactment of this legislation. Thus it is probable that compartments on aircraft for which halon fire suppression is provided to protect against safety fire threats and for which such compartments are also vulnerable to ballistically induced fire, no live fire testing had been performed, and that such halon systems were certified solely by suppressant concentration measurement.

---

<sup>xxxii</sup> There are several versions of this type of analyzer that are certified by the FAA for use in performing fire suppression system concentration measurement for the purpose of qualifying or certifying aircraft fire suppression systems. One is the Statham Analyzer, owned and operated by Walter Kidde Aerospace. This is a modified version of the original Statham analyzer described earlier. Another analyzer is the Halonyzer, of which there are currently two versions, Halonyzer 2 and Halonyzer 3. One Halonyzer 3 analyzer is owned and operated by its manufacturer, Pacific Scientific/HTL Kin-Tech. One Halonyzer 3 analyzer is also owned and operated each by Boeing commercial and by the USAF at WPAFB. One Halonyzer 2 analyzer is owned and operated by Airbus Industries in France. Finally, a ‘modified’ Halonyzer 2 analyzer is owned and operated by the FAA Hughes Technical Center Fire Safety Branch.



**Nitrogen Fire Suppression Zones and Controls**

Zone	Spaces Included in Zone	Flight Engineer's Panel Discharge Pushbutton	Nose Wheel Well Panel Discharge Pushbutton
1	Left wing dry bay, left outboard leading edge, left outboard pylon leading edge	Left outboard wing	Left wing
2	Left wing root dry bay, left inboard leading edge, left inboard pylon leading edge	Left inboard wing	Left wing
3	Right wing root dry bay, right inboard leading edge, right inboard pylon leading edge	Right inboard wing	Right wing
4	Right wing dry bay, right outboard leading edge, right outboard pylon leading edge	Right outboard wing	Right wing
5	Nose wheel well	Nose wheel well	–
6	Cargo under floor, forward	Under floor, forward	Under floor, forward
7	Cargo under floor, middle	Under floor, forward	Under floor, forward
8	Left main wheel well	Left main wheel well	–
9	Right main wheel well	Right main wheel well	–
10	Cargo under floor, aft	Under floor, aft	Under floor, aft
11	Left power turbine unit (PTU) compartment	Left PTU	Under floor, forward
12	Right power turbine unit (PTU) compartment	Right PTU	Under floor, forward

**Figure 2-57. Zones Protected by the Nitrogen Fire Suppression System on C-5 Aircraft.**<sup>119</sup>  
 (Reprinted with permission by the USAF Warner Robbins Air Logistics Center)

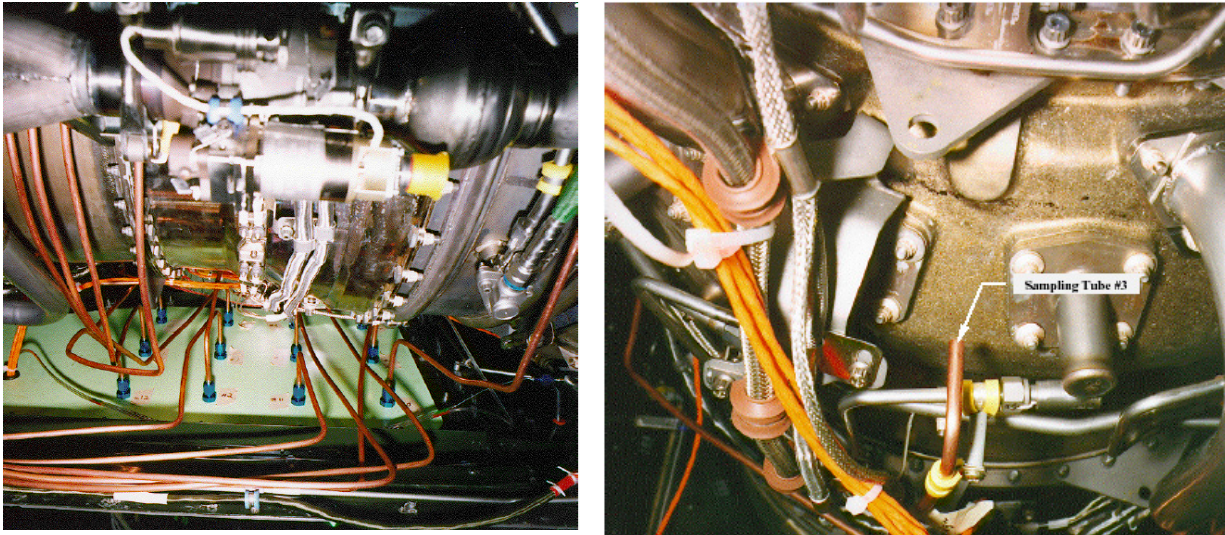


**Figure 2-58. Fire Suppressant Concentration Analyzer Sampling Probe Installation.**  
(Printed with permission of the Naval Air Systems Command.)

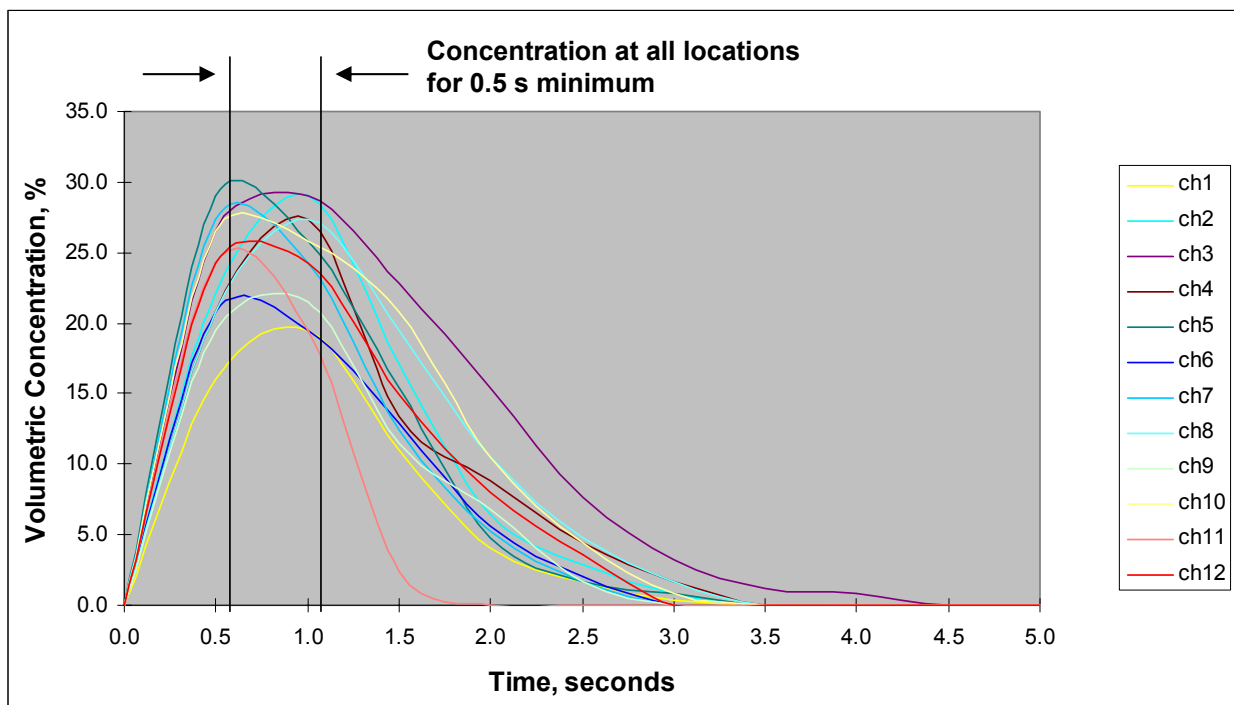


**Figure 2-59. Example Fire Suppression System Suppressant Concentration Measurement.**

Previous testing with halon 1301 for suppression of dry bay compartment fires with ventilation induced by damage from a ballistic projectile indicated that halon 1301 would suppress fires if discharged very fast, on the order of 10 ms, from a fire bottle type used on the United Kingdom CH-47 Chinook helicopters, or if a comparable halon 1301 quantity was discharged from a bottle design typically used for nacelle or APU fire suppression, from which the suppressant will discharge in approximately 1 s. Even though this testing showed that both types of bottle configurations provided halon 1301 concentrations well above 6 % for greater than 0.5 s,<sup>21</sup> no concentration-based dry bay fire suppression system certification requirement was ever established by the DoD. Likewise, even though there is historical reference to the fielding of reactive ullage fire suppression systems, there is no DoD concentration-based qualification requirement for these systems as well. It should be noted that the fast discharge capability of the fire bottle type United Kingdom CH-47 Chinook helicopters is consistent with the design guidance indicated in Figure 2-60 for a confined space (i.e., constant volume), which has existed since 1965.

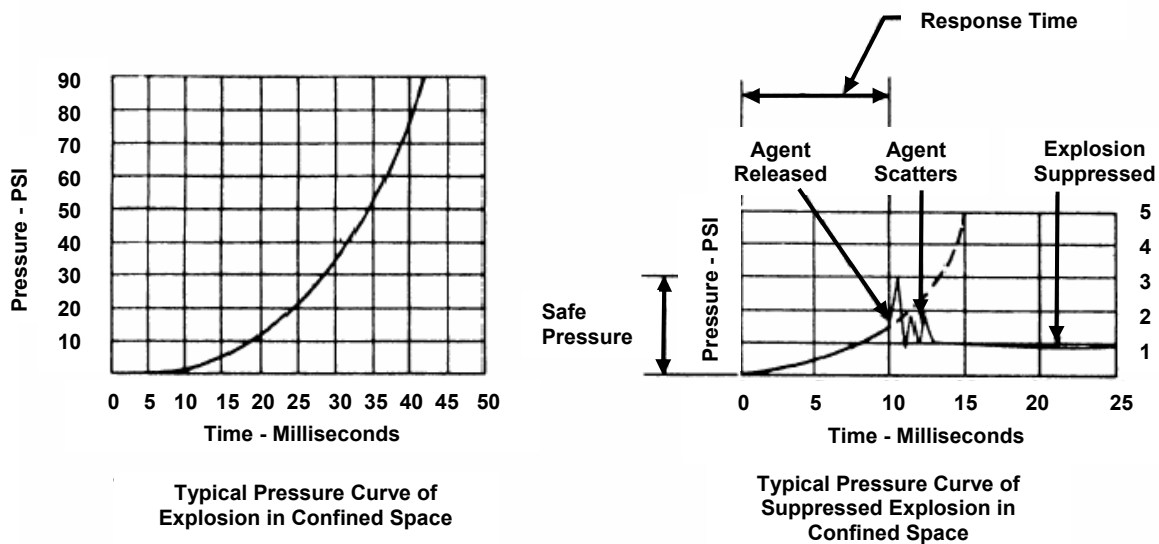


**Figure 2-60. MIL-HDBK-221 Design Guidance for Explosion Suppression.**<sup>120</sup>

In the case of the C-5 nitrogen fire suppression system, which is an extension of the fuel tank LN<sub>2</sub> inerting system and provides dry bay fire protection, the system is required to reduce the oxygen level within the compartment into which it is discharged, ullage or dry bay, to 10 % or less “in the time duration necessary to cope with the particular fire hazard.” (Typically, the DoD will require that ullage inerting systems reduce oxygen concentrations to 9 % or less.). The USN A-6E ullage inerting system was designed to maintain a halon 1301 volumetric concentration of 20 % upon activation.<sup>121</sup>

OBIGGS installations on currently-fielded DoD aircraft were typically certified by measuring the oxygen concentration with a single oxygen sensor installed at the fuel vent interface in one or more fuel tanks or by installing an oxygen sensor on a fill port, as indicated in Figure 2-61. Today, as work continues towards developing OBIGGS for commercial transport aircraft, an oxygen-gas sampling system has been developed by the FAA that is utilized and operates in a manner similar to the concentration measurement analyzers utilized for certifying nacelle fire suppression systems.

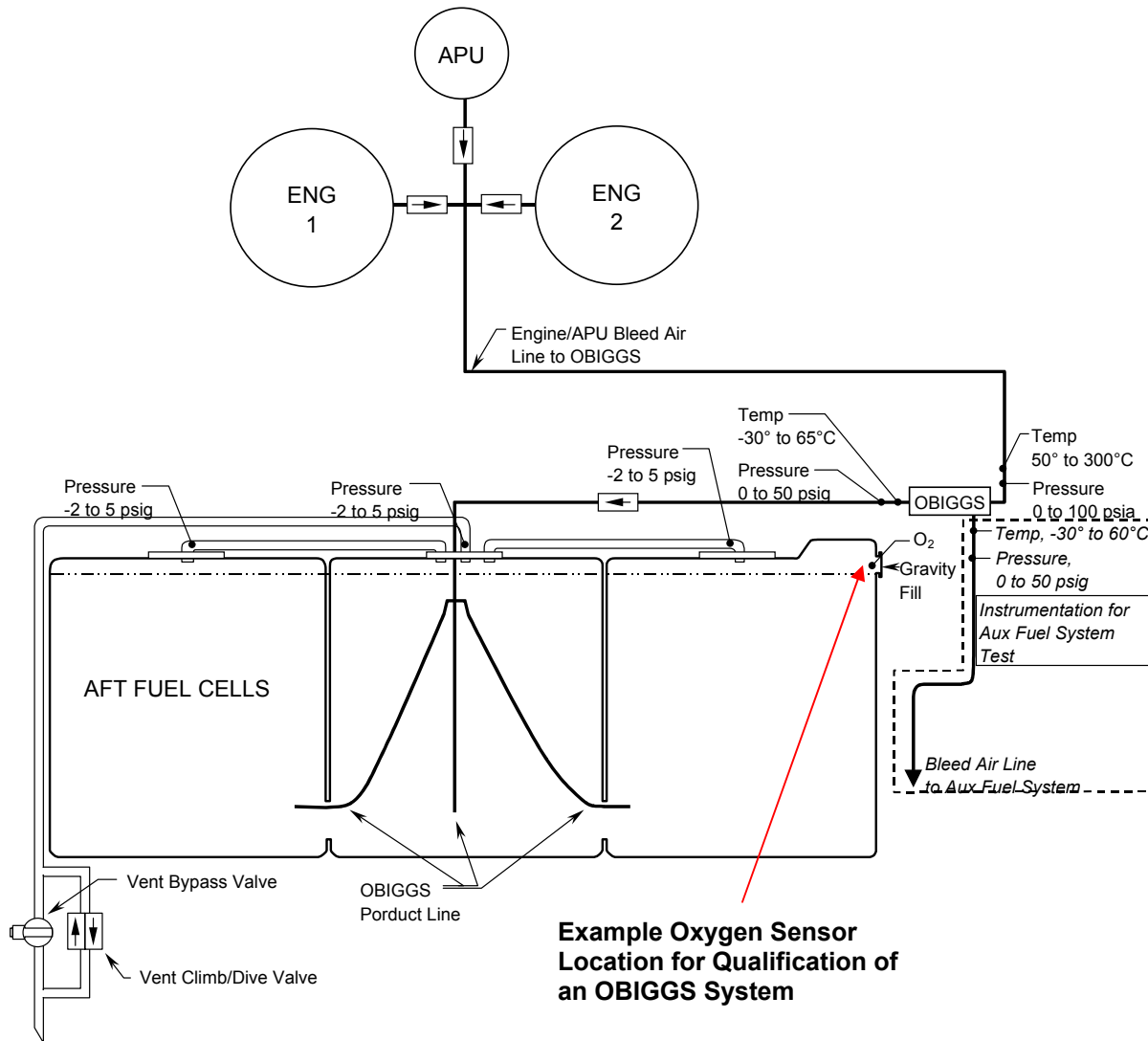


**Figure 2-61. Typical Legacy OBIGGS Qualification Test Oxygen Concentration Measurement Location.**

(Printed with permission of the Naval Air Systems Command.)

## 2.5 HALON ALTERNATIVE TECHNOLOGY DEVELOPMENT PROGRAM (TDP)

Chapter 1 discussed why the DoD initiated the TDP and its goal for identifying near-term, environmentally friendly, and user-safe alternatives to halon for aircraft engine nacelle and dry bay applications, and why the limitations of what had been identified along with new/emerging environmental constraints required continued research and development for these applications. However, the breadth and technical approach of the TDP is historically significant. Like previous efforts related to aircraft fire suppression, the TDP spanned several years and was a collaborative effort involving participants from government agencies, industry, and academia.

Following the DoD's 1989 delineation of its policy on halon replacement research, over 600 potential halon replacement chemicals were assessed.<sup>57,122</sup> This was followed by the USAF initiating the Halon Replacement Program for Aviation in 1992 to develop a non-ozone depleting solution for on-board fire suppression within a timeline to support the F-22 aircraft acquisition program. In addition to the F-22, the V-22 and F/A-18E/F acquisition programs also implemented requirements for fire suppression systems having non-ozone depleting fire suppression agents. Thus, the scope of program was subsequently expanded to address requirements of all DoD and civilian aircraft engine nacelle and dry bay applications and was jointly-sponsored by the USAF, USN, U.S. Army, and the FAA as the TDP. Additionally, an oversight group, the Halon Alternatives Steering Group (HASG), was established to coordinate efforts within the TDP as well as other government research and development (R&D) programs related to fire suppression. This included coordination with related efforts under the EPA's SNAP program, which addressed both environmental acceptability and personnel safety, e.g., toxicity, of candidate halon alternative suppressants. The TDP was a three-phase program, each of which is discussed briefly below. The reader is encouraged to refer the publications referenced in this section for more detailed discussion.

### 2.5.1 Phase 1 – Operational Parameters Study

Phase 1 determined parameters in aircraft engine nacelles and dry bays that have the greatest influence on the quantity of fire suppressant required to extinguish fire in those types of compartments.<sup>123,124</sup> Characteristics of each of these compartment types on then-fielded aircraft were acquired to support development of a test matrix used during this portion of the TDP. A statistical design of experiments (DOX) methodology was employed to reduce the number of possible test configurations to 32 using a Plackett-Burman two-level fractional factorial design to permit study of the effects of 14 parameters related to dry bay compartments and 16 parameters related to engine nacelle compartments along with interactions of factors with only 32 test runs for each compartment. Evaluating two<sup>14</sup> combinations of dry bay compartment factors and two<sup>16</sup> combinations of engine compartment factors was not feasible. The DOX methodology permitted evaluating effects of the parameters for each compartment type within the physical and economic resources available to the TDP as well as to permit concurrent acquisition programs to meet schedule requirements for implementing non-ODS-based fire suppression systems. Table 2-11 lists, in order of significance, the factors found during Phase 1 testing at Wright-Patterson Air Force Base (WPAFB) to influence fire suppression the most in each compartment type. Concurrent studies and testing of candidate halon alternative chemicals were conducted by NIST to evaluate materials compatibility, thermodynamic properties, fluid dynamics associated with discharge, flame suppression effectiveness, flame inhibition chemistry, agent stability under storage, and affects to personnel and the environment.<sup>125</sup> The combined outcome from the WPAFB and NIST efforts resulted in the recommendation that the chemicals listed in Table 2-12 be evaluated during Phase 2.

**Table 2–11. Most Significant Fire Suppression Parameters Identified During Phase 1.**

Engine Nacelle <sup>xxxii</sup>	Dry Bay
Surface Temperature (34 %)	Compartment Volume (48 %)
Fire Suppression Agent (14 %)	Fire Suppression Agent (28 %)
Clearance, or Nacelle Free Volume (12 %)	External Airflow Rate (13 %)

<sup>xxxii</sup> Two additional non-confounded parameters identified were nacelle airflow temperature and fuel temperature. Testing during Phase 1 also highlighted the significance of hot surface reignition.

**Table 2–12. Halon Alternative Fire Suppressants Identified for Phase 2 Evaluation.**

Engine Nacelle	Dry Bay
Pentafluoroethane (HFC-125)	Octafluoropropane (FC-218)
Chlorotetrafluoroethane (HCFC-124)	Pentafluoroethane (HFC-125)
Trifluoroiodomethane (CF <sub>3</sub> I)	Heptafluoropropane (HFC-227ea)
Heptafluoropropane (HFC-227ea)	Trifluoroiodomethane (CF <sub>3</sub> I)

### 2.5.2 Phase 2 – Operational Comparison of Selected Extinguishants

The fire suppressants identified during Phase 1 as the most promising halon alternatives for engine nacelle and dry bay fire suppression applications were subjected to additional testing during Phase 2.<sup>126,127</sup> The DOX methodology was again employed to further evaluate effects of the most significant parameters identified during Phase 1 for each compartment type. Additional factors were also included based on discussion with aviation fire suppression experts. For dry bay fire testing, two additional factors evaluated were fire suppression agent container temperature and clutter (obstructions in the dry bay that inhibit suppressant distribution). For nacelle fire testing, four additional factors were evaluated: fire location in the nacelle, fuel type, nacelle mass airflow rate, and fire suppression agent container temperature. Table 2-13 lists, in order of significance, the factors found during Phase 2 testing at WPAFB to influence fire suppression the most in each compartment type. Additional testing was conducted by NIST to further evaluate fire suppression efficiency, stability during storage, safety following discharge, agent discharge behavior and performance, and interaction with metal fires. Techniques for real-time concentration measurement were also developed along with guidance for engine nacelle fire suppression design and certification.<sup>128,13</sup> The combined outcome from the WPAFB and NIST efforts resulted in the down-selection to pentafluoroethane (HFC-125) as the optimal near-term halon alternative fire suppression agent for both engine nacelle and dry bay applications. This chemical was taken into Phase 3 for detailed evaluation.

**Table 2–13. Most Significant Fire Suppression Parameters Identified During Phase 2.**

Engine Nacelle	Dry Bay
Surface Temperature (39 %)	Compartment Volume (45.3 %)
Fire Suppression Agent (15 %)	Fire Suppression Agent (23.6 %)
Nacelle Airflow Temperature (10 %)	Compartment Volume and Location Interaction (14.3 %)
Surface Temperature and Nacelle Airflow Temperature Interaction (6 %)	Fire Suppressant Bottle Location (5.5 %)
Fire Location (4 %)	

### 2.5.3 Phase 3 – Establishment of Design Criteria Methodologies

During Phase 3, extensive engine nacelle and dry bay fire testing was conducted using HFC-125. The DOX methodology was again employed to evaluate effects of the most significant parameters identified during Phase 2 for each compartment. Extensive statistical analysis of the test data was conducted to develop design models (equations) for aircraft engine nacelle, APU and dry bay applications.<sup>90</sup> The

equations were developed to assist designers in sizing nacelle and dry fire suppression systems using HFC-125. Table 2-14 summarizes the variables that are to be taken into consideration when applying each of the equations.

**Table 2–14. Fire Suppression Parameters in Design Guidance Developed from Phase 3.**

Engine Nacelle	Dry Bay
Surface Temperature (Set at 454.5 °C)	Location – Impact Angle of Ballistic Projectile Relative to the Horizon
Nacelle Airflow Temperature	Dry Bay Free Volume
Nacelle Mass Airflow Rate	External Airflow Rate
Fuel Type	

Evaluation of data from engine nacelle fire testing highlighted the significance of engine surface temperature. Various models were developed to converge on one that would provide a best fit to the experimental data. Curve fits from test data in which the surface temperature was 454.4 °C (850 °F) and lower better modeled the overall test results than curve fits that included test data in which the surface temperature exceeded 454.4 °C. This was attributed to the variability induced from hot surface reignition.

Applying the HFC-125 engine nacelle fire suppression design model is a two-step process. The first step is to calculate the HFC-125 concentration required to certify the system. The equation bounds the resultant concentration to either a minimum of 14.6 % and a maximum of 26 %. Embedded within the concentration equation is a factor for a nacelle hot surface temperature of 454.5 °C. The calculated concentration is then used as an input variable in a sizing equation to estimate the quantity of HFC-125 needed to provide the needed concentration for certification. Though the sizing equation is similar in structure to the current design guidance for halon 1301 in that it contains nacelle mass airflow and nacelle free volume as variables, the testing performed under Phase 3 resulted in this two-step design guidance that includes concentration based on values of nacelle-specific parameters. Previous analyses of the current halon 1301 design guidance had indicated that the concentration variable may have been considered, but it may have been embedded with the concentration value fixed at the halon 1301 flammability limit of 6 %.<sup>63,129</sup>

During dry bay testing, all ballistic shots were initially horizontal with the projectile entering the dry bay compartment from the side. However, additional consideration was given to the fact that some aircraft have belly dry bay compartments. This resulted in testing of vertical shots entering from the bottom of a dry bay. This testing and subsequent data analysis proved that shot angle was an important variable and is one of the variables that must be taken into consideration when applying the HFC-125 dry bay model. During design of an HFC-125 dry bay fire suppression system, the dry bay design model provides an estimate of suppressant quantity needed to suppress a dry bay fire. Prior to the development of this model there had been no design guidance for the sizing of halon 1301 dry bay fire suppression systems, though analysis of results from a previous test effort indicated a halon concentration range between 3 % and 9 % for a protection system incorporating a non-discriminating fire detection sensor, and a range between 6 % and 12 % for a system incorporating a discriminating sensor.<sup>17</sup>

## 2.5.4 Impact of Halon Alternative Fire Suppression to the Aircraft

### Nacelle/APU Fire Suppression Applications

As the DoD has relied heavily on halon 1301 for aircraft fire suppression applications, the impact of what was learned during the TDP as well as from subsequent aircraft-specific development and testing efforts has become clear. Application of the outcomes from the TDP would result in halon alternative fire suppression systems that, relative to halon 1301 systems, would:

- Weigh more, due to both the increased mass of suppressant and the increased size of the bottle required to store the suppressant;
- Be more costly to optimize via enhanced distribution, which itself may lead to an incremental weight increase; or
- Cost more to support over the lifetime of an aircraft, e.g., increased weight translates to increased materials required for fabrication as well as increased fuel consumption and thus increased cost.

For example, on the V-22 fire door, actuators will close off two of three air inlets prior to discharge of the nacelle fire suppression system, which substantially reduces airflow through the nacelle. It was estimated that approximately 1.07 kg (2.35 lb) of halon 1301 would be required to protect each V-22 engine nacelle under this reduced airflow condition, whereas a fire bottle containing 2.72 kg (6 lb) of HFC-125 is installed for each nacelle for this same condition (2.55 times the estimated halon 1301 quantity).<sup>130</sup> At the time of design and qualification of the V-22 nacelle fire suppression system, the TDP design equations had not yet been developed. However, the then-available mass equivalence ratio for HFC-125 mass quantity relative to halon 1301 and a flame suppression number (FSN) were applied in the design analysis for the V-22 system.

Legacy AH-1W/UH-1N aircraft have two fire bottles, primary and reserve, each containing 0.9 kg (2 lb) of halon 1301 for engine nacelle fire protection. The upgraded versions of these aircraft, the AH-1Z/UH-1Y, include exhaust suppression systems. Simply adding such systems can require requalification of a nacelle fire suppression system as nacelle airflow, compartment temperature and suppressant distribution can be impacted. However, these aircraft were also required to implement HFC-125 as the halon-alternative fire suppressant. Examination of the analysis approach to determine the needed HFC-125 mass quantity, which was similar to that used for the V-22, suggested that 1.36 kg (3 lb) of halon 1301 would have been required to protect the nacelles, but these aircraft now have a single fire bottle containing 3.72 kg (8.2 lb) of HFC-125, a single discharge system.<sup>131</sup> This was the mass quantity determined to be necessary to meet a concentration requirement based on application of the TDP concentration equation. Thus relative to a need to only discharge a single fire bottle on the legacy aircraft, the upgrade aircraft HFC-125 suppressant quantity represents an increase of over 2.7 times the potential halon 1301 quantity required and 4 times the halon 1301 installed on legacy aircraft.

For halon 1301, peak flammability limit is indicated by the FAA as the rationale for the 6 % volumetric concentration certification requirement. What the preceding discussion of halon alternative implementation indicates, and what Figure 2-62 illustrates, is that implementing a chemical halon alternative for nacelle fire suppression, in this case HFC-125, is likely to require well over twice the mass quantity of suppressant relative to halon 1301, if typical nacelle fire suppression system design practices are followed. (Figure 2-62 provides a graphical comparison of the current halon 1301 certification

requirements, the minimum and maximum HFC-125 design equation concentrations and the FAA HFC-125 minimum performance standard vs. various published peak flammability limits for both halon 1301 and HFC-125.)

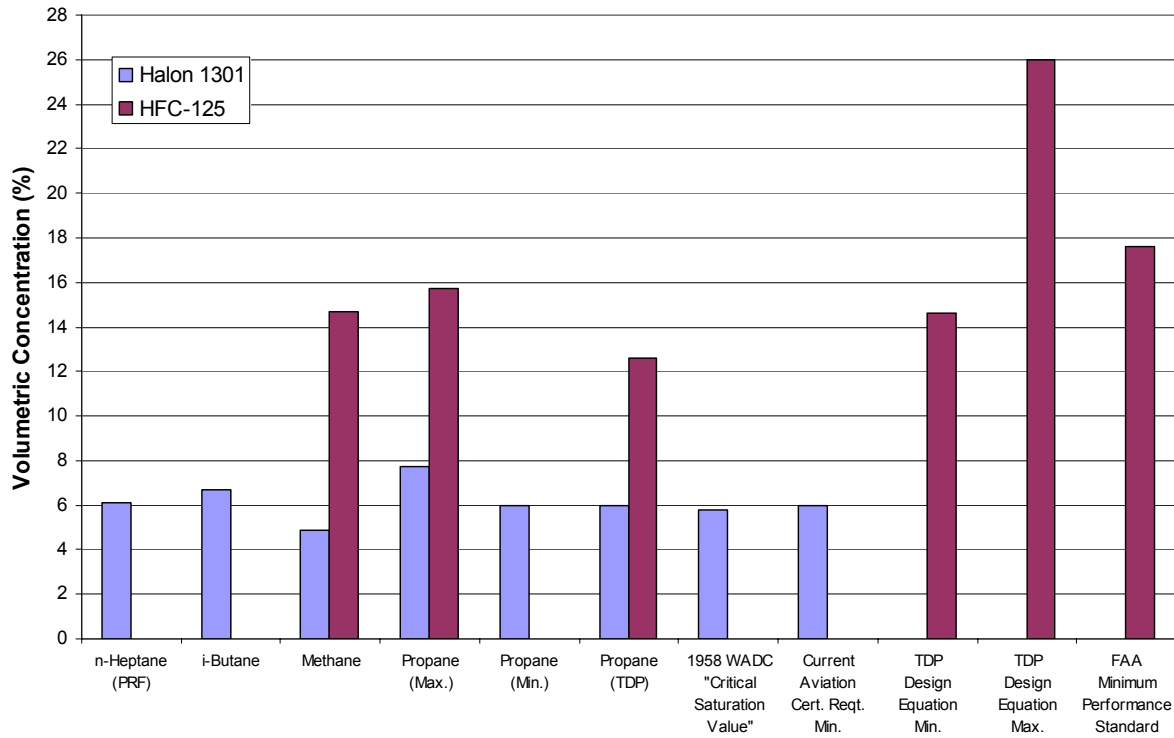


**Figure 2-62. Comparison of Halon 1301 Certification Requirement and HFC-125 Design Equation Limits vs. Published Flammability Limits.**<sup>xxxiii</sup>

Typical design practices usually entail using design guidance (i.e., equations) to estimate suppressant mass quantity needed, conducting analysis of nacelle airflow characteristics for the purposes of designing the suppressant distribution system and discharge location or locations within the nacelle, and then performing qualification tests and, if necessary, adjusting the discharge locations in order to pass qualification; i.e., try different nozzles on the ends of the distribution tubing or changing the orientation of the discharge locations. Though the systems may then meet certification requirements, the entire process can result in non-optimized suppressant distribution, which is illustrated in Figures 2-63 and 2-64.

<sup>xxxiii</sup> In Figure 2-62, the n-heptane flammability limit is from Reference 65. i-Butane, Methane, Propane (max) and Propane (min) flammability limits are from Standard for Clean Agent Fire Extinguishing Systems, NFPA 2001, 2000 Edition. Propane (TDP) flammability limit is from Reference 13. The WADC Critical Saturation Value is from Reference 105. TDP Design Equation Min and Max values are from Reference 90. It is interesting to note that the same halon 1301 volumetric concentration determined by the WADC in 1959 was also indicated in later work described in Dyer, J.H., Marjoram, M.J., and Simmons, R.F., "The Extinction of Fires in Aircraft Jet Engines – Part III, Extinction of Fires at Low Airflows," Fire Technology, 13, 126-138 (1977).

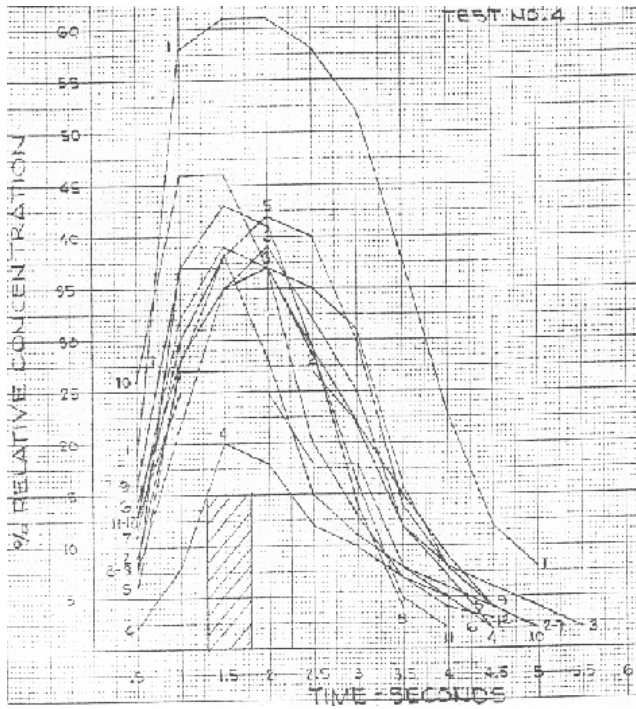


Figure 2-63. Example of Non-Optimized Halon 1301 Nacelle Concentration Distribution.

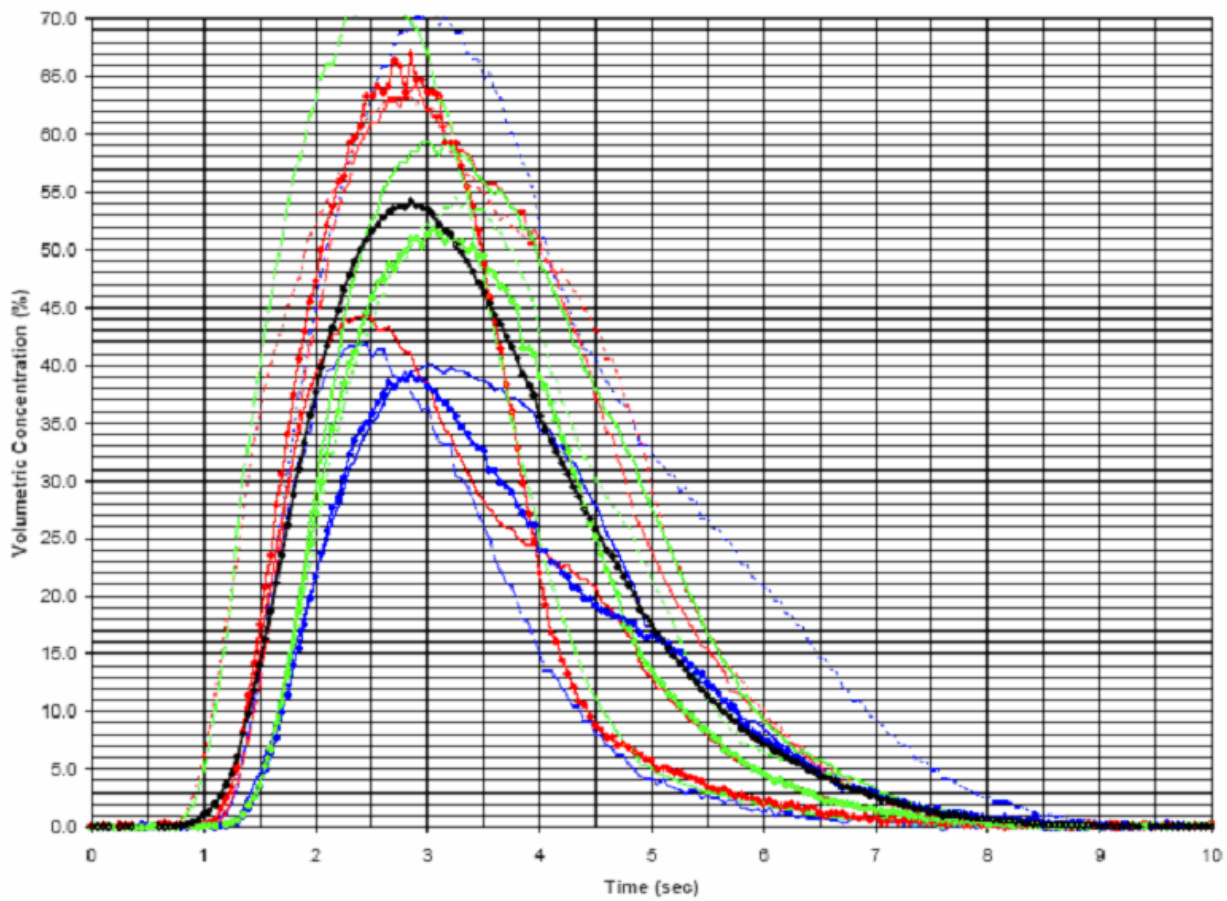
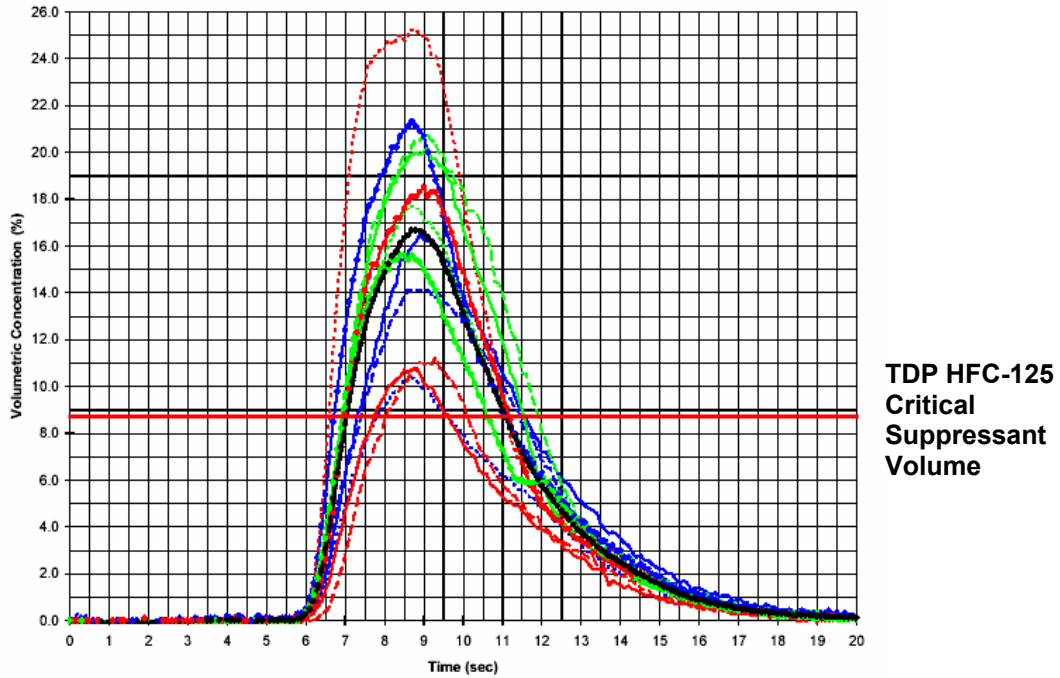


Figure 2-64. Example of Non-Optimized HFC-125 Nacelle Concentration Distribution.

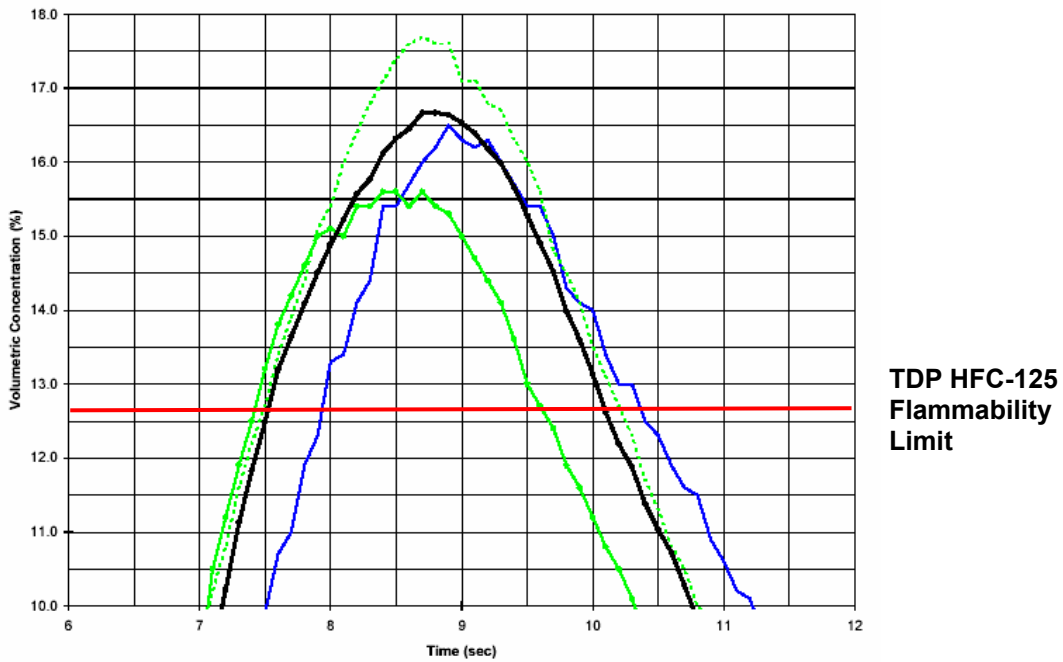
In the case of the F/A-18E/F aircraft, optimizing the nacelle fire suppression system distribution resulted in the fielding of a nacelle fire suppression system with an HFC-125 mass quantity (3.17 kg, 7.0 lb) only 1.27 times that required for the halon 1301 system (2.49 kg, 5.5 lb) on legacy F/A-18 aircraft. While it has been long promoted that the distribution system itself is probably the most important single factor in system design,<sup>132</sup> the distribution system design on the F/A-18E/F resurrects the concept of increased dwell time within the nacelle after discharge. This implementation parallels a recommendation following detailed review of the F-22 full-scale engine nacelle fire test program to maintain suppressant inerting concentrations for an appropriate duration by optimizing delivery and distribution.<sup>133</sup> The F-22 is discussed later in this section. Though the F/A-18E/F system is an HRD system, the suppressant dwell time throughout the entire nacelle is similar to the duration requirement for historical conventional system designs in that the dwell at or above the HFC-125 critical suppressant volume fraction (8.7 %) is maintained for at least 2 s. However, in the portion of the nacelle for which there is a hot-surface ignition threat the suppressant concentration was at or above the flammability limit for at least 0.5 s. An example of this concept is shown in Figure 2-65. Strict application of the HFC-125 concentration equation for the F/A-18E/F would have imposed a certification requirement of 18.5 % volumetric concentration throughout the nacelle for 0.5 s minimum.<sup>47</sup> In the case of the F/A-18E/F aircraft, it was necessary to optimize suppressant distribution to utilize the physical location of the fire bottle, which was to remain unchanged from the legacy F/A-18C/D design unless significant and costly aircraft structural modifications were pursued. It is interesting to note that even if an 18.5 % volumetric concentration requirement were imposed, the design guidance for the HFC-125 equations indicates that they are intended to provide protection for fire events not subject to hot surface reignition.<sup>90</sup>

The F/A-18E/F experience is an example of aircraft program managers trading the impacts associated with various design options. These trades also take into consideration the amount of resources available to evaluate trade options adequately. Thus, limitation of such resources for another aircraft program manager may only permit traditional design practices to be applied. However, either scenario necessitates that the fire suppression system design be optimized to the greatest extent practicable. Chapter 8 provides detailed discussion of the CFD analysis tool developed under the NGP, which is intended for use by aircraft nacelle fire suppression system designers to optimize suppressant distribution.

Another issue that was investigated during the F/A-18E/F testing efforts relates to the use of the Statham and Halonyzer suppressant concentration gas analyzers used currently to certify nacelle fire suppression systems. The issue of response time of such equipment was investigated during the TDP, and during the F/A-18E/F efforts, testing was conducted to show that such equipment may miss the concentration levels that actually result in fire suppression.<sup>134</sup> That this could occur had been noted in early application of the Statham analyzer, for which it was concluded that as the suppressant-air mixture was drawn into a sampling tube, normal gas diffusion would tend to level peak concentrations if the peak is preceded and followed by lower concentrations.<sup>105</sup> A qualitative conclusion derived from the F/A-18E/F evaluation was that such equipment may be a good technique for suppressants that chemically interact with the combustion process, such as halon 1301, but may be limited in use with suppressants such as HFC-125, which physically interact with the combustion process. Thus following traditional design practices, HFC-125-based nacelle fire suppression systems may then be designed to accommodate more mass than is actually required. The NGP has transferred to the DoD test and evaluation community detailed information for the development and use of a Differential Infrared Rapid Agent Concentration Sensor (DIRRACS-2), which is described further in Chapter 5. Application of CFD modeling and DIRRACS-2 can be used to resolve these issues in nacelle fire suppression system design.



(a) Concentration throughout the Entire Nacelle



(b) Concentration at Locations of Hot Surface Reignition

**Figure 2-65. Examples of HFC-125 Nacelle Concentrations.**

Another fire suppression methodology that was developed concurrent with the TDP and subject to HASG oversight was the solid propellant gas generator (SPGG), which disperses an inert gas mixture of nitrogen, carbon dioxide, and water vapor. Similar to gas generators developed for automobile airbags, these devices rapidly generate large quantities of this inert gas mixture, which results from internal combustion of multiple pellets (or grains) of the propellant. The mixture is very hot upon exit from the device but cools rapidly as it expands within the compartment into which it is discharged. Full-scale engine nacelle fire suppression testing for the USAF F-22 evaluated HFC-125 along with inert and chemically-active gas generator technology.<sup>56</sup> The USN had previously evaluated the inert gas generator technology for nacelle fire suppression for the F/A-18E/F and demonstrated that similar mass quantities of halon 1301 and the inert solid propellant would suppress fire and prevent reignition.<sup>135</sup> During testing on the F-22 program, distribution lines from the generators to the nacelle would become white hot during discharge and for a brief period thereafter. In testing performed by the USN using a “single grain” inert gas generator, the same effect of heating of the distribution line during discharge was also noted. Placing inert gas generators within a nacelle and thus eliminating the need for distribution lines had been previously considered impractical due to the potential degrading effect of the nacelle operating temperature environment on the life of the solid propellant. Inconel distribution lines were demonstrated to not melt but would still become white hot. The NGP subsequently developed and performed evaluations of solid propellant formulations that generate cooler effluent that is also more efficient at fire suppression (Chapter 9).

It was during the F-22 nacelle fire suppression evaluations that these newer, chemically-active gas generator propellant formulations were tested in a full-scale application for the first time. In general at least 25 % to 50 % less chemically-active propellant mass was required to suppress nacelle fires relative to the amount of inert propellant mass. For one formulation over 70 % less mass relative to the inert propellant provided successful fire suppression. However, the biggest surprise from the F-22 evaluations was that the same mass quantity of halon 1301 and HFC-125, 6.4 kg (14.1 lb) each, suppressed the worst-case hot-surface reignition fire threat condition in the F-22 nacelle.<sup>133</sup> Though the suppressant mass was similar, in-depth analysis of the suppressant concentrations at the fire zone revealed that the inerting concentration (flammability limit) of halon 1301 was approximately a factor of two smaller than that of HFC-125. It was also noted that 8 s after suppressant discharge, the concentrations in this zone remained above the flammability limit. This 8 s dwell correlated with the criterion established for successful fire suppression, which was no occurrence of reignition within 8 s after suppression.<sup>133</sup> Based on this testing, the USAF implemented nacelle fire suppression for the F-22 aircraft using 14 lb of HFC-125.

The U.S. Army had also conducted an extensive halon alternative test and evaluation effort for the Comanche aircraft program. That effort was still in progress when the Comanche program was cancelled by the DoD. Extensive work had been done to replicate the nacelle conditions during flight modes, create the nacelle fires for those conditions, evaluate the potential hot-surface-reignition threat, and determine the agent quantity necessary to ensure suppression. Requirements for the system included reserve fire suppression capability. HFC-125 and, to a lesser extent, inert gas generators were evaluated. Since the majority of the testing had been conducted using HFC-125, it was selected as the agent for use in system optimization testing that was to be performed. At the time of program cancellation, no HFC-125 mass quantity had been established that would suppress fire under all test conditions, and the program had begun to evaluate trades related to retaining the reserve fire suppression capability, certification metrics and testing, and “fire-out” success criteria in testing.<sup>136</sup> Currently, the Halon Replacement Program of the

U.S. Army Program Executive Office, Aviation, is evaluating use of HFC-125 as the halon replacement on CH-47 Chinook helicopters.

As of the writing of this book, halon alternative testing by the Fire Safety Branch at the FAA Hughes Technical Center had recently been completed. That testing evaluated HFC-125, CF<sub>3</sub>I and, more recently, FK-5-1-12 or dodecafluoro-2-methylpentan-3-one (CF<sub>3</sub>CF<sub>2</sub>C(O)CF(CF<sub>3</sub>)<sub>2</sub>) for nacelle fire suppression applications in commercial aircraft. Findings to date of notable interest for DoD consideration are concentrations required to suppress spray and pool fires and an overpressure phenomenon. Contrasting results from previous testing, higher HFC-125 and CF<sub>3</sub>I concentrations have been required for suppression of nacelle spray fires than pool fires. Also, HFC-125 and another halon alternative tested, bromotrifluoropropene (2-BTP), were observed to produce overpressure phenomena subsequent to reignition within the test fixture flow path. Initial conclusions were that each suppressant appeared to act as a fuel in some instances, and that the phenomenon was not 100 % reliable.<sup>137</sup> The overpressure phenomenon had also been observed with HFC-125 and 2-BTP in cargo compartment fire suppression testing. During simulated aerosol can explosion tests conducted to evaluate explosion suppression performance for aircraft cargo compartments, tests were conducted to provide 2-BTP volumetric concentrations of 3 %, 4 %, 5 %, and 6 %. An overpressure occurred in each test – the associated overpressures were 530 kPa (63 psig), 530 kPa (63 psig), 780 KPa (100 psig), and 7.3 kPa (93 psig), respectively. 2-BTP enhanced the explosion event with as much as 4 times greater pressures than the un-suppressed event and 23 times greater than the halon 1301 benchmark concentration (2.5 %). HFC-125 was also observed to enhance the explosion event when its concentration was below 11.0 %. It doubled the blast pressure pulse peak, and it produced explosion overpressures of 4460 kPa (53 psig) in tests that provided concentrations of 8.9 % and 11 % by volume. No explosion event was observed when the concentration of HFC-125 was 13.5 % by volume.<sup>138</sup> Bromotrifluoropropene evaluation was discontinued in the nacelle fire test program. The FAA minimum performance standard (MPS) for certifying use of HFC-125, CF<sub>3</sub>I or, FK-5-1-12 in nacelle fire suppression applications is now being developed. The reader is referred to the Fire Safety Branch at the FAA Hughes Technical Center to learn more, particularly in regard to flame attachment behavior observed during testing with CF<sub>3</sub>I and FK-5-1-12.<sup>xxxiv</sup>

### Dry Bay Fire Suppression Applications

Both the USAF F-22 and C-130J LFT programs evaluated HFC-125 and gas generator technology for use in dry bay fire suppression. Both programs evaluated inert and chemically-active gas generators. The F-22 testing also evaluated a pyrotechnically-augmented liquid agent system (PALAS) that utilized HFC-227ea. The F-22 testing was specific to the F-22 main landing gear dry bay whereas the C-130J testing evaluated wing dry bays. Figure 2-66 shows a summary of results from the C-130J testing. Results from the F-22 testing are summarized in Table 2-15. These test programs provided the first full-scale comparisons of gas generator fire suppression effectiveness relative to near-term chemical halon alternatives identified during the TDP (HFC-125, HFC-227ea). Both of these test programs clearly showed that on a mass basis, less solid propellant was required to suppress a dry bay fire relative to the chemical alternatives tested, particularly when a chemically-active propellant was used. During the F-22 testing it was found that less than half of the chemically-active propellant was required to effect suppression as compared to the inert propellant.

---

<sup>xxxiv</sup> <http://www.fire.tc.faa.gov/>

	Replica Test Article		Production Test Article	
	# API Shots	Weight Selected (lbs)	# API Shots	Demonstrated Weight (lbs)
<b>Wing Leading Edge</b>				
HFC-125	28	2.16	5	2.16
★ SPGG	10	0.93	4	0.93
<b>Wing Engine Area</b>				
HFC-125	17	2.80	2	2.80
SPGG	8	0.93	2	0.93
<b>Wing Trailing Edge</b>				
HFC-125	16	—	0	—
SPGG	8	1.38	2	1.86

★ Wing Leading Edge SPGG testing included FS01-40 and PAC-3302 agents

**Figure 2-66. Summary of HFC-125 and SPGG Fire Suppression Results from C-130J Live Fire Testing.**<sup>139</sup>

**Table 2-15. Minimum Fire Suppressant Quantities from F-22 Main Landing Gear Dry Bay Live Fire Testing, 150-grain Fragment Threat and Jet Fuel Except Where Noted.**<sup>140</sup>

Suppressant (a)	Delivery System	5 ms Delay	5 ms and 105 ms Delay	400 ms Delay	400 ms and 480 ms Delay	500 ms Delay
HFC-125	Nitrogen Pressurized Bottle	0.68 kg (b)	N/A	N/A	N/A	N/A
HFC-125	Nitrogen Pressurized Bottle	0.91kg	N/A	N/A	N/A	1.5 lb
HFC-125	Nitrogen Pressurized Bottle	N/A	N/A	N/A	N/A	<b>1.13 kg (c)</b>
HFC-227ea	PALAS	1.11kg Fan Nozzle	N/A	N/A	N/A	N/A
HFC-227ea	PALAS	0.89 kg Radial Nozzle	N/A	N/A	N/A	N/A
FS01-40	Inert SPGG	N/A	2 x 0.52 kg (1.03 kg)	N/A	<b>2 x 0.21 kg (0.42 kg)</b>	N/A
FS01-40	Inert SPGG	N/A	N/A	N/A	<b>2 x 0.35 kg (0.70 kg) (c)</b>	N/A
PAC-3302	Chemically Active SPGG	N/A	<b>2 x 0.19 kg (0.38 kg)</b>	0.19 lb	N/A	N/A

(a) A total of 24 tests were conducted using HFC-125, 21 tests were conducted using HFC-227ea, 19 tests were conducted using inert SPGGs, and 10 tests were conducted using chemically-active SPGGs.

(b) Flammable fluid tested was hydraulic fluid.

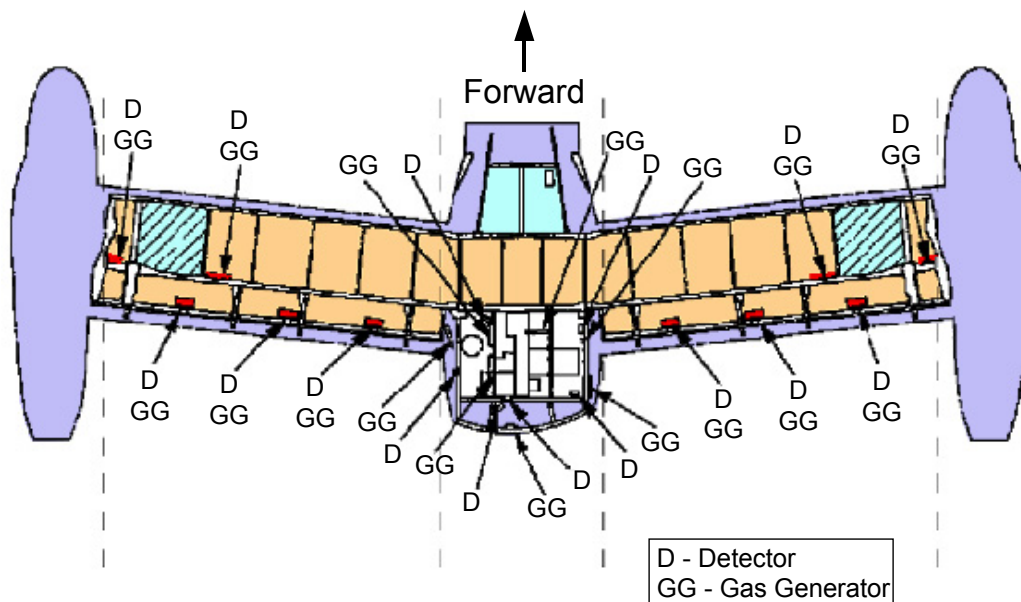
(c) Ballistic threat was 23 mm HEI. Only HFC-125 and inert SPGGs were evaluated against this threat.

Figure 2-67 illustrates the rapidity with which fire suppression is achieved using gas generators for suppression of ballistically-induced fires within an aircraft dry bay compartment.



**Figure 2-67. Time Sequence of Dry Bay Compartment Fire Suppression by Inert Gas Generators, Complete Suppression within 600 ms.**<sup>139</sup>

The inert gas generator technology has been implemented for dry bay fire suppression on the USN F/A-18E/F and MV-22 and on the USAF CV-22; the chemically-active technology was not mature at the time that these systems were required to be developed. Figure 2-68 provides an illustration of the system implementation on the MV-22, without auxiliary wing fuel tanks. On the V-22, this system is referred to as the wing fire protection system (WFPS). The gas generators provide ballistic dry bay fire protection for the various wing dry bays and both ballistic and safety fire protection in the mid-wing compartment, which contains an APU, gearbox, shaft driven compressor, hot air ducting, electrical generators, and other equipment. Discharge of the generators in the mid-wing compartment is sequenced to preclude overpressurization of the compartment. During qualification testing of the WFPS for the mid-wing compartment it was observed that, even though the fires were quickly extinguished, it was noted upon review of the test videotapes from each of the tests that the fire location shifted position around the compartment, i.e., the fire would be pushed to different locations within the compartment as each of the gas generators would discharge until combustion could no longer be sustained.<sup>141</sup>



**Figure 2-68. V-22 Inert Gas Generator Fire Suppression System.**<sup>12</sup>

The V-22 WFPS development effort included a requirement for the capability to measure gas concentration levels within the midwing compartment to demonstrate adequate distribution of the inert gases within the compartment, though no specific gas concentration levels and duration time were set as pass-fail criteria. A gas sampling system was assembled using fast-response CO<sub>2</sub> and oxygen sensors, and gases were drawn from the compartment through 5 m long, 1 mm inside-diameter Tygon tubing. Response time of the concentration measurement sensors was on the order of 120 ms for the CO<sub>2</sub> sensors and 50 ms for the oxygen sensors. In general, lower CO<sub>2</sub> was measured at locations closest to airflow inlets and was greatest at locations near the inert gas generators and where air was drawn out of the compartment, though peak CO<sub>2</sub> concentrations between 13 % and 26 % were recorded.<sup>141</sup> This concentration measurement technique was also utilized during the F-22 engine nacelle test series in an attempt to correlate fire suppression with oxygen and CO<sub>2</sub> concentrations within the nacelle. Analysis of the data could not support any correlation.<sup>56</sup> Detailed analysis of these measurements suggested that the instrumentation could have been contaminated by particulates, water vapor, condensed water vapor, or hydrocarbon vapor. The need to better characterize the mechanisms by which gas generator as well as other fire suppression technology provides fire suppression in a real-world environment such as an engine nacelle led to NGP efforts to develop the Transient Application, Recirculating Pool Fire (TARPF), agent effectiveness screen, which is described in Chapter 6.

Inert gas generators have thus far been proven to be effective though they currently require replacement every five years. On the V-22 there are 17 generators. Given that similarly sized or even larger aircraft could require similar or even larger numbers of these devices, if implemented for dry bay fire protection, the weight and logistics impact (i.e., unit costs, spares provisioning) over the lifetime of an aircraft becomes magnified. As shown in Figure 2-69, fire suppression testing of newer chemically-active solid propellant formulations under the NGP has demonstrated at least a 50 % reduction in propellant mass.

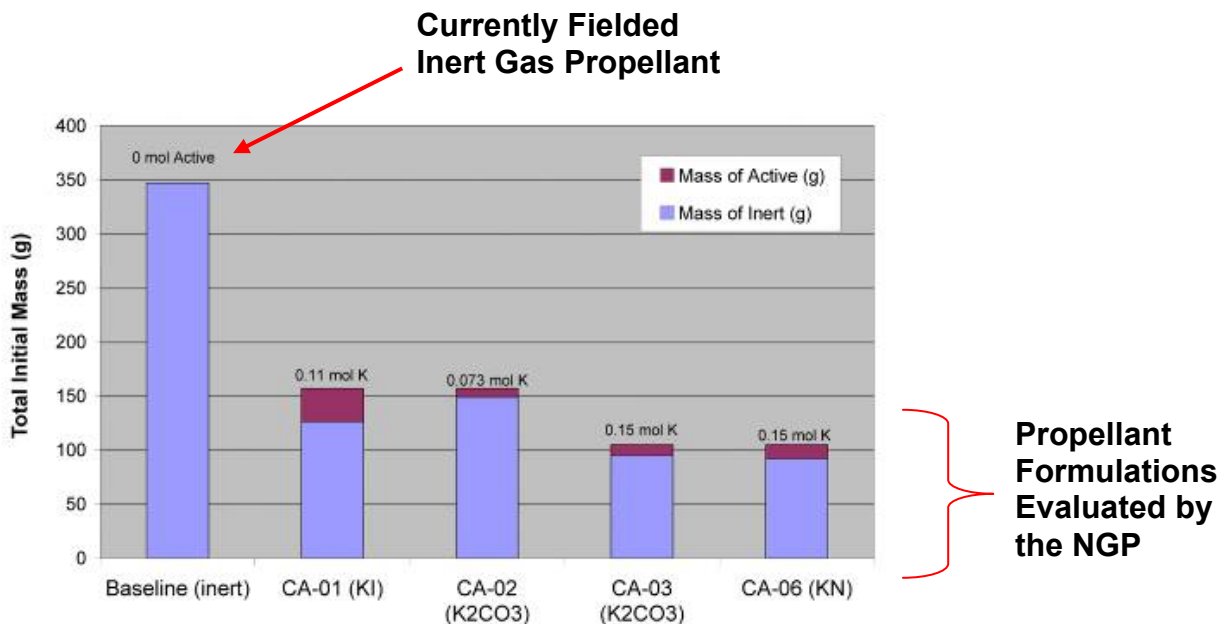


**Figure 2-69 NGP Testing Results Comparing Solid Propellant Inert Gas Generator Propellant Mass vs. Chemically Active Gas Generator Propellant Mass.<sup>142</sup>**

Aircraft dry bay fire testing conducted by the USN using one of the newer propellant formulations has demonstrated on-aircraft fire suppression with such reduction in propellant mass.<sup>143,144</sup> However, application of single passive extinguisher (SPEX) concepts has received increased attention. SPEX concepts focus on system simplification, eliminating the subsystems normally associated with active fire suppression systems (i.e., no fire detection system, no crew alerting and controls, and no system health monitoring). These concepts are a recent emergence within the DoD and testing of several concepts has been sponsored by the Joint Aircraft Survivability Program Office (JASPO). Concepts evaluated to date have been for dry bay fire suppression,<sup>145</sup> and one concept using a plastic, heat sensing tube connected to a low pressure container with monnex dry chemical extinguishant is planned for implementation on the V-22 for wheel well dry bay fire protection. Initially, chemically-active gas generators were one of several options being considered for dry bay fire suppression on the USN P-8 MMA,<sup>34</sup> but SPEX approaches are also being investigated. Chapter 9 describes the inert gas generator technology and the technologies and techniques developed under the NGP related to improving their performance.

### Ullage<sup>xxxv</sup>

Explosion suppression experiments were conducted to determine the ability of the SCS and LFE reactive ullage protection technologies to suppress ballistically-induced ullage fire/explosion events, with FC-218, HFC-227ea, HFC-125, and pentane tested using the LFE and just pentane using the SCS. Ballistic threats tested were single 110-grain fragment, 12.7 mm API, and 23 mm HEI. Detection systems were not integral to the tests and thus the results do not take into consideration detector-related delays. The tests were sponsored by the Joint Technical Coordinating Group for Aircraft Survivability (JCTG/AS), now known as the Joint Aircraft Survivability Program (JASPO), and were conducted by the USN.

SCSs filled with pentane to provide a 47 % concentration (approximately 0.54 mass fraction) suppressed explosions in a 0.85 m<sup>3</sup> (30 ft<sup>3</sup>) volatile ullage simulator when initiated by both a single 110-grain fragment and a 12.7 mm API. Partial suppression only was realized against the 23 mm HEI. In the same ullage simulator partial suppression only was realized against the 12.7 mm API in all tests of FC-218, HFC-227ea, HFC-125, and pentane using the LFE. The greatest concentrations of each were as follows: FC-218, 38.8 % (0.67 mass fraction); HFC-227ea, 42 %, (0.67 mass fraction); HFC-125, 52.5 % (0.64 mass fraction); and pentane, 37.5 % (0.48 mass fraction). Testing of varying amounts of each suppressant allowed definition of the effect of agent concentration and mass fraction on peak pressure in the simulator, as shown in Figure 2-70.

Examination of the concentration data revealed that, of the suppressants tested, pentane edged out FC-218 as having the best suppression efficiency, followed by HFC-227ea, and then by HFC-125. Comparison of peak explosive pressure as a function of suppressant mass fraction revealed that the amount of pentane required to achieve the suppression level of FC-218, HFC-227ea, and HFC-125 was 70 % of the amount needed for those three suppressants (i.e., 30 % less pentane was required).

As of the writing of this book, none of the DoD services has pursued additional evaluation of the reactive suppression technologies using halon alternative suppressants in aircraft fire suppression applications.

---

<sup>xxxv</sup> This section is based on Reference 33. Summary and Conclusions from that report are presented with minor editing for presentation within this chapter.

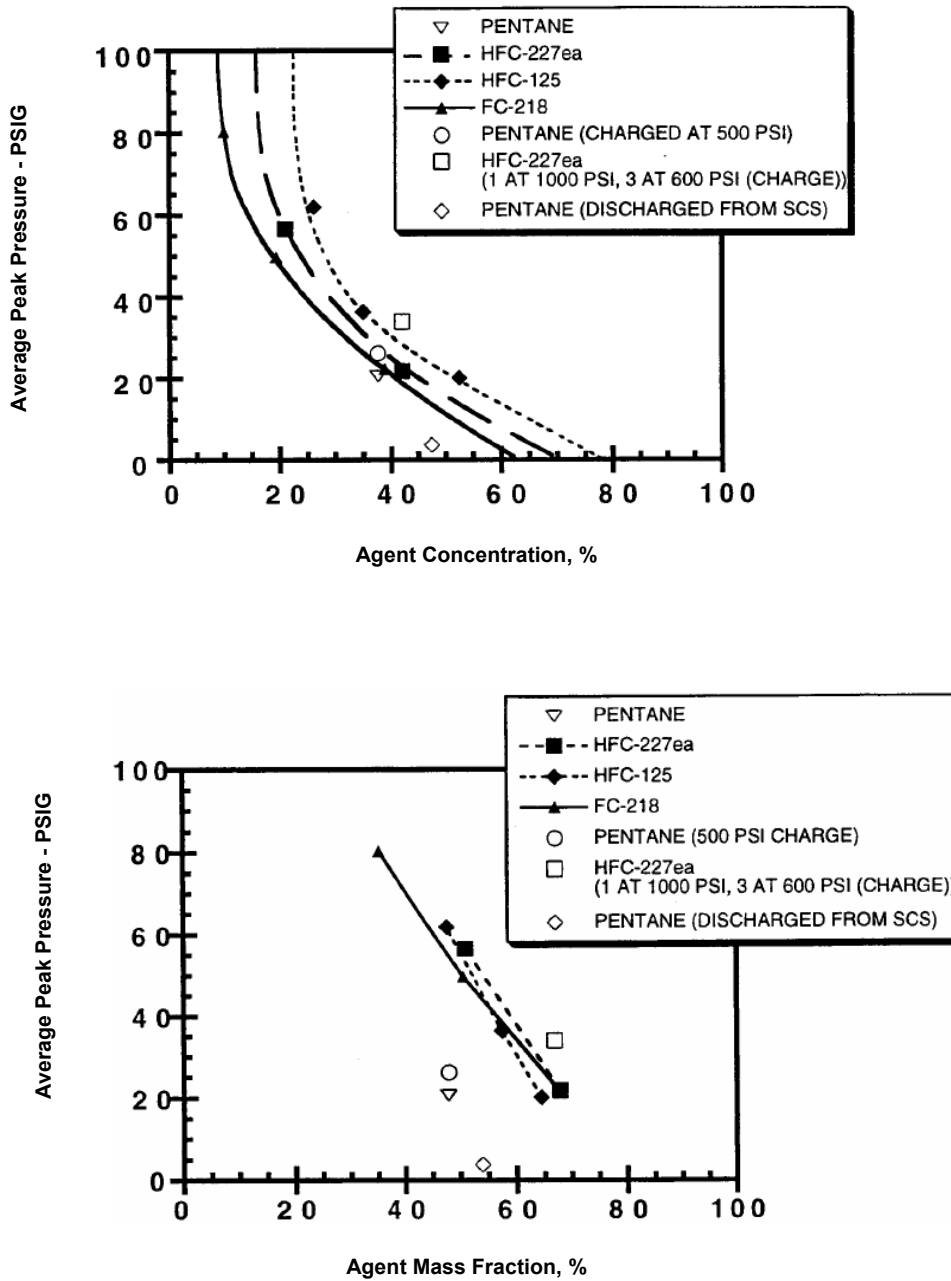


Figure 2-70. Effect of Suppressant Concentration and Mass Fraction on Peak Explosive Pressure for LFEs Pressurized to 1,000 psi, 12.7 mm API Threat and 3 % JP-4S.<sup>33</sup>

**Forward-Looking Considerations**

Major aircraft acquisition programs today include those for unmanned air vehicles (UAV), the USN P-8 MMA program, the USAF-USN-USMC F-35 Joint Strike Fighter (JSF), and the joint USN and U.S. Army Blackhawk/Seahawk Program. UAVs are being utilized with greater frequency during military conflicts. A review of potential cost effective survivability enhancements identified that passive fire suppression for large category UAVs and active fire suppression for Unmanned Combat Aerial Vehicles

(UCAV) are potential cost-effective survivability enhancements for these aircraft.<sup>146</sup> Dry bay fire suppression is planned for the JSF. However, it is a single-engine aircraft, which typically is not provided with nacelle fire suppression. This is because that the typical approach for nacelle fire suppression first involves isolating the nacelle compartment, meaning the pilot shuts off fuel flow, and that the fuel for a nacelle fire is likely that provided to the engine to generate propulsion power for flight. Reduction in or loss of that flow itself can or will lead to loss of thrust and thus lift and flight control. However, given the lessons learned from the Southeast Asia conflict and that a few extra minutes of flight may reduce likelihood of pilot fatality or enemy capture, the DoD's JASPO is currently sponsoring investigation and testing of automatic nacelle fire suppression concepts as a survivability enhancement, particularly for single engine aircraft applications.<sup>147</sup>

As long as the DoD components (Army, Navy, and Air Force) operate current and procure new manned multi-engine aircraft, there will be a requirement for engine nacelle fire suppression. Likewise, for new aircraft procurements, the Live Fire Test law will drive requirements for prevention and suppression of ballistically-induced fires. Aircraft fire suppression systems are categorized as mission critical applications, for which continued use of halon by the DoD has been permitted by law. New production aircraft are required to implement a non-ODS alternative or have had executed an ODS waiver certifying that no viable alternative exists for the application presented by that aircraft. While currently-fielded aircraft would most certainly continue to operate using the fire suppressant (or suppressants) installed currently, there are potential uncertainties (e.g., global warming, depletion or destruction of halon banks) that could impact the type of suppressant implemented in fire suppression systems on these aircraft. With respect to global warming, parties to the Kyoto Protocol, of which the U.S. is currently not a signatory, have developed amendments to reduce emissions of fielded HFC systems that are to become effective in 2007.<sup>148, xxxvi</sup> As of the writing of this book, these requirements would not apply to currently-fielded HFC-based fire suppression systems on DoD aircraft, but DoD environmental activities are likely to monitor the effect of these requirements and whether it is beneficial for DoD to implement similar requirements. The commercial aviation sector is more sensitive to such influences, and it is conceivable that a commercial-derivative aircraft procurement could include a non-halon non-HFC based fire suppression system.

Regardless of potential external regulatory influences, the aircraft program manager is constantly managing risks (i.e., weight, performance, cost, safety and survivability, to name a few). As for any subsystem on an aircraft, there are weight, performance, and cost trades associated with implementing a fire suppression system, and the program manager desires to implement the lightest weight, best performing, lowest cost system. He is concerned with ensuring that aircraft key performance parameters (KPPs) are met. These parameters include weight, performance (range, drag), reliability, and probability of kill (Pk). When weight and/or cost are considered too high, the program manager will trade risk associated with various options, including safety and survivability risks. Such trades receive increased attention and scrutiny when resources (funds) are constrained. For example, if a specific aircraft maneuver drives a worst-case nacelle airflow condition, which in turn drives high the suppressant

---

<sup>xxxvi</sup> The Kyoto Protocol is an agreement made under the United Nations Framework Convention on Climate Change (UNFCCC). Countries that ratify this protocol commit to reduce their emissions of carbon dioxide and five other greenhouse gases, or engage in emissions trading if they maintain or increase emissions of these gases. The five other gases are methane, nitrous oxide, sulfur hexafluoride, hydrofluorocarbons or HFCs, and perfluorocarbons or PFCs. The USAF CV-22 and F-22, the USMC MV-22, and the USN F/A-18E/F use HFC-125 in their nacelle fire suppression systems. HFC-125 is also approved for use by DoD, as well as by the FAA, as a halon 1301 simulant for certification testing of halon 1301 nacelle fire suppression systems.

quantity for a fire suppression system, yet performing such a maneuver is a small exposure over the projected lifetime of the aircraft, the program manager may accept the safety risk associated with fire occurrence during that exposure in order to proceed with a lighter weight fire suppression system. Likewise, from a survivability perspective, the program manager may trade passive protection techniques against active techniques for dry bay fire protection. He may find that the aircraft vulnerable area requirement can be met by implementing passive protection techniques at the risk of not protecting another compartment that requires an active system and yet still meet the aircraft Pk KPP. That the NGP has developed tools such as CFD modeling for design, development and optimization of nacelle fire suppression systems and cost modeling for assessing the life cycle cost benefit of providing nacelle and dry bay fire suppression systems should benefit the program in conducting risk trades. Better performing enhanced powder panels, chemically-active gas generators, and hybrid fire suppression techniques should provide the program manager options previously unavailable in making such trades.

## 2.6 REFERENCES

1. Weiss, S. and Pesman, G.J., "Bibliography of Unclassified Aircraft-Fire Literature," National Advisory Committee for Aeronautics Research Memorandum E9H03, 1949.
2. Weiss, S. and Pesman, G.J., "Bibliography of Classified Aircraft-Fire Literature," National Advisory Committee for Aeronautics Research Memorandum E9H03a, 1949.
3. Dallas, A.W. and Hansberry, H.L., "Determination of Means to Safeguard Aircraft from Powerplant Fires in Aircraft, Part I," Civil Aeronautics Administration Technical Development Report No. 33, 1943.
4. Ball, R.E., *The Fundamentals of Aircraft Combat Survivability Analysis and Design, Second Edition*, American Institute of Aeronautics and Astronautics, Inc., New York, NY, 2003.
5. *Preliminary Survey of the Aircraft Fire Problem*, National Advisory Committee for Aeronautics Research Memorandum E8B18, 1948.
6. Pesman, G.J., "Analysis of Multiengine Transport Airplane Fire Records," National Advisory Committee for Aeronautics Research Memorandum E9J19, 1950.
7. Hughes, D. and Dornheim, M.A., "No Flight Controls," *Aviation Week and Space Technology*, 8 December 2003.
8. *Fire Suppression Substitutes and Alternatives to Halon for U.S. Navy Applications*, National Academy Press, Washington, DC, 1997.
9. Tedeschi, M. and Leach, W., "Halon 1301 Fire Suppression System Effectivity Aboard U.S. Naval Aircraft," 1995, in Gann, R.G., Burgess, S.R., Whisner, K.C., and Reneke, P.A., eds., Papers from 1991-2006 Halon Options Technical Working Conferences (HOTWC), CD-ROM, NIST Special Publication 984-4, National Institute of Standards and Technology, Gaithersburg, MD, 2006.
10. Electronic Communication (email) between Donald Bein, NAVAIR - Naval Air Warfare Center Aircraft Division, Lakehurst, and Joseph Manchor, NAVAIR - Naval Air Warfare Center Weapons Division, China Lake, 15 August 2005, 15 September 2005, and 3 October 2005.
11. Bennett, J.M. and Kolleck, M.L., "Assessing the Cost Impact of Halon Alternatives on Aviation," 1997, in Gann, R.G., Burgess, S.R., Whisner, K.C., and Reneke, P.A., eds., Papers from 1991-2006 Halon Options Technical Working Conferences (HOTWC), CD-ROM, NIST Special Publication 984-4, National Institute of Standards and Technology, Gaithersburg, MD, 2006.

12. O'Bryon, J.F., "Think Globally, Act Globally," 1999, in Gann, R.G., Burgess, S.R., Whisner, K.C., and Reneke, P.A., eds., Papers from 1991-2006 Halon Options Technical Working Conferences (HOTWC), CD-ROM, NIST Special Publication 984-4, National Institute of Standards and Technology, Gaithersburg, MD, 2006.
13. Gann, R.G., ed., *Fire Suppression System Performance of Alternative Agents in Aircraft Engine and Dry Bay Laboratory Simulations*, vol. 2, NIST Special Publication SP 890, National Institute of Standards and Technology, Gaithersburg, MD, 1995.
14. Chamberlain, G. and Boris, P., "Testing of the Engine Compartment Fire Extinguishing System in the F/EF-111," Report No. AFWAL-TR-87-2066, Air Force Wright Aeronautical Labs, Wright Patterson Air Force Base, OH, 1987.
15. *The 737 Information Site*, <http://www.b737.org.uk/>, Copyright Chris Brady, 1999.
16. Doyle, D.D. 1Lt., "F-15 Secondary Power Systems," Wright Patterson Air Force Base Power Division, 2000 Aging Aircraft Conference.
17. Robaidek, M.F., "Aircraft Dry Bay Fire Protection," Flight Dynamics Laboratory, Air Force Wright Aeronautical Laboratories, Prepared by Boeing Military Airplane Company, Report AFWAL-TR-87-3032, 1987.
18. Heinonen, E.W., Moore, T.A., Nimitz, J.S., Skaggs, S.R., Beeson, H.D., and Moussa, N.A., "Fire/Explosion Protection Characterization and Optimization: Phase II – Alternative Dry Bay Fire Suppression Agent Screening," NMERI OC 90/20, Report JTCG/AS-90-T003, 1990.
19. Electronic Communication (email) from Paul Frisinger, 2nd Lt USAF, F-22 System Program Office, Wright Patterson Air Force Base, 1 March 2006.
20. Bernier, R.G., Enoch, W., Lake, R.E., Mowrer, D.W., and Vikestad, W.S., "Aircraft Fuel System Fire and Explosion Suppression Design Guide," U.S. Army Aviation Research and Technology Activity, Aviation Applied Technology Directorate Report USAAVSCOM TR 89-D-16 (JTCG/AS 89-T-005), February 1990.
21. Wong, K. and Fett, C., "Evaluation of Halon 1301 Fire Extinguishing Systems for Dry Bay Ballistic Problems," Report No. AFWAL-TR-84-3112, Wright Patterson Air Force Base Flight Dynamics Laboratory, 1985.
22. *Cyphers, D.C., "Enhanced Powder Panels, "Final Report to SERDP," Skyward, Inc., 2004.*
23. *Technology Development Plan for Alternatives to Ozone-Depleting Substances for Weapons Systems Use*, Final Report, ODUSD (S&T) Weapons Systems, 1998.
24. *Background to Thermal Control Company's Development of Combat Fire Suppression Systems for Aircraft, Fighting Vehicles, and Ships*, AirScrew Ltd, U.K., not dated.
25. *COBRA Primary Fire Suppression System for Fixed and Rotary Wing Aircraft*, AirScrew Ltd, U.K., not dated.
26. Bailey, D.B., Lewinski, D.F., Reynolds, T.L., and Roseburg, C.M., "NAS1-20341 Aircraft and Spacecraft Guidance and Controls Research Task Order 11: Onboard Inert Gas Generation System/Onboard Oxygen Gas Generation System (OBIGGS/OBOGS) Study (Subtask 1) Revision A," Boeing Commercial Airplanes Group, 19 July 2000.
27. Lewinski, D., "Halon Replacement for Airplane Cargo Compartments," 2005, in Gann, R.G., Burgess, S.R., Whisner, K.C., and Reneke, P.A., eds., Papers from 1991-2006 Halon Options Technical Working Conferences (HOTWC), CD-ROM, NIST Special Publication 984-4, National Institute of Standards and Technology, Gaithersburg, MD, 2006.

28. *Fuel Tank Harmonization Working Group (FTHWG) Final Report*, Aviation Rulemaking Advisory Committee (ARAC), 1998.
29. *Fuel Tank Inerting Harmonization Working Group (FTIHWG) Final Report*, Aviation Rulemaking Advisory Committee (ARAC), 2001.
30. Cavage, W.M., "Developing a Fuel-Tank Inerting System for Commercial Transport Airplanes," *Aircraft Survivability*, 2005.
31. Bennett, G., "Review of Technologies for Active Suppression of Fuel Tank Explosions," 2000, in Gann, R.G., Burgess, S.R., Whisner, K.C., and Reneke, P.A., eds., Papers from 1991-2006 Halon Options Technical Working Conferences (HOTWC), CD-ROM, NIST Special Publication 984-4, National Institute of Standards and Technology, Gaithersburg, MD, 2006.
32. *Explosion Suppression*, Aviation Rule Making Advisory Committee (ARAC) Fuel Tank Harmonization Working Group, Task Group 2, 1998.
33. Bernardo, A.B., "Testing of Active Ullage-Suppression Systems with Agents Alternate to Halon 1301," Naval Air Warfare Center Weapons Division Report NAWCWPNS TM 8006 (JTCG/AS-96-V-002), 1998.
34. Legg, D. and Landfield, J., "Addressing Maritime Patrol Aircraft Survivability," *Aircraft Survivability*, 2005.
35. *Joint Service Specification Guide (JSSG), Air Vehicle Subsystems, JSSG 2009, Appendix G: Air Vehicle Fire and Explosion Hazard Protection Subsystem, Requirements and Guidance*, Department of Defense, 1998.
36. *Fuel Tank Inerting*, Aviation Rule Making Advisory Committee (ARAC) Fuel Tank Harmonization Working Group, Task Group 3, 1998.
37. Vanhorn, S.R. and Vitali, J.A., "Fuel Inertion Live Munitions Testing," 1999, in Gann, R.G., Burgess, S.R., Whisner, K.C., and Reneke, P.A., eds., Papers from 1991-2006 Halon Options Technical Working Conferences (HOTWC), CD-ROM, NIST Special Publication 984-4, National Institute of Standards and Technology, Gaithersburg, MD, 2006.
38. Van Horn, S.R., "Final Report, F-16 Fuel Tank Inerting System (Halon 1301) Replacement Chemical Study," Report Number F-16-01-TR-1001, Wright Patterson Air Force Base F-16 System Project Office, 2000.
39. Rupnik, J., Bowman, R.G., and Berrill, P., eds, *Independent Review Panel Report: Suitability of CF<sub>3</sub>I to Replace Halon 1301 as the Inerting Agent in Wing Fuel Tanks on the F-16 Aircraft*, HydroGeoLogic Report No. R09-02.881.doc, 2002.
40. Gann, R.G., "Suitability of CF<sub>3</sub>I to Replace Halon 1301 as the Inerting Agent in Wing Fuel Tanks on the F-16 Aircraft," 2003, in Gann, R.G., Burgess, S.R., Whisner, K.C., and Reneke, P.A., eds., Papers from 1991-2006 Halon Options Technical Working Conferences (HOTWC), CD-ROM, NIST Special Publication 984-4, National Institute of Standards and Technology, Gaithersburg, MD, 2006.
41. Wuebbles, D.J. and Li, Y., "Potential Impacts of CF<sub>3</sub>I on Ozone as a Replacement for CF<sub>3</sub>Br in Aircraft Applications," 2005, in Gann, R.G., Burgess, S.R., Whisner, K.C., and Reneke, P.A., eds., Papers from 1991-2006 Halon Options Technical Working Conferences (HOTWC), CD-ROM, NIST Special Publication 984-4, National Institute of Standards and Technology, Gaithersburg, MD, 2006.
42. *Next-Generation Fire Suppression Technology: Strategy for a National Program*, Office of the Director, Defense Research and Engineering, 1996.

43. Finnerty, A.E., Peregino, P.J., Vande Kieft, L.J., Tucker, J.R., Weiland, D.E., Sheinson, R.S., Gann, R.G., Bennett, M.V., and Wheeler, J.A., "Fires Experienced and Halon 1310 Fire Suppression Systems in Current Weapon Systems," Report SURVIAC TR-00-007, United States Air Force – Air Force Research Laboratory – Survivability and Safety Branch, 2003.
44. Bein, D., "In-Flight Suppressant Deployment Temperatures," 2004, in Gann, R.G., Burgess, S.R., Whisner, K.C., and Reneke, P.A., eds., Papers from 1991-2006 Halon Options Technical Working Conferences (HOTWC), CD-ROM, NIST Special Publication 984-4, National Institute of Standards and Technology, Gaithersburg, MD, 2006. Also available from the Defense Technical Information Center (DTIC), Accession Number ADA444883.
45. *Fixed-Wing Aircraft Fire Protection: Halon 1301 Fire Suppression Systems Effectivity Analysis*, NAWCADLKE-MISC-05-SR-0146, Naval Air Warfare Center Aircraft Division, 1994.
46. *Rotary Aircraft Fire Protection: Halon 1301 Fire Suppression Systems Effectivity Analysis*, NAWCADLKE-MISC-05-SR-0132, Naval Air Warfare Center Aircraft Division, 1994.
47. Leach, W., "Retrofit Opportunities for HFC-125 in Aircraft Engine Nacelles," 1999, Papers from 1991-2006 Halon Options Technical Working Conferences (HOTWC), CD-ROM, NIST Special Publication 984-4, National Institute of Standards and Technology, Gaithersburg, MD, 2006.
48. Electronic Communication (email) from Mike Lupo, Army Materiel Command, Redstone Arsenal, October 1999.
49. Lupo, M., Spreadsheet of January 1985 – December 1995 Army Rotary Wing Fire Incident Data from Appendix E of the *Comanche Halon Alternative Study* prepared by SysTeam, 8 July 1996, Army Materiel Command, Redstone Arsenal, 1999.
50. Leach, W. and Kubina, M., "Halon Alternative Opportunities for H-60 Helicopters," 2006, in Gann, R.G., Burgess, S.R., Whisner, K.C., and Reneke, P.A., eds., Papers from 1991-2006 Halon Options Technical Working Conferences (HOTWC), CD-ROM, NIST Special Publication 984-4, National Institute of Standards and Technology, Gaithersburg, MD (2006).
51. Bowman, H.L., Darwin, R.L., and Williams, F.W., "Halon 1211 Alternatives for Fighting Jet Engine Fires on Flight Decks and Flight Lines," 2000, in Gann, R.G., Burgess, S.R., Whisner, K.C., and Reneke, P.A., eds., Papers from 1991-2006 Halon Options Technical Working Conferences (HOTWC), CD-ROM, NIST Special Publication 984-4, National Institute of Standards and Technology, Gaithersburg, MD, 2006.
52. Beardsley, G.F. and Korl, K., "Report on Japanese Naval Aircraft CO<sub>2</sub> System Design," Report No. F-IR-76-RE, Air Materiel Command, Wright Patterson Air Force Base, 1946.
53. Tyson, J.H. and Barnes, J.F., "The Effectiveness of Ullage Nitrogen-Inerting Systems Against 30-mm High-Explosive Incendiary Projectiles," Naval Weapons Center China Lake Report NWC TP 7129 (JTCG/AS-90-T-004), 1991.
54. Shepherd, J.E., Krok, J.C., and Lee, J.J., *Spark Ignition Energy Measurements in Jet A*, Graduate Aeronautical Laboratories, California Institute of Technology, 1999 Revised 2000.
55. Farenden, P.J., Hirst, R., and Simmons, R.F., "The Extinction of Fires in Aircraft Jet Engines – Part I, Small-Scale Simulation of Fires," *Fire Technology* 12, 266-289, 1976.
56. Gillespie, M.A. (Capt. USAF), *SPGG Assessment Program Data Summary* (Briefing), Wright Laboratory Flight Dynamics Directorate, 1997.

57. Pitts, W.M., Nyden, M.R., Gann, R.G., Mallard, W.G., and Tsang, W., *Construction of an Exploratory List of Chemicals to Initiate the Search for Halon Alternatives*, NIST Technical Note 1279, National Institute of Standards and Technology, Gaithersburg, MD, 1990.
58. *Aircraft Fire Protection/Mishap Investigation Course*, AFP Associates Inc., Dayton, OH.
59. Linford, R.M. and Dillow, C.F., *Optical Emission Properties of Aircraft Combustible Fluids*, Air Force Aero Propulsion Laboratory Report AFAPL-TR-73-83, 1973.
60. Kuchta, J.M., *Investigation of Fire and Explosion Accidents in the Chemical, Mining, and Fuel-Related Industries – A Manual*, U.S. Bureau of Mines Bulletin 680, 1986.
61. Jacobson, E. and Spector, O., “Optical Flame & Gas Detection for the Oil & Gas Industry,” *FS-World.com Fire and Safety Magazine*, Spring 2005, pp 44-51.
62. Keyser, D.R. and Hewson, J.C., “Predicting Fire Suppression in a Simulated Engine Nacelle,” 2004, in Gann, R.G., Burgess, S.R., Whisner, K.C., and Reneke, P.A., eds., Papers from 1991-2006 Halon Options Technical Working Conferences (HOTWC), CD-ROM, NIST Special Publication 984-4, National Institute of Standards and Technology, Gaithersburg, MD, 2006.
63. McClure, J.D. and Springer, R.J., *Environmental and Operating Requirements for Fire Extinguishing Systems on Advanced Aircraft*, Wright Patterson Air Force Base Aero Propulsion Laboratory Report AFAPL-TR-73-122 (JTTCG/AS-74-T-002), 1974.
64. Keyser, D.R. and Hewson, J.C., “Assessment of Fire-Suppression Simulations Using Full-Scale Engine Nacelle Tests,” 2005, in Gann, R.G., Burgess, S.R., Whisner, K.C., and Reneke, P.A., eds., Papers from 1991-2006 Halon Options Technical Working Conferences (HOTWC), CD-ROM, NIST Special Publication 984-4, National Institute of Standards and Technology, Gaithersburg, MD, 2006.
65. Zabetakis, M.G., *Flammability Characteristics of Combustible Gases and Vapors*, Bureau of Mines Bulletin 627, U.S. Department of Interior, 1965.
66. Engibous, D.L. and Torkelson, T.R., *A Study of Vaporizable Extinguishants*, The Dow Chemical Company, WADC Technical Report 59-463, 1960.
67. *Department of Defense Handbook MIL-HDBK-310, Global Climatic Data for Developing Military Products*, 23 June 1997.
68. *Joint Aviation Regulation 1 (JAR-1), Definitions, Change 5*, Joint Aviation Authorities, 15 July 1996.
69. Gann, R., *FY2003 Annual Report, Next Generation Fire Suppression Technology Program (NGP)*, NIST Technical Note 1457, National Institute of Standards and Technology, Gaithersburg, MD, January 2004.
70. *Minutes of the Technology Transition (T2) Meeting*, National Institute of Standards and Technology, 27-28 October 1994.
71. *V-22 EMD Power Plant Installation Temperature Survey Demonstration Test Report*, Bell-Boeing Report No. 901-993-356, 24 January 2000.
72. *SH-2G Helicopter Flight Testing Engine Temperature Survey Test Report*, Kaman Aerospace Corporation Report T-975, 1990.
73. *F/A-18E/F Power Plant Temperature Survey Report*, Northrup-Grumman Corp., Report NOR 98-303 Revision A, 12 March 1999.
74. Daggett, D., “Small Gas Turbine Engine Nacelle Typical Airflows and Temperature Profiles,” International Halon Replacement Working Group, April 1999.

75. Roseburg, C., "Engine Nacelle Halon Alternatives," Halon Alternatives Research Corporation (HARC) Phoenix Meeting, 12 December 2002.
76. Clodfelter, R. G. and Kuchta, J. M., Aircraft Mishap Fire Pattern Investigations, AFWAL-TR-85-2057, August 1985.
77. *White Paper: The PhostrEx™ Fire Suppression System on the Eclipse 500, Pioneering the World's First Commercially Viable Halon Replacement*, Eclipse Aviation Corporation, 2005.
78. *Test Report for Demonstration Flight Tests for Project (SEA) 1411 Fire Extinguishing System Testing*, Kaman Aerospace International Corporation (KAIC) Report T-4006-1, 2000.
79. *F/A-18E/F HFC-125 Fire Extinguishing Test Report*, Northrop Grumman Corp., Report NOR 99-303, 18 February 1999.
80. Kolleck, M. L. and Jeffery, K., *Halon Discharges at Altitude*, June 1994.
81. Nahlen, C.L., "Outside Temperature of Rotary Wing Aircraft Fires Reported Since January 1985," Memorandum for SFAE-AV-RAH-L, 15 December 1995.
82. *Pitot Statics and the Standard Atmosphere*, USAF Test Pilot School Document ADA320216, January 1996.
83. *A Review of the Flammability Hazard of Jet A Fuel Vapor in Civil Transport Aircraft Fuel Tanks*, Federal Aviation Administration Report DOT/FAA/AR-98/26, 1998.
84. Barnett, H.C. and Hibbard, R.R., "Properties of Aircraft Fuels," National Advisory Committee for Aeronautics Technical Note 3276, 1956.
85. *U.S. Standard Atmosphere*, International Civil Aviation Organization, 1976.
86. *Aircraft Ground Operations in Canadian Winter: Taxi Times, Wing Temperatures and Hot De-Icing*, Transport Canada Report TP 12735E, April 1996.
87. *Validation of Methodology for Simulating a Cold-Soaked Wing*, Transport Canada Report TP 12899E, October 1996.
88. Phone conversation between John D'Avirro, APS Aviation, Inc., and Donald Bein, NAVAIR, 31 March 2004.
89. Bein, D., "A Review of the History of Fire Suppression on U.S. DoD Aircraft," 2006, in Gann, R.G., Burgess, S.R., Whisner, K.C., and Reneke, P.A., eds., Papers from 1991-2006 Halon Options Technical Working Conferences (HOTWC), CD-ROM, NIST Special Publication 984-4, National Institute of Standards and Technology, Gaithersburg, MD, 2006.
90. Bennett, J.M and Bennett, M.V., *Aircraft Engine/APU and Dry Bay Fire Extinguishing System Design Model (HFC-125)*, Wright Patterson Air Force Base Flight Dynamics Directorate Report AFRL-VA-WP-TR-1999-3068, May 1997.
91. Grosshandler, W., Hamins, A., McGrattan, K., and Presser, C., *Transient Application, Recirculating Pool Fire, Agent Effectiveness Screen: Final Report*, NGP Project 3A/2/890, NISTIR 6733, National Institute of Standards and Technology, Gaithersburg, MD, 2001.
92. Wright, B.R., Mowery, R.B. and LePera, M.E., "Survivability? It Could be a Matter of Hydraulic Fluid!" American Chemical Society (ACS) Symposium Series 611, pdf file dated 2000.
93. Strasser, A., Waters, N.C., and Kuchta, J.M., *Ignition of Aircraft Fluids by Hot Surfaces Under Dynamic Conditions*, Air Force Aero Propulsion Laboratory Report AFAPL-TR-71-86, 1971.

94. Clodfelter, R.G., "Hot Surface Ignition and Aircraft Safety Criteria," SAE Technical Paper Series 901950, 1990.
95. Warner, E.P., *The Prevention of Fire in Air*, National Advisory Committee for Aeronautics Technical Memorandum 144, 1922.
96. Ingerson, D., "Halon 1301 History," Federal Aviation Administration Fire Safety Branch Website, <http://www.fire.tc.faa.gov/systems/engine/comment.stm>, 1999.
97. Hillman, T.C., Hill, S.W., and Sturla, M.J., *Aircraft Fire Detection and Suppression*, Kidde Aerospace and Defense Technical Paper, 2001.
98. Harper, G., Kay., M. and Feist, G., "Aircraft Dry Bay Fire Protection: A Review of Available Options," 2001, in Gann, R.G., Burgess, S.R., Whisner, K.C., and Reneke, P.A., eds., Papers from 1991-2006 Halon Options Technical Working Conferences (HOTWC), CD-ROM, NIST Special Publication 984-4, National Institute of Standards and Technology, Gaithersburg, MD, 2006.
99. Hansberry, H.L., *Design Recommendations for Fire Protection of Aircraft Powerplant Installations*, U S Department of Commerce, Civil Aeronautics Administration, Technical Development Note No. 31, 1943.
100. Hitchcock, E.B. and Scarlon, E.A., *Use of Monochlorobromomethane by the German Navy and Air Force as a Fire Extinguishing Agent*, U.S. Naval Technical Mission in Europe, Technical Report No. 276-45, 1945.
101. Strasiak, R.R., *The Development History of Bromochloromethane (CB)*, WADC Technical Report 53-279, Wright Air Development Center, Wright Patterson Air Force Base, OH, 1954.
102. Middlesworth, C.M., *Determination of a Means to Safeguard Aircraft from Powerplant Fires In Flight, Part VI, The North American Tornado (Air Force XB-45)*, U S Department of Commerce, Civil Aeronautics Administration, Technical Development Report No. 221, 1954.
103. MIL-E-5352A, *Extinguishing System, Fire, Aircraft, Installation of*, 9 October 1952.
104. Tarbell, L.E., *Determination of a Means to Safeguard Aircraft from Powerplant Fires In Flight, Part V, The Lockheed Constitution (Navy XR60-1)*, U S Department of Commerce, Civil Aeronautics Administration, Technical Development Report No. 198, 1953.
105. Hough, R.L., *Factors Involved in Determining the Efficiency of Fire Extinguishing Agents*, WADC Technical Note 58-281, Wright Air Development Center Aeronautical Accessories Laboratory, 1959.
106. Asadourian, L.A., *Fire Extinguishment Studies of the Convair-340 Powerplant*, U S Department of Commerce, Civil Aeronautics Administration, Technical Development Report No. 265, 1955.
107. *Final Report on Fire Extinguishing Agents for the Period September 1, 1947 to June 30, 1950*, Purdue Research Foundation, Lafayette, IN, 1950.
108. Hansberry, H.L., *Aircraft Fire Extinguishment, Part V, Preliminary Report on High-Rate-Discharge Fire-Extinguishing Systems for Aircraft Power Plants*, U S Department of Commerce, Civil Aeronautics Administration, Technical Development Report No. 260, February 1956.
109. MIL-E-22285, *Extinguishing System, Fire, Aircraft, High-Rate Discharge Type, Installation and Test of*, 11 December 1959.
110. MIL-F-81768 (UASF), *General Specification for Aircraft Fire and Explosion Hazard Protection Systems*, 20 June 1983.

111. Hughes, C.A. and Middlesworth, C.M., *Aircraft Fire Extinguishment, Part IV, Evaluation of Bromochloromethane Fire Extinguishing System for the XB-45 Airplane*, U S Department of Commerce, Civil Aeronautics Administration, Technical Development Report No. 240, 1954.
112. Hughes, C.A., *Aircraft Fire Extinguishment Part II, The Affect of Air Flow on Extinguishing Requirements of a Jet Power-Plant Fire Zone*, U S Department of Commerce, Civil Aeronautics Administration, Technical Development Report No. 205, 1953.
113. New, J.D. and Middlesworth, C.M., *Aircraft Fire Extinguishment Part III, An Instrument for Evaluating Extinguishing Systems*, U S Department of Commerce, Civil Aeronautics Administration, Technical Development Report No. 206, 1953.
114. Young, A.V., *Fire Extinguishment Studies of the Northrop F-89 Powerplant*, Civil Aeronautics Administration Technical Development Report No. 365, 1958.
115. Jaggars, J.F., *Development of Powder-Filled Structural Panels for AH-1S Fuel Fire Protection*, U.S. Army Aviation Research and Development Command Report No. USAAVRADCOM-TR-81-D-32, 1981.
116. *General Guidelines for Measuring Fire Extinguishing Agent Concentrations in Powerplant Compartments*, Department of Transportation/Federal Aviation Administration Advisory Circular 20-100, 1977.
117. Electronic Communications (email) from Alan Randle, Pacific Scientific/HTL Kin Tech, dated 5 September 2006; from James Tucker, SURVICE Engineering Co., dated 5 September 2006; and from Douglass Ingerson, FAA Fire Safety Branch, dated 7 June 2006 and 5 September 2006.
118. Keyser, D.R. and Hewson, J.C., "Fire Suppressant Distribution in an Engine Nacelle," 2004, in Gann, R.G., Burgess, S.R., Whisner, K.C., and Reneke, P.A., eds., Papers from 1991-2006 Halon Options Technical Working Conferences (HOTWC), CD-ROM, NIST Special Publication 984-4, National Institute of Standards and Technology, Gaithersburg, MD, 2006.
119. *Flight Manual, USAF Series C-5A, C-5A(SCM), and C-5B Airplanes*, 1 December 1997 (Change 10, 30 March 2005).
120. *Aircraft Fire Protection Handbook*, MIL-HDBK-221(WP), 3 May 1965.
121. *Technical Manual, Organizational Maintenance, Description and Principles of Operation, Fuel and In-Flight Refueling Systems, Navy Model A-6E TRAM Aircraft*, NAVAIR 01-85ADF-2-30.
122. Gann, R.G., Barnes, J.D., Davis, S., Harris, J.S., Harris, R.H., Herron, J.T., Levin, B.C., Mopsik, F.I., Notarianni, K.A., Nyden, M.R., Paabo, M., and Ricker, R.E., *Preliminary Screening Procedures and Criteria for Replacements for Halons 1211 and 1301*, NIST Technical Note 1278, National Institute of Standards and Technology, Gaithersburg, MD, 1990.
123. Caggianelli, G.M., Bennett, M.J., Kolleck M.L., and Wheeler, J.A., *Halon Replacement for Aviation, Aircraft Engine Nacelle Application Phase I - Operational Parameters Study*, Wright Patterson Air Force Base Flight Dynamics Directorate Report WL-TR-95-3077, April 1997.
124. Poole, B.A. and Wheeler, J.A., *Halon Replacement Program for Aviation, Dry Bay Application Phase I - Operational Parameters Study*, Wright Patterson Air Force Base Flight Dynamics Directorate Report WL-TR-95-3039 (SURVIAC TR-95-010), September 1995.
125. Grosshandler, W.L., Gann, R.G., and Pitts, W.M., eds., *Evaluation of Alternative In-Flight Fire Suppressants for Full-Scale Testing in Simulated Aircraft Engine Nacelles and Dry Bays*, NIST Special Publication SP 861, National Institute of Standards and Technology, Gaithersburg, MD, 1994.

126. Caggianelli, G.M., Bennett, M.J., Kolley M.L., and Wheeler, J.A., *Halon Replacement Program for Aviation, Aircraft Engine Nacelle Application Phase II - Operational Comparison of Selected Extinguishants*, Wright Patterson Air Force Base Flight Dynamics Directorate Report WL-TR-97-3076, May 1997.
127. Caggianelli, G.M., Bennett, M.J., Kolley M.L., and Wheeler, J.A., *Halon Replacement Program for Aviation, Aircraft Dry Bay Application Phase II - Operational Comparison of Selected Extinguishants*, Wright Patterson Air Force Base Flight Dynamics Directorate Report WL-TR-97-3075, December 1996.
128. Gann, R.G., ed., *Fire Suppression System Performance of Alternative Agents in Aircraft Engine and Dry Bay Laboratory Simulations*, vol. 1, NIST Special Publication SP 890, National Institute of Standards and Technology, Gaithersburg, MD, 1995.
129. *Fire Protection Research Program for Supersonic Transport*, Wright Patterson Air Force Base Aero Propulsion Laboratory Report APL TDR-64-105, 1964.
130. *Fire Protection System Description and Analysis Report V-22 EMD Aircraft*, Bell-Boeing Report 901-100-026, 1995.
131. Bein, D., *AH-1Z/UH-1Y HFC-125 Quantity Analysis*, Naval Air Systems Command Internal White Paper, 2000.
132. Chamberlin, G., *Criteria for Aircraft Installation and Utilization of an Extinguishing Agent Concentration Recorder Final Report*, Federal Aviation Administration Report No. FAA-DS-70-3, March 1970.
133. Hamins, A., Cleary, T., and Yang, J., *An Analysis of the Wright Patterson Full-Scale Engine Nacelle Fire Suppression Experiments*, NIST IR 6193, National Institute of Standards and Technology, Gaithersburg, MD, 1997.
134. Kay, M. and Harper, G., "Halon Replacement Program: Test Experience with the F/A-18E/F Engine Bay Fire Extinguishing System," 1999, in Gann, R.G., Burgess, S.R., Whisner, K.C., and Reneke, P.A., eds., *Papers from 1991-2006 Halon Options Technical Working Conferences (HOTWC)*, CD-ROM, NIST Special Publication 984-4, National Institute of Standards and Technology, Gaithersburg, MD, 2006.
135. Budd, L., *F/A-18E/F Engine Nacelle Gas Generator Fire Extinguishing Tests*, NAWCWPNS TM 7859, Naval Air Warfare Center Weapons Division, Survivability Division, 1995.
136. Bein, D., "Topics that Ken MacDonald Requested to be Addressed by the Independent Review Panel Members for the Comanche Halon Alternative Nacelle Fire Suppression System," Naval Air System Command White Paper to Comanche Program Executive Officer, 2003.
137. Ingerson, D., *Engine Nacelle Halon Replacement*, Presentation at the November 2005 International Aircraft Systems Fire Protection Working Group, FAA Fire Safety Branch AAR-440, WJ Hughes Technical Center, 2005.
138. Reinhardt, J.W., *Aerosol Can Explosion, Behavior of BTP and HFC-125 When Subjected to a Simulated Aerosol Can Explosion*, Presentation at the November 2005 International Aircraft Systems Fire Protection Working Group, FAA Fire Safety Branch AAR-440, WJ Hughes Technical Center, 2005.
139. Murphy, J.J. and Vice, J.M., "C-130J Live Fire Test and Evaluation," *Aircraft Survivability*, Summer 2000.
140. Bennett, M.V., *F-22 Dry Bay Fire Suppression Testing*, SURVIAC-TR-98-023, Wright Patterson Air Force Base Air Force Research Laboratory, 1999.

141. *Midwing Fire Protection System Test Data Report for the V-22 Tilt Rotor*, Bell-Boeing Report No. 901-993-027, November 1996.
142. Gann, R., "FY2002 Annual Report, Next Generation Fire Suppression Technology Program (NGP)," NIST Technical Note 1451, National Institute of Standards and Technology, Gaithersburg, MD, 2003.
143. Manchor, J., *Aerojet Chemical Gas Generator Mid-Wing Testing (September 22-24, 2003)*, Internal White Paper, Naval Air Systems Command Survivability Division, 2003.
144. Manchor, J., *Aerojet Active Chemical Gas Generator (ACGG) Testing (August 4-7, 2003)*, Internal White Paper, Naval Air Systems Command Survivability Division, 2003.
145. Manchor, J., *Simple Passive Extinguisher (SPEX) Fire Protection Test Report*, Naval Air Warfare Center Weapons Division Test Report NAWCWPNs TM 851, January 2006.
146. Crosthwaite, K.R., "Unmanned Aerial Vehicle (UAV) Survivability Enhancement Workshop," *Aircraft Survivability*, Fall 2005.
147. Leach, W., "Making Proven Halon Alternatives Even Better for Fixed-Wing Aircraft," 2006, in Gann, R.G., Burgess, S.R., Whisner, K.C., and Reneke, P.A., eds., *Papers from 1991-2006 Halon Options Technical Working Conferences (HOTWC)*, CD-ROM, NIST Special Publication 984-4, National Institute of Standards and Technology, Gaithersburg, MD, 2006.
148. Robin, M.L., "The F-Gas Regulation and its Implications in Fire Suppression Applications," 2006, in Gann, R.G., Burgess, S.R., Whisner, K.C., and Reneke, P.A., eds., *Papers from 1991-2006 Halon Options Technical Working Conferences (HOTWC)*, CD-ROM, NIST Special Publication 984-4, National Institute of Standards and Technology, Gaithersburg, MD, 2006.
149. Snyder, C.E., and Krawetz, A.A., *Determination of the Flammability Characteristics of Aerospace Hydraulic Fluids*, Air Force Materials Laboratory, 1980.
150. Benjamin, R., "Flammability Characteristics of MIL-H-5606 and MIL-H-83282 - A Literature Survey and Critical Review: Implications of Incidences and Hydraulic Fires in Combat and Noncombat Aircraft Operations," Joint Technical Coordinating Groups for Munitions Effectiveness and Aircraft Survivability Report 61 JTCG/ME-9-8 (JLF-TR-88-1), 1988.

---

---

**Chapter 3: FLAME SUPPRESSION  
CHEMISTRY**

**Gregory T. Linteris, Ph.D.  
National Institute of Standards and  
Technology**

---

---

**TABLE OF CONTENTS**

3.1	Introduction.....	120
3.2	Halogen-containing Compounds .....	121
3.2.1	Previous Understanding of the Inhibition Mechanism of CF <sub>3</sub> Br (as of 1995).....	121
3.2.2	Suppression of Nonpremixed Flames by Fluorinated Ethanes and Propanes .....	124
3.3	Metal-containing Compounds.....	142
3.3.1	Background .....	142
3.3.2	Metals with Demonstrated Flame Inhibition Potential.....	155
3.3.3	Flame Inhibition by Iron-containing Compounds .....	156
3.3.4	Flame Inhibition by Tin and Manganese.....	178
3.3.5	Complexation/Matrix Absorption of Super-effective Agents .....	199
3.3.6	Potential for Loss of Effectiveness of Other Metals .....	224
3.3.7	Flame Inhibition and Loss-of-effectiveness Summary .....	232
3.3.8	Conclusions .....	235
3.4	Phosphorus.....	236
3.4.1	Introduction .....	236
3.4.2	Inhibition of Non-premixed Flames by Phosphorus-containing Compounds.....	238
3.4.3	Effects of Dimethyl Methylphosphonate on Premixed Methane Flames.....	267
3.4.4	Summary: Phosphorus-containing Compounds in Flames .....	281
3.5	Comparative Flame Inhibition Mechanisms of Candidate Moieties .....	282
3.5.1	Introduction .....	282
3.5.2	Spectroscopic Studies of Inhibited Opposed Flow Propane/Air Flames .....	282
3.5.3	CF <sub>3</sub> Br and Other Suppressants: Differences in Effects on Flame Structure .....	291
3.5.4	Influence of Bond Energies on Catalytic Flame Inhibition.....	299
3.5.5	Temperature Regions of Optimal Chemical Inhibition of Premixed Flames.....	307

3.6 Insights on Flame Inhibition .....	316
3.7 References.....	318

### 3.1 INTRODUCTION

This chapter describes NGP research agents which work primarily through chemical means. As a prelude to this, it is useful to delineate the different terminology often used to describe the extinguishing of a flame. *Flame inhibition* usually refers to a weakening of a flame, i.e., a lowering of the overall exothermic reaction rate in the flame. This weakening may or may not lead to extinguishment, depending upon the flow field in which the flame exists. In contrast, the terms *fire suppression*, *flame extinguishment*, or *flame extinction* are often used to refer to the case in which the flame has been weakened to the point where it can no longer stabilize in the relevant flow field. Flame quenching refers to flame extinguishment for which heat losses to a surface was a precipitating factor.

The first three sections of the chapter group the research according to the active moiety in the chemical agent: halogens, metals, or phosphorus.

- The section on halogens starts with a description of what was known about the flame inhibiting action of  $\text{CF}_3\text{Br}$  prior to NGP research, and follows with research describing some alternative agents based on fluorine.
- The section on metals also first gives some background, and then provides extensive data on flame inhibition by iron-containing compounds - primarily because these agents have been shown to be the strongest flame inhibitors ever found. Detailed results for the effect of iron (and other agents) on flame radicals are also presented, followed by results for tin and manganese. Since most of the metals in these previous studies were added as toxic organometallic agents, the next section describes work to investigate metal moieties in various forms which are non-toxic. Since it was discovered fairly early in NGP research that metal compounds lose their effectiveness due to the formation of particles, additional research was aimed at finding other metals which were effective but did not suffer that same consequence. The remaining parts of that section describe the potential of other metals to be effective yet not to lose their effectiveness.
- The third section describes extensive research to characterize the potential and effectiveness of phosphorus-containing compounds. It starts with a description of a new experimental approach in counterflow diffusion flames which is helpful with aspirated samples of trimethyl phosphate (TMP) and dimethyl methylphosphonate (DMMP). Following that is a description of how varying the agent transport rates into the flame (through changes to the stoichiometric mixture fraction and the location of agent addition) changes the effectiveness of DMMP. In this section, a temperature dependence of the effectiveness is also described, which is further explored in the following section which describes spectroscopic measurements of OH and numerical modeling of counterflow diffusion flames of methane and air with DMMP added. The numerical model is further validated in the final subsection, where experiments and calculations are performed for premixed flat flames of methane and air with added DMMP.

The final section of the present chapter discusses studies aimed at finding unified principles to describe the fire suppression effectiveness of alternative chemical moieties:

- Comparison of spectroscopically measured reductions in the concentration of the chain-carrying radical OH and in peak temperature in opposed flow, atmospheric pressure, propane/air flames brought to near-extinction conditions through addition of several agents ( $\text{CF}_3\text{Br}$ ,  $\text{N}_2$ ,  $\text{Fe}(\text{CO})_5$ ,  $\text{C}_3\text{F}_7\text{H}$ ,  $\text{C}_3\text{F}_6\text{H}_2$ , DMMP, and PN (cyclo- $\text{P}_3\text{N}_3\text{F}_6$ )).
- Description of additional spectroscopic tests to delineate the reduction in  $[\text{OH}]$  with addition of  $\text{Fe}(\text{CO})_5$  (and, for comparison,  $\text{CF}_3\text{Br}$ ) to low-pressure methane-air flames.
- Discussion of the merits of using  $\text{CF}_3\text{Br}$  as a benchmark for comparison of other fire suppressants.
- A discourse on the use of inhibitor molecule bond energies as a criterion by which the flame inhibition efficiency can be predicted and understood.
- Examination of the regions of a premixed flame which are most susceptible to chemical inhibition.

The NGP research described here has moved the science of flame inhibition and suppression chemistry forward in very large measure. Entirely new, detailed, comprehensive chemical kinetic mechanisms were developed specifically for the NGP, and the use of these kinetic mechanisms in detailed numerical simulations for the present investigations has led to great insight into the action of chemically acting agents in fire suppression. New experimental techniques were developed, as well as new methods of using existing approaches. In fact, much of the present work has been cited in fields external to fire research due to their utility beyond the present needs. The work presented below will provide an outstanding basis for those future researchers who will continue the search for new fire-fighting materials. The new unified insights on fire suppression developed through NGP research are summarized at the end of this chapter.

## 3.2 HALOGEN-CONTAINING COMPOUNDS

### 3.2.1 Previous Understanding of the Inhibition Mechanism of $\text{CF}_3\text{Br}$ (as of 1995)

In previous studies,  $\text{CF}_3\text{Br}$  (and related compounds) have been the subject of much fundamental research, for example in flow reactors,<sup>1,2</sup> premixed flames,<sup>3-11</sup> co-flow diffusion flames,<sup>12-14</sup> and counterflow diffusion flames.<sup>9,15-20</sup> Much recent research has been aimed at finding both short-<sup>21,22</sup> and long-term<sup>23</sup> replacements for  $\text{CF}_3\text{Br}$ . As a result,  $\text{CF}_3\text{Br}$  itself has been the continuing subject of many studies<sup>24-27</sup> since an improved understanding of its mechanism of inhibition will help in the search for alternatives, and nearly all assessments of new agents use  $\text{CF}_3\text{Br}$  as a baseline for comparison of the new agents.

As outlined above, the flame configurations used to study flame inhibition mechanisms have tended to be premixed and counterflow diffusion flames. Premixed flames have been selected mainly because the overall reaction rate, heat release, and heat and mass transport in these flames can be described with a single fundamental parameter - the laminar burning velocity, and because over certain regions, the flow field can be considered one-dimensional (greatly simplifying data collection and numerical simulation). Similarly, counterflow diffusion flames can be considered one-dimensional along the centerline, and the extinction strain rate has been commonly used as the characteristic suppression parameter. In principle, such fundamental parameters can ultimately be used to relate the behavior of the agent in the laboratory flame to its behavior in suppressing a large-scale fire<sup>28</sup>, although this scaling is difficult in practice.

## Premixed Systems

Early studies of the inhibitory effects of halogenated hydrocarbons on flames were conducted in premixed systems. Numerous research groups<sup>12,29-31</sup> determined the influence of halogenated methanes on the flammability limits of hydrocarbon-air mixtures. The magnitude of the inhibitory effect and its dependence on halogen type and stoichiometry generally indicated a chemical rather than thermal mechanism. Simmons and Wolfhard<sup>12</sup> studied the flammability limits of methane-air mixtures with bromine and methyl bromide inhibitors and showed that methyl bromide influenced the limits of flammability in the same manner as equivalent amounts of bromine and methane, indicating that the decomposition products of the halogenated methanes were responsible for the action. Garner et al.,<sup>32</sup> Rosser et al.,<sup>33</sup> Lask and Wagner<sup>34</sup> and Edmondson and Heap<sup>35</sup> measured the reduction in burning velocity of various burner – stabilized hydrocarbon-air flames with addition of several halogenated methanes, halogen acids and halogen dimers. In later work, Niioka *et al.*<sup>36</sup> experimentally investigated the effect of CF<sub>3</sub>Br on the extinction velocity of opposed premixed C<sub>2</sub>H<sub>4</sub> flames. The inhibitory effect was found to be more effective in rich flames than in lean flames. Mitani<sup>37</sup> used experimental results on the decrease of flame propagation speeds of premixed H<sub>2</sub>-O<sub>2</sub>-N<sub>2</sub> and C<sub>2</sub>H<sub>4</sub>-O<sub>2</sub>-N<sub>2</sub> flames with CF<sub>3</sub>Br addition to derive overall activation energies for the inhibition reactions, which correlated well with measured energies for key inhibition steps. All studies were in consensus that the magnitude of the inhibition was related to the number and type of halogen atoms present in the reactants, the concentration of the inhibitor, and the equivalence ratio,  $\phi$ , and that the effect was generally too large to be accounted for by thermal dilution effects. This conclusion was based on supporting calculations or measurements showing that the final temperatures in the inhibited flames were not low enough to account for the burning velocity reductions observed.

Detailed information on the inhibition mechanism of brominated species has been provided by flame structure measurements. Mass spectrometric measurements of stable species concentrations in premixed flames of methane and air were conducted by several investigators: Levy et al.<sup>38</sup> used HBr to inhibit a Bunsen flame and found that HBr inhibited methane consumption but not CO oxidation; Wilson<sup>4</sup> and Wilson et al.<sup>39</sup> performed low-pressure inhibited premixed flame studies with methyl bromide, HCl, HBr, Cl<sub>2</sub>, and concluded that both CH<sub>3</sub>Br and HBr act to reduce radical concentrations in the preheat region of the flame by competing with the chain branching reaction  $H + O_2 = OH + O$ , and that CH<sub>3</sub>Br lowers the peak OH concentration to near equilibrium values, while uninhibited flames have the characteristic super-equilibrium OH concentrations. Biordi et al.<sup>5,40</sup> used a molecular-beam mass spectrometer to obtain stable and radical species concentrations as a function of position in low-pressure premixed flat flames of methane and air with and without addition of CF<sub>3</sub>Br, and Safieh et al.<sup>7</sup> performed similar experiments with a low-pressure CO-H<sub>2</sub>-O<sub>2</sub>-Ar flame. The data and analyses of these researchers provided detailed kinetic information on the mechanisms of Br and CF<sub>3</sub> inhibition under low-pressure premixed, burner-stabilized conditions. Day et al.<sup>41</sup> and Dixon-Lewis and Simpson<sup>42</sup> studied the burning velocities and the rich flammability limits of H<sub>2</sub>-O<sub>2</sub>-N<sub>2</sub> and H<sub>2</sub>-O<sub>2</sub>-N<sub>2</sub>O flames. Their experiments and numerical modeling showed that the thermodynamic equilibrium relationship for the reaction  $H + HBr = H_2 + Br$  together with recombination steps involving bromine atoms are primarily responsible for the inhibition effect of HBr compared to HCl and HF, rather than competition of the H atom-hydrogen halide reaction with the branching reaction  $H + O_2 = OH + O$ . Westbrook<sup>8,43</sup> developed a detailed chemical kinetic mechanism for HBr, CH<sub>3</sub>Br, and CF<sub>3</sub>Br inhibition and performed numerical calculations of flame structure, testing the mechanism using experimental burning velocity reductions and, to some extent, using measured species concentration profiles.

## Diffusion Flames

Early investigations of the effects of chemical inhibitors on diffusion flames used the co-flow configuration. Creitz<sup>44</sup> determined the blow-off limits with CH<sub>3</sub>Br and CF<sub>3</sub>Br added to either the fuel or oxidizer stream for various oxygen volume fractions, and found that oxygen volume fractions approaching 0.30 required over 20 % CF<sub>3</sub>Br in the oxidizer for flame detachment. Simmons and Wolfhard<sup>12</sup> found the blow-off limits for CH<sub>3</sub>Br addition to the fuel and air streams for alkane and hydrogen flames, and showed that blow-off required different amounts of inhibitor for different burner geometries. Their measurements, as well as more recent ones with CF<sub>3</sub>Br,<sup>45,46</sup> have shown that lower gas velocities require greater amounts of inhibitor. Simmons and Wolfhard<sup>12</sup> also performed accompanying spectroscopic measurements in a slot-burner with CH<sub>3</sub>Br added to the air stream and found enhanced C<sub>2</sub> formation as well as a secondary reaction zone (observed via Br<sub>2</sub> emission) on the air side with either CH<sub>3</sub>Br or ethane and bromine added to the air stream.

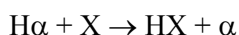
The above jet diffusion flame studies have all shown that a higher volume fraction of the brominated agent was required when it was added to the fuel stream rather than the air stream. Friedman and Levy<sup>15</sup> were the first to use the extinction of counterflow diffusion flames to assess the inhibitory effect of CF<sub>3</sub>Br and CH<sub>3</sub>Br added to the methane stream. Milne et al.<sup>16</sup> added CF<sub>3</sub>Br to either the fuel or air stream of several hydrocarbon-air flames, again showing that addition to the air stream extinguished the flames at lower volume fraction than addition to the fuel stream. Ibiricu and Gaydon<sup>47</sup> made spectroscopic measurements with addition of CH<sub>3</sub>Br and other inhibitors to flames of various fuels. They found OH emission to be decreased, while C<sub>2</sub> and HCO emission were increased. Niioka et al.<sup>36</sup> correlated the extinction conditions of counterflow diffusion flames of ethylene inhibited by CF<sub>3</sub>Br in the air or fuel stream with the estimated mass flux of inhibitor to the reaction zone.

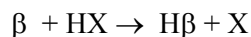
The first measurements of inhibited counterflow flames with liquid fuels were made by Kent and Williams<sup>17,48</sup> for CF<sub>3</sub>Br in the oxidizer stream against a heptane pool. These were followed by extensive measurements for the same agent with numerous condensed-phase fuels by Seshadri and Williams.<sup>49</sup> Among other results and analyses, these investigations characterized the extinction flow velocity as a function of the oxygen mass fraction in the oxidizer stream, found the extinction flow with added inhibitor, and measured stable species mass fractions with gas chromatography. The amount of inhibitor required for flame extinction was found to increase with decreasing air flow velocity (i.e. strain) and the results were highly fuel dependent. In later work, Seshadri and co-workers<sup>50</sup> determined the extinction strain rate for a large number of fluorinated agents in a similar counterflow heptane-air pool burner.

Some of the above diffusion flame studies also show increased soot production with addition of halogenated inhibitors. The laser-induced incandescence and fluorescence measurements of Smyth and Everest<sup>51</sup> have quantified both the increased soot and decreased peak OH in such flames, although the mechanism of higher soot formation for CF<sub>3</sub>Br was not resolved.

## Mechanism of Inhibition

The basic mechanism of halogen flame inhibition was suggested by Rosser et al.<sup>33</sup> and further justified and refined by Butlin and Simmons,<sup>31</sup> Dixon-Lewis and co-workers,<sup>41,42</sup> Westbrook,<sup>8,13,43</sup> and Babushok and co-workers.<sup>52</sup> The reaction mechanism is:





in which X is a halogen,  $\alpha$  is a hydrocarbon, and  $\beta$  is a reactive radical such as H, O, or OH. The hydrogen atom is typically affected most by the catalytic radical recombination cycles above, and its decrease leads to a lowering of the chain-branching reaction  $\text{H} + \text{O}_2 \rightarrow \text{OH} + \text{O}$  and the CO consumption reaction  $\text{CO} + \text{OH} \rightarrow \text{CO}_2 + \text{H}$ . It was demonstrated fairly early<sup>41</sup> that for Br and Cl, the equilibrium condition of the first reaction was key, as was the necessity of the regeneration steps (in the form of the second reaction or some alternatives).

As described above, there has been fairly extensive past research on  $\text{CF}_3\text{Br}$  itself, as well as some simple small hydrofluorocarbon (HFC) short-term replacements. These include phenomenological tests with cup burners as well as fundamental studies. Nonetheless, tests with larger HFCs appear less frequently in the literature, with very little fundamental data from diffusion flames. The following work remedies that deficiency.

### 3.2.2 Suppression of Nonpremixed Flames by Fluorinated Ethanes and Propanes

#### Introduction

The need for environmentally acceptable substitutes for bromine-containing halons (halogenated hydrocarbons) has led to a number of studies on alternative fire suppression agents encompassing a variety of experimental geometries and scales,<sup>21,53</sup> as well as to the development of chemical kinetic models for these agents.<sup>54-56</sup> Models are instrumental in guiding the search for effective halon replacements in that they facilitate the identification of mechanisms key to suppression. Such models must be validated using experimental data. Data sets that can directly be compared to numerical results are therefore particularly valuable. For models of suppression in particular, the usefulness of experimental and numerical studies depends on how well they capture the characteristics of real fire scenarios. Most experimental studies on hydrofluorocarbons (HFCs), used as near-term halon replacements, have focused on inhibited premixed flames, usually with methane fuel, measuring parameters such as flame speed<sup>57,58</sup> or profiles of intermediate species.<sup>59-61</sup> However, most fire-fighting scenarios involve higher hydrocarbon fuels, non-premixed flames, and aim to achieve extinction rather than inhibition. In order to extend laboratory results to more realistic situations, a broad range of data sets is needed to provide adequate model validation for suppression by both HFCs and other classes of alternative agents now being identified.

Research by Williams and co-workers<sup>62</sup> focused on the suppression effectiveness of HFCs in extinguishing non-premixed flames. Although less effective fire suppressants than brominated halons, these agents are currently used as near-term replacements. They possess many of the same favorable physical properties as brominated halons, but do not destroy the stratospheric ozone layer.<sup>21,50</sup> Previously, the Naval Research Laboratory (NRL) investigated non-premixed counterflow methane/air and propane/air flames suppressed by  $\text{CF}_4$ ,  $\text{CHF}_3$ , and  $\text{CF}_3\text{Br}$ .<sup>63</sup> The NGP extended the methane/air and propane/air extinction studies to include all fluorinated ethanes containing at least four fluorine atoms, and ten fluorinated propanes containing at least five fluorine atoms. The fluorinated ethane and fluorinated propane data sets were generated to provide additional input to validate chemical kinetic models such as those developed recently for HFCs.<sup>54-56, 59</sup> Also tested were sulfur hexafluoride ( $\text{SF}_6$ ,

largely inert<sup>13</sup>), nitrogen, three bromine-containing halons, and one iodine-containing halon. All compounds investigated are listed in Table 3-1.

**Table 3-1. Agents Tested.**

Agent	Chemical Formula	$C_p^{300\text{ K}}$ (J/mol.K) <sup>a</sup>	$H^{1600\text{ K}}-H^{300\text{ K}}$ (kJ/mol) <sup>b</sup>	Flames <sup>e</sup>
HFC-134	CHF <sub>2</sub> CHF <sub>2</sub>	90.9	183 <sup>[31]</sup>	M,P,H
HFC-134a	CF <sub>3</sub> CH <sub>2</sub> F	87.2	186 <sup>[31]</sup>	M,P,H
HFC-125	CF <sub>3</sub> CHF <sub>2</sub>	95.9	195 <sup>[31]</sup>	M,P,H
FC-116	CF <sub>3</sub> CF <sub>3</sub>	107.7	206 <sup>[31]</sup>	M,P,H
HFC-245ca	CHF <sub>2</sub> CF <sub>2</sub> CH <sub>2</sub> F	123.7	244 <sup>c</sup>	M,P
HFC-245cb	CF <sub>3</sub> CF <sub>2</sub> CH <sub>3</sub>	123.0	242 <sup>c</sup>	M,P
HFC-245eb	CF <sub>3</sub> CHFCH <sub>2</sub> F	123.0 <sup>c</sup>	242 <sup>c</sup>	M
HFC-245fa	CF <sub>3</sub> CH <sub>2</sub> CHF <sub>2</sub>	122.0 <sup>[35]</sup>	241 <sup>[35]</sup>	M
HFC-236cb	CF <sub>3</sub> CF <sub>2</sub> CH <sub>2</sub> F	130.0 <sup>c</sup>	256 <sup>c</sup>	M,P,H
HFC-236ea	CF <sub>3</sub> CHFCHF <sub>2</sub>	129.8	256 <sup>c</sup>	M,P,H,A
HFC-236fa	CF <sub>3</sub> CH <sub>2</sub> CF <sub>3</sub>	128.1	253 <sup>c</sup>	M,P,H,A
HFC-227ca	CF <sub>3</sub> CF <sub>2</sub> CHF <sub>2</sub>	140.0 <sup>c</sup>	276 <sup>c</sup>	M,P,H
HFC-227ea	CF <sub>3</sub> CHFCF <sub>3</sub>	139.8	275 <sup>[38]</sup>	M,P,H,A
FC-218	CF <sub>3</sub> CF <sub>2</sub> CF <sub>3</sub>	150.6	289 <sup>c</sup>	M,P,H
Halon 1301	CF <sub>3</sub> Br	70.5	125 <sup>[36]</sup>	P,H,A
Halon 13001	CF <sub>3</sub> I	61.3 <sup>[36]</sup>	126 <sup>[36]</sup>	P,H
Halon 1211	CF <sub>2</sub> ClBr	74.6 <sup>d</sup>	133 <sup>[39]</sup>	P,H
Halon 1201	CHF <sub>2</sub> Br	58.7 <sup>d</sup>	120 <sup>[39]</sup>	P,H
Sulfur Hexafluoride	SF <sub>6</sub>	97.4 <sup>[36]</sup>	185 <sup>[36]</sup>	M,P,H
Tetrafluoromethane	CF <sub>4</sub>	61.2	122 <sup>[36]</sup>	H,A
Nitrogen	N <sub>2</sub>	29.1 <sup>[36]</sup>	42 <sup>[36]</sup>	M,P,H,A

<sup>a</sup> Specific heat at 300 K. The numerical superscripts in square brackets indicate reference numbers. If no superscript is present, the value is from Reference 64.

<sup>b</sup> Sensible enthalpy required to raise the agent's temperature from 300 K to 1600 K. The sources for the data used to derive the sensible enthalpy values are indicated by the numerical superscripts in square brackets.

<sup>c</sup> Estimated.

<sup>d</sup> From Reference 65, evaluated at 298 K.

<sup>e</sup> Flames in which given agent was tested: M, methane counterflow; P, propane counterflow; H, n-heptane cup burner; A, methanol cup burner.

An experimental geometry that captures many characteristics of pool fire threats is that of the cup burner, which is described more fully in Chapter 6. Bench-scale co-flow burners operated with a liquid fuel, cup burners are widely used for estimating agent concentrations required to combat fires.<sup>66</sup> Hamins et al.<sup>50</sup> compared a number of HFC agents in cup burner tests using five different fuels: n-heptane, two types of jet fuel, and two types of hydraulic fluid. For nearly all agents tested, the concentrations required to

extinguish the n-heptane flame exceeded those required for the other fuels by less than 10 %. Thus, n-heptane cup burner studies provide extinction data applicable to many hydrocarbon flames.

For validation of kinetic models, treating detailed chemical mechanisms in the two-dimensional model required to describe cup burner flames is computationally difficult. An alternative to cup burners for suppression mechanism studies is provided by non-premixed counterflow flames. This configuration is computationally tractable since it can be modeled quasi-one-dimensionally, along the axis of symmetry of the flame, by invoking a similarity transform.<sup>67</sup> Experimentally, it is also advantageous in that it allows control of the strain rate imposed on the flame. In this paper, the strain rate in a counterflow burner is defined as the maximum axial gradient in axial velocity on the oxidizer side of the flame zone. The strain rate is easily adjusted by changing the gas flows. The effects of suppression agents can then be quantified over a range of flame conditions by measuring the extinction strain rate as a function of agent concentration. Hamins *et al.*<sup>50</sup> and Saso *et al.*<sup>68</sup> found that HFC extinction concentrations for low strain rate n-heptane counterflow flames were similar to those obtained in n-heptane cup burners. Since the cup burner configuration is relevant to many fire scenarios, the results of Hamins *et al.* and Saso *et al.* suggest that agent extinction concentrations in low strain rate non-premixed counterflow flames are pertinent to these same scenarios.

The choice of a model fuel compound for suppression studies involves a trade-off between representative extinction properties and computational tractability. Gaseous fuels including methane, ethane, and propane are attractive to use from both experimental and modeling standpoints, but their relevance to fires involving long chain hydrocarbons needs to be determined. Furthermore, no model fuel is representative of all fire threats. Indeed, alcohol fires, methanol fires in particular, are very difficult to extinguish, even with  $\text{CF}_3\text{Br}$ .<sup>69</sup> The extinction behavior of methane/air counterflow, propane/air counterflow, n-heptane cup burner and methanol cup burner flames are compared in this study to identify systematic trends in the suppression effectiveness of selected agents as a function of the fuel used. In addition to providing experimental data for HFC model validation, another objective of the current investigation is to assess whether methane or propane counterflow burner extinction studies are appropriate models for HFC suppression of liquid hydrocarbon fires.

Tanoff *et al.*<sup>70</sup> recently computed the extinction strain rate of methane/air counterflow flames suppressed by several  $\text{C}_1$  and  $\text{C}_2$  HFCs. One of their major conclusions was that most HFCs investigated, with the exception of  $\text{CHF}_3$ , would be better suppressants in methane flames if they were chemically inert. Also, agents predicted to form  $\text{CF}_2\text{O}$  in the counterflow flame, principally from  $\text{CF}_3$  radicals, were found to be better suppressants than those that do not. The chemical contribution to suppression of the  $\text{CF}_3$  group was reported by Sheinson *et al.*,<sup>13</sup> who attributed 25 % of  $\text{CF}_3\text{Br}$ 's suppression ability to this moiety. The present study further investigates the impact of  $\text{CF}_3$  groups in an agent on suppression by comparing the performance of four sets of HFC isomers.

In counterflow burners, flows at extinction are apparatus dependent. Comparisons between results obtained from different experimental and numerical counterflow flame studies must therefore be made through extinction strain rates. While flows are easily determined, velocity profile measurements are required to determine local extinction strain rates. Here, a burner-specific relationship between local strain rate and flow conditions was obtained. All strain rates quoted herein are therefore traceable to an experimental determination of the local velocity field.

## Experiment

The counterflow burner and experimental methodology have been described previously.<sup>63</sup> The burner consisted of two vertically-mounted open straight tubes, approximately 50 cm long, having an inner diameter of 1 cm. The tube exits were spaced  $10.0 \text{ mm} \pm 0.5 \text{ mm}$  apart. The gap size was determined by translating the burner assembly with respect to a laser beam perpendicular to the tube axis, and measuring the height at which the beam was blocked by the tubes. The top tube was equipped with a cooling jacket to prevent the hot combustion products from preheating the upper reactant stream. The tubes were housed in a Plexiglas chamber, which was continuously purged with nitrogen to dilute combustion products and unburned reactants before they entered the exhaust.

For experiments with methane, the fuel was introduced through the top tube while air/agent mixtures were introduced through the bottom. For experiments with propane, air/agent mixtures were delivered from the top, fuel from the bottom. These configurations were used because they produced the most stable flames at low strain rates. For propane, inverting the reactant streams did not significantly affect the extinction strain rate of the uninhibited flame. Flows of all gases were regulated by mass flow controllers (Sierra Instruments), which were calibrated using a piston flowmeter (DC-2, Bios International). All flow conditions were laminar, with tube Reynolds numbers never exceeding 2100.

During extinction measurements, the flows of fuel and air were set to obtain a flame midway between the tubes. The agent flow was then slowly increased at intervals of 30 s to 45 s, with periodic adjustments of the fuel and air flows to maintain the flame's position, until the flame extinguished. The flame's position was determined by monitoring its image on a video screen. The stagnation plane was always slightly toward the fuel tube from the flame zone. In experiments with methane, the flame typically extinguished completely. For propane, local extinction typically occurred along the centerline, leaving a ring-shaped flame with a hole along the burner axis, similar to that described by Potter and Butler.<sup>71</sup> In all tests, the agent was added to the air stream. This mode of application most closely resembled actual situations, in which an agent is introduced into the air around the fire, with the fuel burning in a non-premixed flame.

The cup burner apparatus and methodology have been described in detail elsewhere.<sup>13</sup> The design was virtually identical to that of Hamins et al.<sup>50</sup> The piston flow meter was used to measure the agent and air flows after each extinction measurement. The total flow of air + agent was  $20 \text{ L/min} \pm 1 \text{ L/min}$  for all extinction measurements, giving a flow velocity, averaged over the 105 mm inner diameter chimney, of  $4.1 \text{ cm/s} \pm 0.2 \text{ cm/s}$  past the 28 mm outer diameter cup. Experiments were conducted on both n-heptane and methanol flames. The fuel level was kept within 0.5 mm of the top of the cup without overflowing, as low liquid levels led to attachment of the flame to the heated rim of the Pyrex cup, resulting in anomalously high extinction values.

The agents listed in Table 3-1 were obtained from the following suppliers: HFC-245eb and halon 13001, Flura; HFC-245fa, AlliedSignal; HFC-236ea and HFC-236fa, Dupont; HFC-227ea and halon 1201, Great Lakes; FC-218, Scott Specialty Gases; halon 1301 and  $\text{CF}_4$ , Matheson. The nitrogen was obtained from the Naval Research Laboratory's in-house supply. The remaining agents were from PCR. The stated purity of the agents was at least 97 %. All agents were used as supplied, with the exception of HFC-245ca, HFC-245eb and HFC-245fa. These pentafluoropropanes have boiling points close to room temperature: 25 °C, 23 °C, and 15 °C, respectively. They were therefore premixed with air in a 1:3 ratio before being tested. The pressure increase ensured that stable flows of these agents were delivered to the

burners. Extinction data was also collected with HFC-245fa unmixed with air. These data were consistent with those obtained using the agent/air mixture.

All of the agents in Table 3-1 were tested in the propane counterflow flame with the exception of HFC-245eb, HFC-245fa, and  $\text{CF}_4$ . All of the agents were tested in the methane counterflow flame with the exception of halon 1301, halon 13001, halon 1211, halon 1201, and  $\text{CF}_4$ . All of the agents with the exception of the pentafluoropropanes were tested with n-heptane in the cup burner. HFC-236ea, HFC-236fa, HFC-227ea, halon 1301,  $\text{CF}_4$ , and nitrogen were tested with methanol in the cup burner.

### Extinction Strain Rate Determination

Many researchers performing studies in counterflow burners have characterized extinction conditions in terms of global or imposed parameters, such as flow rates and gap size,<sup>72</sup> or global strain rates calculated from these parameters.<sup>50,73</sup> These global parameters representing the imposed flow conditions can be compared to the same parameters obtained from numerical calculations of extinction conditions.<sup>74</sup> Because the local flow field near the flame determines extinction, the comparison of global parameters is valid only as long as the relationship between the local strain rate and the global conditions are the same for the experiment and the calculations. Recent measurements<sup>67,75</sup> have cast doubts on the adequacy of representing counterflow experimental boundary conditions by either plug or potential flow in numerical calculations. Comparisons of measured and numerical local strain rates in the vicinity of the flame should show less sensitivity to boundary conditions than comparisons of measured and numerical global strain rates.

The most direct approach in determining strain rate is to measure the local velocity fields. As velocities cannot be measured at extinction, determination of local extinction strain rate involves a series of velocity measurements in increasingly strained flames, and extrapolation to extinction.<sup>63</sup> This sequence of measurements must be repeated for each fuel/oxidizer/additive system and each additive loading, requiring large numbers of velocity profile measurements.

In the present study, air stream local strain rates were determined by measuring the centerline axial velocity as a function of axial position by an LDV system (QSP Digital). The oxidizer stream was seeded with 0.3  $\mu\text{m}$  alumina particles (Buehler). The velocity profile on the oxidizer side of the flame was fit to a 6<sup>th</sup> order polynomial, and the relevant local strain rate was taken to be the maximum value of the derivative of this function. Velocity profiles were measured for propane/air, methane/air, methane/(air + HFC-227ea), and propane/(air +  $\text{SF}_6$ ) flames.

Based on these measurements, an empirical, burner-specific relationship to convert global parameters into local strain rates was determined. Figure 3-1 shows the data used in obtaining this correlation. Measured local strain rate is plotted versus the plug flow global strain rate parameter derived by Seshadri and Williams<sup>76</sup>, and restated by Chelliah et al.<sup>67</sup> in Equation 3-1.

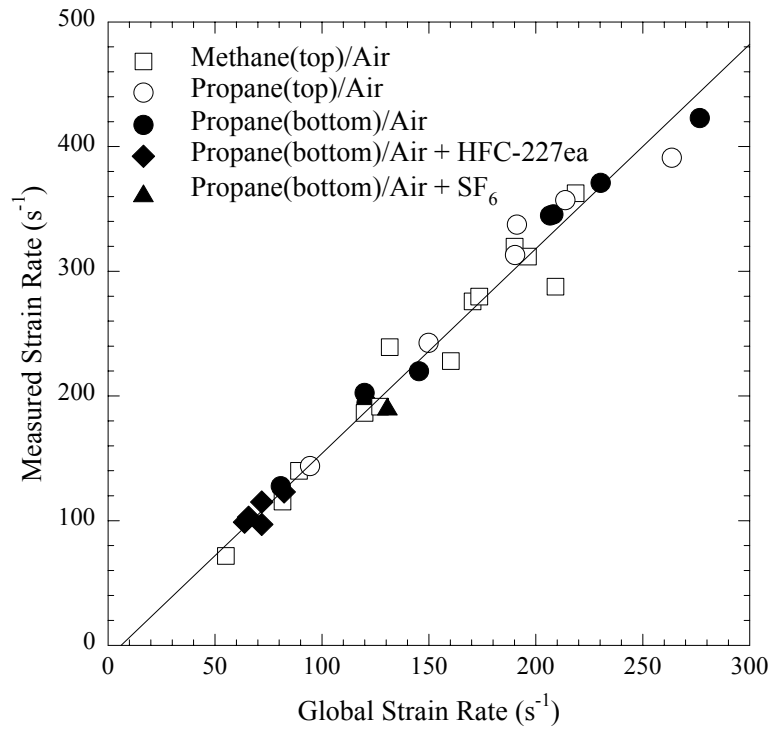


**Figure 3-1. Comparison of Local Strain Rates Measured by Laser Doppler Velocimetry in Non-premixed Counterflow Flames and Global Strain Rates Calculated from Equation 3-1. (The solid line corresponds to the linear regression given in Equation 3-2.)**

$$K_{global,plug} = \frac{2|V_o|}{L} \left( 1 + \left( \frac{\rho_f V_f^2}{\rho_o V_o^2} \right)^{0.5} \right), \quad (3-1)$$

where  $L$  is the gap size (1 cm), and  $\rho_{f,o}$  and  $V_{f,o}$  are the densities and velocities of the fuel and oxidizer streams, respectively.  $V$  is as the *average* velocity across the tube exit. Measured local strain rates for all flame conditions, including those with suppressants present, were proportional to  $K_{global,plug}$  from Equation 3-1,

$$K_{local} = (1.57 \pm 0.02) K_{global,plug}, \quad (3-2)$$

where the velocities used in the global expression are averages based on measured volumetric flows. The local extinction strain rates discussed in the present study were obtained using Equations 3-1 and 3-2.

Seshadri and Williams' plug flow global strain rate expression is for the axial gradient in axial velocity at the stagnation plane calculated for inviscid non-reacting flow, with plug flow boundary conditions imposed at the burner exits. The current apparatus, with straight burner tubes, has velocity boundary conditions significantly different from plug flow. Measurements near the tube exits indicated a nearly parabolic profile for an individual tube in isolation, with some flattening of the profile when the opposing flow from the second tube was introduced. The centerline velocity of a parabolic profile in tube flow was twice the average velocity determined from the volumetric flow and the cross-sectional area. At a given flow, the tube exit centerline velocities in the current apparatus were therefore expected to be between once and twice the plug flow values. Hence, the coefficient relating  $K_{local}$  and  $K_{global,plug}$  was predicted to lie between 1 and 2. The factor of 1.57 obtained was consistent with this prediction. Pellett et al.<sup>77</sup> also determined that local and global strain rates were linearly related in their opposed-tube burners: local

strain rates were found to be 3 times larger than their global counterparts. Pellett et al. used burners with a ratio of gap size to tube diameter equal to 2. For the burner considered here, this ratio was equal to 1.

### Non-Premixed Counterflow Flame Experiments

Figure 3-2 and Figure 3-3 show how local extinction strain rate varied with agent molar concentration for methane and propane non-premixed counterflow flames, respectively. Figure 3-2a and Figure 3-3a show the suppression effects of the fluorinated ethanes, SF<sub>6</sub> and N<sub>2</sub>. The N<sub>2</sub> extinction concentrations have been divided by two for presentation in the figures. Figure 3-2b and Figure 3-3b show results for the fluorinated propanes. Figure 3-3c shows the effects of halon 1301, halon 13001, halon 1211 and halon 1201 on the extinction strain rate of a propane flame. The error bars shown in Figure 3-2a and Figure 3-3a for the HFC-134 data are at the 99.7 % (3 $\sigma$ ) confidence level. Horizontal error bars represent uncertainties in air and agent flows. Vertical error bars represent uncertainties in air, agent and fuel flows, gap size, room temperature and pressure, and the constant of proportionality between local and global strain rates (Equation 3-2). At comparable concentrations or extinction strain rates, uncertainties in the data for the other agents are similar to those shown for HFC-134. The N<sub>2</sub> extinction concentration uncertainties are similar to those for HFC-134 at comparable loadings. They increase to  $\pm 1.7$  mole % at the highest concentrations.

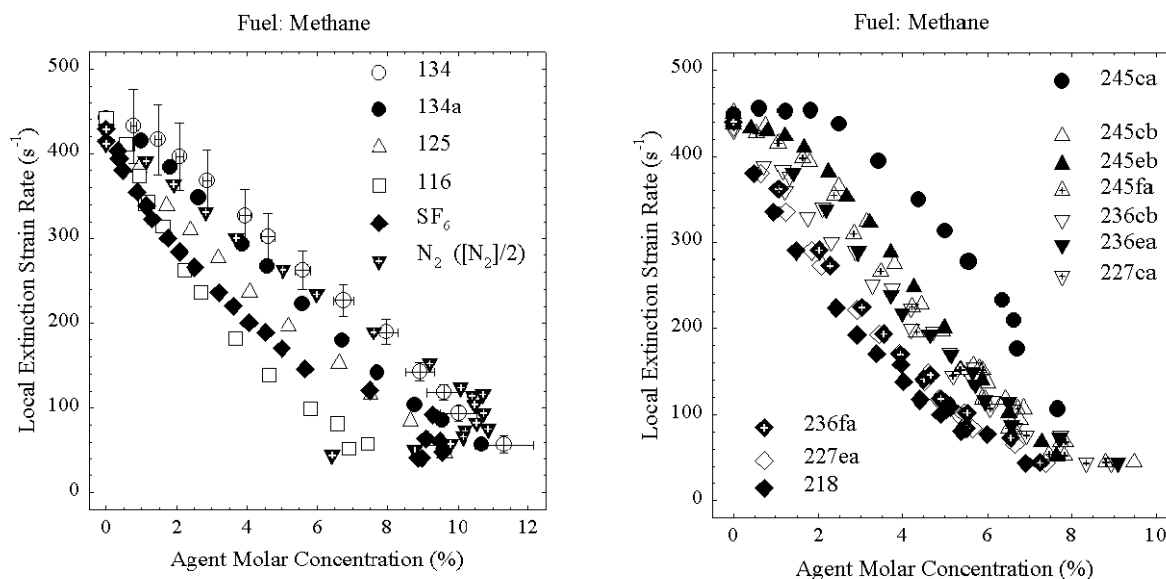


**Figure 3-2. Extinction Strain Rate vs. Agent Molar Concentration for Non-premixed Methane-air Flames Suppressed by: a) Fluorinated Ethanes, SF<sub>6</sub>, and N<sub>2</sub>; and b) Fluorinated Propanes.**

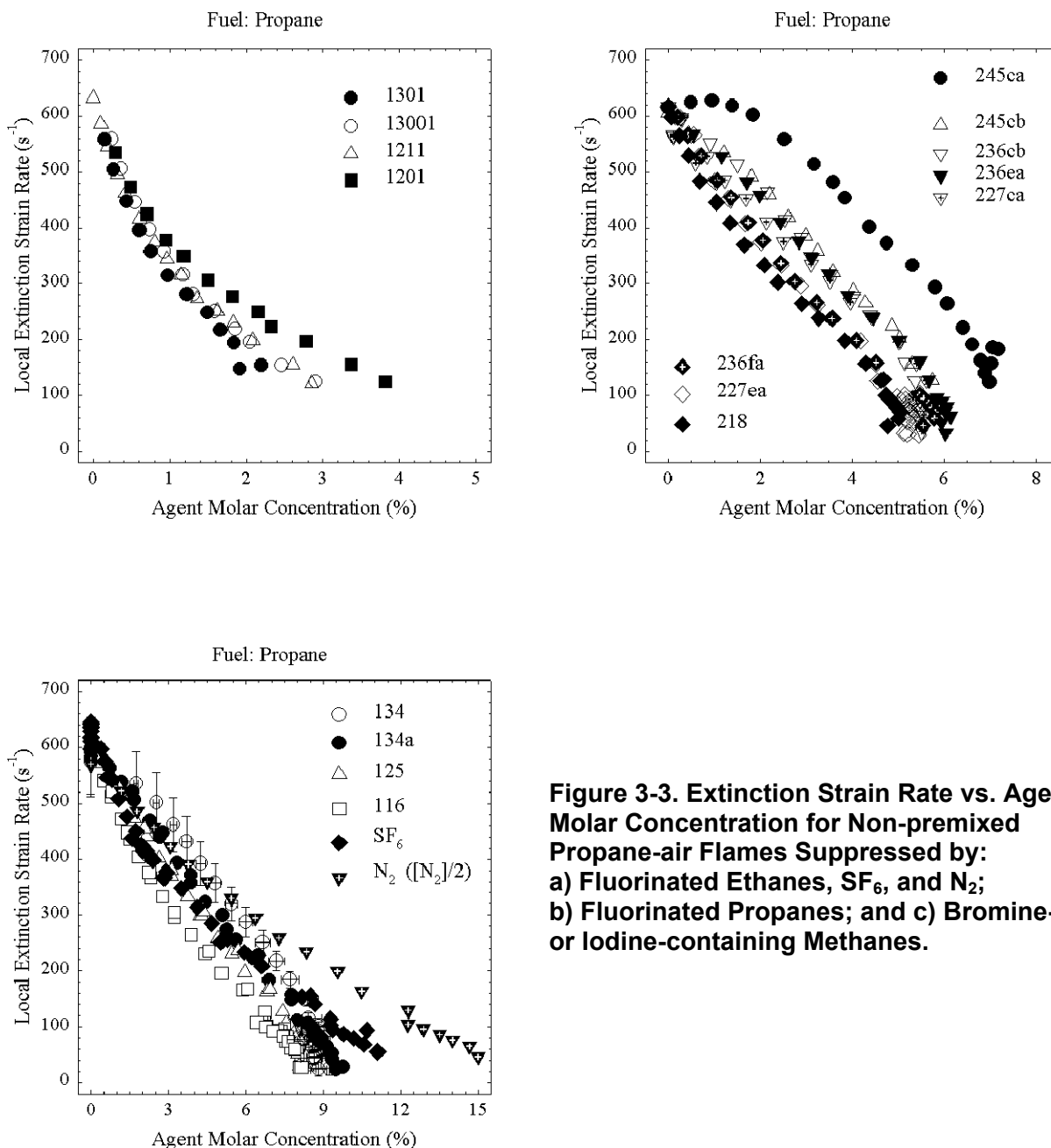


**Figure 3-3. Extinction Strain Rate vs. Agent Molar Concentration for Non-premixed Propane-air Flames Suppressed by:**  
**a) Fluorinated Ethanes,  $SF_6$ , and  $N_2$ ;**  
**b) Fluorinated Propanes; and c) Bromine- or Iodine-containing Methanes.**

### *Extinction of Uninhibited Methane and Propane Flames*

The average uninhibited non-premixed counterflow methane/air and propane/air flame local extinction strain rates were compared to values found in the literature. Pellett et al.<sup>77</sup> used two different opposed-nozzle burners to obtain extinction strain rates of  $384 s^{-1}$  and  $396 s^{-1}$  for methane/air flames. Furthermore, Chelliah et al.<sup>67</sup> measured the local extinction strain rate of their non-premixed counterflow methane/air flame to be  $380 s^{-1}$ . Yang and Kennedy<sup>78</sup> measured theirs to be  $340 s^{-1}$ . Both of these values were obtained for flames having strain rates below that required for extinction. They correspond to lower

bounds for the values that would be calculated from an extrapolation to extinction, and are consistent with the results of the present study. Yang and Kennedy indicated that the strain rate they report is approximately 10 % lower than that which would be obtained through extrapolation; and that the uncertainty in their critical strain rate is approximately +10 % and -5 %.

Global extinction strain rates for uninhibited counterflow non-premixed methane/air and propane/air flames have also been reported. MacDonald et al.<sup>79</sup> reported a global extinction strain rate of 296 s<sup>-1</sup> for methane. The corresponding global value obtained in the present study was 273 s<sup>-1</sup>. Since the experimental geometries in both studies are similar, the values are expected to be comparable. MacDonald et al. indicate that variations of up to 80 s<sup>-1</sup> were observed in their uninhibited global extinction strain rates, due to variations in their air's oxygen content. The global methane extinction number collected in the present study is thus consistent with theirs. Puri and Seshadri<sup>80</sup> report global extinction values, but for a different experimental geometry. The results cannot be directly compared.

### ***Agent Suppression Effectiveness***

Figure 3-2 and Figure 3-3 show that, in general, the extinction strain rate of both methane and propane flames decreased as agent loading increases. Thus, the agents inhibited the flames. For HFC-245ca, however, the extinction strain rates at concentrations below 2 % are higher than those for the uninhibited flames. At these loadings, this agent increased flame strength. Nevertheless, above 2 %, extinction occurred at strain rates below the uninhibited values, and extinction strain rates decreased with increases in concentration: in larger quantities, HFC-245ca acted like a suppressant. The extinction data presented in Figure 3-2 and Figure 3-3 are limited to strain rates above 70 s<sup>-1</sup>. Below this value, considerable scatter was observed and, for several agents, extinction concentrations began to decrease with diminishing strain rate. At low strain rates, the flames became more susceptible to both conductive and radiative heat losses to the burner, and to fluctuations in the flow currents present in the surrounding chamber gases.

A secondary flame zone about 1 mm on the air side of the principal non-premixed flame was observed in tests with HFC-245ca, particularly at high loadings. Hamins et al.<sup>50</sup> also found separate agent and fuel consumption zones in their numerical investigation of the structure of halon 1301 inhibited n-heptane/air non-premixed counterflow flames. In the current study, the secondary flame zone appeared to be caused by the agent burning in the air in a premixed fashion. Yang et al.<sup>81</sup> predicted this phenomenon for CH<sub>3</sub>Cl addition to the oxidizer stream of a methane/air counterflow flame. Although HFC-245ca is non-flammable at ambient temperature and pressure, heat release from the non-premixed flame was apparently sufficient to support its premixed combustion. Grosshandler et al.<sup>82</sup> investigated the flammability of HFC-245ca, and concluded that a stoichiometric mixture of HFC-245ca and air could sustain combustion if preheated 100 K above ambient temperature. A secondary flame zone was also observed in tests with a more effective suppressant, HFC-245cb, but was less pronounced than in the HFC-245ca case.

The relative suppression effectiveness of the fluorinated propanes can be assessed from Figure 3-2b and Figure 3-3b. The most effective fluorinated propanes were FC-218, HFC-227ea, and HFC-236fa, all of which contain two CF<sub>3</sub> groups. HFC-227ca, HFC-236ea, HFC-236cb, and HFC-245cb, along with HFC-245fa and HFC-245eb in the methane case, were less effective and contain one CF<sub>3</sub> group. HFC-245ca has no CF<sub>3</sub> groups and was clearly less effective than the other fluorinated propanes tested. The extinction strain rate curves clustered together in terms of the number of CF<sub>3</sub> groups present in the agent.

Among agents with the same number of  $\text{CF}_3$  groups, compounds with higher fluorine to hydrogen atom (F:H) ratios were slightly more effective agents, particularly at low concentrations: FC-218 was slightly more effective than HFC-227ea and HFC-236fa; and HFC-227ca, HFC-236ea and HFC-236cb were more effective than the pentafluoropropanes. At higher concentrations, agent suppression effectiveness was not as affected by the F:H ratio. The impact on suppression of substituting an F atom for an H atom in the agent molecule is both chemical and physical in nature. F atoms can scavenge H atoms in flames to form HF, reducing the number of H's that participate in flame propagation reactions.<sup>61</sup> Furthermore, as shown in Table 3-1, substituting one F for one H in a fluorinated propane led to a 5 % to 8 % increase in its specific heat at 300 K, enhancing the molecule's sensible enthalpy. Higher F:H ratios were therefore expected to increase the physical suppression effectiveness of fluorinated propanes. However, as the data show, the effect of substituting one H for an F was minor compared to that of arranging the fluorine atoms to provide a  $\text{CF}_3$  group: HFC-236fa was more effective than HFC-227ca, which has one more fluorine atom but one less  $\text{CF}_3$  group.

The impact of  $\text{CF}_3$  groups on suppression is further illustrated by the fluorinated ethane results shown in Figure 3-2a and Figure 3-3a. FC-116, which has two  $\text{CF}_3$  groups, was more effective than HFC-125 and HFC-134a, which only have one. HFC-134, which contains no  $\text{CF}_3$  groups, was the least effective of the fluorinated ethanes for most flame conditions. The presence of additional fluorine atoms in FC-116 and HFC-125 could explain their enhanced effectiveness relative to HFC-134a and HFC-134. However, the tetrafluoroethanes have the same number of fluorine atoms. At strain rates above  $100 \text{ s}^{-1}$ , HFC-134a was more effective than HFC-134, which correlates with the presence of a  $\text{CF}_3$  group in the former. At lower strain rates, the extinction concentrations of these two agents were comparable.

The presence or absence of a  $\text{CF}_3$  group also influenced the suppression effectiveness of the halons shown in Figure 3-3c. This figure shows that halon 1201 ( $\text{CHF}_2\text{Br}$ ) was less effective than both halon 1301 ( $\text{CF}_3\text{Br}$ ) and halon 13001 ( $\text{CF}_3\text{I}$ ), particularly at higher loadings; and halon 1211 ( $\text{CF}_2\text{ClBr}$ ) was slightly less effective than halon 1301. Sheinson et al.<sup>13</sup> investigated the chemical suppression effectiveness of the  $\text{CF}_3\text{Y}$  and  $\text{SF}_5\text{Y}$  ( $\text{Y} = \text{F}, \text{Cl}, \text{Br}, \text{I}$ ) series in an n-heptane cup burner. They concluded that, for  $\text{CF}_3\text{Cl}$ , the  $\text{CF}_3$  moiety made a greater chemical contribution to suppression than the Cl atom. This conclusion is consistent with the greater effectiveness of halon 1301 relative to halon 1211 observed here.

### ***Fluorinated Ethanes vs. Fluorinated Propanes***

The effectiveness of the fluorinated ethanes relative to that of the fluorinated propanes can be assessed by comparing Figure 3-2a to Figure 3-2b, and Figure 3-3a to Figure 3-3b. At strain rates below  $100 \text{ s}^{-1}$ , fluorinated ethanes extinguished methane flames at concentrations between 5 % and 10 %. Loadings between 4 % and 8 % were required for the fluorinated propanes. In the case of propane flames, below  $100 \text{ s}^{-1}$ , extinction concentrations for the fluorinated ethanes ranged from 6 % to 10 %. For the fluorinated propanes, they ranged from 4 % to 8 %. The steeper extinction strain rate curves for the fluorinated propanes indicate that, as a group, they were more effective agents on a molar basis than the fluorinated ethanes. Table 3-1 shows that the specific heats at 300 K of the fluorinated propanes range from 122.0 to 150.6  $\text{J}\cdot\text{mol}^{-1}\cdot\text{K}^{-1}$ , as opposed to 87.2 to 107.7  $\text{J}\cdot\text{mol}^{-1}\cdot\text{K}^{-1}$  for the fluorinated ethanes. The greater effectiveness of the fluorinated propane agents is consistent with their greater sensible enthalpy relative to the fluorinated ethanes.

### ***Methane Flames vs. Propane Flames***

Figure 3-2 and Figure 3-3 can also be compared to assess the differences between suppression of methane and propane non-premixed counterflow flames. The uninhibited propane flame was more difficult to extinguish, requiring an average strain rate of  $583 \text{ s}^{-1}$  vs.  $415 \text{ s}^{-1}$  for methane. However, the extinction strain rates of flames fueled with propane decreased more rapidly with increases in suppressant loading such that, at strain rates below  $100 \text{ s}^{-1}$ , methane and propane flames were extinguished by similar fluorinated agent loadings. If the extinction strain rates are normalized by the corresponding uninhibited strain rates and compared, the sensitivity of both methane and propane flames to agent addition is found to be similar. The propane flames were slightly more sensitive to the suppressants. Figure 3-2 and show that extinction strain rate curve shapes are different for the two fuels.

### **Numerical Investigation of Tetrafluoroethane Isomer Effectiveness**

The kinetic model developed at NIST<sup>83</sup> for fluorinated hydrocarbons has been used to numerically investigate the effects of halogenated compounds on C1 and C2 organic flames.<sup>52,54,58,70</sup> With this model, Tanoff et al.<sup>70</sup> predicted extinction strain rates for methane/air counterflow flames suppressed by  $\text{CF}_4$ ,  $\text{CHF}_3$ ,  $\text{CF}_3\text{CF}_3$  (FC-116),  $\text{CF}_3\text{CHF}_2$  (HFC-125), and  $\text{CF}_3\text{CH}_2\text{F}$  (HFC-134a). The NIST model was also used by Linteris et al.<sup>57</sup>, who reported both experimental and computational flame speeds for methane/air mixtures containing FC-116, HFC-125, and HFC-134a. Reaction pathway analyses of agent decomposition showed that  $\text{CF}_2\text{O}$  was an important intermediate for FC-116, which initially decomposes to form two  $\text{CF}_3$  radicals. The numerical calculations predicted that as the hydrogen content of the fluorinated ethane increased, less  $\text{CF}_2\text{O}$  was produced. To our knowledge, no previous modeling studies have compared different isomers. In the present form of the kinetic mechanism, only fluoroethane isomers may be compared, because the fluorocarbon kinetic mechanism, in its original form, does not include C3 species. Recently, the mechanism has been extended to cover HFC-227ea.<sup>55,56,84</sup> Kinetic mechanisms for other fluoropropanes have not yet been developed.

In the present study, calculations were conducted using the NIST model to predict flame speeds of stoichiometric methane/air mixtures doped with 3.81 mole % of either HFC-134 or HFC-134a. The goal of these calculations was to determine if the current kinetic model predicts isomeric differences between the two agents, and why these differences may exist. Although extinction strain rate predictions, such as those performed by Tanoff et al., are more relevant to the measurements of Figure 3-2a and Figure 3-3a, they are computationally more demanding. It is generally acknowledged that flame speed is closely related to extinction strain rate.<sup>71</sup> The current calculations, which predict isomeric differences in suppression, should therefore carry over to non-premixed flames.

The flame speed calculations were performed on a domain extending 25 cm from the flame into the cold reactants, and 60 cm into the hot products. The calculations used multicomponent viscosities, thermal diffusivities for H and  $\text{H}_2$ , and windward differencing for the convective terms. The initial temperature of the reactants was set to 298.2 K. The ultimate solutions were obtained on meshes having 150 grid points.

The kinetic mechanism used was essentially that developed by NIST, modified according to L'Espérance et al.<sup>61</sup> The reactions

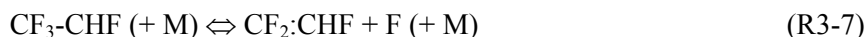


were taken from Linteris et al.<sup>57</sup> Furthermore, the reactions



were also added. These latter two reactions were not present in the NIST mechanism, although the analogous reactions for all other pairs of fluorinated methyl radicals were included. The kinetic rates of reactions R3-5 and R3-6 were estimated by taking the geometric mean of the rates of the analogous reactions for  $\text{CH}_3 + \text{CF}_3$  and  $\text{CHF}_2 + \text{CF}_3$ . R3-5 represents an additional destruction pathway for HFC-134a not considered in the modeling of Reference 57.

Finally, the thermal decomposition reaction



was added using the high pressure kinetic expression from Reference 56 and estimated low pressure kinetics from Reference 84. This reaction proved very important in modeling suppression by HFC-227ea, in which the  $\text{CF}_3\text{-CHF}$  radical is formed from the parent agent by C-C bond dissociation. From HFC-134a, this radical is produced by hydrogen abstraction.

The predicted flame speeds for the mixtures containing HFC-134 and HFC-134a were 18.9 cm/s and 15.5 cm/s, respectively, or 48 % and 39 % of the calculated uninhibited methane/air flame speed of 39.4 cm/s. For the HFC-134a case, the experimental measurement and numerical prediction of Linteris et al.<sup>57</sup> were 38 % and 29 %, respectively. Flame speed measurements for methane/air/HFC-134 mixtures have not been reported. Thus, the kinetic model predicted a substantial difference in inhibition effectiveness between the two tetrafluoroethane isomers. The refinements in the kinetic mechanism greatly improved agreement with the experimental flame speed measurement for HFC-134a.

Reaction pathway diagrams for HFC-134 and HFC-134a are shown in Figure 3-4a and Figure 3-4b. The major removal pathway for  $\text{CHF}_2\text{-CHF}_2$  is thermal dissociation of the C-C bond. For  $\text{CH}_2\text{F-CF}_3$ , the major removal pathways are hydrogen abstraction by H and OH, and HF elimination. Sensitivity analysis indicated that these initial reaction steps had the greatest influence on the difference in flame speed between the two isomers. This may be a consequence of the major removal pathways for HFC-134a consuming H or OH and generating less reactive species, while the dominant HFC-134 pathway generates radicals.

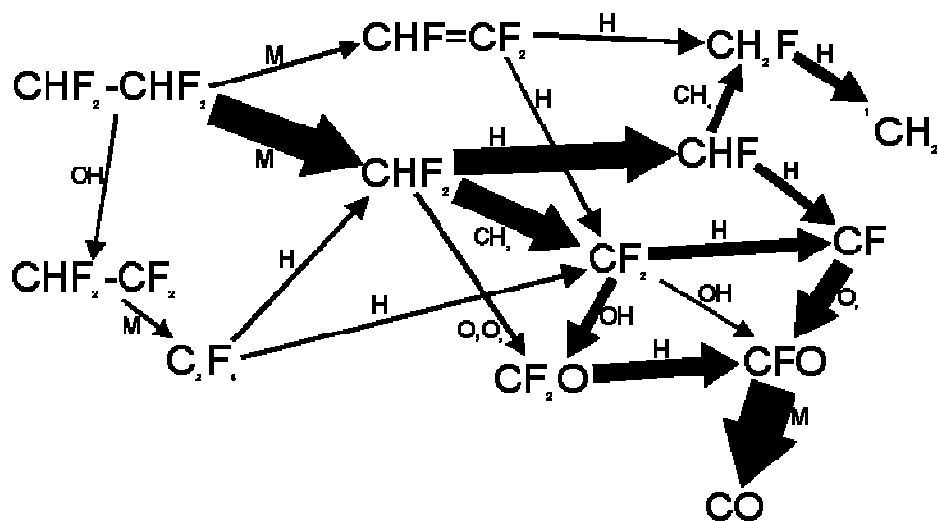
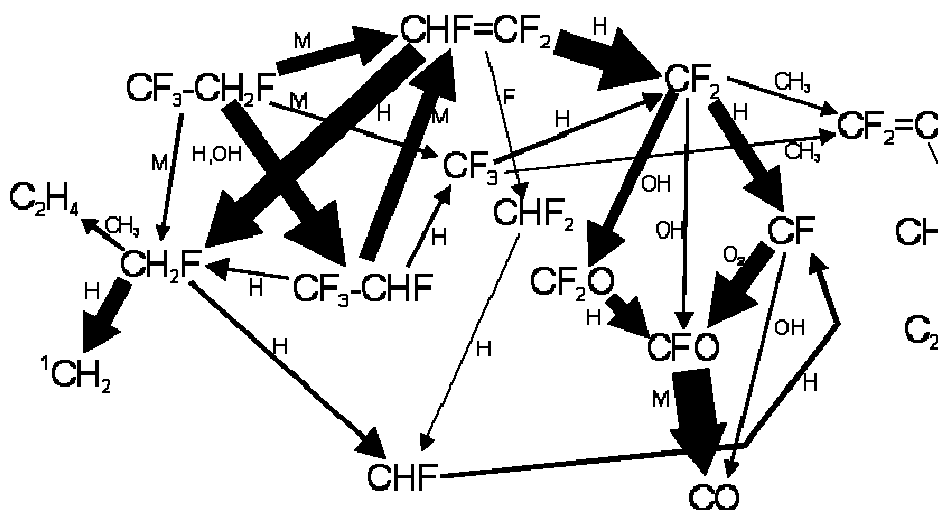


Figure 3-4. Reaction Pathways for Premixed Methane/air Flames Doped with 3.81 Volume % of: (a) HFC-134 and (b) HFC-134a.



The reaction pathways associated with HFC-227ea should be representative of those of other fluorinated propanes. HFC-227ea, under most conditions, is consumed by thermal decomposition, not radical attack. The decomposition pathways are HF elimination and C-C bond removal. The latter process dominates in near-stoichiometric, high temperature flames.<sup>84</sup> For asymmetric isomers, more than one product channel exists for most agent destruction reactions. If a fluorinated ethyl radical is produced by thermal decomposition, it is likely to decompose through H atom elimination from the methyl group, if one is present. Otherwise, F atom elimination will be the dominant process.<sup>84</sup> H and F are both reactive species. However, H has a higher diffusivity and participates in the  $\text{H} + \text{O}_2$  chain branching reaction, while F reacts primarily in a chain propagating reaction with  $\text{H}_2\text{O}$ . These considerations provide one possible explanation for the observed isomeric differences among fluoropropanes. Kinetic mechanisms for these agents must be developed and validated before a more definitive analysis can be conducted.

## Cup Burner Experiments

The n-heptane and methanol cup burner extinction concentrations obtained in Reference 62 are provided in Table 3-2. Concentrations based on both volumetric and molar proportions are included. The two sets of values are not identical as several of the agents deviate from ideal gas behavior at ambient conditions. Each concentration represents the average of at least 3 runs. At the 99.7 % confidence level ( $3\sigma$ ), the uncertainties associated with the cup burner values were estimated to be  $\pm 0.6$  mole %, with the exception of those for  $\text{CF}_4$  and  $\text{N}_2$ , estimated to be  $\pm 1.5$  mole %. Table 3-2 also shows the n-heptane cup burner data (vol. %) of Hamins et al.<sup>50</sup> Extinction concentrations from the two data sets are within 7 % of each other for all agents except HFC-236fa, for which they differ by 11.5 %.

**Table 3-2. Cup Burner Extinction Concentrations.**

Agent	n-Heptane Cup Burner (Present Study)		n-Heptane Cup Burner (Reference 50)	Methanol Cup Burner (Present Study)	
	Vol. %	Mol. %	Vol. %	Vol. %	Mol. %
Halon 1301	3.1 <sup>a</sup>	3.1	3.0	6.3	6.4
Halon 13001	3.2 <sup>a</sup>	3.2			
Halon 1211	3.6	3.7			
Halon 1201	4.1	4.1			
FC-218	6.1 <sup>b</sup>	6.3	6.4		
HFC-236fa	6.1	6.3	6.8	8.0	8.2
HFC-227ea	6.4	6.6	6.3	8.9	9.2
HFC-227ca	6.9	7.1			
HFC-236ea	7.2	7.5		9.9	10.3
HFC-236cb	7.4	7.7			
FC-116	7.9 <sup>a</sup>	8.0	8.4		
HFC-125	8.8	8.9	8.8		
HFC-134a	10.0	10.2	10.2		
Sulfur Hexafluoride	10.6	10.9			
HFC-134	10.9	11.1			
Tetrafluoromethane	16.0 <sup>a</sup>	16.0		22.0	22.1
Nitrogen	30.0 <sup>a</sup>	30.0	31.8	41.6	41.6

<sup>a</sup> From Reference 13.

<sup>b</sup> From Reference 13, but corrected for typographical error.

Hamins et al.<sup>50</sup> and Saso et al.<sup>68</sup> compared cup burner values to extinction data collected in liquid n-heptane counterflow flames. Both studies found that counterflow extinction concentrations at low strain rates were similar to those obtained in a cup burner. To assess the impact of fuel type on extinction loadings, methane and propane counterflow values at low strain rates were compared in the present study

to n-heptane and methanol cup burner values. An appropriate counterflow extinction strain rate must be selected to make the comparison. Hamins et al. used a global strain rate of  $50 \text{ s}^{-1}$ . Saso et al. used a global strain rate of  $30 \text{ s}^{-1}$ , but defined their global strain rate as half that used by Hamins et al. In this investigation, a local strain rate of  $80 \text{ s}^{-1}$  was chosen.

Figure 3-5a, b, c, and d show n-heptane cup burner, methanol cup burner, methane counterflow, and propane counterflow extinction results, respectively. For each fuel, the agents are presented in decreasing order of effectiveness, with the most effective agent being the top bar. The methane and propane counterflow extinction values for  $\text{N}_2$  were divided by two for presentation in the figure. The counterflow extinction concentrations for agents not tested at strain rates as low as  $80 \text{ s}^{-1}$  were extrapolated from the curves of Figure 3-2 and Figure 3-3. The predicted agent extinction concentrations represent the loadings that would be required to suppress the given flames assuming that the agents were inert, and that they extinguished the flames at the same sensible enthalpy per mole of oxygen as  $\text{CF}_4$  and  $\text{SF}_6$ .

### ***Physical Versus Chemical Contributions to Suppression***

Physical versus chemical contributions to suppression for different agents are compared following the formalism of Tucker et al.<sup>69</sup> and Sheinson et al.<sup>13</sup> Physical contributions attributed to agent addition include increased thermal mass, oxygen dilution, and increased conductive heat losses for agents with high thermal conductivities such as helium. Sheinson et al. found that the dominant physical effect of most fluorinated agents is to add thermal mass.  $\text{CF}_4$  and  $\text{SF}_6$ , essentially inert, both extinguish n-heptane cup burner flames when the amount of agent added is such that the energy required to raise the temperature of the nitrogen and agent present, from 300 K to 1600 K, exceeds a critical value. This critical value is proportional to the amount of oxygen supplied, and is similar for  $\text{CF}_4$  and  $\text{SF}_6$ . It is lower for non-fluorinated agents such as Ar, He,  $\text{N}_2$ , and  $\text{CO}_2$ , due to greater contributions of thermal conductivity and oxygen dilution to suppression for these agents.

In the present study, the extinction concentration for  $\text{CF}_4$  was used to estimate the sensible enthalpy per mole of oxygen required to extinguish a methanol flame. The estimated extinction sensible enthalpy for this flame was found to be 322 kJ/mol  $\text{O}_2$ . Similarly,  $\text{SF}_6$  extinction concentrations were used to obtain extinction sensible enthalpies for methane and propane flames of 254 kJ/mol  $\text{O}_2$  and 258 kJ/mol  $\text{O}_2$ , respectively. In the case of n-heptane, both  $\text{CF}_4$  and  $\text{SF}_6$  extinction concentrations were available. The  $\text{SF}_6$  data led to a sensible enthalpy value 1 % lower than that estimated from the  $\text{CF}_4$  data. The average of the two values, 267 kJ/mol  $\text{O}_2$ , was chosen as the extinction sensible enthalpy for the n-heptane flame.

Physical contributions to suppression of other compounds can be estimated by assuming that they are inert and that they extinguish a given flame at the same sensible enthalpy per mole of oxygen as  $\text{CF}_4$  and  $\text{SF}_6$ . The method is valid for compounds with physical contributions to suppression dominated by thermal mass addition, as they are for  $\text{SF}_6$  and  $\text{CF}_4$ . Physical predictions for the extinction concentrations of the agents tested in this study are shown in Figure 3-5. The sensible enthalpies required to raise agent temperature from 300 K to 1600 K are provided in Table 3-1. A comparison of the measured and predicted extinction data reveals that the bromine- and iodine-containing compounds suppress flames mostly through chemical means, with physical contributions to suppression not exceeding 30 % regardless of fuel type. For all of the other agents, the chemical contribution to suppression does not exceed 35 %. The differences between the measured and predicted values for  $\text{N}_2$  are consistent with the findings of Sheinson et al. For HFC-134 and HFC-245ca in methane, the actual extinction concentrations

are larger than the sensible enthalpy predictions. The net effect of fluorocarbon chemistry for these agents, which do not contain  $\text{CF}_3$  groups, is to promote combustion.

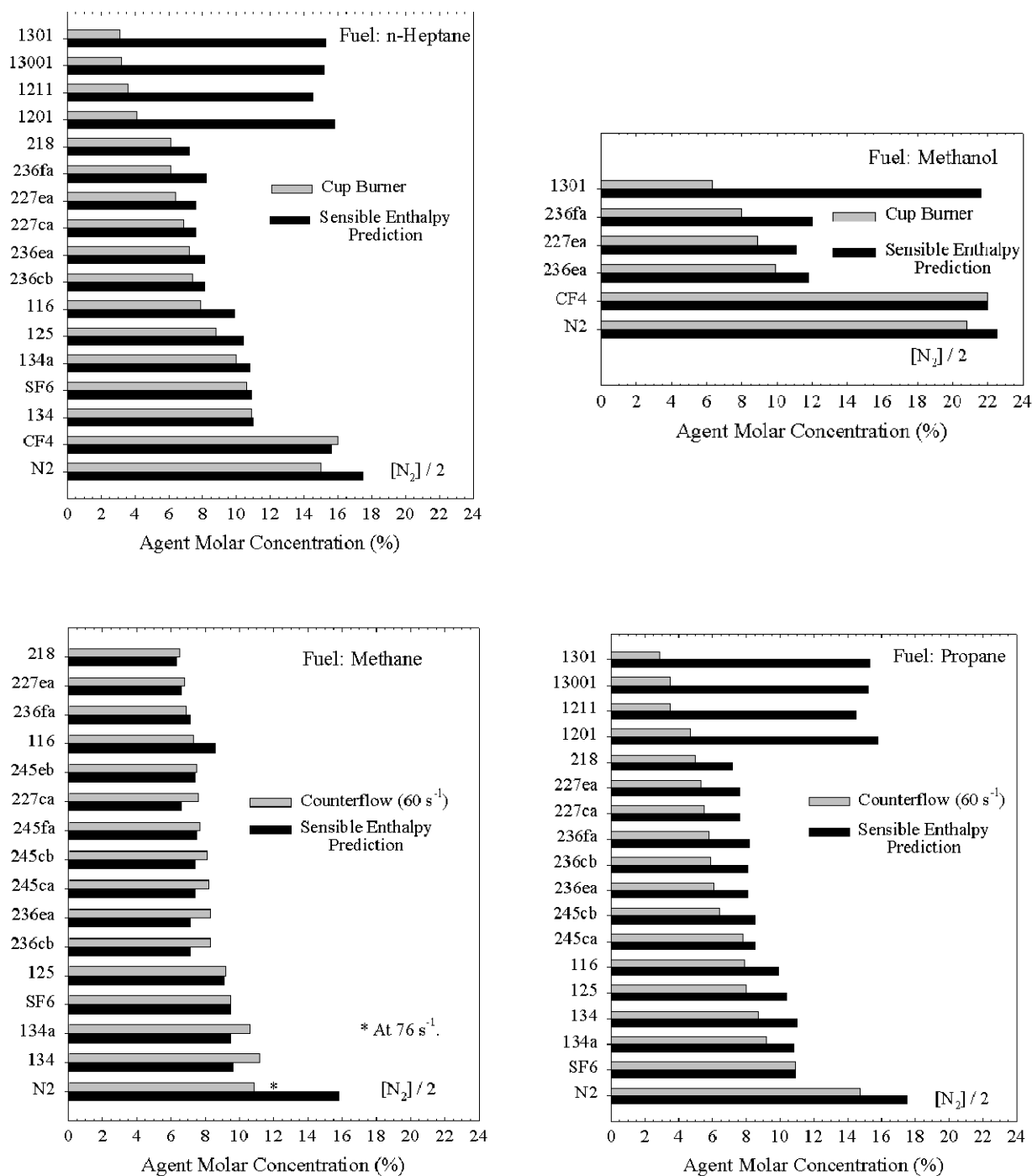


**Figure 3-5. Extinction Concentrations for Agents Suppressing: (a) n-heptane/air Cup Burner Flames; (b) Methanol/air Cup Burner Flames; (c) Methane/air Counterflow Flames at a Strain Rate of 80 s<sup>-1</sup>; (d) Propane/air Counterflow Flames at a Strain Rate of 80 s<sup>-1</sup>.**

### ***Effect of Fuel Type on Suppression Effectiveness Ranking***

The extinction data of Figure 3-5 show that agent effectiveness rankings were similar for the fuels tested. The bromine- or iodine-containing agents formed the most effective group of suppressants. FC-218, HFC-227ea, HFC-227ca and HFC-236fa constituted the next most effective group, followed by the remaining hexafluoropropanes and the pentafluoropropanes. HFC-245ca was the least effective of the fluorinated propanes tested, but was more effective than FC-116 and HFC-125. The tetrafluoroethanes and SF<sub>6</sub> were only more effective than CF<sub>4</sub> and N<sub>2</sub>. The effectiveness ranking for methane, although similar to that of the other fuels, did exhibit some peculiarities. First, FC-116 appeared more effective than most of the fluorinated propanes. Second, within the 3 $\sigma$  experimental uncertainty of  $\pm 0.8$  mole %, all of the fluorinated propanes tested containing less than two CF<sub>3</sub> groups were equal in their ability to suppress methane flames at 80 s<sup>-1</sup>.

Although the relative effectiveness of the various suppressant groups was similar for all the fuels tested, the exact ranking within a group depended on the fuel. Furthermore, the rankings extracted from the counterflow data were somewhat strain rate dependent. The position of the SF<sub>6</sub> extinction strain rate curve relative to those of the fluorinated ethanes illustrates this dependence.

Figure 3-3a shows that at strain rates between 400 s<sup>-1</sup> and 500 s<sup>-1</sup>, in a propane flame, SF<sub>6</sub> was more effective than HFC-125. Below 100 s<sup>-1</sup>, it was less effective than both HFC-134 and HFC-134a. These extinction concentrations are all expressed on a molar basis. On a mass basis, the bromine- and iodine-containing agents were still the most effective suppressants, with all of the other agents tested, including N<sub>2</sub>, exhibiting similar effectiveness.

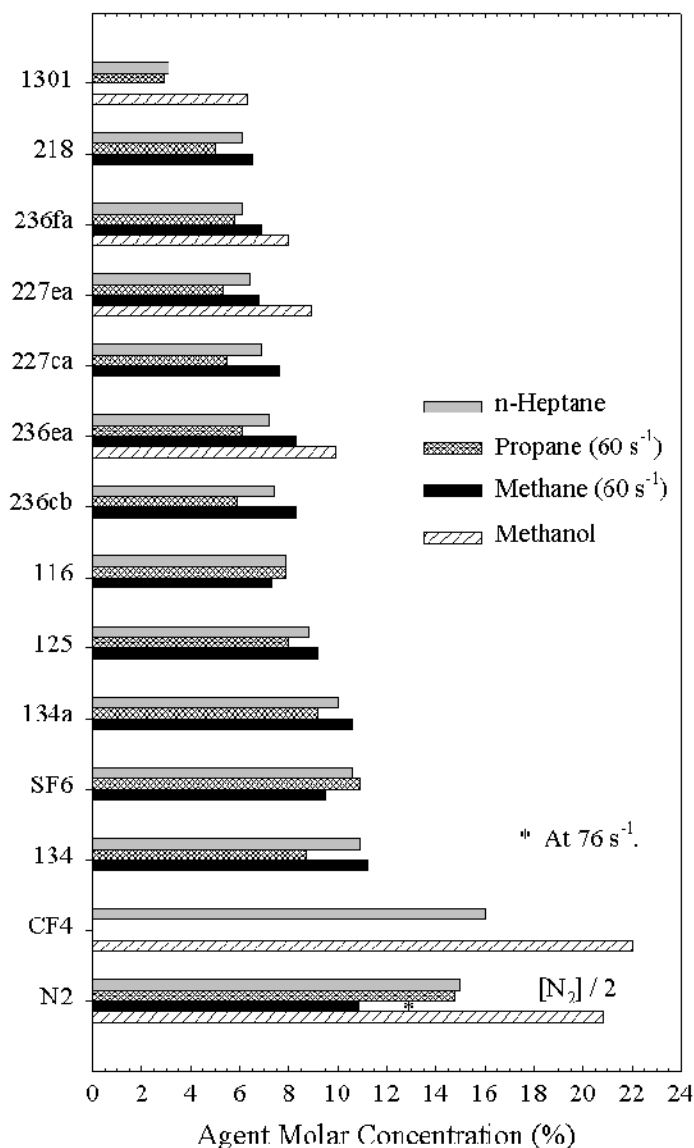
### ***Effect of Fuel Type on Agent Extinction Concentrations***

Figure 3-5 shows that fuel type had an impact on the magnitude of the extinction concentrations, but not on the effectiveness ranking of the agents tested. The extinction concentrations obtained in the four different fuels are compared for several agents in Figure 3-6. Included are all of the agents tested in the n-heptane cup burner, with the exception of halon 13001, halon 1211, and halon 1201. The agents are ranked in order of decreasing n-heptane effectiveness, with the most effective agent as the top bar.

Figure 3-6 shows that, for the agents tested, methanol flames were more difficult to extinguish than the alkane flames. This was due in part to methanol's high sensible enthalpy of extinction relative to that of the alkanes. For all agents except halon 1301, between 30 % and 40 % more agent was required to suppress methanol flames relative to the n-heptane flames. For halon 1301, the required amount doubled. The greater reduction in the effectiveness of halon 1301 was attributed to a decrease in its chemical contribution to suppression. For n-heptane, chemical factors contribute 80 % to halon 1301's effectiveness. For methanol, they contribute 70 %.

Extinction concentrations for methane and propane non-premixed counterflow flames at 80 s<sup>-1</sup> were similar to those for n-heptane cup burner flames. All 12 of the agents tested in both n-heptane and methane flames were more effective against the latter. The largest deviations between the two fuels occurred with N<sub>2</sub>, 28 %, and HFC-116, 20 %. For 8 out of the 12 agents, the deviations were less than 10 %. In the case of propane, the largest deviations from the n-heptane values occurred with HFC-236cb, 25 %, and HFC-134, 22 %. For 4 out of the 13 agents tested in both fuels in Figure 3-6, the deviations were less than 10 %, with all 13 agents more effective in propane. Halon 1201 and halon 13001 were the

only agents more effective in n-heptane: 10 % more halon 1201 and 3 % more halon 13001 were required for propane flames. Counterflow experiments with both methane and propane at low strain rates yield extinction concentrations, in addition to effectiveness rankings, applicable to n-heptane cup burners.



**Figure 3-6. Effect of Fuel Type on Agent Extinction Concentration. The n-heptane and Methanol Data were Collected in a Cup Burner. The Methane and Propane Data were Collected in a Counterflow Burner at a Strain Rate of 80 s<sup>-1</sup>.**

## Conclusions

Curves relating extinction strain rate to agent molar concentration were obtained for a variety of suppressants in methane/air and propane/air non-premixed counterflow flames. The list included four fluorinated ethanes, ten fluorinated propanes, four bromine- or iodine-containing halons, CF<sub>4</sub>, SF<sub>6</sub> and N<sub>2</sub>.

- The relative effectiveness of the fluorinated propanes correlated with the number of CF<sub>3</sub> groups in the agent's molecular structure. Effectiveness did not correlate significantly with any other structural feature.

- For agents with the same number of  $\text{CF}_3$  groups, compounds with higher fluorine to hydrogen atom ratios were slightly more effective, particularly at low concentrations.
- The presence of  $\text{CF}_3$  groups also correlated with an enhanced suppression performance of agents that contain bromine.
- Numerical predictions of the flame speed of doped methane/air mixtures indicated that HFC-134a, with one  $\text{CF}_3$  group, caused a greater reduction in flame speed than HFC-134. Chemical kinetic analysis indicated that a difference in the major pathway for removal of the parent compound was primarily responsible.
- Overall, the fluorinated propanes were found to be more effective on a molar basis than the fluorinated ethanes. This was consistent with the greater sensible enthalpy of the former. For all the HFCs studied, the chemical contributions to suppression did not exceed 35 %.
- Bromine- or iodine-containing agents were more effective than compounds that contained fluorine as the sole halogen. These bromine- and iodine-containing agents suppressed flames mainly through chemical means, with physical contributions to suppression not exceeding 30 %.
- Fuel type did not affect agent effectiveness ranking, but did affect the magnitude of the extinction concentrations. Methanol flames were more difficult to extinguish than either methane, propane, or n-heptane flames, which were similar to each other. For halon 1301, the agent concentration required to extinguish a methanol cup burner was more than double the amount required to extinguish an n-heptane flame. For HFC-236fa, HFC-227ea, HFC-236ea,  $\text{CF}_4$ , and  $\text{N}_2$ , 30 % to 40 % more agent was required.

### 3.3 METAL-CONTAINING COMPOUNDS

#### 3.3.1 Background

The NGP also conducted research to identify new, non-halocarbon suppressants and to understand the mechanisms of inhibition of known, effective agents.<sup>85-87</sup> Metal-containing compounds were of particular interest. Prior to the NGP, the behavior of metal compounds in flames had been studied with regard to several flame phenomena and had been found to be up to several orders of magnitude more effective flame inhibitors than the halogens.<sup>34</sup> While research had been conducted to understand metals in hydrocarbon flames, and progress had been made, a thorough description of the mechanisms of inhibition provided by these agents had yet to be delineated.

In the most obviously relevant work, metal-containing compounds have been added to flames in a number of screening tests, aimed specifically at assessing their potential as fire suppressants. Results from these tests have helped understand the compounds' influence on flame speed (premixed flames) and extinction (diffusion flames), as well as their effect on ignition. Flame studies have also been used to understand the detailed mechanism of inhibition by metal agents, either by providing direct experimental data on species present in the flame zone, or by validating numerical models which are then used to calculate the flame structure; either of these approaches are then used to develop an understanding of the relevant chemical kinetic mechanisms.

Studies of engine knock suppression by metal-containing compounds provided much early data on metals in flames. Since engine knock is known to occur from the rapid pressure rise (and subsequent detonations) inside an engine cylinder caused by too fast reaction of the homogeneous charge of fuel and air, the mechanisms of engine knock reduction may have clear relevance to fire suppression—in which the goal is again to reduce the overall reaction rate with the addition of the suppressing agent. In engines—as well as in heating applications—research has also been directed at understanding their efficacy at soot reduction. Although both soot formation and the overall reaction rate of flames are known to be related to the location and concentration of radicals in the flame, the effects of metals on soot formation are not reviewed here.

Other systems have been used to understand metal chemistry in flames. A large amount of fundamental work has been done with premixed, atmospheric pressure flat flames. The flat flame provides a nearly one-dimensional system, and the region above the flame (i.e., downstream of the main reaction zone) provides a long residence time, high temperature region for radical recombination. The H-atom concentration typically is measured with the Li-LiOH method (described later in this chapter), and the additive's effect on the radical recombination rate is determined. In addition, much detailed fundamental understanding has come from shock tube studies and flash photolysis studies in reaction vessels. Some studies of fire retardants are also relevant to fire suppression mechanisms of metals, such as when the fire retardant works by suppressing the gas phase reactions (and the subsequent heat release and heat feedback to the solid sample). Finally, after-burning in rocket nozzles provided motivation to understand metal-catalyzed radical recombination reactions, and modeling studies have been performed for those systems.

From these studies, it was clear that metals can have a profound effect on flame chemistry. Further, their effectiveness in these varied applications may well be related. In any event, data from each of the applications can provide insight into possible metals for application to fire suppression as well as provide fundamental data useful for predicting their performance in a range of applications. Work investigating the effect of metals for each of the applications is described in the remainder of this subsection.

The remainder of this section provides background on the current understanding of metal inhibition of flames, identifying metals with fire suppression potential, and presents fundamental data which can be used in future comparison with modeling results.

In particular, iron pentacarbonyl,  $\text{Fe}(\text{CO})_5$ , has been found to be one of the strongest inhibitors, up to two orders of magnitude more effective than  $\text{CF}_3\text{Br}$  at reducing the burning velocity of premixed hydrocarbon-air flames.<sup>88,89</sup> Despite past research, a thorough description of its mechanism of inhibition had not been delineated. Iron pentacarbonyl forms particulates upon passing through a flame. Interestingly, other very effective inhibitors also involve a condensed phase. These inhibitors include those which form the particulates after passing through the flame as well as those which are initially added as a condensed phase. The former category includes other organometallics compounds such as lead tetraethyl and nickel carbonyl and the halometallic compounds  $\text{TiCl}_4$  and  $\text{SnCl}_4$ ,<sup>34</sup> as well as a new class of fire suppressants, pyrotechnically generated aerosols,<sup>90</sup> which may work similarly. The latter category includes the widely used alkali metal salt powders  $\text{NaHCO}_3$  and  $\text{KHCO}_3$ ,<sup>91</sup> other metal salts,<sup>92</sup> and a new type of suppressant, non-volatile organic precursors.<sup>93</sup> These condensed phase agents have many similarities, in particular, their strong inhibiting action and the lack of a complete understanding of their modes of inhibition.

Because  $\text{Fe}(\text{CO})_5$  is so effective, it was selected first for further study under the NGP. Although its toxicity prevents it from being used as a flame suppressant, an understanding of its inhibition mechanism was expected to help in developing new agents, and the experimental and analytical tools being developed would be useful for the study of other heterogeneous inhibitors. The approach was to use simple laboratory flames, both premixed Bunsen-type and counterflow diffusion, to obtain fundamental information on the action of iron pentacarbonyl. The burning velocity and extinction strain rate, both of which provide a measure of the overall reaction rate, were determined with addition of  $\text{Fe}(\text{CO})_5$ , while varying the stoichiometry, oxygen mole fraction, flame temperature, and flame location. These experiments allowed control of the chemical environment, the location where the metal-containing species were formed, and the transport of these species to the reaction zone.

Studies of the inhibition mechanism of the iron are described, and are followed by a description of the reasons why it loses its effectiveness in some flame systems. The equivalent flame inhibiting species of other metal agents are then discussed, and evidence for any potential loss of effectiveness for these other metals is assembled.

## Engine Knock

Agents that reduce engine knock may also be effective flame inhibitors, and it was useful to examine the literature of engine knock to search for possible moieties. Engine knock is the onset of detonation waves in an engine cylinder brought about by the homogeneous ignition of the end-gas region of highly compressed and heated fuel and air. The effect of some agents in reducing knock has been known since the 1920s, including compounds of bromine, iodine, tellurium, tin, selenium, iron, and lead, as well as aniline.<sup>94</sup> Tetraethyl lead (TEL) very early became the anti-knock agent of choice. While much subsequent research was performed to understand its mechanism of knock reduction, the exact mechanism for this agent remains an unsolved problem in combustion research (perhaps because leaded fuels were later banned due to their poisoning effect on exhaust catalytic converters). Although much progress was made, the researchers divided into two camps: those endorsing a heterogeneous mechanism<sup>95</sup> and those promoting a homogeneous radical recombination mechanism.<sup>96</sup>

Several known effects of lead in engines support the heterogeneous mechanism. Muraour<sup>97</sup> appears to have been the first to propose chain-breaking reactions on the surface of a colloidal fog formed from TEL. The particle cloud was subsequently shown to be composed of  $\text{PbO}$ , which is the active species.<sup>98</sup> Since a strong influence of  $\text{PbO}$  coatings on reaction vessel walls has also been observed,<sup>98</sup> a heterogeneous mechanism of  $\text{PbO}$  was assumed. Although other results support the heterogeneous mechanism, the evidence is somewhat circumstantial. The known *metallic* antiknock compounds (tetraethyl lead, tellurium diethyl, iron pentacarbonyl, nickel tetracarbonyl<sup>95</sup>) all produce a fog of solid particles. The alkyls of bismuth, lead, and thallium are anti-knocks, but those of mercury (which does not form particles) are not.<sup>99</sup> Richardson et al.<sup>100</sup> showed that carboxylic acids increase the research octane number of TEL in engines, and argued that they reduced agglomeration of the  $\text{PbO}$  particles in the engine end-gas, but acknowledged that their arguments were qualitative. Zimpel and Graiff<sup>101</sup> sampled end gases in a fired engine for transmission electron microscopy (TEM). They claimed that 1000 nm diameter particles formed prior to the arrival of the flame, proving that the effect of TEL was heterogeneous. Commenters to the paper pointed out, however, that the particles could be forming in the sampling system, that the effect of lead extenders was not captured in the particle morphology, and that even if particles form, the gas phase species can also be present, and it is thus not precluded that they are doing the inhibition.

Based on the work of Rumminger and Linteris,<sup>102</sup> even if particles form, they can re-evaporate in the hot region of the flame if they are small enough. Finally, as described by Walsh,<sup>95</sup> a major shortcoming in the work with TEL is that it is easily absorbed on the way to the reaction vessel, so that it is difficult to know how much TEL actually makes it to the flame. As subsequently described by Linteris and co-workers, the efficiency<sup>103-107</sup> and particle formation<sup>102,108</sup> of organometallic agents are strongly affected by the volume fraction of the metal compound.

In later work, Kuppo Rao and Prasad<sup>109</sup> claimed to prove the heterogeneous mechanism of lead anti-knock agents. They inserted copper fins coated with PbO into the cylinder of an engine, or injected 30  $\mu\text{m}$  particles into the air stream, and found antiknock effects. They interpreted these results as evidence that the mechanism is heterogeneous. Nonetheless, they did not measure for the presence of gas phase lead compounds, so a homogeneous mechanism cannot be ruled out. For the eleven lead compounds tested, they found the effectiveness to vary by a factor of about six, and found similarly sized particles of  $\text{CuO}_2$ ,  $\text{CuO}$ ,  $\text{CuCl}_2$ ,  $\text{NiCl}_2$ , and  $\text{SnCl}_2$  to have equal effectiveness which was less than any of the lead compounds.

The early and strong evidence for a homogeneous gas phase inhibition mechanism of TEL was developed by Norrish.<sup>96</sup> Using flash photolysis of mixtures of acetylene, amyl nitrite, and oxygen in a reaction vessel, with and without TEL, the absorption and emission spectra of amyl nitrate, OH, Pb, PbO, NO, CN, CH, and TEL were obtained as a function of reaction progress. The reactants were chosen since, in the absence of anti-knock compounds, they showed the strong homogeneous detonation characteristic of engine knock. The researchers found that the induction time increased linearly with TEL addition at low TEL partial pressures, but that the effectiveness dropped off at higher pressures. This result was described subsequently for the flame inhibitors  $\text{Fe}(\text{CO})_5$ ,<sup>88,103</sup>  $\text{SnCl}_4$ ,<sup>34,107</sup> and  $\text{CH}_3\text{C}_5\text{H}_4\text{Mn}(\text{CO})_3$  (MMT).<sup>107</sup> After decomposition of TEL, Pb was present in low concentration, followed by large amounts of PbO and OH, which subsequently dropped off. With TEL addition, the formation of OH was retarded, and the increase in OH emission was smoother and better behaved. No particles were reported. Norrish et al. described the action of TEL as a two-stage homogeneous gas phase reaction mechanism. In the first stage, TEL reacts with the peroxide and aldehyde intermediates (characteristic of the end of the cool flame regime of alkane combustion), thus reducing the availability of these species for initiating the well-known second stage of the combustion. Gas phase PbO from the TEL then reacts with the chain-carrying intermediates to reduce the rate of heat release, slow the temperature rise, and reduce detonation. It is noteworthy that many of the features subsequently described by Linteris and Rumminger<sup>110</sup> as necessary for flame inhibition by iron compounds (effectiveness in the absence of particles, decreasing effectiveness with higher inhibitor concentration, key role of the metal monoxide species, and the necessary coexistence of OH and metal monoxide species) were shown in the 1950s by Norrish and co-workers to be necessary for effective knock reduction by TEL. Although it was of the highest quality, the findings of Norrish and co-workers were discredited by the engine community largely because the tests were not done in engines or with typical fuels. This work predated most of the important flame inhibition work of the 1970s by 20 years.

## Flame Screening Tests

Papers describing the results of screening tests clearly demonstrated the superior effectiveness of some metal-containing compounds as flame inhibitors. The seminal work of Lask and Wagner<sup>34</sup> investigated the efficiency of numerous compounds for reducing the burning velocity of premixed Bunsen-type

hexane-air flames stabilized on a nozzle burner. They found the metal halides  $\text{SnCl}_4$  and  $\text{TiCl}_4$  to be quite effective at low volume fraction (and  $\text{GeCl}_4$  about a factor of two less than these). In unpublished work, cited by others,<sup>111</sup> Lask and Wagner provide the measured flame speed reduction with addition of  $\text{SbCl}_3$  to hexane-air flames, showing it to be about twice as effective as  $\text{CF}_3\text{Br}$ . They tested  $\text{Fe}(\text{CO})_5$ ,  $\text{Pb}(\text{C}_2\text{H}_5)_4$ , and  $\text{CrO}_2\text{Cl}_2$  and found these to be spectacularly effective, with volume fractions of only 170  $\mu\text{L/L}$  and 150  $\mu\text{L/L}$  required for the first two to reduce the burning velocity by 30 %. (Although not quantified, they believed the effectiveness of  $\text{CrO}_2\text{Cl}_2$  to be even higher.) They categorized the active species in the compounds they tested into two classes: the halogens, and the much more effective transition metals. Skinner and coworkers,<sup>112</sup> using a burner which produced conical flames, tested 80 compounds for reducing the burning velocity of premixed hydrogen-air flames (fuel-air equivalence ratio  $\phi$  of 1.75). They found the most effective to be: tetramethyl lead TML  $\text{Pb}(\text{CH}_3)_4$ ,  $\text{Fe}(\text{CO})_5$ ,  $\text{TiCl}_4$ ,  $\text{SnCl}_4$ ,  $\text{SbCl}_5$ , and TEL (in that order), with TEL only slightly better than  $\text{CF}_3\text{Br}$ , and TML about 11 times better. A limitation of this work, however, was that the agents were tested at only a single volume fraction. Since the efficiency of many agents is known to vary with their concentration,<sup>103</sup> such an approach can skew the relative performance rankings. Also, in the hotter, faster-burning hydrogen flames, the propensity to form particles from the metal oxides and hydroxides is less than in the slower, cooler hydrocarbon-air flames of other studies (see Rumminger et al.<sup>102</sup>). An additional flame screening test was performed by Miller,<sup>113</sup> who tested 15 compounds added to low-pressure (1.01 kPa) premixed and diffusion flames, and found  $\text{SnCl}_4$ ,  $\text{POCl}_3$ ,  $\text{TiCl}_4$ ,  $\text{Fe}(\text{CO})_5$ ,  $\text{WF}_6$ , and  $\text{CrO}_2\text{Cl}_2$  to have some promise.

Two screening tests involved the inhibition of propagating premixed flames through clouds of small solid particles of inhibitor. Rosser et al.<sup>91</sup> added metal salts as dispersions of fine particles (2  $\mu\text{m}$  to 6  $\mu\text{m}$  diameter) to premixed methane-air flames. They used the reduction in upward flame propagation rate through a vertical tube as a measure of the inhibition effect. They correctly described the effects of flame speed and particle diameter on the particle heating rate, and together with the volatilization rate for each compound, assessed the fraction of the particle which was vaporized. They quantified the effect of particle size on inhibition effectiveness, and showed that while additional agent decreased the flame speed, the effectiveness eventually saturated (i.e., beyond a certain additive mass fraction, additional inhibitor had a greatly reduced effect on the flame speed). They postulated a homogeneous gas phase inhibition mechanism involving H, O, and OH radical recombination reaction with the metal atom and its hydroxide. This mechanism had many of the features of subsequently described mechanisms<sup>107,114-116</sup> which are now believed to be correct. They also correctly understood that catalytic radical recombination relies upon a super-equilibrium concentration of radicals (commonly present in premixed flames and diffusion flames at higher strain), and that this provides an upper limit to the chemical effect of catalytically acting agents. Finally, they suggested that adding an inert compound as a co-inhibitor can overcome this limitation. A number of alkali metal sulfates, carbonates, and chlorides were tested, as well as cuprous chloride  $\text{CuCl}$ , which was found to be about twice as effective as  $\text{Na}_2\text{CO}_3$  (after correcting for the larger size of the  $\text{CuCl}$  particles).

A later study involving premixed flames with particles was performed by deWitte et al.<sup>117</sup> In it, relatively large particles (100  $\mu\text{m}$  diameter) were electrostatically suspended in a tube and then injected into a downward facing premixed Bunsen-type flame, and their effect on the flame temperature, burning velocity, and extinction condition was measured. Various barium, sodium, and potassium compounds were tested, as well as  $\text{AlCl}_3$ ,  $\text{CuCl}_2$ , and  $\text{PbO}$ . The authors noted a thermal and chemical effect of the particles, and assumed that the chemical effect was due to recombination of chain-carrying radicals on the particle surfaces. The authors estimated that for these large particles, little of the particles could be

vaporized. Nonetheless, it is not possible to separate the heterogeneous and homogeneous inhibition effects from their data. The authors found particles of  $\text{CuCl}_2$  and  $\text{PbO}$  to be about two and eight times as effective as particles of  $\text{Na}_2\text{CO}_3$ , and surprisingly, found  $\text{AlCl}_3$  to be about three times as effective.

Flame screening tests of many compounds were performed by Vanpee and Shirodkar<sup>92</sup> to test the relative effectiveness of metal salts. The metal acetonates and acetylacetonates were dissolved in ethanol, and fine droplets of the metal salt solutions were sprayed into the air stream of a counterflow diffusion flame over an ethanol pool. The inhibition effect was quantified, at a given air flow velocity (i.e., strain rate) as the change in the oxygen volume fraction at extinction caused by addition of the inhibitor, normalized by the inhibitor volume fraction (Mole merit number =  $(X_{\text{O}_2,\text{ext}} - X_{\text{O}_2,\text{ext},i})/X_i$ , in which  $X_{\text{O}_2,\text{ext},i}$  and  $X_{\text{O}_2,\text{ext}}$  are the oxygen volume fractions required for extinction, with and without added inhibitor, and  $X_i$  is the volume fraction of inhibitor in the oxidizer stream). Their results are depicted in Figure 3-7, which shows the metal compounds tested, listed from most effective to least. The maximum and minimum values of the mole merit number are listed for the range of oxidizer velocities of the tests (50 cm/s to 60 cm/s).

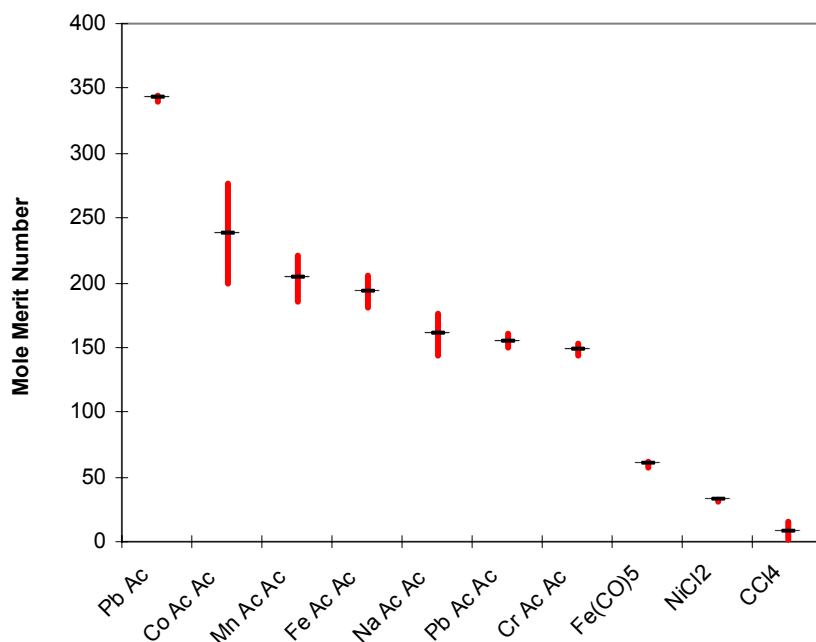


**Figure 3-7. Mole Merit Number of Metal-containing Compounds for the Oxidizer Velocities in the Range of 50 cm/s to 60 cm/s.**<sup>92</sup>

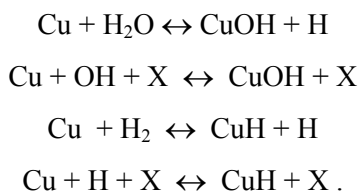
As the figure shows, the metal salts of Pb, Co, Mn, Fe, and Cr all showed some inhibition effect. Interestingly,  $\text{Fe}(\text{CO})_5$  was not as effective as iron acetylacetonate, and for lead, the acetonate was about twice as effective the acetylacetonate. It should be noted, however, that the interpretation of the present data are complicated by several effects. First, changing the oxygen mole fraction changed the temperature, which can change the effectiveness of an agent, as subsequently described in References 103-105, 118, and 119. Since the air stream velocity was changed while holding the nebulizer flow constant, the ethanol concentration changed in these partially premixed diffusion flames. Adding changing amounts of a fuel species (i.e., the carrier ethanol) in the air stream, changed the flame location and the scalar dissipation rate for a given strain rate (i.e., air flow velocity), so that the extinction condition was modified (as discussed in References 73 and 120). The size of the residual particle (which will vary from agent to agent) could affect its ability to vaporize in the flame, affecting the indicated efficiency. Finally, for metal agents that condense, their marginal effectiveness was a very strong

function of the concentration at which they are added. Hence, without knowing what the additive mole fraction was, it is difficult to cross compare the effectiveness of the different agents. For these reasons, the results shown in Figure 3-7 are considered qualitative, rather than quantitative. For example, subsequent studies<sup>121</sup> have rated iron as about 10 times as effective as sodium, in contrast to the results of Vanpee and Shirodkar, which show the acetylacetonate of iron to be only about 20 % more effective than that of sodium.

### Radical Recombination above Premixed Flames

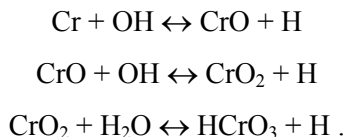
Much of the understanding of the homogeneous gas phase flame inhibition by metals came from studies of H-atom recombination rates above premixed, fuel rich, H<sub>2</sub>-O<sub>2</sub>-N<sub>2</sub> burner-stabilized premixed flames. The techniques, pioneered by Sugden and co-workers,<sup>122-124</sup> involve absorption spectroscopy for OH, and the Li/LiOH technique for H atom. (In the latter technique, the strong absorption lines of Li and Na are simultaneously measured above a flat flame. With the assumptions that Na is present in the flame only in atomic form and that Li is present only as Li and LiOH, the measured ratio of the Li to Na absorption together with the known equilibrium constant for the reaction  $\text{Li} + \text{H}_2\text{O} = \text{LiOH} + \text{H}$  provides [H].) In some of their early relevant work they determined the dominant metal species in H<sub>2</sub>-O<sub>2</sub>-N<sub>2</sub> premixed flames above Meker burners with added dilute sprays from aqueous salts of copper and manganese. Copper was found to exist mostly as Cu in the flame, and the dissociation constants of CuH<sup>125</sup> and CuOH<sup>124</sup> were determined from their concentrations above the flame at different temperatures.

The copper-containing species present above a Meker burner supplied with H<sub>2</sub>-N<sub>2</sub>-O<sub>2</sub> mixtures with added copper salts were found to be Cu, CuO, CuOH, and CuH.<sup>124,125</sup> Their concentrations were related by the balanced reactions:

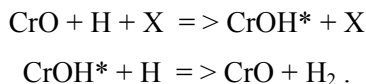


In a detailed study of chromium, Bulewicz and Padley<sup>126</sup> added  $\mu\text{L/L}$  levels of Cr (from either chromium carbonyl or aqueous sprays of chromium salts) to a premixed, fuel-rich, flat-flame burner of H<sub>2</sub>+O<sub>2</sub>+N<sub>2</sub>, and measured the catalytic radical recombination by the chromium compounds. They identified the active chromium species as Cr, CrO, CrO<sub>2</sub>, and HCrO<sub>3</sub> and also detected solid particles, which appeared to have equivalent black-body temperatures up to 500 K higher than the gas. They estimated an *upper limit* for the rate of heterogeneous radical recombination on the particle surfaces, and estimated that, at an upper limit, it was the same order as the natural un-catalyzed recombination rate in the flame. They also found that Cr showed measurable catalytic radical recombination even when added at volume fractions of about  $1\mu\text{L/L}$ , at which heterogeneous particle catalysis cannot be contributing. They cited Jenkins (1969, personal communication) as first showing the catalytic effect of metals (Ca, Sr, Ba) on radical recombination in flames. Interestingly, their data showed a saturation effect in the catalytic radical recombination by Cr species, and their analyses showed that it is due, not to condensation of the active gas phase Cr-containing species to particles, but to reduction in the available radicals to recombine.

Bulewicz and Padley proposed that the following balanced reactions are important in chromium inhibition, but did not develop an explicit mechanism:



Further, they speculated that at very low additive concentrations, the following gas phase reactions might be important:



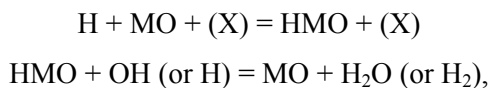
In continuing work, Bulewicz and coworkers<sup>115,116</sup> studied the catalytic effects of 21 metal species for recombining chain-carrying flame radicals present at super-equilibrium levels above premixed, fuel rich, flat flames of  $\text{H}_2 + \text{O}_2 + \text{N}_2$  at 1860 K. Table 3-3 shows the ratio of the catalyzed to uncatalyzed recombination rate for H atom caused by each of the metals, added at 1.3  $\mu\text{L/L}$ .

**Table 3-3. Catalytic Efficiency of Different Metals in Promoting Radical Recombination.**

Values of  $k_{\text{obs}}/k_{\text{uncat}}$  ( $T = 1860 \text{ K}$ ;  $X[\text{M}] = 1.3 \mu\text{L/L}$ ;  $\text{H}_2/\text{O}_2/\text{N}_2 = 3/1/6$ )

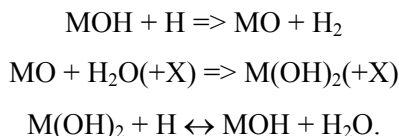
Strong Effect		Some Effect		No Effect	
Cr	2.8	Co	1.1	V	1
U	1.82	Pb	1.1	Ni	1
Ba	1.75	Zn	1.07	Ga	1
Sn	1.6	Th	1.06	Cl	1
Sr	1.35	Na	1.04		
Mn	1.3	Cu	1.04		
Mg	1.25	La	1.04		
Ca	1.25				
Fe	1.2				
Mo	1.16				

The cut-off value for this ratio was arbitrarily set to 1.1, and those above that value were described as having a strong catalytic effect. The possibility of heterogeneous recombination on particles was admitted, but at these low volume fractions, the authors argued primarily for a homogeneous gas phase mechanism involving H or OH reaction with the metal oxide or hydroxide (attributed to Jenkins).



in which M is a metal, and X is a third body.

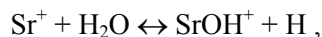
Concurrent with the alkaline earth metals, Cotton and Jenkins<sup>114</sup> showed that Ca, Sr, and Ba added as a fine mist of a salt solution to premixed  $\text{H}_2 + \text{N}_2 + \text{O}_2$  flat flames catalyzed the radical recombination for additive volume fractions in the range of 1  $\mu\text{L/L}$  to 10  $\mu\text{L/L}$ . By estimating the reaction rates in possible recombination mechanisms, they recommended the radical recombination mechanism to be:



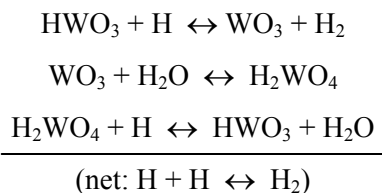
Jenkins and co-workers extended their studies of metal-catalyzed radical recombination in premixed flames to study soot formation in diffusion flames. The strong effect of metals on soot formation in flames is well-known.<sup>127</sup> Cotton et al.<sup>128</sup> added 40 metals to co-flow diffusion flames of propane and N<sub>2</sub>/O<sub>2</sub> mixtures and measured their effect on soot emissions and the smoke point. They postulated a mechanism for soot reduction whereby the catalytic reaction scheme listed above ran backwards, dissociating H<sub>2</sub>O and H<sub>2</sub> into OH and H, which then oxidized the soot particles.

The question of heterogeneous versus homogeneous gas phase chemistry was investigated by Bulewicz et al.<sup>129</sup> Through examination of the variation of the intensity of emitted radiation as a function of wavelength from particles formed above a premixed H<sub>2</sub>+O<sub>2</sub>+N<sub>2</sub> flat flame with added spray of aqueous uranium salt, they determined that the particles (presumably uranium oxide) were up to 500 K above the gas temperature. They interpreted the particle temperature rise to be caused by the catalytic recombination of H and OH on the particle surfaces. Nonetheless, Tischer and Scheller<sup>130</sup> pointed out that the spectral variation of the particle emissivity was unknown, and the gray-body assumption of Bulewicz was probably unjustified. They also argued that the excess temperature may have been due to surface reactions other than radical recombination.

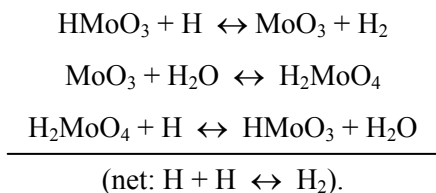
In similar work with premixed, fuel rich, flat flames of H<sub>2</sub>+O<sub>2</sub>+N<sub>2</sub>, Jensen and Jones<sup>131</sup> extended the classic Li + H<sub>2</sub>O ↔ LiOH + H photometric method to include the equilibrium for the reaction



in which [SrOH<sup>+</sup>]/[Sr<sup>+</sup>] was measured mass spectrometrically. Using both this new technique as well as the LiOH photometric method, they studied the catalytic flame radical recombination by tungsten and molybdenum, as well as once again confirming the strong effect of tin. Using flames at temperatures of 1800 K to 2150 K, and with metal addition at 1 μL/L to 110 μL/L, they collected data on the rates of radical recombination in the presence of the metallic catalysts (added as tetramethyl tin, or hexacarbonyls of tungsten or molybdenum), and measured the major species present in flames inhibited by W and Mo. By analogy with the mechanisms they developed for calcium<sup>114</sup> and iron<sup>132</sup> in flames, they then postulated reaction mechanisms for W and Mo, and estimated the rates for the reactions in the catalytic cycles. For the conditions of their flames, the radical recombination cycles, for either W or Mo, were about five times faster than those of tin. (Using the results of Linteris et al.,<sup>107</sup> this translates to an effectiveness about 10 times that of CF<sub>3</sub>Br, or about one-fifth that of Fe(CO)<sub>5</sub>). For tungsten and molybdenum, the cycles are:

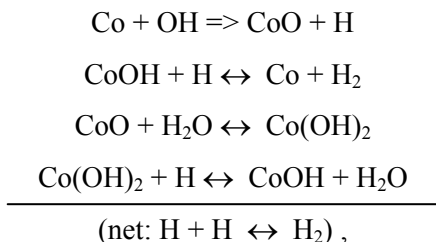


and



Jensen and Jones<sup>131</sup> found the dominant species in tungsten and molybdenum inhibition to be  $\text{WO}_3$ ,  $\text{HWO}_3$ , and  $\text{H}_2\text{WO}_4$ , and  $\text{MoO}_3$ ,  $\text{H MoO}_3$ , and  $\text{H}_2\text{MoO}_4$ .

In continuing work, Jensen and Jones<sup>133</sup> used similar techniques to study the radical recombination by cobalt added to a premixed, fuel rich, flat flame of  $\text{H}_2\text{-N}_2\text{-O}_2$ . With Co added as cyclopentadienylcobalt dicarbonyl at volume fractions of about 0.03  $\square\text{L/L}$  to 145  $\square\text{L/L}$ , and flame temperatures ranging from 1800 K to 2615 K, they spectroscopically identified the dominant cobalt-containing species to be Co, CoO, CoOH, and  $\text{Co(OH)}_2$ , with most of the cobalt being present in the flame as free Co atoms. Again by analogy with the Ca and Fe mechanisms, the Co mechanism was postulated to be:



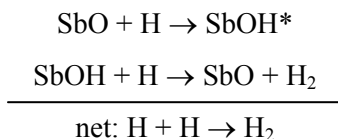
with the first step added since Co is the dominant Co-containing species. The rates of these catalytic steps were again inferred from the experimental data. Cobalt appeared to be about 2/3 as effective as tin in these flames.

### Gas phase Flame Retardants

Insight into mechanisms of metal flame inhibition was gleaned from studies of metal species added to materials as fire retardants (when their mode of action has been found to be in the gas phase). One such system is the antimony - halogen combination. Although they did not unravel the detailed mechanism, Fenimore and coworkers<sup>134-137</sup> showed that the relevant species act in the gas phase; they believed that the antimony moieties poisoned the flame, much as do brominated species. Similarly, Martin and Price<sup>138</sup> observed that the addition of triphenylantimony to certain polymer substrates provided fire retardancy, even in the absence of halogen, and believed the mechanism involved antimony species in the gas phase.

In a series of detailed experiments, Hastie and co-workers determined the mechanism of flame inhibition in the antimony-halogen system. Using a Knudsen effusion cell containing  $\text{Sb}_2\text{O}_3$  over which passed HCl, they showed that  $\text{SbCl}_3$  was evolved through a series of halogenation steps involving successive oxychloride phases.<sup>139</sup> Using a molecular beam mass spectrometer, they studied both the pyrolysis products of polyethylene retarded by antimony-oxide/halogen, as well as intermediate species profiles in premixed  $\text{CH}_4/\text{O}_2/\text{N}_2$  flames with added  $\text{SbCl}_3$  and  $\text{SbBr}_3$ .<sup>140</sup> For the pyrolysis studies, the major effused species from the polymer were  $\text{SbCl}_3$  and  $\text{SbOCl}$ . In the flame studies,<sup>141</sup> they found that  $\text{SbCl}_3$  reacted readily to  $\text{SbOCl}$ , which then reacted with H to form  $\text{SbO}$ . They measured the major intermediate species

of  $\text{SbBr}_3$  flame inhibition to be  $\text{SbO}$ ,  $\text{Sb}$ ,  $\text{HBr}$ , and  $\text{Br}$ . They also measured the decrease in the hydrogen atom volume fraction with addition of  $\text{SbBr}_3$ , and developed a reaction sequence for the formation of the intermediate species, as well as for the gas phase inhibition reactions. They argued strongly that the inhibition effect of antimony-oxide/halogen system was predominantly from the reaction sequence:



with a smaller effect from the usual bromine sequence, and an even smaller contribution from the equivalent chlorine cycle.

### Ignition Studies

The effect of metals on ignition has been studied in both shock tubes and flames. Morrison and Scheller<sup>111</sup> investigated the effect of twenty 20 inhibitors on the ignition of hydrocarbon mixtures by hot wires. They found that  $\text{SnCl}_4$  was the most effective inhibitor tested for increasing the ignition temperature, whereas the powerful flame inhibitors  $\text{CrO}_2\text{Cl}_2$  and  $\text{Fe}(\text{CO})_5$  had no effect on the ignition temperature. Dolan and Dempster<sup>142</sup> studied the effect of small particles (5  $\mu\text{m}$  to 10  $\mu\text{m}$  diameter) of metal compounds on suppressing the spark ignition of premixed natural gas-air mixtures in a vertical 7 cm diameter tube. They found that barium hydroxide octahydrate, barium chloride, and copper acetate monohydrate were each about three times less effective than sodium bicarbonate particles, while cuprous oxide and cobaltous chloride hexahydrate were each about 20 % less effective than  $\text{NaHCO}_3$ . Several studies have shown that metals can actually speed the ignition process in some chemical systems. In shock-tube studies, Matsuda and co-workers<sup>143</sup> found that  $\text{Cr}(\text{CO})_6$  reduced the initiation time for reaction of  $\text{CO}$  or  $\text{C}_2\text{H}_2$  with  $\text{O}_2$  in shock-heated gases. The metal carbonyl was present at 0  $\mu\text{L/L}$  to 50  $\mu\text{L/L}$ , so the presence of any particles was precluded. The mode of action was believed to be gas phase reactions involving  $\text{CrO}$ ,  $\text{CrO}_2$ , and  $\text{CrO}_3$ . In later shock-tube work with  $\text{Fe}(\text{CO})_5$  in mixtures of  $\text{CO-O}_2\text{-Ar}$ , Matsuda<sup>144</sup> found that a volume fraction of  $\text{Fe}(\text{CO})_5$  of few hundred  $\mu\text{L/L}$  greatly accelerated the consumption of  $\text{CO}_2$ . They postulated the effect to be due to oxidation of  $\text{CO}$  by metal oxides via:  $\text{FeO} + \text{CO} \Rightarrow \text{Fe} + \text{CO}_2$ , and noted that these reactions may be of importance since the mixtures were quite dry ( $X_{\text{OH}} \approx 5 \mu\text{L/L}$ ). Interestingly, such accelerating oxidation pathways were also found to be important in the dry reaction of  $\text{CO}$  with  $\text{N}_2\text{O}$  in flames.<sup>145</sup> In recent shock tube studies of  $\text{CH}_4\text{-O}_2\text{-Ar}$  mixtures, Park et al.<sup>146</sup> found that with (500, 1000, or 2000)  $\mu\text{L/L}$  of  $\text{Fe}(\text{CO})_5$ , the ignition time was shorter than without the additive, again indicating a promotion effect of the metal additive; however, they did not determine the cause of the promotion for this moist system. Finally, in flash photolysis studies many years ago, Erhard and Norrish<sup>96</sup> found that unlike  $\text{Pb}(\text{C}_2\text{H}_5)_4$  and  $\text{Te}(\text{CH}_3)_2$  which retarded hydrocarbon combustion,  $\text{Ni}(\text{CO})_4$ ,  $\text{Fe}(\text{CO})_5$ , and  $\text{Cr}(\text{CO})_6$  all greatly accelerated the combustion.

### Radical Recombination in Rocket Nozzles

Jensen and co-workers were motivated to study combustion inhibition by metal compounds largely by the desire to suppress afterburning in rocket nozzle exhausts. Using mechanisms developed for  $\text{K}$ ,  $\text{Ba}$ ,  $\text{Fe}$ ,  $\text{Mo}$ ,  $\text{W}$ ,  $\text{Cr}$ , and  $\text{Sn}$ , Jensen and Webb<sup>147</sup> calculated the amount of inhibitor required to suppress afterburning in the exhaust plume of a double-base propellant (unspecified composition, but usually a

homogeneous mixture consisting of nitrocellulose and nitroglycerine). The products of the propellant reactions consisted of a fuel rich mixture, principally CO and H<sub>2</sub>, much like the recombination region above the fuel-rich premixed H<sub>2</sub>-O<sub>2</sub>-N<sub>2</sub> laboratory flames used to study the metal-catalyzed radical recombination. Their calculations (which did not include the effects of condensation to particles) indicated that W and Mo were about a factor of five less effective than Fe, Cr was about a factor of six less effective, and Sn was more than seven times less effective. These results are consistent with those of the flat flame measurements described above.

Jensen and Webb did not measure particles or calculate the degrading effects of particle formation on the suppression of afterburning in rocket motors, but they did estimate the upper limit for radical recombination by the heterogeneous reactions on the particle surfaces. Their calculations indicated that although significant, the heterogeneous reactions could not suppress the afterburning, even for the smallest particle diameters assumed (10 nm). They also estimated that although the inhibiting species were probably volatilized in the combustion chamber, the characteristic times for condensation were probably of the same order as the residence time in the nozzle, indicating the potential for condensation. Their conclusions were that the metals held good promise for afterburning suppression in rocket motors, and that further work was necessary to estimate the rates of the catalytic cycle reactions and of the condensation rates of the metal derivatives under the conditions in their system.

### Other Relevant Investigations of Metal Compounds in Combustion Systems

There have been a number of recent papers dealing with metals in flames. Crosley and co-workers<sup>148</sup> added MMT to premixed flames with the purpose of studying its effect on NO formation. Adding MMT at volume fractions of about 0.5 μL/L to near-stoichiometric premixed low-pressure (522 Pa) propane-air flat flames in a McKenna burner, they measured the temperature and the relative concentrations of OH, H, O, CH, NO, and CO through the flame. While they observed no discernable effect of the MMT, this may have been due either to the low concentration of the additive, or the low pressure, both of which could limit the influence.<sup>89,107</sup> They did, however, start to develop a mechanism for manganese which served as a basis for future efforts.<sup>107</sup>

Chromium reaction in a atmospheric pressure, premixed hydrogen-air flat flame was studied by Yu et al.<sup>149</sup> Using microprobe gas sampling in the region downstream from the main reaction zone, they collected chromium species in the gas and condensed phase. The particle size distribution and the fraction of Cr as Cr(VI) was determined as a function of position. In addition, they assembled a kinetic mechanism for Cr reaction in flames through analogy with boron and aluminum combustion, and used the mechanism, together with the measured temperature profile, to calculate the fraction of hexavalent Cr in the downstream region from the flame zone. They also modeled the growth (but not the reaction) of the particle phase. For both particle growth and Cr(IV) formation, the calculations were able to predict the experimental trends. They concluded that further kinetic model development was necessary for accurate treatment of Cr speciation in flames. In later work, Kennedy et al.<sup>150</sup> studied the morphology of the particles formed in a hydrogen-air-nitrogen co-flow diffusion flame with added chromium nitrate or chromium hexacarbonyl. They found that the morphology of the particles varied with the temperature of the flame and the source of the chromium.

Kellogg and Irikura<sup>151</sup> performed theoretical calculations to predict the heats of formation as well as the enthalpies and free energies of reaction for the FeO<sub>x</sub>H<sub>y</sub> species thought to be important in iron inhibition.

They found that nearly all of the reactions involving these species and potentially contributing to flame inhibition are exergonic at 1500 K. Hence, they suggested that further refinement of the inhibition mechanisms of iron would require knowledge of the actual kinetic rates of the inhibition reactions to improve upon the preliminary estimates of Rumminger et al.<sup>104</sup>

In a comprehensive review of possible chemicals for use as halon alternatives, Tapscott et al.<sup>152</sup> suggested that of the metals, Cu, Fe, Mn, and Sn, were worthy of further study. Since that time, premixed<sup>107</sup> and co-flow diffusion flame<sup>153</sup> studies have been performed for compounds containing Fe, Mn, and Sn. No additional work has been reported for copper compounds as fire suppressants.

### Detailed Studies with Iron

After the potential effectiveness of iron as a flame inhibitor was indicated,<sup>34,95,99</sup> the behavior of iron pentacarbonyl was investigated in detail in several old investigations. The extraordinary flame inhibiting effectiveness of iron was first identified by Lask and Wagner<sup>34</sup> in their screening study involving methane-, hexane-, and benzene-air premixed Bunsen-type flames with numerous additives. In continuing work,<sup>89</sup> Wagner and co-workers described the superior effectiveness of  $\text{Fe}(\text{CO})_5$  for reducing the burning velocity of hydrocarbon-air flames in nozzle burners. They found that an  $\text{Fe}(\text{CO})_5$  volume fraction of 100  $\mu\text{L}/\text{L}$  reduced the burning velocity by 25 % when added to stoichiometric methane-air flames at atmospheric pressure. With oxygen as the oxidizer, or at reduced pressure, they found the effectiveness to be lowered. For hydrogen-air flames,  $\text{Fe}(\text{CO})_5$  was again much more effective than  $\text{Br}_2$ . They noted that at low volume fractions, the decrease in the burning velocity was proportional to the concentration of  $\text{Fe}(\text{CO})_5$ , whereas for increasing concentrations of  $\text{Fe}(\text{CO})_5$ , the relative influence seemed to decrease. They postulated a homogeneous radical recombination mechanism at low volume fraction, and a heterogeneous one at higher.

To understand the detailed mechanism of  $\text{Fe}(\text{CO})_5$ , Bonne et al.<sup>89</sup> spectroscopically investigated premixed flat flames of methane with air or  $\text{O}_2$ . Unfortunately, at the low pressures for which the flame zone was expanded sufficiently to optically probe the flame (800 kPa), the kinetic effect of  $\text{Fe}(\text{CO})_5$  was very small. Nonetheless, for  $\text{Fe}(\text{CO})_5$  volume fractions up to 100  $\mu\text{L}/\text{L}$  they observed that (1) the peak OH volume fraction  $X_{\text{OH}}$  was unchanged, but shifted slightly downstream from the burner, and (2) the decay rate of  $X_{\text{OH}}$  was increased in the presence of  $\text{Fe}(\text{CO})_5$ , clearly indicating the effect of  $\text{Fe}(\text{CO})_5$  on radical concentrations in the flame. They measured FeO and Fe emission, as well as Fe absorption, and found that Fe and FeO emission peaked in the main high-temperature reaction zone, implicating these species in the radical recombination reactions. Although FeO had a double peak, with a minimum at the location where the rate of OH recombination was greatest, the authors did not feel that the decrease in FeO emission was correlated with a decrease in FeO concentration. They noted that solid particles were forming, that they were attempting to measure them, and said that the results of these measurements would be reported in the future (but no publications subsequently appeared).

In later work, the high effectiveness of iron was confirmed for methane-air premixed Bunsen-type flames, and extended to counterflow diffusion flames, by Reinelt and Linteris.<sup>103</sup> Their work indicated clearly that iron was very effective at low concentration, but that the effectiveness leveled off at higher concentration. Further studies with premixed flames of  $\text{CO}-\text{O}_2-\text{N}_2$  and  $\text{CO}-\text{N}_2\text{O}-\text{N}_2$  confirmed the effectiveness of  $\text{Fe}(\text{CO})_5$  in other systems.

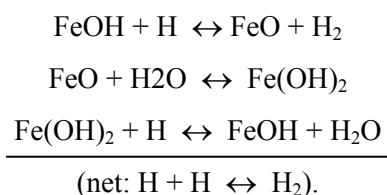


### 3.3.3 Flame Inhibition by Iron-containing Compounds

Recent results provide convincing evidence that the strong flame inhibition by iron is due to a homogeneous gas phase mechanism, which is described below. Following that, the experimental data showing iron's loss of effectiveness is described, along with a discussion of the parameters which most affect the particle formation which is believed to cause the loss of effectiveness.

#### Gas Phase Mechanism

A detailed mechanism for the gas phase iron-catalyzed radical recombination in flames was developed by Jensen and Jones,<sup>132</sup> and later, expanded by Rumminger et al.<sup>104</sup> In both, the main catalytic cycle leading to radical recombination was postulated to be:



This mechanism is shown schematically in Figure 3-8.

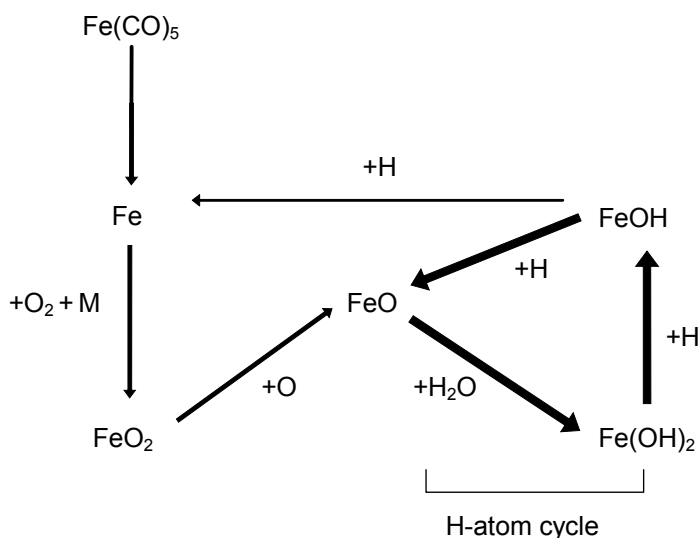
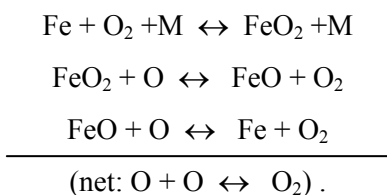


**Figure 3-8. Main Catalytic Radical Recombination Cycle of Iron Found to be Important for Methane-air Flames.**

Although the mechanism described in Rumminger et al. also included other catalytic cycles, they were not found to be particularly important in methane-air flames, premixed or diffusion.<sup>105</sup> In work with premixed  $\text{CO-N}_2\text{-O}_2$  flames, however, the following additional catalytic cycle was found to be much more important than the H-atom cycle:



This new O-atom cycle together with the H-atom cycle are shown in Figure 3-9. Thicker arrows correspond to higher reaction flux. Reaction partners are listed next to each arrow.

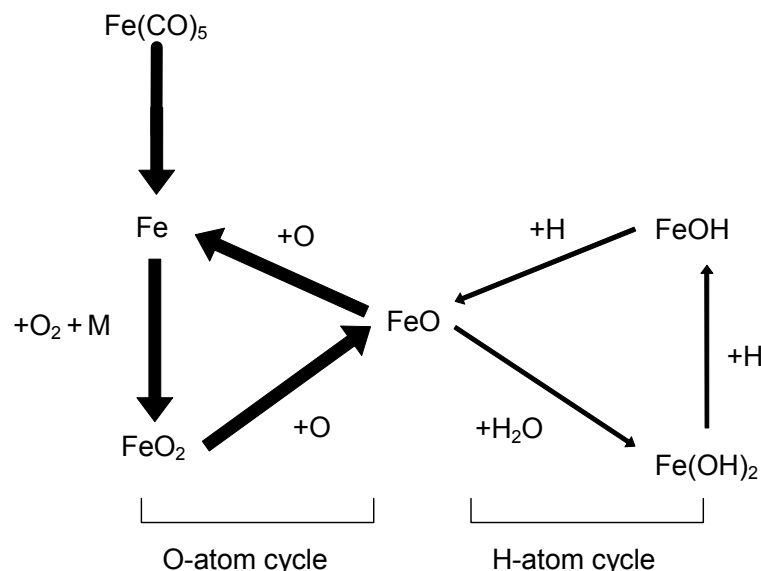


**Figure 3-9. Radical Recombination Reaction Pathways Found to be Important for CO-H<sub>2</sub>-O<sub>2</sub>-N<sub>2</sub> Flames.<sup>118</sup>**

Further, more recent computations of the thermochemistry of iron compounds at flame conditions support the possibility of many more radical recombination cycles.<sup>151</sup> In that study, seven iron species thought to exist at flame temperature were considered: Fe, FeH, FeO, FeOH, FeO<sub>2</sub>, FeO(OH), Fe(OH)<sub>2</sub>,<sup>104</sup> and the heat of reaction at 0 K, and the change in Gibbs free energy at 1500 K were calculated. Based on the results, however, very few of the considered reactions and cycles could be eliminated based on the thermodynamics. The complexity of the situation is illustrated in Figure 3-10, (Kellogg and Irikura<sup>151</sup>), which shows schematically the possible inhibition cycles of iron. (Note that in the figure there are on the order of 50 possible *cycles* since [Fe] can be replaced by Fe, FeH, FeO, or FeOH.)

It is important to observe that even for iron, for which the most research has been performed, the mechanism is in very early stages of development. For example, the rates of the most important reaction steps in the mechanism were selected (within the uncertainty bounds suggested by Jensen and Jones<sup>132</sup>) so as to provide the best agreement with experiments. The mechanism has been tested only for near stoichiometric premixed CH<sub>4</sub>-N<sub>2</sub>-O<sub>2</sub>, CO-N<sub>2</sub>-O<sub>2</sub>, and CO-N<sub>2</sub>O premixed flames, CH<sub>4</sub>-O<sub>2</sub>-N<sub>2</sub> counterflow diffusion flames, and CH<sub>4</sub>-air cup burner flames. Although at low Fe additive mole fraction the agreement was usually good, there were some conditions for which the predicted inhibition was off significantly. These cases include lean premixed CH<sub>4</sub>-air flames ( $\phi=0.9$ ), CH<sub>4</sub>-O<sub>2</sub>-N<sub>2</sub> flames with an oxygen volume fraction in the oxidizer of 0.20, and the cup burner flames with added CO<sub>2</sub> (at very low Fe(CO)<sub>5</sub> volume fraction).

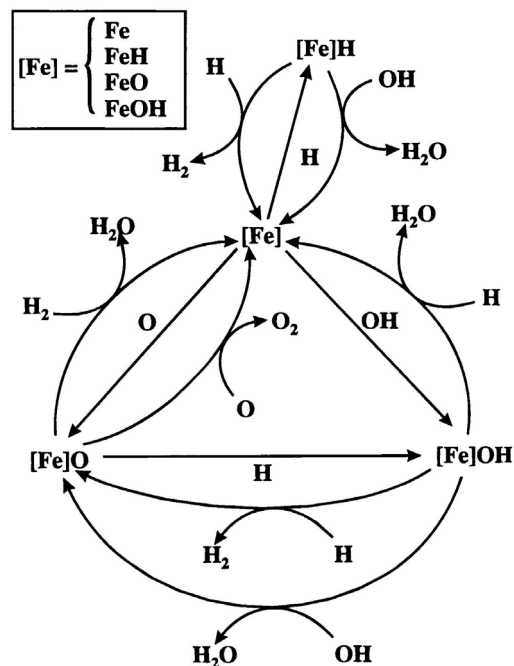


**Figure 3-10. Different Classes of Reactions Which May Contribute to Iron's Super-efficient Flame Suppression Ability through the Catalytic Recombination of Radical Species.<sup>151</sup>**

The main ramification of the above gas phase inhibition mechanism for fire suppression is that lowering radical concentrations lowers the overall reaction rate in the flame, weakening it. In laboratory flames, radical concentrations typically go above equilibrium levels, to super-equilibrium levels. This is particularly true for both premixed and high and moderate strain counterflow diffusion flames. At low strains, however, the radical super-equilibrium is less. (See Figure 3-11.) Radical concentrations in actual fires have not been measured. Nonetheless, recent research using cup burner flames<sup>154</sup> (which, to some extent, resemble small-scale fires) has shown that a stabilization region at the flame base, called the flame kernel, resembles a near-stoichiometric low-temperature premixed flame. Hence, the gas phase *catalytic* radical recombination cycles should be as important in the stabilization of fires as they are for laboratory flames. This is partially confirmed since other gas phase catalytic agents (for example,  $\text{CF}_3\text{Br}$ ) are effective in both laboratory flames and full-scale fires.

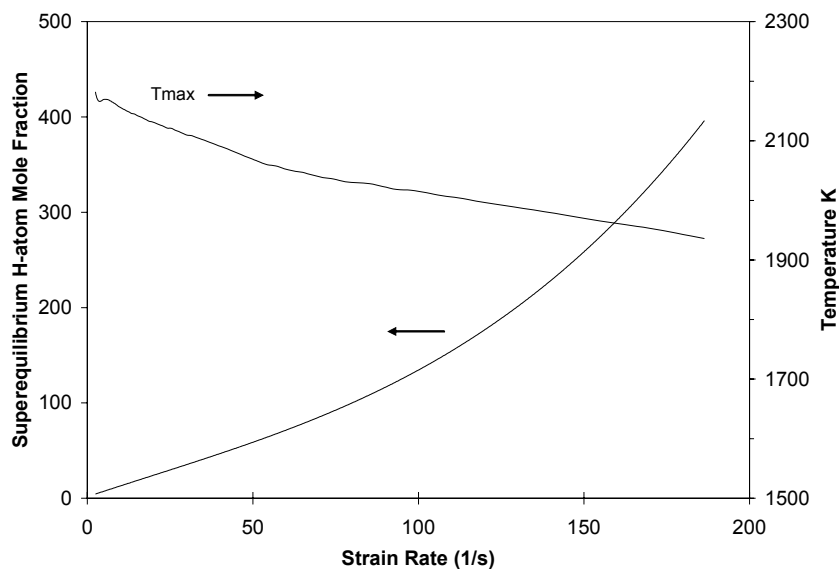


**Figure 3-11. Calculated H-atom Super-equilibrium Ratio and Peak Temperature in a Counterflow Diffusion Flame as a Function of Strain Rate.**

## Inhibition of Low Pressure Opposed-flow Methane-air Flames by $\text{Fe}(\text{CO})_5$

### *Introduction*

For premixed and non-premixed flames, measurements of radical concentrations (O, H, OH) serve as useful indicators of the chemical rates that are being affected, because chemical inhibiting agents act to reduce the super-equilibrium concentration of radicals. Radical concentrations reach their maximum concentrations in the flame reaction zone and then decay toward equilibrium values. Thus, if an inhibitor were present, it would reduce the maximum radical concentrations toward equilibrium values and show the amount of chemical inhibition present.<sup>155</sup> Radical measurements are thus directly related to burning velocity and extinction strain rate measurements.

Prior to the NGP, there had been no laboratory measurements of the change in the concentration of radical species with increasing addition of  $\text{Fe}(\text{CO})_5$  to non-premixed flames. In fact, only limited measurements of radical species in non-premixed flames inhibited by  $\text{CF}_3\text{Br}$  existed.<sup>36,51,156</sup> McNesby and co-workers<sup>157</sup> examined the influence that  $\text{Fe}(\text{CO})_5$  had on the structure of a low pressure, opposed flow,  $\text{CH}_4$ -air flames. OH radical profiles were measured as the concentration of inhibitor was increased, approaching extinguishment. Flames inhibited by  $\text{N}_2$  or  $\text{CF}_3\text{Br}$  were included for reference.

### *Apparatus*

Figure 3-12 presents a schematic diagram of the experimental arrangement. The opposed flow burner apparatus was contained within a 200 L combustion chamber. The combustion chamber was a six-armed stainless steel cross, with the four horizontal arms being 25.4 cm in diameter and the two vertical arms being 30.48 cm in diameter. The opposed jet ducts were mounted in the vertical arms with each head having two axes of motion under computer control. The opposed jet duct diameters were 7.68 cm and the active burner surface was approximately 7.6 cm in diameter. Laminar flow was established in the jet ducts, with the initial gases impinging on a 0.32 cm thick, porous, stainless steel, sintered disk. The gases flowed through a 2.54 cm region before passing through a second, 0.32 cm thick, porous, stainless steel, sintered disk. The second porous disk opened to the combustion chamber. Schlieren images of the gases showed laminar flow from both ducts. The gases and cooling water were fed to the burner ducts via stainless tubing.

Optical access to the chamber was provided on the vertical arms of the chamber through 10.16 cm diameter windows. There were also four additional ports in the horizontal plane, each located between two of the window arms. These ports served as access for pressure monitoring, thermocouple manipulation, and electrical connections. Also mounted on the top and bottom of each window arm were vacuum ports to remove the combustion gases. These eight ports were joined to a single 5.08 cm I.D. tube which fed the gas to a scrubber mounted on a high volume vacuum pump. The scrubbed exhaust gases were then vented to the atmosphere. All flames were studied at a pressure of 6.6 kPa (50 torr), the oxidizer flow consisted of 10 L/min synthetic air (79 %  $\text{N}_2$  + 21 %  $\text{O}_2$ , Matheson UHP Grade) flowing from the upper duct, and the fuel flow was 10 L/min of methane (Matheson UHP Grade) flowing from the lower duct. The gases were regulated and monitored by a gas handling manifold system constructed from a series of flow controllers (Tylan General).

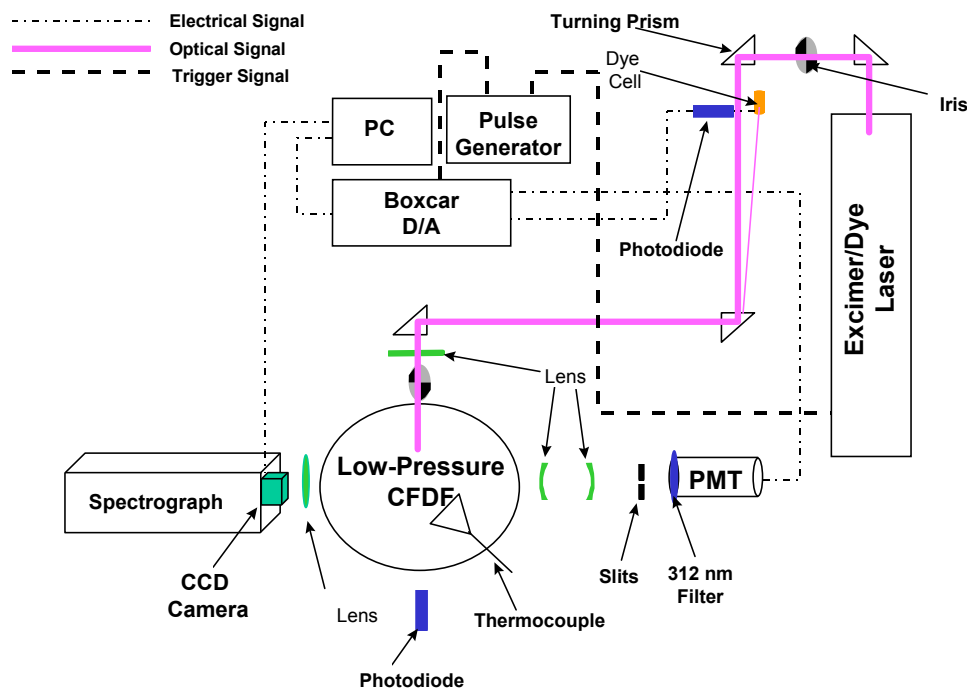


**Figure 3-12.**  
Schematic  
Diagram of the  
Low Pressure  
Burner and  
Optical  
Measurement  
Arrangement.

The oxidizer and fuel ducts were separated 3.8 cm. For the flow conditions and flow duct separation, the luminous flame zone was located on the oxidizer side of the stagnation plane, and the global strain rate was calculated to be  $50.2 \text{ sec}^{-1}$ .<sup>76</sup> The inhibitors were added to the oxidizer flow for delivery to the flame zone.

$\text{Fe}(\text{CO})_5$  is a liquid at room temperature and its introduction into the flame was accomplished by bubbling argon (Ar) through a flask containing 25 ml of  $\text{Fe}(\text{CO})_5$  that was immersed in a constant temperature bath maintained at 13 °C. The resulting Ar/  $\text{Fe}(\text{CO})_5$  mixture consists of  $\approx 2\%$   $\text{Fe}(\text{CO})_5$  and  $\approx 98\%$  Ar. The maximum flow of Ar through the bubbler was 0.41 L/min. At this flow, the effect of Ar on the flame was minimal. The gaseous output of the bubbler apparatus passed through a 5 L/min mass flow meter to monitor the Ar/ $\text{Fe}(\text{CO})_5$  mixture being delivered to the oxidizer stream. The mass flow meter was calibrated for the Ar/ $\text{Fe}(\text{CO})_5$  mixture using a standard soap bubble technique.

### Diagnostics

Flame emission spectra were measured using a Princeton Instruments ICCD camera (Model 120) coupled to a 0.75 m SPEX spectrograph (Model 1702) with a 1200 gr/mm grating controlled by an external Compudrive. A 50 cm focal length lens collected light from the center of the flame and focused it onto the entrance slits (0.05 mm) of the spectrograph. The determined field of view of this optical arrangement was  $1 \text{ cm}^2$ . The ICCD camera, which had an active area of 384 x 576 pixels, was operated in a CW manner and each image recorded was acquired with 50 total accumulations on the camera.

Laser induced fluorescence excitation spectra in the flame were measured using a Lambda Physik excimer/dye laser system. The system consists of a Lambda Physik Compex 102 XeCl excimer laser, a Scanmate 2 dye laser (Rhodamine 6g), and a Second Harmonic Generator (SHG). The fundamental output of the dye laser (580 nm wavelength) was frequency doubled in the SHG unit with a BBO crystal to around 290 nm. The UV laser radiation was tuned to the peak of the  $\text{P}_2(8.5)$  transition at 286.566 nm

((1,0)  $A^2\Sigma^+ \leftarrow X^2\Pi$ ) (References 158-160). The intensity of this transition was slightly temperature dependent,<sup>161</sup> varying by approximately 12 % over the range of maximum temperatures for the flames studied here. The selected transition varied linearly with input energy. Low laser energies were used and the laser was operated in the linear regime. The UV light output of the SHG unit was focused to the center of the burner chamber using a 50 cm focal length fused silica lens and had a vertical and horizontal beam waist of 0.4 mm and 0.5 mm, respectively. Fluorescence was collected at 90 ° to the direction of the excitation laser beam, focused through 0.75 mm horizontal slits to define the collection volume, passed through a band pass filter centered at 312 nm with an 11 nm bandwidth, and detected by a photomultiplier tube (PMT) (Phillips Model XP2018B). Fluctuations in laser power were detected by a photodiode that monitored laser induced fluorescence from a cell containing Rhodamine 6g dye.

The output signals from the PMT and monitor photodiode were directed to gated integrator/boxcar averagers (SRS Model SR-250) operating in a 10 shot average mode. The boxcar gate widths were set to 3 ns. The trigger pulses to the excimer laser and boxcars were supplied by a digital delay pulse generator (SRS Model DG535) at a rate of 10 Hz. Spatially resolved OH LIF profiles were measured by tuning the excitation laser to the peak of the  $P_2(8.5)$  transition and, with the beam location fixed, vertically translating the burner assembly.

### Results

Table 3-5 lists the inhibitor agent concentrations at extinction and the average uncertainties due to measurement variance.

**Table 3-5. Inhibitor Concentrations ( $\mu\text{L/L}$ ) and Uncertainty ( $\pm \mu\text{L/L}$ ) at Flame Extinction.**

Inhibitor	$\text{N}_2$	$\text{CF}_3\text{Br}$	$\text{Fe}(\text{CO})_5$
Extinction Concentration	9426	3735	451
Uncertainty	566	672	77

The large degree of variance was due to changes in the burner cooling. The flow of cooling water to the burner ducts was not monitored precisely, and thus the burner performance probably changed slightly from day-to-day operation. This deficiency was perhaps significant because the burner was operated in a quasi-adiabatic condition, and thus heat losses from the flame to the burner ducts caused decreases in extinction concentrations observed experimentally. Preliminary numerical calculations of extinction concentrations for  $\text{CF}_3\text{Br}$  and  $\text{Fe}(\text{CO})_5$  were 4000  $\mu\text{L/L}$  and 271  $\mu\text{L/L}$ , respectively.<sup>162</sup>

The numerical calculations for both  $\text{CF}_3\text{Br}$  and  $\text{Fe}(\text{CO})_5$  were performed using kinetic models.<sup>52,104</sup> Preliminary numerical calculations by Babushok<sup>163</sup> using the kinetic model for  $\text{Fe}(\text{CO})_5$  inhibition of Rumminger et al.,<sup>104</sup> but corrected for the pressure dependence of the  $\text{FeO} + \text{H}_2\text{O} \leftrightarrow \text{Fe}(\text{OH})_2$  reaction, demonstrated an extinction concentration of 612  $\mu\text{L/L}$ .

All three inhibited flames extinguished in the flat region directly between the opposed flow fuel and oxidizer ducts. Addition of  $\text{N}_2$  or  $\text{CF}_3\text{Br}$  to the 6.6 kPa  $\text{CH}_4$ -air flame did not significantly alter the visual appearance of the flat, axisymmetric, blue disk flame. Addition of  $\text{Fe}(\text{CO})_5$  to the flame caused an orange/yellow luminous zone to appear above the blue luminous zone, similar to what was observed by Reinelt and Linteris.<sup>164</sup> As the  $\text{Fe}(\text{CO})_5$  inhibited flame approached extinction, the blue and the

orange/yellow luminous zones gradually merged, and the flame assumed a uniform bright orange/yellow color. The orange/yellow luminosity in the  $\text{Fe}(\text{CO})_5$  inhibited flame was believed to be caused by iron oxide emission.<sup>89</sup> The dual flame zone observation, which has been observed in previous  $\text{Fe}(\text{CO})_5$  studies,<sup>89</sup> was further characterized using emission spectroscopy.

For the compositional analysis of the solid particles formed in the flame, particle samples were collected and analyzed using a scanning electron microscope (SEM) and X-ray fluorescence (XRF) techniques. Particle samples were taken from the upper cooled burner duct, where large deposits were found, and from an uncoated, 0.2 mm diameter Pt/Pt-10 % Rh wire thermocouple inserted into the visible center of a  $\text{Fe}(\text{CO})_5$  inhibited flame. The collected particulate material appeared as a ruddy orange powder. The XRF showed the elemental composition of the particles to be iron and oxygen. An exact ratio of iron to oxygen was not determined, but the SEM analysis indicated that the size of the particles ranged from 1  $\mu\text{m}$  to 10  $\mu\text{m}$ , with most being 1  $\mu\text{m}$  to 2  $\mu\text{m}$  and quasi-spherical in morphology.

### *Emission Spectroscopy*

Emission spectroscopy was used to qualitatively examine the behavior of OH for each inhibited flame as well as the decomposition of  $\text{Fe}(\text{CO})_5$  upon introduction into the flame. For OH, images were collected at increasing concentrations of inhibitor. Images indicated that for approximately equal inhibitor concentrations added to the flame, the flame to which  $\text{Fe}(\text{CO})_5$  had been added demonstrated the smallest relative OH emission intensity. These observations illustrated that addition of  $\text{Fe}(\text{CO})_5$  to the flame had the greatest effect on the OH population. However further quantification of the results was risky because ground state populations and temperatures calculated from OH emission in flames using a Boltzmann distribution can be misleading. That is, nascent OH that is responsible for the chemiluminescence may not be in thermal equilibrium with ground electronic state OH and other combustion gases.

Figure 3-13 shows a representative emission image collected in the 554 nm wavelength region from the centerline of a flame with 10 % of the experimentally determined extinction concentration of  $\text{Fe}(\text{CO})_5$  added to the oxidizer flow. The addition changed the molecular emission spectra to include iron species such as FeO and FeOH as well as atomic iron lines.<sup>165</sup> These modifications to the molecular emission spectra altered the flame's emission intensity, which is illustrated in Figure 3-13. The spatial mapping indicated that some of the  $\text{Fe}(\text{CO})_5$  had decomposed prior to the luminous flame region at approximately 10.4 mm  $\pm$  1 mm from the oxidizer duct with a majority of the emission in this spectral region attributed to FeO.<sup>166</sup> The lower continuum, at approximately 14.8 mm  $\pm$  1 mm from the oxidizer duct, was due to the broadband luminosity of the hydrocarbon flame. Earlier emission images<sup>165</sup> of CH emission from similar low pressure  $\text{CH}_4$ -air flames seeded with  $\text{Fe}(\text{CO})_5$  showed an additional region of emission intensity closer to the oxidizer duct which was not observed in both uninhibited and inhibited flames seeded with  $\text{N}_2$  or  $\text{CF}_3\text{Br}$ . The additional intensity was identified as iron lines not present in the uninhibited flame.

Recognition of iron oxide particle formation invoked suggestions of heterogeneous chemistry occurring. Work by Babushok et al.,<sup>167</sup> who modeled the effect of an ideal gas phase flame inhibitor using gas kinetic rate constants for a set of radical scavenging and inhibitor-regenerating reactions, indicated otherwise. Calculations were conducted for a premixed flame containing  $\text{Fe}(\text{CO})_5$  and a premixed flame with the ideal gas phase flame inhibitor. The calculations showed that the burning velocities, which were very non-linear as inhibitor concentrations increased, for both flame systems were nearly equal for the

same inhibitor quantities. This result showed that the  $\text{Fe}(\text{CO})_5$  inhibition mechanism was dominated by homogeneous gas phase chemistry when the inhibitor is added in small concentrations.<sup>167</sup>

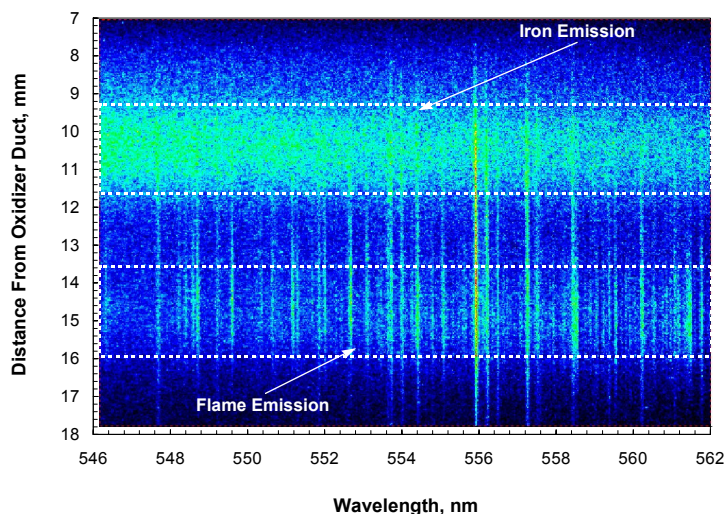


**Figure 3-13. Emission Image Collected from the Centerline of the Low Pressure, Opposed Flow,  $\text{CH}_4$ -air flame with 10 % of the  $\text{Fe}(\text{CO})_5$  Concentration Required to Extinguish the Flame.**

### Laser Induced Fluorescence

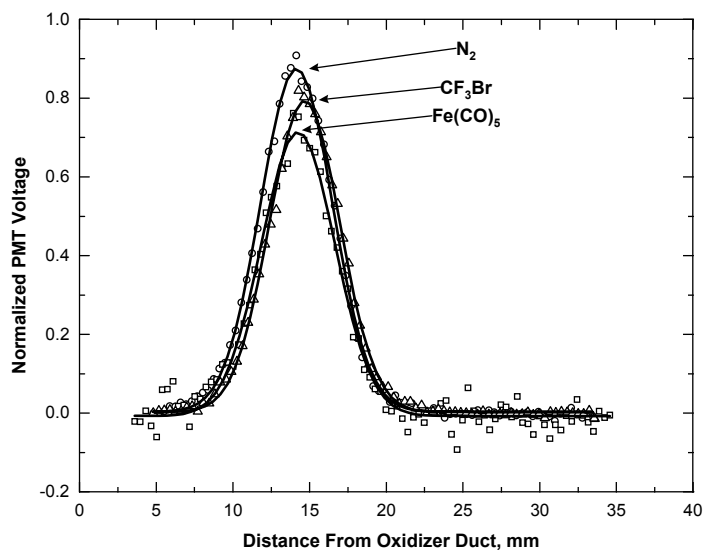


Figure 3-14 shows representative OH LIF profiles measured in flames to which  $\text{Fe}(\text{CO})_5$ ,  $\text{CF}_3\text{Br}$ , or  $\text{N}_2$  had been added.

**Figure 3-14 LIF [OH] Profiles Collected from Inhibited  $\text{CH}_4$ -air Flames Containing Nominally Half of the Concentration Required for Extinguishment.  $\text{N}_2$ : O;  $\text{CF}_3\text{Br}$ :  $\Delta$ ;  $\text{Fe}(\text{CO})_5$ :  $\square$ .**

The inhibitor concentrations and percents of the concentration required for extinguishment were  $\text{N}_2$  (4721  $\mu\text{L}/\text{L}$ , 50 %),  $\text{CF}_3\text{Br}$  (1996  $\mu\text{L}/\text{L}$ , 53 %), and  $\text{Fe}(\text{CO})_5$  (229  $\mu\text{L}/\text{L}$ , 51 %). The data had been normalized to the peak intensity of the OH LIF profile in an uninhibited flame. The  $\text{N}_2$  doped flame had the smallest effect (leaving the highest intensity), followed by  $\text{CF}_3\text{Br}$  and  $\text{Fe}(\text{CO})_5$ .

The addition of an inhibitor to the flame can also change the nature of the flame's reaction zone.

- **Location:** For the uninhibited flame, the location of the average OH LIF maximum from the oxidizer duct was  $14.34 \text{ mm} \pm 0.05 \text{ mm}$ . The addition of  $\text{Fe}(\text{CO})_5$  had a negligible effect on the OH LIF maximum position. The addition of  $\text{CF}_3\text{Br}$  or  $\text{N}_2$  to the flame slightly shifted the position of the OH LIF maximum toward the oxidizer duct to locations of  $14.12 \text{ mm}$  and  $13.65 \text{ mm}$ , respectively. The shifts were small and were largest for the weakest inhibitor, each added at 50 % of its extinguishing concentration. Preliminary numerical calculations<sup>163</sup> using the kinetic model for  $\text{Fe}(\text{CO})_5$  inhibition of Rumminger et al.,<sup>104</sup> but corrected for the pressure dependence of the  $\text{FeO} + \text{H}_2\text{O} \leftrightarrow \text{Fe}(\text{OH})_2$  reaction, predicted the position of the OH maximum concentration at  $13.0 \text{ mm}$  from the oxidizer duct.
- **Width:** Previous studies<sup>168-173</sup> had shown that a decrease in the flame's reaction zone width indicated increased localized strain, which could cause local quenching or flame extinction. The width of the flame's reaction zone may be characterized by the width of a radical profile (Miller, 1996). For the analysis of the radical profile shape modifications, the profiles were fit to a Gaussian function. The width of the flame zone was defined as the distance of one half of the maximum intensity of the Gaussian OH profile, i.e., Full Width Half Maximum (FWHM). The determined [OH] profile width for the uninhibited flame was  $5.67 \pm 0.08 \text{ mm}$ . Addition of  $\text{N}_2$  did not change the profile width. The addition of  $\text{CF}_3\text{Br}$  or  $\text{Fe}(\text{CO})_5$  narrowed the profile width to  $5.50 \text{ mm}$  and  $5.22 \text{ mm}$  respectively. Thus, reduction of the profile widths was small and was largest for the strongest inhibitor, the opposite of the location effect described above.
- **Intensity Trend:** Figure 3-15 presents normalized OH LIF peak intensities vs. inhibitor concentrations. For normalization, the OH maximum intensity from the uninhibited flame was used. The presented data were uncorrected for collisional quenching and temperature dependence, and the major source for error in the peak OH LIF intensities was the laser shot-to-shot variation. The shot-to-shot variance occurred as the laser energy was scanned over the spectral region of interest. The shot-to-shot uncertainty averaged  $\pm 1.5 \%$  which contributed to the overall measurement uncertainty of  $4 \%$ .

Flames inhibited by  $\text{Fe}(\text{CO})_5$  and  $\text{CF}_3\text{Br}$  demonstrated decreases in OH populations that were quasiproportional to the inhibitor concentrations. Flames inhibited by  $\text{N}_2$  demonstrated non-linear behavior, with initially small changes in [OH] and more rapid decreases as extinction was approached. The final measurable [OH] data points, which were near each flame's extinction point concentration, were approximately the same for all three inhibitors: 0.73 to 0.67. Thus, there was an approximately 30 % decrease in the normalized OH intensity at extinction for each inhibitor. The same model used to calculate the peak OH location gave a normalized OH maximum concentration at extinction of 0.73 for  $\text{Fe}(\text{CO})_5$ . The ratio of each inhibitors' concentration relative to  $\text{CF}_3\text{Br}$  near extinction was  $\text{N}_2:\text{CF}_3\text{Br}:\text{Fe}(\text{CO})_5 = 2.5:1:0.11$ , indicating that the  $\text{Fe}(\text{CO})_5$  flame inhibition effectiveness was approximately a factor of 10 greater than  $\text{CF}_3\text{Br}$ . These results were similar to Reinelt and Linteris<sup>103</sup> who observed that  $500 \mu\text{L/L}$  of  $\text{Fe}(\text{CO})_5$  added to the air stream of an atmospheric pressure,  $\text{CH}_4$ -air, counterflow flame reduced the strain by  $\approx 30 \%$ , while addition of  $5000 \mu\text{L/L}$  of  $\text{CF}_3\text{Br}$  reduced the strain about  $20 \%$ .

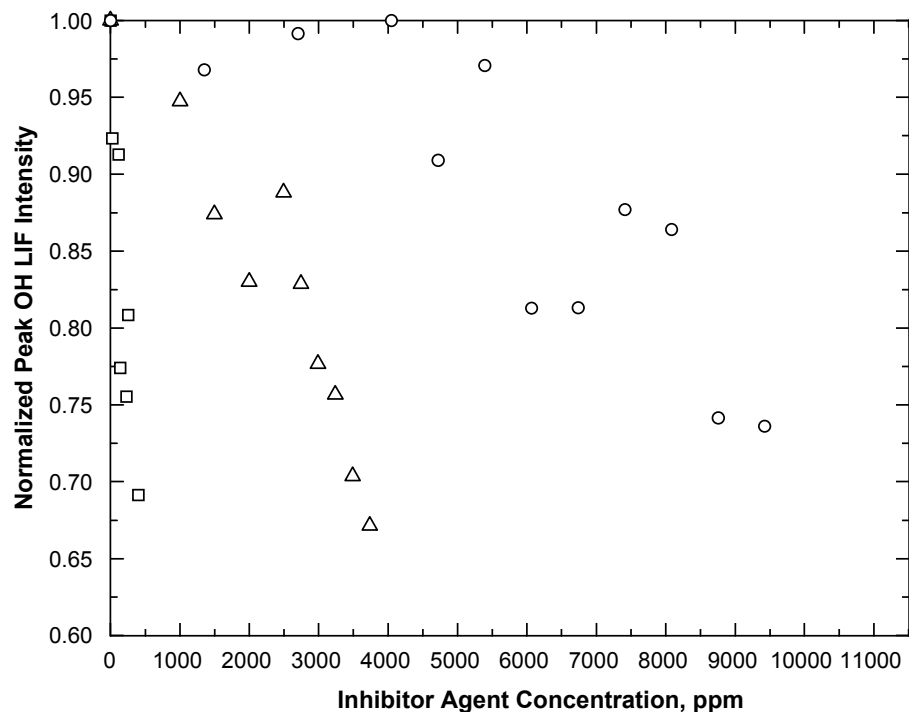


**Figure 3-15.** Dependence of Normalized Maximum OH LIF Intensity on Inhibitor Concentration.  $\diamond$ : N<sub>2</sub>;  $\Delta$ : CF<sub>3</sub>Br;  $\square$ : Fe(CO)<sub>5</sub>. The lowest experimental measurements of OH intensity correspond to near-extinction conditions.

[OH] measurements<sup>156</sup> in non-premixed atmospheric pressure hydrocarbon flames have also shown decreasing OH concentrations with increasing CF<sub>3</sub>Br concentrations.<sup>51</sup> The observed quasimonotonic decrease of [OH] in the current flames with increasing of CF<sub>3</sub>Br and Fe(CO)<sub>5</sub> concentrations was similar to decreases of chain carrier concentrations in the reaction zone of simulated premixed C1-C2 flames with CF<sub>3</sub>Br, CF<sub>3</sub>I, CF<sub>4</sub>, C<sub>2</sub>F<sub>6</sub>, and C<sub>2</sub>F<sub>5</sub>H additives.<sup>52</sup> Uncorrected OH absorption profile measurements by Bonne and co-workers<sup>89</sup> showed a slight decrease in the integrated OH concentrations, i.e., area under curves, with increasing Fe(CO)<sub>5</sub> concentrations for a low pressure (8 kPa), premixed, stoichiometric methane/air flame.

The saturation effect (leveling), which was observed for burning velocities in atmospheric pressure, premixed methane flames seeded with Fe(CO)<sub>5</sub>,<sup>103,104,174</sup> was not observed in this work. Two types of saturation have been discussed in the literature: (1) saturation of chemical influence<sup>52</sup>, and (2) saturation due to condensation processes.<sup>103</sup> Both result in a decrease in inhibitor efficiency with increased inhibitor concentration, but the latter was believed to dominate for Fe(CO)<sub>5</sub> inhibited flames.

The current low pressure, non-premixed flame results show some similarities to the premixed CH<sub>4</sub>-O<sub>2</sub> flame of Bonne et al.<sup>89</sup> at pressures from 101 kPa to 10 kPa. At 101 kPa, addition of 0.03 % Fe(CO)<sub>5</sub> to the Bonne flame decreased the burning velocity  $\approx$  7.5 %, while at 50 kPa, addition of 0.03 % Fe(CO)<sub>5</sub> decreased the burning velocity  $\approx$  6 %. In premixed CH<sub>4</sub>-air flames, addition of 0.01 % Fe(CO)<sub>5</sub> at 101 kPa caused the burning velocity to decrease 24 % while at 50 kPa the decrease in burning velocity was only 8 % to 9 %. Obviously, Fe(CO)<sub>5</sub> had a more pronounced effect in the CH<sub>4</sub>-air flames, but for both systems the decreases in burning velocities were observed to be linear at all pressure conditions and the inhibitor influence of Fe(CO)<sub>5</sub> diminished with decreasing pressure.

## Conclusions

The first LIF measurements of [OH] in the reaction zone of inhibited low pressure, opposed flow flames approaching extinction showed:

- There was a two-zone (blue and orange) luminous flame structure for a  $\text{Fe}(\text{CO})_5$  inhibited flame.
- [OH] levels decreased with increasing  $\text{Fe}(\text{CO})_5$  and  $\text{CF}_3\text{Br}$  concentrations added to the flames.
- $\text{Fe}(\text{CO})_5$  was about 10 times as effective a suppressant as  $\text{CF}_3\text{Br}$ .
- Addition of both chemically active and physically active inhibitors had relatively small effects on the locations of the OH maximum intensities and on the width of the [OH] distribution in the flame front. The weakest inhibitor had the largest effect.
- The addition of  $\text{Fe}(\text{CO})_5$  and  $\text{CF}_3\text{Br}$  slightly narrows the width of the flame reaction zone. The strongest inhibitor had the largest effect.
- Close to extinguishment, flames inhibited with both physically active and chemically active agents showed a 30 % reduction in peak OH concentration.

## Iron's Loss of Effectiveness through Particle Formation

If the gas phase inhibition mechanism of iron were the only consideration, it should be a very effective agent for extinguishing fires. However, NGP research with premixed flames<sup>102</sup> and counterflow diffusion flames<sup>108</sup> indicated that particle formation would limit the effectiveness of iron to those situations in which it was added at high concentration. Subsequent work showed that iron pentacarbonyl at low concentrations was much less effective in cup burner flames than was expected based on the results in premixed or counterflow diffusion flames.<sup>153</sup>

The effectiveness of iron as a flame inhibitor declines as the mole fraction at which it is added is increased. This lower effectiveness had been mentioned briefly by Jost and co-workers,<sup>88</sup> who surmised that a particle inhibition mechanism may be at work at high concentration. They also said that work was underway to understand the role of particle formation; however, subsequent papers did not appear. Many other flame inhibitors also showed lower effectiveness as their concentration increased.<sup>175</sup> However, the loss of effectiveness of iron is much more dramatic. Reinelt and Linteris<sup>103</sup> quantified the loss of effectiveness of iron for premixed and diffusion flames. Rumminger et al.<sup>104</sup> described a gas phase kinetic mechanism for iron inhibition, and showed that the loss of effectiveness was not predicted by a gas phase mechanism (ruling out low radical concentration as the reason for the loss of effectiveness). Linteris et al.<sup>107</sup> have recently described the performance of iron, tin, and manganese in cup burner flames. The loss of effectiveness of iron in each of these flame systems is described below.

Based on the encouraging results for the powerful flame inhibition properties of iron compounds, extinction experiments of ferrocene together with an inert compound generated by a solid propellant gas generator (SPGG) were conducted in an enclosure containing a spray flame.<sup>176</sup> The combination did not have the expected high efficiency. Although it was not possible to extract fundamental information concerning the lack of effectiveness for their flame configuration, the results of Holland and co-workers provided evidence for a loss of effectiveness for iron, and motivated a search for an explanation.

### Premixed Flames

For premixed flames, Figure 3-16 shows that the gas phase mechanism predicts a continuing decrease in the normalized burning velocity ( $S_L/S_{L, \text{uninhibited}}$ ) as  $[\text{Fe}(\text{CO})_5]$  increases, whereas the experiments show a leveling off. (Uncertainties in any experimental data cited throughout this chapter are discussed in the source publication.)

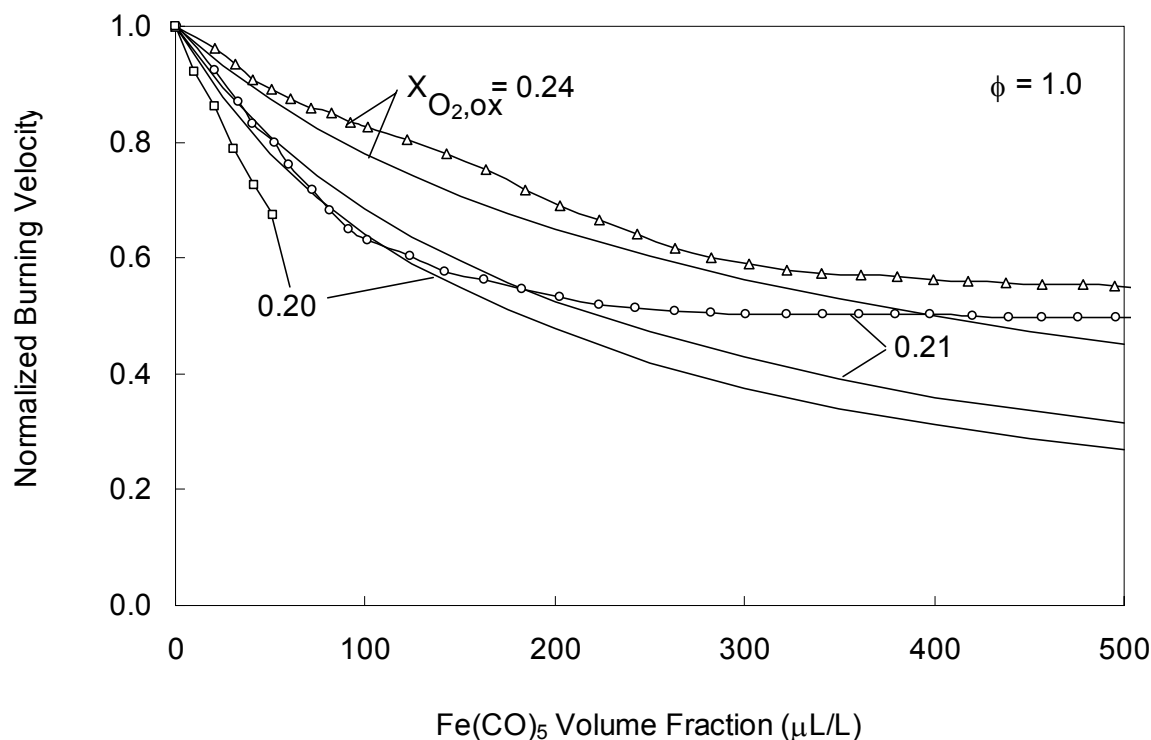


**Figure 3-16. Calculated and Measured Normalized Burning Velocity of Premixed  $\text{CH}_4/\text{O}_2/\text{N}_2$  Flames with  $X_{\text{O}_2, \text{ox}} = 0.20, 0.21, \text{ and } 0.24$  for  $\phi = 1.0$ .**<sup>104</sup>

Subsequent measurements of particles in the premixed flames showed that the loss of effectiveness of the iron was correlated with formation of particles (as illustrated in Figure 3-17 and Figure 3-18), and the scattering from the particles was correlated with the residence time in the flame (necessary for condensation to occur), as shown in Figure 3-19. In addition to measuring the particles with thermophoretic sampling and quantifying their size and agglomeration characteristics with transmission electron microscopy, they also calculated the maximum effect that the particles could have on the burning velocity. Constructing a “perfect heterogeneous inhibitor” model (in which any collision of a radical with a particle recombines the radical to a stable species), they showed that heterogeneous reactions cannot account for the measured flame speed reduction of  $\text{Fe}(\text{CO})_5$ .

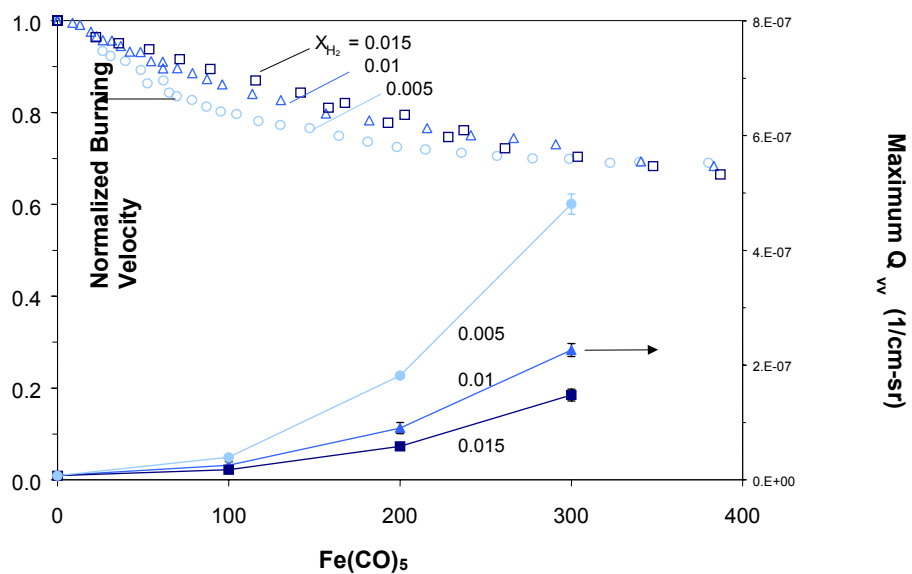


Figure 3-17. Normalized Burning Velocity<sup>103</sup> and Maximum Measured Scattering Signal  $Q_w^{102}$  for  $\phi=1.0$   $\text{CH}_4$  Flame with  $X_{\text{O}_2,\text{ox}} = 0.21$  and  $0.24$ .

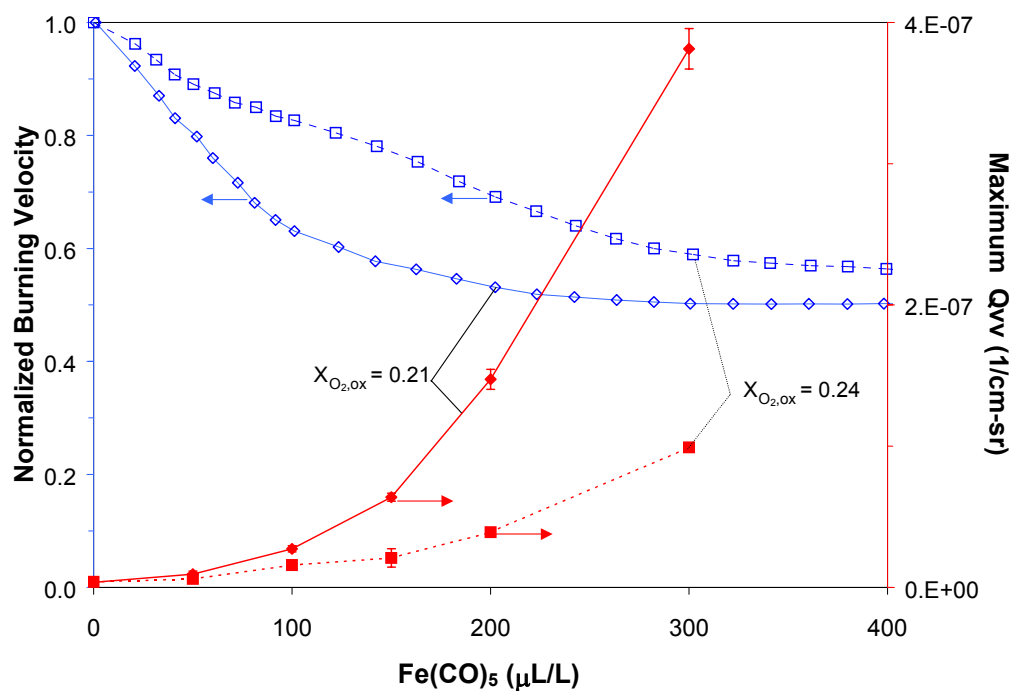
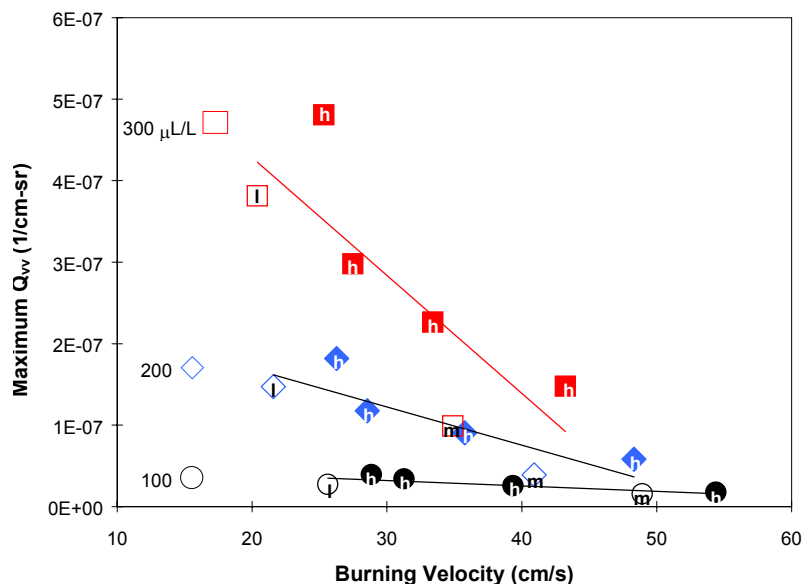
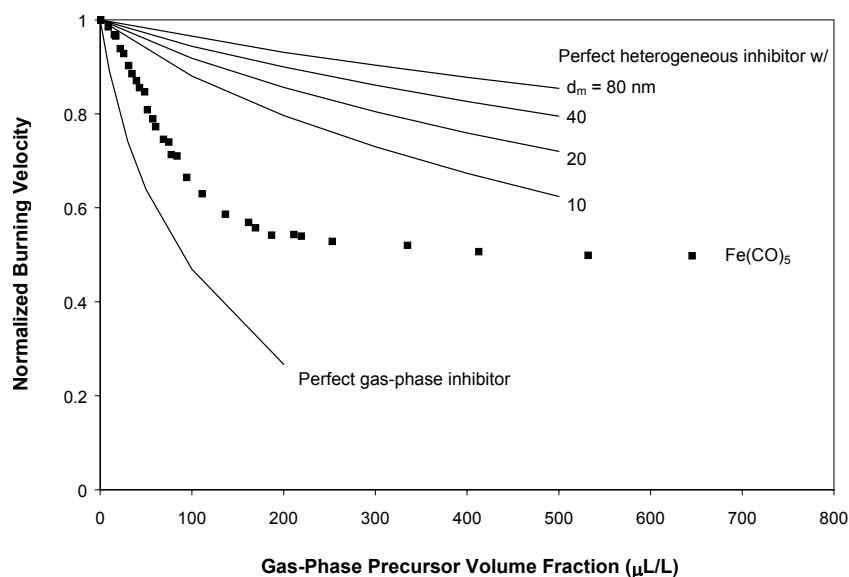


Figure 3-18. Maximum Scattering Signal and Normalized Burning Velocity<sup>118</sup> for  $\text{CO-H}_2$  Flames as  $\text{Fe}(\text{CO})_5$  Concentration Varies.<sup>102</sup>



**Figure 3-19. Maximum  $Q_{vv}$  for Flames of  $\text{CH}_4$  (open symbols) and  $\text{CO}$  (closed symbols) as a Function of the Burning Velocity. The letters correspond to the adiabatic flame temperature ( $l = 2220$  K,  $m = 2350$  K,  $h = 2470$  K); the symbol shape (square, diamond, and circle) corresponds to the loading of  $\text{Fe}(\text{CO})_5$ .**<sup>102</sup>

Figure 3-20 shows the experimental data for normalized flame speed reduction by  $\text{Fe}(\text{CO})_5$  along with the prediction for the perfect gas phase inhibitor and perfect heterogeneous inhibitor (for different assumed particle diameter sizes). As shown, the perfect gas phase inhibitor mechanism shows burning velocity reductions fairly close to that of  $\text{Fe}(\text{CO})_5$ ; whereas, the perfect heterogeneous mechanism does not show enough inhibition, about a factor of eight too low, even for perfect collisions with 10 nm particles. Interestingly, the slope of the  $\text{Fe}(\text{CO})_5$  curve in Figure 3-20 in the “flattening out” region is of the same order as that of the perfect 10 nm diameter particles. Hence, Jost et al.’s<sup>88</sup> postulate that the region of lower effectiveness may be due to radical recombination on particles surfaces may be true. Note also that the slope in the flat region is of the same order as that for  $\text{CF}_3\text{Br}$  in these premixed flames.



**Figure 3-20. Calculated Normalized Burning Velocity for Several Diameters,  $d_m$ , of Ideal Heterogeneous Inhibitor,  $\text{Fe}(\text{CO})_5$  data<sup>103</sup>, and Calculated Normalized Burning Velocity using the Perfect Gas Phase Inhibitor Mechanism.**<sup>102,167</sup>

### Counterflow Diffusion Flames

Similar experimental and modeling results were described for counterflow diffusion flames. As shown in Figure 3-21, the gas phase model predicts more inhibition at higher  $[\text{Fe}(\text{CO})_5]$  than do the experiments. Measured particle scattering signals again showed that the loss of effectiveness (and discrepancy between the measured and gas phase predicted inhibition) increased as particle scattering signal increased; i.e., particle formation was correlated with loss of effectiveness of the  $\text{Fe}(\text{CO})_5$  (Figure 3-22). It is important to note that in the counterflow diffusion flames, the propensity to form condensed-phase iron particles *in the flame region* was not the only mechanism shown to be correlated with loss of effectiveness of iron. If particles formed in one part of the flame, but were unable (due to entrainment or thermophoresis) to be transported to the reaction zone, the active iron species could be sequestered from the region in which they must be present to inhibit the flame. By adding the  $\text{Fe}(\text{CO})_5$  to either the fuel or air stream, and changing the flame location relative to the stagnation plane (by diluting the fuel or oxidizer with  $\text{N}_2$ ), Rumminger et al. clearly showed the effect of drag and thermophoretic forces on reducing particle (and hence iron) transport to the region of radical chain branching.

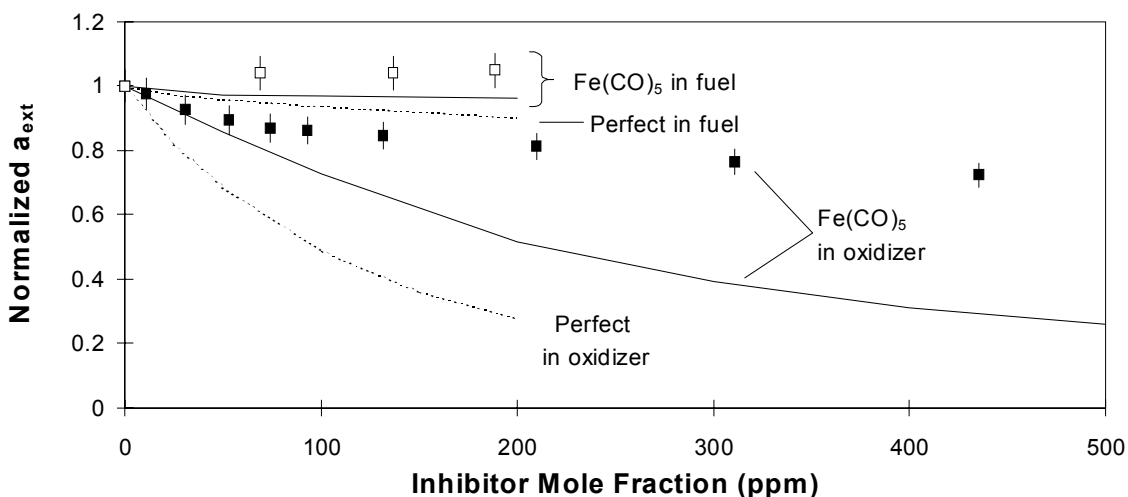


**Figure 3-21. Normalized Extinction Strain Rate for Counterflow Diffusion Flames. Closed symbols: measurements with the  $\text{Fe}(\text{CO})_5$  in the oxidizer; open symbols: measurements with  $\text{Fe}(\text{CO})_5$  in the fuel; solid lines: calculations with  $\text{Fe}(\text{CO})_5$ ; dashed lines: calculation with perfect inhibitor.**<sup>105</sup>

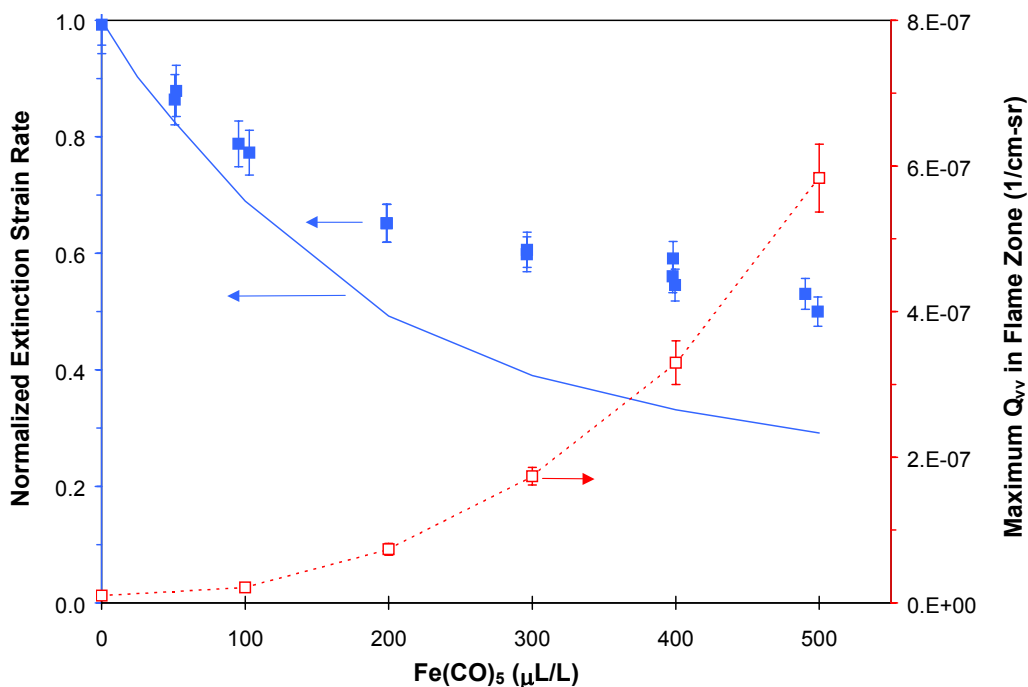


**Figure 3-22. Correlation between Inhibition Effect in Counterflow Diffusion Flames and Maximum Measured Scattering Signal  $Q_{vv}$ .** Filled points are experimental normalized  $a_{ext}$ , solid line is calculated  $a_{ext}$ .<sup>105</sup> Open symbols connected by dotted lines are maximum measured  $Q_{vv}$ . Particle data were collected at 75 % of  $a_{ext}$ .<sup>108</sup>

### Cup Burner Flames

Lintieris et al. tested  $Fe(CO)_5$ , TMT, and MMT in cup burner flames.<sup>85,86,153</sup> Based on the loss of effectiveness at higher  $Fe(CO)_5$  concentrations that was demonstrated in premixed and diffusion flames, it was not expected that iron pentacarbonyl alone would be effective in cup burner flames. However, several publications had suggested that a combination of a good catalytic agent and an inert agent would prove to be effective.<sup>14,91,118,175,177,178</sup> The premise was that the overall reaction rate would be lowered in part through radical recombination by the catalytic agent, and in part through the lower temperature caused by the added diluent. To test these suggestions, Lintieris et al. added  $Fe(CO)_5$ , MMT, or TMT to a cup burner of methane and air, and measured the amount of  $CO_2$  required for extinction.<sup>153</sup> This approach is conceptually the same as the classic oxygen index test used for assessing material flammability.<sup>135</sup> In that test, the oxygen volume fraction in the air stream at blowoff (i.e., the oxygen index) is determined for solid, liquid, or gaseous fuels with chemical additives in either the fuel or oxidizer.

Unfortunately, the effectiveness of  $CO_2$  combined with any of the metal agents was much less than anticipated. Figure 3-23 shows the measured  $CO_2$  volume fraction required for extinction as a function of the catalytic agent volume fraction in the air stream. Data are presented for  $Br_2$ ,  $CF_3Br$ ,  $Fe(CO)_5$ , MMT, and TMT. As shown, although the metals are still more effective than  $CF_3Br$  at low concentration, they are not nearly as effective as expected from the results in premixed and counterflow diffusion flames. The reasons for this loss of effectiveness are described below.

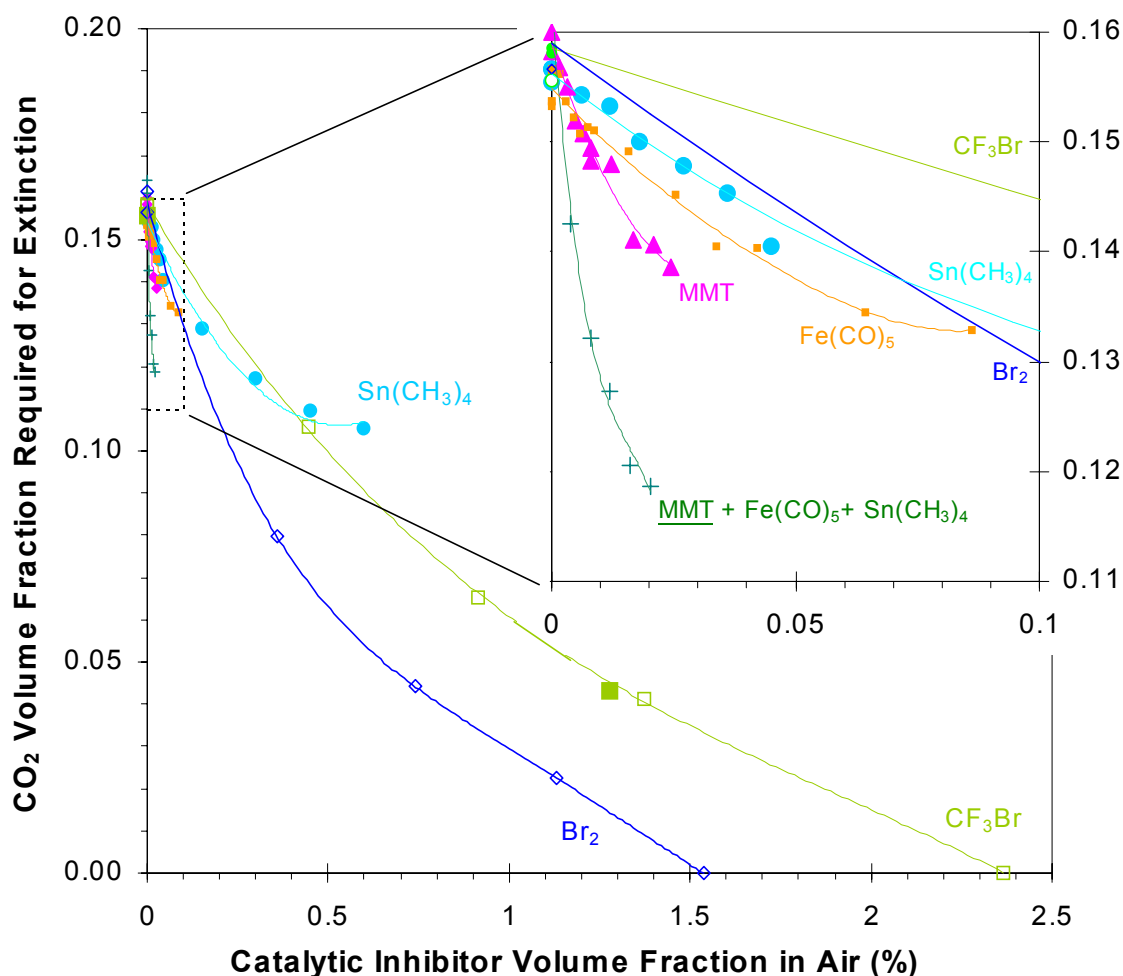


**Figure 3-23. Volume Fraction of CO<sub>2</sub> Required for Extinction ( $X_{\text{CO}_2, \text{ext}}$ ) of Methane-air Cup Burner Flames as a Function of the Volume Fraction of Catalytic Inhibitor Added to the Air Stream. Inset shows region in dotted box with expanded scales.<sup>153</sup>**

In order to understand the lower effectiveness of metals in cup burner flames compared to premixed and counterflow diffusion flames, several steps were taken. First, particle measurements were made in cup burner flames inhibited by Fe(CO)<sub>5</sub>. Shown in Figure 3-24 are scattering cross sections for laser light at 488 nm as a function of radial position and height above the burner in a methane-air cup burner flame with 8 % CO<sub>2</sub> and Fe(CO)<sub>5</sub> in air at four volume fractions.<sup>153</sup> The dotted lines show flame location from a digitized video image of the uninhibited flame. The figures indicated that particles were present both inside and outside (but not coincident with) the luminous flame zone, and that higher Fe(CO)<sub>5</sub> loadings produced higher particle scattering signals.

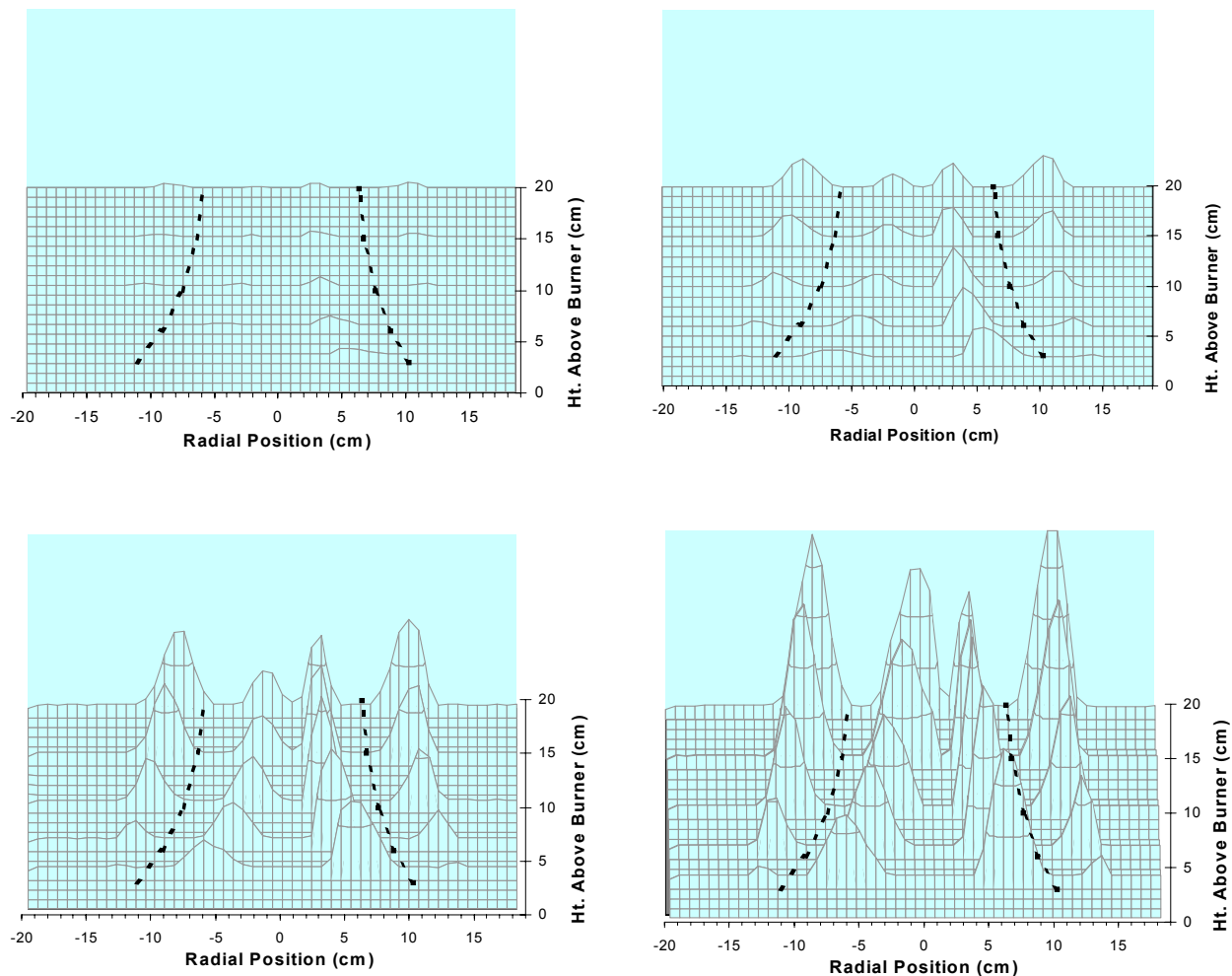


**Figure 3-24. Particle Light Scattering as a Function of Radial Position and Height above Cup Burner for Four Loadings of  $\text{Fe}(\text{CO})_5$ .**<sup>153</sup> Top left: 100  $\mu\text{L/L}$ , top right: 200  $\mu\text{L/L}$ , bottom left: 325  $\mu\text{L/L}$ , bottom right: 450  $\mu\text{L/L}$ .

In order to understand the particle formation and chemical inhibition, numerical modeling of the cup burner flames inhibited by  $\text{Fe}(\text{CO})_5$  were performed,<sup>153</sup> using the gas phase only numerical model developed previously. This model has predicted the blow-off condition of methane and air cup burner flames with added  $\text{CO}_2$ <sup>154</sup> and  $\text{CF}_3\text{H}$ .<sup>179</sup> The temperature field and the velocity vectors for methane-air cup burner flames with 10 %  $\text{CO}_2$ , and 0  $\mu\text{L/L}$  and 100  $\mu\text{L/L}$  of  $\text{Fe}(\text{CO})_5$  are shown in Figure 3-25, while Figure 3-26 shows the calculated blow-off behavior.

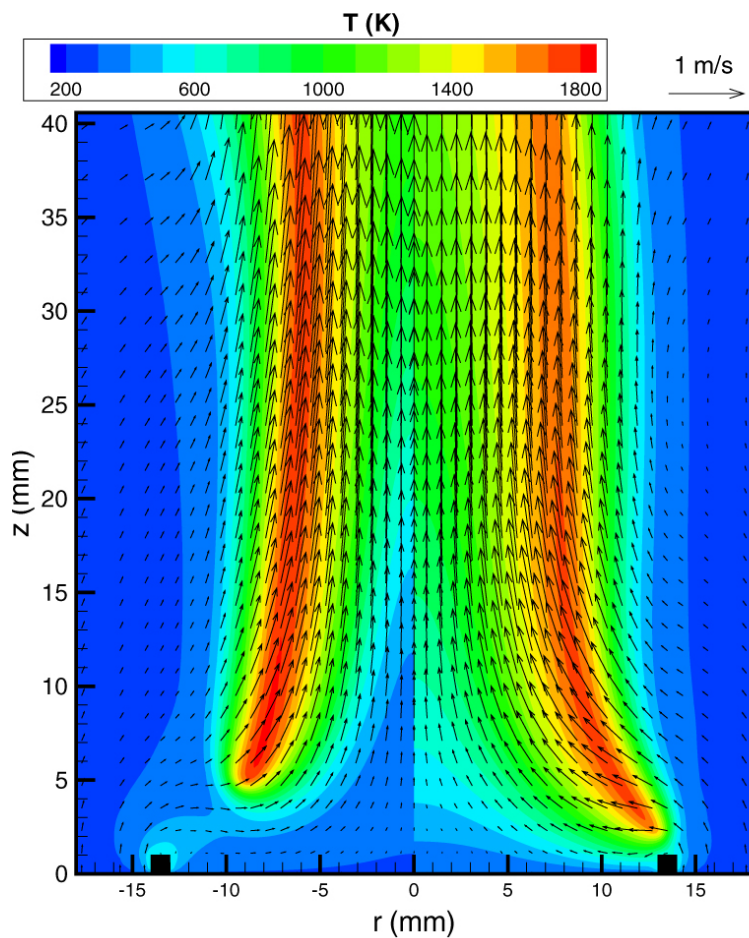


**Figure 3-25. Calculated Temperature (color scale) and Velocity Vectors (arrows) for Methane-air Cup Burner Flame with an Oxidizer Stream  $\text{CO}_2$  Volume Fraction of 0.1, with (left) and without (right) an Added  $\text{Fe}(\text{CO})_5$  Volume Fraction of  $100 \mu\text{L/L}$ .<sup>153</sup>**

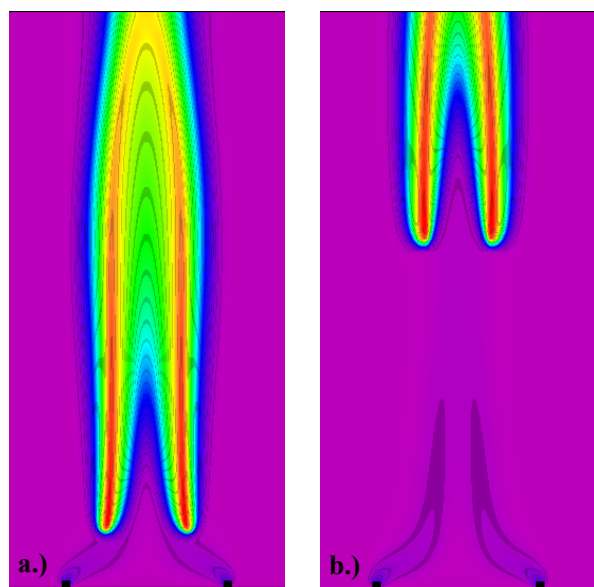


**Figure 3-26. Map of Calculated Temperatures in Cup Burner Methane-air Flames with 10 %  $\text{CO}_2$  in the Oxidizer Stream and (a) 0.011 and (b) 0.012  $\text{Fe}(\text{CO})_5$  Volume Fraction in the Air Stream, Illustrating the Blowoff Phenomenon.<sup>153</sup>**

As in other flame configurations, the loss of effectiveness of iron and a discrepancy between predicted (gas phase model) and measured effectiveness were both correlated with the formation of particles, as shown in Figure 3-27.

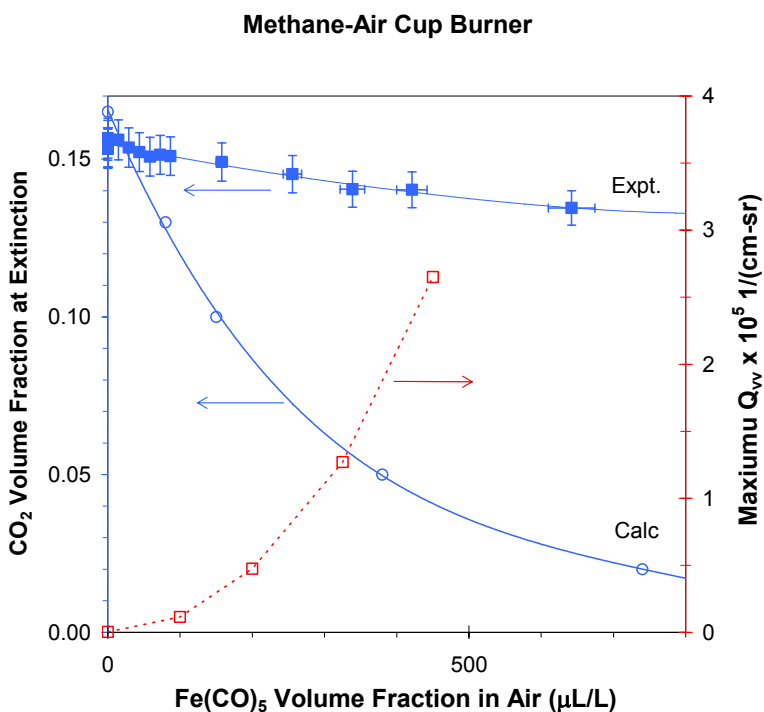


**Figure 3-27. Experimental and Calculated Extinction Volume Fraction of CO<sub>2</sub> (left axis) and Peak Measured Scattering Cross Section (right axis), as a Function of the Volume Fraction of Fe(CO)<sub>5</sub> in the Air Stream.**<sup>85,153</sup>

To understand the propensity for particle formation, the degree of supersaturation of some of the iron-containing intermediates was calculated through the flame, using the detailed flame structure obtained from the model, together with vapor pressure data available from the literature. For a height above the cup burner which passes through the flame kernel (i.e., the stabilization region), Figure 3-28 shows the radial profile of temperature and volume fractions of iron species and radicals, as well as the supersaturation ratio (which is the ratio of the calculated species partial pressure to the planar vapor pressure at the local conditions). The supersaturation ratio is highest for FeO, followed by Fe and Fe(OH)<sub>2</sub>, and the values decrease as the radial location of peak temperature is approached. Note that vapor pressure data for FeOH, FEOOH, and FeO<sub>2</sub> are not available, so their condensation potential has not been assessed. The condensation potential is strong since the temperature of the flame kernel is much lower than the relevant regions of premixed or counterflow diffusion flames.

Finally, the numerical model was extended to include calculation of the particle trajectory for inert particles added to the flame, including the effects of gravity, drag, and thermophoretic forces. This was done since early estimates<sup>180</sup> were that thermophoresis may have been driving the particles away from the flame region. The results of the calculations (Figure 3-29) show that near the flame base, there was some deviation of the particles both up and down around the reaction kernel; however, examination of the estimated radial and axial thermophoretic velocities shows them to have been much less than the gas velocity. Consequently, the particles still passed directly into the reaction kernel, so the effect of thermophoresis near this region is expected to be minor. Nonetheless, the other results described above provided evidence that the loss of effectiveness was due to particle formation.

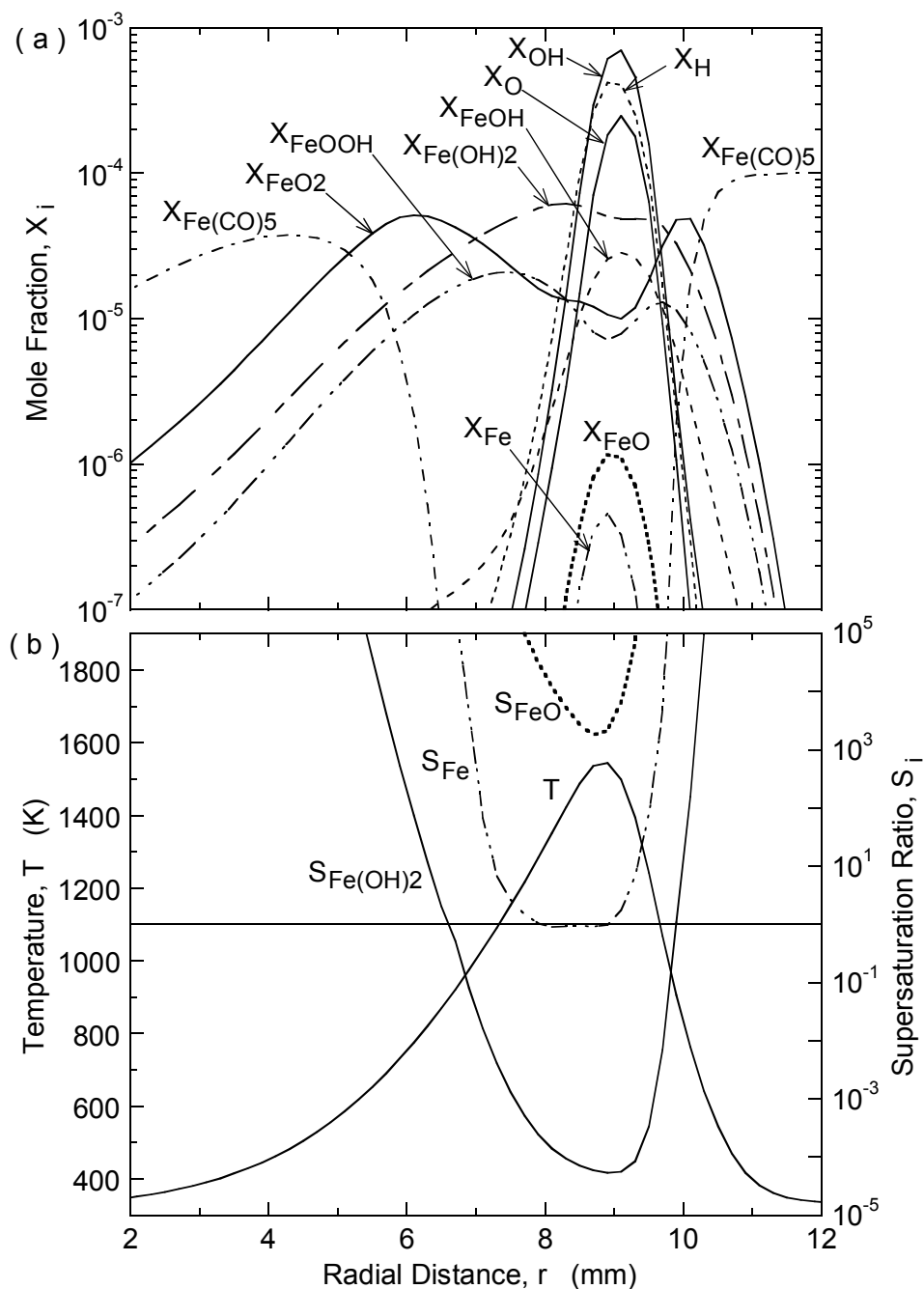


**Figure 3-28. (a) Calculated Volume Fractions,  $X_i$ , of Iron-containing and Other Major Species as a Function of Radial Position at 4.8 mm above the burner (corresponding to the location of the reaction kernel in the flame base); and (b) the Supersaturation Ratio,  $S_i$ , for Fe, FeO, and Fe(OH)<sub>2</sub>.**<sup>153</sup>

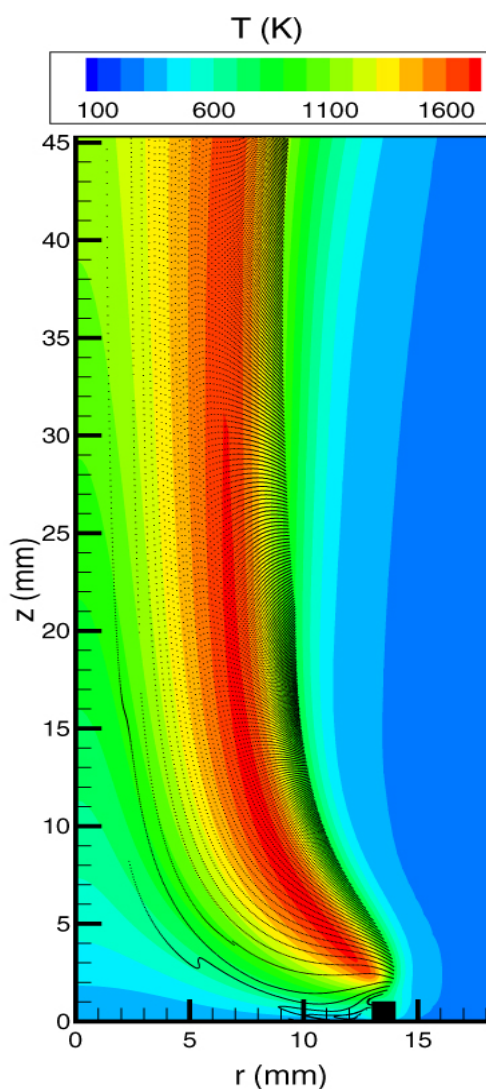


**Figure 3-29. Calculated Particle Trajectories for Free Molecular Regime Particles in a CH<sub>4</sub>-air Flame with 10 % CO<sub>2</sub> in the Oxidizer Stream.**<sup>153</sup>

A review of the results from previous work with particle formation in premixed, counterflow diffusion, and cup burner flames inhibited by Fe(CO)<sub>5</sub> outlined the importance of the following physical effects with respect to effective chemical inhibition:

- Gas phase transport of the active iron-containing species to the region of high H-atom concentration is necessary for efficient inhibition.
- Particle formation near the location of peak [H] can act as a sink for the iron-containing intermediate species and reduce the catalytic effect.
- The volume fraction of inhibitor influences condensation, since at low values, it may be below its saturation value.
- The available residence time affects particle growth.
- If the particles are small enough, they can re-evaporate upon passing into the high temperature region of the flame.
- Thermophoretic forces can be large in the flame and re-distribute particles away from peak [H].

- Convection and drag forces combined with the existing flow field in the flame can prevent particles from reaching the region of peak [H].
- The flame temperature of the stabilization region of cup burner flames is much lower than in premixed or counterflow diffusion flames, exacerbating the condensation potential.

In order to assess the condensation potential of other flame inhibiting metals, it is necessary to know their concentrations in the flame, as well as their local vapor pressure. The availability of these data for the metals listed in Table 3-4 is discussed below.

### 3.3.4 Flame Inhibition by Tin and Manganese

#### Introduction

Faced with the finding that the highly effective flame inhibitor iron pentacarbonyl loses its effectiveness due to condensation of the active species to particles, it became important for the NGP to determine if other metal-containing compounds caused similar strong flame inhibition while not suffering from the loss of effectiveness. Since there had been evidence that manganese- and tin-containing compounds were of high flame inhibition efficiency and since these compounds typically have higher vapor pressures than the corresponding iron compounds, these two families became a subject of NGP research.

Tin compounds are used as fire retardant additives for polymers, and as agents to reduce smoke and CO formation.<sup>127,181</sup> The mechanism of flame inhibition has been attributed to both the promotion of condensed phase char and gas phase flame inhibition.<sup>181,182</sup> Lask and Wagner<sup>34</sup> found  $\text{SnCl}_4$  to be about 1/34 as effective as  $\text{Fe}(\text{CO})_5$  at reducing the burning velocity of premixed n-hexane-air flames by 30 %, and Miller et al.<sup>112</sup> found it to be about 2/3 as effective as  $\text{Fe}(\text{CO})_5$  at reducing the flame speed of hydrogen-air flames by 80 %. Miller<sup>113</sup> measured the amount of inhibitor required to lift-off a premixed  $\text{CH}_4/\text{O}_2/\text{N}_2$  flat flame at low pressure, and found that tetramethyltin ( $\text{Sn}(\text{CH}_3)_4$ , TMT) and  $\text{SnCl}_4$  required a mole fraction of 1.7 % and 1.1 %, respectively; whereas  $\text{Fe}(\text{CO})_5$  and  $\text{Br}_2$  required 0.23 % and 2.3 %, respectively. Morrison and Scheller<sup>111</sup> investigated the effect of 20 flame inhibitors on the ignition of hydrocarbon mixtures by hot wires, and found that  $\text{SnCl}_4$  was the most effective inhibitor tested for increasing the ignition temperature; whereas the powerful flame inhibitors  $\text{CrO}_2\text{Cl}_2$  and  $\text{Fe}(\text{CO})_5$  had no effect on the ignition temperature. As a result of these studies,  $\text{SnCl}_4$  was recommended as a compound deserving further study.<sup>183</sup>

The effects of manganese compounds on flames had also been studied. Vanpee and Shirodkar<sup>92</sup> investigated the influence of many metal chlorides and metal acetates and acetylacetonates on the limiting oxygen index at extinction in a partially premixed counterflow pool burner of ethanol and air. In their experiments, the inhibitor was dissolved in ethanol, which was aspirated into the air stream. They found manganese acetylacetonate to be more effective than acetylacetonates of iron or chromium. Westblom et al.<sup>148</sup> analyzed the consequence of trace amounts of methylcyclopentadienylmanganese tricarbonyl ( $\text{CH}_3\text{C}_5\text{H}_4\text{Mn}(\text{CO})_3$ , MMT) on the flame structure of a premixed propane-air flame at 5.33 kPa, but found no measurable effect. They suggested a kinetic model for the influence of MMT on those flames.<sup>148</sup> In a review article, Howard and Kausch<sup>127</sup> reported that manganese-containing compounds were among the most effective soot-reducing fuel additives. Finally, MMT is a known antiknock agent for gasoline,<sup>184</sup> and an NGP panel<sup>185</sup> suggested manganese compounds as agents for further consideration in studies of fire suppression performance.

This section presents NGP data on flame inhibition by manganese- and tin-containing compounds. The additive influence was analyzed through the effects on the laminar burning velocity of methane-air mixtures for different equivalence ratios and oxygen mole fractions. The kinetic mechanisms of flame inhibition were analyzed by comparing simulation results with experimental data. The relative inhibition efficiencies of TMT, MMT,  $\text{Fe}(\text{CO})_5$ , and  $\text{CF}_3\text{Br}$  were deduced and analyzed. While the manganese and tin compounds tested are too toxic to be used directly as fire suppressants, they provide convenient means for introducing Mn and Sn to a flame, so that the inhibition mechanisms of these elements can be studied.

## Experimental Apparatus

Premixed flames were used for the first tests of new metallic inhibitors. The premixed burning velocity is a fundamental parameter describing the overall reaction rate, heat release, and heat and mass transport in the flame. Furthermore, the inhibitor reaches the reaction zone by convection, so that the amount which enters is unambiguous. The experiments are rapid and relatively straightforward, allowing tests over a wide range of conditions. The flames are easily modeled with existing numerical codes, so that detailed information on the mechanism of chemical inhibition can be determined. There is also a very large data base on the effectiveness of other chemical and inert inhibitors in premixed flames for comparison.

The laminar flame speed  $S_L$  in a premixed flame provides a measure of an agent's reduction of the global reaction rate. While good techniques exist which allow measurement of burning velocity under conditions of controlled stretch rates,<sup>186</sup> they require seeding with particles for determination of the local gas velocity. Since the presence of particles would influence the condensation rates of metallic species, these tests instead employed the total area method with a Bunsen-type flame.<sup>187</sup> The experimental arrangement, described in detail elsewhere,<sup>57,102,106,118,164</sup> was modified to accommodate new evaporators for TMT and MMT. A Mache-Hebra nozzle burner (1.0 cm  $\pm$  0.05 cm diameter) produced a premixed Bunsen-type flame about 1.3 cm tall with a straight-sided schlieren image that was captured by a video frame-grabber board in a PC. Digital mass flow controllers held the oxygen mole fraction in the oxidizer stream  $X_{O_2,ox}$ , the equivalence ratio  $\phi$ , and the flame height constant while maintaining the inlet mole fraction of the inhibitor ( $X_{in}$ ) at the desired value. The average burning velocity was determined from the reactant flows and the schlieren image using the total area method. The fuel gas was methane (Matheson UHP, 99.9 %), and the oxidizer stream consisted of nitrogen (boil-off from liquid  $\text{N}_2$ ) and oxygen (MG Industries,  $\text{H}_2\text{O}$  less than 50  $\mu\text{L/L}$ , and total hydrocarbons less than 5  $\mu\text{L/L}$ ). The inhibitors used were  $\text{Fe}(\text{CO})_5$  (Aldrich), TMT (Alfa Aesar), MMT (Alfa Aesar),  $\text{CF}_3\text{Br}$  (Great Lakes),  $\text{N}_2$  (boil-off), and  $\text{CO}_2$  (Airgas). The catalytic agents were liquids at laboratory conditions. Since they were required in low mole fraction, they were added to the flame in gaseous form rather than as droplets. The  $\text{Fe}(\text{CO})_5$  was added to the carrier gas using a two-stage saturator in an ice bath.<sup>118</sup> Nitrogen was the carrier gas for all agents. The TMT was added using an identical two-stage saturator, with a volume of liquid TMT in each stage greater than 50  $\text{cm}^3$  for all tests. The ice bath was maintained at (0  $\pm$  0.2)  $^\circ\text{C}$  with a maximum carrier gas flow 0.40 L/min. Because of the toxicity of the agents, the  $\text{Fe}(\text{CO})_5$  and TMT saturators, as well as the premixed flame burner, were located in fume hoods. For the MMT, the saturator had three stages, each 20 cm long, 2.36 cm I.D. stainless steel tube, and the entire apparatus was submerged in a controlled temperature bath (Neslab), and vented. The bath temperature was typically (79.2  $\pm$  0.1)  $^\circ\text{C}$ , and the carrier gas flow for this saturator was always <0.5 L/min. The mole fraction of the organometallic inhibitors in the air stream was calculated based on the measured air flow, measured carrier gas flow, and vapor pressure of the agent at the bath temperature, assuming saturated carrier gas. The parameters in the Antoine equation,  $\log_{10}(P)=A-B/(T+C)$  (T in  $^\circ\text{C}$ , P in bar), were (A,B,C): (6.77273, 4.0932, 7.2283),

(1258.22, 1286.16, 1882), and (211.587, 235.846, 200) for  $\text{Fe}(\text{CO})_5$ ,<sup>188</sup> TMT,<sup>189</sup> and MMT,<sup>190</sup> respectively. Since the vapor pressure of MMT is much lower than that of the other agents, experiments with MMT were conducted at a slightly elevated temperature, with the transfer lines and inlet gases maintained at  $(80 \pm 3)^\circ\text{C}$  and the burner tube maintained at  $(80 \pm 1)^\circ\text{C}$ . For the experiments with TMT and  $\text{Fe}(\text{CO})_5$ , the inlet gas temperature  $T_{\text{in}}$  was  $(294.2 \pm 1)$  K. Although the absolute value of the burning velocity is quite sensitive to the inlet temperature, comparisons of agent performance across this range of differing gas inlet temperatures is valid, since the *reduction* in the *normalized* burning velocity with agent addition was relatively insensitive in  $T_{\text{in}}$ . For example, calculations for inhibition by TMT (discussed below), and calculations and experiments with  $\text{CO}_2$  (unpublished data of Reference 106) showed that changing the inlet gas temperature from 294 K to 353 K provided nearly identical curves of normalized burning velocity versus inhibitor mole fraction, differing from each other by less than 2 % for the two inlet temperatures.

Tests were performed for ranges of equivalence ratio and oxygen mole fraction in the oxidizer stream  $X_{\text{O}_2, \text{ox}}$ . The agent mole fraction was calculated relative to the total reactant flow. The test conditions are listed in Table 3-6. The inhibitor for which each of the test conditions was used is included for reference; the values in the table are for uninhibited flames only. Note that while the inlet temperature for the  $\text{Fe}(\text{CO})_5$  and TMT experiments was 294 K, the experimental and numerically calculated burning velocities in the table have been converted to equivalent values at 298 K to facilitate comparison with other values available in the literature.

**Table 3-6. Uninhibited Laminar Burning Velocities  $S_L$  and Adiabatic Flame Temperatures  $T_{\text{AFT}}$  from 1-D Planar Numerical Calculations, Together with the Average Burning Velocity Measured in the Bunsen-type Flames.**

Inhibitor(s)	$\phi$	$X_{\text{O}_2, \text{ox}}$	$T_{\text{in}}$ K	$T_{\text{AFT}}$ K	$S_{L, \text{calc}}$ cm/s	$S_{L, \text{exp}}$ cm/s
TMT	0.9	0.21	298	2159	35.3	$33.9 \pm 1.3$
	1.0	“	“	2235	39.6	$38.0 \pm 2.3$
	1.1	“	“	2193	39.8	$38.0 \pm 1.5$
	1.0	0.20	“	2185	34.7	$33.6 \pm 1.4$
	“	0.244	“	2377	57.0	$58.0 \pm 3.4$
MMT	0.9	0.21	353	2177	48.0	$47.2 \pm 1.5$
	1.0	“	“	2264	53.2	$52.9 \pm 2.9$
	1.1	“	“	2251	53.6	$52.8 \pm 2.0$
	1.0	0.19	“	2167	41.3	$39.9 \pm 1.6$
	“	0.2	“	2220	47.4	$45.5 \pm 1.7$
	“	0.244	“	2396	74.3	$74.7 \pm 4.1$
MMT and $\text{Fe}(\text{CO})_5$	1.0	0.244	353	2396	74.3	$75.9 \pm 4.9$

The burning velocity in Bunsen-type flames is known to vary at the tip and base of the flame; however, these effects are most important over a small portion of the flame. Several steps were taken to minimize the influence of curvature and stretch on interpretation of the action of the chemical inhibitor.

- Use of the schlieren image for the flame area, which was maintained at a constant size (1.3 cm tall) for all tests.
- Normalization of the burning velocity of inhibited flames, i.e., the burning velocity of the inhibited flame divided by the burning velocity of the uninhibited flame, in order to reduce the error caused by flame curvature and stretch.
- Limiting interpretation of the data to inhibitor loading which produced less than 40 % reduction in flame speed.

Determination of the uncertainties in the experimental data using the present apparatus has been described in detail elsewhere.<sup>118</sup> For the present data, the uncertainty (expanded uncertainties with a coverage factor of 2) in the normalized burning velocity were less than  $\pm 5\%$  for all cases. The uncertainty in the equivalence ratio was 1.4 %. Neglecting the uncertainties (unspecified) in the vapor pressure correlation for  $\text{Fe}(\text{CO})_5$ , TMT, and MMT, uncertainties in the bath temperature, ambient pressure and carrier gas flow rate yielded an inhibitor mole fraction uncertainty of 6.5 %.

### Kinetic Mechanisms and Numerical Modeling

There are few data on the chemical kinetics of tin compounds at flame temperatures, although kinetics studies of tin have been conducted for chemical vapor deposition. Studies with  $\text{H}_2\text{-O}_2\text{-N}_2$  flames by Bulewicz and Padley<sup>191</sup> indicated that tin was present as Sn, SnO, and SnOH, with SnO overwhelmingly predominant. Recent spectroscopic data also indicated that tin was present in flames as Sn, SnO, and SnOH,<sup>192</sup> with SnO accounting for approximately 97 % by volume of all tin species.

The present kinetic model for flame inhibition by tin compounds contains reactions of the species Sn,  $\text{SnO}_2$ , SnO, SnH and SnOH. The reaction set was based on the consideration of possible reactions of tin-containing species with the radical pool and with the main species of methane combustion. The mechanism, listed in Table 3-7, consists of 37 reactions of tin-containing species. Rate constants were obtained from the literature when available, or otherwise estimated using empirical procedures and analogies with similar reactions. The reverse rates of the reactions in Table 3-7 were calculated from the forward rate and the equilibrium constant. It was assumed that tin (and manganese) species are non-reactive with hydrocarbon molecules. In the model development, estimates of rate constants were first made, and then the rates of the most important reactions were adjusted (based on sensitivity analysis) to provide agreement with the experimental results. The decomposition of TMT was described by the overall step listed in Table 3-7, but using the rate constant for the reaction  $\text{Sn}(\text{CH}_3)_4 \rightarrow \text{Sn}(\text{CH}_3)_3 + \text{CH}_3$ .<sup>193</sup> Enthalpies of formation for the tin-containing (and manganese-containing) species are presented in Table 3-8. Enthalpies of formation for SnOH and SnH were estimated based on bond energies from References 191 and 194.

**Table 3-7. Reaction Rate Data for Tin Inhibition of Premixed Methane-air Flames.**  
( $k = A T^b \exp(-E/RT)$ , mole, s, cm, kJ)

No.	Reaction	A	b	E	Reference
1	$\text{SnC}_4\text{H}_{12} \Rightarrow \text{Sn} + \text{C}_2\text{H}_6 + \text{C}_2\text{H}_6$	7.94E+13	0.0	230.	193
2	$\text{Sn} + \text{H} + \text{M} = \text{SnH} + \text{M}$	1.00E+15	0.0	0.0	a
3	$\text{Sn} + \text{OH} + \text{M} = \text{SnOH} + \text{M}$	5.36E+18	-0.45	0.0	*
4	$\text{Sn} + \text{OH} = \text{SnO} + \text{H}$	1.00E+13	0.0	27.2	a
5	$\text{Sn} + \text{O} + \text{M} = \text{SnO} + \text{M}$	1.00E+17	0.0	0.0	a
6	$\text{Sn} + \text{O}_2 = \text{SnO} + \text{O}$	3.07E11	0.79	3.63	195
7	$\text{Sn} + \text{O}_2 (+\text{M}) = \text{SnO}_2 (+\text{M})$	2.00E+13	0.0	0.0	a
	Low pressure limit:	1.5E+18	0.0	16.7	
8	$\text{Sn} + \text{HCO} = \text{SnH} + \text{CO}$	3.00E+13	0.0	0.0	a
9	$\text{Sn} + \text{CH}_3\text{O} = \text{SnO} + \text{CH}_3$	2.00E+13	0.0	0.0	a
10	$\text{Sn} + \text{CO}_2 = \text{SnO} + \text{CO}$	1.39E+14	0.0	75.6	195
11	$\text{Sn} + \text{HO}_2 = \text{SnO} + \text{OH}$	1.00E+13	0.0	0.0	a
12	$\text{SnO} + \text{H} + \text{M} = \text{SnOH} + \text{M}$	5.50E+17	0.0	0.0	a
13	$\text{SnO} + \text{O} + \text{M} = \text{SnO}_2 + \text{M}$	1.00E+20	-1.0	0.0	a
14	$\text{SnO} + \text{HCO} = \text{SnOH} + \text{CO}$	9.30E+13	0.0	0.0	a
15	$\text{SnO} + \text{HO}_2 = \text{SnOH} + \text{O}_2$	3.00E+13	0.0	29.3	a
16	$\text{SnO}_2 + \text{H} = \text{SnO} + \text{OH}$	1.00E+14	0.0	8.37	a
17	$\text{SnO}_2 + \text{OH} = \text{SnOH} + \text{O}_2$	3.00E+12	0.0	31.4	a
18	$\text{SnO}_2 + \text{OH} = \text{SnO} + \text{HO}_2$	3.00E+12	0.0	46.0	a
19	$\text{SnO}_2 + \text{O} = \text{SnO} + \text{O}_2$	3.00E+13	0.0	8.37	a
20	$\text{SnO}_2 + \text{CH}_3 = \text{SnO} + \text{CH}_3\text{O}$	3.00E+12	0.0	18.8	a
21	$\text{SnO}_2 + \text{CO} = \text{SnO} + \text{CO}_2$	2.00E+12	0.0	20.9	a
22	$\text{SnOH} + \text{H} = \text{Sn} + \text{H}_2\text{O}$	1.20E+12	0.0	12.6	a
23	$\text{SnOH} + \text{H} = \text{SnO} + \text{H}_2$	7.10E+13	0.0	4.18	a
24	$\text{SnOH} + \text{OH} = \text{SnO} + \text{H}_2\text{O}$	6.30E+13	0.0	0.0	a
25	$\text{SnOH} + \text{O} = \text{SnO} + \text{OH}$	3.00E+13	0.0	0.0	a
26	$\text{SnOH} + \text{O} = \text{SnO}_2 + \text{H}$	5.00E+12	0.0	37.7	a
27	$\text{SnOH} + \text{CH}_3 = \text{SnO} + \text{CH}_4$	2.00E+13	0.0	4.18	a
28	$\text{SnH} + \text{H} = \text{Sn} + \text{H}_2$	5.00E+13	0.0	4.18	a
29	$\text{SnH} + \text{OH} = \text{Sn} + \text{H}_2\text{O}$	3.00E+13	0.0	0.0	a
30	$\text{SnH} + \text{OH} = \text{SnOH} + \text{H}$	5.00E+12	0.0	20.9	a
31	$\text{SnH} + \text{O} + \text{M} = \text{SnOH} + \text{M}$	1.00E+15	0.0	0.0	a
32	$\text{SnH} + \text{O} = \text{Sn} + \text{OH}$	5.00E+13	0.0	4.18	a
33	$\text{SnH} + \text{O} = \text{SnO} + \text{H}$	8.00E+12	0.0	4.18	a
34	$\text{SnH} + \text{CH}_3 = \text{CH}_4 + \text{Sn}$	5.00E+13	0.0	4.18	a
35	$\text{SnH} + \text{HCO} = \text{Sn} + \text{CH}_2\text{O}$	2.00E+12	0.0	18.8	a
36	$\text{SnH} + \text{O}_2 = \text{SnO} + \text{OH}$	3.00E+12	0.0	29.3	a

a Estimates

\* By analogy with reactions of K species in Reference 196

**Table 3-8. Thermodynamic Properties of Tin- and Manganese-containing Species (298 K).**

Species	Enthalpy of Formation kJ/mol	Entropy J/(mol K)	Heat Capacity J/(mol K)	Reference
Mn	283.6	173.6	20.8	197
MnO	161.7	236.0	31.7	197
MnO <sub>2</sub>	23.01	269.3	42.2	197
MnOH	17.32	250.3	45.8	197
Mn(OH) <sub>2</sub>	-373.2	291.2	67.1	e, 198
MnOOH	-116.3	283.3	53.9	e, 198
MnH	197.9	213.6	29.6	197
MMT	-439.3	401.7	149.9	198
Sn	301.2	168.4	21.3	197
SnO	21.91	232.1	31.8	197
SnO <sub>2</sub>	11.69	251.5	49.5	197
SnOH	-15.06	244.8	46.0	e, 191
SnH	268.2	214.7	29.7	e, 194
Sn(CH <sub>3</sub> ) <sub>4</sub>	-17.70	361.2	137.8	199,178
Sn <sub>2</sub>	425.4	267.2	42.1	197

a Estimates

The kinetic mechanism for studying the influence of manganese additives in premixed methane-air flames is presented in Table 3-9. The list of possible Mn-containing species participating in inhibition reactions includes Mn, MnH, MnO, MnOOH, MnHOH, MnOH, MnO, MnO<sub>2</sub> and Mn(OH)<sub>2</sub>. All species except MnH and MnHOH were considered in the mechanism of Smith.<sup>198</sup> The role of MnOH and MnO in radical recombination was discussed by Bulewicz and Padley<sup>116</sup>, and the species MnO and Mn were recently measured in a low pressure propane flame doped by MMT.<sup>148</sup> Hildenbrand and Lau<sup>200</sup> used mass spectrometry to identify the species MnO<sub>2</sub>, MnOH, and Mn(OH)<sub>2</sub>. MnH was included in the current model since equilibrium calculations showed it to be present in significant quantities in MMT-inhibited flames.

The manganese inhibition reaction set was reduced from an initial list of approximately 160 reactions to 61 reactions based on thermochemical considerations and preliminary calculations. The decomposition of MMT followed the overall description suggested in References 148 and 198, and used their rate constants for the Mn-species reactions whenever possible. Rate constants for the remaining reactions were estimated by analogy and based on thermochemical estimates. The main assumptions were the formation of MnO<sub>2</sub> through the reaction of Mn atom with oxygen molecule and the formation of Mn(OH)<sub>2</sub> via reaction of MnO with water (both by analogy to reactions of iron-containing species<sup>104</sup>).

The transport parameters of tin- and manganese-containing species were estimated through analogy with similar metallic species, or based on molecular weight correlations for similar species.

Kinetic models for highly effective flame inhibitors can be considered to consist of two sub-models. The first sub-model includes reactions for the agent decomposition and formation of the active inhibiting species, and the second includes the inhibition reactions. In previous work, it was shown that for the phosphorus-containing compound DMMP and for ferrocene, the decomposition reactions have a small influence on the predicted inhibitor efficiency as long as the overall activation energy of decomposition is less than 250 kJ/mol to 335 kJ/mol.<sup>106,201</sup> In the present work, this was also found to be true for TMT and MMT decomposition.

**Table 3-9. Reaction Rate Data for Manganese Inhibition of Premixed Methane-air Flames.**  
( $k = A T^b \exp(-E/RT)$ , mole, cm, s, kJ)

No.	Reaction	A	b	E	Reference
1	Mn+H+M = MnH+M	1.00E+15	0.0	0.0	a
2	Mn+OH+M = MnOH+M	8.00E+22	-2.2	0.0	198
3	Mn+O+M = MnO+M	1.00E+15	0.0	0.0	a
4	Mn+O <sub>2</sub> = MnO+O	2.50E+14	0.0	125.5	198
5	Mn+O <sub>2</sub> (+M) = MnO <sub>2</sub> (+M)	2.00E+13	0.0	0.0	a
	Low pressure limit:	1.50E+18	0.0	12.6	
6	Mn+HCO = MnH+CO	3.00E+13	0.0	0.0	a
7	MnO+H+M = MnOH+M	7.00E+15	0.0	0.0	198
8	MnO+O+M = MnO <sub>2</sub> +M	2.00E+19	-1.0	0.0	198
9	MnO+H = Mn+OH	1.00E+14	0.0	16.7	a
10	MnO+OH+M = MnOOH+M	3.00E+17	0.0	0.0	a
11	MnO+CH <sub>3</sub> = Mn+CH <sub>3</sub> O	1.00E+14	0.0	29.3	a
12	MnO+H <sub>2</sub> = Mn+H <sub>2</sub> O	3.00E+12	0.0	20.9	202
13	MnO+H <sub>2</sub> O = MnO <sub>2</sub> H <sub>2</sub>	5.40E+12	0.0	0.0	202
14	MnO+CO = Mn+CO <sub>2</sub>	3.00E+11	0.0	0.0	198
15	MnO+HCO = MnOH+CO	2.40E+13	0.0	0.0	198
16	MnO+CH <sub>2</sub> OH = MnOH+CH <sub>2</sub> O	2.40E+13	0.0	0.0	198
17	MnO <sub>2</sub> +H+M = MnOOH+M	2.00E+22	-1.5	0.0	198
18	MnO <sub>2</sub> +H = MnO+OH	1.00E+14	0.0	29.3	a
19	MnO <sub>2</sub> +OH = MnOH+O <sub>2</sub>	3.00E+12	0.0	29.3	a
20	MnO <sub>2</sub> +O = MnO+O <sub>2</sub>	5.00E+13	0.0	8.37	a
21	MnO <sub>2</sub> +CO = MnO+CO <sub>2</sub>	2.00E+12	0.0	20.9	a
22	MnOH+H = Mn+H <sub>2</sub> O	1.20E+12	0.0	2.09	198
23	MnOH+H = MnO+H <sub>2</sub>	3.00E+13	0.0	4.18	a
24	MnOH+OH+M = MnO <sub>2</sub> H <sub>2</sub> +M	1.00E+23	-2.0	0.0	198
25	MnOH+OH = MnO+H <sub>2</sub> O	1.00E+13	0.0	6.28	198
26	MnOH+O+M = MnOOH+M	1.00E+18	0.0	0.0	a
27	MnOH+O = Mn+HO <sub>2</sub>	3.00E+13	0.0	71.1	a
28	MnOH+O = MnO+OH	3.00E+13	0.0	0.0	198

No.	Reaction	A	b	E	Reference
29	$\text{MnOH} + \text{O} = \text{MnO}_2 + \text{H}$	5.00E+12	0.0	37.7	a
30	$\text{MnOH} + \text{CH}_3 = \text{MnO} + \text{CH}_4$	2.00E+13	0.0	12.6	a
31	$\text{MnOOH} + \text{H} + \text{M} = \text{MnO}_2\text{H}_2 + \text{M}$	1.00E+16	0.0	0.0	a
32	$\text{MnOOH} + \text{H} = \text{MnO} + \text{H}_2\text{O}$	2.00E+13	0.0	0.0	a
33	$\text{MnOOH} + \text{H} = \text{MnOH} + \text{OH}$	3.00E+13	0.0	20.9	a
34	$\text{MnOOH} + \text{H} = \text{MnO}_2 + \text{H}_2$	1.00E+13	0.0	16.7	a
35	$\text{MnOOH} + \text{OH} = \text{MnO}_2 + \text{H}_2\text{O}$	6.00E+12	0.0	6.28	198
36	$\text{MnOOH} + \text{O} = \text{MnOH} + \text{O}_2$	2.00E+13	0.0	10.5	a
37	$\text{MnOOH} + \text{O} = \text{MnO} + \text{HO}_2$	3.00E+12	0.0	66.9	a
38	$\text{MnOOH} + \text{O} = \text{MnO}_2 + \text{OH}$	3.00E+13	0.0	18.8	a
39	$\text{MnOOH} + \text{CH}_3 = \text{MnO} + \text{CH}_3\text{OH}$	3.00E+12	0.0	31.4	a
40	$\text{MnOOH} + \text{CH}_3 = \text{MnOH} + \text{CH}_3\text{O}$	1.00E+13	0.0	46.0	a
41	$\text{MnOOH} + \text{CO} = \text{MnOH} + \text{CO}_2$	2.00E+12	0.0	20.9	a
42	$\text{MnO}_2\text{H}_2 + \text{H} = \text{MnOH} + \text{H}_2\text{O}$	6.60E+13	0.0	4.18	a
43	$\text{MnO}_2\text{H}_2 + \text{H} = \text{MnOOH} + \text{H}_2$	5.00E+13	0.0	79.5	a
44	$\text{MnO}_2\text{H}_2 + \text{OH} = \text{MnOOH} + \text{H}_2\text{O}$	1.00E+13	0.0	37.7	a
45	$\text{MnO}_2\text{H}_2 + \text{O} = \text{MnOOH} + \text{OH}$	2.00E+13	0.0	83.7	a
46	$\text{MnO}_2\text{H}_2 + \text{CH}_3 = \text{MnOOH} + \text{CH}_4$	1.00E+13	0.0	87.9	a
47	$\text{MnH} + \text{H} = \text{Mn} + \text{H}_2$	5.00E+13	0.0	12.6	a
48	$\text{MnH} + \text{OH} = \text{Mn} + \text{H}_2\text{O}$	1.00E+14	0.0	0.0	a
49	$\text{MnH} + \text{O} + \text{M} = \text{MnOH} + \text{M}$	1.00E+15	0.0	0.0	a
50	$\text{MnH} + \text{O} = \text{Mn} + \text{OH}$	1.00E+14	0.0	8.37	a
51	$\text{MnH} + \text{CH}_3 = \text{CH}_4 + \text{Mn}$	1.00E+14	0.0	8.37	a
52	$\text{MnH} + \text{O}_2 + \text{M} = \text{MnOOH} + \text{M}$	1.00E+16	0.0	0.0	a

a Estimates

The laboratory flames inhibited by TMT and MMT were numerically modeled as one-dimensional, freely-propagating flames. Solutions were obtained using the Sandia flame code Premix,<sup>203</sup> and the CHEMKIN<sup>204</sup> and transport property<sup>205</sup> subroutines. (Solutions were obtained for values of GRAD and CURV of 0.17 and 0.25 in PREMIX.) The kinetic mechanism for methane combustion was GRIMech 3.0,<sup>206</sup> with the nitrogen chemistry removed. The methane sub-mechanism contained 36 species and 219 reactions.<sup>i</sup> The calculations were for 1-D planar flames, while the experiments determined the average flame speed of Bunsen-type flames which can be influenced by curvature and stretch. To minimize these effects, both the experimental and calculated data are presented as normalized flame speed reduction.

<sup>i</sup> The reaction mechanisms used for the present calculations for flames with manganese or tin compounds should be considered only as a starting point. Numerous changes to both the rates and the reactions incorporated may be made once a variety of experimental and theoretical data are available for testing the mechanism.

## Results

### Observations

The appearance of the flames with added organometallic inhibitors is shown in Figure 3-30. Flames with iron pentacarbonyl were bright orange, with tetramethyltin they were bright pale blue, and with MMT, yellow-green. The intensity of the visible emission increased with inhibitor mole fraction. As the loading of metallic inhibitor increased, there became visible a luminous outer shroud as seen clearly in the last two images on the right in Figure 3-30. These were regions of high particle concentration from inhibitor condensation, leading to broad-band black body radiation, visible here in the orange part of the spectrum. For the TMT-inhibited flames, a white-colored powder (presumably tin oxide) formed on the rim of the quartz burner tube during the tests, especially at high TMT loading. This deposit was removed between collection of each data point. For MMT and  $\text{Fe}(\text{CO})_5$ , a dark red or an orange deposit was formed, respectively. The rate of deposition for these inhibitors, however, was much lower than for the TMT, which was added to the flames at mole fractions about ten times higher.

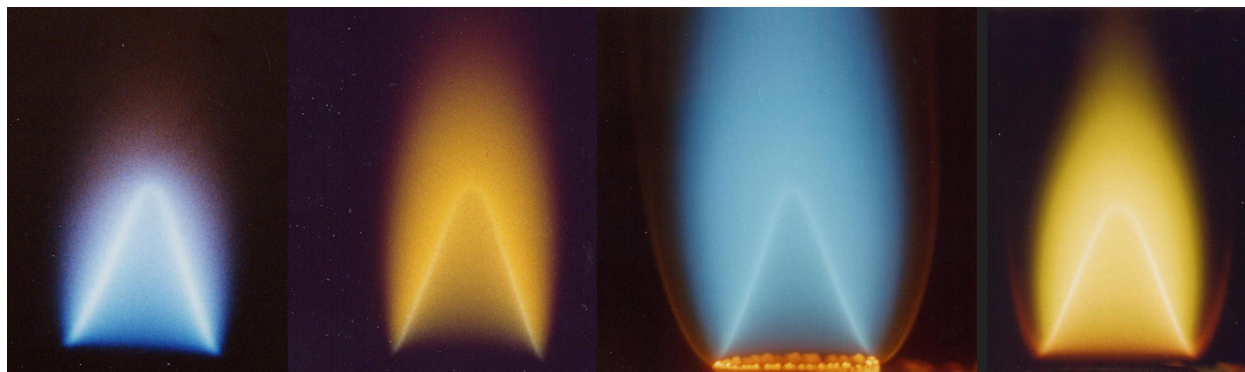


**Figure 3-30. Visible Images of Methane-air Premixed Flames. (From left to right: no inhibitor, 50  $\mu\text{L/L}$  of  $\text{Fe}(\text{CO})_5$ , 4000  $\mu\text{L/L}$  of TMT, and 400  $\mu\text{L/L}$  of MMT).**

### Inhibition by Tetramethyltin

Figure 3-31 shows the relative burning velocity reduction with addition of TMT to methane-air flames ( $X_{\text{O}_2, \text{ox}} = 0.21$ ) for values of equivalence ratio of 0.9, 1.0, and 1.1. The dotted lines are curve fits to the experimental data, and the solid lines are the results of the numerical calculations described above (and discussed below). Data are plotted as normalized burning velocity, which is the burning velocity of the inhibited flame divided by the value for the same flame in the absence of inhibitor. The calculated and experimental burning velocities, along with the calculated adiabatic flame temperatures of the uninhibited flames used for the normalization are listed in Table 3-6. For the uninhibited flames, the experimentally determined average burning velocities for the Bunsen-type flames were within about 4 % of the calculated values for 1-D planar flames. In Figure 3-31 (as well as Figure 3-32, Figure 3-33, Figure 3-34, and Figure 3-36 described below), the last data point shown represents the highest volume fraction of inhibitor for which flames could be stabilized on the present burner (i.e., they extinguished at higher volume fractions). The experimental results in Figure 3-31 demonstrate that for stoichiometric flames, 3000  $\mu\text{L/L}$  of TMT reduced the flame speed by about 41 %, which is about a factor of two better than  $\text{CF}_3\text{Br}$ . The data also showed that, unlike  $\text{Fe}(\text{CO})_5$ , the richer flames were inhibited more strongly by TMT than the leaner flames. (Additional numerical tests with  $\text{SnO}$  as the inhibitor showed that the poorer

inhibition of lean flames was due to the fuel effect from the hydrocarbon portion of the relatively large amounts of  $\text{Sn}(\text{CH}_3)_4$  added to the flames.)

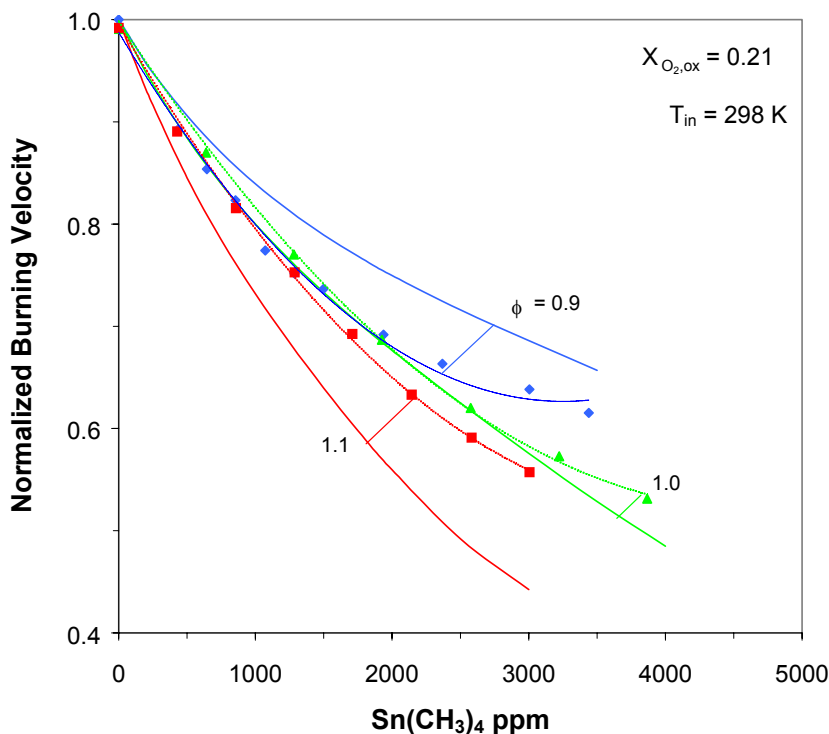


**Figure 3-31. Normalized Burning Velocity of Premixed  $\text{CH}_4/\text{O}_2/\text{N}_2$  Flames Inhibited by TMT for  $X_{\text{O}_2,\text{ox}}=0.21$  and  $\phi=0.9, 1.0,$  and  $1.1$  (Dotted lines: curve fits to data; solid lines: numerical predictions.)**

As described below, the burning velocity reduction caused by tin species was most sensitive to the rates of the reactions:  $\text{SnO} + \text{H} + \text{M} \leftrightarrow \text{SnOH} + \text{M}$ , and  $\text{SnOH} + \text{H} \leftrightarrow \text{SnO} + \text{H}_2$ . Consequently, the pre-exponential factors were adjusted in those rates to provide agreement with the experimental results for stoichiometric mixtures of methane with air. Note, however, the relatively high level of the rate constant for the reaction  $\text{H} + \text{SnO} + \text{M} \leftrightarrow \text{SnOH} + \text{M}$ . Bulewicz and Padley<sup>116</sup> also found that a high rate was required for this process to provide agreement with their experimental data on hydrogen atom recombination in the products of a hydrogen flames. As Figure 3-31 shows, the numerical model predicted the amount of inhibition well for stoichiometric flames. For rich and lean flames, however, the model over- and under-predicted the burning velocity, respectively. For the reaction set considered, reasonable adjustments to the rate constants did not provide better agreement.

Figure 3-32 shows the measured and calculated flame speeds for TMT in stoichiometric flames  $X_{\text{O}_2,\text{ox}}$  equal to 0.20, 0.21, and 0.244. The experimental data and calculations (with adjusted rate constants) show good agreement for the three values of  $X_{\text{O}_2,\text{ox}}$ ; however, for the hottest flames ( $X_{\text{O}_2,\text{ox}} = 0.244$ ), the mechanism slightly overpredicted the inhibition at low mole fraction, and underpredicted it for higher mole fraction. The experimental data show that for the slower and cooler flames (e.g., equivalence ratio is 0.9 or 1.0 and  $X_{\text{O}_2,\text{ox}} = 0.20$  or 0.21), the TMT started to lose its effectiveness above a certain value. For  $\text{Fe}(\text{CO})_5$  inhibited flames, such behavior was shown to be due to condensation of the iron-containing intermediates.<sup>102</sup>

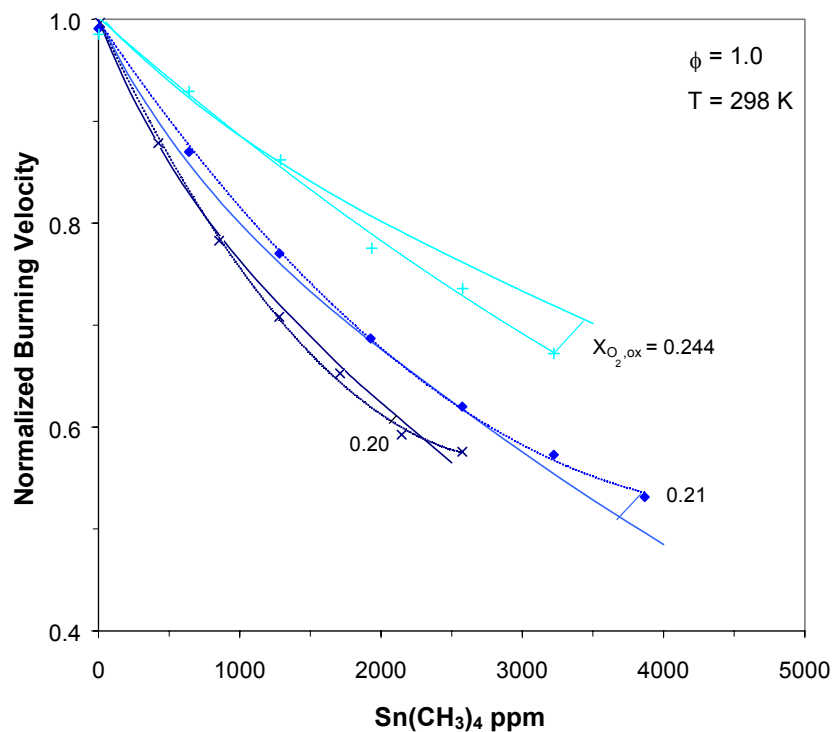


**Figure 3-32 – Normalized Burning Velocity of Premixed CH<sub>4</sub>/O<sub>2</sub>/N<sub>2</sub> flames Inhibited by TMT for  $\phi=1.0$  and  $X_{O_2,ox}=0.20$ , 0.21, and 0.244. (Dotted lines: curve fits to the data; solid lines: numerical predictions)**

### ***Inhibition by MMT***

The premixed flames inhibited by the Mn-containing compound MMT were slightly preheated ( $T_{in} = 80$  °C). The values of the calculated and experimental uninhibited burning velocities, and the adiabatic flame temperatures are shown in Table 3-6. The normalized burning velocities of MMT-inhibited flames with variation in equivalence ratio and  $X_{O_2,ox}$  are shown in Figure 3–33 and Figure 3–34. MMT was about 13 times more efficient at flame inhibition than TMT; however, it too started to lose its effectiveness for flame speed reductions near 50 %. Based on the sensitivity of the burning velocity to the reaction rates, the pre-exponential factors of the reactions  $Mn(OH)_2 + H \leftrightarrow MnOH + H_2O$  and  $MnO + H_2O \leftrightarrow Mn(OH)_2$  were adjusted to provide agreement with experimental data for these methane-air flames at  $\phi=1.0$ . Using the rates shown in Table 3-9, the model predicted the burning velocity reduction quite well. Nonetheless, for the hottest flames ( $X_{O_2,ox} = 0.244$ ) this mechanism also overpredicted the inhibition slightly at low inhibitor mole fraction, and underpredicted the inhibition somewhat at intermediate mole fractions. Also, this gas phase mechanism did not capture the decrease in inhibitor effectiveness which occurred with increasing inhibitor initial mole fraction, likely a result of condensation of Mn-containing species.

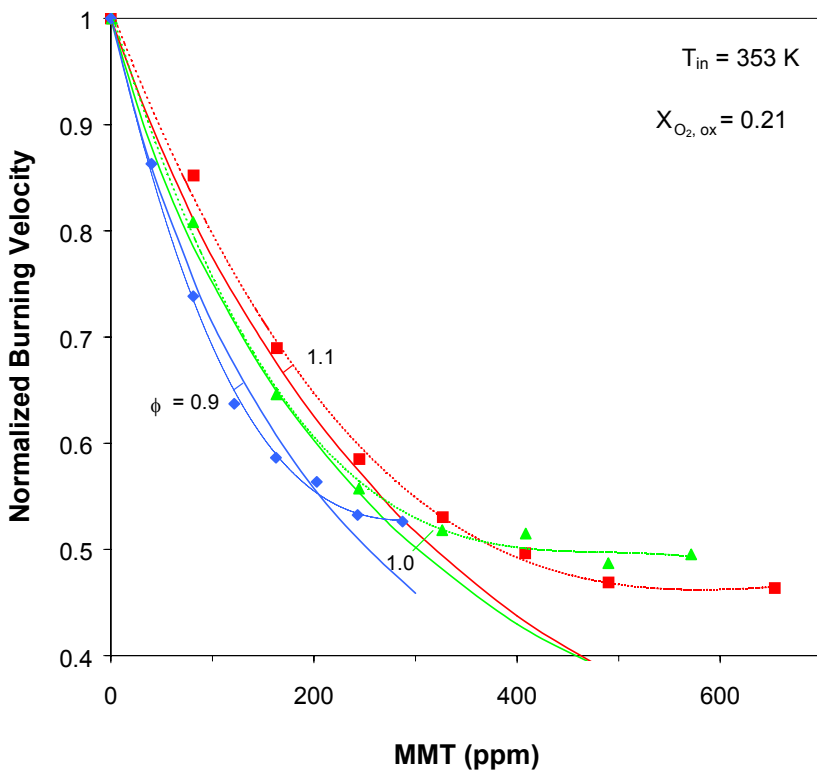


Figure 3-33. Normalized Burning Velocity of Premixed CH<sub>4</sub>/O<sub>2</sub>/N<sub>2</sub> Flames Inhibited by MMT with  $X_{O_2,ox}=0.21$  and  $\phi=0.9, 1.0,$  and  $1.1$ . (Dotted lines: curve fits to data; solid lines: numerical predictions)

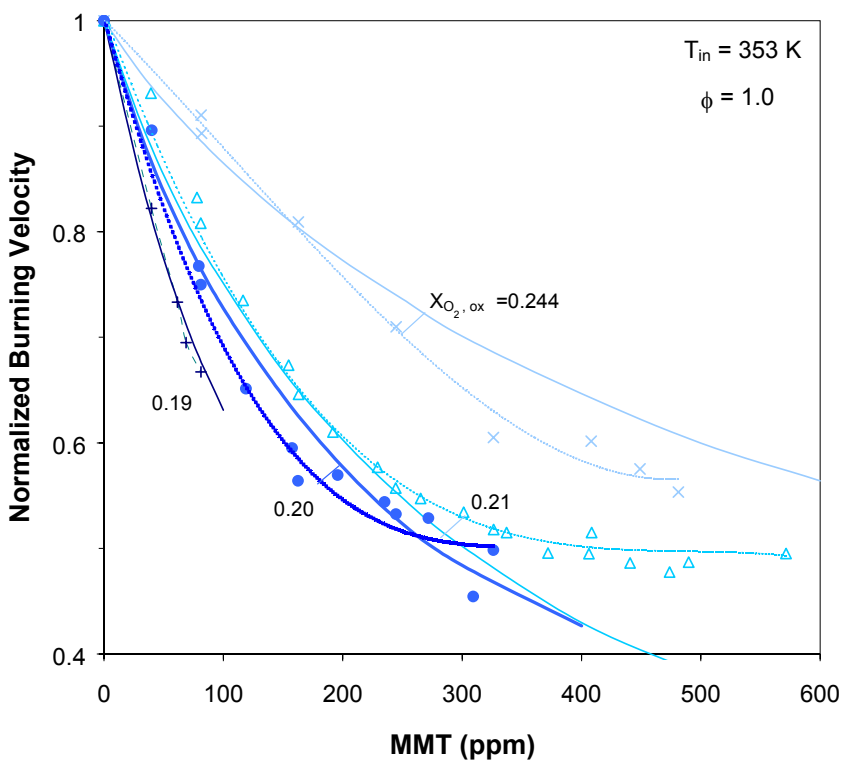
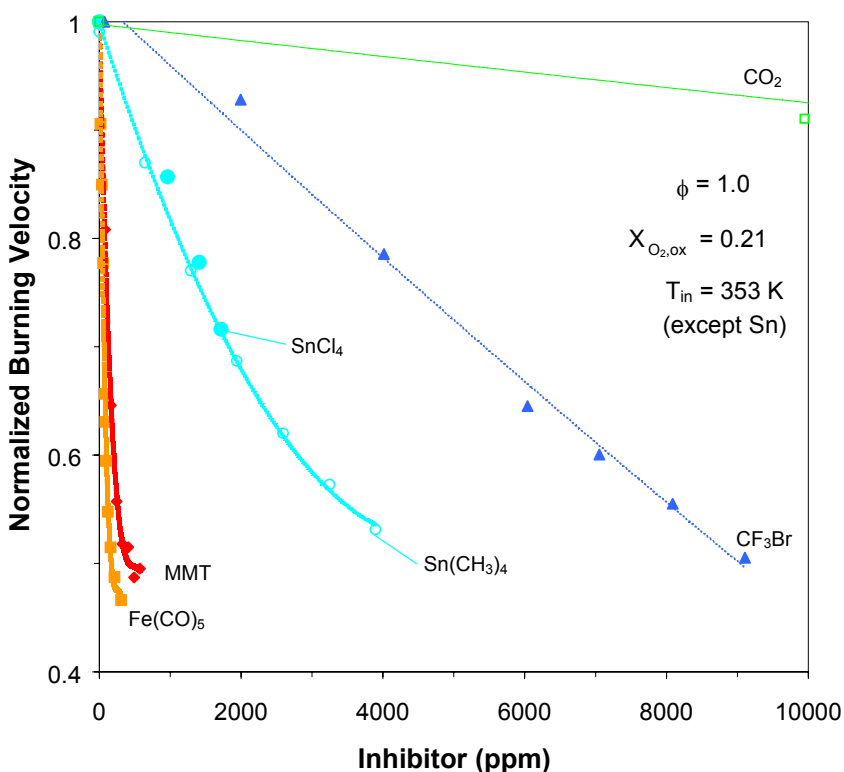


Figure 3-34. Normalized Burning Velocity of Premixed CH<sub>4</sub>/O<sub>2</sub>/N<sub>2</sub> Flames Inhibited by MMT, with  $\phi=1.0$  and  $X_{O_2,ox}=0.19, 0.20, 0.21,$  and  $0.244$ . (Dotted lines: curve fits to the data; solid lines: numerical predictions)

### Comparative Performance of Metals

Figure 3-35 compares the inhibition effectiveness of  $\text{Fe}(\text{CO})_5$ , MMT, TMT,  $\text{SnCl}_4$ ,  $\text{CF}_3\text{Br}$ , and  $\text{CO}_2$ . The data for  $\text{SnCl}_4$  inhibition from Reference 34 show tin tetrachloride was as effective in n-hexane/air flames as TMT was in methane/air flames. Although the experimental data shown for TMT and  $\text{SnCl}_4$  are not for an elevated inlet temperature of 80 °C, numerical calculations showed that the reduction in the *normalized* flame speed caused by TMT addition with  $T_{\text{in}}=298$  K differs from that with  $T_{\text{in}}=353$  K by less than 1 %.  $\text{Fe}(\text{CO})_5$  is significantly more effective than any of the other agents, and all of the metal-based inhibitors had greatly reduced effectiveness for burning velocity reductions greater than 50 %. When the inhibitor mole fractions are re-scaled in Figure 3-35 to provide overlap at 30 % reduction in burning velocity, the normalized burning velocity curves of all inhibitors are nearly coincident for flame speed reductions less than 40 % (i.e., the curves are roughly linear up to this degree of normalized flame speed reduction). Such re-scaling of the experimental data shows that at low mole fraction,  $\text{Fe}(\text{CO})_5$  was about 80 times, MMT 40 times, and TMT three times as effective as  $\text{CF}_3\text{Br}$  at reducing the overall reaction rate of stoichiometric, premixed methane-air flames. For flame speed reductions greater than 40 %, the curves for these five agents diverged. As discussed previously,<sup>175,207</sup> most inhibitors lose their marginal effectiveness at higher mole fractions, but the decrease in inhibition effectiveness is much more dramatic for the organometallic compounds, as was found previously for  $\text{Fe}(\text{CO})_5$ .



**Figure 3-35. Normalized Burning Velocity of Premixed  $\text{CH}_4/\text{O}_2/\text{N}_2$  Flames Inhibited by  $\text{CO}_2$ ,  $\text{CF}_3\text{Br}$ ,  $\text{Sn}(\text{CH}_3)_4$ ,  $\text{SnCl}_4$ <sup>34</sup>, MMT, and  $\text{Fe}(\text{CO})_5$ .  $T_{\text{in}} = 353$  K for all data except  $\text{Sn}(\text{CH}_3)_4$  and  $\text{SnCl}_4$  which are at 298 K. Lines are curve fits to data.**

### Blends of Metals

One approach for overcoming the loss of effectiveness is to add non-condensing amounts of several inhibitors. To test this approach in premixed flames, Linteris and co-workers performed tests with a blend of MMT and  $\text{Fe}(\text{CO})_5$ , added at a molar ratio of 2:1, respectively. Data for pure MMT, pure  $\text{Fe}(\text{CO})_5$ , and their combination are shown in Figure 3-36 ( $T_{\text{in}} = 353 \text{ K}$ ,  $\phi = 1.0$ , and  $X_{\text{O}_2, \text{ox}} = 0.244$ ). The experimental data are represented by the points with a curve fit (dotted line), while the results of the numerical calculations are shown by the solid lines. (The data for the combination of MMT and  $\text{Fe}(\text{CO})_5$  are plotted as a function of the mole fraction of the abundant agent, MMT). The numerical model, which includes both the reactions of manganese-containing species and the iron-containing species from Reference 104 predicts well the normalized flame speed reduction. As the figure shows, adding 0.5 moles of  $\text{Fe}(\text{CO})_5$  for each mole of MMT added did provide additional flame speed reduction over that from MMT alone. This is significant since, as discussed previously,<sup>102</sup> the loss of effectiveness of the metals at higher concentration could be caused either by condensation of active species, or by the loss of radical population by catalytic recombination. Since the addition of iron to the manganese-inhibited flame caused significant additional inhibition, the *strong* loss of effectiveness in the MMT-inhibited flames was likely due to condensation rather than radical depletion. If the cause was radical depletion, addition of  $\text{Fe}(\text{CO})_5$  to the flames already inhibited by high amounts of MMT would have yielded no additional inhibition, since few radicals would be left to recombine. The gas phase kinetic model captured the *mild* reduction of effectiveness of either agent or their blend acceptably well (for flame speed reductions of less than 40 %).

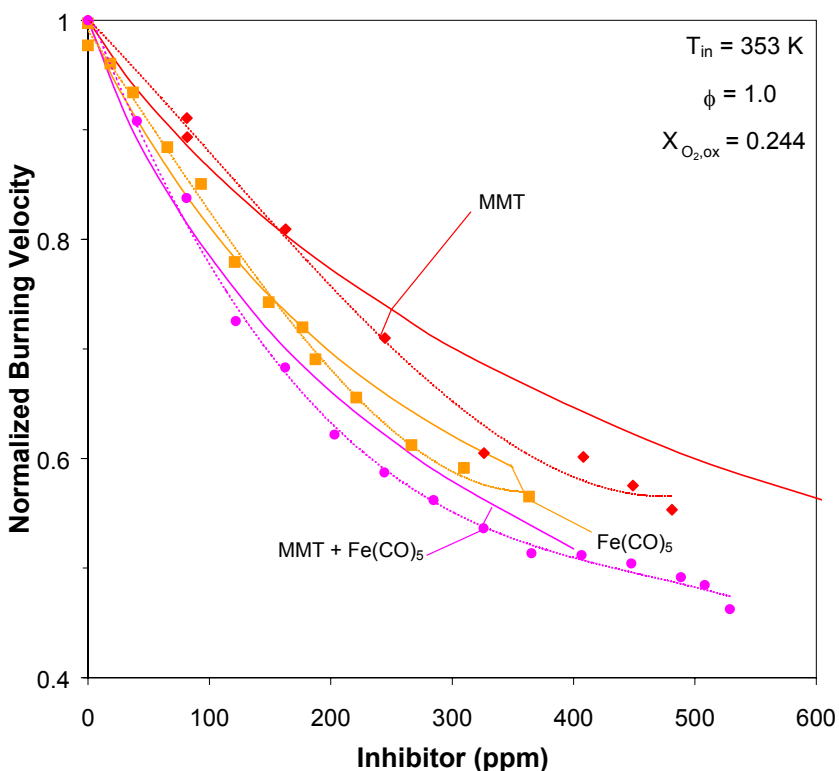


**Figure 3-36. Normalized Burning Velocity of Premixed  $\text{CH}_4/\text{O}_2/\text{N}_2$  Flames Inhibited by Pure MMT and  $\text{Fe}(\text{CO})_5$ , and by a Blend of the Two. Dotted lines are curve fits to the data; solid lines are numerical model calculations.**

## Discussion

One of the benefits of numerical modeling of the flame structure of inhibited flames is that the results of the calculations provide detailed insight into the actual reasons for the strong inhibition. Further, the results for different inhibitors can be used to understand why they each demonstrate a different effectiveness. In the sections below, the inhibition mechanisms of tin and manganese are discussed and compared to that for iron. The difference in efficiency for these systems are shown to be related to the formation reaction and equilibrium relationships for the intermediate metal di-hydroxide species  $\text{Fe}(\text{OH})_2$  and  $\text{Mn}(\text{OH})_2$ .

### *Inhibition Mechanisms of Tin and Manganese*

Examination of species profiles, reaction fluxes, and sensitivity coefficients from the numerically predicted flame structure allows investigation of the mechanisms of inhibition of these metallic compounds. The calculations show that TMT decomposes quickly in the flame, with 90 % consumption at 1000 K. A diagram showing the important reactions for tin inhibition is shown in Figure 3-37 (which also shows in parallel format the reaction paths for MMT, and  $\text{Fe}(\text{CO})_5$  inhibition). In the calculations used to prepare Figure 3-37, TMT, MMT, or  $\text{Fe}(\text{CO})_5$  were present at (1963, 128, or 105)  $\mu\text{L}/\text{L}$ , respectively, in the premixed methane-air flames ( $\phi=1.0$ ,  $T_{\text{in}}=353$  K, and  $X_{\text{ox}}=0.21$ ); these volume fractions produced a 30 % reduction in flame speed.

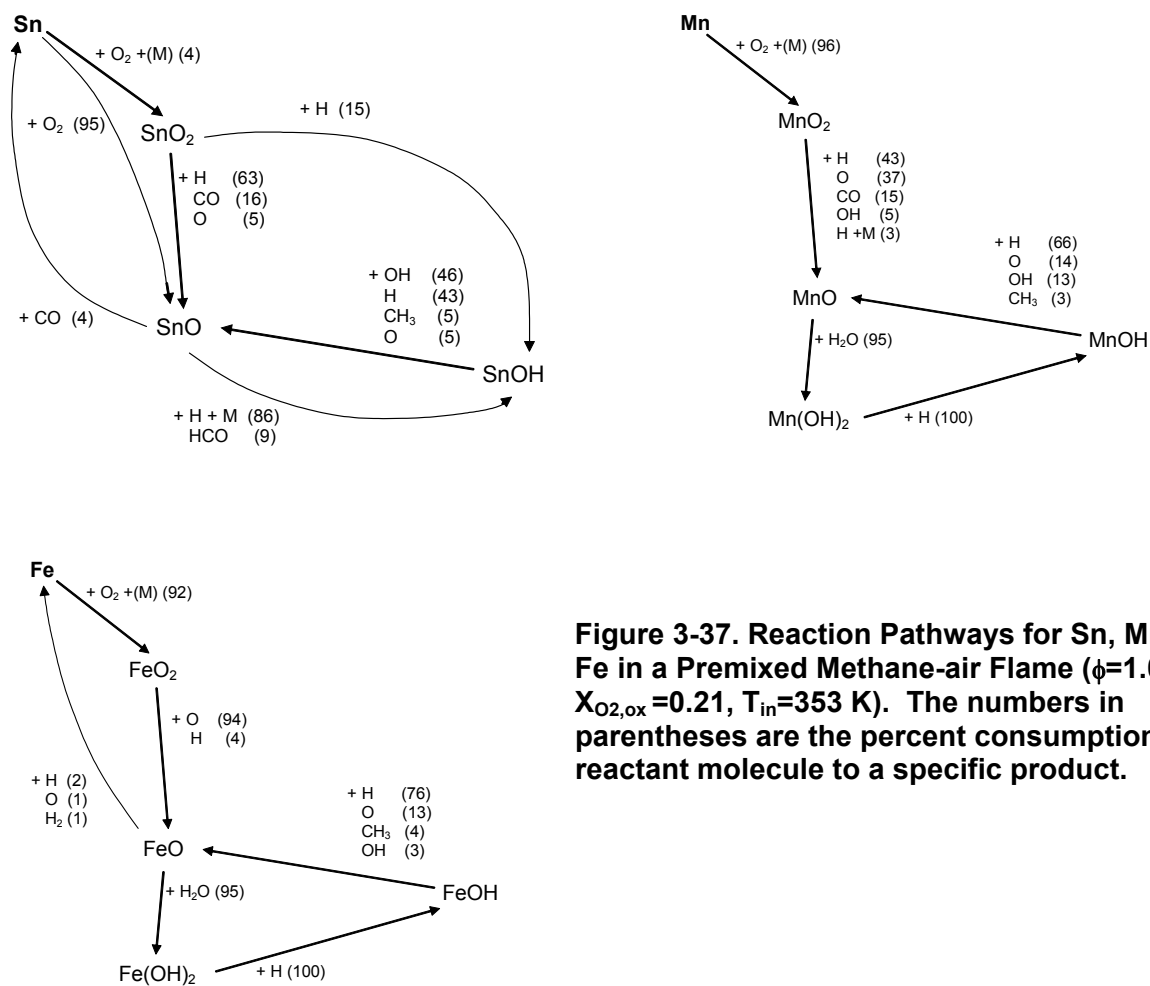
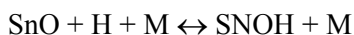


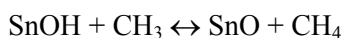
**Figure 3-37. Reaction Pathways for Sn, Mn, and Fe in a Premixed Methane-air Flame ( $\phi=1.0$ ,  $X_{\text{O}_2,\text{ox}}=0.21$ ,  $T_{\text{in}}=353$  K). The numbers in parentheses are the percent consumption of the reactant molecule to a specific product.**

The determination of the important reactions was based on consideration of both the reaction flux and sensitivities. The reaction flux represents the production or consumption of a species by chemical reaction. For a particular reaction, it is defined as the integral of that reaction rate per unit volume over the entire flame domain. The total reaction flux for a species is defined as the sum of the reaction fluxes for the individual reactions which produce or consume it. In Figure 3-37, the pathway for consumption of each species is shown, with arrows connecting the relevant reactant and product species. The number next to each arrow represents the fraction of the total consumption flux for that species which proceeds through that particular reaction.

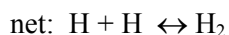
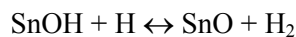
The tin atom formed as a result of TMT decomposition quickly reacts with  $O_2$  through the reactions  $Sn + O_2 (+M) \leftrightarrow SnO_2$ , and  $Sn + O_2 \leftrightarrow SnO + O$ . The former reaction leads to SnO from the reaction of  $SnO_2$  with CO, H, or other radicals. Conversely, the latter reaction forms SnO directly, and is fast at room temperature as compared to the analogous reaction of iron atom. Formation of SnO leads to the following reactions with H and HCO radicals:



which, together with the radical scavenging reactions of SnOH, complete the catalytic radical recombination cycle of tin:



The net effect of the dominant inhibition reactions can be shown as:



Equilibrium calculations show that SnO is the major tin species in the products of a stoichiometric methane–air flame with added TMT. Figure 3-38 presents the sensitivity coefficients of the burning velocity to the rate constants (after adjustment) of tin-containing species for methane/air mixtures with equivalence ratios of 0.9, 1.0, and 1.1. In general, the burning velocity was sensitive to the rates of the catalytic cycle reactions with high fluxes: SnO reaction with H or HCO, and SnOH reaction with H, OH,  $CH_3$ , or O. The burning velocity was most sensitive to the rate of the reaction  $SnO + H + M \leftrightarrow SnOH + M$ , which had a sensitivity about four times less than the chain-branching reaction  $H + O_2 \leftrightarrow OH + O$ . As was found for DMMP and ferrocene additives,<sup>106,201</sup> the burning velocity of flames inhibited by TMT was not particularly sensitive to the rate of the decomposition reaction. Numerical tests showed that changes in the overall activation energy of TMT decomposition in the range 170 kJ/mol to 335 kJ/mol had little effect on the burning velocity with up to 2000  $\mu\text{L/L}$  of TMT. Hence, the inhibition effectiveness of tin compounds is likely to be independent on the parent molecule, as long as rapid decomposition occurs.

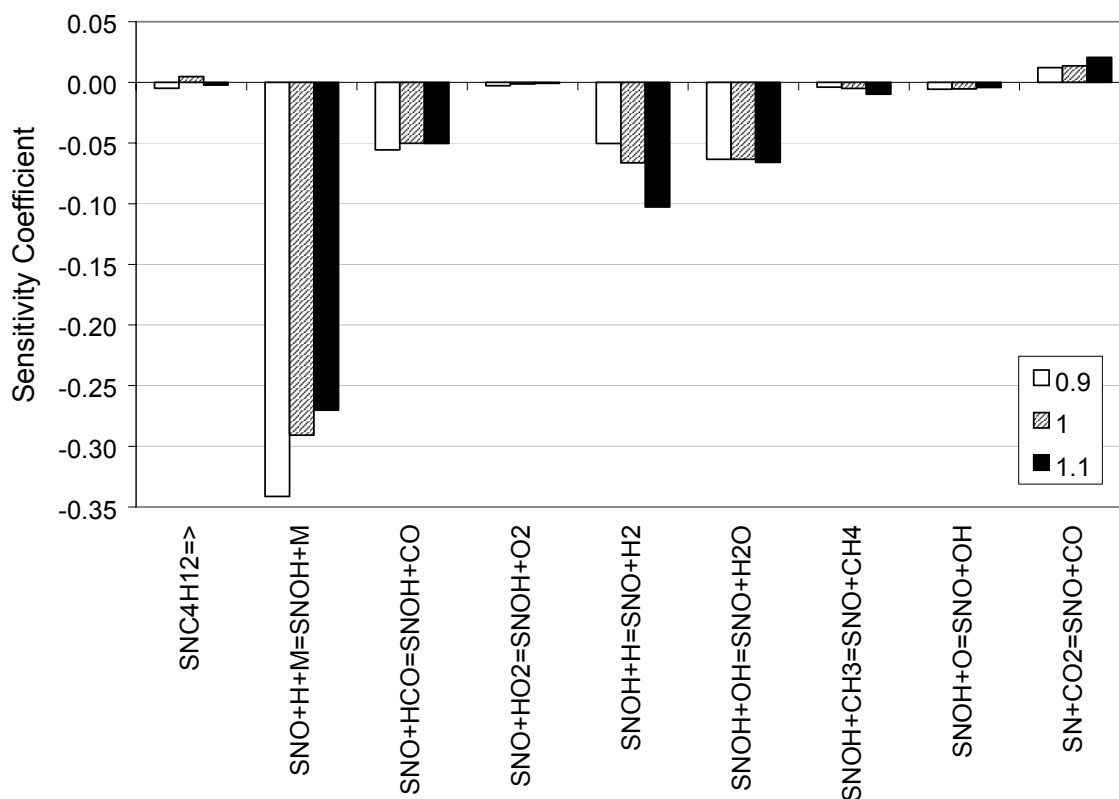
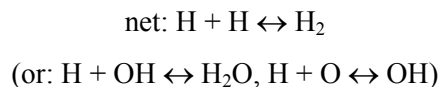
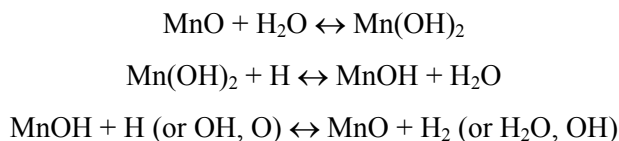


**Figure 3-38. First-order Sensitivity Coefficient of the Burning Velocity to the Specific Reaction Rate Constant for Reactions with Tin-containing Species (1963  $\mu\text{L/L}$  of TMT).**

The reaction  $\text{SnO} + \text{CO} \leftrightarrow \text{Sn} + \text{CO}_2$  (which is followed by  $\text{Sn} + \text{O}_2 = \text{SnO} + \text{O}$ ) is an additional route for CO consumption, and is chain-branching (net:  $\text{CO} + \text{O}_2 = \text{CO}_2 + \text{O}$ ), which reduced the inhibiting effect of SnO in these flames. Similar behavior was found for CO – N<sub>2</sub>O flames inhibited by Fe(CO)<sub>5</sub>.<sup>145</sup> Changes in these rates affected the calculated inhibition efficiency of TMT; nevertheless, the mechanism was dominated by the rate of reaction  $\text{SnO} + \text{H} + \text{M} \leftrightarrow \text{SnOH} + \text{M}$ .

Analysis of the numerical results for inhibition by MMT showed that the behavior of manganese in premixed methane-air flames was similar in many details to that of iron pentacarbonyl. The reaction pathway for manganese species is also shown in Figure 3-37, and the pathway for iron species from Fe(CO)<sub>5</sub> is shown for comparison. As with iron pentacarbonyl, Mn reacts with O<sub>2</sub> to form MnO<sub>2</sub>, which reacts primarily with radicals to form MnO. The catalytic radical recombination cycle consists of:



Although flame equilibrium calculations showed that the species MnH was present at relatively large concentrations, the contribution of reactions of this species to the inhibition effect was relatively small. Figure 3-39 shows the highest absolute values of the sensitivity coefficients of burning velocity to the rate constants (after adjustment) for reactions of manganese-containing species. The burning velocity was sensitive to the rates of the three reactions in the catalytic cycle above, with the rate of the reaction  $\text{Mn}(\text{OH})_2 + \text{H} \leftrightarrow \text{MnOH} + \text{H}_2\text{O}$  having the greatest absolute value. The burning velocity was also somewhat sensitive to the rates of the reactions forming  $\text{MnO}_2$  and  $\text{MnO}$ . The reaction  $\text{MnO} + \text{H} \leftrightarrow \text{Mn} + \text{OH}$  has a positive sensitivity; i.e., increasing its rate increased the burning velocity. This chain propagating reaction temporarily removed MnO from the catalytic cycle above, thus weakening the inhibition.

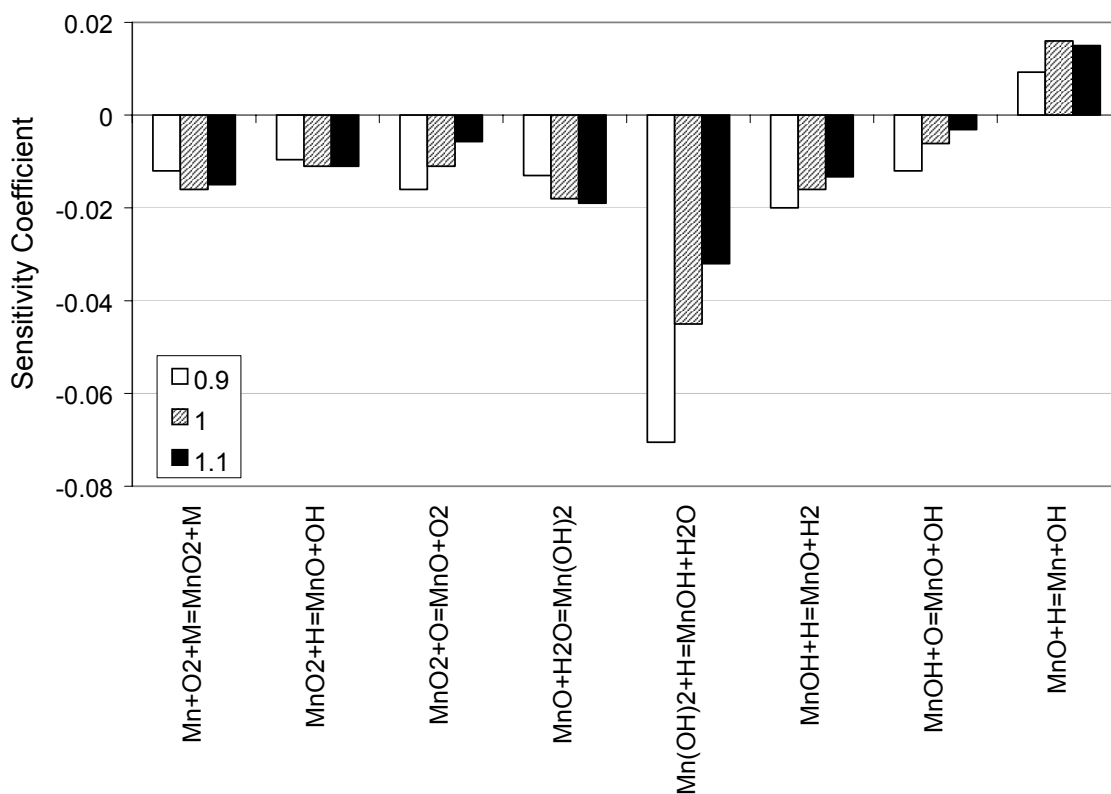


**Figure 3-39. First-order Sensitivity Coefficient of the Burning Velocity to the Specific Reaction Rate Constant for Reactions with Manganese-containing Species (150  $\mu\text{L/L}$  of MMT).**

### *Comparison of inhibition by $\text{Fe}(\text{CO})_5$ , MMT, and TMT*

In order to evaluate the inhibition mechanisms under comparable conditions, the numerical calculations (for  $\phi=1.0$ ,  $X_{\text{O}_2, \text{ox}}=0.21$ , and  $T_{\text{in}}=353$  K) were performed, as above, for initial values of TMT, MMT, and  $\text{Fe}(\text{CO})_5$  which provided an equivalent reduction (30 %) in the normalized burning velocity. These volume fractions were found to be 1963  $\mu\text{L/L}$ , 128  $\mu\text{L/L}$ , and 105  $\mu\text{L/L}$ , respectively. While suppression of a fire would probably require higher agent concentration than that which provides a 30 % flame speed

decrease, this degree of flame speed reduction was selected for two reasons. It provided a significant reduction in overall reaction rate (a factor of two) and kept the agent concentration far enough above the values at which the model and experiments start to diverge (possibly due to condensation). For these flames, the structures were quite similar and the flame speed was the same (37.3 cm/s), allowing straightforward comparison of the inhibition mechanisms.

Based on the calculated results, TMT was required at a mole fraction which was about 17 times greater than iron or manganese compounds for a similar reduction in overall reaction rate. This occurred because the reactions to form SnOH from SnO were rate-limiting and slow. Further, the reverse of the reaction  $\text{SnO} + \text{H} + \text{M} \leftrightarrow \text{SnOH} + \text{M}$  was relatively fast at the location of peak catalytic cycle activity because SnO was a dominant equilibrium product in the high temperature region.

In order to further compare the performance of TMT, MMT, and  $\text{Fe}(\text{CO})_5$ , it was useful to plot the relevant species mole fractions as a function of temperature through the flame. Figure 3-40 shows the mole fractions of the metal species in the inhibition cycles, and the radical species H, OH, and O. The vertical line shows the location of the maximum rate of the  $\text{H} + \text{O}_2$  branching reaction. Note that the locations of the peak fluxes of the inhibition reactions (not shown) were very close to the peak flux of the  $\text{H} + \text{O}_2$  reaction and to the maximum concentrations of H, OH, and O. The bottom figure for TMT inhibition clearly shows the preponderance of SnO as the sink for tin atoms (note the rescaling), hence requiring a large initial TMT mole fraction to achieve both fast reaction of SnO with H atom, and appreciable mole fraction of SnOH for radical scavenging. In Figure 3-40, consider the Mn-containing species at the location of peak H-atom flux. MnO was present in higher mole fraction than FeO. This occurred from the significant backward reaction of  $\text{MnO} + \text{H}_2\text{O} \leftrightarrow \text{Mn}(\text{OH})_2$ , which provided a lower  $\text{Mn}(\text{OH})_2$  concentration for the rate-limiting step  $\text{Mn}(\text{OH})_2 + \text{H} \leftrightarrow \text{MnOH} + \text{H}_2\text{O}$ .

The importance of constraints on equilibrium concentrations as they relate to inhibitor efficiency is illustrated in Figure 3-41, which shows the fraction of all metal species in the flame. For these equilibrium calculations, the metallic element (Sn, Mn, or Fe) was present at a mole fraction of  $1.0 \times 10^{-4}$ , and methane and air were present at stoichiometric proportions. For TMT inhibition, the Sn appeared overwhelmingly as SnO (note the scale change on Sn and SnOH), thus higher levels of TMT were required to yield the required levels of SnOH reaction with H atom, and for the required rates of the slow reaction  $\text{SnO} + \text{H} + \text{M} \leftrightarrow \text{SnOH} + \text{M}$ . Note that since the flames of Figure 3-40 all had equivalent levels of inhibition, the flux of each radical recombining catalytic cycle was about the same; e.g., SnOH, MnOH, and FeOH must have been present at about the same mole fraction since their rates of reaction with H-atom were close, and the rates of reactions forming the hydroxide were approximately the same. Comparing  $\text{Mn}(\text{OH})_2$  and  $\text{Fe}(\text{OH})_2$  in Figure 3-41, in the MMT-inhibited flames, the concentration of  $\text{Mn}(\text{OH})_2$  for temperatures above 1800 K dropped off rapidly, whereas in the  $\text{Fe}(\text{CO})_5$ -inhibited flames,  $\text{Fe}(\text{OH})_2$  did not. Since the reaction of  $\text{Mn}(\text{OH})_2$  with H atom was rate-limiting (Figure 3-39), decreases in the  $\text{Mn}(\text{OH})_2$  mole fraction made MMT less effective as an inhibitor than  $\text{Fe}(\text{CO})_5$ .

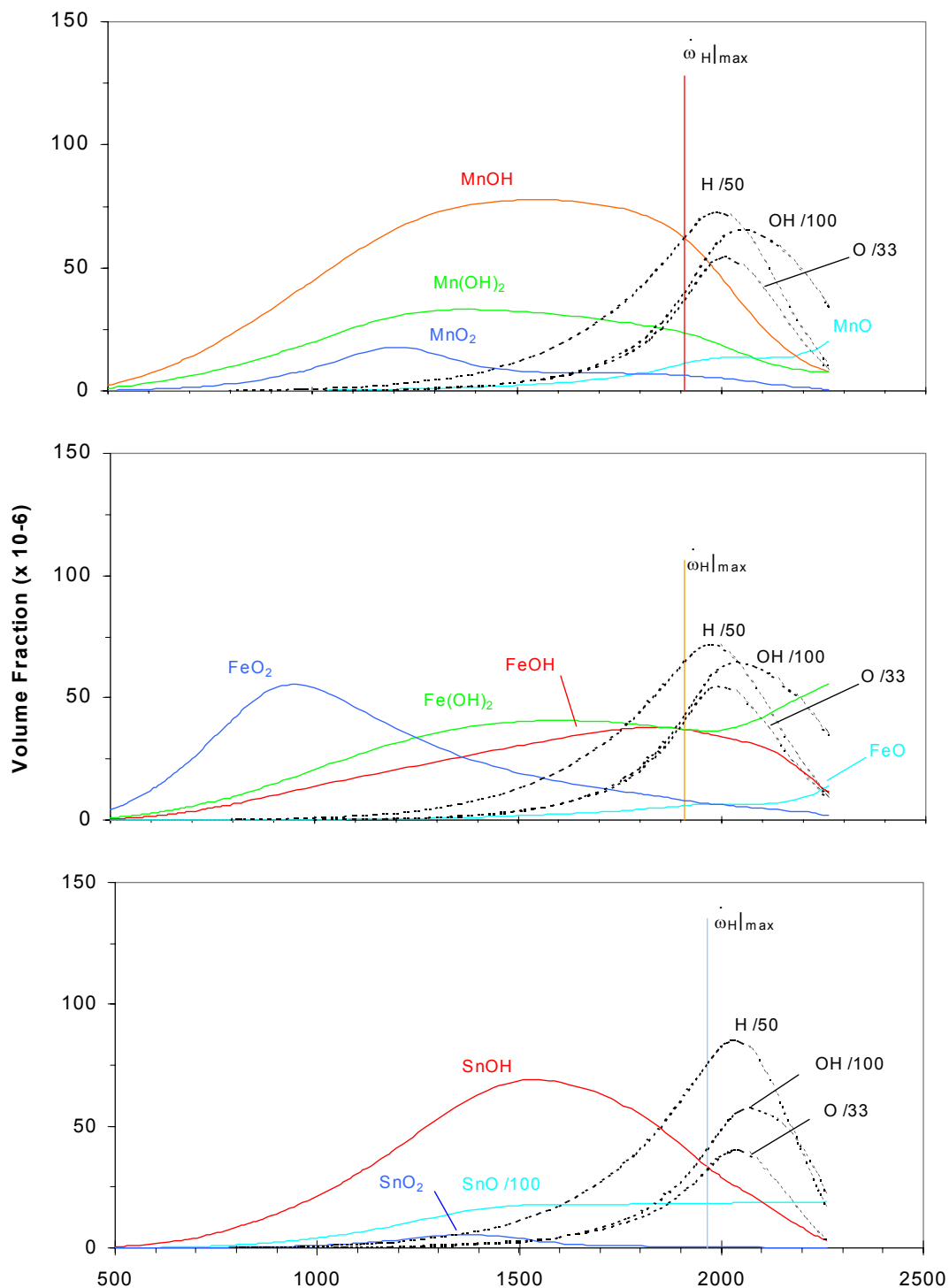


**Figure 3-40. Volume Fractions of O, and OH Radicals and Metal Species Intermediates as a Function of Temperature in Flame for Fe(CO)<sub>5</sub>, MMT, and TMT Added at 105  $\mu\text{L/L}$ , 128  $\mu\text{L/L}$ , and 1963  $\mu\text{L/L}$  (corresponding to a 30 % reduction in flame speed).  $T_{in}=353\text{ K}$ ,  $\phi=1.0$ ,  $X_{O_2,ox}=0.21$ .**

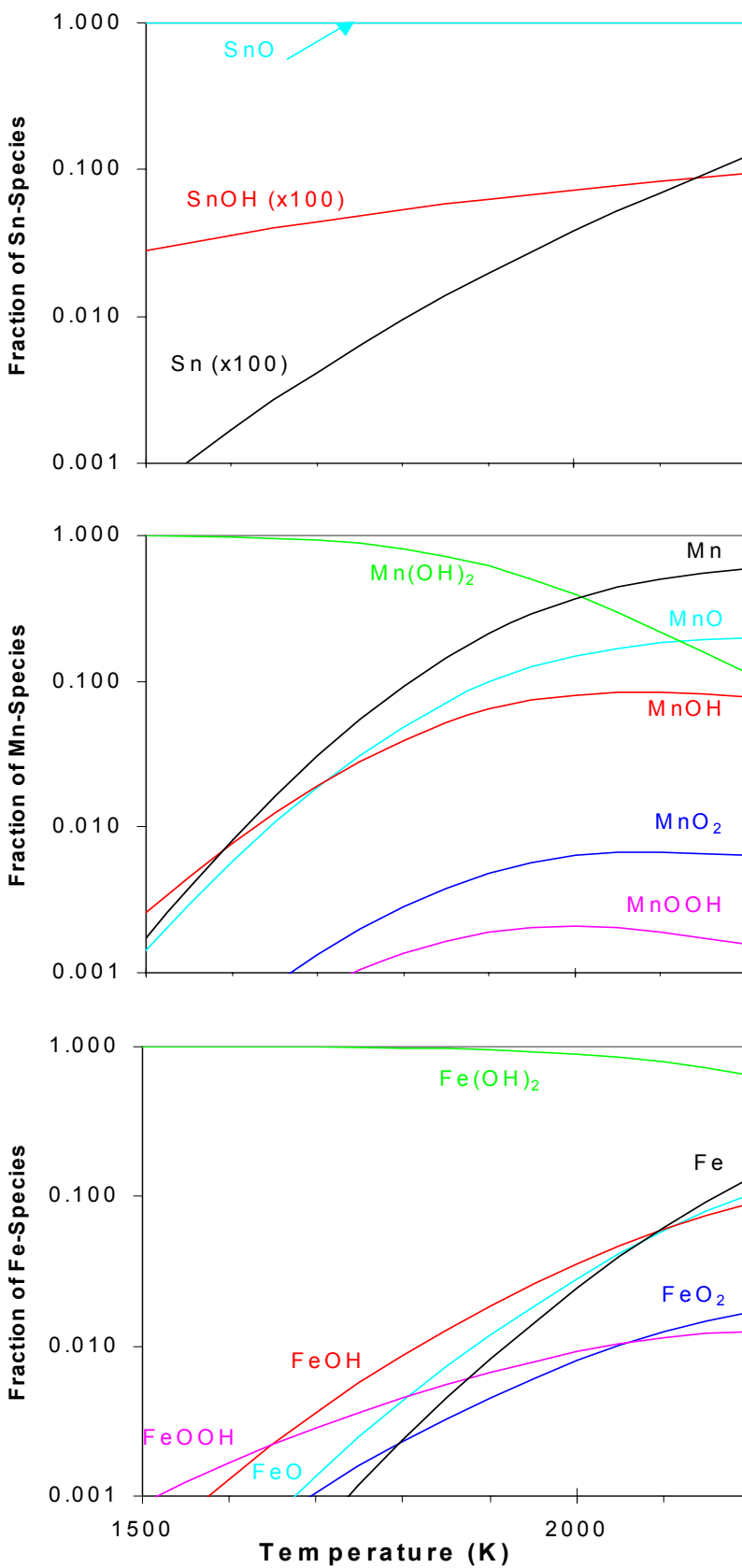


**Figure 3-41 Fractions of Sn-, Mn-, and Fe-species at Equilibrium in Methane-air Flames as a Function of Temperature.**

## Conclusions

This section described the first experimental measurements of the influence of manganese- and tin-containing compounds (MMT, TMT) on the burning velocity of methane/air flames. Comparisons with the agents  $\text{Fe}(\text{CO})_5$  and  $\text{CF}_3\text{Br}$  demonstrated that manganese and tin-containing compounds are effective inhibitors. The inhibition efficiency of MMT was about a factor of two less than that of iron pentacarbonyl. TMT was about 26 times less effective, although it was still about twice as effective as  $\text{CF}_3\text{Br}$ . There were conditions for which both MMT and TMT showed a loss of effectiveness beyond that expected due to radical depletion, and the cause is believed to be particle formation. Kinetic models describing the inhibition mechanisms of MMT and TMT additives were suggested. Simulations of MMT- and TMT-inhibited flames showed reasonable agreement with experimental burning velocity data. The decomposition of the parent molecule for the tin and manganese species was found to have a small effect on the inhibition properties for the range of concentrations used in this work. Calculations confirmed that the main tin-containing species in the flame zone was  $\text{SnO}$ , while the concentrations of  $\text{SnO}_2$ ,  $\text{SnOH}$  and  $\text{Sn}$  were relatively small. The inhibition effect of TMT was determined mostly by the rate of the association reaction  $\text{H} + \text{SnO} + \text{M} \leftrightarrow \text{SnOH} + \text{M}$ , and the catalytic recombination cycle was completed by the reactions  $\text{SnOH} + \text{H} \leftrightarrow \text{SnO} + \text{H}_2$  and  $\text{SnOH} + \text{OH} \leftrightarrow \text{SnO} + \text{H}_2\text{O}$ . The inhibition mechanism of manganese-containing compounds was similar, in many details, to the inhibition mechanism for iron pentacarbonyl:  $\text{MnO} + \text{H}_2\text{O} \leftrightarrow \text{Mn}(\text{OH})_2$ ;  $\text{Mn}(\text{OH})_2 + \text{H} \leftrightarrow \text{MnOH} + \text{H}_2\text{O}$ , and  $\text{MnOH} + \text{OH}$  (or  $\text{H}$ )  $\leftrightarrow \text{MnO} + \text{H}_2\text{O}$  (or  $\text{H}_2$ ). The burning velocity was most sensitive to the rate of  $\text{Mn}(\text{OH})_2 + \text{H} \leftrightarrow \text{MnOH} + \text{H}_2\text{O}$  reaction. Comparison of the mechanisms of inhibition of TMT and MMT to  $\text{Fe}(\text{CO})_5$  showed that the manganese was not as efficient an inhibitor as iron: due to equilibrium constraints, the mole fraction of the intermediate species  $\text{Mn}(\text{OH})_2$  drops off at higher temperature (in comparison to  $\text{Fe}(\text{OH})_2$ ), slowing its rate-limiting reaction with  $\text{H}$  atom in the catalytic cycle. This result illuminated the role of equilibrium constraints on species concentrations in the efficiency of catalytic cycles.

### 3.3.5 Complexation/Matrix Absorption of Super-effective Agents

#### Introduction

While the high flame inhibition effectiveness of these types of compounds would appear to encourage their pursuit as potential fire suppressants, their high toxic potency is a severe deterrent. (See Chapter 6.) To overcome this limitation, the NGP examined means to absorb or adsorb such compounds into an inert matrix for transport to and release in the flame zone. Alternatively, perhaps other, non-toxic compounds of these metals existed which are also superb inhibitors and which maintain their action up to higher mole fractions. Iron-containing compounds, and in particular  $\text{Fe}(\text{CO})_5$ , were the initial focus of the research. They had been found to be the most efficient metallic flame inhibitors, and thus would be most able to overwhelm the additional mass of the matrix material or complexing moiety and contend with halon 1301 in flame suppression efficiency.

#### Absorption Tests of $\text{Fe}(\text{CO})_5$ into Matrix Materials

The objectives of this research<sup>85</sup> were to develop a system for introducing the inhibitor into matrix materials, quantify the absorption and desorption processes of the inhibitor into and out of the matrix, and investigate the thermal stability of the matrix-inhibitor combination.

### ***Matrix Materials and Super Agents Considered***

The selection of matrix material had to consider several key factors:

- Since the primary purpose of the matrix was safe storage and transport of the superagent, it needed to be inert. Porous silica and aerogel fit these criteria well. Zeolite particles have  $\text{Na}^+$  imbedded in the structure and could influence the flame inhibition. Porous carbon particles were not considered, since they could promote flame propagation through oxidation of carbon.
- For efficient loading of agent, the matrix needed to have a high surface area to mass ratio. Zeolite particles have a high ratio of about  $800 \text{ m}^2/\text{g}$ , while crystalline sodium bicarbonate particles have a very low value. The porous silica particles considered had an intermediate value of  $550 \text{ m}^2/\text{g}$ . Aerogel particles have high pore volume to mass, but offer lower agent adsorption surface area.
- The matrix particles had to be seedable into flames. Submicron particles were hard to seed in a steady, consistent manner as opposed to particles above  $5 \mu\text{m}$ . In this regard, zeolite particles with a mean diameter of  $2 \mu\text{m}$  were on the borderline, and the maximum mass loading of seeded zeolite particles did not exceed 0.6 %. In comparison, porous silica particles in the size range of  $15 \mu\text{m}$  to  $40 \mu\text{m}$  were well behaved in the seeder, and a mass loading as high as 6 % was attained in flame experiments.
- The desorption rate of the agent from the pore structure had to be favorable.
- The matrix material had to be stable during the heating and desorption process. A sample of zeolite particles collected after passing through a premixed flame indicated spherical particles greater than the initial size. This perhaps indicated that the matrix material had melted and, through agglomeration, formed large spherical particles.

Because of the superior flame inhibition properties of  $\text{Fe}(\text{CO})_5$ , most of the absorption effort was devoted to this compound. For safety, some experiments were conducted with molecular iodine as a surrogate material for testing the performance of an absorbed agent.

### ***$\text{Fe}(\text{CO})_5$ Absorption Method***

Iron pentacarbonyl was absorbed into particles of zeolite- $\text{NaX}$ , zeolite- $\text{NaY}$ , silica aerogel, and porous silica, as well as  $\text{NaHCO}_3$  and  $\text{Na}_2\text{CO}_3$ . The system developed for introducing the  $\text{Fe}(\text{CO})_5$  into the various matrix materials is shown in Figure 3-42. The technique is a standard method for absorbing compounds into matrix materials. The apparatus was evacuated to a pressure of 7 Pa. In the initial absorption studies, about 1 g of solid support material was first inserted into one of the tubes. This sample was then heated under vacuum for 3 h to 4 h to remove the absorbed gases from the internal pore structure. The support material was then allowed to return to room temperature. The  $\text{Fe}(\text{CO})_5$  to be absorbed was poured into the second tube, with the interconnecting valve closed. While keeping the  $\text{Fe}(\text{CO})_5$  close to its freezing temperature, the valve in the interconnecting tube was opened briefly to remove the gas- $\text{Fe}(\text{CO})_5$  mixture. Finally, the valve to the suction pump was closed and the interconnecting valve was left open, allowing the  $\text{Fe}(\text{CO})_5$  vapor to diffuse and absorb into the pore structure. This process typically took about one to two days.

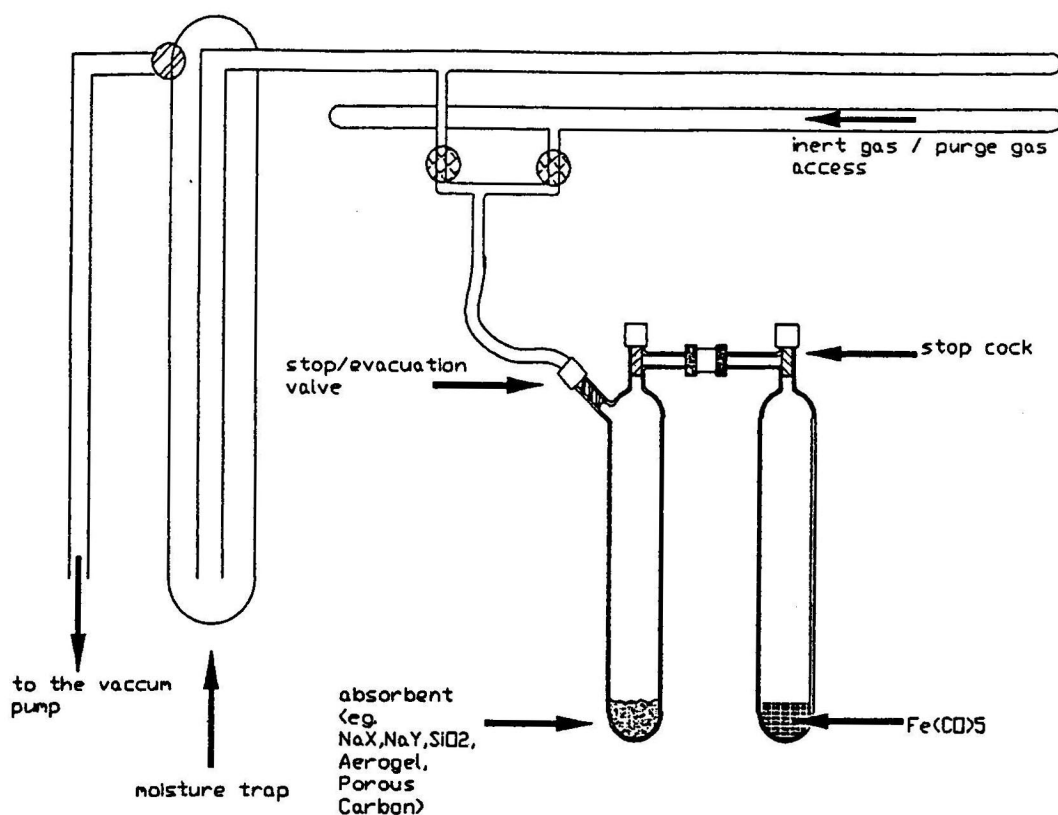


Figure 3-42. Schematic of the Experimental Setup for  $\text{Fe}(\text{CO})_5$  Absorption.

### *Fe(CO)<sub>5</sub> Absorption Results*

For zeolite-NaX with pore volume of  $0.3 \text{ cm}^3/\text{g}$ ,<sup>208</sup> the estimated mass of  $\text{Fe}(\text{CO})_5$  required to completely saturate the internal pore volume was about  $0.3 \text{ g/g}$  of zeolite-X. About 10 % of additional  $\text{Fe}(\text{CO})_5$  was generally poured into the glass tube to ensure complete absorption. Based on the mass increase of the tube containing zeolite-NaX, about 33 % increase in gross mass of the particles was observed, which was consistent with the estimate based on the internal pore volume. This implied that the particles of zeolite-NaX absorb the  $\text{Fe}(\text{CO})_5$  into their pore structure, as opposed to just adsorbing the agent onto the external surface. This amount of mass uptake was encouraging, since only  $100 \text{ }\mu\text{L}$  of  $\text{Fe}(\text{CO})_5$  added to one L of reaction zone volume should reduce the overall reaction rate by a factor of four. Thus, adding a mass loading of particles of 1 % should provide sufficient  $\text{Fe}(\text{CO})_5$  to yield an observable burning velocity or extinction strain rate reduction in our apparatus.

After the  $\text{Fe}(\text{CO})_5$  was absorbed into the zeolite-NaX, the particles changed color to a faint brown/yellow. Based on the color change, the absorption appeared to be uniform in the zeolite particle sample. In addition, a very faint coating (presumably  $\text{Fe}(\text{CO})_5$ ) was observed on the tube walls. When the absorption process was allowed to take place with the chemical hood light on, the color of the  $\text{Fe}(\text{CO})_5$ -absorbed zeolite particles was a darker shade of brown. This was believed to be caused by the decomposition of  $\text{Fe}(\text{CO})_5$  to  $\text{Fe}_2(\text{CO})_9$  (iron nonacarbonyl) in the presence of light.

When the  $\text{Fe}(\text{CO})_5$ -absorbed zeolite-NaX was exposed to air by opening the valve, a reaction front propagated rapidly across the sample, sometimes with a bright orange-colored emission (apparently a flame inside the absorption tube). Hence, it appears that the iron pentacarbonyl reacted pyrophorically with air. Additional experiments were conducted by exposing the  $\text{Fe}(\text{CO})_5$ -impregnated zeolite-NaX particles to either pure oxygen or nitrogen. In oxygen, the particles showed even more violent reaction, whereas in nitrogen, there was no reaction. These tests showed that the decomposition process was related to the oxygen concentration. While these observations were qualitative, this unexpected result indicated that zeolite-NaX may not be an appropriate support matrix for delivering unreacted  $\text{Fe}(\text{CO})_5$  to a flame, and other support materials were pursued.

There is a theoretical basis for believing that zeolite-NaY would be a more desirable support material than would be zeolite-NaX. The surface physical-chemical properties of the zeolite likely have an important role in the  $\text{Fe}(\text{CO})_5$  decomposition process. The general formula for a unit cell of zeolite is given by  $\text{Na}_x\text{Al}_x\text{Si}_{192-x}\text{O}_{384}\cdot y\text{H}_2\text{O}$ , where  $x$  ranges from 48 to 74 for zeolite Y and from 74 to 96 for zeolite X. While the cage structures of zeolite-NaX and -NaY are similar, the difference between them is in the content of cation  $\text{Na}^+$  in the solid matrix. The lower  $\text{Na}^+$  content of zeolite-NaY leads to weaker internal electric fields than in zeolite-NaX, and hence a lower propensity for decomposition of the  $\text{Fe}(\text{CO})_5$  in zeolite-NaY. When exposed to air, the  $\text{Fe}(\text{CO})_5$ -absorbed zeolite-NaY also indicated  $\text{Fe}(\text{CO})_5$  decomposition, but the intensity of the observed reaction was much slower than with zeolite-NaX. Tests with porous silica particles gave weak indication of  $\text{Fe}(\text{CO})_5$  decomposition.

Besides porous silica particles, aerogel particles synthesized at University of Virginia were also tested as a possible support material. These particles were formed by hydrolysis of tetraethyl orthosilicate ( $\text{Si}(\text{OC}_2\text{H}_5)_4$ ) in ethanol, followed by drying to remove extra ethanol and water, leaving behind a solid matrix which was 96 % porous. Three  $\text{Fe}(\text{CO})_5$  absorption experiments were conducted with the aerogel particles produced using the apparatus in Figure 3-42. Prior to absorbing  $\text{Fe}(\text{CO})_5$ , the aerogel particles were heated to 200 °C to 250 °C to remove as much moisture as possible. The first sample indicated a particle mass increase of about 200 %. Two subsequent absorption experiments with aerogels, however, indicated  $\text{Fe}(\text{CO})_5$  absorption of 14 % and 101 % of the aerogel particle mass. (Note that the second sample was from the same batch of aerogel as the first, while the third sample was from a newly synthesized batch of aerogel.) Furthermore, both the second and third samples reacted after about 5 min to 10 minutes exposure to air, while the first sample with substantially larger increase in mass did not react when exposed to air for a long period of time.

The decreased uptake of  $\text{Fe}(\text{CO})_5$  in the second and third aerogel samples and the subsequent reaction when exposed to air led to the hypothesis that either water or ethanol in the aerogel (from the synthesis process described above) was not completely removed. Since  $\text{Fe}(\text{CO})_5$  is known to react violently with water, the absorbed water was perhaps the most likely cause for the above discrepancy in  $\text{Fe}(\text{CO})_5$  absorption and its decomposition.

### ***Quantification of $\text{Fe}(\text{CO})_5$ Absorption/Desorption***

A standard technique for measuring the desorption or the decomposition properties of materials is thermogravimetric analysis TGA. In these tests, the sample is continuously weighed, while its temperature is increased. Zeolite, silica, and aerogel samples were heated to about 500 °C in steps of 5 °C/min, while  $\text{NaHCO}_3$  and  $\text{Na}_2\text{CO}_3$  were heated only to 150 °C because of their propensity to decompose. The TGA analyses required transferring of the  $\text{Fe}(\text{CO})_5$  absorbed particles from the

absorption flask to the weighing pan of the TGA. During this process, some fraction of the particles could react with ambient air, so the transfer time was strongly minimized. TGA analyses were performed for all of the absorbed particles. The  $\text{Fe}(\text{CO})_5$ -absorbed aerogel particles did not react immediately when exposed to air, hence the desorption of  $\text{Fe}(\text{CO})_5$  from these particles measured via TGA was probably the most reliable. However, the desorption from aerogels showed a great variation from sample to sample, ranging from 5 % to 200 %.

The data in Table 3-10 help understand the desorption loss from the various types of  $\text{Fe}(\text{CO})_5$ -laden particles following exposure to air. The elemental analyses (by Southern Testing and Research Laboratories) quantify the amount of Fe and Na remaining in the particles.

- The second column lists the Fe remaining in the sample, based on the weight loss of the sample in the TGA measurements.
- The third and fifth columns provide the Fe and Na remaining in the samples following exposure of the specimens to air at ambient temperature.
- The fourth and sixth columns show the Fe and Na remaining following heating at 500 °C in air for several hours to ensure that  $\text{Fe}(\text{CO})_5$  was fully decomposed.

**Table 3-10. Summary of the Fe and Na Mass Loadings in Unheated and Heated Particles.**

Support Material	From TGA	From Elemental Analysis			
	Fe (% by Mass)	Fe (% by Mass)		Na (% by Mass)	
	Heated	Unheated	Heated	Unheated	Heated
Zeolite-NaX	$7.1 \pm 0.7$	$8.9 \pm 0.9$	$7.1 \pm 0.7$	$11.0 \pm 1.1$	$9.8 \pm 1.0$
Zeolite-NaY	$7.1 \pm 0.7$	$9.7 \pm 1.0$		$6.8 \pm 0.7$	
Porous Silica	$6.0 \pm 0.6$	$12.8 \pm 1.3$	$6.8 \pm 0.7$	< 0.8	< 0.1
Silica Aerogel	4 to 57				
$\text{NaHCO}_3$	$5.0 \pm 0.5$	<0.1	< 0.2	$28.0 \pm 2.8$	$41.0 \pm 4.1$
$\text{Na}_2\text{CO}_3$	$2.0 \pm 0.2$				

- It was not resolved whether the observed weight loss was due to desorption of undissociated  $\text{Fe}(\text{CO})_5$  or decomposed carbonyl.
- Comparison of columns 3 and 4 indicates that heating of the reacted particles had a small effect on the absorbed  $\text{Fe}(\text{CO})_5$  for zeolite particles, but a larger effect for porous silica particles. Hence, it is possible that most of the  $\text{Fe}(\text{CO})_5$  remaining in the unheated zeolite particles was no longer intact  $\text{Fe}(\text{CO})_5$  that could be liberated by heating, but rather was already decomposed.
- For porous silica, about half of the  $\text{Fe}(\text{CO})_5$  was decomposed or unavailable for liberation by heating.
- The Fe and Na mass fractions remaining in the zeolites were considerable and similar. If the Na could be liberated from the zeolite particles in the flame, they might provide flame inhibition even without added iron.

In order to determine whether any unreacted  $\text{Fe}(\text{CO})_5$  remained inside the particle after exposure to air, infrared (IR) spectroscopy analysis was performed. The reacted zeolite or porous silica particles were

crushed and then mixed with potassium bromide particles. This mix was then pressed to form a thin wafer and then tested in the IR spectrometer. The absence of significant absorption of the Fe-CO stretching bond (characteristic of  $\text{Fe}(\text{CO})_5$ ) indicated that there was little  $\text{Fe}(\text{CO})_5$  remaining in the solid support matrices.

The  $\text{Fe}(\text{CO})_5$ -impregnated and reacted zeolite particles were also analyzed using the high-resolution transmission electron microscope (HRTEM). Images of zeolite-NaX particles after absorption of  $\text{Fe}(\text{CO})_5$  and exposure to air showed that a condensed phase substance formed on the exterior surface. For example, the left frame of Figure 3-43 shows an image of a zeolite particle after  $\text{Fe}(\text{CO})_5$  was absorbed and then the sample exposed to air. For comparison, the right frame shows an image of a pure zeolite particle. In the left frame, the zeolite-NaX particle is shown to have a diameter on the order of a micrometer, with pore sizes of the order of 1 nm, while nodules of condensed-phase material (perhaps Fe, FeO, or  $\text{Fe}_2\text{O}_3$ ) have diameters of about 20 nm and are rather well dispersed on the support material. The formation of these condensed-phase nodules implies that  $\text{Fe}(\text{CO})_5$  may not be available from the matrix to provide gas phase Fe, which is required for efficient flame inhibition.

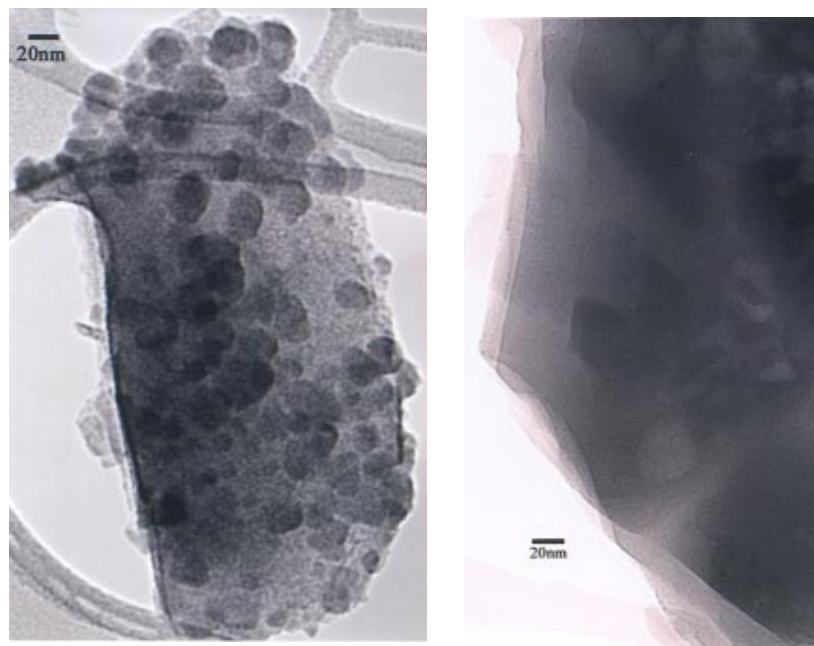


**Figure 3-43. High Resolution Transmission Electron Micrograph Images of Zeolite-NaX Particles. Left: with condensed phase iron species on surface; right: without  $\text{Fe}_2\text{O}_3$  clusters.**

## Methods of Quantifying Suppression Effects by Particulates

### *Test Burners*

Two burner types were selected as test beds for the particles: a premixed Bunsen-type nozzle burner, and a gaseous counterflow diffusion flame burner, also with nozzle-generated flows. These flames were selected for several reasons:

- Both types, unlike co-flow diffusion flame burners (such as a cup burner), allowed unambiguous determination of the amount of agent that reaches the relevant high-temperature reaction region of the flame. This is difficult in cup burner flames, since the transport of agent or particles to the appropriate region of the cup burner is complex; moreover, stabilization (and therefore extinction) of cup burner flames is not presently well understood theoretically.
- Cup burner tests allowed flames at only one strain rate, whereas counterflow diffusion flames allowed tests at variable strain rates.
- The premixed flames mitigated the hazard from  $\text{Fe}(\text{CO})_5$ -impregnated particles contaminating the laboratory space. Premixed flames involved much smaller quantities of gas and particles, and all of the reactants passed through a flame.
- Both counterflow diffusion flames and premixed flames directly provide a measure of the overall reaction rate in the flame, in a configuration which is easily interpreted or modeled. Peters<sup>209</sup> has shown, on a theoretical basis, that for the performance of a chemical catalytic inhibitor, the two burners should be correlated.

### *Particle Seeder*

Chelliah and co-workers designed, built, and tested an effective particle seeding system for introduction of the  $\text{NaHCO}_3$ , silica, zeolite, or aerogel particles to both counterflow diffusion flames and premixed Bunsen-type flames. The design became the basis for particle experiments discussed in Chapter 4.

Because of the challenge in verifying the accuracy of previously reported data with  $\text{NaHCO}_3$  particles,<sup>210,211</sup> considerable attention was devoted to the development of a particle seeder that could provide steady feed rates of particles of various diameters. For the small air flows involved (typically 0.1 L/s), the fluidized bed approach shown in Figure 3-44 gave satisfactory seeder performance for relatively small particles, i.e., less than 30  $\mu\text{m}$  in diameter. This fluidized bed seeder consisted of a 19 mm diameter glass tube with two porous plugs at either end. The air flow to the seeder was controlled through a mass flow controller and split into two streams, which were connected to either end of the glass tube. The flow passing through the bottom, which controlled the fluidization level, was monitored through another flow controller. The fluidized particles and the air entering the fluidization tube (from the top and bottom) were extracted through a small tube located near the middle of the tube. By maintaining the total air flow to the fluidizer tube constant, the particle feed rate was steady, as verified by continuously monitored the light scattered from the particle stream (Figure 3-44). The detection system consisted of a laser diode (671 nm), a high speed silicon detector (Thor Labs DET1-SI ) with a 3 cm focal length collection lens, a laser line filter at 671 nm (Edmund Scientific), and a strip chart recorder (Hewlett-Packard Model 7132) to monitor the detector output.

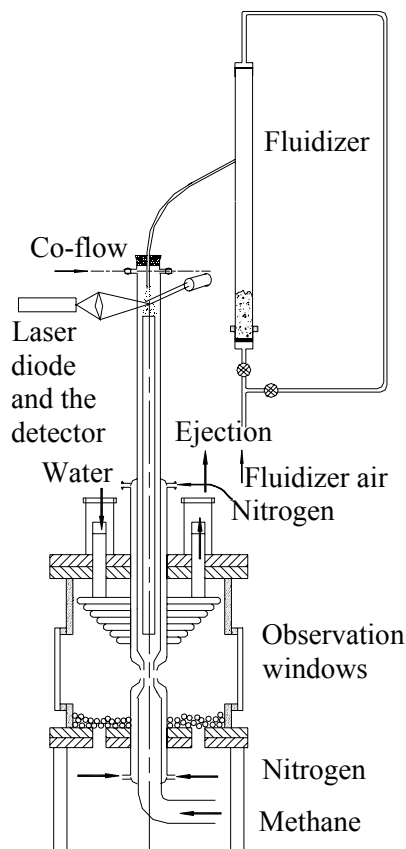


**Figure 3-44. Schematic Diagram of Counterflow Diffusion Flame Burner with Provision for Addition of Particles to the Air Stream.**

### ***Flow Profile Measurement***

For both burners, a laser Doppler velocimetry (LDV) system was used to establish the quality of the top hat velocity profile leaving the nozzle exit and to measure the local strain rate in the counterflow field. Because the enclosed counterflow burner permitted optical access from the two opposing sides, an on-axis forward scattering LDV configuration was selected. The LDV system consisted of an Argon Ion laser (Lexel Model 95) operating at 514.5 nm with a beam splitter and 300 mm focal length transmitting lens (DISA) to obtain two equal intensity beams forming a fringe pattern at the intersection of the focused beams. The probe volume was 0.151 mm wide and 1.51 mm long, with a fringe spacing of 2.57  $\mu\text{m}$ . The collection optic system (DISA) gathered the forward scattered photons from the particles and imaged them on a photomultiplier tube (PMT). The PMT current was amplified (C-Cor Electronics Model 4375A Wideband Video Amplifier) and processed by a timer/counter (TSI Model 1990B) operated in the single burst mode using 8 cycles/burst. The filtered and amplified timer/counter signal was monitored by an oscilloscope (Tektronix Model 2212), and the digital output was interfaced to a personal computer using a digital input card (National Instruments DAQ pad 6510) and processed using data acquisition software (LabView). Measured frequencies were related to particle velocity using the known fringe spacing. To facilitate acquisition of velocity profiles in axial and radial direction of the counterflow field, both fringe generating and collecting optics were mounted on translation stages (Velmex Unislide Model MB2500), which had a minimum step size of 1  $\mu\text{m}$ , with a reported accuracy of 5  $\mu\text{m}$  in 100 mm. Figure 3-45 shows typical velocity profiles at the exit of the premixed burner nozzle for two different volume flows. For comparison, the calculated top-hat velocity profiles are also shown as dotted lines.

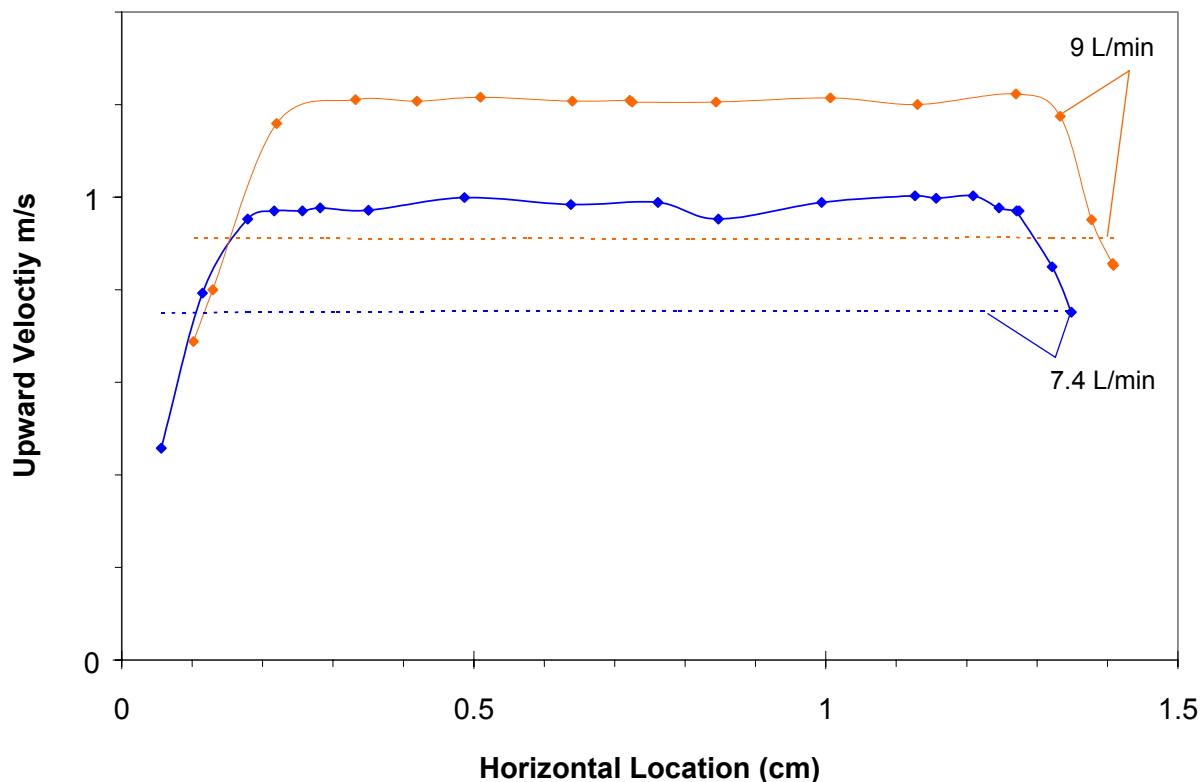
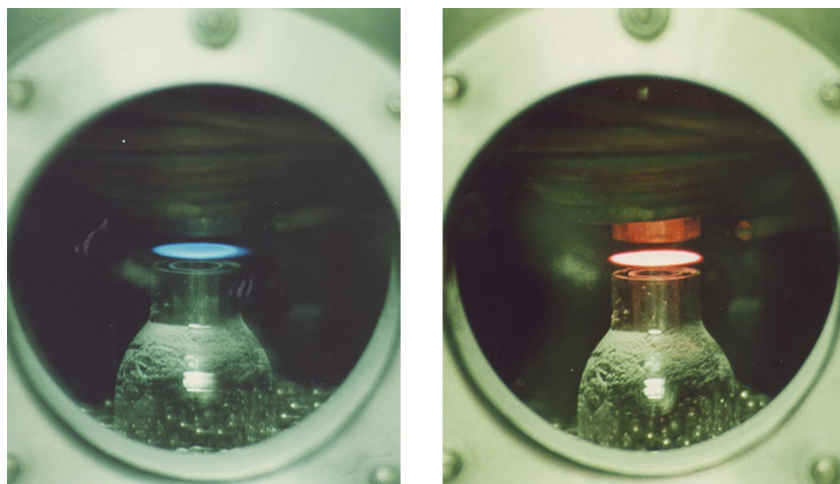


**Figure 3-45. Calculated (dotted lines) and LDV-measured (points) Velocity Profiles at Exit of Premixed Burner Nozzle for Total Flows of 7.4 and 9 L/min.**

#### *Counterflow Diffusion Flames with Inert and NaHCO<sub>3</sub> Particles*

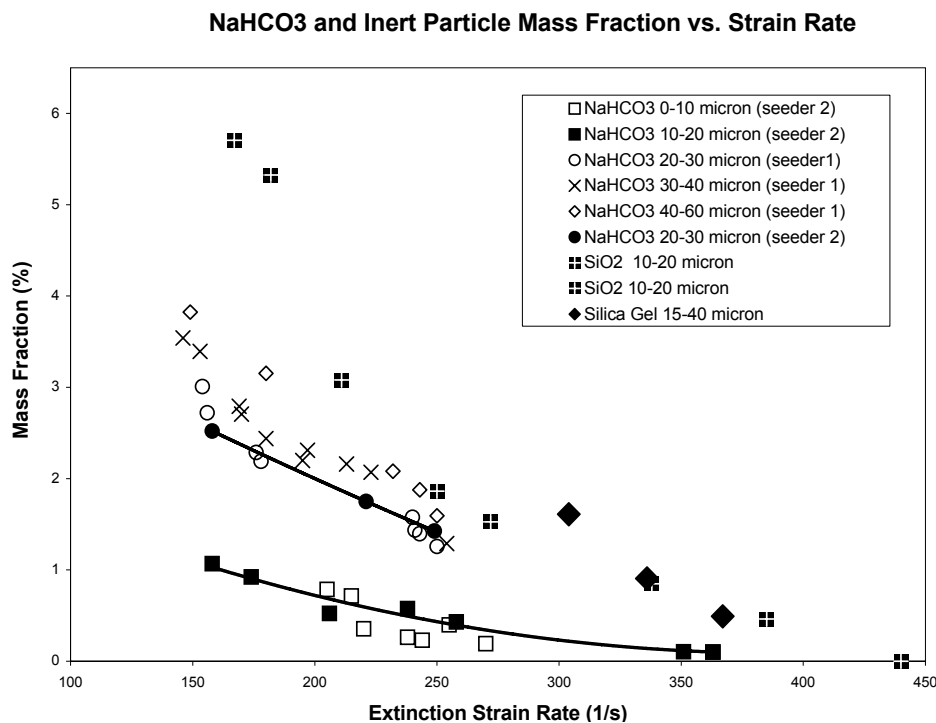
Prior to testing agent-loaded particles, sodium bicarbonate and pure silica particles were used as the test cases for development of the seeding and burner systems.

Figure 3-44 shows the experimental setup of the counterflow burner. A steady, planar, non-premixed flame was established in the mixing layer of counterflowing methane and air streams. The fuel and air nozzles were made from Pyrex glass. The exit diameter of the inner tubes was 15 mm with a nozzle area contraction factor of 6.5, producing a nearly plug flow velocity profile at the nozzle exit. The co-annular nitrogen streams on both fuel and air sides helped maintain a stable planar flame disk. The cylindrical burner chamber included provision for dilution of the chamber with room air at the bottom (to minimize the occurrence of secondary flames), water cooling, and easy adjustment of the nozzle separation distance via o-ring sealed vacuum fittings (MDC). The typical separation distance between the two nozzles was 10 mm to 12 mm. The exhaust gases were evacuated using an air-driven mass flow ejector, with the chamber pressure monitored by a differential pressure gauge. The methane was BOC grade 4.0 with a purity of 99.99 %. The air was supplied by an oil-free compressor and dried by a series of desiccant beds. The flows of fuel and air were controlled using factory-calibrated mass flow meters (Teledyne Hastings-Raydist), with a reported accuracy of  $\pm 1\%$ . Figure 3-46 shows an image of a typical flame disk established without and with NaHCO<sub>3</sub> particles.



**Figure 3-46. Methane-air Counterflow Diffusion Flames: Pure (left), and with NaHCO<sub>3</sub> Particles (right).**

Experiments were conducted to test the system and to establish the effectiveness of particle size on non-premixed flame suppression. These results are shown in Figure 3-47 as the mass fraction of NaHCO<sub>3</sub> needed vs. flow strain rate at extinction, for particle sizes 10 μm to 20 μm, 20 μm to 30 μm, 30 μm to 40 μm, and 40 μm to 60 μm. For comparison, the effectiveness of 10 μm to 20 μm crystalline silica particles are also shown. It is clear that NaHCO<sub>3</sub> particles below 20 μm were significantly more effective in this flow field. As the NaHCO<sub>3</sub> particle size increased, the performance approached that of the inert silica particles.



**Figure 3-47. NaHCO<sub>3</sub> and Silica Mass Fraction vs. Methane-air Nonpremixed Extinction Strain Rate.**

Figure 3-48 shows two photographs of the crossed laser beams from an LDV system penetrating a non-premixed counterflow methane–air flame seeded with 40  $\mu\text{m}$  to 60  $\mu\text{m}$   $\text{NaHCO}_3$  particles. In the upper image, the beams are above the flame, in the region between the flame and the incoming air stream (which is laden with particles), so that the particles have not yet reached the flame. Laser scattering from the particles is clearly visible. In the lower image, the beams are located below the flame and there is still obvious laser light scattering, indicating these large particles survive through the flame. This behavior results in the lower suppression effectiveness as illustrated in Figure 3-47. These results also indicate that even inert particles tend to reduce the flame extinction rate with increasing particle loading. Such effects can be related to the thermal effects associated with heating of these inert particles. (See Chapter 4.)

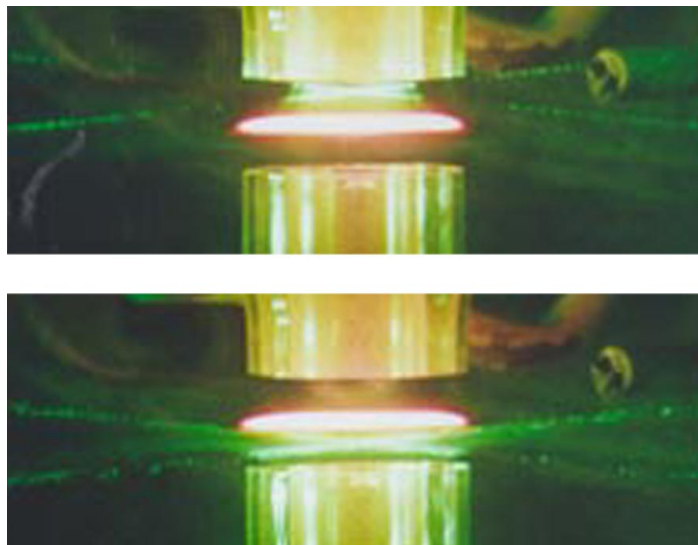


**Figure 3-48 – Laser Scattering of  $\text{NaHCO}_3$  Particles in a Counterflow Diffusion Flame of Methane and Air, Showing that the Particles Pass Through the Flame.**

Parallel modeling efforts have shown that by selecting an appropriate value for the particle decomposition temperature, the experimental results shown in Figure 3-47 can be replicated. With a fixed particle decomposition temperature, the trends observed in Figure 3-47 for the variation in effectiveness due to particle size were then captured. The outcome of such modeling results was that the existence of a critical particle size which was effective in this flow field was directly related to the flow residence time, hence the heating of the particle and its decompositions rate, which would ultimately control the chemical effectiveness.

#### ***Premixed Flames with Inert and $\text{NaHCO}_3$ Particles***

A Mache-Hebra nozzle burner (1.5 cm  $\pm$  0.05 cm diameter) produced a premixed Bunsen-type flame about 1.9 cm tall with a straight sided schlieren image that was captured by a CCD array camera connected through a USB port to a PC. Digital mass flow controllers held the equivalence ratio  $\phi$  and the flame height constant while the mass flow of particles from the seeder was set at the desired value. The average burning velocity was determined from the reactant flows and the schlieren image using the flame angle method<sup>187</sup> from the measured velocity profile. The fuel gas was methane (BOC grade 4.0; 99.99 %), and the oxidizer stream consisted of laboratory air from an oil-free compressor which was dried by a series of desiccant beds. Air and fuel gas flows were set by PC-controlled mass flow controllers (Sierra, 860). Figure 3-49 shows this burner operating with methane-air, with and without  $\text{NaHCO}_3$  particles added to the reactant flow.

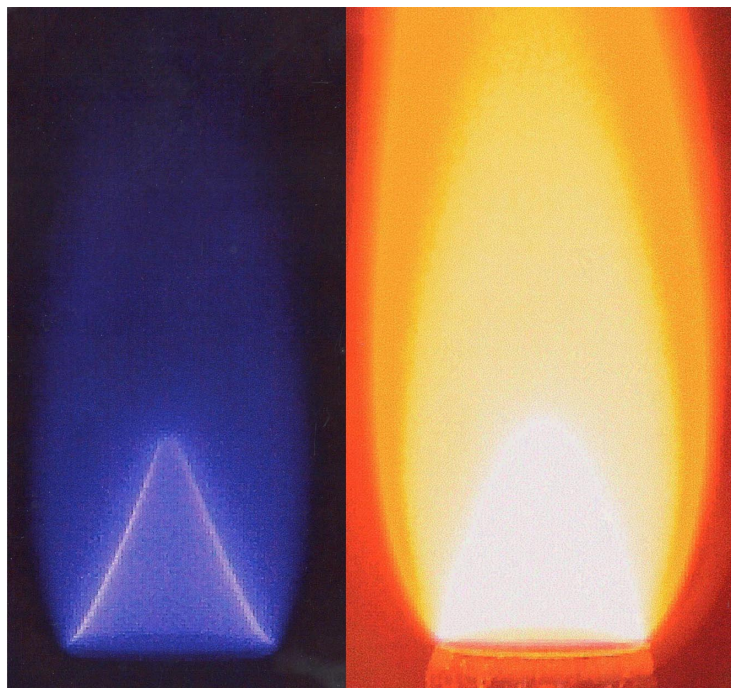


**Figure 3-49. Premixed Methane-air Nozzle Burner Flames: Pure (left) and with NaHCO<sub>3</sub> Particles (right).**

Using the LDV system, the burner exit velocity was characterized in the presence of silica, zeolite, and sodium bicarbonate particles (Figure 3-50). The results indicate that the inert silica particles and zeolite-NaX have a minor effect on the measured burning velocity, while NaHCO<sub>3</sub> has a noticeable effect.

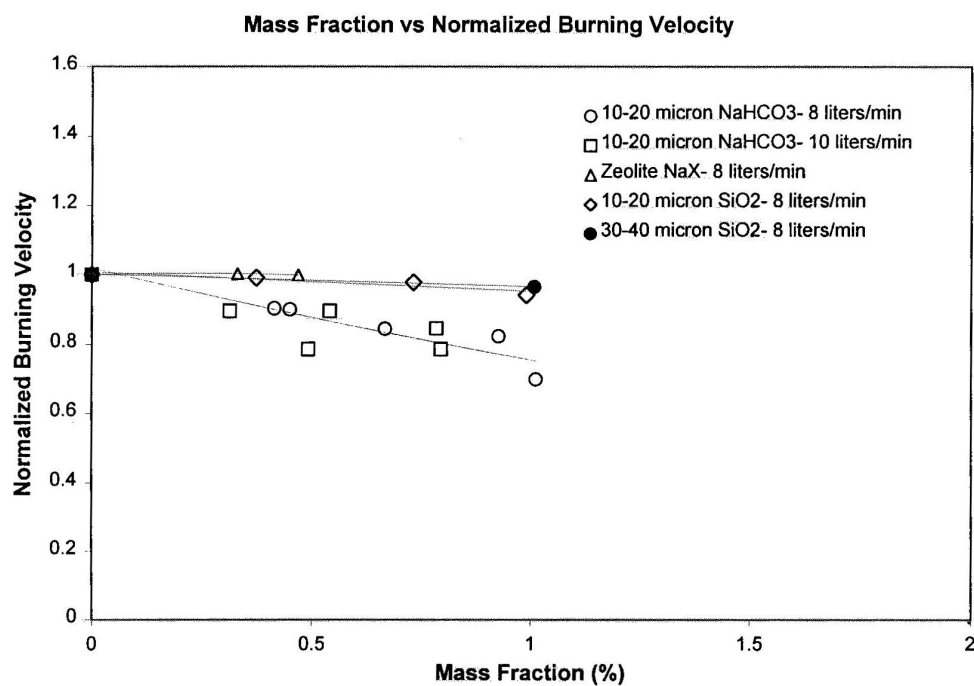


**Figure 3-50. Comparison of Normalized Burning Velocities with Added Particles.**

Comparison of the relative reduction of normalized, non-premixed flame extinction strain rates with normalized premixed burning velocities indicated significant differences. However, such comparisons should take into account the structural differences of the two flames. As shown by Peters<sup>209</sup> and employed by Chelliah et al.<sup>212</sup> for chlorinated hydrocarbon flames, the normalized burning rate is related to the normalized extinction strain rate as  $S_L/S_{L,0} = \sqrt{(a_{ext}/a_{ext,0})}$

Using this correlation, the comparison of the non-premixed and premixed flames inhibited with  $\text{NaHCO}_3$  is shown in Figure 3-51. The disagreement between the two was somewhat greater than the uncertainty in each measurement; however, this disagreement was much less expected based on the significantly different structures of the premixed and diffusion flames. The results suggested that tests with either flame should be roughly comparable in demonstrating the effectiveness of chemically acting agents on the global reaction rate in methane-air flames. On the other hand, the data for inert particles in premixed and counterflow diffusion flames from Figure 3-47 and Figure 3-50, if plotted in Figure 3-51, would show a significant discrepancy. Most likely, these differences are related to the thermal effects associated with varying particle residence time in the two flows considered, and further analysis is required.

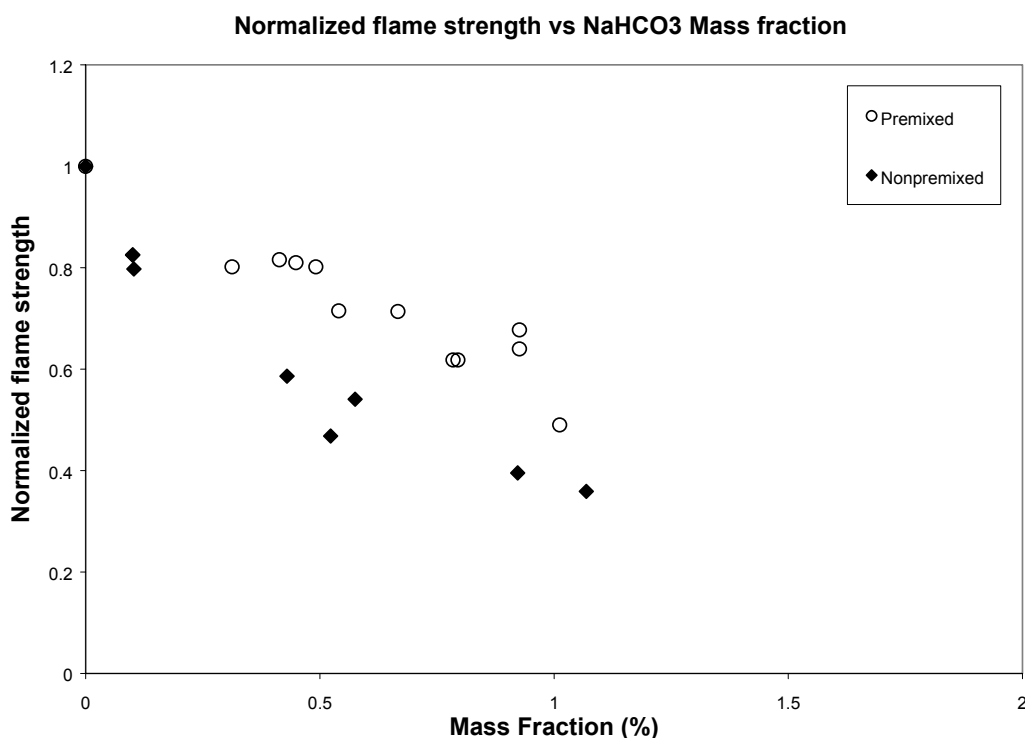


**Figure 3-51. Normalized Flame Strength as a Function of Added  $\text{NaHCO}_3$  Mass Fraction for Premixed and Counterflow Diffusion Flames.**

In summary, this fluidized-bed seeding system described was effective for introducing particles smaller than  $30\ \mu\text{m}$  to the premixed and counterflow burners. The experimental techniques developed were amenable to testing the efficacy of particles with absorbed super-agents in these flames. The effectiveness of particles (which either decompose or release an absorbed agent) was expected to be dependent upon the residence time for this process.

### Premixed Flames with Iodine

Due to the unexpected decomposition of  $\text{Fe}(\text{CO})_5$  within the solid support material and the potential hazard from desorption of this toxic compound, molecular iodine was used as a surrogate to assess the storage concept. The matrix material was selected to be silica gel, based on agent mass loading potential and the seeding properties of the particles in the flow.

- Absorption/desorption investigations indicated that an iodine mass fraction of about 24 % could be loaded into zeolite- $\text{NaX}$  particles. However, the maximum particle seeding achievable with the present apparatus used in the premix flame configuration was about 0.5 % by mass (because of very small size, 2  $\mu\text{m}$ ). Thus, the total iodine mass loading of the air stream was about 0.12 %.
- About 6 % mass fraction of  $\text{I}_2$  could be loaded into the milled and sized (10  $\mu\text{m}$  to 20  $\mu\text{m}$  size range) crystalline silica particles. Here, crystalline silica particles were considered because of their better fluidization and seeding characteristics. In the same premixed flame configuration, more than 2 % by mass of sized 10  $\mu\text{m}$  to 20  $\mu\text{m}$  crystalline silica particles could be introduced. The total iodine mass loading of the air stream was thus 0.12 %, similar to that for zeolite- $\text{NaX}$ .
- Selection of the appropriate matrix material for the particles was based on An iodine mass loading of about 20 % was measured for porous silica gel particles (15  $\mu\text{m}$  to 40  $\mu\text{m}$ ).<sup>ii</sup> Particle seeding of up to 6 % by mass was possible, for a theoretical iodine mass delivery of 1.2 %.

Figure 3-52 shows the normalized flame speed of a methane-air flame for increasing particle mass fraction, for pure silica gel and  $\text{I}_2$ -impregnated silica gel. Iodine-absorbed silica particles do not show any significant reduction in burning velocity compared to chemically inert silica particles.

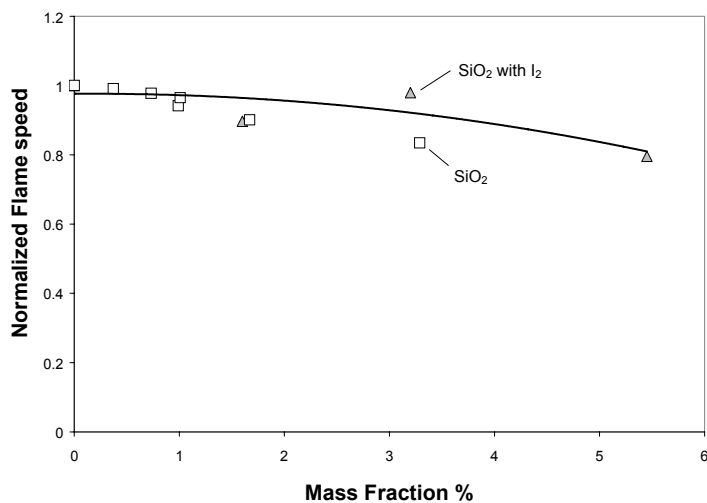


**Figure 3-52. Normalized Flame Speed for a Methane-air Flame with Added Silica Gel Particles (14 to 40) $\mu\text{m}$ , with and without  $\text{I}_2$  Impregnated in the Particles.**

<sup>ii</sup> For porous silica gel particles, TGA analyses of the absorption of iodine were performed on two samples: one tested immediately after the absorption process and the other after the particles had remained in the airflow of the fluidization seeder for several hours. The mass loss from the fresh particles was 19 %, while that from the “aged” particles was about 8 %. There was also a change in the particle color (to a lighter brown shade) after being in the seeder for several hours, a result consistent with the lower mass loss for the post-seeder particles.

This result was not surprising. Based on literature values of the burning velocity reduction of Br<sub>2</sub> in hydrocarbon flames,<sup>186</sup> an estimated I<sub>2</sub> mass loading of 10 % in the air stream would be required to reduce the burning velocity by a factor of two. Hence, even if all of the I<sub>2</sub> in the tested silica gel particles were liberated in the flame, the maximum expected burning velocity reduction would be about 5 % for a 6 % mass loading. In these experiments, such a difference in burning velocity would have been comparable to the experimental uncertainty. For lower iodine desorption rates, the difference between the I<sub>2</sub>-laden and unladen particles would have been undetectable.

Nonetheless, this result was not discouraging. From Table 3-11, the mass loading of Fe(CO)<sub>5</sub> can be about half that of I<sub>2</sub>. However, the flame inhibition effectiveness of Fe(CO)<sub>5</sub> is far higher than I<sub>2</sub>. Thus, further experiments were conducted on alternative means of introducing iron atoms into the flames and on elucidating the potential synergism between super-effective metals and inert additives.

## Complexes of Super-effective Metals

### *Super Agents and Complexing Ligands Considered*

As a first step, the physical and chemical properties of complexes of potential super-effective metal agents were compiled and surveyed. The complexes involved main group metals or transition group metals with different ligands.

**Table 3-11. Components of Metallic Complexes.**

Ligands		Metals	
Organic	Halide	Main Group Metals	Transition Group Metals
acetate (ac)	chloride (Cl)	Group III - aluminum (Al)	copper (Cu)
acetylacetonate (acac)	bromide (Br)	Group IV - tin (Sb), germanium (Ge), lead (Pb)	titanium (Ti)
oxalate (ox)	iodide (I)	Group V - antimony (Sb)	chromium (Cr), molybdenum (Mo)
trifluoroacetylacetonate (TFacac)			manganese (Mn), nickel (Ni), cobalt (Co)
hexafluoroacetylacetonate (Hfacac)			iron (Fe)
methoxide (OMe)			
ethoxide (OEt)			

For the metal-centered halides, it was found that the three most volatile compounds MX<sub>4</sub> were (in order of volatility): TiX<sub>4</sub> < SnX<sub>4</sub> < GeX<sub>4</sub>. The bromides become volatile in the range 70 °C to 150 °C, while the chlorides were higher, in the range (180 °C to 240 °C). Germanium iodide was the iodide compound with the lowest boiling point, estimated near 350 °C.

For the organic-complexes, it was found that the order of volatility was generally



Examples of this include  $\text{Cr}(\text{HFacac})_3$  and  $\text{Cr}(\text{ac})_3$ , which sublime or decompose near 100 °C to 160 °C and 210 °C to 280 °C, respectively, and  $\text{Cu}(\text{HFacac})_2$ ,  $\text{Cu}(\text{TFacac})_2$ , and  $\text{Cu}(\text{acac})_2$ , which sublime or decompose near 130 °C to 180 °C, 180 °C to 210 °C, and 290 °C to 320 °C, respectively.

The relative volatility of complexes was dependent on the metal- or main-group-center atom. The order of volatility for compounds with different ligands varied, dependent upon the ligand. Consequently, a direct ordering was not exact. However, in general the volatility was



That is, aluminum and copper compounds were generally significantly less volatile than lead and germanium compounds.

The selection of a metal complex for initial study was based on the following:

- Known high flame inhibition effectiveness. This narrowed the field to Pb, Cr, and Fe.
- Low toxicity. Pb and Cr compounds are generally toxic in most states, while Fe compounds (other than the pentacarbonyl) are generally of low toxicity.
- The iron atom in the gas phase leads to the inhibiting iron-species intermediates, and that the main property required for the parent molecule is that it readily decomposes at flame temperatures to release iron atom.
- Ferrocene ( $\text{Fe}(\text{C}_5\text{H}_5)_2$  (or Fec) was known to modify the sooting tendency of flames,<sup>127,213-217</sup> was added to materials as a flame retardant,<sup>218</sup> was an antiknock agent, and was used as a source of iron atoms for kinetic studies. It is also far less toxic than  $\text{Fe}(\text{CO})_5$ .

### ***Experimental Apparatus***

Linteris and coworkers performed the first measurements of flame inhibition by ferrocene, and compared its performance with that of  $\text{Fe}(\text{CO})_5$  and  $\text{CF}_3\text{Br}$  in the same flames.<sup>106</sup> They numerically modeled Fec's flame inhibition using the iron-species mechanism developed for studies of  $\text{Fe}(\text{CO})_5$  flame inhibition. They also measured the performance of Fec in combination with other agents, including  $\text{CO}_2$ , and  $\text{CF}_3\text{H}$ .

The tests were performed in premixed flames of methane. Nonetheless, they are relevant to the suppression of practical fires. Babushok and Tsang<sup>219</sup> observed that for a wide variety of hydrocarbons, including methane, the burning velocity is most sensitive to the rates of the same reactions. Since these reactions are the ones most influenced by an inhibitor, the trends in inhibitor effectiveness are the same for most hydrocarbons. While burning velocity measurements are an important first step in assessing an inhibitor's effectiveness and testing mechanism performance, future research should test these highly-effective agents in flames more closely resembling actual fires.

The premixed flame burner was the same as that described in the previous section, modified to accommodate a new evaporator for ferrocene and heating of the gas lines and burner tube.<sup>106</sup> The fuel gas was methane (Matheson UHP, 99.9 %), and the oxidizer stream consisted of nitrogen (boil-off from liquid  $\text{N}_2$ ) and oxygen (MG Industries,  $\text{H}_2\text{O} < 50$  L/L, and total hydrocarbons  $< 5$  L/L). The inhibitors used were Fec (Aldrich),  $\text{Fe}(\text{CO})_5$  (Aldrich),  $\text{CF}_3\text{H}$  (DuPont),  $\text{CF}_3\text{Br}$  (Great Lakes),  $\text{N}_2$ , and  $\text{CO}_2$  (Airgas). The  $\text{Fe}(\text{CO})_5$  was added to  $\text{N}_2$  carrier gas using a two-stage saturator in an ice bath. Because the vapor

pressure of Fec is much lower than that of iron pentacarbonyl, Fec addition at up to 650  $\mu\text{L/L}$  required both higher bath temperature (79.1  $^{\circ}\text{C}$  held within 0.1  $^{\circ}\text{C}$ ) and higher nitrogen carrier gas flows (up to 2800  $\text{cm}^3/\text{min}$ ) relative to  $\text{Fe}(\text{CO})_5$ . Also, the solid state of Fec required an evaporator with larger surface areas for heat and mass transfer. The evaporator design, based upon that of Megaridis<sup>213</sup>, had a  $(30 \pm 5)$   $\text{cm}^3$  packed bed (to provide the bulk of the ferrocene), followed by 30 sublimation stages (to insure that the carrier gas was saturated with Fec at the bath temperature). Each sublimation stage consisted of a 5 mm layer of ferrocene on a 2.36 cm diameter 60 mesh stainless steel screen. A 4 mm gap separated each stage. The vapor pressure correlation of Pelino et al.<sup>220</sup> was used to determine the ferrocene fraction in the carrier gas. Temperature controllers maintained the transfer lines at  $(80 \pm 3)$   $^{\circ}\text{C}$  and the burner tube at  $(80 \pm 1)$   $^{\circ}\text{C}$ . For all flames, the equivalence ratio (in the absence of inhibitor) was 1.0, and agent mole fraction was calculated relative to the total reactant flow. The flows of fuel, oxidizer, Fec- $\text{N}_2$ , and the blended agent ( $\text{CO}_2$ , or  $\text{CF}_3\text{H}$ ) were mixed after the Fec evaporator. The inlet reactant stream temperature was  $(80 \pm 1)$   $^{\circ}\text{C}$ , which corresponded to a calculated adiabatic flame temperature of 2260 K and 2391 K for uninhibited flames at  $X_{\text{O}_2, \text{ox}}=0.21$  and 0.244.

### **Numerical modeling**

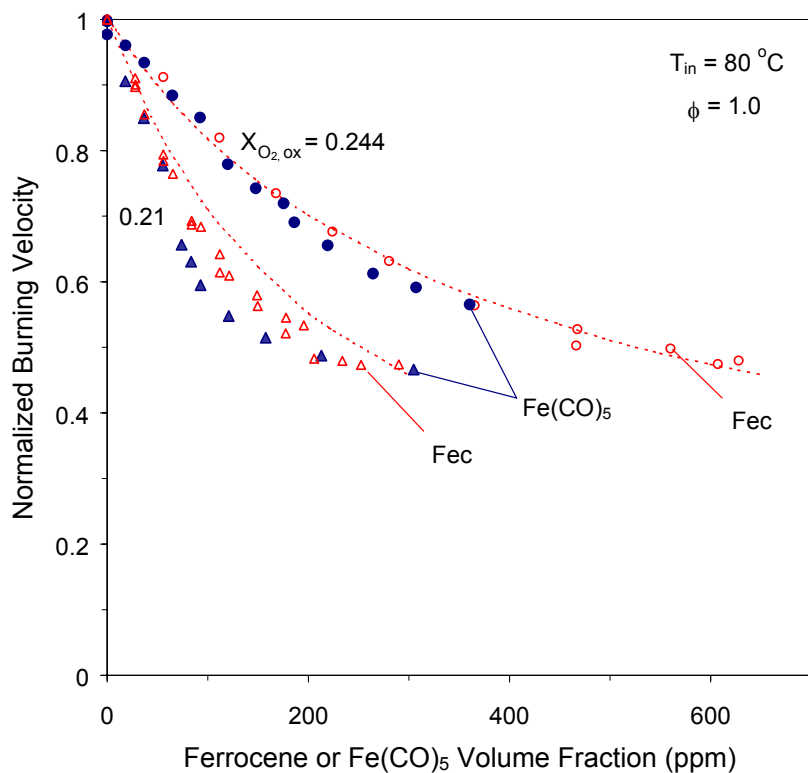
The laboratory flames inhibited by Fec and Fec- $\text{CO}_2$  blends were numerically modeled as one-dimensional freely-propagating flames. Solutions were obtained using the Sandia flame code Premix,<sup>203</sup> and the CHEMKIN<sup>204</sup> and transport property<sup>205</sup> subroutines. Details of the calculations are provided elsewhere.<sup>106</sup> Little was known about the chemical kinetic behavior of ferrocene in flames. A rate constant existed for its thermal decomposition:  $k = 2.188 \cdot 10^{16} \exp(-384 \text{ kJ}/RT) \text{ s}^{-1}$ ,<sup>221</sup> but the activation energy is high, leading one to suspect that reactions with radicals may also be important. Thermodynamic data were available,<sup>222,223</sup> and the transport properties were estimates.<sup>224,225</sup> A reaction set for combustion of methane and larger hydrocarbon fragments was adopted from Sung et al.<sup>226</sup> The iron chemistry was from a mechanism developed for flame inhibition by  $\text{Fe}(\text{CO})_5$ .<sup>104</sup> Overall, the kinetic model contained 105 species and 677 reactions. Calculations showed that addition of  $\text{C}_5\text{H}_5$  at mole fractions up to 400  $\mu\text{L/L}$  had negligible effect on the burning velocity, and that the major effect of Fec was from the iron chemistry. It should be emphasized that the reaction mechanism used for the present calculations should be considered only as a starting point. Numerous changes to both the rates and the reactions incorporated may be made once a variety of experimental and theoretical data are available for testing the mechanism.

### **Flame Inhibition by Ferrocene**

Figure 3-53 shows the relative burning velocity reduction with addition of Fec (open symbols) or  $\text{Fe}(\text{CO})_5$  (closed symbols) to the present slightly pre-heated (80  $^{\circ}\text{C}$ ) methane-air flames. (The uncertainties in the experimental data, described in detail previously,<sup>227</sup> were typically about  $\pm 5\%$ .) The data are plotted as normalized burning velocity, which is the burning velocity of the inhibited flame divided by the value for the same flame in the absence of inhibitor. The uninhibited experimental burning velocities used for the normalizations were  $(53.7 \pm 3)$   $\text{cm/s}$  and  $(75.9 \pm 6)$   $\text{cm/s}$  for  $X_{\text{O}_2, \text{ox}} = 0.21$  and 0.244, respectively. For comparison, the calculations for uninhibited flames using GRI-MECH 1.2 yielded 55.5  $\text{cm/s}$  and 72.6  $\text{cm/s}$ . The effect of the two agents was essentially the same, with very strong initial inhibition followed by a loss of effectiveness above a few hundred  $\mu\text{L/L}$  of agent, as found previously for  $\text{Fe}(\text{CO})_5$  inhibition in flames with reactants at 21  $^{\circ}\text{C}$ .<sup>96</sup>

Figure 3-53 shows that for both Fec and  $\text{Fe}(\text{CO})_5$ , the magnitude of the inhibition is strongly dependent upon the oxygen mole fraction in the oxidizer, with flames with lower mole fraction of  $\text{O}_2$  showing more

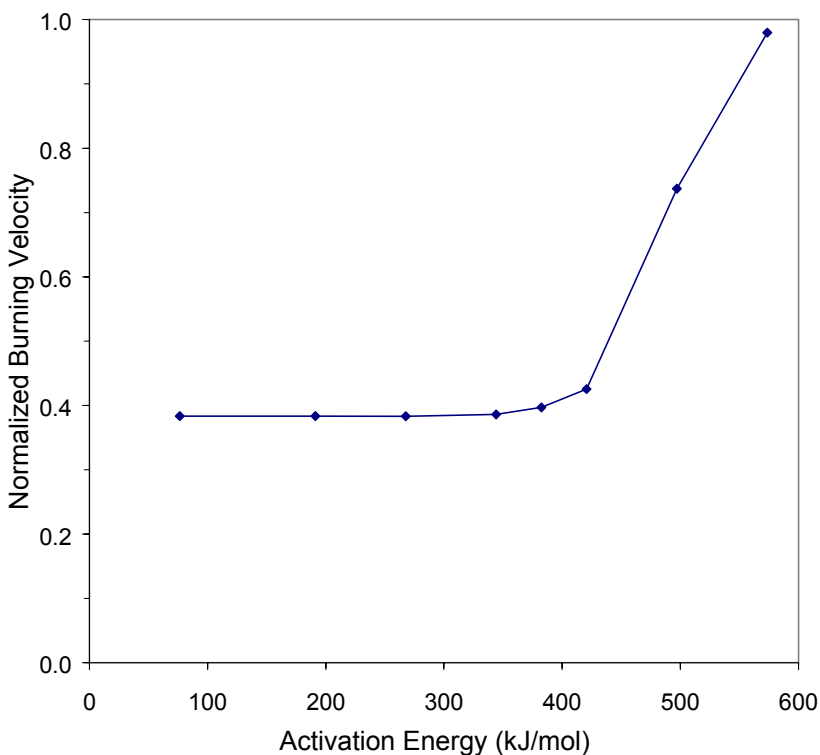
rapid burning velocity reduction. As a result, blends of inert agents with iron-containing compounds may greatly increase the efficiency over that of the inert alone.



**Figure 3-53. Normalized Burning Velocity of Premixed CH<sub>4</sub>/O<sub>2</sub>/N<sub>2</sub> Flames Inhibited by Ferrocene (open symbols) and Fe(CO)<sub>5</sub> (closed symbols) for X<sub>O<sub>2</sub>,ox</sub>=0.21 and 0.244, Together with Modeling Predictions (dotted lines).**

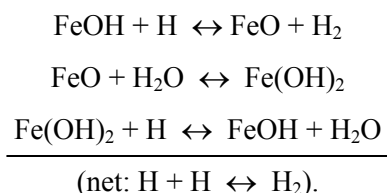
The modeling results for the ferrocene-inhibited flames are also shown in Figure 3-53. The calculations predicted the flame speed reduction caused by ferrocene reasonably well. The major difference between the ferrocene reaction scheme and that for Fe(CO)<sub>5</sub> was in the decomposition of the iron precursor. The mechanism included only the high activation energy thermal decomposition step for Fec consumption:  $\text{FeC}_{10}\text{H}_{10} \rightarrow \text{Fe} + 2 \text{C}_5\text{H}_5$ , which had a peak reaction flux at 1800 K in the present flames. In contrast, iron pentacarbonyl decomposition had a peak reaction flux at about 900 K.

Figure 3-54 shows the normalized burning velocity for a methane-air flame with 400  $\mu\text{L/L}$  of ferrocene as a function of the hypothetical activation energy  $E_a$  of the one-step decomposition reaction. In the temperature range of the stoichiometric methane-air flame of the figure, the predicted inhibition effect of Fec was independent of the overall activation energy of the decomposition of Fec for values of  $E_a$  less than about 400 kJ/mol. Hence, the decomposition rate of Fec used in the model ( $E_a = 384$  kJ/mol) did not influence the predicted behavior. For other conditions, however, (for example non-preheated reactants and highly diluted flames) the decomposition of Fec may need to be modeled more accurately to provide agreement with experimental data.



**Figure 3-54. Normalized Burning Velocity of Stoichiometric CH<sub>4</sub>-O<sub>2</sub>-N<sub>2</sub> Flames at 400 μL/L of Ferrocene as a Function of the Activation Energy of the One-step Ferrocene Decomposition Reaction.**

Since both the Fec and Fe(CO)<sub>5</sub> mechanisms used the same iron sub-mechanism, the mode of flame speed reduction in the model was the same. Decomposition of the ferrocene molecule released iron atom in the gas phase. Iron reacted with O<sub>2</sub> to form FeO<sub>2</sub>, which reacted with O atom to form FeO. FeO is a long-lived intermediate, which together with Fe(OH)<sub>2</sub> and FeOH, entered into the catalytic cycle for H-atom recombination:



The modeling results showed that the stronger burning velocity reduction for the cooler flames ( $X_{\text{O}_2, \text{ox}} = 0.21$ ) was due to their smaller radical pool. In these flames, a given amount of iron removed a larger *percentage* of the hydrogen radicals.

Ferrocene appears to be an alternative to the highly toxic iron pentacarbonyl for addition of gas phase iron to a flame. Unfortunately, its effectiveness also appeared to diminish as the mole fraction increased. For Fe(CO)<sub>5</sub>, the loss of effectiveness was due to the formation of condensed-phase particulates in the reaction zone, and it was presumed that the same mechanism held for ferrocene.

### *Inhibition by Ferrocene and CO<sub>2</sub>*

It is desirable to take advantage of the strong initial flame speed reduction from iron species in the flame, while avoiding the loss of active species due to condensation. Since addition of nitrogen clearly increased the rate of burning velocity reduction at low mole fraction (note the results in Figure 3-53 for  $X_{O_2,ox} = 0.21$  and 0.244), it was logical to determine whether other thermally acting agents could be combined with Fec to mitigate the loss of effectiveness, and perhaps enhance the flame speed reduction at low Fec mole fraction. It was known, however, that addition of an inert, while reducing the burning velocity, also increases the residence time for particle formation in the flame, so that condensation would be increased. It was not known a priori if the net effect of combining thermal and iron-containing agents would reduce the overall reaction rate faster than the increase of the rate of active-species condensation.

Therefore, Linteris and coworkers conducted experiments to resolve this. Using the same apparatus, they added CO<sub>2</sub> to the methane-air-Fec system. Figure 3-55a and Figure 3-55b present the experimental data for tests at  $X_{O_2,ox} = 0.21$  and 0.244. Data are shown for pure CO<sub>2</sub> as well as for CO<sub>2</sub>-Fec blends corresponding to three values of the mole percentage of Fec in CO<sub>2</sub> (0 %, 0.25 %, and 1.5 % in Figure 3-55a, and 0 %, 0.4 %, and 1.5 % in Figure 3-55b).

For the pure compounds, addition of about 10 % of CO<sub>2</sub> (or 25 % N<sub>2</sub>) reduced  $S_L$  by a factor of two at  $X_{O_2,ox} = 0.21$  or 0.244. Adding Fec to CO<sub>2</sub> produced a particularly effective agent. The equivalent of 0.35 % Fec in CO<sub>2</sub> reduced the required CO<sub>2</sub> for a 50 % reduction in the flame speed by about a factor of three at  $X_{O_2,ox} = 0.21$  and about a factor of two at  $X_{O_2,ox} = 0.244$ . The combination of 1.5 % Fec reduced the required CO<sub>2</sub> by 10, making this blend about as effective as CF<sub>3</sub>Br (for which addition of about 1 % halved the burning velocity). Nonetheless, the curvature in the ends of the data sets (particularly for 1.5 % Fec in CO<sub>2</sub>) illustrates condensation was important. Although one might expect the slightly cooler, slower flames with added CO<sub>2</sub> to always show more condensation of iron species, the greater efficiency of the catalytic cycle in the diluted flames predominated for most of the conditions for the flame of Figure 3-55. Higher effectiveness of iron compounds in diluted flames has been observed previously for flames with  $X_{O_2,ox}$  lowered below 0.21.<sup>96</sup>

The condensation behavior of the blends can be discerned from Figure 3-56a and Figure 3-56b, which present additional data for CO<sub>2</sub> and ferrocene in stoichiometric flames with  $X_{O_2,ox} = 0.21$  and 0.244, respectively. In Figure 3-55, CO<sub>2</sub> and ferrocene were added together in proportional amounts, whereas in Figure 3-56, CO<sub>2</sub> is first added at a constant volume fraction (0 %, 2 %, and 6 % in 7a; or 0 %, 4 %, and 12 % in 7b), and then the Fec is added. This approach allows a clearer delineation of the effects of each component of the blend. As the figures show, the curve with 0 % CO<sub>2</sub> (pure Fec) has a decreasing slope magnitude as  $X_{in}$  increases (due to increased condensation). For each of the other curves, the added CO<sub>2</sub> reduces the normalized burning velocity before the Fec is added, so that each curve starts at a value less than unity; addition of Fec further reduces the flame speed. Below an Fec volume fraction of about 70 L/L, the curves are all quite linear, showing that there no loss of effectiveness. But for curves extending beyond this amount of Fec, there is increasing curvature as  $X_{in}$  increases (due to condensation). Nonetheless, at low mole fractions, the inhibition by Fec is actually stronger for conditions of higher CO<sub>2</sub> mole fraction (note the larger magnitude of the slope for the 12 % CO<sub>2</sub> curve in Figure 3-56b). Hence, for some conditions, adding CO<sub>2</sub> makes Fec more effective. As discussed below, once the particles start to form, the deterioration of inhibition may be more rapid with added CO<sub>2</sub>. These results imply that combinations of *non-condensing quantities* of several catalytic agents combined with a thermal agent can be particularly effective.

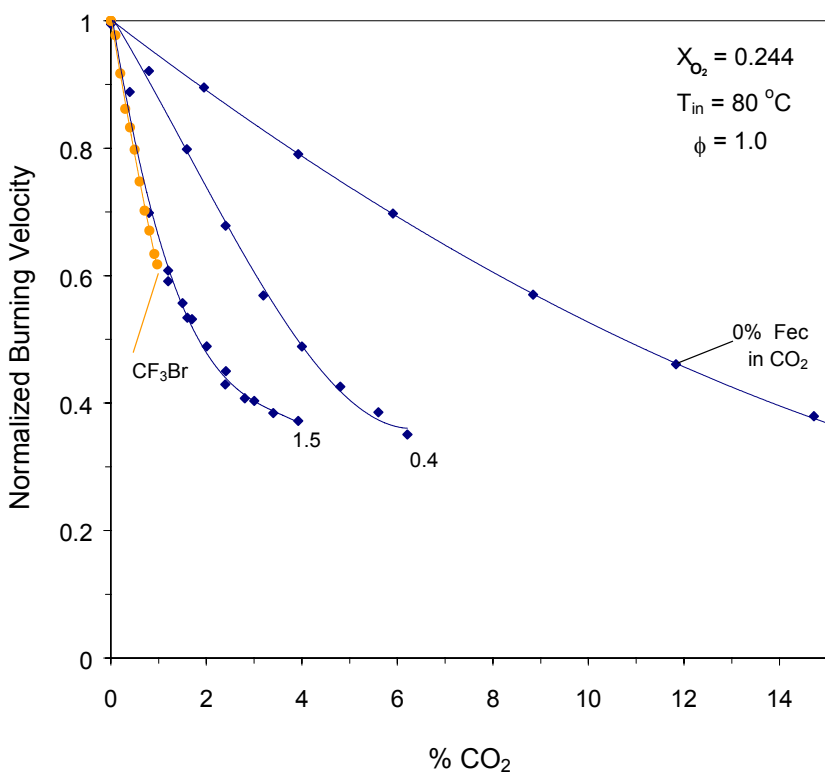
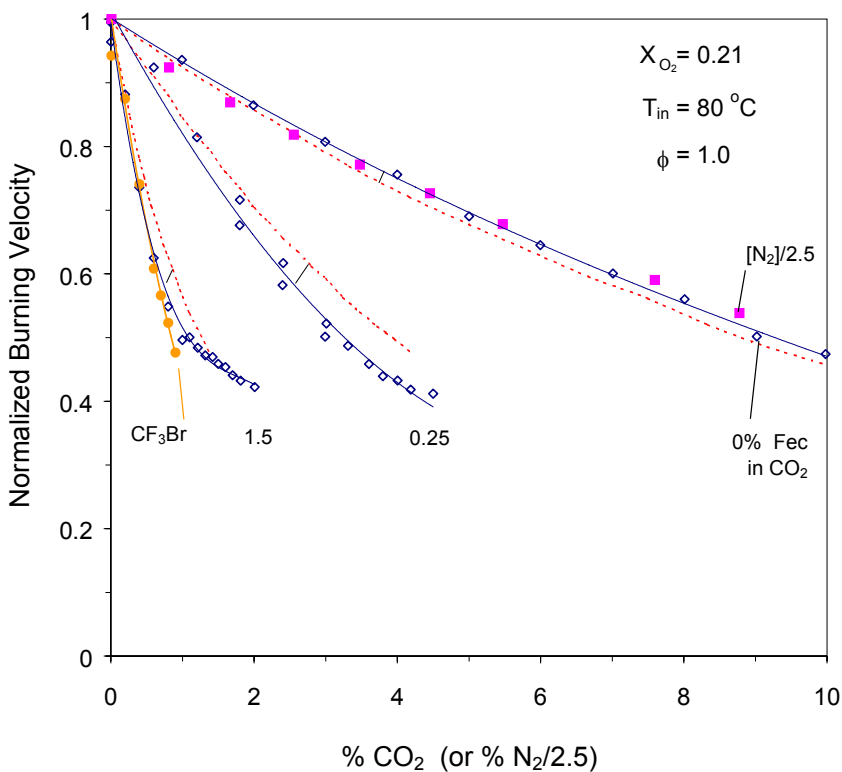


**Figure 3-55. Normalized Burning Velocity of CH<sub>4</sub>/O<sub>2</sub>/N<sub>2</sub> Flames, a)  $X_{O_2,ox} = 0.21$ , b)  $X_{O_2,ox} = 0.244$ , Inhibited by CO<sub>2</sub>, by CO<sub>2</sub>-ferrocene Blends, and by CF<sub>3</sub>Br. (The equivalent percentage of ferrocene in CO<sub>2</sub> (which is constant for each curve) is given. The solid lines are curve fits through the data, and the dotted lines, the calculated results. Data for nitrogen are included in the upper plot by dividing % N<sub>2</sub> by 2.5.)**

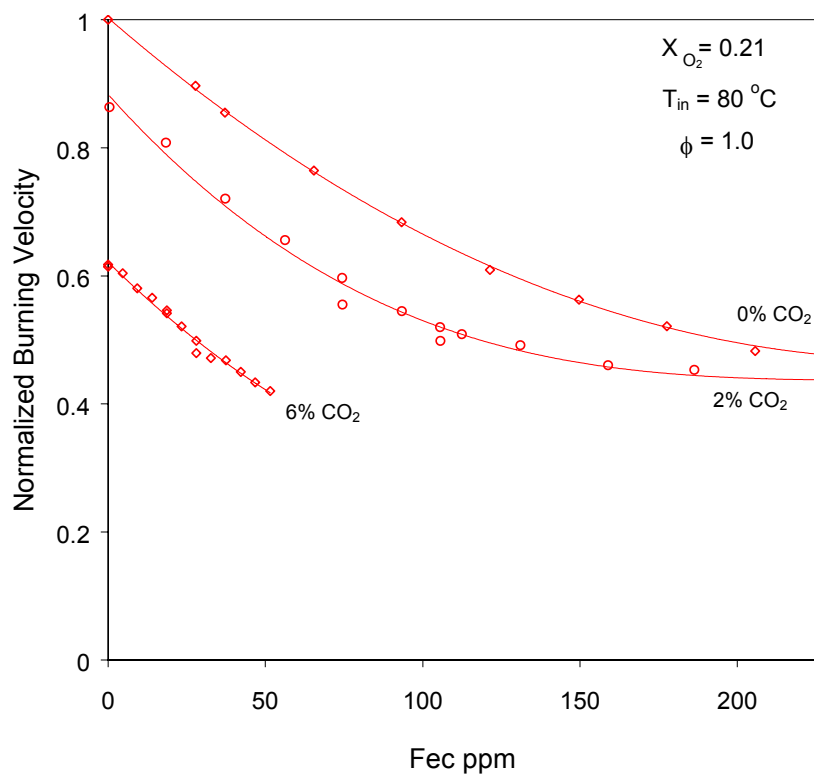
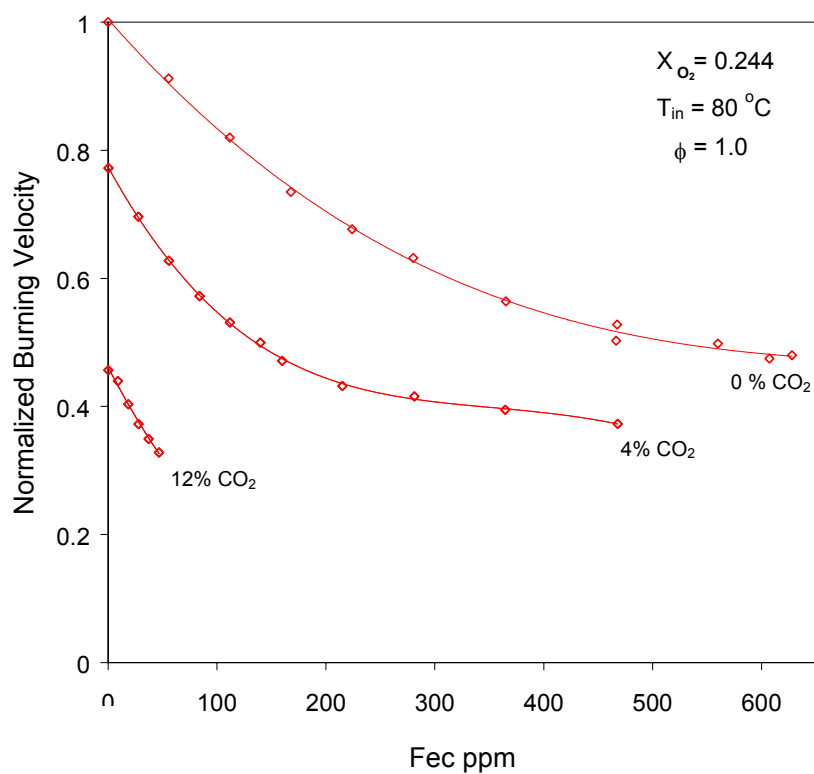


**Figure 3-56. Normalized Burning Velocity of CH<sub>4</sub> / N<sub>2</sub> / O<sub>2</sub> Flames, a.)  $X_{O_2,ox} = 0.21$ , b.)  $X_{O_2,ox} = 0.244$ , with 0, 2, and 6, or 0, 6, and 12 Volume Percent of CO<sub>2</sub>, Respectively, Added to the Reactant Stream, as a Function of Added Ferrocene. (The lines are curve fits to the experimental data.)**



### Inhibition by Ferrocene and $CF_3H$

Many compounds, both thermally and chemically acting, are candidates for blending with catalytic agents. Hydrofluorocarbons, which are easily stored at moderate pressure, were of interest since they were being used as halon replacements. These compounds had been found to reduce the burning velocity of premixed methane-air flames by reducing *peak* H-atom mole fractions by acting as a sink for H atoms through reactions forming HF, and by lowering the temperature of the flame. Since they had also been shown to reduce the *equilibrium* mole fractions of radicals in flames lower than expected based on temperature reduction alone,<sup>58</sup> they might show enhanced performance relative to  $CO_2$  when combined with catalytic agents.

Figure 3-57 presents the burning velocity reduction caused by pure  $CF_3H$  addition to the above flames; a mole fraction of about 5% was required to reduce  $S_L$  by two. Data are also presented for addition of 0.35% Fec in  $CF_3H$ . Unlike ferrocene addition to  $CO_2$ , in which 0.35% Fec in  $CO_2$  reduced the amount of  $CO_2$  required by a factor of about five, this amount of ferrocene in  $CF_3H$  reduced the amount of  $CF_3H$  required only by about one-third. This poor performance may have been due to reactions between iron species and fluorine, which would have reduced the gas phase mole fraction of the active iron-species intermediates, effectively poisoning the iron catalyst.<sup>228</sup>

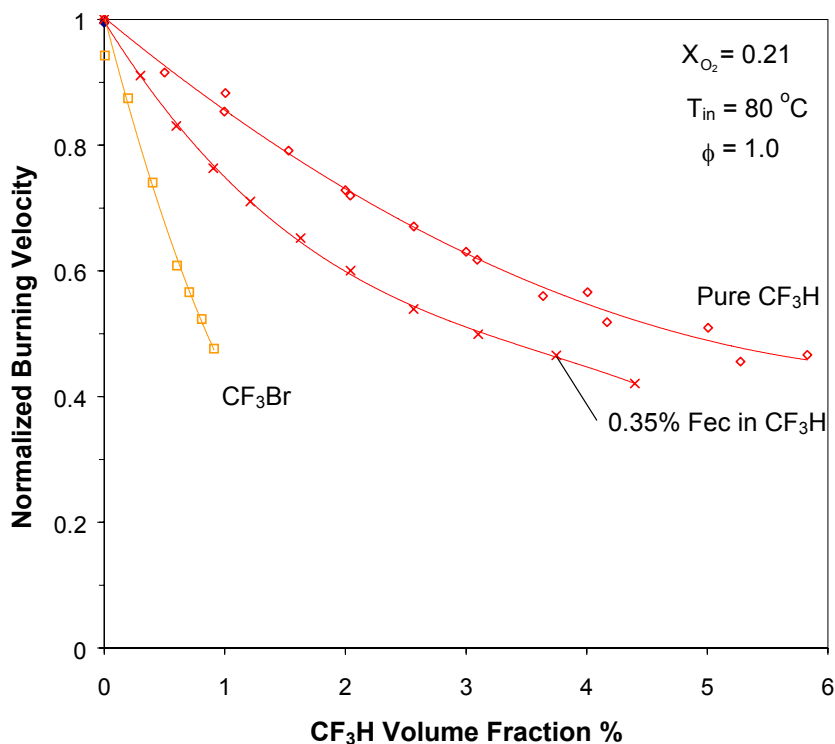


**Figure 3-57. Normalized Burning Velocity of Premixed  $CH_4/O_2/N_2$  Flames Inhibited by Pure  $CF_3H$  and by  $CF_3H$  with 0.35% Ferrocene, Together with Data for  $CF_3Br$ . (Lines are curve fits to the data.)**

Since there existed no experimental data on the rates of reactions of iron species with fluorine containing species in flames, the poisoning effect of fluorinated hydrocarbons on iron-catalyzed radical recombination reactions was assessed through equilibrium calculations for the combustion products. The species included in the calculations were those in the mechanisms for hydrocarbon oxidation, iron-inhibition, and fluorinated hydrocarbon-inhibition,<sup>229</sup> as well as the iron-fluorine species:  $FeF$ ,  $FeF_2$ ,  $FeF_3$ ,

$\text{Fe}_2\text{F}_4$ ,  $\text{Fe}_2\text{F}_6$ .<sup>197</sup> Calculations were performed for the equilibrium products of a stoichiometric methane-air flame with 1 % to 4 %  $\text{CF}_3\text{H}$  containing 0.35 % Fec (the conditions of Figure 3-57). The results of the calculations, shown in Figure 3-58, indicated that  $\text{FeF}$  and  $\text{FeF}_2$  were major product species when  $\text{CF}_3\text{H}$  was added. For 1 % to 4 %  $\text{CF}_3\text{H}$ , the amount of iron taken up by the sum of  $\text{FeF}$  and  $\text{FeF}_2$  increased from 42 % to 84 %, making less iron available in the form of the active iron intermediate species  $\text{Fe}$ ,  $\text{FeO}$ ,  $\text{FeOH}$ ,  $\text{FeO}_2$ , and  $\text{Fe}(\text{OH})_2$ . The formation of fluorinated iron species with strong bonds clearly acted as a sink for iron in the flame, and reduced the mole fractions of active iron-containing species available to participate in the flame inhibition reactions. While the experiments and calculations were performed for  $\text{CF}_3\text{H}$ , the results are likely to be the similar for larger HFCs such as  $\text{C}_2\text{HF}_5$  and  $\text{C}_3\text{HF}_7$  since the decomposition of all of these proceeds largely through the  $\text{CF}_3$ ,  $\text{CF}_2$ , and  $\text{CFO}$  intermediates.<sup>55,57,58</sup>

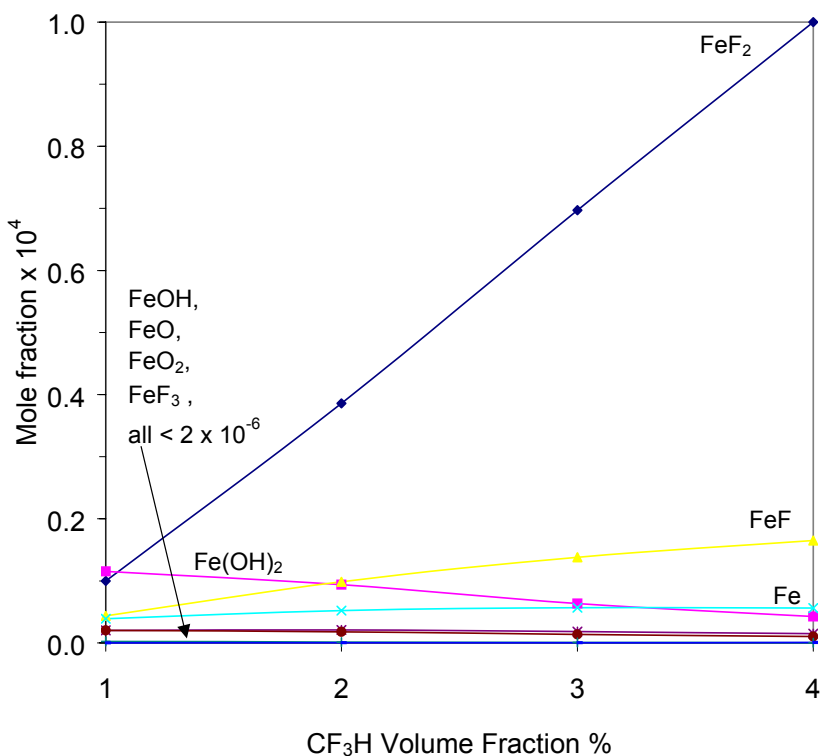


**Figure 3-58. Equilibrium Mole Fraction of Active Inhibiting Species ( $\text{Fe}$ ,  $\text{FeO}$ ,  $\text{FeOH}$ ,  $\text{Fe}(\text{OH})_2$ ) and Iron-fluorine Species with 1 % to 4 %  $\text{CF}_3\text{H}$  (containing 0.35 % Ferrocene) Added to a Stoichiometric Methane-air Reaction Mixture.**

### Comparison of Individual and Blended Performance

The behavior of the blends of agents was investigated by comparing the actual amount of flame speed reduction for the blend to the sum of the inhibition which would result from each agent individually. This approach is illustrated schematically in Figure 3-59. This uses the inhibition index  $\Phi(X_{in})$  of Fristrom and Sawyer,<sup>230</sup> where  $\Phi(X_{in}) = \frac{(V_o - V(X_{in}))}{V_o} \{X_{O_2,ox}/X_{in}\}$  (and using the oxygen mole fraction in the oxidizer). The index  $\Phi(X_{in})$  is seen to be the magnitude of the average slope of the normalized burning velocity curve (times  $X_{O_2,ox}$ ) evaluated at the mole fraction of interest  $X_{in}$ . For a given blend, one can evaluate the amount of normalized burning velocity *reduction* that would have been caused by each individual component of the blend, e.g., components  $a$  and  $b$ . The predicted inhibition index is just a linear combination of the reduction from each component, or  $X_a \cdot \Phi_{a+b}(X_a, X_b)|_{pred} = X_a \cdot \Phi_a(X_a) + X_b \cdot \Phi_b(X_b)$ , in which  $a$  is the major component of the blend, (selected for defining  $\Phi_{a+b}(X_a, X_b)$ ). The actual inhibition index  $\Phi_{a+b}(X_a, X_b)|_{actual}$  was evaluated from the normalized flame speed of the blend (using  $X_a$  in its

definition). The ratio of  $X_a \cdot \Phi_{a+b}(X_a, X_b)|_{\text{actual}}$  to  $X_a \cdot \Phi_a(X_a) + X_b \cdot \Phi_b(X_b)$  provided a reasonable indicator of the performance of the blend relative to the individual components.

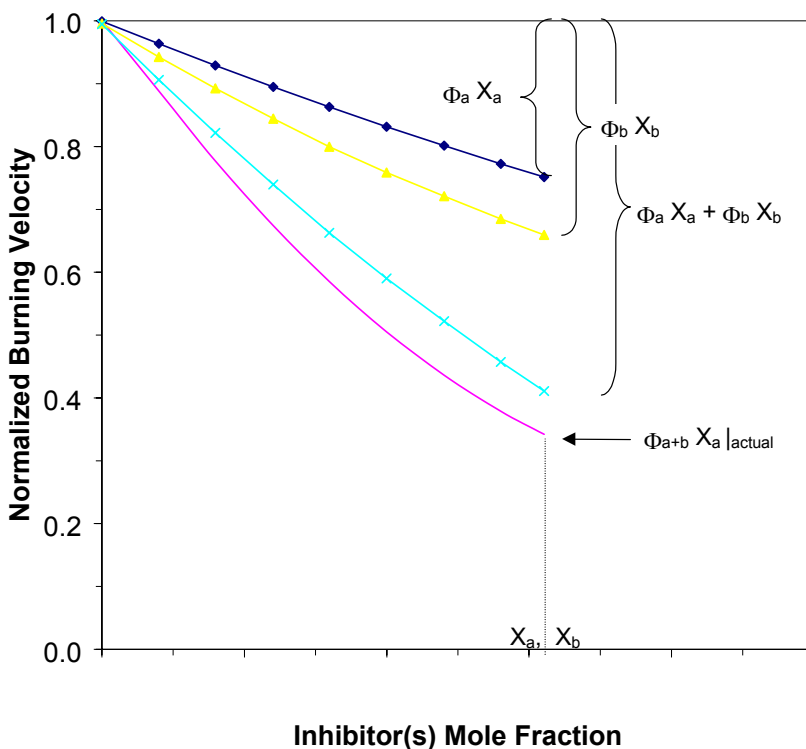


**Figure 3-59. Linear Contribution of Burning Velocity from Each Component of a two-Component Blend of Inhibitors, Together with the Actual Reduction from the Blend.**

As Figure 3-60 shows, a blend of  $\text{CO}_2$  and  $\text{N}_2$  (in the molar ratio of 1:2) provided a performance index of nearly 1.0 for  $\text{N}_2$  added up to 12 % (i.e., containing 6 %  $\text{CO}_2$ ). (The percent amount of the  $\text{N}_2/\text{CO}_2$  mix plotted in Figure 3-60 was divided by two to allow plotting on the same scale.) In contrast, the poor performance of the Fec- $\text{CF}_3\text{H}$  blend is clearly indicated by a decreasing performance index as  $X_{in}$  increases. For the  $\text{CO}_2/\text{Fec}$  blends, the combination worked slightly better than the individual components at low  $X_{in}$  of the blend, and slightly worse at higher  $X_{in}$ . The good performance at low  $X_{in}$  was due to the higher radical super-equilibrium which occurred with flame dilution, as observed previously for  $\text{N}_2$  addition<sup>96</sup>, and the degraded performance at higher  $X_{in}$  was due to the longer residence times for condensation which resulted from the lower flame speeds.<sup>102</sup> In Figure 3-60, the condition at which the curves for Fec/ $\text{CO}_2$  crossover the unity ratio correspond roughly to the location on the curves in Figure 3-55, where the linear behavior has ended and the curvature begins.

### Conclusions

The first data on flame inhibition by ferrocene showed that the efficiency of  $\text{Fe}(\text{CO})_5$  is not unique, and that there may be methods for overcoming its loss of performance.

- Ferrocene was as efficient as  $\text{Fe}(\text{CO})_5$  at reducing the burning velocity of premixed methane flames, but, like  $\text{Fe}(\text{CO})_5$ , lost its effectiveness at a mole fraction above a few hundred  $\mu\text{L}/\text{L}$ . The experimental results were reasonably predicted by a gas phase iron inhibition mechanism. Thus,

similar results can be expected for any rapidly decomposing, iron-containing agent that releases atomic iron in the gas phase

- As with  $\text{Fe}(\text{CO})_5$ , the magnitude of the inhibition by ferrocene had a strong dependence on the oxygen mole fraction. As a result, many combinations of  $\text{CO}_2$  and Fec showed strong inhibition, mitigating the loss of effectiveness observed for pure Fec or  $\text{Fe}(\text{CO})_5$ .
- These results suggest that an inert agent, together with multiple catalytic agents (to keep the absolute mole fraction of each below the saturation point) may prove to be highly effective for all conditions.
- In contrast to the results with  $\text{CO}_2$ , blends of  $\text{CF}_3\text{H}$  and Fec were not effective, implying that iron species and halogens may enter into undesired reactions which poison the catalytic cycles.

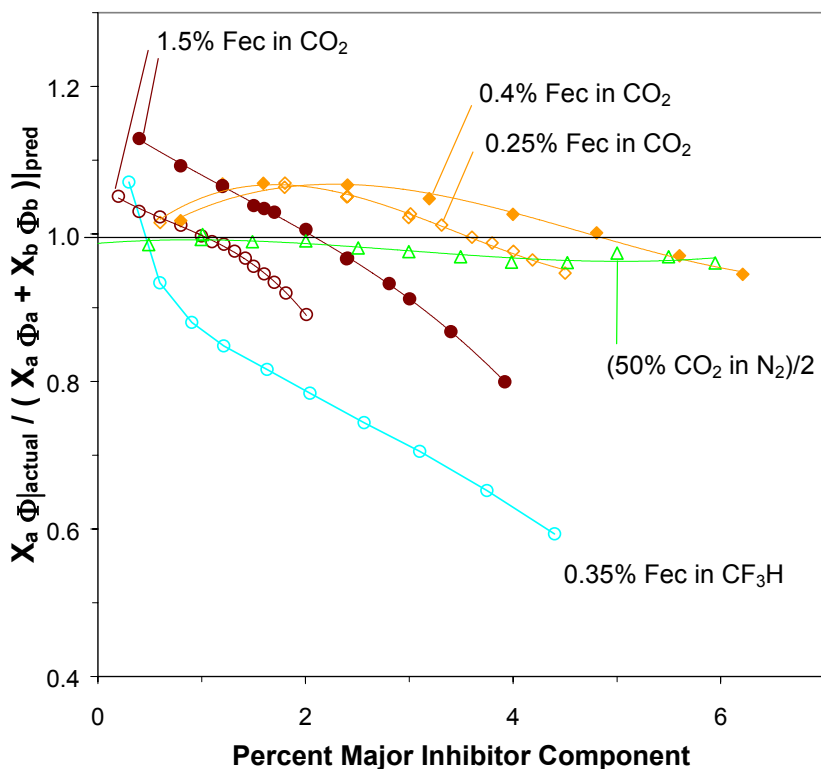


**Figure 3-60. Ratio of the Actual Reduction in  $S_L$  from the Two-component Mix to the Predicted Reduction Based on Linear Combination of the Effect from Each Component. (Open and closed symbols are for  $X_{\text{O}_2, \text{ox}} = 0.21$  and  $0.244$ ; lines are curve fits to the data. The percent  $\text{CO}_2/\text{N}_2$  has been divided by two to fit on the figure.)**

### 3.3.6 Potential for Loss of Effectiveness of Other Metals

There are multiple approaches for determining whether a metal will have a loss of effectiveness similar to that of iron:

- Obtain experimental data for flame systems in which the loss of effectiveness is evident. This requires that the inhibitor be added at volume fractions high enough to allow the loss of effectiveness. Many of the early studies with metal compounds did not provide data to high enough volume fractions to show the loss of effectiveness<sup>34</sup> or the inhibiting effect was not presented as a function of additive volume fraction (so the decreasing effectiveness was not illustrated).<sup>92</sup>

- Note a reported presence of particles in some flame system. Although the presence of particles depends upon the temperature of the flame, the concentration at which the metal moiety is added, and the residence time for particle formation, the observed presence of particles in one flame system is an indication that it may be important in other flame systems as well.
- Consider the local metal species volume fraction compared to the its local vapor pressure in the flame. A limitation of this method is that it relies upon knowledge of the metal species present in a flame system, the mechanism of inhibition, as well as the vapor pressure (or gas phase and condensed-phase thermodynamic data). Often, this information is incomplete. Further, the kinetic rates of the formation of more stable oxides of the metal must be known to assess the contribution of those compounds to condensed-phase particles (since often, the vapor pressure of these oxides is very low; e.g.,  $\text{Fe}_2\text{O}_3$ ).

Below, the available information related to the potential for condensation is presented for each metal species of interest.

## Cr

Bulewicz and Padley<sup>126</sup> found particles in the post combustion region of premixed flat flames inhibited by chromium through visual observation and by detecting continuum radiation from them. They also observed saturation in both the inhibiting effect and in the concentration of gas phase Cr in the flame. In addition, solid deposits were observed on the burner in premixed flames inhibited by  $\text{CrO}_2\text{Cl}_2$ , indicating the potential for particle formation (similar deposits have been observed for premixed flames inhibited by Sn, and Mn<sup>107</sup> and for Fe.<sup>103</sup> Hence, the potential for condensation of Cr species exists and may be important in other flame systems. To further examine this potential, the vapor pressures of Cr, CrO,  $\text{CrO}_2$ , and  $\text{CrO}_3$  above  $\text{Cr}_2\text{O}_3$ , under neutral and oxidizing conditions are shown in Figure 3-61.

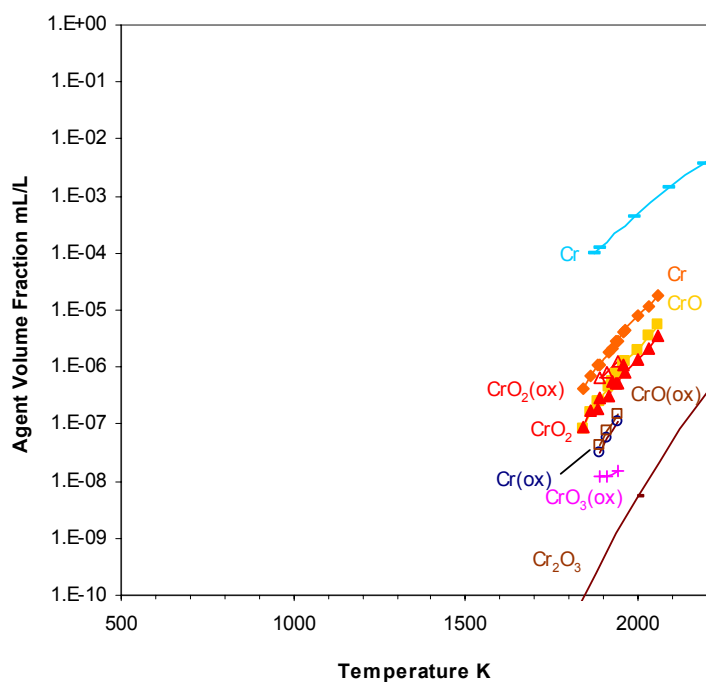


**Figure 3-61. Volume Fraction of Cr-containing Species. Cr, CrO,  $\text{CrO}_2$ , and  $\text{CrO}_3$  above  $\text{Cr}_2\text{O}_3$  at 10.133 kPa under Neutral (closed symbols) and Oxidizing (open symbols). Conditions above  $\text{Cr}_2\text{O}_3$  (reddish hues), and Cr above itself (blue). Data from References 197, 231, and 232**

Note that since  $\text{Cr}_2\text{O}_3$  is a particularly stable oxide, these vapor pressures will be lower than if the equilibrium included other, less stable condensed-phase oxides. For example, in Figure 3-61, the blue curve for Cr is for data for Cr vapor above Cr solid. Nonetheless, since it is not yet known for *any* metal inhibitor what the composition of the condensed phase oxide actually is, the potential for condensation of Cr species is illustrated. That is, many of the chromium oxides appear to have quite low vapor pressures.

## Pb

The presence of PbO particles was detected in many engine knock studies,<sup>94,95,99,109</sup> and it was often argued that the strong inhibition of knock occurred from heterogeneous radical recombination on the particle surfaces. Although lead has been shown to be one of the more effective metal agents in flame screening studies,<sup>34</sup> the additive mole fraction (maximum 150  $\mu\text{L}/\text{L}$ ) was not increased high enough to show the loss of effectiveness that might occur. In the flash photolysis studies of Norrish et al.,<sup>96</sup> however, the TEL concentration was systematically increased, and a drop-off in the effectiveness was observed above a certain volume fraction. Hence, condensation is likely to limit lead effectiveness for at least some applications. It should also be noted, that the high effectiveness of Pb in premixed flames cannot be from particles since, as shown by Rumminger et al.,<sup>102</sup> the collision rate of radicals with solid particles is not high enough to account for the observed inhibition of premixed flames by super-effective agents such as iron or lead. The vapor pressure of Pb and PbO are shown as a function of temperature in Figure 3-62. The data for  $\text{PbO}_2$  are too low to appear on this figure, and hence, condensation is clearly possible for Pb-inhibited flames if  $\text{PbO}_2$  readily forms in the inhibition cycle, or if other higher oxides readily form.

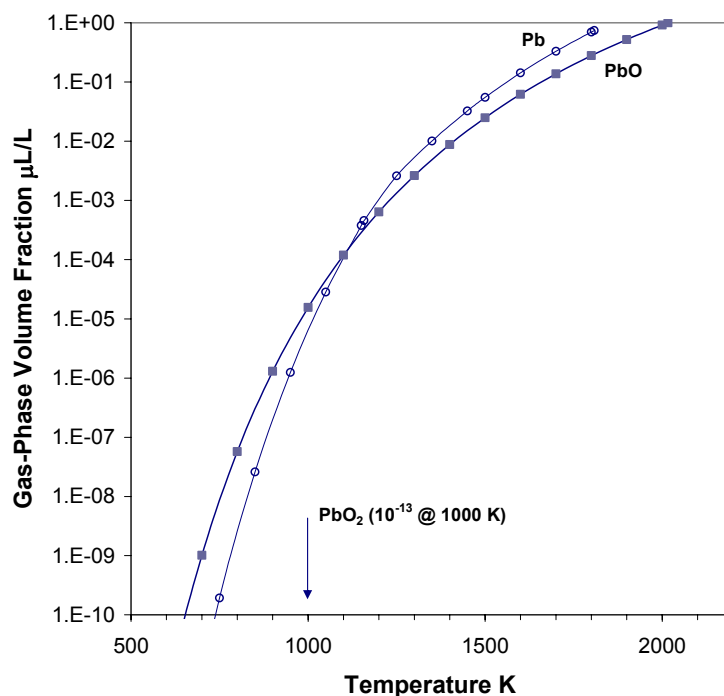


**Figure 3-62. Pb Species Gas Phase Volume Fractions at Equilibrium over the Condensed Phase (at 101.3 kPa). (Vapor pressure of Pb and PbO from Reference 233,  $\text{PbO}_2$  from References 197 and 234.)**

## Mn

The effect of MMT on the flame speed of methane-air mixtures was measured by Linteris et al.,<sup>107</sup> as shown in Figure 3-63. The data clearly show a saturation effect, which was beyond that due to lowering of the radical concentrations. Additional tests in cup burner flames showed a much lower effectiveness than expected, as well as a rapid loss of effectiveness for MMT as its volume fraction was increased. (See Figure 3-23 inset.) The presence of solid particles was also observed visually, as were solid deposits on the burner. The vapor pressure of Mn, MnO, and MnO<sub>2</sub> are shown in Figure 3-64. Since the volume fraction necessary for flame inhibition exceeded 200  $\mu\text{L/L}$ , the potential for condensation was apparent.

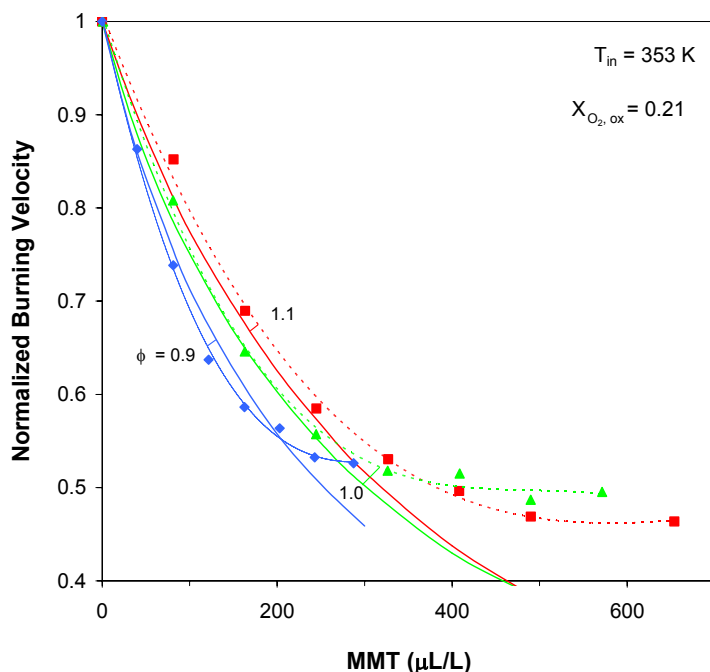


**Figure 3-63. Normalized Burning Velocity of Premixed CH<sub>4</sub>/O<sub>2</sub>/N<sub>2</sub> Flames Inhibited by MMT with  $X_{\text{O}_2, \text{ox}} = 0.21$  and  $\phi = 0.9, 1.0,$  and  $1.1$ .<sup>107</sup> (Dotted lines: curve fits to data; solid lines: numerical predictions.)**

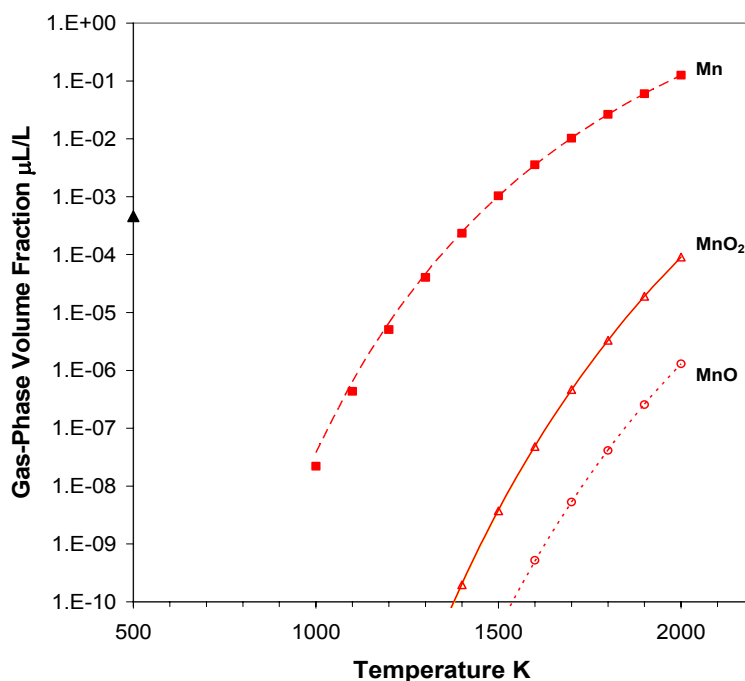


**Figure 3-64. Mn Species Gas Phase Volume Fraction at Equilibrium over the Condensed-phase at 101.3 kPa.<sup>107</sup>**

## W

There are no published data concerning particle formation or loss of effectiveness of flames inhibited by tungsten compounds. A search for vapor pressure or thermodynamic data for tungsten oxides, hydrides, and hydroxides allowed generation of the results in Figure 3-65. As shown,  $\text{WO}_3$  has a quite high vapor pressure at flame temperatures; on the other hand, the vapor pressures of  $\text{WO}_2$  and W are low enough to allow particle formation. Depending upon the flame reactions of W-containing compounds and their rates, as well as the vapor pressures of other compounds which form in flames, condensation may or may not be important.

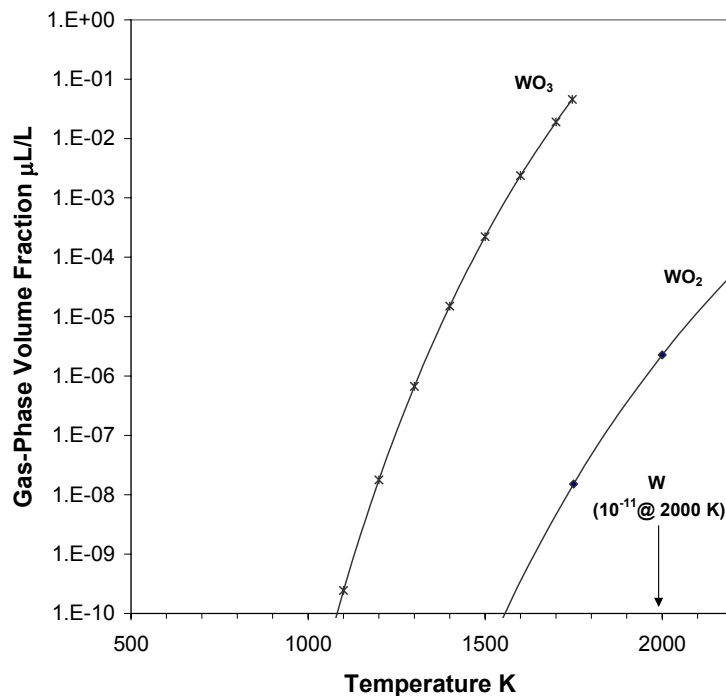


**Figure 3-65. Tungsten-containing Species Gas Phase Volume Fraction at Equilibrium over the Condensed Phase at 101.3 kPa).**<sup>189,197,231</sup>

## Mo

There are likewise no published data concerning particle formation or loss of effectiveness for flames inhibited by Mo-containing species. The vapor pressures of Mo,  $\text{MoO}_2$ , and  $\text{MoO}_3$  for flame conditions are shown in Figure 3-66. As for W compounds, the only species thought to participate in the catalytic cycle for which vapor pressure data are available ( $\text{WO}_3$  and  $\text{MoO}_3$ ) have quite high vapor pressures.

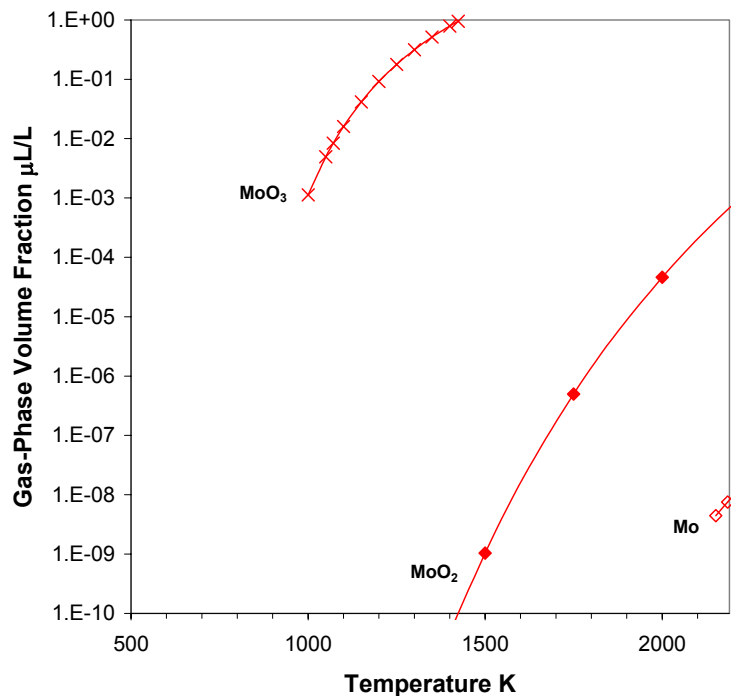


**Figure 3-66. Mo-containing Species Gas Phase Volume Fraction at Equilibrium over the Condensed Phase at 101.3 kPa.**<sup>189,197,231</sup>

## Sn

The results for Sn are similar to that of Mn. At the volume fractions necessary for effective flame inhibition, a loss of effectiveness was observed in premixed flames, although not as dramatic as for Mn (Figure 3-67); particle deposits were observed on the burner. Cup burner tests showed much lower effectiveness than expected, as well as a further loss of effectiveness as the Sn volume fraction increased (Figure 3-23 inset), and solid particles were observed both in the flame and deposited on the burner. The vapor pressures of Sn, SnO, and SnO<sub>2</sub> are shown in Figure 3-68. Clearly, condensation is possible at the 3000 μL/L volume fraction needed for flame inhibition.

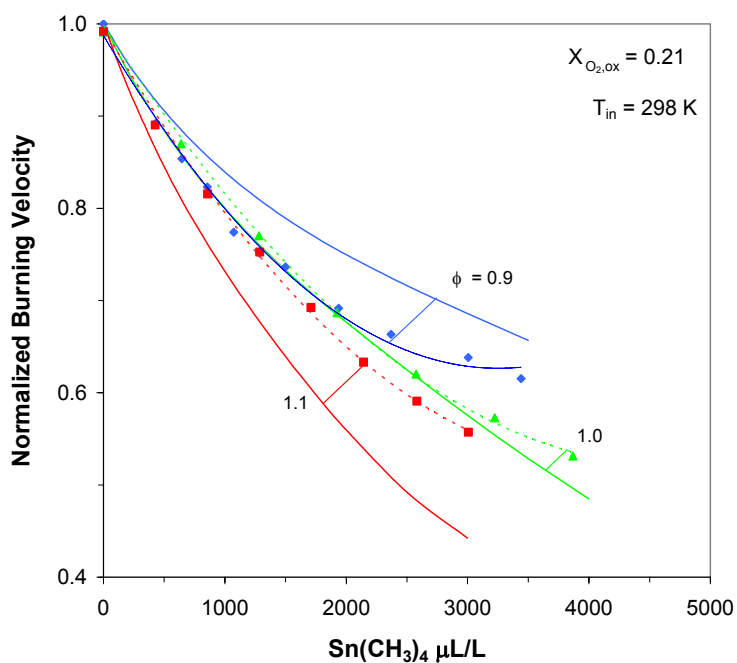


**Figure 3-67. Normalized Burning Velocity of Premixed CH<sub>4</sub>/O<sub>2</sub>/N<sub>2</sub> Flames Inhibited by TMT with  $X_{O_2,ox} = 0.21$  and  $\phi = 0.9, 1.0,$  and  $1.1$ .**<sup>107</sup> (Dotted lines: curve fits to data; solid lines: numerical predictions.)

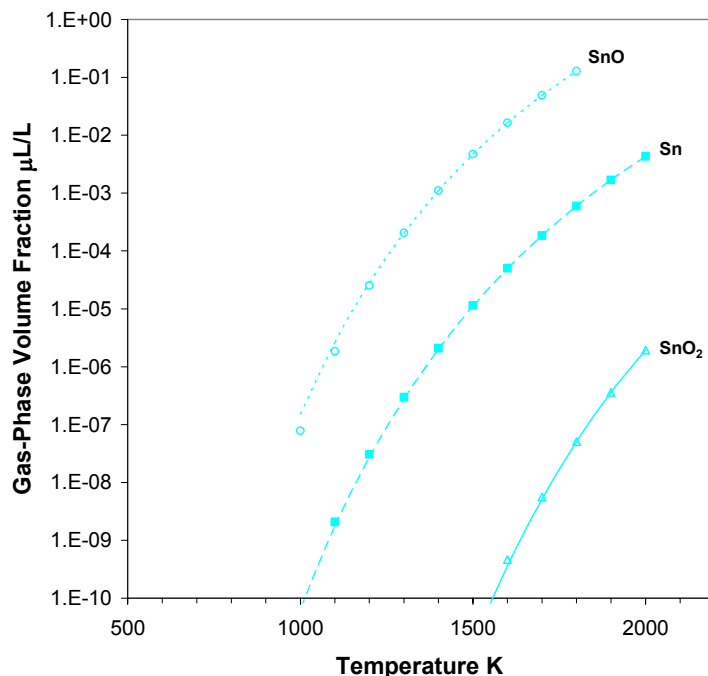


**Figure 3-68. Sn-containing Species Gas Phase Volume Fractions at Equilibrium over the Condensed Phase at 101.3 kPa.**<sup>197</sup>

## Co

The data for Co effectiveness in various flame systems has not been measured as a function of Co concentration. Hence, a loss of effectiveness at higher concentrations has not been demonstrated. Likewise, particle formation in flames with added Co has also not been reported. The available vapor pressure data for Co oxides and hydroxides are shown below. Since CoO is an intermediate species in the proposed inhibition mechanism of Co in H<sub>2</sub>-O<sub>2</sub>-N<sub>2</sub> flames, and total Co loading in the flame is expected to be on the order of several thousand μL/L, condensation may occur. On the other hand, depending upon the relative rates of the inhibition reactions, the volume fraction of CoO may not build up too high, and hence its propensity to condense could be lower than Figure 3-69 might lead one to believe.

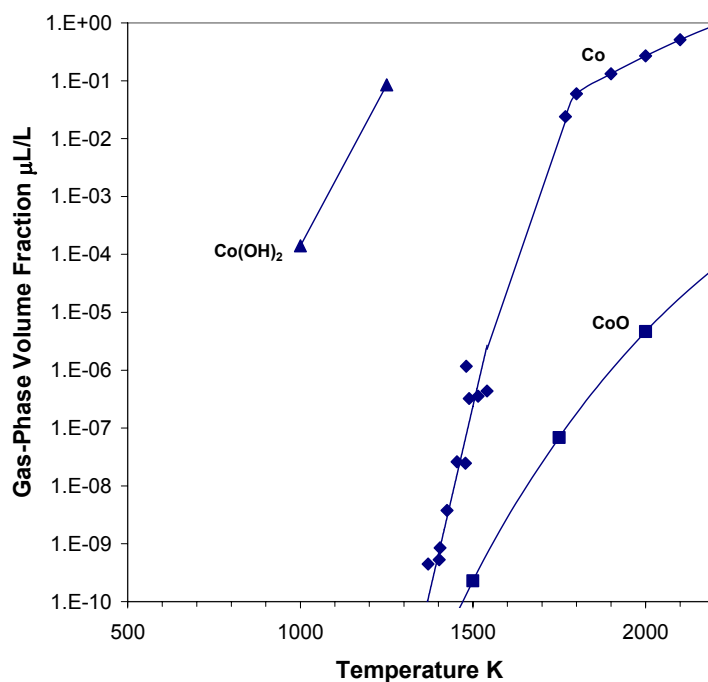


**Figure 3-69 – Co-containing Species Gas Phase Volume Fraction at Equilibrium over the Condensed Phase at 101.3 kPa.**<sup>189,197,231</sup>

## Cu

As shown in Table 3-3, copper salts have been used in experiments on engine knock, ignition suppression, radical recombination above flat flames, as well as in flame screening tests. The compounds were added either as aqueous sprays or directly as particles. There has been no mention in the literature of observed particle formation after decomposition of the additive, or of any loss of effectiveness at higher mole fractions. Only one of these studies ran experiments over a range of additive mole fractions,<sup>91</sup> and in it, they attributed changes in the performance with additive mole fraction to heating effects of the particles (not condensation of active species or saturation of the radical recombination cycle). Hence, it was difficult to assess from previous work if condensation were possible for copper-based inhibitors. To assess the condensation potential, Figure 3-70 assembles the available vapor pressure data for copper compounds which may exist in flames. Although data are not available for other possible hydrides, oxides and hydroxides (e.g., CuH, CuOH) CuO and Cu<sub>2</sub>O have quite high vapor pressures, and that of Cu is also relatively high at flame temperatures.

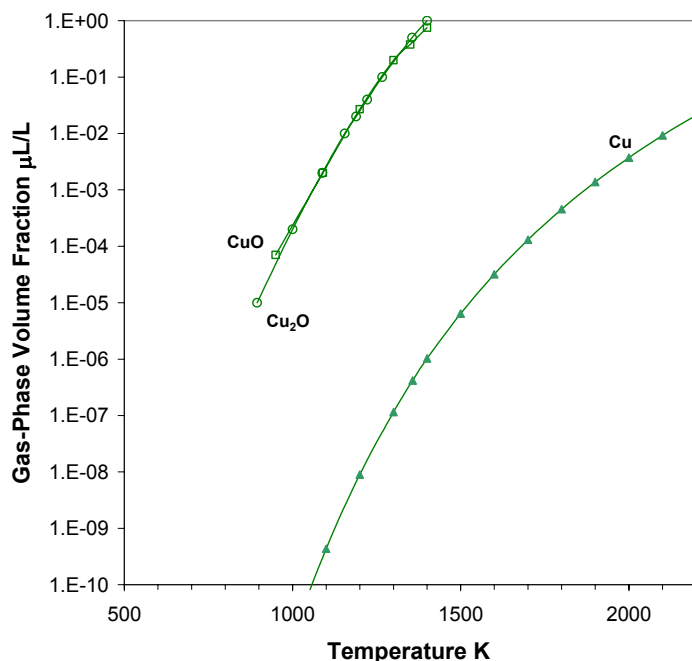


**Figure 3-70. Cu-containing Species Gas Phase Volume Fractions at Equilibrium over the Condensed Phase at 101.3 kPa.**<sup>233,234</sup>

## Sb

Although the only flame data for antimony inhibition<sup>34</sup> did not go to high enough concentrations to show loss of effectiveness, antimony may form condensed-phase particles in flames. In studies of polymers with added Sb<sub>2</sub>O<sub>3</sub> and halogen, Fenimore and Martin<sup>134</sup> showed that the fire retardant effect increases linearly with Sb<sub>2</sub>O<sub>3</sub> at low mass fractions of Sb<sub>2</sub>O<sub>3</sub>, but saturates at some value, above which further addition of Sb<sub>2</sub>O<sub>3</sub> is ineffective. Hence, the fire retardancy effect of antimony shows a strong saturation, much like that for iron, manganese, and tin in cup burner flames.<sup>180</sup> To illustrate this, the data in Figure 3-23 (CO<sub>2</sub> required for extinction with metal species added) are re-plotted below in Figure 3-71 in terms of the limiting oxygen index (based on N<sub>2</sub>). The top of the figure shows the limiting oxygen index for polyethylene/halogen blends as a function of the volume fraction of the metallic inhibitor in the gas phase. The curves for Sb<sub>2</sub>O<sub>3</sub> were calculated based on data available in Fenimore and Martin.<sup>136</sup> The effectiveness of the antimony/halogen system saturated at Sb<sub>2</sub>O<sub>3</sub> volume fractions near 400 μL/L (based

on Sb). On the bottom of the figure, curves for Fe, Mn, and Sn added to the air stream of heptane-air cup burner flames are also shown.<sup>180</sup> Although those experiments were conducted with CO<sub>2</sub> added as the diluent, the data were converted to an equivalent LOI with nitrogen diluent by correcting for the difference in heat capacity between N<sub>2</sub> and CO<sub>2</sub>.

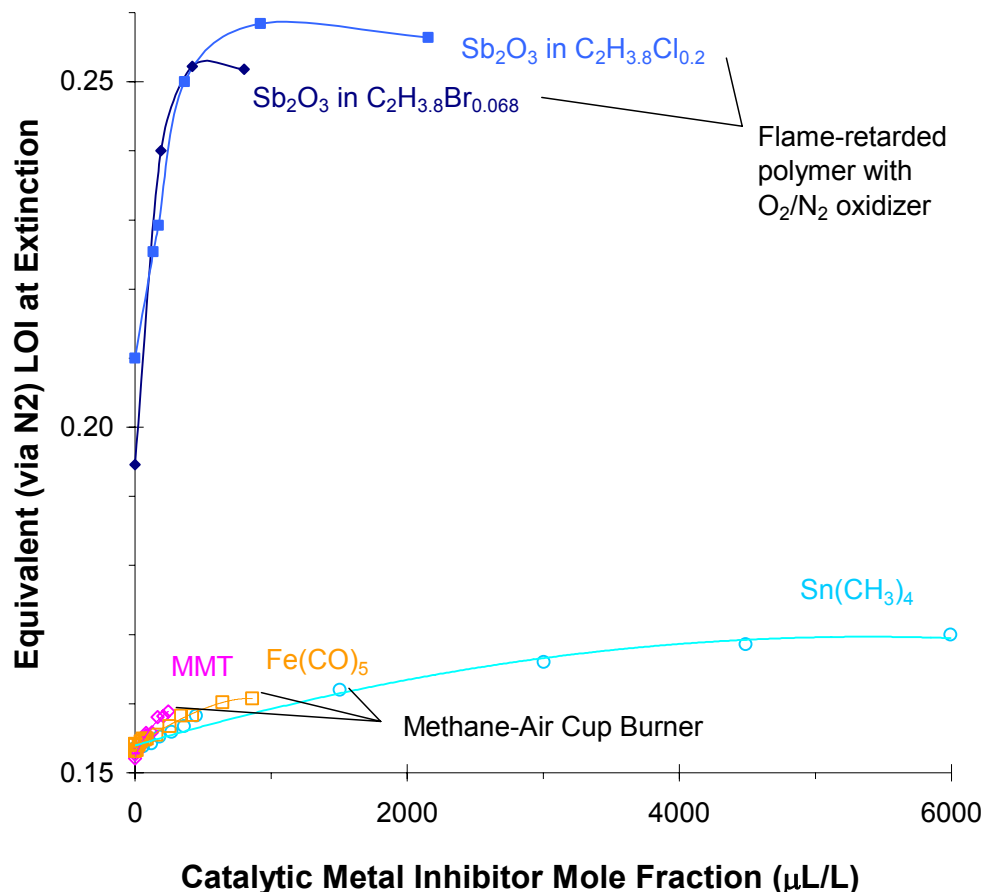


**Figure 3-71. Equivalent N<sub>2</sub>/O<sub>2</sub> Limiting Oxygen Index for Extinction of Polyethylene (PE)-halogen- Sb<sub>2</sub>O<sub>3</sub> Blends<sup>136</sup> and Methane-air Cup Burner Flames with MMT, Fe(CO)<sub>5</sub>, and Sn(CH<sub>3</sub>)<sub>4</sub>.**

Although the influence of Fe, Mn, and Sn on the LOI when added to the air stream of methane-air cup burner flames was much weaker than that of Sb<sub>2</sub>O<sub>3</sub> in halogenated polyethylene, a similar saturation behavior was observed. It would be of value to understand why saturation occurs in the antimony-halogen system, since it has not been explained in the literature.

### 3.3.7 Flame Inhibition and Loss-of-effectiveness Summary

The current state of understanding of the inhibition of flames by metal compounds is summarized in Table 3-12.

**Table 3-12. Current State of Knowledge Relevant to Inhibition Potential of Metals, and Loss of Effectiveness due to Condensation.** ■■■: high, ■■■■: medium, ■■■■■: low, -none.

Element	Inhibition Information					Condensation Information			
	Inhibition Potential		Gas phase Species Identified		Kinetic Mechanism State of Development	Demonstrated Loss-of-Effectiveness		Experimental Evidence of Particles	Experimental Vapor Pressure Data
Cr	■■■		■■■■		■■■■	■■■		■■■	■■■■
Pb	■■■		■■■■		■■■■			■■■	■■■■
Fe	■■■		■■■		■■■■	■■■		■■■	■■■■
Mn	■■■		■■■		■■■■	■■■		■■■■	■■■■
Ni	■■■■								
W	■■■■				■■■■				■■■■
Mo	■■■■				■■■■				■■■■
Cu	■■■■		■■■■						■■■■
Te	■■■■								
Tl	■■■■								
Bi	■■■■								
U	■■■■								
Zn	■■■■								
La	■■■■								
Th	■■■■								
Se	■■■■								
Sn	■■■■		■■■		■■■■	■■■		■■■■	■■■■
Ti	■■■■							■■■■	
Co	■■■■		■■■						■■■■
Ge	■■■■								
Sb	■■■■		■■■■		■■■■	■■■■		■■■■	
P	■■■		■■■		■■■	■■■		■■■■	

The inhibition potential is summarized in terms of the known inhibition behavior, the detection of metal-containing species in flames, and the state of development of a kinetic description of the inhibition. The knowledge of the potential for loss of effectiveness is characterized in terms of the demonstrated loss of effectiveness in flame systems, the presence of particles, and the availability of vapor pressure data for the condensed-phase metal-containing species. In the "Inhibition Potential" column, the *quality* of the information is rated as high, medium, low, and none, not the inhibition ability itself. Even for elements such as iron, which has been the most extensively studied, there were fragmented data on the gas phase species in flames, the gas phase kinetic mechanism had many estimated rate constants and the dominant inhibition cycles were assumed, and vapor pressure data for some of the important intermediates were not available. As the table illustrates, most of the information needed to accurately predict both the inhibition potential as well as the potential for loss-of-effectiveness were incomplete.

The last row in the column shows the state of information relevant to flame inhibition by phosphorus compounds. Due largely to NGP research, the state of understanding of the inhibition potential, the active species for flame inhibition, and the kinetics of the inhibition cycles are fairly well known. However, there is not nearly as complete an understanding of the potential for loss of effectiveness due to condensation of intermediate species formed in a flame. The only data which indicate, indirectly, a potential for condensation are the cup burner extinguishment data from researchers at New Mexico Engineering Research Institute,<sup>235</sup> in which the volume fraction for extinguishment is high relative to other flame systems. In a section below, the NGP work to understand the gas phase flame inhibition mechanism of phosphorus compounds is described in detail.

### Approaches for Ascertaining the Potential of Metal-containing Compounds

Actually calculating the condensation potential of metal inhibitors in flames is quite challenging. To do this in a *quantitative* way requires knowledge of the species present in the flame, the inhibition mechanism with its associated rate constants, the vapor pressures of the metal species, the condensation, agglomeration, and re-evaporation rates for the particles, and the actual species present in the particles. This is far from being achieved even for iron, the most highly studied metal.

An alternative way to assess the potential for condensation of metal inhibitors in flame systems may be simple screening experiments with cup burners. In order to determine both the variation with concentration, as well as the potential benefit of using the metal compounds with inert agents, tests need to be conducted with the added metal compound and a secondary inert agent added together. In such a test, described above and in the literature<sup>86,110,236</sup> the amount of a diluent (e.g., CO<sub>2</sub>, or N<sub>2</sub>) added to the air stream necessary to cause blow-off of the cup burner flame is determined, both with and without the metal agent added at increasing concentration in the oxidizer stream. Since, to some extent, the flames resemble the low-strain conditions of fires, there is expected to be much higher correlation between the behavior in this system and in actual suppressed fires. By adding the metal compounds in the form of organometallic agents (rather than metal salts), the complicating effects of particle evaporation and decomposition are avoided.

A more empirical approach to evaluating metal-containing compounds would be to add them to a solid propellant-based extinguisher. There is inert gas in the effluent, as well as fragmented metal-containing species, so that by proper application to an appropriate fire, the utility of the metal additive could be

assessed at a larger scale. The challenge would be to find a configuration which has the proper sensitivity to the inert gas flow so that the effects of the additive could be quantified.

### Approaches for Overcoming Condensation

There may exist approaches for overcoming the loss of effectiveness of metal compounds due to condensation of metal oxides. For example, halogens could be used to attack the metal oxide and provide metal-halogen species in the gas phase. As described by Hastie and co-workers,<sup>140</sup> the halogen in the antimony-halogen fire retardant system acts to release the antimony from the condensed phase through a series of halogenation steps involving successive oxychloride phases.<sup>139</sup> Bromine has been used in the past to etch off the lead oxide deposits on engine valves, and halogens are used to remove the oxide coating from the incandescent filament in quartz-halogen light bulbs. It is clear that halogens can release metals from solid oxides, and it may be possible to use this property to re-introduce the metals from the condensed oxide into the gas phase where they can again inhibit the flame. Finally, the use of carboxylic acids as extenders of antiknock agents<sup>100</sup> (through the formation of metal salts which can persist in the gas phase) leads naturally to the question of whether such an approach would work for metal-based fire suppressants as well.

### 3.3.8 Conclusions

Extensive analysis of published data and new data obtained from experiments and calculations has enabled new understanding of the flame-inhibiting mechanisms of metal-containing compounds and their potential as successors to halon 1301.

- There are several metal atoms whose compounds have shown very high effectiveness at reducing the rates of the chemical reactions that propagate flames. These are iron, manganese, chromium, antimony, lead, and tin. NGP research has also uncovered additional metals whose compounds are likely to be effective at low concentrations, but which had not been suggested in previous reviews of metal flame inhibition. These are tungsten, molybdenum, and cobalt.
- Most of the metals discussed above have the potential to lose their effectiveness at concentrations below those needed to extinguish flames, due to condensation of the active species. Were this condensation to occur in practical fires, compounds of these metals would likely not demonstrate fire suppression capabilities commensurate with their high flame velocity inhibition efficiency that was observed when added at low concentration to laboratory premixed flames. On the other hand, for the metals W, Mo, Co, and Cu, there is no direct evidence of the potential for loss of effectiveness, and the vapor pressures of the suggested flame-quenching species (for which data are available) are reasonably high. In general, prediction of the potential loss of effectiveness is beyond the current state of the art. Empirical testing in a cup burner or a solid propellant fire extinguisher (Chapter 9) is needed.

## 3.4 PHOSPHORUS

### 3.4.1 Introduction

#### Reasons for Interest

Phosphorus-containing compounds (PCCs) are known to be effective at reducing flammability, with some ambiguity as to whether their effectiveness in these applications can be attributed to gas phase reactions involving phosphorus. The use of various PCCs as fire retardant additives to plastics<sup>237,238</sup> has increased dramatically<sup>239</sup> in recent years, with the 1998 estimated U.S. market for organophosphorus fire retardants at 80 million lb.<sup>240</sup> In this application, the relative importance of gas phase chemistry and solid-phase effects such as char promotion has been debated, with recent work suggesting comparable importance for the two mechanisms, depending on the specific PCC chemistry.<sup>238,241-244</sup> Monoammonium phosphate has been used for many years as a dry chemical fire-extinguishing agent,<sup>245</sup> and has also been found to be very effective in preventing dust explosions.<sup>246,247</sup> Since it is applied as a powder, it is possible that physical properties may contribute substantially to its effectiveness. (See Chapter 4.) Finally, phosphorus is often applied in combination with halogens, making it difficult to assess the contribution of the phosphorus. For example, a mixture of trialkyl phosphates and CF<sub>3</sub>Br for fire-fighting applications has been patented.<sup>248</sup> Phosphorus and halogens often appear in the same molecule as well: a recent evaluation of phosphorus compounds as halon replacements focused on fluorinated phosphazenes and phosphines, showing good flame suppression properties for these compounds in cup burner and streaming tests.<sup>249,250</sup>

The NGP was thus interested in developing further understanding of how PCCs affect flames, with the intent of using this knowledge to identify and screen candidate chemicals as successors to halon 1301. Such foreknowledge was necessary because of potential obstacles to their use as flame suppressants:

- Many, if not all, of these compounds, have low vapor pressures at ambient temperature.<sup>251</sup> (See Chapter 7.)
- Some PCCs have a significant heating value due to alkyl and alkoxy groups attached to the phosphorus atom.
- There are diverse bonding states of the phosphorus atom and a variety of ligand groups within the realm of PCCs. The import of these to flame suppression effectiveness was uncertain.
- PCCs range in their toxicity from non-toxic, essential food constituents and FDA approved additives to some of the most toxic compounds (chemical warfare agents) known.<sup>249,252</sup>

#### Chemical Effects

Well-characterized investigations of the flame inhibition properties of PCCs have been sparse, and in some cases ambiguous or contradictory.

- Korobeinichev et al. investigated the flame structure of low-pressure, premixed stoichiometric H<sub>2</sub>/O<sub>2</sub>/Ar flames with the non-halogenated PCC additives trimethyl phosphate (TMP)<sup>253</sup> and dimethyl methylphosphonate (DMMP).<sup>254</sup> They compared oxygen profiles in flames with and without the PCC additive, interpreting more rapid oxygen consumption as flame promotion and less rapid oxygen consumption as flame inhibition. Both DMMP and TMP acted as inhibitors in

the low-temperature zone near the burner surface and as promoters in the higher-temperature region downstream.

- Fenimore and Jones<sup>255</sup> found that TMP addition produced *no* change in the oxygen consumption rate in a low-pressure, rich, H<sub>2</sub>/O<sub>2</sub>/Ar flame. In a more dilute, rich flame at atmospheric pressure, they observed a reduction in the oxygen consumption rate with increasing TMP loading.
- A more comprehensive study was conducted by Hastie et al.<sup>256</sup> with TMP, triphenylphosphine oxide and POCl<sub>3</sub> additives in premixed and non-premixed atmospheric-pressure propane, methane, and hydrogen flames. PCC effects were evaluated from measurements of H radical concentrations and burning velocities. Inhibition was observed for rich and lean flames with temperatures up to 2350 K. At higher temperatures, flame promotion was observed. Inhibition in premixed flames has been observed in terms of reduced laminar flame speeds for several halogenated PCC additives and one non-halogenated PCC additive, TMP.<sup>34</sup>

A more complete literature review of the influence of PCCs on flames can be found in References 79 and 257.

The emerging premise for flame suppression by PCCs was as follows. Phosphorus-containing radicals, such as HOPO and HOPO<sub>2</sub> (formed from PCCs during combustion<sup>253,254</sup>) catalyze the recombination of the important combustion radicals, H and OH, slowing the overall reaction rate and thus inhibiting the flame.<sup>256</sup> Since it is the phosphorus-containing radicals that participate in the recombination mechanism, and not the parent PCC, the form of the parent compound is relatively unimportant.<sup>19</sup> If supporting evidence were found for this hypothesis, then further studies of flame inhibition by PCCs could investigate alternative forms of the parent compounds that might be less toxic and more amenable for delivery to the flame.

Several mechanisms for catalytic cycles resulting in  $H + OH \rightarrow H_2O$  and  $H + H \rightarrow H_2$ , have been suggested.<sup>140,256,258-260</sup> Partial validation of the radical recombination hypothesis was provided by flow reactor experiments showing that the addition of PH<sub>3</sub> (phosphine) to H<sub>2</sub>-O<sub>2</sub> combustion product gases increased H+OH recombination rates following laser photolysis.<sup>260</sup> Flame experiments have also shown that the presence of PCCs affects radical levels. The addition of small quantities of the POCl<sub>3</sub>, a halogenated PCC, produced lower OH levels in non-premixed methane and ethene flames than did other halogenated compounds not containing phosphorus.<sup>47</sup> The addition of TMP lowered H levels in premixed low-pressure H<sub>2</sub>/O<sub>2</sub>/N<sub>2</sub> flames under rich, dilute conditions, and raised H levels under stoichiometric, less dilute conditions.<sup>256</sup>

## Transport Effects

A key factor affecting suppression is the amount of the additive reaching the non-premixed flame,<sup>261</sup> and several studies<sup>36,45,51,103</sup> of both fuel-side and oxidant-side doping of various fuel/inert vs. oxygen/inert flames have found dramatic changes in additive effectiveness with these changing conditions. When hydrocarbons are burned in air, the stoichiometric contour, where the flame is assumed to be, is situated on the oxidant side of the stagnation plane. Fuel-side additives must diffuse across the stagnation plane to reach the flame, while air-side additives are convected through the flame. The result is that fuel-side additive mole fractions at the flame are substantially reduced from their fuel-stream values, while oxidizer-side additive mole fractions are only slightly reduced from their oxidizer-stream values. The

extent of this additive loading reduction at the flame location varies with the stoichiometric mixture fraction ( $Z_{st}$ ), defined as the mass fraction of material originating from the fuel stream at the location where the concentrations of reactants are in stoichiometric proportions. For hydrocarbon/air flames,  $Z_{st}$  is typically  $< 0.1$ . Considerably different values of  $Z_{st}$  can be achieved by varying the compositions of the fuel and oxidant streams, either via dilution or enrichment. For  $Z_{st} > 0.5$ , the flame is on the fuel side of the stagnation plane, and additive loading reduction at the flame is more severe for oxidant-side additives than for fuel-side additives.

In several experimental studies of flame extinction by  $CF_3Br$ , the effect of additive loading reduction at the flame location has been quantified, assuming unity Lewis number. Results have been mixed. For methane/air opposed-jet diffusion flames, Trees et al.<sup>261</sup> found that  $CF_3Br$  was roughly twice as effective as an air-side additive than as a fuel-side additive, when the quantity of additive at the stoichiometric contour is compared for equal extinction strain rates. Work by Masri<sup>45</sup>, on the other hand, found that oxidizer-side and fuel-side addition of  $CF_3Br$  had very similar effectiveness in extinguishing turbulent natural-gas/air piloted jet flames, when corrected for additive concentrations at the flame location. Niioka et al.<sup>36</sup> reported comparable effectiveness for fuel-side and oxidizer-side addition in extinguishing various ethene/nitrogen vs. oxygen/nitrogen opposed-jet diffusion flames, including one with  $Z_{st} > 0.5$ . Close examination of the Niioka data showed that the fuel-side addition was generally less effective than oxidizer-side addition.

### Temperature Effects

Extinction studies under a variety of flame conditions found a significant temperature dependence for DMMP effectiveness, with higher effectiveness being observed at lower stoichiometric adiabatic flame temperatures.<sup>120</sup> The existence of a temperature dependence for phosphorus-based flame inhibition was first suggested by Hastie and Bonnell in 1980,<sup>256</sup> but since then there has been little investigation of this behavior. There is one computational study on premixed flame speeds,<sup>257</sup> but aside from Reference 79, there has been no experimental work in which flame temperature has been systematically varied.

The influence of flame temperature on inhibition effectiveness is an important consideration in evaluating the feasibility of new phosphorus-based flame suppressants, and has direct bearing on how to maximize their effectiveness in practical applications. The indicated trend implied that a mixture of inert and phosphorus-based suppressants could interact synergistically as the inert component cooled the flame, thus increasing the efficiency of the chemically active component. This would lower the needed quantity of the chemically active component, thus reducing system weight and decreasing environmental concerns and possible health impacts. A similar temperature dependence has been demonstrated for  $CF_3Br$ , including the observation of synergistic interaction with the inert suppressants  $N_2$ ,  $CO_2$  and  $H_2O$ .<sup>14,262</sup> Increased effectiveness at lower flame temperatures has also been observed for the iron-based suppressant  $Fe(CO)_5$ .<sup>103</sup>

#### 3.4.2 Inhibition of Non-premixed Flames by Phosphorus-containing Compounds

Fisher and co-workers<sup>79</sup> examined the inhibiting effects of two PCCs: dimethyl methylphosphonate (DMMP) [CAS #756-79-6,  $P(=O)(CH_3)(OCH_3)_2$ ], and trimethyl phosphate (TMP) [CAS #512-56-1,  $P(=O)(OCH_3)_3$ ], along with other additives for comparison, on a non-premixed methane-air diffusion flame. Their results have led to greater understanding of how a phosphorus-containing fire suppressant

would act to quench flames and developed some guidance for the selection of candidate PCCs for this purpose. Their research:

- Established a novel and sound protocol for conducting such experiments.
- Measured the effectiveness of the two PCCs relative to other, reference suppressants and to each other.
- Determined how the flame inhibition effectiveness of the two additives changed as a function of the agent loading and the adiabatic flame temperature, using the reduction in  $[OH]$  as a marker.

## Experimental

### *Apparatus and Materials*

The opposed-jet burner is shown schematically in Figure 3-72.

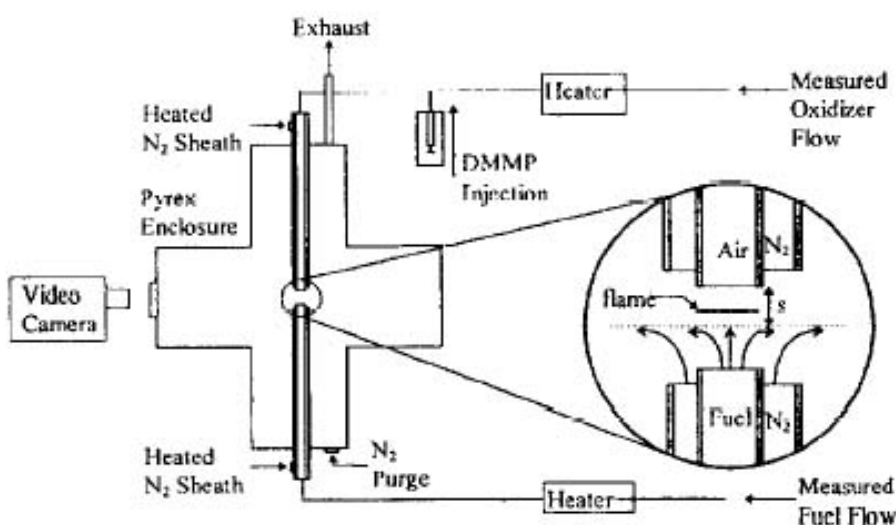


**Figure 3-72.**  
**Schematic of**  
**Opposed-jet Burner.**

The burner was constructed from straight, open glass tubes 30 cm long with an ID of 0.98 cm, and a separation distance of 0.95 cm between opposing nozzles. Annular sheath flows of nitrogen were provided through 2.22 cm ID glass tubes. The sheath tube exits were offset by approximately 1 cm, upstream of the reactant tube exits, to minimize the impact of the sheath flow on the development of the reactant flows. A flat flame was produced when the oxidant and fuel stream velocities were such that the flame was situated in the central portion of the space between the burner nozzles. The entire burner was isolated in a glass enclosure for control of exhaust gases. This enclosure was purged with nitrogen and maintained slightly below atmospheric pressure.

The burner was aligned vertically with the lower tube used as the fuel source and the upper tube as the oxidizer source. The results of a few experiments conducted with the reverse orientation to study the effect of buoyancy showed no significant change in extinction strain rate.

The extreme sensitivity of the extinction strain rate to the mass fraction of oxygen in the oxidizer stream necessitated very precise metering of reactant flows in order to achieve repeatable results. Precision mass

flow controllers, supplied by MKS Industries, were used to measure reactant flows. Even so, to minimize variability, measurements comparing doped and undoped flames were conducted by first evaluating the undoped extinction strain and then adding the dopant to one reactant stream without otherwise altering the composition of either stream.

Most of the extinction measurements were conducted using premixed oxygen and nitrogen (21 %  $\pm$  0.2% oxygen by volume) or Ultra Zero Grade air (21 %  $\pm$  2% oxygen by volume, total hydrocarbon content  $<$  0.1  $\mu$ L/L) as the oxidizer and methane (99 % pure) as the fuel. All gases were supplied by MG industries. For the extinction measurements with flame and stagnation plane coincident, oxygen (99.994 % pure) was mixed with nitrogen (99.998 % pure) in measured proportions to form the oxidizer stream, and the methane fuel was diluted with nitrogen (99.998 % pure).

The chemically active flame inhibitors, DMMP and TMP, were obtained from Aldrich Chemical Company (each 97 % pure). They were liquids at room temperature with low vapor pressures (less than 100 Pa at ambient temperature). In order to maintain sufficient concentrations of the PCC in the vapor phase, the reactant lines were heated to approximately 100 °C with electrical heating tapes. Wall temperatures on the outside surface of the heated lines were measured with adhesive thermocouples. The temperature of the reactant streams 10 cm upstream from the exit of the nozzles was maintained at 100 °C  $\pm$  1 °C via active control of the sheath flow temperature. These final reactant temperatures were measured by sheathed thermocouples in direct contact with the gas flow. The liquid PCC dopant was added to the reactant streams via a syringe pump that provided a constant volume flow. The gas flow at the injection site was preheated to approximately 130 °C for a rapid vaporization of the incoming liquid dopant. The liquid density, syringe size, and motor speed fixed the mass flows of the dopants. Previous pyrolysis experiments with DMMP and TMP<sup>263,264</sup> have shown that thermal decomposition is negligible below 1000 K; thus the preheating of the reactant streams should have had no effect on their chemical composition.

### ***Measurements***

The enclosure had a glass window on one end, approximately 25 cm from the centerline of the flow. A video camera, located a few centimeters from this window, was used to measure flame position. Flame position was measured relative to the oxidizer nozzle exit plane using the separation gap between the nozzles for reference.

OH concentration measurements were made using pointwise LIF. Figure 3-73 shows a schematic of the experimental set up. Profile measurements were made by traversing the laser beam and collection optics simultaneously across the flame in 100  $\mu$ m steps. The translation stages used had a resolution of 10  $\mu$ m. Excitation of the P<sub>1</sub>(9) transition of the A $\leftarrow$ X (1,0) band near 286 nm was made using a frequency-doubled Quanta Ray PDL 2 pulsed dye laser, nominal linewidth of 0.2 cm<sup>-1</sup>, with rhodamine 590 dye. This transition was selected due to the weak temperature dependence of the rotational ground state population in the temperature region of interest ( $<$  10 % variation for 1400 K  $<$  T  $<$  2500 K), which helps maintain a strong LIF signal across the entire OH profile. The dye laser was pumped with a 6 ns to 7 ns pulse at 532 nm provided by a frequency-doubled Spectra Physics DCR 2A Nd:YAG laser operating at 10 Hz.

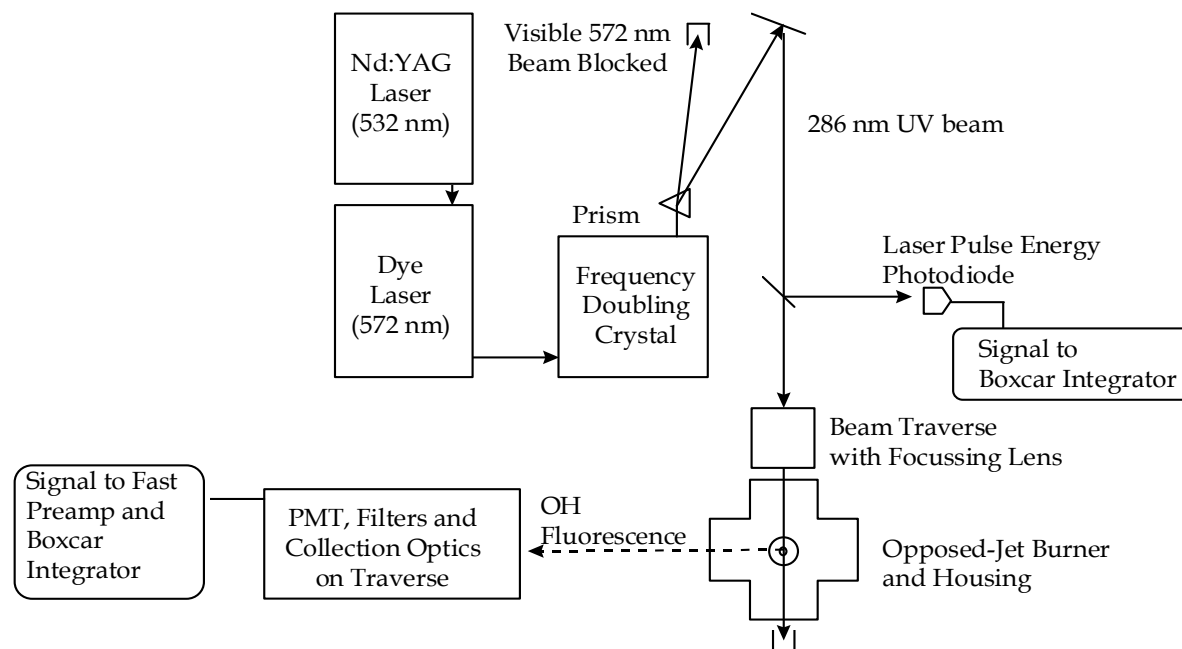


**Figure 3-73. Schematic of LIF Apparatus.**

Detection of OH fluorescence was performed at  $90^\circ$  to the laser beam axis using an RCA 8850 photomultiplier tube and color glass filters (Schott WG305 and UG11) which transmit light in the 305 nm to 371 nm range. The photomultiplier signal was amplified by a SRS240 Fast Pre-amplifier (Stanford Research Systems). The filter combination used blocks elastically scattered laser light (and near-elastic resonant fluorescence) while passing fluorescence emission from the (1,1) band (312-326 nm) and emission from the overlapping (0,0) band (306-320 nm) which can occur following collisionally driven Vibrational Energy Transfer (VET) from the  $v' = 1$  to the  $v' = 0$  states. At atmospheric pressure, VET rates can be significant<sup>265,266</sup> with more than a third of the total measured fluorescence originating from the (0,0) band when using excitation/detection schemes similar to this.<sup>267</sup> Fluorescence trapping of emission from the (1,1) band was negligible due to the small population of the electronic ground state with  $v'' = 1$  over the temperature range under consideration. Some trapping occurred for fluorescence emission originating from the (0,0) band, but the effect was small due to the short path length through the flame (less than 1 cm) and is not expected to influence the measurements.<sup>268,269</sup> PAH fluorescence<sup>268</sup> was expected to be negligible because the moderately strained laminar flames under investigation were virtually soot-free. This was confirmed by measurements taken with the dye laser tuned off resonance. The combination of the focused ( $f = 30\text{cm}$  quartz focusing lens) UV laser beam and slits in the detection optics give a probe volume of less than  $100\ \mu\text{m}$  in diameter and 1.5 mm in length. The opposed-jet burner flame was locally planar near the centerline with the long axis of the probe volume aligned in the plane of the flame surface. Laser pulse energy was monitored using a UV-sensitive photodiode. Both the LIF and laser energy signals were integrated on a shot-by-shot basis using an SRS 250 Boxcar Integrator and Averager (Stanford Research Systems), and recorded on a personal computer using a GW Instruments data acquisition card. Operation within the linear LIF regime was ensured by checking the linearity of LIF signal strengths with pulse energy for all measured data points.<sup>270</sup>

To avoid errors associated with wavelength drift of the dye laser and the resulting changes in the spectral overlap of the laser and molecular absorption line shapes, the output wavelength of the dye laser was

scanned across the  $P_1(9)$  transition at each measurement location using a stepper motor to adjust the grating in the dye laser cavity. 100 measurements of OH fluorescence and laser pulse energy were acquired at each half-step of the motor (corresponding to a wavelength change of approximately 0.0012 nm), and the half-step motor position with the maximum average ratio of fluorescence signal to laser pulse energy was taken to be the absorption line center for the transition. LIF data for that half-step motor position were used for the subsequent evaluation of OH concentration. The repeatability of this procedure was found to be within  $\pm 5\%$  of the mean observed ratio. The average ratio of OH fluorescence signal to laser pulse energy was found by fitting the 100 measurements to a straight line using linear regression analysis. The statistical uncertainty (one standard deviation) in the fitted slopes was less than  $\pm 3\%$ . Additional uncertainty in these slopes arose from statistical uncertainty in the measurement of the zero level in the presence of electrical noise from the Nd:YAG laser. Statistical scatter in the zero measurement ( $\pm$  one standard deviation) corresponded to an uncertainty of  $\pm 3\%$  to  $5\%$  of the peak slope for all data points in the profile. In addition to shot noise and electrical noise, the statistical uncertainty in the measurements reflected fluctuations in flame location. For these aerodynamically stabilized flames, perturbations in the reactant flow can cause small, momentary flame displacements. The 100 shot LIF averaging process largely compensated for these oscillations. The total uncertainty for each measured data point in a given profile due to random errors was found by summing the contribution of the uncertainties described above (assuming statistical independence) and is estimated to be less than  $\pm 10\%$  of the peak value in the profile.

In order to quantify the fluorescence measurements, corrections for collisional quenching and the fraction of the OH population that is in the pumped rotational level must be made. However, the overall effect of these corrections on the profile shape is small, as is expected for our excitation/detection scheme in non-premixed atmospheric-pressure flames.<sup>271-273</sup> Equation 3-3 relates the fluorescence signal to the concentration of OH assuming low laser energy (i.e. negligible saturation of the excited transition):

$$F = CBI f N \Phi \quad (3-3)$$

Here  $F$  is the total fluorescence signal;  $C$  is a constant that incorporates geometric factors such as collection solid angle and probe volume as well as detector efficiencies and gain characteristics of the integrators, amplifiers etc.;  $B$  is the Einstein coefficient for stimulated absorption;  $I$  is the spectral overlap integral between the laser intensity and the molecular absorption line shape, temporally integrated over the duration of the laser pulse;  $N$  is the total OH population, and  $f$  is the fraction of the population that is present in the ground state rotational level excited by the laser; and  $\Phi$  is the fluorescence quantum yield, which depends on the local quenching and VET rates.

Species and temperature profiles from the undoped-flame calculations were used to estimate the required corrections to the linear LIF data for both doped and undoped flames. The fraction of the ground state population in the pumped rotational level is determined using the local gas temperature given by the calculations and assuming rotational thermal equilibrium (Boltzmann distribution), as implemented in the spectral simulation software LIFBASE.<sup>274</sup>

The total fluorescence yield,  $\Phi$ , was estimated using:<sup>267</sup>

$$\Phi = \frac{A_1 + \frac{V_{10}}{Q_0} A_0}{Q_1 + V_{10}} \quad (3-4)$$

where  $A_1$  and  $A_0$  are the spontaneous emission rates for the  $v' = 1$  and  $v' = 0$  vibrational levels, respectively. Equation 3-4 has been simplified by assuming equal transmission and detection efficiencies of the collection optics and PMT for both the (1,1) and (0,0) bands.  $Q_1$  and  $Q_0$  are the total quenching rates for the  $v' = 1$  and  $v' = 0$  levels, and  $V_{10}$  is the total VET rate from  $v' = 1$  to  $v' = 0$ . The influence of VET rates on the fluorescence quantum yield is primarily due to the higher spontaneous emission rate of the  $v' = 0$  state ( $A_1/A_0 \approx 0.575$ )<sup>275</sup>. The quenching and VET rates were evaluated using Equation 3-5.<sup>267,276</sup>

$$Q, V = \left( \frac{P}{k_b T} \right) \sum_i \chi_i \langle v \rangle_{i-OH} \sigma_i^{Q,V}(T) \quad (3-5)$$

where  $P$  is pressure;  $T$  is temperature;  $k_b$  is Boltzmann's constant;  $\chi_i$  is the mole fraction of OH collision partner species  $i$ ;  $\langle v \rangle_{i-OH}$  is the mean relative collision velocity of species  $i$  and OH given by  $\langle v \rangle_{i-OH} = (8k_b T / \pi \mu_{i-OH})^{1/2}$ , where  $\mu_{i-OH}$  is the reduced mass of species  $i$  and OH; and  $\sigma_i^{Q,V}(T)$  is the value of the quenching or VET (superscript  $Q$  or  $V$  respectively) cross section for collisions with species  $i$ , averaged over all rotational levels in a given vibrational level, assuming rotational thermal equilibrium.

Substitution of Equation 3-5 into Equation 3-4 followed by some algebraic manipulation yielded:<sup>267</sup>

$$\Phi = \frac{A_0}{Q_0} \left[ \frac{\left( \frac{A_1}{A_0} \right) \left( \frac{\langle \sigma^Q \rangle_0}{\langle \sigma^Q \rangle_1} \right) + \frac{\langle \sigma^V \rangle_{10}}{\langle \sigma^Q \rangle_0}}{1 + \frac{\langle \sigma^V \rangle_{10}}{\langle \sigma^Q \rangle_0}} \right] \quad (3-6)$$

where  $\langle \sigma^Q \rangle_1$ ,  $\langle \sigma^Q \rangle_0$  and  $\langle \sigma^V \rangle_{10}$  represent the sum over all collision partners of the thermally averaged cross sections for quenching from  $v' = 1$ , quenching from  $v' = 0$ , and VET from  $v' = 1$  to  $v' = 0$ , respectively. Quenching cross-section measurements for the  $v' = 1$  and the  $v' = 0$  state indicated similar values.<sup>265,275</sup> The ratio of averaged VET cross sections to the averaged quenching cross sections was assumed to be independent of position in the flame (e.g.,  $\langle \sigma^V \rangle_{10} / \langle \sigma^Q \rangle_0 \approx \text{constant}$ ). As a result, the quantity in square brackets in Equation 3-6 became a constant, and the fluorescence yield was simply inversely proportional to the quenching rate for the  $v' = 0$  state. The error in the assumption  $\langle \sigma^V \rangle_{10} / \langle \sigma^Q \rangle_0 \approx \text{constant}$  was less than 5%. Values for the quenching rate cross-sections used in this work were taken from temperature-dependent quenching cross-section data compiled by Tamura et al.<sup>277</sup> from the extensive measurements that have been made for the  $v' = 0$  state of OH.

The calculated quenching rate varied by 15% across the OH containing regions in  $N_2$ - $O_2$  flames. This variation was moderated by the presence of a large concentration of  $N_2$  which has a relatively small

gradient in the flame zone. For flames where Ar (a highly inefficient quencher) fully replaced N<sub>2</sub>, the variation was substantially higher at 30 %.

The same quenching environment was assumed for flames both with and without DMMP loading. The maximum phosphorus loading was only 715 μ/L. Since the mole fractions of phosphorus-containing species were small in this case, it was expected that they would not contribute significantly to quenching of OH. Changes in major species profiles due to the presence of DMMP were not expected to be large enough to significantly change the overall quenching environment. Changes in flame temperature due to the addition of these small loadings of DMMP were also found to be negligible (< 10 K).

After correcting for the fluorescence yield and the Boltzmann fraction of the pumped rotational level, the corrected LIF profile was directly proportional to OH concentration. An estimate of the scaling constant relating the corrected LIF measurements to absolute OH concentrations was made by matching the peak of the measured profile from the undoped flame to the peak OH concentration predicted by the flame calculations. This matching did not affect observations of PCC effects on OH, which were all presented normalized to the undoped flame measurements. For profiles measured in flames doped with phosphorus-containing additives, the scaling constant was determined from undoped profiles taken on the same day with the same instrument settings. Because the same constant was used for both doped and undoped flames, quantitative comparisons could be made between the two cases. Determination of the magnitude of the scaling constant was performed by minimizing the mean-square-error between calculated and measured profiles (via a least squares technique). For this minimization, only data points above 50 % of the measured peak value were considered. Minimization of error was performed via adjustment of the scaling constant and a position offset (i.e., the offset between the measured flame center, as indicated by the translation stage micrometers, and the computational flame center). Determination of this scaling constant calibrated the constant C from Equation 3-3, assumed to be constant for a given set of instrument settings. This scaling procedure affected only the magnitude and position of the observed fluorescence profile and not the shape or width.

#### ***Determination of Extinction Strain Rates***

The flame strength can be characterized by the strain rate at extinction,<sup>278,279</sup> and here, the effectiveness of additives as flame inhibitors was determined by measuring the dependence of extinction strain rate on additive loading. The inverse of the strain rate is one of several related measures of the characteristic diffusion time of the flame.<sup>280</sup> The strain rate at extinction was approximated using the following expression involving global flame parameters:<sup>76</sup>

$$a_q = \frac{2V_O}{L} \left( 1 + \frac{V_F \sqrt{\rho_F}}{V_O \sqrt{\rho_O}} \right) \quad (3-7)$$

where L refers to the separation distance between the nozzles, V is the average stream velocity at extinction, ρ is the stream density and the subscripts O and F refer to oxygen and fuel respectively. This expression is equal to the velocity gradient on the oxidant side of the stagnation plane under certain restrictive conditions: reactions, diffusion, and viscous effects must be confined to a narrow region around the stagnation plane, and plug flow boundary conditions must be imposed at the nozzles. Under less restrictive conditions, this expression has been determined experimentally to be nearly proportional to the local oxidant-side velocity gradient. Recent measurements performed in an open-tube burner with

geometry very similar to our own have found a nearly proportional relationship between the  $a_q$  of Equation 3-7 and the maximum local velocity gradient on the oxidant side of the flame, as measured by laser-Doppler velocimetry.<sup>281</sup> The same proportionality was found to hold for methane/air and propane/air flames, with and without flame-inhibiting additives in the air stream. Thus, Equation 3-7 can be used to determine relative changes in extinction strain rates obtained on the same apparatus. In particular, the ratio of doped to undoped  $a_q$  measured using Equation 3-7 should be equal to the same ratio of local oxidant-side velocity gradients. The validity of this approach was borne out by the good agreement between the current data and those of other researchers for inert additives.

In determining extinction conditions for use in calculating  $a_q$ , Fisher and co-workers developed a novel method for approaching extinction, motivated by a need to minimize transient effects of dopant loading. Commonly, extinction studies with opposed-jet burners adjusted the strain rate by varying both the oxidizer and fuel streams simultaneously so that the flame position remained constant,<sup>63</sup> or so that a momentum balance between the two streams was maintained.<sup>80</sup> This required varying the mass flows of both reactant streams, and resulted in changing concentrations of the inhibiting agent when the agent was delivered via a constant-mass-flow syringe pump. The resulting transients in the adsorption/desorption of the agent on walls made it difficult to predict the concentration of agent at the exit plane of the doped reactant stream at extinction.

The new method circumvented the difficulties associated with dopant loading transients. The concentration of dopant in the relevant reactant stream (fuel or oxidizer) was fixed by maintaining constant flows of all the constituents of the doped reactant stream. After waiting a sufficient time for equilibrium conditions to be established, extinction was approached by varying only the flow of the undoped stream. One consequence of using this method is that the position of both stagnation plane and flame varied during the extinction experiment. This was found to have only a minor influence on the measured extinction strain except when the flame or stagnation plane was very close to one of the nozzles.

To validate this method, experiments were performed over a large range of methane and air flows, achieving extinction with the flame in a variety of positions. Figure 3-74 shows the resulting global extinction strain rates ( $a_q$ ) as a function of the observed flame position.

The extinction strain of the undoped flame varied only  $\pm 2\%$  (from a mean value of  $359\text{ s}^{-1}$ ) for flame positions between 0 mm and 7mm. This region of consistent global extinction strain rates was denoted as the *acceptable* region. For experiments in which extinction occurred with the flame outside the acceptable region, large deviations in  $a_q$  occur.

Also shown in Figure 3-74 are sets of data from experiments conducted with a  $300\text{ }\mu\text{L/L}$  doping of DMMP and  $50,000\text{ }\mu\text{L/L}$  doping of  $\text{N}_2$ , both in the oxidizer stream. (The limited number of data points in the DMMP series was a result of the coarsely quantized mass flows of dopant available from the syringe pump.) Because of the inhibitory effect of the DMMP or  $\text{N}_2$  additive, these data sets had markedly lower mean global extinction strain rates than the data for the undoped flames. However, both data sets showed the same systematic trends with flame position, and both had only small variations in extinction strain over the acceptable region.

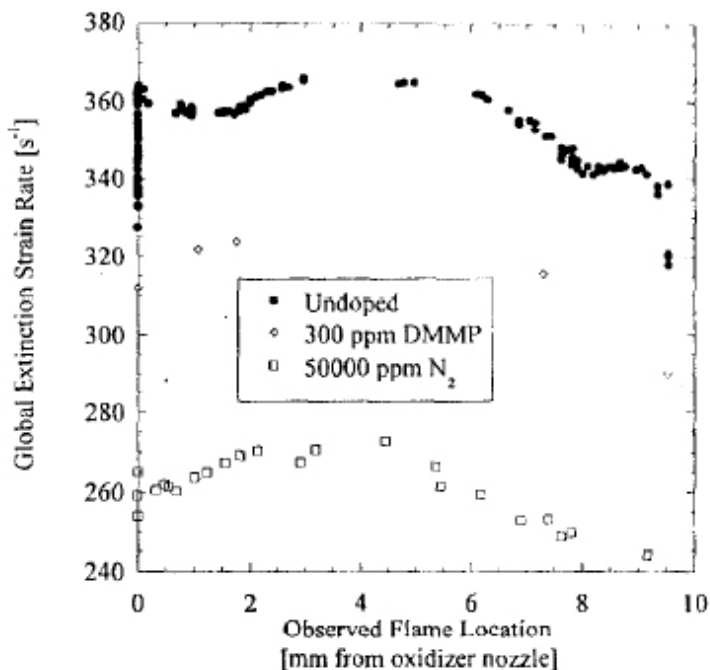


**Figure 3-74. Variation of Global Extinction Strain,  $a_q$ , with Observed Flame Position at Extinction.**

The existence of the same acceptable region for a range of flame extinction strain rates validated this method for approaching extinction. Within this region, the results should be within experimental uncertainty of those obtained using more conventional methods that maintain a nearly constant flame position. The nearly constant extinction strain rates over the central region were consistent with the previous computational findings of Nishioka et al.<sup>282</sup>

The asymmetrical dependence of extinction strain rate on flame position was due to the offsetting of the flame to the oxidant side of the stagnation plane, which was conveniently characterized using the stoichiometric mixture fraction,  $Z_{st}$ . The stoichiometric mixture fraction,  $Z_{st}$ , is the fraction of the material present at the stoichiometric contour that originated in the fuel stream.  $Z_{st}$  was evaluated from reactant compositions in the nozzles and the stoichiometry of the overall combustion reaction, using Equation 3-8:

$$Z_{st} = \frac{Y_{O,-\infty}}{\left( \left( \frac{MW_O \nu_O}{MW_F \nu_F} \right) Y_{F,+\infty} + Y_{O,-\infty} \right)} \quad (3-8)$$

where  $Y$  is mass fraction,  $MW$  is molecular weight,  $\nu$  is the stoichiometric coefficient for complete combustion, the subscripts  $O$  and  $F$  refer to oxygen and fuel, respectively, and the subscripts  $\pm\infty$  refer to conditions at the fuel and oxidizer nozzles. The undiluted flame used for the first series of experiments in Figure 3-74 had  $Z_{st} = 0.054$ . Other researchers have found that, near extinction, this corresponds to a displacement of the flame of approximately 1 mm to the oxidizer side of the stagnation plane.<sup>67,283</sup>

The importance of this displacement was investigated by measurements in which the flame and the stagnation plane were coincident. By varying the dilution of the fuel and oxidizer streams it is possible to move the location of the stoichiometric contour (the presumed flame location), relative to the stagnation

plane. For reactants of equal diffusivities, setting  $Z_{st} = 0.50$  placed the flame at the stagnation plane. Since  $Z_{st}$  depended on two independent variables,  $Y_F$  and  $Y_O$ , fixing  $Z_{st}$  left one degree of freedom on reactant concentrations. Unique conditions for the  $Z_{st} = 0.50$  tests were established by choosing the mass fraction of oxygen to give approximately the same undoped global extinction strain rate as was obtained for the undiluted flame. Results from these conditions,  $Z_{st} = 0.50$  with  $Y_O = 0.387$  and  $Y_F = 0.097$ , are shown in Figure 3-75. During these experiments, in which the oxidizer stream was mixed from separate  $O_2$  and  $N_2$  bottles, it was found that the global extinction strain rate was very sensitive to the concentration of  $O_2$ , consistent with experimental results from Puri and Seshadri for diluted methane-air flames.<sup>80</sup> This sensitivity contributed to the greater scatter in the  $Z_{st} = 0.50$  tests than in the  $Z_{st} = 0.054$  tests, which were conducted with premixed air. Nonetheless, the global extinction strain rate varied less than 3 % of the mean value of  $336 \text{ s}^{-1}$  for flame locations between 0 and 9mm. Within experimental scatter, results with  $Z_{st} = 0.5$  were symmetrical about the center of the region between the two burners.

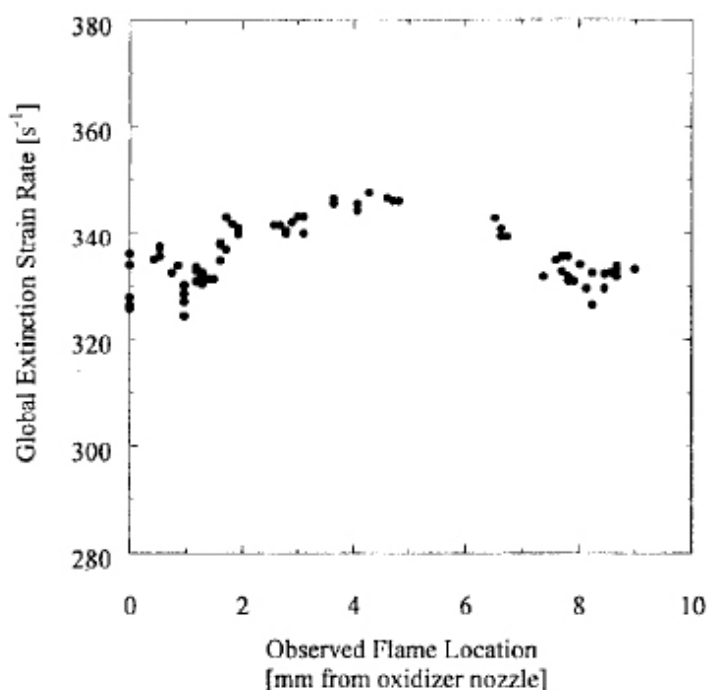


**Figure 3-75. Variation of Global Extinction Strain,  $a_q$ , with Observed Flame Position at Extinction for Non-premixed  $CH_4/N_2$ - $O_2/N_2$  Flames, with  $Z_{st} = 0.50$ .**

Although the acceptable region of Figure 3-74 is defined in terms of the observed flame position, in practice it is not necessary to determine the experimental observation of flame location at extinction for all measurements. Rather, a parameter  $S$  is introduced which can be calculated from the reactant stream properties at the nozzles.  $S$  approximates the distance from the oxidizer nozzle to the stagnation plane and is given by the expression in Equation 3-9, again derived by Seshadri and Williams for plug flow boundary conditions.<sup>76</sup>

$$S = L \left/ \left( 1 + \frac{V_F \sqrt{\rho_F}}{V_O \sqrt{\rho_O}} \right) \right. \quad (3-9)$$

Figure 3-76 shows a plot of observed flame location for both  $Z_{st} = 0.50$  and  $Z_{st} = 0.054$  against the parameter  $S$ . The observed flame location did not vary linearly with the predicted location of the stagnation plane, but instead followed a sigmoidal curve, being much more sensitive to flow variations

when it was near the middle of the separation gap. The data presented in Figure 3-76 show flame positions for only high strain cases ( $275 \text{ s}^{-1}$  to  $360 \text{ s}^{-1}$ ). It was found that, in general, the steepness of the sigmoidal curve increased with increasing strain rates. For purposes of conducting experiments with the new method, it sufficed to observe that the flame location, for each condition, was a well-correlated one-to-one function of this parameter  $S$ . Therefore, one can map the experimentally determined acceptable region in terms of  $S$ , and direct observation of flame position became unnecessary. For  $Z_{st} = 0.0544$ , this region is  $3.50 \text{ mm} < S < 5.25 \text{ mm}$ . All extinction results reported below were for flames inside this acceptable region.

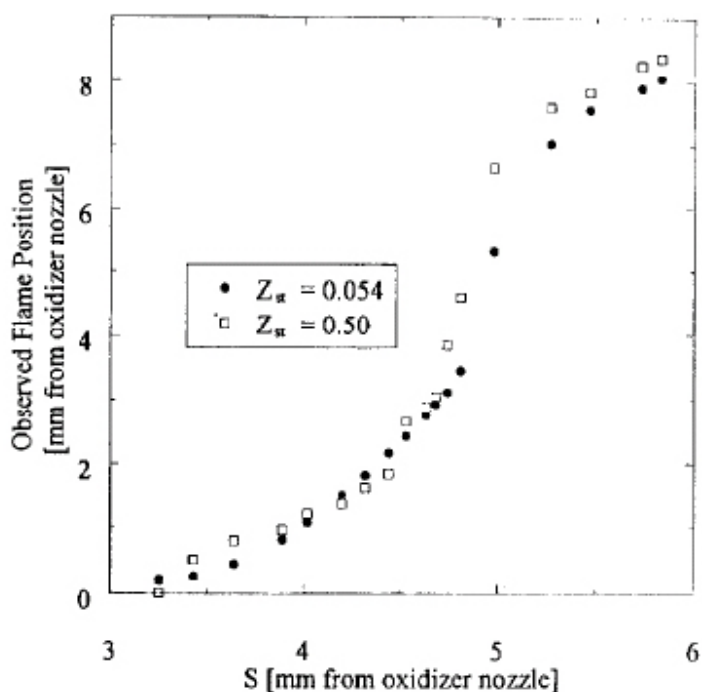


**Figure 3-76. Observed Flame Positions as a Function of Predicted Distance to the Stagnation Plane for Non-premixed Flames of  $\text{CH}_4$ -air ( $Z_{st} = 0.054$ ), and  $\text{CH}_4/\text{N}_2$ - $\text{O}_2/\text{N}_2$  Flames, ( $Z_{st} = 0.50$ ) Near Extinction.**

### Flame Extinction Results

Initial tests were conducted with undoped reactant streams at ambient temperature to compare results with those of other researchers. For undiluted methane burning in air, the measured global extinction strain rate was  $296 \text{ s}^{-1}$ . When the reactant streams were preheated to  $100 \text{ }^\circ\text{C}$ , the measured value for  $a_q$  increased to  $360 \text{ s}^{-1}$ . Extinction measurements on undoped flames using the same oxidizer source were consistent to within  $\pm 5 \text{ s}^{-1}$ . Variation in  $a_q$  up to  $80 \text{ s}^{-1}$  was observed with different bottles of high purity compressed air, and was attributed to slightly different mass fractions of oxygen. All the results for doped flames were normalized to undoped experiments using the same oxidizer source.

The unheated global extinction strain value was comparable to the value found by Puri and Seshadri<sup>80</sup> of  $280 \text{ s}^{-1}$  and to the value of  $255 \text{ s}^{-1}$  computed from flows at extinction reported by Papas et al.<sup>63</sup> using Equation 3-7. All three numbers fell within the range of variation attributed to differences in composition of high purity air batches. This agreement was surprisingly good in light of the significantly different boundary conditions and aspect ratio of the burner used by Puri and Seshadri. Agreement with literature values of local extinction strain rate was not as good; measurements and calculations ranged from  $340 \text{ s}^{-1}$  to  $400 \text{ s}^{-1}$ <sup>63,67,78</sup> and from  $354 \text{ s}^{-1}$  to  $544 \text{ s}^{-1}$ <sup>67</sup>, respectively. We attribute the discrepancy of our measurements with these values to our use of the global strain expression under conditions where it is not

strictly valid. Comparable differences between global and local strain rates have been observed by other researchers.<sup>63</sup>

Further validation experiments were conducted with nitrogen as a chemically inert flame-inhibiting additive. Normalized extinction strain rates for nitrogen addition to the air side of a methane/air flame are shown in Figure 3-77.

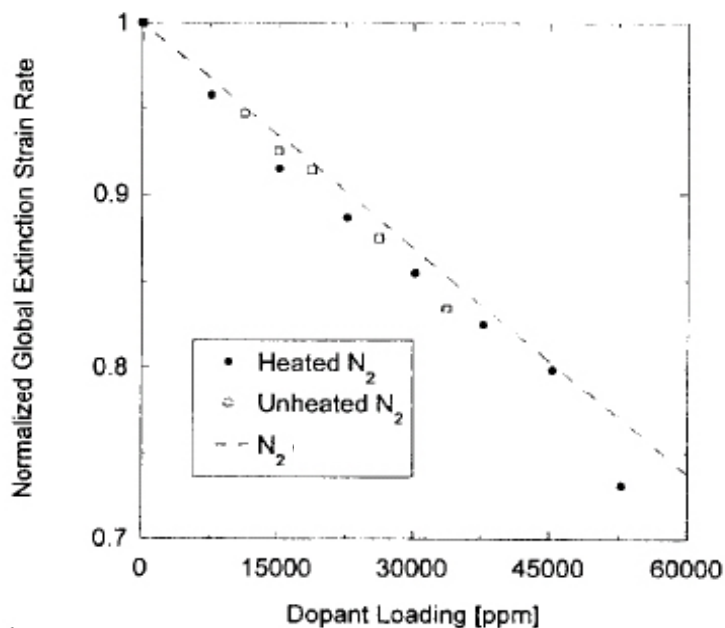


**Figure 3-77. Inhibition of Non-premixed Methane-air Flames, Based on Reduction in the Global Extinction Strain Rate by Oxidizer-side Addition of Nitrogen, with and without Preheated Reactants.**

Each data point represents the average of at least three measurements, and is normalized by the extinction strain rate for a pure methane/air flame. The extinction strain rate dropped linearly with increasing loading of this additive. The results were independent of whether or not the reactants are preheated to 100 °C, consistent with the findings of Trees et al.<sup>284</sup> The nitrogen dilution data can be compared to room-temperature data of Puri and Seshadri,<sup>80</sup> also shown in Figure 3-77. Agreement is good, with least-mean-square slopes agreeing within 7 %. However, it should be noted that the diluted flame experiments of Puri and Seshadri were conducted at a fixed value of  $Z_{st} = 0.0544$ . This required some nitrogen addition to the fuel flow. Here, nitrogen was added only to the oxidizer stream. Previous experiments by Fisher and co-workers<sup>285</sup> indicated that correcting for the effect of this fuel-side addition would lower the present measured extinction strain rates by about 3 %, resulting in an overall discrepancy of 10 % with the Puri and Seshadri data.

Figure 3-78 shows the results for PCC addition to the air stream of methane-air flames. Again, points represent averages of at least three measurements, and were normalized by the undoped extinction strain. For DMMP addition, the global extinction strain rate decreases linearly with additive mole fraction. Experiments indicated that at a volume fraction of 1500  $\mu\text{L/L}$ ,  $a_q$  was reduced by 35 % of the undoped value. Detectable inhibition ( $\approx 3$  % reduction in  $a_q$ ) was found at loadings as low as 100  $\mu\text{L/L}$ . For volume fractions below 100  $\mu\text{L/L}$ , preheating of reactants was not necessary to prevent condensation of DMMP. This allowed for ambient temperature testing of low DMMP loadings which demonstrated inhibition effectiveness similar to that found in the preheated experiments. Figure 3-78 also shows the results from TMP-doped flames. TMP exhibited similar inhibitory properties to DMMP over the common range of loadings. This was consistent with the hypothesis<sup>19</sup> that it is phosphorus radicals

formed in the flame that are important and not the parent compound. Consistent flame inhibition was observed, with no sign of the flame promotion noted by others.<sup>63,254</sup> A possible explanation is that the relatively low peak temperatures typical of highly strained methane vs. air flames<sup>67</sup> were below the 2230 K transition between inhibition and promotion observed by Hastie and Bonnell.<sup>256</sup>

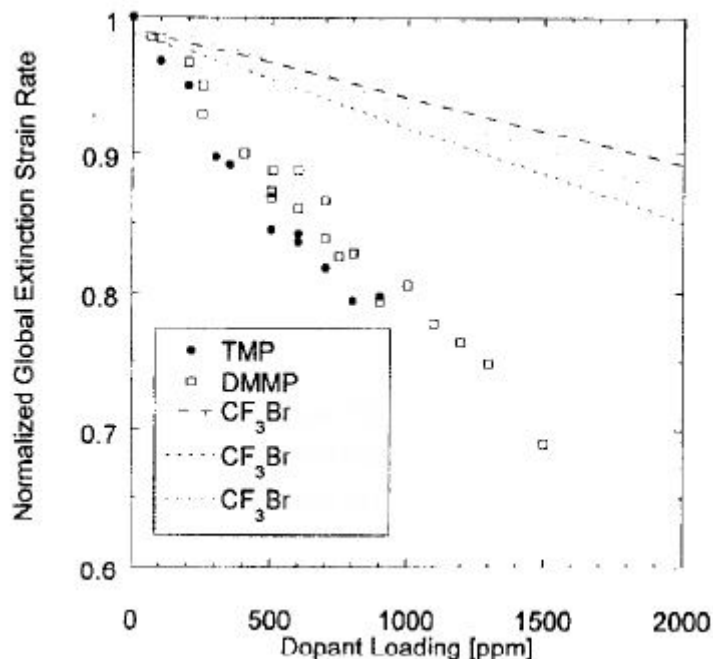


**Figure 3-78. Inhibition of Non-premixed Methane-air flames, Based on Reduction in the Global Extinction Strain Rate, by Oxidizer-side Addition of trimethyl phosphate (TMP), and dimethyl methylphosphonate (DMMP). Also shown are reported literature values for inhibition by CF<sub>3</sub>Br.**

Also shown in Figure 3-78 are published flame inhibition data for CF<sub>3</sub>Br.<sup>16,45,261</sup> The flame inhibition efficiencies of DMMP and TMP are two to four times better, on a molar or mass basis, than those reported for CF<sub>3</sub>Br. Comparisons of these PCCs with Fe(CO)<sub>5</sub>, one of the most effective flame inhibitors known, show that Fe(CO)<sub>5</sub> is a stronger inhibitor at low loadings: inhibition at 200 μL/L<sup>103</sup> is comparable to the PCC's effectiveness at 1500 μL/L. However, Fe(CO)<sub>5</sub>'s effect as an inhibitor plateaus for mole fractions between 200 μL/L and 500 μL/L, the highest gas phase concentration achievable with ambient temperature reactants.<sup>103</sup> The PCCs' inhibition performance can also be compared to the N<sub>2</sub> data presented in Figure 3-77. DMMP and TMP are approximately 40 times more effective than N<sub>2</sub> on a molar basis, ≈10 times as effective on a mass basis. It is important to note that the range of extinction strain rates achieved in these PCC experiments represents only the upper portion of the range of local strain rates encountered in a realistic, turbulent, fire.<sup>21</sup> Extending the experimental range to much lower strains would require a different method of introducing the PCC.

Fisher and co-workers also performed an experiment to determine whether the hydrocarbon content of the PCCs contributed significantly to the inhibition effectiveness. In certain chemical systems, such as carbon monoxide-air combustion, trace amounts of hydrocarbons had been observed to inhibit combustion.<sup>286,287</sup> It is thought that the inhibition occurred because the hydrocarbon acted as a radical sink. Hastie et al.<sup>140,256</sup> attributed 8 % of TMP's inhibition effectiveness in hydrogen flames to this effect. In order to determine whether radical scavenging by the methyl groups, found in the PCCs under investigation, may be responsible in part for the PCCs' inhibition observed here, tests were conducted with isooctane as the dopant. Isooctane has a similar structure to the PCCs, but lacks the central phosphorus atom. It is expected that any contribution from methyl groups to flame inhibition by the

PCCs would be observed during the isooctane tests. However, these tests showed a 4 % increase in the global extinction strain at a loading of 400  $\mu\text{L/L}$ , indicating that the effect of the hydrocarbon was to promote the flame, not to inhibit it. This result provided further support for the hypothesis that the phosphorus atom was crucial to the flame inhibition effects measured in this study.

## Effects of Stoichiometric Mixture Fraction

### Experiments

Fisher and co-workers<sup>120</sup> investigated how the effectiveness of the two additives changed as a function of the adiabatic flame temperature,  $T_{\text{ad}}$ , and the stoichiometric mixture fraction,  $Z_{\text{st}}$ . DMMP is mainly chemically active; argon is inert.

Suppressant effectiveness was defined as the change in extinction strain rate when the additive was introduced, normalized by the undoped extinction strain rate,  $a_{\text{qo}}$ .<sup>79,288</sup> For low loadings, the effectiveness should vary linearly with dopant loading.  $T_{\text{ad}}$  and  $Z_{\text{st}}$  were changed by varying the dilution level of the fuel and oxidizer streams.

For tests of chemically suppressed flames, a constant loading of 500  $\mu\text{L/L}$  of DMMP was added to one of the reactant streams. Argon additive testing was conducted with a loading of 25000  $\mu\text{L/L}$ . The disparity between DMMP and argon concentrations was required because of the stronger suppression effect of DMMP. Experiments were performed for stoichiometric mixture fractions ranging from 0.055 to 0.7. Adiabatic flame temperatures for the various values of  $Z_{\text{st}}$  and overall dilution of the flames were evaluated for the undoped case using the STANJAN code.<sup>9</sup>

To accurately estimate the quantity of dopant at the flame surface, numerical calculations using the OPPDIF code<sup>211</sup> were made with plug flow velocity boundary conditions, multicomponent diffusion but no thermal diffusion, and detailed chemistry (excluding phosphorus compounds), using the GRI mechanism<sup>289</sup> with nitrogen chemistry omitted. The mole fraction of dopant was evaluated at the maximum temperature in the reaction zone, taken to represent the flame location. The estimated diffusivity of DMMP was based on the interaction potentials of similar molecular weight compounds. The numerical calculations were required because this diffusivity was significantly different from the rest of the reactant stream components, making the effect of preferential diffusion important.<sup>261</sup>

In these transport calculations for estimating relevant dopant loadings, the chemically reactive compound DMMP was treated as inert because complete chemical kinetic and transport data were not available for it or its combustion products. This treatment gave a reasonable estimate of the quantity of phosphorus present in all chemical forms.

Two types of experiments were performed. The first varied  $Z_{\text{st}}$  from 0.055 to 0.7. At each  $Z_{\text{st}}$ ,  $a_{\text{qo}}$  was matched to  $350 \text{ s}^{-1} \pm 10 \text{ s}^{-1}$ , by trial-and-error variation of the dilution of both reactants with nitrogen. This process entailed changing the overall dilution, a parameter which is independent of  $Z_{\text{st}}$ . Due to the high sensitivity of  $a_{\text{qo}}$  to reactant composition, this narrow range in allowed  $a_{\text{qo}}$  resulted in an even narrower range of allowed reactant compositions at a given  $Z_{\text{st}}$ . Experimentally determining those allowed compositions accurately became difficult at high  $Z_{\text{st}}$ , where the low methane flows resulted in a higher percentage uncertainty in their values.

As  $Z_{st}$  was increased with fixed  $a_{q0}$ ,  $T_{ad}$  declined steadily, as seen in Figure 3-79. Calculations by Grudno et al.<sup>280</sup> for a fixed  $T_{ad}$ , were qualitatively consistent with this result, finding that  $a_{q0}$  increased monotonically as  $Z_{st}$  was increased from 0.055 to 0.4. This variation in  $a_{q0}$  and  $T_{ad}$  with  $Z_{st}$  was attributed to the changing relationship between the strain rate and the appropriate time scale for diffusion of reactants. While the strain rate is always considered to be a good measure of that time scale, the relationship between the two depends on  $Z_{st}$ .<sup>168,280,290,291</sup> The error bars in Figure 3-79 represent standard deviations of the measurements. The large error at high  $Z_{st}$  represent the methane flow uncertainty described above.

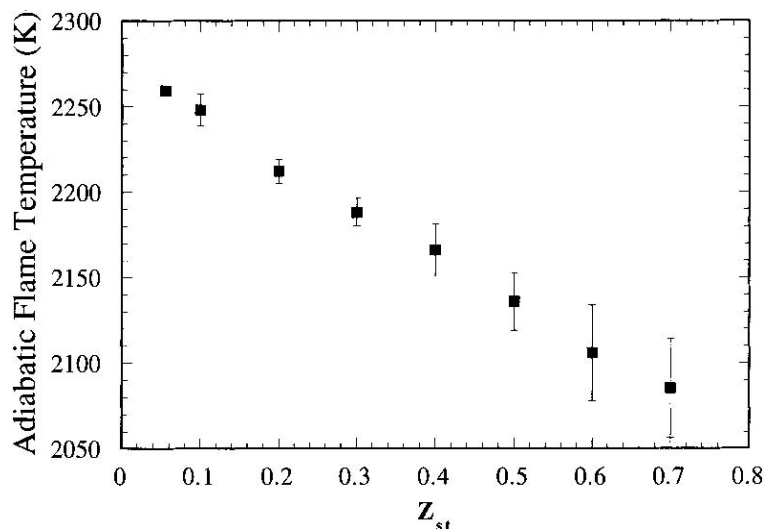


**Figure 3-79. Adiabatic Flame Temperature vs. Stoichiometric Mixture Fraction for a Methane-nitrogen-oxygen-nitrogen Flame with the Extinction Strain Rate Held Constant at  $350 \pm 10 \text{ s}^{-1}$ .**

It was expected that the inert dopant's effectiveness would depend solely on the quantity of dopant present at the flame. Previous experiments had demonstrated that, for a range of loadings greater than that considered here, the effectiveness of the inert suppressant nitrogen increased linearly with dopant loading, at fixed  $Z_{st}$ .<sup>79,80,280</sup> Because flame temperature is reduced by the addition of dopant, this implies temperature invariance of suppression effectiveness over that loading range.

The second type of test varied only the adiabatic flame temperature at a fixed  $Z_{st}$ . This was accomplished in two ways: changing the overall dilution of the flame at a fixed  $Z_{st}$ , and manipulating the temperature of the reactant streams. These experiments were intended to isolate the temperature dependence of the suppression from other effects.

### **Results of Tests with Argon**

Results from the first series of tests are shown in Figure 3-80. The effectiveness of the argon, both oxidizer and fuel side addition, is illustrated. Each data point represents the average of four extinction measurements. The error bars on the figures represent the standard deviation of the observed values, which in this case is larger than the systematic error due to the method of approaching extinction. As expected, effectiveness with oxidant-side doping decreases as the flame moves towards the fuel side (increasing  $Z_{st}$ ). The converse is true with fuel-side doping. Argon has a diffusivity similar to that of the reactants; thus, the quantity present at the stoichiometric contour, which determines its effectiveness, will vary linearly with  $Z_{st}$ .

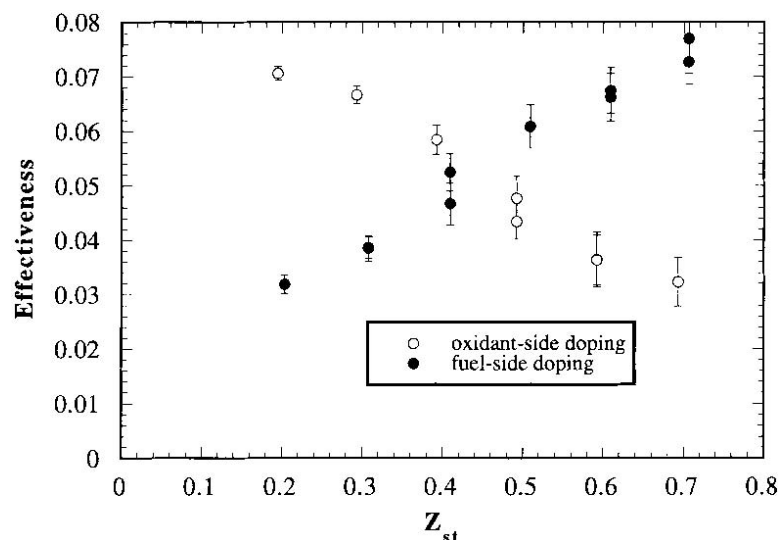


**Figure 3-80. Flame Suppression Effectiveness of 25,000  $\mu\text{L/L}$  Argon as an Oxidant-side or Fuel-side Additive vs. Stoichiometric Mixture Fraction.**

Figure 3-81 depicts the argon effectiveness results. The uncertainty in the calculated mole fraction of dopant at the flame was dominated by the uncertainty in the experimental flow of the dopant, which was  $\pm 10\%$ , as determined by the manufacturer's stated repeatability of the mass flow controller. The smooth trends in the data indicated a significantly better repeatability. The effectiveness curves show no trend with  $Z_{st}$ , indicating that the concomitant changes in  $T_{ad}$  and flame structure, collectively, had no significant influence on the argon effectiveness. Other tests, described below, further demonstrated that the argon effectiveness was independent of  $T_{ad}$ . In addition, Figure 3-81 shows no significant difference, in view of the experimental uncertainty, between the effectiveness of argon with oxidizer- or fuel-side addition, except perhaps at the lowest value of  $Z_{st}$ .

To further clarify the influence of temperature on this system, a series of tests were performed for a fixed  $Z_{st} = 0.055$ .  $T_{ad}$  was manipulated by varying the reactant stream temperature from  $22\text{ }^\circ\text{C}$  to  $112\text{ }^\circ\text{C}$  ( $\pm 1\text{ }^\circ\text{C}$ ). This resulted in a range of  $T_{ad}$  from  $2237\text{ K}$  to  $2283\text{ K}$ . There was a significant influence on the overall flame strength, as seen in the variation of  $a_{q0}$  from  $254\text{ s}^{-1}$  to  $375\text{ s}^{-1}$ . However, the effectiveness for argon at different temperatures varied less than  $4\%$  and showed no trend with  $T_{ad}$ . These results confirmed that argon's effectiveness displayed no dependence on temperature, as well as none on  $Z_{st}$ .

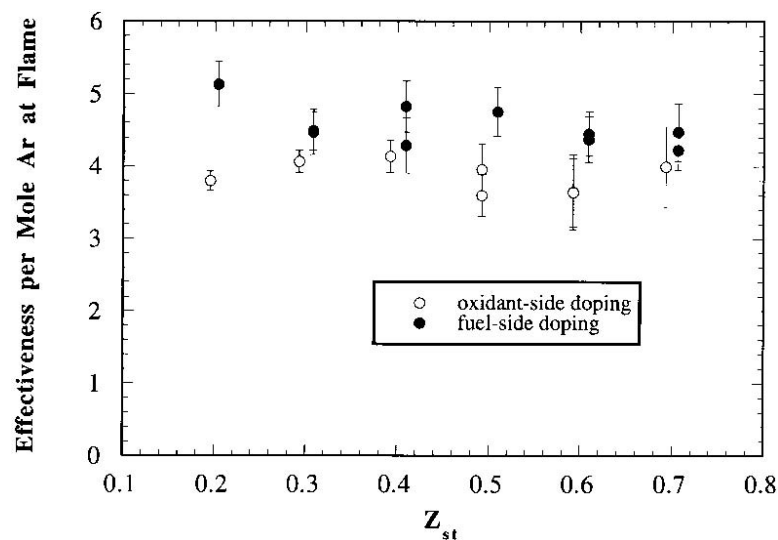


**Figure 3-81. Normalized Flame Suppression Effectiveness of Argon-doped Flames vs. Stoichiometric Mixture Fraction at Fixed  $a_{q0}$ .**

### Results of Tests with DMMP

Figure 3-82 shows the results of extinction measurements performed with DMMP for  $Z_{st}$  between 0.055 and 0.7. The observed effectiveness variation with  $Z_{st}$  was somewhat more complicated than for the inert tests, although it still followed the same general trend. Each data point in Figure 3-82 represents the average of 8 extinction measurements, with error bars representing the standard deviation of the measured values. Differences between individual data points at a given  $Z_{st}$  showed that tests repeated at identical conditions yielded slightly different results. This variation was limited largely by the repeatability of the dopant injection system. The dopant effectiveness may also have been influenced by small changes in flame temperature resulting from lack of repeatability of the reactant stream compositions. The resulting overall experimental scatter was significantly higher than in the inert tests. The systematic uncertainty due to the method of approaching extinction became significant for the oxidizer-side addition tests due to the high observed effectiveness. The result was an estimated overprediction between 3 % and 15 % of DMMP effectiveness for this range of conditions due to this systematic uncertainty. The effect was small for the fuel-side addition data.

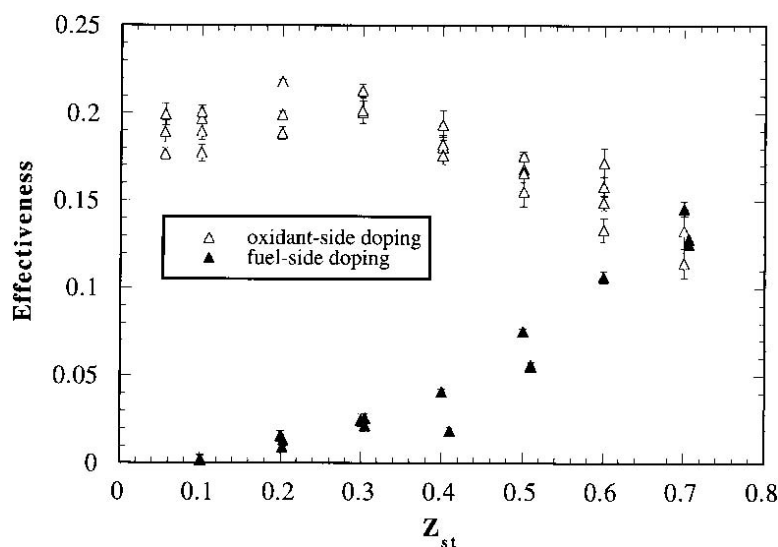


**Figure 3-82. Flame Suppression Effectiveness of 500  $\mu\text{L/L}$  DMMP as an Oxidant-side or Fuel-side Additive vs. Stoichiometric Mixture Fraction.**

The normalized effectiveness results for DMMP, seen in Figure 3-83, have some notable features. Firstly, for a given mole fraction, the DMMP effectiveness is roughly 100 times that of argon, indicating strong chemical suppression by DMMP. Secondly, the curves for oxidizer- and fuel-side addition are offset significantly with respect to one another. This increased oxidizer-side effectiveness has also been observed for the chemically active agent,  $\text{CF}_3\text{Br}$ .<sup>261</sup> The oxidizer-side curve in Figure 3-83 displays an effectiveness roughly triple that of the fuel-side curve. The slight systematic overprediction of the oxidizer-side addition effectiveness, described above, would reduce the magnitude of this disparity, but would not reconcile the difference in these curves. It is possible that since the chemically active suppressant operated by interfering with the radical chemistry rather than as a heat sink within the flame, that the maximum flame temperature contour may not have been the most relevant location for evaluating the mole fraction of dopant. Rather, the appropriate normalization depended on the quantities present in the regions of the flame where the most important radical chemistry occurred. Since key radical reaction rates peaked on the oxidizer side of the flame, a more appropriate normalization might have involved mole fractions at some location to the oxidizer side of the maximum temperature contour. Such an assessment was performed using mole fractions at the point of the maximum reaction rate for the chain branching reaction  $\text{O}_2 + \text{H} \rightarrow \text{OH} + \text{O}$ . Because the concentration gradients of oxidizer- and fuel-side

dopants had opposite directions, this shift in location toward the oxidizer side brought the two curves closer together. However, oxidant-side doping remained more effective.

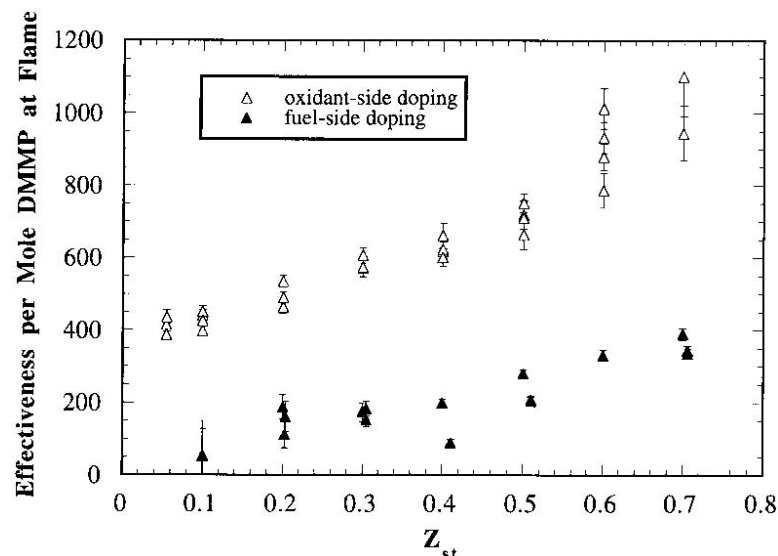


**Figure 3-83. Normalized Flame Suppression Effectiveness of DMMP-doped Flames vs. Stoichiometric Mixture Fraction at Fixed  $a_{qo}$ .**

The disparity between oxidizer- and fuel-side addition may also be associated with the types and quantities of radicals and products that are formed from the parent molecule as it approaches the flame from different directions and their relevance to the suppression action.<sup>45</sup> Assuming that the important suppression action takes place on the oxidizer side of the flame, then additives to the fuel stream must travel through the flame to reach this point. This may have a significant effect on what phosphorus-containing species are present in the region of important radical chemistry for different modes of addition, i.e., oxidizer- or fuel-side doping.

A third feature of Figure 3-83 is that for both the oxidizer- and fuel-side tests, the normalized effectiveness increases with  $Z_{st}$ . The existence of this slope implies that the suppressant effectiveness varied with either temperature, structure of the flame, or both. Studies in a variety of premixed flames had indicated that at high temperatures (above 2350 K),<sup>254,256</sup> DMMP can become a flame promoter. Thus, presumably, the suppression effectiveness of DMMP should decrease with increasing flame temperature. Figure 3-83 is consistent with this expectation, showing decreasing suppressant effectiveness with increasing adiabatic flame temperature (lower  $Z_{st}$  values). However, it is possible that changes in flame structure, which occur at different  $Z_{st}$  values, may also have influenced suppressant effectiveness.

Further tests were conducted to clarify this temperature dependence. Due to condensation of the dopant below 80 °C, control of the reactant temperatures to vary  $T_{ad}$  over a significant range was not possible. Instead, the overall dilution of the flame, at a fixed value of  $Z_{st} = 0.5$ , was used to vary  $T_{ad}$ . In this experiment, the mass fraction of oxygen in the oxidizer stream ranged from 0.39 to 0.44, resulting in a  $T_{ad}$  ranging from 2132 K to 2261 K and an  $a_{qo}$  range of 294 s<sup>-1</sup> to 572 s<sup>-1</sup>. Unfortunately, the variation in reactant stream compositions increased the susceptibility of the results to the sensitivity to random uncertainties in relative flows, producing considerable scatter. The results from this experiment are shown in Figure 3-84, along with the data for oxidizer-side addition at fixed  $a_{qo}$ , but varying  $Z_{st}$  values; all are plotted against  $T_{ad}$ . Although the large experimental scatter makes it difficult to draw quantitative conclusions, there is a clear trend of decreasing effectiveness with increasing  $T_{ad}$ , comparable to that seen

in the constant  $a_{q0}$  data. However, these results did not conclusively eliminate the possibility of flame structure and the detailed chemistry of dopant action influencing dopant effectiveness.

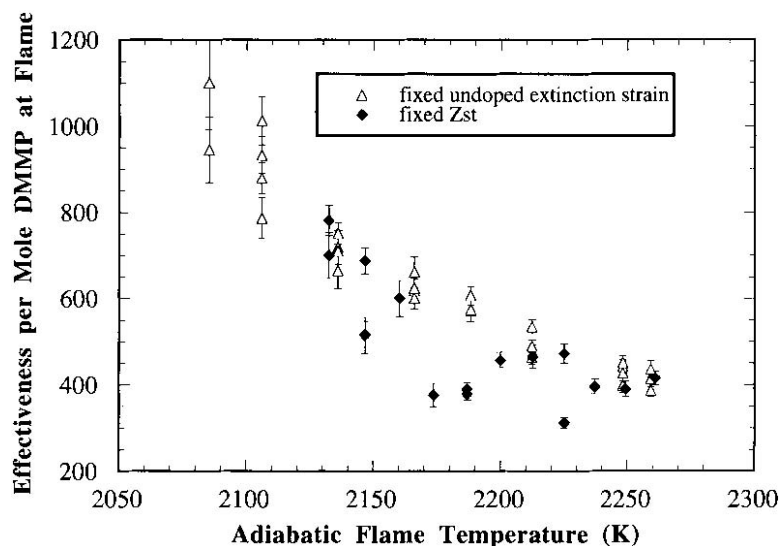


**Figure 3-84. Normalized effectiveness of DMMP-doped Flames as a Function of Adiabatic Flame Temperature.** The symbol  $\Delta$  represents changing  $Z_{st}$  from 0.1 - 0.7, fixed  $a_{q0} = 350 \pm 10 \text{ s}^{-1}$ , while  $\blacklozenge$  represents a fixed  $Z_{st} = 0.5$ , changing  $a_{q0}$  from  $294 \text{ s}^{-1}$  to  $572 \text{ s}^{-1}$  by varying mass fraction of oxygen. Error bars represent standard deviation of data for each set of data runs.

## Effect of Flame Temperature

### Experiments and Calculations

The temperatures of laboratory flames and the flames from real fires can differ significantly. Fisher and co-workers<sup>119</sup> conducted experiments in the same burner used above to quantify the temperature dependence for flame inhibition by DMMP and to gain further insight into the inhibition mechanism. The indicator of inhibition was the degree of decrease in the OH concentration ( $[\text{OH}]$ ) profiles, as measured using LIF. Only a limited number of measurements of  $[\text{OH}]$  in the counterflow configuration have been reported.<sup>271,292-294</sup> A few studies have utilized LIF to observe changes in  $[\text{OH}]$  in flames doped with halogenated suppressants<sup>156, 51,61</sup> work with flames doped with phosphorus-containing agents is far more limited.<sup>294,295</sup>

Here, a series of four non-premixed, atmospheric-pressure flames of methane- $\text{O}_2/\text{N}_2/\text{Ar}$  mixtures were studied (Table 3-13).

**Table 3-13. Flame Conditions.**

Flame #	Oxidizer Composition	$T_{\text{adiabatic}}$ [K]	$T_{\text{calculated peak}}$ [K]	DMMP [ $\mu\text{L}/\text{L}$ ]	$V_{\text{O}}$ [cm/s]	$V_{\text{F}}$ [cm/s]
1	21 % $\text{O}_2$ - 79 % $\text{N}_2$	2261	1967	0 to 572	71	96
2	21 % $\text{O}_2$ - 53 % $\text{N}_2$ - 26 % Ar	2353	2080	0 to 715	71	101
3	21 % $\text{O}_2$ - 26 % $\text{N}_2$ - 53 % Ar	2450	2189	0 to 715	71	106
4	21 % $\text{O}_2$ - 79 % Ar	2547	2286	0 to 715	71	110

Flame temperature was varied by changing the proportions of  $\text{N}_2$  and Ar in the oxidizer side diluent, while maintaining 21 % (by volume)  $\text{O}_2$  and thus a constant stoichiometric mixture fraction of 0.055. The

experimental results were compared to predictions from numerical calculations using a kinetic mechanism<sup>294</sup> for DMMP decomposition and phosphorus-containing radical chemistry. The key reactions in the mechanism responsible for the observed inhibition of OH were identified.

Calculations of the undoped flames were made using the OPPDIF code version 8.5 from the CHEMKIN III Suite.<sup>296</sup> The full GRI-MECH 3.0 mechanism, including nitrogen chemistry, (53 species, 325 reactions)<sup>206</sup> was employed. Mixture-averaged diffusion velocities were used, and thermal diffusion was neglected. Opposed-jet burners are typically modeled as having either potential flow (linear axial velocity gradient) or plug flow (zero axial velocity gradient) boundary conditions, although measurements indicate that the actual velocity field lies somewhere between the two approximations.<sup>67</sup> Calculations were performed for several different boundary conditions. The boundary conditions of potential flow with centerline axial velocities of twice the measured volume averaged velocities for the fuel and oxidizer streams were selected for use in this study, because the resulting OH profiles most closely agreed with the observed profiles. The factor of two for the centerline velocities was appropriate because the flow in the straight-tube reactant nozzles ( $L/D > 30$ ) was expected to be close to Poiseuille flow, in which the centerline velocity is twice the volume average. Temperature profiles predicted by 1D calculations have been found by other researchers to be in good agreement with measurements made in opposed-jet burners under a variety of conditions using spontaneous Raman scattering in  $\text{CH}_4/\text{O}_2/\text{N}_2$ <sup>297</sup> and  $\text{H}_2/\text{air}$ <sup>292</sup> flames, thin SiC filament pyrometry in  $\text{CH}_4/\text{O}_2/\text{N}_2$  flames,<sup>298</sup> and CARS in propane/air flames.<sup>299</sup>

### ***Calculations with Phosphorus Kinetics***

To investigate the cause of the OH concentration changes observed in the LIF experiments, a set of flame calculations was performed using a proposed mechanism for DMMP decomposition and phosphorus-radical chemistry.<sup>294</sup> This mechanism was based on (1) the kinetic data used for the analysis of the influence of  $\text{PH}_3$  on radical recombination rates in the combustion products of a hydrogen flame<sup>258,259</sup> and (2) on kinetic models used for describing DMMP and TMP destruction in a low pressure hydrogen flame.<sup>300,301</sup> Reactions of phosphorus-containing species with radicals and intermediate species of hydrocarbon combustion were included.<sup>294</sup> Reactions were added to the scheme to complete destruction pathways for some species. The used version of this phosphorus mechanism included 27 species and 166 reactions. Thermochemical data compiled by Babushok<sup>302</sup> for phosphorus-containing species were mostly taken from References 197, 303, 304, and 304 {Gurvich & Glushkov 1998 #2420}. Methane- $\text{O}_2$  chemistry was modeled using GRI Mech 3.0 with nitrogen chemistry removed (36 species, 219 reactions retained). The phosphorus mechanism predicted reductions in extinction strain rates for non-premixed methane-air flames due to the presence of DMMP that were in agreement with experimental results from MacDonald et al.<sup>79</sup> An earlier version of the mechanism had also been used to predict the effect of DMMP on premixed flame speeds.<sup>257</sup>

Calculations were performed for all four flames using the combined mechanisms (phosphorus and GRI Mech), both with and without the addition of 572  $\mu\text{L/L}$  of DMMP. Calculations with the combined mechanisms required a higher degree of mesh refinement (both GRAD and CURV parameters for OPPDIF script = 0.1, yielding 250-300 grid points) than the GRI Mech calculations in order to produce [OH] profiles for the doped flames that were independent of grid size. Figure 3-85 illustrates the major species profiles from these calculations for flames 1 and 4 without dopant addition.

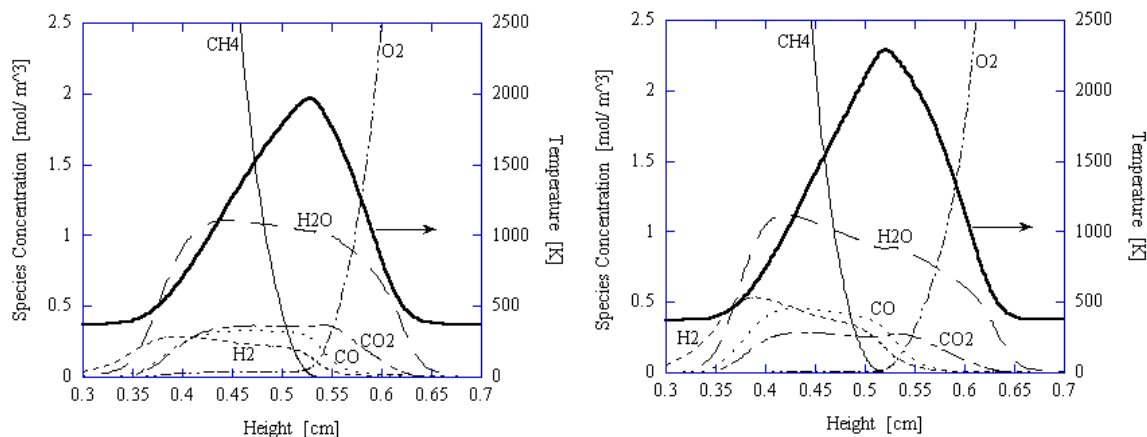


**Figure 3-85. Calculated Major Species and Temperature Profiles for Flame 1 (left) and Flame 4 (right), both undoped.**

### Measurements

Figure 3-86 shows a comparison between measured and calculated [OH] profiles for flames 1 and 4, the coolest and hottest conditions respectively. Multiple profiles, all undoped, are shown to illustrate the repeatability of these measurements.

The agreement between measured and calculated profiles was quite good. The intermediate cases of flames 2 and 3 were in similar agreement between measured and computed profiles. Agreement in peak [OH] was expected since calculated profiles were used to estimate peak concentrations in the measurements for each flame. There was also good agreement in the profile shape, which was not affected by the matching procedure, including the degree of asymmetry, and width (FWHM). The peak concentration, as determined by the calculations, increased by 66 % from  $0.041 \text{ mol/m}^3$  for flame 1 to  $0.069 \text{ mol/m}^3$  for flame 4, which had a stoichiometric adiabatic flame temperature that was 286 K hotter than flame 1. The peak temperatures (Table 3-13), for these moderately strained flames were approximately 300 K cooler than the stoichiometric adiabatic flame temperatures, although the difference in calculated peak temperatures for flames 1 and 4 (319 K) were comparable to the change in the stoichiometric adiabatic flame temperature (286 K).

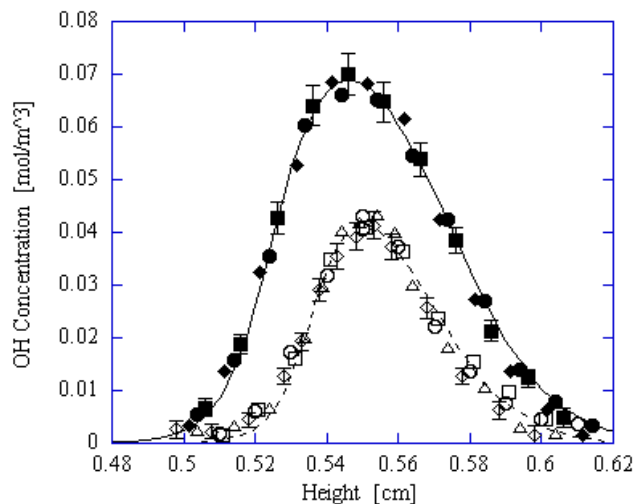


**Figure 3-86. Calculated and Measured OH Concentration Profiles for Flames 1 and 4. Flame 1: dashed line – computations; open symbols - four measured profiles. Flame 4: solid line - computations; filled symbols - three measured profiles. Error bars represent statistical uncertainty in the measured values.**

Figure 3-87 illustrates the variation in computed and measured OH profile widths (FWHM) with adiabatic flame temperature. All flame conditions are undoped. Both the calculated and measured OH profile widths are observed to increase by approximately 40 %, from 0.4 mm to 0.55mm, across the range of temperatures investigated. Good agreement between calculated and measured profile widths is observed for all undoped flames.

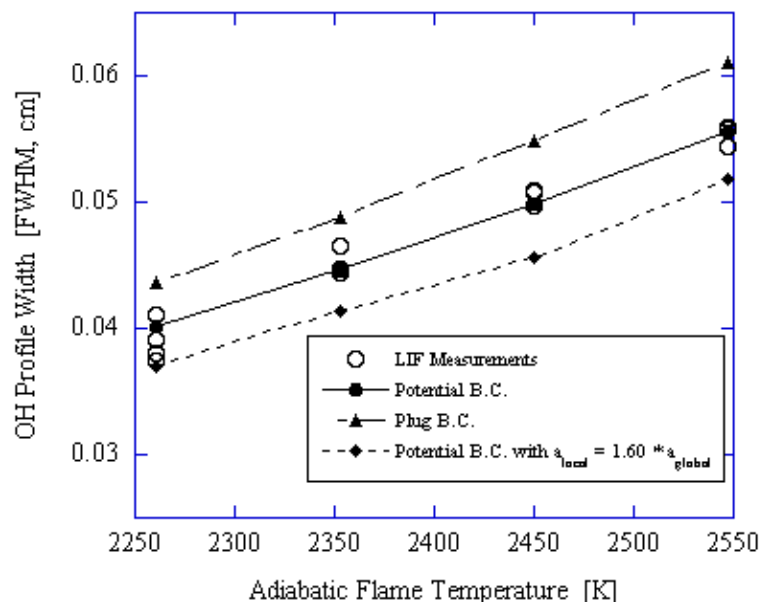


**Figure 3-87. [OH] Profile Widths (FWHM). Open circles: measured values for all undoped flames. Lines with filled symbols: computational values for three different velocity boundary conditions (B.C.). Filled circles: potential flow B.C. with velocities of twice the volume average (Poiseuille flow). Filled triangles: plug flow B.C. with velocities equal to the volume average. Filled diamonds: potential flow B.C. with local strain rate equal to 1.60 times the global strain rate given by Equation 3-7.**

The velocity boundary conditions in the calculations had a noticeable effect on the calculated width of the [OH] profile. In order to investigate the influence of these boundary conditions, two additional sets of calculations were performed, one for plug flow boundary conditions with the measured volume averaged velocities and the other for potential flow while matching the maximum local strain rate to  $480 \text{ s}^{-1}$ , or 1.60 times the global strain rate (Equation 3-1) (which required increasing the centerline velocity for the calculations to 2.8 times the volume averaged value). The higher strain case was motivated by measurements of axial velocity profiles made using Laser-Doppler Velocimetry in a similar burner configuration.<sup>281</sup> These measurements indicated a substantially higher local strain rate (axial velocity gradient on the oxidizer side, evaluated just upstream of the heat release region) of approximately 1.60 times the global strain rate. The original calculations, with boundary conditions of potential flow and velocities of twice the volume average, gave a computed velocity profile with a peak local strain rate of approximately 1.18 times the global strain rate or  $355 \text{ s}^{-1}$ . The calculated [OH] profile widths for the two additional sets of boundary conditions are also shown in Figure 3-87. Both additional sets of boundary conditions predicted similar variation in profile width with flame temperature. However, the plug flow boundary condition overestimated the profile widths by 10 % to 15 %, and the higher strain rate case underestimated the widths by 5 % to 8 %. Finite spatial resolution in the measurements ( $100 \mu\text{m}$ ) limited the accuracy with which the experimental width could be determined. Heat and radical losses to the burner as well as radiation, which were ignored in these calculations, also contributed to the discrepancy between measured and calculated profiles. However, these physical loss mechanisms were significant in these well isolated, non-sooting flames. Uncertainties associated with the chemical

mechanism used influenced the computed profile width and also affected the level of agreement between computed and measured profile widths.

The good agreement between the measured profiles and the calculations made with potential flow boundary conditions with centerline velocities of twice the volume average supported the selection of this boundary condition for use in the quenching and Boltzmann fraction corrections to the LIF data. Because of the relatively small impact of the temperature and quenching correction, the choice of the appropriate boundary conditions did not substantially influence the conclusions below about the influence of phosphorus additives on [OH]. Using profiles calculated with either of the alternate boundary conditions to correct the LIF data changed the observed reductions in total [OH] by less than 1 %, well within the uncertainty of the measurements.

Figure 3-88 illustrates the effect of 572  $\mu\text{L/L}$  of DMMP on OH concentrations in flame 1. With this loading, flame 1 is close to extinction.

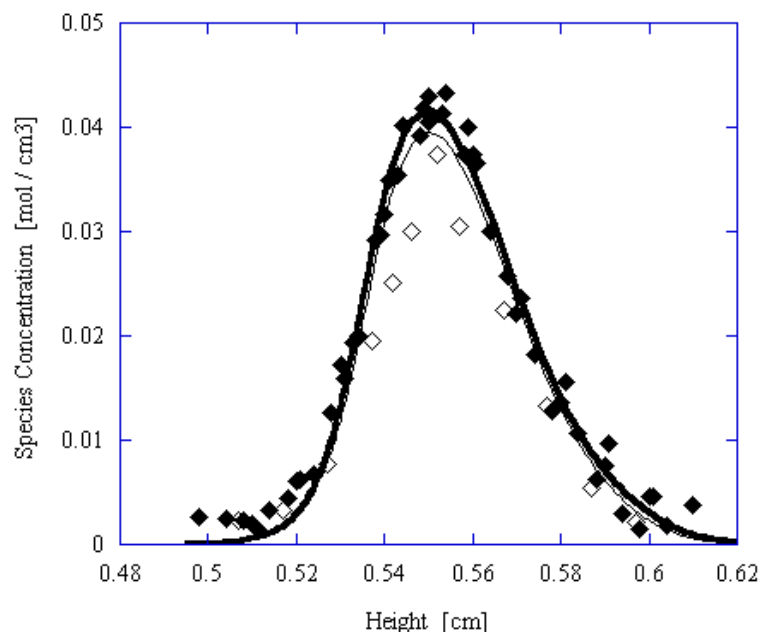


**Figure 3-88. Effect of 572  $\mu\text{L/L}$  of DMMP on [OH] in Flame 1. Filled symbols: undoped profiles. Open symbols: doped profile. Thick line: computational prediction for the undoped profile. Thin line: doped profile. Phosphorus kinetic mechanism from Wainner et al.<sup>294</sup>**

A substantial reduction, approximately 20 %, in OH concentration was observed. The doped profile was smaller in magnitude, but the width was not significantly affected. In order to determine changes in the total flame OH concentration, the profiles were numerically integrated, using a simple trapezoidal rule approximation, across the width of the flame, and then the integrals from the doped and undoped flames were compared. The integration technique was particularly useful for quantifying changes in the higher temperature flames, where the [OH] profile was less affected by the phosphorus-containing additive. There was a  $23 \% \pm 3 \%$  reduction in total OH (by this definition) for the data shown in Figure 3-88. The uncertainty resulted from the estimated statistical uncertainty of the individual data points from the profile, and was closely comparable to the repeatability of the measurement.

OH concentration profiles were measured for all four flames with DMMP loadings up to 715  $\mu\text{L/L}$ , with the exception of flame 1. A loading of 715  $\mu\text{L/L}$  of DMMP in flame 1 caused extinction at the global strain rate used in this study. Therefore, the maximum loading used for that flame was 572  $\mu\text{L/L}$ , the next

highest loading readily achieved experimentally. Figure 3-89 illustrates the ratio of doped to undoped total [OH] for the four flames as a function of loading. Raw data for profiles for all conditions studied in this work can be found in the appendix of Reference 305. Within experimental uncertainty, total [OH] decreased linearly with DMMP addition over this range of loadings. Results from the calculations performed with the phosphorus kinetic mechanism, discussed below, for a range of DMMP loadings from 0  $\mu\text{L/L}$  to 720  $\mu\text{L/L}$ , confirmed the linear variation in the [OH] reduction with loading. The linear trends were consistent with extinction measurements on non-premixed methane-air flames which indicated a linear variation in DMMP effectiveness, defined in terms of reduction in the global extinction strain rate, for loadings up to 1500  $\mu\text{L/L}$ .<sup>79</sup> Linear variation in effectiveness with loading was observed with most flame suppressants at low loadings. Linear regression fits to the data for each flame are also shown in Figure 3-89. The most striking observation from Figure 3-89 is the increase in inhibition effectiveness with decreasing flame temperature. The highest temperature case, flame 4, shows less than 5 % reduction in total [OH] at the maximum loading of 715  $\mu\text{L/L}$ , compared to 23 % reduction in flame 1 for only 572  $\mu\text{L/L}$ .

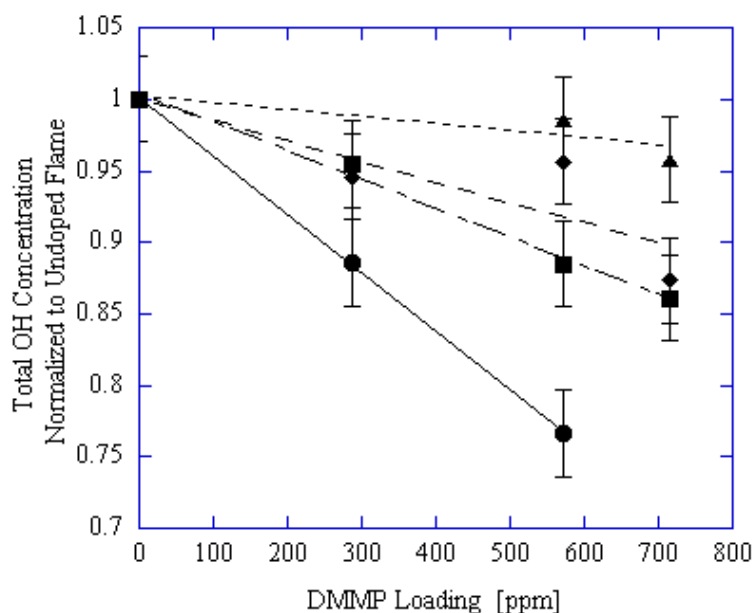


**Figure 3-89. Effect of DMMP Loading for All Flames. Lines are linear regression fits to data. Flame 1: solid line and circles. Flame 2: dot-dash line and squares. Flame 3: dashed line and diamonds. Flame 4: dotted line and triangles. Error bars represent uncertainty in measurements.**

Extinction measurements for the flames were not successful because the high extinction strain rates for flames 2 through 4 required dramatically higher flow velocities that were well into the turbulent flow regime. However, an earlier study had investigated the effect of DMMP on global extinction strain rate for a variety of different flame conditions with different stoichiometric mixture fractions and stoichiometric adiabatic flame temperatures.<sup>120</sup> Effectiveness in terms of extinction strain rates for that work was defined as the fractional reduction in global extinction strain rate divided by the mole fraction of phosphorus in the flame:

$$Effectiveness_q \equiv \frac{(a_{q,0} - a_q)}{a_{q,0}} \frac{1}{\chi_P} \quad (3-10)$$

The subscript q indicates that the measurement was made at extinction conditions, and the subscript 0 denotes the value for the undoped flame. Flame calculations were used to estimate the mole fraction of

phosphorus at the flame surface,  $\chi_p$ , taken to be the maximum temperature contour. There was a similar trend of decreasing effectiveness with increasing temperature. The stoichiometric adiabatic flame temperature in that study was varied in two ways. The first was by changing the stoichiometric mixture fraction from 0.05 to 0.7 while maintaining a fixed undoped global extinction strain rate. The second was by decreasing the overall dilution of the flame while maintaining a stoichiometric mixture fraction of 0.5. The range in adiabatic flame temperatures from that work (2130 K to 2260 K) was substantially lower than that investigated here. Comparing the temperature dependence from the previous investigation to that of the current work requires a measure of effectiveness, analogous to the one used in the previous study, in terms of [OH] reduction as the fractional reduction in total [OH] concentration:

$$Effectiveness_{OH} \equiv \frac{(TotalOH_0 - TotalOH)}{TotalOH_0} \frac{1}{\chi_P} \quad (3-11)$$

Again, the subscript 0 denotes the measured value for the undoped flame. The flame calculations made with the combined GRI Mech and phosphorus mechanisms were used to determine  $\chi_p$ , the total mole fraction of phosphorus (sum of mole fractions of all phosphorus-containing species) predicted at the flame surface, taken to be the maximum temperature contour. Because the stoichiometric mixture fraction was fixed for all flames, changes in  $\chi_p$  were negligible. The use of this parameter did not affect the observed trends and was introduced solely to provide a definition for effectiveness that is analogous to that used in Reference 120 to facilitate a comparison to previous extinction studies. This effectiveness definition is essentially a measure of the slope of the linear trends indicated in Figure 3-89.

Figure 3-90 shows a comparison of this effectiveness based on OH with the one based on the extinction measurements from the previous study. The trends observed in the two data sets are in good qualitative agreement, given that different measures of effectiveness were used. When comparing the two data sets, it should also be noted that for a given stoichiometric adiabatic flame temperature, measurements performed at extinction conditions, such as those from Reference 120, had a peak flame temperature that was cooler than that seen in the LIF measurements, which were performed at a fixed global strain rate of  $300 \text{ s}^{-1}$ , below the value required to extinguish the flame. The effectiveness data in Figure 3-90 show a substantial decrease in DMMP effectiveness with increasing temperature. The unambiguous trends in the LIF data confirmed the hypothesis of Hastie and Bonnell<sup>256</sup> of decreasing inhibition with increasing flame temperature, with nearly a 90 % decrease in effectiveness for a 300 K increase in temperature.

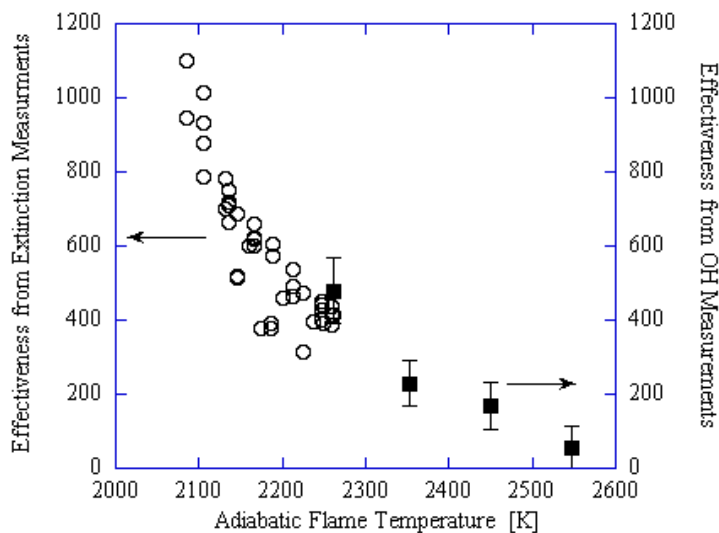


**Figure 3-90. Temperature Dependence of Effectiveness. Open circles: effectiveness data from Reference 9 defined in terms of reduction of global extinction strain. Filled squares: effectiveness data from the current work defined in terms of reduction in OH concentration. Error bars represent uncertainty in the measurements.**

### Calculations with Phosphorus Kinetics:

The combined mechanism of phosphorus kinetics by Wainner et al.<sup>294</sup> and CH<sub>4</sub>-O<sub>2</sub> kinetics from GRI Mech<sup>206</sup> was used to calculate species and temperature profiles for all four flames with and without the addition of 572 μL/L of DMMP. The predicted temperature profiles showed no significant effect from the addition of DMMP (< 10 K change in peak temperature). However, significant changes were observed in OH, H and O profiles. Figure 3-91 illustrates the doped and undoped profiles of OH, H, and O for flame 1. Relative to the undoped profile, the OH profile for the doped flame was lower in magnitude. The change was similar to that observed in the measured data, but not as large. A comparison of computational predictions to measured data is shown in Figure 3-88. The reduction in H and O atom concentrations seen in Figure 3-91 was significantly greater than the reduction for OH, indicating a larger effect of phosphorus chemistry on the concentrations of those species.

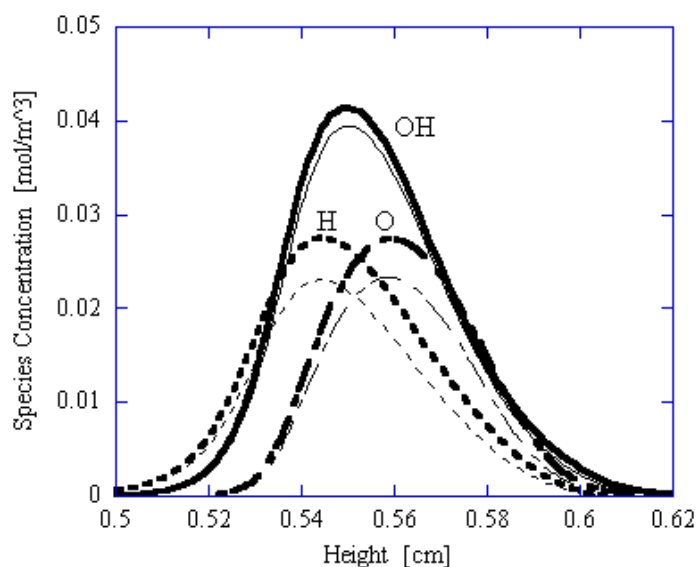


**Figure 3-91. Effect of 572 μL/L of DMMP on Calculated OH, H, and O Concentration Profiles in Flame 1 (CH<sub>4</sub>/O<sub>2</sub>/N<sub>2</sub>). Dark lines are undoped profiles and thin lines are with DMMP addition.**

After performing the spatial integration of the computed profile across the flame, as described above, the change in total OH between the doped and undoped cases was evaluated. Figure 3-92 shows a plot of effectiveness, as defined in terms [OH] reduction (3-11), as a function of the stoichiometric adiabatic flame temperature for both the experiments and the computations. The computational and experimental results in Figure 3-92 showed the same trend of decreasing effectiveness with increasing temperature, although the temperature dependence of the computational results was weaker. The magnitude of effectiveness from the flame calculations agreed well with LIF data from the highest temperature case, flame 4, but the calculations underpredict effectiveness for flames 1 through 3. In these calculations the magnitude of the reduction in OH (i.e., total OH<sub>undoped</sub> - total OH<sub>doped</sub>) was nearly constant for all flames. For these flame calculations, changes in the effectiveness (which was a fractional measure of the reduction of total OH) with temperature were due mainly to the increases in the total OH<sub>undoped</sub>, which was larger by a factor of 2.25 for flame 4 (CH<sub>4</sub>/O<sub>2</sub>/Ar) compared to flame 1 (CH<sub>4</sub>/O<sub>2</sub>/N<sub>2</sub>) in the calculations. This estimate of the increase of total OH for the undoped flames was not sufficient to explain the variation in effectiveness observed in the LIF measurements (reduced by a factor of 10 in flame 4 compared to flame 1).

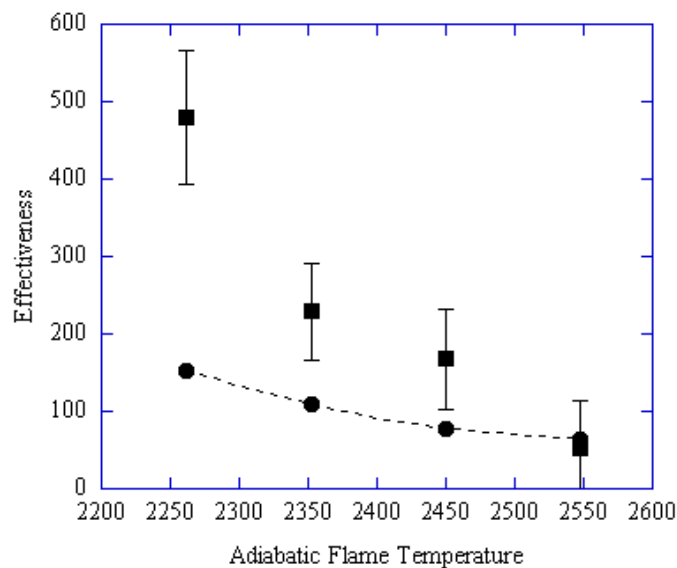


**Figure 3-92. Temperature Dependence of Effectiveness Defined as in Terms of Reduction in total [OH]. Filled circles with the dashed line: computational predictions. Filled squares: measured data. Error bars represent uncertainty in the measurements.**

The processes responsible for the observed reductions in [OH] were determined by analysis of individual reaction rates from the phosphorus mechanism. Since the experimental and computational results both showed a reduction in [OH] with the addition of DMMP, it was expected that the reactions involving phosphorus removed OH from the flame. In fact, for all four flames, the sum of the chemical production rates for OH over all reactions involving phosphorus in the mechanism was positive across most of the [OH] profile, indicating that these reactions directly produced OH rather than destroyed it. Thus, the drop in [OH] upon introduction of phosphorus kinetic sub-mechanism must have occurred indirectly, through an effect on rates of reactions not involving phosphorus-containing species. Poor efficiency for direct recombination of OH by reactions involving suppressant species has been observed previously for iron-based<sup>104</sup> and halogen-based<sup>55,57</sup> suppressants. The net production rates for flame radicals OH, H, and O by all reactions involving phosphorus in flames 1 and 4 are shown in Figure 3-93. It is clear from these figures that the action of the phosphorus-containing species was similar in both flames. The regions of radical production/destruction in flame 4 were somewhat wider, in keeping with the wider flame (see Figure 3-87), but the peak magnitudes of the production rates for H, O, and OH were 5 % to 10 % lower.

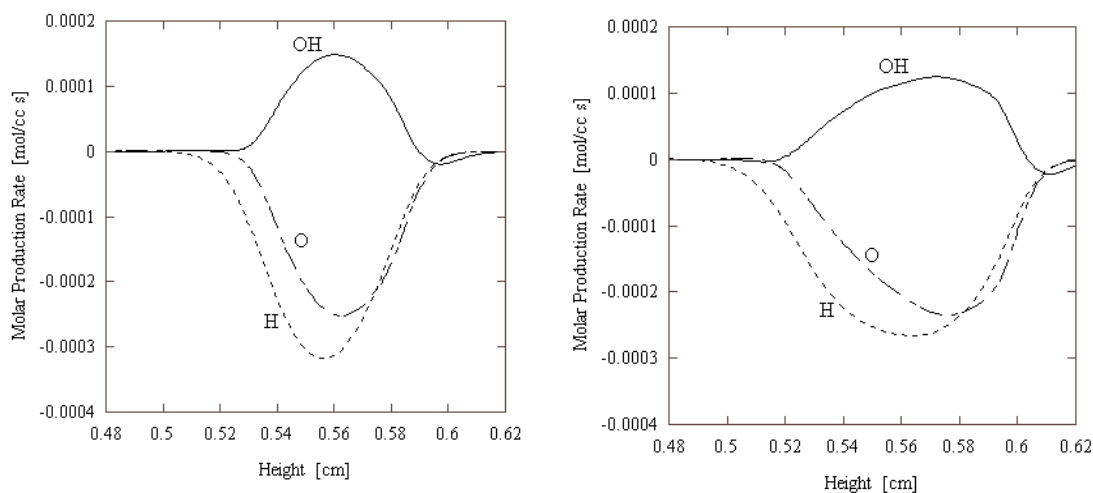


**Figure 3-93. OH, H, and O Production Rates in Flame 1 (left) and Flame 4 (right), Summed over All Reactions Involving Phosphorus.**

The cause of the observed reduction in OH was the fast removal of H and O atoms by the reactions involving phosphorus. Smyth et al.<sup>306</sup> have studied the interrelationships of H, O, and OH concentrations in non-premixed methane-air flames and found that while these species were generally not in equilibrium, their respective populations were still interdependent on one another through a variety of fast radical shuffle reactions. Because of this interdependence, the reductions in H and O atom levels created by the reactions involving phosphorus, observed in Figure 3-91 for flame 1, caused the radical shuffle reactions not involving phosphorus to respond by reducing OH.

Figure 3-94 illustrates the shift in OH production rates by the GRI sub-mechanism (sum of OH production rates over reactions not involving P) due to the addition of 572  $\mu\text{L/L}$  of DMMP to flame 1.

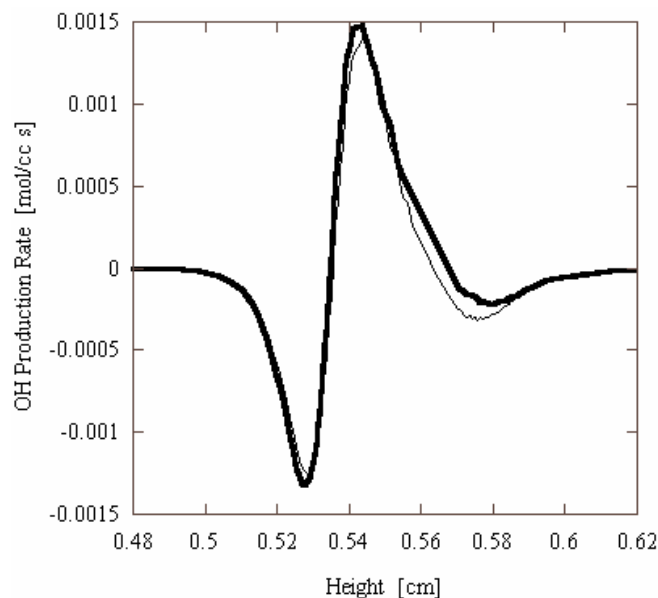


**Figure 3-94. Total OH Production Rates in Flame 1 by Reactions Not Involving Phosphorus. Dark line: Undoped Rate. Thin line: Rate with the Addition of 572  $\mu\text{L/L}$  of DMMP.**

The OH production in the doped flame was generally lower than that in the undoped case, particularly on the oxidizer side of the flame. Three individual reactions that were primarily responsible for the shift seen in Figure 3-94 were identified by comparing the shift in doped and undoped reaction rates for all reactions not involving phosphorus. Two of these reactions, R3-8 and R3-9, underwent a substantial decrease in OH production for the doped flame. R3-8 is one of the important chain branching reactions:



The third reaction that underwent significant changes due to addition of phosphorus is R3-10:



This reaction has been identified by Twarowski<sup>258,259,303</sup> as playing an important role in increased recombination rates  $\text{OH} + \text{H} \rightarrow \text{H}_2\text{O}$  due to the presence of phosphorus containing compounds. In the current non-premixed flames, the overall effect of R3-10 in the presence of phosphorus addition was not clear, as the reaction had regions of increased OH production as well as regions of decreased OH production across the flame width.

Figure 3-95 shows the contribution of individual reactions involving phosphorus to OH production rates and compares them to the changes in the reaction rates of R3-8 R1 and R3-9 R2 (doped rate minus undoped rate) that occurred when DMMP was added to the flame 1.

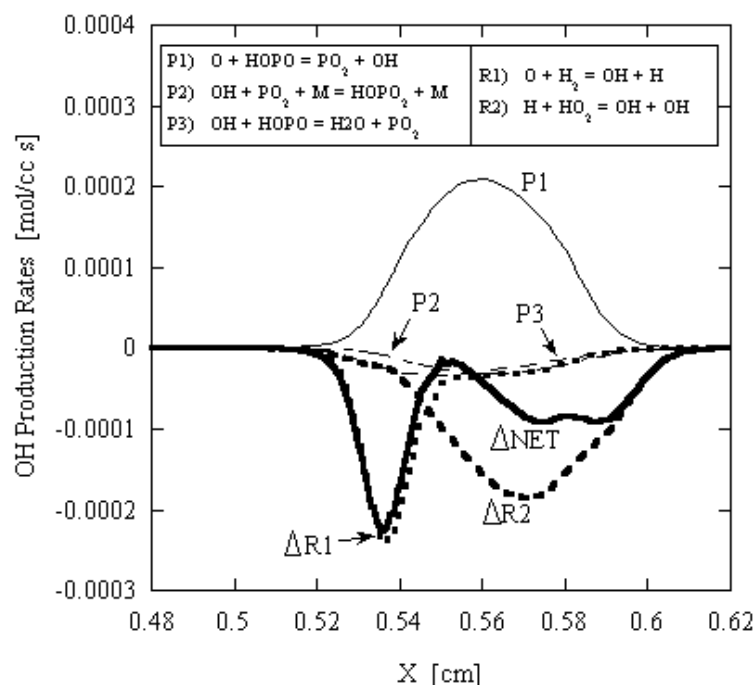


**Figure 3-95. Influence of the Addition of 572 µL/L of DMMP on OH Production Rates in Flame 1. Rates of OH production by reactions involving phosphorus P1 - P3 and changes ( $\Delta R3-8$  and  $\Delta R3-9$ ) in OH production (doped rate - undoped rate) for non-phosphorus containing reactions R3-8 and R3-9. The net effect ( $\Delta NET$ ) of these reactions is shown in bold.**

OH production by reactions involving phosphorus was dominated by R3-11 :



There were two phosphorus containing reactions that consumed OH, but the rates were small (15 % to 30 %) relative to 3-11:



Figure 3-95 also shows the net change in OH production for all reactions in that figure (R3-11, R3-12, R3-13, R3-8 and R3-9). The net rate curve shows overall destruction of OH, indicating that the shift towards decreased production by R3-8 and R3-9 was more than sufficient to balance the direct production of OH by R3-11.

Removal of H and O atoms by reactions involving phosphorus clearly played an important role in the observed inhibition. Calculation results showed that removal of H atoms by reactions involving phosphorus was done primarily by:



and to a lesser extent by:



Figure 3-96 shows the contribution of R3-14 to the total H destruction rate by all reactions involving phosphorus.

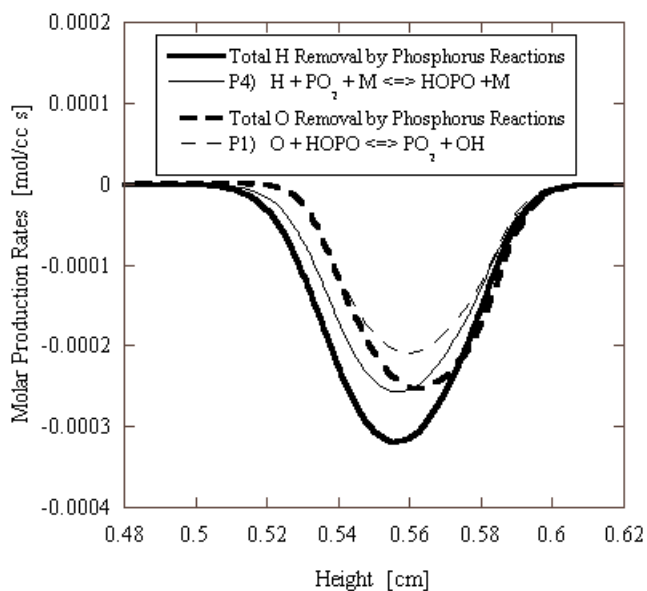


**Figure 3-96. H and O Production Rates by All Reactions Involving Phosphorus (solid lines) and by Individual Reactions (dashed lines) in Flame 1.**

Removal of O atoms by reactions involving phosphorus was done primarily by the OH-producing reaction R3-11. The contribution of R3-11 to O removal was also shown in Figure 3-95. Significant uncertainties remained for the rate coefficients of several of the key reactions involving phosphorus species that have been identified here (R3-11, R3-12 and R3-14).<sup>302</sup> Suggestions that the rate coefficients for the recombination reactions R3-12 and R3-14 might need to be increased by a factor of 2 or more<sup>302</sup> could help reconcile the observed differences in magnitude of effectiveness between the measurements and the computational predictions.

### 3.4.3 Effects of Dimethyl Methylphosphonate on Premixed Methane Flames

#### Introduction

Fire suppression science would benefit from a reliable detailed chemical kinetic mechanism for combustion of organophosphorus compounds. Two mechanisms have recently been proposed for organophosphorus combustion<sup>294,307,307</sup> but they have been validated against only limited experimental data.

Most previous DMMP combustion experiments yielding species data have involved low pressure hydrogen/ oxygen/argon flames. Korobeinichev et al.<sup>254,308</sup> and Werner and Cool<sup>300</sup> both used molecular beam mass spectrometry to study the structure of premixed stoichiometric H<sub>2</sub>/O<sub>2</sub>/Ar flat flames doped with DMMP, between 50 kPa and 100 kPa. They were able to measure DMMP and various stable and unstable products and intermediates. Temperature was measured by thermocouple. DMMP loading was between 1000 μL/L and 11,000 μL/L. Both sets of investigators observed substantial increases in post-flame temperature (approximately 300 K) with the addition of DMMP. Species measurements differed in some respects: certain intermediates observed by each group were not seen by the other. Each group proposed destruction mechanisms for DMMP that formed a basis for further mechanism development.

Aside from species profiles, Korobeinichev et al. also inferred changes in adiabatic flame speed by observing how maximum flame temperature varied with DMMP loading. They found that adding under 5000  $\mu\text{L/L}$  of DMMP increased the flame speed, and above this concentration, the opposite held in low-pressure  $\text{H}_2/\text{O}_2/\text{Ar}$  flames. More recently, Korobeinichev et al.<sup>309</sup> performed experiments in a premixed  $\text{CH}_4/\text{O}_2/\text{Ar}$  flame at 10 kPa with a different organophosphorus compound, TMP. In contrast to their experiments with TMP<sup>310,311</sup> and DMMP<sup>254,308</sup> in hydrogen flames, these experiments showed an inhibitory effect on the flame.

Flame inhibition and suppression effects of DMMP and other organophosphorus compounds have been observed in non-premixed opposed-jet hydrocarbon flames, both through extinction measurements<sup>79,120</sup> and through measurements of flame radical levels.<sup>119</sup> They have also been seen in premixed flames by measuring the heat loss from the flame to a Bunsen burner.<sup>312</sup> Flame suppression effectiveness decreased as temperature increased,<sup>119,120</sup> and appeared to be greatest under near stoichiometric conditions.<sup>312</sup> There has been some agreement on the likely mechanism of flame inhibition by DMMP: phosphorus-containing radicals that are produced from DMMP at flame temperatures participate in catalytic cycles resulting in the recombination of standard flame radicals such as H and OH.<sup>258,260,294,303</sup>

Nogueira and Fisher<sup>313</sup> tested these mechanisms against experimental data under flame conditions that were realistic for flame suppression: a  $\text{CH}_4/\text{O}_2/\text{N}_2/\text{Ar}$  premixed flame doped with DMMP at near ambient pressure. Only stable species not containing phosphorus were measured. The impact of phosphorus on the flame was studied by comparing the undoped with doped profiles of the observed species.

## Experimental

### *Apparatus*

Experiments were conducted using a brass flat-flame burner resembling the one used by Korobeinichev et al.<sup>254,308-311,314,315</sup> In the burner, the premixed reactants entered a plenum from the bottom of the burner, flowed upward through a bed of 3 mm diameter glass beads, and then passed through an array of hexagonally spaced 0.58 mm diameter holes with center-to-center spacing of 0.95 mm in the upper surface of the burner. The use of a perforated plate, rather than a sintered metal plug, made it possible to clean phosphorus-containing products from the burner. The diameter of the flow region was 53.4 mm, and the thickness of the brass plate was 6.35 mm. Surrounding the plenum was an annular passage through which cooling water flowed. A centrifugal pump and resistance heater kept the cooling water, at 91°C, flowing at a rate slightly above 0.3 mL/min through a closed circuit including the water channel of the burner, a rotameter, and an annulus surrounding the reactants gas flow line.

Gas samples and temperature measurements at different heights were obtained by moving the burner relative to stationary probes. The burner was mounted on a motorized linear motion feedthrough, which was controlled by a programmable stepping motor. This device allowed vertical movement with steps of 0.008 mm over a range of 100 mm. The repeatability of returning to a position was about 0.08 mm. The burner and the traverse were sealed within a vertical 146 mm ID stainless steel cylinder that served as a vacuum chamber.

Gaseous reactants ( $\text{CH}_4$ ,  $\text{O}_2$ ,  $\text{N}_2$ , and Ar) were metered with calibrated mass flow controllers and meters. Upstream of the location where the nitrogen mixed with the other gases, liquid DMMP was introduced via a syringe pump (model A with 25 ml Hamilton Syringe; Razel, Stanford, CT). Downstream of the

injection point, a chamber with a residence time of 12 s smoothed out fluctuations in the DMMP loading. The electrical heating and cooling water jacket maintained all reactant streams containing DMMP above 85 °C, high enough to avoid DMMP condensation.

The vacuum chamber pressure was measured at the exhaust line downstream of the vacuum chamber by a capacitance pressure gauge (model PDR-C-1C; MKS, Andover, MA), calibrated using a “U” mercury manometer. For safety reasons, the chamber was maintained at a pressure slightly below ambient and a dry ice/acetone (200 K) cold trap removed PCCs and water from the exhaust stream.

### ***Sampling***

Sampling for species and temperature measurements made use of a stationary quartz microprobe. The probe was 200 mm long and constructed of 6.0 mm OD, 3.8 mm ID quartz tubing, tapering to an orifice. Repeatability tests involved probes of different diameters. The specific probe orifice diameters, measured before each experiment, are listed in Table 3-14. Downstream of the orifice was a 20 mm long vertically oriented section diverging with an angle of 11°. In the following 25 mm, the probe underwent a smooth 90° bend to a horizontal orientation, allowing it to be mounted in a sampling port in the side of the vacuum chamber.

The gases flowed through the probe, lengths of perfluoroalkoxy tubing, a gas cell, and a needle valve, and into a vacuum pump. The pressure downstream of the probe was kept under 20 kPa to guarantee choked flow at the probe’s orifice. A 50 SFM bubble meter (SGE International PTY LTD, Australia) was used to measure the volumetric flow through the probe. The bubble meter was located downstream of the small vacuum pump, where the flow pressure and temperature were close to room conditions. Depending upon the gas temperature and orifice size, between 15 min and 45 min was needed to fill the FTIR cell with the gas sample.

**Table 3-14. Probe Orifice Diameters ( $\mu\text{m}$ ) Used in Specific Experiments.**

DMMP	Fuel-rich Flames	Near-stoichiometric Flames
Doped	61, 66	60, 65
Undoped	56, 67	59, 64

### ***Species Measurements***

Fuel and product gases were measured with a Mattson RS-1 FTIR spectrometer, operating in the wavelength range from 500  $\text{cm}^{-1}$  to 4000  $\text{cm}^{-1}$  with a resolution of 1  $\text{cm}^{-1}$  and signal gain of 4. The sample gases flowed continuously through an 884 mL multi-pass White cell (Infrared Analysis, Madison, WI) with gold-coated mirrors, zinc selenide windows, and a path length of approximately 5.4 m. The cell was maintained near 15 kPa during data acquisition, and was purged and conditioned with gas flow between samples. The scanning time for the FTIR to obtain a sample spectrum was 7.2 min.

Compound concentrations were quantified using an interactive subtraction technique that compared sample spectra to calibration spectra with known species concentrations. Spectral regions were chosen to minimize overlap, but in some cases interfering species had to be subtracted from the spectrum before quantification. Table 3-15 lists spectral regions and sensitivities.

**Table 3-15. FTIR Detection Limits and Wavenumber Ranges.**

Species	Wavenumber Range Used for Quantification (cm <sup>-1</sup> )	Detection limit (μL/L) <sup>a</sup>
CH <sub>4</sub>	3176–3133	400
CH <sub>2</sub> O	2920–2870	100 <sup>b</sup>
CH <sub>3</sub> OH	1060–1010	10
CO	2220–2030	1350
CO <sub>2</sub>	715–670	1200
C <sub>2</sub> H <sub>6</sub>	3000–2950	70 <sup>b</sup>
C <sub>2</sub> H <sub>4</sub>	960–905	60
C <sub>2</sub> H <sub>2</sub>	740–710	10

<sup>a</sup> Lower detection limit could be achieved with a different choice of spectral region for many species.

<sup>b</sup> Quantified after subtraction of CH<sub>4</sub> and CH<sub>3</sub>OH.

Radicals could not be measured with this technique because their lifetimes were too short to persist through the sampling system. Although spectral features associated with DMMP and some of its phosphorus-containing products were observed, their levels were not repeatable. Previous research with extractive FTIR of organic phosphates and phosphonates and their pyrolysis products<sup>263,316,317</sup> suggested that the bulk of the lower-vapor-pressure products were lost by deposition on the surfaces upstream of the FTIR cell. DMMP itself should have reached the gas cell, but at these low flows, transients associated with wall adsorption and desorption resulted in a prohibitively long conditioning time requirement for reliable measurements. Reactions of DMMP and other species in the probe also posed problems in obtaining quantitative species profiles. O<sub>2</sub>, N<sub>2</sub>, and H<sub>2</sub> are not detectable via IR absorption.

### **Probe effects**

The choking at the probe orifice was experimentally verified by measuring flows of post-flame gases through the probe while varying the back pressure in the sampling system. The flow did not vary as long as the back pressure was below 25 kPa, confirming that flow was choked under sampling conditions.

Literature correlations<sup>318</sup> indicated that the location from which gases were sampled should be approximately 3 orifice diameters, or 0.18 mm, upstream of the probe tip location. However, this was largely irrelevant to the comparison between calculated and experimental profiles, as the calculated profiles were based on temperatures measured using a choked-probe technique that entailed the same location error, as described below. Within 10 orifice diameters, or 0.6 mm, of the burner surface, surface/probe interactions led to sampling of gas from both *downstream* and upstream of the probe.<sup>319</sup> This effect was seen in the overrepresentation of products and under representation of methane in samples taken near the burner surface.

Experiments with varying back pressure and with different probe designs were performed to assess the extent of reactions inside the probe.<sup>320</sup> In these experiments, dependence of species concentrations on the gas residence time in the hot region of the probe was seen as evidence for probe reactions. For undoped flames, the main distortion introduced by the probe was in the post-flame zone, where some conversion of CO to CO<sub>2</sub> was seen. In the flame zone, C<sub>2</sub>H<sub>2</sub> was the only species affected by a factor of two reduction in residence time: its concentration dropped by a factor of two. For the preheat and flame zones of doped flames, there was evidence of very significant probe reaction involving CH<sub>2</sub>O. All other species changed

concentrations by less than a factor of 1.5 when the probe residence time was lowered by a factor of two (flame zone) or three (preheat zone). Many species concentrations were unchanged, and only  $\text{CH}_3\text{OH}$  changed by more than a factor of 1.3. Under the same conditions,  $\text{CH}_2\text{O}$  concentrations dropped by factors of 4 and 11, respectively, in the flame and preheat zones when residence time was reduced. DMMP conversion to  $\text{CH}_2\text{O}$  by probe reactions was significant in the pre-heat zone. Although  $\text{CH}_2\text{O}$  measurements in this region were not representative of flame concentrations, they were used as an indicator of the presence of DMMP.

### ***Temperature Measurements***

Temperatures in the flame zone were measured using the choked probe technique described by Kaiser et al.<sup>319,321</sup> In this method, measured flows through the choked probe were compared to those obtained under reference conditions with known upstream temperature. Approximating the flow as one-dimensional and inviscid, the ratio of unknown to reference temperature was obtained. Two different reference conditions were used: (1) room conditions, and (2) post-flame conditions, where the temperature was measured with a platinum/platinum-rhodium thermocouple and corrected for radiative losses. Calculations based on the two different reference conditions yielded temperatures that differed by less than 4 %. Approximations to fluid properties were estimated to introduce errors between 1% and 2%, depending on the location in the flame.<sup>320</sup>

### ***Materials***

The reactants, bought from MG industries, were:  $\text{CH}_4$  (99.99 %),  $\text{O}_2$  (99.994 %),  $\text{N}_2$  (99.998 %), and argon (99.998 %). DMMP (97 %) was bought from Aldrich Chemical Co. and used as is. Calibration curves to quantify the FTIR results used the following gases, bought from MG Industries:  $\text{CO}$  (99.5 %),  $\text{CO}_2$  (99.99 %),  $\text{C}_2\text{H}_2$  (99.6 %),  $\text{C}_2\text{H}_4$  (99.9 %), and  $\text{C}_2\text{H}_6$  (99.0 %). Certified methanol (99.9 %) was bought from Fisher Scientific for methanol calibration. A solution of formaldehyde (37 %) with methyl alcohol (14 %) and water (47 %) was bought from Mallinckrodt Baker for formaldehyde calibration.

### ***Operating Conditions***

Table 3-16 shows the operating conditions used in the current work. Four flames in all were studied: fuel-rich doped and undoped, and near-stoichiometric doped and undoped. Doping refers to the addition of a small quantity of DMMP. As can be seen from the table, reactant flows were chosen to match or nearly match several parameters: the reactants' cold flow velocity, the loading of DMMP for the doped cases, the ratio of inerts ( $\text{N}_2$  and Ar) to  $\text{O}_2$ , and the adiabatic flame temperature. In addition, the chamber was at the same pressure and essentially the same inlet gas temperature for all measurements. Within these constraints, conditions were chosen by trial and error to provide a significantly lifted, yet non-cellular flame when DMMP was present.

**Table 3-16. Operating Conditions.**

	Fuel-rich Flames	Near-stoichiometric Flames
Equivalence ratio	1.13	0.95
Flows (L/min): CH <sub>4</sub>	1.61	1.37
O <sub>2</sub>	2.84	2.88
N <sub>2</sub>	12.48	10.80
Ar	0	1.94
DMMP	9.18E-3 (doped) or 0 (undoped)	9.18E-3 (doped) or 0 (undoped)
Ratio of Ar/N <sub>2</sub> to O <sub>2</sub>	4.39	4.42
Cold flow velocity (cm/s)	12.6	12.6
Mole fraction DMMP in doped cases (L/L)	540	540
Adiabatic flame temperature (K)	2093	2139
Pressure (kPa)	0.92	0.92
Inlet gas temperature (K)	376	373

### Computational Method

Premixed flame calculations were performed using the CHEMKIN suite of programs.<sup>296</sup> The steady laminar flame calculations used detailed chemical kinetics with mixture-averaged species diffusivities. Thermal diffusion was neglected. Temperature profiles were specified as their measured values.

Two chemical kinetic mechanisms for DMMP combustion were used, referred to in this work as the Babushok<sup>294</sup> and Glaude<sup>307</sup> mechanisms. The mechanisms had in common the mechanism for destruction for small phosphorus compounds developed by Twarowski<sup>258,260,303</sup> but they differed somewhat in the paths for DMMP conversion into the small phosphorus-containing species. The Babushok mechanism had 32 species and 199 elementary reactions. Many Arrhenius parameters came from Werner and Cool's work. In the Werner-Cool mechanism, there some were estimates by the authors, and some heats of formation and activation energies were evaluated by BAC-MP4 calculation. The Werner-Cool mechanism for DMMP destruction was validated with relative species profile measurements from a low-pressure H<sub>2</sub>/O<sub>2</sub>/Ar premixed flame at 66 kPa,<sup>300</sup> and the Babushok mechanism was validated with data from opposed flow propane/air flames at 85 kPa.<sup>294</sup> Glaude's mechanism for DMMP combustion had 43 species and 537 elementary reactions. It too was based on the work of Twarowski, Melius, Werner and Cool, but included new initial reactions for DMMP destruction. It was validated against Korobeinichev's low pressure premixed flame results.<sup>254,308,310,311</sup> Korobeinichev and coworkers<sup>314</sup> had also proposed an updated kinetic mechanism using the mechanisms of Twarowski and Werner and Cool as their starting point. This mechanism was not evaluated in the present work.

Each of the DMMP combustion mechanisms was combined with the GRI 3.0 methane combustion mechanism,<sup>206,206</sup> from which nitrogen chemistry had been removed. Nogueira and Fisher<sup>320</sup> describe a series of calculations for which GRI 3.0 results were compared to those of a different methane combustion mechanism.<sup>322</sup> GRI 3.0 was selected because it was more successful in reproducing the experimental results for undoped flames, especially for methanol profiles.

## Results and Discussion

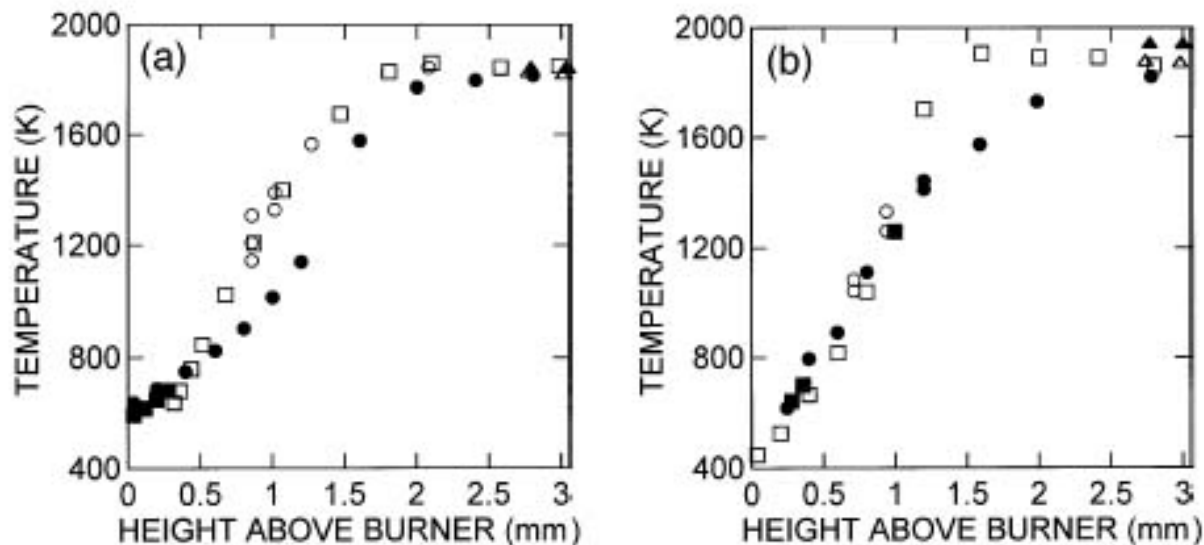
### *Temperature profiles*

Figure 3-97 shows the temperature profiles obtained with and without DMMP doping. Measurements included duplicate data points taken on different days to ascertain repeatability. Choked flow measurements were processed using room conditions as a reference. Post-flame temperatures measured by thermocouple are presented for comparison. In all cases, the lowest measured temperature was about 250 K higher than that of the reactant stream. This was likely a result of the probe/burner interaction near the burner surface, resulting in sampling from both upstream and downstream of the probe orifice.

Both profiles had the same trend. Near the burner surface, doped and undoped temperatures were nearly the same, with doped slightly higher than undoped. The doped temperature increased less rapidly than the undoped one in the early part of the flame, and then increased more rapidly to achieve approximately the same post-flame value as the undoped case.

The shift of DMMP-doped flames away from the burner surface, seen in Figure 3-97, was interpreted by considering the heat transfer interaction between the flame and the burner surface. As there was a negligible change in cold velocity with doping, the change in position indicated that less heat transfer was required to stabilize the doped flame at a given velocity than was required for the corresponding undoped flame. This difference implied that the adiabatic flame speed of the doped mixture was lower than that of the undoped one, or that the overall reaction rate was slowed by the addition of DMMP. This conclusion was consistent with observations of flame suppression effects of organophosphorus compounds in non-premixed methane flames.<sup>79,119,120</sup> In the absence of a change in adiabatic flame temperature with doping, the flame shift away from the burner should have led to lower heat loss and thus a higher post-flame temperature in the doped case. Under these conditions, thermocouple measurements suggested that this was a small effect. Temperatures measured by the choked-orifice method were similar for doped and undoped cases at the highest sampling location, but the undoped flame was actually slightly hotter. However, the shape of the curves suggests that the final post-flame temperature had not been reached for some profiles at that location, leading to uncertainty in the final temperatures.

The shift away from the burner, or broadening of the reaction zone, was consistent with the results of Korobeinichev et al. for TMP in a  $\text{CH}_4/\text{O}_2/\text{Ar}$  flame at 10 kPa.<sup>309</sup> The lack of significant effect of the additive on final temperature, however, was different from Korobeinichev's observations, which indicated that doped final temperatures exceed the corresponding undoped ones by about 200 K. Korobeinichev et al. attributed this higher temperature to the lower heat loss and more complete combustion in the doped case. As observed by Korobeinichev,<sup>309</sup> organophosphorus additives had a distinctly different effect on lower-pressure hydrogen flames, narrowing the reaction zone and raising the final temperature by 350 K to 450 K.<sup>254,300,310</sup> This change from promotion to inhibition behavior was predicted by low pressure flame speed calculations performed by Korobeinichev and coworkers,<sup>309</sup> who offered a qualitative explanation for it based on the effect of radical termination reactions on the heat release rate. Korobeinichev and coworkers<sup>309</sup> observed that the inhibitory behavior of organophosphorus compounds increased with pressure, and was greater in methane than in hydrogen flames. The current experiments, performed at still higher pressures, confirmed this trend.



**Figure 3-97. Temperature Profiles Measured in (a) Rich and (b) Near-stoichiometric Flames. Filled symbols: doped flames. Open symbols: undoped flames. Squares: data from larger probe. Circles: data from smaller probe. Triangles were taken with thermocouples.**

### *Comparison of Doped and Undoped Profiles*

Figure 3-98 through Figure 3-105 are profiles for the eight measured species. Each profile shows undoped and doped experimental results (symbols), along with computational results (lines). In each figure, the dashed line is the undoped calculation using the GRI 3.0 mechanism, while the dotted and solid lines are the doped calculations with Glaude and Babushok mechanisms, respectively. Each profile includes some data points acquired on a different day, with a different probe orifice diameter, as indicated in the figure captions.

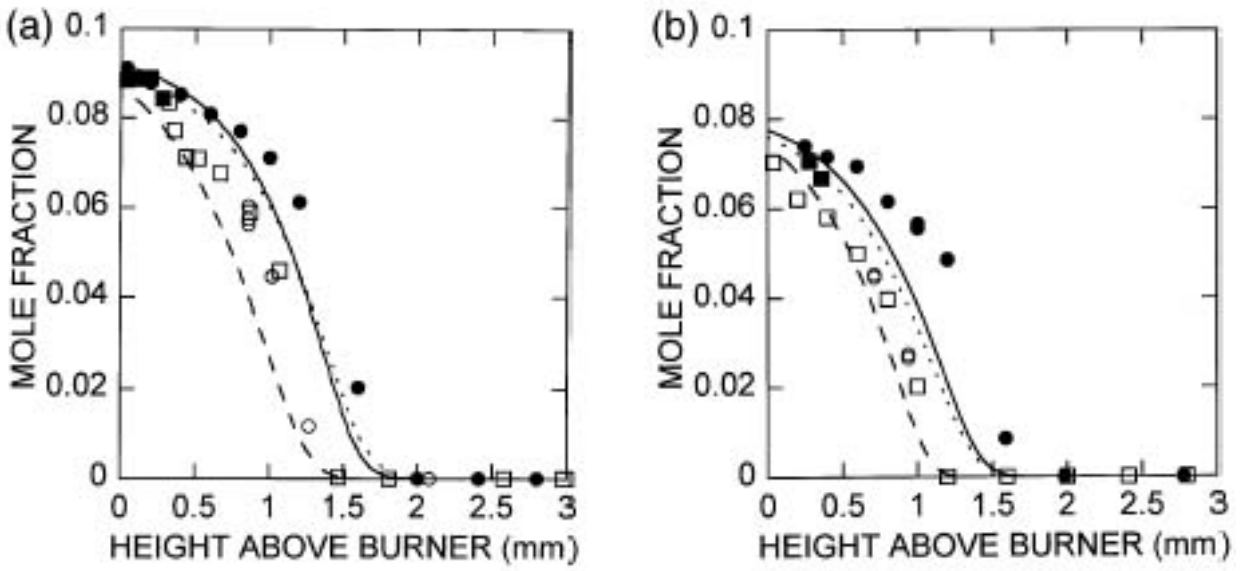


Figure 3-98.  $\text{CH}_4$  in Doped and Undoped (a) Rich and (b) Near-stoichiometric Flames, with GRI (undoped) and Babushok and Glaude (doped) Predictions.

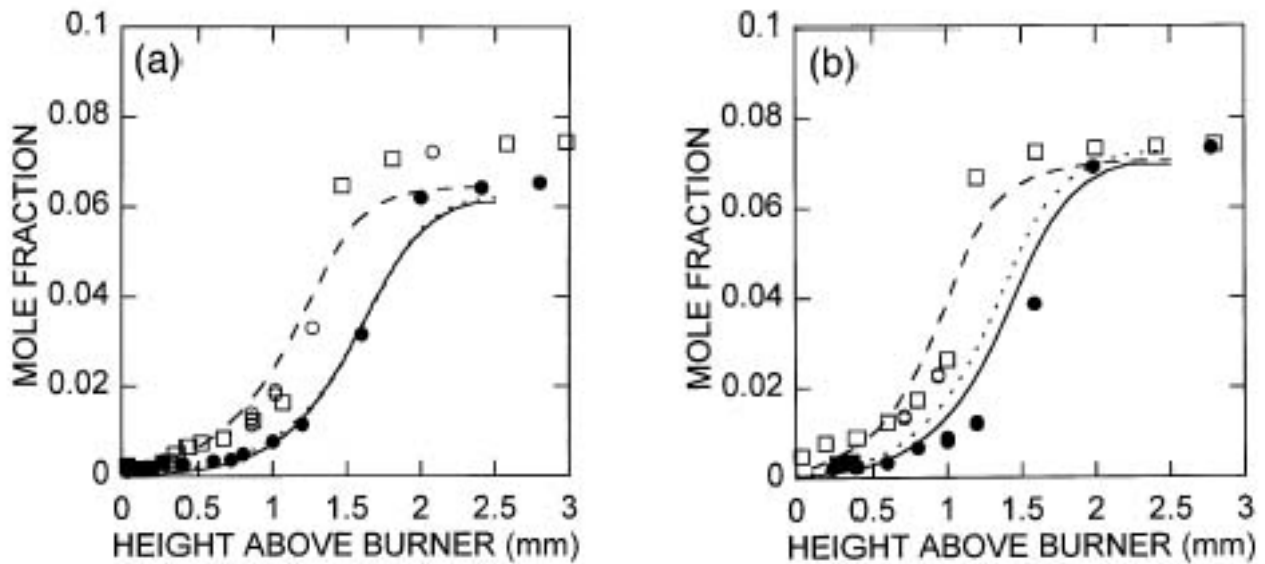


Figure 3-99.  $\text{CO}_2$  in Doped and Undoped (a) Rich and (b) Near-stoichiometric Flames, with GRI (undoped) and Babushok and Glaude (doped) Predictions.

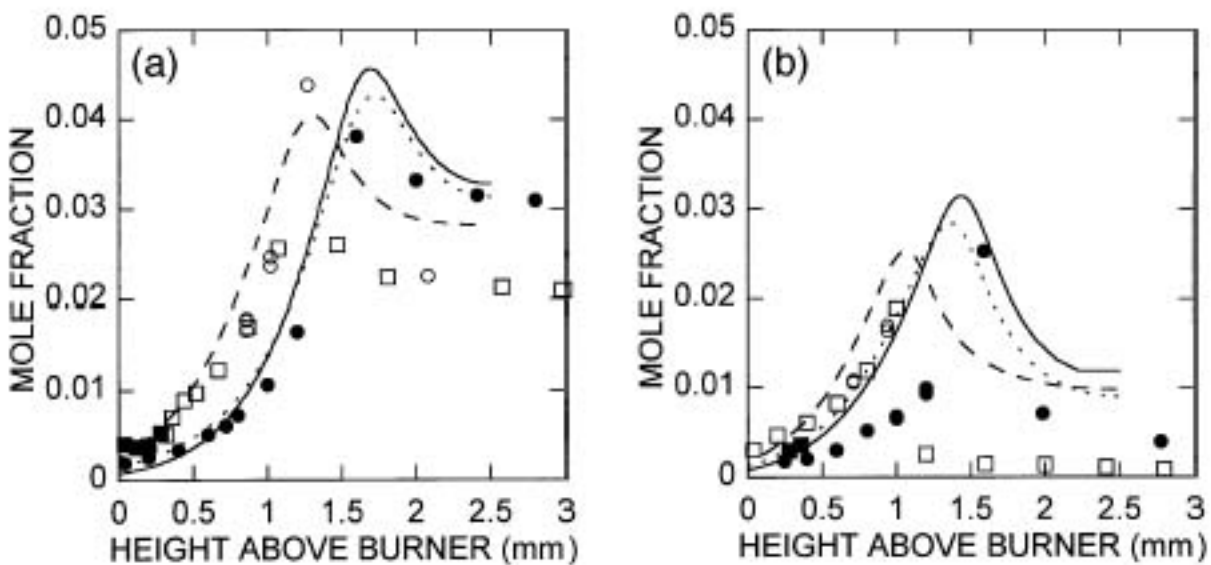


Figure 3-100. CO in Doped and Undoped (a) Rich and (b) Near-stoichiometric Flames, with GRI (undoped) and Babushok and Glaude (doped) Predictions.

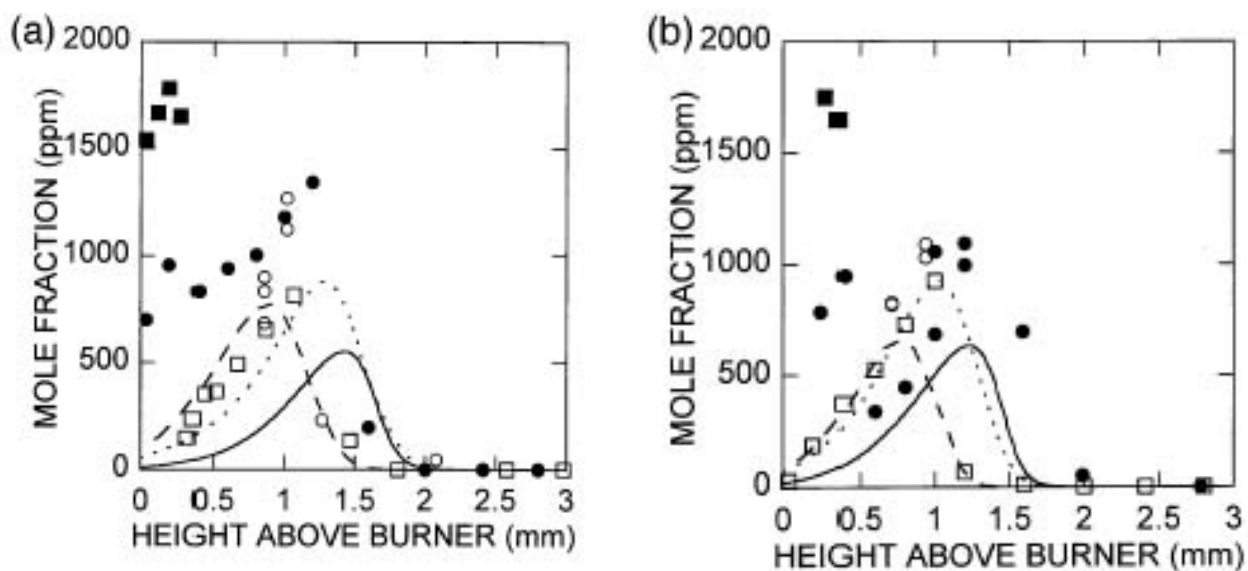


Figure 3-101. CH<sub>2</sub>O in Doped and Undoped (a) Rich and (b) Near-stoichiometric Flames, with GRI (undoped) and Babushok and Glaude (doped) Predictions.

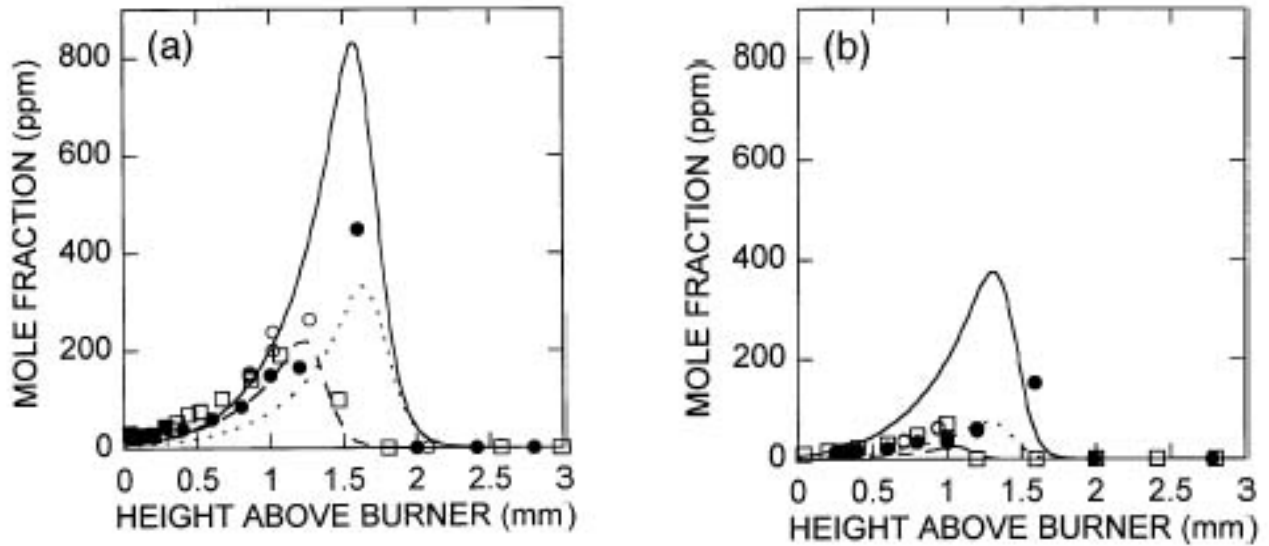


Figure 3-102.  $C_2H_2$  in Doped and Undoped (a) Rich and (b) Near-stoichiometric Flames, with GRI (undoped) and Babushok and Glaude (doped) Predictions.

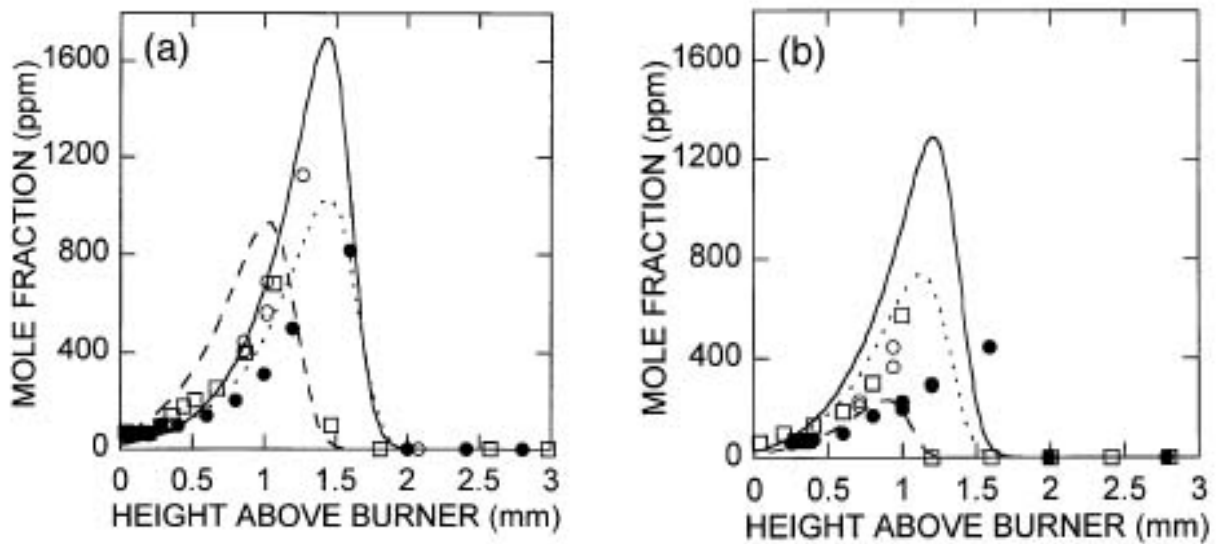


Figure 3-103.  $C_2H_4$  in Doped and Undoped (a) Rich and (b) Near-stoichiometric Flames, with GRI (undoped) and Babushok and Glaude (doped) Predictions.

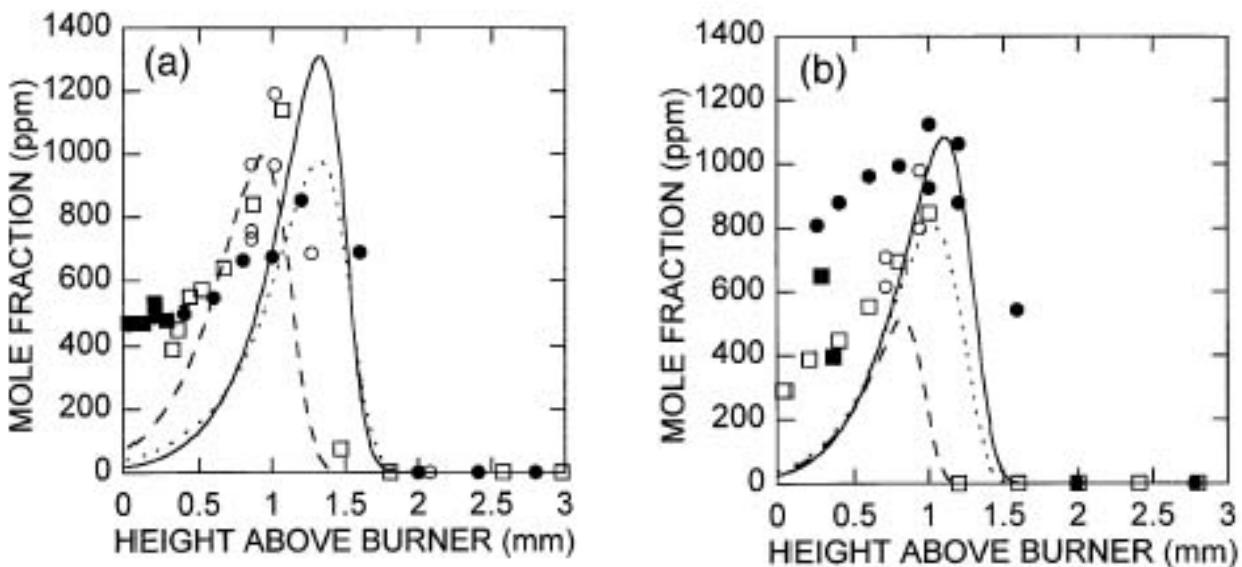


Figure 3-104.  $C_2H_6$  in Doped and Undoped (a) Rich and (b) Near-stoichiometric Flames, with GRI (undoped) and Babushok and Glaude (doped) Predictions.

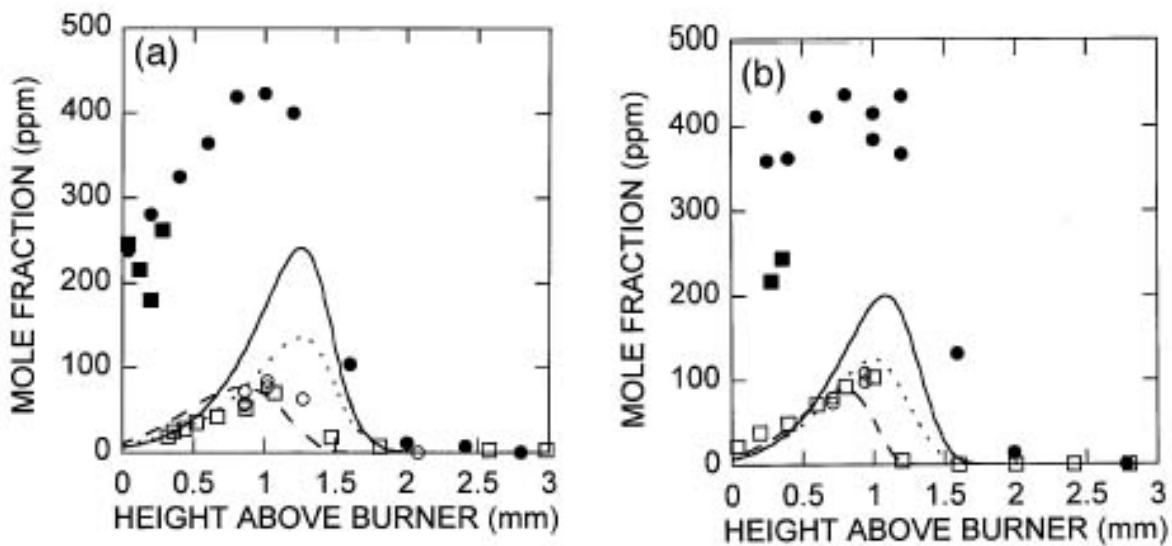


Figure 3-105.  $CH_3OH$  in Doped and Undoped (a) Rich and (b) Near-stoichiometric Flames, with GRI (undoped) and Babushok and Glaude (doped) Predictions.

Doping the flame shifted all species profiles downstream, similar to the behavior of the temperature as described above. The magnitude of this shift was best evaluated from the monotonic  $\text{CH}_4$  or  $\text{CO}_2$  profiles, as the axial spacing of sampling locations was too large to allow reliable comparisons of peak locations for intermediate species. These profiles were fitted to a scaled Weibull cdf form to reduce the impact of noise. Defining the shift as the change in position in the curve fit where half the initial methane was consumed, the experimental values were 0.33 and 0.49 mm for the rich and near-stoichiometric flames, respectively. Similarly, using the location where  $\text{CO}_2$  reached half its maximum value, the experimental shifts were 0.34 and 0.53 mm, respectively. Thus, DMMP consistently had a larger effect on flame location for the near-stoichiometric than for the rich flame under these conditions, and defining flame position in terms of fuel or product profiles yielded similar shifts.

The sampling technique produced artifacts in some profiles, most notably  $\text{CH}_2\text{O}$ . For this species, two peaks can be seen in each of the experimental doped profiles, while the undoped experimental profiles and all the computational profiles show single peaks. The earlier doped peak occurs 0.25 mm from the burner for both equivalence ratios, and was likely due to probe reactions. The location of the first peak close to the burner surface suggested that the upstream peak came directly from DMMP destruction, but the low temperatures (700 K) and presumed low radical levels there implied that destruction of significant quantities of DMMP in the free stream was very unlikely.<sup>264</sup> The magnitude of this peak increased strongly with probe residence time, as shown in the back pressure experiments described in the previous section. The current data set showed further evidence of this dependence: The highest values of  $\text{CH}_2\text{O}$  in Figure 3-101 were repeat data points measured using slightly smaller probe orifice diameters than the other data points. The points taken with the smaller probe orifice (and corresponding longer residence time in the probe with choked flow) had much higher  $\text{CH}_2\text{O}$  levels than the points taken with the larger probe orifice. Although it was a sampling artifact, this upstream  $\text{CH}_2\text{O}$  peak provided information about the DMMP profile. The drop in  $\text{CH}_2\text{O}$  levels at 0.25 mm above the burner indicated that DMMP levels in the gas stream entering the probe began to drop at this location.

For most intermediates, there was no clear change in peak height due to doping. The measured peak height changed with doping by about a factor of two for  $\text{C}_2\text{H}_2$ , about a factor of 1.5 for CO and for the second peak of  $\text{CH}_2\text{O}$ , and by smaller amounts for  $\text{C}_2\text{H}_2$  and  $\text{C}_2\text{H}_6$ . In each of these cases, a narrow peak along with limited spatial resolution made it hard to determine whether the true height had been sampled.

$\text{CH}_3\text{OH}$  levels, on the other hand, showed a dramatic change in peak height with doping, increasing by factors of seven and four for the rich and near-stoichiometric cases, respectively. The broad peak shape (see Figure 3-105) greatly reduced uncertainty due to limited spatial resolution of sampling. Accounting for probe reactions would have increased the difference between doped and undoped profiles, as can be seen from the doped data points taken with smaller probe orifice size (longer residence time). Werner and Cool<sup>300</sup> did not measure methanol and formaldehyde because the energy needed for their ionization was above the capability of their apparatus. Korobeinichev and co-workers<sup>254,308,310</sup> did not report profiles for these species.

### ***Comparison between Experimental and Computational Profiles***

Figure 3-98 through Figure 3-105 also show how successful the two chemical kinetic mechanisms for phosphorus<sup>313</sup> combustion (Babushok and Glaude) were at duplicating experimental data in doped flames. (The first experimental  $\text{CH}_2\text{O}$  peak was excluded from the comparison below as it was considered a sampling artifact.) Using the GRI-MECH predictions of undoped species profiles as a benchmark, the

phosphorus mechanisms were as successful as the GRI mechanism. All mechanisms successfully predict the direction of change in peak height when the equivalence ratio changed from rich to near-stoichiometric for  $\text{CH}_2\text{O}$ ,  $\text{CO}$ ,  $\text{C}_2\text{H}_2$ , and  $\text{C}_2\text{H}_4$ , and all mechanisms failed for  $\text{C}_2\text{H}_6$ . For  $\text{CH}_2\text{OH}$ , GRI failed while the Babushok and Glaude mechanisms succeeded. None of the mechanisms succeeded in predicting the ranking of peak heights in a particular doped or undoped flame.

More quantitatively, in predicting peak heights, the Glaude mechanism for doped flames was roughly equally successful to the GRI mechanism for undoped flames. Glaude's fractional differences in peak height between experiment and calculation were smaller than or about the same magnitude as the corresponding GRI values for all species except  $\text{CH}_3\text{OH}$ . Babushok's mechanism was less successful, producing larger fractional differences than GRI for all cases except  $\text{C}_2\text{H}_6$  in the near-stoichiometric flame and  $\text{CO}$  in both flames. In the case of over-predictions, these discrepancies must be viewed with some caution because true peaks may not be sampled experimentally. Another explanation for some differences was probe reactions, which produced changes of 30 % or so in most species concentrations in the flame zone. The discrepancies between experiment and calculations with the Babushok mechanism clearly exceeded errors due to probe reactions (i.e., exceeded the observed sensitivity to probe residence time) only for  $\text{C}_2\text{H}_2$ ,  $\text{C}_2\text{H}_4$ , and  $\text{CH}_3\text{OH}$ .

Methanol computational results showed large discrepancies with experiment for both phosphorus combustion mechanisms. Qualitatively, the mechanisms succeeded in predicting that the doped  $\text{CH}_3\text{OH}$  peak was higher than the undoped peak. However, they predicted the peak to be too narrow and located too far downstream, and they substantially underpredicted its height. Babushok and Glaude mechanisms predicted that the  $\text{CH}_3\text{OH}$  peak height increased, respectively, by factors of 1.4 to 1.8 and 2.2 to 3.2 over the undoped calculated values. The experimental increase was by factors of 4 (near-stoichiometric) and 7 (rich). This difference indicated an area in which improvements to both mechanisms are needed. The early location of the start of the doped  $\text{CH}_3\text{OH}$  peaks suggested that  $\text{CH}_3\text{OH}$  was an important intermediate in the early decomposition process for DMMP.

Both phosphorus mechanisms agree with experiments in predicting that doping produced a downstream shift of species profiles. The magnitude of the shift was similar for the two mechanisms, an expected result, as calculations with both mechanisms made use of the same specified experimental temperature profiles. The two calculations predicted almost identical shifts in the rich case for all species. In the near-stoichiometric flame, the shift was somewhat larger for Babushok than for Glaude, especially for  $\text{CH}_2\text{O}$ . With the measures of shift size based on the position where  $\text{CH}_4$  concentration was half of the initial concentration as described in the previous section, Glaude and Babushok gave almost identical shifts for the rich case, while Babushok's shift was 30 % larger in the near-stoichiometric flame. In comparison to experimental shifts, calculations were about 20 % too large in the rich flame, and about 45 % too small in the near-stoichiometric flame. Both mechanisms failed to predict that the shift in the near-stoichiometric flame was greater than the one in the rich flame. The magnitudes of the shifts were predicted slightly better by Babushok than by Glaude.

It is important to note that in the current work Glaude's and Babushok's phosphorus mechanisms were combined with the same methane combustion mechanism (GRI 3.0). It is possible that either mechanism would make more successful predictions when used with the methane combustion mechanism with which it was developed.

### 3.4.4 Summary: Phosphorus-containing Compounds in Flames

A novel method for performing repeatable extinction measurements was developed to maintain constant loadings of phosphorus-containing compounds (PCCs) in the oxidizer stream using syringe pump delivery. This method requires that the locations of the flame and stagnation plane relative to the nozzles change during an extinction measurement. The global extinction strain rate was invariant (within  $\pm 2\%$ ) over a broad range of flame locations for methane-air non-premixed flames. Findings using these flames and this technique included:

- Extinction measurement and OH reduction were equivalent markers of agent effectiveness.
- Phosphorus-containing compounds can be 40 times more effective than nitrogen and 2 to 4 times more effective than  $\text{CF}_3\text{Br}$  at quenching non-premixed hydrocarbon flames.
- DMMP and TMP were roughly equivalent in suppression efficiency, independent of the differences in their ligands.
- DMMP was more effective when added to the air side – as in fire suppression.
- The effectiveness of DMMP has a strong temperature dependence, with lower effectiveness at higher adiabatic flame temperatures.
  - These very high temperatures were well above those in ordinary hydrocarbon fires.
  - A mixture of inert and phosphorus-based suppressants could interact synergistically as the physical agent cools the flame, thus increasing the efficiency of the chemically active component.
- Current computational models adequately (but somewhat under-) predicted the effect of DMMP on flame extinguishment. This may have been due to the significant uncertainties in several of the reaction rate coefficients in the phosphorus mechanism.
  - The direct role of the phosphorus-containing species in the flame was the fast removal of H and O atoms, leading indirectly to a decrease in OH.
  - Inhibition was due to the phosphorus-containing radicals,  $\text{PO}_2$ , HOPO, and HOPO<sub>2</sub>, formed after the decomposition of the parent compound.
  - PCC flame inhibition does not depend on the form of the parent compound, provided that the parent breaks down in the flame. Thus, a broad class of potential PCC fire suppressants should exist, from which an alternative to halons with minimal health and environmental impact may be selected.

Additional experiments with methane-nitrogen-oxygen-argon premixed flames showed:

- DMMP addition caused a downstream shift of temperature profiles and all species profiles except  $\text{CH}_3\text{OH}$ . This shift was a consequence of the flame inhibition properties. The magnitude of the shift was over 50 % greater for a near-stoichiometric flame than for a rich flame.
- Flame calculations again were reasonably successful in predicting the effects of DMMP on the flame.

## 3.5 COMPARATIVE FLAME INHIBITION MECHANISMS OF CANDIDATE MOIETIES

### 3.5.1 Introduction

A goal of NGP research was to develop a unified understanding of flame inhibition and extinguishment, so that basic principles could then be used to interpret data from a wide range of inhibitors, as well as a wide range of fire scales. The following sections present work to that end. Since the mechanisms of chemically acting fire suppressants were widely believed to involve recombination of free radicals in the flame, radical concentrations measurements were made for flames with addition of various inhibitors, including  $\text{CF}_3\text{Br}$ . Since  $\text{CF}_3\text{Br}$  was often used as the benchmark for comparison of new agents, an analytical study was undertaken to determine if its mechanism is representative of chemically acting inhibitors in general, or a special case. Further work sought to correlate the effectiveness of agents with the bond strength of the active intermediates. Finally, an idealized inhibitor was used to investigate the properties of the flames themselves which lead to the most effective inhibition.

### 3.5.2 Spectroscopic Studies of Inhibited Opposed Flow Propane/Air Flames

#### Introduction

Skaggs and co-workers<sup>93</sup> applied optical diagnostics and chemical modeling to a propane-air, opposed flow, non-premixed flame to investigate the similarities and differences among the characteristics of flames inhibited and extinguished by a diversity of additives:

- $\text{N}_2$  represented purely physical influence on flame inhibition since it has no chemical inhibition capability.
- HFC-227ea ( $\text{C}_3\text{F}_7\text{H}$ ) and HFC-236 ( $\text{C}_3\text{F}_6\text{H}_2$ ). Hydrofluorocarbons, although they typically increase the heat release rate in the flame, also remove H atoms from the reaction zone and reduce the overall reaction rate.<sup>323</sup>
- $\text{Fe}(\text{CO})_5$  is a highly efficient flame inhibitor. It is chemically active and representative of a class of metal-containing compounds.
- DMMP ( $\text{CH}_3\text{P}(\text{O})(\text{OCH}_3)_2$ ) and PN (cyclo- $\text{P}_3\text{N}_3\text{F}_6$ ) are also efficient chemically active inhibitors, representative of phosphorus-containing compounds.
- Halon 1301 ( $\text{CF}_3\text{Br}$ ) is both an efficient halogenated fire suppressant and the reference agent for the NGP.

#### Experimental

The flame imaging experiments were conducted using the arrangement presented in Figure 3-106. All flames were at atmospheric pressure and consisted of 7.0 L/min synthetic air (79 %  $\text{N}_2$  + 21 %  $\text{O}_2$ ) flowing from the lower duct, and 5.6 L/min of propane flowing from the upper duct. The oxidizer and fuel ducts were separated by a distance of 1.2 cm, and the duct diameters were each 2.54 cm. The inhibitors were added to the oxidizer flow in gaseous form at room temperature with the exception of  $\text{Fe}(\text{CO})_5$ , which was cooled to 11°C and DMMP which was heated to 70°C. Based on the flow conditions

and duct separation, the luminous flame zone was located on the oxidizer side of the stagnation plane, and the global strain rate was calculated to be  $72.5 \text{ sec}^{-1}$ .<sup>76</sup> The burner apparatus was located inside a stainless steel hood to contain any toxic fumes that were exhausted from the burner.

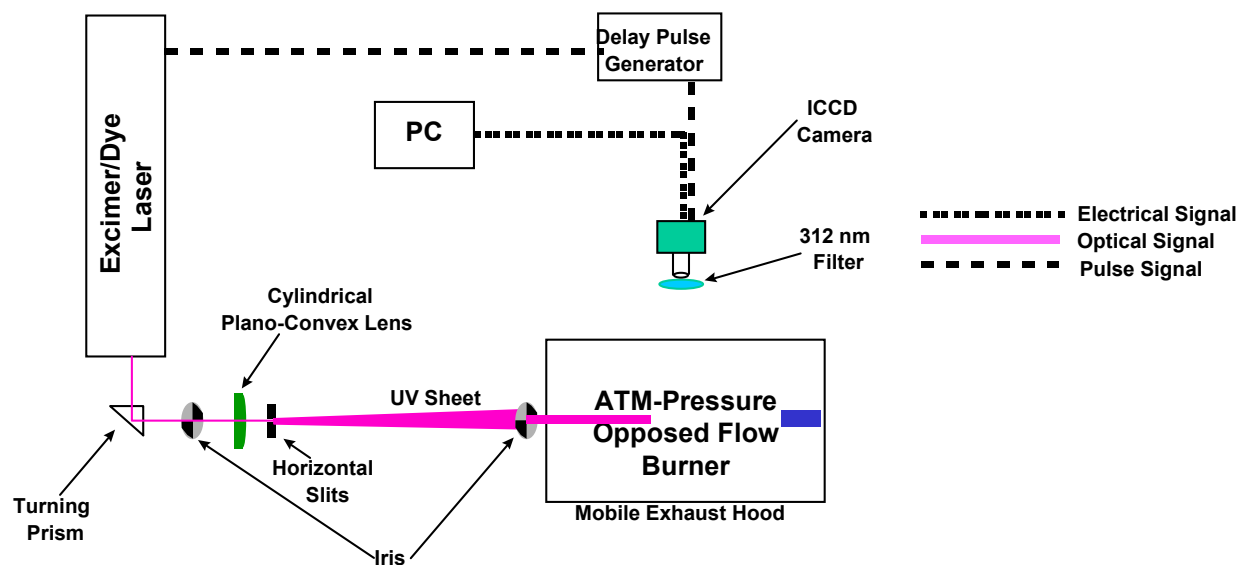


**Figure 3-106. Schematic Diagram of the Experimental Apparatus.**

Previous studies of non-premixed propane/air flames had experimentally determined global extinction strain rates of  $489 \text{ s}^{-1}$ .<sup>324</sup> A decrease in the extinction strain rate was used as an indicator of an inhibitor's efficiency.

Planar laser induced fluorescence (PLIF) and laser induced fluorescence (LIF) were used to measure the H atom, O atom, and OH radical species concentrations as flame extinction was approached. These measurements complemented the extinction strain rate by illustrating an inhibitor's influence on the radical concentration profiles in the flame zone which indicated if the flame's radical chemistry was being perturbed by agent addition.

PLIF images were measured using a Lambda Physik excimer/dye laser system. This system consisted of a Lambda Physik Compex 102 XeCl excimer laser, a Scanmate 2 dye laser (Coumarin 153) and a Second Harmonic Generator (SHG). The fundamental output of the dye laser (560 nm wavelength) was frequency doubled in the SHG unit with a BBO crystal to approximately 281 nm. The UV laser radiation was tuned to the peak of the  $R_2(9.5)$  transition at 281.8 nm ( $(1,0) A^2\Sigma^+ \leftarrow X^2\Pi$ ).<sup>158-160</sup> The UV light output of the SHG unit entered an optical train where the beam is turned  $90^\circ$ , apertured by a sub mm iris, projected through a cylindrical plano-convex lens to form the UV beam into a vertical sheet. To create a uniform sheet width, the sheet was apertured with 0.5 mm vertical slits as it was projected toward the center of the burner. The UV sheet was apertured just before the burner to produce a vertically uniform intensity that was 1.2 cm in height, allowing passage through the entire burner flow field. The OH fluorescence passed through a band pass filter centered at 312 nm with a 11 nm bandwidth and was detected with a Princeton Instruments ICCD camera (Model 120) coupled with a Nikon UV lens located at  $90^\circ$  with respect to the UV sheet. The ICCD camera, which had an active area of  $384 \times 576$  pixels, had a field of view with this optical arrangement of approximately  $33 \text{ cm}^2$  and each image recorded was acquired with 25 total

accumulations on the camera. With this arrangement, the entire relative OH concentration profile was obtained.

Laser induced fluorescence excitation spectra were measured in the flame using the same excimer/dye laser system. This arrangement has been utilized before for similar measurements.<sup>157</sup> The UV laser radiation was scanned from 281.5 nm to 282 nm.<sup>158-160</sup> Low laser energies were used, and the laser was operated in the linear regime. The UV light output of the SHG unit was focused to the center of the burner 30 cm focal length fused silica lens and had a vertical and horizontal beam waist of 0.4 and 0.5 mm, respectively. Fluorescence was collected at 90° to the direction of the excitation laser beam, focused through an 0.5 mm iris to define the collection volume, passed through a band pass filter centered at 312 nm with an 11 nm bandwidth, and detected by a photomultiplier tube (PMT) (Phillips Model XP2018B).

Before inhibitor addition, the uninhibited flame was profiled using LIF between the fuel and oxidizer ducts to obtain a profile of the uninhibited temperature values. To expedite measurements upon addition of an inhibitor, the burner was translated about  $\pm 1$  mm around the OH maximum, and excitation spectra were collected. Each excitation spectrum was fit using a non-linear least squares algorithm to obtain the OH rotational temperature for the spectral measurement.<sup>160</sup>

## Results

Figure 3-107 presents two representative, two-dimensional images of OH fluorescence for an uninhibited propane-air flame and for a propane-air flame to which  $\text{CF}_3\text{Br}$  was added (1.5 % by volume).

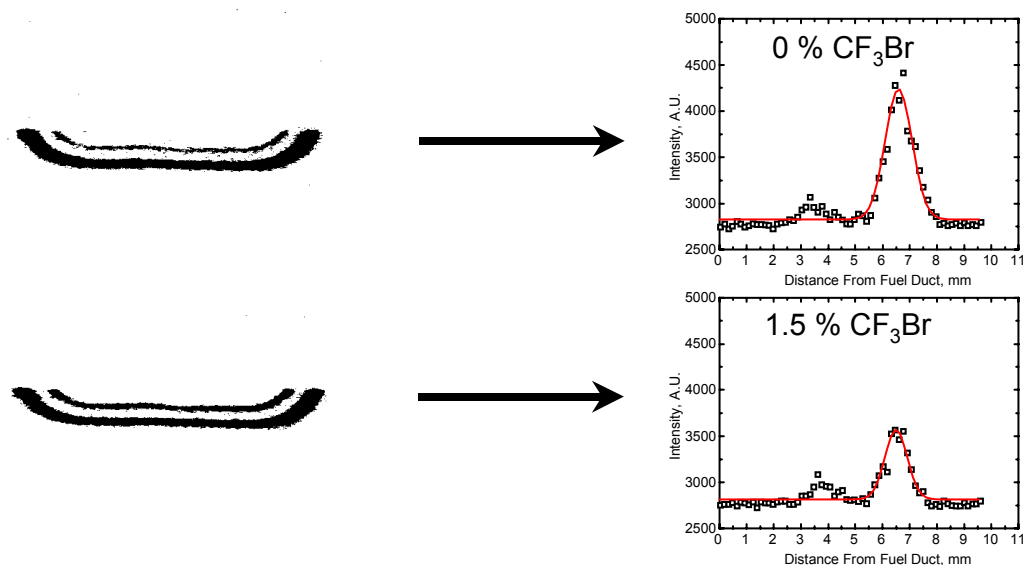


**Figure 3-107. Representative PLIF Images and the Corresponding OH Intensity Profiles from an Opposed Flow Propane-air Flame Seeded with 0 % (by volume)  $\text{CF}_3\text{Br}$  and 1.5 % (by volume)  $\text{CF}_3\text{Br}$ . The fuel and air ducts are at the top and bottom of each PLIF image.**

Both images, which were uncorrected for laser energy fluctuations and local quenching rates, illustrated the presence of two luminous zones as the UV sheet passed through the flame. The lower, thicker zone

was the fluorescence from the OH transition while the upper, thinner zone was the broadband fluorescence due to derivative fuel species such as polycyclic aromatic hydrocarbons. To construct a spatially resolved OH LIF profile from an OH PLIF image, as shown on the right hand side of Figure 3-107, the pixel intensity corresponding to a given height between the fuel and oxidizer ducts (spatial resolution approximately 0.149 mm/pixel) was summed and averaged over a 1 mm horizontal width. The two-dimensional images and LIF profiles illustrated that addition of CF<sub>3</sub>Br to the propane flame caused a decrease in the OH fluorescence signal while the broadband fluorescence increased just slightly. Similar results had been observed previously for CF<sub>3</sub>Br addition to hydrocarbon diffusion flames.<sup>51,156</sup>

Table 3-17 lists the measured inhibitor concentrations in the air stream at extinction and their estimated uncertainties.

**Table 3-17. Inhibitor Concentrations (% by volume) and Uncertainty (± % by volume) at Flame Extinction.**

	Inhibitor						
	N <sub>2</sub>	CF <sub>3</sub> Br	HFC-236	HFC-227ea	PN	DMMP	Fe(CO) <sub>5</sub>
Extinction Concentration	23.1	2.3	6.1	5.3	2.7	0.3	0.2
Estimated Uncertainty	8.20	0.93	1.29	1.08	1.00	0.04	0.03

- The extinction concentration for CF<sub>3</sub>Br was similar to cup burner values, 2.90 %<sup>325</sup>, but slightly lower than values obtained in a co-flowing propane-air flame and a co-flowing propane-air cup burner, 4.1 % and 4.3 %, respectively.<sup>21,51</sup>
- HFC-227ea and HFC-236 had extinction concentrations that were above double that for CF<sub>3</sub>Br, consistent with cup burner values of 6.3 % and 6.6 %, respectively.<sup>325</sup>
- For the phosphorus compounds, PN had an extinction concentration similar to CF<sub>3</sub>Br, while DMMP's value was seven to eight times lower than CF<sub>3</sub>Br. Previous studies by MacDonald et al.<sup>79,120</sup> had shown DMMP to be two to four times more effective than CF<sub>3</sub>Br. However, Fisher et al.<sup>324</sup> reported that for an opposed flow propane-air flame with DMMP added to the air stream, a 25 % decrease in the normalized extinction strain rate corresponded to a DMMP concentration ≈ 1200 μL/L. Linear extrapolation of the cited Fisher et al. data<sup>324</sup> to the strain rate used for the opposed flow, propane-air flame studied here gave a DMMP concentration of 4080 μL/L to 6500 μL/L or 0.4 % to 0.65 % by volume. The DMMP concentration obtained from the extrapolated strain rate data supported the DMMP extinction concentration determined in this study. For PN, cup burner experiments had found an extinction concentration of 1.08 % by volume.<sup>249</sup> The results reported here for PN and DMMP were of concern for several reasons. First, the obtained value for PN was higher, while the DMMP value was lower than other cited experiments. Second, it was assumed prior to these experiments, that if a given compound contained a phosphorus atom, then regardless of its chemical structure, similar extinction concentrations would be observed. A possible explanation for the contrasting behavior between the two phosphorus agents is that the resonant P-N ring structure of PN could be very stable and thus less efficient at delivering phosphorus to the flame.<sup>326</sup>

Figure 3-108 contains the results of the analyzed OH profile areas vs. each agent's concentration as the flames were stepped towards extinction. The reported OH profile areas were averaged over three or more

separate inhibitor extinction experiments, where the data for each experiment were normalized to the [OH] profile area measured in the uninhibited flame acquired prior to each inhibitor extinction experiment to account for changes in burner and camera conditions. The data indicated that there were both physical and chemical modes of inhibition being observed for the agents studied. That is,  $N_2$  which is chemically inert, had the least impact on [OH] with respect to the other agents studied. For the concentration range plotted in Figure 3-108, the flame was not even extinguished by  $N_2$ . Similar results were observed for the two fluorinated propanes which showed initially small declines in [OH], but more rapid decreases just before extinction. Addition of the other inhibitors showed precipitous decreases in the measured [OH] values up to the extinction concentrations where the data decreased more gradually, as highlighted for DMMP and  $Fe(CO)_5$  with the inserted graph in Figure 3-108.

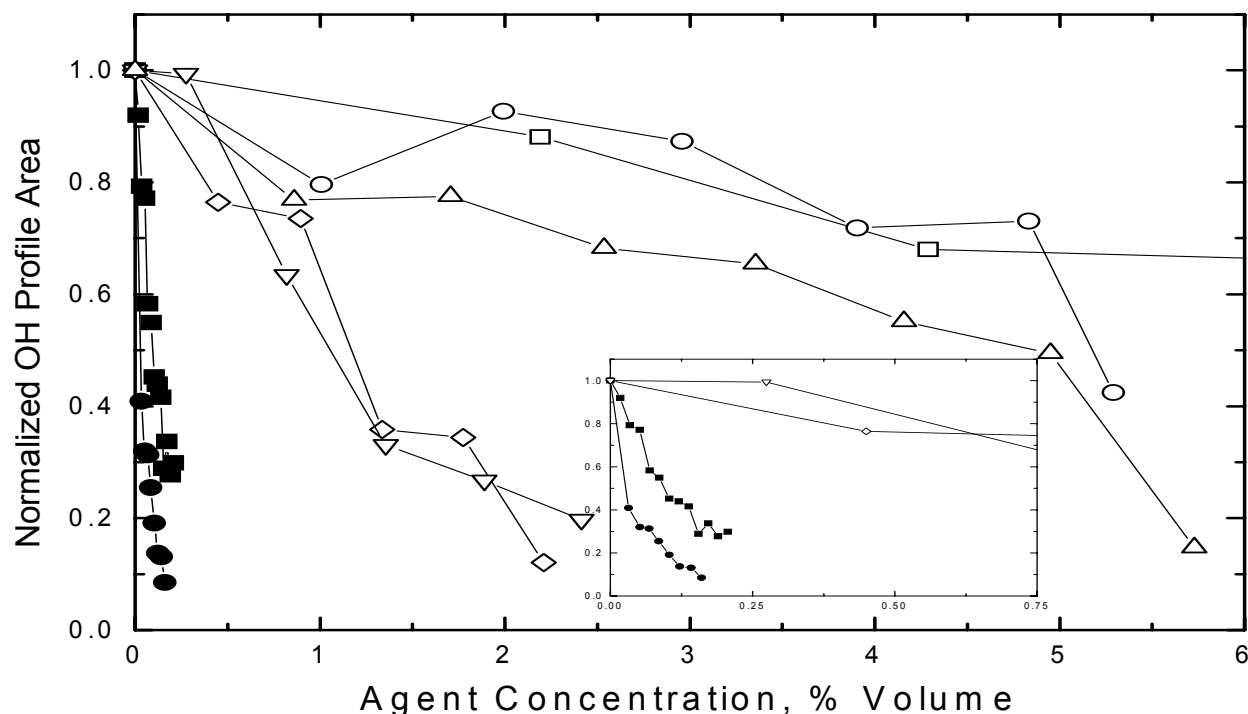


**Figure 3-108. Normalized OH LIF Profile Areas vs. Inhibitor Agent Delivery Concentrations.** □:  $N_2$ , ○: HFC-227ea, △: HFC-236, ▽: PN, ◇:  $CF_3Br$ , ■: DMMP, and ●:  $Fe(CO)_5$ . Insert: Expanded data for PN,  $CF_3Br$ , DMMP, and  $Fe(CO)_5$  Concentrations up to 0.75 % by Volume.

The addition of an inhibitor can change the position and width of the flame's reaction zone. Previous studies had shown<sup>168-170,172,173</sup> that a decrease in the flame's reaction zone width indicated increased localized strain, which can cause local quenching or flame extinction.<sup>171</sup> For the analysis of reaction zone modifications and relative OH concentrations, each OH intensity profile was fit to a Gaussian function. The area under the Gaussian profile curve provided a general indicator of the entire OH population for a given flame condition. The width of the flame's reaction zone was characterized by the width of a radical profile.<sup>173</sup> The width of the flame's reaction zone was defined here as the distance of one half of the maximum intensity of the Gaussian OH profile which was similar to previous studies<sup>170</sup> that estimated the width of a laminar flame reaction zone using one half of the maximum value of a temperature profile.

Table 3-18 lists the measured flame widths determined from the relative OH concentration profiles for each flame situation studied. For the inhibited flames, the widths were measured at 50 % of each agent's determined extinction concentration. The uncertainty in the reported widths due to measurement variance was 11 %.

**Table 3-18. Measured OH Profile Widths (FWHM, mm) for the Uninhibited Flame and Inhibited Flames at 50 % of the Inhibitor Extinction Concentrations.**

Agent	OH Profile Width, mm
Uninhibited	1.30
N <sub>2</sub>	1.24
FE-36	1.31
FM-200	1.26
CF <sub>3</sub> Br	0.96
PN	0.96
DMMP	1.04
Fe(CO) <sub>5</sub>	0.83

The Table 3-18 width values indicated that the widths for N<sub>2</sub>, FE-36, and FM-200 were not significantly different from the uninhibited flame. By contrast, CF<sub>3</sub>Br, PN, DMMP, and Fe(CO)<sub>5</sub> exhibited width changes that were at least 20 % of the uninhibited width value. The OH width trends suggested that inhibitor agents with more physical inhibition capabilities exhibited less effect on the flame structure than inhibitors with enhanced chemical inhibiting capabilities.

Similar trends were expected for the peak flame temperatures. Figure 3-109 presents a plot of peak LIF measured flame temperatures vs. agent delivery concentrations for each inhibited flame. The peak flame temperature for the uninhibited flame was between 2125 K and 2200 K. The obtained temperature values for N<sub>2</sub> and FM-200 were not statistically different from those measured in the uninhibited flame with an estimated uncertainty of  $\pm 300$  K. For CF<sub>3</sub>Br and PN, temperature differences with respect to the uninhibited flame were not observed until near extinction concentrations were added. Previous studies of an atmospheric pressure, axisymmetric propane/air flame inhibited by addition of CF<sub>3</sub>Br to the oxidizer flow, found only small temperature differences in comparison with the uninhibited flame.<sup>36,51</sup> By contrast, Masri et al.<sup>156</sup> reported for a non-premixed atmospheric pressure CH<sub>4</sub>-air flame, that higher temperatures existed in the reaction zone of a CF<sub>3</sub>Br inhibited flame than in the reaction zone of an uninhibited flame near extinction. With mixed results from previous investigations and the large degree of uncertainty in these measurements, the only creditable temperature values are those close to extinction. For Fe(CO)<sub>5</sub> and DMMP, temperature decreases with respect to the uninhibited flame were not observed until proximal extinction concentrations were reached as well. On a concentration basis, Fe(CO)<sub>5</sub> and DMMP had decreased flame temperatures,  $T \approx 1700$  K, at agent concentrations lower than the other agents studied. For Fe(CO)<sub>5</sub>, small decreases in flame temperatures had been observed by Brabson et al.<sup>327</sup> in studies of low-pressure premixed flames inhibited by Fe(CO)<sub>5</sub>.

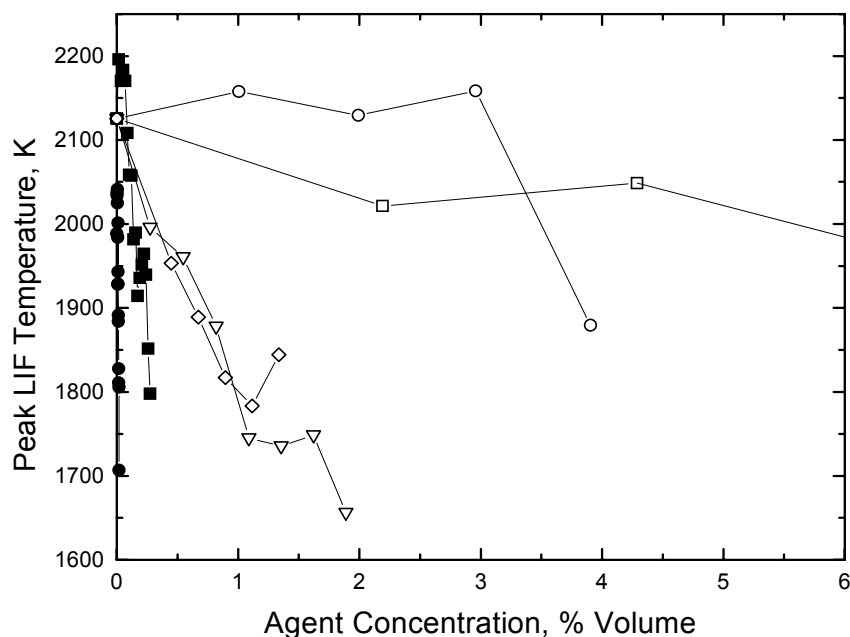
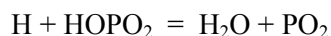
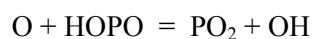
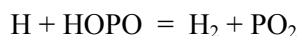
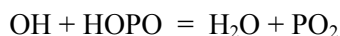


**Figure 3-109. Peak LIF Measured Temperatures (K) vs. Inhibitor Delivery Concentrations. Data Legend: □: N<sub>2</sub>, O: HFC-227ea, Δ: HFC-236, ▽: PN, ◇: CF<sub>3</sub>Br, ■: DMMP, and ●: Fe(CO)<sub>5</sub>.**

### Numerical Modeling

Numerical modeling of a stoichiometric, premixed, propane-air flame inhibited by DMMP, Fe(CO)<sub>5</sub>, CF<sub>3</sub>Br, and N<sub>2</sub> flame was carried out using the CHEMKIN suit of programs.<sup>204</sup> For the simulations, a kinetic model for propane combustion developed by Marinov et al.<sup>328-330</sup> was slightly modified and combined with a C1-C2 hydrocarbon kinetic model<sup>52</sup> that had been employed in earlier inhibition studies. For routine calculations, a simplified model was used to decrease computational time. The kinetic mechanism for phosphorus containing species was based on the model suggested for the analysis of the influence of PH<sub>3</sub> products on the recombination of hydroxyl and hydrogen atoms in a hydrogen flame.<sup>331</sup> and kinetic models<sup>254,300,301</sup> developed to simulate destruction of DMMP and TMP in low pressure hydrogen flames. Additional reactions were added to the phosphorus mechanism to complete the reaction pathways for the consumption of some of the P-containing species. For the modeling of Fe(CO)<sub>5</sub> and CF<sub>3</sub>Br inhibition, previously developed mechanisms for these two species<sup>42,104</sup> were added to the hydrocarbon model.

Computations of the propane flame inhibited by DMMP demonstrated that the consumption of DMMP led via a sequence of reactions to the formation of CH<sub>3</sub>PO<sub>2</sub>. Reactions of CH<sub>3</sub>PO<sub>2</sub> with H and OH created HOPO and HOPO<sub>2</sub>. At this stage, reactions of HOPO, HOPO<sub>2</sub>, and PO<sub>2</sub> with chain carriers formed the following two inhibition cycles:



These inhibition cycles represent the catalytic scavenging cycles that accelerate radical recombination in combustion products containing phosphorus compounds.<sup>260</sup> It is well known that the addition of an inhibitor decreases the burning velocity for premixed flames. Numerical results for burning velocity decreases of 20 % to 30 % using the original rate constants given by Twarowski,<sup>259</sup> indicated that DMMP decreased the flame's burning velocity by a factor of 1.5 to 2 relative to  $\text{CF}_3\text{Br}$  in a methane-air flame. Sensitivity analysis revealed that the burning velocity was receptive to changes in the rate constants for the reactions of  $\text{PO}_2$  radical:  $\text{H} + \text{PO}_2 + \text{M} = \text{HOPO} + \text{M}$  and  $\text{OH} + \text{PO}_2 + \text{M} = \text{HOPO}_2 + \text{M}$ . Reasonable adjustment of rate constants led to agreement with experimental data.

Phosphorus compounds have a wide range of thermal stability. Activation energies of decomposition reactions are in the range 15 kcal/mol to 90 kcal/mol. The influence of the decomposition rate was studied using global kinetics for the decomposition to  $\text{PO}_2$  to HOPO species by varying the overall activation energy for the decomposition reaction. Calculations showed that for the compounds with global activation energies less than 50 kcal/mol, the burning velocity was not affected by the stability of the phosphorus compounds.

Suppression calculations were carried out with increasing additive loadings until suppression concentration levels were achieved (burning velocity  $\leq 5 \text{ cm/s}$ <sup>332</sup>). The calculations were conducted for a gas phase model without taking into account possible condensation processes. Calculation results, Figure 3-110, show that DMMP had less effect in reducing the burning velocity in comparison with  $\text{Fe}(\text{CO})_5$ , but relative to  $\text{CF}_3\text{Br}$  both were more effective. For increases in the concentration of  $\text{Fe}(\text{CO})_5$  and DMMP, both agents exhibited increasing saturation effects. Typically, two types of saturation have been discussed in the literature: (1) saturation of chemical influence,<sup>52</sup> and (2) saturation due to condensation processes.<sup>104</sup>

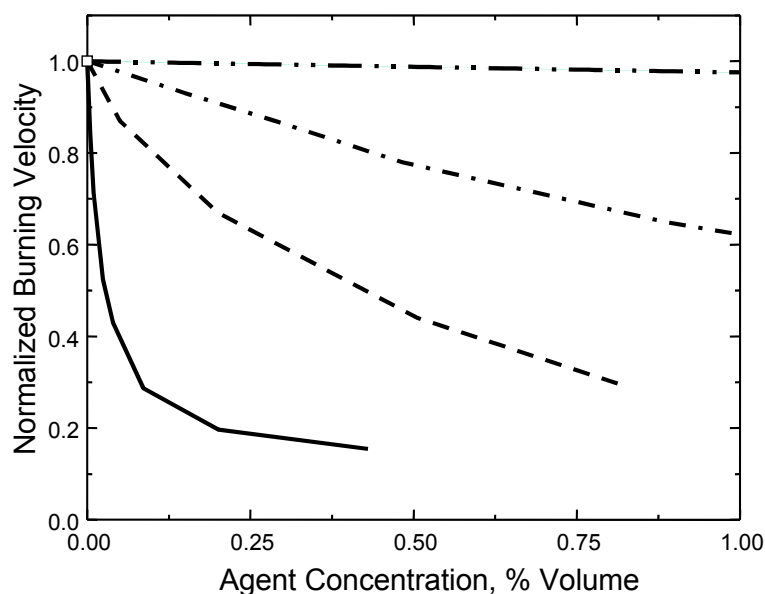


**Figure 3-110. Calculated Burning Velocities vs. Delivered Inhibitor Concentration for a Numerical, Stoichiometric, Premixed, Propane-air Flame. Dashed line: DMMP data. Solid line:  $\text{Fe}(\text{CO})_5$  data. Dashed dot dashed line:  $\text{CF}_3\text{Br}$  data. Near-horizontal Dashed Dot Dot Dashed Line:  $\text{N}_2$  data trend.**

Both processes resulted in a decrease in inhibitor efficiency with increased inhibitor concentration. For example, to decrease the burning velocity to 10cm/s required a DMMP loading of approximately 0.9 %, but an additional 1.2 % of DMMP was needed to decrease the burning velocity to the extinction level of 5 cm/s. Such a strong saturation effect led to a substantial increase in extinction concentrations and a decrease in inhibitor efficiency relative to  $\text{CF}_3\text{Br}$ . The calculated extinction concentrations, in units of % volume, for the numerical propane/air flame were: DMMP: 2.1;  $\text{CF}_3\text{Br}$ :  $\approx 3.5$ ;  $\text{Fe}(\text{CO})_5$ : 0.4 to 0.5; and  $\text{N}_2$ :  $\approx 40$ . The modeling results supported DMMP and  $\text{Fe}(\text{CO})_5$  exhibiting superior inhibition capabilities relative to  $\text{CF}_3\text{Br}$ .

Finally, comparison of the normalized OH concentrations dependency on inhibitor concentrations demonstrated a correlation between experimental and calculated OH concentrations. Figure 3-111 illustrates that two different propane flames inhibited by the same agents had normalized OH concentrations that tracked more or less with one another. At the experimental OH extinction level, i.e., 0.3 to 0.1, both data sets (experimental/computational) had similar normalized OH reductions.

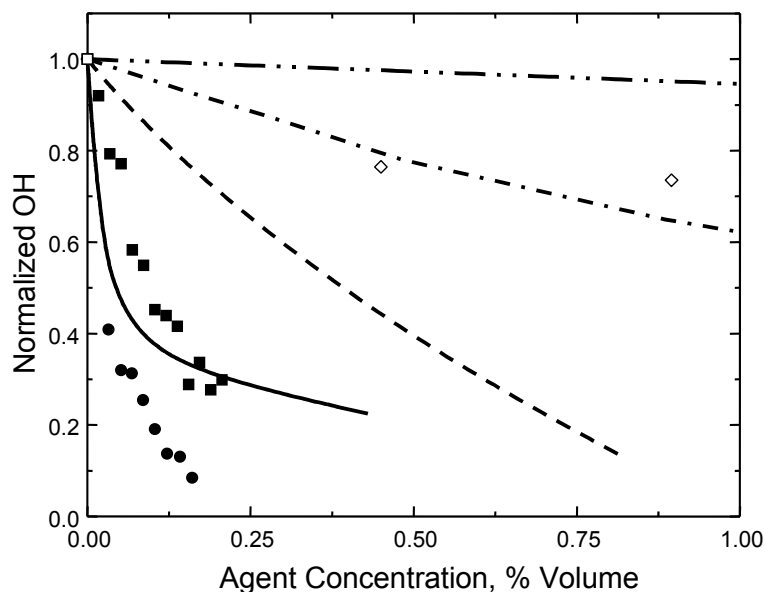


**Figure 3-111. Normalized OH Concentrations vs. Delivered Inhibitor Concentrations. Data legend: experimental (●) and numerical (solid line)  $\text{Fe}(\text{CO})_5$  data; experimental (■) and numerical (dashed line) DMMP data; experimental (◻) and numerical (dash-dot line)  $\text{CF}_3\text{Br}$  data; dashed dot dot dashed line,  $\text{N}_2$  data trend.**

## Conclusions

The experimental results presented here showed for the first time changes in  $[\text{OH}]$  profiles as extinction was approached in a series of inhibited, atmospheric pressure, non-premixed, propane/air flames. There was a good relationship between the narrowing and peak intensity of  $[\text{OH}]$  profiles in these flames with the degree of chemical activity of added inhibitors.  $\text{N}_2$ , HFC-236, and HFC-227ea, with little chemical activity, showed no peak narrowing relative to the uninhibited flame. By contrast,  $\text{CF}_3\text{Br}$ , PN, DMMP and  $\text{Fe}(\text{CO})_5$  demonstrated chemical inhibition capabilities and significant decreases in the  $[\text{OH}]$  peak width.

Contrary to prior hypothesis, there was a difference among PCCs in their flame extinguishment concentrations, on a per-phosphorus atom basis. PN, with the phosphorus atoms in its resonance-stabilized ring structure, was less efficient than DMMP.

### 3.5.3 CF<sub>3</sub>Br and Other Suppressants: Differences in Effects on Flame Structure

#### Introduction

With some exception, the working hypothesis of the NGP was that significant catalytic scavenging of flame-propagating free radicals was necessary to match or exceed the efficiency of halon 1301. A logical issue was the extent to which the knowledge of the flame inhibition mechanism of CF<sub>3</sub>Br, itself a catalytic scavenger, was applicable to identifying alternative suppressants. Was CF<sub>3</sub>Br “typical” of efficient fire suppressants in general? Would all promising replacements for CF<sub>3</sub>Br show similar behavior? Was commonality of properties with CF<sub>3</sub>Br a useful guide in the search for alternatives?

To this end, Williams and co-workers<sup>26</sup> performed modeling studies of premixed flames containing substances representative of different classes of inhibitors, including inert gases, fluorocarbons, and catalytic scavengers of flame radicals. While suppression of nonpremixed flames is the typical scenario in fire extinguishment, the behavior of suppression agents in premixed flames is important in mitigating deflagrations and protecting against re-ignition. Furthermore a large body of suppression data in different types of flames compiled by Babushok and Tsang<sup>333</sup> had shown that for many agents, extinction of nonpremixed flames correlated with reduction of burning velocity in premixed flames.

Williams and co-workers compared the effects on burning velocity and flame structure of CF<sub>3</sub>Br with those of the catalytic inhibitor NaOH, the non-catalytic hydrofluorocarbons CF<sub>3</sub>CHFCF<sub>3</sub> (HFC-227ea) and CF<sub>3</sub>CH<sub>2</sub>F (HFC-134a), and the inert agents N<sub>2</sub> and CF<sub>4</sub>. (CF<sub>4</sub> undergoes little decomposition in the reaction zone of most flames,<sup>61</sup> and is thus predominantly a physical agent). For exploratory purposes, they also considered an idealized, constrained version of Fe(CO)<sub>5</sub> inhibition which includes only the much less effective iron catalytic cycles for O-atom recombination.

#### Computational Methodology

The PREMIX code<sup>203</sup> was used to compute burning velocities and flame structures of atmospheric pressure, stoichiometric methane-air flames with and without suppressants. A domain of 85 cm was used in the calculations, extending 25 cm from the reaction zone on the cold boundary and 60 cm from the reaction zone on the hot boundary. The mesh extension and refinement were such that the spacing between the outermost grid points on each boundary was 1 cm, to minimize any temperature or species gradients at the boundaries. Multicomponent transport formulations, as well as the Soret effect for the species H and H<sub>2</sub>, were used for all calculations. Refinement tolerances of 0.1 for the normalized species gradient (GRAD keyword) and 0.2 for the normalized second derivative (CURV keyword) were used for all calculations. The final meshes typically contained 90 to 125 grid points, depending on the number of additional species introduced by the inhibitor chemistry.

Comparison of the PREMIX results with thermal equilibrium calculations for several inhibited and uninhibited flames showed that, at the final grid point, temperatures were within 5 K and that radical concentrations of H, OH, and O were within a few percent of their equilibrium values. Thus, the radical equilibrium values and adiabatic temperatures were assumed to be those calculated at the hot boundary. All flames were stoichiometric, with the inhibitors listed above added in various concentrations. For the hydrocarbon chemistry, the GRIMEch 2.11<sup>334</sup> (excluding nitrogen chemistry) was used as the chemical

kinetic mechanism. For the uninhibited, stoichiometric methane air flame, a predicted burning velocity of  $39.5 \text{ cm/s} \pm 0.2 \text{ cm/s}$  was obtained.

The fluorocarbon chemistry was based on the mechanism developed by Westmoreland et al., as refined in previous studies performed at the Naval Research Laboratory<sup>61,335</sup>. The bromine chemistry used in the modeling of  $\text{CF}_3\text{Br}$  was that developed by Noto et al.<sup>175</sup>. The kinetic mechanism for  $\text{NaOH}$  was based on that of Zamansky et al.,<sup>335</sup> while that for  $\text{Fe}(\text{CO})_5$  was described by Rumminger and Linteris.<sup>118</sup>  $\text{NaOH}$  must vaporize before being able to participate in the flame chemistry, but the PREMIX code had no provision for inclusion of condensed phase species. To simulate the evaporation effect, the sodium hydroxide was therefore assumed to initially consist of the gas phase dimer  $\text{Na}_2\text{O}_2\text{H}_2$ , which was required to dissociate ( $\Delta H_f = 42 \text{ kcal/mol}$ ) before inhibition chemistry could proceed.  $\text{N}_2$  and  $\text{CF}_4$  were assumed inert: no nitrogen or fluorine chemistry was included in the respective calculations.

### Inhibition Parameter

The effectiveness of an inhibitor at reducing burning velocity in a fuel/oxidizer mixture may be placed on a quantitative basis in terms of the inhibition parameter,  $\Phi$ , proposed by Rosser et al.<sup>33</sup> and modified by Noto et al.<sup>175</sup>

$$\Phi = \ln(U_0/U_i) (X_{\text{O}_2}/X_i) \quad (3-12)$$

where  $U_0$  and  $U_i$  are the burning velocities of the uninhibited and inhibited flames, respectively, and  $X_{\text{O}_2}$  and  $X_i$  are the reactant mole fractions of oxygen and inhibitor. In Reference 175, the burning velocity of a given fuel/air mixture was found to exhibit an exponential dependence on concentrations of several inert and fluorocarbon inhibitors, including  $\text{CF}_3\text{Br}$ . A constant value of  $\Phi$  with inhibitor concentration indicated that the exponential behavior found in Reference 175 held.

Catalytic radical scavengers necessarily manifest saturation effects, because catalysis cannot reduce concentrations of flame radicals below the thermal equilibrium level at the local flame temperature. The existence of a similarity transform, obtained by solving Equation 3-12 for  $U_i$ <sup>175</sup>, which caused the flame speed reduction curves for  $\text{CF}_3\text{Br}$  and non-catalytic agents to coincide, was thus somewhat unexpected.

Changes in burning velocity, adiabatic flame temperature, radical super-equilibrium, and  $\Phi$  are plotted as a function of  $(\text{NaOH})_2$  concentration in Figure 3-112 and  $\text{CF}_3\text{Br}$  concentration in Figure 3-113. The error bars for  $\Phi$  were determined by propagating a change of  $0.2 \text{ cm/s}$  in the inhibited flame speed (the estimated computational uncertainty for the mesh refinement tolerances used) to determine the change in  $\Phi$  in Equation 3-12. The points at low inhibitor concentrations had high uncertainties in  $\Phi$  due to the small reductions in burning velocities. The radical super-equilibrium was defined as the ratio of the peak concentrations of the radical to its concentration at thermal equilibrium at the adiabatic flame temperature. The value for this ratio is always unity or greater; a value greater than unity means the radical exists in super-equilibrium concentration somewhere in the flame.

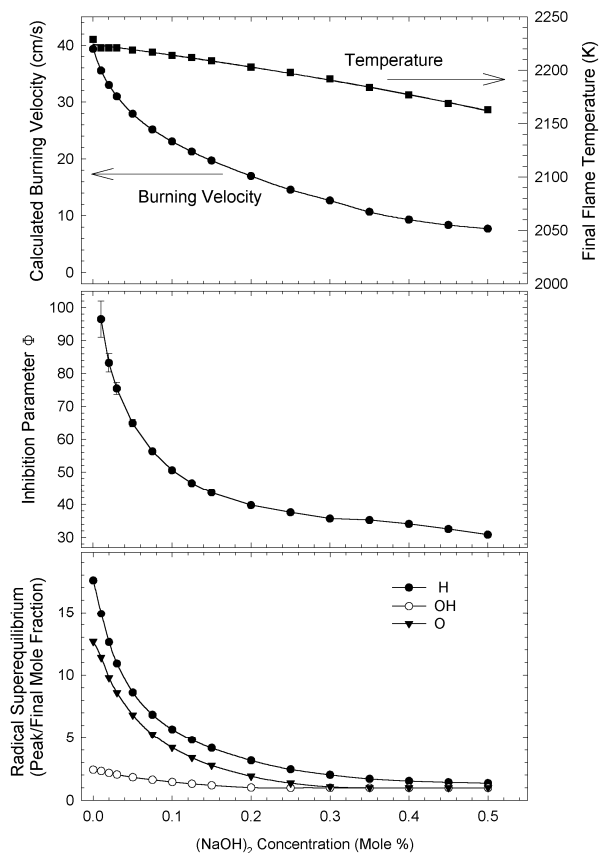


**Figure 3-112. Burning Velocity, Final Flame Temperature, Inhibition Parameter, and Superequilibrium Concentrations of Flame Radicals Computed for Atmospheric Pressure Stoichiometric Methane-air Mixtures Inhibited by NaOH.**

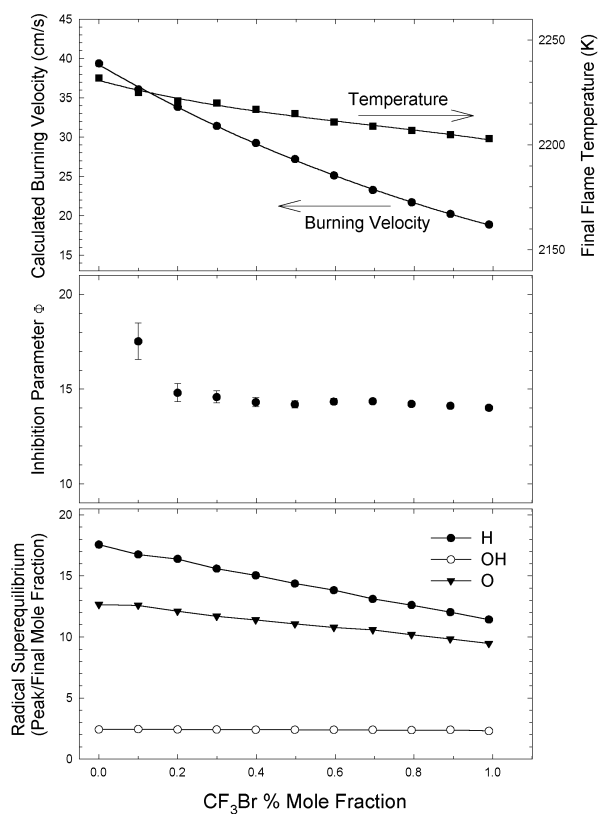


**Figure 3-113. Burning Velocity, Final Flame Temperature, Inhibition Parameter, and Superequilibrium Concentrations of Flame Radicals Computed for Atmospheric Pressure Stoichiometric Methane-air Mixtures Inhibited by  $\text{CF}_3\text{Br}$ .**

The behavior of the inhibition parameter in Figure 3-112 was different from that in Figure 3-113. For sodium, the inhibition parameter was not constant as a function of inhibitor concentration, but varied by more than a factor of three over the range of sodium concentrations considered here. The similarity relationship identified in Reference 336 did not hold for sodium. For  $\text{CF}_3\text{Br}$ , by contrast, the inhibition parameter was nearly constant as a function of inhibitor concentration. For comparison, the inhibition parameter of  $\text{N}_2$ , up to a 50 % reduction in burning velocity maintained an almost constant value of 0.5 (data not shown). The results for  $\text{CF}_3\text{Br}$  agreed with the findings of Noto et al.<sup>336</sup> although the modifications to the fluorocarbon kinetics yielded better agreement with the experimental value of 14.0 for the inhibition parameter, compared to the value of 11.1 reported in Reference.<sup>336</sup> The value of approximately 100 for the inhibition parameter of  $(\text{NaOH})_2$  per sodium atom at low concentrations is comparable to measured values for various sodium compounds ranging from 114 to 200.<sup>336</sup>

### Radical Super-equilibrium

In Figure 3-112, the radical super-equilibrium was drastically reduced with increasing  $\text{NaOH}$ . For inert agents, by contrast, the radical super-equilibrium was increased as the flame is inhibited. When the flame speed was reduced by 40 % by the addition of  $\text{N}_2$ , for example, the H atom super-equilibrium increased from 17 to 70. Although peak radical concentrations decreased as an inert agent was added, the reduction in flame temperature reduced the equilibrium concentrations proportionately more.

For inhibition by  $\text{CF}_3\text{Br}$  (Figure 3-113), the degree of radical super-equilibrium was also reduced with increasing agent concentration, although not as dramatically as for sodium.  $\text{CF}_3\text{Br}$  reduced the H atom super-equilibrium by only 30 % for a 50 % reduction in burning velocity;  $\text{NaOH}$  reduced the H atom super-equilibrium by nearly 80 % at a 50 % burning velocity reduction. This finding supported the conclusion of Saso et al.<sup>337</sup> that saturation was a minor effect in the suppression effectiveness of  $\text{CF}_3\text{Br}$ /inert mixtures. Saturation was not as pronounced for  $\text{CF}_3\text{Br}$  inhibition because the peak radical concentrations remained far from equilibrium for substantial reductions in burning velocity.

Another factor contributing to the lack of a saturation behavior for  $\text{CF}_3\text{Br}$  was that the bromine catalytic cycle involved the sequence of reactions<sup>332</sup>



as an important pathway in regeneration of HBr. The direct reaction



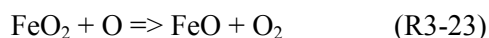
has slow kinetics. This has two consequences: the second order dependence of reaction R3-19 on the bromine concentration compensates for the saturation effect with increasing  $\text{CF}_3\text{Br}$  concentration. Also, a high concentration of bromine is required for this reaction to be significant, leading to a much smaller inhibition parameter for bromine than for iron and sodium,<sup>333</sup> whose scavenging cycles are not thought to depend on second order kinetics.

## Synergism Between Catalytic and Physical Agents

Several experimental and modeling studies had observed that the effectiveness of  $\text{CF}_3\text{Br}$ <sup>91,337</sup> as well as other chemical agents<sup>14,106</sup> could be enhanced by the addition of a physical agent. Saso et al.<sup>337</sup> attributed synergism in mixtures of  $\text{CF}_3\text{Br}$  and inert inhibitors to a temperature effect on the inhibition effectiveness of  $\text{CF}_3\text{Br}$ , rather than a saturation phenomenon. Over a range of adiabatic flame temperatures, Saso et al. found  $\text{CF}_3\text{Br}$  to have virtually identical inhibition parameters at loadings of 0.5 % and 1 % (by volume) in methane/oxygen/inert mixtures, indicating the absence of significant saturation effects.

To extend the computational investigation of synergy to other combinations of agents, inhibition by iron was modeled in combination with nitrogen. For this modeling, iron was considered to participate in a three step mechanism involving only  $\text{O} + \text{O}$  recombination. This pathway was identified by Rumminger and Linteris<sup>118</sup> but was usually secondary in importance to an  $\text{H} + \text{H}$  recombination pathway. This model was not intended as an accurate description of iron's combustion chemistry, but rather to consider whether synergism occurred in the absence of a temperature dependence on the inhibition kinetics.

Of the three reactions making up the  $\text{O} + \text{O}$  catalytic cycle of iron:



R3-23 and R3-24 were assumed to have rate coefficients independent of temperature. The reaction R3-22 had a slight increase in rate with increasing temperature, but the product of the rate coefficient and the number density of third body colliders varied by less than 10 % over the temperature range from 1400K and 2500K.

The iron + nitrogen combination exhibited synergy, as seen in Figure 3-114, which plots burning velocity, flame temperature, and differential inhibition parameter of the  $\text{O} + \text{O}$  cycle of 500  $\mu\text{L/L}$   $\text{FeO}_2$  as a function of nitrogen addition.

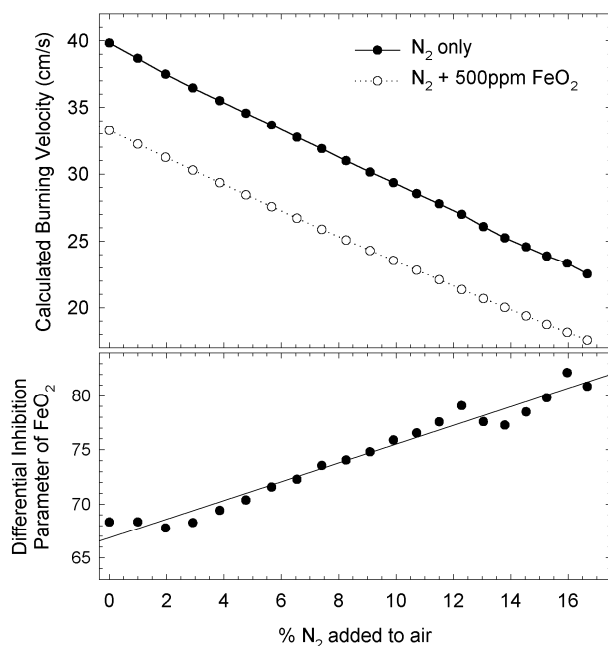


**Figure 3-114. Burning Velocity and Differential Inhibition Parameter computed for Atmospheric Pressure Stoichiometric Methane-air Mixtures Inhibited by  $\text{N}_2$  and  $\text{FeO}_2$  in Combination.**

The differential inhibition parameter for inhibitor B in the presence of inhibitor A is

$$\Phi = \ln(U_A/U_{A+B}) (X_{O_2}/X_B) \quad (3-13)$$

where  $U_A$  and  $U_{A+B}$  are the burning velocities in the flames inhibited by inhibitor A alone and A and B in combination, respectively. The differential inhibition parameter of 500  $\mu\text{L/L}$   $\text{FeO}_2$  increased by about 23 % as the flame temperature was lowered by nitrogen addition from 2230 K to 2010 K. Saso et al.<sup>337</sup> found that the inhibition parameter of  $\text{CF}_3\text{Br}$  increased by some 45 % at loadings of both 0.5 volume % and 1.0 % volume % over the same range of final flame temperatures.

While the findings of synergism agreed qualitatively between  $\text{CF}_3\text{Br}$ /inert and  $\text{Fe}$ /inert mixtures, the final flame temperature influenced the inhibition parameter of  $\text{CF}_3\text{Br}$  twice as much as that of the  $\text{O} + \text{O}$  recombination cycle of iron, due to the lack of explicit temperature dependence of the  $\text{Fe}$  kinetic cycle. Thus, these results showed that synergism in catalytic/inert mixtures did not require temperature dependence of the inhibition cycle, although this could influence its magnitude.

### Correlation of Burning Velocities with Changes in Flame Structure

Padley and Sugden<sup>338</sup> observed in studies of  $\text{H}_2\text{-O}_2\text{-N}_2$  flames that the burning velocity correlated with the partial pressure of atomic hydrogen in the reaction zone. More recently, this correlation had been observed to hold also for hydrogen flames inhibited by  $\text{CF}_3\text{Br}$ .<sup>339</sup> Figure 3-115 plots the peak H atom concentration against burning velocity for a variety of inhibited methane/air flames. For methane flames inhibited by  $\text{N}_2$ ,  $\text{CF}_4$ , and  $\text{CF}_3\text{Br}$ , there was a nearly identical linear relationship between the peak H atom mole fraction and burning velocity, as with the hydrogen flames.

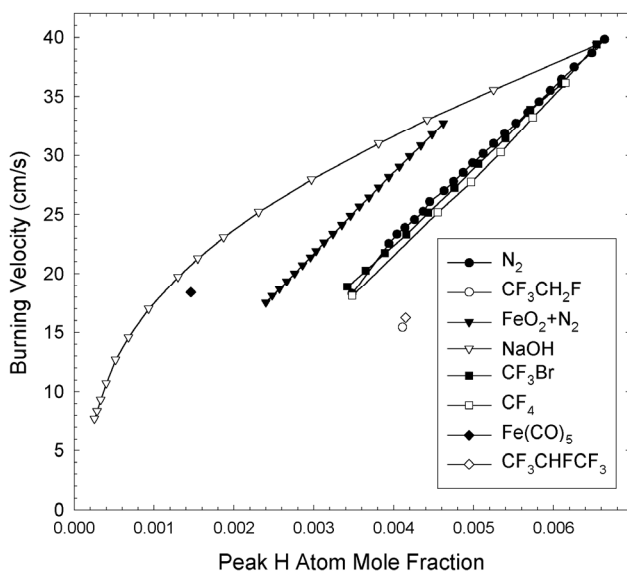


**Figure 3-115. Relationship between Burning Velocity and Peak Concentration of Atomic Hydrogen for Methane-air Flames Inhibited by Various Compounds.**

Examination of the effect of other inhibitors, however, demonstrated that this correlation was not a general one. The fluorocarbon agents  $\text{CF}_3\text{CHFCF}_3$  and  $\text{CF}_3\text{CH}_2\text{F}$  both reduced burning velocity more

than would be expected based on the peak H atom concentrations. Inhibition by sodium or iron produced the opposite effect. Noteworthy in the sodium data was the curvature which coincided with the onset of saturation. The coincidence of the CF<sub>3</sub>Br data points with those of the inert agents appears to have been accidental. The calculations for the fluorocarbons and catalytic agents lay on opposite sides of those of the inert agents, and CF<sub>3</sub>Br was in some sense a combination of the two.

An alternate correlation between burning velocity and flame structure was based on the proportionality between the burning velocity and the square root of the overall reaction rate.<sup>337</sup> In modeling the burning velocity of a large number of inhibited flames, the burning velocity correlated in almost all cases with the product of the peak H atom mole fraction and a global activation energy:

$$S_L^2 = A^2 X_H \exp(-E_a/kT_f) \quad (3-14)$$

where  $S_L$  is the laminar burning velocity,  $X_H$  the peak mole fraction of atomic hydrogen, and  $T_f$  the final flame temperature. The fitted parameters  $A$  and  $E_a$ , obtained by considering the flame inhibited by nitrogen, were  $A=7940$  cm/s,  $E_a=103$  kJ/mol. The same empirical correlation held for inhibition by other inert gases, by iron and sodium, by nitrogen and iron in combination (Table 3-19), and by artificially increasing the H + OH recombination rate. For catalytic agents which did not significantly change the final flame temperature, the burning velocity correlated with the square root of the H atom peak mole fraction, but not with those of atomic oxygen or OH radicals. The effect of catalytic agents on reducing burning velocity proceeded through reduction of the atomic hydrogen concentration, whether or not the scavenging cycle directly involved H atom recombination (as in the O + O cycle of iron).

**Table 3-19. Comparison of Calculated Burning Velocities.**

Flame Condition	$T_{adiabatic}$	$X_{Hmax} \times 10^3$	$S_{premix}$	$S_{eqn}$	$\Delta S_{premix} / \Delta S_{eqn}^a$
CH <sub>4</sub> -air (uninhibited)	2234	6.64	39.8	39.8	---
+9.09 % N <sub>2</sub>	2121	5.12	30.2	30.2	1.00
+16.67 % N <sub>2</sub>	2015	3.94	22.6	22.7	1.01
+8.26 % CF <sub>4</sub> (inert)	1968	3.50	18.4	19.9	1.07
+200 $\mu$ L/L Fe(CO) <sub>5</sub>	2223	1.46	18.4	18.6	1.01
+1.0 % CF <sub>3</sub> Br	2203	3.42	18.9	27.6	1.71
+0.5 % HBr	2221	5.36	30.3	35.2	2.08
+3.8 % CF <sub>3</sub> CH <sub>2</sub> F	2031	4.11	15.5	23.9	1.54
+2.9 % CF <sub>3</sub> CHFCF <sub>3</sub>	2161	3.86	16.3	26.1	1.73
+0.05 % (NaOH) <sub>2</sub>	2219	2.97	28.0	26.2	0.87
+0.40 % (NaOH) <sub>2</sub>	2177	0.33	9.4	8.3	0.97
Increase H+OH+M rate x 100	2234	1.35	19.8	18.0	0.92

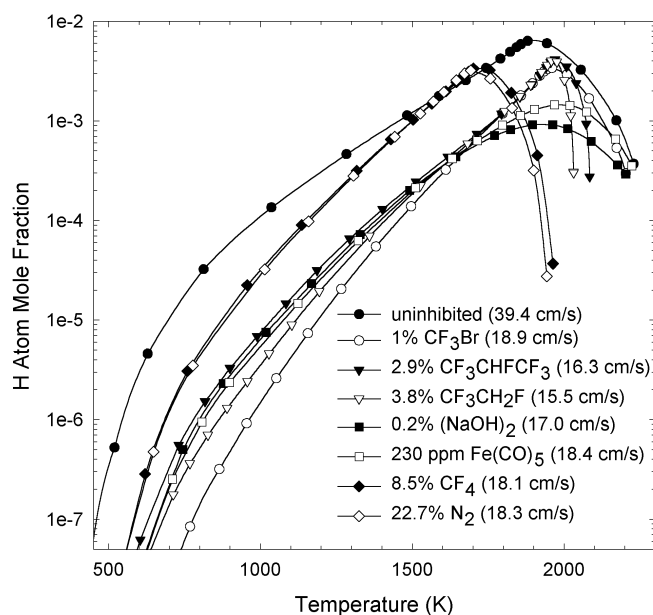
<sup>a</sup>  $39.6 - S_{premix} / (39.6 - S_{eqn})$

Table 3-19 compares the burning velocities estimated using Equation 3-14 to the calculated values for a variety of flame inhibitors. In 6 of the 11 cases, the reduction in burning velocity relative to the uninhibited flame, predicted by Equation 3-14 was within 13 % of the result of the PREMIX calculation. However, the correlation stated in Equation 3-14 greatly underpredicted flame speed reduction by the fluorocarbons CF<sub>3</sub>CH<sub>2</sub>F and C<sub>3</sub>HF<sub>7</sub>, as well as CF<sub>3</sub>Br and HBr. Flame structure modeling indicated that

the breakdown of this relationship involving the peak H atom concentration was a consequence of these agents reducing the H atom concentration mostly in the early part of the flame, prior to the peak concentration, as discussed below.

### Changes in Flame Structure Due to Different Agents

Insight into why the correlation between burning velocity, H atom concentration, and temperature did not hold for either fluorocarbons or bromine-containing compounds was gained from examination of these compounds' effects on flame structure. In Figure 3-116, the mole fraction of atomic hydrogen is plotted against the local temperature for flames inhibited by a variety of agents. All the inhibited flames had burning velocities approximately 50 % that of the uninhibited flame, whose structure is also plotted for comparison. For all these flames, the temperature monotonically increased with position passing from reactants to products.



**Figure 3-116. Mole Fraction of Atomic Hydrogen as a Function of Local Flame Temperature for an Uninhibited and Uninhibited Atmospheric Pressure Methane-air Flame.**

The relationship between H atom mole fraction and local temperature shown in Figure 3-116 was characteristic of each type of agent except for  $\text{CF}_3\text{Br}$ . The physical agents reduced the final flame temperature, but the H atom mole fraction at a given isotherm (above approximately 1300 K) was changed very little from its value in the uninhibited flame. Both iron and sodium reduced the H atom mole fraction by a relatively constant factor throughout the reaction zone. The fluorocarbons reduced the H atom mole fraction early in the flame (in the region below about 1200 K) but had relatively little impact on the peak concentration. This diminished effectiveness at the location of maximum hydrogen atom concentration also occurred for  $\text{CF}_3\text{Br}$ ; in this respect  $\text{CF}_3\text{Br}$  bore more resemblance to nonbrominated fluorocarbons than it did to other catalytic agents such as iron and sodium. Since Babushok et al.<sup>167</sup> found that iron approached the performance of an “ideal” catalytic inhibitor, the different effect of  $\text{CF}_3\text{Br}$  on flame structure from that of iron and sodium indicated a departure from ideality, in particular it only scavenged radicals significantly in low temperature regions of the flame. All the flames inhibited by chemically active suppressants showed nearly equal reductions in H atom mole fraction at 1700 K. In the flames inhibited by inert agents, the H atom concentration at this isotherm was essentially the same as in the uninhibited flame. Therefore, the H atom mole fraction at 1700 K (or any other fixed temperature)

cannot be used as a predictor of burning velocity which is applicable to all inhibited flames. Given the different influences of the suppressants on flame structure, it seemed unlikely that an empirical relationship between flame speed and some other quantity can be found which applies to all suppressed flames.

The depletion of radical species early in the flame had a marked influence on the burning velocity. It is for this reason that fluorocarbons and bromine compounds are better inhibitors than the changes in temperature and peak H atom concentrations predicted. This observation suggested that agents which deplete radicals in high temperature regions but not early in the flame were likely to be less effective inhibitors than would otherwise be expected. This may be the case for condensed-phase agents which must vaporize before inhibition can begin.

## Conclusions

In several respects,  $\text{CF}_3\text{Br}$  is not representative of catalytic fire suppressants in general. Several features of its kinetics, including the strong temperature dependence of the catalytic suppression cycle and the preferential reduction of atomic hydrogen concentrations in low temperature regions of the flame, were not shared by other catalytic suppressants. In these regards, sodium and iron exhibited behavior much more typical of this class of suppressants. For these reasons, caution is required in using specific kinetic properties observed for  $\text{CF}_3\text{Br}$  as a basis for identifying other efficient fire suppressants.

### 3.5.4 Influence of Bond Energies on Catalytic Flame Inhibition

#### Introduction

The suppression effectiveness of  $\text{CF}_3\text{Br}$  and related compounds is primarily due to the chemical activity of bromine,<sup>13,332,340</sup> which participates in a catalytic cycle and reduces concentrations of the free radicals involved in flame propagation. As documented earlier in this Chapter, several chemical elements besides bromine have been shown to exhibit catalytic radical scavenging in flames, sometimes much stronger than that of bromine,<sup>333</sup> although practical issues have limited their implementation. Among the halogens, iodine is a good catalytic scavenger.<sup>20,167</sup> Among non-halogens, good suppression efficiency has been demonstrated for alkali metals,<sup>341</sup> phosphorus,<sup>79</sup> and several transition metals including iron,<sup>104</sup> lead,<sup>92</sup> chromium,<sup>126</sup> and manganese.<sup>107</sup> The elements comprising this list vary greatly in their chemical properties, while other elements in the same groups of the periodic table (e.g., nitrogen, fluorine) do not cause efficient catalytic suppression of flames.

Finding a common basis for efficient chemical suppressants, whose results can be extrapolated to other elements with combustion chemistry which has not yet been thoroughly explored, was of importance to the NGP. Previous work had pointed to the binding energy of a suppressant (or one of its decomposition products) to one or more flame radicals as an important parameter.<sup>42,342</sup> This approach has been used previously to explain, for instance, the greater suppression effectiveness of bromine compared to chlorine.<sup>42</sup> Under the NGP, Fleming and co-workers<sup>343</sup> broadened the scope of the previous work by focusing on a common thermodynamic basis for catalytic suppression by different families of elements, and different types of catalytic cycles. The rationale for revisiting the effect of bond energies at the present time was threefold:

- Computational tools had become available to model the effect of thermodynamics directly, rather than resorting to simplifying approximations such as zone modeling of flame structure<sup>342</sup> or partial equilibrium assumptions of species concentrations.<sup>42</sup>
- The NGP objective was to assess the fire suppression potential of elements that had not yet been extensively investigated, rather than to explain the behavior of elements whose properties were already (empirically) known. By contrast, the work which elucidated the suppression kinetics of bromine was performed after halons were identified and implemented as fire suppressants.
- A great deal of additional chemical kinetic data had become available, including provisional suppression mechanisms for a number of non-halogen-containing species.

Simplified but representative catalytic cycles for known inhibitors (bromine, sodium, iron) were used in conjunction with detailed kinetic modeling of the hydrocarbon flame structure.

### General Features of Catalytic Scavenging Cycles

In most flames, the peak concentrations of the radicals H, O, and OH are much higher than the thermal equilibrium concentrations at the adiabatic flame temperature. This is a consequence of the kinetic rates of the chain branching reactions, for example

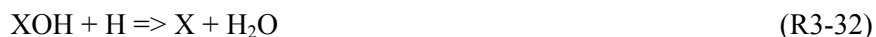


exceeding the rates of chain termination reactions such as



which require a third body for stabilization of the product.<sup>344</sup> Chemical fire suppressants generally participate in a catalytic cycle whose net effect is equivalent to one of the recombination reactions.

For a substance to scavenge flame radicals, there must exist some species X derived from the inhibitor which can bond to H, O, or OH. The species XR, where R is one of the flame radicals, must react with another flame radical R' to form X and RR', where RR' is usually a stable molecule such as H<sub>2</sub>, H<sub>2</sub>O, or O<sub>2</sub>. Possible scavenging reactions include.<sup>345</sup>



To complete the cycle, X must then be converted back to XR through one or more steps. For significant inhibition to occur, the kinetic rate of the scavenging cycle must exceed that of the equivalent direct recombination reaction.

Inhibition by bromine occurs primarily through (R3-30) and to a lesser extent (R3-31),<sup>346</sup> while alkali metals operate primarily through (R3-32).<sup>347</sup> Reaction (R3-33) is likely to occur for metallic elements.<sup>118</sup> Some elements, including iron<sup>118</sup> and phosphorus,<sup>258</sup> are thought to participate in more than one cycle.

### Computational Methodology

The computer code PREMIX<sup>203</sup> was used to model freely propagating atmospheric pressure premixed flames. The baseline condition consisted of stoichiometric methane/air, with an initial reactant temperature of 298.2 K. Tolerances for mesh refinements in PREMIX were set as follows: GRAD = 0.10, CURV = 0.20, up to a maximum of 150 grid points. Multicomponent viscosities and thermal diffusion (Soret effect) were used. The computational domain extended 25 cm from the flame into the reactants gases, and 60 cm into the exhaust gases. The domain was extended in such a way that on both boundaries, the second last grid point was 1 cm from the boundary.

The reaction set given in GRI-MECH 2.11<sup>289</sup> (without nitrogen chemistry) was used for modeling the uninhibited flames. Calculations were carried out using bromine, sodium, and iron as examples of chemical inhibitors. Kinetics of chemical inhibition for these elements were added to the hydrocarbon mechanism as described below.

### Kinetic Mechanisms of Specific Inhibitors

The inhibition cycle of bromine is believed to proceed by H atom scavenging.<sup>42,342</sup> The reaction



is thought to be the primary scavenging reaction, with the reaction with OH



also contributing. The conversion of Br to HBr involves several pathways. The direct recombination



has rather slow kinetics and is typically not the predominant pathway. Atomic bromine can abstract hydrogen atoms from such species as HO<sub>2</sub>, HCO and CH<sub>2</sub>O; these play an important role in most flames.

Two simplified kinetic mechanisms describing inhibition by bromine were constructed and are listed in Table 3-20. Both mechanisms included Br and HBr as the only bromine-containing species. For these calculations, HBr was chosen as the bromine-containing reactant. In the first mechanism, HBr was assumed to react only with atomic hydrogen to form Br, which was converted back to HBr by a direct recombination with H, as well as abstraction of H from HO<sub>2</sub>, HCO, and CH<sub>2</sub>O. The second mechanism was identical, except that HBr was allowed to react only with OH, rather than H.

**Table 3-20. Kinetic Mechanisms for Suppressants ( $k = AT^b \exp(-E_a/kT)$ ).**

Reaction	A (cm <sup>3</sup> /mol-s)	b	E <sub>a</sub> (kcal/mol)	Source
Mechanism for Na (H + OH cycle only)				
(NaOH) <sub>2</sub> + M = NaOH + NaOH + M <sup>a</sup>	3.0E14	0.0	48	
NaOH + H = Na + H <sub>2</sub> O	1.0E13	0.0	1.97	
Na + OH + M = NaOH + M <sup>a</sup>	1.8E21	-1.0	0	
Mechanism for Br (reactions in common for all cycles)				
H + Br + M = HBr + M <sup>a</sup>	1.92E21	-1.86	0	348
Br + CH <sub>2</sub> O = HBr + HCO	1.02E13	0.0	1.59	349
Br + HO <sub>2</sub> = HBr + O <sub>2</sub>	8.43E12	0.0	1.17	349
Br + HCO = HBr + CO	1.69E14	0.0	0	350
Addition for Br (H + H cycle):				
HBr + H = H <sub>2</sub> + Br	6.25E13	0.0	2.40	348
Addition for Br (H + OH cycle):				
HBr + OH = H <sub>2</sub> O + Br	6.62E12	0.0	0	351
Mechanism for Fe (O + O cycle):				
Fe + O <sub>2</sub> + M = FeO <sub>2</sub> + M <sup>a</sup>	1.57E18	0.0	4.05	352
FeO <sub>2</sub> + O = FeO + O <sub>2</sub>	1.73E13	0.0	0.0	a
FeO + O = Fe + O <sub>2</sub>	1.73E13	0.0	0.0	b

<sup>a</sup> No reaction rate reported; assumed equal to the rate in the next row.

<sup>b</sup> Based on reverse reaction of Reference 353.

For iron-containing compounds, Rumminger and Linteris<sup>118</sup> identified catalysis of H atom recombination as the most important scavenging cycle in hydrocarbon flames. In addition, they found that an O atom recombination cycle could be significant in moist CO flames. The three-step cycle is shown in the last three rows of Table 3-20. This mechanism was not intended as an accurate depiction of the overall inhibition chemistry of iron, only the contribution of the O + O scavenging cycle (which is small for hydrocarbon fuels). Analogous O + O cycles may exist for other transition metal elements as well.

For sodium and other alkali metals, Jensen and Jones<sup>347</sup> propose the primary cycle:



The simplified mechanism for sodium consisted of (R3-37) and (R3-38), together with a reaction converting the NaOH dimer (specified as the reactant) to the monomer to simulate an evaporation step.<sup>26</sup> Comparisons of thermal equilibrium calculations with NaOH(s) and (NaOH)<sub>2</sub> as reactants indicate that the very minor reduction in the adiabatic flame temperature caused by the addition of NaOH dimer was about 70 % that of adding an equal amount of solid NaOH.

Using the simplified mechanism, the predicted flame speed of a stoichiometric methane/air mixture inhibited by 0.1 % mole fraction of (NaOH)<sub>2</sub> was 25.0 cm/s, compared to 23.1 cm/s using a more comprehensive mechanism<sup>26</sup> adapted from Zamansky et al.,<sup>335</sup> and 39.4 cm/s for the uninhibited flame.

This result confirmed that the OH + H cycle identified by Jensen and Jones was indeed the most important for suppression of near stoichiometric hydrocarbon flames.

### **Influence of Bond Energies on Suppression Cycles**

For an efficient scavenging cycle to exist, the bond energy between the scavenging atom or radical X and a flame radical R must satisfy certain conditions. If it is too high, the scavenging reaction (R3-30) to (R3-33) would be endothermic. This is the case for fluorine, which binds irreversibly to hydrogen and thus cannot sustain a catalytic cycle. On the other hand, if the bond were too weak, the equilibrium between XR and X + R would be so far toward dissociation that there would be insufficient XR to participate in the scavenging reactions. Stated another way, the rates of the reverse reactions must be small compared to those of the forward reactions, since any catalytic recombination cycle would become a catalytic chain branching cycle if it ran backwards.

These considerations indicated that there would be a limited range of bond energies for which an efficient scavenging cycle could exist. Putting these qualitative arguments on a quantitative basis by computational investigation of the effect of hypothetical changes in bond energies on suppression efficiencies allowed the determination of the bond energies compatible with efficient suppression. Suppression depends on kinetic as well as thermodynamic factors, so appropriate bond energies by themselves do not guarantee good suppression properties. The elements chosen as examples, however, were known to have good suppression properties, so they possess kinetics favorable to scavenging.

Bromine was used as the example element for Reactions (R3-30) and (R3-31), sodium for (R3-32), and iron for (R3-33). During the combustion process, each of these elements can have multiple binding partners and thus could have several bond energies hypothetically relevant to combustion. In order to simplify the situation so that sensitivity to bond energy can be determined in a relatively straightforward way, it was assumed that only one catalytic cycle involving one type of bond existed for each element.

For each set of calculations, the thermodynamic functions for the species XR were not altered, but the heat of formation of the species X at 298 K was varied, while keeping the heat capacity and entropy unchanged. This had the effect of changing the dissociation energy of X-R. In the kinetic mechanisms, the chemical reactions for the scavenging cycle were written in the exothermic direction, and the Arrhenius parameters of the forward reaction were unchanged. All reactions were assumed to be reversible, however, so changing the heat of formation altered the activation energy of the reverse reaction, even without any explicit changes to the kinetic parameters.

In the PREMIX code, the facility existed for determining the sensitivity of the solution vector, including the flame speed eigenvalue, to changes in the heats of formation of species (HSEN keyword). This was distinct from sensitivities with respect to changes in the kinetic rates (ASEN keyword) which have been more commonly reported in modeling studies. Sensitivity analysis, however, only provided the first derivative of the flame structure with respect to thermodynamic or kinetic quantities. The dependence of suppression efficiency on heats of formation is non-monotonic. A small sensitivity coefficient for the enthalpy of a particular species on the flame speed may mean that the species in question is unimportant to suppression, or it could mean that its enthalpy is very close to the optimal value, leading to a vanishing first derivative.

### Bromine: $H + H$ and $H + OH$ Recombination

For this series of calculations HBr was chosen as the bromine-containing reactant. The kinetic mechanism was chosen to model the effect of a single catalytic mechanism, with Br and HBr as the only bromine species. Two sets of calculations were performed, the difference being whether HBr was assumed to react with H or with OH. Figure 3-117 shows the predicted flame velocity of a stoichiometric methane/air mixture inhibited by 0.5 volume % of HBr. The catalytic cycle was found to be most efficient for H-Br bond energies (which were artificially varied in the calculations) between 65 kcal/mole and 90 kcal/mole.

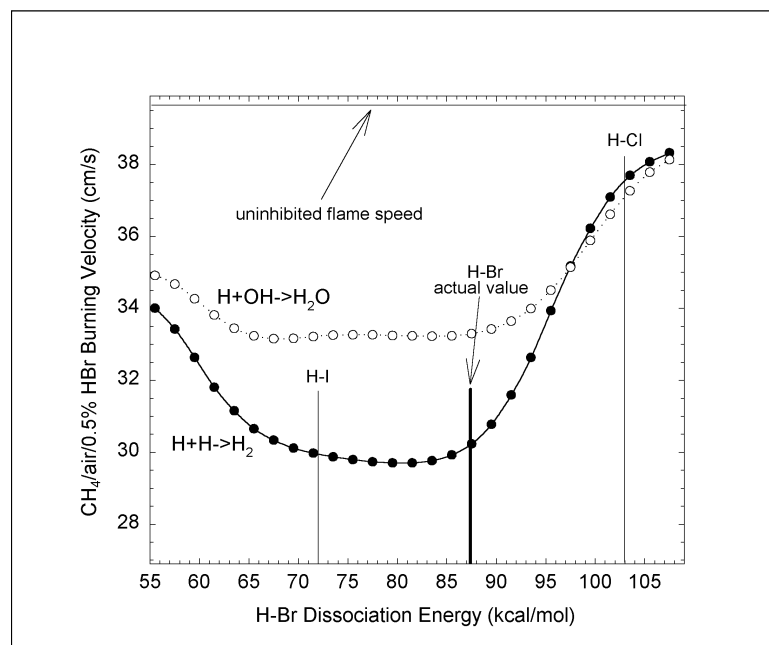


**Figure 3-117. Calculated Flame Velocity as a Function of Hypothetical Variation of the H-Br Bond Energy for Premixed Methane-air Flames Inhibited by 0.5 % HBr Using the  $H + H$  and  $H + OH$  Scavenging Cycles of Table 3-20. The accepted values for the bond energies of H-Br, H-Cl, and H-I are indicated by vertical lines.**

The accepted value of the H-Br bond energy lies near the upper limit of the range, which permits an optimally efficient catalytic cycle (Figure 3-117). The bond energy of H-I is near the lower limit of the optimal range, while the H-Cl bond is too strong for good suppression. The bond energy of H-F (135 kcal/mole) is so high that the molecule is completely inert in this environment. Although the kinetics of the analogous reactions are somewhat different for the other halogens, the bond energy factor by itself led to the correct prediction that the measured suppression effect of iodine was nearly equal that of bromine<sup>20</sup>, while chlorine had a much smaller effect.<sup>354</sup>

### Sodium: $OH + H$ Recombination

The effect of hypothetical variation of the Na-OH bond energy is illustrated in Figure 3-118. There was a more pronounced falloff in suppression efficiency with bond energy than for either of the bromine scavenging cycles. The Na-OH bond energy was close to the optimal value for good suppression, as were the bond energies for all the other alkali metals except lithium. Experimental studies have found that potassium is a considerably more efficient flame suppressant than sodium.<sup>333</sup> In view of the similarity of the thermodynamic properties, this difference may be due to differences in kinetic rates between the two elements, particularly for the recombination step (R3-37).

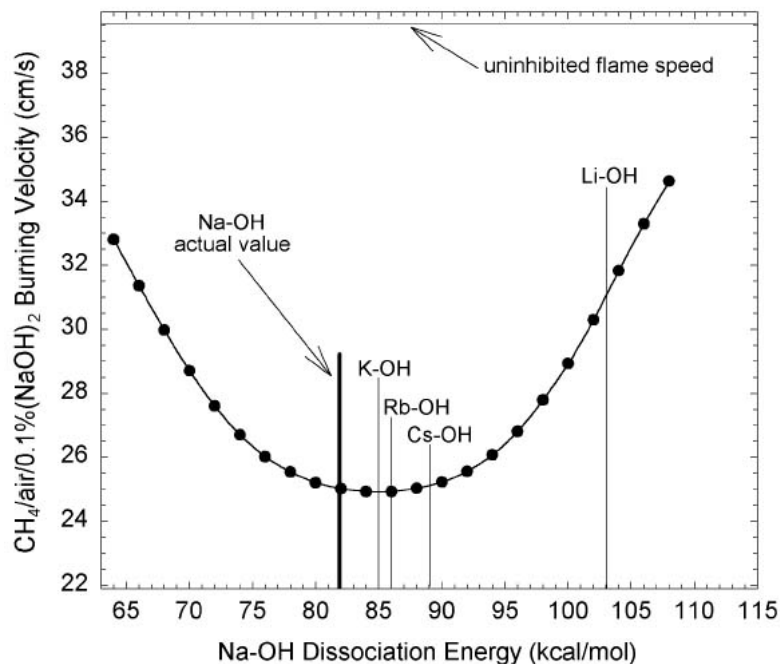


**Figure 3-118. Calculated Flame Velocity as a Function of Hypothetical Variation of the Na-OH Bond Energy for Premixed Methane-air Flames Inhibited by 0.1 % (NaOH)<sub>2</sub> using the H + OH scavenging cycle of Table 3-20. The accepted values of X-OH bond energies for the alkali metals are indicated by vertical lines.**

### **Iron: O + O Recombination**

The three step O + O catalytic cycle modeled for iron had two relevant bond energies, Fe-O and OFe-O, which differed by about 3 kcal/mole. The bond energies were varied in the calculation by keeping the standard state enthalpy of FeO fixed, while varying those of Fe and FeO<sub>2</sub> in opposite directions from their “normal” values. For FeO<sub>2</sub>, the “normal” standard state enthalpy used was not the actual value, but was chosen such that the bond energy of OFe-O was equal to that of Fe-O, 99 kcal/mole.

In the calculation, FeO<sub>2</sub> was chosen as the reactant. For most iron-containing compounds such as Fe(CO)<sub>5</sub>, the parent agent was quickly converted to Fe,<sup>104</sup> which then combined with oxygen through R3-22, making the original identity of the iron compound unimportant. Because of iron's high suppression efficiency, a smaller concentration of suppressant was used (500 μL/L) than for the calculations with sodium or bromine.

Results of the calculations are shown in Figure 3-119. The accepted bond energies of both Fe-O (99 kcal/mol) and OFe-O (96 kcal/mol) are close to the optimal value for efficiency of the catalytic cycle.

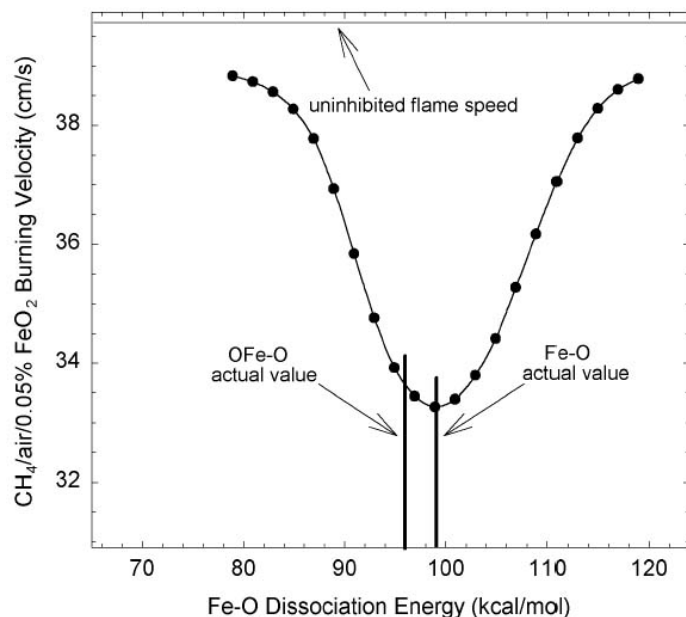


**Figure 3-119. Calculated Flame Velocity as a Function of Hypothetically Variation of Fe-O Bond Energy for Premixed Methane-air Flames Inhibited by 500  $\mu\text{L/L}$   $\text{FeO}_2$  Using the Three-step O + O Scavenging Cycle of Table 3-20. The accepted values of the Fe-O and OFe-O bond energies are indicated by vertical lines.**

## Discussion

These calculations indicated that for an efficient scavenging cycle, the bond energy between a catalytic scavenger and a flame radical must lie in the range of 70 kcal/mol to 100 kcal/mol, the optimal value varying somewhat for different net recombination reactions. This range of values was consistent with the expectation that the bond must be strong enough to be thermodynamically stable at flame temperatures, but not so strong as to prevent regeneration of the active scavenging radical. Table 3-21 shows that the more efficient a scavenging cycle (in terms of the inhibition parameter<sup>175</sup>), the more sensitive it is to changes in bond dissociation energies.

**Table 3-21. Efficiencies and Sensitivities to Bond Energies of Catalytic Cycles.**

Element	Net Cycle	Inhibition Parameter <sup>175</sup>	$\Delta D(\text{kcal/mol})^a$	$D_{\text{max}}(\text{kcal/mol})^b$	$\Delta D/D_{\text{max}}$
Br (0.5%)	H + OH	6.9	39	77	0.51
Br (0.5%)	H + H	11.5	33	77	0.43
Na (0.2%)	H + OH	46	29	85	0.34
Fe (0.05%)	O + O	66	14	99	0.14

<sup>a</sup> Range of bond energies for which the suppression index is at least 75 % of its maximum value.

<sup>b</sup> Bond energy at which the maximum value of the suppression index is achieved.

Other factors also play a role in suppression efficiency, although less definitive than does the bond energy. In most catalytic cycles, there is likely to be at least one recombination step, e.g.,  $\text{Na} + \text{OH} = \text{NaOH}$ ,  $\text{Fe} + \text{O}_2 = \text{FeO}_2$ . In many cases, the recombination reaction may be the rate limiting step in the catalytic cycle. This recombination step must have a faster rate than the direct radical-radical recombination for the catalyst to cause inhibition. In general, the recombination complex is more likely to be stabilized by third body colliders if it is polyatomic, rather than diatomic. Also, if the recombination reaction involves a stable, rather than a radical flame species, it is likely to proceed faster due to the higher reactant concentrations. This is the case for the  $\text{Fe} + \text{O}_2$  recombination step.

Many transition metals whose compounds showed good suppression properties exhibit more than one stable valence. This did not appear to be a fundamental requirement for efficient suppression, since alkali metals only exhibit one valence yet are efficient suppressants. The existence of multiple valences greatly increases the number of possible species, increasing the likelihood that an efficient catalytic cycle may occur. Multiple valences may also facilitate recombination reactions. If the reactant and product of a recombination reaction corresponded to two stable valences of the inhibitor element, then the kinetics of the reaction might be more favorable.

### 3.5.5 Temperature Regions of Optimal Chemical Inhibition of Premixed Flames

#### Introduction

Unwanted fires vary considerably in the spatial distributions and peak values of their temperatures. Hence, understanding the temperature sensitivity of chemical inhibition can aid in the search for halon alternatives. Premixed flames<sup>4,39,150,332,346,355</sup> are a useful medium to resolve any temperature effects. These flames have commonly been divided into various zones or regions, and prior to the NGP there was some knowledge of the flame chemistry in these zones.<sup>356-359</sup>

Analysis of the region of a flame most sensitive to chemical or thermal inhibition has been an active area of flame inhibition research for many years.<sup>4,26,38,39,41-43,150,230,304,346,360</sup> Several investigations have indicated that the important region of action for halogenated agents is the low-temperature region of the flame.<sup>360</sup> It was deemed worthwhile to examine this claim and determine if it applied either to CF<sub>3</sub>Br or to other chemicals.

Numerical simulations of flame inhibition chemistry using complex kinetics and *model* inhibitors would allow simulations of inhibitors which had not yet been identified or synthesized. Linteris and co-workers perturbed the reaction rates of selected chemical reactions in a region that was defined by temperature, species concentration, time, and space.<sup>361</sup> Using model inhibitors introduced at concentrations below those typically used to suppress fires, they calculated the magnitude of the burning velocity reduction for two types of perturbations: impulsive or stepwise. The perturbations were induced by addition of CF<sub>3</sub>Br, addition of a perfect inhibitor, variation of the rate of chain branching, or variation of the heat release rate from CO oxidation.

#### Numerical Technique

##### *Perturbation Mechanics*

The reacting system was perturbed by modifying selected reaction rates in a region or regions, also called bands. In some cases, reactions were turned “on” in the band, and in others, they were turned “off” in the band. In this study, a band was defined by a temperature range. The perturbations were designed to limit the chemical action of an inhibitor in one or more of these bands. A perturbation could affect a single reaction (e.g.,  $\text{H} + \text{O}_2 \leftrightarrow \text{OH} + \text{O}$ ), a class of reactions (e.g., CO<sub>2</sub> formation reactions), or a portion of a chemical mechanism (e.g., reactions involving Br-containing species).

A perturbation factor,  $B_i$ , was defined for the selected group of reactions as, e.g.:

$$\begin{aligned} B_i &= 1 & T < T_b \\ 0 < B_i < 1 & & T_b \leq T \leq (T_b + \Delta) \\ B_i &= 1 & T > (T_b + \Delta) \end{aligned}$$

where  $T$  is the gas temperature,  $T_b$  is the temperature at the low edge of the band, and  $\Delta$  is the width of the band. Figure 3-120a illustrates the band shape for this example. The reaction rates of the selected reactions were multiplied by  $B_i$ , and the rest of the reactions were not directly disturbed (i.e.,  $B_i=1$ ). To study different types of perturbations, the band depth (the magnitude of  $B_i$ ), width ( $\Delta$ ), and shape (the variation of  $B_i$  with  $T$ ) were varied.

For the study of flame inhibition, the pertinent reactions were turned off outside the band ( $B_i=0$ ) and turned on inside the band ( $B_i=1$ ), as illustrated in Figure 3-120b. For modeling of activation or deactivation of an inhibitor, a forward-facing or backward-facing step function was used; the inhibition reactions were turned off (or on) below a certain temperature and turned on (or off) above that temperature, as shown in Figure 3-120c and d.

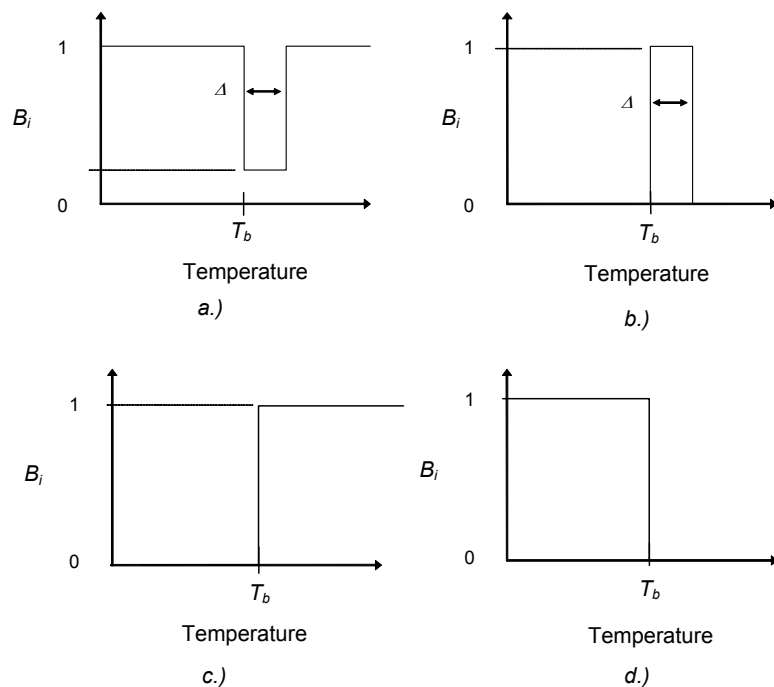


**Figure 3-120. Shapes of the Reaction Rate Profile  $B_i$  Used to Describe: a) Perturbation of Chain Branching and Heat Release Rates, b) Addition of Perfect Inhibitor or  $\text{CF}_3\text{Br}$ , c) Rapid Inhibitor Activation, and d) Rapid Inhibitor Deactivation.**

The band was smoothed at the edges to avoid numerical convergence problems caused by infinite gradients. The smoothing function was  $B_i = a - b \operatorname{erf}(-c T^* + d)$ , where  $T^* = (T - T_b) / \Delta$  at the low temperature edge and  $T^* = (T_b + \Delta - T) / \Delta$  at the high temperature edge. The constants  $a$ ,  $b$ ,  $c$ , and  $d$  were selected such that the width of the smoothed portion of the band was approximately  $0.1 \cdot \Delta$  at each end.

### Flame Modeling Approach

The Sandia flame code Premix<sup>203</sup>, with the kinetic<sup>204</sup> and transport<sup>205</sup> subroutines, was used to simulate the freely-propagating premixed flame. The CHEMKIN subroutine CKRAT was modified to accommodate the chemical behavior of the model inhibitors. Part of the post-processing was performed using a graphical postprocessor.<sup>362</sup> For all calculations, the initial reactant temperature was 300 K and the pressure was 0.10133 MPa. The “GRAD” parameter was set to 0.15, and “CURV” was set to 0.35 for all of the calculations except those involving CF<sub>3</sub>Br, where higher values of GRAD (0.35) and CURV (0.55) were used to reduce the calculation time. The former values of GRAD and CURV yielded 90 to 125 active grid points in the calculation, and the latter, 65 grid points. As discussed in Reference 57, the calculated burning velocity was estimated to be reduced about 6 % relative to a calculation with a (computationally more intensive) infinite number of grid points.

The kinetic and thermodynamic data of GRI-MECH 1.2<sup>334</sup> (32 species and 177 chemical reactions) served as a basis for describing the methane combustion, except when the inhibitor was CF<sub>3</sub>Br. In that case, the mechanism of Babushok et al.<sup>52</sup> described the C<sub>1</sub>/C<sub>2</sub> hydrocarbon chemistry and the halogen chemistry (70 species and 595 reactions). Reference 52 also provided experimental verification of the CF<sub>3</sub>Br mechanism.

The perfect inhibitor model<sup>167</sup> represented an upper limit to the catalytic action of an inhibitor. The model assumed that the inhibitor-containing species In and InX (in which X is a flame radical H, O, or OH), reacted with radicals at gas-kinetic rates. All reactions were bimolecular, with an activation energy and temperature exponent of 0, and a pre-exponential factor of  $1 \times 10^{14} \text{ cm}^3/\text{mol}\cdot\text{s}$ ; the transport properties of Ar were used for the species In and InX. The perfect inhibitor species were present at low concentrations, so their contribution to the energy balance was small. Also, since the reactions for these species were listed as forward and reverse rates, the choice of thermodynamic properties for these species did not affect their reaction rates. The perfect inhibitor reactions<sup>167</sup> were combined with those of GRI-MECH 1.2. Since the perfect inhibitor mechanism was a theoretical construct, it could not be experimentally verified. However, it had been compared with the experimental results for inhibition by the very powerful flame inhibitor Fe(CO)<sub>5</sub>, and found to give burning velocity reductions reasonably close to that agent.<sup>167</sup>

A stoichiometric, freely-propagating premixed CH<sub>4</sub>-air flame was perturbed in temperature bands of  $\Delta = 300 \text{ K}$ . The following four types of perturbation were used:

- Reduction of the rate of chain branching by  $\text{H} + \text{O}_2 \leftrightarrow \text{OH} + \text{O}$  (referred to as “H+O<sub>2</sub>” below), because it provided a majority of the chain branching at high temperature.
- Reduction of the rate of heat release by  $\text{CO} + \text{OH} \leftrightarrow \text{CO}_2 + \text{H}$  (referred to as “CO+OH” below), because of its importance in determination of the final flame temperature.
- Catalytic scavenging of radicals (O, OH, and H) by a perfect inhibitor,<sup>167</sup> to investigate the maximum inhibition effect.
- Inhibition by CF<sub>3</sub>Br, because it was a benchmark in flame inhibition studies.

The band width of 300 K was selected after conducting extensive numerical experiments with different band widths ranging from 50 K to 2000 K. The results consistently showed that the location of maximum inhibition was independent of the width of the band. The minimum burning velocity decreased as the

band became wider, but the band-center temperature of minimum burning velocity remained nearly constant for the perturbation considered. The choice of a 300 K bandwidth was made as a compromise between having too little effect (a 100 K band only decreased burning velocity by 15 %) and being too wide to provide insight into the inhibition mechanisms. Selected input parameters and calculated results are listed in Table 3-22.

**Table 3-22. Input Parameters and Calculated Temperatures and Flame Speeds.**

Perturbation	$\phi$	$B_i$ Inside Band	$B_i$ Outside Band	Inhibitor Volume Fraction	$T_{max}$ (K)	$S_{L,0}^a$ (cm/s)	$S_{L,all}^b$ (cm/s)	$S_{L,min}^c$ (cm/s)	$T_c$ for $S_{L,min}$ (K)
H+O <sub>2</sub>	0.7	0.45	1.0	n.a.	1850	20.7	n.c.	15.5	1550
H+O <sub>2</sub>	1.0	0.45	1.0	n.a.	2235	41.2	n.c.	31.0	1800
H+O <sub>2</sub>	1.3	0.45	1.0	n.a.	2056	25.2	n.c.	18.0	1850
CO+OH	1.0	0.1	1.0	n.a.	2235	41.2	n.c.	29.1	1850
Perfect	0.7	1.0	0.0	$2.0 \cdot 10^{-5}$	1850	20.7	13.8	16.2	1650
Perfect	1.0	1.0	0.0	$4.0 \cdot 10^{-5}$	2235	41.2	27	30.9	1950
Perfect	1.3	1.0	0.0	$2.6 \cdot 10^{-5}$	2056	25.2	16.8	18.3	2000
CF <sub>3</sub> Br	1.0	1.0	$10^{-4}$	0.00755	2235	41.2 <sup>d</sup>	26.4	29.2	1750

<sup>a</sup> Flame speed of the unperturbed or uninhibited flame.

<sup>b</sup> Flame speed with perturbation throughout flame.

<sup>c</sup> Minimum flame speed with perturbation in a bandwidth of 300 K.

<sup>d</sup> The flame speed is 39.0 cm/s when the halogen chemistry is turned off throughout the flame because of the physical effects of CF<sub>3</sub>Br.

n.a. = not applicable.

n.c. = not calculated.

For H+O<sub>2</sub> and CO+OH, the smoothing function constants are a=0.55, b=0.45, c=60, d=57.

For the perfect inhibitor, the smoothing function constants are a=0.5, b=0.5, c=60, d=57.

For the H+O<sub>2</sub> and CO+OH perturbation, the reaction of interest was unaffected outside the band ( $B_i = 1$ ) and damped inside the band ( $B_i = 0.45$  for H+O<sub>2</sub>,  $B_i = 0.1$  for CO+OH). Thus, the reduction in heat release for the CO+OH reaction was achieved through a reduction in the rate of this reaction within the band. For the perfect inhibitor, reactions involving the perfect inhibitor were turned off outside the band ( $B_i = 0$ ), and turned on inside the band ( $B_i = 1$ ). The volume fraction of the perfect inhibitor in the unburned gas was  $4.0 \cdot 10^{-5}$ , which resulted in a flame speed ( $S_L$ ) of 27 cm/s when the inhibitor was active throughout the flame. (For comparison,  $S_L = 41$  cm/s for the uninhibited flame.)

For inhibition by CF<sub>3</sub>Br, the reactant stream consisted of a stoichiometric mixture of methane and air a volume fraction of added CF<sub>3</sub>Br of 0.0755, resulting in a one-third reduction in flame speed (to 26.4 cm/s) when the inhibitor was active throughout the flame. Ideally, when simulating the model inhibitors, the reactions involving Br- and F-containing species would be turned on ( $B_i = 1$ ) in the band and turned off outside the band ( $B_i = 0$ ). Because of convergence problems compounded by the size of the mechanism, a very small value of  $B_i$  ( $= 10^{-4}$ ) for the halogen chemistry was used outside the band.

## Results and Discussion

Figure 3-121 shows the response of the flame to each of the four perturbations. The calculated volume fractions of OH, H, and O (right axis) are shown for an uninhibited stoichiometric methane-air flame. The minimum flame speed occurred at a band-center temperature ( $T_c$ ) of 1750 K for  $\text{CF}_3\text{Br}$ , 1800 K for  $\text{H}+\text{O}_2$ , 1850 K for  $\text{CO}+\text{OH}$ , and 1950 K for the perfect inhibitor. Using reaction flux analyses, it was possible to *infer* that the burning velocity of the flames would be most strongly perturbed at these temperatures: for  $\text{H}+\text{O}_2$  and  $\text{CO}+\text{OH}$ , these temperatures correspond to the maximum reaction rate of the affected reaction (as shown in Figure 3-122). Similarly, for the perfect inhibitor, the temperature is near the temperature corresponding to the peak volume fractions of O, H, and OH (as shown in Figure 3-121). In this figure,

- “ $\text{CF}_3\text{Br}$  baseline” refers to the flame speed when the halogen chemistry is damped by  $10^{-4}$ .
- The band width  $\Delta$  is 300 K, so the band extends 150 K below and above the temperature shown on the x-axis.
- The kinks in some of the curves in Figure 3-121, as well as in Figure 3-123 and Figure 3-125, were caused by a somewhat coarse progression of calculated band-center temperatures, and would not be present for a finer series of calculations.
- The reduction in flame speed for  $\text{H}+\text{O}_2$  and  $\text{CO}+\text{OH}$  can only be compared qualitatively to results for the perfect inhibitor and  $\text{CF}_3\text{Br}$ , because of the different value of  $B_i$  in the bands.

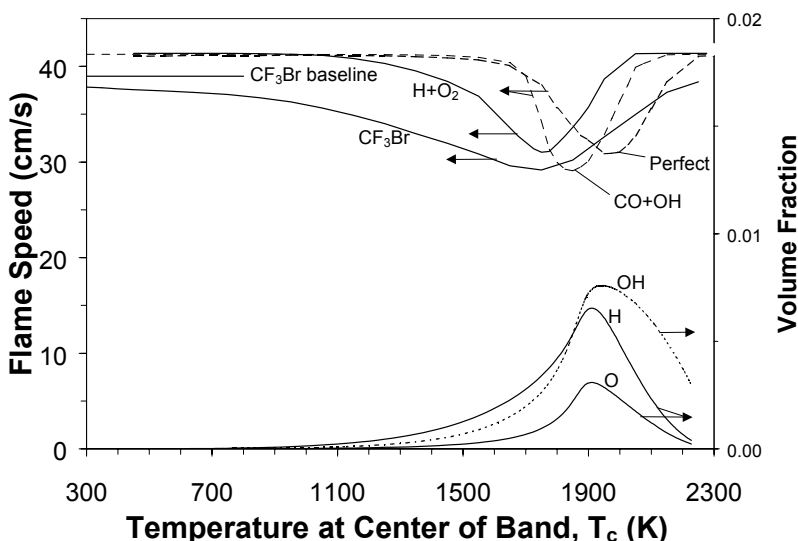


**Figure 3-121. Variation of Flame Speed for Four Types of Perturbation. The calculated volume fraction of OH, H, and O (right axis) is shown for an uninhibited stoichiometric methane-air flame.**

The difference in location of peak effectiveness of  $\text{CF}_3\text{Br}$  vs. the perfect inhibitor was caused by the shift of the partial equilibrium of the scavenging reactions. For  $\text{CF}_3\text{Br}$  at higher temperature, the equilibrium for the inhibition reaction  $\text{H}+\text{HBr} \leftrightarrow \text{H}_2+\text{Br}$  shifted to the left,<sup>41</sup> reducing the effectiveness.

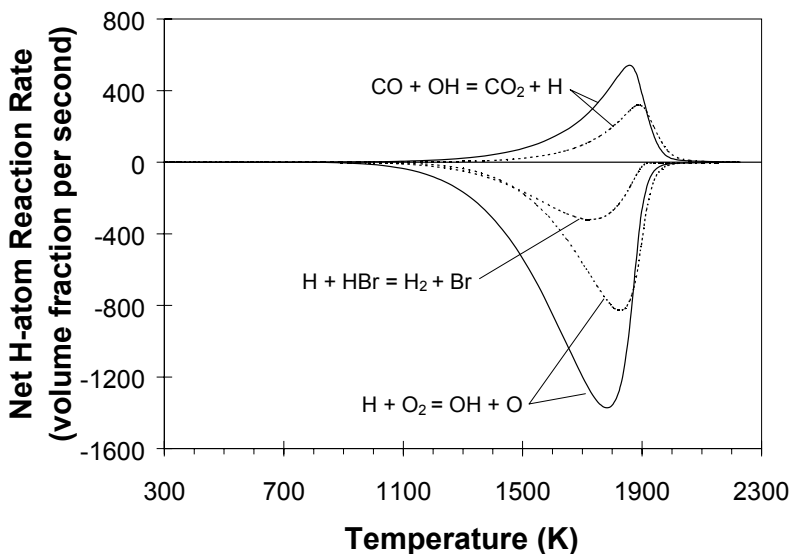


**Figure 3-122. Net H-atom Reaction Rate for Three Important Reactions in Stoichiometric Methane-air Flames. Solid lines: uninhibited flame; dashed lines:  $\text{CF}_3\text{Br}$ -inhibited flame (agent volume fraction of 0.00755).**

These results show that, although some of the inhibition effect of HBr and  $\text{CF}_3\text{Br}$  occurred upstream of the locations of the maximum rates for the chain branching and heat release reactions, the most sensitive temperature region (1600 K to 1900 K) was higher than had been found in prior work. In studies of inhibition of premixed flames by  $\text{CH}_3\text{Br}$ ,  $\text{CF}_3\text{Br}$  and HBr, it had been argued that the primary inhibition occurred upstream of the main reaction zone. Wilson<sup>4</sup> and Wilson et al.<sup>39</sup> investigated inhibition of low pressure (5.1 kPa) methane-oxygen flames inhibited by  $\text{CH}_3\text{Br}$  and HBr. Based on flame structure measurements and calculations, they suggested that inhibition occurred through reduction of radical generation in the “pre-ignition” part of the flame. In a numerical modeling study, Westbrook<sup>332</sup> argued that HBr had its maximum effect in a temperature range between about 1000 K and 1400 K, where the reaction of H atom with HBr competed with its reaction with  $\text{CH}_4$  or  $\text{O}_2$ . Williams and Fleming<sup>26</sup> also described  $\text{CF}_3\text{Br}$  as reducing H-atom concentrations significantly in the lower temperature regions of the flame (< 1200 K); nonetheless, their data showed that the largest absolute reduction in the H-atom volume fraction occurred near 1700 K. Casias and McKinnon<sup>346</sup> also contended that reactions in the low temperature region were of highest importance for inhibition by  $\text{CF}_3\text{Br}$ , although the conditions of their calculated flames (ethylene-air with 1 %  $\text{CF}_3\text{Br}$ ) were somewhat different.

Figure 3-123 shows the effect of chain branching perturbation ( $\Delta = 300$  K) on normalized flame speed for three equivalence ratios: lean ( $\phi = 0.7$ ), stoichiometric ( $\phi = 1.0$ ), and rich ( $\phi = 1.3$ ). Table 3-22 lists calculated maximum temperatures and flame speeds for uninhibited flames at each equivalence ratio. The normalized flame speed was defined as the ratio of the flame speed of a band-inhibited flame to the flame speed of the corresponding uninhibited flame. The temperature of minimum flame speed of the different flames followed the relative position peak of the H-atom volume fraction (Figure 3-124a). The temperature range of maximum influence varied with  $\phi$ , however, because the final temperature of the flame changed with  $\phi$  (Table 3-22).

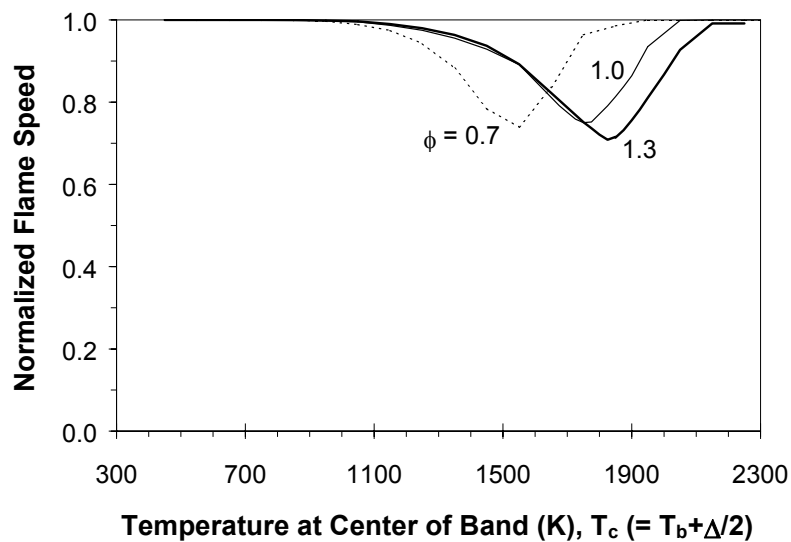


**Figure 3-123 Effect of damping the rate of the H+O<sub>2</sub> reaction on normalized flame speed for  $\phi=0.7, 1.0,$  and  $1.3.$**

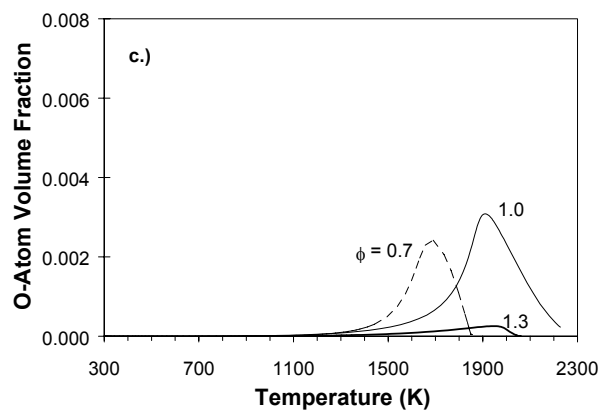
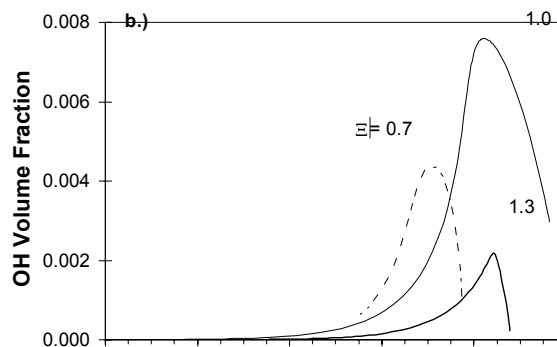
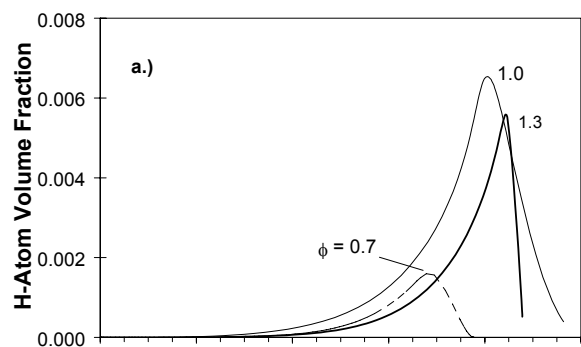


**Figure 3-124. Calculated Volume Fraction Profiles for H, OH and O in Uninhibited Methane-air Flames for Three Stoichiometric Ratios.**

The flame speeds for stoichiometric, rich, and lean flames inhibited by the perfect inhibitor are shown in Figure 3-125. The initial volume fraction of perfect inhibitor used for the calculations was the amount needed for a one-third reduction of flame speed (with the inhibiting reactions active throughout the flame) from the uninhibited condition (see Table 3-22). For band inhibition at the three values of  $\phi$ , the perfect inhibitor showed flame speed reductions qualitatively similar to the results for H+O<sub>2</sub> suppression (as indicated in Table 3-22): the temperature range for maximum effect was lowest for the lean flame, and was higher for stoichiometric and rich flames, which were nearly the same. The ordering followed that of the peak radical volume fractions that are shown in Figure 3-124a-c. The calculations generally demonstrated that inhibition in only a small portion of the flame was responsible for most of the inhibitory effect. For example, as shown in Figure 3-125, when the inhibiting reactions in the lean flame were turned on between 1500 K and 1800 K ( $T_c = 1650$  K), the reduction in flame speed was 65 % as much as when the inhibiting reactions occurred over the entire flame domain. The equivalent results for stoichiometric and rich flames were 72 % and 82 %.

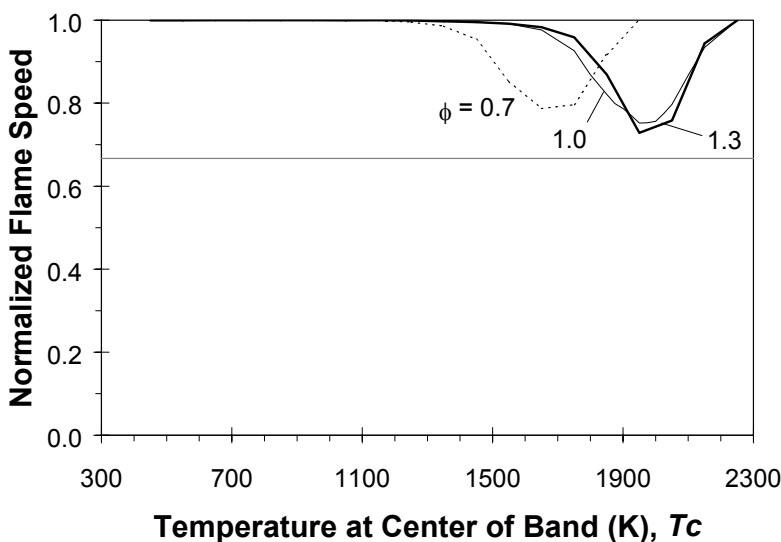


**Figure 3-125. Effect of the Location of Perfect Inhibition on Normalized Flame Speed for  $\phi=0.7$ , 1.0, and 1.3. The horizontal line marks the normalized flame speed when the flames are inhibited throughout the flame.**

A general result of the calculations for the perfect inhibitor was that perturbation near the region of high radical volume fraction had the strongest effect on flame speed. In other words, removing H atoms from the high temperature region before they could diffuse upstream had the strongest effect on flame speed because inhibition reactions are faster in regions of high radical volume fraction and high temperature. The results for CF<sub>3</sub>Br however, showed that the shift of the partial equilibrium at high temperature for certain reactions could influence the region of maximum influence of the agent.

A special, pertinent case evaluated by Linteris and co-workers was that of a potential new fire suppressant that could be inert at storage temperature and release an effective fire suppressant via decomposition or evaporation when added to a fire.<sup>85</sup> This would be analogous to the commonly used powder NaHCO<sub>3</sub>, which decomposes to release the active scavenging species into the gas phase. To simulate such a system, they used a step function perturbation (as opposed to the impulse function in the previous section). The shape of the  $B_i$  function is illustrated in Figure 3-120c. Below the “activation temperature,” the inhibition reactions were turned off, and above the activation temperature, the inhibition reactions were turned on. For ease of calculation, they used the perfect inhibitor model (with inhibitor volume fraction of  $4.0 \cdot 10^{-5}$ ).

The curve labeled “activation” in Figure 3-126 shows the flame speed resulting from inhibitor activation at different temperatures between 300 K and 2200 K. The flame speed was fairly constant up to about 1700 K, but then started to increase. The location of the increase coincided with the peak radical concentration. As the activation occurred later in the flame, the inhibitor had less time to scavenge radicals.

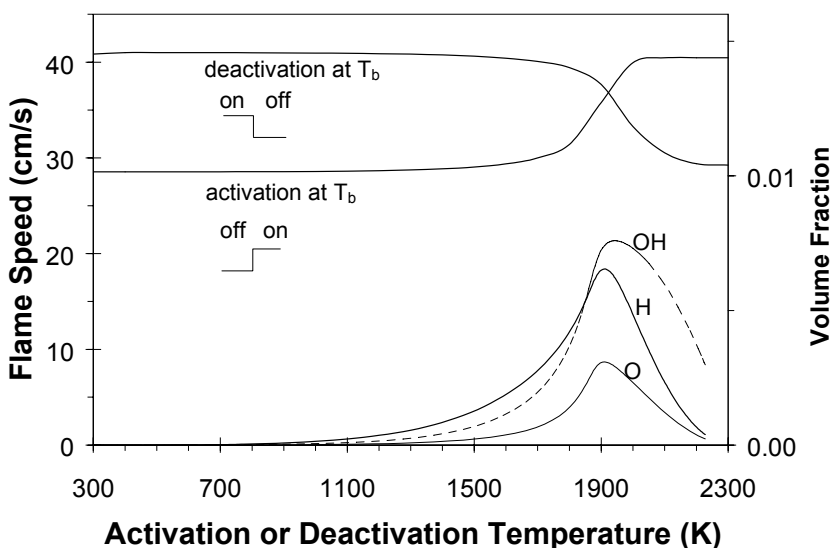


**Figure 3-126. Variation of Flame Speed for Stepwise Inhibitor Activation or Deactivation for a Stoichiometric Methane-air Mixture. Also shown are calculated volume fractions of OH, H, and O in an uninhibited stoichiometric methane-air flame.**

A second special case was that of an active inhibitor that decomposed at a certain temperature and lost its inhibition power. This was exemplified by  $\text{Fe}(\text{CO})_5$  inhibition, in which the active gas phase species were lost because of condensation to particles at some point in the flame. Since the particle formation was related to the residence time, the deactivation might occur over a range of temperatures. The stepwise deactivation was simulated with a band in which the  $B_i$  function (Figure 3-120d) was a mirror image of the previous example. Above the “deactivation” temperature, the inhibition reactions were turned off, and below the deactivation temperature, the inhibition reactions were turned on. As in the stepwise activation calculations, the effect of the inhibitor was more or less constant until about 1700 K. The very small reduction in flame speed when the inhibitor is active between 300 K and 1700 K reaffirmed the importance of the high temperature reactions. The most important region for the perfect inhibitor was above 1700 K for a strong effect on the flame speed; hence, particle formation for  $\text{Fe}(\text{CO})_5$  inhibition must be retarded until after the active species have reached the region of about 1700 K.

## Conclusions

Numerical simulations of perturbed, premixed  $\text{CH}_4$ -air flames using model inhibitors with reaction rates spatially varied in the flame demonstrated the following:

- For agents which catalytically recombine radicals, the flame speed was most reduced when the inhibitor was allowed to act near (a) the region of maximum radical volume fraction or (b) the region of maximum rates of the radical scavenging reactions, depending upon the kinetic mechanism of the particular inhibitor.

- For  $\text{CF}_3\text{Br}$ -inhibited flames, the temperature of maximum influence was near 1750 K, significantly higher than previously suggested. The perturbations had a negligible effect in the region of the flame temperature below 1200 K.
- Inhibition in a relatively small portion of the flame caused a significant reduction in flame speed. In some cases, inhibition in a band spanning only 300 K caused nearly as much reduction in flame speed as when the inhibiting reactions were turned on everywhere.
- Perturbation of the  $\text{H}+\text{O}_2\leftrightarrow\text{OH}+\text{O}$  reaction rate or addition of the perfect inhibitor had a maximum burning velocity reduction in a temperature region which followed the relative position of the peak H-atom volume fraction. This was independent of whether the flame was rich, stoichiometric, or lean.
- The effect of sudden activation and deactivation of the perfect inhibitor was small when the activation or deactivation temperature was above or below 1700 K, respectively. Hence, new inhibitors that may be developed need not become active until near 1700 K, and must not lose their effectiveness until about 2150 K if they are to retain their maximum potential effectiveness.

It is important to note that these conclusions might be different for other fuels, inhibitors, or flame types.

### 3.6 INSIGHTS ON FLAME INHIBITION

Flame inhibition research has been conducted for more than 50 years, providing a technical base on which the NGP was able to build. As a result, the NGP has generated a unified view of chemical flame inhibition.

- Efficient chemical inhibition and suppression of flames results from reduction of the concentrations of flame propagating radicals (H, O, and OH) toward their equilibrium concentrations. This can result from (a) reaction of the inhibitor breakdown products with the radicals, forming stable product species which are relatively inert in the flame, and/or (b) catalytic radical recombination, in which intermediate species formed from the inhibitor breakdown products form more stable molecules from the radicals in a gas phase catalytic cycle.
- An effective catalytic inhibitor must:
  - Break down in the flame with a relatively low activation energy so that the proper intermediates for the catalytic cycle can be present with sufficient time to interact with the radical pool. NGP research has shown that alternate forms of parent molecules can be used as long as they readily breakdown and form the same intermediate species.
  - Form intermediates that regenerate themselves in the catalytic cycle and undergo reactions that are nearly thermally neutral and fast.
  - Break down to intermediate species which can then make it to the right part of the flame, which is the location of the peak chain branching reactions (and hence, peak radical volume fractions). This is generally in the temperature regime between 1700 K and 2100 K.
- Fuels with larger radical pools will be less affected by addition of a catalytic inhibitor.

- Flow-field effects can limit effectiveness, for example through the formation of a condensed phase, followed by entrainment or thermophoresis which limit the agent's transport to the radical pool location.
- Thermodynamic constraints can keep the active moiety from forming the necessary intermediates at the radical pool location by:
  - Driving the active moiety into less active chemical forms, or creating an imbalance in the distribution of species in the catalytic cycle.
  - Causing the intermediates to form a less active condensed form, such as liquid NaOH, or particles of metal oxides.
  - Forming non-active stable species, such as the conversion of Fe to iron fluorides.

NGP research has also developed solid understanding of the flame quenching activity of chemicals built around certain highly effective atoms.

- Extinction measurement and OH reduction were equivalent markers of agent effectiveness.
- Compounds of iron, manganese, chromium, antimony, lead, and tin were very effective at reducing the rates of the chemical reactions that propagate flames.
- Additional metals whose compounds are likely to be effective at low concentrations, but which had not been suggested in previous reviews of metal flame inhibition, are tungsten, molybdenum, and cobalt.
- Phosphorus-containing compounds can be 40 times more effective than nitrogen and 2 to 4 times more effective than  $\text{CF}_3\text{Br}$  at quenching non-premixed hydrocarbon flames.
- DMMP and TMP were roughly equivalent in suppression efficiency, independent of the differences in their ligands. PN was decidedly less effective, likely due to the resonant bonding of the phosphorus atoms in the parent molecule.
- Catalytic inhibitors in general have a strong temperature dependence, with lower effectiveness at higher adiabatic flame temperatures.
- Current computational models adequately (but somewhat under-) predicted the effect of DMMP on flame extinguishment. This may have been due to the significant uncertainties in several of the reaction rate coefficients in the phosphorus mechanism.

### 3.7 REFERENCES

1. Battin-Leclerc, F., Walravens, B., Come, G.M., Baronnet, F., Sanogo, O., Delfau, J.L., and Vovelle, C., "The Chemical Inhibiting Effect of Some Fluorocarbons and Hydrofluorocarbons Proposed As Substitutes for Halons," in Miziolek, A.W. and Tsang, W., eds., *Halon Replacements: Technology and Science* ACS Symposium Series 611, American Chemical Society, Washington, D.C., 1995.
2. Li, K., Kennedy, E.M., Moghtaderi, B., and Dlugogorski, B.Z., "Experimental and Computational Studies on the Gas-Phase Reaction of CF<sub>3</sub>Br With Hydrogen," *Environmental Science & Technology* **34**, 584-590 (2000).
3. Simmons, R.F. and Wolfhard, H.G., "The Influence of Methyl Bromide on Flames, Part 1.-Pre-Mixed Flames," *Combustion and Flame* **1**, 155-161 (1957).
4. Wilson, W.E., "Structure, Kinetics, and Mechanism of a Methane-Oxygen Flame Inhibited With Methyl Bromide," *Proceedings of the Combustion Institute* **10**, 47-54 (1965).
5. Biordi, J.C., Lazzara, C.P., and Papp, J.F., "Flame-Structure Studies of CF<sub>3</sub>Br-Inhibited Methane Flames," *Proceedings of the Combustion Institute* **14**, 367-381 (1973).
6. Hayes, K.F. and Kaskan, W.E., "Inhibition by CH<sub>3</sub>Br of CH<sub>4</sub>-Air Flames Stabilized on a Porous Burner," *Combustion and Flame* **24**, 405-407 (1975).
7. Safieh, H.Y., Vandooren, J., and Van Tiggelen, P.J., "Experimental Study of Inhibition Induced by CF<sub>3</sub>Br in a CO-H<sub>2</sub>-O<sub>2</sub>-Ar Flame," *Proceedings of the Combustion Institute* **19**, 117-126 (1982).
8. Westbrook, C.K., "Inhibition of Hydrocarbon Oxidation in Laminar Flames and Detonations by Halogenated Compounds," *Proceedings of the Combustion Institute* **19**, 127-141 (1982).
9. Reynolds, W.C., "The Element Potential Method for Chemical Equilibrium Analysis: Implementation in the Interactive Program STANJAN," ME 270 HO no 7, Stanford University, Stanford, CA, (1986).
10. Sanogo, O., Delfau, J.L., Akrich, R., and Vovelle, C., "A Comparative Study of the Structure of CF<sub>3</sub>Br- and CF<sub>3</sub>I-Doped Methane Flames," *Journal De Chimie Physique Et De Physico-Chimie Biologique* **93**, 1939-1957 (1996).
11. Kim, C.H., Kwon, O.C., and Faeth, G.M., "Effects of Halons and Halon Replacements on Hydrogen-Fueled Laminar Premixed Flames," *Journal of Propulsion and Power* **18**, 1059-1067 (2002).
12. Simmons, R.F. and Wolfhard, H.G., "The Influence of Methyl Bromide on Flames, Part 2.-Diffusion Flames," *Transactions of the Faraday Society* **52**, 53-59 (1956).
13. Sheinson, R.S., Penner-Hahn, J.E., and Indritz, D., "The Physical and Chemical Action of Fire Suppressants," *Fire Safety Journal* **15**, 437-450 (1989).
14. Lott, J.L., Christian, S.D., Sliepcevich, C.M., and Tucker, E.E., "Synergism Between Chemical and Physical Fire-Suppressant Agents," *Fire Technology* **32**, 260-271 (1996).
15. Friedman, R. and Levy, J.B., "Inhibition of Opposed-Jet Methane-Air Diffusion Flame. The Effects of Alkali Metal Vapours and Organic Halides," *Combustion and Flame* **7**, 195 (1963).
16. Milne, T.A., Green, C.L., and Benson, D.K., "The Use of the Counter-Flow Diffusion Flame in Studies of Inhibition Effectiveness of Gaseous and Powdered Agents," *Combustion and Flame* **15**, 255-264 (1970).
17. Kent, J.H. and Williams, F.A., "Effect of CF<sub>3</sub>Br on Stagnation-Point Combustion of a Heptane Pool," *Proceedings of the Western States Section Meeting*, pp. 73-24, Combustion Institute, Pittsburgh, PA, 1973.

18. Seshadri, K. and Williams, F.A., "Effect of  $\text{CF}_3\text{Br}$  on Counterflow Combustion of Liquid Fuel With Diluted Oxygen," in Gann, R.G., ed., *Halogenated Fire Suppressants* ACS Symposium Series 16, American Chemical Society, Washington, D.C., 1975.
19. Marolewski, T.A. and Weil, E.D., "A Review of Phosphate Ester Fire Resistance Mechanisms and Their Relevance to Fluid Testing, Vol. ASTM STP 1284," in Totten, G.E. and Jürgen, R., Eds., *Fire Resistance of Industrial Fluids* American Society for Testing and Materials, Philadelphia, 1996.
20. Babushok, V., Noto, T., Burgess, D.R.F., Hamins, A., and Tsang, W., "Influence of  $\text{CF}_3\text{I}$ ,  $\text{CF}_3\text{Br}$ , and  $\text{CF}_3\text{H}$  on the High-Temperature Combustion of Methane," *Combustion and Flame* **107**, 351-367 (1996).
21. Grosshandler, W.L., Gann, R.G., and Pitts, W.M., "Evaluation of Alternative In-Flight Fire Suppressants for Full-Scale Testing in Simulated Aircraft Engine Nacelles and Dry Bays," NIST SP 861, National Institute of Standards and Technology, Gaithersburg, MD, (1994).
22. Gann, R.G., "Fire Suppression System Performance of Alternative Agents in Aircraft Engines and Dry Bay Laboratory Simulations," NIST SP 890, vols. I and II, National Institute of Standards and Technology, Gaithersburg MD, (1995).
23. Gann, R.G., "FY2003 Annual Report -- Next Generation Fire Suppression Technology Program (NGP)," NIST Technical Note 1457, National Institute of Standards and Technology, Gaithersburg, MD, (2004).
24. Saso, Y., "Roles of Inhibitors in Global Gas-Phase Combustion Kinetics," *Proceedings of the Combustion Institute* **29**, 337-344 (2003).
25. Vora, N. and Laurendeau, N.M., "Analysis of  $\text{CF}_3\text{Br}$  Flame Suppression Activity Using Quantitative Laser-Induced Fluorescence Measurements of the Hydroxyl Radical," *Combustion Science and Technology* **166**, 15-39 (2001).
26. Williams, B.A. and Fleming, J.W., " $\text{CF}_3\text{Br}$  and Other Suppressants: Differences in Effects on Flame Structure," *Proceedings of the Combustion Institute* **29**, 345-351 (2003).
27. Bundy, M., Hamins, A., and Lee, K.Y., "Suppression Limits of Low Strain Rate Non-Premixed Methane Flames," *Combustion and Flame* **133**, 299-310 (2003).
28. Williams, F.A., "A Unified View of Fire Suppression," *Journal of Fire and Flammability* **5**, 54-63 (1974).
29. Burgoyne, J.H. and Williams-Lier, G., "The Influence of Incombustible Vapours on the Limits of Inflammability of Gases and Vapours in Air," *Proceedings of the Royal Society* **A193**, 525-539 (1948).
30. Belles, F.E. and O'Neal, C., Jr., "Effects of Halogenated Extinguishing Agents on Flame Quenching and a Chemical Interpretation of Their Action," *Proceedings of the Combustion Institute* **6**, 806-813 (1957).
31. Butlin, R.N. and Simmons, R.F., "The Inhibition of Hydrogen-Air Flames by Hydrogen Bromide," *Combustion and Flame* **12**, 447-456 (1968).
32. Garner, F.H., Long, R., Graham, A.J., and Badakhshan, A., "Effect of Certain Halogenated Methanes on Premixed and Diffusion Flames," *Proceedings of the Combustion Institute* **6**, 802 (1957).
33. Rosser, W.A., Wise, H., and Miller, J., "Mechanism of Combustion Inhibition by Compounds Containing Halogen," *Proceedings of the Combustion Institute* **7**, 175-182 (1959).
34. Lask, G. and Wagner, H.G., "Influence of Additives on the Velocity of Laminar Flames," *Proceedings of the Combustion Institute* **8**, 432-438 (1962).
35. Edmondson, H. and Heap, M.P., "The Burning Velocity of Methane-Air Flames Inhibited by Methyl Bromide," *Combustion and Flame* **13**, 472-478 (1969).

36. Niioka, T., Mitani, T., and Takahashi, M., "Experimental Study on Inhibited Diffusion and Premixed Flames in a Counterflow System," *Combustion and Flame* **50**, 89-97 (1983).
37. Mitani, T., "Flame-Retardant Effects of  $\text{CF}_3\text{Br}$  and  $\text{NaHCO}_3$ ," *Combustion and Flame* **50**, 177-188 (1983).
38. Levy, A., Droege, J.W., Tighe, J.J., and Foster, J.F., "The Inhibition of Lean Methane Flames," *Proceedings of the Combustion Institute* **8**, 524-533 (1960).
39. Wilson, W.E., O'Donovan, J.T., and Fristrom, R.M., "Flame Inhibition by Halogen Compounds," *Proceedings of the Combustion Institute* **12**, 929-942 (1969).
40. Biordi, J.C., Lazzara, C.P., and Papp, J.F., R.G. Gann, "The Effect of  $\text{CF}_3\text{Br}$  on a  $\text{CO-H}_2\text{-O}_2\text{-Ar}$  Diffusion Flame," *Halogenated Fire Suppressants*, American Chemical Society, Washington, D.C., 256-294 (1975).
41. Day, M.J., Stamp, D.V., Thompson, K., and Dixon-Lewis, G., "Inhibition of Hydrogen-Air and Hydrogen-Nitrous Oxide Flames by Halogen Compounds," *Proceedings of the Combustion Institute* **13**, 705-712 (1971).
42. Dixon-Lewis, G. and Simpson, R.J., "Aspects of Flame Inhibition by Halogen Compounds," *Proceedings of the Combustion Institute* **16**, 1111-1119 (1977).
43. Westbrook, C.K., "Numerical Modeling of Flame Inhibition by  $\text{CF}_3\text{Br}$ ," *Combustion Science and Technology* **34**, 201-225 (1983).
44. Creitz, E.C., "Inhibition of Diffusion Flames by Methyl Bromide and Trifluoromethyl Bromide Applied to the Fuel and Oxygen Sides of the Reaction Zone," *Journal of Research of the National Bureau of Standards A. Physics and Chemistry* **65A**, 389-396 (1961).
45. Masri, A.R., "Chemical Inhibition of Nonpremixed Flames of Hydrocarbon Fuels With  $\text{CF}_3\text{Br}$ ," *Combustion Science and Technology* **96**, 189-212 (1994).
46. Masri, A.R. and Clarke, T.C., "Lifted Flames and the Effects of Inhibitors," *Combustion Science and Technology* **105**, 345-355 (1995).
47. Ibiricu, M.M. and Gaydon, A.G., "Spectroscopic Studies of the Effect of Inhibitors on Counterflow Diffusion Flames," *Combustion and Flame* **8**, 51-61 (1964).
48. Kent, J.H. and Williams, F.A., "Extinction of Laminar Diffusion Flames for Liquid Fuels," *Proceedings of the Combustion Institute* **15**, 315-325 (1974).
49. Seshadri, K. and Williams, F.A., "Effect of  $\text{CF}_3\text{Br}$  on Counterflow Combustion of Liquid Fuel With Diluted Oxygen," in Gann, R.G., ed., *Halogenated Fire Suppressants* ACS Symposium Series 16, American Chemical Society, Washington, D.C., 1975.
50. Hamins, A., Trees, D., Seshadri, K., and Chelliah, H.K., "Extinction of Nonpremixed Flames With Halogenated Fire Suppressants," *Combustion and Flame* **99**, 221-230 (1994).
51. Smyth, K.C. and Everest, D.A., "The Effect of  $\text{CF}_3\text{I}$  Compared to  $\text{CF}_3\text{Br}$  on OH Soot Concentrations in Co-Flowing Propane/Air Diffusion Flames," *Proceedings of the Combustion Institute*, 1385-1393, The Combustion Institute, Pittsburgh, 1996.
52. Noto, T., Babushok, V., Burgess Jr., D.R., Hamins, A., Tsang, W., and Miziolek, A.W., "Effect of Halogenated Flame Inhibitors on C1-C2 Organic Flames," *Proceedings of the Combustion Institute* **26**, 1377-1383 (1996).
53. Miziolek, A.W. and Tsang, W., eds., *Halon Replacements*, ACS Symposium Series 611, American Chemical Society, Washington, D.C., 1995.

54. Westmoreland, P.R., Burgess, D.R.F. Jr., Zachariah, M.R., and Tsang, W., "Fluoromethane Chemistry and Its Role in Flame Suppression," *Proceedings of the Combustion Institute* **25**, 1505 (1994).
55. Hynes, R.G., Mackie, J.C., and Masri, A.R., "Inhibition of Premixed Hydrogen-Air Flames by 2-H Heptafluoropropane," *Combustion and Flame* **113**, 554-565 (1998).
56. Hynes, R.G., Mackie, J.C., and Masri, A.R., "Shock-Tube Study of the Pyrolysis of the Halon Replacement Molecule  $\text{CF}_3\text{CHF}_3$ ," *Journal of Physical Chemistry a* **103**, 54-61 (1999).
57. Linteris, G.T. and Truett, L., "Inhibition of Premixed Methane-Air Flames by Fluoromethanes," *Combustion and Flame* **105**, 15-27 (1996).
58. Linteris, G.T., Burgess, D.R., Babushok, V., Zachariah, M., Tsang, W., and Westmoreland, P., "Inhibition of Premixed Methane-Air Flames by Fluoroethanes and Fluoropropanes," *Combustion and Flame* **113**, 164-180 (1998).
59. Sanogo, O., Delfau, J.L., Akrich, R., and Vovelle, C., "Experimental and Computational Study of the Effect of  $\text{C}_2\text{F}_6$  on Premixed Methane Flames," *Proceedings of the Combustion Institute* **25**, 1489 (1994).
60. Vandooen, J., da Cruz, F.N., and Van Tiggelen, P.J., "The Inhibiting Effect of  $\text{CF}_3\text{H}$  on the Structure of a Stoichiometric  $\text{H}_2/\text{CO}/\text{O}_2/\text{Ar}$  Flame," *Proceedings of the Combustion Institute* **22**, 1587-1595 (1988).
61. L'esperance, D., Williams, B.A., and Fleming, J.W., "Intermediate Species Profiles in Low Pressure Premixed Flames Inhibited by Fluoromethanes," *Combustion and Flame* **117**, 709-731 (1999).
62. Zegers, E.J.P., Williams, B.A., Fisher, E.M., Fleming, J.W., and Sheinson, R.S., "Suppression of Nonpremixed Flames by Fluorinated Ethanes and Propanes," *Combustion and Flame* **121**, 471-487 (2000).
63. Papas, P., Fleming, J.W., and Sheinson, R.S., "Extinction of Non-Premixed Methane- and Propane-Air Counterflow Flames Inhibited With  $\text{CF}_4$ ,  $\text{CF}_3\text{H}$ , and  $\text{CF}_3\text{Br}$ ," *Proceedings of the Combustion Institute* **26**, 1405-1411 (1996).
64. Huber, M., Gallagher, J., McLinden, M., and Morrison, G., NIST Thermodynamic Properties of Refrigerants and Refrigerant Mixtures Database (REFPROP), National Institute of Standards and Technology, Gaithersburg, MD, 1996.
65. Wagman, D.D., Evans, W.H., Parker, V.B., Schumm, R.H., Halow, I., Bailey, S.M., Churney, K.L., and Nuttall, R.L., "The NBS Tables of Chemical Thermodynamic Properties: Selected Values for Inorganic and C1 and C2 Organic Substances in SI Units.," *Journal of Physical Chemistry Reference Data* **11**, 1982).
66. Booth, K., Melia, B.J., and Hirst, R., "Critical Concentration Measurements for Flame Extinguishment of Diffusion Flames Using Laboratory "Cup Burner" Apparatus," ICI Mond Division, Warrington Laboratory, (1973).
67. Chelliah, H.K., Law, C.K., Ueda, T., Smooke, M.D., and Williams, F.A., "An Experimental and Theoretical Investigation of the Dilution, Pressure and Flow-Field Effects on the Extinction Condition of Methane-Air-Nitrogen Diffusion Flames," *Proceedings of the Combustion Institute* **23**, 503-511 (1991).
68. Saso, Y., Saito, N., Liao, C.H., and Ogawa, Y., "Extinction of Counterflow Diffusion Flames With Halon Replacements," *Fire Safety Journal* **26**, 303-326 (1996).
69. Tucker, D.M., Drysdale, D.D., and Rasbash, D.J., "The Extinction of Diffusion Flames Burning in Various Oxygen Concentrations by Inert-Gases and Bromotrifluoromethane," *Combustion and Flame* **41**, 293-300 (1981).
70. Tanoff, M.A., Dobbins, R.R., Smooke, M.D., Burgess, D.R., Jr., Zachariah, M.R., Tsang, W., and Westmoreland, P.R., "C1 and C2 Fluorinated Hydrocarbon Effects on the Extinction Characteristics of

Methane Vs. Air Counterflow Diffusion Flames,” in Gann, R.G., Burgess, S.R., Whisner, K.C., and Reneke, P.A., eds., *Papers From 1991-2006 Halon Options Technical Working Conferences (HOTWC)*, CD-ROM, NIST SP 984-4, National Institute of Standards and Technology, Gaithersburg, MD, (2006).

71. Potter, A.E., Jr. and Butler, J.N., “A Novel Combustion Measurement Based on the Extinguishment of Diffusion Flames,” *American Rocket Society Journal* **29**, 54-56 (1959).

72. Konnov, A.A., Idir, M., Delfau, J.L., and Vovelle, C., “Experimental Study of Extinction of Nonadiabatic Counterflow Premixed Flames,” *Combustion and Flame* **105**, 308-320 (1996).

73. Fallon, G.S., Chelliah, H.K., and Linteris, G.T., “Chemical Effects of CF<sub>3</sub>H in Extinguishing Counterflow CO/Air/H<sub>2</sub> Diffusion Flames,” *Proceedings of the Combustion Institute* **26**, 1395-1403 (1996).

74. Balakrishnan, G., Trees, D., and Williams, F.A., “An Experimental Investigation of Strain-Induced Extinction of Diluted Hydrogen-Air Counterflow Diffusion Flames,” *Combustion and Flame* **98**, 123-126 (1994).

75. Rolon, J.C., Veynante, D., Martin, J.P., and Durst, F., “Counter Jet Stagnation Flows,” *Experiments in Fluids* **11**, 313-324 (1991).

76. Seshadri, K. and Williams, F.A., “Laminar Flow Between Parallel Plates With Injection of Reactant at High Reynolds Number,” *Int. J. of Heat and Mass Transfer* **21**, 137-150 (1978).

77. Pellett, G.L., Isaac, K.M., Humphreys, W.M., Gartrell, L.R., Roberts, W.L., Dancey, C.L., and Northam, G.B., “Velocity and Thermal Structure, and Strain-Induced Extinction of 14 to 100% Hydrogen-Air Counterflow Diffusion Flames,” *Combustion and Flame* **112**, 575-592 (1998).

78. Yang, G.S. and Kennedy, I.A., “The Effect of Strain on Laminar Diffusion Flames of Chlorinated Hydrocarbons,” *Combustion and Flame* **92**, 187-192 (1993).

79. Macdonald, M.A., Jayaweera, T.M., Fisher, E.M., and Gouldin, F.C., “Inhibition of Nonpremixed Flames by Phosphorus-Containing Compounds,” *Combustion and Flame* **116**, 166-176 (1999).

80. Puri, I.K. and Seshadri, K., “Extinction of Diffusion Flames Burning Diluted Methane and Diluted Propane in Diluted Air,” *Combustion and Flame* **65**, 137-150 (1986).

81. Yang, M.H., Hamins, A., and Puri, I.K., “The Structure of Inhibited Counterflowing Nonpremixed Flames,” *Combustion and Flame* **98**, 107-122 (1994).

82. Grosshandler, W., Donnelly, M., and Womeldorf, C., “*Lean Flammability Limit As a Fundamental Refrigerant Property. Final Technical Report*,” Report No. DOE/CE/23810-98, US Department of Energy, Washington, DC, (1998).

83. Burgess, D.R., Zachariah, M.R., Tsang, W., and Westmoreland, P.R., “*Thermochemical and Chemical Kinetic Data for Fluorinated Hydrocarbons*,” NIST TN 1412, National Institute of Standards and Technology, Gaithersburg, MD, (1995).

84. Williams, B.A., L'esperance, D.M., and Fleming, J.W., “Intermediate Species Profiles in Low-Pressure Methane/Oxygen Flames Inhibited by 2-H Heptafluoropropane: Comparison of Experimental Data With Kinetic Modeling,” *Combustion and Flame* **120**, 160-172 (2000).

85. Linteris, G.T. and Chelliah, H.K., “*Powder-Matrix Systems for Safer Handling and Storage of Suppression Agents*,” NISTIR 6766, National Institute of Standards and Technology, Gaithersburg, MD, (2001).

86. Linteris, G.T., Rumminger, M.D., Babushok, V., Chelliah, H., Lazzarini, A.K., and Wanigarathne, P., “*Effective Non-Toxic Metallic Fire Suppressants*,” NISTIR 6875, National Institute of Standards and Technology, Gaithersburg MD, (2002).

87. Linteris, G.T., "Limits to the Effectiveness of Metal-Containing Fire Suppressants," NISTIR 7177, National Institute of Standards and Technology, Gaithersburg MD, (2004).
88. Jost, W., Bonne, U., and Wagner, H.G., "Iron Carbonyl Found to Be Powerful Flame Inhibitor," *Chemical & Engineering News* **39**, 76 (1961).
89. Bonne, U., Jost, W., and Wagner, H.G., "Iron Pentacarbonyl in Methane-Oxygen (or Air) Flames," *Fire Research Abstracts and Reviews* **4**, 6-18 (1962).
90. Kimmel, E.C., Smith, E.A., Reboulet, J.E., Black, B.H., Sheinson, R.S., and Carpenter, R.L., "Physical and Chemical Characteristics of SFE Fire Suppressant Atmospheres: Comparison of Small-With Large-Scale Laboratory Atmospheres," in Gann, R.G., Burgess, S.R., Whisner, K.C., and Reneke, P.A., eds., *Papers From 1991-2006 Halon Options Technical Working Conferences (HOTWC)*, CD-ROM, NIST SP 984-4, National Institute of Standards and Technology, Gaithersburg, MD, (2006).
91. Rosser, W.A., Inami, S.H., and Wise, H., "The Effect of Metal Salts on Premixed Hydrocarbon-Air Flames," *Combustion and Flame* **7**, 107-119 (1963).
92. Vanpee, M. and Shirodkar, P., "A Study of Flame Inhibition by Metal Compounds," *Proceedings of the Combustion Institute* **17**, 787-795 (1979).
93. Skaggs, R.R., Daniel, R.G., Miziolek, A.W., McNesby, K.L., Babushok, V.I., Tsang, W., and Smooke, M.D., "Spectroscopic Studies of Inhibited Opposed-Flow Propane-Air Flames," in Gann, R.G., Burgess, S.R., Whisner, K.C., and Reneke, P.A., eds., *Papers From 1991-2006 Halon Options Technical Working Conferences (HOTWC)*, CD-ROM, NIST SP 984-4, National Institute of Standards and Technology, Gaithersburg, MD, (2006).
94. Kovarik, B., "Charles F. Kettering and the Development of Tetraethyl Lead in the Context of Alternative Fuel Technologies," *Fuels and Lubricants*, Society of Automotive Engineers, New York, 1994.
95. Walsh, A.D., "The Mode of Action of Tetraethyllead As an Antiknock," in *Six Lectures on the Basic Combustion Process* Ethyl Corp., New York, NY, 1954.
96. Erhard, K.H.L. and Norrish, R.G.W., "Studies of Knock and Antiknock by Kinetic Spectroscopy," *Proceedings of the Royal Society (London) A* **234**, 178-191 (1956).
97. Muraour, H., "La Theorie Des Anti-Detonants," *Chem. et Industr.* **14**, 1911 (1925).
98. Chamberlain, G.H.N. and Walsh, A.D., "The Inhibiting Effect of Lead Tetraethyl. 1. The Effect of Lead Compounds on the Vapour Phase Slow Oxidation of Diisopropyl Ether and on the Ignition of Diethyl Ether.," *Proceedings of the Royal Society A* **215**, 175-186 (1952).
99. Cheaney, D.E., Davies, D.A., Davis, A., Hoare, D.E., Protheroe, J., and Walsh, A.D., "Effects of Surfaces on Combustion of Methane and Mode of Action of Anti-Knock Containing Metals," *Proceedings of the Combustion Institute* **7**, 183-187 (1959).
100. Richardson, W.L., Ryason, P.R., Kautsky, G.J., and Barusch, M.R., "Organolead Antiknock Agents-Their Performance and Mode of Action," *Proceedings of the Combustion Institute* **9**, 1023-1033 (1962).
101. Zimpel, C.F. and Graiff, L.B., "An Electron Microscopic Study of Tetraethyllead Decomposition in an Internal Combustion Engine," *Proceedings of the Combustion Institute* **11**, 1015-1025 (1967).
102. Rumminger, M.D. and Linteris, G.T., "The Role of Particles in the Inhibition of Premixed Flames by Iron Pentacarbonyl," *Combustion and Flame* **123**, 82-94 (2000).
103. Reinelt, D. and Linteris, G.T., "Experimental Study of the Inhibition of Premixed and Diffusion Flames by Iron Pentacarbonyl," *Proceedings of the Combustion Institute* **26**, 1421-1428 (1996).

104. Rumminger, M.D., Reinelt, D., Babushok, V.I., and Linteris, G.T., "Numerical Study of the Inhibition of Premixed and Diffusion Flames by Iron Pentacarbonyl," *Combustion and Flame* **116**, 207-219 (1999).
105. Rumminger, M.D. and Linteris, G.T., "Numerical Modeling of Counterflow Diffusion Flames Inhibited by Iron Pentacarbonyl," *Fire Safety Science: Proceedings of the Sixth International Symposium*, 289-300, Int. Assoc. for Fire Safety Science, Marne-La-Vallee, France, 2000.
106. Linteris, G.T., Rumminger, M.D., Babushok, V.I., and Tsang, W., "Flame Inhibition by Ferrocene and Blends of Inert and Catalytic Agents," *Proceedings of the Combustion Institute* **28**, 2965-2972 (2000).
107. Linteris, G.T., Knyazev, V.D., and Babushok, V.I., "Inhibition of Premixed Methane Flames by Manganese and Tin Compounds," *Combustion and Flame* **129**, 221-238 (2002).
108. Rumminger, M.D. and Linteris, G.T., "The Role of Particles in the Inhibition of Counterflow Diffusion Flames by Iron Pentacarbonyl," *Combustion and Flame* **128**, 145-164 (2002).
109. Kuppu Rao, V. and Prasad, C.R., "Knock Suppression in Petrol Engines," *Combustion and Flame* **18**, 167-172 (1972).
110. Linteris, G.T. and Rumminger, M.D., "Particle Formation in Laminar Flames Inhibited by Metals," *Proceedings of the Western States Section Meeting*, Paper 030, Combustion Institute, Pittsburgh, PA, 2002.
111. Morrison, M.E. and Scheller, K., "The Effect of Burning Velocity Inhibitors on the Ignition of Hydrocarbon-Oxygen-Nitrogen Mixtures," *Combustion and Flame* **18**, 3-12 (1972).
112. Miller, D.R., Evers, R.L., and Skinner, G.B., "Effects of Various Inhibitors on Hydrogen-Air Flame Speeds," *Combustion and Flame* **7**, 137-142 (1963).
113. Miller, W.J., "Inhibition of Low Pressure Flames," *Combustion and Flame* **13**, 210-212 (1969).
114. Cotton, D.H. and Jenkins, D.R., "Catalysis of Radical-Recombination Reactions in Flames by Alkaline Earth Metals," *Transactions of the Faraday Society* **67**, 730-739 (1971).
115. Bulewicz, E.M., Padley, P.J., Cotton, D.H., and Jenkins, D.R., "Metal-Additive-Catalysed Radical-Recombination Rates in Flames," *Chemical Physics Letters* **9**, 467-468 (1971).
116. Bulewicz, E.M. and Padley, P.J., "Catalytic Effect of Metal Additives on Free Radical Recombination Rates in  $H_2+O_2+N_2$  Flames," *Proceedings of the Combustion Institute* **13**, 73-80 (1971).
117. deWitte, M., Vrebosch, J., and van Tiggelen, A., "Inhibition and Extinction of Premixed Flames by Dust Particles," *Combustion and Flame* **9**, 257-266 (1964).
118. Rumminger, M.D. and Linteris, G.T., "Inhibition of Premixed Carbon Monoxide-Hydrogen-Oxygen-Nitrogen Flames by Iron Pentacarbonyl," *Combustion and Flame* **120**, 451-464 (2000).
119. Macdonald, M.A., Gouldin, F.C., and Fisher, E.M., "Temperature Dependence of Phosphorus-Based Flame Inhibition," *Combustion and Flame* **124**, 668-683 (2001).
120. MacDonald, M.A., Jayaweera, T.M., Fisher, E.M., and Gouldin, F.C., "Variation of Chemically Active and Inert Flame-Suppression Effectiveness With Stoichiometric Mixture Fraction," *Proceedings of the Combustion Institute* **27**, 2749-2756 (1998).
121. Babushok, V.I. and Tsang, W., "Inhibitor Rankings for Hydrocarbon Combustion," *Combustion and Flame* **123**, 488-506 (2000).

122. James, C.G. and Sugden, T.M., "Photometric Investigations of Alkali Metals in Hydrogen Flame Gases. 3. The Source of the Alkali Metal Continuum," *Proceedings of the Royal Society A* **248**, 238-247 (1958).
123. Bulewicz, E.M., James, C.G., and Sugden, T.M., "Photometric Investigations of Alkali Metals in Hydrogen Flame Gases. 2. The Study of Excess Concentrations of Hydrogen Atoms in Burnt Gas Mixtures," *Proceedings of the Royal Society A* **235**, 89-106 (1956).
124. Bulewicz, E.M. and Sugden, T.M., "Determination of the Dissociation Constants and Heats of Formation of Molecules by Flame Photometry; Part 3.-Stability of Gaseous Cuprous Hydroxide," *Transactions of the Faraday Society* **52**, 1481-1488 (1956).
125. Bulewicz, E.M. and Sugden, T.M., "Determination of the Dissociation Constants and Heats of Formation of Molecules by Flame Photometry; Part 2.-Heat of Formation of Gaseous Cuprous Hydroxide," *Transactions of the Faraday Society* **52**, 1475-1480 (1956).
126. Bulewicz, E.M. and Padley, P.J., "Photometric Investigations of the Behavior of Chromium Additives in Premixed  $H_2+O_2+N_2$  Flames," *Proceedings of the Royal Society London A* **323**, 377-400 (1971).
127. Howard, J.B. and Kausch, W.J., "Soot Control by Fuel Additives," *Progress in Energy and Combustion Science* **6**, 263-276 (1980).
128. Cotton, D.H., Friswell, N.J., and Jenkins, "The Suppression of Soot Emission From Flames by Metal Additives.," *Combustion and Flame* **17**, 87-98 (1971).
129. Bulewicz, E.M., Jones, G., and Padley, P.J., "Temperature of Metal Oxide Particles in Flames," *Combustion and Flame* **13**, 409-412 (1969).
130. Tischer, R.L. and Scheller, K., "The Behavior of Uranium Oxide Particles in Reducing Flames," *Combustion and Flame* **15**, 199-202 (1970).
131. Jensen, D.E. and Jones, G.A., "Mass-Spectrometric Tracer and Photometric Studies of Catalyzed Radical Recombination in Flames," *Journal of the Chemical Society-Faraday Transactions I* **71**, 149-160 (1975).
132. Jensen, D.E. and Jones, G.A., "Catalysis of Radical Recombination in Flames by Iron," *Journal of Chemical Physics* **60**, 3421 (1974).
133. Jensen, D.E. and Jones, G.A., "Aspects of Flame Chemistry of Cobalt," *Journal of the Chemical Society-Faraday Transactions I* **72**, 2618-2630 (1976).
134. Fenimore, C.P. and Martin, F.J., "Flammability of Polymers," *Combustion and Flame* **10**, 135-139 (1966).
135. Fenimore, C.P. and Jones, G.W., "Modes of Inhibiting Polymer Flammability," *Combustion and Flame* **10**, 295-301 (1966).
136. Fenimore, C.P. and Martin, F.J., "Candle-Type Test for Flammability of Polymers," *Modern Plastics* **12**, 141-192 (1966).
137. Fenimore, C.P. and Martin, F.J., "Burning of Polymers," in Wall, L.A., Ed., *The Mechanisms of Pyrolysis, Oxidation and Burning of Organic Materials* National Bureau of Standards, Washington, D.C., 1972.
138. Martin, F.J. and Price, K.R., "Flammability of Epoxy Resins," *Journal of Applied Polymer Science* **12**, 143 (1968).
139. Hastie, J.W., "Molecular Basis of Flame Inhibition," *Journal of Research of the National Bureau of Standards - A. Physics and Chemistry* **77A**, 733-754 (1973).

140. Hastie, J.W. and McBee, C.L., "Mechanistic Studies of Halogenated Flame Retardants: The Antimony-Halogen System," in Gann, R.G., ed., *Halogenated Fire Suppressants* American Chemical Society, Washington, DC, 1975.
141. Hastie, J.W., "Mass Spectroscopic Studies of Flame Inhibition: Analysis of Antimony Trihalides in Flames," *Combustion and Flame* **21**, 49-54 (1973).
142. Dolan, J.E. and Dempster, P.B., "The Suppression of Methane-Air Ignitions by Fine Powders," *Journal of Applied Chemistry* **5**, 510-517 (1955).
143. Matsuda, S. and Gutman, D., "Shock-Tube Study of  $C_2H_2-O_2$  Reaction. Acceleration of Reaction in the Presence of Trace Amounts of  $Cr(CO)_6$ ," *Journal of Physical Chemistry* **75**, 2402-2404 (1971).
144. Matsuda, S., "Gas Phase Homogeneous Catalysis in Shock Waves. II. The Oxidation of Carbon Monoxide by Oxygen in the Presence of Iron Pentacarbonyl," *Journal of Physical Chemistry* **57**, 807-812 (1972).
145. Linteris, G.T., Rumminger, M.D., and Babushok, V.I., "Premixed Carbon Monoxide-Nitrous Oxide-Hydrogen Flames: Measured and Calculated Burning Velocities With and Without  $Fe(CO)_5$ ," *Combustion and Flame* **122**, 58-75 (2000).
146. Park, K., Bae, G.T., and Shin, K.S., "The Addition Effect of  $Fe(CO)_5$  on Methane Ignition," *Bulletin of the Korean Chemical Society* **23**, 175-176 (2002).
147. Jensen, D.E. and Webb, B.C., "Afterburning Predictions for Metal-Modified Propellant Motor Exhausts," *AIAA Journal* **14**, 947-954 (1976).
148. Westblom, U., Fernandezalonso, F., Mahon, C.R., Smith, G.P., Jeffries, J.B., and Crosley, D.R., "Laser-Induced Fluorescence Diagnostics of a Propane Air Flame With a Manganese Fuel Additive," *Combustion and Flame* **99**, 261-268 (1994).
149. Suyuan Y., Jones, A.D., Chang, D.P.Y., Kelly, P.B., and Kennedy, I.M., "The Transformation of Chromium in a Laminar Premixed Hydrogen-Air Flame," *Proceedings of the Combustion Institute* **27**, 1639-1645 (1998).
150. Kennedy, I.M., Zhang, Y., Jones, A.D., Chang, D.P.Y., Kelly, P.B., and Yoon, Y., "Morphology of Chromium Emissions From a Laminar Hydrogen Diffusion Flame," *Combustion and Flame* **116**, 233-242 (1999).
151. Kellogg, C.B. and Irikura, K.K., "Gas-Phase Thermochemistry of Iron Oxides and Hydroxides: Portrait of a Super-Efficient Flame Suppressant," *Journal of Physical Chemistry a* **103**, 1150-1159 (1999).
152. Tapscott, R.E., Sheinson, R.S., Babushok, V., Nyden, M.R., and Gann, R.G., "Alternative Fire Suppressant Chemicals: a Research Review With Recommendations," NIST TN 1443, National Institute of Standards and Technology, Gaithersburg MD, (2001).
153. Linteris, G.T., Katta, V.R., and Takahashi, F., "Experimental and Numerical Evaluation of Metallic Compounds for Suppressing Cup-Burner Flames," *Combustion and Flame* **138**, 78-96 (2004).
154. Katta, V.R., Takahashi, F., and Linteris, G.T., "Numerical Investigations of  $CO_2$  As Fire Suppressing Agent," *Fire Safety Science: Proceeding of the Seventh International Symposium*, 531-542, Int. Assoc. for Fire Safety Science, Boston, MA, 2003.
155. Fallis, S., Holland, G.F., McCormick, J.L., Reed, R., and Wilson, K.A., "Advanced Propellant/Additive Development for Fire Suppressing Gas Generators: Hybrid Systems," in Gann, R.G., Burgess, S.R., Whisner, K.C., and Reneke, P.A., eds., *Papers From 1991-2006 Halon Options Technical Working Conferences (HOTWC)*, CD-ROM, NIST SP 984-4, National Institute of Standards and Technology, Gaithersburg, MD, (2006).

156. Masri, A.R., Dally, B.B., Barlow, R.S., and Carter, C.D., "The Structure of Laminar Diffusion Flames Inhibited With  $\text{CF}_3\text{Br}$ ," *Combustion Science and Technology* **114**, 17-34 (1996).
157. Skaggs, R.R., McNesby, K.L., Daniel, R.G., Homan, B., and Miziolek, A.W., "Spectroscopic Studies of Low-Pressure Opposed Flow Methane/Air Flames Inhibited by  $\text{Fe}(\text{CO})_5$ ,  $\text{CF}_3\text{Br}$ , or  $\text{N}_2$ ," *Combustion Science and Technology* **162**, 1-17 (2001).
158. Chidsey, I.L. and Crosley, D.R., "Calculated Rotational Transition Probabilities for the A-X System of OH," *Journal of Quantitative Spectroscopy and Radiative Transfer* **23**, 187 (1980).
159. Dieke, G.H. and Crosswhite, H.M., "The Ultraviolet Bands of OH Fundamental Data," *Journal of Quantitative Spectroscopy and Radiative Transfer* **2**, 97 (1962).
160. Kotlar, A., Personal Communication, 1998.
161. Eckbreth, A.C., *Laser Diagnostics for Combustion Temperatures and Species*, Abacus Press, Cambridge MA, 1998.
162. Smooke, M.D., Yale University, Personal Communication, 1997.
163. Babushok, V., NIST, Personal Communication, 1999.
164. Rumminger, M.D., Reinelt, D., Babushok, V., and Linteris, G.T., "Inhibition of Flames by Iron Pentacarbonyl," in Gann, R.G., Burgess, S.R., Whisner, K.C., and Reneke, P.A., eds., *Papers From 1991-2006 Halon Options Technical Working Conferences (HOTWC)*, CD-ROM, NIST SP 984-4, National Institute of Standards and Technology, Gaithersburg, MD, (2006).
165. Daniel, R.G., McNesby, K.L., Skaggs, R.R., Sagar, P., and Miziolek, A.W., "Spectroscopy of Inhibited Counterflow Diffusion Flames Proceedings," *1997 JANNAF Combustion Subcommittee Meeting*, 1997.
166. Gaydon, A.G., *The Spectroscopy of Flames*, John Wiley and Sons, New York, NY, 1972.
167. Babushok, V.I., Tsang, W., Linteris, G.T., and Reinelt, D., "Chemical Limits to Flame Inhibition," *Combustion and Flame* **115**, 551-560 (1998).
168. Peters, N., "Local Quenching Due to Flame Stretch and Non-Premixed Turbulent Combustion," *Combustion Science and Technology* **30**, 1-17 (1983).
169. Liew, S.K., Bray, K.N.C., and Moss, J.B., "A Stretched Laminar Flamelet Model of Turbulent Non-Premixed Combustion," *Combustion and Flame* **56**, 199 (1984).
170. Haworth, D.C., Drake, M.C., and Blint, R.J., "Stretched Laminar Flamelet Modeling of a Turbulent Jet Diffusion Flame," *Combustion Science and Technology* **60**, 287-318 (1988).
171. Bilger, R.W., "The Structure of Turbulent Non-Premixed Flames," *Proceedings of the Combustion Institute* **22**, 450-488 (1988).
172. Roberts, W.L., Driscoll, J.F., Drake, M.C., and Ratcliffe, J.W., "OH Fluorescence Images of The Quenching of a Premixed Flame During an Interaction With a Vortex 169," *Proceedings of the Combustion Institute* **24**, 169 (1992).
173. Miller, J.H., "Applications of Conserved Scalars to Combustion Chemistry," *Proceedings of the Eastern States Section Meeting*, pp. 1-10, Combustion Institute, Pittsburgh, PA, 1996.
174. Reinelt, D., Babushok, V., and Linteris, G.T., "Numerical Study of the Inhibition of Premixed and Diffusion Flames by Iron Pentacarbonyl," *Proceedings of the Eastern States Section Meeting*, pp. 273-276, Combustion Institute, Pittsburgh, PA, 1996.
175. Noto, T., Babushok, V., Hamins, A., and Tsang, W., "Inhibition Effectiveness of Halogenated Compounds," *Combustion and Flame* **112**, 147-160 (1998).

176. Fallis, S., Reed, R., Lu, Y.-C., Wierenga, P.H., and Holland, G.F., "Advanced Propellant/Additive Development for Fire Suppressing Gas Generators," *Halon Options Technical Working Conference*, 361-370, Albuquerque, NM, 2000.
177. Rosser, W.A., Inami, S.H., and Wise, H., "Study of the Mechanisms of Fire Extinguishment of Liquid Rocket Propellants," WADC Technical Report 59-206, ASTIA Document No. AD 216355, 1959).
178. Lippincott, E.S. and Tobin, M.C.J., "The Vibrational Spectra and Thermodynamic Functions of Lead Tetramethyl, Tin Tetramethyl and Germanium Tetramethyl," *Journal of the American Chemical Society* **75**, 4141-4147 (1953).
179. Katta, V.R., Takahashi, F., and Linteris, G.T., "Extinction Characteristics of Cup-Burner Flame in Microgravity," *41st Aerospace Sciences Meeting and Exhibit*, AIAA Paper No. 2003-1150, AIAA, 2003.
180. Linteris, G.T., "Extinction of Cup-Burner Diffusion Flames by Catalytic and Inert Inhibitors," *Second NRIFD Symposium - Science, Technology and Standards for Fire Suppression Systems*, Tokyo, Japan, 2002.
181. Cusack, P.A. and Killmeyer, A.J., "Inorganic Tin-Compounds As Flame, Smoke, and Carbon-Monoxide Suppressants for Synthetic-Polymers," in Nelson, G.L., ed., *Fire and Polymers, Hazards Identification and Prevention* ACS Symposium Series 425, American Chemical Society, Washington, DC, 1990.
182. Hornsby, P.R., Mitchell, P.A., and Cusack, P.A., "Flame Retardation and Smoke Suppression of Polychloroprene Containing Inorganic Tin-Compounds," *Polymer Degradation and Stability* **32**, 299-312 (1991).
183. Pitts, W.M., Nyden, M.R., Gann, R.G., Mallard, W.G., and Tsang, W., "Construction of an Exploratory List of Chemicals to Initiate the Search for Halon Alternatives," NIST Technical Note 1279, National Institute of Standards and Technology, Gaithersburg MD, (1990).
184. Nesmeyanov, A.N., Ed., *Manganese containing antiknock compounds*, Nauka, Moscow, 1971.
185. Tapscott, R.E., Heinonen, E.W., and Brabson, G.D., "Advanced Agent Identification and Preliminary Assessment," NMERI 95/38/32350, NMERI, University of New Mexico, Albuquerque, NM, (1996).
186. Chao, B.H., Egolfopoulos, F.N., and Law, C.K., "Structure and Propagation of Premixed Flame in Nozzle-Generated Counterflow," *Combustion and Flame* **109**, 620-638 (1997).
187. Andrews, G.E. and Bradley, D., "Determination of Burning Velocities: a Critical Review," *Combustion and Flame* **18**, 133-153 (1972).
188. Gilbert, A.G. and Sulzmann, K.G.P., "The Vapor Pressure of Iron Pentacarbonyl," *Journal of the Electrochemical Society* **121**, 832 (1974).
189. Stull, D.R., "Vapor Pressure of Pure Substances Organic Compounds," *Industrial Engineering Chemistry* **39**, 517-540 (1947).
190. Hollrah, D., Ethyl Corp., Personal Communication, 2001
191. Bulewicz, E.M. and Padley, P.J., "Photometric Observations on the Behaviour of Tin in Premixed H<sub>2</sub>-O<sub>2</sub>-N<sub>2</sub> Flames," *Transactions of the Faraday Society* **67**, 2337-2347 (1971).
192. Goodings, J.M. and Chen, Q.-F., "Chemical Kinetics and Thermodynamics of Tin Ionization in H<sub>2</sub>-O<sub>2</sub>-N<sub>2</sub> Flames and the Proton Affinity of SnO," *Canadian Journal of Chemistry* **76**, 1437-1446 (1998).

193. Taylor, J.E. and Milazzo, T.S., "Synthesis of Nanoscale Metal-Oxide Particles Using Laser Vaporization Condensation in a Diffusion Cloud Chamber," *Journal of Physical Chemistry* **82**, 847-852 (1978).
194. Gurvich, L.V., Karachevtsev, G.V., Kondratiev, V.N., Lebedev, Yu., A., Medvedev, V.A., Potapov, V.K., and Hodeev, Ya.S., *Bond energies. Ionization Potentials and Electron Affinities*, Nauka, Moscow, 1974.
195. Fontijn, A. and Bajaj, P.N., "Kinetics of the SN(P-3(0)) Reactions With CO<sub>2</sub> and O<sub>2</sub> Over Wide Temperature Ranges," *Journal of Physical Chemistry* **100**, 7085-7089 (1996).
196. Husain, D., Plane, J.M., and Xiang, C.C., "A Direct Kinetic Study of the Reaction K + OH + He = 3D KOH + He by Time-Resolved Molecular Resonance-Fluorescence Spectroscopy, OH(A<sub>2</sub>=ABSIGMA=BB+-X 2=ABPI=BB), Coupled With Steady Atomic Fluorescence Spectroscopy, K(5 2PJ-4 2S1/2)," *Journal of the Chemical Society, Faraday Transactions II* **80**, 1465-1483 (1984).
197. Gurvich, L.V. and Glushkov, V.P., "Thermodynamic Properties of Individual Substances," NIST special database 5, IVTHANTHERMO-PC, National Institute of Standards and Technology, Gaithersburg, MD, (1998).
198. Smith, G.P., SRI, Personal Communication, 1999
199. J.A. Martinho Simões, "Organometallic Thermochemistry Data," in Mallard, W.G. and Linstrom, P.J., Eds., *NIST Chemistry WebBook, NIST Standard Reference Database Number 69* National Institute of Standards and Technology, Gaithersburg, MD 20899 (<http://webbook.nist.gov>), 2000.
200. Hildenbrand, D.L. and Lau, K.H., "Thermochemistry of Gaseous Manganese Oxides and Hydroxides," *Journal of Chemical Physics* **100**, 8377-8380 (1994).
201. Babushok, V.I. and Tsang, W., "Influence of Phosphorus-Containing Additives on Methane Flames," *Proceedings of the Joint Meeting of the United States Sections*, pp. 587-590, The Combustion Institute, Pittsburgh, PA, 1999.
202. Jensen, D.E., "Condensation Modeling for Highly Supersaturated Vapours: Application to Iron," *Journal of the Chemical Society, Faraday Transactions* **76**, 1494 (1980).
203. Kee, R.J., Grear, J.F., Smooke, M.D., and Miller, J.A., "A Fortran Computer Program for Modeling Steady Laminar One-Dimensional Premixed Flames," SAND85-8240, Sandia National Laboratories, Livermore, CA, (1991).
204. Kee, R.J., Rupley, F.M., and Miller, J.A., "CHEMKIN-II: A Fortran Chemical Kinetics Package for the Analysis of Gas Phase Chemical Kinetics," SAND89-8009B, Sandia National Laboratories, Livermore, CA, (1989).
205. Kee, R.J., Dixon-Lewis, G., Warnatz, J., Coltrin, R.E., and Miller, J.A., "A Fortran Computer Package for the Evaluation of Gas-Phase, Multicomponent Transport Properties," SAND86-8246, Sandia National Laboratories, Livermore, CA, (1986).
206. Smith, G.P., Golden, D.M., Frenklach, M., Moriarty, N.W., Eiteneer, B., Goldenberg, M., Bowman, C.T., Hanson, R.K., Song, S., Gardiner, Jr., W.C., Lissianski, V.V., and Qin, Z., "GRI Mech 3.0," 2000.
207. Linteris, G.T., "Effect of Inhibitor Concentration on the Inhibition Mechanism of Fluoromethanes in Premixed Methane-Air Flames," in Miziolek, A.W. and Tsang, W., eds., *Halon Replacements* ACS Symposium Series 611, American Chemical Society, Washington, D.C., 1995.
208. Breck, D.W., "Correlations of Calculated Intracrystalline Void Volumes and Limiting Absorption Volumes in Zeolite," in Meier, W.M. and Uytterhoeven, J.B., Eds., *Molecular Sieves* American Chemical Society, Washington, D.C., 1973.

209. Andersen, S.O., "Halon and the Stratospheric Ozone Issue," *Fire Journal* **81**, 56-62 (1987).
210. Reed, M.D., Williams, B.A., Sheinson, R.S., and Fleming, J.W., "Behavior of Bicarbonate Powders in Counterflow Diffusion Flames," *Proceedings of the Eastern States Section Meeting*, pp. 83-86, Combustion Institute, Pittsburgh, PA, 1997.
211. Lutz, A.E., Kee, R.J., Grcar, J.F., and Rupley, F.M., "OPPDIF: A Fortran Computer Program for Computing Opposed-Flow Diffusion Flames," SAND96-8243, Sandia National Labs., Albuquerque, NM, (1996).
212. Chelliah, H.K., Yu, G., Hahn, T.O., and Law, C.K., "An Experimental and Numerical Study on the Global and Detailed Kinetics of Premixed and Nonpremixed Flames of Chloromethane, Methane, Oxygen and Nitrogen," *Proceeding of the Combustion Institute* **24**, 1083-1090 (1993).
213. Zhang, J. and Megaridis, C.M., "Iron/Soot Interaction in a Laminar Ethylene Nonpremixed Flame," *Proceedings of the Combustion Institute* **25**, 593-600 (1994).
214. Zhang, J. and Megaridis, C.M., "Soot Suppression by Ferrocene in Laminar Ethylene/Air Nonpremixed Flames," *Combustion and Flame* **105**, 528-540 (1996).
215. Carty, P., Grant, J., and Metcalfe, E., "Flame-Retardancy and Smoke-Suppression Studies on Ferrocene Derivatives in PVC," *Applied Organometallic Chemistry* **10**, 101-111 (1996).
216. Kasper, M. and Siegmann, K., "The Influence of Ferrocene on PAH Synthesis in Acetylene and Methane Diffusion Flames," *Combustion Science and Technology* **140**, 333-350 (1998).
217. Kasper, M., Sattler, K., Siegmann, K., Matter, U., and Siegmann, H.C., "The Influence of Fuel Additives on the Formation of Carbon During Combustion," *Journal of Aerosol Science* **30**, 217-225 (1999).
218. Kishore, K., Kannan, P., and Iyanar, K., "Synthesis, Characterization, and Fire Retardancy of Ferrocene Containing Polyphosphate Esters," *Journal of Polymer Science Part a-Polymer Chemistry* **29**, 1039-1044 (1991).
219. Zheng, R., Bray, K.N.C., and Rogg, B., "Effect of Sprays of Water and NaCl-Water Solution on the Extinction of Laminar Premixed Methane-Air Counterflow Flames," *Combustion Science and Technology* **126**, 389-401 (1997).
220. Pelino, M., Tomassetti, M., Piacente, V., and D'Ascenzo, G., "Vapor Pressure Measurements of Ferrocene, Mono- and 1,1 Di-Acetyl Ferrocene," *Thermochemica Acta* **44**, 89-99 (1981).
221. Lewis, K.E. and Smith, G.P., "Bond Dissociation Energies in Ferrocene," *Journal of the American Chemical Society* **106**, 4650-4651 (1984).
222. Turnbull, A.G., "Thermochemistry of Biscyclopentadienyl Metal Compounds. 1.) Preparation and Thermal Stability," *Australian Journal of Chemistry* **20**, 2059-2067 (1967).
223. Sabbah, R. and Perez, J.A.G., "Contribution a L'Etude Thermochemique De Ferrocene," *Thermochemica Acta* **297**, 17-32 (1997).
224. Reid, R.C., Prausnitz, Y.M., and Sherwood, T.K., *The Properties of Gases and Liquids*, McGraw-Hill, New York, 1987.
225. Wang, H. and Frenklach, M., "Transport Properties of Polycyclic Aromatic Hydrocarbons," *Combustion and Flame* **96**, 163-170 (1994).
226. Sung, C.J., Li, B., Law, C.K., and Wang, H., "Structure and Sooting Limits in Counterflow Methane/Air and Propane/Air Diffusion Flames From 1 to 5 Atmospheres," *Proceedings of the Combustion Institute* **27**, 1523-1529 (1998).

227. Zachariah, M.R., Westmoreland, P.R., Burgess, D.R., and Tsang, W., "BAC-MP4 Predictions of Thermochemical Data for C-1 and C-2 Stable and Radical Hydrofluorocarbons and Oxidized Hydrofluorocarbons," *Journal of Physical Chemistry* **100**, 8737-8747 (1996).
228. Tsang, W., NIST, Personal Communication, 1999
229. Burgess, D.R., Zachariah, M.R., Tsang, W., and Westmoreland, P.R., "Thermochemical and Chemical Kinetic Data for Fluorinatedhydrocarbons," *Progress in Energy and Combustion Science* **21**, 453-529 (1995).
230. Fristrom, R.M. and Sawyer, R.F., "Flame Inhibition Chemistry," *AGARD Conference Proceedings No. 84 on Aircraft Fuels, Lubricants, and Fire Safety, AGARD-CP 84-71*, 12-2 to 12-17, North Atlantic Treaty Organization, Neuilly-sur-Seine, France, 1971.
231. Nesmeianov, A.N., *Vapour Pressure of the Elements.*, New York, Academic Press, 1963.
232. Grimley, R.T., Burns, R.P., and Inghram, M.G., "Thermodynamics of the Vaporization of  $\text{Cr}_2\text{O}_3$ : Dissociation Energies of  $\text{CrO}$ ,  $\text{CrO}_2$ , and  $\text{CrO}_3$ ," *Journal of Chemical Physics* **34**, 664-667 (1961).
233. Barin, I. and Knacke, O., *Thermochemical Properties of Inorganic Substances*, Springer-Verlag, Berlin, New York, 1973.
234. Barin, I., Knacke, O., and Kubaschewski, O., *Thermochemical Properties of Inorganic Substances*, Springer-Verlag, Berlin, New York, 1977.
235. Tapscott, R.E., Mather, J.D., Heinonen, E.W., Lifke, J.L., and Moore, T.A., "Identification and Proof Testing of New Total Flooding Agents: Combustion Suppression Chemistry and Cup-Burner Testing," NMERI 97/6/33010, Albuquerque, NM, (1998).
236. Fay, J.A., "The Distributions of Concentration and Temperature in a Laminar Jet Diffusion Flame," *Journal of Aeronautical Sciences* **21**, 681-689 (1954).
237. Staendeke, H. and Scharf, D.J., "Halogen-Free Flame-Retardant Based on Phosphorus-Compounds," *Kunststoffe-German Plastics* **79**, 1200-1204 (1989).
238. Avondo, G., Vovelle, C., and Delbourgo, R., "Role of Phosphorus and Bromine in Flame Retardancy," *Combustion and Flame* **31**, 7-16 (1978).
239. Sherman, L.M., "Flame Retardants Update: Phosphorus Expands Its Niche," *Plastics Technology* **38**, 102-105 (1992).
240. Shelley, S., "Keeping Fire at Bay," *Chemical Engineering* **100**, 71-73 (1993).
241. Brauman, S.K., "Phosphorus Fire retardance in Polymers. I. General Mode of Action," *Journal of Fire Retardant Chemistry* **4**, 18-37 (1977).
242. Green, J., "Mechanisms for Flame Retardancy and Smoke Suppression: A Review," *Journal of Fire Sciences* **14**, 426-442, 1996).
243. Kashiwagi, T., Gilman, J.W., McGrath, J.E., and Wan, I.-Y., "Flammability Properties of Phosphine Oxide Copolymers and of Commodity Polymers With New Flame Retardant Additives," *1996 FRCA Fall Meeting*, 1996.
244. Peters, E.N., "Flame-Retardant Thermoplastics .1. Polyethylene-Red Phosphorus," *Journal of Applied Polymer Science* **24**, 1457-1464 (1979).
245. Haessler, W., "Dry Chemical Agents and Application Systems," in Cote, A.E. and Linville, J.L., Eds., *Fire Protection Handbook* National Fire Protection Association, Quincy, MA, 1986.
246. Kordylewski, W. and Amrogowicz, J., "Comparison of  $\text{NaHCO}_3$  and  $\text{NH}_4\text{H}_2\text{PO}_4$  Effectiveness As Dust Explosion Suppressants," *Combustion and Flame* **90**, 344-345 (1992).

247. Amrogowicz, J. and Kordylewski, W., "Effectiveness of Dust Explosion Suppression by Carbonates and Phosphates," *Combustion and Flame* **85**, 520-522 (1991).
248. Song, C. E., Kim, I. O., Lee, J. K., Kim, T. K., and Lee, S. G., "Liquid Fire Extinguishing Composition," U.S. Patent 5219474 (1990).
249. Kaizerman, J.A. and Tapscott, R.E., "*Advanced Streaming Agent Development, Volume II: Phosphorus Compounds*," NMERI 96/5/32540, New Mexico Engineering Research Institute, Albuquerque, NM, (1996).
250. Lifke, J. L., Moore, T. A., and Tapscott, R. E., "*Advanced Streaming Agent Development, Volume V: Laboratory-Scale Streaming Tests*," NMERI 96/2/32540, New Mexico Engineering Research Institute, Albuquerque, NM, (1996).
251. Jordan, T.E., "Metal Organic Compounds," in *Vapor Pressure of Organic Compounds, 1st Ed.* Interscience Publishers, New York, 1954.
252. Weil, E.D., "Phosphorus-Based Flame Retardants," in Engel, R., Ed., *Handbook of Organophosphorus Chemistry* Marcel Dekker, Inc., New York, 1992.
253. Korobeinichev, O.P., Chernov, A.A., and Shvartsberg, V.M., "Destruction Chemistry of Trimethyl Phosphate in H<sub>2</sub>/O<sub>2</sub>/Ar Flame Studied by Molecular Beam Mass-Spectrometry," *3rd Asia-Pacific International Symposium on Combustion and Energy Utilization*, 1995.
254. Korobeinichev, O.P., Ilyin, S.B., Mokrushin, V.V., and Shmakov, A.G., "Destruction Chemistry of Dimethyl Methylphosphonate in H<sub>2</sub>/O<sub>2</sub>/Ar Flames Studied by Molecular-Beam Mass Spectrometry," *Combustion Science and Technology* **116**, 51-67 (1996).
255. Fenimore, C.P. and Jones, G.W., "Phosphorus in the Burnt Gas From Fuel-Rich Hydrogen-Oxygen Flames," *Combustion and Flame* **8**, 133-137 (1964).
256. Hastie, J.W. and Bonnell, D.W., "*Molecular Chemistry of Inhibited Combustion Systems. Final Report.*" NBSIR 80-2169, National Bureau of Standards, Gaithersburg, MD, (1980).
257. Babushok, V.I. and Tsang, W., "Influence of Phosphorus-Containing Fire Suppressants on Flame Propagation," *International Conference on Fire Research and Engineering, Third*, 257-267, Society of Fire Protection Engineers, Boston, MA, 1999.
258. Twarowski, A., "Reduction of a Phosphorus Oxide and Acid Reaction Set," *Combustion and Flame* **102**, 41-54 (1995).
259. Twarowski, A., "The Effect of Phosphorus Chemistry on Recombination Losses in a Supersonic Nozzle," *Combustion and Flame* **102**, 55-63 (1995).
260. Twarowski, A., "Photometric-Determination of the Rate of H<sub>2</sub>O Formation From Hand OH in the Presence of Phosphine Combustion Products," *Combustion and Flame* **94**, 341-348 (1993).
261. Trees, D., Grudno, A., and Seshadri, K., "Experimental and Numerical Studies on Chemical Inhibition of Nonpremixed Methane Flames by CF<sub>3</sub>Br," *Combustion Science and Technology* **124**, 311-& (1997).
262. Saso, Y., Zhu, D.L., Wang, H., Law, C.K., and Saito, N., "Laminar Burning Velocities of Trifluoromethane-Methane Mixtures: Experiment and Numerical Simulation," *Combustion and Flame* **114**, 457-468 (1998).
263. Zegers, E.J.P. and Fisher, E.M., "Gas-Phase Pyrolysis of Diethyl Methylphosphonate," *Combustion Science and Technology* **116**, 69-89 (1996).
264. Zegers, E.J., "*Flow Reactor Pyrolysis of Alkyl Phosphates and Phosphonates, Ph.D. Thesis, Mechanical Engineering*," Cornell University, Ithaca, NY, 1997.

265. Beaud, P., Radi, P.P., Franzke, D., Frey, H.M., Mischler, B., Tzannis, A.P., and Gerber, T., "Picosecond Investigation of the Collisional Deactivation of OH A(2)Sigma+(V' = 1, N' = 4, 12) in an Atmospheric-Pressure Flame," *Applied Optics* **37**, 3354-3367 (1998).
266. Smith, G.P. and Crosley, D.R., "Vibrational-Energy Transfer in A2-Sigma+ OH in Flames," *Applied Optics* **22**, 1428-1430 (1983).
267. Allen, M.G., McManus, K.R., Sonnenfroh, D.M., and Paul, P.H., "Planar Laser-Induced-Fluorescence Imaging Measurements of OH and Hydrocarbon Fuel Fragments in High-Pressure Spray-Fame Combustion," *Applied Optics* **34**, 6287-6300 (1995).
268. Puri, R., Moser, M., Santoro, R.J., and Smyth, K.C., "Laser-Induced Fluorescence Measurements of OH Concentration in the Oxidation Region of Laminar, Hydrocarbon Diffusion Flames," *Proceedings of the Combustion Institute* **24**, 1015-1022 (1996).
269. Arnold, A., Bombach, R., Kappeli, B., and Schlegel, A., "Quantitative Measurements of OH Concentration Fields by Two-Dimensional Laser-Induced Fluorescence," *Applied Physics B-Lasers and Optics* **64**, 579-583 (1997).
270. Kelman, J.B. and Masri, A.R., "Quantitative Imaging of Temperature and OH in Turbulent-Diffusion Flames by Using a Single Laser Source," *Applied Optics* **33**, 3992-3999 (1994).
271. Barlow, R.S. and Collignon, A., "Linear LIF Measurements of OH in Nonpremixed Methane-Air Flames: When Are Quenching Corrections Unnecessary," *29th Aerospace Sciences Meeting, AIAA 91-0179*, Reno, 1991.
272. Kollner, M. and Monkhouse, P., "Time-Resolved LIF of OH in the Flame Front of Premixed and Diffusion Flames at Atmospheric Pressure," *Applied Physics B-Lasers and Optics* **61**, 499-503 (1995).
273. Norton, T.S., Smyth, K.C., Miller, J.H., and Smooke, M.D., "Comparison of Experimental and Computed Species Concentration and Temperature Profiles in Laminar, 2-Dimensional Methane Air Diffusion Flames," *Combustion Science and Technology* **90**, 1-34 (1993).
274. Luque, J. and Crosley, D.R., "LIFBASE: Database and Simulation Program (v 1.6)," SRI International Report MP 99-009, 1999).
275. Paul, P.H., "Vibrational-Energy Transfer and Quenching of OH A(2)Sigma+(V'=1) Measured at High Temperatures in a Shock Tube," *Journal of Physical Chemistry* **99**, 8472-8476 (1995).
276. Paul, P.H., "A Model for Temperature-Dependent Collisional Quenching of OH A(2)Sigma+," *Journal of Quantitative Spectroscopy & Radiative Transfer* **51**, 511-524 (1994).
277. Tamura, M., Berg, P.A., Harrington, J.E., Luque, J., Jeffries, J.B., Smith, G.P., and Crosley, D.R., "Collisional Quenching of CH(a), OH(a), and NO(a) in Low-Pressure Hydrocarbon Flames," *Combustion and Flame* **114**, 502-514 (1998).
278. Carrier, G.F., Fendell, F.E., and Marble, F.E., "Effect of Strain Rate on Diffusion Flames," *Siam Journal on Applied Mathematics* **28**, 463-500 (1975).
279. Linan, A., "The Asymptotic Structure of Counterflow Diffusion Flames for Large Activation Energy," *Acta Astronautica* **1**, 1007-1039 (1974).
280. Grudno, A. and Seshadri, K., "Characteristic Residence Times of Laminar Nonpremixed Flames at Extinction," *Combustion Science and Technology* **112**, 199-210 (1996).
281. Fisher, E.M., Williams, B.A., and Fleming, J.W., "Determination of the Strain in Counterflow Diffusion Flames From Flow Conditions," *Proceedings of the Eastern States Section Meeting*, pp. 191-194, Combustion Institute, Pittsburgh, PA, 1997.

282. Nishioka, M., Law, C.K., and Takeno, T., "A Flame-Controlling Continuation Method for Generating S-Curve Responses With Detailed Chemistry," *Combustion and Flame* **104**, 328-342 (1996).
283. Otsuka, Y. and Niioka, T., "*Combustion and Flame* **21**, 163-176 (1973).
284. Trees, D., Seshadri, K., and Hamins, A., "Experimental Studies of Diffusion Flame Extinction With Halogenated and Inert Fire Suppressants," in Miziolek, A.W. and Tsang, W., eds., *Halon Replacements: Technology and Science* ACS Symposium Series 611, American Chemical Society, Washington, D.C., 1995.
285. MacDonald, M.A., Jayaweera, T.M., Fisher, E.M., and Gouldin, F.C., "Inhibited Counterflow Non-Premixed Flames With Variable Stoichiometric Mixture Fractions," *Proceedings of the Eastern States Section*, pp. 91-94, Combustion Institute, Pittsburgh, PA, 1997.
286. Baldwin, R.R., Hopkins, D.E., and Walker, R.W., "Addition of Ethane to Slowly Reacting Mixtures of Hydrogen and Oxygen at 500°C," *Transaction of the Faraday Society* **66**, 189-203 (1970).
287. Yetter, R.A. and Dryer, F.L., "Inhibition of Moist CO Oxidation by Trace Amounts of Hydrocarbons," *Proceedings of the Combustion Institute* **24**, 757 (1992).
288. Grudno, A. and Seshadri, K., "Rate-Ratio Asymptotic Analysis of Inhibition of Nonpremixed Methane-Air Flames by CF<sub>3</sub>Br," *Combustion and Flame* **112**, 418-437 (1998).
289. Bowman, C.T., Hanson, R.K., Davidson, D.F., Gardiner, W.C., Lissianski, V., Smith, G.P., Golden, D.M., Frenklach, M., and Goldenberg, M., "*GRI-MECH: Ver. 2.11 - an Optimized Detailed Chemical Reaction Mechanism for Methane Combustion and NO Formation and Reburning*," No. GRI-95/0058, [http://www.me.berkeley.edu/gri\\_mech](http://www.me.berkeley.edu/gri_mech), The Gas Research Institute, Chicago, IL, (1995).
290. Li, S.C., Libby, P.A., and Williams, F.A., "Experimental and Theoretical Studies of Counterflow Diffusion Flames," *Proceedings of the Combustion Institute* **24**, 1503-1512 (1996).
291. Kim, J.S. and Williams, F.A., "Structures of Flow and Mixture-Fraction Fields for Counterflow Diffusion Flames With Small Stoichiometric Mixture Fractions," *Siam Journal on Applied Mathematics* **53**, 1551-1566 (1993).
292. Brown, T.M., Tanoff, M.A., Osborne, R.J., Pitz, R.W., and Smooke, M.D., "Experimental and Numerical Investigation of Laminar Hydrogen-Air Counterflow Diffusion Flames," *Combustion Science and Technology* **129**, 71-88 (1997).
293. Arnold, A., Becker, H., Hemberger, R., Hentschel, W., Ketterle, W., Kollner, M., Meienburg, W., Monkhouse, P., Neckel, H., Schafer, M., Schindler, K.P., Sick, V., Suntz, R., and Wolfrum, J., "Laser in-Situ Monitoring of Combustion Processes," *Applied Optics* **29**, 4860-4872 (1990).
294. Wainner, R.T., McNesby, K.L., Daniel, R.G., Miziolek, A.W., and Babushok, V.I., "Experimental and Mechanistic Investigation of Opposed-Flow Propane/Air Flames by Phosphorus-Containing Compounds," in Gann, R.G., Burgess, S.R., Whisner, K.C., and Reneke, P.A., eds., *Papers From 1991-2006 Halon Options Technical Working Conferences (HOTWC)*, CD-ROM, NIST SP 984-4, National Institute of Standards and Technology, Gaithersburg, MD, (2006).
295. Skaggs, R.R., Daniel, R.G., Miziolek, A.W., and McNesby, K., "Spectroscopic Studies of Inhibited Opposed Flow Propane/Air Flames," *Proceedings of the First Joint Meeting of the U.S. Sections*, pp. 575-578, Combustion Institute, Pittsburgh, PA, 1999.
296. Kee, R.J., Rupley, F.M., and Miller, J.A., CHEMKIN Collection, Release 3.5, Reaction Design, Inc., San Diego, CA, 1999.
297. Sung, C.J., Liu, J.B., and Law, C.K., "Structural Response of Counterflow Diffusion Flames to Strain-Rate Variations," *Combustion and Flame* **102**, 481-492 (1995).

298. Ravikrishna, R.V. and Laurendeau, N.M., "Laser-Induced Fluorescence Measurements and Modeling of Nitric Oxide in Methane-Air and Ethane-Air Counterflow Diffusion Flames," *Combustion and Flame* **120**, 372-382 (2000).
299. Magre, P., Aguerre, F., Collin, G., Versaevel, P., Lacas, F., and Rolon, J.C., "Temperature and Concentration Measurements by Cars in Counterflow Laminar Diffusion Flames," *Experiments in Fluids* **18**, 376-382 (1995).
300. Werner, J.H. and Cool, T.A., "Kinetic Model for the Decomposition of DMMP in a Hydrogen/Oxygen Flame," *Combustion and Flame* **117**, 78-98 (1999).
301. Mokrushin, V.V., Bol'shova, T.A., and Korobeinichev, O.P., "A Kinetic Model for the Decomposition of DMMP in a Hydrogen/Oxygen Flame", Personal Communication, 1998.
302. Babushok, V., NIST, Personal Communication, 2000
303. Twarowski, A., "The Influence of Phosphorus Oxides and Acids on the Rate of H+OH Recombination," *Combustion and Flame* **94**, 91-107 (1993).
304. Linstrom, P.J. and Mallard, W.G., Eds., *NIST Chemistry WebBook, NIST Standard Reference Database Number 69* National Institute of Standards and Technology, Gaithersburg MD, 20899 (<http://webbook.nist.gov>), 2001.
305. MacDonald, M.A., " *Inhibition of Non-Premixed Flames by Phosphorus-Containing Compounds*," , Ph.D. Dissertation, Cornell University, Ithaca, NY, 2000.
306. Smyth, K.C., Tjossem, P.J.H., Hamins, A., and Miller, J.H., "Concentration Measurements of OH. and Equilibrium Analysis in a Laminar Methane Air Diffusion Flame," *Combustion and Flame* **79**, 366-380 (1990).
307. Glaude, P.A., Curran, H.J., Pitz, W.J., and Westbrook, C.K., "Kinetic Study of the Combustion of Organophosphorus Compounds," *Proceedings of the Combustion Institute* **28**, 1749-1756 (2000).
308. Korobeinichev, O.P., Ilyin, S.B., Shvartsberg, V.M., and Chernov, A.A., "The Destruction Chemistry of Organophosphorus Compounds in Flames - I: Quantitative Determination of Final Phosphorus-Containing Species in Hydrogen-Oxygen Flames," *Combustion and Flame* **118**, 718-726 (1999).
309. Korobeinichev, O.P., Bolshova, T.A., Shvartsberg, V.M., and Chernov, A.A., "Inhibition and Promotion of Combustion by Organophosphorus Compounds Added to Flames of CH<sub>4</sub> or H<sub>2</sub> in O<sub>2</sub> and Ar," *Combustion and Flame* **125**, 744-751 (2001).
310. Korobeinichev, O.P., Shvartsberg, V.M., Chernov, A.A., and Mokrushin, V.V., "Hydrogen-Oxygen Flame Doped With Trimethyl Phosphate, Its Structure and Trimethyl Phosphate Destruction Chemistry.," *Proceedings of the Combustion Institute* **26**, 1035-1042 (1996).
311. Korobeinichev, O.P., Shvartsberg, V.M., and Chernov, A.A., "The Destruction Chemistry of Organophosphorus Compounds in Flames - II: Structure of a Hydrogen-Oxygen Flame Doped With Trimethyl Phosphate," *Combustion and Flame* **118**, 727-732 (1999).
312. Riches, J., Grant, K., and Knutsen, L., "Laboratory Testing of Some Phosphorus-Containing Compounds As Flame Suppressants," in Gann, R.G., Burgess, S.R., Whisner, K.C., and Reneke, P.A., eds., *Papers From 1991-2006 Halon Options Technical Working Conferences (HOTWC)*, CD-ROM, NIST SP 984-4, National Institute of Standards and Technology, Gaithersburg, MD, (2006).
313. Nogueira, M.F.M. and Fisher, E.M., "Effects of Dimethyl Methylphosphonate on Premixed Methane Flames," *Combustion and Flame* **132**, 352-363 (2003).

314. Korobeinichev, O.P., Ilyin, S.B., Bolshova, T.A., Shvartsberg, V.M., and Chernov, A.A., "The Chemistry of the Destruction of Organophosphorus Compounds in Flames - III: The Destruction of DMMP and TMP in a Flame of Hydrogen and Oxygen," *Combustion and Flame* **121**, 593-609 (2000).
315. Korobeinichev, O.P., Chernov, A.A., and Bolshova, T.A., "The Chemistry of the Destruction of Organophosphorus Compounds in Flames - IV: Destruction of DIMP in a Flame of  $H_2+O_2+Ar$ ," *Combustion and Flame* **123**, 412-420 (2000).
316. Zegers, E.J.P. and Fisher, E.M., "Pyrolysis of Triethyl Phosphate," *Combustion Science and Technology* **138**, 85-103 (1998).
317. Zegers, E.J.P. and Fisher, E.M., "Gas-Phase Pyrolysis of Diisopropyl Methylphosphonate," *Combustion and Flame* **115**, 230-240 (1998).
318. Yi, A.C. and Knuth, E.L., "Probe-Induced Concentration Distortions in Molecular-Beam Mass-Spectrometer Sampling," *Combustion and Flame* **63**, 369-379 (1986).
319. Kaiser, E.W., Rothschild, W.G., and Lavoie, G.A., "Effect of Fuel-Air Equivalence Ratio and Temperature on the Structure of Laminar Propane-Air Flames," *Combustion Science and Technology* **33**, 123-134 (1983).
320. Nogueira, M.F.M., "Effects of Dimethyl Methylphosphonate of Premixed Methane Flames, Ph.D. Thesis, Mechanical Engineering," Cornell University, Ithaca, NY, 2001.
321. Kaiser, E.W., Wailington, T.J., Hurley, M.D., Platz, J., Curran, H.J., Pitz, W.J., and Westbrook, C.K., "Experimental and Modeling Study of Premixed Atmospheric-Pressure Dimethyl Ether-Air Flames," *Journal of Physical Chemistry a* **104**, 8194-8206 (2000).
322. Karbach, V. and Warnatz, J., "Http://Nathan.Ca.Sandia.Gov/Tdf/3rdWorkshop/Ch4mech. Html. "Proceedings of the 3rd International Workshop on Measurement and Computation of Turbulent Nonpremixed Flames, Boulder, CO, 1998.
323. Williams, B.A. and Fleming, J.W., "Extinction Studies of Hydrocarbons in Methane/Air and Propane/Air Counterflow Diffusion Flames: The Role of the  $CF_3$  Radical," in Gann, R.G., Burgess, S.R., Whisner, K.C., and Reneke, P.A., eds., *Papers From 1991-2006 Halon Options Technical Working Conferences (HOTWC)*, CD-ROM, NIST SP 984-4, National Institute of Standards and Technology, Gaithersburg, MD, (2006).
324. Fisher, E.M., Gouldin, F.C., Jayaweera, T.M., and MacDonald, M.A., "Flame Inhibition by Phosphorus-Containing Compounds," Final Technical Report Distributed by the Defense Advanced Research Projects Agency, Arlington, VA, (1998).
325. *Cup Burner Flame Extinguishment Concentrations*," NMERI/CGET Technical Update Series (CGET-a) 1995 20/a, 1998).
326. Gann, R.G., NIST, Personal Communication, 1999
327. Brabson, G.D., Walters, E.A., Gennuso, A.R., Owen, J.P., and Tapscott, R.E., "Molecular Beam Mass Spectroscopy of Low-Pressure Flames Seeded With Iron Pentacarbonyl," *Journal of Physical Chemistry* (submitted), 1998).
328. Marinov, N.M., Castaldi, M.J., Melius, C.F., and Tsang, W., "Aromatic and Polycyclic Aromatic Hydrocarbon Formation in a Premixed Propane Flame," *Combustion Science and Technology* **128**, 295-342 (1997).
329. Marinov, N.M., Pitz, W.J., Westbrook, C.K., Castaldi, M.J., and Senkan, S.M., "Modeling of Aromatic and Polycyclic Aromatic Hydrocarbon Formation in Premixed Methane and Ethane Flames," *Combustion Science and Technology* **116**, 211-287 (1996).

330. Marinov, N.M., Pitz, W.J., Westbrook, C.K., Vincitore, A.M., Castaldi, M.J., Senkan, S.M., and Melius, C.F., "Aromatic and Polycyclic Aromatic Hydrocarbon Formation in a Laminar Premixed N-Butane Flame," *Combustion and Flame* **114**, 192-213 (1998).
331. Ewing, C.T., Hughes, J.T., and Carhart, H.W., "The Extinction of Hydrocarbon Flames Based on the Heat-Absorption Processes Which Occur in Them," *Fire and Materials* **8**, 148-156 (1984).
332. Westbrook, C.K., "Inhibition of Methane-Air and Methanol-Air Flames by HBr," *Combustion Science and Technology* **23**, 191-202 (1980).
333. Simmons, R.F. and Wolfhard, H.G., "The Influence of Methyl Bromide on Flames, Part 1.-Pre-Mixed Flames," *Transactions of the Faraday Society* **1**, 1211-1217 (1955).
334. Frenklach, M., Wang, H., Yu, C.-L., Goldenberg, M., Bowman, C.T., Hanson, R.K., Davidson, D.F., Chang, E.J., Smith, G.P., Golden, D.M., Gardiner, W.C., and Lissianski, V., "GRI-MECH: an Optimized Detailed Chemical Reaction Mechanism for Methane Combustion," Gas Research Institute Topical Report No. GRI-95/0058, [http://www.me.berkeley.edu/gri\\_mech](http://www.me.berkeley.edu/gri_mech), The Gas Research Institute, Chicago, IL, (1995).
335. Zamansky, V.M., Lissianski, V.V., Maly, P.M., Ho, L., Rusli, D., and Gardiner, W.C., "Reactions of Sodium Species in the Promoted SNCR Process," *Combustion and Flame* **117**, 821-831 (1999).
336. Babushok, V., Tsang, W., and Noto, T., "Propargyl Type Radicals As Precursors for Polychlorinated Aromatic Hydrocarbons During Incineration," *Proceedings of the Combustion Institute, Vol. 28*, (to appear), The Combustion Institute, Pittsburgh, PA, 2000.
337. Saso, Y., Ogawa, Y., Saito, N., and Wang, H., "Binary CF<sub>3</sub>Br- and CHF<sub>3</sub>-Inert Flame Suppressants: Effect of Temperature on the Flame Inhibition Effectiveness of CF<sub>3</sub>Br and CHF<sub>3</sub>," *Combustion and Flame* **118**, 489-499 (1999).
338. Padley, P.J. and Sugden, T.M., "Chemiluminescence and Radical Re-Combination in Hydrogen Flames," *Proceedings of the Combustion Institute* **7**, 235-244 (1959).
339. Kim, C.H., Kwon, O.C., and Faeth, G.M., "Effects of Fire Suppressants on Hydrogen-Fueled Laminar Premixed Flames," *Proceedings of the Joint Meeting of the U.S. Sections*, paper #219, Combustion Institute, Pittsburgh, PA, 2001.
340. Westbrook, C.K., "Numerical Modeling of Flame Inhibition by CF<sub>3</sub>Br," *Combustion Science and Technology* **34**, 201-225 (1983).
341. Hamins, A., "Flame Extinction by Sodium Bicarbonate Powder in a Cup Burner," *Proceedings of the Combustion Institute* **29**, 2857-2864 (1998).
342. Fristrom, R.M. and Van Tiggelen, P., "An Interpretation of the Inhibition of C-H-O Flames by C-H-X Compounds," *Proceedings of the Combustion Institute* **17**, 773-785 (1978).
343. Williams, B.A. and Fleming, J.W., "Influence of Bond Energies on Catalytic Flame Inhibition: Implications for the Search for New Fire Suppressants," NRL/MR/618003-8728, Naval Research Laboratory, 2003).
344. Griffiths, J.F. and Barnard, J.A., *Flame and Combustion, 3rd Edition*, Blackie Academic and Professional, Glasgow, 1995.
345. Glassman, I., *Combustion*, Academic Press, Orlando, FL, 1987.
346. Casias, C.R. and McKinnon, J.T., "A Modeling Study of the Mechanisms of Flame Inhibition by CF<sub>3</sub>Br Fire Suppressant Agent," *Proceedings of the Combustion Institute* **27**, 2731-2739 (1998).
347. Jensen, D.E. and Jones, G.A., "Kinetics of Flame Inhibition by Sodium," *Journal of the Chemical Society-Faraday Transactions I* **78**, 2843-2850 (1982).

348. Baulch, D.L., Duxbury, J., Grant, S.J., and Montague, D.C., "Evaluated Kinetic Data for High-Temperature Reactions, Vol. 4, - Homogeneous Gas-Phase Reactions of Halogen-Containing and Cyanide-Containing Species," *Journal of Physical and Chemical Reference Data* **10**, 1-721 (1981).
349. Atkinson, R., Baulch, D.L., Cox, R.A., Hampson, R.F., Kerr, J.A., Rossi, M.J., and Troe, J., "Evaluated Kinetic, Photochemical and Heterogeneous Data for Atmospheric Chemistry .5. IUPAC Subcommittee on Gas Kinetic Data Evaluation for Atmospheric Chemistry," *Journal of Physical and Chemical Reference Data* **26**, 521-1011 (1997).
350. Poulet, G., Laverdet, G., and Lebras, G., "Kinetics of the Reactions of Atomic Bromine With HO<sub>2</sub> and HCO at 298 K," *Journal of Chemical Physics* **80**, 1922-1928 (1984).
351. DeMore, W.B., Sander, S.P., Golden, D.M., Hampson, R.F., Kurylo, M.J., Howard, C.J., Ravishankara, A.R., Kolb, C.E., and Molina, M.J., "*Chemical Kinetics and Photochemical Data for Use in Stratospheric Modeling. Evaluation Number 12*," JPL Publication 97-4, 1997).
352. Helmer, M. and Plane, J.M.C., "Experimental and Theoretical Study of the Reaction Fe+O<sub>2</sub>+N<sub>2</sub>=FeO<sub>2</sub>+N<sub>2</sub>," *Journal of the Chemical Society, Faraday Transactions* **90**, 395-401 (1994).
353. Akhmadov, U.S., Zaslanko, I.S., and Smirnov, V.N., "Mechanism and Kinetics of Interaction of Fe, Cr, Mo, and Mn Atoms With Molecular-Oxygen," *Kinetics and Catalysis* **29**, 251-257 (1988).
354. Fuss, S.P. and Hamins, A., "Determination of Planck Mean Absorption Coefficients for HBr, HCl, and HF," *Journal of Heat Transfer-Transactions of the ASME* **124**, 26-29 (2002).
355. Williams, B.A. and Fleming, J.W., "On the Suitability of CF<sub>3</sub>Br As a Benchmark for Replacement Fire Suppressants," in Gann, R.G., Burgess, S.R., Whisner, K.C., and Reneke, P.A., eds., *Papers From 1991-2006 Halon Options Technical Working Conferences (HOTWC)*, CD-ROM, NIST SP 984-4, National Institute of Standards and Technology, Gaithersburg, MD, (2006).
356. Fristrom, R.M. and Westenberg, A.A., *Flame Structure*, McGraw-Hill, New York, 1965.
357. Glassman, I., *Combustion*, Academic Press, New York, NY, 1977.
358. Westbrook, C.K. and Dryer, F.L., "Chemical Kinetic Modeling of Hydrocarbon Combustion," *Progress in Energy and Combustion Science* **10**, 1-57 (1984).
359. Williams, F.A., *Combustion Theory*, Benjamin/Cummings Publishing Company, Menlo Park, California, 1985.
360. Pownall, C. and Simmons, R.F., "The Effect of Hydrogen Bromide on the Structure of Propane-Oxygen Flames Diluted With Argon," *Proceedings of the Combustion Institute* **13**, 585-592 (1971).
361. Rumminger, M.D., Babushok, V.I., and Linteris, G.T., "Temperature Regions of Optimal Chemical Inhibition of Premixed Flames," *Proceedings of the Combustion Institute* **29**, 329-336 (2002).
362. Burgess, D.R., *XSenkplot, an Interactive, Graphics Postprocessor for Numerical Simulations of Chemical Kinetics*, <http://Www.Nist.Gov/Cstl/Div836/Xsenkplot>, National Institute of Standards and Technology, Gaithersburg, MD, 1997.

---

---

## Chapter 4: AEROSOL PROPERTIES

James W. Fleming, Ph.D. and  
Ronald S. Sheinson, Ph.D.,  
U.S. Naval Research Laboratory

---

---

### TABLE OF CONTENTS

4.1	Introduction.....	340
4.2	Previous Knowledge.....	340
4.2.1	Water.....	340
4.2.2	Powders.....	341
4.2.3	Combined Agents - Water Additives.....	342
4.2.4	Burning Surfaces.....	344
4.2.5	Large-scale Studies.....	345
4.2.6	Modeling.....	348
4.3	The Nature of Aerosols.....	348
4.3.1	Quantitative Descriptors.....	348
4.3.2	Generation Techniques.....	350
4.3.3	Quantification of Aerosols.....	351
4.3.4	Aerosol Size and Velocity Characterization.....	351
4.3.5	Aerosol Properties Affecting Behavior.....	355
4.4	The Nature of Flames.....	358
4.4.1	Flame Characteristics.....	358
4.4.2	Premixed Bunsen Type Flames.....	359
4.4.3	Non-premixed Flames.....	360
4.5	Aerosol Flame Suppression Studies.....	363
4.5.1	Water, a Physical Suppression Agent.....	363
4.5.2	Alkali Metal Bicarbonates, Chemically Active Fire Suppressants.....	397
4.5.3	Aqueous Metal Salt Solutions, Combined Chemical and Physical Suppression.....	412
4.5.4	Dendrimers, Combined Chemical and Physical Flame Suppression.....	430
4.6	Surface Cooling.....	438
4.6.1	Introduction.....	438
4.6.2	Evaporation of Liquid Droplets.....	440
4.6.3	Spray Cooling.....	443
4.6.4	Convective Regime.....	444
4.6.5	Nucleate Boiling Regime.....	445
4.6.6	Critical Heat Flux.....	446
4.6.7	Transition and Film Boiling Regimes.....	446
4.6.8	Summary.....	448
4.7	Aerosols and Burning Surfaces.....	448
4.7.1	Flame Spread Studies.....	449
4.7.2	Droplet Interaction with a Hot Surface.....	458

4.7.3 Summary and Conclusions.....	466
4.8 The New State of Knowledge of the Mechanism of Flame Extinguishment by Aerosols .....	467
4.9 Relation of Findings to Practical Fires.....	468
4.10 References.....	469

## 4.1 INTRODUCTION

From the beginning of the Next Generation Fire Suppression Technology Program (NGP), it was expected there would be condensed phase compounds that might offer sufficiently efficient fire protection that could be considered as replacements for halon 1301. These compounds would be delivered to the fire as aerosols. An aerosol is a suspension of small diameter solid particles and/or liquid droplets in a gas. Fog and dust clouds are examples of liquid and solid aerosols, respectively. The term particle is often used to refer to the individual solid components or the individual liquid drops that make up the aerosol.

The realm of fire suppressant aerosols includes two-phase fluid combinations of air with water, halogenated organic chemicals, or solids such as alkali metal compounds or transition metal salts. Because of the influence of gravity, the size of the individual liquid droplets or solid particles must be sufficiently small in order to be carried or suspended by a finite flow of air. Unlike gaseous fire suppression agents, aerosol agents must rely on their environment and delivery method in order to remain suspended and reach the fire location.

Complementing the understanding of the chemical action of fire suppression compounds as described in Chapter 3 with an understanding of the role of the colligative properties of aerosols was recognized as a central factor to the search for suitable replacements. However, the published data describing the fire suppression behavior of aerosols were often difficult to interpret, especially for larger-scale fire tests. It was difficult to separate possible chemical suppression effects from the physical effects which are almost always present. It was known that the aerosol particle size was an important parameter in suppression effectiveness although a quantitative understanding as to the exact role particle size played was hard to determine. In short, the phenomenon of fire suppression using aerosols needed further exploration.

The NGP research described in this chapter was undertaken to address the lack of quantitative information on aerosol suppression behavior. Studies targeted the effects of aerosol size, aerosol droplet or particle velocity behavior in various flow fields, the physical and chemical properties of liquid and powder aerosols, and the predictive capabilities of aerosol suppression behavior. Most of the research predates the NGP focus on aircraft fire protection (Chapter 1) and is directed at a wider range of halon replacement applications.

## 4.2 PREVIOUS KNOWLEDGE

### 4.2.1 Water

Certainly the fire fighting agent that has been used the longest is water (Chapter 1). The interactions of water droplets of various diameters with flames have been studied for almost four decades.<sup>1,2,3,4,5</sup> Many of the early studies examined the effectiveness of water sprays on liquid fires. The suppression of liquid fuel

counterflow flames by water was experimentally investigated by Seshadri<sup>6</sup> using very small droplets that vaporized completely. McCaffrey<sup>7</sup> in the 1980s examined the effect of water introduced in the form of a mist of small droplets on natural gas diffusion flames of various sizes. He introduced the mist outside the base of the flame, where it was entrained along with the fuel. Mass flows of water mist approximately equal to the fuel flows extinguished the flame. In this instance, fine water mist was as effective as halon 1301. In 1977, the U.S. Naval Research Laboratory (NRL) examined some of the advantages of water mist for shipboard use.<sup>8</sup> In addition to pointing out the physical roles (oxygen dilution and high molar heat absorption), the report also noted that aqueous solution of salts would form fine solid particles upon evaporation of the water.

Although there was consensus in the community on the fundamental fire suppression mechanism of water, little detailed quantitative information on the various physical effects operating or any possible chemical effects of water mist was available. Such information underpins the ability to identify when a water-based suppression should be considered, how best to deliver the water, and how one might enhance the fire suppression ability of water mist. Aerosol fire suppression understanding was in its infancy at the beginning of the NGP.

#### 4.2.2 Powders

In addition to the liquid aerosol properties that affect suppression (heat capacity, vaporization and possible additional chemical suppression pathways) powder aerosols possess additional properties that impact fire extinguishment including crystal decrepitation, decomposition, and surface mediated reaction.<sup>9</sup> In interpreting fire suppression results for early studies with various dry powders,<sup>10,11,12</sup> researchers were able to utilize the surface area of the particles to explain thermal vs. chemical effectiveness of finely divided particles.

Rosser et al.<sup>13</sup> examined the effect of finely divided metal salts on the burning velocity of premixed hydrocarbon-air flames in the early 1960s. While several of the powders they studied were not effective, several compounds of sodium, potassium, and copper were effective. They observed that the measured inhibition correlated with the degree of particle evaporation. Successive steps were identified for successful suppression: particle heating, particle evaporation, particle decomposition, and chemical flame inhibition by the added metal compounds.

Fischer et al.<sup>14</sup> at NRL in the early 1980s studied methane flame extinction in a laboratory scale Bunsen burner flame apparatus for a number of powders including monoammonium phosphate, potassium bicarbonate, potassium chloride, sodium bicarbonate, and Monnex<sup>TM</sup> (primarily  $K_2C_2N_2H_3O_3$ ). Extinguishment efficiency increased rapidly with decreasing powder particle diameter with transition diameters ranging from 40  $\mu\text{m}$  to 60  $\mu\text{m}$  depending on the specific inorganic salt compound. Of the powders studied, Monnex<sup>TM</sup> displayed the largest size,  $\sim 60 \mu\text{m}$ , for onset of higher efficiency (probably related to the tendency of Monnex<sup>TM</sup> to undergo decrepitation).

In the early 1980s, Ewing, Hughes, and Carhart<sup>15</sup> at NRL developed an empirical predictor for the flame suppression effectiveness of liquid, gaseous, and solid agents. They observed a large increase in suppression efficiency with decreasing particle size. They concluded that suppression of a methane fire was achieved predominantly by heat extraction from the flame by means of heat capacity sinks and endothermic reaction sinks, such as vaporization, dissociation, and decomposition for the powders they

investigated. They generalized that the extinguishing potential of a powder agent could be predicted from its thermodynamic properties. In later tests, Ewing et al.<sup>16</sup> extinguished heptane pan fires in a 420 L test chamber. Both  $\text{NaHCO}_3$  and  $\text{KHCO}_3$  agents were applied to the fires via a pressurized discharge nozzle. From the tests, a critical size below which particles fully decomposed in their fire scenario was determined for each agent. In a companion effort, Fischer and Leonard<sup>17</sup> performed extinction studies on 21 agents in a premixed flame and also observed a distinct transition region from effective to ineffective particle sizes. Similar experiments were performed by Chattaway et al.<sup>18</sup> in evaluating the efficiency of very small aerosol particulates.

Knuth, Ni, and Seeger<sup>19</sup> studied the flame inhibition effectiveness of several dry chemicals, including  $\text{KHCO}_3$  and  $\text{NaHCO}_3$ , solely in the  $38\mu\text{m}$  to  $43\mu\text{m}$  size range, by adding powders to a counterflow diffusion flame and measuring species and temperature profiles. Their conclusions were primarily based on the decrease in flame temperature and production of the major combustion product species,  $\text{H}_2\text{O}$  and  $\text{CO}_2$ . The powders tested were then ranked in increasing reaction-inhibition effectiveness:  $\text{Al}_2\text{O}_3$  (least effective),  $\text{NaHCO}_3$ ,  $\text{KHCO}_3$ ,  $\text{NH}_4\text{H}_2\text{PO}_4$ , and  $\text{KCl}$  (most effective). Hamins et al.<sup>20</sup> used a counterflow burner to study extinction of liquid pool fires of n-heptane and JP-8 by 13 gaseous agents and sodium bicarbonate. Powder sample in three nominal size ranges were tested:  $0\mu\text{m}$  to  $10\mu\text{m}$ ,  $10\mu\text{m}$  to  $20\mu\text{m}$ , and  $20\mu\text{m}$  to  $30\mu\text{m}$ . Results were not reported for powders above  $30\mu\text{m}$ . They concluded that the  $0\mu\text{m}$  to  $10\mu\text{m}$  size range was the most effective, followed by the  $20\mu\text{m}$  to  $30\mu\text{m}$  and then the  $10\mu\text{m}$  to  $20\mu\text{m}$  range. No explanation for the non-monotonic behavior of effectiveness with size was proposed. Using a cup burner, Hamins showed that, on a mass basis, small  $\text{NaHCO}_3$  particles (sub- $10\mu\text{m}$  diameter particles) which act both as a physical and a chemical suppressant, are three times more effective than halon 1301 ( $\text{CF}_3\text{Br}$ ) and five times more effective than nitrogen.<sup>21</sup>

#### 4.2.3 Combined Agents - Water Additives

A brief, general discussion on the uses of water additives for fire fighting can be found in Wahl.<sup>22</sup> The general intent of adding salts to water was to improve the thermophysical properties of neat water. An example is the lowering of the normal freezing point of water so that it can be used at sub-zero temperatures. For fire suppression, it had long been recognized that additives could significantly reduce the mass of water needed to quench flames.

Monson et al.<sup>23,24</sup> investigated various water additives for fire fighting. Several formulations were identified, which included the following aqueous solutions: 24 % by mass of  $\text{LiCl}$ , 5 %  $\text{LiCl}$ , 26 %  $\text{CaCl}_2$ , 10 %  $\text{Ca}(\text{NO}_3)_2$ , 27 %  $\text{CaCl}_2$ , and 5 %  $\text{FeCl}_3$ , 29 %  $\text{CaCl}_2$ . Only the first of these formulations was actually tested for fire suppression effectiveness. Using a spray nozzle directed at a wood crib fire, the solution extinguished the fire 1.4 times faster than neat water applied at the same rate.

In a series of reports, Grove and co-workers<sup>25,26,27,28,29,30,31,32,33</sup> evaluated the effect of the addition of a viscosity modifier, a surfactant, and/or an opacifier to water on improving the fire suppression effectiveness of water (applied in the form of a spray). The purpose of using a viscosity modifier was to improve the blanketing and runoff properties of water. The opacifier additives were used to mitigate the radiative feedback from the fire to the burning fuel surface. The surfactant was used to facilitate the dispersion of opacifiers in water. Based on the experimental results of their scaled model Class A (solid fuel) fires, it was concluded that:

- The major contribution to the improvement of the fire suppression effectiveness was attributed to the viscosity modifier.
- Viscous water produced more rapid initial control of the fires than neat water.
- The rate of extinguishment of the fires was more rapid with viscous water; the extinguishment time decreased as the viscosity of water was increased.
- The danger of re-ignition was reduced when the fires were extinguished with viscous water, as a result of less water runoff.
- Reduced runoff of viscous water provided better water utilization for fire control and minimized collateral water damage.
- The addition of an opacifier to viscous water further improved the fire fighting properties of water.
- The surfactants used in the study had very little effect on the improvement of the extinguishing properties of water.

In an attempt to improve the effectiveness of water to control and suppress forest fires, Davis et al.<sup>34,35</sup> added several viscosity modifiers to plain water. The results from their controlled field and laboratory fire tests also indicated that fire suppression effectiveness was related to the viscosity of water.

Fine spray solutions of sodium and potassium carbonates and bicarbonates were studied by Friedrich<sup>36</sup> to evaluate the effectiveness of these aqueous solutions in suppressing liquid pool fires. Concentrations ranging from a mass fraction of 0.01 to 0.1 were used in the study, which involved the application of the solution from a spray nozzle located at a fixed distance from the liquid pool. The salt solutions with the highest concentration exhibited the highest effectiveness; however, no improvement in the effectiveness was observed when the concentration was less than a mass fraction of 0.05. No comparison of the fire suppression effectiveness among various salt solutions was given in the cited reference. The author attributed the increase in fire suppression effectiveness of these aqueous solutions to the chemical inhibition ability of the salts and suggested that other compounds such as the oxalates would probably be more effective than the carbonates (albeit low solubility in water and toxicity are potential issues).

Investigation of very high mass fraction additives to water was motivated by the need for fire suppression at low theater temperatures. At the Army Research Laboratory, Elkins studied the use of ethylene glycol anti-freeze as an additive to water.<sup>37</sup> At a volume fraction of 0.3, the ethylene glycol/water solution was found to be approximately three to four times *less* effective (in terms of extinguishment time) than pure water. The author recommended that the concentration of ethylene glycol should not exceed a volume fraction of 0.3, lest the solution lose its fire fighting capability.

The fire suppression effectiveness of aqueous solutions of KBr, KCl, NH<sub>4</sub>Cl, Na<sub>2</sub>CO<sub>3</sub>, NaHCO<sub>3</sub>, K<sub>2</sub>CO<sub>3</sub>, KHCO<sub>3</sub>, and HCOOK of various concentrations were examined by Kida.<sup>38</sup> The solutions were sprayed vertically downward to a small hexane pool fire, and the extinction times were measured. Despite large scatter in the data, a 0.20 volume fraction KHCO<sub>3</sub> solution was found, on the average, to be at least twice as effective (in terms of the extinction times) as pure water. The performance of the other aqueous solutions was not reported in the cited reference.

In a United Kingdom Patent by Ball et al.,<sup>39</sup> potential water additives such as phosphates, carbonates, amino compounds, citrates, anti-freeze agents, and surfactants were suggested to increase the solubility of CO<sub>2</sub> in water for fire suppression applications.

Finnerty et al.<sup>40</sup> evaluated the fire suppression effectiveness of 13 water additives using an airless paint sprayer and a small JP-8 pan fire. Solutions of potassium lactate (0.60 mass fraction) and potassium acetate (also at 0.60 mass fraction) were found to be superior to the other additives and at least four times more effective than pure water in terms of extinguishment time. Although these two solutions had the same overall fire suppression efficiency, the acetate has a sufficiently higher normal freezing point as to render it undesirable for low temperature applications. The superior performance of the potassium lactate and acetate solutions was further demonstrated using the dispersed liquid agent fire screen apparatus developed by NIST<sup>41</sup> under the NGP (Chapter 6).

The significant enhancement in flame suppression ability of aqueous NaOH solutions (almost a factor of five for 17.5 % of NaOH by mass in water)<sup>40</sup> was found to be consistent with previous experiments reported by Zheng et al.<sup>42</sup> for premixed counterflow flames using aqueous NaCl solutions.

Experiments by Mitani and Niioka<sup>43</sup> considered inhibition of premixed flames with ultra fine water droplets (less than 2.4 μm mean diameter) containing NaOH and NaHCO<sub>3</sub>, indicating a flame inhibition/extinction with addition of chemical agents. In particular, their slower C<sub>2</sub>H<sub>4</sub>/O<sub>2</sub>/N<sub>2</sub> premixed flame experiments (as opposed to faster H<sub>2</sub>/O<sub>2</sub>/N<sub>2</sub> flames) showed distinct chemical inhibition effects, but the saturation effects due to condensation of the inhibitor species were not explored. Zheng et al.<sup>42</sup> documented a significant enhancement in counterflow premixed flame suppression from fine droplets of solutions of water/ NaCl over that of pure water.

Fire suppression studies relevant for protecting shipboard machinery spaces conducted by the British Royal Navy in Great Britain examined the suppression effect of adding proprietary wetting agents, Aqueous Film Forming Foam (AFFF), and Film Forming Fluoro Proteins (FFFP) to water sprays.<sup>44</sup> They found that the additives did shorten the fire extinguishing times over neat water, yet the surface tension lowering actually resulted in a slight *increase* in the mean droplet size of the resulting water spray. In this case, the foam forming attributes and possible chemical suppression properties of the additives likely played a more significant role in the suppression effectiveness than the influence of the additive on the surface tension and subsequent droplet formation of the liquid.

#### 4.2.4 Burning Surfaces

There have been numerous studies on flame spread velocities in opposed and counter flow configurations during the last three decades.<sup>45,46,47,48,49,50,51</sup> These studies have shown that the flame spread velocity depends on the fuel thickness, flow configuration, oxygen concentration, and the size of the wind tunnel. Therefore, for flame suppression studies, it is best to obtain data with and without the suppressant in the same facility.

Studies describing spray-target interactions have primarily focused on application of paint coatings to surfaces.<sup>52,53</sup> These studies have shown that high gas phase strain rates where the spray impinges on the target dramatically affect turbulent transport of small droplets (diameter less than 25 μm), and hence the deposition of the droplets on the intended surface. In addition, the deposited droplet size distribution can be significantly different from that of the initial spray. Finally, droplet transport is dependent on initial

droplet momentum, aerodynamic drag, and the gravitational force, with aerodynamic drag being dominant.

Many studies have been performed that quantify the vaporization process of both single and multiple droplet arrays impacting on hot surfaces.<sup>54,55</sup> These studies have identified the need for spatially and temporally resolved data describing the droplet trajectory as it approaches a hot surface (including buoyancy effects), as well as the temperature distribution of the surface material. The NGP studies addressing the interaction of droplets with surfaces are described in Section 4.6 and 4.7.

## 4.2.5 Large-scale Studies

### Need for Testing at Realistic Scale

A candidate halon replacement (in-kind, i.e., vaporizing liquid) or alternative (not in-kind, e.g., aerosol, such as water mist or fine powder) may demonstrate great promise based on laboratory or small-scale evaluations. Implementation effectiveness will hinge on a number of additional considerations including applicability, compatibility, stability, shelf-life, toxicity, and dispersal. Performance against a full-scale, realistic threat and long-term certification is often needed to provide confidence that what looked good in the laboratory will work reliably in practice.

In practice, gaseous fire suppressants deployed as total flooding agents are generally expected and required to disperse throughout a space. Even so, there will remain distribution inhomogeneities due to finite agent release locations and the effects of obstacles. NRL studies in a real-size simulated ship machinery space (840 m<sup>3</sup>) found that, even for a very carefully designed gaseous agent discharge system, there were agent concentration inhomogeneities of at least  $\pm 20\%$  that impacted the fire extinguishment time.<sup>56</sup> For fire suppression agents that are solids or liquids at the application temperature, dissemination and distribution challenges become much more difficult than for gaseous agents.

### Liquid Aerosols - Water Mist

Full-scale total flooding water mist extinguishment tests, including mists with additives such as AFFF, were conducted by NRL in the early 1980s in 83 m<sup>3</sup> and 324 m<sup>3</sup> highly instrumented compartments.<sup>57</sup> The testing demonstrated the effectiveness of a fresh water mist with a high fraction of droplet diameters under 50  $\mu\text{m}$  in diameter. Fixed arrays of commercial nozzles, mainly Bete Fog Nozzles, were evaluated at discharge pressures up to 2 MPa (300 psi). Suppression challenges were included in a variety of Class A (solid) and Class B (liquid) fuels in compartments configured as very obstructed and cluttered machinery spaces or torpedo rooms. Except for occasional malfunctions, all Class B fires were extinguished in 15 s to 40 s. Some Class A fires in the 324 m<sup>3</sup> compartment were fully extinguished with one or two bursts of water mist of 1 min to 2 min duration. The flames from other Class A fires were extinguished, but smoldering continued. Flaming combustion reappeared after the water mist system was turned off. Even with slow extinguishment, significant cooling was achieved; the fires were “slowed down” and re-entry by protected firefighters would have been possible. Even for the largest tests, the total quantities of water used for extinguishment were usually less than 190 L to 265 L (50 gal to 70 gal). For comparison, a conventional 38 mm (1½ in) fire hose delivers about 380 L/min (100 gal/min), and a single hose would hardly begin to quench these fires, especially in the obstructed geometries. With the

water mist, cleanup was minimal. The experience showed the great merit of water mist for total flooding applications and the potential for optimization.

### **Solid Aerosols - Powders**

Early NRL studies in the 1950s provided quantitative data on the effectiveness advantage of potassium bicarbonate ( $\text{KHCO}_3$ ) over sodium bicarbonate ( $\text{NaHCO}_3$ ), and addressed practical techniques for allowing better implementation of powders. In large-scale powder studies in the 1980s, Ewing et al. at NRL found that the increased efficiency with decreasing powder particle size observed in small, bench top experiments was also valid when extinguishing large heptane pool fires ( $0.29 \text{ m}^2$  and  $2.32 \text{ m}^2$ ).<sup>58,59</sup> Momentum factors for getting the particles into the flame sheet were considered.

### ***Pyrogenic Generated Aerosols***

Pyrogenic generation of fire suppression agents is one method of generating and dispersing aerosol agents in large-scale. The “Halon 90 - Second Conference on the Fire Protecting Halons and the Environment” in Geneva on 1-3 October 1990 presented Russian fine solid aerosol fire suppressant efforts via videos of pyrotechnic devices in operation. These combustion devices released a very hot product stream that produced very small solid aerosol particles by condensation. Also presented were a number of Russian pyrotechnic aerosol efforts, including work by Russian émigrés and further studies in Israel and the USA. Initial U.S. Navy evaluation at the Spectronix Israeli site in August 1992 confirmed that the buoyancy of the exothermically produced aerosol is a significant distribution issue in employing a heterogeneous fuel/oxidant propellant product as a total flooding agent in large spaces.

Follow-up experiments at NRL measured aerosol generation temperatures and pressures and evaluated two approaches to removing heat: passive water bath and water spray generators. Fire threats included n-heptane pool fires of various sizes. In the  $56 \text{ m}^3$  ( $2000 \text{ ft}^3$ ), 4.3 m (14 ft) tall instrumented compartment tests,<sup>60</sup> aerosol concentrations were determined from optical density measurements at three heights: 0.5 m, 2.0 m, and 4.1 m (1.7 ft, 6.7 ft, and 13.5 ft).

In tests of uncooled aerosol generation, 1/4 to 1/3 of the solid agent containing pyrotechnic material was aerosolized with over 200 L of  $\text{CO}_2$  per kg of original material. There was also considerable energy emitted. Visible flame plumes 30 cm long exited the generator horizontally, but then quickly rose almost vertically due to buoyancy effects. The highest and middle optical probes were quickly engulfed using 1 kg of material. Only after almost 90 s did the aerosol cloud descend to within 0.5 m of the floor. The aerosol densities took over 4 min to equilibrate and maintain these levels at the three heights. There was little visible residue.<sup>61</sup>

Rapidly bubbling the hot aerosol through water for cooling produced both a rising buoyant plume and a dropping cooled cloud. The two layers did not coalesce until after 2 min, and the aerosol densities were lower with water removal of the aerosol.

The generators utilizing water spray cooling dispensed agent horizontally for over 1 m. However, the 1 kg aerosol charge was not cooled sufficiently by 1.6 L water injection and exited the generator at close to  $1000^\circ\text{C}$ . The horizontal momentum thrust dissipated and buoyancy forces still dominated dispersion. Thus, the elevated temperatures of pyrotechnic-produced aerosols remained a concern.

Large-scale fire extinguishment tests evaluated both liquid and solid aerosols. Hot gas generators were found to extinguish 0.23 m<sup>2</sup> pan fires in 45 s with 4 kg of pyrotechnic material, equivalent to 71 g of solid fire extinguishing agent per m<sup>3</sup>. Water bath cooled generators could not extinguish the fires with 3 kg of material; extinguishment required 5 kg and more than 115 s (equivalent to 89 g/m<sup>3</sup>). In contrast, the water spray cooled generators extinguished a 0.23 m<sup>2</sup> pool fire in 65 s using just 3 kg of agent (equivalent to 54 g/m<sup>3</sup>).

Larger, 1.1 m<sup>2</sup> pan fires were extinguished more quickly and required powder concentrations as low as 15 g/m<sup>3</sup>. However, the larger pan fires were partially self-inhibited by oxygen depletion and were thus easier to extinguish. Even then, aerosol generation and fire extinguishment took significant lengths of time. Much faster generator mixture burning rates are possible with other compositions. However, the increased energy release rates can exceed pressure and temperature safety level requirements, requiring greatly improved aerosol cooling mechanisms to obtain uniform distributions.

Researchers did note that dry chemical fire extinguishing powders exhibited suppression vs. size behavior similar to water aerosols. For a fixed mass of extinguishant, larger particles were found to be less effective and were observed to fall out faster than smaller ones. Very small pyrotechnically generated particles, with estimated diameters ranging from 0.5 μm to 4 μm, propelled at a fire, should be easily swept away by fire-generated convection currents. The small particle size and high concentration aerosol cloud should also cause concern in occupied enclosures. Particles less than 5 μm in diameter can penetrate deep into the lung and cause pulmonary complications, physically clogging the small pulmonary air paths. Some aerosol formulations that have been pursued, while possibly more efficient as fire extinguishants, may generate more toxic and abrasive products. A U.S. Navy toxicological evaluation of a pyrotechnic fire extinguishing formulation with rats showed short-term breathing difficulties although no residual health effects were observed. For the protected area, the hygroscopic nature of some aerosol residues may lead to corrosion and electrical problems.

Additional pyrotechnic approaches were pursued in England, the U.S., and the former Soviet Union. Detailed results were often not available due to the proprietary nature of the materials tested. Solid energy absorbers, evaluated by various producers, increased weight penalties. "VNIIPO" (Moscow) studied nine different types of pyrotechnic-generated aerosol units from "GABAR," "GRANIT," "PERM," "SOYUS," and "Technology," in October 1993. Tests were conducted on 5A and 13B challenges in a 64 m<sup>3</sup> volume. Only the two GABAR single units succeeded in extinguishing both test fires and preventing reignition.<sup>62</sup> Dr. Baratov claimed his GABAR company units addressed the concerns of ignition of combustibles by hot propellant exhaust, cooled aerosol generation for better total volume distribution, and effectiveness on smoldering combustion. One U.S. Army test series on tank engine compartment fires found a pyrotechnic agent successfully extinguished the fire only to later reignite it. The weights of the heat abstracting units can be considerably more than the pyrotechnic charge weights. Still, total system weight was low compared to the pressure vessels and piping of halon-like systems.

Achieving homogeneous distribution can be a significant implementation problem for pyrogenic approaches in large spaces. However, such fire suppression strategies may be quite satisfactory for smaller spaces with lower ceiling heights, such as small rooms, cabinets or storage closets.

## 4.2.6 Modeling

For most of the 20<sup>th</sup> century, there were few basic models that described details of aerosol/flame interactions for non-combustible aerosols. Prior to the NGP, there were no detailed models describing the size reduction and evaporation of droplets in flames, or their effect on surface reaction kinetics. Even models that predict what size droplets could reach burning surfaces were not generally available. Understandably, there was interest in understanding the overall performance of larger-scale water mist systems.<sup>42,63</sup> In 1955, Braidech et al.<sup>1</sup> concluded that, in most cases, the efficacy of water mist is predominantly due to the oxygen displacement effect of the water evaporating, rather than to thermal cooling. In the late 1990s, modeling research began to examine the interactions of droplets with flames. Chen et al.<sup>64</sup> considered the motion of droplets in a non-premixed counterflow field. They considered both n-heptane and water droplets. For the droplet sizes considered, Chen et al. showed that a droplet can penetrate through the stagnation plane established by the gaseous streams and reverse its trajectory at some point in the opposing side of the flow. Prasad et al.<sup>65</sup> modeled water mist suppression of diffusion flames, including the dependence on the droplet trajectories into the flame.

## 4.3 THE NATURE OF AEROSOLS

### 4.3.1 Quantitative Descriptors

#### Particle Diameter

Aerosols are almost never monodisperse (all drops/particles of exactly the same size). Real aerosols can be nearly monodisperse, but more typically exhibit a range of particle sizes. A mean or average diameter is useful for providing specific information relating to a particular phenomenon controlling the process under investigation.<sup>66</sup> (See Table 4–1) These definitions are strictly true only for spherical aerosol particles or liquid drops.

**Table 4–1. Mean Diameter Definitions, Symbols, and Notations used to Describe Aerosol Size Distributions.**

Mean Diameter Basis	Symbol	Notation
Arithmetic or length	$D_{10}$	$\Sigma N_i D_i / \Sigma N_i$
Surface area	$D_{20}$	$(\Sigma N_i D_i^2 / \Sigma N_i D_i)^{1/2}$
Volume	$D_{30}$	$(\Sigma N_i D_i^3 / \Sigma N_i)^{1/3}$
Sauter (SMD)	$D_{32}$	$\Sigma N_i D_i^3 / \Sigma N_i D_i^2$

The arithmetic or length mean,  $D_{10}$ , is simply the mean diameter of the spherical particles. The Sauter Mean Diameter (SMD) is that diameter for a single particle whose ratio of volume to surface area is the same as that of the entire aerosol. While  $D_{10}$  and the SMD values can be used to compare the mean diameters or surface area ratios of various aerosols, they do not convey information regarding the distribution of particle sizes.

Aerosols can also be described by defining a mass accumulation diameter such that all droplets below this diameter make up a certain percentage of the total mass of the aerosol. For instance,  $D_{0.5}$  is that droplet size such that half (0.5) of the liquid volume is in droplets of smaller diameter. The  $D_{0.5}$  diameter

is also referred to as the mass median diameter (MMD). Other common mass accumulation diameters are for 10 %,  $D_{0.1}$ , and for 90 %,  $D_{0.9}$ .

### Particle Size Distribution

Aerosols with similar  $D_{10}$  values,  $D_{0.5}$  values,  $D_{30}$  values, or SMDs can have very different size distributions. Since aerosols of different size can exhibit different degrees of fire suppression effectiveness, characterization of the range of sizes or size distribution is necessary to compare the suppression performance of different aerosols and to make valid comparisons between experimental observations and modeling predictions. Several mathematical expressions for size distributions have been proposed, although each of them has some shortcomings. The expression to use is the one that best characterizes the relevant properties of the mist under study.

A simple and practical method for displaying droplet size information is to plot a histogram where the number of droplets in a defined size bin is plotted for that bin. In practice, the minimum size plotted is dictated by the physical limitation of the instrument settings. A water mist histogram (obtained with a phase Doppler interferometer as discussed below) is presented in Figure 4-1. Values for the mean diameters defined in Table 4-1 for this mist are indicated in the table. In the limit of small bin size, the histogram becomes a frequency or size distribution.

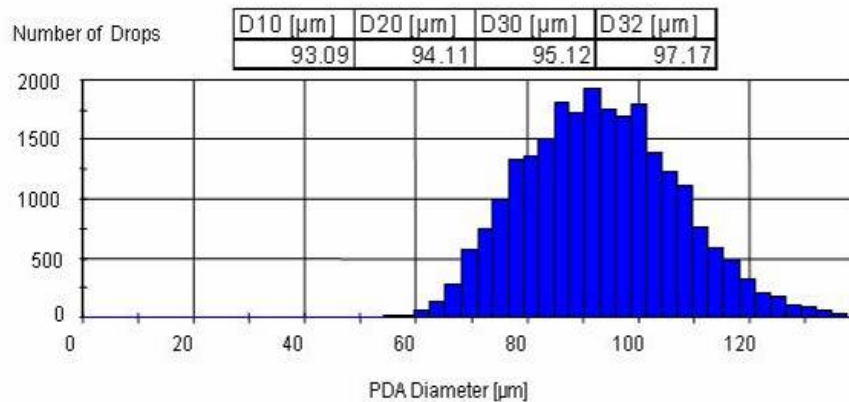


**Figure 4-1. Water Mist Size Histogram and Values of Several Mean Diameters.**

Two commonly used functional expressions describe the droplets as (a) a Gaussian distribution or (b) a mass accumulation.<sup>67</sup> These simple expressions cannot be used to describe bi- or multi-modal distributions. For these, linear combinations of the different single expressions are sometimes used.

The Gaussian or normal distribution with respect to the natural logarithm (lognormal) of the diameter is given in Equation (4-1). This expression is often sufficient to fit observed experimental droplet size distributions, where  $d_{mn}$  is the number geometric mean droplet diameter  $D_{10}$ , and  $s$  is the corresponding standard deviation describing the spread in the distribution.

$$N(d) = \frac{0.399}{s * d} \exp\left(\frac{\{\log(d) - \log(d_{mn})\}^2}{2s^2}\right) \quad (4-1)$$

The Rosin-Rammler equation (mass accumulation expression) describes the aerosol by relating the mass of aerosol material contained in particles up to a certain diameter. The Rosin-Rammler expression is given in Equation (4-2). In this expression,  $a$  and  $b$  are constants related to a mean diameter and the spread, respectively.

$$N(d) = \frac{b}{a^b} d^{b-4} \exp\left(\left(\frac{d}{a}\right)^b\right) \quad (4-2)$$

Note that each expression includes two parameters to describe the distribution. One advantage of using the Rosin-Rammler expression is that all of the representative diameters (e.g.  $D_{0.1}$ ,  $D_{0.5}$ , etc.) can be related to each other through the spread.

Both of these two mathematical descriptions of the histogram in Figure 4-1 are presented in Figure 4-2. The values of the two parameters are:  $D_{10} = 93 \mu\text{m}$ ,  $s=0.15$  (lognormal) and  $a=101$ ,  $b=9.4$  (Rosin-Rammler). Both expressions qualitatively describe the mist, although the lognormal expression is a better match for this mist in both the peak position and spread in the distribution.

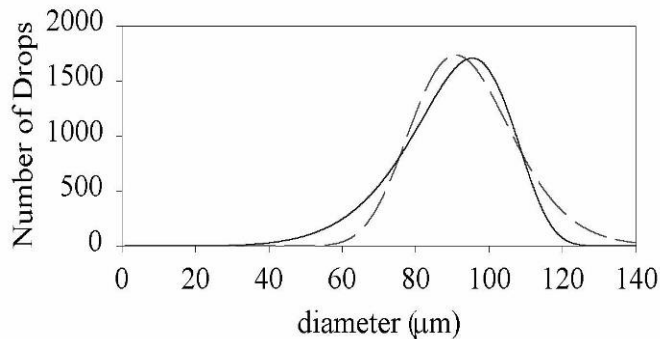


**Figure 4-2. Lognormal (dashed line) and Rosin-Rammler (solid line) Expressions Fit to the Water Mist Histogram Presented in Figure 4-1.**

### 4.3.2 Generation Techniques

Generating, controlling, and measuring aerosols are challenging but necessary tasks for studying fire suppression as well as evaluating fire suppression systems. Although concentration standards are straightforward for gases, there is no aerosol standard. An aerosol generation system that could reproducibly produce a uniform distribution of a monodisperse (or polydisperse) aerosol would be extremely useful.

Aerosols of liquid droplets can be produced using ultrasonic agitation of the liquid, either disrupting the liquid surface or modulation of a liquid jet stream. NGP studies employed both methods; the specifics are outlined in Chapters 7 and 8. Assisted breakup of liquid jets can produce aerosol droplet size distributions that are narrow, approaching a single, monodisperse droplet size for all of the drops. This

generation method is ideal for small, bench-top studies only requiring a small number of drops. The number of droplets produced is in general not sufficient for large-scale suppression applications.

Powder aerosol samples are typically produced by physically crushing solid samples, followed by size separation using various sieving protocols. Sample crushing often results in a range of particle shapes in a given size bin, where individual shape differences will depend on the nature of the powder and the crushing/sieving protocol. Sample drying is often required to improve the flow properties, especially for very small particles. Small concentrations of flow enhancers such as silica can improve flow properties.

Large masses of powder particles can be generated using pyrogenic methods discussed in Section 4.2.5. Particle size and composition (including the addition of chemical suppressant moieties) can be varied depending on the type of generator and the particular propellant formula. Because of the high particle momentum and often high gas temperatures exiting the generators, pyrogenic powder aerosol generation techniques are rarely practical for bench-scale studies. However, in large-scale applications, the high particle momentum can be very useful in aiding agent dispersal.

### **4.3.3 Quantification of Aerosols**

Gaseous fire suppression agents can generally be monitored and controlled by regulating the volumetric flow of the agent. Gaseous agents generally distribute throughout the measurement volume so that agent spatial distribution issues are generally dictated by the physical constraints of the application geometry. Aerosol agents will not uniformly fill the application space, especially very large, obstructed spaces. In order to determine the amount of aerosol agent in the application area, measurement techniques must be employed that are applicable and can provide relevant, valid information. Relevant information includes data on how the aerosol is distributed spatially in the application area, especially in and around any fires that may be present.

### **4.3.4 Aerosol Size and Velocity Characterization**

One of the most challenging aspects of working with aerosols is characterizing the aerosol that has been generated in order to obtain relevant, quantitative information. Such quantitative information, even on a relative basis, is required in order to make valid suppression effectiveness comparisons. A general discussion of the characterization methods used in NGP aerosol fire suppression studies is outlined below. Specific details are given in the individual studies.

### **Diffraction Method**

Diffraction-based systems are capable of providing size information (either mass or volume) of an aerosol.<sup>68</sup> The experimental layout is fairly simple, as shown in Figure 4-3. A coherent light source (i.e., a laser) and a two-dimensional detector (i.e., a linear array of detectors or a charge coupled device, CCD, camera) are needed. The laser light, directed at the detector, passes through the sample volume containing the aerosol. Laser light diffracts around individual droplets in the aerosol (Fraunhofer diffraction). The light intensity pattern falling on the camera is a superposition of all of the single droplet diffraction patterns. By deconvoluting the diffracted intensity from the ensemble of drops, the mass or volume distribution can be derived. Diffraction methods do not rely on a spherical droplet or particle,

although the determination of volume or mass must assume some shape. The ease of set-up and straightforward calibration requirement make diffraction methods attractive.

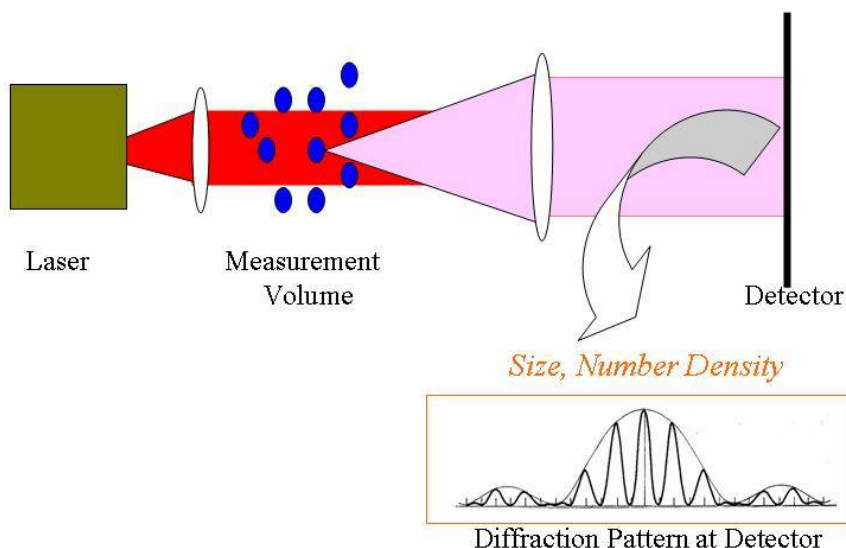


**Figure 4-3.**  
**Schematic Diagram**  
**for Diffraction-based**  
**Particle Sizing.**

Diffraction methods lack the spatial resolution of other optical approaches. They measure everything that lies in the beam path. Because they rely on diffraction, higher power laser sources are often needed. Diffraction methods also do not provide velocity information, and thus cannot provide flux information directly. Although the lack of velocity information is an issue, diffraction methods can provide droplet size distribution and density information. An effective mass flux can be estimated for well-characterized flows.

### Phase Doppler Interferometry Method

Phase Doppler Interferometry (PDI, also referred to as phase Doppler anemometry, PDA) is an established technique that can provide velocity information or both velocity and size for individual, spherical particles.<sup>69</sup> PDI systems which only provide velocity information are called Laser Doppler Velocimetry (LDV) systems. PDI measurement times can be as short as 1  $\mu$ s, so that statistically significant size histograms can be generated in less than a second depending on the particle number density. Droplet sizes from  $\sim 1 \mu\text{m}$  to several mm can be measured, although not with a single system configuration.

PDI droplet sizing relies on the phase difference between two signals originating from the same point and arriving at two spatially separated detectors. Each signal is generated by a droplet passing through a set of parallel grating lines produced from the overlap of coherent laser beams. The technique is depicted schematically in Figure 4-4 with a representation for the ellipsoidal "grating" measurement volume. PDI determined diameters are only strictly valid for spherical drops. A third detector, providing a second phase difference, is used to check the sphericity assumption.

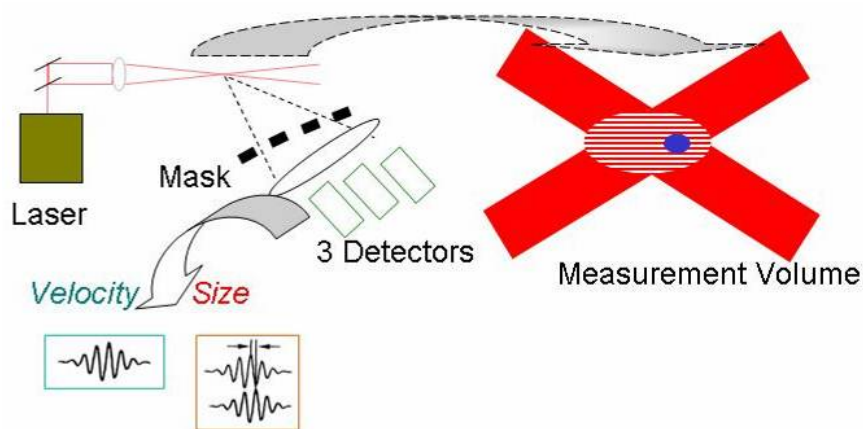


**Figure 4-4. Diagram for 1-D Phase Doppler Interferometry System for Obtaining Size and Velocity of “Spherical” Aerosol Particles.**

The size of the ellipsoidal measurement volume depends on the wavelength of the laser, the beam diameter at focus, and the crossing angle. Typical measurement volumes are  $\approx 1$  mm long by 0.2 mm diameter for droplet sizes relevant to water mist suppression. Only a single droplet can be present in this volume during the measurement period for the measurement to be valid. This requirement can be problematic for very large number densities (e.g.,  $> \approx 10^4$  drops/cm<sup>3</sup> for uniformly dispersed 50  $\mu$ m diameter drops).

The laser wavelength and beam-crossing angle control the grating line spacing. Passage of the droplet through the grating generates a Doppler burst pattern containing the droplet 1-D velocity information perpendicular to the fringes. Additional hardware is required for 2-D and 3-D velocity information. The grating fringe spacing must be reasonable for the droplet size in order to determine a valid burst pattern and provide the corresponding velocity. For closely spaced lines and large drops, there may not be sufficient modulation in the signal to qualify as a valid burst. Large spacings and small droplets may not provide enough modulations for the phase shift validation. PDI signals can originate from light reflected from the droplet surface or refracted through the drop. The angle of the refracted light exiting the droplet is dependent on the liquid index of refraction that must be known. Reflected light does not depend on the index of refraction but signals are generally much weaker. The choice of scattering angle will determine which scattering mode is dominant. When a single scattering mode is dominant there will be a linear correlation of the droplet diameter with the phase difference. If more than one scattering mode significantly contributes to the signal, the phase angle/diameter relationship will not be linear. For water droplets in air, first order refraction dominates light scattered at 30° in the forward direction. A scattering angle of 30° was used for measuring water droplets in the NGP studies.

Uncertainties in the PDI size determinations associated with the scattering angle and refractive index are generally less than a few percent. Because of the finite range for the detector and the non-linear dependence of the scattering intensity on the droplet size, the usable dynamic range dictates a droplet size dependent precision in the determination of the sizes. Additional potential limiting factors are the laser power, detector gain setting, and S/N ratio. These combined effects typically limit the uncertainty for a PDI size determination to at least 0.5 % of the full-scale reading. Velocity uncertainties depend on the processor settings, primarily the need to divide the velocity space into a finite number of bins. Binning depends on the size range to be measured, which depends on the optical configuration used. In addition to the dependence on processor settings, uncertainties in the velocity determination depend also on the

instrument A/D resolution, fringe spacing uncertainty, and sampling frequency. Velocity uncertainties can be as high as  $\pm 25\%$ .

The mass flux determination relies on the droplet size, velocity, and the probe volume. The droplet number density also relies on the probe volume. However, the probe volume is droplet size dependent, requiring a correction for both number density and mass flux. The dynamic range for a single PDI system configuration is typically 40:1. This value depends on several factors, including the optical system, laser power, detector gain and dynamic range, and system S/N ratio. Obtaining accurate size information becomes a compromise between the size resolution desired and the range of droplet sizes that can be determined.

### Imaging Method

Capturing an image of the aerosol particle can provide both size and velocity information. Unlike diffraction-based techniques, imaging techniques can be used to “size” non-spherical particles or spherical objects such as drops. Imaging techniques have been used extensively to study and understand sprays and spray formation and development.<sup>70</sup> In its basic form, an imaging configuration is fairly simple, as shown in Figure 4-5. It consists of a light source and a recording medium, either photographic film or more typically a CCD camera. The light source is normally a laser, which provides sufficient spectral brightness in a short time period to “freeze” the motion of the drop. Droplets can either be back illuminated in shadow method, as indicated in Figure 4-5, or illuminated from the front. The shadow method is more often used, as the droplet size dependent back-reflected light can complicate data collection. In the shadow method, droplet images appear as dark spots on a light background. The 2-D velocity information in the image plane can be determined from timing droplet exposure “tracks” or by double pulsing the light source, creating two images of the same droplet displaced according to its velocity and the illumination time delay. The two images can be in the same camera frame or in sequential frames. Software algorithms correlate the images, permitting both speed and trajectory information. Algorithms permit false shadow rejection from images that remain in the same location frame after frame (e.g., a spot on a lens or window).

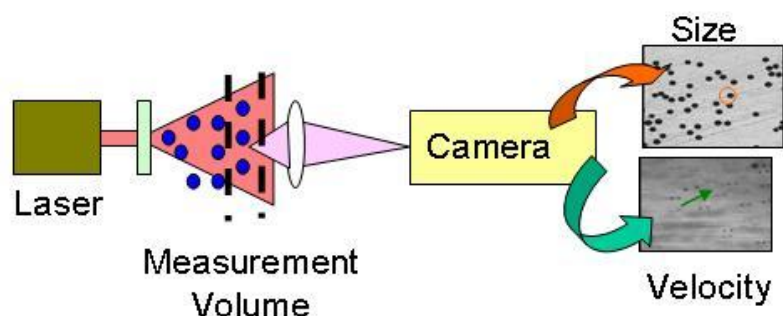


**Figure 4-5. Schematic Diagram for Imaging-based Particle Sizing.**

Although cameras with photographic film can be used, CCD cameras provide greater flexibility. Cameras can be digital or analog. Digital imaging requires a large data storage capacity if the raw images are saved. This may limit the time for continuous data collection. Images can be processed either on-line or off-line. On-line image processing generally saves time but unless the images are also stored, valuable information may be lost. Off-line processing requires that the raw images be stored. Analog cameras

with tape storage (usually super VHS) offer the advantage of long data collection times (several hours). Acquiring the raw images and performing off-line data reduction is an added time expense, but can be an advantage. Repeated data reduction using different fitting parameters can sometimes identify issues with the data collection or point out systematic problems.

Droplets from a few  $\mu\text{m}$  to several mm may be imaged but the total size range requires a change of optics. The measurement region that can be imaged depends on the magnification but is typically  $1\text{ mm}^2$  for detecting  $\sim 4\text{ }\mu\text{m}$  to  $300\text{ }\mu\text{m}$  diameter drops. Similar to microscope optics, imaging magnification factors must be greater than one, requiring that the distance of the droplets from the focusing lens be much shorter than the distance of the image from the lens. In practice, this means that the sample volume must lie fairly close to the collection lens for the smallest droplets.

Size and velocity measurement accuracy is controlled by the lens focusing system, the media resolution (photographic grain limit or camera pixel resolution), and the determination of degree of focus. Since the data obtained are a mixture of in-focus and out-of-focus images, image analysis schemes must be employed to decide which images are valid and then render sizes. The degree of focus impacts both the location of the droplet edges and also the determination of the measurement volume.

The uncertainty in the measurement volume is the largest source of uncertainty for imaging detection. Both the droplet number density and mass flux determination are impacted by this uncertainty. The derived particle volume depends on the size of the drop but fortunately, computers can aid in eliminating the human bias in the decision-making. The key to achieving a reasonable accuracy lies in the calibration and validation processes.

Particle Image Velocimetry (PIV) is the macroscopic analog of droplet size imaging.<sup>71</sup> In PIV, the marker particle image is not resolved since size resolution is not desired. Marker particles are illuminated with two temporally delayed laser sheets. Small particles, typically  $< 1\text{ }\mu\text{m}$ , are used to insure that the marker particles validly represent the flow field. Large areas ( $\geq 1\text{ m}$  by  $1\text{ m}$ , depending on the spectral brightness of the laser source and the collection optics) can be characterized. By recording two shots in the same frame or in sequential frames, both speed and direction of movement of the particle can be derived through image analysis. PIV is typically used to monitor bulk gas or liquid flows. It can also be used to monitor the flow behavior of larger aerosol particles that, because of their size, do not follow the flow field streamlines. As is shown in this chapter, suppression aerosol particle velocity (speed and trajectory) controls the overall aerosol effectiveness. Such velocity information becomes key in understanding the suppression mechanism for aerosol agents.

### **4.3.5 Aerosol Properties Affecting Behavior**

#### **Evaporation/decomposition behavior**

Rosser et al.<sup>13</sup> and Mitani and Niioka,<sup>43</sup> based on observations for particle suppression behavior in premixed flames, described the flame suppression mechanism in terms of particle size and residence times. Generalizing these findings to both liquids and solids, four steps with their characteristic times relevant to suppression behavior of an aerosol (liquid droplet or solid particle) can be assumed:

Step I: aerosol heating,

Step II: aerosol evaporation (solid or liquid) and/or decomposition (primarily solids),

Step III: generation of the inhibitor radical species in the gas phase, and

Step IV: inhibition of the gas-phase combustion process.

Optimum inhibition efficiency requires completion of all four steps. The slower steps determine the extent of inhibition and what aspects of the condensed phased suppression mechanism contribute to the inhibition process. The times for Steps III and IV involving gas-phase reactions are typically much shorter than the drop/particle heating times or the decomposition/evaporation times for Steps I and II.

Heating of the aerosol in Step I needs to raise the temperature to the aerosol's boiling/decomposition temperature. The particle heating will depend on the size of the particle, the particle thermal conductivity and that of the surrounding gas, and the gas temperature. Flames temperatures encountered are typically  $\approx 1800$  K. Assuming the aerosol particles are small, the heating time for Step I is typically short,  $\ll 1$  ms.

The evaporation of the aerosol particle in Step II involves losing mass (vapor) to the surroundings. Several models have been proposed for treating the evaporation of liquid drops, depending on what regimes are relevant and what assumptions are appropriate. One model suitable for the experimental conditions under consideration here is<sup>72</sup>

$$d^2(t) = d_0^2 - Kt \quad (4-3)$$

where  $K$ , the evaporation constant, is given by

$$K = \frac{8\lambda}{\rho c_p} \ln \left[ 1 + (T - T_{boil}) \frac{c_p}{h_{vap}} \right] \quad (4-4)$$

The time for complete evaporation to occur can be estimated from:

$$t_{vap} = \frac{d_0^2}{K} \quad (4-5)$$

Equation (4-3) is referred to as the d-square law for droplet evaporation and predicts the droplet diameter,  $d$ , at any time,  $t$ , in terms of the original droplet diameter,  $d_0$ . The mass transfer is dependent on the temperature,  $T$ , and thermal conductivity,  $\lambda$ , of the surrounding gas as well as on the properties of the drop: heat capacity at constant pressure,  $c_p$ ; density,  $\rho$ ; enthalpy of evaporation,  $h_{vap}$ ; and boiling point,  $T_{boil}$ . According to Equation (4-5), the time required for the droplet to evaporate completely is dependent on the original diameter of the drop.

Evaporation times for water as a function of droplet size for temperatures ranging from 1100 k to 2200 K are shown in Figure 4-6. The evaporation time for a 30  $\mu\text{m}$  diameter water droplet in an air stream at 2100 K is predicted to be  $\approx 2.5$  ms. The thermal conductivity data for air are from Kays and Crawford.<sup>73</sup>

Whether the droplet will have sufficient time to evaporate partially or completely will depend on how long the droplet resides in the higher temperature region. This time depends on the specifics of the flow field configuration.

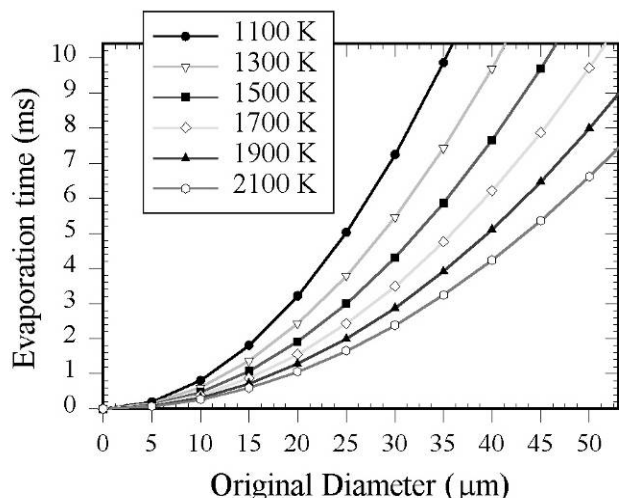


**Figure 4-6. Predicted Evaporation Times using Equations (4-3) through (4-5) for Water Droplets in Air at the Indicated Temperature as a Function of Initial Droplet Diameter.**

**Flow Entrainment**

Generation of the aerosol is only a first step in producing an aerosol suitable for further study. For flame studies, the aerosols must be seeded or entrained into a flow that hopefully results in as uniform a distribution as practical. Both uniformity in the particle mass flow as well as uniformity of the distribution of particle sizes representative of the entire distribution are needed to be able to make valid comparisons and quantitative evaluations. In order to entrain the aerosol particle in the carrier gas flow with a minimal difference in the particle and gas velocities, the gas flow velocity must equal or exceed the particle’s terminal settling velocity<sup>74</sup> in that gas.

The terminal settling velocity assuming Stokes flow for a spherical particle can be expressed as

$$v_T = gd^2 \frac{(\rho_p - \rho_{gas})}{18\eta_{gas}} \tag{4-6}$$

The terminal velocity,  $v_T$ , depends on the acceleration due to gravity,  $g$ , the density difference between the particle,  $\rho_p$ , and the carrier gas,  $\rho_{gas}$ , and the viscosity of the carrier gas,  $\eta_{gas}$ . Values of  $v_T$  for water droplets and sodium bicarbonate particles, two aerosols studied in the NGP program, are shown in Figure 4-7. Terminal settling velocities are centimeters per second depending on diameter and have a quadratic dependence on particle diameter.

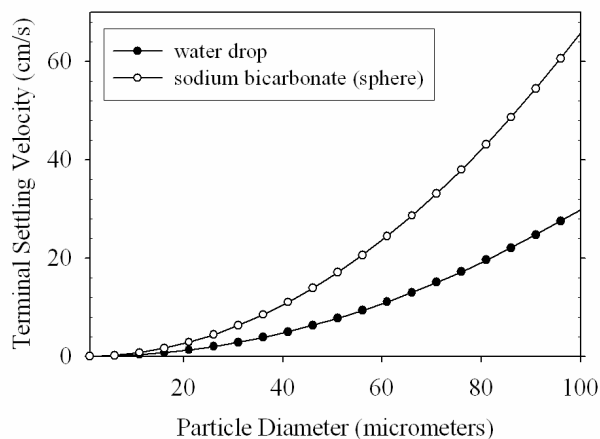


**Figure 4-7 Predicted Terminal Settling Velocity for Water Droplets and Sodium Bicarbonate Particles in Air at 20 °C.**

Entrainment velocities adequate for studying water droplets may be insufficient for studying the same size sodium bicarbonate particles. Thus, the particle terminal settling velocity put limits on the size of aerosol particles that can be entrained and/or delivered to the experiment in a primarily vertical flow. For aerosols whose size distributions are non-monodisperse, low entrainment velocities can result in particle size discrimination. In some cases, velocity discrimination can be used to restrict the aerosol particle sizes introduced to the experiment. Thus, entrainment flow conditions must be considered when carrying out experiments as well as in the interpretation of data.

Particles moving in a flow with a thermal gradient will also tend to experience a thermophoretic force pushing them in the direction of lower temperature. The effect is greater for smaller particles and large temperature gradients. High temperature environments are exactly the conditions that favor rapid disappearance of the condensed phase aerosol agents due to evaporation or decomposition.

## **4.4 THE NATURE OF FLAMES**

### **4.4.1 Flame Characteristics**

Suppression of fires involves heat extraction, oxygen reduction, and, for chemical agents, kinetic effects at the molecular level that involve heat production and the concentration and distribution of key flame and inhibitor species. Despite the studies carried out prior to the NGP, considerable uncertainties existed in the assessment of aerosol suppression pathways, especially in the quantitative interpretation of suppression behavior. Early literature alluded to a dependence of aerosol suppression effectiveness on the fundamental aerosol size (liquid droplets or solid particles), and properties (composition, thermal stability, reactivity). In addition, the application environment (flow field, flow orientation, flame temperature) of the various fires investigated imposed characteristic residence times controlling the performance of the aerosols. Thus, characterizing these flame conditions is necessary to interpret and understand the aerosol suppression results.

For a system that undergoes combustion, the fuel and oxidizer can either be premixed (combined) or non-premixed (kept separate) upon entering the reaction region. Real fires often exhibit a combination of both mixing protocols. Figure 4-8 compares gaseous flame configurations to each other and the variation in the flow field complexity needed to describe and understand them. In general, the greater the complexity of the flow field, the more computationally challenging it is to include both the details of the flow and the details of the chemistry in the modeling treatment of the flame process. This is even more apparent in multiphase flow problems, such as the interaction of solids or liquids with gaseous flames. In order to understand the extinction mechanism of aerosols and approach a quantitative understanding of the aerosol/flame interaction, NGP researchers studied a number of flames depicted in Figure 4-8. This sometimes required a re-examination of key experiments in the literature with the focus on minimizing the number of parameters that might vary and exploring the dependence of several of these parameters on the overall suppression performance. Researchers paid close attention to the control of experimental parameters that could influence the results. In this way, the new data could be used more directly to validate the predictions of multi-phase flame suppression codes as well as aid in their development. The next sections address the different flame configurations explored under the NGP aerosol studies, discuss the metrics used to determine suppression effectiveness, and explore the nature and impact of the imposed residence times on the suppression properties of the aerosols investigated.

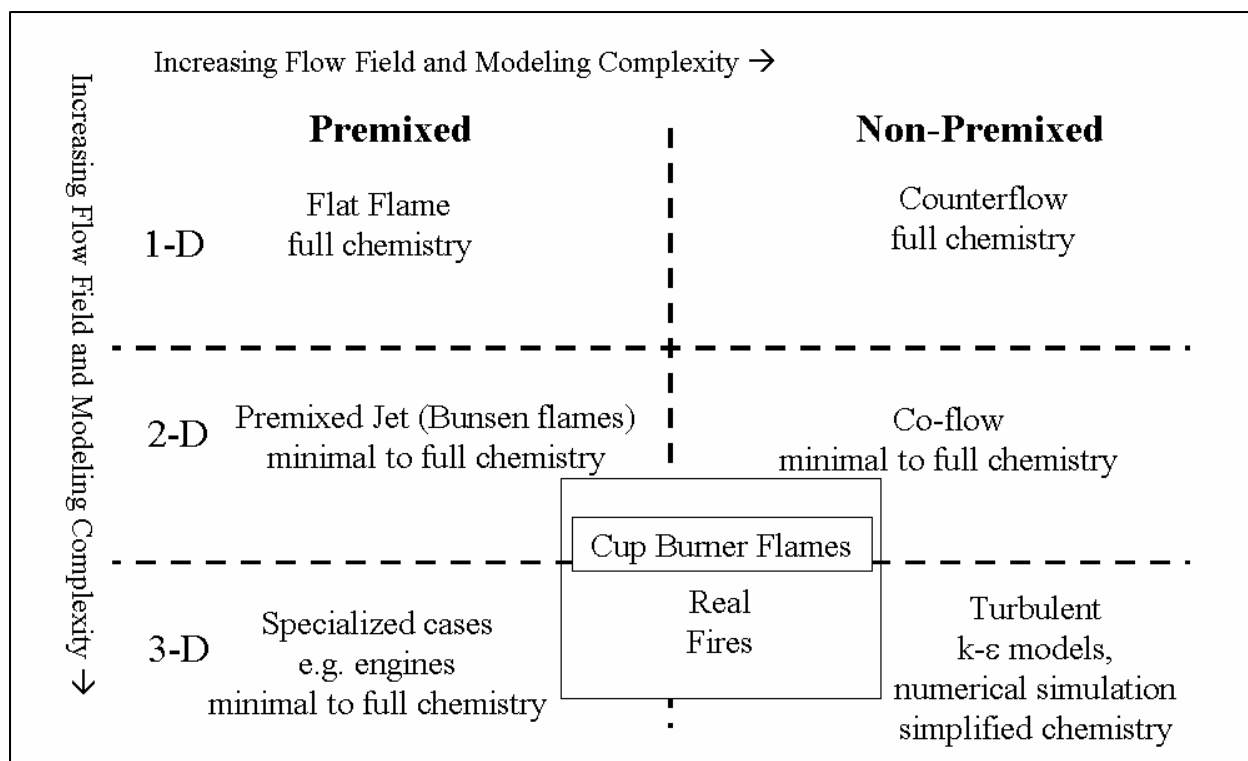


**Figure 4-8. Relationship of Flame Dimensionality and Modeling Complexity.**

#### 4.4.2 Premixed Bunsen Type Flames

Premixed flames offer the least complicated flow field for gaseous flames since they can be configured to give flat, essentially one-dimensional flames. Two such flames are shown schematically in Figure 4-9 from Reference 75. The ideal one dimensional flat flame shown at the left can be experimentally achieved with gaseous reactants and gaseous suppression agents. This configuration is difficult to achieve when aerosols must be introduced uniformly into the flame. Experimentally seeding aerosols into the premixed flow and maintaining the flat, one-dimensional geometry is very difficult.

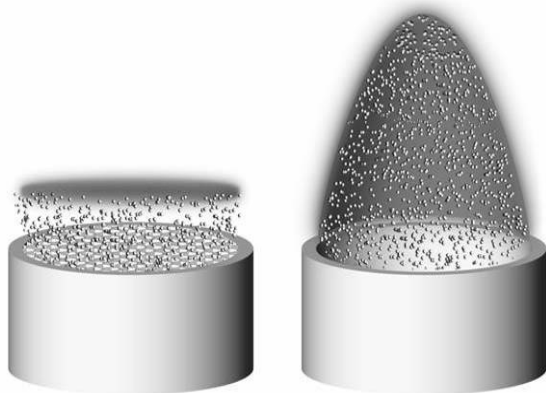


**Figure 4-9. Representations of Aerosol Suppressed Premixed Flames: (left) Ideal Mist Inhibited Flat Flame as Simulated in 1-D Modeling; (right) Bunsen-type Flame Typically Studied Experimentally.**

The air/fuel flow in a premixed Bunsen-type flame, shown on the right, can be fairly easily seeded with aerosols. The figure shows introduction of the aerosol which are seeded into the premixed gases. This is the experimental flame more typically studied with aerosols.

The laminar burning velocity is a fundamental property of a flammable gas mixture and is frequently used as an indicator of the effectiveness of an inhibiting agent.<sup>76</sup> There are various methods to measure laminar burning velocity.<sup>77</sup> Each method involves recording some aspect related to the burning region. The visible flame emission can be converted into a total burning surface area as can schlieren images of density gradients in the flame region due to regions of varying temperature. Both have been used to quantify the burning velocity. Although each gives a slightly different absolute surface area, they provide the same information when comparing suppressed flames to the unsuppressed flame. Ratio comparison minimizes systematic differences between various methods for burning surface derivation.

### 4.4.3 Non-premixed Flames

#### Counterflow

The counterflow or opposed flow flame configuration provides an excellent experimental and modeling arrangement to study the effects of aerosols on a flame and the effects of high temperature environments on the aerosol.<sup>64,78 79</sup> This configuration has been used to study the effect of aerosols on premixed flames by using two opposing premixed fuel and oxidizer flows.<sup>64</sup> Advantages of the counterflow arrangement include the ability to investigate variable flow residence times and potentially to separate chemical from physical effects.

The counterflow flame configuration is depicted schematically in Figure 4-10. The delivery tubes can be converging nozzles or straight tubes. The counterflow burner can be used to study gaseous and aerosol agents. In the non-premixed mode, fuel is introduced through one inlet and oxidizer through the other.

Non-premixed flames of hydrocarbon fuels in air burn near the fuel/air stagnation plane in a region that contains the stoichiometric composition for complete combustion. For hydrocarbon fuels, the flame resides on the air side of the stagnation plane, as depicted in Figure 4-10. The fuel can enter from the top or bottom for non-premixed flames, with air introduced from the opposite tube. The aerosol can be added to either the fuel or the air. Air side introduction of the aerosol is relevant to total flooding fire suppression scenarios and is the configuration most often studied. Transport and composition dependent suppression effects can be studied by comparing extinction results of air-introduced aerosols with results obtained when the aerosol is introduced into the fuel.

Representative centerline temperature and axial velocity profiles are indicated, as is the strain rate,  $a$ , the maximum gradient in the axial velocity on the air side of the flame. In this flow field, stable flames can be maintained if sufficient amounts of heat and flame radicals generated from the combustion process can be conducted to the unreacted fuel and air as they flow into the reaction zone. Extinction occurs when the flow is too fast to maintain the flame. Under these conditions, the flame strain rate exceeds a critical value referred to as the *extinction strain rate*. Suppression agents lower the extinction strain rate and this reduction is a direct measure of the suppression effectiveness. The flame strain rate can be estimated from the global strain rate.<sup>80</sup> Since the global strain rate can vary between burner designs, the local strain rate, determined by experimentally measuring the local velocity field, is used for absolute comparisons.

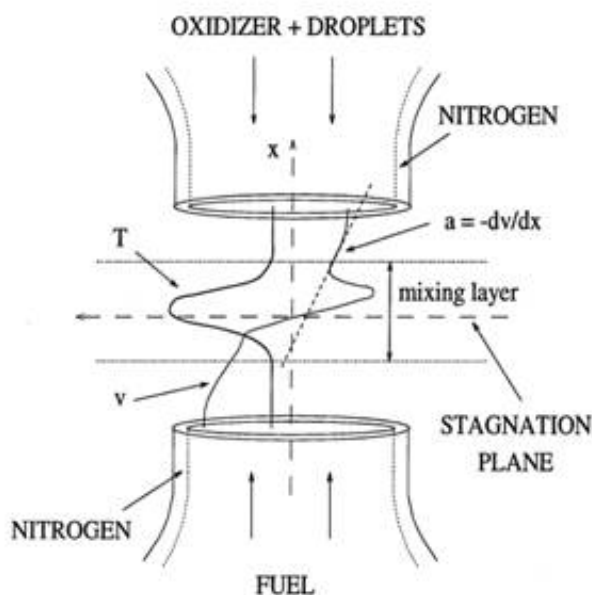


**Figure 4-10. Experimental Schematic for Studying the Effects of Aerosols on the Extinction Strain Rate of Counterflow Non-Premixed Flames.<sup>81</sup>**

The reciprocal of the strain rate can be used to estimate a characteristic residence time for an aerosol particle in this flow field. Depending on burner design, the local strain rate can range from  $\sim 10 \text{ s}^{-1}$  to the value for extinction in the absence of any inhibitor ( $\sim 600 \text{ s}^{-1}$  for propane/air flames). Thus, the particle residence time can be varied by an order of magnitude. Chen et al.<sup>64</sup> note that for certain conditions the aerosol particles can often be trapped and oscillate in the opposing streams, thereby increasing their effective residence times.

Another design for studying suppression of non-premixed flames in opposed flow is the Tsuji burner.<sup>41</sup> Gaseous fuel is introduced through a porous tube perpendicular to the air flow as seen in Figure 4-11. NIST incorporated a variant of this design to develop a suitable NGP screening test for condensed phase agents.<sup>82</sup> Details of that work can be found in Chapter 8.

In the Tsuji configuration, flames can be established in the forward, stagnation region or downstream of the air flow in the fuel tube wake. In the forward direction, the two-dimensional flames are very stable and can be accessed readily with various diagnostic probes. The Tsuji flame established in this flow field also lends itself to modeling. Since the fuel and oxidizer flows can be independently controlled, flame strain rate can also be easily varied and studied. The air stream velocity required to blow-off the forward, stagnation flame is used to evaluate suppressant effectiveness.

In the Tsuji configuration, as in the premixed and opposed flow configurations introduced above, aerosols introduced with the air stream (or their decomposition products) are restricted to enter the flame. This flow arrangement assures the optimum effectiveness for the added agent. Aerosol particles that are too large to completely evaporate or decompose in the flame could potentially collide with the porous fuel tube, requiring periodic tube cleaning or replacement.

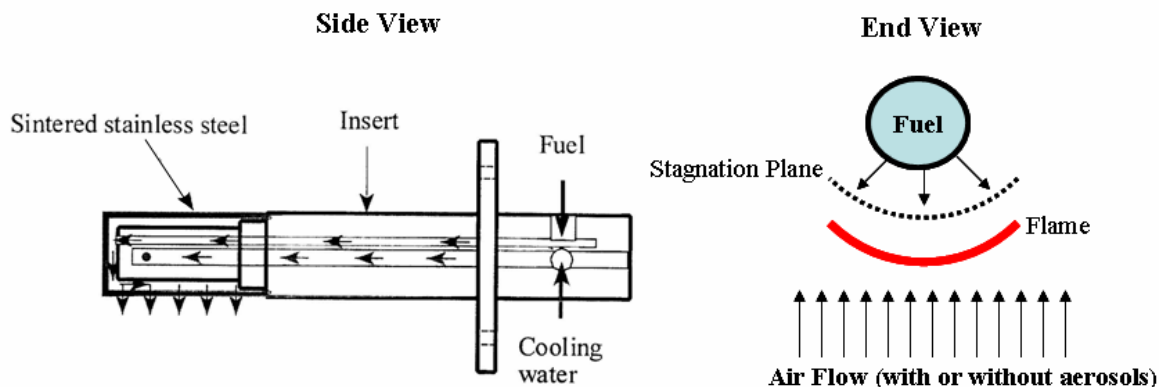


**Figure 4-11. Schematic of Tsuji Burner (left<sup>41</sup>) and Flame Configuration (right).**

### Cup Burner Co-flow Flames

Cup burner flame extinction results are commonly used in the fire protection industry for suppression agent effectiveness ranking as well as for suppression system design guidance. The cup burner flame is a non-premixed flame stabilized on a cylindrical cup that holds liquid fuel or delivers a low-velocity gas jet. A surrounding laminar co-flow of air carries the suppression agent of interest.<sup>83</sup> The majority of the agents studied have been gaseous.

Cup burner flames have many similarities to real fires: initial separation of reactants, flame flickering, and regions of varying strain rates. These similarities make cup burner extinction results useful for suppression agent ranking and for evaluating extinction requirements in real fire scenarios. These similarities also make the cup burner flames challenging for studying aerosol suppressants. Nonetheless, researchers had investigated the suppression behavior and effectiveness of condensed-phase particles in cup burner flames prior to the NGP. (See the work of Hamins et al.<sup>20,21</sup>)

A cup burner apparatus modified to study the suppression properties of water mist is shown in Figure 4-12.<sup>84</sup> Water droplet entrainment and flow conditioning occur in the lower section, water quantification occurs in the middle section, and the flame is located in the uppermost section.

Under the NGP, Linteris et al. studied the effects of various metallic compounds on cup burner flames. Several of the metallic compounds were found to be less effective than expected, surprisingly less effective compared to their performance in premixed or opposed flow flames. Even though the agents are introduced in the gas phase, their poor fire suppression effectiveness has been attributed to the formation of condensed phase particles in the cup burner flow field. Details of that work are presented in Chapter 3.

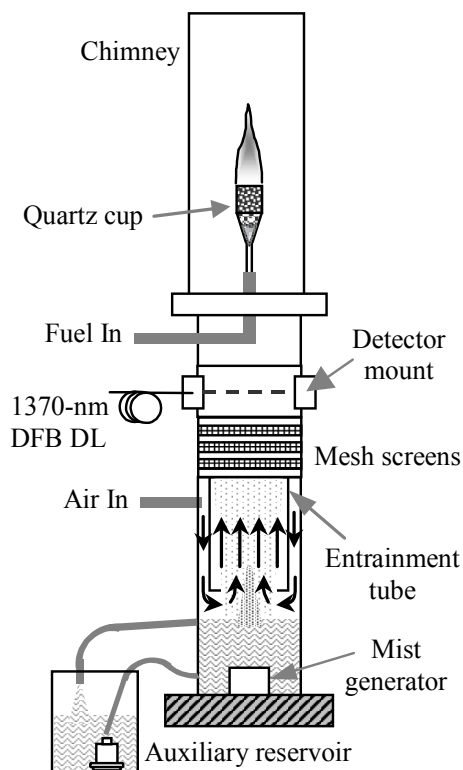


**Figure 4-12. Cup Burner Apparatus Modified for Water Mist Suppression Studies.**<sup>84</sup>

## 4.5 AEROSOL FLAME SUPPRESSION STUDIES

### 4.5.1 Water, a Physical Suppression Agent

#### Water Mist Studies in Premixed Flames

##### *Experimental*

NGP researchers at NRL studied the flame suppression properties of water mist as a function of droplet size, measuring the effectiveness of the mist on reducing the burning velocity of methane/air flames.<sup>85</sup> Mists were generated using various methods. Droplets smaller than  $1\ \mu\text{m}$  in diameter were generated using a venturi-based nebulizer (TSI Model 3076). A schematic of the nebulizer is shown in Figure 4-13. Pressurized air, flowing through a small orifice, produced a high velocity air jet. The resulting pressure drop drew liquid from a reservoir through a small tube and entrained it in the air jet, breaking the liquid into drops. Larger droplets impacted the nebulizer wall and returned to the reservoir. Droplets small enough to remain entrained in the air flow were carried from the nebulizer. The amount of mist exiting the nebulizer was determined by measuring the change in mass of the liquid reservoir with time for a fixed air flow. Mists of polydisperse droplets in the range of  $1\ \mu\text{m}$  to  $20\ \mu\text{m}$  were produced using a second venturi-based nebulizer (Airlife Nebulizer with Air Entrainment and Heater Adapter), requiring a minimum air flow of  $\approx 2.9\ \text{L/min}$  to generate drops.

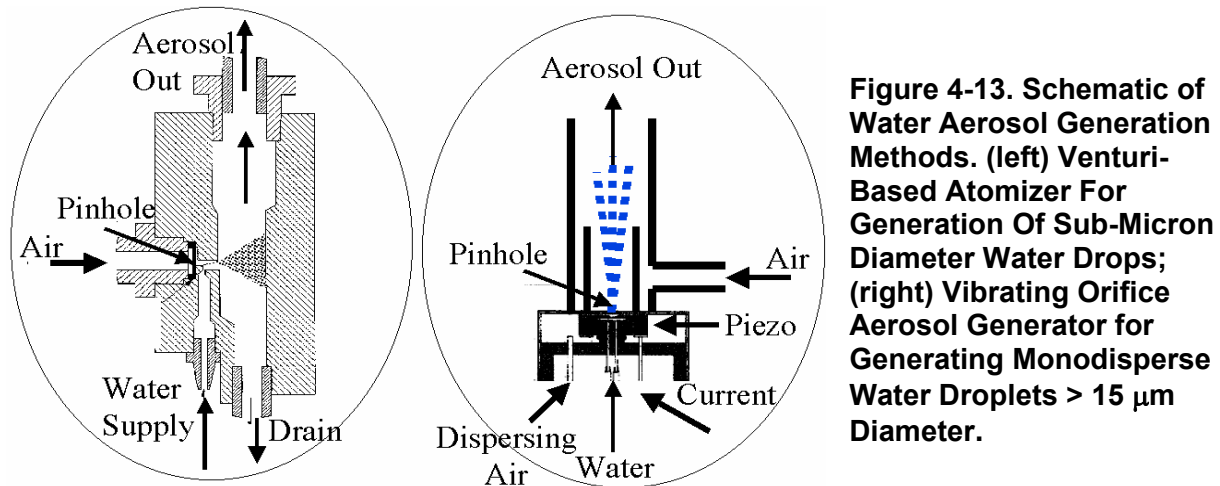


**Figure 4-13. Schematic of Water Aerosol Generation Methods. (left) Venturi-Based Atomizer For Generation Of Sub-Micron Diameter Water Drops; (right) Vibrating Orifice Aerosol Generator for Generating Monodisperse Water Droplets  $> 15 \mu\text{m}$  Diameter.**

Monodisperse droplets of larger size ( $> 15 \mu\text{m}$  diameter) were generated using a vibrating orifice aerosol generator (VOAG, TSI Inc. Model 3450). A schematic of the droplet generator is shown in Figure 4-13 (left). To generate the mist, liquid was forced through a pinhole using either a syringe pump or a plastic bag under pressure. Limited control over the liquid flow was accomplished using either method. The size of the pinhole ultimately determined how much liquid could be delivered to the burner. The pinhole was acoustically excited by a piezoelectric ceramic driven at specific frequencies to break up the liquid jet into a stream of extremely monodisperse drops. The droplet size depended on the pinhole diameter, the liquid flow, the forcing frequency, and the liquid properties. A dispersion cap was used to distribute the droplet stream uniformly into a three-dimensional mist. This sacrificed some of the size monodispersity as shown in Figure 4-14 for the three water mists that were studied. In the absence of the dispersion cap and dispersing air, all droplets occupied a single PDPA size bin.

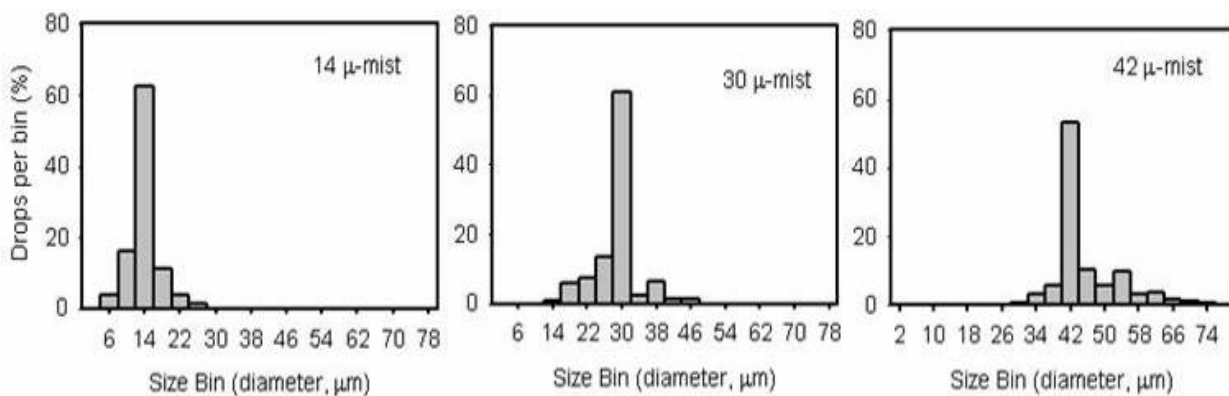


**Figure 4-14. PDPA-determined Droplet Diameter Histogram 2 mm above the Air Tube Exit for Three Water Mists.<sup>85</sup>**

Droplet size, velocity, and number density for droplets greater than  $\approx 2 \mu\text{m}$  in diameter were measured using a phase Doppler interferometry system (Phase Doppler Particle Anemometer – PDPA, Dantec Measurement Technology). For droplets smaller than  $\approx 1 \mu\text{m}$  diameter, water concentration in the

reactant stream was monitored by  $90^\circ$  scattering of a Helium-Neon laser at a wavelength of  $0.6328 \mu\text{m}$  as shown in Figure 4-15. The scattered laser light was detected with a photomultiplier tube (PMT) using a narrow-line optical filter. The laser beam was modulated at 1 kHz by passing the beam through a rotating slotted wheel. The laser beam was positioned just above the burner exit. A reference beam was split off just before the burner and monitored by a photodiode. The scattered and reference signals were processed with a lock-in amplifier (EG&G Instruments, Model 7265 DSP) and integrated over a period of 0.5 s. The scattering intensity was calibrated to a mist delivery rate by correlating the scattering signal with the change in water mass of the reservoir.

The total flame surface area derived by visible flame imaging was used to quantify the reduction in burning velocity as a function of added mist for suppressed premixed conical flames. A schematic of the arrangement is shown in Figure 4-15.

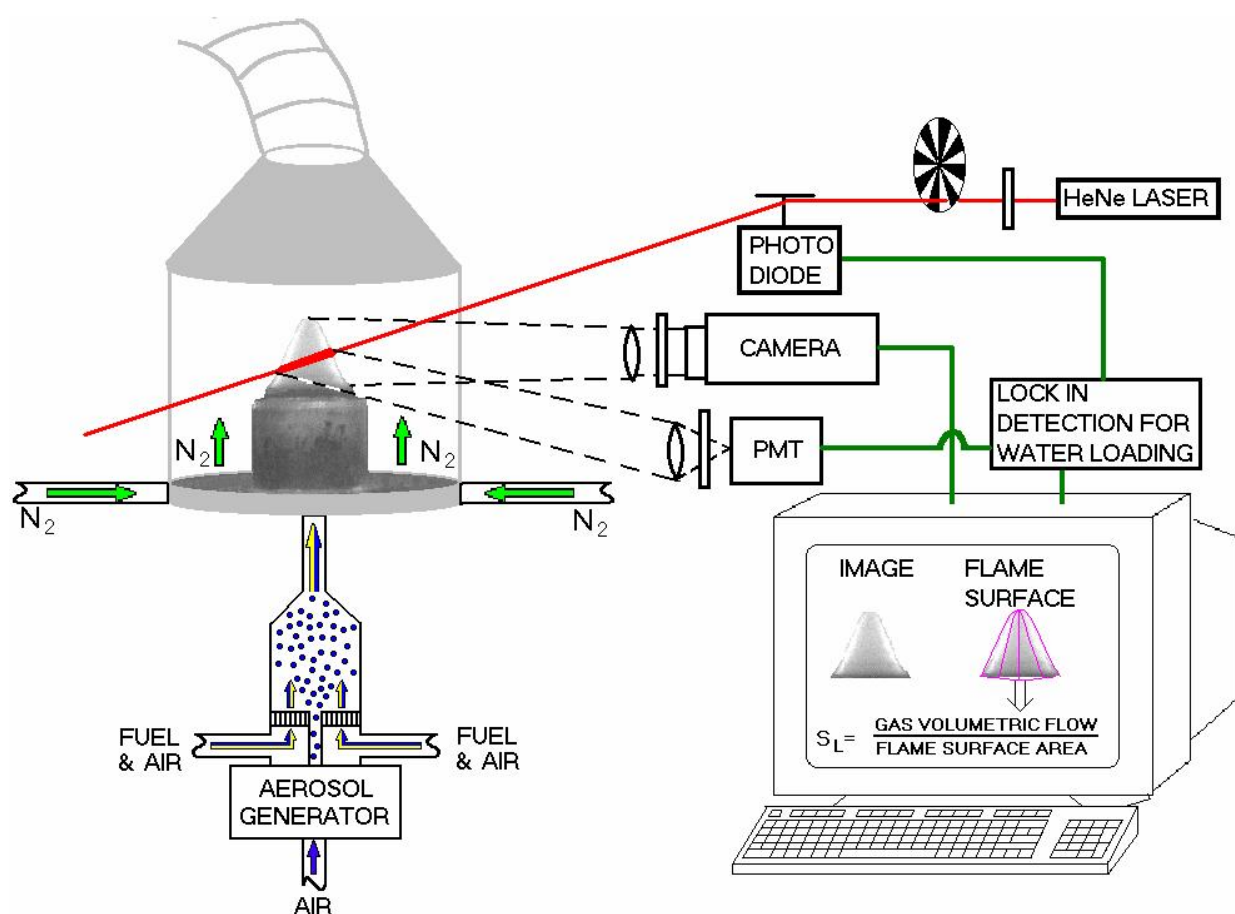


**Figure 4-15. Schematic for Liquid Aerosol Inhibited Burning Velocity Determination in Premixed Flames.**<sup>75</sup>

The burner was a converging nozzle with an exit diameter of 1.0 cm. An entrainment device to straighten the flow and uniformly seed droplets in the premixed gas flow utilized a perforated disk. The sub-micron size mist droplets were small enough to pass through the  $\approx 0.16$  cm diameter perforation holes. Larger droplets ( $> 5 \mu\text{m}$  diameter) were introduced through an opening in the middle of the perforated disk. The burner was enclosed inside a 13 cm diameter inner diameter acrylic tube that allowed optical access to the

flame. The acrylic chamber was vented to an exhaust hood through a conical metal covering open at the top. A nitrogen flow of approximately 3 L/min was introduced through a sintered disk in the bottom of the chamber. This purged the chamber of excess oxygen and product gases. Flame images were recorded using a CCD camera and a value for the total flame surface was determined by fitting the shape and then mathematically generating a three dimensional surface. Burning velocities were determined by comparing the total flame surface to the volumetric flow of gases in the burner. Light from a modulated He-Ne laser, scattered from the aerosol in the premixed flow and detected with a lock-in detector, was used to determine the amount of water aerosol in the form of small droplets introduced into the flame. PDPA was used to quantify the water concentration for mists of larger drops.

Burning velocities for the inhibited flames were reported relative to the uninhibited burning velocity, thereby minimizing systematic errors in determining an absolute value for the burning velocity. Relative values derived from schlieren images for some of the flames were in good agreement with values derived from the visible flame surface. The presence of the aerosol reduced the flame burning velocity, which resulted in a taller flame with a larger flame surface area for a fixed fuel-air flow. To minimize any systematic effects due to varying flame height, fuel and air flows were adjusted to maintain a stoichiometric mixture and a flame height of  $1.0 \text{ cm} \pm 0.15 \text{ cm}$ . The measured burning velocities of nitrogen-inhibited flames were found to be insensitive to flame height over this range.

### ***Modeling***

Both theoretical<sup>86,87</sup> and computational<sup>88,89</sup> models have been developed to predict premixed flame structure and extinction characteristics as a function of water-mist properties. NGP modeling of sub-micron mists in premixed flames was done in collaboration with Prof. Robert Kee at the Colorado School of Mines. The suppression effects of gas-phase agents were modeled using PREMIX<sup>90</sup> and OPPDIFF.<sup>91</sup> The chemical reaction mechanism and the associated thermodynamic and transport properties were taken from GRI-Mech 3.0,<sup>92</sup> but with the nitrogen chemistry removed. The inhibition effects of water aerosols on premixed flames were calculated using a multiphase combustion model.<sup>89</sup> The multi-phase model solves the conservation equations for mass, momentum, and energy for the water droplets within a Lagrangian framework. One-dimensional conservation equations in an Eulerian framework were used to solve the physics of the gas-phase flame propagation. Coupling of the two phases was achieved through addition of drop-evaporation related source terms in the PREMIX software. Boundary conditions for the drop-evaporation dynamics were obtained from the PREMIX solution.

Figure 4-16 illustrates the predicted dependence of the burning velocity on droplet size and water loading.<sup>89</sup> For small drops, the burning velocity decreases monotonically as a function of water loading. For sufficiently small drops, the burning velocity becomes independent of droplet size but still depends on water loading. For stoichiometric, methane-air, premixed flames, this small-droplet limit is achieved for a droplet diameter of approximately  $10 \text{ }\mu\text{m}$ .<sup>89</sup>

### ***Results and Discussion***

Figure 4-17(a) shows the image of a premixed methane-air flame with no mist. Figure 4-17(b) shows mist of nominal  $0.3 \text{ }\mu\text{m}$  drops as they exit the burner nozzle in the absence of the flame. The drops are illuminated with a doubled Nd:YAG laser sheet. In Figure 4-17(c), both the illuminated drops and the flame image are shown although no mist drops are observed leaving the visible flame zone. The inhibition effect of this mist on the flame normalized burning velocity is plotted in Figure 4-18. Details

of the experiment and results are reported in Reference 93. Also shown are the inhibition effect of  $N_2$ ,  $CF_4$ , and  $CF_3Br$ . The  $CF_3Br$  data are modeling results considering full chemistry.<sup>76,94</sup> On a mass basis, the inhibition effectiveness of water mist was comparable to that of  $CF_3Br$ .

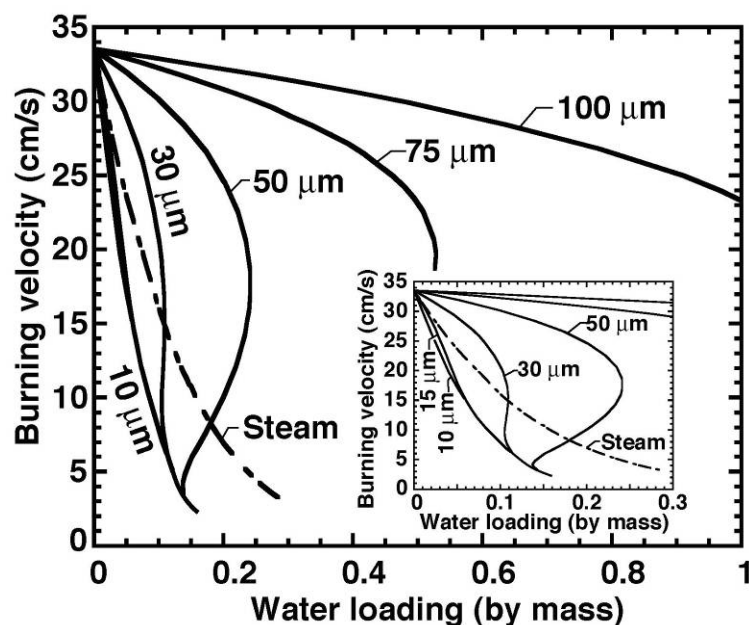


Figure 4-16. Predicted Burning Velocity for a Stoichiometric, Premixed, Methane-air Flame as a Function of Initial Droplet Diameter and Water Mass Loading. (Reference 90)<sup>89</sup>

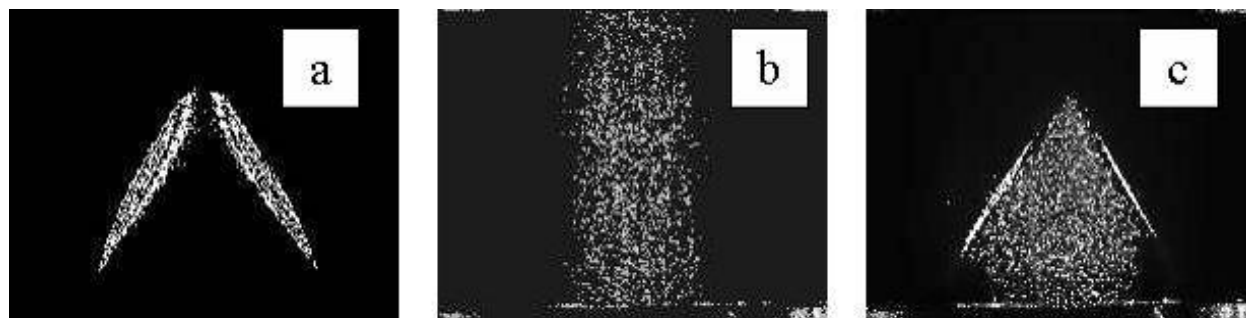


Figure 4-17. (a) Image of Premixed Methane-air Flame Stabilized on Burner; (b) Image of Water Mist (no flame) as it Exits the Burner; (c) Image of Laser-illuminated Water Mist and Methane-air Flame Showing Disappearance of the Mist at the Flame Boundary. (Reference 93)

A summary of an evaluation of the thermodynamic properties of the agents investigated in Figure 4-18 is listed in Table 4-2. Columns 2 and 3 list the sensible enthalpy, per unit mass and per mole, respectively, required to raise the temperature of each agent from 300 K to 1600 K.<sup>95</sup> On a mass basis,  $N_2$  and  $CF_4$  should contribute similarly to the inhibition. The sensible enthalpy for water mist, including the heat of vaporization at 101 kPa (1 atm), is almost twice that of water vapor and 3.5 times higher than for the same mass of  $N_2$  or  $CF_4$ . These predictions are consistent with the experimental observations. The mass of inhibitor required to reduce the burning velocity by a fixed amount (20 % was chosen here) is listed in Column 4 and the molar amount in Column 5.

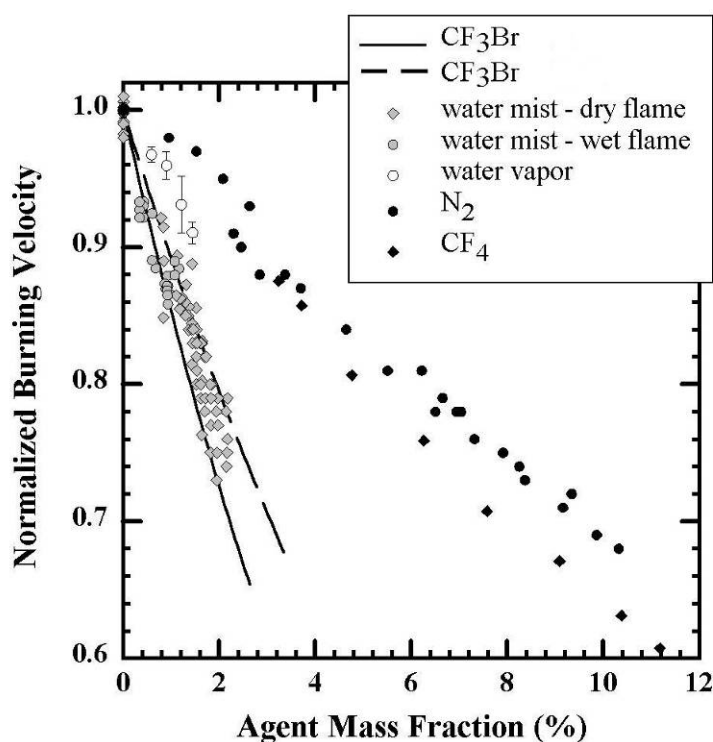


Figure 4-18. Normalized Burning Velocity Reduction vs. Mass of Added Inhibitor for an Inhibited Methane-Air Premixed Flame. (Reference 93)

The mass of liquid water needed to reduce the burning velocity by 20 % is one-third that required for N<sub>2</sub> or CF<sub>4</sub>, which is in good agreement with the thermodynamic estimate. The value for water is comparable to published measurements for CF<sub>3</sub>Br. Thus, small water droplets acting thermally exhibit a comparable effectiveness on a mass basis in premixed flames as CF<sub>3</sub>Br with its chemical effect. Modeling prediction of the small-droplet limiting behavior is presented in Figure 4-19 along with the experimental results of Figure 4-18. The sub-micron mist inhibition results are in excellent agreement with modeling predictions of Yang and Kee, requiring no adjustable parameters.<sup>93</sup> Water vapor was both observed and predicted to be less effective than water aerosols of droplet diameters smaller than  $\approx 15 \mu\text{m}$ . An increase in the effectiveness of liquid water is predicted as the droplet size is reduced to  $\approx 10 \mu\text{m}$ . Below this size limit, no increase in suppression effectiveness with decreasing droplet size is predicted. This limiting droplet size correlates with those droplets that completely evaporate in this flow field and is consistent with the observations in Figure 4-17.

Table 4-2. Thermodynamic Quantities for Physical Suppressants Compared to CF<sub>3</sub>Br.

Agent	$(H_f^{1600\text{K}} - H_f^{300\text{K}})^a$		Mass Fraction to Reduce Burning Velocity by 20 %	Mole Fraction to Reduce Burning Velocity by 20 %
	kJ/g	kJ/mol		
N <sub>2</sub>	1.5	42	0.063 ± 0.004	0.062 ± 0.004
CF <sub>4</sub>	1.4	122	0.055 ± 0.004	0.019 ± 0.002
H <sub>2</sub> O (vapor)	2.9	53	0.033 ± 0.002	0.050 ± 0.003
H <sub>2</sub> O (mist)	5.2	93	0.017 ± 0.001	0.026 ± 0.002
CF <sub>3</sub> Br	0.85	126	0.019 <sup>b</sup>	0.004 <sup>b</sup>

<sup>a</sup> Calculated from data in Chase et al.<sup>95</sup>

<sup>b</sup> Data from Noto et al.<sup>96</sup>

PDPA measurements for larger droplets as a function of position above the burner were recorded for the methane-air premixed flame: diameter vs. position are shown in Figure 4-20(a) and number density vs. position in Figure 4-20(b). Droplets larger than  $27\ \mu\text{m}$  in diameter (generated using the VOAG) were reasonably monodisperse and survived travel through this flame (peak temperature  $\approx 2100\ \text{K}$ , determined using a radiation-corrected, coated Pt/Pt-Rh thermocouple). The smaller droplets generated with a nebulizer (average diameter  $6\ \mu\text{m}$ ,  $Dv_{0.9} < 10\ \mu\text{m}$ ) completely evaporated at the flame front. Thus, the experimental droplet size for onset of complete evaporation in this flame is between  $6\ \mu\text{m}$  and  $27\ \mu\text{m}$ . These measurements are consistent with the predicted nominal  $10\ \mu\text{m}$  limiting droplet size of the multi-phase model.

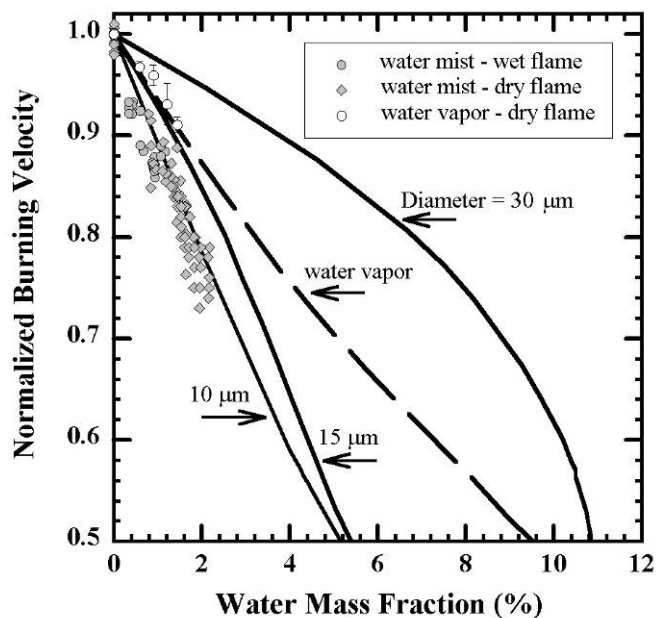


**Figure 4-19. Premixed Methane-air Burning Velocity as a Function of Agent Mass Fraction, Normalized by the Uninhibited Burning Velocity. Water data from Figure 4-18 (symbols), multiphase flame modeling results for humidified flames inhibited with mists of indicated drop size (solid lines), and PREMIX modeling results for humidified flames inhibited with additional water vapor (dashed line).<sup>93</sup>**

Modeling predictions for the experimental conditions presented in Figure 4-20 are shown in Figure 4-21. Droplet size vs. position is shown in Figure 4-21a, and relative droplet number density vs. position is shown in Figure 4-21b. The water mass fraction is 0.05. (The 0 mm position is the 300 K left boundary for the freely propagating flame solution.) Droplet size behavior is in reasonable agreement in the post flame region. However, the experimental droplet number density decay rates are much slower than the model predicts; note that the distance plotted in Figure 4-20b is four times that of Figure 4-21b. The source of the difference lies in the different residence times of the droplets in the flame. In the experiments, droplets are traveling at the same speed as the gas phase, about  $140\ \text{cm/s}$ . In the one-dimensional, freely propagating flame model, droplets also travel at the same speed as the gas phase, but this is about  $30\ \text{cm/s}$ . Thus, the prediction of a higher evaporation rate (shorter evaporation time) for the longer residence time in the model is consistent. Experiments to quantify the effect of larger droplets on the burning velocity are needed.

The model predicts a turning-point behavior for the effect of moderate and larger sized droplets (above  $25\ \mu\text{m}$  for stoichiometric, premixed, methane flames) on burning velocity as seen in Figure 4-16. At the turning point, the derivative of burning velocity with respect to the water mass loading is infinite. Turning points are caused by the droplet dynamics within the flame. Specifically, longer droplet residence time in a suppressed flame causes further increase of efficiency in flame suppression. Mathematically, at a turning point, an infinitesimally small increase of water mass loading causes the

burning velocity to fall to the lower branch of the suppression curve. Such very-low-burning-velocity branches are experimentally not achievable due to the various heat-loss mechanisms that would prevent these flames from stabilizing. Therefore, it may be safe to interpret such turning points as flame extinction points.

The theoretical and computational analyses predict that the burning-velocity curves join together in the lower-burning-velocity region. This behavior can be attributed to a greater droplet residence time in the slow-burning flames. If the burning velocity is sufficiently low, any droplet can totally evaporate within the flame, leading to equivalent efficiency for flame suppression.

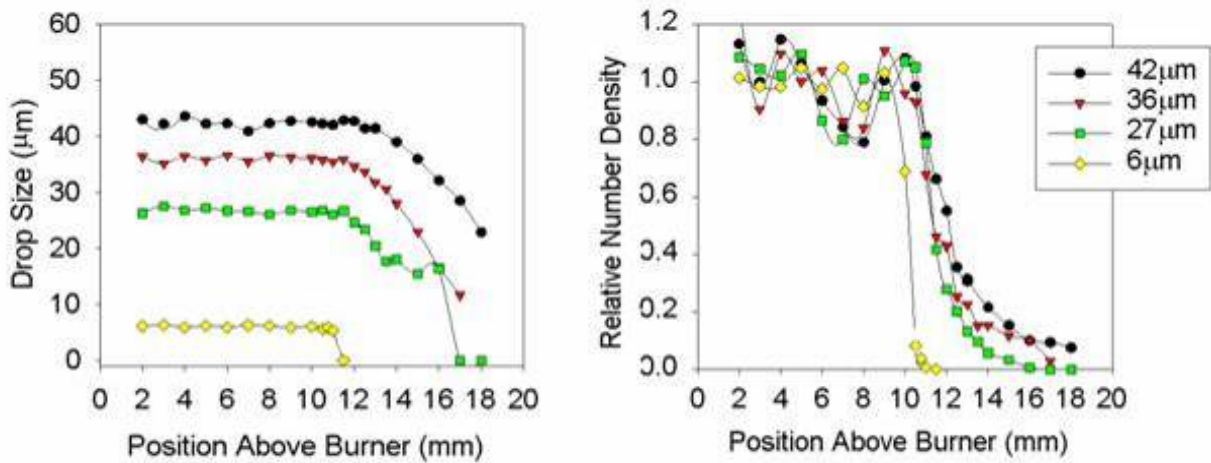


**Figure 4-20. Experimental Measurements of Water Droplet Diameter and Number Density in a Stoichiometric Premixed Methane-air Flame as a Function of Height above the Burner Exit.**<sup>75</sup>

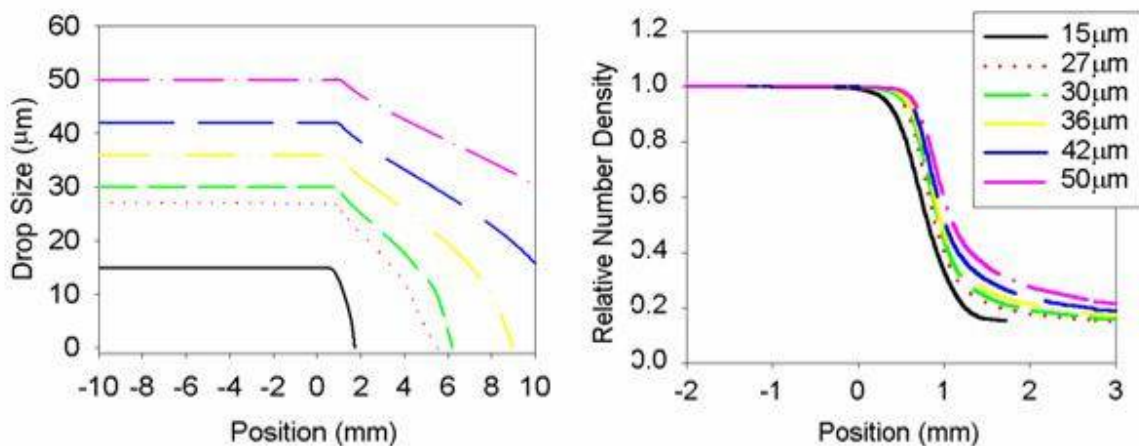


**Figure 4-21. Multi-phase Predictions of Water Mist Droplet Diameter and Number Density in a Stoichiometric Premixed Methane-air Flame.**<sup>75</sup>

The turning points predicted for larger droplets seen in Figure 4-16 can be important in fire suppression. Unfortunately, no direct observation or measurement of such behavior for inhibited premixed flames has been reported. The challenges to realizing such experiments include the generation of the monodisperse mists, the high water-mass loading required at turning points, and controlling the non-ideal conditions such as buoyancy and heat loss to the environment. Experiments that focus on the inhibition effects of larger droplets are needed.

Understanding the inhibited flame structure and droplet dynamics provided considerable insight into the mechanisms of flame suppression. The computational model predicted temperature, species concentration, number density, and droplet history profiles throughout the flame. These variables represent the underlying factors that control the overall burning velocity. Therefore, detailed measurements of flame structure were extraordinarily valuable. Unfortunately, both creating the flame and developing the required diagnostics are significant challenges. For these studies, flame structure, burning velocity, and extinction characteristics were modeled as an ideal flat flame. The experiment was a Bunsen-like configuration that allowed droplets to be introduced through the open tube. The burning velocity in these flames was inferred from analysis of the flame area. In addition, flame profile data were measured, for example, on the centerline. This configuration and modeling approach are valid for sub-micron droplets that fully evaporate prior to entering the flame. However, for larger droplets or particles, data from such experiments cannot be compared directly to one-dimensional flat-flame models. The gas and particle/droplet velocities, for example, were much greater in the Bunsen-like flame. It appears that there are two choices for modeling the inhibition effect of larger particles/droplets in premixed flames: configure a “flat” premixed, burner-stabilized flame that can be seeded with large water particles/drops, or directly model the three-dimensional Bunsen-like flame. The success of uniformly seeding particles/droplets into a flat flame is highly unlikely considering the particle/droplet sizes to be studied. Success seems more likely for alternative modeling approaches. This area is one that still requires further development.

### **Modeling of Counterflow, Non-premixed Flames<sup>i</sup>**

One of the NGP objectives was to understand the trajectories of condensed-phase, monodisperse aerosols in a reacting counterflow field and investigate their effect on the flame extinction condition. Several modeling approaches were explored to aid in the understanding of the observed suppression behavior. One publicly available code advertised as capable of modeling suppression of counterflow flames by aerosols is RUN-1DL (Rogg and Wang, Cambridge, England). Available documentation on the treatment of droplets was very sparse. The code as delivered only treated a single droplet stream and was not immediately capable of modeling flame conditions involving an ensemble of water drops. Further development and code modification to model the range of NGP experimental conditions were deemed too time consuming in light of the limited documentation.

PHOENICS (CHAM, London), a finite volume code for calculating fluid flow, was also considered for modeling the interaction of droplets in the counterflow flame. NRL staff had previously used this to model the flow field in this counterflow burner.<sup>97</sup> PHOENICS was configured to treat the full flame chemistry. Stable gas-phase flames could be modeled. The calculation was very sensitive to the

---

<sup>i</sup> The model described here was developed and predictions made before much of the experimental data was available. Subsequent experimental work presented later in this chapter benefited greatly from the modeling studies. The experimental studies in large part validated the modeling approach and subsequent predictions.

inclusion of the aerosol/flame interaction due to the time and spatial scale dynamic ranges. Further development and code modification were not pursued as part of this project.

Chelliah and co-workers at the University of Virginia developed a two-phase hybrid Eulerian–Lagrangian formulation for treating the interaction of droplets and counterflow non-premixed flames.<sup>80,98,99</sup> The details of the hybrid Eulerian-Lagrangian formulation and the solution algorithm developed to predict the interaction between water mist and a laminar counterflow flame are described in Reference 80. The model predictions were validated against experimental non-premixed counterflow flame extinction conditions and low-pressure flame structure data for both propane and methane flames, as well as indirect comparison to experimental methane-air burning velocity results.<sup>100</sup> A reduced chemical kinetic mechanism was used, which was derived from a much more comprehensive one proposed by Wang and co-workers.<sup>101,102</sup> The Wang mechanism had been validated based on global flame propagation/extinction experiments and flame structure measurements for a variety of fuels.<sup>101</sup> For water mist suppression of propane or methane counterflow flames, extinction strain rate predictions using both mechanisms agreed within  $5 \text{ s}^{-1}$ . Both mechanisms predicted a non-premixed propane-air flame extinction strain rate of  $\approx 580 \text{ s}^{-1}$ , in excellent agreement with the experimental measurements.

For the model, water droplets were introduced into the air stream. The water droplet loadings were small, i.e., the mass of liquid water was less than 3 % of the air flow. Thus, the ratio of droplet separation distance to droplet diameter was greater than 20, and collisional effects between droplets were neglected. The reduced gas-phase chemical kinetics mechanism involved 17 species and 39 elementary reactions with variable thermochemical and transport data. The discretized gas phase equations were solved using an algorithm that includes Newton and fixed point iteration steps.

The flow configuration was shown earlier in Figure 4-10. When ignited, a steady laminar flame was established within the mixing layer. The exit velocity profiles of both air and fuel streams were assumed to be of the plug flow type. The droplets were introduced through the upper nozzle at a steady rate with the air stream and were assumed to be monodisperse. Droplet velocities at the nozzle exit were assumed to be the same as that of air. (For the two-phase system considered here, the gas velocity can differ from that of droplets.) The response of droplet trajectories for different flow strain rates was addressed by varying the nozzle exit velocities of methane and air streams. For plug flow boundary conditions (corresponding to viscous, rotational flow formulation), the flow strain rate,  $a$ , is defined as the negative of the axial velocity gradient of the gas in the air side (i.e.,  $2dv/dx$ ), just outside the mixing layer (Figure 4-10). At flame extinction, the critical value of the flow strain rate was identified here as  $a_{ext}$ . In the experiments, the outer air flow was known to deviate slightly from the plug flow boundary conditions,<sup>103</sup> but explicit detailed laser Doppler velocimetry data at the boundary can be easily implemented in the model.

### ***Effect of Water Vapor on Flame Extinction***

In a real-life fire situation, or in laboratory experiments, when water droplets are introduced into a dry air stream, there will be some evaporation. Consequently, the fraction of oxygen displaced (or diluted) by the water vapor can reduce the flame strength, or the extinction strain rate,  $a_{ext}$ , of the counterflow flame considered here. Figure 4-22 shows a comparison of the predicted variation of maximum flame temperature,  $T_{max}$ , for a methane-air flame as a function of the flow strain rate,  $a$ , for some selected water vapor concentrations. The circle symbol corresponds to a dry case, whereas the star symbol corresponds to a fully saturated case at a room temperature of 300 K and atmospheric pressure (i.e., partial pressure of

water  $p_{\text{H}_2\text{O},\text{sat}} = 0.0351$  atm or, in mass fractions,  $Y_{\text{H}_2\text{O},u} = 0.0222$ , with  $Y_{\text{O}_2,u} = 0.2278$  and  $Y_{\text{N}_2,u} = 0.7500$ ). Based on this figure, if the asymptotic value of highest strain rate for each case is taken as the extinction strain rate,  $a_{\text{ext}}$ , then the results indicate that saturated water vapor alone can decrease the flame extinction strain rate by 25 %. This enhanced effect is not solely due to dilution, but is partly due to the high thermal capacity of water.

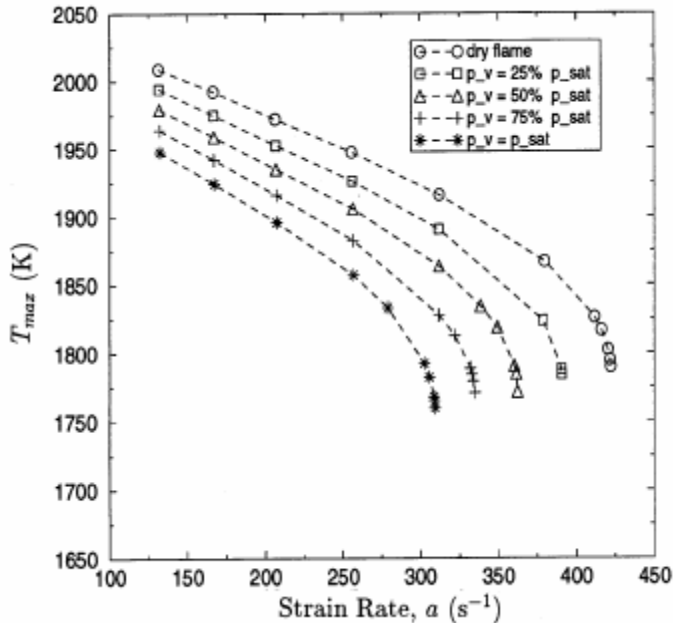


**Figure 4-22. Predicted Comparison of the Maximum Flame Temperature,  $T_{\text{max}}$ , vs. Flow Strain Rate,  $a$ , for a Dry Flame and for Four Flames with Different Inflow Water Vapor Partial Pressures.<sup>80</sup>**

#### **Dynamics of Water Droplets without Interaction**

If the amount of water being injected into the air stream is greater than  $p_{\text{H}_2\text{O},\text{sat}} = 0.0351$  atm (or  $Y_{\text{H}_2\text{O}} > 0.0222$ ), then the excess water will be in condensed form, i.e., in the form of droplets. The mass fraction of water associated with such droplets leaving the air nozzle can be defined using

$$Y_0 = \frac{m_{d0}n_{d0}v_{d0}}{m_{d0}n_{d0}v_{d0} + \rho_u v_u} \quad (4-7)$$

where  $m_{d0}$  is the initial mass of the droplet,  $n_{d0}$  the initial number density,  $v_{d0}$  the initial velocity of the droplet, and  $\rho_u$  and  $v_u$  are the density and velocity of air leaving the nozzle, respectively. All the results shown here are obtained by assuming that the droplet velocity leaving the air nozzle is same as that of the gas, i.e.,  $v_{d0} \equiv v_u$ , but other inflow conditions can be easily analyzed with the model as developed.

Various monodisperse water mists for three different fixed water mass fractions in air ( $Y_0 = 0.01$ ,  $0.02$ , and  $0.03$ ) were considered. Table 4-3 shows the number density of water droplets leaving the air nozzle,  $n_0$  (number/cm<sup>3</sup>), for three different values of  $Y_0$  and for the three different monodisperse droplet sizes selected.

For all the combinations of water mass fraction in condensed phase and droplet sizes, the ratio of droplet separation length to the droplet diameter,  $l_0/d$ , was fairly large ( $>20$ ) and was of uniform order. It was thus reasonable to neglect droplet-droplet interactions for all the cases considered. Further justification is

presented below.<sup>ii</sup> For dilutely loaded droplets, the gas displacement by water droplets can also be neglected because of the large density ratio between the condensed water and the gas. Under such conditions, the only interaction between the droplets and the gas is from source terms due to mass, momentum and enthalpy transfer per unit volume from the droplets to the gas. (See Equations 2 through 5 in Reference 80.) When these terms are included in the numerical calculations, the flame structure and extinction strain rate are affected dramatically, depending on the amount of condensed water added and the droplet sizes. Thus, for the purpose of illustrating and comparing the trajectories of various droplet sizes in the counterflow field and their associated source terms, a fixed, low strain rate case ( $a = 130 \text{ s}^{-1}$ ) where the droplet source terms are excluded (or the source terms turned “off” in the numerics) is considered first. It should be mentioned here that the profiles of droplet trajectories and source terms presented below remain essentially the same for high-strain rates as well.

**Table 4–3. Number Density and Droplet Separation Lengths for Some Selected Water Mass Fractions.<sup>80</sup>**

$Y_o$	$d$ ( $\mu\text{m}$ )	$N_o$ ( $\text{cm}^{-3}$ )	$N_o^{1/3}$ ( $\text{cm}^{-1}$ )	$l_o$ (cm)	$l_o/d$
0.01	5	178,000	56.3	0.0177	35
	20	2,790	14.1	0.0711	36
	50	178	5.6	0.178	35
0.02	5	360,000	71.2	0.0141	28
	20	5,630	17.8	0.0562	28
	50	360	7.1	0.141	28
0.03	5	546,000	81.7	0.0122	24
	20	8,530	20.4	0.0485	24
	50	546	8.2	0.122	24

Figure 4-23 shows a comparison of the axial velocity along the axis of symmetry of the gas and droplets of different sizes for the selected low-strain rate case. Although the coupling arising from the droplet source terms on gas-phase structure was neglected, in solving equations for droplet trajectory shown in Figure 4-23, the droplet vaporization effects were included. (See Equations 18 through 23 in Reference 80.) In Figure 4-23, the 5  $\mu\text{m}$  droplets followed the gas fairly closely, whereas large droplets deviated considerably. The droplet lag became slightly worse for high-strain rates, especially near extinction conditions. The 5  $\mu\text{m}$  droplets were completely vaporized soon after they entered the hot mixing layer, whereas 50  $\mu\text{m}$  droplets penetrated through the flame and also the stagnation plane and then reversed their direction somewhere in the fuel stream. When the droplet vaporization was suppressed, then the penetration of 50  $\mu\text{m}$  droplets became much more pronounced, with multiple crossings at the stagnation plane. These predictions are consistent with those reported earlier by Chen et al.<sup>64</sup>

<sup>ii</sup> In actual water mist systems, it is highly unlikely that the water droplets generated are monodisperse. However, the predictions performed here with monodisperse droplets provide a better mechanism to analyze and understand the basic droplet dynamics and interactions with the gas-phase processes, which can be easily extended to polydisperse droplet flows in the future.

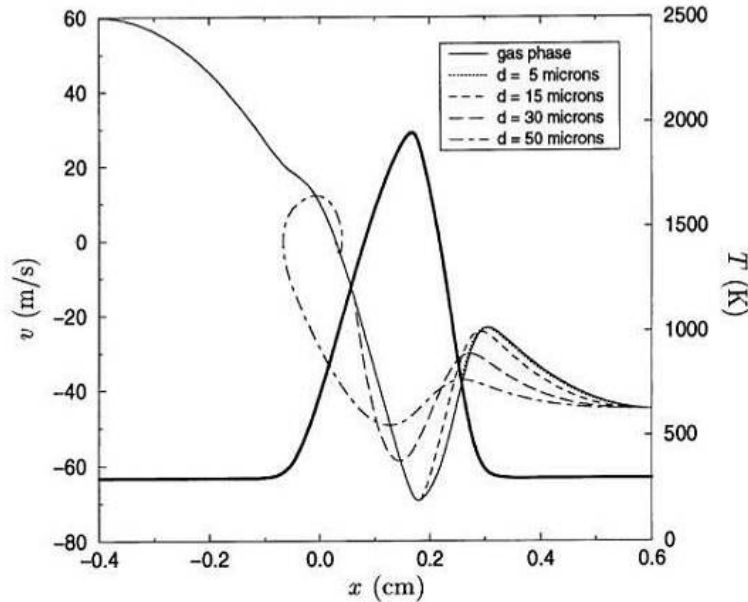


**Figure 4-23. Calculated Gas Velocity, Velocities for Varied Water Droplet Diameters, and Gas Temperature (thick solid line) in a  $130 \text{ s}^{-1}$  Methane/air Flame with Droplet Source Terms turned “off.”<sup>80</sup>**

The droplet response to the variation in gas-phase flow conditions was characterized by the Stokes number,  $S_t$ . By defining the flow residence time in the outer air flow as  $t_f = 1/a$ , and deriving an expression for the droplet response time ( $t_d$ ) based on Stokes drag, the following expression was derived for  $S_t$ :

$$S_t = \frac{18\mu}{a\rho_d d^2} \quad (4-8)$$

where  $\mu$  is the gas viscosity,  $d$  is the aerodynamic diameter of the drop and  $\rho_d$  is the drop density. For the strain rate of  $130 \text{ s}^{-1}$  considered in Figure 4-23 the variation of  $S_t$  for different droplet sizes in the outer oxidizer flow is shown in Table 4-4. The  $5 \mu\text{m}$  droplets have truly small  $S_t$  number, consistent with the results shown in Figure 4-23. As the droplet size approaches about  $15 \mu\text{m}$ , the  $S_t$  number approaches about 0.1, indicating slower response of the droplet to the gas, as seen in Figure 4-23.

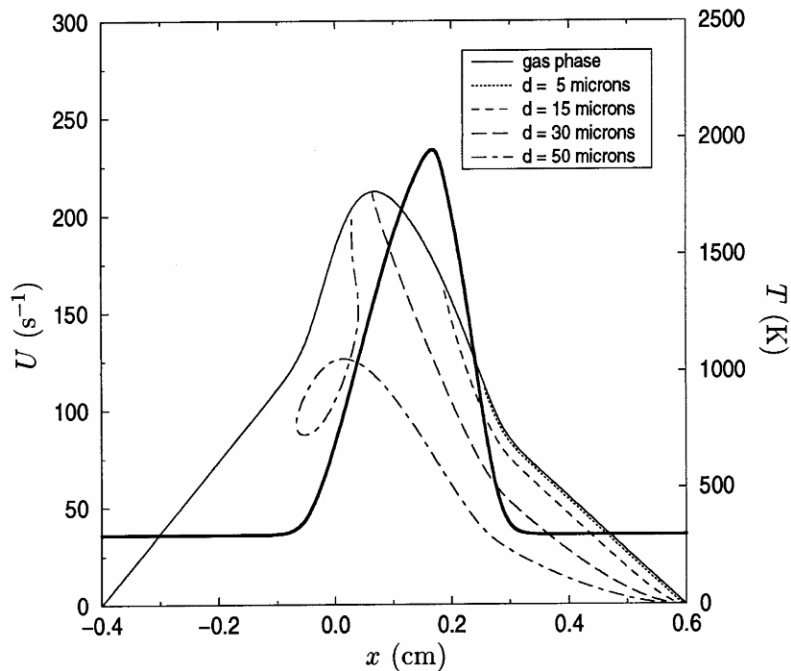
Figure 4-24 through Figure 4-26 show the variation of other variables associated with the droplet, (evaluated from Equations 20, 21, and 23 in Reference 80), along the axis of symmetry. These results were obtained under the same conditions as in Figure 4-23. Figure 4-24, for example, shows that  $U_d$  was always less than  $U$ , which is expected, as the gas was accelerating radially from the axis of symmetry and is consistent with experimental measurements of methanol droplets in a counterflow by Li et al.<sup>104</sup>

Figure 4-25 shows that the temperature of  $5 \mu\text{m}$  droplets ( $T_d$ ) followed that obtained assuming thermal equilibrium (solid line), whereas other droplets showed a small thermal lag. However, this lag had insignificant effect on the flame structure and extinction condition considering the small temperature difference and the energy associated with it. The variation of flux fraction,  $\mathcal{F}$ , as a function of the axial location, shown in Figure 4-26, however, played a very important role in the droplet source terms (see Equation 17 in Reference 80), and therefore the state of the flame. The reduction in  $\mathcal{F}$  seen as the droplet approached the stagnation plane was because of the flow divergence or straining effect.

**Table 4–4. Stokes Number ( $S_t$ ) for Different Droplet Sizes for  $a = 130 \text{ s}^{-1}$ .<sup>80</sup>**

$d$ ( $\mu\text{m}$ )	$t_d$ ( $\text{s}^{-1}$ )	$t_f$ ( $\text{s}^{-1} \times 10^2$ )	$S_t$
5	$0.75 \times 10^{-4}$	0.77	0.0098
10	$0.30 \times 10^{-3}$	0.77	0.039
15	$0.68 \times 10^{-3}$	0.77	0.089
20	$0.12 \times 10^{-2}$	0.77	0.16
25	$0.19 \times 10^{-2}$	0.77	0.25
30	$0.27 \times 10^{-2}$	0.77	0.35
40	$0.48 \times 10^{-2}$	0.77	0.63
50	$0.75 \times 10^{-2}$	0.77	0.99
60	$0.108 \times 10^{-1}$	0.77	1.42

If the droplet vaporization were neglected, the curves shown for different droplet sizes would shift somewhat, but the dramatic reduction of  $\mathcal{F}$  seen with droplet location does not change. Similar results for axial liquid methanol volume flux were observed experimentally by Li et al.<sup>104</sup> with and without a flame.



**Figure 4-24. Comparison of  $U$  of Gas and  $U_d$  of Different Droplet Diameters, with Droplet Source Terms Turned "off."<sup>80</sup> Thick line: gas temperature.**

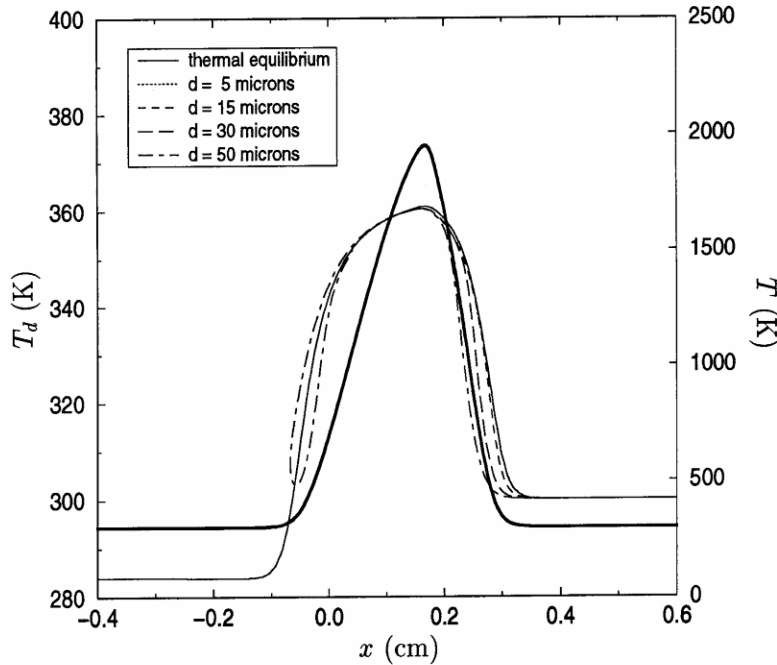


**Figure 4-25. Comparison of Droplet Temperature,  $T_d$ , of Different Droplet Diameters, with Droplet Source Terms Turned "off."<sup>80</sup> Thick line: gas temperature.**

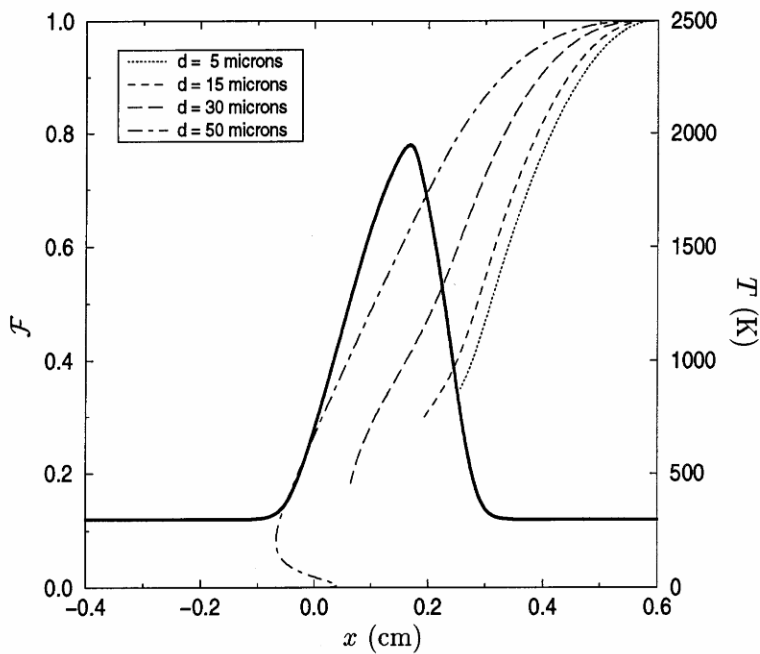


**Figure 4-26. Comparison of Flux Fraction Function,  $\mathcal{F}$ , of Different Droplet Diameters, with Droplet Source Terms Turned "off."<sup>80</sup> Thick line: gas temperature.**

**SOURCE TERMS WITHOUT INTERACTION.** Once the solution of droplet variables was obtained (i.e.,  $d$ ,  $v_d$ ,  $U_d$ ,  $T_d$ , and  $\mathcal{F}$ ), the source terms contributing to the gas phase were evaluated. (See Equation 17 in Reference 80.) Here, such contributions were shown, once again by turning "off" the interaction of such source terms with the gas-phase calculations to keep the flame structure condition the same for

different droplet sizes considered further in the next section. Figure 4-27 through Figure 4-29 show the variation of mass, momentum, and energy source terms, i.e.,  $S_m$ ,  $S_U - US_m$ , and  $S_h - 2h_i S_m$ , along the axis of symmetry for different droplet sizes. Figure 4-27 shows apparently strange profiles, especially on the air side before the flame, where evaporation effects were negligible. It is seen that smaller droplets exerted a greater radial force per unit volume on the gas than larger droplets. This is, however, easily explained by the fact that larger droplets shoot through that region faster than smaller droplets, so that they have much shorter residence times. Comparison of Figure 4-28 and Figure 4-29 indicates the profiles of  $S_m$  and  $S_h - h_i S_m$  to be very similar (except for the change of the sign). This suggested that heat transfer to the droplets and evaporation were well correlated; the implications of such correlations are discussed further in the next section.

**EFFECT OF WATER DROPLETS ON FLAME EXTINCTION.** An important question that was probed by the two-phase model developed here was the effect of water droplets (i.e., their size and mass loading) on the flame extinction condition, with the source terms turned “on.” Such effects were shown by plotting the variation of maximum flame temperature as a function of the flow strain rate, as shown in Figure 4-30. Figure 4-30 also shows the effect of water vapor. Profiles for  $T_{max}$  are plotted for a single mass fraction ( $Y_0$ ) of 0.01 for different droplet sizes. For comparison, the saturated water vapor at room conditions is shown as a solid line.

Figure 4-30 indicates that 50  $\mu\text{m}$  droplets were the least effective of those sizes studied, with a relatively high extinction strain rate. They were still more effective than air saturated with water vapor (mass fraction of 0.022). The 15  $\mu\text{m}$  droplets were the most effective, with the lowest extinction strain rate. As the diameter of monodisperse droplets was decreased below 15  $\mu\text{m}$ , they became less effective. The lowest size considered was 5  $\mu\text{m}$ , as the mass and enthalpy source terms approached a  $\delta$ -function, as seen in Figure 4-27 and Figure 4-28, introducing severe convergence problems of the numerical model.

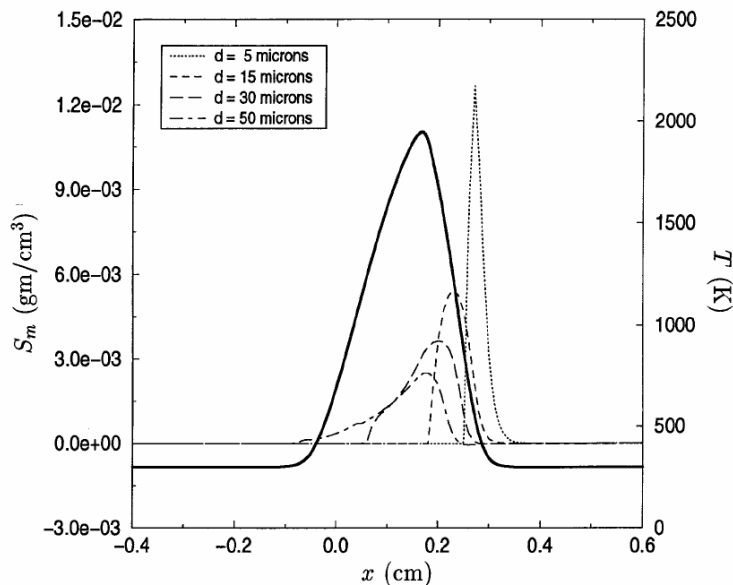


**Figure 4-27. Typical  $S_m$  Profiles of Different Droplet Diameters, with  $Y_0 = 0.02$  and Droplet Source Terms Turned “off.”** Thick line: gas temperature.<sup>80</sup>

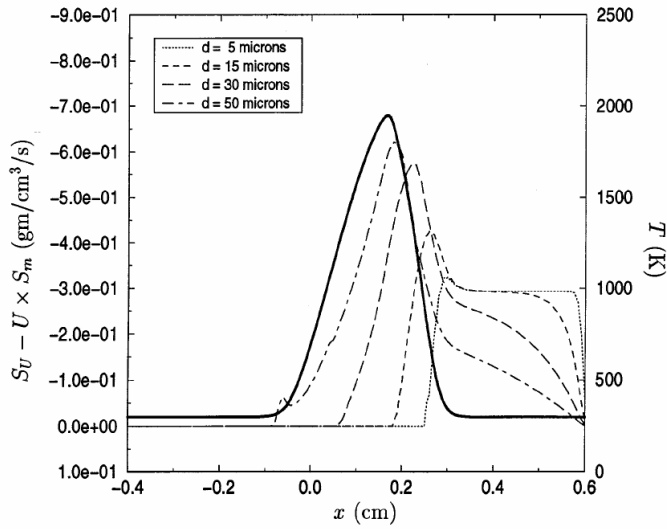


Figure 4-28. Typical  $S_U - US_m$  Profiles of Different Droplet Diameters, with  $Y_0 = 0.02$  and Droplet Source Terms Turned "off." Thick line: gas temperature.<sup>80</sup>

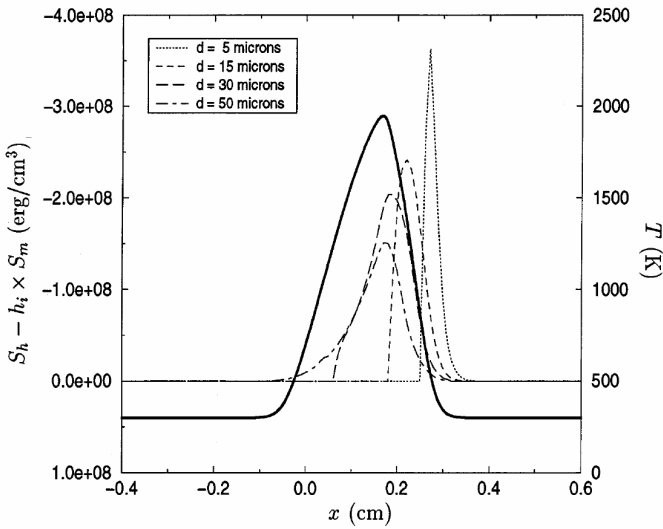


Figure 4-29. Typical  $S_h - h_i S_m$  Profiles of Different Droplet Diameters, with  $Y_0 = 0.02$  and Droplet Source Terms Turned "off."<sup>80</sup> Thick line: gas temperature.

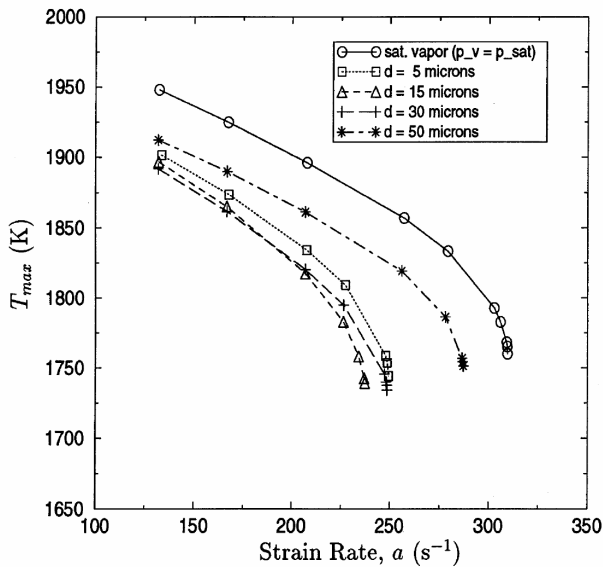
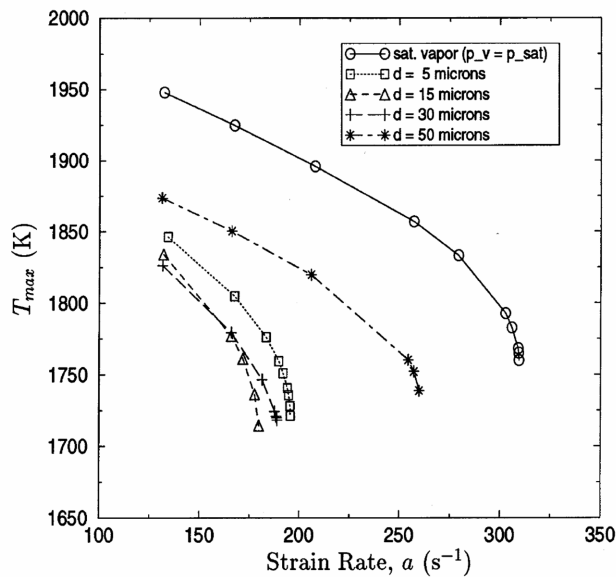


Figure 4-30. Comparison of  $T_{max}$  vs. strain rate  $a$ , for Different Droplet Diameters, with water mass fraction = 0.01.<sup>80</sup>

In fact, droplets of 5  $\mu\text{m}$  and below should approach the limit where all the water considered is in the vapor phase at the air side boundary of the mixing layer, provided the inflow temperature of air is not affected. Irrespective of this difficulty, this most interesting nonmonotonic effect of droplet diameter was captured well by the two-phase model developed here for steady, laminar, counterflow, nonpremixed flames.

For higher water mass fractions in the condensed phase, similar profiles were obtained for  $T_{max}$  as a function of flow strain rate, as shown in Figure 4-31 and Figure 4-32. The extinction strain rate decreased significantly with increasing water droplet loading.



**Figure 4-31. Comparison of  $T_{max}$  vs. strain rate  $a$ , for Different Droplet Diameters, with water mass fraction = 0.02.**<sup>80</sup>

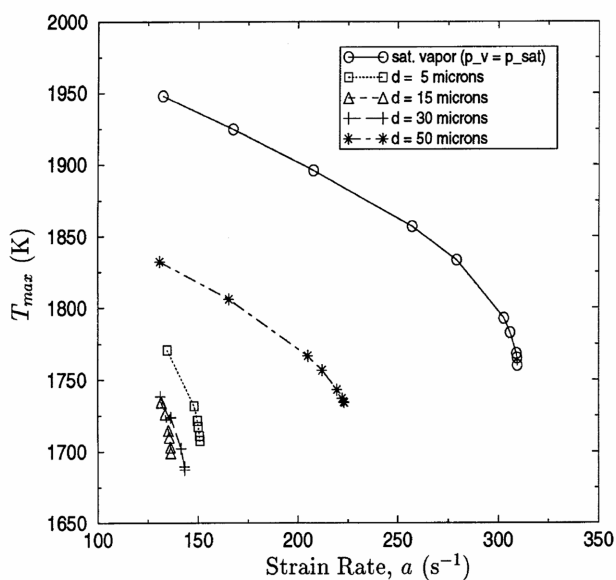


**Figure 4-32. Comparison of  $T_{max}$  vs. strain rate  $a$ , for Different Droplet Diameters, with water mass fraction = 0.03.**<sup>80</sup>

For the mass fractions considered here, the nonmonotonic effect of droplet diameter on the extinction strain rate can be better illustrated by Figure 4-33. For all the conditions considered here, 15  $\mu\text{m}$  to 20  $\mu\text{m}$  droplets were the most effective.

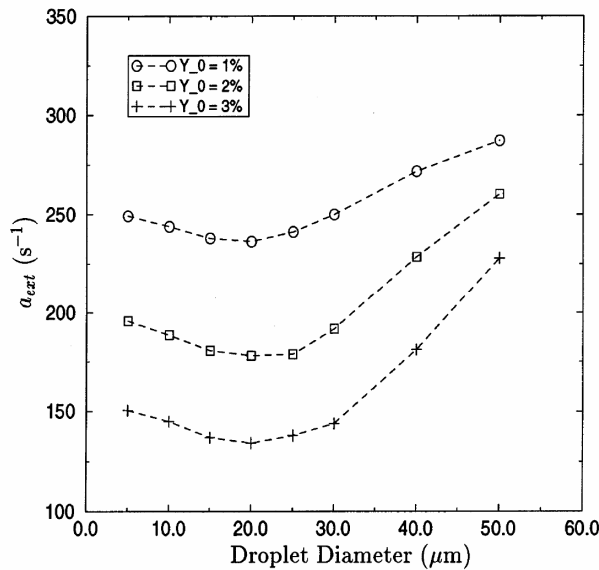


**Figure 4-33. Comparison of  $a_{ext}$  vs. Droplet Diameter for Different Droplet Mass Fractions in the Condensed Phase at Inflow.**<sup>80</sup>

This superior effectiveness of 15  $\mu\text{m}$  to 20  $\mu\text{m}$  droplets can be explained by the location of the mass source term seen in Figure 4-27. In the case of 15  $\mu\text{m}$  droplets, the peak value of  $S_m$ , and also of  $S_h - h_i S_m$ , occurs at the oxygen consumption or radical production layer. The effect of  $S_h - h_i S_m$  on flame temperature resulted in lower radical production and hence early flame extinction.<sup>105,106</sup> The exact physical, thermal, and chemical contributions responsible for flame extinction condition in the presence of water droplets are being investigated separately, with comparison to that of traditional chemical agents, such as halon 1301.

The concept of flow strain rate as defined here, i.e.,  $a = -d_v/d_x$ , is strictly applicable to constant density or nonreactive mixing layer flows. However, it is a useful fluid dynamical parameter for comparison with near extinction experimental velocity data obtained with nonintrusive laser Doppler velocimetry techniques.<sup>103</sup> For theoretical studies, a more useful fluid dynamical parameter is the diffusion time scale defined by the inverse of the scalar dissipation rate:<sup>106,107</sup>

$$\chi = 2D|\nabla Z|^2 \quad (4-9)$$

where  $D$  is an appropriate diffusion coefficient (e.g.,  $D = \lambda/(\rho c_p)$  for unity Lewis number) and  $Z$  is the mixture fraction. For small stoichiometric mixture fractions,  $Z_s$ , an analytical expression relating the stoichiometric scalar dissipation rate,  $\chi_s$ , with  $a$  taking into account the thermal expansion effects, has been derived by Kim and Williams.<sup>108</sup> Instead of using such an analytical expression, the scalar dissipation rate at the stoichiometric point at extinction was directly computed here by solving for a conservation equation for mixture fraction.

The resulting variation of  $(\chi_s)_{ext}$  as a function of the initial droplet size and water mass fraction in condensed phase is shown in Figure 4-34, indicating a trend similar to that of  $a_{ext}$  shown in Figure 4-33.

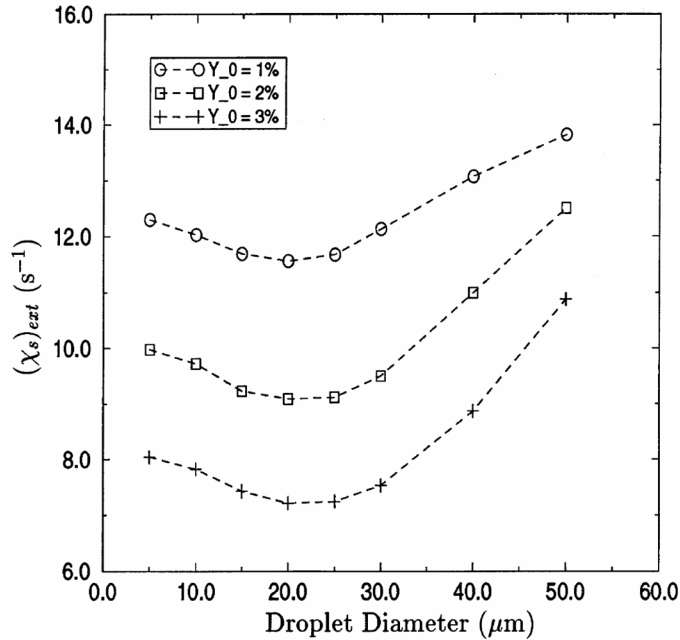


**Figure 4-34. Comparison of  $(\chi_s)_{ext}$  vs. Droplet Diameter for Different Droplet Mass Fractions in Condensed Phase at Inflow.**<sup>80</sup>

The results presented here need to be validated with careful experimentation. Furthermore, the generation of truly monodisperse droplets is a challenging task, and methods of extending the present modeling work to polydisperse droplets also need to be pursued.

**DROPLET-DROPLET COLLISIONS.** A key assumption in the numerical model developed was that droplets are transported without collision with other droplets. This assumption allowed for a fairly simple description of the droplet flow field and derivation of a self-similar solution for both droplets and the gas phase. It relied on the idea that the droplets leaving the air nozzle were monodisperse with the same exit velocity ( $n_{d0}$ ) and, hence, similar dynamics in the counterflow field. Although such ideal conditions are difficult to accomplish in experimental situations, if the initial droplet separation distance to droplet diameter is large, as seen in Table 4-3, the fraction of droplets colliding before evaporation can be neglected.

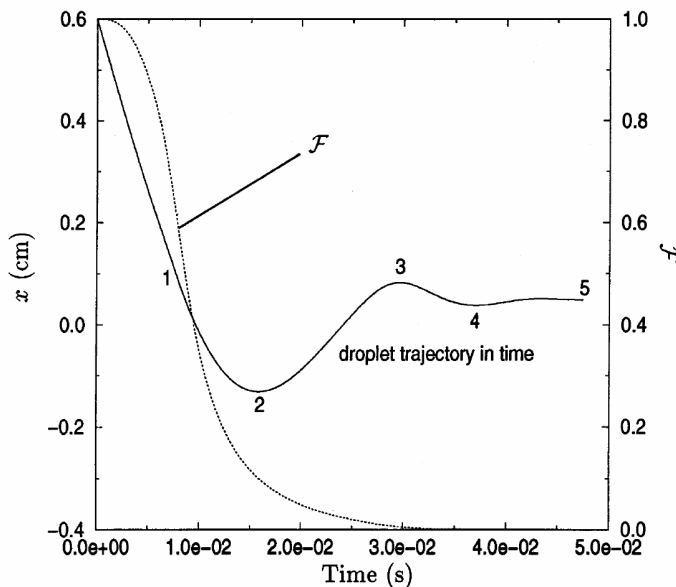
It is valuable to test the validity of this assumption under the worst case for this type of laboratory configuration. This occurs when large droplets at high droplet loading penetrate the stagnation plane and reverse their trajectory, creating a region where opposed flow of droplets exists near the axis of symmetry. Such a region existed for 50 μm droplets considered here, as seen in Figure 4-23.

Figure 4-35 shows the calculated trajectory of 50 μm droplets along the x-axis as a function of time and the corresponding flux fraction function for  $Y_0 = 0.03$ . With  $v_{d0} \approx 60$  cm/s and an average distance  $l_0 = 0.12$  cm (see Table 4-3), each droplet was estimated to be preceded and followed by a droplet before and after a time  $1.8 \times 10^{-3}$  s. Thus, assuming that droplets were leaving the air nozzle at every  $1.8 \times 10^{-3}$  s, then the region between points 1 and 2 (the region where each droplet group would see a group of droplets flowing in the opposing direction) in Figure 4-35 consists of  $\approx 17$  layers. By taking the average value of droplet flux fraction,  $\mathcal{F}$ , in region 1  $\rightarrow$  2 as 1/2 and in region 2  $\rightarrow$  3 as 1/4, the probability of droplet collision in this worst case region was roughly estimated as

$$P_{coll} < 17 \frac{1}{2} \frac{1}{4} \left( \frac{d}{l_o} \right)^2 \approx 0.4\% \quad (4-10)$$

This estimate for collision probability was even smaller for smaller droplets because of evaporation and the increased straining of droplet flux. Hence, the assumption of negligible droplet collision was reasonable.

Several other simplifications and approximations were also used in the development of the analytical model. The implication of the approximations introduced and possible inaccuracies arising from these approximations were addressed in detail in Reference 80.



**Figure 4-35. Calculated Droplet Trajectory as a Function of Time, for  $d = 50 \mu\text{m}$  and  $Y_0 = 0.03$ .**<sup>80</sup>

#### SUMMARY FOR MODELING AEROSOL SUPPRESSANTS IN COUNTERFLOW FLAMES.

This work developed a new two-phase numerical model to analyze the effectiveness of monodisperse, condensed phase fire suppressants in extinguishing counterflow flames. The model overcame the singularities associated with solving the droplet number density equation in a counterflow field accurately and in a very robust manner. This was achieved using a hybrid Eulerian–Lagrangian formulation for the gas-droplet flow, with the introduction of droplet flux fraction to describe the droplet number density equation. The model was applied to a case where monodisperse water droplets were introduced with the air stream to a nonpremixed counterflow methane/air flame. Several cases with droplet diameters ranging from  $5 \mu\text{m}$  to  $50 \mu\text{m}$  and mass loadings of liquid water in the air stream from 0.01 to 0.03 were considered. The model predicted that small droplets ( $< 20 \mu\text{m}$ ) tended to follow the gas closely and went through rapid evaporation in the hot mixing layer, never crossing the stagnation plane. The  $50 \mu\text{m}$  droplet crossed the stagnation plane several times before being completely vaporized. The important finding was that the flame extinction strain rate showed nonmonotonic behavior for different monodisperse droplet sizes considered for several water mass loadings. Assuming that the droplets were introduced with the air stream at the same velocity as the gas,  $15 \mu\text{m}$  droplets were predicted to be the most effective. Addition of 3 % of water by mass in condensed phase (in addition to 2.22 % as water vapor due to saturation) was shown to reduce the extinction strain rate to  $130 \text{ s}^{-1}$  from  $\approx 400 \text{ s}^{-1}$  for the dry air case. The nonmonotonic

suppression effect of droplet size favoring 15  $\mu\text{m}$  droplets was attributed to the droplet dynamics in the counterflow field and to the large mass evaporation and heat sink observed near the oxygen consumption layer. Sensitivity analyses of the approximate analytical models used to simplify the numerical integrations showed that mass evaporation and heat transfer terms needed to be more accurately modeled. Methods of improving the accuracy of these models were left for future pursuits.

## Non-Premixed Counterflow Flame Studies

### Experimental Setup

NRL researchers quantified water mist suppression effectiveness in non-premixed flames by determining the extinction strain rate in counterflow propane/air flames.<sup>109</sup> A schematic of the experimental configuration is shown in Figure 4-36.

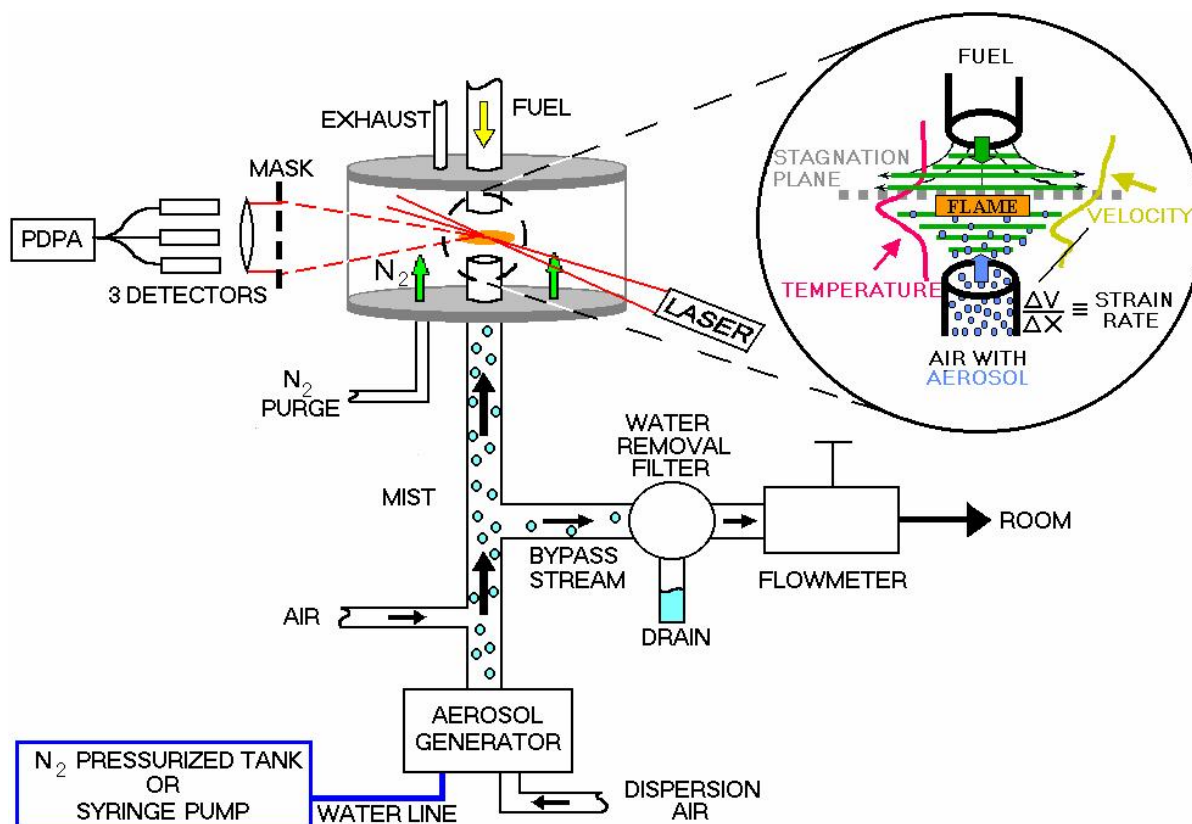


**Figure 4-36. Apparatus for Aerosol-inhibited, Non-premixed Counterflow Flames.**<sup>75</sup>

The burner consisted of two 50 cm long stainless steel tubes (1 cm inner diameter), with outer concentric tubes for a co-flow. The upper tube had a jacket for cooling water. The two tubes were aligned vertically and collinearly with a separation of  $1.00 \text{ cm} \pm 0.05 \text{ cm}$ . Air or fuel exited from a single tube with a parabolic velocity profile. Flow straighteners were not used. The air and fuel velocity profiles near the tube exits when opposing each other were flattened slightly from a parabolic profile due to the presence

of the other opposing flow. In the configuration used for the experiments, the luminous flame zone was fairly flat. The end of the each tube was plumbed through the center of stainless steel plates on the top and bottom of a 22 cm inner diameter, 19 cm long acrylic tube. The acrylic tube had flat windows for good optical access. These windows were critical to both the position of the laser beam overlap for the aerosol velocity and sizing measurements and the detection angle of the scattered light. A  $\approx 4$  SLPM purge flow of nitrogen was introduced into the bottom of the chamber. All gases exited through the top plate of the combustion chamber through a 5 cm diameter exhaust port. Representative centerline temperature and axial velocity profiles are indicated in the “blow-out” section of Figure 4–36, as is the strain rate. For gaseous reactants in this configuration, a relationship between the local strain rate (i.e., the maximum gradient of axial velocity on the air side of the reaction zone), the burner gap size distance, reactant velocities and densities were determined.<sup>110</sup> This burner-specific relationship was used to calculate local strain rates, and had been previously shown to remain valid for the addition of gaseous agents of high molecular weight to the air stream. For a condensed phase agent, the situation became more complicated, because under some conditions the condensed phase comprised a substantial fraction of the total momentum of the flow, and did not have the same velocity as the surrounding gas. In determining strain rates in the present study, it was assumed that the gas flow field was unchanged by the presence of the water mist. This approximation is only valid if the mass fraction of water in the air stream is small. For larger water mass fractions, the gas flow field must be measured in the presence of the water drops. The velocities of the water droplets themselves could not be used to determine the gas flow velocity, however, because they were too large to follow the gas flow field. For these reasons, the water mass fractions in the air stream were no larger than 0.03.

Liquid mist aerosols were generated and seeded in the air flow in the lower tube. Air side introduction of the mist is relevant to real fire, total flooding fire suppression scenarios. Fuel was introduced from the top, water-cooled tube. Flames were started using an arc igniter for a standard fuel and air flow configuration and stabilized in a 1 cm gap between the two tubes. For hydrocarbon fuels burning in air, stoichiometry dictates that the non-premixed flame reside on the air side of the stagnation plane. Phase Doppler Particle Anemometry was used to measure droplet size distribution, number density, and droplet velocities through the flow field by vertically translating the burner assembly. The aerosol generator required a  $\approx 1$  L/min to 1.5 L/min flow of air for proper operation. In order to examine flames of lower strain rate, part of the air stream containing droplets was diverted from the burner. Droplets from the excess stream were removed by filtering, and the resulting air flow was measured to determine the amount of air sent to the burner.

The mists were produced using a vibrating orifice aerosol generator (TSI Inc. Model 3450), based on the design of Berglund and Liu.<sup>111</sup> A schematic of the droplet generator is shown in Figure 4-13. Water was forced through a pinhole that was acoustically excited by a piezoelectric ceramic. At specific resonant frequencies, the water jet broke up into a monodisperse droplet stream. This stream exited the generator through a hole in the dispersion cap. By forcing air to exit through this same hole, the droplet stream was dispersed into a cloud as it exited the droplet generator and entered the counterflow burner’s bottom tube. Measurements of droplet number density as a function of radial position at the tube exit indicated that the droplets were evenly distributed except near the tube wall. The mass flow of water was adjusted primarily by controlling the backing pressure of water entering the orifice. The use of the small orifice in this type of droplet generator placed limitations on the achievable water flow. In general, the smaller the orifice used, the smaller the maximum flow of water that could be obtained.

To obtain flame conditions of high strain and low water mass fraction, the aerosol was mixed with a secondary (dry) air stream. The mixture was then introduced up the tube toward the reaction zone. For low strain rate conditions, the air flow through the droplet generator required to accomplish droplet dispersal often exceeded the desired total air flow to the burner. Under these conditions, a portion of the air/droplet stream was diverted to bypass the burner. The analysis below assumes that no collisions between droplets occurred. The volume fraction occupied by droplets for these operating conditions was typically  $\approx 2 \times 10^{-5}$ . The assumption that a significant number of collisions did not occur is consistent with the droplet size histograms, which did not show appreciable droplet growth, as would be the case if collisions were to occur.

The aerosol generator used in the present study produced droplets having very narrow size distributions. When the dispersion air is used, 95 % of the droplets had diameters within  $\pm 2.5 \mu\text{m}$  of the mean. (The size distribution was even narrower in the absence of dispersion air.)

Droplet size and velocity distributions were monitored using a Phase Doppler Particle Anemometer (PDPA-Dantec Measurement Technology). For the mists studied, all droplets in the original droplet stream were characterized by a single  $4 \mu\text{m}$  wide PDPA bin size. In order to distribute the stream into a mist, a dispersion cap and entrainment assembly were employed. Mist dispersion and air entrainment of the highly-monodisperse droplet stream into a mist in the burner tube degraded the monodispersity slightly. As shown in Table 4–5,  $> 50 \%$  of the water mass for each mist was still contained in three  $4 \mu\text{m}$  wide bins, centered on the title bin. For the  $14 \mu\text{m}$  mist, this value was 90 %.

**Table 4–5. PDPA Derived Diameter Information for the Experimental Mists Studied Measured at 2 mm from the Air Tube Exit.** <sup>113</sup>

Mist Name	% Water Droplets within $\pm 2 \mu\text{m}$ of Nominal Diameter	% Water Mass within $\pm 2 \mu\text{m}$ of Nominal Diameter	% Water Mass within $\pm 6 \mu\text{m}$ of Nominal Diameter
14 $\mu\text{m}$	63	47	90
30 $\mu\text{m}$	61	60	72
42 $\mu\text{m}$	53	38	51

One disadvantage of this generator was that the droplet diameter could not be continuously adjusted: monodisperse droplets could only be produced at specific sizes, corresponding to piezoelectric driver frequencies that match acoustic resonances of the orifice. Using a  $5 \mu\text{m}$  diameter pinhole, for example, monodisperse droplet streams with a size distribution peak at diameters of  $14 \mu\text{m}$ ,  $18 \mu\text{m}$ , and  $24 \mu\text{m}$  were produced. With a  $10 \mu\text{m}$  diameter pinhole, monodisperse streams of  $25 \mu\text{m}$ ,  $30 \mu\text{m}$ , and  $37 \mu\text{m}$  droplets were obtained. If the piezoelectric driver frequency were nonresonant, a bimodal or multimodal droplet size distribution was generally produced.

Using the PDPA, droplet diameters, axial velocities, and number densities were measured at discrete points at a single point in the flame by recording each droplet which crossed the laser probe volume during a specified time period. Laser light scattered by the droplets was collected through a window mounted in the Plexiglas chamber. The burner was mounted on a three-axis translation stage, such that the laser probe volume could be positioned anywhere in the gap between the opposed tubes to record droplet characteristics as a function of position. The axial position of the flame was determined by centering the PDPA probe volume in the middle of the flame's visible emission zone.

The droplet size distribution was monitored during the experiments to ensure that the piezoelectric driving frequency was correctly chosen to yield a monodisperse droplet distribution. The droplet volume density determined by the PDPA was the primary determination of the amount of liquid water delivered to the flame. Comparison runs between the PDPA determination of the water delivery rate, and direct measurements of the accumulated mass of water exiting the droplet generator, yielded agreement within a few percent. The PDPA system was capable of acquiring data at higher droplet loadings than those reported here. This was verified in the case of the larger droplet sizes (the achievable mass fraction of the smaller droplets was limited by the generator). The limit imposed on the water mass fraction was due to the effect of the water droplets on the strain rate, not a limitation of the PDPA diagnostic.

### ***Droplet Behavior***

Figure 4-37 and Figure 4-38 show the evolution of the droplet size distribution, in these propane/air counterflow flames, of initially monodisperse water mists of 30  $\mu\text{m}$  and 18  $\mu\text{m}$ , respectively. The figures plot number densities of droplets in various size ranges as a function of axial position ( $x$ ) along the burner's axis ( $r = 0$  mm). The local axial strain rate,  $a$ , imposed on the flames corresponds to approximately 30 % of the extinction strain rate measured in the present apparatus<sup>110</sup> for the uninhibited flame ( $a_{\text{ext}} = 608 \text{ s}^{-1} \pm 65 \text{ s}^{-1}$ ). The air and droplets exited the lower tube at  $x = 0$  mm; the propane exited the upper tube at  $x = 10$  mm. The luminous zones of the flames were located at  $x = 5.0$  mm and 4.5 mm, respectively, in the experiments employing 30  $\mu\text{m}$  and 18  $\mu\text{m}$  mists. For both initial sizes, the diameter of the droplets changed very little until the flame was reached, with the 30  $\mu\text{m}$  or 18  $\mu\text{m}$  droplets dominating the size distribution.

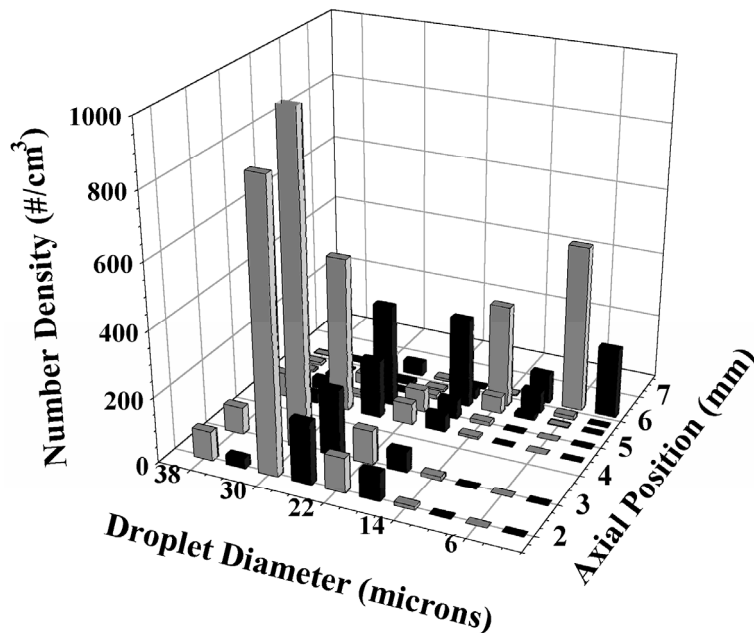


**Figure 4-37. Droplet Diameter Distribution Evolution of a 30  $\mu\text{m}$  Mist in a 170  $\text{s}^{-1}$  Strain Rate Flame; the luminous flame is centered at 5 mm.**<sup>109</sup>

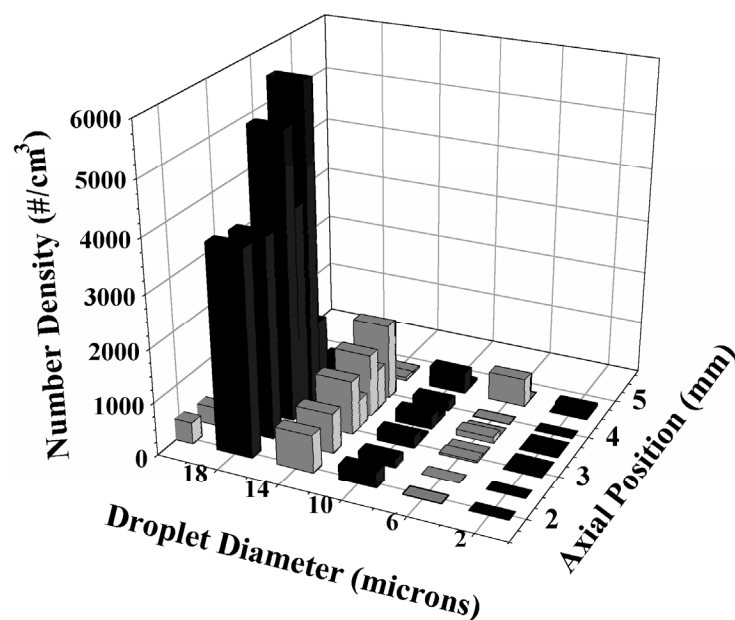


**Figure 4-38 Droplet Diameter Distribution Evolution of an 18  $\mu\text{m}$  Mist in a  $170 \text{ s}^{-1}$  Strain Rate Propane/air Counterflow Flame. The luminous flame is centered at 4.5 mm.**<sup>109</sup>

In the flame region, the two droplet sizes showed somewhat different behaviors. In both cases, the droplets evaporated; and the total number density of droplets, summed over all size ranges, decreased. For the 18  $\mu\text{m}$  initial droplet size, virtually no droplets of any size were detected once the flame was reached. For the 30  $\mu\text{m}$  initial size, the total number density decreased, though not as dramatically, in passing through the flame zone. The droplets that were detected in or beyond the flame zone had a broad size distribution and a much smaller average size than did the incident drops. These observations indicate that, for this flame condition, the 18  $\mu\text{m}$  mist underwent essentially complete vaporization once it entered the reaction zone, while the 30  $\mu\text{m}$  mist appeared to be near the threshold size above which droplets were not completely evaporated. When incident droplets of 42  $\mu\text{m}$  diameter were used, a larger number of droplets were detected beyond the flame zone, supporting the assertion that 30  $\mu\text{m}$  is close to the minimum size capable of just penetrating the flame.

Figure 4-39 and Figure 4-40 focus specifically on the number density profiles of the 30  $\mu\text{m}$  and 18  $\mu\text{m}$  droplets respectively. Number density is plotted vs. axial position. In both experiments, the density first increases with axial position; then quickly drops in the flame region.

Three effects combine to explain the shape of the number density profiles. The main effect is related to the velocity profiles of the 30  $\mu\text{m}$  and 18  $\mu\text{m}$  drops, provided in Figure 4-39 and Figure 4-40, respectively. At the lower tube exit, the droplets had roughly the same velocity as the gas stream. As the gas stream's axial velocity changed in the counterflow field, the equilibrium in velocity between the liquid and gas phases was lost, and the drag forces acted to reestablish it. The droplet velocity profile therefore followed that of the gases; the velocity initially dropped as the gases moved towards the stagnation plane. It then increased when the hot gases expanded in the reaction zone, before it dropped down again, close to the stagnation plane. In regions where the droplets were decelerating, faster droplets caught up to slower ones, and the number density tended to increase. In the flame region, the droplets accelerated, which tended to reduce their number density. Figure 4-39 and Figure 4-40 show that the impact of axial velocity gradients on droplet number density was significant, with variations in number density well correlated with variations in velocity.

Furthermore, as the air exited the lower tube, the flow streamlines began to diverge in the counterflow field, producing radial drag forces on the mist. Due to this effect, the droplets moved away from the burner axis. The divergence of the air flow therefore acted to reduce the droplet number density along the centerline. The third effect is evaporation in the flame region, which caused the droplet size to decrease, and thus also contributed to the decrease in the number densities of the 30  $\mu\text{m}$  and 18  $\mu\text{m}$  droplets.

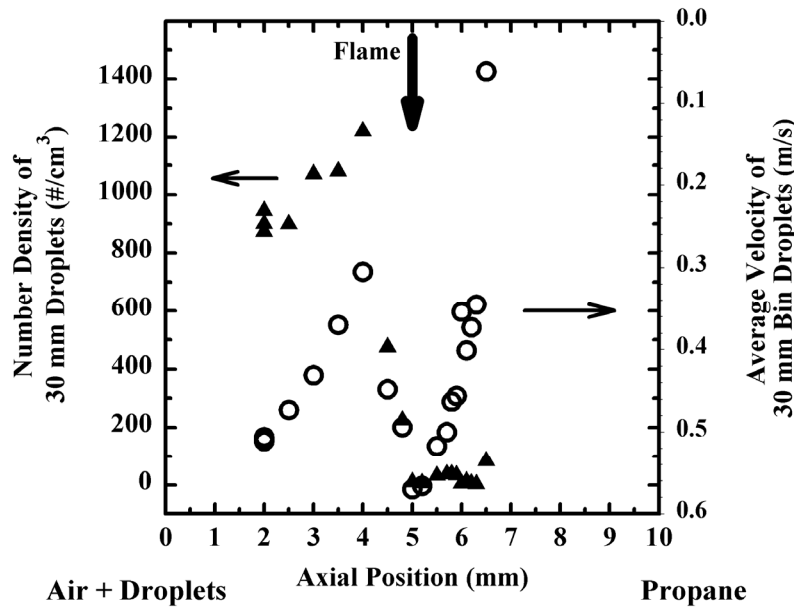


**Figure 4-39. Profiles of Number Density (triangles) and Velocity (circles) of 30  $\mu\text{m}$  Droplets vs. Location in a  $170 \text{ s}^{-1}$  Strain Rate Propane/air/ $30 \mu\text{m}$  Mist Counterflow Flame.**<sup>109</sup>

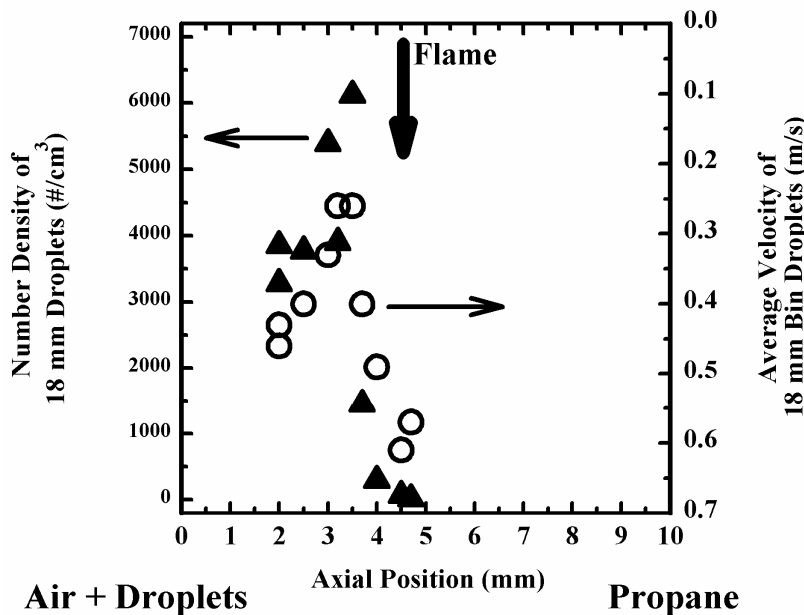


**Figure 4-40. Profiles of Number Density (triangles) and Velocity (circles) of 18  $\mu\text{m}$  Droplets vs. Location in a Propane/air/water mist Counterflow Flame.**<sup>109</sup>

When the data of Figure 4-39 and Figure 4-40 are plotted in terms of droplet flux rather than number density, the peak just before the reaction zone is not present. Figure 4-41 shows the droplet flux profile for the 30  $\mu\text{m}$  mist. The flux was determined from the PDPA software by summing over all droplets detected within the measurement time, with the sum weighted by the velocity of each drop. The droplet

flux decreased slightly as the flame was approached, under the effects of the diverging flow and evaporation. The flux then decreased dramatically in passing through the high temperature zone. For the 18  $\mu\text{m}$  incident droplet size, the plot of flux vs. position is qualitatively similar to that of the 30  $\mu\text{m}$  drops, except that the flux is reduced to essentially zero once the reaction zone is reached. In the plots of droplet flux, scatter in the data was attributed in part to experimental uncertainties, in the PDPA concentration measurements in particular. Slight variations in the position of the flame over the course of the experiment also contributed to the scatter.

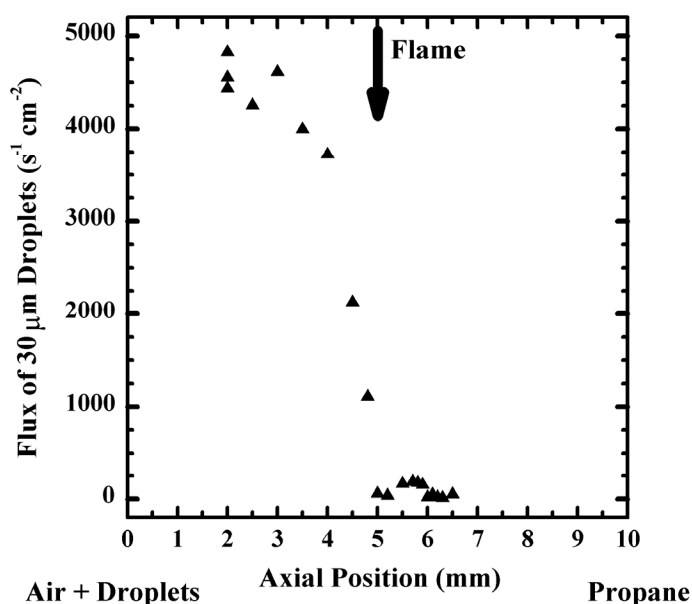


**Figure 4-41. Droplet Flux Profile for a 30  $\mu\text{m}$  Mist in a 170  $\text{s}^{-1}$  Strain Rate Propane/air Flame.**

### *Flame Extinction*

The core data set comprised measurements of the extinction strain rates of non-premixed propane/air counterflow flames at various water mass fractions (up to 0.03) at droplet sizes of 14  $\mu\text{m}$ , 30  $\mu\text{m}$ , and 42  $\mu\text{m}$ . Droplet fluxes were measured by the PDPA instrument along the burner axis 2.0 mm from the air tube exit, at strain rates within 10 % of extinction. Local strain rates were determined from the gas flows as discussed above. The results are plotted in Figure 4-42. For comparison, extinction mass fractions of halon 1301 ( $\text{CF}_3\text{Br}$ ) vs. local strain rate in the propane/air counterflow flame<sup>110</sup> are also plotted. The 42  $\mu\text{m}$  water droplets were clearly much less effective in reducing the extinction strain rate than were the 14  $\mu\text{m}$  or 30  $\mu\text{m}$  droplets. The 14  $\mu\text{m}$  droplets were slightly more effective than the 30  $\mu\text{m}$ , but direct comparison was difficult because only a very limited mass fraction of water was obtainable in the 14  $\mu\text{m}$  droplet size with the present generator. Both of the smaller droplet sizes appeared to be more effective in reducing the extinction strain rate than was halon 1301.

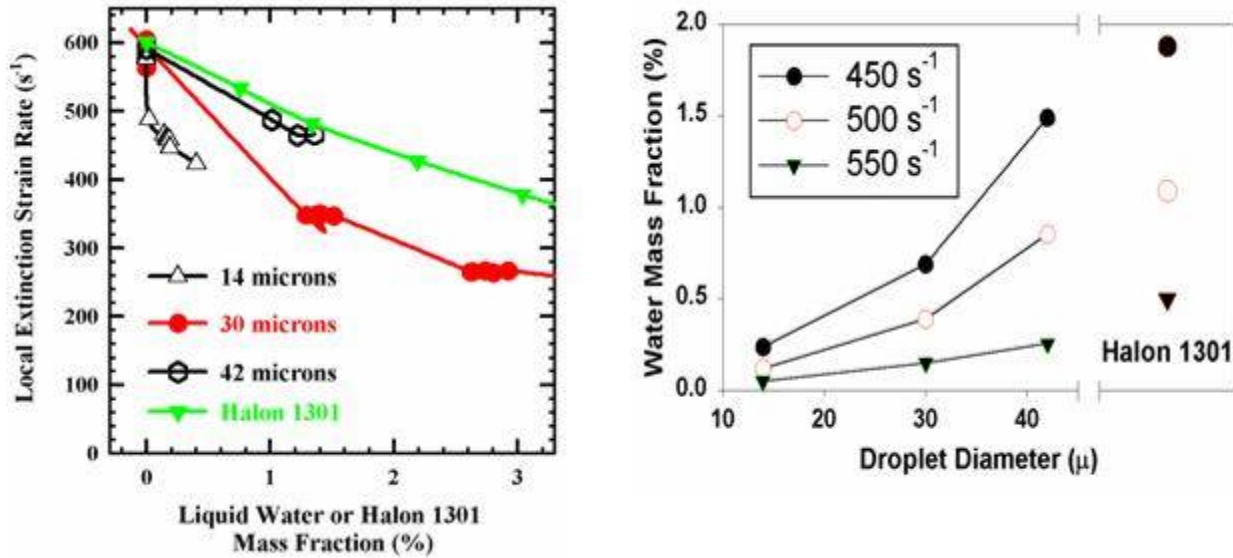


**Figure 4-42. Water Mist Effects on the Extinction of Non-premixed, Counterflow Propane/air Flames: (a) Flame Extinction Strain Rate as a Function of Mass of Water or Halon 1301 in the Air Flow; (b) Mass Fraction of Water Needed to Extinguish the Flames as a Function of Droplet Diameter, Compared to Mass of Gas-phase Halon 1301.**<sup>75</sup>

#### Maximum Droplet Evaporation Diameter

Li, Libby, and Williams<sup>104</sup> performed both numerical and analytical modeling, as well as experimental measurements, of the behavior of methanol droplets in opposed flows, both in the presence and absence of a flame. Clearly, there are differences between the interaction of a fuel droplet with a flame and that of a suppressant droplet. Nevertheless, the effects of evaporation and of viscous drag imparted by the local gas flow field have analogies between the two cases. Li et al.<sup>104</sup> analyzed the phenomenon of "pushback" previously described by Chen et al.<sup>64</sup> in which droplets in certain size ranges exhibited oscillatory motion in the vicinity of the stagnation plane. For a given flow field, large droplets tended to oscillate, while small droplets asymptotically approached an equilibrium position slightly below the stagnation plane. Under the assumptions of the Stokes drag law, neglect of evaporation, and an axial strain rate independent of axial position, the minimum droplet radius for oscillation to occur is given by

$$R_{\min} = \left( \frac{9\mu}{8\rho K} \right)^{\frac{1}{2}} \quad (4-11)$$

where  $\mu$  is the absolute viscosity of the surrounding gas,  $\rho$  is the droplet density, and  $K$  is the axial strain rate. For a water droplet in air at a strain rate of  $150 \text{ s}^{-1}$ , the minimum diameter for oscillation to occur was approximately  $30 \text{ }\mu\text{m}$ . In practice, this threshold represents a lower bound because all droplets lose mass by evaporation, and water droplets with initial sizes smaller than the oscillation threshold usually undergo complete vaporization upon entering the flame zone.<sup>80</sup> The size ranges of droplets investigated in the present study bracketed the threshold size for oscillation for the flow field conditions. Furthermore, the threshold size was similar to the size predicted by Lentati and Chelliah to be most effective at

suppression, although this could be a consequence of the relative importance of viscous drag and evaporation for water in particular.

The experimental results were consistent with the numerical predictions of Lentati and Chelliah<sup>80</sup> for monodisperse droplet streams in a number of respects. For a methane/air counterflow flame with a local strain rate of  $130 \text{ s}^{-1}$ , Lentati and Chelliah<sup>80</sup> predicted that a  $30 \text{ }\mu\text{m}$  water droplet should just pass through the reaction zone before evaporating completely, while droplets having diameters  $15 \text{ }\mu\text{m}$  or less should completely evaporate before reaching the location of maximum temperature. The data shown in Figure 4-37 and Figure 4-38 were taken with a different fuel (propane vs. methane) and at a slightly higher strain rate ( $165 \text{ s}^{-1}$  to  $175 \text{ s}^{-1}$  vs.  $130 \text{ s}^{-1}$ ), but show the same qualitative behavior as a function of droplet size. Furthermore, Lentati and Chelliah<sup>80</sup> predicted that appropriately sized water droplets could be more effective on a mass basis than halon 1301 in suppressing combustion, but that the effectiveness of water was likely to decrease significantly with increasing droplet size for diameters  $>30 \text{ }\mu\text{m}$ . Both of these predictions were consistent with the data presented in Figure 4-42. There were approximations made in the modeling as well as non-ideality in the present experiment. Nevertheless, the results of these experiments supported the predictions of Lentati and Chelliah<sup>80</sup> in those aspects for which there was an adequate comparison.

The degree of evaporation (or decomposition) of an aerosol particle or droplet in a flame depends on the residence time of the aerosol in the high temperature environment. In the flame, the evaporation rate and droplet size are spatially dependent since the aerosol is moving in a non-uniform temperature field. Solution of the problem requires full consideration of the flow field. However, the evaporation model can be used to estimate a droplet size in the premixed and opposed flame configurations for the onset of complete droplet evaporation. In the flame temperature field, droplets begin to evaporate at the lower temperature and the resulting smaller drop, traveling into the higher temperature region, will experience a higher evaporation rate and consequently a shorter total evaporation time.

Consideration of the burning velocity and flame thickness of the methane-air premixed flames reported earlier in this section suggested that the water droplets should experience a residence time in the range of 1 ms to 2 ms. Consideration of the temperature field and the results of Figure 4-6 indicated a droplet size limit for complete evaporation (and the corresponding onset of water droplet limiting effectiveness) at  $\sim 15 \text{ }\mu\text{m}$  in premixed flames. This upper limit estimate was consistent with the water droplet size profiles observed in the premixed flame and with predictions of the multiphase model.

For counterflow flames, transit time in the flame was estimated from the inverse of the strain rate.<sup>80</sup> For a strain rate of  $450 \text{ s}^{-1}$  (high strain rate for methane, mid strain rate for propane) the residence time was  $\approx 2.2 \text{ ms}$ . The estimated droplet size for the onset of complete evaporation was  $\approx 25 \text{ }\mu\text{m}$ . This value agreed with the experimental water droplet size survival properties in propane-air flames<sup>63</sup> and was consistent with the modeling predictions for methane-air flames.<sup>80</sup>

### ***Modeling the Effect of Water Vapor***

NRL staff collaborated with Chelliah and co-workers to understand the observed suppression behavior of water vapor and water droplets on propane-air non-premixed counterflow flames. Comparison of the predictions of the model described in Section 3.5.1 with experimental results provided valuable insights regarding the experimental observations.<sup>112</sup> The collaboration also served to validate the multi-phase flame suppression model further.

During the application of water mist to a fire or a laboratory flame, an enclosed or semi-enclosed chamber will be saturated with water vapor. The time required to attain the saturation condition depends on several factors, including the air temperature, original humidity level, and the total surface area of the droplets applied. For the same condensed water mass, smaller droplets have a higher surface area per unit volume (or mass), leading to a more rapid saturation of the initially dry air, while larger droplets with lower surface area/volume are expected to take considerably longer. Consequently, different levels of water vapor content in air are realizable (i.e., saturated to partially saturated), depending on the droplet size, droplet number density or mass added, gas temperature, and the elapsed time.

The model assumed that the room temperature was constant at 300 K and that the air feed stream was completely saturated with water vapor. The latter implied that droplets traveled with the air stream long enough to attain equilibrium conditions. At 300 K, the mole fraction of water vapor in saturated air is 0.0352; the mass fraction is 0.0224. This corresponds to mole fractions of oxygen of 0.2026, nitrogen of 0.762, and water of 0.0352 in the oxidizer stream.

Results of the two-phase model for non-premixed counterflow propane-air flames are shown in Figure 4-43. Indicated in the figure are flame temperature vs. strain rate curves for flames with dry 300 K air, saturated 300 K air, and saturated 300 K air containing a 14  $\mu\text{m}$ , 30  $\mu\text{m}$ , or 42  $\mu\text{m}$  diameter monodisperse water mist. The water masses for the individual aerosols were based on the experimental determinations shown in Table 4-5. The extinction condition is defined by the curve turning point; the value of the strain rate at the turning point is the predicted extinction strain rate for each suppressed flame condition.

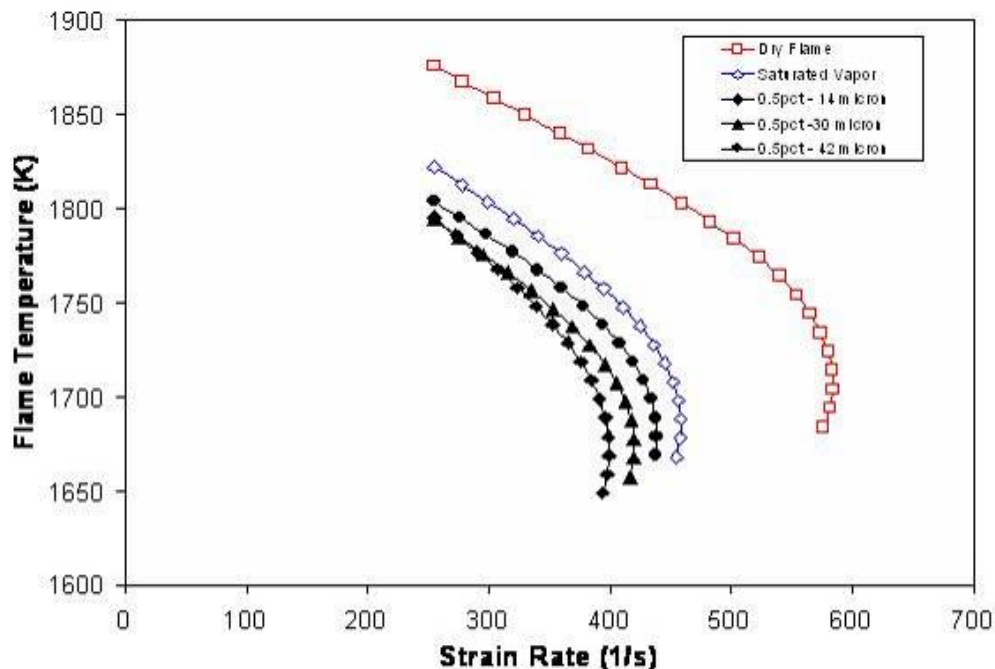


**Figure 4-43. Variation of the Predicted Flame Temperature as a Function of the Flow Strain Rate for Propane-air, Non-premixed Counterflow Flames for Dry Air, Air Saturated with Water Vapor, and Saturated Air with Monodisperse Water Droplets.** <sup>113</sup>

The reduction of oxygen mole fraction from 0.209 (dry air) to 0.2026 (saturated air) due to displacement by water vapor at 300 K yields a decrease in the predicted flame extinction strain rate from  $584 \text{ s}^{-1}$  to  $458 \text{ s}^{-1}$ , a 22 % reduction in the extinction condition, as shown in Figure 4-43. At elevated oxidizer stream temperatures, assuming complete saturation, the increase in partial pressure of water vapor and the resulting decrease in oxygen concentration would lead to an even lower flame extinction strain rate. Likewise, a lower level of humidification in the incoming air stream would result in a smaller reduction in the extinction strain rate than that of the completely saturated air condition.

### *Modeling the Effects of Condensed Water and Droplet Size*

When condensed water droplets were added to an already saturated air stream, the interaction of droplets with the flame front reduced the flame extinction condition further, as seen in Figure 4-44. However, the degree of reduction of the flame extinction condition depended on the droplet size, consistent with previous modeling and experiments involving the methane-air system.<sup>80</sup> Unlike the methane-air counterflow system where the optimal droplet size was predicted to be between  $15 \text{ }\mu\text{m}$  and  $20 \text{ }\mu\text{m}$ , the present predictions and experiments indicated that the optimal droplet size for the propane-air counterflow system was below  $15 \text{ }\mu\text{m}$ . The difference in optimal size was related to the higher flame extinction condition of propane-air flames, about 50 % greater than that of methane-air counterflow flames. The lower flow residence times at higher strain rates provided less time for a given droplet size to completely evaporate. For higher strain rates, droplets need to be correspondingly smaller to optimally interact with the flame front.

A comparison of the modeling and experimental results is presented in Figure 4-44.

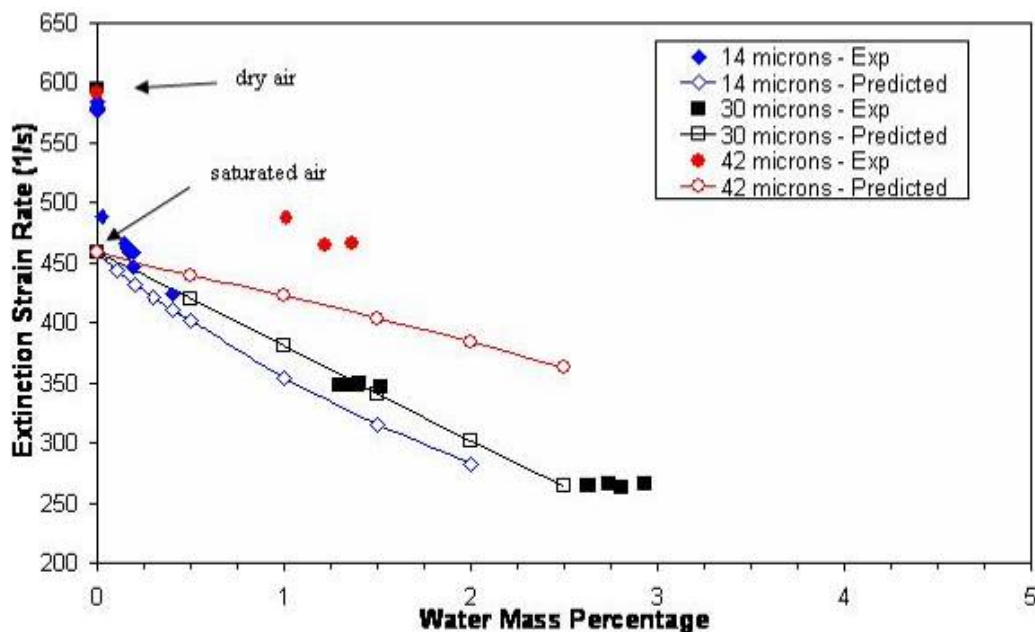


**Figure 4-44. Measured Extinction Strain Rate for Water Mist Suppressed Propane-air, Non-premixed Counterflow Flames vs. % Mass of Condensed-phase Water in the Air<sup>109</sup> and Calculated Results for  $14 \text{ }\mu\text{m}$ ,  $30 \text{ }\mu\text{m}$ , and  $42 \text{ }\mu\text{m}$  Diameter Monodisperse Water Mists in Saturated Air at 300 K.<sup>113</sup>**

Comparison of the results for the three different mists suggests the occurrence of several phenomena. In the experiments, droplets were entrained into dry air. The very rapid reduction in extinction strain rate with only a very small mass of water droplets at the flame, followed by a less dramatic fall off with subsequent water droplet addition suggested a fair degree of humidification. This was particularly noticeable for the 14  $\mu\text{m}$  mist. The experimental data for 14  $\mu\text{m}$  mist at greater than 0.005 mass fraction of added water and for the 30  $\mu\text{m}$  mist data at greater than 0.015 mass fraction of added water droplets were in very good agreement with the model predictions. The 42  $\mu\text{m}$  data were  $\approx 12\%$  higher than the calculation predicted at 0.015 mass fraction of added water drops. This disagreement was consistent with the degree of humidification for this larger droplet size. A quantitative prediction of the degree of air saturation expected for the experimental conditions follows below.

### Humidification Effects of Air Stream

In order to quantify the degree of droplet evaporation for the different droplet sizes and the effect on flame extinction, evaporation times for the 14  $\mu\text{m}$ , 30  $\mu\text{m}$ , and 42  $\mu\text{m}$  diameter droplets were calculated. The calculation incorporates the droplet evaporation equations given in Chin and Lefebvre.<sup>113</sup> Droplet evaporation times in air at 296 K were determined for a range of relative humidity for each of the experimental droplet sizes. For each droplet size, the variation in droplet evaporation times between 0% and 100% relative humidity was fit to a second order polynomial.

The evaporation over time of an ensemble of monodisperse droplets at a specified initial mass fraction in dry air was determined by direct time integration. For each 1 ms time step, the amount of vaporization was calculated based on the instantaneous relative humidity, the droplet number density, and the D-squared evaporation law. The amount of water vaporized impacted the relative humidity and consequently the evaporation rate for the next time step.

The predictions of the total amount of evaporation for a residence time of 750 ms are shown in Figure 4-45.

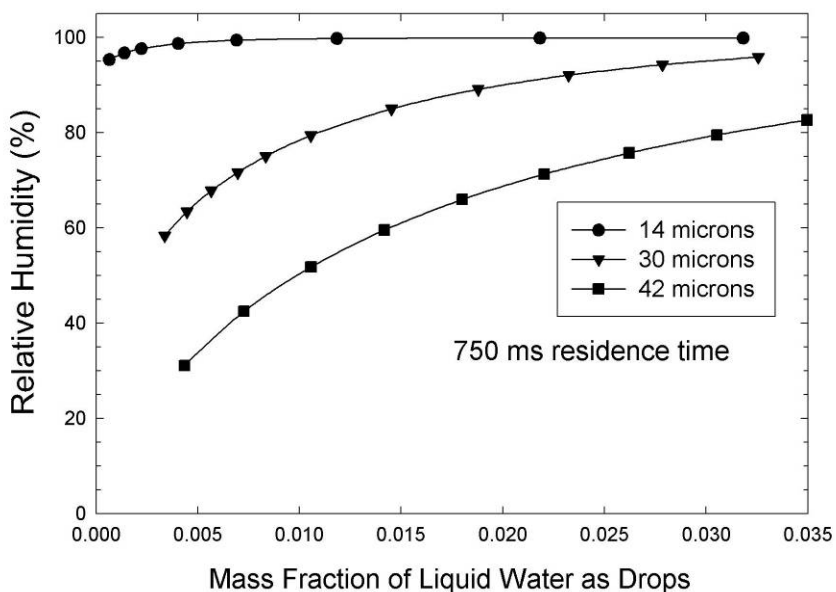


**Figure 4-45 Calculated Humidification Levels of a 296 K Air Stream Containing 14  $\mu\text{m}$ , 30  $\mu\text{m}$ , or 42  $\mu\text{m}$  droplets, Following a Residence Time of 750 ms Starting in Dry Air, as a Function of the Mass Fraction of Liquid Water Remaining after Droplet Evaporation.**<sup>113</sup>

The residence time considered here was the time required to transport the mist after entrainment in originally dry air up the 50 cm long inlet tube. A residence time of 750 ms is the shortest value studied and corresponds to the air exit velocity necessary to produce flames with a local strain rate of  $\approx 600 \text{ s}^{-1}$ . The shortest residence time provided a lower bound for the degree of humidification. Figure 4-45 plots the relative humidity (saturated air having a water mass fraction of 0.018 at the experimental temperature of 296 K) against the mass fraction of liquid water remaining after the specified residence time. The liquid water delivered to the flame as determined via PDPA measurements 2 mm above the air tube exit was reported by Zegers et al.<sup>110</sup>, rather than the initial mass fraction of water introduced by the droplet generator. Figure 4-45 shows that in the case of 14  $\mu\text{m}$  drops, for any liquid water to remain after 750 ms, the air stream relative humidity must be at least 95 %. Thus, the assumption of saturated air in the extinction calculation was valid and was consistent with the rapid reduction in extinction strain rate observed for this droplet size. For the 30  $\mu\text{m}$  drops, two sets of experimental points were collected, clustered at liquid mass fractions of 0.015 and 0.028. For the 0.015 mass fraction tests, the relative humidity after a 750 ms residence time was predicted to be approximately 85 %, while for the 0.028 mass fraction tests it was 95 %. Since the extinction strain rates for the flames inhibited by the 30  $\mu\text{m}$  droplets were approximately  $350 \text{ s}^{-1}$ , this implies a droplet residence time in the air stream prior to arrival at the flame of approximately 1250 ms. The degree of saturation for a 0.015 mass fraction of residual liquid at 1250 ms was predicted to be 96 % (data not shown). For the 42  $\mu\text{m}$  droplets the experimental measurements all had liquid mass fractions in the vicinity of 0.012. For this condition, the calculation predicted a relative humidity of only 55 %; assumption of a residence time of 1000 ms, based on the measured extinction strain rate, gives a relative humidity of 66 %. The calculation assuming 100 % relative humidity was expected to overpredict the extinction strain reduction (lower extinction strain rate), due to the additional heat capacity from the water vapor that was not present in the experiment. This underestimate in the extinction strain rate was in quantitative agreement with the results for the 42  $\mu\text{m}$  mist, as shown in Figure 4-44.

### Conclusions

Using piezoelectric generation of aerosol drops, NRL investigated the evolution of velocity and size distributions of initially monodisperse, 30  $\mu\text{m}$  and 18  $\mu\text{m}$  water mists in non-premixed propane/air counterflow flames. For both size mists, the peak in the droplet size distribution did not change until the flame zone was reached. The peak then shifted to smaller diameters due to evaporation. Variations in number density with axial position were strongly correlated with variations in droplet axial velocity. The fluxes of both 30  $\mu\text{m}$  and 18  $\mu\text{m}$  droplets decreased between the air tube exit and the stagnation plane, due to the effects of the diverging flow and evaporation. None of the 18  $\mu\text{m}$  droplets and very few of the 30  $\mu\text{m}$  droplets survived the flame, suggesting that for this range of droplet sizes in a counterflow flame at moderate strain rate, most of the suppression potential of the mist is used.

On a mass basis, both 14  $\mu\text{m}$  and 30  $\mu\text{m}$  diameter mists were found to be more effective than halon 1301 at suppressing non-premixed propane/air counterflow flames. The flame inhibition properties of the 42  $\mu\text{m}$  diameter mist were considerably poorer than those of the 14  $\mu\text{m}$  or 30  $\mu\text{m}$  mists. The lower suppression efficiency of the 42  $\mu\text{m}$  mist paralleled previous predictions of numerical modeling, and appeared to be caused by incomplete droplet vaporization during passage through the reaction zone. Comparison of the computational extinction strain rates with the reported experimental measurements showed good agreement in consideration of the degree of mist evaporation in the experimental air stream entering the flame. These results explained the observed droplet dependent suppression behavior in the

range of 14  $\mu\text{m}$  to 42  $\mu\text{m}$  in suppressing counterflow propane air flames. The agreement between the predictions and experiments was remarkable, considering the high effectiveness of the small amount of water mass introduced to the flame with the air stream. The hybrid Eulerian-Lagrangian multi-phase flame suppression model and chemical kinetic propane combustion mechanism well predicted the measured local propane-air extinction strain rate. Water droplet suppression modeling of the flames and consideration of the amount of humidification of the air stream for the reported experimental mists quantitatively accounted for the observed response of the flames to the added liquid water mass as well as the effect of water droplets in this size range. Because of the higher strain rate at extinction, the optimum size water droplet was  $\leq 15 \mu\text{m}$ , somewhat smaller than for methane air flames. This smaller optimum size may be anticipated for other fuels considering the similarity of the extinction properties of propane to that of many other higher hydrocarbon “typical” fuels. The present findings indicated that, if the delivery issues inherent to a condensed phase fire suppressant were successfully addressed, aerosols of water composed of fairly small droplets have the potential to be comparable to that of  $\text{CF}_3\text{Br}$ .

#### 4.5.2 Alkali Metal Bicarbonates, Chemically Active Fire Suppressants

Fire suppression by chemically active particulates such as the alkali metal bicarbonates had been investigated for a number of years prior to the NGP.<sup>1,2,3,4</sup>  $\text{NaHCO}_3$  powder (effective diameter  $< 10 \mu\text{m}$ ) was known to be far more effective than any other gaseous chemical agent being considered to replace halon 1301, but the exact physical and chemical mechanism was unquantified. Explicit understanding of the suppression behavior was also lacking. Two NGP projects explored the suppression behavior of these powders in counterflow flames, providing quantitative information that contributed to the development of suitable chemical and physical models describing the behavior of these aerosols.

##### Study I: Extinguishment of Flames with $\text{KHCO}_3$ and $\text{NaHCO}_3$

###### *Experimental*

NRL staff examined the fire suppression effectiveness of solid aerosols of sodium bicarbonate ( $\text{NaHCO}_3$ ) and potassium bicarbonate ( $\text{KHCO}_3$ ) in extinguishing non-premixed counterflow propane air flames using the counterflow burner described in Section 4.5.1 and shown schematically in Figure 4–36.<sup>114,115</sup> For the powder aerosol suppression studies, air was supplied through the top tube and propane through the bottom tube as is shown in Figure 4-46. This figure also shows the location, relative to the stagnation plane, of the visible flame, and predicted profiles of the temperature and the flame radicals H, O and OH. Experimental strain rates were evaluated using laser Doppler velocimetry (LDV) following the procedure outlined by Zegers et al.<sup>109</sup> Uninhibited propane/air flames had an extinction strain rate of  $\approx 600 \text{ s}^{-1}$ . Powder suppression efficiency was evaluated by adding powder to flames whose uninhibited strain rates were  $180 \text{ s}^{-1}$ ,  $305 \text{ s}^{-1}$ , and  $475 \text{ s}^{-1}$ , referred to as low, medium, and high. The flows and strain rates are summarized in Table 4–6.

The powder delivery system provided a steady flow of agent, with controlled variability from  $\approx 10 \text{ mg/min}$  to  $300 \text{ mg/min}$ . The system, shown in Figure 4-47, consisted of a glass metering valve with an adjustable orifice and a tee above the valve where the powder could be introduced. The valve was made from a tapered brass rod inserted into a matching tapered glass orifice. The system was airtight and the orifice could be changed by screwing the tapered rod in or out. A hose clamp holding a piece of teflon was fastened to the glass metering valve at about the position of the valve. The teflon was used to

contact a rotating wheel of variable frequency. A modulated helium-neon laser beam, monitored with a lock-in detector, was used to measure the powder flow. The laser beam was positioned perpendicular to the flow of powder just below the top tube exit. Scattered laser light created by the powder flow was collected by a photomultiplier tube and collection lens at 90°. The intensity of the scattered light was calibrated to the powder flow by collecting and massing powder with no flame. Because the particle scattering intensity is a function of the air velocity and the size distribution of the particles, a calibration was obtained for each powder size and at each flow tested.

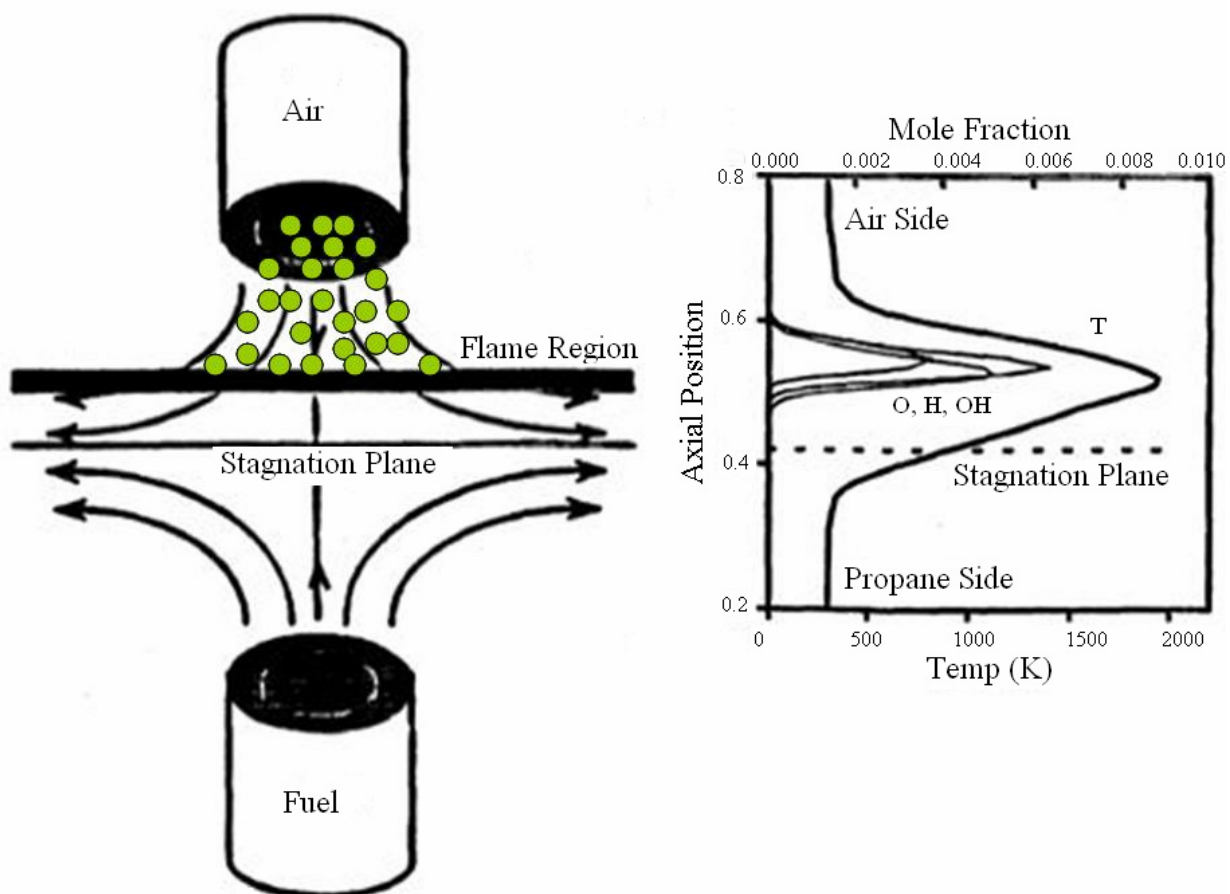


**Figure 4-46. Schematic of the Non-premixed Counterflow Burner and Calculated Temperature, O, H, and OH Profiles for the Low Strain Flame.**<sup>114</sup>

**Table 4-6. Flow and Strain Rate Conditions for Extinction Experiments.**<sup>114</sup>

	Low Strain Flame	Medium Strain Flame	High Strain Flame
Air Flow (L/min)	1.5	2.4	3.5
Fuel Flow (L/min)	1.0	1.7	2.8
Global Strain Rate <sup>a</sup> (s <sup>-1</sup> )	110	180	290
Measured Strain Rate (s <sup>-1</sup> )	180	305	475

<sup>a</sup> Calculated strain rate following Zegers et al.<sup>110</sup>

A video system was used to determine the exact time that the flame was extinguished. Using a fiber optic positioned on the video screen, the intensity of a portion of the flame was monitored and recorded simultaneously with the powder scattering intensity using a LabView controlled A/D board. The addition of powder to the flame dramatically increased the excited  $C_2$  emission from the flame. A suitable optical filter was used to block this emission from the video monitor. Extinction of the flame was evidenced by a dramatic change in light intensity from the video signal. The corresponding powder scattering signal was evaluated to determine the powder flow rate at extinction.

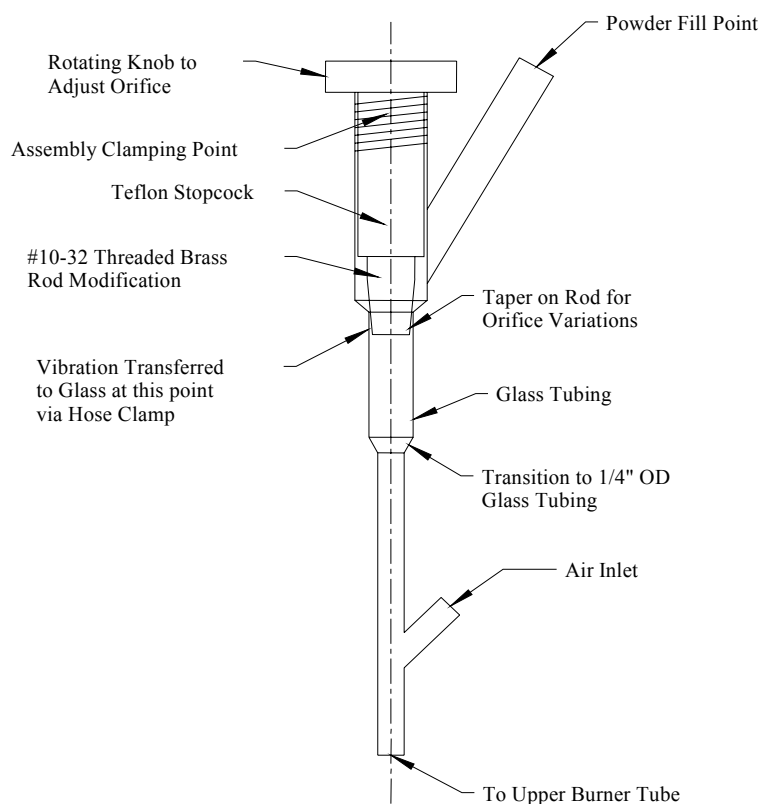


**Figure 4-47. Powder Delivery System.**<sup>115</sup>

Prior to each test, the chamber and tubes were cleaned to remove any excess powder. The flame was ignited and established midway between the two tubes, and the flows adjusted to produce the desired strain rate per Table 4–6. Once the system was acquiring data, the powder was turned on, mixing into the air stream from above the flame to simulate total flooding agent delivery systems. Particle delivery from the top also minimized any size dependent particle entrainment/flow issues. The flow was gradually ramped up until the flame extinguished. In this flow configuration (air on top, fuel on bottom) the propane/air flames tended to extinguish only along the centerline, leaving an annular flame attached to the upper tube. However, the extinction strain rates determined from the centerline extinction were consistent with other studies and have been shown to be valid.<sup>110</sup> Total extinguishment occurred for the propane/air flames only after an excessive amount of powder was delivered to the flame to sufficiently overwhelm it. The flat horizontal burning region of the flame was centered along the axis and positioned at the location determined by the momenta of the flows. However, the flame was rounded at the edges and had a bowl-like shape. The top of the flame curved around and attached to the outer rim of the upper burner tube. Upon extinction, the flat horizontal region of the flame disappeared, but the upper curved region of the flame remained stabilized to the upper burner tube. The flame would continue to burn in the annular

configuration even after the flow of powder was stopped as the flame had attached and stabilized itself on the upper tube. The air and fuel flows were decreased to destabilize the annular flame and recover the original flame structure. The process was repeated until 8 to 10 extinction points were obtained. This procedure was repeated for the same powder at the remaining two strain rates.

Tests were conducted with both sodium bicarbonate ( $\text{NaHCO}_3$ ) and potassium bicarbonate ( $\text{KHCO}_3$ ). Both powders were mechanically sieved into size ranges of  $<38\ \mu\text{m}$ ,  $38\ \mu\text{m}$  to  $45\ \mu\text{m}$ ,  $45\ \mu\text{m}$  to  $53\ \mu\text{m}$ ,  $53\ \mu\text{m}$  to  $63\ \mu\text{m}$ , and  $63\ \mu\text{m}$  to  $75\ \mu\text{m}$  using a commercial sieving unit. Silica was added to the powder samples (2 % by mass) as a drying additive. Both powders seemed to flow very freely with almost no agglomeration noticed. Representative micrographs of the  $\text{NaHCO}_3$  powders are shown in Figure 4-48; micrographs for the  $\text{KHCO}_3$  powders, ground and sieved at  $45\ \mu\text{m}$  to  $53\ \mu\text{m}$  are shown in Figure 4-49.

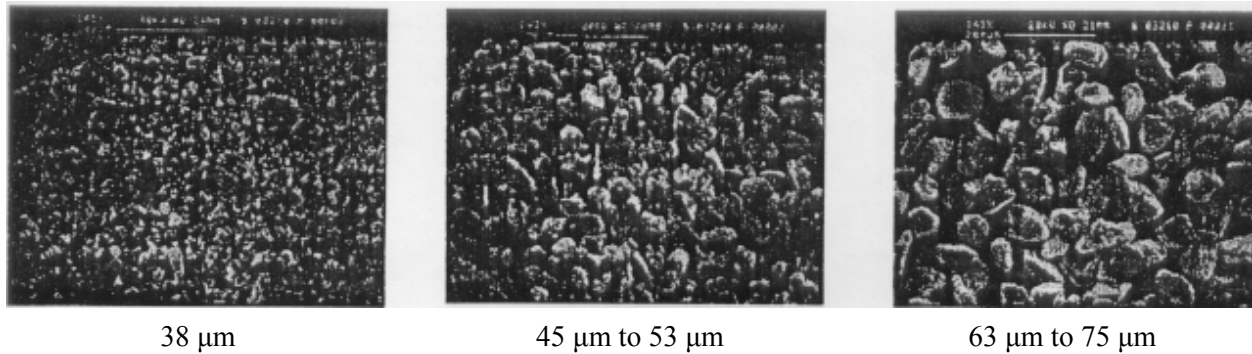


**Figure 4-48. Typical Micrographs of  $\text{NaHCO}_3$  Powder Samples.** <sup>115</sup>

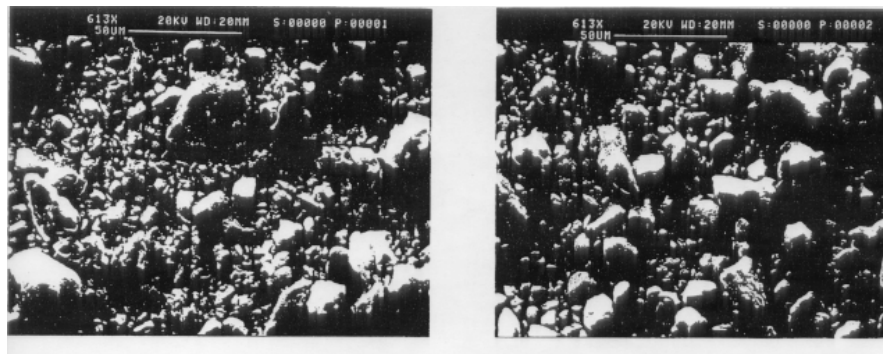


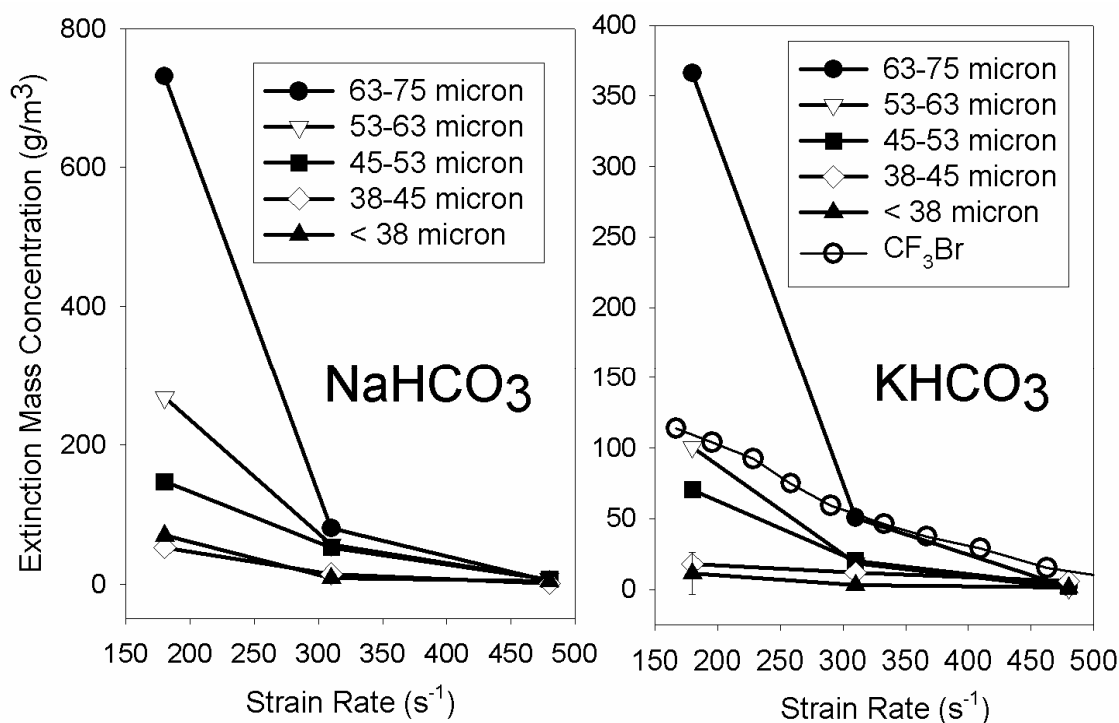
**Figure 4-49. Typical Micrographs of  $\text{KHCO}_3$  Powder.** <sup>115</sup>

## Results and Discussion

Extinction mass concentration measurements as a function of the measured strain rate and particle size bin are tabulated in Table 4-7 and plotted in Figure 4-50. The halon 1301 data were derived from Zegers et al.<sup>109</sup>

**Table 4-7. Propane-air Counterflow Non-premixed Flame Extinction Mass Concentrations for Powders and Halon 1301.**<sup>114</sup>

Chemical	Measured Strain rate (s <sup>-1</sup> )	Extinction Mass Concentration for Specified Size Bin (g/m <sup>3</sup> )				
		< 38 μm	38 μm to 45 μm	45 μm to 53 μm	53 μm to 63 μm	63 μm to 75 μm
NaHCO <sub>3</sub>	180	70	52	150	270	730
	310	8	15	53	56	80
	480	4	1	7	7	4
KHCO <sub>3</sub>	180	12	18	70	100	370
	310	3	12	20	18	51
	480	1	6	3	1	2
Halon 1301	180	110				
	310	56				
	480	15				

**Figure 4-50. Extinction Mass Concentration as a Function of Strain Rate for Various Particle Sizes Ranges of NaHCO<sub>3</sub> and KHCO<sub>3</sub> Powders in a Propane/air, Counterflow, Non-premixed Flame.**<sup>114</sup>

In general, the extinction mass concentration varied inversely with the strain rate of the flame and directly with the particle size of the powder. KHCO<sub>3</sub> was approximately 2.5 times more effective than NaHCO<sub>3</sub> on a mass basis in extinguishing the flame (3 times more effective on a molar basis). The data in Figure 4-50 are replotted in Figure 4-51, showing the extinction mass concentration vs. average particle

diameter for each strain rate flame for  $\text{NaHCO}_3$  and  $\text{KHCO}_3$ . The most dramatic increase in performance for the smaller particles was observed for the low strain rate flame.

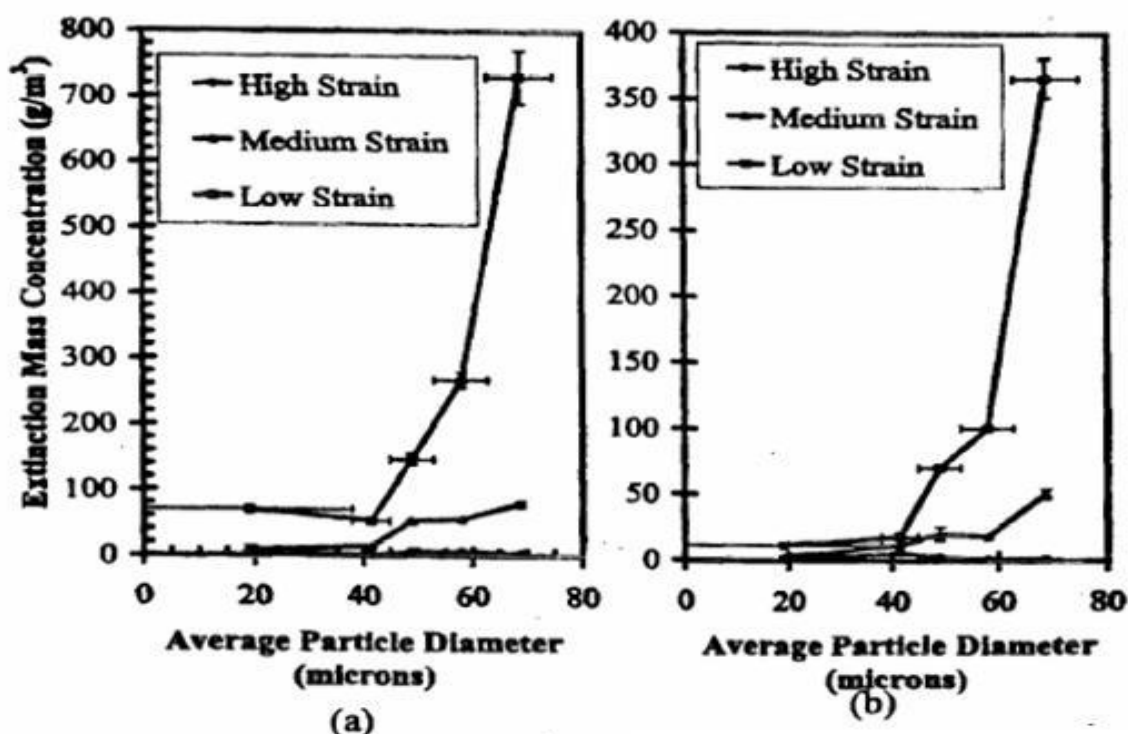


Figure 4-51. Data from Figure 4-50 Plotted to Show Extinction Mass Concentration as a Function of Particle Size Range for Each Flame Strain Rate and Added Powder.<sup>114</sup>

A number of factors have been postulated to contribute to the inhibition of fires by powders although the exact mode of the alkali metal bicarbonates' effectiveness is still not completely understood. The powder adds a great deal of heat capacity to the flame, and solid particles are often effective infrared radiators, leading to radiation cooling of the flame zone. In addition, the alkali metal bicarbonates undergo endothermic decomposition at elevated temperatures, releasing carbon dioxide. The residual alkali hydroxide vaporizes and decomposes at a much higher temperature. The difference in effectiveness between sodium and potassium is also partially due to differences in decomposition temperatures and enthalpies, and possibly to differences in catalytic scavenging cycles between the two elements. The possibility of free radical scavenging processes involving either the solid surface of the particle (heterogeneous) or gaseous by-products of the decomposition (homogeneous) have been postulated. Catalytic reactions would involve the alkali metal ion (i.e., Na, K) and proceed as  $A + R + M \rightarrow AR + M$  followed by  $AR + R' \rightarrow A + RR'$  where  $A$  is the alkali metal ion,  $R$  and  $R'$  are  $H$ ,  $O$ , or  $OH$ , and  $M$  is a third body. These reactions are exothermic and add heat to the flame. However, under favorable thermochemistry, scavenging of the radicals inhibits the flame more than the additional heat promotes it. The possibility of catalytic recombination on the surface of the solid particle has also been suggested.<sup>11,116</sup>

Plots of the extinction mass concentration as a function of average particle diameter and surface area can be found in Figure 4-52a and Figure 4-52b, respectively, for the medium strain rate flames for both powders. The average particle diameter was calculated as the arithmetic mean of each particle size bin,

assuming an even distribution. This average particle diameter was then used in the calculation of the average particle surface area.

Ewing et al.<sup>16</sup> concluded that the fire extinguishing effectiveness of dry chemicals could be fully explained on the basis of particle size and distribution. They found that the effectiveness of the agent increased gradually as the particle diameter decreased until reaching a critical diameter. At this diameter there was a dramatic increase in the flame suppression efficiency and the effectiveness remained constant for all particles below the limit size. The limit sizes reported were 16  $\mu\text{m}$  and 22  $\mu\text{m}$  for  $\text{NaHCO}_3$  and  $\text{KHCO}_3$ , respectively. NRL noticed a dramatic increase in the efficiency at about 45  $\mu\text{m}$  for the  $\text{NaHCO}_3$  sample at medium strain rate. A sizable increase was also noted for  $\text{KHCO}_3$ , but at a much larger particle size of about 65  $\mu\text{m}$ . The higher value found for  $\text{KHCO}_3$  may be influenced by the large percentage of very small particles in all size bins of this agent, as evidenced in representative photomicrographs of the various size bins.

Figure 4-52a shows that the measured extinction concentration increases with the diameter, although a linear correlation between extinction mass concentration and diameter was not found at the medium strain rate. There did appear to be a linear correlation at the medium strain rate case for the extinction mass concentration vs. average particle surface area as seen in Figure 4-52b. For this strain rate, the particle surface area available to interact with the flame more closely correlated with suppression effectiveness than particle diameter.

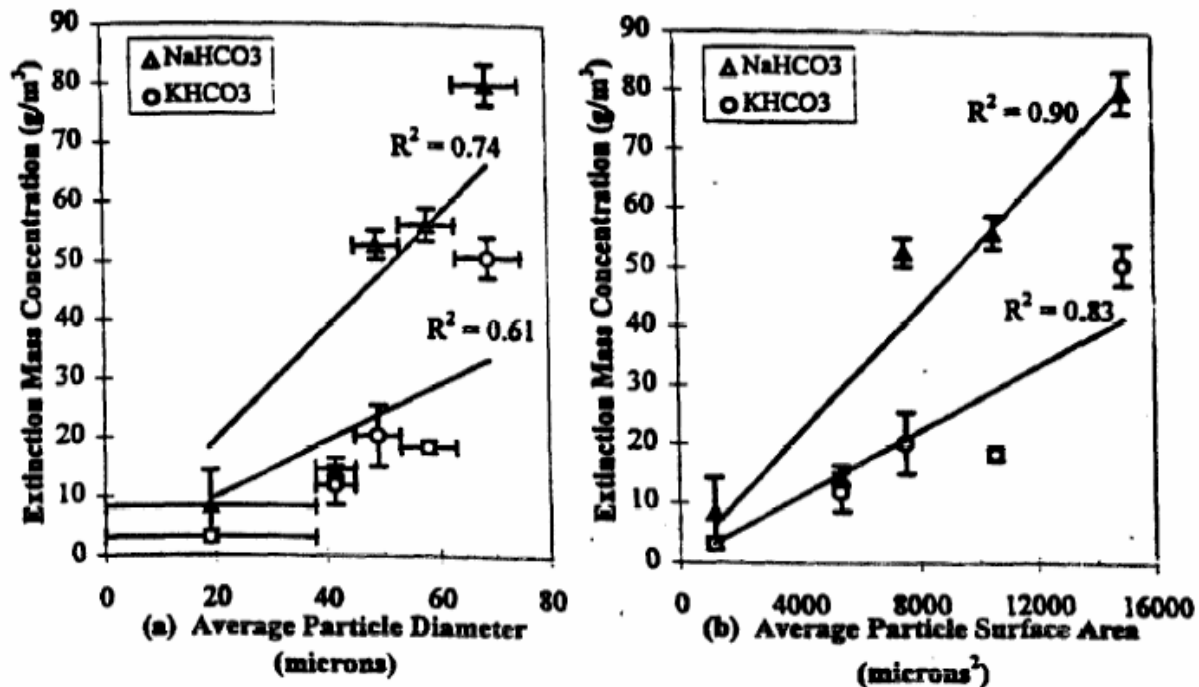


Figure 4-52. Extinction Mass Concentration as a Function of (a) Average Particle Diameter and Average Particle Surface Area for  $\text{NaHCO}_3$  and  $\text{KHCO}_3$  Powders in a Medium Strain Rate ( $310 \text{ s}^{-1}$ ) Propane/air Counterflow Non-premixed Flame.<sup>114</sup>

For the high and low strain rate cases, the correlation between surface area and effectiveness was less clear. For the low strain rate flame, the largest particles fell directly through the flame and into the bottom tube, as they were too large to remain suspended near the stagnation plane by the opposing fuel flow. A dramatic falloff in effectiveness was observed for the two largest particle bins, which likely resulted from the reduced residence time near the flame for these particle sizes. For the high strain rate case, the amount of powder required to extinguish the flame was so small that the particle delivery was difficult to accurately measure and control with our seeding apparatus, leading to a larger uncertainty. It was thus difficult to quantify a relationship between particle size or nominal surface area and extinction effectiveness for these two strain rates, although smaller particles were more effective in both cases. Effectiveness appeared to correlate more closely with surface area than with diameter. The determination of surface area in this study was based on the assumption of a spherical particle of the average diameter for the sieve fraction. A more accurate determination of the effect of surface area on suppression requires direct measurement of surface area (e.g., by gas adsorption), and a more monodisperse size distribution would be useful. However, the extinction results for the 1-D flames of uniform strain rate are consistent with “real world” observations that smaller particles are preferable presumably due to the increased surface area.

Suppression effectiveness should scale with particle surface area for most powder suppression modes. This includes heat transfer, radiation, decomposition/vaporization, and surface catalysis. Therefore, for a specified total powder mass, small particles are expected to be more effective at fire suppression, in accord with our experimental observations. Any dependence on surface area does not, however, allow determination of the primary means by which these particles extinguish fires, due to the interrelated operating suppression modes.

Sodium bicarbonate and potassium bicarbonate have different decomposition temperatures.  $\text{KHCO}_3$  has a decomposition temperature between 100 °C and 200 °C, whereas  $\text{NaHCO}_3$  decomposes at approximately 270 °C. Thus,  $\text{KHCO}_3$  would require less time to reach its decomposition phase than  $\text{NaHCO}_3$ , under similar strain rate and particle size distribution. Also, according to data compiled by Ewing, Hughes, and Carhart<sup>15</sup>, the reaction heat sinks, those associated with the decomposition, vaporization and dissociation, are reported to be 59.7 kcal/mole and 128.6 kcal/mole for  $\text{NaHCO}_3$  and  $\text{KHCO}_3$ , respectively, based on vaporization of non-decrepitating solids. Non-decrepitating solids are defined as those which decompose or vaporize without breaking up. The sensible enthalpies of the decomposition/vaporization products of the two powders over a temperature range from ambient to the extinction temperature of a methane fire, were reported by Ewing, Hughes, and Carhart<sup>15</sup> to be 57.3 kcal/mole and 47.2 kcal/mole for  $\text{NaHCO}_3$  and  $\text{KHCO}_3$ , respectively. The total sensible enthalpies (phase change and heating of the decomposition/evaporation products) are 117.0 kcal/mole for  $\text{NaHCO}_3$  and 175.8 kcal/mole for  $\text{KHCO}_3$ . On a mass basis, the values are 1.39 kcal/g for  $\text{NaHCO}_3$  and 1.76 for  $\text{KHCO}_3$ . For comparable powder sizes based on this thermal analysis,  $\text{KHCO}_3$  should be some 30 % more effective than  $\text{NaHCO}_3$ . The comparable suppression effectiveness of small particles of sodium or potassium bicarbonate compared to halon 1301 and the much higher effectiveness of potassium vs. sodium shown in Figure 4-50 can be attributed to the chemical effectiveness of alkali metal bicarbonates.<sup>117</sup>

For the counterflow flame configuration, *where* the particles reside as they decompose is very important. As the particles exit the top tube of the burner, they position themselves in the counterflowing field at different locations based on their size and mass and the magnitude of the velocity field. Assuming that the particles behave as spherical bodies, the smaller, less massive particles are expected to follow the flow

field as it changes direction to flow radially outward because of the matching opposed fuel flow. Li, Libby, and Williams<sup>104</sup> mathematically examined the behavior of droplets in an opposed flow field. They observed that large droplets fall through the stagnation plane and are turned around by the opposing flow, if the drag force is greater than the gravitational force. The smallest particles always followed the gas velocity streamlines (assuming minimal thermophoretic effects). Slightly larger particles penetrated the stagnation plane and could be “pushed back” by the opposing flow and could exhibit a decaying oscillatory behavior near the stagnation plane. The amplitude for this oscillation was a function of the particle size. Lentati and Chelliah<sup>80</sup> calculated different trajectories for water droplets as a function of size in a counterflow burner. Their calculations indicated that the oscillatory amplitude is essentially zero for a 30  $\mu\text{m}$  (non-evaporating) water drop. For smaller drops, the resulting oscillatory motion was essentially confined to a plane. It should be noted that these calculations are valid only for the particular conditions (e.g., strain rate, spherical drops, fuel density) of the models used. However, comparison to particles is qualitatively similar.

The proximity of the oscillatory “plane” to the stagnation plane depends on the particle shape and size and the strain rate of the flow but not on the original direction of the particle trajectory. Figure 4-53 shows the axial positions of the oscillatory planes relevant to bicarbonate spheres, 10  $\mu\text{m}$  to 70  $\mu\text{m}$  in diameter, in a potential non-reacting counterflow field model assuming the experimental flows for the medium strain rate flame studied. The drag forces on the particles were assumed to obey Stokes law. The 0 cm and 1 cm positions corresponded to the propane and air tube exits, respectively. Ratios of experimental flow to tube cross section were used as model exit velocities, yielding a stagnation plane at 0.39 cm.

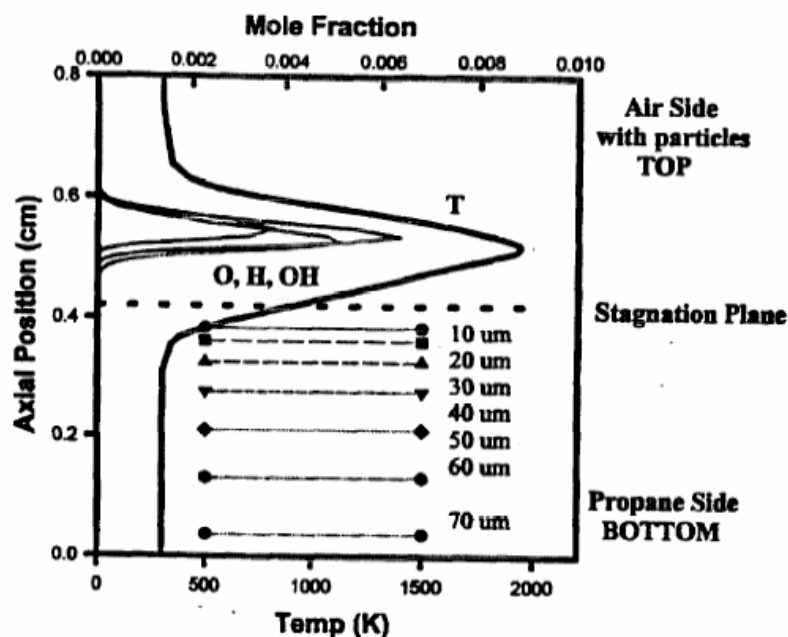


Figure 4-53. Calculated Particle Asymptotic Location as a Function of Particle Diameter for the Flow Conditions of the Low Strain Propane/air Flame.<sup>114</sup>

Also shown in Figure 4-53 are calculated axial temperature and O, H, and OH radical profiles for the propane/air flame at the medium strain rate. For particles introduced into the upper flow *or* the lower flow, the contribution of gravity dictates that the particle will asymptotically oscillate in a plane below the stagnation plane. Smaller particles were predicted to lie closer to the stagnation plane. The location of the oscillatory plane becomes significant if the opposing flow supports a flame. Stoichiometry dictates that the propane/air non-premixed flame be located on the air side, as shown in Figure 4-53. With air

(and powder particles) on the top and propane on the bottom, the flame is located above the stagnation plane. All particles will then pass through the flame and those particles within a certain range of diameters ( $\sim 20 \mu\text{m}$  to  $60 \mu\text{m}$  for the low strain rate flows) can oscillate below the stagnation plane and hence below the center of the flame but still in an elevated temperature region. As the particles decompose, they become smaller, and the opposing flow will move them closer to the stagnation plane, but never in the flame center if delivered with the air from the top.

With propane on top and air on the bottom, the flame is located below the stagnation plane on the air side. In this configuration, some of the particles oscillate at the flame maximum temperature, and hence also at the peak of the key flame radicals. This oscillatory location should lead to greater decomposition because the particle would experience a greater residence time in the higher temperature region and ultimately generate a higher inhibitor concentration closer to the maxima of the key flame radicals. Following this analysis, one might expect that there should be an optimum delivery particle size which would allow the particle to locate at the flame maximum. Since the distance of the flame center to the stagnation plane is a function of the strain rate, one might predict that the optimum particle size might also vary with strain rate. Experimentally, delivering powders via the lower tube is more complicated than delivering powders from the top. Top delivery is essentially “dropping” the particles on the flame; there is no restriction on how big a particle can be and entrainment is straightforward. Bottom, upward delivery, for the gas velocities and particles in this study, cannot deliver the largest particles to the flame since these particles cannot be supported and carried “up” by the entrainment flow velocity.

Flame extinguishment by dry chemical agents is due to a combination of both thermal and chemical mechanisms. The relative contribution of each mechanism is difficult to determine since effectiveness depends on the nature of the particle *and* the particle size and the flame conditions. Both suppression mechanisms rely on the degradation of the solid particles to achieve the maximum effect on the flame. The degree of degradation is a function of the particle size which with the gas velocity determines eventual location of the particles in and near the flame. Smaller particles decompose faster and this degradation increases suppression effectiveness in two ways: heat abstraction due to highly endothermic processes, including decomposition and vaporization; and production of gas-phase atoms that can promote scavenging of the important flame propagation radicals. Since all of the flow is forced to go through the flame, the location of the thermal extraction in the flow is probably less important than where the chemical players (if any) are released.

### **Conclusions**

In propane/air counterflow non-premixed flames,  $\text{KHCO}_3$  was shown to be more effective at extinguishment on a mass basis than  $\text{NaHCO}_3$  for all particle sizes tested. The effectiveness of the powder agent varied inversely with the particle size for the size range tested; smaller particles were more effective in suppressing the flames than the larger ones. Model predictions addressing the behavior of particles in counterflowing fields were consistent with the observed behavior for the suppression effectiveness when the fuel is on the bottom. An explanation of the high effectiveness observed for the alkali metal bicarbonate particles required a significant contribution from a chemical suppression mechanism.

## Study II: Modeling and Flame Extinguishment Measurements of $\text{NaHCO}_3$

Contrary to the extinction behavior observed for  $\text{NaHCO}_3$  reported in the prior section, Trees and Seshadri<sup>118</sup> found a non-monotonic variation of  $\text{NaHCO}_3$  particle mass fraction with particle size required to extinguish a non-premixed counterflow flame for the size range  $\approx 0 \mu\text{m}$  to  $30 \mu\text{m}$ . Chelliah and co-workers conducted NGP studies to address the uncertainties regarding the effect of  $\text{NaHCO}_3$  particle size on flame extinction and developed a rigorous method of quantifying various physical, thermal, and chemical contributions.<sup>119</sup>

### *Flame Suppression with $\text{NaHCO}_3$*

Figure 4-54 shows the apparatus for generating non-premixed, methane air counterflow flames. The  $\text{NaHCO}_3$  particles were separated into five size ranges:  $<10 \mu\text{m}$ ,  $10 \mu\text{m}$  to  $20 \mu\text{m}$ ,  $20 \mu\text{m}$  to  $30 \mu\text{m}$ ,  $30 \mu\text{m}$  to  $40 \mu\text{m}$ , and  $40 \mu\text{m}$  to  $60 \mu\text{m}$  using a vortex separation technique. Particles of a given size were introduced with the air stream at a relatively steady rate. The typical particle mass fraction was about 0.01, corresponding to a particle flow of about 0.1 g/min. For a selected  $\text{NaHCO}_3$  loading, the flame extinction effectiveness of  $\text{NaHCO}_3$  particles was characterized by the extinction flow strain rate, measured by two methods: a global formula based on the nozzle exit velocities and nozzle separation distance<sup>81</sup> and local velocity field measurements using laser Doppler velocimetry (LDV).

Because of the need to establish the accuracy of previously reported data with  $\text{NaHCO}_3$  particles, considerable attention was devoted to the development of a particle seeder that could deliver steady feed rates of particles of specified sizes. Two approaches were used.

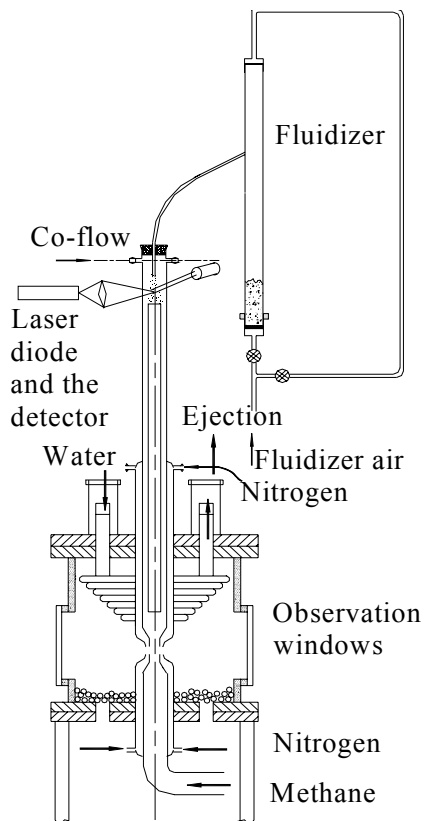


**Figure 4-54. Schematic of the Counterflow Flame Apparatus with the Particle Seeder.**<sup>119</sup>

For the small air flows (typically 0.1 L/s), the fluidized bed approach shown in Figure 4-54 gave satisfactory seeder performance, but only for particles less than 30  $\mu\text{m}$ . The fluidized bed seeder consisted of a 19 mm diameter glass tube with two porous plugs connected at either end. The air inflow to the seeder, controlled through a mass flow controller, was split into two streams and connected to either end of the glass tube. The flow passing through the bottom, which controlled the fluidization level, was monitored through another flow controller. The fluidized particles and the total air entering the fluidization tube were ejected through a small tube located toward the middle of the tube. By maintaining the total air flow through the fluidizer tube constant, the mass fraction of particles attained a steady state. The particle feed rate was continuously monitored using a Mie scattering detection system located at the exit of the seeder air, as shown in Figure 4-54. This detection system consists of a laser diode operating at 671 nm, a Thor Labs DET1-SI High Speed Silicon Detector with collection by a 3 cm focal length lens, background radiation filtering using an Edmund Scientific 671 nm interference filter, and a Hewlett-Packard Model 7132 strip chart recorder. Because the seeder air flow was held fixed, the scattering signal was independent of the total air flow exiting through the air nozzle and was primarily dependent on the particle delivery rate of the seeder. The scattered signal was observed to decay slightly over 20 min to 30 min periods, but could be controlled by shifting part of the bottom fluidizing air to the top. Different particle flows were obtained by controlling the fraction of seeder air flowing through the top and the bottom. The actual mass fraction of the particles in the air stream was determined by calibrating the recorded scattering signal by a separate gravimetric analysis, usually performed before and after each flame extinction experiment.

For particles greater than 20  $\mu\text{m}$ , a positive feed auger system (not shown) was employed. This seeder arrangement consisted of a multi-start Teflon screw (7 mm outer diameter and 5 mm inner diameter) in a high-precision stainless steel tube, where the screw was driven by speed-locked variable speed motor. This seeder was vibrated pneumatically to assist the particle flow, but the particle feed rate was primarily controlled by the motor speed. Part of the total air flow was diverted through a screw-driven particle seeder and was then mixed with the remaining air prior to exiting through the air nozzle. As before, air flow through the seeder was held constant while the total air flow through the nozzle was varied to attain different flame strain rates. For particle sizes above 20  $\mu\text{m}$ , the Mie scattering signal varied less than  $\pm 10\%$ . Particles smaller than 20  $\mu\text{m}$  had a tendency to clump, and consequently significant variation of the scattering signal was observed. Hamins et al.<sup>20</sup> had overcome such clumping by adding about 1 % by mass of 10 nm silica particles to the  $\text{NaHCO}_3$  particles. Due to the uncertainty of the effect of adding the silica particles and the associated safety issues, no silica was added.

Without particles, the measured global flame extinction strain rate was about  $470\text{ s}^{-1}$ , while the measured local LDV strain rate was about  $390\text{ s}^{-1}$ . These values are consistent with those reported previously by Chelliah et al.<sup>103</sup> As  $\text{NaHCO}_3$  particles were added to the air stream, the flame extinction strain rate was expected to decrease because of the physical, thermal, and chemical effects of the particles.

The measured variation of flame extinction strain rate vs. the  $\text{NaHCO}_3$  particle mass fraction in the air stream is shown in Figure 4-55 for the five particle size groups. All five groups demonstrated a clear decrease in the extinction strain rate with increasing particle loading. For a given particle mass fraction, the smallest particles (0  $\mu\text{m}$  to 10  $\mu\text{m}$  and 10  $\mu\text{m}$  to 20  $\mu\text{m}$ , which gave indistinguishable results) produced the lowest extinction strain rate, indicating their highest effectiveness as a flame suppressant.

Trees and Seshadri<sup>118</sup> had reported a similar variation of the mass of particle required with varying extinction strain rate, for each size group. However, they found that while 0  $\mu\text{m}$  to 10  $\mu\text{m}$  particles were the most effective, 10  $\mu\text{m}$  to 20  $\mu\text{m}$  particles were the least effective, with 20  $\mu\text{m}$  to 30  $\mu\text{m}$  particles showing an intermediate effectiveness. There were two differences between the studies that could have affected the results: (a) The fuels were different. Seshadri used a liquid heptane fuel pool, while the present experiments used gaseous methane. (b) Seshadri added about 1 % by mass of 10 nm silica particles to minimize the clumping of particles and help fluidize the smaller particles.

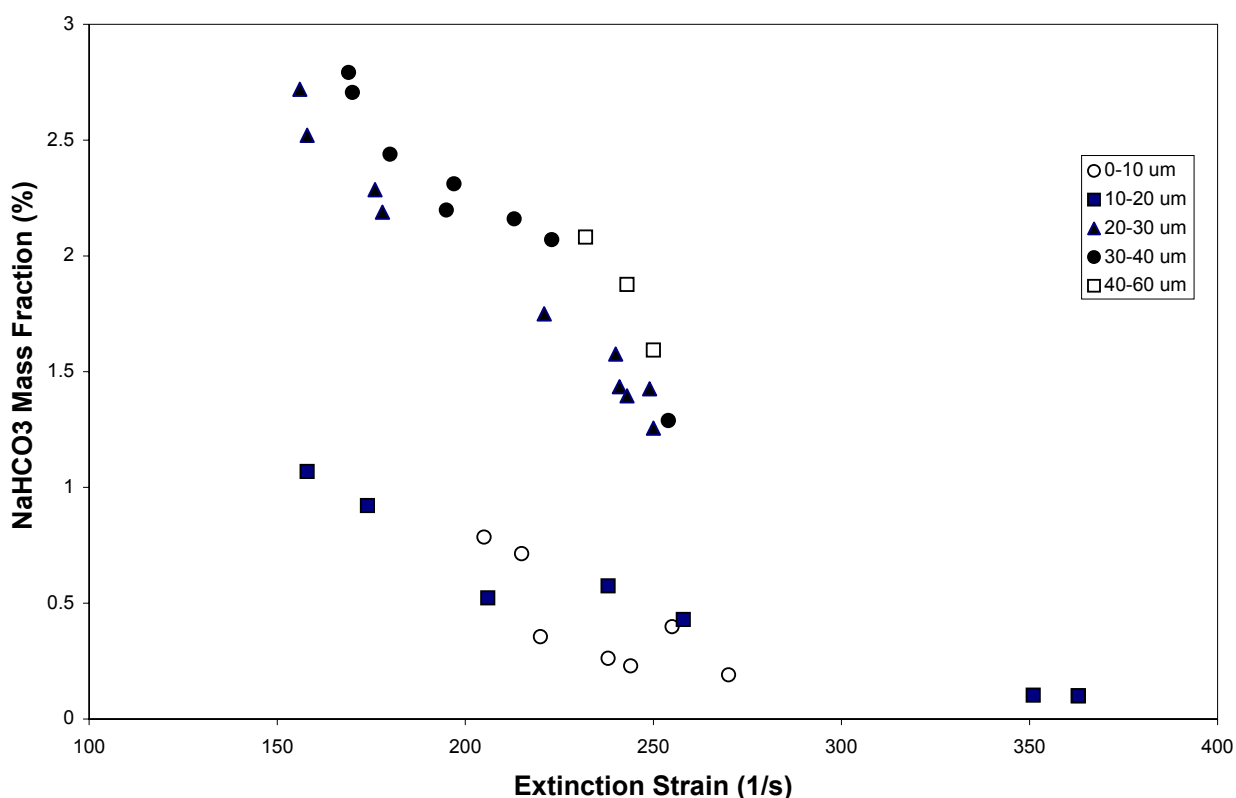


**Figure 4-55. % NaHCO<sub>3</sub> by Mass in air as a Function of Extinction Strain Rate for Different Size Groups of Particles.**<sup>119</sup>

When sodium bicarbonate particles are heated, they are known to decompose into oxides of Na in two stages. In the first stage, NaHCO<sub>3</sub> decomposes to solid sodium carbonate (Na<sub>2</sub>CO<sub>3</sub>), H<sub>2</sub>O, and CO<sub>2</sub> around 543 K. (Note that the global decomposition temperature can vary depending on the particle heating rate, e.g., smaller particles are expected to heat rapidly when exposed to the flame environment because of their higher surface area/volume ratios than the larger particles.) In the second stage, Na<sub>2</sub>CO<sub>3</sub> is known to decompose at 1170 K, leading to formation of Na<sub>2</sub>O and CO<sub>2</sub>. In the presence of water, however, Na<sub>2</sub>CO<sub>3</sub> and Na<sub>2</sub>O are known to react to form sodium hydroxide (NaOH).<sup>120</sup> The NaOH formed promotes catalytic recombination of the radicals species needed for flame propagation, causing the flame to extinguish readily.<sup>121</sup>

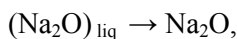
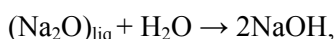
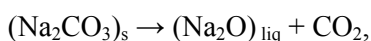
### *Numerical Simulation of NaHCO<sub>3</sub> Particle Effects*

The numerical model described earlier in Section 4.5.1 was extended to include the effects of sodium bicarbonate particle transport, heating, decomposition and subsequent interaction of decomposed gaseous species with the homogeneous flame chemistry. The detailed gas-phase kinetic model for methane-air was augmented with a 20-step elementary mechanism for Na from Jensen and Jones.<sup>121</sup> The model developed for sodium bicarbonate particles involved considerable additional uncertainties. These included the non-spherical nature of the particles, the transient heating effect of the particles, the heterogeneous decomposition mechanism of sodium bicarbonate, and the gas-phase chemical inhibition mechanism by intermediate species formed from the decomposition.

Previous studies had indicated that sodium bicarbonate decomposes at a low temperature of about 543 K to form sodium carbonate through the reaction:<sup>10</sup>



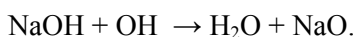
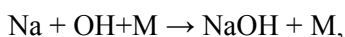
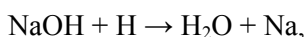
For particle temperatures above 1124 K, the sodium carbonate formed can decompose further to form other reaction intermediates of Na. Based on these observations, Friedman and Levy<sup>120</sup> had postulated that NaOH is the primary inhibiting compound responsible for flame extinction and proposed the following reaction pathways leading to formation of NaOH



followed by the homogeneous reaction:

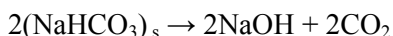


Once the alkali metal hydroxide was formed, the following catalytic radical scavenging cycle was known to be responsible for reduction of the radical pool



The relative importance of these reactions was not well established and the literature indicates some conflicting results.<sup>117,120,121,122</sup>

In the initial NGP simulations, a fast global decomposition reaction of the form,



was employed. The particle temperature at which the decomposition occurred (defined here as  $T_{decomp}$ ) was varied to obtain the sensitivity of the particle size. Although such a global model can be fine tuned to a narrow range of conditions (e.g., narrow particle size range), it should be cautioned that extension of such models to a wider range of conditions may lead to physically unrealistic results. For the homogeneous chemistry associated with NaOH, a detailed reaction model involving 6 species in 20 elementary reactions proposed by Jensen and Jones<sup>121</sup> was employed, in conjunction with the detailed chemistry model for methane oxidation.<sup>80</sup>

Figure 4-56 shows the predicted variation of  $\text{NaHCO}_3$  mass fraction as a function of flame extinction strain rate, for selected  $\text{NaHCO}_3$  particle size groups. For comparison, a plot of equivalent NaOH mass fraction for different extinction strain rates is also shown. The predicted curve with NaOH indicates the absolute maximum inhibition possible, based on the homogeneous model employed. Different NaOH reaction mechanisms were expected to modify this curve, but the predicted trends were not expected to change. The results clearly indicate that particles above 20  $\mu\text{m}$  have a small effect on flame extinction, but as the particle size decreased below 20  $\mu\text{m}$ , the extinction strain rate decreased significantly, indicating a remarkable increase in the effectiveness. This effect was attributed to the rapid heating of the particle and fast decomposition processes.

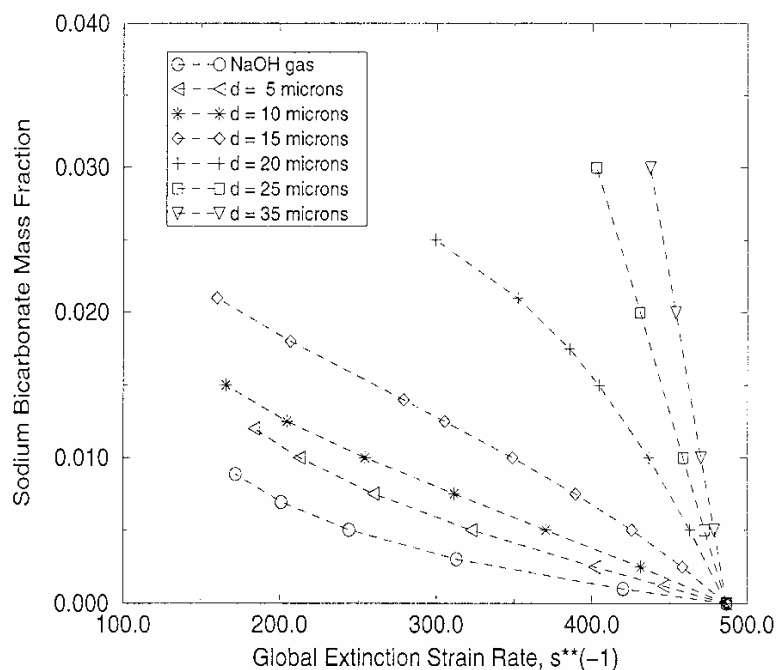


**Figure 4-56. Numerical Prediction of  $\text{NaHCO}_3$  Mass Fraction as a Function of Extinction Strain Rate, for Selected Particle Sizes.**<sup>119</sup>

By varying the  $T_{decomp}$  described earlier, the location at which these particles were rapidly decomposing in the flow field was varied. As a consequence, the amount of Na released to the homogeneous phase is affected, leading to a varying degree of chemical inhibition. To quantify the contributing thermal and chemical effects, the source terms were selectively turned “off” in the model. Unlike previously reported fine-water droplet simulations, these results indicated a significant chemical effect in the presence of  $\text{NaHCO}_3$  particles. For the dilute particle loading considered here, the physical effects were found to be negligible. Improved methods of treating the particle heating and subsequent heterogeneous particle decomposition need to be developed in order to provide more accurate flame extinction predictions.

## Conclusions

All the  $\text{NaHCO}_3$  particle sizes considered ( $< 10 \mu\text{m}$ ,  $10\mu\text{m}$  to  $20\mu\text{m}$ ,  $20\mu\text{m}$  to  $30\mu\text{m}$ , and  $40\mu\text{m}$  to  $60 \mu\text{m}$ ) indicated a decrease in flame extinction strain rate with increasing particle mass fraction, consistent with the NRL results. The effectiveness of flame suppression (quantified here based on the  $\text{NaHCO}_3$  mass fraction needed) varied monotonically with particle size, with the smallest size group being the most effective. Two independent approaches to particle seeding yielded identical results for the overlapping particle size range of  $20 \mu\text{m}$  to  $30 \mu\text{m}$ , providing considerable confidence in the measured results.

Numerical predictions taking into account the detailed homogeneous chemistry and global particle decomposition model indicated a trend in particle effectiveness very similar to that obtained from the experiments. By varying the temperature at which the particles decompose to gaseous products, the predictions showed that the smallest particles are more effective because of their rapid heating, leading to complete decomposition of the particles. By manipulating various source terms in the model, the superior effectiveness of  $\text{NaHCO}_3$  particles was attributed to the homogeneous catalytic radical scavenging by  $\text{NaOH}$  formed, while thermal effects associated with particle heating played a minor role.

## Co-flow, Non-premixed Flames – Cup Burners

The effectiveness of aerosol agents in a cup burner apparatus was not explicitly investigated under the NGP. What was investigated and is reported in Chapter 3, was the role of particle *formation* in the flame after agent introduction which limits the effectiveness of chemical agents. This is a fundamental thermodynamic limitation regardless of whether the agent enters the flame as a gaseous species or a condensed liquid or solid. The cup burner flame still remains a challenging yet relevant configuration for understanding aerosol effectiveness in general. Thus, work continues in a number of labs including the NRL<sup>84</sup> to understand the behavior of aerosols agents in a cup burner apparatus and other co-flow flame configurations.

### 4.5.3 Aqueous Metal Salt Solutions, Combined Chemical and Physical Suppression

#### Non-Premixed Flames

##### Introduction

Chelliah and coworkers, using both experimental and modeling approaches, examined the interactions of small droplets of water and water/ $\text{NaOH}$  solutions with steady, laminar counterflow methane/air non-premixed flames.<sup>98</sup> To compare to the experimental studies, the previously developed hybrid Eulerian-Lagrangian numerical model for monodisperse droplet distributions was generalized to account for more realistic, polydisperse size distributions.

### Experimental Method

The counterflow burner, shown in Figure 4-57, was similar to that described in Study II in Section 1.5.2. A steady, planar, non-premixed flame was established in the mixing layer of counter flowing methane and air streams. The fuel and air nozzles (Pyrex glass) each had an area contraction ratio of 6.5 and an exit diameter of 1.5 cm, producing nearly plug flow velocity profiles at their exits. Co-flowing nitrogen streams on both fuel and air sides helped to maintain a very stable planar flame disk. The nozzles were enclosed in a cylindrical burner chamber, in which water cooling coils and air dilution of the post combustion gases eliminated secondary flames. The nozzle tubes entered the chamber through vacuum fittings which permitted easy adjustment of the nozzle separation distance, which is typically set to 12 mm. An air-driven mass flow ejector evacuated the product gases, while a differential pressure gauge monitored the chamber pressure, which was typically 120 Pa (12 mm water) below atmospheric pressure.

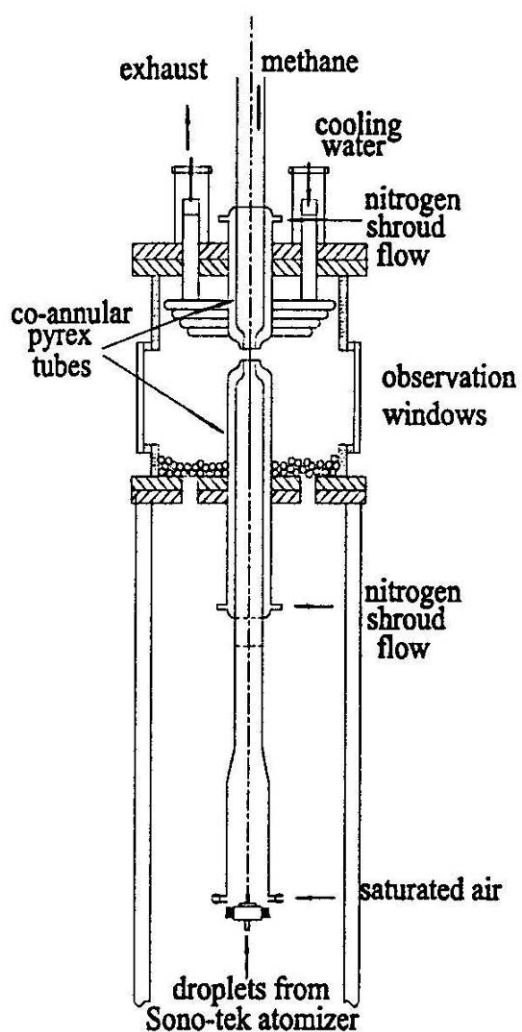


Figure 4-57. Schematic of the Counterflow Burner Configuration with the Water Droplet Atomizer.<sup>98</sup>

An oil-free shop compressor followed by a series of desiccant beds provided the air; the fuel gas was methane (BOC grade 4.0, 99.99% purity). Mass flow meters (Teledyne Hastings-Raydist, factory calibrated with a reported accuracy of  $\pm 1\%$  of full-scale reading) indicated the volumetric flows of the methane and air. For experiments involving water vapor or water droplets, the metered dry air was saturated with water vapor prior to the nozzle exit by bubbling the air through a water bath. A bath

heated to 5 °C above ambient produced an air stream at the nozzle exit at ambient temperature and at least 97 % relative humidity (verified with a hygrometer, Testo 605-H1).

The droplet atomizer was located at the base of the bottom (air) tube, and the droplets were entrained in the airflow. The glass tubes allow easy detection of any water condensation on the tube walls. The droplet size distribution is measured using a PDPA (Aerometrics, two-component; model, DSA).

Two types of droplet generators were tested: (1) a piezoelectrically excited fluid jet atomization system (Fluid Jet Associates)<sup>123</sup> and (2) an ultrasonic fluid surface breakup system (Sono-Tek, Model 8700-120). The first atomizer was capable of generating truly monodisperse droplets (variable by changing the orifice diameter), but the small, 10 μm holes needed for generating 20 μm droplets proved susceptible to clogging and erosion. The second atomizer was found to be relatively simple to use and did not clog, but the droplets generated had a much wider size distribution. The median droplet size was varied by selecting a different length nozzle tip and resonance frequency. All the experimental flame extinction data were obtained using the ultrasonic droplet generator.

The ultrasonic droplet generation system consisted of the ultrasonic nozzle and a broadband ultrasonic frequency generator. A syringe pump (Instech Model 2000) with a plastic 10 cc syringe fed water to the atomizer. In the experiments, the water mass flow was fixed, and the air and fuel flows were increased until the flame extinguished. The flame was found to be very stable until the extinction point. The water mass flow at the nozzle exit was measured gravimetrically by carefully collecting all of the saturated air stream (with droplets) and impinging the droplets on a collection surface. These tests showed that while only about 70 % of the mass of water injected to the atomizer reached the nozzle exit, the operation of the droplet injection system was very consistent over the entire range of water and air flows of the tests.

The droplet number distribution ( $f$ ) as a function of size ( $d$ ) in the vicinity of the ultrasonic atomizer nozzle was characterized by the manufacturer and was believed to follow a log-normal distribution:

$$f(d) = \frac{1}{\sqrt{2\pi}d\sigma} \exp\left[-\frac{\ln d - \ln \mu}{2\sigma^2}\right] \quad (4-12)$$

with a median diameter ( $\mu$ ) of about 20 μm and a Sauter mean diameter (SMD) of about 30 μm (for  $\sigma = 0.6$ ). This normalized distribution, separated into 12 discrete sections for modeling purposes, is shown in Figure 4-58a. Nonetheless, based on the estimated settling velocities of different droplet sizes and the flow velocities in the air tube, it was found that not all the droplets produced by the atomizer would be convected out of the air nozzle. For example, for an airflow corresponding to a flow strain rate of about 285 s<sup>-1</sup>, the estimated maximum droplet size that could be carried in the air stream was about 75 μm, whereas for a strain rate of 160 s<sup>-1</sup>, the corresponding maximum droplet size was about 55 μm. Thus, the air flow velocity up the air-nozzle would modify the generated droplet size distribution. PDPA measurements verified the droplet sizes at the air nozzle exit. Figure 4-58b shows the measured droplet size distribution for a high strain rate of 285 s<sup>-1</sup>, and Figure 4-58c shows a similar plot for a lower strain rate of 160 s<sup>-1</sup>. The shift in maximum size of droplets was consistent with estimates, and the general shape of the distribution remained log-normal.

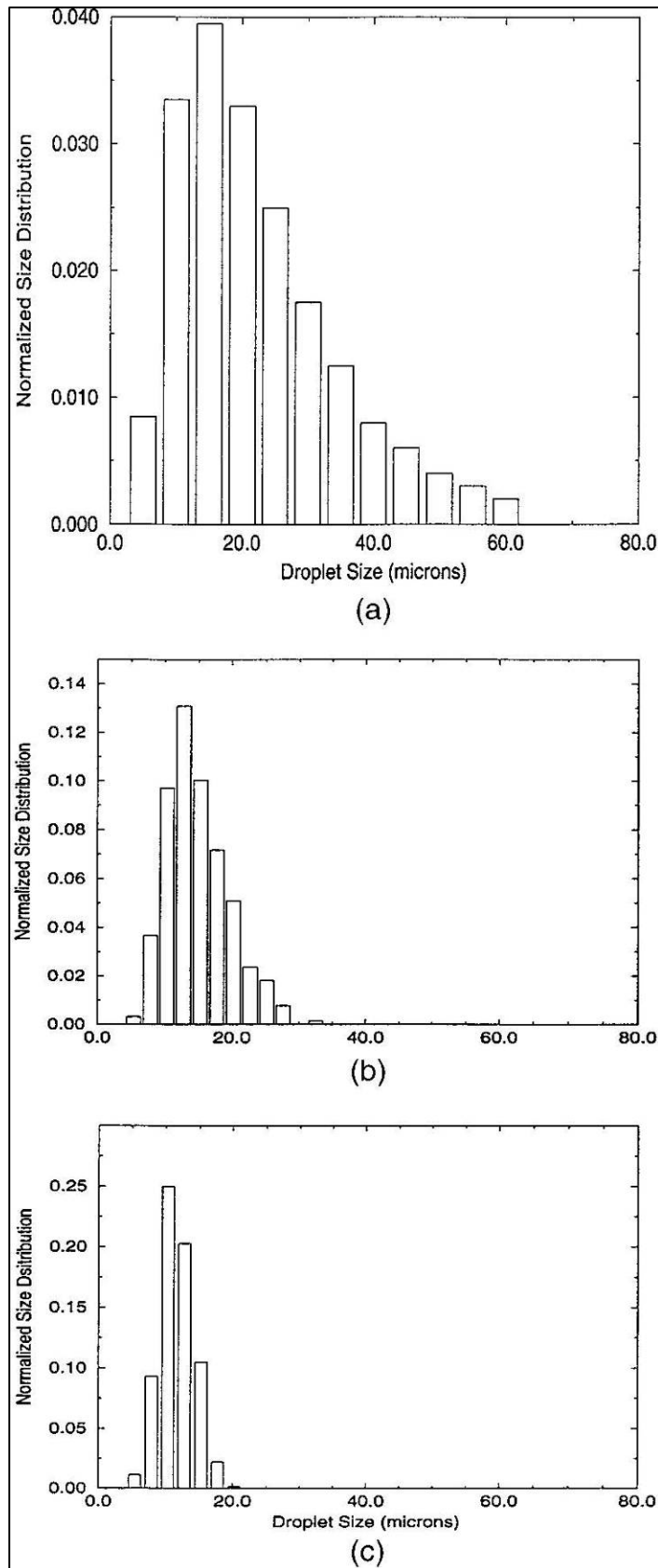


**Figure 4-58. (a) Normalized Droplet Diameter Distribution of the Ultrasonic Atomizer as Reported by the Manufacturer; (b) and (c) Normalized Water Droplet Diameter Distributions Measured Using a PDA at the Exit of the Air Nozzle for an Air Flow Corresponding to Counterflow Strain Rates of  $285 \text{ s}^{-1}$  and  $160 \text{ s}^{-1}$ , respectively.<sup>98</sup>**

Flame extinction experiments were conducted by increasing the air and methane nozzle exit velocities such that the momentum of the two streams was balanced, that is,

$$(\rho v^2)_{air} = (\rho v^2)_{CH_4} \quad (4-13)$$

where  $\rho$  is the density and  $v$  is the axial velocity. Knowing the nozzle separation distance  $L$ , the flow strain rate was defined by the global formula<sup>81</sup>

$$a = 4 \frac{|v_{air}|}{L} \quad (4-14)$$

For non-premixed methane/air flames, the measured global flame extinction strain rate of  $470 \text{ s}^{-1}$  was obtained, while the measured local flow velocity using a laser Doppler velocimetry system yielded a local flow strain rate of about  $390 \text{ s}^{-1}$ . Both of these numbers were highly reproducible and consistent with previous experiments and modeling efforts.<sup>103</sup> The experimental flame extinction results are all based on the global strain rate formula unless otherwise noted.

### Results

The presence of condensed-phase water implied that at equilibrium, the air stream was saturated with water vapor, and this was verified using a hygrometer. At atmospheric pressure and a room temperature of 300 K, the saturated water vapor mole fraction in air is 0.0351 (mass fraction  $Y_{vap} = 0.0224$ ). The saturated water vapor can have a significant effect on the flame extinction condition. Previously, detailed modeling efforts had indicated that the predicted local flame extinction strain rate reduced from  $420 \text{ s}^{-1}$  for a methane/air flame to  $365 \text{ s}^{-1}$  for methane and air saturated with water vapor (a reduction in extinction strain of 12 %).<sup>80</sup> Present experiments with saturated water vapor in the air stream yielded a global extinction strain rate of  $405 \text{ s}^{-1}$  (i.e., a reduction of 13 % from  $470 \text{ s}^{-1}$  measured for methane and dry air), in excellent agreement with the predictions.

Lazzarini et al.<sup>98</sup> also examined the effect of water droplets of  $20 \text{ }\mu\text{m}$  median diameter on the extinction condition for the flames. With increasing droplet number density (or mass fraction of water droplets in the air stream), it was expected that flame extinction would occur more readily, resulting in a lower extinction strain rate. Figure 4-59 plots the mass fraction of water in the condensed phase ( $Y_0$ ) as a function of the flame extinction strain rate.

Note that the zero water droplet mass fraction corresponds to the case where the air stream is saturated with water vapor (i.e.,  $Y_{vap} = 0.0224$ ). The predicted variations of water droplet mass fraction as a function of global extinction strain rates assumed  $20 \text{ }\mu\text{m}$  monodisperse droplets. Irrespective of the assumption of monodisperse droplet size distribution in the simulations, the predicted trend is seen to be in reasonable agreement with experiments.

The experiments and predictions agreed well for pure water vapor. The agreement grew poorer with increasing droplet mass loading. In predictions, relaxation of the monodisperse size distribution approximation based on the measured distributions shown in Figure 4-58 was not expected to rectify this difference because  $20 \text{ }\mu\text{m}$  monodisperse droplets have been predicted to be the most effective. As discussed later in the numerical section, any broadening of the size distribution about  $20 \text{ }\mu\text{m}$  led to predicted higher mass fraction of water in the condensed phase for the same flame extinction strain rate. Thus, differences seen in Figure 4-59 between experiments and modeling were likely due to other causes.

In experiments, calibration of the water droplet mass flow through gravimetric analysis introduced errors; however, considerable care was taken to address uncertainties associated with the approach adopted.

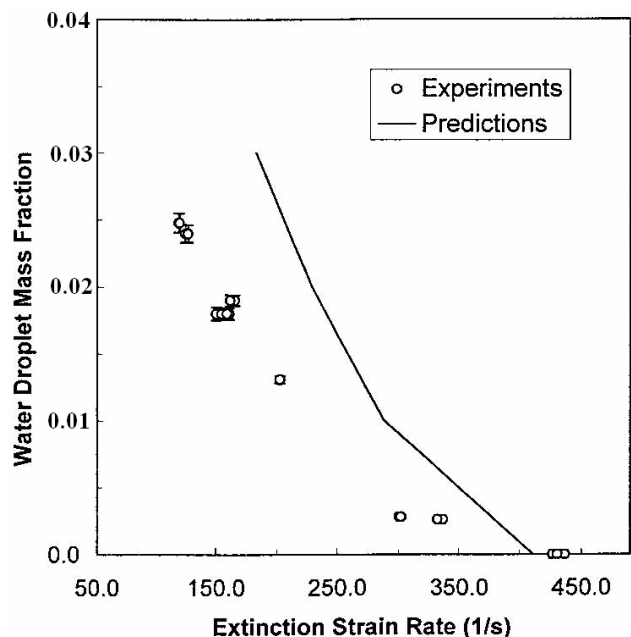


**Figure 4-59. Variation of Water Droplet Mass Fraction in the Condensed Phase as a Function of Flame Extinction Strain Rate.**<sup>98</sup>

Experiments and simulations also examined the effect of the addition of NaOH to the water droplets. The primary mechanism of flame extinction by pure water droplets is through the thermal cooling of the flame front, leading to slower chemical reaction rates. For example, in a counterflow field of methane and air, the 20  $\mu\text{m}$  droplets were shown to be most effective because most of the droplet mass was predicted to evaporate near the oxygen consumption or radical species production region.<sup>105,106</sup> This thermal effect of water droplets can be considerably enhanced by including a chemically active fire-suppressing compound in water. NaOH was selected, as it was known to be the primary compound in the catalytic radical recombination path of sodium bicarbonate fire suppression.<sup>121</sup> Since the solubility of NaOH in cold water is about 30 % of the total mass,<sup>124</sup> a significant amount of NaOH can be released at the flame front, provided that the droplets consisting of water/NaOH are completely vaporized. As noted earlier in this chapter, 20  $\mu\text{m}$  droplets were fully evaporated in this flame system. The same ultrasonic was used to deliver various aqueous solutions of NaOH and investigate their effect on suppressing counterflow methane/air flames.

Figure 4-60 plots the experimentally measured water/NaOH mass fractions as a function of the flame extinction strain rate. As before, the air flowing into the nozzle tube was saturated with pure water vapor. Because the NaOH vapor pressure is very small, less than 130 kPa (1 mm Hg) at room temperature<sup>124</sup>, air saturated with pure water vapor was not expected to affect the evaporation of NaOH. The measured results indicated that with increasing NaOH mass fraction in water, the amount of water/NaOH mass fraction needed for flame extinction decreased significantly - almost a factor of 5 for 17.5 % NaOH by mass in water at the lowest strain rate considered. Combining thermal and chemical suppression effects leads to a significant increase in fire suppression ability, as shown in Figure 4-60.

For a selected extinction strain rate, Figure 4-60 also shows an interesting nonlinear decrease in total water/NaOH mass fraction with increasing NaOH fraction in the solution. Such a phenomenon may be related to saturation of NaOH in the vapor phase and must be addressed through future modeling efforts.

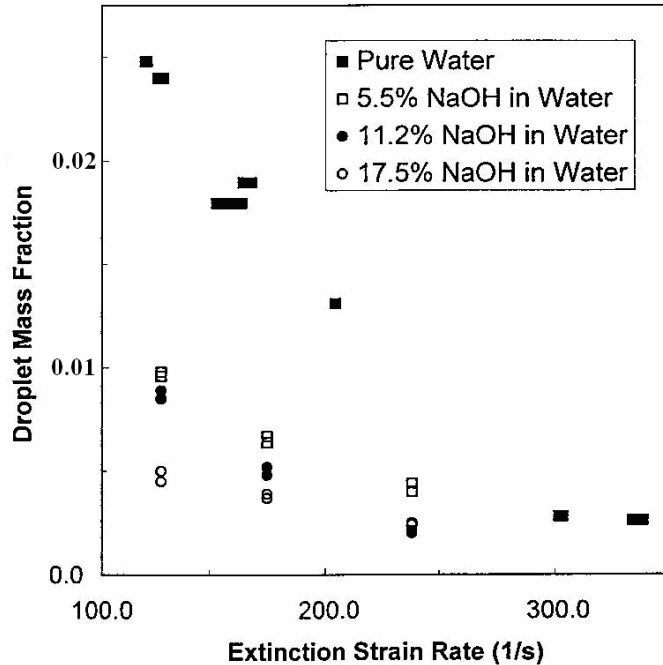


**Figure 4-60. Droplet Mass Fraction in the Condensed Phase as a Function of Flame Extinction Strain Rate for Different Mass Loadings of NaOH in Water.**<sup>98</sup>

### Numerical Predictions

The hybrid Eulerian-Lagrangian formulation for gas and liquid phases described in Section 4.5.3 was used here.<sup>80</sup> This model includes a detailed reaction model for methane oxidation and transport of species and energy across the mixing layer. In this approach, knowing the gas-phase solution, the Lagrangian equations for mass, momentum, energy, and particle flux fraction (normalized by that at the air nozzle exit) were integrated in time to determine the droplet location and source terms contributing to the gas-phase conservation equations. With these new source terms, the Eulerian equations describing the gas phase were then integrated using a standard approach.<sup>125</sup> Finally, the two sets of coupled equations were iterated until a predetermined convergence criterion was reached.

As described in the experimental section, the flame extinction was realized by increasing the flow of methane and air (saturated with water vapor), while the mass flow of condensed water droplets ( $m_{H_2O,c}$ ) was held constant by the syringe pump. During this process, the mass fraction of water droplets

$$Y_0 = \frac{m_{H_2O,c}}{m_{air} + m_{H_2O,c}} \quad (4-15)$$

in air changed because of the varying air mass flow ( $m_{air}$ ). In previous numerical predictions, it was assumed that the condensed phase water mass fraction ( $Y_0$ ) was held constant at all strain rates. The predicted flame temperature variation as a function of flow strain rate for constant  $m_{H_2O,c}$  and for constant  $Y_0$  are shown in Figure 4-61 for 20  $\mu\text{m}$  monodisperse droplets. In the absence of radiative losses, usually only one extinction condition is realized for constant  $Y_0$ . Two flame extinction points are predicted if strain rate is changed in a proportional manner to keep the momentum balanced as depicted in Figure 4-61. Changing the strain rate by varying only the air and fuel flows for a constant  $m_{H_2O,c} = 2.65 \text{ mg/s/cm}^2$  generated the innermost closed oval in Figure 4-61. Starting at some strain rate away from extinction (e.g. point P), extinction conditions were predicted depending on whether strain rate was

increased (point E1) or strain rate was decreased (point E2). This phenomenon was purely a consequence of the two-phase system considered, and its occurrence was observed for water/NaOH solutions. In practice, this second extinction point (E2) can be realized by decreasing the oxidizer transport while the droplet transport is held constant.

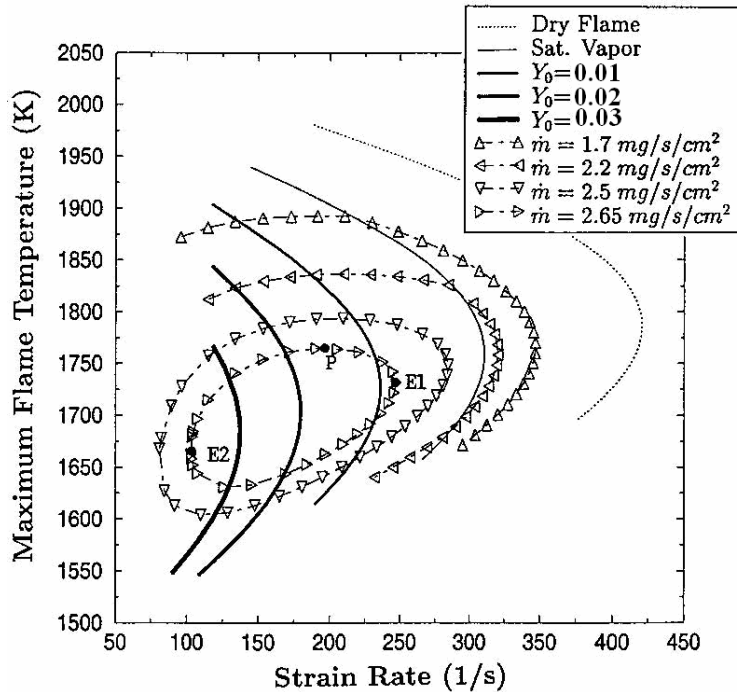


**Figure 4-61. Variation of the Maximum Flame Temperature as a Function of Local Flow Strain Rate for Constant Droplet Mass Fractions (lines) and Constant Water Mass Flux Rates (Lines with Symbols).<sup>98</sup>**

The model developed previously to simulate the interaction of fine water droplets with the counter flow flame assumed monodisperse droplets.<sup>80</sup> This assumption made the computations less demanding, but more importantly, the analyses of the results on droplet size effects became considerably simpler. Because of the experimental difficulties in realizing truly monodisperse water droplets, the above model was generalized here to include the polydisperse size effects. It was shown previously that for water mass loadings similar to those considered here, the ratio of droplet-to-droplet separation distance to droplet size was over 20. Under such conditions, the equation for droplet mass flux ( $\mathfrak{S}$ ) (i.e., the spray equation), written in the form for the present quasi-one-dimensional counterflow field<sup>80</sup>

$$\frac{d\mathfrak{S}}{dt} + 2\mathfrak{S}U_d = \Gamma \quad (4-16)$$

was simplified by setting the droplet collision source term  $\Gamma = 0$ . Thus, by treating the droplet size distribution as composed of several discrete size groups<sup>126,127</sup>, the simulation simplified to solving several Lagrangian equations for these discrete droplet size groups, with initial conditions corresponding to each discrete size group specified at the air nozzle exit.

For 0.01 mass fraction of water in the condensed phase, flame extinction calculations were performed with the three different discrete polydisperse size distributions shown in Figure 4-58. A comparison of these flame extinction results with the ideal 20  $\mu\text{m}$  droplet size for this flow configuration is shown in Table 4-8. The predicted extinction strain rates indicate that any broadening of the size distribution of droplets from the ideal 20  $\mu\text{m}$  size led to a higher flame extinction strain and a further deviation from the

experiments. At higher water mass loadings and decreasing flow strain rates, the thermal radiation effects are known to increase and may also have an influence in the present predictions. However, the strain rates indicated in Table 4–8 are rather moderate, and it is unlikely that the significant differences between experiments and modeling can be solely attributed to radiation heat loss effects.

**Table 4–8. Experimental and Predicted Global Flame Extinction Strain Rates ( $s^{-1}$ ) for Different Droplet Size Distributions and Water Droplet Mass Fraction of 0.01.<sup>98</sup>**

	Experiment	20 $\mu\text{m}$ Monodisperse Droplets	Distribution from Figure 4-58a	Distribution from Figure 4-58b	Distribution from Figure 4-58c
Global strain rate ( $s^{-1}$ )	180	286	297	291	292

### Conclusions and Summary

The main purpose of the work reported in this section was to provide experimental data to validate predictions of the effectiveness of fine water droplets in extinguishing counterflow non-premixed flames. On a mass basis, the predicted ability of fine water mist to suppress gaseous fires with similar or better effectiveness than halon 1301 was verified. Although the original goal was to obtain results using monodisperse droplets as assumed in previous theoretical investigations, this task became rather challenging because of difficulties associated with clogging of very small orifices ( $\approx 10 \mu\text{m}$ ). Instead, an ultrasonic water atomizer generating log-normal distribution of droplet sizes, with a median droplet size of about  $20 \mu\text{m}$ , was employed. The actual droplet size distribution was expected to deviate from the prescribed distribution at the atomizer depending on the convective velocity in the air tube in the counterflow burner, and this variation was characterized using a PDPA. The hybrid Eulerian–Lagrangian numerical model was extended to include such polydisperse droplet size distributions, subject to the assumption that the droplet collisions were negligible based on the large separation distance between droplets compared to their diameter.

When the air stream was saturated with water vapor only, the counterflow non-premixed flame extinction condition measurements agreed well with the corresponding numerical predictions. With addition of condensed phase water droplets, the trends agreed well; however, considerable quantitative differences exist between the experimental results and the modeling predictions. The observed differences were shown to be mildly affected by the polydispersivity of the atomizer employed. This led to the conclusion that other submodels in the numerical model, including radiative heat losses, need to be evaluated.

Addition of NOH to water complemented the thermal fire suppression effectiveness of water. At low strain rates ( $\approx 125 s^{-1}$ ), 17.5% by mass of NaOH in the solution reduced the flame extinction strain rate by almost a factor of five. Inclusion of alkali metal compounds to water mist may not be desired in many applications because of corrosive effects. Yet combining the chemical-acting powder agent with the physical-acting liquid can enhance the suppression effectiveness of the liquid and provide a potentially more convenient delivery method for the powder agent.

### Comparing Non-Premixed and Premixed Flame Suppression Behavior

Flame inhibition and extinguishment have been studied in a wide variety of laboratory flames, often with conflicting results. Chelliah and co-workers examined the effectiveness of water droplets and droplets of

water with three alkali metal compounds in both premixed and non-premixed opposed flow flames, with the intent of constructing a unified phenomenology.<sup>128,129</sup>

### **Experimental**

Two apparatus were used, producing non-premixed and premixed methane/air flames. The burners were designed to be modular, so that the same water-generation and gas-supply systems could be used with either. The counterflow burner was as described in the previous section.<sup>98</sup> As before, the water mass flow was fixed, and the air and methane flows were increased together until the flame was extinguished. The fuel and air flows were adjusted so as to balance their momentum; according to Equation (4-13). The global flow strain rate was defined by Equation (4-14) providing a suitable parameter that describes the non-premixed flame extinction condition.<sup>81</sup> The total water (or solution) droplet mass fraction in the air + saturated water vapor stream was denoted as  $Y_0$ , while the mass fraction of the additive (i.e., NaOH, KOH, NaCl, or FeCl<sub>2</sub>) was denoted as  $y_{add}$ . In the experiments, variation of  $a_{ext}$  with  $Y_0$  as well as  $y_{add}$  were measured.

The premixed burner consisted of a straight-sided conical flame established at the exit of a Mache-Hebra-type nozzle. A schlieren imaging system provided the flame cone angle, which was used to determine the burning velocity.<sup>77</sup> The nozzle exit flow profile was characterized by laser Doppler velocimetry measurements. The typical half-cone angle of the flame was about 20°. With addition of the solution droplets, the flame height was maintained constant at about 2.0 cm by adjusting the total flow of reactants while maintaining the equivalence ratio at the desired value. For the present data, the expanded uncertainties (with a coverage factor of 2) in the burning velocity were  $\pm 6.0\%$ .

The inhibition of a laminar premixed flame was characterized by the relative decrease in the burning velocity (denoted here by  $S_L$ ) with respect to that of an uninhibited flame ( $S_L$ ). The simple conical premixed flame stabilized above the Mache-Hebra nozzle, and the associated flame cone angle measurement technique adopted here is one of many traditional methods of obtaining the laminar flame speed.<sup>77</sup> While curvature and stretch effects did exist in the flame, they were considered minor, particularly since all results were reported as normalized flame speed,  $S/S_0$ . The uninhibited methane and air flame speed obtained from the present burner was 35 cm/s  $\pm$  1.2 cm/s. Because the ultrasonic atomizer and the length of the Pyrex tube delivering the reactant gas mixture were the same as in the counterflow burner, the median droplet diameter was not expected to be different from that of the counterflow flames.

The ultrasonic atomizer was that described above. Droplets of pure water and water containing NaOH, KOH, and FeCl<sub>2</sub> were generated with a diameter range of 10  $\mu$ m to 20  $\mu$ m, except as noted.

### **Extinction of Non-Premixed Flames with Water Solutions**

Figure 4-62 shows a comparison of droplet mass fraction in air ( $Y_0$ ) as a function of the global extinction strain rate ( $a_{ext}$ ), with varying NaOH mass fraction in water ( $y_{NaOH}$ ). Similar results were reported above for NaOH mass fractions in water of  $y_{NaOH} = 0.055, 0.112, \text{ and } 0.175$ .<sup>98</sup> Earlier experiments at the lowest flow strain rate of 125 s<sup>-1</sup> and 0.175 NaOH in water showed a significantly higher effectiveness over the 0.055 and 0.112 NaOH cases (i.e.,  $Y_0 = 0.005$  for  $y_{NaOH} = 0.175$  vs.  $Y_0 = 0.010$  for  $y_{NaOH} = 0.055$  and 0.112). However, for higher extinction strain rates ( $>125$  s<sup>-1</sup>), the earlier experiments showed a negligible differences in extinction condition with varying NaOH mass fraction.

The difference between the new  $y_{NaOH} = 0.175$  data and previous results was found to be caused by a temperature dependence of the ultrasonic nozzle performance. When the nozzle tip was allowed to reach a steady operating temperature, typically about 40 °C after about 15 min of continuous operation, the resulting flame extinction data were consistent and reproducible. While the revision of  $y_{NaOH} = 0.175$  data can be attributed to ultrasonic atomizer nozzle performance, the observation that the mass fraction of NaOH above 0.055 yields no apparent increase in flame suppression is rather interesting. The differences in the effectiveness with varying NaOH mass fractions pointed to the importance of the residence time in the flow field and the requirement that both the droplets evaporate *and* the residue particles evaporate or decompose. Only after the drops have evaporated can the residue particles begin to decompose in order to release the chemical suppression agent. Higher concentration of additives for the same drop size resulted in a larger particle after drop evaporation. At a fixed strain rate (i.e. drop and resulting particle residence time) higher additive concentrations were expected to take longer to release all of the chemical agent.

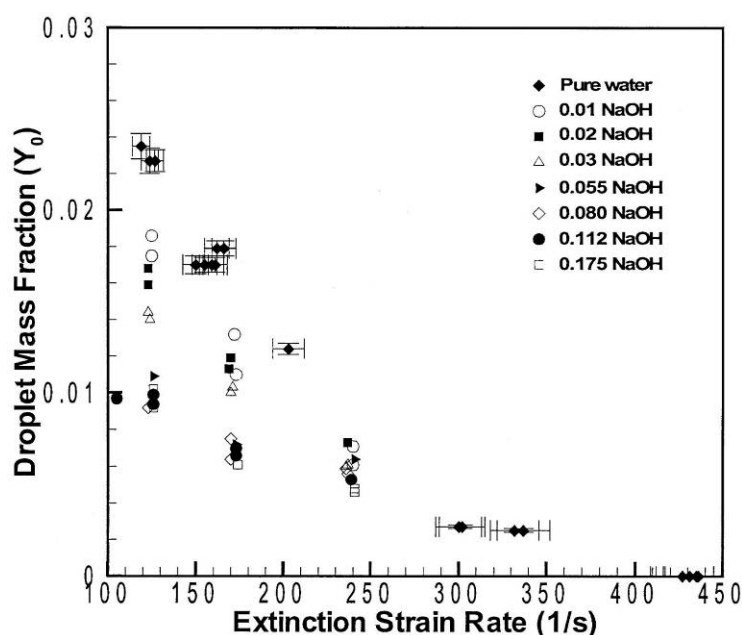


**Figure 4-62. Droplet Mass Fraction as a Function of Extinction Strain Rate of a Methane/air Non-premixed Flame for Several NaOH Mass Fractions in Water.**<sup>129</sup>

Also important to the degree of suppression effectiveness was a thermodynamic limit to the amount of responsible chemical catalytic scavenger that could be achieved in the gas phase at the flame conditions. Agent saturation behavior has been reported in premixed flames with iron, manganese, and tin organometallic compounds<sup>130,131</sup> and metal salts added as particles.<sup>13</sup> For sodium compounds, NaOH is the active chemical catalytic species for Na-based chemical suppression. Thus, the gas phase concentration of NaOH controlled the amount of suppression achievable. The flame extinction results shown in Figure 4-62 at the strain rate of 125 s<sup>-1</sup> are replotted in Figure 4-63, according to the variation of droplet mass fraction ( $Y_0$ ) vs. NaOH mass fraction in water ( $y_{NaOH}$ ). As the  $y_{NaOH}$  in the water was increased above 0.08, the total droplet mass fraction ( $Y_0$ ) needed for flame extinguishment became invariant with the NaOH mass fraction in the droplets. Also shown in Figure 4-63 is the mole fraction of NaOH in air ( $X_{NaOH}$ ), *assuming* that all of the NaOH in the water droplets was completely released to the gas phase. As pointed out above, the amount of additive released is controlled by the residence time. In addition, the maximum  $X_{NaOH}$  that can exist in the gas phase is controlled by temperature and thermodynamics.

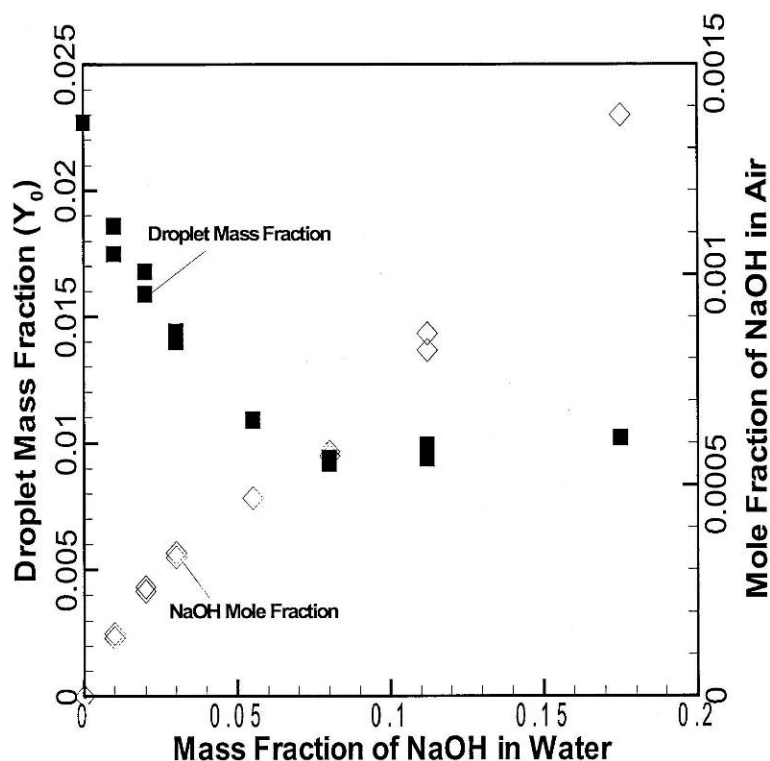
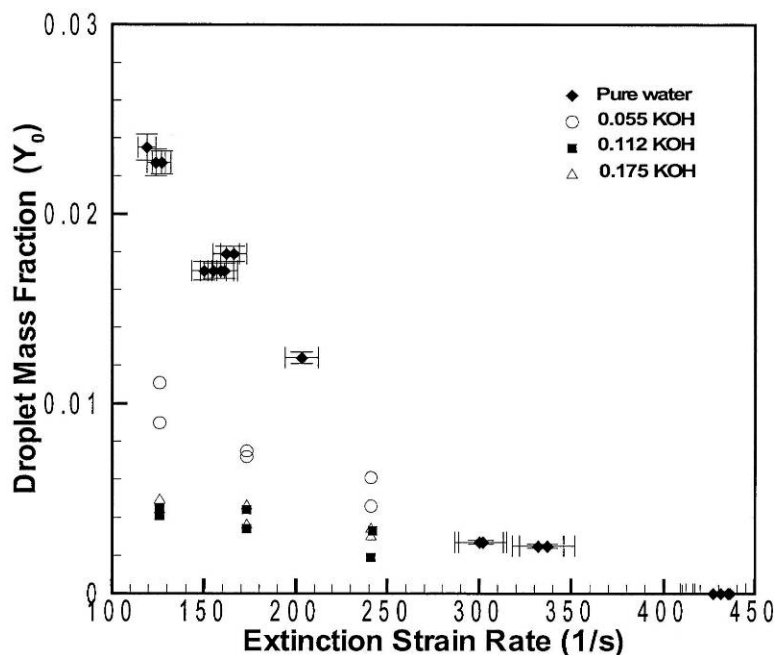


Figure 4-63.  $Y_0$  and Mole Fraction of NaOH in Air as a Function of  $y_{NaOH}$  for the Extinction Strain of  $125 \text{ s}^{-1}$  in Figure 4-62.<sup>129</sup>

Thermochemical data for NaOH were used to estimate the maximum amount of gas phase NaOH achievable. Assuming that NaOH exists as a monomer in the gas phase, an equilibrium liquid-vapor calculation based on the Clausius-Clapeyron equation yielded an NaOH saturation temperature of 1125 K.<sup>132</sup> This vapor-liquid equilibrium temperature is about 400 K to 500 K below the characteristic temperature within the rate-limiting oxygen-consumption, radical-production region of the flame.<sup>106</sup> Because of the thermal boundary layer surrounding each evaporating droplet, it is conceivable that an effective temperature below the flame temperature may control the saturation of excess NaOH vapor. Alternatively, loss of active inhibiting species to condensation may be controlled by a compound with a lower vapor pressure than NaOH. In experiments, resolving the appropriate effective temperature that controls saturation of condensation of the relevant species is perhaps impossible, and therefore, only detailed numerical simulations can provide better understanding of the saturation phenomenon occurring. Although numerical simulations that include detailed interactions between the condensed phase and the gas phase have recently been developed to describe water droplet interactions,<sup>80</sup> analytical models for droplet evaporation of binary mixtures in flames have not. In this case, modeling the evaporation of binary liquid droplets with highly disparate boiling temperatures (373 K for water vs. 1663 K for NaOH) may require further simplifications. Only experimental results are presented here.

Besides NaOH, other alkali metal compounds are known to be chemically effective fire suppressants. In particular, potassium-containing compounds have been shown to be more effective than sodium.<sup>13</sup> Figure 4-64 shows experimental extinction strain rates of a methane/air non-premixed flame with similar sized water/KOH droplets containing varying mass fractions of KOH. For the lowest extinction strain rate considered (i.e.,  $125 \text{ s}^{-1}$ ), the data show increasing flame suppression up to about  $y_{KOH} = 0.112$ . Further increase in the KOH mass fraction in water up to 0.175, however, yielded no further increase in the flame suppression ability of the water/KOH solution. Following the analysis of water/NaOH saturation vapor conditions, current water/KOH results indicated that KOH saturates at a gas-phase mole

fraction of about  $x_{KOH} = 0.0003$  for  $y_{KOH} = 0.112$ . Liquid-vapor equilibrium data for KOH indicated that this mole fraction corresponds to a gas temperature of about 1025 K, which is about 100 K lower than that obtained for the NaOH case. The lower effective saturation temperature for KOH was consistent with the lower boiling temperature of KOH (1597 K) compared to that of NaOH (1663 K).



**Figure 4-64. Droplet Mass Fraction as a Function of Extinction Strain Rate of a Methane/air Non-premixed Flame for Several KOH Mass Fractions in Water.**<sup>129</sup>

Non-premixed methane/air flame extinction experiments were also conducted with NaCl. Water/NaCl droplets have been considered previously by Zheng et al.,<sup>42</sup> but only in the context of extinction of counterflow premixed flames as a function of fuel-air equivalence ratio. The flame suppression trends shown in Figure 4-64, with increasing NaCl mass fraction in water, were consistent with previous data with NaOH and KOH.

Compounds containing the metal Fe has previously been shown to be very effective at flame inhibition.<sup>133</sup> Here, exploratory experiments were conducted to test the efficacy of an  $Fe^{2+}$  compound dissolved in water. An  $FeCl_2$  mass fraction of an  $y_{FeCl_2} = 0.15$  in water was tested, and this water/ $FeCl_2$  solution clearly indicated a chemical inhibition effect, as seen in Figure 4-65. Although  $FeCl_2$  was not as effective as NaCl on a mass basis, experiments with lower mass fractions of  $FeCl_2$  must be performed to evaluate the occurrence of saturation phenomenon, as observed in water/NaOH solutions.

In order to relate the chemical inhibition of the agents considered here to previous studies, the non-premixed flame extinction results were analyzed on a molar basis of the additive. To avoid uncertainties related to saturation effects, only additive mass fractions below the saturation condition were considered. Since water/NaOH extinction results showed saturation of NaOH vapor was approached for additive mass fractions above 0.055, the molar comparisons between NaOH and KOH were performed at  $y_{add} = 0.055$ . For the extinction data points considered, the mole fraction of alkali metal hydroxide ( $AmOH$ ) was evaluated and is plotted as a function of flame extinction strain rate, as shown in the upper panel of Figure 4-66.

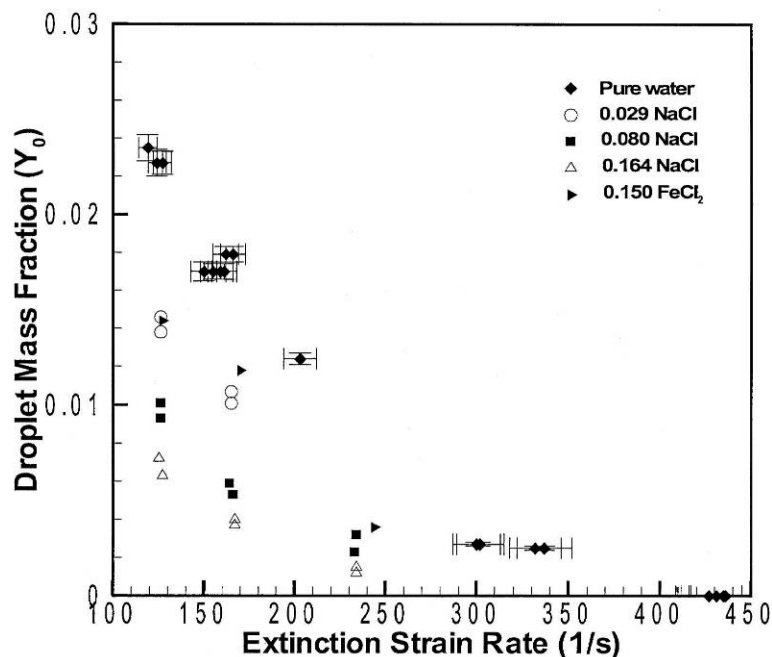


Figure 4-65. Droplet Mass Fraction as a Function of Extinction Strain Rate of a Methane/air Non-premixed Flame for NaCl and  $\text{FeCl}_2$  in Water.<sup>129</sup>

These molar comparisons indicated a roughly double performance benefit of KOH over NaOH as an additive to water droplets, similar to what has been reported based on flames inhibited with particulates.<sup>13</sup> Kinetic studies indicated that recombination of K with OH is about 30 % faster than Na with OH and that recombination of K with  $\text{O}_2$  is in fact 2 to 3 times faster than Na with  $\text{O}_2$ .<sup>134</sup> Thus, differences in the reaction kinetics was perhaps the primary reason for the more effective flame suppression of KOH over NaOH.<sup>117</sup>

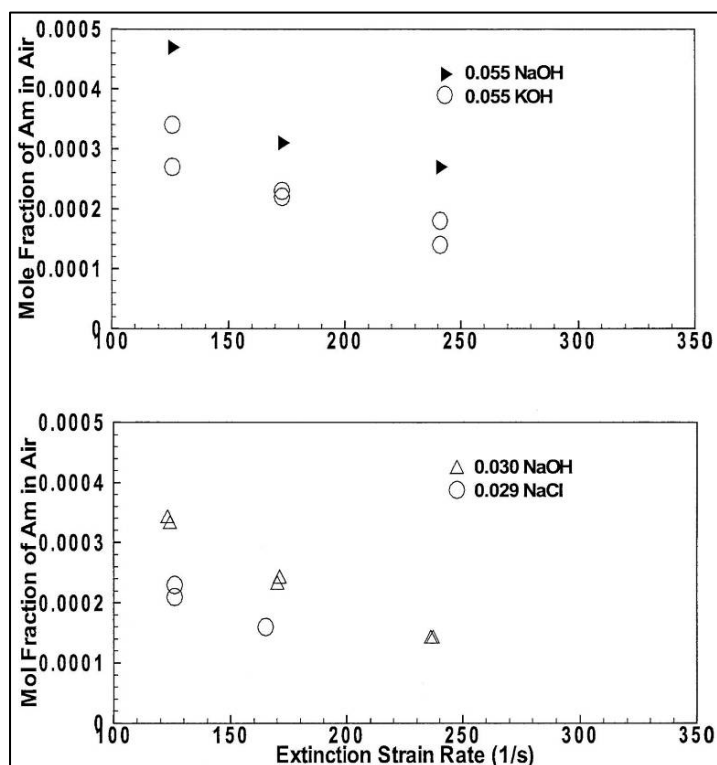


Figure 4-66. Upper panel: Mole Fraction of Alkali Metal atom in Air as a Function of Non-premixed Methane/air Flame Extinction Strain Rate for NaOH and KOH Mass Fractions of 0.055 shown in Figure 4-63 and. Lower panel: Mole Fraction of Am in Air as a Function of Non-premixed Methane/air Flame Extinction Strain Rate for NaOH and NaCl Mass Fractions of 0.03 Shown in Figure 4-63 and Figure 4-66 (upper panel).<sup>129</sup>

Comparison of molar plots of NaCl vs. NaOH, shown in the lower panel of Figure 4-66, indicates a surprisingly superior flame suppression ability of NaCl over NaOH. The difference in effectiveness is not due to the vapor pressure of the parent compounds, since NaCl has a lower vapor pressure than NaOH. Although Cl can display an inhibiting effect similar to Br, a quantitative comparison between NaCl and NaOH requires additional studies and more detailed modeling to understand their suppression differences.

For a droplet mass loading of  $Y_0 = 0.014$  and an extinction strain rate of  $125 \text{ s}^{-1}$ , a comparison of the mole fraction of chemical agent needed in air ( $X_i$ ) yielded the following order:  $X_{KOH} = 0.00021 < X_{NaCl} = 0.00023 < X_{NaOH} = 0.00034 < X_{FeCl_2} = 0.00056$  (assuming linear interpolation between available data). These values indicated that on a molar basis KOH is the most effective chemical agent, followed by NaCl and NaOH. For water/ $FeCl_2$ , the interpolation assumed that  $y_{FeCl_2} = 0.15$  is unsaturated at this high molar loading, which is certainly questionable. If  $FeCl_2$  does condense at a lower additive mass fraction (e.g.,  $y_{FeCl_2} < 0.05$ ), then on a molar basis water/ $FeCl_2$  would be the most effective solution as  $X_{FeCl_2}$  would approach 0.00018 (instead of 0.00056 above).

### ***Extinction of Premixed Flames with Water Solutions***

The inhibition of premixed flame propagation with various chemical fire-suppressing agents is well documented.<sup>130,135,136</sup> Chelliah and coworkers<sup>129</sup> investigated the inhibition of a conical premixed flame with fine water/NaOH droplets. Based on phenomenological reasoning,<sup>137</sup> it is well known that the burning velocity is proportional to the square root of the chemical reaction rate.

$$S = \left( \frac{S_L}{S_L^0} \right)^2 \quad (4-17)$$

Consequently, Figure 4-67 shows the square of normalized burning velocity vs. droplet mass fraction ( $Y_0$ ) for varying the NaOH mass fraction in water ( $y_{NaOH}$ ). With increasing  $y_{NaOH}$ , these results do not show any significant increase in flame inhibition compared to the inhibition with pure water droplets. This was a rather unexpected finding because of the close similarities (described below) between the premixed and non-premixed flames considered.

The insensitivity of higher NaOH mole fractions in water droplets in the premixed flame configuration can be explained by considering the droplet residence times in the flame. Because of the vast difference in the boiling temperature between water and NaOH (373 K vs. 1663 K), water is expected to evaporate first. If the flow residence time of droplets through the premixed flame were less than that through a counterflow flame, a partially vaporized droplet (smaller than the initial  $\sim 20 \mu\text{m}$  at the inflow boundary) with a much higher concentration of NaOH would emerge. Therefore, the lack of chemical inhibition observed in the premixed experiments with water/NaOH solutions may be caused by partially vaporized droplets. To test this hypothesis, the flow residence times of droplets through premixed and non-premixed flames, inhibited with pure water droplets, were investigated.

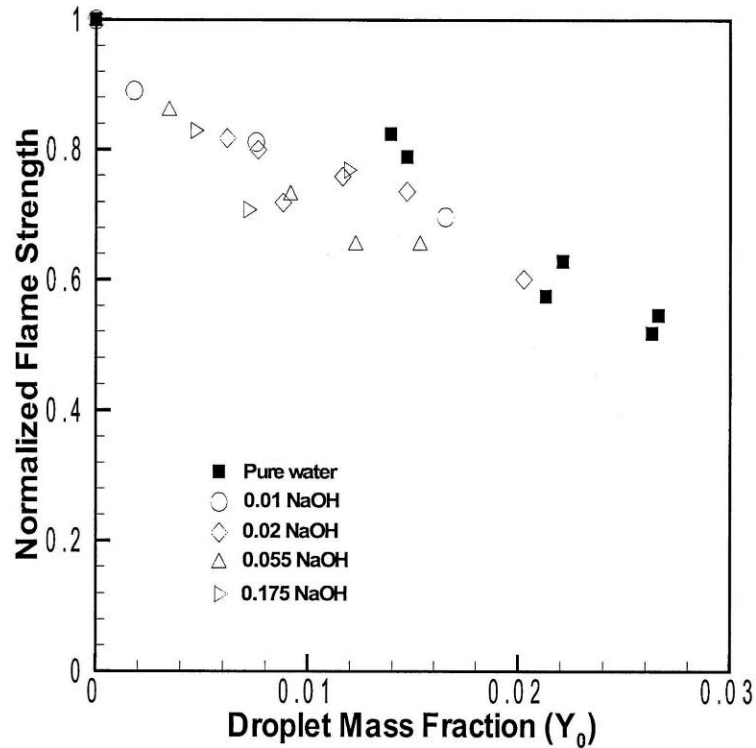


Figure 4-67. Square of the Normalized Burning Velocity of a Premixed Flame Inhibited with Fine Droplets of Water Solution for Several NaOH Mass Fractions in Water.<sup>129</sup>

#### Comparison of Premixed and Non-Premixed Flames with Pure Water Droplets

As described above, the premixed flame burning velocity is proportional to the square root of the overall chemical reaction rate. The non-premixed flame extinction strain rate, however, is directly proportional to the chemical reaction rate. A formal asymptotic analysis,<sup>107</sup> assuming that the overall reaction of the form fuel + oxidizer  $\rightarrow$  products is applicable to both premixed and non-premixed flames, yielded the following relationship between the burning velocity and extinction strain rate

$$(\rho_0 S_L^0)^2 \propto \left( \frac{\rho \lambda}{c_p Z_{st}^2} \right) a_{ext} \quad (4-18)$$

where  $Z_{st}$  is the stoichiometric mixture fraction (assumed to be a small parameter),  $k$  the thermal conductivity, and  $c_p$  the specific heat. Based on this relationship and assuming that the mixture fraction, transport, and thermodynamic properties were not affected by the small fraction of condensed-phase agent added,<sup>138</sup> a direct comparison of the extinction/inhibition of non-premixed and premixed flames was accomplished by defining normalized flame strength as

$$S = \left( \frac{S_L}{S_L^0} \right)^2 = \left( \frac{a_{ext, inhib}}{a_{ext, uninhib}} \right) \quad (4-19)$$

Its applicability for droplets of pure water was examined in Figure 4-68, which shows the normalized flame strength for the premixed and non-premixed flames as a function of the mass fraction of water. The data indicate that the 13  $\mu\text{m}$  median diameter droplets are not equally effective in inhibiting the premixed flame. (Note that for proper normalizations,  $S_L^0$  corresponds to a case in which the premixed methane/air stream is saturated with water vapor, and  $a_{ext, uninhib}$  to a case in which the non-pre-mixed air stream is saturated with water vapor.)

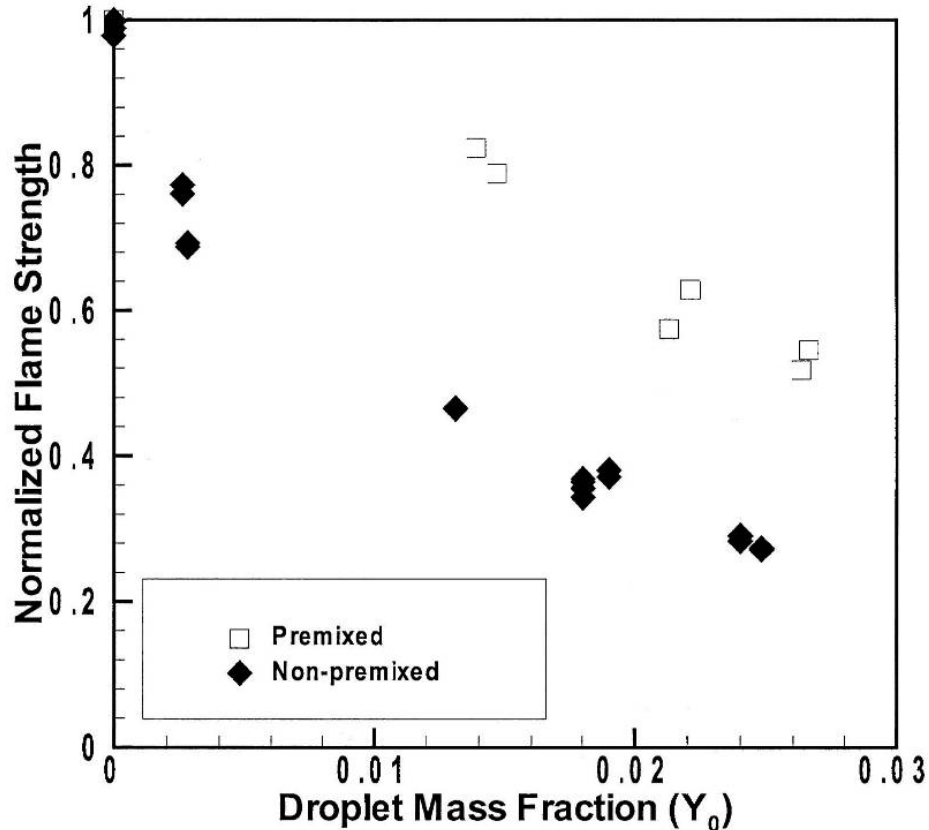


**Figure 4-68.** Normalized Flame Strength of Non-premixed and Premixed Methane/air Flames Inhibited with Droplets of Water with a Median Diameter of  $20\ \mu\text{m}$ .<sup>129</sup>

The aforementioned differences between the inhibition of non-premixed and premixed flames by pure water droplets, as well as the disparate results for droplets of water/NaOH in premixed flames, was explained based on the flow residence time as associated with each flame structure and its effect on the evaporation of fine water droplets. Figure 4-69 shows the numerically obtained flame structure of a premixed and a non-premixed flame, corresponding to conditions in which the flame was inhibited by  $13\ \mu\text{m}$  droplets with a droplet mass fraction of  $Y_0 = 0.01$ .

The estimated flow residence time of these droplets through the thermal layer, from the cold boundary up to the peak flame temperature, differed substantially: 4 ms for the premixed vs. 14 ms for the non-premixed. This implied that the time available for the droplets to vaporize in premixed flames was considerably less, and that the  $13\ \mu\text{m}$  droplets were not necessarily the ideal size for inhibiting the premixed flame considered. Consequently, the maximum thermal cooling was not achieved compared to the counterflow flame, resulting in the lower flame inhibition observed in Figure 4-68 for premixed flames.

Residence time considerations may also explain the much poorer relative effectiveness of either NaOH or KOH at  $a = 240\ \text{s}^{-1}$  vs.  $a = 125\ \text{s}^{-1}$ , as shown in Figure 4-62 and Figure 4-64. The higher strain flames present lower residence times, possibly preventing release of all of the additive to the gas phase.

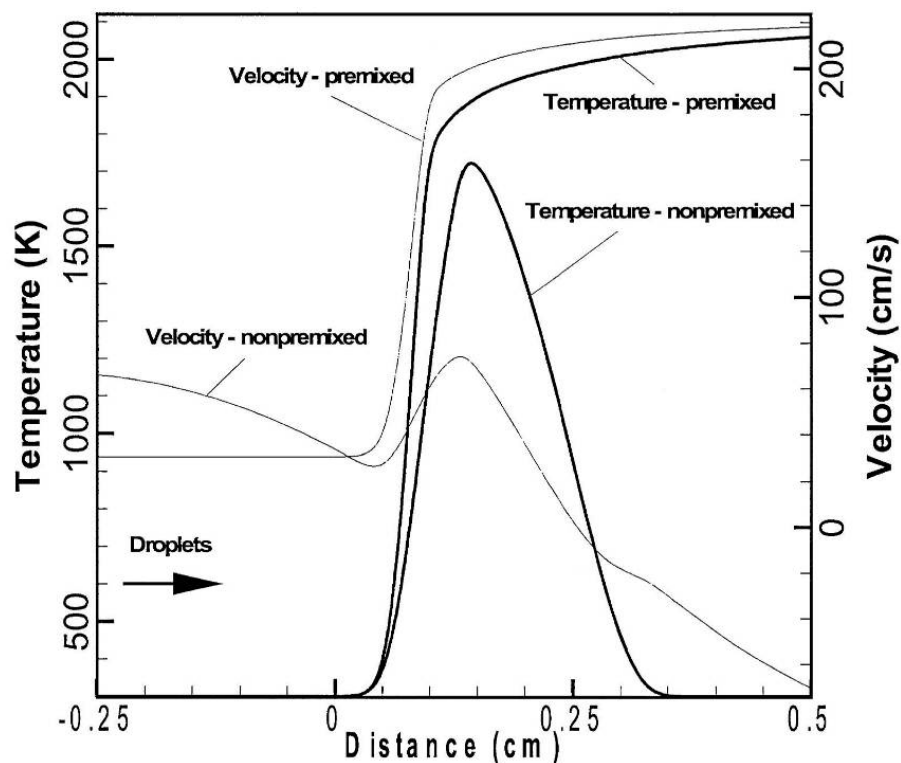


Figure 4-69. Non-premixed and Premixed Flame Structures Corresponding to Inhibited Conditions of Water Droplet Mass Fraction of  $Y_0 = 0.01$ .<sup>129</sup>

### Conclusions and Summary

The low vapor pressure of alkali metal salts at normal room temperature requires their delivery to a flame as a powder or as a droplet spray, if suppression is to be efficient. However, efforts to combine the thermal fire suppression ability of fine water droplets with the chemical inhibition of alkali metal compounds indicated the existence of an upper limit for agent effectiveness perhaps due to condensation of some intermediate inhibitor species. Inclusion of NaOH in water (up to 17.5 % by mass) significantly enhanced the fire suppression ability of water by complementing its thermal effects with chemical catalytic radical recombination effects of NaOH. When the mass fraction of an alkali metal hydroxide in water was below this condensation limit, comparison of the chemical effectiveness indicated that KOH was twice as effective as NaOH on a molar basis for a wide range of flow strain rates. Comparison of the effectiveness of water/NaOH with water/NaCl on a molar basis indicated the superior effectiveness of NaCl over NaOH.

The relationship between droplet size and flow residence time was found to be important, both for comparing the behavior of condensed-phase agents between flame types, as well as for evaluating the efficacy of chemically active additives. Comparison of the effects of water/NaOH droplets on the extinction of non-premixed and inhibition of premixed flames implied that if the droplets were not completely evaporated before reaching the chemical reaction layer (because of non-optimal droplet size or insufficient droplet residence times), then the full chemical effectiveness of the agent was not realized. When the same water droplets were introduced to non-premixed and premixed flames, with no velocity lag between the droplets and the gas phase, the characteristic flame extinction/inhibition conditions of the two flames differed. Flame structure analysis revealed a distinct flow residence time of droplets (with a median diameter of 13  $\mu\text{m}$ ) through each flame structure: 14 ms for the non-premixed flame, 4 ms for the premixed flame. This time difference was the cause for the observed differences in the two flames.

The predicted results for polydisperse size distributions were consistent with previous monodisperse predictions. However, differences observed between experiments and modeling could not be explained solely on the basis of the size distribution effects.

The results illustrate the importance of understanding the particular reacting flow field and temperature conditions in order to assess the intricate coupling between droplet size and its residence time through the flame structure. In real fires with turbulent flow fields, the flow residence times of droplets can be quite varied; optimum droplet sizes might be different than the 10  $\mu\text{m}$  to 20  $\mu\text{m}$  observed in these studies. Therefore, design of optimal fire-suppression systems using droplets of water solutions must consider the flow residence times and flame structures of each application carefully.

#### 4.5.4 Dendrimers, Combined Chemical and Physical Flame Suppression<sup>iii</sup>

##### Introduction

At the beginning of the NGP, dendritic polymers or dendrimers were a new polymer technology coming to fruition as commercial products. They are ultra-branched, three-dimensional polymeric molecules possessing a low-density core surrounded by a crowded, high density surface.<sup>139,140</sup> Typical dendrimers were of the order of 5 nm to 10 nm in diameter. The interior of the dendrimer has tens to hundreds of branching junctions, depending on the overall degree of polymerization of the dendrimer. In the chemistries most commonly synthesized, these branching points were tertiary amines. Thus, the nitrogen at the branch junction has a lone pair of electrons that could be used for “complexation.” The ends of these branching paths are located on the dendrimer's surface and may also number in the tens to hundreds. The chemistry of these end groups is easily tailored to incorporate a desired chemical moiety or to encourage complexation with a specific ion.

Previous research had shown that transition metal complexes and alkali metal salts may act as super-agents for fire suppression, performing as much as 60 times more efficiently than halon 1301.<sup>141,142</sup> Unfortunately, the most effective of the complexes also suffer from such problems as high toxicity and reactivity with metal surfaces. By encapsulating the metal ion inside the dendrimer or by attaching it to a dendrimer surface, it might be possible to create a super-effective agent encapsulated in an inert, bio-compatible shell that would decompose upon contact with flame.

Beck Tan *et al.*<sup>143</sup> of the Army Research Laboratory (ARL) assessed the applicability of aqueous aerosols of dendritic polymeric for fire suppression effectiveness on gaseous laboratory flames (using the dispersed liquid agent fire fighting screen described in Chapter 8) and on liquid pool fires.

##### Materials

Poly(amidoamine) dendrimers were purchased from Dendritech, Inc., of Midland, Michigan. Two types of dendrimers were used in this study. The G3.5-ONa dendrimers had 64 -COONa end groups per molecule and a nominal molecular weight of 14,000 g/mole. These materials were used in the as-received condition. Four derivatives of G4.0 dendrimers were synthesized and tested. They were designated G4.SA (no metal added) or G4.SA-X, where X indicated the added metal ion: Cr, Fe, or K. Each of the

---

<sup>iii</sup> Text and figures in Section 4.5.4 are taken mainly from Reference 143 unless otherwise noted.

added ions had indicated significant flame inhibition potential (Chapter 3). The base molecular weight of the G4.SA dendrimer was 19,300 g/mole. Each potassium dendrimer contained 64 potassium ions; each other metal dendrimer contained 21 metal ions. Elemental analyses of the five dendrimers are given in Table 4–9.

**Table 4–9. Elemental Composition of Pure Dendrimers and Dendrimer Salt Complexes.**

Element	Quantity	Dendrimer				
		G4.SA	G4.SA-Cr	G4.Sa-Fe	G4.SA-K	G3.5-ONa
H	Mass %	8.08	6.94	6.81	6.7	7.38
	Atom %	53.09	51.2	51	50.9	52.5
C	Mass %	48.03	42.07	37.9	42.2	43.37
	Atom %	26.7	25.6	23.7	26.7	25.7
N	Mass %	14.7	12.76	16.63	12.61	12.9
	Atom %	7.0	6.72	7.29	6.84	6.55
O	Mass %	29.1	33.6	37.3	28.7	29.4
	Atom %	12.5	15.5	17.5	13.6	13.1
Cr	Mass %	--	4.63	--	--	--
	Atom %	--	0.66	--	--	--
Fe	Mass %	--	--	4.37	--	--
	Atom %	--	--	0.6	--	--
K	Mass %	--	--	--	9.8	--
	Atom %	--	--	--	1.9	--
Na	Mass %	--	--	--	--	13.1
	Atom %	--	--	--	--	2.14

## Fire Suppression Experimentation

The fire suppression effectiveness for aqueous solutions of the five dendrimers was evaluated using two techniques.

One set of tests involved the dispersed liquid agent fire suppression screen (DLAFSS) apparatus developed at NIST for screening experimental fire suppressants; it is described fully in Chapter 8. Briefly, the apparatus consists of a cylindrical, opposed flow, propane burner located in a vertical wind tunnel. A nebulizer was used as a droplet generation device. Liquid agents were entrained into the air flow in the wind tunnel and traveled upward where they impinged on the propane flame. When the air velocity reached a critical value, the stable, blue enveloped flame at the burner was blown off, forming a wake flame. The transition to a wake flame was equivalent to extinguishing the fire. All experiments using the DLAFSS apparatus were conducted with the propane flow set at 2.0 L/min and the nebulizer air flow at 0.25 L/min.

Some data were collected for solutions of 25 % (by weight) dendrimer in water and a sample delivery rate of 0.3 mL/min. However, due to the high viscosity of the solutions, the sample delivery pump stalled repeatedly. The remainder of the tests were conducted using more dilute solutions (15 % by weight) and increased sample delivery rate of 0.5 mL/min. These settings allowed for the same delivery rate of sample without causing the sample delivery device to stall.

Although this was by far the best method found for screening experimental liquid fire suppression agents, the dendrimer residue frequently clogged the burner pores, necessitating changing the burner. This also added substantial variation to the test results. (The blow-off velocity for air alone was 220 cm/s. The range of scatter between runs and for the different burners was about  $\pm 20$  cm/s. For water droplets, the blow-off velocity was 200 cm/s, with scatter of  $\pm 20$  cm/s.) To improve the ability to discern differences among the tested aerosols, data for air blow-off velocity and water blow-off velocity for a given burner collected on a given day were averaged and used in calculating blow-off velocity ratios of water to air, sample to air, and sample to water for samples that were evaluated using that same burner. Then, the ratios calculated for each sample were averaged. These average ratios were the parameters used to evaluate the candidate suppressant's performance.

The second method used was a modification of the JP-8 fuel fire suppression agent screening method developed by Finnerty at ARL.<sup>144</sup> A test involved spraying a stream of the agent directly onto a 160 mm diameter pan containing 200 mL of JP-8. A Binks Model 15 paint spray gun was used as the agent delivery device, with a 1.58 mm nozzle operating at a pressure of 275 kPa (40 psi). This gun produced a fine stream of fluid droplets entrained in a forced air flow from a relatively small volume (50 mL) of fluid. The apparatus was adjusted so that the droplet spray distribution pattern covered the entire surface of the fuel container. For water, the flow out of the spray gun was 4.6 mL/s, while the rate of collection in the fuel container was 1.7 mL/s.

The time to extinguish the fire was the criterion used to evaluate the effectiveness of various agents. Additional data included the volume of agent fluid remaining in the spray gun, and the volume of fluid remaining in the fuel pan. All experiments were recorded using a video camera, and exact fire-out times were extracted from the recordings. A photograph of an experiment in progress is shown in Figure 4-70.

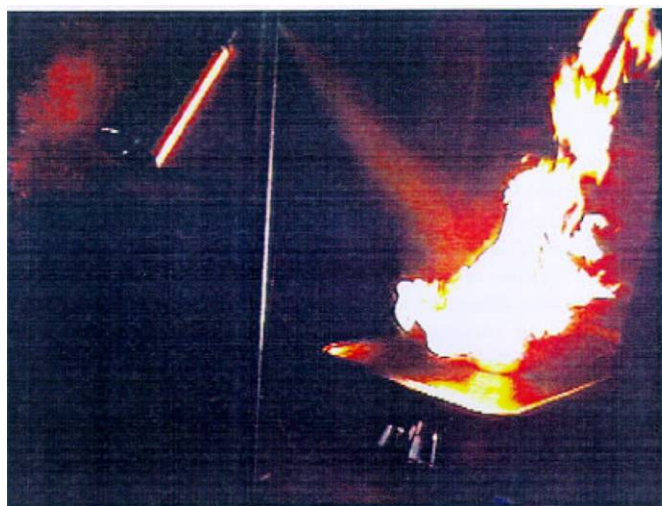


**Figure 4-70. Setup for JP-8 Fire Suppression Experiments.**

### **DLAFSS Results**

Fire suppression screening experiments were conducted on water and aqueous solutions of pure dendrimer, dendrimer Na salts, dendrimer K salts, dendrimer Fe complexes, dendrimer Cr complexes, NaAc,  $K_2CO_3$ , chromium (+3) chloride hexahydrate, and ammonium iron (+2) sulfate hexahydrate. In the case of the salt solutions, the salt concentrations were adjusted so that the atom concentration of the metal

ion was either equivalent to that in the corresponding dendrimer-metal complex solution (Na, Fe, and Cr salts) or set at 10 times the equivalent weight (K salts).

The values of average blow-off velocities calculated for each agent screened are shown in Table 4–10. These values are similar to those collected by Yang et al.<sup>145,146</sup> for a variety of potassium and sodium small molecule salts. A lower blow-off velocity indicates a more efficient flame suppressant.

**Table 4–10. Average Blow-off Velocities for of Various Candidate Agents.**

Agent	Blow-off Velocity (cm/s) @ 0.3 mL/min	Blow-off Velocity (cm/s) @ 0.5 mL/min	Sample-to-water Blow-off Ratio
Water			1.00
10 % G4.SA	170		0.91
25 % G4.SA-K	152		0.82
4.8 % K <sub>2</sub> CO <sub>3</sub>	189		0.98
15 % G4.SA		193	0.96
15% G4.SA-K		180	0.94
3.23 % K <sub>2</sub> CO <sub>3</sub>		204	0.98
15 % G3.5-ONa		152	0.78
0.65 % CH <sub>3</sub> CO <sub>2</sub> Na		171	0.87

The results of the DLAFSS flame suppression experiments are summarized in Figure 4-71 and Figure 4-72. To avoid misinterpretation of the data, the water-to-air blow-off velocity ratio measured during the same conditions as the sample-to-air blow-off velocity ratio is given in each case. The effectiveness of the agent should be interpreted based on that reference.

Figure 4-71 summarizes the results of fire suppression experiments conducted with a sample delivery rate of 0.3 mL/min. The most interesting result from the 0.3 mL/min experiments was from comparison of the 25 % G4.SA-K and the 4.8 % K<sub>2</sub>CO<sub>3</sub> solutions. Although the K<sub>2</sub>CO<sub>3</sub> aerosol contained 10 times the K ions of the G4.SA-K dendrimer salt solution, the dendrimer solution was more efficient as a fire suppression agent. Another important finding was that the pure dendrimer solution, 10 % G4.SA, had fire suppression capacity that was comparable to pure water. This was significant because there were initial concerns that the polymer might act as a fuel and thereby be detrimental to fire suppression effectiveness.

The DLAFSS results for the 15 % solutions and a sample delivery rate of 0.5 mL/min are summarized in Figure 4-72. The results from small molecule K and Na salts are also included for comparison. The results for the 15 % G4.SA solution indicate that once again, the addition of the pure dendrimer to water was not detrimental to fire suppression effectiveness. The fire suppression effectiveness of the 15 % G4.SA and the 15 % G4.SA-K samples was the same as water, within experimental uncertainty. Comparison of G4.SA-K to the K<sub>2</sub>CO<sub>3</sub> solution showed that the dendrimer salt solution was perhaps a little better than the pure salt, but the former contains one-tenth the K ion concentration.

The agent that showed the most significantly enhanced fire suppression capability was the G3.5ONa dendrimer K salt. The blow-off velocity of the dendrimer-sodium salt was reduced nearly 20 % relative to the blow-off velocity ratio for water measured under the same conditions. The 0.65% NaAc, which had the same Na ion concentration as the G3.5-ONa dendrimer salt, also showed promise for enhancing the fire suppression effectiveness of water, but to a lesser extent than the dendritic salt solution.

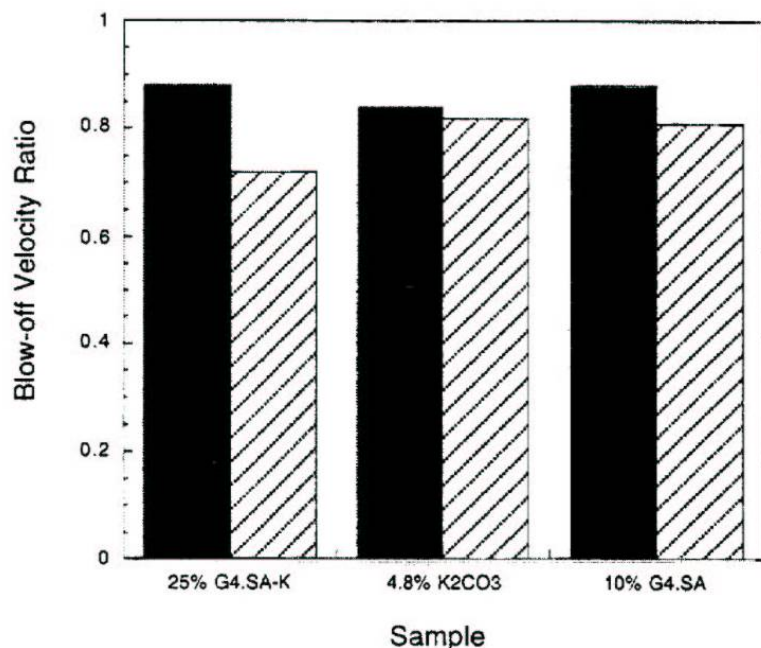


**Figure 4-71. Blow-off Velocity Ratios for Various Candidate Agents to Air, and Reference Ratios for Water to Air Measured under the Same Conditions. Solid bars: water to air; lined bars: sample to air.**

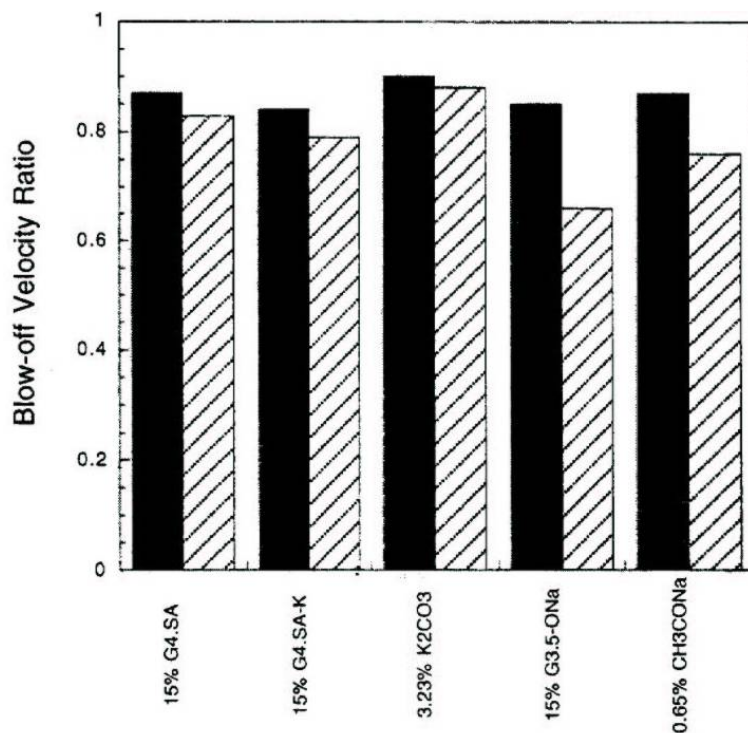


**Figure 4-72. Blow-off Velocity Ratios for Various Candidate Agents to Air, and Reference Ratios for Water to Air Measured under the Same Conditions. Solid bars: Water to air; lined bars: sample to air.**

The blow-off velocity ratios of sample fire suppression effectiveness to water fire suppression effectiveness measured when the same conditions were used are tabulated in Table 4-10. All ratios were comparable to or less than 1.0, indicating that all the experimental agents performed at least as well as water. In particular, the Na salts (both dendrimer and small molecule) and the dendrimer-potassium salt delivered at 0.3 mL/min from 25% solution were considerably more effective than water.

In the case of the Na salts, it appears that the Na cation was the active species. Both the small molecule salt and the dendrimer salt showed promise as fire suppression agents. It is noteworthy that the NaAc showed an effect when present at only  $\approx 0.65\%$  by weight. Since this salt is inexpensive, non-hazardous and readily available, it may be prudent to investigate its fire suppression effectiveness more fully. The G3.5-ONa dendrimer performed somewhat better than the small molecule salt solution of equivalent Na ion concentration. A similar effect was observed in comparing the 25 % G4.SA-K and the 4.8 %  $K_2CO_3$  solutions. Since the pure dendrimer solutions were not found to be significantly more effective than water, the observed effect must be related to the combination of the cation with the dendrimer "carrier." This is the type of effect that motivated the project and offers some proof of the concept that the use of dendritic polymers as carriers for active fire suppressant species could be beneficial.

The mechanism responsible for observed enhancement in the fire suppression effectiveness of the Na and K through coupling with the dendrimer carrier cannot be easily extracted from the data. One possibility was that the organization of the cations on the dendrimer surface, which resulted in an extremely high local concentration of them, had a beneficial effect on the kinetics of the radical recombination reaction believed to be responsible for flame suppression. This type of kinetic effect had been observed for other situations in which an active species was localized on the surface of a dendrimer.<sup>147</sup> A second possibility was that the size and size distribution of the droplets being delivered to the flame were altered by the dendrimers in such a way as to improve the fire suppression effectiveness of the fluid, based on purely geometrical considerations. The droplet diameter from a nebulizer, which was the sample delivery device incorporated into the DLAFSS device, is known to be related to the properties of the nebulizing fluid, such as density, surface tension, and viscosity.<sup>148</sup> The density of the dendrimer solutions was not substantially different from that of water, and the surface tension of polymer and salt solutions was generally not changed by more than about 10 % to 20 %. However, the viscosity of dendrimer solutions was much greater than that of water. Other recent work on poly(amidoamine) dendrimers<sup>149</sup> indicated that the viscosity of 15 % to 25 % dendrimer solutions at room temperature should be on the order of tens of centipoise, an order of magnitude greater than that of pure water ( $\sim 1.0$  cP).<sup>150</sup> A third possibility may be the thermodynamic saturation limits to the amount of inhibitor species permitted in the gas phase discussed in Section 4.5.3.

The idea that the viscosity effects may alter the fire suppression effectiveness through changes in the delivery spray may explain the apparent discrepancy between the fire suppression effectiveness observed for 25 % G4.SA-K dendrimer solution delivered at 0.3 mL/min and the 15 % G4.SA-K solution delivered at 0.5 mL/min (Figure 4-71 vs. Figure 4-72). The mass flow of polymer into the flame was identical, but the fire suppression effectiveness of the 25 % solution was considerably better than the 15 % solution. This may have been a reflection of the viscosity difference between the two fluids, which could be as much as a factor of 6 to 8, and its effect on the droplet size and distribution in the sample delivery spray. Although results by Yang et al.<sup>151</sup> indicated that the droplet size and distribution generated in the DLAFSS experiment are not strongly dependent on fluid viscosity in low viscosity solutions ( $\sim 1$  cP to 4 cP), they did not measure droplet size distributions in polymer solutions that have viscosities that are much greater than that of water.

Although it is likely that viscosity played a role in the determination of apparent fire suppression effectiveness, in the sodium salt and sodium dendrimer systems, chemical mechanisms are also probably contributing significantly. Both the 15 % pure dendrimer solution and the 15 % G4.SA-K solution were much less effective than the 15 % G3.5-ONa solution, though the viscosities should be of similar

magnitude (see Table 4–10). Given this evidence of chemical interaction, it is in the sodium-containing systems where the kinetic benefits of localizing the active species on the surface of a dendrimer should be most readily apparent. The results from the G3.5-ONa solution provide the most concrete evidence that using a dendrimer carrier to deliver active species into a flame can have a positive effect on the fire suppression effectiveness of that active species.

### Pan Fire Suppression Results

The analysis of data from the JP-8 fuel fire screening experiments was straightforward. The relevant parameters recorded were the time to extinguish the fire and the mass of agent that was dispersed in extinguishing the fire. Because a relatively large mass of agent was required to perform each experiment and the results were not found to be highly reproducible, these experiments were used only for the dendrimer-iron complexes that could not be studied using the DLAFSS apparatus because of their high viscosity. The associated transition metal salt and pure dendrimer controls were also studied (chromium [III] chloride hexahydrate, ammonium iron [II] sulfate hexahydrate, and G4.SA). The dendrimer chromium complexes could not be studied because the supply of material was insufficient.

The results from the JP-8 fuel fire screening experiments are summarized in Figure 4-73 and Figure 4-74.

Although the masses of the various agents required to extinguish the JP-8 fires varied from 40 g to 65 g (Figure 4-74), the measurement uncertainty precluded drawing definitive conclusions regarding the relative fire-out times for any of the agents studied. It was not possible to judge the relative efficiency of the agents from these experiments also due to the discrepancy in the agent delivery rates. These rates were calculated from the mass deployed and the time of deployment and are plotted in Figure 4-75. The paint sprayer was delivering higher viscosity solutions at slower rates. This difficulty in uniform agent dispersion for solutions of varying viscosity is a challenge to be addressed during the development of screening techniques for experimental fire suppression agents.

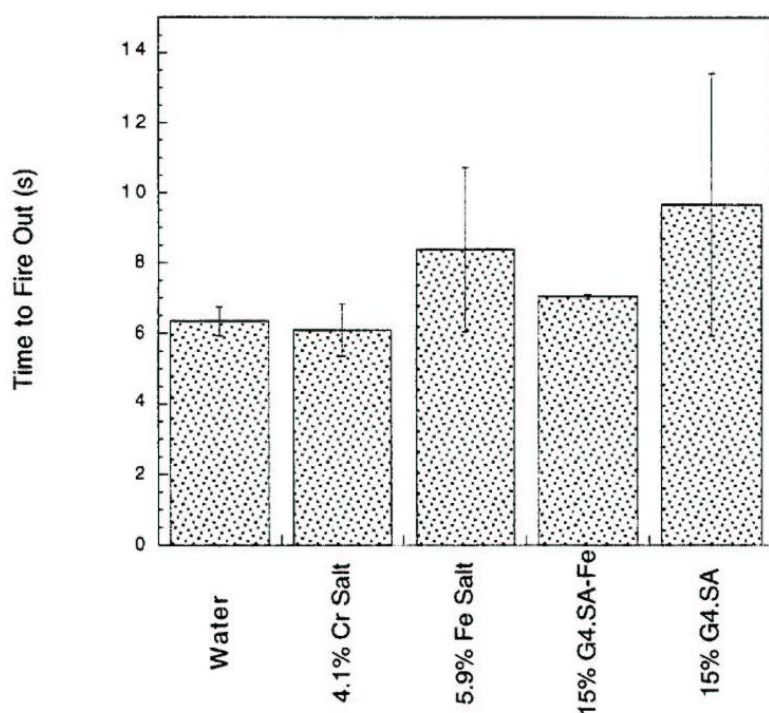


**Figure 4-73. Times for Various Experimental Fire Suppressants to Extinguish a 200 mL JP-8 Pan Fire. The error bars represent  $\pm$  one standard deviation.**

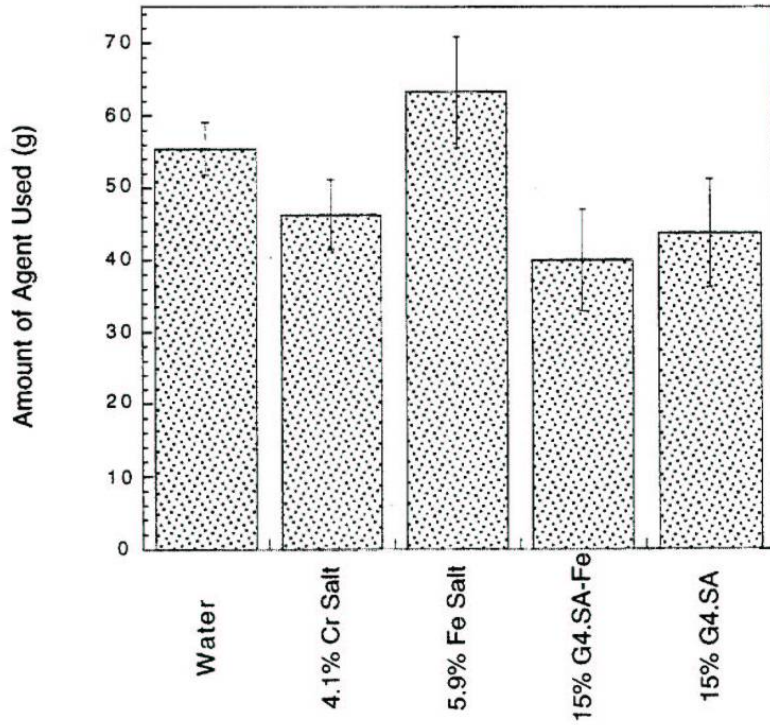


**Figure 4-74. Mass of Various Experimental Fire Suppressants to Extinguish a 200 ml JP-8 Pan Fire. The error bars represent  $\pm$  one standard deviation.**

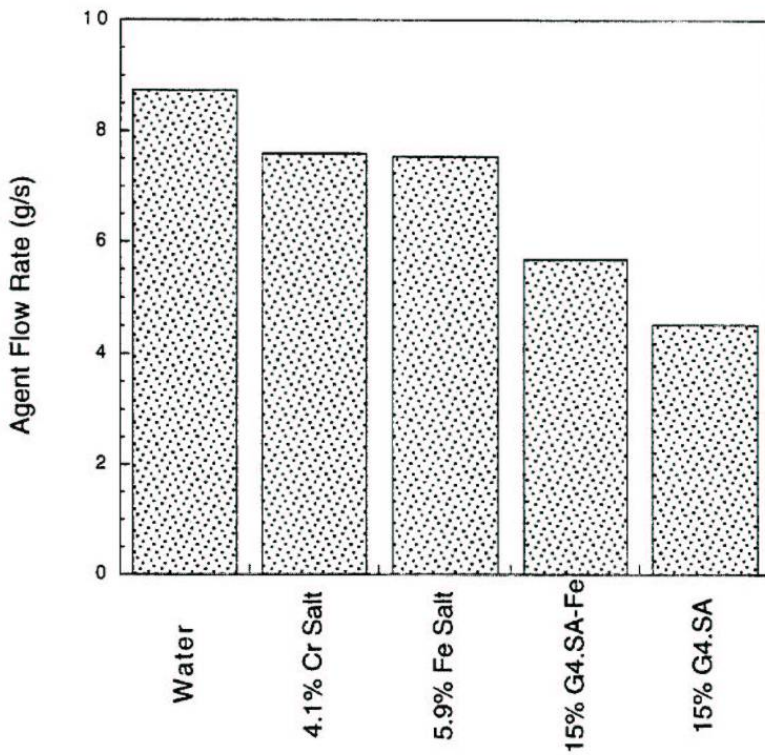


**Figure 4-75. Mass flows for Various Fire Suppressants Deployed during JP-8 Screening Experiments.**

Because of the difficulties encountered in investigating the transition metal complexes using the JP-8 fuel fire experiments, it was not possible to draw any strong conclusions regarding the fire suppression effectiveness of the dendrimer-transition metal complexes. However, the experiment was sensitive enough so that the effect of a super-agent would have been noticeable. This study indicated that the dendrimer-iron complexes did not exhibit the super-agent performance previously observed for iron pentacarbonyl and other volatile transition metal complexes.<sup>143</sup>

## Important Findings

This exploratory study found that:

- Poly(amidoamine) dendrimers added to water at substantial concentrations have no deleterious effect on the fire suppression effectiveness of water and can marginally improve the flame suppression effectiveness of water. Any contribution of polymer combustibility was at least offset by the flame suppression contribution.
- The use of dendritic polymer carriers to deliver agents containing potassium and sodium ions can increase the effectiveness of these agents on laboratory flames.
- Dendrimer-sodium salts were more effective flame suppression agents than dendrimer potassium salts. This is in contrast to the greater observed effectiveness of potassium over sodium in all other (non-dendrimer delivery) suppression studies and may be due to saturation limits in the dendrimer experiments.
- The addition of sodium acetate to water improved its flame suppression effectiveness significantly, even at loadings of less than 1 % by weight.
- Potassium carbonate did not significantly improve the flame suppression effectiveness of water at concentrations as great as 5 % by weight for the droplet size and flow conditions studied.
- More work is needed in the development of versatile experiments for screening experimental aerosol fire suppressants.

## 4.6 SURFACE COOLING<sup>iv</sup>

### 4.6.1 Introduction

When liquid suppressant droplets released from a discharge port approach a fire, several things can happen.<sup>152</sup> Droplets with sufficient momentum to penetrate the flame, depending on their sizes, can either be consumed in the flame (participate directly in the suppression processes through physical and/or chemical mechanisms) or reach the fuel surface. Droplets with little momentum (e.g., very small droplets) may not penetrate the fire and will be deflected away by the rising hot plume.<sup>153</sup> These deflected droplets will eventually evaporate or strike adjacent objects. For droplets landing outside the burning area, the cooling of the adjacent and surrounding surfaces could mitigate or contain the flame spread. Therefore, droplet interaction with surfaces is an integral part of the overall suppression process.

---

<sup>iv</sup> Large portions of the text of Section 4.6, as well as the figures, have been used from Reference 152 without further attribution. The reader should consult the original document for additional details.

Surface heat extraction and burning surface area reduction are generally regarded as the dominant mechanism for extinguishment of burning solid fuels by water sprays.<sup>154</sup> The cooler liquid droplets can interact with the relatively hot fuel surface, extract heat during vaporization, and thereby reduce the surface temperature. With surface cooling, the burning rate falls, which leads to a decrease in heat feedback to the fuel surface. Eventually, a critical burning rate is reached beyond which combustion can no longer be sustained. The deposited droplets also reduce the mass transfer area on the fuel surface, which also causes a reduction in burning rate.

In order to understand surface cooling without resorting to a detailed analysis of the coupling between the transient thermal response of the fuel bed as a result of the application of liquid agent and the heat feedback from the flame to the fuel, the transient coupling process is considered as a series of quasi-steady steps. At any instant in time, a steady-state energy balance at the fuel surface can be written as:

$$\dot{m}''_{fuel} \Delta H_{fuel} = Q''_{cond} + Q''_{conv} + \epsilon_{flame} \sigma T_{flame}^4 - \epsilon_s \sigma T_{surf}^4 - q'' \quad (4-20)$$

where  $\dot{m}''_{fuel}$  is the fuel burning mass flux,  $\Delta H_{fuel}$  is the effective heat of gasification of the fuel,  $Q''_{cond}$  is the conductive heat flux to the fuel surface,  $Q''_{conv}$  is the convective heat flux to the fuel surface,  $\epsilon_{flame}$  is the flame emissivity,  $\sigma$  is the Stefan-Boltzmann constant,  $T_{flame}$  is the average flame temperature,  $\epsilon_s$  is the surface emissivity,  $T_{surf}$  is the fuel surface temperature, and  $q''$  is the heat flux removal from the fuel surface due to surface cooling.

The surface cooling heat flux,  $q''$ , depends on the interaction of the liquid droplets with the surface. There are many different scenarios of droplet impact on a surface. The impacting processes depend on the thermophysical and geometrical properties of the droplet and of the target surface and on the magnitude and direction of the impact velocity vector. In addition, for a flaming surface, the droplet will traverse through an environment different from that of a non-burning surface before impact. However, in the literature, droplet/surface interaction studies focus almost exclusively on non-burning surfaces.

When relatively cool liquid droplets impact a solid surface, cooling of the surface occurs as a result of heat transfer between the surface and the droplets. A liquid droplet impacting a solid surface has been extensively studied in the literature.<sup>155,156,157,158,159,160,161,162,163</sup> Maps that identify the various impact and heat transfer regimes over a wide range of experimental conditions have been constructed. Spray cooling or quenching of hot metallic surfaces has also been extensively studied.<sup>164,165,166,167,168,169</sup> Many empirical heat transfer correlations for spray cooling applications exist.

For a liquid droplet interaction with a *liquid* surface, several scenarios need to be considered. The impact dynamics are complicated by the ability of the liquid surface to deform and to displace in response to the impinging droplet. There is also internal fluid motion of the liquid pool initiated by the impact processes.<sup>170</sup> If the droplet has a very high impact velocity, it can cause a crater in the liquid pool and a splash upon impact. For a burning liquid pool, the splash may result in a sudden increase in burning rate due to an increase in the liquid surface area caused by the splash droplets. If the droplet is soluble in the liquid, mass transfer between the penetrating droplet and the liquid will occur. Depending on droplet impact parameters, differences in miscibilities and physical properties (surface tension and viscosity) between the droplet and the target liquid, and the depth of the liquid layer, several phenomena are likely following impact. The droplet may float on the surface, may coalesce into the liquid pool with little or no splashing and produce a vortex ring, may rebound or splash forming a crater and a small jet or column of liquid at the surface, or may dissolve into the liquid pool. Most work in the literature has examined the

isothermal impact of a liquid droplet onto a surface of the same liquid (e.g., see the review article of Rein<sup>170</sup> and the references therein). In a fire suppression scenario, the impacting droplet encounters a different liquid target (suppression fluid vs. fuel) with different physical properties. The temperature of the droplet can be much lower than that of the liquid surface (especially, in the case of burning), and the contact between a cold droplet with a hot liquid may sometimes results in vapor explosion,<sup>171</sup> an unwanted situation. All of these complicated interactions render the study of heat transfer processes between liquid droplets and a liquid surface an arduous and daunting task. Appropriate heat transfer correlations do not exist in the literature; therefore, liquid surface cooling calculations, in spite of the importance of the process, are not attempted here.

This section discusses droplet evaporation and solid surface cooling by droplets, an integral part of the surface cooling problem. If the droplets evaporate completely before reaching the fuel surface, the heat removal from the surface will decrease significantly due to the fact that the liquid latent heat of vaporization does not play a role. Under this circumstance, the surface will only be cooled by a vapor jet, which is not an effective cooling mechanism.

Another important aspect in surface cooling is the ability of the droplets to reduce the surface temperature of components in the vicinity of a fire to prevent re-ignition, which is a potential problem in suppressing aircraft engine nacelle fires. If sufficient cooling of any hot surfaces in the vicinity does not occur, re-ignition of residual fuel vapor/air mixture may result.

In the following discussion, the five fluids (water, lactic acid, C<sub>3</sub>F<sub>5</sub>H<sub>3</sub>O, HFE-7100, and R338mccq) identified in Pitts et al.<sup>152</sup> as having the highest mass-based  $\Delta H^{total}$  (total heat absorbed including enthalpy of evaporation in going from room temperature to 1400 K) were considered to evaluate their droplet vaporization and surface cooling characteristics. Low boiling-point fluids were not considered because under typical operating conditions, these fluids flash-vaporize soon after they leave the discharge opening and arrive at the surface in the form of a vapor.

#### 4.6.2 Evaporation of Liquid Droplets

The estimation of liquid droplet evaporation is based on the classical d<sup>2</sup>-law, which gives the droplet diameter as a function of time as

$$D^2 = D_o^2 - Kt, \quad (4-21)$$

where  $D$  is the instantaneous droplet diameter,  $D_o$  is the initial droplet diameter,  $t$  is the time, and  $K$  is the evaporation constant. The evaporation constant was calculated by

$$K = \frac{8k_g \ln(1+B)}{\rho_F C_{pg}}, \quad (4-22)$$

where  $B$  is the transfer number,  $k_g$  is the gas-phase thermal conductivity,  $C_{pg}$  is the gas-phase heat capacity, and  $\rho_F$  is the liquid density. The  $B$  number based on mass transfer considerations is given by

$$B_M = \frac{Y_{FS} - Y_{F\infty}}{1 - Y_{FS}}, \quad (4-23)$$

where  $Y_{FS}$  and  $Y_{F\infty}$  are the vapor-phase mass fraction at the droplet surface and ambiance, respectively. The mass fraction,  $Y_{FS}$ , was evaluated by

$$Y_{FS} = \frac{P_{FS} M_F}{P_{FS} M_F + (P - P_{FS}) M_A}, \quad (4-24)$$

where  $P_{FS}$  is the liquid vapor pressure at the droplet surface,  $P$  is the ambient pressure, which is equal to the sum of the liquid vapor pressure and partial pressure of air at the droplet surface, and  $M_F$  and  $M_A$  are the molecular weights of liquid and air, respectively.

The  $B$  number based on heat transfer considerations was given by

$$B_T = \frac{C_{pg} (T_\infty - T_s)}{\Delta H_{vap}}, \quad (4-25)$$

where  $T_\infty$ ,  $T_s$ , and  $\Delta H_{vap}$  are the ambient temperature, droplet surface (wet-bulb) temperature, and latent heat of vaporization of the liquid, respectively. Under steady-state conditions,  $B_M = B_T$ , and either Equation (4-23) or Equation (4-25) may be used to calculate the evaporation constant in Equation (4-22).

If  $T_s$  is known, the calculation of the evaporation constant is straightforward; however, under normal circumstances it is necessary to determine  $T_s$  in order to evaluate  $B$  and  $K$ . The calculation procedure can be found in References 113, 172 and 173. The basic idea was to find  $T_s$  such that  $B_M = B_T$ . Spalding<sup>172</sup> and Kanury<sup>173</sup> used a graphical approach. By plotting  $B_M$  and  $B_T$  against  $T_s$ , the intersection of these two curves defined the wet-bulb temperature and the corresponding  $B$ . An iterative method was used by Chin and Lefebvre.<sup>113</sup> The calculations presented here used the latter approach.

To calculate  $K$ , the reference temperature ( $T_r$ ) and mass fractions ( $Y_{Fr}$  and  $Y_{Air}$  for the fluid and air, respectively), based on the one-third rule,<sup>113</sup> were used to estimate the gas phase thermophysical properties.

$$T_r = T_s + \frac{T_\infty - T_s}{3} \quad (4-26)$$

$$Y_{Fr} = Y_{FS} + \frac{Y_{F\infty} - Y_{FS}}{3} \quad (4-27)$$

$$Y_{Air} = 1 - Y_{Fr}. \quad (4-28)$$

The equation for calculating the gas-phase heat capacity,  $C_{pg}$ , was given by

$$C_{pg}(T_r) = Y_{Air} C_{pA}(T_r) + Y_{Fr} C_{pF}(T_r) \quad (4-29)$$

where  $C_{pA}$  is the heat capacity of air and  $C_{pF}$  is the gas-phase heat capacity of the fluid, all evaluated at  $T_r$ . The thermal conductivity of the gas phase was estimated using the following equation,

$$k_g(T_r) = Y_{Air} k_A(T_r) + Y_{Fr} k_F(T_r), \quad (4-30)$$

where  $k_A$  is the thermal conductivity of air and  $k_F$  is the gas-phase thermal conductivity of the liquid, all evaluated at  $T_r$ .

The conditions used in the calculations were: (1)  $T_\infty = 1400$  K (to simulate a flaming ambiance), (2)  $Y_{F_\infty} = 0$ , and (3)  $P = 0.101$  MPa. The thermophysical properties of air, water, and lactic acid were obtained from the database of the Design Institute for Physical Properties I.<sup>174</sup> The properties of  $C_3F_5H_3O$ , HFE-7100, and R338mccq were estimated by methods described in Reid et al.,<sup>175</sup> the modified Rackett technique was used for  $\rho_F$ , the method of Joback for  $C_{pF}$ , the method of Lee and Kesler for  $P_{FS}$ , the method of Pitzer's acentric factor correlation for  $\Delta H_{vap}$ , and the method of Ely and Hanley for  $k_F$ .

Figure 4-76 shows droplet evaporation times,  $t_b$ , as a function of initial droplet diameter. The droplet evaporation time was easily obtained by assigning  $D = 0$  in Equation (4-21) once  $K$  is known,

$$t_b = \frac{D_o^2}{K}. \quad (4-31)$$

For a given initial droplet diameter under the same ambient conditions, the evaporation time for a water droplet was the longest and for a R338mccq droplet the shortest. For the five fluids examined, the ranking based on droplet evaporation times was

$$t_{b,R338mccq} < t_{b,HFE7100} < t_{b,C_3F_5H_3O} < t_{b,lacticacid} < t_{b,water}. \quad (4-32)$$

How fast a droplet evaporates determines whether it will still remain as a droplet upon reaching the surface. However, if *flame cooling* is the dominant fire suppression mechanism, then it would be better to have the droplet completely vaporized in the flame.

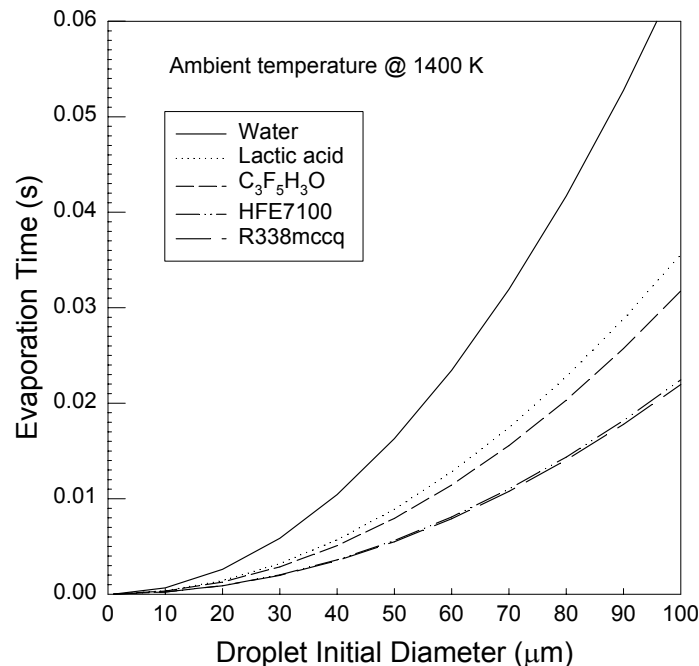


**Figure 4-76. Droplet Evaporation Time as a Function of Initial Droplet Diameter for Five Fluids.**

### 4.6.3 Spray Cooling

In order to assess surface cooling, we consider the literature on spray cooling and quenching of hot metallic surfaces. The application of spray-cooling correlations to fuel surface cooling is only appropriate when the fuel surface is solid (e.g., a PMMA or wood slab). Even in this case, care should be exercised because subtle differences in cooling mechanisms exist. A burning PMMA surface in reality is in a molten state, and wood forms a porous char layer. The interactions of droplets with molten and porous surfaces remain very difficult problems to tackle. Differences also arise between fuel surface cooling and quenching of metallic surfaces. In the latter, radiative heat transfer to the droplets only occurs from the heated surface; however, in the former, it also occurs from the flame. Strictly speaking, the following calculations are more applicable to the cooling of a hot surface to prevent re-ignition than to the cooling of a burning fuel surface.

Depending on the surface temperature, when a hot surface is being quenched by a liquid spray, it will experience several distinct heat transfer regimes which can be followed along the “boiling curve.” Such a curve is a plot of surface heat flux vs. surface temperature and represents the strong relationship between heat flux and surface temperature during quenching. The characteristics of the boiling curve are classified as (with increasing surface temperature): (1) convective, (2) nucleate boiling, (3) critical heat flux, (4) transition boiling, (5) Leidenfrost point, and (6) film boiling. Detailed descriptions are available.<sup>164,165</sup> Figure 4-77 is an illustration of a boiling curve associated with spray cooling of a hot surface. The general features of the curve are similar to those for a pool boiling curve.

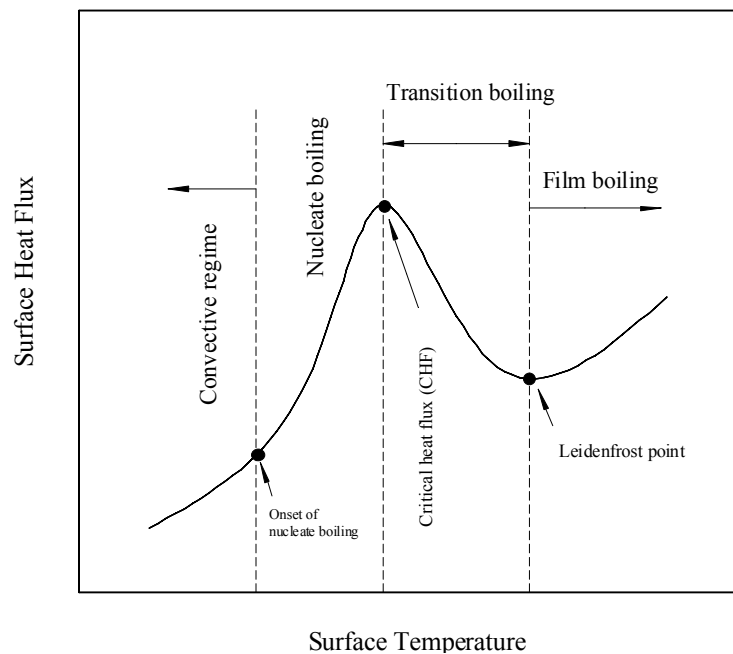


**Figure 4-77. Typical Boiling Curve Associated with Quenching of a Hot Surface by Liquid Droplets.**

Since the boiling curve of one fluid may differ from that of other fluids, there are several important assumptions that have to be made in the following analysis.

- When a comparison of surface heat fluxes is made, it is assumed that for the prevailing surface temperature, these fluids are in the *same* regime on the boiling curve. This assumption may not be valid because, for example, the surface temperatures at which the critical heat flux and Leidenfrost phenomena occur may be significantly different among the fluids studied; therefore, while one fluid may be at the critical heat flux, the other fluid may be in the nucleate boiling regime at the prevailing surface temperature. Unfortunately, in most cases, it is not possible *a priori* to determine the demarcation point (surface temperature) from one cooling regime to another without resorting to experimental observations.
- The second assumption is that the dimensionless heat transfer correlations obtained in the literature using water (in most cases) are applicable to the other fluids considered here.
- A third assumption is that the effect of surface roughness on surface heat flux is not considered. Furthermore, the spray parameters used in the following calculations were chosen to be within the range of applicability of the empirical correlations. These operating parameters, though encountered in spray quenching applications, may not be identical to those appropriate for fire fighting applications. In addition, since different droplet generation techniques (sprays vs. mono-dispersed droplet streams) have been used to obtain the heat transfer correlations in various regimes, it is imperative that a comparison among the calculated surface heat fluxes should be made with these fluids in the *same* regime.

#### 4.6.4 Convective Regime

Mudawar and co-workers<sup>164,165</sup> had performed extensive studies on cooling of metal surface in this regime using water sprays. Their heat transfer data were correlated using the Nusselt number (Nu), the Reynolds number (Re), and the Prandtl number (Pr) by the following expression,

$$\frac{hD_{32}}{k_f} = Nu = 2.512 \left[ \frac{Q'' D_{32}}{\nu_f} \right]^{0.76} \left[ \frac{C_{pf} \mu_f}{k_f} \right]^{0.56} = 2.512 Re^{0.76} Pr^{0.56}, \quad (4-33)$$

where  $h$  is the heat transfer coefficient,  $k_f$  is the thermal conductivity of the liquid,  $\nu_f$  is the liquid kinematic viscosity,  $C_{pf}$  is the liquid heat capacity, and  $\mu_f$  is the liquid viscosity. The Reynolds number is based on the volumetric spray flux,  $Q''$ , and the Sauter mean diameter,  $D_{32}$ , of the spray. All the liquid properties are evaluated at  $(T_{surf} + T_f)/2$  where  $T_f$  is the droplet temperature before impact.

Figure 4-78 shows the calculated heat flux as a function of  $T_{surf} - T_f$ . The calculations were performed using  $Q'' = 0.005 \text{ m}^3/\text{m}^2\text{-s}$ ,  $T_f = 295 \text{ K}$ , and  $D_{32} = 0.5 \text{ mm}$ . The thermophysical properties of water and lactic acid were obtained from the DIPPR.<sup>174</sup> The properties of  $\text{C}_3\text{F}_5\text{H}_3\text{O}$ , HFE-7100, and R338mccq were estimated by methods described in Reid et al.,<sup>175</sup> the boiling point method of Sato was used for  $k_f$ , the corresponding states method of Rowlinson for  $C_{pf}$ , and the method of Brule and Starling for  $\mu_f$ . In this regime, water removed heat from the surface more efficiently than the other four fluids. It may not be feasible in practice to maintain the same  $D_{32}$  with a fixed  $Q''$  (the conditions used in the calculations) for the five fluids because the atomization characteristics at the spray nozzle would be vastly different among the fluids owing to their thermophysical properties, thus resulting in different  $D_{32}$ .<sup>66</sup>

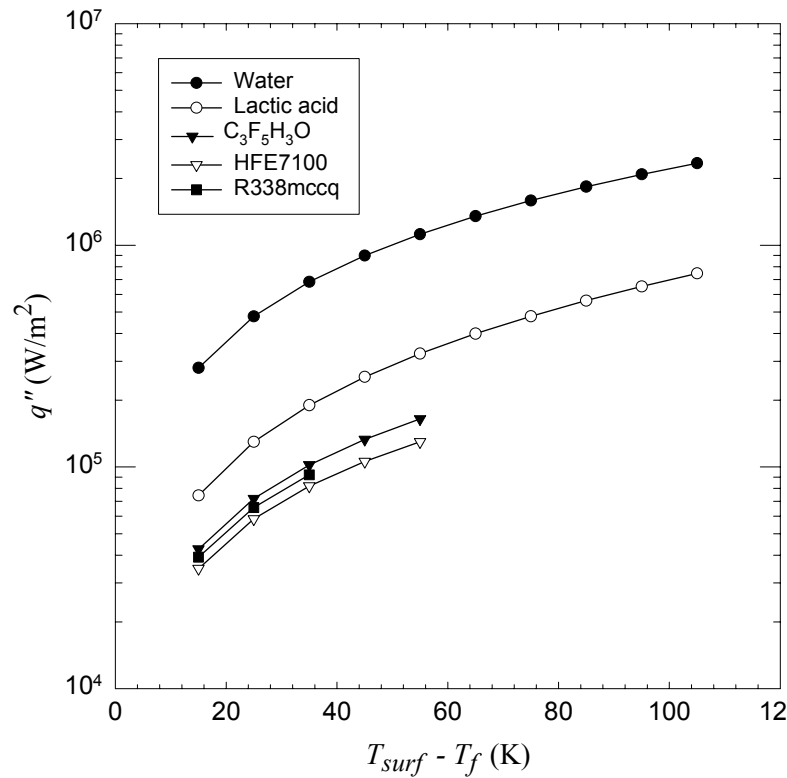


Figure 4-78. Calculated Boiling Curves in the Convective Regime for Five Liquids.

#### 4.6.5 Nucleate Boiling Regime

Compared to other regimes on the boiling curve, the nucleate boiling regime in spray cooling has probably been the least studied. In this regime, the heat flux removal from the surface was found to scale only with  $T_{surf} - T_f$  in the studies by Mudawar and co-workers<sup>164,165</sup> where a water spray was used. The heat flux,  $q''$ , was correlated in the form of

$$q'' = 1.87 \times 10^{-5} (T_{surf} - T_f)^{5.55}. \quad (4-34)$$

In the work of Qiao and Chandra<sup>176</sup> on nucleate boiling enhancement using a surfactant/water solution, the heat flux measurements could also be correlated well by scaling with  $T_{surf} - T_f$  in a form similar to Equation (4-34),

$$q'' = 0.56 \times 10^{-5} (T_{surf} - T_f)^6. \quad (4-35)$$

Assuming that the proportionality constant and the power in the scaling law do not change significantly among the five chemical compounds and that the heat flux can be scaled with  $(T_{surf} - T_f)$ , then the heat flux removal from the surface in the nucleate boiling regime using these five liquids should be similar for a given  $T_{surf}$ .

#### 4.6.6 Critical Heat Flux

The dimensionless correlation developed by Mudawar and Valentine<sup>164</sup> for water spray cooling over a wide range of flows was used to estimate the critical heat flux (*CHF*),

$$\frac{CHF}{\rho_g \Delta H_{vap} Q''} = 122.4 \left\{ 1 + 0.0118 \left[ \frac{\rho_g}{\rho_F} \right]^{1/4} \left[ \frac{\rho_F C_{pf} (T_{sat} - T_f)}{\rho_g \Delta H_{vap}} \right] \right\} \left( \frac{\sigma_f}{\rho_F Q''^2 D_{32}} \right)^{0.198}, \quad (4-36)$$

where  $\rho_g$  is the vapor density of the fluid,  $T_{sat}$  is the saturation temperature of the fluid, and  $\sigma_f$  is the surface tension of the fluid. All the fluid properties were evaluated at the fluid saturation temperature.

Using  $Q'' = 0.005 \text{ m}^3/\text{m}^2\text{-s}$ ,  $T_f = 295 \text{ K}$ , and  $D_{32} = 0.5 \text{ mm}$ , the resulting *CHF*s for water, lactic acid,  $\text{C}_3\text{F}_5\text{H}_3\text{O}$ , HFE-7100, and R338mccq are  $0.63 \times 10^7 \text{ W/m}^2$ ,  $0.86 \times 10^7 \text{ W/m}^2$ ,  $0.33 \times 10^7 \text{ W/m}^2$ ,  $0.23 \times 10^7 \text{ W/m}^2$ , and  $0.21 \times 10^7 \text{ W/m}^2$ , respectively. In the calculations, surface tensions of water and lactic acid were obtained from the DIPPR,<sup>174</sup> while those of  $\text{C}_3\text{F}_5\text{H}_3\text{O}$ , HFE-7100, and R338mccq were estimated using the method of Brock and Bird.<sup>175</sup> Although lactic acid and water have the highest and second highest *CHF*s, respectively, under the conditions used in the calculations, it should be noted that it is inappropriate to compare the *CHF*s unless they occur at the same surface temperature for the five fluids, a situation highly unlikely given the differences in the thermophysical properties of these fluids.

#### 4.6.7 Transition and Film Boiling Regimes

Based on dimensional analysis, Deb and Yao<sup>177</sup> statistically derived an equation for heat transfer effectiveness ( $\varepsilon$ ) in terms of droplet Weber number ( $We$ ), dimensionless wall superheat ( $B_w$ ) and vapor parameters ( $K_d$ ), and surface factor ( $SF$ ) for surface material effect,

$$\varepsilon = 0.027 \exp \left[ \frac{0.08 \sqrt{\ln \left( \frac{We}{35} + 1 \right)}}{\left( B_w + \frac{SF}{60.5} \right)^{1.5}} \right] + 0.21 K_d B_w \exp \left[ -\frac{90}{We + 1} \right], \quad (4-37)$$

with

$$We = \frac{\rho_F V_i D_o}{\sigma_f} \quad (4-38)$$

$$B_w = \frac{C_{pF} (T_{surf} - T_{sat})}{\Delta H_{vap}} \quad (4-39)$$

$$K_d = \frac{k_F}{C_{pF} \mu_v} \quad (4-40)$$

and

$$SF = \sqrt{\frac{k_s \rho_s C_{ps}}{(k \rho C_p)_{steel}}} - 1, \quad (4-41)$$

where  $V_i$  is the droplet impact velocity,  $K_d$  is the dimensionless vapor parameter,  $\mu_v$  is vapor viscosity, and  $k_s$ ,  $\rho_s$ , and  $C_{ps}$  are the thermal conductivity, density, and heat capacity of the surface material, respectively. All liquid and vapor properties are evaluated at  $T_{sat}$ . The heat transfer effectiveness is defined as the ratio of actual heat transfer from the hot surface to the total heat transfer required for complete evaporation of the droplets. Therefore, the heat flux from the surface is

$$q'' = \varepsilon G [\Delta H_{vap} + C_{pf}(T_{sat} - T_f)], \quad (4-42)$$

where  $G$  is the liquid mass flux.  $\varepsilon$  was obtained from Equation (4-37) by fitting data mainly from experiments using a single stream of droplets. The experimental conditions covered the film boiling regime and to some extent the adjacent transition boiling regime and Leidenfrost point.

Figure 4-79 shows the calculated heat fluxes for the five fluids as a function of the surface temperature. The calculations were performed using  $T_f = 295$  K,  $V_i = 2.5$  m/s,  $D_o = 0.3$  mm, and  $G = 0.5$  kg/m<sup>2</sup>-s. For illustration, a stainless steel, SS 304, was used as the target surface. Under the conditions used in the calculations, the resulting droplet  $We$  were 31, 97, 181, 297, and 339 for water, lactic acid, C<sub>3</sub>F<sub>5</sub>H<sub>3</sub>O, HFE-7100, and R338mccq, respectively. The range of surface temperatures used in the calculations was chosen so that the calculated  $\varepsilon$  did not exceed 1. The three boiling regimes (transition boiling, Leidenfrost condition, and film boiling) are apparent in Figure 4-79. If it is assumed that at  $T_{surf} \geq 800$  K, all five fluids exhibit film boiling, and lactic acid has the highest surface heat flux.

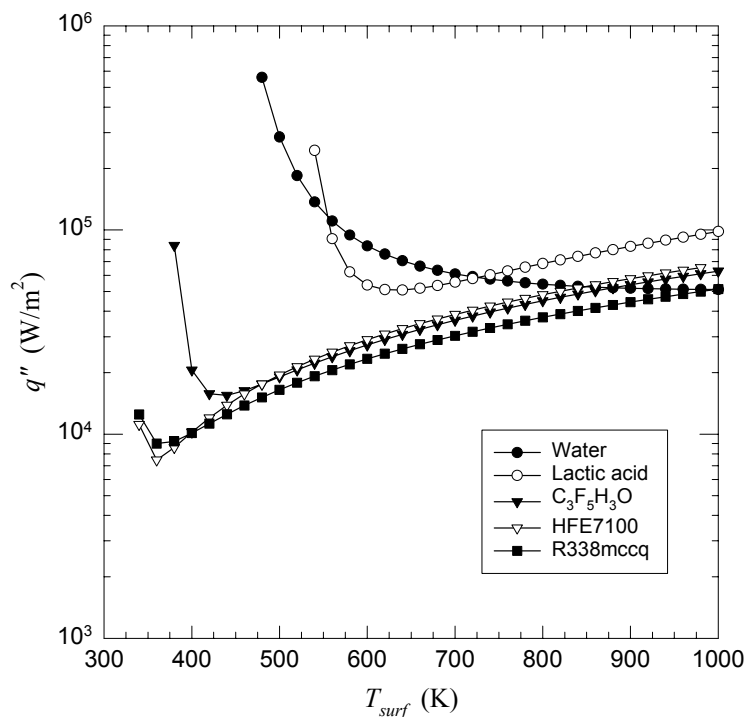


**Figure 4-79. Calculated Boiling Curves for Five Liquids for the Transition and Film Boiling Regimes.**

Figure 4–79 also demonstrates again the difficulty in comparing the heat fluxes at a given surface temperature. For example, at  $T_{surf} = 550$  K,  $C_3F_5H_3O$ , HFE-7100, and R338mccq are in the film boiling regime, whereas, water and lactic acid are in the transition boiling regime. As stated above, unless the surface temperature at which the onset of a particular boiling regime is known a priori, it is not possible to know which heat flux correlation pertaining to which boiling regime should be applied in the estimation.

#### 4.6.8 Summary

A suppression mechanism possibility for aerosol agents (and not generally for gaseous agents) is the potential to cool any burning surfaces or hot surrounding surfaces. Surface cooling by liquid droplets is a very complicated heat transfer process because it depends on so many parameters: the thermophysical properties (surface tension, density, viscosity, heat of vaporization, etc.) of the liquid, droplet size, droplet impact velocity, spray mass flux, and surface properties. Even for non-burning, smooth surfaces, calculations of surface heat fluxes from first principles are not possible without resorting to experimental observations. Empirical heat transfer correlations under conditions encountered in fires are lacking, and the quantification of surface cooling as a means to extinguish the burning fuel remains elusive, especially when the fuel is a liquid. Nonetheless, the greatest benefit will arise from those agents that are efficient thermal agents, particularly aerosols that have large heats of vaporization per gram of agent.

### 4.7 AEROSOLS AND BURNING SURFACES

There are four key physical phenomena involved in the interaction of aerosols with burning surfaces: (1) buoyancy effect on the trajectory of the aerosol particles, (2) evaporation/decomposition effect on the trajectory of the particles, (3) cessation of reaction and reduction in flame spread caused by the aerosol on flaming surface combustion, and (4) reduction in surface temperature caused by the particle impingement, spreading, and evaporation/decomposition on surface. The NGP study on the interaction of aerosol with burning surfaces addressed the interactions of liquid droplets with surfaces. The NGP study experimentally determined the key water droplet properties, such as surface loading and droplet diameter, that affect flame spread rate, and through numerical and experimental comparison sought to determine the effect of droplet size and velocity on droplet buoyancy and evaporation as the droplets approach a hot surface or fire. The work is summarized here and can also be found in References 178, 179, 180 and 181.

Monte Carlo methods are widely used to solve for the heat transfer in a wide variety of problems<sup>182,183</sup> due to their simplicity and accuracy. There are many methods to improve the accuracy of Monte Carlo simulations including improved sampling,<sup>184</sup> weighing and biasing,<sup>185</sup> and the discrete probability function method.<sup>186</sup> Therefore, the simulation of the problem utilizing Monte Carlo methods is straightforward, once the important rates that govern the physical processes are understood.

The different components that describe both the droplet trajectory and the temperature distribution over the surface as a function of time are studied in detail in this project by separating the various physical processes and integrating them to obtain an experimentally validated model that can be used in Monte Carlo simulations. Experiments were conducted with non-evaporating and evaporating particles of controlled density injected at controlled velocities towards a variably heated surface. Particle velocity as a function of the impressed buoyancy forces were measured, thereby determining the likelihood of a particle reaching a burning surface. Evaporation effects were also examined. Both monodisperse and polydisperse droplets were injected over PMMA flames or over heated polyurethane foam, using droplet

loading, delay time after ignition, and location of the spray from the leading edge as parameters. Such conditions provided data for examining any correlation between spray characteristics and flame spread. Surface temperature changes as a function of aerosol impingement were determined using a Two Color Planar Pyrometer. Finally, Monte Carlo simulations of the mist/surface interactions were investigated to develop fuller understanding of the dominant processes and identify the key aerosol properties that impact efficient suppression of the fire.

#### 4.7.1 Flame Spread Studies

##### Experimental

Flame spread experiments were carried out in a wind tunnel, whose photograph is shown in Figure 4-80. The wind tunnel measured 45 cm high, 76 cm wide, and 175 cm long. The roof had three rectangular slots 7.6 cm wide x 28 cm long for observation of the flame by means of a video camera. The slots were covered with 1.25 cm thick glass windows during the experiments. The velocity inside the tunnel was controlled by an exhaust fan.

Honeycomb flow straighteners of polycarbonate, placed at the mouth of the duct, were used to remove large scale turbulent eddies and create uniform flow conditions in the test section. Each flow straightener had a diameter of 0.64 cm and is 25 cm in length. This L/D ratio, yielded a maximum Reynolds number of 64 and was sufficient to establish a fully developed laminar flow in the straighteners.<sup>187</sup> A 0.16 cm thick ceramic paper was applied to the interior of the tunnel to reduce heat transfer to the walls.



**Figure 4-80. Wind Tunnel Used for Fire Spread Studies.**

PMMA sheet was used as the fuel. PMMA supports surface combustion, and the flame spread rate over it is steady and well characterized. The properties of PMMA, such as density, specific heat at constant pressure, and heat of combustion, are consistent and well known. PMMA test specimens were 30 cm x 20 cm sheets of thickness 0.32 cm or 0.64 cm. The PMMA sheets were ignited with a small methanol trough before placing them into the wind tunnel. The experiments were carried out at four opposing wind speeds of 69 cm/s, 84 cm/s, 121 cm/s, and 153 cm/s. Three air flows, ranging from 9.5 cm<sup>3</sup>/min to 15.5 cm<sup>3</sup>/min, and three inlet pressures (880 kPa, 1375 kPa, and 2115 kPa) were used to vary the mass loading and the droplet size of the water spray used for suppression.

Initially, the fire suppression experiments were carried out with one surface in contact with an insulating ceramic material. This is the conventional method, called here “with backing” mode or one-sided combustion mode. When fire suppression experiments were begun, it was realized that the ceramic backing was quick to absorb water and was instrumental in extinguishing the flame almost as soon as the water spray was turned on. Therefore, the present studies were carried out with the PMMA sample supported along its sides with air flowing above and below the specimen. A photograph of the flame suppression experiment with the water mist applied is shown in Figure 4-81.



**Figure 4-81. Flame Spread Experiment with Water Mist.**

Calculations showed that the Blasius boundary layer thickness over the surface of the aluminum platform has a maximum value of about 1.4 cm. A 6 cm gap between the bottom surface of the PMMA specimens and the support platform ensured that free stream conditions existed on both the top and bottom and that the flame spread was unaffected by the boundary layer on the support platform.

A hollow cone spray was generated using a pressure atomizer which delivered good atomization quality over a large range of flows at the same inlet pressure. The nozzle was mounted on a bracket at a distance of about 60 cm upstream of the sample and at a height of about 17.5 cm above the surface of the PMMA. The droplets were carried downstream and onto the flame by the airflow present in the wind tunnel.

To obtain local surface loading of the water spray, pieces of absorbent tissue paper were taped onto the surface of a PMMA sample in a 4 x 4 grid. The spray was established at a given test condition and the difference in weight of the tissues was determined after a suitable interval of time. A Phase Doppler Particle Analyzer was used to obtain the droplet size and droplet mean velocity data. The PDPA was operated in forward scatter mode ( $\theta = 30^\circ$ ). The probe volume was 14 cm downstream of the nozzle exit.

A black-and-white 8-bit CCD camera was used to track the motion of the flame. The camera was mounted on a bracket above the observation window and looked down perpendicularly onto the burning samples. It was observed that the edges of the PMMA samples burned faster than the center. In order to avoid erroneous estimates of flame spread rate on account of edge effects, the camera focused on the central 23 cm of the flame.

During a typical experiment, the flame spread images were obtained 8 s apart. The location of the flame was assigned to be the pixel of maximum intensity. The difference in location of the flame in a particular row of pixels between two frames (that were separated by a known time interval) yielded the flame spread rate for that row. To reduce the discretization errors, the flame spread was calculated from images separated by 160 s. The mean velocity of the flame calculated for all the rows was designated to be the velocity of the flame at that time.

The reduction in flame temperature due to droplet loading was obtained using a two-color planar pyrometer (TCPP). A schematic diagram of the two color planar pyrometer is shown in Figure 4-82. The TCPP had an imaging lens that was used to collect broad band radiation from the fire. The radiation was split into two beams that were spectrally differentiated using band pass filters. An array imaging camera was used to obtain the spectral image of the flame at two wavelengths. The band pass filters were centered at approximately 900 nm and 1000 nm, and each had a band width of 80 nm. The TCPP was calibrated using a standard laboratory black body source.

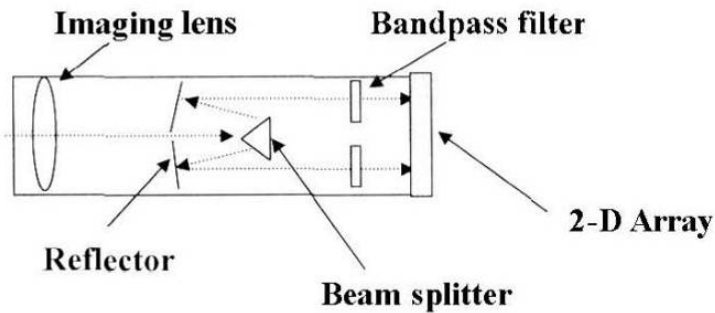


**Figure 4-82. Schematic of the Two-color Planar Pyrometer.**

## Results and Discussion

The first issue addressed was the measurement uncertainty. If  $x$  is the position of the flame and  $t$  is the time interval between measurements, the velocity is given by  $v = x/t$ . The uncertainties in the measurement of flame position ( $w_x$ ) and time ( $w_t$ ) were used to estimate the uncertainty in the flame spread rate ( $w_v$ )<sup>188</sup>

$$w_v = \left[ \left( \frac{\partial v}{\partial T} w_T \right)^2 + \left( \frac{\partial v}{\partial x} w_x \right)^2 \right]^{\frac{1}{2}} \quad (4-43)$$

For the imaging system, the uncertainty in position was  $\pm 1$  pixel, and that in time (provided by the camera timer) was 1  $\mu$ s. Therefore, for a typical flame event lasting 160 s, with the flame moving about 12 pixels, the uncertainty in velocity was:

$$\frac{w_v}{V} = \frac{w_x}{X} = 8.3\% \quad (4-44)$$

Typical flame velocity data obtained using the imaging system is shown in Figure 4-83. The imaging system started recording at a rate of 1 image every 8 s immediately following flame ignition. During the first few minutes, the flame spread rate rapidly decreased until a steady state was reached. At steady

state, the flame spread velocity changed approximately 10 % due to the small-scale fluctuations in the flame front and the uncertainty of the measurement.

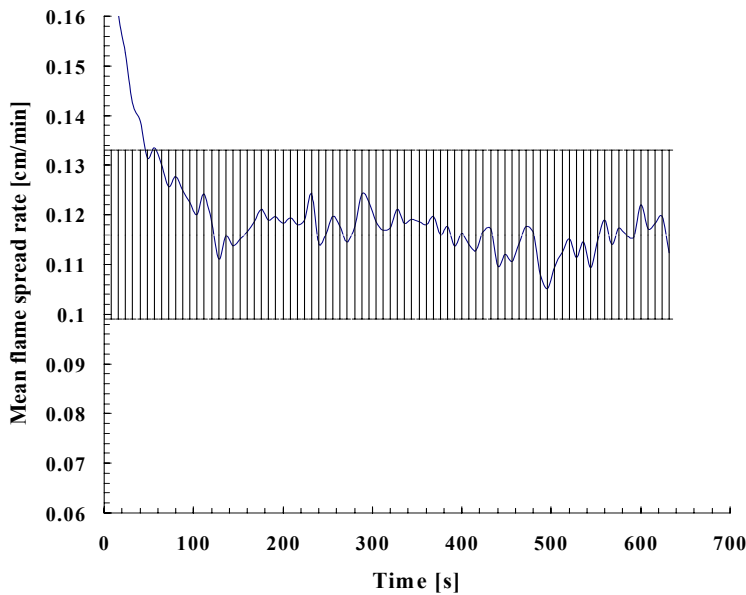


**Figure 4-83. Typical flame spread time trace obtained using Focal Plane Array Imaging.**

The flame spread rate as a function of opposing wind speed is shown in Figure 4-84. The vertical bars represent one standard deviation in the statistical variation of the data on each side of the mean (approximately 60 points per run). The experimental uncertainty is less than 10 % of the mean.

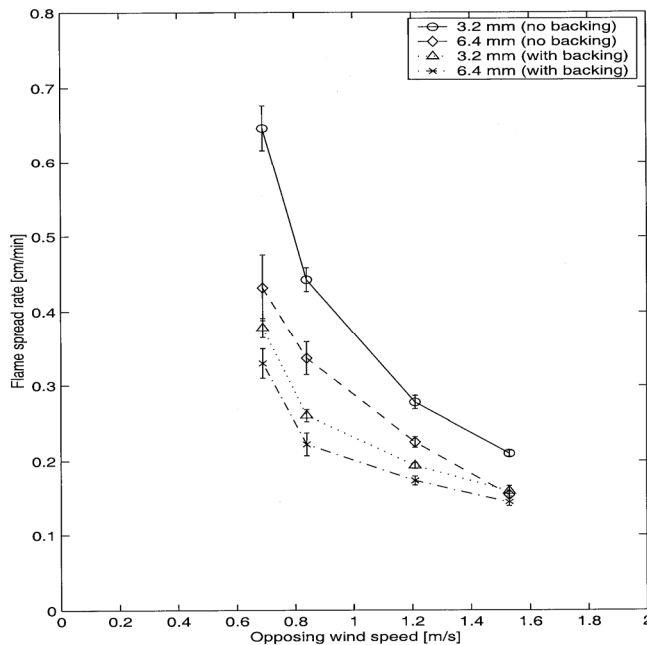


**Figure 4-84. Flame Spread Rates without Water Mist.**

As expected, the flame spread rate without backing was higher than that with backing for the same sample thickness, since burning was allowed to take place on both sides in the 'without backing' mode. Also in 'with backing' mode, some amount of heat loss occurred to the supporting aluminum plate since the ceramic paper (on which the PMMA is burned) was not a perfect insulator.

Another observation is that the flame spread rate decreased as the opposing wind speed increased. This can be explained by realizing that the forward heat transfer by gas-phase conduction from the flame to the unburned fuel decreased. Convective heat transfer from the unburned fuel surface also increased. This result is therefore expected. It was also found that the flame spread rate was higher for the thinner fuel than the thicker fuel. Since the heat transfer required to raise the temperature of the unburned fuel to its vaporization temperature is less for a thin fuel, this finding was also expected. These three results were consistent with the observations reported by previous investigators.

The flame spread rate results found in this work were approximately 20 % greater than the findings of Fernandez-Pello et al.<sup>48</sup> for the 0.64 cm thickness PMMA at 70 cm/s opposed flow velocity. At flow velocities of 85 cm/s and 120 cm/s, the results in the present work were lower than the findings of Reference 48 by about 9 % and 6 %, respectively. The results at the two higher flows were within the limits of experimental uncertainty.

Differences at the lower flow velocity were outside of the experimental uncertainty and can be explained as follows. At the lower opposed wind speeds, the flame stand-off height was more than at the higher opposed wind speeds. As the width of the sample in the present work (30 cm) was much greater than that in Reference 48, there was greater radiation heating of the unburned fuel surface by the flame. Hence the measured flame spread rate was greater.

At the higher opposing wind speeds the flame stand-off height was much less. At these high wind speeds, radiation from the flame was much lower, due to a small view factor. It is believed that it was the size of the experimental facility that was responsible for differences in the measured flame spread velocities between this study and the work of Reference 48. In particular, the wind tunnel duct used by Reference 48 was 5 cm x 4 cm in cross-section and 100 cm long, while the duct used in the present work had a cross-section of 45 cm x 76 cm and was 175 cm long. The greater re-radiation from the walls of the duct in the work of Reference 48 was believed to be the reason for the difference in the findings.

Another reason for the differences between the current measurements and those of Reference 48 could be different diagnostic and analytical techniques used to determine the flame spread rate. The progress of the flame in the experiments of Reference 48 was measured visually as it passed over previously ruled marks on the PMMA surface, whereas in the present work a CCD camera tracked the flame motion. The data analysis method used by Reference 48 is not known, but in the present work the estimate of flame spread rate is over a rather large length of time (160 s) rather than being "instantaneous."

The flame spread rate as a function of surface loading for the 0.32 cm thickness sample is shown in Figure 4-85. Similar results for the 0.64 cm thick PMMA are shown in Figure 4-86. The systematic decrease in flame spread rate with increasing surface loading on the PMMA can be clearly seen in all cases.

The effect of surface loading was greatest in the case of low opposing wind speeds, viz. 69 cm/s and 84 cm/s. The reason may be that the flame spread rate was low to begin with at the higher opposing wind speeds and with increasing loading there was a practical limit to the flame spread rate that can exist and still be measurable. It was conjectured that a threshold value of flame spread rate exists, between 0.15 cm/min and 0.20 cm/min, below which the flame would be rapidly extinguished.

The role of surface loading on the flame spread rate was explained in terms of heat transfer effects. On account of surface cooling, there was a reduction in pyrolysis of the fuel ahead of the flame front. As the rate of fuel vapor production decreased, less heat was liberated in the exothermic chemical reaction between the fuel vapor and oxygen. This resulted in a net decrease in heat transfer to the unburned PMMA ahead of the flame. As a result, the flame spread rate dropped.

In order to determine the effect of spray operating parameters on the droplet size, namely the atomizer inlet pressure and flow, measurements of droplet size and velocity were performed using a Phase Doppler Particle Analyzer. Droplet size and velocity data are presented in Figure 4-87.

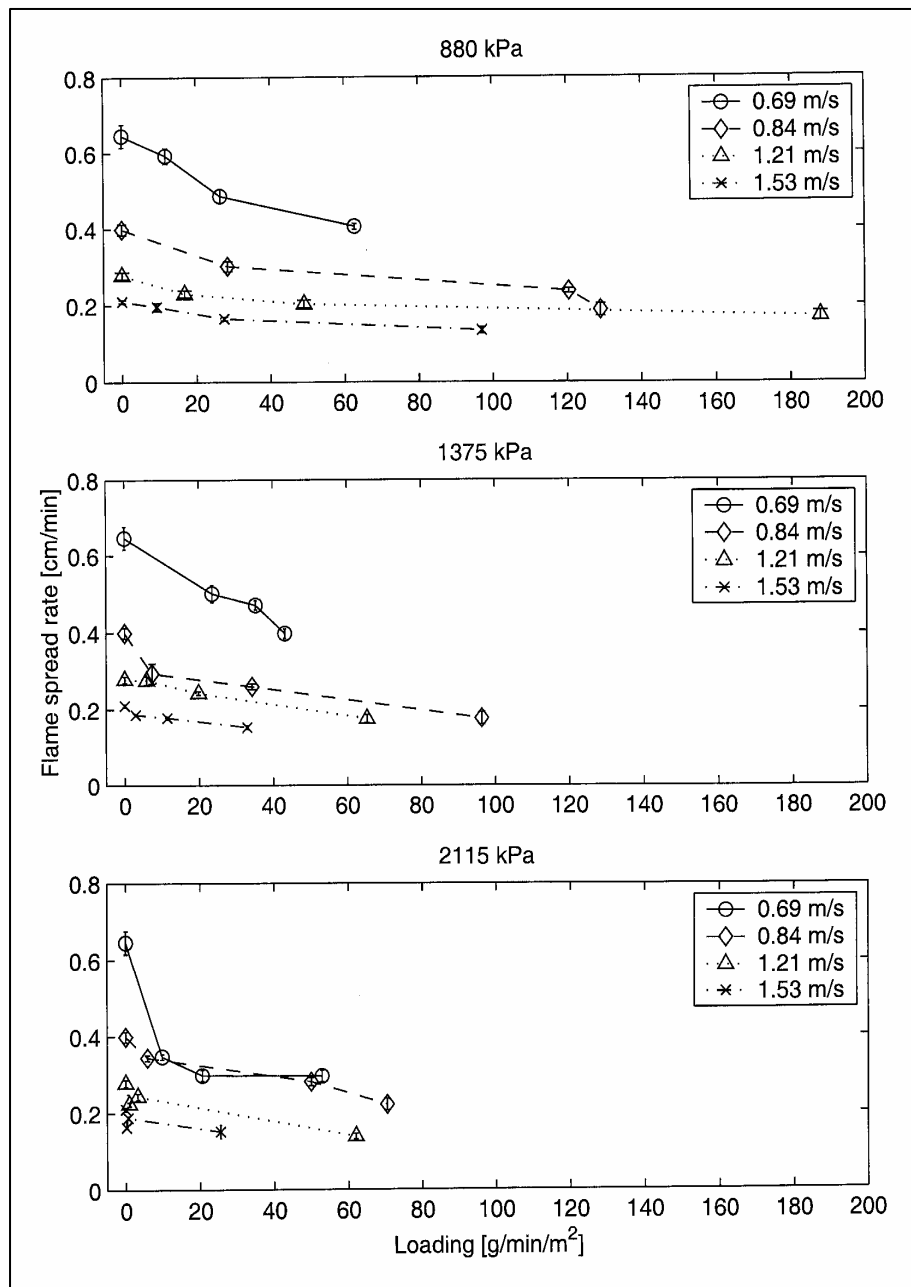


**Figure 4-85. Flame Spread Rate as a Function of Surface Loading for 3.2 mm Thick PMMA.**

From Figure 4-87, it is seen that both the droplet size and the mean velocity increased as the mass flow rate through the nozzle increased for a constant inlet pressure. At the same flow through the nozzle, the droplet size was smaller and the mean velocity greater at the higher pressure. The difference in the mean droplet diameter at 10 cc/min flow at the three different pressures was approximately  $2.5 \mu\text{m}$ ; at 15 cc/min flow rate it was approximately  $1 \mu\text{m}$ . By the  $d^2$ -law of droplet evaporation the ratio of evaporation times of droplets  $27.5 \mu\text{m}$  and  $25 \mu\text{m}$  in diameter is 1.2. Therefore, a notable impact due to evaporative cooling in the flame vicinity cannot be expected. Consequently, the droplet size variation should not be a significant factor in flame spread rate variations for the conditions considered here.

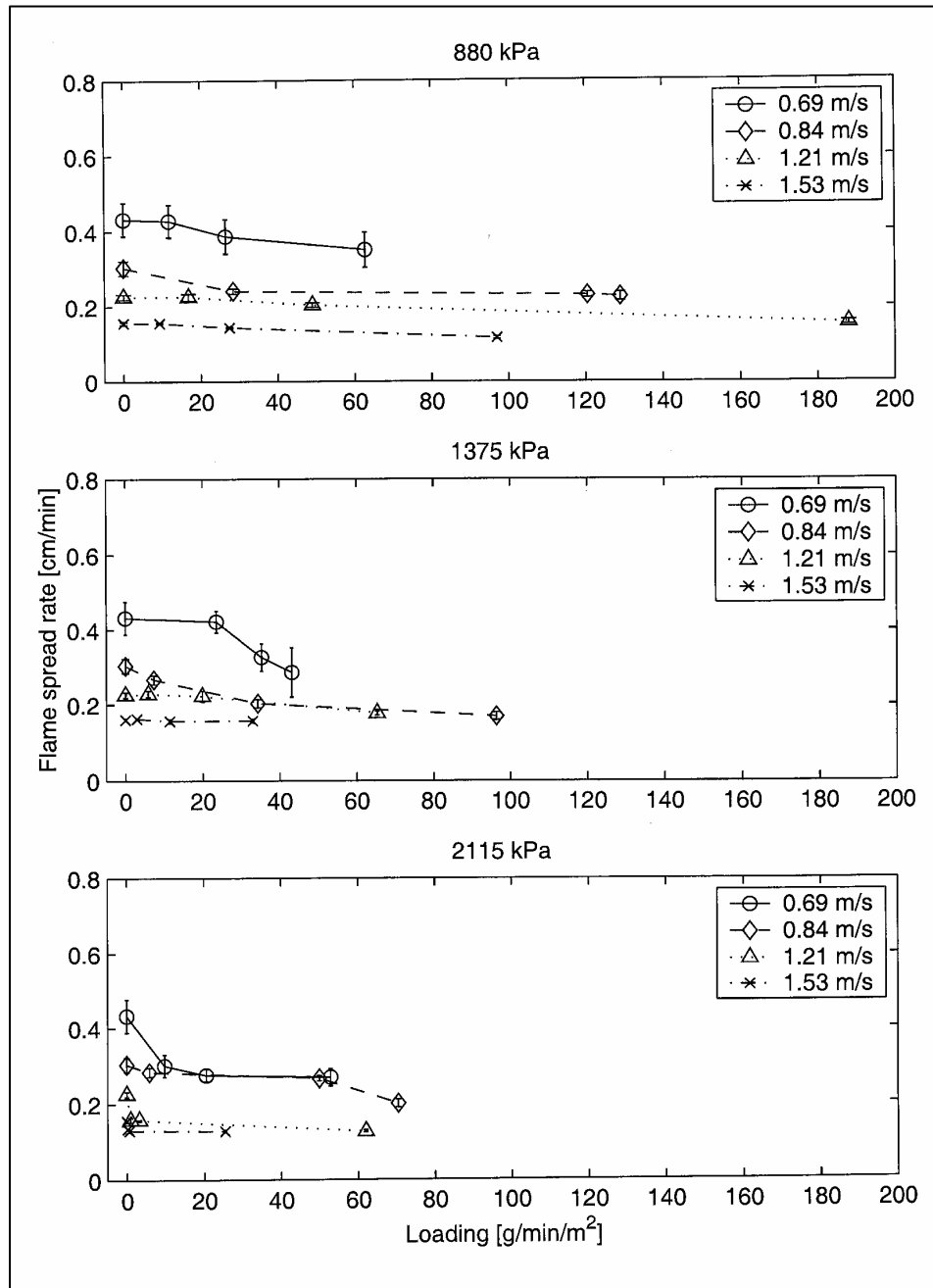


**Figure 4-86. Flame Spread Rate as a Function of Surface Loading for 0.64 cm Thick PMMA.**

The droplet mean velocity measurements provided an explanation as to why the flame spread rate increased with increasing nozzle discharge rate at low opposing wind speeds. The reason is that the droplet mean velocity increased as the flow rate increased. This reduced drift due to the cross-wind and led to deposition of the spray in the collection pan (placed below the spray nozzle) upstream of the target. The surface loading on the PMMA was thus reduced and, consequently, the flame spread rate increased. The data obtained from all tests were used to develop an empirical correlation. The normalized flame spread rates for all conditions are shown in Figure 4-88. Three different injection pressures (corresponding to different droplet diameters), two different PMMA thicknesses, and four different opposed flow velocities were used in developing the empirical correlation.

Data represented by open symbols shown in Figure 4-87 were obtained with 0.32 cm thick PMMA, and those represented by closed symbols were obtained with 0.64 cm thick PMMA sheets.

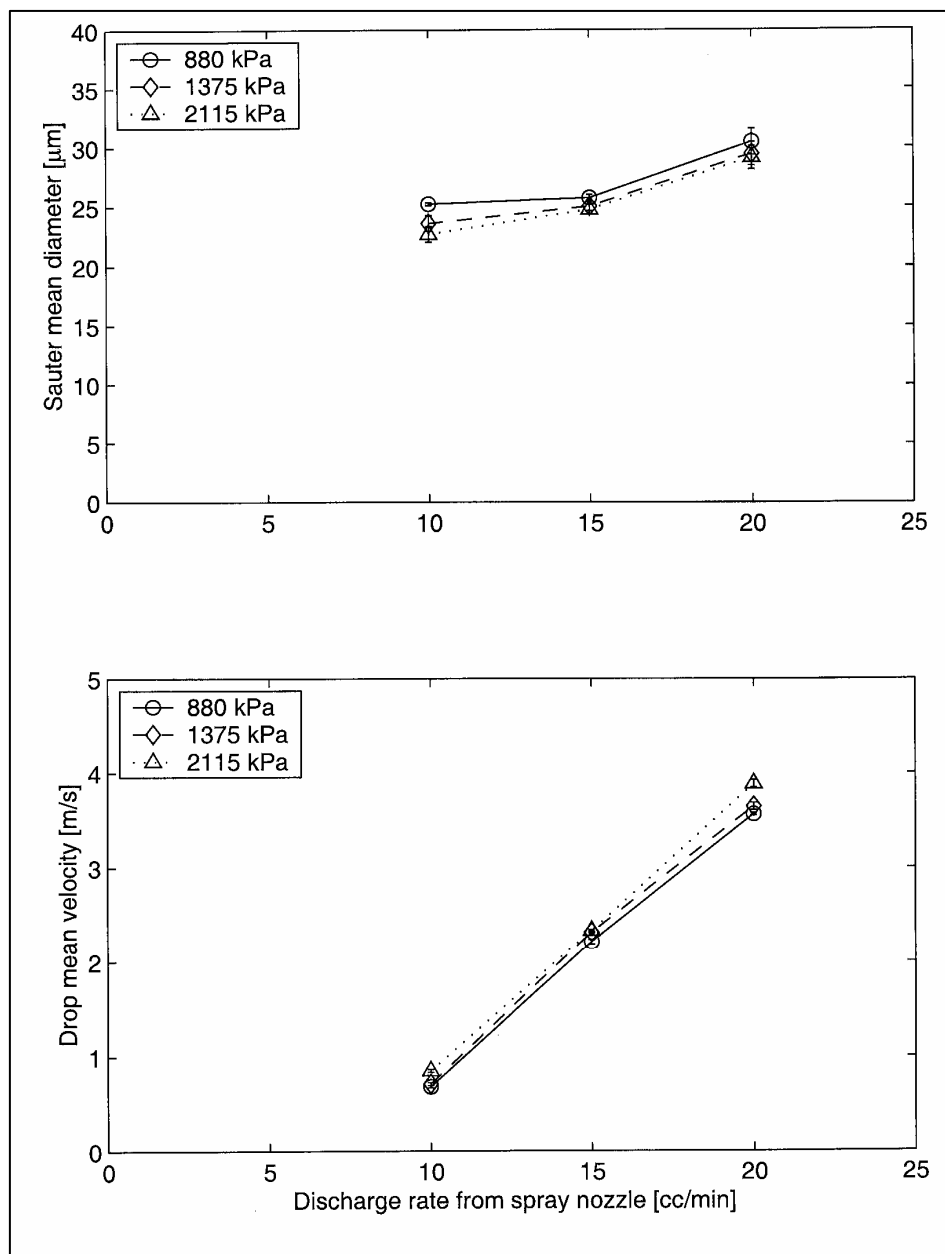


**Figure 4-87. Mean Droplet Size and Velocity as a Function of Spray Nozzle Discharge Rate.**

The regression analysis for the normalized flame spread in the thinner samples provided an approximately 85 % correlation with liquid mass loading. For the thicker samples, the correlation of the normalized flame spread with the liquid mass loading was approximately 75 %. The correlation obtained for all twenty-four conditions showed that the normalized flame spread rate was roughly a function of the local liquid mass loading alone. Correlations for flame spread rates with zero liquid mass loadings are readily available in the literature.

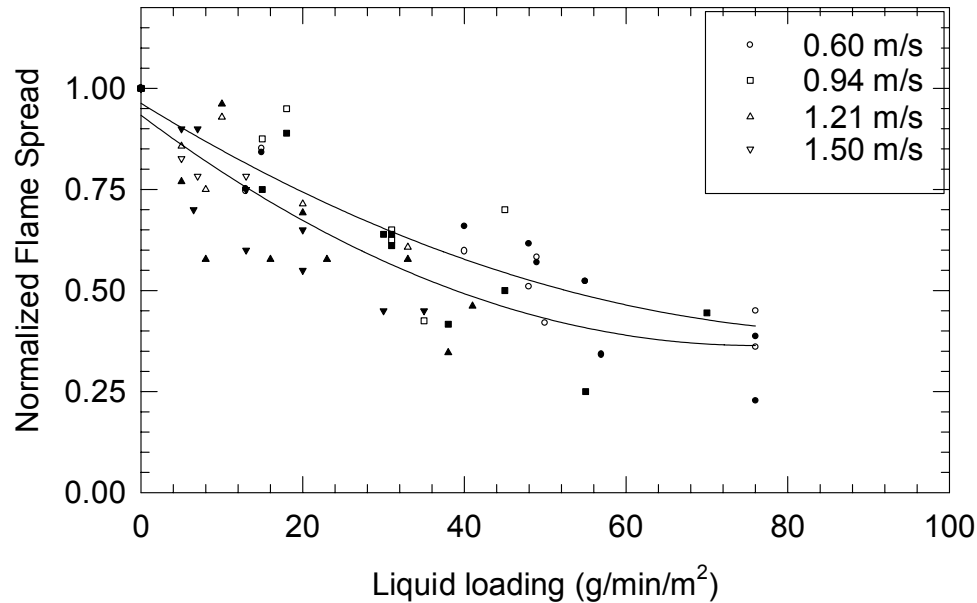


**Figure 4-88.**  
Variation in  
Normalized  
Flame Spread  
with Liquid  
Loading.

Therefore, the current results can be used to estimate (within a factor of two) what the local liquid mass flux should be to achieve extinction. This information is useful, since it provides a direct estimate of the optimal suppressant mass required to extinguish the fires. The effect of water loading on the decrease in the mean flame temperature is shown in Figure 4-89. The mean temperature of the flame without any water loading varied between 1200 K and 1400 K depending on the opposing wind velocity. The temperature dropped rapidly with increasing water loading, and the flame was extinguished at approximately 1000 K.

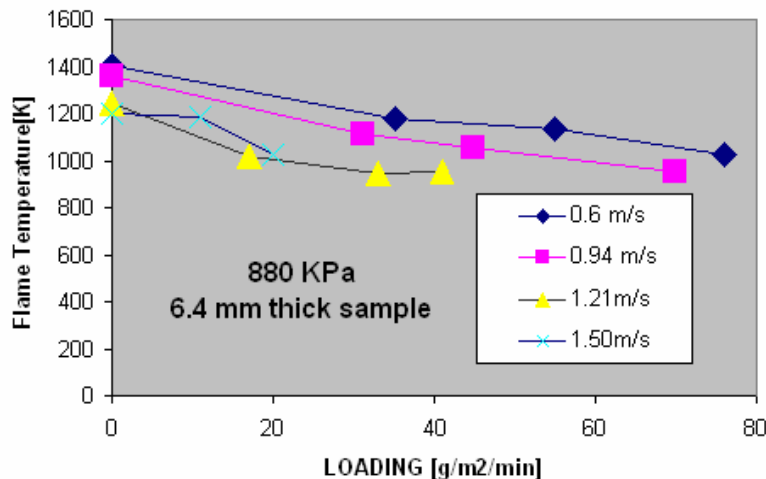


**Figure 4-89.** Mean Flame  
Temperature Obtained Using  
the TCPP. (880 kPa, 0.64 cm  
thick PMMA)

## 4.7.2 Droplet Interaction with a Hot Surface

### Experimental

Schematics of the experimental arrangement are shown in Figure 4-90 through Figure 4-93. The experimental apparatus consisted of six main parts: the liquid supply system, the piezoelectric ceramic atomizer and its power supply system, the heater assembly and its power supply system, the temperature data acquisition system, the Phase Doppler Particle Sizer (PDPA) spray characterization system, and the spray imaging system.

Compressed shop air was reduced to an appropriate pressure by a regulator then introduced into a thick-walled plastic reservoir in which the liquid was stored. Liquid flowed out of the reservoir and passed through a filter and a rotameter, before finally reaching the piezoelectric ceramic atomizer. The filter had a pore size of 10  $\mu\text{m}$ . The mass flow ranged from 0.1 g/s to 1.0 g/s, and the inlet pressure ranged from 27.6 kPa to 82.7 kPa. They were adjusted simultaneously using the rotameter. Distilled water was used for evaporation experiments. Dow Corning 510, a non-evaporative fluid, was used for the buoyancy experiments.

A piezoelectric atomizer (purchased from Universitat Erlangen-Nurnberg, Germany) was used to produce monodisperse droplets with flows up to 4 g/s.<sup>189</sup> A schematic of the atomizer is shown in Figure 4-91. A 2 MHz function generator (Wavetek, Model 19) was used with an amplifier to supply square wave signals (approximately 30 V peak to peak) to the atomizer. The output frequencies ranged from 3 kHz to 2 MHz.

Three round stainless steel plates with orifices of different diameters made by laser drilling were used as nozzles in the atomizer. The plates were 50  $\mu\text{m}$  thick, and were supported by a 1 mm thick stainless plate with a 1 mm hole in the center. The orifice diameters were 100  $\mu\text{m}$ , 50  $\mu\text{m}$ , and 20  $\mu\text{m}$ . The atomizer was placed above the center of the heater in a fixture that allowed 360° rotation. In addition, the atomizer was capable of being moved in both the vertical and horizontal direction.

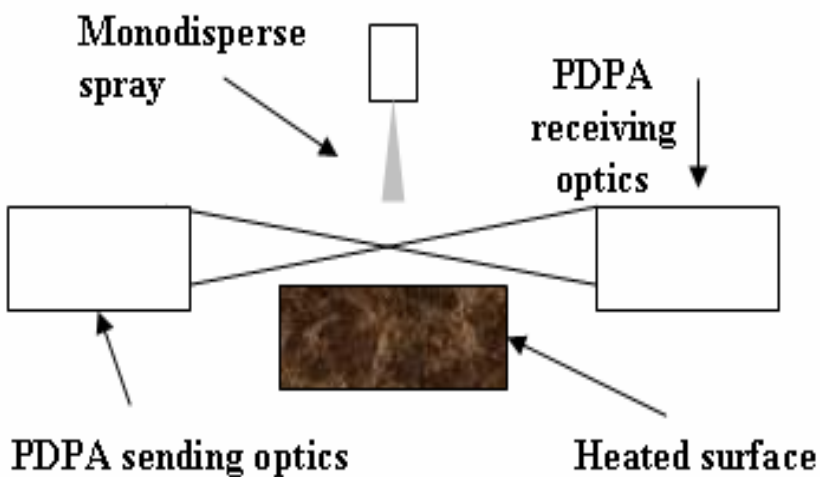
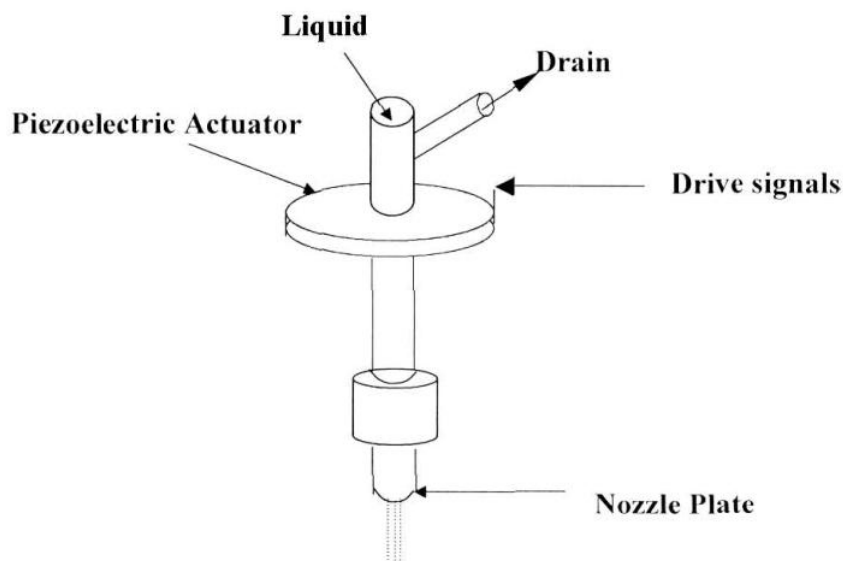


Figure 4-90. Experimental Arrangement for the Measurements.



**Figure 4-91.**  
**Configuration of the**  
**Piezoelectric Atomizer.**

A heat source was necessary to provide a surface temperature as uniform as possible. A modified design of a hot plate was used in the experiments.<sup>190</sup> A schematic of the heater assembly is shown in Figure 4-92. The main components were an exterior aluminum ring with top and bottom cover plates, a copper block with inside cartridge heaters, and insulation material. To reduce oxidization of the heated surface and clogging in the orifices and pipes, distilled water was used. The plate used was taken out of the atomizer after each experiment and cleaned using an ultrasonic cleaner before the next test.

The arrangement of the oxygen-free copper block and the thermocouples is shown in Figure 4-93. The block was 10 cm in diameter. The exposed surface was nickel-plated to a thickness of 50  $\mu\text{m}$ . Twenty-three cartridge heaters were obtained from OMEGA, each rated at 100 W maximum. They were arranged to heat the block as uniformly as possible. Twelve type K subminiature thermocouples were inserted into the copper block at 4 radial locations. There were 3 in each group, located at different depths to extrapolate the surface temperature. Holes for the cartridge heaters were 0.94 cm in diameter, and a total of 23 were arranged in three concentric circles as shown in Figure 4-93. The holes for the thermocouples were 0.16 cm in diameter, and a total of 12 were located as shown in Figure 4-93.

The copper block was surrounded by Cotronics Rescor 360 Ceramic Board insulation. This insulation was selected for low thermal conductivity (0.055 W/m-K at 260  $^{\circ}\text{C}$ , 0.108 W/m-K at 600  $^{\circ}\text{C}$ ), resistance to high temperature (continuous operating temperature limit of 1260  $^{\circ}\text{C}$ ), rigidity, and machinability. There was a center hole in each insulation layer below the copper block to allow the thermocouples and cartridge heater leads to pass through.

A square, 1.59 mm thick Macor machinable ceramic cover was placed above the uppermost piece of the insulation layer, with a hole 10.16 cm in diameter in it for the exposed nickel-plated copper surface. The Macor sat on a ridge machined into the top aluminum cover plate. The exposed heater surface was maintained flush with the surrounding Macor plate by adjusting three screws beneath the insulation at the very bottom of the assembly. High temperature sealant 906 (Megnesia Adhesive from Cotronics) was used to fill the gap between the Macor and the aluminum cover plate. Excess water flowed down along the exterior surface of the aluminum ring and was drained out through a hole in the slot, which was formed by the cylinder and the short ring mounted on the bottom plate.

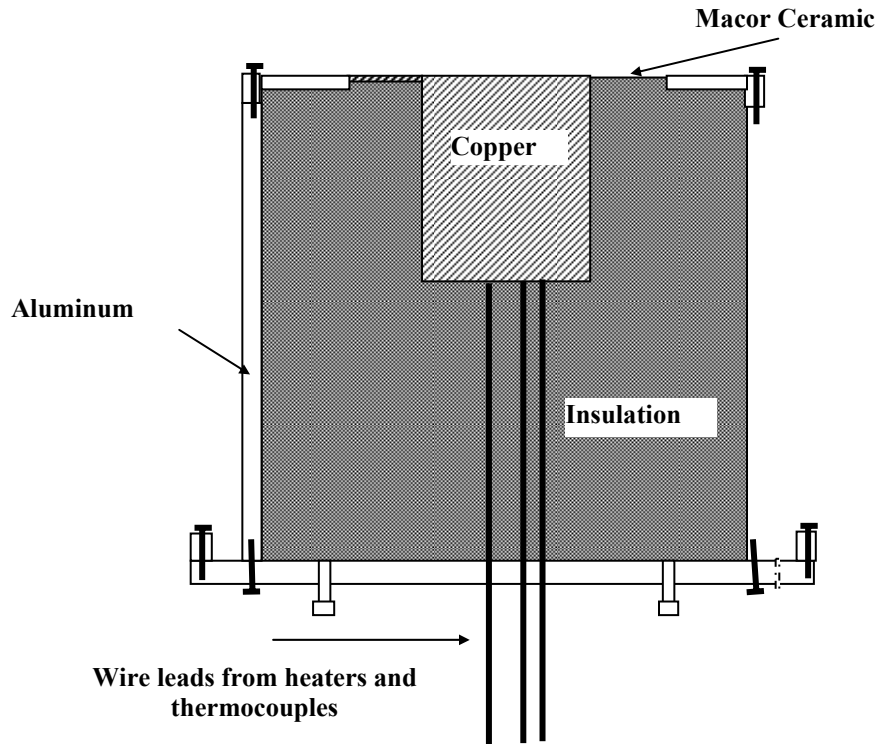


**Figure 4-92.**  
Schematic  
Diagram of the  
Heater Assembly.

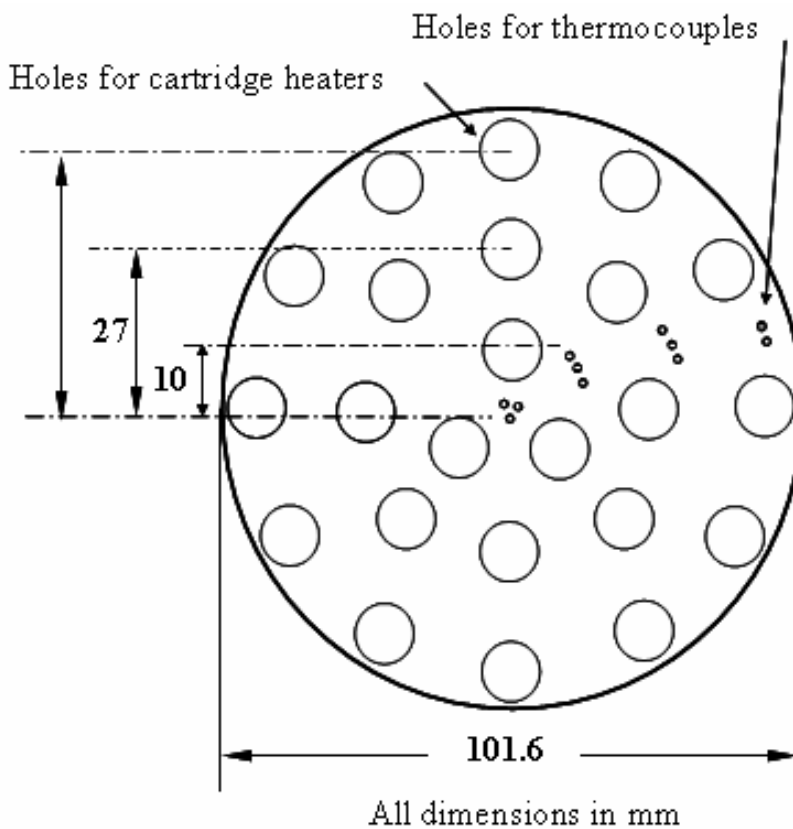


**Figure 4-93.** Temperature  
Measurement Locations  
on the Heater.

A PDPA was used to measure the sizes and velocities of the droplets (See Section 4.3.4). The PDPA transmitter (Model 11 00) contained a 10 mW, polarized Helium-Neon laser. The collimating lens was 300 mm, and the receiver lens was 1000 mm to permit the largest range for measuring droplet sizes. The forward scattering mode was used to obtain data. The position of the Phase Doppler Particle Analyzer (PDPA) was fixed. The heater and the atomizer were moved together to measure droplets at different axial and radial locations. A three-dimensional motor controller was used to provide accurate relative positioning of the laser probe volume.

The 12 voltage signals from the thermocouples were received by the EXP-16 board (Computer Boards) and multiplexed into a single signal for amplification. A gain of 100 was used to achieve the largest voltage measurable and programmable by the CIO-DAS1402/12 board (Computer Boards). The EXP-16 also contained a CJC (cold junction compensation) circuit for correcting thermocouple readings.

Experiments were performed for different liquids, nozzle plates, flows, and operating frequencies. The initial surface temperature of the copper was chosen to be 600 °C for water and 250 °C for Fluid 510. In addition, a base line data set with the heater at 25 °C was also obtained. For a given a nozzle plate and a given flow, the operating frequencies were changed to get different droplet sizes and velocities. A frequency was chosen by visually observing the jet shape and ensuring that there were no satellite droplets breaking away from the main stream. A plastic curtain was used in the experiments to reduce the ambient disturbances. Measurements at different axial and radial locations within the spray were obtained by moving the heater and the nozzle assembly using a slide.

## Modeling

For designing suppression systems, models are routinely used to calculate droplet trajectories. Since droplets arriving at a fire location have to pass through a hot environment, the models also have to account for buoyancy and evaporation. The data obtained using the PDPA can be used for assessing the accuracy of these models. During the course of the project, a model based on Lund et al.<sup>191</sup> that accounts for coalescence and evaporation of droplets was evaluated using the data.

The influence of evaporation was evaluated through use of the  $d^2$  law as described by<sup>192</sup>

$$\frac{dm}{dt} = 2\pi D_V \frac{p_v}{RT} ShD \quad (4-45)$$

where  $m$  is droplet mass,  $t$  is time,  $D_V$  is the mass diffusion coefficient,  $p_v$  is the vapor pressure,  $R$  is the ideal gas constant for the vapor,  $T$  is the temperature,  $Sh$  is the Sherwood number, and  $D$  is the droplet diameter.

A change of variables converted the change in mass with respect to time in Equation (4-45) to a change in diameter with respect to axial location. The resulting equation was:

$$\frac{dD}{dz} = \frac{4D_V p_v Sh}{\rho_L D R T V} \quad (4-46)$$

The remaining unknown variable, the Sherwood number, was calculated using the correlation found in Ranz and Marshall:<sup>193</sup>

$$Sh = 2 + 0.6 Re^{0.5} Sc^{0.33} \quad (4-47)$$

where  $Re$  is the Reynolds number and  $Sc$  is the Schmidt number.

Calculations were made using Equations (4-46) and (4-47), plus the definitions of  $Re$  and  $Sc$ , to determine the change in droplet diameter with axial location for a particular size class. Since droplet diameter was found to decrease by only 0.015  $\mu\text{m}$  for every 1 cm of axial distance, it was concluded that the influence of evaporation was negligible for the hydrocarbon oil used in this investigation.

The extent to which droplet coalescence played a role in increasing SMD was determined via a kinetic theory-based model. The model neglected viscous, gravitational and pressure forces. It was based on the coalescence of a droplet of size-velocity class  $i$  with a droplet of size-velocity class  $j$  to yield a droplet of size-velocity class  $k$ :

$$D_i + D_j \rightarrow D_k \quad (4-48)$$

From this relationship the rate equation for change in number of droplets of class  $i$  was:

$$\frac{dn_i}{dz} = \varepsilon \left( - \sum \frac{k_{ij} \eta_i \eta_j}{V_i} + \sum \frac{k_{ij} \eta_i \eta_j \alpha_{ij}}{V_i} \right) V_p \quad (4-49)$$

where  $n_i$ , the counts per unit volume for droplet class  $i$ , was defined as

$$\eta_i = \frac{n_i}{A_p t_{run} V_i} \quad (4-50)$$

The collision frequency for droplets of class  $i$  colliding with those of class  $j$ , was defined as:

$$k_{ij} = \frac{\pi}{4} (D_i + D_j)^2 V_{ij} \quad (4-51)$$

The probability of a collision leading to coalescence,  $\varepsilon$ , was determined by extrapolating the work of Jiang et al.<sup>194</sup> to the fluids studied here, and then approximating the impact parameter vs. Weber number curves as straight lines. Such a procedure overestimated the probability of a collision leading to coalescence.

In Equations (4-49) through (4-51),  $n_i$  represents the number of droplets in class  $i$ ,  $A_p$  is the PDPA probe area normal to the flow,  $t_{run}$  is the run time,  $V_i$  is the velocity of class  $i$ ,  $V_p$  is the PDPA probe volume, and  $a_{ij}$  represents the diameter  $D_k$  that results from coalescence in Equation (4-48).

Equations (4-49) through (4-51) were used to calculate the change in number of droplets for a particular class  $i$  with respect to axial location. Care was taken when distributing the product mass and momentum over the appropriate size-velocity bins. The coarse-grained PDF technique of Sivathanu and Gore<sup>186</sup> was employed to keep computational evaluation of Equation (4-49) tractable while ensuring spray mass and momentum conservation. Having calculated  $dn_i/dz$  in this fashion,  $dSMD/dz$  was determined by taking the derivative of  $SMD$  with respect to  $z$ .

$$\frac{dSMD}{dz} = - \frac{\left( \sum D_i^2 \frac{dn_i}{dz} \right) \left( \sum n_i D_i^3 \right)}{\left( \sum n_i D_i^2 \right)^2} \quad (4-52)$$

Equation (4-52) was then used to calculate a change in the *SMD* due to coalescence of droplets with axial location. The results were compared with those obtained using the PDPA instrument.

## Results and Discussion

The temperature field above the hot plate is shown in Figure 4-94. The temperature was 600 °C just above the hot plate and rapidly decreased due to buoyancy induced entrainment. At an axial distance of 100 mm, the temperature was less than 200 °C at the center line. The buoyancy induced velocity field was unsteady. (The time-resolved velocity field was not quantified.) The injector was located 250 mm above the hot plate in the centerline.

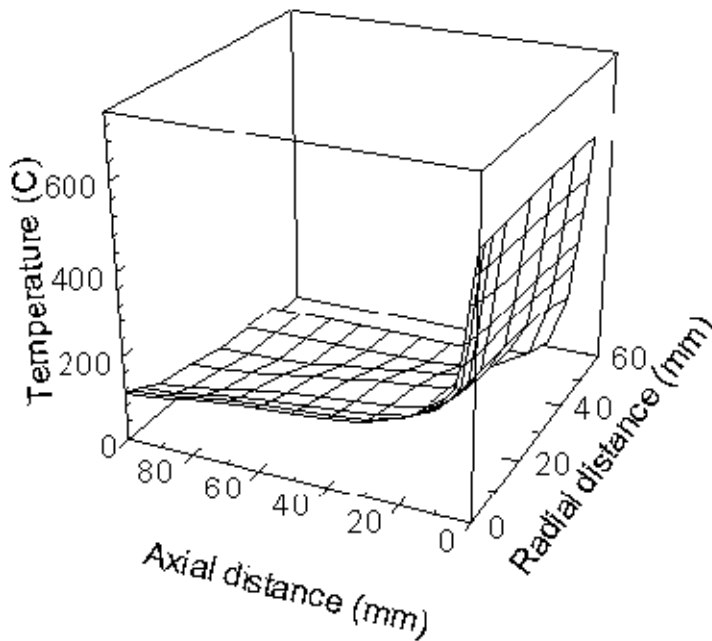


**Figure 4-94. Steady State Temperature Field above the Hot Plate.**

A steady state k-ε-g model, assuming a boundary layer flow, was used to try to predict the temperature field. However, even under steady state conditions, the local velocity field had both positive and negative values. The model did not have a mechanism to account for flow reversals. Therefore, the model predictions showed very large divergence from the experimental observations and are not provided here. A 3-D large eddy simulation code is needed to improve the model predictions.

The change in droplet diameter with distance from the injector is shown in Figure 4-95. The PDPA results obtained using a cold plate and a hot plate are also shown. The effects of coalescence are readily apparent. For both cases, the mean diameter of the droplets increased by approximately a factor of three by the time they arrived at the hot plate. For the hot surface, the droplet diameter increased only by a factor of two. The smaller droplet diameters in the hot environment are likely due to evaporation. They may also be due to decreased coalescence. If the buoyancy induced flow field affects the local velocities

significantly, this could lead to lower coalescence and reduce the SMD. These two effects can be separated using non-evaporating droplets.

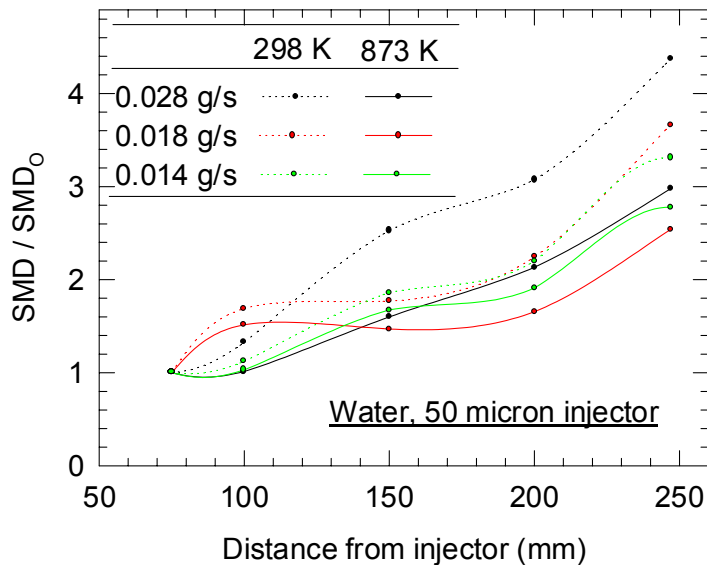


**Figure 4-95. Change in Sauter Mean Diameter of the Water Droplets with Axial Distance.**

Fluid 510 was used to determine evaporation effects on the droplet size history. When the fluid was sprayed onto the surface at 600 °C, a thick smoke was formed. This smoke prevented the PDPA from obtaining droplet velocity and size data. In addition, the fluid formed a very hard coating on the copper plate. Therefore, the plate was cleaned, and the temperature reduced to 250 °C (below the flash point of Fluid 510).

The change in droplet diameters with axial locations for Fluid 510 is shown in Figure 4-96. Two different excitation frequencies, representing two different droplet diameter distributions were used for the experiments. For both cases, it was found that the variation in SMD was identical, irrespective of the temperature of the plate. Therefore, the buoyancy induced flow field did not significantly affect the coalescence of droplets. It was evaporation that was responsible for the lower SMD when the plate was hot.

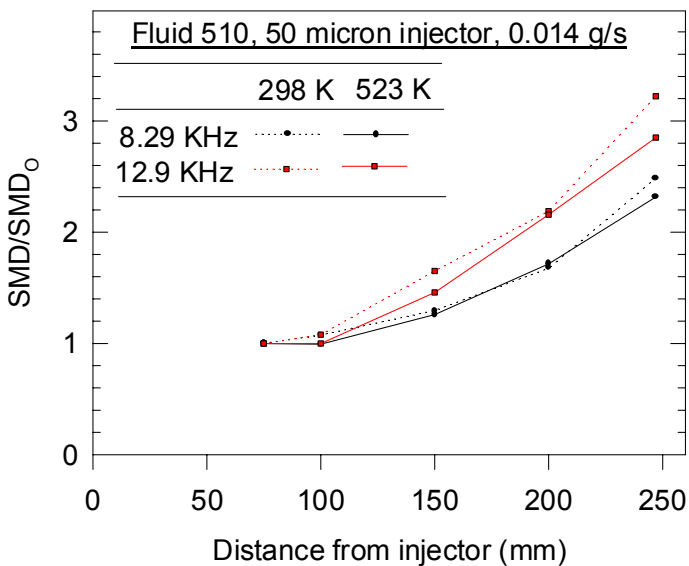


**Figure 4-96. Change in Sauter Mean Diameter of the Droplets with Axial Distance for Fluid 510.**

To evaluate the coalescence model, the velocity and number density of the droplets was required. The velocity of the water droplets is shown in Figure 4-97. It is clearly evident that the velocity of droplets was affected significantly by buoyancy. The velocities are much lower when the plate was hot. This usually increased the droplet SMD since the lower velocities provided a longer time interval for coalescence.

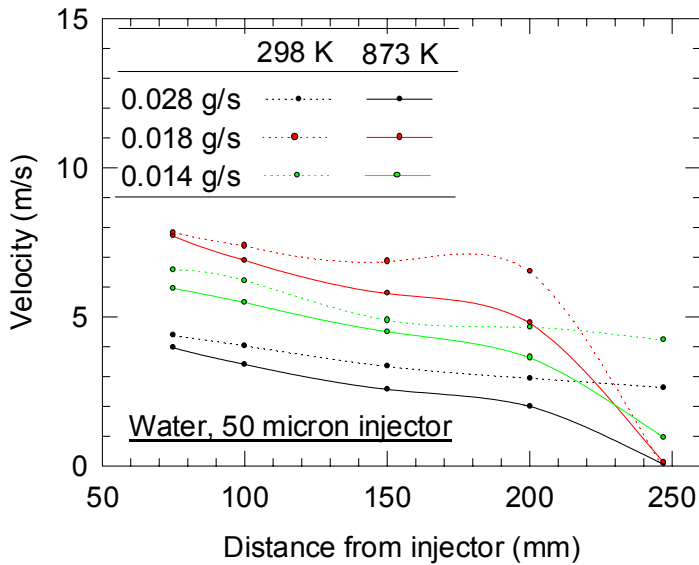


**Figure 4-97. Variation in Velocity with Axial Distance for Water Spray.**

The change in velocity with axial distance for three conditions using Fluid 510 is shown in Figure 4-98. Due to the lower temperatures attained, the change in velocity due to the buoyancy induced upward velocity of air was minimal. Similar results were obtained for the 20  $\mu\text{m}$  nozzle. In all cases, the droplet diameter increased a factor of two or higher with downstream distance. Coalescence was the primary reason for the increase in droplet diameter.

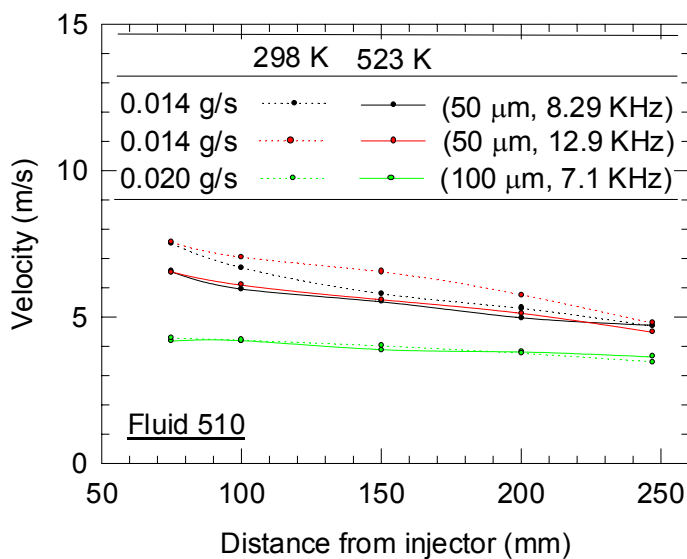


**Figure 4-98. Variation in Velocity with Axial Distance for Fluid 510.**

Modeling results of the change in SMD with diameter using Equation (4-46) for coalescence and Equation (4-52) for droplet evaporation differed significantly from the experimental data. The coalescence model predicted approximately two orders of magnitude lower changes in SMD with axial distance. The evaporation model suggested that the SMD of droplets would change by less than 2 % in all cases.

Improvements in the model using a Monte Carlo-based approach are needed to delineate the effects of coalescence and evaporation. Also needed is a more rigorous method of predicting the temperature field above the hot surface to implement the Monte Carlo simulations. Finally, wake effects are important in this study and should be incorporated into the models.

### 4.7.3 Summary and Conclusions

This research examined the effect of water mist on the reduction in the flame spread velocity into an opposing wind. Flame spread velocities with and without water mist were obtained for a solid fuel, polymethylmethacrylate (PMMA), using Focal Plane Array Imaging. PMMA sheets of different thickness were burned in an opposed flow configuration, with varying wind velocities. The flame spread rate for the 'without backing' tests was found to be greater than for the 'with backing' tests due to flame spread on both sides in the 'without backing' case. At ambient oxygen concentration, the heat transfer effect on the fuel vapor evolution rate was the dominant factor controlling the flame spread rate.

A spray nozzle, suspended over the PMMA sheets, was used to vary the water loading at the flame front. Flame spread in the presence of a water mist indicated a strong influence of surface loading in reducing flame spread rate. The effect was more pronounced at low values of opposing wind speeds. The flame spread rate for a given liquid loading decreased slightly for smaller droplets. Water loading, rather than the droplet size, is the more important parameter for reducing flame spread. The reduction in flame spread rate in the presence of the mist can be modeled empirically using the experimental parameters.

Droplet diameter and velocity measurements from a monodisperse spray onto a hot plate showed that buoyancy had a significant impact on both droplet velocities and diameters. A non-evaporating spray (Dow Thermal Fluid 510) was used to assess the effects of buoyancy and an evaporating spray (water) was used to study the combined effects of buoyancy and evaporation on the droplet trajectories. For both fluids, coalescence was the dominant mechanism by which droplets changed size during their flight to a hot surface. For the temperature range achieved during the study, the change in water droplet diameters due to evaporation was much smaller than due to coalescence. Two coalescence and evaporation models developed were not successful in predicting droplet coalescence and evaporation. The models need to be improved significantly before they can be used in fire suppression studies. Temperature reduction of burning surfaces inhibited with water mist has to be measured for more conditions to obtain a more accurate assessment of the optimal water loading required for fire extinguishments.

The results of the study are applicable to design considerations for aerosol-based fire suppression devices to ensure optimum operation.

#### 4.8 THE NEW STATE OF KNOWLEDGE OF THE MECHANISM OF FLAME EXTINGUISHMENT BY AEROSOLS

NGP research has greatly advanced the understanding of the processes by which aerosols in the form of solid particles or liquid droplets suppress flames, the aerosol properties that control these processes, and the values of the properties that promote efficient extinguishment. The interrelated dependencies of particle size and flame conditions explain why seemingly contradictory suppression results appeared in the earlier literature exploring the effectiveness of aerosols in differing flame systems. Experimental quantification of the aerosol particle size distributions, number densities, and particle velocities actually delivered to the flames was key to establishing valid correlations between observed suppression effectivenesses with modeling predictions. Comparison of experimental data in combination with modeling predictions permitted the exploration of suppression in aerosol parameter space that would have been much more difficult to explore solely with either approach alone.

- Rosser and co-workers summarized the extinction mechanism of powders of metal compounds based on experiments in the 1960s.<sup>13</sup> NGP assessment of subsequent works combined with detailed NGP experimental and modeling studies concluded that with some modification these conclusions can be extended to qualify the suppression mechanism of aerosols in general.
- To achieve maximum suppression effectiveness, individual components of an aerosol must pass through a succession of steps: I - Heating; II - Evaporation/decomposition; III - Generation of the chemical inhibitor specie(s) for chemical agents; IV - Flame inhibition.
- Evaporation/decomposition leads to dilution of the available oxygen and lowers the temperature which alters the flame chemistry (dominates for those aerosols with no chemical inhibitor).
- Any generated chemical inhibitor species must directly participate in the flame radical chemistry.
- Small particles are favored; evaporation/decomposition must be close to or in the flame.
- The transition diameter from effective, small particles to larger, less effective larger ones depends on the time to complete steps I and II (i.e., complete evaporation of the aerosol material).
- Suppression effectiveness is controlled by the time required for the aerosol particles to progress through each step AND the amount of time allowed, i.e. the residence time.
- For premixed flames, higher flame temperatures imply higher burning velocities and shorter particle residence times.
- For non-premixed counterflow flames, the particle residence time is related to the inverse of the strain rate; particles can oscillate near the stagnation plane and lengthen the effective residence time for certain particle sizes and strain rates.
- For non-premixed co-flow flames with air-stream entrainment of the aerosol (e.g. cup burner flames), the residence times are dictated by the air stream velocity through the flame.
- Residence time requirements are greater for liquid aerosols with a chemical inhibitor additive than for the pure liquid; liquid with additive aerosols must complete steps I and II for the liquid followed by steps I and II again for the additive residue.

- For chemical inhibitor species, thermodynamic limitations can impose restrictions on the gas phase chemical inhibitor specie(s) (see Chapter 3); complete evaporation/decomposition and/or longer residence times may offer no advantage.
- Aerosols are generally less effective in premixed flames than in non-premixed flames of the same fuel.
- For achievable aerosol suppression effectiveness there is a tradeoff between flame temperature, flow field velocity, particle residence time, and particle physical and chemical properties; this tradeoff can lead to non-monotonic effectiveness behavior with particle size.
- Specific flame type, nature of fuel, and aerosol properties ultimately determine the magnitude of the aerosol suppression effectiveness.

## 4.9 RELATION OF FINDINGS TO PRACTICAL FIRES

The conclusions in this chapter are based for the most part on observations in laboratory-scale flame suppression studies. Aerosol particles were typically injected directly into the flame. For real-scale fires, the conclusions outlined above will include a critical additional first step; the aerosol must first get to the fire to begin the process. The type of aerosol generation system and what happens in aerosol transport to the fire will also impact suppression performance. Thus, in addition to answering what aerosol properties are optimum at the fire, one must also address what properties should the aerosol exhibit when generated in order to achieve the optimum suppression properties at the fire. The required set of aerosol characteristics can change as the fire changes, especially as the fire grows in size involving more of its surroundings. Transport and delivery topics are presented and discussed in Chapter 8.

Spaces where real fires occur are generally distinctly larger than the dimensions of a laboratory flame apparatus. Aerosol travel distances are longer; changes will occur in the size distribution and particle velocities from generation point to the fire location. This location is not known in advance so there is also a need to consider the effective dispersion throughout the area requiring protection. Higher aerosol densities need to be generated in order to fill the space adequately. This often impacts the resulting particle size distributions.

Small fires in large spaces, especially small, obstructed fires, are particularly challenging for gaseous agents. These fires are even more challenging for aerosol suppression agents. Smaller fires generate less heat, resulting in lower overall temperatures and lower aerosol evaporation or decomposition rates. Entrainment currents around smaller fires are less intense and less likely to draw large amounts of aerosol into the fire. For a given aerosol, the smaller particles are more likely to follow the weaker airstream trajectories than the larger particles, but smaller particles evaporate more quickly. A bi-modal aerosol distribution (or other combination) may address this issue. A bi-modal distribution may also address the aerosol requirements for protecting a wider range of fire threats and protecting against fires in varying stages of development.

## 4.10 REFERENCES

1. Braidech, M.M., Neale, J.A., Matson, A.F., and Dufour, R.E., *The Mechanism of Extinguishment of Fire by Finely Divided Water*, Underwriters Laboratories Inc. for the National Board of Fire Underwriters, N.Y., 1955.
2. Rasbash, D.J., Rogowski, Z.W., and Stark, G.W.V., "Mechanisms of Extinction of Liquid Fires with Water Sprays," *Combustion and Flame* **4**, 223-234, (1960).
3. Lugar, J.R., "Preliminary Test Results of Fine Water Mist Fire Protection Systems Study," David W. Taylor Naval Ship Research and Development Center, MD, 1980.
4. Coppalle, A., Nedelka, D., and Bauer, B., "Fire Protection: Water Curtains," *Fire Safety Journal* **20**, 241-255, (1993).
5. Mawhinney, J.R., Dlugogorski, B.Z., and Kim, A.K., "A Closer Look at the Fire Extinguishing Properties of Water Mist," *Proceedings of the Fourth International Symposium on Fire Safety Science*, The International Association for Fire Safety Science, pp. 47-60, 1994.
6. Seshadri, K., "Structure and Extinction of Laminar Diffusion Flames Above Condensed Fuels with Water and Nitrogen," *Combustion and Flame* **33**, 197-215, (1978).
7. McCaffrey, B.J., "Momentum Diffusion Flame Characteristics and the Effects of Water Spray," *Combustion Science and Technology* **63**, 315-335, (1989).
8. Fielding, G.H., Williams, F.W., and Carhart, H.W., *Fire Suppression – Why Not Water?*, NRL Memorandum Report No. 3435, Naval Research Laboratory, Washington, DC, February 1977.
9. Friedman, R., "On the Mechanisms of Flame Extinguishment by Dry Powders," *Journal of Fire Protection Engineering* **5**, 290-318, (1993).
10. Dolan, J.E., and Dempster, P.B., "The Suppression of Methane-Air Ignitions by Fine Powders," *Journal of Applied Chemistry* **5**, 510-517, (1955).
11. DeWitte, M., Verbosch, J., and van Tiggelen, A., "Inhibition and Extinction of Premixed Flames by Dust Particles," *Combustion and Flame* **8**, 257-266, (1964).
12. Birchall, J.D., "On the Mechanism of Flame Inhibition by Alkali Metal Salts," *Combustion and Flame* **14**, 85-96, (1970).
13. Rosser, W.A., Jr., Inami, S.H., and Wise, H., "The Effect of Metal Salts on Premixed Hydrocarbon-Air Flames," *Combustion and Flame* **7**, 107-119, (1963).
14. G. Fischer and J. T. Leonard, *The Effectiveness of Fire Extinguishing Powders Based on Small Scale Fire Suppressant Tests*, Internal NRL Progress Report, 1984.
15. Ewing, C.T., Hughes, J.T., and Carhart, H.W., "The Extinction of Hydrocarbon Flames Based on the Heat-Absorption Processes which Occur in them," *Fire and Materials* **8**, 148-156, (1984).
16. Ewing, C.T., Faith, F.R., Hughes, J.T., and Carhart, H.W., "Flame Extinguishment Properties of Dry Chemicals: Extinction Concentrations for Small Diffusion Pan Fires," *Fire Technology* **25**, 134-149, (1989).
17. Fischer, G., and Leonard, J.T., *Effectiveness of Fire Extinguishing Powders Based on Small Scale Fire Suppression Tests*, Naval Research Laboratory, NRL/MR/6180-95-7778, Washington, D.C., 1995.
18. Chattaway, A., Dunster, R.G., Gall, R., and Spring, D.J., "The Evaluation of Non-Pyrotechnically Generated Aerosols as Fire Suppressants," 1995, in Gann, R.G., Burgess, S.R., Whisner, K.C., and

Reneke, P.A., eds., *Papers from 1991-2006 Halon Options Technical Working Conferences (HOTWC)*, CD-ROM, NIST SP 984-4, National Institute of Standards and Technology, Gaithersburg, MD, 2006.

19. Knuth, E.L., Ni, W.F., and Seeger, C., "Molecular-Beam Sampling Study of Extinguishment of Methane-Air Flames by Dry Chemicals," *Combustion Science and Technology* **28**, 247-262, (1982).

20. Hamins, A., Gmurczyk, G., Grosshandler, W., Rehwoldt, R.G., Vazquez, I., Cleary, T., Presser, C., and Seshadri, K., "Flame Suppression Effectiveness," in *Evaluation of Alternative In-Flight Fire Suppressants for Full-Scale Testing in Simulated Aircraft Engine Nacelles and Dry Bays*, National Institute of Standards and Testing, No. NIST SP 861, pp. 345-465, April 1994.

21. Hamins, A., "Flame Extinction by Sodium Bicarbonate Powder in a Cup Burner," *Proceedings of the Combustion Institute* **27**, 2857-2864, (1998).

22. Wahl, A.M., "Water and Water Additives for Fire Fighting," Section 6, Chapter 1, in *Fire Protection Handbook*, 18th edition, A.E. Cote (editor), National Fire Protection Association, Quincy, MA, 1997.

23. Monson, W.L., Reid, L.J., Schreiner, M., Jr., Bonney, D.T., and Huff, W.J., *Research on Water Additives for Fire Fighting*, Quarterly Report No. 3, U.S. Army Engineer Research and Development Laboratories, Fort Belvoir, Virginia, December 15, 1953.

24. Monson, W.L., Reid, L.J., Schreiner, M., Jr., Bonney, D.T., and Huff, W.J., *Research on Water Additives for Fire Fighting*, Quarterly Report No. 4, U.S. Army Engineer Research and Development Laboratories, Fort Belvoir, Virginia, March 15, 1954.

25. Grove, C.S. et al., "Additives to Improve the Fire-Fighting Characteristics of Water," *Fire Research Abstracts and Reviews* **1**, 18, (1958).

26. Aidun, A.R., Walker, E.J., Gabriel, S., Buckman, W.R., and Grove, C.S., Jr., "Additives to Improve the Fire-Fighting Characteristics of Water," *Fire Research Abstracts and Reviews* **1**, 58, (1958).

27. Walker, E.J., Aidun, A.R., and Grove, C.S., Jr., "Additives to Improve the Fire-Fighting Characteristics of Water," *Fire Research Abstracts and Reviews* **1**, 129, (1958).

28. Walker, E.J., Aidun, A.R., and Grove, C.S., Jr., "Additives to Improve the Fire-Fighting Characteristics of Water," *Fire Research Abstracts and Reviews* **2**, 71, (1960).

29. Aidun, A.R. and Grove, C.S., Jr., "Additives to Improve the Fire-Fighting Characteristics of Water," *Fire Research Abstracts and Reviews* **3**, 91, (1961).

30. Aidun, A.R. "Additives to Improve the Fire-Fighting Characteristics of Water," *Fire Research Abstracts and Reviews* **3**, 93, (1961).

31. Aidun, A.R., "Additives to Improve the Fire-Fighting Characteristics of Water," *Fire Research Abstracts and Reviews* **3**, 213, (1961).

32. Grove, C.S., Jr., Grove, S.T., and Aidun, A.R., "Improving the Effectiveness of Water for Fire Fighting," *Fire Research Abstracts and Reviews* **4**, 54, (1962).

33. Aidun, A.R. and Grove, C.S., Jr., "Additives to Improve the Fire-Fighting Characteristics of Water," *Fire Research Abstracts and Reviews* **5**, 34, (1963).

34. Davis, J.B., Dibble, D.L., and Phillips, C.B., "Firefighting Chemicals—New Weapon for the Fire Suppression Crew," *Fire Research Abstracts and Reviews* **5**, 37, (1963).

35. Davis, J.B., Dibble, D.L., Phillips, C.B., and McBride, R.S., "Viscous Water and Algin as Fire Control Materials," *Fire Research Abstracts and Reviews* **5**, 37, (1963).

36. Friedrich, M., "Fire Extinguishing Experiments with Aqueous Salt Solution Sprays," *Fire Research Abstracts and Reviews* **6**, 44, (1964).
37. Elkins, G.H.J., "Use of Anti-Freeze in Water Extinguishers," *Fire* **57**, 448, (1965).
38. Kida, H., "Extinction of Fires of Liquid Fuel with Sprays of Salt Solutions," *Fire Research Abstracts and Reviews* **11**, 212, (1969).
39. Ball, D.N., Spring, D.J., and Davis, S.J., "Fire Extinguishing Substance," UK Patent GB 2,233,226A, June 21, 1990.
40. Finnerty A.E., McGill, R.L., and Slack, W.A., *Water-Based Halon Replacement Sprays*, ARL-TR-1138, Army Research Laboratory, Aberdeen Proving Ground, July, 1996.
41. Yang, J.C., Donnelly, M.K., Prive, N.C., and Grosshandler, W.L., *Dispersed Liquid Agent Fire Suppression Screen Apparatus*, NISTIR 6319, National Institute of Standards and Technology, Gaithersburg, MD, July 1999.
42. Zheng, R., Bray, K.N.C., and Rogg, B., "Effect of Sprays of Water and NaCl-Water Solution on the Extinction of Laminar Premixed Methane-Air Counterflow Flames," *Combustion Science and Technology* **126**, 389-401, (1997).
43. Mitani, T., and Niioka, T., "Extinction Phenomenon of Premixed Flames with Alkali Metal Compounds," *Combustion and Flame* **55**, 13-21, (1984).
44. Edwards, M., Watkins, S., and Glockling, J., "Low Pressure Water Mist, Fine Water Spray, Water Source and Additives: Evaluation for the Royal Navy," *Proceedings of the 8th International Fire Science and Engineering Conference, Interflam '99*, Edinburgh, Scotland, Vol. 1, pp. 639-650, 29 June-1 July, 1999.
45. De Ris, J.N., "Spread Of A Laminar Diffusion Flame," *Proceedings of the Combustion Institute* **12**, 241-252, (1969).
46. Lastrina F.A., Magee R.S., and McAlevy III, R.F., "Flame Spread Over Fuel Beds: Solid-Phase Energy Considerations," *Proceedings of the Combustion Institute* **13**, 935-948, (1971).
47. Fernandez-Pello, A.C., Ray, S.R., and Glassman, I. "Downward Flame Spread In An Opposed Forced Flow," *Combustion Science and Technology* **19** (1-2), 19-30, (1978).
48. Fernandez-Pello, A.C., Ray, S.R., and Glassman, I., "Flame Spread in an Opposed Forced Flow: The Effect of Ambient Oxygen Concentration," *Proceedings of the Combustion Institute* **18**, 579-589, (1981).
49. Apte, V.B., Bilger, R.W., Green, A.R. and Quintiere, J.G., "Wind-Aided Turbulent Flame Spread and Burning Over Large-Scale Horizontal PMMA Surfaces," *Combustion and Flame* **85**, 169-184, (1991).
50. Loh, H.-T. and Fernandez-Pello, A.C., "A Study Of The Controlling Mechanisms Of Flow Assisted Flame Spread" *Proceeding of the Combustion Institute* **20**, 1575-1582, (1984).
51. Perzak, F.J. and Lazzara, C.P., "Flame Spread Over Horizontal Surfaces of Polymethylmethacrylate," *Proceedings of the Combustion Institute* **24**, 1661-1668, (1992).
52. Kwok, K.C., *A Fundamental Study of Air-Spray Painting*, Ph. D. Thesis, Mechanical Engineering Department, University of Minnesota, 1991.
53. Hicks, P.G., and Senser, D.W., "Simulation of Paint Transfer in an Air Spray Process," *Journal of Fluids Engineering* **117**, 713-719, (1995).

54. DiMarzo, M., Kavooosi, and Klassen, M., *Transient Cooling of a Hot Surface by Droplets Evaporation*, Report prepared for the National Institute of Standards and Technology, NISTGCR- 89-559, University of Maryland, College Park, MD, 1989.
55. DiMarzo, M., and Evans, D.D., *Evaporation of Water Droplet Deposited on a Hot High Thermal Conductivity Solid Surface*, NBSIR 86-3384, National Institute of Standards and Technology, Gaithersburg, MD, 1986.
56. Sheinson, R.S., Maranghides, A., Eaton, H., Barylski, D., Black, B., Friderichs, T., Peatross, M., Salmon, G., and Smith, W., "Total Flooding Agent Distribution Considerations," 1995, in Gann, R.G., Burgess, S.R., Whisner, K.C., and Reneke, P.A., eds., *Papers from 1991-2006 Halon Options Technical Working Conferences (HOTWC)*, CD-ROM, NIST SP 984-4, National Institute of Standards and Technology, Gaithersburg, MD, 2006.
57. Carhart, H.W., Sheinson, R.S., Tatem, P.A., and Lugar, J.R., "Fire Suppression Research in the U.S. Navy," Proceedings - First International Conference on Fire Suppression Research, Stockholm and Boras, Sweden, May 5-8, 1992.
58. Ewing, C.T., Faith, F.R., Romans, J.B. Hughes, J.T. and Carhart, H.W., "Flame Extinguishment Properties of Dry Chemicals: Extinction Weights for Small Diffusion Pan Fires and Additional Evidence for Flame Extinguishment by Thermal Mechanisms," *Journal of Fire Protection Engineering* **4**, 35-52, (1992).
59. Ewing, C.T., Faith, F.R., Romans, J.B., Siegmann, C.W, Ouellette, R.J., Hughes, J.T., and Carhart, H.W., "Extinguishing Class B Fires with Dry Chemicals: Scaling Studies," *Fire Technology* **31**, 1-16, (1995).
60. Sheinson, R.S., Eaton, H.G., Black, B.H., Brown, R., Burchell, H., Salmon, G., St. Aubin, J., and Smith, W.D., "Total Flooding Fire Suppressant Testing in a 56 m<sup>3</sup> (2000 ft<sup>3</sup>) Compartment," 1993, in Gann, R.G., Burgess, S.R., Whisner, K.C., and Reneke, P.A., eds., *Papers from 1991-2006 Halon Options Technical Working Conferences (HOTWC)*, CD-ROM, NIST SP 984-4, National Institute of Standards and Technology, Gaithersburg, MD, 2006.
61. Sheinson, R.S., Eaton, H.G., Zalosh, R.G., Black, B.H., Brown, R., Burchell, H., Salmon, G., and Smith, W.D., "Intermediate Scale Fire Extinguishment By Pyrogenic Solid Aerosol," 1994, in Gann, R.G., Burgess, S.R., Whisner, K.C., and Reneke, P.A., eds., *Papers from 1991-2006 Halon Options Technical Working Conferences (HOTWC)*, CD-ROM, NIST SP 984-4, National Institute of Standards and Technology, Gaithersburg, MD, 2006.
62. Discussions between R.S. Sheinson and A. Baratov, 12 April, 1994.
63. Zegers, E.J.P., Williams, B.A., Sheinson, R.S., and Fleming, J.W., "Dynamics and Suppression Effectiveness of Monodisperse Water Droplets in Non-Premixed Counterflow Flames," *Proceedings of the Combustion Institute* **28**, 2931-2937, (2000).
64. Chen, N.H., Rogg, B., and Bray, K.N.C., "Modelling Laminar Two-Phase Counterflow Flames with Detailed Chemistry and Transport," *Proceedings of the Combustion Institute* **24**, 1513-1521, (1992).
65. Prasad, K., Li, C., Kailasanath, K., Ndubizu, C., Ananth, R., and Tatem, P.A., "Numerical Modeling of Water Mist Suppression of Methane-Air Diffusion Flames," *Combustion Science and Technology* **132**, 325-364, (1998).
66. Lefebvre, A.H., *Atomization and Sprays*, Hemisphere Publishing Corporation, pp. 91-92, 1988.
67. Sirignano, W.A., *Fluid Dynamics and Transport of Droplets and Sprays*, Cambridge University Press, Cambridge, United Kingdom, pp. 5-6, 1999.

68. Black, D.L., McQuayt, M.Q., and Bonint, M.P., "Laser-Based Techniques for Particle-Size Measurement: A Review of Sizing Methods and their Industrial Applications," *Progress in Energy and Combustion Science* **22**, 267-306, (1996).
69. Durst, F., Brenn, G., and Xu, T.H., "A Review of the Development and Characteristics of Planar Phase-Doppler Anemometry," *Measurement Science and Technology* **8**, 1203-1221, (1997).
70. Chigier, N., "Optical Imaging of Sprays," *Progress in Energy and Combustion Science* **17**, 221-262, (1991).
71. Rafel, M., Willert, C.E., Kompenhans, J., *Particle Image Velocimetry: A Practical Guide*, Springer-Verlag Berlin, 1998.
72. Turns, S., *An Introduction to Combustion: Concepts and Applications*, 1st ed., McGraw Hill, Inc., New York, p. 314, 1996.
73. Kays, W.M. and Crawford, M.E., *Convective Heat and Mass Transfer*, 2nd ed., McGraw-Hill Book Company, New York, p 388, 1980.
74. Perry, R.H., Green., D.W., Maloney, J.O., *Perry's Chemical Engineers' Handbook*, Seventh Edition, The McGraw-Hill Companies, Inc., New York, p. 6-51, 1997.
75. Fleming, J.W., Williams, B.A., Sheinson, R.S., Yang, W., Kee, R.J., "Water Mist Fire Suppression Research: Laboratory Studies", *Proceedings of the Second National Research Institute for Fire Disaster Symposium: Technology Standards for Fire*, Tokyo, Japan, Paper 23, 17-19 July 2002.
76. Noto, T., Babushok, V., Burgess Jr., D.R., Hamins, A., Tsang, W., and Miziolek, A., "Effect of Halogenated Flame Inhibitors on C1-C2 Organic Flames," *Proceedings of the Combustion Institute* **26**, 1377-1383, (1996).
77. Andrews, G.E., and Bradley, D., "Determination of Burning Velocities: A Critical Review," *Combustion and Flame* **18**, 133-153, (1972).
78. Continillo, G., and Sirignano, W.A., "Counterflow Spray Combustion Modeling", *Combustion and Flame* **81**, 325-340, (1990).
79. Lacas, F., Darabiha, N., Versaevel, P., Rolon, J. C., and Candel, S., "Influence of Droplet Number Density on the Structure of Strained Laminar Spray Flames," *Proceedings of the Combustion Institute* **24**, 1523- 1529, (1992).
80. Seshadri, K. and Williams, F.A., "Laminar Flow Between Parallel Plates with Injection of a Reactant at High Reynolds Number," *International Journal of Heat and Mass Transfer* **21**, 251-253, (1978).
81. Lentati, A.M. and Chelliah, H.K., "Dynamics of Water Droplets in a Counterflow Field and their Effect on Flame Extinction," *Combustion and Flame* **115**, 158-179, (1998).
82. Yang, J.C., Donnelly, M.K., Prive, N.C., Grosshandler, W.L., An Apparatus For Screening Fire Suppression Efficiency Of Dispersed Liquid Agents," *Fire Safety Journal* **36**, 55-72, (2001).
83. Hirst, R. and Booth, K., "Measurement of Flame-Extinguishing Concentrations," *Fire Technology* **13**, 296-315, (1977).
84. Fisher, B.T., Awtry, A.R., Sheinson, R.S., and Fleming, J.W., "Flow Behavior Impact on the Suppression Effectiveness of sub-10- $\mu\text{m}$  Water Drops in Propane/Air Co-flow Non-Premixed Flames", *Proceedings of the Combustion Institute* **31**, 2731-2739, (2007).
85. Fuss, S.P., Chen, E.F., Yang, W., Kee, R.J., Williams, B.A., Fleming, J.W., "Inhibition of Premixed Methane/Air Flames by Water Mist," *Proceedings of the Combustion Institute* **29**, 361-368, (2002).

86. Mitani, T., "A Flame Inhibition Theory by Inert Dust and Spray," *Combustion and Flame* **43**, 243-253, (1981).
87. Blouquin, R. and Joulin, G., "On the Quenching of Premixed Flames by Water Sprays: Influences of Radiation and Polydispersity", *Proceedings of the Combustion Institute* **27**, 2829-2837, (1998).
88. Kee, R.J., Grcar, J.F., Smooke, M.D., and Miller, J.A., *A Fortran Program for Modeling Steady Laminar One-Dimensional Premixed Flames*, Sandia National Laboratories, SAND85-8240, 1987.
89. Yang, W. and Kee, R.J., "The Effect of Monodispersed Water Mists on the Structure, Burning Velocity, and Extinction Behavior of Freely Propagating, Stoichiometric, Premixed, Methane-Air Flames," *Combustion and Flame* **130**, 322-335, (2002).
90. Kee, R.J., Grcar, J.F., Smooke, M.D., and Miller, J.A., *A Fortran Program for Modeling Steady Laminar One-Dimensional Premixed Flames*, Sandia National Laboratories, SAND85-8240, 1987.
91. Lutz, A.E., Kee, R.J., Grcar, F.M. and Rupley, F.M., *OPPDIF: A Fortran Program for Computing Opposed-Flow Diffusion Flames*, Sandia National Laboratories, SAND96-8243, 1997.
92. Smith, G.P., Golden, D.M., Frenklach, M., Moriarty, N.W., Eiteneer, B., Mikhail Goldenberg, M., Bowman, C.T., Hanson, R.K., Song, S., Gardiner, Jr., W.C., Lissianski, V.V., and Qin, Z., *GRI-Mech 3.0*, [http://www.me.berkeley.edu/gri\\_mech/](http://www.me.berkeley.edu/gri_mech/), 2001.
93. Fuss, S.P., Chen, E.F., Yang, W., Kee, R.J., Williams, B.A., Fleming, J.W., "Inhibition of Premixed Methane/Air Flames by Water Mist," *Proceedings of the Combustion Institute* **29**, 361-368, (2002).
94. Parks, D.J., Alvares, N.J., and Beason, D.G., "Fundamental Flame-Speed Measurements in Combustion Gases Containing CF<sub>3</sub>Br," *Fire Safety Journal* **2**, 237-247, (1979/80).
95. Chase Jr., M.W., Davies, C.A., Downey Jr., J.R., Frurip, D.J., McDonald, R.A., and Syverud, A.N., *JANAF Thermochemical Tables*, 3rd Edition, *Journal of Physical And Chemical Reference Data* **14**, 927-1856, Suppl. 1, 1985.
96. Noto, T., Babushok, V., Hamins, A., and Tsang, W., "Inhibition Effectiveness of Halogenated Compounds," *Combustion and Flame* **112**, 147-160, (1998).
97. Davis, M.P., Fleming, J.W., Williams, B.A., and Ladouceur, H.D., "Flow Field Considerations for Counter Flow Burners", *Proceedings of the Eastern States Section*, The Combustion Institute, Pittsburgh, PA, pp. 200-203, Oct 1999.
98. Lazzarini, A.K., Krauss, R.H., Chelliah, H.K., and Linteris, G.T., "Extinction Conditions of Non-Premixed Flames with Fine Droplets of Water and Water/NaOH Solutions," *Proceedings of the Combustion Institute* **28**, 2939-2945, (2000).
99. Chelliah, H.K., Lazzarini, A.K., Wanigarathne, P.C., and Linteris, G.T., "Inhibition of Premixed and Non-Premixed Flames with Fine Droplets of Water and Solutions," *Proceedings of the Combustion Institute* **29**, 369-376, (2002).
100. Chelliah, H.K., Williams, B.A., Mowrey, R.C., and Fleming, J.W., "Water Mist Suppression Of Propane-Air Flames: Modeling And Experimental Study," *Proceedings Of The Eastern States Section*, The Combustion Institute, Pittsburgh, PA, 26-29 October 2003.
101. Davis, S.G., Law, C.K., and Wang, H., "Propene Pyrolysis and Oxidation Kinetics in a Flow Reactor and Laminar Flames," *Combustion and Flame* **119**, 375-399, (1999).
102. H. Wang, U. Delaware, private communication with H.K. Chelliah.

103. Chelliah, H.K., Law, C.K., Ueda, T., Smooke, M.D., and Williams, F.A., "An Experimental and Theoretical Investigation of the Dilution, Pressure and Flow-Field Effects on the Extinction Condition of Methane-Air-Nitrogen Diffusion Flames," *Proceedings of the Combustion Institute* **23**, 503-511, (1990).
104. Li, S.C., Libby, P.A., and Williams, F.A., "Spray Structure in Counterflowing Streams with and without a Flame," *Combustion and Flame* **94**, 161-177, (1993).
105. Seshadri, K., and Peters, N., "Asymptotic Structure and Extinction of Methane-Air Diffusion Flames," *Combustion and Flame* **73**, 23-44, (1988).
106. Chelliah, H.K., and Williams, F.A., "Aspects of the Structure and Extinction of Diffusion Flames in Methane-Oxygen-Nitrogen Systems," *Combustion and Flame* **80**, 17-48, (1990).
107. Peters, N., "Local Quenching due to Flame Stretch and Non-Premixed Turbulent Combustion," *Combustion Science and Technology* **30**(1-6), 1-17, (1983).
108. Kim, J.S., and Williams, F.A., "Structures of Flow and Mixture-Fraction Fields For Counterflow Diffusion Flames With Small Stoichiometric Mixture Fractions," *SIAM Journal of Applied Mathematics* **53**(6), 1551-1566, (1993).
109. Zegers, E.J.P., Williams, B.A., Sheinson, R.S. and Fleming, J.W., "Dynamics and Suppression Effectiveness of Monodisperse Water Droplets in Non-Premixed Flames," *Proceedings of the Combustion Institute* **28**, 2931-2937, (2000).
110. Zegers, E.J.P., Williams, B.A., Fisher, E.M., Fleming, J.W., and Sheinson, R.S., "Suppression of Nonpremixed Flames by Fluorinated Ethanes and Propanes," *Combustion and Flame* **121**, 471-487, (2000).
111. Berglund, R.N. and Liu, B.Y.H., "Generation Of Monodisperse Aerosol Standards", *Environmental Science and Technology* **7**(2), 147-153, (1973).
112. Chelliah, H.K., Williams, B.A., and Fleming, J.W., "Water Mist Suppression of Propane-Air Flames: Interpretation of Experimental Results," NRL/MR/6180--05-8853, March 10, 2005.
113. Chin and Lefebvre, "Steady-State Evaporation Characteristics of Hydrocarbon Fuel Drops," *AIAA* **21**(10), 1437- 1443, (1983).
114. Fleming, J.W., Reed, M.D., Zegers, E.J.P., Williams, B.A., and Ronald S. Sheinson, R.S., "Extinction Studies of Propane/Air Counterflow Diffusion Flames: The Effectiveness of Aerosols," *Proceedings of the Halon Options Technical Working Conference*, 403-414, (1998).
115. Reed, Mark D., *A Study of the Behavior of Bicarbonate Powder Extinguishants in a Counterflow Propane/Air Diffusion Flame*, M.S. thesis, Worcester Polytechnic Institute, Fire Protection Engineering, Worcester, MA, (work carried out at the NRL), 1997.
116. Seeger, P.G., "A Laboratory Test Method for Evaluating the Extinguishing Efficiency of Dry Powder," *AGARD Conference Proceedings* Vol. **166**, Paper 24, 1975.
117. Williams, B.A. and Fleming, J.W., "Suppression Mechanisms of Alkali Metal Compounds," 1999, in Gann, R.G., Burgess, S.R., Whisner, K.C., and Reneke, P.A., eds., *Papers from 1991-2006 Halon Options Technical Working Conferences (HOTWC)*, CD-ROM, NIST SP 984-4, National Institute of Standards and Technology, Gaithersburg, MD, 2006.
118. Trees, D. and Seshadri, K., "Experimental Studies of Flame Extinction by Sodium Bicarbonate (NaHCO<sub>3</sub>) Powder," *Combustion Science and Technology* **122**, 215-230, (1997).
119. Wanigarathne, P.A., Krauss, R.H., Chelliah, H.K., and Davis, R.J., "Fire Suppression by Particulates Containing Metallic Compounds," 2000, in Gann, R.G., Burgess, S.R., Whisner, K.C., and Reneke, P.A.,

eds., *Papers from 1991-2006 Halon Options Technical Working Conferences (HOTWC)*, CD-ROM, NIST SP 984-4, National Institute of Standards and Technology, Gaithersburg, MD, 2006.

120. Friedman, R. and Levy, J.B., Inhibition of Opposed-Jet Methane Air Diffusion Flames - the Effects of Alkali Metal Vapors and Organic Halides, *Combustion and Flame* **7**, 195-201, (1963).

121. Jensen, D.E., and Jones, G.A., "Kinetics of Flame Inhibition by Sodium," *Journal of the Chemical Society, Faraday Transactions I* **78**, Part 9, 2843-2850, (1982).

122. McHale, E.T., "Flame Inhibition by Potassium Compounds," *Combustion and Flame* **24**, 277-279, (1975).

123. Takahashi, F., Schmoll, W. J., and Dressler, J. L., "Characterization of a Velocity-Modulation Atomizer," *Review of Scientific Instruments* **65**, 3563-3569, (1994).

124. Lide, D.R., ed, *CRC Handbook of Chemistry and Physics*, 81st edition., CRC Press, Boca Raton, FL, p. 8-108, 2000.

125. Smooke, M.D., "Solution of Burner-Stabilized Premixed Laminar Flames by Boundary-Value Methods," *Journal of Computational Physics* **4**, 72-105, (1982).

126. Greenberg, J.B., Silverman, I., and Tambour, Y., "On the Origins of Spray Sectional Conservation Equations," *Combustion and Flame* **93**, 90-96, (1993).

127. D'Angelo, Y., Silverman, I., Gao, L. P., Gomez, A., and Smooke, M. D., "Computational and Experimental Study of Counterflow Spray Diffusion Flames," *Proceedings of the Eastern States Section, The Combustion Institute*, Pittsburgh, PA, 1996.

128. Wanigarathne, P.C., *Fire Suppression in Studies with Particulates Containing Metallic Compounds*, M.S. thesis, University of Virginia, Charlottesville, VA, 2001.

129. Chelliah, H.K., Lazzarini, A.K., Wanigarathne, P.C., and Linteris, G.Y., "Inhibition of Premixed and Non-premixed Flames with Fine Droplets of Water and Solutions," *Proceedings of the Combustion Institute* **29**, 369-376, (2002).

130. Reinelt, D., and Linteris, G.T., "Experimental Study of the Inhibition of Premixed and Diffusion Flame by Iron Pentacarbonyl," *Proceedings of the Combustion Institute* **26**, 1421-1428, (1996).

131. Linteris, G.T., Knyazev, V., and Babushok, V., "Inhibition of Premixed Methane Flames by Manganese and Tin Compounds," *Combustion and Flame* **29**, 221-238, (2002).

132. *NIST Chemistry WebBook*, no. 69, <http://webbook.nist.gov/chemistry/>, release July 2001.

133. Vanpee, M., and Shirodkar, P.P., "A Study of Flame Inhibition by Metal Compounds," *Proceedings of the Combustion Institute* **17**, 787-795, (1978).

134. Patrick, R., and Golden, D.M., "Termolecular Reactions of Alkali Metal Atoms with O<sub>2</sub> and OH," *International Journal of Chemical Kinetics* **16**, 1567-1574, (1984).

135. Lask, G., and Wagner, H.G., "Influence Of Additives On The Velocity Of Laminar Flames," *Proceedings of the Combustion Institute* **8**, 432-438, (1962).

136. da Cruz, F.N., Vandooren, J., and Van Tiggelen, P., "Comparison Of The Inhibiting Effect Of Some Halogenomethane Compounds On Flame Propagation," *Bull. Soc. Chim. Belg.* **97**, 1011-1030, (1988).

137. Williams, F.A., *Combustion Theory*, 2nd ed., Benjamin/Cummings, Menlo Park, CA, 1985.

138. Chelliah, H.K., Yu, G., Hahn, T.O., and Law, C.K., "An Experimental and Numerical Study on the Global and Detailed Kinetics of Premixed and Nonpremixed Flames of Chloromethane, Methane, Oxygen and Nitrogen," *Proceedings of the Combustion Institute* **24**, 1083-1090, (1992).

139. Tomalia, D.A., "Dendrimer Molecules," *Scientific American* **272**, 62-66, (1995).
140. Tomalia, D.A., Naylor, A.M., and Goddard, W.A., "Starburst Dendrimers - Molecular Level Control of Size, Shape, Surface Chemistry, Topology, and Flexibility from Atoms to Macroscopic Matter," *Angewandte Chemie. International Edition* **29**, 138-175, (1990).
141. Tapscott, R.E., "Current Topics on New Halon Replacements," National Industrial Research Institute, Agency of Industrial Science and Technology, Nagoya, Japan, 10 April 1997.
142. Babushok, V.I. and Tsang, W., "Inhibitor Rankings for Hydrocarbon Combustion," *Combustion and Flame* **123**, 488-506 (2000).
143. Beck Tan, N.C., DeSchepper, D.C., and Balogh, L., *Dendritic Polymers as Fire Suppressants*, ARL-TR-2071, Army Research Laboratory, Aberdeen Proving Ground, October, 1999.
144. Finnerty, A.E., McGill, R. L., and Slack, W.A., Technical Report ARL-TR-1138, Aberdeen Proving Ground, Maryland, 1996.
145. Yang, J.C., Donnelly, M.K., Prive, N.C., and Grosshandler, W.L., "An Apparatus for Screening Fire Suppression Efficiency of Dispersed Liquid Agents," 1998, in Gann, R.G., Burgess, S.R., Whisner, K.C., and Reneke, P.A., eds., *Papers from 1991-2006 Halon Options Technical Working Conferences (HOTWC)*, CD-ROM, NIST SP 984-4, National Institute of Standards and Technology, Gaithersburg, MD, 2006.
146. Yang, J.C., Donnelly, M. K., Prive, N.C., and Grosshandler, W.L., "*Dispersed Liquid Fire Suppression Screen Apparatus*," NISTIR-6319, Gaithersburg, MD, 1999.
147. Chen, C.Z., Beck Tan, N.C., and Cooper, S.L., "Incorporation of Dimethyldedecylammonium Chloride Functionalities onto Poly(propylene) Dendrimers Significantly Enhances Their Anti-bacterial Properties," *Chemical Communications* **16**, 1585-1586, (1999).
148. Nukiyama and Tanasawa, "Experiments on the Atomization of Liquids in Air-Stream," *Transactions of the Society of Mechanical Engineers* **4,5,6**, (1938-1940).
149. Uppuluri, S. , Dvornic, P. R., Beck Tan, N. C., and Hagnauer, G., "*The Properties of Dendritic Polymers II: Generation Dependence of the Physical Properties of Poly(amidoamine) Dendrimers*," ARL-TR-1774, Aberdeen Proving Ground, Maryland, 1999.
150. Lide D.R., ed., *CRC Handbook of Chemistry and Physics*, 81st edition, CRC Press, Inc., Boca Raton, FL, p.6-3, 2000.
151. Yang, J.C., Prive, N.C., Donnelly, M.K., and Grosshandler, W.L., "Recent Results from the Dispersed Liquid Agent Fire Suppressant Screen," 1999, in Gann, R.G., Burgess, S.R., Whisner, K.C., and Reneke, P.A., eds., *Papers from 1991-2006 Halon Options Technical Working Conferences (HOTWC)*, CD-ROM, NIST SP 984-4, National Institute of Standards and Technology, Gaithersburg, MD, 2006.
152. Pitts, W.M., Yang, J.C., Bryant, R.A., Blevins, L.G., and Huber, M., *Characteristics and Identification of Super-Effective Thermal Fire-Extinguishing Agents*, Final Report, NGP Project 4C/1/890, NIST Technical Note 1440, National Institute of Standards and Technology, Gaithersburg, MD, June 2001.
153. Downie, B., Polymeropoulos, C., and Gogos, G., "Interaction of a Water Mist with a Buoyant Methane Diffusion Flame," *Fire Safety Journal* **24**, 359-381, (1995).
154. Rasbash, D.J., "The Extinction Of Fire With Plain Water: A Review," *Proceedings of the First International Symposium of Fire Safety Science*, C. E. Grant And P.J. Pagni, Editors, Hemisphere, Washington, pp. 1145-1163, 1986.

155. Engel, O. G., "Waterdrop Collisions With Solid Surfaces," *Journal of Research of the National Bureau of Standards* **54**, 281-298, (1955).
156. Chandra, S. and Avedisian, C.T., "On The Collision Of A Droplet With A Solid-Surface," *Proceedings of the Royal Society of London A-Mathematical Physical and Engineering Sciences* **432**, 13-41, (1991).
157. Chandra, S. and Avedisian, C.T., "Observations of Droplet Impingement on a Ceramic Porous Surface," *International Journal of Heat and Mass Transfer* **35**, 2377-2388, (1992).
158. Mundo, C., Sommerfeld, M., and Tropea, C., "Droplet-Wall Collisions - Experimental Studies of the Deformation and Breakup Process," *International Journal of Multiphase Flow* **21**, 151-173, (1995).
159. Yarin, A.L. and Weiss, D.A., "Impact of Drops on Solid-Surfaces - Self-Similar Capillary Waves, and Splashing as a New-Type of Kinematic Discontinuity," *Journal of Fluid Mechanics* **283**, 141-173, (1995).
160. Bernardin, J.D. and Mudawar, I., "Experimental and Statistical Investigation of Changes in Surface Roughness Associated with Spray Quenching," *International Journal of Heat and Mass Transfer* **39**, 2023-2037, (1996).
161. Bernardin, J.D., Stebbins, C.J., and Mudawar, I., "Effects of Surface Roughness on Water Droplet Impact History and Heat Transfer Regimes," *International Journal of Heat and Mass Transfer* **40**, 73-88, (1997).
162. Bernardin, J.D., Stebbins, C.J., and Mudawar, I., "Mapping of Impact and Heat Transfer Regimes of Water Drops Impinging on a Polished Surface," *International Journal of Heat and Mass Transfer* **40**, 247-267, (1997).
163. Bernardin, J.D. and Mudawar, I., "Film Boiling Heat Transfer of Droplet Streams and Sprays," *International journal of Heat and Mass Transfer* **40**, 2579-2593, (1997).
164. Mudawar, I. and Valentine, W.S., "Determination Of The Local Quench Curve For Spray Cooled Metallic Surfaces," *ASME Journal of Heat Treating* **7**, 107-121, (1989).
165. Klinzing, W.P., Rozzi, J.C., and Mudawar, I., "Film And Transition Boiling Correlations For Quenching Of Hot Surfaces With Water Sprays," *ASME Journal of Heat Treating* **9**, 91-103, (1992).
166. Mudawar, I. and Deiters, T.A., "A Universal Approach to Predicting Temperature Response of Metallic Parts to Spray Quenching," *International Journal of Heat and Mass Transfer* **37**, 347-362, (1994).
167. Hall, D.D. and Mudawar, I., "Experimental and Numerical Study of Quenching Complex-Shaped Metallic Alloys with Multiple, Overlapping Sprays," *International Journal of Heat and Mass Transfer* **38**, 1201-1216, (1995).
168. Estes, K.A. and Mudawar, I., "Correlation of Sauter Mean Diameter and Critical Heat Flux for Spray Cooling of Small Surfaces," *International journal of Heat and Mass Transfer* **38**, 2985-2996, (1995).
169. Mudawar, I. and Estes, K.A., "Optimizing And Predicting Chf In Spray Cooling Of A Square Surface," *ASME Journal of Heat Transfer* **118**, 672-679, (1996).
170. Rein, M., "Phenomena Of Liquid-Drop Impact On Solid And Liquid Surfaces," *Fluid Dynamic Research* **12**, 61-93, (1993).
171. Henry, R.E. and Fauske, H.K., "Nucleation Processes In Large-Scale Vapor Explosions," *ASME Journal of Heat Transfer* **101**, 280-287, (1979).

172. Spalding, D.B., *Some Fundamentals of Combustion*, Butterworths Scientific Publications, London, 1955.
173. Kanury, A.M., *Introduction to Combustion Phenomena*, Gordon & Breach, New York, 1975.
174. *DIPPR Data Compilation of Pure Compound Properties Database*, V9.02, NIST Standard Reference Data Program #11, NIST, Gaithersburg MD, 1995.
175. Reid, R.C., Prausnitz, J.M., and Poling, B.E., *The Properties of Gases & Liquids*, 4th ed., McGraw-Hill, New York, 1987.
176. Qiao, Y.M., and Chandra, S., "Spray Cooling Enhancement by Addition of a Surfactant," *ASME Joournal of Heat Transfer* **120**, 92-98, (1998).
177. Deb, S. and Yao, S.-C., "Analysis on Film Boiling Heat Transfer of Impacting Sprays," *International Journal of Heat and Mass Transfer* **32**, 2099-2112, (1989).
178. Fu, C., Sojka, P.E., and Sivathanu, Y.R., "Water Mist Impingement onto a Heated Surface," *Proceedings of the 5th Joint ASME/JSME Joint Thermal Engineering Conference*, 1999.
179. Fu, C., Sojka, P.E., and Sivathanu, Y.R., "On the Interaction Between Evaporating Sprays and Heated Surfaces," *Proceedings of the 12th Annual Conference on Liquid Atomization and Spray Systems*, 1999.
180. Oke, H.P., *An Experimental Study of Flame Spread over PMMA Subject to a Water Mist*, M.S. Thesis, School of Mechanical Engineering, Purdue University, November, 1999.
181. Chunming Fu., *Droplet Interactions with a Hot Surface*, M.S. Thesis, School of Mechanical Engineering, Purdue University, March 2000.
182. Howell, J.R., "Application Of Monte Carlo To Heat Transfer Problems Advances in Heat Transfer," in *Advances In Heat Transfer*, Vol. 5, J. P. Hartnett and T. Irvine, Eds., Academic Press, New York, p. 1, 1968.
183. Haji-Sheik, *Handbook of Numerical Heat Transfer*, John Wiley & Sons Inc., NY, 1988.
184. Kahn, H., and Marshall, A. W., "Methods Of Reducing Sample Size In Monte-Carlo Computations," *Journal of the Operations Research Society of America* **1**, 263-278, (1953).
185. Lanore, J.M., "Weighting and Biasing of a Monte Carlo Calculation for Very Deep Penetration Of Radiation," *Nuclear Sciene and Engineering* **45**, 66-72, (1971).
186. Sivathanu, Y.R., and Gore, J.P., "A Discrete Probability Function-Method for the Equation of Radiative-Transfer," *Journal of Quantitative Spectroscopy and Radiative Transfer* **49**, 269-280, (1993).
187. Fox, R.W., and McDonald, A.T., *Introduction to Fluid Mechanics*, John Wiley & Sons (SEA) Pte. Ltd., Singapore, 1995.
188. Kline, S.J., and McClintock, F.A., "Describing Uncertainties In Single-Sample Experiments," *ASME Mechanical Engineering* **75**, 3-8, (1953).
189. Brenn, G., Helpio, T., and Durst, F. , "A New Apparatus for the Production of Monodisperse Sprays at High Flow Rates," *Chemical Engineering Science* **5**, 237-244 , (1997).
190. Dingel, B.E., *An Experimental and Theoretical Study of Air and Water Mist Impingement Cooling*, M.S. thesis, Mechanical Engineering, Purdue University, 1997.
191. Lund, M.T., Sojka, P.E., Lefebvre, A.H., Gosselin, P.G., "Effervescent Atomization at Low Mass Flow Rates. Part I: The Influence Of Surface Tension," *Atomization and Sprays* **3**, 77-89, (1993).

192. Masters, K., *Spray Drying*, 2nd Edition, John Wiley and Sons, New York, 1976.
193. Ranz, W.E., and Marshall, W.R, "Evaporation from Drops," *Chemical Engineering Progress* **48**, 173-180, (1952).
194. Jiang, Y.J., Umemura, A., and Law, C.K., "An Experimental Investigation on the Collision Behavior of Hydrocarbon Droplets," *Journal of Fluid Mechanics* **234**, 171-190, (1992).

---

---

**Chapter 5: INSTRUMENTATION FOR  
BENCH- AND LARGE-SCALE  
TEST FIXTURES**

---

---

**Kevin L. McNesby, Ph.D.  
U.S. Army Research Laboratory**

**TABLE OF CONTENTS**

5.1 Introduction.....	482
5.2 Laser Induced Breakdown Spectroscopy for Measurement of Fire Suppressants.....	483
5.3 Tunable Diode Laser Absorption Spectroscopy (TDLAS) for Measurement of Combustion products, Fuels, and Oxygen .....	485
5.3.1 General .....	485
5.3.2 HF .....	486
5.3.3 Oxygen .....	490
5.3.4 Fuels .....	490
5.3.5 Observations.....	501
5.4 Measurement of Fire Suppressant Concentration Using a Differential Infrared Rapid Agent Concentration Sensor (DIRRACS) .....	502
5.4.1 Introduction .....	502
5.4.2 Original Instrument Design – DIRRACS I .....	502
5.4.3 Improved Hardware Design – DIRRACS II .....	505
5.4.4 Data Acquisition and Analysis.....	507
5.4.5 Calibration Experiments.....	507
5.4.6 Release Tests of HFC-125 in the TARPF Facility .....	508
5.4.7 HFC-125 Release Tests in a Bradley Vehicle .....	509
5.4.8 Assessment .....	513
5.5 Conclusion .....	513
5.6 References.....	514

## 5.1 INTRODUCTION

A projectile penetrating the hull and fuel cell of a land combat vehicle may result in a fine mist of fuel being dispersed into the crew compartment. By military specification, the ensuing “mist fireball explosion” must be extinguished within 250 ms of detection, using the onboard chemical fire suppression system.<sup>1</sup> A similar hazard occurs upon the penetration of a projectile into an aircraft dry bay and adjacent fuel cell. The fire extinguishing agent must be distributed throughout the interior region surrounding the fuel tank and flame extinguishment accomplished within a time interval similar to that for ground vehicles. This speed is necessary to prevent structural damage to the aircraft wing or fuselage to the point where the plane would crash.

Live-fire tests of ground vehicles and aircraft (or representations of sections of these) are frequently conducted in order to characterize the performance of a fire suppression system in quenching such fires. In these tests, it is particularly important to monitor the distribution of the fire suppressant agent in real time. This enables judgment on the extent to which the time to flame extinguishment was limited by the effectiveness of the agent, the agent dispersion system, or both. To obtain the desired information from these very short duration tests, it is necessary to use instrumentation that provides data that are resolved on a time scale shorter than the suppression event, generally in tens of milliseconds.

The instruments currently used for monitoring the concentration of halon 1301 are the Statham analyzer and the Halonyzer.<sup>2</sup> Each has a time response on the order of 200 ms or longer. Clearly they are not capable of monitoring the rapid distribution of the agent in a dry bay or crew compartment environment.

There are additional gases whose time-dependent concentrations reflect on the efficacy of the fire suppression process. These include the local oxygen and fuel concentrations, which control the extent of the burning. They also include the concentrations of toxic or corrosive combustion products. Chief among these, for both halon 1301 and most of the halocarbon replacement chemicals, is hydrogen fluoride (HF).<sup>3</sup> As various fluorine-containing suppressants emerged, minimization of HF gas production during fire suppression became an important design criterion.<sup>4</sup> The extreme reactivity of this gas dictated the additional requirement that the measurement be made in-situ, which, in turn, mandated the use of optical techniques.

The NGP performed research to develop and adapt measurement techniques, apparatus and procedures for real-time, in-situ measurements of combustible gases, combustion by-products, and suppressant concentrations during the quenching of deflagrations in ground vehicles and aircraft.

Each of the techniques was based on the absorption of light from infrared sources: near-infrared tunable diode lasers (NIR-TDL), near infrared pulsed lasers, and resistively-heated coils (or “Nernst” glowers). In the following text, the infrared region of the spectrum is considered to encompass wavelengths from 1  $\mu\text{m}$  to 30  $\mu\text{m}$ . Table 5–1 lists the techniques used, the gases measured, the absorption wavelengths, and the approximate limits of detection (LoD). All LoD values listed are the best achievable laboratory values. Experience indicated that the LoDs in field measurement were at least one order of magnitude worse than in laboratory measurements.

Limited descriptions of the methods appear in the following sections, with more extensive detail available in the references. In each case, the procedure was studied in a laboratory to determine the measurement

linearity and the limits of detection. Some of the apparatus were then hardened and installed for use on a real-scale test fixture.

**Table 5–1. Optical Diagnostics for Fire Species.**

Method	Molecule	Wavelength (μm)	LoD (μL/L)
Tunable Diode Laser Absorption Spectroscopy (TDLAS)	HF	1.31	0.04
TDLAS	O <sub>2</sub>	0.76	100
TDLAS	CH <sub>4</sub>	1.65	0.6
TDLAS	CO	1.55	5
TDLAS	JP-8 DF-2 gasoline	1.71	100
Laser-induced Breakdown Spectroscopy (LIBS)	O <sub>2</sub>	Emission	1000
LIBS	CF <sub>3</sub> Br	Emission	1000
LIBS	CF <sub>3</sub> H	Emission	1000
Differential Infrared Rapid Concentration Sensor (DIRRACS)	C <sub>2</sub> HF <sub>5</sub>	8.3 to 9.0	5000

## 5.2 LASER INDUCED BREAKDOWN SPECTROSCOPY FOR MEASUREMENT OF FIRE SUPPRESSANTS

In this technique, a pulsed Nd:YAG laser, typically with pulse energy > 50 mJ, is focused onto a gas mixture with sufficient intensity that molecular breakdown takes place in the focal volume of the laser. The high electric field at the laser focus causes an ionization of a small number of gas molecules (usually air). Free electrons within this plasma then absorb laser radiation (inverse Brehmstrahlung<sup>5</sup>), resulting in further ionization accompanied by collisional heating. Temperatures within the laser focal volume may reach 20,000 K, resulting in atomization of any molecules within the focal volume. After the laser pulse, rapid deceleration of the electrons within the plasma leads to an initial emission of broadband radiation (Brehmstrahlung<sup>5</sup>) lasting tens to hundreds of nanoseconds, followed by emission of discrete wavelengths of light as the atomic species present in the plasma return to their ground states (in tens to hundreds of microseconds). A schematic showing the application of LIBS to laboratory measurements is shown in Figure 5–1.

First, the technique was used for measurement of linearity and determination of limits of detection for mixtures of halogenated fire suppressants in air.<sup>6,7</sup> Figure 5–2 shows that the intensity of F atom emission near 400 nm, measured using LIBS is nearly directly proportional to vapor concentration. The limit of detection for each gas, using LIBS, was approximately 1000 μL/L. Following these tests, a series of experiments was performed to determine if the LIBS measurement process could initiate combustion in combustible hydrocarbon/air mixtures. Tests were performed on flowing streams of pure methane and pure propane in air. In most cases, the LIBS spark provided sufficient energy to cause the gas mixture to begin burning. Following these tests, it was decided that the LIBS technique was inappropriate for use in enclosed areas that may contain hydrocarbon/air mixtures approaching the lower explosion limit (LEL), and was therefore inappropriate for measurement of oxygen concentrations immediately following fire suppression, when reflash conditions may exist.

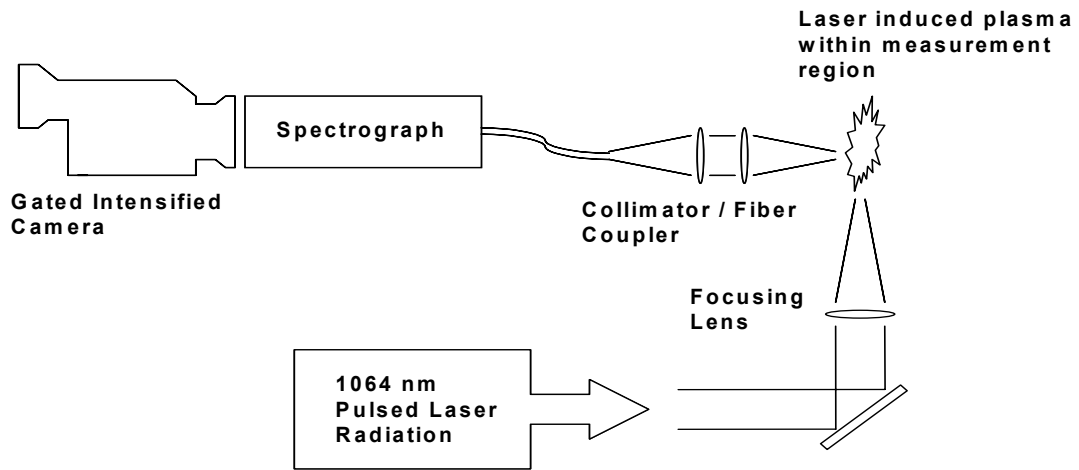


Figure 5–1. Schematic of Laser Induced Breakdown Spectroscopy (LIBS) Measurement Apparatus.

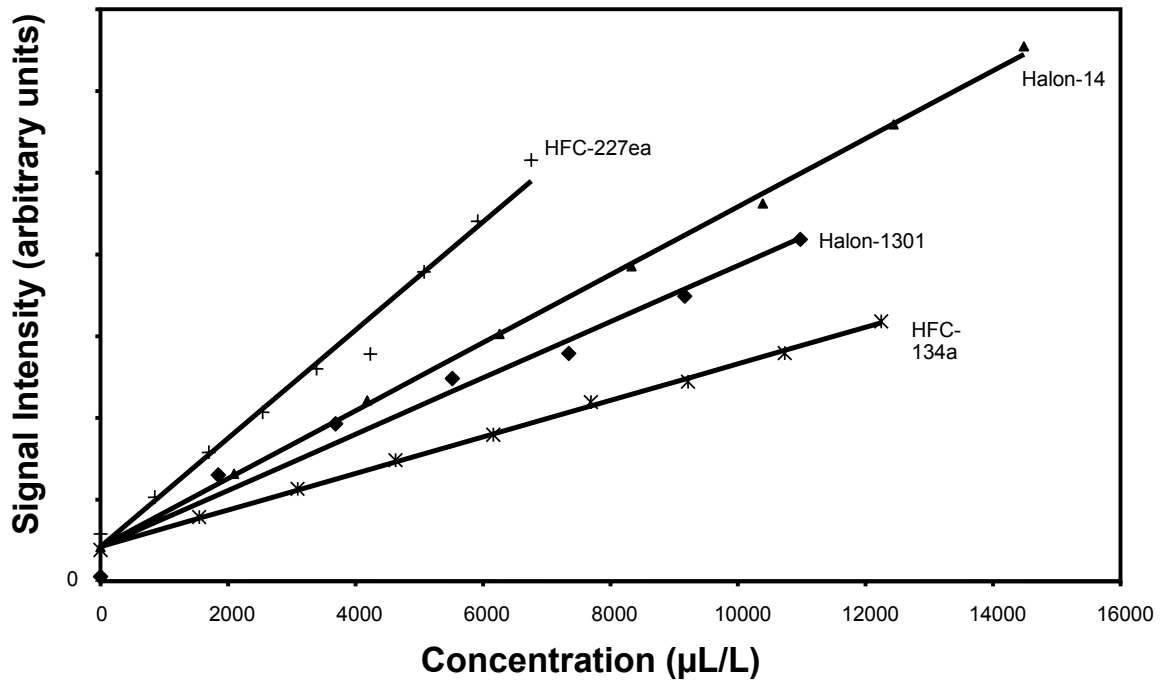


Figure 5–2. Measured Concentrations of Fluorinated Fire Suppressants using LIBS.

As of the date of this book, laser induced breakdown spectroscopy (LIBS) has not been transitioned to field measurement of suppressant concentrations (in non-flammable environments) in armored vehicles at the Aberdeen Test Center. The main reason for this is that optical fibers necessary for delivering pulsed radiation to the measurement site were found to be unreliable, failing at fewer than 200 shots. However, several manufacturers are now offering fibers for delivering pulsed radiation at 1.06  $\mu\text{m}$ . These high power delivery fibers can transmit a pulse of up to 80 mJ at 10 ns, which may enable LIBS of gases at remote locations.

### **5.3 TUNABLE DIODE LASER ABSORPTION SPECTROSCOPY (TDLAS) FOR MEASUREMENT OF COMBUSTION PRODUCTS, FUELS, AND OXYGEN**

#### **5.3.1 General**

In static laboratory environments, a widely used standard method for detection and measurement of gases has been Fourier transform infrared (FTIR) spectroscopy.<sup>8</sup> In conventional Fourier transform spectrometers, each “discrete” wavelength of light emitted by the glowbar source, generally a resistively heated tungsten coil, is power modulated by a Michelson interferometer. As a result, the output at any individual wavelength, as measured at the detector, is cosinusoidal, with a frequency in the kHz (acoustic) range. The signal measured at the detector is a superposition of cosinusoidal waveforms called an interferogram. The amplitude and frequency of each cosine wave composing the interferogram is a function of the moving mirror displacement and of the wavelength of the incident light. The measurement interval is ultimately determined by the velocity of the moving mirror, and may only approach 20 ms for a single scan. Spectral resolution is a function of the moving mirror displacement, and gas sensitivities may exceed parts per million. Although highly refined, the net effect of this design is to necessitate complicated electromechanical mirror transport systems, limit measurement applications to repeatable or static events, and thus limit the use of these instruments to the laboratory.

To overcome these limitations for in-situ gas measurement during and following a ballistic event on board a land-based vehicle, NGP researchers at the Army Research Laboratory pursued a solid-state measurement system, while attempting to maintain the sensitivity and broad spectral coverage of interferometer-based infrared spectroscopy. The design criteria for gas detection and measurement employing infrared light sources and detectors were mid-range sensitivity (50  $\mu\text{L/L}$  to 5000  $\mu\text{L/L}$ )<sup>9</sup>, time for collection of a full spectrum of 10 ms or less, and, in the near infrared, the ability to use low replacement cost optics, optical fibers, and detectors necessary for data sampling in hostile environments. For example, commercially available diode lasers, initially produced for optical communication, began to see use for measurement of HF gas in the early 1980s.<sup>10</sup> By 2000, relatively low cost narrow band diode lasers emitting near-infrared radiation (near-infrared tunable diode lasers, NIR-TDL) at wavelengths absorbed by most atmospheric gases and many radical species (e.g., HF gas near a wavelength of 1.3  $\mu\text{m}$ ) were commercially available. Use of NIR-TDLs for gas measurement became a widely accepted method for industrial applications.<sup>10,11</sup> Wavelength modulation techniques and the ability of inexpensive optical fibers to deliver light to hostile environments allowed sensitive optical components and electronics to be remotely located.

There were significant challenges to be overcome for these NIR-TDLs to become practical. The first involved the ability to measure and store data continuously with a new data point acquired every 10 ms. Secondly, it was unclear how the sensor equipment would perform in the harsh environment for field

testing, in which the sensor assembly in the vehicle was subjected to shock (explosion) and heat (fire). The third involved developing a method that enabled the narrow band light source (the diode laser) to measure a broad band absorber (JP-8 vapor), while maintaining the signal to noise enhancement achievable with phase sensitive detection.<sup>12,9</sup>

The following sections describe the technique and results for the detection of HF, various fuels, and molecular oxygen.

### 5.3.2 HF

HF gas concentrations were measured using a stand-alone spectrometer system assembled at the Army Research Laboratory.<sup>13</sup> This system used a single, distributed feedback (DFB) tunable diode laser emitting near infrared radiation at a wavelength near 1.31  $\mu\text{m}$ . This wavelength coincides with the P2 line of the first overtone absorption of HF gas, and is free of overlap by water lines present in most combustion environments [10]. Typically, the laser was modulated (wavelength tuned) at 100 Hz for a range of approximately  $0.5 \text{ cm}^{-1}$ , such that the center of this tuning range coincided with the center of the absorption by the P2 transition in HF gas (absorption linewidth approximately  $0.1 \text{ cm}^{-1}$ ). Superimposed upon this “slow” modulation was a fast (50 kHz to 100 kHz) sinusoidal wavelength modulation. The wavelength range of the fast modulation was adjusted so that it was a small ( $< 0.25$ ) fraction of the absorption linewidth of the P2 transition (1<sup>st</sup> overtone) in HF gas. This dual modulated light beam was then launched onto an optical fiber, and the fiber used to transmit the beam from a control room (located a safe distance from the measurement site) to the measurement site. For field work, this usually meant the beam was transported approximately 100 m to the measurement site. At the measurement site, the fiber was terminated with a gradient index (GRIN) lens, causing the light beam to be collimated while it passed through free space (the measurement region). After passing through free space for approximately 10 cm to 15 cm, the modulated light beam impinged upon a room temperature operation semiconductor light detector (typically InGaAs). The signal from the biased (12 V) photodetector was returned to the control room via a BNC cable, demodulated using a lock-in amplifier, and recorded on a laptop computer running LabView software. The amplitude (height) of the second derivative-like signal output by the lock-in amplifier was proportional to the amount of light-absorbing gas (HF) present in the measurement region. The steps involved in laser modulation and demodulation are shown in Figure 5–3.

The experimental protocol, lab results, field results, and data analysis methods are detailed in several publications.<sup>14,15,16,17,18,19</sup> Early in the experimental cycle, an effort was made to use a second optical fiber to capture the light after it had passed through the measurement region, allowing the photodetector to remain in the control room. However, it was found that the alignment of the two optical fibers for the “pitch and catch” setup at the site (typically, the crew compartment of a Bradley Fighting Vehicle) was extremely sensitive. So, it was decided to place the photodetector at the measurement site, since tests showed that small misalignments in the open path fiber-to-detector line of sight were less important than small misalignments in open path fiber-to-fiber line of sight. Additionally, the costs associated with replacing either the fiber-to-detector or fiber-to-fiber setup within the vehicle were similar (hundreds of dollars). Using this system, the measurement duration was 10 ms (100 scan/s); however, the time between measurements was approximately 100 ms, caused by the delay in transferring information from the lock-in amplifier to an oscilloscope, and from the oscilloscope to the laptop computer running LabView software. Figure 5–4 shows the equipment used for monitoring the real-scale fires in ground vehicles.

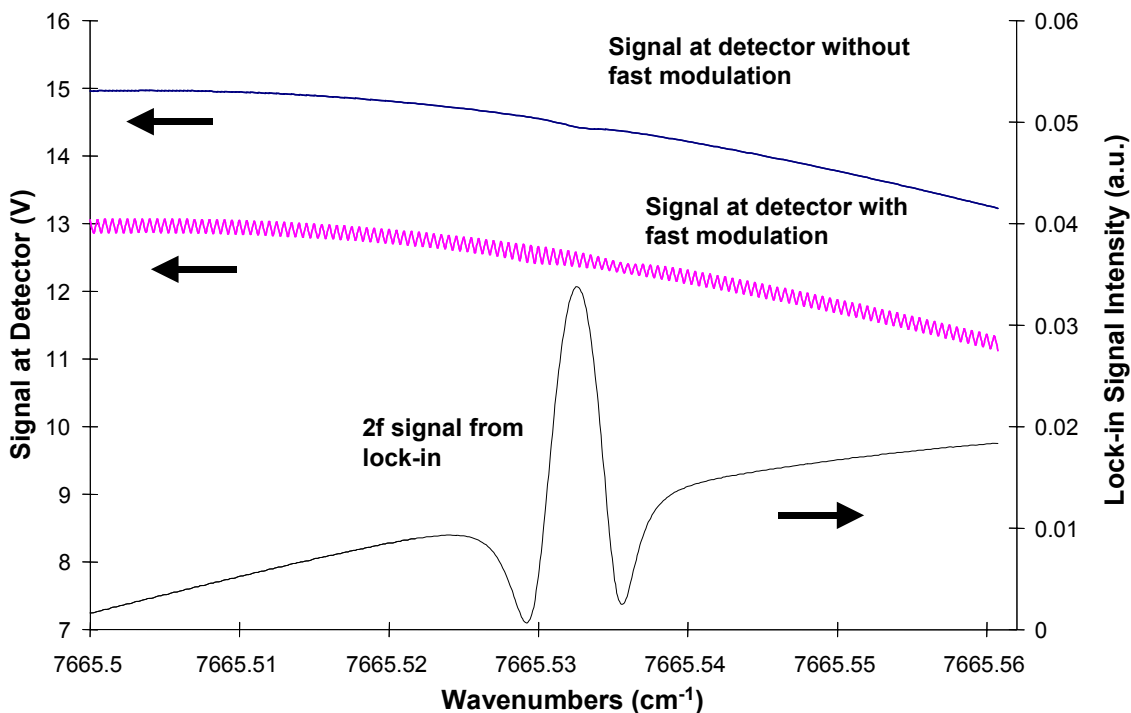


Figure 5–3. Successive Signal Improvements in the Detection of HF using TDLAS.

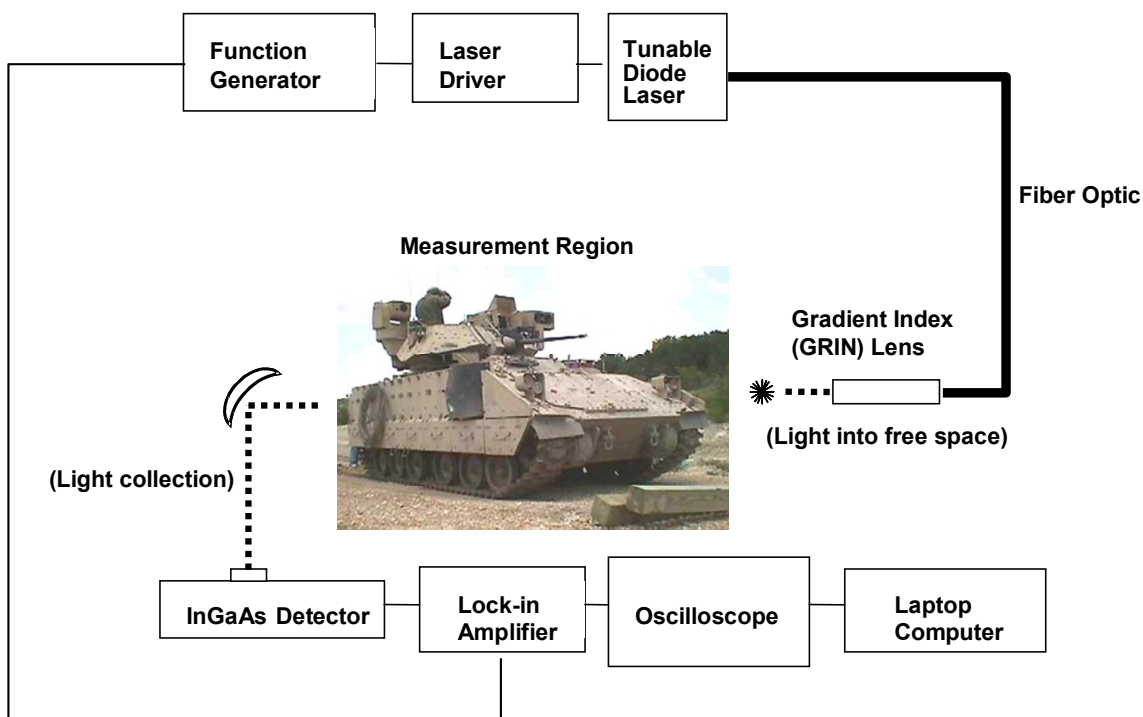


Figure 5–4. Schematic of TDLAS Apparatus for Measurement of Gases Produced during Fire Suppression in Ground Vehicles.

This single gas stand-alone spectrometer system for HF gas measurement was used for three types of testing:

1. Suppression of JP-8 pool fires, using a handheld extinguisher charged with HFC-227ea.
2. Suppression of heptane pan fires in an enclosure, using a mechanically actuated bottle charged with a series of fluorinated propanes.
3. Suppression of spark initiated or ballistically initiated JP-8 fires in the crew compartment of a Bradley Fighting Vehicle hull, using  $\text{CF}_3\text{Br}$  or HFC-227ea.

For these tests, measurements of HF gas (and other combustion products) were also measured using extractive Fourier transform infrared spectroscopy as a check. In all cases, reasonable agreement was obtained. For the JP-8 pool fire measurements, the objective was to obtain a measurement of the approximate exposure to HF experienced by a firefighter while suppressing the fire using a hand held extinguisher. The HF measurement location was approximately 5 m from the pool fire, allowing the firefighter full access to the pool fire, as he was attempting to extinguish the fire as rapidly as possible. For these tests, the HF gas concentration that was measured ranged from 0  $\mu\text{L/L}$  to approximately 1000  $\mu\text{L/L}$ . As only one measurement site was used, the measurement was largely a function of wind direction, although the time-averaged exposure was always beyond acceptable levels.

For the heptane pan fires, the objective was to understand the temporal behavior of HF gas concentration following release of the suppressant. These tests of approximately 30 kW fires were conducted in a cubic 1.5 m<sup>3</sup> enclosure. The heptane pan was located under an 0.5 m high steel table, on which the NIR-TDLAS apparatus was placed. A handheld bottle extinguisher charged with the extinguisher and perhaps a scavenging agent was situated on top of the enclosure, with a spray nozzle protruding into the enclosure. The fires were extinguished by application of HFC-236 ( $\text{C}_3\text{F}_6\text{H}_2$ ), HFC-227ea ( $\text{C}_3\text{F}_7\text{H}$ ), HFC-236 plus APP, or HFC-227ea plus APP. APP (ammonium polyphosphate) powder, itself an effective flame extinguishant, was added as both a possible synergist for the less efficient fluorocarbons and as a possible means of reducing HF yields.

The heptane fire was ignited using a butane electric match and allowed to burn for 15 s before the contents of the extinguisher were dumped into the enclosure. A video camera monitored the fire event and enabled determination of the time of extinguishment. HF data were collected for 180 s after ignition of the fuel at rate of 1 spectrum/s. In addition, spectroscopic measurements of the amount of light attenuation (obscuration) that occurs as a hand held fire extinguisher containing powder fire fighting agent is released in the crew space of a M1 land combat vehicle were performed.

The effectiveness of APP as a HF reduction and potential scavenging agent was examined by comparing the HF concentrations from fires extinguished with HFC-236/APP or HFC-227ea/APP mixtures and fires extinguished by HFC-236 or HFC-227EA alone. The two mechanisms by which HF gas concentrations can be decreased during and following fire extinguishment by the addition of the APP to the fluorinated agents are:

- Reducing the time required to extinguish the fire, thereby minimizing the time that the fluorine-containing suppressant is exposed to flame temperatures, or
- Scavenging the HF after it is produced.

Figure 5–5 shows the results of one such test. The application of 7 % APP clearly affects a significant reduction in HF. What is important is that a nominal doubling of the APP level virtually eliminated the HF. If this were principally a scavenging effect, one would expect that the green line in Figure 5–5 would rise further initially and then decline more steeply than the red curve. The observed behavior favors enhanced quenching of the flames and the accompanying reduction in the thermal generation of the HF.

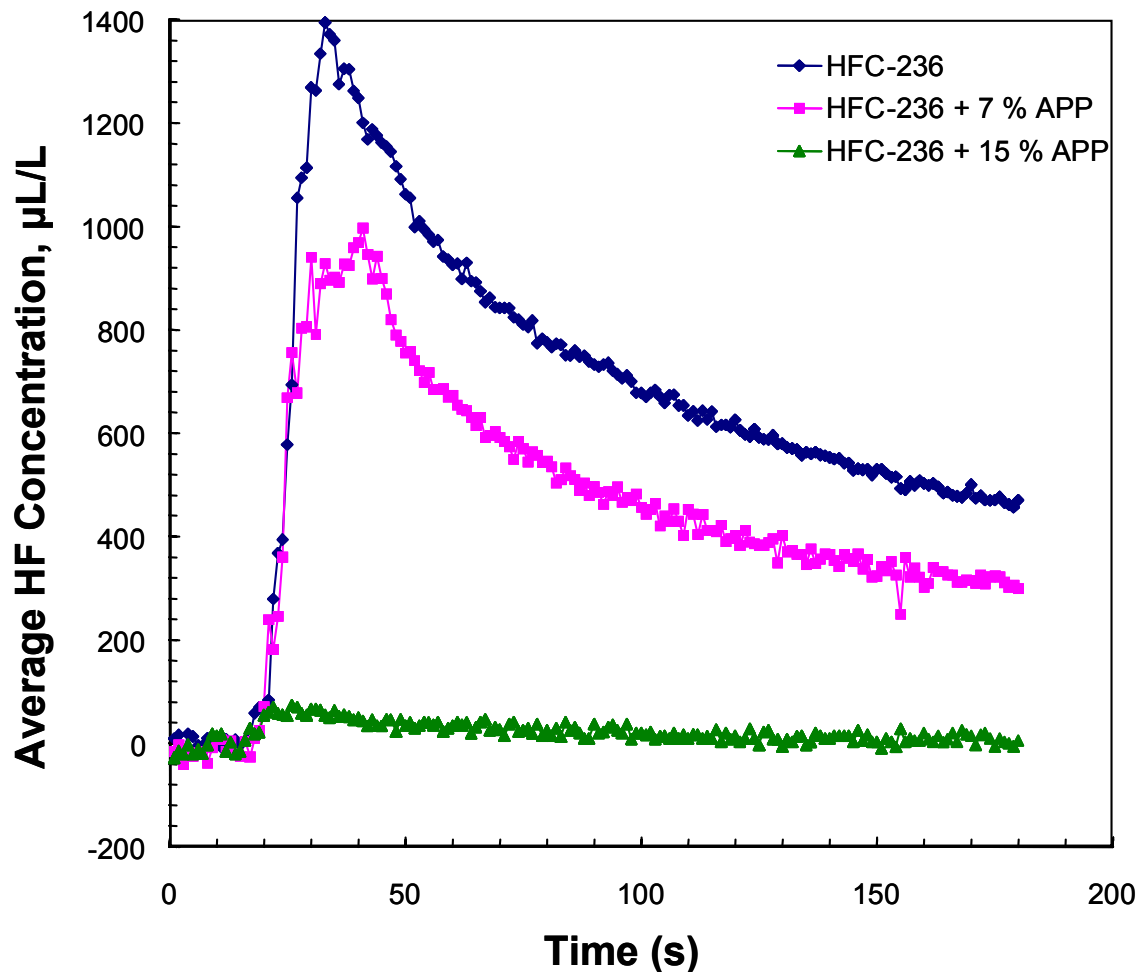


**Figure 5–5. HF Gas Produced during Suppression of Heptane Pan Fires by HFC-236 with and without the Addition of Ammonium Polyphosphate).**

In the tests conducted in the ground vehicles, the HF measurement location approximated the seating location of a passenger within the vehicle. The results indicated that HF concentrations produced from fires extinguished by HFC-236 plus APP and HFC-227ea plus APP were reduced in the test facility and that the presence of APP accelerated the reductions. Production of HF gas ranged from hundreds to thousands of ( $\mu\text{L/L}$ )-min, depending on how quickly the fire was extinguished. For successful tests (fires extinguished within 250 ms of the suppressant being deployed), HF levels were typically in the hundreds of  $\mu\text{L/L}$ . For tests where the fire was not extinguished or suppression was not complete after 250 ms (resulting in suppressant being burned), the HF levels were often beyond the measurement range of both instruments (usually 5000  $\mu\text{L/L}$  for TDLAS). Visibility reduction during extinguisher deployment was

measured inside the combat vehicle for extinguishers containing HFC-236 plus APP and  $\text{NaHCO}_3$  plus  $\text{N}_2$ . (HFC-227ea was not available for these tests.)

### 5.3.3 Oxygen

Measurement of the fuel and oxygen concentrations is especially important after the suppression event in order to predict the possibility of reignition. Minimum acceptable detection limits for fuel/oxygen gas mixtures were projected to be about  $600 \mu\text{L/L}$  (0.06 %) for the fuel and  $3000 \mu\text{L/L}$  oxygen (0.3 %), for a 10 cm optical path length at room temperature. These values would ensure the ability to make accurate concentration measurements near the lean flammability limit. The oxygen measurements are described in this section, the fuel measurements in the next.

A fully automated, multi-position, multi-laser instrument, built by Southwest Sciences, Inc., was originally designed to measure concentrations of  $\text{CO}$ ,  $\text{O}_2$ , HF, and  $\text{NO}_2$  gases at four different locations within the crew compartment of a Bradley Fighting Vehicle, achieving near continuous measurement with data points every 10 ms. Housed in a trailer adjacent to the control room at the test site, this instrument used the same technique of dual modulation spectroscopy employed by the stand alone HF measurement system described earlier. However, it used a 10 kHz ramp for the “slow” modulation and a 1MHz sine wave for the “fast” modulation. During the course of development of this instrument, it was decided to focus exclusively on measuring HF and  $\text{O}_2$  within the Bradley hull, during suppression by HFC-227ea of spark initiated JP-8 fires.

For these fires, a heated ( $\approx 70 \text{ }^\circ\text{C}$ ) spray of JP-8 liquid was begun within the crew compartment of the Bradley hull. The fuel nozzles were located along one interior wall. About 1 s later, this fuel spray was ignited by a series of spark plugs located along the wall of the interior of the vehicle. Approximately 1 s after ignition, two onboard bottles containing the pressurized suppressant (HFC-236, HFC-227ea, or FC-36,  $\text{C}_3\text{F}_8$ ) were released.

At the crew seating location, a sharp drop in  $\text{O}_2$  concentration occurred during the fire and suppression event. Following suppression,  $\text{O}_2$  levels returned to ambient in a few seconds. It was not clear whether the decrease in  $\text{O}_2$  levels during the fire and suppression event was due to depletion of oxygen by combustion or displacement of oxygen by the hot fuel vapors/expanding HFC-227ea vapor. Results from a typical test measuring oxygen concentration as a function of time in the crew compartment of the Bradley fighting vehicle are shown in Figure 5–6.

Test difficulties related to reliability of the visible diode lasers operating near 760 nm limited the data obtained in spray fires in vehicles. During the course of this project, fiber pigtailed lasers became commercially unobtainable at this wavelength.

### 5.3.4 Fuels

The third measurement capability to be developed was for the quantification of hydrocarbon fuels in fuel/air mixtures: heptane ( $\text{C}_7\text{H}_{16}$ ), as a model fuel, and two realistic fuels: DF-2 (a diesel fuel), and JP-8. The apparatus was a multi-point, field worthy, fiber-coupled, near-infrared tunable diode laser-based sensor. The system was to provide concentration data before (minimum five data points prior to agent

release), during, and after the suppression event, for a nominal event time of 250 ms, with a time resolution better than 10 ms.

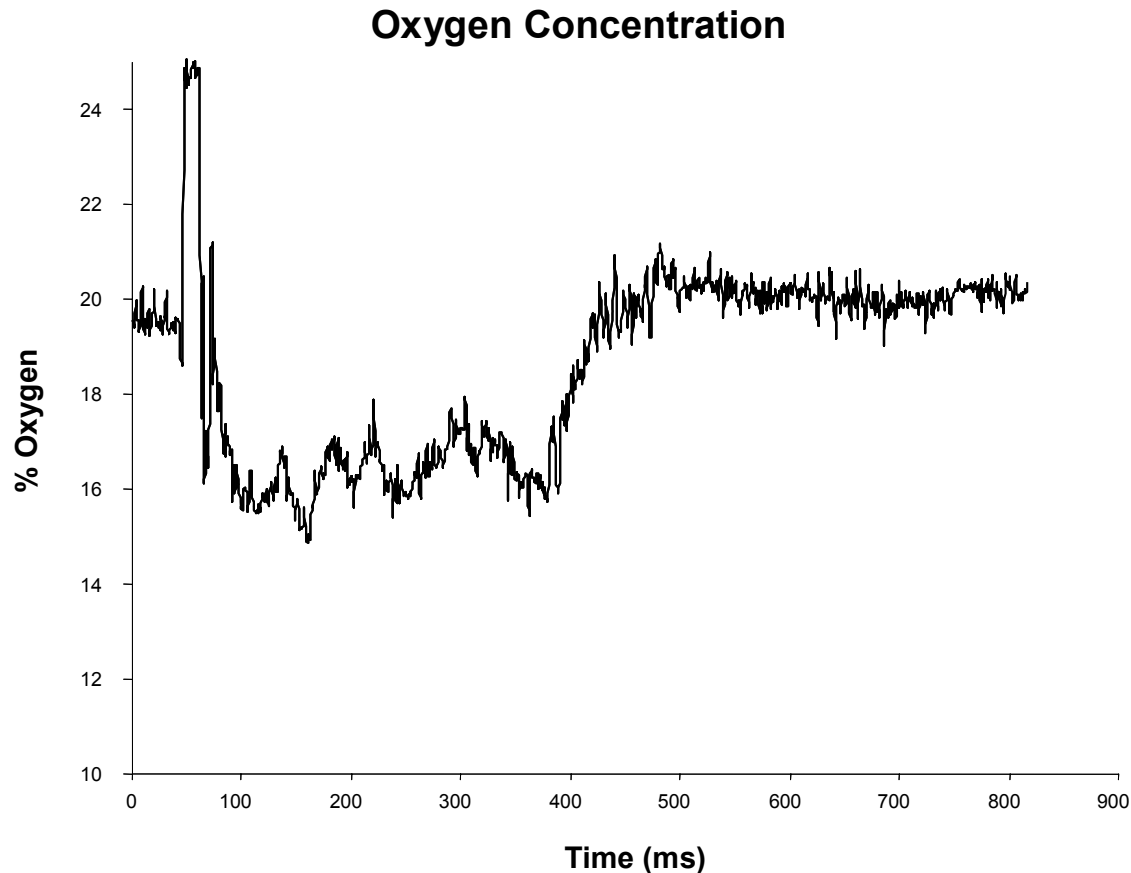


**Figure 5–6. Oxygen Concentration Measured Within the Crew Compartment of a Bradley Fighting Vehicle During Suppression by C3F8 of a Spark-Initiated JP-8 Spray Fire.**

Field worthy detectors for hydrocarbon vapor measurements typically rely upon infrared techniques: DOAS (differential optical absorption spectrometry), FT-IR (Fourier transform infrared emission/absorption)<sup>20,21,22</sup> or electrochemical/electrothermal techniques.<sup>23</sup> These methods give good results, but have found limited use for measurements in fires. FT-IR and DOAS spectrometers are usually bulky, require careful placement/alignment of interferometer/source optics and detector or retro-reflector, and are generally limited to a single line of sight. Placement of the instrument within the test environment (crew compartment) is not feasible (potential damage), looking across the entire measurement space does not isolate the region of interest, and although extractive sampling has been shown to be useful,<sup>24</sup> it does not provide the necessary temporal information. Additionally, the interferometer temporal resolution is limited by the mirror scan speed (although some new designs are approaching scan rates near 1 kHz).<sup>25</sup>

Nevertheless, use of FT-IR and DOAS for measurement of the fundamental C-H stretch in hydrocarbon fuels near 3.4  $\mu\text{m}$  can yield sensitivities in the nL/L (ppb) range, and because the full spectrum may be measured (when using FT-IR), it is often possible to determine species of hydrocarbons present in a simple mixture. For stable, relatively safe sampling sites with an accessible line of sight, incoherent

infrared absorption techniques (FT-IR, DOAS) are often the techniques of choice. Electrothermal/electrochemical detectors are generally inexpensive (\$2000 to \$5000), are often transportable by a single person, and have sensitivities ( $\approx 100\text{s } \mu\text{L/L}$ ) well below lower explosion limits for most hydrocarbon vapors.<sup>26,27,28,29</sup> Time sensitivity is typically from 1 s to 15 s. Some units may have accuracy problems when used in the presence of methane gas, and may be less sensitive to heavier hydrocarbon vapors.<sup>23</sup> For measurement sites requiring full portable instrumentation with time resolution from one second to tens of seconds, these instruments can also provide excellent results.

Gas detection methods using near-infrared tunable diode lasers can use optical fibers and relatively inexpensive (room temperature operation) semiconductor detectors to separate electronics and laser sources from hazardous testing locations. Using modulation techniques and phase sensitive detection methods, temporal resolution routinely exceeds 1 ms per measurement. As previously mentioned, detection methods employed (typically wavelength modulation spectroscopy (WMS) and balanced ratiometric detection (BRD) techniques)<sup>8,9</sup> give good results for gas phase concentration measurements of small molecules with well resolved ro-vibrational absorption lines, such as hydrogen fluoride, methane, carbon monoxide, water, etc.<sup>30</sup> However, large and/or heavy molecules may not possess well resolved ro-vibrational absorption bands because of overlap between fundamental, combination, and/or overtone vibrations, and because of rotational constants which may be less than typical gas phase linewidths.<sup>31</sup> For mixtures of heavy molecules, e.g., the middle distillate fuels, the spectra may be even less structured. Figure 5–7 shows the near-infrared gas phase absorption spectrum of dry air saturated at 294 K by the hydrocarbon fuels JP-8, DF-2, and gasoline, measured using a Fourier transform spectrometer, with an optical path of 0.75 m.

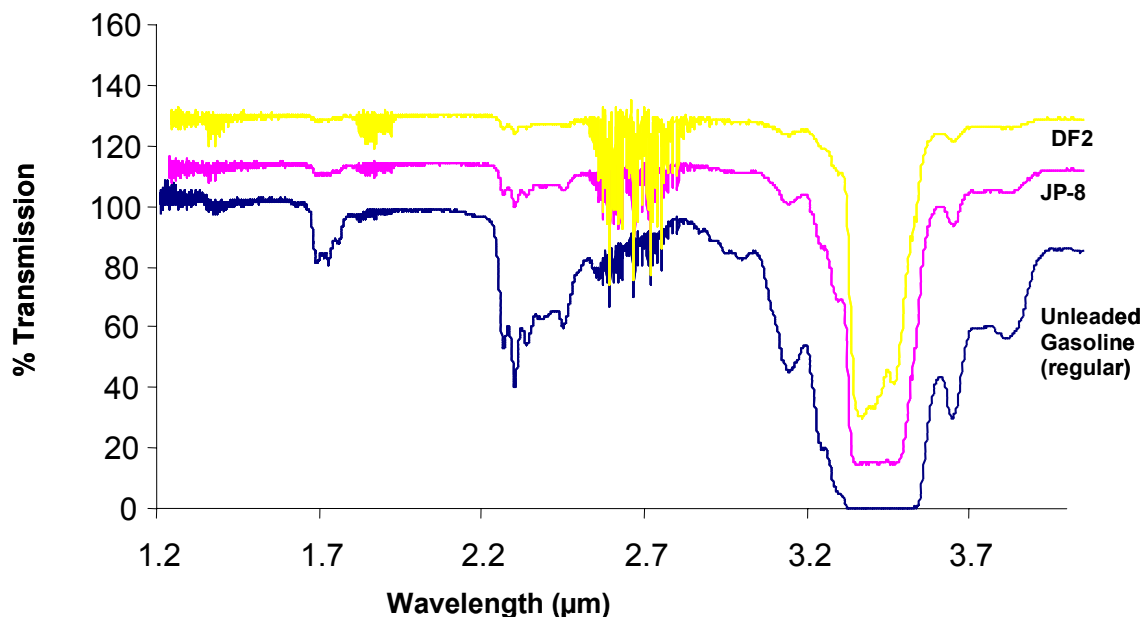


**Figure 5–7. FT-IR Spectra of Dry Air Saturated at 294 K with Vapor from Unleaded gasoline, JP-8, and DF2.**

(The spectra have been offset for clarity. Structured absorptions near 1.9 and 2.7  $\mu\text{m}$  are from water vapor.)

As suggested by the spectra shown in Figure 5–7, the vapors from each fuel fit criteria<sup>32</sup> to be classified as a gas having unstructured absorption spectra (often called a "broad band absorber"). Both WMS and BRD, as usually employed, are not suitable for gases that exhibit broad, unstructured absorption spectra.<sup>8,9,30</sup> For both techniques, the main limitation for fuel sensing is the narrow tuning range of the diode laser. Because the tuning range of the DFB lasers is usually several orders of magnitude smaller than the width of the spectral feature in broad band absorbers ( $0.4 \text{ cm}^{-1}$  vs.  $> 100 \text{ cm}^{-1}$ ), it is not possible using commercially available DFB lasers to tune from the region of maximum absorption to a region of zero absorption.

McNesby and co-workers developed a technique to overcome this limitation for measurement of such molecules, while approaching the sensitivity and time response of WMS and BRD methods. The approach took advantage of the residual amplitude modulation (RAM) that occurs as the wavelength of a semiconductor tunable diode laser is varied by modulating the laser injection current. Typically (for WMS and BRD), RAM is a nuisance, and what is important is the wavelength modulation. For this method, the RAM is what enables the technique to work, and the relatively small variation of wavelength during the modulation is largely ignored (but will be commented upon below). For this method, two different DFB lasers are driven using a sinusoidally varying injection current. Each laser injection current is modulated at the same frequency, but the two lasers are out of phase by  $180^\circ$ .<sup>32</sup> The light output of the two lasers is combined to produce the probe beam used for the line-of-sight measurement. When the power output amplitudes of each sinusoidally modulated laser are the same, the combined output of the two lasers will have an amplitude that is (ideally) invariant with time. The key to the method is selection of one laser wavelength coincident with a wavelength absorbed by the gas of interest, and selection of the second laser wavelength in a region where no absorption is anticipated. When the mixed, modulated probe beam is passed through a gas which preferentially absorbs the laser radiation from only one of the lasers, the signal at the detector is modulated at the injection current modulation frequency and, for small absorptions, has an amplitude whose magnitude is proportional to the concentration of absorbing gas.

The simple mathematical description begins by considering Beer's law for narrow band laser radiation exiting an absorbing sample gas of concentration  $c$  molecules per  $\text{cm}^3$ , for a path length of  $l$  cm. The absorption coefficient ( $\text{cm}^2/\text{molecule}$ ) at the most intense region of absorption (the resonant wavelength,  $\lambda_R$ ), is  $\alpha(\lambda_R)$ .  $I_0(\lambda_R)$  is the intensity of the incident radiation at the resonant wavelength.  $I(\lambda_R)$  is the intensity of radiation at the resonant wavelength after exiting the sample gas:

$$I(\lambda_R) = I_0(\lambda_R) \exp(-\alpha(\lambda_R)cl) \quad (5-1)$$

If the incident radiation at the resonant wavelength is now power modulated sinusoidally at frequency  $a$ , and time  $t$ , with depth of modulation  $D_R$ , the intensity of the radiation at the resonant wavelength after exiting the gas becomes:

$$I(\lambda_R) = I_0(\lambda_R)(1 + D_R \sin(at)) \exp(-\alpha(\lambda_R)cl) \quad (5-2)$$

To get a measurement of transmission off resonance (important to generate a differential signal and to discriminate against scattering by particles such as smoke), we add a second laser source at a wavelength not absorbed by the gas,  $\lambda_{NR}$ . This non-resonant wavelength is mixed with the resonant wavelength, power modulated at the same frequency but  $180$  degrees out of phase with the resonant wavelength

modulation, and has a depth of modulation  $D_{NR}$ . If the radiation exiting the gas is now focused on an (ideally) wavelength-insensitive detector, the power at this detector,  $I(\lambda_R + \lambda_{NR})$ , may be given by:

$$I(\lambda_R + \lambda_{NR}) = [I_0(\lambda_R)(1 + D_R \sin(at)) \exp(-\alpha(\lambda_R)cl) + I_0(\lambda_{NR})(1 + D_{NR} \sin(at + \pi))] \quad (5-3)$$

To process this signal, we multiply by a reference sine wave of amplitude  $p$  in phase with and at the same frequency,  $a$ , as the power modulation of the two lasers. We then integrate over  $C$  periods of power modulation:

$$C \int_0^\pi \{ [I_0(\lambda_R)(1 + D_R) \exp(-\alpha(\lambda_R)cl) - I_0(\lambda_{NR})(1 + D_{NR})] \sin(at) p \sin(at) \} dt \quad (5-4) \\ = (C/2)p\pi [I_0(\lambda_R)(1 + D_R) \exp(-\alpha(\lambda_R)cl) - I_0(\lambda_{NR})(1 + D_{NR})]$$

Rearranging, assuming  $\exp(-\alpha(\lambda_R)cl) \ll 1$  and using  $A$  (Absorbance) equal to  $\alpha(\lambda_R)cl$ :

$$2C \int_0^\pi \{ [I_0(\lambda_R)(1 + D_R) \exp(-\alpha(\lambda_R)cl) - I_0(\lambda_{NR})(1 + D_{NR})] \sin(at) p \sin(at) \} dt \quad (5-5) \\ = Cp\pi [I_0(\lambda_R)(1 + D_R) - I_0(\lambda_{NR})(1 + D_{NR}) - I_0(\lambda_R)(1 + D_R)A]$$

For the special case where the power and depth of modulation of the two lasers are equal, Equation 5-5 becomes:

$$2C \int_0^\pi \{ [I_0(\lambda_R)(1 + D_R) \exp(-\alpha(\lambda_R)cl) - I_0(\lambda_{NR})(1 + D_{NR})] \sin(at) p \sin(at) \} dt \quad (5-6) \\ = -Cp\pi [I_0(\lambda_R)(1 + D_R)A]$$

Equation 5-6 is just the output of a lock-in amplifier operating on the first harmonic for measurement of the amplitude of the sine wave created by the differential absorption (for small absorptions) of the mixed laser beam by the gas at concentration  $c$  and path length  $l$ . This output is proportional to the number of periods,  $C$ , over which the integration is carried, the amplitude,  $p$ , of the reference sine wave, the incident power,  $I_0(\lambda_R)$ , of the laser at the resonant wavelength, and the Absorbance,  $A$  (and hence gas concentration when pressure broadening of the spectral feature is not important). It is worth noting that Equation 5-6 also indicates that the lock-in output is increased by increasing depth of modulation ( $D_R$ ). As will also be discussed later, Equation 5-5 shows that it is important that the two laser power amplitudes and depths of modulation are as equal as possible, especially for small values of Absorbance. As mentioned previously, and implied by Equation 5-6, because the measurement relies on differential absorption to quantify gas concentrations, division of the raw signal at the detector by the average laser power should account for pseudo wavelength-independent signal intensity extinction from scatterers, such as smoke particles. However, it should also be mentioned that decreases in overall signal voltage will result in similar decreases in the signal to noise ratio of the measurement.

A diagram of the experimental apparatus employing this method is shown in Figure 5–8. The two DFB laser diodes (Sensors Unlimited) used to produce the mixed wavelength probe beam have nominal wavelengths of 1.307  $\mu\text{m}$  and 1.71  $\mu\text{m}$ . The laser diodes are driven using an ILX LDC-3900 modular laser diode controller. The variable phase sinusoidal injection currents are supplied by two SRS Model DS345 function generators operating on a common time base, Sinusoidally modulated (100 kHz, modulation depth adjusted to near 100 %) laser diode radiation from each diode laser is mixed onto a common fiber using a fiber optic coupler (Gould Fiberoptics) and launched into free space using a single mode fiber that is terminated by a gradient index (GRIN) lens (Sentech Corp.). The output beam is

directed into a variable pathlength gas cell (Laser Photonics L5210) set at the minimum setting of 4 m. Radiation exiting the 4 meter path length cell is detected using a New Focus Model 2034 InGaAs large element photodetector (maximum responsivity near 1600 nm). The detector signal is demodulated at the laser injection current modulation frequency using a lock-in amplifier (SRS 830), displayed on an oscilloscope (LeCroy 7200), and recorded on a laptop computer (Dell Latitude) running LabView software (National Instruments). JP-8 and DF-2 were milspec grade and were obtained from the fuel depot at the Aberdeen Proving Ground. The gasoline was regular grade obtained during the summer months at a commercial vendor in Aberdeen, MD. All were used as supplied. Air was saturated with fuel vapor using a bubbler apparatus based upon a nitrogen sparger. Air flow through the stainless steel frit immersed in the fuel was typically  $100 \text{ cm}^3/\text{min}$  to  $250 \text{ cm}^3/\text{min}$ . Figure 5-9 shows the vapor phase absorption spectrum of air saturated by vapor at 294 K from JP-8, DF-2, and gasoline between wavelengths of  $1.3 \text{ }\mu\text{m}$  and  $1.75 \text{ }\mu\text{m}$  superimposed upon the emission from the optical fiber carrying the mixed wavelength laser beam. The data were recorded using a Bomem DA-8 spectrometer (using a liquid nitrogen-cooled InSb detector) interfaced to a Wilkes 0.75 m path length cell. The near infrared tunable diode laser radiation was transported using optical fibers to the external source port on the FT-IR spectrometer. This figure shows that the emission of the laser at  $1.71 \text{ }\mu\text{m}$  falls near the most intense region of the C-H stretch (first overtone) absorption for the three fuels studied, and that the  $1.3 \text{ }\mu\text{m}$  laser falls in a region where there is no measurable absorption of the laser radiation by the fuels studied. Because of the narrow emission linewidth of the lasers, the reported line shape in this figure is just the instrument line shape (in this case, sinc) of the FT-IR spectrometer.<sup>33</sup>

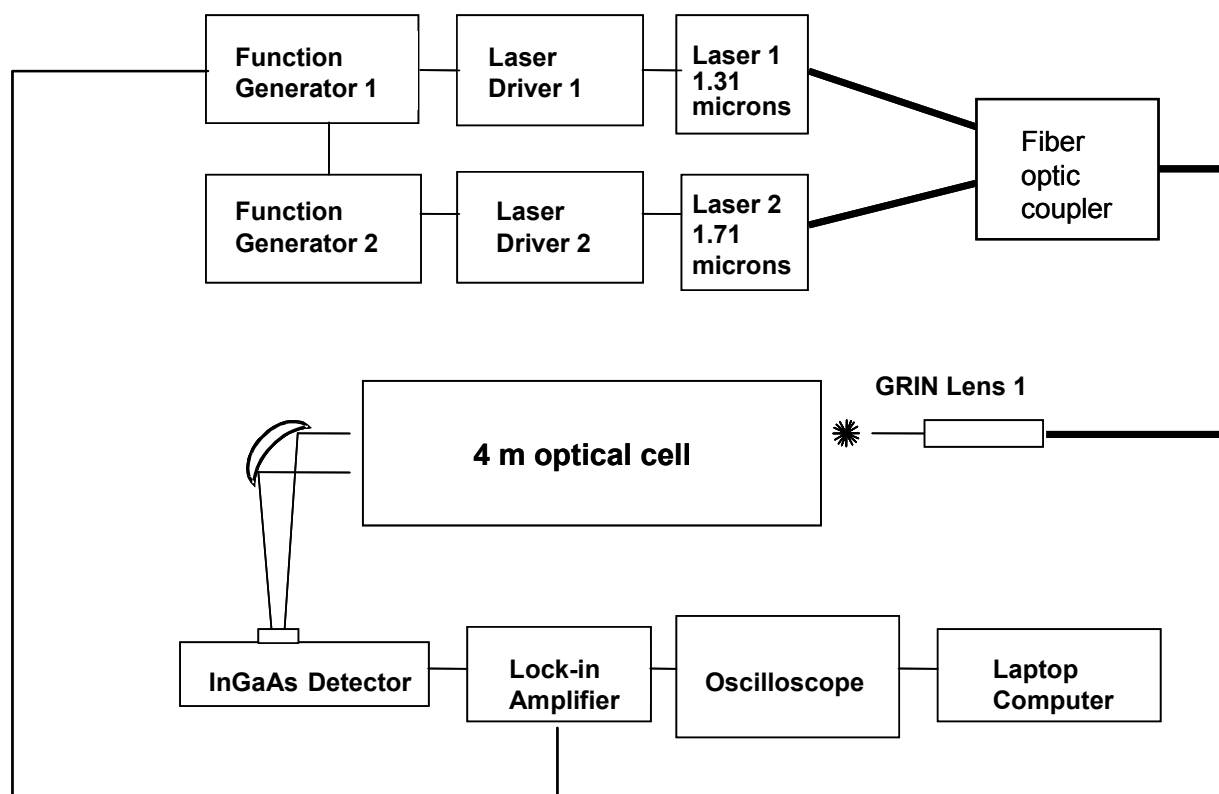


**Figure 5–8. Schematic Diagram of the Laser Mixing Apparatus Used to Measure Fuel Vapor Concentrations.**

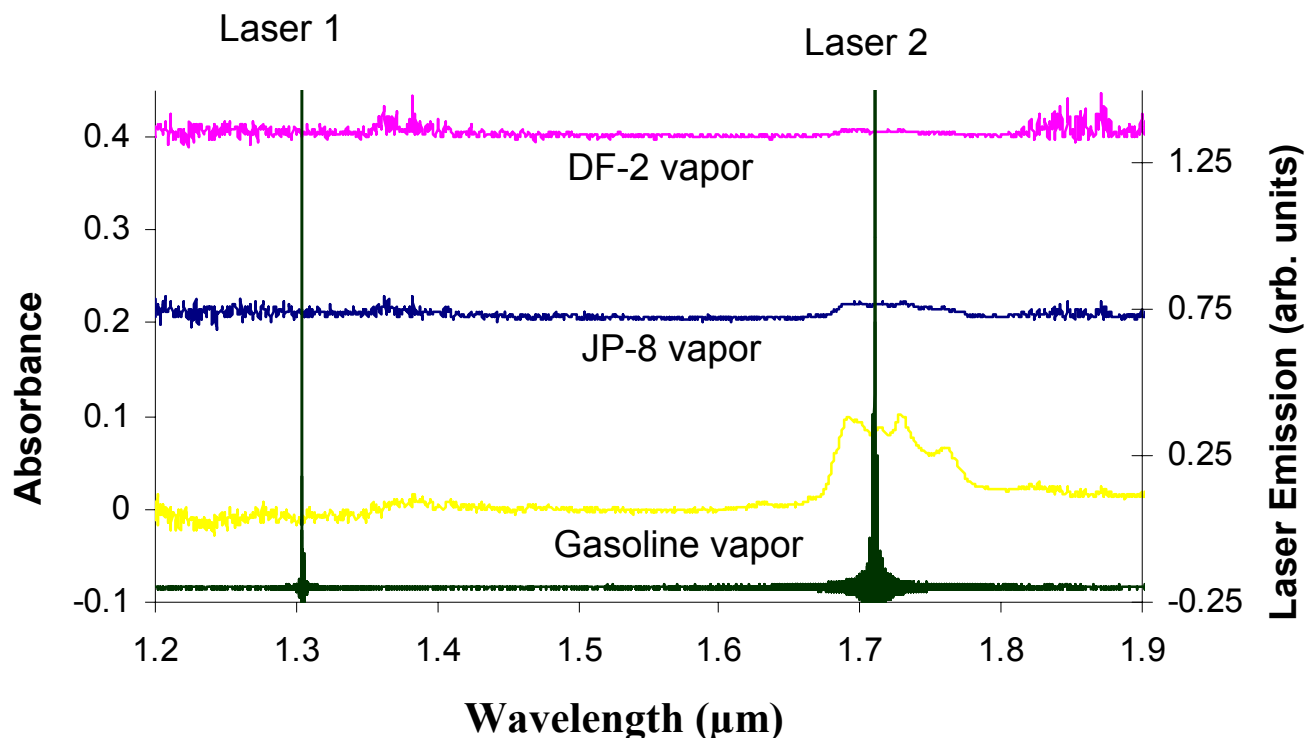


**Figure 5–9. Absorption Spectrum of Air Saturated with JP-8, DF-2, or Gasoline Vapor at 294 K Superimposed upon the Emission from the Optical Fiber Carrying the Mixed Wavelength Laser Beam.**

Figure 5–10 shows the gasoline vapor concentration (measured using the mixed laser sensor) as dry air saturated by gasoline vapor slowly displaces (several hundred  $\text{cm}^3/\text{minute}$ ) the dry air in a 13.7 L optical cell (4 m path length). Also shown in this figure is the change in oxygen concentration that occurs during the displacement (DFB laser-based oxygen sensor courtesy of Oxigraf, Inc., Mountain View, CA). This figure shows the sensor response as the vapor concentration approaches and exceeds the lower explosive limit (LEL) for most hydrocarbon vapors (e.g., for JP-8, the LEL is approximately  $9500 \mu\text{L}/\text{L}$ ).<sup>26,34</sup> Each data point is the average of the lock-in amplifier output measured over 10 ms. All measurements were made at atmospheric pressure. Figure 5–11 shows the measured fuel vapor concentration as the dry air in the 13.7 L optical cell is displaced by air saturated (at 294 K) with JP-8 vapor. The results for DF-2 were similar to those for JP-8. The partial pressures at atmospheric pressure (measured using a capacitance manometer to  $\pm 20\%$ ) for gasoline, JP-8, and DF-2 fuels were found to be approximately 1.7 kPa, 4.7 kPa, and 0.23 kPa, respectively. The C-H stretch first overtone absorption coefficient for the fuel vapors was determined to be approximately  $2.7 (\pm 0.4) \times 10^{-21} \text{ cm}^2/\text{molecule}$ , which is in reasonable agreement with that for the first overtone of the C-H stretch for methane ( $8.7 \times 10^{-22} \text{ cm}^2/\text{molecule}$ ).<sup>11</sup> The estimated limit of detection for each of these fuel vapors, using the mixed laser sensor, was approximately  $100 (\mu\text{L}/\text{L})\text{-m}$ .

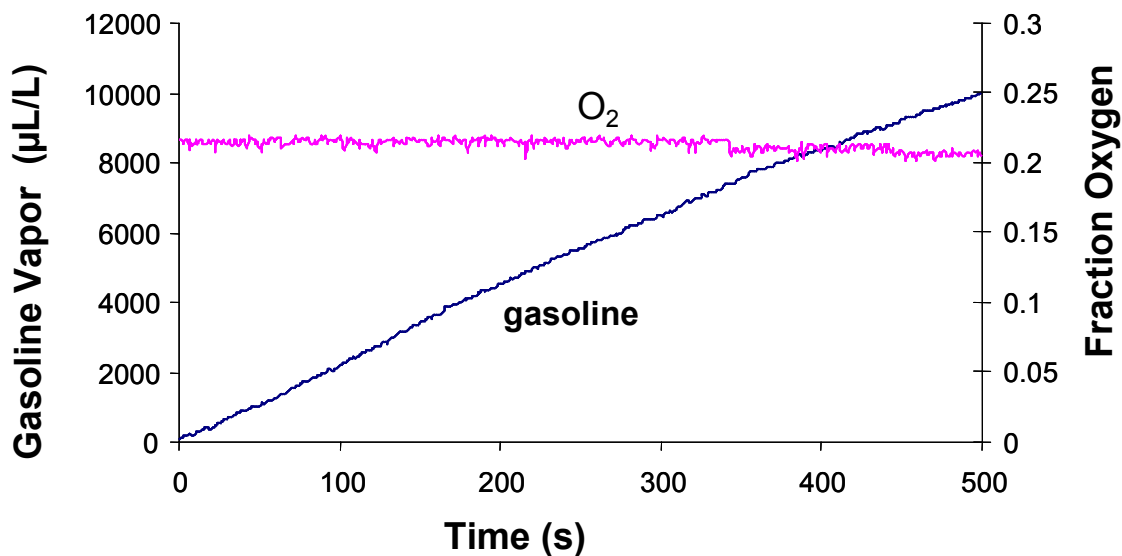


Figure 5–10. Concentrations of Gasoline Vapor and Oxygen, Measured as Dry Air Saturated with JP-8 Vapor Displaces the Dry Air in a 13.7 L Optical Cell.

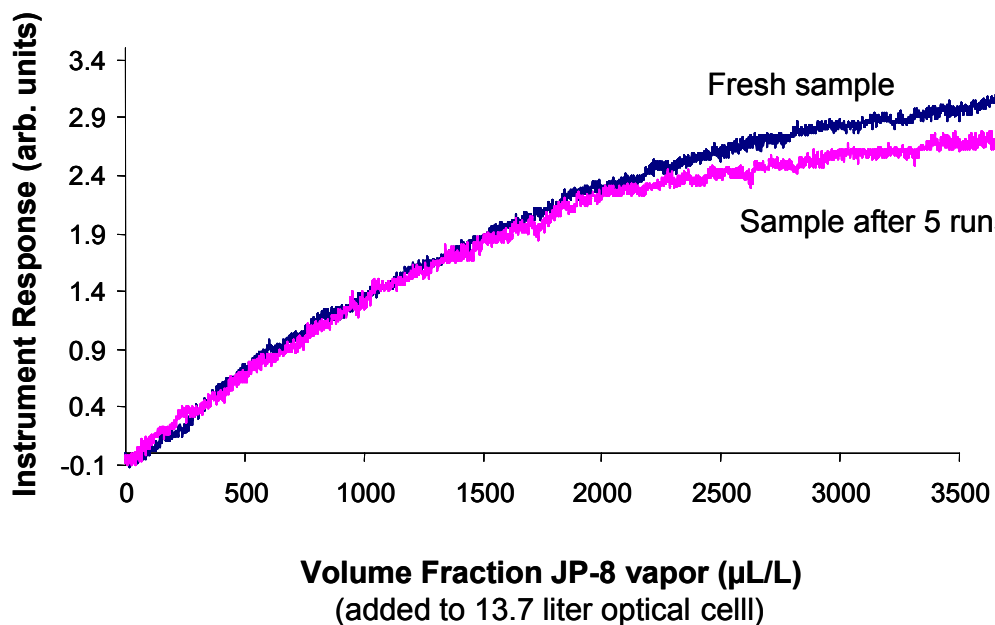
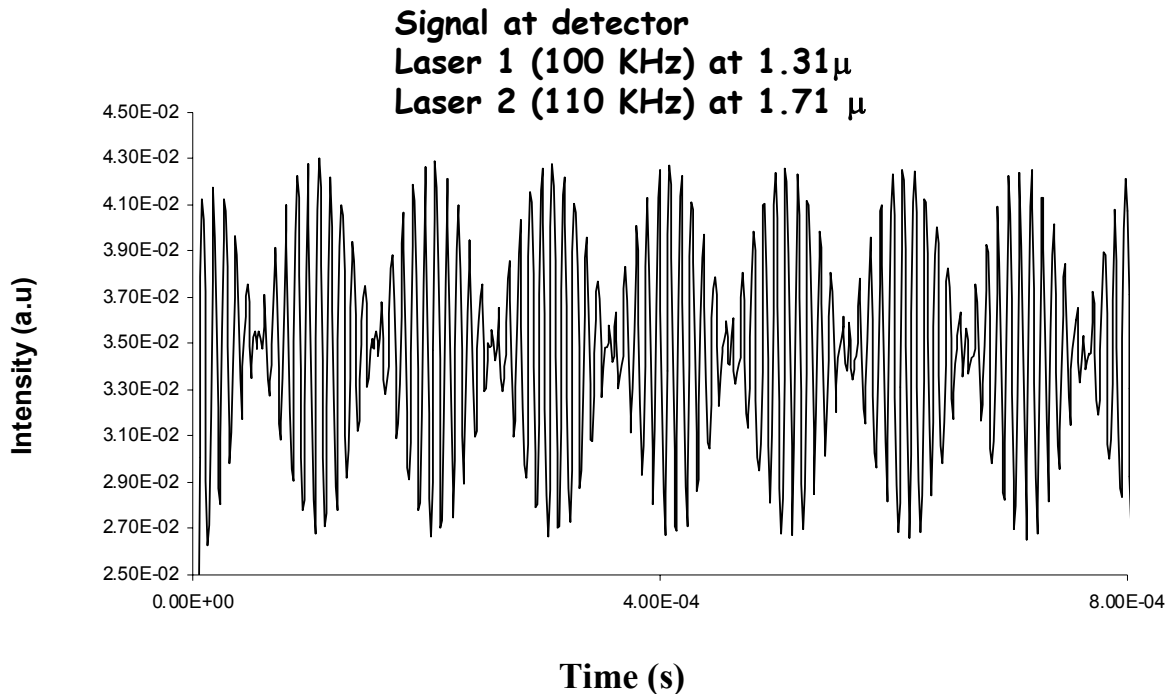


Figure 5–11. Loss of Lighter Hydrocarbons from JP-8 Caused by Repeated Fills of the Optical Cell Used for Testing the Mixed Laser Fuel Vapor Sensor.

Two factors led to the decision that measurement of the full absorption envelope for the C-H stretching vibration was necessary, and that the first generation sensor system was inadequate for general fuel vapor sensing:

- Careful examination of the C-H overtone bands for each of the fuels tested (JP-8, DF-2, and gasoline) shows that the contours of the absorption features, when normalized to each other, were not superimposable. So, being limited to sampling vapors from different fuels using the same single wavelength would be a potential source of error.
- Changes in temperature, storage conditions (aging) and changes in fuel composition between vendors may cause changes in the contour of the unstructured absorption envelope.

Therefore, it was necessary to develop a technique with the simplicity of the first generation sensor but with the capability of expansion to measure the full C-H absorption envelope of the fuel vapor. The approach taken for this second generation sensor uses an array of addressable microphotonic semiconductor lasers, each emitting light at a different wavelength, and power modulated at different frequencies (typically between 100 kHz and 150 kHz). When the modulated light is combined onto a single path, and the combined beam brought to focus on a detector, the signal reported by the detector has the contour of an interferogram. This interferogram is analyzed by standard Fast Fourier Transform (FFT) techniques to yield the amplitudes of the individual component cosine waves.<sup>35</sup> These amplitudes are proportional to the average power of light at each wavelength reaching the detector. Figure 5–12 shows the interferogram generated by a two laser mixed beam.



**Figure 5–12. Two Laser Interferogram Measured at the Detector for the Second Generation Fuel Vapor Sensor.**

Laser 1 emits radiation near a wavelength of 1.31  $\mu\text{m}$  and was power modulated at 100 kHz, with a depth of modulation near 95 %. As with the first generation sensor, this laser wavelength was chosen because it is not absorbed by hydrocarbon vapor or by water vapor. Laser 2 emits laser radiation near a wavelength of 1.71  $\mu\text{m}$  and was power modulated at 110 kHz, with a depth of modulation near 95 %. Also as with the first generation sensor, this laser wavelength was chosen because it is approximately at the center of the 1<sup>st</sup> overtone C-H stretching vibration of most middle distillate fuel vapors.

The output from each fiber coupled laser is launched onto a single, common, single mode optical fiber using a commercially available fiber coupler (Gould Fiber Optics). Each laser is power modulated, each at a different frequency, using digital function generators (Stanford Research Systems DS-345) operating on a common time base. This modulated light beam is passed through a GRIN lens into free space, and the transmitted light detected using an InGaAs (New Focus model 2011) detector. The signal at the detector is demodulated (Agilent Infinium Oscilloscope) using a Fast Fourier Transform (FFT), in a manner similar to that of commercially available Fourier transform infrared (FT-IR) spectrometers.<sup>35</sup> The time for each measurement is user controlled by varying the frequency of power modulation. Resolution is user controlled by varying the number of periods of power modulation measured per “scan.” Figure 5–13 is a schematic drawing of the experimental apparatus for the Fourier transform laser spectroscopy (FT-LS) system.

As with the first generation sensor, the second generation sensor was tested by measuring gasoline vapor concentration as dry air saturated by gasoline vapor slowly displaced (several hundred  $\text{cm}^3/\text{minute}$ ) the dry air in a 13.7 L optical cell (4 m path length). Figure 5–14 shows the sensor response as the vapor concentration approaches and exceeds the lower explosive limit (LEL). For most hydrocarbon vapors (i.e., for JP-8 and most other middle distillate fuels), the LEL is approximately 0.1 % by volume.<sup>26,34</sup> For the absorbance measurement, the background for each laser was the demodulated signal prior to the onset of fuel vapor flow. The flow apparatus was characterized using the first generation sensor, and using that calibration the absorbance reported here is reasonably linear with concentration (within 5 %), but was not explicitly measured for these experiments. All of the factors that determine quality of conventionally measured FT-IR spectra are of importance here (modulation depth, apodization, phase, etc.).<sup>33</sup> Most of the efforts for the prototype were focused on making sure the lasers were modulated in phase, using a common time base. Any effects of varying the modulation depth or of varying the laser power were not investigated. Dynamic range effects were also not investigated, although some improvement was anticipated relative to Michelson interferometer based instruments because the Fourier frequencies for each laser are no longer coupled to the laser wavelength. The time for each measurement point was approximately 1 s. All measurements were made at atmospheric pressure.

The absorption coefficients for most VOCs in the near-infrared spectral region ( $\approx 1 \mu\text{m}$  to  $2 \mu\text{m}$  wavelength, two (or more) vibrational quanta per transition) are typically lower by an order of magnitude than for the mid-infrared spectral region ( $\approx 2 \mu\text{m}$  –  $30 \mu\text{m}$  wavelength, typically 1 vibrational quantum per transition).<sup>36</sup> As indicated in Figure 5–7, the ARL team determined the near infrared absorption coefficients between wavelengths of 1.0  $\mu\text{m}$  and 30  $\mu\text{m}$  for JP-8, finding the maximum absorption coefficient to occur between a wavelength of 1.6  $\mu\text{m}$  and 1.825  $\mu\text{m}$ , with a value of about  $3 \times 10^{-21} \text{ cm}^2/\text{molecule}$ . Using the prototype FT-LS instrument described above, the detection limit was approximately  $200 \mu\text{L}/\text{L m}^{-1}$ , or approximately 50 times worse than the detection limit using a commercial FT-IR spectrometer.<sup>37</sup> It is worth noting that for the prototype sensor described here, the power modulation of each diode laser was not purely cosinusoidal (harmonics in the FFT output), even though

the driver current was supplied by the SRS DG535 function generators. As the number of lasers being power modulated is increased, it is expected the contributions to signal from frequencies other than driver frequencies may limit resolution. A custom driver waveform may be needed to give the best cosinusoidal power modulation.

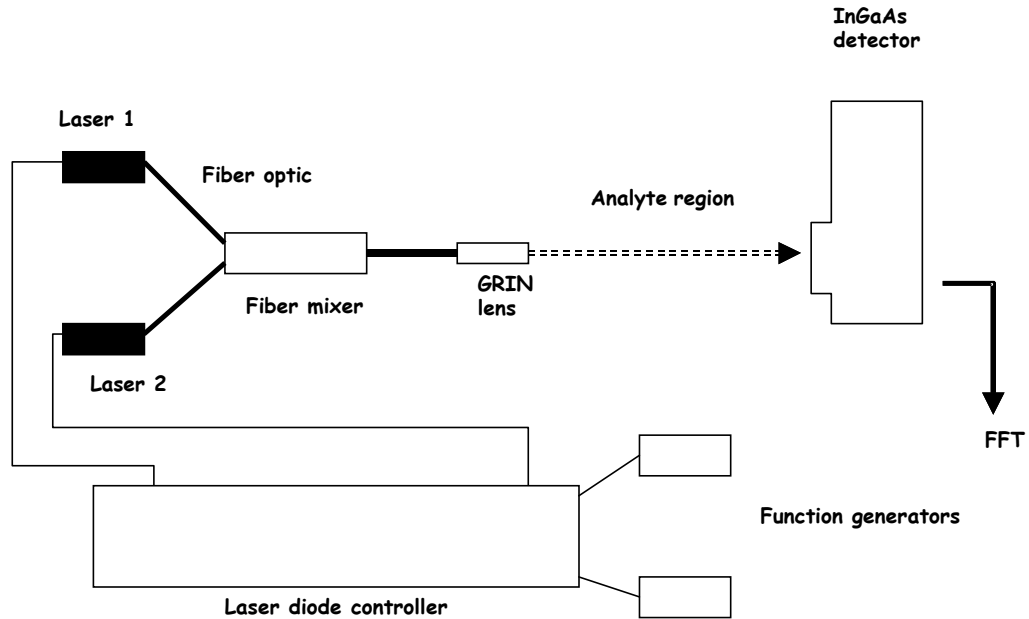


Figure 5–13. Experimental Apparatus Used for Fourier Transform Laser Spectroscopy.

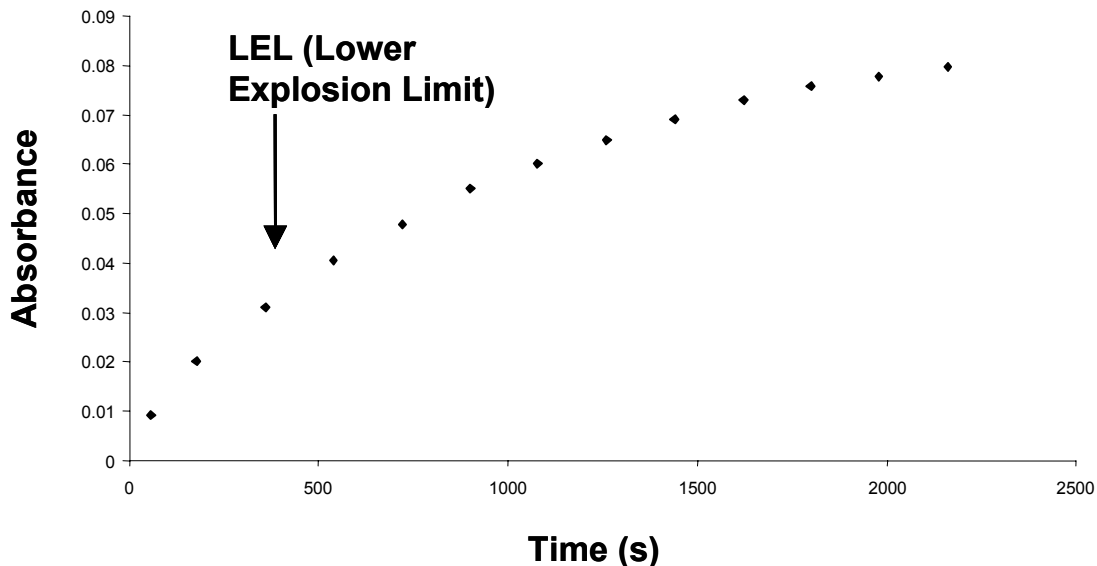


Figure 5–14. Absorption of 1.71  $\mu\text{m}$  Laser Radiation as Air is Displaced by Air Saturated with Gasoline Vapor in a 2 m Cell.

At the time of publication of this book, the ARL team was developing a 10-laser FT-LS source in the near infrared, providing reasonable coverage of the full overtone C-H absorption envelope for hydrocarbon vapors. The basic idea for this sensor is illustrated in Figure 5–15. Analysis similar to PLS techniques already employed for FT-IR spectral data could be used to identify mixture components.<sup>38</sup> Such an instrument may be readily assembled from commercially available telecommunications equipment. The main challenge is finding a vendor for the individual laser diodes, since there is low demand for lasers outside of the fiber windows near 1350 nm and 1550 nm. Provided that the cost of addressable light sources continues to decrease, arrays covering larger spectral windows may become available. While several options exist for wavelength separation, the highly developed FT-IR market may influence the design of new solid state spectrometers, and this approach may warrant further consideration.

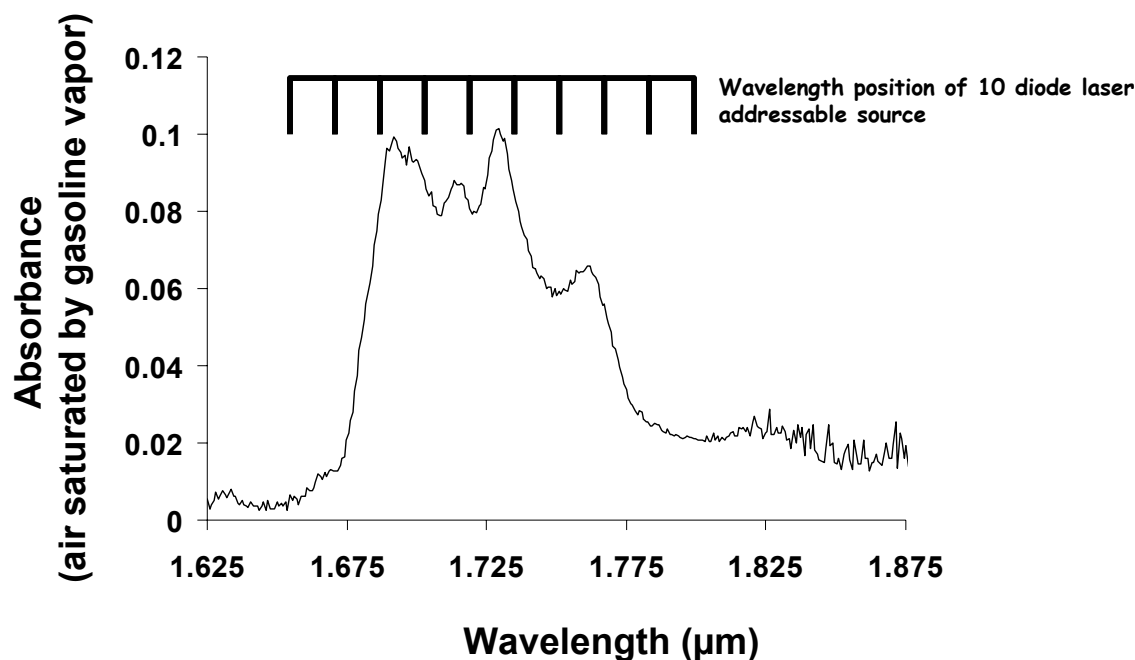


Figure 5–15. Schematic of a 10-laser FT-LS Source in the Near Infrared.

### 5.3.5 Observations

Gas sensing using near-infrared lasers will probably increase steadily in popularity. This is in large part due to the ease of transmission of the IR signals through optical fibers, room temperature operation, high signal to noise ratio through phase sensitive detection techniques, and the large telecommunications infrastructure that continues development of electronics that may easily be adapted to gas sensing. Nonetheless, some changes are potentially at hand:

- The replacement of a single laser detecting a single gas by either an addressable source or by a single, broadly tunable laser.
- The use of room temperature operation, mid-infrared lasers (quantum cascade and interband cascade designs). These offer all of the advantages of phase sensitive detection available

with near-infrared DFBs, and have a huge advantage of gas sensing using the fundamental vibrational transition.

- Microphotonic sensors will employ suites of arrays of near- and mid-infrared devices, and that these devices will gradually displace conventional Michelson interferometer based systems in the laboratory and in the field.

The main technical difficulties associated with this technology center on the availability of DFB lasers. With the contraction of the telecommunications market at the beginning of the 21<sup>st</sup> century, many fabrication facilities discontinued manufacture of lasers at user-specified wavelengths, producing lasers only within the telecommunications bands near 1330 nm and 1550 nm. Although there has been some supply from foreign manufacturers, obtaining lasers for gas sensing (in particular, O<sub>2</sub> near 760 nm) remains challenging. This difficulty exacerbates the main challenge for gas sensing using near infrared DFB lasers, namely, sensing of molecules and mixtures of gases that do not present well resolved vibrational spectra.

## **5.4 MEASUREMENT OF FIRE SUPPRESSANT CONCENTRATION USING A DIFFERENTIAL INFRARED RAPID AGENT CONCENTRATION SENSOR (DIRRACS)**

### **5.4.1 Introduction**

In addition to the LIBS technique described earlier, the NGP developed a second technique for monitoring the concentration of a fire suppressant chemical during a rapidly extinguishment event. This non-dispersive apparatus, the Differential Infrared Rapid Agent Concentration Sensor (DIRRACS), employs a resistively heated source and directly measures the broad, fundamental absorption of the chemical. The design goal was an instrument with a response time of 3 ms that could be used with a variety of fire suppression agents over a concentration range from 1 % to 20 %, with an expanded uncertainty of approximately 10 % of the nominal value. Following an initial design, DIRRACS I, the design goal was met for the fire suppressant HFC-125 (C<sub>2</sub>HF<sub>5</sub>) with the improved DIRRACS II.

### **5.4.2 Original Instrument Design – DIRRACS I**

Figure 5–16 is a schematic drawing of the DIRRACS I. Figure 5–17 depicts the optics. A detailed description of the instrument design and theory of operation is given by Pitts et al. at the National Institute of Standards and Technology (NIST).<sup>39</sup> Briefly, IR radiation from a coil heater source heated to 500 °C is directed through a 2.8 cm long sample volume. The transmitted beam passes through a long-wavelength cut-off filter to remove IR radiation with wavelength longer than 14 μm, through a chopper operating at 500 Hz, a narrow-band-pass filter transmitting from 8.4 to 8.9 μm, to a LiTaO<sub>3</sub> pyroelectric sensor. As shown in Figure 5–18, a narrow-bandpass filter was selected that overlaps with a strong absorption feature for HFC-125. There is also strong IR absorption, resulting from the C-F stretch vibrational modes, in the same spectral region for other agents with C-F bonds including HFC-227ea (C<sub>3</sub>HF<sub>7</sub>), FC-218 (C<sub>3</sub>F<sub>8</sub>), halon 1301 (CF<sub>3</sub>Br), and CF<sub>3</sub>I. The pyroelectric sensor has a built-in FET amplifier. The output signal was increased with a 100x, low-noise amplifier; and frequencies below about 300 Hz were filtered out.

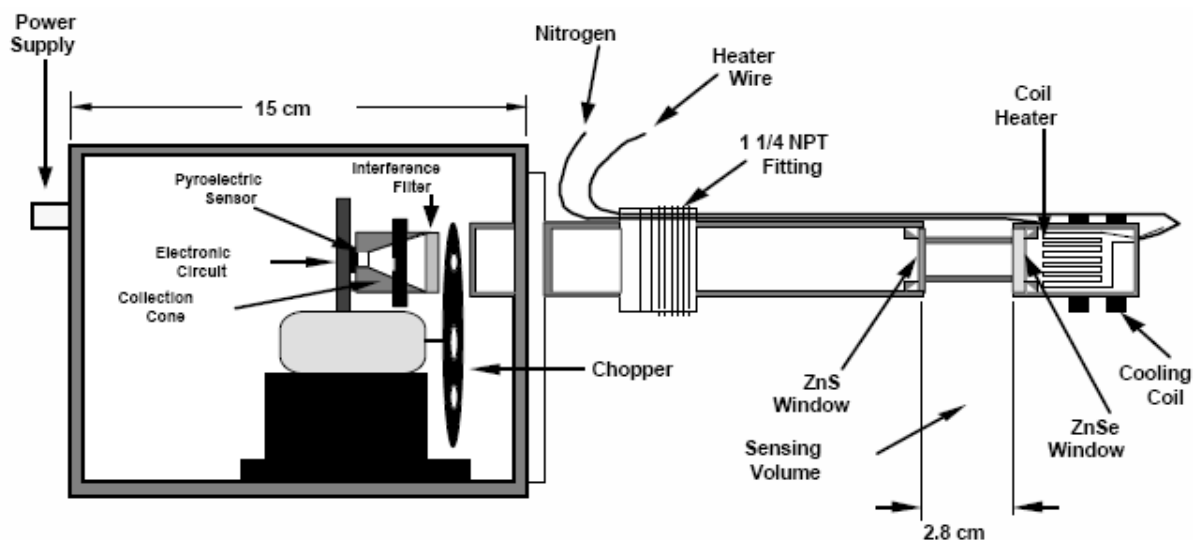


Figure 5-16. Schematic of the DIRRACS I.

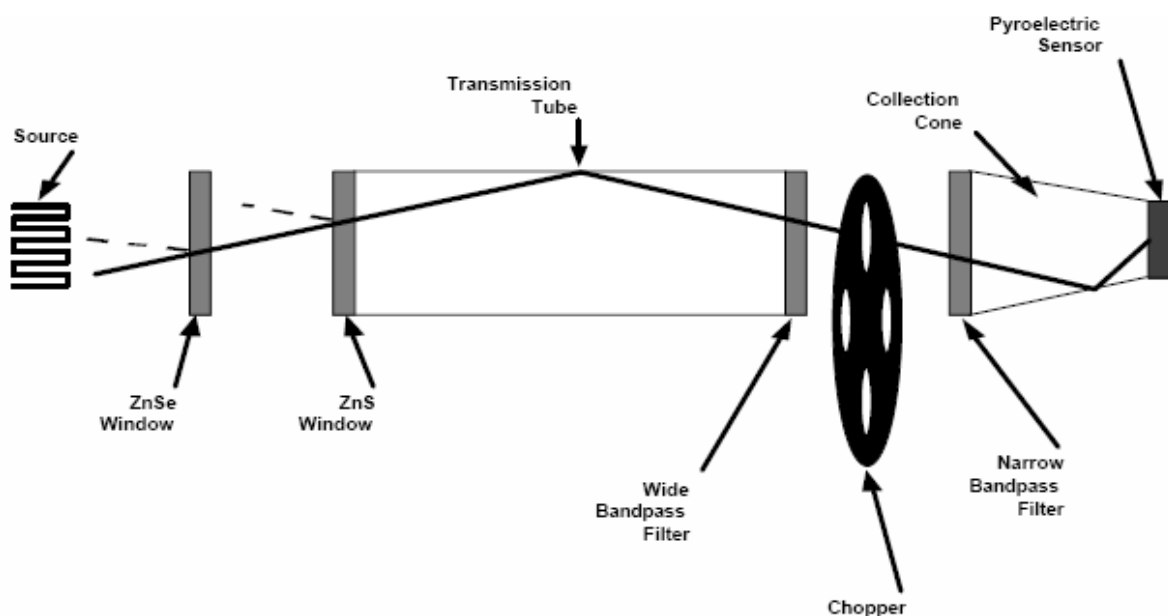
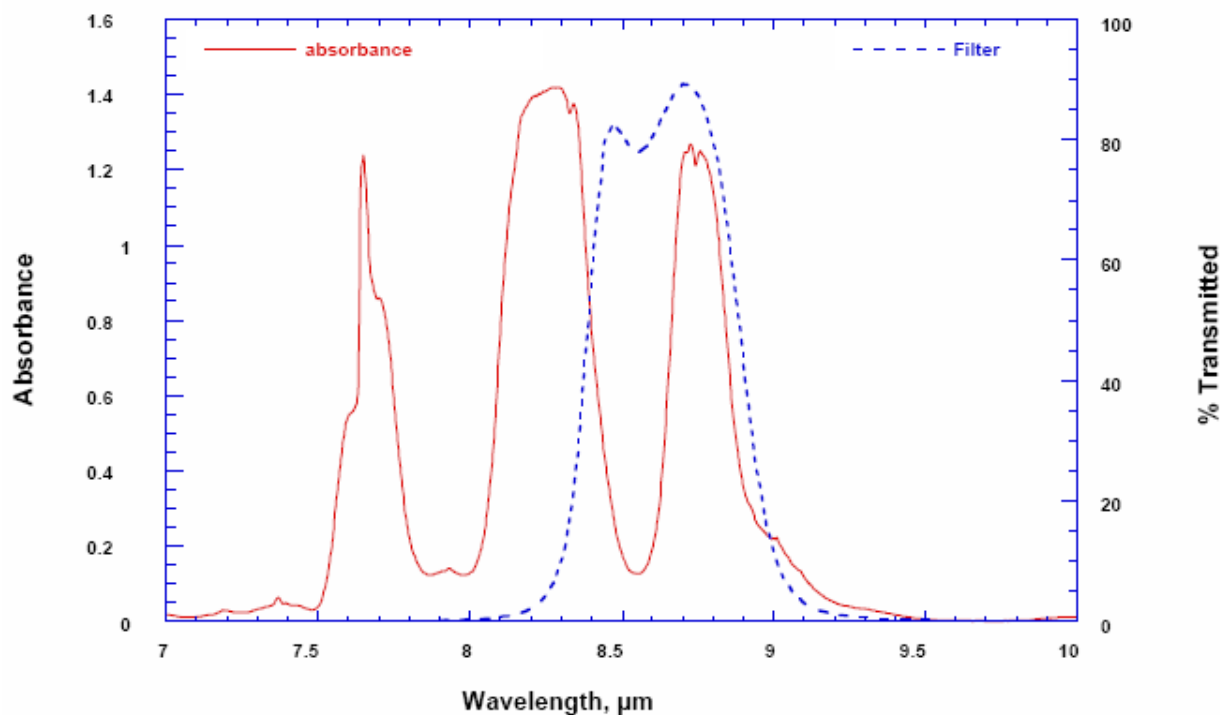


Figure 5-17. Schematic of the Optical Design Used in DIRRACS I.

The detector output was collected at 20 kHz using a digitizing card mounted in a PC and analyzed to determine the peak-to-valley (Pk-Vy) voltage difference. A computer-controlled calibration system (described later) utilizing three mass flow controllers was used for calibrating the Pk-Vy signal versus HFC-125 concentration. For the 2.8 cm optical path length, the instrument is sensitive over a mole fraction range from 0.01 to 0.25. While the calibration measurements indicated a nominal  $\approx 10\%$  uncertainty (coverage factor  $k=2$ ), actual tests using a transient agent release facility indicated a systematic difference between the measured and expected values and much larger noise when compared

to the calibration measurements. Subsequent study indicated that the high flow velocity in the facility caused a change in the instrument response by affecting the source temperature and inducing vibrations in the instrument. An additional limitation of the method was the high background signal from the IR radiation from the walls. Two approaches were used to address the problems. The first approach was to surround the IR source with a cooling coil to minimize the effect of the flow on the source temperature. The second method was to use a second narrow-band-pass filter at a nearby, non-absorbing wavelength. In this case, it was expected that both signals would be affected in the same way by a change in the source temperature so that the ratio would be constant. Neither method solved the flow effect problem, though the cooling coil approach provided some improvement, and neither method addressed the problems with vibration or background radiation from the walls.



**Figure 5–18. Absorption Spectrum of HFC-125 Superimposed with the Transmittance Spectrum for the Bandpass Filter.**

Even with these limitations, useful data have been obtained using the DIRRACS I. Two models of the DIRRACS I were used in the first measurements of the dispersal time of an agent in the dry-bay facility at Wright-Patterson Air Force Base.<sup>39</sup> The preliminary measurements indicated a relatively long time, on the order of a few seconds, for dispersal of the agent throughout the dry bay. This information has important implications about the mechanism of extinguishment when the fire is far from the release point of the agent. If the fire is extinguished under these conditions, the mechanism must not involve a direct interaction of the agent on the fire, if one assumes the presence of the fire does not affect the distribution of the agent. These results showed the value of a fast response agent measurement.

### 5.4.3 Improved Hardware Design – DIRRACS II

The drawbacks of the DIRRACS I necessitated major modifications to the original design. The objectives were to eliminate the temperature and flow sensitivity of the source, detector, and other components; increase the signal-to-noise ratio; and increase the frequency response. Figure 5–19 is a schematic of the DIRRACS II design, and Figure 5–20 is a photograph of the breadboarded instrument as set up to measure a transient agent release in the Transient Application, Recirculating Pool Fire Apparatus (TARPF), described in Chapter 6 of this book. IR radiation is emitted by the source (cylinder with triangle on top at bottom central) toward an elliptical mirror, reflected through the chopper and pinhole, collimated by a parabolic mirror (behind chopper), through the periscope (attached to the duct at left), reflected by a 90° mirror and a focusing mirror, through a narrow-band-pass filter, and finally detected by a HgCdTe detector (under the plate with the hole).

The key design changes in the DIRRACS II are:<sup>40</sup>

- The addition of a periscope, for reducing the high noise level of the DIRRACS I at velocity conditions of 10 m/s to 20 m/s. The periscope also allows the sampling volume to be completely isolated from the rest of the instrument, so convective flow and temperature variations at the measurement location cannot affect the source or detector.
- Reduction in system vibrations by constructing the periscope assembly from standard stainless steel vacuum components. This structure is much more rigid than the previous optical housing.
- Decrease the sample path length by about a factor of two, increasing the practical maximum mole fraction measurable by the instrument from about 0.2 to about 0.5.
- Collimating the IR beam and focusing it through an aperture just before the chopper and using a faster IR detector (HgCdTe), to allow operation of the chopper at frequencies as high as 4000 Hz, while the previous design with a large, unfocussed beam and slow detector was limited to about 400 Hz. This IR source also provided a more stable output with a higher intensity at the wavelength range of interest. The performance of the HgCdTe detector improves with frequency up to 4000 Hz, while the pyroelectric detector response falls off for frequencies above about 50 Hz. The tenfold increase in frequency corresponds to about a tenfold improvement in time response. The new detector also produces nearly square-wave output well above any background signal from extraneous radiation sources. The detector does require liquid N<sub>2</sub> cooling, but one filling provides at least 2 h of stable operation.
- Placing the IR source within the instrument housing, eliminating the problems of the high flow affecting the temperature of the source and the movement of the source.
- The elliptical and parabolic mirrors were used to produce an 8 mm collimated beam, which was ultimately focused on the detector. The background IR radiation contributed little (<1 %) to the IR radiation reaching the detector, while in the previous design as much as 50 % of the IR radiation originated from blackbody radiation from the walls.

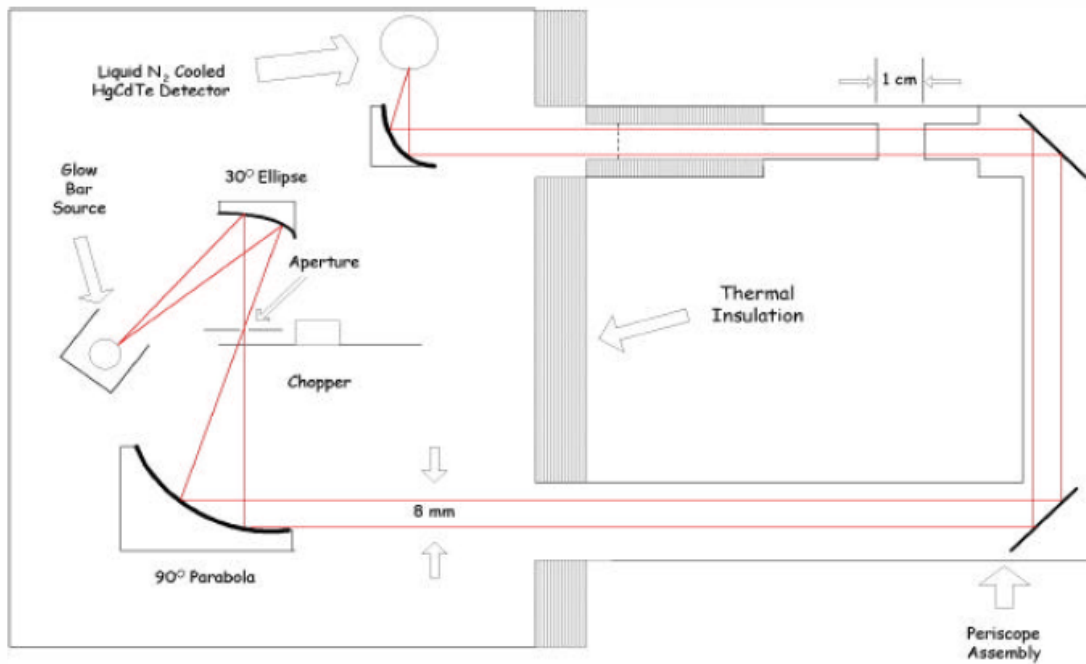


Figure 5–19. Schematic of DIRRACS II.

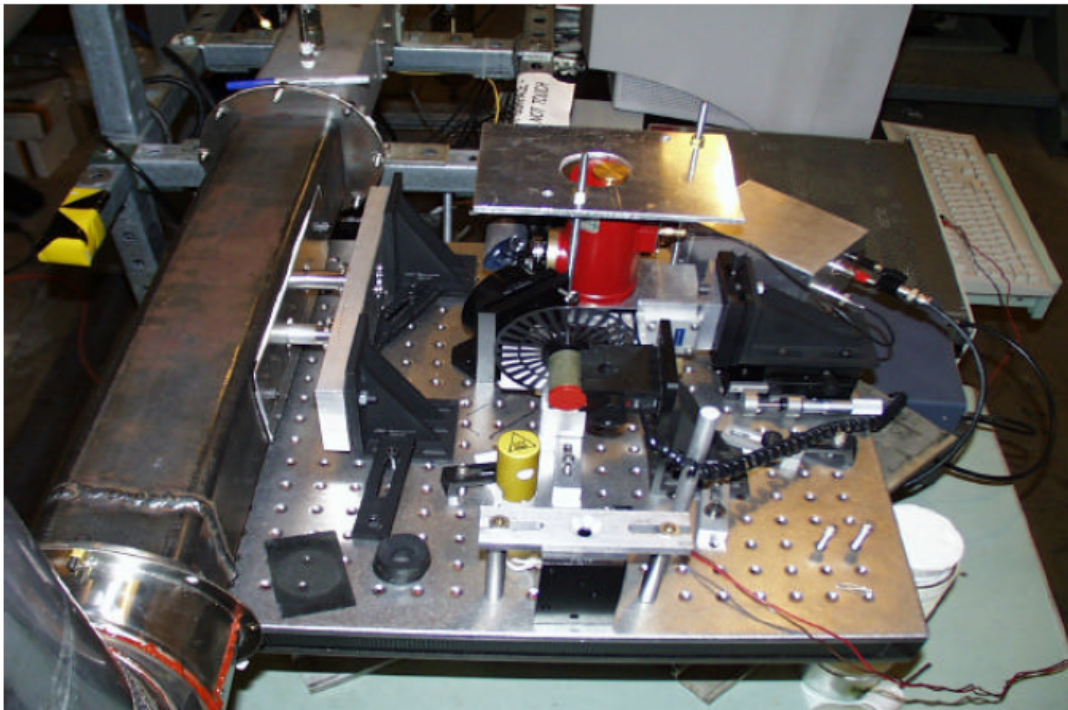


Figure 5–20. Photograph of the DIRRACS II with the Periscope Mounted within the Flow Channel of the TARP Facility.

#### 5.4.4 Data Acquisition and Analysis

In addition to the hardware design improvements, improvements to data acquisition and analysis were also made. The old data acquisition board was limited to about 20 kHz sampling frequency. The new board allows variable data collection rates up to 250,000 samples/s. Most often, a setting of 128,000 samples/s is used to allow data to be collected over a longer time period for a given level of data storage. Either an internal or external trigger can initiate data collection. The previous method of analysis involved postprocessing of the data, which required at least an hour. The current software combines the functions of acquisition and analysis. In conjunction with a faster computer and new data acquisition board, the software reduces the data and displays it within 20 s after acquisition. The software performs preliminary filtering using Fast Fourier Transform analysis to remove DC offset, drift, and 60 Hz noise. The software performs the filtering using digital lock-in amplification with the frequency determined by the chopper output and averages over a discrete and selectable number of cycles.

#### 5.4.5 Calibration Experiments

Calibrations of the DIRRACS II were conducted with a facility fully described in Pitts et al.<sup>39</sup> A summary of the apparatus and procedure are presented here. The calibration facility consists of 3 mass flow controllers and various solenoid and pneumatic valves controlled with a computer, data acquisition board, and analog/digital output board. A 2 L/min mass flow controller and a 10 L/min model are used to meter the agent through the system. The programming prescribes at what point the fraction of agent in the mixture is best supplied through the higher capacity controller. The third controller is a 10 L/min model which is dedicated to air flow.

The program uses equations based on calibrations of each flow controller for agent or air to set the mass flows through each controller to match the user input mass fraction of agent. The system output changes the mixture at the calibration cell within seconds. The sealed cell with an inlet and outlet for agent/air mixture flow was attached to the DIRRACS II periscope around the sampling volume. Because leakage of agent into the periscope through the window seals was suspected, 120 kPa (17 psi) pressure air was blown into the two periscope ends to prevent accumulation of agent which would impact the calibration. Since the cell was not particularly designed for the DIRRACS II, it had a relatively large interior volume and required about 1 min for a mixture to completely change to a new mixture input by the operator. This initial calibration of the DIRRACS II for HFC-125 is shown in Figure 5–21. Each data point represents an average of data collected over 1 s. The standard deviations for 1 s samples of data generated with particular calibration mixtures ranged between 0.1 % and 0.25 % of the averages. The expanded combined standard uncertainty (2 standard deviations) among the average peak-to-valley data points shown in Figure 5–21 is about 2 % of nominal for the calibrations that were conducted, which translates into approximately a 0.005 mole fraction uncertainty.

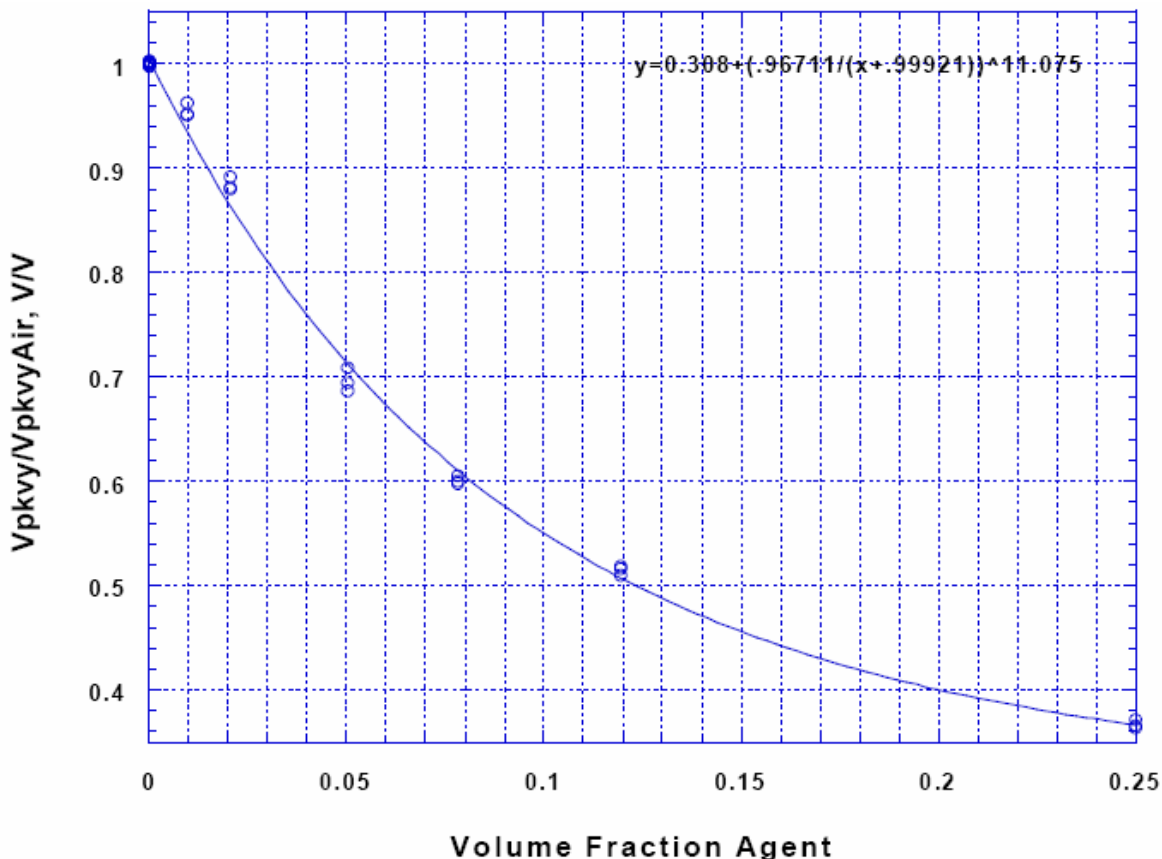


**Figure 5–21. Calibration plot of Average Normalized Peak-to-valley Signals vs. Volume Fraction of HFC-125.**

#### 5.4.6 Release Tests of HFC-125 in the TARP Facility

The NIST TARP facility (Chapter 9) consists of a 2.5 m long duct of 9.2 cm x 9.2 cm square cross section which is connected to a high capacity air compressor. Variable orifice plates allow the compressor to generate air velocities up to 20 m/s in the duct. Various agents can be stored in 1 L and 2 L cylinders. Before a test, a cylinder is filled to a prescribed pressure, which is measured with a pressure transducer inside the cylinder. A release is controlled with a timer that determines the length of time the cylinder solenoid valve is opened. The normal operation of the TARP facility consists of igniting a flame in a test section and releasing various amounts of agent upstream to observe the extinguishment behavior. For the DIRRACS testing, no flame was ignited, but the air flow and agent release capabilities of the system were utilized. The periscope assembly was mounted 0.5 m downstream of the pool fire zone and about 2 m downstream of the region where the agent is mixed into the air stream.

Over 40 release tests were conducted in the TARP Facility.<sup>40</sup> Each test was conducted with specified settings of air flow, agent vessel pressure, and agent vessel valve opening period. In order to capture events of less than 1 s with the data acquisition system, varying combinations of total points collected and sampling frequency were used. The series of tests with the DIRRACS II was used to help characterize the distortion of pulses of agent as they moved downstream after each release.

Two of the HFC-125 release tests that represent the extremes of the series are described here. The first involved a pulse of 100 ms duration from a cylinder a 30 kPa initial agent pressure. The second was a 250 ms pulse from a 330 kPa pressure. In both cases, the air velocity through the duct was 11 m/s. The chopping frequency was 2 kHz and the sampling frequency was 128 kHz.

Figure 5–22 shows the recorded peak-to-valley voltage normalized by the background value, which is proportional to the IR intensity incident on the detector. The abrupt decrease in the voltage is a result of the IR absorption by the HFC-125. The width in the dip in the voltage is slightly larger than the release time because of downstream mixing effects. Figure 5–23 shows the calculated evolution of the volume fractions of the chemical.

The different pulse durations are apparent, although the step releases become significantly spread out. The test data indicate that a 0.005 volume fraction of HFC-125 can easily be detected and differentiated from background noise. Also, turbulent fluctuations on the order of 5 ms to 10 ms are clearly resolved due to a combination of the 2 kHz chopping frequency and the Fourier Transform high frequency filtering. For neat air flowing past the periscope in the TARP facility, the standard deviation normalized by the average of a 1 s sample of data was typically about 0.2 %. This is a substantial improvement over the DIRRACS I, which had a standard deviation of 23 % under the same conditions.

#### 5.4.7 HFC-125 Release Tests in a Bradley Vehicle

A series of 11 agent release tests were carried out in a Bradley armored personnel carrier at the Aberdeen Test Center in order to characterize the DIRRACS II response to temperature and flow effects during transient agent concentration measurements.<sup>40</sup> The vehicle is shown in Figure 5–24. The extinguishing agent, HFC-125, was released in amounts ranging from about 2 kg up to about 4 kg at a fill pressure of 5.2 MPa. All of the releases were from the right, high mounting position just behind the turret. There was only one DIRRACS II unit, so concentration was monitored at two locations in different tests. Figure 5–25 shows the high location, which was near head height for an occupant in the left side of the vehicle, about halfway between the turret and the rear bulkhead. The instrument was located between two rectangular structures representing the location and approximate size of two occupants of the vehicle. The second, low location was at about waist height.

The agent volume fraction and the cylinder pressure are plotted versus time for the DIRRACS II in the high position in Figure 5–26. The HFC-125 reached the measuring position 275 ms after the release. The peak agent volume fraction was 0.22, and decreased to a value of about 0.07 after 1.5 s. Before the agent arrival, the background volume fraction is close to zero and averages about 0.0006. After arrival of the agent, the volume fractions range between 0.05 and 0.21, which overwhelms by two orders of magnitude the background level and by at least a factor of 25 the effect of pressure or vibration noise.

Figure 5–27 compares the HFC-125 concentration in the lower location to the same upper location result in the prior figure. In the lower position, the arrival time increases from 300 ms to about 400 ms, and the peak volume fraction decreases to about 0.12; however, after 1.5 s the volume fraction is slightly higher at the lower position, 0.09 compared to about 0.07. After 2 min, the HFC-125 volume fraction was in the range 0.03 to 0.09 compared to an estimate of 0.095 based on a well mixed distribution throughout the volume of the vehicle.

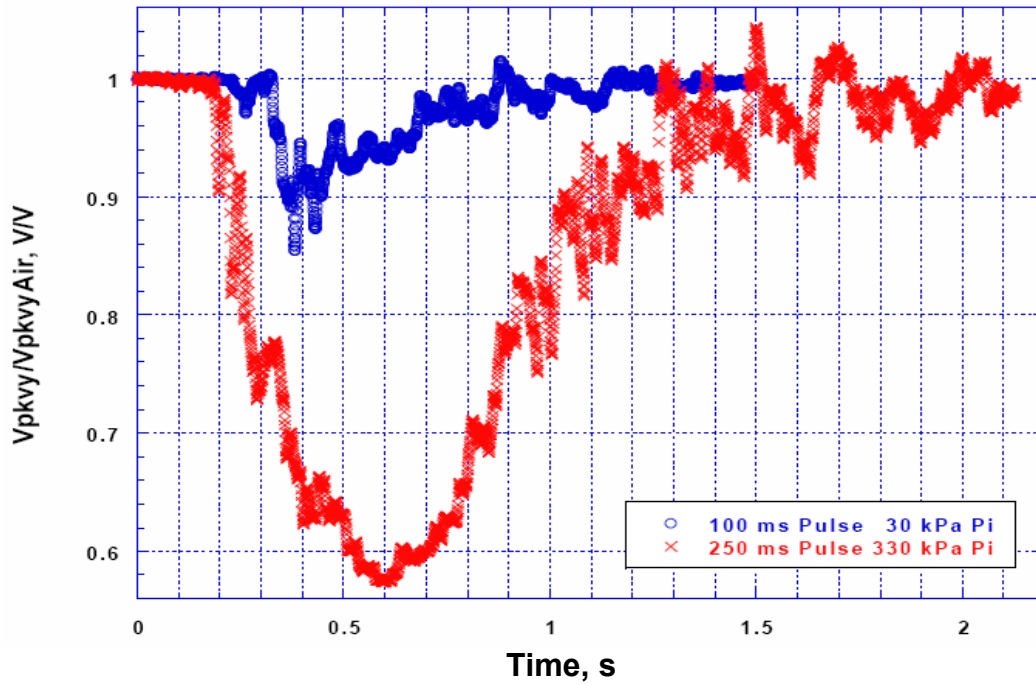


Figure 5–22. Normalized Peak-to-valley Signals Resulting from Processing the Raw Signal from the DIRRACS II for Two Releases of HFC125.

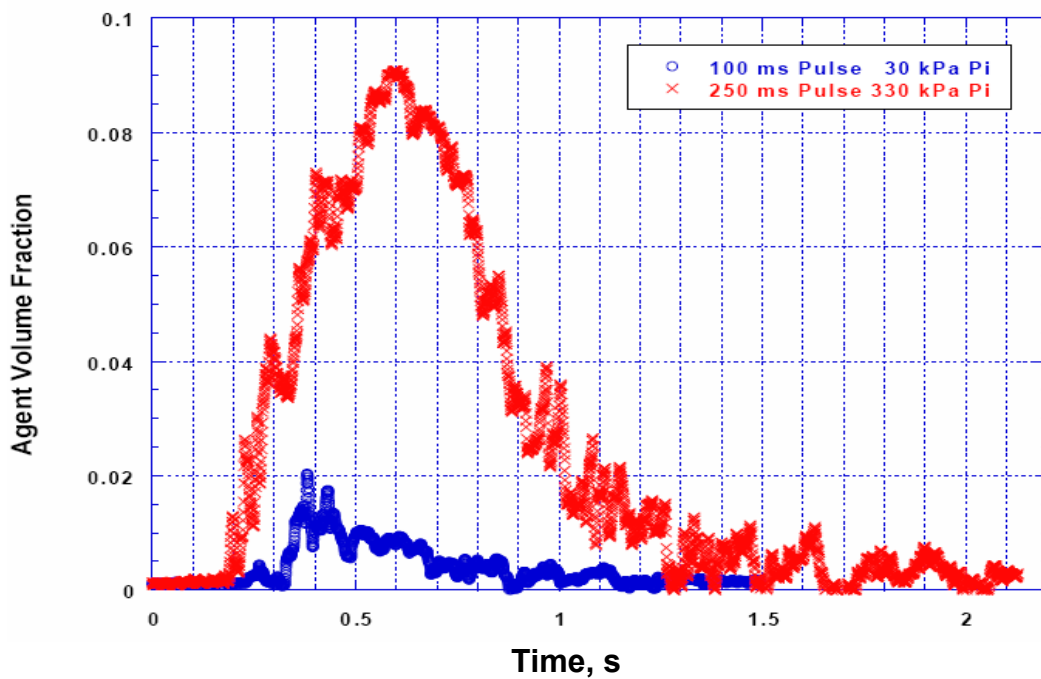
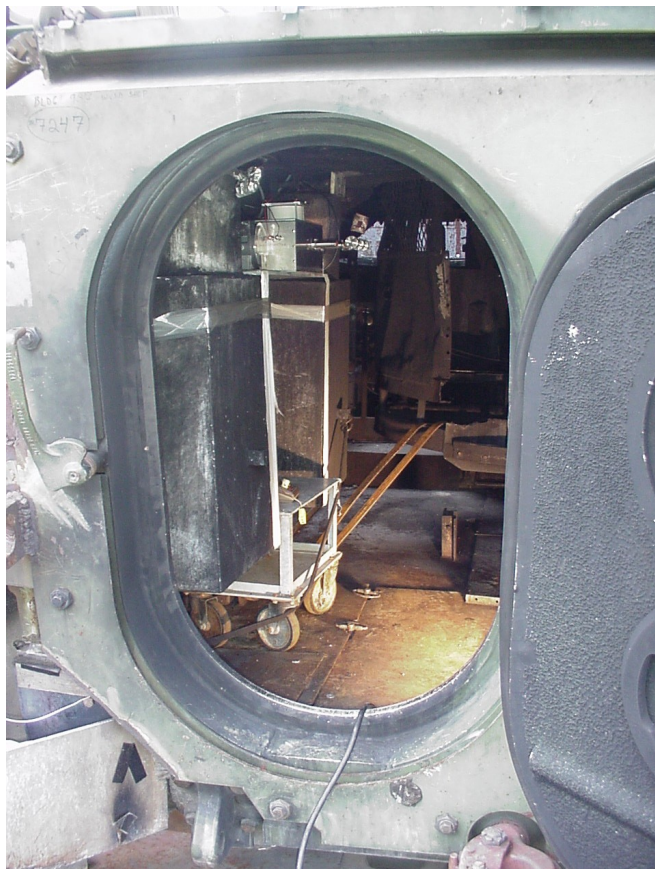


Figure 5–23. HFC-125 Volume Fraction vs. Time for Two Releases of HFC-125 in the TARPF facility.



**Figure 5–24.** Bradley armored personnel carrier modified for performing agent release and fire suppression studies.



**Figure 5–25.** Interior of the Bradley Vehicle Showing the periscope of the DIRRACS II in the “high” location. The Two Rectangular Structures Simulate Occupants.

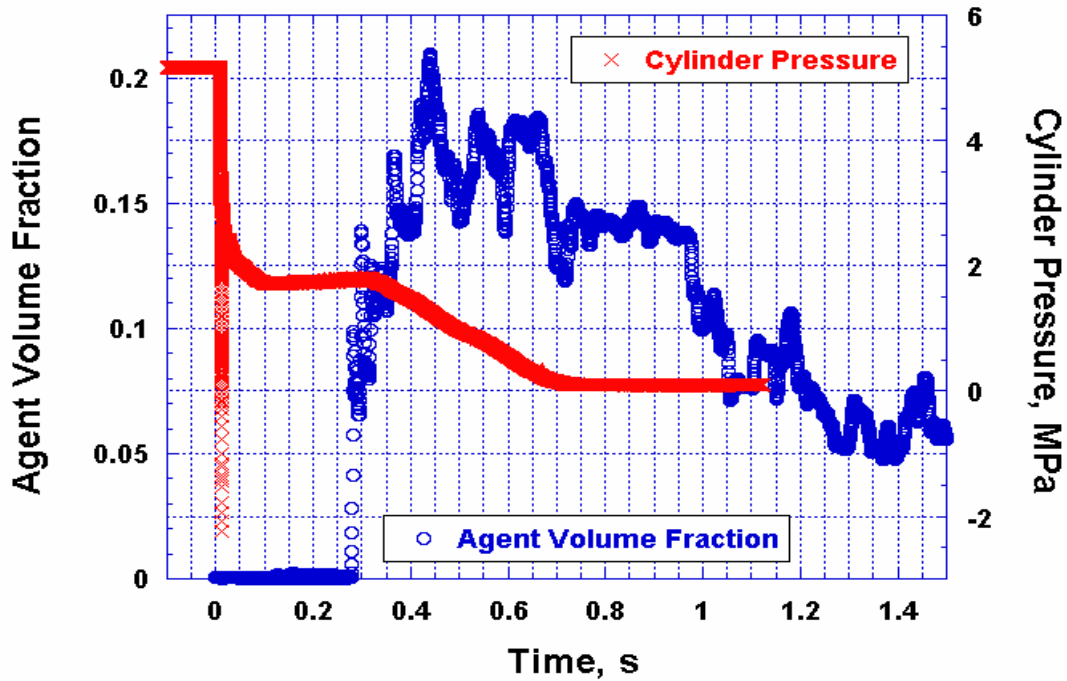


Figure 5–26. HFC-125 Volume Fraction and Cylinder Pressure vs. Time at the Upper Measurement Position.

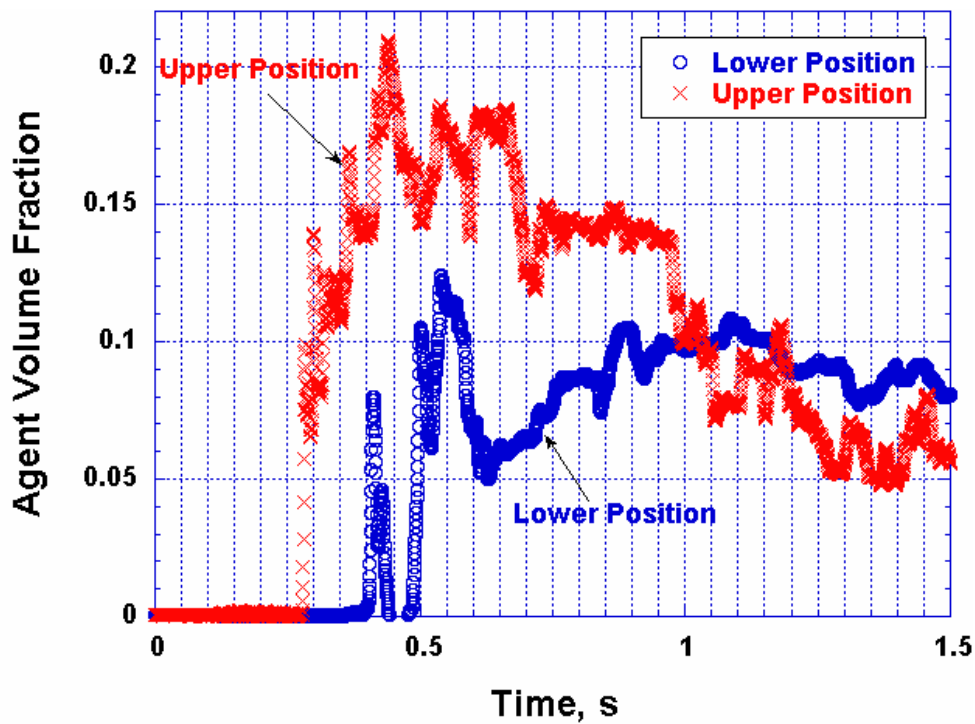


Figure 5–27. HFC-125 Volume Fractions vs. Time At the High and low Positions During Two Different Releases.

### 5.4.8 Assessment

DIRRACS II meets the design needs for monitoring halon replacement chemicals:

- Response time: The instrument monitored agent releases with a 4 ms time response and can capture the structure of distinct events that are less than 10 ms in duration.
- Dynamic range: The instrument measured HFC-125 volume fractions from 0.01 to 0.25 with an expanded uncertainty of 0.005.
- Versatility: The DIRRACS II can be used for any agents with the C-F bond using the current filter or replacing it with one more closely matched to an agent's absorption spectrum.
- Ruggedness: The instrument is portable and withstood the vibration from the agent release. The DIRRACS II could be useful for monitoring agent concentration in a fire environment provided some protection is added to shield the periscope and other exposed components from the corrosive gases produced by decomposition of the agent in the fire.

It was significant that the measured times for the HFC-125 to reach the measuring positions were longer than the desired time to extinguish the fire. This information could be useful for understanding the mechanism of fire suppression for the fire tests performed in the Bradley vehicle.

The design is ready to be adapted for reproduction or commercialization. A manual<sup>41</sup> has been prepared to assist in the fabrication of copies of DIRRACS II and to provide operation instructions to users.

## 5.5 CONCLUSION

Under the NGP, researchers at the Army Research Laboratory and the National Institute of Standards and Technology have developed techniques for measuring the concentrations of fuel vapors, oxygen, hydrogen fluoride, and fire suppressants during real-scale, high-speed fire suppression tests. Full implementation of all of these techniques into routine testing has not yet been realized, but the discrete remaining technological barriers to this have been identified, showing the way to full measurement capability in future fire tests.

The use of these instruments has already produced insights into the fluid dynamics of suppressant release and distribution, the potential for flame re-ignition, and the advantage of rapid flame extinguishment in containing the concentrations of noxious combustion products, all under realistic fire conditions.

## 5.6 REFERENCES

1. "Design of Combat Vehicles for Fire Survivability," MIL-HDBK-684, U.S. Army Tank-Automotive and Armaments Command, AMSTA-TR-T, Warren, MI; February 15, 1995.
2. Yanikoski, F.F., "Gas Analysis Apparatus", United States Patent Office Patent Number 2,586,899, February 26, 1952.
3. Linteris, G.T., and Gmurczyk, G.W., "Prediction of HF Formation during Suppression. NIST SP 890; in *Fire Suppression System Performance of Alternative Agents in Aircraft Engine and Dry Bay Laboratory Simulations*, Volume 2, Gann, R. G., Editor(s), 201-318 pp, 1995.
4. See multiple papers indexed under "Decomposition Products" in Gann, R.G., Burgess, S.R., Whisner, K.C., and Reneke, P.A., eds., *Papers from 1991-2006 Halon Options Technical Working Conferences (HOTWC)*, CD-ROM, NIST SP 984-4, National Institute of Standards and Technology, Gaithersburg, MD, (2006).
5. Brewster, M.Q., *Thermal Radiative Transfer and Properties*, Wiley Interscience, New York. 1992, p. 253.
6. Lancaster, E.D., McNesby, K.L., Daniel, R.G., Miziolek, A.W., "Spectroscopic Analysis of Fire Suppressants and Refrigerants by Laser Induced Breakdown Spectroscopy," *Applied Optics* **38**, 1476 (1999).
7. Williamson, C.K., McNesby, K.L., Daniel, R.G., and Miziolek, A.W., "Laser-Induced Breakdown Spectroscopy for Real-Time Detection of Halon Alternative Agents," *Analytical Chemistry* **70**, 1186-1191, (1998).
8. K.L. McNesby and R.A. Pesce-Rodriguez, "Applications of vibrational spectroscopy in the study of explosives", in *Handbook of Vibrational Spectroscopy*, Vol. 4, (J. Chalmers and P. Griffiths, Ed.), Wiley Interscience, Chichester, England, 2002.
9. Bomse, D.S., Stanton, A.C., and Silver, J.A., "Frequency Modulation and Wavelength Modulation Spectroscopies: Comparison of Experimental Methods Using a Lead-salt Diode Laser," *Applied Optics* **31**, 718-731 (1992).
10. Martinelli, R., Menna, R., Cooper, D., Carlisle, C., and Riris, H., "Near-infrared InGaAs/InP Distributed-feedback Lasers for Spectroscopic Applications," *SPIE Proceedings* **2148**, 292-307, Laser Diode Technology and Applications VI, P.C. Chen, L.A. Johnson, H. Temkin, eds., 1994.
11. Linnerud, I., Kaspersen, P., and Jaeger, T. "Gas Monitoring in the Process Industry Using Diode Laser Spectroscopy," *Applied Physics B* **67**, 297-305, (1998).
12. Reid J., and Labrie, D., "Second-Harmonic Detection with Tunable Diode Lasers - Comparison of Experiment and Theory," *Applied Physics B*, **26**, 203-210, (1981).
13. McNesby, K.L., Skaggs, R.R., Miziolek, A.W., Clay, M., Hoke, S., and Miser, C.S., "Diode Laser-Based Measurements of Hydrogen Fluoride Gas During Chemical Suppression of Fires," *Applied Physics B*, **67**, p443, (1998).
14. McNesby, K.L., Daniel, R.G., Modiano, S.H., and Miziolek, A.W., "Optical Measurement of Toxic Gases Produced During Firefighting Using Halons," *Applied Spectroscopy* **51**, 678-683, (1997).
15. McNesby, K.L., Skaggs, R.R., Miziolek, A.W., and Modiano, S.H., *Optical Measurement of Toxic Gases Produced During Firefighting Using Halons*, ARL-TR-1349, Army Research Laboratory, Aberdeen, MD, 1997.

16. McNesby, K.L., Skaggs, R.R., Miziolek, A.W., Daniel, R.G., and Miser, C.S., "Near-Infrared Tunable Laser Diagnostics in Laboratory Scale Flames," *Proceedings of the Sixth Topical Meeting on Laser Applications to Chemical and Environmental Analysis*, Optical Society of America, Orlando, FL, p. 203, March, 1998.
17. McNesby, K.L., Skaggs, R.R., Miziolek, A.W., Clay, M., Hoke, S., and Miser, C.S., "Diode Laser-Based Measurements of Hydrogen Fluoride Gas During Chemical Suppression of Fires," *ARL-TR -1785*, Army Research Laboratory Aberdeen, MD, 1998.
18. Skaggs, R.R., Daniel, R.G., Miziolek, A.W., McNesby, K.L., Herud, C., Bolt, W.R., and Horton, D., "Diode Laser Measurements of HF Concentrations Produced From Heptane/Air Pan Fires Extinguished By HFC-236, HFC-227EA, HFC-236 Plus APP, or HFC-227EA Plus APP," *Applied Spectroscopy* **53**, 1143, (1999).
19. McNesby, K.L., Wainner, R.T., Daniel, R.G., Skaggs, R.R., Morris, J.B., Miziolek, A.W., Jackson, W.M., and McLaren, I.A., "Detection and Measurement of Middle-Distillate Fuel Vapors by Use of Tunable Diode Lasers," *Applied Optics*, **40**, 840-845 (2001).
20. Wormhoudt, J, ed., *Infrared Methods for Gaseous Measurements - Theory and Practice*, Marcel-Dekker, New York, 1985;
21. Guenther, P.L., Stedman, D.H., Bishop, G.A., Beaton S.P., Bean J.H., and Quine, R.W., "A Hydrocarbon Detector for the Remote Sensing of Vehicle Exhaust Emissions," *Review of Scientific Instruments* **66**, 3024-3029, (1995)
22. Ferraro, J.R., and Basile, L.J., *Fourier Transform Infrared Spectroscopy: Applications to Chemical Systems*, Vols. 1-3, Academic Press, New York, 1978.
23. <http://www.brandtinst.com/biosystems/apnotes/equiv3.htm>.
24. Modiano, S.H., McNesby, K.L., Marsh, P.E., Bolt, W., and Herud, C., "Quantitative Measurements by Fourier Transform Infrared Spectroscopy of Toxic Gas Production During Inhibition of JP-8 Fires by CF<sub>3</sub>Br and C<sub>3</sub>F<sub>7</sub>H," *Applied Optics* **35**, 4004-4008, (1996).
25. Griffiths, P.R., Hirsche, and Manning, C.J., "Ultra-rapid-scanning Fourier Transform Infrared Spectrometry," *Vibrational Spectroscopy* **19**, 165-176, (1999).
26. Naegeli, D.W., and Childress, K.H., "Lower Explosion Limits and Compositions of Middle Distillate Fuel Vapors," Proceedings of the Fall Meeting of the Society of Automotive Engineers, SAE paper # 982485, (1998), pp. 1-7.
27. Kuchta, J.M. and R.G. Clodfelter, *Aircraft Mishap Fire Pattern Investigations. Final Report*, APWAL-TR-85-2057, Aero Propulsion Laboratory, Wright Patterson Air Force Base, OH, 1985.
28. Baer, M.R., and Gross, R.J., "Extended Modeling Studies of the TWA 800 Center-Wing Fuel Tank Explosion," Report SAND2000-0445, Sandia National Laboratories, Albuquerque, NM, 2000.
29. Shepherd, J., "Learning from a Tragedy: Explosions and Flight 800," *Engineering and Science*, **2**, 18-29, (1998).
30. Werle, P., "A Review of Recent Advances in Semiconductor Laser Based Gas Monitors," *Spectrochimica Acta A*, **54**, 197-236, (1998).
31. Hertzberg, G., *Infrared and Raman Spectra*, Van Nostrand Reinhold Co., New York, 1945.
32. McNesby, K.L., Wainner, R.T., Daniel, R.G., Miziolek, A.W., Jackson, W.M., and McLaren, I.A., "High-Sensitivity Laser Absorption Measurements of Broadband Absorbers in the Near-Infrared Spectral Region," *Applied Optics*, **39**, 5006-5011, (2000).

33. Griffiths, P.R., and de Haseth, J.A., *Fourier Transform Infrared Spectrometry*, Wiley-Interscience, New York, 1986.
34. McNesby, K.L., Wainner, R.T., Daniel, R.G., Skaggs, R.R., Morris, J.B., Miziolek, A.W., Jackson, W.M., and McLaren, I.A., "Detection and Measurement of Middle-Distillate Fuel Vapors by Use of Tunable Diode Lasers," *Applied Optics*, **40**, 840-845, (2001).
35. Cooley, J.W., and Tukey, J.W., "An Algorithm for the Machine Calculation of Complex Fourier Series," *Math. Comput.*, **19**, 297, (1965).
36. Rothman, L.S., Gamache, R.R., Tipping, R.H., Rinsland, C.P., Smith, M.A.H., Chris, D., Benner, V., Devi, M., Flaud, J-M., Camy-Peyret, C., Perrin, A., Goldman, A., Massie, S.T., Brown, L.R., and Toth, R.A., "The Hitran Molecular Database: Editions of 1991 and 1992," *Journal of Quantitative Spectroscopy and Radiative Transfer* **48**, 469, (1992).
37. McNesby, K.L., and Miziolek, A.W., "Fourier Transform Laser Spectroscopy," *Applied Optics*, **42**, 2127-2131, (2003).
38. Zhu, X., and Cassidy, D.T., "Liquid Detection with InGaAsP Semiconductor Lasers Having Multiple Short External Cavities," *Applied Optics-LP* **35**, 4689-4693, (1996).
39. Pitts, W. M.; Mulholland, G. W.; Breuel, B. D.; Johnsson, E. L.; Chung, S.; Harris, R. H., Jr.; Hess, D. E., "Real-Time Suppressant Concentration Measurement," in *Fire Suppression System Performance of Alternative Agents in Aircraft Engine and Dry Bay Laboratory Simulations. Volume 2*, Gann, R. G., ed., NIST SP 890, National Institute of Standards and Technology, Gaithersburg, MD, 1995.
40. Johnsson, E.L., Johnsson, Mulholland, G.W., Fraser, G.T., Leonov, I.I., and Golubiatnikove, G.Y., *Development of a Fast-Response Fire Suppressant Concentration Meter*, NIST TN 1464, National Institute of Standards and Technology, Gaithersburg, MD, 2004.
41. Johnsson, E.L., Mulholland, G.W., Fraser, G.T., Leonov, I.I., and Golubiatnikove, G.Y., *Description and Usage of a Fast-Response Fire Suppressant Concentration Meter*, NIST TN 1463, National Institute of Standards and Technology, Gaithersburg, MD, 2004.

---

---

## Chapter 6: SCREENING TESTS FOR CANDIDATE FIRE SUPPRESSANTS

Richard G. Gann, Ph.D.  
National Institute of Standards and  
Technology

J. Douglas Mather, Ph.D.  
Chemical Development Studies, Inc.

---

---

### TABLE OF CONTENTS

6.1	The Need for Screening Tests.....	518
6.2	General Approach.....	519
6.3	Agent Properties to be Screened.....	519
6.4	Fire Suppression Efficiency Screening.....	521
6.4.1	Estimation of Values.....	521
6.4.2	Cup Burner.....	522
6.4.3	Dispersed Liquid Agent Fire Suppression Screen (DLAFSS).....	525
6.4.4	Transient Application, Recirculating Pool Fire Apparatus (TARPF).....	535
6.4.5	Summation.....	557
6.5	Atmospheric Lifetime Screen.....	557
6.5.1	Factors Affecting Atmospheric Harm.....	557
6.5.2	Prior Estimation Methods.....	558
6.5.3	The Screening Protocol.....	561
6.5.4	Removal by Hydroxyl Radical Reaction.....	561
6.5.5	Measurement of Photolysis Rates.....	565
6.5.6	Estimation of Reactivity.....	568
6.5.7	Solution of Fluoroalkylamines.....	571
6.5.8	Reactivity of Alkyl Phosphates towards Radicals in Water.....	571
6.6	Volatility Screen.....	572
6.6.1	Extinguishant Volatility.....	572
6.6.2	Extinguishant Evaporation Equilibrium.....	572
6.6.3	Extinguishant Evaporation Rate.....	574
6.6.4	Boiling Temperature.....	576
6.7	Toxicity Screen.....	577
6.7.1	Hazards and Regulation.....	577
6.7.2	Screening Process.....	578
6.7.3	Literature Values.....	579
6.7.4	Quantitative Structure Activity Relationships.....	581
6.7.5	Non-animal Laboratory Testing.....	584
6.7.6	<i>In Vitro</i> Tests.....	589
6.7.7	PBPK Modeling of Cardiotoxic Effects.....	590
6.7.8	Limit Tests.....	596
6.8	Application of Screen Tests.....	597

6.9 References.....	598
---------------------	-----

## 6.1 THE NEED FOR SCREENING TESTS

A primary component of the Next Generation Fire Suppression Technology Program (NGP) was the survey of the "world" of chemistry, seeking to identify chemicals that merited examination under practical fire suppression conditions or to enable a finding that no previously unidentified such chemicals existed. This entailed consideration of thousands of compounds, a task detailed in the next chapter of this book. While full-scale testing of chemicals is eventually necessary to demonstrate acceptability, it is impractical to use such tests to narrow the large list of candidates. Full-scale tests are strongly influenced by the initial and boundary conditions surrounding the fire and suppression event. Complex, non-linear relationships among the agent, the flow field, and the fire cannot be unraveled from these full-scale suppression tests because critical parameters cannot be controlled tightly enough, and the number of tests is constrained by cost, time, safety and environmental considerations. Rather, performing this survey required a protocol for rapid and inexpensive screening of this large number of chemicals to identify those relatively few agents worthy of further examination as alternative fire suppressants.

There are multiple, critical chemical properties whose beneficial values promoted the widespread use of halon 1301 ( $\text{CF}_3\text{Br}$ ) and which would contribute to the consideration of alternative fire suppressants. These properties were listed in Chapter 1 and will be discussed further below. A testing hierarchy was needed to ensure that the most important properties were considered first. Estimation of values of these properties, for comparison with appropriately selected target values, needed to be obtained using minimal mass of the chemicals since:

- The purchase of testing quantities of this many chemicals would be prohibitively expensive,
- Many compounds would need to be custom synthesized, at significant cost, and
- Some compounds would be of unknown toxicity.

Prior to the NGP, various methods had been used to screen chemicals. Some of these were explicit, others were informal or ill-defined. Shortly before the start of the NGP, a pilot effort had arrived at preliminary screening procedures and criteria for alternatives to both halon 1301 and halon 1211 ( $\text{CF}_2\text{ClBr}$ ).<sup>1</sup> These screening procedures were able to distinguish between gases and liquids of varying degrees of performance. The authors noted the importance of the purity of the chemical being examined. They also developed classes of performance for new chemicals, related to the values for halons 1211 and 1301.

The NGP development of a screening protocol built on this and other formal and informal procedures. The first item of business was to review the existing protocols. In this pursuit, the NGP conducted a Workshop on Agent Compatibility with People, Materials and the Environment on November 14 and 15, 1997.<sup>2</sup> Approximately 40 experts from government, academia, and industry participated in the evaluation and revision of current test methods for application to screening candidates for the next generation of fire suppressants. A distinction was made between screening and evaluation/analysis tests. Screening tests are meant to provide guidance in the identification of suitable compounds (and the elimination of unsuitable

compounds) from a long list of candidates, whereas evaluation/analysis tests are performed as part of the risk assessment process that is required for qualifying all halon replacement chemicals. This chapter describes the set of screening tests used by the NGP research team.

## 6.2 GENERAL APPROACH

For a single candidate suppressant, performing a full battery of screening tests for the 12 properties listed in Chapter 1 could require about 4 moles of chemical, about 8 days, and \$15,000 (in 1990 dollars).<sup>1</sup> This was beyond the resources of the NGP. Thus, the first order of business was to identify which of the 12 properties should be the subjects for initial screening. This decision was based on the properties deemed most important for a successful chemical, most likely to disqualify a chemical, and easiest to determine. A second task was to identify or develop efficient and reasonably accurate screening tests, recognizing that these would not necessarily be the tests used in the final acceptance of an agent. The selection was based on ease of operation for these types of chemicals, the extent of prior data available, the amount of chemical required, and the relevance of the figure(s) of merit to the NGP applications. Existing methods were adapted or new methods were developed to meet anticipated needs. The third task was to set an order of screening tests to perform. As will be seen in Section 6.9, not all of the screening tests were routinely used.

For each property to be screened, a three-step process was followed:

1. Determine whether there was a value in the published literature.
2. Estimate the value of the property from the values for analogous compounds. If available, make use of quantitative structure-activity relationships (QSARs).
3. Perform the selected screening test.

The expanse of organic and inorganic chemistry was sorted into chemical families. Each family was characterized by one or more chemical features, e.g., the presence of a carbon-carbon double bond or a bromine atom. Since a family might include hundreds of individual chemicals, a small number of most likely prospects were identified that had desirable values of the screening properties, estimated using the first two of the steps above. For instance, chemicals with low boiling points were preferred, since they would be most likely to disperse rapidly (see below). If commercially available, small quantities of these chemicals were purchased. Otherwise, source(s) for custom synthesis were identified. (This is detailed in Chapter 7.) The laboratory tests were then performed as described in the remainder of this chapter.

## 6.3 AGENT PROPERTIES TO BE SCREENED

In reviewing the 12 properties identified as affecting the desirability of a chemical compound as a halon 1301 alternative, the following evaluation emerged:

- Fire suppression efficiency. This was a property that needed to be screened. Halon 1301 quenches most flames at a concentration of about 3 volume % in air. HCF-125 ( $C_2HF_5$ ), noted in Chapter 1 as the best commercially available alternative under the DoD Technology Development program, has acceptable values of other key chemical properties, but typically quenches flames at about 8 volume % in air, with some modest variation depending on the fuel.<sup>3</sup> It was dissatisfaction with the additional required mass and storage volume that led to the formulation of the NGP. The target for the screen results of candidate chemicals was a

- fire suppression efficiency better than HFC-125 and preferably comparable to that of halon 1301.
- Effective quenching of flame re-ignition. It was presumed that a chemically active suppressant (see Chapter 3) would require little agent mass beyond that needed for open flame quenching. A physical flame suppressant would need an increase similar to that for HFC-125. Thus, no screen testing was deemed necessary.
  - Atmospheric lifetime. Environmental effects were the problem that provoked the search for halon alternatives. Since the focus of the NGP was on identifying volatile candidate fire suppressants that would disperse well, compounds were screened for atmospheric effects only. Atmospheric lifetime became the key environmental figure of merit, since chemicals with short residence times in the troposphere would make minimal contributions to ozone depletion, global warming, and other, as yet unknown, types of environmental pollution. The Environmental Protection Agency (EPA) required a low value for approval under its Significant New Alternatives Policy (SNAP) Program.<sup>4,i</sup> Manufacturers could expect a continuing market in a chemical with a low value (assuming desirable values of the other chemical properties). Similarly, fire suppression systems owners did not want to be required to replace their systems yet another time. For screening purposes, the NGP aimed for lifetime estimates of the order of one month. Halon 1301 has an estimated atmospheric lifetime of 65 years.<sup>5</sup>
  - Effectiveness of low-temperature dispersion. Because in-flight fires often occur at operational altitudes where temperatures are low, a successful agent must have high volatility.<sup>ii</sup> NGP experiments established that excellent dispersion was achieved for chemicals whose boiling points were below the ambient temperature in the engine nacelle or dry bay (Chapter 8). The military specification for this minimum operating temperature is -40 °C, although operating temperatures in actual halon 1301 releases have generally been significantly higher (Chapter 2). Halon 1301 and HFC-125 have boiling points below -50 °C, and flashing does occur. Thermodynamic calculations showed that a typical suppressant chemical will have an equilibrium concentration of at least 5 volume % at -40 °C if its boiling point is below 20 °C. However, at these temperatures, the evaporation rate may be too slow for effective dispersion to all parts of the engine nacelle or dry bay before the agent is flushed from the space. Nonetheless, the NGP used a maximum boiling point criterion of 20 °C for screening purposes. As a peripheral benefit, a low boiling point generally means that an agent would eventually evaporate with little or no residue. Thus, no additional screen for agent residue was used.

---

<sup>i</sup> The EPA is responsible for assuring that no halon replacement presents an unacceptable risk to human health or the environment. For toxicity, the primary focus has been to assure the potential for timely egress from the immediate environment generated by the discharge of a fire suppressant. Although the EPA has no requirements on screening candidates, the EPA does characterize the risks associated with halon replacement agents. As part of this process, information on the toxic properties of chemical agents is compiled and combined with the exposure assessment results to estimate risk. The EPA requests toxicity data on a case-by-case basis for the risk characterization. Because many of the current halon replacement agents have been halogenated hydrocarbons, information related to acute toxicity, cardiac sensitization, subchronic toxicity, developmental toxicity and genetic toxicity have been required. Inert gas agents have had a different set of requirements, such as the concentration that produces hypoxia. The EPA, however, does not state specific methods to use for these tests. Ideally, the methods used to screen chemicals advanced as fire suppressants will address the endpoints which the EPA will use to regulate them.

<sup>ii</sup> Halon 1301 is referred to as a total flooding agent. When discharged, it rapidly fills the space it is protecting, becoming able to quench flames in virtually any location. This is contrasted with streaming agents, which are (as the name implies) squirted at a fire. For these fluids, low volatility generally enhances performance by allowing a greater focus of the stream without loss by evaporation.

- Low toxicity of the chemical and its combustion and decomposition products. Most engine nacelle and dry bay fires occur during flight and no people are exposed to the released agent or its by-products. The same is true for in-flight accidental discharges (of which there are very few) in unoccupied spaces. However, there is the potential for a fire or an accidental discharge when the aircraft is on the ground, e.g., during maintenance operations or fire suppression system re-charging. Then, there is the possibility of exposure of people. For halogenated compounds, the primary risk from exposure to low concentrations is cardiac irregularity. The NGP screening criterion was the suppressing concentration should be lower than the lowest observed acute exposure level (LOAEL) for inducing cardiac arrhythmia.

These properties are not entirely independent. For example, the molecules in fluids with low boiling points are generally small, i.e., composed of relatively few atoms. Some of the molecular features that lead to short atmospheric lifetime, such as a carbon-carbon double bond, increase the number of atoms over the simplest single-carbon compounds, which generally increases the boiling point. The presence of atoms that provide efficient flame extinguishment, such as a bromine atom, may increase toxicity.

The following properties were not included in the initial screening. However, preferred measurement methods were identified.<sup>2</sup>

- Low electrical conductivity
- Low corrosivity to metals
- High compatibility with polymeric materials
- Stability under long-term storage

## 6.4 FIRE SUPPRESSION EFFICIENCY SCREENING

### 6.4.1 Estimation of Values

The first step in obtaining an approximate value for the concentration of a chemical compound needed to extinguish a flame was based on prior measurement of the compound itself or the known efficiency of analogous compounds. In general, candidate compounds belonged to one of three categories:

- Physically active molecules. These compounds absorb heat into their vibration-rotational modes. In some cases, the breakage of chemical bonds (without immediate recombination) may result in additional endothermicity. The heat absorption removes enthalpy from the flame and its environment, cooling the flame. The effectiveness of such compounds typically increases with an increasing number of atoms, and the more effective compounds tend to have higher boiling points. (See below.) Pitts<sup>6</sup> had performed a thorough study of these chemicals (Chapter 7), and his compilation became the basis for assessing any further candidates of this type.
- Reactive molecules. There are some atoms, such as fluorine, that can be extracted from the suppressant molecule by a hydrogen atom from the flame. The resulting HF bond is sufficiently strong that the fluorine atoms play no further role in the quenching of the flame. There were flame extinguishment data for some fluorocarbons and hydrofluorocarbons, and these values provided a reference for considering additional such compounds.

- Catalytic molecules. Certain atoms were known to participate in chain reactions that lead to the recombination of flame-propagating free radicals. The bromine atom, present in  $\text{CF}_3\text{Br}$ , is one of these. Iodine and phosphorus atoms were known to be of high effectiveness, as were some metal atoms. Chlorine atoms are also known to be catalytic, but with a shorter chain length and thus lower effectiveness than bromine atoms. The presence of one or more of these atoms in a candidate chemical suggested the potential for flame suppression efficiency near that of halon 1301. NGP research and testing refined this list as the Program evolved.

### 6.4.2 Cup Burner

The most commonly used apparatus for examining fire suppressant chemicals is the cup burner, and it was the workhorse of this Program. In 1961, Creitz published a bench-scale apparatus that could be used to measure the effectiveness of chemicals at extinguishing a small, gaseous diffusion flame that was housed in a vertical glass chimney.<sup>7</sup> His apparatus was the predecessor of the cup burners that were to follow. By 1973, workers at ICI had adapted this to enable the use of a burning liquid pool.<sup>8</sup> Today, there are numerous cup burners in use around the world, not all of which are identical. There is a project underway to create an NFPA standard for the cup burner design and procedure for its use. A schematic is shown in Figure 6–1; close-up photographs appear in Figure 6–2.

A similar burner was used at the Factory Mutual Research Corporation (FMRC).<sup>9</sup> Researchers at the National Institute of Standards and Technology (NIST) replaced the liquid pool with a stick of polymethylmethacrylate<sup>1</sup>, and Tapscott and co-workers at the New Mexico Engineering Research Institute (NMERI) developed a liquid cup burner of smaller diameter that would use less agent.<sup>10</sup> In this apparatus, the cup diameter was 13 mm and the chimney diameter was 50 mm.

For gaseous or volatile liquid flame suppressants, the NGP used the NMERI cup burner with n-heptane as the fuel. The operation was straightforward.<sup>10</sup> The pure chemical was placed in a Tedlar bag, which was placed in a pressure chamber. To force the agent from the bag, a known flow of air was introduced into the chamber, compressing the bag and causing a known flow of agent vapor to the base of the cup burner. Dilution air, monitored with a mass flowmeter, was also introduced into the burner base.

The level of the burning liquid fuel was set to be flush with the lip of the cup. The air stream was established flowing upward past the cup, typically at about 0.17 L/s (flow velocity about 0.08 m/s) in the NMERI device. After a short pre-burn period, the candidate suppressant was introduced into the air stream at a concentration below the expected value for flame extinguishment. After determining that this concentration did not quench the flame (within about 10 s), the suppressant flow was increased, and the flame was observed for about 10 s again. This stepwise increase was continued until the concentration was sufficient to extinguish the flame. Further tests were sometimes performed to refine the extinguishing value, generally to within about 0.5 volume %. The process typically consumed 0.03 moles of the chemical if the extinguishing concentration was about 5 volume %.

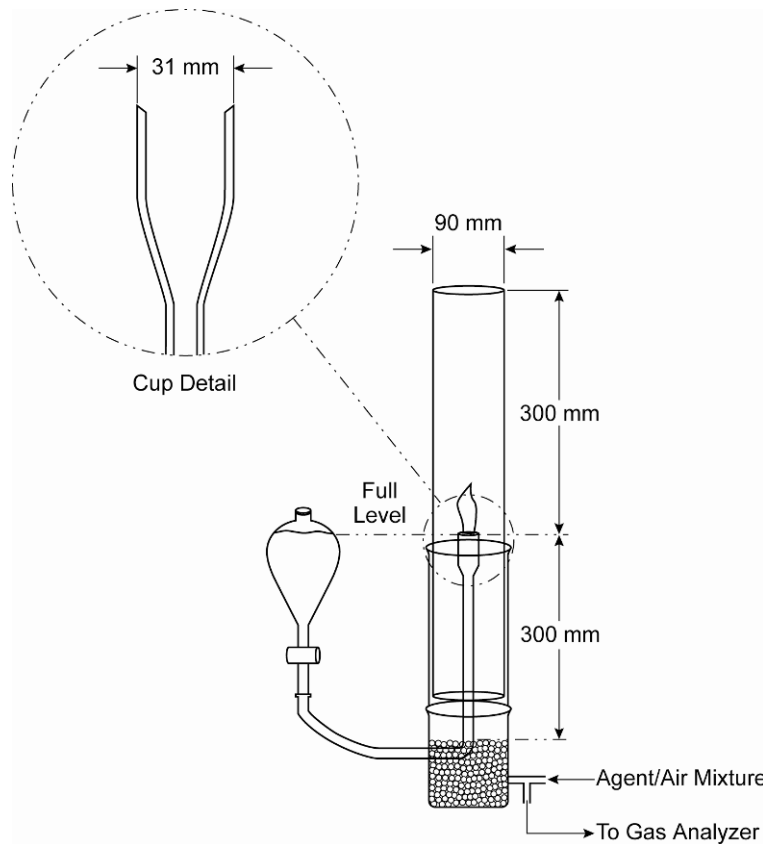


**Figure 6–1. Schematic of the Cup Burner Apparatus.**  
 (Adapted from Kidde-Fenwal drawing, used with permission)

**Figure 6–2. Photographs of a Standard Cup Burner.**  
 (Kidde-Fenwal photographs, used with permission)



A different injection mode was used if the candidate suppressant was of lower volatility, i.e., the boiling point was such that the equilibrium concentration in ambient air was near or below the extinguishing concentration.<sup>10</sup> The liquid sample was discharged by a syringe pump at a measured rate into a nebulizer. The sample reservoir and syringe pump were cooled to depress vaporization and minimize bubble formation within the pump and connective tubing. The nebulized mist was carried by a metered flow of heated air (Figure 6–3) into a heated glass column and fully evaporated. The air-agent mixture entered the cup burner at a temperature between 40 °C and 50 °C. The cup burner chimney was heated to eliminate condensation of the agent on the glass surface. (See Figure 6–4.)

Using these approaches, the apparatus was usable to address compounds with boiling points from at least -58 °C (halon 1301) to 130 °C. In some cases, when it was not possible to obtain a sufficient mass of the chemical for a determination of the extinguishing concentration, the value was estimated, and a single test was performed to establish an upper bound.

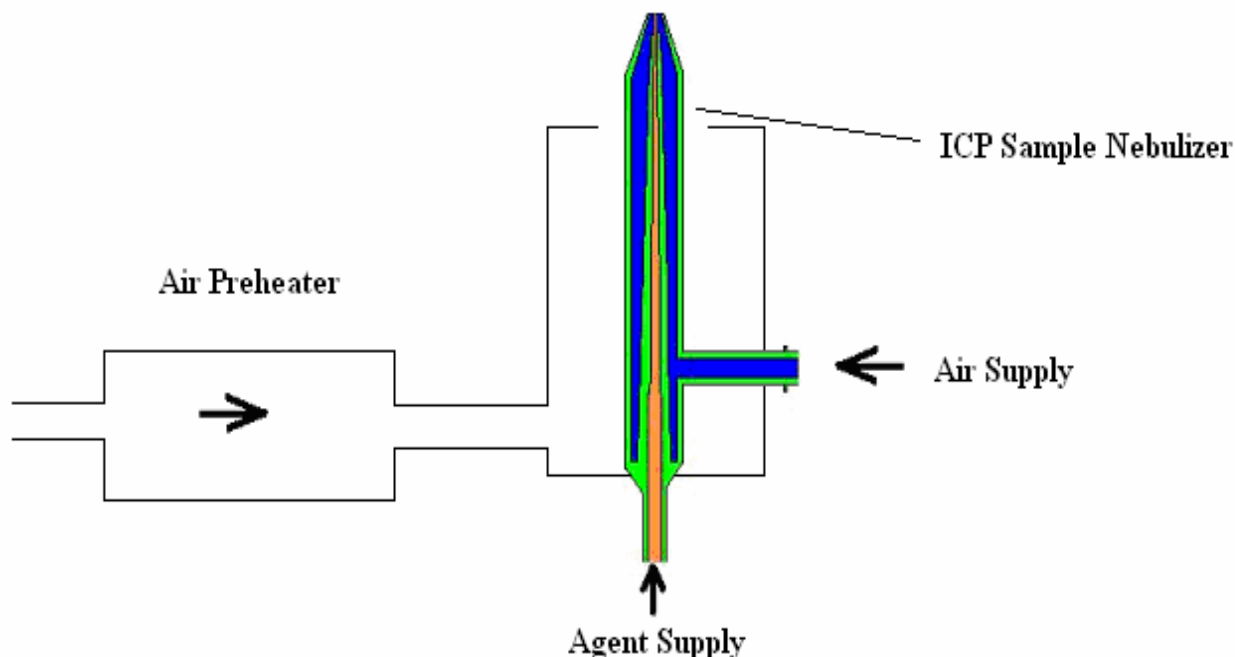


**Figure 6–3. Schematic of Sample Nebulizer.**  
(Chemical Development Studies, Inc. drawing, used with permission)

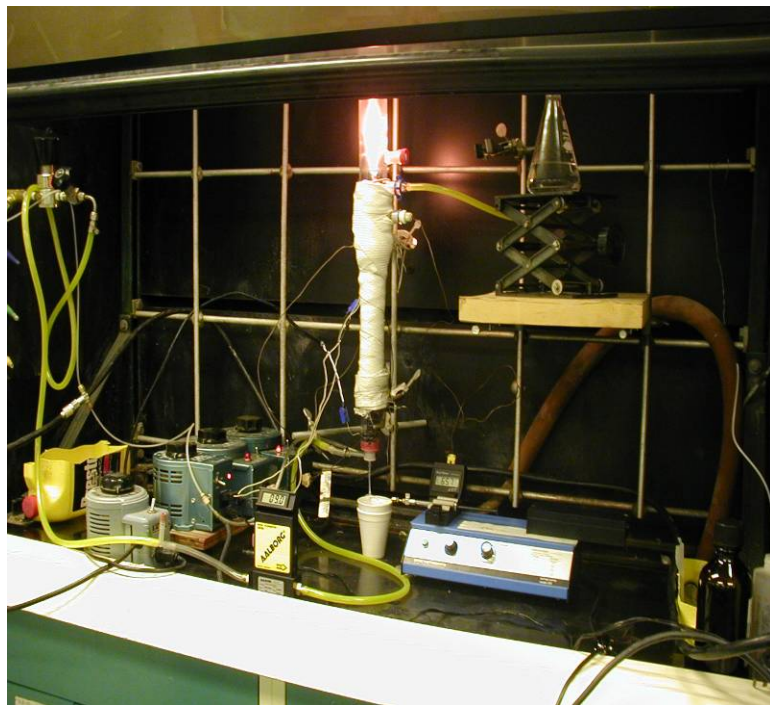


**Figure 6–4. Heated Cup Burner for Appraising High-boiling Flame Suppressants.** (Chemical Development Studies, Inc. photograph, used with permission)

### 6.4.3 Dispersed Liquid Agent Fire Suppression Screen (DLAFSS)

#### Need for a Liquid Agent Screen

In practice, fluid suppressants are stored as liquids under pressure. This enables storing more than 100 times the agent mass in a given volume, compared to storage as a compressed gas. Upon release, the fluid partially vaporizes, with the remaining fraction emerging as droplets of varying size. When they reach the flame zone, the droplets absorb additional heat, cooling the flame as they vaporize. This heat of vaporization can be a significant contribution to the agent's flame suppression efficiency, especially for water or other polar compounds. It was anticipated that some such compounds, with other desirable properties, would merit screening for their fire suppression effectiveness. The cup burner, dispensing only gases, does not capture this additional benefit.

For the NGP, Yang and co-workers designed, constructed, and demonstrated a laboratory-scale apparatus that could perform the screening of liquid agents in a well-controlled experimental setting.<sup>11</sup> The following describes the design and the operational procedure of the Dispersed Liquid Agent Fire Suppression Screen (DLAFSS). Detailed component drawings are documented in the appendices to a more detailed report.<sup>12</sup>

#### General Description

As shown in Figure 6–5 and Figure 6–6, the apparatus consisted of:

- a burner that generated a flame whose properties made it appropriate for examining liquid aerosol suppressants and whose extinguishment was readily observed,

- a wind tunnel that produced a flow field in which the droplets were transported to the flame in a well characterized manner, and
- a liquid droplet generator that generated small amounts of liquid aerosol agent of controlled and known dimension.

The device could also be used to screen gaseous fire suppressants. In principle, the apparatus could be employed to screen powders by incorporating a powder delivery system in lieu of a liquid droplet generator; however, that was not pursued.

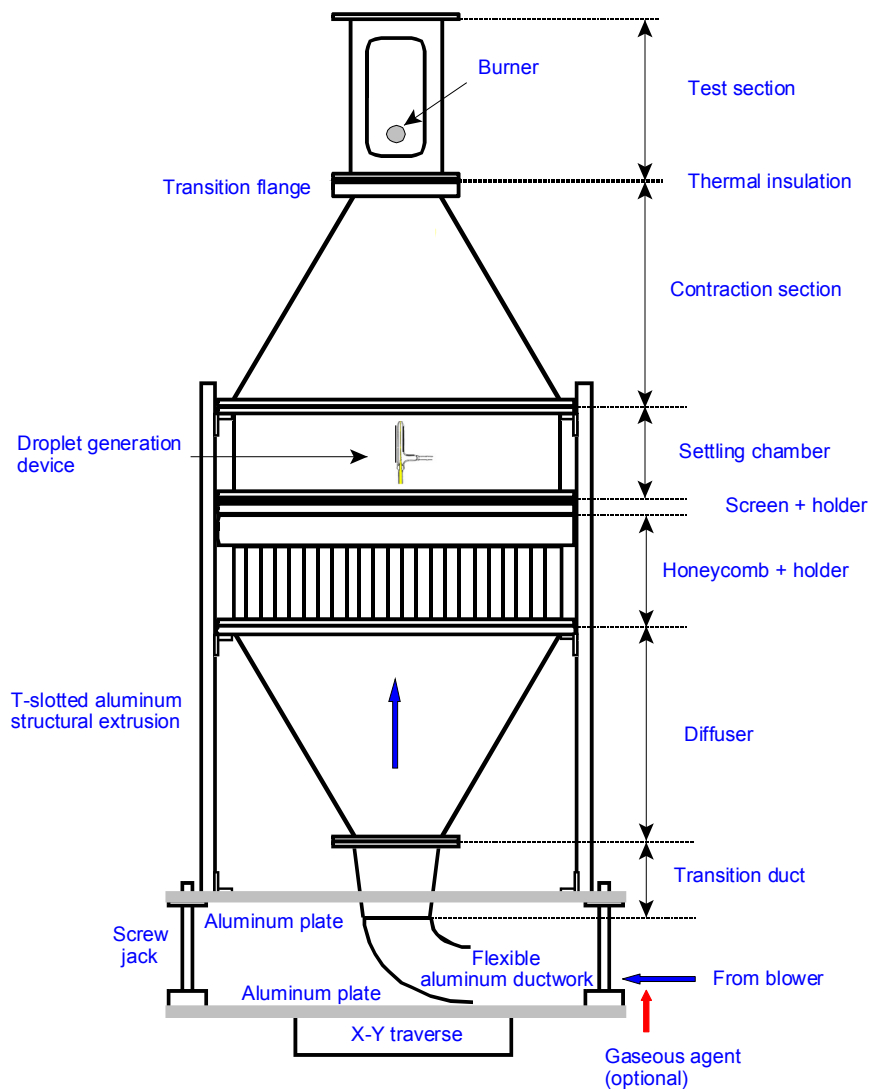
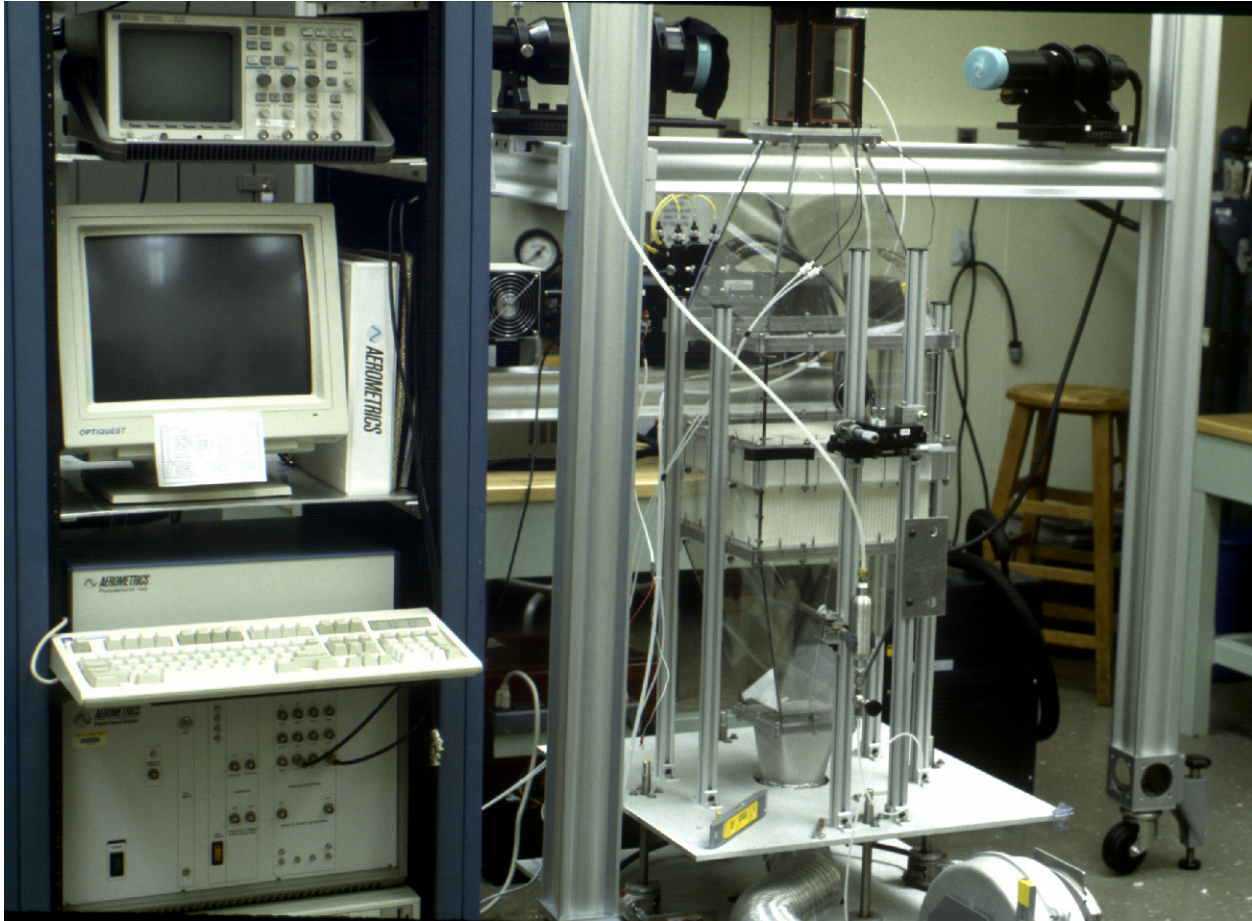


Figure 6–5. Schematic of the DLAFFS Wind Tunnel.<sup>12</sup>



**Figure 6–6. Photograph of the DLAFSS Wind Tunnel.**<sup>12</sup>

The burner was designed to be durable, easily built, installed, operated, and able to generate reliable screen test data. It is shown schematically in Figure 6–7 and photographically in Figure 6–8. The burner was a replaceable, porous (20  $\mu\text{m}$  typical pore diameter) sintered stainless steel, standard  $\frac{1}{2}$ " UNF-threaded cup filter, with a length of 3.18 cm, an inner diameter of 1.12 cm, and an outer diameter of 1.58 cm. The burner was screwed onto an extended water-cooled insert through which fuel was injected. The water was used to cool the burner (to prevent damage to the porous surface structure) and the fuel (to prevent fuel pyrolysis prior to its ejection through the porous surface). A water-cooled, cylindrical brass rod, of the same diameter as the burner, extended the burner cylinder across the test section. The downstream hemicylinder of the burner surface was coated with a thin layer of high-temperature-resistant black paint in order to prevent fuel ejection into the wake region. The high pressure drop across the porous sintered surface assured a very uniform fuel flow over the burner surface.

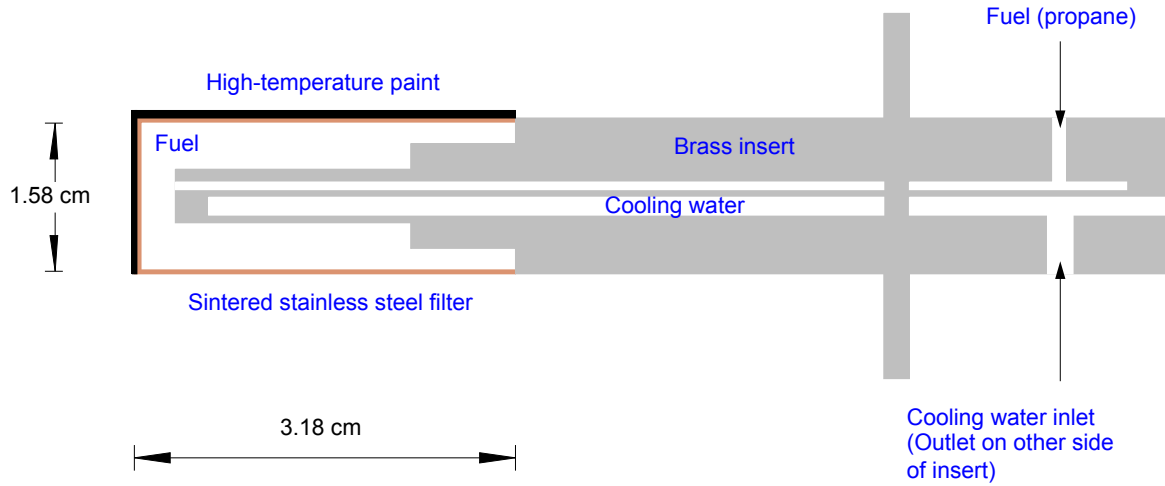


Figure 6–7. Cut-away View of the DLAFSS Burner Insert.<sup>12</sup>

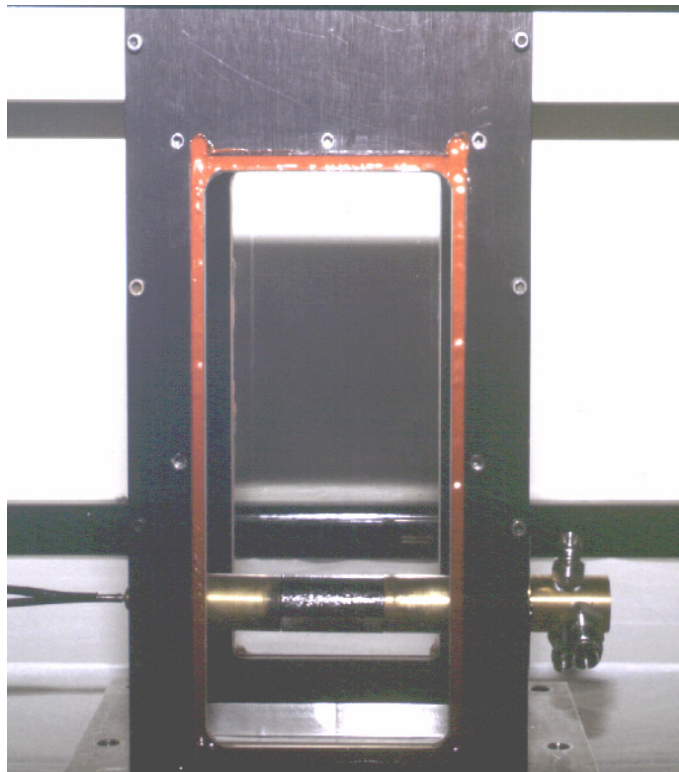
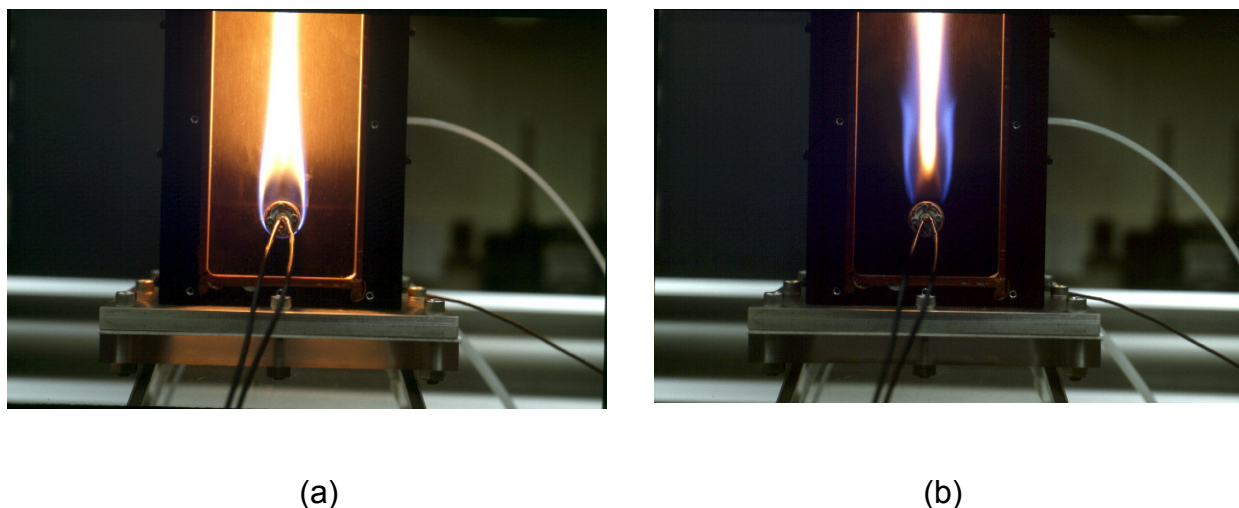


Figure 6–8. Photograph of the DLAFSS Burner Assembly.<sup>12</sup>

Propane, which is moderately sooting, was used as the fuel. Its flow was regulated by a mass-flow controller (with a range of 0 L/min to 4 L/min), which was controlled by a personal computer using a data acquisition board and software. A bubble flow meter was used to calibrate the mass-flow controller. The fuel was ejected uniformly from the cylinder surface, and a counterflow diffusion flame was formed in the forward stagnation region of the burner (Figure 6–9a).

This type of burner, devised by Tsuji<sup>13,14,15,16</sup> and commonly referred to as a "Tsuji burner," has been extensively used to study flame structure and flame extinction using inert gases,<sup>17</sup> halons,<sup>18</sup> and powders.<sup>18</sup> There are many advantages to the use of a counterflow cylindrical burner. The fuel and the oxidizer flows can be independently adjusted. The flame is laminar, two-dimensional, and very stable in the forward stagnation region. The geometry of the burner and the flow field allow for relatively simple analysis of the forward stagnation region.<sup>19,20,21,22,23,24,25</sup> Both enveloped (Figure 6–9a) and wake (Figure 6–9b) flames can be easily maintained over a wide range of fuel and oxidizer flows. The flame is easily observed, and critical stages such as the blow-off limit (abrupt transition from an enveloped flame to a wake flame) can be ascertained with ease and high reproducibility. The flame front can be easily accessed by intrusive<sup>14,15</sup> or non-intrusive<sup>20,25</sup> probing techniques, thus enabling detailed studies of flame structure, if desired.



**Figure 6–9. An Enveloped Flame (a) and a Wake Flame (b).<sup>12</sup>**

The advantage of the current burner design over those used in the past was that burner replacement could be easily performed when clogging of the porous burner surface occurred due to the deposition of soot particles or residue from liquid agents containing dissolved solids.<sup>18</sup>

The wind tunnel provided a uniform, low turbulence intensity oxidizer flow to the porous cylindrical burner. As shown in Figure 6–5, the air flow in the wind tunnel was oriented vertically upwards. There were five major components in the wind tunnel. The tunnel, except the test section, was made of clear polycarbonate and polymethylmethacrylate for visual observation of droplet transport toward the burner.

- The variable speed blower introduced the air flow into the tunnel through an expandable, flexible 10 cm diameter aluminum ductwork. A coupling converted this circular cross section to the square shape of the remainder of the tunnel. A slide gate damper at the blower inlet enabled control of the air intake.

- The 30 cm long diffuser had a 10 cm x 10 cm inlet cross section and an expansion ratio (based on area) of 1:9.
- The flow straightener section, which served to insure that the flow to the test section is laminar and uniform over the entire cross-section, consisted of a polycarbonate honeycomb and a screen. The honeycomb cells had a nominal diameter of 3.2 mm. A 50-mesh center-to-center stainless steel screen with 30 % open area and with wire diameter of 0.23 mm was used.
- The 30 cm long contraction section had a contraction ratio (based on area) of 9:1, with an inlet cross sectional area of 30 cm x 30 cm. A smooth-surfaced transition flange was placed between the outlet of the contraction section and the inlet of the test section, along with a thermal insulation gasket.
- The test section had a cross sectional area of 10 cm x 10 cm and a length of 20 cm. It was made of black-anodized aluminum with three Pyrex observation windows (12 cm x 7 cm x 0.64 cm) mounted flush against the three walls and sealed using high-temperature silicone. The burner was inserted through the fourth wall. The combustion products from the burner were vented to an exhaust hood.

A three-dimensional traverse mechanism was used to position the entire wind tunnel with respect to stationary optical instrumentation for droplet characterization at various locations near the burner. The wind tunnel was mounted on an aluminum base plate, which was placed on four worm-gear screw jacks coupled together via flexible shafts. The jacks were mounted on a second aluminum plate and were driven by a stepping motor and a computer-controlled microstepping indexer drive to raise and lower the tunnel. The horizontal movement of the wind tunnel was provided by mounting the whole wind tunnel assembly on a milling machine index table.

Two droplet generation techniques were developed:

- A piezoelectric droplet generator that created uniform liquid droplets of diameter near 100  $\mu\text{m}$ .<sup>26</sup> The operating principle of the droplet generator is based on the break-up of a nitrogen-pressurized jet ejecting from an orifice as a result of controlled vibration from a piezoelectric transducer driven at a fixed frequency. The droplet generator consisted of a liquid chamber which was connected to a 40 mL stainless steel reservoir, a bleed port (for eliminating any air bubbles trapped inside the chamber during priming), an orifice plate containing a sapphire orifice, and a piezoelectric transducer. The transducer was bonded with conductive epoxy to a circular disc stamped from flat stainless steel shim stock (0.38 mm thick).

Although distilled and de-ionized water and a few very dilute aqueous solutions have been successfully tested with this droplet generator,<sup>27</sup> clogging of the orifice opening constantly plagued the continuous operation of the piezoelectric droplet generator, aggravated by liquids with high loading of dissolved salts. This approach was subsequently not considered for further development.

- A small glass nebulizer was of the type used in inductively-coupled plasma atomic emission spectroscopy and was commercially available. The nebulizer was mounted at the same location (in the settling chamber of the wind tunnel) as the piezoelectric droplet generator. A schematic of the nebulizer is shown in Figure 6–10.

The aerodynamic break-up of a liquid stream issued from the capillary by high-velocity air caused the formation of a fine mist of droplets. Because of the differences in the droplet formation mechanisms, a relatively large opening (diameter  $\approx 100 \mu\text{m}$ ) of the capillary in the nebulizer, compared to the sapphire orifice (diameter  $\approx 30 \mu\text{m}$ ) above, could be used with a wide range of liquids, including those with a relatively high salt concentration. The large capillary opening made the nebulizer less prone to clogging. Fluid was fed to the nebulizer by a small, programmable syringe pump. Air was supplied to the shell of the nebulizer by a mass-flow controller. The resulting mist was entrained upwards toward the flame by the air flowing in the tunnel. The atomizing air flow was set at 0.25 L/min, which was the highest flow that could be used without disturbing the flame at the burner. Because of this limit, the atomization efficiency of the nebulizer dropped when the liquid delivery rate was increased beyond 1.3 mL/min; that is, larger droplets were generated that may not be entrained upward by the air flow in the tunnel.

The droplet generator was located in the settling chamber and was approximately 42 cm upstream of the burner. The presence of the droplet generator in the wind tunnel did not create any significant perturbation or blockage effect on the oxidizer flow field near the burner because the flame characteristics did not change with or without the presence of the droplet generator in the flow stream. By adjusting the location of the droplet generator with respect to the burner, droplet loss to the wind tunnel walls was minimized because the resulting dispersed droplet cloud was confined to a very narrow region near the burner.

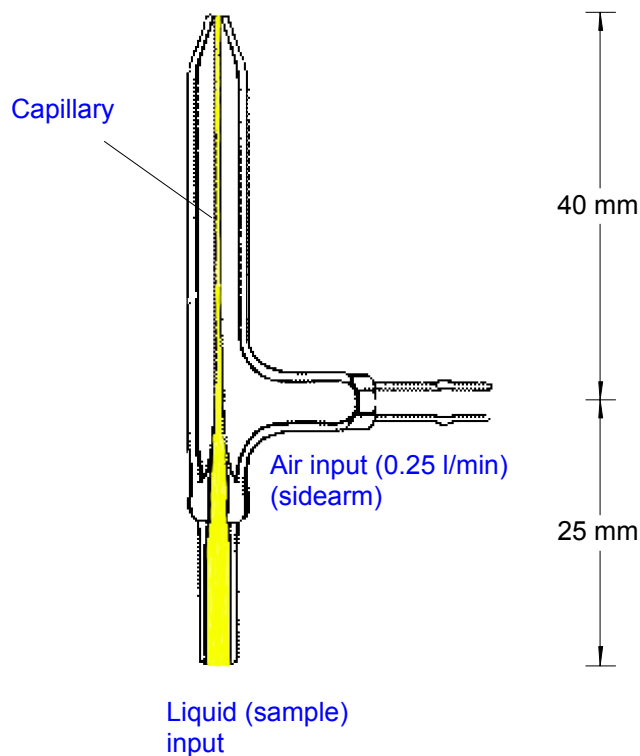


**Figure 6–10. Schematic of the DLAFSS Nebulizer.**<sup>26</sup>

Measurements of droplet size using a two-component Phase Doppler Particle Analyzer with a Doppler Signal Analyzer showed that the Sauter mean diameter is 20  $\mu\text{m}$  to 30  $\mu\text{m}$  for fluids having a range of colligative properties. About 90 % of the droplets fell within  $\pm 5 \mu\text{m}$  of the mean value.

## Operation

There were two ways to perform the screen experiments: (1) increasing the air flow at a fixed liquid agent application rate until blow-off occurs, and (2) increasing liquid agent application rate at a fixed air flow until blow-off occurs. The former was selected because the procedure requires less agent, and there was no need to correct for the lag time from changing the syringe pump setting (to increase the liquid flow) to attaining a steady liquid delivery rate.

For the rapid, *relative* indicator of the performance of candidate liquid suppressants, the fuel flow was fixed at 2 L/min, which corresponds to an ejection velocity of 4.2 cm/s. This value virtually eliminated an effect of fuel flow on blow-off velocity. Once a stable flame has been established, a fixed concentration of agent aerosol was added to the air stream; the concentration was low enough that the stable enveloped flame was maintained. The air velocity was then increased until there was a transition from a stable enveloped flame to a wake flame. This was generally a sharp change. The "figure of merit" for the agent, at that mass fraction in the air stream, was the value of the air velocity at blow-off: the higher the air blow-off velocity, the less effective the fire suppressant.

The following procedure was then used to determine a "standard" mass fraction of agent at flame extinction. Since there were many liquid agent delivery rates that one can use in the screening procedure, a reference delivery rate was needed to compare and interpret the fire suppression effectiveness of various liquid agents in a consistent and meaningful way.

Nitrogen was selected as a reference gas due to the availability of suppression data for both the cylindrical and cup burners. The mass fraction of nitrogen to extinguish a propane cup burner flame is 0.32.<sup>28</sup> DLAFSS experiments<sup>12</sup> have shown that the nitrogen mass fraction at blow-off, equivalent to the cup burner value, corresponded to a reference blow-off velocity of  $\approx 30 \text{ cm/s}$ .<sup>iii</sup> At this velocity and a propane flow of 2 L/min, an enveloped flame could not be stabilized. Therefore, to compare the results obtained from the cylindrical burner to conditions commensurate with cup-burner results, extrapolation to a lower air velocity was required. The procedure was as follows:

- A blow-off air velocity without fluid application (but with air flowing in the nebulizer) was obtained, followed by a blow-off experiment with a fixed fluid application rate.
- The fluid delivery rate at an air velocity of 30 cm/s was then deduced by linear extrapolation. Based on experience, an application rate between 0.6 mL/min and 1 mL/min appeared to be appropriate, which was a compromise between minimizing the fluid consumption for a test and attaining a blow-off velocity close to the reference blow-off velocity of 30 cm/s.

Once the application rate corresponding to the reference blow-off velocity was deduced, the reference mass flow of the liquid agent,  $\dot{m}_{agent,ref}$ , was calculated using the liquid density. The reference mass fraction of the liquid agent in the air stream was then

---

<sup>iii</sup> It is expected that similar reference blow-off velocities will be obtained when the cup burner results for other gases are used because at the *same* low global strain rate in a counterflow flat-flame burner, the agent extinction concentrations agree well with the measurements obtained from a cup burner.

$$Y_{agent,ref} = \dot{m}_{agent,ref} / (\dot{m}_{agent,ref} + \dot{m}_{air,ref}) \tag{6-1}$$

where  $\dot{m}_{air,ref}$  is the mass flow of air, calculated from the cross-sectional area of the test section and an air velocity of 30 cm/s.

**Sample Results with Aqueous Suppressants**

Several test fluids (water, skim milk, 30 % sodium iodide, and 30 % and 60 % potassium lactate) were used to evaluate the performance of the screening apparatus.<sup>11,29</sup> Milk is known to be a fire suppressant,<sup>30</sup> sodium iodide was selected because it may be more effective than sodium bromide<sup>31</sup>, and potassium lactate has been demonstrated to be more effective than water.<sup>31</sup> Figure 6–11 shows the screening results for these test fluids. In each case, only 10 mL of sample was needed to perform a rapid screen with one repeat. For a given fluid, increasing the liquid application rate decreased the blow-off velocity. As expected, a mass fraction of 60 % potassium lactate was more effective than 30 % potassium lactate. Water was the least effective when compared to skim milk, 30 % sodium iodide, and 60 % potassium acetate. Based on this set of data, the coefficient of variation from run-to-run using the liquid screening apparatus was estimated to be better than 20 %.

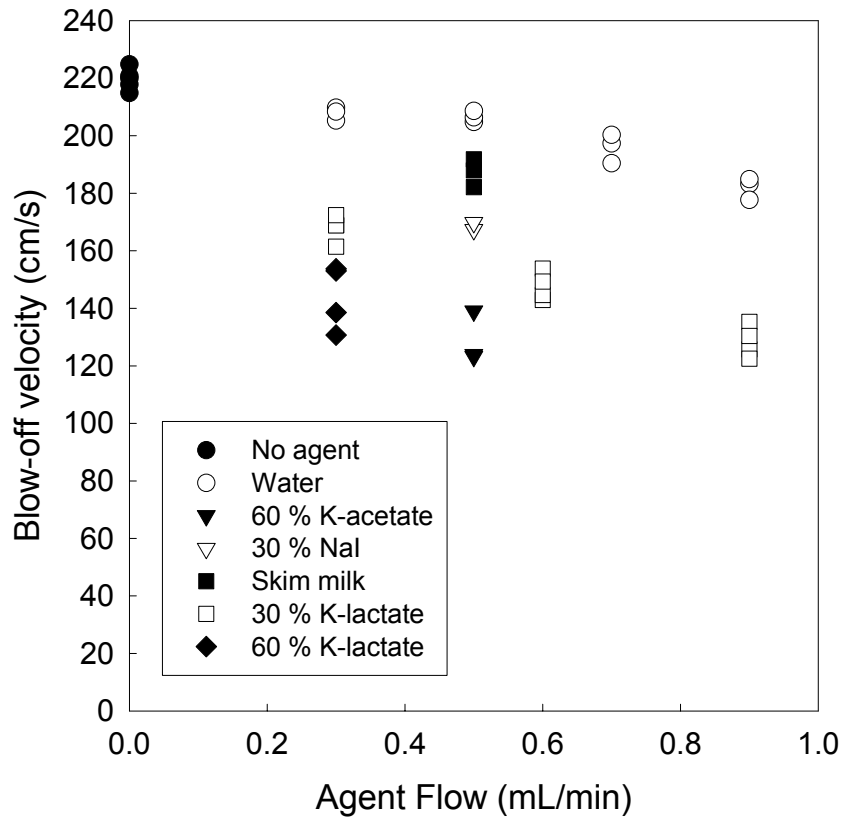


Figure 6–11. Screening Results for Various Aqueous Fluids.<sup>12</sup>

Table 6–1 summarizes the calculations of the reference agent mass fraction in air using the screening results from Figure 6–11 and the approach described above. Average values of the blow-off velocities were used in the extrapolation. For cases where blow-off velocities at more than one liquid application rate were available, linear regressions were used to extrapolate the reference blow-off velocities.

**Table 6–1. Calculated Nominal Agent Mass Fractions at Reference Blow-off Air Velocity of 30 cm/s.**<sup>12</sup>

Agent	$V_{agent,ref}$ (mL/min)	Agent density (g/ mL) @ 20 °C	$M_{agent,ref}$ (g/s)	Nominal agent mass % (%)	$m_{water,ref}/$ $m_{agent,ref}$
Water	4.62	1.00	0.08	2.6	1.0
60 % K-acetate	0.99	1.34	0.02	0.8	4.0
30 % NaI	1.76	1.29	0.04	1.3	2.0
Skim milk	2.78	1.01	0.05	1.6	1.6
30 % K-lactate	1.74	1.15	0.04	1.2	2.0
60 % K-lactate	0.71	1.33	0.02	0.6	4.0

The last column of Table 6–1 lists the ranking indices relative to water. For example, the 60 % K-acetate and 60 % K-lactate solutions were considered to be four times more effective than water at the reference blow-off velocity. If the droplets were not homogeneously dispersed across the total cross-sectional area, the calculated agent mass fraction would be underestimated. The effective area was considered as the effective coverage area of the mist in the test section. Depending on the effective coverage area, a difference of a factor of two to three in the calculated liquid mass fraction resulted. By placing a sheet of filter paper over the exit of the test section for a short duration with the wind tunnel operating (without the burner) and the nebulizer atomizing water with a dye added, the droplet-impact (color) pattern on the filter paper was used as an indicator to determine the mist coverage area in the test section. The color pattern, which was approximately circular, indicated that the mist from the nebulizer completely covered the burner and its vicinity. The mist coverage area was estimated to be about 40 % of the total cross-sectional area of the test section for all the conditions encountered in these screening tests.

Water and the aqueous agents studied were found to be more effective than  $CF_3Br$ , compared to the propane cup burner value (mass fraction of 0.17 for  $CF_3Br$ ).<sup>28</sup> The computational study by Lentati and Chelliah<sup>32</sup> also demonstrated that 20  $\mu m$  water droplets were more effective at extinguishing an opposed-flow methane diffusion flame than  $CF_3Br$  (mass fraction of 4.24 % vs. 5.9 %) at an extinction strain rate of 176  $s^{-1}$ . Although the ratio of the DLAFFSS nominal water mass fraction to the cup burner value for  $CF_3Br$  using propane was smaller, the two studies were in qualitative agreement in terms of the suppression effectiveness of water droplets.

Care should be exercised when extrapolating the screening results in Table 6–1. These were obtained using an idealized laboratory flame and a droplet delivery system such that the transport of fine liquid droplets to the flames was not a factor in determining the suppression effectiveness. In real fires, droplet entrainment and transport to the fire can significantly affect the liquid agent mass concentration required to suppress a fire, especially in highly obstructed enclosure fires.

#### 6.4.4 Transient Application, Recirculating Pool Fire Apparatus (TARPF)

##### Need for the Apparatus

Both the cup burner and the DLAFFSS determine the minimum concentration of agent needed to suppress a flame by increasing the agent flow slowly until a critical volume fraction is achieved in the oxidizer stream and flame extinction is observed. In practice, however, agents designed to replace  $\text{CF}_3\text{Br}$  are discharged rapidly, not steadily. Solid propellant gas generators (SPGGs), for example, typically discharge their effluent in 10 ms to 500 ms. A robust and repeatable means to evaluate the effectiveness of different formulations at these fast application rates requires a non-conventional screening device.

NIST research staff developed a Transient Application, Recirculating Pool Fire (TARPF) suppression facility to screen different agents and prototype systems as an indicator of full-scale performance.<sup>33</sup> The TARPF agent suppression screen was designed to reproduce the most difficult fire situation and to allow control of critical agent discharge parameters, including agent discharge rate and duration, air flow, and obstacle geometry. The performance of gaseous agents, aerosols and SPGGs was examined.

The apparatus derived from prior work by Hirst and Sutton,<sup>34</sup> who developed a wind tunnel to explore the impact of step height, air flow, and pressure on the blow-out of a jet fuel pool fire stabilized behind a backward facing step. Hirst et al.<sup>35</sup> studied the suppression of these types of fires using various halons, and concluded that a liquid pool burning in a flow behind an obstacle is the most difficult fire to extinguish. This was borne out in full-scale tests done later.<sup>36</sup> Experiments by Hamins et al.,<sup>37</sup> in cooperation with Walter Kidde Aerospace, were conducted in a wind tunnel scaled down from the earlier work by Hirst to examine the performance of HFC-125 and HFC-227ea. Investigations at the Air Force Research Laboratory<sup>38</sup> as part of the NGP sought to determine the detailed structure during suppression of a non-premixed methane/air flame stabilized behind a step. The changing character of the flame with step height and air velocity was examined, along with the amount of halon 1301 required to suppress the flame as a function of the flow parameters and injection interval.

A turbulent spray burner had been designed in earlier work at NIST<sup>39</sup> to simulate an engine nacelle spray fire resulting from a ruptured fuel or hydraulic fluid line. Flames were suppressed using gaseous and powdered agents. Hamins et al.<sup>37</sup> redesigned the burner to include a heated disk in the center of the flow downstream of the fuel nozzle. They showed that the concentration of nitrogen necessary to extinguish a turbulent propane flame increased substantially with surface temperature. The same trend, but to a lesser degree, was observed with hydrofluorocarbons.

Previous studies had demonstrated the effectiveness of SPGGs and their hybrids in full-scale fire suppression experiments.<sup>40,41</sup> Solid propellant gas generators undergo rapid solid-phase reactions producing inert gases, principally carbon dioxide, water vapor, and nitrogen, as well as particulates composed of inorganic salts. Each component individually behaves as a fire suppressant. Hybrid generators are particularly attractive for some special situations such as inhabited spaces or cold temperature applications.<sup>42</sup> The hybrids use the hot inert SPGG exhaust to vaporize and expel a secondary suppressant, typically a liquid, such as water or a low boiling point halocarbon, through a nozzle.<sup>43</sup>

## Experimental Facility

### Hardware

As shown in Figure 6–12 and Figure 6–13, the TARPF was a small wind tunnel consisting of a number of sections. The main portion of the tunnel was 2.5 m long with a square cross section 92 mm on a side. (Detailed mechanical drawings of key components of the facility can be found in reference 44.) Air, supplied by a compressor rated for a maximum flow of 180 g/s at 1.0 MPa, could be delivered to the tunnel at speeds, averaged over the 92 mm square cross section, up to 17 m/s. Flow was monitored using a calibrated sonic orifice and a piezoelectric pressure transducer. The inlet air temperature could be heated to above 200 °C. A honeycomb flow straightener and mixing screens were located 1 m upstream of the test section. The burner consisted of a sintered bronze plate, 92 mm wide by 190 mm long. Propane, the primary fuel, could be supplemented with a JP-8 spray. The expanded relative uncertainty<sup>iv,45</sup> in the flows of fuel and air were  $\pm 5\%$  of the measured value, based upon the manufacturers' specifications for the metering orifice and mass flow controllers. Stainless steel baffles between 10 mm and 55 mm high were located upstream of the burner. A ramp could also be inserted to form a 25 mm high backward-facing step.

To investigate different re-ignition scenarios, a hot surface obstruction was set up immediately downstream of the propane porous burner. (See Figure 6–12.) The v-shaped obstruction was 25 mm in height, the base was 25 mm wide, and was centered across 50 mm of the wind tunnel passage. An S-type thermocouple was placed on the external upstream surface of the obstruction. A high-resistance, high temperature ceramic adhesive was used to adhere the thermocouple to the Inconel surface, 15.5 mm thick. An ethane torch was supported underneath the obstruction to heat the inner surface to over 1100 °C. A mass flow controller was used to regulate the obstruction surface temperature. The fire was initiated by a spark across two electrodes protruding from the side wall of the test section 20 mm above the surface of the burner and 20 mm downstream of the step. Heat release rates were up to 10 kW. A 30 Hz video camera could view the flame and the suppression process from above and the side through 6 mm thick Pyrex windows. For some experiments, a 1000 Hz digital camera was used to investigate the flame dynamics. A photograph of a typical flame taken through the window is shown in Figure 6–14. The inclined mirror above the apparatus reflects a top view of the flame.

A stream of JP-8 droplets provided a source of re-ignition for the propane flame as they were directed directly onto the heated obstruction after flame suppression. The droplet array was generated from a 0.14 mm sapphire orifice that was pressure fit into a 3.1 mm tube. The tube was inserted into the wind tunnel passage from the top wall at a position 25 mm upstream of the flame stabilizing obstacle. The end 3.8 mm of the tube was bent 90° into the direction of the air stream, and was centered between the passage top wall and face of the ramp. The JP-8 was forced through the injector with nitrogen back pressure at 170 kPa. The low back pressure and several sintered filters (with a pore size of 7  $\mu\text{m}$  and 2  $\mu\text{m}$ ) were used to help prevent clogging of the injector. Initially, piezo-electric crystals were used to initiate droplet breakup, but impingement of the fuel on the heated obstruction was difficult due to entrainment of the individual droplets into the high-velocity air flow. Impingement was achieved successfully by directing the non-atomized fuel stream on the heated obstruction.

---

<sup>iv</sup> The expanded relative uncertainty on all dimensions and independent parameters described in this chapter is  $\pm 50\%$  of the highest significant place reported, with a coverage factor of 2, unless otherwise stated.

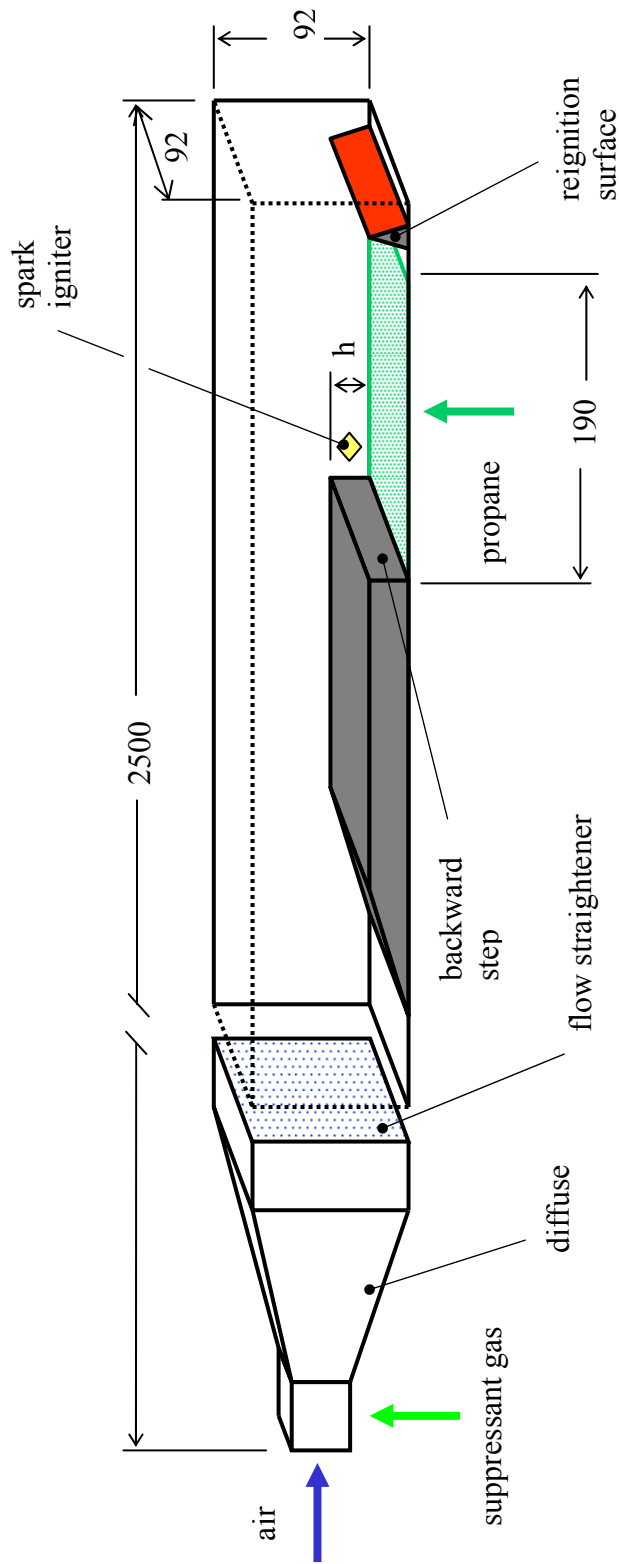
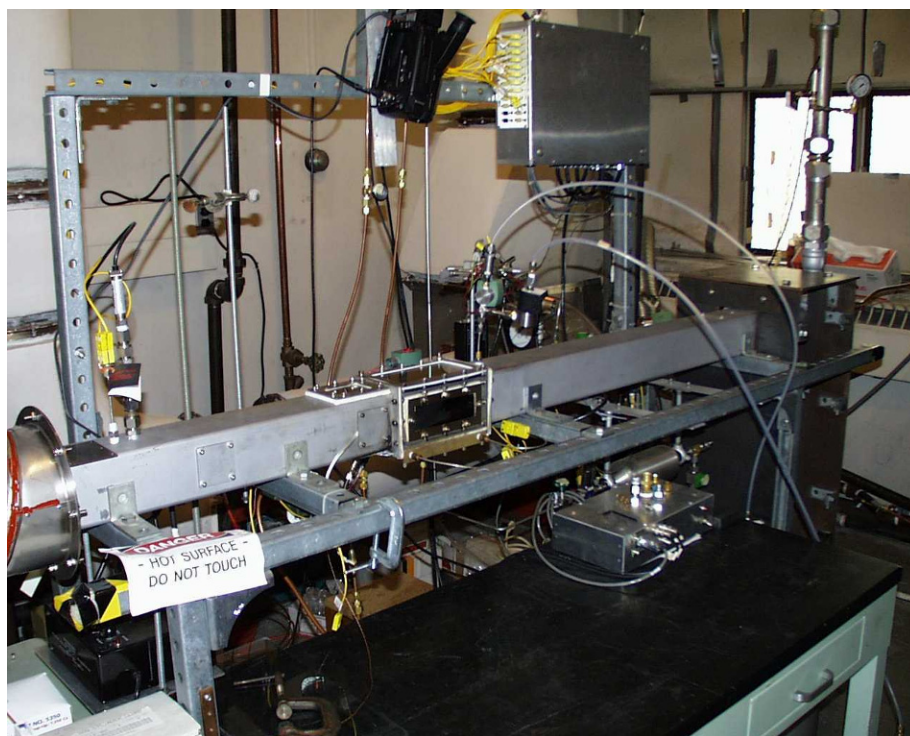
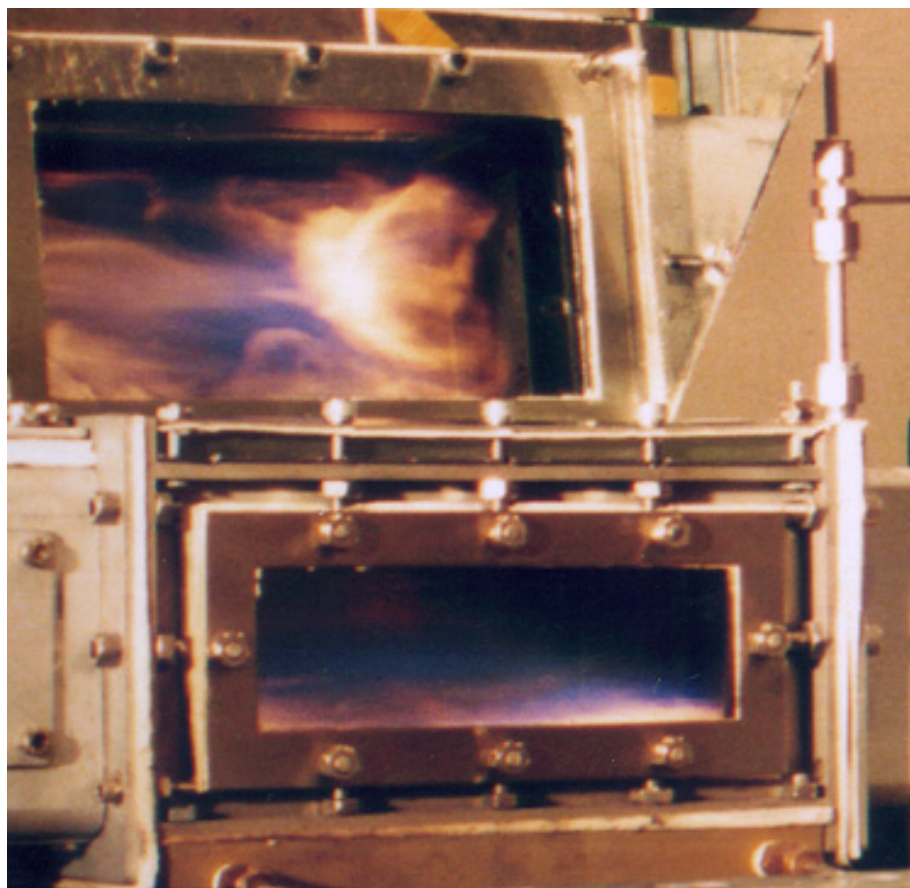


Figure 6–12. Schematic of Step-stabilized Pool Fire Apparatus. <sup>44</sup> Dimensions are in millimeters.



**Figure 6–13.**  
**Photograph of the**  
**TARPF. (NIST photo)**



**Figure 6–14.**  
**Photograph of a**  
**Baffle-stabilized**  
**Propane Flame in the**  
**TARPF. (NIST photo)**

The JP-8 injection time (controlled by a solenoid valve), and flow were varied in order to optimize the impingement process. The impingement of the fuel onto the obstruction surface resulted in a significant decrease in the surface temperature, and care was taken to compensate for this effect during experiments.

The fire suppressing agent was injected downstream of the air metering orifice. Since the air flow was choked by the metering orifice, the introduction of the agent was accomplished without altering the total air flow.

### ***Volatile Agents***

Gaseous agents (nitrogen, CF<sub>3</sub>Br, and HFC-125) were stored in 1 L and 2 L stainless steel vessels with the pressure monitored by a 1 ms response piezoelectric transducer, and the temperature measured with a chromel-alumel thermocouple. An electronic timer controlled the interval (10 ms to 1000 ms) that a solenoid valve on the agent vessel remains open. The agent passed through a 6 mm diameter orifice before it was injected through two opposed radial ports into the air passage upstream of the diffuser. A computer monitored the flow controllers, pressure transducers, and thermocouples, and sent a signal to the electronic timer to open and close the solenoid valve while releasing the flow of suppressant. The mass of the gaseous agent released was determined from the change in pressure and temperature in the storage vessels. The expanded uncertainty in the calculated mass was  $\pm 2\%$ , with a minimum absolute uncertainty of 0.12 g attributable to the resolution of the pressure transducer. The discharge rate and duration were controlled by the initial agent pressure and an electronically actuated solenoid valve. The piezoelectric pressure transducer was able to follow the change within about 5 kPa, but the thermocouple response was too slow. To determine the instantaneous mass discharge, the nitrogen was assumed to be an ideal gas with the expansion inside the bottle occurring isentropically. The uncertainty in  $dm/dt$  was estimated to be  $\pm 2$  g/s.

### ***Aerosol Agents***

Aerosol agents required a totally different injection system than what has been described above or used previously. The flows and injection durations of commercial fuel injectors were not adjustable over the range and with the precision necessary for the current application.

The liquid dispensing system (Figure 6–15) consisted of a liquid reservoir, a compressed air cylinder, two computer-controlled solenoids, and a hollow-cone atomizer. The atomizer was positioned equidistant vertically between the ramp and the upper wall of the wind tunnel, and at discrete locations along the air passage from 65.5 cm upstream of the propane porous burner to a location downstream near the ramp. Several different atomizers were used while trying to obtain a well-dispersed spray of droplets in the air passage. The atomizers were commercially manufactured to the following: (1) a nominal spray angle of 70° when operated at 1.03 MPa with a flow of 1.9 mL/s, and (2) a nominal spray angle of 60° when operated at 0.69 MPa with a flow of 1.1 mL/s. Operating these atomizers at nominal pressures normally resulted in a fully developed spray, and thus an increase above the nominal condition had a small effect on reducing droplet size. When positioned at upstream locations, the spray appeared to fill the entire air passage cross section. To initiate a mist for a fixed duration, the data acquisition system activated the solenoid that was connected to the reservoir. At the end of the discharge, the solenoid was deactivated to terminate the flow to the atomizer. The second solenoid leading to a drain was simultaneously activated to prevent any residual flow to the nozzle and dripping from the nozzle.

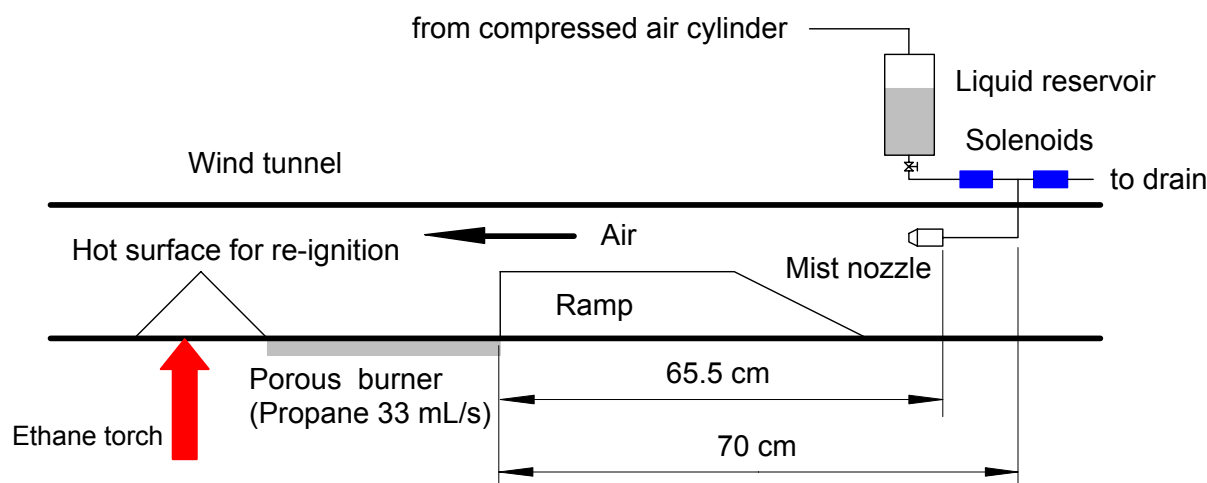


**Figure 6–15. Liquid Aerosol Agent Injection System.**<sup>12</sup>

### *SPGG Facility and Operation*

Gas generators are manufactured in discrete units using specific chemical formulations and orifice sizes that are designed based on the particular application. The TARP operator can control neither the total mass discharged nor the injection time interval of the SPGG. To accommodate this limitation, a custom discharge chamber was designed to allow the operator to select the fraction of the SPGG discharge that is injected into the flame zone. The hardware was designed to allow standard size gas generators (which contain significantly more material than is required for suppression in the TARP) to be evaluated by repeating the test sequence with identical gas generators and incrementally increasing the fraction of SPGG effluent allowed to flow into the TARP air stream. The SPGG effluent passed through a metering orifice and was injected into the air stream using the same manifold as for the compressed gaseous agents. The flow through the bypass port was discarded into a laboratory exhaust hood. The pressure in the discharge chamber was monitored by a 1 ms response piezoelectric transducer and the temperature was measured with a 76  $\mu\text{m}$  type K thermocouple. Figure 6–16 is a schematic diagram of the SPGG injection system; and Figure 6–17 is a close-up photograph.

The housing, enclosing the entire injection system, was made of 6 mm thick stainless steel as a precaution against a premature or explosive discharge. The internal volume was approximately 200 mL. There were four main ports on the discharge chamber as seen in Figure 6–17:

- A  $\frac{3}{4}$  NPT female thread connecting to the gas generator cartridge holder,
- A variable area metering orifice (1.6 mm to 6.4 mm diameter) to limit the flow into the TARP,
- A bypass port tapped for a 2 NPT nipple, and
- A 19 mm port for mounting a pressure relief blow-out diaphragm.

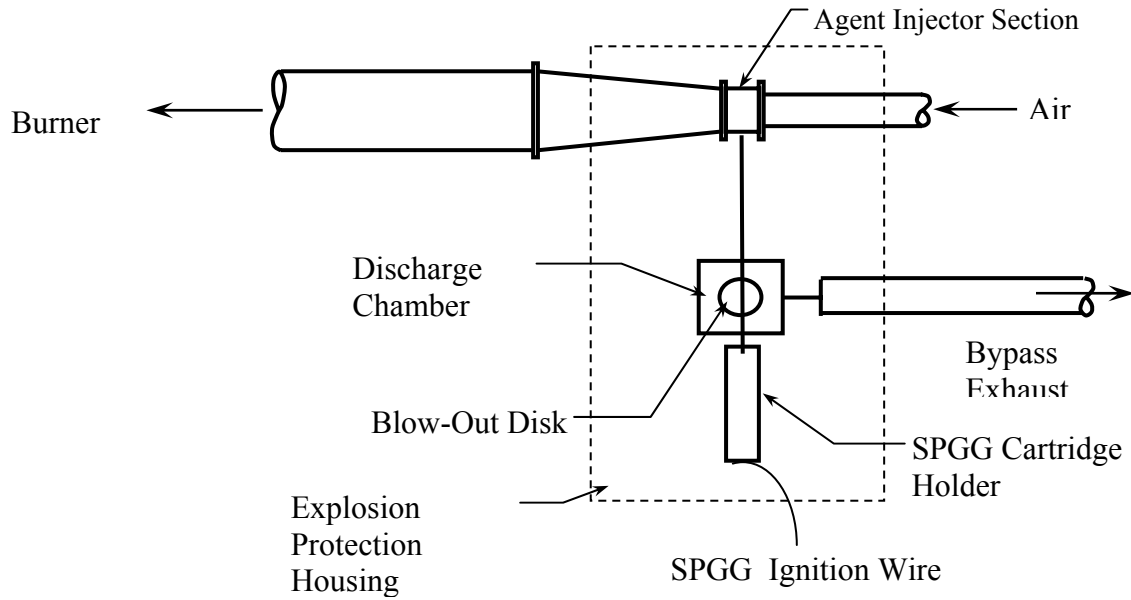


**Figure 6–16. Schematic Diagram of the SPGG Injection System.**<sup>44</sup>

The fraction of the SPGG effluent injected into the TARPF was varied by selecting the size of Ports 3 and 4. In many of the experiments, Port 4 was left open to maximize the bypass area.

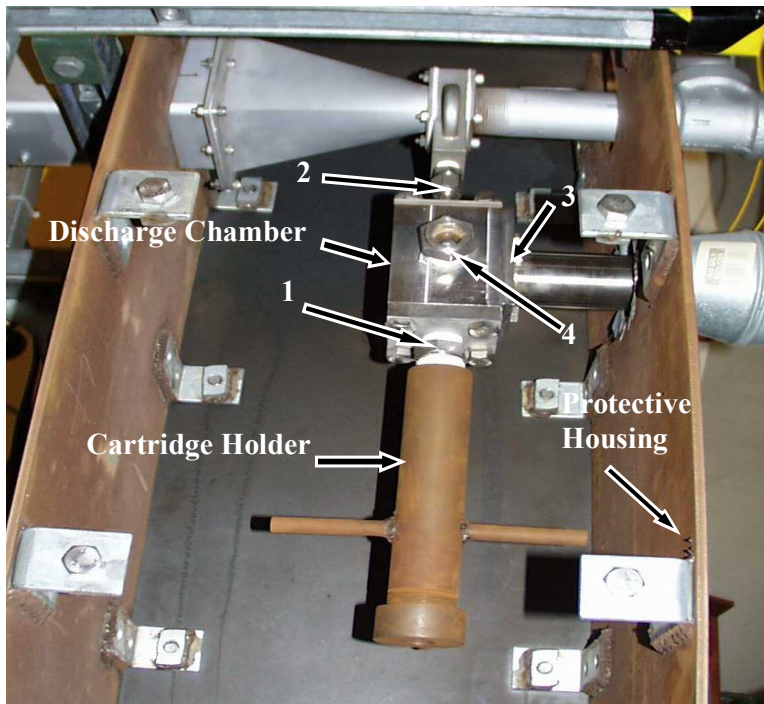


**Figure 6–17. Photograph of TARPF Injection System with Housing Cover Removed. The four ports in the discharge chamber are: (1) SPGG outlet, (2) metering orifice, (3) bypass, and (4) blow-out.**

The mass of the SPGG injected into the TARPF was determined from the total mass discharged and the ratio of the area of the metering orifice to the combined area of the metering orifice and the bypass area. The expanded uncertainty in the calculated mass was  $\pm 2\%$ , with a minimum absolute uncertainty of 0.12 g attributable to the resolution of the pressure transducer. From the temperature and pressure measurements, the rate of suppressant addition to the incoming air,  $dm/dt$ , was estimated within an expanded uncertainty of  $\pm 2$  g/s. The concentration of the SPGG in the air flow was determined from the rate of suppressant addition ( $dm/dt$ ) and the mass flow of air. As in the gaseous agent experiments, the air flow was invariant during the agent discharge due to the use of a sonic orifice.

For the tests performed under the NGP, identical commercial air-bag hybrid gas generators were used, one in each of fifty experiments. Each generator released  $20.7 \text{ g} \pm 0.1 \text{ g}$ . The discharged mass was specified by the manufacturer and confirmed experimentally by weighing the generators before and after each discharge. The agent was composed of 20 g of compressed argon gas and 0.7 g of a solid propellant, which at equilibrium converts to KCl (s), H<sub>2</sub>O, N<sub>2</sub> and a small amount of gaseous CO<sub>2</sub>.<sup>46</sup>

The gas generator was discharged after steady-state fire conditions were achieved in the TARPF. The discharge was controlled by engaging an electronic switch on a control box that completed a circuit leading from a 12 V battery to the electrical connector located on the gas generator. One ampere was required to fire the 40 mg squib, which was an intrinsic part of the gas generator. The squib ignites the solid propellant, which rapidly discharges. The combustion products of the solid propellant propelled the gaseous argon from the generator casing, located within the cartridge holder, into the discharge chamber. SPGG cartridges were changed and prepared for the next run in less than 4 min.

### Numerical Modeling and Analysis

To better understand the fluid dynamics of the suppression event, the first publicly released version of the Fire Dynamics Simulator (FDS)<sup>47</sup>, a computational fluid dynamics model, was used to simulate the baffle or step-stabilized flame in the TARPF facility. The sub-grid scale turbulence model was not used, but rather the coefficients of viscosity, thermal conductivity and mass diffusivity were derived from kinetic theory and empirical extrapolation.<sup>48</sup> Thus, the calculations directly simulated the fluid motion, but not the combustion. Both two-dimensional (higher resolution) and three-dimensional (with turbulent flame structure) simulations were performed. Details of the calculations are presented in References 33 and 44.

Presented in Figure 6–18 are sequences of images separated in time by 0.01 s that are taken from simulations that illustrate the dynamics of the suppression event. Figure 6–18a is a 3-D simulation of a flame stabilized on a 25 mm baffle that is undergoing a successful suppression. Figure 6–18b is a 2-D simulation of flow (moving left to right) over a 25 mm step. The darkness of the image reflects the extent of local heat release. In both Figures, the top images show the flame just prior to discharge of nitrogen into the air stream. Upon injection, the flame was disturbed by a large vortex generated by the pressure pulse. Due to the low Mach number approximation, the gas upstream of the step was essentially incompressible, and the velocity jump from 2.1 m/s to 5.7 m/s was conveyed to all points in the flow domain in 0.02 s, the time of the ramp-up from the base velocity to the injection velocity. Thus, even before the agent arrived at the step, the flame had already been dramatically transformed from its original state. The generation of the large vortex at the step produced a pathway by which the agent could penetrate the region just behind the step, mixing with the gases, cooling and diluting the fuel and oxygen.

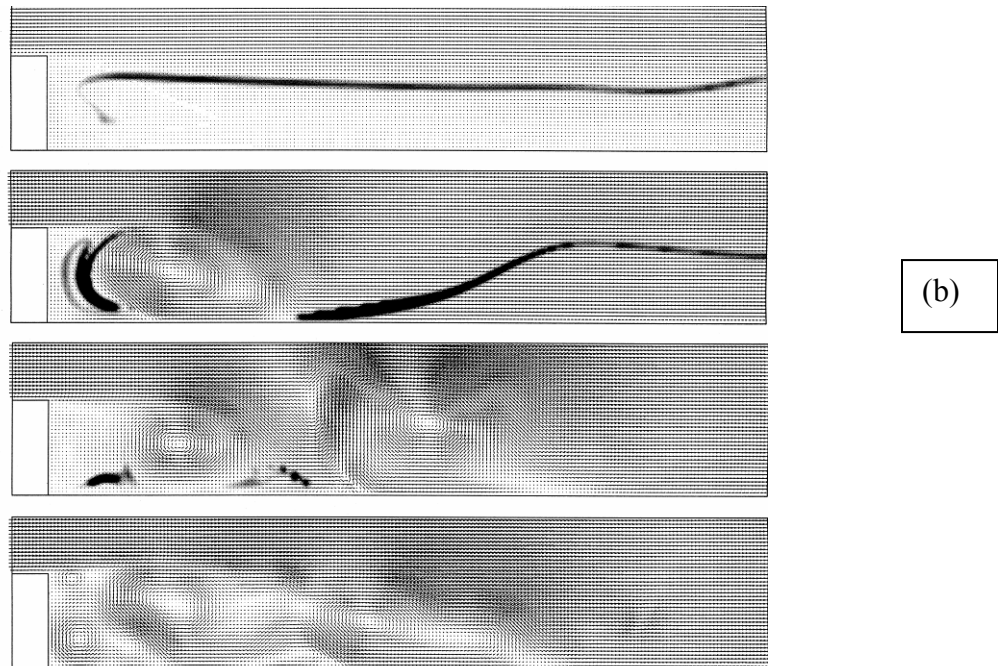
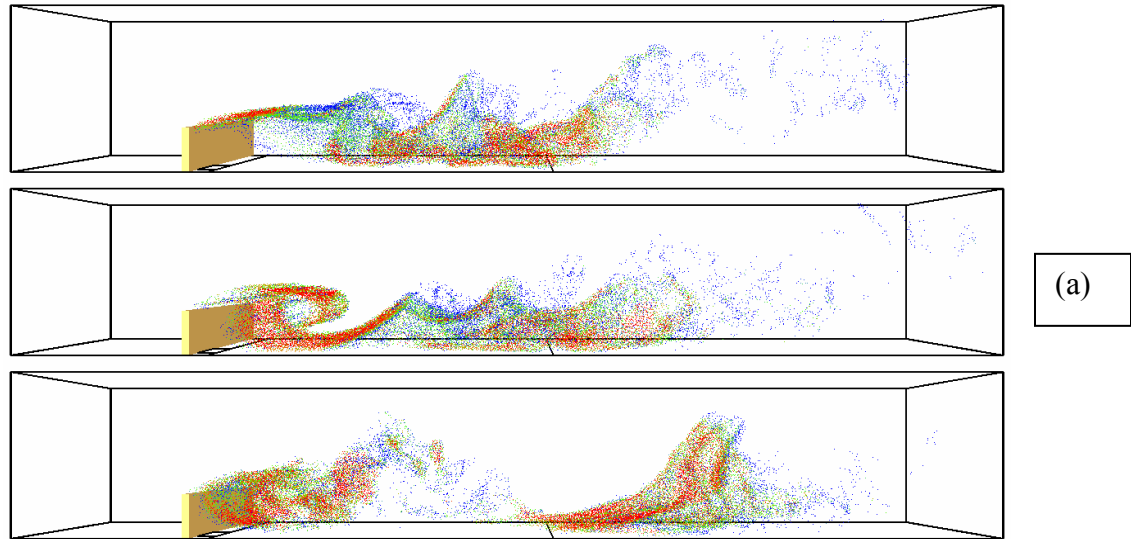


**Figure 6–18. Disruption of a Stabilized Flame by the Injection of Nitrogen Upstream of 25 mm High Obstacle.**

**(a) 3-D Simulation of Flow over Baffle; (b) 2-D Simulation of Flow over Step.**

**The frames are separated by 0.01 s. <sup>12</sup>**

## Flow Characterization

The TARPF facility was operated over a range of propane and air flows to examine the flame behavior. Flame blowout, with no added fire extinguishing agent, was achieved either by increasing the air flow or decreasing the propane flow. At low air velocities, a fluctuating laminar flame was anchored on the top downstream edge of the step or baffle and extended well downstream of the porous plate. As the velocity increases, the flame became turbulent and less luminous. Near blowout, the orange color disappeared and the visible blue flame shrunk. With the backward-facing step installed, an average air velocity above the step of over 23 m/s was necessary to blow out the flame if the propane flow was greater than 33 mL/s, corresponding to a velocity of 1.9 mm/s.

Two air flows were chosen to evaluate the ability of the agents to suppress the propane pool fire stabilized by the backward-facing step:

<u>Mean Air Velocity</u>	<u>Propane Flow</u>	<u>Regime</u> <sup>38</sup>
2.1 m/s $\pm$ 0.2 m/s	33 mL/s $\pm$ 2 mL/s	Regime I (rim-stabilized flame)
5.4 m/s $\pm$ 0.2 m/s	85 mL/s $\pm$ 2 mL/s	Between Regime I and II (intermittent turbulent flame)

The velocity distribution of the air 76 mm upstream of the burner was measured with a 3 mm diameter pitot tube at seven locations across the duct. The velocity profiles were flat within 5 % over the central three-fourths of the duct. The boundary layer above the step appeared to be less than 7 mm thick. The presence of the flame tended to increase the pitot probe signal, which was likely due to a combination of preheating the air upstream by the flame, acceleration in the flow due to partial blockage of the duct caused by the expanding combustion gas, and a possible shift in electrical output due to heating of the pitot probe and transducer.

The mass of suppressant necessary to extinguish a fire in the TARPF depends upon the fuel and air flows chosen to challenge the suppressant. Figure 6–19 shows how the mass of nitrogen necessary to extinguish a 25 mm baffle-stabilized flame varied with the flow of air and fuel. The uncertainty in any given value was estimated to be  $\pm$  0.2 g. When the air speed was less than 5 m/s and the fuel flow was fixed at 45 mL/s  $\pm$  2 mL/s, decreasing the speed reduced the amount of nitrogen necessary to extinguish the flame. No flame extinction occurred between 5 m/s and 15 m/s because the mass of nitrogen necessary exceeded the maximum amount contained in the storage vessel. Above 16 m/s, the strain on the flame was sufficient at times to extinguish the flame without the need for any nitrogen. (The dashed lines are included in the figure to assist the eye in identifying the extinction boundaries.)

The propane flow had less than a 5 % effect on the mass of N<sub>2</sub> needed to extinguish the flame, at fixed injection interval and air flow. There was a lower limit for the propane flow (< 12 mL/s) that led to extinction due to heat loss to the burner, even with no N<sub>2</sub> dilution. The upper flow limit (120 mL/s) was dictated by the maximum safe operating temperature of the burner. Since the mass of N<sub>2</sub> needed to suppress the flame did not appear to increase, there was no need to operate the burner at higher fuel flows.

The total mass of N<sub>2</sub> required for suppression also depended on the injection interval. This relationship is plotted in Figure 6–20 for a 3.9 m/s  $\pm$  0.2 m/s air flow, 45 mL/s  $\pm$  2 mL/s propane flow flame stabilized on the 25 mm baffle. The total number of experiments was more than ten times the number of data points

plotted in this and the following curves; for clarity, only those conditions close to the extinction boundary are included. (For all these figures, the open circles represent the largest mass of N<sub>2</sub> that did not result in extinction; the filled circles are the minimum mass of agent that successfully extinguished the flames.) As the injection interval was increased from 100 ms to 500 ms, the minimum mass required increased over three-fold. The rate of mass addition (total mass/estimated injection interval) decreased with increasing injection interval, as shown in the right-hand figure.

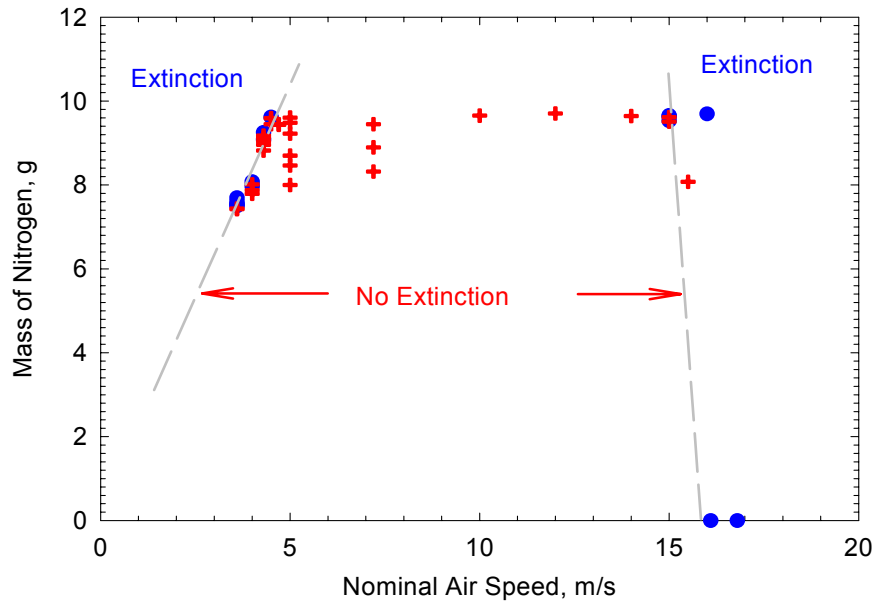


**Figure 6-19. Impact of Air Speed on Extinction of a 25 mm Baffle-stabilized Flame.**<sup>44</sup>  
**Propane Flow: 45 mL/s; N<sub>2</sub> Injection Time: 312 ms.**  
**Circles: Flame Extinction; Crosses: No Extinction**

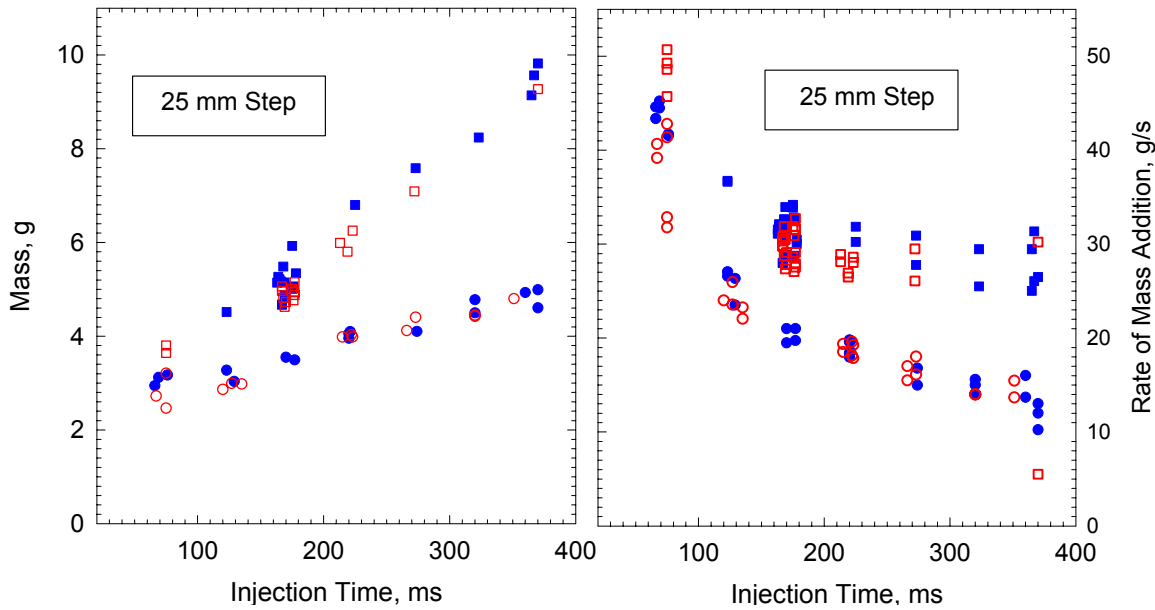


**Figure 6-20. Mass and Rate of Nitrogen Addition to Extinguish a 45 mL/s Propane Flame in 3.9 m/s Air Flow.**<sup>44</sup>

Next, there was an effect of the geometry of the obstruction on the mass of  $N_2$  needed for flame suppression. The data plotted with squares in Figure 6–21 were taken with the ramp placed in front of the 25 mm baffle to form a backward step-stabilized flame, rather than the simple baffle-stabilized flame represented in Figure 6–20. The air flow was the same in these two cases but the propane flow was higher, 85 mL/s, in Figure 6–21. The addition of the ramp and increase in propane flow did not have much influence on the mass of  $N_2$  required for suppression. For both the baffle and backward step, just under 6 g of  $N_2$  are required when the injection interval is 200 ms  $\pm$  10 ms. The data plotted as circles in Figure 6–21 were taken with the nominal air speed reduced to about 1.5 m/s and the propane flow proportionately to 33 mL/s. The squares represent experiments conducted at the high air and propane flows, and circles represent experiments conducted at the lower flows. Less than 4 g  $\pm$  0.2 g of  $N_2$  were needed to extinguish this flame if injected over a 200 ms  $\pm$  10 ms interval. The differences in rates of mass addition to suppress the high flow and low flow flames can also be seen at the right in Figure 6–21.

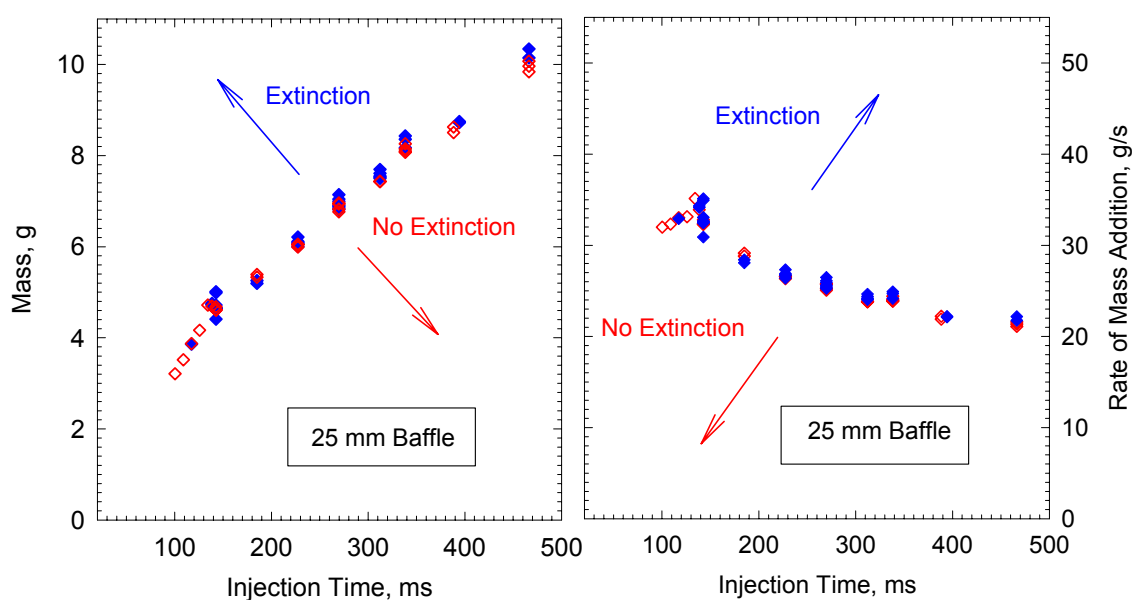


**Figure 6–21. Mass and Rate of Nitrogen Addition Required to Extinguish High Flow (squares) and Low Flow (circles) Propane/Air Flames Stabilized Behind a 25 mm Step.**<sup>44</sup>

Figure 6–22 and Figure 6–23 show what happens to the required nitrogen mass and addition rate if the baffle height is decreased to 10 mm or increased to 55 mm (blockage from 11 % to 60 %), respectively. The symbols have the same meaning as in Figure 6–21. The short baffle produced a fire which was the easiest to extinguish, and the high baffle the most difficult in terms of the amount and rate of  $N_2$  addition.

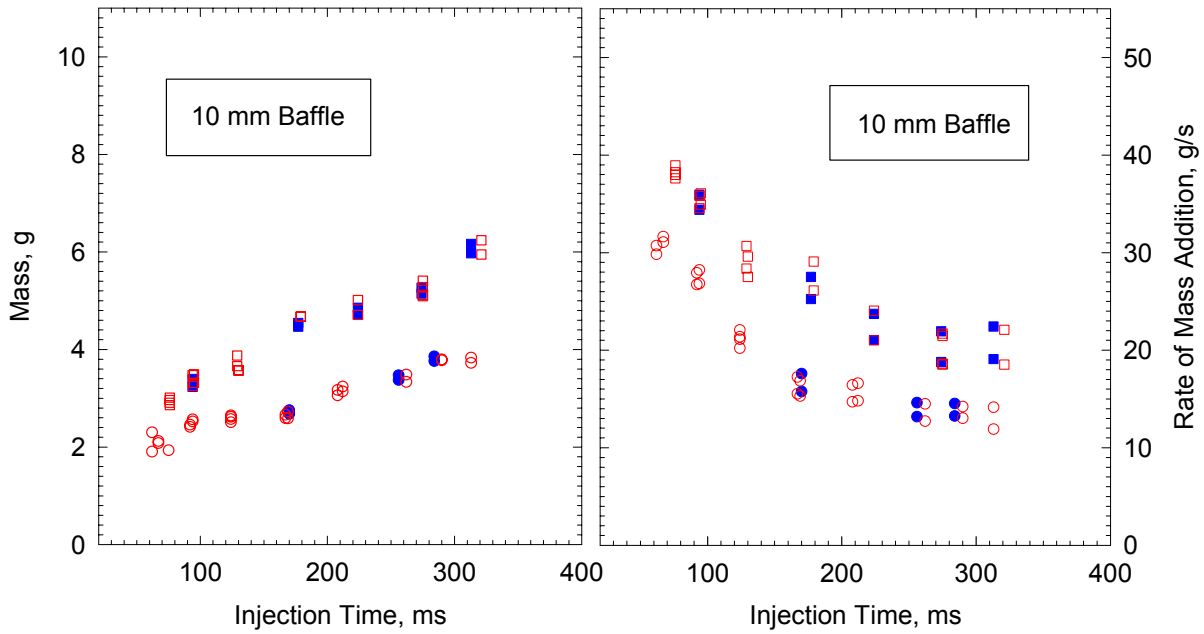


Figure 6–22. Mass and Rate of Nitrogen Addition Required to Extinguish High Flow (squares) and Low Flow (circles) Propane/Air Flames Stabilized Behind a 10 mm Baffle.<sup>44</sup>

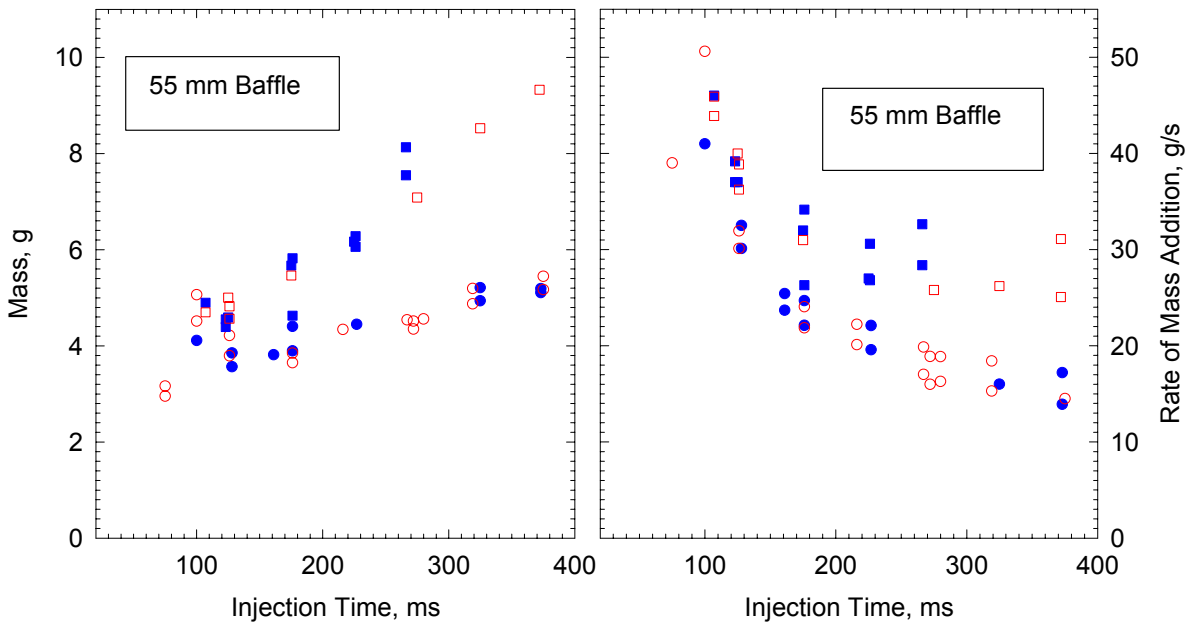
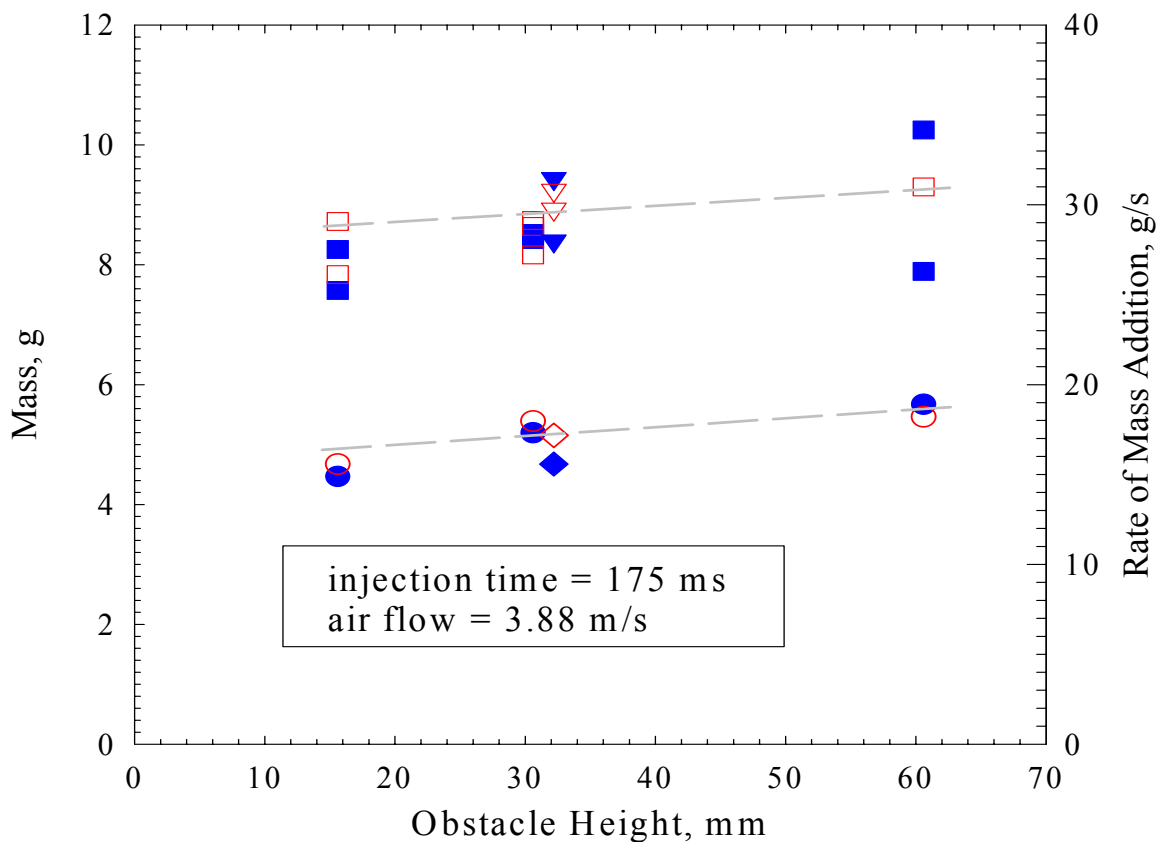


Figure 6–23. Mass and Rate of Nitrogen Addition Required to Extinguish High Flow (squares) and Low Flow (circles) Propane/Air Flames Stabilized Behind a 55 mm Baffle.<sup>44</sup>

The effect of baffle height was not large if the injection interval was at least 150 ms, as can be seen more clearly in Figure 6–24. (Note that 6 mm has been added to the height of each obstacle to account for the distance between the floor of the tunnel and the recessed top surface of the burner.) The bottom curve delineates the minimum amount of nitrogen for suppression when the air flow was fixed at its high value and the agent injection interval was maintained at  $175 \text{ ms} \pm 10 \text{ ms}$ . The open circles represent the largest mass of  $\text{N}_2$  that did not result in extinction for flames stabilized on the different sized baffles; the filled circles are the minimum mass of agent that successfully extinguished the flames. The diamonds are the results for the 25 mm baffle with the ramp in place (backward-facing step). Experiments were also conducted with and without the reignition obstruction shown in Figure 6–12. The amount of  $\text{N}_2$  necessary for suppression was unchanged.

The rate of mass addition is plotted in the upper curve of Figure 6–24 (the triangles are the backward-facing step, and the squares are for the baffles). The data are plotted two ways: the higher value is the rate of nitrogen addition computed during the first 50 ms that the solenoid valve is open; the lower value is the average over the entire open interval measured from the pressure trace. The estimated rate of mass addition varied substantially, especially for the 55 mm baffle, depending upon whether the averaging period was the first 50 ms or the entire time that the solenoid remains open.



**Figure 6–24. Impact of Obstacle Height on the Total Mass and Rate of Addition of Nitrogen Required to Suppress an Obstacle-stabilized Pool Fire.**<sup>44</sup>

### Effect of Type of Gaseous Suppressant

Figure 6–25 is a plot of the minimum agent volume fraction that extinguished the fires ( $X$ ) as a function of the agent injection time interval ( $\Delta t$ ) for both  $N_2$  and  $CF_3Br$ . The parameter  $X$  is defined as the average volume flow of agent during the injection interval divided by the sum of the agent and bulk air flows.

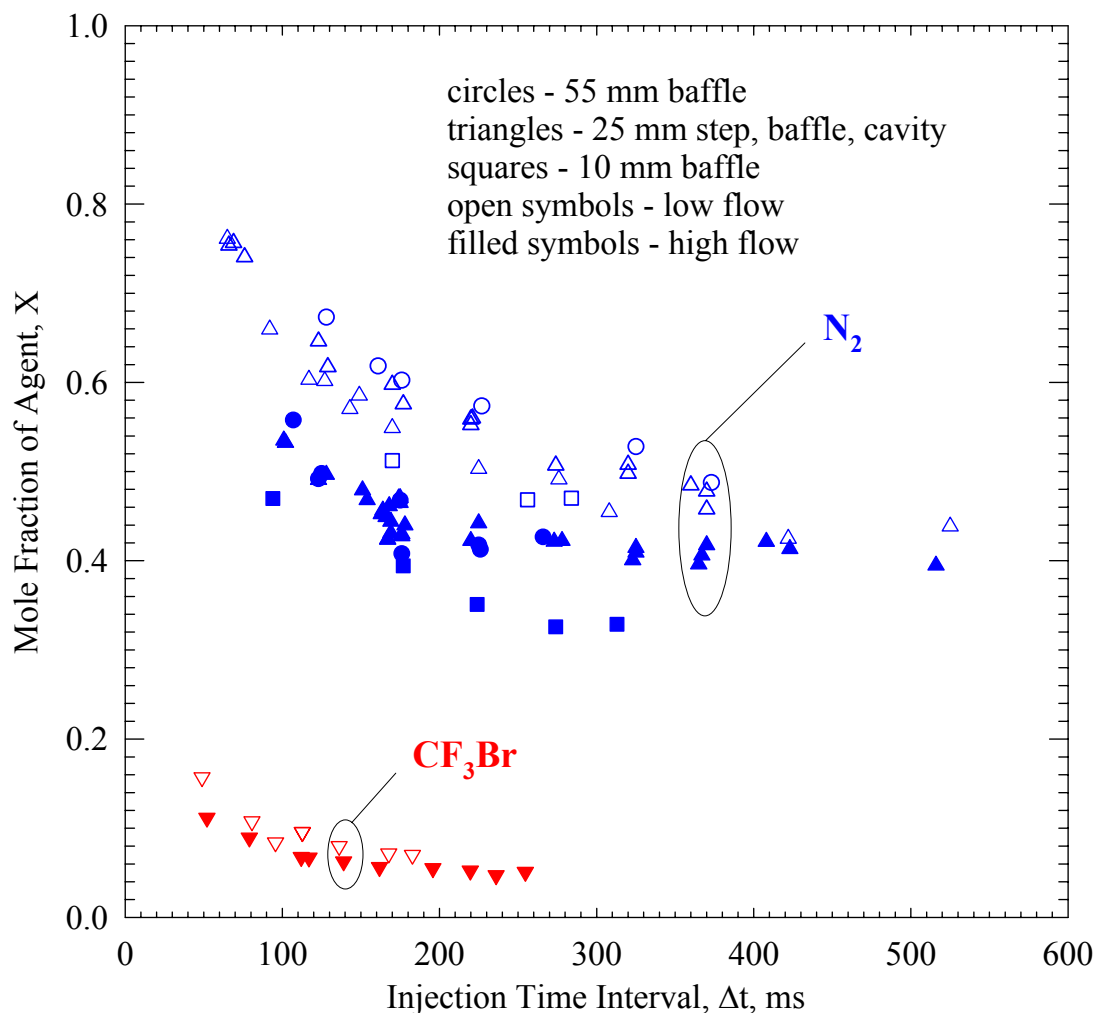


**Figure 6–25. Mole Fraction of Suppressants ( $N_2$  and  $CF_3Br$ ) Added to Air at Extinction Boundary for High and Low Flow Conditions, as a Function of Injection Time Interval and Obstacle Geometry.**<sup>44</sup>

The data represent experiments conducted over a range of conditions including air velocities that varied from 2 m/s to 9 m/s, propane flows from 33 mL/s to 85 mL/s, and baffle heights between 10 mm and 55 mm, in addition to the 25 mm backward step. The open and closed symbols represent the low and high air flow conditions, respectively. Figure 6–25 shows that  $X$  decreased with increasing injection time interval for all obstacle types and both agents. The highest volume fraction requirements were consistently for the low air flow conditions. For some experiments, the value of  $X$  was nearly 0.8 for short injection intervals. The most challenging geometric configuration was the 55 mm baffle, followed by the 25 mm obstacles, and the 10 mm baffles. There was little difference in  $X$  between the 25 mm step, 25 mm

cavity and the 25 mm baffle and those data are presented as one group in Figure 6–25. The effectiveness of  $\text{CF}_3\text{Br}$  was compared to that of  $\text{N}_2$  using the 25 mm high backward step. The 1 L storage vessel was used to accentuate the pressure change associated with the small quantities of  $\text{CF}_3\text{Br}$  required for suppression. Only  $1.6 \text{ g} \pm 0.2 \text{ g}$  of  $\text{CF}_3\text{Br}$  injected for 100 ms was needed to extinguish the flame under the high air flow conditions (corresponding to  $X \approx 0.075$ ), as compared to  $3.9 \text{ g} \pm 0.2 \text{ g}$  for  $\text{N}_2$  as agent ( $X \approx 0.5$ ) under similar conditions. These results were consistent with numerous studies that showed that  $\text{CF}_3\text{Br}$  is a more effective suppressant than  $\text{N}_2$  for both free standing and baffle stabilized flames.

### Effect of Hot Surface

Experiments were conducted to assess the importance of a nearby hot surface (Figure 6–12) on the effectiveness of a fire suppressant. An ethane-fueled torch was used to preheat the upstream surface of the obstacle to produce temperatures in excess of  $1000 \text{ }^\circ\text{C}$  as measured on the exterior face. Pyrometer readings of the interior (i.e., fire-side) surface indicated temperatures were about  $50 \text{ }^\circ\text{C}$  cooler. Experiments determined that hot surface temperatures close to  $1000 \text{ }^\circ\text{C}$  were needed to ignite the propane pool when the air and propane were set to the low flow conditions.

A spray nozzle was located upstream of the stabilizing step that allowed liquid JP-8 to be sprayed over the propane pool and onto the heated inverted-vee surface. The fuel acted to cool the surface approximately  $150 \text{ }^\circ\text{C}$  below the temperature that had been obtained when only the gaseous propane fuel was flowing. The JP-8 was ignited and formed a flame that stabilized behind the vee when the temperature of the surface exceeded  $900 \text{ }^\circ\text{C}$ .

To test for re-ignition of the propane fire, the propane fire was initiated under the operating conditions of an air flow velocity of  $1.5 \text{ m/s}$  and a propane flow of  $33 \text{ mL/s}$ , and the obstruction was heated to the temperature desired. The flame was observed to extend past the obstruction. The agent ( $\text{N}_2$ , HFC-125, or  $\text{CF}_3\text{Br}$ ) was introduced to the system for three different injection times of 75 ms, 100 ms, and 150 ms, and the occurrence of flame suppression was observed. (The agent injection time was varied to observe its effect on re-ignition of the propane fuel.) The agent storage cylinder pressure was increased if suppression did not occur, and the process repeated. In order to determine the efficacy of the JP-8 stream in the re-ignition process, experiments were conducted with the JP-8 stream directed against the heated obstruction while the unignited propane was still flowing into the wind tunnel. If re-ignition did not occur after 10 s, then the propane flow was terminated. A variety of re-ignition results were observed which depended on the injection time interval of the agent and JP-8 stream. Re-ignition was found to occur when the obstruction was above  $900 \text{ }^\circ\text{C}$  (bright red), and was affected by the cooling provided by the agent and JP-8 liquid stream.

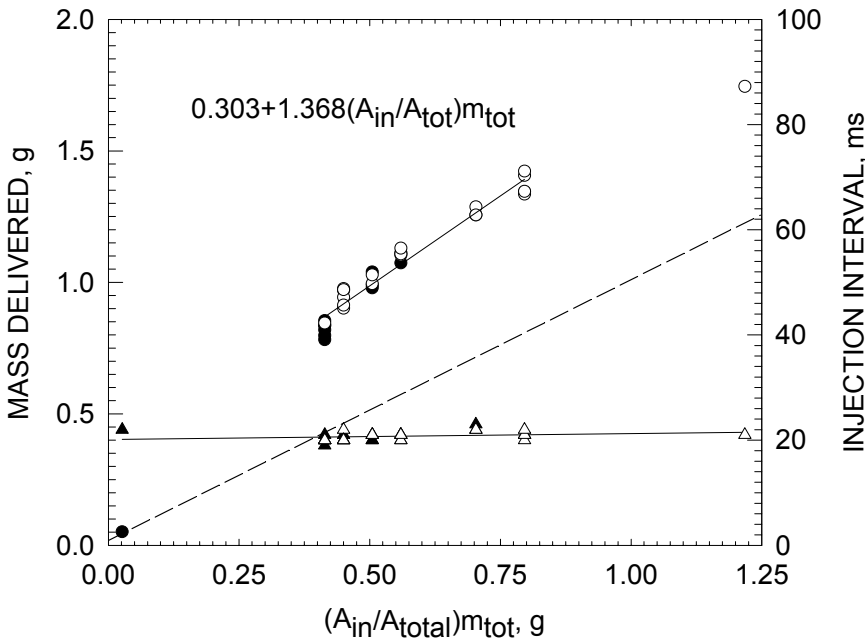
The influence of the surface temperature was found to be bi-modal: when the temperature of the hot surface (with the JP-8 and propane flowing) was below about  $880 \text{ }^\circ\text{C} \pm 10 \text{ }^\circ\text{C}$ , the amount of agent necessary for suppression was the same as when the surface was unheated; and when the temperature was above  $890 \text{ }^\circ\text{C} \pm 10 \text{ }^\circ\text{C}$ , reignition always occurred within about 10 s independent of higher temperatures or the amount of  $\text{N}_2$  added. A similar finding resulted when nitrogen was replaced by  $\text{CF}_3\text{Br}$ , although the measured dividing temperature was about  $50 \text{ }^\circ\text{C}$  higher. This difference may have been associated with a build-up of carbon on the hot surface that insulated the fire-side surface from the ethane torch, making an accurate determination of the surface temperature more difficult.

A few experiments were conducted with the temperature reduced to the Leidenfrost point (290 °C for JP-8) to determine if an increase in contact time would compensate for the lower temperature. Ignition of the JP-8 and propane did not occur. Satcunanathan and Zaczek<sup>49</sup> measured the ignition delay of kerosene and diesel fuels on a hot metal surface and found that ignition could occur in less than 1 s for a 2 mm diameter droplet, but that the ignition time increased for temperatures between about 500 °C and 550 °C due to surface boiling. No ignition of the JP-8 droplets was observed in the TARPF when the vee-surface temperature was maintained in the range between 360 °C and 440 °C. However, Jomaas et al.<sup>50</sup> found that ignition of a JP-8 pool fire occurred in their step-stabilized burner for temperatures in the same range.

**SPGG Results**

For the SPGG experiments, the nominal velocity of the air above the backward-facing step was maintained constant at 5.4 m/s; the propane flow was 85 mL/s (at standard temperature and pressure). The high pressures (typically 1000 kPa to 3000 kPa) produced in the SPGG discharge chamber and the known area of the metering orifice allowed the mass flow of agent added to the air stream of the TARPF to be estimated by assuming that the flow through the orifice is choked. Five replicate tests produced virtually indistinguishable mass flow and thermocouple temperature traces.

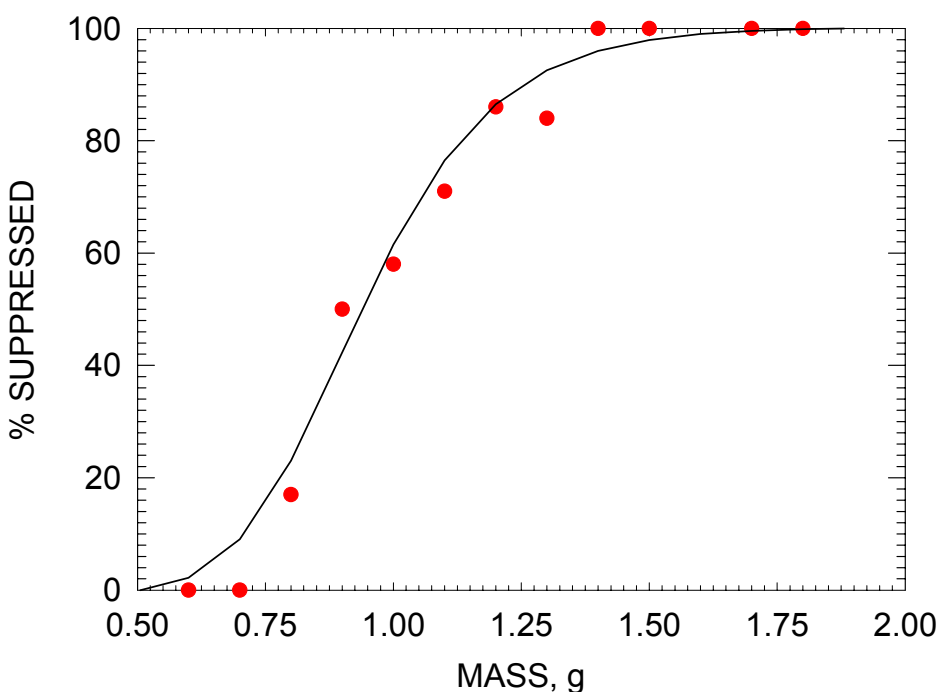
The SPGG discharge time was consistently 20 ms ± 1 ms, which is over three times faster than the shortest N<sub>2</sub> or CF<sub>3</sub>Br injection interval, and was not much affected by the bypass port area. The bypass ratio ( $A_{in}/A_{tot}$ ) is the area of the inlet metering orifice (port 2) divided by the total open area available for flow to exit the discharge chamber (ports 2, 3, and 4). The time interval,  $\Delta t$ , is shown in Figure 6–26 as a function of the estimated discharge mass. The total mass delivered to the air stream during the discharge process was found by integrating  $dm/dt$  over  $\Delta t$ . Excluding the highest and lowest area ratios, the estimated mass delivered can be seen in Figure 6–26 to be linearly proportional to the area ratio; however, almost 50 % more mass was estimated than one would expect. The dashed line in Figure 6–26 indicates that a 1-to-1 relation would exist if the mass were directly proportional to the area ratio.



**Figure 6–26. Injection interval (triangles) and Calculated Mass Delivered to Flame (circles) as a Function of Area Ratio Times Total Mass of Gas Generated (20.7 g).<sup>44</sup>**

There are several factors that contributed to an uncertainty in the estimate of the deployed mass of agent. First, uncertainties in the gas composition and temperature upstream of the metering orifice affected the estimate since the mass was proportional to the square root of the molecular weight divided by the temperature. A factor of two underestimate in this parameter would cause a 40 % over-estimate in mass, which, if corrected for, would cause the data plotted in Figure 6–26 to more closely align with the dotted line. A second source of uncertainty was the complexity of the flow within the discharge chamber created by the jet emanating from the SPGG. The calculation assumed that the upstream flow was steady and parallel to the axis of the metering orifice, but the flow was highly transient and more perpendicular.

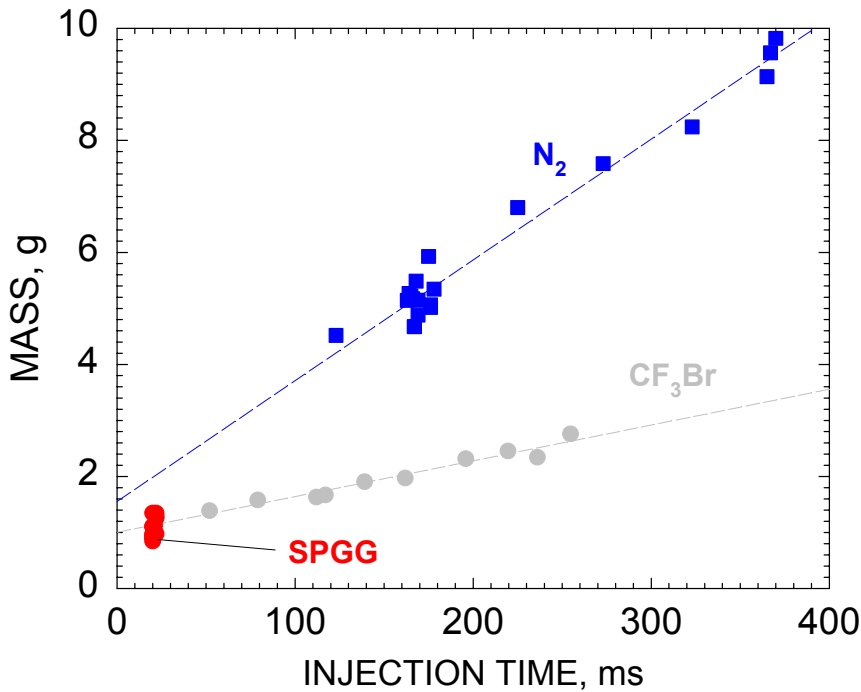
Suppression of the propane pool fire with the hybrid gas generators occurred when at least 1.5 g of agent was injected into the fire; conversely, extinction never occurred when less than 0.7 g was added. The % of the fires suppressed varied when the agent mass was between these limits, as shown in Figure 6–27. The suppression statistics were generated by lumping the mass from thirty-three discharges into bins 0.2 g wide, centered about the data plotted. The solid line is a fit to the data assuming that the shape is sigmoidal. It is apparent from the curve that there was a 50 % chance that suppression would be successful if the amount of agent were  $0.9 \text{ g} \pm 0.1 \text{ g}$ , and there was a 90 % success rate for  $1.3 \text{ g} \pm 0.1 \text{ g}$  of agent.



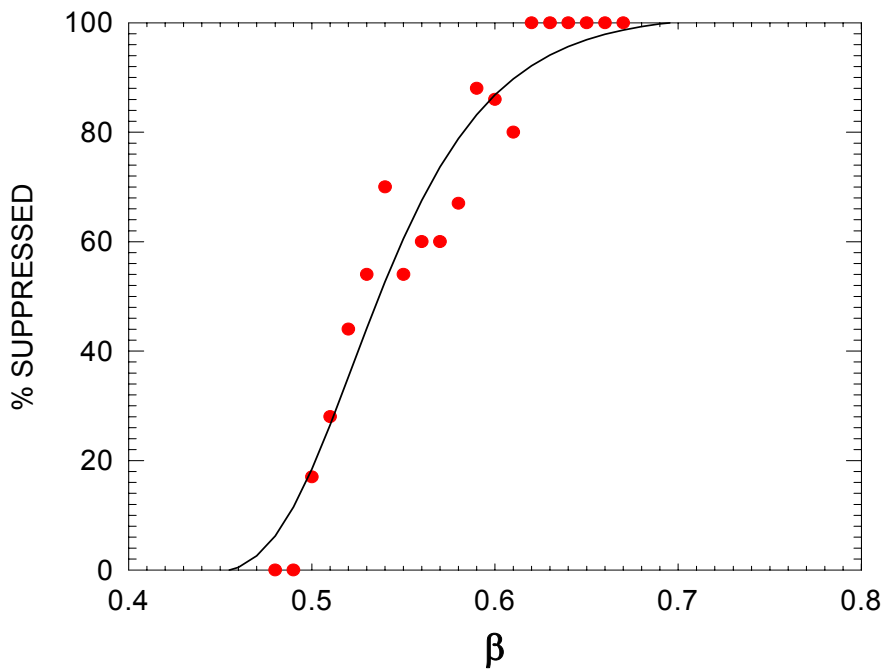
**Figure 6–27.**  
**Percentage of**  
**Flames**  
**Extinguished as a**  
**Function of Mass**  
**Delivered to Flame**  
**by an SPGG.**<sup>44</sup>

Figure 6–28 is a plot of the mass of agent required for suppression versus the injection time interval. All of the SPGG data are lumped around 20 ms since the injection time was fixed. Linear fits to the nitrogen and halon 1301 data yielded intercepts of 1.6 g for nitrogen and 1.2 g for halon 1301. The SPGG data fall close to the halon results. The significance of the linear shape and the value of the intercept was unclear; however, the superior performance of the gas generator was undeniable.

The mass fraction of agent,  $\beta$ , is defined as the total mass injected divided by the injection duration,  $\Delta t$ , over the sum of the mass flow of air plus the mass flow of agent. The percentage of occasions that the flame was extinguished is plotted in Figure 6–29 as a function of  $\beta$ .



**Figure 6–28. Impact of Injection Time Interval on the Mass of Agent Required to Suppress a Step-stabilized Propane Pool Fire.**<sup>44</sup>



**Figure 6–29. Percentage of Flames Extinguished as a Function of Estimated Mass Fraction of Agent.**<sup>44</sup>

All of the fires were extinguished when  $\beta$  was greater than 0.62; none for a mass fraction below 0.49. The definition of  $\beta$  for the SPGG differs somewhat from the definition as applied to the gaseous agents because the mass discharge profiles for SPGG and the gaseous agents were different. Whereas the mass

injection rate of the gaseous agents was controllable through selection of the injection hardware, the SPGG mass injection rate was practically dependent on the propellant effluent generation rate (i.e., the propellant burning rate). For the same mass, variation of the discharge profile led to variation in agent effectiveness. Optimization of the rate of agent discharge is an area that would benefit from further study, which could be approached from analytic, numerical, and experimental perspectives.

### Data Correlation

The effectiveness of the gaseous agents was compared to that of the SPGG through use of a simple agent mixing model to describe the suppression phenomena. A more detailed description of the model can be found in Grosshandler et al.<sup>51</sup> and Hamins et al.<sup>37</sup> A characteristic time,  $\tau$ , for mixing of the agent into the flame zone was defined in terms of the air and agent volume flows,  $(V'_{air} + V'_{agent})$ , and the step height,  $h$ , as

$$\tau = \gamma h / \{(V'_{air} + V'_{agent}) / [(L-h)L]\} \quad (6-2)$$

where  $L$  is the width of the tunnel and  $\gamma$  is an empirical non-dimensional parameter that relates the ratio of the distance that a fluid element travels within the recirculation zone to the obstacle height. Takahashi et al.<sup>38</sup> measured the characteristic mixing time in a similar facility and found  $\gamma$  to be around 40. Evaluating Equation 6-2 for the range of flows and baffle heights examined in the current study and using a value of 40 for  $\gamma$ ,  $\tau$  was found to vary between 0.04 s and 0.40 s.

Hamins et al.<sup>37</sup> found that for a specified injection duration it is possible to relate the volume fraction of agent required to achieve extinction,  $X$ , to the characteristic mixing time,  $\tau$ , according to the following relation:

$$X/X^* = [1 - \exp(-\Delta t/\tau)]^{-1} \quad (6-3)$$

where  $X^*$  can be found experimentally by flowing agent continuously into the air stream at increasing rates until extinction occurs. If the air flow is low enough, the value of  $X^*$  is expected to be similar to the cup burner extinction requirements. For propane in a cup burner, Trees et al.<sup>52</sup> found the value of  $X^*$  to be 0.32 for  $N_2$ , 0.41 for Ar, and 0.039 for  $CF_3Br$ . Others have found similar results.<sup>53</sup>

Figure 6–30 compares the suppression results for  $N_2$ ,  $CF_3Br$ , and SPGG through use of Equation 6-3, where the normalized volume fraction is plotted as a function of the non-dimensional injection interval. For the SPGG results,  $X^*$  is assumed to equal the  $X^*$  value for argon. While the data do not fall exactly on the model, the trend of the results are well represented by the single curve when one considers run-to-run variations due to the statistics associated with suppression of a turbulent flame. The results show that the effectiveness of the SPGG hybrid significantly exceeds the model predictions.

For laminar diffusion flames strained at intermediate rates, Trees et al.<sup>52</sup> showed that the minimum extinction volume fraction of agent in a counterflow flame decreases from the cup burner value when the strain rate is  $50 \text{ s}^{-1}$  to much smaller values for a strain rate of  $400 \text{ s}^{-1}$ . Although the flow in the recirculating region behind a step is much more complicated than in a counterflow flame, the strain rate in the current study should scale with  $1/\tau$ . When the flow of air is increased sufficiently, the flame becomes strained to the point that agent is not needed for extinguishment and the flame blows out. In other words,

as the air flow in the TARPF increases, the model represented by Equation 6-3 in Figure 6–30 must be adjusted not only for changes in  $\tau$ , but also for changes in the value of  $X^*$ .

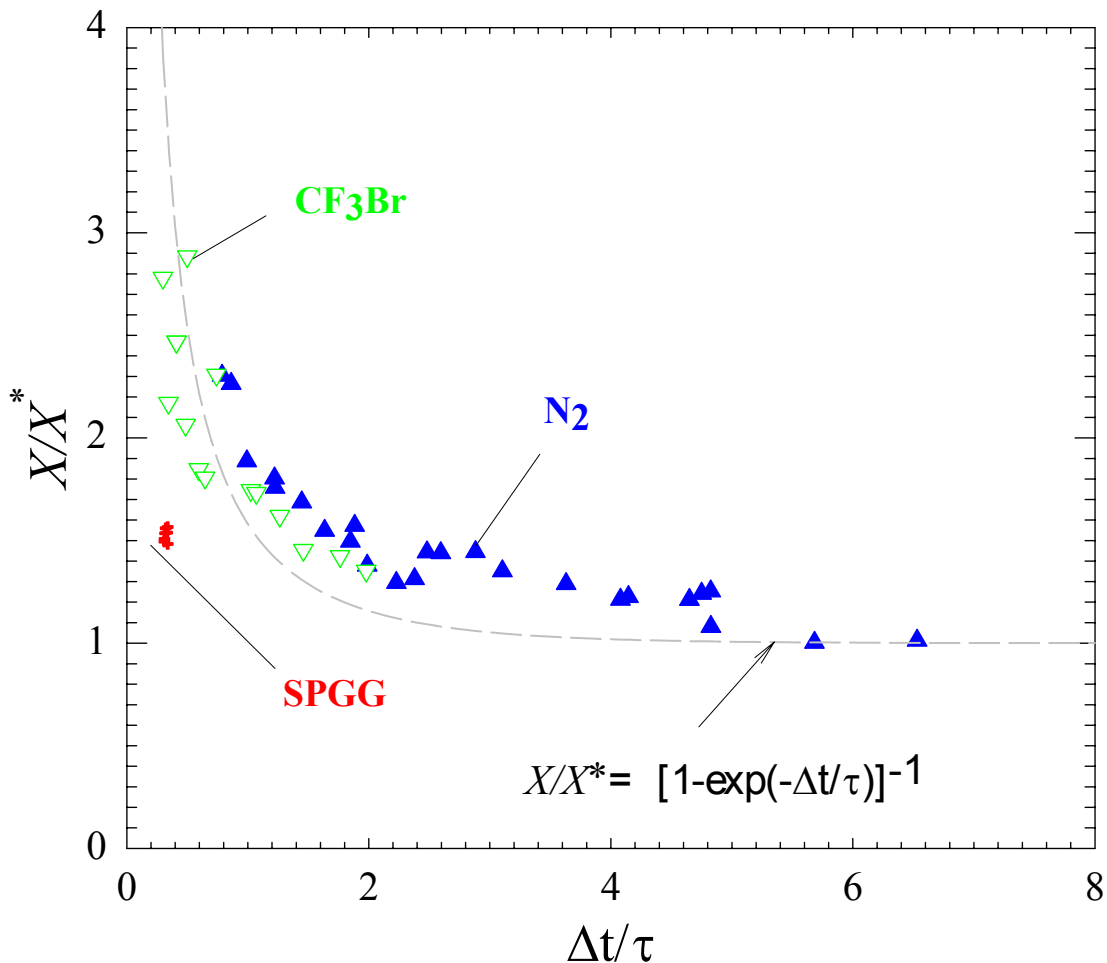


**Figure 6–30. Normalized Volume Fraction as a Function of Non-dimensional Injection Interval, Comparing N<sub>2</sub>, CF<sub>3</sub>Br, and SPGG.** <sup>44</sup>

A number of direct numerical simulations of N<sub>2</sub> suppressing the step-stabilized flame were conducted assuming a finite reaction rate with one step chemistry. The injection interval and volume fraction of nitrogen were varied, and the flame structure was followed through the transient period. Either the flame was extinguished, or it was reestablished following the passage of the N<sub>2</sub> pulse. Figure 6–31 summarizes the results. Open diamonds indicate that no suppression occurred; solid diamonds imply that suppression was successful. The gray symbols refer to the experimental N<sub>2</sub> and CF<sub>3</sub>Br data for all geometries examined. The dotted line is from Equation 6-3.

The computations were able to distinguish regimes of extinction and non-extinction in the case of nitrogen as an agent. The numerical model could not predict what would happen when a chemically active agent like CF<sub>3</sub>Br is introduced into the flame. The cooling and dilution of the flame by the agent

could be predicted, and hopefully, simplified combustion mechanisms for various chemically-active agents can be developed that will lead to a better understanding of the dynamics of fire suppression.

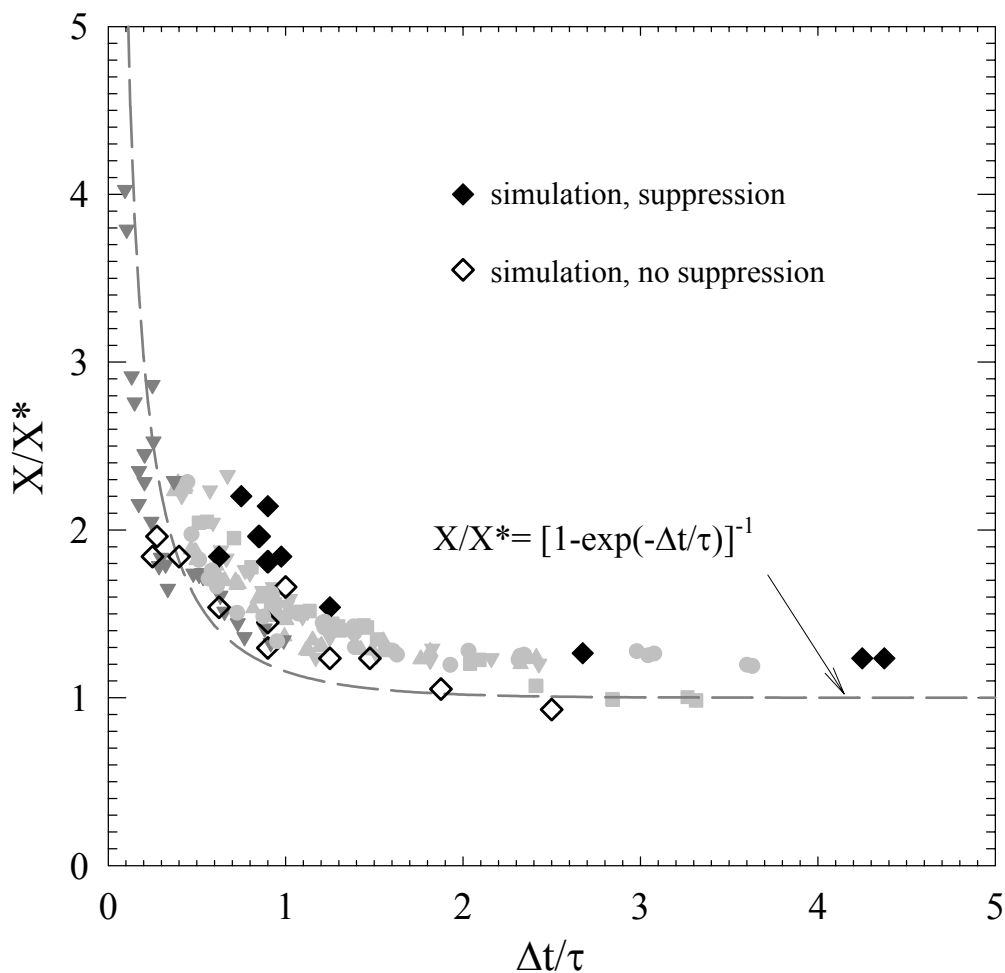


**Figure 6–31. Suppression Volume Fraction of Agent ( $N_2$  or  $CF_3Br$ ) Normalized by Cup Burner Values ( $X^*$ ) as a Function of Injection Time Interval Normalized by Characteristic Residence Time ( $\tau$ ). Gray symbols: experimental results keyed to Figure 6–25; black diamonds: direct numerical simulations with  $N_2$ .<sup>44</sup>**

### Important Findings

- The minimum volume fraction of agent for suppression, normalized by the cup burner value, correlated with  $[1 - \exp(-\Delta t/\tau)]^{-1}$ , where  $\Delta t$  is the injection time interval and  $\tau$  characterizes the mixing time behind the obstacle in the flow.
- The general character of the flame and its extinction by a thermal gaseous agent was captured by a direct numerical simulation of the flow based upon single-step chemistry, and numerical experiments have corroborated the simple correlation of the experimental data for  $N_2$ .

- The measured difference between the decrease in agent storage bottle pressure and the arrival of the agent at the fire highlighted the importance of determining the agent concentration locally and the difficulty in relating changes in bottle pressure to actual mixing conditions.
- For the first time, both compressed and solid-propellant generated gases could be compared side by side, and the effect on performance of different formulations, particle loadings and burning rates for various SPGG designs could be unambiguously discriminated.
- When the temperature of a hot surface downstream of the pool was above 800 °C, the flame, following suppression, reignited and stabilized on the hot surface. At a temperature below 800 °C, the number of reignitions approached zero. This result was in contrast to when the hot surface was located between the stabilizing step and the fuel pool, in which a delayed reignition was observed at temperatures as low as 400 °C.

#### 6.4.5 Summation

Because of the expected diversity of physical and chemical properties of candidate fire suppressants, the NGP developed three apparatus for screening fire suppression efficiency. The cup burner was the workhorse for examination of the chemicals, as discussed further in Chapter 7. The DLAFSS was available for assessing those chemicals with high boiling points and high heats of vaporization. The TARP was available for appraising those chemicals and delivery systems for which it was expected that burst delivery would significantly modify the interpretation of data obtained using the cup burner.

### 6.5 ATMOSPHERIC LIFETIME SCREEN

#### 6.5.1 Factors Affecting Atmospheric Harm

The NGP screening protocol had its roots in the 1990 development of screening procedures for ozone depletion potential (ODP)<sup>v</sup> and global warming potential (GWP).<sup>vi, 1</sup> It was updated and refined as the result of a 1997 NGP workshop<sup>2</sup> and constraints on the agent chemistry resulting from the other properties being screened.

A comprehensive discussion of atmospheric chemistry and the effects of pollutants can be found in reference<sup>54</sup>. The principles that determined the NGP screening protocol were:

- Both ODP and GWP are directly related to the lifetime of a test substance in the atmosphere. The greater the persistence of a chemical, particularly within the troposphere, the greater the potential for adverse effects on the global environment. It was assumed that other, as yet undetermined effects would also be directly related to atmospheric lifetime.
- The tropospheric lifetime of a chemical is determined by the rates of physical and chemical removal processes. The most important of these are the reactivity with respect to OH radicals and absorption of solar radiation in the VIS-UV region of the solar spectrum. For each such process, it must be established that the products are rapidly removed from the atmosphere, e.g., by rainout. In general, OH reactions are important if there are abstractable H atoms

---

<sup>v</sup> The ozone depletion potential of a gas is defined as the change in total ozone per unit mass emission of the gas, relative to the change in total ozone per unit emission of CFC-11 (CFCl<sub>3</sub>).

<sup>vi</sup> The global warming potential of a gas is defined as the change in irradiance at the tropopause (the boundary between the stratosphere and the troposphere) per mass of the gas emitted relative to the change in irradiance per mass of carbon dioxide.

available or if the test compound has unsaturated C-C bonds (aromatic or aliphatic). Fully halogenated alkanes are unreactive with respect to OH radicals. The mechanism whereby most CFCs and halons are destroyed in the atmosphere is by absorption of solar radiation in the 170 nm to 300 nm region. For a replacement chemical, photolysis in the troposphere could also be important if the chemical absorbs solar radiation in the VIS-UV part of the spectrum. For example, photolysis efficiently removes organic iodine compounds within the troposphere. Other removal processes, including physical removal (*i.e.*, rainout, aerosol scavenging and solvation) are significantly slower. Methods for estimating lifetimes due to these physical processes are discussed in Reference 55.

- Ozone depletion potential is also directly related to the numbers and kinds of certain atoms in a compound's chemical formula. If a test substance does not contain chlorine, bromine, iodine, or nitrogen, the current knowledge of stratospheric chemistry indicates that the ozone depletion potential is zero. Each of these four atoms can have a deleterious effect on stratospheric ozone, and many molecules containing them will have a positive ODP value. The calculation of ODP requires the use of an atmospheric model with a complete input of chemistry, solar irradiation, and transport. Comparison of the results of various models, ranging from the most elaborate three dimensional models to the much simpler one dimensional models, indicates that in the case of the halocarbons, simple models give results adequate for use in developing screening tests.<sup>56</sup> Halon 1301 has an estimated ODP value of about 13.
- Global warming potential is directly related to the capability of a test compound to absorb radiation in the region of the "atmospheric window" between 7  $\mu\text{m}$  and 13  $\mu\text{m}$ . Test compounds which are weak absorbers in this region are unimportant with regard to global warming.

## 6.5.2 Prior Estimation Methods

### Stratospheric Ozone Depletion

Skaggs and Nimitz<sup>57</sup> proposed a method for estimating ODP values for halocarbons of containing one or two carbon atoms and no bromine atoms. The method related the ODP to two factors: a reactivity factor, related to the number of chlorine atoms in the molecule, and a survival factor, *i.e.*, the fraction of molecules reaching the stratosphere. The relationship is shown in Equation 6-4.

$$\text{ODP} = c_1 n^{c_2} e^{-(c_3/t)} \quad (6-4)$$

where:

$n$  is the number of chlorine atoms

$t$  is the atmospheric lifetime

$n^{c_2}$  is the reactivity factor

$c_2$ , and  $c_3$  are parameters to be fit

$e^{-(c_3/t)}$  is the survival factor

$c_1$  is a normalizing constant

This equation gave values that were relatively close to the rigorously calculated ODPs used in fitting the parameters. Since the rigorously calculated ODP values and atmospheric lifetimes used in the parameter fitting have changed since the equation was originally proposed, the reported parameters are not given here.

Iikubo and Robin<sup>58</sup> extended this formulation to include estimation of ODP values for bromine-containing compounds.

$$\text{ODP} = A E P [(\#\text{Cl})^B + C(\#\text{Br})] D^{(\#\text{C}-1)} \quad (6-5)$$

Here, P is the photolysis factor, which was set equal to 1.0 if there were no special structural features that made the molecule subject to tropospheric photolysis. Otherwise, P = 0.180 for a bromine geminal to a chlorine (e.g., Br-C-Cl), P = 0.015 for geminal bromine atoms (Br-C-Br), or P = 0.370 for vicinal bromine atoms (Br-C-C-Br). The fitting parameter values were: A = 0.446, B = 0.740, C = 32.000, and D = 1.120. The hydrogen factor, E, was set equal to 1.000 if there were no hydrogen atoms; otherwise it was set equal to 0.0625. #C, #Br, and #Cl are the numbers of carbon, bromine, and chlorine atoms, respectively.

Use of Equation 6-5 gave, at best, rough approximations, even if the equation was restricted to simple saturated halocarbons (Table 6–2). The trends, however, were preserved. It may be that a better fit of parameters could be obtained with a larger set of more recent data as a basis.

**Table 6–2. Estimated and Reported ODP Values (Relative to CFC-11) for Selected Halocarbons.**

Compound	Formula	Calculated ODP	Reported ODP	Reference
Halon 1301	CBrF <sub>3</sub>	14.3	12	59
Halon 1211	CBrClF <sub>2</sub>	2.6	5.1	59
Halon 2402	CBrF <sub>2</sub> CBrF <sub>2</sub>	17.4	6.6	60
HBFC-22B1	CHBrF <sub>2</sub>	0.89	0.74	61
HBC-30B2	CH <sub>2</sub> Br <sub>2</sub>	0.03	0.17	62
HBC-40B1	CH <sub>3</sub> Br	0.89	0.64	59
HCFC-123	CHCl <sub>2</sub> CF <sub>3</sub>	0.050	0.014	59

## Atmospheric Lifetime

To a great extent, values of ODP and GWP are determined by the tropospheric lifetimes of the compounds. Regardless of the chemical, the ODP and GWP values will be negligible if tropospheric removal is efficient. Tropospheric removal reactions can be either bimolecular or unimolecular. Bimolecular reactions involve reaction with atmospheric species such as hydroxyl free radicals ( $\bullet\text{OH}$ ), tropospheric ozone ( $\text{O}_3$ ), oxygen atoms ( $\bullet\text{O}$  in  $^3\text{P}$ ,  $^1\text{D}$  electronic states), etc. Unimolecular reactions include photolysis, thermal dissociation, and heterogeneous absorption (aqueous or particulate aerosols).

The rate of disappearance of a species, C, due to a bimolecular reaction with an atmospheric species A can be expressed as shown in Equation 6-6, where [C] and [A] are the concentrations of species C and A,

and  $k_2$  is a second-order reaction rate constant. Similarly, the rate of removal through unimolecular reactions is expressed by a first-order differential equation with the first-order reaction rate constant  $k_1$  as shown in Equation 6-7. Typical units for  $k_2$  and  $k_1$  are, respectively,  $\text{cm}^3/\text{molec}\cdot\text{s}$  and  $\text{s}^{-1}$ , with concentrations in  $\text{molec}/\text{cm}^3$ . The rate constants  $k_1$  and  $k_2$  are constant only under a given set of conditions. For example, for photolysis,  $k_1$  depends on the radiation flux and wavelength; for reaction with atmospheric particulate,  $k_1$  depends on the concentration (and composition and other characteristics) of the particulate.

$$\frac{d[C]}{dt} = -k_2[C][A] \quad (6-6)$$

$$\frac{d[C]}{dt} = -k_1[C] \quad (6-7)$$

Careful consideration shows that all reactions can actually be considered “bimolecular” in form since the concentration of particulate, for example, is incorporated into  $k_1$  for particulate removal, and the “concentration” (actually, the flux) of photons is incorporated into  $k_1$  for photolysis.

The concentration of a species undergoing reaction, as shown in Equation 6-6 or Equation 6-7, decays exponentially as given by Equation 6-8. Here  $[C]_0$  is the initial concentration,  $[C]_t$  is the concentration at any time  $t$ , and  $t_{1/e}$  is the “e-folding” atmospheric lifetime, i.e., the time required for the concentration of an atmospheric species to decay to  $1/e$  (approximately 0.369) of its initial value. The e-folding lifetime is related to the reaction rate constant by or depending on whether the reaction is bimolecular (Equation 6-9) or unimolecular (Equation 6-10).

$$[C]_t = [C]_0 e^{-t/t_{1/e}} \quad (6-8)$$

$$t_{1/e} = 1/k_2[A] \quad (6-9)$$

$$t_{1/e} = 1/k_1 \quad (6-10)$$

Using these equations, one can estimate the atmospheric lifetime due to various removal processes by using globally averaged values for concentrations of reactant species.

A globally averaged tropospheric hydroxyl free radical concentration of  $9.7 \times 10^5$  molecules/ $\text{cm}^3$  and a globally averaged tropospheric ozone concentration of  $5.0 \times 10^{11}$  molecules/ $\text{cm}^3$  have been used for such estimations.<sup>63,64</sup> In the global averaging approximation, one uses reaction rate constants for a mean tropospheric temperature. Values around 298 K are often used<sup>65</sup> and were used in the NGP estimations.

In the global average approximation, atmospheric lifetime is directly proportional to the second-order rate constant ( $k_{OH}$ ) for reaction with  $\bullet\text{OH}$ , when this is the primary tropospheric removal process. Thus, an alternative way to estimate the atmospheric lifetime for a compound  $B$  removed only by reaction with  $\bullet\text{OH}$  was to use Equation 6-11 to relate the lifetime of  $B$  ( $t_{1/e}^B$ ) to that ( $t_{1/e}^C$ ) of a reference compound  $C$ .<sup>66</sup> Here,  $k_{OH}^B$  and  $k_{OH}^C$  are the second-order hydroxyl reaction rate constants for the two materials. Methyl chloroform ( $\text{CH}_3\text{CCl}_3$ ) is usually the reference compound. This method is equivalent to using the globally averaged  $\bullet\text{OH}$  concentration when this concentration has been determined from measurements of

atmospheric removal of methyl chloroform, as in the case of the value used in this report.<sup>63</sup> Note that with the appropriate rate constants, one could use an equation similar to Equation 6-11 when a removal mechanism other than reaction with a hydroxyl free radical predominates, as long as the removal mechanism for the compound of interest (B) is the same as that for the reference compound (C).

$$t_{1/e}^B = t_{1/e}^C (k_{OH}^C / k_{OH}^B) \quad (6-11)$$

Attempts to use Quantitative Structure-activity Relationships (QSARs) to predict  $k_{OH}$  values have not been highly successful.<sup>67</sup> A procedure based on the C-H bond energy (and, thus, related to the activation energy for hydrogen atom abstraction by  $\bullet OH$ ) gave disappointing fits to rigorously calculated atmospheric lifetimes, though re-parameterization with more recent data might help.<sup>57</sup> Since many of the compounds of interest as halon replacements contain fluorine atoms, there was one trend of interest. Examination of rate constants for a variety of fluorinated compounds indicated that fluorine substitution activated hydrogen atoms on the same carbon atom toward  $\bullet OH$  abstraction, but deactivated hydrogen atoms on carbon atoms immediately adjacent. The reaction of  $\bullet OH$  with  $CH_3CH_2F$ , for example, proceeds primarily (85 %) with hydrogen atom abstraction from the  $CH_2F$  group.<sup>68</sup>

Better results may be available through quantum mechanical calculations. There was strong evidence that  $k_{OH}$  values vary linearly with the calculated values for the highest occupied molecular orbital in hydrofluorocarbons.<sup>69</sup>

### 6.5.3 The Screening Protocol

Estimation of the atmospheric impact of candidate fire suppressant considered several properties. The following is the sequence that was typically followed:

- A small molecule that did not contain chlorine, bromine, iodine, or nitrogen was generally "passed."
- For a larger molecule or one that contained one or more of the four atoms, but contained a feature that bespoke a high rate of reactivity in the troposphere (see below), its reaction rate with OH was estimated. The potential of the molecule to absorb VIS-UV radiation was also estimated.
- The reaction rate was measured for a molecule that fared well in the prior step and in the screens for fire suppression effectiveness and volatility.

The following sections relate the methods to be used in such appraisals.

### 6.5.4 Removal by Hydroxyl Radical Reaction

Hydroxyl radicals can transform and remove trace atmospheric substances from the troposphere by abstracting hydrogen atoms or by addition/displacement reactions at unsaturated sites in the molecule. The reaction of any substance, X, with OH can be written as



and the rate of one of these reactions is given by:

$$\frac{-d(X)}{dt} = k_{OH}(OH)(X) , \quad (6-13)$$

where  $k_{OH}$  is the rate constant for reaction,  $(X)$  the concentration of species  $X$ , and  $(OH)$  is the average tropospheric  $OH$  concentration. Since  $(OH)$  is essentially constant (concentration independent of the presence of the trace substance  $X$  in the atmosphere), the expression can be written as:

$$\frac{-d(X)}{(X)} = k_{OH}(OH)(dt) \quad (6-14)$$

or:

$$\ln \left( \frac{X_0}{X_t} \right) = k_{OH}(OH) t , \quad (6-15)$$

where  $X_0$  is the concentration at some zero of time, and  $X_t$  the concentration at time  $t$ . The time for the concentration to decay from  $X_0$  to  $X_t$  is thus given by:

$$t = \frac{\ln \left( \frac{X_0}{X_t} \right)}{k_{OH}(OH)} . \quad (6-16)$$

The atmospheric half-life (where  $X_0/X_t$  has been set equal to 2.718, the base of natural logarithms), or atmospheric lifetime, can be defined as:

$$t = \frac{\ln(2.718)}{k_{OH}(OH)} \text{ or } t = \frac{1}{k_{OH}(OH)} . \quad (6-17)$$

Using an average atmospheric hydroxyl radical concentration of  $10^6 \text{ molec cm}^{-3}$  <sup>(70)</sup>, the tropospheric lifetime becomes:

$$t_{OH}(trop) = \frac{3 \times 10^{-14}}{k_{OH}} , \quad (6-18)$$

where the units of  $t_{OH}(trop)$  are years ( $1 \text{ year} = 3 \times 10^7 \text{ s}$ ) and of  $k_{OH}$  are  $\text{cm}^3 \text{ molec}^{-1} \text{ s}^{-1}$ . For the identification of compounds with tropospheric lifetimes of the order of a month or less, desirable values of  $k_{OH}$  are  $3 \times 10^{-13} \text{ cm}^3 \text{ molec}^{-1} \text{ s}^{-1}$  or higher.

Values of  $k_{OH}$  may be determined by direct laboratory measurement of the rate constant of reaction, or may be estimated using structure-activity relationships. The latter is preferred for screening those compounds for which appropriate data are available, since the measurements are quite labor intensive and the calculation is faster and less expensive and uses none of the compound.

## Experimental Measurement of OH Rate Constants

The method of choice for this determination was the flash-photolysis resonance fluorescence technique.<sup>71,72,73</sup> It is a precise, reliable, and commonly used method for the measurement of OH rate constants over the range of rate constants of about  $10^{-14}$  to  $10^{-9}$   $\text{cm}^3 \text{molec}^{-1} \text{s}^{-1}$ . This method measures the loss of OH under conditions of excess test compound and yields an absolute measurement of the OH rate constant. It is mandatory that the sample of the test compound be free of impurities that are significantly more reactive than the test substrate, e.g., unsaturated compounds or compounds with many easily abstracted hydrogen atoms. The method requires the participation of senior scientific staff. A schematic of a typical apparatus is shown in Figure 6–32.

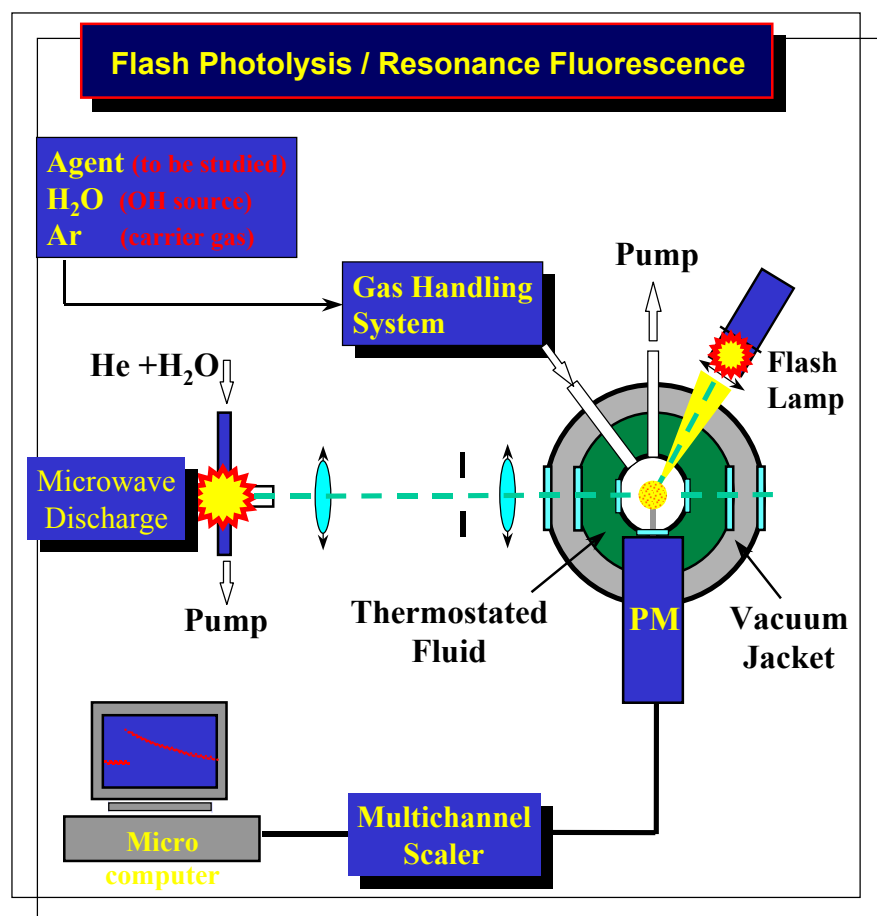


Figure 6–32. Schematic of Flash Photolysis Resonance Fluorescence Apparatus for Measuring Reactivity of Compound with OH Radicals.<sup>2</sup>

The apparatus consisted of a stainless steel or glass cell surrounded by an outer wall between which fluid was circulated to a temperature regulator to maintain a fixed temperature, measured by means of a thermocouple. The cell had four window ports at 90° positions around the cell, and one additional window port on the base of the cell. The entire cell was mounted within a vacuum housing. Gases were admitted to the cell through inlets connected to a gas handling system. A hydroxyl radical resonance lamp, consisting of a microwave powered discharge in 130 Pa of a mixture of He saturated with water vapor, and a pulsed N<sub>2</sub> discharge flash lamp, which was powered by discharge capacitors and a power supply, were located at right angles to each other and to a photomultiplier detector.

Hydroxyl radicals were produced by the flash photolysis of H<sub>2</sub>O. The OH radical resonance lamp was used in cw mode to excite a small fraction of the hydroxyl radicals which then emitted resonance radiation at 308 nm which was detected by the photomultiplier. The signal output was then fed to pulse counting electronics, and ultimately to a computer for signal averaging and subsequent statistical analysis and graphical display. The measurement process was initiated by a photomultiplier (PM) which was triggered by the visible light from the flash lamp. A delay gate introduced a delay time of 100 μs to 300 μs to eliminate any scattered light interference from the flash lamp. Fluorescence signal from 50 to 500 flashes were typically averaged to generate a suitable decay curve.

In a typical experiment, reaction mixtures containing the test compound, argon, and water vapor (prepared manometrically in a 5 L bulb before admission to the reaction cell) were flowed slowly (at about 100 cm<sup>3</sup> s<sup>-1</sup>) through the cell. The quantity measured in this test was the rate of loss of OH radicals in the presence of a great excess of the test compound. Under these conditions, the rate expression can be written as:

$$\frac{-d(OH)}{dt} = k(OH)(S), \quad (6-19)$$

where OH is the concentration of OH radicals, S is the concentration of the test substance, k is the rate constant, and t is the reaction time. Under conditions where (OH) << (S), S is essentially constant, and the OH decay is first order, and the rate expression becomes:

$$\frac{-d(OH)}{(OH)} = k(S) dt = k' dt, \quad (6-20)$$

where k', the apparent first-order rate constant, is obtained directly from a measurement of the exponential rate of decay of OH. The true rate constant is then:

$$k = \frac{k'}{(S)}. \quad (6-21)$$

However, since there are OH diffusional losses from the reaction zone, in practice the first order decay was measured as a function of the concentration of the test compound, and from a plot of first order rate constant against concentration, the second order rate constant was obtained from the slope.

Tests for impurity effects must be included as part of the screening protocol. The effect of reactive impurities on test results can be illustrated by considering a test compound which has a rate constant for reaction with OH radicals of about 1 x 10<sup>-15</sup> cm<sup>3</sup> molec<sup>-1</sup> s<sup>-1</sup>, corresponding to an atmospheric lifetime of 30 years. If the test sample contained a 1 % impurity in the form of an alkene, which typically may have a rate constant for reaction with OH of about 1 x 10<sup>-12</sup> cm<sup>3</sup> molec<sup>-1</sup> s<sup>-1</sup>, then the apparent OH rate constant would be about 1 x 10<sup>-14</sup> cm<sup>3</sup> molec<sup>-1</sup> s<sup>-1</sup>, corresponding to a lifetime of 3 years. Purity was thus of great importance in carrying out these tests, and it was desirable for the test compounds to have impurity levels for alkenes and other unsaturated compounds of less than about 0.1 %. If the purity was not known, then the following test procedure was followed:

- Measure the rate constant.

- If  $k < 3 \times 10^{-15} \text{ cm}^3 \text{ molec}^{-1} \text{ s}^{-1}$ , the test results were acceptable.
- If  $k > 3 \times 10^{-15} \text{ cm}^3 \text{ molec}^{-1} \text{ s}^{-1}$ , check the test sample for impurities. This was done initially by carrying out a trap-to-trap distillation and then remeasuring the rate constant. If the rate constant decreased, the sample was impure, and an analysis was necessary. Only after analysis and, if necessary, purification, were additional measurements be undertaken.

### 6.5.5 Measurement of Photolysis Rates

Photolysis is the process whereby a molecule is chemically transformed following the absorption of light. For photolysis to be important in the troposphere, the molecule must be able to absorb photons in the VIS-UV region of the solar spectrum (between about 290 nm and 700 nm), and the resultant energy-rich molecule must be chemically transformed rather than being physically quenched back to the original state. The rate of photolysis depends upon the flux of solar photons in the VIS-UV region, the absorption cross section of the substance over the same region, and the quantum yield for dissociation as a function of wavelength. The rate of photolysis is:

$$-\frac{dX}{dt} = k_p(X) = f\sigma\phi(X), \quad (6-22)$$

where  $f$  is the flux of solar photons in  $\text{cm}^{-2} \text{ s}^{-1}$ ,  $\sigma$  is the cross section in  $\text{cm}^2$ ,  $\phi$  is the quantum yield for dissociation,  $k_p$  is the effective first order rate constant in  $\text{s}^{-1}$ , and  $(X)$  is the concentration of substance  $X$  in  $\text{molec cm}^{-3}$ . Thus:

$$k_p = f\sigma\phi. \quad (6-23)$$

The rate constant must actually be determined as the integral of this quantity over the whole range of atmospherically-accessible solar radiation. The process is considerably simplified by carrying out the calculation for discrete intervals of the solar spectrum of interest and summing to obtain the total rate constant. Other factors including solar zenith angle, season, latitude, altitude, and surface albedo also enter into the calculation.

The lifetime with respect to photolysis is defined as,

$$t_p(\text{trop}) = \frac{I}{k_p}, \quad (6-24)$$

or, numerically,

$$t_p(\text{trop}) = 3 \times 10^8 k_p^{-1} \quad (6-25)$$

where the units of  $t_p(\text{trop})$  are years and the units of  $k_p$  are  $\text{s}^{-1}$ .

To determine  $k_p$ , it is necessary to know the atmospheric flux of solar photons and their wavelength distribution, the absorption cross section of the compound over the same spectral range, and the quantum yield for dissociation, also as a function of wavelength. The first quantity is tabulated and available.<sup>54</sup> The second quantity is readily measured in the laboratory. The third quantity, however, is not easily

obtained. For the purpose of developing a screening test, the quantum yield was conservatively taken to be unity at all wavelengths, and the screening test was based on measurement of the absorption cross section.

Then,

$$k_p \leq f\sigma \text{ and } t_p(\text{trop}) \geq k_p^{-1}. \quad (6-26)$$

and since  $f$  is a tabulated quantity, the test measurement involved measurement of the absorption cross section in the VIS-UV region of the spectrum.

The measurement can be undertaken using a variety of spectrometer configurations. Design options include single pass or multipass for the absorption train, and also single beam or double beam for the detection system. Double beam instruments consist of true double beam configurations employing two identical monochrometers and two detection systems, virtual double beam configurations employing a beam splitter at the exit of the monochromator followed by two detection systems, and broad-band referencing, where the wavelength dispersed signal is referenced to the non-dispersed incident light source. Any of these experimental configurations are acceptable. Of particular relevance are the measurements of Molina and coworkers<sup>74</sup>, using a double-beam instrument to measure absorption cross sections for several brominated methanes and ethanes, and those of Gillotay and coworkers<sup>75</sup> who measured absorption cross sections for some bromine-containing compounds using both multiple reflection and single pass single-beam instruments.

The choice of instrument is dictated by the requirement that it be able to measure absorption cross sections as low as  $10 \text{ cm}^2$  to  $24 \text{ cm}^2$ . Absorption cross section is defined in terms of the fractional absorption of light passing through a defined path length of a given concentration of absorber.

One can define a figure of merit for the measurement system based on the quantity  $\sigma pP$  (the optical depth), where  $\sigma$  is the absorption cross section (wavelength dependent),  $p$  the pressure (or concentration) of the test compound, and  $P$  the path length. Highest precision cross section measurements are made with an optical depth of about one (30 % to 40 % absorption). For weak absorbers,  $\sigma pP$  will be much smaller. In addition, for a fixed path length, absorption depends on the pressure (or concentration) of the test substance in the optical path. Under nominal conditions of "room" temperature (298 K), absorption may be limited by the available vapor pressure of the test substance.

To measure the cross section for a weak absorber requires high pressure, and/or long path length, and/or high accuracy in measuring very small amounts of absorption. For screening purposes, the accuracy or reproducibility of the measurements should be about 25 %, and this should define the smallest possible value of  $\sigma pP$  suitable for making the measurements.

The measurement method described here was based on the use of a single beam monochromator.<sup>76</sup> The absorption cross section is defined as:

$$\sigma(\lambda) = \left( \frac{I}{c} \ln \left( \frac{I_\lambda}{I_0} \right) \right), \quad (6-27)$$

where  $\sigma_\lambda$  is the cross section at a given wavelength, ( $c$ ) the concentration of absorbing test substance in molec  $\text{cm}^{-3}$ ,  $\ell$  the path length in cm,  $I_\lambda$  the intensity of light passing through the cell containing the absorber, and  $I_0$  the intensity of light passing through the empty cell, both in arbitrary units. The test measurement thus involved measuring and taking the ratio of the quantities  $I_\lambda$  and  $I_0$ .

A schematic of a suitable apparatus is shown in Figure 6–33.

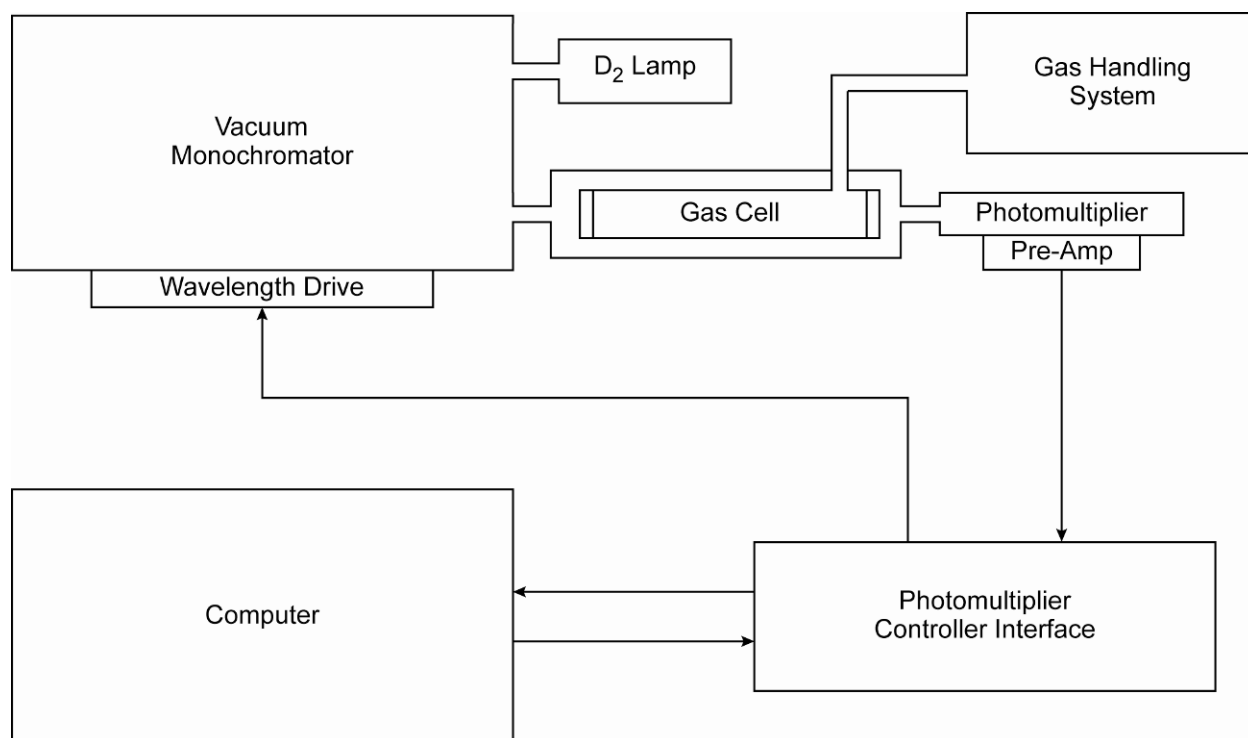


**Figure 6–33. Apparatus for Measuring the Absorption Cross Section of Candidate Fire Suppressants.**<sup>1</sup>

The apparatus consisted of a 1 m incidence McPherson vacuum monochromator employing a 600 lines/mm grating blazed at 150 nm. The lamp shown in the figure was a Hamamatsu deuterium lamp with a highly stabilized power supply. This provided a convenient source of radiation over the 290 nm to 400 nm range. For measurements further into the red region of the spectrum, a tungsten lamp was used. The detector was a Hamamatsu solar blind side-on multiplier tube. Five absorption cells having a range of path lengths ranging from 0.2 cm to 20 cm were chosen by use of the turret assembly. The monochromator wavelength drive was controlled by a stepping motor with 800 steps per revolution. The gear train used was such that 16 pulses were equivalent to 0.1 nm wavelength change. Gas pressure in the cell was monitored with a diaphragm type gauge.

The signal from the photomultiplier tube, which was observed in real time during a measurement, was processed and fed to a controller interface module which was part of an IBM compatible personal

computer system. A spectrum was first measured with no gas in the cell, then with an appropriate amount of gas in the cell, and finally with the cell again empty. The deuterium lamp was very stable, and this procedure led to a very reliable measurement of the adsorption cross section down to about  $10^{-23}$  cm<sup>2</sup>.

The procedure was to measure the absorption cross section from 290 nm to 700 nm using the definition of absorption cross section given above. The absorption cross section as a function of wavelength was then related to photolysis rate constant using procedures outlined by Finlayson-Pitts and Pitts.<sup>54</sup>

The experimentally measured absorption cross section was averaged over discrete wavelength intervals. Over the same intervals, Table A7 in Reference 1 provided values of the solar flux, corresponding to a cloudless day, zenith angle of 0°, surface albedo zero, uncorrected for latitude or season. For each discrete spectral region the rate of absorption was calculated as the product of columns 2 and 3 or that table, and the result entered into column 4. The summation of column 4 then gave the total rate of absorption. This was an upper limit to the number of photons absorbed. Following Molina and coworkers<sup>74</sup>, it was recommended that the maximum rate of absorption be divided by 3 to provide a more realistic estimate of the average atmospheric absorption rate. This absorption rate constant was an upper limit to the true rate constant for photolysis:

$$k_p \leq k_a. \quad (6-28)$$

The problem of test sample purity was of concern here as well as with respect to OH reactivity. Low levels of a strongly absorbing impurity will give an incorrect set of cross section results. Therefore, when the purity was not known, the following test procedure was followed:

- Measure the absorption cross section as a function of wavelength, and calculate  $k_p$ .
- If  $k_p < 3 \times 10^{-9}$  s<sup>-1</sup>, the test results were acceptable.
- If  $k_p > 3 \times 10^{-9}$  s<sup>-1</sup>, check the test sample for impurities by carrying out a trap-to-trap distillation and then re-measuring the absorption cross section. If the absorption cross section changed significantly, the sample was impure, and an analysis was necessary. Only after analysis and if necessary, purification, were additional measurements undertaken.

The test value derived for lifetime with respect to photolysis provided only a lower limit to the true lifetime, and if the quantum yield were low, the test compound could have a much longer lifetime.

### 6.5.6 Estimation of Reactivity

The estimation method was based on an analysis of the structure of the molecule and its breakdown into component structural sub-units. The reactivity was expressed in terms of (a) abstraction of H atoms, (b) addition at double or triple C-C bonds, and (c) addition to aromatic structures. The total rate constant was obtained by summing the contributions of the different groups. In some cases, the reactivity and hence lifetimes of certain classes of compounds were estimated without going through a detailed estimation calculation or making laboratory measurements. For instance, the completely halogenated (with F, Cl, Br, or I) alkanes are essentially inert with respect to reaction with OH radicals. On the other hand, reactions of OH radicals at unsaturated sites (aliphatic or aromatic in character) are always very much faster than abstraction<sup>77</sup>, and therefore, unsaturated substances have short atmospheric lifetimes. Thus, the estimation methods were presented only with reference to saturated compounds containing at least one abstractable hydrogen atom.

The reactions of OH radicals have been the most studied of all classes of gas-phase reactions, and, as a result, there was a very large body of reliable kinetic data. Atkinson<sup>78</sup> used this database to develop a group method for estimating OH radical rate constants for hydrogen atom abstraction. He also provided a basis for estimating rate constants for attack at double and triple C-C bonds, and attack at unsaturated aromatic sites. Examination of his database showed that the rate constants for the latter classes of reactions were all very fast compared to those for abstraction reactions.

The basis for the Atkinson method was the separation of the molecule into defined structural units. The rate constants for -CH<sub>3</sub>, -CH<sub>2</sub>-, and >CH- groups are dependent on the nature of the substituents alpha and beta to the group. In general, rate constants for the groups can be written as:

$$\begin{aligned}k(CH_3 - X) &= k_p F(X), \\k(Y - CH_2 - X) &= k_s F(X) F(Y), \\k(X - CH(Z) - Y) &= k_t F(X) F(Y) F(Z), \text{ and} \\k(X - OH) &= k_{OH} F(X),\end{aligned}$$

where  $k_p$ ,  $k_s$ ,  $k_t$ , and  $k_{OH}$  refer to the rate constant for abstraction from nominal primary, secondary, tertiary, and hydroxyl groups, respectively, and the factors  $F(X)$ ,  $F(Y)$ , and  $F(Z)$  are correction factors to account for the effects of substituent groups. Using values for group rate constants and correction factors tabulated by Atkinson, rate constants for test compounds were derived.

Nimitz and Skaggs also estimated ODP values and atmospheric lifetimes of one- and two-carbon hydrofluorocarbons and hydrochlorofluorocarbons on the basis of quantitative structure activity relationships.<sup>79</sup> Their values were based on estimates of the OH reactivity with the hydrogen atom(s). They were able to predict the results one- and two-dimensional atmospheric calculations within about a factor of two for compounds with atmospheric lifetimes under 30 years.

However, experimental studies had demonstrated that the reactivity of the hydroxyl radical with many, more complex types of halogenated organic compounds was not adequately correlated by simple structure-activity relationships. In particular, when an ether linkage was introduced, even the relative order of reactivity among the various ethers could not be predicted correctly.<sup>80</sup> This implied that it would be necessary to measure rate constants for a large number of members of any new class of reactants. A better method of screening candidate molecules was clearly needed.

Under the NGP, Huie and coworkers developed a refined method to predict atmospheric lifetimes for new classes of halogenated compounds.<sup>81,82,83</sup> At the heart of the method was a computational scheme for OH reaction rate constants for those compounds for which hydrogen abstraction would be expected to be the dominant reaction mechanism. They established accuracy of this approach utilizing a set of compounds for which reliable experimental data were available. Combining calculations with new measurements of ultraviolet absorption spectra, they then estimated atmospheric lifetimes of a set of bromine-containing compounds for which no data had been reported.

At the core of the method was the establishment of a level of theory that would predict the reactivity of the hydroxyl radical with a series of simple molecules, seeking the lowest possible degree of computational difficulty. This level would then be applied to more complex molecules and, ultimately,

applied to the new families of candidate fire suppressants. The results would be validated by a limited number of experimental determinations, but extensive experimentation and synthesis could be avoided.

In the initial study, several levels of theory were explored for the reaction of OH with  $\text{CH}_2\text{Br}_2$ .<sup>81</sup> This molecule was chosen both because of the importance of bromine as a fire suppressant and because the relatively large electron system of the molecule made this reaction a serious test of the various levels of theory. This study included the treatment of tunneling, making use of three different methods of approximating this correction. A low level of *ab initio* structure calculations was found to be more than adequate for screening purposes. Building on the results of this study, the reactions of OH with the other halogen-substituted methanes, up to bromine, were also calculated<sup>82, 83</sup> and compared with experimental results where available. Huie and coworkers also performed measurements on some bromopropanes<sup>84</sup> and bromofluoroalkenes.<sup>85</sup> Table 6–3 summarizes the results of these calculations and measurements.

**Table 6–3. Atmospheric Lifetimes (years), from Theory and from OH Reactivity Measurements, for Selected Molecules.**

	Atmospheric Lifetime (theory)	Atmospheric Lifetime (from meas.)	Theory/Meas.
$\text{CH}_2\text{Br}_2$	0.1	0.25	0.5
$\text{CH}_3\text{F}$	6.4	2.9	2.2
$\text{CH}_3\text{Cl}$	1.5	1.5	1.0
$\text{CH}_3\text{Br}$	2.5	2.0	1.3
$\text{CH}_2\text{F}_2$	3.6	5.6	0.6
$\text{CH}_2\text{FCl}$	1.7	1.4	1.2
$\text{CH}_2\text{Cl}_2$	0.43	0.46	0.9
$\text{CH}_2\text{ClBr}$	0.54	0.49	1.1
$\text{CH}_2\text{Br}_2$	0.57	0.42	1.4
$\text{CHF}_3$	400	263	1.5
$\text{CHF}_2\text{Cl}$	13.2	12.7	1.0
$\text{CHF}_2\text{Br}$	6.0	5.6	1.1
$\text{CHFCl}_2$	1.2	2.1	0.6
$\text{CHCl}_3$	0.15	0.51	0.3
$\text{CH}_2\text{FBr}$	1.9	Unknown	
$\text{CHFBr}_2$	0.49	Unknown	
$\text{CHFClBr}$	0.73	Unknown	
$\text{CHCl}_2\text{Br}$	0.16	Unknown	
$\text{CHClBr}_2$	0.12	Unknown	
$\text{CH}_2\text{BrCH}_2\text{CH}_3$		14 days	
$\text{CH}_3\text{CHBrCH}_3$		19 days	
$\text{CF}_2=\text{CF}_2$		1.1 days	
$\text{CFBr}=\text{CF}_2$		1.4 days	
$\text{CHBr}=\text{CF}_2$		2.4 days	
$\text{CH}_2=\text{CBr}-\text{CF}_3$		2.8 days	
$\text{CH}_2=\text{CBr}-\text{CF}_2-\text{CF}_3$		3.2 days	
$\text{CH}_2=\text{CH}-\text{CF}_2-\text{CF}_2\text{Br}$		7.0 days	

In summary, the calculated rate constants for the reaction of OH with halomethanes were in good agreement with their experimental counterparts, establishing the viability of *ab initio* calculations as the basis of a screening tool. Calculations for the reactions of OH with several fluoroethanes and the ethers derived from them have reproduced the experimental trends, with predictions in absolute reactivity within a factor of three. Calculations are being extended to ethers with several carbons and containing fluorine along with one or more bromine atoms.

### 6.5.7 Solution of Fluoroalkylamines

Fluorinated alkylamines were considered as possible alternate fire suppressants. In this case, a possible atmospheric loss mechanism was solution into atmospheric droplets and subsequent rainout. To investigate the likelihood of this process, Huie and coworkers calculated Henry's Law constants ( $K_H$ ) for a series of fluoroalkylamines, using the SM5.42 solvation model at the PM3 level of theory. Based on comparisons of the results of calculations for similar alkylamines with experiment, they estimated that these results were valid to within a factor of three. Based on these results, rainout is likely not to be a very effective removal mechanism for the more highly fluorinated species.

### 6.5.8 Reactivity of Alkyl Phosphates towards Radicals in Water

Some suggested fire suppressants are not volatile but their environmental fate is still of concern. Alkyl phosphates are a class of chemicals that have been extensively investigated as fire suppression agents. They have very low volatility and are unlikely to be degraded in the atmosphere. They are, however, soluble in water and their environmental fate is likely to involve reactions in this medium. As part of this project, Huie and coworkers measured the rate constants for their reactions with the radicals important in aqueous phase degradation processes: the carbonate radical,  $\text{CO}_3^-$ , and the dichloride radical,  $\text{Cl}_2^-$ . The reactivity towards the sulfate radical,  $\text{SO}_4^-$ , was also measured for comparison. The procedure used was pulse radiolysis, in which a high-energy electron pulse is utilized to generate the radicals, whose temporal history is monitored by the use of optical absorption. The results of this study are presented in Table 6-4 (in units of  $\text{L mol}^{-1} \text{s}^{-1}$ ).

**Table 6-4. Reactions of Phosphates.**

Compound	$\text{SO}_4^-$	$\text{Cl}_2^-$	$\text{CO}_3^-$
Triethyl phosphate	$1.6 \times 10^6$	$< 7 \times 10^4$	$< 1 \times 10^4$
Diethyl Phosphate	$8.7 \times 10^6$		$< 1 \times 10^4$
Trimethyl Phosphate	$1.3 \times 10^5$	$< 4 \times 10^4$	$< 3 \times 10^3$
Dimethyl Phosphate	$7 \times 10^4$		

Although the sulfate radical reacted at a measurable rate with all the compounds, only upper limits could be obtained for the reactions of the two other radicals. The results indicated that both hydrogen abstraction and electron transfer reactions took place for the very strong oxidant  $\text{SO}_4^-$ , but that the reduction potentials of  $\text{CO}_3^-$  and  $\text{Cl}_2^-$  were not high enough to react with these phosphates and neither of these radicals had a strong propensity for hydrogen abstraction. The reactions of the two radicals,  $\text{CO}_3^-$  and  $\text{Cl}_2^-$ , were too slow for this degradation mechanism to be of importance in the environment.

## 6.6 VOLATILITY SCREEN

### 6.6.1 Extinguishant Volatility

For a chemical to be successful as a total flooding agent, it must evaporate and fill a space to the desired concentration within the time available for extinguishment. As determined by Pitts et al.<sup>86</sup>, and noted earlier in this chapter, if the boiling point of the fluid is below the ambient temperature, the dispensed fluid will flash and disperse rapidly. For fluids of higher boiling point, estimation of the capability to flood a volume entailed two determinations: (1) the equilibrium vapor pressure at the ambient temperature in the fire compartment and (2) the rate of evaporation to achieve that vapor pressure.

### 6.6.2 Extinguishant Evaporation Equilibrium

Estimation of whether a given compound can achieve the required extinguishment concentration upon discharge entailed a thermodynamic analysis.<sup>87</sup> The logarithm of the ratio of the vapor pressure ( $p$ ) at two different temperatures,  $T_2$  and  $T_1$  (in Kelvins), can be estimated from Equation 6-29, the Clausius-Clapeyron equation, where  $R$  is the ideal gas constant and  $\Delta H_{\text{vap}}$  is the heat of vaporization. This equation is based on the assumptions that (1)  $\Delta H_{\text{vap}}$  is temperature independent and (2) the vapor is an ideal gas. The ratio of  $\Delta H_{\text{vap}}/T_b$ , where  $T_b$  is the boiling point temperature, is equal to the molar entropy of vaporization  $\Delta S_{\text{vap}}$  at the boiling point. For closely related compounds,  $\Delta S_{\text{vap}}$  at the boiling point is nearly constant (Equation 6-30). Thus, by selecting  $T_1$  as the boiling point ( $T_b$ ) at  $p_1 = 101 \text{ kPa}$  (1 atm), one can estimate the vapor pressure at other temperatures.

$$\log_{10}(p_2/p_1) = (\Delta H_{\text{vap}} (T_2 - T_1) / 2.303 RT_2 T_1) \quad (6-29)$$

$$\Delta H_{\text{vap}}/T_b = \Delta S_{\text{vap}} \approx t_c \quad (6-30)$$

Combining the two equations for a boiling point,  $T_b$  (K), at a pressure,  $P_b$ , Equation 6-31 is obtained. Trouton's constant,  $t_c$  (J/K-mol), is a variable to be determined for a particular family of compounds.

$$p_2 = P_b 10^{(0.052) t_c [1 - (T_b/T_2)]} \quad (6-31)$$

For example, if  $t_c$  were equal to 88 J/K-mol, which holds for many compounds, then the estimated vapor pressure at 25 °C for a compound with a boiling point of  $T_b = 50 \text{ °C}$  at 101 kPa (1 atm) is 42 kPa. From vapor pressure values, the maximum possible volume % were estimated. These values are listed in Table 6-5. Similar tables can be prepared for other pressures.

The maximum allowable boiling point ( $T_b$ ) able to achieve a desired volume % of a chemical in air at a given ambient temperature,  $T_2$ , was then estimated. Equation 6-32 calculates values of  $T_b$  for temperatures in K,  $P_b$  in kPa, and  $t_c$  in J/K-mol. The calculated estimates in Table 6-6 are for a Trouton's constant of 88 J/K-mol. The results are shown graphically in Figure 6-34.

$$T_b = [1 - (\log(101 * C / 0.13 P_b) / 0.052 t_c)] T_2 \quad (6-32)$$

**Table 6–5. Estimated Equilibrium Vapor Pressure (Volume %) as a Function of Boiling Point and Ambient Temperature.** <sup>87</sup> [Trouton’s Constant = 88 J/K-mol; P = 101 kPa]

T <sub>b</sub> , °C	Ambient Temperature, °C												
	-60	-50	-40	-30	-20	-10	0	10	20	25	30	40	50
-60	100												
-50	61	100											
-40	37	62	100										
-30	23	39	64	100									
-20	14	24	40	65	100								
-10	8	15	26	42	66	100							
0	5	9	16	27	43	67	100						
10	3	6	10	18	29	45	68	100					
20	2	4	7	11	19	30	46	69	100				
30	1	2	4	7	12	20	31	47	70	84	100		
40	1	1	3	5	8	13	21	33	49	59	71	100	
50	0	1	2	3	5	9	14	22	34	41	50	71	100

**Table 6–6. Estimated Maximum Boiling Point That Can Achieve a Given Volume Percent of Chemical in Air.** <sup>87</sup>

Volume %	Ambient Temperature, °C												
	-60	-50	-40	-30	-20	-10	0	10	20	30	40	50	
1	33	47	61	76	90	105	119	133	148	162	176	191	
2	19	33	46	60	74	87	101	115	128	142	156	169	
3	11	24	37	51	64	77	91	104	117	130	144	157	
4	5	18	31	44	57	70	83	96	109	122	135	148	
5	0	13	26	39	52	65	77	90	103	116	129	142	

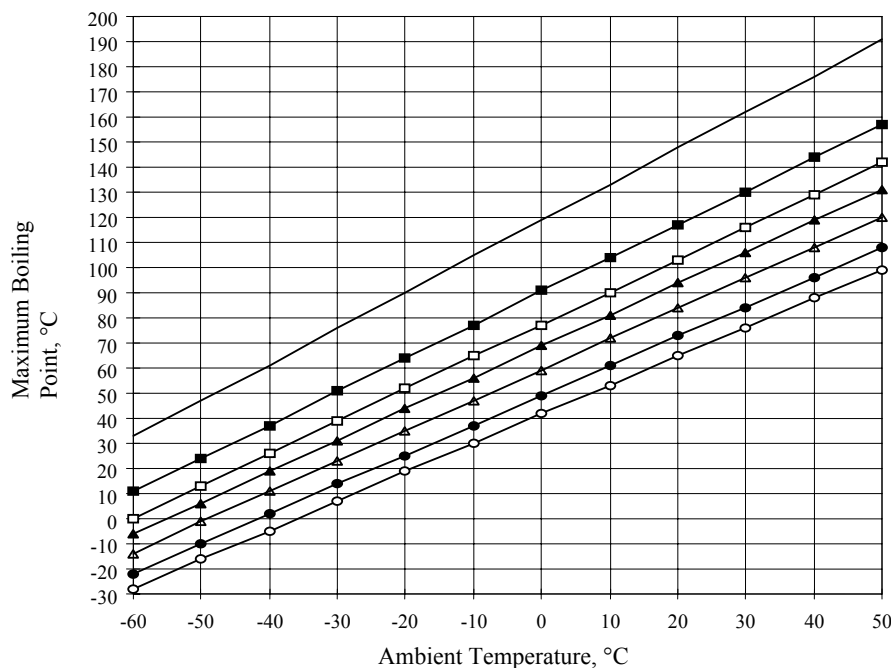


**Figure 6–34. Estimated Maximum Boiling Points That Can Achieve Selected Values of Volume % in Air as a Function of Ambient Temperature.** <sup>87</sup>  
 Top to Bottom:  
 1 %, 3 %, 5 %, 7 %, 10 %, 15 %, 20 %

### 6.6.3 Extinguishant Evaporation Rate

Estimation of evaporation rates is much more difficult than the calculation of equilibrium agent concentrations. The following is an overview of some of the factors that must be considered.<sup>87</sup>

In the simplest case, a spherical droplet of fire suppressant agent of radius,  $r$ , is ejected into stagnant, completely unsaturated air at a velocity,  $U_0$ . The rate of evaporation as a function of the droplet radius and the time for complete evaporation was of interest. It was assumed that the temperature of the droplet was the same as its surroundings, and that the temperature at the surface of the droplet did not change as the droplet evaporated. While neither of these conditions is generally true, considering temperature changes was too complex for a simple analysis. The following uses cgs units.

Fick's first law for one-dimensional diffusion relates the flux ( $J$  in  $\text{g/s}\cdot\text{cm}^2$ ) of a vapor through a gaseous medium to the concentration gradient  $dc/dx$ , where  $c$  is the agent concentration ( $\text{g/cm}^3$ ) and  $x$  is the direction of diffusion (Equation 6-33).

$$J = -D \frac{dc}{dr} \quad (6-33)$$

$D$ , the diffusion coefficient of the vapor in  $\text{cm}^2/\text{sec}$ , is a function of the agent and the ambient conditions. Kinetic theory shows that for ideal gases of density,  $\rho$ , of rigid spherical molecules having a molecular mass,  $m$ , and a diameter,  $\sigma$ , the diffusion coefficient is given by Equation 6-34, where  $k$  is the Boltzmann constant and  $T$  is the absolute temperature.<sup>88</sup>

$$D = \frac{3}{8} \frac{(\pi m k T)^{1/2}}{\pi \sigma^2 \rho} \quad (6-34)$$

Setting the density  $\rho = Pm/kT$ , one obtains Equation 6-35, which shows that the diffusion coefficient is proportional to  $T^{3/2}$  and inversely proportional to the pressure  $P$  for this idealized gas composed of hard-spheres. It is also inversely proportional to the square root of the molecular mass and to the square of the molecular diameter. Real gases, of course, show significant deviations from this relationship, which may be modified to take into account actual molecular interactions.

$$D = \frac{3}{8} \frac{(kT)^{3/2}}{\pi^{1/2} \sigma^2 P m^{1/2}} \quad (6-35)$$

Continuing to use the hard-sphere model, one can relate the diffusion coefficient to the coefficient of viscosity ( $\eta$ ,  $\text{g/cm}\cdot\text{s}$ ), the heat capacity per molecule ( $c_v$ ,  $\text{g}\cdot\text{cm}^2/\text{s}^2\cdot^\circ\text{C}$ ,  $= C_v/N_0$ , where  $N_0$  is Avogadro's number), and the coefficient of thermal conductivity ( $\lambda$ ,  $\text{g}\cdot\text{cm}/\text{s}^3\cdot^\circ\text{C}$ ) (Equations 6-36 and 6-37).

$$D = \frac{12\lambda m}{25\rho c_v} \quad (6-36)$$

$$D = \frac{6\eta}{5\rho} \quad (6-37)$$

Equation 6-33 was rewritten to give the diffusion mass transport through a spherical surface of radius  $r$  (Equation 6-38).

$$\frac{dm}{dt} = -4\pi r^2 \frac{dc}{dr} D \quad (6-38)$$

Equation 6-38 was used to determine the mass transport from the liquid/gas interface surrounding a spherical drop of radius  $r_0$  with a concentration of  $c_0$  to a region far from the drop ( $r_\infty$ ) with a vapor concentration  $c_\infty$ . Since  $dm/dt$ , the mass transport, is independent of  $r$ , integration of Equation 6-38 gives Equation 6-39. If  $r_\infty$  is very large and if  $c_\infty$  is taken as zero, Equation 6-40 results.

$$\frac{dm}{dt} \int_{r_0}^{r_\infty} \frac{dr}{r^2} = -4\pi D \int_{c_0}^{c_\infty} dc \quad (6-39)$$

$$\frac{dm}{dt} = 4\pi D \frac{c_0 - c_\infty}{(1/r_0 - 1/r_\infty)} \quad (6-40)$$

If  $r_4$  is taken as sufficiently large, Equation 6-40 can be rewritten to give Equation 6-41. Note that as  $c_\infty$  approaches  $c_0$  (the air becomes saturated), the rate of evaporation approaches zero.

$$\frac{dm}{dt} = 4\pi D r_0 (c_0 - c_\infty) \quad (6-41)$$

Equation 6-41 can be rewritten to give Equation 6-42.

$$\frac{dm}{dt} = \frac{4\pi r_0 D M (p_0 - p_\infty)}{RT} \quad (6-42)$$

where  $M$  = molecular weight of the vapor, and  $p_0$  and  $p_4$  are the partial pressures of the vapor at the surface of the droplet and at a distance infinitely far from the droplet. In the case of a fire suppressant agent, it was assumed that  $p_\infty$  is initially zero, since no agent has yet been released into the compartment. If  $c_\infty$  is zero, one obtains Equation 6-43.

$$\frac{dm}{dt} = 4\pi D r_0 c_0 \quad (6-43)$$

Equation 6-43 shows that the transport rate increases with drop size and with the concentration of agent at the liquid/vapor interface.

Performing estimates using this equation posed two problems. First, one must determine  $D$  for a real gas (rather than for the hard-sphere idealized gas discussed earlier). Second, and more difficult, one must determine the concentration of agent at the interface.

Since measured values of diffusivity were often not available, the only way to obtain values was to perform estimates based on available equations. Reference 89 lists several correlations for diffusivity. The lowest error was estimated to be from the Fuller-Chapman-Giddings equation, Equation 6-44.

$$D = \frac{0.1013 T^{1.75} \left( \frac{1}{M_1} + \frac{1}{M_2} \right)^{0.5}}{P \left[ \left( \sum v_1 \right)^{1/3} + \left( \sum v_2 \right)^{1/3} \right]^2} \quad (6-44)$$

Here,  $T$  is the temperature of gases in K,  $M_1$  is the molecular weight of the gas diffusing into the air,  $M_2$  is the molecular weight of the air,  $P$  is the pressure of the gases, and  $v_1$  and  $v_2$  are atomic diffusion volumes

which are given in tables. Unfortunately, atomic diffusion volumes are not available for the majority of compounds and must be estimated for many of the compounds of interest in fire suppression.

The question of motionless droplets is academic at best. Droplets of fire suppressant chemicals will be rapidly expelled through the nozzle to ensure complete coverage of the protected area or the fire as well as providing mechanical breakup to smaller droplet sizes. Any realistic evaluation of evaporation must include inertia, gravity, and other forces acting on the droplets. The rapid acceleration of the droplets also distorts the droplets; however, one usually assumes spherical droplets.

The problem quickly escalates from a simple diffusion mechanism to a heat and mass transfer mechanism; it reduces to the calculation of the rate of evaporation or heat transfer from a spherical body in a moving gas stream (in the case of interest, the droplet is in motion within stagnant air, but the mathematics are the same). Solutions to such problems rely on the use of dimensionless numbers such as Reynolds, Nusselt, Prandtl, and Schmidt numbers. The problem is complicated by the fact that flow may be either laminar or turbulent, depending on the value of the Reynolds number; heat and mass transfer are radically different in laminar and turbulent flow.

A simple correction to Equation 6-43 to allow for the increase in evaporation rate due to motion through air is where  $dm/dt$  equals the evaporation rate with flow around the droplet is equal to 0.276, Equation 6-45.

$$\frac{dm}{dt} = 4r\pi D(c_o - c_\infty)(1 + \beta Sc^{1/3} Re^{1/2}) = I_o f \quad (6-45)$$

(measured for a sphere),  $Re$  is the Reynolds number characterizing the flow of the air around the drop, and  $Sc$  is the Schmidt number. The term  $f$  is usually called the wind or ventilation factor. It is reported that Equation 6-45 accurately represents the evaporation rate of droplets in moving air.<sup>90</sup> For very small droplets falling in air,  $f$  is small, approaching 1; for larger droplets in moving streams,  $f$  can be rather large, reflecting the higher heat and mass transfer rates at higher velocity.

#### 6.6.4 Boiling Temperature

From this analysis, it became clear that the estimation of evaporation rates was far beyond the capability for screening candidate fire suppressants. Thus, the NGP utilized a compound's boiling point as the screen for volatility.

A chemical's boiling temperature is one of the most fundamental properties, and literature values were available for many of the compounds under consideration by the NGP. Yang and coworkers reported on the use of a software package to estimate boiling points.<sup>91</sup>

For those compounds that were custom synthesized for the NGP (see Chapter 7), frequently the supplier measured the boiling point.

For those instances where a measurement was needed, it was generally necessary that the measurement use very little sample. Available techniques for determinations involving higher boiling compounds include a microscale method<sup>92</sup>, based on determination of the temperature at which the pressure above the boiling liquid is large enough to overcome its vapor pressure in an inverted capillary tube. This method

typically employs a melting point apparatus and melting point capillary tubes. Boiling point determination methods applicable to low boiling compounds include the vapor pressure based isoteniscope method.<sup>93</sup> Both methods are applicable to very small samples.

## 6.7 TOXICITY SCREEN

### 6.7.1 Hazards and Regulation

There are a variety of acute toxic effects that can result from exposure to a fire suppressant chemical. These include sensory irritation, incapacitation, or even death. The NGP was concerned with the full range of such effects.

It has been recognized for decades that a principal toxic effect of halocarbon agents is cardiac sensitization.<sup>94,vii</sup> This is the sudden onset of cardiac arrhythmia caused by a chemical sensitization of the heart to epinephrine (adrenaline). Cardiac sensitization is a particularly important concern in fires because under the stress of the fire event, or even an accidental discharge of a fire suppressant, higher levels of epinephrine are secreted in the body, increasing the possibility of sensitization. Since the current firefighting halons and most replacement chemicals were halocarbons, most (but not all) of the NGP screening effort focused on this toxic effect.

Under the EPA SNAP Program,<sup>4</sup> cardiac sensitization values helped define the use restrictions placed on a replacement chemical. For example, when using halon substitutes as total flooding agents, the following conditions, which were adopted from an OSHA safety and health standard (29 CFR 1910 Subpart L), generally applied:

- Where egress from a normally occupied area cannot be accomplished within 1 min, the employer shall not use the agent in concentrations exceeding its NOAEL.<sup>viii</sup>
- Where egress from a normally occupied area takes longer than 30 s but less than 1 min, the employer shall not use the agent in a concentration greater than its LOAEL.<sup>ix</sup>
- Agent concentrations greater than the LOAEL are only permitted in areas not normally occupied by employees provided that any employee in the area can escape within 30 s. The employer shall assure that no unprotected employees enter the area during agent discharge.

There were no regulatory guidelines for conducting a cardiac sensitization study. However, the procedure most often followed for evaluating exposure to agents that might potentially evoke a cardiac sensitization response was the test performed using beagle dogs.<sup>95</sup> In this procedure, an intravenous dose of epinephrine was administered to each dog to establish its cardiac response to an epinephrine challenge alone. The dogs were monitored continually for electrocardiographic changes indicative of the appearance of ventricular fibrillation. The doses were increased from 1 µg per kg of body weight toward 12 µg/kg in steps of 0.1 ml/kg. After a recovery period, the dog was exposed to a selected concentration of the candidate suppressant. At 5 min into the exposure, the dog was injected with an epinephrine dose

---

<sup>vii</sup> See section 6.7.8 for screening for other acute toxic effects.

<sup>viii</sup> NOAEL, the "no observed acute exposure level," is the highest concentration at which no adverse toxicological or physiological effect was observed.

<sup>ix</sup> LOAEL, the "lowest observed acute exposure level, is the lowest concentration at which an adverse toxicological or physiological effect was observed.

just below the value that caused cardiac arrhythmia by itself. It was noted whether the dog experiences a response or not. Exposures at different suppressant concentrations were performed until the onset of an effect was bracketed to the desired precision. The results of this test are expressed in terms of the LOAEL and the NOAEL. The separation of these values was a function of the step size in suppressant concentration used for the cardiac sensitization test. The expense of the test often prevented a small increment from being used.

LOAEL data obtained from the dog-based cardiac sensitization testing are very conservative and, perhaps as a direct result, very rarely have people died as a result of exposure to the halons. The dog-based standard seems to be achieving exactly what it was designed to achieve – ensuring a wide margin of safety to a broad spectrum of end users.

### 6.7.2 Screening Process

The 1997 NGP Workshop on Fire Suppressant Compatibility with People, Materials, and the Environment developed a preferred protocol for obtaining indicative data regarding the various toxic possible effects of candidate agents.<sup>2</sup> The participants noted that there was no checklist to be used in a "cookbook" fashion. Expert judgment was needed to interpret the results of each test and decide what, if any, additional testing was necessary to evaluate the health effects of new agents. The progression of steps they endorsed was:

1. use published values,
2. derive values from quantitative structure-activity relationships (QSARs),
3. conduct non-animal biological tests, and
4. conduct live animal tests.

The steps involve successively more time, cost, and agent. The report on the Workshop contains extensive references to resources for performing the steps.

A protocol containing an even more comprehensive set of toxicity tests was developed by Dodd and co-workers.<sup>96</sup> This included tests for genotoxicity, subchronic toxicity, carcinogenicity, development and reproductive toxicity, among others. However, the NGP identified no compounds that progressed to that level of testing.

With regard to cardiotoxicity, performing the dog exposure tests was not feasible for the large number of chemicals under consideration by the NGP. Only a few laboratories in the world have the equipment and the expertise. Completing the testing takes about two months. The testing cost per chemical is currently approaching \$100 k. The test requires about 30 moles of the test chemical, which generally would have needed to be custom-synthesized. Nonetheless, for the safety of personnel and for obtaining regulatory approval, estimating the cardiac sensitization LOAEL for a candidate fire suppressant was important.

Hence, the NGP conducted an extensive review to identify methods to aid in the selection of compounds with a higher probability of acceptable LOAEL and NOAEL values when actually tested. While any estimation method enabling a ranking of compounds would facilitate compound acquisition efforts, it was felt that the accuracy of the absolute LOAEL values needed to be within 2 volume % for the method to be of much use in final compound selection.

Halogenated compounds have found a variety of uses beyond fire suppression. Cardiac sensitization has surfaced as a consideration in the development of propellants for medical inhalers, it has been observed as a cause of cardiac arrest in substance abuse by inhalation of solvents used in spray paints and hairsprays, and it has occurred in the use of some pharmaceuticals and surgical anesthetics. Thus, there was significant background material to be searched for the current purpose.

At the time of the completion of the NGP, no accurate screening procedure existed to obviate the need for the standard dog exposure test. In fact, such testing of two otherwise promising chemicals generated negative results (Chapter 7). Sections 6.7.3 through 6.7.6 summarize the NGP investigation process.

### 6.7.3 Literature Values

A useful starting place for assessing the toxic properties of a candidate fire suppressant was a compendium of health and safety or toxicological data on chemicals, such as Reference 97. A number of databases also existed, both computerized and non-computerized, which were helpful in determining known toxic properties of a chemical, a set of chemicals, or even a chemical class:

- The Chemical Abstract Services (CAS) ONLINE (<http://info.cas.org/>) database was a pay-for-services, informational compendium of thousands of substances, which included information on chemical and physical properties, structures, synonyms, and in some cases, toxicity values.
- The National Library of Medicine site called MEDLARS (<http://toxnet.nlm.nih.gov>). MEDLARS contained a number of specific databanks including the Registry of Toxic Effects of Chemical Substances (RTECS), Hazardous Substance Databank (HSDB), the Integrated Risk Information System (IRIS), the Genetic Toxicology (Mutagenicity) Database (GENE-TOX), and the Chemical Carcinogenesis Research Information System (CCRIS).
- The National Library of Medicine (NLM) also had a number of other citation databases such as TOXLINE, MEDLINE, or CANCERLIT containing abstracted literature information on various aspects of toxicology. The NLM databases could be accessed free via the Internet (<http://igm-01.nlm.nih.gov/index.html>).
- RTECS was a comprehensive online database developed by the National Institute of Occupational Safety and Health (NIOSH) for the purpose of collecting, collating, and disseminating toxic effects information for “all known toxic substances,” which were considered to be potentially all known chemicals that can elicit abnormal biological effects.
- The Merck Index (<http://www.dupontmerck.com>) contained physical and toxicity data from published literature sources. The Index was free, but limited to only a select few single substances.
- The Environmental Protection Agency’s Office of Pollution Prevention and Toxics holds the Toxic Release Inventory (<http://www.epa.gov/opptintr/tri/>), which was a valuable free source of information about toxic chemicals that were being used, manufactured, treated, transported, or released into the environment.
- The EPA’s GENE-TOX data bank compiled information on mutagenicity and carcinogenicity for several thousand chemicals (found through the MEDLARS online site) and the International Agency for Research on Cancer (IARC) (<http://www.iarc.fr/pub/publist.htm>) published for-fee monographs reviewing the carcinogenic potential of certain chemicals.

- The National Technical Information Service (NTIS) covered government-sponsored research and development efforts and some work may contain toxicological information. Searches for reports could be performed free of charge, but the actual documents could only be obtained for a fee (<http://www.ntis.gov/search.htm>).

For screening purposes, the literature examination was directed at finding any severe toxic effects that occurred at exposures of up to concentrations of the order of 5 volume % for several minutes. If there was insufficient information regarding the specific chemical under consideration, chemically similar compounds were examined.

Table 6–7, Table 6–8, and Table 6–9 list published NOAEL and LOAEL values for members of different families of halocarbons. These data enabled some preliminary insights:

- There were a wide range of values among and within the chemical families.
- The limited data for partially fluorinated methanes (Table 6–7, compounds 6 and 7) demonstrated a relatively low tendency to induce cardiac sensitization.
- The three hydrofluoropropanes (Table 6–7, compounds 3 through 5) showed a wide range of LOAEL values with no obvious correlation with the degree of fluorination. There may be a relationship with the location of the hydrogen atoms, both with this family and the hydrofluoroethanes (compounds 8 through 11).
- In Table 6–8, an iodine atom appeared to lead to a low LOAEL value.
- Many CFCs and HCFCs, which are closely related to the halons, were cardiotoxins.<sup>98</sup> Table 6–9 gives little or no indication of relationships between degree of fluorination or chlorination (or hydrogenation) and LOAEL values. While the highly fluorinated compound,  $\text{CF}_3\text{CF}_2\text{Cl}$ , was notable for its unusually high LOAEL of 15 volume % most values ranged from a low of 0.5 volume % to a more nominal high of 5 volume %.

**Table 6–7. Cardiac Sensitization Values for Fluorocarbons and Hydrofluorocarbons.**

#	Chemical Formula	NOAEL (vol. %)	LOAEL (vol. %)	Reference
1	$\text{CF}_3\text{CF}_2\text{CF}_2\text{CF}_3$	40	>40	99
2	$\text{CF}_3\text{CF}_2\text{CF}_3$	30	>30	62
3	$\text{CF}_3\text{CHFCHF}_2$	2.5	3.5	100
4	$\text{CF}_3\text{CHFCF}_3$	9	10.5	99
5	$\text{CF}_3\text{CH}_2\text{CF}_3$	10	15	99
6	$\text{CH}_2\text{F}_2$	20	25	61
7	$\text{CHF}_3$	30	>50	99
8	$\text{CH}_2\text{FCF}_3$	4	8	61
9	$\text{CH}_3\text{CF}_3$	4	8	62
10	$\text{CHF}_2\text{CF}_3$	7.5	10	99
11	$\text{CH}_3\text{CF}_2\text{H}$	5	15	95

**Table 6–8. Cardiac Sensitization Values for Br-, Cl-, and I-containing Alkanes.**

#	Chemical Formula	NOAEL (vol. %)	LOAEL (vol. %)	Reference
1	CF <sub>3</sub> I	0.2	0.4	101
2	CF <sub>3</sub> Br	5.0	7.5	99
3	CF <sub>2</sub> HBr	2	3.9	99
4	CF <sub>2</sub> BrCl	0.5	1.0	102
5	CF <sub>2</sub> BrCF <sub>2</sub> Br	-	0.1	103
6	CBrClFCBrF <sub>2</sub>		0.5	103
7	CF <sub>3</sub> CF <sub>2</sub> CF <sub>2</sub> I	-	0.1	104

**Table 6–9. Cardiac Sensitization Values for CFCs and HFCs.**

#	Chemical Formula	NOAEL (vol. %)	LOAEL (vol. %)	Reference
1	CF <sub>2</sub> ClH	2.5	5	61
2	CF <sub>2</sub> Cl <sub>2</sub>	2.5	5	95
3	CFCl <sub>3</sub>	-	0.5	105
4	CH <sub>2</sub> =CClH	2.5	5	95
5	CCl <sub>3</sub> CH <sub>3</sub>	0.25	0.5	95
6	CF <sub>2</sub> ClCH <sub>3</sub>	2.5	5	95
7	CFCl <sub>2</sub> CH <sub>3</sub>	-	0.5	106
8	CF <sub>3</sub> CF <sub>2</sub> Cl	-	15	95
9	CF <sub>3</sub> CCl <sub>2</sub> H	1	2	61
10	CFCl <sub>2</sub> CH <sub>3</sub>	-	1	106
11	CF <sub>2</sub> ClCF <sub>2</sub> Cl	-	2.5	95
12	CClF <sub>2</sub> CFCl <sub>2</sub>	0.25	0.5	95
13	CF <sub>2</sub> ClCF <sub>2</sub> CFHCl	-	2.0	107

#### 6.7.4 Quantitative Structure Activity Relationships

Quantitative structure-activity relationships (QSARs), based on scientific judgment by experienced scientists, may be used as an integral part of health hazard characterization. This approach relies on the toxicologist or chemist being able to fit the new chemical into a category of existing chemicals because of similarities in molecular structure or chemical functionality. In order for this approach to be of value, the existing chemicals category or close structural analog must have its own robust toxicology database and the uncertainty of read-across from the close structural analogs or the category to the new chemical must be recognized and, if possible, defined.

Skaggs et al. performed an extensive review of toxicity prediction and screening approaches, identifying chemical attributes employed in the development of QSARs, predictors of relationships between biological activity and chemical properties.<sup>108</sup> The descriptor types included:

- Hydrophobicity, a measure of water insolubility. Neutral, unreactive chemicals exhibit a strong relationship between the hydrophobicity of the compound and its LC<sub>50</sub>. Hydrophobicity is equated to the octanol-water partition coefficient and reflects the ability of a chemical to cross a biological membrane and correlates with toxicity because diffusion through cell walls allows chemicals to influence internal cellular processes and biochemistry. Both the Hammett Constant and the Taft Polar Substituent Constants are measures of

substituent polarity. Steric properties relate to molecular structure and affect the binding of molecules to biological sites.

- Molecular connectivity descriptors describe the number of atoms in a compound and their formally-bonded and spatial relationships. Molecular Connectivity Indices (MCI) associate numerical values with structure of the molecule. Many properties are directly related to the number and connections of atoms in molecules.<sup>109</sup> Molecular connectivity describes structural information and relates to physical properties.
- Linear Solvation Energy Relationship (LSER) analysis is based on the correlation of diverse chemical properties, including toxicity and solvent-solute interactions. The analysis is based on four molecular parameters: intrinsic molecular volume, polarity, and two measures of ability to hydrogen bond as an acceptor or donor. While this measure provides the most accurate QSARs covering the widest range of chemical classes, the parameters are available on only a finite amount of chemicals.<sup>110</sup>
- Molecular connectivity QSARs require that indices based on structure be determined, and generally the amount of data needed is less than that for quantitative property-activity relationships (QPAR). In both cases, sufficient toxicity data must be available with which to develop correlations capable of providing toxicity estimates of unknown substances. These data are not available in the required abundance to perform highly reliable assessments across a broad range of compounds.

Skaggs et al. reported that the key to using any of these techniques was to determine a family of chemicals for which biological indices (for example, LD<sub>50</sub>), as well as physical/chemical properties, molecular structure, or both, are known.<sup>108</sup> In actual QSAR modeling, these sets of data are referred to as “training sets.” By the use of statistical techniques such as multiple regression analysis (MRA), a relationship between the biological indices and property/molecular structure is determined based on the “training set” data. The better or more extensive the training set the more the predictions are apt to be accurate.<sup>111</sup>

Vinegar<sup>112</sup> has extracted some general, but not universal, toxicity trends that have been used to provide a relative toxicity ranking for the candidate compounds and compound groups:

- Toxicity Ranking Criteria
  - Aromatics are more toxic than aliphatics.
  - Asymmetric molecules are more toxic than symmetric molecules.
  - Straight (carbon) chains are more toxic than branched.
  - Ethers are more toxic than alkanes.
  - Short chain ethers are more toxic than long chain ethers.
  - Vinyl ethers are more toxic than saturated ethers.
  - Polyoxyethers are more toxic than monoethers.
- Cardiac Sensitization Ranking Criteria
  - Halogen presence is more potent than hydrogen.
  - Bromine presence is more potent than fluorine presence.
  - Iodine presence is more potent than bromine presence.

QSAR analysis has been formalized and computerized for some health endpoints (e.g., cancer, mutagenicity, and teratogenicity) and may be useful with appropriate recognition of the limitations of these programs. Evaluation of the computerized QSAR programs available commercially has been the subject of a review.<sup>113</sup> The U.S. EPA has grouped chemical substances with similar physical-chemical, structural and toxicological properties into working categories. These groupings enable the user of the NCP Chemical Categories guidance document to benefit from the accumulated data and decisional precedents within EPA's new chemicals review process since 1987, in order to identify areas of health hazard concern. There were 51 chemical categories listed in the table of contents of the EPA document, the detailed summaries of which may be found at: <http://www.epa.gov/opptintr/newchms/chemcat.htm>.

Multiple investigators have developed numerous QSARs to predict the toxicity of chemicals, as indicated in Table 6–10, taken from Reference 2.

**Table 6–10. Availability of QSARs for Various Chemical Classes and Toxic Endpoints.**<sup>2</sup>

Chemical Class	Functional Group	Possible Toxicity Endpoints	References
Alcohols	-C-OH	Irritation	114, 115, 116, 117
Aldehydes and Acetals	> C = O	Irritation, Sensitization, Anesthesia, Mutagenicity and Carcinogenicity	114, 118
Allyl compounds	H <sub>2</sub> C=CH-R	Liver Toxicity, Kidney Toxicity, Neurotoxicity, Sensitization, Carcinogenicity	119
Amides	-CONH <sub>2</sub>	Irritation, and liver, kidney and brain toxicity	120, 121, 122, 123, 124, 125, 126, 127, 128
Amines		Cholinesterase Inhibition, Carcinogenicity	114, 129, 130, 131, 132, 133, 134, 135, 136
Azides	-N <sub>3</sub>	Cardiovascular actions and enzyme inhibition	137
Bromides	Inorganic and organic bromides	Neurotoxicity, Irritation, Hepatotoxicity, Cardiotoxicity	138, 139, 142
Chlorinated Hydrocarbons	Cl-C-R	Carcinogenicity, Anesthesia, Hepatotoxicity	140, 141, 142, 143, 144, 145, 146, 147, 148
Epoxy Compounds		Irritation, Mutagenicity, Neurotoxicity, Hepatotoxicity, Kidney Toxicity, Embryotoxicity	119, 149, 150, 151, 152,
Esters	RCOOR'	Asphyxiants, Narcotics, Irritants	138, 153, 154, 155, 156
Ethers	R-C-O-R'	Anesthesia, Cardiotoxicity, Irritation, Carcinogenicity	157, 139, 158, 159, 160, 161
Ketones	RCOR'	Anesthesia	114, 118, 123, 155, 162, 163, 164
Nitro, Nitrate, and Nitrite	-NO <sub>x</sub>	Irritation, Neuromuscular Dysfunction, Hepatotoxicity, Cardiotoxicity, Mutagenicity, Carcinogenicity	139, 165, 166
Nitroso compounds	C-N=O or N-N=O	Carcinogenicity, Mutagenicity, Teratogenicity	167
Phosphorus compounds		Anesthesia, Cholinesterase Inhibition, GI Dysfunction, Irritation, Neurotoxicity, Kidney Toxicity, Hepatotoxicity, Teratogenicity, Reproductive Toxicity	129, 153, 168
Sulfur Compounds		Irritation, Corrosivity, Cardiotoxicity, Neurotoxicity	138, 124, 126, 139, 128

Because the predictive capabilities of QSARs are based on the quality of the data used in their development and an understanding of the mechanisms of toxicity, these techniques can sometimes be unreliable and should not be the sole criterion for screening decisions. The basic principles behind QSAR technology are well documented and can apply to any class of chemical and any measurable end point.<sup>169</sup>

Several texts describe the basics of QSAR techniques,<sup>170</sup> but briefly, QSARs involve taking a sufficiently large, consistent data set and correlating it with known descriptors of the chemicals within the data set. The correlation techniques are principally multivariate regression and discriminant analysis for weighting descriptors.<sup>171</sup> This leads to a mathematical expression, whereby endpoint data can be predicted for chemicals with known descriptors. For example, one can use a data set of lethal concentration values (e.g.,  $LC_{50}$ )<sup>x</sup> for halogenated hydrocarbons and correlate these values with certain physico-chemical descriptors such as numbers or type of halogens, vapor pressures, and/or octanol-water partition coefficients. The resulting mathematical equation would allow one to calculate the lethal concentration for a new halogenated hydrocarbon knowing only the physico-chemical descriptors for that particular chemical. Several of these approaches have been employed in the search for clean fire suppressants.<sup>172,173</sup>

### 6.7.5 Non-animal Laboratory Testing

#### The Case for Octanol-Water Partition Coefficients

There is some evidence to support a relationship between the tendency of a chemical toward cardiac sensitization and its relative solubility in polar and non-polar liquids.<sup>174</sup> However, the actual mechanism is not yet fully understood.

Frazier reported that some researchers had concluded that cardiac sensitization is a direct result of a physical-chemical interaction of the sensitizing agent with heart cell membrane structures.<sup>175</sup> This mechanistic hypothesis was derived from the observation that a critical blood concentration of agent is needed to elicit a cardiac sensitization response and the effects are immediately reversible, if they are not sufficiently severe to cause death, when the sensitizing agent is removed. Below that critical concentration, the effect does not occur.

Clark and Tinston had reported a possible correlation of cardiac sensitizing potentials of halogenated and some non-halogenated chemicals with selected physiochemical properties.<sup>176</sup> Based on the data in Table 6–11, they suggested that the effect was not a chemical (reactivity based) toxicity but instead a generalized physical property effect that just happened to cause cardiac arrhythmia when sufficient chemical “occupied a constant fraction of the critical biophase,” i.e., was absorbed into heart nerve and muscle cells membranes. For the tested chemicals in the table, the  $EC_{50}$  (volume % of chemical that has an effect, E, on half of the test animals) and vapor pressure at 37 °C data appear to correlate. This hypothesis suggested that if a chemical were preferentially soluble in a barely polar liquid, such as octanol, and less soluble in a polar fluid, such as water, it would be less likely to be flushed from the tissue environment.

---

<sup>x</sup>  $LC_{50}$  (or similar terms indicating various toxicological endpoints) denotes the concentration of a toxic gas statistically calculated from concentration-response data to produce lethality in 50 % of the test animals within a specified exposure and post-exposure time

Tanner et al.<sup>177</sup> provided support for this polarity effect. Using differential scanning calorimetry, they showed that the inhalation anesthetic agent halothane ( $\text{CF}_3\text{CHClBr}$ ) destabilized some proteins in aqueous solution with respect to thermal unfolding, presumably due to halothane binding to the native folded state. Low (millimolar) concentrations of halothane produced significant destabilization of proteins, and they concluded that destabilization of proteins by halothane could be attributed to mainly hydrophobic interactions of halothane with the proteins.

There was further information on the phenomenon of cardiac sensitization from the fields of surgical anesthesia agents and pharmaceutical development. While the published literature was abundant in the former area, not surprisingly, little was found describing the approaches and methods employed by major pharmaceutical companies in their drug development research related to avoiding cardiac sensitizing or arrhythmia inducing drugs.

Anesthesia was an active area of research, with considerable published data on the influence of various compounds on human systems.<sup>178</sup> These studies included data on the relative tendencies of a wide range of current and former anesthesia agents to induce cardiac arrhythmia as well as comparison molecular property data, toxicity information, and models for agent uptake to target tissues. Reviews covering cell membrane ion gate channel effects and the effects of molecular structure were found in studies of pharmacokinetics and molecular physiology.<sup>179, 180</sup> The data presented relate uptake of anesthesia agents and physical properties, such as blood gas ratios (partitioning) of the anesthesia agent based on relative solubility in the two media.

**Table 6–11. Air Concentration Inducing Cardiac Sensitization in 50 % of Animals.**<sup>176</sup>

Compound	Volume % at EC <sub>50</sub>	Partial Pressure at EC <sub>50</sub> , kPa	Vapor Pressure at 37 °C, kPa	Relative Saturation for Cardiac Sensitization
$\text{CCl}_4$	0.53	0.53	25	0.02
$\text{CH}_3\text{CCl}_3$	0.75	0.76	28	0.03
$\text{CCl}_2\text{FCF}_2\text{Cl}$	1.0	1.0	70	0.02
$\text{CFCl}_3$	1.3	1.3	158	0.02
$\text{CF}_3\text{CHClBr}$	2.0	2.0	64	0.01
$\text{CH}_2\text{Cl}_2$	2.4	2.4	88	0.03
$\text{CHFCl}_2$	2.5	2.5	273	0.03
$\text{CH}_2=\text{CHCl}$	5.1	5.1	560	0.01
$\text{CF}_2\text{Cl}_2$	8.1	8.2	900	0.01
$\text{CF}_2\text{ClCF}_2\text{Cl}$	10.0	10.1	307	0.01
$\text{CH}_3\text{CH}_2\text{CH}_3$	20	20	1270	0.03
$\text{CF}_3\text{Br}$	20	20	2030	0.01
$\text{CF}_3\text{Cl}$	80	81	5410	0.01

Evidence for some of the effects of general (volatile) anesthetics on membranes and membrane ion channels were described in terms of a protein binding mechanism.<sup>181</sup> However, this interpretation did not account for the lack of demonstrated differential anesthetic effects of the two stereoisomers (R and S) of isoflurane. The R and S stereoisomers of isoflurane would be predicted to bind quite differently to stereospecific protein sites, yielding marked differences in the relative abilities of the R and S forms of

isoflurane to induce anesthesia. Investigation of the effects of volatile anesthesia agent on voltage gated ion channels was also ongoing and provided evidence for their inhibition of voltage-gated ion channels and to a greater extent on ligand-gated ion channels.<sup>181</sup> These same researchers reported that “we can summarize these findings with the generalization that volatile anesthetics had high-efficacy on ligand-gated ion channels, whereas they had relatively low potency and high efficacy effects on voltage-gated ion channels.” While these observations did not conclusively or perhaps significantly further the identification of one particular mode of interaction they related to the search for cardiac sensitization screening methods, they did provide insight to both the status of current investigations into the interaction of volatile halocarbons and cell membranes.

Anesthesia agents are not unlike halons in elemental composition. Anesthesia agents are represented by lower molecular weight brominated and chlorinated hydrofluoroalkanes and ethers. Some are chlorinated fluorocarbons. Of potential use were studies of the minimum alveolar concentration (MAC) values determined for anesthesia agents<sup>181,182</sup> and clinical observations of the tendency of volatile anesthetics to induce cardiac arrhythmia or premature ventricular contractions (PVCs).<sup>183</sup>

Table 6–12 combines these physiological effects with the hypothesis of Clark and Tinston. These data indicated a potential correlation between the tendency of a compound to induce PVCs and its log( $K_{ow}$ ) value.

Octanol-water partition coefficients have also been used in QSAR analysis and rational drug design as a measure of molecular hydrophobicity and are key parameters in studies of the environmental fate of chemicals. This was because the degree of hydrophobicity of a compound was known to affect its drug absorption, bioavailability, hydrophobic drug-receptor interactions, metabolism of a compound, and toxicity.

Given the compositional and molecular similarities between anesthesia agents and many of the current halon replacement compounds of interest as well as the reports reviewed above linking a compounds hydrophobicity to toxicity, cardiac arrhythmia, protein interaction effects measures of hydrophobicity seemed a clear strong choice for further evaluation and study as potential screening methods for cardiac sensitization. The possibility of a near term screening method based on the comparative hydrophobicities of the candidate compounds seemed worthy of further investigation.

**Table 6–12. Partitioning ( $K_{ow}$ ) and Arrhythmia Properties of Selected Anesthetics.**<sup>184,185</sup>

Property	Halothane	Enflurane	Isoflurane	Desflurane	Sevoflurane
Blood-gas Ratio <sup>a</sup>	2.5	1.9	1.4	0.42	0.6
Oil-water Ratio <sup>b</sup>	220	120	170	19	55
Arrhythmia <sup>c</sup>	+++	+	+	~	~
MAC <sup>d</sup>	0.74 %	1.68 %	1.15 %	6.3 %	2.0 %

a Ratio of the anesthesia agent concentration in the blood over the anesthesia agent concentration in the gas phase. High values indicate more effective transport of the chemical throughout the body and thus to cardiac tissue.

b The "oil" phase is commonly, but not exclusively, octanol.

c The symbols "+++", "+", and "~" reflect, in order, a decreasing tendency of the anesthetic to induce PVCs in human patients during anesthesia. The last of these indicates only a slight tendency. Halothane is notable for its greater tendency to induce PVCs than the other anesthesia agents listed.

d Minimum Alveolar (air) Concentration (MAC) for an anesthesia agent is a measure of the anesthetic potency of the compound, i.e., the air concentration required to immobilize 50 % of patients such that they don't give a motor response to a pain stimulus.

## Measurement of $K_{OW}$

Experimental determination of the octanol-water partition coefficient,  $K_{OW}$ , using reverse phase high pressure liquid chromatography, is rapid and requires only a few mg of the compound.<sup>174</sup> The measured property is the equilibrium constant for the concentrations of the chemical in the two liquids. Referencing the retention times on the chromatographic column of compounds for which  $K_{OW}$  values are known establishes a basis for obtaining partition coefficients for candidate fire suppressants.

## Calculation of $K_{OW}$

Values of  $K_{OW}$  were estimated from the contributions of molecular fragment-based terms plus correction factors.<sup>186</sup> Different algorithms can give different results, so experience was needed to select or develop an appropriate version for the particular chemicals under consideration. Two of the most commonly used algorithms were from Molinspiration Cheminformatics (<http://www.molinspiration.com>) and Syracuse Research Corporation (<http://esc.syrres.com>).

Octanol-water partition coefficients were calculated for the difluorinated bromopropenes using these two molecular fragment contribution-based methods and plotted in Figure 6–35. For this family of compounds, the two methods were in good agreement. Interestingly, the highest  $\log(K_{OW})$  value calculated for this series was for  $\text{CH}_2=\text{CHCF}_2\text{Br}$ , which proved highly toxic in inhalation toxicity tests.<sup>187</sup>

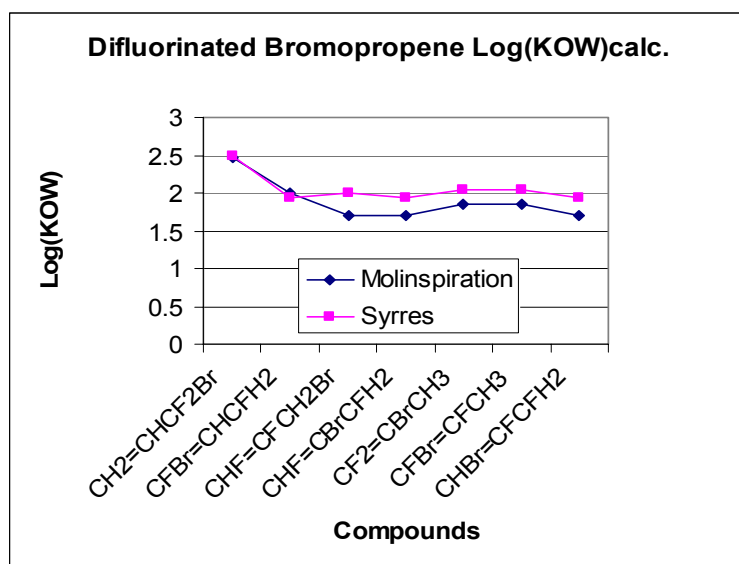


**Figure 6–35. Comparison of Two Difluorobromopropene Log( $K_{OW}$ ) Calculation Methods.**<sup>174</sup>

Octanol-water partition coefficients were also calculated for the trifluorinated bromopropenes using the two methods (Figure 6–36). The plotted data points (line connecting data points from same method calculation) were also roughly comparable.

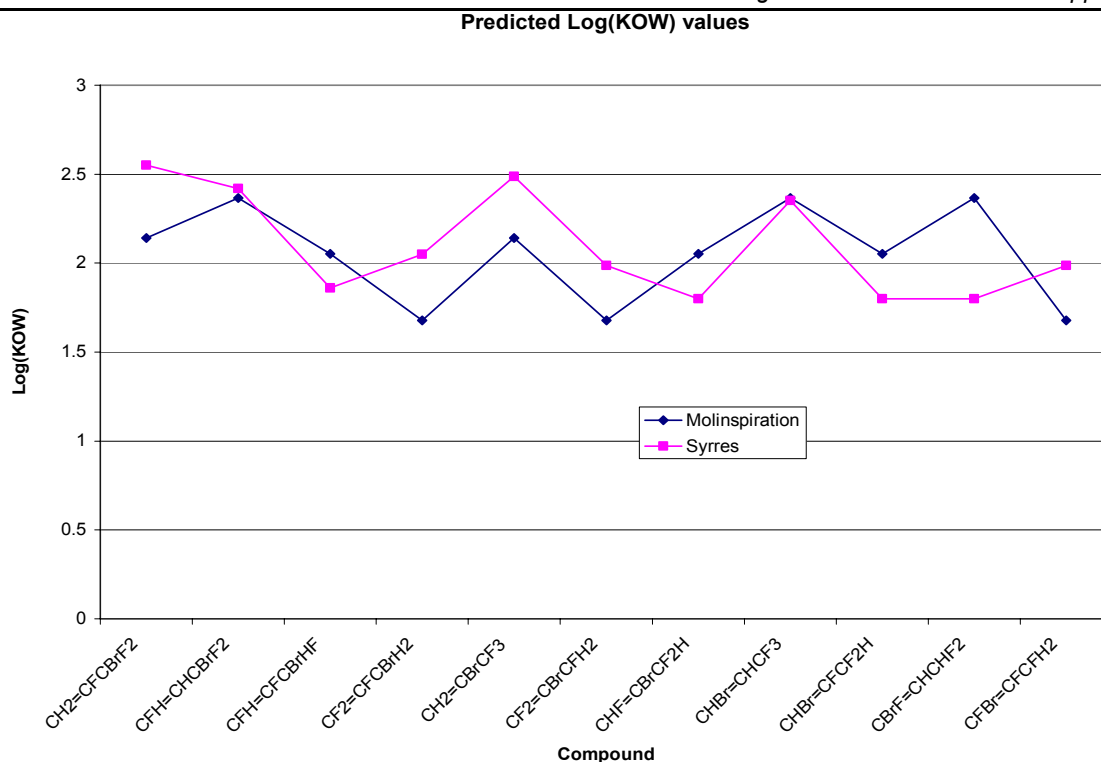


**Figure 6-36. Comparison of Two Trifluorobromopropene Log(K<sub>OW</sub>) Calculation Methods.**<sup>174</sup>

An indication of the disparity as well as trends in the predicted values for the two calculation methods can be seen in Table 6-13.

**Table 6-13. Comparison of Calculated and Measured Values of Log K<sub>OW</sub> of Selected Halocarbons.**<sup>174</sup>

Compound	Log K <sub>OW</sub> * (calculated)	Log K <sub>OW</sub> ** (calculated)	Log K <sub>OW</sub> (measured)	LOAEL (volume %)
CF <sub>3</sub> Br (halon 1301)	1.83	1.59	1.86	7.4
CHBrF <sub>2</sub>	1.85	0.98	NA	3.9
CH <sub>2</sub> =CBrCF <sub>3</sub>	2.14	2.49	NA	1.0
CF <sub>2</sub> ClBr (halon 1211)	2.17	1.90	2.1	1.0
CF <sub>3</sub> I	2.22	2.01	NA	0.4
C <sub>3</sub> HF <sub>7</sub>	2.35			10.5

\* Molinspiration Cheminformatics algorithm

\*\* Syracuse Research Corporation algorithm

It is probable that the use of calculated partition coefficient values to develop predictions of trends in LOAEL performance works best when only applied to narrowly defined groups of compounds (for instance, bromofluoroalkenes) and even then only used as a tentative predictor of LOAEL value. This limitation is demonstrated by the last line of Table 6-13. The calculated log K<sub>OW</sub> value for C<sub>3</sub>HF<sub>7</sub> suggests a LOAEL lower than that any of the other compounds, which is clearly not the case.

Another potential shortcoming of the available calculations is that they do not recognize or differentiate between the cis and trans structural isomers of compounds, such as the 1-bromo-3,3,3-trifluoropropenes

and the 3-bromo-1,3,3-trifluoropropenes. There were no experimental data to establish the actual differences between such isomers.

### 6.7.6 *In Vitro* Tests

A wide range of *in vitro* methods has been developed for specific toxic endpoints, including acute lethality, mutagenicity, anesthesia, kidney toxicity, hepatotoxicity, and teratogenicity.<sup>2</sup> These methods commonly use perfused organ preparations, isolated tissue preparations, single cell suspensions, or tissue culture systems. Upon exposure to the test chemical, the specific response can vary from one species to the next. Thus, preparations should be derived from species that respond to the chemical challenge in ways which are similar to humans. Furthermore, caution should always be exercised when utilizing *in vitro* techniques during the screening process because many factors, such as absorption and transport processes, influence the toxicity of a chemical. Thus, it was not deemed wise to rule out further consideration of a candidate based exclusively on the results of a single *in vitro* test.

The development of an *in vitro* cardiac sensitization screening method requires the development and validation of a system that retains the essential components of the process of cardiac sensitization. Identified requirements<sup>175</sup> for an *in vitro* system include a cardiomyocyte system that:

1. exhibits synchronized and spontaneous contraction,
2. is responsive to exogenous epinephrine,
3. exhibits sensitivity to known cardiac sensitizers, and
4. allows exposure of sensitizing agents to system in a controlled atmosphere.

To this list must be added the ability to accurately rank compounds whose LOAELs differ by as little as a few percent.

Frazier has reviewed a number of studies involving cardiac cell systems.<sup>175</sup> Most of these were performed to assess the effects of certain drugs on cardiac functions or to determine specific of cardiac function itself. These are categorized in Table 6–14.

**Table 6–14. *In Vitro* Cardiac Cell Systems.**

Model	Life stage	Species	Reference
Myocardial cells	Fetal	Human	188
Cardiomyocytes	Neonatal	Rat	189
Ventricular Cardiomyocytes	Neonatal	Rat	190
Ventricular Cardiomyocytes	Neonatal	Dog	191
Cardiomyocytes	Adult	Rat	192
Cardiomyocytes	Adult	Rabbit	193
Cardiomyocytes	Adult	Dog	194
Cardiomyocytes	Adult	Feline	195
Ventricular Cardiomyocytes	Adult	Guinea Pig	196
Ventricular Cardiomyocytes	Adult	Rat	197

Skaggs et al.<sup>108</sup> concluded that, despite the variety of *in vitro* systems available to assess the cardiac toxicity of certain agents, any model selected would have to be characterized with respect to the

expression and response of adrenergic receptors and the ion fluxes (sodium and calcium) before cardiac sensitization validation studies could be initiated. At the time of completion of the NGP, there was no *in vitro* method that was established as predictive of the standard dog exposure test for cardiac sensitization.

### 6.7.7 PBPK Modeling of Cardiotoxic Effects

#### The Time-dependence of Toxic Hazard

Should a suppression system discharge into an area that is either occupied intentionally (such as a ground vehicle crew compartment) or unintentionally (such as during maintenance of an engine nacelle), people could be exposed to a high concentration of the agent for a relatively short time. The methods presented above involve a steady exposure for a long enough time period to see an effect. This masks the kinetic effects of a short exposure.

Figure 6–37 shows a hypothetical time dependence of a toxic response to a short exposure to a discharged fire suppressant. The concentration in the local atmosphere rises sharply following the discharge. Depending on the airtightness of the surroundings, the agent can dissipate quickly (as in the engine nacelle) or moderately (as in the crew compartment). There is a time lag in the concentration of the agent at the body site where the toxic effect will occur. This is due to transport time to that site, a process that could involve multiple steps. As the suppressant dissipates, the occupant breathes a lower concentration. Thus, the eventual dose (the integral of local agent concentration and time) reaching the sensitive site can be far lower than the exposure (the integral of the environmental concentration over the exposure time).

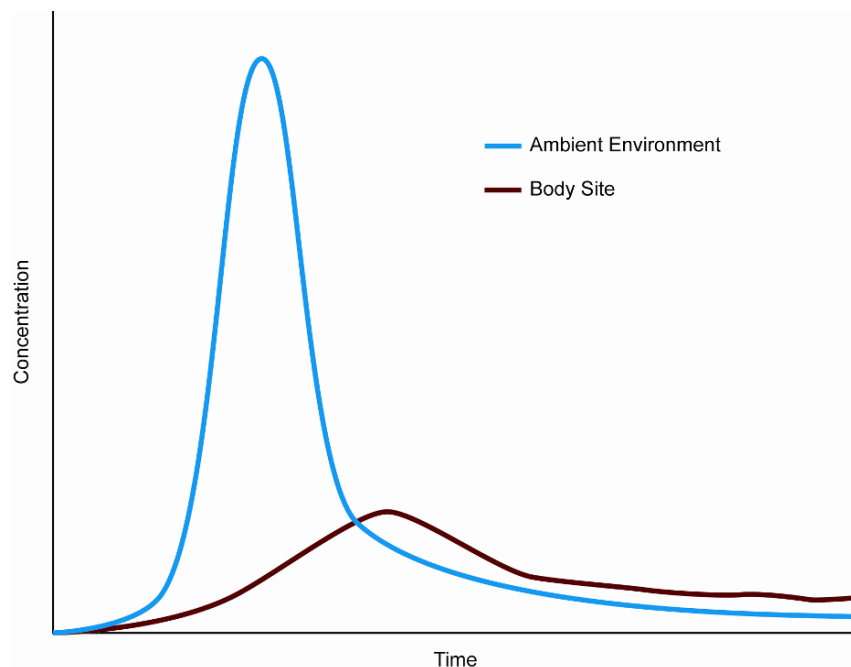


**Figure 6–37. Hypothetical Time Dependence of a Toxic Response to a Fire Suppressant. (NIST drawing)**

#### The PBPK Model

Under sponsorship of the EPA and the NGP, a team of toxicologists at the Air Force Research Laboratory (AFRL) modified a physiologically-based pharmacokinetic (PBPK) model of a human to include time-

dependent representation of the cardiovascular system and lungs that will allow simulation of the outcome of short-term exposures to fire suppressant chemicals.<sup>xi</sup> This was an important improvement over commonly used PBPK models that used steady-state descriptions to describe uptake of chemical via the lung and subsequent transfer of chemical to arterial blood. The principal features of the model<sup>198,199,200,201</sup> are summarized here.

A PBPK model provides the quantitative link between a (possibly time-varying) exposure concentration and the blood levels of the chemical achieved following inhalation. The PBPK model is a mathematical description of the uptake, distribution, metabolism, and elimination of a chemical in the species of interest. The time required for an arterial concentration to reach the LOAEL target arterial concentration is considered the safe (i.e., protective) exposure duration. The physiological compartments that compose the model are based on appropriate physiological and anatomical properties for the species of interest as well as the chemical specific properties of the test compound. The use of PBPK models for kinetic description of chemical interaction with biological systems has been well represented in the scientific literature and is widely accepted by the scientific community as a tool for risk assessment.

The human PBPK model used in this work<sup>198</sup> differed from the more traditional PBPK model in that it included a respiratory-tract compartment containing a dead-space region and a pulmonary exchange area. It was used successfully to simulate the pharmacokinetics of halothane, isoflurane, and desflurane which are structurally similar to many of the chemicals being considered as halon replacements. The pulmonary exchange area had its own air space, tissue, and capillary subregions. Respiration was described on a breath-by-breath basis. This more detailed lung description was necessary to successfully simulate pharmacokinetic data in the 0 min to 1 min range.<sup>198</sup> Additional physiological compartments described in this model were liver, fat, lung, gut, and slowly perfused and rapidly perfused tissues. All model compartments were perfusion limited and metabolism, if present, was assumed to occur in the liver.

The model required a considerable amount of input data:

- Cardiac sensitization LOAEL. This was determined using beagle dogs, as described above. The LOAEL thus determined was conservative in that the epinephrine challenge was well above physiological levels, and the LOAEL value was used without any correction factors. That the effect was due to the peak concentration of chemical rather than the area under the curve has been established by Reinhardt et al.<sup>95</sup>
- Arterial concentration measured after five minutes of exposure of beagles to the LOAEL concentration. Obtaining this information required that studies be done with beagles that have been cannulated for the sampling of arterial blood. At least six beagles should be exposed, without epinephrine challenge, at three exposure concentrations for 10 min at each exposure. The concentrations should be the LOAEL, approximately 25 % above the LOAEL, and approximately 25 % below the LOAEL. Blood samples should be taken at least at (1, 2, 5, 7, and 10) min to check the reliability of the data obtained at 5 min.
- Partition coefficients of the chemical in blood, liver, fat, and muscle. The most sensitive parameter for determination of the correct blood concentration was the blood partition coefficient, and there could be as much as a two-fold difference between human and rat blood. Therefore, since the model was being used to simulate human exposures, AFRL measured human blood partition coefficients. For the other partition coefficients, where much

---

<sup>xi</sup> This model addresses accidental exposure to the suppressant itself, such as might occur following an accidental discharge. It does not include the contribution of any decomposition products that are formed during and following flame extinguishment.

less difference was expected, rat tissue partition coefficient data were used when human data were not available. Details on obtaining these data are presented in reference 201.

- **Metabolic constants.** These were obtained using a gas uptake method using rats, as described by Gargas et al.<sup>202</sup> Fortunately, most of the proposed halon replacements were relatively inert and had extremely low to no measurable metabolism. Furthermore, even with moderate metabolism, there was no noticeable effect on the outcome of short-term simulations required for modeling of cardiac sensitization.
- **Human blood flows and tissue volumes.** There is significant variation in these variables among people. Therefore, Monte Carlo simulations were performed as part of the simulation of the concentration of an inhaled fire suppressant in the bloodstream. The ranges of the variables were compiled in Tables 1 and 2 of Reference 201. The Monte Carlo simulations were performed using ACSL TOX simulation software (Pharsight Corp., Mountain View, CA) operating under Windows 95 and Windows NT (Microsoft Corp., Redmond, WA).

### Simulations of Exposure to Constant Concentration Environments

The combined application of cardiac sensitization data and physiologically based modeling provided a quantitative approach, which could facilitate the selection and effective use of halon replacement candidates. The AFRL team exercised the model, performing the first simulations of short term (0 min to 5 min) effects. They used these results to determine short-term safe exposure times for halon 1301 and four potential replacement chemicals CF<sub>3</sub>I (trifluoroiodomethane), HFC-125 (pentafluoroethane), HFC-227ea (1,1,1,2,3,3,3-heptafluoropropane), and HFC-236fa (1,1,1,3,3,3-hexafluoropropane).<sup>201</sup>

Figure 6–38 and Figure 6–39 show the result of Monte Carlo simulations of the concentration of halon 1301 and HFC-125, respectively, in human blood during exposure to six different constant concentrations of the suppressant in air. The simulation lines represent the results of 1000 Monte Carlo simulations. The horizontal line at 25.7 mg/L represents the lowest arterial blood concentration measured at 5 min in a group of 6 dogs exposed to halon 1301 at the cardiac sensitization LOAEL of 7.5 %. For the six concentrations, Table 6–15 shows the safe exposure times, the time at which the blood concentration of halon 1301 reached the LOAEL for the most sensitive dog. Table 6–15 show such estimates for HFC-125. Similar curves and tables were generated for the other four fire suppressants.

**Table 6–15. Time for Safe Human Exposure at Stated Concentrations for Halon 1301 and HFC-125.**<sup>199</sup>

Halon 1301 Concentration (mole %)	Time (min)	HFC-125 Concentration (mole %))	Time (min)
5.5	5.00	11.5	5.00
6.0	5.00	12.0	1.13
6.5	1.33	12.5	0.73
7.0	0.59	13.0	0.59
7.5	0.42	13.5	0.50
8.0	0.35	11.5	5.00

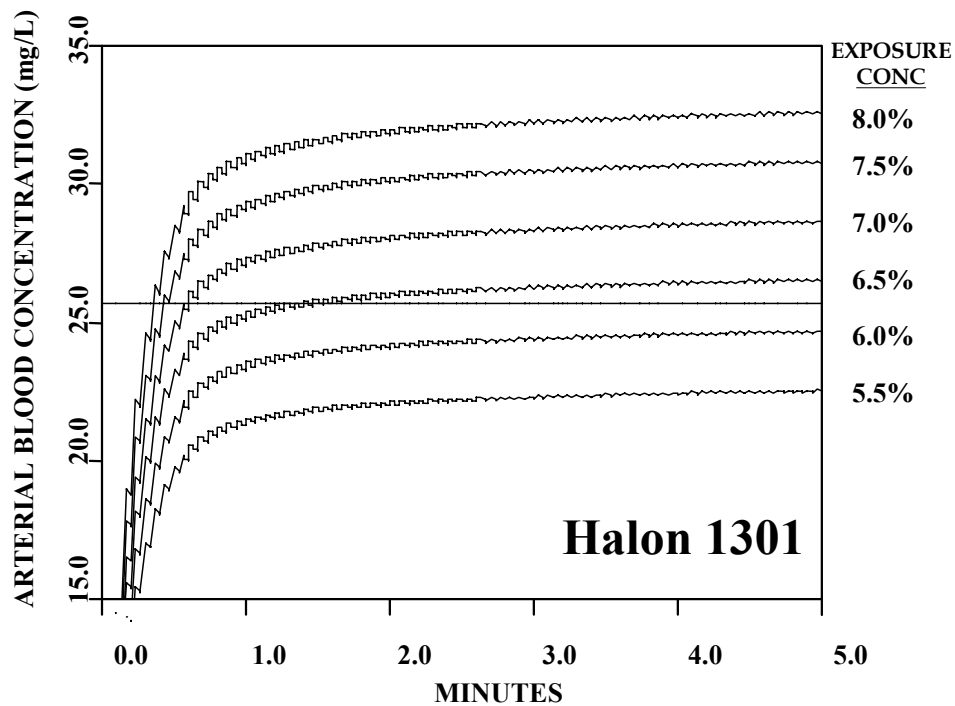


Figure 6-38. Monte Carlo Simulations of Humans Exposed to Halon 1301. <sup>199</sup>

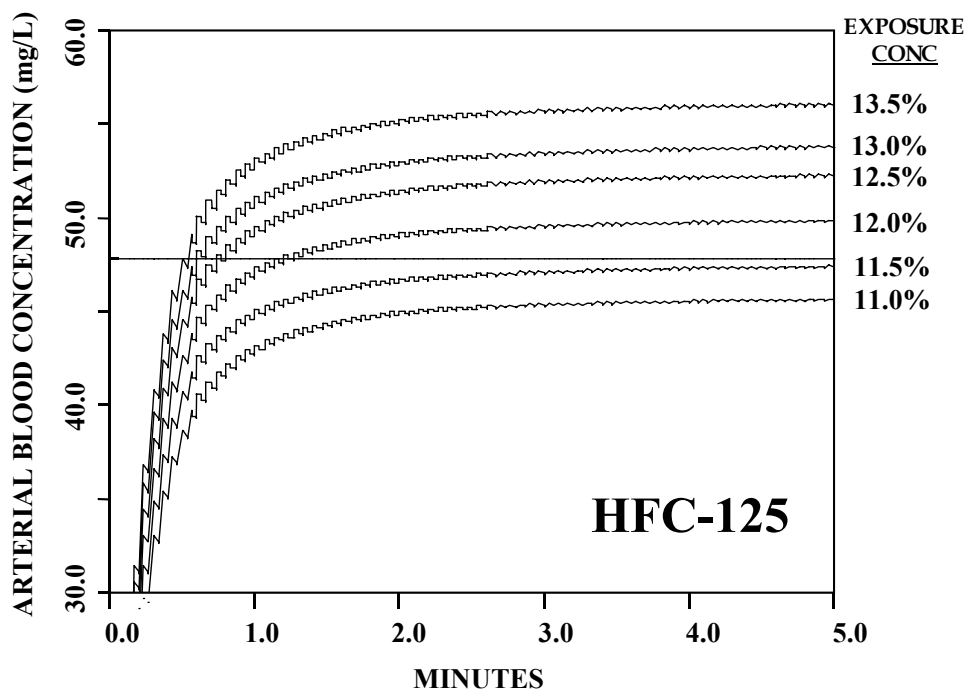


Figure 6-39. Monte Carlo Simulations of Humans Exposed to HFC-125. <sup>199</sup>

The importance of this to approval of a fire suppressant is significant. The specifications for safe exposure design of halon 1301 and potential replacement chemicals for use as total flooding agents in a fire-fighting scenario (section 6.7.1) do not take into consideration the pharmacokinetics of the agents and the relationship between the exposure concentration and the internal concentration actually associated with a cardiac event.

The critical issue in applying any standard for safe exposure is the relationship between the effective concentration of agent necessary to extinguish a fire and the concentration that poses a potential threat for cardiac sensitization. Where the extinguishing concentration approaches the cardiac sensitization concentration, the agent may still be approved for use as a fire extinguishant but only in areas that are normally unoccupied. For candidate agents where the extinguishing concentration is above the cardiac sensitization concentration, there is reluctance by some to risk using the agent because of perceived potential for accidental exposure. An additional consideration is that many of these agents release halogen acids upon contact with heat. The toxicity of these acids is of concern. Levels of release can be reduced if the fire can be put out quickly, which can be done if higher concentrations of extinguishing agent are used.

A comparison was made between the concentration for safe 5 min exposure and the recommended design concentration of agent for extinguishing a fire. As can be seen in Table 6–15, exposure to HFC-125 can occur safely for at least 5 min at an exposure concentration of 11.5 volume %, which is above the LOAEL by 1.5 volume %. The recommended design concentration for fire extinguishment is 10.4 volume % to 11.3 volume %.<sup>99</sup> Thus, the PBPK simulation suggested that it was safe to stay for 5 min in an HFC-125 environment that would put out a fire. From Table 6–15, the safe 5 min exposure for halon 1301 occurred at 5.5 volume % which was below the LOAEL by 2.0 volume %. The design concentration for fire extinguishment was 5 volume %.<sup>203</sup> Thus, the PBPK simulation suggested that it is not safe to stay for 5 min in a halon 1301 environment that would put out a fire. Halon 1301 has a long history of safe use, which points to the conservative nature of the cardiac sensitization endpoint, which ultimately determines the target arterial concentration, which in turn is used for determining safe exposure time.

After a range of chemical concentrations has been evaluated using the cardiac sensitization protocol, the dose-response data can be used to establish the NOAEL and LOAEL. Utilization of the animal testing data for assessing potential risks to humans requires development of appropriate risk assessment methods. These methods must address the unusual exposure circumstances involved in the use of chemicals as fire suppressants. In particular, potential exposures would be for relatively brief, but varying, periods of time at concentrations high enough to effectively extinguish fires. Egress times need to be established for people occupying a facility at the time of chemical agent discharge. The LOAEL determined in dogs has been applied directly by the EPA in evaluating acceptable use and allowable exposure limits for humans. Establishing egress times from the 5 min exposure LOAEL requires careful consideration of the relationship between exposure concentration, duration, and the temporal aspects of the biological response. Under steady state conditions, the concentration in blood and tissues would be constant regardless of the exposure duration.

## Simulations of Exposure to Time-varying Concentration Environments

AFRL demonstrated how to use the method to evaluate the potential for the occurrence of a cardiac-sensitizing event for time-varying concentrations.<sup>199</sup> The examples chosen were exposures to halon 1301 and halon 1211 in three aircraft for which concentration measurements had been reported. These data were used with the PBPK model to see if any of the described scenarios could put passengers or crew at potential risk for cardiac sensitization.

1. A fleet-configured Navy E-2B “Hawkeye” airplane.<sup>204</sup> Using a Statham Laboratories Model GA-2A gas recorder, concentrations of halon 1301 were measured at head level in areas occupied by flight crewmembers and in airplane locations where fire hazard potential posed the greatest threat. Under these conditions at floor level in the equipment area, the concentrations of halon 1301 in arterial blood exceeded the target concentration at about 40 s into the exposure and remained above the target for the duration of the measurements. Arterial concentration simulations remained below target at the other measured sites.
2. A Cessna Model C-421B, a small pressurized aircraft.<sup>205</sup> Halon 1211 and halon 1301 were measured using factory field-modified Beckman Model 865 infrared gas analyzers. Measurements were made at three locations:
  - The actual fire extinguisher discharge location.
  - Knee area – 0.50 m above the floor at the area of discharge. The discharge area for pilot’s and copilot’s seat tests was at knee level where the seat cushion meets the seat back.
  - Nose area – 0.94 m above the floor at the area of discharge.

The releases of halon 1301 resulted in simulated arterial concentrations well below the target concentration. Releases of halon 1211 resulted in simulated arterial concentrations that surpassed the target concentration of 21.0 mg/L in well under a minute.

3. A Cessna Model 210C, a small non-pressurized aircraft.<sup>206</sup> Halon 1211 and halon 1301 were measured using modified Beckman Model 865 infrared gas analyzers. Measurements were made at the point of release and at two other selected sites during each test. Halon 1301 arterial concentrations remained below the target concentration, while halon 1211 arterial concentrations exceeded the target level at all measured locations when the extinguisher was directed under the instrument panel on the pilot’s side with overhead vents open or closed.

The use of halon 1301 for several decades has occurred with an excellent safety record. Retrospective modeling of scenarios such as those illustrated here showed that generally under normal use there has been little to no opportunity for the occurrence of exposure situations where individuals have been put at potential risk of having blood levels of halon 1301 ever reach a target concentration that might predispose for the onset of a cardiac sensitization response. Halon 1211, when used as a streaming agent under open conditions, likewise has posed little risk. However, when used under more confined situations, the potential for cardiac sensitization exists. Several scenarios illustrated above showed situations where arterial concentrations of halon 1211 exceeded the target associated with a potential for cardiac sensitization. The report of an incident by Lerman et al.<sup>207</sup> demonstrated that the risk is real if halon 1211 were used under confined situations where the exposure concentration got high enough to result in highly elevated blood concentrations.

The PBPK model has been used both retrospectively to evaluate previous actual exposure scenarios and prospectively to evaluate potential exposure scenarios. An example of a retrospective evaluation was given in Vinegar et al., where they evaluated an accidental exposure to halon 1211 that had occurred during an Israeli military exercise.<sup>198</sup> In this instance, model predictions were consistent with the outcome where the gunner, having only brief exposure, successfully escaped without incident but the driver, with prolonged exposure, reached levels adequate for cardiac sensitization. The driver, in fact, was observed to be in ventricular fibrillation, never regained consciousness, and died as a result of the incident.

A prospective application of the model was demonstrated by Vinegar et al.<sup>208</sup> In order to evaluate the potential hazard to ground crews of an accidental release of CF<sub>3</sub>I, a discharge test was conducted on an F-15 aircraft to record CF<sub>3</sub>I concentration time histories at various locations near the aircraft. These exposure data were used with the PBPK model to simulate the potential blood levels of workers at various locations around the aircraft during the release. The blood levels were compared to the target arterial blood concentration associated with cardiac sensitization. Results showed that at some locations the target was not reached, but at the open nacelle the blood concentrations could potentially reach double the target. This information was put in perspective with a further retrospective simulation of individuals who had actually inhaled CF<sub>3</sub>I and whose blood concentrations were simulated and estimated to be 100 times the target. These individuals experienced no apparent effect of their exposures.

The code for the PBPK model has been listed in a report by Vinegar and Jepson.<sup>209</sup> It can provide a defensible approach and appropriate tools for decision makers, who are tasked with balancing performance and personnel safety issues, to evaluate the acute toxicity potential of inhaled fire suppressants.

### 6.7.8 Limit Tests

An acute toxicity test is an essential component of a screening protocol, since the EPA's SNAP program requires acute toxicity of a substitute chemical as part of its submission package. However, under DoD Directive #3216.1, stringent policies dictate that the most conservative approaches must be taken with regard to the use of laboratory animals in research programs. The need to spend time and resources to obtain a once traditional "LC<sub>50</sub> value" for a halon replacement candidate is discouraged in favor of a single limit test.

The purpose of the limit test is to evaluate mammalian toxicity following a single dose or exposure of the halon replacement candidate. A traditional limit test involves exposing several rats to a single, conservative dose of chemical for a fixed period of time and determining whether this dose is lethal.<sup>210</sup> For gaseous chemicals, inhalation is the most important route of exposure, whereas for liquids, skin contact may be more important than inhalation. For volatile candidate fire suppressants, a typical exposure is to a concentration of 10 volume % for 15 min, both of which are likely in excess of the exposure of people were the chemical eventually used as a fire suppressant. Following the limit test, the (surviving and dead) animals are typically examined for other adverse effects.

For liquid and solid candidate suppressants, an acute irritancy test could be used to evaluate the potential of a chemical to cause irritation in test animals after a single dose or exposure. These tests are usually performed in rabbits' eyes and skin since rabbits have a well-characterized response to irritants. Standard

protocols for irritation testing are described in the EPA's Office of Prevention, Pesticides, and Toxic Substances Health Effects Test Guidelines. The guidelines for acute eye and skin irritation are 870.2400 and 870.2500, respectively (OPPTS Series 870). The URL is:

[http://www.epa.gov/docs/OPPTS\\_Harmonized/870\\_Health\\_Effects\\_Test\\_Guidelines](http://www.epa.gov/docs/OPPTS_Harmonized/870_Health_Effects_Test_Guidelines).

## 6.8 APPLICATION OF SCREEN TESTS

Table 6–16 summarizes the screening tests as described above, along with the quantities of chemicals needed for their use. In practice, as will be seen in Chapter 7, it was generally easy to eliminate candidate chemicals from further consideration based on the most basic screening procedures.

- The NGP relied most heavily on cup burner data and the presence of one or more chemically active atoms for estimating a chemical's fire suppression efficiency. Only compounds whose extinguishment concentration was measured or estimated to be below 5 volume % were considered further.
- Next, compounds whose boiling points were above 20 °C were eliminated from further consideration. For fluids with slightly higher boiling points, similar fluids were considered to see if there might be a lower boiling member of the chemical family.
- Third, a chemical continued under consideration if it had a feature that rendered it tropodegradable, i.e., likely to have a short atmospheric lifetime.
- Most of the compounds considered were of unknown toxicity, so in relatively few cases could a confident safe exposure value be assigned. For compounds that were successful in the first three properties, a limit test would be performed. Success there would lead to a dog exposure test. In practice, no animal tests were performed for agents for in-flight fire suppression.

**Table 6–16. Nominal Quantities of Chemicals Needed for Screening Tests.**

Property Screened	Method	Total Mass/Volume of Chemical Required
Fire Suppression Efficiency	Cup burner	750 mL (gas)
	DLAFSS	10 mL (liquid)
	TARPF	10 g
Volatility	Boiling point	0.2 mL
Atmospheric lifetime	OH reactivity	5 L (gas)
	Absorption spectrum	10 mL (gas)
Toxicity	Literature	0 g
	Dog test	5 kg

## 6.9 REFERENCES

1. Gann, R.G., Barnes, J.D., Davis, S., Harris, J.S., Harris, R.H., Herron, J.T., Levin, B.C., Mopsik, F.I., Notarianni, K.A., Nyden, M.R., Paabo, M., and Ricker, R.E., *Preliminary Screening Procedures and Criteria for Replacements for Halons 1211 and 1301*, NIST Technical Note 1278, National Institute of Standards and Technology, 1990.
2. Nyden, M.R., and Skaggs, S.R., *Screening Methods for Agent Compatibility with People, Materials, and the Environment*, NISTIR 6323, National Institute of Standards and Technology, Gaithersburg, MD, 1999.
3. Hamins, A., Gmurczyk, G., Grosshandler, W., Rehwoldt, R.P., Vazquez, I., and Cleary, T., "Flame Suppression Effectiveness," in Grosshandler, W.L., Pitts, W.M., and Gann, R.G., eds., *Evaluation of Alternative In-Flight Fire Suppressants for Full-Scale Testing in Simulated Aircraft Engine Nacelles and Dry Bays*, NIST Special Publication 861, National Institute of Standards and Techno, Gaithersburg, MD, 1994.
4. Significant New Alternative Policy (SNAP) Program Final Rule, *Federal Register* **59**, 13044, March 18, 1994.
5. *Climate Change 1995, The Science of Climate Change*, Intergovernmental Panel on Climate Change (IPCC), 1995.
6. Pitts, W.M., Yang, J.C., Bryant, R.A., Blevins, L.G., and Huber, M.L., *Characteristics and Identification of Super-Effective Thermal Fire-extinguishing Agents*, NIST Technical Note 1440, National Institute of Standards and Technology, Gaithersburg, MD, 2006.
7. Creitz, E.C., "Inhibition of Diffusion Flames by Methyl Bromide and Trifluoromethyl Bromide Applied to the Fuel and Oxygen Sides of the Reaction Zone," *Journal of Research of the National Bureau of Standards (U.S.)* **65 (4)**, 389, (1961).
8. Hirst, R., and Booth, K., "Measurement of Flame-extinguishing Concentrations," *Fire Technology* **13(4)**, 296-315 (1977).
9. Bajpai, S.N., *Inerting Characteristics of Halons 1301 and 1211*, Report 22391.3, Factory Mutual Research, Norwood, MA, 1974.
10. Mather, J.D., and Tapscott, R.E., *Tropodegradable Bromocarbon Extinguishants II, Final report to the Strategic Environmental Research and Development Program (SERDP)*, 1994, available on the NGP web site: [www.bfirl.nist.gov/866/NGP](http://www.bfirl.nist.gov/866/NGP).
11. Yang, J.C., Donnelly, M.K., Prive, N.C., and Grosshandler, W.L., "An Apparatus for Screening Fire Suppression Efficiency of Dispersed Liquid Agents," *Fire Safety Journal* **36**, 55-72 (2001).
12. Yang, J.C., Donnelly, M.K., Prive, N.C., and Grosshandler, W.L., *Dispersed Liquid Agent Fire Suppression Screen*, NISTIR 6319, National Institute of Standards and Technology, Gaithersburg, MD, 1999.
13. Tsuji, H. and Yamaoka, I., "The Counterflow Diffusion Flame in the Forward Stagnation Region of a Porous Cylinder," *Proceedings of the Combustion Institute* **11**, 979-984 (1967).
14. Tsuji, H. and Yamaoka, I., "The Structure of Counterflow Diffusion Flames in the Forward Stagnation Region of a Porous Cylinder," *Proceedings of the Combustion Institute* **12**, 997-1005, (1969).
15. Tsuji, H. and Yamaoka, I., "Structure Analysis of Counterflow Diffusion Flames in the Forward Stagnation Region of a Porous Cylinder," *Proceedings of the Combustion Institute* **12**, 723-731 (1971).

16. Tsuji, H., "Counterflow Diffusion Flames," *Progress in Energy and Combustion Science* **8**, 93 (1982).
17. Ishizuka, S. and Tsuji, H., "An Experimental Study of Effect of Inert Gases on Extinction of Laminar Diffusion Flames," *Proceedings of the Combustion Institute* **18**, 695-703 (1981).
18. Milne, T.A., Green, C.L., and Benson, D.K., "The Use of the Counterflow Diffusion Flame in Studies of Inhibition Effectiveness of Gaseous and Powdered Agents," *Combustion and Flame* **15**, 255 (1970).
19. Dixon-Lewis, G., David, T., Gaskell, P.H., Fukutani, S., Jinno, H., Miller, J.A., Kee, R.J., Smooke, M.D., Peters, N., Effelsberg, E., Warnatz, J., and Behrendt, F., "Calculation of the Structure and Extinction Limit of a Methane-Air Counterflow Diffusion Flame in the Forward Stagnation Region of a Porous Cylinder," *Proceedings of the Combustion Institute* **20**, 1893-1904, (1984).
20. Dreier, T., Lange, B., Wolfrum, J., Zahn, M., Behrendt, F., and Warnatz, J., "CARS Measurements and Computations of the Structure of Laminar Stagnation-Point Methane-Air Counterflow Diffusion Flames," *Proceedings of the Combustion Institute* **21**, 1729-1736 (1986).
21. Peters, N. and Kee, R.J., "The Computation of Stretched Laminar Methane-Air Diffusion Flames Using a Reduced Four-Step Mechanism," *Combustion and Flame*, **68**, 17 (1987).
22. Olson, S.L. and T'ien, J.S., "A Theoretical Analysis of the Extinction Limits of a Methane-Air Opposed-Jet Diffusion Flame," *Combustion and Flame*, **70**, 161 (1987).
23. Dixon-Lewis, G. and Missaghi, M., "Structure and Extinction Limits of Counterflow Diffusion Flames of Hydrogen-Nitrogen Mixtures in Air," *Proceedings of the Combustion Institute* **22**, 1461-1470 (1988).
24. Chen, C.H. and Weng, F.B., "Flame Stabilization and Blowoff Over a Porous Cylinder," *Combustion Science and Technology*, **73**, 427 (1990).
25. Sick, V., Arnold, A., Diesel, E., Dreier, T., Ketterle, W., Lange, B., Wolfrum, J., Thiele, K.U., Behrendt, F., and Warnatz, J., "Two-Dimensional Laser Diagnostics and Modeling of Counterflow Diffusion Flames," *Proceedings of the Combustion Institute* **23**, 495-501 (1990).
26. Yang, J.C., Chien, W., King, M., and Grosshandler, W.L., "A Simple Piezoelectric Droplet Generator," *Experiments in Fluids*, **23**, 445 (1997).
27. Yang, J.C., Donnelly, M.K., Privé, N.C., and Grosshandler, W.L., "Fire Suppression Efficiency Screening Using a Counterflow Cylindrical Burner," *Proceedings of the 5th ASME/JSME Joint Thermal Engineering Conference*, San Diego, California, March 1999.
28. Hamins, A., Gmurczyk, G., Grosshandler, W., Rehwoldt, R.G., Vazquez, I., Cleary, T., Presser, C., and Seshadri, K., "Flame Suppression Effectiveness," Chapter 4 in Grosshandler, W., Gann, R.G., and Pitts, W.M., eds., *Evaluation of Alternative In-flight Fire Suppressants for Full-scale Testing in Simulated Engine Nacelles and Dry Bays*, NIST SP 861, National Institute of Standards and Technology, Gaithersburg, MD, 1994.
29. Yang, J.C., Prive, N.C., Donnelly, M.K., Grosshandler, W.L., "Recent Results from the Dispersed Liquid Agent Fire Suppression Screen," in Gann, R.G., Burgess, S.R., Whisner, K.C., and Reneke, P.A., eds., *Papers from 1991-2006 Halon Options Technical Working Conferences (HOTWC)*, CD-ROM, NIST SP 984-4, National Institute of Standards and Technology, Gaithersburg, MD, 2006.
30. Rossotti, H., *Fire*, Oxford University Press, Oxford, UK, 1993.
31. Finnerty, A.E., McGrill, R.L., and Slack, W.A., *Water-Based Halon Replacement Sprays*, ARL-TR-1138, U.S. Army Research Laboratory, Aberdeen Proving Ground, MD, July 1996.

32. Lentati, A.M. and Chelliah, H.K., "Physical, Thermal, and Chemical Effects of Fine-Water Droplets in Extinguishing Counterflow Diffusion Flames," *Proceedings of the Combustion Institute* **27**, 2839-2846 (1998).
33. Grosshandler, W., Hamins, A., McGrattan, K., Charagundla, S.R., and Presser, C., "Suppression of a Non-Premixed Flame Behind a Step," *Proceedings of the Combustion Institute* **28**, 2957-2964 (2001).
34. Hirst, R. and Sutton, D., "The Effect of reduced pressure and Airflow on Liquid Surface Diffusion flames," *Combustion and Flame* **5**, 319-330 (1961).
35. Hirst, R., Farenden, P.J., and Simmons, R.F., "The Extinction of Fires in Aircraft Jet Engines – Part I, Small-scale Simulation of Fires," *Fire Technology* **12**, 266-275 (1976).
36. Hirst, R., Farenden, P.J., and Simmons, R.F., "The Extinction of Fires in Aircraft Jet Engines – Part II, Full-scale Fire Tests," *Fire Technology* **13**, 59-68 (1977).
37. Hamins, A., Cleary, T., Borthwick, P., Gorchov, N., McGrattan, K., Forney, G., Grosshandler, W., Presser, C., and Melton, L., "Suppression of Engine Nacelle Fires," Chapter 9 in *Fire Suppression System Performance of Alternative Agents in Aircraft Engine and Dry Bay Lab. Simulations*, NIST SP 890: Vol. II, Gann, R.G. (ed.), National Institute of Standards and Technology, Gaithersburg, MD, 1995.
38. Takahashi, F., Schmoll, W.J., Strader, E.A., and Belovich, V.M., "Suppression of a Nonpremixed Flame Stabilized by a Backward-Facing Step," *Combustion and Flame* **122**, 105-116 (2000).
39. Hamins, A., Gmurczyk, G., Grosshandler, W., Rehwoldt, R., Vazquez, I., Cleary, T., Presser, C., and Seshadri, K., "Flame Suppression Effectiveness," Chapter 4 in *Evaluation of Alternative In-flight Fire Suppressants for Full-scale Simulated Aircraft Engine Nacelles and Dry Bays*, (Grosshandler, W.L., Gann, R.G., and Pitts, W.M., eds.) NIST SP 861, National Institute of Standards and Technology, Gaithersburg, MD, 1994.
40. W. Leach, Naval Air Systems Command, personal correspondence to W. Grosshandler, National Institute of Standards and Technology, 1998.
41. Hamins, A., Cleary, T., and Yang, J., "An Analysis of the Wright-Patterson Full-Scale Engine Nacelle Fire Suppression Experiments," NISTIR 6193, National Institute of Standards and Technology, Gaithersburg, MD, 1997.
42. Mitchell, M., "Hybrid Fire Extinguisher for Occupied and Unoccupied Spaces," in Gann, R.G., Burgess, S.R., Whisner, K.C., and Reneke, P.A., eds., *Papers from 1991-2005 Halon Options Technical Working Conferences (HOTWC)*, CD-ROM, NIST SP 984-3, National Institute of Standards and Technology, Gaithersburg, MD, (2005).
43. Wierenga, P. H., and Holland, G. F., "Developments in and Implementation of Gas Generators for Fire Suppression," in Gann, R.G., Burgess, S.R., Whisner, K.C., and Reneke, P.A., eds., *Papers from 1991-2006 Halon Options Technical Working Conferences (HOTWC)*, CD-ROM, NIST SP 984-4, National Institute of Standards and Technology, Gaithersburg, MD, 2006.
44. Grosshandler, W., Hamins, A., McGrattan, K., and Presser, C., *Transient Application, Recirculating Pool Fire, Agent Effectiveness Screen: Final Report, NGP Project 3A/2/890*, NISTIR 6733, National Institute of Standards and Technology, Gaithersburg, MD, 2001.
45. Taylor, B.N. and Kuyatt, C.E., *Guidelines for Evaluating and Expressing the Uncertainty of NIST Measurement Results*, NIST Technical Note 1297, National Institute of Standards and Technology, Gaithersburg, MD, (1993).
46. J. Neidert, Atlantic Research Corporation, personal communication to W. Grosshandler, National Institute of Standards and Technology, 2000.

47. McGrattan, K.B., Baum, H.R., Rehm, R.G., Hamins, A., and Forney, G.P., *Fire Dynamics Simulator, Technical Reference Guide*, NISTIR 6467, National Institute of Standards and Technology, Gaithersburg, MD, 2000.
48. Reid, R.C., Prausnitz, J.M. and Poling, B.E., *Properties of Gases and Liquids*, McGraw-Hill, Inc., New York, 4th edition, 1987.
49. Satcunanathan, S., and Zaczek, B.J., "The Spontaneous Ignition and Ignition Delay of Liquid Fuel Droplets Impinging on a Hot Surface," Thermodynamics and Fluid Mechanics Convention, Institution of Mechanical Engineers, London, 27-29 March, 1968.
50. Jomaas, G., Roberts, B.T., DuBois, J., and Torero, J.L., *A Study of the Mechanisms Leading to Re-ignition in a 'Worst Case' Fire Scenario*, Final Report, Cooperative Agreement No. 70NANB8H0043, Department of Fire Protection Engineering, University of Maryland College Park, MD20742-3031, June, 2000. (Also NIST GCR 01-806, National Institute of Standards and Technology, Gaithersburg, MD, 2001.)
51. Grosshandler, W.L., Hamins, A., Charagundla, R., and Presser, C., "Suppression Effectiveness Screening for Impulsively Discharged Agents," in Gann, R.G., Burgess, S.R., Whisner, K.C., and Reneke, P.A., eds., *Papers from 1991-2006 Halon Options Technical Working Conferences (HOTWC)*, CD-ROM, NIST SP 984-4, National Institute of Standards and Technology, Gaithersburg, MD, 2006.
52. Trees, D., Seshadri, K., and Hamins, A.M., "Exp. Studies of Diffusion Flame Extinction with Halogenated and Inert Fire Suppressants," in *Halon Replacements - Technology and Science*, Miziolek, A.W., and Tsang, W. (eds.), ACS Symposium Series 611, American Chemical Society, Washington, DC, 1995.
53. Sheinson, R. S., Penner-Hahn, J. E., and Indritz, D., "The Physical and Chemical Action of Fire Suppressants," *Fire Safety Journal* **15**, pp 437-450 (1989).
54. Finlayson-Pitts, B.J., and Pitts, Jr., J.N., *Chemistry of the Upper and Lower Atmosphere*, Academic Press, New York, 2000.
55. Tapscott, R.E. and Olivares-Sooley, M.G., "Decision Tree for Global Environmental Impact Screening," in Gann, R.G., Burgess, S.R., Whisner, K.C., and Reneke, P.A., eds., *Papers from 1991-2006 Halon Options Technical Working Conferences (HOTWC)*, CD-ROM, NIST SP 984-4, National Institute of Standards and Technology, Gaithersburg, MD, 2006.
56. Fischer, D.A., Hales, C.H., Filkin, D.L., Ko, M.K.W., Sze, N.D., Connell, P.S., Wuebbles, D.J., Isaksen, I.S.A., and Stordal, F., "Relative Effects on Stratospheric Ozone of Halogenated Methanes and Ethanes of Social and Industrial Interest," in World Meteorological Organization, Global Ozone Research and Monitoring Project - Report No. 20, *Scientific Assessment of Stratospheric Ozone: 1989*, Vol. II, Appendix: AFEAS Report, pp. 301-377. (Available from Upper Atmosphere Research Program, NASA Headquarters, Washington, D.C., 20546).
57. Skaggs, S. R., and Nimitz, J. S., "Estimating Tropospheric Lifetimes and Ozone-Depletion Potentials of One- and Two-Carbon Hydrofluorocarbons and Hydrochlorofluorocarbons," *Environmental Science and Technology* **26**, 739-744 (1992).
58. Iikubo, Y., and Robin, M. L., "Fire Extinguishing Methods and Blends Utilizing Hydrofluorocarbons," USA, Patent Number 5,124,053, 23 June 1992. Assigned to Great Lakes Chemical Corporation.
59. *Scientific Assessment of Ozone Depletion: 1994*, Report No. 37, National Oceanic and Atmospheric Administration, National Aeronautics and Space Administration, United Nations Environment Programme, and World Meteorological Organization, February 1995.

60. Connell, P. S., and Wuebbles, D. J., "Ozone Depletion Potential, Halons, and Halon Alternatives," NMERI Halon Alternatives Program Review, Albuquerque, NM, 23-24 Jan 1991.
61. *Risk Screen on the Use of Substitutes for Class I Ozone-Depleting Substances: Fire Suppression and Explosion Protection (Halon Substitutes)*, SNAP Technical Background Document, U.S. Environmental Protection Agency, Washington, DC, March 1994.
62. "Protection of Stratospheric Ozone: Final Rule," *Federal Register*, **60 (113)**, 31092-31107, 13 June 1995.
63. Prinn, R., Weiss, R. F., Miller, B. R., Huang, J., Alyea, F. N., Cunnold, D. M., Fraser, P. J., Hartley, D. E., and Simmonds, P. G., "Atmospheric Trends and Lifetime of  $\text{CH}_3\text{CCl}_3$  and Global OH Concentrations," *Science* **269**, No. 5221, 187-192 (1995).
64. Wuebbles, D. J., and Connell, P. S., *A Screening Methodology for Assessing the Potential Impact of Surface Releases of Chlorinated Halocarbons on Stratospheric Ozone*, UCID-19233, Lawrence Livermore Laboratory, Livermore, California, November 1981.
65. Prather, M. J., and Spivakovsky, C. M., "Tropospheric OH and the Lifetimes of Hydrochlorofluorocarbons," *Journal of Geophysical Research*, **95**, 18723-18729 (1990).
66. Imasu, R., Suga, A., and Matsuno, T., "Radiative Effects and Halocarbon Global Warming Potentials of Replacement Compounds for Chlorofluorocarbons," *Journal of the Meteorological Society of Japan* **73**, No. 6, 1123-1136 (1995).
67. Zhang, Z., Saini, R. D., Kurylo, M. J., and Huie, R. E., "Rate Constants for the Reactions of the Hydroxyl Radical with Several Partially Fluorinated Ethers," *Journal of Physical Chemistry*, **96**, 9301-9304 (1992).
68. Atkinson, R., "Kinetics and Mechanisms of the Gas-Phase Reactions of the Hydroxyl Radical with Organic Compounds," *Journal of Physical and Chemical Reference Data, Monograph No. 1*, American Chemical Society, Washington, DC, and American Institute of Physics, Woodbury, New York, 1989.
69. Cooper, D. L., Cunningham, T. P., Allan, N. L., and McCulloch, A., "Potential CFC Replacements: Tropospheric Lifetimes of C3 Hydrofluorocarbons and Hydrofluoroethers," *Atmospheric Environment* **27A**, No. 1, 117-119 (1993).
70. Prather, M.C., "Tropospheric Hydroxyl Concentrations and the Lifetimes of Hydrochlorofluorocarbons (HCFCs)," in World Meteorological Organization, *op. cit.*, 147-158.
71. Kurylo, M.J., and Braun, W., "Flash Photolysis Resonance Fluorescence Study of the Reaction  $\text{Cl} + \text{O}_3 \rightarrow \text{ClO} + \text{O}_2$  Over the Temperature Range 213-298 K," *Chemical Physics Letters* **37**, 232 (1976).
72. Kurylo, M.J., Cornett, K.D., and Murphy, J.L., "The Temperature Dependence of the Rate Constant for the Reaction of Hydroxyl Radicals with Nitric Acid," *Journal of Geophysical Research* **87**, 3081-3085 (1982).
73. Ravishankara, A.R., Wine, P.H., and Nicovich, J.M., "Pulsed Laser Photolysis Study of the Reaction between  $\text{O}(^3\text{P})$  and  $\text{HO}_2$ ," *Journal of Chemical Physics* **78**, 6629 (1983).
74. Molina, L.T., Molina, M.J., and Rowland, F.S., "Ultraviolet Absorption Cross Sections of Several Brominated Methanes and Ethanes of Atmospheric Interest," *Journal of Physical Chemistry* **86**, 2672-2676 (1982).
75. Gillotay, D., and Simon, P.C., "Ultraviolet Absorption Spectrum of Trifluoro-bromomethane, Difluoro-dibromomethane, and Difluoro-bromo-chloromethane in the Vapor Phase," *Journal of Atmospheric Chemistry* **8**, 41 (1989).

76. Klein, R., Braun, W., Fahr, A., Mele, A., and Okabe, H., "Scattered Light and Other Corrections in Absorption Cross Section Measurements in the Vacuum Ultraviolet: A Systems Approach," *Journal of Research of the National Institute of Standards and Technology* **95**, 337-344 (1990).
77. Kaufman, F., "Kinetics of Elementary Radical Reactions in the Gas Phase," *Journal of Physical Chemistry* **86**, 69 (1984).
78. Atkinson, R., "Kinetics and Mechanisms of the Gas-Phase Reactions of the Hydroxyl Radical with Organic Compounds under Atmospheric Conditions," *Chemical Reviews* **86**, 69-201 (1986).
79. Nimitz, J.S., and Skaggs, S.R., "Estimating Tropospheric Lifetimes and Ozone-depleting Potentials of One- and Two-carbon Hydrofluorocarbons," *Environmental Science and Technology* **26**, 739-744, (1992).
80. Orkin, V. L., Villenave, E., Huie, R. E., and Kurylo, M. J., "Atmospheric Lifetimes and Global Warming Potentials of Hydrofluoroethers: Reactivity Toward OH, UV Spectra, and IR Absorption Cross Sections", *Journal of Physical Chemistry A*, **103**, 9770-9779 (1999).
81. Louis, F., Gonzalez, C., Huie, R. E., and Kurylo, M. J., "An *ab Initio* Study of the Reaction of Halomethanes with the Hydroxyl Radical. Part 1: CH<sub>2</sub>Br<sub>2</sub>", *Journal of Physical Chemistry A*, **104**, 2931-2938 (2000).
82. Louis, F., Gonzalez, C., Huie, R. E., and Kurylo, M. J., "An *Ab Initio* Study of the Kinetics of the Reactions of Halomethanes with the Hydroxyl Radical. Part 2: A Comparison between Theoretical and Experimental Values of the Kinetic Parameters for 12 Partially Halogenated Substituted Methanes," *Journal of Physical Chemistry A*, **104**, 8773-8778 (2000).
83. Louis, F., Gonzalez, C., Huie, R. E., and Kurylo, M. J., "An *Ab Initio* Study of the Kinetics of the Reactions of Halomethanes with the Hydroxyl Radical. Part 3. Reactivity Trends and Kinetics Parameter Predictions for the Potential Halon Replacements CH<sub>2</sub>FBr, CHFBr<sub>2</sub>, CHFClBr, CHCl<sub>2</sub>Br, and CHClBr<sub>2</sub>," *J. Phys. Chem. A*, **105**, 1599-1604 (2001).
84. Kozlov, S. N., Orkin, V. L., Huie, R. E., and Kurylo, M. J., "OH Reactivity and UV Spectra of Propane, n-Propyl Bromide, and Isopropyl Bromide," *Journal of Physical Chemistry A*, **107**, 1333-1338 (2003).
85. Orkin, V. L., Louis, F., Huie, R. E., and Kurylo, M. J., "Photochemistry of Bromine-Containing Fluorinated Alkenes: Reactivity toward OH and UV Spectra," *Journal of Physical Chemistry A*, **106**, 10195-10199 (2002).
86. Pitts, W.M., Yang, J.C., Gmurczyk, G., Cooper, L.Y., Grosshandler, W.L., Cleveland, W.G., and Presser, C., "Fluid Dynamics of Agent Discharge," in Grosshandler, W.L., Pitts, W.M., and Gann, R.G., eds., *Evaluation of Alternative In-Flight Fire Suppressants for Full-Scale Testing in Simulated Aircraft Engine Nacelles and Dry Bays*, NIST Special Publication 861, National Institute of Standards and Technology, Gaithersburg, MD, 1994.
87. Brabson, G.D., Garcia, M.M., Heinonen, E.W., Juarez, G., Mather, J.D., and Tapscott, R.E., *Main Group Compounds as Extinguishants*, Report No. 98/8/33380, New Mexico Engineering Research Institute, Albuquerque, NM, 2001, available on the NGP web site: [www.bfrl.nist.gov/866/NGP](http://www.bfrl.nist.gov/866/NGP).
88. Hirschfelder, J. O., Curtiss, C. F., and Bird, R. B., *The Molecular Theory of Gases and Liquids*, John Wiley & Sons, New York, 1954.
89. Perry, R. H., and Green, D. W., editors, *Perry's Chemical Engineering Handbook*, Seventh Edition, McGraw-Hill, New York, 1997.

90. Green, H. L., and Lane, W. R., *Particulate Clouds: Dusts, Smokes, and Mists*, E. & F. N. Spon Ltd., London, 1964.
91. *NIST Structures and Properties, Version 2.0*, NIST Standard Reference Database 25, National Institute of Standards and Technology, Gaithersburg, MD, January 1994.
92. Pavia, D.L., Lampman, G.M., Kriz, G.S., and Engel, R.G., *Introduction to Organic Laboratory Techniques - A Small Scale Approach*, Brooks/Cole Publishing, 2005.
93. The isoteniscope procedure and equipment are a modification of ASTM D 2879-86, ASTM International, West Conshohocken, PA.
94. *An Appraisal of Halogenated Fire Extinguishing Agents*, National Academy of Sciences, Washington, DC, 1972.
95. Reinhardt, C.F., Azar, A., Maxfield, M.E., Smith, P.E., and Mullin, L.S., "Cardiac Arrhythmias and Aerosol Sniffing," *Archives of Environmental Health* **22**, 265-279 (1971).
96. Dodd, D.E., Jepson, G.W., and Macko, Jr., J.A., *Human Health Safety Evaluation of Halon Replacement Candidates, Section II*" Final Report to the U.S. Department of Defense, Strategic Environmental Research and Development Program, 2000.
97. Lewis, R. J., Sr., *Sax's Dangerous Properties of Industrial Materials*, Ninth Edition, Van Nostrand Reinhold, New York, 1996.
98. Harris, W. S., "Cardiac Effects of Halogenated Hydrocarbons," in *An Appraisal of Halogenated Fire Extinguishing Agents*, National Academy of Sciences, Washington, DC, pp. 114-126, 1972.
99. NFPA 2001, Standard on Clean Agent Fire Extinguishing Systems, NFPA, Quincy, MA, 2004.
100. Gage, C. L., Hendriks, R. V., Smith, N. D., Brna, T. G., *New Chemical Alternative for Ozone-Depleting Substances: HFC-236ea*, EPA-600/R-97-117, NTIS PB98-127384, 1997.
101. *Acute Inhalation Toxicity Study of Iodotrifluoromethane in Rats*, Armstrong Laboratory, Air Force Systems Command, Wright-Patterson Air Force Base, Ohio, March 1994
102. Beck, P. S., Clark, D. G., Tinston, D. J., "The Pharmacologic Actions of Bromochlorodifluoromethane (BCF)," *Toxicology and Applied Pharmacology*, (1973).
103. *Registry of Toxic Effects of Chemical Substances, 1985-86 Edition*, National Institute of Occupational Safety and Health, U.S. Department of Health and Human Services, Washington, DC.
104. Skaggs, S. R., Dierdorf, D. S., and Tapscott, R. E., "Update on Iodides as Fire Extinguishing Agents," *Proceedings of the 1993 CFC and Halon Alternatives Conference*, Washington, DC, pp. 800-809, 1993.
105. Calm, J.M., "Refrigerant Safety," *ASHRAE Journal*, 17-26, (1974).
106. Bogdan, M., "Blowing Agents: Producer and User Perspective," International Chemical Congress of Pacific Basin Societies, 17-22 December, 1996.
107. Davies, R. H., Bagnall, R. D., Bell, W., Jones, W. G. M., "The Hydrogen Bond Proton Donor Properties of Volatile Halogenated Hydrocarbons and Ethers and Their Mode of Action in Anaesthesia," *International Journal of Quantum Chemistry*, Quantum Biology Symposium No. 3, 171-185, (1976).
108. Skaggs, S. R., Tapscott, R. E., Heinonen, E.W., "Advanced Agent Program: Toxicological Screening Methods," NMERI 95/48/31882, Wright Laboratories (WL/FIVCF), Tyndall Air Force Base, Florida, December 1996.

109. Kier, L. B., and Hall, L. H., "The Nature of Structure-Activity Relationships and Their Relation to Molecular Connectivity," *European Journal of Medicinal Chemistry* **12**, 307-312 (1977).
110. Blum, D., and Speece, R., "Determining Chemical Toxicity to Aquatic Species," *Environmental Science and Technology* **24**, 284-294 (1990).
111. Kier, L. B., and Hall, L. H., *Molecular Connectivity in Structure-Activity Analysis*, John Wiley & Sons, Inc., New York, 1986.
112. Vinegar, A., ManTech Environmental Technology Inc., Dayton, Ohio, personal correspondence to R. E. Tapscott, New Mexico Engineering Research Institute, The University of New Mexico, May 1997.
113. Dearden, J.C., Barratt, M.D., Benigni, R., Bristol, D.W., Combes, R.D., Cronin, M.T.D., Judson, P.N., Payne, M.P., Richard, A.M., Tichy, M., Worth, A.P., and Yourick, J.J., "The Development and Validation of Expert Systems for Predicting Toxicity," The Report and Recommendations of ECVAM Workshop 24, Atlanta, pp. 25:223-252, 1997.
114. Alarie, Y., Abraham, M.H., Nielsen, G.D., and Schaper, M., "Structure-activity Relationships of Volatile Organic Chemicals as Sensory Irritants," *Archives of Toxicology* **72(3)**, 125-40, (1998).
115. Wang, G., and Bai, N., "Structure-activity Relationships for Rat and Mouse LD<sub>50</sub> of Miscellaneous Alcohols," *Chemosphere* **36(7)**, 1475-83 (1998).
116. Rucki, M., Tichy, M., "Acute Toxicity of Alcohols: Prediction by QSAR Analysis and by Molecular Similarity," *Central European Journal of Public Health* **5(4)**, 183-187 (1997).
117. Debord, J, et al., "Inhibition of Arylesterase by Aliphatic Alcohols," *Chemical and Biological Interactions* **113(2)**, 105-115 (1998).
118. Cronin, M. T., Schultz, T.W., "Structure-toxicity Relationships for Three Mechanisms of Action of Toxicity to *Vibrio Fischeri*," *Ecotoxicological Environmental Safety* **39(1)**, 65-69, (1998).
119. Politzer, P, et al., "Molecular Properties of the Chlorinated Ethylenes and their Epoxide Metabolites," *Annals of the New York Academy of Sciences* **367**, 478-492, (1981).
120. Boyes, R. N., "A review of the Metabolism of Amide Local Anesthetic Agents," *British Journal of Anaesthesiology* **47 suppl**, 225-230 (1975).
121. Huang, Y., et al., "Synthesis and Quantitative Structure-activity Relationships of N-(1-benzylpiperidin-4-yl) phenylacetamides and Related Analogues as Potent and Selective Sigma1 Receptor Ligands," *Journal of Medicinal Chemistry* **41(13)**, 2361-2370 (1998).
122. Hadjipavlou-Litina, D., "Review, Reevaluation, and New Results in Quantitative Structure-activity Studies of Anticonvulsants," *Medical Research Review* **18(2)**, 91-119 (1998).
123. Nilsson, J., et al. "GRID/GOLPE 3D Quantitative Structure-activity Relationship Study on a Set of Benzamides and Naphthamides, with Affinity for the Dopamine D3 Receptor Subtype," *Journal of Medicinal Chemistry* **40(6)**, 833-840 (1997).
124. Krystek, S.R., Jr., et al., "Three-dimensional Quantitative Structure-activity Relationships of Sulfonamide Endothelin Inhibitors," *Journal of Medicinal Chemistry* **38(4)**, 659-668, (1995).
125. Mager, P.P., "QSAR, Diagnostic Statistics, and Molecular Modelling of Antiallergic Acrylamide Derivatives," *Drug Des. Discov.* **9(2)**, 107-18 (1992).
126. Kaul, S., et al., "Quantitative Structure--pharmacokinetic Relationship of a Series of Sulfonamides in the Rat," *European Journal of Drug Metabolism and Pharmacokinetics* **15(3)**, 211-217 (1990).

127. Lisciani, R., et al., "Structure-analgesic Activity Relationships in a Set of 2-aminobenzamide Derivatives," *Farmaco [Sci]*. **41(2)**, 89-102 (1986).
128. Seydel J.K., et al., "Quantitative Structure-pharmacokinetic Relationships Derived on Antibacterial Sulfonamides in Rats and its Comparison to Quantitative Structure-activity Relationships," *Journal of Medicinal Chemistry* **23(6)**, 607-613 (1980).
129. Recanatini, M., Hansch, C., and Cavalli, A., "A Comparative QSAR Analysis of Acetylcholinesterase Inhibitors Currently Studied for the Treatment of Alzheimer's Disease," *Chemical and Biological Interactions* **105(3)**, 199-228 (1997).
130. Debord, J., et al., "Cholinesterase Inhibition by Derivatives of 2-amino-4,6-dimethylpyridine," *Journal of Enzyme Inhibition* **12(1)**, 13-26 (1997).
131. Akamatsu, M., et al., "Quantitative Analyses of the Structure-hydrophobicity Relationship for N-acetyl di- and tripeptide Amides," *Journal of Pharmaceutical Science* **83(7)**, 1026-1033 (1994).
132. McGuire, E.J., et al., "Peroxisome Induction Potential and Lipid-regulating Activity in Rats. Quantitative Microscopy and Chemical Structure-activity Relationships," *American Journal of Pathology* **139(1)**, 217-229 (1991).
133. Dai, Q.H., et al., "Quantitative Explanation on Structure-carcinogenic Activity Relationship of Aromatic Amines by Di-region Theory," *Sci. China B* **34(5)**, 547-559 (1991).
134. Trieff, N.M., et al., "Aromatic Amines and Acetamides in Salmonella Typhimurium TA98 and TA100: a Quantitative Structure-activity Relation Study," *Molecular Toxicology* **2(1)**, 53-65 (1989).
135. Purdy, R., "The Utility of Computed Superdelocalizability for Predicting the LC<sub>50</sub> Values of Epoxides to Guppies," *Sci Total Environ.* **109-110**, 553-6 (1991).
136. Hatch, F.T., et al., "Quantitative Structure-activity (QSAR) Relationships of Mutagenic Aromatic and Heterocyclic Amines," *Mutation Research* **376(1-2)**, 87-96 (1997).
137. Sabbioni, G., et al., "Quantitative Structure-activity Relationships of Mutagenic Aromatic and Heteroaromatic Azides and Amines," *Carcinogenesis* **13(4)**, 709-73 (1992).
138. Roberts, D. W., Basketter, D. A., "Further Evaluation of the Quantitative Structure-activity Relationship for Skin-sensitizing Alkyl Transfer Agents," *Contact Dermatitis* **37(3)**, 107-112 (1997).
139. Ehring, G.R., et al., "Quantitative Structure Activity Studies of Antiarrhythmic Properties in a Series of Lidocaine and Procainamide Serivatives," *J. Pharmacol. Exp. Ther.* **244(2)**, 479-492 (1988).
140. Chaisuksant Y., et al., "Effects of Halobenzenes on Growth Rate of Fish (*Gambusia Affinis*)," *Ecotoxicology and Environmental Safety* **39(2)**, 120-130 (1998).
141. Waller, C.L., et al., "Modeling the Cytochrome P450-mediated Metabolism of Chlorinated Volatile Organic Compounds," *Drug Metab Dispos.* **24(2)**, 203-210 (1996).
142. Roldan-Arjona, T., et al., "Mutagenic and Lethal Effects of Halogenated Methanes in the Ara Test of Salmonella Typhimurium: Quantitative Relationship with Chemical Reactivity," *Mutagenesis* **8(2)**, 127-131 (1993).
143. Mumtaz, M.M., et al., "A Weight-of-evidence Approach for Assessing Interactions in Chemical Mixtures," *Toxicology and Industrial Health* , 377-406 (1992).
144. Crebelli, R., et al., "The Induction of Mitotic Chromosome Malsegregation in *Aspergillus Nidulans*. Quantitative Structure Activity Relationship (OSAR) Analysis with Chlorinated Aliphatic Hydrocarbons," *Mutation Research* **266(2)**, 117-34 (1992).

145. Benigni, R., et al., "Relationship between Chlorofluorocarbon Chemical Structure and Their Salmonella Mutagenicity," *Journal of Toxicology and Environmental Health* **34(3)**, 397-407 (1991).
146. Devillers, J., et al., "Quantitative Structure-activity Relations of the Lethal Effects of 38 Halogenated Compounds against *Lepomis Macrochirus*," *C. R. Acad. Sci. III*, **303(14)**, 613-616 (1986) French.
147. Weinstein, H., et al., "Determinants of Molecular Reactivity as Criteria for Predicting Toxicity: Problems and Approaches," *Environ. Health Perspective* **61**, 147-162 (1985).
148. Sabljic, A., "Quantitative Structure-Toxicity Relationship of Chlorinated Compounds: A Molecular Connectivity Investigation," *Bulletin of Environmental Contamination Toxicology* **30(1)**, 80-83 (1983).
149. Politzer, P., Trefonas, P., Politzer, I., and R., Elfman, B., "Molecular Properties of the Chlorinated Ethylenes and their Epoxide Metabolites," *Annals of the New York Academy of Sciences* **367**, 478-492 (1981).
150. Hooberman, B.H., et al., "Quantitative Structure-activity Relationships for the Mutagenicity of Propylene Oxides with Salmonella," *Mutation Research* **299(2)**, 85-93 (1993).
151. Purdy, R., "The Utility of Computed Superdelocalizability for Predicting the LC<sub>50</sub> Values of Epoxides to Guppies," *Sci. Total Environ.* **109-110**, 553-556 (1991).
152. Lutz, W.K., "Structural Characteristics of Compounds that can be Activated to Chemically Reactive Metabolites: Use for a Prediction of a Carcinogenic Potential," *Arch Toxicol. Suppl.* **7**, 194-207 (1984).
153. Johnson, M.K. "The mechanism of delayed neuropathy caused by some organophosphorus esters: using the understanding to improve safety," *Journal of Environmental Science and Health [B]* **16(6)**, 823-841 (1980).
154. Jones, S.L., et al., "Quantitative Structure-activity Relationships for Estimating the No-observable-effects Concentration in Fathead Minnows (*Pimephales promelas*)," *Quality Assurance* **4(3)**, 187-203 (1995).
155. Jaworska, J.S., et al., "Quantitative Structure-toxicity Relationships and Volume Fraction Analyses for Selected Esters," *Archives of Environmental Contamination Toxicology* **29(1)**, 86-93 (1995).
156. Kluwe, W.M., "Carcinogenic Potential of Phthalic Acid Esters and Related Compounds: Structure-activity Relationships," *Environmental Health Perspectives* **65**, 271-278 (1986).
157. Nielsen, G. D., et al., "Sensory Irritation Mechanisms Investigated from Model Compounds: Trifluoroethanol, Hexafluoroisopropanol and Methyl Hexafluoroisopropyl Ether," *Archives of Toxicology* **70(6)**, 319-28 (1996).
158. Ren, S., et al., "QSAR Analysis of Membrane Permeability to Organic Compounds," *J Drug Target.* **4(2)**, 103-107 (1996).
159. Hamerton, I., et al., "Development of Quantitative Structure Property Relationships for Poly(arylene Ethers)," *Journal of Molecular Graphics* **13(1)**, 14-17, 51 (1995).
160. Hooberman, B.H., et al., "Quantitative Structure-activity Relationships for the Mutagenicity of Propylene Oxides with Salmonella," *Mutation Research* **299(2)**, 85-93 (1993).
161. Di Paolo, T., "Structure-activity Relationships of Anesthetic Ethers Using Molecular Connectivity," *Journal of Pharmacological Science* **67(4)**, 564-566 (1978).
162. Di Paolo, T., "Molecular Connectivity in Quantitative Structure--activity Relationship Study of Anesthetic and Toxic Activity of Aliphatic Hydrocarbons, Ethers, and Ketones," *Journal of Pharmacological Science* **67(4)**, 566-568 (1978).

163. Cronin, M.T., et al., "Structure-toxicity Relationships for Three Mechanisms of Action of Toxicity to *Vibrio Fischeri*," *Ecotoxicological Environmental Safety* **39(1)**, 65-69 (1998).
164. Wieland, T., "The Use of Structure Generators in Predictive Pharmacology and Toxicology," *Arzneimittelforschung* **46(2)**, 223-227 (1996).
165. Dai, Q.H., et al., "Quantitative Pattern Recognition for Structure-carcinogenic Activity Relationship of N-nitroso Compounds Based upon Di-region Theory," *Sci. China [B]* **32(7)**, 776-790 (1989).
166. Purdy, R., "A Mechanism-mediated Model for Carcinogenicity: Model Content and Prediction of the Outcome of Rodent Carcinogenicity Bioassays Currently Being Conducted on 25 Organic Chemicals," *Environmental Health Perspectives* **104 Supplement 5**, 1085-1094 (1996).
167. Lewis, D.F., Parke, D.V., Walker, R., Ioannides, C., and Brantom, P.G., "Nitrosamine Carcinogenesis: Rodent Assays, Quantitative Structure-activity Relationships, and Human Risk Assessment," *Drug Metabolism Reviews* **29(4)**, 1055-78 (1997).
168. Johnson, M.K., "The Mechanism of Delayed Neuropathy Caused by Some Organophosphorus Esters: Using the Understanding to Improve Safety," *Journal of Environmental Science and Health [B]* **15(6)**, 823-41 (1980).
169. Martin, Yvonne C., "Studies of Relationships between Structural Properties and Biological Activity by Hansch Analysis," in Golberg, Leon, editor, *Structure-Activity Correlation as a Predictive Tool in Toxicology*, Hemisphere Publishing, Washington, DC, 1983, pp. 77.
170. Golberg, Leon, editor, *Structure-Activity Correlation as a Predictive Tool in Toxicology*, Hemisphere Publishing, Washington, DC, 1983.
171. Chan, P. and Hayes, A. W., "Acute Toxicity and Eye Irritancy," in Hayes, A.W., ed., *Principles and Methods of Toxicology*, Third Edition, Raven Press, Ltd., New York, 1994.
172. Grzyll, L. R. and Back, D. D., *Development of Quantitative Structure-Property Relationships for Tropodegradable Halocarbon Fire Suppression Agents*" Final Report, Mainstream Engineering, Inc., Rockledge, FL, March 1997.
173. Grzyll, L. R., Back, D. D., Ramos, C., and Samad, N. A., "Screening and Characterization of Second-Generation Halon Replacements," in Gann, R.G., Burgess, S.R., Whisner, K.C., and Reneke, P.A., eds., *Papers from 1991-2006 Halon Options Technical Working Conferences (HOTWC)*, CD-ROM, NIST SP 984-4, National Institute of Standards and Technology, Gaithersburg, MD, 2006.
174. Mather, J.D., and Tapscott, R.E., *Environmentally Acceptable Extinguishants*, Final Report, NIST GCR 06-901, National Institute of Standards and Technology, Gaithersburg, MD, 2006.
175. Frazier, J. M., Evaluation of *In vitro* Alternatives to the Dog Cardiac Sensitization Assay, ManTech Environmental Technologies, Inc., Toxic Hazards Research Unit, Dayton Ohio, April 1994.
176. Clark, D.G., Tinston, D.J., "Correlation of the Cardiac Sensitization Potential of Halogenated Hydrocarbons with their Physiochemical Properties," Imperial Chemical Industries Limited - Short Communications, May 25, 1973.
177. Tanner, Liebman & Eckenhoff, *Toxicology Letters* **100-101**, 387-391 (1998).
178. Hemmings, Jr., H.C., and Hopkins, P.M., "*Foundations of Anesthesia - Basic and Clinical Science*," Harcourt, 2000.
179. *Ibid.*, Chapter 5, "Molecular Physiology."
180. *Ibid.*, Chapter 8, "Pharmacokinetics of Inhalation Anesthetics."

181. *Ibid.*, Chapter 22, "Mechanisms of Anesthesia."
182. *Ibid.*, Chapter 24, "Inhalation of Anesthetic Agents."
183. [www.virtual-anaesthesia-textbook.com/vat/volatile.htm](http://www.virtual-anaesthesia-textbook.com/vat/volatile.htm). A tutorial website with a wide variety of anesthesia agents' clinical human exposure and cardiac effects information, as well as further reference citations.
184. Hemmings, Jr., H.C., and Hopkins, P.M., *op cit.*, Chapter 41 "Cardiac Anesthesia."
185. [www.virtual-anaesthesia-textbook.com/vat/volatile.htm](http://www.virtual-anaesthesia-textbook.com/vat/volatile.htm). This is an excellent tutorial website with detailed discussions of a wide variety of anesthesia agents including clinical human exposure and cardiac effects information as well as further reference citations.
186. Molinspiration Cheminformatics web site: <http://www.molinspiration.com> and Syracuse Research Corporation web site: <http://esc.syrres.com>.
187. Finch, G.L., Barr, E., Nikula, K., Krone, J., and Mather, J.D., "Acute Inhalation Toxicity of Candidate Halon Replacement Compounds in Rats," Final Report, Lovelace Respiratory Research Institute, Albuquerque, NM, April 22, 1999.
188. Goldman, B. I., and Wurzel, J., "Effects of Subcultivation and Culture Medium on Differentiation of Human Fetal Cardiac Myocytes," *In Vitro Cell Development Biology* **28A**, 109-119 (1992).
189. Mark, G. E. and Strasser, F. F., "Pacemaker Activity and Mitosis in Culture of Newborn Rat Heart Ventricle Cells," *Experimental Cell Research* **44**, 217-233 (1966).
190. Schanne, O.F., Ruiz-Ceretti, E., Rivard, C., and Chartier, D., "Determinants of Electrical Activity in Clusters of Cultured Cardiac Cells From Neonatal Rats," *Journal of Molecular and Cellular Cardiology* **9**, 269-283 (1977).
191. Liu, W., Clarkson, C. W., Yamasaki, S., Chang, C., Stolfi, A., and Pickoff, A. S., "Characterization of the Rate-Dependent Effects of Ethmozine on Conduction, In Vivo, and on the Sodium Current, *In vitro*, in the Newborn Heart," *Journal of Pharmacological Experiments and Theory* **263**, 608-616 (1992).
192. Vahouny, G. V., Wei, R., Starkweather, R., and Davis, C., "Preparation of Beating Heart Cells from Adult Rats," *Science* **167**, 1616-1618 (1970).
193. Dani, A. M., Cittadini, A., and Inesi, G., "Calcium Transport and Contractile Activity in Dissociated Mammalian Heart Cells," *American Journal of Physiology* **6**, C147-C155 (1979).
194. Youker, K., Smith, C. W., Anderson, D. C., Miller, D., Michael, H., Rossen, R. D., Entman, M. L., "Neutrophil Adherence to Isolated Adult Cardiac Myocytes. Induction by Cardiac Lymph collected During Ischemia and Reperfusion," *Journal of Clinical Investigation* **89**, 602-609 (1992).
195. Woosley, R. L., Chen, Y., Freiman, J. P., Gillis, R. A., "Mechanism of the Cardiotoxic Actions of Terfenadine," *Journal of American Medical Association* **269**, 1532-1536 (1993).
196. Failli, P., Fazzini, A., Franconi, F., Stendardi, I., Giotti, A., "Taurine Antagonizes the Increase in Intracellular Calcium Concentration Induced by Alpha-Adrenergic Stimulation in Freshly Isolated Guinea-Pig Cardiomyocytes," *Journal of Molecular and Cellular Cardiology* **24**, 1253-1265 (1992).
197. Eid, H., Larson, D. M., Springhorn, J. P., Attawia, M. A., Nayak, R. C., Smith, T. W., Kelly, R. A., "Role of Epicardial Mesothelial Cells in the Modification of Phenotype and Function of Adult Rat Ventricular myocytes in Primary Coculture," *Circulation Research* **7**, 40-50 (1992).
198. Vinegar, A., G.W. Jepson, and J.H. Overton. "PBPK Modeling of Short-term (0 to 5 min) Human Inhalation Exposures to Halogenated Hydrocarbons," *Inhalation Toxicology* **10**, 411-429 (1998).

199. Vinegar, A., "Modeling Cardiac Sensitization Potential of Humans Exposed to Halon 1301 or Halon 1211 aboard Aircraft," *Aviation, Space, and Environmental Medicine* **72**(10), 928-936 (2001).
200. Vinegar, A., (PBPK Modeling of Canine Inhalation Exposures to Halogenated Hydrocarbons," *Toxicological Sciences* **60**, 20-27 (2001).
201. Vinegar, A., Jepson, G.W., Cisneros, M., Rubenstein, R., and Brock, W.J., "Setting Safe Acute Exposure Limits for Halon replacement Chemicals using Physiologically Based Pharmacokinetic Modeling," *Inhalation Toxicology* **12**, 751-762 (2000).
202. Gargas, M.L., Andersen, M.E., and Clewell, III, H.J., "A Physiologically-based Simulation Approach for Determining Metabolic Constants from Gas Uptake Data," *Toxicology and Applied Pharmacology* **86**, 341-352 (1986).
203. NFPA 12A, *Standard on Halon 1301 Fire Extinguishing Systems*, NFPA , Quincy, MA, 2004.
204. Smith, D.G. and Harris, D.J., "Human Exposure to Halon 1301 (CBrF<sub>3</sub>) During Simulated Aircraft Cabin Fires," *Aerospace Medicine* **44**, 198-201 (1973).
205. Abramowitz, A., Neese, W., and Slusher, G., "Smoke and Extinguisher Agent Dissipation in a Small Pressurized Fuselage," Federal Aviation Administration report DOT/FAA/CT-89/31, 1990.
206. Slusher, G.R., Wright, J., and Demaree, J., "Halon Extinguisher Agent Behavior in a Ventilated Small Aircraft," Federal Aviation Administration report DOT/FAA/CT-86/5, 1986.
207. Lerman, Y., Winkler, E., Tirosh, M.S., Danon, Y., and Almog, S., "Fatal Accidental Inhalation of Bromochlorodifluoromethane (Halon 1211), *Human Experiments in Toxicology* **10**, 125-128 (1991).
208. Vinegar, A., Jepson, G.W., Hammann, S.J., Harper, G., Dierdorf, D.S., and Overton, J.J., "Simulated Blood Levels of CF<sub>3</sub>I in Personnel Exposed During its Release from an F-15 Jet Engine Nacelle and During intentional inhalation," *Journal of the American Industrial Hygiene Association* **60**, 403-408 (1999).
209. Vinegar, A., and Jepson, G., *Toxicological Assessment of Human Health Consequences Associated with Inhalation of Halon Replacement Chemicals; Section I: Physiologically-based Modeling of Halon Replacements for Human Safety Evaluations*, Final Report to the Strategic Environmental Research and Development Program, (2000).
210. "Acute Inhalation Toxicity," Guideline 403, Organization of Economic and Commercial Development (OECD), Paris, France, adopted 12 May 1981.

---

---

## Chapter 7: SEARCH FOR NEW FIRE SUPPRESSANT CHEMICALS

J. Douglas Mather, Ph.D.  
Chemical Development Studies, Inc.

Robert E. Tapscott, Ph.D.  
GlobeTech, Inc.

---

---

### TABLE OF CONTENTS

7.1	Fire Suppressant Replacement Knowledge Prior to the NGP .....	612
7.1.1	Overview of Early Halon Replacement Efforts .....	612
7.1.2	Fire Suppressant Research – 1974 Through 1993.....	613
7.1.3	DoD Technology Development Plan (1993 to 1997).....	615
7.1.4	Advanced Agent Working Group (AAWG) .....	616
7.1.5	Summary: Alternative Agents and Selection Criteria Prior to the NGP .....	622
7.2	The NGP Approach to New Chemicals Screening .....	612
7.3	NGP Surveys of Inorganic Chemical Families.....	612
7.3.1	Main Group Elements - Group I.....	626
7.3.2	Main Group Elements - Group II .....	627
7.3.3	Main Group Elements - Group III.....	627
7.3.4	Main Group Elements - Group IV.....	628
7.3.5	Main Group Elements - Group V.....	634
7.3.6	Main Group Elements - Group VI.....	645
7.3.7	Main Group Elements - Group VIII (Noble Gases).....	646
7.3.8	Transition Metal Based Compounds .....	646
7.3.9	Inorganic Chemicals - Conclusions.....	647
7.4	NGP Surveys of Organic Compounds .....	647
7.4.1	Highly Efficient Thermal Agents.....	647
7.4.2	Tropodegradable Candidate Compounds .....	658
7.4.3	Bromofluoroalkenes .....	662
7.4.4	Fluoroalkoxide and Fluoroalkyl Phosphorus Compounds .....	665
7.4.5	Fluoroalkyl Nitrogen-based Candidates .....	680
7.4.6	Bromofluoroalkyl Nitrogen-based Candidates.....	685
7.4.7	Fluorinated Ethers .....	687
7.4.8	Bromofluoroethers.....	691
7.4.9	Bromofluorooxiranes.....	694
7.4.10	Bromofluoro / Fluorinated Aldehydes and Ketones.....	695
7.4.11	Bromofluoro Alcohols.....	695
7.4.12	Iodinated Hydrocarbons .....	696
7.5	Chemical Family Options and Replacement Issues.....	700
7.5.1	Suppressant Criteria and Selection Constraints.....	700
7.5.2	General Conclusions.....	701
7.6	References.....	702

## 7.1 FIRE SUPPRESSANT REPLACEMENT KNOWLEDGE PRIOR TO THE NGP

### 7.1.1 Overview of Early Halon Replacement Efforts

As described in Chapter 1 of this book, in the years following the Army-Purdue study, there was extensive scientific and engineering research that led to the commercialization and widespread use of halon 1301. Following the adoption of the Montreal Protocol on Substances That Deplete the Ozone Layer in 1987, organized efforts to identify replacements were initiated by a broad range of governmental and non-governmental groups. These efforts were hastened in the United States by the planned phase-out of production of halon 1301 (CF<sub>3</sub>Br) and halon 1211 (CF<sub>2</sub>ClBr) by the end of 1993.

The replacement of halon 1301 presented some daunting challenges. Halon 1301 is unique as a brominated halocarbon. Its -58 °C boiling point is the lowest of the bromofluoroalkane chemical family, and its toxicity is quite low. It is an efficient fire suppressant and explosion inertant. It has great dimensionality (space filling), high tolerance to less than optimal discharge technique, and excellent chemical stability. Early results showed that a small change in the molecule could lead to large and conflicting effects on key performance properties. For example, the replacement of a fluorine atom by a hydrogen atom to produce halon 1201 (CF<sub>2</sub>HBr) reduced the estimated atmospheric lifetime from 65 years to 15 years, but raised the boiling point to -15 °C.

Nonetheless, the search for alternatives to the firefighting halons began as a quest for a "drop-in," a chemical that would fit into existing fire suppression systems and perform just like or better than the halon it was replacing. During the early years of this research, there were frequent changes in thinking among those involved in identifying new chemicals. For instance, it was realized that instead of a single drop-in replacement being identified for halon 1301 (as well as halon 1211) the world of fire suppression applications was going to see a broad range of new agents and technologies. Furthermore, the criteria for environmental acceptability changed. With the emphasis on dramatic reductions in both stratospheric ozone depletion effects and atmospheric global warming potentials, the research focus shifted to identifying short atmospheric lifetime molecules. These compounds incorporate structural components that are reactive with atmospheric constituents of the atmosphere or are photochemically reactive, as shown in Table 7-1.

**Table 7-1. Tropospheric Removal Mechanisms.**

Primary Removal Mechanism	Example Families
Photodegradation	Iodides, carbonyls, bromides
Reaction with hydroxyl radicals	Alkenes, aromatics, hydrogen-containing amines, hydrogen-containing ethers, carbonyls
Physical removal	Ketones, alcohols, esters
Reaction with tropospheric ozone	Alkenes

Risk assessment based toxicity tests and limits were identified, and understanding of situational toxicological constraints underwent considerable evolution. Some chemical options considered for halon replacement (e.g., the perfluorocarbons) were at first embraced, but later discarded as understanding of global warming impact issues developed.

By the time NGP research began in 1997, these efforts had resulted in the birth of new fire extinguishment technologies, a broader view of the chemical options available, and emerging

understanding of the dynamics of fire suppression under the adverse conditions encountered during the suppression of in-flight fires in aircraft. The following is a brief summary of these activities and their outcomes.

### 7.1.2 Fire Suppressant Research - 1974 Through 1993

Scientists at the Naval Research Laboratory had begun investigation of the principles of fire suppression by halon 1301 as early as 1974. This was driven by the Naval Air System Command's desire for a more efficient agent for suppressing in-flight fires. The outcome of this and the few contemporary efforts are summarized in Reference 1. As Rowland and Molina's finding that such compounds could deplete stratospheric ozone became well-known, this research broadened to a variety of fire suppression related topics and potential chemical agents.<sup>2,3</sup> Research at NRL also studied  $\text{CF}_3\text{I}$  flame extinguishment<sup>4,5</sup> and conducted studies of hydrogen fluoride (HF) byproduct formation resulting from halon 1301 fire extinguishment.<sup>6,7</sup>

Beginning in the mid-1980s, the U.S. Air Force (USAF) sponsored research at the New Mexico Engineering Research Institute (NMERI) on "first generation" halon replacement candidates focused on chemicals that were or soon would be readily available and that had a significant amount of known toxicological information.<sup>8</sup> This strategy was adopted for two reasons:

1. Available chemicals could be tested at relatively low cost to determine effectiveness in firefighting scenarios, and
2. Toxicological testing of candidates was expensive and time consuming.

Chemicals developed primarily as chlorofluorocarbon (CFC) replacements were the major focus as first-generation replacements. Relatively large quantities of these chemicals were available, and manufacturers were supporting toxicological testing, as these chemicals were often being considered for applications as refrigerants, solvents, and foam blowing agents, in addition to fire suppression. This strategy proved successful in that a number of halon replacement candidates were identified that were readily available for testing that had a significant amount of toxicity testing already performed.<sup>9,10,11,12,13</sup> Evolving understanding of likely global warming and ozone depletion restrictions as well as the desire for greater agent effectiveness in fire suppression led to a de-emphasis on "first generation" chemicals.

The first generation agents were all halocarbons: hydrochlorofluorocarbons (HCFCs), perfluorocarbons (FCs or PFCs), and hydrofluorocarbons (HFCs). Hydrobromofluorocarbons (HBFC) were also evaluated very early in the program, but were dropped when it became apparent that they would be regulated due to their still significant Ozone Depletion Potentials (ODP). Although the first generation program was successful in identifying available candidates that did not require toxicological testing, the first generation halocarbons were not as effective as the in-use halons and required approximately two to four times more agent. Moreover, some had toxicological and environmental drawbacks. In particular, environmental concerns led to the following restrictions:

- HCFCs would eventually be phased out of production due to their non-zero ODP, and some restrictions are already in place in parts of Europe (and to a limited extent in the USA). The European Community (EC) regulation 3093/94, which entered into force on 1 June 1995, does not allow the use of HCFCs for fire protection.

- Under the Significant New Alternatives Policy (SNAP), the U.S. Environmental Protection Agency (EPA) has applied narrowed limits to the use of perfluorocarbons. PFCs are fully fluorinated compounds, unlike HCFCs or HFCs, and have several attractive features. They are nonflammable, have low toxicity, and do not contribute to stratospheric ozone depletion. The environmental characteristics of concern, however, are their high Global Warming Potentials (GWPs), which are as much as 12,500 times that of carbon dioxide (for a 100 year time horizon), and their long atmospheric lifetimes of up to 50,000 years for CF<sub>4</sub>.<sup>14</sup> Although the actual contributions to global warming depend upon the quantities emitted, the long lifetimes make the warming effects of PFCs irreversible. The EPA is allowing the use of PFCs for only selected applications where no other substitute would meet performance or safety requirements.
- HFCs have been prominent as replacements for ozone depleting substances. Nevertheless, they are receiving increasing attention from environmental organizations. The National Institute of Public Health and Environmental Protection, The Netherlands, has projected a significant increase in greenhouse gas emissions due to the use of HFCs to replace CFCs and HCFCs.<sup>15</sup> Moreover, in 1996 Denmark announced that they planned to phase out all hydrofluorocarbons (HFCs) within the next 10 years due to their contributions to global warming.<sup>16</sup>

Early NMERI research on streaming agent replacements for halon 1211 led to the development of methods of estimating atmospheric lifetime and ozone depletion,<sup>17</sup> laboratory scale test methods,<sup>18</sup> methods for evaluation of materials compatibility and operational validation,<sup>19</sup> and preliminary lists of advanced agents (chemically active suppressants).<sup>20</sup>

In 1989, a number of companies involved in the manufacture, sale, and installation of fire suppressant chemicals formed the Halon Alternatives Research Consortium (HARC, which would evolve into the Halon Alternatives Research Corporation). This group's Technical Committee formulated a research plan that would lead to the identification of alternatives to halon 1301 and halon 1211. The first (and only) projects were sponsored by the USAF at the National Institute of Standards and Technology (NIST). The output was two reports:

1. *Preliminary Screening Procedures and Criteria for Replacements for Halons 1211 and 1301*, which was discussed in Chapter 6 of this book.
2. *Construction of an Exploratory List of Chemicals to Initiate the Search for Halon Alternatives*.<sup>21</sup> This report is the first systematic survey since the late 1940s of chemical families and their potentials as halon replacements. Table 7-2 presents the chemical family recommendations resulting from this analysis.

Guiding attributes required of a replacement for halon 1301 included: fire suppression effectiveness, low residue level, low electrical conductivity, low metals corrosion, high materials compatibility, stability under long term storage, low toxicity (inhalation and contact) of the chemical and its combustion products, and low (or zero) contributions to stratospheric ozone depletion and global warming. The report summarized the various mechanisms of flame extinguishment and listed approaches to altering a chemical to decrease its contribution to ozone depletion, including enhancement of chemical reactivity with atmospheric •OH radicals. Finally, the report listed 103 compounds of immediate interest for further testing in flame extinguishment and explosion suppression. Several of the chemical families identified as well as approaches to selecting environmentally acceptable short atmospheric lifetime compounds identified were successfully employed in later studies.

**Table 7–2. NIST List of Recommended Chemical Families (1990).**

Chemical Family Recommendation	Justification for Further Consideration - Environmental Advantage and Flame Suppression Estimates
Halogenated ketones, anhydrides, esters	Carbonyl absorption max. red shift contributes to photolysis
Unsaturated halocarbons	Reactivity of alkenes to atmospheric •OH radicals
Halogenated ethers and related compounds	Absorption red shift due to C-O-C linkage aides in photolysis
Halons containing iodine	Iodinated halogenated compounds more photochemically reactive and a higher fire suppression efficiency
Sulfur halides	Desirable attributes - Low toxicity, possible significant fire suppression properties
Phosphorus containing compounds	Established fire suppression properties (expected free radical trap mechanism) needs a more volatile or gaseous compound
Silicon and germanium compounds	Silicon in particular (possibly germanium) expected flame suppression effectiveness and short atmospheric lifetime
Metallic compounds	Established flame suppression properties, likely alternative compounds of great interest
Inert gases	Physical suppressant options

The Halon Options Technical Working Conference held its first annual meeting in the spring of 1991. The conference became the premier forum for presentation of research related to halon replacements and, as such, routinely covered topics ranging from new agents and fire suppression equipment to atmospheric science and chemical and suppression by-product toxicology. The compiled papers are available on CD from NIST<sup>22</sup> and at the HOTWC web site, [www.bfrl.nist.gov/866/HOTWC](http://www.bfrl.nist.gov/866/HOTWC).

As early as the first HOTWC, research papers were presented describing the synthesis of compounds which to the present are topics of intense interest. For example, a 1991 paper presented by Dr. J. Adcock of the University of Tennessee detailed his synthesis, under funding by the Electric Power Research Institute, of the low molecular weight brominated fluoroethers that remain of intense interest today.<sup>23</sup> Papers presented by EPA staff covering toxicology and regulatory and toxicological issues provided guidance to the fire research community and those involved in the search for new chemicals. Researchers from private industry presented numerous papers detailing the results of their halon replacement efforts. Many papers detailing agent and equipment development and testing as well as basic extinguishment science were presented by researchers from the military services in the U.S. and overseas.

### 7.1.3 DoD Technology Development Plan (1993 to 1997)

The Technology Development Plan (TDP) was initiated to identify feasible, commercially available alternatives to ozone depleting substances or use in existing weapons systems.<sup>24</sup> The work was divided among seven Technical Plans. Those involving fire fighting were:

- Technical Plan I. Alternative chemicals, processes and/or techniques for extinguishment of slow growth fires in manned spaces of ships and critical command and control facilities. The best chemical for retrofit was identified as HFC-227ea (C<sub>3</sub>HF<sub>7</sub>). Fine water mist was noted as a candidate for future platforms.
- Technical Plan II. Alternative chemicals, processes, and/or techniques for extinguishment of slow growth fires in engine nacelles and dry bays of fixed wing aircraft and helicopters. HFC-125 (C<sub>2</sub>HF<sub>5</sub>) was identified as the optimal chemical for engine nacelle fires. Solid

propellant gas generator technology was promoted for dry bay applications. Perfluorohexane was identified as a streaming agent to replace halon 1211.

- Technical Plan III. Alternative chemicals, processes, and/or techniques for extinguishment of fast growth fires and explosion suppression in unmanned spaces of fixed wing aircraft engine nacelles and dry bays of fixed wing aircraft and helicopters. Completion of this work was deferred.
- Technical Plan IV. Alternative chemicals, processes, and/or techniques for explosion suppression in crew occupied compartments of ground armored vehicles.

All but one of these compounds was less efficient than the halon it would replace, requiring more mass and higher storage volume to achieve comparable performance. Trifluoromethyl iodide ( $\text{CF}_3\text{I}$ ) was found to be as effective as the existing halons. However, cardiac sensitization at levels well below the extinguishing concentration restricted further consideration.

There was, therefore, an increasing incentive to look at compounds other than the usual, saturated halocarbons. These compounds are the non-halocarbon candidates, known as “advanced agents.” The most promising of these were the phosphorus compounds (particularly, the phosphorus nitrides (which include phosphazenes and phosphonitriles), metal compounds, and silicon compounds. In addition, the broad family of tropodegradable bromocarbons included promising candidates.

#### 7.1.4 Advanced Agent Working Group (AAWG)

On August 23, 1994 representatives of the North Slope Oil Producing and Transmission Companies met with members of the “ $\text{CF}_3\text{I}$  Working Group.” The AAWG was formed in the course of this meeting with participating representatives of most of the U.S. military services, NIST, EPA, several fire suppression industry representatives, private consultants, and NMERI. The AAWG funded some of the initial efforts to determine the probability of identifying clean advanced agents for use in normally occupied areas. The work was largely performed at NMERI. Questions posed included:

- What chemically active agent mechanisms were available for protection against fire and explosion?
- What chemical families could provide a replacement for halon 1301 (including preliminary assessments of manufacturability, global environmental impact, and toxicity for these families)?
- What were the prospects for a halon 1301 replacement without major hardware changes?

A listing of specific chemicals was developed for study (Table 7–3). The compounds listed emphasized estimated short atmospheric lifetime and the presence of bromine in the chemical structure. Additional efforts to estimate toxicity, physical properties and more accurately determine fire extinguishment performance through selective testing of some of the compounds listed were initiated.

NMERI assembled physical and toxicological information on the compounds and identified sources and in some cases synthetic methods for these compounds. Toxicological and physical property reviews of this data related toxicity modeling data were performed. Little cardiac sensitization data could be identified at that point and models in existence did not address this particular toxicological end point.

Table 7–3. AAWG Preliminary List of Compounds.

Chemical Formula	Chemical Name	CAS No./Availability
<b>Alkenes</b>		
CH <sub>2</sub> =CHCF <sub>2</sub> Br	3-bromo-3,3-difluoropropene	420-90-6/Commercial sources
CF <sub>2</sub> BrCH=CHCF <sub>3</sub>	<i>cis</i> - and <i>trans</i> -1-bromo-1,1,4,4,4-pentafluoro-2-butene	
CF <sub>2</sub> BrCF <sub>2</sub> CH=CH <sub>2</sub>	4-bromo-3,3,4,4-tetrafluorobutene	18599-22-9/Commercial sources
CF <sub>2</sub> BrC(CF <sub>3</sub> )=CH <sub>2</sub>	3-bromo-3,3-difluoro-2-(trifluoromethyl)propene	
<b>Alcohols</b>		
CF <sub>2</sub> BrCH <sub>2</sub> OH	2-bromo-2,2-difluoroethanol	420-94-0
CF <sub>3</sub> CFBrCH <sub>2</sub> OH	2-bromo-2,3,3,3-tetrafluoropropanol	94083-41-7
CF <sub>2</sub> BrCF <sub>2</sub> CH <sub>2</sub> OH	3-bromo-2,2,3,3-tetrafluoropropanol	
CF <sub>3</sub> CHOHCH <sub>2</sub> Br	3-bromo-1,1,1-trifluoro-2-propanol	Research chemical only
<b>Ethers</b>		
CF <sub>2</sub> H-O-CF <sub>2</sub> HBr	(bromodifluoromethyl)(difluoromethyl)ether	no CAS Number
CF <sub>2</sub> Br-O-CH <sub>3</sub>	(bromodifluoromethyl)(methyl)ether	
CF <sub>2</sub> BrCH <sub>2</sub> -O-CF <sub>3</sub>	(2-bromo-2,2-difluoroethyl)(trifluoromethyl)ether	
CF <sub>2</sub> BrCF <sub>2</sub> -O-CH <sub>3</sub>	(2-bromo-1,1,2,2-tetrafluoroethyl)(methyl)ether	13749-39-8
-CH <sub>2</sub> CF <sub>2</sub> CBrFCH <sub>2</sub> -O-	3-bromo-2,2,3-trifluorooxolane	
<b>Amines</b>		
(CBrF <sub>2</sub> )(CHF <sub>2</sub> ) <sub>2</sub> N	bis(difluoromethyl)(bromodifluoromethyl)amine	no CAS Number
(CBrF <sub>2</sub> )(CF <sub>3</sub> )(CH <sub>3</sub> )N	(bromodifluoromethyl)(trifluoromethyl)(methyl)amine	no CAS Number
(CF <sub>3</sub> ) <sub>2</sub> (CH <sub>2</sub> CBrF <sub>2</sub> )N	bis(trifluoromethyl)(2-bromo-2,2-difluoroethyl)amine	
(CBrF <sub>2</sub> )(CF <sub>3</sub> ) <sub>2</sub> N	bis(trifluoromethyl)(bromodifluoromethyl)amine	
<b>Carbonyl Compounds</b>		
CBrF <sub>2</sub> CH <sub>2</sub> C(O)H	3-bromo-3,3-difluoropropanal	
CH <sub>3</sub> C(O)CH <sub>2</sub> CF <sub>2</sub> Br	4-bromo-4,4-difluoro-2-butanone	
CBrF <sub>2</sub> CH <sub>2</sub> C(O)OCH <sub>3</sub>	methyl 3-bromo-3,3-difluoropropionate	99953-33-0
CBrF <sub>2</sub> CH <sub>2</sub> C(O)OCF <sub>3</sub>	trifluoromethyl 3-bromo-3,3-difluoropropionate	
<b>Aromatics</b>		
C <sub>6</sub> F <sub>5</sub> Br	bromopentafluorobenzene	344-04-7/Commercial sources
C <sub>6</sub> F <sub>5</sub> CBrF <sub>2</sub>	(bromodifluoromethyl)pentafluorobenzene	35523-39-8
C <sub>6</sub> BrF <sub>4</sub> CF <sub>3</sub>	bromoheptafluorotoluene	113601-46-0
	2-bromoheptafluorotoluene	66820-64-2
	3-bromoheptafluorotoluene	5360-80-5
	4-bromoheptafluorotoluene	17823-46-0

A toxicological quantitative structure-activity relationship (QSAR) relies on the establishment of a statistically significant mathematical correlation between chemical toxicity and a particular chemical, structural, or physical property of a group of similar compounds in order to be used to predict the toxicity of untested chemicals. Further, the predictive accuracy of values and trends is greatest for only for compounds in the same group or very similar groups. QSAR models also included proprietary models for halon property estimation which attempted the estimation of cardiac sensitization LOAEL values.<sup>25</sup>

QSAR modeling of 25 brominated compounds was performed by the U.S. Army Center for Health Promotion and Preventative Medicine (CHPPM) and the British Ministry of Defence (MOD) DERA. U.S. Army CHPPM employed TOPKAT to model QSAR toxicity predictions of acute LD<sub>50</sub>, LC<sub>50</sub>, eye sensitization and chronic LOAEL, mutagenicity, DPT, and carcinogenicity.<sup>26</sup> The results of this study are presented in Table 7–4.

**Table 7–4. TOPKAT Toxicity Predictions.**

Chemical Formula	Acute Toxicity <sup>a</sup>			Chronic Toxicity <sup>a</sup>			
	LD <sub>50</sub>	LC <sub>50</sub>	Eye	LOAEL	Mut.	DTP	Carc.
<b>Alkenes</b>							
CH <sub>2</sub> =CHCF <sub>2</sub> Br	o		o	o	X	o	(X)
CF <sub>2</sub> BrCH=CHCF <sub>3</sub>	o	o	X	o	o	o	X
CF <sub>2</sub> BrCF <sub>2</sub> CH=CH <sub>2</sub>	o	o	o	o	o	o	X
CF <sub>2</sub> BrC(CF <sub>3</sub> )=CH <sub>2</sub>		o	X	o	X	o	(X)
<b>Alcohols</b>							
CF <sub>2</sub> BrCH <sub>2</sub> OH	o	o	o	o	o	X	(X)
CF <sub>3</sub> CFBrCH <sub>2</sub> OH	o	o	o	o	o	X	X
CF <sub>2</sub> BrCF <sub>2</sub> CH <sub>2</sub> OH	o	o	o	o	o	X	X
CF <sub>3</sub> CHOHCH <sub>2</sub> Br	o	X		X	X		(X)
<b>Ethers</b>							
CF <sub>2</sub> H-O-CF <sub>2</sub> HBr				X	o		X
CF <sub>2</sub> Br-O-CH <sub>3</sub>				o	o	o	X
CF <sub>2</sub> BrCH <sub>2</sub> -O-CF <sub>3</sub>				o		o	X
CF <sub>2</sub> BrCF <sub>2</sub> -O-CH <sub>3</sub>	o	o		o	o		X
-CH <sub>2</sub> CF <sub>2</sub> CB <sub>r</sub> FCH <sub>2</sub> -O-				X	X	o	X
<b>Amines</b>							
(CBrF <sub>2</sub> )(CHF <sub>2</sub> ) <sub>2</sub> N				o			o
(CBrF <sub>2</sub> )(CF <sub>3</sub> )(CH <sub>3</sub> )N	o			o			(X)
(CF <sub>3</sub> ) <sub>2</sub> (CH <sub>2</sub> CBrF <sub>2</sub> )N				o	o		X
(CBrF <sub>2</sub> )(CF <sub>3</sub> ) <sub>2</sub> N				o			X
<b>Carbonyls</b>							
CBrF <sub>2</sub> CH <sub>2</sub> C(O)H	o			o			
CH <sub>3</sub> C(O)CH <sub>2</sub> CF <sub>2</sub> Br	o	X	o	o		X	
CBrF <sub>2</sub> CH <sub>2</sub> C(O)OCH <sub>3</sub>	o	o		o			(X)
CBrF <sub>2</sub> CH <sub>2</sub> C(O)OCF <sub>3</sub>		o		o			(X)
<b>Aromatics</b>							
C <sub>6</sub> F <sub>5</sub> Br		X	o	X			o
C <sub>6</sub> F <sub>5</sub> CB <sub>r</sub> F <sub>2</sub>		o	X				o
C <sub>6</sub> BrF <sub>4</sub> CF <sub>3</sub>		X*	X				o

o meaningful estimates

\* moderate confidence

Eye eye irritation

Mut mutagenicity

X possibly unacceptable toxicity levels

() mixed results on different models

Carc carcinogenicity

DERA employed DEREK (Deductive Estimation of Risk from Existing Knowledge), version 15.1,<sup>27</sup> to evaluate the same list of compounds. DEREK is a rule-based software system designed for qualitative prediction of potential toxicity hazards by a chemical based on known structure-activity relationships.

The program does not estimate cardiac sensitization.<sup>28</sup> Four endpoints were evaluated by DEREK, as shown in Table 7–5: carcinogenicity, mutagenicity, sensitization (presumably respiratory) and skin sensitization. In addition, the “rules” incorporated into model skin sensitization (where the program has a tendency to predict false positives) as well as respiratory sensitization, irritation and corrosivity. Acute toxicity is of the highest concern for halon alternatives, but unfortunately is not addressed by the program.

These estimation methods are both highly dependent on the existence of a “training set” of data for similar chemical structures and chemical functional groups in order to establish the correlations and weightings needed to be predictive. Such information is limited, rendering this approach of little use.

**Table 7–5. DEREK Toxicity Predictions.**

Chemical Family	Chemical Formula	DEREK Prediction
Alkenes	CH <sub>2</sub> =CHCF <sub>2</sub> Br	Skin irritation
	CF <sub>2</sub> BrCH=CHCF <sub>3</sub>	Skin irritation
	CF <sub>2</sub> BrCF <sub>2</sub> CH=CH <sub>2</sub>	Skin irritation, mutagenicity
	CF <sub>2</sub> BrC(CF <sub>3</sub> )=CH <sub>2</sub>	Skin irritation
Alcohols	CF <sub>2</sub> BrCH <sub>2</sub> OH	Skin irritation
	CF <sub>3</sub> CFBrCH <sub>2</sub> OH	Skin irritation, mutagenicity
	CF <sub>2</sub> BrCF <sub>2</sub> CH <sub>2</sub> OH	Skin irritation, mutagenicity
	CF <sub>3</sub> CHOHCH <sub>2</sub> Br	Skin irritation, mutagenicity
Ethers	CF <sub>2</sub> H-O-CF <sub>2</sub> HBr	Skin irritation
	CF <sub>2</sub> Br-O-CH <sub>3</sub>	Skin irritation
	CF <sub>2</sub> BrCH <sub>2</sub> -O-CF <sub>3</sub>	Skin irritation
	CF <sub>2</sub> BrCF <sub>2</sub> -O-CH <sub>3</sub>	Skin irritation
Amines	-CH <sub>2</sub> CF <sub>2</sub> CBrFCH <sub>2</sub> -O-	Skin irritation, mutagenicity
	(CBrF <sub>2</sub> )(CHF <sub>2</sub> ) <sub>2</sub> N	Skin irritation
	(CBrF <sub>2</sub> )(CF <sub>3</sub> )(CH <sub>3</sub> )N	Skin irritation
	(CF <sub>3</sub> ) <sub>2</sub> (CH <sub>2</sub> CBrF <sub>2</sub> )N	Skin irritation, mutagenicity
Ethers	(CBrF <sub>2</sub> )(CF <sub>3</sub> ) <sub>2</sub> N	Skin irritation
	CBrF <sub>2</sub> CH <sub>2</sub> C(O)H	Skin irritation, mutagenicity
	CH <sub>3</sub> C(O)CH <sub>2</sub> CF <sub>2</sub> Br	Skin irritation
	CBrF <sub>2</sub> CH <sub>2</sub> C(O)OCH <sub>3</sub>	Skin irritation
Aromatics	CBrF <sub>2</sub> CH <sub>2</sub> C(O)OCF <sub>3</sub>	Skin irritation
	C <sub>6</sub> F <sub>5</sub> Br	None
	C <sub>6</sub> F <sub>5</sub> CBrF <sub>2</sub>	Skin irritation, skin sensitization
	C <sub>6</sub> BrF <sub>4</sub> CF <sub>3</sub> (ortho, meta, para isomers)	None

As an alternative approach, Tapscott and Mather identified some general toxicity trends for alkanes, based on non-quantitative structure activity relationships (SARs) and published toxicity information, from comprehensive reviews of toxicity literature.<sup>29</sup> The identified trends are shown below in rows, with the compound formula followed by ln(LC<sub>50</sub>) values in mice for 30 min exposures. General trends relating the number of fluorine or hydrogen atoms needed to impart favorable toxicity were not identified. This study indicated that location of substituents appeared to play a more important role than the number of fluorine or hydrogen atoms.

- Toxicity increases in the order F < Cl < Br, for example:

CHF <sub>2</sub> CH <sub>2</sub> Cl, 2.00	CHF <sub>2</sub> CH <sub>2</sub> Br, 1.52	CF <sub>3</sub> CHBrCl, 0.18
CF <sub>3</sub> CHFCl, 3.8	CF <sub>3</sub> CHCl <sub>2</sub> , 2.00	

- For haloethanes, H adjacent to a –CF<sub>3</sub> group increases toxicity, therefore, CF<sub>2</sub>XCHF<sub>2</sub> is preferred over CF<sub>3</sub>CHX<sub>2</sub> (the X's can be identical or dissimilar halogens and follow the same trend as outlined above). For example:

CF <sub>2</sub> ClCHFCl, 2.20	CF <sub>3</sub> CHCl <sub>2</sub> , 2.00	CF <sub>3</sub> CHBrCl, 1.10
CF <sub>2</sub> BrCHFBr, 0.45	CF <sub>3</sub> CHBr <sub>2</sub> , 0.18	
CF <sub>2</sub> ClCHFBr, 1.42	CF <sub>2</sub> BrCHFCl, 1.22	

- For halopropanes, the –CH<sub>3</sub> group reduces toxicity (at least when opposite a –CF<sub>3</sub> group); therefore, CF<sub>3</sub>CXRCH<sub>3</sub> is preferred over CF<sub>3</sub>CRHCH<sub>2</sub>X, where R can be either a halogen or H. For example:

CF <sub>3</sub> CCl <sub>2</sub> CH <sub>3</sub> , 2.30	CF <sub>3</sub> CH <sub>2</sub> CHCl <sub>2</sub> , 0.88	CF <sub>3</sub> CHClCH <sub>2</sub> Cl, 0.79
CF <sub>3</sub> CHBrCH <sub>3</sub> , 2.03	CF <sub>3</sub> CH <sub>2</sub> CH <sub>2</sub> Br, 1.50	

- For halopropanes, –CH<sub>2</sub>– groups are favored over –CF<sub>2</sub>– groups, for example:

CHF <sub>2</sub> CH <sub>2</sub> CClF <sub>2</sub> , 3.00	CHF <sub>2</sub> CF <sub>2</sub> CH <sub>2</sub> Cl, 1.62
CF <sub>2</sub> ClCH <sub>2</sub> CH <sub>3</sub> , 2.77	CH <sub>2</sub> ClCF <sub>2</sub> CH <sub>3</sub> , 2.13

To decrease the toxicity, it is essential that carbon atoms alpha to the carbonyl group contain no halogen atoms. Carbonyl compounds exhibit a range of toxicities depending on whether the carbonyl group is in an aldehyde, ketone, carboxylic acid, or ester.

### Toxicity Studies of Tropodegradable Bromofluoroalkenes

Extremely promising inhalation exposure acute toxicity testing at 5 volume %, Table 7–6, of eight bromofluoroalkenes demonstrated no adverse effects in five of the tested compounds.<sup>30</sup> The surprisingly good results from this round of initial testing provided impetus for a greatly expanded program of testing for selected bromofluoroalkenes. The AAWG provided a large part of the funding for this exposure study.

The Ames Mutagenicity test results<sup>31</sup> on the more promising compounds selected based on boiling point were equally reassuring, Table 7–7, as were the results of the chromosomal aberration tests, Table 7–8.<sup>32</sup>

Cardiac sensitization is a property that has been associated with both halogenated and non-halogenated compounds. It has surfaced as a prime consideration in the development of solvents, fire suppressants, and propellants for medical inhalers. It was observed as a cause of cardiac arrest in substance abuse by inhalation of solvents used in spray paints, lubricants, glues and hairsprays, and it has been associated with some pharmaceuticals and volatile surgical anesthesia agents. Known cardiac sensitizing or arrhythmogenic compounds are represented by a wide range of chemical families including alkanes, alkenes, ethers, fluorocarbons, iodocarbons, and bromocarbons.

**Table 7–6. Acute Inhalation Toxicity Tropodegradable Bromofluoroalkenes.**

Chemical Name	Chemical Formula	Deaths <sup>a</sup> during (post) exposure
1-Bromo-3,3,3-trifluoropropene	CF <sub>3</sub> CH=CHBr	0
2-Bromo-3,3,3-trifluoropropene	CF <sub>3</sub> CBr=CH <sub>2</sub>	0
4-Bromo-3,3,4,4-tetrafluorobutene	CF <sub>2</sub> BrCF <sub>2</sub> CH=CH <sub>2</sub>	0
2-Bromo-3,3,4,4,4-pentafluorobutene	CF <sub>3</sub> CF <sub>2</sub> CBr=CH <sub>2</sub>	0
2-Bromo-3,3,4,4,5,5,5-heptafluoropentene	CF <sub>3</sub> CF <sub>2</sub> CF <sub>2</sub> CBr=CH <sub>2</sub>	0 (1)
3-Bromo-3,3-difluoropropene	CH <sub>2</sub> =CHCBrF <sub>2</sub>	7
2-Bromo-3-trifluoromethoxy-3,4,4,4-tetrafluorobutene	CH <sub>2</sub> =CBr(OCF <sub>3</sub> )CFCF <sub>3</sub>	10
2-Bromo-3-trifluoromethyl-3,4,4,4-tetrafluorobutene	CH <sub>2</sub> =CBrCFC(CF <sub>3</sub> ) <sub>2</sub>	10

a 10 rats and a 30 min exposure at 5 volume % agent in air

**Table 7–7. Ames Mutagenicity Test Results.**

Chemical Name	Chemical Formula	Ames Test Result
2-Bromo-3,3,3-trifluoropropene	CF <sub>3</sub> CBr=CH <sub>2</sub>	Negative
4-Bromo-3,3,4,4-tetrafluorobutene	CF <sub>2</sub> BrCF <sub>2</sub> CH=CH <sub>2</sub>	Negative
2-Bromo-3,3,4,4,4-pentafluorobutene	CF <sub>3</sub> CF <sub>2</sub> CBr=CH <sub>2</sub>	Negative

**Table 7–8. Chromosomal Aberration Test Results.**

Chemical Name	Chemical Formula	Test Result
2-Bromo-3,3,3-trifluoropropene	CF <sub>3</sub> CBr=CH <sub>2</sub>	Negative
4-Bromo-3,3,4,4-tetrafluorobutene	CF <sub>2</sub> BrCF <sub>2</sub> CH=CH <sub>2</sub>	Negative

The cardiac sensitization test data presented in Table 7–9 represent the only two such tests attempted on bromofluoropropenes.<sup>33,34</sup> While the 1 volume % LOAEL value observed for 2-bromo-3,3,3-trifluoropropene was disappointingly low, making the compound not usable as a halon 1301 replacement, the compound may well be able to serve as a halon 1211 replacement, usable in unoccupied areas. Testing of 1-bromo-3,3,3-trifluoropropene was terminated due to severe adverse effects including tremor.

**Table 7–9. Cardiac Sensitization Testing of Bromofluoropropenes.**

Chemical Name	Chemical Formula	NOAEL	LOAEL
2-Bromo-3,3,3-trifluoropropene	CH <sub>2</sub> =CBrCF <sub>3</sub>	0.5 volume %	1.0 volume %
1-Bromo-3,3,3-trifluoropropene	CHBr=CHCF <sub>3</sub>	a	a

a Determination aborted due to adverse effects on dogs

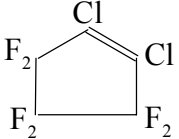
Further fluorination of these molecules was desirable to reduce boiling points. However, it was unclear where the optimum in degree and pattern of fluorination and site of bromination lay. Given the many additional compounds that had yet to be tested, it was hoped that at least one would have acceptable cardiac sensitization and other toxicity properties to be acceptable for use in occupied areas.

### Significant Toxicity Data Source – Inhalation Anesthetic Development

Early compound toxicity efforts were greatly aided by research in anesthesiology, where limited testing results on halogenated alkenes had been reported (Table 7–10).<sup>35</sup> Where provided, the concentrations

used were high. The observations in the comments section provided useful compound selection guidance and indicated that study of the related brominated alkenes was worthwhile.

**Table 7–10. Anesthesiology Testing of Fluoroalkenes.**

Chemical Formula	Animals	Anesthesia	Comments
 <chem>ClC(Cl)=C(F)F</chem>	2 rats	no	Extreme depression, analgesia, respiratory depression and failure. Death within 18 hours.
<chem>CClF=CClCF3</chem>	4 dogs	yes	Induction quiet, recovery uneventful, heart slowed with no fall of blood pressure. Brachycardia.
<chem>CF2=CClCF3</chem>	1 dog	no	Concentration of 75 %. Marked struggle, gasping, respiratory arrest, revived by artificial respiration.
<chem>CCl2=CClCF3</chem>	1 dog	no	Muscular rigidity, pulmonary edema, death after a few hours.
<chem>CHCl=CClCF3</chem>	2 rats	no	Respiratory depression and failure, one rat died, the other recovered quickly.
<chem>CCl2=CClCF3</chem>	3 rats	<sup>a</sup> no/yes	Depression, pulmonary edema, eye irritation, convulsions and death within 1 hour.
<chem>CF2=CFCF3</chem>	2 dogs	no	Concentrations of 50 % and 75 %. No demonstrable effect. Tremors, respiratory irritation.
<chem>CH2=CHCF3</chem>	2 dogs	no	Tremors, lack of coordination.

a Anesthesia observed for one rat at a higher concentration.

2-Bromo-3,3,3-trifluoropropene, CH2=CBrCF3, was reported to be an excellent anesthetic with a rapid, uneventful recovery.<sup>36</sup> As the concentrations used were unknown, it was difficult to determine the potency of this chemical as an anesthetic; however, that no adverse effects were observed indicated that this material may have a low toxicity. Studies of 3-chloro-3,3-difluoropropene, CF2ClCH=CH2, as an anesthetic in dogs showed cardiac arrhythmia with ventricular extra systole, blood pressure decrease, and tremor. Interestingly, inhalation studies later demonstrated that the brominated analogue, CF2BrCH=CH2, was quickly lethal to rats at an air concentration of 5 volume %.<sup>30</sup>

Overall, the reported live animal toxicity testing performed in the course of anesthesia research provided useful guidance in evaluation candidate compound acute inhalation toxicities and aided early efforts to down-select and target compounds for further synthesis and testing. Efforts to identify suitable anesthesia agents confronted challenges similar to those of interest to the halon replacement community. Suitable anesthesia agents for inhalation needed to be non-flammable and also have low acute toxicity. Low acute toxicity attributes would preferably have included little tendency to induce cardiac arrhythmia.

### 7.1.5 Summary: Alternative Agents and Selection Criteria Prior to the NGP

The status of alternative agents and development of selection criteria prior to the start of NGP research efforts was dominated by non-brominated fluorocarbons and dry powder extinguishants. In addition, blends of HFCs and HCFCs, combinations of dry powders and fluorocarbons including jelled, agents were in various stages of either commercialization or SNAP approvals. The use of brominated compounds with short atmospheric lifetimes was under consideration for use in streaming applications

and as replacements for halon 1301 in massive fire suppression applications such as protection of petroleum production facilities. An almost universal goal of all researchers was the demand by the halon user community for a drop-in replacement agent.

The history of halon replacement development through the mid 1990s reflected concurrent progress in fire technology and basic environmental and atmospheric research areas. In a very real way, halon alternatives development in this era has the appearance of a sequential process of research-based discovery, environmental selection criteria revision followed by rejection of developed alternatives, and a resumption of applied research.

The non-brominated and non-iodinated compounds under consideration were often in commercial use for other purposes. They all suffered from various shortcomings. While they were not ozone depleters because they did not have bromine or iodine in their structures, they did not have short atmospheric lifetimes, and in some cases had significant global warming potentials. Other common weaknesses included significantly higher boiling points, higher toxicity, and high flame extinguishment concentrations. The functional fire suppression related shortcomings were generally highlighted through comparison to halon 1301.

The development of  $CF_3I$  reached a critical point prior to the start of the NGP with the announced results of cardiac sensitization LOAEL performance far lower than that of even halon 1211. Use of  $CF_3I$  was questioned, and limited risk assessments were performed. The applicability of the test involving epinephrine-challenged dogs was challenged, and the resulting discussion continues. Further, the lack of a useable screening method for cardiac sensitization represented a major financial barrier to the candidate chemical selection process.

Toward the end of the pre-NGP period, the concept arose of incorporating bromine in short atmospheric lifetime (tropodegradable) compounds as a means of achieving more aggressive flame suppression and hopefully reducing agent weight requirements. This desire led to preliminary lists of potentially tropodegradable compounds. These incorporated molecular features susceptible to attack by atmospheric  $\bullet OH$  or  $\bullet H$  radicals or tropospheric ozone, photolysis by solar radiation, hydrolysis by atmospheric moisture, or sufficient polarity to dissolve in rain water. Retaining fluorine in the molecule in order to achieve non-flammability and to an extent to reduce boiling point was deemed essential.

## 7.2 THE NGP APPROACH TO NEW CHEMICALS SCREENING

The NGP search for alternative fire suppressants and, in particular, replacements for halon 1301, was broad in scope, covering nominally the world of chemistry. To ensure that the most optimal chemicals were identified efficiently, a comprehensive search and assessment of a broad array of chemical families and elements was performed.

The 1997 statement of objectives of the nine-year NGP effort was to develop and demonstrate, by 2005, replacements for halon 1301 that were, retrofitable, economically feasible, environmentally acceptable and user-safe processes and techniques and fluids that meet the operational requirements currently satisfied by halon 1301 systems in aircraft, ships, land combat vehicles, and critical mission support facilities. The results were to be specifically applicable to fielded weapons systems. By FY2000 this comprehensive goal was restructured and focused on aircraft alone. This change in targeted systems refocused chemical selection efforts on chemical families with the capability to address fire suppression

needs in the extreme low temperature conditions experienced by in-flight aircraft. As part of this refocused effort, NGP evaluations of agent low temperature dispersion, aircraft fire incidence and fire risk assessment were conducted. These studies are detailed in Chapters 2 and 8, and they significantly reduced the sole chemical selection boiling point criterion at a midway point in the Program.

As noted in Chapter 6, these surveys typically began with an assessment of available literature information on physical properties, toxicity, and flame suppression. A second step involved estimation of these properties, where possible. Promising chemical families were subject to increased scrutiny, and in some cases representative compounds were obtained and flame suppression tests run. Where unusually interesting, and especially previously unexamined, chemical families were identified, limited mechanistic studies were performed and often individual projects were largely dedicated to their study.

The criteria for further serious consideration of a compound as a candidate for suppression for in-flight aircraft fires were delineated in Chapter 6:

- Cup burner flame extinguishment level measured or estimated to be below 5 volume %. To better this 5 volume % limit, a compound had to catalytically suppress combustion or have a high heat capacity.
- Boiling points below about 20 °C. For fluids with slightly higher boiling points, similar fluids were considered to see if there might be a lower boiling member of the chemical family.
- Inclusion of a chemical feature that rendered the chemical tropodegradable, i.e., likely to have a short atmospheric lifetime.
- Absence of any toxicological data showing that serious effects on people could occur at a concentration lower than that needed to effect flame extinguishment.

As the early NGP research progressed, some chemical families were found unsuitable, while others of promise were identified.<sup>37,38</sup> About one-third of the way into the Program, the NGP performed a detailed analysis of the state of knowledge of the chemical families.<sup>39</sup> The goal of this review was to identify chemical families still in need of scrutiny as potential flame suppressants and halon replacements, to list those chemical families for which sufficient knowledge existed to select the best candidates, and to identify those families unlikely to contain useable alternative fire suppressing chemicals. Allowance for otherwise desirable candidates with somewhat elevated boiling points was made. The available data for each family was reviewed and a consensus reached on chemicals for further investigation and those for which further study was not warranted. Priorities were divided into three groups, as shown in Table 7–11:

- High Priority: Families that had not been extensively studied and for which there was high promise to yield one or more candidates.
- Further Study: Families for which limited data indicated promise to yield one or more candidates.
- Quick Look: Families that were relatively unstudied and whose potential was unclear or for which the cost of the compounds might prohibit a full study.

Table 7–12 lists the wide range of chemical families for which further study was not recommended and the primary reasons for those decisions.

**Table 7–11. Chemical Families Selected for Further Study.**

Chemical Family	Recommendation		
	High Priority	Further Study	Quick Look
Iodine containing alkanes and alkenes		X	
Bromine containing alkenes	X		
Iodine containing ethers			X
Bromine containing ethers		X	
Bromine containing alcohols			X
Fluorine containing aldehydes and ketones		X	
Nitriles			X
Fluoro- and bromofluoroamines	X		
Sulfoxides			X
Phosphorus containing Acids and Esters			X
Phosphonitriles and Phosphorus halides		X	
Copper containing Compounds			X
Manganese containing Compounds	X		
Iron containing compounds		X	
Tin containing compounds	X		

**Table 7–12. Chemical Families Not Pursued Further.**

Chemical Family	Major Disqualifying Finding		
	Well Studied	Toxicity, Colligative Property or Other Drawback	Suppression Efficiency or Flammability
Brominated, chlorinated and fluorinated alkanes	X		
Chlorinated alkenes		X	X
Fluorinated alkenes			X
Alkynes			X
Iodinated ethers		X	
Chlorinated ethers			X
Fluorinated ethers	X		
Iodinated or chlorinated alcohols		X	
Fluorinated alcohols		X	X
Iodinated or brominated aldehydes & ketones		X	
Chlorinated aldehydes & ketones		X	X
Halogenated (I, Br, F) aromatics		X	
Nitro compounds		X	X
Nitrates, nitrites, nitroso compounds		X	
Hexavalent sulfur		X	X
Difluorosulfur compounds		X	
Phosphines or pentacoordinate Phosphorus		X	
Alkali metal or alkaline earth compounds	X		
Boron and aluminum compounds			X
Titanium, antimony, germanium or silicon - containing compounds		X	

A summary of the several broad survey efforts to identify chemical families with the potential to yield suitable effective and environmentally acceptable halon replacements is presented in the following sections. The material presented describes selection approaches, chemical family evaluations, and the limited testing done to confirm extinguishment performance.

Separate presentations of the focused studies of fluoroalkyl phosphorus compounds and low boiling tropodegradable chemical families of flame suppression performance are located in Section 7.4. A limited presentation of work on phosphorus halide extinguishants such as  $\text{PBr}_3$  is discussed later in Section 7.3.5. A broad discussion of phosphorus and metal fire extinguishment chemistry is presented in Chapter 3 of this book.

## 7.3 NGP SURVEYS OF INORGANIC CHEMICAL FAMILIES

### 7.3.1 Main Group Elements - Group I

The term “main group elements” is used to denote any elements other than transition metals. Figure 7–1 represents a periodic table with the elements being considered in boldface. Note that carbon, oxygen, and the halogens may be (in some cases, are likely to be) present; however, such elements do not form the primary structural features of the compounds considered here. As noted earlier, some nitrogen compounds were examined in earlier work; others are discussed in section 7.4. Helium, neon, and argon were considered in their elemental form. Due to their toxicity, the radioactive elements were excluded. Though they were included, the Group I and Group II elements were unlikely to have utility as defined here since most compounds of these are solids.

Group I elements comprise the alkali metals: lithium (Li), sodium (Na), potassium (K), rubidium (Rb), cesium (Cs), and francium (Fr). The last element is radioactive and was not considered. Compounds of the alkali metals, in particular potassium and sodium salts, have long been used as fire extinguishing agents. A thorough review of the literature on fire extinguishment by compounds of the Group I elements has been prepared,<sup>40</sup> and these elements have also been discussed in a report prepared for the USAF.<sup>20</sup> These compounds were highly effective extinguishants but the suppression mechanism was uncertain. Extinguishment may be due to heat absorption, free-radical recombination on particulate surfaces, or homogeneous free-radical removal. Heat extraction did not account for the high extinguishment efficiencies of these elements.

I	II		III	IV	V	VI	VII	VIII
<b>Li</b>	<b>Be</b>		<b>B</b>	C	N	O	F	<b>He</b>
<b>Na</b>	<b>Mg</b>		<b>Al</b>	<b>Si</b>	<b>P</b>	<b>S</b>	Cl	<b>Ne</b>
<b>K</b>	<b>Ca</b>	Transition Metals	<b>Ga</b>	<b>Ge</b>	<b>As</b>	<b>Se</b>	Br	<b>Kr</b>
<b>Rb</b>	<b>Sr</b>		<b>In</b>	<b>Sn</b>	<b>Sb</b>	<b>Te</b>	I	<b>Xe</b>
<b>Cs</b>	<b>Ba</b>		<b>Tl</b>	<b>Pb</b>	<b>Bi</b>	Po	At	Rn
Fr	Ra							

Figure 7–1. Groups and Elements Studied.

Nearly all compounds of the Group I elements are solids at room temperature, and, therefore, past work has been on either dry chemical powders or aqueous solutions. Exceptions are some of the lithium alkyls,

which are flammable. Some eutectic mixtures of alkali metal salts have melting points near room temperature; however, the vapor pressures are negligible. Studies have shown that aqueous solutions of some alkali metal compounds are extremely effective fire extinguishants,<sup>41</sup> as are alkali metal powders (Chapter 4). However, these have been rejected for aircraft application due to their corrosion threat. Given the more mature state of knowledge and demonstrated effectiveness of sodium, potassium, and phosphorus based powders, any less efficient powders of other elements did not warrant consideration.

### 7.3.2 Main Group Elements - Group II

No flame extinguishment data have been found for compounds of beryllium. However, compounds of the other Group II elements (excluding, of course, radium) have been shown to have lower fire extinguishing efficacies than those of the Group I compounds. Since these Group II compounds are also solids, compounds of the Group II elements were not considered further.

### 7.3.3 Main Group Elements - Group III

#### Boron

A number of boron compounds are gases or liquids; however, apparently without exception all are either flammable, highly toxic, or act merely as carriers where, as a part of the molecule, they bring halogen atoms into the combustion zone. The known gaseous and liquid boranes (boron hydrides) are flammable. Many of the simple halides, such as  $\text{BF}_3$ ,  $\text{B}_2\text{Cl}_6$ , etc., are highly unstable in the presence of moisture and are all highly toxic.

Fire extinguishment testing using standard handheld extinguishers had shown that finely divided borax ( $\text{Na}_2\text{B}_4\text{O}_7$ , degree of hydration not specified) was approximately equal to sodium bicarbonate in fire extinguishment effectiveness.<sup>42</sup> The fire suppression efficiency of this compound may be due to the presence of sodium.

Common flame retardants for fabrics and plastics are sodium borate pentahydrate (borax pentahydrate,  $\text{Na}_2\text{B}_4\text{O}_7 \cdot 5\text{H}_2\text{O}$ ), boric acid ( $\text{B}(\text{OH})_3$ ), boric oxide ( $\text{B}_2\text{O}_3$ ), disodium octaborate tetrahydrate ( $\text{Na}_2\text{B}_8\text{O}_{13} \cdot 4\text{H}_2\text{O}$ ), ammonium pentaborate octahydrate [ $(\text{NH}_4)_2\text{B}_{10}\text{O}_{16} \cdot 8\text{H}_2\text{O}$ ], and the zinc borates (e.g.,  $\text{Zn}_4\text{B}_{12}\text{O}_{22} \cdot 7\text{H}_2\text{O}$ ).<sup>43</sup> In an extensive study of boron compounds, sodium tetrafluoroborate ( $\text{NaBF}_4$ ), a solid, was the most effective single compound for reducing fabric flammability.<sup>44</sup> These flame retardants are all solids.

In this study, no liquid or gaseous boron compounds were found that have a reasonable toxicity and that are nonflammable. There was also no evidence that boron has any catalytic fire suppression capability.

#### Aluminum

Aluminum oxide trihydrate ( $\text{Al}_2\text{O}_3 \cdot 3\text{H}_2\text{O}$ ) is a widely used fire retardant in elastomers,<sup>45</sup> where it operates primarily by endothermic release of water to provide cooling. Gaseous aluminum chloride had been shown to be an effective inhibitor of premixed methane/air flames,<sup>46</sup> and the dispersed powder effectively inhibited spark ignition of methane/air mixtures.<sup>47</sup> This activity was probably due to the presence of chlorine rather than to the aluminum itself. To date, no evidence that aluminum has any catalytic fire

suppression capabilities has been presented. Moreover, the few gaseous or liquid aluminum compounds that exist have serious drawbacks (toxicity, flammability, and/or stability).

### Gallium, Indium, and Thallium

No fire extinguishing studies have been reported for these three relatively rare elements. This may be due to the realization that toxicity would present a serious barrier to use of any thallium or indium compounds as extinguishants.

## 7.3.4 Main Group Elements - Group IV

### Carbon

Carbon is the structural core of organic compounds, which are discussed in Section 7.4. There is no reason to expect that solid carbon particles are effective fire suppressants, as they would act as fuel and oxidize to CO and CO<sub>2</sub>. It is possible that flame radiation absorption by particulate carbon may aid in suppression, but no evidence exists that carbon imparts any catalytic fire suppression capability.

### Silicon

Silicon compounds have been examined in several projects,<sup>37,38,48,49</sup> and there is little evidence that silicon offers any inherent fire suppression capabilities. The presence of silicon may, in some cases, offer desirable environmental (improved rain-out due to hydrolysis to polar species) and toxicological (through chemical decomposition) characteristics or physical properties.

The chemistry of silicon compounds related to compounds of interest in the development of fire suppressants has been reviewed in detail.<sup>49</sup>

Due to the complexity of the syntheses, no attempt was made to prepare fluoroalkyl-containing silicon compounds during the NGP. Table 7–13 lists those silicon compounds selected for testing to obtain at least some baseline data.<sup>49</sup>

**Table 7–13. Silicon-containing Compounds.**

Chemical Name	Formula	$T_b$ (°C)	Flash Point, °C
Silicon tetrachloride	SiCl <sub>4</sub>	57.6	None
Bromotrimethylsilane	SiBr(CH <sub>3</sub> ) <sub>3</sub>	79	32
Silicon tetrabromide	SiBr <sub>4</sub>	153	None

Silicon tetrachloride (SiCl<sub>4</sub>) has a relatively low boiling point; however, this compound caused problems with the Standard NMERI Cup Burner. During the first test, the metering valve on the cup burner apparatus became increasingly difficult to adjust and finally froze. Upon disassembly, the valve and line leading to the valve were found to be clogged with particulate matter. It is likely that silicon dioxide was formed by hydrolysis. No further testing was attempted; however, with care, it is likely that the Modified NMERI Cup Burner could be used for this or similar compounds in the future.

Bromotrimethylsilane ( $\text{SiBr}(\text{CH}_3)_3$ ) was tested using the Modified NMERI Cup Burner. With a boiling point of 79 °C, this compound was relatively easily volatilized; however, the material is flammable. Two tests gave cup burner extinguishment concentrations of 2.3 volume %. As the flow of the compound was increased, there appeared to be some effect on the flame, although no distinct lifting of the flame off the fuel cup was observed. The flame wandered around, occasionally falling down the side of the cup. When the flow reached 0.043 g/s, the flame behaved erratically and traveled to the bottom of the chimney (to the glass beads). The flame in the fuel cup was extinguished, but the compound continued to burn on the surface of the glass beads. A small amount of the compound was found to sustain a flame.

Silicon tetrabromide ( $\text{SiBr}_4$ ), as expected, was more effective than the other silicon compounds tested. The first test with the Modified NMERI Cup Burner gave an extinguishment concentration of 2.0 volume %. During subsequent testing, however, serious problems with clogging of the syringe pump were encountered. Cleaning the syringe completely and repeating the test resulted in the same problem. This cast doubt on the extinguishment value of 2.0 volume % obtained in the first test. If the syringe were sticking, the measured flow would have been less than the actual flow, because the syringe pump was allowed to slip for safety. This would have resulted in a low cup burner value.

### ***Silicon Compound Fire Suppression Mechanism***

A past review of the chemistry and fire suppression properties of silicon compounds had been presented in Reference 49. Except as otherwise stated, all of the information presented here was newly acquired or is an expansion of information contained in that source. Of particular interest as fire suppressants were silicon-containing compounds with fluorinated alkyl groups. Fluoro-organosilicon polymers have been of some commercial interest.<sup>50</sup>

Many organosilicon materials are relatively stable, inert, have a low toxicity, and have lower atmospheric lifetimes than do closely related carbon compounds. This allows the incorporation of bromine in silanes and siloxanes without having unacceptably large ODP values. While silicon compounds without bromine do not appear to have significant fire suppression capabilities, the addition of bromine could provide a compound with good fire suppression capability while maintaining good environmental characteristics.

Overall, there was little evidence that silicon itself plays a significant role in flame extinguishment, even though one could propose combustion free radical recombination cycles such as those in Reactions 7-1 and 7-2, similar to those proposed for other metals.<sup>51</sup>



The combustion and explosive properties of dichlorosilane ( $\text{SiH}_2\text{Cl}_2$ ) have been thoroughly studied.<sup>52</sup> Polyorganosiloxanes and inorganic silicates have been examined as potential flame retardants.<sup>53</sup> The major mode of reaction is the formation of protective surface coatings during a fire. The flammability of silicone polymers has been reduced through addition of fluorine, bromine, and  $\text{CCl}_3$  groups.<sup>54</sup>

Claims have been made that liquid fire extinguishing compositions containing haloalkanes and cyclic polysiloxanes increase penetration and throw distance.<sup>55</sup> However, there has been no claim that the silicon-containing compounds actually increase the intrinsic fire suppression capability.

### ***Silicon Compound Atmospheric Lifetime, ODP, and GWP***

Silicon, and other metalloids and metals, are known to be deposited in the upper atmosphere by meteors; however, it is believed that only the more polar metal oxides (e.g., sodium oxide) are likely to have any direct homogeneous chemical effect on atmospheric chemistry since these compounds have weak metal-oxygen bonds and can regenerate free atoms through photolysis and reactions with  $\bullet\text{O}$  and  $\bullet\text{OH}$ .<sup>56</sup> On the other hand, it must be recognized that silicon-containing particulates could play a significant role in heterogeneous atmospheric chemistry.<sup>57</sup> The silicon-oxygen bond is quite strong compared with the sodium-oxygen bond in the simple diatomics (Si-O, 799.6 kJ/mole; Na-O, 256.1 kJ/mole).<sup>58</sup> Thus, reactions proposed for ozone depletion by sodium (Reactions 7-3 and 7-4) are unlikely for ozone depletion by silicon.<sup>59</sup> Sodium atoms generated in the atmosphere may also enhance ozone depletion by chlorine<sup>60</sup> although it is not known whether similar enhancement by silicon takes place. Note, however, that since approximately 40 metric tons to 300 metric tons of metals are deposited daily by meteorites<sup>61</sup> and since silicon is one of the more abundant elements in meteorites<sup>60</sup> it is unlikely that anthropogenic silicon would produce a significant atmospheric effect in comparison to other sources.



Rate constants for reactions of some silicon compounds with  $\bullet\text{OH}$  free radicals and estimated lifetimes based on those rate constants are presented in Table 7-14.

Methane ( $\text{CH}_4$ ) has a rate constant of  $0.0836 \times 10^{-12} \text{ cm}^3/\text{molec}\cdot\text{s}$  at 298 K<sup>62</sup>, a value considerably smaller than that found for silane ( $\text{SiH}_4$ ). This is, however, undoubtedly due to the lower Si-H bond strength in  $\text{SiH}_4$  (bond strengths: H-SiH<sub>3</sub>, 384.1 kJ/mole; C-CH<sub>3</sub>, 438.9 kJ/mole).<sup>58</sup> Of greater interest are rate constants for silicon-containing molecules with no Si-H bonds. 2,2-Dimethylpropane ( $\text{C}(\text{CH}_3)_4$ ) has an  $\bullet\text{OH}$  rate constant of  $0.875 \times 10^{-12} \text{ cm}^3/\text{molec}\cdot\text{s}$  at 298 K, which is slightly smaller than that of tetramethylsilane ( $\text{Si}(\text{CH}_3)_4$ ). Unfortunately, other data allowing a direct comparison between C-H bond rate constants for carbon and silicon compounds were unavailable. Thus, there appeared to be no reason to assume that, in the absence of Si-H bonds, silicon compounds were inherently more reactive toward  $\bullet\text{OH}$  than are carbon compounds.

Maximum rate constants (no reaction observed) on the order of  $10^{-21} \text{ cm}^3/\text{molec}\cdot\text{s}$  have been determined for the reaction of  $\text{O}_3$  with silicon-containing compounds.<sup>63</sup> These data gave minimum estimated lifetimes of the order of 2500 days. Thus, there would be little, if any, removal by tropospheric ozone.

In general, silicon compounds are considerably more unstable toward hydrolysis than are carbon compounds, and this property may provide an effective removal route for many of these materials. The Si-halogen bond hydrolyzes readily; however, the rapidity of this hydrolysis (and the resulting formation of toxic products) eliminates the consideration of compounds containing halogens bonded directly to

silicon as fire suppressants (other than for basic laboratory studies). Compounds containing Si-H bonds also hydrolyze relatively easily when the pH is greater than 7, but are relatively stable in acidic solution. The alkoxy-Si bond is subject to hydrolysis and cleavage can cause condensation to higher polymers. Note, however, that this is highly dependent on the absence of steric hindrance. Alkoxy-substituted silanes with larger alkoxy groups are much more stable toward hydrolysis.<sup>64</sup> Silanes containing only carbon bonded to silicon are relatively hydrolytically stable.

**Table 7-14. •OH Rate Constants for Silicon Compounds.**

Chemical Formula	$k_{OH}, \text{cm}^3/\text{molec}\cdot\text{s}$	Atmospheric Lifetime, days <sup>a</sup>
$\text{SiH}_4^b$	$12.2 \times 10^{-12}$	0.97
$\text{Si}(\text{CH}_3)\text{H}_3^b$	$34.3 \times 10^{-12}$	0.35
$\text{Si}(\text{CH}_3)_2\text{H}_2^b$	$44.8 \times 10^{-12}$	0.27
$\text{Si}(\text{CH}_3)_3\text{H}^b$	$26.7 \times 10^{-12}$	0.45
$\text{Si}(\text{CH}_3)_4^b$	$1.09 \times 10^{-12}$	10.9
$\text{SiH}_4^c$	${}^d12.4 \pm 1.9 \times 10^{-12}$	0.96
$\text{Si}(\text{C}_2\text{H}_5)_4^c$	${}^e75 \times 10^{-12}$	0.16
$\text{Si}(\text{CH}_3)_4^f$	${}^d1.00 \pm 0.09 \times 10^{-12}$	11.9
$(\text{CH}_3)_3\text{SiOSi}(\text{CH}_3)_3^f$	${}^d1.38 \pm 0.09 \times 10^{-12}$	8.6
$[(\text{CH}_3)_2\text{SiO}]_3^f$	${}^d5.2 \pm 1.1 \times 10^{-13}$	22.9
$[(\text{CH}_3)_2\text{SiO}]_4^f$	${}^d1.01 \pm 0.20 \times 10^{-12}$	11.9
$[(\text{CH}_3)_2\text{SiO}]_5^f$	${}^d1.55 \pm 0.30 \times 10^{-12}$	7.7
$(\text{CH}_3)_3\text{SiOSi}(\text{CH}_3)_2\text{OH}^f$	${}^d1.89 \pm 0.36 \times 10^{-12}$	6.3

a Lifetimes estimated using globally averaged •OH model.

b Personal communication from Dr. Paul Marshall, Department of Chemistry, University of North Texas, Denton, to Dr. Robert E. Tapscott, 27 May 1997. Values are at 295 K.

c Reference 62

d Value at 297 K

e Value at 793 K

f Reference 63

Silicon compounds are expected to be more susceptible to photolysis than are the corresponding carbon compounds. The laser-induced photodissociation of silanes is one method used for vapor deposition of silicon films in the production of microelectronics.<sup>65</sup>

A few, scattered, and, in some cases suspect, lifetime and GWP data have been reported for silicon-containing compounds.<sup>49</sup> Siloxanes have been reported to have atmospheric lifetimes of from 10 days to 30 days.<sup>66</sup>

It was concluded that silicon compounds are unlikely sources of stratospheric ozone depletion due to the presence of silicon only. When hydrogen atoms are present, limited data indicated effective removal by tropospheric •OH and short atmospheric lifetimes. Insufficient data were available to judge tropospheric removal and atmospheric lifetimes for silicon compounds containing no hydrogen, with one exception. Silicon compounds containing direct Si-halogen bonds hydrolyze rapidly and give short atmospheric lifetimes; however, such compounds were unsuitable for halon substitutes due to their expected high toxicity. Photolysis may be a potential route to atmospheric removal in some cases. Of particular interest was possible photolytic "synergism" when both silicon and bromine were present; however, no data existed to evaluate such "synergism." Unfortunately, there were no atmospheric data for fully halogenated organosilicon compounds containing no Si-H or Si-halogen bonds (and, in particular,

compounds containing primarily fluorine as the halogen). Such compounds are unlikely to be removed rapidly by hydrolysis, rainout, or other processes, with the possible exception of photolytic decomposition. In summary, although there was no evidence that silicon compounds will have unacceptable global atmospheric environmental properties (e.g., unacceptable ODP, GWP, or lifetime), this may not be true for fully halogenated silicon compounds containing no Si-H or Si-halogen bonds.

Finally, silicon compounds were expected to have few if any global atmospheric impacts. This may be the case even when bromine is present. There is, however, a real need for studies of the photochemistry of bromine-containing silicon compounds.

### ***Silicon Compounds - Toxicity***

Compounds containing silicon bonded to halogens are highly toxic owing to rapid hydrolysis of the silicon-halogen bond, although the inhalation toxicity of  $\text{SiCl}_4$  is moderate.<sup>67</sup> Limited testing of industrial chemicals indicated that stable silane derivatives have a low toxicity. A number of siloxanes used industrially have a low toxicity.<sup>67</sup>

One paper not presented in Reference 39 reported that no toxic signs were found for four male rats to a single 6-hour exposure at 8000  $\mu\text{L/L}$  or to 15 6-hour exposures at 1000  $\mu\text{L/L}$  for tetramethylsilane,  $\text{Si}(\text{CH}_3)_4$ .<sup>68</sup> In the same study, 20 6-hour exposures of four female rats to diphenyldimethoxysilane,  $\text{Si}(\text{C}_6\text{H}_5)_2(\text{OCH}_3)_2$ , at its saturation vapor pressure showed no adverse effects.

A recent EPA final action on significant new uses listed potential toxicity hazards for a number of silicon compounds.<sup>69</sup> The final rule stated that alkoxy silanes can cause lung toxicity and severe irritation to skin, eyes, and mucous membranes. Of particular interest is the finding that "Based on analogy to alkoxy silanes and perfluoro compounds,"  $\text{Si}(\text{OCH}_3)_3(\text{CH}_2\text{CH}_2\text{CF}_2\text{CF}_2\text{CF}_2\text{-CF}_2\text{CF}_2\text{CF}_2\text{CF}_2\text{CF}_3)$  may cause lung toxicity, irritation to mucous membranes, liver toxicity, blood toxicity, immunosuppression, and reproductive toxicity. In part, this finding may have been due to the analogy between the fluoroalkyl chain and some HFCs; it may have had little or nothing to do with the silicon atom.

There is only a relatively small amount of toxicity data available for the silicon compounds of primary interest here (compounds containing halogenated alkyl groups and no direct Si-halogen bonds). In general, siloxanes have moderately low toxicities. Alkoxy-containing silicon compounds could cause irritation to skin, eyes, and mucous membranes. The presence of Si-halogen bonds is expected, in all cases, to cause severe toxicity problems due to hydrolysis with formation of hydrohalic acids. Such compounds are probably unacceptable as halon substitutes.

### ***Silicon Compound Chemistry***

Silicon chemistry has been the subject of a number of relatively recent reviews (e.g., the papers in Reference 70); however, the number of nonflammable silicon compounds that can be considered for halon replacement is small.

Silicon compounds offer relatively little promise. The silicon itself contributes little to fire suppression effectiveness, and many of the most interesting compounds (e.g., those containing bromofluoroalkyl and/or fluoroalkyl groups) have been difficult to synthesize. Of particular concern was the instability of compounds containing  $-\text{CF}_3$  groups immediately adjacent to the silicon atom, and such compounds were

not considered further. Compounds in which -OR and/or -OCF<sub>2</sub>Br groups are attached to the silicon atom have low volatility and high viscosity.

A series of bromoalkylsilanes were prepared in a two-step synthesis from a halomethane and a bis(trimethylsilyl)amide.<sup>71</sup> The preparation is shown in Reactions 7-5 and 7-6, where “M” is sodium or potassium and “R” is a nonfluorinated (compounds containing fluorine on a carbon atom adjacent to silicon are usually unstable) haloalkyl group.



The reaction of trialkylchlorosilane (SiClR<sub>3</sub>) with chlorotrifluoroethene (CClF=CF<sub>2</sub>) allowed the synthesis of a number of trifluorovinylsilanes (CF<sub>2</sub>=CFSiR<sub>3</sub>).<sup>72</sup> Bromination or hydrobromination of the double bond may permit the formation of the compounds CBrF<sub>2</sub>CBrFSiR<sub>3</sub>, CBrF<sub>2</sub>CHFSiR<sub>3</sub>, and CHF<sub>2</sub>CBrFSiR<sub>3</sub>.

A series of tetra(fluoroalkoxy)silanes (Si(OR)<sub>4</sub>) have been prepared by reaction of the appropriate fluorinated alcohol with silicon tetrafluoride (SiF<sub>4</sub>).<sup>73</sup> All of the compounds are liquids at room temperature, Table 7-15; the melting points are low, (less than -68 °C except for Si(OCH<sub>2</sub>CF<sub>3</sub>)<sub>4</sub>). However, the boiling points and viscosities are high. One major problem with such alkoxy compounds is that they hydrolyze readily and then polymerize.

**Table 7-15. Tetra(fluoroalkoxy)silanes.**

Chemical Name	Formula	<i>T<sub>b</sub></i> °C (kPa)	Liquid density g/mL (°C)	Liquid viscosity, 20 °C (cp)
Tetrakis(2,2,2-trifluoroethoxy)silane	Si(OCH <sub>2</sub> CF <sub>3</sub> ) <sub>4</sub>	155.5 to 157 (99)	1.5107 (20)	2.2089
Tetrakis(2,2,3,3-tetrafluoropropoxy)silane	Si(OCH <sub>2</sub> CF <sub>2</sub> CHF <sub>2</sub> ) <sub>4</sub>	117 to 118 (0.5)	1.5927 (20)	18.92
Tetrakis(2,2,3,3,4,4,4-heptafluorobutoxy)silane	Si(OCH <sub>2</sub> (CF <sub>2</sub> ) <sub>2</sub> CF <sub>3</sub> ) <sub>4</sub>	96 to 97 (0.5)	1.5740 (71.1)	7.613
Tetrakis(2,2,3,3,4,4,5,5-octafluoropentoxy)silane	Si(OCH <sub>2</sub> (CF <sub>2</sub> ) <sub>3</sub> CHF <sub>2</sub> ) <sub>4</sub>	156 to 159 (0.3)	1.8150 (20)	42.75
Tetrakis(2,2,3,3,4,4,5,5,6,6,7,7-dodecafluoropentoxy)silane	Si(OCH <sub>2</sub> (CF <sub>2</sub> ) <sub>5</sub> CHF <sub>2</sub> ) <sub>4</sub>	201 to 204 (0.4)	1.7181 (71.1)	108.8
Tetrakis(2,2,3,3,4,4,5,5,6,6,7,7,8,8,9,9-hexadecafluorononoxo)silane	Si(OCH <sub>2</sub> (CF <sub>2</sub> ) <sub>7</sub> CHF <sub>2</sub> ) <sub>4</sub>	<sup>a</sup> 235 to 240 (0.3)	Not reported	Not reported

a With decomposition.

Overall it was determined that there was insufficient basis for continued consideration of silicone-based compounds as halon replacements.<sup>39</sup>

## Germanium, Tin, and Lead

The only germanium compound studied as a fire extinguishant was germanium tetrachloride,  $\text{GeCl}_4$ ,<sup>74</sup> whose extinguishing capability was primarily due to the presence of the chlorine atoms. On the other hand, there is evidence of strong chemical inhibition for compounds of tin and lead (Chapter 3). Thus, lead tetra-acetate ( $\text{Pb}(\text{CH}_3\text{COO})_4$ ) and lead acetylacetonate,  $\text{Pb}(\text{CH}_3\text{C}(\text{O})\text{CHC}(\text{O})\text{CH}_3)_2$ , neither of which contain halogens, are effective extinguishants.<sup>75</sup> A catalytic mechanism has been proposed for fire extinguishment by tin.<sup>76</sup> A recent paper presented results indicative of a weak catalytic flame suppression action by tin compounds.<sup>77</sup>

Despite the scattered indications of catalytic effects for compounds of the heavier Group IV elements, germanium is too costly to be considered, and tin and lead are environmentally unacceptable as well as toxic to animals. Heavy metal toxicity is a well recognized and extensively documented environmental concern.

### 7.3.5 Main Group Elements - Group V

#### Inorganic Nitrogen

The chemistry and flame suppression of nitrogen compounds (with an emphasis on fluoroalkyl amines) was discussed in earlier work performed under the NGP.<sup>37,38</sup> One cycle that has been proposed to catalyze recombination of hydrogen atoms and hydroxyl free radicals is given in Reactions 7-7 through 7-9.<sup>78</sup> The NO cycle, however, appears to be relatively inefficient.<sup>79</sup>



#### Inorganic Phosphorus

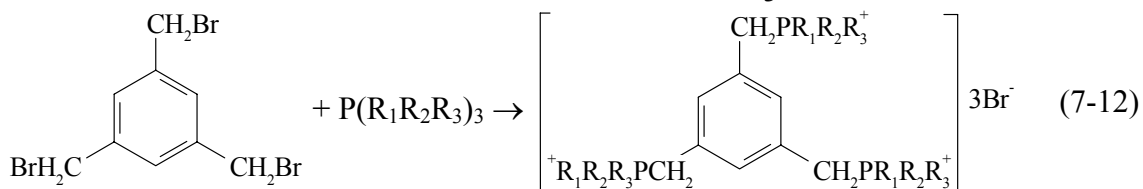
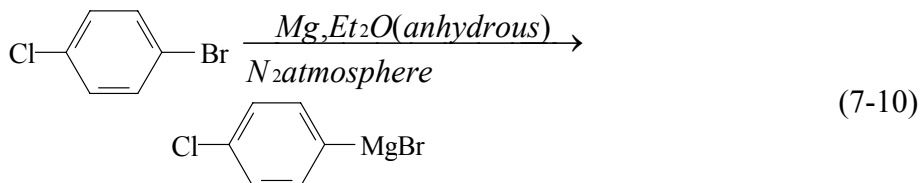
A search of the Chemical Abstracts Database for the key words “flame,” “fire,” and “flammable” coupled with “phosphonitriles” and related terms yielded 366 references, nearly all of which were for fire retardants for polymers. These included reviews of cyclo- and polyphosphazenes as fire retardants and as fire resistant materials.<sup>80,81</sup>

The mechanisms of fire retardancy of solids by phosphorus-containing compounds have been studied for decades.<sup>82</sup> Depending on the specific compound and the host polymer, these additives act in the gas and/or condensed phases.<sup>83</sup> The details of the mechanism are still debated, as evidenced in papers presented at the annual Business Communications Company (BCC) Conference on Flame Retardancy.

Phosphorus and bromine behave as synergistic flame retardants, and the greatest synergism appears to be when the two elements are combined in the same molecule.<sup>84,85</sup> It has been proposed that in polyesters,

compounds containing both phosphorus and bromine act in two separate roles as flame retardants.<sup>86</sup> The work cited indicated that the phosphorus induced formation of aromatic residues and char, which reduced the transport of gases to the flame. The bromine was believed to reduce the overall oxidation rate, reducing the heat transported back to the solid.

The preparation of halogenated triaryl phosphines as flame retardants has been reported.<sup>87</sup> An example is shown in Reactions 7-10 and 7-11 for tris(parachlorophenyl)phosphine (solid, melting point 106 °C). A number of phosphonium salts have also been prepared, as shown in Reaction 7-12, where R<sub>1</sub>, R<sub>2</sub>, and R<sub>3</sub> are various alkyl and aryl groups. All of these materials are solids.



Resorcinol bis(diphenyl phosphate) (Figure 7-2, n = 1 to 8), a polymeric material containing no halogen, has been reported to act as a flame retardant additive.<sup>88</sup> The material, which is made from phosphorus oxychloride, resorcinol, and phenol, is a colorless to light yellow liquid with a viscosity of 600 cp at room temperature and 100 cp at 55 °C.

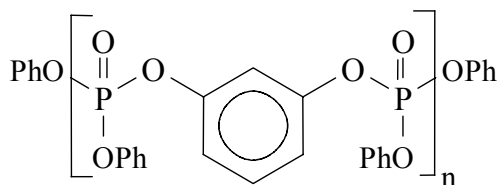
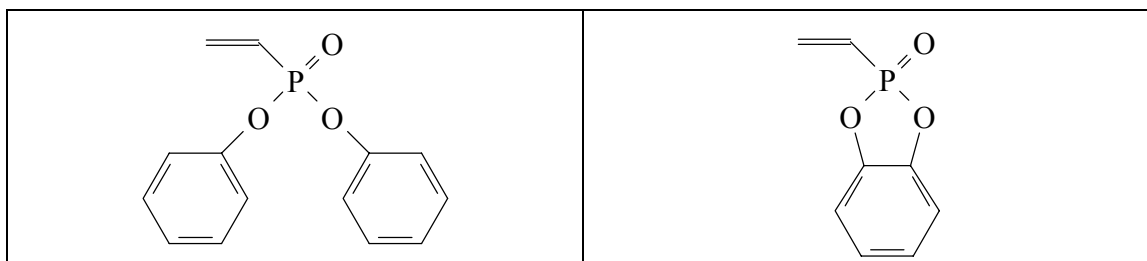


Figure 7-2. Resorcinol.

Phosphorus-containing groups have been incorporated directly onto polymeric molecules rather than using phosphorus additives to provide flame retardancy. Fire resistant organosilicon polymers have been prepared by incorporation of phosphazenes.<sup>89</sup> Resins containing melamine combined with triethylphosphate and dimethylmethylphosphonate have been reported as flame retardants.<sup>90</sup> A number of compounds containing vinyl groups attached to phosphorus have been prepared to permit copolymer formation (e.g., Figure 7-1<sup>91</sup>). It is believed that when incorporated directly into a polymer, these materials provide flame retardancy primarily by char formation.



**Figure 7-3. Vinyl Phosphonates.**

The large variability in toxicity of phosphorus compounds and the possibility of cholinesterase inhibition raised toxicity concerns with these compounds. In general, their toxicity decreases as the oxidation state of the phosphorus increases, i.e., phosphines are generally the most toxic and phosphates are the least toxic. Phosponitriles appear to have relatively low toxicities, but mutagenicity may be of concern. Compounds with phosphorus-halogen bonds are probably unacceptable as halon substitutes. Phosphorus chemistry has been the subject of a number of relatively recent reviews (e.g., the papers in Reference 92); however, most of this work has been on nonvolatile or flammable chemicals.

Chapter 3 and Reference 93 provide good overviews of phosphorus chemistry as it applies to chemicals of interest as fire suppressants. A review of NGP testing of phosphorus compounds is consolidated in Section 7.4.4.

### ***Phosponitriles***

Among the phosphorus compounds, phosponitriles have been of primary interest as replacement fire suppressants in the past; however, there are relatively few that have sufficiently high volatility to replace halon 1301. There may, however, be some interest in using these materials in carriers for some applications.

The linear phosponitriles, for which preparations have been reported,<sup>94</sup> are considerably more reactive than the cyclic compounds, particularly toward hydrolysis.<sup>95</sup> This makes them somewhat less attractive than the cyclic materials for study as halon 1301 replacements. The reactivity of the 3-membered ring system  $P_3N_3Cl_6$  toward chloride exchange is lower than that of the four-membered and larger cyclics.<sup>96</sup>

Of particular interest are the fluorinated phosponitriles. Fluorination normally occurs as geminal substitution; however, procedures for making nongeminal derivatives have been reported.<sup>97</sup> Although a number of chloro- and fluoro-substituted bis(dimethylamino)-cyclotriphosponitriles have been reported<sup>98</sup> most of these are solids. The fluoro-substituted bis(dimethylamino)cyclotriphosponitriles compound, Figure 7-4, is however, a liquid.

Bromine-containing phosponitriles are of some interest due to the potential for fire extinguishment contribution by bromine and for possible synergism between bromine and phosphorus. The fully brominated compounds are solids or oils<sup>99</sup> and are, therefore, unlikely to be appropriate for investigation as fire extinguishants, though they may have other uses (e.g., flame retardants). Crown ether complexes have been used to prepare the highly colored solid compound  $NP_2Br_9$  from  $KBr$  and hexachlorocyclotriphosponitrile ( $P_3N_3Cl_6$ ).<sup>100</sup> This compound can then be heated to form the more stable  $NP_2Br_7$ . Structures have not been published for either of these materials. The preparation of mixed

fluorine- and bromine-substituted phosphonitriles by reaction of silver fluoride with  $P_3N_3Br_6$  have been reported,<sup>101</sup> but the chemical and physical properties were not given.

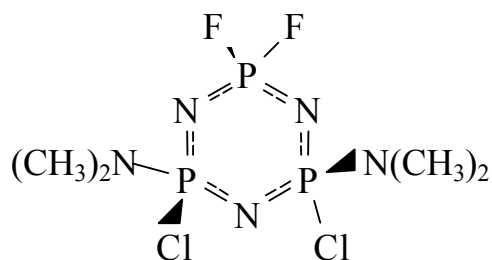


**Figure 7–4. Example of a Fluoro-substituted Bis(dimethylamino) Cyclotriphosphonitrile.**

Mixed methyl- and fluorine-substituted phosphonitriles have been prepared by reaction of octafluorocyclotetraphosphonitrile with methyl lithium.<sup>102,103</sup> The compounds are high boiling liquids and solids. Derivatives with tert-butyl and n-butyl substituents<sup>104,105</sup> and with 1- and 2-propenyl substituents<sup>106</sup> have also been reported.

Acquired phosphonitriles were reported to have attractively low cup burner flame extinguishment concentrations (Table 7–16).<sup>93</sup> The first of these compounds was even more efficient at extinguishing an opposed flow diffusion flame.<sup>3</sup> A number of polyfluoroalkoxy-substituted compounds (e.g.,  $P_3N_3(OCH_2CF_3)_6$ ) have also shown very good extinguishments characteristics.

**Table 7–16. Phosphonitrile Flame Extinguishment**

Chemical Formula	Cup Burner Extinguishing (volume %)
$P_3N_3F_6$	$1.08 \pm 0.07$
$P_3N_3ClF_5$	$0.91 \pm 0.02$
$P_3N_3Cl_2F_4$	$0.96 \pm 0.08$

### *Phosphoranes*

A number of fluorophosphoranes (pentacoordinate phosphorus(V) compounds), including some amino-substituted products have been described.<sup>107,108</sup> Although all of these contain phosphorus-fluorine bonds (making them unlikely candidates as halon replacements), the boiling points are in the acceptable range for a number of compounds. Unfortunately, none of the alkyl derivatives in the sources cited was fluorinated.

### *Phosphorus Halides*

As shown in Table 7–17, some of these compounds are four to eight times as efficient as halon 1301 as flame suppressants. However, the boiling points are too high for aircraft use, except perhaps  $PF_3$ . Moreover, the toxicity and corrosiveness of these compounds is expected or known to be high. Nonetheless, it would be useful to examine the possibly more stable, totally fluorinated compounds,  $PF_3$  and  $O=PF_3$ .

**Table 7–17. Phosphorus Halide Flame Extinguishment.**

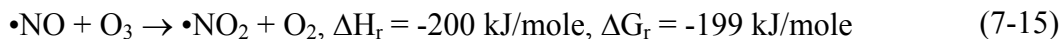
Chemical Formula	$T_b$ (°C)	Efficiency Relative to Halon 1301
PCl <sub>3</sub>	75	6.7, 6.9
PBr <sub>3</sub>	173	4.6, 6.9
PF <sub>2</sub> Br	23.9	
PF <sub>3</sub>	16.5	
O=PCl <sub>3</sub>	34.4	5.2
O=PF <sub>2</sub> Br	32	
S=PCl <sub>3</sub>		8
S=PBr <sub>3</sub>		6.7, 6.9

**Phosphorus-containing Compounds – Atmospheric Lifetime, ODP, and GWP**

The effect of phosphorus on stratospheric ozone has not been reported. A general cycle that may enable ozone depletion by phosphorus is shown in Reactions 7-13 and 7-14. Note, however, that the large stability and expected reluctance to add additional oxygen atoms make  $\bullet\text{PO}_3$  and higher oxides unlikely candidates for direct participation in ozone depletion.  $\bullet\text{NO}_3$  is known to photolyze sufficiently rapidly that at least some possible reactions are believed to be insignificant in atmospheric chemistry, and the higher oxides of phosphorus are likely to photolyze even more rapidly.<sup>109</sup>



Nitrogen oxides are believed to deplete stratospheric ozone by the reactions shown in Reactions 7-15 through 7-17.<sup>110</sup> Here and elsewhere in this chapter, enthalpies of reaction ( $\Delta H_r$ ) and free energies of reaction ( $\Delta G_r$ ) were calculated from standard enthalpies of formation ( $\Delta H_f^\circ$ ) and standard free energies of formation ( $\Delta G_f^\circ$ ) at 298.15 K taken from Reference 111 unless otherwise indicated. By analogy, one might propose Reactions 7-18 and 7-19 for ozone depletion by phosphorus. Reaction 7-18 is highly exothermic and has been proposed as the cause for the chemiluminescence observed for the reaction of ozone with phosphine.<sup>112</sup> Here, however, the relatively large O-PO bond dissociation enthalpy (calculated as 540 kcal/mol from the standard enthalpies) compared to the O-NO bond dissociation energy (306 kJ/mole) makes the second reaction in the cycle (Reaction 7-19) unfavorable at 298.15 K. The higher stability of phosphorus dioxide can be seen from the total enthalpy of 1129 kJ/mole for dissociation of  $\text{PO}_2$  into its constituent atoms compared with the calculated value of 938 kJ/mole for  $\text{NO}_2$ .





An alternative mechanism is described in Reactions 7-20 and 7-21, where the second reaction is again distinctly unfavorable. This cycle is similar to the chlorine ozone depletion cycle in Reactions 7-22 and 7-23. Here, again, the large phosphorus-oxygen bond strength is an obstacle. The bond strength in diatomic PO is 599.1 kJ/mole compared with 269 kJ/mole for  $\bullet\text{ClO}$ .<sup>58</sup>



Bromine and chlorine jointly provide a highly effective mechanism for stratospheric ozone depletion through a cycle of Reactions 7-17 and 7-24 through 7-26.<sup>113</sup> Here,  $\Delta H_r$  and  $\Delta G_r$  for  $\bullet\text{BrO}$  were taken from Reference 58. A similar cycle can be proposed for phosphorus by coupling Reactions 7-20, 7-24, and 7-27. The free energy change for Reaction 7-27, however, is very large, positive, and, thus, unfavorable.



The analysis presented above provides a strong indication that any ozone depletion must involve reaction of  $\text{O}_3$  with  $\bullet\text{PO}$  (e.g., Reactions 7-18 and 7-19). The phosphorus-oxygen bond in this diatomic molecule is too strong to allow formation of significant concentrations of atomic phosphorus. As noted above, however, the second reaction in the cycle (Reaction 7-19) is unfavorable at 298.15 K. The minimum stratospheric temperature (at the tropopause) varies from approximately 193 K to 223 K depending on the latitude, and the maximum stratospheric temperature (at the mesopause) is approximately 285 K depending on the season and latitude.<sup>114</sup> Data from the JANAF tables<sup>111</sup> indicate that the reaction becomes even less favorable ( $\Delta H_r$  and  $\Delta G_r$  both become more positive) as the temperature decreases from 298.15 K. A major question is how fast  $\bullet\text{PO}$  is removed by reaction with  $\text{O}_3$  (Reaction 7-18) before it reacts with  $\text{O}_2$  (the reverse of Reaction 7-19). Ozone concentrations vary widely in the stratosphere; however, we can take the concentration of ozone in the stratosphere to be approximately

$10^{10}$  molecules/cm<sup>3</sup> to  $10^{11}$  molecules/cm<sup>3</sup> compared to a maximum of around  $10^9$  molecules/cm<sup>3</sup> for  $\bullet\text{O}(^3\text{P})$ .<sup>i,115,116</sup> Thus, the mixing ratio (the ratio to air) for  $\bullet\text{O}(^3\text{P})$  is calculated as approximately 1  $\mu\text{L/L}$  in the stratosphere. This implies that Reaction 7-19 would lie far to the left and that the concentration of  $\bullet\text{PO}$  would be small.

Missing, of course, from this analysis is an assessment of kinetics for Reactions 7-18 and 7-19. Also missing is any discussion of other reactions of  $\bullet\text{PO}$  and  $\bullet\text{PO}_2$ , both of which are highly polar and are likely to be absorbed onto ice crystals. Despite the shortcomings of this analysis, it is obvious that stratospheric ozone depletion by phosphorus-containing compounds is very unlikely.

Relatively few data are available on atmospheric lifetimes for phosphorus compounds. Atkinson has reported the rate constants for several phosphorus compounds,<sup>117</sup> and these are shown in Table 7-18 along with atmospheric lifetimes estimated from the globally averaged tropospheric  $\bullet\text{OH}$  concentration. Very limited data indicate that the presence of a phosphorus atom increases  $\bullet\text{OH}$  reactivity. Thus, for example, methane ( $\text{CH}_4$ ) has a rate constant of  $0.0836 \times 10^{-12}$  cm<sup>3</sup>/molec-s at 298 K,<sup>117</sup> a value considerably smaller than that found for phosphine ( $\text{PH}_3$ ), even though methane has one more reactive site (i.e., one more hydrogen atom). The activation energy for hydrogen atom abstraction decreases (as expected) with decreasing dissociation energy of the M-H bond, and this undoubtedly explains the higher rate constant for  $\text{PH}_3$  (bond strengths: H-PH<sub>2</sub>, 351.0 kJ/mol; C-CH<sub>3</sub>, 438.9 kJ/mol).<sup>58,118,119</sup> It is difficult to compare compounds with and without phosphorus and containing hydrogen bonded only to carbon, since there are no isostructural compounds. The rate constant of  $3.92 \times 10^{-12}$  cm<sup>3</sup>/molec-s at 298 K for 2,2-dimethoxypropane ( $\text{C}(\text{CH}_3)_2(\text{OCH}_3)_2$ ) is smaller than that of trimethylphosphate ( $(\text{CH}_3\text{O})_3\text{PO}$ ), which has three fewer hydrogen atoms. The rate constant of  $11.7 \times 10^{-12}$  cm<sup>3</sup>/molec-s at 298 K for 2,2-diethoxypropane ( $\text{C}(\text{CH}_3)_2(\text{OC}_2\text{H}_5)_2$ ) is smaller than that of triethyl phosphate ( $(\text{C}_2\text{H}_5\text{O})_3\text{PO}$ ), which has nearly the same number of hydrogen atoms.<sup>117</sup> Since the predominant mechanism for reaction with the compounds in Table 7-18 appears to be hydrogen atom abstraction<sup>117</sup> it may be that a decreased bond strength accounts for the possibly higher reactivity for phosphorus-containing compounds; however, bond strength data to confirm this are lacking.

**Table 7-18. Rate Constants  $\bullet\text{OH}$  Reactions With Phosphorus Compounds.**

Chemical Formula	$k_2$ at 297 K, cm <sup>3</sup> /molec-s	Estimated Tropospheric Lifetime, days
$\text{PH}_3$	$13 \pm 3 \times 10^{-12}$	0.9
$(\text{CH}_3\text{O})_3\text{PO}$	$7.37 \pm 0.74 \times 10^{-12}$	1.6
$(\text{C}_2\text{H}_5\text{O})_3\text{PO}$	$55.3 \pm 3.5 \times 10^{-12}$	0.2
$(\text{CH}_3\text{O})_2\text{P}(\text{O})\text{SCH}_3$	$9.29 \pm 0.68 \times 10^{-12}$	1.3
$(\text{CH}_3\text{S})_2\text{P}(\text{O})\text{OCH}_3$	$9.59 \pm 0.75 \times 10^{-12}$	1.2
$(\text{CH}_3\text{O})_3\text{PS}$	$69.7 \pm 3.9 \times 10^{-12}$	0.2
$(\text{CH}_3\text{O})_2\text{P}(\text{S})\text{SCH}_3$	$56.0 \pm 1.8 \times 10^{-12}$	0.2
$(\text{CH}_3\text{O})_2\text{P}(\text{O})\text{N}(\text{CH}_3)_2$	$31.9 \pm 2.4 \times 10^{-12}$	0.4
$(\text{CH}_3\text{O})_2\text{P}(\text{S})\text{N}(\text{CH}_3)_2$	$46.8 \pm 1.4 \times 10^{-12}$	0.3
$(\text{CH}_3\text{O})_2\text{P}(\text{S})\text{NHCH}_3$	$233 \pm 15 \times 10^{-12}$	0.05
$(\text{CH}_3\text{O})_2\text{P}(\text{S})\text{NH}_2$	$244 \pm 9 \times 10^{-12}$	0.05
$(\text{CH}_3\text{O})_2\text{P}(\text{S})\text{Cl}$	$59.0 \pm 3.8 \times 10^{-12}$	0.2

<sup>i</sup> The concentration of oxygen atoms in other than the <sup>3</sup>P ground state would be even smaller.

Phosphorus compounds studied to date are quite unreactive toward ozone. An upper limit of  $6 \times 10^{-20}$  cm<sup>3</sup>/molecules has been determined for reaction of trimethylphosphate ((CH<sub>3</sub>O)P=O) with ozone at 296 K.<sup>120</sup> Using a globally averaged tropospheric ozone concentration, one estimates from this value a minimum lifetime of 386 days for reaction of trimethylphosphate with tropospheric ozone. Atkinson has reported rate constants with upper limits on the order of  $10^{-19}$  at 296 K to 298 K for gas-phase reactions of O<sub>3</sub> with phosphorus-containing compounds, giving estimated minimum lifetimes of around 200 days. In none of these cases was a reaction observed.<sup>121</sup>

It is likely that many phosphorus compounds are sufficiently polar that rainout is an important tropospheric removal mechanism. Atmospheric hydrolysis is possible for phosphonitriles containing direct P-halogen bonds even when the halogen is fluorine, and this is likely to be an effective tropospheric removal mechanism for such compounds. Photolysis is more important for compounds containing phosphorus than for corresponding carbon compounds; however, insufficient data are available to determine whether photolysis provides effective atmospheric removal.

No rigorous calculations of atmospheric lifetimes or GWPs of phosphorus-containing compounds have been reported. A 3 day lifetime has been estimated for trimethylphosphate based on the rate constant for reaction with •OH.<sup>120</sup> This value differs slightly from that given in Table 7–18 due to the use of a slightly different globally averaged •OH.

In summary, phosphorus compounds are unlikely sources of stratospheric ozone depletion due to the presence of phosphorus only. When hydrogen atoms are present, limited data indicate effective removal by tropospheric •OH and short atmospheric lifetimes. Insufficient data are available to judge tropospheric removal and atmospheric lifetimes for phosphorus compounds containing no hydrogen; however, it is likely that rainout and/or hydrolysis will give short atmospheric lifetimes. In summary, there is no evidence to suggest that phosphorus compounds will have unacceptable global atmospheric environmental properties (i.e., unacceptable ODP, GWP, or lifetime).

### ***Toxicity of Phosphonitrilic Compounds***

A general review of the toxicity of phosphorus compounds is also accessible in Reference 93. One concern is that a number of phosphorus compounds (particularly phosphite esters) are cholinesterase inhibitors. The following summarizes results from tests of this particular class of compounds.

Hexakis(2,2,2-trifluoroethoxy)cyclotriphosphazene toxicity: An acute oral toxicity assessment utilizing male and female Fischer 344 rats and genotoxicity testing utilizing the Ames assay has been performed on hexakis(2,2,2-trifluoroethoxy)cyclotriphosphazene (P<sub>3</sub>N<sub>3</sub>(OCH<sub>2</sub>CF<sub>3</sub>)<sub>6</sub>).<sup>122</sup> No deaths or signs of toxic stress were observed in any of the rats orally dosed at the limit test value of 5 g of P<sub>3</sub>N<sub>3</sub>(OCH<sub>2</sub>CF<sub>3</sub>)<sub>6</sub> per kg body weight. Body weights of the male rats during the subsequent 14 day observation period appeared unaffected by treatment. In the Ames assay, P<sub>3</sub>N<sub>3</sub>(OCH<sub>2</sub>CF<sub>3</sub>)<sub>6</sub> produced no mutagenicity (base-pair substitution or frameshift mutation) in the bacterial (Salmonella) system. In summary, P<sub>3</sub>N<sub>3</sub>(OCH<sub>2</sub>CF<sub>3</sub>)<sub>6</sub> produced no toxicity via the oral route of administration and was determined not to be genotoxic.

Phosphonitrilic Chloride Compounds (Chlorophosphazene): In 1979, Ethyl Corporation submitted to the U. S. Environmental Protection Agency (EPA) the results of in vitro and in vivo studies on two similar phosphonitrilic chloride compounds, each with the same CAS (Chemical Abstracts Service) No. (25034-79-1). In all, there were 16 reports, each covering a separate toxicological test for each compound:

- a. *In vitro* mammalian cell transformation assay.<sup>123,124</sup>
- b. *In vitro* mammalian cell transformation assay in the presence of exogenous metabolic activation assay.<sup>125,126</sup>
- c. *In vivo* mammalian cell point mutation assay.<sup>127,128</sup>
- d. *In vitro* mammalian cell point mutation assay in the presence of exogenous metabolic activation assay.<sup>129,130</sup>
- e. *In vivo* cytogenetic assay in rodents for mutagenicity.<sup>127</sup>
- f. *Salmonella*/Microsomal assay for bacterial mutagenicity assay.<sup>131,132</sup>
- g. Differential inhibition of repair deficient and repair competent strains of *Escherichia Coli*: DNA (deoxyribonucleic acid) repair assay.<sup>133,134</sup>
- h. Dominant lethal assay in rodents for mutagenicity assay.<sup>135,136</sup>

Table 7–19 paraphrases the results of the eight toxicity tests for each compound. Due to the limited solubility of the test compounds in vehicles compatible with mammalian cell culture systems, it was difficult to establish the exact concentration of the chemical in solution for the *in vitro* tests, a problem noted in the reports cited.

**Table 7–19. Toxicity Studies of Chlorophosphazenes.**

3899-A	3899-B
<b><i>In Vitro</i> Mammalian Cell Transformation Assay</b>	
a. Although the cytotoxicity tests were not reproducible in showing the toxic effects of the test compound with target cells, a dose response effect was observed in each of the cytotoxicity studies. b. The test compound was incapable of inducing morphological transformants (Type III foci) in the BALB/3T3 clone A31 cell system.	a. The cytotoxicity studies demonstrated a dose response effect. b. The test chemical was demonstrated to be positive in producing a Type III foci at 60 µg/mL concentration. Relative to solvent (acetone), the number of morphologically transformed (Type III) foci present at this concentration was statistically significant (P<0.05).
<b><i>In vitro</i> Mammalian Cell Transformation Assay in the Presence of Exogenous Metabolic Activation</b>	
a. Cytotoxic effects of the test agent appeared to increase in the presence of an exogenous source of metabolizing activity (S-9). b. The test chemical was effective in inducing morphological transformation (Type III foci) at the 30 µg/mL concentration. Relative to the negative control, the number of morphologically transformants per number of cells at risk at the 30 µg/mL concentration was not statistically significant (P>0.05).	a. Cytotoxic effects of the test agent appeared to increase in the presence of an exogenous source of metabolizing activity (S-9). b. The test chemical was effective in inducing morphological transformation (Type III foci) in the BALB/3T3 Clone A31 cell system at all concentrations employed.
<b><i>In Vitro</i> Mammalian Cell Point Mutation Assay</b>	
a. Although the cytotoxicity tests were not reproducible in showing the toxic effects of the test compound with target cells, a dose response effect was observed in each of the cytotoxicity studies. b. The test compound was incapable of inducing ouabain-resistant colonies at all of the doses tested.	a. The cytotoxicity tests demonstrated a dose response effect. b. The test chemical was incapable of inducing ouabain-resistant colonies at all concentrations.

3899-A	3899-B
<b><i>In Vitro</i> Mammalian Cell Point Mutation Assay with Exogenous Metabolic Activation</b>	
a. Cytotoxic effects of the test agent appeared to increase in the presence of an exogenous source of metabolizing activity (S-9). b. The test chemical was ineffective in inducing ouabain-resistant colonies in the BALB/3T3 Clone A31 cell system at all concentrations employed.	a. The cytotoxic effects of the test agent appeared to increase in the presence of an exogenous source of metabolizing activity (S-9). b. The test chemical was ineffective in inducing ouabain-resistant colonies at all concentrations employed.
<b><i>In Vitro</i> Cytogenetic Assay in Rodents for Mutagenicity</b>	
The test compound exhibited little or no clastogenic activity. No dose response was observed. Under the conditions of this test, the data suggest that the test compound exhibits little or no mutagenic activity.	The test compound exhibited moderate clastogenic activity. A dose response was observed. Under the conditions of this test, the data suggest that the compound exhibits mutagenic activity.
<b>Dominant Lethal Assay in Rodents for Mutagenicity</b>	
Test compound appeared to exhibit minimal activity in total implantations, number of live implantations per pregnant female, and pre-implantation losses. No significant dose response was observed and little or no mutagenic activity in the dominant lethal test.	Test compound appeared to exhibit minimal activity in total implantations, number of live implantations per pregnant female, and pre-implantation losses. No significant dose response was observed and little or no mutagenic activity in the dominant lethal test.
<b><i>Salmonella</i>/Microsomal Assay for Bacterial Mutagenicity</b>	
a. The test agent did not induce a significant increase in the number of point mutations in <i>Salmonella</i> typhimurium strains in the absence of activating system for strains TA1535, TA1537, TA1358, TA100, and TA98. b. It did not induce a significant increase in the number of point mutations with the addition of an exogenous source of liver enzymes for metabolic activation in strains of TA1535, TA1537, TA1358, TA100, and TA98.	a. Test agent did not induce significant increase in number of point mutations in <i>Salmonella</i> typhimurium strains in the absence of activating systems for TA1535, TA1537, TA100, TA98. b. Induced a significant increase in the number of point mutations in the absence of the activating system for strain TA1538. c. Did not induce a significant increase in the number of point mutations with the addition of an exogenous source of liver enzymes for activation.
<b>Differential Inhibition of Repair Deficient and Repair Competent Strains of <i>Escherichia Coli</i> (<i>E. coli</i>): DNA Repair</b>	
The test chemical did not produce a statistically significant difference in its ability to produce cell death between repair deficient ( <i>polA</i> <sup>-</sup> ) and repair competent ( <i>polA</i> <sup>+</sup> ) strains in <i>E. coli</i> .	Test chemical produced statistically significant difference at 2 $\mu$ L per plate in production of cell death between repair deficient ( <i>polA</i> <sup>-</sup> ) and repair competent ( <i>polA</i> <sup>+</sup> ) strains in <i>E. coli</i> .

The fact that a positive effect was obtained in a number of *in vitro* tests indicates that the material may be a potential mutagen, and thus this class of materials may be mutagenic. Note that compound 3899-B (the less refined compound) generally appeared more toxic. This indicated that impurities and other chemicals may increase toxicity to an unacceptable level even if the pure compounds are not unacceptably toxic.

**Other Phosphorus Compounds:** In a study of a number of phosphorus compounds, no toxic signs were observed following 15 6 h exposures of two male and two female rats to 200  $\mu$ L/L tributyl phosphite, P(OC<sub>4</sub>H<sub>9</sub>)<sub>3</sub>.<sup>137</sup> The blood, urine, and organs (upon autopsy) were normal. The same study showed that tris(hydroxymethyl)propane bicyclic phosphite, Figure 7-5, has an unexpectedly high toxicity and was stated to be "one of the most toxic compounds handled in this laboratory." All rats died following a 1 h

exposure to 10  $\mu\text{L/L}$ . The action on the central nervous system was probably due to its sufficient stability to penetrate cell membranes as a non-ionized molecule, possibly with subsequent hydrolysis. Note, however, that its hydrolysis product, dihydroxybutylphosphonic acid, has a low oral and parental toxicity.

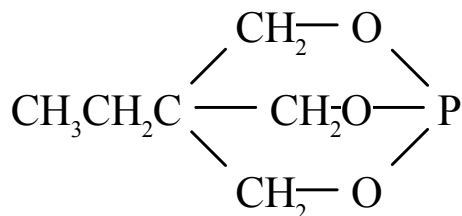


**Figure 7-5. Tris(hydroxymethyl)propane Bicyclic Phosphite.**

### ***Phosphorus Tribromide (PBr<sub>3</sub>)***

In spite of its contact toxicity and corrosive hazards, documented in material safety data sheets<sup>67,138</sup>, the attraction of a reactive molecule containing four catalytic atoms (three bromine atoms and a phosphorus atom) led to several studies of the efficacy of phosphorus tribromide (PBr<sub>3</sub>) molecule as a fire extinguishant.<sup>84,85,92</sup> The high boiling point (173 °C) and low vapor pressure (1.3 kPa @ 48 °C) of PBr<sub>3</sub> indicated that in fire suppression applications the compound would have no dimensionality, and unless the compound were applied in sufficient quantity directly on the burning surface, it was unlikely that complete and reliable flame extinguishment would be obtained. These physical properties led to the conclusion that PBr<sub>3</sub> had no promise as a total flooding agent. The alternative study of low boiling bromine carriers such as the alkenes and ethers was judged more likely to yield a more toxicologically and environmentally acceptable halon replacement with greater dimensionality, and therefore no further effort to study PBr<sub>3</sub> was made.

Nonetheless, studies continued. In the 1990s, there were limited press releases of some studies of PBr<sub>3</sub>, along with poster session presentations at the annual Halon Options Technical Working Conferences in the 1990s. A report to the Air Force conveyed some technical documentation.<sup>139</sup>

Recently, it was announced that a commercial aircraft engine nacelle fire extinguishment system would employ this chemical, in very small quantity relative to halon 1301.<sup>140</sup> The described approach utilized focusing a spray of the PBr<sub>3</sub> onto a location where the fire was assumed to occur. This approach gained its advertised agent mass and volume advantage because halon 1301 is typically discharged to flood the entire engine nacelle. Total flooding mitigates the risk that the fire might start in an obstructed location and not be extinguished. In addition, the discharge of HFCs and halons is accompanied by significant cooling of hot surfaces in and around the flame zone. This is credited with diminishing or even eliminating the potential for relight of hot liquids and vapors present in the burn zone. There was no presentation of same-test-fixture comparison of the PBr<sub>3</sub> system to halon 1301 extinguishment.

### **Arsenic, Bismuth, and Antimony**

Antimony has been extensively used in flame retardants, usually in conjunction with bromine-containing compounds.<sup>48</sup> No studies on fires suppression by arsenic or bismuth compounds have been found. Arsenic and antimony compounds are too toxic to meet that screening criterion.

### 7.3.6 Main Group Elements - Group VI

#### Oxygen

Oxygen compounds are included under other headings and are not covered here. The use of water (H<sub>2</sub>O) as an extinguishant dates to before the earliest historical written records. There is no indication that simple inorganic oxygen compounds provide any type of catalytic fire suppression capability.

#### Sulfur

A sulfur dioxide cycle (Reactions 7-28 and 7-29) has been proposed to inhibit combustion by removal of hydrogen atoms.<sup>79</sup>



However, no fire suppression tests have been conducted on these compounds, and there is no evidence indicating that the sulfur atom imparts any chemical fire suppression capability. The nonhalogenated sulfur-containing compounds are generally flammable. Thus, attention was directed at highly halogenated compounds.

It appeared possible that brominated fluorosulfur compounds could be efficient fire suppressants and have short atmospheric lifetimes. However, no affordable sources of these compounds could be located, and there was also expectation that their volatility would be insufficient.

The perfluoroalkyl sulfur compounds have relatively high oxidation and hydrolysis stability. Bis(trifluoromethyl)sulfide (CF<sub>3</sub>-S-CF<sub>3</sub>) is prepared by heating bis(trifluoromethyl)disulfide (CF<sub>3</sub>-SS-CF<sub>3</sub>) at 425 °C for 3 days to 4 days.<sup>141</sup> This and other perfluoroalkylsulfides can also be prepared by heating or photolysis of R<sub>f</sub>OC(O)R<sub>f</sub>, where R<sub>f</sub> is a perfluoroalkyl group.<sup>142,143</sup> The ester is prepared by reaction of R<sub>f</sub>-S-Cl and silver perfluorocarboxylates (AgOOCR<sub>f</sub>). The derivatives R<sub>f</sub>-SF<sub>2</sub>-R<sub>f</sub> are prepared by fluorination of the corresponding sulfide with ClF or F<sub>2</sub>, followed by hydrolysis to give R<sub>f</sub>-S(O)-R<sub>f</sub>.<sup>144,145</sup> These compounds are generally hydrolytically and oxidatively stable.<sup>141,143,144</sup>

As can be seen in Table 7-20, only the first two sulfides are sufficiently volatile to meet the screening criterion for aircraft use.

A major drawback of sulfur compounds is the expected formation of toxic sulfur oxides or hydrogen sulfide during fire extinguishment. Toxicity concerns, a lack of availability of test chemicals, and likely long atmospheric lifetime of the fully fluorinated thioalkanes resulted in further examination of this family being abandoned.

**Table 7–20. Perfluoroalkyl Sulfur Compounds.**

Chemical Name	Formula	$T_b$ (°C)
1,1,1,3,3,3-hexafluoro-2-thiopropene	CF <sub>3</sub> -S-CF <sub>3</sub>	<sup>a</sup> -22
1,1,1,3,3,3,4,4,4-octafluoro-2-thiobutane	CF <sub>3</sub> -S-CF <sub>2</sub> CF <sub>3</sub>	<sup>b</sup> 6.3
1,1,1,3,3,3,4,4,5,5,5-decafluoro-2-thiopentane	CF <sub>3</sub> -S-CF <sub>2</sub> CF <sub>2</sub> CF <sub>3</sub>	<sup>b</sup> 38.6
1,1,1,2,2,3,3,3-octafluoro-2-thiopropene	CF <sub>3</sub> SF <sub>2</sub> CF <sub>3</sub>	<sup>b</sup> 21.0
1,1,1,2,2,3,3,3,4,4,4-decafluoro-2-thiobutane	CF <sub>3</sub> SF <sub>2</sub> CF <sub>2</sub> CF <sub>3</sub>	<sup>b</sup> 44.1
1,1,1,2,2,3,3,3,4,4,5,5,5-dodecafluoro-2-thiopentane	CF <sub>3</sub> SF <sub>2</sub> CF <sub>2</sub> CF <sub>2</sub> CF <sub>3</sub>	<sup>b</sup> 69.3
1,1,1,2,2,3,3,3,4,4,5,5,6,6,6-dodecafluoro-3-thiopentane	CF <sub>3</sub> CF <sub>2</sub> SF <sub>2</sub> CF <sub>2</sub> CF <sub>3</sub>	<sup>b</sup> 69.5
1,1,1,3,3,3-hexafluoro-2-oxo-2-thiopropene	CF <sub>3</sub> S(O)CF <sub>3</sub>	<sup>b</sup> 37.3
1,1,1,3,3,3,4,4,4-octafluoro-2-oxo-2-thiobutane	CF <sub>3</sub> S(O)CF <sub>2</sub> CF <sub>3</sub>	<sup>b</sup> 58.2
1,1,1,3,3,3,4,4,5,5,5-decafluoro-2-oxo-2-thiopentane	CF <sub>3</sub> S(O)CF <sub>2</sub> CF <sub>2</sub> CF <sub>3</sub>	<sup>b</sup> 64.0

a Reference 141.

b Reference 143.

## Selenium and Tellurium

The only compound containing one of these elements for which fire extinguishment capabilities have been reported is perfluoroselenolane.<sup>146</sup> There was no indication that selenium or tellurium compounds exhibited catalytic flame inhibition or that such compounds would have particular utility as halon replacements. Selenium toxicity was of great concern.<sup>67,138</sup>

### 7.3.7 Main Group Elements - Group VIII (Noble Gases)

Of the non-radioactive Group VIII elements (helium, neon, argon, krypton, and xenon), only xenon and, to a much lesser extent, krypton are known to form compounds. These compounds are strong oxidizing agents and would probably act to increase flame intensity rather than decrease it. At any rate, these are not stable at ordinary temperatures, so only the atoms would reach the flame. Like nitrogen, the noble gases extinguish flames by dilution and cooling. They thus did not meet the efficiency screening criterion.

### 7.3.8 Transition Metal Based Compounds

The 2001 NGP review<sup>39</sup> of the status of knowledge of fire suppressants recommended a further look at compounds of copper, iron, manganese, and tin. A more detailed and more current review (including extensive NGP research) of the chemistry of transition metal compounds appears in Chapter 3 of this book. That chapter notes data supporting high flame inhibition efficiency for a longer list of metals, adding chromium, cobalt, lead, molybdenum, and tungsten. Unfortunately, most metal-containing compounds from this larger set have the potential to lose their ability to quench flames due to condensation of the active species. There was no direct evidence for salts of cobalt, copper, molybdenum, and tungsten to lose their flame quenching potential.

All compounds containing these metals are solids or dense liquids at flight temperatures and are thus not sufficiently volatile for total flooding as gases. Thus, the NGP did not perform a systematic flame extinguishment study of these compounds. They could be dispensed by incorporation in a solid propellant fire extinguisher, as described in Chapter 9. The addition of K<sub>2</sub>CO<sub>3</sub> has significantly improved

the performance of a prototype device, and salts of these metals would need to be at least as beneficial for further consideration.

### 7.3.9 Inorganic Chemicals - Conclusions

Nearly all of the inorganic compounds are insufficiently volatile and/or have not shown even moderate fire suppression efficiency. They thus do not meet primary screening requirements for replacing halon 1301 in aircraft applications. A few compounds are moderately volatile, but are toxic or corrosive. Some phosphorus halides have boiling points that might be sufficient for use should the operational temperature criterion be raised significantly above the -40 °C extreme at which halon 1301 alternatives are expected to perform.

## 7.4 NGP SURVEYS OF ORGANIC COMPOUNDS

### 7.4.1 Highly Efficient Thermal Agents

#### Screening

The NGP conducted extensive research to determine whether other organic compounds could be as efficient at flame extinguishment as halon 1301 simply by absorbing heat from the flames, i.e., without any chemical or catalytic activity.<sup>147</sup> A number of reports by Pitts et al. describe specific aspects of and the conclusions resulting from this research.<sup>148,149,150,151,152,153,154</sup> In this effort, two existing thermodynamic databases maintained by NIST were searched in order to identify chemical compounds predicted to extract large amounts of heat from a combustion zone:

- Design Institute for Physical Properties database (DIPPR), which contains 1458 compounds from 83 chemical families (Table 7–21) and
- REFPROP, which contains 43 compounds tailored to alternate refrigerant applications, including many candidates for replacing HCFCs.

This search also included representative compounds from some families of chemicals not well represented in existing thermophysical property databases. These were compounds having high heat of vaporization, liquid phase heat capacity, total heat absorption due to a phase change, and/or heat needed to raise the liquid or gas to combustion temperatures. Fluorinated ethers were important to consider, since their atmospheric lifetimes may be significantly lower than those of chlorofluorocarbons,<sup>155</sup> and some of these had been identified as possible replacements for blowing agents, refrigerants, fire suppression agents, and solvents.<sup>21,156,157,158,159,160</sup> Additional compounds were several cyclic fluorinated ether compounds (fluorinated oxiranes, oxetanes, and furans), some non-cyclic methyl ethers (HFE-116, HFE-125), fluorinated methyl ethyl ethers with two or fewer hydrogen atoms (HFE-227me, HFE-236me), and some larger fluorinated ethers (methoxy-nonafluorobutane, C<sub>4</sub>F<sub>9</sub>OCH<sub>3</sub>, HFE-7100; perfluorodimethoxymethane, CF<sub>3</sub>OCF<sub>2</sub>OCF<sub>3</sub>; perfluoropropyltrifluoromethyl ether, CF<sub>3</sub>OCF<sub>2</sub>CF<sub>2</sub>CF<sub>3</sub>; and heptafluoropropyl-1,2,2,2-tetrafluoroethyl ether, CF<sub>3</sub>CHFOCF<sub>2</sub>CF<sub>2</sub>CF<sub>3</sub>). Lastly, the list of compounds considered included two fluorinated amines, the alternative refrigerant HFC-338mccq (CH<sub>2</sub>FCF<sub>2</sub>CF<sub>2</sub>CF<sub>3</sub>), and the fluorinated alcohol 2,2,3,3,3-pentafluoropropanol (CF<sub>3</sub>CF<sub>2</sub>CH<sub>2</sub>OH).

Table 7–21. Family Types in the DIPPR Database

#	Family Type	#	Family Type	#	Family Type
1	n-Alkanes	29	Cycloaliphatic alcohols	57	Other amines, imines
2	Methylalkanes	30	Aromatic alcohols	58	Nitriles
3	Dimethylalkanes	31	Polyols	59	C,H,NO <sub>2</sub> compounds
4	Other alkanes	32	<i>n</i> -Aliphatic acids	60	Isocyanates/diisocyanates
5	Cycloalkanes	33	Other aliphatic acids	61	Mercaptans
6	Alkylcyclopentanes	34	Dicarboxylic acids	62	Sulfides/theophenes
7	Alkylcyclohexanes	35	Aromatic carboxylic acids	63	Polyfunctional acids
8	Multi-ring cycloalkanes	36	Anhydrides	64	Polyfunctional esters
9	1-Alkynes	37	Formates	65	Other polyfunctional C,H,O
10	2,3,4-Alkenes	38	Acetates	66	Polyfunctional nitriles
11	Methylalkenes	39	Propionates & Butyrates	67	Nitroamines
12	Ethyl and higher alkenes	40	Other saturated aliphatic esters	68	Polyfunc. amides/amines
13	Cycloalkenes	41	Unsaturated aliphatic esters	69	Polyfunctional C,H,O,N
14	Dialkenes	42	Aromatic esters	70	Polyfunctional C,H,O,S
15	Alkynes	43	Aliphatic ethers	71	Polyfunc. C,H,O,halides
16	<i>n</i> -Alkylbenzenes	44	Other ethers and diethers	72	Polyfunc. C,H,N,halides
17	Other alkylbenzenes	45	Epoxides	73	Other polyfunc. organics
18	Other monoaromatics	46	Peroxides	74	Elements
19	Napthalenes	47	C1/C2 aliphatic chlorides	75	Silanes/siloxanes
20	Other condensed rings	48	C3 & higher aliphatic chlorides	76	Organic-inorganic
21	Diphenyl/polyaromatics	49	Aromatic chlorides	77	Inorganic acids
22	Terpenes	50	C,H,Br compounds	78	Inorganic bases
23	Other hydrocarbon rings	51	C,H,I compounds	79	Organic salts
24	Inorganic gases	52	C,H,F compounds	80	Sodium salts
25	Aldehydes	53	C,H multihalogen compounds	81	Other inorganic salts
26	Ketones	54	<i>n</i> -Aliphatic primary amines	82	Inorganic halides
27	<i>n</i> -Alcohols	55	Other aliphatic amines	83	Other inorganics

The research approach involved developing a figure of merit for evaluating each compound based on the total enthalpy absorbed by the compound as it was heated from room temperature to flame temperature, represented by 1400 K. The total heat absorbed consists of three contributions (Equation 7-30),

$$\Delta H^{Total} = \Delta H_l + \Delta H_v + \Delta H_g, \quad (7-30)$$

where the first contribution,  $\Delta H_l$ , is the heat involved in taking the liquid from room temperature up to the normal boiling point,  $T_b$ ,

$$\Delta H_l = \int_{298K}^{T_b} C_p^{liquid} dT. \quad (7-31)$$

The value of the liquid heat capacity (Equation 7-31) at the normal boiling point was used, since the heat capacity of a liquid does not change significantly over a small temperature range. If this was unavailable, the liquid phase heat capacity at 20 °C was estimated using the method of Chueh and Swanson.<sup>161162</sup>

The second term,  $\Delta H_v$ , is the latent heat of vaporization at the normal boiling point. If not available, these were estimated using the approach of Fishtine.<sup>163</sup>

The third contribution,  $\Delta H_g$ , is the integral, [Equation 7-32] of the gas-phase heat capacity from the normal boiling point to 1400 K,

$$\Delta H_g = \int_{T_b}^{1400K} C_p^{gas} dT. \quad (7-32)$$

The gas phase heat capacities were estimated using the method of Rihani and Doraiswamy,<sup>164</sup> which was based on structural contributions. For agents with boiling points below 298 K, the total heat involved is just the contribution  $\Delta H_v$ .

Table 7–22 summarizes the results of this computation, comparing the best of the examined chemicals, along with some reference compounds. The listing is in order of their  $\Delta H^{Total}$  expressed on a molar basis (kJ/mol).

**Table 7–22. Compounds with High  $\Delta H^{Total}$  (Molar Basis).**

	$T_b$ (°K)	$\Delta H^{Total}$ (kJ/mol)
perfluoro-2-butyltetrahydrofuran, C <sub>8</sub> F <sub>16</sub> O	375.2	608.4
heptafluoropropyl-1,2,2,2-tetrafluoroethyl ether	315.2	421.9
methoxy-nonafluorobutane, HFE-7100	334	407.6
perfluoropropyltrifluoromethyl ether, CF <sub>3</sub> OCF <sub>2</sub> CF <sub>2</sub> CF <sub>3</sub>	279.9	336.3
perfluoroisobutane, C <sub>4</sub> F <sub>10</sub>	252.5	321.2
1,1,1,2,2,3,3,4-octafluorobutane, HFC-338mccq	301	321.0
decafluorobutane, C <sub>4</sub> F <sub>10</sub>	271	318.5
octafluorocyclobutane, C <sub>4</sub> F <sub>8</sub>	267	303.2
perfluorotrimethylamine, C <sub>3</sub> F <sub>9</sub> N	264	293.8
lactic acid, C <sub>3</sub> H <sub>6</sub> O <sub>3</sub>	455	292.9
perfluorodimethoxymethane, CF <sub>3</sub> OCF <sub>2</sub> OCF <sub>3</sub>	263	286.8
octafluorofuran, C <sub>4</sub> F <sub>8</sub> O	272.4	289.8
2,2,3,3,3-pentafluoropropanol, C <sub>3</sub> F <sub>5</sub> H <sub>3</sub> O	353.15	280.8
octafluoro-2-butene	270	261.9
tris(difluoromethyl)amine, C <sub>3</sub> H <sub>3</sub> F <sub>6</sub> N	275	256.5
trifluoromethyl-1,2,2,2-tetrafluoroethyl ether, HFE-227me	263.6	255.3
octafluoropropane, FC-218	236.4	250.8
difluoromethyl-1,2,2,2-tetrafluoroethyl ether, HFE-236me	296.5	239.4
1,1,1,2,2,3,3,3-heptafluoropropane, HFC-227ea	257.5	236.5
1,1,1,2,2,3,3-hexafluoropropane, HFC-236ea	279.7	222.2
bis(trifluoromethyl)ether, HFE-116	257	196.2
pentafluorodimethylether, HFE-125	235	183.8
hexafluoroethane, FC-116	194.95	181.1
1,1,2,2-tetrafluorodimethylether, HFE-134	279.4	170.2
<b>pentafluoroethane, HFC-125</b>	<b>225.2</b>	<b>166.8</b>
1,1,1,2-tetrafluoroethane, HFC-134a	247	156.8
1,1,2,2-tetrafluoroethane, HFC-134	250	152.8
<b>bromotrifluoromethane, halon 1301</b>	<b>215.26</b>	<b>110.9</b>
Water, H <sub>2</sub> O	373.1	87.5
carbon dioxide, CO <sub>2</sub>	N/a	56.2
Nitrogen, N <sub>2</sub>	77.4	34.7
Argon, Ar	87.3	22.9

Table 7–23 gives the same quantity, but expressed on a mass basis (kJ/kg). Compounds that were identified as flammable or toxic, or that had known ozone depletion problems, have been eliminated. The DIPPR database does not contain any information on toxicity or other health effects. This information came from manufacturers' safety data sheets and Hawley.<sup>165</sup> Since the information on toxicity was incomplete, further investigation of some chemicals would be needed. The web site at <http://chemfinder.camsoft.com/> provided OPD and GWP information. Perfluorocarbons are included for reference, although the EPA has indicated they may be used only when all other compounds are inappropriate. Halon 1301 and HFC-125, two reference compounds, are shown in boldface.

**Table 7–23. Compounds with High  $\Delta H^{Total}$  (Mass Basis).**

Chemical Name, Formula	$T_b$ (°K)	$\Delta H^{total}$ (kJ/kg)
Water, H <sub>2</sub> O	373.1	4855.7
lactic acid, C <sub>3</sub> H <sub>6</sub> O <sub>3</sub>	455	3251.6
2,2,3,3,3-pentafluoropropanol, C <sub>3</sub> F <sub>5</sub> H <sub>3</sub> O	353.15	1872.0
methoxy-nonafluorobutane, HFE-7100	334	1630.4
1,1,1,2,2,3,3,4-octafluorobutane, R338mccq	301	1588.7
1,1,1,2-tetrafluoroethane, HFC-134a	247	1536.8
tris(difluoromethyl)amine, C <sub>3</sub> H <sub>3</sub> F <sub>6</sub> N	275	1535.5
octafluorocyclobutane, C <sub>4</sub> F <sub>8</sub>	267	1515.8
1,1,2,2-tetrafluoroethane, HFC-134	250	1497.6
heptafluoropropyl-1,2,2,2-tetrafluoroethyl ether	315.2	1475.0
perfluoro-2-butyltetrahydrofuran, C <sub>8</sub> F <sub>16</sub> O	375.2	1462.3
1,1,1,2,3,3-hexafluoropropane, HFC-236ea	279.7	1461.4
1,1,2,2-tetrafluorodimethylether, HFE-134	279.4	1442.0
difluoromethyl-1,2,2,2-tetrafluoroethyl ether, HFE-236me	296.5	1424.7
1,1,1,2,3,3,3-heptafluoropropane, HFC-227ea	257.5	1390.9
<b>pentafluoroethane, HFC-125</b>	<b>225.2</b>	<b>1389.8</b>
trifluoromethyl-1,2,2,2-tetrafluoroethyl ether, HFE-227me	263.6	1372.4
pentafluorodimethylether, HFE-125	235	1351.3
perfluoroisobutane, C <sub>4</sub> F <sub>10</sub>	252.5	1349.6
octafluorofuran, C <sub>4</sub> F <sub>8</sub> O	272.4	1341.5
decafluorobutane, C <sub>4</sub> F <sub>10</sub>	271	1338.2
octafluoropropane, FC-218	236.4	1333.8
perfluorotrimethylamine, C <sub>3</sub> F <sub>9</sub> N	264	1329.3
perfluoropropyltrifluoromethyl ether, CF <sub>3</sub> OCF <sub>2</sub> CF <sub>2</sub> CF <sub>3</sub>	279.9	1323.9
hexafluoroethane, FC-116	194.95	1312.2
octafluoro-2-butene	270	1309.2
perfluorodimethoxymethane, CF <sub>3</sub> OCF <sub>2</sub> OCF <sub>3</sub>	263	1303.5
carbon dioxide, CO <sub>2</sub>	n/a	1276
bis(trifluoromethyl)ether, HFE-116	257	1273.9
nitrogen, N <sub>2</sub>	77.4	1238.3
bromotrifluoromethane, halon 1301	215.26	744.7
Argon, Ar	87.3	573.2

The results of Table 7–22 indicate that the top candidates for use in moderate (ground level) ambient temperature environments or as streaming agents (defined here as having boiling points higher than 293 K), on a molar basis, are perfluoro-2-butyltetrahydrofuran, methoxy-nonafluorobutane, heptafluoropropyl-1,2,2,2-tetrafluoroethyl ether, and 1,1,1,2,2,3,3,4-octafluorobutane.

Table 7–23 indicates that methoxy-nonafluorobutane (HFE-7100) is also high on the list when expressed on a mass basis. It is available commercially.<sup>166</sup> The others are not, but have been synthesized and used for research.<sup>167, 168,169</sup> The top total-flooding candidates (defined as having boiling points lower than 293 K) are perfluoropropyltrifluoromethyl ether, perfluoroisobutane, decafluorobutane, and octafluorocyclobutane. Of these, the last two are available commercially.<sup>170</sup> The latter three are perfluorocarbons and thus not reasonable to consider further.

HFE-7100 was developed as a replacement for ozone-depleting chemicals used in a variety of applications. It has been estimated to have a zero ozone depletion potential, a relatively low global warming potential, low toxicity, and good materials compatibility.<sup>166</sup> It has been approved under the Significant New Alternatives Policy (SNAP) of the United States Environmental Protection Agency. There is an existing patent dealing with use of HFE-7100 as a fire-extinguishing agent. Based on these favorable properties, it was decided to characterize the extinguishing capability of HFE-7100 experimentally.

The data included in Table 7–23 indicate that lactic acid is predicted to be highly effective as a thermal agent. Clearly, this compound is not a potential candidate as a replacement for halon 1301 for in-flight fires due to its high boiling and melting points and caustic nature. It is also an organic compound and may be combustible. However, based solely on its ability to extract heat, it is predicted to be nearly twice as effective on a mass basis as any of the other potential thermal agents considered, except water. Its ability to extract heat is predicted to be roughly two-thirds of that of water on a mass basis and 3.5 times greater on a molar basis. Since lactic acid is soluble in water, it was deemed worthwhile to investigate the suppression characteristics of mixtures of these two polar liquids.

### Effectiveness of Thermal Agents

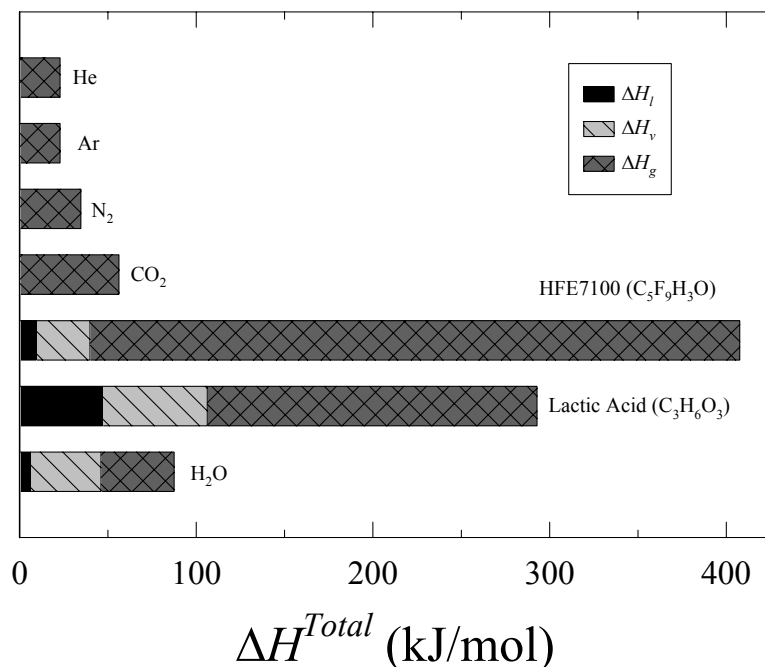
In order to understand the effectiveness of thermal agents better, experimental and modeling investigations were performed for flame extinguishment by water, lactic acid, and HFE-7100. Prefatory measurements and calculations for simpler, gaseous thermal agents (nitrogen, carbon dioxide, argon, and helium) were used to establish the viability of the approach.<sup>147</sup>

Figure 7–6 shows the relative contributions of the various heat extraction mechanisms in Equation 1 for the seven agents in terms of heat extraction per mole of agent and per mass of agent. On a molar basis HFE-7100 is predicted to be the most effective, with lactic acid a close second. The contribution of liquid processes to the total heat extraction is relatively small for HFE-7100. Liquid water is predicted to be the next most effective due primarily to the relatively high heat absorbed during evaporation. The four gaseous agents are predicted to be relatively ineffective and are ordered  $\text{CO}_2 > \text{N}_2 > \text{Ar} = \text{He}$ .

On a per mass basis, the plot has a very different appearance. The most effective agent in these terms is helium followed by water and lactic acid. On this plot the role of heat extraction by heating and vaporization of the liquid agents is clear. It can be seen that for water, over half of the heat extraction arises from the liquid processes. For lactic acid, the contribution of liquid vaporization to the total heat

extraction is significant, but greatly reduced as compared to water. The large differences between the HFE-7100 and lactic acid and water are due to hydrogen bonding that exists in water and lactic acid. This bonding significantly increases the amount of heat energy required to vaporize liquids when it is present.

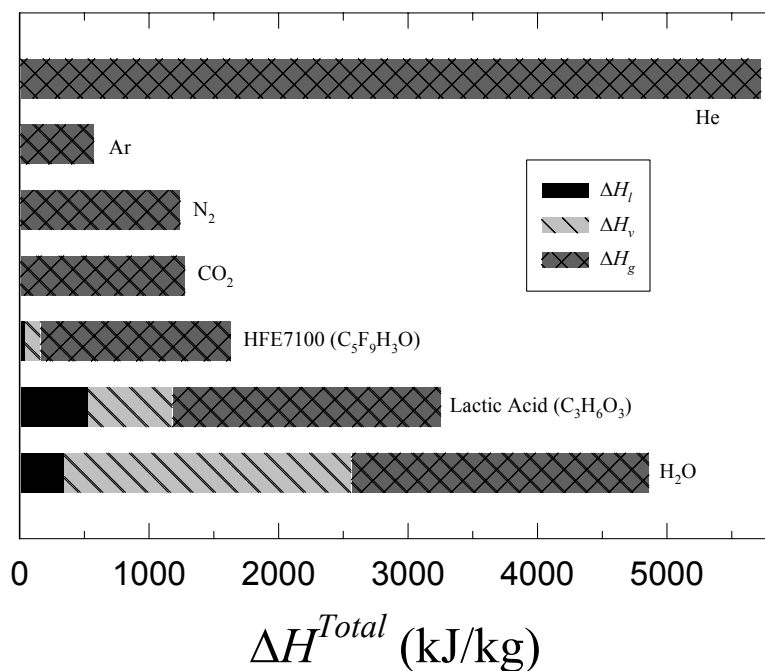
### Estimated Total Heat Extraction (kJ/mol)



**Figure 7–6. Relative Contributions of Liquid Heating, Vaporization, and Gas Heating to 1400 K to the Total Heat Absorbed by Various Thermal Agents.**

(top: mole basis; bottom: mass basis)

### Estimated Total Heat Extraction (kJ/kg)



Nitrogen and carbon dioxide were predicted to extract roughly the same amount of heat per kg, while the amount extracted by gaseous HFE-7100 was only slightly higher. In fact, it has been found that for a number of gaseous species expected to act primarily as thermal agents the mass required to extinguish a fire is roughly constant.<sup>171</sup> However, it is clear from these plots that this criterion should only be used to provide guidance and that it is not generally applicable to a wide range of molecular species.

The performance of HFE-7100 and lactic acid was evaluated using the Dispersed Liquid Agent Fire Suppression Screen (DLAFSS, Chapter 8). Despite lactic acid's expected ability to withdraw significant levels of heat from a flame zone, it is flammable. Thus, there will be competitive effects between the heat release and heat extraction in the suppression processes. To mitigate the effect of the heat release, lactic acid was mixed with water, also a good thermal agent, but nonflammable. Both the ether and the aqueous solution were introduced as droplets.

Figure 7–7 shows the test results for three lactic acid solutions. The undiluted stock solution was not tested because it was so viscous it caused the syringe pump, used to deliver the liquid to the nebulizer, to stall. Each data point represents an average of five or more tests; the error bars represent one standard deviation. The blow-off velocity decreased with increasing liquid application rate. In other words, as more of the acid mixture was delivered to the flame, less airflow was required to induce extinction.

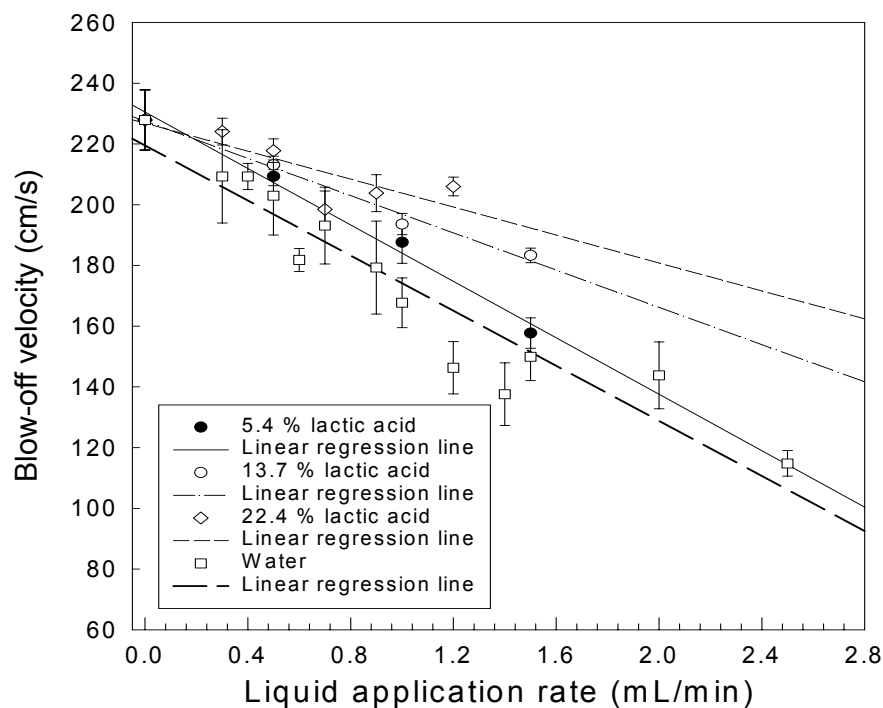


**Figure 7–7. Air Velocities at Extinguishment of the DLAFSS Flame as a Function of Liquid Application Rate for Lactic Acid/water Mixtures.**

The slopes of the lines in Figure 7–7 are a measure of the effectiveness of a liquid in suppressing a flame. The steeper the slope, the more effective is the liquid. The three lactic acid/water mixtures showed no improvement of fire suppression effectiveness over neat water. In fact, the fire suppression effectiveness decreased as the lactic acid mass fraction was increased. Given that no chemical effects were expected for fire suppression with lactic acid, it was concluded that the increased heat extraction due to lactic acid was being overwhelmed by heat release due to its combustion.

Figure 7–8 is a similar plot for HFE-7100. The shallower slope indicates a less efficient agent than water.

HFE-7100 was also studied in the Transient Application Recirculating Pool Fire (TARPF) facility (Chapter 8) to understand its performance under flow conditions typical of those present in aircraft engine nacelles. The airflow in the tunnel was fixed at  $6.67 \text{ H } 10^{-3} \text{ m}^3/\text{s}$ . The porous burner was operated with a propane flow of 33 mL/s. The mist nozzle had a flow of 1.9 mL/s at 1.03 MPa. The mist discharge duration was varied from 1 s to 10 s. The hot surface used to investigate re-ignition was not activated. The only heating of this surface came from the impinging flame.

For these operating conditions, it was found that the pool fire stabilized behind the backward-facing step could not be completely suppressed by the HFE-7100 mist. Furthermore, the nominal effective mass fraction of the HFE-7100 for the TARPF experiments was more than twice as high as that required to extinguish a propane flame in the DLAFFS. A similar behavior was observed when water was tested. The difference is almost certainly associated with agent distribution and entrainment in the TARPF. It is likely that droplets of agent dispersed in the high-speed air flow had sufficient momentum to pass above the recirculating zone without being entrained. In this way, it would be possible to have an extinguishing concentration of liquid agent in the air above the flame, but a lower concentration in the actual location where the flame is stabilized. In either case, the results demonstrated the importance of agent distribution for effective flame extinguishment.

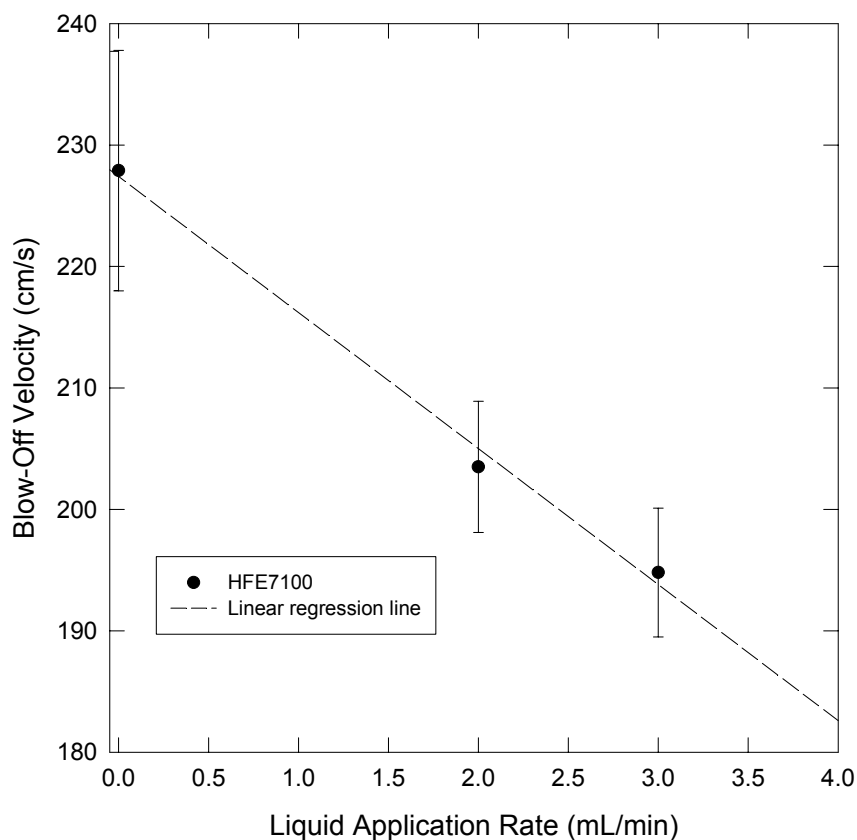


**Figure 7–8. Air Velocities at Extinguishment of the DLAFFS Flame as a Function of Liquid Application Rate for HFE-7100.**

## Chemical Kinetic Modeling of Thermal Agents

To obtain further insights into the effectiveness of thermal agents and their mechanisms of flame extinguishment, detailed chemical-kinetic computations were performed in which various thermal agents were added to the air side of laminar opposed-flow diffusion flames.<sup>147</sup> The flames were simulated using OPPDIF,<sup>172</sup> a computer code developed by Sandia National Laboratories. OPPDIF is built on a number of general purpose subroutines, collectively known as CHEMKIN-III.<sup>173</sup> GRI-Mech 1.2, which had been developed with the support of the Gas Research Institute, provided the detailed kinetics for the methane/air flame.<sup>174</sup>

GRI-Mech 1.2 consisted of 32 chemical species undergoing 177 reactions. One- and two-carbon species were included. Thermodynamic and transport data were provided as separate files. The mechanism was created by starting with appropriate estimates for the rate constants and then optimizing to provide the best agreement with experimental measurements in such systems as premixed flames, shock tubes, and flow reactors.<sup>174</sup> The mechanism was not optimized using diffusion flame results. The extinction behavior for the propane/air flame was calculated using the mechanism of Babushok and Tsang.<sup>175</sup>

In the simulations, the goal was to identify the flow conditions just sufficient to cause extinction of a flame formed by fuel and either air or air with added agent. The approach was based on the hypothesis that the maximum flame temperature at extinguishment for a given fuel is a unique value as long as the agent is non-reactive in the flame. Most of the calculations were for methane/air flames, but some were performed for the computationally more intensive propane/air flames. An arbitrary, but stringent, criterion was adopted which defined the extinction velocity as that for which a burning solution was still obtained, but for which an increase of only 0.01 cm/s in the fuel and air initial velocities either resulted in (a) a failure to find a solution or (b) a non-burning solution. Additional small increases in velocity always resulted in non-burning solutions.

The general procedure was to find a solution for a given type of diffusion flame by first solving an isothermal case and using the solution as the input for a calculation in which the energy equation was added. Once that solution was available, it was used as the starting point for calculations in which such parameters as the oxidizer and flow velocities were changed. Only the formulation including the energy equation was solved for the “restarted” cases. The new solution then became the starting point for cases involving further changes in the controlling parameters. For a given set of initial conditions (fuel, agent fraction, etc.), higher and higher flow velocities were used until the above extinction criterion was met.

Checks against later GRI-Mech releases 2.11 and 3.0 showed no more than a minimal effect of the specific release on the calculated results.

Figure 7–9 shows the similarity of the calculated maximum flame temperatures at extinction, which were uniform at  $1794\text{ }^{\circ}\text{C} \pm 7\text{ }^{\circ}\text{C}$ . The three calculations of the strain rate of the flame at extinction were also close at  $500\text{ s}^{-1} \pm 6\text{ s}^{-1}$ . Other reported calculations show similar results, while reported experimental values from seven laboratories averaged  $384\text{ s}^{-1} \pm 21\text{ s}^{-1}$ .<sup>147</sup> Since all the calculations invoke similar chemistry, it is presumed that the difference between the (consistent) calculated values and the (consistent) measured values results from the particular chemical kinetic mechanism used. The uncertainties in the rate constants could readily account for the roughly 20 % difference.

For the propane/air flames, the calculated strain rate at extinction was  $621 \text{ s}^{-1}$ . The three reported values were  $510 \text{ s}^{-1}$ ,  $583 \text{ s}^{-1}$ , and  $721 \text{ s}^{-1}$ .<sup>147</sup> This range of measured values is wider than that for the methane/air flames and encompasses the calculated value for the propane/air flame.

Table 7–24 lists the added volume fractions of inert gases calculated to extinguish a buoyancy dominated, methane/air diffusion flame. Previously published and NGP-measured values for each of the inert gases are included. Note that prior to the NGP, there was just one published value for flame extinguishment by the inert gases other than nitrogen. Details of all the measurements are included in Reference 147. Table 7–25 is a similar table for propane/air flames.

The following observations follow from the above data:

- For both fuels, the extinguishment values show some dependence on the type of burner.
- The calculated values agree with DLAFSS values, as expected since the extinguishing concentrations are tied to the experimental values for porous burners in opposed flow configurations.
- The helium results are consistently lower than the predicted values.
- Detailed chemical kinetic modeling, combined with the concept of a limit temperature, does a good job of capturing the relative effectiveness of thermal agents for extinguishing diffusion flames as well as the effects of using different fuels.

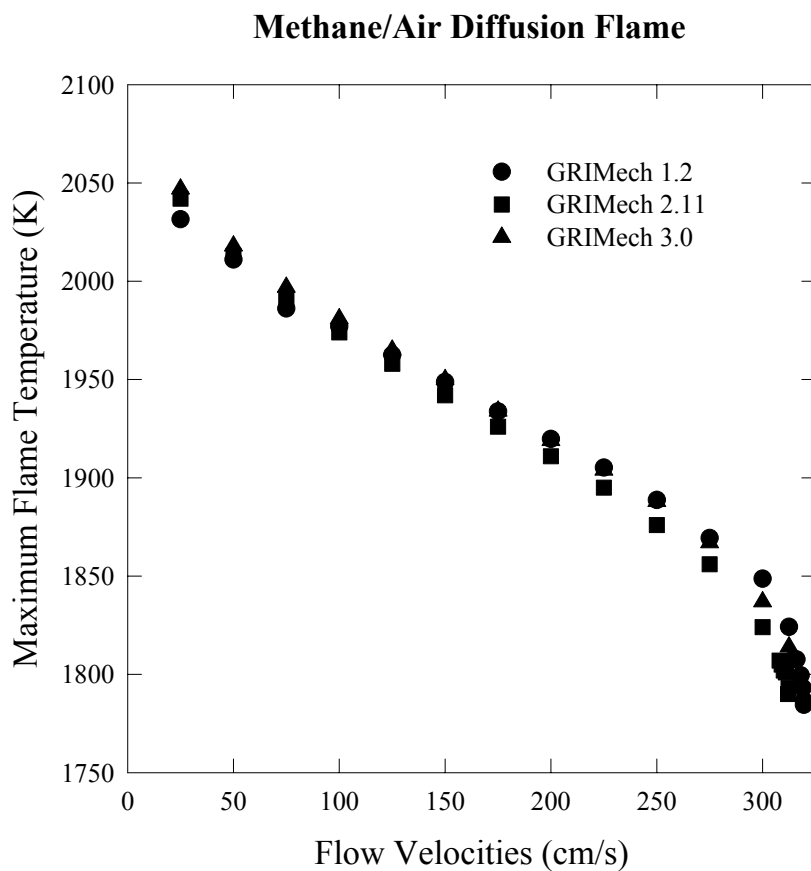


**Figure 7–9. Maximum Flame Temperatures as a Function of the Equal Fuel and Air Velocity Magnitudes for a Methane/Air Opposed-Flow Diffusion Flame for Three Versions of the GRI-Mech Mechanism.**

**Table 7–24. Extinguishing Volume Fractions of Inert Gases for CH<sub>4</sub>/Air Diffusion Flames.**

Burner	N <sub>2</sub>	Ar	He	CO <sub>2</sub>	Reference
Calculated	0.33	0.43	0.33	0.22	147
Counterflow	0.34				179
Counterflow	0.32				176
Opposed Jet	0.29				177
Opposed Jet	0.30			0.19	178
Coflow	0.27				181
DLAFSS	0.33	0.47	0.21	0.24	147
Coflow	0.23	0.31	0.20	0.13	147

**Table 7–25. Extinguishing Volume Fractions of Inert Gases for C<sub>3</sub>H<sub>8</sub>/Air Diffusion Flames.**

Burner	N <sub>2</sub>	Ar	He	CO <sub>2</sub>	Reference
Calculated	0.39	0.50	0.39	0.28	147
Counterflow	0.39				179
Opposed Jet	0.35				177
Coflow	0.32				171
Coflow	0.33			0.20	180
Coflow	0.33				181
DLAFSS	0.26	0.55	0.22	0.26	147
Coflow	0.28	0.37	0.28	0.18	147

### Chemical Kinetic Modeling of HFE-7100

In order to obtain some idea of the concentrations that might be required for extinguishment by a more general thermally acting agent, a series of calculations was carried out for HFE-7100. This calculation assumed that the only mechanism for heat extraction was the heat capacity of the gaseous agent, even though significant heat could also be removed by evaporation if the agent were released as a liquid at room temperature. This molecule was likely to decompose upon entering the high temperature region of the flame and then react to form final products. Reaction of the agent was not modeled. Due to the presence of a large number of fluorine atoms, it was also likely that the extinguishing efficiency would include a small chemical component.<sup>182,183,184,185</sup> On this basis, the result of this calculation was an upper limit for the required extinguishing concentration.

It is noteworthy that a relatively small volume fraction of C<sub>4</sub>F<sub>9</sub>OCH<sub>3</sub>, 0.055, was required to lower the maximum flame temperature to the extinguishment temperature of 1550 K. The high heat capacity of this molecule, due to its large number of atoms, makes it a particularly effective thermal agent in molar terms. If liquid vaporization and chemical effects improved its effectiveness still further, this species might approach the effectiveness of halon 1301, which has an extinguishing volume fraction of 0.029 % on a molar basis.<sup>186</sup> On a mass basis, this fluorinated ether is less effective, based on the molecular weights of 148.9 g/mol for halon 1301 and 250 g/mol for C<sub>4</sub>F<sub>9</sub>OCH<sub>3</sub>, but not dramatically so. It might be expected that the mass fraction of C<sub>4</sub>F<sub>9</sub>OCH<sub>3</sub> that must be added would be similar to other agents that do not have a strong component of chemical effectiveness.<sup>171</sup>

Two experimental measurements of the volume fractions of this compound required to extinguish diffusion flames have been identified. Unpublished measurements from the New Mexico Engineering Research Institute using a standard cup burner with heptane fuel yielded an extinguishing volume fraction of 0.061.<sup>187</sup> In a patent disclosure, Flynn and Scott also reported that a volume fraction of 0.061 was sufficient to extinguish a butane flame in a “micro-cup burner.”<sup>188</sup> Given the limitations of the chemical kinetic simulation, there was reasonably good agreement.

At 300 K and atmospheric pressure, the saturation volume fraction of the ether in air was calculated to be 0.29. Thus, the saturation pressure at room temperature should be more than sufficient to extinguish a diffusion flame. Whether there would be time to establish this equilibrium would depend on the particular fire scenario. For example, in the event of an office building fire, there might well be time for sufficient evaporation to occur. Conversely, for an in-flight fire in an aircraft engine nacelle, the air flow through the nacelle would likely flush the agent faster than evaporation could establish an extinguishing concentration (Chapter 8).

### Summary of Thermally Active Agents

There appear to be no gaseous chemicals that achieve a flame extinguishing efficiency comparable to halon 1301 purely through absorption of heat from flames. There may well be some liquid chemicals whose enthalpies of vaporization could augment the other thermal effects and achieve the desired efficiency.

HFC-7100 (methoxy-nonafluorobutane ( $C_4F_9OCH_3$ )) appears to be the best of these liquid compounds. Its high boiling point suggests it would show promise as a streaming agent. Its equilibrium vapor pressure at room temperature is sufficiently high that it might be applicable for fires in enclosed spaces. As will be seen in Chapter 8, its high boiling point probably precludes its consideration for timely extinguishment of in-flight fires in cold engine nacelles and dry bays.

HFC-125 was a key reference compound due to its selection as the best commercially available agent under the TDP. On a mass basis, it is in an effectiveness class with the better non-aqueous thermal suppressants. Its boiling point, nearly as low as that of halon 1301, ensures superior low temperature dispersion. There is thus no clear reason to replace it with another compound that has no chemical fire suppression activity.

## 7.4.2 Tropodegradable Candidate Compounds

### Atmospheric Chemistry and Tropodegradable Processes

The long atmospheric life of  $CF_3Br$  allows time for this chemical to travel from the earth's surface to the stratosphere where it is fragmented by ultraviolet radiation. The bromine atom then catalyzes ozone conversion to molecular oxygen. The initial reaction to the potency of the bromine catalysis was to search for replacement fire suppressants that were bromine-free.

Early in the 1990s, a halon replacement strategy emerged to reintroduce the chemical suppression effectiveness of bromine. This approach employed a “carrier molecular structure” with intrinsically very low atmospheric lifetime (on the order of days or weeks) to act as a carrier or base structure. To this, a

bromine atom was added, resulting in a tropodegradable brominated fire extinguishant or tropodegradable bromocarbon. Since, in general, GWP and ODP values decrease with decreasing atmospheric lifetime, tropodegradable bromocarbons potentially solved the environmental problems (global warming and ozone depletion) while providing efficient fire suppression. Tropodegradable compound atmospheric lifetimes had in some cases been measured, but generally were estimated based on data generated for functional groups such as sites of unsaturation, numbers of C-H bonds, and substitution patterns. Early estimates of atmospheric lifetime for alkenes, which were as low as a few days, have since been demonstrated to be accurate.

The carrier compounds selected were generally partially fluorinated and incorporated chemical features that are reactive with atmospheric -OH or O<sub>3</sub>, are photochemical reactive, or are inherently polar and therefore subject to atmospheric removal by the rainout process (Table 7–26).

**Table 7–26. Tropodegradable Brominated Candidates.**

Tropodegradable Base Structure	Corresponding Tropodegradable Bromocarbon
CF <sub>3</sub> -O-CF <sub>2</sub> H	CF <sub>3</sub> -O-CF <sub>2</sub> Br
CF <sub>3</sub> -O-CFH <sub>2</sub>	CF <sub>3</sub> -O-CFBrH
CF <sub>2</sub> H-O-CF <sub>2</sub> H	CF <sub>2</sub> H-O-CF <sub>2</sub> Br
CH <sub>2</sub> =CHCF <sub>3</sub>	CH <sub>2</sub> =CBrCF <sub>3</sub> , CHBr=CHCF <sub>3</sub>
CH <sub>2</sub> =CFCF <sub>3</sub>	CHBr=CFCF <sub>3</sub>
CH <sub>2</sub> =CFCF <sub>2</sub> H	CH <sub>2</sub> =CHCF <sub>2</sub> Br, CHBr=CFCF <sub>2</sub> H
CHF=CHCF <sub>3</sub>	CFBr=CHCF <sub>3</sub> , CHF=CBrCF <sub>3</sub>

The reactions that cause atmospheric decomposition of a molecule differ for alkenes, ethers, and amines, as summarized in Table 7–1. For alkenes, reaction with hydroxyl free radicals or with tropospheric or ground level ozone target the double bond, while ethers and amines are subject to hydrogen abstraction reactions by the -OH radical. Photolysis of the C-I bond is the predominant reaction pathway for iodinated fluoroalkanes such as CF<sub>3</sub>I. Direct physical removal of alcohols through rainout is not contingent on the reactivity of the compound.

Compounds can also be degraded by reaction with a number of other atmospheric species, including oxygen atoms in the <sup>3</sup>P and <sup>1</sup>D electronic states, NO<sub>x</sub>, nitric acid, and peroxy species. Such reactions are relatively minor tropospheric sinks for the chemicals considered here.<sup>189</sup>

A rate constant can be assigned to each of these processes: k<sub>OH</sub> for reaction with hydroxyl free radicals, k<sub>physical</sub> for physical removal, k<sub>photo</sub> for photolysis, and k<sub>O<sub>3</sub></sub> for reaction with tropospheric ozone. These rate constants vary not only with the chemical being removed from the troposphere, but are also a function of the atmospheric position (which determines the hydroxyl free radical concentration, temperature, and solar flux). As an approximation, one can use, for all but k<sub>photo</sub>, the globally averaged rate constants. An overall pseudo first-order rate constant k<sub>1</sub> can be written, where  $k_1 = k_{OH}[\bullet OH] + k_{physical} + k_{photo} + k_{O_3}[O_3]$ , [•OH] is a globally averaged tropospheric hydroxyl free radical concentration (9.7 x 10<sup>5</sup> cm<sup>3</sup>/molec-s),<sup>190</sup> and [O<sub>3</sub>] is the globally averaged tropospheric ozone concentration (5.0 x 10<sup>11</sup> cm<sup>3</sup>/molec-s).<sup>191</sup>

### ***Hydroxyl Free Radical Hydrogen Atom Abstraction***

All compounds containing a hydrogen atom (e.g., hydrocarbons, HFCs, and HCFCs) are subject to reaction with tropospheric  $\bullet\text{OH}$ . The organic free radical  $\bullet\text{R}$  formed rapidly reacts with diatomic oxygen ( $\text{O}_2$ ) to form a peroxy radical ( $\text{ROO}\bullet$ ), which further reacts to give a series of products. In most cases, these final products are rapidly removed by physical processes so that they do not contribute significantly to ozone depletion or global warming. For most saturated haloalkanes, this process is too inefficient to be considered as giving tropodegradable compounds.

For the compounds of interest here, a hydroxyl free radical can abstract a hydrogen atom and/or add to an unsaturated molecule to yield products (Reaction 7-33). The effectiveness of  $\bullet\text{OH}$  reactions in removing compounds from the atmosphere depends on the reaction rate constant ( $k_{\text{OH}}$ ) and the atmospheric concentration of  $\bullet\text{OH}$ . The rate constant  $k_{\text{OH}}$  gives the time rate of change of the concentration of a compound C in the atmosphere due to reaction with  $\bullet\text{OH}$  only (Equation 7-34) and can be written as the sum of the rate constants for hydrogen atom abstraction ( $k_{\text{OH}}^1$ ) and for hydroxyl addition to an unsaturated compound ( $k_{\text{OH}}^2$ ). The atmospheric half-life of a chemical for which the sole removal mechanism is reaction with  $\bullet\text{OH}$  is given by Equation 7-35, which can be rewritten to yield the atmospheric lifetime (i.e., the e-folding lifetime), Equation 7-36.



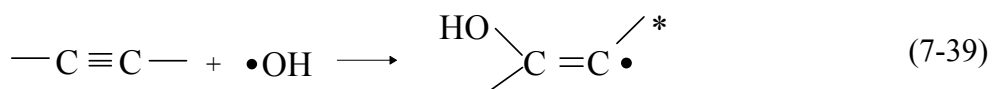
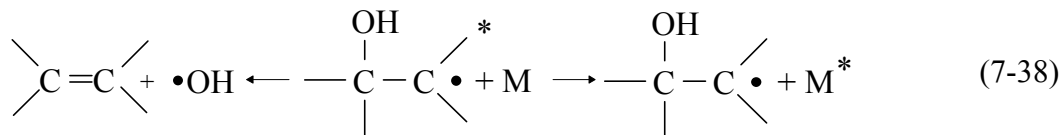
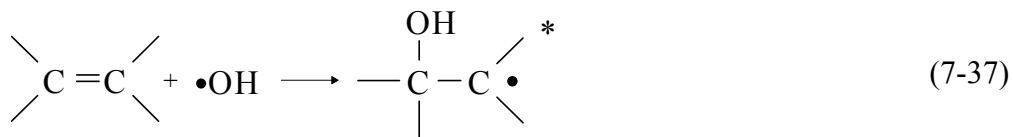
$$\frac{d[\text{C}]}{dt} = -k_{\text{OH}}[\text{C}][\bullet\text{OH}] \quad (7-34)$$

$$t_{1/2} = \frac{\ln 2}{k_{\text{OH}}[\bullet\text{OH}]} \quad (7-35)$$

$$t_{1/e} = \frac{1}{k_{\text{OH}}[\bullet\text{OH}]} \quad (7-36)$$

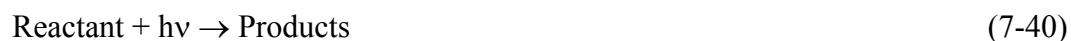
### **Addition of $\bullet\text{OH}$ Free Radicals to Unsaturated Chemicals**

Addition of  $\bullet\text{OH}$  free radicals to unsaturated chemicals is a highly effective removal process. For alkenes, the  $\bullet\text{OH}$  adds to give a highly energetic product radical (Reaction 7-37), where the asterisk indicates an activated species. If it does not lose another group, the energetic product can then either revert back to reactants, or it can be stabilized by collision with another molecule (M), which can carry off the excess energy (Reaction 7-38). The reverse reaction is probably not important below 100 °C, higher than temperatures found in the troposphere. Hydroxyl free radicals can also add to a triple bond (Reaction 7-39) and to aromatics. Due to potential manufacturing difficulties and stability problems, alkynes (compounds containing triple bonds) are not considered as halon replacement candidates; however, aromatic compounds are.



### Photolysis

Photolysis (also called photodegradation and photolytic decomposition) requires absorption of electromagnetic radiation with resulting molecular decomposition. The photodecomposition reactions have the form shown in Reaction 7-40, where the products are fragments of the original reactant molecule. Planck's constant ( $h$ ) multiplied by the frequency of the electromagnetic radiation ( $\nu$ ) gives the energy of a single photon of radiation with that frequency, and " $h\nu$ " is often used as a symbol for a photon in a chemical equation (e.g., Reaction 7-40). As the frequency of the electromagnetic radiation increases and the wavelength ( $\lambda$ ) decreases, the energy per photon increases. Thus, shorter wavelength electromagnetic radiation, such as ultraviolet (UV), is usually more effective in effecting photodegradation than is longer wavelength radiation, such as visible and infrared (IR). Photolysis of a molecule depends on two parameters, the absorption cross section ( $\sigma$ ) (which determines how much of the available light is absorbed) and the quantum yield ( $\phi$ ) (the fraction of the absorbed photons that affects photolysis). If every photon absorbed produced a reaction,  $\phi = 1$ .



Most organic compounds exhibit decreasing absorption cross sections as the radiation wavelength increases (at least for the ultraviolet and visible spectral regions). Since much of the lower wavelength, higher energy solar radiation is removed by stratospheric ozone before sunlight reaches the troposphere (particularly UV-B radiation, with wavelengths between 180 nm and 320 nm many molecules do not encounter electromagnetic radiation of a sufficiently short wavelength for absorption until they reach the stratosphere. For example, the CFCs (chlorofluorocarbons) absorb little if any of the solar radiation required for photolytic decomposition as they pass through the troposphere. However, in the stratosphere, where short wavelength UV radiation is intense, the CFCs photodecompose to release chlorine atoms.

Photodissociation in the troposphere requires that a compound absorb radiation in the wavelength range from 299 nm to 700 nm. The photodissociation rate constant  $k_{\text{photo}}$  is determined by Equation 7-41, where  $\sigma(\lambda)$  is the absorption cross section as a function of the wavelength,  $\lambda$ ,  $I(\lambda)$  is the solar intensity as a function of  $\lambda$ , and  $\phi(\lambda)$  is the photodissociation quantum yield. Thus, a chemical compound has two characteristics that determine the importance of photolysis: (1) the absorption cross section (how well it absorbs electromagnetic radiation encountered in the troposphere) and (2) the quantum yield. Both of

these are a function of the electromagnetic radiation wavelength. The atmospheric lifetime for photodissociation only is then given by Equation 7-42.

$$k_{\text{photo}} = \int_{290\text{nm}}^{700\text{nm}} \sigma(\lambda)I(\lambda)\phi(\lambda)d\lambda \quad (7-41)$$

$$t_{1/e} = 1/k_{\text{photo}} \quad (7-42)$$

In general, halocarbons require one of the groups shown in Figure 7–10 to be present for significant absorption and photodissociation in the troposphere (i.e., absorption for  $\lambda = 299 \text{ nm}$  to  $700 \text{ nm}$ ).

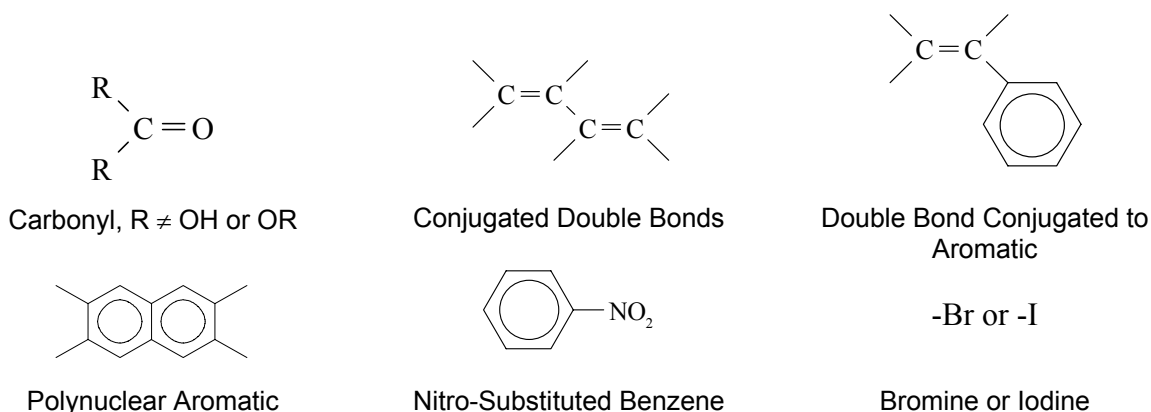


**Figure 7–10. Groups Required for Significant Tropospheric Photodissociation.**

Only the ketones and iodides were of major interest; however, compounds with conjugated double bonds (i.e., double bonds that allow some delocalization of the  $\pi$  electron cloud) and compounds containing a double bond conjugated to an aromatic could form the basis for more “exotic” fire suppressants, albeit with likely higher boiling points. In addition, photolysis of bromine compounds assists in lowering the atmospheric lifetimes for bromine-containing compounds (those proposed herein).

### 7.4.3 Bromofluoroalkenes

#### Criteria for Acquisition

The chemical family of bromofluoroalkenes represents an extensive array of structural possibilities. The examination began with an exhaustive listing and assessment of structural options, including structural isomers. Table 7–27 shows the range of variety just for  $C_3$  compounds with 3, 4, or 5 fluorine atoms.

From the overall list, the following were concepts used to determine which compounds would be acquired for screening:

- Lowest boiling points in a given subgroup. Ideally, a compound’s boiling point was published; some were estimated. The lowest boiling points were likely to be found among the more heavily fluorinated compounds (3, 4 or 5 atoms) and those with the fewest carbon atoms (2 or 3).

- Variation in chemical structure. This helped develop guidance for isomeric effects on flame extinguishment efficiency and volatility.
- Estimation of tendency to cause cardiac arrhythmia.
- Availability and cost from a commercial supplier or laboratory synthesis.
- Expected flame suppression efficiency. Since the bromine atom is always released in the flame zone, all the bromofluoroalkenes were expected to extinguish flames at 3 volume % to 4 volume %. This estimate was expected to be improved by increasing fluorination and decreasing hydrogenation. However, some fluoroalkenes were reported to be spontaneously flammable (e.g.,  $\text{CF}_2=\text{CFBr}^{192}$ ), complicating selection and prediction of effectiveness.

**Table 7–27 Bromofluoropropenes.**

Chemical Name	Chemical Formula	cis/trans Isomers
2-bromo-1,1,3,3,3-pentafluoropropene	$\text{CF}_2=\text{CBrCF}_3$	
3-bromo-1,1,2,3,3-pentafluoropropene	$\text{CF}_2=\text{CFCF}_2\text{Br}$	
1-bromo-1,2,3,3,3-pentafluoropropene	$\text{CFBr}=\text{CFCF}_3$	Y
3-bromo-1,1,3,3-tetrafluoropropene	$\text{CF}_2=\text{CHCF}_2\text{Br}$	
2-bromo-1,3,3,3-tetrafluoropropene	$\text{CFH}=\text{CBrCF}_3$	Y
1-bromo-1,2,3,3-tetrafluoropropene	$\text{CFBr}=\text{CFCF}_2\text{H}$	Y
1-bromo-1,3,3,3-tetrafluoropropene	$\text{CFBr}=\text{CHCF}_3$	Y
3-bromo-1,2,3,3-tetrafluoropropene	$\text{CHF}=\text{CFCF}_2\text{Br}$	Y
3-bromo-1,1,2,3-tetrafluoropropene	$\text{CF}_2=\text{CFCFHBr}$	
2-bromo-1,1,3,3-tetrafluoropropene	$\text{CF}_2=\text{CBrCF}_2\text{H}$	
2-bromo-3,3,3-trifluoropropene	$\text{CH}_2=\text{CBrCF}_3$	
3-bromo-1,3,3-trifluoropropene	$\text{CFH}=\text{CHCBrF}_2$	Y
2-bromo-3,3,3-trifluoropropene	$\text{CHBr}=\text{CHCF}_3$	Y
2-bromo-1,1,3-trifluoropropene	$\text{CF}_2=\text{CBrCFH}_2$	
2-bromo-1,3,3-trifluoropropene	$\text{CFH}=\text{CBrCF}_2\text{H}$	Y
3-bromo-1,1,2-trifluoropropene	$\text{CF}_2=\text{FCBrH}_2$	
3-bromo-1,2,3-trifluoropropene	$\text{CFH}=\text{CFCFBrH}$	Y
3-bromo-1,1,3-trifluoropropene	$\text{CF}_2=\text{CHCFBrH}$	
3-bromo-2,3,3-trifluoropropene	$\text{CH}_2=\text{CFCF}_2\text{Br}$	
1-bromo-2,3,3-trifluoropropene	$\text{CHBr}=\text{CFCHF}_2$	Y
1-bromo-1,2,3-trifluoropropene	$\text{CFBr}=\text{CFCFH}_2$	Y
1-bromo-1,3,3-trifluoropropene	$\text{CBrF}=\text{CHCHF}_2$	Y
1-bromo-2,3,3,3-tetrafluoropropene	$\text{CHBr}=\text{CFCF}_3$	Y

It was presumed that the atmospheric lifetimes would be short. In the case of the halogenated propenes, atmospheric lifetimes are limited primarily by atmospheric OH radical reactions and estimated to be on the order of a week. For example, 2-bromo-3,3,3-trifluoropropene was estimated to have an atmospheric lifetimes of 4 days.<sup>193</sup>

### Cup Burner Extinguishment

Several of these compounds were acquired in small (5 g) quantities and their cup burner extinguishment evaluated. As the first of the tropodegradable families examined, two groups were investigated.

Table 7–28 includes chemicals with a range of carbon content (3 atoms to 5 atoms) and structural variation, and three or more fluorine atoms. While these differences had significant impact on the boiling points, there was essentially no effect on the concentration needed to extinguish a cup burner flame.<sup>194,195,196</sup> The values were as expected and acceptable, given the presence of a bromine atom and some hydrogen fuel in each molecule.

The second group involved the most volatile compounds. Flammability, air reactivity, or markedly higher cup burner extinguishment values in the fluorinated ethenes eliminated further consideration of these lowest boiling alkenes. Table 7–29 shows the cup burner values and boiling points of the most volatile propenes (and one ethene). None of the substituted propenes met the volatility criterion. There was no effect of structure on the extinguishing concentrations.

**Table 7–28 Bromofluoropropene Cup Burner Flame Extinguishment Data.**

Compound Name	Chemical Formula	T <sub>b</sub> (°C)	Vol. %
1-Bromo-3,3,3-trifluoropropene	CF <sub>3</sub> CH=CHBr	40	3.5 <sup>a</sup>
3-Bromo-3,3-difluoropropene	CBrF <sub>2</sub> CH=CH <sub>2</sub>	42	4.5
2-Bromo-3,3,3-trifluoropropene	CF <sub>3</sub> CBr=CH <sub>2</sub>	34	2.6
4-Bromo-3,3,4,4-tetrafluorobutene	CF <sub>2</sub> BrCF <sub>2</sub> CH=CH <sub>2</sub>	54	3.5
2-Bromo-3,3,4,4,4-pentafluorobutene	CF <sub>3</sub> CF <sub>2</sub> CBr=CH <sub>2</sub>	56	3.8 <sup>a</sup>
2-Bromo-3-trifluoromethyl-3,4,4,4-tetrafluorobutene	CF <sub>3</sub> C(CF <sub>3</sub> )FCBr=CH <sub>2</sub>	78	3.3 <sup>a</sup>
1-Bromo-2-trifluoromethyl-3,3,3-trifluoropropene	(CF <sub>3</sub> ) <sub>2</sub> C=CHBr	63	2.6 <sup>a</sup>
1-Bromo-4,4,4,3,3-pentafluorobutene	CF <sub>3</sub> CF <sub>2</sub> CH=CHBr	58	3.1 <sup>a</sup>
2-Bromo-3,3,4,4,5,5,5-heptafluoropentene	CF <sub>3</sub> CF <sub>2</sub> CF <sub>2</sub> CBr=CH <sub>2</sub>	78	3.7 <sup>a</sup>
2-Bromo-3-trifluoromethoxy-3,4,4,4-tetrafluorobutene	CF <sub>3</sub> CF(CF <sub>3</sub> O)CBr=CH <sub>2</sub>	75	3.8 <sup>a</sup>

a Testing performed using premixed agent/air mixtures

**Table 7–29 Low Boiling Bromofluoroalkene Cup Burner Values.**

Compound Name	T <sub>b</sub> (°C)	Volume %
1-Bromo-pentafluoropropene	27	3.1
2-Bromo-pentafluoropropene	25	3.5
3-Bromo-1,1,3,3-tetrafluoropropene	33	3.3
2-Bromo-1,3,3,3-tetrafluoropropene	29	3.5
2-Bromo-1,1,3,3-tetrafluoropropene	29	3.3
1-Bromo-2,3,3,3-tetrafluoropropene	30 (est.)	3.3
2-Bromo-3,3,3-trifluoropropene	32-34	3.1
1-Bromo-1,2-difluoroethene	20 to 24 (est.)	8.4

The cup burner extinguishment performance of the substituted ethene was outside the range for continued consideration. The isomeric compound (1-bromo-2,2-difluoroethene, CHBr=CF<sub>2</sub>) is flammable. This demonstrated the potential for strong effects of structural isomerism on flammability in these very small molecules. While 1-bromo-1,2-difluoroethene serves as a bromine carrier, this was clearly not sufficient to assure an acceptable cup burner value.

In summary, there are trifluorinated, tetrafluorinated and pentafluorinated bromopropenes that all are good extinguishants with no indications of flammability. However, bromofluoropropene boiling points

lower than 25 °C are extremely unlikely. If the low temperature limit were raised, these compounds could prove useful in aircraft applications, subject to atmospheric lifetime and toxicity testing.

#### 7.4.4 Fluoroalkoxide and Fluoroalkyl Phosphorus Compounds

##### Criteria for Acquisition

The approach to compound selection was similar to that for the bromocarbons in Section 7.4.3. However, there were multiple toxic effects, rather than a focus on cardiac arrhythmia. The substitution of F atoms for H atoms was expected to lower the boiling point and increase flame suppression efficiency. Syntheses for many of the compounds were complex or untried, and this was a limiting factor in the research.

##### Toxicity

There is a large amount of toxicity data available for phosphorus compounds. In part, this is because a number of phosphorus compounds (particularly phosphite esters) are cholinesterase inhibitors. The toxicity of phosphorus compounds is highly variable. Thus, toxicity must be given careful consideration. There is limited information indicating that toxicity may increase from phosphates to phosphites to phosphines. Phosphonitriles appear to have relatively low toxicities, but some show indications of mutagenicity. The presence of P-halogen bonds can cause severe irritation and lung damage owing to hydrolysis with formation of phosphorus-containing and hydrohalic acids. For this reason, compounds containing direct halogen atom bonds to phosphorus atoms are poor candidates as halon substitutes.

Table 7–30 contains information on the toxicity and safety of some phosphorus-containing chemicals related to compounds of interest here.

**Table 7–30 Phosphorus Compound Toxicity (Safety) Information.**

Compound Name	Formula	CAS No.	Observations <sup>a</sup>
Bis(trifluoromethyl)-chlorophosphine	$\text{PCl}(\text{CF}_3)_2$	650-52-2	[BLO280] Ignites spontaneously in air. HR = 3.
Dibutylphosphate	$\text{O}=\text{P}(\text{OH})(\text{OC}_4\text{H}_9)_2$	107-66-4	{RTECS HS630000} [DEG600] LD <sub>50</sub> (rat, oral) = 3200 mg/kg. Moderately toxic by ingestion. HR = 2.
Dibutylphosphonate	$\text{O}=\text{PH}(\text{OC}_4\text{H}_9)_2$	1809-19-4	{RTECS HS6475000} [DEG800] LD <sub>50</sub> (rat, oral) = 3200 mg/kg, LD <sub>50</sub> (rabbit, skin) = 1990 mg/kg. Moderately toxic by ingestion, skin contact. Severe eye irritant. HR = 2.
Diethylphosphonate	$\text{O}=\text{PH}(\text{OC}_2\text{H}_5)_2$	762-04-5	{RTECS TG7875000} [DJW400] LD <sub>50</sub> (rat, oral) = 3900 mg/kg, LD <sub>50</sub> (rabbit, skin) = 2165 mg/kg. Moderately toxic by ingestion, skin contact. HR = 2.

Compound Name	Formula	CAS No.	Observations <sup>a</sup>
Diisopropyl methylphosphonate	$O=P(CH_3)-[OCH(CH_3)_2]_2$	1445-75-6	{RTECS SZ9090000} [DNQ875] LD <sub>50</sub> (rat, oral) = 826 mg/kg, LD <sub>50</sub> (mouse, oral) = 1041 mg/kg. Moderately toxic by ingestion, skin contact. HR = 2.
Diisopropylphosphonate	$O=PH[OCH(CH_3)_2]_2$	1809-20-7	{RTECS SZ7660000} [DNQ600] LD <sub>50</sub> (rat, oral) = 3100 mg/kg, LD <sub>50</sub> (rabbit, skin) = 5700 mg/kg. Moderately toxic by ingestion. Mildly toxic by skin contact. HR = 2.
Dimethyl(1,2-dibromo-2,2-dichloroethyl) phosphate	$O=P(OCH_3)_2-(OCHBrCBrCl_2)$	300-76-5	{RTECS TB9540000} [DRJ600] LD <sub>50</sub> (rat, inh) = 7700 μg/kg, LD <sub>50</sub> (mouse, inh) = 156 mg/kg, LD <sub>50</sub> (rat, oral) = 250 mg/kg, LD <sub>50</sub> (rabbit, skin) = 1100 mg/kg. Poison by ingestion, inhalation. Moderately toxic by skin contact. Skin irritant. Insecticide of the cholinesterase inhibitor type. HR = 3.
Dimethyl(2,2-dichloroethyl)-phosphate	$O=P(OCH_3)_2-(CH=Cl_2)$	62-73-7	{RTECS TC0350000} [DRK200] LC <sub>50</sub> (rat, inh, 4 hr) = 15 mg/m <sup>3</sup> , LC <sub>50</sub> (mouse, inh, 4 hr) = 13 mg/kg, LD <sub>50</sub> (rat, oral) = 25 mg/kg, LD <sub>50</sub> (rabbit, skin) = 107 mg/kg. Poison by ingestion, inhalation, skin contact, intraperitoneal, intravenous, subcutaneous. Experimental teratogen, suspected carcinogen Cholinesterase inhibitor. HR = 3.
Dimethylphosphonate	$O=PH(OCH_3)_2$	868-85-9	{RTECS SZ7710000} [DSG600] LD <sub>50</sub> (rat, oral) = 3050 mg/kg, LD <sub>50</sub> (rabbit, skin) = 2400 mg/kg. Moderately toxic by ingestion, skin contact. Experimental carcinogen. Skin, eye irritant. HR = 3.
Hexaethyltetraphosphate	$OP(OC_2H_5)_2-[OP(O)(OC_2H_5)]_2-OP(O)(OC_2H_5)_2$	757-58-4	{RTECS XF1575000} [HCY000] LD <sub>50</sub> (rat, oral) = 7 mg/kg, LD <sub>50</sub> (mouse, oral) = 56 mg/kg, LD <sub>LO</sub> (rat, skin) = 15 mg/kg. Poison by ingestion, skin contact, intraperitoneal, subcutaneous, intravenous, intramuscular. HR = 3.
Tris(2-chloroethyl) phosphite	$O=P(OCH_2CH_2Cl)_2-(CH_2CH_2Cl)^b$	140-08-9	{RTECS KK2810000} [PHO000] LD <sub>50</sub> (rat, oral) = 100 mg/kg, LD <sub>50</sub> (rabbit, skin) = 810 mg/kg. Poison by ingestion, intraperitoneal. Moderately toxic by skin contact. Severe eye irritant. HR = 3.

Compound Name	Formula	CAS No.	Observations <sup>a</sup>
Tris(2-fluoroethyl) phosphite	$O=P(OCH_2CH_2F)_2-(CH_2CH_2F)^b$	63980-61-0	{RTECS KL1925000} [PHO250] LC <sub>LO</sub> (rat, inh, 10 min) = 500 mg/m <sup>3</sup> , LC <sub>LO</sub> (mouse, inh, 10 min) = 1000 mg/m <sup>3</sup> . Poison by inhalation. HR = 3.
Triethylphosphite	$O=P(C_2H_5)(OC_2H_5)_2^b$	122-52-1	{RTECS TH1130000} [TJT800] LD <sub>50</sub> (rat, oral) = 3200 mg/kg. Moderately toxic by ingestion. Skin, eye irritant. HR = 2.
Tris(1-bromo-3-chloroisopropyl)-phosphate	$O=P[OCBr-(CH_3)(CH_2Cl)]_3$	7328-28-1	{RTECS TC8600000} [TNE500] Mutagenic data. HR = D (insufficient data).
Triisooctylphosphite	$O=P[(CH_2)_5CH-(CH_3)_2]-[O(CH_2)_5CH(CH_3)_2]_2^b$	25103-12-3	{RTECS TH1150000} [TKT000] LD <sub>50</sub> (rat, oral) = 9200 mg/kg, LD <sub>50</sub> (rabbit, skin) = 3970 mg/kg. Moderately toxic by skin contact. Mildly toxic by ingestion. Skin irritant. HR = 2.
Triisopropylphosphite	$O=P[CH(CH_3)_2]-[OCH(CH_3)_2]_2^b$	116-17-0	{RTECS TH2800000} [TKT500] LD <sub>50</sub> (rat, oral) = 167 mg/kg. Poison by ingestion. Moderately toxic by intraperitoneal. HR = 3.
Trimethylphosphite	$O=P(CH_3)(OCH_3)_2^b$	121-45-9	{RTECS TH1400000} [TMD500] LD <sub>50</sub> (rat, oral) = 1600 mg/kg, LD <sub>LO</sub> (rabbit, skin) = 2200 mg/kg. Moderately toxic by ingestion, skin contact. Experimental teratogen. Severe skin, eye irritant. HR = 2.
Tributylphosphine oxide	$O=P(C_4H_9)_3$	814-29-9	{RTECS SZ1575000} [TNE750] Poison by intravenous route. Eye irritant. HR = 3.
Tritolylphosphate (tricresylphosphate)	$O=P(OC_6H_5CH_3)_3$	1330-78-5	{RTECS TD0175000} [TNP500] LD <sub>50</sub> (rat, oral) = 5190 mg/kg, LD <sub>50</sub> (mouse, oral) = 3900 mg/kg. Poison by ingestion. Moderately toxic by skin contact. Eye, skin irritant. HR = 3.
Tri-2-tolylphosphate (tri-o-cresylphosphate)	$O=P(OC_6H_5CH_3)_3$	78-30-8	{RTECS TD0350000} [TNP750] LD <sub>50</sub> (rat, oral) = 1160 mg/kg. Poison by ingestion, subcutaneous, intramuscular, intravenous, intraperitoneal. Moderately toxic by ingestion. HR = 3.
Dimethylfluorophosphate	$C_4H_{10}FO_3P$	358-74-7	{RTECS TE5600000} [DJJ400] LC <sub>50</sub> (rat, inh, 10 min) = 7 g/m <sup>3</sup> , LC <sub>50</sub> (mouse, inh, 10 min) = 500 mg/m <sup>3</sup> . Poison by inhalation, skin. HR = 3.

Compound Name	Formula	CAS No.	Observations <sup>a</sup>
Dimethylfluorophosphate	C <sub>2</sub> H <sub>6</sub> FO <sub>3</sub> P	5954-50-7	{RTECS TE6125000} [DSA800] LC <sub>50</sub> (rat, inh, 1 min) = 1800 mg/m <sup>3</sup> , LC <sub>50</sub> (mouse, inh, 10 min) = 290 mg/m <sup>3</sup> . Poison by inhalation, skin contact, intravenous. HR = 3.
2-Ethyl-2(hydroxymethyl)- 1,3-propane-diol, cyclic phosphate (1:1)	C <sub>6</sub> H <sub>11</sub> O <sub>4</sub> P	1005-83-2	{RTECS TX6475000} [ELJ500] LC <sub>50</sub> (rat, inh, 1 hr) = 30 mg/m <sup>3</sup> . Poison by ingestion, inhalation, skin contact, intraperitoneal and intravenous routes. HR = 3.
Ethyl isopropyl fluorophosphonate	C <sub>5</sub> H <sub>12</sub> FOP	None assigned	{RTECS SZ8552000} [ELX100] LC <sub>50</sub> (rat, inh, 10 min) = 260 mg/m <sup>3</sup> , LC <sub>50</sub> (mouse, inh, 5 min) = 245 mg/m <sup>3</sup> . Poisonous by inhalation, skin contact, and subcutaneous routes. HR = 3.
Hexamethyl phosphoramidate	C <sub>6</sub> H <sub>18</sub> N <sub>3</sub> OP	680-31-9	{RTECS TD0875000} [HEK000] TC <sub>LO</sub> (rat, inh, 52 wk continuous) = 50 ppb, carcinogenic. An experimental carcinogen and tumorigen. Moderately poisonous by ingestion, skin contact, intraperitoneal, intravenous. Experimental reproductive effects. Human mutagenic data. HR = 3.
Triphenylphosphite	O=P(C <sub>6</sub> H <sub>5</sub> )(OC <sub>6</sub> H <sub>5</sub> ) <sub>2</sub> <sup>b</sup>	101-02-0	{RTECS TH1575000} [TMU250] LD <sub>50</sub> (rat, oral) = 1600 mg/kg, LD <sub>50</sub> (mouse, oral) = 1333 mg/kg. Poison by intraperitoneal, subcutaneous. Moderately toxic by ingestion. Severe skin irritant. HR = 3.
Tris(2-bromoethyl) phosphate	O=P(OCH <sub>2</sub> CH <sub>2</sub> Br) <sub>3</sub>	27568-90-7	{RTECS TC8480000} [TNE600] LC <sub>LO</sub> (rat, inh) = 260 mg/m <sup>3</sup> . Poison by inhalation. Mutagenic data. HR = 3.
Isopropyl methyl fluorophosphonate	C <sub>4</sub> H <sub>10</sub> FO <sub>2</sub> P	107-44-8	{RTECS TA8400000} [IPX000] LD <sub>50</sub> (rat, inh, 10 min) = 150 mg/m <sup>3</sup> , LD <sub>50</sub> (mouse, inh, 30 min) = 5 mg/m <sup>3</sup> , TC <sub>LO</sub> (man, inh) = 90 μg/m <sup>3</sup> (eyes), LC <sub>50</sub> (human, inh) = 70 mg/m <sup>3</sup> . Deadly human poison by skin contact and inhalation. HR = 3.
Mevinphos (2-carbomethoxy-1- methylvinyl dimethyl phosphate)	C <sub>7</sub> H <sub>13</sub> O <sub>6</sub> P	7786-34-7	{RTECS GQ5250000} [MQR750] LC <sub>50</sub> (rat, inh, 1 hr) = 14 ppm. Poison by ingestion, inh, skin contact, subcutaneous, intravenous, intraperitoneal. HR = 3.

Compound Name	Formula	CAS No.	Observations <sup>a</sup>
Monocrotophos (3-hydroxy-N-methyl-cis-crotonamide, dimethyl phosphate)	C <sub>7</sub> H <sub>14</sub> NO <sub>5</sub> P	6923-22-4	{RTECS TC4375000} [MRH209] LC <sub>50</sub> (rat, inh, 4 hr) = 63 mg/m <sup>3</sup> . Poison by ingestion, inh, skin contact, intraperitoneal, subcutaneous, and intravenous routes. Mutagenetic data. HR = 3.
Tetraethylpyrophosphate	P(O)(OC <sub>2</sub> H <sub>5</sub> ) <sub>2</sub> -OP(O)(OC <sub>2</sub> H <sub>5</sub> ) <sub>2</sub>	107-49-3	{RTECS UX6825000} [TCF250] LD <sub>50</sub> (rat, oral) = 500 µg/kg, LD <sub>50</sub> (mouse, oral) = 7 mg/kg, LD <sub>50</sub> (rat, skin) = 2400 µg/kg. Poison by ingestion, skin contact, intraperitoneal, intramuscular, other. Cholinesterase inhibitor. HR = 3.
Triethylphosphate	O=P(OC <sub>2</sub> H <sub>5</sub> ) <sub>3</sub>	78-40-0	{RTECS TC7900000} [TJT750] LD <sub>LO</sub> (rat, oral) = 1600 mg/kg, LD <sub>LO</sub> (mouse, oral) = 1600 mg/kg. Moderately toxic by ingestion, intraperitoneal, and intravenous. Reproductive effects. Mutagenic data. Cholinesterase inhibitor. HR = 2.
1,1,1-Trishydroxy-methylpropane bicyclic phosphite	C <sub>6</sub> H <sub>11</sub> O <sub>3</sub> P	824-11-3	{RTECS TY6650000} [TNI750] LC <sub>LO</sub> (rat, inh, 4 hr) = 10 ppm. A poison by ingestion, inhalation, skin contact, intraperitoneal, and intravenous routes. HR = 3.

a The SAX No. (Reference 67) is given in brackets followed by information from that reference; the RTECS No. (Reference 138) is given in braces. "HR" denotes the SAX Hazard Rating.

b The most probable (phosphonate) structure is given for these compounds, which can also be assigned the phosphite structure (P(OR)<sub>3</sub>). Both forms may exist.

## Flame Chemistry and Flammability

A description of the inhibition chemistry of phosphorus appeared in Chapter 3, and Section 7.3.5 of this chapter described the behavior of largely inorganic phosphorus-containing compounds. Over 40 years ago, it was proposed that the flame extinguishment action of POCl<sub>3</sub> was due to the chlorine and that its high efficiency was due to ready formation of HCl in the flame.<sup>197</sup> Subsequent research found that POCl<sub>3</sub> was about 10 times more effective than an equivalent amount of chlorine.<sup>198</sup>

Liquid halocarbons containing both phosphates and phosphites had been claimed as fire extinguishants.<sup>199</sup> Phosphates and phosphate esters had been of particular interest as fire suppressants since they are difficult to ignite and self-extinguish.<sup>200</sup> Trimethylphosphate ((O=P(OCH<sub>3</sub>)<sub>3</sub>) showed a more pronounced effect on flame velocity than Cl<sub>2</sub> or Br<sub>2</sub>.<sup>201</sup> In an opposed-jet burner, dimethylmethylphosphonate (DMMP, O=P(CH<sub>3</sub>)(OCH<sub>3</sub>)<sub>2</sub>) was about 4 times more effective than halon 1301.<sup>202</sup> However, studies on flat H<sub>2</sub>/O<sub>2</sub>/Ar flames indicated that DMMP acted as a flame promoter.<sup>203</sup> No cup burner values have been determined for DMMP, and it would be difficult to obtain such values because of its very high boiling point (181 °C<sup>58</sup>) and low vapor pressure (160 Pa at 25 °C<sup>204</sup>).

The estimated extinguishment concentrations of a broad range of organophosphates and phosphonates were estimated using a screening method based on the Flame Ionization Detector (FID) response of each

compound (Table 7–31).<sup>205,206,ii</sup> The data presented in Table 7–31 indicate that in general the non-fluorinated phosphates and phosphonates may well be efficient extinguishants. However, many of the compounds are flammable, and they all have high boiling points.

**Table 7–31. FID Extinguishment Estimates of Phosphorus Acids and Esters.**

Compound Name	Structure	FID Extinguish. (volume %)
Trimethyl phosphate	$O=P(OCH_3)_3$	0.6 – 2.8
Dimethyl methylphosphonate	$O=P(OCH_3)_2CH_3$	0.7
Diethyl methylphosphonate	$O=P(OC_2H_5)CH_3$	0.9
Dimethyltrifluoroethyl phosphate	$O=P(OCH_3)_2OCH_2CF_3$	0.7
Diethyltrifluoroethyl phosphate	$O=P(OC_2H_5)_2OCH_2CF_3$	0.7
Diethylpentafluoropropyl phosphate	$O=P(OC_2H_5)_2OCH_2CF_2CF_3$	0.7
Diethylhexafluoroisopropyl phosphate	$O=P(OC_2H_5)_2OCH(CF_3)_2$	0.7
Diethylheptafluorobutyl phosphate	$O=P(OC_2H_5)_2OCH_2CF_2CF_2CF_3$	0.6
Diethyloctafluoropentyl phosphate	$O=P(OCH_2H_5)_2OCH_2CF_2CF_2CF_2CF_2H$	1.1
Bis(2,2,2-trifluoroethyl)-2,2,3,3,3-pentafluoropropyl phosphate	$O=P(OCH_2CF_3)_2OCH_2CF_2CF_3$	0.7
Tris(2,2,2-trifluoroethyl) phosphate	$O=P(OCH_2CF_3)_3$	0.8
Tris(2,2,3,3,3-pentafluoro-1-propyl) phosphate	$O=P(OCH_2CF_2CF_3)_3$	1.0
Tris(2,2,3,3,4,4,4-heptafluoro-1-butyl) phosphonate	$O=P(OCH_2CF_2CF_2CF_3)_3$	1.8

Laboratory studies had also found that decomposition of organophosphorus compounds could generate additional fuel. Gas phase studies in nitrogen found that diethylmethylphosphonate (DEMP,  $O=P(CH_3)(OCH_2CH_3)_2$ ) pyrolyzed to form ethene ( $CH_2=CH_2$ ), ethanol ( $CH_3CH_2OH$ ), and ethylmethylphosphonate ( $O=P(OH)(CH_3)(OCH_2CH_3)$ ).<sup>207</sup> Formation of ethene may have resulted from formation of a six-membered ring transition state or by scission of a  $PO-CH_2CH_3$  bond with subsequent loss of a hydrogen atom from the ethyl radical ( $\bullet CH_2CH_3$ ). Similar results have been found in pyrolysis studies of diisopropylmethylphosphonate (DIMP), which generated propene ( $CH_2=CHCH_3$ ), 2-propanol ( $CH_3CH(OH)CH_3$ ), isopropylmethylphosphonate (IMP,  $O=P(OH)(CH_3)(OCH(CH_3)_2)$ ), and methylphosphonic acid (MPA,  $O=P(OH)_2(CH_3)$ ).<sup>208</sup> A six-membered ring transition state (Figure 7–11) was proposed for formation of 2-propene. Derivatization followed by gas chromatography-mass spectrometry has identified DMP, (dimethylphosphate ( $O=P(OH)(OCH_3)_2$ ), monomethylphosphate ( $O=P(OH)_2(OCH_3)$ ), MPA, orthophosphoric acid ( $O=P(OH)_3$ ), phosphorous acid ( $P(OCH_3)_3$ ), and phosphonic acid ( $O=PH(OH)_2$ ) as combustion products in a  $CH_4/O_2/N_2$  flame doped with DMMP.<sup>209</sup>

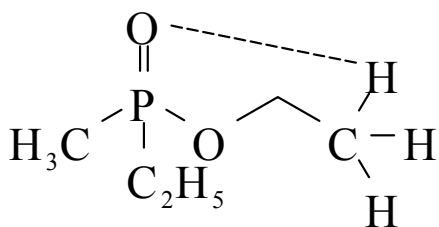


**Figure 7–11. Formation of a Six-membered Ring Transition State.**

<sup>ii</sup> The FID extinguishment values are quite different from those obtained using a cup burner. This is because the gas chromatograph FID technique enables estimation of relative extinguishment performance for a small hydrogen flame. This is not equivalent to the extinguishment of a heptane pool.

Attempts to determine a cup burner extinguishment value for a high volatility, nonfluorinated compound, trimethylphosphite ( $\text{P}(\text{OCH}_3)_3$ ) have also been unsuccessful, due to its flammability. Each of the phosphorus compounds discussed above is, in fact, flammable at some concentration.

Nonetheless, there was good reason to expect efficient flame suppression from a phosphorus-containing compound (PCC), as long as (a) it decomposed to release the phosphorus atom and (b) the flammability was mitigated. This expectation led to extensive NGP examination of a range of families of PCCs in which a significant portion of the molecule was organic.

There are two ways around the flammability problem. One is to blend the material with a nonflammable carrier; the other is to work with fluorinated alkyl derivatives of phosphorus. The NGP examined both of these approaches using the cup burner.

### Preliminary Fluoroalkoxide Phosphorus Flame Suppression Testing

Examination of prior studies and materials properties indicated that alkylphosphonitriles were not ideal for testing owing to their low volatility, and that phosphines were likely too toxic to consider, except possibly for mechanistic studies. Table 7–32 presents seven available phosphorus-containing compounds selected for preliminary testing, along with key properties.

**Table 7–32 Properties of Phosphorus-Containing Compounds.**

Compound Name	Formula	$T_b$ , °C (kPa)	Flash Point, °C
Dimethylmethylphosphonate	$\text{O}=\text{P}(\text{CH}_3)(\text{OCH}_3)_2$	181 (101) <sup>210</sup>	68 <sup>210</sup>
Trimethylphosphate	$\text{O}=\text{P}(\text{OCH}_3)_3$	197 (101)	None
Trimethylphosphite	$\text{P}(\text{OCH}_3)_3$	111-112 (101)	27
(Bromodifluoromethyl) diethylphosphonate	$\text{O}=\text{P}(\text{CBrF}_2)(\text{C}_2\text{H}_5)_2$	99-102 (2.1) <sup>211</sup> 220 (101) <sup>a</sup>	Not available
Hexamethylphosphoramide	$\text{O}=\text{P}(\text{N}(\text{CH}_3)_2)_3$	230-232 (98)	Not available
Bis(2,2,2-trifluoroethyl)phosphite	$\text{O}=\text{P}(\text{OCH}_2\text{CF}_3)_2$	43-44 (0.26) <sup>210</sup> 190 (101) <sup>210</sup>	76 <sup>210</sup>
Tris(2,2,2-trifluoroethyl)phosphite	$\text{P}(\text{OCH}_2\text{CF}_3)_3$	130-131 (99) <sup>210</sup>	>110 <sup>210</sup>

a Estimated using pressure-temperature nomograph.

Testing of dimethylmethylphosphonate ( $\text{O}=\text{P}(\text{CH}_3)(\text{OCH}_3)_2$ ) was attempted using the Standard NMERI cup burner but due to its high boiling point, the material was difficult to volatilize. The elevated temperature caused some decomposition to a black, tarry substance. A single test gave an extinguishing value of 5 volume %. This was considered a maximum value because not all the compound was available to extinguish the fire.

Trimethylphosphate ( $\text{O}=\text{P}(\text{OCH}_3)_3$ ) was also difficult to test due to its high boiling point. The extinguishment value of 6.6 volume % is high, as it was observed that a small amount of the compound did not volatilize in the mixing chamber. With a higher chamber temperature (328 °C), an extinguishment value of 6.8 volume % was obtained; however, again, some of the compound in the mixing chamber did not volatilize. At a mixing chamber temperature of 344 °C, a cup burner value of 5.3 volume % was obtained. This value was also suspect, since the n-heptane in the fuel cup boiled and was difficult to control.

Trimethylphosphite ( $\text{O}=\text{P}(\text{OCH}_3)_3$ ) was flammable and ignited. Complete extinguishment of the n-heptane flame was not achieved.

Only a small amount of (bromodifluoromethyl)diethylphosphonate ( $\text{O}=\text{P}(\text{CBrF}_2)(\text{C}_2\text{H}_5)_2$ ) was available. During the first test, the flame extinguished readily at a value of 4.7 volume %. The second test employed approximately one-third that of the first test. Even though the temperature of the heated chamber at the base of the cup burner was 250 °C, it appeared that the compound did not volatilize completely. The flame continued to show some extinguishment from the compound after the syringe pump was turned off, which indicated that the compound in the mixing chamber continued to volatilize even after the agent supply was stopped. The temperature of the heated chamber was therefore increased to 300 °C and the compound appeared to volatilize, but n-heptane boiling was observed at the extinguishment point of 1.4 volume %. Thus, the extinguishment concentration was estimated to be between 1.4 volume % and 4.7 volume %. A test with an increased flow and a slightly lower chamber temperature (270 °C) resulted in an extinguishment value of 3.3 volume %.

Testing of hexamethylphosphoramide ( $\text{O}=\text{P}[\text{N}(\text{CH}_3)_2]_3$ ) was difficult due to its high boiling point and low vapor pressure. An extinguishment value of 8.7 volume % was obtained.

Tris(2,2,2-trifluoroethyl)phosphite was tested at a chamber temperature of 200 °C. An extinguishing value of 1.8 volume % was obtained.

Trimethylphosphite was also blended with either HFC-227ea or HFC-125 to form a nonflammable mixture, and cup burner flame extinguishment concentrations were determined (Table 7–33). These mixtures were 1 % to 2 % lower in extinguishment concentration than the respective pure HFC.

**Table 7–33. Flame Extinguishment Values for Trimethylphosphite Blends with HFCs.**

Compound Name (/Blend)	Formula	Extinguishment Value, volume %
1,1,1,2,3,3,3-Heptafluoropropane (HFC-227ea)	$\text{CF}_3\text{CHF}_2\text{CF}_3$	6.2
Trimethylphosphite/HFC-227ea (7.2 %/92.8 %)	$\text{P}(\text{OCH}_3)_3/\text{CF}_3\text{CHF}_2\text{CF}_3$	5.1
Pentafluoroethane (HFC-125)	$\text{CHF}_2\text{CF}_3$	8.7
Trimethylphosphite/HFC-125 (12.2 %/87.8 %)	$\text{P}(\text{OCH}_3)_3/\text{CHF}_2\text{CF}_3$	6.8

From these data, it was concluded that highly fluorinated PCCs in this family can have flame extinguishment efficiencies comparable to halon 1301. While blending flammable PCCs with an HFC might reduce the flammability hazard, the flame extinguishment concentration was dominated by the HFC, and the mixture concentration offered little advantage over the HFC alone. Moreover, during the discharge process, disproportionation of the mixture is likely, potentially creating a zone in which a flammable PCC concentration exists.

### Second Series Compound Availability and Synthesis

This first set of results led to the selection of a second set of phosphorus-containing compounds for examination. In this process, compounds such as  $\text{PH}_3$  or  $\text{P}(\text{CH}_3)_3$  were ruled out as being flammable, while compounds involving P-F bonds were ruled out due to expected hydrolysis and unacceptable toxicity. The selected compounds represented a range of related structures and included both phosphine

and phosphonate compounds. Including both P(III) and P(V) phosphorus oxidation states, as well as incorporating, where possible, similar fluorinated substituents increased the probability of identifying promising chemical families. Promising compounds would serve as guides to future research and compound synthetic efforts.

Each of the selected compounds needed to be synthesized for the NGP. This was accomplished using utilizing bench top and vacuum line procedures. Each of the products was purified and then characterized, as needed for structure verification, by  $^{19}\text{F}$ ,  $^{31}\text{P}$  and  $^{13}\text{C}$  NMR, infrared and mass spectral measurements and by elemental analysis. The syntheses performed, as well as relevant literature references, are briefly described below. Table 7–37, at the end of the section, summarizes the results.

### ***Phosphites (Phosphonates) and Phosphates***

The most problematic features of these families of PCCs were high boiling points and flammability. Fluorination reduced both. Thus, the most promising additional compounds have formulas such as  $\text{P}(\text{OR}_f)_3$  or  $\text{O}=\text{P}(\text{OR}_f)_3$ , where  $\text{R}_f$  is a fluorinated group, which should have as low a molecular weight and as high a degree of fluorination as possible. Based on this, two logical compounds for further examination were tris(trifluoromethyl)phosphite ( $\text{P}(\text{OCF}_3)_3$ ) and tris(trifluoromethyl)phosphate ( $\text{O}=\text{P}(\text{OCF}_3)_3$ ).

The phosphite was not commercially available, and efforts to obtain a custom synthesized sample were unsuccessful. Protonated phosphites can be synthesized by reaction of  $\text{PCl}_3$  with ROH. Unfortunately, alcohols that could be used to prepare esters containing fluorine bound to the carbon atom adjacent to oxygen are inherently unstable, breaking down by a 1,2-elimination of hydrogen fluoride (HF) to give carbonyl compounds. Alternative synthetic processes were proposed, but with no laboratory willing to undertake the effort.

- Reaction of trifluorophosphine with carbonyl fluoride:  $\text{PF}_3 + 3 \text{O}=\text{CF}_2 \rightarrow \text{P}(\text{OCF}_3)_3$ . The enthalpy of reaction ( $\Delta H_r$ ) was estimated based on published bond energy values.<sup>212,213,214</sup> Table 7–34 provides data used in these calculations. The column marked “Basis” indicates the type of compound or types of compounds used to determine the bond energy.  $\Delta H_r$  was estimated as 92 kJ/mol (22 kcal/mole). Thus, the reaction is slightly endothermic, and the reverse reaction may provide a pathway for decomposition. This is particularly likely since the entropy of the decomposition reaction would almost certainly be positive due to the increase in the number of moles of gas. (Were the material to be formed as the phosphonate structure,  $\text{O}=\text{P}(\text{CF}_3)(\text{OCF}_3)_2$ , the reaction is less endothermic, with  $\Delta H_r$  estimated as to be 58 kJ/mol (14 kcal/mole). Again, however, the reverse reaction should have a positive entropy change. Even though the reactions are predicted to be endothermic, one must recognize that the use of average bond energies is highly suspect.)
- Reaction of phosphorous acid with trifluoromethyl iodide:  $\text{P}(\text{OH})_3 + 3\text{CF}_3\text{I} \rightarrow \text{P}(\text{OCF}_3)_3 + 3\text{HI}$ .

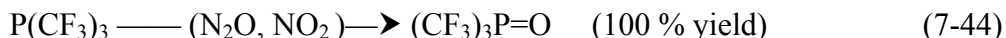
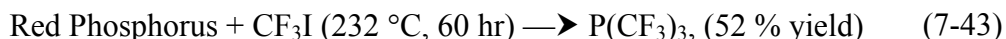
A synthesis for the phosphate has been published, based on oxidation of tris(trifluoromethyl)phosphine ( $\text{P}(\text{CF}_3)_3$ ).<sup>215</sup> It has a boiling point of 52 °C at 101 kPa and a melting point of -86 °C. The vapor pressure,  $p$ , in kPa can be fit to the equation  $\log_{10}p = -1445/T + 4.45$ , where  $T$  is in K, yielding a vapor pressure of 40 kPa (0.4 atm) at 25 °C. This vapor pressure is sufficient for cup burner testing, but the value at -40 °C of 0.02 kPa is far too low for aircraft use. An NGP attempt to produce this compound was unsuccessful.

**Table 7–34. Enthalpy of Reaction for  $\text{PF}_3 + 3 \text{O}=\text{CF}_2 \rightarrow \text{P}(\text{OCF}_3)_3$ .**

Bond				$\Delta\text{H}$ , Total for Bond Formation or Dissociation
Type	Number	Energy, kJ/mol (kcal/mol)	Basis	kJ/mol (kcal/mol)
<b>Reactants</b>				
P-F	3	498 (119)	$\text{PF}_3$	1500 (360)
C-F	6	490 (117)	$\text{CF}_4$	2900 (700)
C=O	3	749 (179)	Ketones	2200 (550)
			Sum	6700 (1600)
<b>Product, Phosphite Structure</b>				
P-O	3	368 (88)	$\text{P}_4\text{O}_6$	1100 (260)
C-F	9	490 (117)	$\text{CF}_4$	4400 (1050)
C-O	3	358 (85.6)	Organics	1070 (260)
			Sum	6600 (1600)
<b>Product, Phosphonate Structure</b>				
P-O	2	368 (88)	$\text{P}_4\text{O}_6$	740 (180)
P=O	1	456 (109)	$\text{O}=\text{PCl}_3$	460 (110)
P-C	1	306 (73)		310 (70)
C-F	9	490 (117)	$\text{CF}_4$	4490 (1100)
C-O	2	358 (85.6)	Organics	720 (170)
			Sum	6600 (1600)

Attention then focused on four phosphite/phosphonate compounds.<sup>iii</sup>

- **Tris(trifluoromethyl) Phosphonate,  $\text{O}=\text{P}(\text{CF}_3)_3$**  (Compound 1, Table 7–37). This two-step synthesis (Reactions 7-43 and 7-44) involved reaction of red phosphorus with  $\text{CF}_3\text{I}$ , forming the flammable intermediate  $(\text{CF}_3)_3\text{P}$ . This was followed by an oxidation insertion reaction with nitrous oxide and nitrogen dioxide to form the phosphonate,  $(\text{CF}_3)_3\text{P}=\text{O}$ .<sup>38</sup>

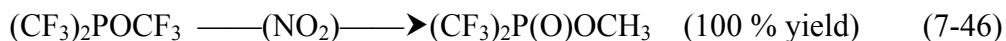


- **Tris(2,2,2-trifluoroethoxy) Phosphite,  $\text{P}(\text{OCH}_2\text{CF}_3)_3$**  (Compound 2, Table 7–37). This synthesis was carried out by adding trifluoroethanol dropwise into a vigorously stirred solution of phosphorus trichloride (slight excess) at 0 °C. After 5 h, fractional distillation gave the desired product. This reaction is summarized in Reaction 7-45.



- **Bis(trifluoromethyl) trifluoromethoxy Phosphonate,  $\text{O}=\text{P}(\text{OCH}_3)(\text{CF}_3)_2$** , (Compound 3, Table 7–37). The  $(\text{CF}_3)_2\text{POCF}_3$  intermediate was oxidized with a slight molar deficiency of nitrogen dioxide as in the synthesis of Compound 1. The NO was removed under vacuum. This reaction is summarized in Reaction 7-46.

<sup>iii</sup> Rearrangements can occur between the phosphite form, e.g.,  $\text{P}(\text{OR})_2\text{R}$ , and the phosphonate form, e.g.,  $\text{O}=\text{P}(\text{OR})\text{R}_2$ .



- **Bis(trifluoromethyl) 2,2,2-trifluoroethoxy Phosphonate,  $(\text{CF}_3)_2\text{P}(\text{O})\text{OCH}_2\text{CF}_3$ ,** (Compound 4, Table 7–37). This synthesis is very similar to that for Compound 3. This reaction is summarized in Reaction 7-47.



### Fluoroalkyl Phosphines

Following the lessons learned from the previous family of compounds, examination of the phosphines focused on the smallest, heavily fluorinated molecules. Table 7–35 shows published data for some of the simplest fully fluorinated organic phosphines.

**Table 7–35. Perfluoroalkyl Phosphines.**

Compound Formula	$T_b$ (°C)	Properties	Reference
$(\text{CF}_3)_3\text{P}$	17	Spontaneously flammable	216
$(\text{CF}_3\text{P})_4$	Not available	Solid, melting point 66.4 °C	220
$(\text{CF}_3\text{P})_5$	190	Not available	220
$(\text{CF}_3)_2\text{PP}(\text{CF}_3)_2$	83 to 84	Flammable	216
$(\text{C}_2\text{F}_5)_3\text{P}$	70	Not available	211

The simplest perfluorinated trialkyl compound is tris(trifluoromethyl)-phosphine ( $(\text{CF}_3)_3\text{P}$ ), which has been prepared as a mixture with trifluoromethyldiiodophosphine,  $(\text{CF}_3)\text{PI}_2$ , and bis(trifluoromethyl)-iodophosphine,  $(\text{CF}_3)_2\text{PI}$ , by reaction of phosphorus with trifluoriodomethane  $(\text{CF}_3\text{I})$ ,<sup>216</sup> and also by reaction of tris(diethylamino)phosphine,  $\text{P}(\text{N}(\text{C}_2\text{H}_5)_2)_3$ , with trifluoromethyl bromide ( $\text{CBrF}_3$ , halon 1301) and triphenylphosphite,  $\text{O}=\text{P}(\text{OC}_6\text{H}_5)_3$ , in tris(dimethylamino)phosphine oxide,  $\text{OP}(\text{N}(\text{CH}_3)_2)_3$ , hexamethylphosphor-amide, HMPA).<sup>217</sup> Unfortunately, this material (like some of its complexes<sup>218</sup>) is spontaneously flammable (Table 7–35). The iodide derivatives are exceedingly useful precursors for a number of compounds of interest here; however, even with optimized procedures,<sup>219</sup> the syntheses are difficult, and the reactants and products are hard to handle. Reaction of  $(\text{CF}_3)_2\text{PI}$  with mercury gives the flammable compound tetrakis(trifluoro-methyl)diphosphine  $(\text{CF}_3)_2\text{PP}(\text{CF}_3)_2$ <sup>216</sup> and the tetrameric and pentameric cyclic compounds  $(\text{CF}_3\text{P})_4$  and  $(\text{CF}_3\text{P})_5$ <sup>220</sup> (Table 7–35). The compounds  $(\text{CF}_3)\text{PF}_2$  and  $(\text{CF}_3)_2\text{PF}$  are also known.<sup>221</sup>

The higher molecular weight perfluoroalkyl derivatives are likely to be more stable than the methyl compounds. Tris(pentafluoroethyl)phosphine ( $(\text{C}_2\text{F}_5)_3\text{P}$ ), with a boiling point of 70 °C, has been prepared by reaction of phosphorus trichloride ( $\text{PCl}_3$ ) with ethyl lithium ( $\text{C}_2\text{F}_5\text{Li}$ ), which can be prepared by reaction of chloropentafluoroethane ( $\text{C}_2\text{F}_5\text{Cl}$ ) with n-butyl lithium ( $\text{C}_4\text{F}_9\text{Li}$ ).<sup>211</sup> The procedure, however, has not been published. It has proven impossible to prepare the tris(heptafluoropropyl)-phosphine ( $(\text{C}_3\text{F}_7)_3\text{P}$ ), apparently due to steric hindrance.<sup>222</sup>

A large number of trifluoromethyl-substituted diphosphorus compounds having the general formula  $(\text{CF}_3)_2\text{PRP}(\text{CF}_3)_2$ , where “R” represents a branched or linear hydrocarbon or fluorocarbon chain, have been synthesized as bidentate ligands starting with  $(\text{CF}_3)_2\text{PP}(\text{CF}_3)_2$ .<sup>223,224</sup> It has been stated that these

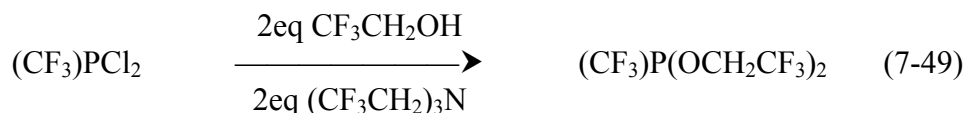
compounds are difficult to prepare owing to difficulty in synthesis of the diphosphine precursor.<sup>211</sup> A similar compound has also been prepared:  $(C_2F_5)_2PCH_2CH_2P(C_2F_5)_2$ , boiling point 105 °C at 11 kPa.<sup>225</sup> The primary interest in these compounds is as bidentate ligands.<sup>226</sup>

Based on this information, the following three compounds were synthesized for further examination.

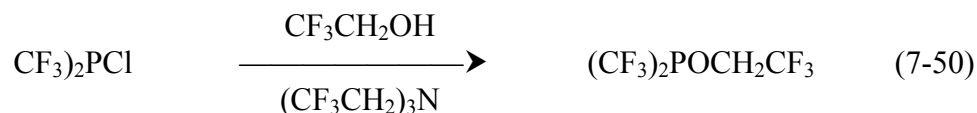
- **Bis(trifluoromethyl)methoxy Phosphine,  $(CF_3)_2POCH_3$** , (Compound 5, Table 7–37). The intermediate,  $(CF_3)_2PI$ , formed as one of the products in 25 % yield from the reaction of  $CF_3I$  and red phosphorus, was reacted at 25 °C with  $AgCl$  to form  $(CF_3)_2PCl$  at an approximately 100 % yield. The chloride was subsequently reacted with methanol in the presence of triethylamine, substituting the methoxide for the iodine.<sup>38</sup> This reaction is summarized in Reaction 7-48.



- **Bis(2,2,2-trifluoroethoxy) trifluoromethyl Phosphine,  $(CF_3)P(OCH_2CF_3)_2$** , (Compound 6, Table 7–37). This synthesis is very similar to the synthesis of Compound 5. This reaction is summarized in Reaction 7-49.



- **Bis(trifluoromethyl) 2,2,2-trifluoroethoxy Phosphine,  $(CF_3)_2POCH_2CF_3$** , (Compound 7, Table 7–37). This synthesis, very similar to Reaction 7-49, is summarized in Reaction 7-50.



### *Amino Fluoroalkylphosphines*

Aminobis(trifluoromethyl)phosphines ( $(CF_3)_2PNR_2$ ,  $R = -H, -CH_3$ ) have been prepared by reaction of chlorobis(trifluoromethyl)phosphine ( $(CF_3)_2PCl$ ) with the appropriate amine.<sup>227</sup> Though these materials are relatively stable liquids (Table 7–36), they are readily oxidized in air. The simplest amino compound is spontaneously flammable, as is the  $(CF_3)_2PCl$  starting material. Amines containing two and three bis(trifluorophosphine) groups<sup>228</sup> and compounds of the type  $[(CF_3)_2N]_nP(CF_3)_{3-n}$ ,  $n = 1$  to 3 (the latter discussed further in Reference 93) have also been prepared (Table 7–36). The starting materials, however, are also spontaneously flammable:  $(CF_3)_2PCl$  or tris(trifluoromethyl)phosphine ( $(CF_3)_3P$ ). Aminobis-(heptafluoropropyl)-phosphine ( $(C_3F_7)_2PNH_2$ ), a high boiling liquid (Table 7–36), has been prepared by reaction of  $(C_3F_7)_2PCl$  with anhydrous ammonia.<sup>222</sup> As is typical for all of these reactions, the starting material was prepared by reaction of heptafluoropropyl iodide with phosphorus at high temperature and pressure followed by replacement of the iodide with chloride using silver chloride.

The volatility of even the simplest of these compounds was insufficient for aircraft use, and this chemical family was not examined further.

**Table 7–36. Amino Fluoroalkylphosphines.**

Compound Formula	$T_b$ (°C) <sup>a</sup>	Properties	Reference
(CF <sub>3</sub> ) <sub>2</sub> PNH <sub>2</sub>	67.1	Spontaneously flammable	227
(CF <sub>3</sub> ) <sub>2</sub> PNH(CH <sub>3</sub> )	72.3	Not available	227
(CF <sub>3</sub> ) <sub>2</sub> PN(CH <sub>3</sub> ) <sub>2</sub>	83.2	Not available	227
((CF <sub>3</sub> ) <sub>2</sub> P) <sub>2</sub> NH	Not available	Vapor pressure 6.2 kPa at 23.9 °C	228
((CF <sub>3</sub> ) <sub>2</sub> P) <sub>2</sub> NCH <sub>3</sub>	Not available	Vapor pressure 2.3 kPa at 25.0 °C	228
((CF <sub>3</sub> ) <sub>2</sub> P) <sub>3</sub> N	Not available	Solid, melting point 36.5 °C to 36.8 °C	228
(CF <sub>3</sub> ) <sub>2</sub> NP(CF <sub>3</sub> ) <sub>2</sub>	51	Stable at room temperature	229
((CF <sub>3</sub> ) <sub>2</sub> N) <sub>2</sub> P(CF <sub>3</sub> )	92.5	Stable at room temperature	229
((CF <sub>3</sub> ) <sub>2</sub> N) <sub>3</sub> P	135	Stable at room temperature	229
(C <sub>2</sub> F <sub>7</sub> ) <sub>2</sub> PNH <sub>2</sub>	143	Not available	222

a 101 kPa (nominal) pressure.

### ***Reactivity in Air***

Upon breaking open their respective glass sealed vials, Compounds 5 and 7 reacted extremely vigorously (i.e., fumed) as air entered and contacted the liquid agent. Some fuming was also noted for Compounds 3 and 6. It may be that compound 7 underwent air oxidation to yield a phosphonate structure, O=P(OCH<sub>2</sub>CF<sub>3</sub>)(CF<sub>3</sub>)<sub>2</sub>, or oxygen insertion reactions at the P-CF<sub>3</sub> bonds.

### ***Cup Burner Flame Extinguishment Testing***

In view of the wide range of boiling points represented by the compounds synthesized, a means was required for preventing the condensation on cooler surfaces and countering the evaporative cooling effects of the nebulized agent as they dispersed into the air stream of the cup burner. Heating the inlet air to between 50 °C and 55 °C counteracted the evaporative cooling effects of the misted agent at the tip of the nebulizer and enhanced droplet vaporization. On mixing with the cooler, nebulized agent/air stream, the column temperature dropped to between 45 °C to 50 °C. The preheated air was also employed to warm the entire cup burner chimney prior to a test run, and as a result no condensation of agent was observed during or following extinguishment testing.

Due to the limited quantities of some agents, each was tested no higher than the screening concentration of 5 % by volume.

### ***Observations***

It is possible that phosphonates having multiple -CF<sub>3</sub> groups are too stable for the phosphorus atom to be released into the cup burner flame. When Compound 1 was tested at 5 volume %, no evidence of flame lift-off was observed. Compound 3, with two -CF<sub>3</sub> groups, showed lift-off and flame extinguishment just below 5 volume %. Compound 4, also with two -CF<sub>3</sub> groups, showed lift-off but no flame extinguishment at 5 volume %.

Only Compound 4 approached the desired boiling point range. In the trade-off between higher degree of fluorination to reduce the boiling point and moderate hydrogenation for efficient fire suppression, there may be limited further promise in this family of compounds. This conclusion must be tempered by the observed low cup burner test value (1.8 %) of compound 7 and the possibility that air reaction is converting it to a very efficient flame suppressant. It cannot, however, be concluded at this point that the

air oxidation produces a complete conversion to a single compound or that the reaction is complete by the time the products enter the flame zone.

In earlier work, Compound 2 had been reported to have a cup burner extinguishment value of 1.78 volume % for n-heptane fuel.<sup>39</sup> This value is much lower than that measured subsequently and reported here. Differences in manner of sample vaporization could well be responsible. In the earlier studies, a hot sand bath (>250 °C) was employed to volatilize the compound as it was introduced into the base of the cup burner. It is possible this method induced thermal decomposition and air reaction of the test compound, yielding a more effective flame suppressant.

Compound 7, though air reactive, yielded an impressively low cup burner value. It is possible this low value might have been due to a breakdown product whose air concentration was even lower than 1.8 volume %. Identification and study of Compound 7 (or Compound 5) air reaction products might lead to significant advancements in phosphorus-based suppressants for aircraft dry bays and other unoccupied areas. If the extinguishing concentration were 1 volume % or lower, significant improvements in the efficiencies of solid propellant fire extinguishers or powder panels (Chapter 9) might be achieved. The nature and toxicity of compound 6 air decomposition products needs to be determined.

The synthesis attempted of (tris(trifluoromethoxy) phosphonate,  $O=P(OCF_3)_3$ ) had been reported in the literature. While the NGP was unable to obtain this compound, a realistic expectation of its synthesis still exists. Its similarity to the structures thought to be the breakdown products from compound 7, that may be contributing to its demonstrated higher effectiveness, make this compound a prime target for further research and testing.

Phosphines provide good materials for mechanistic studies; however, they can be ruled out as candidates owing to their inherent low stability (many are flammable, sometimes spontaneously, even with fluorinated substituents) and high toxicities. Though it is possible to obtain fire extinguishment (sometimes very efficient) with phosphazenes, these compounds have inherently high molecular weights and, therefore, very low volatility.

### **Fluoroalkyl (alkoxide) Phosphorus Compounds - Summary**

No phosphorus-containing compounds were identified that met needed criteria for volatility, stability, and flame suppression efficiency. Some may be useful flame suppressants at temperatures above the current low temperature criterion. Given the high flame suppression efficiency of a chemically liberated phosphorus atom, a well chosen PCC could enhance the effectiveness of solid propellant fire extinguishers. Determination of the decomposition rates and combustion products could further that choice. Some of the phosphorus compounds are polar or reactive (to hydrolysis) and thus are likely to have short atmospheric lifetimes. The environmental fate of their decomposition products fate would need to be assessed.

Table 7–37. Phosphorus-containing Compound Performance.

	Compound Name	Formula	Mass Available(g)	T <sub>b</sub> (°C) <sup>a</sup>	Ext. Conc. (vol. %)	Exposure of Agent to Air
1	Tris(trifluoromethyl) Phosphonate	O=P(CF <sub>3</sub> ) <sub>3</sub>	7.3	32	None @ 5 %	No fumes or ignition
2	Tris(2,2,2-trifluoroethoxy) Phosphite	P(OCH <sub>2</sub> CF <sub>3</sub> ) <sub>3</sub>	50.0	130 (est.)	3.1	No fumes or ignition
3	Bis(trifluoromethyl) trifluoromethoxy Phosphonate	O=P(OCH <sub>3</sub> )(CF <sub>3</sub> ) <sub>2</sub>	5.5	42	4.6	Fumes, no ignition
4	Bis(trifluoromethyl) 2,2,2-trifluoroethoxy Phosphonate	O=P(OCH <sub>2</sub> CF <sub>3</sub> )(CF <sub>3</sub> ) <sub>2</sub>	7.0	130	None @ 5 %	No fumes, did not ignite cloth
5	Bis(trifluoromethyl)methoxy Phosphine	P(OCH <sub>3</sub> )(CF <sub>3</sub> ) <sub>2</sub>	5.3	55	Ignited on air exposure <sup>b</sup>	Ignited spontaneously
6	Bis(2,2,2-trifluoroethoxy) trifluoromethyl Phosphine	P(OCH <sub>2</sub> CF <sub>3</sub> ) <sub>2</sub> CF <sub>3</sub>	7.2	111	3.0	Fumes, no ignition
7	Bis(trifluoromethyl) 2,2,2-trifluoroethoxy Phosphine	P(OCH <sub>2</sub> CF <sub>3</sub> )(CF <sub>3</sub> ) <sub>2</sub>	6.5	25	1.8	Ignited cloth, fumed strongly

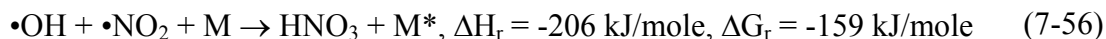
a. Determined at nominally 100 kPa, except Compound 7 at 7 kPa.

b. In view of the low cup burner test value of Compound 7, the structurally similar Compound 5 was preserved in order to provide a future opportunity to identify the product of its reaction with air.

### 7.4.5 Fluoroalkyl Nitrogen-based Candidates

#### Atmospheric Lifetime, ODP, and GWP

The fact that nitrogen oxides could be direct depleters of stratospheric ozone was recognized earlier than that halocarbons posed an environmental threat.<sup>230</sup> The first concerns were about direct injection of nitrogen oxides into the stratosphere by high altitude aircraft.<sup>231</sup> Nitrogen compounds, however, play other roles in atmospheric chemistry involving ozone depletion. The ozone chemical balance depends directly on the total amount of active nitrogen species.<sup>232</sup> Nitric oxide (NO) releases chlorine from chlorine monoxide (Reaction 7-52).<sup>233</sup> Nitrogen oxides can also decrease stratospheric ozone depletion by the formation of the chlorine nitrate (ClONO<sub>2</sub>) reservoir (Reaction 7-53)<sup>233</sup> and by the removal of •OH (Reactions 7-54 through 7-56).<sup>234</sup> Hydroxyl free radicals convert HCl and HBr to free chlorine and bromine atoms, which are potent depleters of stratospheric ozone. Removal of nitric acid by condensation is believed to play a major role in the Antarctic ozone hole.<sup>234</sup>



Since some highly fluorinated amines have long atmospheric lifetimes, it is possible that anthropogenic amines of interest in this research could deplete stratospheric ozone.

A relatively large amount of data are available for reactions of atmospheric •OH radicals with nitrogen-containing compounds; however, few experimental data (as opposed to estimations) are available for compounds that might be useful as halon 1301 replacements, i.e., those containing fully or partially fluorinated alkyl groups (to improve toxicity and flammability characteristics). Amines containing no hydrogen atoms are expected to be inert to attack by •OH, which can be seen in the absence of reaction observed with N,N-bis(pentafluoroethyl)penta-fluoroethanamine (N(CF<sub>2</sub>CF<sub>3</sub>)<sub>3</sub>), for which an •OH rate constant  $k_2 < 6 \times 10^{-16} \text{ cm}^3/\text{molec}\cdot\text{s}$  has been reported.<sup>235</sup> This rate constant corresponds to an estimated atmospheric lifetime of greater than 55 years.

A relatively large amount of data is available for hydrogen-containing, nonfluorinated amines. Nitroalkanes (RNO<sub>2</sub>) have been relatively well studied,<sup>236</sup> but these have little resemblance to amines, which are the most promising of the nitrogen-containing halon replacements. As a result of concerns about health impacts, the atmospheric chemistry of N-nitrosodimethylamine ((CH<sub>3</sub>)<sub>2</sub>N-NO) and dimethylnitramine ((CH<sub>3</sub>)<sub>2</sub>N-NO<sub>2</sub>) has been examined.<sup>237</sup> Table 7-38 presents rate constants for hydroxyl free radicals reactions with several nonfluorinated amines.<sup>119</sup> Where several values were given, the first value cited at or near 298 K was used for consistency. These values were calculated at or near the high

pressure limit. Atmospheric lifetimes in Table 7–38, calculated from a globally tropospheric •OH concentration of  $9.7 \times 10^5$  molecules/cm<sup>3</sup>, are on the order of a few days or less. The reactions of all of the compounds in Table 7–38 probably involve hydrogen atom abstraction from the alkyl groups. Since all of these compounds are highly polar, rainout would also be an effective removal mechanism.

Rate constants have been compiled for gas-phase reactions of O<sub>3</sub> with a number of nitrogen-containing compounds,<sup>238</sup> and the data for amines are shown in Table 7–39. The rate constants increase and lifetimes (estimated from the globally averaged tropospheric O<sub>3</sub> concentration) decrease with increasing alkyl substitution. This is also the direction of increasing proton affinity ( $-\Delta H$  for the reaction  $B + H^+ \rightarrow BH^+$ , where B is a base).<sup>239</sup>

**Table 7–38. •OH Rate Constants for Nitrogen-containing Compounds.**

Compound Name	$k_{OH}$ , cm <sup>3</sup> /molec-s	Temperature (K)	Atmospheric Lifetime (days) <sup>a</sup>
Methylamine, NH <sub>2</sub> (CH <sub>3</sub> )	$22.0 \pm 2.2 \times 10^{-12}$	299	0.5
Ethylamine, NH <sub>2</sub> (CH <sub>2</sub> CH <sub>3</sub> )	$27.7 \pm 2.8 \times 10^{-12}$	299.6	0.4
Dimethylamine, NH(CH <sub>3</sub> ) <sub>2</sub>	$64.5 \pm 6.6 \times 10^{-12}$	298.5	0.2
Trimethylamine, N(CH <sub>3</sub> ) <sub>3</sub>	$60.9 \pm 6.1 \times 10^{-12}$	298.7	0.2
Diethylhydroxylamine N(CH <sub>2</sub> CH <sub>3</sub> ) <sub>2</sub> OH	$101 \times 10^{-12}$	308	0.1
2-(Dimethylamino)ethanol CH <sub>2</sub> (N(CH <sub>3</sub> ) <sub>2</sub> )CH <sub>2</sub> OH	$47 \pm 12 \times 10^{-12}$	$300 \pm 2$	0.3
2-Amino-2-methyl-1-propanol CH <sub>3</sub> C(CH <sub>3</sub> )(NH <sub>3</sub> )CH <sub>2</sub> OH	$28 \pm 5 \times 10^{-12}$	$300 \pm 2$	0.4
N-Nitrosodimethylamine (CH <sub>3</sub> ) <sub>2</sub> N-NO	$02.53 \pm 0.21 \times 10^{-12}$	$298 \pm 2$	4.7
Dimethylnitramine, (CH <sub>3</sub> ) <sub>2</sub> N-NO <sub>2</sub>	$03.84 \pm 0.15 \times 10^{-12}$	$298 \pm 2$	3.1

a Based only on reaction with •OH.

**Table 7–39. Rate Constants for Reactions of O<sub>3</sub> With Amines.**

Compound Formula	$k_2$ at 296 K, (cm <sup>3</sup> /molec-s)	Estimated Tropospheric Lifetime (days)	Proton Affinity (kJ/mole)
NH <sub>2</sub> (CH <sub>3</sub> )	$2.13 \pm 0.29 \times 10^{-20}$	1087	896
NH <sub>2</sub> (CH <sub>2</sub> CH <sub>3</sub> )	$2.76 \pm 0.34 \times 10^{-20}$	839	908
NH(CH <sub>3</sub> ) <sub>2</sub>	$2.61 \pm 0.30 \times 10^{-18}$	008.9	923
N(CH <sub>3</sub> ) <sub>3</sub>	$9.73 \pm 1.02 \times 10^{-18}$	002.4	938

The reactions appear to proceed by addition of O<sub>3</sub> to the nitrogen to give R<sub>3</sub>N+O-O-O-, which then decomposes by uncertain mechanisms. Data for reactions involving halogen-substituted alkyl amines have not been reported; however, it is likely that the reaction rates will decrease with increasing halogen substitution, which makes the nitrogen atom less electron rich.

Rate constants have also been reported for reaction of O<sub>3</sub> with pyridines (approximately  $5 \times 10^{-20}$  cm<sup>3</sup>/molec-s to  $50 \times 10^{-20}$  cm<sup>3</sup>/molec-s) and for unsaturated nitriles ( $< 1 \times 10^{-19}$  cm<sup>3</sup>/molec-s to  $1.38 \times 10^{-19}$  cm<sup>3</sup>/molec-s for acrylonitrile CH<sub>2</sub>=CHCN and  $3.52 \times 10^{-19}$  cm<sup>3</sup>/molec-s for methacrylonitrile CH<sub>2</sub>=C(CH<sub>3</sub>)CN).<sup>121</sup> Ozone is known to react with alkene derivatives, and the results for the acrylonitriles

probably have little to do with the presence of nitrogen. The pyridines, which are, at best, distantly related to the amines of interest, have calculated lifetimes for reaction with tropospheric ozone of approximately 1 year or less. The maximum values of the rate constants for reaction of N-nitrosodimethylamine  $(\text{CH}_3)_2\text{N}-\text{NO}$  and dimethylnitramine  $(\text{CH}_3)_2\text{N}-\text{NO}_2$  with tropospheric ozone are  $1 \times 10^{-20} \text{ cm}^3/\text{molec}\cdot\text{s}$  and  $3 \times 10^{-21} \text{ cm}^3/\text{molec}\cdot\text{s}$  (calculated lifetimes of 6 years and 21 years, respectively) and could be less than this.<sup>237</sup> Photolysis is probably the primary removal mechanism for N-nitrosodimethylamine.

Of particular interest for fire suppression are alkyl-substituted amines, with one or more alkyl groups containing bromine atoms. The primary problem is that fluorination is needed to decrease both the flammability and toxicity of amines. As fluorination increases, both the polarity and the flammability are expected to decrease (for different reasons). The polarity is directly related to toxicity, since highly polar amines are strong bases and therefore irritants. The polarity is, however, also directly related to the effectiveness of atmospheric removal. Nonfluorinated amines are expected to undergo significant rainout.

Reported lifetimes and GWPs were reviewed for several fluoroalkyl amines in Reference 240. However, the values are highly suspect. For example, the lifetime of  $(\text{CH}_3)_2\text{NC}_2\text{F}_5$  is reported as 250 years, while that of the much less hydrogen-rich compound  $(\text{CF}_3)_2\text{NCF}_2\text{CF}_2\text{H}$  is given as 2.10 years.<sup>241</sup> Moreover, the estimation methods for the lifetimes and GWPs were not reported. Eliminating the highly questionable value of 250 years gives estimated lifetimes for hydrofluoroamines (HFAs) of around 0.3 years to 3 years.<sup>241</sup>

While there is nothing inherent in nitrogen compounds that would lead to atmospheric lifetime or GWP problems, individual compounds may have significant effects. Replacement of fluorine atoms with bromine atoms would tend to reduce HFA lifetimes by a factor of 10 in some compounds. Data indicate that for bromine-containing alkanes, each 10-year increase in the atmospheric lifetime increases the ODP by approximately a factor of 2. Therefore, hydrofluorobromoamines should have low ODPs. Any impact from nitrogen on stratospheric ozone would be negligible compared to that from bromine.

Research from the National Industrial Research Institute of Nagoya has focused on fluoroalkylamines, with an emphasis on perfluoroalkyl derivatives, as fire suppressants.<sup>242</sup> All of their fluoroalkylamines inhibited flame propagation less efficiently than  $\text{CF}_3\text{Br}$ , but more efficiently than HFC-227ea. A thorough assessment of the atmospheric impact of fluorinated amines and of bromofluoroamines (based on estimations and calculations) has been presented.<sup>240</sup> For example, the compound  $(\text{CBrF}_2)(\text{CF}_3)\text{NCH}_3$  is estimated to have an atmospheric lifetime of 10 days and an ODP of 0.006 relative to CFC-11.<sup>240</sup> The amine  $\text{N}(\text{CF}_3)_2\text{CF}=\text{CF}_2$  is expected to have a lower atmospheric lifetime due to the presence of its  $-\text{F}=\text{CF}_2$  group.

## Toxicity

The acute inhalation toxicities of some hydrofluoroamines (HFAs) are given in Table 7-40.<sup>29</sup> These have also been reviewed in Reference 240; however, here the  $\text{LC}_{50}$  values are also given as volume percent. Although these lower bounds do not cause any concern, measurements at higher concentrations are needed. In addition to the compounds shown in Table 7-40, the  $\text{LC}_{10}$  for mouse inhalation has been reported as 0.0123 volume % for 2,2,2-trifluoroethylamine  $(\text{CF}_3\text{CH}_2)\text{NH}_2$ ,<sup>67</sup> a value that appears rather low; however, this compound contains hydrogen atoms directly bonded to the nitrogen.

**Table 7–40. Acute Inhalation Toxicity of Hydrofluoroamines.**

Compound Formula	Exposure Time, Subject	LC <sub>50</sub> (mg/L)	Molecular Weight	LC <sub>50</sub> (volume %)
(CF <sub>3</sub> ) <sub>2</sub> NCH <sub>3</sub>	3 h, rat	>20	113.99	>0.43
(CF <sub>3</sub> ) <sub>2</sub> NCF <sub>2</sub> CF <sub>2</sub> H	3 h, rat	>20	253.04	>0.19
(CF <sub>3</sub> ) <sub>2</sub> NCFHCF <sub>3</sub>	3 h, rat	>20	253.04	>0.19
(CF <sub>3</sub> ) <sub>2</sub> NCH <sub>2</sub> CF <sub>3</sub>	3 h, rat	>20	235.05	>0.21
(CF <sub>3</sub> ) <sub>2</sub> NCH <sub>2</sub> CF <sub>2</sub> H	4 h, rat	>20	217.06	>0.23
(CF <sub>3</sub> ) <sub>2</sub> NCH <sub>2</sub> CH <sub>3</sub>	4 h, rat	>20	181.08	>0.27

A review of Reference 67 identified inhalation toxicity data for over 120 compounds containing both nitrogen and fluorine; however, inhalation data are available for only 6 of these (Table 7–41). Nearly every compound in this limited set is given a SAX HR of 3, signifying the worst hazard level. However, none of these compounds is closely related to amines, and most contain groups known to lead to toxicity. Many N-nitroso compounds, such as the nitrosocarbamates, are carcinogens.

**Table 7–41. Toxicity and Safety Information for Selected N, F Compounds.**

Compound Name	Formula	CAS No.	Observations <sup>a</sup>
fluoroacetanilide	C <sub>8</sub> H <sub>8</sub> FNO	330-68-7	{RTECS AE2975000} [FFH000] LC <sub>LO</sub> (mouse, inh, 10 min) = 480 mg/m <sup>3</sup> . Poison by ingestion, intraperitoneal, and possible other routes. Moderately toxic by inhalation. HR = 3.
beta-fluoroethyl-N-(beta-chloroethyl)-N-nitrosocarbamate	C <sub>4</sub> H <sub>8</sub> ClFN <sub>2</sub> O <sub>3</sub>	63884-92-4	{RTECS EZ2275000} [IH000] LC <sub>LO</sub> (guinea pig, inh, 10 min) = 300 mg/m <sup>3</sup> . Poison by inhalation. HR = 3.
2-fluoroethyl-N-methyl-N-nitrosocarbamate	C <sub>4</sub> H <sub>7</sub> FN <sub>2</sub> O <sub>3</sub>	63982-15-0	{RTECS FC6475000} [FIS000] LC <sub>LO</sub> (guinea pig, inh, 10 min) = 100 mg/m <sup>3</sup> , LC <sub>LO</sub> (mouse, inh, 10 min) = 500 mg/m <sup>3</sup> . Poison by inhalation. HR = 3.
3-nitrobenzotrifluoride	C <sub>7</sub> H <sub>4</sub> F <sub>3</sub> NO <sub>2</sub>	98-46-4	RTECS XT3500000} [NFJ500] LC <sub>50</sub> (rat, inh) = 870 mg/kg, LC <sub>50</sub> (mouse, inh, 2 hr) = 880 mg/m <sup>3</sup> . Moderately toxic by ingestion, inhalation, and subcutaneous routes. HR = 3.
(alpha, alpha, alpha-trifluoro- <i>m</i> -tolyl)isocyanate	C <sub>8</sub> H <sub>4</sub> F <sub>3</sub> NO	329-01-1	RTECS NR200000} [KJ250] LC <sub>50</sub> (rat, inh) = 3600 mg/m <sup>3</sup> , LC <sub>50</sub> (mouse, inh) = 3300 mg/m <sup>3</sup> . Moderately toxic by ingestion, inhalation, intraperitoneal routes. HR = 2.
2,4,6-trifluoro- <i>s</i> -triazine	C <sub>3</sub> F <sub>3</sub> N <sub>3</sub>	675-14-9	{RTECS XZ1750000} [TKK000] LC <sub>50</sub> (rat, inh, 4 hr) = 3.1 μL/L. Poison by skin contact, inhalation. HR = 3.

<sup>a</sup> The SAX No. (Reference 67) is given in brackets followed by information from that reference; the RTECS No. (Reference 138) is given in braces. "HR" denotes the SAX Hazard Rating.

No generalities on the toxicity of nitrogen compounds can be made. Amines range in toxicity from poisons to only slightly toxic. In fact, fully fluorinated alkyl amines show no toxicity. Some amines are skin irritants while others are sensitizers.<sup>67</sup> Although LC<sub>50</sub> values have been determined for some hydrofluoroamines (HFA), the test levels are very low and measurements at higher concentrations are needed. ((CH<sub>3</sub>)<sub>2</sub>NCF<sub>2</sub>CBrF<sub>2</sub>) has tested negative for genotoxicity and cytotoxicity.<sup>243</sup>

## Volatility

Generally due to toxicity concerns, the only compounds of interest are amines containing three alkyl groups. Moreover, to decrease toxicity and corrosivity (by decreasing polarity) and to decrease flammability, the alkyl groups should be at least partially fluorinated. This chemical family represents a very broad range of fluorination patterns and alkyl substitution patterns. Table 7–41 indicates that there are some such fluoroalkylamines with boiling points below and near the screening criterion.

## Flame Extinguishment

As the primary question to be addressed was extinguishment performance, and little change in performance was expected amongst the fully fluorinated ethyl and methyl amines, three low boiling compounds were selected for examination.

**Table 7–42. Fluoroalkylamine Boiling Points.**

Compound Formula	$T_b$ (°C)
$N(CF_3)_3$	-10
$N(CF_3)_2CF=CF_2$	13.7
$N(CF_3)_2CH_3$	11 to 12
$N(CF_3)_2CF_2CF_3$	20.5
$N(CF_3)_2CF_2CHF_2$	32.0
$N(CF_3)_2CH_2CH_3$	33 to 34
$N(CF_3)_2CH_2CH_3$	33.3
$N(CF_3)_2CH_2CF_3$	38
$N(CF_3)(CF_2CF_3)_2$	46

- **N,N-bis(trifluoromethyl)pentafluoroethanamine ((pentafluoroethyl)bis(dimethyl)-amine,  $N(CF_3)_2(C_2F_5)$ )**, obtained from Dr. Takashi Abe, National Industrial Research Institute (NIRI), Japan was the product of electrochemical fluorination.<sup>244</sup> This synthetic approach is generally not amenable to the preparation of partially fluorinated compounds. Three cup burner tests were run to give an average extinguishment value of 3.8 volume %.
- **Trifluoroacetonitrile,  $CF_3CN$** , is a commercially available compound.<sup>170,192</sup> It has very low boiling point of -67 °C and seeming potential tropodegradability resulted in an interest in further study. Cup burner tests yielded flame extinguishment at 9 volume %, suggesting that there is no chemical effect from the nitrile group.
- **N,N-bis(trifluoromethyl)-trifluoro-methanamine (tris(trifluoromethyl)amine,  $N(CF_3)_3$ )**, synthesis was attempted unsuccessfully using the procedure shown in Reaction 7-57. No cup burner value therefore was obtained.



## Summary

There is no indication that the presence of a nitrogen atom in a compound significantly improves the fire suppression efficiency relative to other thermally active flame suppressants. The fully fluorinated compounds, which have the lower boiling points, are also likely to have long atmospheric lifetimes. While partially fluorinated amines are likely to have relatively short atmospheric lifetimes, it is difficult to determine whether the lifetime would be sufficiently short to allow bromine substitution (to increase flame suppression efficiency). Toxicity appears to be problematic for the partially fluorinated compounds.

### 7.4.6 Bromofluoroalkyl Nitrogen-based Candidates

There are three families of this type that were considered: amines, imines, and nitriles.

In general, the atmospheric lifetimes of bromofluoro nitrogen-based compounds were expected to be similar to those of analogous non-brominated nitrogen-based compounds. There is no indication that the nitrogen alkyl linkage provides any significant contribution to rainout. The polarity of the nitrogen lone pair may be too small. Perfluorinated saturated amines are expected to have atmospheric lifetimes similar to those of the perfluorinated alkanes, a property that generally makes their use as halon replacements questionable. The atmospheric lifetimes for partially fluorinated amines are much shorter. Atmospheric lifetimes of imines are unknown but may well be limited by their unsaturated bond, though this has not been confirmed. Bromination of the amine or imine structures is not expected to alter this assessment. Cup burner flame extinguishment results suggested that a wide number of these compounds would likely meet extinguishment performance needs.

The toxicity of bromofluoro nitrogen based compounds was expected to be higher than those of analogous non-brominated nitrogen-based compounds.

#### Bromofluoroamines

Amines offer significant promise, particularly as a result of research underway in Japan on the applications of fluoroalkyl amines as halon and CFC replacements.<sup>244</sup> Much of this research appears to be headed toward perfluoroalkyl amines, which are likely to have long atmospheric lifetimes. Nevertheless, the work provides synthetic routes and property evaluations. Incompletely halogenated compounds, such as  $N(CF_3)(CHF_2)(CF_2Br)$ , could provide short atmospheric lifetimes and chemical suppression.

Bromofluoro amines have a wide range of structures, as indicated by the examples in Table 7–43.

**Table 7–43. Bromofluoroamine Candidate Compounds.**

Chemical Formula		
$N(CF_3)_2CFHBr$	$N(CF_2H)(CF_2H)(CFHBr)$	$N(CFH_2)(CFH_2)(CF_2Br)$
$N(CF_3)(CF_2H)CF_2Br$	$N(CFH_2)(CF_3)(CFHBr)$	$N(CFH_2)(CF_2H)(CFHBr)$
$N(CF_3)(CF_2H)CFHBr$	$N(CF_3)(CF_2H)(CH_2Br)$	$N(CH_3)(CF_3)(CFHBr)$
$N(CF_2H)(CF_2H)CF_2Br$	$N(CH_3)(CF_3)(CF_2Br)$	$N(CH_2F)(CF_3)(CH_2Br)$
$N(CFH_2)(CF_3)CF_2Br$	$N(CH_3)(CF_2H)(CF_2Br)$	

There are synthetic pathways to many of these. For instance, N-bromobis(trifluoromethyl)amine  $(CF_3)_2NBr$  adds to the unsaturated compounds tetrafluoroethene  $CF_2=CF_2$ , trifluoroethene  $CHF=CF_2$ , 1,1-difluoroethene  $CH_2=CF_2$ , cis-1,2-difluoroethene  $CHF=CHF$ , ethene  $CH_2=CH_2$ , hexafluoropropene  $CF_2=CFCF_3$ , chlorotrifluoroethene  $CClF=CF_2$ , and 1,2-dichlorodifluoroethene  $CClF=CClF$  under mild conditions, to give the 1:1 adducts in high yield. The  $(CF_3)_2N$  attaches only to the  $CH_2$  group of 1,1-difluoroethene, whereas trifluoroethene gives the isomers  $(CF_3)_2NCHFCF_2Br$  (78 %) and  $(CF_3)_2NCF_2CHFBr$  (22 %). Hexafluorocyclobutene and octafluorobut-2-ene require more drastic conditions, and give the olefin dibromide and tetrakis(trifluoromethyl)hydrazine rather than addition of the N-bromo-compound.<sup>245</sup>

The boiling points of bromofluoroamines range only as low as 22 °C, as indicated in Table 7–44. In the last three rows, the flame extinguishment values for the two compounds and their mixture indicate that the value of the bromine atom and the thermal effects of the complex molecule were both realized. However, because of the N-Br linkage, the lowest boiling of these compounds may be unacceptably toxic.

**Table 7–44. Bromofluoroamine Boiling Points and Flame Suppression Results.**

Chemical Formula	$T_b$ (°C)	Cup Burner Flame Extinguishment (Volume %)
$(CF_3)_2N-Br$	22	---
$(CF_3)_2NCBrF_2$	40.6	---
$(CF_3)_2NCF_2CBrF_2$	59.5	---
$N(CF_3)_2(CHFCF_2Br)$	72	2.4
60 % $N(CF_3)_2(CHFCF_2Br)$ , 40 % $N(CF_3)_2(CF_2CFHBr)$	72	2.4
$N(CF_3)_2(CH_2CF_2Br)$	80	2.4

## Imines

Bromofluoroimines were until recently unstudied. This is in large measure due to a lack of availability of starting materials and facilities willing to attempt the chemistry. Synthetic approaches to some compounds have been developed and reported.<sup>246,247,248</sup>

The simplest of these, N-bromo-difluoromethanimine,  $CF_2=NBr$ , has an attractively low boiling point of 14 °C. However, it too has an N-Br linkage and may be unacceptably toxic.

## Nitriles

As seen in the prior section for  $CF_3CN$ , it is unlikely that nitriles would have an intrinsic chemical fire suppression capability. The addition of bromine or iodine should impart a chemical flame suppression contribution.

Bromodifluoroacetonitrile ( $CF_2BrCN$ ) was the sole brominated fluoroalkyl nitrile obtained for examination. Its boiling point is uniquely low, 3 °C, which is also the lowest boiling potentially tropodegradable brominated compound identified. Cup burner testing of  $CF_2BrCN$  indicated an upper bound flame extinguishment value of 4 volume %, consistent with the effect of the bromine atom and confirming the minor impact of the triple bond on flame extinguishment efficiency. There was an

unconfirmed report that this compound is toxic. Should the minimum in-flight temperature requirement be relaxed, toxicity and atmospheric lifetime determinations for this compound would be in order.

### 7.4.7 Fluorinated Ethers

#### Fire Suppression Properties

Hydrofluoropolyethers (HFPE) are being introduced into the market, and there is some evidence for relatively good fire suppression performance.<sup>249</sup> A large amount of research has been performed on fluoroethers as CFC replacements.

#### Atmospheric Lifetimes, ODP, and GWP

The presence of the ether linkage increases reactivity toward hydrogen abstraction, though fluorine substitution decreases the enhancement.<sup>250</sup> Hydrofluorocarbons show an approximately linear correlation between  $k_{OH}$  and the highest-occupied molecular orbital (HOMO) energies.<sup>251</sup> Rate constants, many estimated, reported for reaction of hydrofluoroethers (HFE) with  $\bullet OH$  are shown in Table 7-45. In the absence of a hydrogen atom, fluorinated ethers exhibit no reaction with  $\bullet OH$ , significantly increasing the atmospheric lifetime.

Very little work has been done on reactions of ethers with ozone, primarily due to their low reactivity. The rate constants for reaction with furan ( $2.42 \times 10^{-18}$  cm<sup>3</sup>/molec-s) and 2,5-dihydrofuran ( $1.61 \times 10^{-17}$  cm<sup>3</sup>/molec-s) are relatively large, owing to the presence of a double bond.<sup>238</sup> For saturated ethers, however, rate constants are expected to be extremely slow,  $\leq 10^{-20}$  cm<sup>3</sup>/molec-s, at room temperature.<sup>238</sup>

The energy of the HOMO has been used to estimate atmospheric lifetimes for a number of HFES.<sup>252</sup> A list of atmospheric lifetimes reported for halogenated ethers, most of which are estimated, Table 7-46.

The degradation products resulting from the alkoxy radicals formed after initial hydrogen atom abstraction from hydrofluoropolyethers (HFPE) have been studied.<sup>253</sup> Chlorine-atom initiated photooxidations of the HFPEs in air ( $HCF_2OCF_2OCF_2OCF_2H$ ,  $HCF_2OCF_2CF_2OCF_2H$  and  $HCF_2OCF_2OCF_2H$ ) produced  $COF_2$  as the only carbon-containing product, with observed average  $COF_2$  molar formation yields of 4.73, 3.77, and 2.82, respectively. In the early stages of the reaction, the  $COF_2$  molar formation yields are close to the number of carbon atoms in each parent HFPE. Based on current knowledge of degradation pathways of hydrofluorocarbons (HFC) and hydrochlorofluorocarbons (HCFC), it is expected that  $COF_2$  will also be produced with near-unit yield per carbon atom from the above HFPEs in the troposphere, where loss processes would be initiated primarily by reaction with  $\bullet OH$  radicals.

#### Toxicity

The toxicity of ethers is relatively low, and the ether linkage has a relatively low biological and chemical reactivity.

Table 7–45. Rate Constants for Hydrofluoroether Reactions with •OH.

Halocarbon No.	Formula	$k_{OH}$ , $\text{cm}^3/\text{molec}\cdot\text{s}$	Reference
HFE-CE225ea	-O-CF <sub>2</sub> CHF CF <sub>2</sub> -	<sup>a</sup> 2.51 x 10 <sup>-15</sup>	250
		<sup>a</sup> 2.4 x 10 <sup>-15</sup>	250
HFE-E	CH <sub>3</sub> -O-CF(CF <sub>3</sub> ) <sub>2</sub>	<sup>a,b</sup> 1.6 x 10 <sup>-14</sup>	254
HFE-E	CH <sub>3</sub> -O-CH(CF <sub>3</sub> ) <sub>2</sub>	<sup>a,b</sup> 2.2 x 10 <sup>-13</sup>	254
HFE-E	CHF <sub>2</sub> -O-CH(CF <sub>3</sub> ) <sub>2</sub>	<sup>a,b</sup> 1.8 x 10 <sup>-14</sup>	254
HFE-E	CH <sub>2</sub> F-O-CH(CF <sub>3</sub> ) <sub>2</sub>	7.3 x 10 <sup>-14</sup>	255
HFE-E125	CHF <sub>2</sub> -O-CF <sub>3</sub>	<sup>a</sup> 3.38 x 10 <sup>-15</sup>	250
		<sup>a</sup> 3.56 x 10 <sup>-15</sup>	250
		<sup>c</sup> 4.2 x 10 <sup>-16</sup>	249
HFE-E134	CHF <sub>2</sub> -O-CHF <sub>2</sub>	<sup>a</sup> 2.53 x 10 <sup>-14</sup>	2500
		<sup>a</sup> 2.41 x 10 <sup>-14</sup>	250
		<sup>a,b</sup> 3 x 10 <sup>-15</sup>	254
		<sup>c</sup> 2.3 x 10 <sup>-15</sup>	249
HFE-E143a	CH <sub>3</sub> -O-CF <sub>3</sub>	<sup>a</sup> 2.14 x 10 <sup>-14</sup>	250
HFE-E227ca1	CHF <sub>2</sub> -O-CF <sub>2</sub> CF <sub>3</sub>	<sup>b,d</sup> 1.95 x 10 <sup>-15</sup>	251
HFE-E227ca2	CHF <sub>2</sub> CF <sub>2</sub> -O-CF <sub>3</sub>	<sup>b,d</sup> 4.5 x 10 <sup>-15</sup>	251
HFE-E227ea1	CF <sub>3</sub> CHF-O-CF <sub>3</sub>	<sup>a,b</sup> 5.1 x 10 <sup>-15</sup>	254
		<sup>b,d</sup> 3.5 x 10 <sup>-15</sup>	251
HFE-E236ca1	CHF <sub>2</sub> -O-CF <sub>2</sub> CHF <sub>2</sub>	<sup>b,d</sup> 1.15 x 10 <sup>-14</sup>	251
HFE-E236ca12	CHF <sub>2</sub> -O-CF <sub>2</sub> -O-CHF <sub>2</sub>	1.3 x 10 <sup>-15</sup>	249
HFE-E236ea1	CHF <sub>2</sub> -O-CHF CF <sub>3</sub>	<sup>a,b</sup> 9.5 x 10 <sup>-15</sup>	254
		<sup>b,d</sup> 7 x 10 <sup>-15</sup>	251
HFE-E236ea2	CHF <sub>2</sub> CHF-O-CF <sub>3</sub>	<sup>b,d</sup> 3 x 10 <sup>-14</sup>	251
HFE-E236mf1	CF <sub>3</sub> CH <sub>2</sub> -O-CF <sub>3</sub>	<sup>a,b</sup> 1.5 x 10 <sup>-14</sup>	254
HFE-E245ca2	CHF <sub>2</sub> -O-CF <sub>2</sub> CH <sub>2</sub> F	<sup>b,d</sup> 7 x 10 <sup>-15</sup>	251
HFE-E245cb1	CH <sub>3</sub> -O-CF <sub>2</sub> CF <sub>3</sub>	<sup>c</sup> 1.07 x 10 <sup>-14</sup>	256
		<sup>a,b</sup> 4.6 x 10 <sup>-14</sup>	254
		<sup>b,d</sup> 5.5 x 10 <sup>-14</sup>	251
HFE-E245cb2	CH <sub>3</sub> CF <sub>2</sub> -O-CF <sub>3</sub>	<sup>b,d</sup> 1.5 x 10 <sup>-15</sup>	251

a 296 K

b Estimated from HOMO energy.

c 298 K

d Average

Table 7–46. Atmospheric Lifetimes for Fluorine-containing Ethers.

Halocarbon No.	Chemical Formula	Atmospheric Lifetime ( years)	Reference
FE-CE216	-O-CF <sub>2</sub> CF <sub>2</sub> CF <sub>2</sub> -	<sup>a</sup> >330	250
HCFE-E235ca2	CHF <sub>2</sub> -O-CF <sub>2</sub> CHClF	<sup>a</sup> 6	255
HCFE-E235da1	CHF <sub>2</sub> -O-CHClCF <sub>3</sub>	<sup>a</sup> 5	255
HFE-CE225ea	-O-CF <sub>2</sub> CHF CF <sub>2</sub> -	<sup>b,c</sup> 26	250
HFE-E	CHF <sub>2</sub> -O-CH(CF <sub>3</sub> ) <sub>2</sub>	<sup>a</sup> 3.8	257
HFE-E	CH <sub>3</sub> -O-CF(CF <sub>3</sub> ) <sub>2</sub>	4.9	257
		<sup>b,c</sup> 3.5	250

Halocarbon No.	Chemical Formula	Atmospheric Lifetime ( years)	Reference
		4.3	258
HFE-E	CH <sub>3</sub> -O-CH(CF <sub>3</sub> ) <sub>2</sub>	<sup>b,c</sup> 0.25	254
HFE-E	CH <sub>2</sub> F-O-CH(CF <sub>3</sub> ) <sub>2</sub>	<sup>a</sup> 1.4	255
		<sup>b,c</sup> 3.1	254
HFE-E	HF <sub>2</sub> CO(CF <sub>2</sub> O) <sub>n</sub> (CF <sub>2</sub> CF <sub>2</sub> O) <sub>m</sub> CF <sub>2</sub> H	<sup>e</sup> 8	f
HFE-E125	CHF <sub>2</sub> -O-CF <sub>3</sub>	82	259
		19	250
		<sup>b,c</sup> 156	249
HFE-E134	CHF <sub>2</sub> -O-CHF <sub>2</sub>	8	259
		<sup>b,c</sup> 2.6	250
		<sup>b,c</sup> 19	250
		<sup>b,c</sup> 35	249
HFE-E143a	CH <sub>3</sub> -O-CF <sub>3</sub>	<sup>b,c</sup> 3	250
HFE-E227ca1	CHF <sub>2</sub> -O-CF <sub>2</sub> CF <sub>3</sub>	<sup>b,e,f</sup> 16.05	252
		<sup>b,e,f</sup> 33	251
HFE-E236ca1	CHF <sub>2</sub> -O-CF <sub>2</sub> CHF <sub>2</sub>	<sup>b,e,f</sup> 5.95	252
		<sup>b,e,f</sup> 8.5	251
HFE-E236cb1	CH <sub>2</sub> F-O-CF <sub>2</sub> CF <sub>3</sub>	<sup>b,e,f</sup> 5.9	252
HFE-E227ca2	CHF <sub>2</sub> CF <sub>2</sub> -O-CF <sub>3</sub>	<sup>b,e,f</sup> 12.1	252
		<sup>b,e,f</sup> 17.5	251
HFE-E227ea1	CF <sub>3</sub> CHF-O-CF <sub>3</sub>	<sup>b,c</sup> 11	250
		20	258
		<sup>b,e,f</sup> 23.5	251
		<sup>b,e,f</sup> 14.9	252
HFE-E236cb2	CH <sub>2</sub> FCF <sub>2</sub> -O-CF <sub>3</sub>	<sup>b,e,f</sup> 6.7	252
HFE-E236ea1	CHF <sub>2</sub> -O-CHF <sub>2</sub> CF <sub>3</sub>	<sup>a</sup> 4.04	257
		<sup>b,e,f</sup> 6.5	251
		<sup>b,e,f</sup> 7.5	252
HFE-E236ea2	CHF <sub>2</sub> CHF-O-CF <sub>3</sub>	<sup>b,e,f</sup> 5.1	252
		<sup>b,e,f</sup> 4.55	251
HFE-E236mf1	CF <sub>3</sub> CH <sub>2</sub> -O-CF <sub>3</sub>	<sup>b,c</sup> 3.7	250
		<sup>b,e,f</sup> 4.75	252
HFE-E245ca1	CH <sub>2</sub> F-O-CF <sub>2</sub> CHF <sub>2</sub>	<sup>b,e,f</sup> 3.5	252
HFE-E245ca2	CHF <sub>2</sub> -O-CF <sub>2</sub> CH <sub>2</sub> F	<sup>a</sup> 2.18	257
		<sup>b,e,f</sup> 6.5	251
		<sup>b,e,f</sup> 4.4	252
HFE-E245cb1	CH <sub>3</sub> -O-CF <sub>2</sub> CF <sub>3</sub>	6.5	256
		<sup>b,c</sup> 1.2	250
		<sup>b,e,f</sup> 0.85	251
		<sup>b,e,f</sup> 1.4	252
HFE-E245ea1	CHF <sub>2</sub> -O-CHF <sub>2</sub> CHF <sub>2</sub>	<sup>b,e,f</sup> 2.75	252
HFE-E245eb1	CH <sub>2</sub> F-O-CHF <sub>2</sub> CF <sub>3</sub>	<sup>b,e,f</sup> 2.2	252
HFE-E245eb2	CH <sub>2</sub> FCHF-O-CF <sub>3</sub>	<sup>b,e,f</sup> 3.35	252
HFE-E254ea1	CH <sub>2</sub> F-O-CHF <sub>2</sub> CHF <sub>2</sub>	<sup>b,e,f</sup> 1.3	252

Halocarbon No.	Chemical Formula	Atmospheric Lifetime ( years)	Reference
HFE-E254ea2	CH <sub>2</sub> FCHF-O-CHF <sub>2</sub>	<sup>b,e,f</sup> 1.75	252
HFE-E254eb1	CH <sub>3</sub> -O-CHF <sub>2</sub> CF <sub>3</sub>	<sup>b,f</sup> 0.5	252
HFE-E254ca1	CH <sub>2</sub> F-O-CF <sub>2</sub> CH <sub>2</sub> F	<sup>b,e,f</sup> 3.1	252
HFE-E245cb2	CH <sub>3</sub> CF <sub>2</sub> -O-CF <sub>3</sub>	<sup>b,e,f</sup> 11.2	252
		<sup>b,e,f</sup> 27.5	251
HFE-E245fa1	CHF <sub>2</sub> -O-CH <sub>2</sub> CF <sub>3</sub>	<sup>b,c</sup> 5.2	250
		<sup>b,c</sup> 1.7	251
		<sup>b,e,f</sup> 1.15	251
		<sup>a</sup> 4.7	257
		<sup>b,f</sup> 1.9	252
HFE-E245fa2	CF <sub>3</sub> -O-CH <sub>2</sub> CHF <sub>2</sub>	<sup>c</sup> 2.2	251
		<sup>b,e,f</sup> 1.45	251
		<sup>b,e,f</sup> 2.65	252
HFE-E254cb1	CH <sub>3</sub> -O-CF <sub>2</sub> CHF <sub>2</sub>	<sup>a</sup> 0.47	257
		<sup>b,c</sup> 0.85	251
		<sup>b,e,f</sup> 0.35	251
		<sup>b,e,f</sup> 0.95	252
HFE-E254cb2	CH <sub>3</sub> CF <sub>2</sub> -O-CHF <sub>2</sub>	<sup>b,e,f</sup> 3.85	252
		<sup>b,e,f</sup> 6	251
HFE-E254eb2	CH <sub>3</sub> CHF-O-CF <sub>3</sub>	<sup>b,e,f</sup> 2.45	252
HFE-E254fa1	CHF <sub>2</sub> -O-CH <sub>2</sub> CHF <sub>2</sub>	<sup>b,e,f</sup> 1.05	252
		<sup>b,e,f</sup> 0.45	251
HFE-E356mcf2	CF <sub>3</sub> CH <sub>2</sub> -O-CF <sub>2</sub> CH <sub>2</sub> F	<sup>a</sup> 1.8	257
HFE-E356mec1	CH <sub>3</sub> -O-CF <sub>2</sub> CHF <sub>2</sub> CF <sub>3</sub>	<sup>b,c</sup> 0.94	251
HFE-E356mf2	CF <sub>3</sub> CH <sub>2</sub> -O-CH <sub>2</sub> CF <sub>3</sub>	<sup>a</sup> 0.5	257
HFE-E356pcc1	CH <sub>3</sub> -O-CF <sub>2</sub> CF <sub>2</sub> CHF <sub>2</sub>	<sup>b,c</sup> 0.93	251
HFE-E356pfc1	CHF <sub>2</sub> -O-CH <sub>2</sub> CF <sub>2</sub> CHF <sub>2</sub>	<sup>b,c</sup> 1.3	251
HFE-E356pfc2	CHF <sub>2</sub> CH <sub>2</sub> -O-CF <sub>2</sub> CHF <sub>2</sub>	<sup>b,c</sup> 2	251
HFE-E365mc1	CH <sub>3</sub> -O-CH <sub>2</sub> CF <sub>2</sub> CF <sub>3</sub>	<sup>b,c</sup> 0.11	251
HFE-E365sf2	CH <sub>3</sub> CH <sub>2</sub> -O-CF <sub>2</sub> CF <sub>3</sub>	<sup>a</sup> 0.3	257
HFE-E374pcf2	CH <sub>3</sub> CH <sub>2</sub> -O-CF <sub>2</sub> CHF <sub>2</sub>	<sup>b,c</sup> 0.43	251
HFE-E4-3-10pccc124	CHF <sub>2</sub> -O-CF <sub>2</sub> -O-CF <sub>2</sub> CF <sub>2</sub> -O-CHF <sub>2</sub>	<sup>b,c</sup> 7	249
HFE-E254fb1	CH <sub>2</sub> F-O-CH <sub>2</sub> CF <sub>3</sub>	<sup>b,f</sup> 0.5	252
HFE-E254fb2	CH <sub>2</sub> FCH <sub>2</sub> -O-CF <sub>3</sub>	<sup>b,e,f</sup> 1.6	252
		<sup>b,e,f</sup> 0.7	251
HFE-E263fb1	CH <sub>3</sub> -O-CH <sub>2</sub> CF <sub>3</sub>	<sup>b,c</sup> 0.1	251
		<sup>b,f</sup> <0.1	251
		<sup>b,c</sup> 0.1	251
HFE-E263fb2	CH <sub>3</sub> CH <sub>2</sub> -O-CF <sub>3</sub>	<sup>b,f</sup> 0.3	251
HFE-E329p2	CHF <sub>2</sub> CF <sub>2</sub> -O-CF <sub>2</sub> CF <sub>3</sub>	<sup>b,c</sup> 6.8	251
HFE-E338mf2	CF <sub>3</sub> CH <sub>2</sub> -O-CF <sub>2</sub> CF <sub>3</sub>	<sup>b,c</sup> 4.3	251
HFE-E347pf1	CHF <sub>2</sub> -O-CH <sub>2</sub> CF <sub>2</sub> CF <sub>3</sub>	<sup>a</sup> 1.62	257
HFE-E347pf2	CF <sub>3</sub> CF <sub>2</sub> -O-CH <sub>2</sub> CHF <sub>2</sub>	<sup>b,c</sup> 2.8	251
HFE-E347s1	CH <sub>3</sub> -O-CF <sub>2</sub> CF <sub>2</sub> CF <sub>3</sub>	6.4	241

Halocarbon No.	Chemical Formula	Atmospheric Lifetime ( years)	Reference
		<sup>b,c</sup> 1.3	251
		5.6	258
HFE-E449s1	CF <sub>3</sub> CF <sub>2</sub> CF <sub>2</sub> CF <sub>2</sub> -O-CH <sub>3</sub>	4.1	260
HFE-E569sf2	CF <sub>3</sub> CF <sub>2</sub> CF <sub>2</sub> CF <sub>2</sub> -O-CH <sub>2</sub> CH <sub>3</sub>	1.2	261

a Estimated

b For reaction with •OH only.

c Non-rigorous calculation.

d See Reference

e Average

f Estimated from HOMO energy.

## Extinguishment Testing

1-Methoxynonafluorobutane, HFE-7100, was obtained from 3M Company. Hydrofluoropolyether was obtained as an experimental product from Ausimont S.p.A. in Milano, Italy. As expected and indicated in Table 7–47, neither of these compounds exhibited extinguishment performance suggesting a chemical extinguishment mechanism. The flame extinguishing results are comparable to HFCs.

**Table 7–47. Fluoroether Cup Burner Extinguishment Data.**

Compound Name	Formula	$T_b$ (°C)	Cup Burner Flame Extinguishment (Volume %)
1-Methoxynonafluorobutane	CF <sub>3</sub> CF <sub>2</sub> CF <sub>2</sub> CF <sub>2</sub> -O-CH <sub>3</sub>	60	6.1
Hydrofluoropolyether	HF <sub>2</sub> CO(CF <sub>2</sub> O) <sub>n</sub> (CF <sub>2</sub> CF <sub>2</sub> O) <sub>m</sub> CF <sub>2</sub> H	100	5.1

## Assessment Summary

There was little reason to pursue hydrofluoroethers or perfluoroethers further. The fire suppression efficiencies were comparable to the HFCs, and the larger molecular weights led to higher boiling points. There was no indication that the ether linkage provided any significant contribution to rainout; the polarity is too small. Perfluorinated saturated ethers were expected to have atmospheric lifetimes similar to those of the perfluorinated alkanes, a property that generally made their use as halon replacements questionable. The atmospheric lifetimes for partially fluorinated ethers were much shorter. The low reactivity of the ether linkage causes ethers to be relatively biologically benign, though there are many exceptions; anesthesia is a problem in some cases.

### 7.4.8 Bromofluoroethers

#### Atmospheric Lifetime, ODP, and GWP

The atmospheric lifetimes of bromofluoroethers are expected to be similar to those of the base fluoroether. The only bromofluoroether whose atmospheric lifetime has been studied is Roflurane, CH<sub>3</sub>-O-CF<sub>2</sub>CFBrH ( $T_b$  = 89 °C), a compound once employed as an anesthesia agent.<sup>262</sup> The reported estimate of atmospheric lifetime was 14 days.

## Toxicity Assessment Summary

Toxicity data for the bromofluoroethers are scarce. However, Roflurane has been shown to have a very low toxicity.<sup>263</sup> This is a hopeful sign that other members of the bromofluoroether family would be of acceptable toxicity.

## Volatility and Availability

The boiling point screening criterion of 20 °C severely limited the number of bromofluoroethers considered. Bromofluoroethers with one or both of the alkyl groups having two or more carbons and with the bromine atom on a carbon atom not adjacent to the ether linkage typically have boiling points above 60 °C. Thus attention focused on the halogenated dimethyl ethers and a limited number of methyl ethyl ethers. Having at least a one-to-one ratio of fluorine atoms to hydrogen atoms ensured non-flammability.

With variation in site of bromination and fluorination, a large number of structural isomers are possible even with this very limited range of ethers. The number of compounds was reduced through a selection process which focused on the most symmetrically substituted compounds (lower expected boiling point) and those compounds expected to be the least polar based on calculated octanol water partition coefficients. This latter criterion was expected to help select the least toxic compounds (Chapter 6).

Synthesis of the brominated dimethyl ethers was first presented by Adcock and co-workers in 1991.<sup>23</sup> Further clarification and elaboration from Prof. Adcock enabled the successful synthesis of bromodifluoromethyl difluoromethyl ether,  $\text{CF}_2\text{Br-O-CF}_2\text{H}$ .<sup>264</sup> This information indicated that elemental bromine did not substitute in these ethers in good yields without decomposition, and that the more reactive interhalogen compound, bromine chloride, should be employed. In this method, equimolar amounts of chlorine and bromine formed bromine chloride during short pre-irradiation of the halogen mixture prior to introduction of the fluorinated ether. While a small excess of bromine suppressed virtually any chlorination, too large an excess of bromine significantly slowed the rate of reaction. Stepwise bromination of the dihydriyl fluoroether,  $\text{HCF}_2\text{-O-CF}_2\text{H}$  was observed under these conditions. Additional synthetic information provided valuable guidance and enabled the successful synthesis of adequate amounts of  $\text{CF}_2\text{Br-O-CF}_2\text{H}$  for very limited extinguishment testing. That guidance included:

- Employ a high pressure Hg lamp. The high pressure lamp gave a pressure broadened spectrum, unlike the older medium pressure or low pressure lamps, and therefore provided an increased rate of reaction. Medium and low pressure lamps did not work in this reaction.
- Eliminate all  $\text{O}_2$  and  $\text{H}_2\text{O}$  from the bromine and chlorine reactants and the bisdifluoromethyl ether. Remove all air ( $\text{O}_2$  and  $\text{H}_2\text{O}$ ) from all glassware and photolysis equipment. These were extremely important steps, and failure of the reaction resulted when they were not followed.
- Adjust the  $\text{Br}_2/\text{Cl}_2$  ratio such that  $\text{Br}_2$  is in very slight excess to  $\text{Cl}_2$ . The amount of  $\text{Br}_2$  employed was approximately stoichiometric to the fluoroether being brominated. This method was reported to require only a couple of hours of photolysis. In the reaction, chlorine abstracted hydrogen and bromine, then added to form the product. When too high a  $\text{Br}_2$ :halocarbon ratio was employed, the reaction slowed down due to light absorption. When too much chlorine was present, chlorination of the ether occurred instead of the desired bromination.

The reaction is tricky, and several attempts were needed to optimize the synthetic conditions. With recycling of unreacted reactants, a high yield may well be achieved.

### Flame Extinguishment

The contribution from the bromine atom was expected to dominate suppression of flame chemistry, with some thermal contributions to flame suppression from the more heavily fluorinated alkyl groups.

Prior to the NGP, only two measurements of flame suppression by the higher boiling hydrobromofluoroethers (HBFES) had been carried out.  $\text{CH}_2=\text{CBr}(\text{OCF}_3)\text{CF}_2\text{CF}_3$ , which is unsaturated, had a cup burner extinguishment concentration of 3.8 volume %.<sup>240</sup> Roflurane,  $\text{CH}_3\text{-O-CF}_2\text{CHBrF}$ , was estimated to have a heptane cup burner volume fraction of 4.2 % and a short atmospheric lifetime.<sup>240</sup> Table 7–48 summarizes the NGP cup burner test data for five of the lowest molecular weight compounds in this family. All confirmed the flame extinguishment expectation.

**Table 7–48. Bromofluoroether Cup Burner Testing Summary.**

Compound Name, Formula	Chemical Formula	T <sub>b</sub> (°C)	Cup Burner Extinguishment (volume %)
1-Bromo-1,2,2-trifluoroethyl trifluoromethyl ether	$\text{CF}_3\text{-O-CFBrCF}_2\text{H}$	42	< <sup>c</sup> 4.5
2-Bromo-1,1,2-trifluoroethyl trifluoromethyl ether	$\text{CF}_3\text{-O-CHF}_2\text{CF}_2\text{Br}$	37	< 4.5
Bromomethyl trifluoromethyl ether	$\text{CH}_2\text{Br-O-CF}_3$	39	3.2
Bromodifluoromethyl difluoromethyl ether	$\text{CF}_2\text{Br-O-CF}_2\text{H}^{\text{a}}$	20-24 (est.)	3.7 (2.4) <sup>b</sup>
Bromomethyl difluoromethyl ether	$\text{CH}_2\text{Br-O-CF}_2\text{H}$	70	3.6

a Impure sample 65 % bromodifluoromethyl difluoromethyl ether, 25 % bisdifluoromethyl ether, 10 % other ethers

b Estimated extinguishment value based on a 65 % purity

c < signify upper limit extinguishment value.

The cup burner flame extinguishment performance of the sample of 65 volume % bromodifluoromethyl difluoromethyl ether was initially calculated as if the sample were 100 % pure. When the observed 3.7 volume % extinguishment value was corrected for the actual 65 % purity of the sample, an extinguishment value of 2.4 volume % was obtained. It was unlikely that the major impurity in this sample (bisdifluoromethyl ether) contributed significantly to extinguishment at its effective low concentration of 0.9 volume %. The remaining impurities in this sample included predominantly chlorinated analogues to the desired product.

Substituting additional fluorine for a hydrogen on  $\text{CH}_2\text{Br-O-CF}_3$  might yield a compound (probably a mixture of two structural isomers) with a boiling point in the vicinity of 20 °C to 30 °C. This might be worthwhile if the low temperature performance requirement were eased (Chapter 2). Bromofluoromethyl trifluoromethyl ether ( $\text{CFHBr-O-CF}_3$ ) was also of interest. However, the fluoroether starting material ( $\text{CFH}_2\text{-O-CF}_3$ ) was not available. Other possible low boiling chemicals in this family are  $\text{CF}_2\text{Br-O-CH}_2\text{F}$ ,  $\text{CHFBr-O-CHF}_2$ ,  $\text{CF}_2\text{Br-O-CF}_3$ , and  $\text{CF}_2\text{Br-O-CHF}_2$ .

## Assessment Summary

There is some potential for the bromofluoroethers as total flooding fire suppressants. While the lowest boiling points are not low enough for effective dispersion under the current operational requirement, there are some structural isomers with boiling points as low as 20 °C to 24 °C. There is reason to expect that some of these compounds might have relatively low toxicity. Limited atmospheric lifetime estimates suggest the possibility of acceptable performance.

### 7.4.9 Bromofluorooxiranes

The propene oxides (or oxiranes) were expected to be stable, low boiling compounds. As carriers of bromine, there was potential for them to exhibit acceptable flame extinguishment properties as well. Testing indicated that the non-brominated perfluoropropene oxide has a cup burner value of 9.6 volume %.<sup>265</sup> The toxicities of these compounds are unknown. Since they may be readily attacked by OH radicals, their atmospheric lifetimes may well be short, but this is unconfirmed.

There are three possible bromine locations in the pentafluorinated propene oxide molecule. Further isomerism due to the formation of one or more optically isomeric carbons results in further isomeric complexity. This complexity yields a total of eight unique compounds, Figure 7–12.

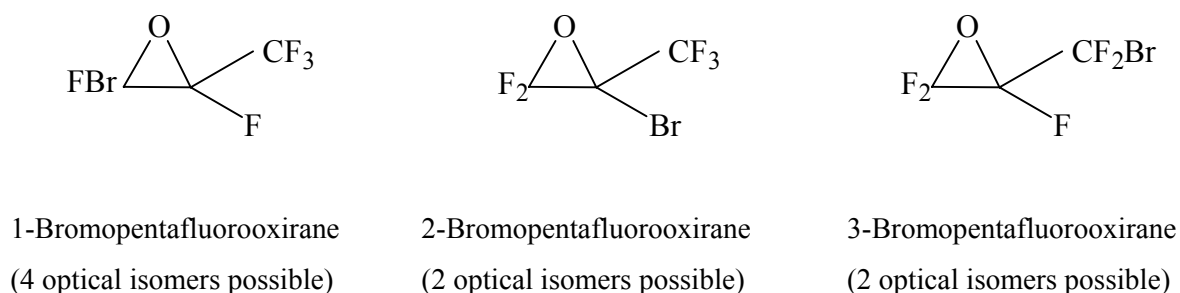


**Figure 7–12. Structural and Optical Isomerism of Bromopentafluoropropene Oxide.**

Synthesis of 3-bromopentafluorooxirane has been reported.<sup>266</sup> A brief survey of the literature also revealed that 30 % hydrogen peroxide in a basic medium had been used successfully in the epoxidation of fluorinated alkenes such as hexafluoropropene.<sup>267</sup> These compounds might also potentially be synthesized in a single step from existing bromofluoropropenes by a partial oxidation of the alkene bond.  $\text{CF}_2(\text{O})\text{CBrCF}_3$  (2-bromo-1,2-perfluoropropene oxide) was successfully sourced and its flame extinguishment properties determined, as indicated in Table 7–49. Since the cup burner results was higher than generally expected of a brominated compound and since the boiling point was marginal, NGP investigation of the bromofluoropropene oxides was halted.

**Table 7–49. Bromofluoropropene Oxide Cup Burner Testing Summary.**

Compound Name	T <sub>b</sub> (°C)	Cup Burner Extinguishment (volume %)
2-Bromopentafluorooxirane	20 (est.)	4.9
1-Bromopentafluorooxirane	Unknown	Sourced, not acquired
3-Bromopentafluorooxirane	Unknown	Sourced, not acquired

#### 7.4.10 Bromofluoro / Fluorinated Aldehydes and Ketones

##### Fluorinated Aldehydes and Ketones

An analysis of the potential suitability of fluorinated aldehydes and ketones as halon replacements concluded that further study was warranted.<sup>39</sup> This determination resulted in the “Highly Efficient Thermal Agents” research briefly described earlier in section 7.4.1 of this chapter.<sup>147</sup>

The suitability of fluoroketones was also demonstrated during the course of the NGP by 3M Corporation with their successful commercialization of the perfluoroketone, dodecafluoro-2-methylpentan-3-one, CF<sub>3</sub>CF<sub>2</sub>C(O)CF(CF<sub>3</sub>)<sub>2</sub>, FK-5-1-12. This compound has a cup burner heptane extinguishment of 4.5 volume %, <sup>268</sup> but a boiling point (49 °C) well above that required for efficient dispersion under in-flight conditions. Its short atmospheric lifetime yields a lower GWP value than those of the HFCs. Other than the reported data for FK-5-1-12, fire suppression data are almost completely unknown for fluorinated carbonyl compounds.

##### Bromofluoro Aldehydes and Ketones

2-Bromo-2,2-difluoroethanal, CBrF<sub>2</sub>CHO, was the sole representative compound that had been studied. The cup burner value for this compound was reported to be 4.4 volume %, and the boiling point was about 40 °C.<sup>269</sup> As all other examples of bromofluoro aldehydes would likely have higher boiling points, further consideration of this family was not pursued.

#### 7.4.11 Bromofluoro Alcohols

Initial evaluations of bromofluoro alcohols were conducted by the Advanced Agent Working Group, which found that chemical instability of this family was problematic. NGP research identified no additional compounds worthy of study, as the boiling points of the brominated fluoroalcohols were higher than required for in-flight fire suppression (Table 7–50).

It appeared that extinguishment might not be obtainable for alcohols in which the hydrogen content is significant. Thus, better flame extinguishment might be found for compounds such as CBrF<sub>2</sub>CF<sub>2</sub>OH and CBr<sub>2</sub>FCF<sub>2</sub>OH. While the alcohols have the advantage of being highly susceptible to “rain out” and would therefore have a lower atmospheric lifetime, they also have boiling points well above those required for aircraft applications and were not pursued further under the NGP.

**Table 7–50. Bromofluoro Alcohol Boiling Points.**

Compound Formula	$T_b$ (°C)	Cup Burner Flame Extinguishment Value (volume %)	Reference
$\text{CBrF}_2\text{CH}_2\text{OH}$	67 (2 kPa)	did not always extinguish	270
$\text{CF}_3\text{CHOHCH}_2\text{Br}$	124	4.1	271
$\text{CHBrFCH(OH)CF}_3$	124		
$\text{CHFBrCF}_2\text{CH}_2\text{OH}$	149		
$\text{CF}_3\text{CBrFCH}_2\text{OH}$	97		
$\text{CF}_3\text{CHBrCH}_2\text{OH}$	108		
$\text{CF}_3\text{CH(OH)CHBrCH}_3$	66		
$\text{CF}_3\text{CBrFCH(CH}_3\text{)OH}$	112		
$\text{CF}_3\text{CBrFC(CH}_3\text{)}_2\text{OH}$	128		
$\text{CF}_3\text{CH(OH)CHBrCH}_2\text{CH}_3$	94		
$\text{CF}_3\text{CH(OH)CBr(CH}_3\text{)CH}_3$	68		
$\text{CF}_3\text{CBrClC(CH}_3\text{)}_2\text{OH}$	137		
$\text{CF}_3\text{CBr}_2\text{C(CH}_3\text{)}_2\text{OH}$	152		
$\text{CF}_3\text{CHOHCHBr}_2$	155-158	4.78	270
$\text{CBr}_2\text{FCH}_2\text{OH}$	85 (2.7 kPa)	4.56, appeared flammable	270

## 7.4.12 Iodinated Hydrocarbons

### Iodofluoroalkanes

Nearly all the attention in this family has been directed at  $\text{CF}_3\text{I}$ .  $\text{CF}_3\text{I}$  has a boiling point that is uniquely low (Table 7–51), perhaps low enough for consideration for in-flight applications (although, see Chapter 8). In addition, the iodine atom imparts cup burner flame extinguishment effectiveness to these compounds that is comparable to the bromine atom in halon 1301. When released in the lower atmosphere, the fluorinated iodoalkanes all degrade by photolysis of the carbon–iodine bond and are expected to have short atmospheric lifetimes.<sup>19</sup> These factors led to expectation that  $\text{CF}_3\text{I}$  would be a near drop-in replacement for  $\text{CF}_3\text{Br}$ , which has a cup burner value of 2.9 volume %.

However, experiments revealed unsatisfactory low temperature distribution of  $\text{CF}_3\text{I}$  (Chapter 8 and Reference 272) and raised concerns over its materials compatibility and chemical stability.<sup>273,274,275,276,277</sup> In addition, this compound's LOAEL was measured to be 0.5 volume %, <sup>278,279</sup> resulting in it being deemed unacceptable for use in normally occupied areas.

There have been studies that indicate a reduced cardiac sensitization hazard from an inadvertent release of  $\text{CF}_3\text{I}$ . An early report of experimental discharge modeling of the potential for  $\text{CF}_3\text{I}$  exposure attempted to quantify the potential for aircraft service ground crew exposure to  $\text{CF}_3\text{I}$  during inadvertent agent discharge in one of the engine nacelles during maintenance operations, or pre-take-off inspection.<sup>280</sup> Employing differential IR imaging and sampling of the  $\text{CF}_3\text{I}$  plume, the study's authors provided evidence of a  $\text{CF}_3\text{I}$  plume at the LOAEL concentration and suggested a need for further investigation. Extensive efforts to model human inhalation exposure effects employed a physiologically-based

pharmacokinetic (PBPK)<sup>281</sup> approach, described in Chapter 6, that yielded a better understanding of the relationship between exposure concentration and the resulting blood levels following exposure to CF<sub>3</sub>I.

**Table 7–51. Iodoalkane Boiling Points.**

Chemical Formula	$T_b$ (°C)	Cup Burner Flame Extinguishment Value <sup>265</sup> (volume %)
CF <sub>3</sub> I	-22.5	3.0
CHF <sub>2</sub> I	21.6	
CH <sub>2</sub> FI	53.5	
CH <sub>3</sub> I	42.5	
C <sub>2</sub> F <sub>5</sub> I	12	2.1
CHF <sub>2</sub> CF <sub>2</sub> I	39.4	
C <sub>3</sub> F <sub>7</sub> I	41.2	3.0
C <sub>4</sub> F <sub>9</sub> I		2.8
C <sub>6</sub> F <sub>13</sub> I		2.5
C <sub>4</sub> F <sub>8</sub> I <sub>2</sub>		2.1

One potential application of CF<sub>3</sub>I was for inerting aircraft fuel tanks, particularly in the F-16, against in-flight fires and explosions. Considerable controversy arose over this use. As a result, at the request of the Under Secretary of Defense (Acquisition, Technology and Logistics), the Director of Defense Research and Engineering convened an Independent Review Panel (IRP) to assess the four critical technical issues and comment on how they might affect implementation of CF<sub>3</sub>I as a viable substitute for halon 1301 in the F-16 inerting application.<sup>282</sup> This assessment of the suitability of CF<sub>3</sub>I as a replacement for halon 1301 as an inerting agent in F-16 wing fuel tanks concluded, based on an analysis of materials compatibility, low temperature performance, human toxicology, and atmospheric chemistry, that:

- CF<sub>3</sub>I is more chemically reactive than halon 1301. After further qualification testing, it may be possible to specify materials that could be used in service with CF<sub>3</sub>I.
- CF<sub>3</sub>I is inadequate as a replacement for halon 1301 in the existing F-16 system due to its higher boiling point and resultant reduced delivery pressure at low temperatures.
- CF<sub>3</sub>I is more toxic than halon 1301. It would be unwise to replace a chemical with a more toxic one. More rigorous toxicity testing of CF<sub>3</sub>I would provide a more quantitative estimate of its toxicity in realistic exposure scenarios.
- Ozone depletion from F-16 application of CF<sub>3</sub>I could be as small as 1/8 that of halon 1301 (at lower altitudes) or as large as 1 2/3 times as damaging as halon 1301 (at higher altitudes). In any case, CF<sub>3</sub>I use onboard an F-16 would be a Class I substance if significant amounts are released above 6,000 m (20,000 ft), and the U.S. Clean Air Act bans use of Class I substances.

This last finding was based on (a) the historical altitudes at which halon 1301 was emitted to the atmosphere following deployment for inerting fuel tanks and (b) the ozone depleting effectiveness of CF<sub>3</sub>I. The latter is very sensitive to the altitude of release, since this compound degrades efficiently at low altitudes, but is even more effective than halon 1301 at destroying ozone should it reach the stratosphere following a high altitude release. For fuel tank inerting, the outcome of a detailed analysis was not favorable to the implementation of CF<sub>3</sub>I as a halon 1301 replacement.

Since the NGP was responsible for identifying potential candidates for replacing halon 1301 for fire suppression in aircraft engine nacelles, it was important to know whether the different release altitudes for this application might lead to different ozone depletion results. Wuebbles and co-workers at the University of Illinois used a two-dimensional atmospheric model (the 2004 version of the UIUC 2D Chemical Transport Model, CTM) to calculate the effect of CF<sub>3</sub>I on stratospheric ozone for this application. For comparison, they re-visited the use of this agent for fuel tank inerting.<sup>283,284</sup>

The 2004 version of the CTM determined the atmospheric distribution of 89 chemically active atmospheric trace constituents with 70 photolytic reactions, 189 thermal reactions, and heterogeneous reactions. Reaction-rate constants and photochemical data in the model were primarily based on the recommendations compiled by the NASA Panel for Data Evaluation.<sup>285,286</sup> The model domain extended from pole to pole and from the ground to 84 km in altitude. A grid box was 5 degrees of latitude and 1.5 km in log-pressure altitude.

The altitude profile of releases of halon 1301 for engine nacelle (and auxiliary power unit) fire suppression was from Bein's compilation of historic data from the military Safety Centers (Chapter 2 and Reference 287). The data encompass over 6,000 incidents from 1980 through 2002. Table 7-51 shows the distribution as inserted into the CTM.

**Table 7-52. Compilation of Historic Firefighting Emissions of CF<sub>3</sub>Br.**

Flight Height (km)	Model Layer	Emission (kg)	Percent of Total Emissions
12 to 13.5	layer 9	8.7	0.57
10.5 to 12	layer 8	13.3	0.87
9 to 10.5	layer 7	77.9	5.07
7.5 to 9	layer 6	22.4	1.46
6 to 7.5	layer 5	142.3	9.26
4.5 to 6	layer 4	45.0	2.93
3 to 4.5	layer 3	61.5	4.00
1.5 to 3	layer 2	115.6	7.52
0 to 1.5	layer 1	1050.0	68.3

Wuebbles and co-workers ran three cases for the latitudes at which the emissions occurred. For 0 °N to 10 °N, the ODP value was 0.084; for 30 °N to 40 °N, the ODP value was 0.028; and for 55 °N to 65 °N, the ODP value was 0.036. All were well below the control value of 0.2 in the U.S. Clean Air Act, but near the cautionary value of 0.05 used by the U.S. Environmental Protection Agency (EPA). In general, since most of CF<sub>3</sub>I emissions in this estimate occurred at lower altitudes, they did not tend to deplete atmospheric ozone severely. Therefore, provided this CF<sub>3</sub>I emission profile continues to be representative of the actual release characteristics, CF<sub>3</sub>I released from aircraft for fighting engine nacelle fires should have a low impact on the ozone layer relative to that of CF<sub>3</sub>Br.

In revisiting the effect of replacing CF<sub>3</sub>Br with CF<sub>3</sub>I for fuel tank inerting, Wuebbles and co-workers used an updated (2004) version of the CTM. They also used two different altitude distributions of suppressant release, thus performing a sensitivity analysis. The first distribution was that used in the original calculations described in Reference 282. The second was an alternative distribution from Van Horn et al.<sup>288</sup> The two are shown graphically in Figure 7-13; the calculated ODP values are shown in Table 7-53.

In the original estimate, the resulting ODPs were in the range of 0.07 to 0.25, mostly below the control value of 0.2 in the U.S. Clean Air Act, but above the EPA value of concern of 0.05. With respect to the Van Horn estimate, all the resulting ODPs were no more than 0.05. Given the fact that aircraft were typically operated at mid-latitudes (the two southern cases calculated here) in the Northern Hemisphere, CF<sub>3</sub>I emissions following the Van Horn estimate would not have a substantial impact on ozone.

The model calculations show that the altitude where CF<sub>3</sub>I is released from aircraft is a dominant factor in its ozone depletion effects. However, using either distribution, the aircraft-released CF<sub>3</sub>I would have much lower impact on the ozone layer than CF<sub>3</sub>Br.

These computation estimates are subject to specific uncertainties. Iodine chemistry is not as well understood as that for chlorine and bromine. Heterogeneous reactions between reactive iodine and other active atmospheric reactants on the surface of aerosols could accelerate the ozone destruction rate of iodine catalytic cycles, which could result in much larger ODP values for CF<sub>3</sub>I. Extensive studies using a three-dimensional global transport model of the troposphere and stratosphere would enhance confidence in the results from this two-dimensional model.

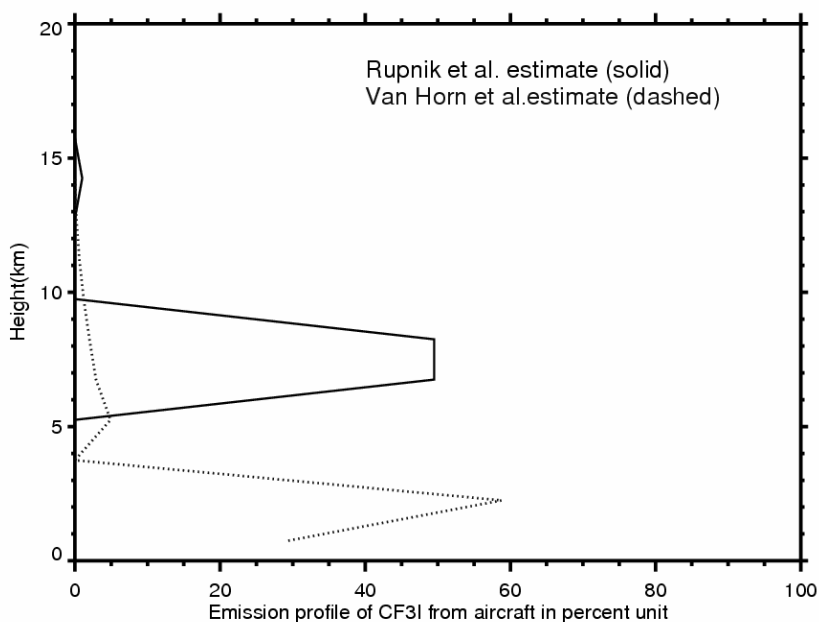


**Figure 7-13. Vertical Profiles of CF<sub>3</sub>I Emissions for Fuel Tank Inerting in Military Aircraft.** Percent unit is mass-weighted.

**Table 7-53. Estimated Ozone Depletion Effects of CF<sub>3</sub>I for Two Emission Profiles.**

Latitude Range	ODP	
	Reference 282 (Rupnik et al.)	Reference 288 (Van Horn et al.)
0 °N to 10 °N	0.254	0.050
30 °N to 40 °N	0.084	0.019
55°N to 65 °N	0.071	0.025

In summary, technical issues with CF<sub>3</sub>I remain, as far as aircraft use is concerned. While the ODP contribution is much lower than that of halon 1301, it is still close to being a Class 1 substance, depending

on the specific altitudes at which it is deployed. The industrial hygiene issues from maintenance discharge persist. Dispersion is questionable in cases of low temperature nacelle and dry bay use.

### Iodofluoroalkenes

A prior estimate of the suitability of iodinated alkenes to perform as halon replacements concluded that further study was warranted.<sup>39</sup> No extinguishment studies have been carried out on any iodoalkene, and the effect of the double bond on extinguishment is unknown. As with bromofluoroalkenes, it is possible that some highly halogenated, lower molecular weight iodoalkenes may be flammable.<sup>289</sup> Examples of some of the simplest iodofluoro ethenes are  $\text{CF}_2=\text{CFI}$ ,  $\text{CFH}=\text{CHI}$ ,  $\text{CF}_2=\text{CHI}$ ,  $\text{CH}_2=\text{CFI}$ , and  $\text{CFH}=\text{CFI}$ ,

A review of physical property data indicated that boiling points would likely be much higher than acceptable. For example,  $\text{CF}_2=\text{CFI}$ , expected to be one of the most volatile compounds in this family, has a  $T_b$  of 30 °C.<sup>192</sup> The values for partially hydrogenated iodofluoroethenes would be higher. There was a lack of sources for these compounds, along with expectation of chemical instability. These ended consideration of these compounds.

### Iodine-containing Ethers

Prior analysis of the suitability of iodinated ethers as potential halon replacements concluded that limited further study was warranted.<sup>39</sup> There were no published data regarding the fire suppression effectiveness of these iodinated derivatives. However, as with brominated compounds, the cup burner values should reflect the presence of the iodine atom and should be in the vicinity of 3 volume %.

The lightest iodine-containing ether, iodomethyl methyl ether (iodomethoxymethane) has a relatively high boiling point of 122 °C at 101 kPa.<sup>290</sup> It is expected that due to the higher molecular weight (all compounds must contain at least two carbon atoms and an oxygen atom) and the presence of iodine, all these compounds will have volatilities that are unsuitable for total flood application. This undesirable attribute of these compounds resulted in a decision to direct efforts to more promising areas.

## 7.5 CHEMICAL FAMILY OPTIONS AND REPLACEMENT ISSUES

### 7.5.1 Suppressant Criteria and Selection Constraints

In this part of the NGP, researchers built on prior work, assessed the state of knowledge, and greatly extended understanding of fire suppression as well as the potential of both inorganic and organic compounds to serve as halon replacements for suppressing in-flight fires in aircraft. Using the screening criteria discussed in Chapter 6 and listed earlier in this chapter, NGP research appraised a near-universal range of chemistries, focusing on those most likely to provide acceptable replacements. Operationally, these criteria were:

- Cup burner flame extinguishment level measured or estimated to be below 5 volume %. This was to obtain fire suppression and reignition quenching efficiency comparable to halon 1301 and higher than the HFCs. To better this 5 volume % limit, a compound must catalytically suppress combustion or have a high heat capacity.

- Boiling points below about 20 °C. For fluids with slightly higher boiling points, similar fluids were considered to see if there might be a lower boiling member of the chemical family. As discussed in Chapter 8, highly effective dispersion at the lowest in-flight temperatures would require boiling points below -40 °C. However, analysis of the altitudes of historical CF<sub>3</sub>Br discharges (Chapter 2) indicated that significantly higher boiling points might well be tolerated. Dispensing the agent as a fine mist might also allow for the use of higher boiling fluids, although establishing a sufficiently high dispensing rate is likely to require more extensive and weighty distribution hardware.
- Inclusion of a chemical feature that rendered the chemical tropodegradable, i.e., likely to have a atmospheric lifetime on the order of a month or less.
- Absence of any toxicological data showing that serious effects on people could occur at a concentration lower than that needed to effect flame extinguishment.

During the nearly two decades of searching for halon alternatives since the signing of the Montreal protocol, there has been a major evolution of the most limiting performance criterion. Initially, there was concern that compounds with halon-like fire suppression efficiency and low ozone depletion contribution would be difficult to find. Later, toxicity became prominent, as several potential alternatives to ozone depleting chemicals performed poorly in cardiotoxicity testing (Chapter 6). For suppressing in-flight fires in aircraft, identifying chemicals that would disperse readily emerged as a principal limiting factor.

The premium on compounds with effective dispersion at low temperatures frequently led to conflict with the other screening criteria. Chemicals with a high heat capacity generally were of high molecular weight and high boiling point. Chemicals with a feature that led to tropospheric reactivity were often polar or were composed of a large number of atoms, both of which typically led to higher boiling points.

Finally, many of the compounds that appeared promising in theory were not available commercially. For some of these, the NGP was able to identify a laboratory that was willing to try to synthesize enough chemical for screening tests. This was not always successful. For still other compounds, the NGP was unable to find any source.

## 7.5.2 General Conclusions

During the formulation of the NGP and continuing through the research stages, the expectation of identifying a true drop-in replacement for halon 1301 for the suppression of in-flight fires in aircraft was quite low. After appraising thousands of compounds, the NGP was indeed unable to identify such a chemical. The requirement that all the properties of the replacement chemical be so similar to those of halon 1301 as to ensure compatibility with existing weapons platforms was too stringent.

The more realistic objective was to identify chemicals that had promise to perform significantly better than HFC-125. Even that proved difficult:

- No strictly thermally active compounds had a boiling point below -40 °C and a fire suppression efficiency superior to that of HFC-125. As will be seen in Chapter 8, a much higher mass of a higher boiling compound would be needed to compensate for condensation losses on cold surfaces. Even if the temperature requirement were relaxed, as discussed in Chapter 2, there were no strictly thermally active compounds that were deemed worthy of further consideration.

- Only one compound,  $\text{CF}_3\text{CN}$ , with a boiling point of  $-67\text{ }^\circ\text{C}$ , met the strictest volatility criterion. However, it required about 9 volume % to suppress a cup burner flame, about the same as HFC-125.
- A few iodoalkanes had boiling points near  $0\text{ }^\circ\text{C}$  and extinguished cup burner flames at about 3 volume %. However, it was expected they would be no less toxic than  $\text{CF}_3\text{I}$ .
- There were two other compounds with boiling points near or below  $0\text{ }^\circ\text{C}$ . Attempts were unsuccessful to synthesize  $\text{N}(\text{CF}_3)_3$  ( $T_b = -10\text{ }^\circ\text{C}$ ).  $\text{CF}_2\text{BrCN}$  ( $T_b = 3\text{ }^\circ\text{C}$ ) extinguished cup burner flames at less than 4 volume %.
- There were some bromoalkenes with cup burner values about 3 volume % to 4 volume % and with boiling points of  $25\text{ }^\circ\text{C}$  or slightly above. These temperatures are not likely to lead to effective dispersion at cold temperatures, and two similar compounds had performed poorly in cardiotoxicity testing.

Were the low temperature requirement to be relaxed modestly,  $\text{N}(\text{CF}_3)_3$  and  $\text{CF}_2\text{BrCN}$  would have sufficient volatility. However, for the former, a synthesis path is needed, along with an assessment of whether the nitrogen oxides formed following decomposition pose an ozone threat comparable to halon 1301. For the latter, toxicity and atmospheric lifetime data are lacking. Some bromofluoroalkenes would be eligible if the low temperature requirement were relaxed substantially and toxicity data were developed.

The development of hybrid solid propellant fire extinguishers (Chapter 9) presents an alternative means of dispensing a chemically active fire suppressant. In these devices, the compound is either mixed in with the solid propellant or is added to the high temperature exhaust from the unit. In either mode, the boiling point and toxicity are unimportant. What matters is that the additive be chemically effective at flame suppression, that the chemical species that effects the suppression be present in the exhaust flow, and that the mass of the additive be minimized. The NGP has affirmed or established that effective chemical activity is characteristic of compounds containing P, Br, I, Na, or K atoms. Low mass compounds of some of these atoms have significantly increased the effectiveness of SPFEs (Chapter 9).

## 7.6 REFERENCES

1. Gann, R.G., ed., *Halogenated Fire Suppressants*, ACS Symposium Series 16, American Chemical Society, Washington, DC, 1975.
2. Sheinson, R.S., "Laboratory Through Full Scale: The U. S. Navy Halon Total Flooding Replacement Program," Chapter 16 in *Halon Replacements: Technology and Science*, ACS Symposium Series 611, Miziolek, A. W., and Tsang, W., Eds., American Chemical Society, Washington, DC, 1995, ISBN 0-8412-3327-6, pp. 175-188.
3. Sheinson, R.S., Hahn, J.E., Geary, K., and Williams, F.W., "Quantification of Physical Fire Suppression of Heptane Pool Fires," *Proceedings of the Chemical and Physical Processes in Combustion Symposium*, Eastern Section Combustion Institute, The Combustion Institute, Pittsburgh, PA, (1977).
4. Sheinson, R.S., Gellene, G.J., Williams, F.W. and Hahn, J.E., "Quantification of Fire Suppressant Action on Liquid Pool Fires," *Proceedings of the Eastern States Combustion Institute*, The Combustion Institute, Pittsburgh, PA, (1978).
5. Sheinson, R.S., Penner-Hahn, J.E., and Indritz, D., "The Physical and Chemical Action of Fire Suppressants," *Fire Safety Journal* **15**, 437, (1989).

6. Sheinson, R.S., Carhart, H.W., Musick, J.K., and Williams, F.W., "Halon Acid Production from Full Scale  $\text{CF}_3\text{Br}$  Pool Fire Suppression Tests," *Proceedings of the Eastern States Combustion Institute*, The Combustion Institute, Pittsburgh, PA, (1979).
7. Sheinson, R.S., J.K. Musick, and Carhart, H.W., "HF and HBr Production from Full Scale  $\text{CF}_3\text{Br}$  (Halon 1301) Fire Suppression Tests)," *Journal of Fire & Flammability*, **12**, 229-235, (1981).
8. Floden, J.R., and Tapscott, R.E., "The Quest for Chemical Alternatives to Halon 1211," *The Military Engineer*, **82(537)**, 13-15, August 1990.
9. Nimitz, J.S., Tapscott, R.E., Skaggs, S.R., and Moore, T.A., *Halocarbons as Halon Replacements: Technology Review and Initiation*, ESL-TR-89-38, Vol. 1 of 5, Wright Laboratories (WL/FIVCF), Tyndall Air Force Base, Florida, July 1990.
10. Tapscott, R.E., Dierdorf, D.S., Moore, T.A., and Skaggs, S.R., *Halocarbons as Halon Replacements: Technology Review and Initiation, Halon 1301 Replacements*, ESL-TR-89-38, Vol. 2 of 5, Wright Laboratories (WL/FIVCF), Tyndall Air Force Base, Florida, March 1993.
11. Tapscott, R.E., Nimitz, J.S., Walters, E.A., and Arneberg, D.L., *Halocarbons as Halon Replacements: Laboratory Testing of Halon 1211 Replacements*, ESL-TR-89-38, Vol. 3 of 5, Wright Laboratories (WL/FIVCF), Tyndall Air Force Base, Florida, March 1993.
12. Dierdorf, D.S., Tapscott, R.E., Skaggs, S.R., and Moore, T.A., *Halocarbons as Halon Replacements: Laboratory Testing of Halon 1301 Replacements*, ESL-TR-89-38, Vol. 4 of 5, Wright Laboratories (WL/FIVCF), Tyndall Air Force Base, Florida, March 1993.
13. Tapscott, R.E., and Lee, M.E., *Halocarbons as Halon Replacements: Medium-Scale Testing of Halon 1211 Replacements*, ESL-TR-89-38, Vol. 5 of 5, Wright Laboratories (WL/FIVCF), Tyndall Air Force Base, Florida, May 1993.
14. *Radiative Forcing to Climate Change: The 1994 Report of the Scientific Assessment Working Group of IPCC*, Intergovernmental Panel on Climate Change, Cambridge University Press, Cambridge, UK, 1994.
15. *RIVM Study Assesses HFC Policy Options and Effects*, Global Environmental Change Report, Vol. 7, No. 2, p. 4, 27 January 1995.
16. "Denmark to Propose Phaseout for HFCs," *Ozone Depletion Today*, 7 November 1996.
17. Skaggs, S.R., and Nimitz, J.S., "Estimating Tropospheric Lifetimes and Ozone-Depletion Potentials of One- and Two-Carbon Hydrofluorocarbons and Hydrochlorofluorocarbons," *Environmental Science and Technology* **26**, 739-744, 1992.
18. Lifke, J.L., Moore, T.A., and Tapscott, R.E., *Advanced Streaming Agent Development, Volume V: Laboratory-Scale Streaming Tests*, Wright Laboratory (WL/FIVCF) and Applied Research Associates, Inc., Tyndall Air Force Base, Florida, June 1996. NMERI 96/2/32540, Vol. 5 of 5.
19. Moore, T.A., Dierdorf, D.S., Skaggs, S.R., and Tapscott, R.E., *Materials Compatibility and Agent Operational Validation for Halon 1301 Replacement: Phase IV*, Vol. 2, NMERI S.S. 2.32(4), March 1993.
20. Tapscott, R.E., Heinonen, E.W., and Brabson, G.D., *Advanced Agent Identification and Preliminary Assessment*, NMERI 95/15/31883, Wright Laboratory (WL/FIVCF), Tyndall Air Force Base, Florida, April 1996.
21. Pitts, W.M., Nyden, M.R., Gann, R.G., Mallard, G.W., and Tsang, W., *Construction of an Exploratory List of Chemicals to Initiate the Search for Halon Alternatives*, Technical Note 1279, National Institute of Standards and Technology, Gaithersburg, MD, (1990).

22. Gann, R.G., Burgess, S.R., Whisner, K.C., and Reneke, P.A., eds., *Papers from 1991-2006 Halon Options Technical Working Conferences (HOTWC)*, CD-ROM, NIST SP 984-4, National Institute of Standards and Technology, Gaithersburg, MD, (2006).
23. Adcock, J.R., Mathur, S. B, Huang, H.Q, Mukhopadhyay, P., Wang, B., "Fluorinated Ethers – A New Family of Halons," in Gann, R.G., Burgess, S.R., Whisner, K.C., and Reneke, P.A., eds., *Papers from 1991-2006 Halon Options Technical Working Conferences (HOTWC)*, CD-ROM, NIST SP 984-4, National Institute of Standards and Technology, Gaithersburg, MD, (2006).
24. *Technology Development Plan for Alternatives to Ozone-depleting Substances for Weapons Systems Use, Final Report*, Office of the Deputy Secretary of Defense (Science and Technology)/Weapons Systems, September 1998.
25. Grzyll, L.R., and Back, D.D., *Development of Quantitative Structure-Property Relationships for Tropodegradable Halocarbon Fire Suppression Agents*, Final Report, SSG Subtask 3.20, Subcontract S-5000.48, Applied Research Associates, Inc., Tyndall Air Force Base, Florida, Mainstream Engineering Corporation, Rockledge, Florida, March 1997.
26. Bausum, H.T., *QSAR Estimates of Toxicity of Candidate Halon Replacement Compounds*, Health Effects Program, U.S. Army Center for Health Promotion and Preventive Medicine, 10 January, 1997.
27. DEREK, copyright by the President and Fellows of Harvard College and LHASA UK Ltd., (1990-1995).
28. Brittain, A.J., *A Toxicological Assessment of 24 Potential Halon Replacement Agents Using Structural Activity Relationship Analysis*, INM Technical Report (Health & Hygiene) N. 97006, The Institute of Naval Medicine, Alverstoke, GOSPORT, Hants, PO12 2DL.
29. Tapscott, R.E., and Mather, J.D., *Toxicity Assessment of Tropodegradable Halocarbons*, Final Report NMERI 97/4/32930, Center for Global Environmental Technologies, prepared for Wright Laboratories, April 1997.
30. Finch, G.L., Barr, E., Nikula, K., Krone, J., Mather, J.D., *Acute Inhalation Toxicity of Candidate Halon Replacement Compounds in Rats*, Lovelace Respiratory Research Institute, Final Report April 22, 1999.
31. Gladnick, N.L., *AAWG #873, AAWG #903, and AAWG #1116: Bacterial Reverse Mutation Test in Salmonella Typhimurium and Escherichia Coli*, DuPont Pharmaceuticals Company, February 29, 2000.
32. Curry, P.T., *AAWG #873: In vitro Chromosome Aberration Test in Human Peripheral Blood Lymphocytes*, DuPont Pharmaceuticals Company - Stine-Haskell Research Center, November 20, 2000.
33. Horrell, P.J., *Agent 873, An Inhalation Study to Investigate the Cardiac Sensitization Potential in the Beagle Dog*. Huntingdon Life Sciences Limited, Final Report - September 16, 2002.
34. AAWG Minutes reporting results of cardiac sensitization testing of 1-bromo-3,3,3-trifluoropropene, Halon Alternatives Research Corporation, Arlington, VA.
35. Lu, G.G., Ling, J.S.L., and Krantz, J.C., Jr., "Anesthesia. XLI: The Anesthetic Properties of Certain Fluorinated Hydrocarbons and Ethers," *Anesthesiology* **14**, 466-472, (1953).
36. Krantz, J.C., Jr., and Rudo, F.G., "The Fluorinated Anesthetics," in *Handbook of Experimental Pharmacology*, Vol. 20/1, Eichler, O., Farah, A., Herken, H., and Welch, A. D., editors, Springer-Verlag, Berlin, Germany, Chapter 10, pp. 501-564, (1966).
37. Tapscott, R.E., Heinonen, E.W., and Mather, J.D., *Identification and Proof Testing of New Total Flooding Agents: Toxicity and Global Environmental Assessment*, Interim Report, NMERI Report No.

- 97/29/33010, U. S. Department of Defense, Strategic Environmental Research and Development Program and Defense Advance Research Projects Agency, Arlington, Virginia, February 1998.
38. Tapscott, R.E., Mather, J.D., Heinonen, E.W., Lifke, J.L., and Moore, T.A., *Identification and Proof Testing of New Total Flooding Agents: Combustion Suppression Chemistry and Cup Burner Testing*, Final Report, NMERI Report No. 97/6/33010, U. S. Department of Defense, Strategic Environmental Research and Development Program and Defense Advance Research Projects Agency, Arlington, Virginia, May 1998.
39. Tapscott, R.E., Sheinson, R.S., Babushok, V., Nyden, M.R., and Gann, R.G., *Alternative Fire Suppressant Chemicals: A Research Review with Recommendations*, NIST Technical Note 1443, National Institute of Standards and Technology, Gaithersburg MD, (2001).
40. Patterson, R.A., Gobeli, G.W., Brabson, G.D., and Tapscott, R.E., *Advanced Streaming Agent Development, Volume II: Metal Compounds*, WL-TR-96-XX, NMERI Report No. 96/3/32540, Vol. 2 of 5, Wright Laboratories (WL/FIVCF), Tyndall Air Force Base, Florida, and Applied Research Associates, Inc., Tyndall Air Force Base, Florida, June 1996.
41. Moore, T.A., and Weitz, C.A., *Laboratory Optimization and Medium-Scale Screening of Halide Salts and Water Mixtures*, NMERI Report No. 96/12/32590, U. S. Army Tank-Automotive and Armament Command (TACOM), Warren, Michigan, June 1996.
42. McCamy, C.S., Shoub, H, and Lee, T.G., "Fire Extinguishment by Means of Dry Powder," *Proceedings of the Combustion Institute* **6**, 795-801, (1957).
43. Shen, K.K., and Ferm, D.J., "Boron Compounds as Fire Retardants," *Proceedings, Flame Retardants—101: Basic Dynamics*, Baltimore, Maryland, pp. 137-146, 24-27 March 1996.
44. Kasem, M.A., and Richards, H.R., "Flame-Retardants for Fabrics," *Industrial and Engineering Chemistry, Product Research and Development* **11**, 114-133, (1972).
45. Raether, L.O., "Flame Retardant Markets, Products, Regulations, a Historical Perspective," *Proceedings, Flame Retardants—101: Basic Dynamics*, Baltimore, Maryland, pp. 1-11, 24-27 March 1996.
46. Friedman, R., and Levy, J.B., "Inhibition of Methane-Air Flames by Gaseous Aluminum Chloride," *Combustion and Flame* **2**, 105-107, (1958).
47. Dolan, J.E., and Dempster, P.B., "The Suppression of Methane-Air Ignitions by Fine Powders," *Journal of Applied Chemistry* **5**, 510-517, (1955).
48. Tapscott, R.E., Heinonen, E.W., and Brabson, G.D., *Advanced Agent Identification and Preliminary Assessment*, WL-TR-95-XX, NMERI Report No. 1995/15/31883, Wright Laboratory (WL/FIVCF), Tyndall Air Force Base, Florida, December 1996.
49. Gobeli, G. W., Tapscott, R. E., and Kaizerman, J. A., *Advanced Streaming Agent Development, Volume I: Silicon Compounds*, WL-TR-96-XX, NMERI Report No. 96/1/32540, Vol. 1 of 5, Wright Laboratory (WL/FIVCF), Tyndall Air Force Base, Florida and Applied Research Associates, Inc., Tyndall Air Force Base, Florida, May 1996.
50. Caporiccio, G., "Chemically Reactive Fluorinated Organosilicon Compounds and Their Polymers," U.S. Patent Number 5,041,588, 20 August 1991, assigned to Dow Corning Corporation, Midland, MI.
51. Hastie, J.W., "Chemical Inhibition of Flames," in *High Temperature Vapors*, Academic Press, New York and London, Chapter 5, pp. 332-357, 1975.

52. Ryzhkov, O.T., Azatyan, V. V., Rubtsov, N.M., and Temchin, S.M., "A Kinetic Study of Chain Branching in Dichlorosilane Oxidation," *Kinetics and Catalysis*, Vol. 36, No. 1, pp. 99-102, 1995, and references therein.
53. Metcalfe, E., Feng, Z., Kendrick, D, and Sejourne, S., "Silicon-Based Flame Retardants," *Proceedings, BCC Conference on Flame Retardancy*, Stamford, Connecticut, 2-4 June 1997.
54. Pierce, O.R., and Kim, Y.K., "High-Temperature Fluorosilicone Elastomers," *Applied Polymer Symposium*, No. 22, pp. 103-125, 1973.
55. Languille, P., Vitat, J.C., Guillemont, A.R., and Remond, J.-P., "Liquid Fire Extinguishing Composition," USA, Patent Number 3,879,297, 22 April 1975. Assigned to Rhone-Progil, Paris, France.
56. Kurylo, M.J., Kaye, J.A., Hampson, R.F., and Schmoltner, A.M., *Present State of Knowledge of the Upper Atmosphere 1993: An Assessment Report*, NASA RP-1337, NASA Office of Mission to Planet Earth Science Division, National Aeronautics and Space Administration, Washington, DC, January 1994.
57. "Atmospheric Chemistry: Measurements, Mechanisms and Models: General Discussion," *Faraday Discussions* **100**, 441-457, (1995).
58. Lide, D.R., ed., *CRC Handbook of Chemistry and Physics*, 86th Edition, CRC Press, Inc., Boca Raton, Florida, USA, 2005.
59. Watson, R.T., Prather, M.J., and Kurylo, M.J., *Present State of Knowledge of the Upper Atmosphere 1988: An Assessment Report*, NASA Reference Publication 1208, National Aeronautics and Space Administration, Washington, DC, August 1988.
60. Plane, J.M.C., "The Chemistry of Meteoric Metals in the Earth's Upper Atmosphere," *International Reviews in Physical Chemistry* **10** (1), 55-106, (1991).
61. Plane, J.M.C., and Helmer, M., "Laboratory Studies of the Chemistry of Meteoric Metals," in *Research in Chemical Kinetics*, Vol. 2, Compton, R. G., and Hancock, G., editors, Elsevier Scientific Publishing Company, Amsterdam, pp. 313-367, 1994.
62. Atkinson, R., "Kinetics and Mechanisms of the Gas-Phase Reactions of the Hydroxyl Radical with Organic Compounds," *Journal of Physical and Chemical Reference Data, Monograph No. 1*, American Chemical Society, Washington, DC, and American Institute of Physics, Woodbury, New York, 1989.
63. Atkinson, R., "Gas Phase Tropospheric Chemistry of Organic Compounds," *Journal of Physical and Chemical Reference Data, Monograph No. 2*, American Chemical Society, Washington, DC, and American Institute of Physics, Woodbury, New York, 1994.
64. Fordham, S., ed., *Silicones*, Philosophical Library, Inc., New York, NY, p. 32, 1960.
65. Y. Sawado, T. Akiyama, T. Ueno, K. Kamisako, K. Kuroiwa, and Y. Tarui, "Contributions of Silicon-Hydride Radicals to Hydrogenated Amorphous Silicon Film Formation in Windowless Photochemical Vapor Deposition System," *Japanese Journal of Applied Physics* **33**, 950-955, (1994).
66. Swanson, S.P., Cull, R.A., Bryant, D., and Moore, J., "New Technologies and Cleaning Performance Based on Volatile Methyl Siloxanes," *Proceedings, International Conference on Ozone Protection Technologies*, Washington, DC, 21-23 October 1996.
67. Sax, N.I., and Lewis, R.J., Sr., *Dangerous Properties of Industrial Materials*, Vol. 1-3, Seventh Edition, Van Nostrand Reinhold, New York, 1989.
68. Gage, J.C., "The Subacute Inhalation Toxicity of 109 Industrial Chemicals," *British Journal of Industrial Medicine* **27**, 1-18, (1970).

69. "Significant New Uses of Certain Chemical Substances: Final Rule," *Federal Register* **63**(41), 393-3441, 22 January 1998.
70. Michl, J., ed., "Silicon Chemistry," *Chemical Reviews* **95**(5), (1995).
71. Martel, B., and Hiriart, J.M., "Nouveaux Intermediaires  $\alpha$ -Halomethylmetalliques Stables: Formation et Stabilité Remarquable D' $\alpha$ -Halomethylsodium et D' $\alpha$ -Halomethylpotassium," *Tetrahedron Letters* **29**, 2737-2740, (1971).
72. Hiyama, T., Nishide, K., and Obayashi, S., "Practical Synthesis and Polymerization of Trifluorovinylsilanes. A Possible Precursor of Poly(difluoroacetylene)," *Chemistry Letters*, 1765-1768, 1984.
73. Froberger, C.F., "Synthesis of Tetra(perfluoroalkoxy)silanes," *Journal of Organic Chemistry* **25**, 311-312, (1960).
74. Morrison, M.E., and Scheller, K., "The Effect of Burning Velocity Inhibitors on the Ignition of Hydrocarbon-Oxygen-Nitrogen Mixtures," *Combustion and Flame* **18**, 3-12, (1972).
75. Vanpee, M., and Shirodkar, P.P., "A Study of Flame Inhibition by Metal Compounds," *Proceedings of the Combustion Institute* **17**, 787-795, (1978).
76. Bulewicz, E.M., and Padley, P.J., "Catalytic Effect of Metal Additives on Free Radical Recombination Rates in  $H_2+O_2+N_2$  Flames," *Proceedings of the Combustion Institute* **13**, 73-80, (1971).
77. Linteris, G. T., "Suppression of Cup Burner Diffusion Flames by Super-Effective Chemical Inhibitors and Inert Compounds," 2001, in *Papers from 1991-2006 Halon Options Technical Working Conferences (HOTWC)*, CD-ROM, NIST SP 984-4, National Institute of Standards and Technology, Gaithersburg, MD, (2006).
78. Bulewicz, E.M., and Sugden, T.M., "Flame Photometric Studies of Reactions Induced by Nitric Oxide in Hydrogen-Oxygen-Nitrogen Flames I. The Catalyzed Recombination of Atomic Hydrogen and Hydroxyl Radicals," *Proceedings of the Royal Society of London, Section A* **277**, 143-154, (1964).
79. Babushok, V., Tsang, W., Linteris, G.T., and Reinelt, D., "Chemical Limits to Flame Inhibition," *Combustion and Flame* **115**, 551-560, (1998).
80. Allen, C.W., "The Use of Phosphazenes as Fire Resistant Materials," *Journal of Fire Sciences* **11**, 320-328, (1993).
81. Kobayashi, E., "Flame Retarder in Phosphorus Chemistry—Focusing On Phosphazene Derivative," *Kinokairyo* **4**, 60-71, (1989).
82. Lyons, J.W., *The Chemistry and Use of Fire Retardants*, Wiley-Interscience, New York, (1970).
83. Levchik, S.V., "Mechanistic Studies of Fire Retardancy in Aliphatic Nylons," *Proceedings, BCC Conference on Flame Retardancy*, Stamford, Connecticut, 2-4 June 1997.
84. Green, J., "Phosphorus-Bromine Flame Retardant Synergy in a Polycarbonate/Polyethylene Terephthalate Blend," *Journal of Fire Sciences* **12**, 257-267, (1994).
85. Green, J., "A Phosphorus-Bromine Flame Retardant for Engineering Thermoplastics—A Review," *Journal of Fire Sciences* **12**, 388-408, (1994).
86. Avondo, G., Vovelle, C., and Delbourgo, R., "The Role of Phosphorus and Bromine in Flame Retardancy," *Combustion and Flame* **31**, 7-16, (1978).

87. Howell, B.A., Uhl, F.M., Liu, C., and Johnston, K.F., "Highly Halogenated Phosphorus-Containing Compounds as Potential Flame Retardant Agents," *Proceedings, BCC Conference on Flame Retardancy*, Stamford, Connecticut, 2-4 June 1997.
88. Bright, D.A., Dashevsky, S., Moy, P.Y., and Williams, B., "Resorcinol bis(diphenyl phosphate), a Non-Halogen Flame-Retardant Additive," *Proceedings, BCC Conference on Flame Retardancy*, Stamford, Connecticut, 2-4 June 1997.
89. Babcock, L.M., Bard, J.K., Leibfried, R.T., "Flame-Retardant Organosilicon Polymers, Their Manufacture and Articles Produced from Them, European Patent Application EP 556844, 1993, assigned to Hercules (*Chemical Abstracts* 136160f, **120**, 1994).
90. Weil, E.D., and Kim., H.K., "Flame Retardant Unsaturated Resins—An Overview and New Developments," *Proceedings, BCC Conference on Flame Retardancy*, Stamford, Connecticut, 2-4 June 1997.
91. Ebdon, J.R., Joseph, P., Hunt, B.J., Price, D., Milnes, G.J., and Gao, F., "Flame Retardance in Styrenic and Acrylic Polymers with Covalently-Bound Phosphorus-Containing Groups," *Proceedings, BCC Conference on Flame Retardancy*, Stamford, Connecticut, 2-4 June 1997.
92. "Phosphorus Chemistry," *Chemical Reviews* **94**(5), (1994).
93. Kaizerman, J. A., and Tapscott, R. E., *Advanced Streaming Agent Development, Volume III: Phosphorus Compounds*, Vol. 3 of 5," NMERI 96/5/32540, Wright Laboratory (WL/FIVCF) and Applied Research Associates, Inc., Tyndall Air Force Base, Florida, May 1996.
94. Zhivukhin, S.M., Tolstoguzov, V.B., Kireev, V.V., and Kuznetsova, K.G., "Preparation of Chlorophosphazenes," *Russian Journal of Inorganic Chemistry* **10**, 178-180, (1965).
95. Lund, L.G., Paddock, N.L., Proctor, J.E., and Searle, H.T., "Phosponitrilic Derivatives. Part I. The Preparation of Cyclic and Linear Phosponitrilic Chlorides," *Journal of the Chemical Society*, 2542-2547, (1960).
96. Sowerby, D.B., "Cyclic Inorganic Compounds. Part I. Chlorine Exchange Reactions with the Chlorophosponitriles," *Journal of the Chemical Society*, 1396-1400, (1965).
97. Green, B., and Sowerby, D.B., "Fluorination of Aminochlorotriphosponitriles and the Preparation of Non-geminal Chlorofluorotriphosponitriles," *Chemical Communications*, 628, (1969).
98. Green, B., and Sowerby, D.B., "Cyclic Inorganic Compounds. Part IX. Fluorination of Bisdimethylaminotetrachlorophosponitrile," *Journal of the Chemical Society (A)*, 987-991, (1970).
99. John, K., and Moeller, T., "Phosponitrilic Bromides," *Journal of Inorganic and Nuclear Chemistry* **22**, 199-204, (1961).
100. Walsh, E.J., Derby, E., and Smegal, J., "Nucleophilic Substitutions on Hexachlorocyclotriphosphazene Using 18-Crown-6 Ether Complexes," *Inorganica Chimica Acta* **16**, 9-10, (1976).
101. Steger, E., and Klemm, D., "Beitrag zur Kenntnis von Fluoro-Bromo-Cyclotriphosphaz-enen," *Journal of Inorganic and Nuclear Chemistry* **29**, 1812-1813, (1967).
102. Ranganathan, T.N., Todd, S.M., and Paddock, N.L., "Reaction of Octafluorocyclotetraphosponitrile with Methylithium," *Inorganic Chemistry* **12**, 316-323, (1973).
103. Paddock, N.L., Ranganathan, T.N., and Todd, S.M., "Reaction of Methyl-lithium with Phosponitrilic Fluorides: A Novel Orientation Pattern," *Canadian Journal of Chemistry* **49**, 164-165, (1971).

104. Ramachandran, K., and Allen, C.W., "Organophosphazenes. 15. Reactions of Hexafluorocyclotriphosphazene with *tert*- and *n*-Butyllithium Reagents," *Journal of the American Chemical Society* **104**, 2396-2399, (1982).
105. Moeller, T., Failli, A., and Tsang, F.Y., "Observations on the Butylation of Trimeric and Tetrameric Phosphonitrilic Fluorides," *Inorganic Nuclear Chemistry Letters* **1**, 49-52, (1965).
106. DuPont, J.G., and Allen, C.W., "Organo-Substituted Phosphazenes. 10. Reactions of Hexafluorocyclotriphosphazene with Propenyllithium Reagents," *Inorganic Chemistry* **17**, 393-3096, (1978)
107. Schmutzler, R., "Chemistry and Stereochemistry of Fluorophosphoranes," *Angewandte Chemie International Edition* **4**, 496-508, (1965).
108. Schmutzler, R., "Fluorophosphoranes," *Inorganic Syntheses* **9**, 63-73, (1968).
109. Boodaghians, R.B., Canosa-Mas, C.E., Carpenter, P.J., and Wayne, R.P., "The Reactions of NO<sub>3</sub> with OH and H," *Journal of the Chemical Society, Faraday Transactions 2* **84**, 931-948, (1988).
110. Rowland, F.S., "Stratospheric Ozone Depletion," in *Annual Review of Physical Chemistry*, Vol. 42, Strauss, H. L., Babcock, G. T., and Leone, S. R., editors, Annual Reviews, Inc., Palo Alto, California, pp. 731-766, (1991).
111. Chase, M.W., Davies, C.A., Downey, J.R., Frurip, D.J., McDonald, R.A., and Syverud, A.N., *JANAF Thermochemical Tables*, 3rd Edition, *Journal of Physical and Chemical Reference Data*, **14**, Supplement 1, (1985).
112. Stedman, D.H., and Fraser, M.E., "Spectroscopy and Mechanism of Chemiluminescent Reaction Between Group V Hydrides and Ozone," *Journal of the Chemical Society, Faraday Transactions 1* **79**, 527-542, (1983).
113. McElroy, M.B., Salwitch, R.J., Wofsy, S.C., and Logan, J.A., "Reductions of Antarctic Ozone Due to Synergistic Interactions of Chlorine and Bromine," *Nature* **321**, 759-762, (1986).
114. Boville, B.W., "Environmental Aspects of Stratospheric Ozone Depletion," UNEP Ozone Meeting, Washington, DC, March 1977.
115. Wofsy, S.C., "Temporal and Latitudinal Variations of Stratospheric Trace Gases: A Critical Comparison Between Theory and Experiment," *Journal of Geophysical Research* **83**, 364-378, (1978).
116. Anderson, J.G., "The Absolute Concentration of O(<sup>3</sup>P) in the Earth's Stratosphere," *Geophysical Research Letters* **2**, 231-234, (1975).
117. Atkinson, R., "Kinetics and Mechanisms of the Gas-Phase Reactions of the Hydroxyl Radical with Organic Compounds," *Journal of Physical and Chemical Reference Data, Monograph No. 1*, American Chemical Society, Washington, DC, and American Institute of Physics, Woodbury, New York, 1989.
118. Heicklen, J., "The Correlation of Rate Coefficients for H-Atom Abstraction by HO Radicals with C-H Bond Dissociation Enthalpies," *International Journal of Chemical Kinetics* **13**, 651-665, (1981).
119. Atkinson, R., "Estimations of OH Radical Rate Constants from H-Atom Abstraction from C-H and O-H Bonds Over the Temperature Range 250-1000 K," *International Journal of Chemical Kinetics* **18**, 555-568, (1986).
120. Tuazon, E.C., Atkinson, R., Aschmann, S.M., Arey, J., Winer, A.M., and Pitts, J.N., Jr., "Atmospheric Loss Processes of 1,2-Dibromo-3-Chloropropane and Trimethyl Phosphate," *Environmental Science and Technology* **20**, 1043-1046, (1986).

121. Atkinson, R., "Gas Phase Tropospheric Chemistry of Organic Compounds," *Journal of Physical and Chemical Reference Data, Monograph No. 2*, American Chemical Society, Washington, DC, and American Institute of Physics, Woodbury, New York, 1994.
122. Wolfe, R.E., Ellis, D.H., Leahy, H.F., Vinegar, A., and Sharma, S., *Acute Oral Toxicity Evaluation and Genotoxicity Testing of Hexakis(2,2,2-trifluoroethoxy)cyclotri-phosphazene, a Replacement Candidate for Ozone Depleting Substances*, AL/ OE-TR-1997-0054, Armstrong Laboratory, Occupational and Environmental Health Directorate, Toxicology Division, Human Health Systems Center, Air Force Materiel Command, Wright-Patterson AFB, Ohio, ManTech - GEO-CENTERS Joint Venture, Toxic Hazards Research, Dayton, Ohio, May 1997.
123. Weir, P., *Activity of 3899-A Chlorophosphazene in in vitro Mammalian Cell Transformation Assay*, Ethyl Corporation, Baton Rouge, Louisiana, Microbiological Associates, Bethesda, Maryland, October 1978.
124. Weir, P., *Activity of 3899-B Chlorophosphazene in in vitro Mammalian Cell Transformation Assay*, Ethyl Corporation, Baton Rouge, Louisiana, Microbiological Associates, Bethesda, Maryland, October 1978.
125. Weir, P., *Activity of T1352A in in vitro Mammalian Cell Transformation Assay in the Presence of Exogenous Metabolic Activation*, Ethyl Corporation, Baton Rouge, Louisiana, Microbiological Associates, Bethesda, Maryland, March 1979.
126. Weir, P., *Activity of T1356A in in vitro Mammalian Cell Transformation Assay in the Presence of Exogenous Metabolic Activation*, Ethyl Corporation, Baton Rouge, Louisiana, Microbiological Associates, Bethesda, Maryland, March 1979.
127. Weir, P., *Activity of T1350 in the in vivo Cytogenetic Assay in Rodents for Mutagenicity*, Ethyl Corporation, Baton Rouge, Louisiana, Microbiological Associates, Bethesda, Maryland, 1979.
128. Weir, P., *Activity of T1355 in the in vivo Cytogenetic Assay in Rodents for Mutagenicity*, Ethyl Corporation, Baton Rouge, Louisiana, Microbiological Associates, Bethesda, Maryland, 1979.
129. Weir, P., *Activity of T1351A in in vitro Mammalian Cell Point Mutation Assay in the Presence of Exogenous Metabolic Activation*, Ethyl Corporation, Baton Rouge, Louisiana, Microbiological Associates, Bethesda, Maryland, March 1979.
130. Weir, P., *Activity of T1357A in in vitro Mammalian Cell Point Mutation Assay in the Presence of Exogenous Metabolic Activation*, Ethyl Corporation, Baton Rouge, Louisiana, Microbiological Associates, Bethesda, Maryland, March 1979.
131. Weir, P., *Activity of 3899-A-CPP in the Salmonella/Microsomal Assay for Bacterial Mutagenicity*, Ethyl Corporation, Baton Rouge, Louisiana, Microbiological Associates, Bethesda, Maryland, October 1978.
132. Weir, P., *Activity of 3899-B-CPP in the Salmonella/Microsomal Assay for Bacterial Mutagenicity*, Ethyl Corporation, Baton Rouge, Louisiana, Microbiological Associates, Bethesda, Maryland, October 1978.
133. Weir, P., *Activity of 3899-A Chlorophosphazene in a Test for Differential Inhibition of Repair Deficient and Repair Competent Strains of Escherichia Coli: DNA Repair*, Ethyl Corporation, Baton Rouge, Louisiana, Microbiological Associates, Bethesda, Maryland, September 1978.
134. Weir, P., *Activity of 3899-B Chlorophosphazene in a Test for Differential Inhibition of Repair Deficient and Repair Competent Strains of Escherichia Coli: DNA Repair*, Ethyl Corporation, Baton Rouge, Louisiana, Microbiological Associates, Bethesda, Maryland, September 1978.

135. Weir, P., *Activity of T1349 in the Dominant Lethal Assay in Rodents for Mutagenicity*, Ethyl Corporation, Baton Rouge, Louisiana, Microbiological Associates, Bethesda, Maryland, January 1979.
136. Weir, P., *Activity of T1354 in the Dominant Lethal Assay in Rodents for Mutagenicity*, Ethyl Corporation, Baton Rouge, Louisiana, Microbiological Associates, Bethesda, Maryland, January 1979.
137. Gage, J.C., "The Subacute Inhalation Toxicity of 109 Industrial Chemicals," *British Journal of Industrial Medicine* **27**, 1-18, (1970).
138. Sweet, D.V., ed., *Registry of Toxic Effects of Chemical Substances*, Report Number DHHS (NIOSH) 87-114, Vols. 1-5, U. S. Department of Health and Human Services, National Institute for Occupational Safety and Health, Washington, DC, April 1987.
139. Haaland, P.D., and Huntington, J.H., *Halon Replacement for Aircraft Fire Suppression Systems*, Final Report - AFRL-ML-WP-TR-1998-4120, June 1998.
140. Eclipse Aviation press release, August 2005.
141. Lawless, E.W., and Harman, L.D., "Bis(trifluoromethyl)sulfide," *Journal of Inorganic and Nuclear Chemistry* **31**, 1541-1542, (1969).
142. Haas, A., and Oh, D.Y., "Perhalogenierte Sulfenylcarboxylate," *Chemische Berichte* **102**, 77-82, (1969).
143. Sauer, D.T., and Shreeve, J.M., "Bis(Perfluoroalkyl)Sulfur Difluorides and Bis(Perfluoroalkyl)Sulfoxides," *Journal of Fluorine Chemistry* **1**, 1-11, (1971/72).
144. Sauer, D.T., and Shreeve, J.M., "Bis(perfluoroalkyl)sulphur Difluorides and Bis(perfluoroalkyl)Sulphoxides," *Chemical Communications*, 1679-1680, (1970).
145. Lawless, E.W., "Perfluorodimethyl Sulfoxide and Bis(trifluoromethyl)sulfur Difluoride," *Inorganic Chemistry* **9**, 2796-2798, (1970).
146. Krespan, C.G., "Fluorocarbon Metalloid Compounds of Tetrafluoroethylene and Sulfur, Selenium, or Phosphorus and Their Preparation," U.S. Patent 2,931,803, 5 April 1960, assigned to E.I. du Pont de Nemours and Company, Wilmington, DE.
147. Pitts, W.M., Yang, J.C., Bryant, R.A., Blevins, L. G., and Huber, M.L., *Characteristics and Identification of Super Effective Fire Extinguishing Agents, Final Report, NGP project 4C/1*, NIST Technical Note 1440, National Institute of Standards and Technology, Gaithersburg, MD, 2006..
148. Pitts, W.M. and Blevins, L.G., "An Investigation of Extinguishment by Thermal Agents Using Detailed Chemical Kinetic Modeling of Opposed Jet Diffusion Flames," pp. 215-249, Fifteenth Meeting of the UJNR Panel on Fire Research and Safety, NISTIR 6588, National Institute of Standards and Technology, Gaithersburg, MD, (2000).
149. Pitts, W.M. and Blevins, L.G., "An Investigation of Extinguishment by Thermal Agents Using Detailed Chemical Modeling of Opposed Flow Diffusion Flames," 1999, in Gann, R.G., Burgess, S.R., Whisner, K.C., and Reneke, P.A., eds., *Papers from 1991-2006 Halon Options Technical Working Conferences (HOTWC)*, CD-ROM, NIST SP 984-4, National Institute of Standards and Technology, Gaithersburg, MD, (2006).
150. Pitts, W.M. and Blevins, L.G., "An Investigation of Extinguishment by Thermal Agents Using Detailed Chemical Kinetic Modeling of Opposed Flow Diffusion Flames," *Proceedings of the Fall Technical Meeting of the Eastern Section of the Combustion Institute*, pp. 184-187, The Combustion Institute, Pittsburgh, PA, (1999).

151. Yang, J.C., Bryant, R.A., Huber, M.L., and Pitts, W.M., "Experimental Investigation of Extinguishment of Laminar Diffusion Flames by Thermal Agents," 2000, in Gann, R.G., Burgess, S.R., Whisner, K.C., and Reneke, P.A., eds., *Papers from 1991-2006 Halon Options Technical Working Conferences (HOTWC)*, CD-ROM, NIST SP 984-4, National Institute of Standards and Technology, Gaithersburg, MD, (2006).
152. Pitts, W.M. and Blevins, L.G., "An Investigation of Extinguishment by Thermal Agents Using Detailed Kinetic Modeling of Opposed Jet Diffusion Flames," Work in Progress Poster 1-K10, Presented at the Twenty-Eight Symposium (International) on Combustion, Edinburgh, Scotland, July 31-August 4, 2000.
153. Pitts, W.M., Bryant, R.A., and Yang, J.C., "Thermal Agent Extinguishment of Two Types of Diffusion Flames," *Proceedings of the Second Joint Meeting of the United States Sections*, The Combustion Institute, Pittsburgh, PA, 2001.
154. Pitts, W.M., Yang, J.C., and Bryant, R.A., "Fuel Effects on the Extinguishment of Laminar Diffusion Flames by Thermal Agents," 2001, in Gann, R.G., Burgess, S.R., Whisner, K.C., and Reneke, P.A., eds., *Papers from 1991-2006 Halon Options Technical Working Conferences (HOTWC)*, CD-ROM, NIST SP 984-4, National Institute of Standards and Technology, Gaithersburg, MD, (2006).
155. Heathfield, A.E., Anastasi, C., Pagsberg, P., and McCulloch, A., "Atmospheric Lifetimes of Selected Fluorinated Ether Compounds," *Atmospheric Environment* **32**, 711-717 (1998).
156. Grzyll, L. R., Back, D. D., Ramos, C., and Samad, N.A., *Development of a Rapid Screening Technique for Second-Generation Halon Alternatives*, SBIR Phase II Final Report, Contract Number DAAH01-93-C-R150, (1996).
157. Minor, B., "Compositions Including a Three Carbon Cyclic Fluoroether," U.S. Patent No. 5480572 (1996).
158. Minor, B., "Compositions Including a Fluoroamine and a Second Component," U.S. Patent No. 5441659 (1995).
159. Minor, B., Chisolm, T. E. C., and Shealy, G. S., "Azeotrope (Like) Compositions with Fluoromethyl Trifluoromethyl Ether and Dimethyl Ether," U.S. Patent No, 5607616 (1997).
160. Sekiya, A. and Misaki, S., "A Continuing Search for New Refrigerants," *Chemtech* **26**, 44-48 (1996).
161. Chueh, C.F. and Swanson, A.C., "Estimation of Liquid Heat Capacity," *Canadian Journal of Chemistry* **51**, 596-600, (1973).
162. Church, C.F., and Swanson, A.C., "Estimating Liquid Heat Capacity," *Chemical Engineering Progress* **69**, 83-85. (1973).
163. Fishtine, S.H., "Reliable Latent Heats of Vaporization," *Industrial and Engineering Chemistry* **55(4)**, 20-28 (1963).
164. Rihani, D.N. and Doraiswamy, L.K., "Estimation of Heat Capacity of Organic Compounds from Group Contributions," *Industrial and Engineering Chemistry Fundamentals* **4**, 17-21 (1965).
165. Hawley, G.G., *Condensed Chemical Dictionary*, Eighth Ed., Van Nostrand Reinhold Company, New York (1971).
166. 3M Corporation; web site <http://www.mmm.com/fluids/7100.html>.

167. Salvi-Narkhede, M., Adcock, J.L., Gakh, A., and Van Hook, W.A., "Vapor Pressures, Liquid Molar Volumes, Vapor Non-ideality, and Critical Properties of  $\text{CF}_3\text{OCF}_2\text{CF}_2\text{CF}_3$ , *c*- $\text{CF}_2\text{CF}_2\text{CF}_2\text{CF}_2\text{O}$ ,  $\text{CF}_3\text{OCF}_2\text{OCF}_3$ , and  $\text{CF}_3\text{OCF}_2\text{CF}_2\text{H}$ ," *Journal of Chemical Thermodynamics* **25**, 643-647 (1993).
168. Wang, B.H., Adcock, J.L., Mathur, S.B., and Van Hook, W.A., "Vapor Pressures, Liquid Molar Volumes, Vapor Non-Idealities, and Critical Properties of Some Fluorinated Ethers:  $\text{CF}_3\text{OCF}_2\text{OCF}_3$ ,  $\text{CF}_3\text{OCF}_2\text{CF}_2\text{H}$ , *c*- $\text{CF}_2\text{CF}_2\text{CF}_2\text{O}$ ,  $\text{CF}_3\text{OCF}_2\text{H}$ , and  $\text{CF}_3\text{OCH}_3$ ; and of  $\text{CCl}_3\text{F}$  and  $\text{CF}_2\text{ClH}$ ," *Journal of Chemical Thermodynamics* **3**, 699-710 (1991).
169. Matsuo, S., Tanaka, Y., Takada, N., Yamamoto, H., and Sekiya, A., "Gaseous Thermal Conductivities of Fluorinated Methyl Ethyl Ethers," *Journal of Chemical and Engineering Data* **43**, 473-476 (1998).
170. Apollo Scientific, Derbyshire, UK; <http://www.apolloscientific.co.uk/>.
171. Hamins, A., Gmurczyk, G., Grosshandler, W., Rehwoldt, R. G., Vazquez, I., Cleary, T., Presser, C., and Seshadri, K., "4. Flame Suppression Effectiveness," in *Evaluation of Alternative In-Flight Fire Suppressants for Full-Scale Testing in Simulated Aircraft Engine Nacelles and Dry Bays*, Grosshandler, W. L., Gann, R.G., and Pitts, W.M., eds., NIST SP 861, pp. 345-465, National Institute of Standards and Technology, Gaithersburg, MD (April, 1994).
172. Lutz, A.E., Kee, R.J., Grcar, J.F., and Rupley, F.M., *OPPDIF: A Fortran Program for Computing Opposed-Flow Diffusion Flames*, SAND96-8243, Sandia National Laboratories, Livermore, CA (1996).
173. Kee, R.J., Rupley, F.M., Meeks, E., and Miller, J.A., *CHEMKIN-III: A FORTRAN Chemical Kinetics Package for the Analysis of Gas-Phase Chemical and Plasma Kinetics*, SAND96-8216, Sandia National Laboratories, Livermore, CA (1996).
174. Frenklach, M., Wang, H., Yu, C.-L., Goldenberg, M., Bowman, C.T., Hanson, R.K., Davidson, D.F., Chang, E.J., Smith, G.P., Golden, D.M., Gardiner, W.C., and Lissianski, V., *GRI-MECH 1.2*, [http://www.me.berkeley.edu/gri\\_mech/](http://www.me.berkeley.edu/gri_mech/).
175. Babushok, V. and Tsang, W., "Inhibitor Rankings for Alkane Combustion," *Combustion and Flame* **123**, 488-506 (2000).
176. Ishizuka, S., and Tsuji, H., "An Experimental Study o the effect of Inert Gases on extinction of laminar Diffusion Flames," *Proceedings of the Combustion Institute* **18**, 695-703m (1981).
177. Puri, I., and Seshadri, K., "Extinction of Diffusion Flames Burning Diluted Methane and Diluted Propane in Diluted Air," *Combustion and Flame* **65**, 137-150 (1986).
178. Hamins, A. Building and Fire Research Laboratory, National Institute of Standards and Technology, Gaithersburg, MD, private communication.
179. Simmons, R.F., and Wolfhard, H.G., "The Influence of Methyl Bromide on Flames, Part 1 – Pre-Mixed Flames," *Combustion and Flame* **1**, 155-161 (1957).
180. Babb, M., Gollahalli, S.R., and Sliepcevich, C.M., "Extinguishment of Liquid Heptane and Gaseous Propane Diffusion Flames," *Journal of Propulsion and Power* **15**, 260-265 (1999).
181. Ural, E.A., "Measurements of the Extinguishing Concentrations of Gaseous Fuels Using the Cup Burner Apparatus," in Gann, R.G., Burgess, S.R., Whisner, K.C., and Reneke, P.A., eds., *Papers from 1991-2006 Halon Options Technical Working Conferences (HOTWC)*, CD-ROM, NIST SP 984-4, National Institute of Standards and Technology, Gaithersburg, MD, (2006).
182. Noto, T., Babushok, V.I., Burgess, D.R.F., Hamins, A., Tsang, W., and Miziolek, A., "Effect of Halogenated Flame Inhibitors on  $\text{C}_1$ - $\text{C}_2$  Organic Flames," *Proceedings of the Combustion Institute* **26**, 1377-1383, 1996.

183. Linteris, G.T., Burgess, Jr., D.R., Babushok, V., Zachariah, M., Tsang, W., and Westmoreland, P., "Inhibition of Premixed Methane–Air Flames by Fluoroethanes and Fluoropropanes," *Combustion and Flame* **113**, 164-180 (1998).
184. Saso, Y., Zhu, D.L., Wang, H., Law, C.K., and Saito, N., "Laminar Burning Velocities of Trifluoromethane–Methane Mixtures: Experiment and Numerical Simulation," *Combustion and Flame* **114**, 457-468 (1998).
185. Papas, P., Fleming, J.W., and Sheinson, R.S., "Extinction of Non-premixed Methane- and Propane-air Counterflow Flames Inhibited with CF<sub>4</sub>, CF<sub>3</sub>H, and CF<sub>3</sub>Br," *Proceedings of the Combustion Institute* **26**, 1405-1411, 1996.
186. Moore, T.A., Weitz, C.A., and Tapscott, R.E., "An Update of NMERI Cup Burner Test Results," 1996, in Gann, R.G., Burgess, S.R., Whisner, K.C., and Reneke, P.A., eds., *Papers from 1991-2006 Halon Options Technical Working Conferences (HOTWC)*, CD-ROM, NIST SP 984-4, National Institute of Standards and Technology, Gaithersburg, MD, (2006).
187. Tapscott, R.E., New Mexico Engineering Research Institute, unpublished data, 1997.
188. Flynn, R.M. and Thomas, S.D., "Fire Extinguishing Process and Composition," U. S. Patent 5,718,293, February 17, 1998.
189. Cohen, N., *Structure-Reactivity Relationships for Predicting Environmentally Hazardous Chemicals*, EPA/600/3-86/072, Environmental Protection Agency, Office of Research and Development, Research Triangle Park, North Carolina, prepared by the Aerospace Corporation, El Segundo, California, December 1986.
190. Prinn, R., Weiss, R.F., Miller, B.R., Huang, J., Alyea, F.N., Cunnold, D.M., Fraser, P.J., Hartley, D.E., and Simmonds, P.G., "Atmospheric Trends and Lifetime of CH<sub>3</sub>CCl<sub>3</sub> and Global OH Concentrations," *Science*, **269** (5221), 187-192, (1995).
191. Wuebbles, D.J., and Connell, P.S., *A Screening Methodology for Assessing the Potential Impact of Surface Releases of Chlorinated Halocarbons on Stratospheric Ozone*, UCID-19233, Lawrence Livermore Laboratory, Livermore, California, November 1981.
192. SynQuest Laboratories, Inc. online catalog, <http://www.synquestlaboratories.com>.
193. Huie, R.E., Orkin, V.L., Louis, F.L., Kozlov, S.N., Kurylo, M.J., "Effect of Bromine Substitution on the Lifetimes and Ozone Depletion Potentials of Organic Compounds," 2002, in Gann, R.G., Burgess, S.R., Whisner, K.C., and Reneke, P.A., eds., *Papers from 1991-2006 Halon Options Technical Working Conferences (HOTWC)*, CD-ROM, NIST SP 984-4, National Institute of Standards and Technology, Gaithersburg, MD, (2006).
194. Tapscott, R.E., and Mather, J.D., "Tropodegradable Fluorocarbon Replacements for Ozone Depleting and Global Warming Chemicals," *Proceedings of the International Conference on Fluorine Chemistry '99*, Tokyo, (1999).
195. Tapscott, R.E., Mather, J.D., "Tropodegradable Fluorocarbon Replacements for Ozone Depleting and Global Warming Chemicals," *Journal of Fluorine Chemistry* **101**, 209-213 (2000).
196. Lifke, J., Martinez, A., Tapscott, R.E., and Mather, J.D., *Tropodegradable Bromocarbon Extinguishants*, Final Report to the Strategic Environmental Research and Development Program, Report 99/8/33350, New Mexico Engineering Research Institute, Albuquerque NM, 2001.
197. Ibiricu, M.M., and Gaydon, A.G., "Spectroscopic Studies of the Effect of Inhibitors on Counterflow Diffusion Flames," *Combustion and Flame* **8**, 51-62, (1964).

198. Hastie, J.W., "Chemical Inhibition of Flames," in *High Temperature Vapors*, Academic Press, New York and London, Chapter 5, pp. 332-357, 1975.
199. Song, C.E., Kim, I.O., Lee, J.K., Kim, T.K., and Lee, S.G., "Liquid Fire Extinguishing Composition," USA, Patent Number 5,219,474, 15 June 1993. Assigned to Korea Institute of Science and Technology, Seoul, Republic of Korea.
200. Weil, E.D., and Marolewski, T.A., "A Review of Phosphate Ester Fire Resistance Mechanisms and Their Relevance to Fluid Testing," in *Fire Resistance of Industrial Fluids*, ASTM STP 1284, Totten, G.E., and Reichel, J., eds., American Society for Testing and Materials (ASTM), Philadelphia, Pennsylvania, 1996.
201. Lask, G., and Wagner, H.G., "Influence of Additives on the Velocity of Laminar Flames," in *Proceedings of the Combustion Institute* **8**, 432-438, (1962).
202. MacDonald, M.A., Jayaweera, T.M., Fisher, E.M., and Gouldin, F.C., "Inhibition of Non-Premixed Flames by Dimethyl Methylphosphonate," *Proceedings of the Central States Section*, The Combustion Institute, Pittsburgh, PA, 1997.
203. Korobeinichev, O.P., Ilyin, S.B., Mokrushin, V.V., and Shmakov, A.G., "Destruction Chemistry of Dimethyl Methylphosphonate in H<sub>2</sub>/O<sub>2</sub>/Ar Flame Studied by Molecular Beam Mass-Spectrometry," *Combustion Science and Technology* **116-117**, 51-67, (1996).
204. Information Handling Services, Material Safety Data Sheets Service, Microfiche Edition, Bimonthly Updates #1060-028, A-04, August/September 1989
205. Riches, J., Grant K., and Knutsen L., "Laboratory Testing of Some Phosphorus-Containing Compounds as Flame Suppressants," 1999, in Gann, R.G., Burgess, S.R., Whisner, K.C., and Reneke, P.A., eds., *Papers from 1991-2006 Halon Options Technical Working Conferences (HOTWC)*, CD-ROM, NIST SP 984-4, National Institute of Standards and Technology, Gaithersburg, MD, (2006).
206. Riches, J., Grant K., Morey, E. and Knutsen L., "A Flame Ionization Detector As A Screening Tool For Halon Alternatives," 2000, in Gann, R.G., Burgess, S.R., Whisner, K.C., and Reneke, P.A., eds., *Papers from 1991-2006 Halon Options Technical Working Conferences (HOTWC)*, CD-ROM, NIST SP 984-4, National Institute of Standards and Technology, Gaithersburg, MD, (2006).
207. Zegers, E.J.P., and Fisher, E.M., "Gas-Phase Pyrolysis of Diethyl Methylphosphonate," *Combustion Science and Technology* **116-117**, 69-89, (1996).
208. Zegers, E.J.P., and Fisher, E.M., "Gas-Phase Pyrolysis of Diisopropyl Methylphosphonate," *Combustion and Flame* **115**, 230-240, (1998).
209. Rapp, D.C., Nogueira, M.F.M., Fisher, E.M., and Gouldin, F.C., "Identification of Stable Phosphorus-Containing Combustion Byproducts by Gas Chromatography/Mass Spectrometry Preceded by Derivatization," *Environmental Engineering Science* **14** (2), 133-140, (1997).
210. Martin, B.L., and Graves, D.J., "Hydrolysis of Trifluoroethyl Phosphate as Evidence that the Serine and Tyrosine Phosphatase Activities of Calcineurin Share the Same Specificity Determinant," *Biochemical and Biophysical Research Communications* **194**, 150-156, (1993).
211. Roddick, D.M., and Schnabel, R.C., "(Fluoroalkyl)phosphine Coordination Chemistry," in *Inorganic Fluorine Chemistry: Toward the 21st Century*, Thrasher, J.S., and Strauss, S.H., eds., American Chemical Society, Washington, DC, pp.421-437, 1994.
212. Johnson, D.A., *Some Thermodynamic Aspects of Inorganic Chemistry*, Ebsworth, E.A.V., Padley, P.J., and Schofield, K., eds., Cambridge University Press, London, UK, 1968, Table 7.2.
213. Sanderson, R.T., *Polar Covalence*, Academic Press, New York, NY, (1983).

214. Sanderson, R.T., *Chemical Bonds and Bond Energy*, Academic Press, New York, NY, (1976).
215. Mahler, W., "Oxidation of Tris(trifluoromethyl)phosphine," *Inorganic Chemistry* **18** (2), 352-354, (1979).
216. Bennett, F.W., Emeléus, H.J., and Haszeldine, R.N., "Organometallic and Organometalloidal Fluorine Compounds. Part VII. Trifluoromethyl Compounds of Phosphorus," *Journal of the Chemical Society*, 1565-1571, (1953).
217. Görg, M., Rösenthaller, G.-V., and Kolomeitsev, A.A., "Facile Syntheses of Tris(trifluoromethyl)phosphine and Difluorotris(trifluoromethyl)phosphorane," *Journal of Fluorine Chemistry* **79**, 103-104, (1996).
218. Emeléus, H.J., and Smith, J.D., "Substitution Compounds of Tristrifluoromethylphosphine with Nickel Carbonyl," *Journal of the Chemical Society*, 527-528, (1958).
219. Burg, A.B., Mahler, W., Bilbo, A.J., Haber, C.P., and Herring, D.L., "The Synthesis of Fluorocarbon Phosphorus Iodides," *Journal of the American Chemical Society* **79**, 247, (1957).
220. Mahler, W., and Burg, A.B., "The Cyclopolyposphines (CF<sub>3</sub>P)<sub>4</sub> and (CF<sub>3</sub>P)<sub>5</sub>, and Related Chemistry," *Journal of the American Chemical Society* **80**, 6161-6167, (1958).
221. Burg, A.B., and Street, G.B., "Perfluoromethylphosphine-Nickel Compounds, Including a New Volatile Heterocycle," *Inorganic Chemistry* **5** (9), 1532-1537, (1966).
222. Emeléus, H. J., and Smith, J.D., "The Heptafluoropropylidodiphosphines and Their Derivatives," *Journal of the Chemical Society*, 375-381, (1959).
223. Phillips, I.G., Ball, R.G., and Cavell, R.G., "Synthesis and Coordination Chemistry (with Platinum(II) and Molybdenum(0)) of New Bis(bis(trifluoromethyl)phosphano)-alkanes. Structure of a New Bis(phosphano)methanide Complex," *Inorganic Chemistry* **27**, 4038-4045, (1988).
224. Cooper, P., Fields, R., and Haszeldine, R.N., "Organophosphorus Chemistry. Part XII. Reactions of Tetramethylbiphosphine and Tetrakis(trifluoromethyl)biphosphine with Olefins," *Journal of the Chemical Society (C)*, 3031-3035, (1971).
225. Ernst, M.F., and Roddick, D.M., "Synthesis and Coordination Properties of Bis(bis(pentafluoroethyl)phosphino)ethane," *Inorganic Chemistry* **28**, 1624-1627, (1989).
226. Brookhart, M., Chandler, W.A., Pfister, A.C., Santini, C.C., and White, P.S., "Synthesis and Reactivity of [(C<sub>2</sub>F<sub>5</sub>)<sub>2</sub>PCH<sub>2</sub>CH<sub>2</sub>P(C<sub>2</sub>F<sub>5</sub>)<sub>2</sub>]Fe(CO)<sub>3</sub>," *Organometallics* **11**, 1263-1274, (1992).
227. Harris, G.S., "Reactions of Halogenobistrifluoromethylphosphines with Amines and Ammonia; and their Behavior with Phosphine and Hydrogen Sulphide," *Journal of the Chemical Society*, 512-519, 1958.
228. Burg, A.B., and Heners, J., "The New Phosphinoamines HN[P(CF<sub>3</sub>)<sub>2</sub>]<sub>2</sub>, CH<sub>2</sub>N[P(CF<sub>3</sub>)<sub>2</sub>]<sub>2</sub>, and N[P(CF<sub>3</sub>)<sub>2</sub>]<sub>3</sub>," *Journal of the American Chemical Society* **87** (14), 3092-3097, (1965).
229. Ang, H.G., and Emeléus, H.J., "Preparation of Bistrifluoromethylamino-derivatives of Phosphorus(III) and Arsenic (III)," *Chemical Communications*, 460, (1966).
230. McElroy, M.B., Wofsy, S.C., Penner, J.E., and McConnell, J.C., "Atmospheric Ozone: Possible Impact of Stratospheric Aviation," *Journal of the Atmospheric Sciences* **31**, 287, (1974).
231. Johnston, H.S., Kinnison, D.S., and Wuebbles, D.J., "Nitrogen Oxides from High Altitude Aircraft: An Update of Potential Effects on Ozone," *Journal of Geophysical Research* **94**, 16351-16363, (1989).
232. Guy B., and De Rudder, A., "The Potential Impact on Atmospheric Ozone and Temperature of Increasing Trace Gas Concentrations," *Journal of Geophysical Research* **92**, 10903-10920, (1987).

233. Miller, C., Steed, J.M., Filkin, D.L., and Jesson, J.P., "The Fluorocarbon Ozone Theory-VII. One-Dimensional Modeling-an Assessment of Anthropogenic Perturbations," *Atmospheric Environment* **15**, 729-742, (1981).
234. Crutzen, P.J., and Arnold, F., "Nitric Acid Cloud Formation in the Cold Antarctic Stratosphere: A Major Cause for the Springtime 'Ozone Hole'," *Nature* **324**, 651-655, (1986).
235. Ioue, G., Izumi, K., and Lozovsky, V.A., "OH Reaction Rate of Halon and CFC Substitutes," in *Development and Evaluation of Countermeasure Technologies for the Stratospheric Ozone Depletion*, Mizuno, K., and Igarashi, M., eds. Environment Agency of Japan, pp. 192-193, 1996.
236. Nelsen, O.J., Sidebottom, H.W., O'Farrell, D.J., Donlon, M., and Treacy, J., "Rate Constants for the Gas-Phase Reactions of OH Radicals and Cl Atoms with  $\text{CH}_3\text{CH}_2\text{NO}_2$ ,  $\text{CH}_3\text{CH}_2\text{NO}_2$ ,  $\text{CH}_3\text{CH}_2\text{CH}_2\text{CH}_2\text{NO}_2$ , and  $\text{CH}_3\text{CH}_2\text{CH}_2\text{CH}_2\text{CH}_2\text{NO}_2$ ," *Chemical Physics Letters* **156**(4), 312-318, (1989).
237. Tuazon, E.C., Carter, W.P.L., Atkinson, R., Winer, A.M., and Pitts, J.N., Jr., "Atmospheric Reactions of N-Nitrosodimethylamine and Dimethylnitramine," *Environmental Science and Technology* **18**, 49-54, (1984).
238. Atkinson, R., and Carter, W.P.L., "Kinetics and Mechanisms of the Gas-Phase Reactions of Ozone with Organic Compounds under Atmospheric Conditions," *Chemical Reviews* **84**, 437-470, (1984).
239. Huheey, J.E., *Inorganic Chemistry*, 3rd Edition, Harper & Row, New York, New York, p. 301, 1983.
240. Heinonen, E.W., Lifke, J.L., and Tapscott, R.E., *Advanced Streaming Agent Development, Volume IV: Tropodegradable Halocarbons, Vol. 4 of 5*, NMERI 96/4/32540, Wright Laboratories (WL/FIVCF) and Applied Research Associates, Inc., Tyndall Air Force Base, Florida, May 1996.
241. Misaki, S., and Sekiya, A., "Development of a New Refrigerant," presented at the International Chemical Congress of Pacific Basin Societies, Honolulu, Hawaii, 17-22 December 1995.
242. Takahashi, K., Inomata, T., Fukaya, H., and Abe, T., "New Halon Replacements Based on Perfluoroalkylamines. An Approach from the Other Side of Fluorine Chemistry," in *Halon Replacements Technology and Science*, ACS Symposium Series 611, Miziolek, A.W., and Tsang, W., eds., American Chemical Society, Washington, DC, Chapter 13, pp. 139-150, (1995).
243. Yasuhara, A., Kaya, K., and Shiraishi, F., "Human Impact of Halon Alternatives," in *Development and Evaluation of Countermeasure Technologies for the Stratospheric Ozone Depletion*, Mizuno, K., and Igarashi, M., eds., Environment Agency of Japan, pp. 190-191, (1996).
244. Abe, T., Hayashi, E., Ono, T., Nishida, M., Fukaya, H., Hayakawa, Y., Terasawa, N., Inomata, T., and Takahashi, K., "Development of Halon Replacements and Their Evaluation as Fire Extinguishers," in *Development and Evaluation of Countermeasure Technologies for the Stratospheric Ozone Depletion*, Mizuno, K., and Igarashi, M., editors, Environment Agency of Japan, pp. 187-189, (1996).
245. Haszeldine, R.N., and Tipping, A.E., "Perfluoroalkyl Derivatives of Nitrogen. Part XVII. The Reaction of N-Bromobis(trifluoromethyl)amine with Olefins," *Journal of the Chemical Society*, 6141-6145, (1965).
246. DesMarteau, D., O'Brien, "An Efficient Synthesis of N-Bromo perhalo-1-alkanamines," *Journal of Organic Chemistry* **49**, 1467-1469, (1984).
247. Bauknight, C.W., and DesMarteau, D., "Reactions of N-Bromodifluoromethanimine," *Journal of Organic Chemistry* **53**, 4443-4447, (1988).
248. O'Brien, B., Thrasher, J., Bauknight, C., Robin, M., and DesMarteau, D., N-Bromodifluoromethanimine, *Journal of the American Chemical Society* **105**, 4266-4267, (1984).

249. Visca, M., Silvani, R., and Marchionni, G., "Hydrofluoropolyethers: Another Alternative to CFCs," *Chemtech* **27** (2), 33-37, (1997).
250. Zhang, Z., Saini, R.D., Kurylo, M.J., and Huie, R.E., "Rate Constants for the Reactions of the Hydroxyl Radical with Several Partially Fluorinated Ethers," *Journal of Physical Chemistry* **96**, 9301-9304, (1992).
251. Cooper, D.L., Cunningham, T.P., Allan, N.L., and McCulloch, A., "Potential CFC Replacements: Tropospheric Lifetimes of C3 Hydrofluorocarbons and Hydrofluoroethers," *Atmospheric Environment* **27A** (1), 117-119, (1993).
252. Suga, A., Mochizuki, Y., Gotoh, Y., Ito, H., Takahashi, M., Yamashita, M., Aoyagi, M., Sekiya, A., Kondo, S., and Hakuta, T., "Estimated Lifetimes of Fluorinated Ethyl Methyl Ethers in Atmosphere," *Chemistry Express* **8** (4), 205-208, (1993).
253. Tuazon, E.C., "Tropospheric Degradation Products of Novel Hydrofluoropolyethers," *Environmental Science and Technology* **31**, 1817-1821, (1997).
254. Imasu, R., Suga, A., and Matsuno, T., "Radiative Effects and Halocarbon Global Warming Potentials of Replacement Compounds for Chlorofluorocarbons," *Journal of the Meteorological Society of Japan* **73** (6), 1123-1136, (1995).
255. Brown, A.C., Canosa-Mas, C.E., Parr, A.D., Pierce, J.M.T., and Wayne, R.P., "Tropospheric Lifetimes of Halogenated Anaesthetics," *Nature* **341**, 635-637, (1989).
256. Misaki, S., and Sekiya, A., "Update on Fluorinated Ethers as Alternatives to CFC Refrigerants," *Proceedings, International Conference on Ozone Protection Technologies*, Washington, D.C., 21-23 October 1996, pp. 65-70.
257. Misaki, S., and Sekiya, A., "Development of a New Refrigerant," presented at the International Chemical Congress of Pacific Basin Societies, Honolulu, Hawaii, 17-22 December 1995.
258. Sekiya, A., and Misaki, S., "Development of Hydrofluoroethers as Alternative Refrigerants and Other Applications," *Proceedings, International Conference on Ozone Protection Technologies*, Baltimore, Maryland, 12-13 November 1997, pp. 26-33.
259. *Climate Change 1995, The Science of Climate Change*, Houghton, J.T., Meira Filho, L.G., Callander, B.A., Harris, N., Kattenberg, A., and Maskell, K., eds., Intergovernmental Panel on Climate Change, Cambridge University Press, Cambridge, England, 1996.
260. "Protection of Stratospheric Ozone: Notice of Acceptability," *Federal Register* **61**(173), 47012-47018, 5 September 1996.
261. Grenfell, M.W., Klink, F.W., Owens, J.G., and Yanome, H., "New Fluorinated Solvent Alternatives," presented at Precision Cleaning '95, Rosemont, Illinois, 15-17 May 1995.
262. Russell, J.P., Szur, A.J., and Terrell, R.C., "Process for making Fluorinated Ethers," U.S. patent 3,897,502, July 29, 1975, assigned to Airco, Inc., Montvale, NJ.
263. Larsen, E.R., *Fluorine Chemistry Reviews*, 1969, pp. 1-44.
264. Personal communications to J. D. Mather from Dr. J. Adcock, University of Tennessee, June/July 2005.
265. Moore, T.A., Weitz, C.A., Tapscott, R.E., "An Update on NMERI Cup Burner Test Results," 1996, in Gann, R.G., Burgess, S.R., Whisner, K.C., and Reneke, P.A., eds., *Papers from 1991-2006 Halon Options Technical Working Conferences (HOTWC)*, CD-ROM, NIST SP 984-4, National Institute of Standards and Technology, Gaithersburg, MD, (2006).

266. Darst, K.P., Ezzell, B.R., and Ishibe, N., "Preparation of a 2,3-dihaloperfluorocarbonyl halide," U.S. Patent 5,557,010), CAS# 181951-69-9, September 17, 1996, assigned to Dow Chemical Co., Midland, MI.
267. Millauer, H., Schwertfeger, W., and Siegemund, G., "Hexafluoropropene Oxide - A Key Compound in Organofluorine Chemistry," *Angewandte Chemie International Edition (English)* **24**, 161-179, (1985).
268. Carnazza, B.P., Owens, J.G., Rivers, P.E., and Schmeer, J.S., "FK-5-1-12 Performance Characteristics: Recent Developments," 2004, in Gann, R.G., Burgess, S.R., Whisner, K.C., and Reneke, P.A., eds., *Papers from 1991-2006 Halon Options Technical Working Conferences (HOTWC)*, CD-ROM, NIST SP 984-4, National Institute of Standards and Technology, Gaithersburg, MD, (2006).
269. Heinonen, E.W., Kaizerman, J.A., Lifke, J.L., Mather, J.D., Moore, T.A., and Tapscott, R.E., *Advanced Streaming Agent Development, Phase 1B: Syntheses, Toxicity, and Decomposition Products*, Final Report, NMERI 96/13/32760, Wright Laboratory, WL-TR-97-XX, 1997.
270. Personal correspondence from Carrie Weitz, NMERI, University of New Mexico, 11 November 1996, to Robert Tapscott, New Mexico Engineering Research Institute.
271. Tapscott, R. E., and Mather, J. D., "Development of a Tropodegradable Total-Flooding Agent, Phase II: Initial Screening," NMERI Report Number 96/22/30930, Advanced Agent Working Group, July 1997.
272. Yang, J.C., Manzello, S.L., Nyden, M.R., and Connaghan, M.D., "Cold Discharge of CF<sub>3</sub>I in a Simulated Aircraft Engine Nacelle," *Proceedings of the Seventh International Symposium on Fire Safety Science*, International Association for Fire Safety Science, pp. 715-726, (2003).
273. Forbes, Lt. Col. S., "Air Force Rationale for Rejecting CF<sub>3</sub>I as a Halon 1301 Replacement for F-16 Fuel Tank Inerting," SAF/AQRE, 12 July 2002.
274. "Suitability of CF<sub>3</sub>I to Replace Halon 1301 as the Inerting Agent in Wing Fuel Tanks on the F-16 Aircraft," Independent Review Panel Report, HydroGeoLogic, Inc., Herndon, VA, 2002. A long summary of this report is available as Gann R. G., "Suitability of CF<sub>3</sub>I to Replace Halon 1301 as the Inerting Agent in Wing Fuel Tanks on the F-16 Aircraft," 2003, in Gann, R.G., Burgess, S.R., Whisner, K.C., and Reneke, P.A., eds., *Papers from 1991-2006 Halon Options Technical Working Conferences (HOTWC)*, CD-ROM, NIST SP 984-4, National Institute of Standards and Technology, Gaithersburg, MD, (2006).
275. Grosshandler, W.L.; Gann, R.G.; Pitts, W.M., eds., "Evaluation of Alternative In-Flight Fire Suppressants for Full-Scale Testing in Simulated Aircraft Engine Nacelles and Dry Bays," Chapters 6, 7, and 8, NIST Special Publication 861, pp. 643-763, National Institute of Standards and Technology, Gaithersburg, MD, 1994.
276. Gann, R.G. ed., "Fire Suppression System Performance of Alternative Agents in Aircraft Engine and Dry Bay Laboratory Simulations," Volume, Chapters 5, 6, and 7, Special Publication 890, pp. 121-404, National Institute of Standards and Technology, Gaithersburg, MD, 1995.
277. Price, H.M., *Compatibility of F-16 Integral Fuel Tank Materials with CF<sub>3</sub>I*, Report MPLR-2686, Lockheed Martin Tactical Aircraft System, October 4, 1999.
- Dante, J.F., Air Force Research Laboratory Memo to Lockheed Martin, 18 Aug 2000.
278. Kenny T.J., Sheperd C.K., Hardy C.J., *Iodotrifluoromethane and Iodoheptafluoropropane Assessment of Cardiac Sensitization Potential in Dogs*, Huntingdon Research Centre. UK, for Armstrong Laboratories, Toxicology Division, Wright-Patterson AFB, OH, 1995.
279. Dodd, D.E. and Vinegar, A., "Cardiac Sensitization Testing of the Halon Replacement Candidates Trifluoroiodomethane (CF<sub>3</sub>I) and 1,1,2,2,3,3,3-Heptafluoro-1-iodopropane (C<sub>3</sub>F<sub>7</sub>I)," *Drug and Chemical Toxicology* **21**(2), 137-149, (1998).

280. Hammann, S.J., Kay, M., Harper, G., Dierdorf, D., Wilson, F., "An Experimental Evaluation of CF<sub>3</sub>I Gas Dispersion," 1997, in Gann, R.G., Burgess, S.R., Whisner, K.C., and Reneke, P.A., eds., *Papers from 1991-2006 Halon Options Technical Working Conferences (HOTWC)*, CD-ROM, NIST SP 984-4, National Institute of Standards and Technology, Gaithersburg, MD, (2006).
281. Vinegar, A., G.W. Jepson, and J.H. Overton. "PBPK Modeling of Short-term (0 to 5 min) Human Inhalation Exposures to Halogenated Hydrocarbons," *Inhalation Toxicology* **10**, 411-429 (1998).
282. Rupnik, J., Bowman, R.G., and Berrill, P., eds., *Suitability of CF<sub>3</sub>I to Replace Halon 1301 as the Inerting Agent in Wing Fuel Tanks on the F-16 Aircraft*, Independent Review Panel Report, HydroGeoLogic, Inc., Herndon, VA, 2002. A long summary of this report is available as Gann R. G., "Suitability of CF<sub>3</sub>I to Replace Halon 1301 as the Inerting Agent in Wing Fuel Tanks on the F-16 Aircraft," 2003, in Gann, R.G., Burgess, S.R., Whisner, K.C., and Reneke, P.A., eds., *Papers from 1991-2006 Halon Options Technical Working Conferences (HOTWC)*, CD-ROM, NIST SP 984-4, National Institute of Standards and Technology, Gaithersburg, MD, (2006).
283. Li, Y., and Wuebbles, D.J., "Potential Impacts of CF<sub>3</sub>I as a Replacement for CF<sub>3</sub>Br in Aircraft Applications," 2005, in Gann, R.G., Burgess, S.R., Whisner, K.C., and Reneke, P.A., eds., *Papers from 1991-2006 Halon Options Technical Working Conferences (HOTWC)*, CD-ROM, NIST SP 984-4, National Institute of Standards and Technology, Gaithersburg, MD, (2006).
284. Li, Y., Patten, G., Youn, D., and Wuebbles, D.J., "Potential Impacts of CF<sub>3</sub>I on Ozone as a Replacement For CF<sub>3</sub>Br in Aircraft Applications," *Atmospheric Chemistry and Physics* **6**, 4559-4568, (2006).
285. DeMore, W.B., Sander, S.P., Golden, D.M., Hampson, R.F., Kurylo, M.J., Howard, C.J., Ravishankara, A.R., Kolb, C.E., and Molina, M.J., *Chemical Kinetics and Photochemical Data for Use in Stratospheric Modeling*, Evaluation Number 12, Jet Propulsion Laboratory (JPL) Publication 97-4, Pasadena, California, 1997.
286. Sander, S.P., Friedl, R.R., Golden, D.M., Kurylo, M.J., Huie, R.E., Orkin, V.L., Moortgat, G.K., Ravishankara, A.R., Kolb, C.E., Molina, M.J., and Finlayson-Pitts, B.J. *Chemical Kinetics and Photochemical D for Use in Atmospheric Studies*, NASA/JPL Publication 02-25, Pasadena, California, 2003.
287. Bein, D.P., "In-Flight Suppressant Deployment Temperatures," 2004, in Gann, R.G., Burgess, S.R., Whisner, K.C., and Reneke, P.A., eds., *Papers from 1991-2006 Halon Options Technical Working Conferences (HOTWC)*, CD-ROM, NIST SP 984-4, National Institute of Standards and Technology, Gaithersburg, MD, (2006).
288. Van Horn, S.R., Vitali, J., Capt. Tucker, J., Delgado, M., and Rodriguez, B., *CF<sub>3</sub>I Agent for Fire Extinguishment in Unoccupied Areas – Aircraft Fuel Tank Inerting Application*, Technology Transition Briefing, AFRL# 99P10VA, ASC Program #292, ASC Validated Technology # 131, 1999.
289. Chattaway, A., Grigg, J., and Spring, D.J., "The Investigation of Chemically Active Candidate Halon Replacements," 1998, in Gann, R.G., Burgess, S.R., Whisner, K.C., and Reneke, P.A., eds., *Papers from 1991-2006 Halon Options Technical Working Conferences (HOTWC)*, CD-ROM, NIST SP 984-4, National Institute of Standards and Technology, Gaithersburg, MD, (2006).
290. Weast, R.C., and Grasselli, J.G., eds., *CRC Handbook of Data on Organic Compounds*, CRC Press, Inc., Boca Raton, FL, (1989).

---

---

## Chapter 8: FLUID DISPENSING AND DISPERSION

Giann C. Yang, Ph.D.  
National Institute of Standards and  
Technology

David Keyser, Ph.D.  
Naval Air Systems Command (retired)

---

---

### TABLE OF CONTENTS

8.1	Introduction.....	722
8.1.1	Characteristics of Aircraft Engine Nacelle Fires.....	722
8.1.2	Summary of Suppressant Fluid Dynamics.....	723
8.1.3	Scope.....	724
8.2	Fluid Storage.....	725
8.3	Fluid Transport through Piping.....	726
8.3.1	Introduction.....	726
8.3.2	Previous Work.....	729
8.3.3	Base Code Selection.....	730
8.3.4	Code Development Work.....	732
8.3.5	Code Theory.....	733
8.3.6	Supporting Laboratory Data.....	753
8.3.7	Comparison of Code Predictions to Experimental Data.....	786
8.3.8	Assessment of Fluid Transport Model.....	804
8.4	Dynamics of Fluid Transport in Cluttered Spaces.....	805
8.4.1	Spray Transport past Generic Clutter Elements.....	805
8.4.2	Spray Interaction with Unheated and Heated Clutter Elements.....	809
8.4.3	Transport around Clutter and Recirculation Zones.....	821
8.4.4	Low Temperature Effects on Agent Dispersion.....	829
8.5	Modeling of Fluid Dispersion in a Nacelle.....	839
8.5.1	Background.....	839
8.5.2	CFD Models.....	839
8.5.3	Code Assessment Using Quarter-Scale Nacelle Tests and Simulations.....	847
8.5.4	Assessment of VULCAN Fire Suppression Sub-model.....	854
8.5.5	Assessment of VULCAN in Suppressant Distribution in a Full-Scale Nacelle.....	863
8.5.6	Assessment of VULCAN in Pool Fire Suppression in a Full-Scale Nacelle.....	868
8.6	Full-Scale Nacelle Fire Suppression Tests.....	871
8.6.1	Experimental Design.....	871
8.6.2	Test Facility.....	872
8.6.3	Test Matrices and Decision Tree.....	876
8.6.4	Actual Test Program.....	878
8.6.5	Instrumentation.....	879
8.6.6	Test Procedure.....	879

8.6.7 Test Results and Comparisons to Simulations .....	882
8.7 Improved Transport of Water to Fires .....	889
8.7.1 Background .....	889
8.7.2 Electrically Charged Water Mist.....	889
8.7.3 A Self-Atomizing Form of Water .....	909
8.8 Summary of Lessons Learned.....	916
8.9 References.....	918

## 8.1 INTRODUCTION

### 8.1.1 Characteristics of Aircraft Engine Nacelle Fires

Serious fires in aircraft engine nacelles, sufficient to terminate a mission, usually involve liquid fuel, either jet fuel or hydraulic fluid, supplied by a leak in its supply system. The primary types of fire are spray fires and pool fires. Fuel sprays occur when a pressurized line develops a relatively small opening, caused by battle or other damage, which results in a misting or atomized discharge of droplets. Fuel from larger openings in pressurized lines may flow over the hot surfaces and ignite there, or end up in pools below the engine contained by aircraft structure or other clutter. Typical ignition sources are electrical sparking and hot surfaces. Because aircraft engines normally produce and reject a lot of heat, the consequence is many and large hot surfaces on the outside of the engine. The air required to maintain combustion is furnished by flow from the atmosphere for which the original purpose is to cool the engine.

The most likely region for fires in engine nacelles is the long, narrow, annular space between the engine core and the outer aerodynamic skin. A large number of components are located within this region, resulting in a complex, cluttered geometry. The nacelle design typically includes ventilation airflow, either via an external scoop or other source, to both cool the nacelle and to avoid the build-up of flammable mixtures. In general, this engineered airflow has sufficient momentum to dominate the buoyancy produced by burning. The dynamics of a fire within an aircraft engine nacelle are typically dominated by the designed airflow.

Presently, aircraft survivability and suppression system proving tests are performed under conditions intended to replicate the nacelle airflow while the aircraft is in flight. Test fixtures, such as the Aircraft Engine Nacelle Fire Test Simulator (AEN) at Wright-Patterson Air Force Base (WPAFB) in Dayton, Ohio, have been constructed to represent variable geometries typical of aircraft nacelles. Extensive sets of experiments and live-fire tests with varying degrees of complex internal geometry have been conducted to evaluate the performance of suppression systems and new agents. These tests and experiments have provided significant insight into the essential features of successful systems and serve as the basis for present system acceptance. However, the results from these tests, particularly when fire extinguishment (as opposed to merely the concentration of agent) is the criterion, are often difficult to understand given the lack of a well-characterized flow field.

Adding to the difficulty in extinguishing fires in nacelles, especially in flight, is their cluttered interiors. These bluff bodies create many “flame-holders” regions with various sizes and shapes downstream of the recirculating zones into which the suppression agents have difficulty penetrating. In the case of pool fires resulting from flammable liquid accumulating at the bottom of the nacelle, one can encounter an unwanted situation where the pool fire is temporarily suppressed by an agent but rapidly flares up again

after the agent is exhausted from the nacelle. The re-ignition of the liquid pool is probably due to continuing fuel vapor generation from the pool and adjacent hot nacelle surfaces not being cooled below the ignition point of the fuel vapor as a result of the suppression action.

A phenomenon, termed *accelerated burning*, has been observed in a diversity of fire suppression tests and was witnessed in this test program as well. It resulted from slow injection of insufficient agent to suppress nacelle engine fires. The injection transient only served to facilitate mixing of fuel vapor and air for combustion. In these cases, the resulting fire could be more intense than if nothing had been done. This phenomenon has been studied by Hamins et al.<sup>1</sup>

### 8.1.2 Summary of Suppressant Fluid Dynamics

Conventional fire suppression systems for aircraft engine nacelle protection typically consist of a pressure vessel, in which a liquid fire suppressant is stored and pressurized with an inert gas, such as nitrogen or carbon dioxide. The fire-suppressant is released remotely by a fast-opening valve upon the indication of fire. The pressurized agent is ejected into the piping manifold and is distributed to the locations in the nacelle, which have been selected by design and analysis for optimum delivery and dispersion of the agent in order to suppress any foreseen fire. A schematic of a fire suppressant system is shown in Figure 8-1.

The pressure vessel governs the initial conditions for agent discharge that affect the subsequent dispersion of the suppressant. The aspects of fluid storage in a pressure vessel are related to the determination of the thermodynamics state of the fluid in the bottle and the sizing of the bottle required to accommodate adequate amount of agent required for fire suppression without compromising the bottle's structural integrity.

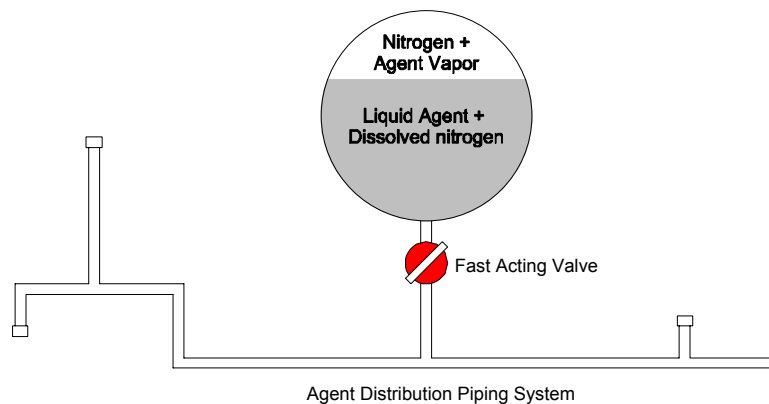


**Figure 8-1. Schematic of Storage and Distribution System for Fire Suppression.**

Once the valve is opened, the pressurized liquid agent is forced out into the distribution system (straight pipes, bends, tees, etc.), which may be at a temperature greater than the boiling point and at ambient pressure. This can cause a multi-component, two-phase flow, which is quite complicated to analyze and measure.

A gaseous suppressant can be easily dispersed throughout the protected space. If a superheated liquid agent is released, flashing will occur, which will greatly facilitate the agent dispersion. Halon 1301, with a boiling point of  $-58\text{ }^{\circ}\text{C}$ , is an example of such a fluid. Because of its flashing characteristics and rapid evaporation, the dispersion of halon 1301 in an enclosure, even cluttered with obstacles, is rapid and effective.

If the suppressant has a high normal boiling point and/or is released at temperatures below its normal boiling point, the liquid droplets formed at the discharge nozzle will persist as they flow through the nacelle. The actual droplet size distribution delivered to the fire will be different from the initial distribution at the discharge nozzle. After liquid droplets form, depending on the droplet number density and droplet ballistics (velocities and trajectories) and even before they arrive at the fire zone, droplet-droplet and droplet-surface interaction may happen in an aircraft engine nacelle due to its highly cluttered environment. These processes may alter the initial droplet size and velocity distributions significantly. The presence of high-speed airflow can also affect the droplet size and velocity distributions. If the dispersing spray encounters a solid obstacle, pooling, dripping, splitting, splashing, or shattering of the droplets will result. Dripping and pooling causes local retention of liquid on the nacelle bottom surface, cutting or splitting of the droplet due to impact at the edge of the surface may result in smaller droplets, and droplet splashing and shattering can generate smaller daughter or satellite droplets. The nacelle surface temperature also plays a role in the droplet-surface interaction.

### 8.1.3 Scope

The NGP determined that, following the discharge of a suppressant from the storage bottle, more needed to be understood about the behavior of the two-phase suppressant flow in the distribution plumbing and the subsequent dispersion of the suppressant from the plumbing outlets to the fire location through the cluttered environment in a nacelle. This chapter presents new understanding of and bases for improvements in the storage, the distribution, delivery, and dispersion of fire suppressants in an aircraft engine nacelle. Prior to the NGP, such a comprehensive approach to the study of fluid dispensing and dispersion for nacelle fire protection applications had never been attempted.

The two-phase distribution flow is discussed in detail in section 8.3. A two-phase computer code, based on a code widely used in the nuclear industries, was developed further for this application. The program was benchmarked against transient experimental data available in the literature, as well as experiments conducted in the NGP study.

The phenomena of liquid suppressant interacting with cluttered elements are discussed in section 8.4. In addition, the effects of liquid boiling point, storage bottle temperature, and nacelle and airflow temperatures on agent dispersion were examined using  $\text{CF}_3\text{I}$  as a surrogate.

Sections 8.5 and 8.6 focus on the study of agent dispersion in a nacelle using computer simulations and full-scale nacelle fire tests. Computational fluid dynamics (CFD) programs were used to simulate these processes, to aid the design of the experiment, to facilitate the formulation of the test matrices, and to predict the outcomes of fire-tests. CFD simulations provide detailed visualization of agent dispersion throughout the nacelle to optimize the locations and number of agent discharge nozzles needed for prototype fire suppression system designs. Agent concentration and agent interaction with probable flame loci can also be predicted to determine the appropriate amount of agent to be stored and the agent

injection duration. Such information leads to the design pressure for the storage bottle and design guidance for efficient agent deployment and provides a high degree of confidence in using simulation tools to guide fire protection system design for nacelles. These advances will also benefit other applications of complex geometry where flame extinguishment must be accomplished in time frames of the order of seconds or faster.

In section 8.7, two other potential strategies to facilitate fluid dispersion have been explored and will be discussed. One involves the use of an electrically charged, water-mist system, and the other examines a self-atomizing form of water employing CO<sub>2</sub> hydrates. Given the geometrical and physical constraints of a nacelle, these two techniques have not been proven to be promising for nacelle applications.

## 8.2 FLUID STORAGE

When the fire suppressant is a fluid, it will most likely be stored in a pressure vessel. In most applications, the release or discharge of the bottle content depends solely on the prevailing internal pressure within the bottle ullage. Yang and coworkers<sup>2</sup> have developed a methodology for predicting this pressure.

For a pure fluid, the ullage pressure will be the vapor pressure of the fluid at the prevailing temperature. If the applications are limited to room temperature or above, fluids with high vapor pressures at room temperature can be released at a moderate rate with adequate driving force within the bottle. However, the discharge can become problematic at very low temperatures where the vapor pressure becomes sub-atmospheric. The conventional way to alleviate this problem is to use a suppressant gas (*e.g.*, nitrogen) to enhance the ullage pressure above the vapor pressure of the fluid at room temperature. In this case, the ullage pressure is maintained at a relatively high level, even at low temperatures, to facilitate the discharge processes. An alternative way to address the low ullage pressure problem at low temperatures is to use the so-called hybrid system wherein an SPGG (solid propellant gas generator), upon activation, provides the pressure source to drive the fluid out of the bottle (see Chapter 9). The focus of this section is on a pure fluid pressurized with a suppressant gas.

The prevailing ullage pressure is critical to the discharge of the bottle content. The pressure can be derived from the thermodynamic state of the suppressant fluid with the pressurized gas under different ambient conditions. The myriad ambient conditions are the result of bottle location and in-flight or on-the-ground environments of an aircraft. The thermodynamic state of the fluid in the bottle not only determines the initial conditions for fluid agent discharge in case of a fire, but also provides data for bottle design in terms of its size and ability to withstand increased internal pressure at elevated temperature.

The ullage pressure in the bottle is a complex function of ambient temperature because of the temperature dependence of the fluid vapor pressure, the partial pressure of pressurized gas in the ullage, and the solubility of the pressurized gas in the fluid. For halon 1301, the bottle pressure-temperature relationship and the solubility of pressurized gas nitrogen in the agent have been well characterized. By contrast, such a relationship and solubility data are scarce or do not exist for many of the halon alternative fluids.

The thermodynamic state of the storage container can be determined by an appropriate equation of state applicable to mixtures (fluid and pressurized gas) with empirical binary interaction coefficients.<sup>3</sup> Other thermodynamic frameworks have also been used.<sup>4</sup> In the following, a brief discussion of the development of a computer code, named PROFISSY, in the Technology Development Program (TDP) to calculate the

thermodynamics state of the bottle will be presented. Detailed description of the code can be found in Yang et al.<sup>2</sup>

PROFISSY (acronym for Properties Of Fire Suppression Systems) was developed for the primary purpose of helping fire suppression bottle designers or users to obtain temperature-pressure characteristics of bottle contents. Simply put, given a vessel charged with agent and nitrogen at room temperature, one would like to know what the final vessel pressure will be when the vessel is at a different temperature. Only four pieces of input information are required to run the program: (1) agent mass, (2) vessel volume, (3) fill temperature, and (4) either nitrogen mass needed to pressurize the vessel, or the fill pressure of the vessel.

The program also predicts whether a liquid-full condition (i.e., the storage vessel is completely filled with liquid with no ullage) would occur at elevated temperatures for a given initial fill density, defined as the amount of liquid divided by the vessel volume. When the initial fill density is above the critical density of the fluid, a liquid-full condition will result due to the thermal expansion of the liquid, to the point that the vessel becomes completely filled as it is heated. A liquid-full condition is undesirable and must be avoided because the internal pressure of the vessel will rise sharply with temperature once a liquid-full condition has been reached.<sup>4</sup> This could result in rupture of the vessel.

PROFISSY incorporates a thermodynamics model known as “extended corresponding states” (ECS).<sup>5</sup> The central idea of extended corresponding states is that all points on the *PVT* (pressure-volume-temperature) surface of any fluid may be represented by scaling the *PVT* surface of a reference substance. These “scale factors” involve the critical properties of the fluid of interest and the reference fluid and may also be functions of temperature and density. The ECS model is a powerful tool, applicable to the entire range of fluid states, from dense liquid to dilute gas, as well as to the supercritical fluid regime. It may be used with only minimal information on a fluid: the critical point, the normal boiling point, and the molecular weight. Additional information on a fluid, such as vapor pressures, saturated liquid densities, and liquid viscosities can be used to refine the model predictions.

The current PROFISSY code, running on a PC, supports thermodynamics state calculations for halon 1301, FC-218, CF<sub>3</sub>I, HFC-125, and HFC-227ea. Experimental data have been obtained to compare to the code predictions for these fluids.<sup>6</sup> In general, the predictions were found to be within 10 % of the measurements.<sup>6</sup> The code can be easily extended to include other fluid/nitrogen systems, if desired.

## 8.3 FLUID TRANSPORT THROUGH PIPING

### 8.3.1 Introduction

As stated above, the current halon delivery systems generally consist of a suppressant vessel connected to the delivery location by a piping network. Prior to the NGP, there was no publicly available simulation tool for transient, two-phase flow through a complex pipe system. There is a need to determine whether the existing piping system for halon 1301 can be used for a replacement agent. For the NGP, Tuzla and coworkers<sup>7</sup> have developed a computer code for two-phase fire suppressant flow in a complex piping system.

Since halon and its potential replacement fluids are in a vapor state at standard pressure and temperature, at the discharge location the fluid will be a two-phase mixture of superheated liquid and vapor. Thus significant thermodynamic and thermal non-equilibrium can be expected between the phases. Also, due to the large pressure difference between upstream source vessel and downstream exit, continuous flashing is anticipated as the fluid travels through the piping, and two-phase critical (choked) flow can occur at various locations.

There has been some work conducted on modeling halon 1301 flows. In a 1988 summary of the state-of-the-art, DiNunno and Budnick<sup>8</sup> indicated that most of the flow calculations were performed using proprietary methods. These methods were verified against standard NFPA procedures for calculations and by discharge testing in sealed tests. However, there were significant uncertainties in the calculations and also in extrapolation of test results to actual configurations.

Pitts et al.<sup>9</sup> described a mathematical model for calculating the discharge of fire-suppressant fluids from a pressurized discharge tank across an orifice at the exit and showed that the transient pressure history in the discharge vessel calculated by the model compared reasonably well to data from experiments. Elliott et al.<sup>10</sup> developed a computer program called HFLOW for predicting the discharge of halon 1301 from a discharge vessel through a piping system. The results of the program compared favorably to the results of experiments conducted with halon 1301 in several piping arrangements. The theoretical model was based on a homogeneous model of two-phase flow. Elliott et al.<sup>10</sup> also modified an existing computer program called SOLA-LOOP,<sup>11</sup> which was originally written for steam-water flows, to be able to model halon 1301. This computer program was a non-equilibrium, non-homogeneous model of two-phase flow, using the drift flux approach to calculate slip between the phases. It was shown that this program, modified to account for halon 1301 properties, was able to capture the physics of the agent discharge more accurately than its predecessor.

The methods described by Yang et al.<sup>2</sup> and Elliott et al.<sup>10</sup> appear to be the only methods available in the public domain for calculating performance of fire-suppressant fluid delivery systems. One way to develop a general, flexible computer program that would be able to model a variety of piping networks and handle several candidate fluids would be to extend this work by modifying these methods. Another approach is to take advantage of the advances in two-phase flow modeling that have taken place in the nuclear power industry, which have resulted in several computer codes available in the public domain. The development of the computer code described here followed the latter approach.

Hence, to predict the performance of the delivery system accurately, a computer code should be a transient two-phase code, which allows for phase non-equilibrium. The short delivery times require fairly high flows, which promote homogeneous two-phase flow, i.e., little slip. However, in imbalanced piping networks, with side tees and other fittings, some separated flow could occur (stratified flows, slug/plug flow, etc.). Hence, the code should be able to predict slip between phases and the corresponding effect on pressure drop. This can be especially important when separated flow encounters directional change, such as at a side tee. The ability to predict the transport of non-condensable gas is also important. The fluid, pressurized with a driver gas, is initially saturated with the gas. During the delivery, as the system depressurizes, the driver gas comes out of the solution and expands. This gas evolution phenomenon needs to be accounted for. One additional requirement is that the code should be useful for estimation of the transient hydrodynamic loads in the piping network. Thus, the momentum equations need to be sufficiently detailed to estimate the unbalanced force in piping sections between locations of elbows and other fittings.

A key technical approach in the present program was utilization of advancements made in other applications that deal with multi-phase flows. In particular, the highly sophisticated computer codes that have been developed for thermal-hydraulic analysis of nuclear power systems have all the characteristics required for analysis of fire suppressant systems. These include models that account for relative slip between liquid and vapor phases, thermodynamic non-equilibrium between the phases, changes in two-phase flow regimes, critical choke flows, and transport of non-condensable gases. Such codes are also structured for numerical analysis of fast transients, well capable of the transients anticipated for suppressant systems.

Since the fluids being considered for use in fire suppressant systems are different from the water/steam system of nuclear power systems, physical property packages need to be modified and expanded. Here again, the NGP leveraged existing technology by borrowing from existing property packages. Specifically, the REFPROP package, developed by NIST<sup>12</sup>, covers many refrigerant fluids, including those that are potential candidates for the fire suppressant systems.

The effort contained an experimental task to obtain data needed to assess the code. The experimental program utilized a discharge loop using several proposed fire suppressants. Major flow parameters, which have not been measured heretofore, were successfully measured. These include measurements of instantaneous discharge flow rate, fluid temperature, and void fraction at various locations along a discharge pipe.

The program is based on a one-dimensional, two-fluid model of two-phase flow. In this model, separate conservation equations are written for the liquid and gas phases for mass, momentum, and energy. Constitutive relationships are specified for interphase transport of mass, momentum, and energy. Heat transfer between the fluid and passive structures such as pipe walls are modeled. The program also contains built-in models for wall friction and two-phase critical flow. The transport of non-condensable gas in the system, namely the nitrogen fill gas, as well as the nitrogen released from solution during agent discharge, is modeled via separate mass conservation equations, with constitutive relations to specify the rate of gas release. The conservation equations are solved using a semi-implicit numerical method, with user-supplied boundary and initial conditions.

The program was deliberately made flexible in terms of types of fluids and piping layout. The current version of the program allows the user to select any one of five fluids: water, halon 1301, CO<sub>2</sub>, HFC-227ea or HFC-125. Modules are available in the program with which the user can model a delivery system, including one or more supply tanks and a combination of piping networks. The user can also model valves in the system, with specified valve opening times if needed.

The suppressant discharge is a highly transient process, generally lasting from less than a second to a few seconds. The program was benchmarked against transient experimental data available in the literature, as well as experiments conducted as a part of this project, on the discharge of HFC-227ea and HFC-125 in a specially prepared discharge loop. The present experiments lasted between 1.5 s to 6 s. In addition to transient system pressure at various points, these experiments also measured critical parameters, such as the transient mass discharge history, fluid temperature, and the void fraction near the exit. These are the first dynamic measurements of mass flow, fluid temperatures, and void fraction during suppression discharge. These new data allowed a more comprehensive assessment of the computer program than possible with previously available experimental data. The results of the assessment showed that the program is capable of predicting the performance of various delivery systems with several fluids.

Detailed description of the development of the computer code can be found in Tuzla et al.<sup>7</sup>, which comprises two volumes. The first volume provides a detailed description of the experimental work and discussion of the results. It also includes a brief description of the theory and numerical solution method, instructions for installation on a personal computer with the WINDOWS operating system, and instructions on preparation of the input needed to describe the system being analyzed. The second volume consists of three appendices: (a) an input manual for the computer program, (b) information on the experimental data, and (c) comparison of the present data to predictions of the computer program. A copy of the computer code can be found in the CD-ROM enclosed in that report.

### 8.3.2 Previous Work

To fully test the computer code developed in this research, comparisons of code predictions against experimental data were made. A literature survey was conducted to find possible sources for experimental data for transient two-phase flows. One widely referenced study is "The Marviken Tests," conducted using water/steam for the nuclear reactor industry and documented in the two reports.<sup>13,14</sup> These tests used a liquid/vapor-filled vessel under high pressure and measured the vertical discharge characteristics as this system was released to atmospheric conditions. A similar test was carried out by Edwards and O'Brien<sup>15</sup>, but focused on the effects of a horizontal discharge. Even though the Marviken and Edwards tests were conducted with water/steam systems, they still provide some means for assessing portions of the code, which use mechanistic models for predicting non-homogeneous, non-equilibrium two-phase flows. These mechanistic models are fluid-independent and can be invoked for all fluids.

Three studies, which more closely reflect the intentions of the current study, have used fire suppressants as their test fluids, rather than water and steam. The work undertaken by Elliot et al.<sup>10</sup> in 1984 includes both theoretical and experimental investigations. In this work, halon 1301 was used as the suppressant fluid. The tests discharged halon under nitrogen gas pre-pressure, resulting in flow of a liquid/vapor/non-condensable-gas mixture through a configuration of piping and an end nozzle. This study provides data on pressure decay as a function of time, allowing for the estimation of discharge flow rates, which are useful for accessing code predictions. This study also provides observations of experimental phenomena as the discharge proceeded. An example is the phenomenon of evolution of the dissolved nitrogen from the liquid halon, which causes an increase in the pressure of the discharge vessel and an increase in the driving force propelling the discharge of the fluid.

The most comprehensive tests conducted to this date were launched in the mid 1990s by the National Institute of Standards and Technology (Yang et al.<sup>2</sup> and Pitts et al.<sup>9</sup>). Their tests not only utilized halon 1301 as a test fluid, but also utilized HFC-125, HFC-227ea, and CF<sub>3</sub>I. They conducted several experimental runs with each fluid, providing extensive data for various pipe configurations and operating conditions. Experiments with different initial fill volumes, pressures, and temperatures were performed to determine their effects on the two-phase system. Their findings provide important information about the characteristics of the two-phase transient flow as it discharges from the source vessel and through the piping. The pressure histograms from this earlier program are used as a benchmark in gauging the effectiveness of the code being developed in the current program.

These prior studies provided the beginning of an experimental database. However, there were no data on several key parameters important to computational code assessment. Primary among these is the instantaneous mass discharge rate and void fraction, both at the exit of the source vessel and at the exit of

the distribution pipe. Such parameters reflect the mechanisms of phase change (vaporization) and interfacial momentum transfer (slip velocity) that must be correctly modeled in the computer code. Without specific experimental measurements of such key parameters, it is impossible to fully assess the validity of any prediction. This is the reason why the current experimental program was structured to obtain a number of additional measurements, above and beyond the usual measurement of pressure decay.

Two-phase flow calculations require thermodynamic and transport properties of the fluid. These properties are required for single-phase liquid, for single-phase vapor, and for saturated vapor/liquid mixtures. The following thermodynamic properties are needed as functions of absolute pressure:

- Saturation temperature
- Specific heat for gas and liquid phases
- Thermal expansion coefficient for gas and liquid phases
- Isothermal compressibility for gas and liquid phases
- Specific volume for gas and liquid phases
- Specific entropy for gas and liquid phases

In addition, the following transport properties are also required for two-phase flow calculations:

- Dynamic viscosity for gas and liquid phases
- Thermal conductivity for gas and liquid phases
- Surface tension

Most fire suppressants are also used as refrigerants. The refrigerant property package REFPROP developed at NIST by Gallagher et al.<sup>12</sup> covers most of the fire suppressants. For example, it contains properties of halon 1301, and present fire suppressant candidate HFC-227ea. After evaluation, it was found that REFPROP was a suitable package for determining the properties required by the new code for two-phase flow calculations with suppressant fluids.

### 8.3.3 Base Code Selection

#### Desired Feature of the New Code

The base code was developed with some specific features in terms of its technical ability to model the basic phenomena of two-phase flows. In addition, user convenience and ease of development were also desirable features. The present development sought to include the following features in the new code.

Required features:

- Non-proprietary, publicly available
- Portable to various computer and operating systems
- Ease of development (well-documented, flexible architecture)

Desired features:

- Non-homogeneous two-phase flow accounting for relative slip between phases
- Non-equilibrium two-phase flow, allowing for metastable conditions during flashing
- Choking under single and two-phase conditions
- Non-condensable (dissolved gas) transport
- Multi-component mixtures (liquids, gases, powders)
- Flexible system modeling capability (choice of piping components and layout)
- Robust set of equations, for simulation of fast transient two-phase flows (for example, momentum equation to include frictional losses, energy equation to include dissipation)
- Demonstrated ability to model representative systems (assessment against experiments)
- Ease of application (user-friendly inputs)

There are other intangible features that have also been considered, such as the existence of an active user group, which would facilitate future modifications and developments.

### **Two-phase Codes Considered**

The relevant codes are those used in the nuclear industry for loss-of-coolant accident analyses (LOCA). These codes address the major phenomena of interest (non-homogeneous, non-equilibrium two-phase flows, choking conditions, fast transients). The survey was limited to codes developed and available in the United States and consisted of RELAP5, RETRAN, TRAC-P, TRAC-B and GOTHIC. Codes developed in other countries that could be used (ATHLET, CATHARE) were not considered because easy access to these codes may not be available.

All these codes have many of the required and desirable features for the present application. They are all based on a two-fluid model of two-phase flow, with constitutive equations to specify the interfacial transport terms. Although some of them have multi-dimensional modeling capability, they are predominantly used in a one-dimensional mode. A brief history of these codes is presented below, with some relevant information:

RELAP5. The version examined of this code was RELAP5/MOD3, version 3.2, available since 1995, RELAP5/MOD3 Code Manual.<sup>16,17</sup> This code was developed at the Idaho National Engineering and Environmental Laboratories (INEEL) under sponsorship of the U.S. Nuclear Regulatory Commission (USNRC). It is used for a variety of reactor accident analyses, including LOCA analyses, for a variety of types of reactors. It is also used in a variety of general thermal-hydraulic analyses in nuclear and non-nuclear systems. It is non-proprietary, and is publicly available, for a transmittal fee, from the USNRC. An active user group, including U.S. and international organizations, meets once a year. Information on user problems, error correction, etc. is transmitted to user group members once every three months.

RETRAN. The version examined of this code was RETRAN-03, RETRAN-03 (1992).<sup>18</sup> This code was developed by Computer Simulations and Analysis, Inc., under sponsorship of the Electric Power Research Institute (EPRI). It is used primarily for analyses of reactor systems, with focus on the primary cooling system, and usually for non-LOCA scenarios. It is proprietary, and can be obtained from EPRI,

with license fees and user group membership fees. The user group, including U.S. and international organizations, is active and meets regularly.

TRAC-P. The examined version of this code was TRAC-PF1/MOD2, TRAC-PF1/MOD2 Code (1992).<sup>19</sup> It was developed by the Los Alamos National Laboratory (LANL) under USNRC sponsorship. It is used primarily for LOCA analysis of pressurized water reactors. It is non-proprietary and can be obtained, for a transmittal fee, from the USNRC. There are a relatively small number of users and no regular user group meetings.

TRAC-B. The version examined of this code was TRAC-BF1/MOD1, TRAC-BF1/MOD1 Code (1992)<sup>20</sup> and TRAC-BF1/MOD1 Models (1992).<sup>21</sup> It was developed by INEEL under USNRC sponsorship. It is used for accident analyses of boiling water reactors. It is non-proprietary and can be obtained from the USNRC for a transmittal fee. The user group is active and meets regularly.

GOTHIC. The version examined of this code was GOTHIC version 5.0, GOTHIC Containment Analysis Package Version 5.0 (1995).<sup>22</sup> It was developed by Numerical Applications, Inc., under EPRI sponsorship. It is used primarily for analysis of reactor containments. It was developed from the COBRA series of codes originally developed at the Pacific Northwest Laboratory under USNRC sponsorship. The original COBRA series of codes are non-proprietary, but were not maintained by the USNRC after the mid-1980's, and are now difficult to obtain. The GOTHIC code is proprietary and can be obtained from EPRI for license fees and user membership fees. The user group is active and meets regularly.

## **Code Selected**

The documentation for each of the candidate codes was reviewed. It was concluded that all the codes listed above have many of the required and desirable features, but none have all of them. The RELAP5 code (MOD3, version 3.2) had more of the required and desirable features than the other codes. In addition, the code had been adapted previously for operation with a fluid other than water, and the code architecture to accomplish this was available in the latest version of the code. This was especially helpful for insertion of new property packages for suppressant fluids. In addition, significant operating and code development experience with RELAP5 had been accumulated, thus providing confidence that the program objectives could be met successfully with this code. Based on these characteristics, RELAP5/MOD3, version 3.2 was selected as the base code platform for the present development.

### **8.3.4 Code Development Work**

#### **Scope of Program**

The FSP computer code, which was derived by modifying the RELAP5/MOD3.2 computer code, is referred to in this section as the base code or, sometimes, as RELAP5. A detailed description of the code, particularly the numerical solution method, is not given here because the base code has been documented extensively.<sup>16,17</sup> Most of the RELAP5 documentation applies to the FSP code. Users interested in the details of the solution method should refer to that documentation.

The main modifications to the base code in developing the FSP code were:

1. **Fluid Properties:** The base code was based on water-steam systems. This was supplemented in the FSP code by using the REFPROP fluid properties package.<sup>12</sup> In this version of FSP, four fluids have been incorporated, halon 1301, CO<sub>2</sub>, HFC-227ea, and HFC-125. Any of these alternate fluids can be selected by the user. Water properties, which were the default option in the base code, have not been removed, and hence water is also one of the fluid options in FSP.
2. **Constitutive Relationships:** The code requires specification of constitutive relationships, such as for the calculation of wall drag and interphase drag, to provide closure for the basic two-phase flow conservation equations used by the two-fluid model. In the base code, several of these relationships were based on experimental data from water-based systems and were uniquely applicable to these systems. These relationships were modified in FSP to be fluid-independent. The specific areas modified were the interphase drag models in vertical flow, and wall heat transfer models for critical heat flux and transition boiling.
3. **Release of Dissolved Gas:** The base code contained transport equations for non-condensable gas in the gas phase and also for a solute (boron) in the liquid phase. In FSP, these transport equations were modified. The noncondensable gas transport equation was modified to include a source term to account for release of dissolved gas. The boron transport equation was altered to reflect transport of dissolved gas as the solute instead of boron. A sink term was added to this equation for conserving the total amount of noncondensable gas in the system. This approach allowed modeling the release of gas anywhere in the system based on local conditions. New constitutive relations were added to represent the gas release rate. This requires specification of two additional parameters, a critical bubble radius for initiating the gas release, and a rate constant. These parameters have been implemented in FSP as user input variables.

The above major modifications were made to the base code to develop the FSP code. There were some additional minor modifications, primarily for making the code usable on PC-based computer platforms. This version of FSP runs on a WINDOWS 95/98 operating system. Installation and detailed code implementation instructions can be found in Tuzla et al.<sup>7</sup>

### 8.3.5 Code Theory

The base code, RELAP5, was originally written in Standard FORTRAN-77 to run on the UNIX Operating System, but had been adapted to other operating environments. The version of RELAP5 chosen for further development is generally considered to be machine-independent and portable to a variety of commonly used operating systems.

To run this program, the user generates an input file. This input file is essentially the description of the problem to be executed. It contains the geometrical description of the system under analysis, the necessary boundary and initial conditions, and other constraints imposed by the user, such as partition of the system into control volumes (nodalization), selection of particular code options and control of the time step used in the numerical solution.

During execution, FSP generates two files, an output file that can be read by the user, and a restart file written in binary format. The output file provides information at time intervals requested by the user in

the input file. The restart file contains all the information the code needs such that the user can restart the code to run for a longer time period, with or without additional changes to the problem description, and is also used for generating graphical output.

The RELAP5 code also contains many user-convenient features and special models, which were developed primarily for nuclear plant analyses, such as the definition of specific components in nuclear systems, and code models to capture the transient behavior of nuclear fuel rods. Some of these are useful for the intended application to fire suppressant fluids and fluid systems, and some are not. In the development of the FSP code, most of the existing features of RELAP5 were retained, although not necessarily useful in modeling fire suppressant delivery systems.

The description of the code presented here is a brief summary, intended to provide basic information for the user. The base code has been documented in great detail,<sup>16,17</sup> and the user is referred to that documentation for additional information, particularly the numerical solution method.

## Governing Equations

The thermal-hydraulic model solves eight field equations for eight primary variables as a function of time ( $t$ ) and distance ( $x$ ). The eight primary dependent variables are pressure ( $P$ ), phasic specific internal energies ( $U_g, U_f$ ), vapor volume fraction or void fraction ( $\alpha_g$ ), phasic velocities ( $v_g, v_f$ ), noncondensable quality ( $X_n$ ), and solute density ( $\rho_b$ ). Note that the noncondensable quality is defined as the mass fraction of noncondensables in the gas phase, the remaining fraction being the mass fraction of fluid in the gas phase. Of these eight variables, six are state variables ( $P, U_g, U_f, \alpha_g, X_n, \rho_b$ ) and two are velocities ( $v_g, v_f$ ). The corresponding eight field equations are the conservation equations for mass, momentum and energy for each phase, and the conservation of mass for the noncondensables in the gas and liquid phases. The equations are described in detail in RELAP5-1, 1995. The simple forms of these equations are shown below, as one-dimensional area-averaged equations, on a per unit volume basis.

### Conservation of Mass:

Gas Phase:

$$\frac{\partial}{\partial t}(\alpha_g \rho_g) + \frac{1}{A} \frac{\partial}{\partial x}(\alpha_g \rho_g v_g A) = \Gamma_g + \Gamma_N \quad (8-1)$$

Liquid Phase:

$$\frac{\partial}{\partial t}(\alpha_f \rho_f) + \frac{1}{A} \frac{\partial}{\partial x}(\alpha_f \rho_f v_f A) = \Gamma_f \quad (8-2)$$

The terms on the right hand side of Equation 8-1 are the interfacial vapor generation per unit volume, and the noncondensable gas released from solution per unit volume. The terms on the right hand side of Equation 8-2 are the corresponding terms for the liquid phase. For continuity across the interface,  $\Gamma_g + \Gamma_f = 0$ . The source term for noncondensable gas,  $\Gamma_N$ , which is the rate of dissolved gas release per unit volume, is treated similar to an external source term. Thus, there is no corresponding term in the liquid phase mass conservation equation. Essentially, this assumes that the liquid density is not affected by the presence of dissolved gas.

**Conservation of Momentum:**

Gas Phase:

$$\begin{aligned} \alpha_g \rho_g A \frac{\partial v_g}{\partial t} + \frac{1}{2} \alpha_g \rho_g A \frac{\partial v_g^2}{\partial x} = & -\alpha_g A \frac{\partial P}{\partial x} + \alpha_g \rho_g B_x A - (\alpha_g \rho_g A) FWG(v_g) \\ & + \Gamma_g A (v_{gf} - v_g) - \Gamma_N A v_g - (\alpha_g \rho_g A) FIG(v_g - v_f) \\ & - C \alpha_g \alpha_f \rho_m A \left[ \frac{\partial (v_g - v_f)}{\partial t} + v_f \frac{\partial v_g}{\partial x} - v_g \frac{\partial v_f}{\partial x} \right] \end{aligned} \quad (8-3)$$

Liquid Phase:

$$\begin{aligned} \alpha_f \rho_f A \frac{\partial v_f}{\partial t} + \frac{1}{2} \alpha_f \rho_f A \frac{\partial v_f^2}{\partial x} = & -\alpha_f A \frac{\partial P}{\partial x} + \alpha_f \rho_f B_x A - (\alpha_f \rho_f A) FWF(v_f) \\ & + \Gamma_f A (v_{fl} - v_f) - (\alpha_f \rho_f A) FIF(v_f - v_g) \\ & - C \alpha_f \alpha_g \rho_m A \left[ \frac{\partial (v_f - v_g)}{\partial t} + v_g \frac{\partial v_f}{\partial x} - v_f \frac{\partial v_g}{\partial x} \right] \end{aligned} \quad (8-4)$$

On the right hand side of Equation 8-3, the second term is the body force and the subsequent terms are the wall friction, momentum transfer due to mass transfer (from vapor generation as well as dissolved gas release), interfacial frictional drag and force due to virtual mass.

**Conservation of Thermal Energy:**

Gas Phase:

$$\begin{aligned} \frac{\partial}{\partial t} (\alpha_g \rho_g U_g) + \frac{1}{A} \frac{\partial}{\partial x} (\alpha_g \rho_g U_g v_g A) = & -P \frac{\partial \alpha_g}{\partial t} - \frac{P}{A} \frac{\partial}{\partial x} (\alpha_g v_g A) \\ & Q_{wg} + Q_{ig} + \Gamma_g h_g + \Gamma_N h_N - Q_{gf} + DISS_g \end{aligned} \quad (8-5)$$

Liquid Phase:

$$\begin{aligned} \frac{\partial}{\partial t} (\alpha_f \rho_f U_f) + \frac{1}{A} \frac{\partial}{\partial x} (\alpha_f \rho_f U_f v_f A) = & -P \frac{\partial \alpha_f}{\partial t} - \frac{P}{A} \frac{\partial}{\partial x} (\alpha_f v_f A) \\ & Q_{wf} + Q_{if} + \Gamma_f h_f + Q_{gf} + DISS_f \end{aligned} \quad (8-6)$$

On the right hand side of Equation 8-5, the third to last terms are the wall heat transfer, interfacial heat transfer, energy transfer due to mass transfer (vapor generation as well as release of dissolved gas), sensible heat due to presence of noncondensables, and dissipation.

**Conservation of Mass for Noncondensables in Gas Phase:**

$$\frac{\partial \alpha_g \rho_g X_n}{\partial t} + \frac{1}{A} \frac{\partial}{\partial x} (\alpha_g \rho_g X_n v_g A) = \Gamma_N \quad (8-7)$$

where

$X_n$  = mass fraction of noncondensable gas in the gaseous phase

$\Gamma_N$  = noncondensable gas generation rate

This equation conserves mass of noncondensables in the gas phase, and allows transport/distribution of the noncondensables along with the gas phase. It is assumed that the noncondensables are transported at the same velocity as the fluid in the gas phase, that they are in thermal equilibrium with the vapor, and that the properties of the gas phase are mixture properties of the vapor/noncondensable mixture. The sensible heat transfer terms due to the presence of noncondensables in the energy equations represent heat transfer at the noncondensable gas-liquid interface. This is necessary because the interfacial terms use saturation temperature based on the local vapor partial pressure.

**Conservation of Mass for Noncondensables in Liquid Phase (Dissolved Gas):**

$$\frac{\partial \rho_s}{\partial t} + \frac{1}{A} \frac{\partial}{\partial x} (\rho_s v_f A) = \Gamma_s \quad (8-8)$$

where

$\rho_s$  = density of the dissolved nitrogen (solute), i.e., mass of dissolved nitrogen per unit volume

$\Gamma_s$  = negative of mass rate of nitrogen released per unit volume, or solute generation rate

This equation provides the means to model the release of dissolved gas at any location based on local conditions. The gas release model itself is described in a subsequent section, along with the assumptions used in its implementation in the code.

In the base code, it is assumed that at the gas-liquid interface, there is no storage of mass, momentum or energy. In FSP, the dissolved gas release term is modeled similar to that for an external source. It is assumed separately that  $\Gamma_g + \Gamma_f = 0$  (similar to the base code), and that  $\Gamma_N + \Gamma_s = 0$ . Summing Equations 8-3 and 8-4 provides a relationship between the interfacial drag terms  $FIG$  and  $FIF$ . Summing Equations 8-5 and 8-6 provides a relationship between the interfacial mass transfer and interfacial heat transfer. These are essentially the interface jump conditions needed for closure of the conservation equations. Note that in FSP, because of the way in which the dissolved gas release term has been treated, the conservation of mass, momentum and energy at the gas-liquid interface is only approximately satisfied. This is an inherent assumption in the code. The results of executing the code for typical FSP applications have not shown significant effects due to this approximation. If new applications show significant effects, this assumption would have to be re-visited.

To complete the equation set, several terms on the right hand side of the conservation equations need to be specified, such as  $FWG$ ,  $FIG$ ,  $Q_{wg}$ , and  $Q_{ig}$ . These are the constitutive relations, described in a subsequent section. Typically, these are based on mechanistic models and empirical correlations, and are written in terms of velocities, thermodynamic and transport properties, and the temperatures of the liquid and gas phases. Thus, additional relationships have to be defined to relate these to the primary dependent variables of the code.

## Numerical Solution

To solve the above set of equations, the differential conservation equations are cast into a numerically convenient set of finite difference equations, using a staggered spatial mesh arrangement. In this method, mass and energy are conserved over a control volume while momentum is conserved over a cell bounded by the mass and energy cell centers. A semi-implicit method is used for time advancement, where the implicit terms are formulated to be linear in the dependent variables at the new time. Essentially, this requires specification of the partial derivatives of fluid density with respect to the primary dependent variables. Most of the source terms on the right hand side of the equations are also treated semi-implicitly. The noncondensable dissolved gas release term is treated explicitly.

Figure 8-2 shows the staggered mesh concept used in the numerical solution. In the method, scalar variables (pressure, internal energies and void fraction) are defined at the cell centers, at  $K$ ,  $L$ , and so on. Vector quantities (velocities) are defined at the cell boundaries, at the junctions connecting the cells, at  $j$ ,  $j + 1$ , and so on. In this method, to define the flux terms at the boundaries of the mass and energy conservation cells, the void fraction and fluid properties are “denoted” from the upstream cells. Similarly, to estimate friction losses needed in the momentum conservation, “volume velocities” are estimated at cell centers using an averaging procedure of the velocities at the junctions connecting to each cell. The documentation of the base code (RELAP5) provides a detailed description of the method.<sup>16,17</sup> Here, it is noted that the user can access “junction properties” as well as “volume properties” in developing the input model and examining the output of the code.

The governing equations, together with the interface jump conditions, constitutive relations, thermodynamic and transport properties, and property derivatives, as a function of the primary dependent variables, form a closed set of equation. The code solves this set for the primary dependent variables as a function of time and spatial location. Details of derivation of the finite difference equations and the numerical solution method are described in the base code documentation.<sup>16,17</sup>

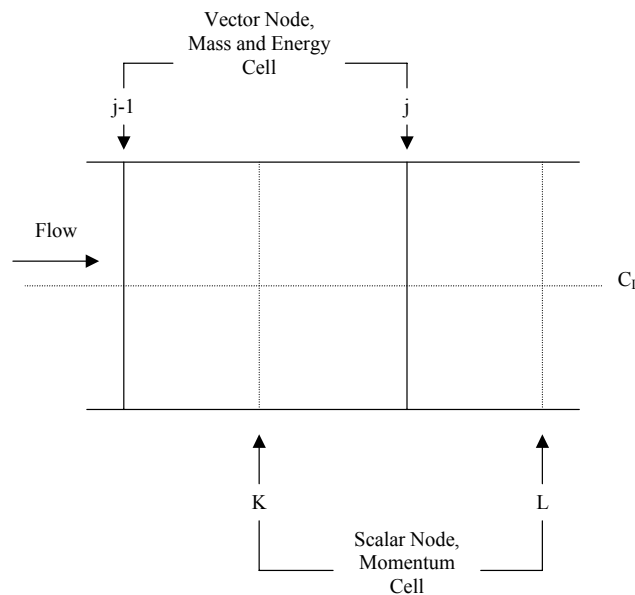


**Figure 8-2. Staggered Mesh Numerical Method.**

## State Relationships and Fluid Properties

As discussed previously, the code uses five primary dependent state variables:

- $P$ : total pressure
- $\alpha$ : gas phase volume fraction
- $U_g$ : gas phase specific internal energy
- $U_f$ : liquid phase specific internal energy
- $X_n$ : mass fraction of noncondensable gas in the gas phase

All thermodynamic variables are expressed in terms of the above five state variables. In addition, several state derivatives are needed for the numerical scheme. Detailed descriptions of fluid property estimation and calculations of thermodynamic variables for the code can be found in Tuzla et al.<sup>7</sup>

## Constitutive Models

The constitutive relations include models for defining two-phase flow regimes and flow-regime-related models for interphase drag and shear, the coefficient of virtual mass, wall friction, wall heat transfer, and interphase heat and mass transfer. Heat transfer regimes are defined and used for wall heat transfer. For the virtual mass, a formula based on the void fraction is used.

Note that while the FSP code contains models for wall heat transfer, these models have not been exercised or assessed with the various new fluids that have been implemented into the code. In addition, wall heat transfer is not expected to play a significant role in the analysis of typical suppressant delivery systems because of the short time period of the expected transient. If a user encounters a special application of FSP where wall heat transfer may need to be included in the model, the base code documentation contains the needed information.<sup>16,17</sup>

The constitutive relations needed are for the terms:  $\Gamma_g$ ,  $\Gamma_f$ ,  $\Gamma_N$ ,  $FWG$ ,  $FWF$ ,  $FIG$ ,  $FIF$ ,  $C$ ,  $Q_{wg}$ ,  $Q_{wf}$ ,  $Q_{ig}$ ,  $Q_{if}$ ,  $Q_{gf}$ ,  $DISS_g$ , and  $DISS_f$ . In general, these relationships are dependent on the thermodynamic state, void fraction, fluid properties and velocities. As shown in Figure 8-2, the thermodynamic state, void fraction and fluid properties are defined at volume centers, while the velocities are defined at the junctions. Fluid properties and the void fraction are “donored” to junctions, and volume velocities are estimated by momentum flux weighting of the velocities at the junctions that connect to each volume. It is convenient to use flow regimes to characterize the two-phase flow. This allows specifying a more mechanistic form to the various constitutive relations, which is desirable since the code is structured to handle various different fluids.

Four flow regime maps are included in the base code, but only two of these are relevant for applications of FSP. The other flow regime maps will not be encountered by the user and are not discussed here. The flow regime maps in FSP address flow regimes and transitions between flow regimes for horizontal flow and vertical flow.

The flow regime maps are based on the work of Taitel et al.<sup>23</sup> and Mishima and Ishii<sup>24</sup>, who have developed flow regime classifications and mechanistic models to describe flow regime transitions.

However, some of their transition criteria are quite complex, and further simplification has been carried out in order to efficiently apply these criteria in the code. When wall heat transfer is not modeled, the flow regimes and the transition criteria are dependent on hydrodynamic conditions only. When wall heat transfer is modeled, there is a possibility that the wall may encounter the condition of critical heat flux (CHF). In the post-CHF condition, the wall will mostly not be wetted by the liquid. This alters the flow regime. To capture this effect, the code recognizes the effect of wall heat transfer explicitly, and if post-CHF conditions are indicated, a separate flow regime map is used to characterize the two-phase flow patterns. Again, note that the post-CHF regimes would be invoked only if the user models wall heat transfer, and the local fluid and wall conditions indicate post-CHF conditions. As discussed above, wall heat transfer is not expected to be required in most applications of the FSP code. Hence, these flow regimes are not described here, and the base code documentation contains detailed description, if needed.<sup>16,17</sup>

The vertical flow regime map (for both up and down flow) is for volumes whose elevation angle  $\phi$  is such that  $45^\circ < |\phi| < 90^\circ$ . This map is modeled as nine regimes – four for pre-CHF heat transfer, four for post-CHF heat transfer, and one for vertical stratification. As noted previously, the post-CHF regimes will not be encountered if wall heat transfer is not modeled by the user. The pre-CHF regimes are the same flow regimes as would exist if there was no wall heat transfer. For pre-CHF heat transfer, the regimes modeled are the bubbly, slug, annular mist, and mist-pre-CHF regimes.

The horizontal flow regime map is for volumes whose elevation angle  $\phi$  is such that  $0^\circ < |\phi| < 45^\circ$ . This map does not distinguish between pre- and post-CHF regimes. Otherwise it is similar to the vertical flow regime map. The horizontal flow regime map consists of horizontally stratified, bubbly, slug, annular and mist-pre-CHF regimes.

In reviewing the base code, RELAP5/MOD3.2, it was found that most of the constitutive relations were structured to be reasonable for the fluids included in FSP. The only areas where correlations specific to water were used were in the computation of interphase drag in vertical flow, and in wall heat transfer. Thus only these calculations were modified. In the description presented below, the emphasis is on providing the user with basic information on what is contained in FSP. Details of the various models can be found in the base code documentation.<sup>16,17</sup> Additional information is provided below in the specific areas where the base code was modified. The dissolved gas release model was developed especially for FSP, and so it is described in more detail than the other models.

### **Wall Friction**

The relevant wall friction terms are *FWG* and *FWF* in the phasic momentum equations. Note that the wall friction force terms include only wall shear effects. Losses due to abrupt area change are calculated using mechanistic form loss models. Other losses due to elbows or complicated flow passage geometry are modeled using energy loss coefficients supplied by the user in the input for junction information.<sup>7</sup> These terms are also directly used in computing the energy dissipation terms,  $DISS_g$  and  $DISS_f$  in the phasic thermal energy equations.

The approach was to first calculate an overall two-phase frictional pressure drop. This was done using a standard two-phase multiplier method (as shown in Wallis<sup>25</sup>). The two-phase friction was then partitioned between the phases (Chisolm<sup>26</sup>) to get the phasic wall friction components. A further adjustment was made to incorporate flow regime effects, using a wetted wall fraction. This provides a more physical

representation for certain regimes where it is clear that one phase would be more influenced by wall friction than the other, as in annular flow, where the wall is fully wetted by the liquid phase.

The model uses the hydraulic diameter and surface roughness data provided by the user for each volume. There is an option for the user to turn off wall friction altogether, but this is not recommended unless as a sensitivity study to debug results from a specific analysis.

### ***Interphase Friction***

The interphase friction (or drag) per unit volume in the phasic momentum equations is expressed in terms of a phasic interphase friction coefficient as:

$$F_{ig} = \alpha_g \rho_g FIG (v_g - v_f) \quad (8-9)$$

and

$$F_{if} = \alpha_f \rho_f FIF (v_g - v_f) \quad (8-10)$$

The magnitude of the interphase drag force per unit volume on the liquid is assumed to be equal to that on the gas phase. This provides a relationship between *FIG* and *FIF*,

$$\alpha_g \rho_g FIG = \alpha_f \rho_f FIF \quad (8-11)$$

The interphase drag force per unit volume represents the interphase momentum transfer rate and is due to the difference between the phasic velocities. Thus, analogous to the transfer of heat or mass, it can be expressed as:

$$F_{i,gf} = F_i (v_g - v_f) \quad (8-12)$$

where  $F_i$  is a momentum conductance term, and can be expressed as:

$$F_i = A_{gf} B_{gf} \quad (8-13)$$

where  $A_{gf}$  is the interfacial area per unit volume, and  $B_{gf}$  is a momentum transfer coefficient.

The code uses the flow regime characterization to derive relationships for  $A_{gf}$  and  $B_{gf}$  in terms of fluid properties, flow geometry, phasic velocities and the void fraction. These are then related back to the terms *FIG* and *FIF* needed in the phasic momentum equations.

The base code, RELAP5/MOD3.2, uses mechanistic models for the above calculations, except for vertical flow in the pre-CHF regimes. In this case, the base code uses a correlation developed empirically from water data. In FSP, to make this independent of the fluid type, the empirical correlation (called the Drift Flux correlation or the EPRI correlation) has been replaced with the mechanistic models. The models are similar to what exists in the base code for the various flow regimes and therefore are not further described here. It is noted that for the calculation of interphase drag in vertical flow in FSP, the vertically stratified regime is not explicitly used. Vertical stratification is recognized primarily for the calculation of interphase heat and mass transfer.

In building the input file, there is a parameter,  $b$ , that allows the user to select an optional interphase drag modeling approach for rod bundles. In FSP, in addition to replacing the interphase drag models for

vertical flow, this option has been essentially de-activated. Thus choosing a value of 0 or 1 for this parameter will not have an effect. It is recommended that the user choose the default value, which is zero.

### ***Interphase Heat and Mass Transfer***

The interphase heat and mass transfer rates are related by the assumption that energy is not stored at the interface. It should be noted that the code separately recognizes interphase mass transfer in the bulk fluid and at an interface near the wall. This allows the code to mechanistically treat some special cases, such as subcooled boiling. In this case, there is a radial temperature gradient within the liquid, and boiling occurs near the wall, while there is condensation in the bulk fluid. Thus, the general treatment is:

$$\Gamma_g = \Gamma_{ig} + \Gamma_w \quad (8-14)$$

where  $\Gamma_w$  is computed by the wall heat transfer models. When wall heat transfer is not modeled, this term is zero.  $\Gamma_{ig}$  is computed from the heat transfer at the bulk interface. The interface is assumed to be at the saturation temperature. The heat transfer at the bulk interface is then:

$$Q_{ig} = H_{ig} (T^s - T_g) \quad (8-15)$$

$$Q_{if} = H_{if} (T^s - T_f) \quad (8-16)$$

$$Q_{ig} + Q_{if} + \Gamma_{ig} (h_g - h_f) = 0 \quad (8-17)$$

where  $h_g$  and  $h_f$  can be at saturation or at the value corresponding to the local pressure and temperature, depending on whether the process is one of boiling or condensation.

The terms  $H_{ig}$  and  $H_{if}$  are the interphase heat conductance terms and are conveniently modeled as products of the interphase area per unit volume and the interphase heat transfer coefficient. These are in turn determined as a function of the flow regime, and modeled as a function of fluid properties, flow geometry, velocities and the void fraction.

### ***Wall Heat Transfer***

The total wall heat flux,  $q''$ , is modeled as a sum of heat fluxes to the vapor and liquid phases:

$$q'' = h_g (T_w - T_{ref,g}) + h_f (T_w - T_{ref,f}) \quad (8-18)$$

where  $h_g$  and  $h_f$  are heat transfer coefficients to the gas and liquid phases respectively (per unit wall surface area), and  $T_{ref,g}$  and  $T_{ref,f}$  are gas and liquid reference temperatures. The reference temperatures can be the local gas or liquid temperature or the saturation temperature, depending on the correlation used for the heat transfer coefficient.

A heat transfer surface concept is used, based on the heat flux, wall temperature and saturation temperature, to decide the mode of heat transfer (such as convection to single phase liquid, bulk nucleate boiling, condensation). Correlations are used for the heat transfer coefficients in the various heat transfer regimes to compute the heat flux. The total heat flux is ensured to be continuous over the heat transfer-wall temperature surface, to avoid numerical difficulties as the heat transfer regimes go through transitions.

Also calculated is the portion of the wall heat flux ( $Q_{ig}^w$  and  $Q_{if}^w$ ) that contributes directly to mass transfer. Then the interphase mass transfer due to wall heat transfer is calculated from:

$$Q_{ig}^w + Q_{if}^w + \Gamma_w (h_g - h_f) = 0 \quad (8-19)$$

where, as before,  $h_g$  and  $h_f$  can be either at saturation conditions or at the local pressure and temperature, depending on whether the process is boiling or condensation.

The base code, RELAP5/MOD3.2 contains generic models for the heat transfer coefficients in most of the heat transfer regimes that can be considered to be reasonably fluid-independent. In two areas, the correlations are more empirical and also based solely on water data. Hence, these have been modified in the FSP code. One area is the critical heat flux (CHF). The base code uses a table look-up procedure for calculating CHF, using data obtained for water at a variety of conditions. This was replaced in FSP by a simpler model, based on a modification to the Zuber correlation (Zuber et al.<sup>27</sup>).

$$q_{CHF} = 1.31(0.96 - \alpha_g) \rho_g h_{fg} [\sigma g (\rho_f - \rho_g) / \rho_g^2]^{1/4} \quad (8-20)$$

Zuber's correlation has been shown to match CHF data for a variety of fluids under pool boiling conditions. The modification to Zuber's correlation is the term  $(0.96 - \alpha_g)$  and has shown to match flow data with water and Freon. Note that this condition of CHF is normally one that is associated with hydrodynamic dryout of a heated surface. This is the type of CHF one may expect when wall heat transfer is modeled with only passive heat structures, such as typical pipe walls in fire-suppressant delivery systems. In implementing the above model in FSP, a lower limit of 1000 W/m<sup>2</sup> was imposed to prevent negative values, at high void fractions.

The other area modified is in the correlation for wetted area fraction used for computing post-CHF heat transfer. This correlation utilizes an exponential decay form to capture the decrease of wetted area fraction as the wall temperature increases. The decay constant was derived as a function of flow rate and void fraction, from water data. In FSP, the decay constant has been set to a fixed value. This is considered reasonable because this heat transfer regime is rarely encountered, and will provide continuity for the heat transfer surface if encountered.

### ***Coefficient of Virtual Mass***

The last term in the phasic momentum equations is the dynamic drag term due to virtual mass effects, also called the inertial drag force per unit volume. In the base code, in the numerical solution procedure, the spatial dependence of the velocities in this term was neglected. Thus the term only includes the time-dependent portion. This was a compromise, because the spatial terms were dependent on the nodalization selected by the user to represent a particular system, and there was some user experience that suggested that this led to numerical errors. The main intent of this term is to capture sudden accelerating flows, and the time-dependent term provides that capability. The coefficient,  $C$ , in this term is called the coefficient of virtual mass. It is given as:

$$C = 0.5 (1 + 2\alpha_g) / (1 - \alpha_g) \quad \text{for } 0 \leq \alpha_g \leq 0.5$$

and,

$$C = 0.5 (3 - 2\alpha_g) / \alpha_g \quad \text{for } 0.5 \leq \alpha_g \leq 1$$

### Release of Dissolved Gas

The liquid agent in the storage vessel is stored under pressure of a noncondensable gas ( $N_2$ ). It is assumed that the agent has been stored for a long enough period for the liquid to be saturated with  $N_2$  (equilibrium condition). At equilibrium, the concentration of dissolved  $N_2$  in the liquid medium is proportional to the partial pressure of  $N_2$  in the gaseous space above the liquid. This is Henry's law:

$$x_N^* = H P_N \quad (8-21)$$

where  $x_N^*$  is the equilibrium concentration (mole fraction of solute in solution),  $H$  is Henry's constant and  $P_N$  is the partial pressure of  $N_2$  above the liquid.  $H$  is usually a function of temperature and the liquid type.

As the system is depressurized, nitrogen will come out of the solution since the partial pressure decreases. According to Henry's law, the corresponding concentration of nitrogen in the solution must also decrease. Hence the excess must be released. In a fast depressurization transient, the excess can still be in solution due to surface tension. Considering a micro-bubble of dissolved gas with radius  $r_c$ , the difference between the pressure inside and outside the bubble is given by

$$\Delta P_{NUC} = \frac{2\sigma}{r_c} \quad (8-22)$$

where  $\sigma$  is the surface tension. As the pressure outside decreases, the pressure difference builds up until a point where surface tension can no longer hold the bubble together, and the excess  $N_2$  is then released. This initiation mechanism is similar to nucleate boiling, in which the liquid is superheated before boiling can occur. The radius of the micro-bubble can be empirically determined by observing the point at which  $N_2$  release occurs. In this model, this radius is assumed known (user input). The release pressure is then given by

$$P_{rel} = P_i - \Delta P_{NUC} = P_i - \frac{2\sigma}{r_c} \quad (8-23)$$

where  $P_i$  is the initial system pressure.

The above determines the initiation of release. The rate of release is determined as follows. Henry's law determines the equilibrium concentration for given conditions. As the system is depressurized, the corresponding partial pressure decreases. The corresponding equilibrium concentration will be less. The solution is therefore at a state of non-equilibrium. The release is a means to achieve a new equilibrium. Thus, the release rate is postulated to be proportional to the difference between the actual concentration and the equilibrium concentration (dictated by Henry's law) as follows:

$$\Gamma_{rel} = \Gamma_0 (x_N - x_N^*) \quad (8-24)$$

where  $\Gamma_0$  is some release coefficient,  $x_N$  is the actual concentration, and  $x_N^*$  is the equilibrium concentration as given by Henry's law. Thus

$$\Gamma_{rel} = \Gamma_0 (x_N - H P_N) \quad (8-25)$$

The release will be zero when the actual concentration approaches the equilibrium concentration, as it should be. The release model is similar to other transfer phenomena, such as heat transfer and mass transfer.

The model requires that users specify, as input, the parameters  $r_c$  and  $\Gamma_0$ , and the initial pressure  $P_i$  and temperature  $T_i$ .

The numerical implementation of the release rate model poses a problem, since the partial pressure is not the local value, but the value above the liquid-gas interface. A compromise is made by using the local total pressure in place of the partial pressure in calculating the equilibrium concentration using Henry's law. This over-predicts the equilibrium concentration, and hence under-predicts the release rate. It may be compensated by using a larger release coefficient. Thus, the release rate is numerically implemented as, for the  $k^{th}$  volume:

$$\Gamma_{rel,k} = \Gamma_0 (x_{N,k} - H P_k) \quad (8-26)$$

$HP_k$  is the mole fraction of  $N_2$  in solution. To convert to mass of  $N_2$  per unit mass of solvent, one gets

$$\text{Mass Fraction } N_2 = \frac{H P_k W_N}{(1 - H P_k) W_f} \quad (8-27)$$

where  $W_N$  is the molecular weight of nitrogen (28.0) and  $W_f$  is the molecular weight of the fluid. The actual concentration is related to the solute density as

$$x_{N,k} = \left( \frac{\rho_s}{\alpha_f \rho_f} \right)_k \quad (8-28)$$

The solute generation rate is therefore the negative of the release rate:

$$\Gamma_{s,k} = -\Gamma_{N,k} = -\Gamma_0 \left[ \left( \frac{\rho_s}{\alpha_f \rho_f} \right)_k - \frac{H P_k W_N}{(1 - H P_k) W_f} \right] \quad (8-29)$$

The above is only valid if the local concentration is greater than the equilibrium concentration. Otherwise the release rate should be zero. Hence

$$\Gamma_{s,k} = \min(\Gamma_{s,k}, 0.0) \quad (8-30)$$

Also, the amount of release in one time step should not be more than the total amount dissolved in the volume. Thus the maximum release rate is given by

$$\Gamma_{rel,k,max} = \frac{\rho_s}{\Delta t} \quad (8-31)$$

where  $\Delta t$  is the current time step. Hence the final expression for the solute generation term is

$$\Gamma_{s,k} = \max \left\{ \min(\Gamma_{s,k}, 0.0), -\frac{\rho_s}{\Delta t} \right\} \quad (8-32)$$

The Henry's constant is estimated from the PROFISSY Code (see Yang et al.<sup>2</sup>) as follows. Assuming Henry's law to be valid, the equilibrium concentration is given by

$$x_N = H P_N \quad (8-33)$$

In PROFISSY, the concentration of nitrogen in the agent liquid ( $x_N$ , mole fraction) is calculated given the system pressure ( $P$ ), temperature ( $T$ ), total volume ( $V$ ), and total agent mass ( $m_a$ ). The partial pressure of nitrogen can be determined from

$$P_N = P - P_v \quad (8-34)$$

where  $P_v$  is the saturation pressure of the agent fluid at  $T$ . Table 8-1 lists the output from PROFISSY, and the calculation of  $H$  as described above. Three fluid systems are considered: HFC-227ea, HFC-125 and halon 1301. As can be seen, the solubility of nitrogen in all three agents is very similar, and Henry's constant can be correlated as a quadratic function of temperature, as shown in Figure 8-3. The analytical form of the correlation is given by

$$H = H_0 + C_1 T + C_2 T^2 \quad (8-35)$$

where  $H$  is in mol/Pa, and  $T$  is in K and  $H_0 = 2.35 \times 10^{-7}$ ,  $C_1 = -1.55 \times 10^{-9}$ , and  $C_2 = 2.96 \times 10^{-12}$

**Table 8-1. PROFISSY Results for Henry's Constants.**

	HFC-227ea/N <sub>2</sub>	Halon 1301/N <sub>2</sub>	HFC-125/N <sub>2</sub>
<i>T</i> (K)	<i>H</i> (mol/Pa)	<i>H</i> (mol/Pa)	<i>H</i> (mol/Pa)
190	n/a	4.70E-08	n/a
200	n/a	4.20E-08	n/a
210	n/s	3.87E-08	3.65E-08
220	3.77E-08	3.67E-08	3.80E-08
230	3.62E-08	3.59E-08	3.37E-08
240	3.52E-08	3.30E-08	3.37E-08
250	3.47E-08	3.45E-08	3.47E-08
260	3.30E-08	3.15E-08	3.41E-08
270	3.34E-08	3.27E-08	3.25E-08
280	3.29E-08	3.28E-08	3.48E-08
290	3.29E-08	3.22E-08	3.40E-08
300	3.36E-08	3.35E-08	3.76E-08
310	3.49E-08	3.74E-08	3.90E-08
320	3.58E-08	3.96E-08	4.45E-08
330	3.79E-08	4.88E-08	5.39E-08
340	4.15E-08	n/a	n/a
350	4.59E-08	n/a	n/a
360	5.42E-08	n/a	n/a

Figure 8-4 shows the calculated bottle pressure as a function of time for various release coefficients. The critical radius was specified at  $7.5 \times 10^{-9}$  m. The initial concentration was estimated as 0.02916 kg N<sub>2</sub>/ kg liquid phase. This value is comparable to the reported initial concentration of Test 146 in Elliott et al.<sup>10</sup> At about 0.1 s, as the pressure decreases to a value of about 4 MPa, there is a noticeable change in the rate of pressure decrease. This is the pressure at which gas begins to be released from the liquid, and experimental results generally indicate that this would happen at about the same pressure for a given fluid type and system configuration. As discussed earlier, this pressure is controlled by the value of the critical gas bubble radius,  $r_c$ , chosen by the user. The lower the value of  $r_c$  specified, the lower the pressure at which gas release would be initiated.

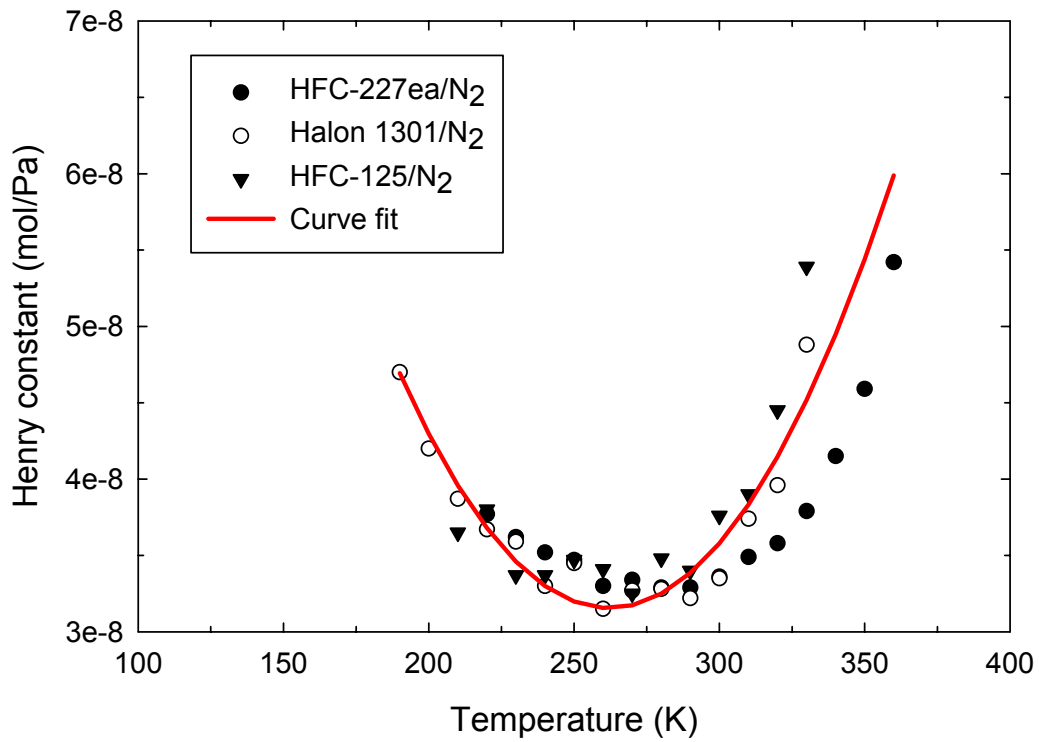


Figure 8-3. Curve Fit for Henry's Constant.

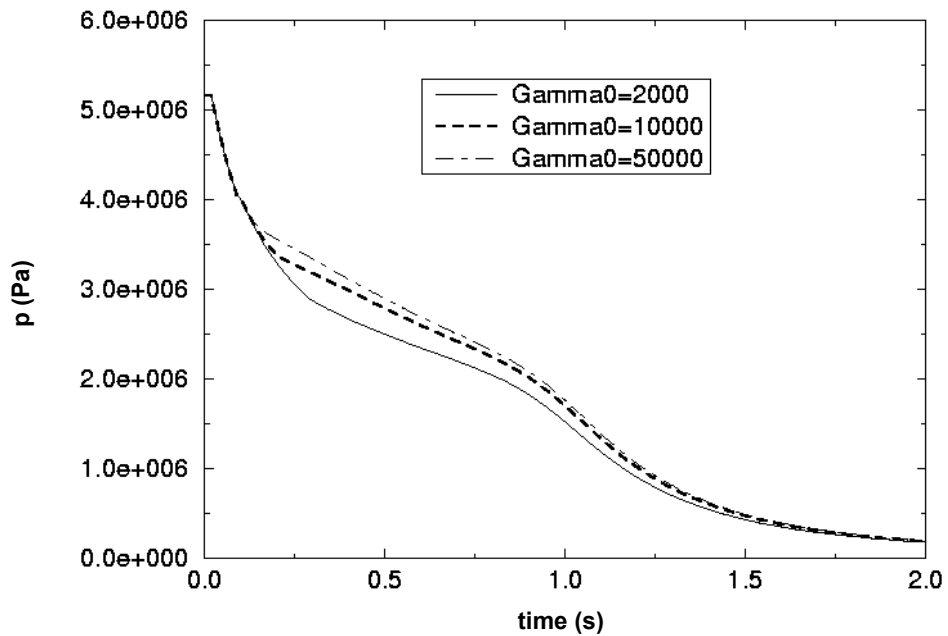


Figure 8-4. Effect of Release Coefficient on Calculated Pressure Response.

The value of  $\Gamma_0$  controls the rate of gas release. At low values of  $\Gamma_0$ , the rate of release is small, and the pressure continues to decrease monotonically below the pressure at which gas release was initiated. As the value of  $\Gamma_0$  is increased, there is a noticeable decrease in the depressurization rate at the gas release pressure (at about 0.1 s). This is the expected trend. Test runs of the code indicate that this method of modeling the gas release works relatively smoothly, and the code appears to handle a wide range of release coefficients without numerical difficulty.

One of these sensitivity cases, corresponding to a  $\Gamma_0$  of 10,000 kg/m<sup>3</sup> s and an initial concentration of 0.02196 kg N<sub>2</sub>/kg liquid, was used to further check out the model. Figure 8-5 compares the calculated pressure with experimental measurements. Figure 8-6 shows the void fraction responses for the various cells used to model the supply bottle. Volume 203-01, not shown in the figure, is at the top of the bottle, and Volume 203-10 is at the bottom. The figure shows a relatively smooth emptying of the bottle, with the void fractions in the lower cells increasing to 1.0 subsequent to the void fractions in the cells above them. The void fraction in the last cell, Volume 203-10, increases to 1.0 after all the other cells, at about 1.0 s. This represents the time in the calculation when the bottle is emptied.

This calculation was also used to check out other parameters. The solute concentration profiles showed smooth changes, following expected trends. A mass balance was carried out to ensure that the code conserved the mass of nitrogen, between the initial amount and the additional amount released from the liquid. Essentially, these checks ensured that the gas release model was implemented in the code as intended, and the mechanistic gas release model produced the expected trends. There is of course some uncertainty in how to specify the correct values for the parameters  $r_c$  and  $\Gamma_0$ . However, as shown in other sections of this report, comparisons to experiments with different fluids and system configurations indicate reasonably good agreement between code calculations and experimental data, with these parameters varying over a relatively narrow range. This has been useful in arriving at a range of recommended values for these parameters. Further, from a design perspective, while variation of these parameters causes a noticeable variation in the initial pressure history, there is not much variation in the time required to empty the supply bottle. Hence it is believed that this gas release model, used with the range of recommended values for  $r_c$  and  $\Gamma_0$ , would adequately serve the needs of a design engineer evaluating the performance of a suppressant delivery system.

## Special Process Models

This section describes certain models in the code that simulate special processes. The user can select many of these processes via input. A detailed description of these process models can be found in the base code documentation.<sup>16,17</sup> The information below is a brief summary, to provide some basic information and where appropriate, some user guidelines on the use of these models.

### *Choked Flow*

Choking is defined as the condition where the mass flow rate becomes independent of the downstream conditions. Choking occurs because acoustic signals can no longer propagate upstream as the fluid velocity equals or exceeds the propagation velocity. In typical FSP applications, choking can occur at the bottle exit, as soon as the discharge begins, and also at the discharge location from the system. The choked flow model in FSP is by Trapp and Ransom<sup>28</sup> and is used to calculate the mass discharge from the

system. The model can also be used to predict the existence of and calculate choked flow at interior points in the system.

The user can select the choking model as a part of the junction control flag information in the input file. The user can select this option at all junctions. In fact, the default option will select the choked flow model. It is recommended, however, that the user only select this model at the system exit location(s) and at the junction representing the exit of the supply vessel. The model should be turned off at all other internal junctions. This is because the sonic velocity (propagation velocity) in two-phase flow can be a strong function of the void fraction, and the choked flow model imposes an external criterion on the code's normal numerical solution method. This can lead to difficulties in code execution and a drastic reduction in the computational time step.

Also note that the input for junctions allows the use of discharge coefficients for subcooled liquid, saturated fluid and single-phase vapor. Current assessment of the code against experiments suggests that best results are obtained by using a subcooled discharge coefficient of 1.0, a two-phase discharge coefficient of 0.8 to 0.9, and a single-phase vapor discharge coefficient equal to the two-phase discharge coefficient.

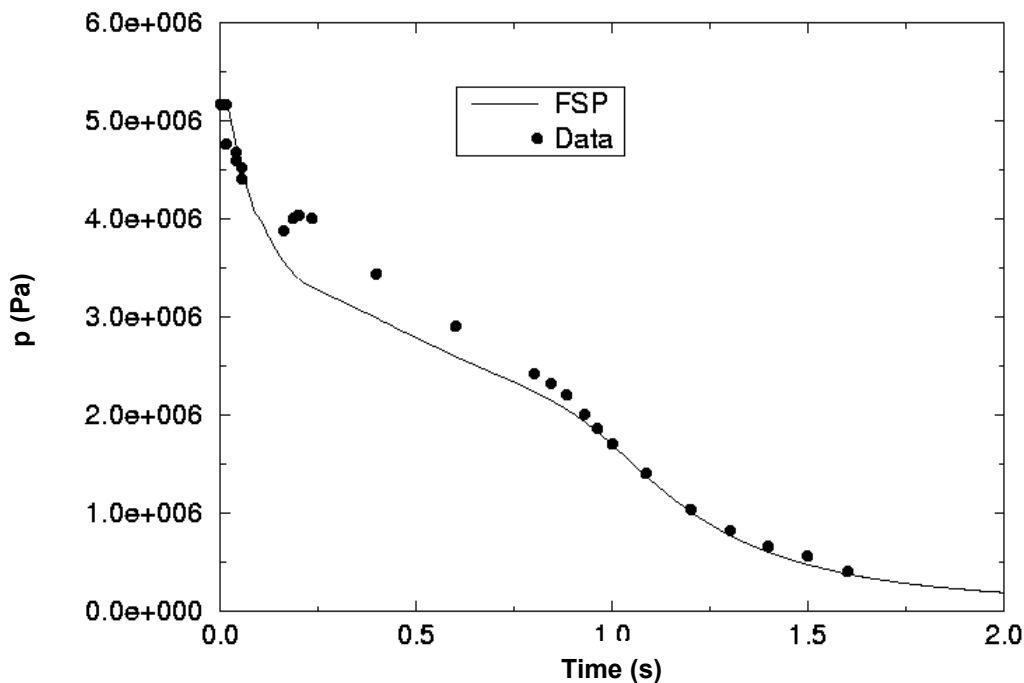


**Figure 8-5. Comparison of Calculated and Measured Bottle Pressure for Test 146.**

### *Horizontal Stratification and Entrainment*

Flow at low velocity in a horizontal pipe can be stratified due to buoyancy forces. The horizontal flow regime map in the code contains a mechanistic model to predict when stratification occurs. When the flow is stratified, the area average pressures are affected by the nonuniform transverse distributions of the phases. The normal code equations are based on assuming uniform transverse pressure distribution. To account for the nonuniform pressure distribution, adjustments are made to the momentum equations to

consider area average pressures for the vapor and liquid phases, and the interfacial pressure between them. This model is always active in the code, but becomes significant only when the code's stratification criterion is met. The code then calculates a liquid level in the channel (circular pipe geometry is assumed) and uses this information to estimate the hydrostatic pressure in the transverse direction.

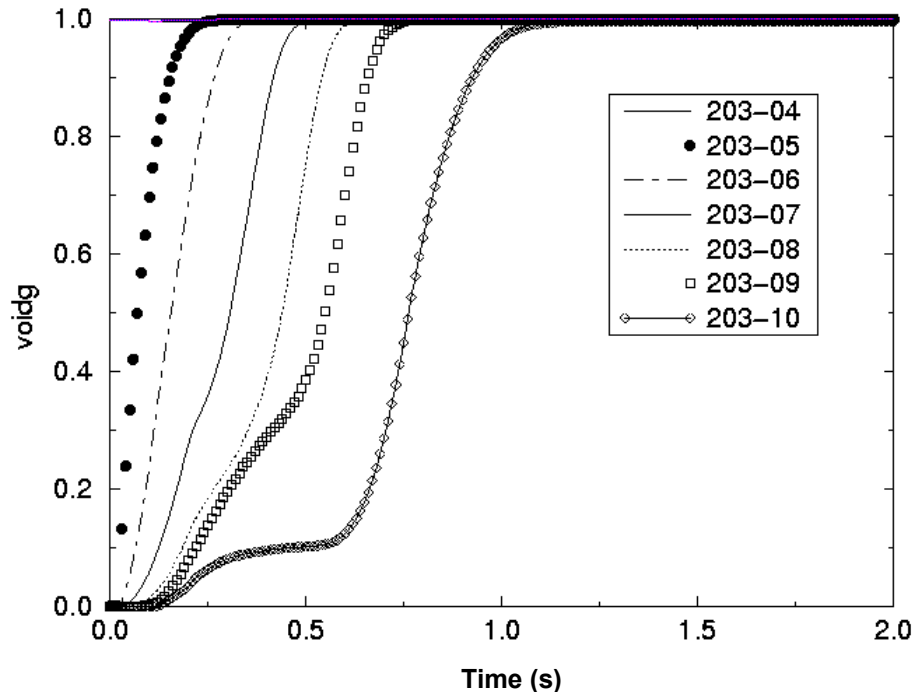


**Figure 8-6. Void Fraction Responses in Lower Portion of Bottle.**

Also, when the flow is stratified, the void fraction flowing in a junction may be different than the upstream volume void fraction. A typical example would be when there is an area contraction. With stratified conditions in the upstream volume, if the level is below the pipe centerline, the void fraction in the junction would be significantly higher than the upstream volume. If the level is above the pipe centerline, the junction void fraction would be lower than the upstream volume. In addition to the formation of a level and its effect, the vapor can entrain liquid through the junction, and similarly the liquid can pull through some gas. The code considers these possibilities, and adjusts the junction void fraction to be different than the upstream volume void fraction when the upstream volume is calculated to be stratified.

The user does not actively engage these models. It is part of the code's internal structure and will automatically be invoked as needed.

### ***Abrupt Area Change***

A general piping network system can contain sudden area changes and orifices. The code contains built-in models for the user to access in simulating these geometries. The basic hydrodynamic model in the code is formulated for slowly varying flow area. Hence, special models are needed when the flow area undergoes an abrupt change, such as at an orifice.

Basically, the user can select the abrupt area change option at any junction in the model, as a part of the junction control flag input information. The code will calculate the energy loss coefficients associated with the abrupt area change internally. In a case where the flow is going through a sudden contraction, the code will also internally compute the losses associated with the formation of a vena contracta. Along with selecting the abrupt area change option, if the user also enters form loss coefficients, these will be added to the internally calculated form losses.

### ***User-Specified Form Losses***

In the junction control flag information card, the user can specify a junction to be a smooth or abrupt area change junction. The user can also specify form loss coefficients at the junction. For standard geometries, and configurations such as elbows and tees, these form loss coefficients can be obtained from standard handbooks. If the user has frictional pressure drop data for a particular system at known flow rates, that can be used to back out form loss coefficients.

The user can also enter flow dependent form loss coefficients. Typically, the form losses would be a function of the Reynolds Number. The code input allows a standard form and the user has to enter the desired constants for the Reynolds Number dependence.

### ***Cross Flow Junction***

The code's numerical method is generally formulated using one-dimensional elements. However, there are applications where an approximate treatment of transverse flow can provide an improved physical simulation. The crossflow junction component provides this feature.

A typical place to use the crossflow junction would be in modeling a standard 90° tee. The crossflow junction would be used to model the connection to the branch line, as shown in Figure 8-7. In this case, the momentum flux in the side branch is assumed to be perpendicular to the main flow stream. Thus the mainstream momentum flux does not contribute to the crossflow momentum formulation. Essentially, in the crossflow junction formulation, there is no transport of axial direction momentum due to the flow in the transverse direction.

The user selects the crossflow junction option by specifying the appropriate connection code when describing the 'From' and 'To' volumes for a junction.

## **Component Models and Systems**

The code contains a variety of generic components that are used to build system models. These include components such as Single Volume, Time-Dependent Volume, Single Junction, Pipe, Valve, etc. Most of these are self-explanatory. This section provides some additional information on building a system model and the use of some of the components and features.

### ***Branch***

There are several ways to simulate branching flows. Several single junctions can be connected to the exit of a single volume to simulate flow splits. A BRANCH component is also provided in the code. Essentially, this functions no differently than a single volume to which more than two junctions are

connected. Primarily, it is a user-convenience, which allows all the junction information to be entered along with the volume information in one component instead of using several separate components. A crossflow junction can be used to connect a branch component to another component. Two typical uses are in modeling branching flows in a one-dimensional branch, and a tee branch.

A one-dimensional branch is one where more than two normal junctions connect to a volume, and where it is assumed that multidimensional effects are small compared to system interaction effects. Typically, this would be used in branched flows that occur in headers or plena. Fluid entering a header and then splitting into several parallel paths would be modeled as a one-dimensional branch.

A tee branch is formed by the arrangement shown in Figure 8-7, where the crossflow junction was used. In this case, the Volume  $V_2$  may be specified as a branch component, and the crossflow junction connecting to it could be defined by the appropriate connection code, described in the input manual in Tuzla et al.<sup>7</sup> The tee connection could also be modeled without a crossflow junction, by using a branch component with normal junctions, as shown in Figure 8-8. This approach has the advantage that fewer volumes are used. The disadvantage is that if the tee is really a standard 90° tee, then it may not be the best representation of the physical process. In typical FSP applications, very little difference has been observed between the two approaches. Hence, either approach seems acceptable.

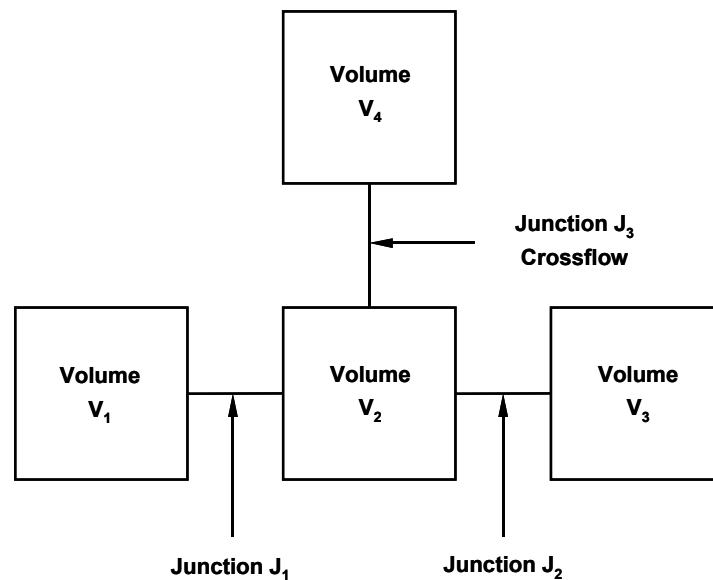


**Figure 8-7. 90° Tee Model with Crossflow Junction.**

Note that a volume with more than two junctions connected to it is treated by the code as a branch component, even if it has not been defined as such in the input. What this really means is that the volume velocity in this volume is determined as a momentum flux weighted average of the flows in the junctions connecting to it. Also, the volume cross-sectional area is apportioned between the various streams in proportion to the volumetric flow in these streams. The consequence is that, if one stream has a very high velocity, there would be excess error in conserving momentum (and mechanical energy) around this volume. One place where this has an impact is if one of the junctions connecting to the branch is the exit junction for the system and it is choked at a high velocity. To avoid this situation, it is recommended that the user allow some straight pipe length connected to all the junctions of a branch. It is also

recommended that when the BRANCH component is used, the junctions of the component use the abrupt area change option.

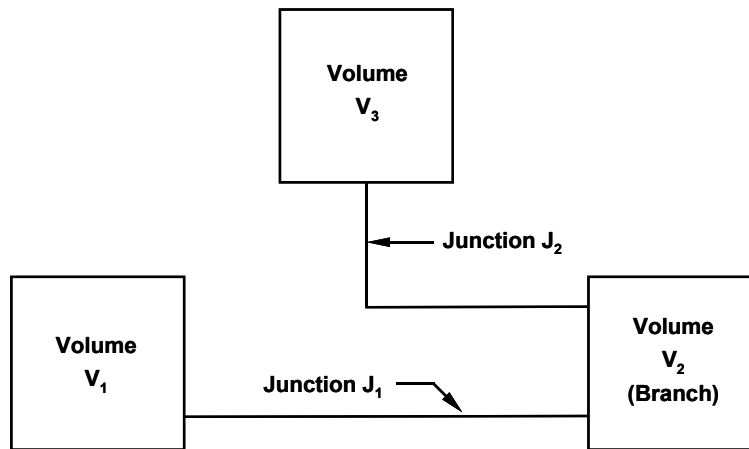


**Figure 8-8. Tee Model with Normal Junctions.**

### *Valves*

Valves are quasi-steady models that are used to either specify an option in a system model or to simulate control mechanisms. They are essentially treated as single junctions and the input required to describe them is similar. There are two categories of valves, those that open and close instantly or those that open and close gradually. The base code contains several types of valves. Only two types are envisioned to be useful in modeling typical fire suppressant delivery systems, and these are described here.

A Trip Valve is one that is fully open or fully closed based on a trip setting. The opening or closing will occur in one time step following the trip signal. The trip signal can be structured to latch the valve in an open or closed position, if desired.

A Motor Valve has the ability to control the junction flow area as a function of time. The operation of this valve is controlled by two trips, one to open and one to close. A user-specified rate parameter controls the rate at which the valve area changes. The abrupt area change option is normally used with this component to allow the code to automatically compute the form loss coefficient as a function of the valve area.

Typical use of this component in FSP applications would be to describe the junction that connects the suppressant supply vessel to the piping system. The valve could be opened as fast as desired by the user to simulate the initiation of the discharge transient.

### *Trip Systems*

The Trip System consists of the evaluation of logical statements. Each trip statement has a true or false result, and an associated variable, TIMEOF. This variable is the time in the transient at which the trip became true and has a value of  $-1.0$  when the trip is false. This variable can be used to set time delays based on events during the transient. Within the code structure, the trip system only evaluates the logical statements (such as, is the transient time greater than 2.0 s?). The decision of what action is needed based

on the trip status resides within other models. In the above example, the trip system would assign a true or false value to a particular trip number depending on whether the transient time was less or greater than 2.0 s. If this trip number is invoked by a valve component, the valve models would decide whether to close or open the valve, at what rate, etc. Using the trip system is fairly self-explanatory, and directions are provided in Tuzla et al.<sup>7</sup>

### **Control Systems**

The control system provides the capability to evaluate simultaneous algebraic and differential equations. This allows simulation of control systems typically used in hydrodynamic systems. Another use is to define auxiliary output quantities, which can then be extracted from the output or restart files as tables or plots.

In typical FSP applications, no complicated trip and control logic is required. Hence, control systems are primarily used to define auxiliary output variables. For example, enthalpy is not a normal code variable, and if it is needed for some reason, it can be computed using several control systems (such as the SUM and MULTIPLIER components) to calculate it from the internal energy, pressure and specific volume, which are all normal code variables. Another example would be if a user wanted to know the Froude Number at the system exit, for evaluating mixing characteristics in the discharge area. A variety of control systems are provided in Tuzla et al.<sup>7</sup>

### **Code Architecture**

The FSP code was developed from the base code RELAP5/MOD3.2, which was written in FORTRAN 77 for a variety of 64-bit and 32-bit computers. In developing FSP from the base code, RELAP5/MOD3.2, the source code was obtained from the Idaho Engineering National Laboratory. This code was adaptable to other computing environments. The code was configured to work on a PC with WINDOWS 95 operating system and tested to ensure that the code options would function properly. The hardware chosen for installation was a laptop PC with a Pentium 233 MHz processor, 64 MB RAM and 3.2 GB hard drive. The compiler used was the Digital<sup>TM</sup> Visual FORTRAN compiler (Standard Edition, Version 5.1) for WINDOWS 95 operating system. The coding is modular, using top-down structuring. The various models and procedures are isolated in separate subroutines. Detailed description of the top-level organization of the code, code installation and execution, input file processing, and graphics for output can be found in Tuzla et al.<sup>7</sup>

### **8.3.6 Supporting Laboratory Data**

Experiments were performed to obtain data for several baseline fire suppressants and to establish a protocol for obtaining such data for any future candidate fluids. These data were then used in the assessment of the product code for simulating possible suppressant delivery systems. Descriptions of pertinent dimensions and design features of the test facility are provided below.

#### **Experimental Test Facility**

The test facility consists of a source vessel for the suppressant fluid, a quick opening discharge valve, a holding rack, a piping network, and a collection tank. This arrangement allows the system to be operated

as a closed loop to recycle the test fluid. A simple schematic is provided in Figure 8-9, showing the layout of the facility. The dimensions of this test system adhere as closely as possible to standard sizes used in present-day fire suppression systems.

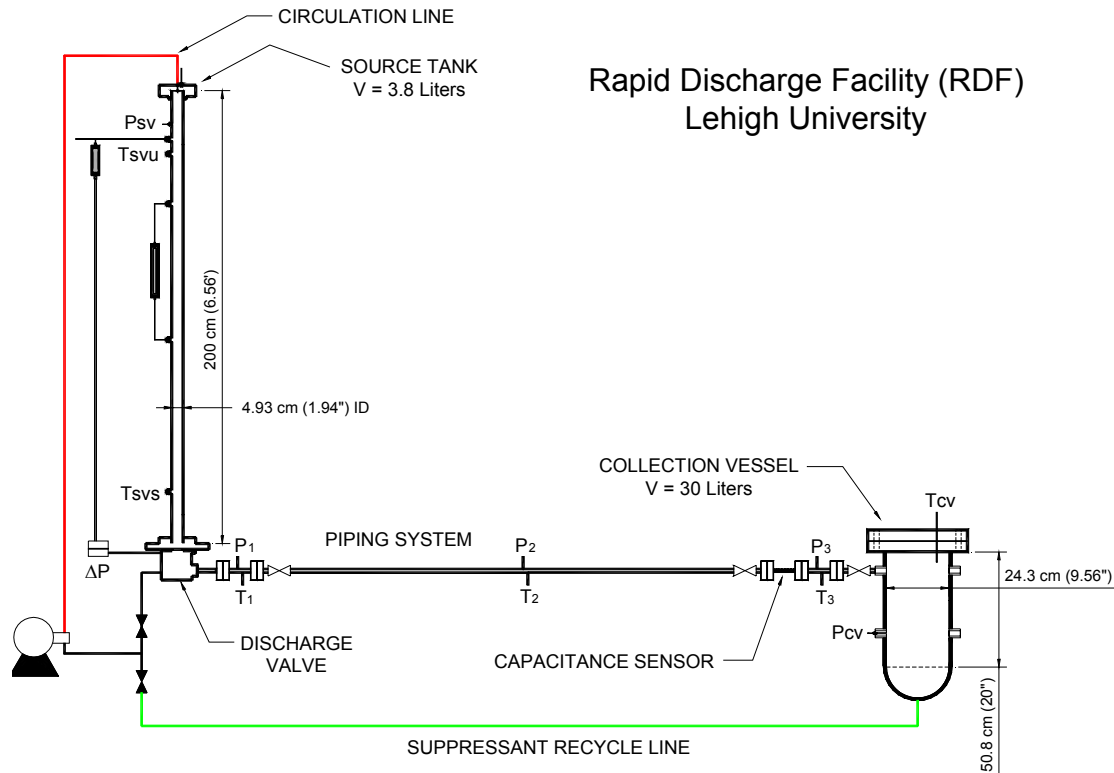


**Figure 8-9. Schematic of Test Facility: Source Vessel, Discharge Piping, and Collection Vessel.**

The source vessel, one of the main components of the facility, is shown in Figure 8-10. The source vessel has a total internal volume of 3.81 L and was initially charged with liquid to about 60 % of that volume. The source vessel was constructed from a 2 m long piece of 5.08 cm nominal diameter stainless steel pipe with an internal diameter of 4.93 cm and a wall thickness of 0.55 cm. Using a vessel of large length-diameter ratio improves the accuracy of measuring liquid inventory. A pressure difference associated with the static head of the liquid in the vessel is used to measure the liquid inventory in the vessel at any time during the experimental run. The long length, or height, of the source vessel provides a greater range of static head measurements, thus increasing the accuracy of determining the transient liquid inventory. This pipe was positioned vertically and capped at both ends by stainless steel pipe flanges approximately 2.54 cm thick. Two slip-on flanges with O-ring grooves for the pressure seals were welded to either end of the pipe so that the top and bottom plates could be bolted in place. The top plate has an identical outer diameter as the flanges, at 16.51 cm, and was tapped to allow for a mixing line inlet and a fill/relief line. The bottom plate has a larger diameter of 27.94 cm for the purpose of anchoring the vessel to the holding rack while minimizing any vibration or movement during operation. This plate was also tapped to allow the discharge valve to be screwed into place and sealed with a crushable, tempered aluminum gasket. Other features incorporated into the source vessel include pressure and temperature

ports, a liquid level gauge, a mixing line, and the differential pressure transducer with fluid transmission line for measurement of liquid inventory.

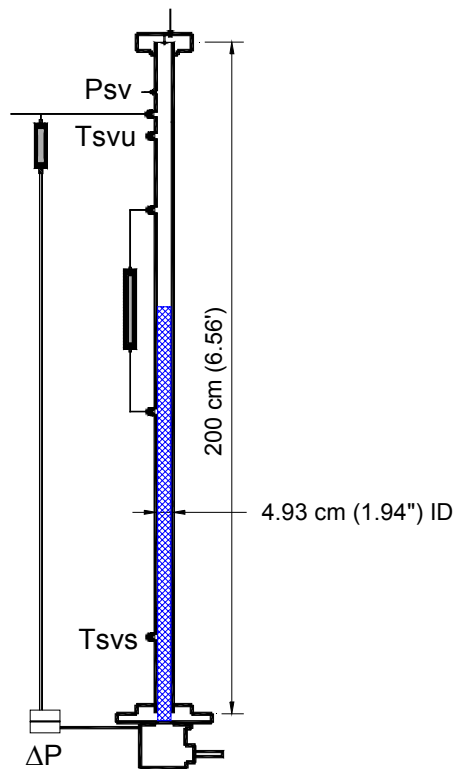


**Figure 8-10. Schematic of Source Vessel Showing Mass Inventory Measurement.**

Since tests required pressures up to (4.04 to 5.05) MPa in the source vessel, pressurization by nitrogen was employed. As shown in Figure 8-11, for HFC-227ea, the equilibrium vapor pressure of suppressant fluids only reaches about 0.505 MPa at room temperature, insufficient for the desired pressure without the additional partial pressure of an inert pressurization gas such as nitrogen. A potential problem with this method is that the total pressure in the vessel will not reach equilibrium until the liquid has become saturated with dissolved nitrogen. In order to expedite this process, a mixing system has been incorporated into the design, using a pump to recycle liquid suppressant from the bottom of the source vessel to a spray nozzle located in the vapor/gas space. By spraying small droplets of liquid through the nitrogen gas, the surface area of liquid in contact with nitrogen will increase, therefore increasing the rate at which nitrogen can be dissolved into the liquid.

Additional ports in the source vessel include an opening near the top, which serves as the connection to the nitrogen supply and as one leg of the transmission line for the differential pressure transducer. A liquid level gauge made of armored glass has also been attached to the middle section of the vessel to visually determine the liquid fill level in the vessel at the beginning of each experimental run. Also, there are two thermocouple ports for the vapor and liquid spaces and a pressure port in the vapor space. The last port is in the top plate, providing access for filling of the vessel and also serving as a connection for a safety pressure-relief device.

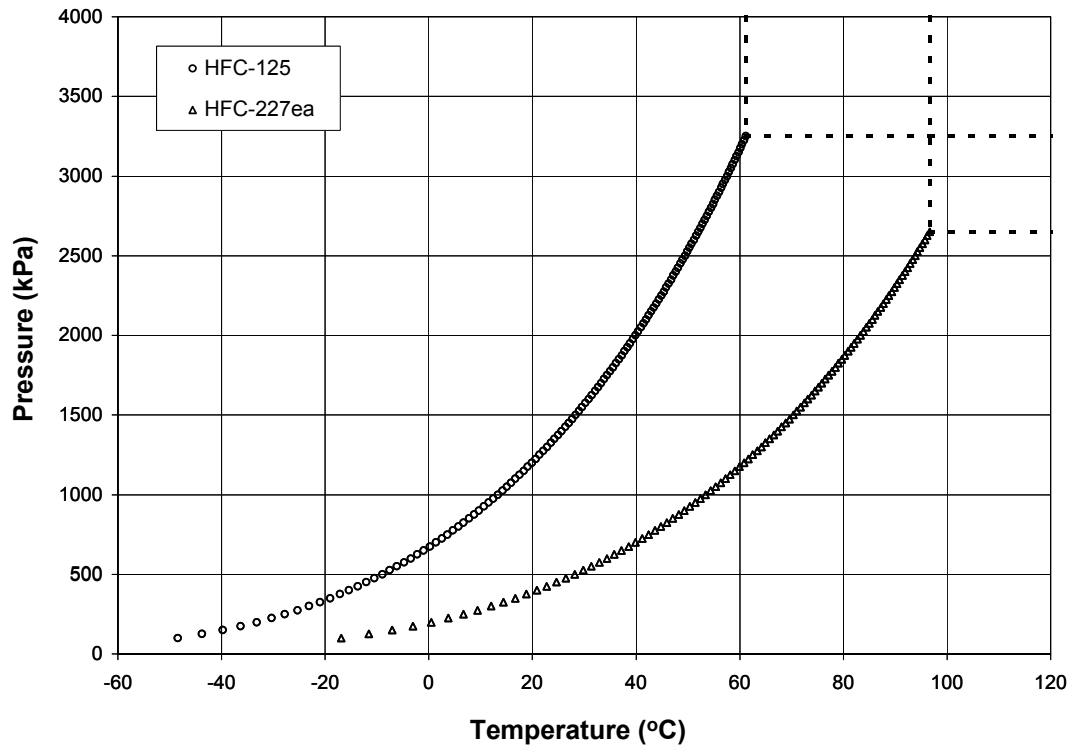


**Figure 8-11. Pressure vs. Temperature Saturation Curve for HFC-227ea and HFC-125.**

The next pertinent item in the design is the release mechanism of the source vessel, for initiating discharge of the test agent. A quick-opening plunger valve with an inlet diameter of 3.18 cm and an exit diameter of 4.45 cm was used for this purpose. This valve, shown in Figure 8-12, is a Model MV121KJ-2 valve made by Marotta Scientific Controls Inc. A feature of this valve is the use of the fluid pressure to drive the plunger upon command; thereby eliminating the need for springs or motors. To set or close the valve, the plunger is pushed up into its armed position and held in place by a small locking latch. Two O-rings are attached to the plunger to form a pressure seal along the valve casing. Pressure must then be provided on the inlet side of the valve for the valve to operate properly. To open the valve, an electrical charge provided by a 20V DC power source releases the latch, allowing the fluid pressure to rapidly drive open the plunger. This release is much faster than that of traditional solenoid valves, and is similar to that of a burst diaphragm or explosive-charge release, which is used in present-day suppression systems. The valve is connected to the 1/2-in discharge piping in the loop by a tapered transition piece. This transition incorporates a flange connection to permit access to the O-ring seals on the plunger for lubrication.

The piping in the test facility consists of 1.27 cm nominal diameter stainless steel pipe with an internal diameter of 1.39 cm and a wall thickness of 0.38 cm. There are five other pieces, including the adapter piece described above, which make up the discharge piping system. Two of these pieces are approximately 30.5 cm in length with flanges at either end to provide for easy disassembly. All the flanges are machined with an O-ring groove to provide an adequate seal against the high pressures experienced in the tests. These 30.5-cm sections will be used as access points at the beginning and end of the piping system, as indicated in Figure 8-13. They will also be the first and last locations of the pressure and temperature measurement ports. Ports for the pressure transducers and film thermocouples used for these measurements required special weld fittings in order to insure a complete pressure seal in

the loop. These fittings were specially designed to cause minimal disturbance to the flow, while allowing for the sensor to be as close to the flow as possible. See Figure 8-14 for a schematic diagram of these fittings.

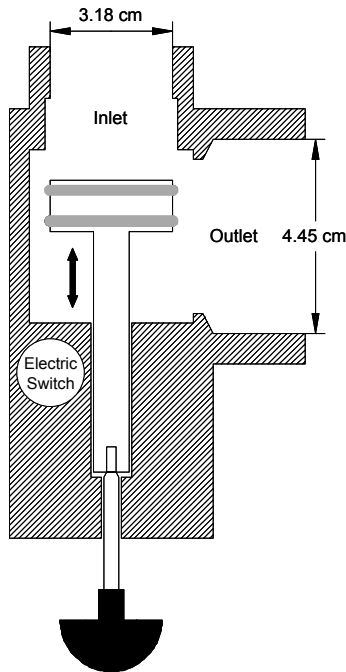


Figure 8-12. Schematic of a Marotta valve.

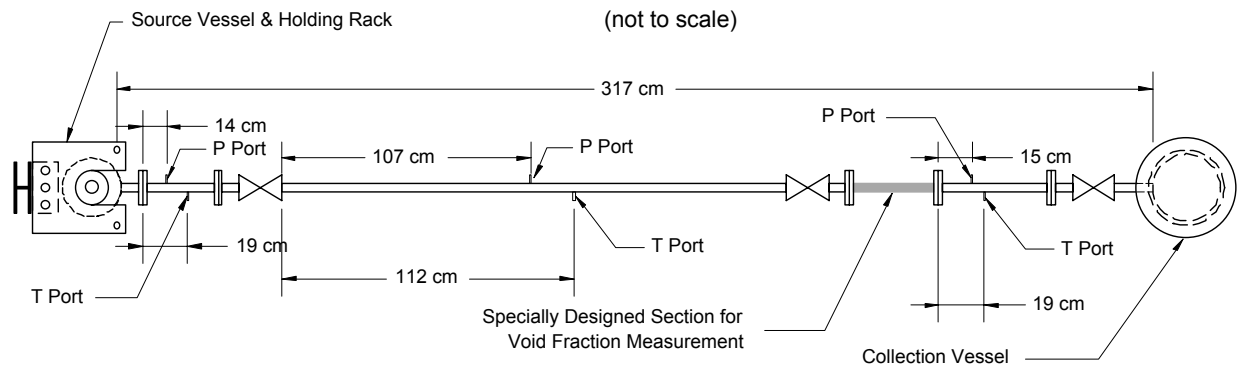
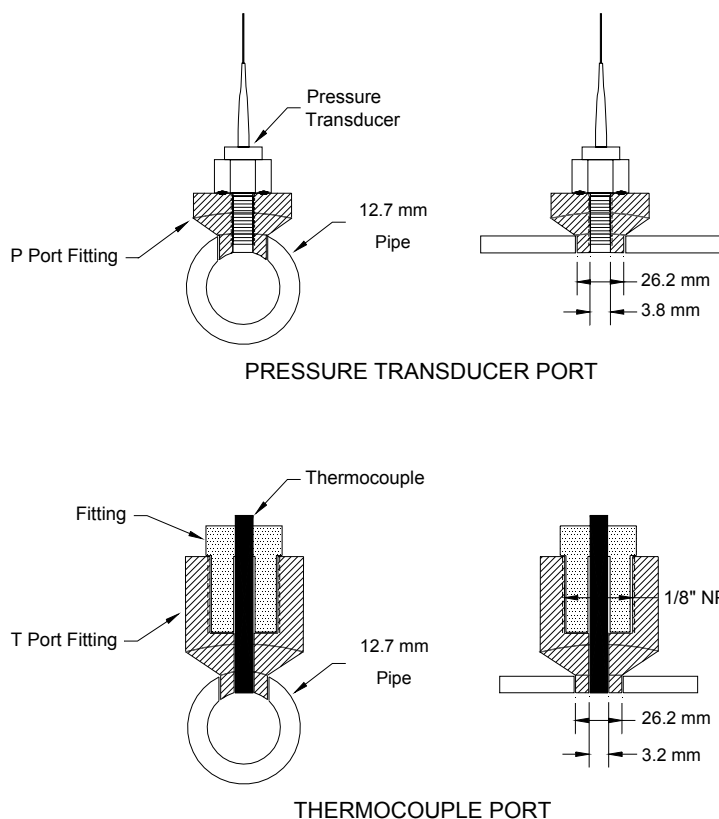


Figure 8-13. Top View of Test Facility; Schematic of Discharge Piping System.

The other two pieces in the piping system include a special section used for the void fraction measurement and a long middle section of pipe. The long middle section of pipe represents the distribution spool piece often found in fire-suppressant piping systems. Both ends are flanged and are capped by valves, allowing for the isolation of this section when dismantling. The middle piece will be tapped in the middle for temperature and pressure ports as described previously. This middle piece of long discharge piping allows for easy reconfiguration to different piping schemes (i.e., inclusion of tees or elbows). This whole piping system is then connected by a flange to the collection vessel, providing a closed flow path from the source vessel, through the piping system, to the collection vessel.



**Figure 8-14. Schematic of Pressure Fittings for Temperature and Pressure Ports.**

The collection vessel is designed to serve two purposes: to catch the test fluid for recycle and to enable monitoring of the transient discharge pressure during test runs. The collection vessel has an internal volume of approximately 30 L, chosen to limit the final pressure after discharge to less than 1.01 MPa to 1.212 MPa. This vessel is made of a 25.4 cm diameter stainless steel pipe with an internal diameter of 24.3 cm and a wall thickness of 1.50 cm. The bottom of the collection vessel is a hemispheric cap with a 1.27 cm port, to be used for emptying the contents. At the top end is a pair of 4.445 cm thick flanges sealed by an O-ring. The outside flange has access holes to allow for a cooling coil, a vacuum line, and a temperature measurement port. The cooling coil can carry either cold water or liquid nitrogen for the purpose of condensing the spent suppressant fluid for recycling. The vacuum line is connected to the top of the vessel for the purpose of relieving the excess pressure before the next run. The line is connected to a knock-back condenser to prevent a minimal amount of suppressant from escaping. Additional ports in the sides of the vessel provide connections for the piping system and a fast-response pressure transducer.

In anticipation of potentially large reaction forces during fluid discharge, a rugged framework was designed to support the test facility. As shown in Figure 8-15, a 20.3 cm I-beam, 305 cm high, was chosen to give a rigid backing for the source vessel while being heavy enough to dampen any vibrations exhibited during the test runs. This rack I-beam is directly bolted to the building structure for rigidity. The rack I-beam has three welded shelves for use in supporting the source vessel. The first is positioned just below the middle of the beam and is used to hold the source vessel from the bottom. Since this area experiences most of the forces during the discharge tests, the shelf in this area is bolted to the large flange at the bottom of the source vessel. This shelf is equipped with support legs for added stability. The next shelf is located near the top of the rack and anchors the top section of the source vessel by clamping to the 5.08 cm pipe. The last shelf, positioned lower down on the beam, is used to hold the mixing pump. The

I-beam is also equipped with bolt holes along its face in order to add support structures for the level gauges and mixing lines. As for the piping system, it is supported by a metal framework, which has provisions for clamping the pipe and preventing movement in both horizontal and vertical directions. The collection vessel is attached to a movable dolly to allow for opening of the piping system when access is necessary. To account for substantial forces associated with the fluid discharging into the vessel, the collection vessel is held in place by support braces attached to a building I-beam. A picture of this entire system is shown in Figure 8-16, where the source vessel, straight piping system, collection vessel, support structure and instrumentation can be seen.

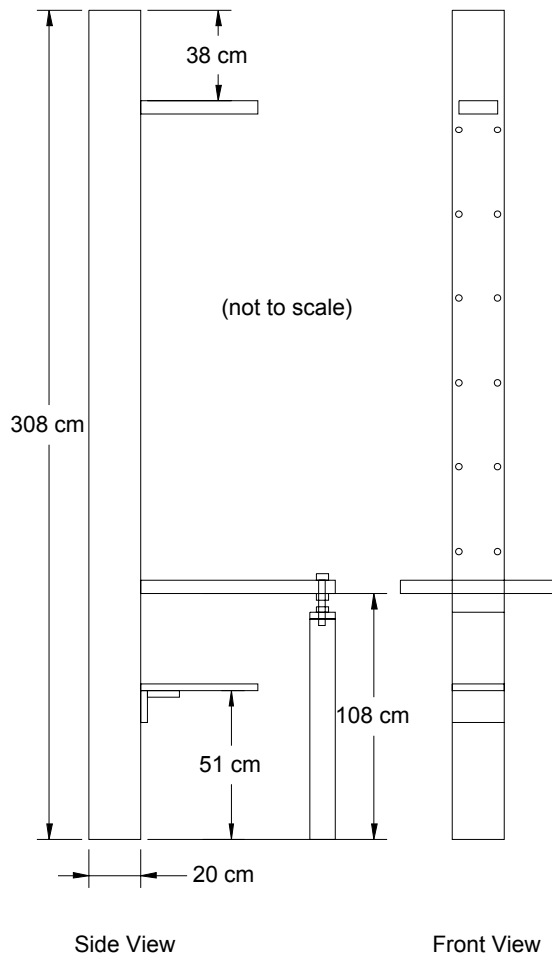
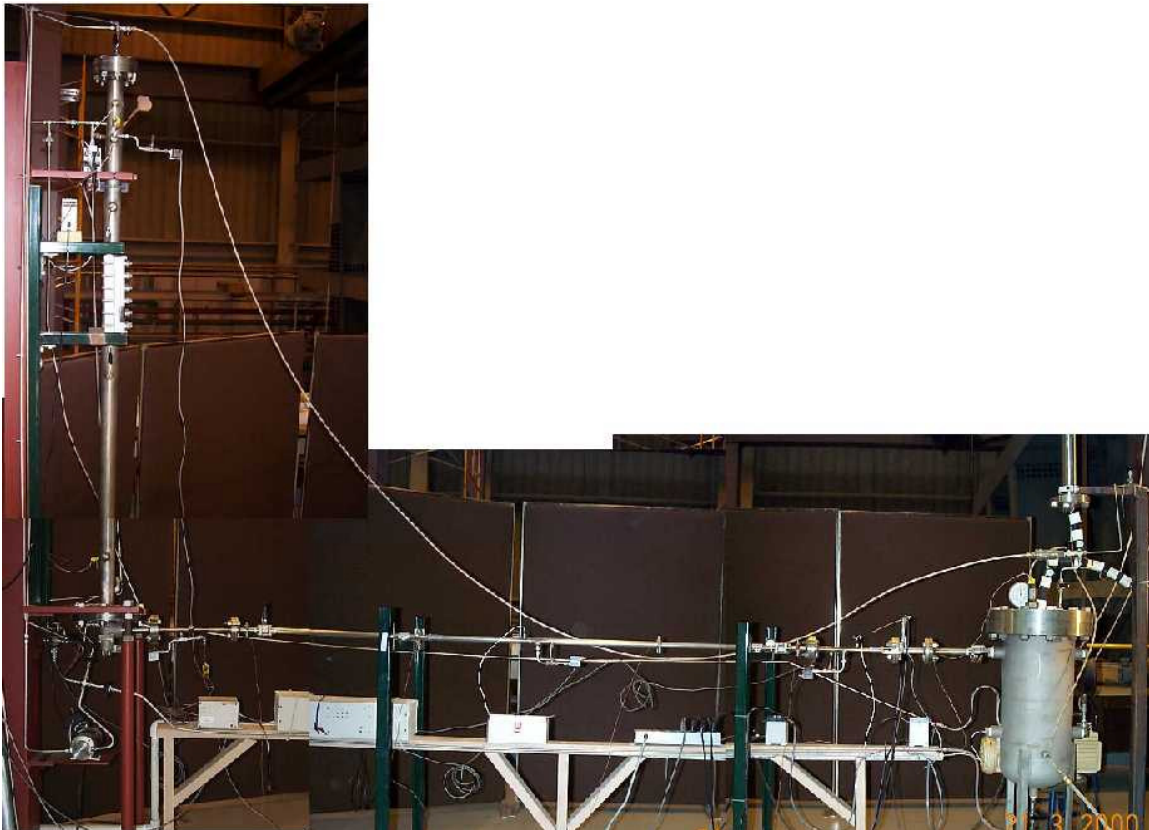


**Figure 8-15. Schematic of Rack Used to Hold the Source Vessel.**

### ***Pressure Sensors***

The test facility is equipped to measure instantaneous pressure readings in the source vessel, along the piping system, and in the collection vessel by means of fast response pressure transducers. Two types of transducers were used in the experiments conducted, the Entran Model EPX-V01 with a range of (0 to 6.87) MPa-g and the Validyne Model DP15 with varying ranges from (0 to 6.87) MPa-g. The Entran transducers were primarily used in the early runs when the temperature drop during operation was not a concern. The Validyne transducers were used for both pressure drop measurements and absolute pressure measurements. The Validyne transducers were used with a transmission fluid for speed of transmitting the pressure wave in the pressure drop readings and also for insulation when the temperature drop was

considerable, as in the HFC-125 tests. The Entran transducers have a diaphragm, which deflects according to the difference of the pressures experienced at its front and backsides, and provides an output through a strain gauge bridge located on the backside of the diaphragm. The Validyne transducers used a magnetically permeable diaphragm, which when deflected caused a magnetic reluctance, which was then interpreted by the inductance value of coils in the transducer body. In order to install these transducers at measurement locations, special fittings had to be designed and fabricated. It is desirable to locate the transducers as flush to the inside surface of the pipe as possible, in order to minimize disturbances to the flow. This was accomplished with the specially designed fittings shown in Figure 8-14. With these fittings welded into place on the pipe, the transducers can be screwed into the tapped hole, allowing an O-ring to seal against the high fluid pressures. Bench top experiments were conducted to determine whether the transducers had appropriate response times for the fast transient tests conducted. Both transducers were found to have response times at acceptable level of 140 ms for pressurization and 190 ms for depressurization when operating at 2.02 MPa to 3.03 MPa. The best test for the instrumentation was to view their performance in actual testing situations.



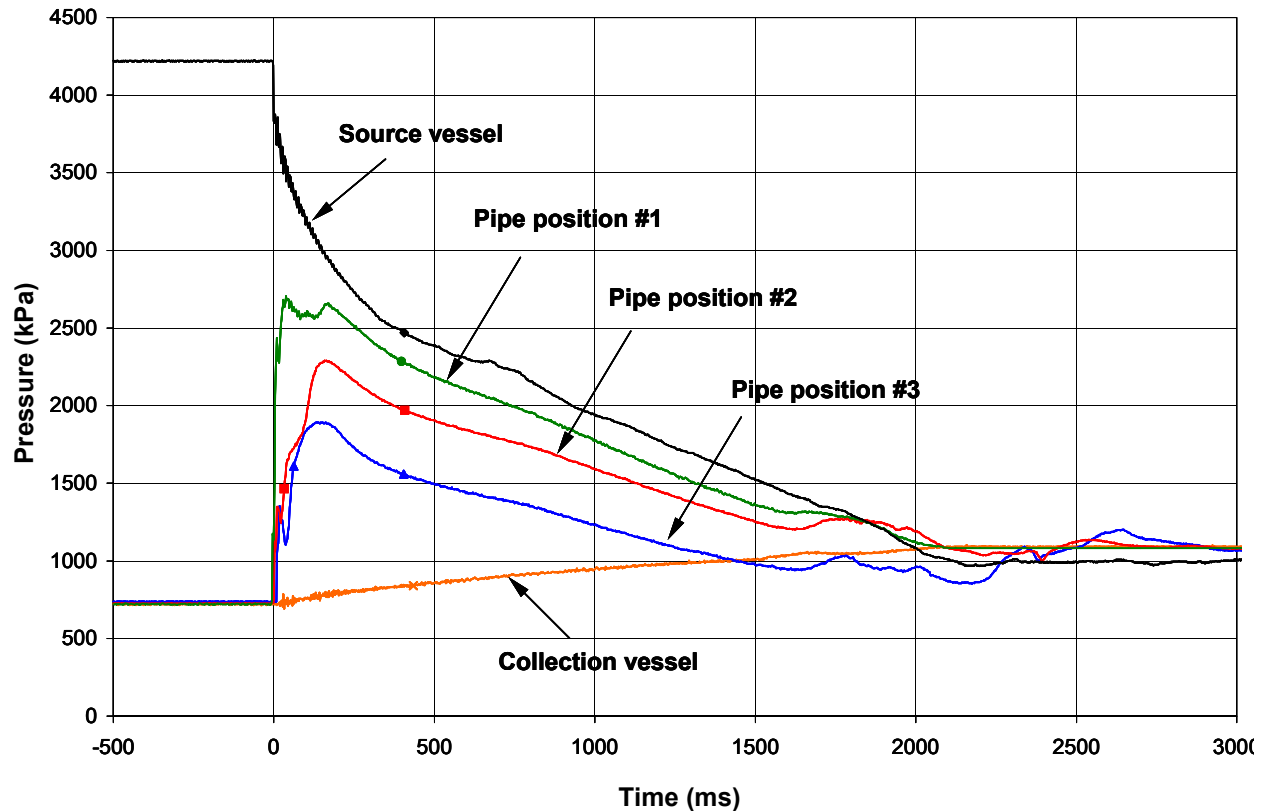
**Figure 8-16. Picture of Test Facility: Source Vessel, Discharge Piping, Collection Vessel, Support Structure and Instrumentation.<sup>7</sup>**

Figure 8-17 shows a typical output (Run #5) from the pressure transducers installed in the test facility. This run used HFC-227ea as a test fluid and was initially charged to a source vessel pressure of 4.22 MPa. As shown in the figure, the pressures in the source vessel, pipe, and collection vessel remained constant until the moment when the valve was actuated (time = 0 ms). Then the pressure in the source vessel dropped quickly while the pressures in the rest of the facility rose. This occurred until the pipe was filled

with fluid (time  $\approx 200$  ms) and then there was a steady decrease in all of the pressures until all of the fluid was discharged from the source vessel (time  $\approx 1500$  ms). At this point a small pressure increase or “bump” was prevalent in the piping pressure traces due to the exit of the remainder gas contents of the source vessel. A set of runs with similar initial conditions was also carried out to check the repeatability of the measurements and the reliability of the instrumentation. The operating conditions are shown in Table 8-2.

**Table 8-2. Operating Condition for Repeatability Tests.**

Run	Fill volume (mL)	Ambient temperature (°C)	Source vessel pressure (kPa)	Downstream pressure (kPa)
#3	2358	32	4180	720
#4	2370	29	4195	525
#5	2388	31	4220	720



**Figure 8-17. Pressure Traces for Experimental Run #5.**

All the tests used HFC-227ea. The repeatability was very good as shown by Figure 8-18, which compares the source vessel pressure traces of the three experimental runs. The slight discrepancies are most likely caused by differences in the initial and environmental conditions and are believed to be not due to the instrumentation. The transducers did a good job in tracking the pressure fluctuations during the experimental runs.

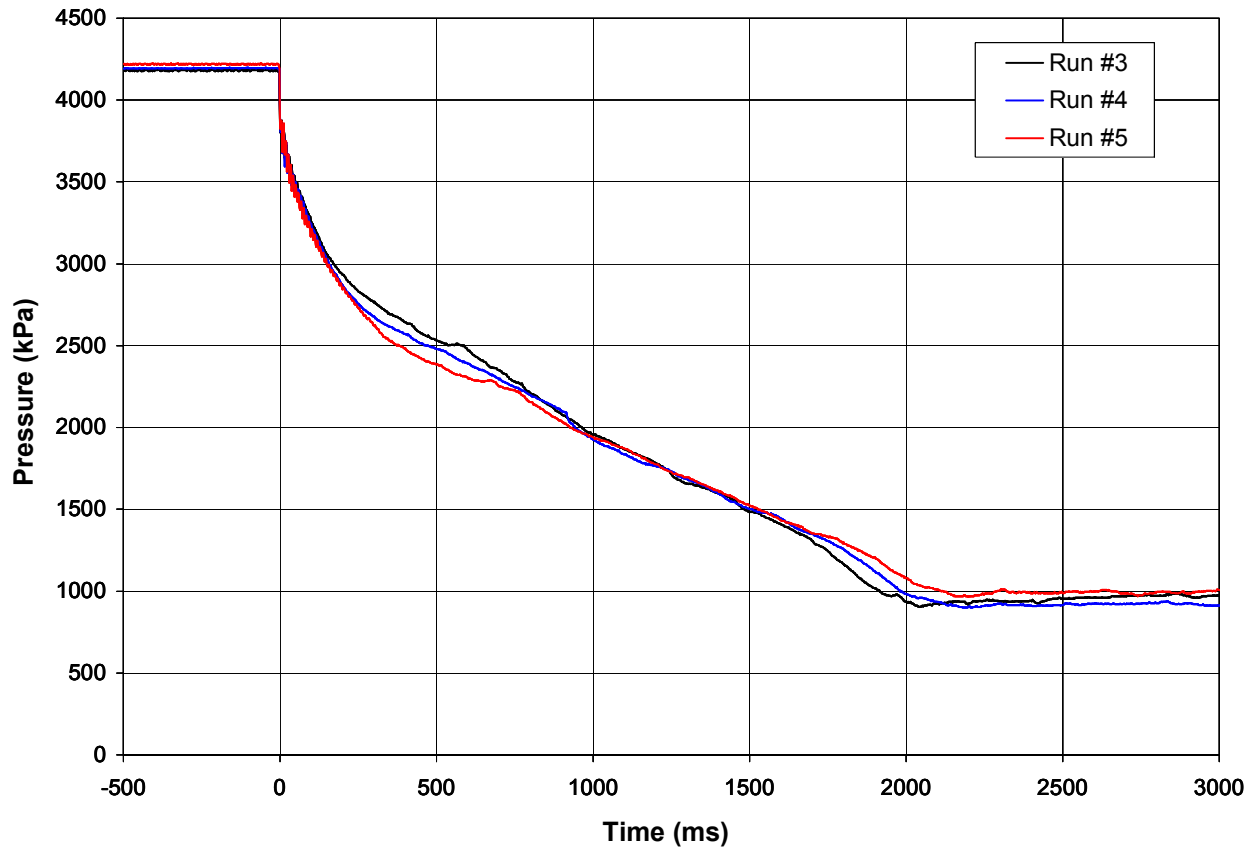


**Figure 8-18. Repeatability of the Source Vessel Pressure Traces.**

There was also a necessity to measure the pressure drop across particular sections of the piping system. While the absolute measurements at different locations allowed us to measure the variation of absolute pressure across the discharge pipe, there was also an interest in measuring pressure drops across fittings in order to determine frictional losses across these piping elements. Figure 8-19 and Figure 8-20 show the two other piping configurations tested in this study in addition to the straight pipe configuration. Validyne pressure transducers were connected on either side of the fittings to measure the distinct pressure drop associated with these fittings. This can be seen by the ports specifically designated to the fittings shown on the diagrams (i.e., PT2-PT3 across a 90° elbow). A typical output from this measurement is shown in Figure 8-21, where pressure drop versus time is displayed. This plot shows the pressure drop across a 90° elbow from Run #9 using HFC-227ea as a test fluid and an initial pressure of 3915 kPa. There is a notable pressure drop instantly as the fluid front passes through the elbow, which deteriorates as time passes. This continues until approximately 2300 ms when the last liquid is discharged and the remaining gas leaves the system, denoted by the sudden drop in pressure attributed to a reduction in the frictional component of pressure drop associated with gas flow over liquid flow. Similar plots were made for the pressure drop across capped tees, through tees and unions. Also, a comparison was done between the vertical branches of a through tee to study the effect of phasic composition on the separation of the flow. With these measurements, it was possible to successfully analyze the effects of different fittings on the pressure losses in the discharge piping.

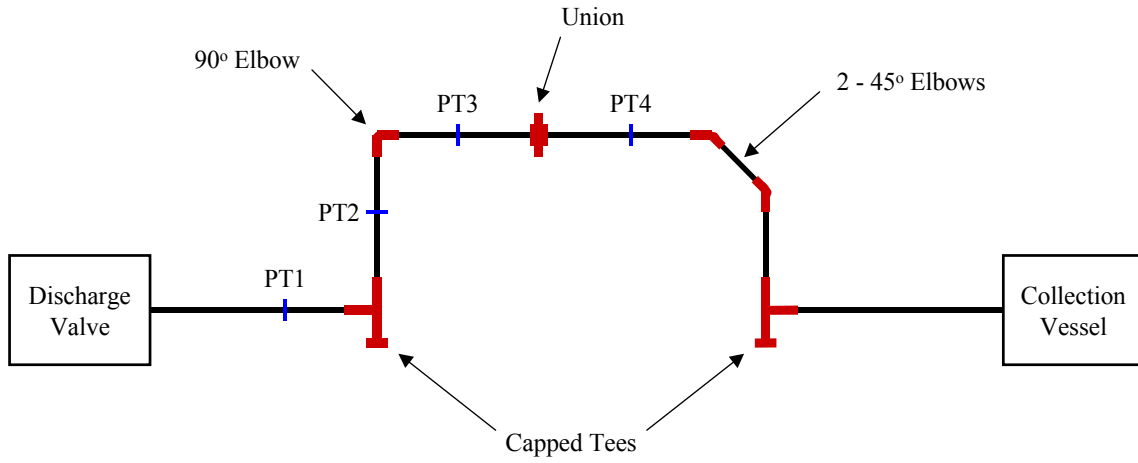


Figure 8-19. Schematic of Alternate Piping Configuration #1.

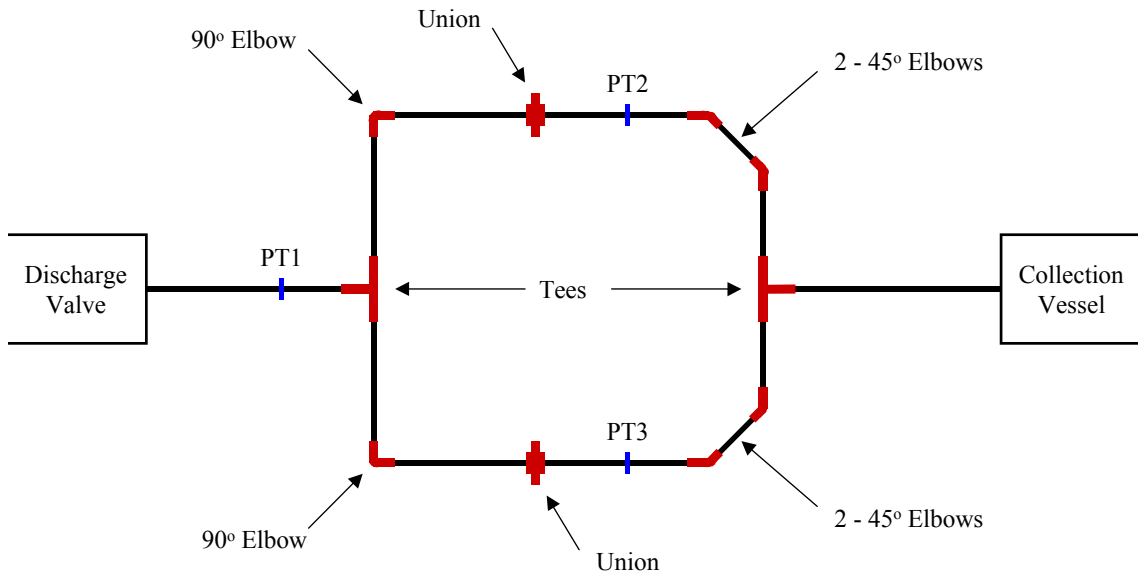
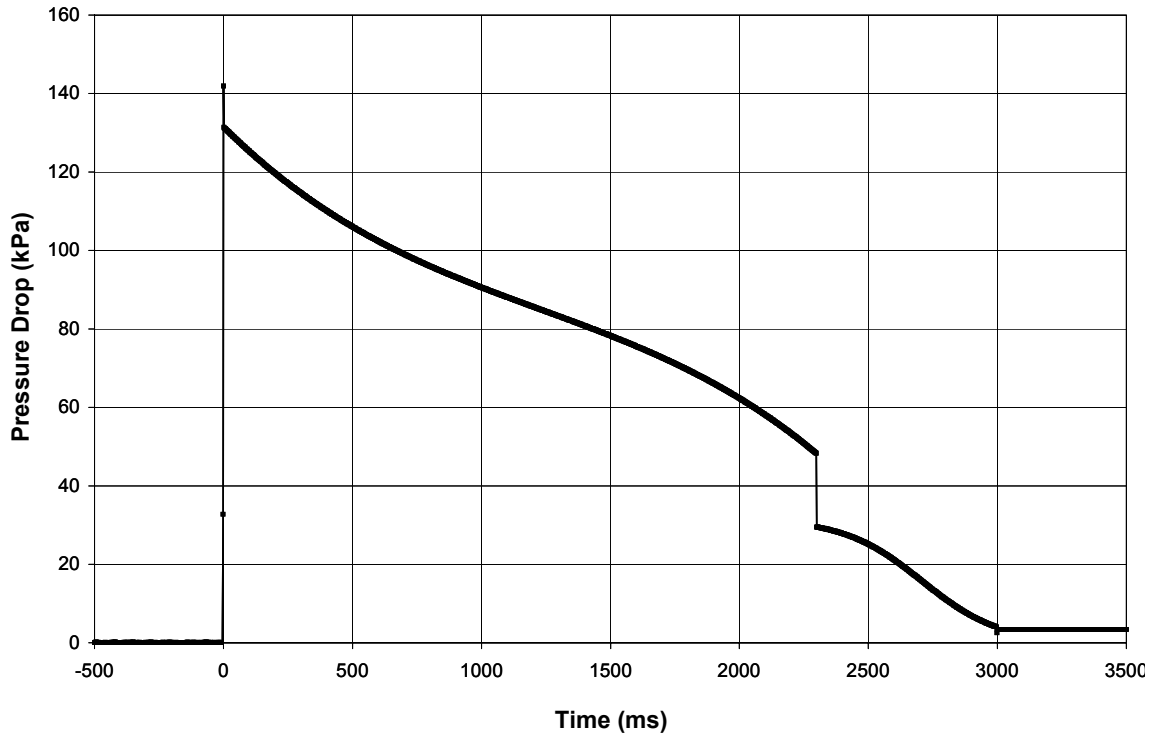


Figure 8-20. Schematic of Alternate Piping Configuration #2.



**Figure 8-21. Transient pressure drop across a 90° elbow from Run #9.**

### *Flow Rate Sensor*

As mentioned previously, a key parameter to measure is the instantaneous mass flow rate of fluid during transient discharge from the source vessel. This has not been successfully measured in prior experiments due to its inherent difficulty. If fluid inventory in the source vessel could be measured as a function of time, then the rate of discharge would be given by the gradient of inventory versus time. Because of possible void generation in the liquid (due to gas evolution) and associated level swelling, observation of the liquid level does not provide an indication of fluid inventory. The approach is to measure the static head of fluid in the source vessel, as a dynamic function of time. Since frictional and kinetic terms are negligible in the overall momentum balance for conditions in the vessel, the fluid inventory in the vessel can be obtained directly from static head measurements:

$$M = \frac{A}{g} \Delta P \quad (8-36)$$

where  $M$  is the fluid inventory,  $A$  is the cross-sectional area of the vessel,  $g$  is gravitational acceleration, and  $\Delta P$  is the pressure difference from the bottom to the top of the vessel (static head). The instantaneous rate of mass flow out of the vessel is then obtained from the time derivative:

$$\dot{m} = \frac{dM}{dt} = \frac{A}{g} \frac{d\Delta P}{dt} \quad (8-37)$$

In order to obtain the desired accuracy for the rate of mass flow, a precise measurement of  $\Delta P$  is necessary. A Validyne Model DP15 differential pressure transducer was used to obtain this static head  $\Delta P$ . As shown in Figure 8-10 and Figure 8-22, this transducer was connected to the vapor space and the liquid volume at the top and bottom of the source vessel, respectively. The transmission line connecting the vapor space to the liquid space was filled with a Meriam Red fluid with a specific gravity of 2.95 to maximize response time. The theory behind this was that the pressure signals would be transmitted to the transducer at the speed of sound in liquid, sufficiently fast to obtain dynamic data during suppressant discharge and much quicker than through a compressible gas volume. Therefore, the connections to the liquid and vapor spaces were made at the wall of the Marotta valve and the wall of the source vessel, respectively. This allowed for an almost flush-mounted differential pressure transducer with an excellent response time for measuring liquid inventory. Figure 8-22 shows a diagram of the setup for this differential pressure transducer. Note that it was attempted to fill the transmission line as close to the source vessel as possible, therefore reducing any pockets of fire suppressant vapor and making a more accurate measurement.

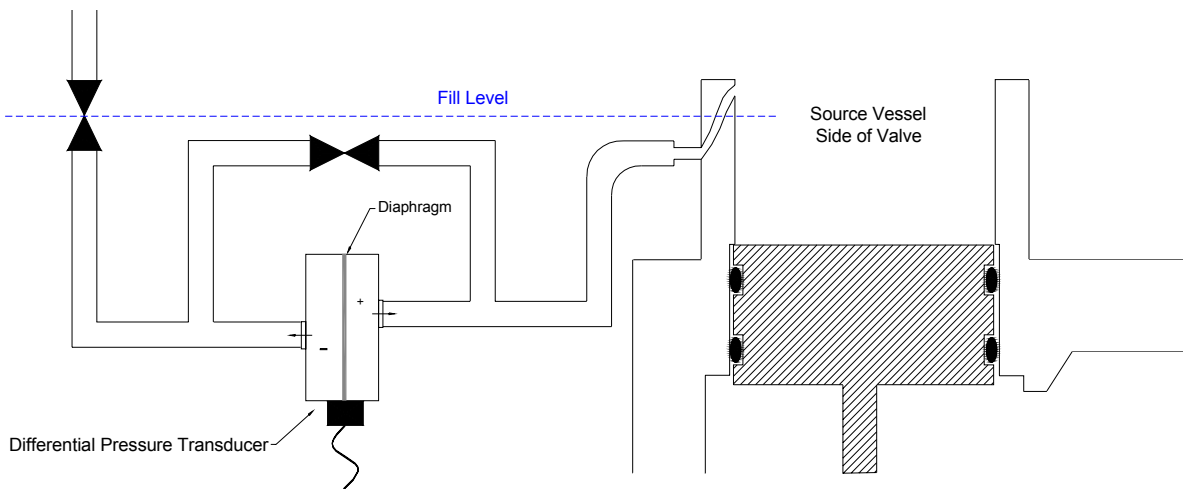


**Figure 8-22. Diagram of Transducer Setup for Mass Inventory Measurement.**

This technique worked very well, as shown in Figure 8-23, a plot of the cumulative mass leaving the source vessel versus time. This example shows the same experimental run described in the previous section. It shows that at the point when the valve was actuated, a quick release of test fluid left the source vessel and continued gradually until the source vessel was empty, at approximately 3.37 kg. This corresponded with the pressure drop in the source vessel shown in Figure 8-17 and with the end of the liquid flow and beginning of the gas flow at a time of  $\approx 1500$  ms. This is what one would expect; the fact that the pressure trace did not fluctuate very much indicated that there was a steady flow of fluid through the facility. Once again, this method for measuring the instantaneous liquid inventory gave excellent repeatability.

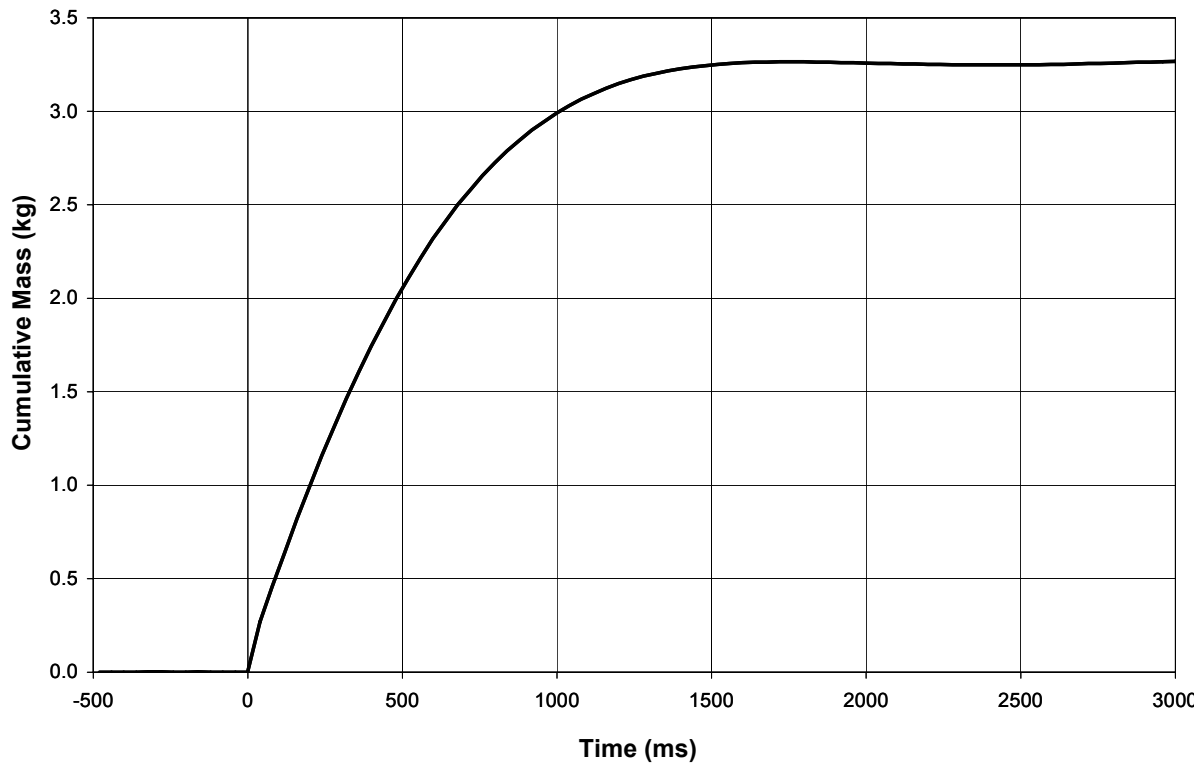


**Figure 8-23. Transient Mass Inventory of Run #5.**

### *Temperature Measurement Sensors*

Fluid temperatures along the discharge pipe were measured using film thermocouples. It has been experimentally shown,<sup>29</sup> that this type of thermocouple can provide response times on the order of milliseconds. A schematic of the film thermocouple is shown in Figure 8-24. Since the hot junction of the thermocouple is comprised of the metallic film, it is essential to maintain a continuous electric conductive-path through that film. Two issues are involved: compatibility of the film material to the test fluid, and the erosive effects of the flow on the film. In past experiments, a metallo-organic paint was used to make the film at the tip of the thermocouple. This film worked well in experiments with high temperature steam and water. The same material was used for the junction film in the test series. A bench setup was prepared to test the thermocouple with this film junction. After forming the film, the thermocouple assembly was exposed to test liquids for durations of up to five minutes. Tests with the primary test fluid, HFC-227ea, indicated that the junction film holds up well to such exposure. No bench test for erosion of the film was attempted prior to the running of the test facility, due to the significant effort involved. It was found that the film held up for anywhere from 5-10 experimental runs before deterioration in the film deemed it necessary to remove the thermocouple from the facility and reapply the metallic film. The need for reapplication of the metallic film was determined by an increased fluctuation in the output signal of the thermocouple or in some cases a loss in the signal altogether. Many of the failures in the thermocouple were not attributed to the metallic film at all, but to the disintegration of the inner wiring of the thermocouple. This was most likely due to the vibration encountered in the test facility when the experimental runs were conducted and the tight seal on the thermocouple casing needed to hold the thermocouple in place during testing.

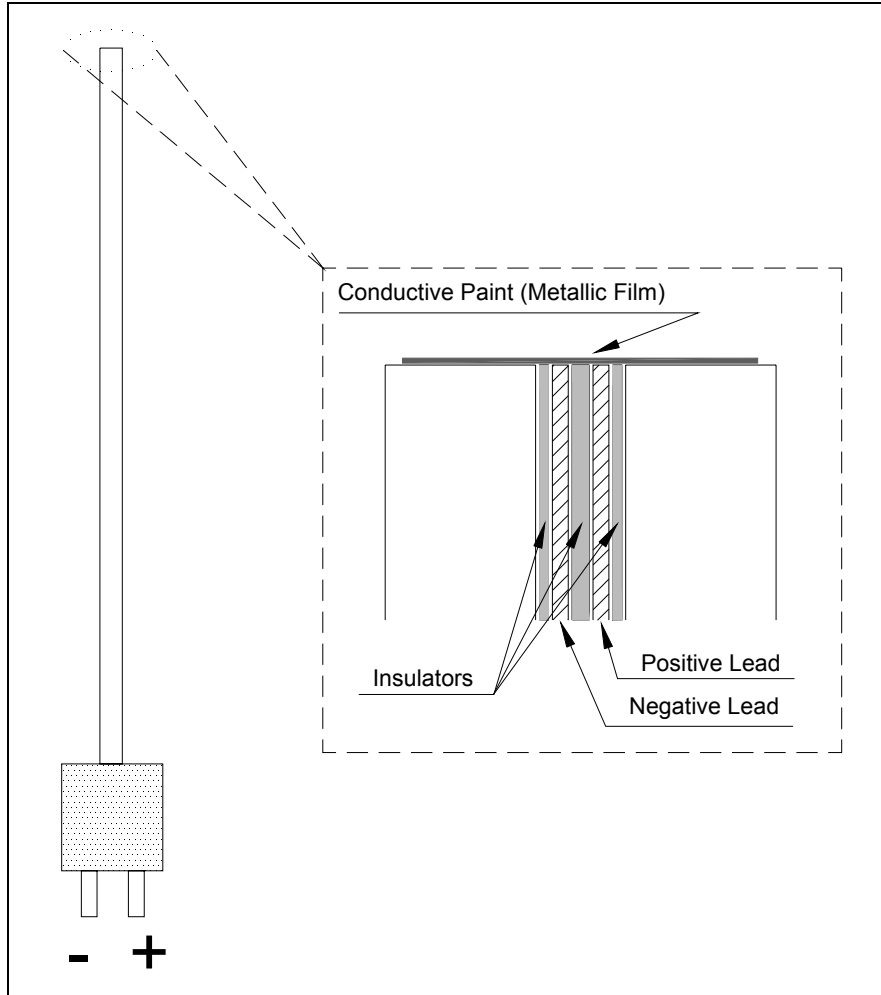


**Figure 8-24. Schematic of Thermocouple Construction.**

An example of a typical output from the four film thermocouples located throughout the test facility is shown in Figure 8-25. The top set of data is the signal from the film thermocouple located in the vapor space of the source vessel. The next three sets are from the film thermocouples in pipe positions #3, #2, and #1, respectively from top to bottom. This plot shows no significant temperature change in the vapor space, which is due to the fact that there was only a gas expansion involved in this region. While an adiabatic gas expansion from a volume of 1.5 L to 34 L should have resulted in a large decrease in temperature, this was not an adiabatic expansion due to the availability of a large heat sink in the stainless steel walls. With the considerable warming from the facility walls and the thermocouple's location at the top most portion of the entire facility, the only temperature drop experienced is minimal. As for the other set of thermocouple traces, it is believed the most significant reason for the difference in temperature drop along the pipe is also due to the warming effects.

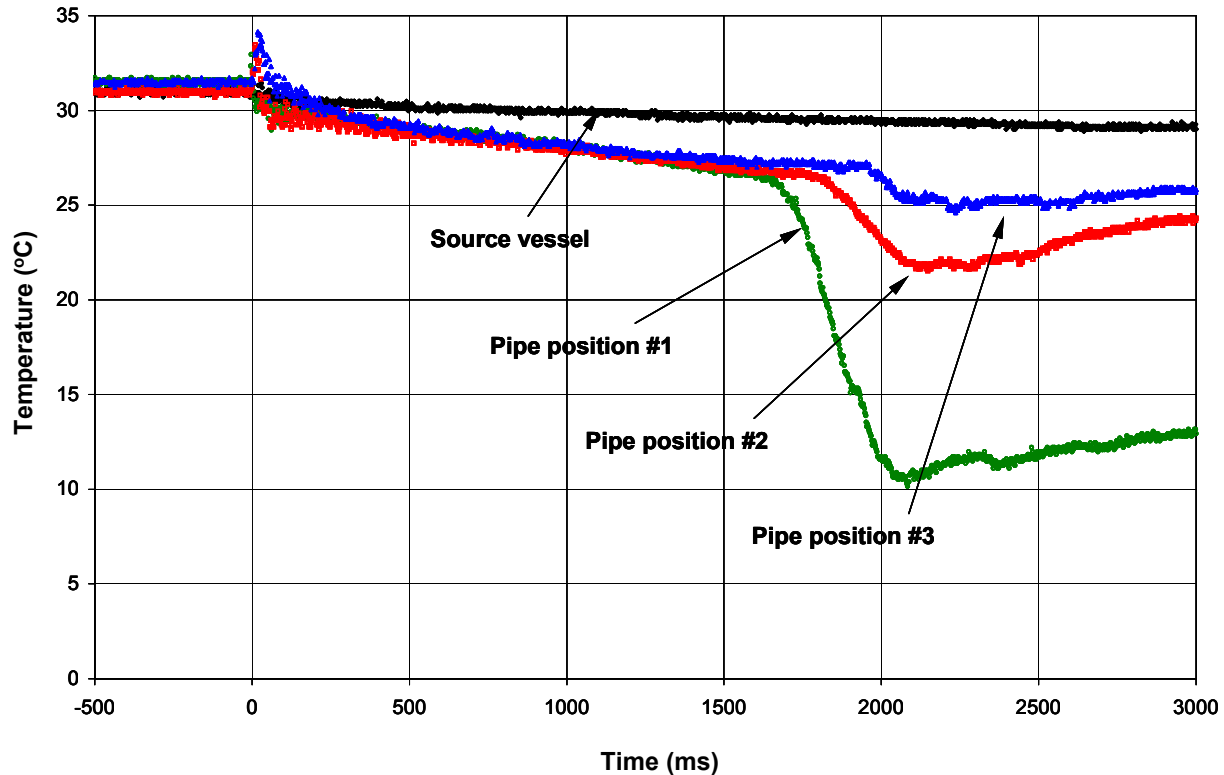


**Figure 8-25. Transient Temperature Trace from Film Thermocouples of Run #5.**

There were also two standard 0.79 mm diameter, shielded thermocouples in the source and collection vessels. Figure 8-26 shows a typical temperature trace from these thermocouples, again from Run #5. The two traces shown in this diagram are significantly different from each other. The collection vessel temperature does a quick dip and then warms back up to room temperature. This is due to the filling of the vessel with cold fluid, which is probably still going through the process of dissolution of nitrogen from liquid suppressant. Also, there is an energy loss associated with the phase change of the suppressant fluid as it goes from liquid in the pipe to gas in the collection vessel. This goes on until the collection vessel reaches the saturation pressure of the suppressant fluid, and then the vessel begins to heat up due to compression of the gas in the volume. On the other hand, the thermocouple located at the bottom of the source vessel initially does not change much since it is submersed in liquid suppressant. Then as the liquid in the source vessel runs out, it experiences the vaporization of the suppressant fluid on its surface and the expansion of the remaining gas in the system. To fully understand the complete picture of the changes of phase taking place in the experimental runs, a representation of the void in the facility is needed, which is described below.

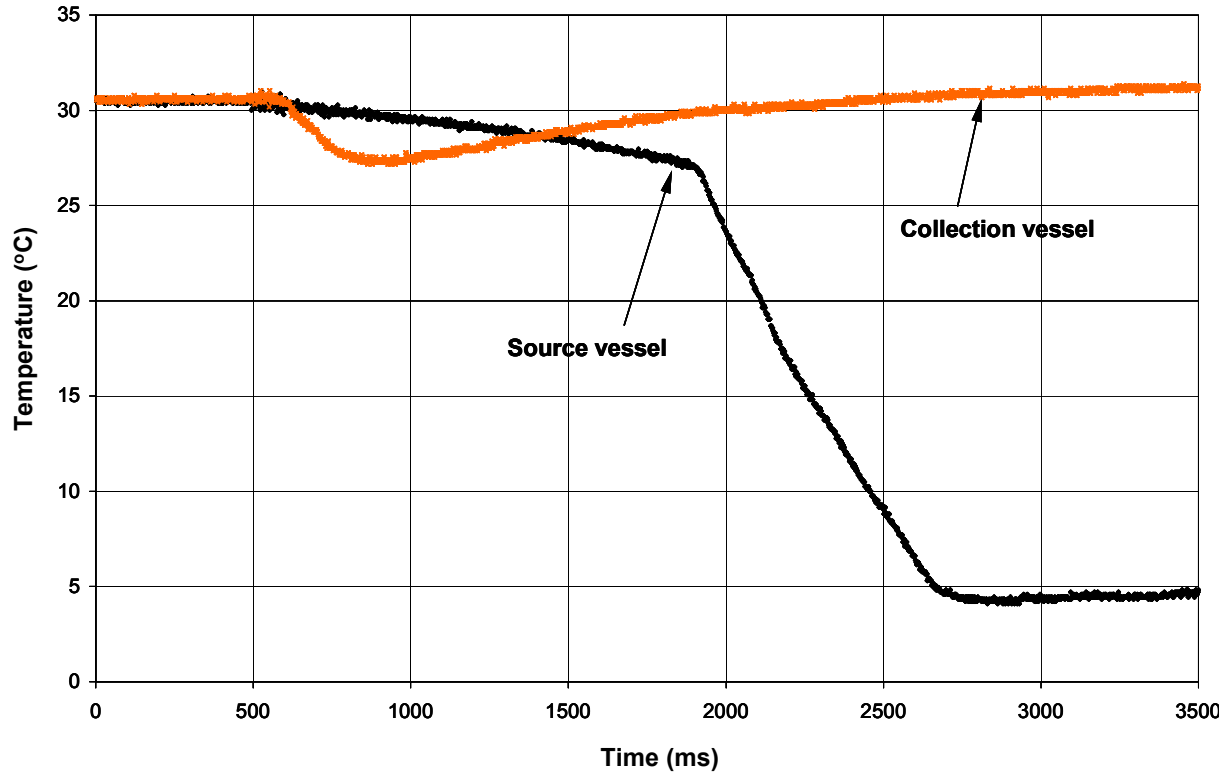


**Figure 8-26. Transient Temperature Trace from Shielded Thermocouples of Run #5.**

### *Void Fraction Sensor*

One of the major flow variables for two-phase flow is the void fraction. Many flow parameters, such as thermodynamic quality, vapor and liquid mass fluxes, and transport properties of vapor and liquid affect the void fraction. In turn, the void fraction strongly affects pressure drop, holdup inventory, and flow rate for any given operating condition. Thus, it is desirable to experimentally measure the void fraction during the transient discharge of suppressant. Once again, this is a difficult measurement in two-phase flows and was not attempted in prior experiments of suppressant flow. In the present work, an attempt was made to measure the transient void fraction at the end of the discharge pipe. The desirable features of a sensor for void fraction are:

- No disturbance on flow
- Integrate the void fraction over the cross-section
- Fast response

Based on previous experience, a capacitance sensing method for this measurement was selected, in expectation that this method would satisfy all of the above desirable features.

A number of different capacitance probes were designed, fabricated, and bench tested. The final probe configuration is shown schematically in Figure 8-27. As indicated the probe consists of a positive electrode and a ground electrode, both placed on the outside surface of the discharge pipe. The section of the discharge pipe at this location needs to be electrically nonconductive to allow capacitance

measurements. For the purpose of these bench tests, a glass tube was used as the pipe material. The positive electrode is a strip of copper in contact with the outer surface of the pipe. The electrode span is as wide as the ID of the pipe. The ground electrode is placed on the opposing side of the pipe. When powered by a high-frequency voltage, this probe would measure an overall capacitance between the two electrodes, which includes the whole cross-section of the tube. This capacitance can then be calibrated to give the void fraction of the vapor/liquid mixture in the pipe. There is a guard electrode around the positive electrode to prevent/reduce stray capacitance.

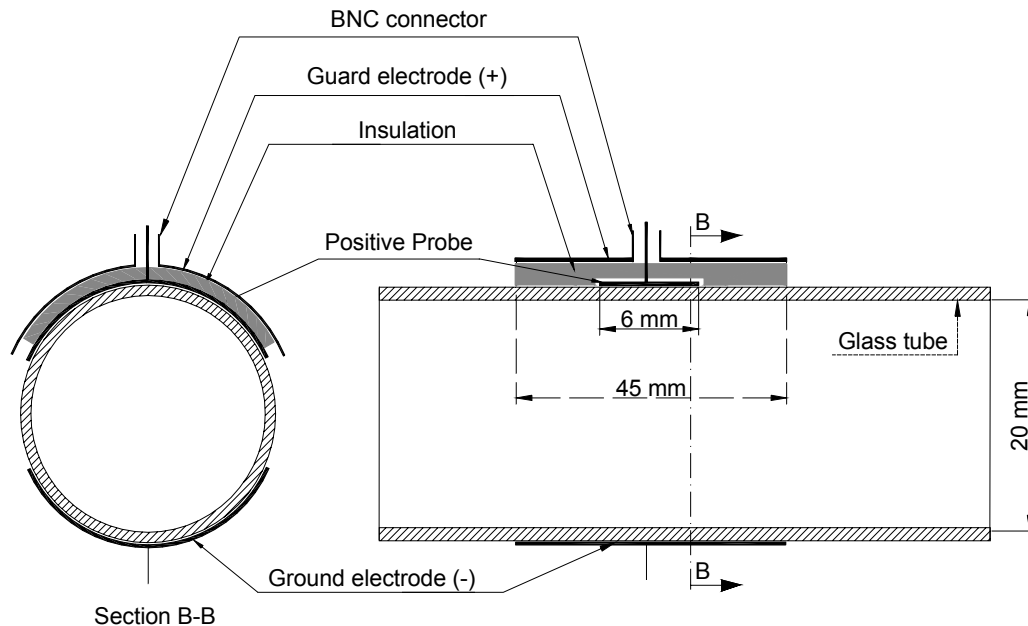


**Figure 8-27. Schematic of Capacitance Probe for Bench Setup.**

This probe was tested on a bench loop with water and HFC-134a. The schematic of the bench setup is shown in Figure 8-28. The test started with the glass tube filled with water. During the test, the tube was emptied from the bottom so that the liquid level receded with a constant speed. The recorded signal from the capacitance sensor was compiled as a voltage signal from the capacitance meter and then reduced into void fraction with a calibration using the signals associated with all liquid and all vapor. An example of the output from this test is shown in Figure 8-29. It is seen that initially the probe senses 100 % liquid in the tube. As the liquid level approaches the top edge of the sensor, the signal slowly starts to show some void in the sensing volume (edge effect). When the liquid level is within the sensing volume, the variation of measured void fraction is linear with liquid level. Again, there is an edge effect when the liquid level is close to the bottom edge of the sensing volume. Later, when the liquid level falls clear of the sensing volume, the probe senses all air in the tube. Despite the fact that the sensing area is guarded, there are some edge effects in the axial direction. The above test was repeated with HFC-134a under pressure and similar results were observed.

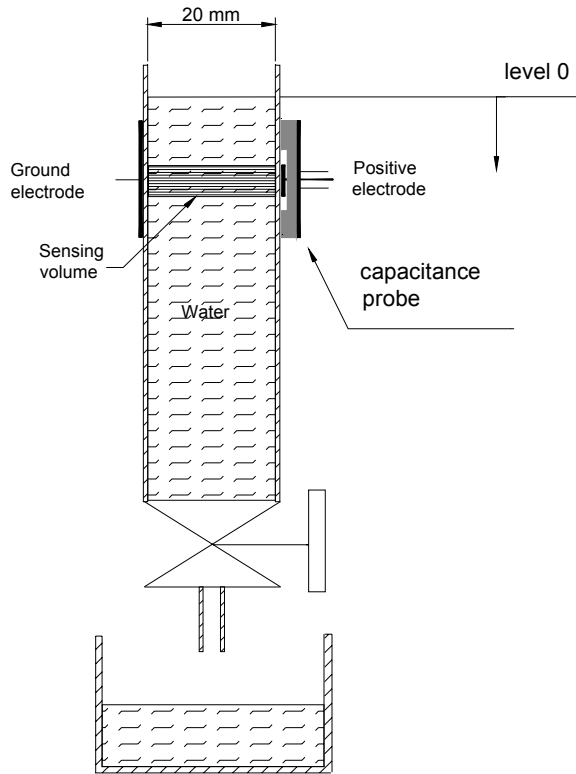


**Figure 8-28. Bench Setup to Test Capacitance Sensor.**

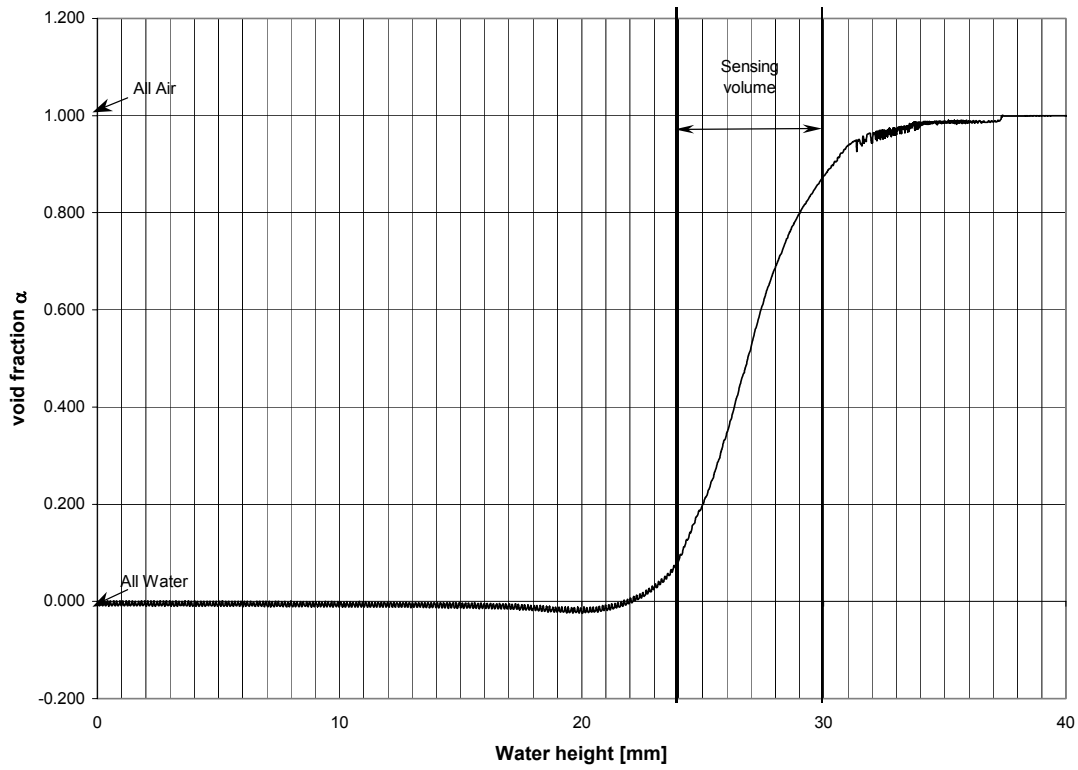


**Figure 8-29. Void Fraction from Bench Tests of Capacitance Sensor.**

The biggest problem with changing this design to fit the conditions experienced in the experimental test facility was to contain the higher pressures. In the previous bench examples, only low-pressure systems were dealt with and in the present application the system pressure was as high as 1250 kPa at the location of the void probe. The other difficulty was that an electrically conductive surface between the probe and the tested medium was not allowed. Due to these limitations, a design that would be constructed on the inner surface of the pipe was developed, as shown in Figure 8-30. There were three main pieces to this design; the first was the electrical plug welded to the metal pipe, which served as a pressure seal and as an electrical connection to the capacitance meter. The next two pieces were the guard and the probe separated by a small layer of insulation. To insure that these pieces were not washed away in the flow during the runs, they were covered in a thin layer of epoxy. This capacitance probe used the pipe wall as its ground creating an electrical field similar to the one shown in Figure 8-31.

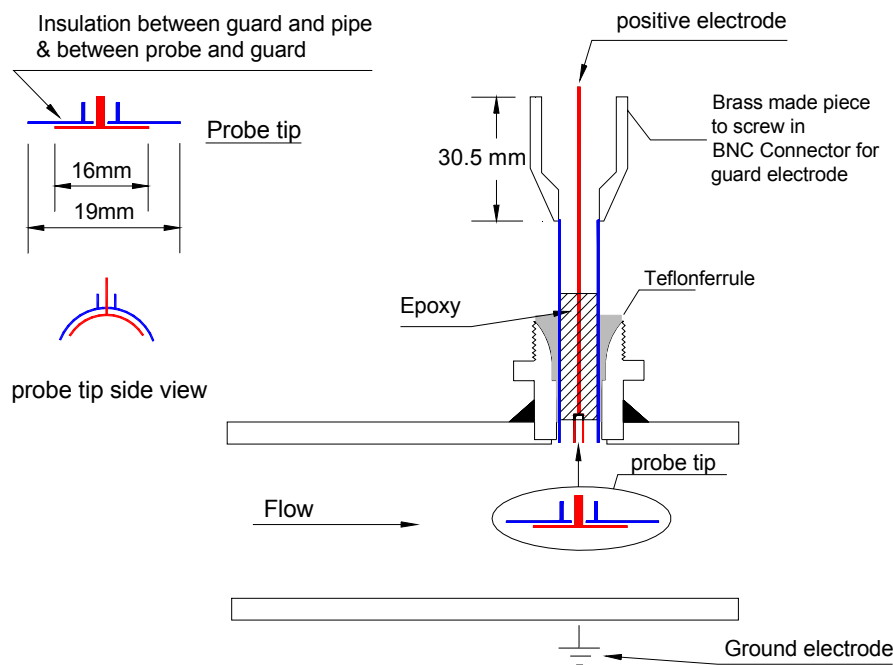
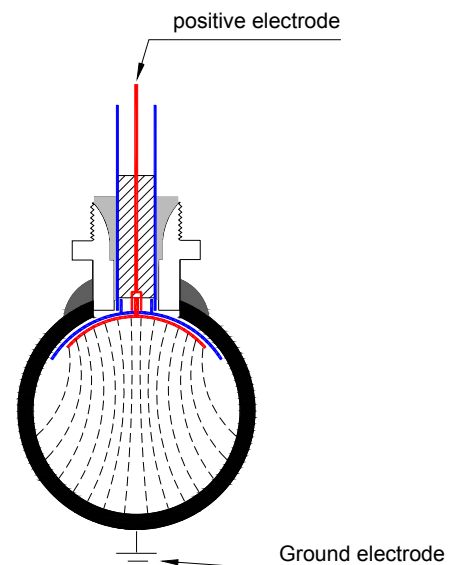


**Figure 8-30.**  
**Schematic of**  
**Capacitance Probe for**  
**Test Facility.**

**Figure 8-31. Cross-section of Capacitance**  
**Setup Showing Electrical Field.**



While the orientation of this design was horizontal as compared to vertical in the bench test setup, it was believed that the results were similar. An in situ calibration by filling the area with all liquid suppressant and then letting it run out so that only suppressant vapor remained was conducted.

An example of the final output of an actual experimental run is provided in Figure 8-32, where void fraction versus time for Run #5 is shown. The signal initially starts out at a void fraction of 1.0 (all vapor) and then shoots down to approximately 0.4 as the area is flooded with the transient flow of two-phase fluid. The signal fluctuates as the mixture of the two phases changes depending on the speed and location of the dissolution of the nitrogen from the liquid suppressant. As the flow slows down, so do the fluctuations in the capacitance signal, until the liquid runs out (time = 1700 ms), and the remaining gas is vented into the collection vessel, causing the signal to abruptly go back to the 1.0 region. The largest problem with the capacitance signal resulted from the static charge build up of the fast moving dispersed flow. It caused the signal to jump out of range and required a significant filtering effort to be conducted. This is also the reason for the offset in the final value at the end of the run. Despite these slight problems, it was felt that the capacitance probe design gave an excellent representation of the void fraction values experienced during the experimental runs.

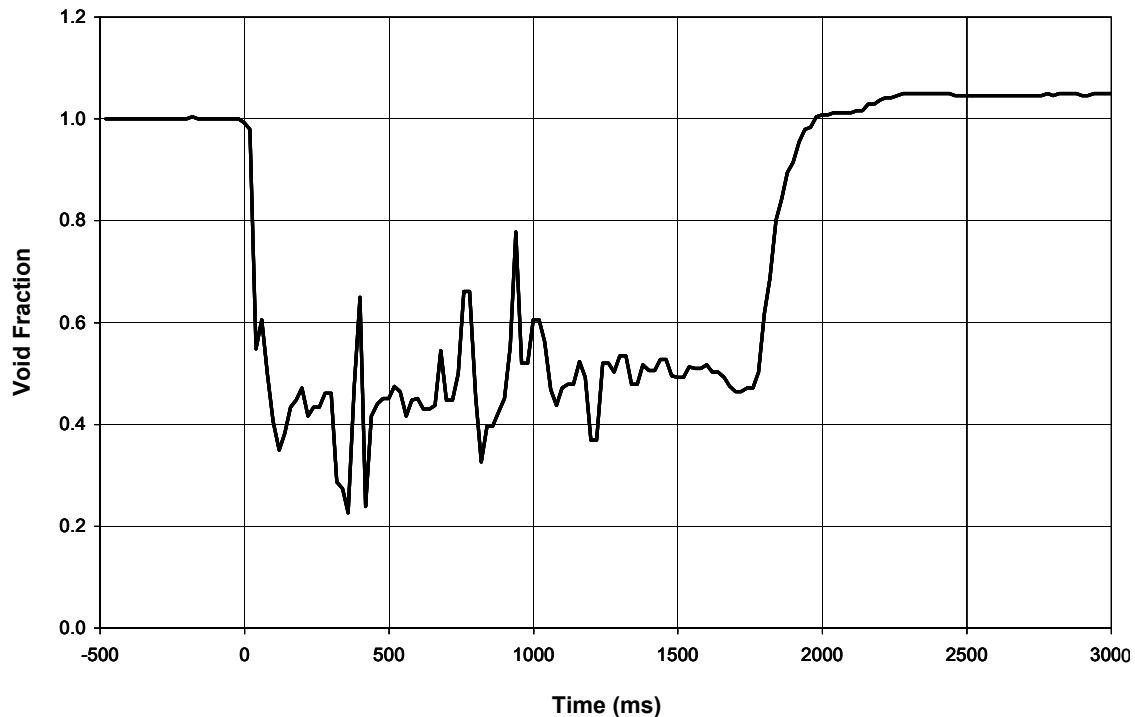


**Figure 8-32. Transient Void Fraction of Run #5.**

### Test Matrix Performed in Study

After the completion of the test facility, it was necessary to choose the appropriate initial conditions in which to conduct the experimental runs. The main goal was to encompass a wide variety of test parameters while keeping the total number of runs at a minimum to lessen the wear on the instrumentation. Table 8-3 shows the experimental runs conducted in this study. HFC-227ea was used as

the primary test fluid since it was recommended at the time as the alternative fire suppressant with the best fire-retarding ability. HFC-125 was also used since it had been studied recently, and there was some test data that could be used for future comparison. In the preliminary experiments, water and carbon dioxide were used to test the new instrumentation after installation. For example, Run #19 used water as a test fluid and was undertaken to test the capacitance sensor and film thermocouple without exposing them to high pressure or a corrosive fluid. Run #18 also used water and had the intent of testing the mass flow sensor response and all of the thermocouples in the facility. In a similar manner, Runs #20 and #21, which used CO<sub>2</sub>, were used to measure the response of the film thermocouples to a sudden drop of temperature as low as -40 °C, while also allowing us to gauge the error encountered by the pressure transducers at this temperature. These four runs utilized the straight pipe configuration in the test facility shown previously in Figure 8-13. The HFC-125 Runs (#14-#17) were conducted with only one objective, to test the influence of changing the source vessel pressure. The four runs were carried out at source vessel pressures varying from 2050 kPa to 5000 kPa. It must also be noted that any runs using source vessel pressures with initial conditions using low pressures were conducted at fill levels between 85 % and 90 %. This was done in an attempt to facilitate as much vaporization during the flow discharge as possible since the downstream pressure would remain at a lower pressure with the smaller amount of nitrogen gas available to expand.

The majority of the experimental runs used HFC-227ea as a test fluid and was broken into three main piping configuration groups. First, there were the tests using the straight pipe configuration. These tests had three different goals: (1) to test the repeatability of the instrumentation, (2) to observe the effect of changing the source vessel pressure, and (3) to determine the effect of a heat source or “hotspot” along the piping system. The repeatability Runs (#3 to #5) were conducted at an initial source vessel pressure of about 4.242 MPa. The result of the source vessel pressure trace is shown in Figure 8-18. While the “hotspot” Run (#7), was conducted at a similar starting pressure with a foot long section at 55 °C between the 2<sup>nd</sup> and 3<sup>rd</sup> instrumentation ports on the pipe, only one such run was needed since it was determined that a minimal effect resulted from the heat addition under such rapid transient conditions. The third goal was to observe the effect of varying the initial source vessel pressure from 2125 kPa to 4910 kPa (Runs #1 to #6). The second main piping configuration group used the piping configuration shown in Figure 8-19, where a vertical “U” turn was built into the piping system to allow the measurements of the effect of pipe fittings on the pressure loss in the system. The pressure drops across a capped tee, 90° elbow and union were measured with varying initial source vessel pressures from 2120 kPa to 4910 kPa in Run #8 to Run #10. The third piping configuration group used a complete vertical split as shown in Figure 8-20, where the tee was no longer capped but used to join two symmetric piping sections. The two sections were identical to the one used in the previous grouping although this time the pressure drop across the split was measured. A sensor was placed before the tee and after the 90° elbows on either arm of the split to test whether there was an effect from the splitting of the flow. These tests were also conducted at three varying initial source vessel pressures from 2140 kPa to 4910 kPa in Run #11 to Run #13. These tests examined the effects of changing the initial source vessel pressures, changing the test fluids, changing the piping configurations and the repeatability of the instrumentation.

### **A Typical Experimental Run**

First the plunger in the Marotta valve is set into the closed position using the arming tool. Once the valve is closed, the next task is to recycle any fluid remaining in the collection vessel back to the source vessel using a magnetically driven centrifugal pump. If there is not enough test fluid in the collection vessel to

reach the desired initial fill level for the next run, then the recycle line is closed and a line to a fresh-supply tank above the test facility is opened, allowing the remaining liquid needed for the run to be pumped into the source vessel. Once this is accomplished, the supply line is closed and a circulation line is opened allowing the liquid at the bottom of the source vessel to be pumped to a spray nozzle at the top of the vessel. The spray nozzle then creates a fine mist of liquid to float through the vapor space of the vessel before joining the rest of the liquid. At this point, nitrogen gas is slowly added to the source vessel through a connection at the top of the vessel. The circulation pump is continuously run until the liquid is saturated with nitrogen. This is recognized by a constant pressure in the source vessel, which usually takes about 120 min. The circulation pump is then turned off, and the contents of the source vessel are allowed to settle and cool down to room temperature. The data acquisition system is initiated and run for 500 ms before the Marotta valve is actuated. This allows for the collection of the initial conditions of the system. Once the valve is actuated, the contents of the source vessel discharge through the Marotta valve into the piping system and finally collect in the collection vessel.

**Table 8-3. Matrix of Experimental Runs Conducted.**

Run #	Test Fluid	Piping Configuration	Fill Volume (mL)	P <sub>svo</sub> (kPa)	P <sub>cvo</sub> (kPa)	Temperature (°C)
1	HFC-227ea	Straight Pipe	3571	2125	10	32
2	HFC-227ea	Straight Pipe	2340	3235	635	33
3	HFC-227ea	Straight Pipe	2358	4180	720	32
4	HFC-227ea	Straight Pipe	2370	4195	525	29
5	HFC-227ea	Straight Pipe	2388	4220	720	31
6	HFC-227ea	Straight Pipe	2150	4910	715	31
7	HFC-227ea	Straight Pipe w/ Hotspot @ 55°C	2200	4230	710	27
8	HFC-227ea	Capped Tee (Config. #1)	3420	2120	125	21
9	HFC-227ea	Capped Tee (Config. #1)	2500	3915	575	24
10	HFC-227ea	Capped Tee (Config. #1)	2450	4910	615	25
11	HFC-227ea	Through Tee (Config. #2)	3507	2140	600	26
12	HFC-227ea	Through Tee (Config. #2)	2400	3935	655	24
13	HFC-227ea	Through Tee (Config. #2)	2460	4910	615	25
14	HFC-125	Straight Pipe	2900	2050	110	26
15	HFC-125	Straight Pipe	2363	3635	175	26
16	HFC-125	Straight Pipe	2400	4245	165	26
17	HFC-125	Straight Pipe	2467	5000	125	24
18	Water	Straight Pipe	3585	2875	120	28
19	Water	Straight Pipe	3100	4150	100	23
20	CO <sub>2</sub>	Straight Pipe	~1000	5215	100	20
21	CO <sub>2</sub>	Straight Pipe	~1000	5360	100	20

To fully understand the output from a single run, a typical experimental run (Run #5) will be examined in more detail. The pressure traces can be seen in Figure 8-17 where the traces go from the source vessel at the top, to the collection vessel at the bottom, and the pipe ports in the middle. Specifically, the black line (diamond) is the source vessel trace and the green (circle), red (square) and blue (triangle) traces are the first, second and third pipe positions, respectively, with the orange (cross) line being the trace for the collection vessel. Initially the source vessel is at 4220 kPa and the pressure downstream of the closed

valve is at 720 kPa. After the valve is opened, the pressure in the source vessel quickly drops as its contents fill the piping system, explaining the sudden rise in pressure there. At the point when the pipe is completely filled,  $\approx 200$  ms, there is a consistent drop in pressure as the fluid empties into the collection vessel. At  $\approx 1600$  ms, the fluid begins to run out and the flow in the system is predominately vapor. This quickly causes the entire system to equilibrate to the same ending pressure,  $\approx 1100$  kPa.

Not only can the pressure traces be followed for the discharge, but the temperature change also can be followed throughout the system. Figure 8-25 shows the output of the highly sensitive film thermocouples placed at the top of the source vessel in the vapor space and along the bottom of the piping system at the three port locations. The same color and symbol scheme is used as in the pressure traces with the source vessel being on top, followed by the third, second, and first pipe positions, respectively. There was little temperature change experienced in the fluid flow portion of the discharge since there was little flashing of the suppressant. The main temperature drop occurs at the point when the vapor discharge begins ( $\approx 1600$  ms). This is due to the sudden expansion of the remaining nitrogen gas and falls as low as  $10^\circ\text{C}$  at the first pipe position. There are lesser temperature drops farther down the pipe due to the increased distance from the initial point of expansion and the warming of the vapor by the system walls. There were also two 0.79 mm shielded thermocouples placed in both the source vessel and collection vessel. The outputs of these are shown in Figure 8-26, where the black (diamond) symbols are for the bottom, fluid space of the source vessel, and the orange (cross) symbols are for the top, vapor space of the collection vessel. There is a small dip in the temperature of the collection vessel as the fluid initially reaches the large volume of the vessel and then it warms back up to room temperature rather quickly. As for the source vessel temperature, this thermocouple experiences a temperature drop due to the expansion of the gas that the film thermocouple in the vapor space did not. This is most likely due to the fact that the film thermocouple at the top of the vessel is in contact with stagnant gas and did not have enough time to sense its temperature, while the lower thermocouple experienced the shock of the quick expansion from the fast flowing gas.

The next insight derived from this study was provided by the differential pressure transducer, which measured the mass flow rate of the discharge. As seen in Figure 8-23, this instrumentation allowed for the measurement of the cumulative mass of liquid leaving the system. This provides a good estimate of how much liquid has left the source vessel and might possibly land on the desired destination, in this case, into the collection vessel. Ideally, one would have liked to locate such a sensor near the desired destination, but since an accurate, quick response method of measuring the collected fluid could not be developed, this seemed the most suitable alternative. Figure 8-23 verifies what has been already observed from the previous measurements of pressure and temperature. At first there is a primarily liquid flow, starting rapidly and slowly dying out as the inventory is relinquished to the piping system, until no liquid is left at  $\approx 1600$  ms. Along with this additional measurement to backup other assessments, the void fraction leaving the pipe was also measured by use of a capacitance sensor located at the end of the pipe. This instrument obtained an electrical signal, which pertained to a capacitance measurement of the flow passing through this section. This signal was then converted into a measurement of void fraction through a previous calibration where a value of 0.0 denotes all liquid flow and a value of 1.0 denotes all vapor flow with everything in the middle being a mixture of the two. Figure 8-32 shows the output from this sensor during the experimental run. Once again, the main liquid flow seems to end in the 1600 ms to 1800 ms range. The slight discrepancy between this measurement and the mass inventory measurement is most likely caused by the fact that they are on either ends of the pipe. This trace shows that at the beginning there is a flow of predominately liquid, void fraction of 0.4-0.2, which slowly rises to a more

consistent value of 0.5 until the liquid runs out and the value jumps back up to an all vapor level. There are many peaks in the trace due to the fact that the flow is highly turbulent at this period in the flow, with the phasic composition changing with the rate of nitrogen coming out of the solution. The flow slows down a little near the end, and the trace smoothes out until the end when there is no more flow. These four different methods of taking measurements indicate that the transport processes occurring during the rapid transient phase of the experimental runs can be adequately assessed. The detailed output of all of the experimental runs conducted in this study can be found in Appendix B of the report by Tuzla et al.<sup>7</sup>

## Observations and Conclusions

The analysis of the full range of experiments conducted in this study provided many findings and observations. The most exciting developments in this study pertained to the previously unsuccessful measurements of mass flow, void fraction, and local temperature. The transient fluid inventory method gave excellent results, providing not only another check for the computer code developed in this work, but also an innovative technique currently unavailable in two-phase flow experiments. The void fraction measurement using a capacitance sensor has been used in other applications, but never in such a rapid-transient setting. In addition, most methods used in previous studies required the probe to extend out into the measured flow, which causes obstruction to the flow and obvious changes in the resulting flow characteristics. The current method provides a quick, accurate signal with minimal disturbance to the flow, resulting in the measurement of more realistic flow characteristics. Last, the film thermocouples used in this study also allowed measurements to be made without disturbing the fluid flow. In previous studies, thermocouples were always extended into the middle of the pipe in order to get the most accurate representation of the local temperatures, causing them to break and deflect the fluid as it flowed. These techniques had another shortcoming of not allowing a fast response due to the thermocouple sheathing. In the current case, only a paper-thin layer was present to shield the thermocouple junction from the flow while having no effect on the flow, due to their flush-mounted design. These techniques allowed this study to provide a more comprehensive data set for the computer code simulations to be tested against.

The experiments in this study primarily focused on the use of HFC-227ea as a test fluid. The first set of experimental runs examined the effect of changing the initial source vessel pressure on the flow characteristics through a straight, 12.7 mm nominal diameter pipe, see Figure 8-13. The main difference between these runs was the speed at which the source vessel discharged its contents into the piping system and hence, into the collection vessel. All the runs exhibited the same basic phenomena as seen in Figure 8-17: (1) a quick pressure drop as the pipe filled, (2) a continuous drop in the pressure as the source vessel discharged its remaining fluid, and (3) a slight pressure “bump” in the pressure measurements in the pipe due to the venting of the remaining gas and vapor in the source vessel. Similar behaviors are evident when examining the void fraction and mass flow measurements. The lowest void fraction is seen at the beginning of the runs (Figure 8-32) when the liquid content in the flow is the greatest. Near the end of the run, a marked increase in the void fraction is observed as more nitrogen comes out of solution causing it to rise. The corresponding mass flow measurement (Figure 8-23) shows the fastest discharge at the beginning of the run when the source vessel pressure is at its highest value, thus providing the greatest driving force. Once the pressure begins to wane, so does the flow, until it ends at the end of the liquid flow for the run.

The second set of experiments was conducted using an alternative piping system which contained tees, elbows, and a union as shown in Figure 8-19. The main goal for these runs was to measure the pressure

drop associated by adding specific pipe fittings into the piping network. As expected, the flow was significantly reduced by the pipe fittings, as shown in Figure 8-33. The comparison shows that Run #1 with the straight pipe finishes discharging its contents at approximately 4600 ms compared with Run #8 that used the piping layout containing two capped tees, a 90° elbow, a union and two 45° elbows, which finished at about 7500 ms. To study these pressure drop measurements, a comparison to literature values for non-compressible, turbulent flow through pipe fittings using the friction loss factor method was conducted. This method is based on the procedure where pipe fittings are set equal to equivalent lengths of pipe depending on the anticipated pressure drop associated with the fitting. In the experimental setup, the pressure ports used to measure the pressure drop across the fittings included not only the fitting but also some piping in between (see Figure 8-19). In each case the additional piping plus the fitting between the pressure ports was included in order to remain as accurate as possible. For example, the 90° elbows were made up of the pressure port then 5.08 centimeters of piping, then the elbow, then 7.62 more centimeters of piping and the final pressure port. Therefore, the designation, “90° elbow”, is actually the elbow plus 12.7 cm of piping. Predicted literature values were obtained by using the literature value for the friction loss factor,  $K$ , for the particular fitting and adding it to the calculated value for the additional piping, found by using Equation 8–38.

$$K = 4f_f \frac{L}{D} \quad (8-38)$$

where  $f_f$  is the friction factor of the pipe found by using a chart in the literature with the diameter and estimated roughness of the pipe,  $L$  and  $D$  are the length and diameter of the pipe, respectively. Once a total  $K$  is found for the fitting and additional piping, it can be used in Equation 8–39 to find the literature value for  $\Delta P$ .

$$\Delta P = \frac{K \rho v^2}{2} \quad (8-39)$$

where  $\rho$  is the mixture density calculated using the experimental void fraction measurements, and  $v$  is the flow mixture velocity calculated from the experimental values of mass flow through the pipe and the mixture density.

Since the experiments took place under two-phase conditions, the mixture density was used in order to get as close to the actual conditions in the pipe as possible. The one drawback of this method was that the void fraction sensor was not located at the local position of the fitting, but at the end of the pipe so it might not be a precise representation of the void conditions at the fitting. For this reason and because the literature values for  $K$  were developed using liquid turbulent flow, a comparison to values using the liquid density and liquid velocity in place of the mixture density and mixture velocity was also included. See Table 8-4 for the detailed values of this comparison. As the comparison shows, there are some discrepancies between the literature and the experimental values, with the calculations using liquid density being in reasonable agreement. In order to compare whether the mixture or the liquid density is best used when calculating the literature value for  $\Delta P$ , the error has been provided in parentheses. This error was determined using the experimental value as the actual value. The experimental values for pressure, void fraction, density and velocity were taken in the middle of the runs, with Run #8 being from 1500 ms to 3500 ms and Runs #9 and #10 being from 500 ms to 1500 ms. Some of the possible reasons for the discrepancies in the comparison between the calculations using the liquid density and those using the mixture density may be:

1. The phasic composition of the flow at the particular time during the run. For example, at the beginning of the run there is a large amount of liquid flowing, but there is also a large quantity of nitrogen degassing, so it is hard to tell how this will effect the calculations.
2. The capped tee is near the beginning of the piping layout, while the void sensor that is used for the calculation of the mixture density is at the end.
3. The fact that the literature value for the union is actually considered as if the fitting is just a section of straight pipe. In theory, this should be the case since the union when assembled should not interfere with the flow, but there are still ridges from the male and female sections connecting on the inside of the union, possibly causing disturbances to the flow.
4. The role of the two-phase flow in the experiments. An assumption made when modeling two-phase flow through pipe fittings is that the differences from single-phase liquid flow are marginal, but this may not be the case. The void fraction may play a large part in the pressure drop experienced through a pipe fitting since it will influence the flow conditions through the fitting.

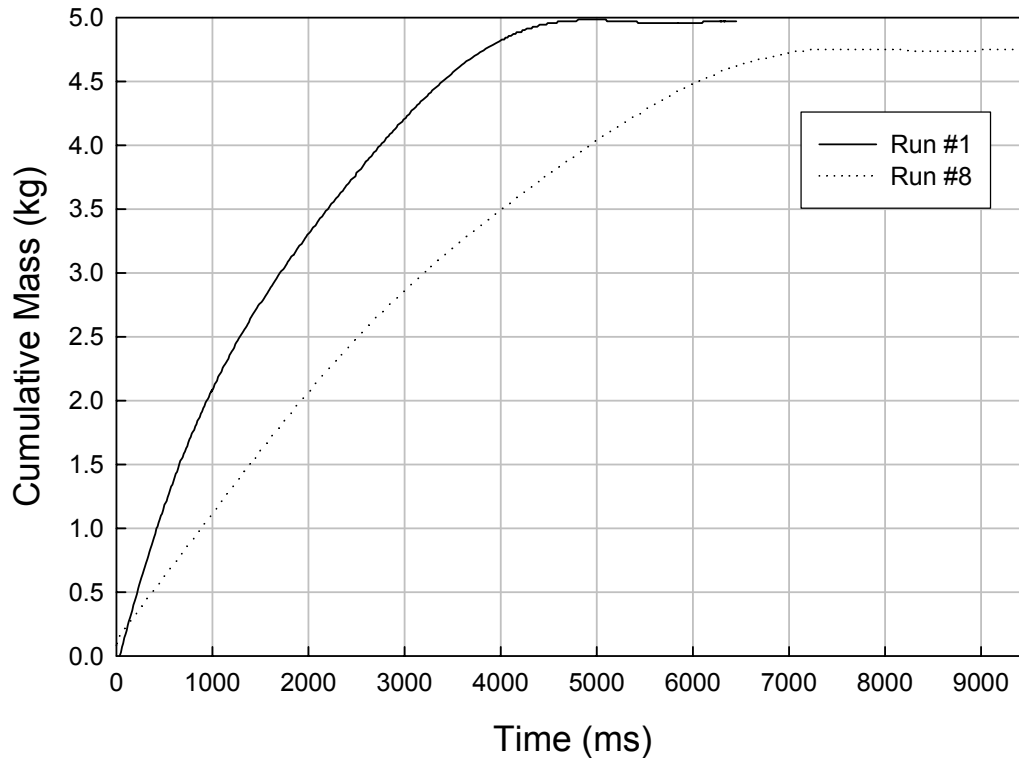


**Figure 8-33. Cumulative Mass as a Function of Time for Runs #1 and #8.**

Overall, the liquid density yielded a better calculation than the mixture assumption with an average error of 47 % compared with 155 %. These findings suggests that the phasic composition of the flow through the fitting plays a major role in the pressure drop experienced at any instantaneous time during the discharge and that local flow characteristics will play a large role in determining the magnitude of the pressure drop.

**Table 8-4. Comparison of Experimental Pressure Drop Values to Literature Values.**

	Run #8	Run #9	Run #10
Initial source vessel pressure (kPa)	2120	3915	4910
Void fraction	0.649	0.507	0.485
Liquid density (kg/m <sup>3</sup> )	1403.5	1392.8	1389.0
Mixture density (kg/m <sup>3</sup> )	514.43	704.73	733.18
Velocity (m/sec)	3.446	9.007	7.630
<b>90° Elbow</b>			
Experimental $\Delta P$ (kPa)	9900	27800	36000
Literature value $\Delta P$ (mixture $\rho$ ) (kPa)	21594 (118 %)	106073 (282 %)	72775 (102 %)
Literature value $\Delta P$ (liquid $\rho$ ) (kPa)	7915 (20 %)	53673 (93 %)	38414 (7 %)
<b>Capped Tee</b>			
Experimental $\Delta P$ (kPa)	11300	40400	62600
Literature value $\Delta P$ (mixture $\rho$ ) (kPa)	29778 (164 %)	195398 (384 %)	134059 (114 %)
Literature value $\Delta P$ (liquid $\rho$ ) (kPa)	14580 (29 %)	98871 (145 %)	70763 (13 %)
<b>Union</b>			
Experimental $\Delta P$ (kPa)	11100	31500	50400
Literature value $\Delta P$ (mixture $\rho$ ) (kPa)	17048 (54 %)	83742 (166 %)	57454 (14 %)
Literature value $\Delta P$ (liquid $\rho$ ) (kPa)	6248 (44 %)	42373 (35 %)	30327 (40 %)

The third set of experiments also used an alternative-piping configuration, which included a vertical split of the flow (see Figure 8-20). The goal of these runs was to examine whether there would be any difference in pressure drop between the two legs of the split. At slower flow velocities, separation of the flow may occur based on the flow regime of the discharge. For example, if the flow were stratified then all the liquid may flow through the bottom leg of the split and the entire vapor may travel through the top leg. This would be evident from the difference in pressure drop between the two legs since the vapor would have a much lower pressure drop than the liquid. In the experimental runs, no such trend was observed, as can be seen in Figure 8-34, which depicts the pressure drop across both legs after a vertical tee split. The plots for both the top and bottom branch are almost identical, which was the case for the entire tested pressure range of 2140 kPa to 4910 kPa. At these high velocities the flow is in the bubbly flow regime resulting in an even split between the two branches.

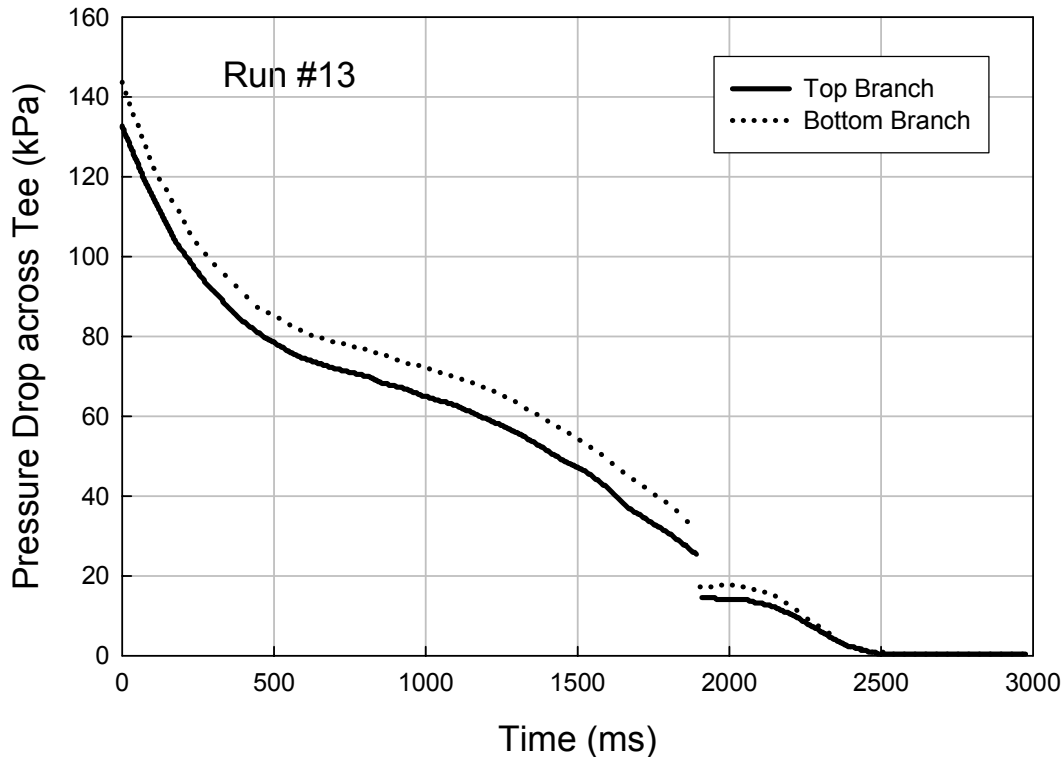


**Figure 8-34. Pressure drops across top and bottom branch tees from Run #13.**

The fourth set of experiments used the same piping configuration as the first set, the straight pipe, but the test fluid was changed to HFC-125. The main difference observed in these runs over the HFC-227ea runs was the drop in temperature as the liquid vaporized. If a comparison is made between Run #5 (HFC-227ea) and Run #16 (HFC-125), which have initial source vessel pressure within 5 kPa of each other, there is an undeniable difference in the temperature traces in the collection vessel.

As Figure 8-35 shows, the temperature in Run #5 only drops about 3 °C compared to a temperature drop of almost 35 °C in Run #16. The other temperature traces between these runs are similar. This may be due to the fact that the flow passes through the pipe at a fast rate with a high convective heat transfer coefficient, which causes the fluid to warm up. However, in the collection vessel, the volume/surface ratio is much larger and convective heat transfer to surface area is smaller. Although, it would have been beneficial to measure the temperature at the end of the pipe to justify this theory, it was unable to take this measurement due to a thermocouple failure. Once the liquid reaches the collection tank, it must vaporize to reach the saturation conditions in the collection vessel, causing a drop in temperature. These conditions did not significantly effect the other measurements near the end of the pipe for either fluid. For instance, for either fluid, the void fraction followed a similar trend as expected from the previous runs, it dropped off as the initial flow passed the sensor and then rose slowly until the liquid ran out, then it returned to the all vapor value, as shown in Figure 8-36 and Figure 8-37. During runs with both of these fluids, a noticeable pressure recovery due to the degassing of the nitrogen was not observed, which was seen in previous studies. Although, when examined closely, a sudden slow down in the pressure decay after the initial pressure drop was observed, which might indicate a slight recovery.

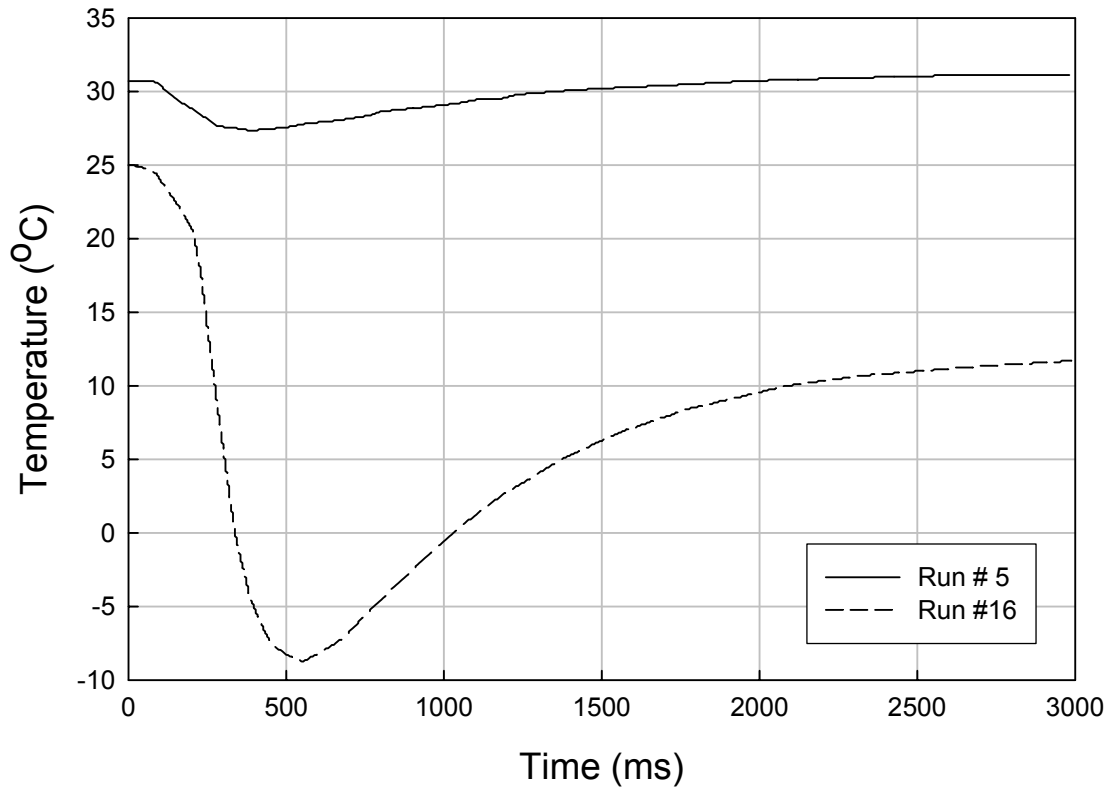


**Figure 8-35. Comparison of Temperature Traces in the Collection Vessel from Runs #5 and #16.**

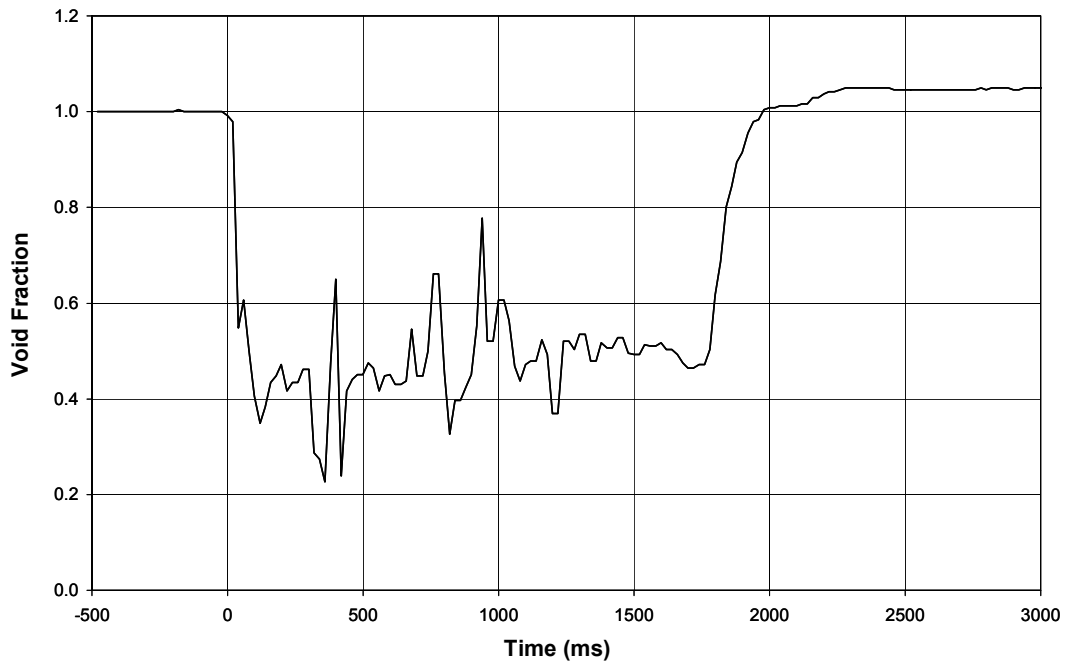


**Figure 8-36. Void Fraction Measurements from Run #5.**

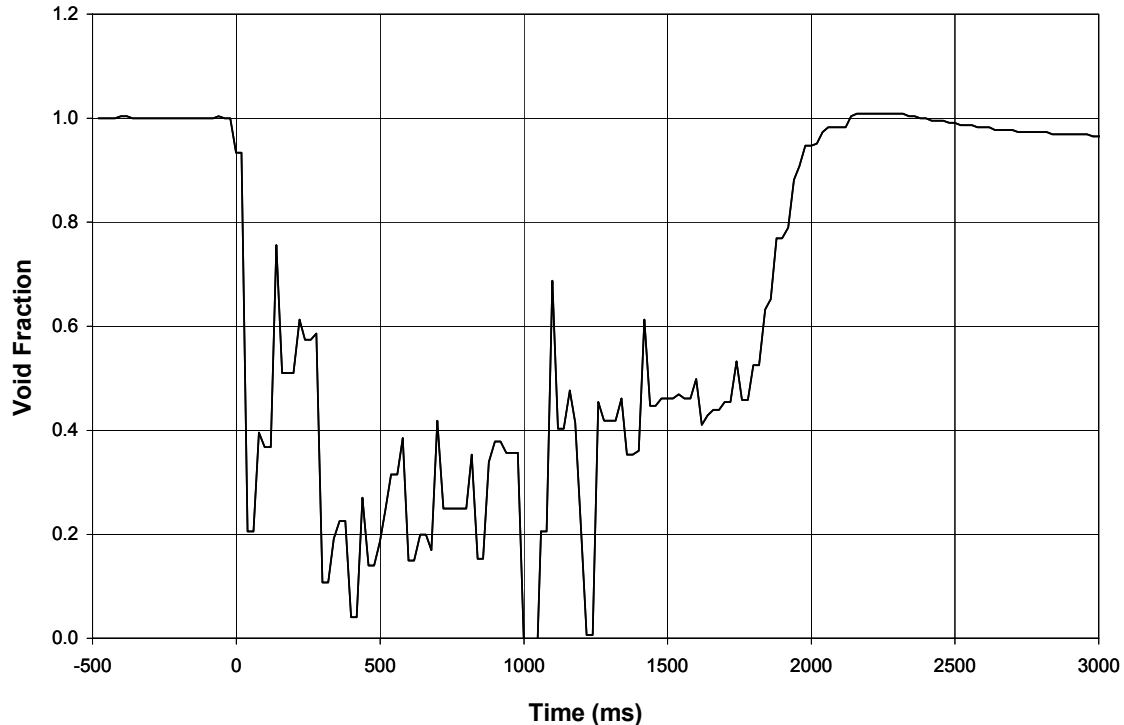


**Figure 8-37. Void Fraction Measurements from Run #16.**

This conclusion is supported by the fact that in the HFC-227ea runs there was a much smoother transition shown on the source vessel pressure trace between the initial pressure drop and the filling of the pipe. This can be seen best by once again comparing Runs #5 & #16, where there is a slight “bump” in the source vessel pressure trace at about 400 ms of Run #16, as shown in Figure 8-38 and Figure 8-39. The absence of a more pronounced pressure recovery due to the degassing of nitrogen can be accounted for by either of two reasons: the speed of the flow is too great for a noticeable increase in pressure from degassing to be observed at any one point, or the degassing took place so gradually over the run preventing any noticeable increase. It was unknown whether the degassing occurred at some point since the void fraction validated that a two-phase flow existed. However, it was certain that this was not due to vaporization since there was no temperature drop.

The last sets of runs were conducted during preliminary tests of the instrumentation after installation in the system. The first test using water, Run #18, allowed for testing the mass flow rate sensor. As can be seen in Figure 8-40, this test worked out very well and gave an excellent representation of the instantaneous mass inventory in the source vessel. This test also showed that the thermocouples could pick up quick drops in temperature, as shown in the pipe position 1 trace of the film thermocouple, which picked up the nitrogen expansion at the end of the run, as shown in Figure 8-41. The second test, Run #19, provided an excellent sample of the capabilities of the capacitance probe for measuring void fraction. Since there was no vaporization or dissolution of gas in this run, the void fraction should go from a value of 1.0 to 0.0 as the liquid flowed. This is exactly what was found at the beginning of the run until it stopped at precisely the same point as the temperature dropped, signifying the start of the nitrogen expansion through the system, as can be seen in Figure 8-42. The final set of experimental runs used carbon dioxide as a test fluid and was conducted with an open collection vessel to prevent a high pressure

at the end of the run. The goal of these tests was to get a grasp on the response time of the film thermocouples and what range of temperature drop they could collect. The thermocouples were able to pick up a quick drop in temperature of up to  $-40\text{ }^{\circ}\text{C}$ .

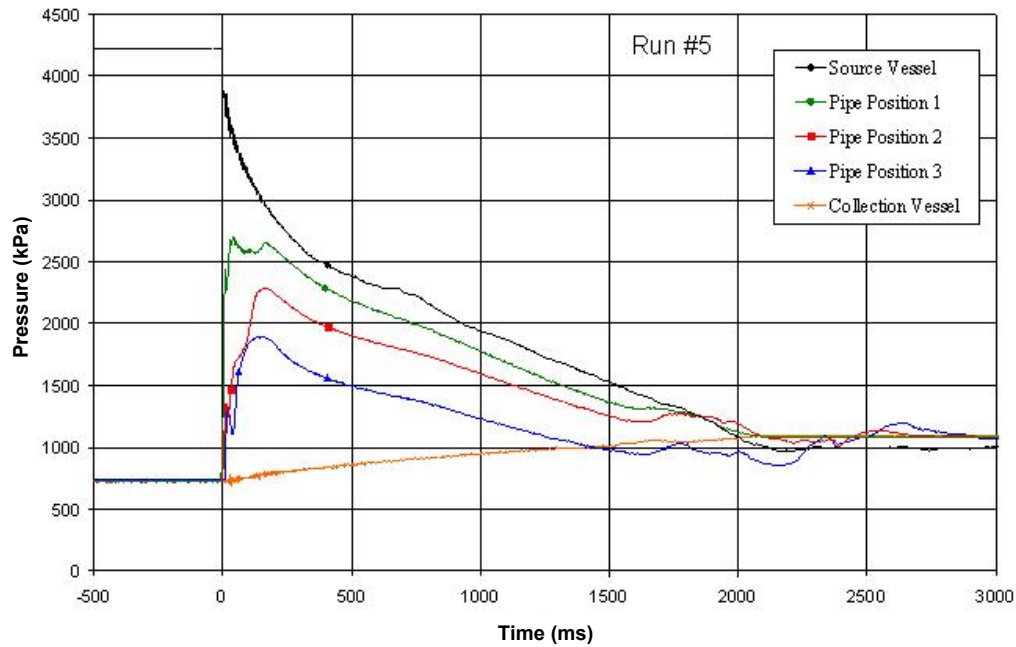


Figure 8-38. Pressure Traces from Run #5.

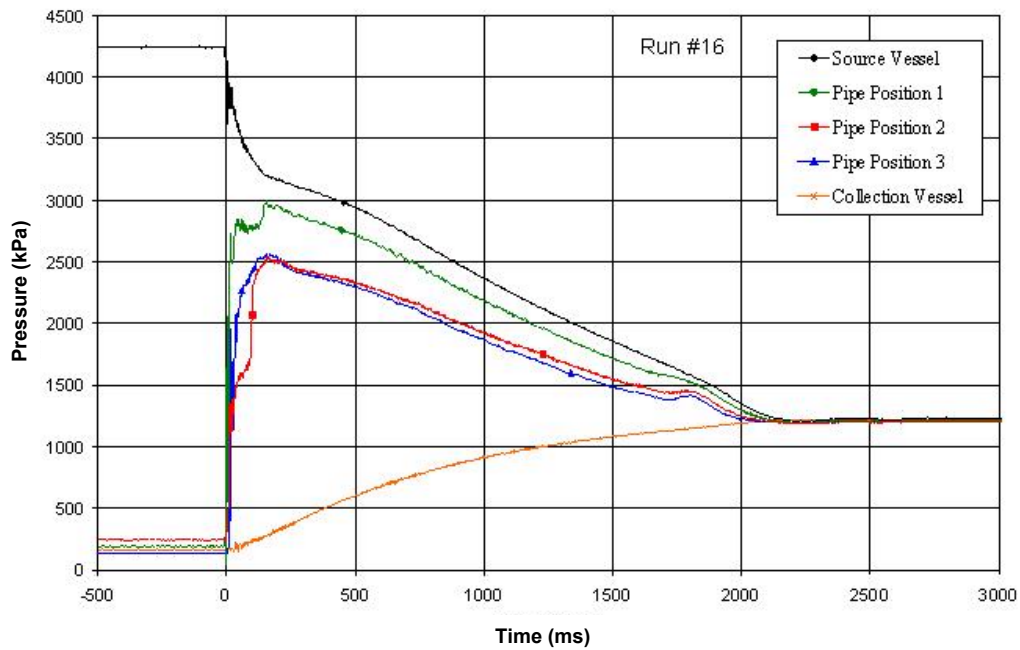


Figure 8-39. Pressure Traces from Run #16.

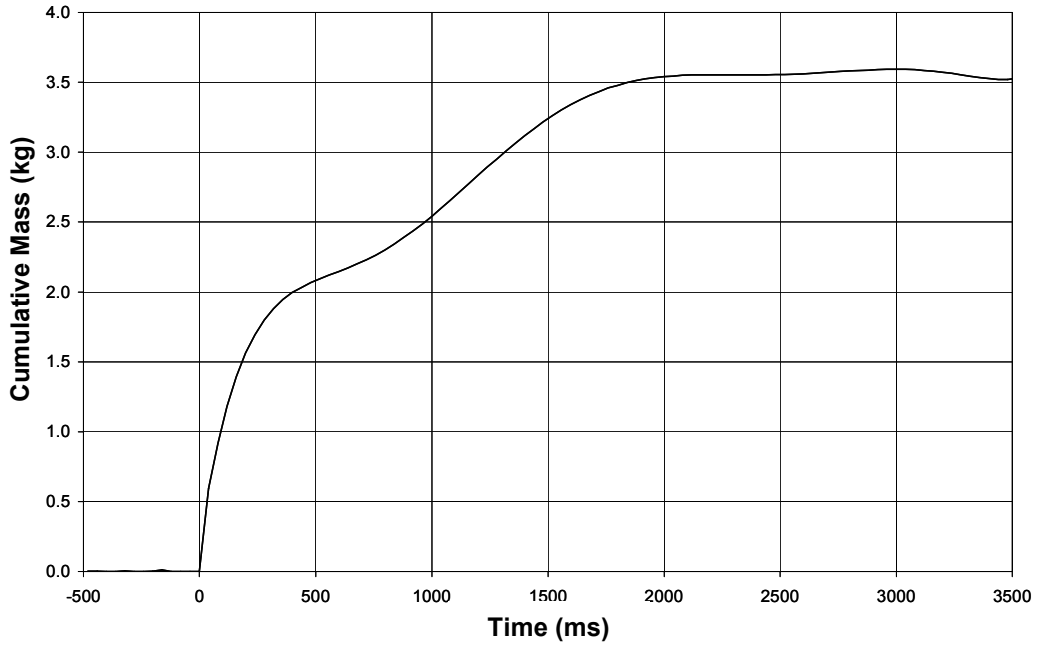


Figure 8-40. Mass Inventory in the Source Vessel from Run #18.

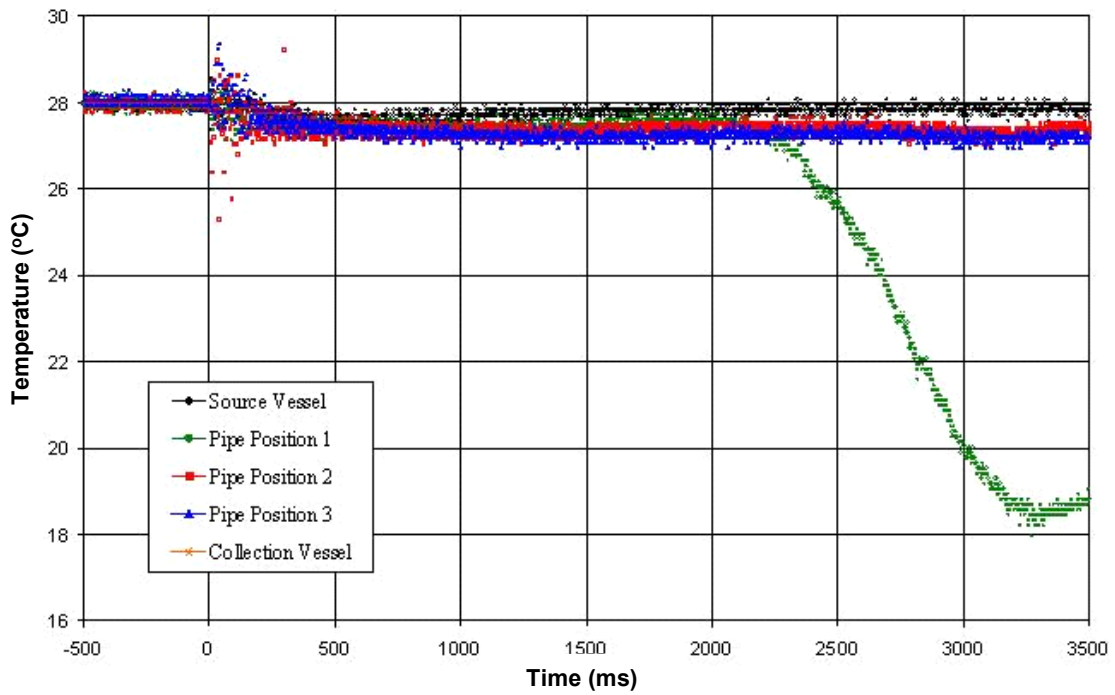
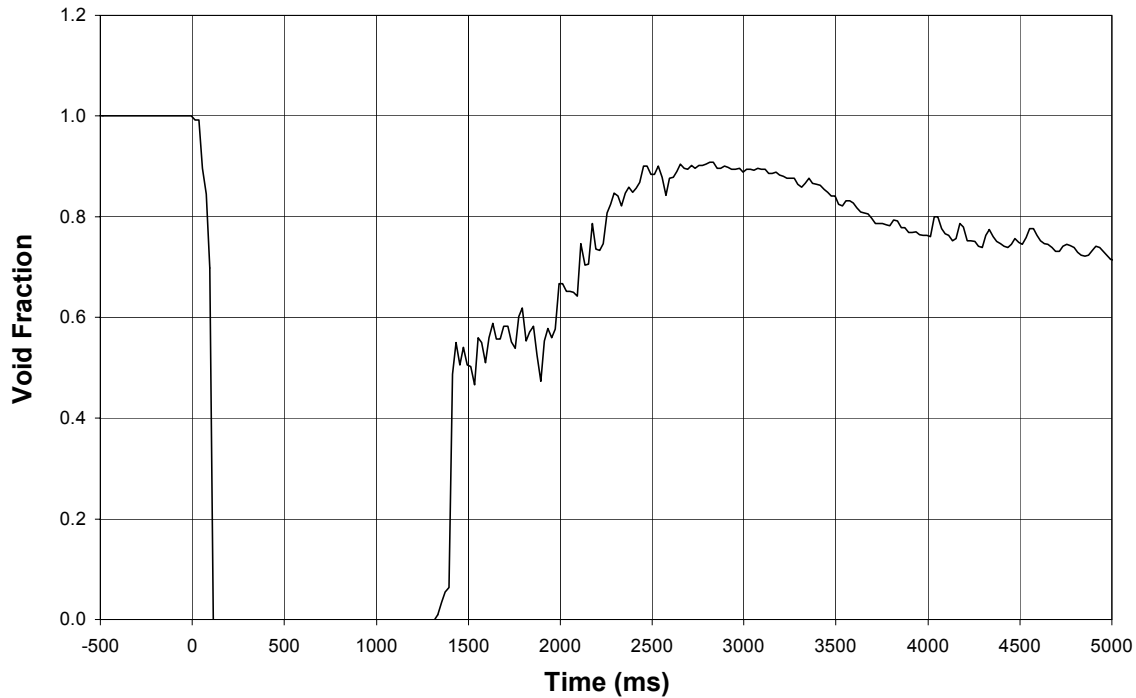


Figure 8-41. Temperature Traces at Various Positions from Run #18.



**Figure 8-42. Void Fraction Measurements from Run #19.**

### 8.3.7 Comparison of Code Predictions to Experimental Data

This section discusses some of the code assessments carried out against experiments. Early assessment of the FSP code was against halon 1301 discharge experiments reported by Elliott et al.<sup>10</sup> These tests were carried out with three different system configurations. These included a bottle-nozzle arrangement, a bottle with straight pipe, and a bottle with a straight pipe branching to two separate exit legs. Test 146 from Elliott et al.<sup>10</sup> was a bottle-nozzle arrangement. This test was used in early assessment of FSP for the gas release model. The other configurations tested by Elliott et al.<sup>10</sup> were also simulated during various developmental stages of the code. The results generally showed good agreement between code calculations and experimental data. A re-assessment of the final code version against data from these configurations was not carried out. This was primarily because the tests were conducted with halon 1301, and the intent of code development was for alternate fluids. The expectation is that the final version of FSP would be able to simulate these tests quite well. Other experimental data on suppressant discharge through typical delivery systems have been compiled and reported by Yang et al.<sup>2</sup> and Pitts et al.<sup>9</sup>

This section presents the assessment of the code carried out against some of the experiments reported in Yang et al.<sup>2</sup> The experiments were conducted at NIST, and included a series of discharge tests using several agents (including halon 1301). The code was also assessed against current experiments carried out as a part of this code development project by examining several piping configurations, with HFC-227ea and with HFC-125. These experiments are particularly useful for code assessment because, in addition to the usual measurement of pressure, the experiments were able to estimate the mass flow rate of discharge, and also measured the void fraction near the pipe exit.

### Code Assessment against NIST Test Data

The basic design of the NIST experimental apparatus consisted of a storage vessel (or pressure vessel), discharge piping, and a recovery tank. A nitrogen make-up tank was connected to the pressure vessel to simulate constant-head discharge if needed. The pressure vessel was fitted with a quick release valve at the bottom. Figure 8-43 shows the test apparatus. The data included vessel pressure and pressures at various locations along the discharge piping. Several discharge piping configurations were used. These included: (1) 3.5 m straight pipe discharge; (2) 3.5 m pipe with 90° bend; (3) 4.5 m pipe with 90° bend; (4) 3.5 m straight pipe with expansion from 9.5 mm ID to 15.9 mm ID; (5) 3.5 m straight pipe with contraction from 15.9 mm ID to 9.5 mm ID; and (6) 4.5 m, 15.9 mm ID tee configuration. Two pipe sizes were used for all configurations, unless otherwise stated, and these were 9.5 mm ID and 15.9 mm ID. The various configurations are shown in Figure 8-44.

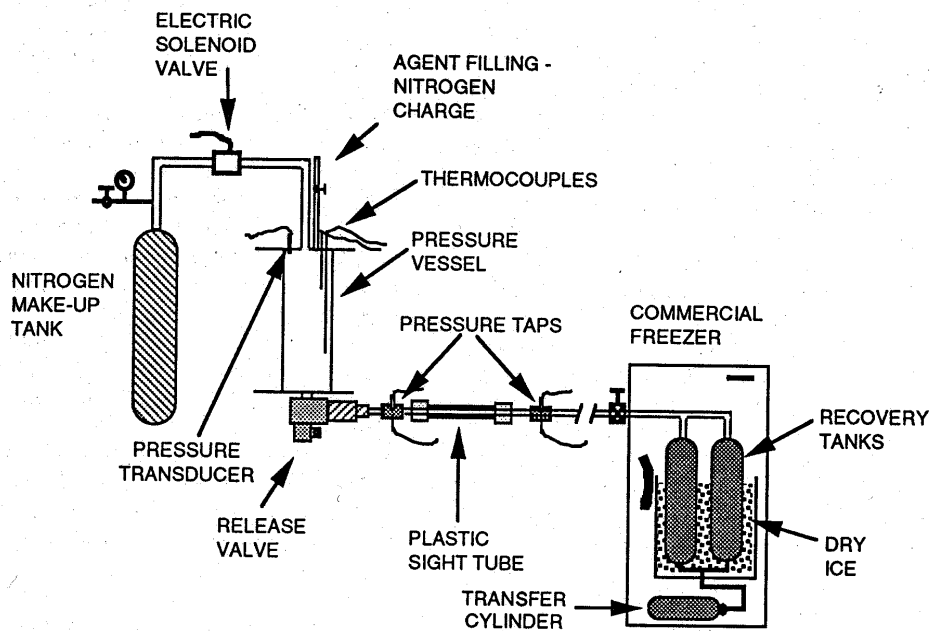


**Figure 8-43. NIST Test Apparatus.<sup>2</sup>**

Four agents were tested in these experiments. These were halon 1301, HFC-125, HFC-227ea and CF<sub>3</sub>I. The assessment presented here is only for the HFC-227ea experiments. Table 8-5 lists the tests conducted with HFC-227ea. Note that the test identifier in the first column is actually the Figure Number in Appendix II of the NIST Report (Yang et al.<sup>2</sup>).

Four tests were simulated using FSP. These are Tests B-59, B-68, B-61, and B-60. Together they represent a variety of piping configurations. The results of the simulations are presented below.

A FSP input model for each discharge piping configuration was developed. The following geometrical information was obtained from Yang et al.<sup>2</sup>

Storage Vessel Volume:	$4.06 \times 10^{-3} \text{ m}^3$
Storage Vessel ID:	100 mm
Discharge Valve:	31.8 mm inlet to 44.5 mm exit
Discharge Valve Stroke:	order of 10 ms
Nitrogen Make-up Tank:	$88 \times 10^{-3} \text{ m}^3$
Nitrogen Charge Tubing:	19.1 mm ID
Nitrogen Solenoid Valve:	30 kPa pressure difference opening, stroke 50 ms
Discharge Piping Sizes:	9.5 mm and 15.9 mm ID
Discharge Piping Lengths:	3.5 m and 4.5 m
Recovery Tank Volume:	$15 \times 10^{-3} \text{ m}^3$

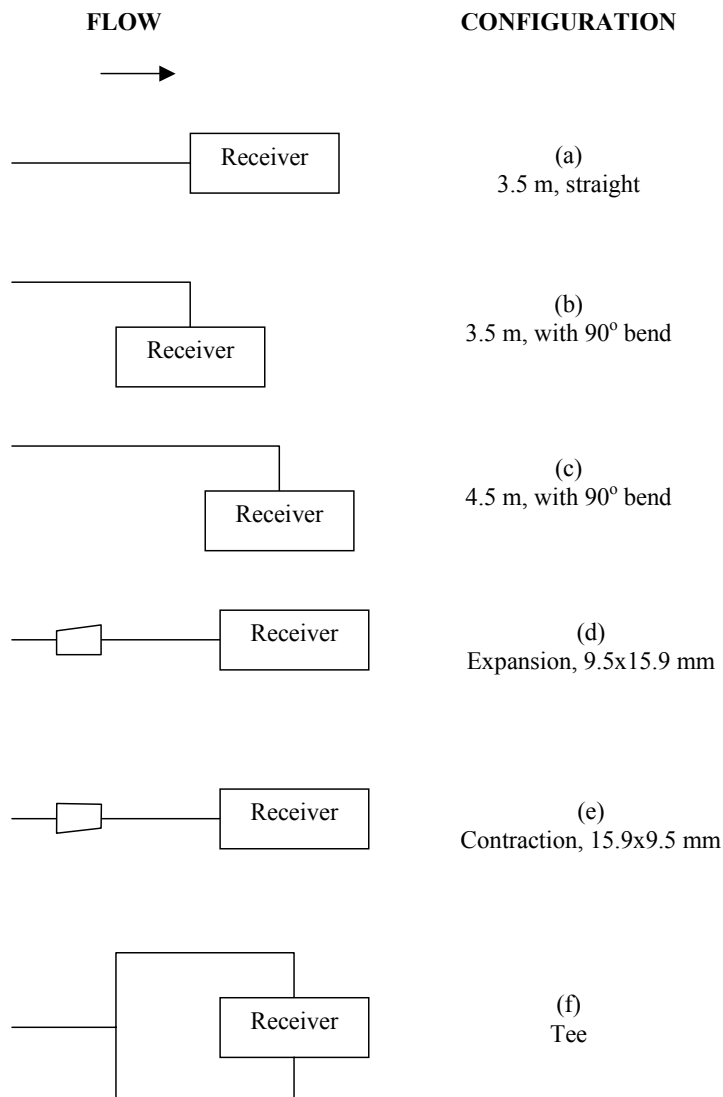
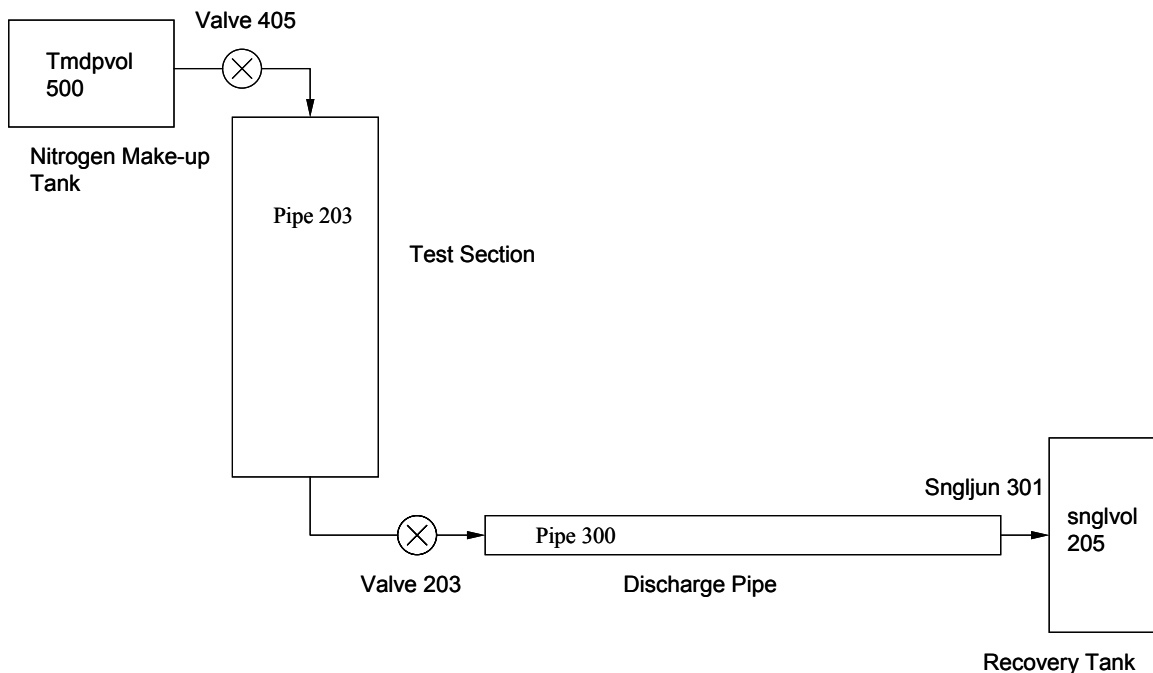


**Figure 8-44. Piping Configurations for NIST Experiments.**

**Table 8-5. Test Matrix from NIST Experiments.**

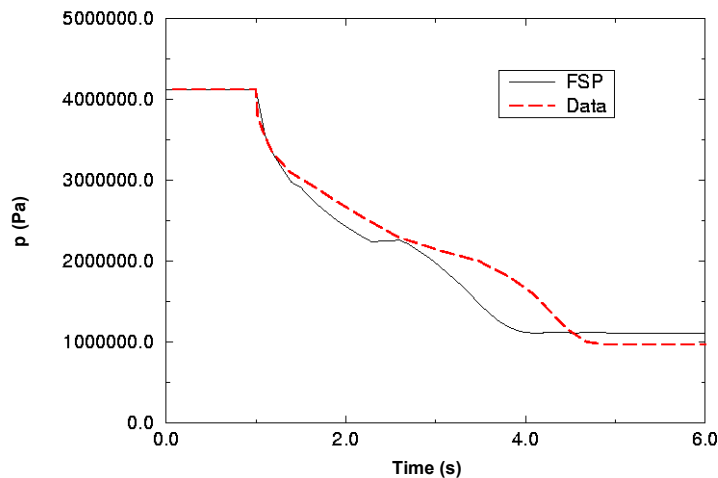
Test Identifier	Pressure (MPa)	Fill Volume (%)	Configuration
B-54	2.75	56.5	straight pipe, 9.5 mm ID, 3.5 m long
B-56	4.12	60.2	straight pipe, 9.5 mm ID, 3.5 m long
B-58	4.12	49.2	3.5 m, 90-deg bend, 9.5 mm ID
B-59	4.12	49.2	4.5 m, 90-deg bend, 9.5 mm ID
B-60	4.12	49.0	straight pipe with contraction
B-61	4.12	49.0	straight pipe with expansion
B-66	2.75	54.1	straight pipe, 15.9 mm ID, 3.5 m long
B-68	4.12	49.4	straight pipe, 15.9 mm ID, 3.5 m long
B-71	4.12	49.4	3.5m, 90-deg bend, 15.9 mm ID

The above information was used to develop the input models for FSP for each of the tests. The models are not described in detail or presented here. They were very similar, conceptually, to the sample problem described in detail in Tuzla et al.<sup>7</sup> The supply vessel (called storage tank in these tests) and discharge piping were each modeled with PIPE components, with a VALVE component in between them, simulating the initiation of the discharge process. In modeling the discharge piping, junctions were located at the physical locations of area changes (contraction or expansion) and bends. Appropriate loss coefficients were entered to simulate the energy losses at these locations. Figure 8-45 shows the general FSP model used for these simulations.



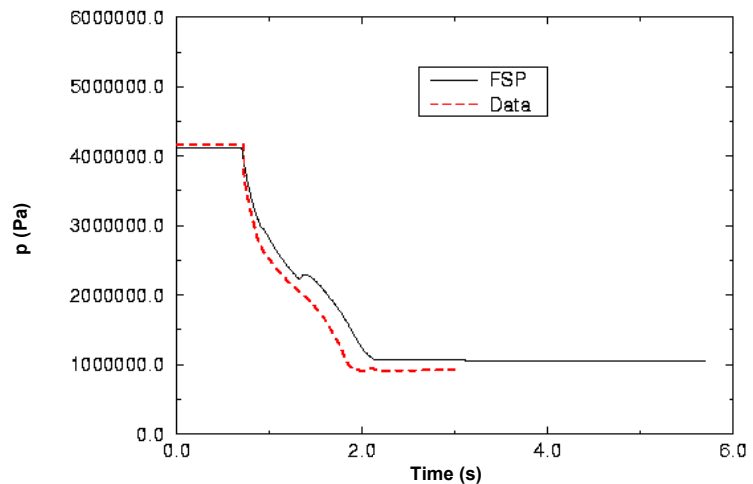
**Figure 8-45. FSP Input Model.**

These cases were all run with the value of  $r_c$  in the range of  $7.5 \times 10^{-9}$  m to  $1.0 \times 10^{-8}$  m. The discharge coefficients at the system exit were chosen as 1.0, 0.8 and 0.8 for the subcooled, two-phase, and single phase vapor conditions, respectively. The value of  $\Gamma_\theta$  was set at 10,000 for the tests. Figure 8-46, Figure 8-47, Figure 8-48, and Figure 8-49 respectively show the calculated and measured pressure responses in the supply vessel, for Test B-59, B-68, B-61, and B-60. Not shown here are the pressure histories at various locations along the discharge piping. Generally, at these locations, the measured pressure would increase sharply as the discharge was initiated, and then decrease gradually as the fluid left the system. This trend was picked up by the code. Overall, the code picks up the qualitative trends in the pressure history. If the time for complete discharge of the agent is taken as the time at which the pressure drops to its lowest value, the code seems to calculate this generally within about 25 %. A better agreement between calculation and data could probably be obtained by varying  $r_c$  and  $\Gamma_\theta$ . This has not been attempted here, primarily because there are inherent uncertainties in these parameters, and a code user would normally vary these parameters in design calculations to get conservative results for design purposes. Generally, a higher value of  $\Gamma_\theta$  would release more dissolved gas earlier in the transient. This would generally delay the complete discharge of the bottle slightly. Users can utilize this information to develop conservative designs in applying the FSP code.



**Figure 8-46. Comparison of Calculated and Measured Bottle Pressure for B-59.**

**Figure 8-47. Comparison of Calculated and Measured Bottle Pressure for B-68.**



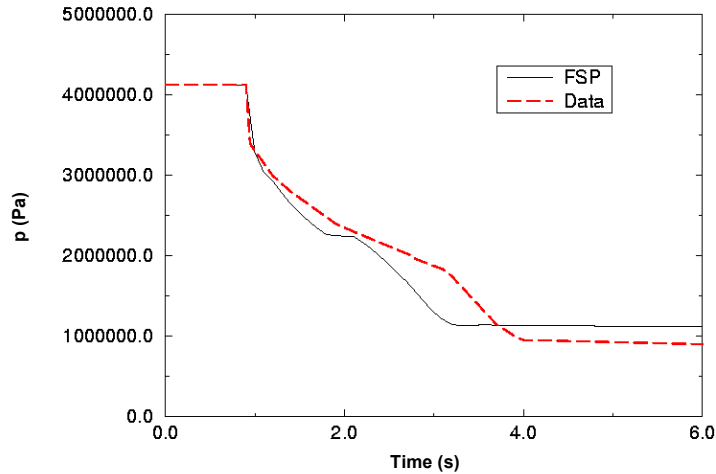
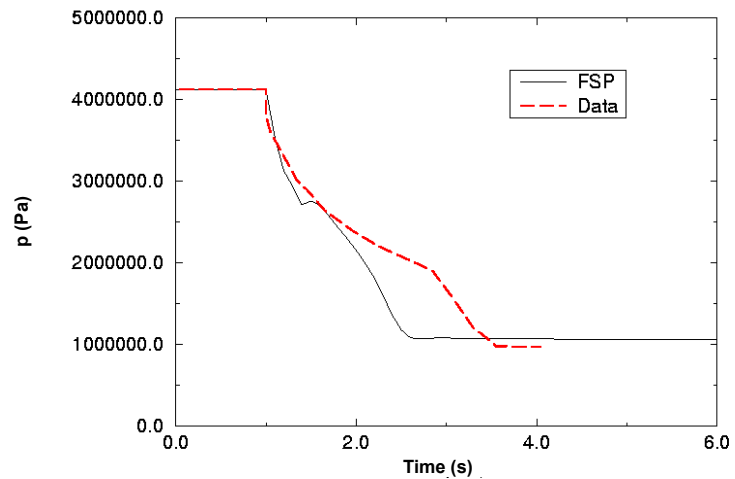


**Figure 8-48. Comparison of Calculated and Measured Bottle Pressure for B-61.**

**Figure 8-49. Comparison of Calculated and Measured Bottle Pressure for B-60.**



### Code Assessment Against Current Test Data

In this section a detailed comparison of the computer code predictions and the experimental values for a rapid transient discharge of a suppressant flow will be examined. To fully test the code, all aspects of an actual suppressant discharge must be considered. For this reason, the current experimental data should be the benchmark for comparison since it includes the most extensive experimental data to date. This is due to the fact that data for local temperatures, void fraction, and mass flow rate which, were previously unavailable, were measured. In addition, extensive data for a number of different flow conditions and piping configurations have been obtained.

When using the computer code to make predictions, it was necessary to determine a few operating parameters to represent the operating conditions of a specific run. Some of these parameters are straightforward and pertinent to the piping configuration, such as diameters, lengths, etc., and operating conditions such as initial pressure, temperature, etc. However, some of these parameters are part of the modeling used in the code. One of these models is the gas dissolution model, as discussed above.

Dependent on the fluid used during the discharge, the gas dissolution model requires two constants: the critical bubble radius when nitrogen is released from the fluid and the release rate of nitrogen.

The critical radius can be found for a specific run by estimating when the release of nitrogen begins. This is the point near the beginning of the run when the pressure stops dropping rapidly, represented as a change in slope in the pressure trace. With this pressure and the surface tension of the fluid, a critical radius can be calculated as described earlier. After examining the first set of experimental Runs (#1-#7), it was determined that the value was in the range of 5 nm to 20 nm. The second parameter, the rate of degassing, was found to fall in the range from 1000-10,000, depending on the system. The last parameter that needs to be defined as input to the code is the discharge coefficient for choked flow conditions. Since the default is 1.0, it is expected that the value must be relatively close to this value.

For ease in use and consistency, it is desirable to choose one value for each of these parameters to run the computer code. To determine the appropriate values for these parameters, a sensitivity analysis of the effects of varying these parameters on the code's output was performed, and the results were compared with experimental data. The experimental Run #4 was used for this purpose. This run was chosen over the others because it was one of the repeatability tests and was in the range of typical suppressant discharge applications.

The first sensitivity study examined the effect of critical radius on the computer code output. To isolate the effect of changing this parameter, the values for the gas release rate and the discharge coefficients were kept constant at 1000 and 0.8, respectively. The calculations showed that a lower value for the critical radius caused the slope change in the source vessel pressure trace to occur later. Therefore, this parameter is important for determining when the gas begins to release from the liquid. By comparing the calculations using critical radii of 7.5 nm and 10 nm with the experimental results, as seen in Figure 8-50, a critical radius of 10 nm was chosen.

The second sensitivity study was to identify a value for the rate of nitrogen gas release, with the discharge coefficient and the critical radius kept constant at 0.8 and 7.5 nm, respectively. This rate influences the speed at which the nitrogen gas is released once the process begins, thus changing the shape of the pressure-time history. As shown in Figure 8-51, the pressure trend remains straight and uniform at lower gas release rates; however, there is a pressure recovery or "bump" in the trace at higher release rates. Based solely on the pressure-time history results, it is hard to determine the best value to use for this parameter so other output parameters from the calculations were examined. The void fraction results are shown in Figure 8-52, which indicates that average void fraction increases with the gas release rate parameter. This figure, the other does not, shows that a value just below 2500 kg/m<sup>3</sup> s appears to be appropriate. Based on the observations from the above two figures, a gas release rate value of 2000 kg/m<sup>3</sup> s was chosen.

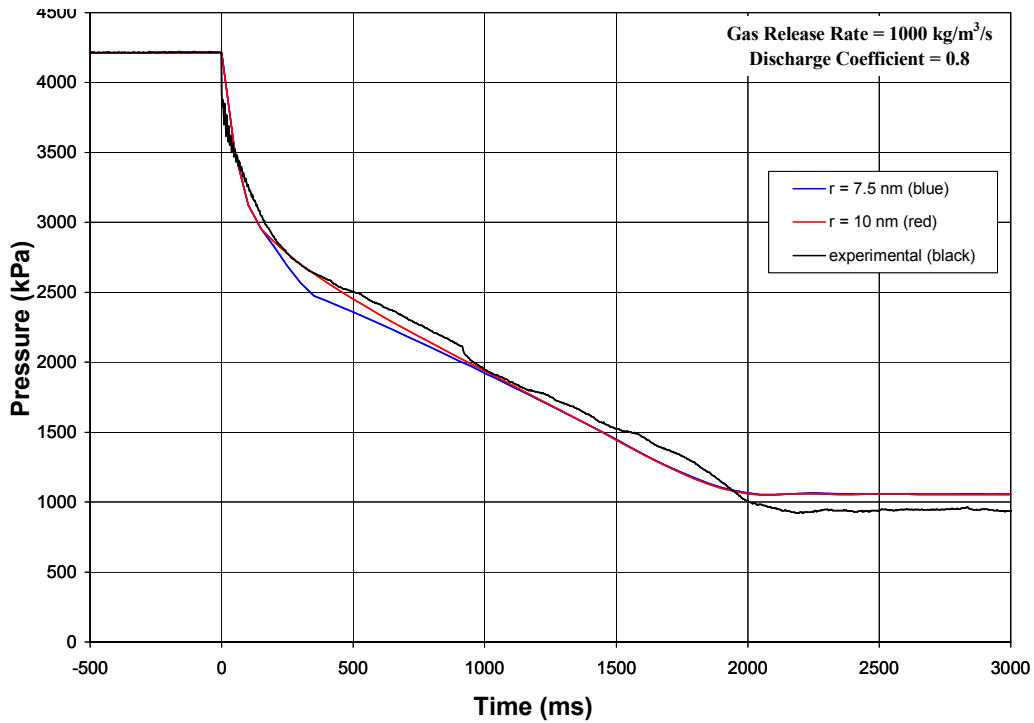


Figure 8-50. Comparison of Experimental and Predictive Source Vessel Pressure Data in Sensitivity Study on Critical Radius Value for Conditions of Run #4.

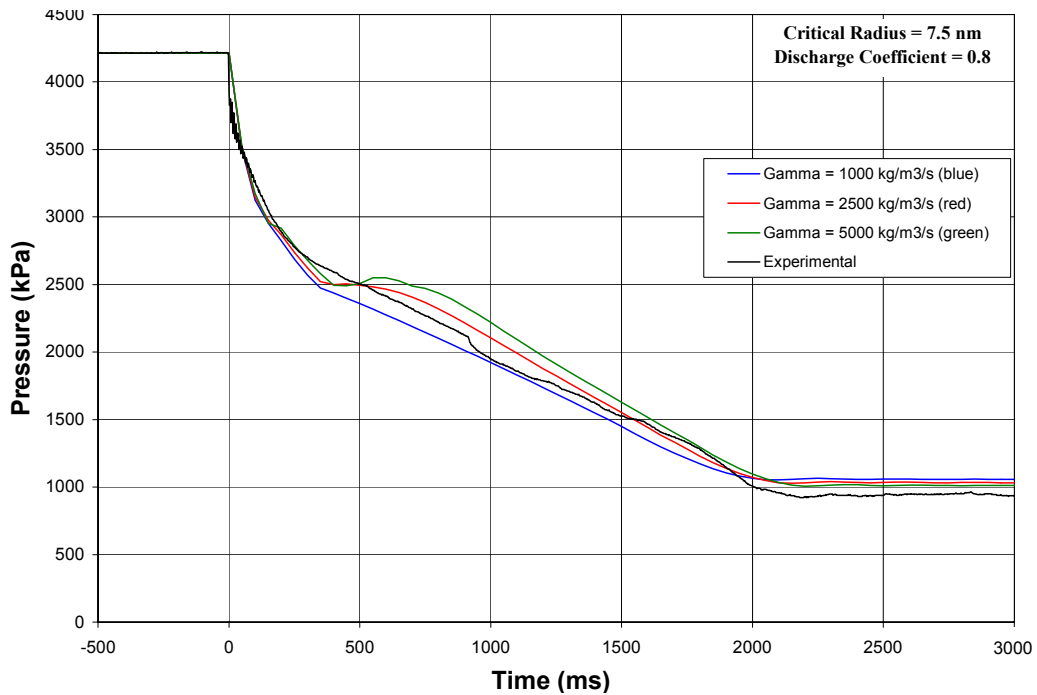
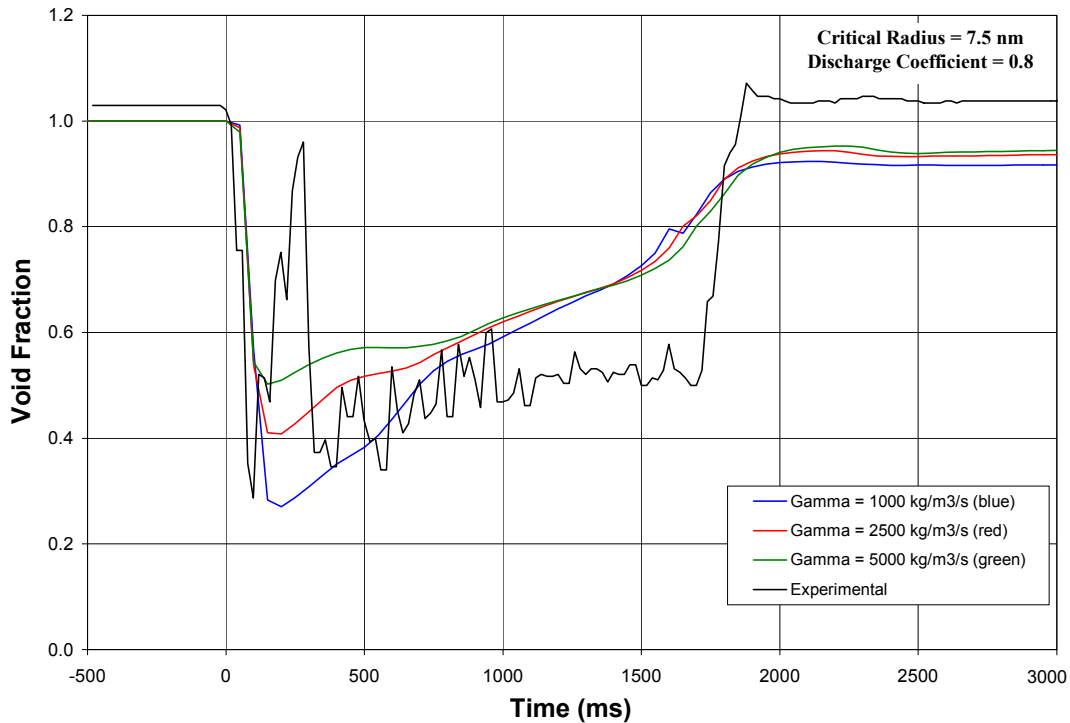


Figure 8-51. Comparison of Experimental and Predictive Source Vessel Pressure Data in Sensitivity Study on Gas Release Rate Value for Conditions of Run #4.



**Figure 8-52. Comparison of Experimental and Predictive Void Fraction Data in Sensitivity Study on Gas Release Rate Value for Conditions of Run #4.**

The last sensitivity analysis was to pick a value for the discharge coefficient. This parameter influences when and where choking occurs in the system. Values ranging from 0.75 to 1.15 were tried, and there were only negligible differences in the output. Therefore, it was decided to use a value of 0.9 for the discharge coefficient.

With all of the operating parameters chosen, a final comparison with the experimental data of Run #4 was conducted. The calculations show good agreement with the experimental results, as shown in Figure 8-53 and Figure 8-54.

In the following discussion, the focus is on comparing the computer code prediction with an entire experimental run (Run #5). The results for cumulative mass in the source vessel as a function of time are shown in Figure 8-55. The prediction agrees well with the experimental measurements. The only noticeable difference is the final mass value and the speed of the discharge represented by the different slope gradients. Even with these differences, the prediction gives an end-of-liquid flow at approximately 1800 ms compared to a measured time of 1600 ms in the experiment, a very good estimate of discharge time.

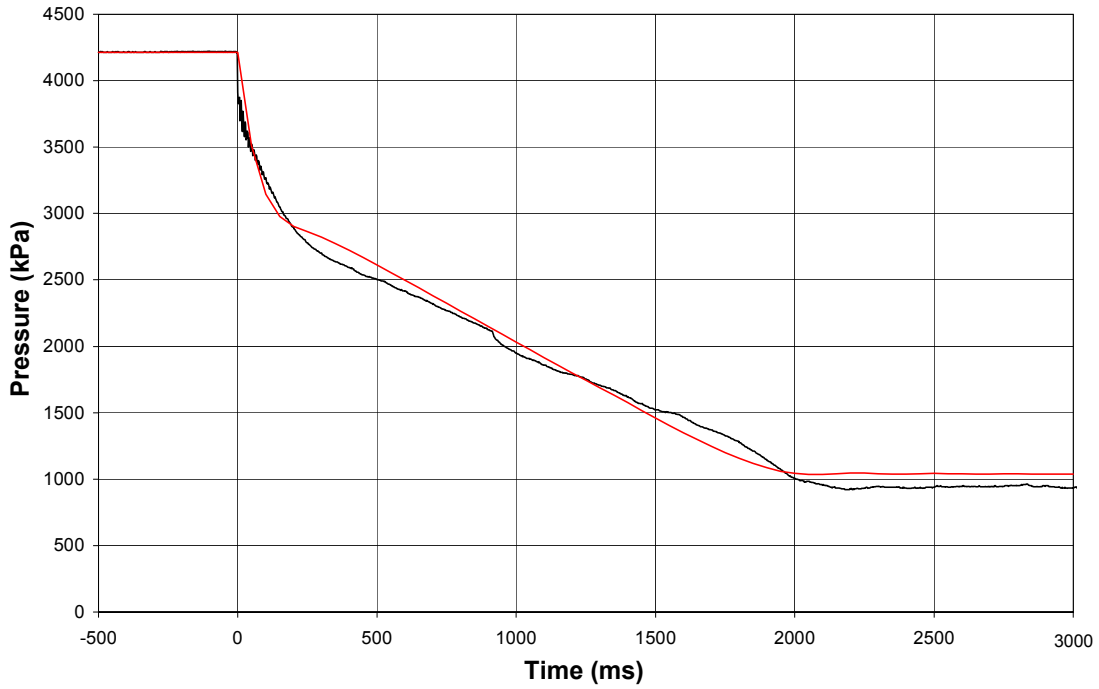


**Figure 8-53. Comparison of Experimental (in black) and Predictive (in red) Pressure Data Using Final Values for Code Operating Parameters for Conditions of Run #4.**

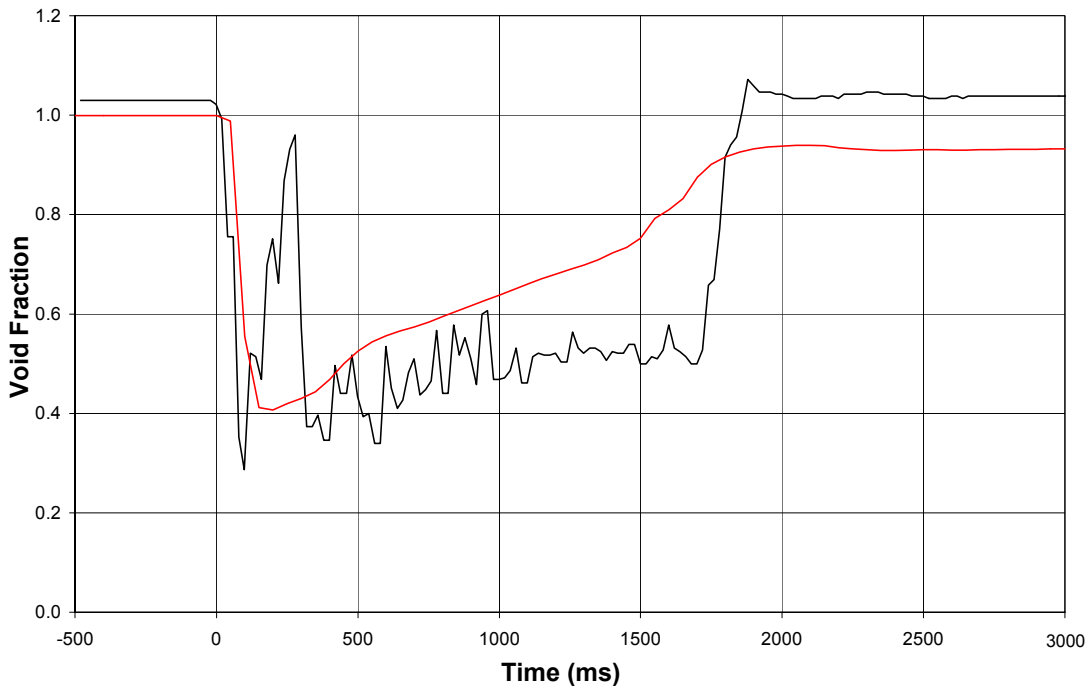


**Figure 8-54. Comparison of Experimental (in black) and Predictive (in red) Void Fraction Data Using Final Values for Code Operating Parameters for Conditions of Run #4.**

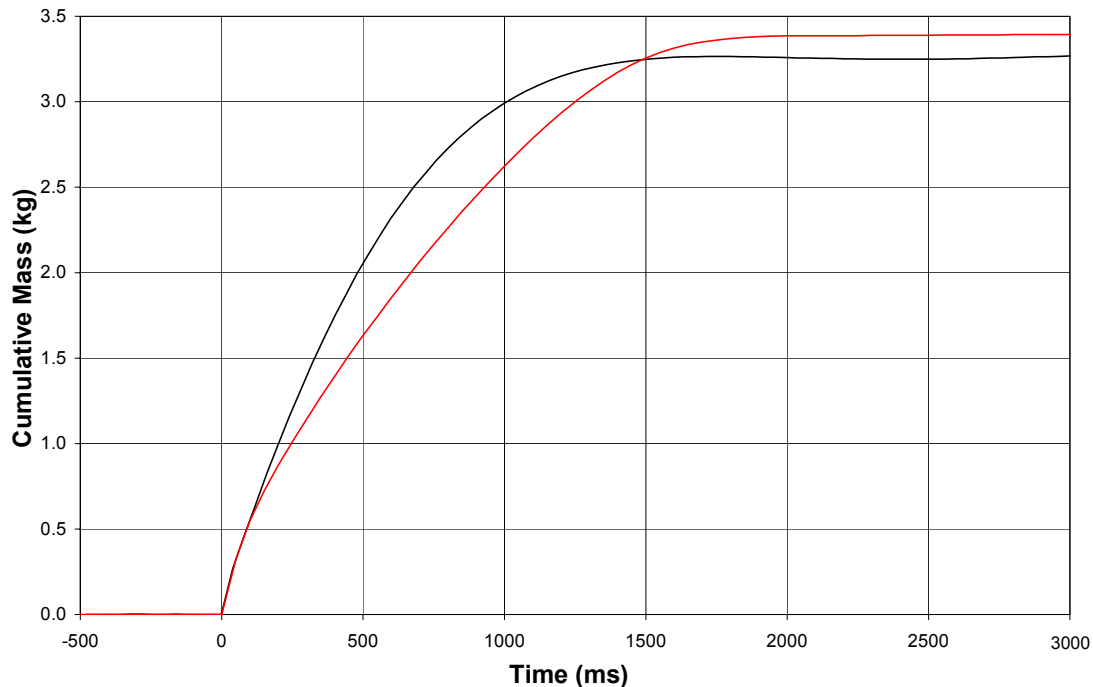


**Figure 8-55. Comparison of Cumulative Mass for Experimental Run #5 (black) and Predictive Computer Code Data (red).**

The next comparison examined is the void fraction experienced at the end of the piping system before the discharge reached the collection vessel. Again, the agreement between the prediction and experiment is good, as shown Figure 8-56. While the experiment was influenced by the local flow regime giving the output a fluctuating appearance, the prediction has a smooth trace due to the fact that the void fraction was calculated based on mass balance terms giving an average void fraction value for the amount of liquid and vapor present in the system. A similar trend can be seen in both, a sudden drop as the pipe is filled with liquid and then an increase as nitrogen comes out of solution and raises the average amount of gas in the flow until the run ends with no more liquid flowing. The only glaring difference is in the final value reached at the end of the run. The prediction never goes back to an all-vapor reading of 1.0, indicating that in the simulation there is still liquid present in the pipe. In a realistic situation, the liquid would eventually drain into the collection vessel since it is the lowest part of the system, but the prediction is finding this value through a mathematical simulation, so it may not account for this. Neglecting this problem, a good representation of the void fraction can be found using the prediction.

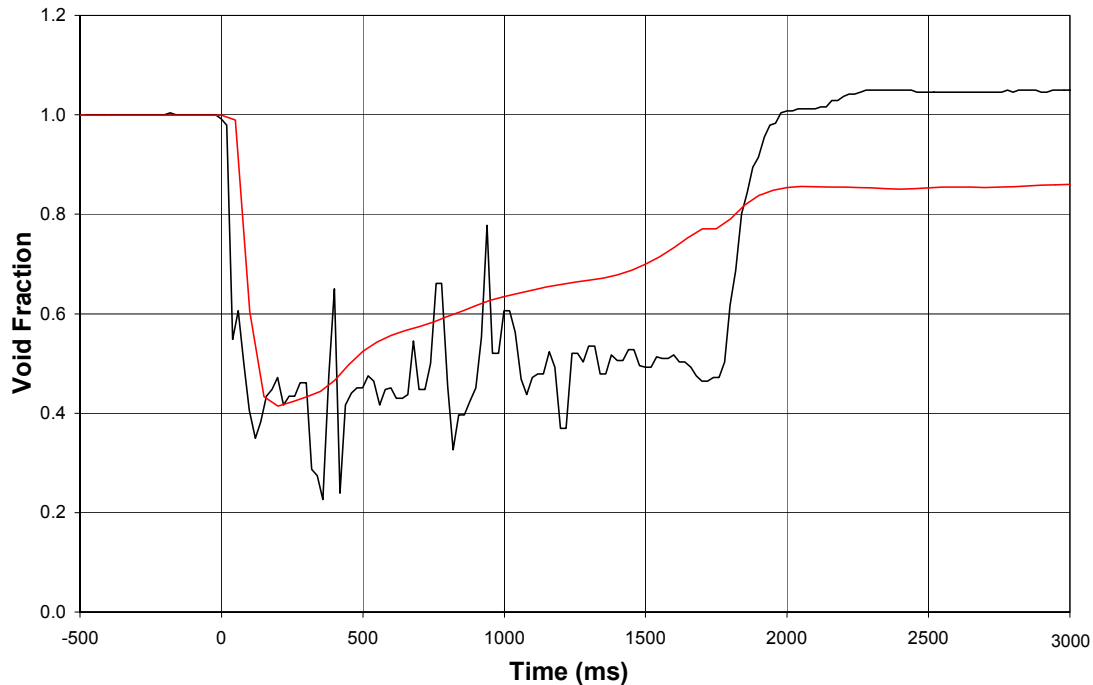


**Figure 8-56. Comparison of Void Fraction for Experimental Run #5 (black) and Predictive Computer Code Data (red).**

The most important comparison for this study is a comparison of the experimental and calculated pressure traces since pressure is what drives the discharge and delivers the suppressant to the fire. Figure 8-57, Figure 8-58, Figure 8-59, Figure 8-60, and Figure 8-61 show the prediction compared to the experiment for the pressures in the source vessel, at pipe position #1, at pipe position #2, at pipe position #3, and in the collection vessel, respectively. They all agree very well with the experimental data, with the only discrepancy being the final pressure at the end of the run. While the shape of the curves varies slightly, they all show the same trend and a similar slope as the pressure decreases during the discharge. This observation is most exciting since most of the experimental data available is in the form of pressure traces, allowing for the code to be more widely used in comparisons and in simulating the output of various system configurations.

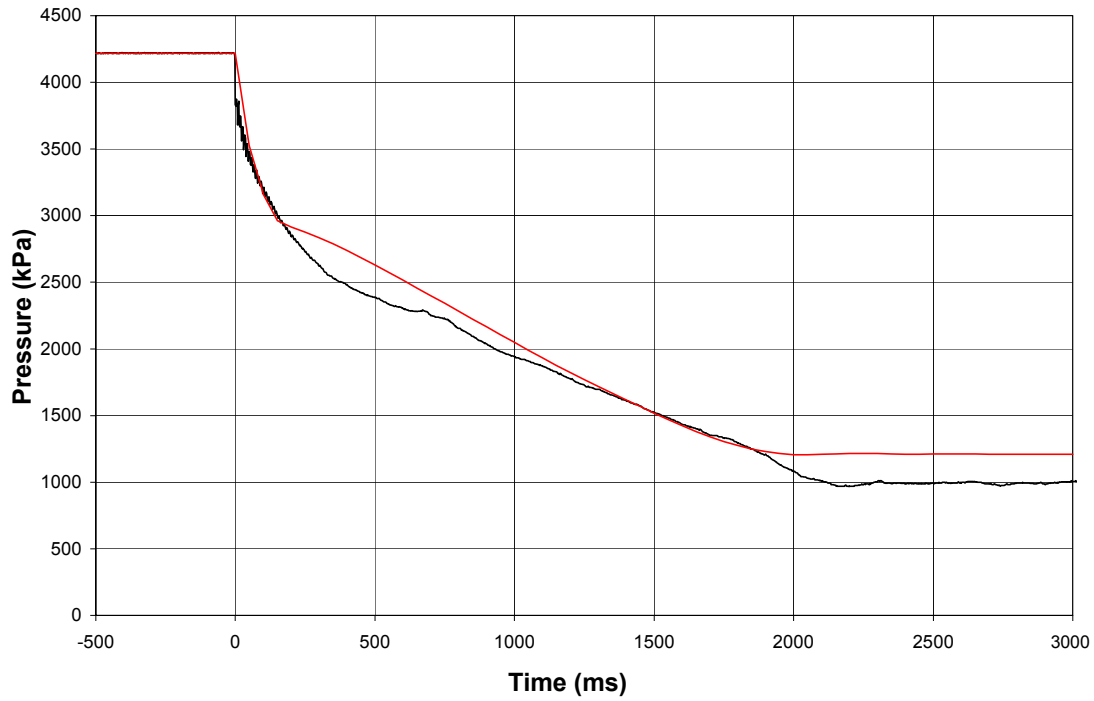


**Figure 8-57. Comparison of Source Vessel Pressure for Experimental Run #5 (black) and Predictive Computer Code Data (red).**

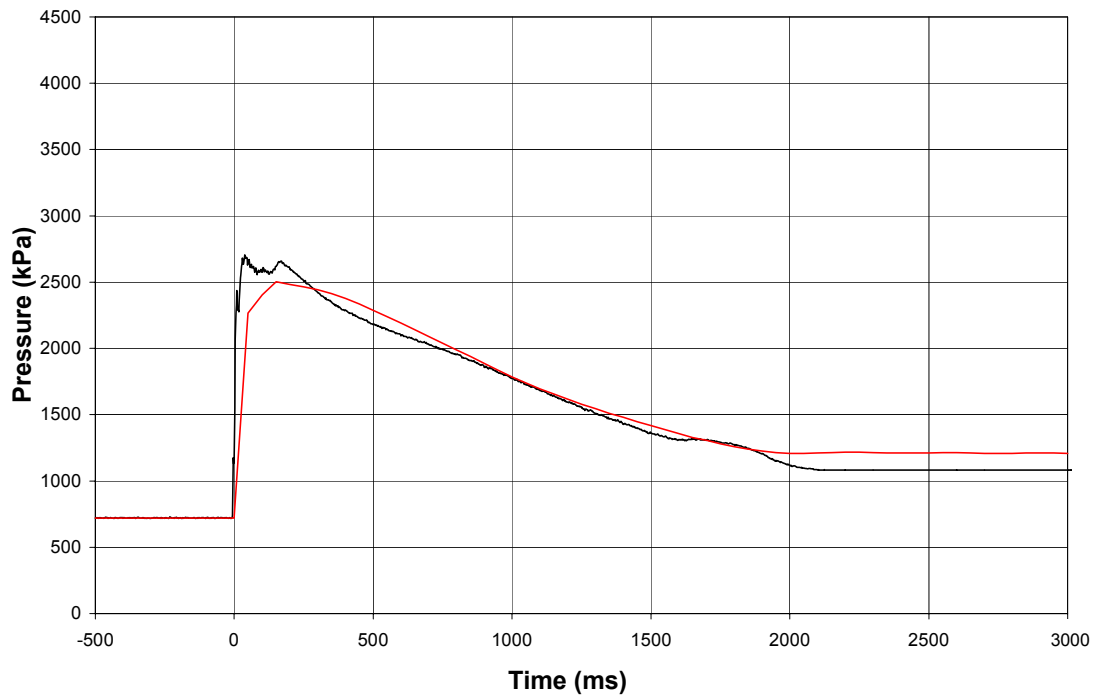


**Figure 8-58. Comparison of Pipe Position #1 Pressure for Experimental Run #5 (black) and Predictive Computer Code Data (red).**

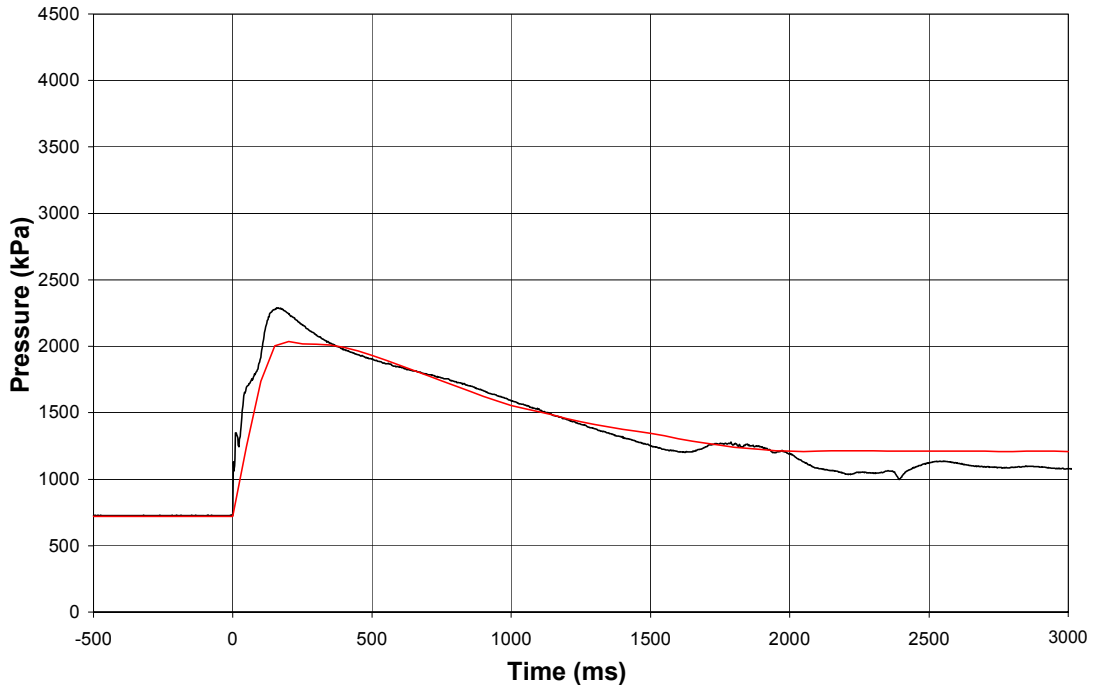


**Figure 8-59. Comparison of Pipe Position #2 Pressure for Experimental Run #5 (black) and Predictive Computer Code Data (red).**

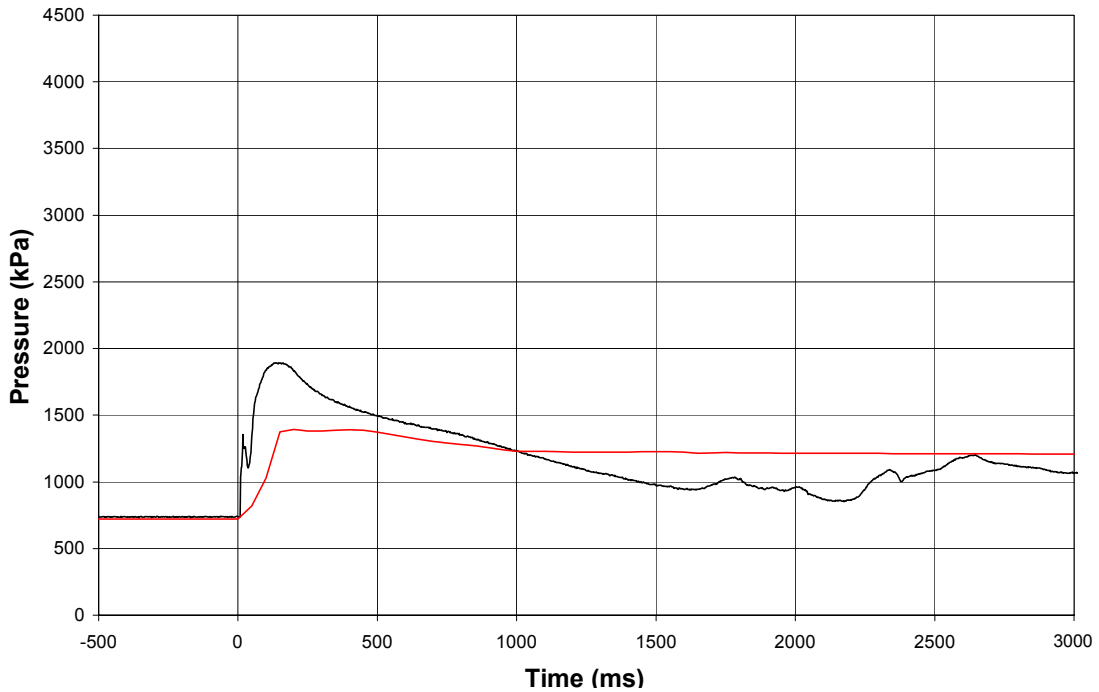


**Figure 8-60. Comparison of Pipe Position #3 Pressure for Experimental Run #5 (black) and Predictive Computer Code Data (red).**

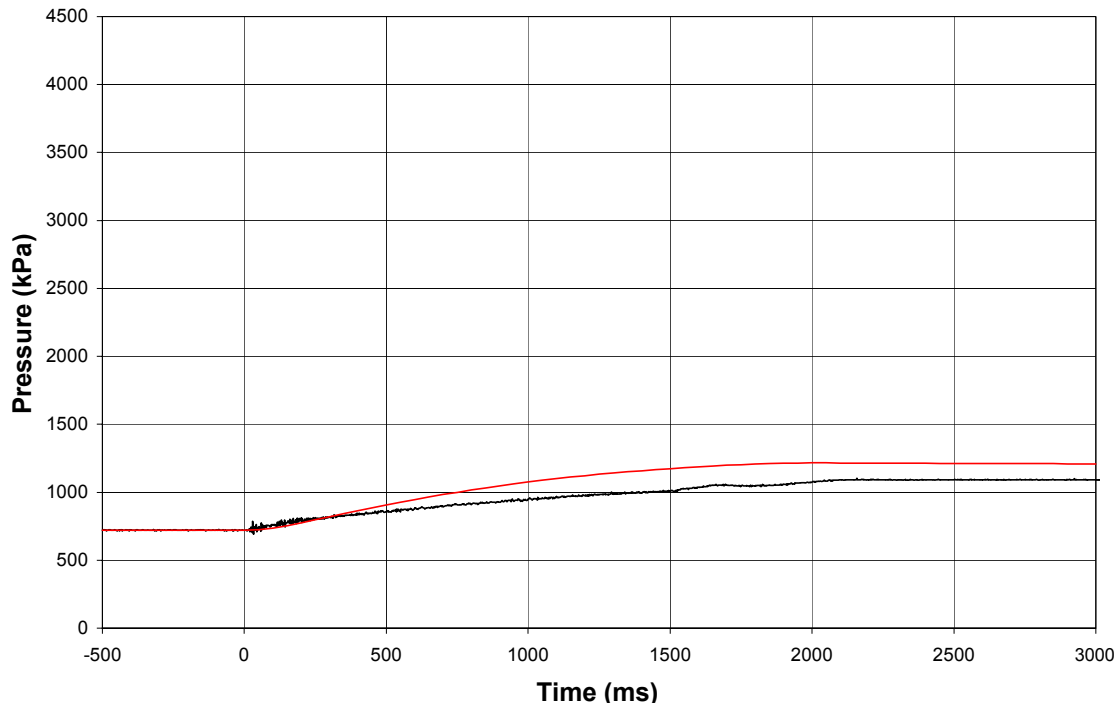


**Figure 8-61. Comparison of Collection Vessel Pressure for Experimental Run #5 (black) and Predictive Computer Code Data (red).**

While these comparisons were available with all of the runs conducted in this study, there were also special measurements made in some cases. For instance, experimental measurements of the pressure drop across different pipe fittings were conducted. While the prediction used a literature value for the friction loss factor associated with the fittings, comparison of the pressure drop across these fittings could still be made. This provides an indication of whether the literature values are accurate for a two-phase flow through different pipe configurations. Figure 8-62, Figure 8-63, and Figure 8-64 show the experimental data for Run #9 compared to the predicted data for the pressure drop across a capped tee, 90° elbow, and connecting union, respectively. This run used the simpler of the two alternative piping configurations (see Figure 8-19). The comparisons generally show reasonable agreement; however, the predicted pressure starts to fall earlier than the measurement. The experimental pressure trace exhibits a sudden drop when the liquid runs out at the initiation of the vapor/gas flow. Although the calculation does not predict a sudden drop in pressure at the end of the liquid flow, it shows an end of the run in the same general vicinity as the experimental trace, implying that it is most likely at the end of the liquid flow.

The last comparison made dealt with the temperature measurements. Since the predictive code does not consider heat transfer between the fluid and the piping, the only real temperature variation comes from any phase change in the system or any compression or expansion of the contents of the system. Specifically, degassing of the dissolved nitrogen and the adiabatic expansion of the nitrogen near the end of the run will be the main contributors. Because the code is not influenced by the ambient temperature of the system, it predicts a much lower temperature than the experimental measurements. The comparisons in this analysis are for experimental Run #16, which used HFC-125 as a test fluid. The largest temperature changes were experienced for this fluid.

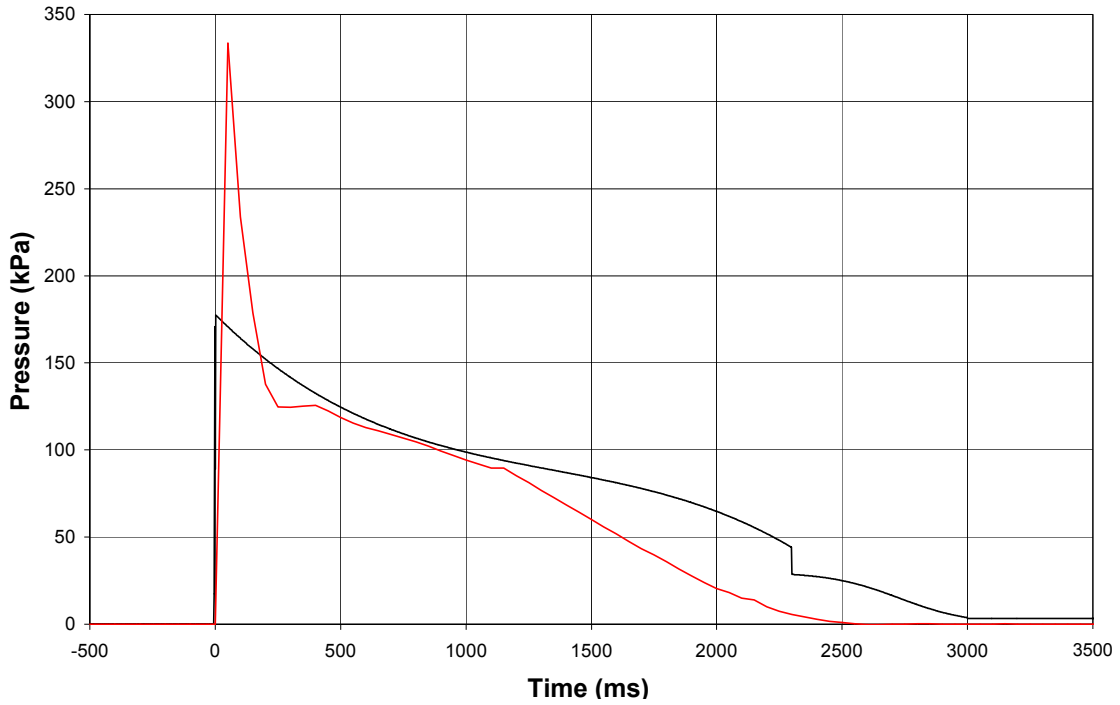


**Figure 8-62. Comparison of Pressure Drop across a Capped Tee for Experimental Run #9 (black) and Predictive Computer Code Data (red).**

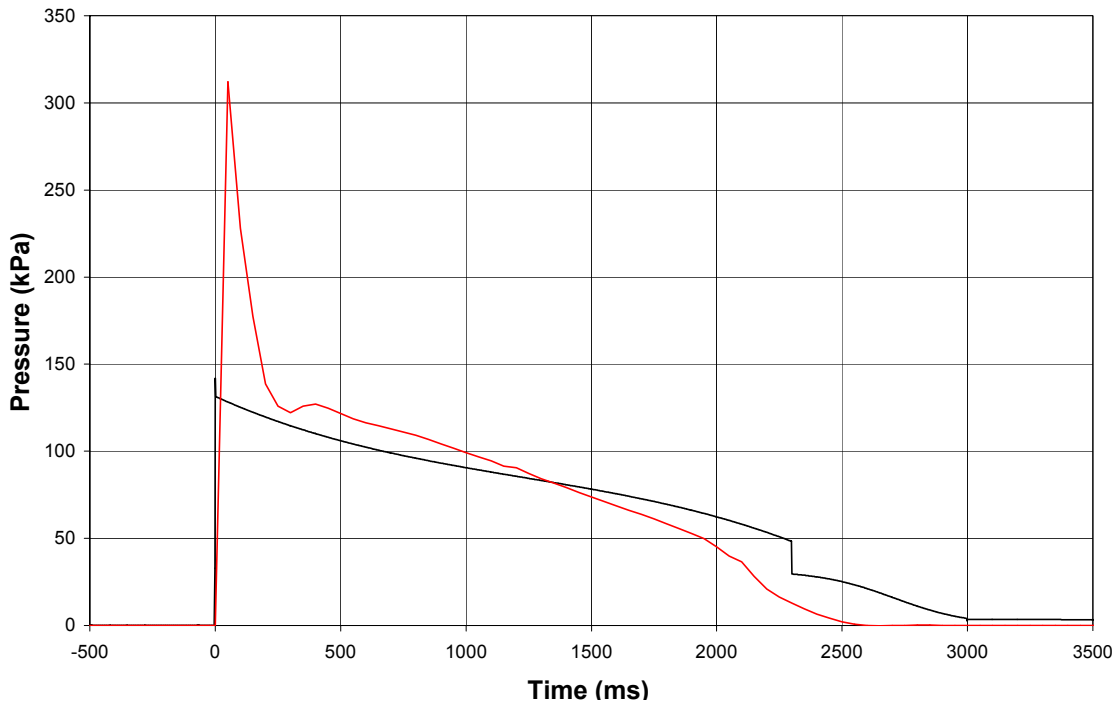


**Figure 8-63. Comparison of Pressure Drop across a 90° Elbow for Experimental Run #9 (black) and Predictive Computer Code Data (red).**

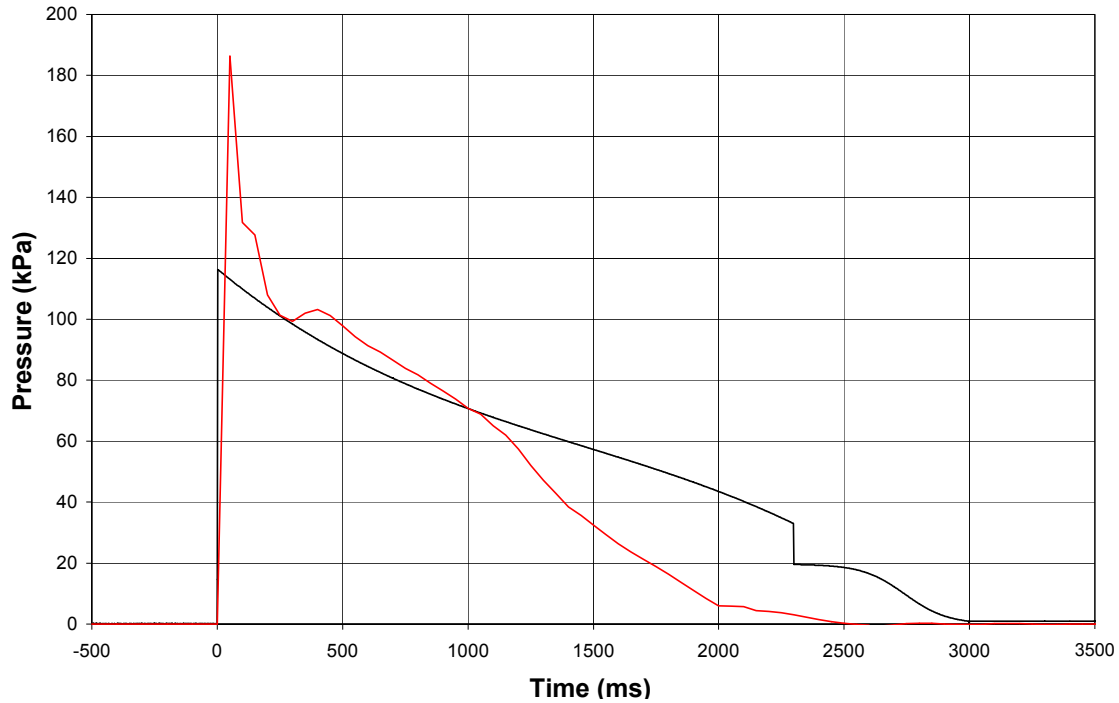


**Figure 8-64. Comparison of Pressure Drop across a Union for Experimental Run #9 (black) and Predictive Computer Code Data (red).**

In Figure 8-65, a comparison is made between the experimental measurements of the source vessel temperature using shielded thermocouple placed at the bottom of the vessel and immersed in the fluid and the fluid temperature predicted by the code. The trends in the predictions and measurements show good qualitative agreements. Figure 8-66 illustrates a temperature comparison between predictions and measurements for the pipe position #1 in the piping system. In this case, the differences between calculated and measured values are more pronounced than in the source vessel comparison. As expected, the heat transfer coefficient in the pipe is greater than anywhere else in the system, and the short-comings of excluding fluid-to-pipe heat transfer in the code are most noticeable in this region. A comparison of predicted and measured gas temperature in the collection vessel is shown in Figure 8-67. The initial temperature drop is due to the fact that the liquid is evaporating to raise the pressure to its saturation equilibrium value. This trend stops when the pressure rises high enough that there is no longer any need for the liquid to evaporate. Both the prediction and the experiment capture such trend in the temperature traces.

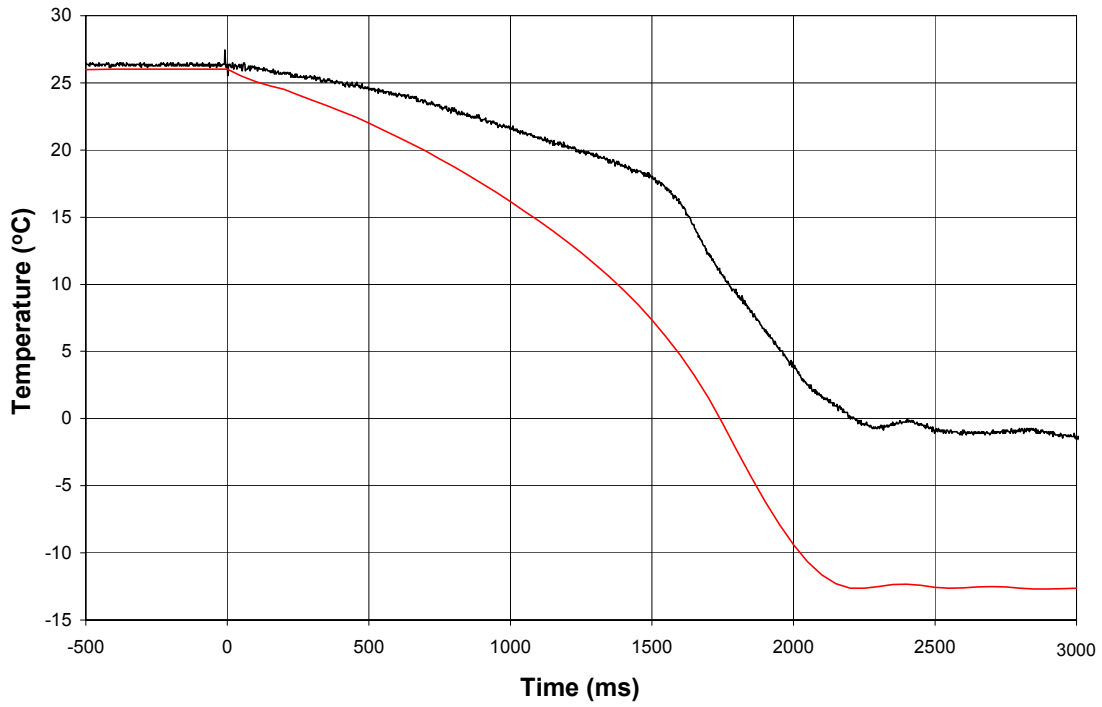


**Figure 8-65. Comparison of Source Vessel Fluid Temperature for Experimental Run #16 (black) and Predictive Computer Code Data (red).**

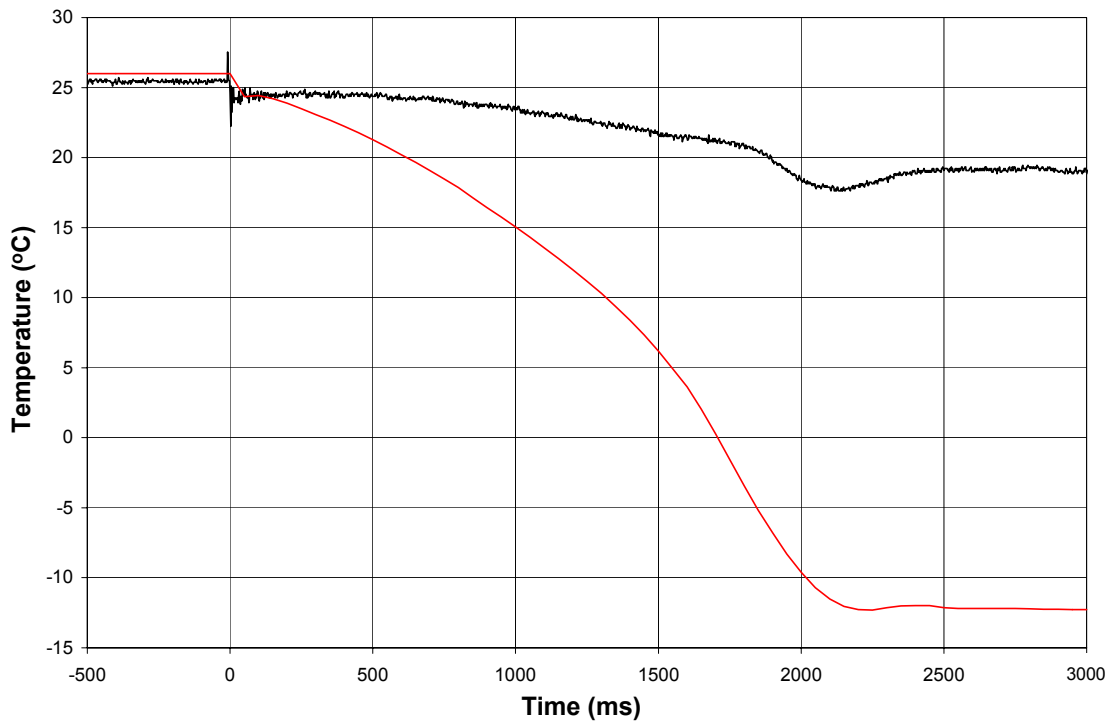


**Figure 8-66. Comparison of Pipe Position #1 Fluid Temperature for Experimental Run #16 (black) and Predictive Computer Code Data (red).**

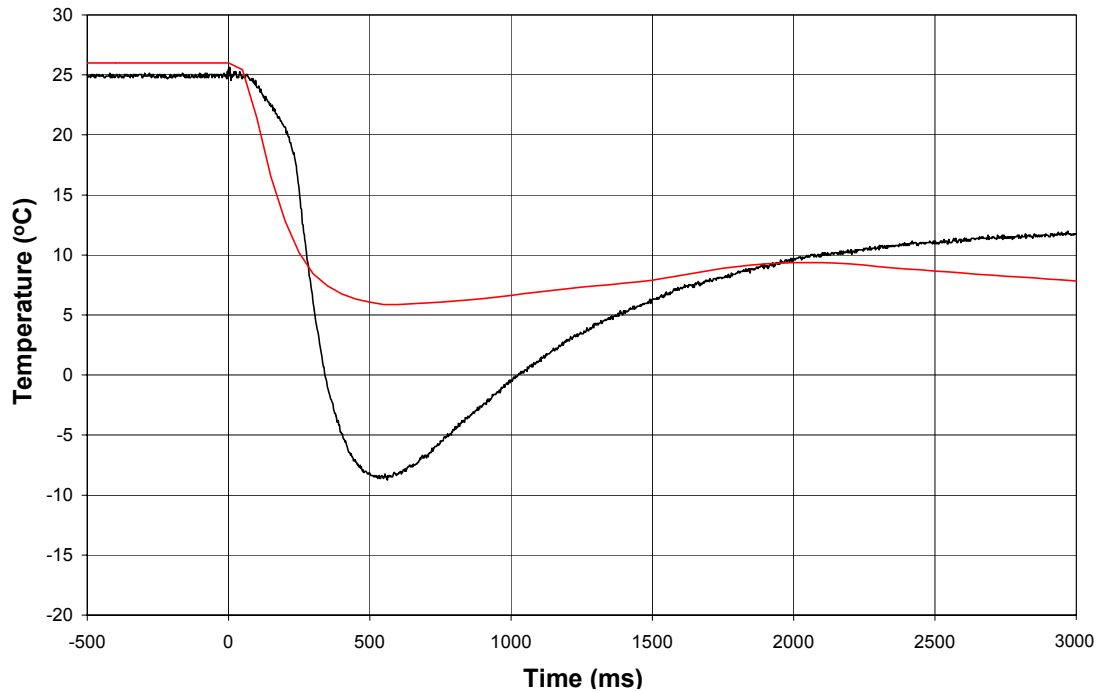


**Figure 8-67. Comparison of Collection Vessel Gas Temperature for Experimental Run #16 (black) and Predictive Computer Code Data (red).**

### 8.3.8 Assessment of Fluid Transport Model

Overall, comparisons between the predictions and the experimental runs generally show reasonable agreements. In most cases, the prediction gives good estimation of the physical characteristics of a two-phase flow in a model system. The code even handles two different test fluids with reasonable accuracy. It also predicted three different piping configurations well, demonstrating its versatility in modeling other potential systems. While these points support the code's robustness for use with suppressant systems, it must also be noted that there are a few limitations of the code. The most notable one is that the code would not always work for some initial conditions for a specific test fluid. This is most likely due to some limitation on the thermodynamics package. If this situation occurs, the user must slightly adjust the actual run condition in order to fall into a region of the thermodynamics package that will yield an output. For example, an error occurred before the program could complete the simulation for the experimental Run #5. However, changing the ambient temperature from 31 °C to 30 °C in the initial conditions enabled the simulation to completion. This was only a minor change, but it still made the simulation a bit cumbersome.

Another area that caused problems was to simulate low-pressure runs (2000 kPa to 2500 kPa, initial source vessel pressure). There were two problems which arose during these tests. The first was similar to the problem stated previously due to the thermodynamics package. These experimental runs (Runs #1 & #8) were conducted with low downstream pressures so that flashing could occur in the pipe directly after the start of the run and the actuation of the valve. The code would not accept these conditions to run the simulation due to the fact that it identified a non-equilibrium condition in the downstream areas. The downstream pressure had to be raised to a pressure closer to the saturation conditions of the test fluid in

order for the code to run. The other problem associated with these low-pressure test runs was the high fill level used in the source vessel. In experimental Runs #1, #8, #11, #14, and #18, a fill level of 80 % to 90 % was used to try and to reduce the amount of nitrogen present in the system. The hope was to keep the system pressure low enough to facilitate flashing of the suppressant during discharge. While the initial conditions did not cause the code to stop running with an error, it did provide unexpected results. For example, in Run #1, the total mass of test fluid (HFC-227ea) placed in the source vessel at the beginning of the run was about 4.9 kg. However, the code prediction never approached that value during the predicted discharge; it reached a final value of about 3.1 kg. It is unclear at this time why the code ran reasonably well with a fill level of about 60 %, instead of the test fill level of about 85 %. This problem would limit the applicability of the code to moderately fill conditions.

The last problem encountered executing the code was the high-pressure runs (4750 kPa to 5000 kPa, initial source vessel pressure). Once again, it was believed that the problem was caused by the properties package. The only way to get the code to run using these initial conditions was to lower the source vessel temperature considerably, while keeping the downstream temperature around the ambient value. Even then, the desired operating pressure could not always be reached. For example, in Run #6, the source vessel temperature was dropped from 31 °C to 2 °C with an initial source vessel pressure of 4860 kPa in place of 4910 kPa. In addition, the code tends to under-predict the total duration of discharge due most likely to the temperature dropping below the range of the thermodynamics package. Despite these observed problems, the code did a reasonable job in predicting the parameters (e.g., void fraction, mass inventory, etc.) for most runs with initial source vessel pressures from 3000 kPa to 4500 kPa and a fill level of about 65 %.

The FSP code can, in principle, be extended to include other candidate fluids that exhibit transient two-phase flow in piping system. The procedure outlined in Tuzla et al.<sup>7</sup> for the incorporation of halon 1301, CO<sub>2</sub>, HFC-227ea, and HFC-125 into FSP should be followed. In addition, a computational thermodynamic tool similar to REPROP or PROFISSY is needed to predict fluid properties for performing FSP calculations. Estimation of other input parameters like critical bubble radius and release rate of dissolved gas for the fluid of interest can be made through sensitivity analysis of these parameters in FSP calculations and comparison to experimental data.

## **8.4 DYNAMICS OF FLUID TRANSPORT IN CLUTTERED SPACES**

### **8.4.1 Spray Transport Past Generic Clutter Elements**

As discussed in Chapter 7, the NGP examined a wide range of potential candidates as alternatives to halon 1301. Should the transport of a chemical from the distribution plumbing to the fire site be inefficient, additional chemical (and the accordant larger storage bottle, piping, etc.) would be needed, an undesirable outcome. In particular, high boiling suppressants (which tend to have high heat extraction capacity) would be discharged in a liquid state, breaking into liquid droplets, and be entrained within the flow passing through the nacelle, impinging on various objects prior to reaching the fire zone. Since halon 1301 was so efficient, research into understanding the engine nacelle airflow offered little advantage. Today, however, a better understanding of the nacelle airflow and how it influences the spread of fires and fire extinguishing agents can have a large impact on the effectiveness of a halon replacement system. NGP research expanded the fundamental knowledge of spray interactions with

clutter (e.g., obstacles representing fuel and hydraulic lines, electrical wire bundles, etc.) to learn how well agents of low volatility might reach an unspecified downstream fire location.

Disimile and coworkers conducted experiments focusing on the ability of sprays to pass through a series of cylindrical obstacles, representing generic clutter, while moving in a turbulent coflow.<sup>31</sup> Since only transport, and not flame extinguishment, was to be studied, water was used as the test fluid. A low-speed flow facility, with the test section air speed ranging up to 12.0 m/s, was modified for the current program. The major components of this facility include an inlet contraction, turbulence generator, test section, clutter section, and the return and separation plenum (Figure 8-68). The flow is from left to right. They collected three-dimensional velocity and diameter data at two locations downstream for nine combinations of clutter spacing and coflow airspeed.

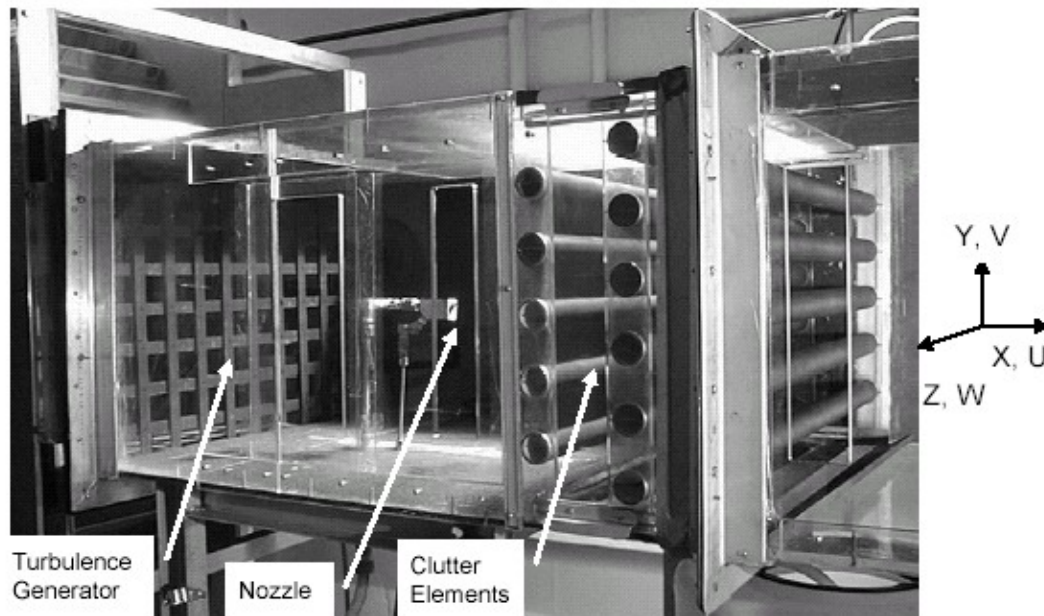


**Figure 8-68. Zone A of the Test Section.**

A large grid consisting of several 25.4 mm wide, 6.4 mm thick, sharp-edged flat steel slats, spanning the cross-sectional area of Zone A of the test section, was assembled in a checkerboard pattern with open cell dimension between the slats of 51 mm  $\times$  51 mm. This grid is also visible in Figure 8-68. Velocity surveys using constant temperature anemometry were acquired downstream of the turbulence generator, at  $x = 711.2 \text{ mm} \pm 0.8 \text{ mm}$ . A wave-like distribution of the streamwise component of the mean velocity was observed, with velocities ranging from approximately 3.7 m/s to 5.0 m/s. Although general symmetry was observed, it appeared that the lower portion of the test section had a greater degree of unsteadiness. It is believed that the additional unsteadiness was a result of smoke generation supply tubes positioned at the entrance of the inlet contraction. In a similar manner, turbulent intensities were recorded and ranged between 10 % and 14 %.

The clutter package used in the current test series can be seen installed within Zone A of the test section (Figure 8-68). The clutter package consisted of 16 two-dimensional elements, spanning the width of the test section. These elements were cylindrical segments made from PVC. The elements had an outer

diameter  $D$  of  $50.8 \text{ mm} \pm 0.8 \text{ mm}$  and were assembled to form three separate arrays with equally spaced rows of 5, 6, and 5 tube elements, separated vertically by  $0.94 D$  between each cylindrical element. The streamwise spacing between each clutter array was variable, ranging in terms of element diameter, from  $0.25 D$  to  $2.00 D$  with an uncertainty of  $\pm 0.06 D$ .

The clutter arrangement was selected based on its geometric similarity to common elements found within aircraft engine nacelles. Many cylindrical elements fill the nacelle environment with various local densities. With the capability of varying the streamwise distance between each array of clutter elements in the chosen clutter package, the clutter densities found within larger aircraft engine nacelles was simulated.

A three-dimensional phase Doppler interferometer (PDI) was used to simultaneously acquire velocity components and the diameter of the liquid drops exiting the suppressant spray nozzle. Water and air are mixed by the dual fluid nozzle and travel toward the leading edge of the clutter package. The droplets not captured by the clutter package proceeded downstream, where their three-dimensional velocity and diameters were measured. The measurement volume of the PDI system was located at 2.0 and 5.5 clutter diameters downstream of the trailing edge of the clutter.

The spray nozzle water flow was set and maintained at  $(17.1 \pm 0.4) \text{ L/min}$ , with a corresponding nozzle water pressure of  $(158 \pm 14) \text{ kPa}$ . The water flow was monitored using a turbine type flowmeter positioned directly upstream of a pressure gage. The incoming air was regulated to a pressure of  $(172 \pm 3) \text{ kPa}$ . The test matrix consisted of 18 experimental conditions. This included 13 air speeds, five clutter densities, and two downstream measurement locations. Clutter package densities were varied by changes in the streamwise spacing between individual clutter arrays. Since the leading edge of the clutter package was fixed, changing the array spacing affected the location of the trailing edge of the last clutter element. Therefore, to maintain a fixed downstream location of the PDI measurement volume with respect to the trailing edge of the clutter, the PDI measurement volume had to be moved correspondingly.

To determine the volume of water transmitted through the clutter array as a function of the streamwise spacing of the clutter array and air speed, 13 air speeds were investigated ranging from  $0.5 \text{ m/s}$  to  $6.5 \text{ m/s}$  in increments of  $0.5 \text{ m/s}$ . To measure the volume of water passing through the clutter configuration accurately, a repeatable procedure for measuring the liquid water volume was followed. This included the water supply tanks being filled to the same initial starting volume of 303 L, the air speed and the nozzle air pressure set. A clock was then energized when the water pump was powered on such that the water flow through the nozzle was set to  $(17.1 \pm 0.4) \text{ L/min}$ . Water drops that wetted the clutter pooled on the individual elements and dripped down to a collection pan located beneath the clutter. Water droplets that passed through the clutter into Zone B were deposited within the return plenum. The volume of water collected directly under the clutter package was carefully measured, as was the water collected in the return plenum by using graduated containers.

Figure 8-69 shows the percentage of water recovered directly under the clutter package as a function of element spacing and air speed. The general trend of the data suggests that the volume of the liquid collected decreased with increasing air speed. In fact, above  $4.5 \text{ m/s}$  less than 5 % of the liquid was captured, and the differences between the five clutter densities converged. However, with the air speed set to  $0.5 \text{ m/s}$ , the amount of water collected under the clutter ranged from 61.25 % (at  $0.25 D$  spacing) to 37.50 % (at  $2.0 D$ ). As the spacing between the individual clutter rows was reduced, the amount of water

captured increased. Specifically, as the streamwise spacing was reduced from  $2.0 D$  to  $0.25 D$ , the captured water increased to over 50 %.

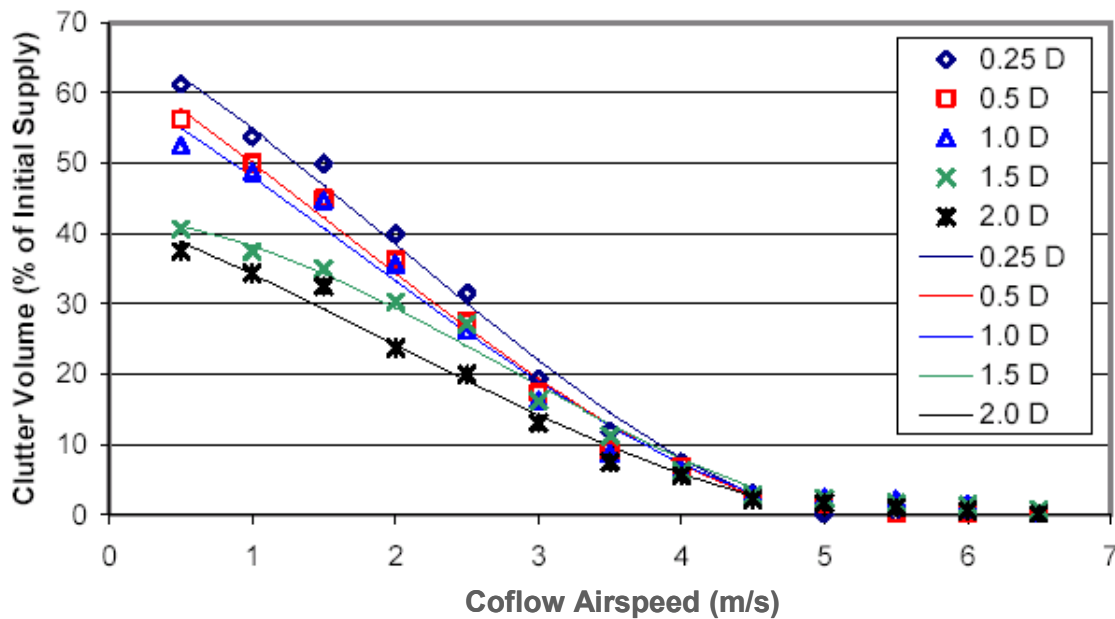


Figure 8-69. Clutter Recovery vs. Airspeed.

Likewise, Figure 8-70 indicates the amount of water collected in the return plenum as percent of the initial volume. All five clutter densities are represented in this figure. The volume collected in the plenum increases as the air speed increases. It can be seen that the volume recovered in the plenum approaches 100 % as the air speed increases.

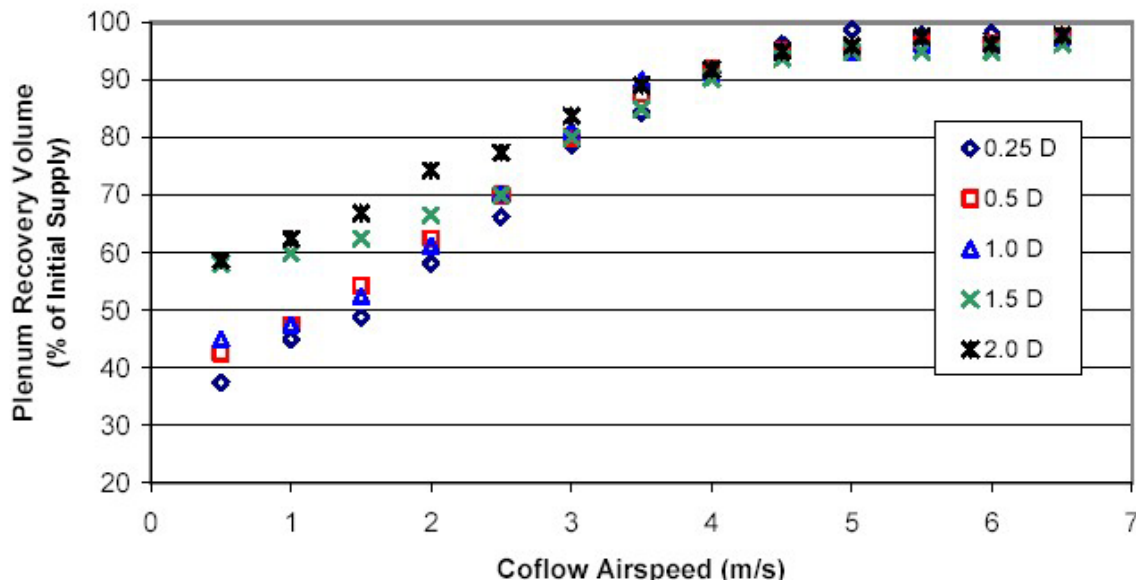


Figure 8-70. Plenum Recovery vs. Airspeed.

During the test evaluation of five clutter spacings and 13 air speeds, the percent of unaccounted water volume was determined. In all cases, the difference was random and less than 4 %. As a measure of repeatability, no less than 96 % of the total supply volume was recovered in the combined clutter and plenum return recovery tanks.

The results of these experiments clearly show the effect of cylindrical clutter elements on the transport of liquid droplets and provide benchmark data to develop first-generation computer models to aid in the design of fire suppression systems for aircraft engine nacelles. Although this work only addresses round elements of uniform size and distribution, it provides a framework to generate a database for examining the effects of different size, geometry, and density of clutter elements as well as different levels of turbulence on droplet transport for nacelle applications.

#### 8.4.2 Spray Interaction with Unheated and Heated Clutter Elements

For the next level of understanding, Presser and coworkers injected liquid fire suppressants into a well-characterized, homogenous, turbulent flow field, and investigated the droplet transport processes under a variety of conditions, as well as the interaction of the spray with different obstacles.<sup>32</sup> Also of interest was determining whether droplets rebounded and/or shattered off the surface of an obstacle.

The experimental arrangement is shown in Figure 8-71. The experiment was oriented horizontally to enable estimating the mass of liquid agent impinging on the obstacle, the mass that dripped off the obstacle, and the mass transported past the obstacle. This geometry also prevented liquid droplets downstream of the obstacle from falling back upstream into the oncoming stream.

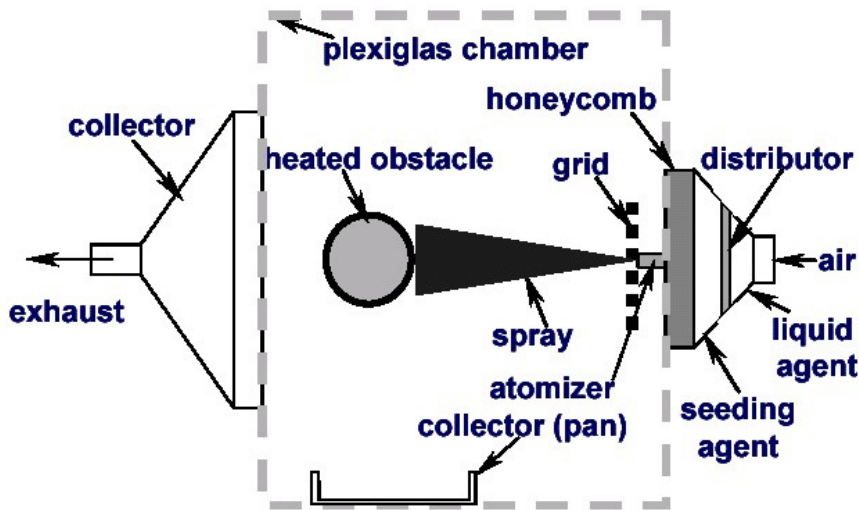


Figure 8-71. Heated Cylinder Test Section.

The initial agent was water and was supplied to the flow field with a 60° hollow-cone pressure-jet atomizer. In the octagon-shaped PMMA chamber, the front face supported the inlet passages for the liquid agent and air, and the back face supported the exhaust passage, which served to form a closed system with defined boundaries. A honeycomb layer was used to straighten the air flow, which was co-positioned around an injector for the agent. Grid-generated turbulence was imposed on the air stream by placing a square layer of wire mesh screen downstream of the honeycomb. For these experiments, the incoming air was directed entirely through a distributor plate with steel wool, circular cross-sectional area

of the honeycomb, and then through wire mesh screen (placed 25 mm downstream of the honeycomb), as shown in Figure 8-71. The face of the liquid atomizer was placed flush with the upstream side of the grid, and centered within one mesh cell so that the liquid spray would be unimpeded by the grid. The stepper-motor-driven traversing system translated the entire assembly, and permitted measurements of the flow field properties at selected locations downstream of the injector. Measurements included particle image velocimetry (PIV), PDI (to obtain spatial and temporal profiles of the size and velocity distributions), and visualization of the flow field. Measurements in the spray and flow field were carried out upstream and downstream of the obstacles.

Measurements were carried out with two obstacles, an aluminum cylinder and a more complex body-centered cube (BCC) arrangement of wooden spheres and connecting posts. (See Figure 8-72 and Figure 8-73, respectively.)

The cylinder had a diameter of 32 mm (305 mm in length), which was chosen because its diameter was larger than the integral length scale of turbulence. The cylinder was heated to study the effects of a heated surface on droplet vaporization and transport, as a droplet approached the heated surface. A hole was bored through the center for placement of a 250 W cartridge heater. The rod was also cut into two halves and 1 mm deep channels bored along one segment for placement of five K-type thermocouples. The thermocouples had an inconel sheath, ungrounded, and 0.8 mm in diameter (305 mm long). The thermocouples were placed in a cross pattern in the center of the rod (each separated by a distance along the surface of 6.4 mm, with the thermocouple junctions placed about 3.2 mm of the surface with bored holes at each location). The central thermocouple was used for temperature control of the heater, which was positioned behind the thermocouples.

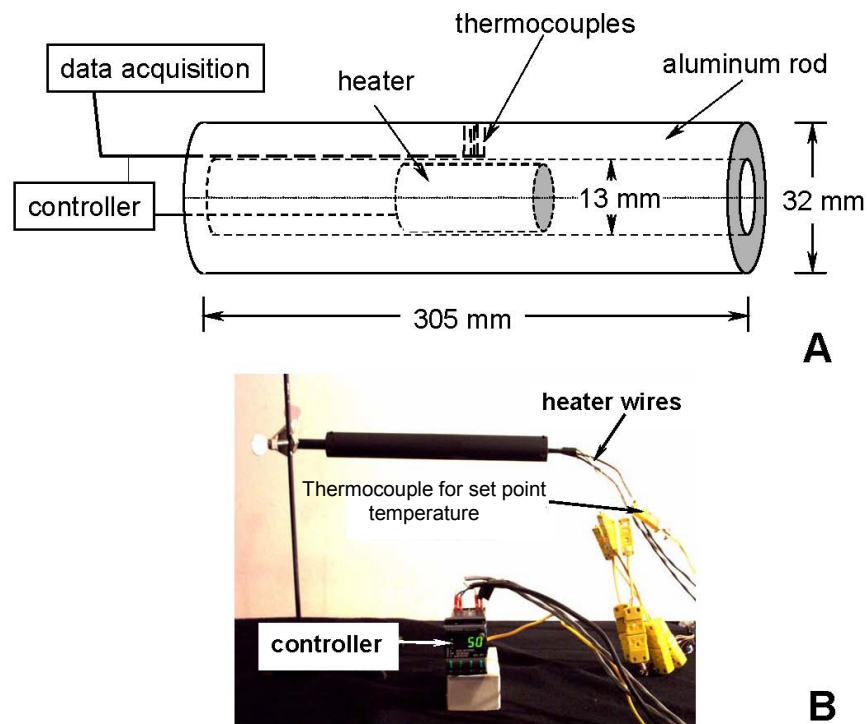


**Figure 8-72. Heated Cylinder. (A) Schematic and (B) Front View.**

The BCC was composed of nine wooden spheres with a nominal diameter of 28 mm, all interconnected with posts, as shown in Figure 8-73. The blockage ratio, or obstructed cross-sectional area for an equivalent area encompassing a face of the BCC, was about 64 %. The obstacles were placed nominally 182 mm downstream of the honeycomb, and centered with the atomizer centerline.

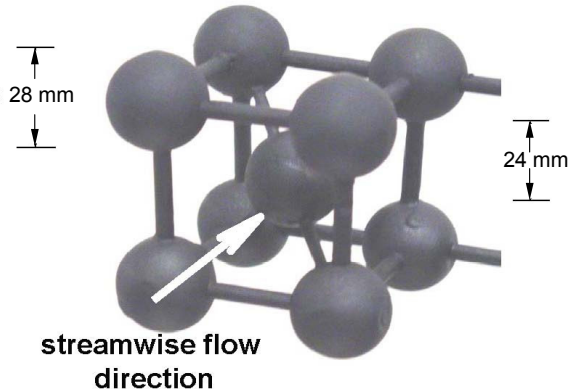
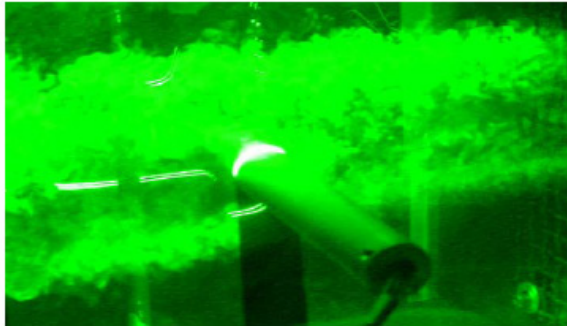


**Figure 8-73. Body-centered Cube of Spheres.**

PIV measurements were carried out in the droplet-laden, homogeneous turbulent flow over both the unheated and heated cylinder, and body-centered cube arrangement of spheres. Transport of both water droplets and seed particles was characterized upstream and downstream of these obstacles. Data were recorded for the cylinder at ambient temperature and after being heated to 150 °C to estimate the effects of the hot cylinder surface on droplet transport. The results indicated that smaller droplets were entrained into the recirculation region behind the cylinder while the larger droplets impacted the cylinder surface, accumulated and dripped off, and/or rebounded off the surface and dispersed radially outward into the free stream. The Weber number was too low to lead to droplet shattering. Significant spray cooling of the surface was observed for the heated cylinder, in addition to the presence of a vapor stream downstream of the cylinder along the shear layer region between the recirculation zone and free stream. Surface cooling that resulted from spray impingement was around 50 % of the preset cylinder temperature. For the BCC (with a blockage ratio of about 64 %), there was both transport of droplets and seed particles around and through the BCC, as well as significantly more liquid accumulation and dripping than for the cylinder.

The droplet-laden flow field over each obstacle was recorded with a digital movie camera at 9 frames/s. Examples of the observed droplet/particle transport processes are shown in Figure 8-74 for (a) seeded only and (b) droplet only flow over the unheated cylinder, and (c) combined droplet and seeded flow over the BCC. The seed was entrained in the turbulent flow field (see Figure 8-74A) and a relatively high concentration of particles was observed in the wake behind the cylinder. On the other hand, the droplets in the center of the spray were found to impinge on the surface of the cylinder while those droplets at larger radial positions were transported around or past the cylinder with an increased radial component of velocity (see Figure 8-74B). Few droplets were observed behind the cylinder in its wake. Droplets that impinged and wetted the cylinder surface dripped off at a rate of approximately one drop every 5 s. The transport of droplets through the BCC (see Figure 8-74C) was interesting in that both the spheres and connecting rods (that simulate cylinders) block the droplets, while the flow field traversing through the obstacle provided an unobstructed path for the entrained droplets. Dripping was observed from each sphere at a rate of approximately 1 droplet/s. If one assumes that droplets fall off each sphere at this rate, one can determine that this liquid represents approximately 4.5 % of the inlet water flow (assuming a

dripped droplet diameter of 8.5  $\mu\text{m}$ , which was an estimated largest droplet size observed from digital movies). Although the BCC had more dripping of liquid than the cylinder, the major portion of the spray was still able to traverse the obstacle.



**A** Figure 8-74. Photographs of Seed/droplet-laden Flow Fields around Obstacles.



**A: Unheated Cylinder; B: Heated Cylinder; C: Body-centered Cube of Spheres. Flow Direction is from Right to Left.**

**B**



**C**

The above-mentioned laser sheet images indicated that dispersion of droplets/particles around the obstacle was dependent on its size. Comparison of the PIV velocity fields obtained with water droplets from the pressure-jet atomizer and 1  $\mu\text{m}$  size seed particles formed from the fogging device also supported this finding. For example, the three components of droplet velocity for the flow over the unheated cylinder are presented in Figure 8-75. In this figure, three cases are presented that represent the flow with the seed only, both seed and spray, and spray only. The black circle represents the position and size of the cylinder. The black contour lines represent stream traces (i.e., direction) of the in-plane velocity vectors. Comparison of the two cases with spray to the seed-only case indicated that the recirculation zone was somewhat larger for the spray cases. Larger size droplets required a longer distance to interact with the turbulent flow field, reduce their higher momentum, and be entrained into the recirculation zone, if at all. The stream trace (contour lines) also showed an unexpected pattern behind the cylinder near the stagnation point. Instead of presenting closed loops that indicate a time-integrated recirculating pattern,

the contours appear to emanate from the stagnation region. One possible explanation is that there is a strong spanwise flow along the length of the cylinder. It appeared to be generated by the cylinder and may be related to the finite cylinder length (with an aspect ratio of about 10:1).

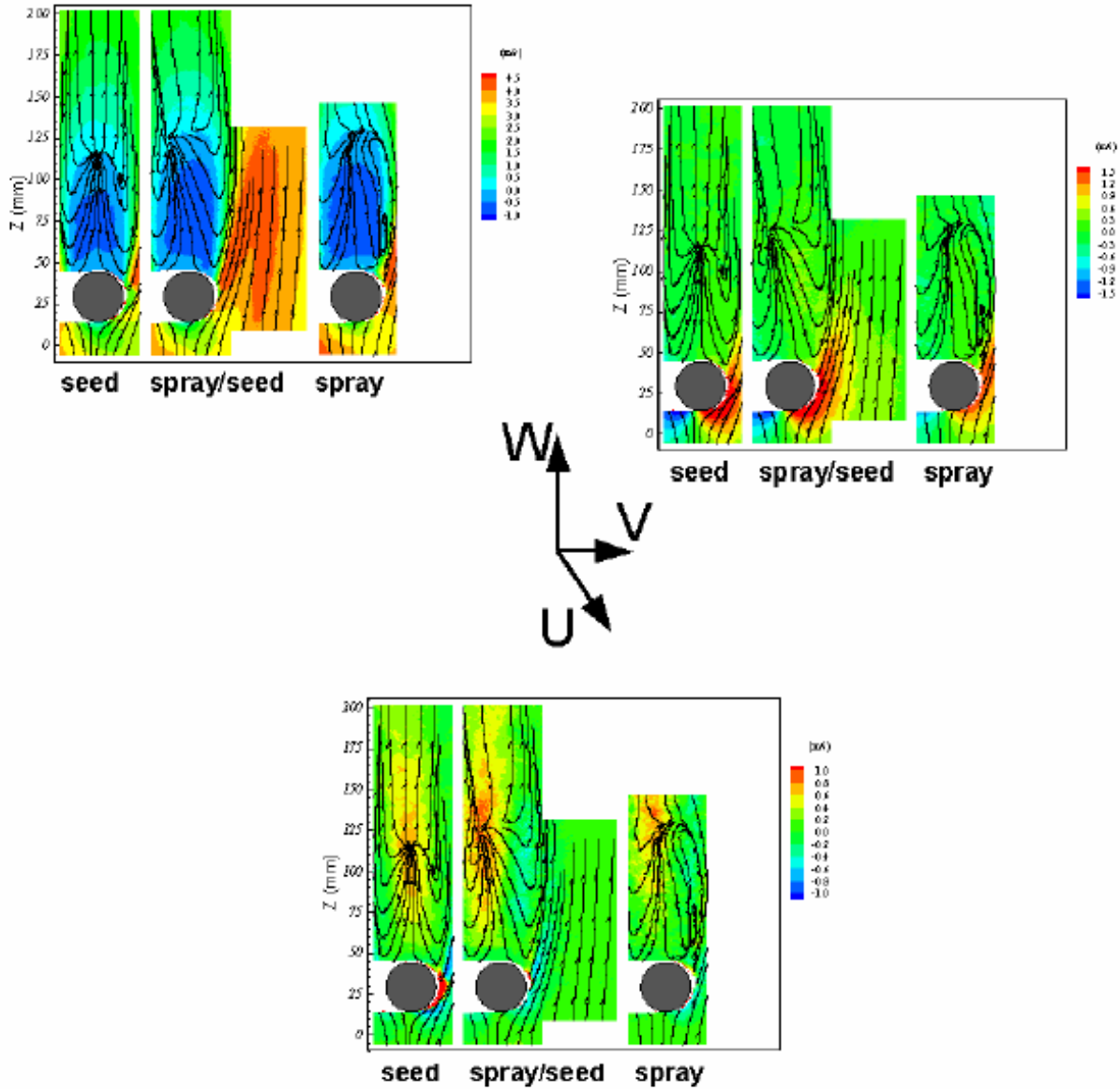


**Figure 8-75. Variation of the Mean Streamwise and Cross-stream Velocities with Downstream Distance for the Unheated Cylinder. Contours are the Stream Traces of the In-plane Vectors Obtained from the Axial and Radial Components of Velocity.**

Figure 8-76 presents the velocity field around the BCC for the combined spray/seed case. Although the configuration was more complicated, there were still similar features to the cylinder case. The flow accelerated around the spheres and there was reverse flow in the wake region. In addition, the presence of a cross-stream component of the flow was evident around the spheres. This cross flow may be a result of

the three-dimensional nature of the spheres and flow field, and the transport of entrained droplets and aerosol particles through convoluted pathways of this obstacle.

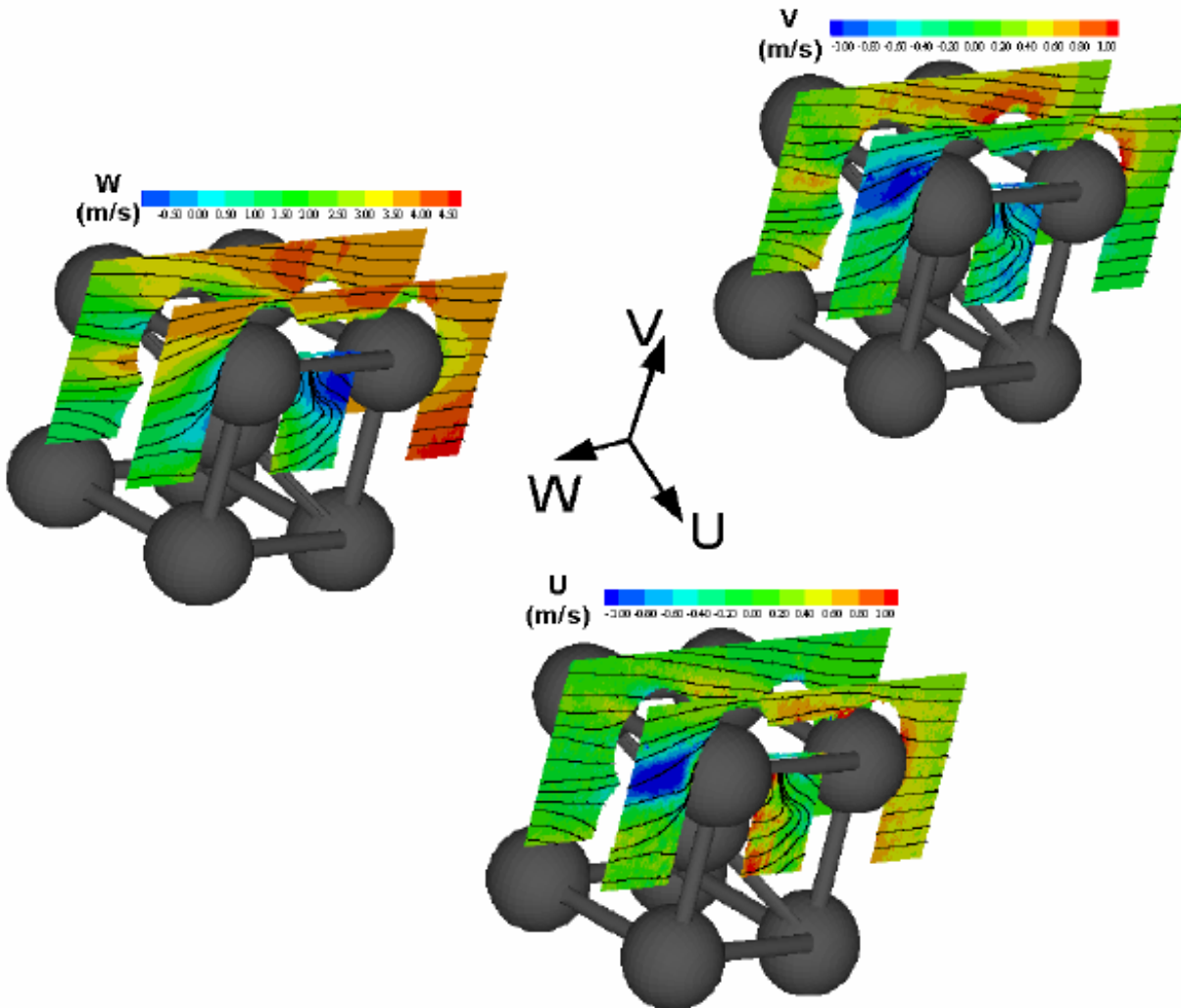


**Figure 8-76. Variation of the Mean Streamwise and Cross-stream Velocities with Downstream Distance for the Body-centered Cube of Spheres. Contours are the Stream Traces of the In-plane Vectors Obtained from the Axial and Radial Components of Velocity.**

### Droplet Size and Velocity Distributions

The aforementioned results indicated that droplet surface impact, vaporization, and transport behind the cylinder were dependent on droplet size. Measurements of spatially and temporally resolved droplet size and velocity distributions in the upstream and downstream vicinity of the cylinder, using PDI, were needed. Three agents with different boiling points were examined: water (with a boiling point of 100 °C), HFE-7100 (with a boiling point of 61 °C) and HFE-7000 (with a boiling point of 34 °C). Several strategies may be used to detect size dependent effects in regions where droplets rebound or vaporize. For example, a droplet near the upstream surface of the cylinder with a negative streamwise velocity

(i.e., a droplet transported against the flow) would be indicative of a droplet rebounding off of the cylinder surface, and thus PDI would be used to obtain the associated droplet size. If the size distribution near the heated cylinder surface is devoid of relatively smaller size droplets, as compared to other locations away from the cylinder, then this result may be indicative of the effects of vaporization. These strategies were used in interpretation of the measurements.

Phase Doppler techniques involve creating an interference pattern in the region where two laser beams intersect, and results in a region consisting of alternating light and dark fringes. The region where the laser beams intersect is called the probe volume or sample volume. Due to the interference pattern, a droplet passing through the probe volume scatters light that exhibits an angular intensity distribution, which is characteristic of the size, refractive index, and velocity of the droplet. For a droplet with known refractive index, the size and velocity can be determined by analyzing the scattered light collected with several photomultiplier tubes (PMT). The PDI is a single-point (or spatially resolved) diagnostic instrument in that it obtains information about the spray at a single point in space. The PDI is also a single-particle instrument in that information is obtained for only one droplet at a time. This offers advantages over integrating techniques because the characteristics of a particular droplet (size, velocity, etc.) can be recorded and the data can be separated into classes (size classes, velocity classes) to further characterize the spray system.

The experiments were conducted using a two-component phase Doppler interferometer with a Real-time Signal Analyzer (RSA) available from TSI, Inc. A 5 W argon ion laser, operating in multi-line mode, was used as the illumination source. The blue (wavelength = 488 nm) and green (wavelength = 514.5 nm) lines of the argon ion laser were separated by beam conditioning optics, and focused by the transmitting optics to intersect and form the probe volume. The transmitting optics were coupled to the beam conditioning optics, using fiber optic cables to permit the transmitter to be located near the experiment. The front lens on the transmitter had a focal length of 500 mm. The green and blue beams had a beam separation distance of 39.9 mm and 40.2 mm, fringe spacing of 6.45 mm and 6.07 mm, and beam waist of 164 mm and 155 mm, respectively. Frequency shifting was set at 40 MHz. The receiver was located at a scattering angle of  $30^\circ$  measured from the direction of propagation of the laser beams. To accommodate the horizontal orientation of the experimental apparatus, the transmitter and receiver were positioned in a vertical plane, as shown in Figure 8-77. Due to the large size of the receiver, the transmitter was positioned with the laser beams angled at  $30^\circ$  to the cylinder, which required correction of the cross-stream velocity. The front lens on the receiver had a focal length of 1000 mm. The spacing for the three PMT detectors (A, B, and C) that were used to carry out the sizing measurements was 34.8 mm for detectors A and B, and 101 mm for detectors A and C. A 150 mm slit aperture was located within the receiver to limit the length of the probe volume.

The measurements were carried out at several radial ( $R$ , cross-stream) positions and over a range of axial ( $Z$ , streamwise) positions upstream and downstream of the cylinder. Figure 8-78 illustrates the measurement grid that was used and the location of the cylinder relative to the grid mesh. Measurements were carried out from approximately 50 mm upstream of the cylinder to a downstream position of 100 mm. An increment of 2.5 mm was used for  $-25.4 \text{ mm} < Z < 38.1 \text{ mm}$ , and an increment of 12.7 mm for all other axial positions. In the radial direction, measurements were carried out in increments of 5 mm from 0 mm to 20 mm in the upper hemisphere (i.e., in the positive radial direction). Data were not obtained immediately downstream of the cylinder (i.e., for  $\approx 25 \text{ mm} < Z < 14.6 \text{ mm}$ ) because the signals were too low to detect any droplets.

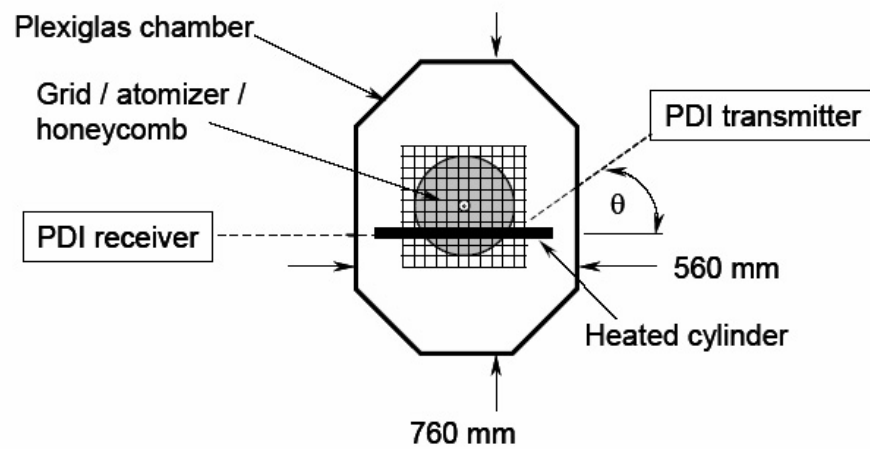
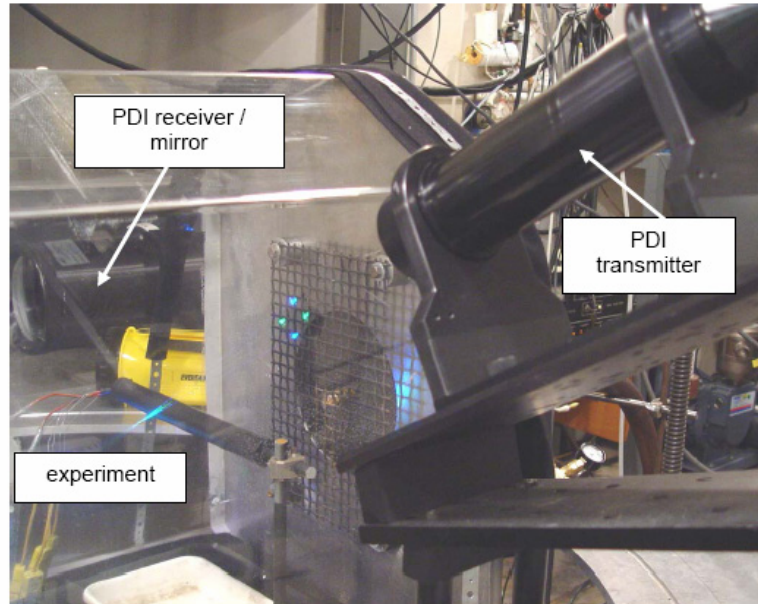


**Figure 8-77. View and Schematic of the Experimental Arrangement with the Laser from the Phase Doppler Interferometry System.**

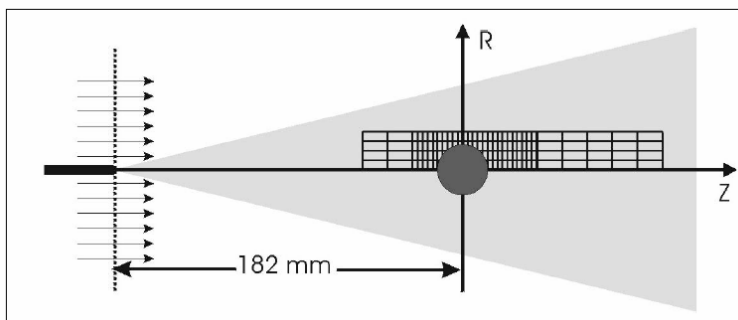


**Figure 8-78. Schematic of the Measurement Grid around the Cylinder.**

The droplet-laden flow field over both the unheated and heated obstacle was recorded with a high-resolution digital camera (providing both still-images and movies at 9 frames/s). Droplets were observed in the center of the spray impinging on the surface of the cylinder and dripping off at the bottom of the cylinder, while those droplets at larger radial positions were transported around the cylinder. Movies obtained with a high-speed digital camera at 1000 frames per second indicated that many impinging droplets rebounded off the surface and into the free stream. More rebounding droplets were observed when the air velocity was zero. Few larger size droplets were observed behind the cylinder in its wake, but were abundant with the smaller size aerosol seeds that were introduced to the flow through the air stream. There was no evidence of secondary breakup of the droplets, which was expected because the Weber number was much smaller than the critical value for droplet shattering.

When the cylinder was heated to 150 °C (i.e., well above the boiling point of water), the droplet-laden flow over the cylinder appeared to be similar to the unheated case except along the shear layer downstream of the cylinder. In this region, as mentioned earlier, a vapor layer formed which was presumed to be the result of vaporization of the liquid that wets the hot surface. It was expected that vaporization of liquid near the cylinder surface may influence locally the transport of droplets behind the cylinder by vaporizing the smaller size droplets, and thus was a focus of this segment of the investigation.

A solid-cone nozzle was used to increase the number of droplets impinging on the cylinder surface (a hollow-cone atomizer was used earlier with PIV measurements). It was observed that drippings off the cylinder occurred at a rate of approximately 6.5 mL/min for the unheated cylinder, while there was no dripping for the heated cylinder due to droplet vaporization. It was also observed by the PDI laser beam intensity that the concentration of droplets behind the cylinder was significantly reduced. For the heated cylinder, the cylinder surface temperature varied significantly with time after the spray was introduced to the flow field. However, it is unknown at this time whether these changes are attributable to time-varying changes in the response time of the cylinder heater during droplet impingement, or to some other systemic issue.

The PDI was used to provide information on: (1) droplets rebounding off the upstream face of the cylinder, (2) vaporization of droplets near the heated cylinder, (3) droplet sizes entrained into the recirculation region behind the cylinder, and (4) the effect of agent boiling point on droplet transport. The unheated cylinder results for the Sauter mean diameter ( $D_{32}$ ) and droplet mean streamwise component of velocity ( $U$ ) are presented in Figure 8-79. The rectangle located on the abscissa at an axial position of  $Z \cong \pm 14.6$  mm represents the location of the cylinder. The gap in the data for the radial positions  $R = 0, 5$  mm, and 10 mm indicates the presence of the cylinder. For Figure 8-79A, the general trends were: (1) a decrease in mean size on the downstream side of the cylinder, as compared to the upstream side, and (2) an increase in mean size with increasing radial distance from the central plane of the cylinder. The latter was indicative of the presence of more smaller size droplets near the center of the spray, as exemplified by the results obtained at the upstream axial position of  $Z = -50$  mm, which was attributed to the design characteristics of the atomizer. For the droplet mean streamwise velocity (Figure 8-79B), the values increased with decreasing radial position at the upstream position of  $Z = -50$  mm. These higher velocities correlate with the smaller droplet mean size near the center of the spray. As droplets approach the upstream surface of the cylinder, there is a decrease in the streamwise velocity component and an increase in the cross-stream component. There is an increase in the droplet streamwise velocity over the cylinder for  $R = 15$  mm, and 20 mm, which is also characteristic of the accelerated flow over the cylinder, as described earlier. At locations near the upstream surface of the cylinder, negative values for the

streamwise velocity are detected (see Figure 8-80), which may be indicative of droplets rebounding off the surface. However, positive values of velocity are obtained for the abundance of droplets, which indicates that these impinging droplets either adhere to the cylinder surface or rebound at an angle that maintains their momentum in the downstream direction over the cylinder. Note that the symbols in Figure 8-80 are sized according to the actual droplet diameter.

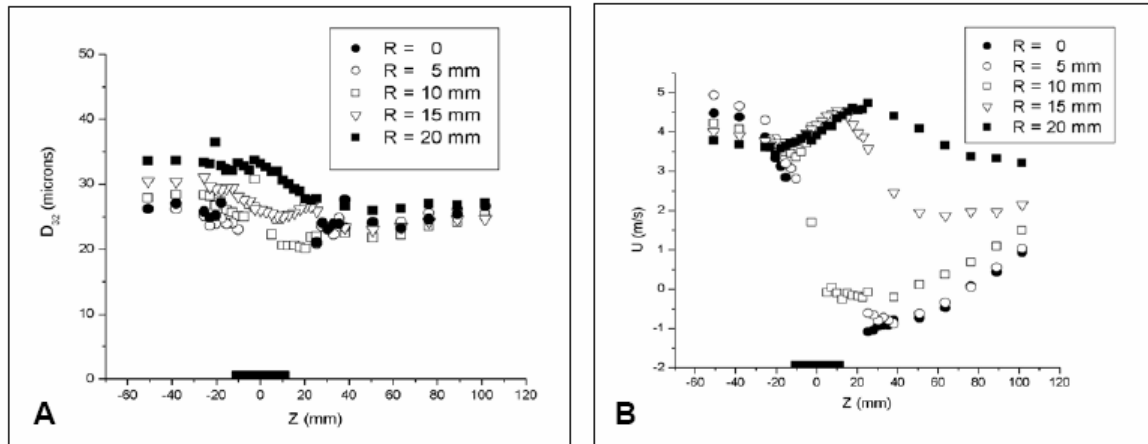


**Figure 8-79. Variation of Water Droplet (A) Sauter Mean Diameter and (B) Mean Streamwise Velocity with Streamwise Position at Different Cross-stream Positions for the Unheated Cylinder.**

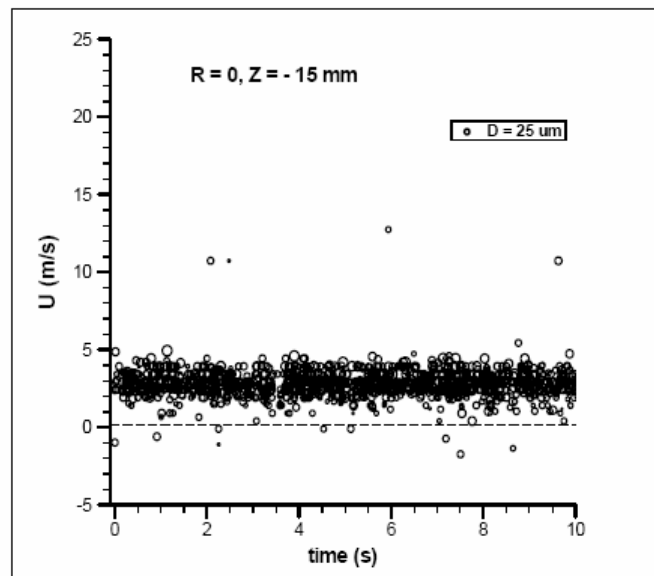


**Figure 8-80. Variation of the Streamwise Velocity with Time upstream of the Unheated Cylinder at Z = -15 mm and along the Centerline.**

The droplet streamwise velocities decrease and become negative values for  $R = 0, 5$  mm, and  $10$  mm on the downstream side of the cylinder, which is indicative of the presence of a recirculation zone and the entrainment of these droplets into this zone. Although the magnitude of the droplet mean streamwise velocity downstream of the cylinder is negative, indicating the presence of a recirculation region, it is clear that the mean is representative of a distribution of velocities and associated droplet sizes. This point is highlighted in Figure 8-81, which presents the droplet streamwise velocity with respect to droplet interarrival time into the probe volume at two points downstream of the cylinder within the recirculation region. One measurement location along the centerline, at  $Z = 25$  mm (see Figure 8-81A), represents a measurement close to the cylinder, while the other, at  $Z = 76$  mm (see Figure 8-81B), represents a location near the downstream edge of the recirculation pattern. The results for  $Z = 25$  mm indicate that many droplets are recirculated upstream toward the cylinder (because  $U < 0$ ), as expected, but also indicate that several droplets at this location are transported in the downstream direction (i.e.,  $U > 0$ ). One can speculate that these latter droplets either originate in the recirculation zone or are transported around the cylinder surface and penetrate directly into the recirculation region. In addition, the droplet size does not provide additional information since the size for these droplets varies between  $5 \mu\text{m}$  and  $30 \mu\text{m}$ , and this range is similar to that for the size distribution for the entire population for this measurement. In a similar vane, the results in Figure 8-81B indicate that the abundance of droplets are transported in the downstream direction at this point (i.e., for  $U > 0$ ). However, a few droplets are entrained into the recirculation region (i.e., for  $U < 0$ ).

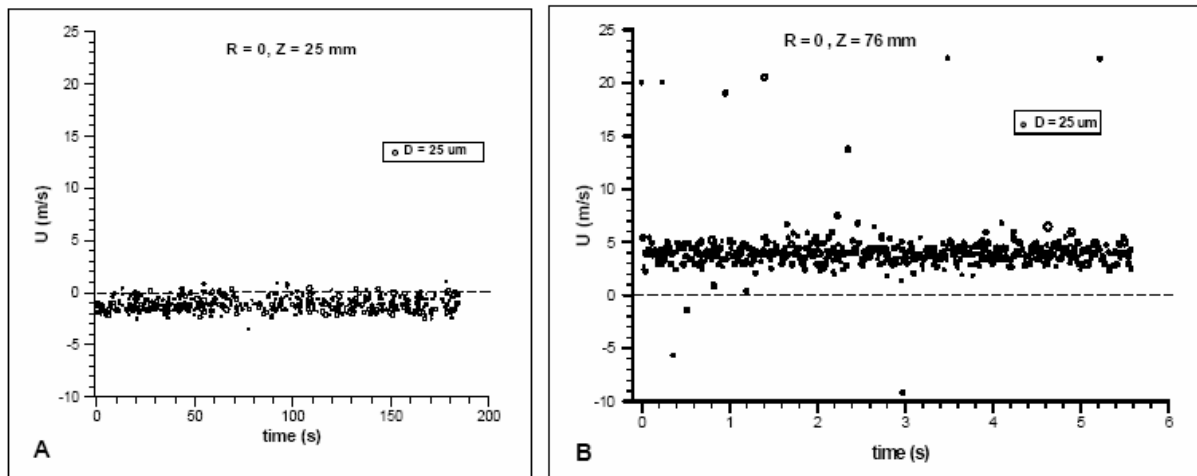


**Figure 8-81. Variation of the Streamwise Velocity with Time at Two Streamwise Positions of (A)  $Z = 25$  mm and (B)  $Z = 76$  mm along the Centerline, downstream of the Unheated Cylinder within the Recirculation Region.**

Comparison of results for the unheated and heated cylinders indicates consistently that the value of  $D_{32}$  are smaller for the heated case as the droplets are transported past the cylinder surface. The droplet streamwise and cross-stream components of velocity are also lower for the heated case. The unheated and heated results are compared in Figure 8-82 for  $D_{32}$  and  $U$  at  $R = 20$  mm. The decrease in the values of both  $D_{32}$  and  $U$  for the heated case indicates that droplet vaporization does not result in the complete removal of the smaller size droplets from the distribution, but instead a decrease in the size of all droplets

(which results in an overall decrease in both the mean size and velocity). In fact, the droplet size distributions illustrate clearly the shift of the entire distribution to smaller sizes for the heated cylinder.

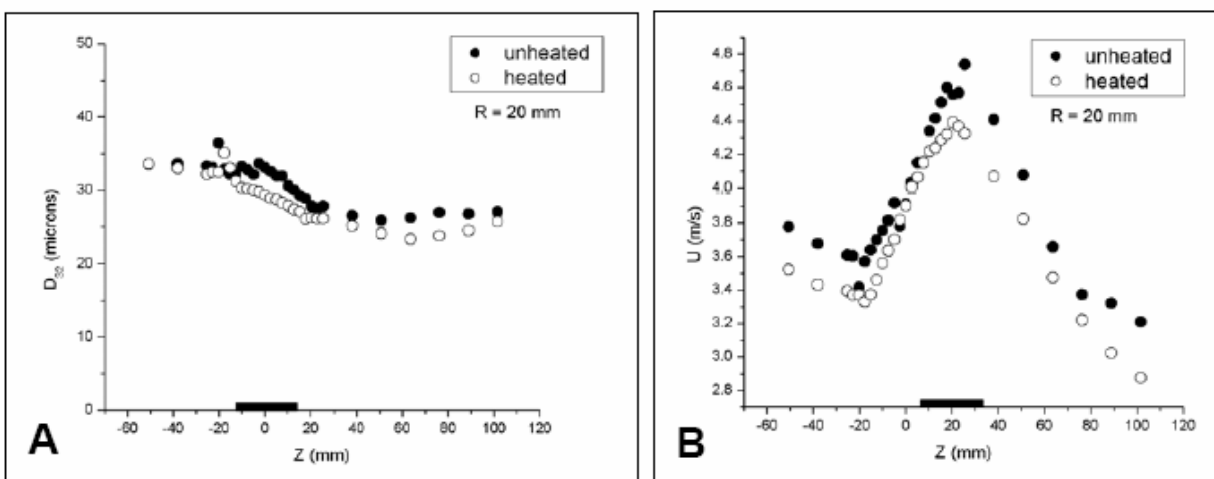


**Figure 8-82. Variation of Water Droplet (A) Sauter Mean Diameter and (B) Mean Streamwise Velocity for the Unheated (22 °C) and Heated (150 °C) Cylinders.**

Droplets with lower boiling points (i.e., the HFE agents as compared to water) were observed to vaporize more readily, resulting in vaporization of droplets before reaching the obstacle, and the absence of dripping off the cylinder surface. Comparison of results for the three agents indicates that droplet size increases and velocity decreases with increasing agent boiling point. Figure 8-83 presents a comparison of the droplet mean size and streamwise velocity with streamwise position for the three agents at  $R = 20$  mm. The size distribution for each agent is also found to shift to larger sizes for increasing agent boiling point.

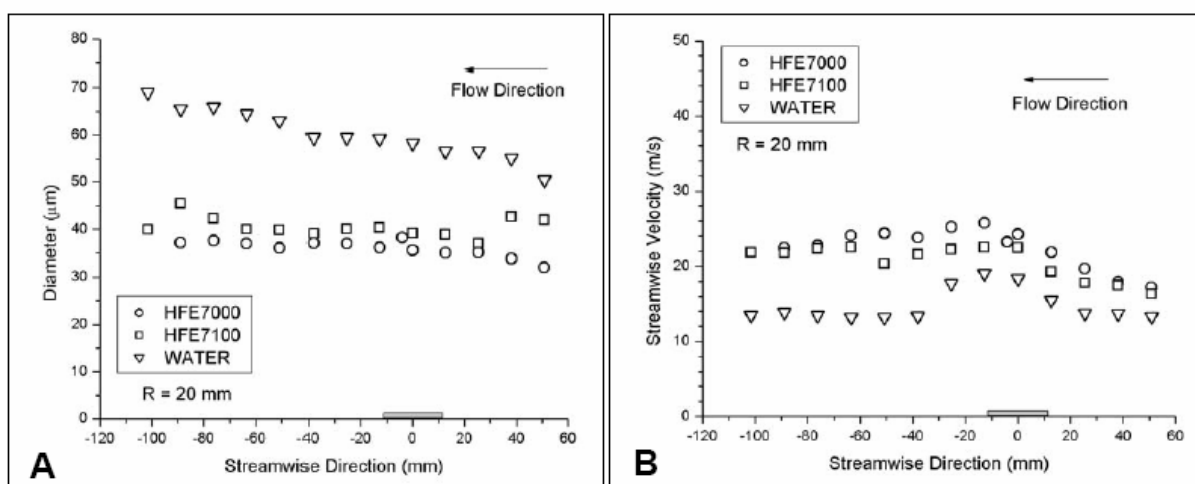


**Figure 8-83. Comparison of the Droplet (A) Mean Size and (B) Streamwise Velocity for the Three Agents.**

This study shows the effects of agent thermophysical properties on droplet transport processes through clutter elements. Other parameters, such as initial droplet size and velocity distributions, initial droplet number density, clutter surface temperature, and geometry of clutter elements, also govern droplet interaction with clutter elements and droplet transport through the elements. All these factors together with the nacelle airflow and potential fire location need to be considered when designing a fire suppression system using a liquid fire suppressant for nacelle applications.

### 8.4.3 Transport around Clutter and Recirculation Zones

There is a dearth of data of flow around basic bluff-body shapes immersed in the low speed, turbulent free streams characteristic of engine nacelles. Therefore, wind tunnel models of basic shapes were manufactured and tested in a high-turbulence, low-speed wind tunnel.<sup>33</sup> The data were analyzed to obtain mean velocities, turbulence intensities, and drag coefficients. In addition, the data time history was analyzed to gage the Strouhal number of the bluff-body wake. The data from these tests were used to develop and validate a sub-grid-scale CFD model to account for the effects of small objects in the engine bay that are difficult to resolve using a CFD mesh.

Circular cylinders (single and in tandem), spheres (single and tandem), a simulated wire bundle, a structural rib, and a cubic arrangement of spheres with cylindrical connectors were tested from 1 m/s to 10 m/s in a free-stream turbulence intensity of approximately 10 %. A circular cylinder was also tested in laminar flow at a turbulence intensity of 0.6 % for comparison with published data. Drag measurements were estimated using a momentum deficit approach.

### Experimental Setup

The tests were conducted in the low-speed, high-turbulence wind tunnel located at the United States Naval Academy (USNA). The test facility is an open jet wind tunnel powered by three 3.73 kW motors and has a speed range from 0 m/s to 18 m/s. A turbulence grid, consisting of 5 cm (2 inch) PVC plumbing pipe, was installed at the jet exit and a 0.99 m long by 0.69 m high by 0.18 m wide extension was added to condition the flow downstream of the turbulence grid. Empty test section tests found that the flow had average turbulence intensities across the test section of 9.78 %, 9.32 %, and 9.65 %. Test section flow non-uniformities of 0.16 m/s, 0.08 m/s, and 0.02 m/s were measured at average free stream velocities of 10.21 m/s, 5.08 m/s, and 1.19 m/s, respectively. The wind tunnel free stream velocity was analyzed in the absence of the turbulence grid also and found to have a test section flow non-uniformity of 0.03 m/s at a velocity of 9.87 m/s. The turbulence intensity across the “clean” test section averaged 0.58 %.

The clutter models were placed at the jet exit (Figure 8-84 and Figure 8-85), and a thermal anemometry probe was traversed upstream one model diameter from the leading edge of the model and one, three, and six model diameters downstream from the trailing edge of the model. Various shaped models were tested.

Table 8-6 gives details of the models and test conditions. The cylinder models were manufactured from PVC or copper pipe. Representative surfaces of the pipe material were measured and found to have a surface finish 0.4  $\mu\text{m}$ , rms.

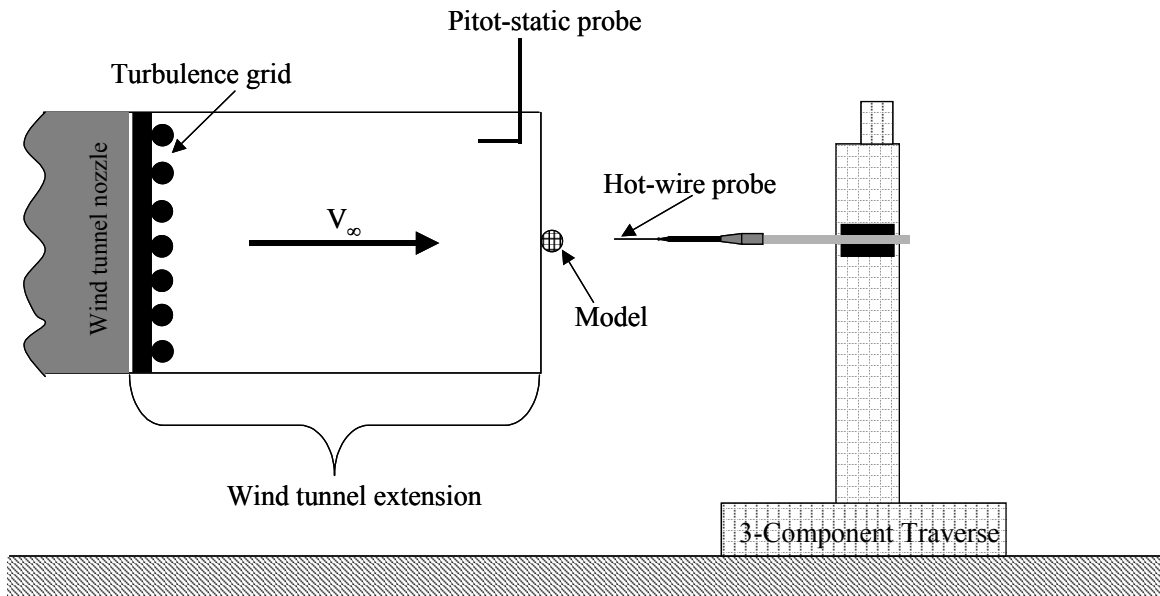


Figure 8-84. USNA Wind Tunnel Schematic.



Figure 8-85. Low-speed, High-turbulence, Open Jet USNA Wind Tunnel.

**Table 8-6. Model Geometry and Test Conditions.**

Type	Diameter (mm)	Velocity (m/s)	Reynolds Number	Material	Laminar	Turbulent	Spacing	Model Location from Ceiling (mm)
Empty TS	N/A	10, 5, 1	NA	N/A	× (10 m/s)	×		306.8 (297.3 laminar)
Cylinder	48.4	10 5 1	32600 16200 3250	PVC	×	×		297.3
Cylinder	28.8	10 5 1	19550 9800 2200	Copper		×		318.4
Cylinder	9.6	10 5 1	6400 3200 760	Copper		×		323.9
Tandem cylinder	28.8	5	9800	Copper		×	1 <i>d</i>	277.8
Sphere	50.8	5	16900	Wood		×		342.9 (CL)
Tandem sphere	50.8	5	16900	Wood		×	1 <i>d</i>	342.9 (CL)
Rib	38.1	5	12800	Aluminum		×		Tunnel floor
Wire bundle	47.6 (9.5 mm wire)	10	32000	Wire around PVC		×		306.4
Cube	63.5 (25.4 mm spheres)	5	12800	Wood		×		342.9 (CL)

***Wire Bundle Model***

This model was created using approximately 1.3 cm diameter wires secured around a 2.54 cm PVC pipe, see Figure 8-86. The outer diameter of the wire bundle is roughly equivalent to the large cylinder model. The mean velocity and turbulence intensity data were little affected by a 1 in 24 rotation of the wire bundle model. In comparison to the large cylinder data, the wake of the wire bundle model had a greater velocity deficit and an increase in the turbulence intensity.

***Tandem Medium Cylinder Model***

The tandem cylinder model, seen in Figure 8-87, was tested, and the results were compared to those from the medium cylinder model at 5 m/s. The tandem medium cylinder model had a significantly wider wake and more of a velocity decrement. The turbulence intensity of the tandem medium cylinder model was higher than the medium cylinder model turbulence intensity. Tandem cylinder drag (and correspondingly, the shed wake) is very much dependent upon the spacing between the cylinders. The

data depicted is for a cylinder spacing of one diameter. New data may prove to be markedly different for another cylinder spacing.

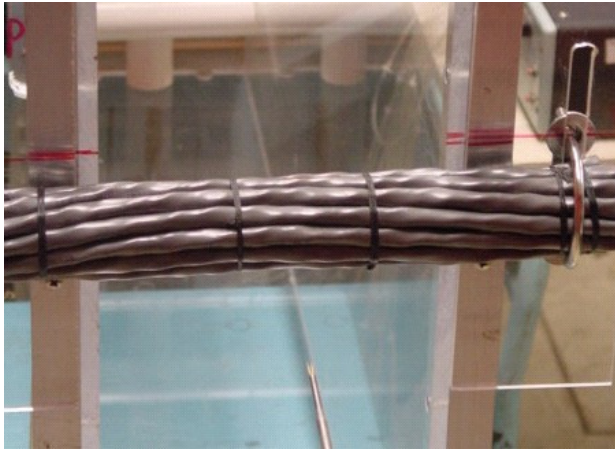
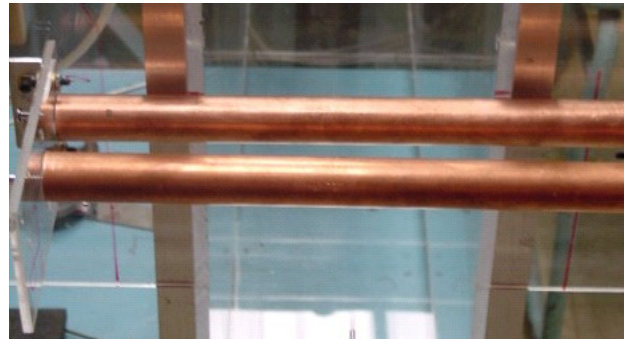


**Figure 8-86. Photograph of the Wire Bundle Model.**

**Figure 8-87. Photograph of the Tandem Medium Cylinder Model.**



### ***Sphere Model***

To obtain an accurate assessment of the drag coefficient, horizontal traverses were accomplished for all of the three-dimensional models (sphere, tandem sphere, and cube). For each location, six traverses (three horizontal and three vertical) were obtained. In general, the sphere exhibited a smaller wake with less turbulence intensity as compared to a similar sized two-dimensional cylinder at a similar Reynolds number. The effect of the model wake on the flow quickly dissipated downstream of the model, approaching the free stream tunnel conditions.

### ***Tandem Sphere Model***

This model was compared to the sphere model; the tandem sphere model had a wider wake but less of a velocity deficit immediately behind the model. However, the tandem sphere model had a slightly greater velocity deficit farther downstream. Turbulence intensity levels were less than the single sphere model immediately downstream but were slightly more at the farther downstream location.

### ***Cube Model***

A cube arrangement of spheres with connecting rods, as shown in Figure 8-88 was meant to simulate the many porous, three-dimensional objects found in an engine bay. The mean velocity and turbulence intensity were measured at different upstream and downstream traverse locations at a free stream velocity of 5 m/s. Unlike the sphere data, the wake of the cube was not seen to dissipate as quickly at the downstream traverse locations. In addition, the wake immediately downstream was wider but with a smaller velocity deficit than seen for the sphere. Turbulence intensity immediately aft of the cube was noticeably less than that of the sphere. However, the turbulence intensity of the cube far downstream was noticeably higher than the sphere's.

### ***Rib Model***

A representative aircraft rib, affixed to a flat plate was tested to determine mean velocity and turbulence intensity data. Limited data were also obtained on the flat plate alone. As expected, there is a sizeable velocity deficit seen near the flat plate and behind the rib. Recovery to the free stream velocity is delayed as the vertical traverse location moves downstream. The turbulence intensity data is chaotic near the flat plate and behind the rib. Recovery to the free stream turbulence intensity is delayed.

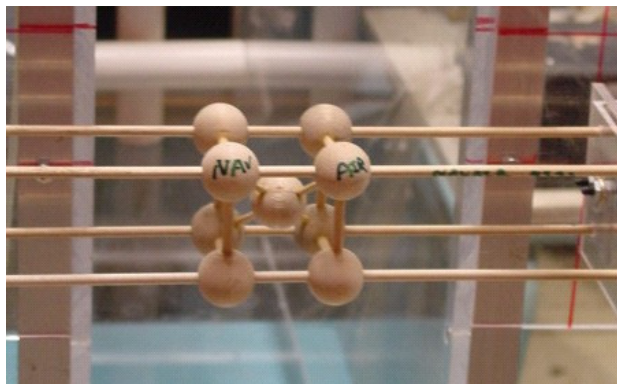


**Figure 8-88. Photograph of the Cube Model.**

### **Drag Estimates**

The drag coefficient estimates are presented in Table 8-7 along with the uncertainty estimates. In general, the models in a turbulent free stream had lower values of drag coefficient compared to the published values for similar models in a low-turbulence free stream. The analysis used the velocity data and takes into account the wind tunnel velocity jet dissipation, effects of the walls and jet boundaries, and momentum losses vertically as well as horizontally. The present tests and historical data yielded similar drag coefficient values for a cylinder in low turbulence flow (1.23 for the present test, 1.20 from the literature). The estimate for the tandem sphere data in a “clean” flow field was estimated from Hoerner<sup>34</sup> assuming the models to be flat disks. The estimate for the cube in a “clean” flow field was based on a porous model composed of spheres and rods, weighted by area. Analyzing data with a similar amount of scatter<sup>35, 36</sup> for a circular cylinder and applying the same uncertainty/bias estimates yielded an uncertainty of 13.2 % at 95 % confidence.

**Table 8-7. Summary of Drag Coefficients.**

<b>Model Type</b>	<b><math>C_D</math> (present test)</b>	<b>Velocity (m/s)</b>	<b>95 % Confidence (%)</b>	<b><math>C_D</math> (published; low turbulence)</b>	<b>Reynolds Number</b>	<b>Size (mm)</b>
Large cylinder	0.555	9.540	8.4	1.20	30812	48.41
Large cylinder	0.792	4.731	11.3	1.20	15279	48.41
Large cylinder	1.130	1.012	10.8	1.00	3268	48.41
Cylinder low turbulence	1.228	9.534	7.1	1.20	30793	48.41
Medium cylinder	1.040	9.237	8.2	1.20	17611	28.80
Medium cylinder	0.858	4.618	8.6	1.06	8804	28.80
Medium cylinder	1.084	1.089	12.6	1.00	2077	28.80
Tandem medium cylinder	0.939	4.630	11.3	1.06	8826	28.80
Small cylinder	0.368	9.556	8.4	1.04	6089	9.55
Small cylinder	0.444	4.825	9.0	1.00	3074	9.55
Small cylinder	0.635	1.128	9.5	1.30	719	9.55
Sphere	0.467	4.950	26.8	0.47	16775	50.80
Tandem sphere	0.703	4.907	8.9	0.71	16633	50.80
Rib	0.921	5.086	15.9	1.30	12930	38.10
Wire bundle	1.039	9.334	8.6	1.14	29662	47.63
Cube	0.242	4.531	15.9	0.28	19195	63.50

Generally, for a given Reynolds number, the smaller the size of the model, the lower the drag coefficient. For the small cylinder, the drag coefficient was found to be significantly lower than for the large and medium cylinders at a roughly equivalent Reynolds number. Although the length of the wind tunnel extension was thought sufficient to ensure that the generated turbulence was well-mixed, perhaps the nature of the eddies created by the 5.08 cm diameter turbulence grids causes differences in the local flow field around the various models, thus causing a violation in the similarity parameter.

The wire bundle model was seen to have significantly higher drag (approaching the drag coefficient of the cylinder in low turbulence flow field) compared to a similar sized cylinder. This is a different trend than seen in a similar model in a low turbulence flow field. A wire bundle in a low turbulence flow field has been shown to decrease the drag coefficient compared to a smooth cylinder of the same diameter.

The tandem sphere had nearly double the drag coefficient of the single sphere model. For each estimate, the same frontal area was used in the drag coefficient calculations. In a similar manner, the same frontal area was used for estimating the drag coefficients for the medium cylinder and tandem medium cylinder.

### Strouhal Number

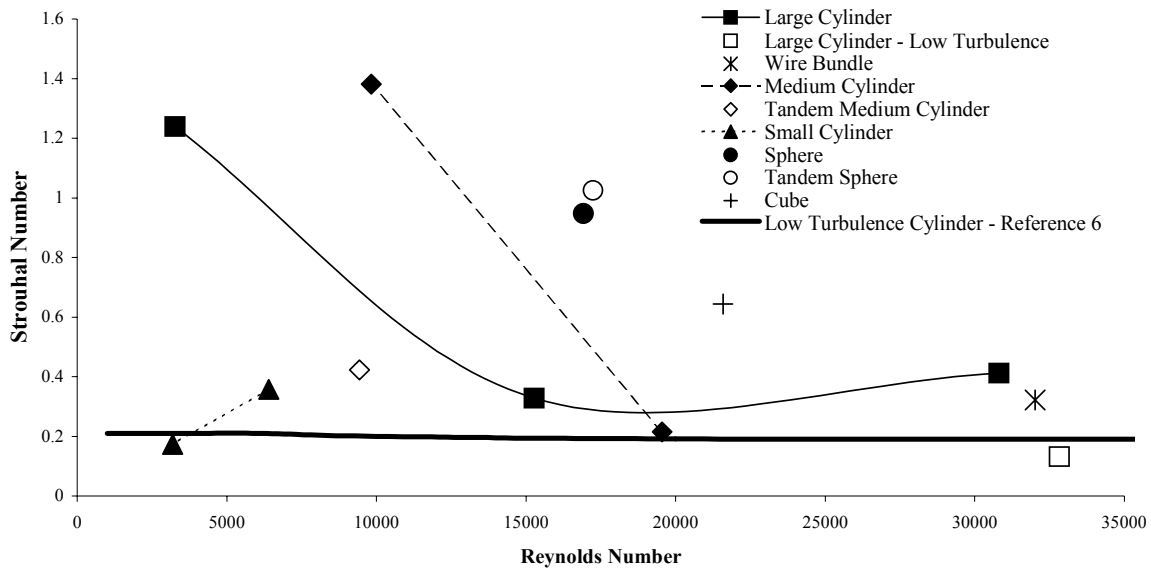
The algorithm to determine the power spectrum density (PSD) was based on the method by Welch.<sup>37</sup> The data were segmented into windows to allow eight averages. No data overlapping was employed, and a Hanning filter was used with a window length the same size as the data segments. The mean was eliminated from the PSD calculations and a 95 % confidence criterion was used to gage the PSD assessment.

Table 8-8 gives the frequency and Strouhal number resolution. The Strouhal number is a dimensionless characteristic of vortex-shedding off bluff bodies, such as clutter. This shedding of vortices downstream affects the mixing of agent into the recirculation regions as well as the major downstream flows. In cases where a comparison of models needed to be consistent (e.g., a medium cylinder model and the tandem medium cylinder model), the analysis was performed over the same data record length.

**Table 8-8. Frequency and Strouhal Number Resolution.**

Model Type	Reynolds Number	Velocity (m/s)	$\Delta f$ (Hz)	$\Delta St$
Large cylinder	32,605	10.0126	8.492	0.041
Large cylinder	16,208	4.9936	4.069	0.039
Large cylinder	3,253	1.0000	1.424	0.069
Medium cylinder	19,553	10.0157	10.851	0.031
Medium cylinder	9,826	4.9664	21.701	0.126
Medium cylinder	2,175	1.1070	3.255	0.085
Small cylinder	6,395	9.9710	13.021	0.012
Small cylinder	3,193	4.9840	13.021	0.025
Cylinder-low turbulence	32,338	10.0126	11.182	0.054
Tandem medium cylinder	9,435	4.8953	21.701	0.128
Sphere	16,917	4.9866	8.492	0.087
Tandem sphere	17,426	5.0994	8.492	0.085
Wire bundle	32,019	10.0131	8.492	0.040
Cube	21,585	5.0647	4.069	0.051

To gage the coherence, the empty test section data were analyzed to determine the pulse frequency peaks in the tunnel. This was used as a guide to cull non-model frequencies from the spectrum. The Strouhal number corresponding to the dominant frequency is plotted against Reynolds number in Figure 8-89. It was found that the Strouhal number of the cylinder model in a low-turbulence flow field was lower, than that reported in the literature, 0.13 versus 0.19, (see Schlichting<sup>36</sup>).



**Figure 8-89. Strouhal Number versus Reynolds Number for the Various Tested Configurations.**

It should be noted that model size had an effect on the Strouhal number. That is, the large circular cylinder at 1 m/s has the approximate Reynolds number of the small circular cylinder at 5 m/s. However, the Strouhal number was significantly different: 1.2 for the large cylinder at 1 m/s and 0.2 for the small cylinder at 5 m/s.

The fundamental frequency of the empty test section data was: 25.8 Hz ( $St = 0.125, 0.074, \text{ and } 0.025$  based upon the large, medium, and small cylinder diameter, respectively) at 10 m/s, 17.3 Hz ( $St = 0.167, 0.100, \text{ and } 0.033$  based upon the large, medium, and small cylinder diameter, respectively) at 5 m/s, and 8.7 Hz ( $St = 0.419, 0.249, \text{ and } 0.083$  based upon the large, medium, and small cylinder diameter, respectively) at 10 m/s. The different flow fields most likely caused the differences in Strouhal numbers and drag coefficients.

The Strouhal numbers of the sphere and tandem sphere models were equal. However, there was a notable difference between the medium cylinder and tandem medium cylinder models. The wire bundle model was found to have a similar Strouhal number as the similarly sized cylinder. No dominant frequency was noted for the rib model. In general, the Strouhal number was higher for cylinders in a turbulent flow field compared to cylinders in low turbulence.

### Summary and Implications

Fundamental measurements of mean velocity, turbulence intensity distributions, drag coefficient estimates, and wake shedding frequency were obtained for basic aerodynamic shapes. A limited comparison to data obtained for a circular cylinder in a low-turbulence flow field was also conducted. The results show that the wake structure behind a circular cylinder in a turbulent flow field was smaller compared to the same cylinder in low-turbulence flow. Turbulence intensity increased with decreasing Reynolds number. The drag coefficient estimates were generally lower than those obtained in low-

turbulence flow fields. Strouhal number variation with Reynolds number was generally higher for cylinders in a turbulent flow field, when compared to cylinders in low-turbulence. Model size was seen to affect the similarity parameters of the Strouhal number and Reynolds number due to differences in the shedding characteristics of the turbulence grid in the wind tunnel. The results also show higher turbulence intensity behind the bluff body when compared to the same configuration in a laminar flow field. Also, the drag coefficients for the same configuration were seen to be lower than those in a laminar flow. These latter two points imply that the clutter impedes the flow of agent and air less (proportionally) in a turbulent flow than in a laminar one and that the mixing of agent into the flow as a result of interacting with the clutter is less sensitive to Reynolds number than was expected. Subsequent testing, described below, indicates that clutter usually facilitates the mixing of agent in the protected space.

#### 8.4.4 Low Temperature Effects on Agent Dispersion

##### Introduction

Should a fire suppressant be discharged into a sufficiently cold engine nacelle or dry bay, it is expected that some of the chemical will condense on the cold surfaces. Gravity would then lead to puddling of the condensate at a low point in the volume, and the agent would then volatilize at a rate determined by its vapor pressure at the local temperature and the local air flow. This behavior would necessitate the storage and distribution of additional suppressant, which would result in increased storage weight and volume, as well as a longer time to fire extinguishment. The cold temperature release finds its applications in the cold start of an engine in a cold environment or in high-altitude cruising conditions.

Yang and coworkers<sup>38</sup> conducted a series of tests in a simulated engine nacelle to verify this phenomenon and to estimate the magnitude of its impact. In these tests, the key variable was the difference between the boiling point of the suppressant and the ambient temperature in the nacelle. The temperature of the suppressant storage bottle was also treated as an independent variable.

For the NGP, a criterion for low temperature applications for a fire suppressant was set at  $-40\text{ }^{\circ}\text{C}$ . To study the effect of low temperature on agent dispersion, it was necessary to identify a surrogate agent that has a normal boiling point higher than the  $-40\text{ }^{\circ}\text{C}$  minimum temperature criterion. Trifluoroiodomethane ( $\text{CF}_3\text{I}$ ), which has been proposed as a potential replacement for halon 1301 in aircraft engine nacelle and dry bay fire protection applications,<sup>4,39</sup> meets this criterion and was selected as a surrogate for the study.  $\text{CF}_3\text{I}$  has a normal boiling point of  $-22\text{ }^{\circ}\text{C}$ , which is almost  $20\text{ }^{\circ}\text{C}$  higher than the  $-40\text{ }^{\circ}\text{C}$  minimum temperature criterion. The dispersion of  $\text{CF}_3\text{I}$  into air at temperatures down to  $-40\text{ }^{\circ}\text{C}$  may not be as effective as halon 1301, which has a normal boiling point of  $-57.8\text{ }^{\circ}\text{C}$ . In addition,  $\text{CF}_3\text{I}$  can be detected using UV absorption spectrometer, which was the available method for measuring temporal  $\text{CF}_3\text{I}$  concentration in this study. Table 8-9 lists some of the physical properties of  $\text{CF}_3\text{I}$  and  $\text{CF}_3\text{Br}$ .

**Table 8-9. Selected Thermophysical Properties of  $\text{CF}_3\text{I}$  and  $\text{CF}_3\text{Br}$ .<sup>2</sup>**

Agent	Molecular Weight (kg/mol)	$T_b$ ( $^{\circ}\text{C}$ )	$T_c$ ( $^{\circ}\text{C}$ )	$P_c$ (MPa)	$\rho_c$ ( $\text{kg}/\text{m}^3$ )	$\Delta H_v$ (kJ/kg)
$\text{CF}_3\text{I}$	0.196	$-22.0$	122.0	4.04	871	106
$\text{CF}_3\text{Br}$	0.149	$-57.8$	67.0	4.02	745	111

$T_b$  is the normal boiling point;  $T_c$  is the critical temperature;  $P_c$  is the critical pressure;  $\rho_c$  is the critical density;  $\Delta H_v$  is the latent heat of vaporization at  $T_b$ .

Although the release of  $\text{CF}_3\text{I}$  (at room temperature or chilled to about  $-40\text{ }^\circ\text{C}$ ) into a fire compartment and an engine nacelle simulator at ambient room temperature has been examined,<sup>2,40</sup> the discharge of cold  $\text{CF}_3\text{I}$  into a cold ambience has not been performed, or at least has not been documented in open literature. There is only one corporate internal report,<sup>41</sup> which describes a study of the release of cold  $\text{CF}_3\text{I}$  into a well-mixed cold *enclosure* with no airflow. Careful examination of the data indicated some deterioration in the distribution of  $\text{CF}_3\text{I}$  within the enclosure when compared to room temperature conditions. To assure that there is no substantial deterioration in dispersion performance under cold temperature applications, discharge tests in an aircraft engine nacelle at temperatures below the agent boiling point are needed. The temperature of  $-40\text{ }^\circ\text{C}$  was selected in this study because it was below the normal boiling point of  $\text{CF}_3\text{I}$  and was the lowest operating temperature for some of the equipment used in the experiments.

### Experimental Apparatus (ELEFANT)

The experimental apparatus (called Extremely Low-temperature Environment For Aircraft Nacelle Testing) consisted of a simulated engine nacelle with baffles, an agent release port, four observation windows, and two measurement ports. Figure 8-90 is a schematic of the simulator. The annulus of the simulator had an inside diameter of 0.6 m and an outside diameter of 0.9 m, resulting in a cross-sectional area of  $0.35\text{ m}^2$ . The length (2 m) of the simulator was comparable to the distance between the agent injection port and the downstream end of a typical small engine nacelle. The baffle height was 0.075 m. The baffles were used to mimic a complicated flow path for the agent as in the case of a real nacelle. Two longitudinal ribs with the same height as the baffles were placed on the outer surface of the inner core of the nacelle between the inner forward and aft baffles. The ribs were used as barriers to the agent flowing circumferentially. The simulator was fabricated of 3.2 mm thick stainless-steel sheet metal.

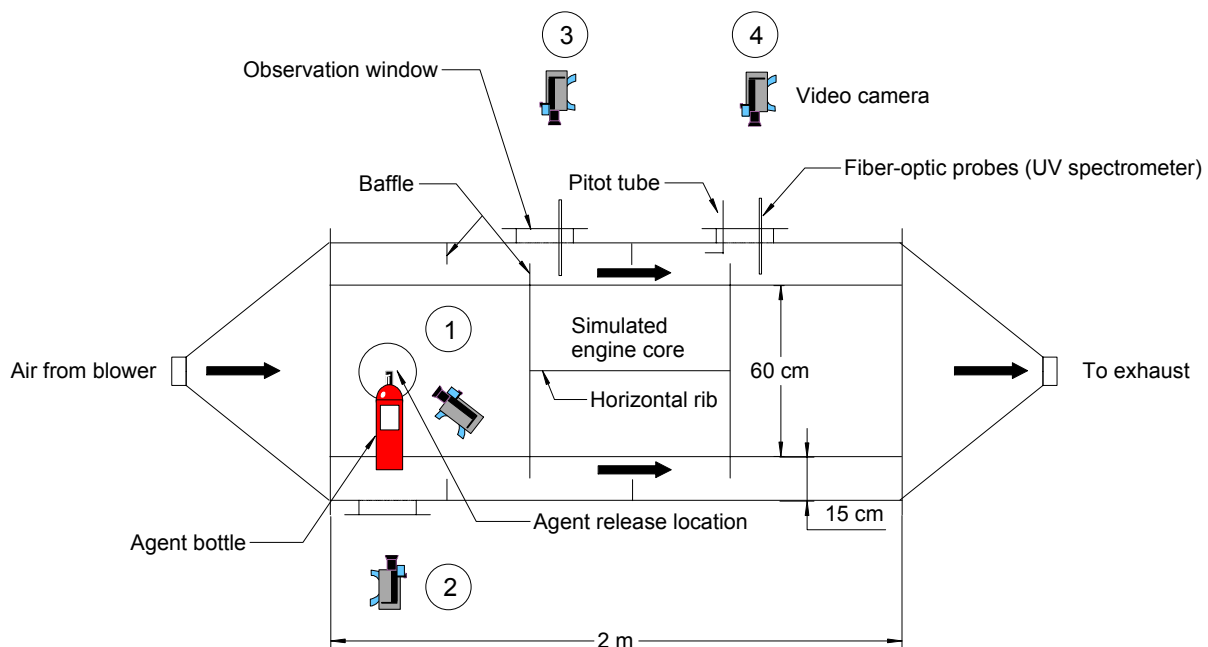


Figure 8-90. Schematic of the Test Fixture (ELEFANT).

A bottle with an internal volume of 2.36 L was used to store  $\text{CF}_3\text{I}$  for discharge. A fast-response static pressure transducer (uncertainty  $\pm 10$  kPa specified by the manufacturer) was mounted on the receiver bottle to monitor the pressure inside the bottle during filling and discharge. A K-type thermocouple (uncertainty  $\pm 1$  °C) was inserted into the bottle to record the temperature of the liquid agent before discharge. A quick-acting solenoid valve was used to release the agent. To tailor the agent discharge time ( $\approx 0.5$  s), a reducer was placed at the valve exit. The agent was released through a vertical tee at the end of a short stainless-steel tubing (i.d. = 15.9 mm, o.d. = 19.1 mm) connected to the reducer. Four CCD cameras (30 frames/s) were used to observe the agent discharge behavior at the release port (Camera 1), at a location in the bottom of the simulator to observe any pooling of agent (Camera 2), and at the two concentration measurement locations (Cameras 3 and 4). A frequency-controlled, variable-speed blower provided airflow through the nacelle simulator. The maximum air speed at room temperature in the annulus, measured using a pitot tube, can reach 9.2 m/s.

To achieve an operating temperature of  $-40$  °C, the entire facility was placed inside the U.S. Army environmental test chamber at Ft. Belvoir, and the cold discharge experiments were conducted inside the chamber. The chamber has an interior dimension of 2.74 m (H)  $\times$  3.35 m (W)  $\times$  3.66 m (L) and a 1.83 m  $\times$  1.83 m sliding door. The lowest temperature attainable in the environmental test chamber is  $-54$  °C. Discharge experiments in room temperature were also conducted inside the chamber with the refrigeration unit turned off to establish baselines for comparisons.

The experimental procedure involved the following steps. The receiver bottle was first immersed in dry ice and connected to the  $\text{CF}_3\text{I}$  supply bottle, which was placed on an electronic balance (uncertainty of  $\pm 1$  g) to monitor the amount of agent transferred to the receiver bottle. The dry ice was used to condense the  $\text{CF}_3\text{I}$  vapor in the receiver bottle. The supply bottle was slightly warmed using two 120 V floodlights to increase the vapor pressure to facilitate the transfer of  $\text{CF}_3\text{I}$  vapor to the receiver bottle. When the amount of agent in the receiver bottle reached the target mass, the bottle was then removed from the dry ice, warmed back to room temperature, and weighed on the electronic balance to determine the actual mass in the bottle. The receiver bottle was then pressurized with nitrogen to 4.12 MPa. Shaking the bottle intermittently and vigorously was required before the final equilibrium pressure was attained. The amount of nitrogen added was obtained by weighing the filled bottle. The bottle was now ready for the discharge experiments. For cold temperature conditions, the environmental test chamber and the receiver bottle were cooled down to approximately  $-40$  °C before a test was commenced. Two contact K-type thermocouples were attached on the front and aft of the simulator external skin to monitor the ambient temperature of the chamber. In addition, a bare-beaded K-type thermocouple was placed in the annulus to measure the airflow temperature through the nacelle.

Given the simulated nacelle volume and airflow, the amount of agent required for a fixed injection period ( $< 0.5$  s for typical nacelle applications) was estimated using the generic nacelle modeling results discussed in Hamins et al.<sup>66</sup> The agent bottle was charged with  $\approx 1$  kg of  $\text{CF}_3\text{I}$  and then pressurized with nitrogen to the desired pressure (4.21 MPa) at room temperature. Table 8-10 lists the experimental matrix. The airflow through the simulator was maintained at  $1.5$  kg/s  $\pm$  0.1 kg/s (mean  $\pm$  standard deviation).

**Table 8-10. Experimental Matrix.**

Nominal Initial Conditions of Vessel	Nominal Conditions of Vessel Before Discharge	Nominal Conditions in the Simulator
22 °C and 4.12 MPa	-40 °C at prevailing <i>P</i>	-40 °C
22 °C and 4.12 MPa	22 °C and 4.12 MPa	22 °C (baseline)
22 °C and 4.12 MPa	22 °C and 4.12 MPa	-40 °C

The dispersion effectiveness of CF<sub>3</sub>I was assessed based upon concentration measurements at the two locations inside the engine nacelle simulator (see Figure 8-90). The number of measurement locations could be easily increased; however, the intent of this work was not to address the certification process, which requires twelve measurement locations. The measurements were made using two Ocean Optics S2000 UV/VIS fiber-optic spectrometers. The optical components consisted of a deuterium/tungsten source, four (UV grade quartz) collimating lenses, and 300 μm diameter optical fibers. These were arranged to provide two measurement locations (coincident with Cameras 3 and 4) approximately 0.75 m apart along the direction of the airflow in the engine nacelle testing apparatus. A bifurcated fiber (1 m in length, coupled with a 5 m extension) was used to connect the source to a pair of collimating lenses secured by brackets to the Plexiglas® viewing windows located on the top of the apparatus. The source radiation emanating from each lens was transmitted over a 0.038 m optical path (perpendicular to the airflow) to an opposing set of collimating lenses connected by independent optical fibers (5 m in length) to the master and slave spectrometers. Although the manual indicated that these optical components should have a spectral range from 200 nm to 850 nm, very little throughput at wavelengths shorter than 250 nm was found.

The spectrometer settings used for the measurements in the nacelle testing apparatus were as follows. The spectrometers were triggered by an electronic timer. The integration time (analogous to the shutter speed) was set at 30 ms, and the pixel resolution of the analogue to digital converter (ADC) was set at 10, which amounts to a spectral resolution of only about 3 nm. With this configuration, it was able to achieve a data acquisition rate of approximately 12 single scan spectra (6 at each location) per second to capture the time dependent details of the agent discharge. An estimate of the uncertainty (one standard deviation) of the measurements was obtained by comparing results at these settings to more accurate values obtained after signal averaging 100 scans at the full resolution of the spectrometer (≈ 0.3 nm). Based on this analysis, the CF<sub>3</sub>I partial pressures reported in this paper are accurate to ± 15 %.

The UV spectrometer was calibrated at 295 K using a quartz cell with an optical path length of 0.075 m. The cell was first evacuated to 1.33 Pa. Then, a fixed amount of CF<sub>3</sub>I vapor was metered into the cell by monitoring the cell pressure. Spectra were taken using an integration time of 30 ms and a pixel resolution of 10. Figure 8-91 shows a typical CF<sub>3</sub>I absorption spectrum at 295 K. Note that the peak absorbance for CF<sub>3</sub>I centers around 270 nm. The calibration curve (at λ = 300 nm and 22 °C), which is a plot of absorbance (*A*) against concentration (*C*, molecules cm<sup>-3</sup>), is shown in Figure 8-92.

The Bouguer-Beer-Lambert law is expressed as

$$A(\lambda) = -\log \left[ \frac{I(\lambda)}{I_o(\lambda)} \right] = \frac{C\sigma(\lambda, T)L}{2.303} \quad (8-40)$$

where  $I(\lambda)$  and  $I_o(\lambda)$  are the incident and transmitted intensities through the cell respectively,  $\sigma(\lambda, T)$  is the absorption cross section ( $\text{cm}^2$ ),  $L$  is the optical path length (cm),  $T$  is the temperature, and  $\lambda$  is the wavelength. Note that the absorption cross-section is a function of wavelength and temperature. Using the ideal gas law, Equation 8–41 gives the relationship between  $C$  and the partial pressure  $p$  (Pa) at 22 °C.

$$C = 2.44 \times 10^{14} p \quad (8-41)$$

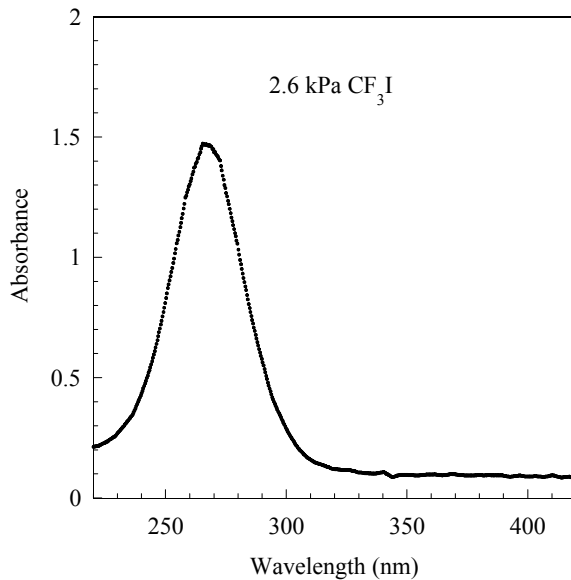


Figure 8-91. Absorption Spectrum of  $\text{CF}_3\text{I}$ .

From Equation 8–40, the absorption cross section can be obtained from the slope of the calibration curve. A linear regression line is fitted through the data points in Figure 8-92, and the absorption cross-section of  $\text{CF}_3\text{I}$  is  $8.1 \times 10^{-20} \text{ cm}^2$ , which is comparable to the value of  $8.9 \times 10^{-20} \text{ cm}^2$  at  $\lambda = 300 \text{ nm}$  and 22 °C to 27 °C in the literature.<sup>42</sup> Since the calibration was performed at 22 °C, a correction for the temperature effect on the absorption cross section is necessary to obtain the  $\text{CF}_3\text{I}$  partial pressure at other prevailing temperature, using the following equation:<sup>42</sup>

$$\sigma(\lambda, T) = \sigma(\lambda, 25 \text{ }^\circ\text{C}) \exp[B(\lambda)(T - 25)] \quad -63 \text{ }^\circ\text{C} < T < 27 \text{ }^\circ\text{C} \quad (8-42)$$

The concentration  $C$  of  $\text{CF}_3\text{I}$  at any temperature was calculated from the absorbance measurement using Equations 8–40 and 8–42. At 300 nm,  $B = 4.876 \times 10^{-3} \text{ }^\circ\text{C}^{-1}$  from DeMore et al.<sup>42</sup> The partial pressure of  $\text{CF}_3\text{I}$  was then obtained using the ideal gas law at the *prevailing* temperature. However, the temperature effect on the absorption cross section was found to be negligible in the concentration calculations.

An electronic timer was used to coordinate the experimental sequence of events. At  $t = 0 \text{ s}$ , a signal was sent from the timer to trigger the data acquisition system to record the pressure of the discharge bottle and the pitot tube output at a sampling rate of 200 Hz. At  $t = 1 \text{ s}$ , the timer initiated the two UV spectrometers, and at  $t = 2 \text{ s}$ , the solenoid valve was activated to discharge the  $\text{CF}_3\text{I}$ /nitrogen mixture from the bottle into the engine nacelle simulator.

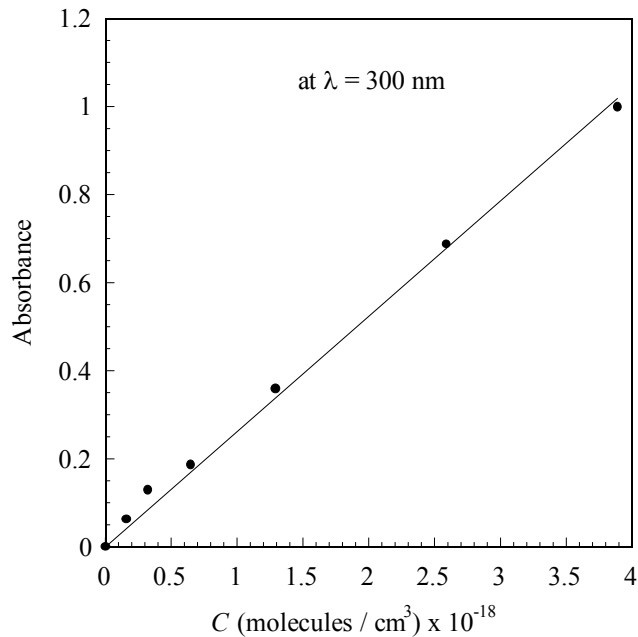


**Figure 8-92. Calibration Curve at 300 nm.**

## Results and Discussion

Figure 8-93 shows the temporal variation of pressure inside the bottle during a typical discharge. The initial time ( $t = 0$ ) corresponds to the time when the solenoid valve was opened. In the figure, the prevailing bottle pressure before discharge at  $\approx -40$  °C is much lower than that at room temperature. Due to the reduction in the initial bottle pressure, the discharge time ( $\approx 0.24$  s) of the cold *liquid* agent is much longer than that ( $\approx 0.16$  s) of the baseline case; the liquid discharge time corresponds to the transition point in the pressure vs. time curve.<sup>43</sup> The observations from Camera 1 also showed that the agent discharge time at  $\approx -40$  °C was longer than that at room temperature.

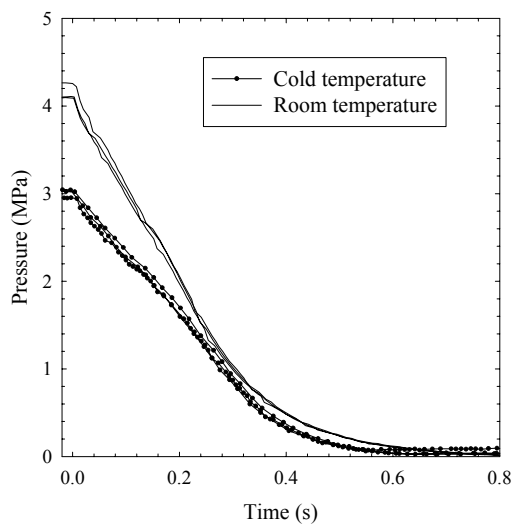


**Figure 8-93. Variation of Bottle Pressure during Discharge at Room and Cold Temperatures.**

When  $\text{CF}_3\text{I}$  was discharged at room temperature, the observations obtained from Camera 2 showed that a small amount of  $\text{CF}_3\text{I}$  pooled in the bottom of the simulator upon release, and the liquid  $\text{CF}_3\text{I}$  boiled off within 66 ms. When  $\text{CF}_3\text{I}$  was discharged at  $-40\text{ }^\circ\text{C}$ , a significant amount of liquid  $\text{CF}_3\text{I}$  pooled at the bottom of the nacelle upon release. The liquid  $\text{CF}_3\text{I}$  evaporated slowly and remained for many seconds ( $> 60\text{ s}$ ) before complete evaporation. The observations from Cameras 3 and 4 showed that a cloud of  $\text{CF}_3\text{I}$  passed through the field of view of the cameras after agent discharge. The observations from Cameras 3 and 4 were qualitatively similar for the discharge of  $\text{CF}_3\text{I}$  at room temperature and  $-40\text{ }^\circ\text{C}$ .

The difference in pooling tendency described above can be explained as follows. Consider a 2.36 L container with 1 kg of  $\text{CF}_3\text{I}$  pressurized with nitrogen to 4.12 MPa at  $22\text{ }^\circ\text{C}$ . If the container is cooled down to  $-40\text{ }^\circ\text{C}$  before release, the final pressure of the container is estimated to be 2.8 MPa using the computer code (PROFISSY).<sup>2,6</sup> The code is based on the calculations of vapor-liquid phase equilibria using the extended corresponding-states principle. Assuming the discharge of the liquid agent from the container is an isentropic process from the initial container pressure to atmospheric pressure, the final states of the agent can be calculated using the computer code (FISSYCS)<sup>2</sup>, which is a modified version of PROFISSY. Table 8-11 tabulates the calculated results for the two conditions. The liquid mole fraction (the percent of agent/nitrogen mixture still remaining in the liquid phase after the isentropic expansion process) is substantially higher at  $-40\text{ }^\circ\text{C}$  than at  $22\text{ }^\circ\text{C}$ . Such a high liquid fraction should result in significant pooling upon agent release from the bottle. The combined effects of liquid pooling and slow evaporation at  $-40\text{ }^\circ\text{C}$  will have an adverse impact on the subsequent dispersion of the agent/nitrogen mixture in the nacelle.

**Table 8-11. Liquid Fraction of  $\text{CF}_3\text{I}/\text{N}_2$  Mixture after Isentropic Expansion to 0.101 MPa.**

Initial Conditions	Liquid Fraction (%)
$22\text{ }^\circ\text{C}$ at 4.12 MPa	70
$-40\text{ }^\circ\text{C}$ at 2.8 MPa	90

Although full  $\text{CF}_3\text{I}$  spectra were obtained in each test, a common practice used is to base concentration measurements on the wavelengths at the peak absorbance or its vicinity. The absorbance at 300 nm was used to obtain the  $\text{CF}_3\text{I}$  concentration because saturation of the detector at  $\approx 280\text{ nm}$  was observed under certain test conditions. The concentration of  $\text{CF}_3\text{I}$  thus obtained is shown for both the room and cold temperature releases in Figure 8-94 and Figure 8-95 for the two measurement locations, respectively. The initial time ( $t = 0$ ) in the figures corresponds to the initiation of the agent release. Although three runs were performed at each condition with similar observations, only a single run for each condition is shown in the figure for clarity. The arrival times of the agent at the two measurement locations were clearly captured in the figures. Some salient features are noted in the two figures.

For the room temperature release, an initial spike was observed at the forward measurement location. This was due to the presence of a two-phase (liquid droplet-laden) flow because the off-resonance spectral measurement at 500 nm also showed a peak at the same time. The two-phase flow was the result of break-up of the liquid core at the discharge port into droplets. The off-resonance extinction at 500 nm indicated that liquid  $\text{CF}_3\text{I}$  droplets were present for only a short period of time ( $< 2\text{ s}$ ) immediately following the discharge. Therefore, it can be argued that the concentration measurements after the initial spike in Figure 8-94 was due largely to the  $\text{CF}_3\text{I}$  vapor, with minimal or negligible contribution from the droplets.

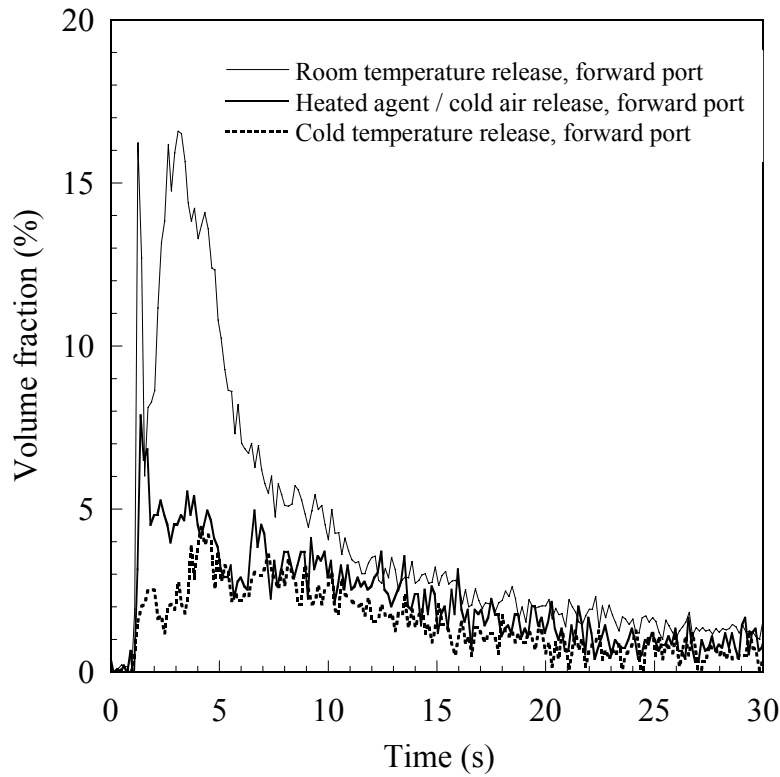
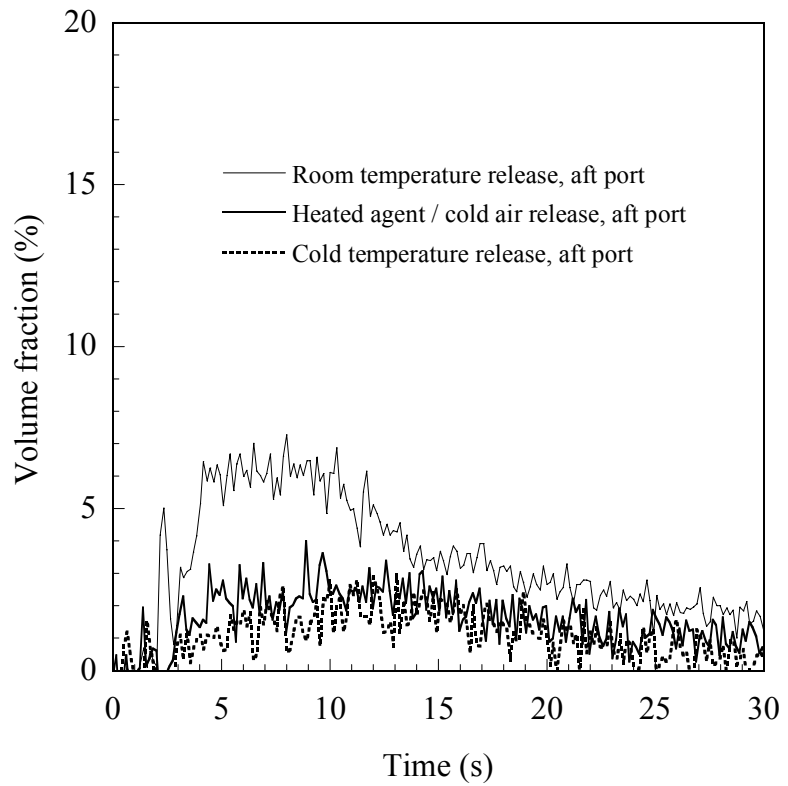


**Figure 8-94.  $\text{CF}_3\text{I}$  Concentration Profiles at the Forward Port.**

**Figure 8-95.  $\text{CF}_3\text{I}$  Concentration Profiles at the Aft Port.**



The off-resonance spectral measurement at 500 nm in the aft location indicated that no droplets were present. The absence of the droplets and the much lower  $\text{CF}_3\text{I}$  concentration (Figure 8-95) at this location indicated that the current nacelle simulator had indeed created a very challenging environment for agent dispersion, a condition which is generally true for a real engine nacelle. Furthermore, the generic nacelle model<sup>66</sup> provided a reasonable estimate of the amount of agent needed to achieve the required extinguishing concentration at two measurement locations in the current nacelle. Halon 1301 and  $\text{CF}_3\text{I}$  have similar heptane cup-burner extinguishing values, a volume fraction of 0.032 from Grosshandler et al.<sup>4</sup> Assuming that the military specification for halon 1301 can be applied to  $\text{CF}_3\text{I}$ , the measurements in Figure 8-94 and Figure 8-95 suggest that a volume fraction of 0.06 can be attained over a duration of 0.5 s in both locations at room temperature.

For cold temperature release, the off-resonance spectral measurements at 500 nm did not indicate the initial presence of droplets at both forward and aft measurement locations. The absence of the droplets was due partly to the reduction in the initial bottle pressure ( $\approx 3$  MPa vs.  $\approx 4.1$  MPa at room temperature), which would impart less momentum to the droplets upon the release of the agent. Droplets with less momentum were less likely to be transported to the two measurement locations. The combined effect of low bottle pressure and large liquid fraction in cold temperature release (see discussion above) might generate larger droplets as a result of poor atomization of the liquid core, thus hindering the ability of the droplets to follow the airflow. Similar to the room temperature release, the concentration at the forward location was higher than that at the aft. However, the difference was not as significant as in the case of room temperature release. The most important finding from this study was that there was a significant reduction in the agent concentration in the cold temperature release. At the forward measurement location, a reduction of a factor of almost 3 was observed at the peak concentration. At both locations, the agent concentration measurements were always *below* a volume fraction of 0.06.

One operational strategy to mitigate the poor dispersion of  $\text{CF}_3\text{I}$  for cold temperature applications has been proposed, namely, warming the bottle before being released into the cold ambience. Figure 8-94 and Figure 8-95 illustrate, respectively, the concentration measurements at the two locations in the nacelle simulator when the agent was released at  $\approx 20$  °C and the airflow through the nacelle was maintained at  $\approx -40$  °C. The concentration levels obtained under this condition were still much lower than those at room temperature; however, some improvement was clearly noted when compared to the results at cold temperature.

To further illustrate the potential of this approach, thermodynamic calculations were performed using PROFISSY, FISSYCS, and the same initial bottle conditions at room temperature. (1 kg of  $\text{CF}_3\text{I}$  in a 2.36 L bottle, pressurized with nitrogen to 4.12 MPa at 22 °C, see discussion above.) Note that in the following analysis, the heat transfer between the flashing spray and the nacelle surroundings was not considered. The calculations were performed as follows. First, a final state of the bottle was obtained using PROFISSY to simulate heating or cooling of the bottle. The state was then used as input for FISSYCS to obtain the amount of liquid fraction resulting from an isentropic process taking the fluid from the prevailing pressure to 0.101 MPa.

Figure 8-96 shows the calculated liquid fraction as a function of temperature. The liquid fraction decreases with increasing bottle temperature. However, there is a discontinuity at about 94 °C. At temperatures below the discontinuity temperature, the initial state is liquid-phase, the isentropic process results in a liquid-vapor system.

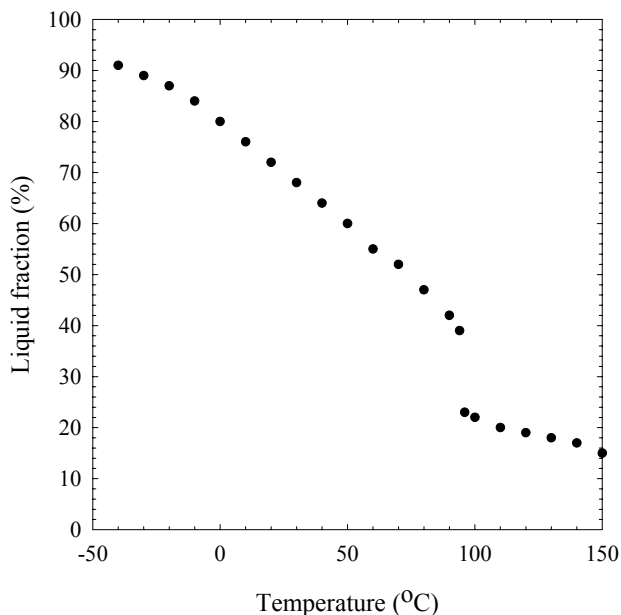


**Figure 8-96. Calculated Liquid Fraction as a Function of Bottle Temperature.**

At temperatures above the discontinuity temperature, PROFISSY predicted a single-phase gaseous state before the isentropic process. The discontinuity is the result of the occurrence of a two-phase system due to the isentropic process. If the strategy is to decrease the liquid fraction, heating the bottle up to a temperature before the discontinuity temperature is reached seems to be an option. Although heating the bottle above the discontinuity temperature appears to be a better choice from the figure, a dichotomy exists. On the one hand, the resulting liquid fraction is much lower than that at any temperature below the discontinuity temperature. On the other hand, the isentropic process inadvertently transforms a gaseous phase, which facilitates the dispersion of the agent, back to a liquid-vapor phase, which may hinder agent transport through cluttered space in the nacelle. However, system constraints (*e.g.*, bottle operating pressure and space) on a specific aircraft platform may ultimately limit the implementation of either approach because the bottle pressure is a function of temperature. Although the above argument provides some thermodynamic basis for examining the feasibility of heating the bottle to improve dispersion for cold temperature applications, the interaction of a flashing spray with cold nacelle surfaces may also play an important role in determining subsequent agent dispersion. Further experiments are needed to validate the concept.

The results from the two measurement locations in the nacelle have shown that the dispersion of  $\text{CF}_3\text{I}$  under this condition with the equipment and the discharge nozzle used is not very effective and there is substantial deterioration in agent concentration. If the military specification for halon 1301 extinguishing concentration can be applied to  $\text{CF}_3\text{I}$  (volume fraction of 0.06 for 0.5 s), the concentration levels at the two measurement locations in the nacelle never exceed the extinguishing concentration requirement. The situation worsens at the location further away from the agent injection port. If the extinguishing concentration for the nacelle is designed based on room-temperature test data, the measurements indicate that the dispersion and performance of the agent are likely to deteriorate when the agent is used at a temperature below its normal boiling point.

## Implications

This study using  $\text{CF}_3\text{I}$  as a surrogate shows that the agent's normal boiling point and the prevailing bottle and nacelle conditions are critical to the agent dispersion processes for low temperature applications. Halon 1301 and HFC-125, with their respective normal boiling points lower than  $-40\text{ }^\circ\text{C}$ , will disperse efficiently. The benefit of a more efficient suppressant chemical with a high normal boiling point will be readily offset by the poor dispersion performance (puddling and slow evaporation) in a nacelle when the agent is expected to be used at temperatures below its normal boiling point. Heating the storage bottle before agent discharge could improve agent dispersion performance at low temperatures. For agents with high normal boiling points, nacelle fire suppression system design should not be solely based on the agent dispersion performance data obtained at room temperature, and low-temperature dispersion tests should also be conducted.

## 8.5 MODELING OF FLUID DISPERSION IN A NACELLE

### 8.5.1 Background

The focus of this research was to develop engineering models of flow, fire, and fire suppression and extinguishment in cluttered environments. These models will advance the fundamental knowledge of fire dynamics and suppression and provide a foundation for optimizing the distribution of suppressants for newly designed or retrofit fire safety systems in aircraft engine nacelles. This work was carried out in a joint, iterative computational/experimental approach to develop engineering subgrid models for use in integral CFD and fire field simulations. Models were developed using detailed CFD calculations performed at Sandia National Laboratories and discovery and validation experiments performed at Air Force and Naval laboratories. Only gaseous agents were investigated initially. The end goal was to provide computational tools to improve suppressant delivery and develop guidance to system designers.

### 8.5.2 CFD Models

During the course of the NGP, several CFD codes, which include VULCAN, CFD-ACE, Fire Prediction Model (FPM), and Fire Dynamics Simulator (FDS), have been assessed for use in modeling of fluid dispersion and fire suppression in aircraft engine nacelle environment. The simulation effort in this project focused mainly on the use of VULCAN because of its many newly developed sub-models specifically for aircraft engine nacelle applications.

### Basic Features of VULCAN

VULCAN has been developed at Sandia National Laboratories (SNL) in collaboration with the SINTEF Foundation and the Norwegian University of Science and Technology. VULCAN is derived from the KAMELEON Fire model<sup>44, 45</sup> and uses an extension of the SIMPLEC method of Patankar and Spalding<sup>46</sup> to solve the conservation equations on a structured, staggered, three-dimensional Cartesian, finite-difference grid. The brick mesh is employed to facilitate rapid solutions of radiative heat transfer. The ability to resolve the geometry of the system is only limited by the ability to construct the appropriate grid with the Cartesian grid generator available in VULCAN. First- and second-order upwind schemes can be used for the convective terms. Turbulence is modeled using a standard two-equation  $k-\varepsilon$  model. The

VULCAN code has the capability of performing fire simulations, and the combustion simulation is based on Magnussen's Eddy Dissipation Concept (EDC) assuming infinitely fast combustion.<sup>47</sup> Models of soot generation and oxidation are also included.

The wide range of length-scales in reacting flows presents a significant modeling challenge. Where air flows are high enough that the flow is turbulent (as is typical in most terrestrial fire environments), fluid-mixing length-scales may span several decades from the geometric scale down to the Kolmogorov scales. Chemical length-scales may be even smaller, typically less than a millimeter. Because it is not possible to resolve the full range of dimensions, models of subgrid-scale processes are employed. Within the VULCAN fire-field model, the  $k$ - $\epsilon$  model is employed to predict the effect of turbulent fluctuations on the flow, and the EDC model predicts the chemical evolution using a collection of perfectly stirred reactors (PSR).

### *Modeling Fire Suppression*

Combustion in VULCAN is modeled using the EDC that can be thought of as a distribution of PSRs that relate the fuel-consumption rate to the fluid-mixing rate, the latter obtained from turbulent time scales. The submodels within VULCAN assume that the fuel-air mixing rates scale with the inverse of the Kolmogorov time scale ( $\tau_K$ ). The actual mass rate of reactant mixing is proportional to  $\tau_K$  and is also a function of the local mass fractions of reactants. In high-fidelity modeling of turbulent diffusion flames, the fluid time scales corresponding to extinction are found to be very close to the Kolmogorov time scales.<sup>48</sup> Conversion of reactants to products and the associated heat release occur at a rate determined by either the mixing rate or some maximum chemical rate that is a function of the composition. Fires are typically limited by mixing, but if the ratio of time scales is sufficiently small (fast mixing), then conversion of reactants to products and the associated heat release cannot proceed to completion. This results in a reduction in temperature leading to a reduction in chemical rates. Continued reduction in the mixing time relative to the chemical time leads to a state where no combustion is possible, and the flame is extinguished. The ratio between fluid and chemical mixing times is generally referred to as the Damköhler number. A suitable chemical time relevant to flame extinction can be defined as the value of PSR extinction time corresponding to a switch from combustion occurring to combustion being impossible, which is the chemical time scale representing the fastest possible chemical reaction rates. For Damköhler numbers smaller than a critical value, the flame will be extinguished. The critical Damköhler number that relates  $\tau_K$  and the extinction time is not known *a priori* and is determined empirically by matching blow-off criteria for an ethane jet flame.<sup>49</sup> The suppression model takes advantage of this Damköhler number criterion by determining values corresponding to extinction from detailed chemical-kinetic calculations in the PSR configuration.

The chemical time scale is a function of the reactant mass or mole fractions, enthalpy, and pressure, assuming these reactants originate at ambient pressures and temperatures, neglecting enthalpy changes. While it is straightforward to make the chemical time scale a function of the enthalpy (and this has been done with the suppression model), the results then depend strongly on heat flux through walls, a quantity that is not well known for the experimental configurations. Two neglected thermal effects are of moderate significance: For JP-8 pool fires, the initial fuel vapor temperature is somewhat greater than ambient; this tends to reduce the chemical time scale. Radiative thermal losses and losses to the walls, while included in VULCAN, are neglected in the suppression model because the magnitude of these losses is dependent on the heat flux through the wall, which is unknown. Estimates indicate that heat losses to obstructions are significant here and tend to increase the chemical time scale.

Within VULCAN, chemical reactions are greatly simplified, reflecting the predominance of mixing processes in fires. This simplified treatment of kinetics is not necessarily sufficient for suppression predictions, and chemical time scales corresponding to the addition of suppressant are calculated off-line. These off-line calculations use the CHEMKIN PSR capability<sup>50</sup> with a detailed chemical mechanisms for iso-octane from Curran et al.,<sup>51</sup> coupled with a mechanism for halogenated suppressants from Babushok et al.<sup>52</sup> Chemical time scales have been obtained for iso-octane combustion in air with HFC-125, N<sub>2</sub>, H<sub>2</sub>O, CO<sub>2</sub> and CF<sub>3</sub>Br, although only results with the first suppressant are described here. Chemical time scales relevant to suppression are obtained by conducting PSR simulations at successively shorter residence times until combustion is extinguished, thereby defining the extinction time. To facilitate use in CFD simulations, values for the extinction time are fitted to a suitable functional form as a function of the mole fraction of HFC-125 added to the inlet air. For iso-octane, the selected surrogate for JP-8, the curve fit is inverted to express the magnitude required to extinguish the mixture. Given the chemical time scale as a function of the fluid cell composition and the mixing rate based on the dissipation rate and viscosity (through the Kolmogorov time scale), the magnitude of the Damköhler number in that cell determines whether combustion takes place in that cell or not. In the numerical implementation, given  $\tau_K$  in a fluid cell, the time required to extinguish the flame is obtained using a comparison with the HFC-125 mole fraction in the fluid cell to indicate whether suppression occurs. A similar approach was used by Byggstoyl and Magnussen for local quenching in the absence of suppressants.<sup>53</sup> A detailed description of the fire suppression model can be found in Hewson et al.<sup>54</sup>

#### *Subgrid Scale Clutter Model*

The release and transport of an agent into an engine nacelle is sensitive to local geometrical features or “clutter” that is difficult to resolve numerically without using an excessively large CFD grid. Examples include wire bundles or hydraulic lines. Capturing these features in a grid will result in extremely small time steps for accurate numerical simulations of agent release and subsequent fire suppression. An alternative is to use a sub-grid scale (SGS) model to represent the macroscopic effects of these small features using reasonably sized CFD grid-cells. For agent dispersal in a cold flow environment, the macroscopic flow effects of sub-grid clutter cells must have two main effects. The first is to provide a momentum sink due to viscous and pressure drag forces. The second is to either increase or decrease the turbulent kinetic energy, depending on the local clutter size relative to the characteristic length-scale of turbulence. In general, if the size of the clutter is smaller than the turbulent length-scale, the turbulent kinetic energy will decrease, and vice versa. Regarding flame suppression, the clutter serves as either a mechanism for flame attachment or for local extinction depending on the local time scales of the heat transfer to the clutter and chemical kinetics for ignition.

Specifically, the effects of subgrid scale (SGS) clutter on the momentum and turbulent kinetic energy transport were developed with application to engine nacelles.<sup>55, 56</sup> The modeling methodology was based on a two-phase averaging procedure introducing expressions that required SGS modeling. The SGS models were formulated using a combination of well-established constitutive relations borrowed from the porous media literature and classical relations for drag on bluff bodies. The modeling methodology was exercised for two classes of problems. The first was flow in a porous media for which the obstructions were relatively dense. For this problem, predictions using the SGS clutter model were compared to established correlations taken from the porous media literature. The second class of problems was a cylinder in cross-flow for which both detailed experimental measurements and detailed CFD calculations of velocity deficit and kinetic energy profiles were available. Results from the experimental

measurements revealed that the effect of upstream turbulence had a significant effect on the drag coefficient. Comparisons of the detailed CFD predictions to experimental measurements showed reasonable agreement for the mean and RMS streamwise velocity indicating that extracting phase-averaged quantities from the detailed computations, as part of future efforts, was a sound approach for determining unknown clutter model constants in a bluff body drag limit.

### **Basic Features of CFD-ACE**

CFD-ACE, a commercial computational fluid dynamics model with a body-fitted coordinate grid, is a pressure-based commercial code<sup>57,58</sup> that solves the Favre-averaged Navier-Stokes equations. The code uses a cell-centered control volume approach to discretizing the governing equations. It employs an iterative solution scheme in which the assembled equations for each dependent variable are solved sequentially and repeatedly to reduce errors to acceptably low values.

Various modeling options are available. In the present calculations, the governing equations were solved until a steady-state solution was reached. Heat transfer was not modeled. The code was applied using the incompressible option with a single fluid (air) and the  $k$ - $\epsilon$  turbulence model of Launder and Spalding<sup>59</sup> with wall functions. In addition, the  $k$ - $\omega$  turbulence model of Wilcox<sup>60</sup> and the Low Reynolds number  $k$ - $\epsilon$  turbulence model of Chien and Smith<sup>61</sup> were used in sensitivity calculations. First-order upwind spatial differencing was used for the turbulence quantities and 90 % second-order upwind spatial differencing (with 10 % first order blend) was used for the velocity and density. The structured grid utilized a body-fitted coordinate system with multiple domains.

### **Basic Features of FPM**

The Fire Prediction Model (FPM)<sup>62</sup> simulates the events occurring during the penetration of a single ballistic threat into an aircraft and subsequent penetration of a fuel tank. The model describes the principal processes involved the initiation and sustainment of fires, or ullage explosions in a dry bay. The model runs on personal computers, and queries the user for specific information about the conditions to be analyzed. No off-line computations by the user are required; the model contains pre-determined threat, fluid, and target material data encompassing a wide range of conditions of interest. The FPM was designed specifically to provide a tool to examine dry bay fires and ullage explosions over a wide range of conditions rapidly and apply directly to the needs for live-fire testing predictions, planning, and post-test analysis; vulnerability estimates (probability of kill given a hit,  $P_{k/h}$ ); and aircraft design guidelines. The simulation principally relies on basic physical principles which are supplemented by empirical data as needed. Study conditions that can be examined by the FPM are grouped into 9 categories and briefly described below.

*Flammable Liquid Container Type* The user can select an integral or non-integral tank or a liquid line.

*Run Setup* The run setup option allows the user to tailor the run to their needs. The user can select single-shot or parametric runs, specify the flow field cell size, and modify the time step to increase speed or accuracy.

*Target Vehicle* The FPM allows the user to specify either an air or ground target vehicle. Selections of threats, liquids, and target materials are restricted based on the vehicle selected.

*Ignition Source* The FPM simulates spray ignition by either a ballistic threat, hot surface, or electrical spark. Ignition by a hot surface can occur directly by sprayed droplet impinging directly onto the hot surface or indirectly as liquid vapor previously released into the bay is carried past the hot surface.

*Ballistic Threat* Four types of ballistic threats can be simulated by the FPM: Armor-Piercing Incendiary (API) projectiles, High Explosive Incendiary (HEI) projectiles, warhead or bomblet fragments, or shaped charges. Because the functioning of an API projectile can vary depending on impact conditions, four types of function can be simulated: complete, partial, slow burn, or delayed.

*Flammable Liquid* Seven flammable liquids can be selected by the user. Three military jet fuels (JP-4, JP-5, or JP-8, two different flash points) a diesel fuel (DF-2), or two military hydraulic fluids (MIL-H-5606 and MIL-H-83282) are available. In addition, the user is given the option to describe the characteristics of some liquid of interest, other than what is available.

*Encounter Conditions* The user may define a wide range of environmental conditions under which the simulation is to be run, including target altitude, fuel and ambient air temperatures, ventilation air velocity, external pressure, and target velocity. For altitudes above sea level, the model will compute ambient conditions using the standard atmosphere. External air pressures will be computed by the model based on the target surface and location impacted and orientation of the damage-hole to airflow.

*Dry Bay Description* The FPM provides the user with a large number of options and features to describe the dry bay. First, the dry bay dimensions and location are defined. The dry bay is assumed to be a rectangular parallelepiped. Other items needed to define the bay include wall material and thickness; internal clutter locations and dimensions; structural barrier locations, dimensions, and orientation; ventilation flow areas and locations; and the presence of an ECS duct. As part of the dry bay description, a fire-suppression system can be specified. The user has a wide range of options to describe the fire-suppression system. Ten agents can be selected, including both cooling and reactive agents. Next, the number, location, and type of injector can be specified. The type can be spherical (agent injected radially from location) or directional (agent injected in a specified direction). The duration of the agent injection and mass-rate of injection are also needed. Finally, the injection can be activated by an IR sensor or manually, at the user's discretion. The clutter option is sufficiently general to allow the user to shape the bay into various shapes and/or multiple compartments. If a hot surface is present within the bay, the clutter is used as the hot component, and the user can describe the hot surface by its location and temperature.

*Impact Condition* The FPM requires a description of the impact conditions, including threat impact velocity, threat approach direction, and point of impact on the target's surface. In addition, the model can simulate the threat function to be on the dry-bay surface or internal to the bay.

As part of this effort, the FPM was modified to allow ignition of a spray fire with a user-described ignition source, bypassing the ballistic-impact routines of the model. The approach used by the FPM to simulate a spray fire is known as a separated-flow (two phase) model. This approach treats the finite rates of exchange of mass, momentum, and energy between the liquid and gas phases. In general, there are three approaches to separated flow models, reflecting differences in simulating evaporating and combusting sprays. The FPM uses the discrete-droplet approach. In this approach, the entire spray is divided into many representative samples of discrete drops whose motion and transport through the flow-field are found using a Lagrangian formulation in determining the drop's history, and an Eulerian

formulation is used to solve the governing equations for the gas phase. It is assumed that the spray is dilute; i.e., although the droplets interact with the gas phase, they do not interact with each other. Thus, droplet collisions are ignored and empirical correlations for single droplets can be employed for interphase transport rates.

In two-phase models, the liquid droplet flow is divided into a finite number of classifications: Each drop class is assigned an initial diameter, velocity, direction, temperature, concentration, position, and time of injection. The temporal evolution of each class is then determined throughout the flow.

The FPM uses this approach, adapting it to the FPM dry-bay flow-field. In effect, the FPM tracks the position of each class of droplet, computing the vaporization for each class dependent on the droplet location and bay conditions at that location, and the model's flow-field computes the conservation equations. The position of a given group is calculated from:

$$\begin{aligned}x_p &= x_{p_o} + \int v_{p_x} dt \\y_p &= y_{p_o} + \int v_{p_y} dt \\z_p &= z_{p_o} + \int v_{p_z} dt\end{aligned}\quad (8-43)$$

The instantaneous velocity is determined by the solution of the equation of motion.

$$m \frac{dV}{dt} = -\frac{1}{2} C_d \rho A V^2 + mg \quad (8-44)$$

The standard drag coefficient for solid spheres is employed for sprays.

$$C_D = \begin{cases} \frac{24}{\text{Re}_{d_p}} \left[ 1 + \frac{\text{Re}_{d_p}^{2/3}}{6} \right] & \text{for } \text{Re}_{d_p} < 1000 \\ 0.44 & \text{for } \text{Re}_{d_p} > 1000 \end{cases} \quad (8-45)$$

The Reynolds number is defined as:

$$\text{Re}_{d_p} = \frac{d_p |v_p - v|}{\nu} \quad (8-46)$$

The simulation of the transport properties involved in fire involves the application of the conservation equations of mass, momentum, energy, and species for that system. These equations simply describe a balance of the net rate of inflow and outflow of some particular parameter, its rate of storage, and its rate of production and destruction within a volume. The FPM describes the motion of the fluid within the bay by the Eulerian approach where the composition, velocity, and state of the fluid everywhere in the bay occupied by the fluid at all instants are determined. To derive the Eulerian equations of motion, a stationary coordinate system is chosen and fluid is observed entering and exiting a volume of arbitrary shape and size. This control volume is found within the fluid and is at rest with respect to the coordinate system. In the FPM, the volume is a cube whose length is specified by the user.

The FPM uses a staggered grid concept where the scalar properties of pressure, temperature, mass, and species mass are determined at the cell center and fluid velocities are established at each cell edge in each coordinate direction.

Solutions are obtained on a numerical grid of elementary control volumes which fill the entire dry bay. This approach ensures local balances in the many small control volumes, subject only to the particular boundary conditions. To improve computational efficiency and reduce model run-time, the FPM utilizes a multi-cell, three-dimensional dual grid system; a diffusion and convection grid. Within the diffusion grid, the simulation of fire is performed by the solution of the conservation equations of mass, momentum, species, and energy. Because convective currents work over much larger scales than the processes of diffusion and combustion, the conservation of momentum (the convective mass and energy flow) is performed in the convective grid and results superimposed into the diffusion grid by the prorating the flow.

The mass-rate of change of chemical fire suppressant can occur by convection, depletion by chemical reaction, or injection into the bay. The FPM simulates both chemical and "cooling" types of agents. Cooling agents such as CO<sub>2</sub> and H<sub>2</sub>O extinguish flame by the rapid introduction of mass into the combustion zone, which absorbs heat through changes of heat capacity and the heat of vaporization as described above. Chemical agents extinguish fires by the removal of free radicals throughout the combustion process, precluding complete combustion as well as providing some cooling effect.

The FPM treats the chemical reaction of fuel vapor, oxygen, and suppressant as a one-step, third-order reaction, as shown below.



where  $k$  is the specific reaction rate constant and follows the Arrhenius law

$$k = A \exp\left(\frac{E}{RT}\right) \quad (8-48)$$

### Basic Features of FDS

Fire Dynamics Simulator (FDS), developed by NIST, is a CFD model of fire-driven fluid flow. The formulation of the equations and the numerical algorithm and a user's guide can be found in McGrattan et al.<sup>63,64</sup> In conjunction with FDS, an OpenGL graphics program called Smokeview was also developed by NIST to visualize the numerical output generated by FDS. Smokeview performs this visualization by presenting animated, traced, particle flow, animated contour slices of computed gas variables, and animated surface data. Smokeview also presents contours and vector plots of static data anywhere within a scene at a fixed time. A detailed description of Smokeview can be found in Forney and McGrattan.<sup>65</sup>

Since its first release in February 2000, about half of the applications of FDS have been for design of smoke-handling systems and sprinkler/detector activation studies. The other half consists of reconstructing residential and industrial fires. Throughout its development, FDS has been aimed at solving practical problems in fire-protection engineering, while at the same time providing a tool to study

fundamental fire-dynamics and combustion. Some of the major components and sub-models used in FDS are briefly described below.

*Hydrodynamic Model* FDS solves numerically a form of the Navier-Stokes equations appropriate for low-speed, thermally driven flow with an emphasis on smoke and heat transport from fires. The core algorithm is an explicit predictor-corrector scheme, second order accurate in space and time. Turbulence is treated by means of the Smagorinsky form of Large Eddy Simulation (LES). It is possible to perform a Direct Numerical Simulation (DNS) if the underlying numerical grid is fine enough. LES is the default mode of operation.

*Multi-blocking* This is a term used to describe the use of more than one rectangular mesh in a calculation. FDS calculations can prescribe more than one rectangular mesh to handle cases where the computational domain is not easily embedded within a single block.

*Combustion Model* For most applications, FDS uses a mixture-fraction model for combustion. The mixture fraction is a conserved scalar quantity that is defined as the fraction of gas at a given point in the flow-field that originated as fuel. The model assumes that combustion is controlled by mixing, and that the reaction of fuel and oxygen is infinitely fast. The mass-fractions of all of the major reactants and their products can be derived from the mixture by means of “state relations,” empirical expressions derived from a combination of simplified analysis and measurement.

*Radiation* Radiative heat transfer is included in the model via the solution of the radiation equation for a nonscattering gray gas, in some limited cases using a wide-band model. The equation is solved using a technique similar to finite-volume methods for convective transport, thus the name given to it is the “Finite Volume Method” (FVM). Using approximately 100 discrete angles, the finite-volume solver requires about 15 % of the total CPU time of a calculation, a modest cost given the complexity of radiative heat transfer. Water droplets absorb thermal radiation. This is important in cases involving mist sprinklers, but it also plays a role in all sprinkler cases. The absorption coefficients are based on Mie theory.

*Geometry* FDS approximates the governing equations on a rectilinear grid. The user prescribes rectangular obstructions that are forced to conform with the underlying grid.

*Boundary Conditions* All solid surfaces are assigned thermal boundary conditions, plus information about the burning behavior of the material. Usually, material properties are stored in a database and invoked by name. Heat and mass transfer to and from solid surfaces is usually handled with empirical correlations, although it is possible to compute directly the heat and mass transfer when performing a Direct Numerical Simulation (DNS).

*Heat-Conduction through a Wall* In early versions, heat that was conducted into a wall was lost to an infinite void. Now it is possible to transfer the heat from one room to another through a one-cell-thick wall.

*Thin Walls* It is possible to prescribe a thin sheet barrier to impede the flow. This is particularly useful when the underlying grid is coarse, or when the barrier is indeed very thin, like a window. However, FDS will reject obstructions that are too small relative to the numerical grid.

*Suppression* The suppression algorithm is a necessary adjustment to the mixture-fraction model of that prevents combustion from occurring in cool, oxygen-depleted environments. Recall that the basic mixture-fraction model assumes that fuel and oxygen burn when mixed. This is a good assumption in many fire scenarios, but when compartments become under-ventilated, or when agents are injected, the “mixed is burnt” model is not appropriate.

*Initial Conditions* It is possible to prescribe some non-trivial initial conditions. For example, certain parts of the domain can have temperatures different from ambient, and an initially constant flow-field can be prescribed.

### 8.5.3 Code Assessment Using Quarter-Scale Nacelle Tests and Simulations

To evaluate the fidelity of these CFD codes and their suitability for highly-cluttered engine nacelle applications, an initial exploratory effort was to investigate the flow field in a simplified, quarter-scale nacelle of typical shape. Calculations were performed using both the CFD-ACE and VULCAN codes. Flow conditions examined correspond to the same Reynolds numbers as test data from the full-scale nacelle simulator used by the 46<sup>th</sup> Test Wing of the United States Air Force (USAF). These flow conditions were examined using both models prior to fabrication of a test fixture. Based on the pre-test simulations, a quarter-scale test fixture was designed and fabricated for the purpose of obtaining spatially resolved measurements of velocity and turbulence intensity. Post-test calculations have been performed for comparison to the experimental results obtained from the quarter-scale test fixture. Because of geometric complexities, efforts to characterize the flow field in engine nacelles using computational fluid dynamics have been limited to simplified cases. Calculations performed to date include the analysis performed by Hamins et al.<sup>66</sup> of agent transport for the extensive set of tests performed in the Aircraft Engine Nacelle (AEN) test facility for the Halon Alternatives Research Program for Aircraft Engine Nacelles and Dry Bays. Marginal agreement between calculation results and experimental data was obtained. In some cases, opposite trends were observed in the calculations and experimental results. Additional calculations were performed by Lopez et al.<sup>67</sup> of a typical fighter nacelle geometry simulating agent release via solid propellant gas generator.

Quarter-scale experiments (to allow access of appropriate diagnostics guided by pre-test calculations) were performed at WPAFB.<sup>68</sup> Flow conditions were scaled to match the Reynolds numbers in the extensive set of experiments performed in the AEN facility as part of the Halon Alternatives Program. Calculations were performed and compared with experimental data at multiple cross sections within the flow field. The pre-test calculations assisted in the design and execution of the experiments required to gain the necessary knowledge for these kinds of flows. Then the post-test simulations, using both CFD-ACE and VULCAN, and the exact geometry and boundary conditions from the experiments compared CFD results with the experimental results.

The primary flow-field calculations used the CFD-ACE code because of its body-fitted coordinate features to represent smooth circular geometries. Although capable of simulating reacting flows, the CFD-ACE code does not contain models for radiative heat transfer, turbulent combustion, and soot production needed to simulate fires. These fire-physics models are included in VULCAN; however, the VULCAN model approximates the geometry by using a rectangular brick grid to facilitate the solution for radiation. Although many nacelle fire cases can be addressed without modeling the fire-physics, it is ultimately desirable to be able to represent the heat transfer from the fire and the fire-suppression effects,

such as the influence of turbulent flame strain combined with fuel/air mixtures. Both models have been applied in the pre-test and post-test calculations. The flow solution yielded by the approximate mesh used in the VULCAN code is compared with the results provided by the CFD-ACE modeling to quantify the effect of the Cartesian VULCAN mesh.

### Simplified Nacelle Tests and Simulations

A photograph of the experimental test fixture is shown in Figure 8-97. The fuselage stations where experimental velocity data were obtained are shown in Figure 8-98.

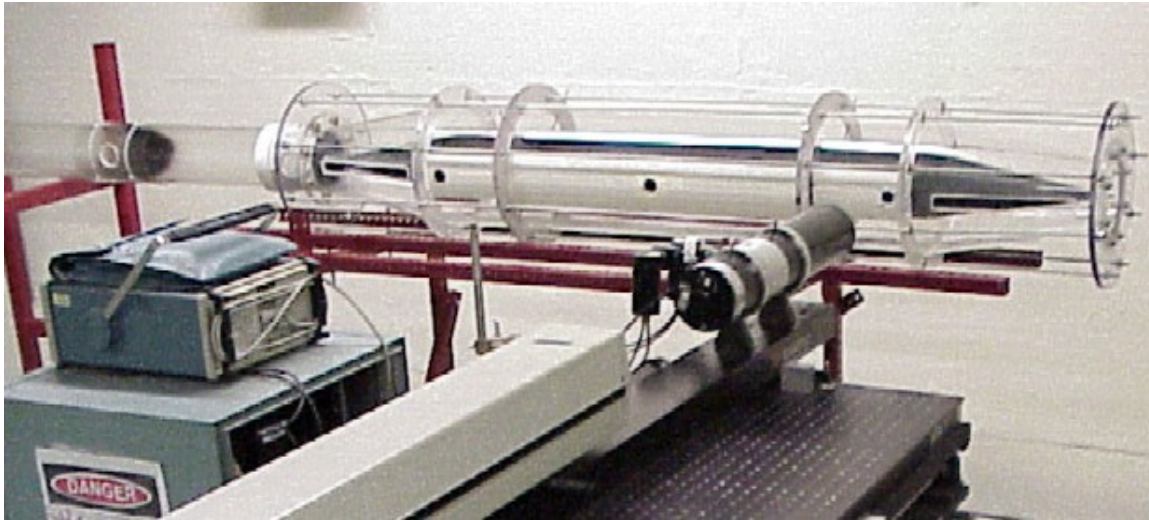


Figure 8-97. Photograph of the Quarter-Scale Nacelle Test Facility with LDV apparatus.

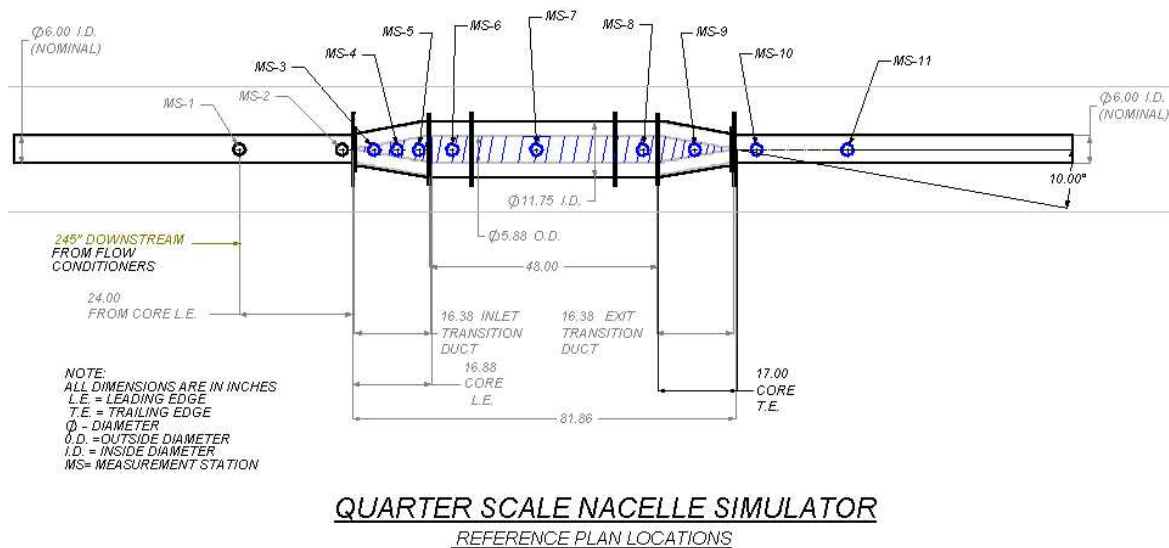


Figure 8-98. Measurement Stations in the Quarter-Scale Nacelle.

The CFD codes modeled the nacelle geometry starting at measurement station #1 (MS-1), where experimental data were used as an exact initial and boundary condition. The modeled geometry ended 10 pipe diameters downstream of the core region.

Upon entering the quarter scale nacelle, the flow undergoes a change from a pipe flow to an annular flow. This change in flow geometry is induced by a fluoropolymer cone, with a sharp leading edge centered within the nacelle. The cone is approximately 432 mm long and 149 mm at its base. The base of the cone is attached to the 149 mm teflon core which resides within the nacelle proper.

In the present simulator, the cone half-angle was machined at 10 degrees. As a result of the cone angle and transition duct wall offset, the flow is redirected away from the simulator centerline. This geometrical change occurs abruptly at the interface between the air supply duct and nacelle, and is therefore considered to be a sharp or discontinuous surface boundary.

Further, this divergence increases the flow cross-sectional area by a factor of approximately three. After passage through this transition duct the flow is abruptly redirected towards the simulator centerline by 10°. This occurs at a second discontinuity on both the inner surface (simulating the engine core) and outer surface. This next element, referred to as the nacelle proper is configured as an annular channel of constant spacing,  $H$ , between inner and outer surfaces – 74.7 mm. The nacelle proper extends downstream 1.22 m, approximately 16  $H$ .

Exiting the nacelle proper the flow is redirected toward the simulator centerline through another 10-degree offset. This offset occurs at the entrance of a second cone, designated as the Exit Transition Duct (ETD). At the entrance of the ETD, the inner core of the nacelle proper undergoes a discrete transition back to a conical surface with a sharp trailing edge, thereby producing a transition from a converging annular channel back into a pipe flow.

Flow conditions upstream of the quarter-scale engine nacelle were determined by matching the Reynolds number (based on diameter) between the full-scale and quarter-scale nacelle simulators, for a specified mass flow. Air within the test range at ambient temperature and pressure was used to supply the flow facility in all tests. Supply air density was computed using the local temperature and pressure of the surrounding air resulted in a computed density of 1.2 kg/m<sup>3</sup>. From this density, a mass flow for the quarter-scale nacelle was determined to be approximately 0.344 kg/s. Assuming uniform flow, the average velocity within the 152.4 mm air supply tube was computed and estimated to be 15.7 m/s. Under these conditions the Reynolds number based on tube diameter,  $Re_D$  was estimated to be 172,000.

Velocity measurements were accomplished using both hot-wire anemometry and laser-Doppler velocimetry (LDV). Several hot-wire traverses were obtained to confirm that the air supplied to the simulator using an external blower was adequately conditioned. Verification of the flow conditioning section consisted of the acquisition of velocity data at the exit of the inlet supply tube with a typical hot-wire, nominally 4 microns in diameter and 1.25 mm-long, positioned normal to the mean flow. Velocity profiles were obtained by horizontally traversing across the tube diameter. Each velocity traverse consisted of measurements at 38 locations across the tube diameter. At each spatial location, 5000 samples were acquired from which a mean velocity and turbulence fluctuation level were computed. Once the supply airflow was considered to represent a fully-developed pipe flow, the simulator was attached to the inlet supply tube, and velocity traverses utilizing an LDV were initiated, which locations

or measurement stations were determined from prior simulations conducted by Sandia National Laboratories (SNL).

For VULCAN, the extreme length of the geometry created a grid with many computational cells (Figure 8-99). The final Cartesian grid consisted of 196 ( $X$ -direction) by 45 ( $Y$ -direction) by 45 ( $Z$ -direction) grid points for a total of 396,900 cells in the simulation. The cells in the cross-section were  $0.007 \times 0.007 \text{ m}^2$ , while the minimum cell length in the axial direction was 0.0085 m and varied along the pipe (refined in transition regions and stretched in the exit pipe and other straight sections). The simulation time was approximately 5 days utilizing a 250 MHz processor. The solution was converged such that all residuals were reduced 5 orders of magnitude.

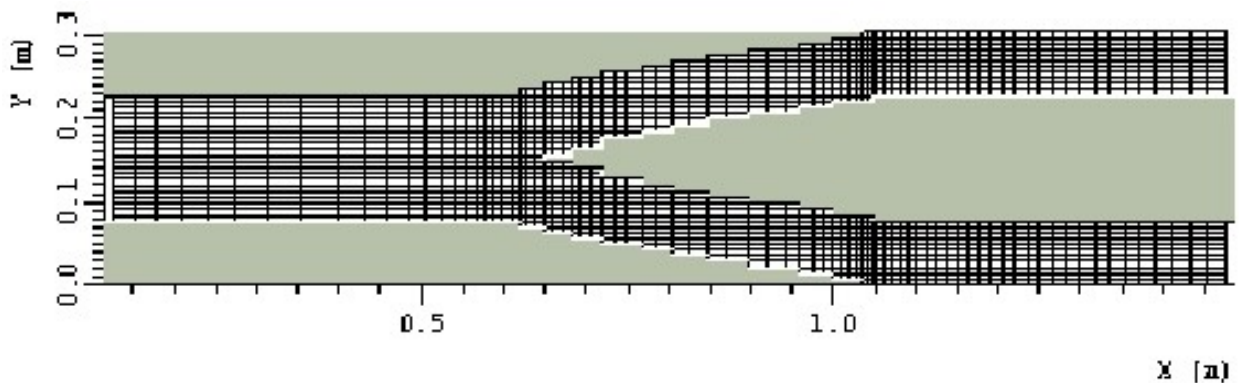


**Figure 8-99. VULCAN Gridding for the Quarter-Scale Nacelle.**

The computational grid used by CFD-ACE consisted of 301 axial (primary flow direction) points, 25 radial points, and 48 circumferential points, for a total of 361,200 grid points. Example slices from the grid are shown in Figure 8-100. Axial grid spacing in the annular (nacelle/core) region varied from 0.6 cm near the corners of the expansion/contraction regions to 1.8 cm in the middle section. Radial spacing was approximately 0.2 cm throughout the annulus. Circumferential spacing was constant at 7.5 degrees, which relates to arc dimensions of 2.0 cm at the maximum nacelle diameter to 1.0 cm at the maximum core diameter. In addition to the fine three-dimensional solution, a coarser mesh solution was obtained. The coarse mesh was generated by extracting every other grid point in all three directions from the fine mesh. The coarse mesh contained 151 axial points, 13 radial points, and 24 circumferential points, for a total of 47,112 grid points. In both cases, convergence was obtained such that all residuals of interest (velocity, pressure, turbulence) were reduced by more than 5 orders of magnitude. The fine mesh solution required 400 Mbytes of memory, 2200 iterations and 15 days computing time on a 250 MHz processor.

The boundary conditions used in the CFD simulations were carefully applied to represent the experimental conditions. In some cases, a slight deviation from the experimental conditions was necessary. The boundary conditions are fully discussed in Black et al.<sup>69</sup>

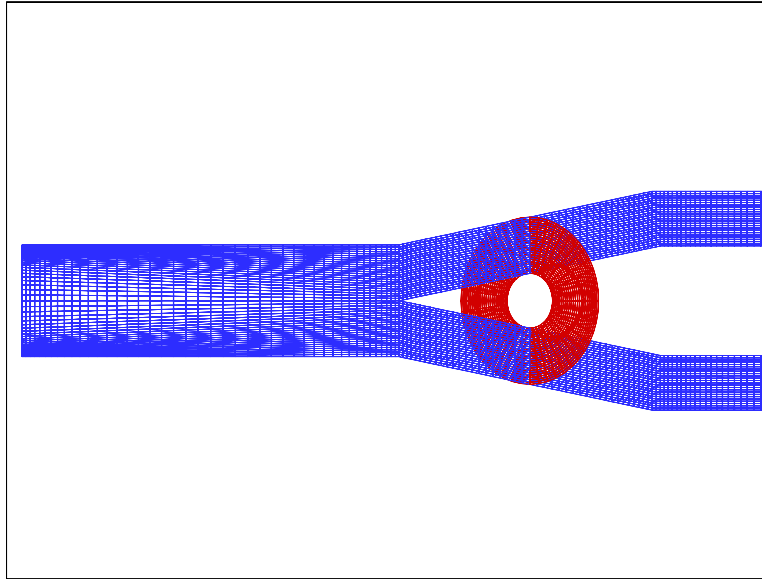


**Figure 8-100. Section of the CFD-ACE Grid Used in the Simulation.**

The data measured at the inlet (MS-1) showed a slight asymmetry in the velocity profile. It was not possible to use this asymmetric velocity profile as an inlet boundary condition in the calculations since only a radial profile was required. Instead, a logarithmic symmetrical profile was used to fit the data.

$$\frac{u}{u_{\max}} = \left(\frac{y}{R}\right)^{0.12} \tag{8-49}$$

The agreement with measured inlet profile is shown in Figure 8-101. In both cases, the maximum velocity is 20.07 m/s. Similar to the inlet velocity, the inlet turbulence intensity was also asymmetric. The simulations used a symmetric inlet turbulence intensity based on a parabolic curve fit of experimental data. This was accomplished by splitting the experimental data set at the midpoint, mirroring both sides across the centerline, and fitting a parabolic curve to these data in Figure 8-102. The resulting equation for the inlet turbulence intensity is shown on the plot as the solid curve.

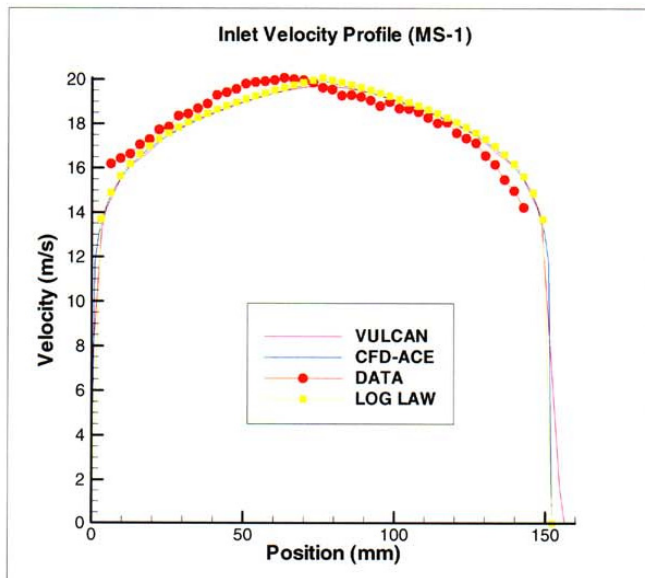


**Figure 8-101. Inlet Velocity Profile.**

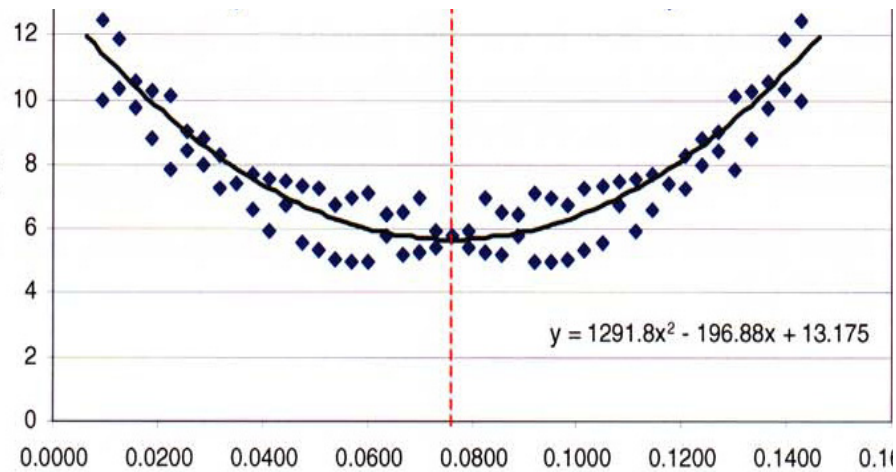


Figure 8-102. Inlet Turbulence Intensity Profile.

### Comparison with Experimental Data

At the outlet of the nacelle geometry, constant pressure was specified using standard ambient conditions of 98,700 Pa and 293 K. The outlet was located 10 pipe diameters downstream from the nacelle's core. Along the surfaces of the core there was no surface roughness, and the temperature was likewise 293 K.

The experimental velocities at MS-4 are slightly larger than the CFD-ACE predictions and show oscillations near the nacelle wall and core wall (Figure 8-103). The VULCAN velocity predictions show a very narrow band of high velocity flow with rapid decreases in velocity away from the center of the channel because the VULCAN grid is not smooth along the angled walls and is blocking more of the flow. The experimental data shows poorer resolution near the walls. The experimental turbulence intensity values agree with the CFD predictions in the center of the channel but deviate near the walls.

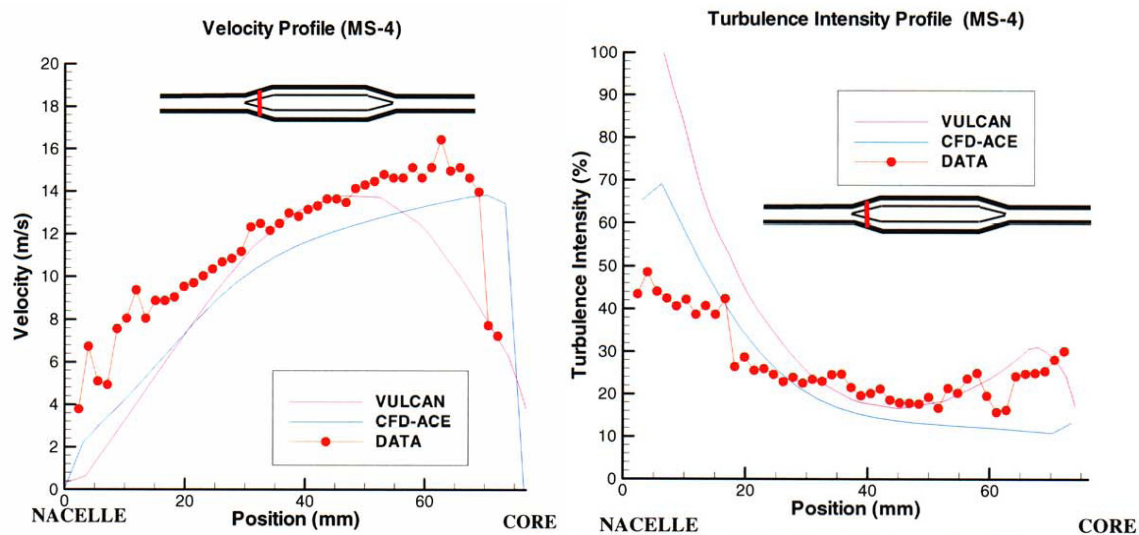
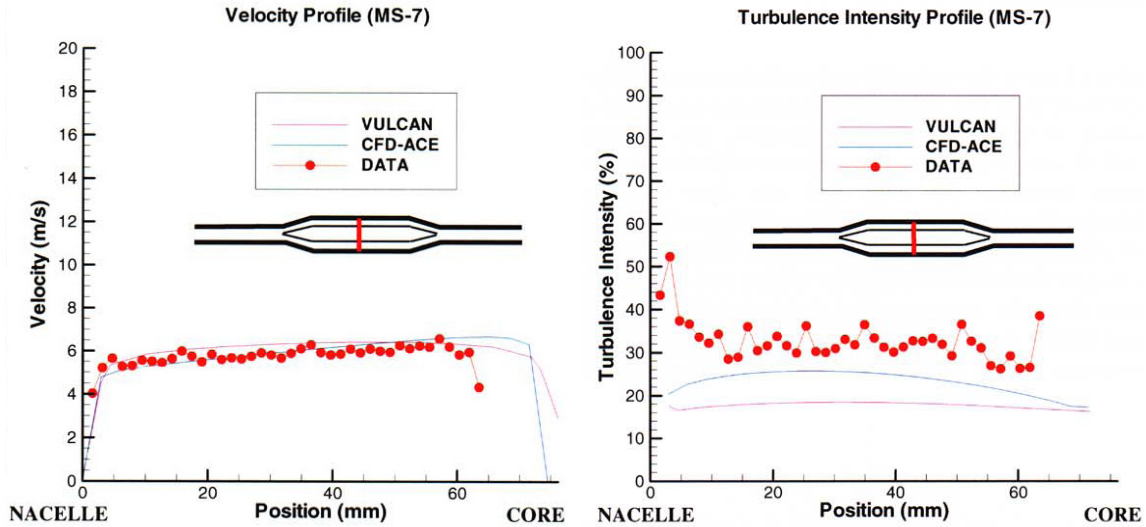


Figure 8-103. Velocity and Turbulence Intensity Profiles at Measurement Station 4.

The velocity predictions at MS-7 are in very good agreement with the experimental data, and the CFD predictions of turbulence intensities also show good agreement, with the data showing slightly larger turbulence intensity. It should be noted that the experimental data does not span the entire distance to the core (Figure 8-104).



**Figure 8-104. Velocity and Turbulence Intensity Profiles at Mid-nacelle.**

The CFD-ACE velocity predictions shown in Figure 8-105 are in very good agreement with the experimental data, whereas, the VULCAN predictions show the flow slowing down near both the nacelle wall and the core wall and increasing in the center of the channel. This is caused by the stair-stepped grid along the angled walls which tend to squeeze the flow into center of the channel. Both CFD-ACE and VULCAN predict ~10 % lower turbulence intensity values than the experimental data, similar to the previous measurement plane (MS-8).

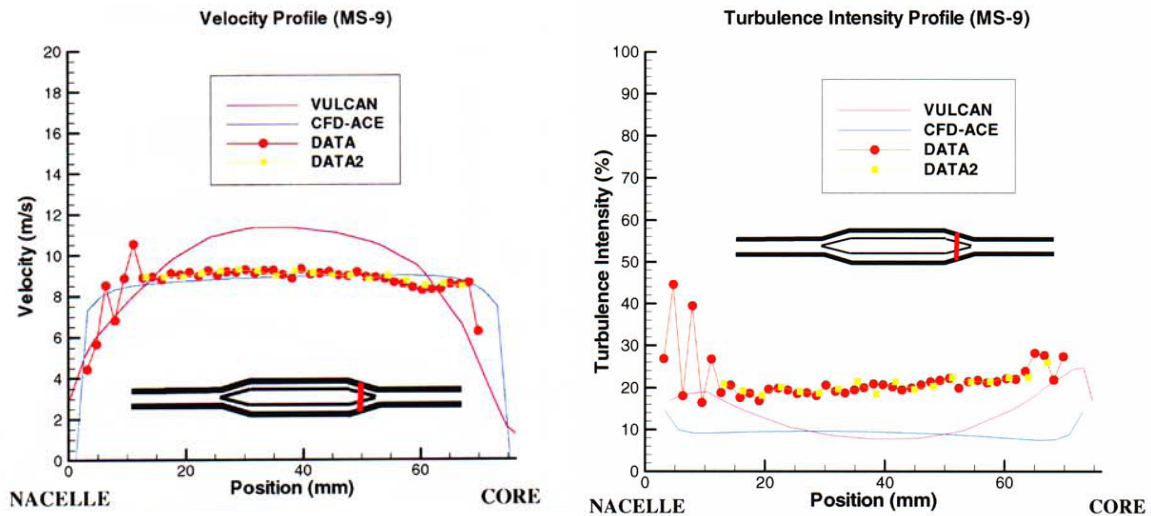


**Figure 8-105. Comparison of Simulation and Experimental Data at the Exit Cone.**

At the final measurement plane, MS-11, in the outlet pipe the predicted velocity profiles show the wake diminishing with increasing distance from the core, as shown in Figure 8-106. In addition, the measured turbulence intensity is considerably higher than CFD-ACE predicted, which is a constant turbulence intensity below 10 % for the majority of the flow across the pipe.

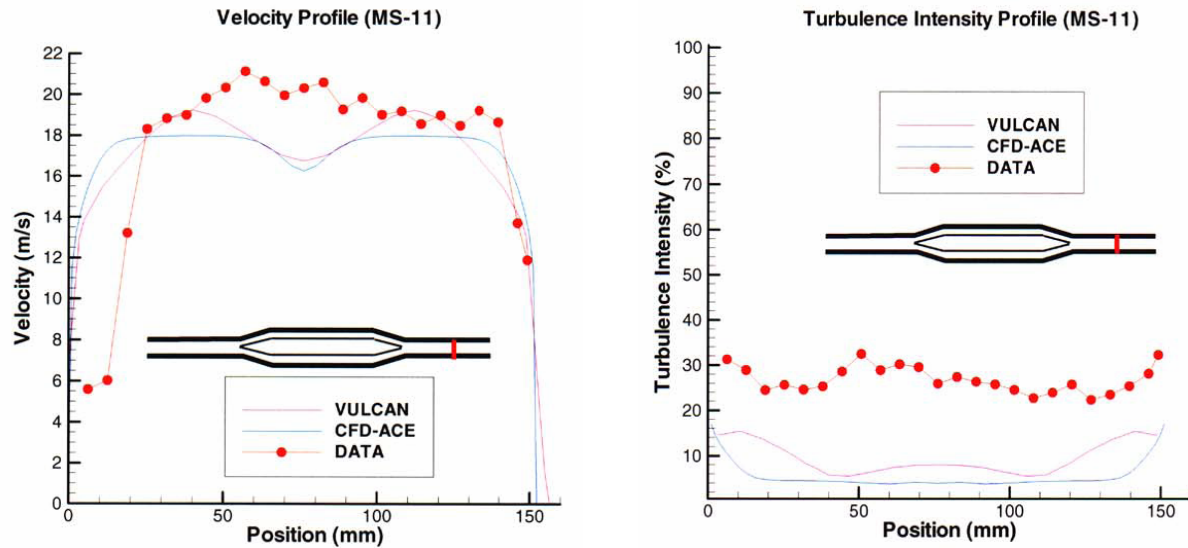


**Figure 8-106. Velocity and Turbulence Intensity Profiles Flow in the Exit Pipe.**

The comparisons of the numerical predictions with the experimental data, in general, showed good agreement with the velocity, and the turbulence intensity predictions also showed good agreement in the inlet pipe section and in the inlet transition section. However, the numerical predictions showed larger turbulence intensity near the corner region between the inlet transition duct and straight core section. Then, downstream the data consistently showed larger turbulence intensity at the remaining measurement planes, although the trends were similar. In addition, there were some differences between VULCAN and CFD-ACE results due to the Cartesian grid structure used by the VULCAN code. These differences mainly occurred in the inlet transition duct and the outlet transition duct where the walls are smoothly angled, but the grid is stepped. Also, the experimental data tended to show poorer resolution near the walls of the transition ducts because of the physical difficulties in measuring near these surfaces.

#### 8.5.4 Assessment of VULCAN Fire Suppression Sub-model

The optimization of fire suppression systems in aircraft engine nacelle applications is made more challenging by the fact that clutter in the form of structural supports, wiring, piping, machinery and similar items can adversely affect the suppressant flow. Furthermore, recirculation zones that form on the downstream sides of clutter have been identified as favorable for flame stabilization.<sup>70,71,72</sup> Of the various stabilized fires, liquid pool fires established behind obstructions such as structural ribs have been identified as some of the most challenging to suppress.<sup>70,71,72</sup>

Flow obstructions can act as flame holders, stabilizing flames and making suppression difficult. Stabilization is aided by creating a recirculation region with relatively low dissipation rates, and thus large  $\tau_k$ , and hot products. Suppression is made more difficult because it takes significantly more time for

suppressant to penetrate the recirculation zone than it takes for the suppressant to pass over an unobstructed flame. Hamins et al. and others<sup>66,75,73</sup> have taken advantage of a simple mixing model in the form of the conservation equations for an unsteady PSR that predicts the suppression delay associated with the delay in mixing suppressant into a recirculation zone.<sup>50</sup> The model predicts that the mole fraction of suppressant in the recirculation zone varies as

$$X_{recirc} = X_{\infty} [1 - \exp(-t / \tau_{mix})] \quad (8-50)$$

where  $X_{\infty}$  is the suppressant mole fraction outside the recirculation region and  $\tau_{mix} \propto h / u^*$  is the mixing time, proportional to the quotient of the velocity past the recirculation zone and the recirculation zone thickness, here taken to be the step height,  $h$ . Takahashi et al.<sup>74</sup> measured the proportionality constant for their configuration to be  $\tau_{mix} = 34.7(h / u^*)$  where  $u^*$  is explicitly given as the average of the mean flow velocity over the step and the mean flow without the step.

In this section, the efficacy of the VULCAN fire suppression sub-model for the suppression of pool fires stabilized behind obstructions was assessed. The suppression model was evaluated using measurements of the agent required to suppress a fire stabilized behind a rearward-facing step.<sup>75</sup> The CFD code was then used to indicate ways in which the arrangement of clutter within an environment resembling an aircraft engine nacelle may change suppressant requirements, suggesting potential design practices that might be confirmed with further experimental measurements.

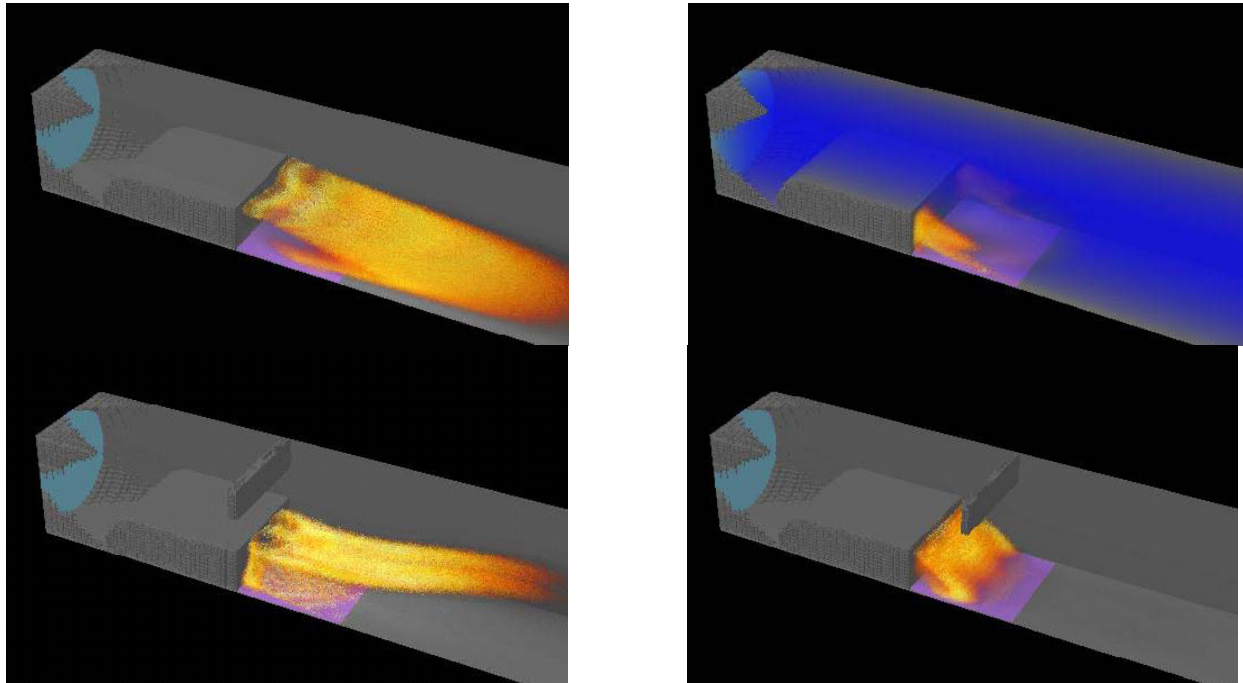
For a CFD model to adequately predict suppression in the presence of obstructions, it will be important that the model can reasonably predict (1) the suppressant required to extinguish flames at a given fluid mixing rate, and (2) the rate of suppressant mixing into recirculation regions. To address these questions, simulations using the suppression model described above were conducted for JP-8 pool fires stabilized behind a backwards-facing step, and results are compared with measurements of Takahashi et al.<sup>75</sup> Those simulations for which there are experimental data available and that are involved in model evaluation are referred to as Case A1; see Table 8-12. All simulations denoted as Case A are conducted in a 154 mm by 154 mm square wind tunnel, 770 mm long, with a 64 mm tall backwards-facing step placed in front of a 150 mm by 150 mm JP-8 pool. Airflow through the wind tunnel was 10100 standard L/min, the turbulence level at the entrance was set to 6 % and the turbulent length scale, used to calculate the initial dissipation rate was set to 3 mm based on the turbulence generators employed in the experiments.

**Table 8-12. Description of Simulations of Pool Fires Stabilized behind a Backwards-facing Step.**

Case	Description	$\tau_{mix}$
A1*	As in Takahashi et al. <sup>75</sup> with the fuel being JP-8 and the suppressant being HFC-125.	0.23 s
A3	As in A1 but with a 42 mm rib on the upper wall collocated with the backwards-facing step.	0.15 s
A5	As in A1 but with a 42 mm rib on the upper wall 84 mm behind the backwards-facing step.	0.24 s
B1	22.5 cm high, 180 cm wide, and 180 cm long wind tunnel with 5 cm rib located 60 cm from entrance. A 45 cm long by 30 cm wide JP-8 pool was centered on the lower surface.	0.30 s
B2	As in B1 but with two 5 cm high longitudinal ribs each located 20 cm from the centerline.	0.30 s
C1	As in B1 but with the tunnel height reduced to 10 cm.	0.23 s
C2	As in B2 but with the tunnel height reduced to 10 cm.	0.23 s

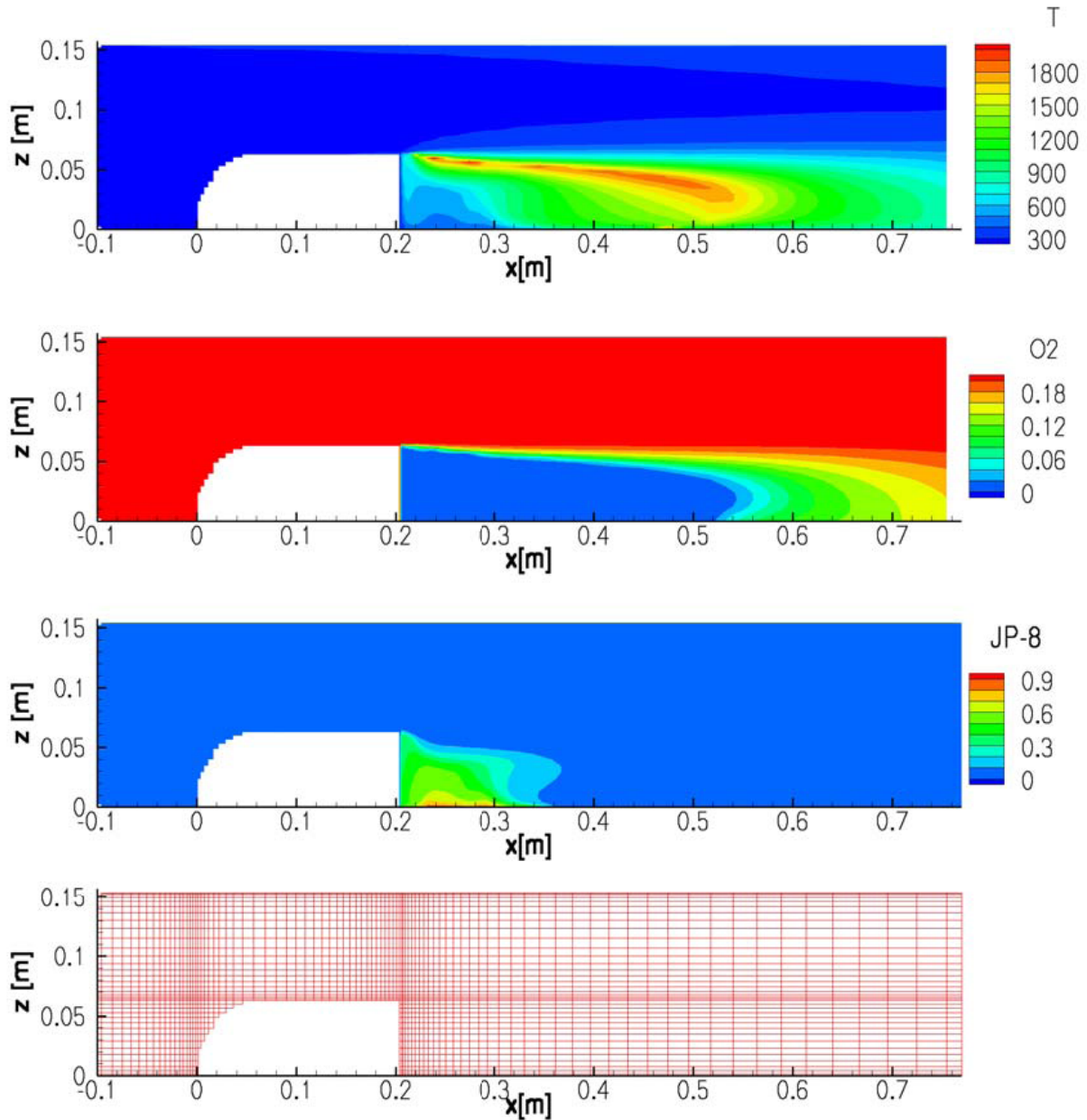
\*Used in model validation.

Figure 8-107 provides an overview of the simulation geometry, showing the location of the flame behind the step. Simulations were brought to a steady state with fires established, after which suppressant was injected, thoroughly mixed with the incoming air.



**Figure 8-107. Ray Tracing Image of Case A1 before Agent Injection (top left) and 0.2 s after Injection of 10% HFC-125 (top right). Images of Case A3 (lower left) and A5 (lower right) before Agent Injection. The air/suppressant inlet is light blue, the pool is purple, the suppressant is deep blue, and the flame is orange to yellow.**

Figure 8-108 shows the state along the wind tunnel centerline just prior to agent injection with the high temperature flame mainly located at the edge of the recirculation zone between the fuel and air. Fuel vaporization is determined by the rate of heat flux to the pool surface, moderated by an estimate of heat losses, for example to the porous plate through which the fuel passes. The flame location relative to the edge of the recirculation zone is somewhat sensitive to these heat losses. It was assumed that 40 % of the heat flux to the pool resulted in fuel vaporization. Greater heat losses result in reduced fuel vaporization, bringing the flame closer to the pool. This effect tends to increase the heat flux to the pool, partially offsetting the heat losses. The sensitivity to heat loss is not very large, but it is enough to move the flame in and out of the recirculation zone given 80 % to zero heat losses. Also shown in Figure 8-108 is a cross-section of the computational mesh, showing grid points clustered around the step to capture relevant details of the boundary layer in these regions. Grid sensitivity studies are in process, although refinement in regions around the step to date has not resulted in measurable differences in the results for Case A1. Injection of suppressant is conducted by keeping the air mass flow rate through the domain constant and increasing the total mass flow rate as required to inject the desired quantity of suppressant.



**Figure 8-108. Centerline Contour Plots Showing (from top to bottom) the Temperature, Oxygen Mass Fraction, Fuel Mass Fraction and the Computational Grid for Case A1.**

Rather than conduct a number of simulations for each suppressant mole fraction to determine the minimum injection time, as was done in the experiments, the suppressant was continually injected and the time to suppression was measured. Suppression was defined as the time at which the maximum temperature throughout the domain dropped below 1000 K. Figure 8-109(a) shows the evolution of the maximum temperature for various suppressant mole fractions. The selection of 1000 K as the temperature corresponding to suppression seems justified since the temperature rapidly drops around this point, and there is no evidence of tendency to reignite for temperatures below 1200 K. It is evident that an HFC-125 mole fraction of 0.075 is insufficient to suppress this flame, while 0.08 is sufficient.

Successively greater mole fractions lead to a monotonic reduction in the time required to suppress the flame. These results are summarized in Figure 8-109(b) where they are also compared with the results of Takahashi et al.<sup>75</sup>

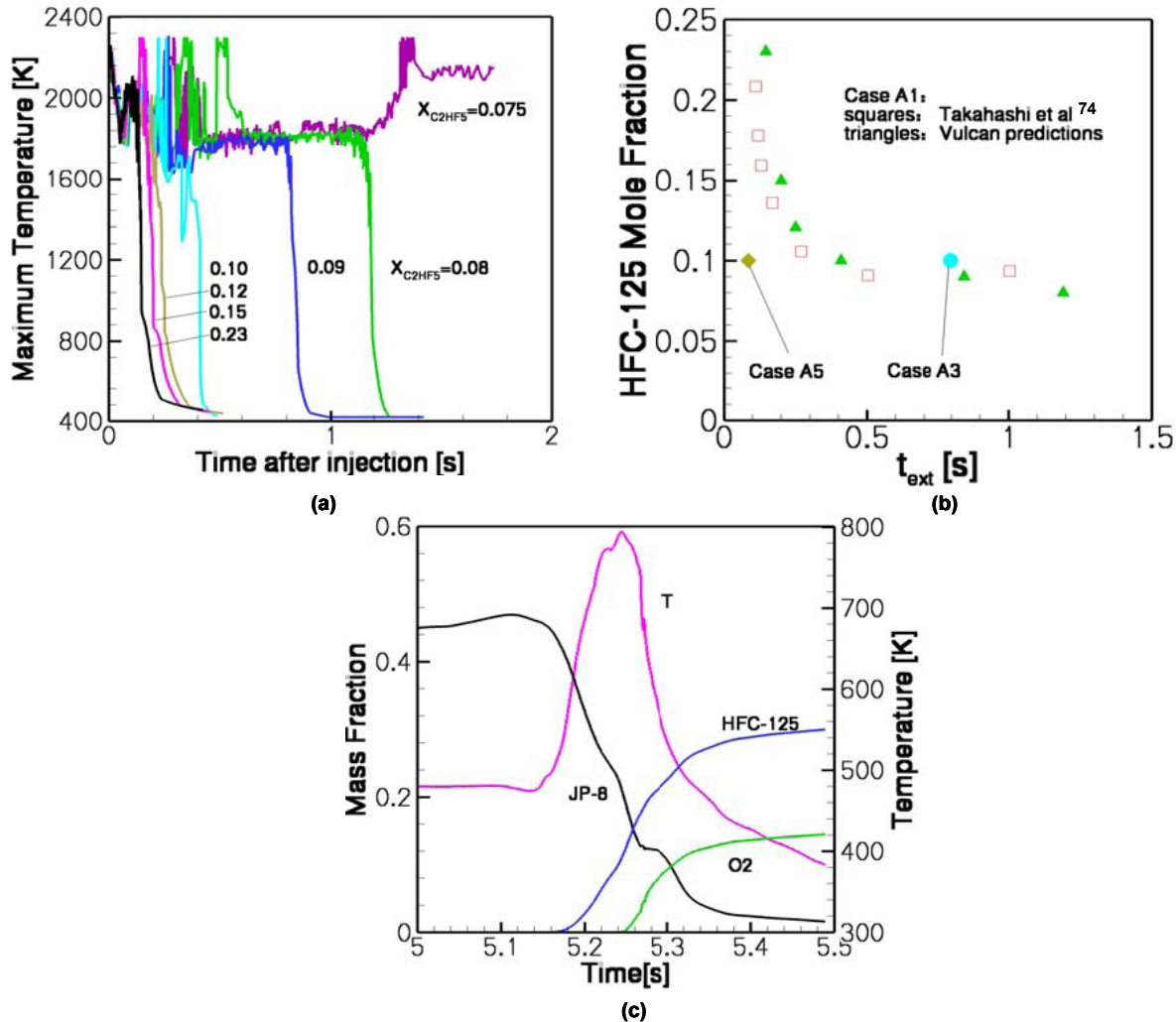


**Figure 8-109. (a) Evolution of the Maximum Fluid Cell Temperature in the Domain for Case A1 for Various HFC-125 Mole Fractions. (b) Suppression Times as a Function of Added HFC-125 for Cases A1, A3 and A5. (c) Mass Fraction and Temperature Evolution in the Recirculation Zone (8 mm above pool and 8 mm behind step) for Case A1 with 10 % HFC-125 by Volume Injected at 5 s.**

The maximum temperature shown in Figure 8-109(a) fluctuates greatly during the transient suppression process because of a combination of the refined grid and the delta-function nature of the EDC model: at certain instants of time the model treats a particular cell as almost entirely stoichiometric flame. This behavior occurs as the flame moves through the finely gridded region behind the step during the suppressant injection. While this behavior would not be observed when averaging over integral time or length scales, this can occur in the context of the EDC model when the cell thickness is comparable to the Kolmogorov scale as it is in the present grid at some locations. In fact, for better EDC model

applicability, it is desirable to coarsen the mesh, but high levels of grid refinement are used to reduce reliance on log-linear wall models in regions of adverse pressure gradients.

Figure 8-109(c) shows the local smoothness of the temperature evolution deep in the recirculation region along with major species. This figure and Figure 8-110 show key aspects of the suppression dynamics for the particular case A1 with 0.1 HFC-125 mole fraction. The suppressant rapidly flows over the top of the recirculation zone, but dilatation associated with combustion initially reduces recirculation behind the step. As the upper portions of the flame are suppressed (within the first 0.1 s) recirculation gradually increases, bringing suppressant in to extinguish regions that are still burning. As the fire suppression progresses, the flame is observed in Figure 8-109(c) and Figure 8-110 to move deeper into the recirculation zone as fuel vaporization is reduced and oxygen moves into the recirculation zone with the suppressant. It is found that an inner, secondary recirculation zone forms in the corner between the pool and the step into which some air is entrained, primarily from the sides, but into which suppressant penetration is exceedingly slow. With wall heat losses treated in the suppression model, this region is generally the last to be suppressed.

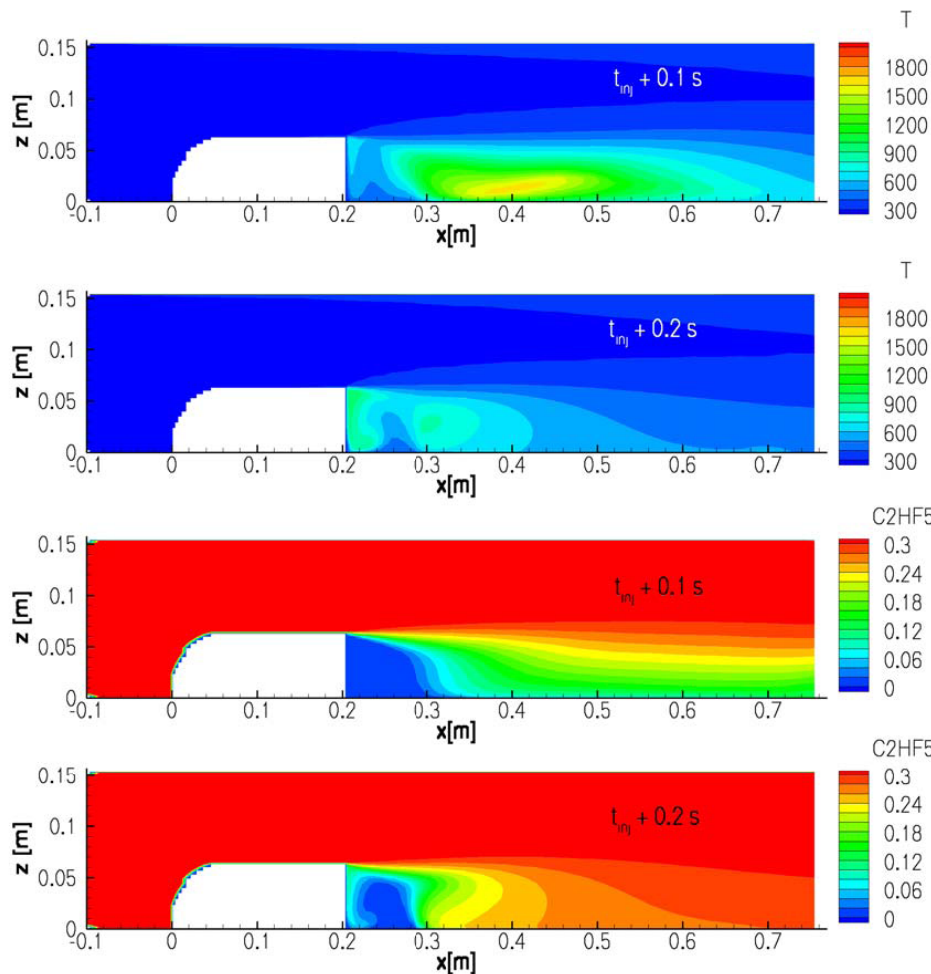


**Figure 8-110.**  
Centerline Contour  
Plots of Temperature  
and HFC-125 Mass  
Fraction at 0.1 s and  
0.2 s after  
Suppressant  
Injection for Case A1  
with 0.1 HFC-125  
Mole Fraction  
Injected.

Using the same basic configuration as the experiments conducted by Takahashi et al.,<sup>75</sup> simulations were conducted to investigate the effect of additional clutter, in the form of a small rib on the upper wall, opposite the backwards-facing step behind which the fire is stabilized. Specifically, a rib protruding from the upper surface with a height of 42 mm is located either directly above the end of the backward facing

step or two rib heights behind the back of the step; these configurations are denoted A3 and A5; the simulations are otherwise similar to those in A1. These scenarios reflect the existence of additional clutter on the side of a passage opposite the flame-stabilizing obstruction. Additional obstructions result in the acceleration of the flow over the step and past the fire. The correlation between flow velocities over obstructions and suppressant mixing rates<sup>66,73,74,75</sup> would suggest that collocated obstructions would result in accelerated suppression. In Figure 8-109(b), suppression times are plotted for cases A3 and A5 with 10% HFC-125 suppressant in the free stream along with the results for Case A1 where there is no additional obstruction. The results are not completely intuitive: there is a strong reduction in suppression time for case A5 but no reduction and possibly an increase in suppression time for case A3. This trend goes against a simple implementation of Equation 8–50 that would suggest reduced suppression times in accordance with the changes of  $\tau_{mix}$  in Table 8-12. Equation 8–50 would imply that case A3 should have the shortest suppression time while it is observed to have the longest.

The results for cases A3 and A5, relative to A1, can be explained by consideration of the pressure field, shown in Figure 8-111, that determines the extent of the recirculation regions.

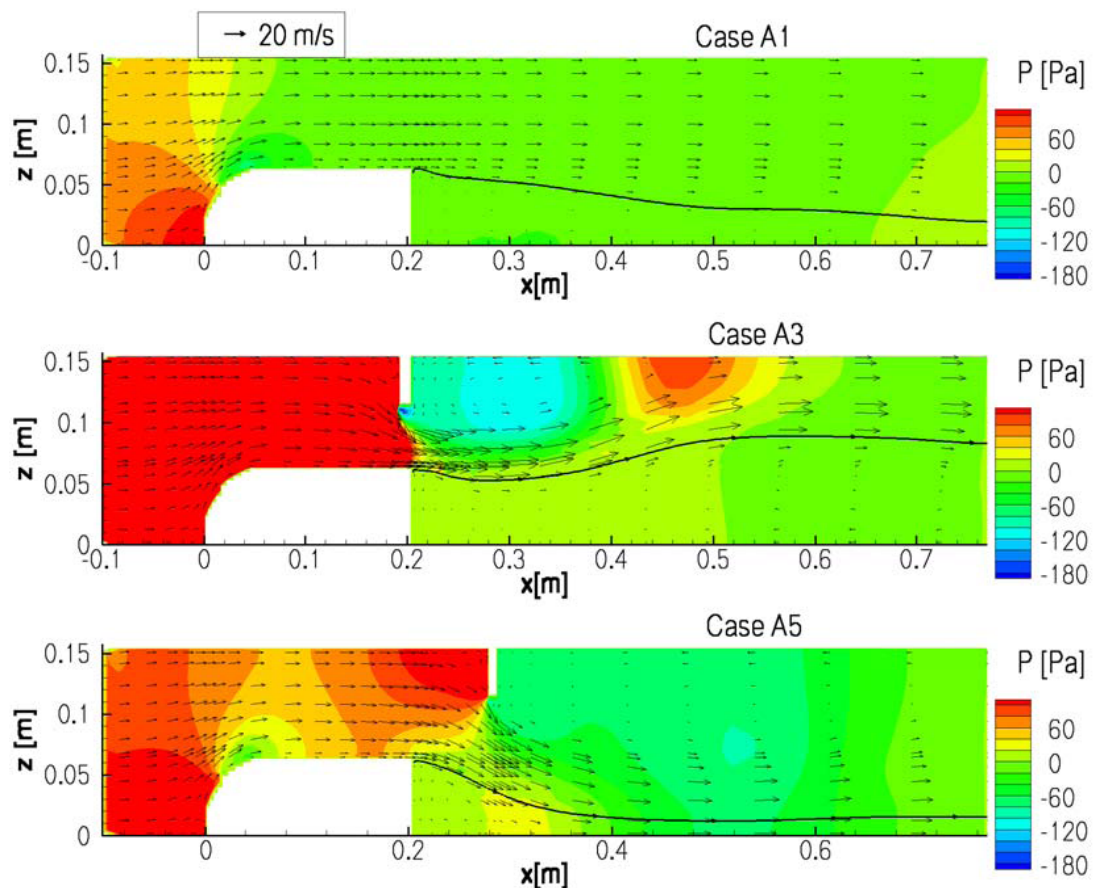


**Figure 8-111. Centerline Pressure Contours and Velocity Vectors for Cases A1, A3 and A5 prior to Suppressant Injection. (Contour levels are equal for all panes and space at  $2 \times 10^6$  Pa intervals. Solid lines represent streamline traces from just behind the corner of the step.)**

Also shown in Figure 8-111 are velocity vectors and streamline traces from behind the corner of the step to provide rough indications of recirculation zone sizes. In case A3, flow past a flat plate oriented against the flow results in a greater pressure loss than flow over the backwards-facing step. The greater pressure loss tends to pull the mean flow upward, reducing the mixing in the lower recirculation zone where the fire is stabilized. Shifting the upper obstruction past the step results in significant reductions in the suppression time. This result occurs because the high-pressure region in front of the upper rib is coincident with the low-pressure region behind the backwards-facing step, accelerating the flow downward and increasing suppressant mixing into the recirculation zone. Thus, despite the fact that the area available for flow past the lower recirculation zone is greater and the velocity  $u^*$  correspondingly lower in Case A5 relative to Case A3, the suppression time is reduced because the flow is directed into the recirculation zone, thereby increasing mixing in the recirculation zone. The key result is that the suppression time is strongly dependent on recirculation zone size, and that multiple factors affect the recirculation zone size. Given a single obstruction, recirculation zone mixing is primarily dependent on  $h/u^*$ , but pressure gradients can change the effective recirculation zone thickness. Given this, recirculation region mixing times should be a function of  $h^*/u^*$ , where  $h^* = h^*(h, \nabla p)$ , indicating the dependence of the effective recirculation zone length scale on the pressure gradient. As is typical for separated flows, favorable (accelerating) pressure gradients reduce recirculation zone length scales while adverse pressure gradients have the opposite effect. Pressure drop past obstructions is related to the drag coefficient, and there is extensive literature on the subject that may be useful in identifying the magnitude of pressure changes across obstructions. It is noted here that the  $k-\epsilon$  model is known to have limited success in adverse pressure-gradients, but the conclusions reached here are not dependent on the validity of the  $k-\epsilon$  model. Rather, the conclusions depend on the relevance of pressure gradients in directing fluid flow, and on the result from dimensional analysis that mixing times can be related to  $\mu$  and the characteristic scale of the recirculation zone.

The model validation experiments described above and others for studying fire suppression of obstruction-stabilized flames<sup>66,75</sup> were conducted in roughly square wind tunnels. In certain applications such as aircraft engine nacelles, the width to height aspect ratio tends to be large. In preparation for studies of actual engine nacelle environments and to plan an additional series of experiments to be conducted at WPAFB by the USAF 46<sup>th</sup> Test Wing, a series of simulations using dimensions characteristic of the wind tunnel available at WPAFB and an F-18 engine nacelle were conducted. The characteristic dimensions identified are obstruction heights on the order of 5 cm in wide channels with heights on the order of 10 cm to 30 cm. The resulting series of simulations, cases B1, B2, C1 and C2 are summarized in Table 8-12. In each of these simulations, the inlet velocity was 5 m/s, the turbulence intensity was 10 % and the turbulent length scale was 0.025 m. Significantly, pool sizes are narrow relative to the channel width. Simulations indicate that dilatation from a pool fire behind a rib induces secondary recirculation regions that sweep the fire outward and along the rib transverse to the flow. Observation of these flow fields indicates that they may reduce the suppressant penetration into certain portions of the flame-stabilization region. However, within aircraft, structural supports and clutter are observed to be oriented in both transverse and longitudinal directions. The consequences of longitudinal (streamwise) ribs are examined by adding longitudinal ribs just outside of the pool (Cases B1 and C1 becoming Cases B2 and C2). It is observed that for both Cases B2 and C2 the longitudinal ribs do not prevent spread of the fire beyond the ribs, as shown in Figure 8-112. Mass fraction profiles in the recirculation zone indicate, however, that longitudinal ribs do affect the flow because rate of transport of agent is greater with ribs for Case B2 relative to B1 and for Case C2 relative to C1, shown in Figure 8-113(a). Further, the time to suppress the fire is reduced as shown in Figure 8-113(b). The result that

longitudinal ribs reduce the time required to suppress a fire suggest a series of experiments in high aspect ratio wind tunnels to evaluate their validity. If the experiments are consistent with the simulation results, then both the potential reduced suppression ability due to dilatation and the possibility that longitudinal clutter ameliorates it are considerations in system design.

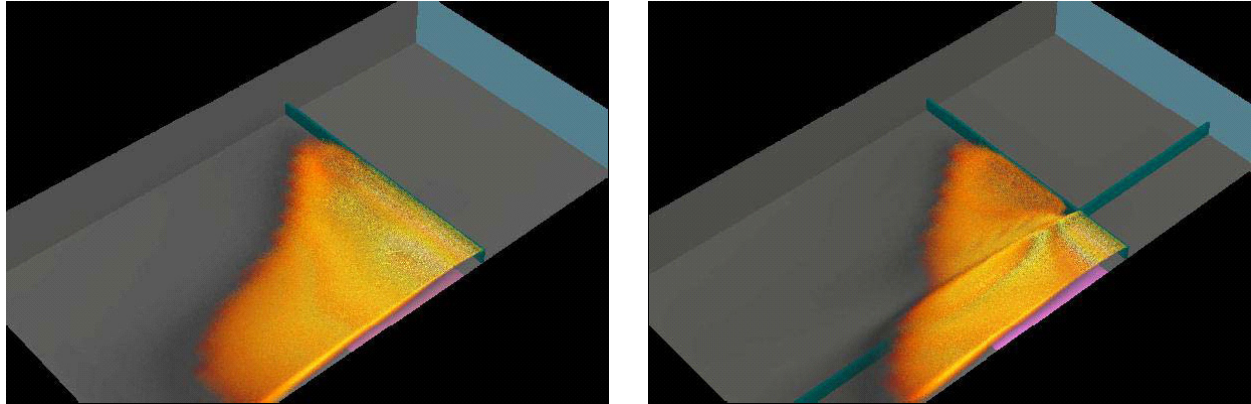


Figure 8-112. Raytracing images of Cases B1 (left) and B2 (right). (Colors as in Figure 8-107. Simulations take advantage of symmetry, and only the calculated half of the domain is shown.)

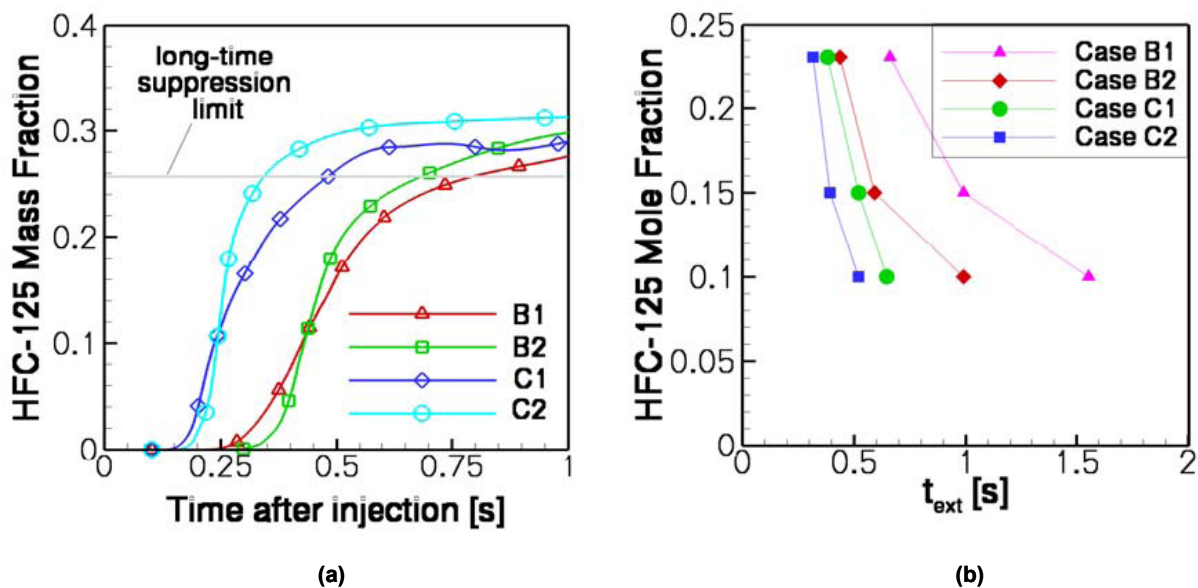


Figure 8-113. (a) Temporal Evolution of HFC-125 Mass Fraction in the Recirculation Zone at a Point 0.012 m above the Lower Surface and 0.05 m behind the Rib along the Centerline. (b) Suppression Times as a Function of HFC-125 Mole Fraction for Cases B1, B2, C1, and C2.

### 8.5.5 Assessment of VULCAN in Suppressant Distribution in a Full-Scale Nacelle

The flow inside an engine nacelle ground test simulator was studied for the purpose of understanding and optimizing the distribution of suppressant.<sup>76, 77</sup> One objective of the study was to identify conditions for which suppression would or would not be successful in order to test the ability of VULCAN to discriminate between various scenarios and to provide input on experimental design for full-scale nacelle fire tests. To accomplish this, the distribution of fire suppressant during cold flow (without a fire) was first examined to identify regions of low concentration using VULCAN.

The overall nacelle geometry used in the VULCAN simulations was based on the “Iron Bird” full-scale nacelle simulator (to be described in detail below), which was a mock up of a port engine nacelle. In the absence of fires and suppressant flow, the flow field in the nacelle was dominated by flow through an inlet air scoop located near the front of the nacelle coming up through the nacelle bottom. The inlet air flowed from the inlet across the engine toward the upper aft of the nacelle. For the purposes of the simulations, an air mass flow rate of 1.0 kg/s was used. The inlet air mass flow rates determined the air exchange times, the time over which the mass of air entering and leaving the nacelle equaled the mass of air in the nacelle. For the simulation, the internal volume of the nacelle, neglecting clutter objects, was just over 1.4 m<sup>3</sup>. This volume gave an air-exchange time of 1.6 s. The inlet cross section was approximately 0.008 m<sup>2</sup> and the inlet airflow velocity was approximately 150 m/s. This resulted in an inlet Reynolds number of  $9 \times 10^5$  resulting in strong turbulence even without the clutter-enhanced mixing.

The ground simulator was outfitted with a set of four suppressant discharge nozzles that were found to be sufficient to suppress a fire when 3.2 kg of fire suppressant was discharged.<sup>78</sup> These are denoted by the numbers 1 through 4 with higher numbers corresponding to nozzles that are located toward the rear of the nacelle (Figure 8-114). Numerical simulations were conducted for suppressant injection through these nozzles into the nacelle in the absence of a fire to obtain information on the distribution through the nacelle.<sup>76</sup> The suppressant was assumed to enter the nacelle in the vapor phase or to vaporize fast relative to other time scales. The suppressant mass flux for each nozzle was assumed to be proportional to the nozzle area.

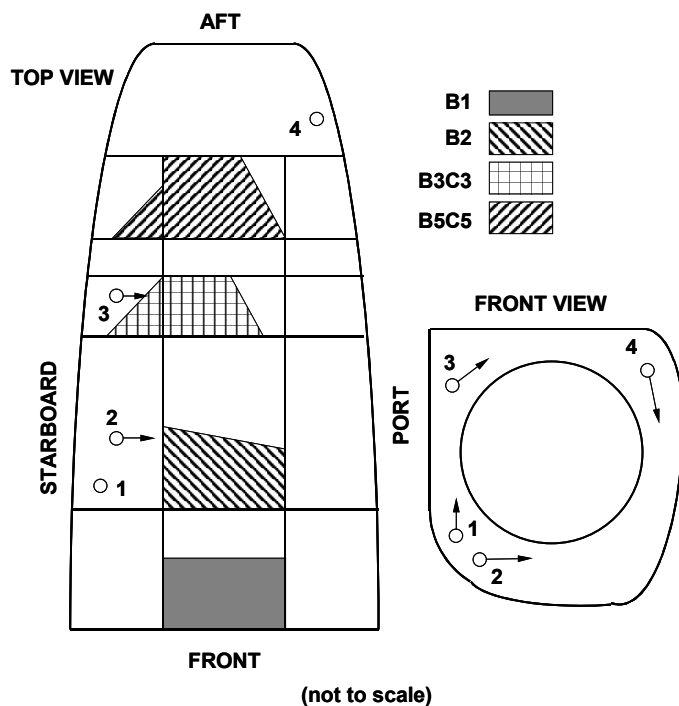


**Figure 8-114. Locations of the Suppressant Nozzles and the Pools in the Nacelle Simulator.**

The mass fraction of HFC-125 in vertical planes near the nacelle center and near the starboard and port sides are shown in Figure 8-115 at the end of the 3 s suppressant injection period.

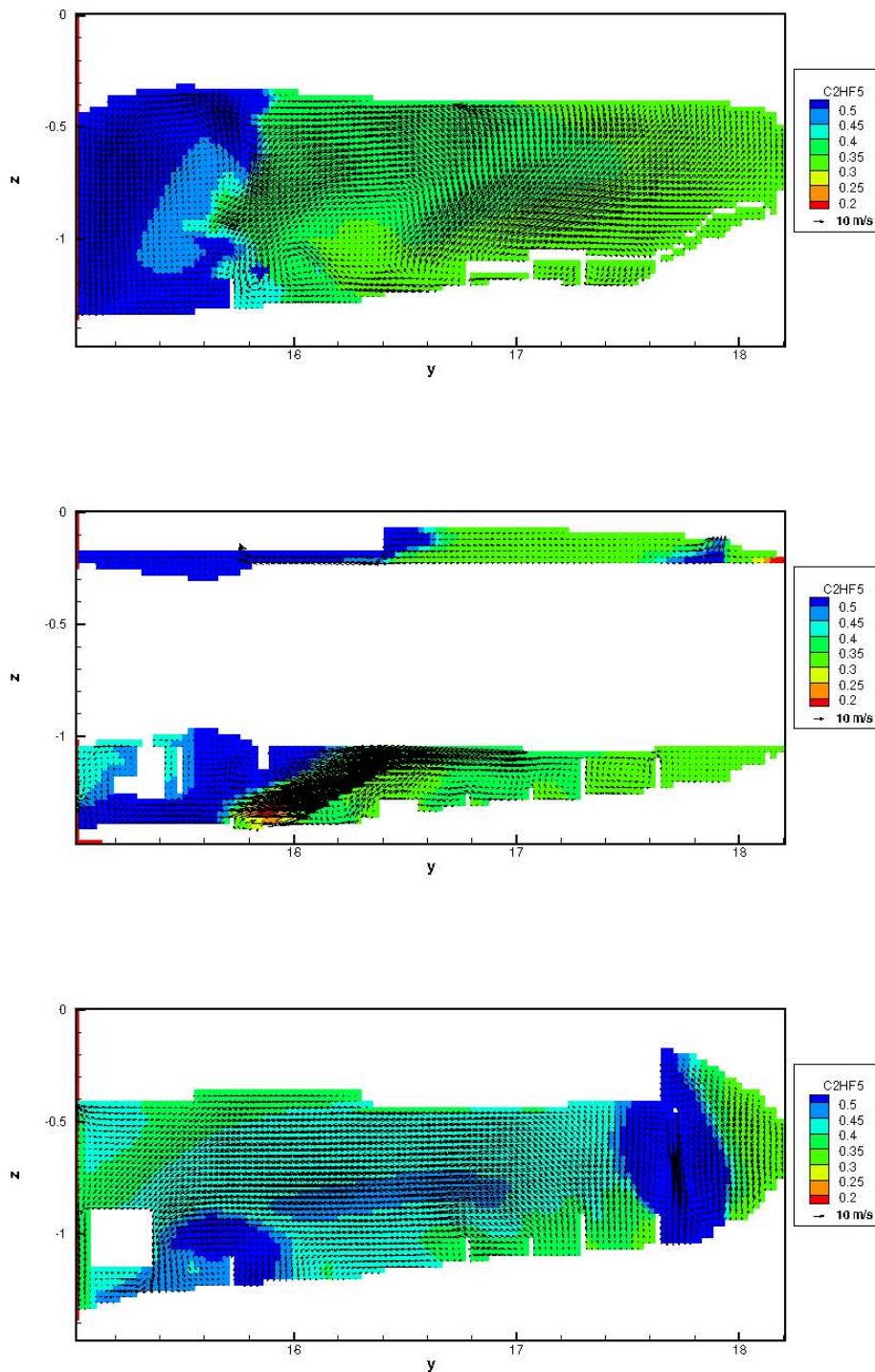


**Figure 8-115. Contour Plots of  $C_2HF_5$  at 3.0 s after Start of Suppression Injection in Vertical Planes near Starboard Side (top), near Nacelle Centerline (center), and near Port Side (bottom). (Airflow is 1.0 kg/s, and suppressant flow is 3.2 kg/s over 3 s.)**

In these contour plots the computational cells representing the nacelle, the engine, and the clutter are blanked (white). The mass fractions are colored in such a manner that blue and green (cool) colors indicate likely suppression and red (hot) colors indicate that suppression is unlikely. The critical mass fraction for suppression in the absence of intense mixing is somewhat less than 0.3 (closer to 0.25, so that this is a conservative estimate), and so the dividing line for likely suppression can be taken to be the dividing line between yellow-green and green. Depending on the turbulent mixing rates, suppression may occur for lower mass fractions of HFC-125. Velocity vectors are also provided in Figure 8-115 to indicate the general flow direction.

Nozzle 1 is located on the starboard side of the nacelle in the forward section and is directed upward. The suppressant from Nozzle 1 fills the upper forward nacelle and is advected into the lower forward nacelle. Nozzle 2 is located near Nozzle 1 on the starboard side of the nacelle and directed towards the port side beneath the engine and across the top of the inlet airflow. Suppressant from nozzle 2 is dispersed aftward by the inlet jet along the nacelle. Nozzle 3 is located just past the mid-point of the nacelle, in between the second and third ribs, on the upper starboard side of the engine. Suppressant flow is directed at roughly a 45° angle upward across the top of the engine, and the majority of suppressant follows the mean flow forward along the upper nacelle. Nozzle 4 is located on the port side of the engine near the aft of the nacelle just behind the fifth rib. The suppressant is directed downward along the side of the engine in a direction that is counter to the general upward flow toward the upper diamond vent; this recirculation results in oscillations as the injecting gases are turned around by the mean flow.

### **Distribution of Suppressant throughout the Nacelle**

As a measure of sufficient distribution in the nacelle, the portion of the nacelle volume for which the suppressant mass fraction exceeds 30 % has been used for characterization. Even with low-intensity mixing, this amount is generally sufficient for suppression and represents a conservative estimate of suppressibility. Figure 8-116 shows this fraction when the airflow is 1.0 kg/s with varying rates of injection (same mass over different durations). The mass of suppressant to be injected was fixed at 3.2 kg, and the period over which it was released varied from 2 s to 6 s. Shorter injection periods correspond to higher bottle pressures. To the extent that suppressant vaporization is slow, the effective period of injection increases. Figure 8-116 shows that the entire volume is essentially filled for at least one second for injection durations of 3 s or less. For longer periods of injection, the volume is not filled with high concentrations (> 30 %) because suppressant is continually advected out the various vents. The failure to fill the nacelle completely does not indicate that suppression will not occur, but rather reduces the confidence in suppression.

The average peak mass fractions for the simulations shown in this figure are 0.59, 0.51, 0.44 and 0.35. Smaller mass fractions correspond to the longer injection duration. If the turbulent mixing in the nacelle were sufficient to create homogeneity, the mass fraction throughout the nacelle would exceed 0.3 for all of these scenarios. Clearly, inhomogeneities arising from imperfect mixing are significant. This indicates that the CFD analysis can provide significant information on the degree of inhomogeneity. Specifically it can provide an estimate of the volume that fails to meet a criteria such as the one indicated here (suppressant mass fractions exceeding 0.3).

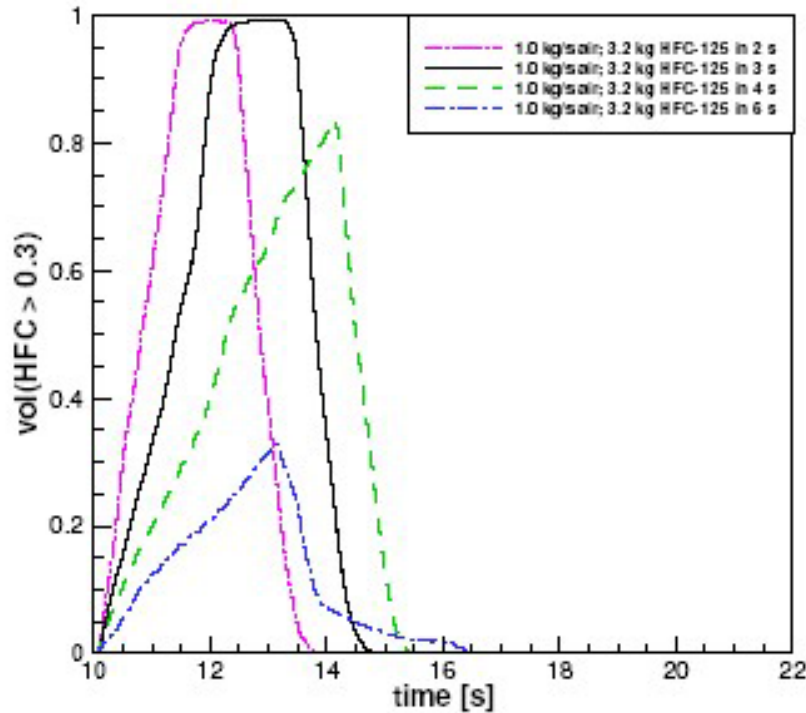


**Figure 8-116. Simulation Results of Various Injection Periods.**

### Influence of Nozzles on Distribution of Agent

Simulations were conducted to ascertain the effect of removing a single suppressant nozzle, while keeping the overall mass of injected suppressant constant at 3.2 kg injected uniformly over 3 s. For these conditions, the nacelle volume in which the fraction exceeds 0.3 is evaluated. These results were compared to those shown for all four nozzles functioning; the nacelle was completely filled, according to this criterion, for the range of flows considered.

In conducting simulations with specific nozzles removed, the mass flow out of the remaining nozzles was kept at the same values used in the previous simulations. This corresponds to an assumption that the pressure driving the suppressant is not affected by the removal of a nozzle and that the nozzle cross-sections have not changed. The duration is thus increased to allow release of the full 3.2 kg of HFC-125.

The volume fraction of the nacelle where the suppressant mass fraction exceeds 0.3 is indicated in Figure 8-117 for an airflow of 1.0 kg/s. In these and other scenarios, it appears that removing Nozzle 3 has no detrimental effect, since the complete volume is indicated as filled, and the duration for which it is filled is increased because of the slightly slower rate of injection using three nozzles. Based on the criteria shown in Figure 8-117, removing Nozzle 4 also has little effect on the sufficient distribution of the suppressant. Note that the lower diamond vent in the nacelle simulator is modeled as essentially blocked, based on observations of the test simulator. Assuming that this vent is not blocked on similar fleet aircraft, the removal of suppressant in the aft region may be substantially faster, making the retention of Nozzle 4 highly desirable. On the other hand, the additional vent in the aft region would mean that a greater portion of the suppressant injected through Nozzle 4 would leave the nacelle rapidly.

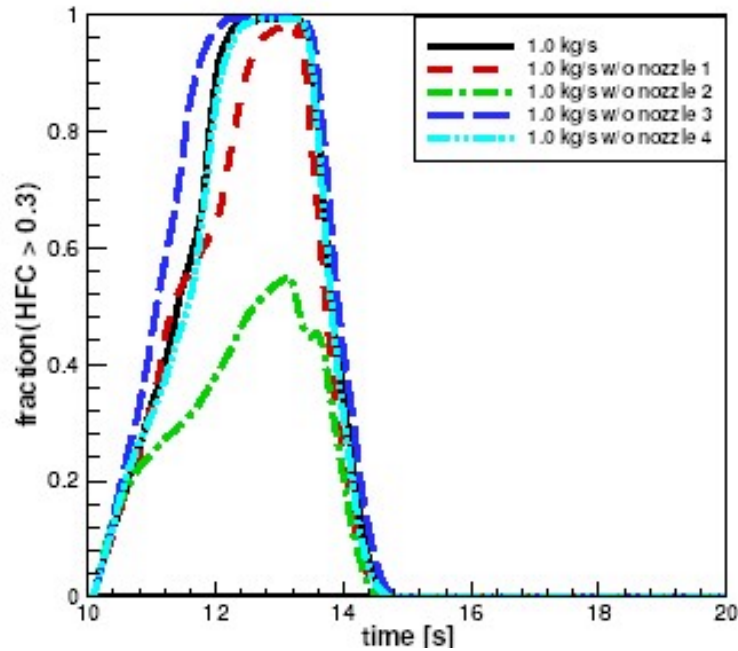


**Figure 8-117. Simulation Results Showing the Effect of Nozzles on Agent Distribution.**

The removal of Nozzles 1 or 2 does appear to have a significant effect on the distribution of suppressant throughout the nacelle. Suppressant from these nozzles is entrained in the inflow; this entrainment by the air significantly helps distribute suppressant throughout the nacelle.<sup>67</sup> The distribution of suppressant along the centerline is shown in Figure 8-118 with Nozzle 2 assumed to be capped; this can be compared with the distribution using 4 nozzles. Nozzle 2 is located in the forward starboard area of the nacelle and directed across the lower nacelle outboard. Without Nozzle 2 present, the inlet air jet entrains relatively little suppressant, and this results in little suppressant along the lower nacelle where pool fires might exist. It is clear that Nozzle 2 plays a key role in distributing the suppressant throughout the nacelle as it mixes with the air inlet.

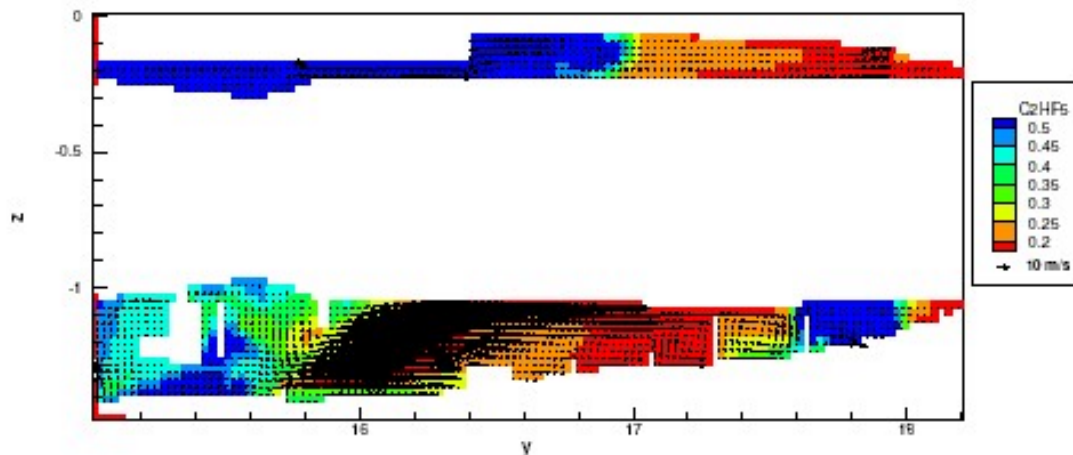


**Figure 8-118. Simulated Agent Distribution along the Nacelle Centerline.**

### 8.5.6 Assessment of VULCAN in Pool Fire Suppression in a Full-Scale Nacelle

Pool fires stabilized behind obstructions have been identified as among the most challenging fires to suppress.<sup>71,72</sup> Obstructions such as structural ribs provide a region of recirculating flow where hot products help stabilize the flame that suppressant is relatively slow to penetrate. In certain scenarios, such as those described in References 54, 66, and 75, the suppressant concentration must be maintained at an elevated level in the flow past the stabilization region for a substantial period of time to ensure that adequate suppressant penetrates the stabilization region.

The approximate locations of the pools used for VULCAN are shown in Figure 8-114. These sections are delineated from the forward to the aft end with increasing numbers as each rib is passed. The letter “B” is applied as a prefix to the pool location to indicate that the pool is located between the two central longerons. These are the only locations where substantial quantities of fuel can be collected. To augment the quantity of fuel, the basin just to the port of that indicated by “B” is sometimes assumed to hold some fuel also; this basin is denoted with the prefix “C”. The pool located at B1 is between the forward end of the nacelle and the first rib. That denoted B2 is located just aft of the first rib; the inlet air flows partially over this pool. The pool denoted B3 is located behind the second rib. The pool denoted B5C5 is located between the fourth and fifth ribs; these are the two larger ribs. The simulations indicate that pool fires at locations B4 and B6 are difficult to stabilize because of the particular predicted circulation. The surface areas of the largest possible pools in each section were measured in the ground-test simulator. Similar pool areas have been used in the simulations; the pool areas are indicated in Table 8-13.

The pools are assumed to be filled with JP-8, and the evaporation rate based on heat feedback to the pool. In general, it is difficult to predict the thermal feedback to a pool from a fire, because these fires are partially advected beyond the pools by the convective flows in the nacelle. It is particularly difficult to determine the evaporation rates without measurements. The uncertainty of the evaporation rate may be as high as 50 %. As a measure of the degree to which fires in different sections spread throughout the nacelle, Table 8-13 also shows the volume over which combustion is occurring and high temperatures exist. Heat release from pool fires B2 and B3C3 is substantially distributed throughout the nacelle by the main air inlet that passes over the fires in these regions.

**Table 8-13. Pool Characteristics.**

Pool	Area (m <sup>2</sup> )	Predicted Evaporation Rate (kg/s)	Volume of Combustion (%)	Volume where $T > 700$ K (%)
B1	0.084	0.0089	5.9	4.6
B2	0.100	0.011	4.6	22
B3C3	0.094	0.0082	5.5	37
B5C5	0.043	0.0043	1.5	5.2

#### Suppression Using Four nozzles

Suppression was predicted for all pool fires in the nacelle using the four-nozzle configuration and 3.2 kg of suppressant when this mass was injected over 3 s or 4 s. Results of these tests are summarized in Table 8-14.

**Table 8-14. Summary of Test Results with Four Nozzles.**

Pool	Mass HFC-125 (kg)	Injection Rate (kg/s)	Active Nozzles	Suppression Time (s)
B1	3.2	1.07	1,2,3,4	0.8
B1	2.2	1.07	1,2,3,4	0.8
B2	3.2	1.07	1,2,3,4	0.9
B2	2.2	1.07	1,2,3,4	0.9
B3C3	3.2	1.07	1,2,3,4	1.2
B3C3	2.2	1.07	1,2,3,4	1.2
B3C3	3.2	0.53	1,2,3,4	None
B3C3	3.2	0.64	1,2,3,4	None
B3C3	3.2	0.71	1,2,3,4	None
B3C3	2.2	0.73	1,2,3,4	None
B5C5	3.2	1.07	1,2,3,4	1.8
B5C5	2.2	1.07	1,2,3,4	1.8

To examine the effect of varying the mass of suppressant injected and the rate of injection, a series of additional simulations for fires in pool B3C3 were conducted. When the rate of suppressant injection is reduced to just below 0.75 kg/s, no suppression was predicted in the simulations, although sustained burning would certainly be described as tenuous for these conditions since the fire was restricted to a corner of the pool C3. As the rate of suppressant injection is reduced, the fire stability increases, and at 0.53 kg/s the fire is clearly stabilized, at least near the corner of pool C3. The fire tends to stabilize in this location because the mixing rates are lower, as indicated in the following section. It is noteworthy that the mass of suppressant injected plays little role in determining the occurrence of suppression here. For the two cases with suppressant injection rates of 0.71 and 0.73, the resulting tenuous burning region is very similar. There will be a lower bound in terms of suppressant mass injected over a short period, although this has not been identified here. More significant in practice is the duration over which suppressant will act to inhibit reignition and allow cooling of heated surfaces. Thus the suppressant requirements are likely to be dictated by a combination of the rate required to flood the compartment with a high enough concentration and the mass required to maintain that concentration to inhibit potential reignition sources.

There is one complication that arises with high-boiling point agents, however. For high boiling point agents, the relevant parameter will not be the rate at which liquid suppressant is injected, but rather the rate at which the liquid suppressant vaporizes. The physics of the evaporation process are not captured in the present simulations but will be considered in subsequent simulations.

Though the detailed results are not presented here, suppression is sensitive to heat flux from the fire to the pool. If the heat flux and, hence, the fuel evaporation are reduced by 50 %, suppression is substantially easier for the cases considered in this section. For example, the reduced suppressant injection rates shown in Table 8-14 that fail to suppress the fire in pool B3C3 do succeed in suppressing the fire if the heat flux to the pool is reduced by 50 %. The fire can be completely separated from the fuel source with slower evaporation rates. Similar results are expected if the fuel is cold or if there are substantial heat losses through the nacelle under the pool. While relatively high engine temperatures are expected during operations, temperatures during ground tests may be such that reduced evaporation is experienced.

## Suppression with Individual Nozzles Capped

The capping of various nozzles causes inhomogeneities that left certain regions with little suppressant. A series of simulations was conducted where one nozzle was assumed to remain capped. To examine the effects of these inhomogeneities for the majority of these simulations, the flow from each of the other nozzles was maintained at previous values when all nozzles were open, giving a reduced rate for the sum of the three remaining nozzles and an increased duration of injection. Results of these tests are summarized in Table 8-15. For fires in the extreme forward and aft pools, the removal of various nozzles did not alter the prediction of suppression.

**Table 8-15. Summary of Test Results with Individual Nozzles Capped.**

Pool	Mass HFC-125 (kg)	Injection Rate (kg/s)	Active Nozzles	Suppression Time (s)
B1	3.2	0.83	2,3,4	1.3
B1	2.2	0.83	2,3,4	1.3
B1	3.2	0.74	1,3,4	1.5
B1	2.2	0.74	1,3,4	1.5
B1	3.2	1.07	1,3,4	1.1
B1	3.2	1.07	1,3,4	1.1
B2	3.2	0.83	2,3,4	None
B2	2.2	0.83	2,3,4	None
B2	3.2	0.74	1,3,4	4.6
B2	2.2	0.74	1,3,4	3.2
B3C3	3.2	0.83	2,3,4	1.6
B3C3	2.2	0.83	2,3,4	1.6
B3C3	3.2	0.74	1,3,4	None
B3C3	2.2	0.74	1,3,4	None
B5C5	3.2	0.74	1,3,4	2.4
B5C5	3.2	0.90	1,2,3	1.7

For pool B1 the removal of either Nozzle 1 or Nozzle 2 has little effect beyond delaying the suppression. For pool B5C5, the removal of Nozzle 2 results in an increase in the suppression time because suppressant from Nozzle 2 is entrained in the air and carried back across the ribs surrounding the pool. Without Nozzle 2, the suppression is delayed until suppressant from other nozzles flows around the nacelle to be entrained by the air inlet. The removal of Nozzle 4, which is closest to pool B5C5 and injects suppressant around the aft section of the nacelle, has minimal effect on suppression of this pool because the major flow is under the engine aftward.

For pool B3C3, the removal of Nozzle 1 has little effect other than to delay the suppression. Removing Nozzle 2, however, results in a failure to suppress fires in pool B3C3. As indicated in Figure 8-118, the removal of Nozzle 2 leaves a significant volume directly over the pool B3C3 with little suppressant. Thus, Nozzle 2 is necessary to suppress fires in this region.

For a pool located at B2, Nozzle 1 is critical for suppression. Suppressant from Nozzle 1 is entrained across pool B2 by the air, and in the absence of that nozzle the suppressant's concentrations just over the

pool are too low. Capping Nozzle 2 also leaves a region deficient in suppressant there as well, but the air influx over this region (approaching 100 m/s) is sufficient to extinguish any fire in that region.

As the rate of injection is reduced by a third or more, many volumetric regions of the nacelle do not have sufficient suppressant for all fires. This is caused by inhomogeneities in the concentration, since the average concentrations in the nacelle are sufficient to suppress all fires. Suppression also fails as the rate of injection is reduced by one third or more. The removal of Nozzles 1 and 2 causes substantial inhomogeneities in the distribution of agent. When Nozzle 3 is assumed to be capped, there is no apparent degradation in suppression.

Sensitivity studies in these simulations have disclosed that the pool vaporization rate is very sensitive to fuel temperature, heat losses, details of the geometry, and the momentum associated with injection.

## 8.6 FULL-SCALE NACELLE FIRE SUPPRESSION TESTS

### 8.6.1 Experimental Design

Results from the VULCAN pretest simulations (see above VULCAN assessment sections) and simplified analyses helped guide the design of the experimental test plan and matrix for fire suppression tests in a full-scale nacelle. These results estimated the overall concentration of suppressant in the nacelle, the duration of the transients as the concentrations rise and fall, and the magnitude of the distribution of suppressant. A simplified analysis of the relative masses of air and suppressant flowing into the nacelle can provide some guidance on the overall suppressant concentration and the transients. The suppressant mass-injection rate relative to the total injection rate provides a characteristic mean mass fraction within the nacelle,  $Y_{ss}$ . The injection must proceed for a long duration for the mean mass fraction to reach this characteristic steady-state value, but the mean mass fraction approaches this value in an exponential manner with an exponential time constant that is proportional to the total nacelle volume divided by the total volumetric influx. This time constant indicates the time scale for transients. In the tests conducted here, it was found that suppression was less sensitive to the total injected mass than it was to the rate of injection.

The VULCAN predictions indicated, and the test results subsequently confirmed, that the overall or average mass fraction of suppressant resulting in fire suppression was substantially greater than the cup burner value, which was  $Y_{cb} = 0.28$ .<sup>79</sup> In general, the estimated average fraction required for suppression is on the order of 30 % to 40 % greater than the cup-burner value, according to the VULCAN simulations. A similar excess was required for the tests. The fact that a greater overall mass fraction is required indicates that inhomogeneities are significant. In other words, the suppressant's mass fraction in certain regions of the flow is substantially less than the mean. It is noted that the high rates of mixing present in the nacelle tend to reduce the mass fraction required to suppress the fire. It has been found for HFC-125 that strained laminar flames are indicated to be suppressed at mass fractions as low as 0.16.<sup>79</sup>

One of the primary objectives of the study was to ascertain the predictive capabilities of VULCAN regarding the degree of inhomogeneity in the nacelle. To this end, it was noted that predictions with VULCAN were very successful at reproducing extinction in a geometry where the suppressant was introduced in a uniform manner and the only mixing processes were related to a fire-stabilizing recirculation zone.<sup>54</sup> The nacelle simulator geometry was appreciably more complicated, and the leading

challenge was expected to be the transport of the suppressant rather than the well-established suppression model itself. In order to evaluate the mixing process for several scenarios, simulations and tests were conducted with different rates of injection and with different nozzle configurations. As an added variable, the air inflow was varied to simulate varying flight conditions. As indicated above, the ratio of the suppressant injection rate to the combined, total mass rates was indicative of the mean of the suppressant mass fractions in the nacelle.

Based on the results of VULCAN model simulations of various test conditions, it was predicted that the suppression would be more sensitive to the rate of injection of agent than to the amount of suppressant, or equivalently the duration of injection. Further, suppression was indicated to be sensitive to the distribution of nozzles about the nacelle. With these results, a test plan was generated in the form of a rule-based sequence of tests. The test sequence was initiated with an approximation of a scenario, which was expected to result in successful suppression. From this point, subsequent tests reduced the effectiveness of that system by either:

- reducing the injection rate by reducing the bottle pressure so that the suppressant's mass fraction was reduced, or
- removing a nozzle so that the distribution of suppressant was less uniform, or
- reducing the mass of suppressant injected for a given bottle pressure so that the peak mass fraction was reduced and held for a shorter duration.

### 8.6.2 Test Facility

The NAVAIR's full-scale "Iron Bird" nacelle at Navel Air Station (NAS) Patuxent River, Maryland, which is typical of an advanced tactical aircraft, was used for this effort. Figure 8-119 shows the fire test simulator. The air inlet source is seen in the lower left coming up into the bottom of the nacelle. There are two vents in the top: a diamond-shaped vent in the aft, and a balance piston round vent about 1/3 aft of the face. On the front face, there are four exit holes simulating connections from the nacelle to the Airframe Mounted Accessory Drive (AMAD) bay and other parts of the aircraft. These four holes are arrayed around the engine as shown in Figure 8-120.

The flow areas of the top vents, the diamond aft vent and the balance piston vent, are 248 cm<sup>2</sup> and 22.8 cm<sup>2</sup> respectively. The ground test simulator is a mock up of a port engine nacelle. Therefore, the port side corresponds to the outboard side of the engine, where air is introduced in flight, and the starboard side corresponds to the inboard side of the engine. The nacelle is roughly 3.18 m long. The width and height vary significantly along the length, but are contained within a region 1.45 m high and 1.15 m wide. Coordinates are measured from a reference point on the top starboard side of the simulator test fixture so that all vertical coordinates are negative while other coordinates are positive.

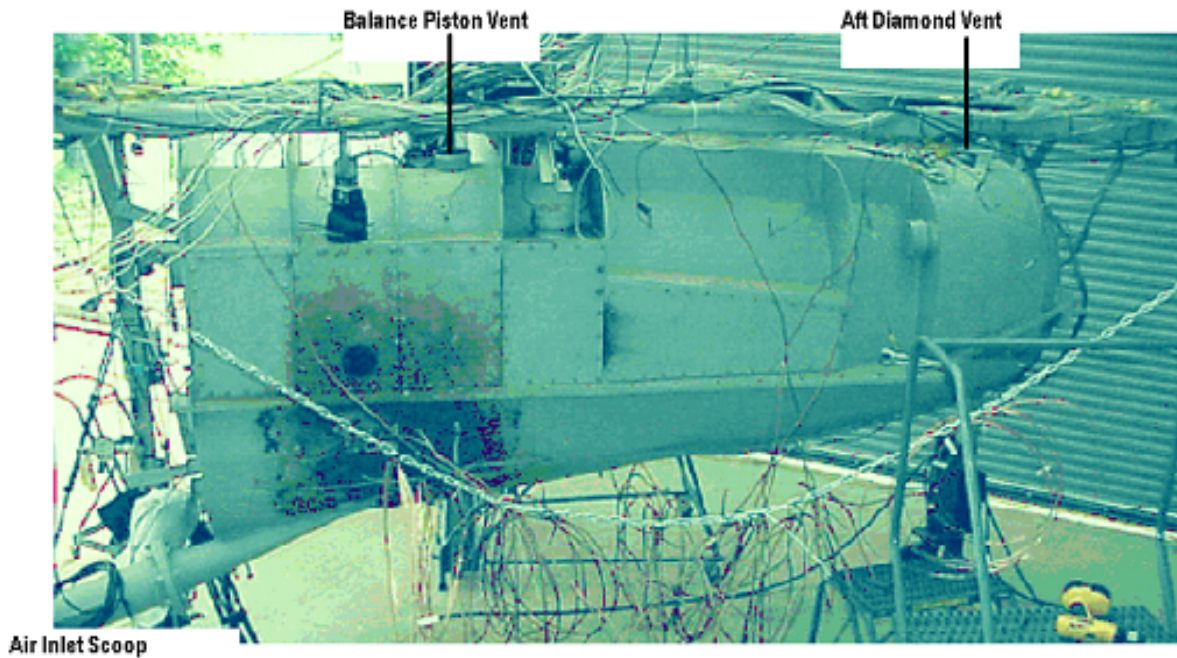


**Figure 8-119. Ground Test Nacelle 'Iron Bird' Simulator.**

In conjunction with the rearward taper of the airframe, the nacelle is generally tallest and widest near the forward end, narrowing towards the aft. At various sections, there are larger cavities around the engine sides and top with additional space for air circulation. The lower nacelle surface slopes smoothly up from the forward to the aft, crossed by five ribs of varying heights. There are roughly four longerons running along the lower nacelle surface. The two central longerons end about 0.6 m before the aft end. The engine, a hollow cylinder in the ground simulator, extends from the forward to the aft of the nacelle. The engine diameter is nominally 0.77 m with a slight narrowing over the front 0.61 m to a minimum diameter of 0.62 m. From 0.81 m aft to the aft end of the nacelle, the engine is uniformly 0.77 m in diameter.

The outer surface of the engine is generally smooth, although various clutter items are attached as described below. In addition to the ribs and longerons, the most significant clutter is located near the forward end of the nacelle. It is dominated by a gearbox assembly located from 0.1 m to 0.75 m behind the forward end and primarily below the engine. The gearbox assembly is a collection of several parallelepiped and cylindrical objects of varying sizes that obstruct the flow in the large space between the engine and the lower nacelle in the vicinity of the air inlet scoop. Additional large parallelepiped clutter objects are located along the engine, particularly on the port side as far back as 1.5 m behind the forward end. Smaller clutter, primarily tubing and wire bundles, exists along the lower half of the engine across the length of the nacelle. Some of this smaller clutter has been identified as a potential reflight surface because of the relatively low thermal capacity and rapid heating to very high temperatures. The afterburner control vanes at the aft end of the nacelle have not been included in the computational model because the setup (initially) focused on fire scenarios near the forward end of the nacelle.

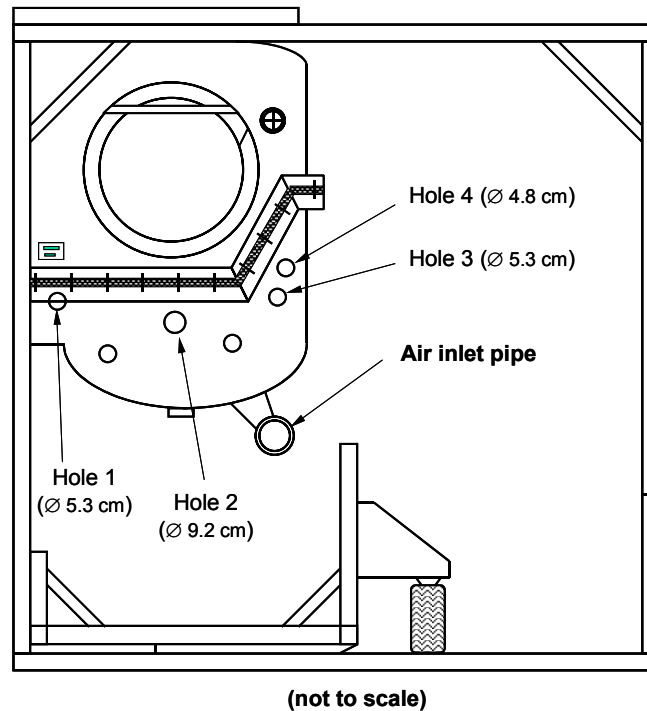


**Figure 8-120. Drawing of Front Face of Ground Test Nacelle.**

In order to apply realistic boundary conditions for the VULCAN simulations, it was necessary to measure the inlet and outlet flows from the nacelle simulator under ambient conditions without fire. The openings shown in Figure 8-119 and Figure 8-120 are not the geometric ventilation paths. The various ventilation paths, such as the balance piston vent, aft diamond vents (both upper and lower), and AMAD bay ventilation paths in the front, have been "sized" to provide the flow distributions predicted in the airflow analysis conducted by Northrop-Grumman.<sup>80</sup> The simulator is designed for testing at one flight condition, traveling at 0.55 M (Mach number) at sea level. Given this restriction, three nominal flows were selected to correspond to three major flight conditions: high-speed, high-altitude cruise, loiter, and precision approach. These flows are 0.96 kg/s, 0.68 kg/s, and 0.57 kg/s, respectively. The air is supplied from a centrifugal compressor driven by a gas turbine. The inlet flow is measured using a calibrated turbine meter. There is adequate straight pipe, according to ASME Standards,<sup>81</sup> and a flow straightener between the compressor and the turbine meter. Likewise, there is adequate straight pipe downstream of the turbine meter, and downstream of the 45° elbow, there is an Etoile swirl-removing conditioner in the straight pipe leading to the nacelle. The supply air pressure was measured with a water manometer immediately downstream of the turbine meter. The air effluxes were measured at each of the outlets separately under steady state. The air temperatures in the nacelles were measured with thermocouples at four locations, one on each side and near each end of the nacelle. The airflow out the aft diamond vent was measured with a pitot rake. The airflow in the other outlets was measured with a calibrated vane anemometer and stopwatch. Air pressures in the nacelle were measured at three locations using an inclined water manometer. All airflow data were corrected to ambient conditions at the time of test in order to determine the mass balance.

The nominal mass flow of air was set on the control console by setting the speed of the gas turbine driving the blower. There was some small variation in flow, less than 6 %, with a period of many seconds resulting from the gas turbine-mounted controls. During the test run at each rate, at least four readings were observed from each thermocouple and manometer. Considerably more data were recorded from the turbine meter. The vane anemometer, which was used for all air efflux measurements, except that from the aft diamond vent on top, was equipped with a mechanical totalizer. Consequently, a stopwatch was used to record the period of observation in order to obtain the average flow. The pitot rake and its converging ductwork came equipped with an electronic data output of its own, and the readout that was selected was that of volumetric flow at atmospheric conditions. Its period of observation was about 1 min, and two such observations were recorded for each test condition. All data were observed and recorded manually in view of the steady-state conditions. The automatic data acquisition system is designed for capturing transient fire events in the nacelle simulator and, therefore, would generate far more data than were required for this test. All data were averaged to provide a mean for each steady state. The observations could not be made simultaneously, and since there was some long-period variation in the flow, this introduced an additional uncertainty.

The proportional distribution of air effluxes remained nearly constant throughout the range of inlet flows and, therefore, the actual mass flows are nearly proportional to the total inflow. There were several surprising observations during the tests. The first was that there was no perceptible flow in or out of the bottom aft vent. It could be that the very fine mesh screen ( $\approx 50$  /cm) which covered this vent was clogged with soot and rust particles or that the flow pattern inside the nacelle was directed away from this vent by the interior ribs. The second was the rather large variation, proportionately speaking, in the average pressures measured inside the nacelle, the range being greater than the mean. The third observation was a highly asymmetric velocity profile across the top aft vent. Most of the flow was exiting from the port side of the diamond; the velocity out the starboard side was measured with the vane anemometer to be  $\approx 20$  % of that out the port side. The pitot rake apparatus was designed to observe an overall average of that efflux collected by the converging duct.

The only corrections made to the pretest VULCAN model were the fact that no flow from the aft bottom vent and the actual, measured vent areas were used instead of their previous estimates. In retrospect, the only assumption which had any consequence was that of a uniform pressure throughout the interior of the nacelle simulator. As mentioned above, these large variations were unexpected, and they contributed significantly to the differences between the actual flow distribution at the boundaries and those predicted. It was predicted that half the flow would exit from the top aft vent. In fact, closer to two-thirds of the flow exited at that location. Consequently, the model predicted about 6.5 % more flow leaving via the Balance Piston Valve and 8.5 % more by the four AMAD vents in the front bulkhead. The test predictions of the model as adjusted for the actual vent areas are shown in Table 8-16.

In discussing the agreement between model and test in the total flow and average pressures, the test was a calibration of the nacelle simulator. In constructing the model, it was assumed that the balance piston vent and aft top vent would behave as parallel orifices and that the AMAD vents would behave more like nozzles. A weighted average of these coefficients of discharge was predicted to be 0.733. By actual test and calibration, it was determined that the effective coefficient of discharge equals 0.614. This value implies that all the vents behave essentially as sharp-edged orifices. This value of the coefficient of discharge correlates very well within the published data for the vent Reynolds number range, during test, of 1680 to 6800, for which the coefficient is 0.613 to 0.605, respectively.<sup>81</sup>

**Table 8-16. Comparison of Predicted vs. Measured Pressures and Flows.**

Inflow (kg/s)	Predicted Pitot Pressure (Pa)	Measured Pitot Pressure (Pa)	Measured Average Nacelle Pressure (Pa)	Predicted Average Nacelle Pressure (Pa)	Bias Ratio
0.92	145.2	93.0	380.6	380.4	-0.00041
0.65	71.4	53.7	181.6	187.3	0.03151
0.52	47.1	too small	118.2	123.6	0.04570

### 8.6.3 Test Matrices and Decision Tree

The test plan and test matrices were made to correspond to VULCAN simulations previously run to predict the test results. Twenty-five fire tests were conducted in the NAVAIR ground nacelle simulator to validate VULCAN simulations. This simulator was equipped with a four-nozzle suppressant distribution system. JP-8 pool fires (see Table 8-13 for pool areas) were considered in a variety of locations in the nacelle where the collection of fuel was likely, and both the suppressant flow and the overall air flow through the nacelle were varied to simulate a wide range of operating conditions. Tests were run also for reduced air flow. However, because of limitations on the rate of injection imposed by the HFC-125 vapor pressure, it was not possible to reach a condition where suppression failed at lower air flows. That was in agreement with the predictions that for lower airflows the overall mass fraction of agent for the attainable injection rates was always sufficient to extinguish the fires. The effects of varying the inhomogeneities were also investigated by capping individual nozzles.

The planning for the tests and the computer simulations resulted in the following test matrices with decision tree:

In test sequences 1 through 5, there are 11 to 14 tests indicated with no repeats.

1. First sequence: Pools in B1, B2, and B3C3. Airflow: 1 kg/s. All nozzles. Vary the suppressant injection rate. (3 tests)
  - a. Standard suppressant injection rate.
  - b. If 1.a. suppressed, 50 % injection rate.
  - c. If 1.b suppressed, 25 % injection rate. End.
  - d. If 1.b fails to suppress, 75 % injection rate. End
  - e. If 1.a fails to suppress, 150 % injection rate.
  - f. If 1.e suppressed, 125 % injection rate. End.
  - g. If 1.e fails to suppress, 200 % injection rate. End.
  - h. General procedure: Given the results of a test, with the first test nominally at the standard injection rate, successful suppression will lead to a 50 % reduction in the rate of injection and failed suppression will lead to a 50 % increase. A possible sequence of injection rates (suppression results) would be “std” (suppress), “50 %” (fail), “75 %” (?). If the second test had resulted in suppression, then the final injection rate would be “25 %.”

2. Second sequence: Cap Nozzle 2. Airflow: 1 kg/s. (2 or 3 tests) 4 are listed
  - a. If 1.a. fails to suppress, try with pool B3C3 only. Standard injection rate.
  - b. Pools in B1, B2, and B3C3. Standard injection rate.
  - c. If 2.b. is suppressed, try reduction in suppressant injection for 2.b (only pool B3C3). Suggest intermediate injection rate from Sequence 1.
  - d. If 2.a suppressed, try reduced suppressant rate for all pools that gave suppression in the first sequence.
3. Third sequence: Cap Nozzle 1. Airflow: 1 kg/s. (2 or 3 tests)
  - a. If 3.a. fails to suppress, try with pool B2 only. Standard injection rate.
  - b. Pools in B1, B2, and B3C3. Standard injection rate.
  - c. If 3.b. is suppressed, try reduction in suppressant injection for 3.b (only pool B2). Suggest the intermediate injection rate from Sequence 1.
  - d. If 3.a suppressed, try reduced suppressant rate for all pools that gave suppression in the first sequence.
4. Fourth sequence: Cap Nozzle 3. Air standard injection rate. (1 or 2 tests). Pools in B1, B2 and B3C3. Use lowest injection rate where suppression succeeded in the first sequence if this differs from standard injection rate.
  - a. 75 % injection rate.
  - b. 50 % injection rate.
5. Fifth sequence: Repeat first sequence with airflow at 0.5 kg/s. (3 tests). This sequence might best be done before capping any nozzles to help map out the operation space.
  - a. 50 % injection rate.
  - b. 75 % injection rate.
6. Repeat tests in all sequences that bracket suppression.
7. Tests with reduced masses of agent (70 %, 43 %, and 32 %). Airflow: 1 kg/s.
8. Tests with 100 % agent at reduced injection rate. Airflow: 0.75 kg/s.
  - a. Minimum injection rate of agent.
  - b. Slightly lower airflow; 0.73 kg/s.

Suppressant injection rate was defined as “standard” for the standard rate of injection nominally used in the qualification tests, “50 %” for half that rate of injection, “75 %” for  $\frac{3}{4}$  that rate, etc. The procedure for changing the suppressant injection rate was to change the bottle pressure with a fixed suppressant mass. If any set of the pool fires were unstable, the air flow was reduced. When capping nozzles, the agent flow for a given bottle pressure was reduced somewhat. The bottle pressures led to suppression without the inhomogeneities caused by removing nozzles.

### 8.6.4 Actual Test Program

As the tests progressed through the decision tree and matrices, the sequence of tests was modified to adjust to the findings, in particular the seeming dependence of the success of extinguishments on the agent injection rate of the agent. As a result, the enumeration of Test Series 7 and 8 above were changed to Test Series 5 and 1 below. Series 8 was a repeat of certain tests in Series 1 (e.g., 8b = 1b). The actual path was:

1. First sequence: Pools in B1, B2, and B3C3. Airflow: 1 kg/s. All nozzles. Vary the suppressant injection rate. (3 tests)
  - a. Standard suppressant injection rate.
  - b. If 1.a. suppressed, 50% injection rate.
  - c. If 1.b fails to suppress, 75% injection rate.
  - d. Repeated b and c for replication assurance.
2. Second sequence: Cap Nozzle 2. Air flow: 1 kg/s.
  - a. Try with pool B3C3 only. 75% injection rate.
  - b. Pools in B1, B2, and B3C3. 75% injection rate.
  - c. If 2.b suppressed, 50% suppressant rate for pool B3C3.
  - d. Standard injection rate.
3. Third sequence: Cap Nozzle 1. Air flow: 1 kg/s.
  - a. Pools in B1, B2, and B3C3. 50% injection rate.
  - b. Pools in B1, B2, and B3C3. 75% injection rate.
  - c. Pools in B1, B2, and B3C3. 75% injection rate and 0.75 kg/s air flow.
  - d. Pool B3C3 only. 75% injection rate.
  - e. Pool B1 only. 75% injection rate.
4. Fourth sequence: Cap Nozzle 3. Air flow: 1 kg/s.
  - a. Pools in B1, B2, and B3C3. 75% injection rate.
  - b. Pools in B1, B2, and B3C3. 50% injection rate.
5. Fifth sequence: Reduced mass of agent and airflow 1 kg/s.
  - a. 50% injection rate.
  - b. 75% injection rate.
6. Repeat tests in all sequences that bracket suppression.
7. Reduce agent mass. Airflow: 1 kg/s
  - a. 69% of agent and standard injection rate.
  - b. 69% of agent and 75% injection rate.

- c. 43 % of agent and standard injection rate.
  - d. 32 % of agent and 116 % standard bottle pressure.
8. Test with 100 % agent at reduced injection rate. Airflow: 0.75 kg/s
- a. Minimum agent injection rate.

### 8.6.5 Instrumentation

Supply airflow measurement was made using a 15.24 cm turbine meter (Sponsler Co., Inc., Model SP6-CB-PH7-C-4X, S/N 130619). When calibrated in water, the meter had an relative uncertainty of  $\pm 0.75\%$ . Temperature measurements were made using 21 type K thermocouples with an uncertainty of  $\pm 1\text{ }^{\circ}\text{C}$ . Two digital stopwatches with an uncertainty of less than 0.1 s over 15 min period were used for time measurements. Fuel quantities for the pools were metered using graduated cylinders with an uncertainty of  $\pm 5\text{ mL}$ . Four video cameras were used to record the existence of fire and its extinguishment inside the nacelle. Other instruments included a dead weight tester from Druck Co. with a range of (0 to 71) MPa and an uncertainty of  $\pm 0.02\text{ MPa}$ , a pressure gage from NoShok with a range of (0 to 7.1) MPa and an uncertainty of  $\pm 0.04\text{ MPa}$ , and a pressure transducer from Patriot Gage Co. with a range of (0 to 20.7) MPa and an uncertainty of  $\pm 0.1\text{ MPa}$ .

### 8.6.6 Test Procedure

These tests focused on extinguishing JP-8 pool fires contained by structural ribs and longerons along the lower nacelle surface. Prior to the testing, the bottom of the nacelle was lowered and the spaces between the ribs were sealed from their normal drain holes so that each could become a container for fuel. In the tests, three pools (Figure 8-114) were used: B1, B2 and B3 (or B3C3, indicating that the pool crossed one longeron). Prior to the tests, measured quantities of water were added to each pool, and the dimensions of the resulting pools were recorded to document the surface area of each pool as a function of liquid contained in the pool.

In most of the tests, all three pools were ignited because this provided the strongest fire source. In several tests, only the first or third pool was used in conjunction with fewer agent-distribution nozzles in order to assess the spatial distribution of the agent in both the VULCAN model and the real nacelle. The burning rate and the nacelle temperatures were observed to be substantially lower when a single pool was burned, as predicted in the VULCAN pretest simulations.

The mass of agent to be used in each test was measured by the difference over the tare of the empty bottle on a calibrated scale. HFC-125 was the agent used in all tests. The rate of injection was controlled by the nitrogen pressure in this bottle, and three rates of injection were targeted by setting the bottle pressure to one of three values: 3.55 MPa, a rate roughly 75 % of standard design, 1.9 MPa, and a rate roughly 50 % of the standard 0.85 MPa. At these ambient temperatures the vapor pressure of HFC-125 was about 0.85 MPa so that no nitrogen charge was added for the lowest pressure and rates. Nitrogen is somewhat soluble in this agent, and consequently the fire-suppression agent in these tests was a mixture of both HFC-125 and nitrogen; the latter was ignored in the VULCAN simulations. The suppressant bottle discharges downward so that the initial discharge is driven by the nitrogen pressure, which drops adiabatically as liquid agent is displaced from the bottle. At an intermediate pressure, the rate of pressure change slows; this is associated with agent discharge driven largely by the boiling of the agent or the

dissolved nitrogen. For the lowest bottle pressure there is no nitrogen-driven stage. The last stage of the discharge is gaseous agent and nitrogen flowing from the bottle together. The pressure profiles from several tests, using all of the nozzles, are shown in Figure 8-121. The discharges from the two tests denoted 1a(21) and 1a(25) are essentially the same conditions, as are the four tests denoted 1b(21), 5d(25), 8a(26) and 1b(26). The scatter in these pressure profiles is indicative of uncertainties attributable to, for example, ambient temperature changes that may heat the bottle during the few minutes that the test is being set up. Such uncertainties were estimated to be roughly  $\pm 10\%$ .

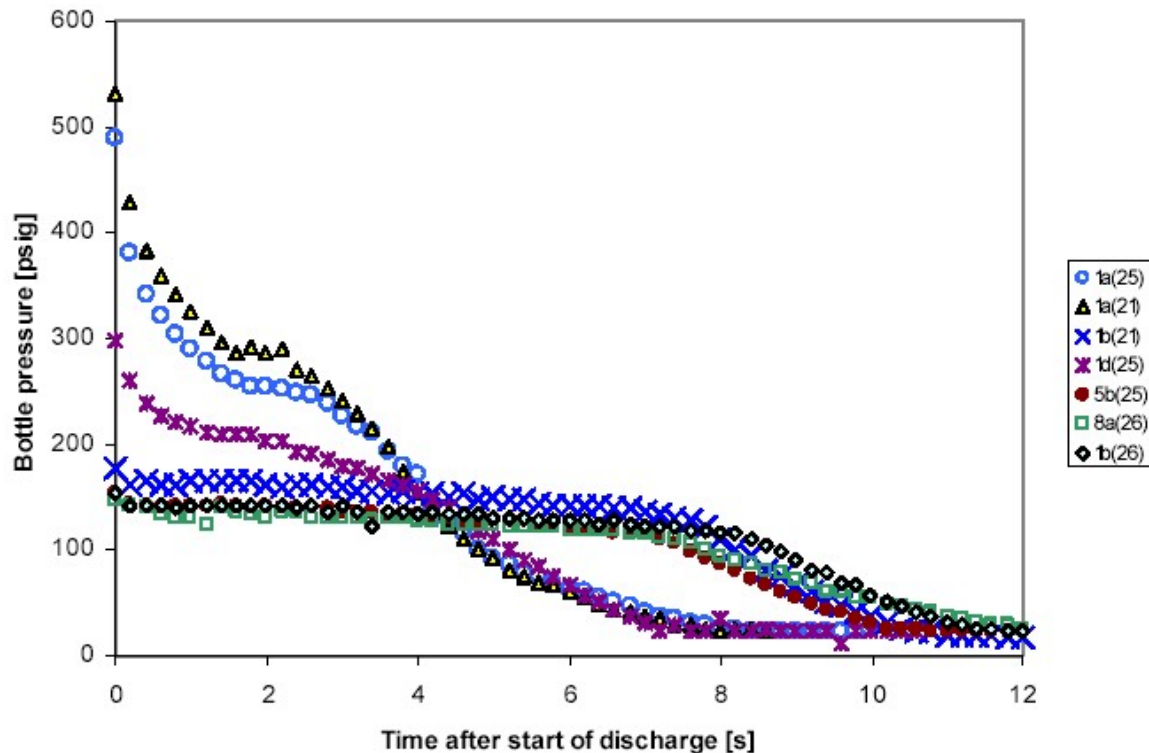


**Figure 8-121. Transient Bottle Pressure during Discharge for Various Initial Pressures with Nozzles Discharging a Total of 3.2 kg of HFC-125.**

Once the bottle was filled, it was installed into the distribution piping on the nacelle, and its manual safety valve was opened. Predetermined quantities of fuel were poured from graduated cylinders into the pools chosen for each test. At the end of each test, the remaining fuel was drained from each pool so that the amount consumed could be accounted; these data, along with the elapsed time of the test, gave an estimate of the heat-release rate during the test.

Igniting the pools of JP-8 fuel at ambient temperatures was challenging. The bottom of the nacelle was warmed with hot air to enhance the volatility of the fuel and to reduce heat losses. A minimum airflow from the blower at idle was established to provide sufficient air for combustion. An electric igniter was inserted over each pool in turn while a more volatile fuel, pure ethanol, was sprayed onto the pool. Once the pool ignited, it required about 30 s to begin vigorously burning. After all pool flames had been established, the airflow was ramped up to the predetermined rate, either 1 kg/s or 0.5 kg/s, according to the turbine meter. This steady flow was maintained for about 15 s to 30 s before the agent was released. The elapsed period of burning was recorded with stopwatches as well as by the digital data acquisition system.

This system also recorded the signals from the array of 21 thermocouples in the nacelle. The indicated temperatures did not attain steady state over the duration of the fires. Four video cameras recorded the views inside and outside the nacelle, from which elapsed times for extinguishment were extracted.

After each release of agent, a reduced airflow was maintained to cool the nacelle and remove potentially inflammable vapor. Then the remaining fuel was collected and measured in the graduated cylinders.

For the tests in which a nozzle was removed by capping the end, the sequence was repeated also by lowering the bottle pressure until suppression failed. The general sequence for changing the injection rate was to reduce the injection rate by 50 % if the previous attempt succeeded and to increase the injection rate back to 75 % of the standard rate if the previous attempt failed to extinguish. The lowest attainable injection rate was 50 % of the nominal designed rate, so this process results in bracketing the suppression in proximity to 100 %, 75 %, and 50 % of normal injection rates. The nominal bottle pressures corresponding to these tests were 0.84 MPa, 1.9 MPa, and 3.55 MPa. While these were relatively wide margins, the available resources did not allow for additional tests to narrow these bands. The tests actually conducted are summarized in Table 8-17.

**Table 8-17. Summary of Full-Scale Tests Conducted.**

Test Indicator*	Air Inflow (kg/s)	Pools	Nozzles	Suppressant Mass (kg)	Bottle Pressure (MPa)	Target Suppressant Discharge Rate (kg/s)
1a (25)	0.91	All	All	3.18	3.55	1.1
1a (21)	0.91	All	All	3.18	3.55	1.1
1b (21)	0.91	All	All	3.18	0.84	0.5
1d (25)	0.91	All	All	3.18	1.83	0.8
5b (25)	<b>0.46</b>	All	All	3.18	1.83	0.8
5d (25)	<b>0.46</b>	All	All	3.18	0.84	0.5
7a (26)	0.91	All	All	<b>2.20</b>	3.16	1.1
7d (26)	0.91	All	All	<b>2.20</b>	1.86	0.8
8b (26)	<b>0.68</b>	All	All	3.18	0.83	0.5
1b (26)	0.91	All	All	3.18	0.9	0.5
2d (27)	0.91	<b>B3C3</b>	<b>No Nozzle 2</b>	3.18	3.55	0.7
2b (27)	0.91	All	<b>No Nozzle 2</b>	3.18	1.9	0.6
2d (27)	0.91	All	<b>No Nozzle 2</b>	3.18	3.55	0.7
2a (27)	0.91	<b>B3C3</b>	<b>No Nozzle 2</b>	3.18	1.9	0.6
3d (27)	0.91	All	<b>No Nozzle 1</b>	3.18	1.9	0.6
3b (27)	0.91	All	<b>No Nozzle 1</b>	3.18	3.55	0.8
3c (28)	<b>0.68</b>	All	<b>No Nozzle 1</b>	3.18	1.9	0.6
3e (28)	0.91	<b>B1</b>	<b>No Nozzle 1</b>	3.18	1.9	0.6
3d (28)	0.91	<b>B3C3</b>	<b>No Nozzle 1</b>	3.18	1.9	0.6
4a (28)	0.91	All	<b>No Nozzle 3</b>	3.18	1.9	0.6
4b (28)	0.91	All	<b>No Nozzle 3</b>	3.18	0.84	0.4
7c (28)	0.91	All	All	<b>1.36</b>	3.55	1.1
7d (28)	0.91	All	All	<b>1.02</b>	4.14	1.1

Note: Variations from the baseline conditions, apart from bottle pressure, are indicated in bold face.

\* The alpha-numeric indicates the test conditions described in the Actual Test Program. The number in the parentheses is the date when the tests was conducted.

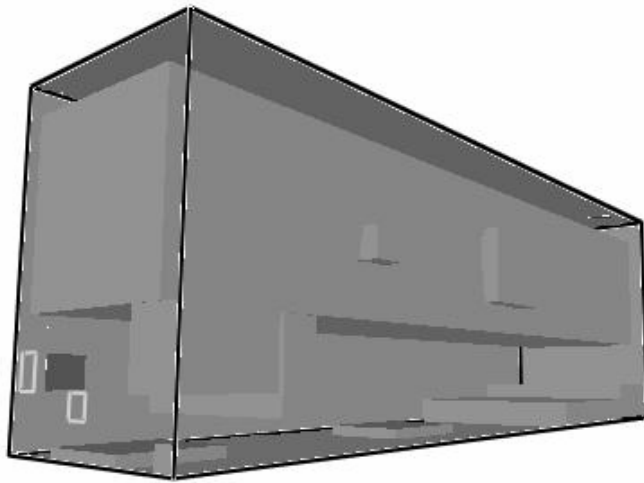
### 8.6.7 Test Results and Comparisons to Simulations

The tests are enumerated in Table 8-18 in chronological order; these test numbers will be used in the discussion that follows. In addition to VULCAN, simulations were also performed using FDS and FPM to predict the results of the fire tests. Figure 8-122 and Figure 8-123 show the nacelle configurations used in the FDS and FPM simulations, respectively. The rectilinear shape of the nacelle simulator is the result of the Cartesian coordinate system used in FDS and FPM.

**Table 8-18. Comparison of Fire Test Results and Pretest Simulations.**

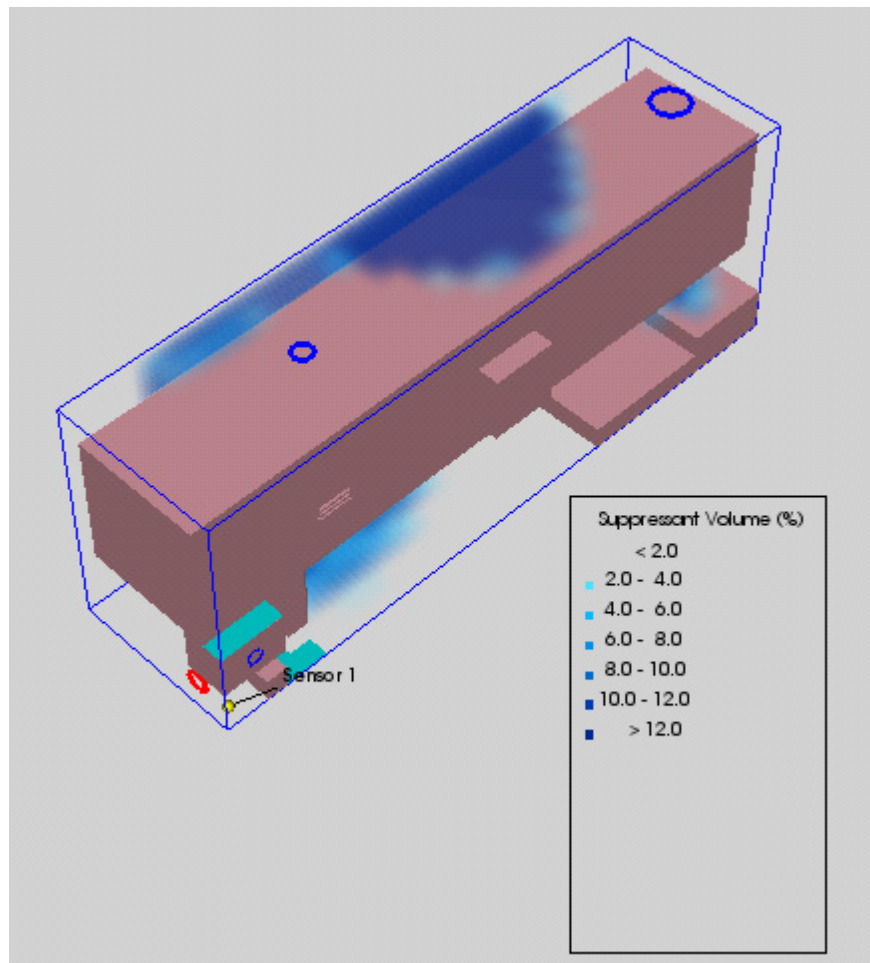
Test Plan		Fire Test		VULCAN	FPM	FDS
Test Number	Alpha-numeric Designator	Measured Time to Extinguish (s)	Agent Injection, Rise Time (s)	Predicted Time to Extinguish (s)	Predicted Time to Extinguish (s)	Predicted Time to Extinguish (s)
2	1a	Out in 1.3 s	6.8	1.1 (e)	2.0	2.0
3 & 12	1c	Accelerated burning	10.0	Marginal out	Not out	Not out
5	1d	Out in 5.2 s	7.0	1.9 (e)	2.0 to 3.0	2.6
6	5d	Out, no data	No data	1.9 (e)	1.0 to 2.0	2.6
7	5b	Out in 4.4 s	9.5	Out	1.0	< 5.0
8	5a	Out >6.3 s	4.4	1.9 (e)	< 3.0	1.9
9	5b	Out in 4.85 s	5.0	n/av	1.0	3.0
10 & 11	8b	Out in 2.3 s	9.6	n/av	< 2.0	3.6
13	2a	Out in 11.2 s	6.5	Not out	Not out	6.5
14	2d	Not out	10.4	Not out	Not out	> 4.0
15	2b	Out in 28.9 s	7.2	3.4 (e)	Relight > .6	7.0
16	2c	Not out	9.3	Not Out	2.0 to 3.0	13.0
17	3a	Not out	10.8	Not out	Not out	Not out
18	3b	Out in 6.0 s	5.6	1.5 (e)	7.0	18.6
23	4b	Not out	13.8	n/av	2.0	19.5
24	7a	Out in 3.9 s	3.8	n/av	4.0	16.8
25	7b	Out in 1.8 s	2.4	n/av	3.0, relight @ 6.0 ?	18

Table 8-18 also shows a condensation of all tests for which simulations were available. The primary observations therein include whether or not the fire was extinguished, the model predictions, the period of agent injection, and an estimate of the observed times-to-extinguish versus the predictions. These latter required interpretive judgment and the application of “rules of thumb” unique to each simulation program to decide when extinction was complete. Similarly, for the actual fire test data, while the injection period was acquired, the link between the recording video and the data-acquisition system had failed, unbeknownst to the test engineers. Consequently, the synchronization of the visual data to the agent-injection transient was not available during post-processing. The time of extinction was clearly observable with an uncertainty of  $\pm 0.1$  s, but the initiation of mixing the agent could be observed only by a sudden increase in the intensity of the fire. The uncertainty of this observation is estimated to be  $\pm 2$  s.



**Figure 8-122. Nacelle Configuration Used in FDS Simulations.**

**Figure 8-123. Nacelle Configuration Used in FPM Simulations.**



Test 2 was the “standard” test arrangement. It used the full bottle pressure, the full mass of agent, and all the discharge nozzles and all the discharge locations that were used to qualify the system. As expected and predicted, the fires were extinguished.

In Test 3, the rate of injection was reduced to the minimum, which was the vapor pressure of HFC-125, pre-calculated to be about 50 % of the standard rate. For replication, this test was repeated a few days later, as Test 12. What was observed seemed to be accelerated burning. At this lowest rate of injection, flames came shooting out of every opening in the test nacelle, and the fires did not go out. From the video records and personal observations, it seemed that the injected agent only served to stir up the gases in the nacelle in such a way as to promote better mixing. In consequence, a much more intense fire resulted until the end of the injection period.

The only difference between Tests 5 and 6, which were otherwise a replicate pair, was the order in which the pools were filled. Normally (and in Test 5) they were filled from the front (B1) aft. In Test 6 they were filled front, back, and then middle last, in order to control for loss by evaporation during the period of filling. The reason for this change was the observation that more fuel disappeared from the middle pool than from the other two. There was no change in the test result, and this confirmed observations both during the test and from the viewing the video records that the airflow in the nacelle blew the fuel out of the second pool (B2) in visible drops toward the flame front over the pool B3C3. In both these tests, the agent was injected at about 75 % of the standard rate; in both cases the fires were extinguished.

In Test 7, a proportionality question was investigated. Here, the injection rate was again set at about 50 % of standard, but the airflow also was reduced by half. Even with the extended injection period, the fires were extinguished promptly. In this test, the concentration of agent in the ventilating airflow was identical to that of Test 2, and the obvious conclusion may be drawn. Following this test, the question arose whether or not the vigorous airflow itself was a major factor in “blowing out” the fires. In this test, the pool B3C3 was filled to the standard 2 L, and after the fire was established and stable there, the airflow was increased to the standard rate. The observed result was the most vigorous blow-torch seen, and it was concluded that range of airflows in these tests were insufficient to “blow out” the fires.

Test 8 was the first to investigate the possibility of using less agent; the mass of agent was reduced to 2.2 kg. Using the standard airflow and injection rates, again the fires were extinguished promptly, as in Test 2. Test 9 was identical, except that the injection rate was reduced to about 75 %. As in Test 5, the fires again were extinguished, proving that the “standard” mass of agent was more than sufficient to extinguish these pool fires.

In Tests 10 and 11, the question of proportionality was investigated further. In this replicate pair, the airflow was reduced to 75 % and the injection rate to 50 % (the minimum). In terms of agent concentration relative to airflow, these tests were similar to Test 5, and in the end the result was the same. However, visual observations of the test showed that it took perceptibly longer to extinguish under these conditions, which indicated that the edge of the extinction envelope was near.

In some tests, the standard, successful distribution system of four nozzles discharging the agent was degraded by capping one nozzle at a time and discharging the agent into the nacelle through the remaining three. In Tests 13 through 16, Nozzle 2, which discharged athwart near the front of the nacelle, was capped. In Tests 16 through 21, Nozzle 1, which discharged upwards at the same location as Nozzle 2,

was capped. In Tests 22 through 23, Nozzle 3 was capped. Nozzle 4 was so remote from the fires, toward the aft, outboard end of the nacelle, that it was never altered.

Test 13 was conducted to verify fire-modeling predictions on the effect of poor distribution of agent. Nozzle 2 discharged athwart under the engine. It was predicted by two out of three simulations that this pool fire would not be extinguished, since the only pool fueled and enflamed was B3C3. This was a configuration which was close to the edge of the extinction envelope. The injection rate was set at 75 % of standard, as in Test 5, except in this case the critical nozzle was capped, and only one pool instead of three was used. In fact, the fire did finally go out, but it took more than 11 s to extinguish.

In Test 14, all three pools were lit, and the injection rate was reduced to about 50 %. The model predictions were the same for this case as for Test 13, but this time the fires were not extinguished. This means that FDS, which predicted correctly for Test 13, gave the only “wrong” result this time. In conclusion, it seems that when the models predict different outcomes, the edges of the actual extinction envelope are nearby.

To illustrate how close to the edge of the extinction envelope these tests were, Test 15 replicated Test 13, except that all three pools were lit. In this case, the fires were extinguished. However, the elapsed time to extinction was abnormally long, almost 30 s. Perhaps the greater mass of products of combustion acted to suppress the fires further.

The varied outcomes of the three prior tests led to conducting Test 16, in which only one pool, B3C3, was lit, and the injection rate was reduced to about 50 %. In this case, all three models predicted extinction, and the fires did indeed go out.

In the next series of tests the original, logical sequence was followed with Nozzle 1 capped. As before, in Test 17 the injection rate was set at 50 %, and all three models correctly predicted the outcome. Likewise, in Test 18 the same configuration was set except that the injection rate was set to 75 %. In this test also, all three models correctly predicted the same outcome of extinguishment.

The next three tests, all with Nozzle 1 capped, are not shown in Table 8-18. Test 19 established an airflow of 75 % of standard and an injection rate at 75 %, and even with Nozzle 1 capped the fires were extinguished. This one presented an equivalent proportion of agent to airflow as if both were standard. In Test 20, only pool B1 was enflamed, and with standard airflow and a 75 % injection rate, that fire was extinguished, but with difficulty because it took several seconds to go out. This test was similar to Test 13 except for which pool was fueled. In the same manner, Test 21 was similar to Test 13 including that the fire was in pool B3C3 only, but in this case the fire did not go out. No simulations of these tests were done.

Nozzle 3 was capped in Tests 22 and 23; otherwise Test 22 was a replicate of Test 5, and Test 23 was a replicate of Test 3. For these configurations, Nozzle 3 made no difference: the two tests in each pair had the same outcomes. The fires in Tests 5 and 22 were extinguished; the fires in Tests 3 and 23 did not. The injection period of Test 23 was the longest of any test. A simulation in VULCAN was not run; FPM predicted extinguishment, as did FDS, but again note the elapsed time before extinction, which indicates that this test also approached the edge of the envelope.

All the tests conducted with less agent were successful in extinguishing the fires in all three pools. Standard conditions were set for all these tests. The first instances were reported above for Tests 8 and 9. In Test 24, the mass of agent was reduced to 1.36 kg, and the bottle was at standard pressure. In Test 25, the mass of agent was reduced to 1.02 kg, and the bottle pressure was increased to 4.14 MPa to increase the rate of injection. All fires were promptly extinguished. The most likely deduction may be that the rate of injection is the most important factor in extinguishing fires.

The 25 tests were conducted to explore the edges of the extinguishment envelope for this ground nacelle simulator. Two of these tests were conducted to determine whether or not fires could be stabilized in individual pools (B1 and B3). It was demonstrated that these pools could sustain a fire, which agreed with VULCAN simulations, although the VULCAN simulations indicated that the stability of fires in individual pools was sensitive to heat losses. Specifically, if the heat losses associated with conduction through the pool to the nacelle were 50 % of the heat flux to the pool (essentially reducing the vaporization rate by 50 %), then certain pools, not employed in the present series of tests, could fail to sustain fires. In the test, it was necessary to apply heat sources (heat lamps) to the nacelle under the pools to minimize heat losses just to get the fires stabilized, and this lends support to the VULCAN observations.

Of the remaining tests, two were replicates of the first two tests in order to gain confidence in the results; in each replicate pair, the results were identical. Because of the vapor pressure of HFC-125 and the inability to light or stabilize fires in certain pools, some pretest VULCAN simulations could not be investigated. Consequently certain tests were run without pretest simulations. However, across a similar range of parameters, these results were in agreement with the trends of the VULCAN simulations.

Ideally, the pressure data shown in Figure 8-121 could be used to determine the actual suppressant discharge rate to a level of accuracy similar to the accuracy of the inlet airflow meter. During the post-test data processing, this was done by calculating the adiabatic discharge of liquid agent from the bottle and assuming that the flashing and two-phase flow occurred at the throats of the nozzles, as reported in Smith et al.<sup>82</sup> However, during the tests the discharge rate had to be estimated. For this purpose, discharge rates identical to those in the VULCAN simulations were employed. Specifically, with all nozzles discharging, the 3.2 kg of HFC-125 was presumed to discharge uniformly over 3 s, 4.5 s, and 6 s for bottle pressures of 3.55 MPa, 1.9 MPa, and 0.85 MPa. The discharge rate was presumed to be reduced in accordance with the reduction in the total nozzle area when nozzles were capped. The assumption of constant discharge rates in the VULCAN model would be a source of disagreement with the test results. This uncertainty in the rates varies over the duration of the injection period, and the errors in the estimates provided here are likely to be greatest in the earliest fraction of a second and during the latter periods. If the rate of suppressant injection were averaged over the significant few seconds, say the first 2 s to 3 s of the injection process, the uncertainties are on the order of  $\pm 15\%$ .

The results of the tests employing all nozzles are shown in Figure 8-124. Blue bars represent successful extinction, while red bars represent a failure to suppress the fire. In all of these cases, the VULCAN predictions were in agreement with the test results.

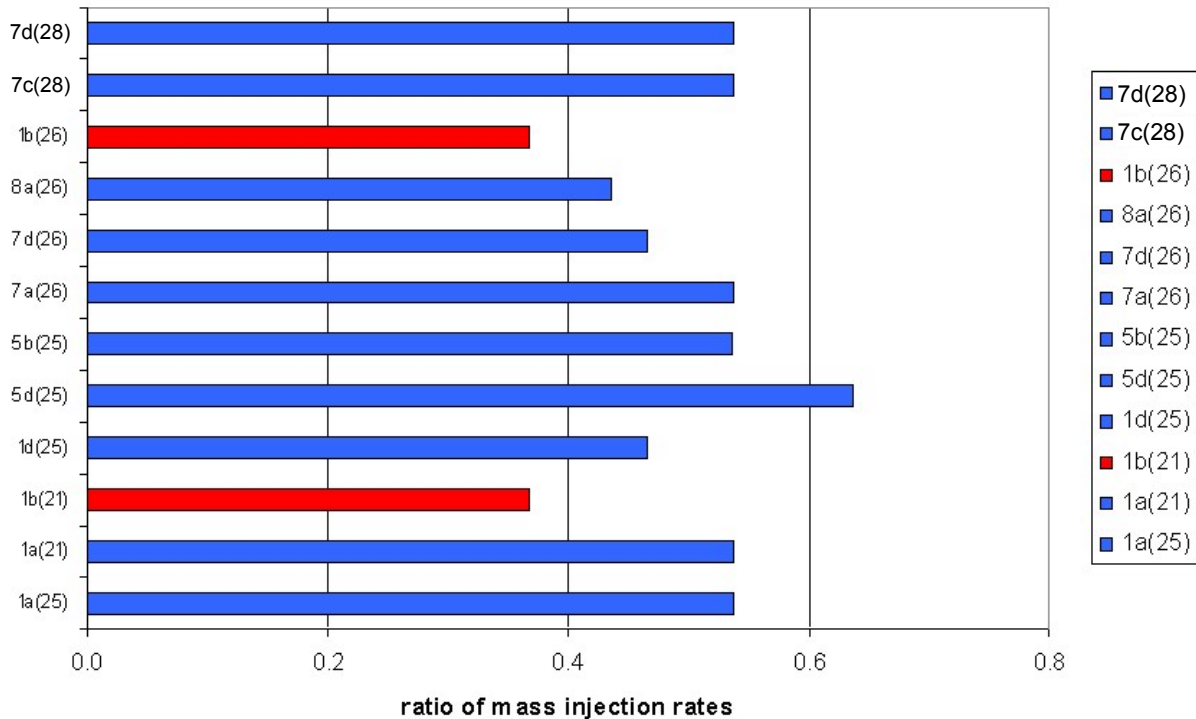


**Figure 8-124. Results of Tests with All Nozzles Used.**

The results of tests with labels starting in “1”, “5”, or “8” correspond to baseline cases using approximately 3.2 kg of suppressant at varying bottle pressures and airflows. This series can be viewed as varying the ratio of the suppressant mass injection rate to the total (air + suppressant) mass influx. Suppression is observed to fail when this ratio is below (approximately)  $0.4 \pm 0.04$ . Where the airflow is greatest and the bottle pressure is lowest, the total uncertainty is estimated to be  $\pm 19\%$ . For reduced airflows (0.68 kg/s) or increased bottle pressures (1.82 MPa), suppression was always successful. That the ratio of injection rates exceeds the cup burner mass fraction<sup>4</sup> by a factor of 1.4 (0.4/0.28) probably indicates the degree of inhomogeneous agent distribution in the system.

In Figure 8-124, the four tests with labels starting “7” are where the mass of suppressant was reduced from 3.2 kg to 2.2 kg, 1.4 kg, and 1 kg. All of these tests resulted in successful suppression of the fire. In each of these cases, the rate of injection was close to that for the designed conditions. It was estimated that the bulk of the suppressant was injected in 3 s for 3.2 kg, in 2 s for 2.2 kg, and in 1 s for 1 kg to 1.7 kg, which reinforced the importance of the ratio of injection rates. The VULCAN simulations were conducted only with 3.2 kg and 2.2 kg of agent, and these simulations agreed with the tests. No VULCAN simulations were run for agent masses less than 2.2 kg.

Figure 8-125 summarizes results for which one of the four nozzles was capped. Blue bars represent successful extinction, while red bars represent a failure to suppress the fire. In all of these cases, the VULCAN predictions were in agreement with the test results. Green bars indicate cases where suppression was successful in the tests but was indicated to fail in the VULCAN simulations.

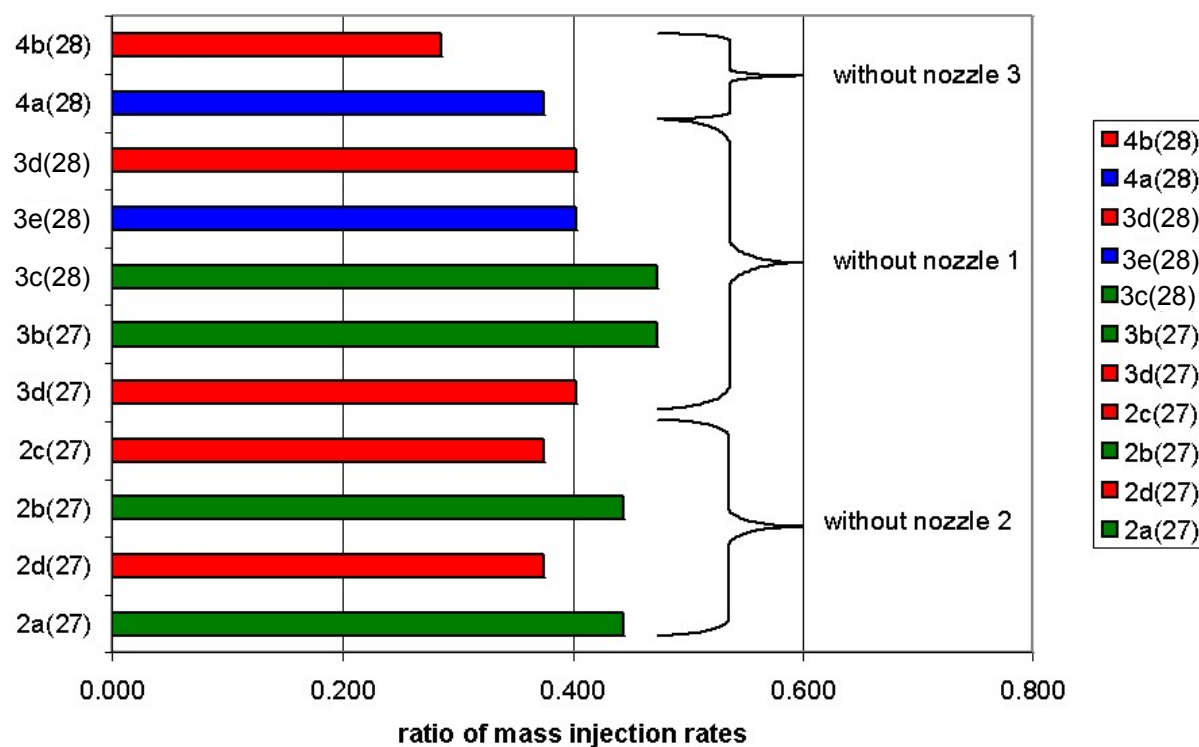


**Figure 8-125. Results of Tests with One Nozzle Capped.**

Capping a nozzle has two effects. First, the total nozzle area is reduced so that, for the same bottle pressure, the suppressant injection rate is reduced proportionally. The second effect of capping a nozzle is to increase the inhomogeneity of the distribution inside the nacelle. Greater inhomogeneity requires a greater ratio of injection rates to achieve successful suppression. VULCAN simulations predicted that higher inhomogeneity would result by capping either Nozzle 1 or Nozzle 2, but not Nozzle 3.

The results of tests, with Nozzle 3 capped, are indicated by the labels with the prefix “4” at the top of Figure 8-125. The ratio where suppression fails trended toward lower values than with all nozzles. Whether or not the degree of inhomogeneous distribution actually decreased and performance of the system increased by capping Nozzle 3, should not be concluded based on the present results, even if implied by the tests. Nozzle 3 injected suppressant into the upper nacelle, far from any of the pool fires. For this reason, a reduced concentration of suppressant in the upper nacelle may not have influenced agent effectiveness at the locations of the fires. The uncertainties in the suppressant injection rate and the lack of replicate tests do not allow definitive conclusions to be drawn. Tests where Nozzle 1 was capped are indicated with the prefix “3” in Figure 8-125. In some tests only specific pools were ignited in order to find the locations where fires failed to be extinguished (Table 8-17). The tests where all pools were ignited are 3b, 3d, and 3c. In these cases, there was a difference between the VULCAN results and the tests. The VULCAN simulations predicted a failure to suppress the fire in test 3b, although the fire was extinguished in the tests. (The VULCAN prediction for 3c was not actually run, but extrapolated.) Reducing the injection rate to a ratio 20 % less led to a successful prediction, as in case 3d. VULCAN tended to predict failure to suppress before it actually occurred. This may be because the mixing rate within the VULCAN simulation erred on the low side. In highly cluttered areas bounded by walls, the current clutter model did not account properly for enhanced mixing near the wall. Clutter models may

improve these predictive capabilities, but the fact that the VULCAN predictions tended to be conservative, with a safety factor on the order of 20 %, is preferred and acceptable. In terms of the ratio of the mass injection rates, the tests indicated a critical value between 0.4 and 0.45, a statistically insignificant increase over the 0.4 ( $\pm 15$  %) found in tests employing all nozzles. The VULCAN predictions indicated that the critical ratio of mass injection rates was between 0.45 and 0.55. Tests 3e and 3d, in which only pools B1 and B3 were filled, were done to ascertain the regions of the inhomogeneous agent distribution that led to failed suppression. The results indicate that low concentrations occur in the vicinity of pool B1 but not pool B3, which agrees with the VULCAN simulations. The ability of VULCAN to identify regions where fires cannot be suppressed is very useful.

The results of tests for which Nozzle 2 was capped are indicated by the labels with the prefix “2” in Figure 8-125. As with the previous examples, the VULCAN simulations indicated a failure to suppress at the higher injection rates because of a reduced homogeneity of agent distribution. Test results showed that the failure to suppress occurred at the next decrement in the injection rate, the same as when Nozzle 1 was capped. This likewise indicates a 20 % safety factor relative to the VULCAN simulations. The failure to suppress when either nozzle is capped occurs at a ratio of injection rates again spanning 0.4, the same as in the tests with all nozzles. VULCAN simulations capping Nozzle 2 did indicate greater inhomogeneity in the fire region.

The pretest VULCAN simulations correctly predicted the success or failure of extinction in nearly all cases. In only two cases were there disagreements between the VULCAN predictions and the test results. In both of these cases, when either of the two forward nozzles was capped, the test results found that the fires were suppressed using a bottle pressure 25 % lower than the VULCAN simulations had predicted. This indicates that the VULCAN simulations were somewhat conservative in their predictions of the mixing in the forward nacelle region.

## **8.7 IMPROVED TRANSPORT OF WATER TO FIRES**

### **8.7.1 Background**

As noted in Chapter 1, initially the NGP research was directed at the full range of weapons systems in which halon 1301 systems had been installed. Water sprays or mists were (and are) viable alternatives for some of those platforms. Accordingly, the NGP supported efforts aimed at improving the efficiency of getting water sprays or mists to the fires. In particular, two techniques for improving water droplet transport to fires will be described and discussed: (1) electrically charged water mist and (2) a self-atomizing form of water.

### **8.7.2 Electrically Charged Water Mist**

#### **Background**

It is well known that hydrocarbon flames contain electrical charges because of the process of chemiionization.<sup>83</sup> In chemiionization, flame radicals react to form electrons and positive ions at temperatures much lower than those required for thermal ionization. In a normal flame, both positive and negative ions (primarily formed by electron attachment) are formed in addition to the electrons. The high mobility of the electrons results in the outer region of the flame being negatively charged by the electrons

and the bulk of the flame region being positively charged by the preponderance of positive ions. Much of what is known about flame ionization has been learned from studies of premixed flames<sup>83,84,85,86</sup> although some diffusion flame studies have been conducted.<sup>87</sup>

For real fuels and real fires (almost always diffusion flames) there are a number of considerations which could lead to either increases or decreases in the flame ionization, but these cannot be quantified at this time. For example, real fuels contain impurities (e.g., metals) which can greatly increase the ion concentration. On the other hand the formation of soot particles in cooler regions of a fire act as sites to which electrons will attach. This keeps the negative charge closer to these regions of the fire than would occur if the electrons were free to diffuse away on their own. Thus, electron attachment may reduce the charge separation (at least in the fire plume) that normally makes flames appear to be positive.

While it cannot be certain which effects will dominate in real fires, there is no doubt that diffusion flames in air behave as though they are positively charged since they are strongly pulled by negatively charged objects.<sup>88, 89</sup>

The application of an external electric field in the vicinity of the flame results in the motion of electrons and negative ions towards the positive electrode and the motion of positive ions in the opposite direction towards the negative electrode. More momentum is generally exchanged by collisions between the positive ions and the neutral gas molecules as compared to the momentum exchanged by collisions with the negative species dominated by electrons. This momentum exchange results in the production of an ionic wind<sup>90</sup> which is a flow towards the negative electrode. This ionic wind is responsible for the large flame displacements reported above, and the effect has been used to control blowoff stability,<sup>89</sup> which can be increased or decreased depending on the orientation of the electrodes that produce the electric field. These effects can be produced with extremely low electrical power levels, on the order of  $10^{-2}$  % of the power released during combustion.

There are several different scenarios in which electric charging of the water mist droplets can interact with real fires. A negatively charged droplet approaching the vicinity of the fire will repel electrons and negative ions, and there will be an attraction between the negatively charged droplets and positive ions.

To distinguish whether the charged mist droplets move toward the flame or the flame moves towards the droplets, the overall mass of water mist per unit volume in a spray based on assumed droplet velocities was computed and compared it to the density of air under the assumption of a water application rate of (1 to 2) L/ (min-m<sup>2</sup>), which is considered to be sufficient to extinguish a heptane pool fire.<sup>91</sup> For example, the mass of the water mist droplets contained in a unit volume is 1.3 % of the mass of air in the same volume for a water flux of 1 L/ (min-m<sup>2</sup>) and a droplet velocity of 1 m/s. The water density relative to air varies proportionately with the water flux and inversely with the droplet velocity. The effective mass per unit volume of the ions was taken as the density of the air since the ions pull the air or other flame gases along with them when they move.

The mass of liquid water per unit volume can vary from a small to a moderate fraction of the mass of the flame gases per unit volume depending on the velocity of the droplets and the temperature of the gases. Of course, the actual droplet flux, and thus the liquid water mass, is decreased if the droplets are evaporating as they approach the flame. Thus, if the water flows are low and/or the droplets experience a great deal of evaporation near the flame, the droplet mass is low compared to that of the ions and the air that contains them so that the droplets can move towards the flame.

Without a mechanism for charge removal, charge would build up and retard the attractive motion between the negative mist and the positive flame gases. This removal can be accomplished if there is an electrical ground in the vicinity of the fire. In many cases the circuit is closed by a conducting floor or wall in contact with the electrical ground. This would be the case for a fire on a ship deck or on metal shelving.

The voltage drop,  $\Delta V$ , across a surface is given by

$$\Delta V = \frac{\rho t I}{A} \quad (8-51)$$

where  $\rho$  is the volume resistivity of any insulating layer such as paint,  $t$  is the thickness of the insulating layer,  $I$  is the total electrical current and  $A$  is the total surface area available through which current passes to ground. Because the currents involved in droplet charging are so small, and the surface area available for current flow to ground through floors and walls is so large, the voltage drop caused by current flow through wall or deck paint should be small. For aircraft applications such as fire extinguishment in engine nacelles, the surfaces are generally not painted so that there is no problem in obtaining a good electrical ground.

Even if the fire's net positive charge is small, the fire can still be a relatively better electrical conductor than the surrounding air due to the presence of charges in it. Thus, the droplets will still try to ground themselves through the fire, and the excess charge that they carry will eventually proceed to an earth ground near the base of the fire.

In addition to water droplets being individually drawn to the flame ions, the presence of a large number of charged droplets results in electrostatic repulsion between the droplets. An electrical ground allows a steady state current composed of the droplet charges to be established under the action of this self-repulsion. The current path could be composed of droplets striking the floor or wall, droplets evaporating and the electrons they carry either passing directly to ground or attaching to a molecule which travels to ground under the influence of the charge induced electric field. Positive ions could move toward the droplets and neutralize them, leaving a net negative charge composed of the fire's electrons and negative ions which are discharged through the electrical ground near the fire's base.

The presence of cooler soot particles in the upper regions of a fire plume may act as sites for flame electron attachment. Repulsion of the negatively charged droplets by the negatively charged soot particles, could be beneficial from the point of view that those droplets might not be swept away by high velocity plume gases. If those droplets are redirected to lower velocity regions outside of the main plume, then they might be pulled in closer to the base of the flame by the positive flame ions or the presence of a surface electrical ground. In any case there are a number of possible situations in which electrical charging will cause water mist to come into closer contact with reacting flame gases.

Safety considerations present only a small concern with the droplet charging method used in this work because the currents involved in mist charging are extremely small. In this program two power supplies were used: a high voltage (15 kV) unit which is not capable of delivering any significant current (200  $\mu$ A) and a lower voltage (5 kV) unit which can deliver 10 mA. The first unit is safe and the second unit can be made safe by installing current limiting resistors. While this is not life threatening in itself, any significant shock could be distracting or disorienting in an emergency situation. The only way such a shock could occur is by direct contact with the charged electrode. For this reason it is recommended that the high voltage electrodes be physically shielded to prevent direct contact with them.

Two references of particular interest for the present study are those of Patterson et al.,<sup>91</sup> performed at the New Mexico Engineering Research Institute (NMERI), and Gottuk et al.,<sup>92</sup> performed at Hughes Associates, Inc. Patterson et al.<sup>91</sup> obtained a large database on uncharged mist extinguishment of heptane pool fires in a well-controlled test chamber environment. Gottuk et al.<sup>92</sup> compared fire extinguishment of heptane pool fires with and without electric charging.

Patterson et al.<sup>91</sup> used water mist to extinguish 5.08 cm diameter heptane pool fires in a 1.07 m × 1.07 m × 2.06 m chamber. Following establishment of the fire for 30 s, the chamber was closed so that there was no further ventilation once the mist was turned on. In spite of their great care in achieving a uniform water flux over their chamber and the absence of ventilation currents, their data exhibits a tremendous amount of variability in extinguishment time as a function of water flux (Figure 8-126), especially for low values of the flux. The curve shown is a cubic fit to the extracted data.

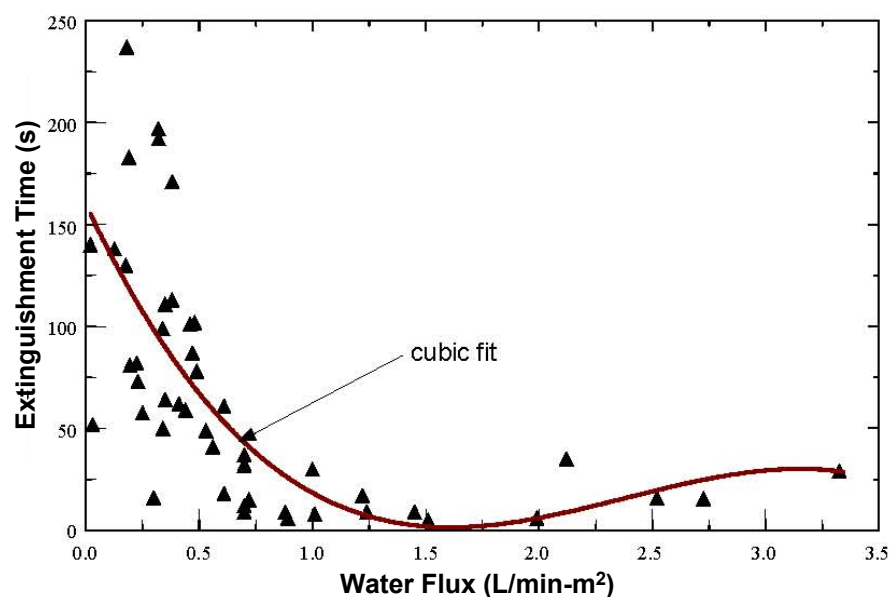


**Figure 8-126. Extinguishment of Heptane Pool Fires by Uncharged Water Mist.**<sup>91</sup>

Gottuk et al.<sup>92</sup> studied the effects of electric charging of water mists on extinguishment of heptane fuel fires. A single mist nozzle was used in an open environment to extinguish a heptane fire in a 10 cm diameter pan. Water was collected to determine the water flux in the same size pan as used for the fuel. Gottuk et al.<sup>92</sup> arbitrarily selected the criterion that a fire was considered to be extinguished if the extinguishment occurred within 20 s after application of the water flow. They reported that this was a useful criterion for their experiments on the basis that fires that were not extinguished in that time were never extinguished, except for one case with electrical charging in which extinguishment occurred in 34 s. Results were reported as groups of the number of cases in which a fire was extinguished out of the number of tests within a range of water collection rates for a given voltage.

Table 8-19 reproduces the fire extinguishment results that appear in Table 3 of the report of Gottuk et al.<sup>92</sup> in the units of water flux used by Patterson et al.<sup>91</sup> Their table shows three ranges of water mist flux and the fraction of the tests in which a fire was extinguished for each flux.

**Table 8-19. Effectiveness of Charged Water Mist Expressed as Percent of Successful Pool Fire Extinguishments.<sup>92</sup>**

	Water Application Rate (L/min-m <sup>2</sup> )		
	5.0 to 5.9	6.0 to 6.4	6.5 to 7.0
Uncharged (0)	0/0	6/13 (46 %)	9/10
+ Charged	0/3	2/6 (33 %)	0/3
- Charged	0/9	3/4 (75 %)	0/0

For the lowest water flux range, no fires were extinguished by the charged sprays; thus no improvement from the charging could have been seen. For the highest water application rate, the positively charged spray was significantly less effective than the uncharged sprays.

It is difficult to draw a conclusion for the middle range of water application rates. A change of a single test result for either type of charged spray gives results that are similar to the uncharged spray tests. It would take more extensive tests in this range to reveal a real effect.

Gottuk et al.<sup>92</sup> concluded that no significant increase in fire extinguishing capability resulted from charging the water sprays and that the most notable effect of charging the spray was spray divergence, resulting in lower water application rates to the fire. Gottuk et al.<sup>92</sup> were also concerned with the safety of the electrical system. However, their observation that charging makes the mist spread out could actually be beneficial, since small uncharged droplets have short horizontal stopping distances which determine how far they can spread from the centerline of a spray nozzle. Charged droplets produce a force on each other that can disperse them to greater horizontal distances. Without charging, extremely high pressures would be needed, or there would have to be an array of a great number of nozzles to achieve a wide distribution of fine water mist spray.

For the NGP, Berman and coworkers<sup>93</sup> at AeroChem Research Laboratories carried out exploratory research to further assess whether electrical charging of water mist could substantially reduce both the time and the amount of water required to extinguish a small pool fire by taking advantage of the electrical properties of flames. The specific objectives of the study were to:

- compare the motion of charged and uncharged water mist droplets near a flame
- determine the reduced time for fire extinguishment due to electric charging of the water mist. The current program addressed ceiling sprinkler extinguishment of compartment fires, and the same principles should hold for aircraft engine nacelle fires. The main technical problem encountered was achieving a uniform distribution of water mist over a significant surface area both with and without charging. Promising results were obtained despite this difficulty, which may be correctable with additional work.

### Experimental Set-up

The fire test chamber used for the experiment is shown in Figure 8-127. The chamber had a steel frame, polycarbonate walls, and a metal flame hood at its top that leads to a duct flow booster exhaust fan. The chamber plan view dimensions were 1.2 m × 1.2 m, and the viewable height through the Lexan window was about 1.8 m. The bottom of the chamber was open with a vertical height of at least 0.3 m, around the periphery of the bottom of the chamber for fresh air to enter. A horizontal beam located about 0.5 m

above the bottom of the sidewalls was used to mount all of the burners and fuel pans. A translating beam located 0.13 m above the fuel pan held the water collection pans used to determine the water distribution. The translating beam was moved out of the way when fire extinguishment tests were performed. The booster fan was at its half point power position for all extinguishment tests. The chamber's metal structural elements, the flame hood, the spray nozzles, the water pipes, the fuel pans, and the water collection pans were all electrically grounded.

### Water Droplet Motion Due to Charging

The hypothesis of this project was that there is an attraction between the negatively charged droplets and the positively charged flame. The first step was to verify that the droplets were being charged and to estimate the magnitude of the charging effect and the corresponding induced motion. Once this was established, tests were performed to detect additional motion of the charged droplets near the flame.

#### *Estimates of Electric Charging and Field Effects*

Initial tests were implemented to determine the electric forces on charged droplets in terms of their motion near a grounded metal screen. A Cone Jet TX-1 hollow cone nozzle was chosen to observe the attraction of the charged mist to grounded objects and fires. It was expected that the droplets dispersed in the hollow cone pattern would be easier to track compared to a solid cone spray nozzle. The characteristics of the TX-1 are given in Table 8-20.

**Table 8-20. Hollow Cone Nozzle Characteristics.**

TX-1 Hollow Cone Nozzle				
Pressure (kPa-g)	206	275	344	412
Mean volume diameter ( $\mu\text{m}$ )	108	101	97	93
Flow rate (L/min)	0.056	0.063	na	0.095
Total spray angle (degree)	na	54	na	na

Charging was produced by an inductive principle in which an electric field is established between a positively charged ring and three grounded wire tips in a pitchfork configuration formed by three soft copper wires that were twisted to form a single basic wire shaft (see Figure 8-128). The positive ring induces electron emission from these grounded wires, and these electrons attach to the droplets. The process is aided by the fact that the electric field also aligns polarized droplets so that the positive ends of droplets point toward the grounded wires. The proximity of a positive end of a nearby droplet produces extra field strength to remove additional electrons from the wire. From principles stated by Kelly,<sup>94</sup> the charges will distribute themselves among the available droplets.

This electrode configuration was typically operated between 5 kV to 15 kV with a Gamma High Voltage Research Inc. dc power supply. This power supply delivered 1 kV output for each 1 V input so that it could be operated with batteries or the low voltage dc normally found in fire control systems (typically 24 V). At 15 kV many droplets tended to head back toward the grounded nozzle body. The maximum effective spreading of the spray pattern occurred at around 10 kV.

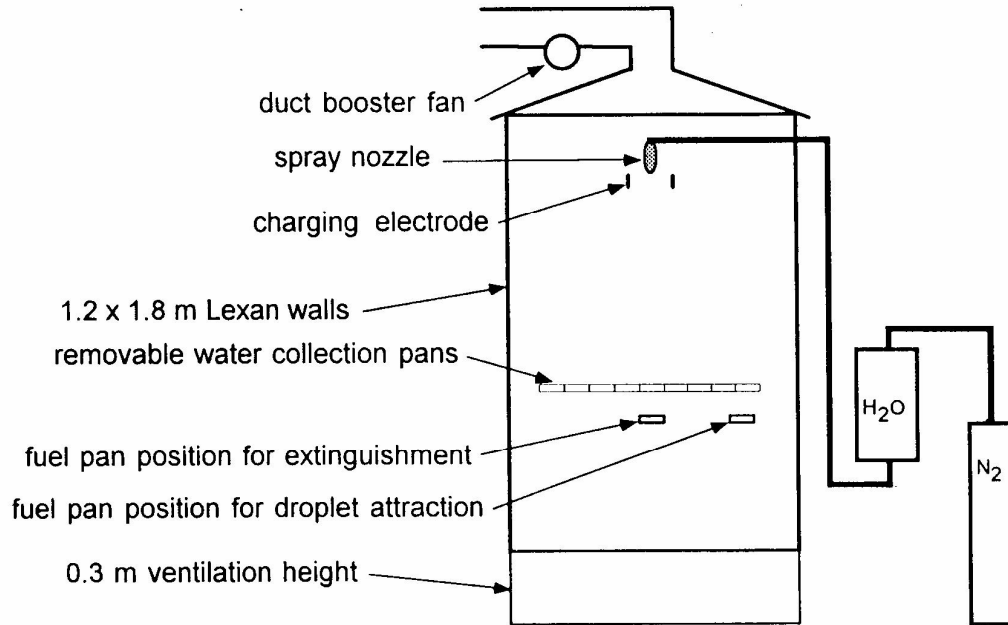


**Figure 8-127. Schematic Sketch of Fire Test Chamber. Metal chamber structure, water nozzle, fuel pan, and water collection pans are all electrically grounded.**

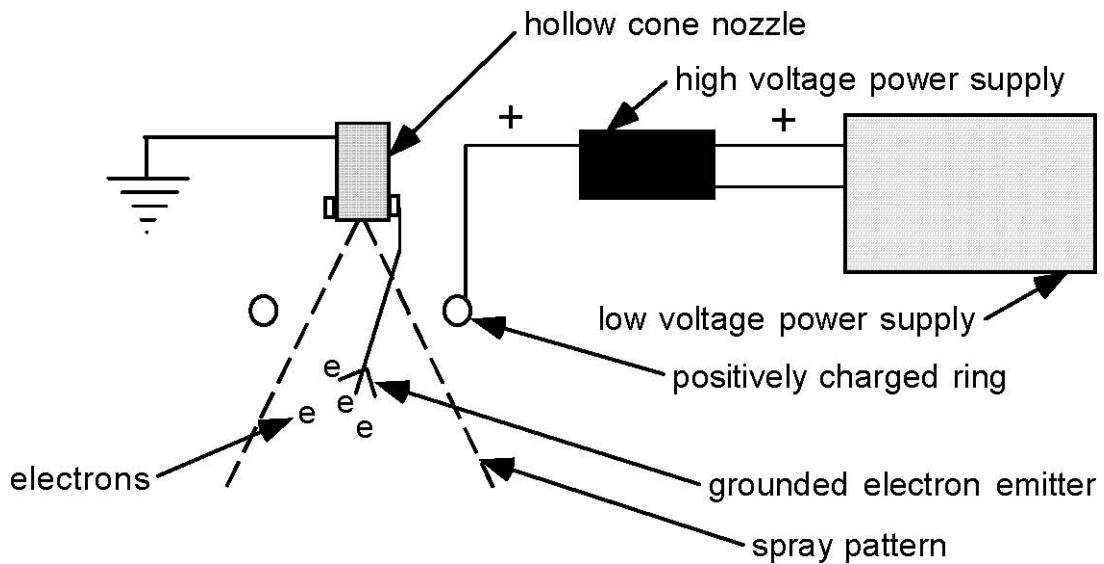


**Figure 8-128. Electron Induction Electrode.**

The metal screen was positioned vertically and displaced about 13 cm away from the nozzle centerline (see Figure 8-129). Applications of 5 kV to 15 kV to a positive inductive electrode showed that the droplets from the TX-1 hollow cone nozzle were strongly attracted to the screen. Moving the grounded electrodes as a whole to different locations in the spray, e.g., directly underneath the nozzle or off to the side, did not seem to make a big difference in the charging effect. Because the droplets traveled nearly horizontally towards the screen, the electrostatic force on them due to their charge and the electric field generated by the bulk of the charged droplets greatly exceeded the net gravitational force on them.

Estimate of the amount of droplet charging can be obtained by assuming that the ratio of the horizontal component of the droplet velocity to its vertical component is the same as the ratio of the droplet's horizontal electrical force to its gravitational force.

$$\frac{F_{\text{electrical}}}{F_{\text{gravitational}}} = \frac{V_{\text{horizontal}}}{V_{\text{vertical}}} \quad (8-52)$$

This relation is valid if the droplet velocities are based on either of two extreme physical limits: (1) the two accelerating forces are equal to the corresponding component of the droplet drag force or (2) the drag is small compared to the accelerating forces.

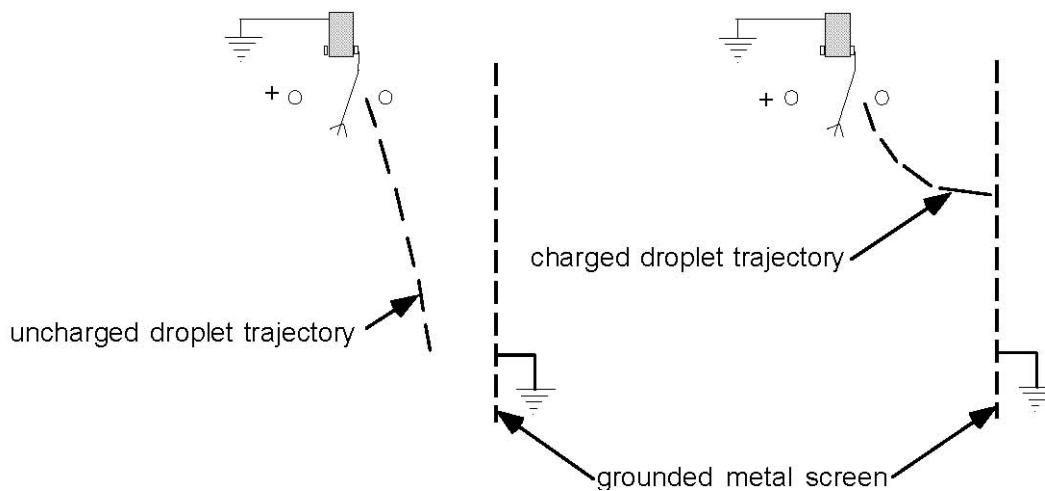


**Figure 8-129. Attraction of Charged Droplets to Grounded Metal Screen.**

The ratio of the forces is

$$\frac{F_{\text{electrical}}}{F_{\text{gravitational}}} = \frac{3q_d E}{4\pi R_d^3 \rho_d g} \quad (8-53)$$

where  $q_d$  is the electrical charge on a droplet,  $R_d$  is the droplet diameter,  $E$  is the electric field strength,  $\rho_d$  is the droplet density, and  $g$  is the gravitational acceleration. An important characteristic droplet charge value is the Rayleigh limit droplet charge  $q_{\text{Rayleigh}}^{95}$ , defined as

$$q_{\text{Rayleigh}} = \sqrt{64 \epsilon_0 \sigma \pi^2 R_d^3} \quad (8-54)$$

where  $\epsilon_0$  is the free space electrical permittivity constant and  $\sigma$  is the droplet's surface tension. The droplet will break up into smaller ones if the droplet charge exceeds  $q_{Rayleigh}$ . For this case,  $q_{Rayleigh}$  is around  $4 \times 10^7$  electrons per droplet. It is common practice to describe the actual droplet charge as a percent of the Rayleigh limit charge. Thus, 1 % of the Rayleigh limit still corresponds to  $4 \times 10^5$  electrons.

The electric field is determined by the distribution of all the charged droplets and the positioning of the high voltage electrode and all the grounded surfaces. Since the charge distribution is not known, it is not possible to determine  $E$  without making some important assumptions and additional computations. However, the product of  $q_d E$  can be estimated from Equation 8-53, and some possible combinations of  $q_d$  and  $E$  can be compared.

Using Equation 8-52 to describe the force ratio and writing  $q_d$  as a percent of the Rayleigh limit value, the electric field vector in volts/meter is

$$E = 71,970 \frac{V_{vertical}}{V_{horizontal}} \frac{1}{\% q_{Rayleigh}} \quad (8-55)$$

It is difficult to estimate the velocity ratio since it is so large, and it varies at different locations. If the ratio is arbitrarily set at 100 and the droplets are charged to 1 % of the Rayleigh limit, then  $E = 7.197 \times 10^6$  V/m, which is more than twice the breakdown voltage value for air of  $3.0 \times 10^6$  V/m. Thus, a droplet charging value of 3 % to 4% (with a correspondingly lower value of  $E$ ) would not be unreasonable. Gottuk et al.<sup>92</sup> estimated that the charging in their case was 4 % for a spray with a similar droplet size. By rearranging Equation 8-55 to solve for percent of Rayleigh charge as a function of  $E$ , the estimate for the percent charging increases if the electric field strength is lower and decreases if the velocity ratio is lower.

### ***Attraction of Droplets to Flames***

Tests were performed with the same positive inductive electrode and TX-1 hollow cone nozzle with flames positioned off to the side of the nozzle centerline instead of a metal screen. First, a small propane diffusion flame was positioned a little over 0.30 m from the centerline of the nozzle (see Figure 8-130). Application of a 15 kV voltage changed the droplet trajectories from a vertically downward direction to a nearly horizontal orientation directed towards the base of the diffusion flame.

Similar tests were instituted for pool fires in a 9 cm diameter pan using heptane in one case and methanol in a second. While there was a noticeable increase in the spray angle due to charging, the trajectories did not display the large horizontal motion observed for the propane diffusion flame and appeared to be more continuously vertical near the fire. Charging seemed to increase the amount of water reaching the pool fire, but this may be due to the effect of self-repulsion which would increase the diameter of the region covered by the spray.

There are indeed differences between the gas diffusion and pool flames. The heptane flame produces more soot particles which can attach electrons after the particles cool. The methanol flame is not expected to produce chemiions.

Estimates can be made for the electric field and charging using the velocity ratio in Equation 8-55, typically on the order of 0.5. If the charging level is the same as in the case of attraction to a metal ground, then the electric field will be on the order of a hundred times weaker relative to the estimates

made in the previous section. In making these estimates, one should be aware that air currents, which have not been accounted for, will also have an effect on the velocity components.

### Fire Extinguishment Tests

Extinguishment time as a function of water flux with and without electric charging for a different nozzle and nozzle arrangement, a different size fire, and a different chamber was obtained in the present study. The fire extinguishment study by Gottuk et al.<sup>92</sup> in an open environment pointed out the importance of charging in changing the water flux. For this reason, almost all measurements of extinguishment time, both with and without charging, were either immediately preceded or followed by a measurement of the water collected at the location of the fuel pool pan.

#### 10 cm Diameter Pool Fire

Much effort was needed to develop a spray system that would provide a uniform distribution of water over a diameter of 1 m, ten times the diameter of the 10 cm diameter fuel pans to be used. A special consideration was that droplets carrying the same sign of electrical charge would tend to repel each other. The effect of the self-repulsion would be to produce spreading of the droplets and reduce the water flow per unit area.

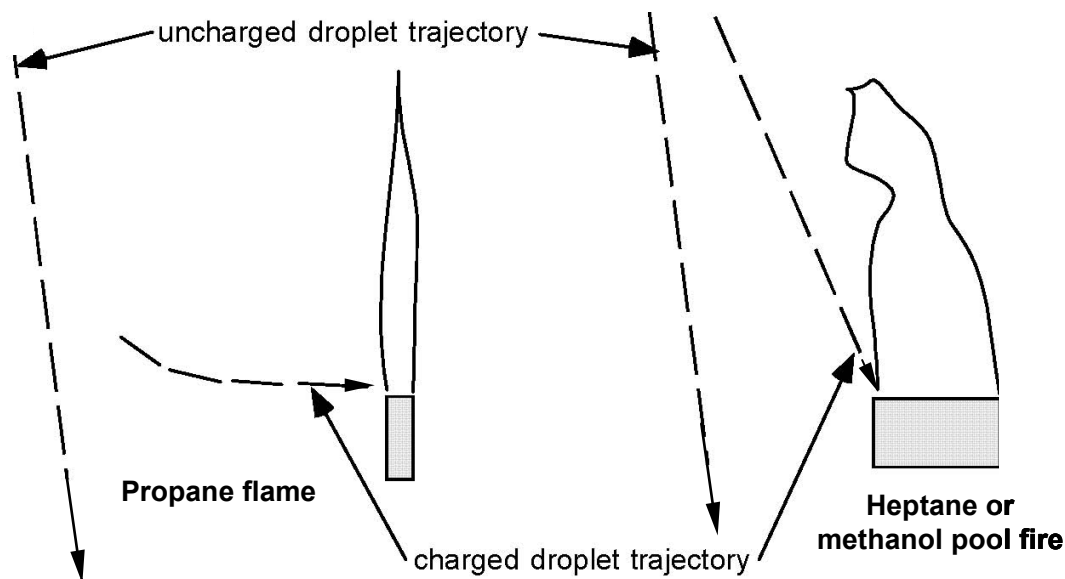


**Figure 8-130. Motion of Charged Droplets near Fires.**

A single nozzle assembly called the 7N, recommended by Spraying Systems, Inc., was used for the experiments (see Figure 8-131). The 7N assembly, which held 7 individual hollow cone nozzles, had a single 2.54 cm water pipe connection which fed one central nozzle and six outer nozzles at a constant radius from the center one. The axes of the outer nozzles were canted away from the centerline. The manufacturer asserted without specific size measurements that the droplets from the individual nozzles crossed paths so that a somewhat uniform spray was produced. Following the manufacturer's guidelines, the operating range was limited to between 687 kPa and 1031 kPa. A water feed system was designed

and assembled with the water pressurized by nitrogen from a regulated high pressure cylinder to cover the range of pressures to be used with the 7N nozzles.

It was expected that different sized nozzles might be needed to cover the range of conditions for the tests. Based on a preliminary test of fire extinguishment with a single nozzle, 0.095 L/min nozzles were selected for the 7N assembly. The plan was to install the 7N assembly with 0.095 L/min nozzles, observe its fire extinguishment performance with and without charging, and purchase one or more additional 7N assemblies with the appropriate flow capacity nozzles to cover the range of testing. Thus, in all cases the overall geometry would remain unchanged whether or not the droplets were electrically charged or the water flow rates were to be changed by replacement of the 7N assembly or individual nozzles. The water flow per unit area would be controlled by varying the water pressure and changing the nozzles. There was little change in droplet diameter in going up or down one size in nozzle flow capacity.

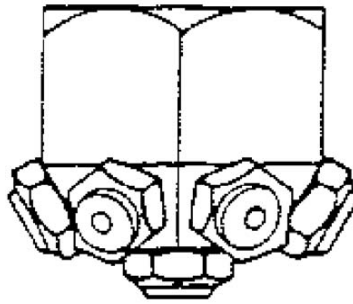


**Figure 8-131. 7N Seven Hollow Cone Nozzle Setup.**

Since extinguishment times with the 0.095 L/min nozzles were found to be short, a lower capacity 7N supplied with seven 0.063 L/min nozzles was obtained to cover the range of lower flow rates and longer extinguishment times. The characteristics of the 7N system with 0.095 L/min nozzles are given in Table 8-21 and those of the 0.063 L/min 7N system are given in Table 8-22.

**Table 8-21. High Flow Capacity Seven Nozzle Assembly.**

7N – 1.5 Seven Hollow Cone Nozzle Assembly			
Pressure (kPa-g)	687	859	1031
Mean volume diameter ( $\mu\text{m}$ )	69	62	59
Flow rate (L/min)	1.060	1.174	1.287
Spray coverage diameter (m)	0.76	0.76	0.76

**Table 8-22. Low Flow Capacity Seven Nozzle Assembly.**

7N – 1 Seven Hollow Cone Nozzle Assembly			
Pressure (kPa-g)	687	859	1031
Mean volume diameter ( $\mu\text{m}$ )	59	57	55
Flow rate (L/min)	0.680	0.794	0.869
Spray coverage diameter (m)	0.61	0.61	0.61

Charging the spray from the 7N nozzles was challenging because of the close proximity of the nozzles to each other. In a more typical setting in which water was supplied separately to a number of individual nozzles, rather than an assembly, it would be relatively easy to assure that the droplets from each nozzle were charged using an individual charging electrode. For the 7N, a single circular large diameter charging electrode was positioned coaxially around the 7N assembly.

A 3.8 cm wide strip of wire screening material was rolled into a circular hoop and fastened on the inside of an 0.2 m diameter ring made of copper tubing (see Figure 8-132). The orientation of the screening material was vertical. It was hoped that this would decrease water collection on the screening and large droplet formation. This strip produced electron emission from both the top and bottom rows.

The cut screen mesh provided approximately 250 sharp points on the top and the same number on the bottom of the electrode to charge the droplets from the outer set of six nozzles with the 7N grounded. The question was if the center nozzle mist would become charged. The rationale was that since the outer and central nozzle sprays crossed over, some charged outer nozzle spray would find its way to the center of the system, and some inner nozzle spray would move out and become charged due to its proximity to the charged outer nozzle droplets. In addition, earlier tests using the inductive approach with grounded wires as the electron source indicated that the ability to charge droplets was not strongly linked to the position of those electrodes.

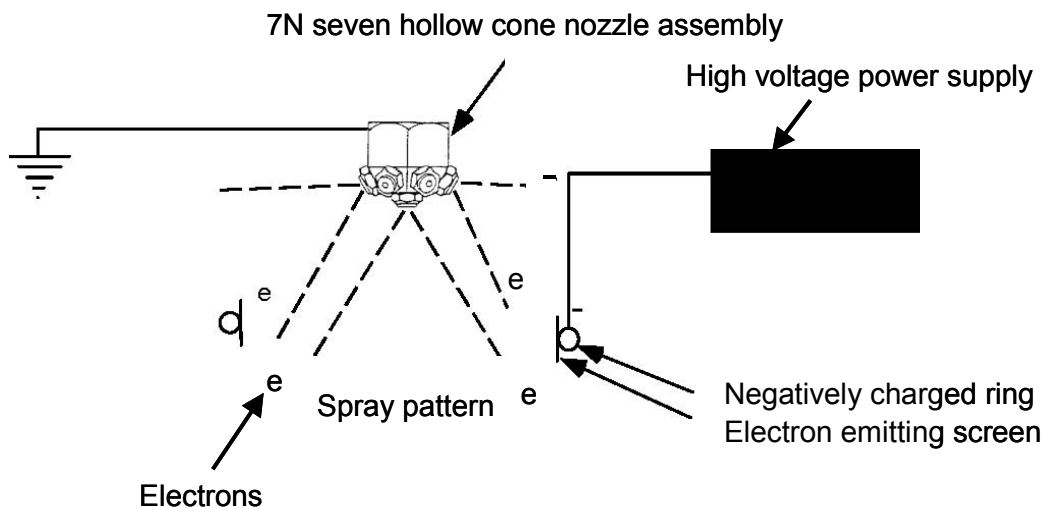


**Figure 8-132. Spray Charging Set-up.**

One might think of an individual multiply-charged droplet near an uncharged droplet as an inductive source of electrons in the sense of inductive wire electrodes. Thus, an uncharged droplet will become polarized when it passes close to a charged droplet. The positive end of a polarized droplet will become aligned with the negatively charged droplet. The additional electric field strength associated with this alignment will result in the transfer of electrons from the charged to the uncharged droplet. In this way, it was hypothesized that a cascade effect could transfer electrons from regions of charged to regions of uncharged droplets. Despite precautions, some large drops formed on the strip electrode and dripped off, but they did not fall into the fuel pan and thus did not affect fire extinguishment. These larger drops were less susceptible to the effects of airflow induced by the ventilation fan or the fire plume. In a more

realistic environment with individual chargers for each nozzle, dripping would not be expected to be important.

Water flux uniformity tests were made using nine 10 cm diameter pans to collect the water (these were identical to the pan used to hold the fuel for the pool fire). These were placed side by side on a beam that could be slid on a rail into position above the fuel pan, and then be moved easily out of the way when fire extinguishment tests were performed. This array of collection pans was about 13 cm above the plane of the fuel pan, and the entire array of pans spanned a distance of 0.9 m.

With all seven of the 0.095 L/min nozzles installed in the 7N, the flow was quite peaked with its maximum off slightly from the centerline of the nozzle (Figure 8-133). Note that Spraying Systems, Inc. asserted that the spray was uniform over a diameter of 0.75 m if the assembly was more than 0.9 m above the collection plane. Thus, the assembly did not operate as anticipated. It was unclear whether this pattern was characteristic of all 7N assemblies or whether it was influenced by the particular chamber in which it was installed. When the 0.2 m diameter multiple nozzle design electrode ring was placed around the nozzle, the spray pattern appeared to be more symmetric, but was still peaked. Dripping from the electrode contributed significantly to the water collected on either side of the main peak at  $\pm 10$  cm from the centerline. While these drops did have a major effect on the water collection, they did not appear to play any significant role relative to fire extinguishment because the water they carried did not interact with the fire and did not splash the fuel surface.

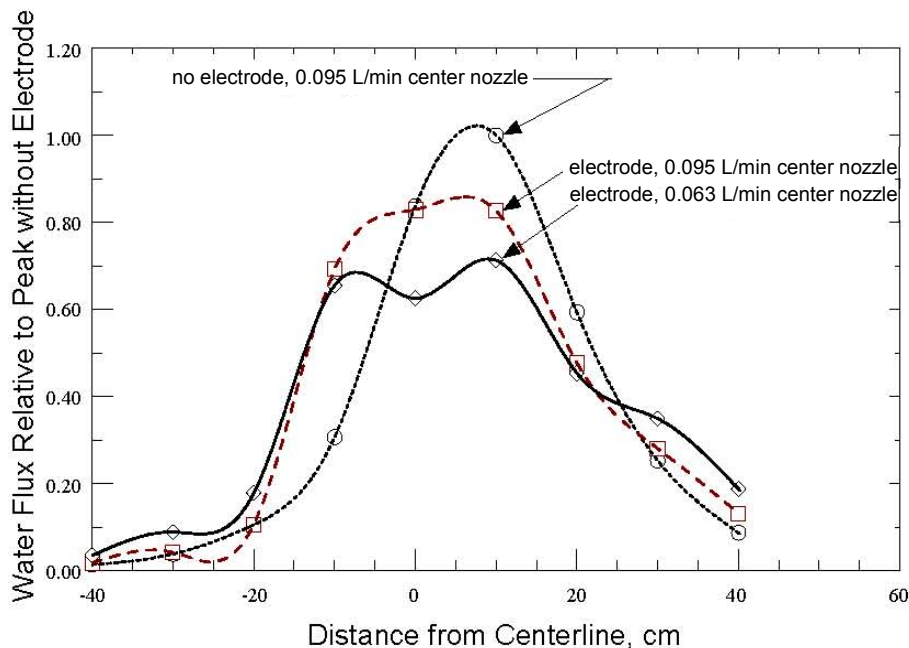


**Figure 8-133. Effect of Center Nozzle Size on 7N Nozzles Water Flux.**

Plugging the center nozzle produced a fairly uniform water flow distribution. In this case, the spray patterns of the 6 remaining nozzles appeared to project further out radially so that the walls of the chamber became wet at a greater height above floor than had been experienced before. It thus appeared that the central nozzle played an important role in determining the spray patterns of the other six nozzles.

Possibly, air entrained by the central nozzle affected the airflow environment that the other nozzle sprays experienced. Unfortunately, the water flux without the center nozzle flow was too small to extinguish the fire being studied. For this reason, a compromise was reached to replace the center nozzle with a 0.063 L/min capacity nozzle and to retain the six other 0.095 L/min orifices in the 7N assembly. This did not produce any dramatic change in the water distribution (Figure 8-133), but it did allow a pressure to be set to provide extinguishment times in a good range for the measurements.

The water flux distribution of the 7N nozzles with the 0.063 L/min center nozzle is shown in Figure 8-134 when the electrode is uncharged and at -5kV. Charging reduces the center water flux and increases that at the edges of the spray pattern slightly. These changes are much less than those observed by Gottuk et al.<sup>92</sup> for a single nozzle. In the case of the 7N nozzles, charging of the outer portion of the spray makes those droplets spread out in all directions, and the outer spray droplet charge density restricts the spread of the inner charged spray.

Experiments to determine the effect of mist droplet charging on the extinguishment of a heptane pool fire were performed in the test chamber. The water spray system consisted of an electrically grounded 7N nozzle containing a central 0.063 L/min nozzle and six circumferential 0.095 L/min nozzles located 1.1 m above the pool fire. A 0.2 m diameter electron emission charging electrode, described previously, was placed coaxially around the water spray system centerline and located about 10 cm below the bottom of the nozzle assembly.

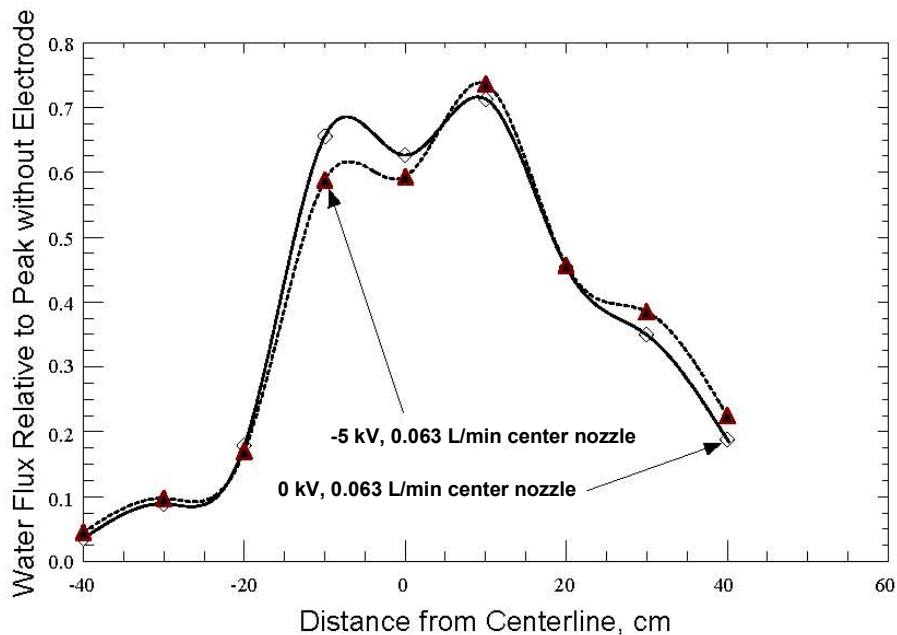


**Figure 8-134. Effect of Electrical Charging on Water Flux Distribution of the 7N Nozzles with the 0.063 L/min Center Nozzle.**

Heptane was poured into a 10 cm diameter, 2.8 cm tall seamless and electrically grounded tin pan until the fuel level was 0.8 cm from the open end. The fuel was ignited and the fire was allowed to burn for 3 min in order to develop a steady state structure. A water flow at pressures between 687 kPa and 1031 kPa was supplied to the 7N nozzles immediately following the initial heating period. Measurements

of extinguishment time were made separately with and without dc electric field charging of the mist. Water flow measurements were made both with and without dc electric field mist charging by replacing the fuel pan with a water pan of the same size as the fuel pan and the nine pans used previously for water distribution measurements.

Since some previous tests had found large effects with low voltage charging, the tests began with voltages on the order of -1 kV and -2 kV at 1031 kPa. Measurements were then continued at -5 kV at this pressure as well as at pressures of 687 kPa and 859 kPa.

Frequent water flow measurements were needed since it was clear that the water flux at a fixed nozzle pressure varied. These variations develop due to changing airflow patterns in the chamber or deposits found in the nozzle, in spite of the use of a 2  $\mu\text{m}$  filter in the water line.

Extinguishment time is plotted in Figure 8-135 as a function of water flux with and without electric charging. Because the voltage level at 1031 kPa did not produce a clear trend for values between -1 kV and -5 kV, all of the charged mist data is plotted together for these experiments. The voltage was maintained at -5 kV for all of the other droplet charging cases. At the higher flows, it does not appear that there is an effect of electric charging. However, electric charging did produce major improvements over the performance of uncharged droplets in the lower water flux range. As the flux was lowered without charging, a flow was reached where significantly greater times were needed to extinguish the fires. The curves can be interpreted as showing a decreased extinguishment time at constant water flux or reduced water flux to achieve a given extinguishment time. This behavior would be beneficial in cases where the water supply for fire extinguishment is limited. It was speculated that the extinguishment time with charging would also increase if the water flux were lowered much more. Data were not taken for smaller fluxes with this nozzle because the water collection values were inconsistent for pressures below 687 kPa.

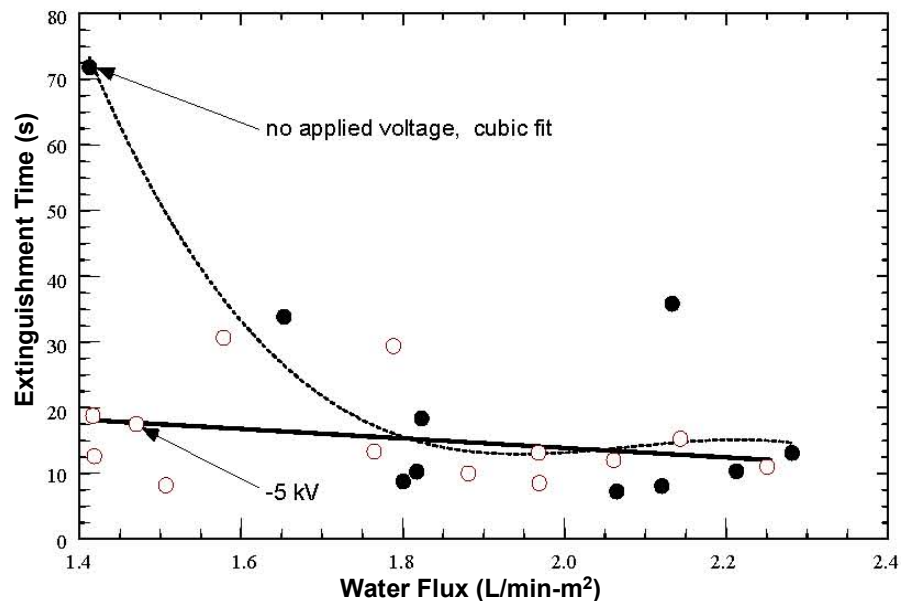


**Figure 8-135. Initial Data on Effect of Electrical Charging for a 10 cm Diameter Heptane Pool Fire.**

The nozzle and electrode were removed, cleaned, and then reinstalled after the above initial set of data had been analyzed to obtain a second set of data. In the new tests, the water collected in the single pan directly below the nozzle increased due to charging, which was different from other observations including the previously mentioned water flux distribution measurements recorded in Figure 8-134. These new data points were added to those previously displayed in Figure 8-135, and the total data set is presented in Figure 8-136. The trend of rapidly growing extinguishment time with decreasing water flux is not as apparent for the uncharged case as in Figure 8-135. For this reason, linear fits to both the charged and uncharged data sets are displayed in Figure 8-136. Again, there is little difference in extinguishment time due to charging when that time is generally small at the higher water fluxes, but the uncharged case still has extinguishment times that are significantly higher, by a factor of nearly 2, than the charged case in the low water flux regime where extinguishment times are larger. The standard deviation of the uncharged data is nearly twice that of the charged results. Thus, the complete set of data still indicates improvement in extinguishment due to charging, even though the validity of the additional data was questionable because of the higher water collection.

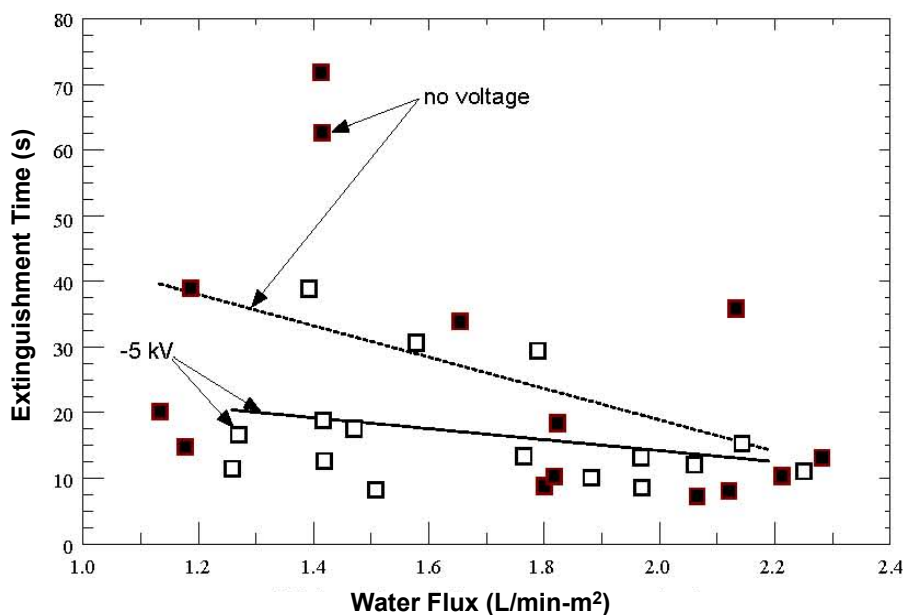


**Figure 8-136. All Electrical Charging Data for a 10 cm Diameter Heptane Pool Fire.**

### *5 cm Diameter Pool Fire*

Because of difficulties in holding the 7N nozzle water flow constant in the water collection pan and the possibility that the center nozzle mist might not be receiving as much charging as the outer nozzle mist, it was decided to perform additional work with a single water mist nozzle and a smaller, 5 cm diameter, fuel pan. More repeatable water collection rates and more effective charging of the mist were expected with the single nozzle. The smaller fuel pan was chosen to maintain the ratio of the spray diameter to the pan diameter much larger than unity.

The lowest flow solid cone from Spraying Systems, Inc. nozzle was the TG-0.3 whose flow characteristics are given in Table 8-23. A coverage area for the TG-0.3 nozzle was not given in the

specifications. However, the spray visually appeared to be relatively uniform over a diameter of 0.25 m to 0.30 m at a distance of 0.7 m from the nozzle. Based on this observation, the ratio of the spray diameter to pan diameter was between 5 and 6.

A new electrode for these tests consisted of a wire screen with a 8.9 cm diameter circle cut out of its center. The cut inside edges of the screen formed the array of wires that emit electrons (Figure 8-137). This screen was positioned horizontally with its center point coincident with the spray nozzle centerline. It was secured to the circular ring electrode that had been used in the positive inductive electrode system discussed previously (Figure 8-128). With the nozzle grounded, an easily visible spreading of the spray pattern was observed with the application of -3 kV. This spreading was increased considerably when the voltage was increased to the maximum value of -5 kV.

**Table 8-23. Solid Cone Nozzle Characteristics.**

TG-0.3 Solid Cone Nozzle				
Pressure (kPa-g)	206	275	344	412
Mean volume diameter ( $\mu\text{m}$ )	250	210	180	160
Flow rate (L/min)	0.195	0.233	N/A	0.277
Total spray angle (degree)	51	54	N/A	59

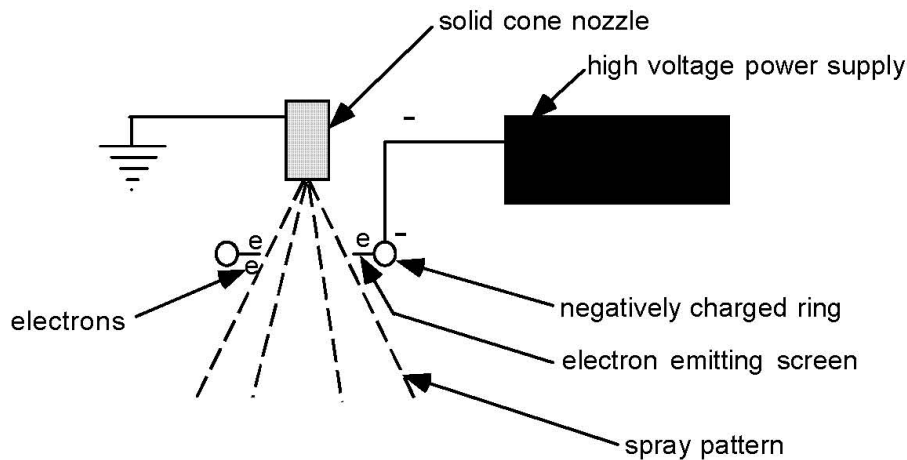


**Figure 8-137. Schematic of Single Nozzle Electron Emission Electrode.**

Heptane was poured into a 5 cm diameter, 1.6 cm tall seamless and electrically grounded tin pan until the fuel was 0.6 cm from the open end (this is almost the same diameter as used in the study of Patterson et al.<sup>91</sup>). The fuel was ignited, and the fire was allowed to stabilize for 1 minute. Water flow at pressures between 206 kPa and 412 kPa was supplied to the TG-0.3 nozzle immediately following the preheat period. Measurements of extinguishment time were made separately with and without dc electric field charging of the mist. In most cases the extinguishment time measurements were followed by water flux measurements in a separate 5 cm diameter pan that was identical with the fuel pan and was placed in the holder that supported the fuel pan.

The distance between the nozzle and the fuel pan was set as 0.7 m. Extinguishment time was then measured as a function of the water flux collected in the 5 cm diameter pan at zero voltage and at -5kV.

When the electrode was charged, there was a considerable decrease in the water flux collected in the pan because of mist spreading. Thus, the nozzle was operated at a higher pressure when charging was applied to obtain the same range of collected water flux rates that had been obtained at lower pressures without charging.

The results plotted in Figure 8-138 show that the expected rise in extinguishment time for the charged case occurred at a lower level of water flux than for the uncharged case. The solid line is a linear fit of the three water flux points for the charged case. A dashed line with the same slope is shifted to the right of the solid line to indicate the general upward trend for the uncharged case. This confirms the general trend seen for the 10 cm diameter fuel pan fire, which also found improved extinguishment with charging. As it was noted for the 10 cm case, the extinguishment times were significantly shorter with charging for the low water flux range in which the uncharged extinguishment times began to grow.

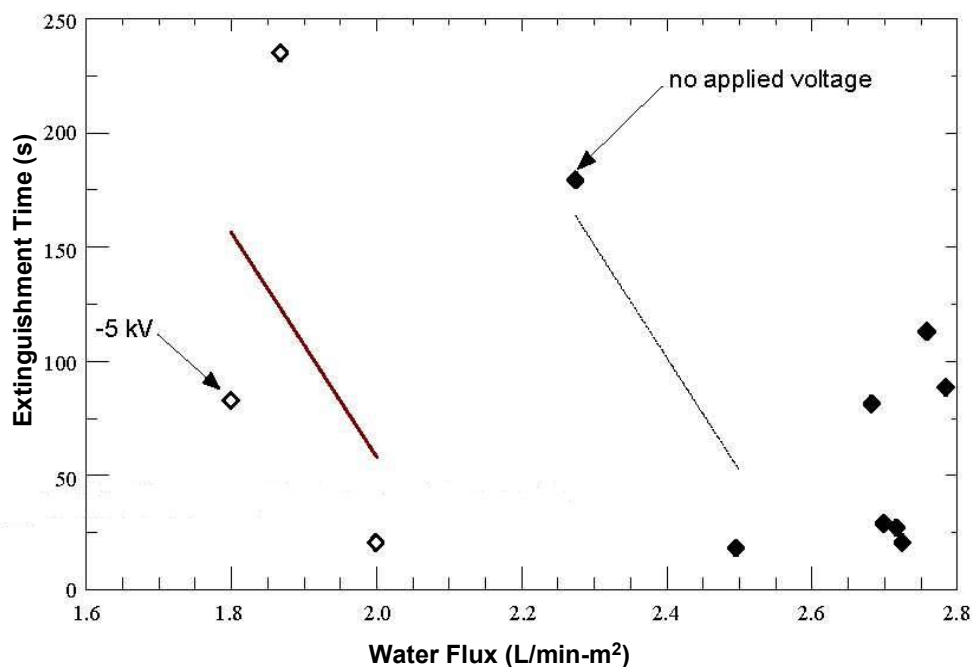


**Figure 8-138. Effect of Electrical Charging on Extinguishment for a 5 cm Diameter Heptane Pool Fire.**

### Discussion of Results

The present results are compared with other data obtained by Patterson et al.<sup>91</sup> and Gottuk et al.<sup>92</sup> The fitted curve results of Patterson et al.,<sup>91</sup> the fitted data shown in Figure 8-136, and the trend lines in Figure 8-138 are plotted together in Figure 8-139. The experiments of Gottuk et al.<sup>92</sup> occurred for water flux rates that were more than twice those treated in current experiments and thus outside of the range of Figure 8-139. Patterson et al.<sup>91</sup> did not consider charging, and their data show the general feature of the rise in extinguishment time as water flux is reduced beyond some point and substantiates the present observations of a rapid rise in extinguishment time for the case without charging. Note that the results of the experiments using high water fluxes (small extinguishment time) closely follow the data of Patterson

et al.<sup>91</sup> Although they were careful to establish uniform water flux, and they did not have additional air motion due to ventilation, their extinguishment time data are at least as scattered as the present data. The apparent randomness appears to be inherent to this kind of problem, and it appears that the water flux is a rational basis for comparing and interpreting extinguishment results when using water mists.

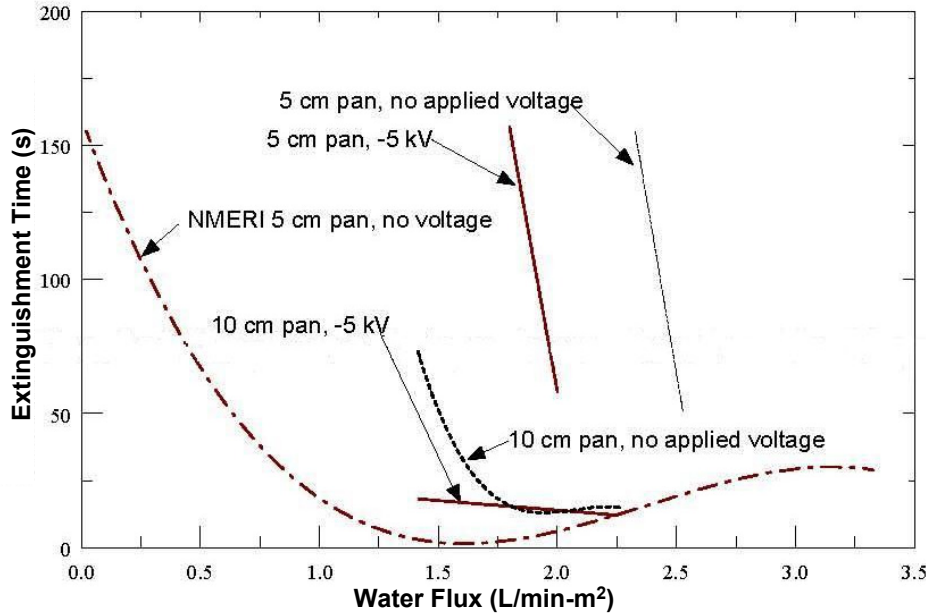


**Figure 8-139. AeroChem 5 cm and 10 cm and NMERI 5 cm Heptane Extinguishment Data. Hughes Associates, Inc. 10 cm tests ranged from (5 to 7) L/(min m<sup>2</sup>).**

It was also found that charging the mist reduced the water flow directly under the single TG-0.3 nozzle to around 75 % of its value without charging. The data of Gottuk et al.<sup>92</sup> show a reduction to around 85 %. For the multiple nozzle configuration, the reduction of the water flux directly below the nozzle assembly was much smaller, being about 95 % of the uncharged value. In addition, the increases due to charging at large distances were also small as seen in Figure 8-134.

Two possible reasons for the small reduction in water flux below the nozzle assembly compared to the single nozzle case are that: (1) the repulsive forces due to charged droplets at larger diameters restrained the tendency of the smaller droplets to spread and (2) an insufficient amount of charge was available to the multiple nozzle spray, and in particular the central portion of the spray, to grossly affect its geometry. This is not a major concern, as it simply indicates the need for a more effective charging electrode for the 7N nozzle.

The current results confirm the conclusion of Gottuk et al.<sup>92</sup> that charging produces a large amount of spreading in the mist distribution for single nozzles. It is clear that charging applied to an array of single nozzles will enable the use of greater spacing between the nozzles while achieving as uniform a spray pattern as in the case without charging. This is of particular concern for small droplets which are hard to disperse transversely due to their high aerodynamic drag. The electrostatic forces help to spread them out more evenly.

The present results clearly show that application of negative charging to water mist reduces the extinguishment time when the water flux is at its lowest effective values. Within this range the water flux needed to attain a given extinguishment time is also reduced. This is true for both the 5 cm and 10 cm heptane fuel fires and two different nozzle and charging systems. For the 10 cm fire data in Figure 8-136, the variability in extinguishment time, expressed as the standard deviation, was reduced at low values of water flux.

The question of the effect of charging on the total amount of water,  $Q$ , per unit floor area needed to extinguish a fire requires some further discussion.  $Q$  is equal to the product of the water flux,  $f$ , and the extinguishment time  $t_{ext}$  so that

$$Q = f t_{ext} \quad (8-56)$$

and it has the dimensions of a length (or thickness). Patterson et al.<sup>91</sup> refer to  $Q$  as the “de novo thickness.”

Ways in which reductions in  $Q$  can be categorized include: (1) a reduction in the flux,  $f$ , at constant extinguishment time,  $t_{ext}$ , (2) a reduction in the extinguishment time,  $t_{ext}$ , at a constant value of flux,  $f$ , and (3) an absolute maximum reduction of  $Q$  for some combination of  $t_{ext}$  and  $f$ . The first two cases are readily seen by comparing curves with and without charging in Figure 8-139 for either fixed  $f$  or  $t_{ext}$ .

To better understand the condition for an absolute maximum reduction in  $Q$ , note that the case of constant  $Q$  from Equation 8-56. corresponds to

$$t_{ext} = \frac{Q}{f} \quad (8-57)$$

so that in a plot of extinguishment time vs. water flux,  $t_{ext} \rightarrow \infty$  as  $f \rightarrow 0$  and  $t_{ext} \rightarrow 0$  as  $f \rightarrow \infty$ . Since the NMERI data in Figure 8-139 remains finite as  $f \rightarrow 0$ , this data actually shows a trend of decreasing  $Q$  for small  $f$ , although the absolute minimum  $Q$  occurs for an intermediate value of  $f$  close to 1.5 L/min-m<sup>2</sup>. The fitted curve of the NMERI data corresponds to increasing values of  $Q$  for large  $f$  since  $t_{ext}$  levels out in that range.

For the AeroChem data in the case of no charging,  $t_{ext}$  appears to grow without limit in Figure 8-139 for both the 5 cm and 10 cm fires for finite  $f$  so that  $Q$  will become infinite as  $f$  decreases. Charging allows a much smaller flux  $f$  of water to be used to achieve extinguishment in the same time. Here the reduction in  $Q$  due to charging can be accomplished in a limited range of  $f$  at the same  $t_{ext}$  (Figure 8-139). For the 10 cm case, there is insufficient data to make any statement about how small a value of  $f$  can be used to minimize  $Q$ .

Gottuk et al.<sup>92</sup> argue that one can simply increase the flux  $f$  to achieve the same effect as charging. This may be a simple alternative in the single nozzle, well-ventilated case, but there are broader ranges of  $f$  in different problems over which electric charging has a beneficial effect. Increasing  $f$  (without significant reductions in extinguishment time) is the wrong approach in a halon replacement program to minimize the weight of the fire suppressant. Therefore, work should focus on increasing the effectiveness of the technique so that smaller values of  $f$  will be capable of extinguishing a fire.

Although the effects of ventilation and uniformity cannot be fully separated, a shift appears to be occurring in the AeroChem tests relative to the Hughes Associates, Inc. data to move the extinguishment time curves to lower water flux values and to reduce the magnitude of their slope. Because of this, it is anticipated that conditions such as those reported in Figure 8-126 for unventilated chambers and highly uniform water flux will yield significant reductions in extinguishment time  $t_{ext}$  when charging is applied. In that case  $t_{ext}$  would be greatly reduced for low  $f$  so that  $Q$  could be reduced both in the absolute case and for the same extinguishment time according to Equation 8-56.

## Implications for Use

Although there seems to be a potential benefit to electrically charged a water mist to extinguish a small pool fire, the locations of in-flight engine nacelle fires and the highly cluttered nature of an engine nacelle preclude further development of this technique. Essentially, all those surfaces act as grounding plates. Thus, one could expect that some fraction of the droplets will be attracted to the clutter and will pool on the surfaces. Furthermore, it is not clear whether a high voltage field would interfere with the aircraft avionics at a critical time when the pilot is undertaking emergency measures to fight the fire and perhaps to maintain readiness for survival. However, these limitations may not apply to other potential applications.

### 8.7.3 A Self-Atomizing Form of Water

#### Background

For the NGP, Lyon<sup>96</sup> explored the potential use of gas hydrates as another approach to generating water mist and efficiently dispersing it throughout the space to be protected. The hydrate is a loosely bound complex of a host gas and a number of water molecules. It is only stable under high pressure. Thus, when released from its storage container, the ejected droplets of the complex would ideally travel some distance and violently break into water droplets and molecules of the host gas. These would then disperse rapidly from these numerous virtual sources. This is an analog to the flashing observed for halon 1301, HFC-125, and other low boiling point fluids.

The hydrates can form in either of two structures. In both of these structures, the essential unit is a pentagonal dodecahedron of water molecules, the gas molecule occupying the space in the center of the dodecahedron. This structure owes its stability to the fact that each of the twenty apices is occupied by an oxygen atom bonded to four hydrogen atoms at close to tetrahedral angles, i.e. it maximizes hydrogen bonding.

In the type I structure there are 2 smaller and 6 larger cavities for every 46 water molecules. For type II there are 16 smaller cavities and 8 larger cavities for every 136 water molecules. The type II hydrate forms only with gas molecules that are too large for the cavities in the type I structure. While the number of cavities has a definite stoichiometry, the extent to which gas molecules occupy those cavities can vary over a significant range. Furthermore mixed hydrates with two or more different types of gas molecules filling the cavities can readily be formed. For the case of a mixed hydrate of a large molecule such as  $\text{CHCl}_3$  and a small molecule such as  $\text{CO}_2$ , the large molecule occupies some of the large cavities and none of the small cavities while the small molecule occupies some of both.

At 0 °C, a pressure of 1.3 MPa is necessary to form the CO<sub>2</sub> hydrate from pure water. With increasing temperature, the CO<sub>2</sub> pressure needed to form the hydrate increases. At 9.9 °C, 4.39 MPa is needed and at greater temperatures, no hydrate can be formed by CO<sub>2</sub> alone. Mixed hydrates containing substantial amounts of CO<sub>2</sub> can, however, be formed at higher temperatures by using a second gas with a hydrate forming ability greater than CO<sub>2</sub>.

There were no published reports as to what happens when a gas hydrate is suddenly depressurized. It is, however, interesting to note that water under extreme pressure can form 5 solid phases in addition to the familiar ice. One of these, ice III, is blue. While ice III is thermodynamically stable only at pressures in excess of 206 MPa, it can be cooled to liquid nitrogen temperature, and then be depressurized. At 0.101 MPa and very low temperature, ice III is metastable. It can last for an extended period of time if kept cold, but it disintegrates into a fine powder of ordinary ice on contact with anything warm.

From a thermodynamic viewpoint, the decomposition of a CO<sub>2</sub> hydrate offers two quite different cases. The heat of forming a CO<sub>2</sub> hydrate from gaseous CO<sub>2</sub> and liquid water is almost exactly the same as the heat for forming ice from the water. Thus, if a pure CO<sub>2</sub> hydrate at an initial temperature below 0 °C were adiabatically depressurized, it would become unstable with respect to decomposition to ordinary ice and gaseous CO<sub>2</sub> with very little temperature change occurring during this decomposition. This case would appear to be quite similar to the case of ice III in which considerable metastability was possible, i.e., both involve the conversion of one solid to another without the formation of a liquid phase.

If, however, the initial temperature were greater than 0 °C, the hydrate would become unstable with respect to adiabatic decomposition to gaseous CO<sub>2</sub> and a mixture of liquid water and ice, the temperature falling during the decomposition to 0 °C. Since the liquid water can act as a catalyst for the conversion of the solid hydrate to ordinary ice, the hydrate seems less likely to be metastable in this case.

The goals of this project were to determine whether hydrates are capable of delayed self-atomization and that they are consequently potentially useful as replacements for halons in fire fighting.

## **Experimental Procedures**

### ***Sample Preparation***

0.5 L stainless steel sample bombs which were equipped with 0.635 cm ball valves were used to prepare CO<sub>2</sub>/water mixtures which were converted to hydrate. To prepare these mixtures, the sample bomb was weighed, distilled water was transferred into it, and it was reweighed. It was then attached to a vacuum line and evacuated briefly to remove air. The sample bomb valve was then closed, and the bomb was connected to a CO<sub>2</sub> cylinder that was equipped with a dip leg. After liquid CO<sub>2</sub> was added to the bomb, it was reweighed and placed in a refrigerator to convert the CO<sub>2</sub>/water mixture to hydrate.

### ***Video Camera Studies***

During tests the sample cylinders were held vertically with the valve pointed down. A length of 0.635 cm OD stainless steel tubing on the outlet of the ball valve bent to a right angle or to a U shape was attached to the outlet end of the ball valve. This allowed the discharge to be directed vertically downward or upward. A video camera was used to record what occurred. During subsequent analysis of the videotape, the discharge time was measured with a stopwatch while playing the tape at slow speed. Playing speed

was measured by comparing stopwatch readings with time as recorded on the tape by the video camera's clock. Distances were measured on the tape using a reference length.

### *Candle in the Wind Experiments*

Figure 8-140 shows the experimental setup used in this series of tests. In this setup, a 2.22 cm diameter candle was placed inside a transparent plastic tube, 61 cm long by 10.2 cm in diameter. The top of this plastic tube was connected to a blower while the bottom was filled with vertical 10.2 cm long Pyrex tubes, 6 mm OD and 4 mm ID. The blower was used to pull a flow of air through this tube at a rate of 3.54 L/s, i.e. at a velocity of 43.6 cm/s. The small Pyrex tubes served as flow straighteners.

While the bulk of this airflow was vented, some of it was extracted by a sample pump and sent first through a rotameter then to a Fuji NDIR CO<sub>2</sub> meter, which monitored the CO<sub>2</sub> content of the gases exiting the blower. For comparison experiments with halon 1211, the sample was passed through a bed of an oxidation catalyst at 800 °C (CuO on high surface area alumina) to convert the halon to CO<sub>2</sub>. Previous studies have shown that this catalyst is quite efficient for oxidizing halons.

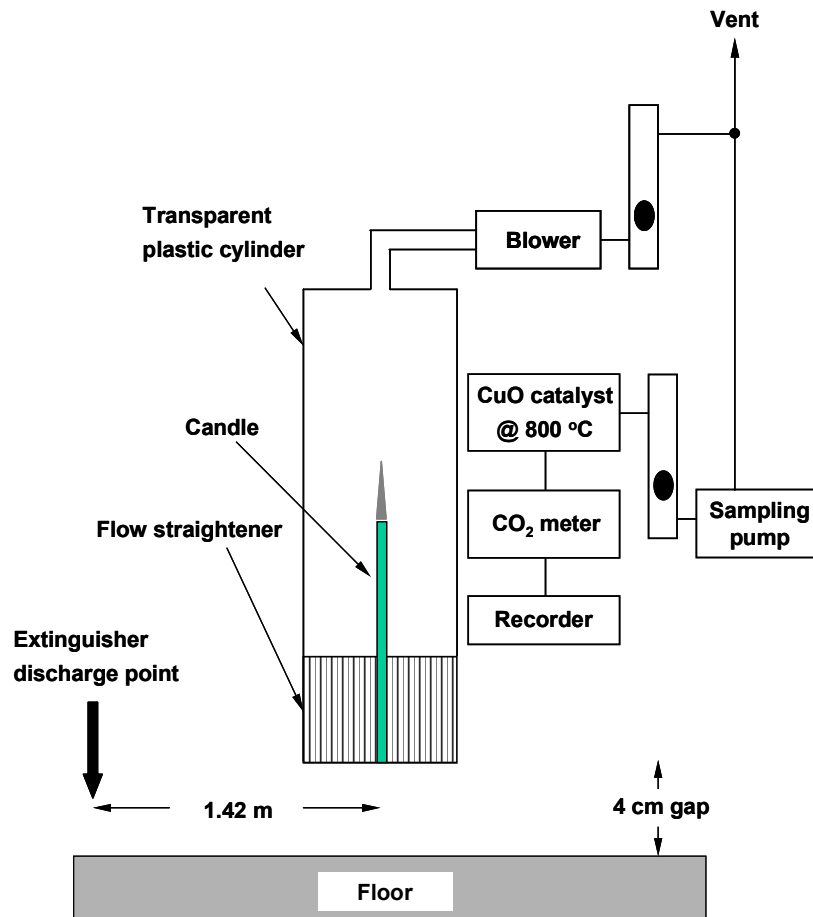


**Figure 8-140. Experimental Setup for Testing the Relative Effectiveness of Fire Extinguishing Agents.**

### *Test with an Obstructed Fire*

The experimental setup shown in Figure 8-141 was used in the extinguishment tests with an obstructed fire using a single burst discharge of the agent. The following procedure was used: a paper wick and 75 cm<sup>3</sup> of diesel fuel were placed in the 6 cm cup. After igniting the wick, the fire was allowed to burn for 3 min, the ball valve was opened, and the result observed.

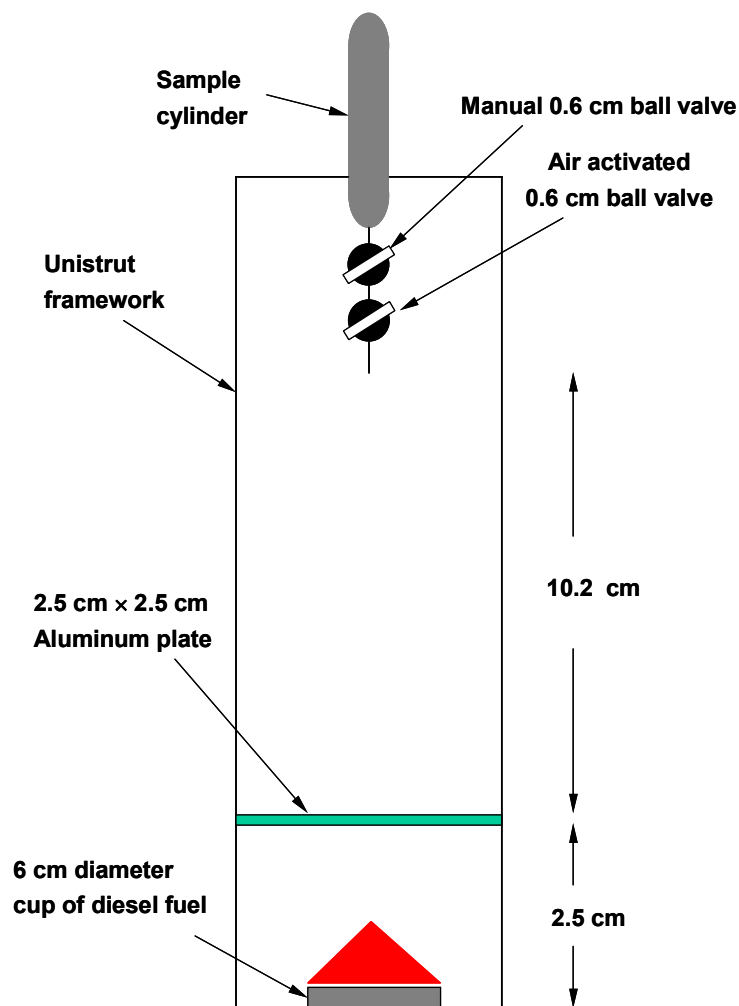


**Figure 8-141. Experimental Setup for Testing Agents Against an Obstructed Flame.**

### *Ambient Pressure Recovery of Hydrates*

To recover CO<sub>2</sub> hydrate, a 2.54 cm OD stainless steel tube with fittings on its ends was used instead of the 0.5 L sample bomb. Hydrate was prepared as above, but then the sample was cooled to -15 °C, depressurized, the fittings were undone, and the hydrate removed. To prepare and recover C<sub>3</sub>F<sub>8</sub> hydrate, the same procedure was used, except that the preparation was done in a Fischer-Porter glass sample bomb.

### ***Discharge Characteristics of CO<sub>2</sub> Hydrate***

Samples in which the ratio of CO<sub>2</sub> to water was low enough to leave a significant portion of the water unconverted to hydrate had reasonably satisfactory discharge characteristics, i.e., when the ball valve was opened the hydrate/water mixture was discharged in a more or less continuous flow. Samples in which the ratio of CO<sub>2</sub> to water was high enough to leave little or no water unconverted did not show satisfactory discharge characteristics, i.e., when the ball valve was opened the hydrate was discharged in discontinuous spurts.

## **Results**

### ***Visual Observations***

A blank experiment was done with 400 mL samples of water in 1000 cm<sup>3</sup> sample bombs pressurized with He at 10.3 MPa. This produced a spray jet with a 0.35 s discharge time, 5 m tall and roughly 15 cm wide at its peak. The droplets formed by this jet showed a readily observable settling rate indicating that they were relatively coarse. Qualitatively similar behavior was observed with helium pressurizations at 6.87 MPa and 3.78 MPa. At 1.57 MPa helium pressurization, however, the discharge resembled that of a common garden hose with little or no atomization.

For a solution of 0.2 mass fraction of CaCl<sub>2</sub> in water saturated with CO<sub>2</sub> at ambient temperature and 5.81 MPa, the spray jet pattern was clearly different, 3 m tall and 50 cm wide. The droplets formed by this jet did not show an observable settling rate, indicating that a desired fine mist was formed.

For samples of CO<sub>2</sub> hydrate/water mixture with an initial pressurization of 1.51 MPa, the discharge was similar in length and width to that of the sample which was pressurized with helium to 1.57 MPa, but the discharge produced a mist with no observable tendency to settle.

### ***Candle Flame Results***

Experiments were conducted using the setup illustrated in Figure 8-140 to determine the threshold for extinguishing candle flames by CO<sub>2</sub>, halon 1211, and fine mists generated by CO<sub>2</sub> hydrate/water mixtures. The results in Figure 8-142 and Figure 8-143 show that these experiments gave a threshold for CO<sub>2</sub> between 6.8 volume % and 7.1 volume % and a threshold for halon 1211 between 1.57 volume % and 1.74 volume %. No thresholds were determined for fine mists generated by the CO<sub>2</sub> hydrate/water mixtures since under all conditions tested these mists were not able to extinguish the candle flame.

In another experiment, a red laser beam was sent through the transparent plastic cylinder. Initially the beam was invisible, but scattering from particles of Ca(OH)<sub>2</sub> (20 μm to 40 μm size) in the plastic cylinder made the beam evident.

### ***The Obstructed Flame Results***

Three tests were done with CO<sub>2</sub> hydrate/water mixtures, and in all three tests the obstructed flame was not extinguished.

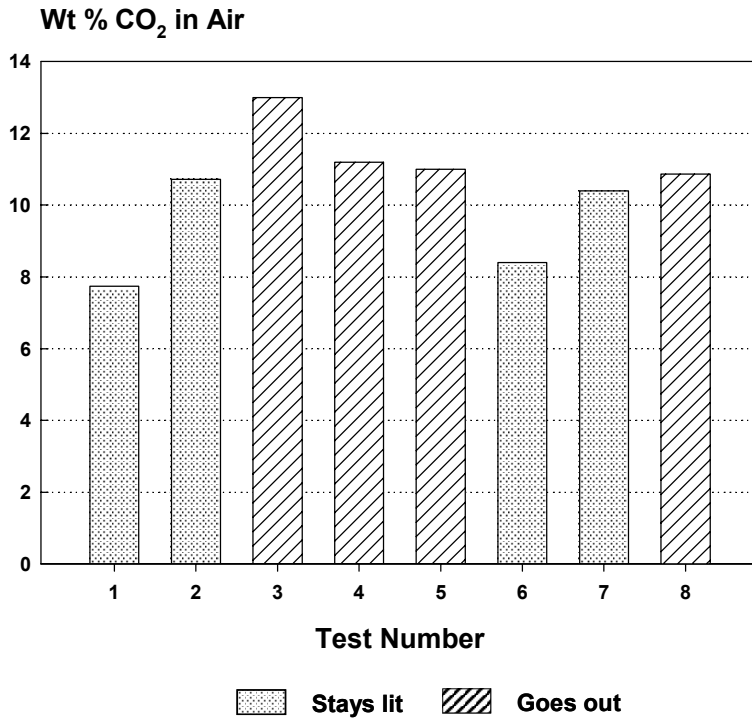
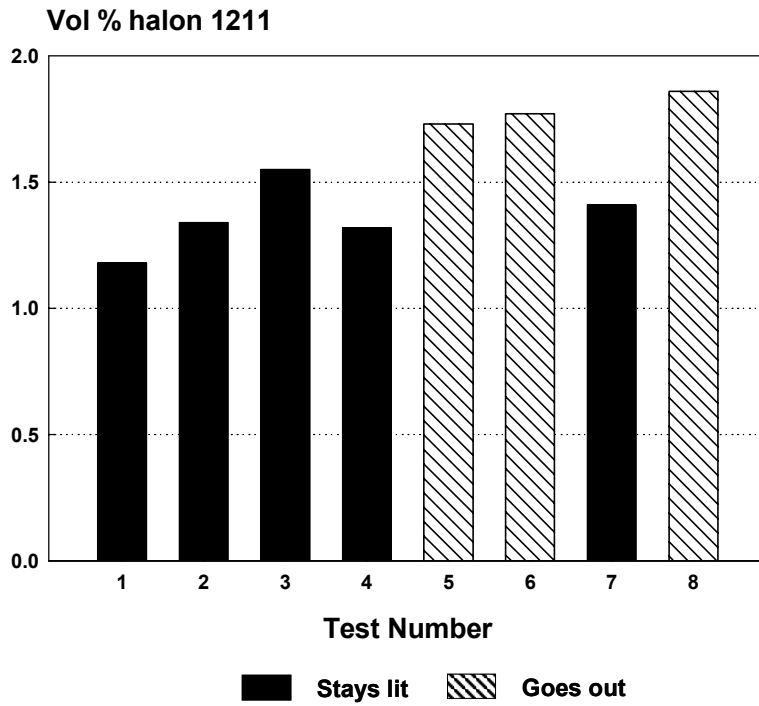


Figure 8-142. Extinction of a Candle Flame by CO<sub>2</sub>.

Cylinder cross section = 84 cm<sup>2</sup>  
 Updraft = 44 cm/s

Figure 8-143. Extinction of a Candle Flame by Halon 1211.



Cylinder cross section = 84 cm<sup>2</sup>  
 Updraft = 44 cm/s

### ***Observations on Hydrate Samples Recovered at Ambient Pressure***

Samples of the CO<sub>2</sub> hydrate looked very much like ice. When they were placed on the surface of a hot plate (surface temperature of 260 °C), they acted much as did samples ice, i.e., they melted and boiled with little or no wetting of the surface. A sample of the CO<sub>2</sub> hydrate placed on an ambient temperature aluminum plate initially melted with bubbling but without producing mist, then suddenly exploded. After the explosion, some fragments of the sample remained on the aluminum plate. They melted with bubbling but without further explosion. A sample of the C<sub>3</sub>F<sub>8</sub> hydrate placed on an ambient temperature aluminum plate melted without explosion or mist production but with bubbling and a continuous snapping sound.

## **Discussion**

### ***Metastability of Gas Hydrates***

As discussed above, gas hydrates might be effective firefighting agents if they were to undergo delayed self-atomization, which in turn might occur if the hydrate were metastable at ambient pressure. One might expect that metastability would or would not lead to self-atomization depending on the circumstance. If a particle of hydrate is traveling through the air at a high velocity, its surface is subject to high shear. As that surface begins to convert to liquid water and gaseous carbon dioxide, any bubbles forming will be broken into fine droplets. Thus for a hydrate particle in flight metastability seems likely to lead to atomization. For a particle at rest, however, the situation is less clear. If the particle can store sufficient strain energy for self-atomization, then it might do so. If the stored strain energy is not this large, it could still be sufficient to cause the hydrate particle to explode into coarse fragments or make snapping sounds as it melts. While the observations with the recovered hydrate samples are consistent with these expectations, the only thing they unambiguously show is that the hydrates are capable of metastability.

### ***Analysis of Visual Observations***

Different spray forming mechanisms exist when a liquid is discharged through a hole at various flow rates. The spray regime map depends on the Ohnesorge and Weber numbers (see Faeth<sup>97</sup>). The results of calculations for the experiments done with water pressurized with helium were consistent with the observation that samples with helium pressurizations of 10.31 MPa, 6.87 MPa, and 3.78 MPa atomized. Samples pressurized with helium to 1.57 MPa, which was observed not to atomize, were calculated to be in the wind-induced range (Faeth<sup>97</sup>).

The theory of spraying presented in Faeth<sup>97</sup> does not consider the possibility that the liquid being sprayed may contain a dissolved gas. Given that helium is only very slightly soluble in water, it is not surprising that the experiments with helium pressurized samples were quite consistent with this theory. The solubility of CO<sub>2</sub> in water at 21 °C and 5.81 MPa is, however, 34 cm<sup>3</sup> STP gas per cm<sup>3</sup> of liquid. The decrease in height, the increase in width and the fact that the droplets did not show observable settling are all consistent with the assumption that the discharge produced coarse droplets which the dissolved CO<sub>2</sub> subsequently or concurrently atomized into fine mist.

There is, however, the problem that droplets of fine mist are far more readily visible than an equal mass of coarse droplets. While the visual observations indicate that spray water saturated with CO<sub>2</sub> at high pressure does indeed produce fine mist, they do not reveal how efficiently this happened.

Since the discharged hydrate/water mixture occurred in the wind induced region, had a similar appearance to the helium pressurized discharge in this region, but still produced a mist that showed no observable settling, the indication of the visual observations is that after a delay the hydrate atomized itself into a fine mist. Here again, however, the data do not indicate how efficient the atomization was.

### ***Fire Extinguishing Tests***

In a previous research project, the ability of water saturated with CO<sub>2</sub> at high pressure to extinguish fires was examined.<sup>98</sup> While the results showed that this was indeed an effective way of extinguishing fires, the mechanism for extinguishing the fires was not clear. Perhaps the fine mist produced by the CO<sub>2</sub> saturated water extinguished the flame by cooling it or perhaps the jet of CO<sub>2</sub>/mist was simply blowing out the flame.

Both sets of experiments reported above were designed to avoid this ambiguity. In both cases the flame was protected from the discharge of the hydrate so that mist from the hydrate arrived in the general vicinity of the flame, but without momentum from the discharge to carry it into the flame itself. Under this condition, the mist from the hydrate was not effective for extinguishing the flame.

While the reasons for this failure are not completely clear, two possibilities are obvious. The present results suggest that CO<sub>2</sub> hydrate does undergo delayed self-atomization but they do not show the efficiency of this process. If the efficiency of mist production is poor, the hydrate will not be an effective extinguishing agent. Secondly, there is the question of the velocity at which the mist enters the flame. Droplets of mist have a diffusion coefficient that is very close to zero. For an ideal diffusion flame this would give them a near zero velocity of approaching the flame and for a real diffusion flame the velocity would be quite low. As the above analysis shown, fine mist might be ineffective in this situation.

The goal of this research was to ascertain whether gas hydrates, especially CO<sub>2</sub> hydrate, could undergo delayed self-atomization and whether this property would make them potentially useful replacements for the halons. While the data indicate the former, the latter now appears to be a remote possibility. Accordingly, further research along this line was not pursued.

## **8.8 SUMMARY OF LESSONS LEARNED**

- Fluid storage in a bottle determines the initial conditions for subsequent discharges into piping distribution systems. Fluid storage problems pertain to thermodynamic vapor-liquid phase equilibrium calculations, which in most cases are straightforward.
- For multi-phase pipe flow calculations, the FSP code is capable of calculating the pressure history and discharge flow rates similar to the measured data. The code is able to pick up the qualitative behavior associated with the release of dissolved gas as the delivery system undergoes rapid depressurization during the discharge of the suppressant agent. The code is very flexible in being able to model different piping systems via user input, and it offers the user many options in developing an appropriate input model to describe the physical system. Because of these characteristics, the code appears to be a viable tool for analysis or design of

suppressant delivery systems. However, the code will only begin the computation if the initial thermodynamic state of the fluid is properly specified by the user. The uncertainties in the model predictions can be attributed to the constitutive relationships for interphase drag and wall heat transfer estimations, the inherent uncertainties in predicting the release rate of dissolved gas, the critical gas bubble radius, and the appropriate discharge coefficients to account for uncertainties in the critical flow model of the code and the geometry of the junction for subcooled liquid, two-phase liquid-vapor, and single-phase vapor. The user should plan to vary these parameters for a specific application and gain understanding of how this would affect the overall time of suppressant discharge.

- Any of the fire simulation programs (VULCAN, FDS, and FPM) investigated in this effort can be used to help design a fire suppression system in practically any space inside an aircraft or ground vehicle. While their application to shipboard spaces was not investigated in this effort, there seems to be no conceptual impediment to such an application, except possibly that the allowable grid sizes might lengthen the computational periods significantly. Each of these software simulations incorporates a slightly different set of assumptions, so that using more than one of them will ameliorate unforeseen effects of the peculiar, embedded assumptions on any particular model. Of the three, only the FPM incorporates a threat-evaluation subroutine which predicts whether or not a fire will be initiated by any of the weapons in its library.
- Any of the fire simulation programs (VULCAN, FDS, and FPM) investigated in this effort can be used to optimize the design of qualification tests which may be required for acceptance of a fire-suppression system for an aircraft or ground vehicle. Such utility allows the planner of tests to focus on those cases for which these simulations show that extinction is marginal, thus reducing the number of tests required to ‘prove’ the system.
- If two or more fire simulation programs agree in the outcome, the tests likely will confirm. If there be disagreement in the predicted outcome from different fire-simulation programs for the same case, then the conditions are approaching the edge of the extinguishment envelope. The simplified chemical analyses incorporated into these fire simulations do not account for nonhomogeneous mixing.
- Because of the strongly oscillatory flow and turbulence inside a typical nacelle, the initial concerns about the adverse effects of clutter on the penetration of suppressants into those spaces have been allayed. The “clutter” enhances the mixing of the suppressant into the flow.
- In full-scale nacelle testing, almost all the predictions of “borderline” extinguishment outcomes were, in fact, extinguished. In other words, the simulation programs used in this effort err on the ‘safe’ side. Simplified homogeneous analysis shows two critical parameters determine successful suppression in nacelles:
  1. Ratio of “suppressant” mass inflow rate to “suppressant plus air” mass inflow rate determines the maximum concentration attainable for “long” injection periods. This ratio should be greater than 0.41 for HFC-125.
  2. The speed of injection is more important than the total mass of agent deployed. Total rate of volumetric displacement by inflowing air plus suppressant determines the elapsed time scale to reach maximum concentrations. (For an F-18 nacelle, air flows are large, so that the time scale to reach maximum concentration is small ( $< 1$  s)). Consequently, if a “wave” of sufficiently high concentration reaches all the potential zones of fire for even a fraction of a second, the fire will be extinguished.

- The temperatures of agent storage bottle, airflow, and nacelle surfaces all play important roles in agent dispersion performance at low temperature applications, especially when the prevailing temperature is below the normal boiling point of the agent. Care should be exercised when extrapolating results from room temperature tests to evaluate agent dispersion performance at low temperatures.
- Neither electrically charged water mist systems nor the use of CO<sub>2</sub> hydrates appear to be promising substitutes for halons.

## 8.9 REFERENCES

1. Hamins, A., McGrattan, K., and Forney, G., "Unwanted Accelerated Burning after Suppressant Delivery," NIST Special Publication 1004, National Institute of Standards and Technology, Gaithersburg, MD, 2003.
2. Yang, J.C., Cleary, T.G., Vázquez, I., Boyer, C.I., King, M.D., Breuel, B.D., Womeldorf, C.A., Grosshandler, W.L., Huber, M.L., Weber, L., and Gmurczyk, G., "Optimization of system discharge," in Gann, R.G., ed., *Fire Suppression System Performance of Alternative Agents in Aircraft Engine and Dry Bay Laboratory Simulations*, NIST SP 890: vol. I, National Institute of Standards and Technology, Gaithersburg, MD, 1995.
3. Walas, S.M., *Phase Equilibrium in Chemical Engineering*, Butterworth, Boston, 1985.
4. Grosshandler W.L., Gann R.G., and Pitts W.M., eds., *Evaluation of Alternative in-Flight Fire Suppressants for Full-Scale Testing in Simulated Aircraft Engine Nacelles and Dry Bays*, NIST SP 861, National Institute of Standards and Technology, Gaithersburg, MD, 1994.
5. Huber, M.L. and Ely, J.F., "A Predictive Extended Corresponding States Model for Pure and Mixed Refrigerants Including an Equation of State for R134a," *International Journal of Refrigeration* **17**, 18-31, 1994.
6. Yang, J.C., Huber, M.L., Vázquez, I., Boyer, C.I., and Weber, L., "Measured and Predicted Thermodynamics Properties of Selected Halon Alternative/Nitrogen Mixtures," *International Journal of Refrigeration* **20**, 96-105, (1997).
7. Tuzla, K., Palmer, T., Chen, J.C., Sundaram, R.K., and Yeung, W.S., "Development of Computer Program for Fire Suppression Fluid Flow," Report number ITF 2000-1, Vols. I and II, Institute of Thermo-Fluid Engineering & Science, Lehigh University, Bethlehem, PA, September 2000.
8. DiNenno, P.J. and Budnick, E.K. Jr., "Halon 1301 Discharge Testing: A Technical Analysis," National Fire Protection Research Foundation, Quincy, MA, 1988.
9. Pitts, W. M., Yang, J. C., Gmurczyk, G. W., Cooper, L. Y., Grosshandler, W. L., Cleveland, W. G., and Presser, C., "Fluid Dynamics of Agent Discharge", in Grosshandler W.L., Gann R.G., and Pitts W.M., eds., *Evaluation of Alternative in-Flight Fire Suppressants for Full-Scale Testing in Simulated Aircraft Engine Nacelles and Dry Bays*, NIST SP 861, National Institute of Standards and Technology, Gaithersburg, MD, 1994.
10. Elliott, D. G., Garrison, P. W., Klein, G. A., Moran, K. M., and Zydowicz, M. P., *Flow of Nitrogen-Pressurized Halon 1301 in Fire Extinguishing Systems*, JPL Publication 84-62, Jet Propulsion Laboratory, California Institute of Technology, Pasadena, California, 1984.
11. Hirt, C. W., Oliphant, T. A., Rivard, W. C., Romero, N. C., and Torray, M. D., *SOLA-LOOP: A Non-Equilibrium, Drift Flux Code for Two-Phase Flow in Networks*, Report No. L-7659, Los Alamos National Laboratory, Los Alamos, NM, 1979.

12. Gallagher, J., McLinden, M., Morrison, G., and Huber, M., "NIST Thermodynamic Properties of Refrigerants and Refrigerant Mixtures Database (REFPROP), Version 4.0," National Institute of Standards and Technology, Gaithersburg, MD, 1993.
13. Marviken Power Station, "The Marviken Full Scale Critical Flow Tests: Volume 1: Summary Report," NUREG/CR-2671, MXC-301, U.S. Nuclear Regulatory Commission, Washington, DC, 1982.
14. EPRI Report NP-2370, "The Marviken Full-Scale Critical-Flow Tests, Volume 1: Summary Report", Electric Power Research Institute, Palo Alto, CA, 1982.
15. Edwards, A.R. and O'Brien, T.P., "Studies of Phenomena Connected with the Depressurization of Water Reactors," *Journal of British Nuclear Energy Society* **9**, 125-135, (1979).
16. RELAP5 Development Team, "RELAP5/MOD3.2 Code Manuals, Volume 1: Code Structure, Models and Numerical Schemes," U. S. Nuclear Regulatory Commission Report NUREG/CR-5535, 1995.
17. RELAP5 Development Team, "RELAP5/MOD3.2 Code Manuals, Volume 2: User Manual," U. S. Nuclear Regulatory Commission Report NUREG/CR-5535, 1995.
18. RETRAN-03: A Program for Transient Thermal-Hydraulic Analysis of Complex Fluid Flow Systems, EPRI NP-7450, Volume 1, May 1992.
19. TRAC-PF1/MOD2 Code Manual, Los Alamos National Laboratory, NUREG/CR-5673 or LA-1203-M, Volume 1-3, 1992.
20. TRAC-BF1/MOD1 Code Manual: An Advanced Best-Estimate Computer Program for BWR Accident Analysis, Idaho National Engineering Laboratory, NUREG/CR-4356 or EGG-2626, Volumes 1-2, 1992.
21. TRAC-BF1/MOD1 Models and Correlations, INEL, NUREG/CR-4391 or EGG-2680, 1992.
22. GOTHIC Containment Analysis Package Version 5.0, Numerical Applications, Inc., User Manual (NAI 8907-02 Rev. 6), and Technical Manual (NAI 8907-06 Rev. 5), 1995.
23. Taitel, Y.A., Bornea, D., and Dukler, A.E., "Modeling Flow Pattern Transitions for Steady Upward Gas-Liquid Flow in Vertical Tubes," *AIChE Journal* **26**, 345-354, (1980).
24. Mishima, K., and Ishii, M., "Flow Regime Transition Criteria Consistent with Two-Fluid Model for Vertical Two-Phase Flow," NUREG/CR-3338, April 1984.
25. Wallis, G.B., *One-Dimensional Two-Phase Flow*, McGraw Hill, New York, 1972.
26. Chisholm, D., "A Theoretical Basis for the Lockhart-Martinelli Correlation for Two-Phase Flow," *International Journal of Heat and Mass Transfer* **10**, 767-1778, (1967).
27. Zuber, N., Tribus, M., and Westwater, J. W., "The Hydrodynamic Crisis in Pool Boiling of Saturated and Subcooled Liquids," *Second International Heat Transfer Conference*, Paper 27, Denver, 1961.
28. Trapp, J. A., and Ransom, V. H., "A Choked Flow Calculation Criterion for Nonhomogeneous, Nonequilibrium Two-Phase Flows," *International Journal of Multiphase Flow* **8**, 669-681, 1982.
29. Cokmez-Tuzla, A.F., Tuzla, K., and Chen, J.C., "High Speed Thermometry for Detection of Transient Liquid Contact on Superheated Surfaces," in Schooley, J., ed., *Temperature Its Measurement and Control in Science and Industry*, vol. 6, pp. 1173-1177, American Institute of Physics, 1993.
30. Welty, J.R., Wicks, C.E., and Wilson, R.E., *Fundamentals of Momentum, Heat, and Mass Transfer*, 3rd edition, John-Wiley & Sons, New York, 1984.
31. Disimile, P.J., Tucker, J.R., Crosswell, B., and Davis, J.M., "The Transport of Water Sprays past Generic Clutter Elements Found within Engine Nacelles," *Fire Safety Journal* **40**, 65-78, (2005).

32. Presser, C., "Parametric Investigation of Droplet Atomization and Dispersion of Liquid Fire Suppressants," Final Report to DoD SERDP, December 2003.
33. Ghee, T.A. and Keyser, D.R., "Basic Aerodynamic Shapes in a Low-Speed, Highly Turbulent Flow," AIAA-2003-3953, 21st AIAA Applied Aerodynamics Conference, Orlando, Florida, June 23-26, 2003.
34. Hoerner, S.F., *Fluid-Dynamic Drag*, Hoerner Fluid Dynamics, Vancouver, WA, 1965.
35. Fage, A. and Warsap, J.H., "The Effects of Turbulence and Surface Roughness on the Drag of Circular Cylinders," ARC RM 1283, 1930.
36. Schlichting, H., *Boundary Layer Theory*, 7th ed., McGraw-Hill, New York, 1987.
37. Welch, P.D., "The Use of Fast Fourier Transform for the Estimation of Power Spectra: A Method Based on Time Averaging over Short, Modified Periodograms," *IEEE Transactions on Audio and Electroacoustics* Vol. **AU-15**, June 1967.
38. Yang, J.C., Manzello, S.L., Nyden, M.R., and Connaghan, M.D., "Cold Discharge of  $\text{CF}_3\text{I}$  in a Simulated Aircraft Engine Nacelle," *Proc. Seventh International Symposium on Fire Safety Science*: 715-726 (2003).
39. Gann R.G. (ed.), *Fire Suppression System Performance of Alternative Agents in Aircraft Engine and Dry Bay Laboratory Simulations*, volumes I and II, NIST SP 890, U.S. Department of Commerce, Washington, DC, November 1995.
40. Guesto-Barnak, D., Sears, R., and Simpson, T., "Engine nacelle fire protection using non-ozone depleting fire suppressants," *Proceedings of International Conference on Ozone Protection Technologies*, pp. 515-524, Washington, D.C., October 21-23, 1996.
41. Personal communication to Yang, J.C. from Meserve, W.J., Pacific Scientific, HTL/KIN-Tech Division, Document Number 51750579, Duarte, California, May 2000.
42. DeMore, W.B., Sander, S.P., Golden, D.M., Hampson, R.F., Kurylo, M.J., Howard, C.J., Ravishankara, A.R., Kolb, C.E., and Molina M.J., *Chemical Kinetics and Photochemical Data for Use in Stratospheric Modeling, Evaluation: Number 12*, JPL Publication 97-4, Jet Propulsion Laboratory, California Institute of Technology, Pasadena, California, 1997.
43. Yang, J.C., Cleary, T.G., Huber, M.L., and Grosshandler, W.L., "Vapor Nucleation in a Cryogenic Fluid/Dissolved Nitrogen Mixture during Rapid Depressurization," *Proceedings of the Royal Society of London* **A455**, 1717-1738, (1999).
44. Holen, J., Brostrom, M., and Magnussen, B.F., "Finite Difference Calculation of Pool Fires," *Proceedings of the Combustion Institute* **23**, 1677-1683, (1990).
45. Magnussen, B.F., Hjertager, B.H., Olsen, J.G., and Bhaduri, D., "Effects of Turbulent Structure and Local Concentrations on Soot Formation and Combustion in  $\text{C}_2\text{H}_2$  Diffusion Flames," *Proceedings of the Combustion Institute* **17**, 1383-1393, (1979).
46. Patankar, S.V. and Spalding, D.B., "A Calculation Procedure for Heat, Mass, and Momentum Transfer in Three-Dimensional Parabolic Flows," *International Journal of Heat and Mass Transfer* **15**, 1787-1806, 1972.
47. Magnussen, B.F., "The Eddy Dissipation Concept," *Proceedings of the Eleventh Task Leaders Meeting*, IEA Working Group on Conservation in Combustion, Lund, Sweden, 1989.
48. Hewson, J.C. and Kerstein, A.R., "Local Extinction and Reignition in Nonpremixed Turbulent  $\text{CO}/\text{H}_2/\text{N}_2$  Jet Flames," *Combustion Science and Technology* **174**, 35-66, (2002).

49. Tieszen, S.R., Stamps, D.W., and O'Hern, T.J., "A Heuristic Model of Turbulent Mixing Applied to Blowout of Turbulent Jet Diffusion Flames," *Combustion and Flame* **106**, 442-466, (1996).
50. Meeks, E., Moffat, H.K., Grcar, J.F., and Kee, R.J., "AURORA: A Fortran Program for Modeling Well Stirred Plasma and Thermal Reactors with Gas and Surface Reactions," Sandia National Laboratories Report SAND96-8218 (1996).
51. Curran, H.J., Gaffuri, P., Pitz, W.J., and Westbrook, C.K., "A Detailed Modeling Study of Iso-Octane Oxidation," *Proceedings of the Combustion Institute* **27**, 381-395, (1999).
52. Babushok, V.I., Noto, T., Burgess, D.R.F., Hamins, A., and Tsang, W., "Influence of  $\text{CF}_3\text{I}$ ,  $\text{CF}_3\text{Br}$ , and  $\text{CF}_3\text{H}$  on the High-Temperature Combustion of Methane," *Combustion and Flame* **107**, 351-367, (1996).
53. Byggstoyl, S. and Magnussen, B.F., "A Model for Flame Extinction in Turbulent Flow," *Proceedings of the Combustion Institute* **17**, 381-395, (1978).
54. Hewson, J.C., Tieszen, S.R., Sundberg, W.D., and DesJardin, P.E., "CFD Modeling of Fire Suppression and Its Role in Optimizing Suppressant Distribution," 2003, in Gann, R.G., Burgess, S.R., Whisner, K.C., and Reneke, P.A., eds., *Papers from 1991-2006 Halon Options Technical Working Conferences (HOTWC)*, CD-ROM, NIST SP 984-4, National Institute of Standards and Technology, Gaithersburg, MD, (2006).
55. DesJardin, P.E., Nelsen, J.M., Gritz, L.A., and Ghee, T.A., "On the Development of a Subgrid Scale Clutter Model," AIAA-2002-0984, 40th AIAA Aerospace Sciences Meeting and Exhibit, Reno, Nevada, January 14-17, 2002.
56. DesJardin, P.E., Nelsen, J.M., Gritz, L.A., Lopez, A.R., Suo-Anttila, J.M., Keyser, D.R., Ghee, T.A., Disimile, P.J., and Tucker, J.R., "Towards Subgrid Scale Modeling of Suppressant Flow in Engine Nacelle Clutter," 2001, in Gann, R.G., Burgess, S.R., Whisner, K.C., and Reneke, P.A., eds., *Papers from 1991-2006 Halon Options Technical Working Conferences (HOTWC)*, CD-ROM, NIST SP 984-4, National Institute of Standards and Technology, Gaithersburg, MD, (2006).
57. CFD-GUI™, CFD-ACE Structured Flow Solver Manual, Version 5, CFD Research Corporation, Huntsville, Alabama, October 1998.
58. CFD-ACE™, Theory Manual, Version 5, CFD Research Corporation, Huntsville, Alabama, October 1998.
59. Launder, B.E. and Spalding, D.B., "The Numerical Calculation of Turbulent Flows," *Computational Methods Applied to Mechanics and Engineering* **3**, 269-289, (1974).
60. Wilcox, D.C., "A Half Century Historical Review of the  $k-\epsilon$  Model," AIAA-91-0615, 29th Aerospace Sciences Meeting, Reno, Nevada, Jan 7-10, 1991.
61. Chien, T. and Smith, A.M.O., *Analysis of Turbulent Boundary Layers*, Academic Press, New York, 1982.
62. Fire Prediction Model, Version 3.1, *Software Analyst's Manual*, Pascal, A.M., SURVIAC Information Analysis Center. Available from Mr. M. Lentz, FPM Model Mgr., 46 OG/OGM/OL-AC 46 OG/OGM/OL-AC, 2700 D. St. Bldg. 1661, WPAFB, OH 45433-7605.
63. McGrattan, K.B., Baum, H.R., Rehm, R.G., Hamins, A., Forney, G.P., Floyd, J.E., Hostikka, S., and Prasad, K., *Fire Dynamics Simulator (Version 3) – Technical Reference Guide*, NISTIR 6783, U.S. Department of Commerce, Washington, DC, November 2002.

64. McGrattan, K.B., Forney, G.P., Prasad, K., Floyd, J.E., and Hostikka, S., *Fire Dynamics Simulator (Version 3) – User’s Guide*, NISTIR 6784, U.S. Department of Commerce, Washington, DC, November 2002.
65. Forney, G.P. and McGrattan, K.B., *User’s Guide for Smokeview Version 3.1 – A Tool for Visualizing Fire Dynamics Simulation Data*, NISTIR 6980, U.S. Department of Commerce, Washington, DC, April 2003.
66. Hamins, A., Cleary T., Borthwick, P., Gorchkov, N., McGrattan, K., Forney, G., Grosshandler, W., Presser, C., and Melton, L., “Suppression of Engine Nacelle Fires,” in Gann, R.G., ed., *Fire Suppression System Performance of Alternative Agents in Aircraft Engine and Dry Bay Laboratory Simulations*, NIST SP 890: vol. II, U.S. Department of Commerce, Washington, DC, 1995.
67. Lopez, A.R., Gritzo, L.A., and Hassan, B., “Computational Fluid Dynamics Simulation of the Air/Suppressant Flow in an Uncluttered F-18 Engine Nacelle,” 1997, in Gann, R.G., Burgess, S.R., Whisner, K.C., and Reneke, P.A., eds., *Papers from 1991-2006 Halon Options Technical Working Conferences (HOTWC)*, CD-ROM, NIST SP 984-4, National Institute of Standards and Technology, Gaithersburg, MD, (2006).
68. Black, A.R., Suo-Anttila, J.M., Gritzo, L.A., Disimile, P.J., and Tucker, J.R., *Numerical Predictions and Experimental Results of Air Flow in a Smooth Quarter-Scale Nacelle*, Sandia National Laboratories Report SAND2002-1319, Albuquerque, New Mexico, 2002.
69. Black, A.R., Suo-Anttila, J.M., Disimile, P.J., and Tucker, J.R., “Numerical Predictions and Experimental Results of Air Flow in a Smooth Quarter-Scale Nacelle,” AIAA-2002-0856, 40th Aerospace Sciences Meeting and Exhibit, Reno, Nevada, January 14-17, 2002.
70. Hirst, R. and Sutton, D., “The Effect of Reduced Pressure and Airflow on Liquid Surface Diffusion Flames,” *Combustion and Flame* **5**, 319-330, (1961).
71. Hirst, R., Farenden, P.J., and Simmons, R.F., “The Extinction of Fires in Aircraft Jet Engines – Part I, Small-Scale Simulation of Fires,” *Fire Technology* **12**, 266-275, (1976).
72. Hirst, R., Farenden, P.J., and Simmons, R.F., “The Extinction of Fires in Aircraft Jet Engines – Part II, Full-Scale Fires,” *Fire Technology* **13**, 59-67, (1977).
73. Hamins, A., Presser, C., and Melton, L., “Suppression of a Baffle-Stabilized Spray Flame by Halogenated Agents,” *Proceedings of the Combustion Institute* **26**, 1413-1420, (1996).
74. Takahashi, F., Schmoll, W.J., Strader, E.A., and Belovich, V.M., “Suppression of a Nonpremixed Flame Stabilized by a Backward-Facing Step,” *Combustion and Flame* **122**, 105-116, (2001).
75. Takahashi, F., Schmoll, W.J., Strader, E.A., and Belovich, V.M., “Suppression Behavior of Obstruction-Stabilized Pool Flames,” *Combustion Science and Technology* **163**, 107-130, (2001).
76. Hewson, J.C. and Keyser, D.R., *Suppression of Pool Fires with HFC-125 in a Simulated Engine Nacelle*, Technical Report SAND2007-3442, Sandia National Laboratories, Albuquerque, NM, 2007.
77. Hewson, J.C. and Keyser, D.R., “Predicting Fire Suppression in a Simulated Engine Nacelle,” 2004, in Gann, R.G., Burgess, S.R., Whisner, K.C., and Reneke, P.A., eds., *Papers from 1991-2006 Halon Options Technical Working Conferences (HOTWC)*, CD-ROM, NIST SP 984-4, National Institute of Standards and Technology, Gaithersburg, MD, (2006).
78. Technical Work Description (TWD) LNV12.01-013, “F/A-18 E/F (HFC-125) Fire Protection System Qualification Test,” Northrop Grumman, El Segundo, California, February 29, 2000.

79. Hamins, A., Gmurczyk, G. W., Grosshandler, W. L., Rehwoldt, R.G., Vazquez, I., Cleary, T., Presser, C., and Seshadri, K., "Flame Suppression Effectiveness", in Grosshandler W.L., Gann R.G., and Pitts W.M., eds., *Evaluation of Alternative in-Flight Fire Suppressants for Full-Scale Testing in Simulated Aircraft Engine Nacelles and Dry Bays*, NIST SP 861, U.S. Department of Commerce, Washington, DC, 1994.
80. Northrop Test Work Description, LN 12.01-011, rev. n/c, "F/A-18 E/F Engine Bay Fire Extinguishing System," 09 July 1997, Contract N00019-92-C-0059, H12-354C-7656.
81. Performance Test Code 19.5-2004, *Flow Measurement*, ASME, New York.
82. Smith, L.T., Murdock, J.W., and Applebaum, R.S., "An Evaluation of Existing Two-Phase Flow Correlations for Use with ASME Sharp Edge Metering Orifices," ASME Paper 76-WA/FM-3, New York, NY, 1977.
83. Calcote, H.F., "Ion Production and Recombination in Flames," *Proceedings of the Combustion Institute* **8**, 184-199, (1962).
84. Wortberg, G., "Ion-Concentration Measurements in a Flat Flame at Atmospheric Pressure," *Proceedings of the Combustion Institute* **10**, 651-655, (1965).
85. Peters, J., Vinhier, C., and Van Tiggelen, A., *Oxidation and Combustion Reviews* (C.F.H., Tipper, Ed.) Elsevier, Amsterdam, Vol. 4, 93, 1969.
86. Calcote, H.F., "Ions and Electron Profiles in Flames," *Proceedings of the Combustion Institute* **9**, 622-637, (1963).
87. Calcote, H.F., Olson, D.B., and Keil, D.G., "Are Ions Important in Soot Formation?," *Journal of Energy and Fuels* **2**, 494-504, (1988).
88. Payne, K.G. and Weinberg, F.J., "A Preliminary Investigation of Field-Induced Ion Movement in Flame Gases and Its Applications," *Proceedings of the Royal Society of London* **A250**, 316-336, (1959).
89. Berman, C.H., Gill, R.J., Keil, D.G., and Calcote, H.F., "Enhanced Soot Radiation Using Electric Fields," AeroChem Final Report TP-466, Gas Research Institute Contract No. 5086-260-1312, 1987.
90. Chattock, A.P., *Philosophical Magazine* **48**, 401, (1899).
91. Patterson, R.A., Brabson, G.D., Schiro, J., and Tapscott, R.E., "Critical Concentration Measurements and Lab-to-Room Scale-Up Water Mist Fire Testing," 1996, in Gann, R.G., Burgess, S.R., Whisner, K.C., and Reneke, P.A., eds., *Papers from 1991-2006 Halon Options Technical Working Conferences (HOTWC)*, CD-ROM, NIST SP 984-4, National Institute of Standards and Technology, Gaithersburg, MD, (2006).
92. Gottuk, D.L., Steel, J.S., Roby, R.J., and Beyler, C.L., "Final Report of Phase II, Energy Fields for Fire Extinguishment," Hughes Associates, Inc., Contract No. F08635-92-C-0015, prepared for Tyndall AFB, 1993.
93. Berman, C.H., *et al.*, "Electrically Charged Water Mist for Extinguishing Fires," Final Report to SERDP NGP, March 1998.
94. Kelly, A.J., "On the Statistical, Quantum, and Practical Mechanics of Electrostatic Atomization," *Journal of Aerosol Science* **25**, No. 6, 1159-1177, (1994).
95. Belan, J. and Harstad, K., "Electrostatic Dispersion and Evaporation of Clusters of Drops of High-Energy Fuel for Soot Control," *Proceedings of the Combustion Institute* **26**, 1713-1722, (1997).
96. Lyon, R.K., "Development of a Self Atomizing Form of Water," Final Report to SERDP NGP, January 1998.

97. Faeth, G.M., "Structure and Atomization Properties of Dense Turbulent Sprays," *Proceedings of the Combustion Institute* **23**, 1345-1352, (1990).
98. Lyon, R.K., Private Communication, Energy and Environmental Research Corporation, Whitehouse, NJ 08888, January 1998.

---

---

## Chapter 9: POWDER PANEL AND PROPELLANT DISCHARGE TECHNOLOGIES

---

---

William L. Grosshandler  
National Institute of Standards and  
Technology

### TABLE OF CONTENTS

9.1	Introduction.....	925
9.2	Enhanced Powder Panels.....	927
9.2.1	NGP Objectives.....	927
9.2.2	Background on Powder Panel Technology.....	928
9.2.3	Operating Principle.....	929
9.2.4	Technical Issues.....	931
9.2.5	Survey of Powder Panel Applications.....	932
9.2.6	Powder Dispersion Screening Experiments.....	935
9.2.7	Live-fire Proof-of-concept Demonstrations.....	945
9.2.8	Optimization Program.....	949
9.2.9	Live-fire Demonstration Testing of Optimized Enhanced Powder Panels.....	955
9.2.10	Mass-trade Comparison Analysis.....	968
9.2.11	Summary of Powder Panel Research Program.....	972
9.3	Solid Propellant Gas Generators”.....	974
9.3.1	Brief History.....	974
9.3.2	Operating Principles.....	975
9.3.3	Experimental Techniques.....	976
9.3.4	Results: General Behavior of Propellants.....	988
9.3.5	Results: Cooled Propellant Formulations.....	992
9.3.6	Results: Chemically Active Fire Suppressants.....	1001
9.3.7	Results: Hybrid Fire Extinguishers.....	1011
9.3.8	Summary of Solid Propellant Gas Generator Research.....	1018
9.4	References.....	1021

### 9.1 INTRODUCTION

Halon 1301 has a vapor pressure high enough to propel it from a storage bottle and through distribution piping rapidly enough to suppress even fast growing fires. Nitrogen gas is used to pressurize halon 1301 storage bottles to ensure that even at temperatures as low as -40 °C, where the halon 1301 vapor pressure has dropped considerably, the total pressure is sufficient for rapid discharge of the fire suppressing fluid.

Hydrofluorocarbon alternatives to halon 1301, such as HFC-125, are discharged in a similar manner, but because around three times the amount of agent is required to ensure the fire is extinguished, a larger

pressure vessel is needed, and the total system is considerably bulkier and heavier than the halon 1301 system.

Two technologies were explored in the Next Generation Fire Suppression Technology Program (NGP) that avoid the need for, and the attendant bulk and safety issues of, a high pressure storage vessel to operate effectively. These technologies are (1) powder panels, and (2) solid propellant gas generators. Both of these technologies have the ability to discharge fire fighting agent in less than 100 ms, which makes them suitable for protecting aircraft dry bays (enclosed spaces adjacent to a fuel cell). The solid propellant gas generator can be adapted to aircraft engine nacelles, as well.

Powder panels consist of powdered fire extinguishing agents sandwiched, unpressurized, between two rigid membranes that, as a unit, can be attached to or used in place of the skin of the aircraft confining a dry bay. The powder is released and dispersed into the dry bay when the panel is pierced by a projectile, forming an aerosol cloud sufficiently dense to prevent ignition or suppress a fire resulting from the rupture of the adjacent fuel tank. The system is entirely passive.

The powder panel designs that existed prior to the NGP were inefficient. The research conducted as part of the NGP was aimed at enhancing the powder panel in three ways:

- using more chemically active fire suppressant materials,
- enhancing the dispersion of the powder, and
- decreasing the system mass.

Solid propellant gas generators (SPGGs, alternatively referred to as SPFEs, solid propellant fire extinguishers, for the current application) contain no fluids and are at atmospheric pressure prior to activation. The propellant within a chamber is activated by an initiator and burns rapidly to produce large quantities of gases. These materials either can be dispersed directly into the volume being protected or through a manifold of piping similar to what is used for halon 1301. Prior to the advent of the NGP, the primary application for SPGGs was for automotive airbags and aircraft inflatable escape slides. As first mentioned in Chapter 2 of this book, the gas mixture is very hot upon exit from the SPGG but cools rapidly as it expands within the compartment into which it is discharged. During testing on the F-22 program, distribution lines from the generators to the nacelle would become white hot during discharge and for a brief period thereafter. In testing performed by the U.S. Navy using a “single grain” inert gas generator, the same effect of heating of the distribution line during discharge was also noted. Placing inert gas generators within a nacelle and thus eliminating the need for distribution lines previously had been considered impractical due the potential degrading affect of the nacelle operating temperature environment on the life of the solid propellant. Inconel distribution lines were demonstrated to not melt, but would still become white hot.

The focus of the NGP research was to develop upgraded SPGG technology for aircraft fire protection by finding ways (1) to reduce the temperature of the gases dispersed by the generator, and (2) to increase the suppression effectiveness of the products (including finely dispersed particulates). The latter involved changing the chemical reactants, their stoichiometry and morphology, the geometry of the containment vessel, and incorporating various additives thought to be adept at retarding ignition or at quenching the combustion process. In addition, the concept of a hybrid fire extinguisher (HFE) was studied, with a

SPGG used as a compact source of high pressure gas to propel a liquid hydrofluorocarbon or aqueous mixture.

## 9.2 ENHANCED POWDER PANELS

### 9.2.1 NGP Objectives

The combat environment for military aircraft or even a terrorist environment for civilian aircraft poses a significant fire hazard when a ballistic threat is introduced. These threats are designed to act as ignition sources upon penetration of onboard flammable fluid containers. As previous combat experience and vulnerability analyses have shown, fire is the most significant vulnerability faced by an aircraft subjected to ballistic threat impact.

One area of focus for the NGP has been improved storage and delivery of fire extinguishing agents. One such technology, the powder panel, passively stores and then delivers agent upon the impact of a ballistic projectile. Powder panels have most often been applied to the lining of aircraft dry bays to provide passive, light mass, effective fire protection against ballistic impact. Projectile penetration of the dry bay and adjacent fuel tank releases agent from the powder panel into the fire zone to inert the space before or as the adjoining fuel spills into the space and is ignited by incendiaries. The recognition of ballistic threat-induced fires as a major contributor to aircraft vulnerability and a need to avoid active halon fire extinguishing systems has led to a renewed interest in powder panels as a fire protection device.

Despite the potential for powder panels, commercial units are of roughly the same design that has existed for decades, and their limited range of effectiveness has prevented further implementation in production aircraft. In 2001, the NGP embarked on an effort to use current technology and new ideas to examine the feasibility of enhanced powder panel designs and demonstrate proofs-of-concept. This section details a two-phase effort to accomplish this work.<sup>1,2,3,i</sup>

The objective of the NGP research was to identify concepts for powder panel enhancement (relative to current capability and to halon 1301) and demonstrate their performance. The basis for this advanced protection consisted of characterization of current powder panel technology and assessment of recently developed improvements in powder panel materials and construction. The expected outcome of this work was enhanced powder panel concepts that are competitive with halon 1301 in critical parameters such as mass, volume occupied, and fire extinguishing capability, and, thus, are candidates for use in its place.

NGP research into enhanced powder panels was performed by Cyphers and co-workers at Skyward, Ltd. The Aerospace Survivability and Safety Flight (46 OG/OGM/OL-AC) was the managing laboratory. In Phase I of the work, background information was gathered on the state of current powder panels, initial concepts for enhanced powder panels were examined, and the feasibility of improved powder panel features was demonstrated. In Phase II, the examination was widened to study whether enhanced powder panels could become practical, while maintaining improved performance. Optimized powder panels were examined for their potential to meet production requirements and their benefits were examined against other fire protection alternatives. The program concluded with live fire demonstration tests of the optimized powder panels.

---

<sup>i</sup> Large portions of the text of Section 9.2, as well as all the figures, have been used from Reference 1 without further attribution. The reader should consult the original document for additional details.

### 9.2.2 Background on Powder Panel Technology

Powder panels are passive fire protection devices for discharging dry chemical agents to prevent or extinguish combat-induced fires in military vehicles. They consist of two walls, an internal rib or core structure, and a fire extinguishing agent, typically a dry chemical powder, that fills the interior space. Historically, commercial powder panels have consisted of thin walls of aluminum foil or composite sheets, with an aluminum or Nomex honeycomb core. Typical thicknesses for commercial powder panels have been reduced to just over 2.5 mm. Powder panels are typically arranged along the walls of a void area in a military vehicle (called a dry bay in an aircraft) adjacent to or on the walls of a flammable fluid container (fuel tank, fuel line, hydraulic fluid reservoir, etc.). Figure 9–1 depicts the typical arrangements of powder panels. They are typically attached directly to the wall of the flammable fluid container by an epoxy adhesive. Testing has shown this arrangement to be more effective than mounting on the walls of the dry bay separated from the fluid container.<sup>4</sup> Upon penetration by a ballistic projectile, powder panels release powder into the fire zone before or as the adjoining fuel spills into the space and is ignited by incendiaries or other ignition sources.

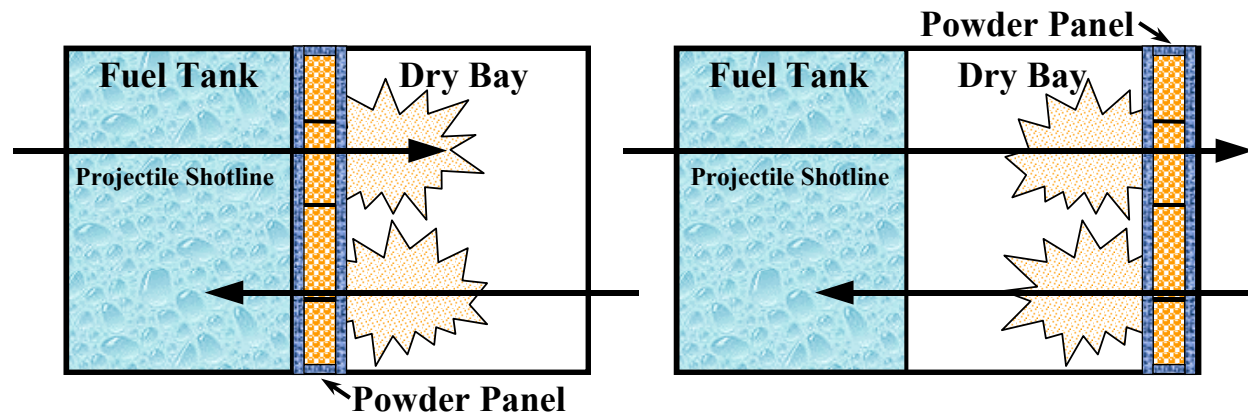


**Figure 9–1. Typical Powder Panel Arrangements.**

The design and acceptability criteria for these devices are different from conventional active fluid suppressant systems. Powder panels add mass based upon the surface area of the fuel wall/fire zone interface, as opposed to the volume of the fire zone, so the relative benefit of the panels is dependent upon the configuration of the particular bay. Typical areal densities (mass/surface area) for commercial powder panels are on the order of 1.95 kg/m<sup>2</sup> to 2.44 kg/m<sup>2</sup>.

Powder panels are not a new concept for extinguishing ballistic threat-induced fires in aircraft, as discussed previously. Powder panels around aircraft fuel tanks were first developed and used by the Royal Aircraft Establishment in England. Some U.S. military helicopters (e.g., the AH-1W/Z and the UH-1N/Y) and the V-22 aircraft have implemented powder panels in their vulnerability reduction designs. Powder panels have also been widely examined for military combat land vehicles, such as tanks and armored personnel carriers, but have been applied in limited circumstances.

Nonetheless, despite testing which has demonstrated the effectiveness of these devices, powder panels have seen limited use in aircraft for several reasons. False discharges do not occur with these passive fire protection devices, but cleanup following a fire or inadvertent damage has been a concern. This concern,

primarily in aircraft, stems from the possibility of corrosion by the contact of chemical powders with vehicle structure. As a result, current powder panels often use an inert fire extinguishing powder, such as aluminum oxide ( $\text{Al}_2\text{O}_3$ ), to prevent reaction with the metal. In military ground vehicles, wide application of powder panels has been limited due to the potential ill, albeit limited, effects on crew members or obscuration of the crew compartment upon activation. Although non-toxic agents can be used, during the period of time the powder particles are suspended in crew areas, the crew may have difficulty breathing and operational effectiveness may be limited. Several other reasons cited for their limited use overall include concerns over durability, potential adverse effects on electromechanical components and optics, their ability to protect highly cluttered areas, airflow influences, and a lack of protection from accidental fires.

Although powder panels have been examined for years, current commercial powder panel designs are in essence very similar to those that have existed for decades. However, a number of factors have renewed interest in powder panel technology. First, the banned production of halon 1301 has created a demand for new techniques to fill its role. Also, new materials, powders, and construction techniques have been developed, which may allow for improved powder panel performance, in terms of both system mass and fire extinguishing capability.

Systems that have used halon 1301 for ballistic threat-induced fire protection in fire zones eventually may require some substitute technique. Powder panel technologies are viable alternatives for some of these applications. They don't require detectors, plumbing, wiring or bottles, and they are false-discharge resistant. Current designs have limitations, particularly limited powder dispersion ability, and problems providing protection against relatively small caliber threats. As a result, most don't compare favorably against halon 1301 in trade-off studies.

Improved powder panels could expand use of this fire protection technology for additional vulnerable fire zones on our critical weapons systems. New powder panel concepts with enhanced characteristics have been proposed recently. These include frangible materials to optimize dispersion, single-piece construction technology, modular designs, pre-dosed sections, lighter mass materials, and lower cost materials. These enhanced powder panels could be used in applications as halon 1301 or other fire extinguishing system replacements, or they could replace existing powder panels with superior technology.

### 9.2.3 Operating Principle

Powder panels work through the release of fire extinguishing powder into the mixing zone of a flammable fluid and an ignition source to essentially inert the zone and prevent a fire from igniting. To assist in the discussion of powder panels and their effectiveness, it is helpful to discuss fire ignition as it relates to an onboard aircraft fire due to ballistic projectile penetration.

For any fire to initiate, the interaction of a flammable fluid, oxidant, and ignition source is required.<sup>5</sup> However, the simple mixing of these three ingredients does not ensure fluid ignition or the initiation of a sustained fire. Fire initiation by a ballistic threat is a complex phenomenon involving a process that sequentially brings together the three ingredients at the right time, in sufficient and properly proportional quantities, and with the needed intensity. The process begins when the ballistic threat penetrates the vehicle, generates an ignition source, and traverses the vehicle penetrating the fluid container, thereby

releasing fluid into the open volume of the vehicle. This open volume is referred to as a dry bay in aircraft. While each threat type is inherently different, the result is the same, i.e., deposition of thermal energy into a volume of air in front of the impact hole and the raising of the temperature of this volume. If the threat impacts a flammable fluid container within the vehicle and releases fluid, the fluid will be injected into the dry bay some distance by the threat/container impact and the container pressure. As the fluid is injected into the dry bay, it atomizes (i.e., breaks up into droplets). As the droplets penetrate into the heated air, they begin to vaporize, and the fluid vapor mixes with the surrounding air and produces a flammable fluid/air mixture. As the fluid/air mixture is heated, a chemical reaction will commence.

As the reaction proceeds, heat is lost to the surrounding air by conduction. If the rate of heat produced by the reaction exceeds the rate of heat lost, the chemical reaction will accelerate until all the oxygen (for fuel rich conditions) within this volume is consumed; a flash is seen more or less simultaneously throughout this volume as ignition occurs. If the rate of heat lost exceeds the rate of heat produced, then the temperature of the volume will begin to decrease, and the rate of reaction will decline as well. Eventually the reaction will cease and ignition will not occur. As such, ignition is simply a reaction that proceeds to consume the available flammable fluid/air mixture contained within the volume encompassed by the ignition source, resulting in a flame visible within this volume. If, after ignition occurs, sufficient oxygen and flammable fluid are available, a sustained fire may result that could lead to a loss of the aircraft.

Fire extinguishing powder introduced into this volume immediately upon impact by the ballistic projectile has the potential to reduce the probability of a fire ignition. The powder must render the fuel/air mixture nonflammable so the chemical reaction does not continue. The powder can do this in two ways. According to Finnerty et al.<sup>6</sup> (and further citations in Reference 6), it is widely believed that fire extinguishing powders can function as both energy-absorbing materials and as solid surfaces on which free radicals can be destroyed. Heat may be absorbed by the heat capacity of the solid, the heat of fusion at the melting point, the heat capacity of the liquid, heat of dissociation from breaking of chemical bonds, and heat of vaporization. These all contribute to the total energy absorbing capability (endothermicity) of the fire extinguishing powder.<sup>7</sup>

From a chemical aspect, it has been found that there is a catalytic path for the destruction of free radicals, especially O, OH and H, by certain fire extinguishing powders that contain alkali metals, such as sodium and potassium.<sup>8,9</sup> Potassium salts have been shown to be more effective than sodium salts, and iodide anions are more effective than chloride anions. Any powder that has a chemical fire extinguishing capability will also have the heat-absorbing capability.<sup>10</sup>

Testing has shown that, for a fixed total mass of powder, smaller and more numerous powder particles, through the increased surface area available, are more effective at reducing the chance of ignition than fewer, larger particles.<sup>7,11</sup> A large total surface area of the powder is important in both heat absorption and chemical interference mechanisms. The former is why even an inert material like aluminum oxide can be effective if it is sufficiently finely divided. Conversely, large particles may actually pass through the flame zone before they can reach flame temperature, further reducing their ability to absorb as much heat as an equivalent mass of finer particles.

The effectiveness of the powder panel can, therefore, be enhanced through the proper use of a fire extinguishing powder (type and particle size), and by maximizing the amount of powder released into the mixing zone consisting of the flammable fluid and the ignition source. The objective of the enhanced

powder panels is to appropriately select a powder and maximize the mass of powder released into the mixing zone.

#### 9.2.4 Technical Issues

In order to become a viable concept for combat fire protection in aircraft, two major technical attributes of powder panels needed to be addressed. These attributes, performance and practicality, are intertwined. Previous testing evaluated a number of different powder panel designs and materials and showed limited ranges of effectiveness.

One consistent factor in many of these designs was the use of a honeycomb structural material as the rib or core material. Honeycomb provides several benefits to powder panels. First, it adds structural integrity to the panel, much as honeycomb has proven valuable for structural design in aircraft construction. Honeycomb also allows for even distribution of the fire extinguishing powder throughout the panel, minimizing concerns over powder settling. It also can be constructed of very light mass materials such as Nomex or aramid fibers. The limiting factor for honeycomb has been its performance. Only cells in the direct path of projectile penetration, and perhaps those just around the penetration area, are torn and allow powder to escape.

Different faces for the powder panel have been tested, focusing on materials such as aluminum foil and several different composites. Many of these efforts have focused on durability in the aircraft environment. However, performance, as quantified through surface area removal or fracturing, has been limited. This is true despite techniques to enhance opening of the powder panel walls, such as weak or selective bonding of the panels to the core, particularly for the front or open face to the fire zone. Very thin sheets or films have also been tried to promote surface removal and allow powder to escape.

Consequently, the NGP needed to demonstrate the feasibility of completely re-designing a powder panel so that it could release a more effective amount of powder. However, production and qualification requirements levied on fire protection methods, such as powder panels, might show these designs to be impractical for aircraft applications. Therefore, additional work was required to optimize these panels for attaining potential design requirements. For example, with aircraft mass restrictions being very demanding, powder panel mass needs to be minimized before it can even be considered competitive as a fire protection solution for a particular aircraft application. This goal involves proper material selection and powder panel thickness determinations. Another key aircraft requirement is durability in the aircraft's harsh operating environment. This includes an ability to survive under extreme (both hot and cold) temperature, vibration, g-loading, and exposure to a variety of chemicals (jet fuel, hydraulic fluid, etc.). These environmental restrictions further reduce the set of materials and design concepts that can be used. Other production requirements may be related to such items as toxicity, maintainability and reliability. Thus, the problem becomes one of developing a powder panel that is competitive with other fire extinguishing technologies by releasing sufficient powder when penetrated by a ballistic projectile to prevent fire ignition, while still remaining acceptable under tightly controlled aircraft environment requirements.

### 9.2.5 Survey of Powder Panel Applications

Cyphers and co-workers began with a survey of powder panel applications in operational U.S. aircraft and investigations of previous powder panel testing. The purpose of the survey was to identify powder panel materials and designs that have been previously evaluated and those that have actually been integrated into aircraft designs. The survey included the collection of all available data; however, it focused on more recent test programs and on testing related to U.S. aircraft applications. Using this information as a baseline, it was then possible to explore potential improvements in powder panel designs.

Powder panels around aircraft fuel tanks were first developed and used by the Royal Aircraft Establishment in England.<sup>12</sup> They have also been examined widely for military combat land vehicles, such as tanks and armored personnel carriers.<sup>13,14,15,16</sup> An example of the integration of powder panels into a U.S. aircraft design is the use of these fire extinguishing devices in the V-22 Osprey. The widest use of powder panels has been in helicopters, for which a number of test programs have been conducted to evaluate powder panel applications. A significant effort was conducted, for example, to evaluate both parasitic (attached to existing structure) and structural (panels themselves function as structure) powder panels in Army AH-1S Cobra helicopters.<sup>12,17,18,19</sup> Although powder panels were never integrated into the AH-1S, they did find their way into the Navy UH-1N Huey and AH-1W Super Cobra.<sup>20</sup> These legacy aircraft are being upgraded to UH-1Y and AH-1Z configurations, both of which also will use powder panels for dry bay protection. Testing was conducted at Boeing to evaluate powder panel applications in the AH-64 Apache. This evaluation examined the use of powder panels along various fuel tank walls. Powder panels have also been evaluated recently for the RAH-66 Comanche helicopter.

The powder panel application survey indicated that no U.S. fixed wing aircraft currently employ powder panels. A number of reasons have been offered for this:

- Powder panels do not assist with accidental fires.
- Low-tech approaches are difficult to sell.
- There are concerns over accidental leakage that could lead to corrosion, durability, volume-filling capability with clutter involved, and detrimental airflow influences.

There have been powder panel test programs relating to U.S. applications extending back to at least the late 1970s.<sup>16</sup> Many of the test programs included evaluations of the fire extinguishing effectiveness of various powder panel designs and various dry powders contained within the panels.<sup>3,21,22</sup> Standard designs included the use of thin aluminum foil, Nomex, or composite panels sandwiching an aluminum or Nomex honeycomb core, which contained the fire extinguishing powder. Typical powders included aluminum oxide ( $\text{Al}_2\text{O}_3$ ), Purple K ( $\text{KHCO}_3$ ), and Monnex ( $\text{KC}_2\text{N}_2\text{H}_3\text{O}_3$ ).  $\text{Al}_2\text{O}_3$  has been extensively used in powder panel testing and is the only powder identified in U.S. aircraft applications, primarily due to its low corrosiveness compared to the other powders.<sup>5,13</sup> A summary of some previously tested powder panel materials is included in Table 9–1.

The literature review revealed some unique powder panel designs and configurations evaluated in previous testing,<sup>23,24</sup> but also more common powder panel materials and designs. Very thin aluminum or aluminum foil and composite materials have most often been evaluated for the front face or the face toward an open dry bay. Similar materials have been evaluated for the back face or the face attached to or directly adjacent to the flammable fluid container. As Table 9–1 indicates and the literature search showed, the most commonly evaluated rib structural design by far has been honeycomb. The honeycomb

has been composed of various materials, but it has most often been evaluated on its ability for even distribution of powder and for its structural rigidity.

**Table 9–1. Examples of Previously Tested Powder Panel Materials.**

Front Face	Rib Structure	Back Face	Panel Thickness (mm)	Powder
0.025 mm 8111-0 aluminum (Al) alloy foil	2024-T2 Al honeycomb	0.025 mm 8111-0 alloy Al foil	1.3	Monnex
0.10 mm Al	fiberglass	0.33 mm Al	1.8	KDKI
0.51 mm 2024-T3 Al	honeycomb	0.51 mm 2024-T3 Al	2.3	Al <sub>2</sub> O <sub>3</sub>
0.025 mm stainless steel	Al foil bags	4.06 mm 2024-T3 Al	2.5	Al <sub>2</sub> O <sub>3</sub> +10 % KI
5.1 mm titanium	Nomex	2-ply fiberglass/ epoxy	3.0	Al <sub>2</sub> O <sub>3</sub> with 1 % silicon oxide
2-ply graphite-epoxy tape	honeycomb	2-ply graphite/ epoxy tape	3.0	Purple K
3-ply (0/90/0) graphite epoxy		3-ply (0/90/0) graphite/epoxy	6.4	potassium bicarbonate
2-ply Kevlar-epoxy cloth polyethylene		2-ply Kevlar/epoxy cloth polyethylene	9.5	10 % acetate in water
Pro-Seal coated ballistic nylon bags		Pro-Seal coated nylon	12.7	
			25.4	

In addition to examining military-specific powder panel testing, an examination of recent powder panel work for non-ballistic applications was performed. Data were obtained for powder panel evaluations using a much wider variety of materials with potential for greater fire extinguishing effectiveness. Drawing upon data from the powder panel survey, a baseline set of materials and designs was established for examination in the first phase of this project.

The second phase of the NGP research involved an expanded survey and investigation that included the identification of aircraft using active halon systems for fire protection, particularly in areas where powder panels could be used. This research was to be used for later comparisons of potential powder panel fire protection systems with current halon systems. The expanded survey also included the identification of design issues for integrating enhanced powder panels into production aircraft and the identification of any necessary qualification testing required before implementation.

The examination of aircraft fire protection systems in the expanded survey revealed that halon systems are infrequently used in dry bay areas.<sup>25</sup> Conversely, powder panels have been demonstrated to be effective almost exclusively in these areas. Active halon fire extinguishing systems are prevalent in engine nacelles or auxiliary power unit compartments for fire protection (e.g., in the A-10, B-2, C-12, C-130, F-14, F-22, P-3 and many other aircraft) or for inerting in fuel tank ullage areas to protect against ullage explosion (e.g., in the A-6, F-16, and F-117). Powder panels have typically been evaluated in aircraft dry bay areas and have only been integrated into production aircraft in these areas (e.g., in the V-22 and AH-1W). Therefore, as a part of the cost-benefit or return-on-investment analysis presented later, a direct comparison of an existing halon fire extinguishing system with an enhanced powder panel system proved to be difficult.

There are only a few potential examples of halon fire protection systems that could provide direct comparisons for a dry bay area. Most of these examples, however, do not offer likely replacement possibilities and are not applicable across a wide range of aircraft. For example, the C-5 aircraft has a center wing leading edge dry bay which is protected by a halon fire extinguishing system. However, this

system was incorporated to protect against overheating or safety-related fires from hydraulic components, not ballistic impact. It is located above the fuselage and would be difficult to hit in most reasonable combat scenarios. Replacement with a passive powder panel fire protection system may not prove practical in this case. As in this example, some of the current halon systems are focused on protecting flammable fluid lines or electronics, which has not been a focus for integrated powder panels thus far. The C-5 has two other dry bay-type areas with halon protection, focusing on electronics protection, not flammable fluid container protection. The B-1 also has an overwing fairing protection system, meant for protection of a hydraulic line and fuel line. It is not an ideal area for comparison with powder panels, either, for the same reasons discussed for the C-5 aircraft. Data were gathered during this survey for other aircraft areas that provide a more practical application for enhanced powder panels.

Discussions were held with various aircraft manufacturers to examine production design requirements or issues, and to provide data to them, which could allow for the consideration of enhanced powder panels in design trade studies. The manufacturers included Bell Helicopter-Textron, Inc., The Boeing Company, Sikorsky Aircraft Corporation, and Lockheed Martin Corporation. The specific aircraft discussed were the V-22, RAH-66, and F-35.

Specific production aircraft requirements were considered proprietary in most cases, but general design requirements were not and are notable. Among the key design criteria often mentioned in the discussions were powder panel thickness, areal density (mass per unit area), and temperature environment. As with any other aircraft component, particularly a forward-fit component, size and mass are big factors. The powder panel must not interfere with existing equipment and cannot create a significant mass penalty. Since design values associated with specific military aircraft are part of the technical specifications for the respective aircraft, these values will not be discussed herein.

However, these values along with current commercial powder panel thicknesses and mass were used as design goals for the Phase II optimization effort. Commercial powder panels used for testing had thicknesses greater than 2.54 mm. The core was composed of a honeycomb design and the face sheets were constructed of a composite material. These panels had areal densities of around 2 kg/m<sup>2</sup>. In repeated conversations with aircraft manufacturers, the temperature range most often quoted as a potential extreme requirement for powder panels was from -40 °C to 104 °C. In many aircraft areas, continuous service temperature would not reach these extremes, but for purposes of the optimization design effort, these temperatures were considered important.

The aircraft prime contractors were also asked if enhanced powder panels would have to undergo any qualification tests such as thermal cycling, impact resistance, vibration or other durability testing, chemical resistance examinations, and moisture absorption evaluations, for example. Based upon their responses, data suggest that commercially available powder panels may have used individual material data to support such qualification, but the assembled powder panels did not appear to be subjected to many of these tests for production qualification. This is not to imply that future powder panel applications may be relieved of such requirements. Some limited production design criteria were considered for the fully assembled enhanced powder panel, such as panel thickness, areal density, and temperature environment, as mentioned above. However, resources in this program did not permit a full examination of many of these other potential production requirements.

## 9.2.6 Powder Dispersion Screening Experiments

### Experimental Setup

Phase I experimental testing was conducted at the Air Force 46<sup>th</sup> Test Wing Aerospace Survivability and Safety Flight's Aerospace Vehicle Survivability Facility (AVSF) at Wright-Patterson Air Force Base (WPAFB), Ohio. An experimental test device (dry bay/fuel tank simulator) was designed and fabricated to enable a direct comparison of powder panel materials and designs, both existing and improved concepts. Through an impact dynamics study, various characteristics critical to the fire extinguishing effectiveness of powder panels were examined. The test device shown in Figure 9–2 allowed for the experimental screening of candidate powder panels by comparing these characteristics in a highly repeatable fashion. Among the characteristics examined were panel impact dynamics, including cracking and material removal, the amount of fire extinguishing powder released into the test article, the dispersion of this powder, and the time the powder remained suspended in the dry bay.

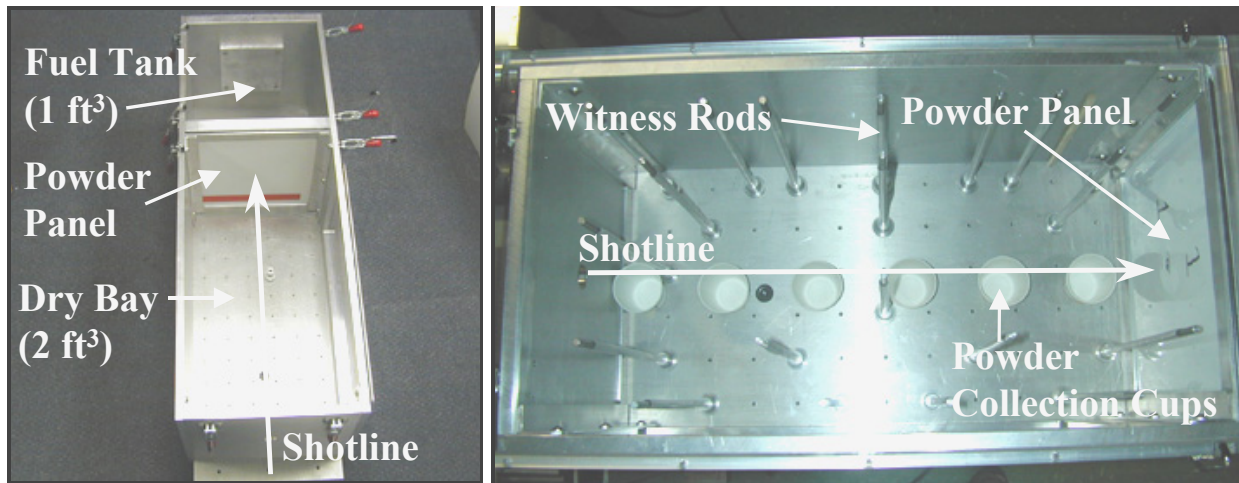


**Figure 9–2. Experimental Test Device and Powder Collection Methods.**

The test device simulates a 0.057 m<sup>3</sup> (2 ft<sup>3</sup>) aircraft dry bay and a 0.028 (1 ft<sup>3</sup>) m<sup>3</sup> fuel tank, with a dry-to-wet shotline. The fuel tank is capable of holding fluid, and the dry bay has Lexan windows to allow for visual observation of each test. Testing in Phase I did not involve fluid in the tank or airflow, to simplify the screening process. Replaceable 7075-T6 aluminum panels of 2.03 mm thickness were inserted to represent the fuel tank wall adjacent to the dry bay. In most of the tests, powder panels were secured directly in front of the fuel tank wall. This offered the worst-case scenario, without fluid in the tank, for evaluating the amount of powder released into the dry bay. The test device also allowed for the installation of powder panels directly behind the dry bay wall where the projectile enters the test article.

The test device was designed to capture powder dispersion information so a direct comparison between candidate powder panels could be made. Figure 9–2 (right side) shows the powder collection methods used in the dry bay. Witness rods are located throughout the dry bay. Plastic tubes are slid over the rods to capture released powder during each test. The rods are placed in a pattern to ensure that the powder dispersion characteristics throughout the dry bay are understood. The plastic tubes are qualitatively examined for signs of powder after each test. Powder collection cups are also located in the dry bay.

These cups are located along the shotline, where the powder concentration is most important during a ballistic projectile impact. The path of the projectile incendiary or impact flash is the location where the mixture of flammable fluid and ignition source is most likely to result in fire initiation. The collection cups were examined and weighed after each test to determine the amount of powder collected. In addition to these collection methods, each panel was weighed before and after each test to determine the amount of powder released. Panel components were also individually weighed to assist in determining the mass of powder loaded into each panel. The removed area of the front face (dry bay side) of the powder panel was also determined. This area was typically a direct correlation with the amount of powder released into the dry bay and provided another measure to compare the panels. The back face (fuel tank side) removed area of the powder panel was also determined for comparison with the front face and to examine the influence of one upon the other. Digital video was captured for each test to assist in determining characteristics related to powder suspension and dispersion.

Figure 9–3 shows the light-gas gun (compressed helium-filled bottle rated at 20.68 MPa) used to launch 0.50 caliber hard steel ball projectiles at velocities of approximately 671 m/s. The kinetic energy of these projectiles was roughly equivalent to a threat greater than a 7.62 mm armor piercing incendiary (API), but just less than a 12.7 mm API projectile.



**Figure 9–3. AVSF Range A Light-gas Gun.**

Testing during Phase I involved only one dry chemical fire extinguishing agent. The powder selected was Purple K ( $\text{KHCO}_3$ ) due to its non-toxic nature, visibility for post-test inspection, and fire extinguishing effectiveness. Corrosion from long-term exposure was not a concern in these tests.

### **Results of Powder Dispersion Screening Tests**

A total of 32 powder panel tests were conducted during the first phase of this program. These tests included components similar to those examined in previously tested powder panel programs to provide some baseline data. Among the materials tested were thin aluminum (0.41 mm thick) and aluminum foil panels. Also examined were 3.2 mm and 6.4 mm thicknesses of 5052 aluminum honeycomb, acting as the rib structure for various panels. A Nomex (aramid fiber paper) honeycomb core of 9.5 mm thickness was also tested. Table 9–2 is a compilation of all systems examined.

**Table 9–2. Phase I Powder Panel Configurations Tested.**

Test No.	Material Description	Total Thickness (mm)	Pretest Mass (g)
1	0.41 mm Al front, 5.3 mm corrugated polyallomer, 0.25 mm Al back	6.0	630
2	0.25 mm Al front, 5.2 mm corrugated polyallomer, 0.41 mm Al back	5.9	594
3	Double wall polypropylene	4.5	427
4	Double wall polycarbonate	6.6	561
5	Double wall polycarbonate, scored	6.6	704
6	1.52 mm ABS faces, 9.5 mm acrylic eggcrate rib	12.4	963
7	1.8 mm (peak) acrylic prismatic faces, 9.5 mm acrylic eggcrate rib	12.9	1038
8	2.0 mm clear acrylic faces, 9.5 mm acrylic tube ribs	13.5	1402
9	1.8 mm textured acrylic front, 1.5 mm ABS back, two ABS ribs (3.0 mm thick) at 102 mm and 203 mm	6.9	769
10	1.8 mm acrylic prismatic front, 1.5 mm ABS back, two ABS ribs (3.0 mm thick) at 102 mm and 203 mm	7.2	830
11	102 mm x 102 mm scored clear 1.5 mm acrylic front, 2.0 mm clear acrylic back, 3.2 mm polycarbonate honeycomb rib	6.9	574
12	51 mm x 51 mm scored clear acrylic, 2.0 mm clear acrylic back, 3.2 mm polycarbonate honeycomb rib	7.6	579
13	1.5 mm ABS faces, 9.5 mm Nomex rib (PN2-1/8-6.0)	13.5	1128
14	1.8 mm textured acrylic front, 2.0 mm clear acrylic back, 6.4 mm Al honeycomb rib (PAMG-XR1-8.1-1/8-002-5052)	10.5	832
15	1.5 mm ABS faces, 6.4 mm Al honeycomb rib (PAMG-XR1-8.1-1/8-00205052)	10.2	764
16	2.0 mm clear acrylic faces, 6.4 mm Al honeycomb rib (PAMG-XR1-8.1-1/8-002-5052)	10.8	942
17	1.5 mm ABS faces, 9.5 mm hollow acrylic tube ribs	13.3	1268
18	51 mm x 51 mm scored 2.03 mm clear acrylic front, 2.0 mm clear acrylic back, 3.2 mm Al honeycomb rib	7.2	638
19	0.08 mm epoxy primer sheet front, 1.5 mm ABS back, two ABS ribs (3.0 mm thick) at 102 mm and 203 mm	5.6	441
20	1.8 mm acrylic prismatic front, 1.5 mm ABS back, 1.6 mm Al corrugation	5.6	434
21	1.8 mm acrylic prismatic front, 1.5 mm ABS back, two ABS ribs (3.0 mm thick) at 102 mm and 203 mm	7.8	552
22	1.8 mm styrene prismatic front, 1.5 mm ABS back, 1.6 mm Al corrugation	5.4	328
23	1.8 mm styrene prismatic front, 1.5 mm ABS back, two ABS ribs (3.0 mm thick) at 102 mm and 203 mm	6.5	517
24	1.5 mm fiberglass polyester resin front, 1.5 mm ABS back, two ABS ribs (3.0 mm thick) at 102 mm and 203 mm	6.3	722
25	1.5 mm polyester resin front, 1.52 mm ABS back, two ABS ribs (3.0 mm thick) at 102 mm and 203 mm	6.5	746
26	Double wall polypropylene, scored, panel - on dry bay wall	4.3	402
27	2.5 mm polyester resin front, 1.5 mm ABS back, two ABS ribs (3.0 mm thick) at 102 mm and 203 mm	7.1	620
28	2.5 mm polyester resin front, 1.5 mm ABS back, two ABS ribs (3.0 mm thick) at 102 mm and 203 mm	7.4	876
29	2.5 mm epoxy resin front, 1.5mm ABS back, two ABS ribs (3.0 mm thick) at 102 mm and 203 mm	7.1	791
30	1.3 mm clear acrylic front, 1.5 mm ABS back, two ABS ribs (3.0 mm thick) at 102 mm and 203 mm	6.7	597
31	1.3 mm clear acrylic front, 1.5 mm ABS back, two ABS ribs (3.0 mm thick) at 102 mm and 203 mm, dry bay clutter	6.2	596

The majority of tests featured unique materials and designs not evaluated in previous powder panel ballistic testing. The goal was to find a front face material and powder panel design that results in significant front face material loss and powder release into the dry bay during a ballistic impact event. Thermoplastic and thermoset materials were the focus of most testing. For the front panel face (dry bay side), materials that exhibited brittle properties upon impact, but durability in handling, were of utmost interest. Front face materials evaluated included a polycarbonate (Lexan), polystyrene, polypropylene, and polymethylmethacrylate (acrylic, Plexiglas). These materials are cost-effective and easily obtainable in off-the-shelf forms. For example, off-the-shelf acrylic and polystyrene overhead fluorescent lighting panels in a variety of faceted designs were tested. These designs may enhance or degrade their brittle nature. The use of intentional surface scoring of flat acrylic panels was also examined using a couple of different scoring patterns and different techniques for implementing the scoring lines. The intent was to determine if surface scoring could be used to enhance the fracture characteristics of the material.

Thermoset polymers were also evaluated for the front face. Tested materials included two polyester resins, an epoxy resin, and a thin epoxy primer. The thin epoxy primer tested was only 0.076 mm (0.003 in.) thick. It is available commercially as a spray and requires a careful procedure for forming it and bonding it to the rib structure. The other thermoset materials are readily available in commercial form, requiring the mixing of a two-part liquid resin.

Plastics were also tested for the back face (fuel tank wall side) and in various configurations for the internal rib structure of the panel. The impetus for experimenting with the back panel was to determine if the fracture characteristics of the back panel influence the front panel in any way. For the dry bay/fuel tank configuration examined, there was a desire to inhibit the back panel hole size to reduce flammable fluid leakage, which could assist in reducing fire ignition probability in an actual production configuration.

Finally, a number of materials and designs were examined for the powder panel internal rib structure. The rib structure adds rigidity and strength to the panel, prevents settling of the powder, and must allow for easy release of as much powder as possible. Some of the panels examined in Phase I were single piece extruded materials that had front and back walls and internal channels. These panel designs were composed of polycarbonate and polypropylene. They were filled with powder in their production form, and the ends were sealed for testing.

As mentioned, honeycomb materials were also examined. One honeycomb material evaluated was 3.2 mm thick, composed of polycarbonate material, and featured a circular cell structure. The honeycomb materials maximized the amount of bonding area to the front panel, which typically inhibited front face cracking. Bonding areas could be reduced to allow for more cracking of the front face, however, the support of the honeycomb structure inhibits flexure, thereby working against crack propagation.

Several other rib designs were conceived to enhance powder release and yet prevent the settling of powder that might reduce its effectiveness to impacts in certain areas. One design included sections of hollow acrylic tubing aligned horizontally and spaced at vertical distances of one inch or less. Both the tubes and the spaces between the tubes were filled with powder to ensure total coverage to threat impact. This rib design provided significant panel stiffness due to the amount of bonding surface area and seemed to provide leverage for sections of the front face to flex and break out. Another design concept was to use strips of solid plastic oriented horizontally in a fashion similar to the tubes. In these trials, the width of the solid strips was minimized since powder would not be present in these locations during a projectile

impact. Tests were conducted with the number of these ribs minimized, the spacing maximized, and the overall panel thickness minimized. These panels were relatively stiff due to the strength of the panel face-to-rib bonds, but allowed for significant flexing of the front face due to the rib spacing. This rib arrangement required several tradeoffs. Ribs that formed channels too far apart allowed powder settling or bulging of the face sheets, but allowed for flexure of the front face during impact, which optimized cracking. Rib channels that were too close together prevented powder settling, but were more prone to function like honeycomb and provide too much support to the front face, reducing the likelihood of significant cracking. In these rib arrangements, powder along the length of the panel could be released from all open channels, which afforded greater performance than a honeycomb design. In a honeycomb design, only the cells penetrated or torn around the perimeter of the impact will release powder, unless significant cracking or area is removed from the front face.

A corrugated aluminum foil with 1.6 mm peak-to-peak height was also examined in some tests. The metal did not show a propensity to break up in these tests, so the front face would need to break up and separate for the panel to be effective. Some of the benefits of this design are similar to the channel design; however, the combination of metal and plastic in these trials may have some operational environment drawbacks, such as significantly different coefficients of thermal expansion. This design, the acrylic tube design, and variations of the horizontal plastic strip design allowed for filling of the powder panel after the panel was nearly assembled. Only the one edge had to be sealed after filling. This design variation could offer some improvement for assembly.

Phase I testing was able to identify novel powder panel designs with enhanced performance over more standard design concepts. Table 9–3 lists some of the more novel and effective designs, while Table 9–4 lists some designs that feature more baseline design concepts and less effective performance.

**Table 9–3. More Effective Powder Panel Designs in Experimental Testing.**

Test No.	Material Description	Thickness (mm)	Panel Mass (g)	Powder Release (g)	% Powder Released	Front Face Area Removed (cm <sup>2</sup> )
8	2.03 mm clear acrylic faces, 9.53 mm acrylic tube ribs	13.5	1402	48	6	32
9	1.78 mm cracked ice acrylic front, 1.52 mm ABS back, two ABS ribs (3.05 mm thick)	6.9	769	23	5	18
12	2.03 mm (50.8 mm x 50.8 mm scored) clear acrylic, 2.03 mm clear acrylic back, 3.18 mm polycarbonate honeycomb rib	7.6	579	9	5	23
21	1.78 mm acrylic prismatic front, 1.52 mm ABS back, two ABS ribs (3.05 mm thick)	7.8	552	30	13	20
23	1.78 mm styrene prismatic front, 1.52 mm ABS back, two ABS ribs (3.05 mm thick)	6.5	517	28	13	26
27	2.49 mm polyester resin front, 1.52 mm ABS back, two ABS ribs (3.05 mm thick)	7.1	620	8	4	25
28	2.49 mm polyester resin front, 1.52 mm ABS back, two ABS ribs (3.05 mm thick)	7.4	876	83	18	81

**Table 9–4. Less Effective Powder Panel Designs in Experimental Testing.**

Test No.	Material Description	Thickness (mm)	Panel Mass (g)	Powder Release (g)	% Powder Released	Front Face Area Removed (cm <sup>2</sup> )
1	0.41 mm Al front, 5.3 mm polyethylene corrugated rib, 0.25 mm Al foil back	6.0	630	0.6	0.2	1
2	0.25 mm Al foil front, 5.2 mm polyethylene corrugated rib, 0.41 mm Al back	5.9	594	0.04	0.01	1
13	1.5 mm ABS faces, 9.5 mm aramid rib	13.5	1128	1.5	0.2	1
14	1.8 mm textured acrylic front, 2.0 mm clear acrylic back, 6.4 mm Al honeycomb rib	10.5	832	1	0.2	1
15	1.5 mm ABS faces, 6.4 mm Al honeycomb rib	10.2	764	1	0.2	1
16	2.0 mm clear acrylic faces, 6.4 mm Al honeycomb rib	10.8	942	3	0.6	2
18	2.0 mm (5.1 cm x 5.1 cm scored) clear acrylic front, 2.0 mm clear acrylic back, 3.2 mm Al honeycomb rib	7.2	638	2	0.8	10

The tables indicate the mass of each powder panel, which were all about 302 mm square. Total powder-filled mass for panels tested in the first year of testing ranged from 428 g to 1,400 g. Most of the mass difference is due to varying thicknesses of the panels, with the mass of the powder contributing significantly because of increased panel internal volume. By contrast, commercial panels obtained during the NGP weighed between 175 g and 189 g for a similar size. Obviously, this was one design feature requiring optimization in Phase II testing.

Some measures of effectiveness are also noted in Table 9–3 and Table 9–4, including powder release or loss as a result of the ballistic test, percentage of the powder released, and the front face area removed. The estimate of the powder release is determined by comparing the panel mass before and after each test and weighing/estimating panel material lost. In cases where the panel was not effective at dispersing the powder, the hole on both faces of the panel may have been virtually the same size as the projectile (12.7 mm diameter). In other cases, a significant amount of the front face material may have been lost (Figure 9–4). Obviously, in these cases, a significant amount of powder was also released from the panel. The amount of powder released during testing varied from a fraction of a gram in some of the more standard designs to over 100 g.

A review of the Phase I test data indicated a wide disparity in the reaction of the panels. In some tests, the powder release was negligible, i.e., no powder was detected on the witness rods and no powder deposited in the cups. In these ineffective powder panel tests, more powder is actually observed exiting the back of the panel, along with the projectile, versus entering the dry bay. In other tests (Figure 9–5), the cloud of powder in the dry bay engulfed the entire dry bay and remained for a matter of minutes. Many tests resulted in some minute residue in the cups that was more likely spall from the powder panel front face and/or ribs, rather than the powder. In tests of effective powder panel concepts, powder was observed on all the witness rods and measurable powder mass was observed in all six cups. The amount of powder deposited in the collection cups varied during testing from no trace to over seven grams by mass.



**Figure 9-4. Test Example of Significant Panel Fracture and Material Loss.**

Typically, 0.05 g or less was captured in any single cup, with the highest concentration of the powder being closest to the powder panel, as expected. Twenty different witness rods were placed throughout the dry bay and visible powder was noticed in more effective tests on all of the witness rods. To further verify the dispersion of the powder for effective designs, several panels were tested with dry bay clutter and powder was still observed on all witness rods, even those in isolated areas.

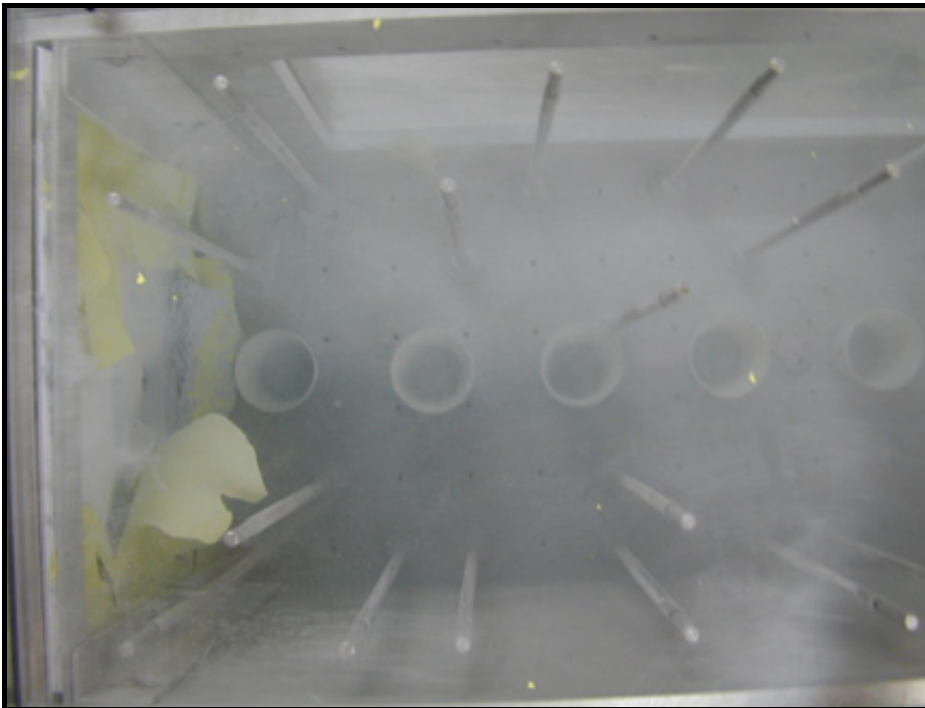


**Figure 9-5. Test Example of Effective Powder Release and Dispersion.**

The most promising of the new powder panel designs examined in this research offer the potential to be competitive with halon 1301 in a wider variety of dry bay designs. In one of these cases (epoxy primer front face), nearly 50 % of the front face area was removed, almost 60 % of the powder was released, and the powder remained suspended throughout the dry bay for over four minutes. This occurred despite the fact that this was one of the thinnest panels tested. This compares with testing of other powder panel designs integrated into operational aircraft, where the powder disperses only along the shotline, dissipates in tenths of a second, and the amount of dispersed powder was limited to the region of projectile penetration (approximate powder release of a few percent).<sup>26</sup>

Figure 9–6 and Figure 9–7 show major performance benefits achievable with some of the enhanced design concepts listed in Table 9–3 (by test number) over more standard powder panel designs (Table 9–4). Results indicated the powder panel front face area removed could be increased by 15 to 20 times over more standard designs (Figure 9–6). Testing also revealed the amount of powder released into a dry bay could be increased 5 to 10 times with an enhanced powder panel design (Figure 9–7). Testing also indicated that powder dispersion could be enhanced, even with dry bay clutter, ensuring the prevention of fire ignition over a wider area (Figure 9-8). In this figure, the number of witness rods with detectable powder residue is indicated for each test. Effective designs resulted in powder being suspended in the dry bay for much longer periods of time than standard powder panels (as much as four minutes in one test compared to one second or less). Finally, the design and fabrication effort revealed enhanced powder panels afforded greater design flexibility, which can be utilized to target mass, durability, and other application-specific design goals. These findings revealed that new powder panel concepts could significantly enhance the fire extinguishing effectiveness of this vulnerability reduction method, thereby demonstrating the feasibility of enhanced powder panels.

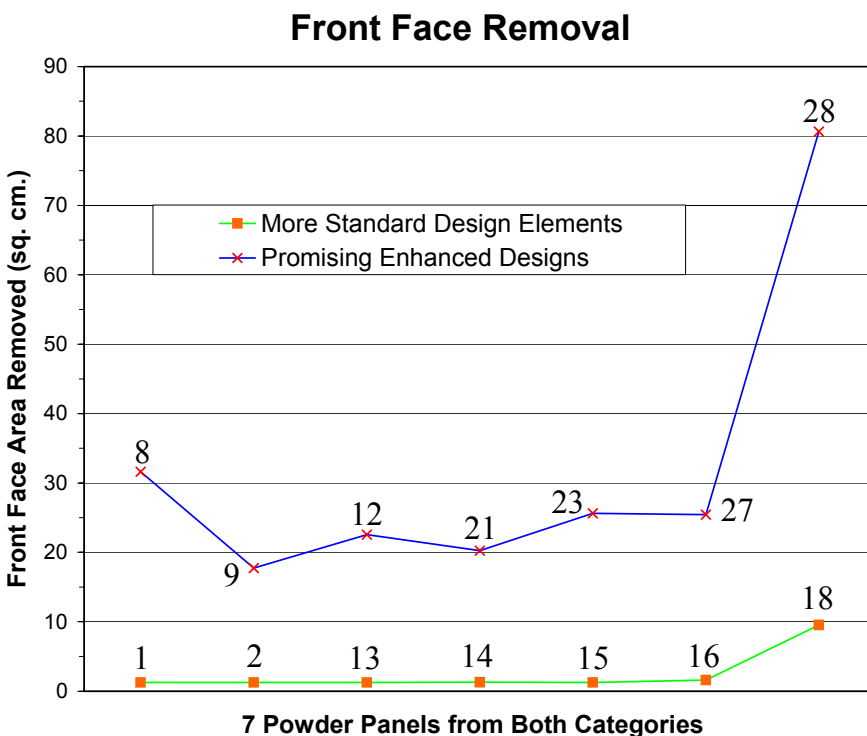


**Figure 9–6. Effect on Powder Panel Fracture Area of Standard Design Features and Enhanced Designs.**

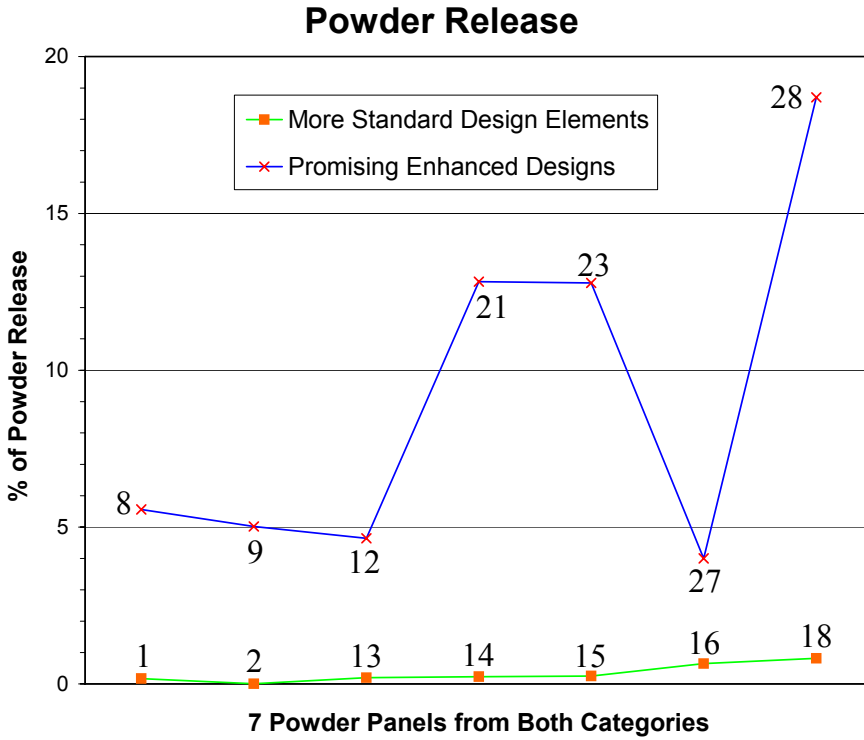


**Figure 9–7. Effect on Powder Delivery of Standard Design Features and Enhanced Designs.**

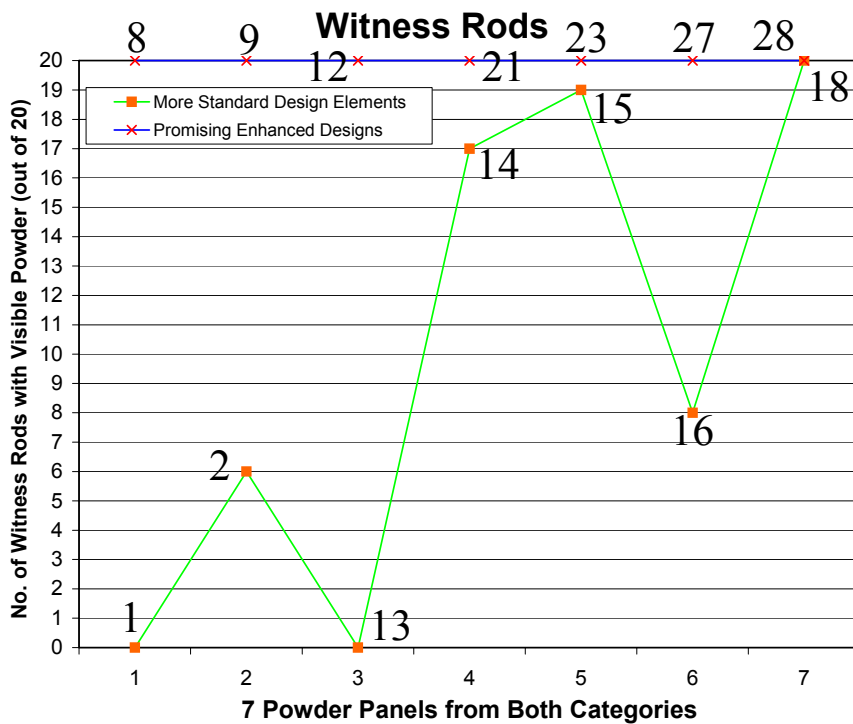


**Figure 9–8. Effect on Powder Dispersion of Standard Design Features and Enhanced Designs.**

Experimental observations indicate, as predicted, that the front face material properties are of utmost importance. More brittle materials outperformed ductile materials (that resist fracturing) by releasing more powder into the dry bay. The projectile seemed to melt its way through polycarbonate and

polypropylene materials, and even some polystyrene materials, resulting in little or no powder released into the dry bay. Acrylic front face panels and faceted acrylic and styrene materials reacted in a much more brittle nature, resulting in lost material or cracking that more effectively released powder into the dry bay. One acrylic panel with a prismatic square pattern actually did not perform very well. It appears that the pattern on the panel inhibited crack growth. Mixed results were found during testing of scored acrylic panels. Some cracking seemed to follow scoring lines in the vicinity of the impact that may have contributed to more material loss. However, comparisons between 5.1 cm and 10.2 cm scoring patterns showed that cracks emanating from the hole area, created directly by the projectile impact, were actually prevented from growing longer, i.e., scoring lines acted as crack stoppers. With appropriate scoring designs, though, it appears crack growth optimization techniques could be used to enhance performance.

A strong synergism was found between the rib structure and the front face. Increasing the bond surface area between the front face and ribs inhibited powder dispersion for the designs tested. Results indicated that standard honeycomb ribs resisted greater front face cracking because of the increased number of bond sites. Experiments on bonding honeycomb materials to the front face in a reduced number of selected areas, such as the panel perimeter, proved effective for polycarbonate honeycomb, but not necessarily for the aluminum honeycomb. It was reasonable to conclude from the testing, weaker and fewer bonding sites would allow both designs to function more effectively, as previous work has shown. Multiple explanations were plausible for the more effective polycarbonate tests. It is probable there was a contribution from the more brittle properties of the polycarbonate, which did fracture in some locations, and the design of the aluminum honeycomb likely distributed the impact energy over a greater surface area without allowing critical flexure of the front face. Design concepts using channels or horizontal ribs proved to be associated with the most effective powder panels, particularly when a more frangible front face was used. Channel designs allowed more powder to be released from the impact location than more segmented or cellular designs. Tradeoffs would be necessary for these designs between rib spacing and powder loading, as sufficient powder must be available at all potential impact sites, but more powder translates to greater mass. Testing indicated three-piece powder panel designs outperformed easy-to-assemble double-wall extrusion designs, as built-in rib channels inhibited cracking.

Variation in the powder panel back face had much less effect on powder panel performance than the front face or rib design. A number of tests involved less brittle ABS material for the back face, since it is postulated that a smaller hole in the back face may actually mitigate the chance of a dry bay fire by reducing fuel leakage and confining it to an area along which most of the powder is released. This would provide a second means to increase powder panel effectiveness. The first being the use of a more brittle front face to maximize fire extinguishing powder release, while the flammable fluid leakage is minimized. Experimental testing did reveal that the front face of the powder panel can be designed to fracture and release large amounts of powder, while minimizing the damage to the panel back face. Phase I testing did not involve a fluid-filled tank, thereby eliminating hydrodynamic ram pressures on the fuel tank wall and reducing the chance of damage to the back face. In the tests involving ABS, the damage sustained by the back face was a hole just larger than the diameter of the 12.7 mm diameter ball projectile.

## 9.2.7 Live-fire Proof-of-concept Demonstrations

### China Lake Testing Facilities

Following Phase I experimental testing, Skyward, Ltd. was afforded the opportunity to participate in several live fire demonstration tests of enhanced powder panels. These proof-of-concept tests were conducted in two different test series simulating aircraft dry bays and involving the potential ignition of a fuel fire. These tests provided Skyward with an opportunity to select some of the more effective enhanced powder panel design features identified in Phase I, perform some quick optimization, add some unique design features not previously evaluated, and perform live fire testing, all in advance of the initiation of Phase II. The promising results of these demonstration tests provided a leap forward for the initiation of Phase II.

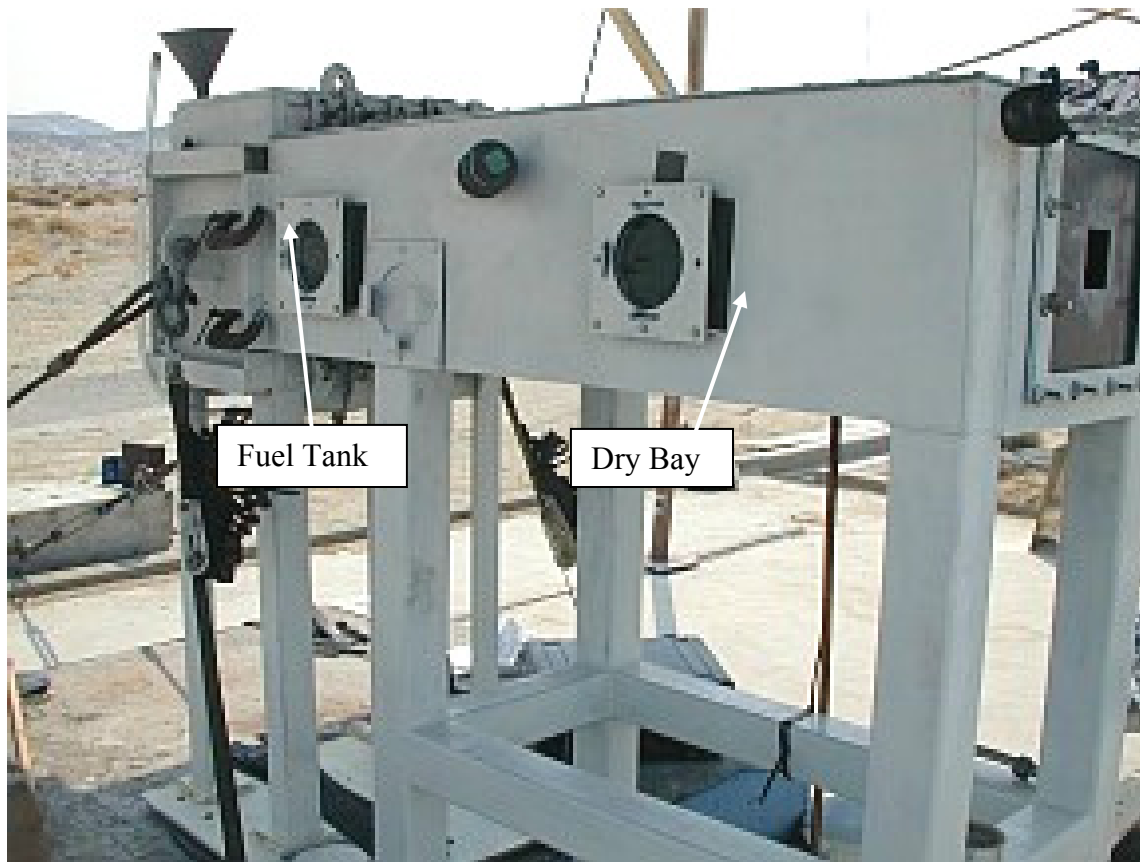
#### *JTCG/AS Demonstration Testing*

The ability of enhanced powder panels to prevent fire ignition was first demonstrated in a Joint Technical Coordinating Group on Aircraft Survivability (JTCG/AS), since renamed Joint Aircraft Survivability Program Office (JASPO), test program examining reactive powder panel concepts, which is a method of using a reactive energetic backing with any powder panel design to enhance powder delivery effectiveness.<sup>27</sup> These tests were conducted at the Naval Air Warfare Center-Weapons Division Weapons Survivability Laboratory in China Lake, California. Four tests of enhanced powder panels without reactive backing were conducted. These tests involved the firing of 12.7 mm API projectiles into a dry bay/fuel tank simulator containing JP-8 fuel. Projectiles were fired at approximately 757 m/s at a 0° angle into the dry bay, impacting an aluminum striker plate, which was separated from the powder panel/fuel tank by approximately 0.30 m. The projectiles then continued through the powder panel, penetrating the fuel tank and releasing JP-8 fuel. A 0.46 m wide x 0.61 m high x 1.22 m long dry bay (right side of Figure 9–9) was connected to a 1.22 m x 1.22 m x 1.22 m fuel tank (left side of Figure 9–9).

A 3.18 mm thick 2024-T3 simulated fuel tank bulkhead was positioned on the front or initial impact side of the fuel tank. The powder panel was attached to this removable bulkhead panel with a 2-part epoxy adhesive. Tests were also conducted with commercial powder panels in this test series to provide a basis of comparison with the enhanced powder panel tests, as well as to tests with no protection.

#### *FAA Demonstration Testing*

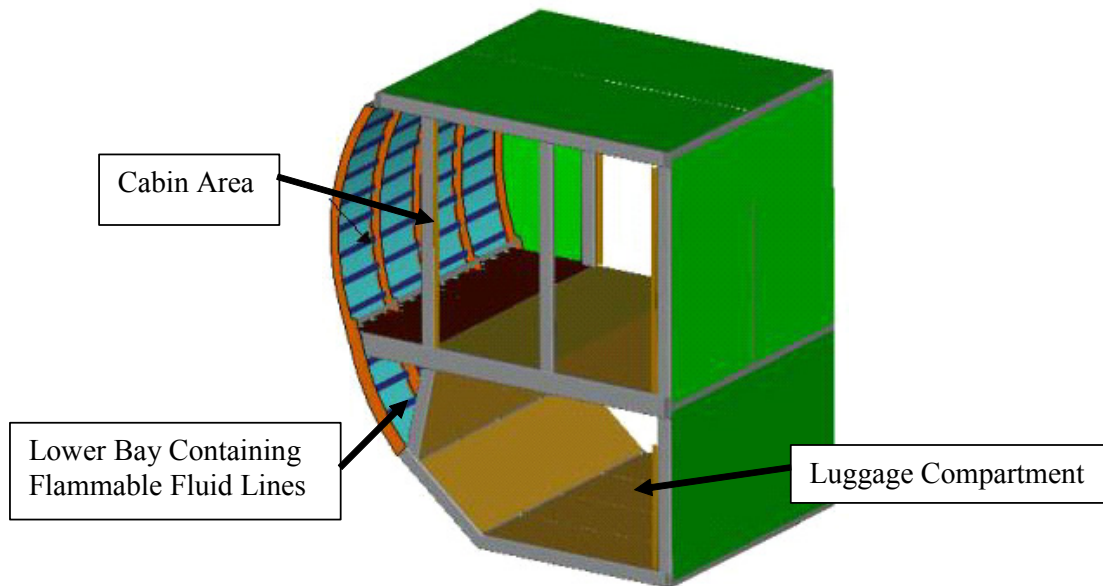
A second demonstration test series of an enhanced powder panel was conducted in a Federal Aviation Administration (FAA) program.<sup>28</sup> This test series was also conducted at China Lake, just after the JTCG/AS series. This test examined the feasibility of powder panels in preventing fuselage fires in commercial aircraft caused by the release and impact of an uncontained engine rotor blade with flammable fluid lines. Figure 9-10 shows a schematic of the test article. A simulated rotor blade was fired through the lower bay and into the luggage compartment and an ignitor initiated a fire in the presence of leaking fuel as the rotor blade penetrated the lower bay. An enhanced powder panel successfully prevented a fire from igniting in one of the tests. A second test was invalidated due to problems with the timing sequence, but unrelated to the powder panel. Two commercial powder panel tests were also conducted during this test series to evaluate their effectiveness and allow comparison of the results with those of the enhanced powder panel test.



Fuel Tank

Dry Bay

Figure 9–9. JTCG/AS Test Article.



Cabin Area

Lower Bay Containing  
Flammable Fluid Lines

Luggage Compartment

Figure 9–10. Schematic of the FAA Test Article.

**Live Fire Test Results**

Following the experimental testing of Phase I, the opportunity for demonstrating enhanced powder panels arose at the Navy’s Weapons Survivability Laboratory. Lessons learned from the NGP Phase I experimental testing were used to design and fabricate some new, slightly more optimized powder panels. These panels again incorporated thermoplastic materials. However, thinner panels and reduced powder loading resulted in reduced mass, and new panel designs were utilized. Masses were decreased on average 100 g to 200 g from those designs evaluated in experimental testing for 30.2 cm x 30.2 cm panels. The mass of the panels tested at China Lake varied from 320 g to 422 g, and the thicknesses ranged from 2.4 mm to 3.3 mm. In both the JTCG/AS and FAA test programs, the enhanced powder panels showed solid improvement over current powder panel designs. Fire ignition was prevented in all five valid tests involving enhanced powder panels (four JTCG/AS tests and one FAA test). Conversely, fires resulted in all four valid commercial powder panel tests (two JTCG/AS and two FAA tests).

The powder releases from both the commercial and enhanced panel designs in the China Lake tests were as much as ten times those experienced in the light gun tests conducted at WPAFB due to a number of significant differences in the two facilities and test protocols: the energy of the projectile used at China Lake was about 17% larger; the striker plate at China Lake caused the projectile to spall and yaw; and, most significantly, fuel was present in the China Lake tests that applied extra pressures from the hydraulic ram effect, distorting the wall and imparting additional forces on the panel.

Figure 9–11 shows some images captured from high-speed video in JTCG/AS testing demonstrating the fire mitigation capability of enhanced powder panel designs. Powder discharge was estimated to be at least 90 % of the pretest powder loading for the enhanced powder panels, compared to 5 % to 10 % for commercial powder panels. Greater powder dispersion throughout the dry bays was also evident for the enhanced powder panels. Figure 9–12 compares the amount of fire extinguishing powder released from an enhanced powder panel with a commercially available powder panel in the JTCG/AS tests.

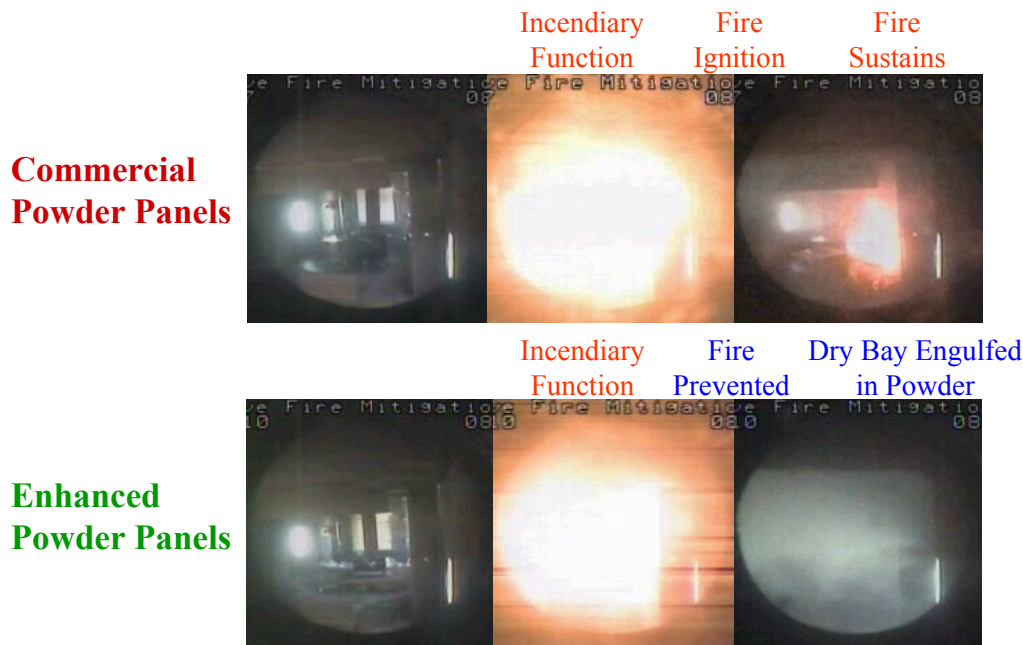


**Figure 9–11. Enhanced Powder Panel Fire Mitigation Capability.**

Figure 9–13 shows that impact of the enhanced powder panel by a rotor blade in the FAA test resulted in release of all the fire extinguishing agent, as it prevented fire ignition. Baseline testing showed that unprotected fuselage areas did indeed result in sustained fires.

**Commercial Powder Panel  
~5-10% Powder Release**



**Enhanced Powder Panel  
~90% Powder Release**



**Figure 9–12. Comparison of Commercial and Enhanced Powder Panel Agent Release in JTCG/AS Dry Bay Fire Extinguishing Testing.**



**Figure 9–13. Entire Contents of Enhanced Powder Panel Released During FAA Test in Which the Fire Was Prevented.**

## 9.2.8 Optimization Program

### Optimization Testing Methodology

In Phase II, Skyward continued their impact dynamics research, with a focus on optimizing the enhanced powder panels, parametrically examining design variations, and then demonstrating the optimized panels. Panel materials, thickness, and construction techniques were optimized to reduce the panel mass and thickness, while maintaining effective powder release and dispersion.

Testing was conducted in the same simulated dry bay experimental device used for concept evaluations in Phase I, and with the same light gas gun launching 12.7 mm diameter ball projectiles. Optimization test variables included panel materials and thicknesses, fire extinguishing powder loading (mass of powder inserted into a given panel size), rib designs, and the assembly process. Optimization testing focused on three primary areas of investigation:

- effectiveness optimization (maximize front face fracture and powder release);
- practicality enhancement (reduce mass, decrease panel thickness, address production issues); and
- reliability improvement (quantify reliability of measures of effectiveness, increase durability, and reduce risk of accidental leakage).

Maximizing powder release into the dry bay continued to be the defining goal, but other requirements were levied on the design effort to ensure that the enhanced powder panels were as practical and reliable as possible. Mass was reduced, panel thickness was minimized, and other potential production requirements were considered. An areal density (mass per unit area) target was provided by one of the vehicle manufacturers for the design effort.

Phase II testing primarily involved the use of aluminum oxide ( $\text{Al}_2\text{O}_3$ ) over Purple K ( $\text{KHCO}_3$ ) or other powders, even though these other powders have been demonstrated to be more effective as fire extinguishing agents. At least two of the aircraft manufacturers in the powder panel survey expressed doubt that any potentially corrosive chemical powder would be acceptable by their aircraft, so there was a conscious effort made to demonstrate the effectiveness of  $\text{Al}_2\text{O}_3$  during the optimization testing.  $\text{Al}_2\text{O}_3$  is the only known powder panel agent to be incorporated into an aircraft due to its lack of reactivity with aircraft structure. Additionally, since  $\text{Al}_2\text{O}_3$  has a much higher specific gravity than  $\text{KHCO}_3$  (3.95 compared to 0.88), it was thought to be worst-case and would help with determining success in mass reduction efforts. The  $\text{Al}_2\text{O}_3$  tested was 5  $\mu\text{m}$  in average particle diameter, compared to an average of approximately 30  $\mu\text{m}$  for the  $\text{KHCO}_3$ , which may also mean the former could pack more tightly.

Certain front face materials evaluated in Phase I testing proved to be effective and remained a focus in Phase II. These materials included thermoplastics with brittle material properties and some thermoset resins. Other unique materials were also examined that more appropriately targeted optimization requirements. Efforts were made to minimize front face and overall thickness and yet maintain sufficient strength to avoid accidental fracture. Lower density materials were compared to more dense materials.

Various new and unique designs were examined for the rib structure in Phase II, including the thickness of the ribs and attachment methods to the front and back faces. The rib design was examined in detail because it directly affects the potential fire extinguishing powder loading, which can be the primary mass

driver in the overall design. Various rib materials were examined for influence on powder panel performance, including some materials evaluated in the more effective Phase I designs.

Phase II testing also included examinations of back face materials and thicknesses and their influence on powder panel effectiveness. Materials examined in Phase I were once again tested along with some materials not previously evaluated. Testing included designs where the front and rear faces and the rib materials were the same and others where dissimilar materials were used.

Bonding techniques were also examined, with an emphasis on ensuring a robust overall design that reduced the risk of accidental leakage. In addition, rib-to-face bonding was examined for its influence on the performance of the powder panel. This influence was noted in Phase I testing and further examined in Phase II. Bonding materials were examined, as well as bonding patterns or techniques.

### Parametric/Optimization Experimental Results

A total of 25 tests were conducted in Phase II optimization tests in Range A at the AVSF. Table 9–5 lists the panels tested and includes pretest panel masses and areal densities, along with the mass of powder released, the percentage of powder released, and the estimated front face area removed. The panels are listed in descending order by the mass of powder released in each test.

**Table 9–5. Phase II Optimization Tests.**

Test No.	Material Description	Total Thickness (mm)	Pretest Mass (g)	Areal Density (kg/m <sup>2</sup> )	Powder Release (g)	% Powder Released	Face Area Removed (cm <sup>2</sup> )
5	0.64 mm polystyrene front 1.3 mm polycarbonate ribs 0.51 mm polycarbonate back	2.4	295	3.24	5.2	3.2	11
22	0.76 mm acrylic front 0.76 mm polycarbonate ribs 0.76 mm polycarbonate back	2.3	215	2.37	4.0	8.4	6
24	0.51 mm composite front 0.76 mm polycarbonate ribs 0.38 mm polycarbonate back	1.6	141	1.55	3.0	6.3	1
8	0.76 mm acrylic front 1.3 mm polycarbonate ribs 0.76 mm polycarbonate back	3.0	348	3.82	3.0	1.8	12
18	0.64 mm polystyrene front 0.76 mm polycarbonate ribs 0.51 mm polycarbonate back	1.9	332	3.65	2.5	1.2	2
14	0.64 mm polystyrene front 1.3 mm polycarbonate ribs 0.76 mm polycarbonate back	2.7	368	4.05	2.2	1.9	10
2	0.64 mm polystyrene front 0.76 mm polycarbonate ribs 0.51 mm polycarbonate back	2.4	252	2.77	2.2	1.8	5
10	0.76 mm acrylic front 1.3 mm polycarbonate ribs 0.76 mm polycarbonate back	2.8	453	4.98	2.1	0.7	1

Test No.	Material Description	Total Thickness (mm)	Pretest Mass (g)	Areal Density (kg/m <sup>2</sup> )	Powder Release (g)	% Powder Released	Face Area Removed (cm <sup>2</sup> )
4	0.64 mm polystyrene front 1.3 mm polycarbonate ribs 0.51 mm polycarbonate back	2.4	330	3.63	1.7	0.8	24
23	0.51 mm composite front 0.76 mm polycarbonate ribs 0.38 mm polycarbonate back	1.6	140	1.54	1.6	2.8	2
17	0.64 mm polystyrene front 0.76 mm polycarbonate ribs 0.51 mm polycarbonate back	1.9	330	3.63	1.5	0.8	2
6	0.64 mm polystyrene front 0.76 mm ABS ribs 0.76 mm ABS back	2.2	201	2.21	1.4	1.5	10
11	0.64 mm polystyrene front 1.3 mm polycarbonate ribs 0.76 mm polycarbonate back	2.7	404	4.44	1.0	0.7	7
13	0.64 mm polystyrene front 1.3 mm polycarbonate ribs 0.76 mm polycarbonate back	2.7	410	4.51	0.8	0.5	3
16	0.64 mm polystyrene front 0.76 mm polycarbonate ribs 0.51 mm polycarbonate back	1.9	306	3.37	0.8	0.4	2
7	0.64 mm polystyrene front 0.76 mm ABS ribs 0.76 mm ABS back	2.2	194	2.13	0.8	0.9	6
21	0.64 mm polystyrene front 0.76 mm polycarbonate ribs 0.76 mm polycarbonate back	2.2	192	2.10	0.6	1.2	1
9#	0.08 mm glass epoxy front 0.1" Nomex honeycomb ribs 0.08 mm glass epoxy back	2.7	175	1.92	0.3	0.2	1
15#	0.08 mm glass epoxy front 2.5 cm Nomex honeycomb ribs 0.08 mm glass epoxy back	2.7	175	1.92	0.2	0.2	0.5
19	1.0 mm polycarbonate front 0.76 mm polycarbonate ribs 0.76 mm polycarbonate back	2.5	270	2.96	0.1	0.3	0.7
20*	1.0 mm polycarbonate front 0.76 mm polycarbonate ribs 0.76 mm polycarbonate back	2.5	261	2.87	N/A	N/A	0.7
25*	0.51 mm composite front 0.76 mm polycarbonate ribs 0.38 mm polycarbonate back	1.6	124	1.36	N/A	N/A	19

# Existing powder panel designs.

\*Tests conducted with water in fuel tank; not able to accurately determine powder release.

A summary of the designs is also provided in Table 9–5, listing the front and back face materials and the material thickness. Effective front face materials tested in Phase I were evaluated, including a textured polystyrene. Some other materials were also examined, including other thermoplastics and some composite materials not evaluated in Phase I. Materials used for the back face concentrated on polycarbonate, which proved to be effective in Phase I, although some tests were conducted with ABS, a more ductile material. Table 9–5 also shows the rib materials tested and the thicknesses of the internal section of the panel. Different rib designs and manufacturing processes were examined in the optimization testing. Rib materials most often mirrored the back face material.

Optimization testing indicated significant decreases in mass were possible from Phase I test panels, while maintaining improved powder release. Panel masses were reduced as much as 57 % from the lightest panel tested in the first phase, with an increase in powder release. Figure 9–14 compares the lightest Phase II panel with the lightest Phase I panel and a commercial powder panel. Two of the lightest pretest filled panel masses were 124 g and 140 g. By comparison, commercial powder panels tested in Phase II weighed approximately 175 g. Therefore, the enhanced powder panels were reduced as much as 29 % below the commercial panel mass. Enhanced powder panel thicknesses ranged between 1.6 mm and 3.0 mm in optimization evaluations. This was a reduction of more than 60 % from the thinnest panel tested in Phase I. Commercial panels evaluated in Phase II were 2.7 mm in thickness. The enhanced powder panels were, therefore, reduced about 39 % in thickness below the commercial powder panel.

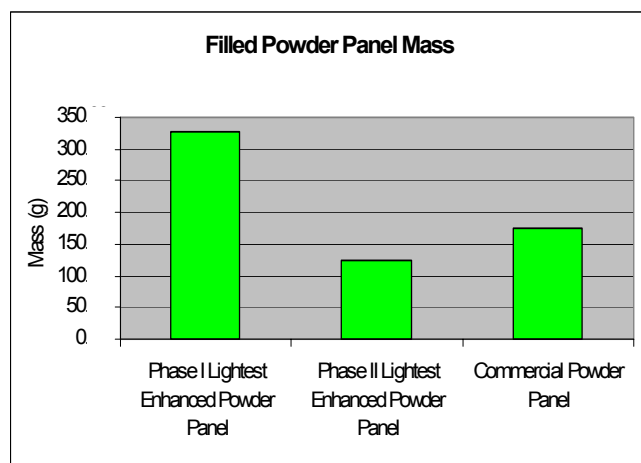


**Figure 9–14. Enhanced Powder Panel Mass Reduction.**

Figure 9–15 compares the thinnest panels tested in Phase I and Phase II with the commercial powder panels. Reductions in thickness reduce the amount of powder in the panel, which is the significant mass consideration. However, a thicker panel along the shotline also reduces the potential powder release, which obviously affects powder panel effectiveness. Therefore, there is a balance necessary between panel thickness, which affects panel mass, and the effectiveness of the panel, as measured by powder release or loss. Front and back face materials and the rib structure design were other variables examined to increase performance without increasing mass.

Powder release is an important factor in the testing because the greater the amount of powder dispersed in the dry bay, particularly along the shotline, the lower the chance of an ignited fire. The amount of powder released in Phase II testing ranged from as low as 0.1 g to as much as 5.2 g. This powder release or loss is not as much as the most effective panels in Phase I testing, but the panel thickness and available powder has been significantly reduced to meet likely design goals. Powder release for the commercial

powder panel tests was 0.2 g and 0.3 g. Figure 9–16 compares the best performing Phase II enhanced powder panel (no water in the tank) with the best performing commercial powder panel. These data show the amount of powder released from the enhanced powder panels was as much as 21 times greater than the commercial powder panels.

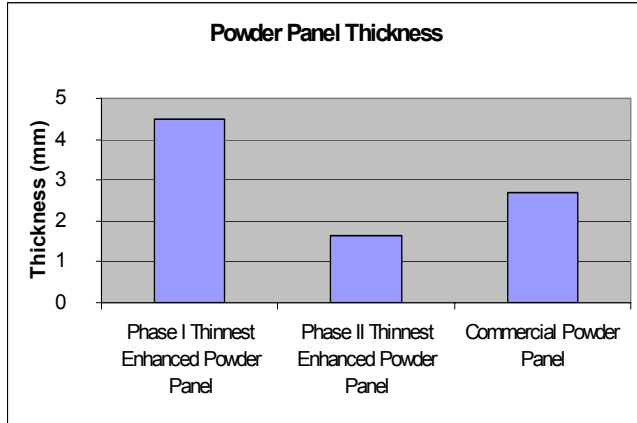


**Figure 9–15. Enhanced Powder Panel Thickness Reduction.**

The percentage of powder released (powder released or lost divided by pretest total powder loading multiplied by 100) has also been used as a measure of powder release effectiveness. The enhanced panel design attempts to maximize the release of the available powder in the panel. Optimized panels tested ranged from 0.3 % to 8 % of the total powder released. The commercial panels released approximately 0.2 % of the total powder contained.

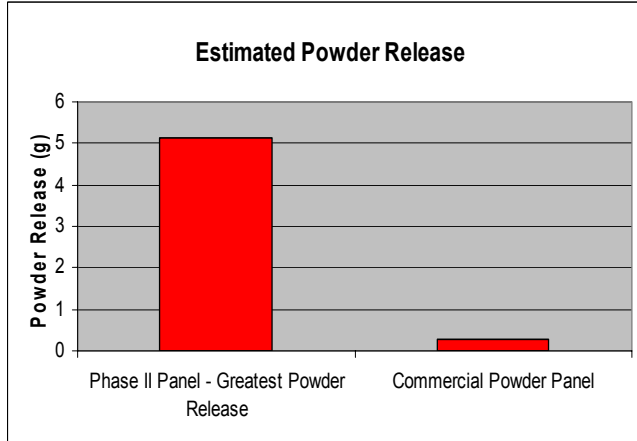


**Figure 9–16. Comparison of Enhanced and Commercial Panel Powder Released.**

Figure 9–17 compares the best performing Phase II enhanced panel (no water in the tank) with the best performing commercial panel. These data show the enhanced panels could increase the percentage of total powder released by as much as 42 times. A ranking of the panels using percentage of powder released does not track directly with a ranking of the panels by total powder released, since there was some considerable variance in overall pretest panel mass.

Tests 9 and 15 in Table 9–5 were conducted on the commercially available powder panels. As mentioned previously, these panels are composed of a honeycomb core and two thin composite face sheets. The commercial powder panels were among the lighter panels tested (empty mass and with powder), but also released nearly the least amount of powder and the smallest percentage of powder. Except for one test

examining a ductile front face, the powder release and percentage of powder released for the commercial panels is less than half the next enhanced powder panel. As discovered in previous testing with Nomex honeycomb cores, powder is released from those cells directly penetrated by the projectile and those torn on the perimeter of the penetration either by the penetrating projectile or hydrodynamic ram forces acting on the fuel tank panel. However, the damage area is relatively well contained and powder is not able to escape from the rest of the panel. Enhanced powder panels offer the potential for a much greater percentage of the panel's contents to be released. It was anticipated at this point in the program that the effects of hydrodynamic ram on the powder panel will only increase the amount of improvement an enhanced powder panel can offer. Further testing would verify this assertion.

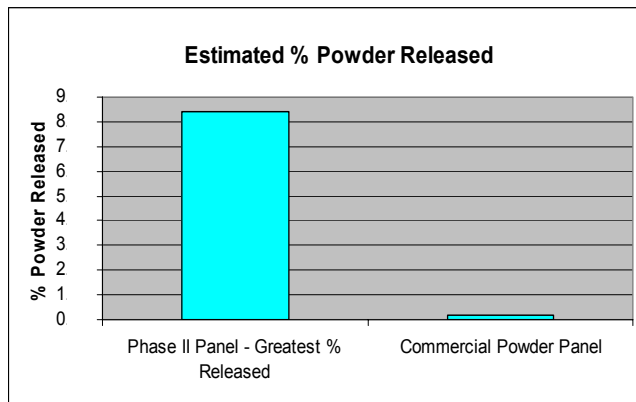


**Figure 9–17. Comparison of Enhanced and Commercial Panel Percent Powder Released.**

The outlier enhanced powder panel (Test 19) utilized polycarbonate throughout the design, including the front face. In this test, the entrance hole in the front face and exit hole in the rear face essentially self-sealed together and prevented virtually any powder from escaping, except through the penetration area alone. This design was also examined in Test 20 with water in the fuel tank and yielded the same damage. The front face area removed for these tests was approximately  $0.7 \text{ cm}^2$ , the least effective performance by an enhanced powder panel. By contrast, Test 4 resulted in almost  $25 \text{ cm}^2$  of the front face removed and Test 25, with water, resulted in over  $19 \text{ cm}^2$  being removed.

Figure 9–18 compares the enhanced powder panel experiencing the greatest front face area removal (no water in the tank) with the better performing commercial powder panel ( $1.1 \text{ cm}^2$ ). An improvement of over 22 times is shown with this enhanced powder panel.

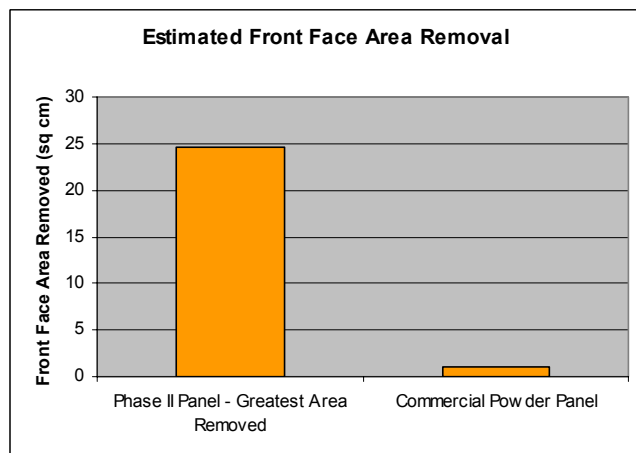


**Figure 9–18. Comparison of Enhanced and Commercial Panel Front Face Area Removal.**

For Tests 20 and 25, conducted with water in the fuel tank, a post-test mass of the panel to determine powder release or loss was not practical. The powder in both panels absorbed water as a result of the test. These two tests, however, demonstrated that hydrodynamic ram would significantly enhance front face fracture for a more brittle front face, leading to greater powder release, but would not likely assist fracture for a ductile front face. Front face area removal was increased for the same panel design by as much as 12 times (comparing Test 24 to Test 25) due to the additional forces and fuel tank panel deformation associated with hydrodynamic ram. This result demonstrated that in cases where the powder panel will be attached to a flammable fluid container, and hydrodynamic ram is expected when the container is punctured, the powder panel can be designed to take advantage of the expected hydrodynamic ram event.

In summary, the Phase II data showed that an enhanced powder panel (Test 24) can be 19 % lighter and 39 % thinner than a commercial powder panel, yet release over 10 times more powder mass, 30 times greater the percentage of powder originally contained in the panel, and sustain at least 32 % greater front face area removal. The data also showed that the effects of hydrodynamic ram would further increase the performance of an enhanced powder panel.

### **9.2.9 Live-fire Demonstration Testing of Optimized Enhanced Powder Panels**

#### **Testing Objective**

At the end of Phase II, a series of live fire demonstration tests was conducted of the optimized designs. These tests were to demonstrate (a) that the most promising enhanced powder panel designs could prevent fire ignition and be competitive with commercial powder panels in vital design criteria such as mass and thickness; and (b) that powder dispersion and fracture mechanics results shown in the small experimental test article could be extrapolated to a larger, more realistic test article. They also examined attachment techniques for the panels, the effectiveness of  $\text{Al}_2\text{O}_3$  (historically the preferred dry chemical powder in aircraft applications), and the effect of certain variables on enhanced powder panel effectiveness.

#### **Wright-Patterson AFB Facility**

Phase II live fire demonstration testing was conducted by the Air Force 46<sup>th</sup> Test Wing Aerospace Survivability and Safety Flight. The tests were conducted in outdoor Range 2 at their Aerospace Vehicle Survivability Facility, Wright-Patterson Air Force Base (WPAFB), Ohio (Figure 9–19).

Baseline testing was conducted to ensure that fire could be ignited when a powder panel was not present. One test was conducted with a standard commercial powder panel to evaluate its effectiveness for the same test variables. Finally, six enhanced powder panel tests were conducted. Figure 9–20 shows the test article setup.



**Figure 9–19. Range 2 at the WPAFB Aerospace Vehicle Survivability Facility.**

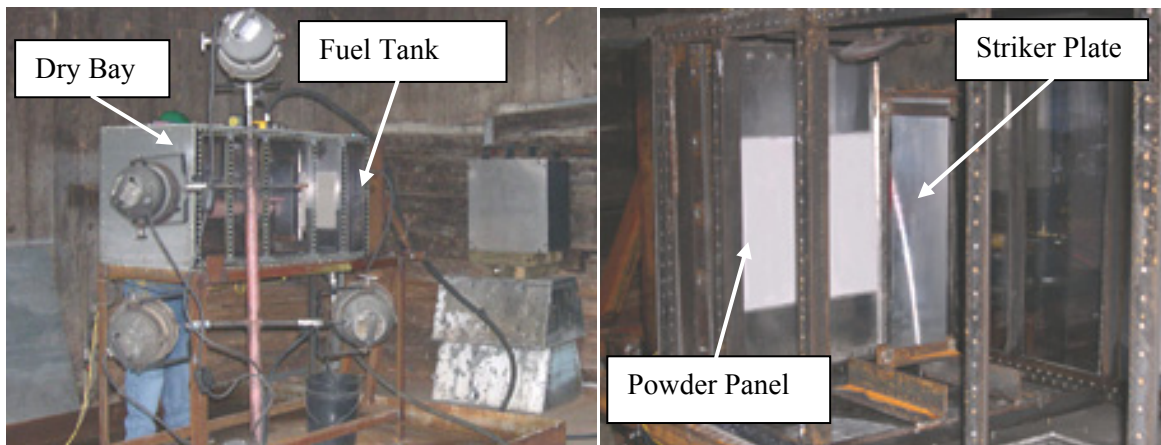


**Figure 9–20. Test Article.**

### ***Instrumentation***

Threat Velocity Measurement Equipment - The projectile velocity at impact was calculated for each test by measuring the elapsed time required to travel from the gun barrel muzzle to the striker plate. A gun break wire was installed in a small hole drilled in the side of the barrel near the exit end. The wire was

severed as the projectile exited the muzzle. A break-paper grid was located at the intended impact point on the striker plate, and was broken when the projectile impacted the target. With the break wire and break paper time increments determined and the standoff distance known, the impact velocity could be calculated. If the paper grid and strain gage failed before impact, the projectile velocity could still be estimated using the gun break signal and the pressure transducer signal recorded on the Nicolet data acquisition system.

**Thermocouples** - Temperature-time histories were collected to obtain a temperature profile for the dry bay test article. Thermocouples were located within the dry bay. All thermocouples operated in the  $-18^{\circ}\text{C}$  to  $1330^{\circ}\text{C}$  range with a 1 kHz sampling rate. One thermocouple was located on the back side of the striker plate below the target location and the other near the fuel tank wall above the powder panel.

**Optical Records** - A high-speed video camera (approximately 500 frames/s) was mounted beside the test article to record the view looking through a Lexan panel on the side of the test device. Skyward provided a digital video camera (approximately 30 frames/s) that also recorded the event through the Lexan panel. Both cameras were aimed toward the powder panel, but covered as much of the dry bay as possible. A standard video camera (30 frames/s) was positioned more distant to focus on the overall test article and capture the entire event.

### **Test Article and Procedures**

Nine ballistic tests were conducted, including unprotected and powder panel-protected configurations of the dry bay/fuel tank simulator. The test article and test setup were similar to the enhanced powder panel demonstration tests conducted at the Weapons Survivability Laboratory at China Lake, California. A simulated dry bay/fuel tank test article (Figure 9–21) was used of a larger size than the experimental test device. The dry bay measured 0.61 m wide x 0.61 m high x 1.22 m long. The fuel tank attached to one end of the dry bay measured 0.36 m wide x 1.22 m high x 0.61 m long. The powder panels were connected to a simulated fuel tank wall composed of 1.8 mm thick 2024-T3 for most tests. A striker plate was located 0.30 m in front of the powder panel/fuel tank wall to ensure projectile functioning. Lexan panels in the test article allowed test results to be observed directly.

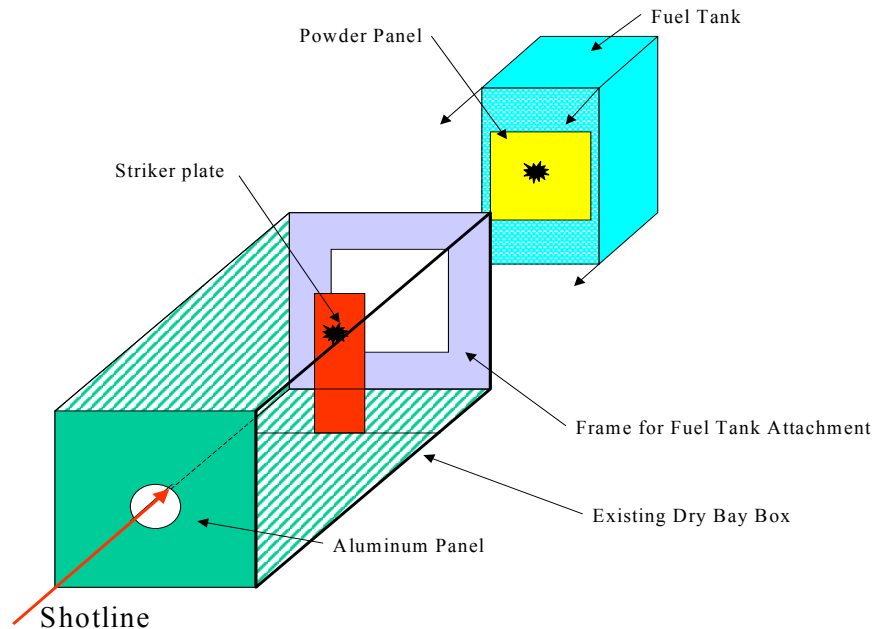


**Figure 9–21.**  
**Schematic of Test**  
**Article. (Top and Lexan**  
**Side Removed for**  
**Clarity)**

The test article was placed near the east wall of AVSF Range 2, with the fuel tank on the east side. The gun was positioned to the west of the test article, and fired from the west toward the east wall of the range. This configuration ensured projectiles did not leave the range enclosure. Figure 9–22 shows the relative position of the test article and gun setup.

A single threat type was used for each of the enhanced powder panel tests. The 12.7 mm API Type B-32 projectile was fired through the center of the test article at a velocity of approximately 760 m/s. A physical description of the projectile is provided in Figure 9–23. The projectiles were fired from Mann barrels at close range to minimize targeting error, and the projectile powder mass was modified, as necessary, to achieve the desired impact velocity.

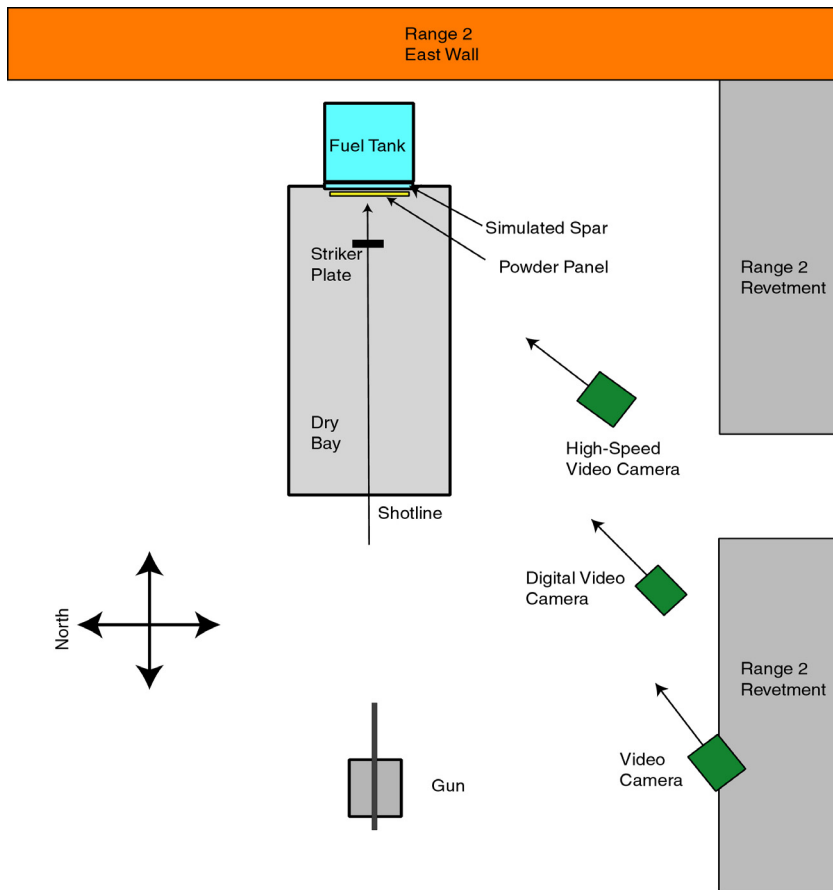


**Figure 9–22. Test Article Setup in Range 2.**

The setup was reviewed prior to each test to ensure that the appropriate powder panel was installed in the proper location, the fuel tank was filled, and the appropriate impact location on the striker plate was targeted. The principal safety issue with this testing was the safe containment of the ballistic threat. The principal method of stopping the threat was through a catch plate located on the back wall of the fuel tank test article. The east wall of Range 2 was behind the test article if the projectile were to escape. An external catch plate was positioned on this wall as well.

The powders that were used for testing were non-toxic; however, because the dry powder is a finely divided solid material, it can become suspended in the air causing a mild discomfort similar to that

experienced in any dust-laden atmosphere. To minimize the exposure to the dust, all participants used dust masks during test clean-up.

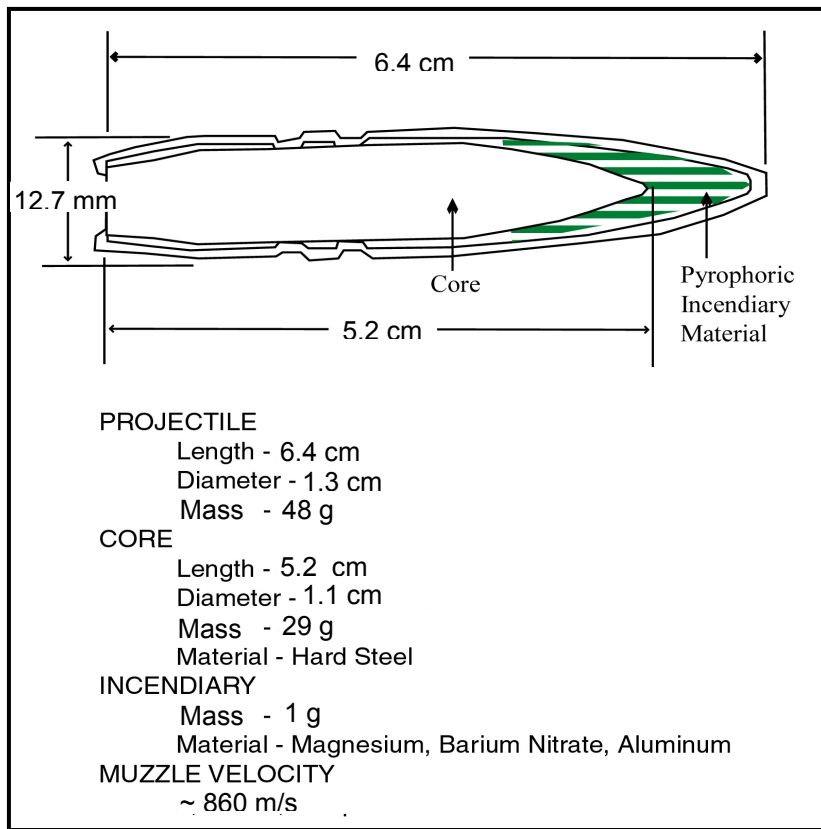


**Figure 9–23. 12.7 mm API Type B-32 Projectile Description.**

### Live Fire Demonstration Test Results of Optimized Enhanced Powder Panels

Some of the more practical, yet effective enhanced powder panels were evaluated in live fire demonstration tests conducted at the end of Phase II. This testing involved many of the same elements involved in proof-of-concept testing after Phase I. However, in these tests, the thinner and lower mass Phase II optimized panels were evaluated. A total of nine tests were conducted, as summarized in Table 9–6. The test was set up to ensure a threat function for each powder panel test. A successful powder panel test was considered to be one where no fire ignition occurred, assuming both fuel leakage and functioning of the ballistic threat. Estimates of the front face area removed and the percentage of powder released were made. Due to the presence of JP-8 fuel, it was not possible to weigh the precise amount of powder released or lost, so an estimate of the percentage of the original powder released was made. This was a rough estimate based upon a post-test examination of the panel and area calculations. It was impossible to determine the influence of leaking fuel on remaining powder in the panel immediately after the test, but the estimates do correlate well with powder dispersion evidence and fire ignition results.

Two different enhanced powder panel designs were evaluated in the demonstration tests, with the primary differences involving material composition. Enhanced Design 1, in Table 9–6, was lighter with potentially better thermal resistance capability. Enhanced Design 2 was heavier, with features to make it

more durable. Test EPP-08 varied in design somewhat from the Enhanced Design 1, utilizing a self-sealing back face material, but was essentially the same in other respects.

**Table 9–6. Phase II Enhanced Powder Panel Live Fire Demonstration Tests.**

	<b>Powder Panel</b>	<b>Panel Mass (g)</b>	<b>Panel Thickness (mm)</b>	<b>Powder</b>	<b>Threat Function?</b>	<b>Fire Ignition?</b>	<b>Front Face Area Removed (cm<sup>2</sup>)</b>	<b>Estimated % Powder Released</b>
EPP-01	No Panel - Baseline	N/A	N/A	N/A	Yes	No	N/A	N/A
EPP-02	No Panel - Baseline	N/A	N/A	N/A	Yes	Yes	N/A	N/A
EPP-03	Commercial	189.0	2.69	Al <sub>2</sub> O <sub>3</sub>	Yes	Yes*	50	8
EPP-04	Enhanced Design 1	145.4	1.90	Al <sub>2</sub> O <sub>3</sub>	Yes	No	156	70
EPP-05	Enhanced Design 1	140.8	1.90	Al <sub>2</sub> O <sub>3</sub>	Yes	Yes*	146	83
EPP-06	Enhanced Design 2	186.5	1.90	Al <sub>2</sub> O <sub>3</sub>	Yes	No	309	88
EPP-07	Enhanced Design 2	227.0	1.90	KHCO <sub>3</sub>	Yes	Yes, but powder extinguished fire	329	83
EPP-08	Enhanced Design 1	157.1	2.13	Al <sub>2</sub> O <sub>3</sub>	Yes	No	54	61
EPP-09	Enhanced Design 2	226.3	2.16	KHCO <sub>3</sub>	Yes	No	252	62

\* Panel dislodged from fuel tank wall during test

Two baseline tests were conducted at the beginning of the test program. The purpose of these tests was to ensure threat functioning and the ignition of a fire in an unprotected or inadequately protected dry bay. For these conditions, a successful powder panel would prevent fire ignition, despite the functioning threat, and an unsuccessful powder panel would not prevent fire ignition. In the first baseline test, the fuel tank panel was a 2.0 mm thick 7075-T6 plate. This was the same material and thickness used as the simulated fuel tank panel in all Range A experimental tests. In EPP-01 a fire was not ignited, as a large deluge of fuel was seen engulfing the dry bay almost immediately, creating an extremely fuel rich environment. The threat did function, but the fuel tank panel resisted the significant hydrodynamic ram pressures and peeled away from the fasteners attaching it to the fuel tank. The fuel tank panel deformed significantly before its edges at the fastener locations tore through, but the impact hole was not significantly larger than the threat size. The toughness of this material was also evident in the Range A tests, where hydrodynamic ram was most often not a variable and worst-case conditions were desired. In these demonstration tests, it was desired to allow hydrodynamic ram damage to occur. Without hydrodynamic ram forces and minimized fuel spurting, it is possible an inaccurate judgment could be made regarding powder panel effectiveness. In this first baseline test, the panel resisted hydrodynamic ram forces such that the weakest failure point was the fuel tank panel attachment mechanism.

Since a fire was not ignited in this first test (and the potential for fire was essential for the powder panel evaluations), modifications were made to the test article and setup to better ensure fire ignition. For the second baseline test, the fuel tank material was changed to 1.8 mm thick 2024-T3 and a structural frame

was used to hold the fuel tank panel to the fuel tank without interfering with the powder panel positioned between its boundaries. In addition, the planned projectile velocity was lowered to 762 m/s to mirror proof-of-concept testing after Phase I and to reduce energy somewhat. The fuel level was lowered from completely full (about 64 l) to about three-fourths full (49 l) to permit pressure relief in an ullage area and reduce the amount of fuel that might immediately spill out into the ignition zone and create another over-rich condition. These modifications proved worthwhile, as EPP-02 did result in a fire. The fire was visible for about 4 s, but appeared to be self-extinguishing near that time. This would provide an adequate burn time for an evaluation of the powder panels, but an alteration to the test article was envisioned to be necessary.

The third test (EPP-03) involved a commercial powder panel, as Table 9-6 indicates. The threat functioned as planned, however a fire was ignited. The fire only lasted a short duration, as the fire appeared to be and seeking oxygen. A long jet of flame actually shot out of the entrance hole at the front of the dry bay. The fire lasted over 1 s, but thick black smoke from the combustion filled the dry bay and lasted for many minutes afterward. The temperature in the dry bay climbed about 49 °C. The conclusion was that the panel was not successful in inhibiting fire ignition or preventing a sustained fire, rather a self-extinguishing fire occurred due to a lack of oxygen. Closer inspection of the dry bay and the high-speed video revealed the commercial powder panel did not remain adhered to the fuel tank panel with the two-part epoxy used. The panel was dislodged after the threat flash and started coming loose as the fire was ignited below and almost behind the panel as it flew off. The powder release was not sufficient to allow powder to remain suspended in the dry bay; however, its effectiveness could remain in question since it did not adhere properly. Black markings evident of not only a flash, but of an ignited fire, were present in the dry bay. No powder residue was found in the dry bay following the test, although the panel did break up better than in non-fluid tests in Range. The damage area was approximately 10.2 cm high x 6.4 cm wide. It is estimated from an inspection of the panel that the front face area removed was approximately 50 cm<sup>2</sup> and about 8 % of the powder was released.



**Figure 9–24. Post-Test Damage Image of EPP-03 Commercial Powder Panel.**

The fourth test (EPP-04) involved an enhanced powder panel. For this test, modifications to the test article were considered to allow more venting or fresh oxygen to be available to the combustion process. However, since more enhanced powder panel tests were to be conducted, it was desired to conduct at least

one with the exact same conditions as the commercial powder panel for a direct comparison. In this test, the threat functioned as expected, with the high-speed video indicating a flash duration of approximately 0.008 seconds or more, which was comparable to the previous two tests. However in this test, as soon as the flash dissipated, the dry bay was engulfed in fire extinguishing powder, and no fire ignition occurred. The temperature in the dry bay around the flash climbed only about 10 °C. A review of the video confirmed that no combustion occurred after the threat function. Powder was visible on the walls of the dry bay, with powder on the Lexan window all the way to the end of the 1.2 m long dry bay. A significant amount of powder also covered the striker panel on the surface facing the powder panel. Powder was also visible in the dry bay for a number of minutes after the test. The panel was adhered with a two-part, fast curing epoxy, which was the same adhesive used in the commercial panel test. However, in this case the panel held fairly well, although some loss of adhesion occurred. Figure 9–25 shows a post-test image of the powder panel, demonstrating the front face fracture. The damage area was approximately 14 cm high x 18 cm wide. It is estimated from an inspection of the panel that the front face area removed was approximately 156 cm<sup>2</sup> and about 70 % of the powder was released.



**Figure 9–25. Post-Test Damage Image of EPP-04 Enhanced Powder Panel.**

In preparation for EPP-05, the dry bay test article was modified to allow for more fresh air to vent into the fire zone. A 7.62 cm diameter hole was drilled into the aluminum side wall of the dry bay. It was centered along the length of the dry bay, 0.61 m from the fuel tank wall and down about 13.3 cm from the top of the dry bay. In this test, a double-sided adhesive tape was used to adhere the powder panel, versus a two-part epoxy. The threat functioned in the test, as planned, and the high-speed video showed a fire ignited about 0.02 seconds after the flash dissipated. The fire lasted several seconds and the temperature climbed about 194 °C in the dry bay near the fuel tank. In the real-time and high-speed video, the powder panel was visible being dislodged from the fuel tank and slamming into the side Lexan panel. The fire started behind the powder panel in the corner opposite the direction the powder panel flew off. Powder was visible in the video emanating from the panel into the Lexan and down onto the floor. As the panel lay against the Lexan, continued powder leakage was visible onto the floor, and it suspended in the vicinity of the dry bay. It is unclear if the continued release of powder was responsible for the fire extinguishing later or if the fire self-extinguished. Inspection of the test article did indicate some black residue around the new dry bay opening, so the extra vent did provide an oxygen source to the fire. In this test, the powder panel design was exactly the same as in EPP-04. In addition, the powder panel broke

up at least as effectively as in EPP-04, so it was surmised that if the panel had not dislodged from the fuel tank wall, it would likely have prevented a fire. However, further tests were required to determine if the additional oxygen available would hinder the effectiveness of the enhanced powder panels. The post-test damaged powder panel is shown in Figure 9–26. The front face damage area was approximately 18 cm high x 15 cm wide. The front face area removed was approximately 145 cm<sup>2</sup>. About 83 % of the powder was released, but as described, much of this may have exited the panel as it flew into the Lexan side panel and then rested against it.



**Figure 9–26. Post-Test Damage Image of EPP-05 Enhanced Powder Panel.**

Test EPP-06 involved a different enhanced powder panel design, primarily involving a change to the front face material. It also marked the first test using MIL-S-8802 aircraft sealant, rather than a faster curing epoxy sealant, as the adhesive to attach the powder panel to the fuel tank wall. All tests conducted after EPP-05 used this adhesive. This powder panel and all the panels utilizing this sealant remained well adhered to the fuel tank during testing. In this test, the flash was visible in the high-speed video, and then powder was seen once again engulfing the dry bay with no fire ignition occurring. The temperature in the dry bay climbed no more than about 14 °C near the flash. Powder seemed to distribute well and quickly.

Powder was still lingering in the dry bay nearly fifteen minutes after the test, when the side panel was removed (Figure 9–27). Upon inspection of the fuel tank, powder was visible along the length of the Lexan window and across the surface of the striker plate facing the powder panel (Figure 9–28).

Some large pieces of the powder panel front surface were actually stuck to the striker plate along with the powder. Powder was also detected on the aluminum side panel nearly the length of the dry bay. Powder was also visible on the structural framework of the dry bay. In all of the powder panel tests, sufficient fuel leaked into the dry bay to make visible powder on the surface of the fuel very difficult to distinguish.

As shown in Figure 9–29, the powder panel was fractured in EPP-06 similar to the previous enhanced powder panel tests. The front face damage area extended nearly to the edges of the panel, measuring approximately 30 cm high by 27 cm wide. The front face area removed was approximately 309 cm<sup>2</sup> and about 88 % of the powder was released.

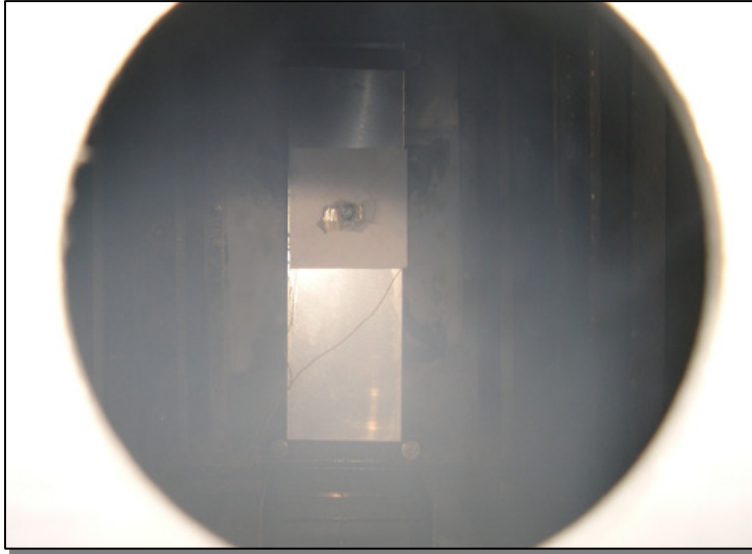


**Figure 9–27. Powder Suspension in the Dry Bay Well After the Test.**

In Test EPP-07,  $\text{KHCO}_3$  was used as the fire extinguishing powder, rather than  $\text{Al}_2\text{O}_3$ , to examine any difference in powder release or powder dispersion and suspension within the dry bay. The panel design was the same as in EPP-06. In this test, however, powder loading was increased and the panel weighed approximately 22 % more. In this test, the threat functioned as planned for a duration of less than 0.016 s.

**Figure 9–28. Powder Dispersion on Striker Plate and Side Lexan Panel.**



After the flash dissipated, the powder was seen in the video beginning to engulf the dry bay. However, a fire was ignited in the lower corner of the dry bay near the fuel tank panel and Lexan panel. It lasted only about 0.28 s as the powder was seen reaching this area about the time it was extinguished. The temperature in the dry bay climbed no more than 17 °C near the fuel tank. A small leak was evident from the fuel tank in pretest preparations and it occurred in this corner. It is plausible that some fuel remained in this corner of the dry bay after the leak was fixed. This likely allowed for an ignition of fuel already present in the dry bay, before fuel from the threat penetration hole fully began to spray into the dry bay. Based upon the evidence provided, this powder panel was considered successful, despite the brief ignition of a fire, because the powder was considered responsible for extinguishing the fire. Upon inspection of the test article, powder was evident on the Lexan panel and aluminum side panel similar to the previous

test. Powder was also evident on the dry bay structural framework, top panel, and striker plate. As expected, the  $\text{KHCO}_3$  was somewhat easier to distinguish than the  $\text{Al}_2\text{O}_3$ . The powder panel front face fracture was similar to EPP-06, as shown in Figure 9–30. The front face damage area extended nearly to edges of the panel again, measuring approximately 30 cm high x 27 cm wide. The front face area removed was approximately 329  $\text{cm}^2$  and about 83 % of the powder was released.



**Figure 9–29. Post-Test Damage Image of EPP-06 Enhanced Powder Panel.**

Test EPP-08 utilized  $\text{Al}_2\text{O}_3$  and used the same front face material evaluated in Tests EPP-04 and EPP-05. This panel had a slightly larger total thickness (2.1 mm) than these previously tested enhanced powder panels, but still weighed less than the commercial powder panel tested. This test also involved the use of a self-sealing material for the back face. In this test, the threat functioned as planned and no fire was ignited. The cloud of powder quickly moved throughout the dry bay. The temperature in the dry bay climbed no more than 13 °C. Powder was evident along the length of the Lexan panel and the other aluminum side panel. It was also found on the striker plate facing the powder panel and the dry bay top wall and back wall. The front face area removal was somewhat reduced from previous panels using the same front face, but cracking was extensive, allowing large flaps of material to easily release powder (Figure 9–31). The damage area extended about 29 cm high x 24 cm wide. The front face area removed was approximately 54  $\text{cm}^2$  and about 61 % of the powder was released. The hole in the back face of the powder panel was approximately 1.3 cm x 1.3 cm, resulting in an area removal about 66 % less than any of the other enhanced powder panel tests. It is, therefore, likely that less fuel was immediately available for fire ignition than in tests without a self-sealing back face. It is believed the thickness of the back face could be increased for such a design to improve self-sealing capability, while still maintaining an overall mass and thickness comparable to commercial powder panels. A test to verify this assertion was not possible during this test program.

The final Phase II live fire demonstration test (EPP-09) again involved  $\text{KHCO}_3$ . The same design used in Tests EPP-06 and EPP-07 was used, except the panel internal width was wider, and, therefore the overall panel was wider (2.16 mm). Despite the increased thickness, powder loading was such that it was very close in mass to EPP-07, which also examined  $\text{KHCO}_3$ . A large flash was evident in this test upon review of the high-speed video. However, no fire was ignited. The temperature in the dry bay near the flash climbed on average around 20 °C. A large cloud of powder enveloped the dry bay and powder was

visible striking the Lexan wall. Both side walls had visible powder deposits, as well as the top panel beyond the striker plate, and the striker plate itself. When the side wall was removed more than five minutes after the test, a large cloud of powder was still evident in the dry bay (Figure 9–32).

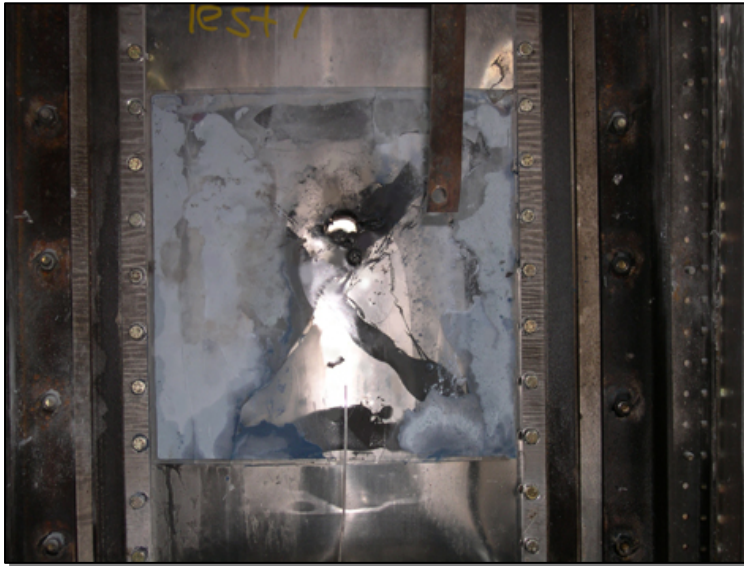


**Figure 9–30. Post-Test Damage Image of EPP-07 Enhanced Powder Panel.**

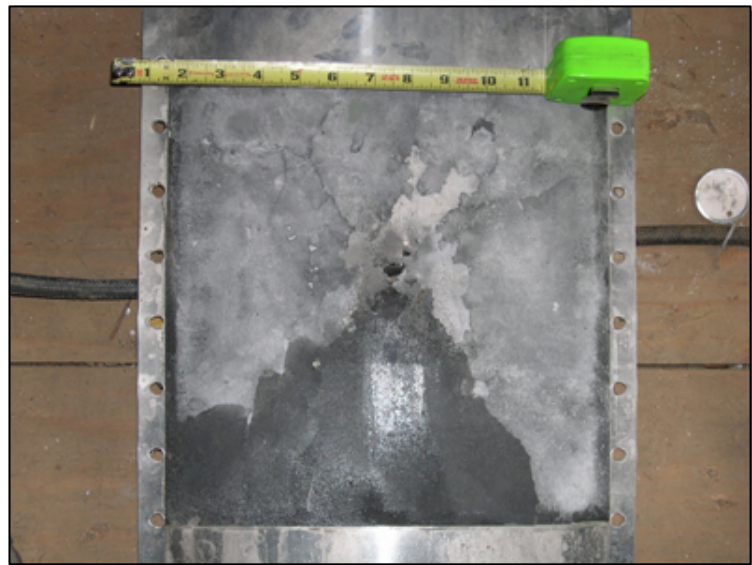


**Figure 9–31. Post-Test Damage Image of EPP-08 Enhanced Powder Panel.**

The damage to the enhanced powder panel front face was significant, as shown in Figure 9–33. The damage area extended about 30 cm high x 26 cm wide. The front face area removed was approximately 252 cm<sup>2</sup> and about 62 % of the powder was released.

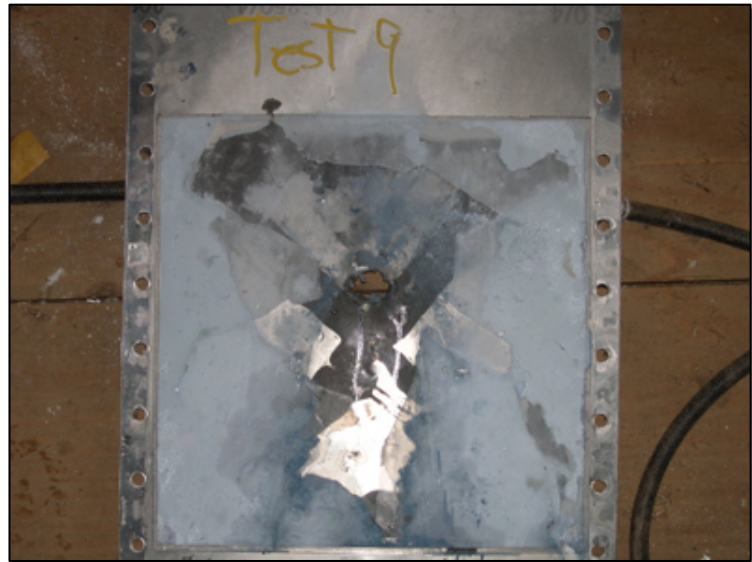
The results of the Phase II live fire demonstration tests were very promising. Out of six enhanced powder panel tests, only one test was considered unsuccessful, and it was likely due to the lack of adherence of the panel to the fuel tank. This problem was associated with the selection of adhesive for attaching the panel to the fuel tank, not the panel design itself. The same panel design was able to prevent fire ignition in two other tests. The commercial powder panel was unsuccessful in preventing fire ignition, but it too

failed to adhere to the fuel tank panel. Demonstration testing after Phase I at China Lake, with many of the same test conditions including the ballistic threat, showed these panels were not effective under these conditions. In these NGP demonstration tests, the enhanced powder panels released at least 87 % more powder than the commercial powder panel. Except for one enhanced powder panel, which still released significantly more powder, the size of the front face area removed was at least 34 % better for the enhanced powder panels compared to the commercial powder panel.



**Figure 9-32. Powder Evident in Dry Bay More Than 5 min after EPP-09 Test. (Side Wall Removed)**

**Figure 9-33. Post-Test Damage Image of EPP-09 Enhanced Powder Panel.**



Thinner enhanced powder panels appeared to release more of the total panel's powder content. However, they also likely contained less powder, so the total powder release may have been fairly close to the thicker panels. The powder panel utilizing a self-sealing back face (EPP-08) did appear to sustain less front face break-up than other enhanced powder panels. This could have been a result of this design variation. However, the reduction in the size of the back face hole, also likely contributed to the panel effectiveness by reducing immediate fuel leakage.

Both tests with  $\text{KHCO}_3$  resulted in successes, although Test EPP-07 did show evidence of a very brief fire ignition. It appeared the powder release did, however, result in the fire being extinguished.  $\text{KHCO}_3$  was expected to be at least as effective as  $\text{Al}_2\text{O}_3$ , however, the grain size of the  $\text{KHCO}_3$  was on average around 30  $\mu\text{m}$  compared to the 5  $\mu\text{m}$   $\text{Al}_2\text{O}_3$ . As previous testing has shown, a smaller grain size has proven to be more effective in fire extinguishing. It is inconclusive, however, in these few tests, whether or not grain size was even a factor.

It was conclusive that sufficient powder was released from each of the enhanced powder panels to significantly reduce the likelihood of a dry bay fire, regardless of the powder type. It was estimated that at least 40 g of powder was released in most of the enhanced powder panel tests, with as much as 70 g from the heavier panels. By contrast, it was estimated the commercial powder panel likely released less than 10 g of powder.

### 9.2.10 Mass-trade Comparison Analysis

Combat-related aircraft dry bay fires are a known vulnerability for many aircraft. However, the cost, mass, maintenance, and/or performance parameters have infrequently justified the installation of halon fire extinguishing systems for these areas. Other fire protection methods such as solid propellant gas generator systems, void space foam fillers, or even commercial powder panels have been implemented in some cases, but many dry bay areas still go unprotected. It is possible that a more effective powder panel could offer a justifiable option for previously unprotected dry bay areas or a well-supported alternative to areas protected by other means.

Cyphers and co-workers performed a comparison of an enhanced powder panel protection system with a halon fire extinguishing system to demonstrate its potential as a halon alternative. The powder panel survey had revealed that it was very difficult to find a practical example for which to perform a direct comparison. In addition, obtaining design information for certain areas that might provide a comparison was very difficult within the resources of this program. To further complicate this task, when information was obtained on a potential aircraft area or an alternative system used in trade studies, the information was often considered proprietary and was not releasable. Therefore, an emphasis was placed on generating some estimates for integrating powder panels into forward-fit or currently unprotected areas. When possible, active system information was estimated for possible integration into the same areas. It turned out that the most practical comparisons were with current powder panels and other currently-fielded active fire extinguishing systems, such as solid propellant gas generators (SPGGs) that generate a mixture of nitrogen, carbon dioxide and water vapor.

Comparisons with halon fire extinguishing systems in engine nacelles or APU compartments were considered, but rejected because significant additional work would be necessary to demonstrate that powder panels would even work in such an area, where airflow and hot surface ignition are concerns. Additionally, in these areas where accidental fires are of an equal or greater concern than ballistic threat-induced fires, powder panel protection is not currently a consideration due to the passive nature of powder panels. This eliminated some potential comparisons on the C-5 and B-1 aircraft, for example.

One forward-fit example explored was the C-130 Hercules aircraft. The C-130 outer wing leading edge is not currently protected by a fire extinguishing system. The wing is divided into two segments, the center wing section (CWS) and the outer wing section (OWS). Since the outer wing fuel tanks are vulnerable to

enemy fire, but currently have no fire protection, and because data were available (including wing geometry) for an estimated active fire extinguishing system, it was practical to use this example.

A preliminary analysis was conducted for the OWS leading edge dry bays circa 1996 to estimate the mass of an SPGG fire extinguishing system using then off-the-shelf components. The masses were estimated for the wing leading edge dry bays between engines #1 and #2 and between #3 and #4 (referred to as inboard leading edge dry bay) and outboard of the #1 and #4 engines (referred to as outboard leading edge dry bay). This analysis also included estimates for the engine area dry bays, but for purposes of this study, the comparison is limited to the leading edge dry bays. It was estimated one inboard leading edge dry bay would require about 1,070 g of agent and an outboard leading edge dry bay would require about 1,190 g. To provide this agent to each dry bay would require three 420 g unit generators each. The mass for each unit is about 1,300 g, for a total generator mass on one wing of 7,810 g. One controller would weigh about 1,920 g, which would be capable of controlling all the SPGGs in both wings. It is estimated both the inboard leading edge and the outboard leading edge would each require three optical sensors. Each sensor weighs approximately 177 g, for a total mass on one wing of 1,060 g. For purposes of this study, the cables and braces or mounting hardware required was arbitrarily assumed to weigh about 10 % of the SPGG and sensor mass for each dry bay. This mass could be more significant, depending upon where the controller is located, but should provide a slightly better estimate than ignoring this mass.

Feasibility and demonstration testing of SPGGs was conducted in the C-130 Vulnerability Reduction Program, as part of C-130J Live Fire Test & Evaluation, and determined that the mass of agent in the 1996 preliminary analysis was likely overestimated.<sup>29</sup> However, the estimates provided are the best available since a fully optimized system has not been examined. Table 9–7 provides mass estimates for each of the SPGG system components for the C-130 outer wing's leading edge dry bays.

Table 9–7 also provides estimates for enhanced powder panel fire protection systems. Estimates are shown for both a lower mass version (areal density of 1.60 kg/m<sup>2</sup>) and a heavier version (2.05 kg/m<sup>2</sup>), both of which have been demonstrated to be effective in this program. Areal densities for the commercial powder panels tested in this program ranged from 1.92 kg/m<sup>2</sup> to 2.08 kg/m<sup>2</sup>. An estimate using the lower mass 175 g commercial powder panel is shown. An estimate is also provided for the mass of adhesive to attach either enhanced or commercial powder panels. Finally, Table 9–7 shows estimated areas and volumes for the OWS wing leading edge dry bays. The SPGG agent requirements are estimated based upon volume, and the powder panel requirements are based upon wetted front spar area.

Table 9–8 summarizes total mass estimates for each wing leading edge fire extinguishing system for an entire C-130 aircraft (both wings). The data show that enhanced powder panels can be very competitive with SPGGs in terms of mass for such a system. For this example, the 1.60 kg/m<sup>2</sup> enhanced powder panel system would weigh about 0.8 kg more than the SPGG system for the entire aircraft. The lighter mass enhanced powder panel would obviously be a design objective, since for this application it could be as much as 5.6 kg lighter than its higher areal density counterpart. Future work will determine if further optimization is possible. The lighter commercial powder panel evaluated in this program was just under the mass of the heavier enhanced powder panel by 1.6 kg. The powder panel mass was calculated, as if they were applied across the entire surface area of the leading edge spar. With external stiffeners located across the surface of the spar, it is likely modular powder panel sections would be inserted between stiffeners. This would further reduce powder panel mass. Also, the mass of protective foam and tape typically used in the vicinity of SPGG discharge areas was not estimated, so the SPGG system mass would likely be higher. For a full analysis of this example, other issues such as cost and complexity

would also need to be examined. Obviously, the powder panel systems should be relatively simple to apply and maintenance free once applied. The complexity of integrating an active fire extinguishing system would be more complicated and involve some power requirements, safety concerns, and perhaps integration issues with other systems.

**Table 9–7. C-130 Wing Leading Edge Dry Bay Fire Extinguishing System Component Mass Estimates.**

Description	Inboard Leading Edge	Outboard Leading Edge
Volume	1.52 m <sup>3</sup>	1.68 m <sup>3</sup>
Area	2.73 m <sup>2</sup>	3.43 m <sup>2</sup>
SPGG Propellant Required	1,070 g	1,190 g
Number of SPGGs (420 g Units)	3	3
SPGG Mass (3)	3,910 g	3,910 g
Number of Optical Sensors	3	3
Optical Sensor Mass (3)	530 g	530 g
SPGG Controller Mass	1,920	-
Wiring, Brackets and Mounting Hardware (Estimate 10 % of SPGG/Sensor Mass)	444g	444g
Light Enhanced Powder Panel Mass - 1.60 kg/m <sup>2</sup>	4,370	5,490
Heavier Enhanced Powder Panel Mass - 2.05 kg/m <sup>2</sup>	5,600	7,030g
Commercial Powder Panel Mass - 1.92 kg/m <sup>2</sup>	5,240g	6,590
Adhesive Mass for Powder Panels (Estimate 10 % of Heaviest Panel Mass)	560 g	700 g

**Table 9–8. C-130 Wing Leading Edge Dry Bay Total Fire Extinguishing System Mass Estimates.**

Fire Extinguishing System	Total System Mass
Solid Propellant Gas Generator System Mass	21.4 kg
Lighter Enhanced Powder Panel Design 1 Mass - 1.60 kg/m <sup>2</sup> (0.327 lb/ft <sup>2</sup> )	22.2 kg
Heavier Enhanced Powder Panel Design 2 Mass - 2.05 kg/m <sup>2</sup> (0.420 lb/ft <sup>2</sup> )	27.8 kg
Commercial Powder Panel Mass - 1.92 kg/m <sup>2</sup> (0.394 lb/ft <sup>2</sup> )	26.2 kg

Data were available for a second comparison of enhanced powder panels, in this case with a current gas generator system on the V-22 aircraft. The outboard tip rib dry bay on this aircraft has a volume of approximately 0.260 m<sup>3</sup>. No airflow passes through this dry bay. Other relevant design details are part of the aircraft technical specifications and will not be described in detail. The active fire suppression system in this area consists of a 626 g inert SPGG, including 189 g of agent, and a 284 g sensor/detector. Testing was conducted on a larger inboard tip rib dry bay and this system was sized according to successful configurations in that area. The dry bay is monitored by a control box that currently monitors other areas of the aircraft, so no new mass was added for this equipment. Wiring and mounting hardware was added to the mass estimate, since this equipment is necessary specifically for this dry bay. The wiring would have to run to the control box in a central location. In the previous example, approximately 444 g was added for wiring and accessories. For this single generator and sensor, the mass for this estimate was reduced to 33 % of this estimate or 148 g for one wing, which is likely a favorable estimate. The total mass estimate for one wing would, therefore, be approximately 1060 g. For comparison, masses for both

enhanced powder panel designs discussed previously were estimated for this dry bay. The lighter mass powder panel, with an areal density of  $1.60 \text{ kg/m}^2$ , would weigh about 710 g per wing. Incorporation of the heavier enhanced powder panel, with an area density of  $2.05 \text{ kg/m}^2$ , would weigh about 910 g. The commercial powder panel by contrast, with an areal density of  $1.92 \text{ kg/m}^2$ , would weigh approximately 860 g. Table 9–9 summarizes these mass estimates.

**Table 9–9. V-22 Outboard Tip Rib Dry Bay Fire Extinguishing System Component Mass Estimates.**

Description	Outboard Tip Rib Dry Bay
Solid Propellant Gas Generator Mass(1)	630 g
Sensor/Detector Mass (1)	280 g
Wiring, Brackets and Mounting Hardware Mass (Estimate 33 % of Previous Example with 3 SPGGs)	150 g
Lighter Enhanced Powder Panel Design 1 Mass - $1.60 \text{ kg/m}^2$	710 g
Heavier Enhanced Powder Panel Design 2 Mass - $2.05 \text{ kg/m}^2$	910
Commercial Powder Panel Mass - $1.92 \text{ kg/m}^2$	860 g
Adhesive Mass for Powder Panels (Estimate 10 % of Heaviest Panel Mass)	90 g

Table 9–10 tabulates the total mass for the aircraft (both wings) for each of the fire protection systems. These data show the lightest enhanced powder panel weighs about 500 g less than the inert SPGG system. Even the heavier enhanced powder panel design would be very comparable, weighing about 100 g less than the inert SPGG system. The commercial powder panel system would weigh about 280 g more than the enhanced powder panel design, but still less than the SPGG system. Obviously, one major difference in this example was the existence of a controller on the aircraft for the active system, which did not add mass, but the overall active system still weighed a little more. Although the differences in mass for both comparisons are quite small, it is well known that aircraft mass increases carry large price tags. A judgment would need to be made based upon system cost and the savings in complexity, whether or not the mass differences (savings or cost) for the enhanced powder panel system would be worthwhile. Further optimization of these enhanced powder panel designs in subsequent programs may further reduce the mass differences between this passive fire extinguishing system and this active fire extinguishing system. Many other comparisons are possible between the enhanced powder panels and other fire protection methods. However, the purpose of the examples provided above was to simply demonstrate that enhanced powder panels, which have been demonstrated in live fire tests to be effective, have also been optimized to levels that make consideration of this vulnerability reduction technique valuable.

**Table 9–10. V-22 Outboard Tip Rib Dry Bay Total Fire Extinguishing System Mass Estimates.**

Fire Extinguishing System	Total System Mass
Solid Propellant Gas Generator System	2,120 g
Lighter Enhanced Powder Panel Design 1 Mass - $1.60 \text{ kg/m}^2$	1,610 g
Heavier Enhanced Powder Panel Design 2 Mass - $2.05 \text{ kg/m}^2$	2,010 g
Commercial Powder Panel Mass - $1.92 \text{ kg/m}^2$	1,900 g

### 9.2.11 Summary of Powder Panel Research Program

This NGP research has led to major gains in efficiency and effectiveness of powder panels, and has reached the point where there are alternatives to halon-like compressed systems suitable for controlling fires in aircraft dry bays. Although additional work is necessary to address manufacturing issues and ensure enhanced powder panels meet the requirements of individual aircraft programs, powder panel technology is a viable option for future fire protection of aircraft dry bays.

Findings from this research revealed that realistic powder panel concepts can significantly enhance the fire extinguishing effectiveness of this vulnerability reduction method. Enhanced powder panel designs can afford the following benefits over current commercial powder panel designs:

- greater front face area removal to allow more powder to escape,
- greater powder release into the dry bay,
- better dispersion of powder to prevent ignition off-shotline,
- longer powder suspension to prevent fire ignition for longer periods of time,
- design flexibility to target mass, durability, and application-specific design goals, and
- significantly improved fire extinguishing effectiveness over commercial powder panels, achieved at an equal or lighter mass and thickness.

Optimization goals were achieved for enhanced powder panels in this project. These goals were to lower enhanced powder panel mass and thickness to the levels of current commercial powder panels or below and to demonstrate greater performance in live fire testing. Enhanced powder panels evaluated in final demonstrations ranged in mass from 140 g to 230 g, with four of the six panels being lighter than the commercial powder panel evaluated (190 g). Thicknesses ranged from 1.9 mm to 2.2 mm, while the commercial powder panel thickness was 2.7 mm.

Live fire testing conducted in a dry bay of realistic size for an aircraft (0.45 m<sup>3</sup>), with an actual ballistic threat (12.7 mm API), and about 50 l of JP-8, resulted in the prevention of fire ignition in four out of six tests. In a fifth test, a fire starting from an existing pool of fuel was quickly extinguished (after only 0.28 s) by an enhanced powder panel. The cause of a lone unsuccessful test resulting in a fire was attributed to an inadequate attachment adhesive on the back of the enhanced powder panel. The test of a commercial powder panel resulted in a fire; however, the attachment adhesive again failed to hold. Although the commercial panel test was not conclusive, a further examination of the test results indicated a significant increase in vital performance characteristics for the enhanced powder panels. Despite being as much as 26 % lighter and 29 % thinner, the enhanced powder panel tests resulted in at least 34 % greater front face area removal and at least four times greater powder release. Powder was evident on surfaces throughout the dry bay following enhanced powder panel tests and was visibly suspended in the dry bay up to five minutes after some of the enhanced powder panel tests. No evidence was present of dispersed and/or suspended powder in the commercial powder panel test.

A number of lessons were learned about effective powder panel design. Some, previously discovered, were reaffirmed. Among the key lessons learned were:

- Brittle or frangible front face materials outperform ductile or tough materials.

- Front face crack growth optimization can be designed into the powder panel through the use of particular front face materials, thicknesses, rib designs, attachment methods to the ribs, and even surface scoring.
- A strong synergism exists between the rib structure and the front face design.
- The back face can be designed to aid in powder dispersion and/or reduce fluid leakage.

Another key finding in this program is that there are design features associated with enhanced powder panels that can make them very resistant to accidental leakage. With the use of plastics and certain composites, there are adhesives to attach the various elements of the panel that form extremely tight bonds. The selection of a front face material and thickness can take into account the likely harsh environment to which the powder panel will be exposed. Accidental leakage has been a significant concern for aircraft designers considering powder panels and is the primary reason that  $\text{Al}_2\text{O}_3$  has been the only chemical fire extinguishing powder finding production usage. With this resistance to accidental leakage in certain designs, perhaps other lighter mass and improved performance fire extinguishing agents can be considered. Not only are other powders lighter in mass, but improved effectiveness of these powders may lead to reduced requirements for powder loading.

To fully take advantage of the potential benefits from enhanced powder panels, further examination of the more promising designs should be performed for potential qualification test requirements. These may include, but are not limited to, operating temperature, chemical exposure, vibration, impact resistance, and moisture absorption. These issues were considered in the selection of materials for Phase II optimization testing, but qualification testing for these parameters was not conducted.

Despite significant increases in powder release for enhanced powder panels, a balance must be achieved between mass/thickness and effectiveness. For protection against larger threats, it may be warranted to consider higher powder loading, which is the significant mass driver. For strict mass restrictions, testing may be required for the given powder panel to determine the type and size of the threat for which protection is afforded.

As the previous section detailed, enhanced powder panels have been developed with increased effectiveness over current powder panel designs at equivalent or better mass and size. These enhanced powder panel designs can now be examined for various applications, particularly in military aircraft, as a trade-off with other fire extinguishing systems. Additional work will be required with the examination of production design requirements, which may cause some adjustments in the selection of materials or sizing, but the design principles should be in place. Some manufacturing concepts were developed and others conceived as a result of this work, which will need to be optimized for production application.

The potential of enhanced powder panel designs for increasing effectiveness without negatively impacting mass and other concerns has generated renewed interest by several aircraft programs. Among the programs inquiring about enhanced powder panel development are the F-35 Joint Strike Fighter, CH-53E Super Sea Stallion, RAH-66 Comanche, and the V-22 Osprey. Successful live-fire tests have been conducted on a production AH-1Z Super Cobra.

## 9.3 SOLID PROPELLANT GAS GENERATORS<sup>30,31,ii</sup>

### 9.3.1 Brief History

Solid propellant gas generators (SPGGs) are devices designed to produce gases of a desired composition (e.g., nitrogen, water vapor, and carbon dioxide) from condensed reactants similar to those used in solid rocket motors. SPGGs are compact, they can generate gases that are inert in fires, they do this quickly (fractions of a second) and on demand, and they produce gas temperatures that are very hot (greater than 1200 °C). The first three attributes (compactness, inert gases, and release on demand) are what make SPGGs attractive for fire suppression applications in aircraft; the fourth attribute (high exhaust temperature) is a limitation.

Prior to the advent of the NGP and its predecessor program to identify alternatives to halon 1301 for aircraft fire suppression applications, gas generators had been used primarily for automobile airbags and for inflatable slides for emergency evacuation of airplanes. In the early 1990s, development of the F/A-18 E/F and V-22 aircraft demanded a non-halon fire protection system to mitigate the hazard of fires due to equipment failures, accidents and enemy attack. Testing performed at the Weapons Survivability Lab of the Naval Air Warfare Center-Weapons Division (NAWCWD)-China Lake demonstrated that SPGGs could be integrated into a system that provided an effective alternative to halon 1301 for fire protection in military aircraft dry bays.<sup>32,33,34,35</sup>

Between 1993 and 1996, the Naval Air Systems Command (NAVAIR) sponsored live fire testing of SPGG systems develop by the Rocket Research Company (now Aerojet Redmond). The tests demonstrated the effectiveness of SPGGs in suppression of various fires in the F/A-18 E/F dry bays and the V-22 wing dry bays. Since the original F/A-18 E/F and V-22 programs, new propellants have been developed that implement some degree of chemical activity into the formulation.<sup>36,37,38,39</sup>

The SPGG program sponsored by the NGP was a collaborative effort between a group at Aerojet (that had been with its predecessor companies) and the Naval Air Warfare Center-Weapons Division. The objectives of this program were to develop new highly efficient, environmentally acceptable, chemically active fire suppressant capabilities based upon solid propellant gas generators; and to improve understanding of propellant and additive effectiveness in fire suppression. The program was designed to accomplish the following:

1. Establish baseline SPGG performance with Aerojet propellant designated FS-0140 (EPA SNAP-approved for use in normally occupied spaces).
2. Develop techniques for reducing the combustion temperature of the propellant, such as tailoring the propellant formulations, and for incorporating chemical additives (radical traps and re-light inhibitors).
3. Develop techniques for cooling the combustion products (e.g., coolant beds) to allay such problems as physical deformation or failure of distribution lines and threat to occupants.

---

<sup>ii</sup> Section 9.3 is based on References 30 and 31. Large portions of the text from these documents, along with the figures shown here (except as noted), have been used without further attribution.

4. Characterize the extinguishment mechanisms of solid propellant systems by examining the relative contributions of oxygen displacement, cooling and flame strain effects upon the SPGG-driven suppression event.
5. Modify existing hybrid extinguisher technology using additional gaseous and liquid suppressants, assuring operability at low ambient operating temperatures.
6. Measure the exhaust temperature, burning rates, and suppression effectiveness of the new propellants with and without additives.
7. Correlate laboratory- and mid-scale results.
8. Perform tests on real platforms defined by the weapon systems community (through JTCG/AS) on those agents that performed best in mid-scale tests.

### 9.3.2 Operating Principles

Conceptually, both SPGGs and pressure-bottle (blow-down) systems deliver agent according to the same analytical expression, whereby the rate of agent delivery  $m'_d$  is related to the discharge coefficient  $C_d$  of the agent, the throat area  $A_t$  and the pressure inside the delivery device  $P_c$ , i.e.

$$m'_d = C_d \times A_t \times P_c. \quad (9-1)$$

In a blow-down system, the initial bottle pressure is given by the sum of agent vapor pressure  $P_{vap}$  plus that of a pressuring gas (typically nitrogen)  $P_{pressurant}$ :

$$P_c = P_{vap} (\text{agent}) + P_{pressurant} \quad (9-2)$$

Here,  $P_c$  is at its maximum in the pre-discharge condition, and both  $P_c$  and  $m'_d$  decrease rapidly upon initiation of the discharge process. Where the SPGG differs from the blow-down bottle is its ability to store agent at zero internal pressure, and then to generate high pressures internally by the combustion of the solid propellant to form a blend of inert gases.

For solid propellants,  $P_c$  is directly related to the product of the burning surface area  $A_{surface}$  and the rate at which gas is generated from the propellant, referred to as the burn rate ( $BR$ , in units of cm/s), raised to a power. The logarithm of  $BR$  typically increases linearly with  $\log(P_c)$  with slope determined by the pressure exponent,  $n$ :

$$\log BR = n \log (P_c/A_{surface}) + \text{constant} \quad (9-3)$$

A pressure exponent less than one assures that high combustion-induced internal pressures can be maintained, translating into sustained high rates of agent discharge. Pressure exponents in the range of 1 to 2 result in extremely unstable combustion, with the relevant chemistry dominated by gas phase reactions.

Solid propellants are typically comprised of an intimate mixture of finely ground solid fuels and oxidizers, often blended together with a polymeric binder. The component fuel and oxidizer combine to create exhaust gases, with the generation of heat. For typical solid propellant reactions, exhaust temperatures are in the range of 1700 °C to 2200 °C.

Propellants used in SPGG fire extinguishers are designed to produce an inert gas blend of carbon dioxide, nitrogen and water vapor and to yield cooler exhaust temperatures. The Aerojet propellant FS-0140 used

as the baseline for the current study has  $\text{CH}_3\text{N}_5$  as its fuel and  $\text{Sr}(\text{NO}_3)_2$  as its oxidizer, with  $\text{MgCO}_3$  added to absorb heat and reduce the exhaust temperature. The exhaust product gases from FS-0140 consist of about 45 %  $\text{N}_2$ , 35 %  $\text{CO}_2$ , and 20 %  $\text{H}_2\text{O}$  by volume. The strontium and magnesium form solid oxides in the process. Peak chamber temperatures are around 1200 °C, and are reduced to about 775 °C in the exhaust stream.

Exhaust temperatures can be reduced further by mixing the fuel and oxidizer in off-stoichiometric proportions, by selecting less exothermic fuel/oxidizer combinations, or by adding materials that absorb heat through dilution, phase change, or endothermic decomposition. Propellant additives are also used to increase the radical scavenging propensity of the exhaust products, which, in turn, improve the efficiency by which the fire is suppressed. The temperature and chemical activity of an SPGG fire extinguisher can also be tailored through a hybrid arrangement (a so-called Hybrid Fire Extinguisher), with the propellant exhaust used to pressurize, disperse, and vaporize a liquid agent such as a hydrofluorocarbon or an aqueous solution.

While the mechanisms described above for controlling the exhaust temperatures and chemical activity of the effluent are easy to state on a theoretical basis, the effect of changing the propellant mixture is far from being predictable. This means that many combinations of propellants, additives, pressures and geometries need to be explored experimentally over a range of scales.

### 9.3.3 Experimental Techniques

#### Propellant Screening Tests

The developmental propellants described here were made up in batches less than 1 kg. In a typical process, individual ingredients were pulverized and then wet-mixed in an inert fluorocarbon medium with a polymeric binder. The solid was then collected, dried and compression molded into pellets. Larger batches of propellant were manufactured and pressed on an automated rotary press.

Propellant development for the Aerojet-NAWS China Lake effort generally took place according to (a) initial computational evaluation of candidate mixtures of fuel, oxidizer, processing additives and coolants, followed by (b) small-scale processing of compositions down-selected from (a), and then (c) scale-up of formulations down-selected from (b) in order to facilitate fire suppression effectiveness testing.

Computational evaluation consisted of thermodynamic analysis of the solid propellant compositions using the NAWC Propellant Evaluation Program (PEP)<sup>40</sup> augmented by the JANNAF Thermodynamic Database. PEP models the combustion process in a gas generator in two steps, the first determining equilibrium of the input mixture at a fixed combustion pressure, and the second calculating the equilibrium condition of that combustion chamber mixture upon expansion to atmospheric pressure. Computational inputs consisted of:

- chemical composition of individual ingredients
- enthalpy of individual ingredients
- density and mass fraction of individual ingredients in the mixture
- equilibrium chamber pressure (generally 6.9 MPa)

- equilibrium exhaust pressure (generally 101 kPa)

The outputs were:

- chemical constituents (and their respective fraction) at specified equilibrium conditions
- bulk adiabatic temperatures of combustion products formed at equilibrium at combustion chamber pressure (6.9 MPa) and exhaust pressure (101 kPa)

Preparations followed standard practices for any new propellant mixture, with initial preparation of small (1 g to 5 g) batches of propellant by hand grinding, to verify adequate safety properties (standard propellant testing includes sensitivity to impact, friction, and electrostatic discharge, ESD). Suitable mixtures were then scaled up to batches of 50 g to 1 kg for further evaluation.

New propellant formulations tested under the NGP were prepared by either dry or wet techniques. In a typical dry process, individual ingredients were weighed, combined with ceramic grinding media in a mechanical ball mill for dry-blending, and then dry-pressed into tablets for burn rate testing. Individual components were normally pre-ground to specific particle sizes and then added to the mixture for blending to a uniform composition, and then pressed on an automated rotary press. In a typical wet process, ingredients were weighed, pulverized and then wet-mixed in an inert fluorocarbon medium, where polymeric binder was deposited upon the powder and the mixture precipitated. The solid was then collected, dried and compression molded into pellets.

Preliminary characterization of the different propellant blends typically included analysis according to a burn rate test. Burn rate testing, when taken together with the gas output from PEP thermochemical calculations, provides a measure of the rate of gas/agent evolution from different solid propellant compositions. Most propellant burn rates were evaluated over a range of pressures between 3.4 MPa and 21 MPa.

Burn rate testing was performed by either a strand burner or a window bomb. In the strand burner technique, compression molded cylindrical grains (pills) of approximately 12.7 mm diameter and 12.7 mm thickness were prepared with a non-burning inhibitor (e.g., epoxy). The inhibitor was coated onto the outside circumference of the cylinder, as well as on one circular face. The inhibited grains were placed in a closed bomb, pressurized to a predetermined level (usually 6.9 MPa and 17.2 MPa). The uncoated face of the grain was ignited using an electric match and the time was measured from ignition to the end of the linear burn event. The burn distance/burn time yielded the burn rate.

Initial testing at China Lake was performed in a high pressure window bomb (Figure 9–34). This is a closed vessel, filled with an inert gas to a static pressure, and equipped with two optical windows. The full assembly is shown in the center, with the window for viewing and filming near the bottom. Single burn rate samples (e.g., single extruded grains) were ignited by a hot wire (seen on the left of Figure 9-34) and the rate at which the burning front advanced through the sample was recorded on film. For evaluating burn rate temperature sensitivity, a variable temperature stage was used, with a flow of liquid and gaseous nitrogen through the holes in the copper block surrounding the sample (right side of Figure 9–34) used to control temperature. This film was calibrated and analyzed to determine burn distance, burn time and hence burn rate. The pressure limit of this apparatus extends to 55 MPa, the higher end of nominal gas generator internal pressure maximum. More promising candidates were scaled up to larger batches, and the most promising up to several kilograms in size.

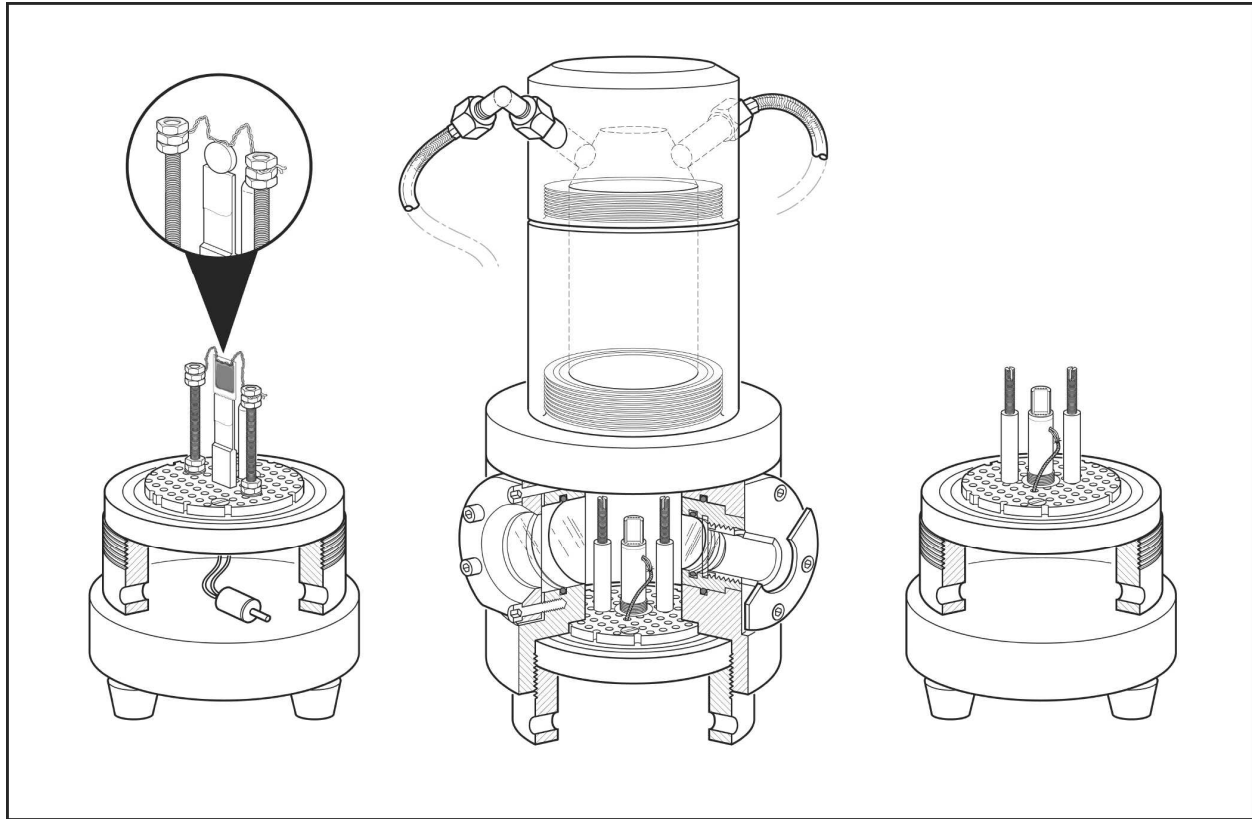


**Figure 9–34. NAWS-China Lake Propellant Burn Rate Apparatus.**

### Fire Test Fixture

The mid-scale Fire Test Fixture (FTF) developed by Aerojet was used to test the effectiveness of various agents under repeatable test conditions. The FTF fixture (shown in Figure 9–35 and Figure 9–36) is 1.87 m long x 0.61 m wide x 0.61 m high and is located in a concrete reinforced test cell with the floor coated with fuel-resistant, non-absorbing material. A schematic of the FTF test facility is shown in Figure 9–37. It consists of several major subsystems including:

- Main test chamber
- Air supply system
- Fuel supply system
- Ignition system
- Suppressant discharge system
- CO<sub>2</sub> emergency extinguishing system
- Control and data acquisition system

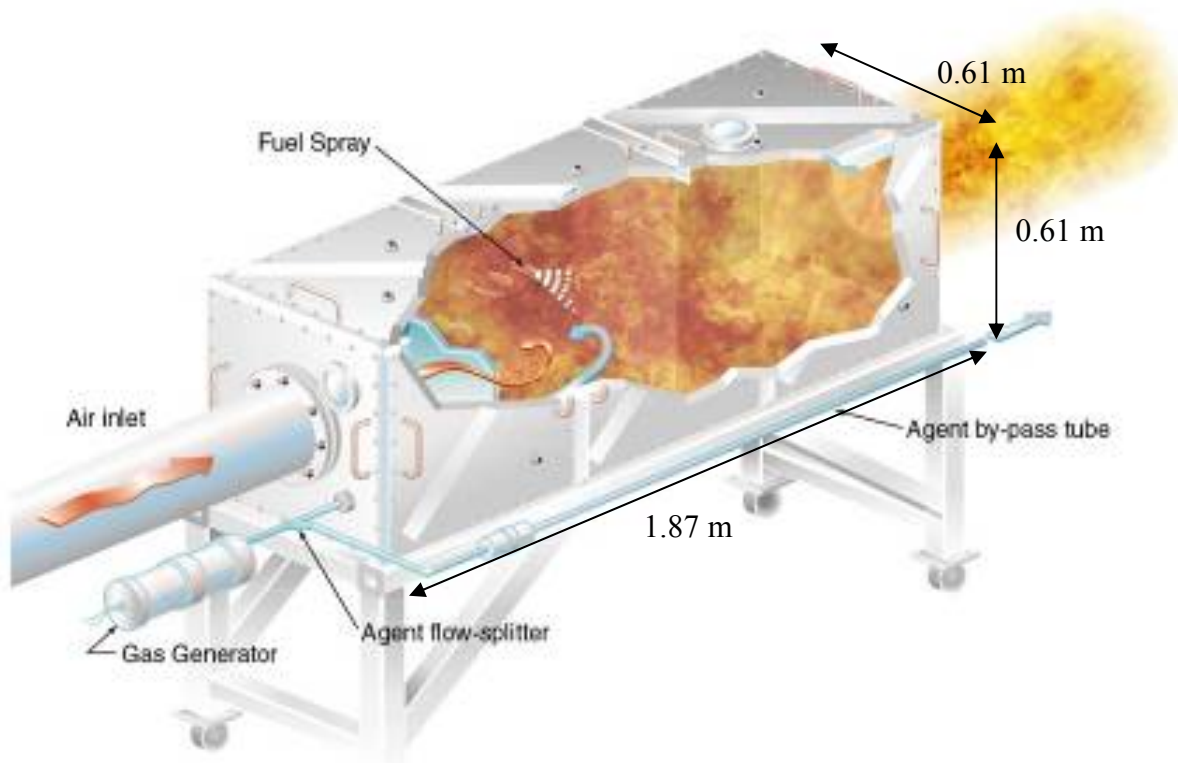


Figure 9–35. Aerojet Fire Test Fixture (FTF).

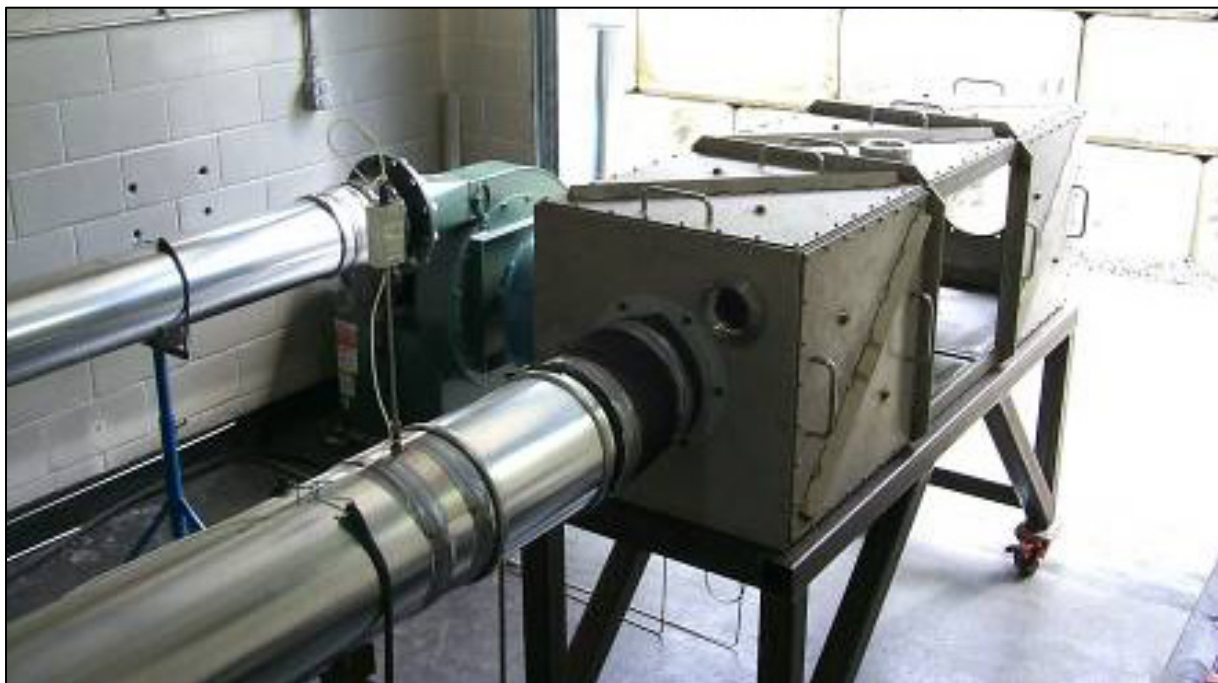


Figure 9–36. Photograph of Fire Test Fixture.

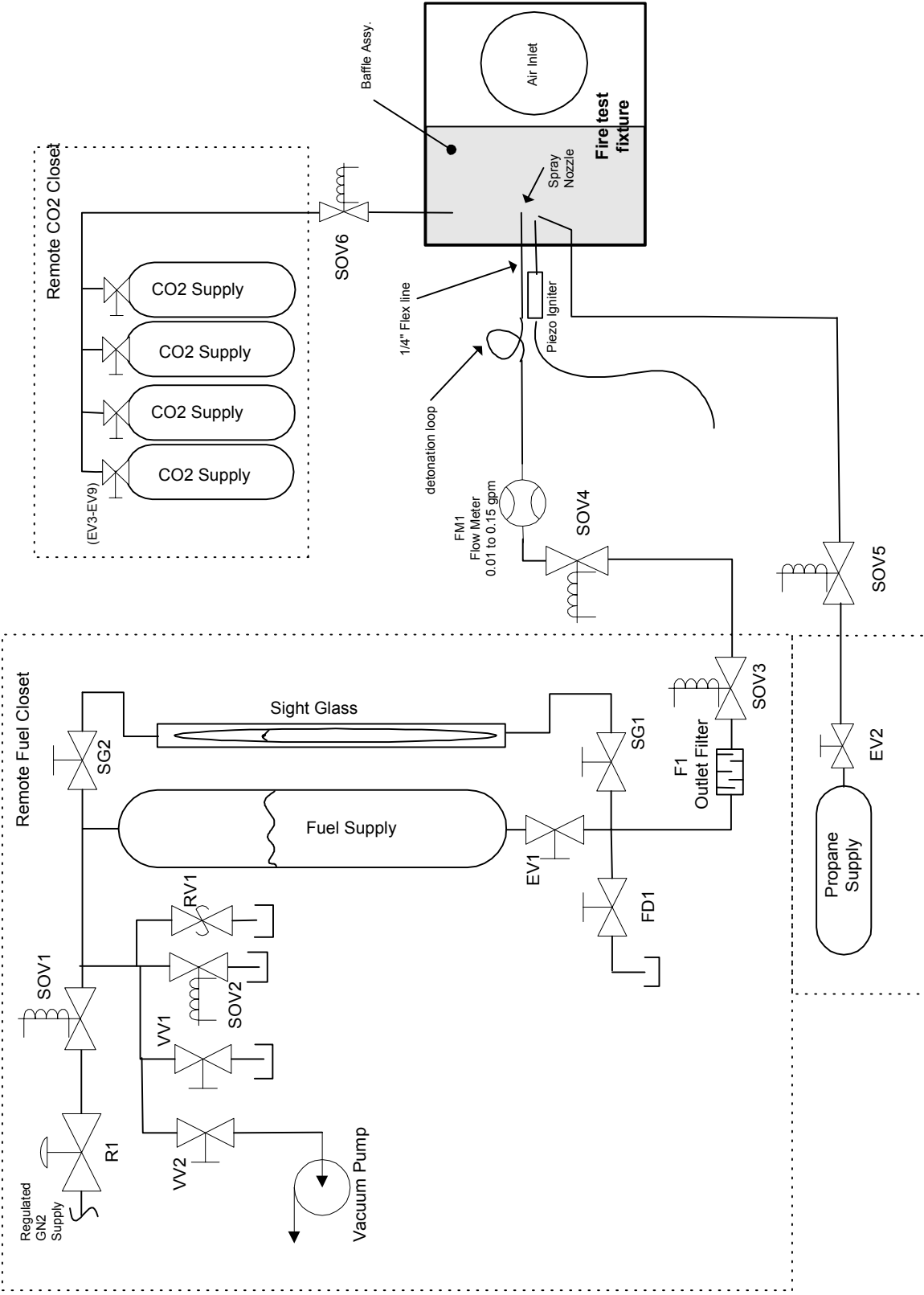
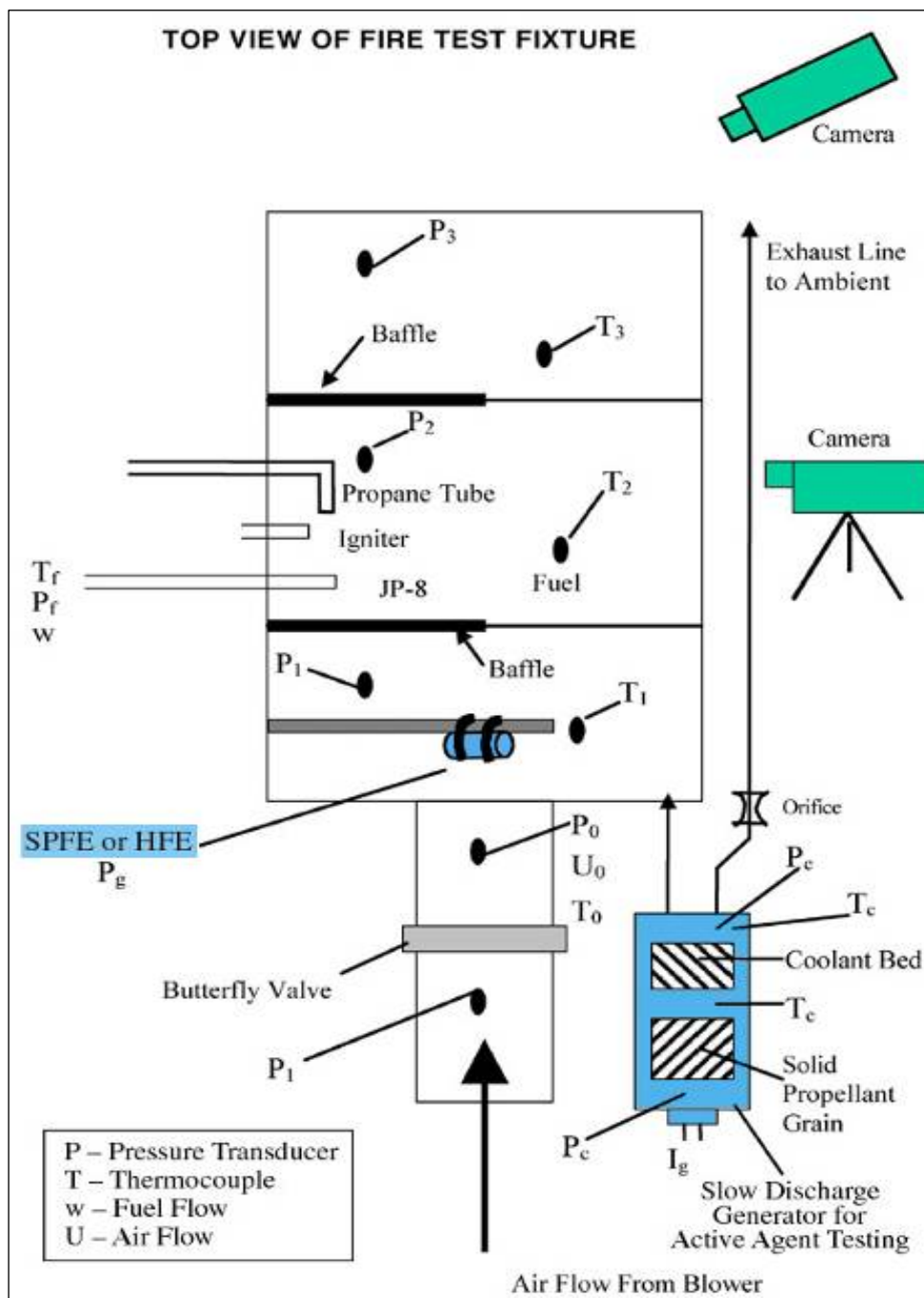


Figure 9-37. FTF Test Facility Schematic.

Various instruments were installed in the solid propellant fire extinguisher and FTF to monitor and control test variables, and to make sure they were in the similar ranges from test to test. These instruments included a pressure transducer in the hybrid fire extinguisher chamber, and thermocouples, pressure transducers, and flow meters in the FTF. The instrumentation layout is presented in Figure 9–38.



**Figure 9–38. Fire Test Fixture Operational Configurations.**

JP-8 was used as the fuel in all of the tests conducted in the FTF. The fuel mass flow was 20.3 g/s, which produced a nominal heat release rate of 1000 kW. The air mass flow was 385 g/s, producing a global

equivalence ratio of 0.80, if one assumes the stoichiometric air-to-fuel mass ratio for JP-8 is 15.18. Table 9–11 provides a summary of the operating conditions for the FTF and Table 9–12 compares these to the operating conditions of other fire test fixtures used in the NGP.

**Table 9–11. Fire Test Fixture Operating Conditions.**

Parameter		Value	
Flow Conditions		Air	JP-8
	Mass flow, m', g/s	385	20.3
	Volumetric Flow, L/s	316	25
	Linear Flow in pipe, cm/s	670	-
Stoichiometry			
	Air-fuel Ratio ( $m'_{\text{air}}/m'_{\text{fuel}}$ )	19	
	Equivalence Ratio	0.8	
Flame Zone Conditions			
	Flame Temperature, K	1200	
	Heat release rate, kW	1000	
	Length, cm	180	
	Cross-Sectional Area, cm <sup>2</sup>	3700	
	Volume, L	670	
	Residence time, s	0.27	
	Agent Injection Interval, ms	Up to 8000	

**Table 9–12. Comparison of Aerojet FTF to Other Fire Test Fixtures.**

Fixture 6	Turbulent Spray Burner <sup>41</sup>	Turbulent Spray Burner <sup>42</sup>	Baffle Stabilized Pool Fire <sup>43</sup>	Baffle Stabilized Pool Fire <sup>44</sup>	FTF
Characteristic					
Length (cm)	5.5	7.5	190	190	180
Cross-Sectional Area (cm <sup>2</sup> )	13.0	19.6	84.6	84.6	3716
Volume (L)	0.09	0.15	16.1	16.1	670
Air Mass Flow (g/s)	21.8	33.0	539	539	385
Residence Time (ms)	5	5	112	35	270
Fuel	JP-8	JP-8	Propane	Propane	JP-8
Fuel Mass Flow (g/s)	0.28	0.34	0.15	0.15	20.3
Equivalence Ratio	0.19	0.16	0.01	0.005	0.80
Fire Heat Release Rate (kW)	13	15.8	7	7	943

The nominal inlet air velocity in the FTF was 6.7 m/s, which, assuming a well-stirred model, leads to a characteristic residence time under cold conditions of about 1.3 s. The residence times when hot or along streamlines that pass by the baffles would be significantly shorter.

Once the desired SPGG device was mounted, the JP-8 spray was initiated and ignited with a propane pilot flame, and the air flow was set to the standard condition. Experience showed that a steady fire could be attained in about 4 s to 5 s. At that time the SPGG was fired, and the agent was discharged.

Depending upon the design, the gas generator device either was located within the FTF in the forward chamber (on a metal bar in the middle of the air flow, shielded from and upstream of the fire), or mounted outside of the FTF adjacent to the air inlet. Figure 9–38 illustrates the gas generator device placement within and outside of the FTF.

Tests were performed using two distinctly different configurations of suppressors mounted to the FTF. In the first configuration, the relative performance of several chemically active additives was determined. This testing utilized a slow discharge (5 s to 8 s) gas generator located outside the FTF; igniting this unit resulted in entrainment of candidate chemically-active agents into a SPGG exhaust stream for delivery to the fire. A neutral-burning solid-propellant gas generator, shown in Figure 9–39 and Figure 9–40, was mounted in the external location; the slow discharge was used in an attempt to minimize flame strain and mixing effects anticipated in rapid discharge tests, thereby emphasizing the performance difference among the various candidates. The discharge of the SPGG for these initial tests had a duration of approximately 5 s. Fine-grid metallic meshes and porous plates were used downstream of the agents to enhance the mixing between the SPGG exhaust and agents prior to entering a distribution tube. The distribution tube was split into two lines, one entered the test fixture, and the other discharged directly to ambient. (See Figure 9–38.) By varying the flow ratio between these two lines, the amount of agent entering the fire zone could be controlled. In the tests, the split ratio was fixed to be 50 %, and the initial agent quantity in the SPGG was varied.

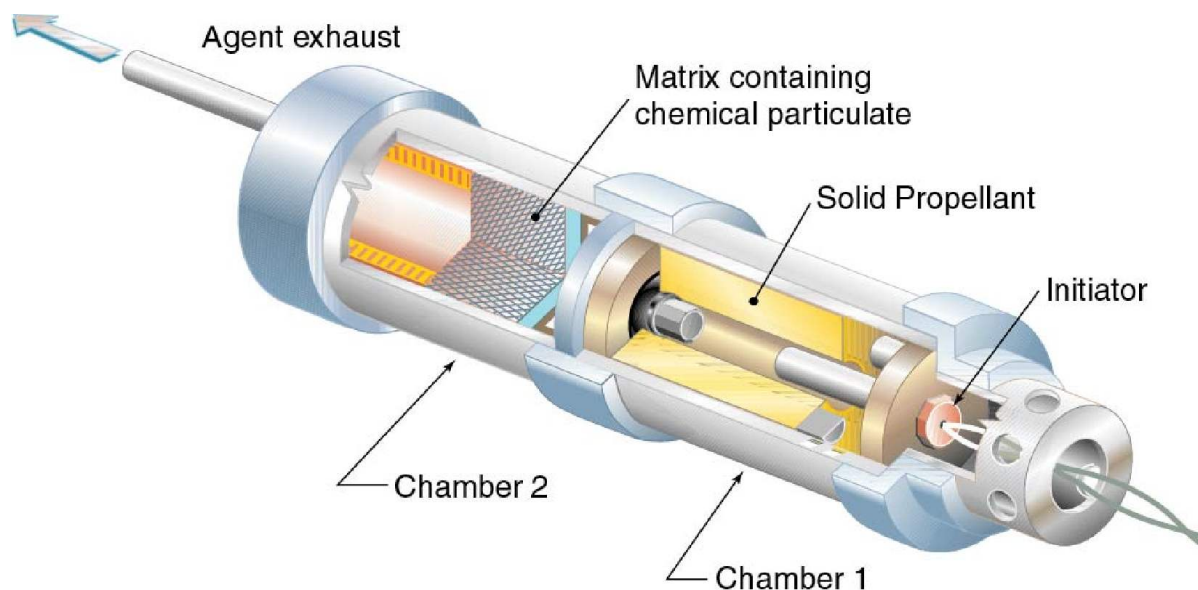


**Figure 9–39. Aerojet Slow Discharge Solid Propellant Gas Generator Test Unit.**

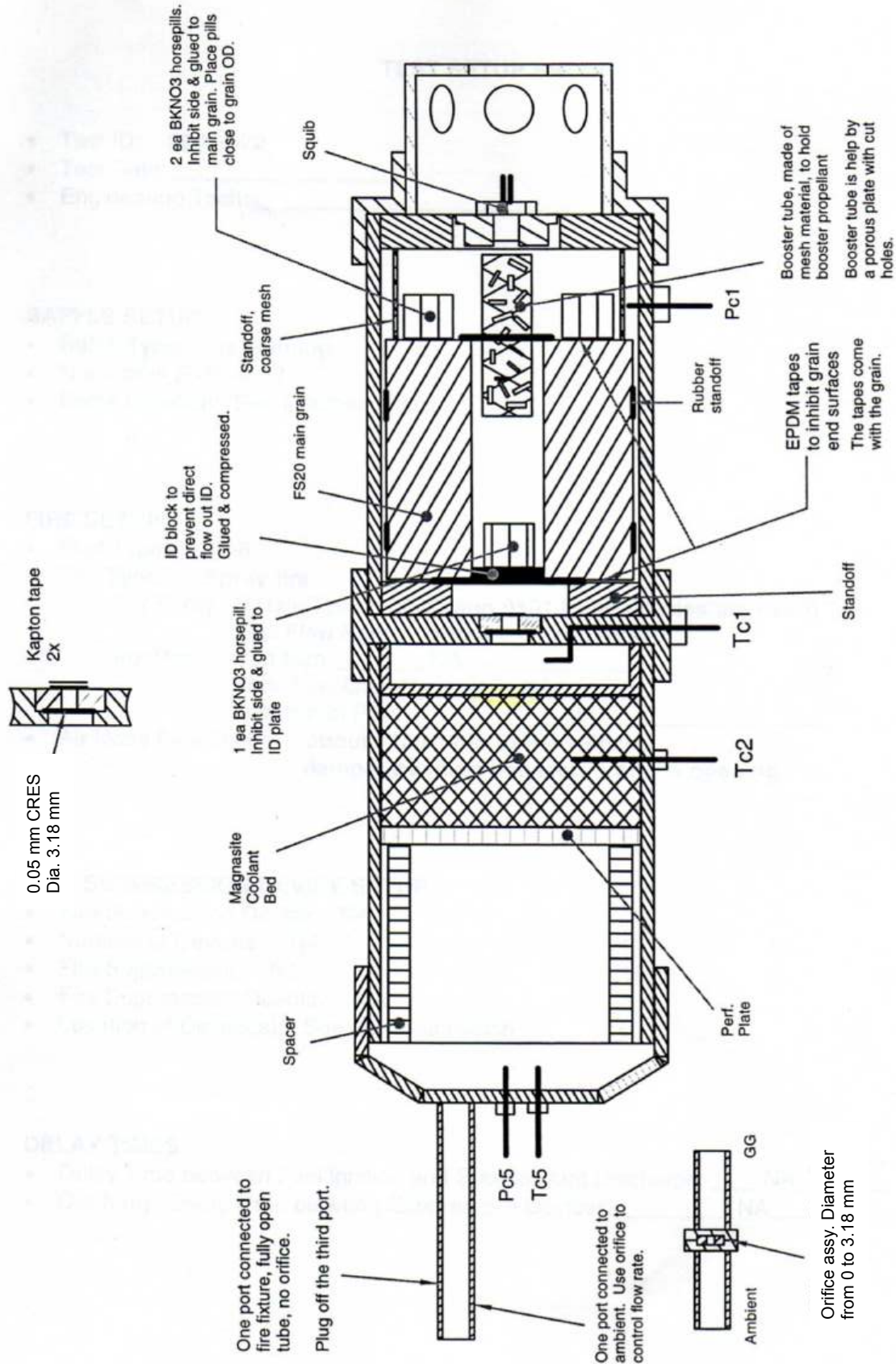
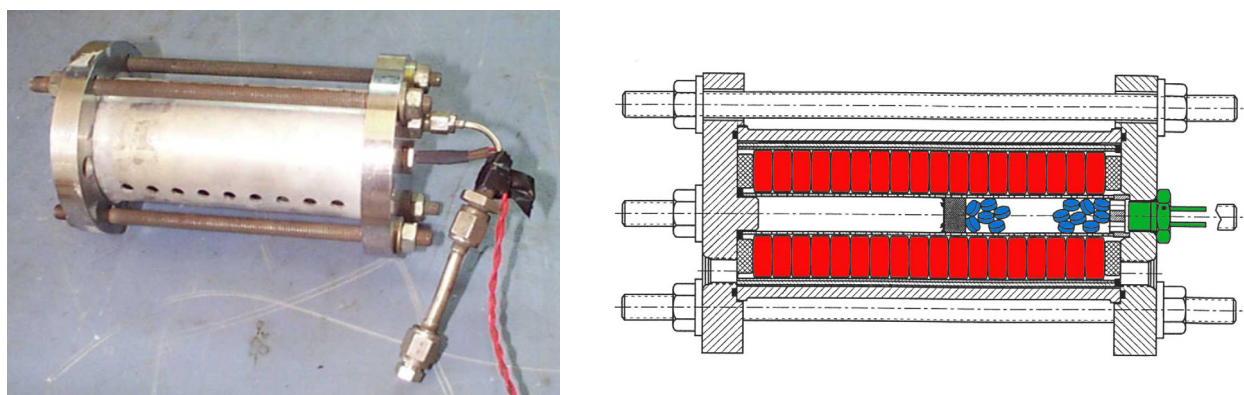


Figure 9-40. Cutaway of Aerojet Slow Discharge Solid Propellant Gas Generator Test Unit.

The second test configuration used the fire extinguisher mounted within the FTF in a chamber upstream of the fire. For this testing, the SPGG discharge times were generally maintained between 150 ms and 200 ms for ease of comparison with the original data. The SPGG used for this testing, shown in Figure 9–41, was mounted within the FTF and could be disassembled after a test, refurbished between runs, loaded with weighed quantities of test propellant, readily reassembled, and re-used for additional testing. For the hybrid extinguisher, the hybrid fluid typically surrounds the SPGG, resulting in a bottle within a bottle configuration, as shown in Figure 9–42.<sup>45</sup>

The relative efficiency of different suppressants was ranked based upon their threshold quantity. The threshold was defined as the amount of agent needed to extinguish the fire at least two out of three times. Typically three tests were conducted at the threshold amount and three additional tests were conducted at an agent load greater than the threshold amount. In the first (external SPGG) configuration, a “bleed” line with an orifice to ambient was used to adjust the percentage of agent delivered to the fire; the orifice in this line is gradually closed until testing yields a fire-out time of  $\approx 5$  s. In the second (internal SPGG/hybrid extinguisher) configuration, total agent loads were adjusted up (or down) until threshold levels were achieved. In Figure 9–43 are consecutive frames of a successful suppression event in the FTF.



**Figure 9–41. Aerojet Reusable Rapid Discharge Solid Propellant Fire Extinguisher Unit.**

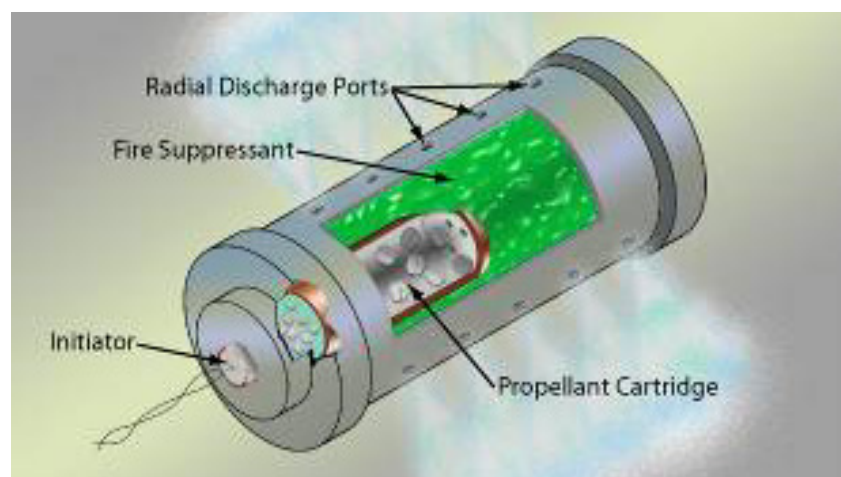


**Figure 9–42. Arrangement of a Typical Hybrid Fire Extinguisher.**

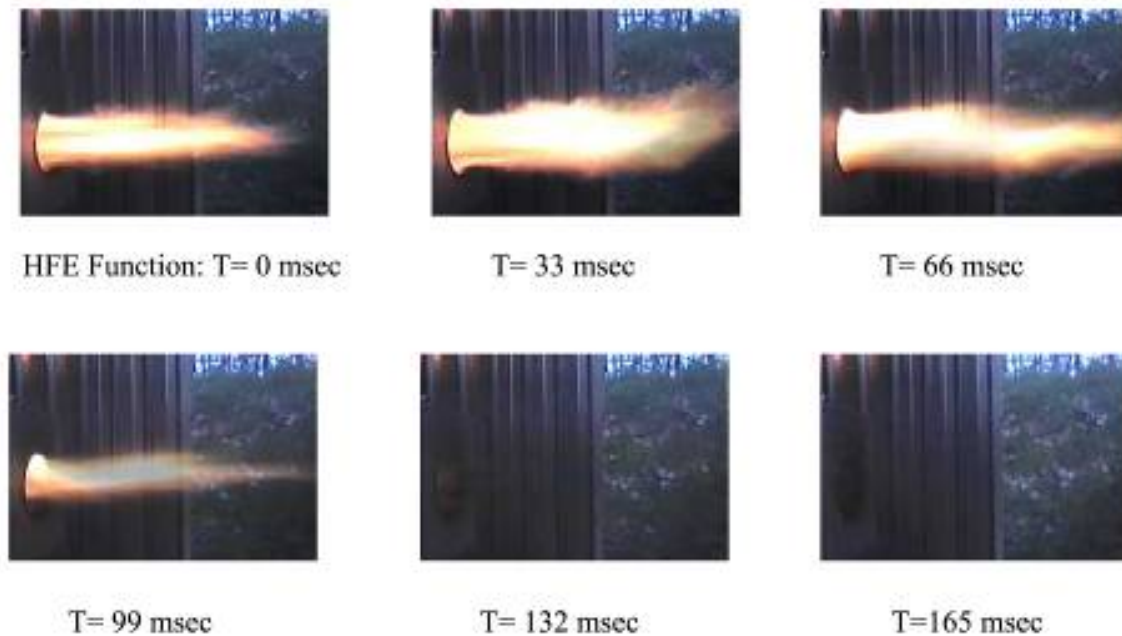


**Figure 9-43. Consecutive Frames during SPGG Suppression of a Fire in the FTF.**

#### **Full-scale Demonstration Tests at China Lake**

Although not included in the NGP-funded program, it is relevant to briefly describe the live-fire testing conducted by Aerojet for NAVAIR to demonstrate SPGG fire suppression technology on full-scale aircraft dry bays. The tests were conducted at China Lake on mid-wing sections and landing gear sponsons.

Figure 9-44 shows an SPGG fire extinguisher with 210 g of chemically active propellant mounted in the landing gear sponson test article. JP-8 filled the fuel line. The main landing gear door was either open or closed, and the external airflow was run up to about 120 m/s. The gun was then loaded, and fired. The projectile impacted the striker plate and fuel line, resulting in a fuel spray that immediately ignited. The SPGG extinguishers were initiated either automatically or following a set delay period after initial impact.

The intent of the mid-wing testing was to evaluate the potential for a common size gas generator for the entire aircraft. Testing evaluated the extinguishment performance of a common sized generator extinguisher at the most challenging fire location of the aircraft (the high airflow mid-wing compartment). The chemical gas generators were installed at various positions, with a typical installation shown in Figure 9-45.



**Figure 9–44. SPGG Installed in Sponson Test Article for Live-fire Demonstration.**<sup>46</sup>  
(Photograph reprinted with permission of the Naval Air Systems Command.)



**Figure 9–45. SPGGs Installed in Mid-wing Test Article for Live-fire Demonstration.**<sup>47</sup>  
(Photograph reprinted with permission of the Naval Air Systems Command.)

### 9.3.4 Results: General Behavior of Propellants

#### General

This research explored several complementary approaches directed toward identifying more effective solid propellant-based fire extinguishers. All of these approaches utilized a solid propellant gas generator to deliver the suppression agent to the fire, including:

- development and characterization of new, cooler solid propellant compositions
- development and characterization of new chemically active solid propellant compositions, and
- development and characterization of new hybrid fire extinguishers.

The benchmark by which all these improvements were measured was the first solid propellant composition manufactured by Aerojet and used on the F/A-18 E/F Dry Bay Fire Extinguisher and the V-22 Wing Fire Protection System. This propellant is referred to as FS01-40.

The thermodynamics, burn rate, and fire suppression effectiveness were studied using the techniques and apparatus described in the previous section, and the results of these studies are reported in this section for each of the three above approaches. The exhaust temperature and momentum, and the temperature of the propellant during discharge, are also important parameters that were examined.

#### SPGG Temperatures and Discharge Pressures

SPGG exhaust temperatures for different propellant compositions were measured at several points along the exit streamline. These measurements indicated gas temperatures varied widely with distance from the gas generator exit, with values near 600 °C directly outside the generator to below 200 °C at points ~ 30 cm from the gas generator. Temperature measurement of SPGG exhaust is complicated by the need for rapid (ms) response in the face of high velocity, high temperature gases. Fine wire thermocouples, while giving good response times, eroded/broke during testing near the gas generator exit; hence, no temperature data for this region are reported.

In a series of hybrid SPGG tests with propellant-to-liquid suppressant mass ratios ranging from about 1:10 to 1:5, exhaust temperatures were much lower than for the SPGG alone, dropping to values between 50 °C and 65 °C. The tests were conducted as “vise shots,” where a hybrid SPGG is mounted in a bench-top vise and held there for functioning (Figure 9–46).

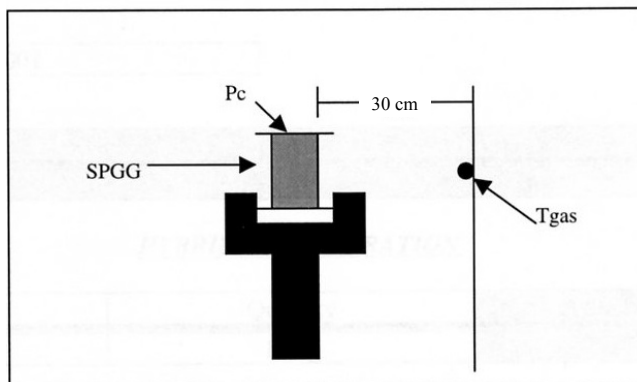


**Figure 9–46. Typical Setup of Preliminary Vise Shot for Hybrid Extinguisher.**

The hybrid configuration used a fixed mass (18 g) of inert solid propellant and different quantities of the HFE-1230 hybrid fluid. The quantity of hybrid fluid varied from 176 g (the standard 1:10 propellant:hybrid mass ratio) to 103 g (a 1:5 ratio).

For each of the tests, the following performance characteristics were recorded: chamber pressure ( $P_c$ ) and temperature of gas downstream of the discharge orifices ( $T_{\text{gas}}$ ). Type-K thermocouples were mounted on a screen  $\approx 30$  cm from the gas outlet (location was aligned with one set of gas outlet orifices) and data were collected at 100 Hz.

Temperatures recorded for the standard 1:10 propellant:hybrid mass ratio were reduced significantly as compared to all-SPGG configurations (55 °C to 60 °C vs.  $\approx 200$  °C, respectively). The recorded performance characteristics reveal that as the quantity of hybrid fluid is reduced (from 176 g to 103 g), the measured internal suppressor pressures are reduced proportionally (17.2 MPa to 9.9 MPa). Temperatures of the mixed air-suppressant exhaust blend, however, vary only slightly, with the reduced quantity of hybrid fluid yielding temperatures of  $\approx 65$  °C as compared to 57 °C for the 1:10 mass ratio.

Discharge rates were varied across a range to determine if this parameter played a role in suppression effectiveness. The rate of mass discharged from a gas generator is related to the internal pressure, which increases with the exposed area of the propellant. Different discharge rates were prepared by using a common propellant but varying the relative surface areas available for burning by making use of different sizes of tablets, while keeping the burning rate constant.

The three tablet sizes considered were small (9.5 mm diameter x 2.4 mm thick); standard or medium (12.7 mm diameter x 6.4 mm thick); and large (12.7 mm diameter x 12.7 mm thick). For the standard sized tablet (CA-04), internal pressures reached 12.4 MPa, and the device discharged the agent in about 0.2 s. For a fixed gas generator load (mass of propellant), the smaller pellet size had a larger total surface area, resulting in faster pressurization (peak pressure of 17.7 MPa) and a discharge time of 0.1 s, which can be seen in Figure 9–47. The large tablets had a smaller surface area (per unit mass) that produced a very uneven burn (yellow trace, Figure 9–47), and peak pressures reached only 5.5 MPa. In some cases the pressures were too low to rupture the burst disks, and when the disks did rupture, burn times stretched out to almost 1 s.

In an attempt to improve discharge characteristics of the larger tablet size, the gas generator orifice area was reduced by  $\approx 50\%$ . This reduction in area results in a less than two times higher internal pressure and a more regular and well-behaved pressurization curve, while retaining the longer discharge time desired. Even with the variations in peak pressures, all the SPGGs evaluated in Figure 9-46 were able to extinguish the fire in the FTF.

Figure 9–48 portrays the temperatures measured using Type K thermocouples tack-welded to the SPGG surface. Measured temperatures appear to peak at about 120 °C. While different tablet sizes do yield different performance times (as seen in the pressurization curve above), the heat output is expected to be unchanged with tablet size, which is approximately the case for the blue and yellow traces in Figure 9–48. The significantly different surface temperatures shown in the pink trace appear to be the result of differences in measurement location and thermocouple attachment quality.

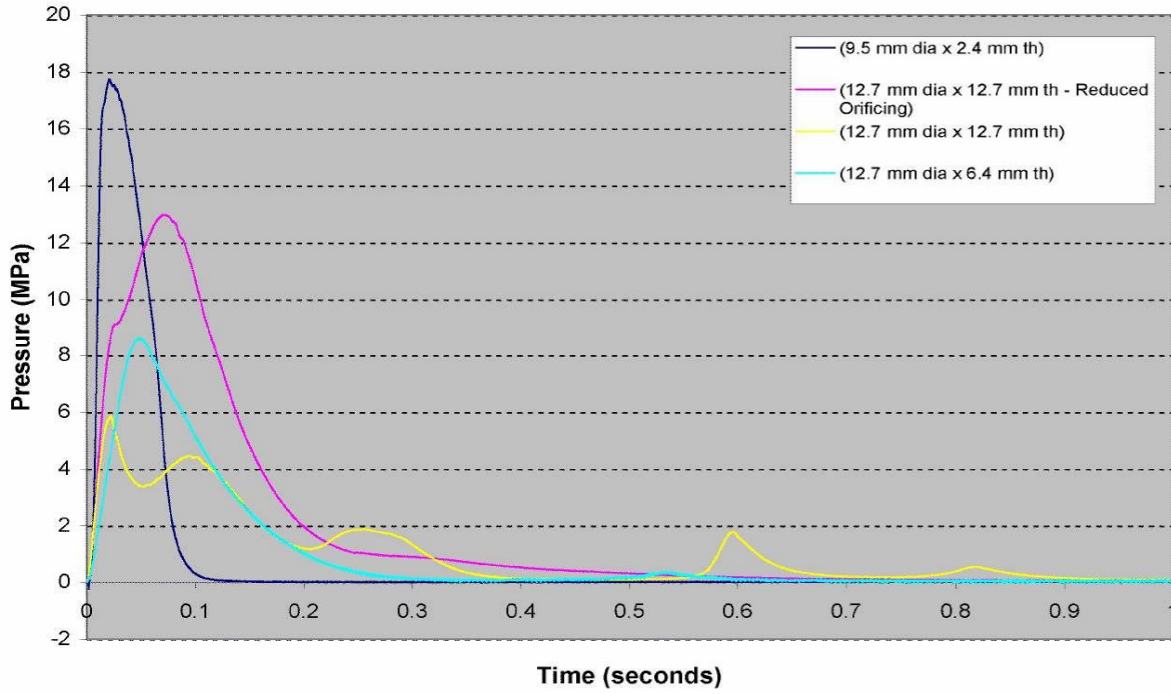


Figure 9–47. Chamber Pressure for Different Propellant Surface Areas (CA-04).

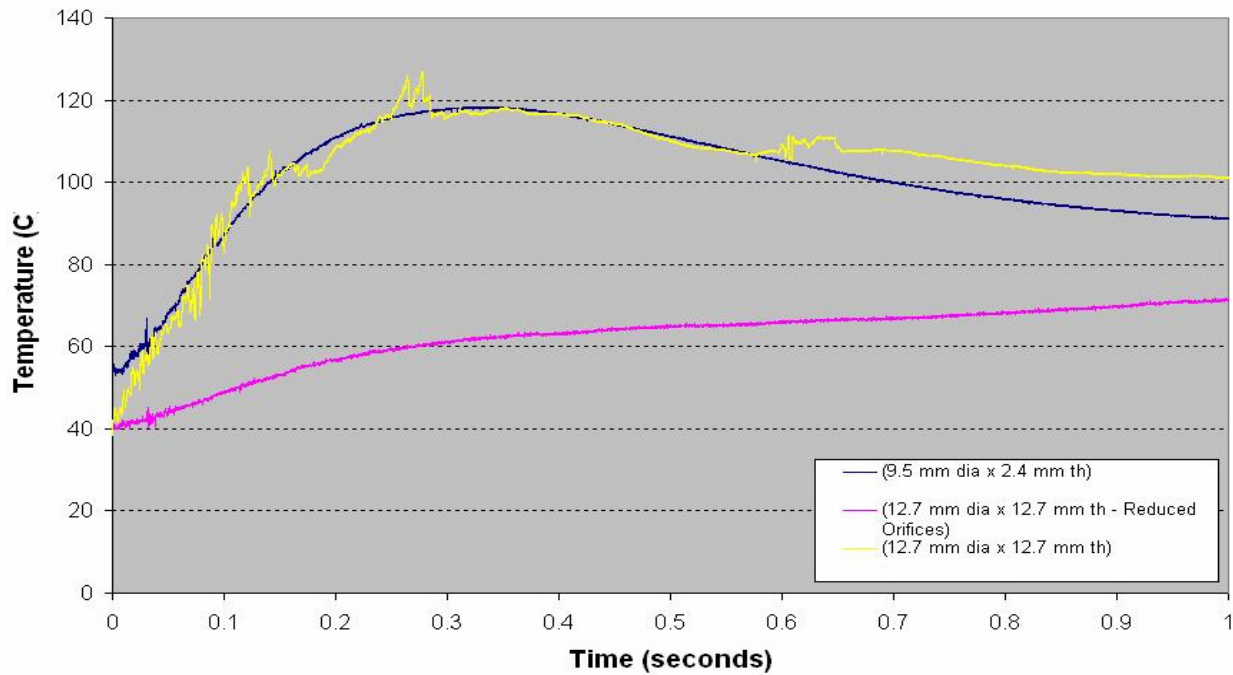


Figure 9–48. Housing Temperatures for Different Propellant Surface Areas (CA-04).

## Effects of Propellant Temperature on Burn Rate

Besides pressure, the burn rate is also dependent on the initial temperature at which the propellant is burned. Higher temperatures generally result in increased burn rates, as is typical for activated processes. Given that most propellant applications require functioning of the propellant device over temperature extremes as wide as  $-50\text{ }^{\circ}\text{C}$  to  $75\text{ }^{\circ}\text{C}$ , a low sensitivity of burning rate on temperature is desirable. Two parameters are typically used to describe this temperature sensitivity of burn rate, the derivative of the linear burn rate with respect to temperature at fixed pressure,  $\sigma_p$ , and the variation in combustion chamber pressure with temperature at fixed propellant geometry,  $\pi_k$ . These parameters are dependent on the nature of the propellant composition, its burn rate and the combustion mechanism of the given propellant, and are defined as follows:<sup>48</sup>

$$\sigma_p = \left( \frac{1}{r} \frac{r_1 - r_0}{T_1 - T_0} \right)_p = \left( \frac{\partial \ln r}{\partial T} \right)_p$$

and

$$\pi_k = \left( \frac{1}{P} \frac{P_1 - P_0}{T_1 - T_0} \right)_{K_n} = \left( \frac{\partial \ln P}{\partial T} \right)_{K_n},$$

where  $r$  is the linear burn rate,  $r_0$  and  $r_1$  are the burn rates at  $T_0$  and  $T_1$ , respectively, and  $K_n$  is defined as the ratio of burning surface area to exit orifice area,  $A_b/A_t$ . For conventional propellants,  $\sigma_p$  ranges between  $0.002/\text{K}$  to  $0.008/\text{K}$ ; for AP-based propellants,  $\sigma_p$  is typically  $\approx 0.0015$ , while for AN-based propellants,  $\sigma_p$  is often in the vicinity of  $0.002/\text{K}$ .

These two parameters can be related to each other through the pressure exponent defined previously,  $n$ .

$$\pi_k = \frac{1}{1-n} \sigma_p$$

Note that in the case of  $n$  approaching 1,  $\pi_k$  can become very large even for small  $\sigma_p$ ; i.e., large changes in chamber pressure can be expected with even small temperature variations.

Table 9–13 shows the measured burning rates at various initial temperatures for the baseline propellant composition used in the current study, along with the derived temperature sensitivity parameters and pressure exponent. These findings reveal that the burn rate increases with temperature in a predictable manner.

**Table 9–13. Temperature Dependence of Burn Rate for Baseline Propellant, FS-0140.**

T, °C	BR <sub>1000</sub> (mm/s)	P <sub>max</sub> (MPa)
-25	12.7	7.83
25	14.0	10.3
75	15.2	12.8
$\sigma_p = 0.13\text{ } \%/^{\circ}\text{C}$	$\pi_k = 0.48\text{ } \%/^{\circ}\text{C}$	$n = 0.73$

### 9.3.5 Results: Cooled Propellant Formulations

The hot exhaust gases of typical solid propellant compositions are not efficient suppressants for combustion reactions. Additionally, the quantity of gases required for suppression may result in over-pressurization conditions when released in enclosed bays, as well as resulting in greater concerns for materials compatibility for the structure surrounding the suppressor. For these reasons and others, cooler solid propellant fire extinguisher compositions are highly desired.

This research explored three different routes towards achieving cooler solid propellant fire extinguisher compositions:

- reducing the enthalpy of the combustion process through selection of various fuels/oxidizer blends;
- altering the stoichiometry and enthalpy of the propellant reactions through various fuel:oxidizer ratios; and
- seeking faster-burning solid propellant compositions, to which one could add coolant to reduce the overall exhaust gas temperature.

### Solid Propellant Combustion Thermodynamics

The impact of different fuels upon calculated adiabatic flame temperatures was explored. The selection of fuels focused on those with nitrogen-nitrogen bonding in the fuels' molecular structure. N–N bonding was considered to provide two distinct advantages: N–N molecular bonds are often kinetically labile and therefore susceptible to rapid reaction with an oxidant; and additional nitrogen atoms in the fuel increases the production of the molecular nitrogen in the exhaust.

Several high-nitrogen fuels were considered. (See Figure 9–49.) A more negative enthalpy of formation generally leads to cooler exhaust products; however, one must also consider the enthalpy of the equilibrium products that are formed. In particular, a higher N:C and N:H ratio in a fuel results in the formation of a greater proportion of N<sub>2</sub> vs. CO<sub>2</sub> and H<sub>2</sub>O gas; the lesser enthalpy associated with N<sub>2</sub> (vs. CO<sub>2</sub> or H<sub>2</sub>O) results in a cooler solid propellant exhaust composition.

Thermodynamic equilibrium calculations of the adiabatic flame temperature (typically conducted at 6.9 MPa) are precise and straightforward. On the other hand, predictive solid propellant kinetics modeling is very poorly developed and unreliable. Hence, characterization of viability of cooler propellant compositions requires complementary thermodynamic modeling together with experimental measurement of combustion kinetics, or burn rate.

The effect of different fuels upon exhaust gas temperatures was determined for a common oxidizer in a stoichiometric mixture. The calculations were performed using the NAWC PEP<sup>40</sup> computer code, and the results are shown in Table 9–14. A review of these data shows that all but the GAZT (bisguanidium azotetrazole)/strontium nitrate blend exhibit adiabatic combustion temperatures well in excess of 2000 K.

Among the fuels studied, 5-amino-tetrazole (5AT) is the most readily available; it and its derivatives are used in several commercially viable automotive airbag formulations. Many of the other fuels considered have limited commercial availability. Preliminary evaluations suggested that bis(5-aminotetrazolyl) tetrazine (BTATZ) would be an attractive candidate for further study because of its high nitrogen content.

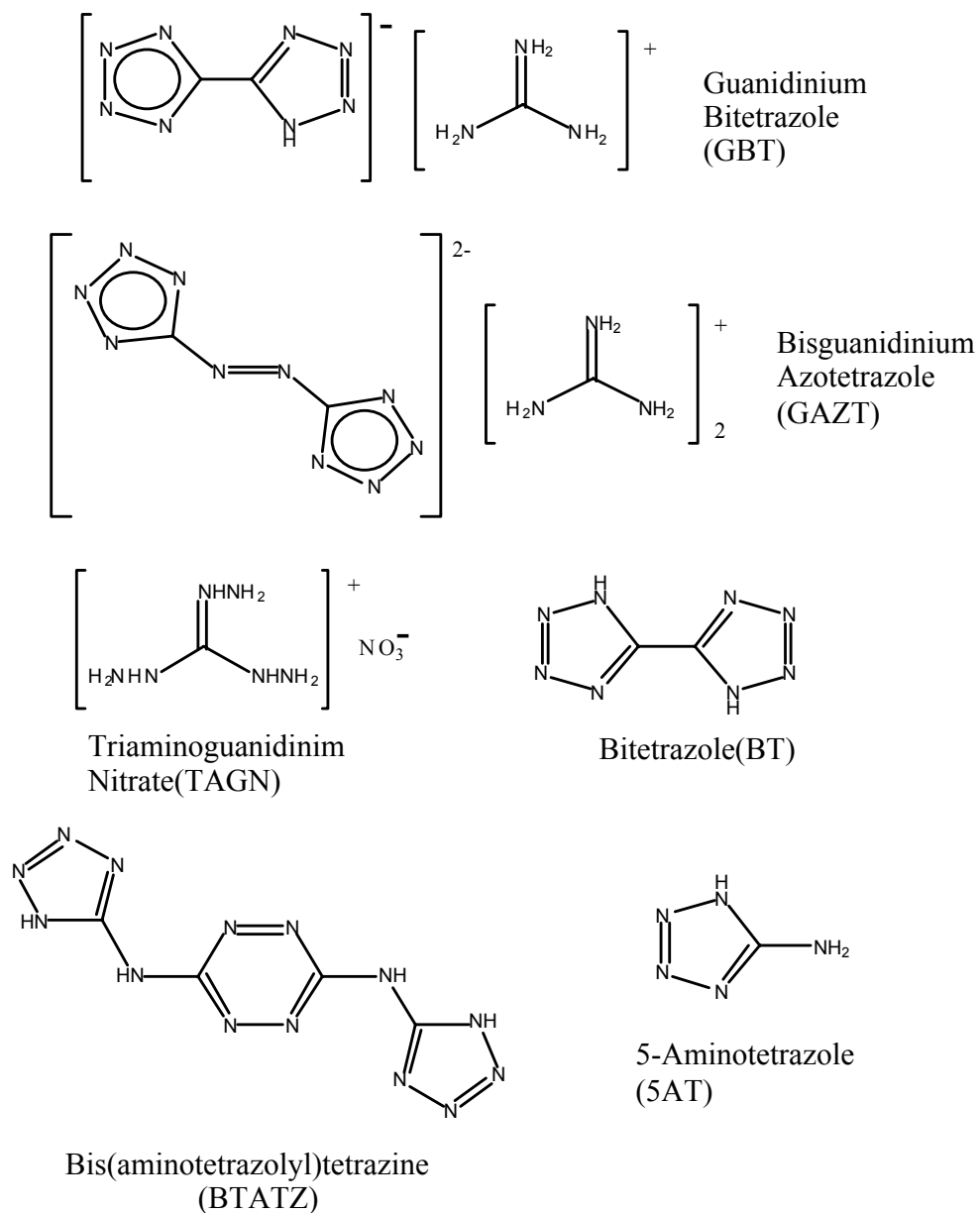


**Figure 9–49. High-nitrogen Fuels Used in China Lake/Aerojet Propellant Development.**

BTATZ was discovered recently by Hiskey et al.<sup>49,50</sup> at Los Alamos National Laboratory (LANL). Its promise as a high-nitrogen, highly reactive fuel led to an extensive NGP effort to explore its utility for solid propellant compositions, and to work to scale up synthesis of this material from the several gram, laboratory level to kilogram quantities.

**Table 9–14. Adiabatic Temperatures of High Nitrogen Propellant Fuels in Stoichiometric Mixtures with Sr(NO<sub>3</sub>)<sub>2</sub> Oxidizer.**

Fuel	Molecular Formula	$\Delta H$ (J/g)	Density (g/cm <sup>3</sup> )	T <sub>c</sub> (K)
5AT	CH <sub>3</sub> N <sub>5</sub>	2450	1.65	2650
BTATZ	C <sub>4</sub> H <sub>4</sub> N <sub>14</sub>	3560	1.74	2750
TAGN	CH <sub>9</sub> N <sub>7</sub> O <sub>3</sub>	-290	1.54	2680
BT	C <sub>2</sub> H <sub>2</sub> N <sub>8</sub>	3350	1.79	2750
GBT	C <sub>3</sub> H <sub>7</sub> N <sub>11</sub>	1540	1.57	2520
GAZT	C <sub>4</sub> H <sub>12</sub> N <sub>16</sub>	-1110	1.66	1930
GN	CH <sub>6</sub> N <sub>4</sub> O <sub>3</sub>	-3530	1.39	2250
NQ	CH <sub>4</sub> N <sub>4</sub> O <sub>2</sub>	-880	1.73	2720

BTATZ is synthesized from commercially available ingredients in a four-step procedure furnished by LANL and outlined in Figure 9–50.<sup>49,50</sup> Reaction of guanidine hydrochloride with three equivalents of hydrazine hydrate yields triaminoguanidine hydrochloride (TAG•HCl) in almost quantitative yield. Reaction of TAG•HCl with 2,4-pentanedione leads to dihydroDMPTZ which upon oxidation with N<sub>2</sub>O<sub>4</sub> gives DMPTZ. Very careful control of the reaction conditions is required for the final step. The solvent used for the reaction (sulfolane) is a solid at room temperature (melting point 28 °C). The solvent is heated to 40 °C and DMPTZ and 5AT are added. This temperature is maintained for 2 hours and then the temperature increased over a six-hour period to 135 °C and held at that temperature for 18 hours. BTATZ precipitates from the reaction mixture during this time. The reaction mixture is allowed to cool to 70 °C and ethanol is added to prevent the mixture from freezing upon further cooling. BTATZ is collected on a medium porosity glass frit and is washed with copious amounts of ethanol. The crude product is purified by trituration with dimethylformamide (DMF) or ethanol, with ethanol giving a higher recovery but providing slightly less pure material. The yield for this last step in a typical experiment is in the 70 % to 75 % range with ethanol purification versus  $\approx$  50% when DMF is employed. The synthesis of BTATZ was carried out initially at quantities of about 1 g for review by the safety committee, as is common for the synthesis of energetic materials. The results and procedures used were reviewed by a panel of experienced energetic materials researchers before any scaling up of the synthesis was permitted. Typically, if upon review, the procedures are deemed safe and the material itself has no hazardous properties that cannot be mitigated through the use of appropriate handling techniques, the reaction can be scaled up by a factor of five. Several results at each level were required for review.

Using these guidelines NSWC staff preceded through the 1 g, 5 g, 25 g, 100 g, 250 g and 450 g levels. All of these reactions were carried out in a laboratory fume hood. At this level, 6 L of solvent were used in a 12 L flask. On the 450 g scale, the product was collected by filtration on two 3 L medium porosity filter funnels. In order to carry out the syntheses described above we needed a large amount of the immediate precursor DMPTZ (C<sub>12</sub>H<sub>14</sub>N<sub>8</sub>). This material is not an energetic material and is not subject to the scale-up limitations described for the synthesis of BTATZ. NSWC staff used a published procedure to carry out the synthesis of approximately 4.5 kg of this material. A further 4.5 kg were supplied by the Los Alamos National Laboratory. Modifications to the purification process provided material with acceptable properties but in higher yield than that using the standard method.

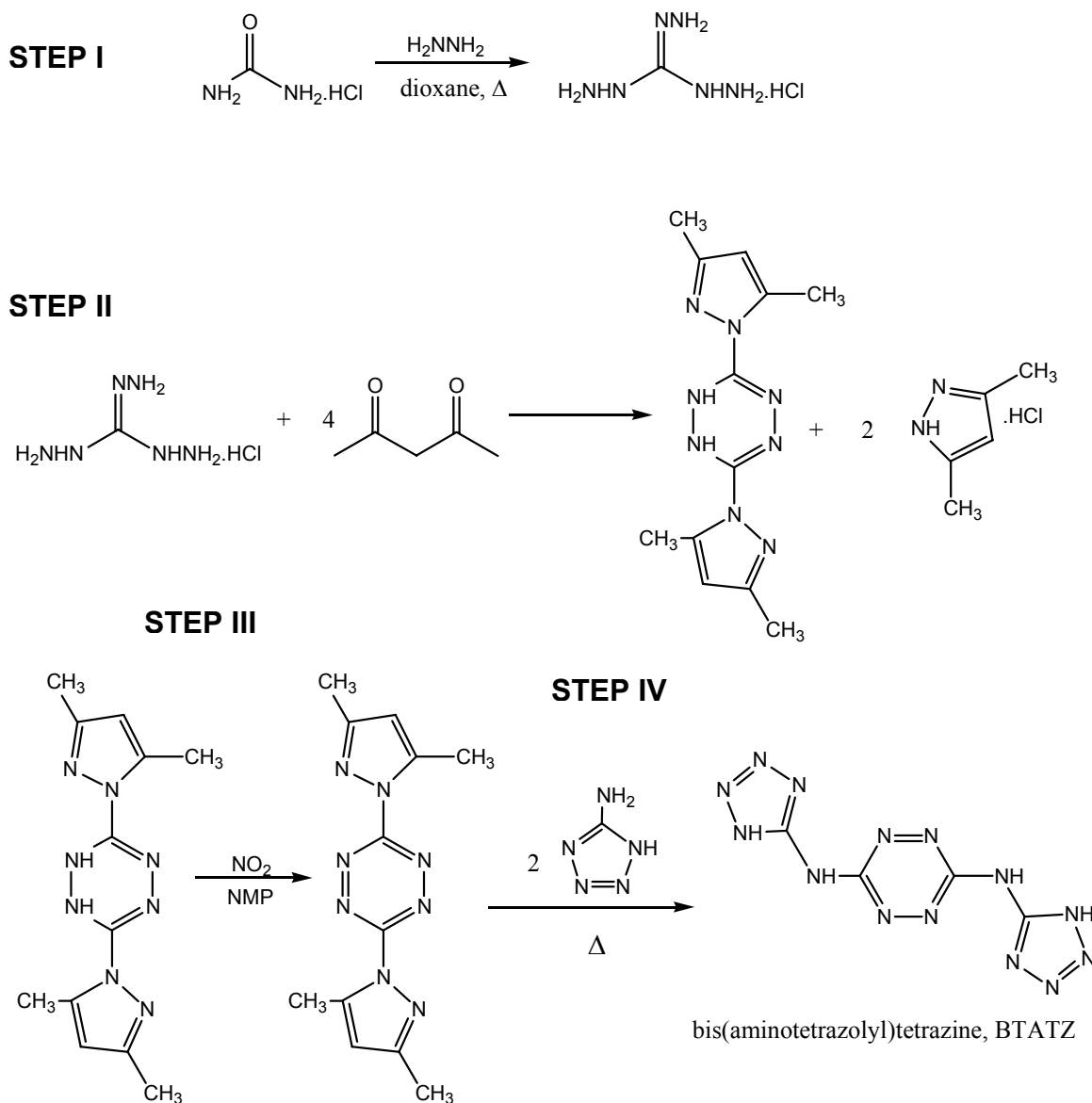


**Figure 9–50. Synthetic Route to BTATZ.**

Further safety data on BTATZ itself has been obtained. BTATZ shows acceptable friction and impact sensitivity but is somewhat sensitive to electrostatic initiation. When formulated into a molding powder with poly(ethyl acrylate) (3 % as a binder) electrostatic sensitivity is still a concern, even when 0.5 % carbon black is added; however when pressed into pellets or deposited as a thin layer the material meets the criteria set for routine handling of energetics. However, shipments of these new energetic materials is still limited to small quantities.

In order to assess the effect of the choice of oxidizer on exhaust gas temperatures, thermodynamic calculations were performed using the NAWC PEP<sup>40</sup> computer code, with different oxidizers and a common fuel (5-aminotetrazole, or 5AT) in stoichiometric proportions. Combustion was assumed to be complete. The results are compiled in Table 9–15.

Among the oxidizers considered, strontium nitrate and potassium perchlorate produced the hottest exhaust gases. The ammonium nitrate/5AT blend, while it produces a lower adiabatic flame temperature, has poor thermal stability, rendering it impractical for use in a fire extinguisher on DoD weapons platforms.

**Table 9–15. Adiabatic Temperatures of Oxidizers in Stoichiometric Mixtures with 5-aminotetrazole.**

Oxidizer	Molecular Formula	$\Delta H$ , J/g	Density, g/cc	Calculated $T_c$ , K
Strontium Nitrate	$Sr(NO_3)_2$	-4610	2.99	2650
Potassium Nitrate	$KNO_3$	-4880	2.12	2150
Potassium Perchlorate	$KClO_4$	-3210	2.52	2970
Ammonium Nitrate	$NH_4NO_3$	-4980	1.72	2390

### High Nitrogen Propellant Burning Characteristics

While fuel and oxidizer thermodynamic studies provide a useful means of predicting appropriate solid propellant compositions having cooler exhaust gases, actual use of a composition requires that it be kinetically robust; i.e., the composition must burn at an appropriate rate.

For different DoD fire suppression applications, agent discharge rates can be expected to extend over a broad range, from 50 ms to 500 ms for aircraft dry bay applications, to 0.5 s to 5 s for aircraft engine bay applications. The focus of this NGP research was the shorter timeframe associated with aircraft dry bays.

The chemical reaction proceeds with a rate that is directly proportional to the pressure raised to the  $n^{\text{th}}$  power. When taking place inside a closed vessel – e.g., a gas generator – pressures typically build to  $\approx 6.9$  MPa to 34 MPa in order to produce consistent performance. The burn rate at 6.9 MPa (1000 psi) is often used as a standard condition for comparison of different solid propellants; this  $BR_{1000}$  is typically in the range of 5 mm/s to 15 mm/s. For the sake of ease of manufacturability (of both the gas generator and enclosed propellant grains),  $n$  is preferred to be less than 0.6. Propellant compositions exhibiting pressure exponents greater than unity were not considered for further evaluation, as this pressure dependence is not suitable for practical applications.

For this project, several different combinations of fuels, oxidizers and coolants have been modeled and tested. A summary of several cooler propellant compositions is presented in Table 9–16. The baseline solid propellant fire extinguisher composition (FS-0140) can be seen to have a moderately high combustion temperature (1450 K), a moderate burn rate (1.27 cm/s), and a moderate pressure exponent ( $n \approx 0.5$ ). Most of these compositions contain, low levels of the processing/combustion aids including PBA (poly(butyl acetate) binder), C-black (carbon black combustion aid) and mica (a lubricant); oxidizers were typically KP (potassium perchlorate) or KN (potassium nitrate).

**Table 9–16. Development Propellant Compositions and Burning Parameters.**

Propellant Composition (wt %)	Exhaust Species, vol % @ T <sub>c</sub>	Temperature (K)		Calculated Density (g/cm <sup>3</sup> )	Gas Output (mol/100 g)	Measured BR <sub>1000</sub> (cm/s)	Measured Pressure exponent, n
		T <sub>c</sub>	T <sub>exh</sub>				
<b>Baseline:</b> 5AT, 21.9, Sr(NO <sub>3</sub> ) <sub>2</sub> 19.1, MgCO <sub>3</sub> 60.0	N <sub>2</sub> 45, CO <sub>2</sub> 35, H <sub>2</sub> O 20	1450	1000	2.55	2	1.27	0.5
<b>5AT:</b> 5AT 86.0, KP 10.0, PBA 3.0, C-black 0.5, Mica 0.5	N <sub>2</sub> 61, H <sub>2</sub> 29, CO 3, CH <sub>4</sub> 3, KCl(s) 5.3 g	1667	874	1.68	4.41	0.43	0.80
<b>BTATZ-1:</b> BTATZ 97.0, PBA 2.0, C-black 0.5, Mica 0.5	N <sub>2</sub> 75, H <sub>2</sub> 24, CO, CH <sub>4</sub>	2349	1151	1.72	3.66	5.44	0.51
<b>BTATZ-2:</b> BTATZ 86.0, KP 10.0, PBA 3.0 C-black 0.5, Mica 0.5	N <sub>2</sub> 68, H <sub>2</sub> 23, CO 9	2290	1135	1.76	3.68	5.46	0.55
<b>BTATZ-3:</b> BTATZ 86.0, KN 10.0, PBA 3.0, C-black 0.5, Mica 0.5	N <sub>2</sub> 69, H <sub>2</sub> 23, CO 8	2085	1088	1.74	3.72	4.57	0.57
<b>5AT/BTATZ-1:</b> 5AT 48.0 BTATZ 48.0, PBA 3.0, C-black 0.5, Mica 0.5	N <sub>2</sub> 68, H <sub>2</sub> 29	1939	908	1.66	4.14	1.40	1.6 (3.45-6.89 MPa)
<b>5AT/BTATZ-2:</b> BTATZ 72.0, 5AT 24.0, PBA 3.0 C-black 0.5, Mica 0.5	N <sub>2</sub> 70, H <sub>2</sub> 28	2118	995	1.69	3.94	4.52	0.71
<b>5AT/BTATZ-3:</b> 5AT 43.0, BTATZ 43.0, KP 10.0, PBA 3.0, C-black 0.5, Mica 0.5	N <sub>2</sub> 63, H <sub>2</sub> 28, CO 6, KCl (s) 5.3 g	1961	967	1.72	4.01	3.85	0.7 (6.89-18.9 MPa)
<b>5AT/BTATZ-4:</b> 5AT 43.0, BTATZ 43, KN 10.0, PBA 3.0, C-black 0.5, Mica 0.5	N <sub>2</sub> 65, H <sub>2</sub> 29, CO 4 K <sub>2</sub> CO <sub>3</sub> (s) 5.3 g	1799	965	1.70	4.10	1.55	1.6
<b>GAZT:</b> GAZT 33.6, KP 62.4, PBA 3.0 C-black 0.5, Mica 0.5	N <sub>2</sub> 28, CO <sub>2</sub> 13, H <sub>2</sub> O 28 H <sub>2</sub> 26, CO 24, KCl(s) 32.6 g	1723	964	1.92	2.51	>6.4	ND
<b>BT:</b> BT 33.6, KP 62.4, PBA 3.0, C-black 0.5, Mica 0.5	N <sub>2</sub> 31, CO <sub>2</sub> 12, H <sub>2</sub> O 10, H <sub>2</sub> 13, CO 29, KCl(s) 32.6 g	2479	1761	1.92	2.13	>6.4	ND
<b>GBT:</b> GBT 33.6, KP 62.4, PBA 3.0, C-black 0.5, Mica 0.5	N <sub>2</sub> 28, CO <sub>2</sub> 10, H <sub>2</sub> O 9, H <sub>2</sub> 23, CO 29, KCl(s) 32.6 g	2000	1457	1.88	2.19	>6.4	ND
<b>TAGN:</b> TAGN 33.6, KP 62.4, PBA 3.0, C-black 0.5, Mica 0.5	N <sub>2</sub> 21, CO <sub>2</sub> 17, H <sub>2</sub> O 30, H <sub>2</sub> 11, CO 13, KCl(s) 32.6 g	2646	1421	1.86	2.44	>6.4	ND

In addition to its high nitrogen content, BTATZ has a high burn rate with a low pressure exponent and burns well even without any added oxidizer. This is attractive because addition of oxidizer leads to a much hotter effluent gas mixture as the product. In contrast, 5AT does not sustain combustion at atmospheric pressure and requires added oxidizer and significant pressure to a burn steadily.

BTATZ was included in several formulations in combination with 5AT in an attempt to increase the efficiency of combustion while keeping oxidizer content to a minimum. A composition with 10 % KP has a very low dependence of burn rate on pressure, with a calculated combustion temperature of approximately 1700 K, and yields over 4 mol gas/100 g, nearly 60 % of which is N<sub>2</sub>.

A concern in most of these compositions is the high fraction of un-oxidized gases in the exhaust. Hydrogen levels are typically in the 10 % to 30 % range, with CO levels 5 % to 10 %. Although these gases are always diluted in N<sub>2</sub>-dominated exhaust, their presence would seem to represent a challenge in suppression applications. The CO levels would render their use unattractive in occupied spaces.

Over the range 6.89 MPa to 18.9 MPa the pressure exponent for formulation 5AT/BTATZ-3 is 0.5 and decreasing. This formulation is a promising candidate as the burn rate is relatively high at low pressures and has a decreasing pressure dependence of the burn rate. Formulations BTATZ-2 and BTATZ-3 also exhibit ideal burning characteristics for gas generator applications with pressure exponents around 0.5 and with relatively high burn rates.

BTATZ and its blends offer the potential for SPGG formulations with higher gas output and cooler effluents at low pressure. Low-pressure operation offers the possibility of constructing hardware from lighter mass materials resulting in an overall significant reduction in mass of the system. Evaluation of these compositions did not result in truly applicable, cooler solid propellant fire extinguisher compositions. However, several of these compositions offered promise for applicability when additives are used to promote cooler exhaust gases.

### **Additives and Formulations for Cooler Exhausts**

The temperature of an otherwise hot solid propellant exhaust can be reduced if it is intermixed with a heat sink or cooling agent. This cooling agent can be included within the fuel-oxidizer blend, or it can be implemented externally to the combustion chamber. These two approaches are considered, in order, in this section.

Coolants are materials that undergo an endothermic reaction (or phase change) upon exposure to heat. Several endothermically active agents were considered, including MgCO<sub>3</sub>, Al(OH)<sub>3</sub>, CaCO<sub>3</sub> and hydrated clays. When dispersed within a propellant blend, these solids absorb heat and decompose endothermically, producing inert gases such as CO<sub>2</sub> and H<sub>2</sub>O. The combination of lower temperatures from heat absorption and inert gas production contributes directly to more effective fire suppression.

The effect of different coolants upon calculated adiabatic combustion temperature for fully-oxidized stoichiometric blends was calculated using the NAWSC PEP<sup>40</sup> thermodynamics code. The fuel-oxidizer blend (5AT- Sr(NO<sub>3</sub>)<sub>2</sub>) and mass fraction of coolant (40 %) were maintained constant for the different coolants. Relative effectiveness for heat absorption of the different coolants can be seen in Table 9–17 through the lowered adiabatic flame temperature. Magnesium carbonate was selected for the baseline propellant mixture because of its strong cooling performance. The benefits of other coolants are not

always realized in propellant formulation; aluminum hydroxide, for instance, while offering attractive cooling properties has the unattractive feature of excessive reduction in propellant burn rates. The calculated adiabatic flame temperature for calcium carbonate should be lower than that of  $MgCO_3$ ; this discrepancy suggests there are gaps in the thermodynamic reference data used in the PEP code. Note that relative heat absorption capabilities are less than the evaporative cooling from water, but can approach 80 % that of water in the case of calcium carbonate.

**Table 9–17. Effect of Different Coolants on Adiabatic Flame Temperature of 5AT-Sr(NO<sub>3</sub>)<sub>2</sub> Propellant Mixture.**

Coolant	Molecular Formula	Endothermic Process	$\Delta H$ , J/g	Density, g/cm <sup>3</sup>	$T_c$ , K
Magnesium carbonate	$MgCO_3$	decomposition to MgO	1390	3.05	1440
Aluminum Hydroxide	$Al(OH)_3$	decomposition to $Al_2O_3$	970	2.42	1480
Copper(II) Oxalate	$Cu(C_2O_4) \cdot 0.5H_2O$	decomposition to Cu	83	2.21	1910
Calcium Carbonate	$CaCO_3$	decomposition to CaO	1780	2.71	1440
Water	$H_2O$	evaporation	2260	1.00	not determined

The benefits of decreased exhaust temperatures are often offset by a decrease in the burn rate of the propellant, which in turn decreases the rate of suppressant delivery. This is illustrated in Figure 9–51, where  $\ln(BR_{1000})$  is plotted as a function of  $1/T_c$  for five proprietary formulations. The linear relationships indicate that an Arrhenius-type activated process is occurring, as might have been anticipated.

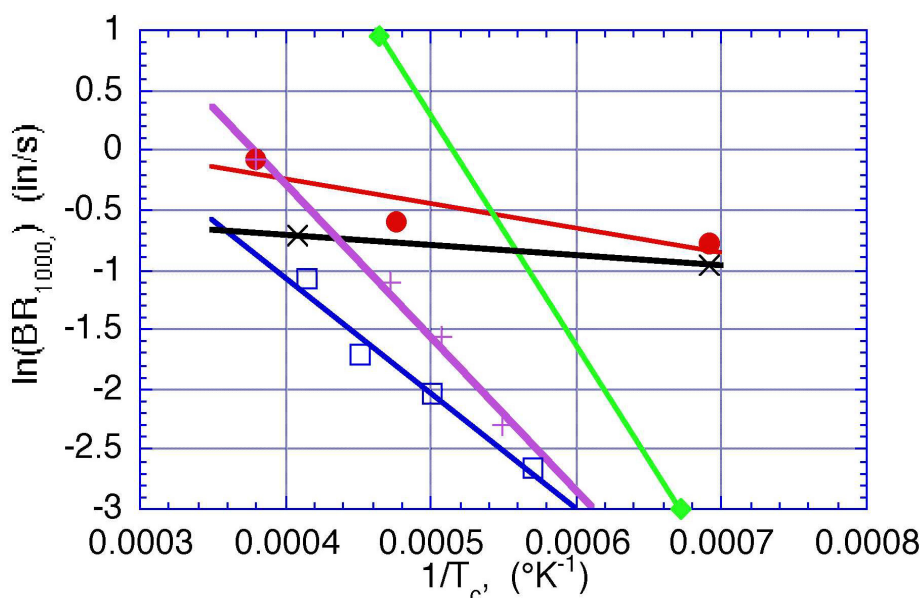


**Figure 9–51. Temperature Dependence of Propellant Burn Rates for Different FS01-40/additive Combinations.**

A number of high nitrogen component formulations based on BTATZ have been evaluated for their suitability in agent generation devices as a function of the amount of coolant added ( $MgCO_3$ ). The results are presented in Table 9–18 and in Figure 9–52. These data again illustrate the falloff in burn (agent generation) rate with decreased adiabatic combustion temperature.

**Table 9–18. High Nitrogen Content Developmental Propellants with MgCO<sub>3</sub> Coolant: Compositions and Burning Parameters.**

Propellant Composition (wt %)	Exhaust species (vol % @ T <sub>c</sub> )	Temperature (K)		Calculated Density (g/cm <sup>3</sup> )	Gas output (mol/100 g)	Measured BR <sub>1000</sub> (cm/s)	Measured Pressure exponent, n
		T <sub>c</sub>	T <sub>exh</sub>				
<b>Baseline:</b> 5AT, 21.9, Sr(NO <sub>3</sub> ) <sub>2</sub> 38.1, MgCO <sub>3</sub> 40.0	N <sub>2</sub> 45, CO <sub>2</sub> 35, H <sub>2</sub> O 20	1450	1000	2.55	2	1.27	0.5
<b>BTSN-00:</b> BTATZ 36.0, Sr(NO <sub>3</sub> ) <sub>2</sub> 63.0, PBA 3.0, C-black 0.5, Mica 0.5	N <sub>2</sub> 59, CO <sub>2</sub> 26, H <sub>2</sub> O 13	2770	1590	2.38	2.27	2.77	nd
<b>BTSN-10:</b> BTATZ 32.4, Sr(NO <sub>3</sub> ) <sub>2</sub> 56.6, PBA 3.0, C- black 0.5, Mica 0.5	N <sub>2</sub> 56, CO <sub>2</sub> 30, H <sub>2</sub> O 12	2560	1460	2.43	2.12	TBD	nd
<b>BTSN-20:</b> BTATZ 28.8, Sr(NO <sub>3</sub> ) <sub>2</sub> 50.3, PBA 3.0, C-black 0.5, Mica 0.5	N <sub>2</sub> 55, CO <sub>2</sub> 34, H <sub>2</sub> O 13	2260	1440	2.49	2.00	0.75	nd
<b>BTSN-30:</b> BTATZ 25.1, Sr(NO <sub>3</sub> ) <sub>2</sub> 43.9, PBA 3.0, C- black 0.5, Mica 0.5	N <sub>2</sub> 54, CO <sub>2</sub> 33, H <sub>2</sub> O 12	1890	1410	2.55	1.89	TBD	nd
<b>BTSN-40:</b> BTATZ 21.4, Sr(NO <sub>3</sub> ) <sub>2</sub> 37.6, PBA 3.0, C-black 0.5, Mica 0.5	N <sub>2</sub> 49, CO <sub>2</sub> 40, H <sub>2</sub> O 11	1500	1140	2.61	1.79	0.89	nd
<b>BTSN-50:</b> BTATZ 17.8, Sr(NO <sub>3</sub> ) <sub>2</sub> 31.2, PBA 3.0, C-black 0.5, Mica 0.5	N <sub>2</sub> 42, CO <sub>2</sub> 48, H <sub>2</sub> O 9	1444	964	2.67	1.54	0.38	nd

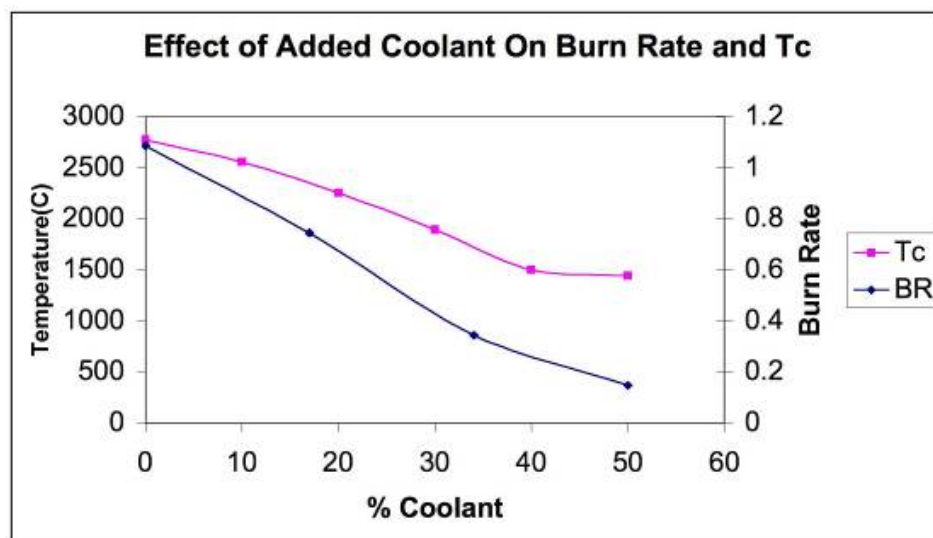


**Figure 9–52. Effect of Coolant Percentage on Burning Rate (in./s) and Adiabatic Temperature of High Nitrogen Propellants Listed in Table 9-18.**

The cooler, high gas output propellant compositions described in Table 9–18 represent an important step towards increased efficiency SPGG fire suppression devices. Gas temperatures were reduced in some

cases by up to 20 % when compared to the current baseline. The findings of increased burn rate compositions, while maintaining relatively low gas temperatures, provides a means for further increases in agent cooling when these compositions are further modified with endothermic chemical coolants. In general, the most successful energetic fuels were high in nitrogen, based upon BTAZ, with atomic N:C ratios of at least 3:1, as well as significant levels of unsaturation. These features combined to enable the cooler exhaust temperatures and N<sub>2</sub>-dominated exhaust gases at the expense of the more exothermic CO, CO<sub>2</sub>, and H<sub>2</sub>O.

The relative fire suppression effectiveness of some of these new, cooled solid propellant fire extinguisher compositions was not evaluated in this program due to excessive costs associated with addressing US Department of Transportation (DoT) restrictions on the shipping of energetic BTATZ materials from where they were prepared (China Lake, California) to where they were to be tested in the FTF (Redmond, Washington). A DoT classification requires several kg of propellant for testing, with its associated costs, plus the fees for DoT witnessing and licensing.

Further testing of BTATZ blends in the FTF is certainly warranted due to the potential of these materials to produce lower temperature products. In addition, it is necessary to confirm that, because of the relatively high hydrogen levels in the exhaust of some of these blends, the presence of H<sub>2</sub> does not diminish suppression effectiveness. China Lake presented calculations that the H<sub>2</sub> did not promote additional combustion; experiments to validate these have not yet been conducted.

### 9.3.6 Results: Chemically Active Fire Suppressants

#### Candidate Active Agents

The great fire suppression effectiveness of halon 1301 is due largely to its combination of high chemical activity and ease of dispersion (Chapter 8). Many other bromine- and iodine-containing compounds would have similar chemical effectiveness, but disperse less effectively due to significantly higher boiling points.

In addition, there are other compounds known to be effective fire suppressants, including some "superagents" which exhibit fire suppression effectiveness much greater than halon 1301 (Chapter 3).<sup>51</sup> The foremost example of these agents is iron pentacarbonyl, Fe(CO)<sub>5</sub>, but other examples include chromyl chloride, CrO<sub>2</sub>Cl<sub>2</sub>, and tetraethyl lead, Pb(C<sub>2</sub>H<sub>5</sub>)<sub>4</sub>. These agents have very high boiling points and are highly toxic, and so are not used in general suppression applications.

Solid propellant compositions offer a potent means of delivering such chemically active materials to a fire. These chemicals can be incorporated directly into the propellant composition. Upon combustion of the solid propellant, its product gases carry the additive and its radical-trapping reaction products into the fire zone. To enable testing of this concept in SPGG formulations, a broad review of potential candidates was undertaken in this project, including the examples presented in Table 9–19.

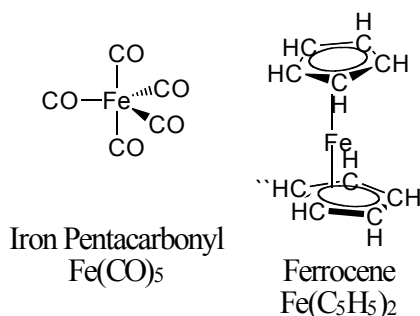
Among halide-containing species, Br- and I-containing compounds were considered to offer the most promise. Among these compounds, the alkali-metal salts offered appealing combinations of availability, and volatility; further, those potassium-based halides appeared to offer the most suitable levels of hygroscopicity – where low moisture-affinity is desired.

**Table 9–19. Candidate Chemically Active Agents.** (Data from References 52, 53)

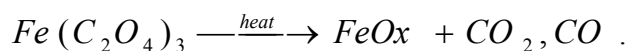
Compound	Active Species	MP (°C)	BP (°C)	Comments
<b>HALOGEN VEHICLES</b>				
NaI	I	660	1304	deliquescent powder
KI	I	681	1330	
KIO <sub>3</sub>	I	560		sometimes used as propellant oxidizer; partial decomposition at MP, releasing O <sub>2</sub>
NaBr	Br	747	1390	forms a dihydrate - NaBr·2H <sub>2</sub> O
KBr	Br	734	1435	
C <sub>12</sub> Br <sub>10</sub> O	Br	294	unknown	
NaCl	Cl	801	1413	
KCl	Cl	770	1500 sublimes	
KClO <sub>4</sub>	Cl	610 (controlled conditions)		used frequently as a propellant oxidizer; decomposes at 400 °C
<b>ALKALI VEHICLES</b>				
CaCl <sub>2</sub>	Ca	772 anhy	1935 anhy	forms mono-, di-, tetra-, & hexahydrates; highly hygroscopic
LiBr	Li	550	1265	forms mono-, di-, and trihydrates
LiCl	Li	605	1360	
LiI	Li	449	1180	forms mono-, di-, and trihydrates
RbBr	Rb	693	1340	
RbCl	Rb	718	1390	
RbI	Rb	647	1300	
Na <sub>2</sub> CO <sub>3</sub>	Na	851	decomposition	forms mono- and decahydrates; begins to loosen CO <sub>2</sub> well before melting
K <sub>2</sub> CO <sub>3</sub>	K	891	decomposition	
Li <sub>2</sub> CO <sub>3</sub>	Li	723	1310 (decomp.)	
Rb <sub>2</sub> CO <sub>3</sub>	Rb	837	900 (decomp.)	very hygroscopic; readily forms monohydrate
NaHCO <sub>3</sub>	Na	50 (decomp.)		begins to lose CO <sub>2</sub> at 50 °C; converts to Na <sub>2</sub> CO <sub>3</sub> at 100 °C
KHCO <sub>3</sub>	K	>100		Decomposition
LiHCO <sub>3</sub>	Li	no data	No data	
RbHCO <sub>3</sub>	Rb	no data	No data	
NaNO <sub>3</sub>	Na	308	380	
KNO <sub>3</sub>	K	334	400 (decomp.)	evolves O <sub>2</sub> at decomposition
LiNO <sub>3</sub>	Li	264	600 (decomp.)	hygroscopic
RbNO <sub>3</sub>	Rb	305		
NOAC	Na	58		decomposition, forms trihydrate
KAc	K	292		deliquescent crystals
LiAc	Li	70	decomposition	
RbAc	Rb	246		hygroscopic
Na <sub>2</sub> SO <sub>4</sub>	Na	884		forms a decahydrate; hygroscopic
K <sub>2</sub> SO <sub>4</sub>	K	1069	1689	
Li <sub>2</sub> SO <sub>4</sub>	Li	845 subl		forms a monohydrate

Compound	Active Species	MP (°C)	BP (°C)	Comments
Rb <sub>2</sub> SO <sub>4</sub>	Rb	1050		
<b>TRANSITION METAL (Iron) VEHICLES</b>				
FeO	Fe <sup>+2</sup>	1377		readily oxidizes to Fe <sub>3</sub> O <sub>4</sub> ; insoluble in H <sub>2</sub> O
Fe <sub>2</sub> O <sub>3</sub>	Fe <sup>+3</sup>	1565		insoluble in H <sub>2</sub> O
Fe <sub>3</sub> O <sub>4</sub>	Fe <sup>+2</sup>	1594		insoluble in H <sub>2</sub> O
Fe(C <sub>2</sub> H <sub>5</sub> ) <sub>2</sub>	“Fe”			ferrocene
Fe <sub>2</sub> (CO) <sub>9</sub>		100 (decomp.)		iron nonacarbonyl; toxic
Fe <sub>3</sub> (CO) <sub>12</sub>		140 (decomp.)		iron dodecacarbonyl; toxic
FeCl <sub>2</sub>	Fe <sup>+2</sup>	677	1023	forms di- and tetrahydrate; hygroscopic
FeCl <sub>3</sub>	Fe <sup>+3</sup>	306	315 (decomp.)	hygroscopic

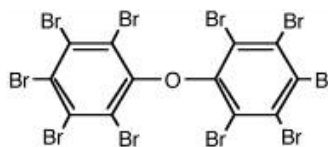
Fe(CO)<sub>5</sub> was considered too hazardous for handling in the Aerojet test fixture due to its toxicity and the large scale of the test fixture. Alternative vehicles for the iron atom were considered, including ferrocene, bis(cyclopentadienyl)iron, and Fe(C<sub>5</sub>H<sub>5</sub>)<sub>2</sub>, shown here:



Additional iron-containing compounds that were considered included several oxides and the oxalate. At elevated temperatures, the oxalate is known to decompose according to



Decabromodiphenyl ether (DBPE) was also investigated:



This material has been used in many plastic formulations as a flame inhibitor. On thermal degradation, C-Br bond breakage results in formation of volatile Br compounds.

### Suppression Effectiveness of Entrained Chemicals

Some of the candidate chemical agents were tested in the FTF to evaluate their effectiveness in fire suppression for a controlled JP-8 fire. The agents were delivered into the fire zone using the slow discharge SPGG displayed in Figure 9–40, whereby powdered candidate agents were entrained by high-

temperature exhaust gases produced by a neutral-burning solid-propellant gas generator producing a blend of CO<sub>2</sub>, N<sub>2</sub>, and H<sub>2</sub>O with constant discharge rate of exhaust gases to carry the candidates into the fire. Discharge rates for this testing were purposefully slow in order to minimize strain and mixing effects associated with rapid SPGG discharges. A representative discharge (pressure-time) profile for these tests is presented in Figure 9–53.

Initial tests of this type used a coolant bed to support the candidate agents. Aqueous solutions of the candidate were mixed with the coolant material (magnesite, 6 mesh to 10 mesh) and heated until the water had evaporated. This yielded loadings of  $\approx 20\%$  candidate agent on magnesite. The fraction of agent carried to the fire could again be controlled by varying a downstream orifice leading to ambient.

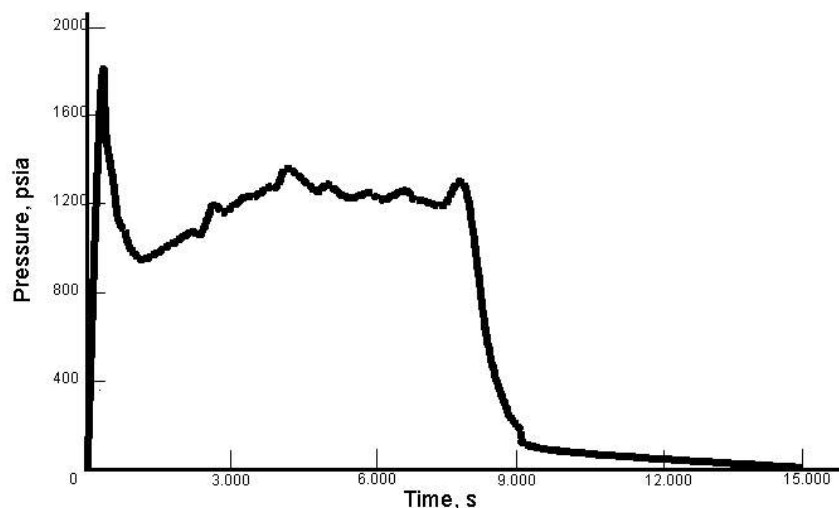


**Figure 9–53.**  
**Representative SPGG**  
**Pressure-time Curve**  
**Obtained During Delivery**  
**of Candidate Chemically**  
**Active Agents.**

An alternate approach gave more reproducible performance. In this case, powdered candidate agents were supported on a metal grid in the downstream chamber that formerly housed the coolant bed. Upon activation of the gas generator, the resultant exhaust would pass thru the chamber and entrain the powder and carry it to the fire. Test results using the latter method are shown in Table 9–20.

**Table 9–20. Summary of SPGG Fire Suppression Testing with Chemically Active Agents.**

Agent	Mass, g	Test No.	Result	Agent	Mass, g	Test No.	Result
<b>KI</b>	20	027-06	fire not out	<b>Fe<sub>2</sub>O<sub>3</sub></b>	40	038-01	fire not out
	40	027-07	fire not out		80	038-02	fire not out
	40	027-05	fire out				
	60	027-04	fire out				
<b>KBr</b>	40	032-02	fire not out	<b>Ferrocene</b>	40	039-01	fire not out
	60	032-03	fire not out		80	039-02r	fire not out
	60	032-01	fire not out				
<b>K<sub>2</sub>CO<sub>3</sub></b>	20	035-03	fire not out	<b>Iron Oxalate</b>	40	040-01	fire not out
	40	035-02r	fire out				
	60	035-01	fire out	<b>DBPE</b>	60	041-01	fire not out

The iron-based agents and DBPE were less effective than KI and K<sub>2</sub>CO<sub>3</sub>, at least within Aerojet's FTF. The results also indicated that K<sub>2</sub>CO<sub>3</sub> and KI were more effective than KBr. The threshold amount for

successful fire extinguishment seemed to be around 40 g of neat  $K_2CO_3$  or KI powder used in each solid propellant extinguisher.

The similarity in performance between the iodide and the carbonate reflects the observations in turbulent spray burner testing;<sup>54</sup> those data were interpreted as reflective of the greater role of the potassium ion in suppression effectiveness rather than the anion. A possible explanation for this trend is the more facile vaporization of the chemically relevant potassium species from the  $K_2CO_3$ . This is inconsistent with the higher melting point of  $K_2CO_3$  vs. KI (891 °C vs. 681 °C), but may be consistent at higher temperatures where  $K_2CO_3$  decomposes before boiling whereas KI melts without decomposing at 1330 °C. Another possibility is that there is an antagonistic interaction between the halogen and alkali metal species in the flame region.

Testing with ferrocene yielded some unexpected results. Based on its chemical similarity to iron pentacarbonyl, ferrocene would be expected to be a potent suppressant. However, multiple tests in which powdered ferrocene was swept into the hot solid propellant exhaust did not result in fire suppression when loads were increased to levels well in excess of the KI, KBr, or  $K_2CO_3$  suppression loads. Furthermore, ferrocene delivery was accompanied by growth of needles of ferrocene crystals on the exit port of the delivery tube. These findings imply that the ferrocene is quite stable in air/combustion conditions, and further that this material could not be entrained for a sufficient length of time into the flame zone. Iron oxide, likewise, was ineffective as an active suppressant. While only one test with iron oxalate was attempted with a 40 g load, the results did not indicate that this iron-containing compound could reach superagent status in this mode of operation.

The lesser performance of the iron- and decabromo-containing species, known to be excellent flame inhibitors in other circumstances, indicates that an adequate agent delivery mechanism needs to be carefully designed and implemented in the solid propellant fire extinguisher in order to fully utilize the chemical capabilities of such agents.

### **Burning Characteristics of Active Propellant Compositions**

Chemical additives selected from Table 9–19 were incorporated into formulations wherein the chemically active agent is liberated upon combustion of the solid propellant, the exhaust consisting of inert gases plus entrained additives. These additives (or their precursors) were blended directly into the propellant, or the additive (or precursor) was blended into a hybrid fluid. Several compositions were developed, such that a common composition family evolved having different levels of additive. Burning properties of several of these compositions are summarized in Table 9–21. Compositions incorporating combustion inhibitors were demonstrated to burn efficiently and were subsequently shown to be effective in fire suppression. The incorporation of species to suppress fires did not prevent combustion of the propellant.

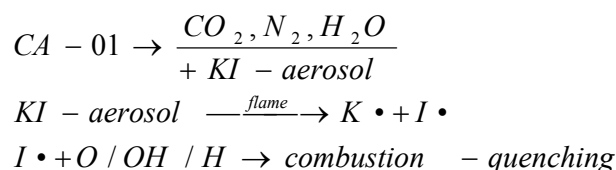
**Table 9–21. Chemically Active Developmental Propellants.**

Propellant Composition (wt %)	Exhaust species (vol % @ T <sub>c</sub> )	Temperature (K)		Calculated Density (g/cm <sup>3</sup> )	Gas output, mol/100 g	Measured BR <sub>1000</sub> (cm/s)	Measured Pressure exponent, n
		T <sub>c</sub>	T <sub>exh</sub>				
<b>Baseline:</b> 5AT, 21.9, Sr(NO <sub>3</sub> ) <sub>2</sub> 18.1, MgCO <sub>3</sub> 40.0	N <sub>2</sub> 45, CO <sub>2</sub> 35, H <sub>2</sub> O 20	1450	1000	2.55	2.00	1.27	0.5
<b>CA-01:</b> 5AT 17.2, Sr(NO <sub>3</sub> ) <sub>2</sub> 30.0, MgCO <sub>3</sub> 30.0, KI 21.3, Graphite 0.5	N <sub>2</sub> 47, CO <sub>2</sub> 31, H <sub>2</sub> O 22	1450	970	2.66	1.47	1.27	0.55
<b>CA-02:</b> 5AT 20.8 , Sr(NO <sub>3</sub> ) <sub>2</sub> 36.2, MgCO <sub>3</sub> 38.0, K <sub>2</sub> CO <sub>3</sub> 5.0	N <sub>2</sub> 47, CO <sub>2</sub> 31, H <sub>2</sub> O 22 KI 21.3 g 0.13 mol K	1440	1200	2.54	1.67	1.40	0.48
<b>CA-03:</b> 5AT 20.0, Sr(NO <sub>3</sub> ) <sub>2</sub> 34.7, MgCO <sub>3</sub> 36.4, K <sub>2</sub> CO <sub>3</sub> 8.9	N <sub>2</sub> 47, CO <sub>2</sub> 31 H <sub>2</sub> O 22, <b>K<sub>2</sub>CO<sub>3</sub> 9.0 g</b> <b>0.13 mol K</b>	1450	1210	2.54	1.78	1.32	0.59
<b>CA-04:</b> 5AT 19.7 Sr(NO <sub>3</sub> ) <sub>2</sub> 34.3, MgCO <sub>3</sub> 36.0, K <sub>2</sub> CO <sub>3</sub> 10.	N <sub>2</sub> 47, CO <sub>2</sub> 32, H <sub>2</sub> O 22 K <sub>2</sub> CO <sub>3</sub> 10.0 g 0.15 mol K	1440	1110	2.54	1.75	1.27	0.44
<b>CA-05:</b> 5AT 17.52, Sr(NO <sub>3</sub> ) <sub>2</sub> 30.5, MgCO <sub>3</sub> 32.0, K <sub>2</sub> CO <sub>3</sub> 20.0	N <sub>2</sub> 47, CO <sub>2</sub> 31 H <sub>2</sub> O 22 K <sub>2</sub> CO <sub>3</sub> 20.0 g 0.30 mol K	1480	1180	2.52	1.55	0.64	0.77
<b>CA-06:</b> 5AT 22.1, Sr(NO <sub>3</sub> ) <sub>2</sub> 24.8, MgCO <sub>3</sub> 39.5, KNO <sub>3</sub> 13.1, Graphite 0.5	N <sub>2</sub> 47, CO <sub>2</sub> 31 H <sub>2</sub> O 22 K <sub>2</sub> CO <sub>3</sub> 9.0 g 0.13 mol K	1440	1100	2.44	1.61	1.04	0.66
<b>CA-07:</b> 5AT 22.1, Sr(NO <sub>3</sub> ) <sub>2</sub> 22.9, MgCO <sub>3</sub> 40.0, KNO <sub>3</sub> 15.0	N <sub>2</sub> 47, CO <sub>2</sub> 31, H <sub>2</sub> O 22 K <sub>2</sub> CO <sub>3</sub> 10.0g 0.15 mol K	1440	1090	2.42	1.78	1.62	0.52
<b>CA-08:</b> 5AT 22.1, Sr(NO <sub>3</sub> ) <sub>2</sub> 22.9, MgCO <sub>3</sub> 40.0, KNO <sub>3</sub> 30.0	N <sub>2</sub> 47, CO <sub>2</sub> 31 H <sub>2</sub> O 22 K <sub>2</sub> CO <sub>3</sub> 20.0 g 0.30 mol K	1470	990	2.30	1.79	.68	1.77
<b>CA-09:</b> 5AT 21.9, Sr(NO <sub>3</sub> ) <sub>2</sub> 38.1, MgCO <sub>3</sub> 34.5, Fe <sub>2</sub> O <sub>3</sub> 5.0 Graphite 0.5	N <sub>2</sub> 48, CO <sub>2</sub> 29, <b>H<sub>2</sub>O 33, Fe<sub>2</sub>O<sub>3</sub> 5g</b> <b>(0.06 mol Fe)</b>	1470	1100	2.59	1.88	1.62	0.62
<b>CA-10:</b> 5AT 81, KP 10, DBPE 5.0, PBA 3.0, C-black 0.5, Mica 0.5	N <sub>2</sub> 60, H <sub>2</sub> 28 CO 3, CH <sub>4</sub> 4 KCl(s) 2.0 g KBr(s) 5.4 g	1630	874	1.71	4.24	0.25	1.0
<b>CA-11:</b> 5AT 19.7, Sr(NO <sub>3</sub> ) <sub>2</sub> 34.3, MgCO <sub>3</sub> 36.0, DBPE 10.0	N <sub>2</sub> 42, CO <sub>2</sub> 30 H <sub>2</sub> O 11, H <sub>2</sub> 6	1440	853	2.57	1.76	nd	nd

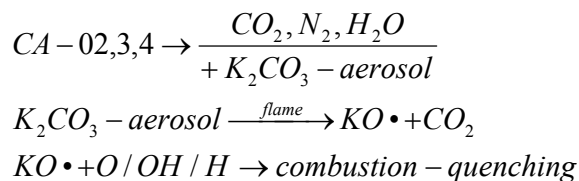
### Potassium-Containing Compositions

Three different approaches were used to incorporate potassium-containing species into propellant blends. These approaches built upon the agent testing efforts already described. The first blended potassium iodide directly into a propellant; the second blended potassium carbonate directly into a propellant, and the third used potassium nitrate blended into a propellant.

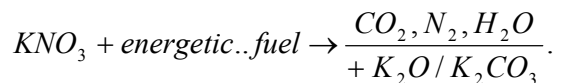
One potassium iodide-containing blend was made, labeled CA-01. This blend had an acceptable BR1000 and pressure exponent  $n$ . This composition was expected to obtain chemical activity by delivering KI aerosol, entrained in a  $CO_2$ ,  $N_2$ ,  $H_2O$  inert gas blend, to the fire, the KI then dissociating in the flame to produce combustion-radical-trapping  $I\bullet$  species according to:



Several potassium-carbonate-containing blends were made, where the mass of  $K_2CO_3$  in the blend was varied from 5 % to 20 %. The rationale for the varied levels of  $K_2CO_3$  was to probe this effect upon fire suppression effectiveness; i.e. varying the extent of chemically active agent within an otherwise nearly-common inert gas blend. All of these blends had acceptable burning properties, although at 20 %  $K_2CO_3$ , BR1000 was dropping to unattractively low levels at the same time that the pressure exponent,  $n$ , was increasing to unattractive levels. As such this propellant, as formulated, would not be ideally suited for commercial application. These compositions were expected to obtain chemical activity by delivering  $K_2CO_3$  aerosol, entrained in a  $CO_2$ ,  $N_2$ ,  $H_2O$  inert gas blend. The  $K_2CO_3$  would dissociate in the flame to produce combustion-radical-trapping  $I\bullet$  species according to:



In an attempt to counteract the fall-off in BR1000 observed in the 20 %  $K_2CO_3$ -containing blends, an alternative approach to potassium incorporation was investigated. Instead of direct incorporation of  $K_2CO_3$  into a propellant blend, we incorporated potassium nitrate ( $KNO_3$ , or KN). When blended into a propellant, KN is an oxidizer for fuels; the potassium product of this reaction is typically either the oxide,  $K_2O$ , or the carbonate,  $K_2CO_3$ :



For the cooled propellant blends under consideration here, the dominant K-containing species is expected to be  $K_2CO_3$ . Hence for K-containing blends based on KN,  $K_2CO_3$  aerosols can also be expected, with KN offering the possibility of circumventing the undesirable burn rates obtained in the higher percentage  $K_2CO_3$  blends. One caveat necessary to keep in mind when comparing the carbonate and the nitrate blends is that the use of KN requires that its oxidizing power be offset by a comparable amount of fuel in

order to maintain the desired CO<sub>2</sub>, N<sub>2</sub>, H<sub>2</sub>O inert gas exhaust blend; this offset is minimal and straightforward to achieve.

The KN-containing blends are listed as CA-6, CA-7, and CA-8 in Table 9–21. At lower levels, these KN blends yielded materials having suitable burning parameters. Unfortunately, attempts to obtain usable quantities of blends containing higher levels of KN (e.g., CA-8) were repeatedly thwarted by a combination of poor burning characteristics and/or poor processability.

### ***Iron-Containing Additives***

As mentioned previously, iron pentacarbonyl Fe(CO)<sub>5</sub>, was not blended into any propellant formulations because of its high toxicity. Ferrocene and its derivatives have been reportedly used in various propellants as burn rate modifiers with great success. However these formulations displayed unsuitable thermal stability. The ferrocene derivatives tended to migrate to the surface of the propellant, where they are oxidized to ferrocenium compounds. Ferrocenium derivatives in combination with propellant ingredients give friction sensitive materials. This limits the use of ferrocene derivatives to hybrid systems where the propellant and the additive are stored separately.

Iron oxide containing formulations do not have the drawbacks of iron pentacarbonyl and ferrocene mentioned above. Although definitive results were not obtained in this project, the routes explored to date involving iron oxide containing discharges have yielded burning characteristics that suggest further study is warranted.

### ***Decabromodiphenyl Ether***

Propellant compositions were formulated both with and without decabromodiphenyl ether (DBPE), added as a chemically active flame inhibitor, and these formulations underwent preliminary burning characterization. Composition CA-11 in Table 9–21 did not have suitable burning properties, with the effect of the DBPE to slow the burn rate and increase the pressure exponent. DBPE was also formulated into a 5AT-Sr(NO<sub>3</sub>)<sub>2</sub>-MgCO<sub>3</sub> blend (CA-11). These formulations were evaluated thermodynamically but not reduced to practice due to lack of resources and because of concerns with regard to DBPE handling during propellant processing and corrosivity during DBPE application.

## **Suppression Effectiveness of Chemically Active Propellant Compositions**

Chemically active propellant compositions were prepared in kilogram quantities to provide sufficient material for repeated testing. Propellant was typically pressed into 12.7 mm diameter x 6.4 mm thick tablets. The tablets were loaded into heavy mass, refurbishable gas generators, with some booster propellant ignition aid added, and then fitted with pyrotechnic initiators. Upon activation, the initiator ignites the booster propellant and then the main propellant. The internal pressure rises (Figure 9–54) until it exceeds the burst pressure of the material sealing the orifices of the device; this occurs at approximately 6.9 MPa. Internal pressures continue to rise, reaching a maximum of up to 10 MPa before the propellant completes its burn. Complete discharge of the agent from the SPGG is achieved within about 200 ms of initiation. Acceptable discharge times were achieved provided the pressures were maintained in the 6.8 MPa to 13.6 MPa range. Representative FTF pressure-time curves showing the impact of the SPGG discharge on the fixture pressure are shown in Figure 9–55 for two successful and one unsuccessful suppression event using the CA-04 propellant formulation.

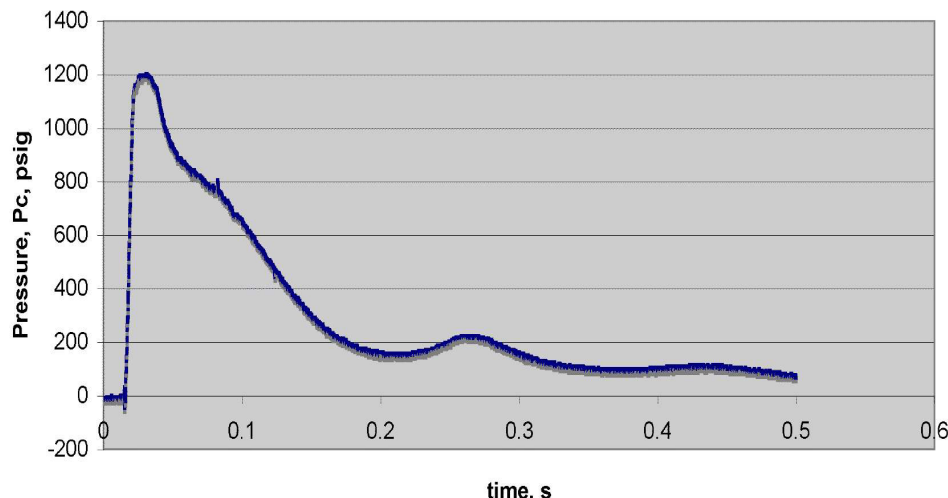


**Figure 9–54.**  
**Representative P-t**  
**Curve for SPGG**  
**Chamber**  
**Pressure.**

Peak SPGG chamber pressures below 6.8 MPa did not in general yield reproducible discharge behavior, and peak pressures much above 10.2 MPa in general yielded too rapid a discharge event and sometimes SPGG over pressurization (and rupture). The target peak pressure was 10.2 MPa, which yielded a discharge time of  $\approx 100$  ms. For ease of test turnaround, SPGG orifices for maintaining this sort of discharge rate were modeled after Aerojet proprietary designs used in the V-22/F-18 fire suppression systems. These designs use several different orifice diameters ranging from 2 mm to 4.8 mm with burst seal material consisting of 0.1 mm aluminum. Total orifice area was 168 mm<sup>2</sup> for a 210 g test SPGG. This total area is scalable to larger and smaller SPGG sizes.

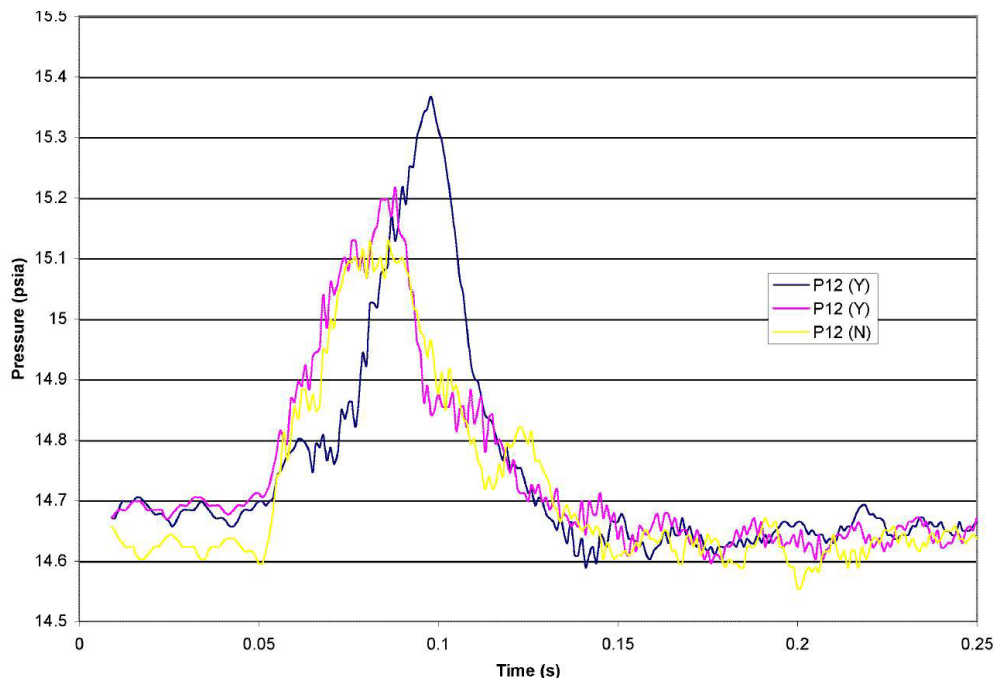


**Figure 9–55.**  
**Representative**  
**P-t Curve for**  
**Fire Test**  
**Fixture**  
**Pressure**  
**before, during,**  
**and after**  
**SPGG**  
**discharge.**

Figure 9–56 summarizes the test results and shows how the test configurations compare on a total agent mass basis and also on a K-molar basis. FTF testing with various inert and chemically active solid propellant compositions demonstrated that incorporation of 0.1 % additive (expressed as a fraction of the gaseous molar output) into inert fire suppressants has a dramatic positive effect on fire suppression

efficiency. The otherwise similar propellant compositions examined during this testing indicated a 50 % to 70 % (by mass) reduction of agent loading for suppression of identical fires when the propellant composition contained as little as 0.1 %. On an equimolar basis, potassium carbonate appears to be a more effective chemical additive than potassium iodide. Table 9–22 summarizes the threshold values of the most promising active agents. The threshold is defined as the amount of agent needed to extinguish the fire in the FTF at least two out of three times. Typically, three tests were conducted at the threshold amount and three additional tests were conducted at an agent load greater than the threshold amount.

The results indicate that  $K_2CO_3$  and KI yield significantly improved suppression effectiveness when compared to the inert propellant composition. For a composition containing 0.1 mole KI per 100 g propellant, the threshold propellant load was  $\approx 45$  % that of the baseline inert propellant composition, given similar discharge conditions and mass flows. A composition containing a similar amount of  $K_2CO_3$  (0.1 mole K per 100 g propellant) required only 30 % of the mass of the baseline propellant.

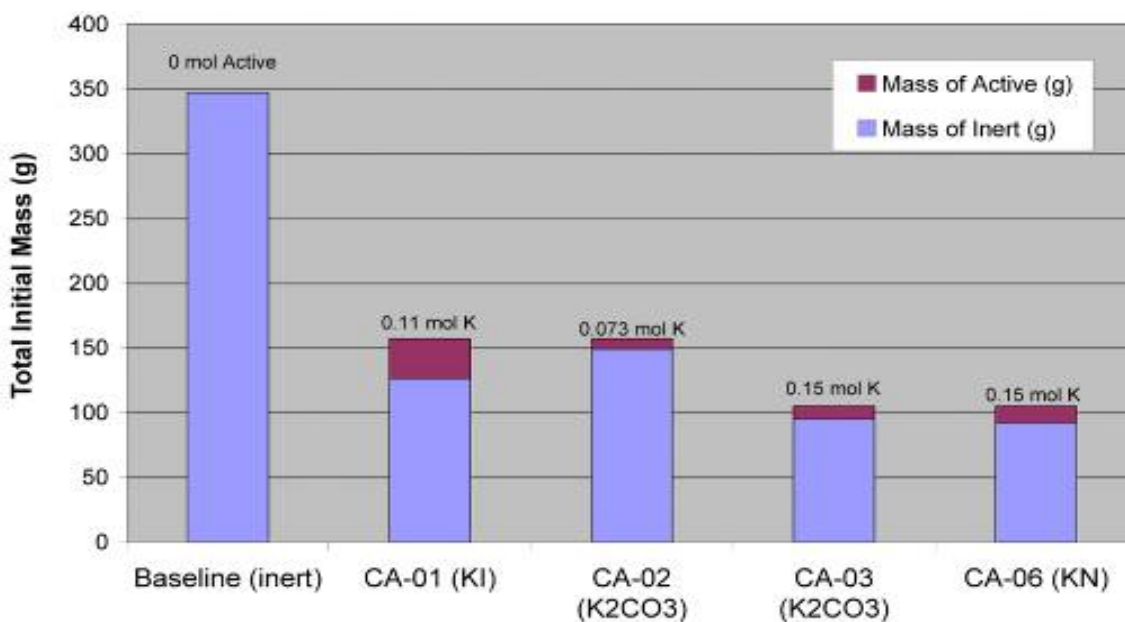


**Figure 9–56. Threshold Mass of Inert Propellant Plus Potassium Compound for Suppression in the FTF.**

The defined threshold level criterion of agent required for suppression (two out of three fires suppressed) was met for the baseline, CA-01, and CA-02 compositions; for CA-03 and CA-06, this criterion was exceeded and the fires were always suppressed, down to the minimum load capable for our equipment. This suggests that actual performance improvements for CA-03 and CA-06 were greater than a factor of three over the inert baseline propellant. A comparison of the suppression findings for CA-02 and CA-03 indicate that suppression effectiveness increased with higher levels of potassium content. CA-03 and CA-06, with comparable molar levels of potassium, appear to have similar suppression effectiveness. On the contrary, comparison of CA-01 with CA-02 suggests that the KI-containing composition (CA-01) may have some canceling contributions from the K and I portions of the additive.

**Table 9–22. Threshold Mass of Propellant and Potassium-based Additive for Fire Suppression in the FTF.**

Agent/Additive	Baseline/ none	CA-01/ KI	CA-02/ K <sub>2</sub> CO <sub>3</sub>	CA-03/ K <sub>2</sub> CO <sub>3</sub>	CA-06/ K <sub>2</sub> CO <sub>3</sub> (from KN)
Gas Fraction	50 %	50 %	50 %	50 %	50 %
MW, g/mole	30	30	30	30	30
Mole active (K)/100 g	0	0.127	0.073	0.145	0.145
Mole active (K) discharged	0	0.199	0.114	0.152	0.152
Threshold gas generator Load, g	347	157	157	105	105
Powder discharge mass, g (Threshold)	173.5	78.5	78.5	52.5	52.5

Table 9–22 and Figure 9–56 are subject to some uncertainty due to the nature of large-scale fire tests. The threshold quantity may not be a sharp line separating the regions between fire-out and fire-not-out, but more of a band due to variations in test parameters.

Larger pellets of the chemically active decabromodiphenyl ether formulation were burned and the temperature of the gaseous products measured. The SPGG outlet temperature was approximately 675 °C, which was in good agreement with the temperature predicted from thermochemical calculations. The chemically active formulation was found to be impact, friction and electrostatically insensitive. The PBDE formulations was able to successfully suppress a JP-8 pool fire in a small vented box, but was not able to suppress the JP-8 flame in the FTF at a loading of 60 g.

### 9.3.7 Results: Hybrid Fire Extinguishers

Hybrid Fire Extinguisher suppression effectiveness tests employed a set of re-usable “workhorse” generators, with size varying from 56 mL to 110 mL internal volume. A schematic of this test article is shown in Figure 9–57.

Exhaust orifices provided an outlet for the fluid; there were typically eight 3.1 mm to 3.4 mm orifices (oriented 90° apart on all four sides to ensure non-propulsive behavior) sealed with 0.05 mm thick Al 1100-T1 shim material. Propellant loads were typically 10 g to 20 g, and the nominal propellant:fluid mass loading ratio was 1:6 to 1:10.

The tests were conducted on combinations of the fluid suppressants listed in Table 9–23 with the following propellants: Baseline (FS-0140, inert); CA-01 (chemically active – KI); and CA-04 (chemically active – K<sub>2</sub>CO<sub>3</sub>). Halon 1301 was not tested, but is included in Table 9–23 for reference.

In order to ensure safe operation within the test fixture, all new propellant-fluid configurations underwent functional testing first to ensure proper performance of the propellant/fluid combination. These tests consisted of the assembly of the desired propellant/fluid combination, mounting the hybrid extinguisher unit in a vise anchored to a bench, and operating the hybrid extinguisher.

Accurate definition of threshold level loads for the hybrid extinguisher testing was found to be best accomplished using various combinations (single and/or different hybrid extinguisher sizes) mounted upstream of the flame in the test fixture, as shown in Figure 9–58. The results of hybrid extinguisher testing are presented in two separate categories: fluorocarbon systems and aqueous systems.

Hybrid Unit

Side View

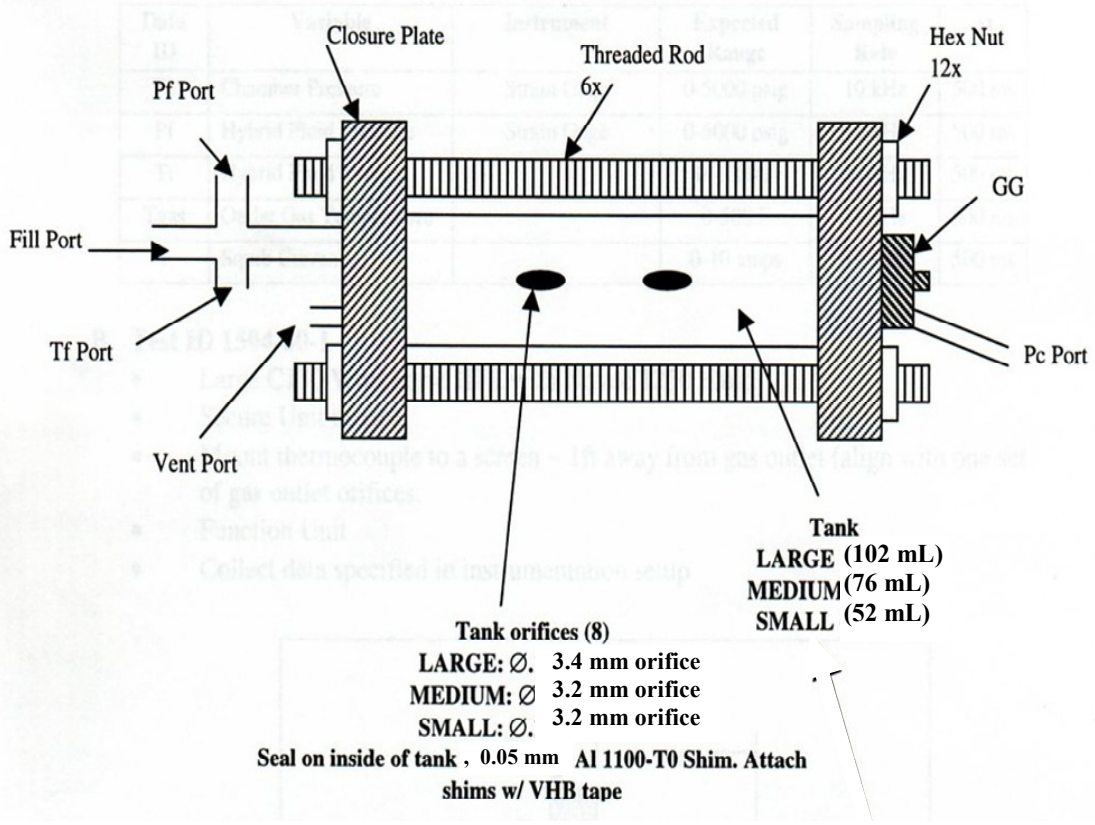


**Figure 9–57. Schematic of Hybrid Extinguisher Workhorse Hardware Configuration.**

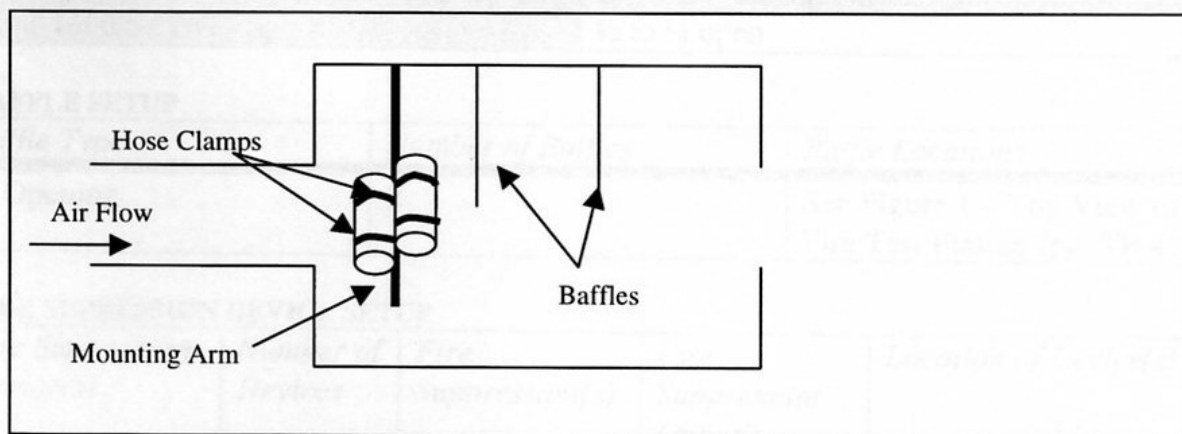


**Figure 9–58. Mounting Configuration of Multiple Hybrid Extinguishers Used to Bracket Threshold Levels.**

**Table 9–23. Properties of Hybrid Fluid Candidates.**

Property	Halon 1301	HFC-125	Water	HFC-227ea	HFE-7100	HFE-1230	CF <sub>3</sub> I
Chemical formula	CF <sub>3</sub> Br	C <sub>2</sub> F <sub>5</sub> H	H <sub>2</sub> O	C <sub>3</sub> F <sub>7</sub> H	C <sub>4</sub> F <sub>9</sub> OCH <sub>3</sub>	C <sub>6</sub> F <sub>12</sub> O	CF <sub>3</sub> I
Molecular wt.	149	120	18	170	250	316	196
Boiling pt.(°C)	-58	-48	100	-16	61	49	-21
Freezing point (°C)	-168	-102.8	0	-131	-135	-108	
Density @25° C (g/cm <sup>3</sup> )	1.55	1.19	1.00	1.4	1.52	1.6	2.1
Vapor pressure (kPa) @ 25° C	1510	1370	3	460	27	6	538
Specific heat (kJ/kg°C)		1.26	4.18	1.184		0.89	
(J/g) Heat of vaporization	117	113	2255	134	201	88	113
Cup-burner (vol %) fire extinguishing concentration	3.1	8.7	25 <sup>#</sup>	6.5	6	5	3.1
Fire extinguishing design concentration (g/m <sup>3</sup> )	305	516		590		776	401
Ozone depletion potential (relative to CFC-11)	12	0	0	0	0	0	0.0001
Global warming potential (relative to CO <sub>2</sub> )	5400	2800	0	2900	320	1	<5
Atmospheric lifetime (yr)	65	33	n/a	37	4.1	0.014	<0.005
Cardio-sensitization LOAEL (vol%)	10	10	n/a	10.5		10	0.4
Cardio-sensitization NOAEL (vol%)	7	7.5	n/a	9		10	0.2
EPA SNAP approved for unoccupied	No	Yes	Yes	Yes	Yes	Yes	Yes

# assumes full recovery of enthalpy of vaporization

### Fluorocarbon Hybrid Extinguishers

The fluorocarbon test results are listed in Table 9–24. The threshold values were determined for the hybrid extinguisher initially at ambient temperature. The baseline hybrid extinguisher against which the other propellant/fluids were compared consisted of the FS-0140 propellant (21.9 % 5AT, 38.1 % Sr(NO<sub>3</sub>)<sub>2</sub>, 40.0 % MgCO<sub>3</sub>) with HFC-227ea fluid. The threshold suppression level for this baseline hybrid extinguisher was 358 g. (The fire suppression number (FSN) reported in the table is the ratio of the threshold determined for the other hybrid extinguisher combinations normalized by the baseline mass.) Replacing the HFC-227ea with HFE-1230 led to a similar threshold level. Interestingly, this threshold level value is nearly identical to the value obtained for testing of the FS-0140 propellant alone in a standard SPGG.

Hybrid extinguisher tests with HFE-7100 and a total load of 358 g did not extinguish the fire. Further testing with this agent was suspended since the amount of agent needed would have been more than the base system, with no particular advantage. In addition, measurements in the test fixture revealed higher bay pressures than the norm and the flame seemed to be enhanced by the fluid discharge.

**Table 9–24. Hybrid Extinguisher Fluorocarbon System Data Summary.**

Agent	FS-0140/ HFC- 227ea	FS-0140/ HFE/ 1230	FS-0140/ HFE- 7100	CA-01/ HFC- 227ea	CA-04/ HFC- 227ea	FS-0140/ HFC-227ea + KHCO <sub>3</sub>	FS-0140/ HFC- 227ea + NaHCO <sub>3</sub>	FS- 0140/ CF <sub>3</sub> I
Active additive	-	-	-	K <sub>2</sub> CO <sub>3</sub>	K <sub>2</sub> CO <sub>3</sub>	KHCO <sub>3</sub>	NaHCO <sub>3</sub>	CF <sub>3</sub> I
MW, g/mol	170	316	250	170	170	170	170	196
Load, g	358	358	-	228	228	265	228	98 <sup>b</sup>
Discharge mass, g	340	340	-	217	217	252	220	93
Mole (K or I) discharged	0	0	-	0.040	0.046	0.040	0.052	0.429
FSN	1	1	>1 <sup>a</sup>	0.637	0.637	0.740	0.637	0.274

a. Tests conducted using 358 g (same agent mass as the FS01-40/HFC-227ea system) did not extinguish the fire.

Testing was suspended since the amount of agent needed would be more than the baseline system.

b. Anticipated threshold value: two tests were conducted using 130 g (both fires out) and two tests were conducted using 98 g (one fire out, one fire not out).

Several combinations of chemically active hybrid extinguishers were tested. Combinations of the chemically active propellants CA-01 and CA-04 with HFC-227ea were found to yield  $\approx 40\%$  enhancement in performance when compared to the baseline hybrid extinguisher. This finding indicates that significant reductions in hybrid extinguisher agent levels can be achieved by combining chemically active solid propellant compositions with inert fire suppression agents.

Chemically active hybrid extinguishers were also constructed using the FS-0140 propellant with HFC-227ea plus the chemically active powders KHCO<sub>3</sub> and NaHCO<sub>3</sub> (potassium bicarbonate and sodium bicarbonate, respectively). These systems exhibited performance enhancement of about  $\approx 40\%$ , similar to the results from the CA-01/HFC-227ea and CA-04/HFC-227ea tests. Note that each of these chemically active hybrid extinguisher combinations maintained similar levels of chemically active additive (0.04 mol to 0.05 mol), implying that in each case the benefit of this chemical activity is independent of the form in which that additive is delivered.

Testing of the inert FS-0140 propellant with the chemically active suppressant CF<sub>3</sub>I resulted in the most effective hybrid combination, with an approximate threshold value  $\approx 25\%$  of the baseline propellant/fluid combination. This represents an approximate threshold value since two tests were conducted using 130 g (both fires out) and two tests were conducted using 98 g (one fire out, one fire not out), as opposed to the standard two-out-of-three successful fire suppression events used to define the threshold. Fire extinction coincided with the formation of brilliant purple smoke exhausting from the test fixture, evidence of the formation of elemental iodine, I<sub>2</sub>, fumes during the suppression process.

Hybrid extinguisher testing with CF<sub>3</sub>I proved problematic because this agent tended to dissolve common adhesives not affected by other fluids like HFC-227ea. Because some leakage of agent around/through the Mylar burst tape occurred during these tests, the burst shims were moved to outside the hybrid extinguisher, thereby minimizing exposure of the adhesive to CF<sub>3</sub>I.

An additional test of the 130 g FS-0140 propellant/CF<sub>3</sub>I hybrid extinguisher was conducted after cold soaking; the fire was successfully extinguished. In this test the hybrid extinguisher was conditioned to -65 °C; however, the CF<sub>3</sub>I temperature rose to -27 °C before the extinguisher was operated.

### Aqueous Hybrid Extinguishers

The results of the aqueous-based hybrid extinguisher combinations are summarized in Table 9–25.

**Table 9–25. Hybrid Extinguisher Aqueous System Data Summary.**

Agent	CA-01/ Water	CA-04/ Water	Baseline/ Water:KOAc:Soap <sup>b</sup>
Active additive	KI	K <sub>2</sub> CO <sub>3</sub>	KC <sub>2</sub> H <sub>3</sub> O <sub>2</sub>
MW, g/mol	18	18	30
Load	-	-	228
Discharge mass, g	-	-	217
Mole (K) discharged	-	-	0.96
FSN (Baseline/HFC-227ea)	>1 <sup>a</sup>	>1 <sup>a</sup>	0.637

a. Testing conducted using 358 g (same agent mass as the FS01-40/HFC-227ea system) did not extinguish the fire. Testing was suspended since the amount of agent needed would be more than the baseline system.

b. 48:48:4 mass ratio of water:potassium acetate:soap.

Tests conducted at ambient temperature using pure water with a total load of 358 g (same agent mass as the FS-0140/HFC-227ea system) did not extinguish the fire. Testing of hybrid extinguishers charged with chemically active CA-01 and CA-04 propellants in conjunction with pure water also did not successfully extinguish the fire with agent loads up to the baseline mass. Substituting a water-potassium acetate-soap (surfactant) blend (48:48:4 mass ratio) for pure water, and pressurizing with the CA-04 chemically active propellant did yield successful flame extinction at levels approximately 60 % that of the Baseline hybrid extinguisher. Potassium acetate, KO<sub>2</sub>CCH<sub>3</sub>, or “KOAc,” is a well known freezing point suppressant for aqueous solutions, and as it contains potassium ions, also contributes a chemically active agent to the suppressant mix. The improved performance of these KOAc blends vs. pure water is presumably due to the chemical activity contributed by the potassium; assuming this is the case, one would expect to see a range of performance thresholds for this hybrid extinguisher given variations in KOAc levels. However, testing of different levels of KOAc in water was not attempted in this effort as the focus was on KOAc loadings suitable for meeting typical low temperature performance requirements of -40 °C.

Testing of aqueous hybrid extinguishers was often plagued by poor performance/distribution of the agent. A frequent occurrence was the collection of puddles of water upstream of the flame zone in the FTF. While this means that flame suppression was accomplished with less than the full hybrid extinguisher load, it also means that the given test articles would benefit from design modifications to yield improved distribution, e.g., through use of screens to improve mixing of the SPGG exhaust with the fluid, or by varying the ratio of propellant to fluid.

### Summary of Hybrid Extinguisher Results

A summary of the hybrid extinguisher testing is presented in Figure 9–59. On a mass-to-mass basis, the inert hybrid extinguisher and SPGG systems appear to provide similar suppression protection, requiring

≈ 360 grams to suppress the 1 MW FTF fire. The higher molar efficiency of the hybrid testing reflects the higher molecular mass of the HFC-227ea. As in the pure SPGG, incorporation of chemically active species into the propellant improves the suppression efficiency for the hybrid extinguisher configuration. Testing conducted with  $\text{KHCO}_3$  added into the hybrid fluid of the system produced results similar (based on moles of K) to results with active agents (KI,  $\text{K}_2\text{CO}_3$ ) added into the propellant. This indicates that active additives in the hybrid fluid may be just as effective as active additives in the propellant.

Testing hybrid extinguishers with HFE-7100 and HFE-1230 did not lead to reductions in total propellant-plus-fluid mass (when compared to HFC-227ea), but it did demonstrate that higher boiling point fluids could be successfully discharged when pressurized by a solid propellant gas generator. This opens opportunities for alternate suppression fluids that, on the basis of vapor pressure alone, would not appear to be desirable candidates as fire suppressants.

The lowest hybrid extinguisher agent loads were found when using  $\text{CF}_3\text{I}$  as the hybrid fluid. Coupling this agent with a solid propellant gas generator also overcame the low temperature dispersion problem encountered in previous testing with conventional pressurized fire bottles.<sup>55</sup>

Hybrid extinguisher testing with aqueous agents provided additional insight into necessary levels of active agent required for suppression. Tests using an inert propellant configuration with pure water were found to require agent loads in excess of threshold levels of inert propellants and HFC-227ea. Similar findings were obtained when the active CA-04 propellant was used in conjunction with pure water. This relatively poor performance of the water hybrids is likely a function of insufficient distribution of the hybrid stream into the fire compartment of the FTF. However, while poor dispersion in the case of water-based hybrid extinguishers probably resulted in their lackluster performance, this effect was found to be offset by blending in potassium acetate.

The improvement found from the addition of chemically active species to the propellant mixture in the hybrid extinguisher systems (an approximate 36 % reduction in suppressant mass) appears to be less than that found in the SPGGs (70 %). Note, however, that the propellant is 100% of the total agent mass for the SPGG configuration, but only 14 % of the total agent mass for the hybrid extinguisher configuration, thus limiting the molar fraction of chemically active additive to ≈ 2 volume %. It is likely that if the amount of active additive in the hybrid extinguisher systems were optimized, these systems would show a mass reduction similar to the SPGG systems.

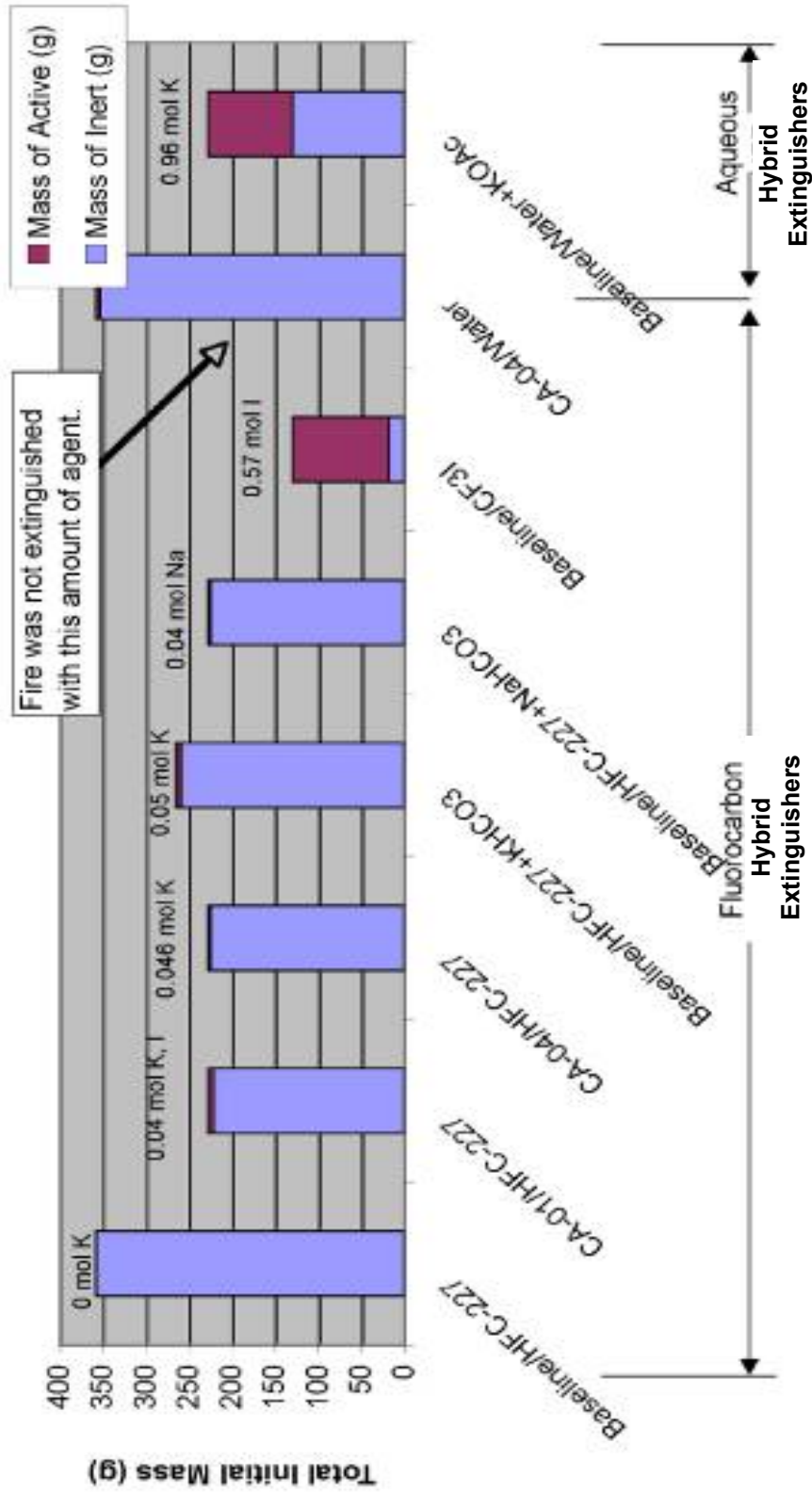


Figure 9-59. Effectiveness of Various Hybrid Extinguisher Propellant/fluid Combinations.

### 9.3.8 Summary of Solid Propellant Gas Generator Research

The Aerojet/NAWSC/NGP advances in solid propellant-based fire suppression technology include:

- Developing a methodology for screening candidate propellants.
- Developing a medium scale Fire Test Facility to evaluate alternative SPGG fire suppression technologies for a cluttered space such as a dry bay or engine nacelle.
- Scaling up the production of the high nitrogen propellant fuel, BTATZ, to half kilogram quantities.
- Calculating exhaust temperature and composition of new, high nitrogen propellants.
- Measuring burning rate and pressure exponent for these new, high nitrogen propellants.
- Tabulating the effect of different coolants on the effect of propellant burning rate and exhaust temperature.
- Examining the effect of various halogen, alkali, and iron compounds on fire suppression effectiveness of SPGG fire extinguishers.
- Determining the effectiveness of SPGG hybrid fire extinguishers using fluorocarbon and aqueous fluids.

Three different paths to cooler propellant compositions were demonstrated: by reducing the enthalpy of the combustion process through selection of various fuels/oxidizer blends; by altering the stoichiometry of the propellant reactions; and by seeking faster-burning solid propellant compositions, to which one could add coolant to reduce the overall exhaust gas temperature. Cooler propellant compositions have been used in conjunction with chemically active additives, or combustion radical scavengers. Adding radical traps to the exhaust provides means for cooling, dilution and chemical termination of the combustion process, hence increasing the overall effectiveness of the fire suppressant.

Propellant formulations incorporating the new high nitrogen compound BTATZ ( $C_4H_4N_{14}$ ) appear to provide increased means for reducing propellant combustion temperatures. The preparation of BTATZ has progressed to the half kilogram scale. This increased production capability plus the attractive burn rate and pressure sensitivity of BTATZ formulations make them good candidates for future work, including re-formulation with additional chemical coolants, as well as suppression effectiveness testing in the FTF. Direct incorporation of coolant species into the propellant composition reduced exhaust temperatures by as much as 30 % vs. current baselines.

Testing of propellant compositions containing potassium iodide and potassium carbonate as chemically active additives demonstrated enhanced effectiveness in the FTF as compared to chemically inert compositions. FTF testing with various inert and chemically active solid propellant compositions demonstrated that incorporation of 0.1 mole % additives into inert fire suppressants can have a dramatic effect upon suppression efficiency. The otherwise similar propellant compositions examined during this testing indicated a 50 % to 70 % reduction (by mass) of agent loading for suppression. On an equimolar basis, potassium carbonate appears to be a more effective chemical additive than potassium iodide. The greater effectiveness of potassium carbonate (vs. potassium iodide) may be related to more facile vaporization of the carbonate-based species after melting, or to an antagonistic interaction between the halogen and alkali metal species in the flame region.

Fire testing with chemically active compositions indicate that the CA-04 composition (20 % 5AT, 34 %  $\text{Sr}(\text{NO}_3)_2$ , 36 %  $\text{MgCO}_3$ , 10 %  $\text{K}_2\text{CO}_3$ ) is the most effective. This composition is three times more effective per unit mass than the inert baseline propellant (22 % 5AT, 19 %  $\text{Sr}(\text{NO}_3)_2$ , 60 %  $\text{MgCO}_3$ ), with no  $\text{K}_2\text{CO}_3$ . Testing with compositions of lower active-agent loading resulted in less effective performance. This indicates that the additive loading in CA-04 is below (or at) the saturation level reported in sub-scale testing with numerous other chemically active suppressants.

Testing of hybrid SPGGs with HFE-1230 indicates that high boiling point, low vapor pressure agents can be delivered efficiently to the fire zone by heating and pressurizing the liquid with an SPGG. Suppression tests with HFE-7100 were not as encouraging, and in fact resulted in flashback in fire tests. Both the HFE-1230 and HFC-227ea gave comparable results (on a mass basis) in fire suppression tests. Incorporation of  $\text{CF}_3\text{I}$  into a hybrid extinguisher proved convenient for overcoming poor cold-temperature dispersion. The water-based hybrid extinguishers did not perform as well as the fluorocarbon-based hybrid extinguishers; however, blending potassium acetate into the water was shown to significantly improve suppression effectiveness in the FTF.

On a mass basis, the inert hybrid extinguisher and SPGG systems appear to provide similar suppression protection. Incorporation of chemically active species into the hybrid extinguisher propellant improves the suppression efficiency. Testing conducted with additives incorporated into the hybrid fluid of the system produced results similar to results with active agents added into the propellant. This indicates that active additives in the hybrid fluid may be just as effective as active additives in the propellant.

Since initiation of this research in 1999, when inert SPGGs were installed in the first V-22 and F/A-18 dry bay fire protection systems, gas generator devices using advanced propellants and advanced additives have been demonstrated, developed and manufactured for three new platforms.<sup>56,57</sup> Developments in improved, chemically active SPGGs are being implemented over the course of 2005-2008 on the JSF F-35 dry bay fire protection system. Testing in 2005 validated the effectiveness of chemically active HFC-227ea hybrid devices in suppressing fires from ballistic events upon the US Army's M1114 HMMWV.

Figure 9-60 summarizes how the performance of SPGGs, as measured by suppression effectiveness, has improved over this period. This research has enabled system mass reductions by over a factor of two, with still greater reductions possible by optimizing the findings.

Finally, SPGG technology has also crossed over from military to civilian applications. Devices using chemically active, water-based hybrid extinguishers have moved from development to production and integration in commercial automobiles manufactured for the Ford Motor Company's Crown Victoria Police Interceptor.<sup>58</sup> A conceptual flow of this evolution and application is presented in Figure 9-61. (Note that in Figure 9-60 and Figure 9-61, the term "SPFE" for Solid Propellant Fire Extinguisher is used to distinguish these systems from a Hybrid Fire Extinguisher or "HFE.")

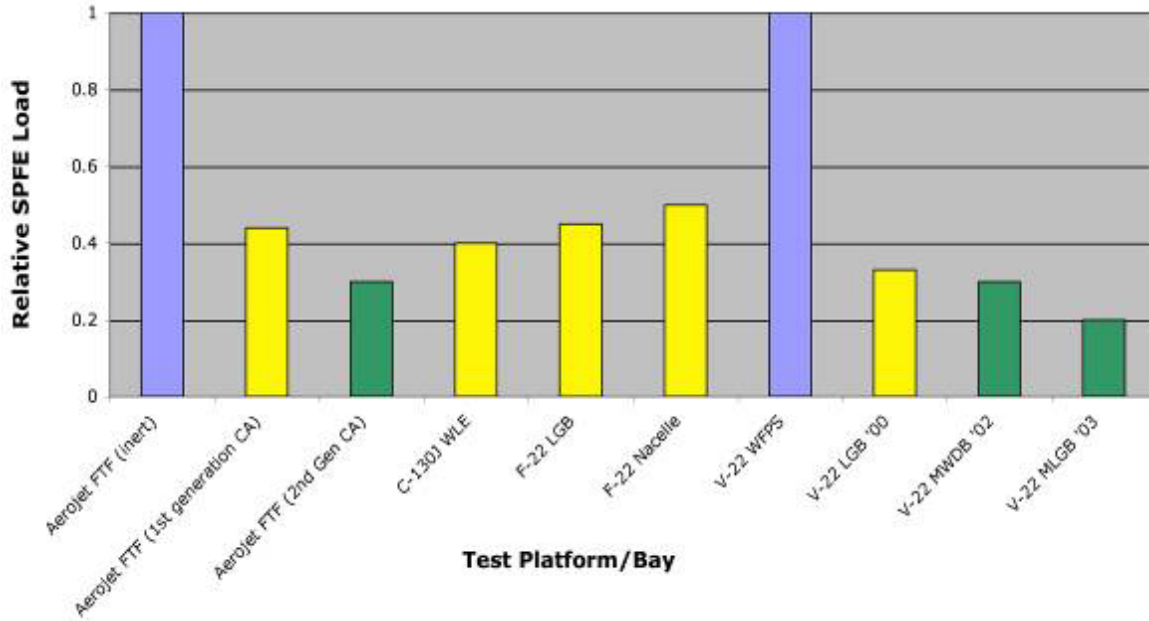


Figure 9–60. Relative Effectiveness of Various SPGG Fire Extinguishers over the Span of the NGP Research. Blue bars: inert effluent; yellow bars: 1<sup>st</sup> generation Chemically Active Systems; green bars: 2<sup>nd</sup> generation Chemically Active Systems.

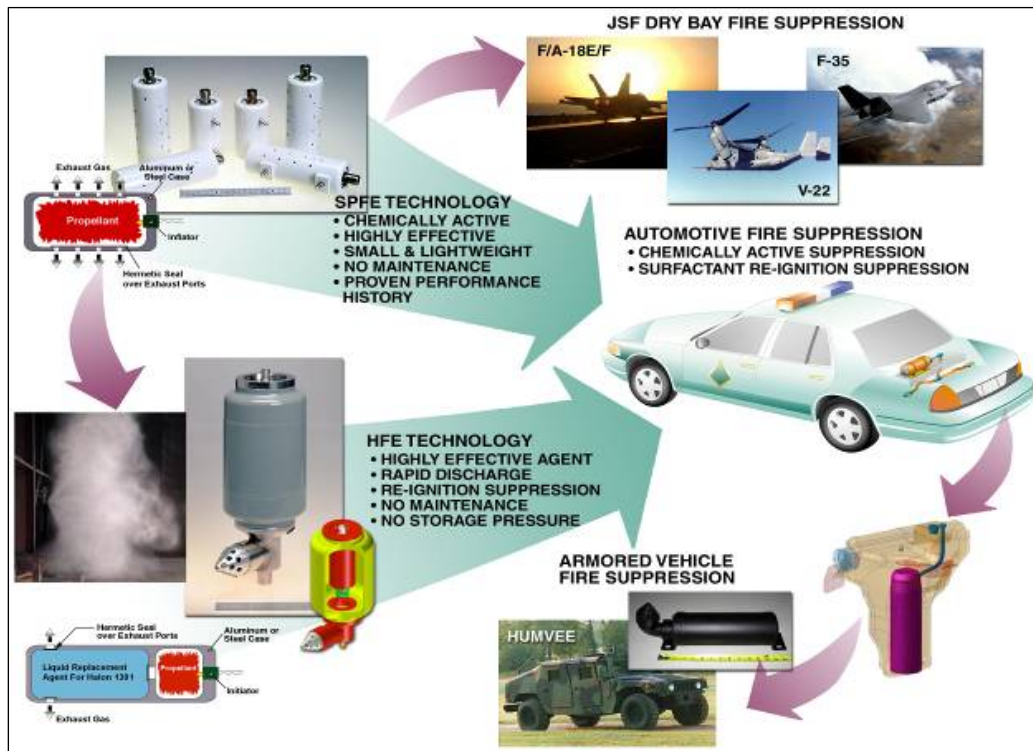


Figure 9–61. Evolution of SPGG Fire Suppression Application Technologies.

## 9.4 REFERENCES

1. Cyphers, D.C., *Enhanced Powder Panels: Final Technical Report*, report SKY-03-01, Skyward, Ltd, Dayton OH, December 2003.
2. Cyphers, D.C., Frederick, S.A., and Haas, J.P., "Enhanced Powder Panels," 2002, in Gann, R.G., Burgess, S.R., Whisner, K.C., and Reneke, P.A., eds., *Papers from 1991-2006 Halon Options Technical Working Conferences (HOTWC)*, CD-ROM, NIST SP 984-4, National Institute of Standards and Technology, Gaithersburg, MD, (2006).
3. Cyphers, D.C., Frederick, S.A., and Haas, J.P., "Demonstrating Enhanced Powder Panels," 2003, in Gann, R.G., Burgess, S.R., Whisner, K.C., and Reneke, P.A., eds., *Papers from 1991-2006 Halon Options Technical Working Conferences (HOTWC)*, CD-ROM, NIST SP 984-4, National Institute of Standards and Technology, Gaithersburg, MD, (2006).
4. Seymour, T.J. and Ellenwood, P.S., *Powder Pack Fire Protection for Aircraft Dry Bays*, AFWAL-TR-84-3119, June 1985.
5. Pascal, A., *B-1B LFT&E Dry Bay Fire Test Series Data Analysis*" (U), Enthalpy Corporation, June 1997.
6. Finnerty, A.E., Vande Kieft, L.J., and Drysdale, A., *Physical Characteristics of Fire-Extinguishing Powders*, ARL-TR-1450, Army Research Laboratory, August 1997.
7. Ewing, C.T., Highes, J.T., and Carhart, H.W., "The Extinction of Hydrocarbon Flames Based on the Heat-absorption Processes That Occur in Them," *Fire and Materials* **8**, 148-156, (1984).
8. Dolan, J.E., "The Suppression of Methane/Air Ignitions by Fine Powders," *Proceedings of the Combustion Institute* **6**, 787-801, (1957).
9. Altman, R.L., Teng, A.C., Mayer, L.A. and Myronuk, D.J., *Development and Testing of Dry Chemicals in Advanced Extinguishing Systems for Jet Engine Nacelle Fires*, Report JTCG/AS-82-T-002, Joint Technical Coordinating Group for Aircraft Survivability, 1983.
10. Finnerty, A.E., and Vande Kieft, L.J., "Powders as Halon Replacements," 1997, in Gann, R.G., Burgess, S.R., Whisner, K.C., and Reneke, P.A., eds., *Papers from 1991-2006 Halon Options Technical Working Conferences (HOTWC)*, CD-ROM, NIST SP 984-4, National Institute of Standards and Technology, Gaithersburg, MD, (2006).
11. Fischer, G., and Leonard, J.T., *Effectiveness of Fire Extinguishing Powders Based on Small Scale Suppression Tests*, NRL/MR/6180-95-7778, Naval Research Laboratory, October 19, 1995.
12. Jagers, Jerry F., *Development of Powder-Filled Structural Panels for AH-1S Fuel Fire Protection*, USAAVRADCOTR-81-D-32, Bell Helicopter Textron, October 1981.
13. Peregino II, P.J., Finnerty, A.E., Adkins, T., McGill, R., Cline, T., Gault, W., and Saunders, D., *Fire Protection for External Fuel Cells*, ARL-MR-413, U.S. Army Research Laboratory, October 1998.
14. Finnerty, A.E. and Polyanski, S., *Powder Packs – A Passive Approach to Extinguishing Fire in Combat Vehicles*, Technical Report BRL-TR-3191, U.S. Army Ballistic Research Laboratory, January 1991.
15. Finnerty, A.E., and Dehn, J.T., *Alternative Approaches to Fuel-Fire Protection for Combat Vehicles*, ARL-TR-377, U.S. Army Research Laboratory, April 1994.
16. Finnerty, A.E., McGill, R.L., Slack, W.A., and Saunders, D.M., *Fuel Cells in a Composite Armored Vehicle*, ARL-TR-1911, March 1999.

17. Pedriani, C.M., Ballistic Testing of Advanced Fire Suppression Systems Designed to Protect Helicopter Fuel Tanks from 23mm High Explosive Incendiary-Tracers (HEI-T), USAAVRADCOTM 80-D-3, February 1980.
18. Jagers, J. Fox, R., Johnson, J., and Liardon, D., *Development of Survivability and Vulnerability Improvement Modifications (SAVIM) for the AH-1S Helicopter, Appendix C – Vulnerability Analysis and Crew Protection*, USAAVRADCOTR-81-D-29, Bell Helicopter Textron, May 1982, CONFIDENTIAL.
19. Kiser, B. L., *Helicopter SAVIM Advanced Development Program*, USAAVSCOM TR-84-D-14, Bell Helicopter Textron Inc., October 1984.
20. Keane, C.A., *Vulnerability Reduction Technology for Rotary Wing Aircraft*, Master's Thesis, Naval Postgraduate School, June 1998.
21. Robaidek, M.F., *Aircraft Dry Bay Fire Protection*, AFWAL-TR-87-3032, Boeing Military Airplane Company, July 1987.
22. Pedriani, C.M., *Testing of Powder Packs and Powder-Filled Structures for Aircraft Fire Protection*, USAAVRADCOTR-82-D-12, JTCG/AS-81-T-002, July 1982.
23. Mercer, M., *A Ballistic Evaluation of Lightmass Void Fillers*, JTCG/AS-87-T-004, Naval Weapons Center, September 1987.
24. Finnerty, A.E., *Preliminary Evaluation of Powder Packs*, Memorandum Report BRL-MR-3641, Army Research Laboratory, December 1987.
25. Kolleck, M.L., *Halon Fire Protection Systems for Aviation - Existing System Configuration and Operational Environment Specifications*, Preliminary Report, prepared for Halon Replacement Program for Aviation Team, December 1992.
26. Manchor, J.A., *Reactive Powder Panel Ballistic Demonstration*, briefing, JTCG-AS Project V-1-04, NAVAIR (NAWCWD Code 418300D), January 2001.
27. Manchor, J.A., *V-1-04 Reactive Powder Panels*, briefing, JTCG-AS Project V-1-04, NAVAIR, September 2002.
28. Lundin, S.J., *Uncontained Engine Debris Tests - Fuselage Fire - Advanced Powder Panel Data CD-ROM*, NAVAIR and FAA, October 28, 2002.
29. Haas, J.P., Murphy, Jr., J.J., *C-130 Vulnerability Reduction Program/C-130J Live Fire Test Program Test Report, Phase IA - Wing Leading Edge Dry Bay Testing, (U)*, AAC TR 00-14, February 2001 (SECRET).
30. Fallis, S., Reed, R., McCormick, J.L., and Holland, G.F., "Advanced Propellant/Additive Development for Fire Suppressing Gas Generators: Development + Test," 2002, in Gann, R.G., Burgess, S.R., Whisner, K.C., and Reneke, P.A., eds., *Papers from 1991-2006 Halon Options Technical Working Conferences (HOTWC)*, CD-ROM, NIST SP 984-4, National Institute of Standards and Technology, Gaithersburg, MD, (2006).
31. *Advanced Propellant/Additive Development for Gas Generators*, Report Number D03008, Aerojet, Redmond, WA, March 2006.
32. Reed, R., Chan, M. L., and Moore, K. L., "Pyrotechnic Fire Extinguishing Method," U.S. Patent No. 4,601,344; 1986.
33. Galbraith, L. D., Holland, G. F., Poole, D. R., and Mitchell, R. M., "Apparatus for Suppressing a Fire," U.S. Patent No. 5,423,384; 1995.

34. Galbraith, L.D., "Apparatus & Method for Suppressing a Fire," U.S. Patent No. 5,449,041, 1995.
35. Galbraith, L.D., Holland, G.F., Poole, D.R., and Mitchell, R.M., "Apparatus for Suppressing a Fire," U.S. Patent No. 5,613,562, 1997.
36. Holland, G.F., Wilson, M.A., "Chemically Active Fire Suppression Composition," U.S. Patent No. 6,024,889, 1998.
37. Wucherer, E.J., and Holland, G.F., "Chemically Active Fire Suppressants and Device," U.S. Patent No. 6,217,788, 2001.
38. Williams, B., Wheatley, B., Neidert, J., Lynch, R., and Martin, R., "Fire Suppressant," U.S. Patent No. 6,045,726, 2000.
39. Scheffe, R., Neidert, J., Black, R., Lynch, R., and Martin, R., "Fire Suppressant Compositions," U.S. Patent No. 6,277,296, 2001.
40. Cruise, D.R., *Theoretical Computations of Equilibrium Compositions, Thermodynamic Properties, and Performance Characteristics of Propellant Systems*, NWC TP-6037, Naval Weapons Center, China Lake, CA, 1979.
41. Holland, G., Aerojet Report 98-R-2134, 1998.
42. Grosshandler, W., Gann, R., and Pitts, W., eds, "Evaluation of Alternative In-flight Fire Suppressants for Full-scale Testing in Simulated Aircraft Engine Nacelles and Dry Bays," NIST SP 861, National Institute of Standards and Technology, Gaithersburg, MD, April 1994.
43. Grosshandler, W., Donnelly, M., Charagundla, S.R., and Presser, C., "Suppressant Performance Evaluation in a Baffle-stabilized Pool Fire," 1999, in Gann, R.G., Burgess, S.R., Whisner, K.C., and Reneke, P.A., eds., *Papers from 1991-2006 Halon Options Technical Working Conferences (HOTWC)*, CD-ROM, NIST SP 984-4, National Institute of Standards and Technology, Gaithersburg, MD, (2006).
44. Grosshandler, W., Hamins, A., Charagundla, S.R., and Presser, C., "Suppression Effectiveness Screening for Impulsively Discharged Agents," 2000, in Gann, R.G., Burgess, S.R., Whisner, K.C., and Reneke, P.A., eds., *Papers from 1991-2006 Halon Options Technical Working Conferences (HOTWC)*, CD-ROM, NIST SP 984-4, National Institute of Standards and Technology, Gaithersburg, MD, (2006).
45. Fallis, S., Reed, R., McCormick, J.L., Wilson, K.A., and Holland, G.F., "Advanced Propellant/Additive Development for Fire Suppressing Gas Generator: Hybrids," 2001, in Gann, R.G., Burgess, S.R., Whisner, K.C., and Reneke, P.A., eds., *Papers from 1991-2006 Halon Options Technical Working Conferences (HOTWC)*, CD-ROM, NIST SP 984-4, National Institute of Standards and Technology, Gaithersburg, MD, (2006).
46. Manchor, J., "Aerojet Active Chemical Gas Generator (ACGG) Testing (August 4-7, 2003)," Internal White Paper, Naval Air Systems Command Survivability Division, 2003.
47. Manchor, J., "Aerojet Chemical Gas Generator Mid-Wing Testing (September 22-24, 2003)," Internal White Paper, Naval Air Systems Command Survivability Division, 2003.
48. Sutton, G., and Biblarz, O., *Rocket Propulsion Elements*, 7th ed. John Wiley & Sons, Inc. New York 2001.
49. Chavez, David E.; Hiskey, Michael A., "1,2,4,5-Tetrazine-based Energetic Materials," *Journal of Energetic Materials* **17**(4), 357-377 (1999)..
50. Chavez, David E.; Hiskey, Michael A.; Naud, Darren L., "Tetrazine Explosives," *Propellants, Explosives, Pyrotechnics*, **29**(4), 209 -215, (2004).

51. Linteris, G.T., Rumminger, M.D., and Babushok, V.I., "Premixed Carbon Monoxide-Nitrous Oxide-Hydrogen Flames: Measured and Calculated Burning Velocities with and without  $\text{Fe}(\text{CO})_5$ ," *Combustion and Flame* **122**, 58-75 (2000).
52. Patnaik, P., *Handbook of Inorganic Chemicals*, Knovel.com, 2003.
53. Lide, David R. ed. *Handbook of Chemistry and Physics*, 73rd edition, Taylor & Francis, New York, 1993.
54. Aerojet Internal Research and Development Report, H00016 (Proprietary to Aerojet)
55. Yang, J.C., Nyden, M.R., and Manzello, S.L., "Cold Discharge of  $\text{CF}_3\text{I}$  in a Simulated Aircraft Engine Nacelle," 2001 in Gann, R.G., Burgess, S.R., Whisner, K.C., and Reneke, P.A., eds., *Papers from 1991-2006 Halon Options Technical Working Conferences (HOTWC)*, CD-ROM, NIST SP 984-4, National Institute of Standards and Technology, Gaithersburg, MD, (2006).
56. Wierenga, P.H., and Holland, G.F., "Developments in and Implementation of Gas Generators for Fire Suppression," 1999, in Gann, R.G., Burgess, S.R., Whisner, K.C., and Reneke, P.A., eds., *Papers from 1991-2006 Halon Options Technical Working Conferences (HOTWC)*, CD-ROM, NIST SP 984-4, National Institute of Standards and Technology, Gaithersburg, MD, (2006).
57. Wierenga, P.H., "Further Advances in the Development of Hybrid Fire Extinguisher Technology," 2000, in Gann, R.G., Burgess, S.R., Whisner, K.C., and Reneke, P.A., eds., *Papers from 1991-2006 Halon Options Technical Working Conferences (HOTWC)*, CD-ROM, NIST SP 984-4, National Institute of Standards and Technology, Gaithersburg, MD, (2006).
58. Dierker, J.B., Jr., Thompson, R.H., Wierenga, P.H., and Schneider, M.A., "Fire Suppression System Development for the Ford Crown Victoria Police Interceptor," 2005, in Gann, R.G., Burgess, S.R., Whisner, K.C., and Reneke, P.A., eds., *Papers from 1991-2006 Halon Options Technical Working Conferences (HOTWC)*, CD-ROM, NIST SP 984-4, National Institute of Standards and Technology, Gaithersburg, MD, (2006).

---

---

## Chapter 10: LIFE CYCLE COSTING OF FIRE SUPPRESSION SYSTEMS

---

---

J. Michael Bennett, Ph.D.  
Bennetech, LLC

### TABLE OF CONTENTS

10.1	Background.....	1025
10.1.1	Technical Concept .....	1025
10.1.2	NGP Tasks .....	1026
10.1.3	General Methodology .....	1027
10.2	Agent properties.....	1027
10.3	Current System Description (Halon 1301) for Legacy Aircraft .....	1028
10.3.1	Cargo Aircraft .....	1028
10.3.2	Fighter Aircraft .....	1034
10.3.3	Rotary-wing Aircraft.....	1038
10.4	Proposed System Description (HFC-125) for Future Aircraft.....	1042
10.4.1	Design Guide .....	1042
10.4.2	Cargo Aircraft .....	1045
10.4.3	Fighter Aircraft .....	1048
10.4.4	Rotary-wing Aircraft.....	1052
10.5	Costs Of Current and Replacement Systems .....	1054
10.5.1	Life Cycle Cost Estimate (LCCE) Summary for Legacy Aircraft.....	1056
10.5.2	Life Cycle Cost Estimate (LCCE) Summary for Future Aircraft .....	1058
10.5.3	Detailed Cost Element Structure (CES).....	1061
10.5.4	Cost Element Structure Data Development .....	1061
10.6	Cost Savings.....	1066
10.7	Cost Analysis Using Altered Fire Suppression Performance .....	1068
10.7.1	Factor of Safety Testing.....	1068
10.7.2	System Description .....	1069
10.7.3	Altered Fire Suppression Performance .....	1070
10.7.4	Cost Analysis .....	1073
10.8	Conclusions.....	1082
10.9	References.....	1083

### 10.1 BACKGROUND

#### 10.1.1 Technical Concept

Aircraft fires impose a significant cost impact on the military. Fire is either the primary cause or a contributing factor in a large portion of mishaps that result in injuries to personnel, material loss of

aircraft assets, and loss of mission capability. Methods and technologies to mitigate these costs or "design them out" are a major component in aircraft design, retrofit, and maintenance.

To determine the preferred fire extinguishing medium, system or method for any application, the holistic approach is to compare alternatives based upon an overall cost of ownership, or "life cycle cost," either over an aircraft's projected useful life or some fixed period of use. This approach incorporates the various costs associated with procuring, installing and maintaining such equipment, including non-hardware costs such as development and certification, as well as repair and parts replacement. Fire protection equipment that functions successfully will prevent damage to personnel and property, resulting in an offsetting cost savings. The magnitude of these savings depends on the success rate and speed of suppression (thereby minimizing physical damage), and the cost of the protected assets themselves. The net cost or savings of each alternative can then be compared to determine the best choice, in this case as a replacement for the halon 1301 fire extinguishing chemicals.

This process can also serve other purposes:

- Estimation of whether a new fire protection technology is sufficiently superior to the state of the art, in cost effectiveness, to warrant further pursuit.
- Justification of the use of any fire protection system at all for an application of interest. This entails a comparison of the cost savings in terms of assets preserved against the total life cycle cost of the fire protection technology.
- Determination of the economics of an optimal degree of effectiveness of a firefighting system. Historically, fielded fire suppression systems have been less than 100 % effective. There are costs (dollars, mass carried, and volume occupied) that generally increase with an enhanced degree of surety that a firefighting system will protect the aircraft and its occupants.

### 10.1.2 NGP Tasks

To demonstrate the applications of life cycle costing to aircraft fire extinguishing systems, Bennett, Kolleck and co-workers at Booz Allen & Hamilton:

1. Established a life cycle cost baseline for typical halon 1301 (CF<sub>3</sub>Br) fire extinguishing systems that are used on aircraft today, by considering several varied aircraft platform type representatives (both legacy (existing) and future platform types), to establish a life cycle cost equivalence goal for any halon 1301 replacement derived from or considered by the NGP.
2. Performed a similar cost analysis for the same platforms using a different fire suppressant. These systems used the "first generation" halon 1301 replacement, HFC-125, C<sub>2</sub>HF<sub>5</sub>, (see below) for which extensive data existed. The HFC-125 system was sized to the same level of performance as the existing halon 1301 systems. This established a threshold cost-of-ownership level that any halon 1301 replacement technology must exceed to be preferred over the pre-existing use of HFC-125 and thus maintain further interest for research and implementation.
3. Performed cost of ownership studies by varying the performance levels of such systems, by adjusting the size capacities (with resultant weight and size impacts on life cycle cost), to determine an optimal performance level in terms of life cycle cost by balancing firefighting effectiveness with the size/capacity/cost implications.

4. Evaluated the merits of halon 1301 and HFC-125 systems (and, by extension, or any other fire protection system) in terms of their ability to pay for themselves by determining if the cost savings in terms of assets saved historically actually exceeded the life cycle costs of developing, installing and supporting such systems in the field. This enabled confirming if the systems actually provide a tangible monetary benefit to their aircraft customers, to determine which aircraft configurations (if any) provide such benefits, and to quantify any perceived benefits.

The methodologies developed, modified and demonstrated under the NGP have been documented in References 1, 2, and 3, whose distribution is restricted, and in References 4, 5, 6, 7, and 8, which are available to the public. The methodologies were fashioned to serve as stand-alone products, to provide the framework to build modified models for future halon 1301 replacements, and to serve as analysis tools to identify key indicators of desirable halon 1301 replacement properties to consider in later research on new technologies. Since their formulation, these methodologies have been used to perform trade-off studies and to assist in the selection of the most affordable halon replacement agent and system design for aircraft recently under development.

### 10.1.3 General Methodology

A methodology was developed to determine the net cost of the fire suppression system. This methodology incorporates the cost of the system, which is a function of system size/weight, and the cost savings provided by the system, which are a function of extinguishant effectiveness and the resultant aircraft saved and their value. The net cost is the cost of the system minus the cost savings.

Fire system characterization was first necessary to understand and appreciate the system cost information fully. This was accomplished for the current halon 1301 systems and estimated for the proposed HFC-125 systems. Information regarding the current systems was available through previous NGP efforts.<sup>9,10</sup> Estimates regarding the proposed systems were made using information generated as a part of the Halon Replacement Program for Aviation.<sup>11</sup> Impact estimates (sensitivity analyses) were also made for the potential increase in bottle size/distribution plumbing.

System cost information was developed utilizing the data contained in the Federal Logistics (FEDLOG) system and various traditional costing factors. The Defense Logistics Agency provided access to this system. It contains part numbers, suppliers, and other logistical information specifically for the Service of interest. It is not releasable to the general public because of the proprietary nature of some of the data.

Cost savings information was obtained by utilizing the Annual Fire Protection Cost Model [1966-1995; 1996-2025]<sup>12</sup> and other peacetime incident data.

## 10.2 AGENT PROPERTIES

Halon 1301 is considered by many to be a nearly perfect compound for fire suppression in challenging and high performance applications, such as aircraft. This compound can be stored compactly as a liquefied gas at room temperature and a 1.61 MPa storage pressure, but quickly flash vaporizes at atmospheric pressure and ambient temperatures. It remains stable for years, which is important for satisfactory storage in fielded use. The electrical conductivity of the gas is low (permitting its use in

electrical and electronics areas), it is non-corrosive in its pure state, and it is an effective fire suppressant at concentrations well below levels that pose toxicity concerns to humans.

HFC-125 was the “first generation” halon 1301 alternative chemical recommended for immediate use after intensive research efforts of the U.S. Air Force/Navy/Army/Federal Aviation Administration funded, multiyear Halon Replacement Program for Aviation to identify near-term substitutes for halon 1301 for aircraft platforms needing an immediate replacement.<sup>13</sup> The selection had been made following testing in generic and reconfigurable engine nacelle and dry bay mockups, representing the wide range of aircraft fire zone configurations of interest to the sponsors. Statistical experimental design techniques were used to translate the experiments representing a subset of all the possible combinations of fire zones and scenarios into the determination of the extinguishant with the best firefighting performance i.e., lowest agent mass required to extinguish the fires, for all the applications and conditions of interest. In addition to fire suppression performance results, other data on the extinguishants’ storage and discharge characteristics, toxicity and materials compatibility traits were considered in the final decision. Once this decision was made, additional experiments were performed to develop a more precise system sizing model, again using statistical experimental design, for HFC-125 that would facilitate the sizing of extinguishing systems using it for various aircraft engine nacelle and dry bay applications.

HFC-125 has many characteristics similar to halon 1301. It leaves no residue in the event of accidental discharge, and thus requires negligible cleanup support. It is non-reactive with steel, aluminum, or brass, and no adverse effects are expected on plastics. Most importantly, it fills heavily cluttered spaces quickly and easily, even at cold temperatures, and under high ventilation air flow conditions. Its atmospheric lifetime is 26.4 years.<sup>10</sup>

For these two chemicals, Table 10–1 lists the properties that were used in the cost estimates.

### **10.3 CURRENT SYSTEM DESCRIPTION (HALON 1301) FOR LEGACY AIRCRAFT**

#### **10.3.1 Cargo Aircraft**

The typical legacy cargo aircraft fire protection system layout is described below. The basic design approach placed emphasis on the prevention and containment of fire. The engine nacelle and APU compartments are designated as fire zones, where combustible fluids (fuel, hydraulic fluid, and engine oil) and ignition sources coexist, and a single failure in the combustible fluid system could result in a fire.<sup>14</sup>

#### **Aircraft Engine Nacelle Fire Protection System Components and Procedures**

Provided below are realistic fire protection system configuration data for current (legacy) cargo aircraft currently being procured and operated by the USAF. It was assumed that fire protection systems for future cargo aircraft would be similar to these. Schematic drawings of the engine nacelle systems are shown in Figure 10–1 through Figure 10–3.

**Table 10–1. Properties of Halon 1301 and HFC-125 Used in Life Cycle Costing.**

Features	Halon 1301	HFC-125
Extinguishant Physical State (ambient)	Gas	Gas
Mechanism of Extinguishment	Chemical, some cooling, inerting	Cooling, inerting
Physical Properties		
Boiling Point (°C) at 101 kPa (1 atm)	-57.8	-48.5
Molecular Weight, g	149	120
Liquid Density, kg/m <sup>3</sup> (lb/ft <sup>3</sup> ) at 70 EF	97.8	75.7
Vapor Pressure, kPa (psia) at 298 K	249	190
Freezing Point, °C (1 atm)	-168	-103
Critical Temperature, °C	4	72
Critical Pressure, kPa (atm)	39	38
Critical volume, cm <sup>3</sup> /mol	200	272
Critical Density, g/cm <sup>3</sup>	0.75	0.44
Liquid Density, g/cm <sup>3</sup>	1.5	1.2
Vapor Density, g/L	8.7	4.9
Liquid Specific Heat, cal/g	0.21	0.3
Vapor Specific Heat, cal/g	0.11	0.19
Liquid Heat Capacity, cal/mol-K	30.9	36.1
Vapor Heat Capacity, cal/mol-K	16.5	22.6
Extinguishant Effectiveness		
Cup Burner Value, volume %	3.3	9.1
Weight Impact (ratio to halon systems)	1	2.2
Volume Impact (ratio to halon systems)	1	2.9
Environmental Considerations		
Ozone Depletion Potential (ODP)	10 to 14	0
Global Warming Potential (GWP)	1.9	0.58

Fire extinguishing protection is provided for each engine by a fixed, high discharge rate, halon 1301 fire extinguishing system on each wing. Two engine vaporizing liquid fire extinguishers are located on the front spar of each wing inboard of the outboard pylon. Each extinguisher has two discharge ports, one directed to each engine on that wing. This arrangement allows either engine to receive fire extinguishing agent from either or both extinguishers (as a two-shot system) if needed.

The distribution lines to the engine core and accessory compartments can terminate with discharge nozzles. However, for halon 1301, this is often a simple open pipe. A pylon fire extinguisher check valve, located in the engine distribution lines, isolates the two compartments from each other. The pylon fire extinguisher check valve opening pressure exceeds the differential pressure between the core and accessory compartments.

Each engine's vaporizing liquid fire extinguisher has two engine aircraft fire extinguisher power device cartridges and one agent pressure switch. There are shutoff valves for each engine's fuel and hydraulic fluid supplies.

When a fire is detected in an engine, the applicable FIRE PULL fire control handle assembly is pulled. Signals are supplied through the handle assembly to close the applicable engine fire fuel and hydraulic shutoff valves, isolating the affected engine.

The agent from the extinguishers is discharged by pulling out the applicable handle assembly. The handle assembly is rotated counterclockwise to discharge the agent from the inboard fire extinguisher and clockwise to discharge the agent from the outboard fire extinguisher. The handle assembly is spring-loaded to the center position. If the use of the first extinguisher does not put out the fire, agent is applied from the second bottle.<sup>14,15,16</sup>

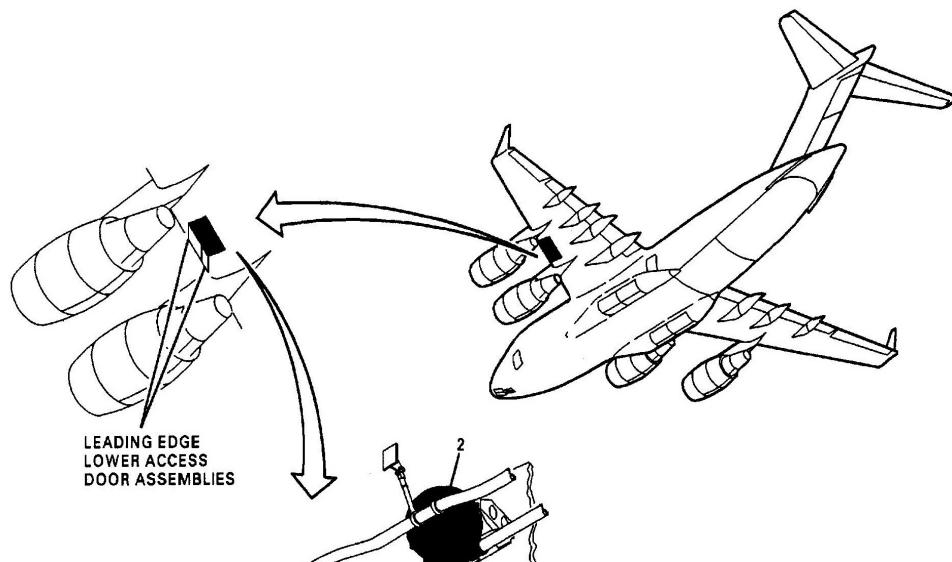


**Figure 10-1.**  
Typical Cargo  
Aircraft Engine  
Nacelle Fire  
Protection  
System Location  
(Wing Leading  
Edge).<sup>16</sup>

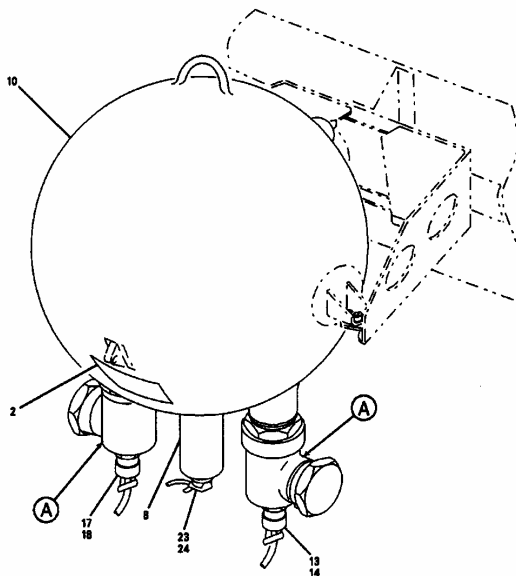


**Figure 10-2.** Close-up of Typical Engine  
Nacelle Fire Protection System Bottle.<sup>16</sup>  
(A: discharge heads)

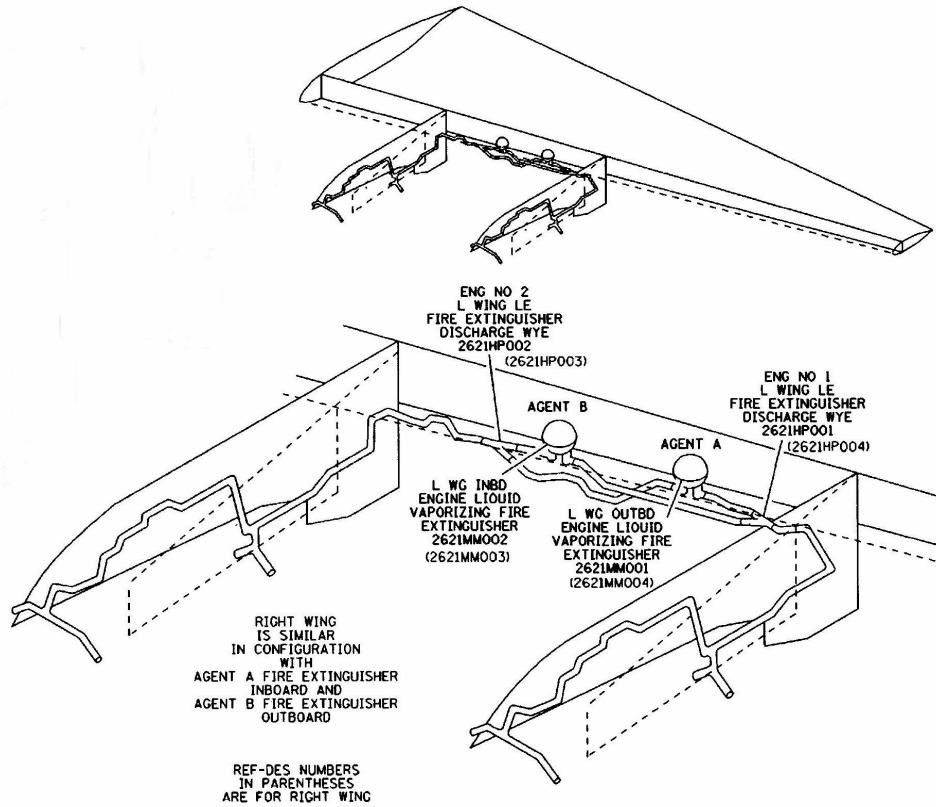


Figure 10–3. Typical Cargo Aircraft Engine Nacelle Fire Suppressant Storage and Distribution System (Wing Leading Edge).<sup>16</sup>

**Additional Legacy Cargo Aircraft Fire Protection System Information**

Table 10–2 displays additional fire suppression system information (engine nacelle and APU) for a typical legacy cargo aircraft.<sup>1</sup>

**Table 10–2. Additional Legacy Cargo Aircraft Fire Protection System Information.**

	Engine Nacelle	APU
<b>GENERIC</b>		
Number of aircraft	121	
Fire types	Spray/pool	
<b>FIRE ZONE</b>		
# of fire zones (# of compartments)	2 (4)	1 (1)
Fire zone free volume (net volume), m <sup>3</sup> (ft <sup>3</sup> )	7.45 (263)	0.623 (22)
Air ventilation at fire site, kg/s (lb/s)	0.29 (0.64)	0.29 (0.64)
<b>EXTINGUISHANT</b>		
# of halon 1301 systems	2	1
Extinguisher trigger mode	Remote	Remote
Extinguisher volume, cm <sup>3</sup> (in <sup>3</sup> )	10,300 (630)	1400 (86)
Diameter of extinguishant container, cm (in)	27.7 (10.9)	14.2 (5.6)

	Engine Nacelle	APU
Storage compartment for extinguishant bottle, m <sup>3</sup> (ft <sup>3</sup> )		0.42 (15)
Free volume in storage compartment, cm <sup>3</sup> (in <sup>3</sup> )		0.43 (260)
Normal charge and pressure of extinguisher container, MPa (psig) @ 21 °C (70 °F) with N <sub>2</sub>	5.6 (800)	4.24 (600)
Max extinguisher container pressure (Burst range of safety disc), MPa (psig)	13.2 to 15.6 (1900 to 2300) @ 96 °C (205 °F)	11.96 to 13.3 (1720 to 1920) @ 96 °C (205 °F)
Extinguisher container percent filled, %	67	69
Extinguisher container orientation	Upright with valves at bottom	
Dimensions of bottles with valves, cm x cm (in x in)	6.9 x 3.5	
Dimensions for present access to bottles	20 in x 13 in = 260 in <sup>2</sup> = 1.81 ft <sup>2</sup>	
Extinguisher container mass without halon 1301, kg (lb)	5.8 (12.8)	1.5 (3.2)
Halon 1301 mass, kg (lb)	9.5 (21.0)	1.1 (2.5)
Extinguisher container location, inside/outside fire zone	Outside	
<b>STRATEGY FOR USE</b>		
# of shots	2	1
Manual/automatic	Manual	Manual
Procedure for Activation	Fire warning light is activated, pilot initiates firing of pyrotechnic squib which releases the contents of the bottle, the agent travels through the system plumbing to the engine nacelle/APU and is discharged as a gas.	
<b>DISTRIBUTION SYSTEM</b>		
Extinguisher dispersion method, @ 21 °C (70 °F)	5.6 MPa, N <sub>2</sub> @ 800 psig	4.24 MPa N <sub>2</sub> @ 600 psig
Extinguisher discharge rate (95 % in 0.9 s), kg/min (lb/min)	544 (1200)	72 (158)
Distribution system plumbing material	Bottle to pylon stub: 6061ALT6; all else: CRES.	CRES 321
Inner diameter, cm (in)	From bottle to pylon stub, 3.8 (1.5) ID; all else, 3.8 (1.5), 2.5 (1.0), and 1.9 (0.75) ID. Wall thickness, 0.24 (0.095)	1.27 (0.5) ID. Wall thickness, 0.071 (0.028)
Length, cm (in)	99.4 (39.14) from outboard bottle to both outlets in core compartments; 41.7 (16.42); from outboard bottle to inboard pylon	Straight length – 12.7 (5) – 78.7 (31)
Shape, bends, elbows	varies	1 bend, 1.5 radius
Number and nature of nozzles/pipe terminations	Two nozzles	One nozzle
<b>MODIFICATION POTENTIAL</b>		
Restriction on alternative fluids, very/modest/slight	slight	slight

	Engine Nacelle	APU
Ease of access of current distribution plumbing for retrofit (0 %-very difficult, 50 %-relatively easy, 100 % easy)	30 % difficult; 70 % easy.	30 % difficult; 70 % easy.
Access & available space for additional distribution plumbing or nozzle modification (0 %-very difficult, 50 %-relatively easy, 100 % easy)	30 % difficult; 70 % easy.	30 % difficult; 70 % easy.
OTHER		
Extinguisher system manufacturer	Walter Kidde	
Evidence of halon 1301 distribution characteristics (from certification tests)	6 % by volume for 0.5 s at cruising condition.	
Range of expected operating temperatures for the bottle and the plumbing, °C (°F)	-60 to 93 (-77 to 200)	
Maximum Air Temperature in the Nacelle, °C (°F)	71 (160)	
MISCELLANEOUS	27.6 kPa (4 psi) is max pressure the protected volume can accept in nacelle. Max pressure in plumbing is 13.8 MPa (2000 psi) allowable. Potential fuels: Jet A and JP-8, Hydraulic Fluid Mil-H-83282, Lube Oil Mil-L-23699.	

### Auxiliary Power Unit (APU) Fire Protection System Components and Procedures

Fire extinguishing is provided for the APU by a fixed, high discharge rate, halon 1301 fire extinguishing system in the APU compartment. The APU fire extinguisher consists of the following components:

- APU vaporizing liquid fire extinguisher,
- APU fire extinguisher agent pressure switch, and
- APU fire extinguisher power device cartridge.

The APU extinguisher is externally mounted on the APU compartment forward firewall. The extinguisher has one discharge port. The discharge head, agent pressure switch and power device cartridge are located on the extinguisher.

To extinguish a fire in the APU, the agent is discharged by any of the following switches:

- AGENT DISCH switch on the APU control panel.
- AGENT DISCH toggle switch on the aft loadmaster APU FIRE control panel assembly.
- AGENT DISCH toggle switch on the ground refueling control panel APU FIRE panel.<sup>5</sup>

An APU fire is indicated by as many as five signals in the aircraft, outside the aircraft, and on the APU itself.<sup>6</sup>

Figure 10–4 shows the typical auxiliary power unit fire protection system location for cargo aircraft.<sup>5, 7</sup>

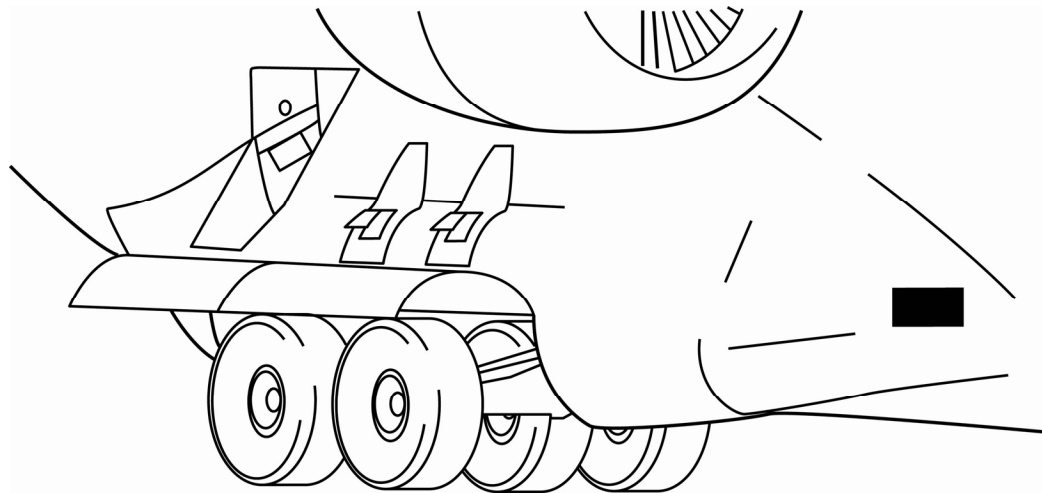


**Figure 10–4.**  
**Typical**  
**Auxiliary**  
**Power Unit**  
**Fire**  
**Protection**  
**System**  
**Location.**<sup>16</sup>

### 10.3.2 Fighter Aircraft

#### Fire Protection System Components and Procedures

The location for the representative legacy fighter aircraft fire protection system is in the aft fuselage between the engines, as shown in Figure 10–5 and Figure 10–6.<sup>17</sup> The single-bottle halon 1301 fire suppression system is designed to provide fire protection for the left and right engine nacelles, the left and right airframe mounted accessory drive (AMAD) bays, and the Auxiliary Power Unit (APU) bay.<sup>1</sup> Therefore, the first fire occurrence in either the engine/AMAD or APU bays will utilize all of the agent. The single cylindrical bottle is approximately 46 cm (18 in.) in length with a 11 cm (4.5 in.) diameter.<sup>18</sup> The general system installation is shown in Figure 10–7.<sup>19</sup>

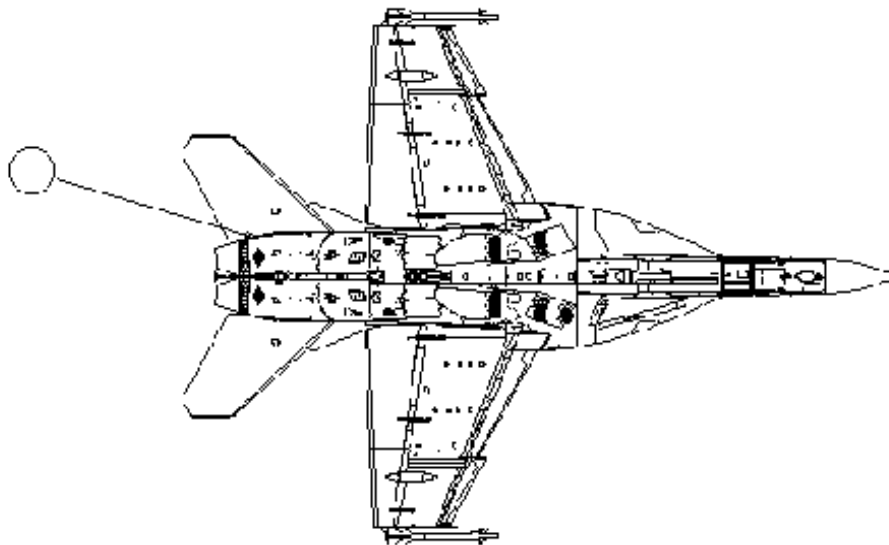


**Figure 10–5.** Typical General Location of Fighter Aircraft Fire Extinguisher Bottle.<sup>17</sup>

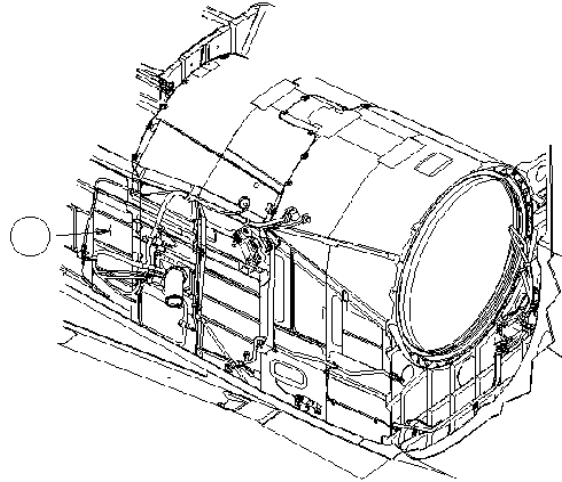


**Figure 10–6. Schematic of Typical Fighter Aircraft Engine Bay.**<sup>17</sup>

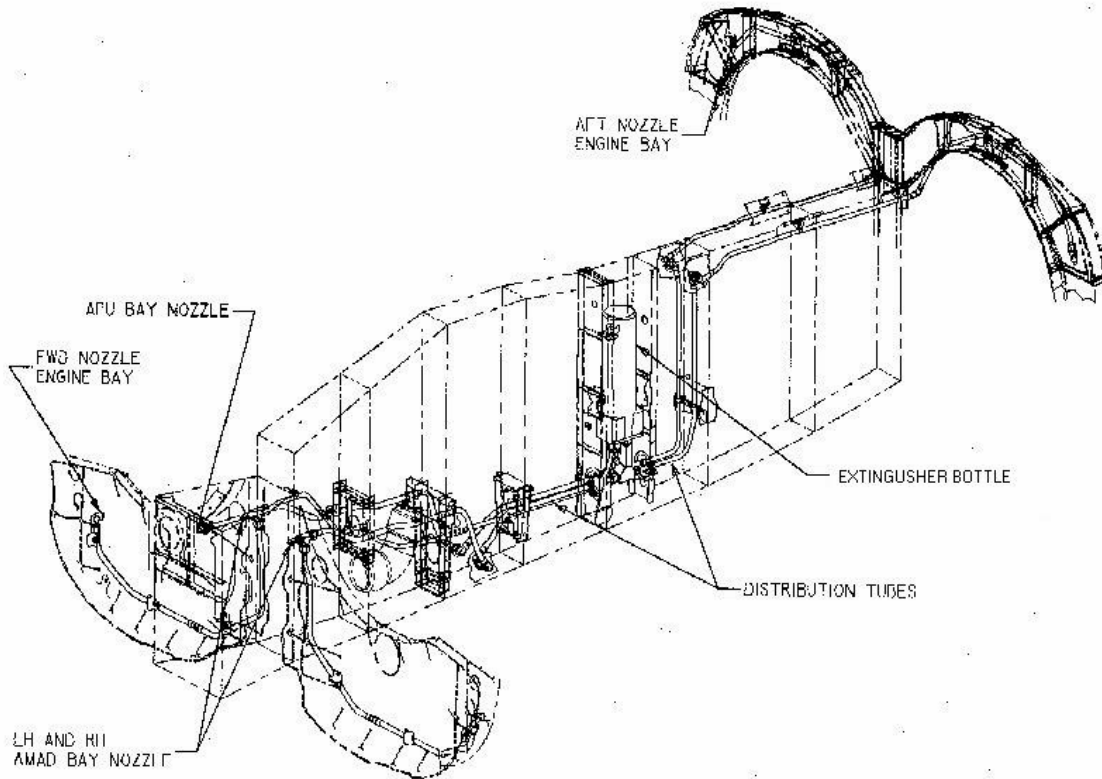


**Figure 10–7. Typical Fighter Aircraft Fire Suppression System Installation.**<sup>19</sup>

The fire detection and extinguishing system is made up of three fire warning/extinguisher lights, a fire extinguisher pushbutton, one fire extinguisher bottle, a fire test switch and dual-loop fire detection sensors. The extinguisher bottle is in the aft fuselage between the engines. The bottle provides a one-shot

extinguishing capability. The system provides engine/AMAD and APU fire warning, emergency shutdown and selective fire extinguishing.<sup>20</sup>

The three fire warning/extinguisher lights are pushbutton switch indicators which come on when a fire condition exists. Two of the fire warning/extinguisher lights are labeled FIRE. One, mounted on the top left corner indicates a fire condition in the left engine bay; the other, mounted on the top right corner of the instrument panel, indicates a fire condition in the right engine bay. The APU FIRE warning/extinguisher light is positioned inboard of the right FIRE light. A voice alert warning is activated anytime a fire warning light comes on. If more than one warning light comes on at the same time, the voice alert warning priority is ENGINE FIRE LEFT, ENGINE FIRE RIGHT, then APU FIRE.<sup>12</sup>

The fire extinguisher pushbutton switch is on the master arm panel and is labeled FIRE EXTGH. The switch has two lights. A yellow light is labeled READY and a green light labeled DISCH (discharge). When READY is on, the fire extinguisher bottle is armed. The READY light comes on when the appropriate fire warning/extinguisher light is pressed. Pressing an engine fire warning/extinguisher light shuts off fuel to the engine at the feed tank. With READY on, pressing the fire extinguisher pushbutton discharges the fire extinguisher bottle and turns on the DISCH light. There is no indication of actual discharge of the fire extinguisher bottle.<sup>12</sup>

The APU fire extinguishing system can be either manually or automatically actuated. To manually actuate the system, the fire extinguisher bottle is first armed and the APU shut down by pressing the APU FIRE warning/extinguisher light. When pressed, the APU FIRE light stays in and a barber pole indicator appears along side the light. The extinguisher bottle is then discharged into the APU bay by pressing the FIRE EXTGH pushbutton with the READY light on. Discharge of the bottle is delayed ten seconds after the light is pressed. This allows the APU time to spool down before the extinguishing agent is introduced. If the aircraft is on the ground, the APU fire extinguishing system is actuated automatically. The result is the same as with manual actuation, with the APU shutting down immediately after a fire is detected and the fire extinguisher discharging into the APU bay ten seconds later. The automatic system is prevented from operating by the action of a relay.<sup>12</sup>

Actuation of the engine/AMAD fire extinguisher can only be performed manually. Lifting the guard and pressing the affected FIRE warning/extinguisher light arms the system. This also shuts off fuel to the engine at the engine feed shutoff valves and closes the cross feed valve. When pressed, the FIRE light stays in, and a barber pole indicator appears in the switch guard. The extinguisher bottle is discharged into the affected engine bay by pressing the FIRE EXTGH pushbutton with the READY light on.<sup>12</sup>

### Additional Legacy Fighter Aircraft Fire Suppression System Information

Table 10–3 displays fire suppression system information (engine nacelle and APU) for the typical legacy fighter aircraft.<sup>9</sup>

**Table 10–3. Additional Legacy Fighter Aircraft Fire Suppression System Information**

Parameter	Engine Bay/APU
FIRE TYPES (pool fires, mist)	Spray/pool
FIRE ZONE	
Number of fire zones	3 (2 engines/AMAD, 1 APU)
Fire zone free volume, m <sup>3</sup> (ft <sup>3</sup> )	1.14 (40.3)

Parameter	Engine Bay/APU
<b>EXTINGUISHANT</b>	
Number of halon 1301 systems	1
Extinguisher trigger mode	Pilot activated
Extinguisher volume, cm <sup>3</sup> (in <sup>3</sup> )	3031 (185)
Size of cylindrical extinguishant container, cm (in)	11.4 cm (4.5 in) diameter, 46 cm (18 in.) long
Storage compartment for extinguishant bottle, cm (in)	206 x 12.7 x 20.3 (81 x 5 x 8)
Free volume in storage compartment, m <sup>3</sup> (in <sup>3</sup> )	0.048 (2953)
Normal charge and pressure of extinguisher container, MPa (psi)	4.3 (625) @ 22.2 °C (72 °F)
Max extinguisher container pressure, MPa (psi)	6.2 (900) @ 16 °C (60 °F)
Extinguisher container percent filled, %	50
Extinguisher container orientation (upright with valves at bottom)	Lateral configuration
Extinguisher container mass without agent, kg (lb)	2.7 (~6)
Halon 1301 mass, kg (lb)	2.5 (5.5)
Extinguisher container location (inside/outside fire zone)	Outside
<b>STRATEGY FOR USE</b>	
Number of shots	1 shot discharges into engine nacelle and AMAD bay or APU.
Manual/automatic	Manual
Procedure for Activation	Fire warning light is activated, pilot initiates firing of pyrotechnic squib which releases the contents of the bottle, the agent travels through the system plumbing to the engine nacelle/APU and is discharged as a gas.
<b>DISTRIBUTION SYSTEM</b>	
Extinguisher dispersion method	Cut-off pipe
Extinguisher discharge rate, kg/s (lb/s)	0.99 (2.2)
Distribution system plumbing	Single pipe discharged into engine and AMAD simultaneously. APU has discharge port, but the first fire occurrence in either the engine/AMAD or APU bays will utilize all halon 1301
Number and nature of nozzles/pipe terminations	Cut-off pipe
Tightness of the bottle space	Only 12.7 cm (5 in) in height available for growth.
Extinguisher Bottle Growth Potential	12.7 cm (5 in) in height
<b>OTHER</b>	
Suppression success fraction	Historical reports show 80% success.
Evidence of halon 1301 distribution characteristics (from certification tests)	Yes
Range of expected operating temperatures for the bottle and the plumbing, °C (°F)	-54 to 316 (-65 to 600)

## Typical Legacy Fighter Aircraft Fire Suppression Concentration Tests

The Certification Section of Chapter 2 describes the traditional methodology utilized to certify an aircraft fire suppression system.

### Historical Fire Suppression System Effectiveness

As discussed in Chapter 2, data have been compiled on the effectiveness of the F/A-18 fire suppression system.<sup>21</sup> The data show where, when, and why fires occurred from 1982 through 1993, as recorded by the Naval Safety Interactive Retrieval System (NSIRS). During this time period, seven F-18 aircraft were lost or destroyed due to fire.

The engine halon 1301 fire suppression systems were shown to be 80 % successful in extinguishing in-flight fires, and this effectiveness was the same for each engine. Eighty-nine percent of all fires in areas protected by halon 1301 fire suppression (engines and AMAD bays) occurred in flight. Fires in halon 1301-protected areas accounted for 84 % of all in-flight fires. Engine fires accounted for 78 % of all in-flight fires, with 19 occurring in the right engine, 15 occurring in the left engine, three in both engines, and three in unspecified engines.

The preponderance (73 %) of F-18 aircraft fires occurred during a peak period between 1986 and 1989. Seventy-five percent of all engine fires occurred during this time period, and it was reported by Government fire protection engineers that the F-18 afterburner liners were faulty and the cause of at least 25 incidents, not all of which were fire incidents.

The majority (87 %) of F-18 fires were caused by material failures. Common material failures included afterburner liner and spray bar pigtail failures, high-pressure compressor failures, fuel leaks, electrical wire insulation breaches, fuel-filler cap mishaps, failures in the AMAD bay (e.g., hydraulic pump failures), as well as failures of various parts due to fatigue or foreign object debris (FOD).<sup>21</sup>

These aforementioned “real world” effectiveness data were considered when estimating the realistic extinguishing “success rates” to be forecast in future use, and the resultant cost of assets saved, to offset the life cycle costs of developing, acquiring and maintaining a fire extinguishing system for an aircraft platform. This approach was used for all of the platform types studied.

### 10.3.3 Rotary-wing Aircraft

#### Fire Protection System Components and Procedures

The general location (between the two engines) of a legacy rotary-wing aircraft fire protection system is shown in Figure 10–8.

The two-bottle halon 1301 fire suppression system is designed to provide dual-shot fire protection for the left and right engine nacelles. Each bottle is cylindrical in shape, and the two bottles are stacked vertically with the long axis of each bottle parallel to the engines themselves.

There are two discharge locations in the engine nacelle, one at the forward firewall, the second at the side. The extinguishing lines truncate with open ended pipes. The inner diameter of the lines is 1.8 cm

(0.69 in. The flame detectors are required to detect a fire within 5 s. Additional time is needed for the pilot to initiate and activate the fire extinguishing system.<sup>22</sup>

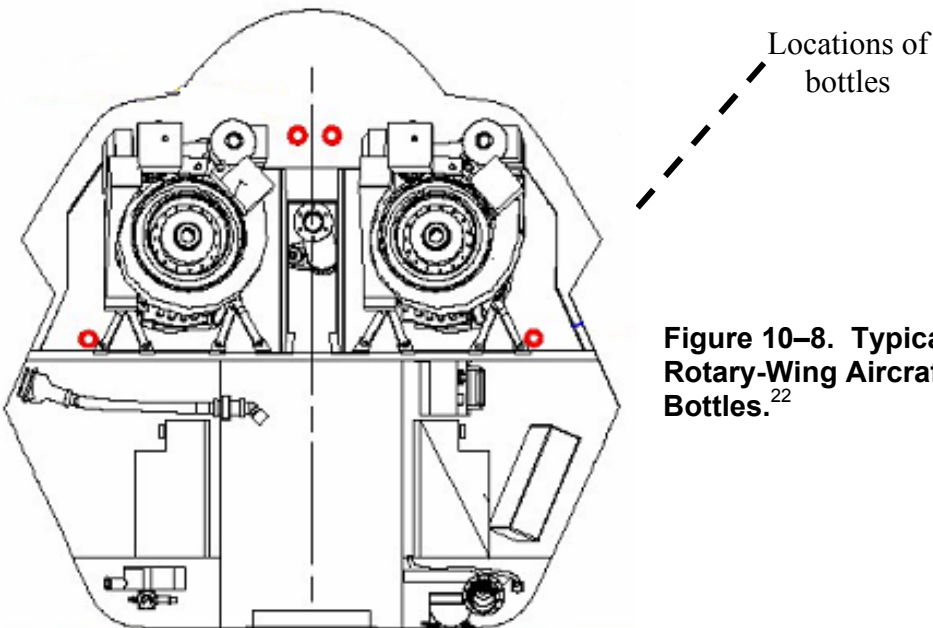


**Figure 10–8. Typical General Location of Rotary-Wing Aircraft Fire Extinguisher Bottles.**<sup>22</sup>

Each engine nacelle bay has a total volume of approximately  $0.85 \text{ m}^3$  ( $30 \text{ ft}^3$ ) and houses a single jet turbine engine. Aside from the turbine engine, the bay is fairly cluttered with fuel lines, control systems, etc. The resulting total free volume in each bay is approximately  $0.46 \text{ m}^3$  ( $16.1 \text{ ft}^3$ ). Each nacelle bay is independently ventilated via four apertures, which provide passive airflow that fluctuates with the helicopter's airspeed and orientation. The airflows inside the nacelle bay range from about  $0.54 \text{ kg/s}$  to  $1.6 \text{ kg/s}$  ( $1.2 \text{ lb/s}$  to  $3.5 \text{ lb/s}$ ).

### Halon 1301 Design Guide Estimation

The total mass of the current representative rotary-wing system is approximately  $6.5 \text{ kg}$  ( $14.3 \text{ lb}$ ). The total extinguishing agent mass is  $0.7 \text{ kg}$  ( $1.5 \text{ lb}$ ) per platform or  $0.3 \text{ kg}$  ( $0.8 \text{ lb}$ ) for each bottle. The present system requires head space (vapor volume in the bottles above the liquid fill line) to pressurize the fluid to  $4.1 \text{ MPa}$  ( $600 \text{ psi}$ ) with nitrogen, and uses  $0.3 \text{ cm}$  ( $1/8 \text{ inch}$ ) thick 304 stainless steel bottles that weigh  $0.8 \text{ kg}$  ( $1.8 \text{ lb.}$ ) each, or  $1.6 \text{ kg}$  ( $3.5 \text{ lb}$ ) for the two bottles. The mass of the fluid distribution manifold, pyrotechnic valves, mounting hardware, and electrical connectors is about  $4.2 \text{ kg}$  ( $9.3 \text{ lb}$ ), with the estimated mass of electrical cables and mounting hardware of  $0.52 \text{ kg}$  ( $1.1 \text{ lb}$ ) per installation (for a total of  $1.0 \text{ kg}$  ( $2.3 \text{ lb}$ ) per platform).<sup>23</sup>

However, it was unclear whether the current design's halon 1301 mass ( $0.3 \text{ kg}$  ( $0.8 \text{ lb}$ ) per bottle, for a total of  $0.7 \text{ kg}$  ( $1.5 \text{ lb}$ ) per platform, used by the rotary-wing representative was sufficient to maintain the necessary concentration of agent of at least 6 % by volume in air in all parts of the affected zone simultaneously for at least  $0.5 \text{ s}$  at normal cruising condition. Due to this uncertainty, the required halon 1301 amount was calculated using the military specification for sizing systems, MIL-E-22285.<sup>24</sup> This specification applies to the installation of high-rate-discharge type fixed fire extinguishing systems for

engine spaces and other potential fire zones in aircraft. As a design guide, the following equations may be used to determine the minimum mass of agent to be discharged into each engine:

1. For “rough” nacelle interior with low air flow, and for a smooth nacelle interior regardless of air flow, using whichever of the following two equations provides the larger value of W:

$$W = 0.05V \quad (10-1)$$

$$W = 0.02V + 0.25WA \quad (10-2)$$

2. For “rough” nacelle interior with high air flow:

$$W = 3(0.02V + 0.25WA) \quad (10-3)$$

3. For a “deep frame” nacelle interior with high airflow:

$$W = 0.16V + 0.56WA \quad (10-4)$$

where:

W (lb) = mass of agent

WA (lb/s) = mass flow air passing through the zone at normal cruising condition.

V (ft<sup>3</sup>) = net volume of the zone (gross volume of the zone less the volume of major items of equipment.<sup>24</sup>)

Figure 10–4 shows the legacy rotary wing aircraft-specific parameters used to estimate the amount of halon 1301 required.

**Table 10–4. Legacy Rotary-wing Aircraft Specific Parameters.**

Parameter	Value
Airflow	0.54 kg/s to 1.59 kg/s (1.2 lb/s to 3.5 lb/s)
fuel source	MIL-H-83282, MIL-H-5606, JP-8
Maximum air temperature	51.7 °C (125 °F)
free volume	0.46 m <sup>3</sup> (16.1 ft <sup>3</sup> )

The resulting halon 1301 system agent capacity per platform ranges from 1.09 kg (2.39 lb.) to 3.26 kg (7.18 lb.), per the guidance of the aforementioned military sizing standards.

### **Additional Legacy Rotary-Wing Aircraft Fire Suppression System Information**

Table 10–5 displays fire suppression system information (engine nacelle and APU) for a typical legacy rotary-wing aircraft.<sup>10</sup>

**Table 10–5. Additional Legacy Rotary-wing Aircraft Fire Suppression System Information.**

Parameter	Value
FIRE TYPES (pool fires, mist)	Spray/pool
FIRE ZONE	
Number of fire zones	2
Fire zone free volume, m <sup>3</sup> (ft <sup>3</sup> )	0.46 m <sup>3</sup> (16.1 ft <sup>3</sup> )
EXTINGUISHANT	
Number of halon 1301 systems	2
Extinguisher trigger mode	Pilot activated
Extinguisher volume, cm <sup>3</sup> (in <sup>3</sup> )	
Size of extinguishant container, cm, cm, cm (in, in, in)	Cylindrical
Normal charge and pressure of extinguisher container, MPa (psi)	4.14 MPa (600 psi)
Extinguisher container percent filled, %	60
Extinguisher container orientation	Stacked vertically and parallel to engines
Extinguisher container mass without halon 1301, kg (lb)	0.79 kg (1.75 lb.) each or 1.59 kg (3.5 lb.) for the two bottles
Halon 1301 mass, kg (lb)	0.68 kg (1.5 lb.) per platform or 0.34 kg (0.75 lb.) for each bottle
Extinguisher container location (inside/outside fire zone)	Outside
STRATEGY FOR USE	
Number of shots	2
Manual/automatic	Manual
Procedure for Activation	Fire warning light is activated, pilot initiates firing of pyrotechnic squib which releases the contents of the bottle, the agent travels through the system plumbing to the engine nacelle and is discharged as a gas.
DISTRIBUTION SYSTEM	
Extinguisher dispersion method	The extinguishing lines end with open ends.
Distribution system plumbing	There are two discharge locations in the engine nacelle, one at the forward firewall, the second at the side. The inner diameter of the lines is 1.76 cm (0.694 in).
Number and nature of nozzles/pipe terminations	Two; The extinguishing lines end with open ends.

### Typical Legacy Rotary-Wing Aircraft Fire Extinguishing Concentration Tests

The protocol for certifying and approving fire suppression systems for rotorcraft via concentration measurements during discharge is the same as previously described for the design of fighter aircraft systems.

## Historical Fire Suppression System Effectiveness

Reference 25 provides information on the historical effectiveness of rotary-wing aircraft fire suppression systems. It discusses where, when, and why fires occurred from 1977 through 1993, as recorded by the Naval Safety Interactive Retrieval System (NSIRS). During this period, 146 of 161 rotary aircraft fires (91 %) did not result in “destruction” of the aircraft – the fires were either extinguished by the on-board fire protection systems or ground crew, or self extinguished. The rotary aircraft fire suppression systems were reported as having extinguished 71% of all fire events in which the system was activated to attempt extinguishment. Analysis of the Safety Center data indicates that, when used, the rotary aircraft fire suppression systems were 71 % effective overall in extinguishing fires, and the engine fire suppression systems were 57 % effective.<sup>25</sup>

## 10.4 PROPOSED SYSTEM DESCRIPTION (HFC-125) FOR FUTURE AIRCRAFT

### 10.4.1 Design Guide

Since current (legacy) aircraft use halon 1301 (and not HFC-125), a potential system description and sizing for retrofit/future aircraft had to be estimated. The Halon Replacement Program for Aviation developed a Design Guide to assist in sizing systems using HFC-125.<sup>11</sup> These systems are intended to provide extinguishant effectiveness equivalent to halon 1301 systems, which were designed using traditional approaches. This Design Guide was used to size a system for future aircraft platforms under consideration. The legacy aircraft-specific parameters were also used to estimate the mass of HFC-125 required for their platforms. The Design Guide provides a two step design process to be used in sizing systems appropriately.

The five-step approach to determine the required design concentration for certification and estimate the necessary mass of extinguishant to meet certification requirements consists of the following procedure:

1. Calculate the customized design concentration required for the configuration of the platform of interest using Equation 5 in the Design Guide, using relevant operational values of air temperature, air mass flow rate, and fuel type used on the platform in the fire zone.
  - a. If the range of air temperature and air mass flow varies considerably in the flight envelope, several combinations of relevant maximum air temperature and corresponding mass flow should be tried to assure the highest concentration calculated to be required over the flight envelope is achieved. In general, the application of the highest air temperature and minimum air mass flow (within acceptable data bounds, as governed by the Design Equation 5) will normally give a conservative worst-case estimate.
  - b. For this equation, the values input for maximum air temperature and air mass flow should never be outside the range of the values upon which the equation was developed (37.8 °C to 135.0 °C (100 °F to 275 °F) and 0.4 kg/s to 1.2 kg/s (0.9 to 2.7 lb/s), respectively). If the actual maximum operating condition is outside of these ranges, the closest extreme value should be used. The impact on the accuracy of the results has been shown in experiments to be minimal.
  - c. If more than one flammable fluid is present in the engine nacelle or APU (such as hydraulic fluids or oils), use the highest fuel constant (coefficient) value corresponding to

the fluids present. (For example, the fuel constant = 0.4053 for hydraulic fluid would be used if it is present, since it has the highest constant.)

- d. If a single system protects one or more engine nacelles and an APU, calculate the required concentration and corresponding mass for either application independently and use the higher of the two mass requirements.
2. Calculate the expected extinguishant mass requirement via Equation 10-6, using the required concentration calculated in Equation 10-5, the volume of the fire zone (nacelle or APU) and the actual air mass flow (even if outside the bounds considered in the previous step).
3. Design the extinguishant container capacity consistent with current design practice and use the mass estimates in Equation 10-6 for use in design trade-study comparisons and as a starting point for certification testing.
4. Perform the certification discharge experiments (using existing Halonyzer or Statham analyzer equipment to measure concentrations real-time, but recalibrated for HFC-125), with the criteria being the attainment of the design concentration calculated in Equation 10-5 at all measurement points in the nacelle simultaneously for at least 0.5 s.
5. If certification is not met, increase the container capacity or modify the distribution system to eventually pass certification.

The concentration calculated using Equation 10-5 will be the concentration used for certification testing of a HFC-125 system designed for engine nacelle or APU protection. Equation 10-5 can give a range of concentration values from 14.5 % by volume to 26 %, by volume,

$$X_e = 21.10 + 0.0185 \text{ AIRT} - 3.124 \text{ WA} + 5.174 (\text{FUEL CONSTANT}) + 0.0023 (\text{AIRT}) \times (\text{FUEL CONSTANT}) + 1.597 (\text{FUEL CONSTANT})^{11} \quad (10-5)$$

where:

$X_e$ (% by volume)	=	Certification Design Concentration
AIRT (°F)	=	maximum ventilation air temperature in the nacelle or APU during operations
WA (lb/s)	=	internal air mass flow in the nacelle or APU during operations
FUEL CONSTANT	=	coefficient to account for presence of JP fuel, hydraulic fluids, or oil

The variable ranges permissible for use in Equation 5 are:

AIRT	37.8 °C to 135.0 °C (100 °F to 275 °F)
$\dot{W}_a$	0.4 kg/s to 1.2 kg/s (0.9 lb/s to 2.7 lb/s)
FUEL CONSTANT (Use highest coefficient of fluids present.)	

If JP fuel, use	0.3586
If hydraulic fluid, use	0.4053
If oil, use	0
If fire resistant hydraulic fluid (SKYDROL), use	0

Equation 10-6 below is a theoretically derived equation to estimate the minimum mass of extinguishant required for a system to pass the certification process while exhibiting at least the minimum design concentration  $X_e$  calculated from Equation 10-5, everywhere in the nacelle simultaneously. The equation was derived using physical flow modeling idealization presumably similar to that used to develop mass sizing formulas used for earlier halon 1301 certification, since the equations are similar in structure. Only one equation now exists for HFC-125, which accounts for the effects of high-speed airflow and compartment obstructions (ribs and other structure), whereas the prior halon 1301 equations had multiple empirical sizing equations for various rib height and clutter classes, since it could exploit a large body of test data with these various configurations. Like its predecessor formula for halon 1301, this theoretical estimation equation assumes optimal distribution and mixing of the extinguishant. It is useful for preliminary sizing of systems for trade studies with other alternatives during the design process and as a starting point to begin certification tests. If a distribution system is not designed to distribute the extinguishant efficiently, certification tests may not be passed initially, and either the distribution system will require modification and improvement or the bottle capacity and extinguishant mass will need to be increased until certification is accomplished. Equation 10-6 will calculate system sizes that will range between 2.3 and 4.3 times the volume of optimally designed halon 1301 systems for identical applications, with a corresponding mass growth ratio only about 80 % of the volume growth ratio compared to a halon 1301 system (due to the lower density of HFC-125 compared to halon 1301). The estimated HFC-125 system size and mass may actually be much closer in size to an existing halon 1301 installation, due to the oversizing of many previous halon 1301 designs.<sup>11</sup>

$$MASS(lb.) = 0.003166X_eV + 4.138 \frac{X_e}{100 - X_e} \dot{W}_{ACTUAL} \quad (10-6)$$

where:

$$\begin{aligned} X_e (\% \text{ by volume}) &= \text{engine/APU concentration for certification (Equation 10-5)} \\ V (\text{ft}^3) &= \text{free volume of nacelle or APU--ft}^3 \\ \dot{W}_{ACTUAL} (\text{lb/s}) &= \text{actual maximum air mass flow (no experimental bounds)} \end{aligned}$$

The two-step approach (per the Design Guide) was followed to determine the required design concentration for certification and estimate the necessary mass of extinguishant to meet certification requirements.

The Design Guide<sup>11</sup> is limited to providing a mass estimate that assumes the HFC-125 is optimally distributed (with just the minimal required concentration at all sites simultaneously, and no wasted excess), which may well be too optimistic, based upon experience with fielded systems. The following analysis was performed to provide an alternative method of estimating of the required mass and increased container volume required, by attempting to replicate the amount of inefficiency currently observed with fielded legacy systems, due to simplifications and design limitations of their distribution systems, or even due to simple overdesigns, that result in excess or “wasted” extinguishant discharged that does not directly satisfy the Design Guide criteria. This is accomplished simply by beginning with pre-existing fielded legacy halon 1301 systems in use, and adjusting their size for HFC-125 (with a similar overdesign, presumably), by merely adjusting their capacities and size by the ratios of the design

concentrations, liquid densities and molecular weights of HFC-125, compared to halon 1301. This alternative scaling approach (a “scale up” coefficient from halon 1301 to HFC-125, for equivalent protection) for realistic, “inefficient” systems is expressed in Equations 10-7 and 10-8 (illustrated for this application to require an HFC-125 design concentration of 24 %).

$$\frac{MW_{HFC-125}}{MW_{Halon1301}} * \frac{[C]_{HFC-125}}{[C]_{Halon1301}} = \frac{120}{149} * \frac{23.8}{6} = 3.2 = WeightRatio \quad (10-7)$$

$$WeightRatio * \frac{v_{HFC-125}}{v_{Halon1301}} = WeightRatio * \frac{\rho_{Halon1301}}{\rho_{HFC-125}} = 3.2 * \frac{97.8}{75.7} = 4.1 = VolumeEstimate \quad (10-8)$$

where:

- MW (g) = Molecular Weight
- [C] (% by volume) = Concentration determined by the Design Guide
- $\rho$  (lb/ft<sup>3</sup>) = Liquid Density @ 70 °F

#### 10.4.2 Cargo Aircraft

Table 10–6 and Table 10–7 show the results of the Design Guide calculations (concentration and mass estimation) for the future cargo aircraft engine nacelle and auxiliary power unit fire systems, respectively.

**Table 10–6. Design Guide Estimates of HFC-125 Concentration and Mass for Future Cargo Aircraft Engine Nacelles.**

Maximum Temperature	Air Mass Flow kg/s (lb/s)	Fuel Constant	Concentration	Mass Estimate (lb)	Mass Estimate (kg)
71.1 °C (160 °F)	Maximum - 1.22 (2.7)	Jet A (0.359)	17.8	N/A	N/A
71.1 °C (160 °F)	Maximum - 1.22 (2.7)	JP-8 (0.359)	17.8	N/A	N/A
71.1 °C (160 °F)	Maximum - 1.22 (2.7)	MIL-H-83282 (0.405)	18.1	N/A	N/A
71.1 °C (160 °F)	Maximum - 1.22 (2.7)	MIL-L-23699 (0.0)	15.6	N/A	N/A
71.1 °C (160 °F)	Minimum – 0.41 (0.9)	Jet A (0.359)	23.4	N/A	N/A
71.1 °C (160 °F)	Minimum – 0.41 (0.9)	JP-8 (0.359)	23.4	N/A	N/A
71.1 °C (160 °F)	Minimum – 0.41 (0.9)	MIL-H-83282 (0.405)	<b>23.8</b>	N/A	N/A
71.1 °C (160 °F)	Minimum – 0.41 (0.9)	MIL-L-23699 (0.0)	21.3	N/A	N/A
71.1 °C (160 °F)	Actual – 0.29 (0.64)	MIL-H-83282 (0.405)	N/A	<b>21.3</b>	<b>9.7</b>

**Table 10–7. Design Guide Estimates of HFC-125 Concentration and Mass for Future Cargo Aircraft Auxiliary Power Units.**

Maximum Temperature	Air Mass Flow kg/s (lb/s)	Fuel Constant	Concentration	Mass Estimate (lb)	Mass Estimate (kg)
71.1 °C (160 °F)	Maximum – 1.22 (2.7)	Jet A (0.359)	17.8	N/A	N/A
71.1 °C (160 °F)	Maximum – 1.22 (2.7)	JP-8 (0.359)	17.8	N/A	N/A
71.1 °C (160 °F)	Maximum – 1.22 (2.7)	MIL-H-83282 (0.405)	18.1	N/A	N/A
71.1 °C (160 °F)	Maximum – 1.22 (2.7)	MIL-L-23699 (0.0)	15.6	N/A	N/A
71.1 °C (160 °F)	Minimum – 0.41 (0.9)	Jet A (0.359)	23.4	N/A	N/A
71.1 °C (160 °F)	Minimum – 0.41 (0.9)	JP-8 (0.359)	23.4	N/A	N/A
71.1 °C (160 °F)	Minimum – 0.41 (0.9)	MIL-H-83282 (0.405)	<b>23.8</b>	N/A	N/A
71.1 °C (160 °F)	Minimum – 0.41 (0.9)	MIL-L-23699 (0.0)	21.3	N/A	N/A
71.1 °C (160 °F)	Actual – 0.29 (0.64)	MIL-H-83282 (0.405)	N/A	<b>2.6</b>	<i>1.2</i>

Note that the concentration estimate is based upon an air mass flow of 0.4 kg/s (0.9 lb/s) (within the bounds relevant for the equation) and the mass estimate is based upon the actual air mass flow of 0.27 kg/s (0.6 lb/s), as directed by the Design Guide. The first eight rows in each table are calculations of the maximum concentration required, evaluated over a range of air flows and fuel types, with the maximum concentration is denoted in bold face. The last row is the calculation of the required mass needed to hold the maximum required concentration, while accounting for airflow dilution at the highest actual operating mass flow, with the mass also being denoted in bold face.

The estimate of the proposed system concentration, mass and volume increase is given in Table 10–8. Table 10–9 shows the current and proposed system extinguishant and bottle masses. This is only an (proportional) estimate because the larger bottles would have to be designed by a fire suppression system manufacturer using factors such as agent density, agent pressure, percent liquid fill, and required container wall thickness.

**Table 10–8. Future Cargo Aircraft Proposed System Estimates.**

	Aircraft Engine Nacelle					Auxiliary Power Unit					Total Agent Per Platform	
	Conc.	Mass		Volume		Conc.	Mass		Volume		lb	kg
	% by vol.	lb	kg	in <sup>3</sup>	L	% by vol.	lb	kg	in <sup>3</sup>	L		
Current halon 1301 system	6.0	21.0	9.5	630	10.3	6.0	2.5	1.1	86.0	1.4	86.5	39.2
Estimated HFC-125-optimally distributed	23.8	21.3	9.7	814	13.3	23.8	2.6	1.2	110.9	1.8	87.9	39.9
Estimated HFC-125-non-optimally distributed	23.8	67.2	30.5	2583	42.3	23.8	8.0	3.6	352.6	5.8	277.0	125.6

**Table 10–9. Future Cargo Aircraft Extinguisher Container and Agent Mass.**

	Current Halon 1301 System				Estimated HFC-125-Optimally Distributed				Estimated HFC-125- Non-Optimally Distributed			
	AEN		APU		AEN		APU		AEN		APU	
	lb	kg	lb	kg	lb	kg	lb	kg	lb	kg	lb	kg
Bottle mass	12.8	5.8	3.2	1.5	13.0	5.9	3.3	1.5	41.0	18.6	10.1	4.6
Agent mass	21.0	9.5	2.5	1.1	21.3	9.7	2.6	1.2	67.2	30.5	8.0	3.6
Total mass	33.8	15.3	5.7	2.6	34.3	15.6	5.9	2.7	108	49.1	18.2	8.3

### Potential Airframe Impact

Depending on the legacy cargo aircraft of interest, the potential airframe impact will vary. Issues to consider include: impact to the airframe weight/volume, maintenance, and modification.

### Weight/Volume Impact

The weight/volume impact depends on the system optimization. As shown in the previous tables, a system that is optimally distributed can have a significant weight and volume reduction versus a non-optimally distributed system. Increases in weight will cause an increase in the fuel required to haul the additional weight. Increases in volume will cause a reduction in weapon system capability (such as reduced storage for munitions).

### Maintenance Impact

During this study, maintenance personnel were contacted for their insight and advice regarding the impact to maintenance procedures. The maintenance personnel provided the following maintenance time estimates and procedures. Two AFSC senior airmen are required to assist in access or removal of the items and to perform retrofit. Access to all five fire bottles requires one man-hour total. The fire bottles require weight checks every 10 years and the explosive actuating squibs are time change items and require time change every five years from date of manufacture or three years from the date of installation. Four man-hours total for all five fire bottles are required to remove the item. Six man-hours total for four fire bottles are required to reinstall and inspect the item.

Current regulation Bottle requires that the bottle mass not exceed 17 kg (37 lb) if it is to be lifted overhead by one person. If the resulting design exceeds this limit, an additional maintenance person would be required and would result in additional operation and support costs.

Any modification to the system must allow access to the fire bottles and distribution system. The areas accessed during normal fire suppression system maintenance include the wing leading edge and engine pylons. The access panels are routinely opened for other maintenance and there are no problems foreseen in removing any of the access panels. Typically, the access panels are the only components that have to be removed to access the fire protection system. The same access panels are typically used to access the

distribution system as are the fire bottles. Access panels may need to be made larger if a larger bottle is used.

### **Modification Impact**

An estimate of the modification impact was difficult to ascertain and depends on the modification required. A more accurate assessment of the impact requires input from the airframe manufacturer, which was not available. Modification to the structure may be significant (and may be cost prohibitive).

If the distribution system is optimally designed, HFC-125 may be able to fit in the existing space. However, if the distribution system is not optimally designed it will require a larger and heavier bottle, which may not be feasible in the current configuration. This may require either modification of the existing structure, a relocation of the bottles, or the optimization of the distribution system. It would need to be determined whether enough access/available space for additional distribution plumbing or nozzle modification exists.

A poorly designed distribution system results in an unnecessary increase weight. Therefore, there is a strong incentive to optimize the system. It is recommended that a distribution optimization study (similar to the Navy's program for the F/A-18 E/F) be performed or else extensive aircraft modification will be required.

Due to the current lack of airframer engineering assistance, the significant cost impact of modifying an aircraft (including structure) to accommodate fire system changes could not be estimated accurately. Therefore, those costs were not included in this study (since it requires a detailed, multi-faceted engineering assessment for engineers familiar with a specific platform and its design details and modification labor estimations, and performed on a case-by-case basis), and any estimates of retrofit costs in this study using larger systems that may require moderate or extensive structure modifications should be considered a very conservative underestimate of actual retrofit costs involved.

Prior to the final design of an HFC-125 system, assistance from extinguisher system manufacturers and from the airframe manufacturer needs to be sought.

### **10.4.3 Fighter Aircraft**

#### **General Description**

Future fighter aircraft fire suppression systems will utilize a four-nozzle HFC-125 system in addition to the agent outlets in the AMAD and APU bays for enhanced agent distribution. The general location for the future fighter aircraft fire suppression system is similar to the legacy fighter aircraft fire suppression system. The extinguisher bottle is in the aft fuselage between the engines and provides a one-shot extinguishing capability. Future fighter aircraft fire suppression systems utilize a single bottle of HFC-125. The four-nozzle distribution system, shown schematically in Figure 10–9 is designed to swirl the agent into the incoming ventilation air and around the engine nacelle.<sup>26</sup>

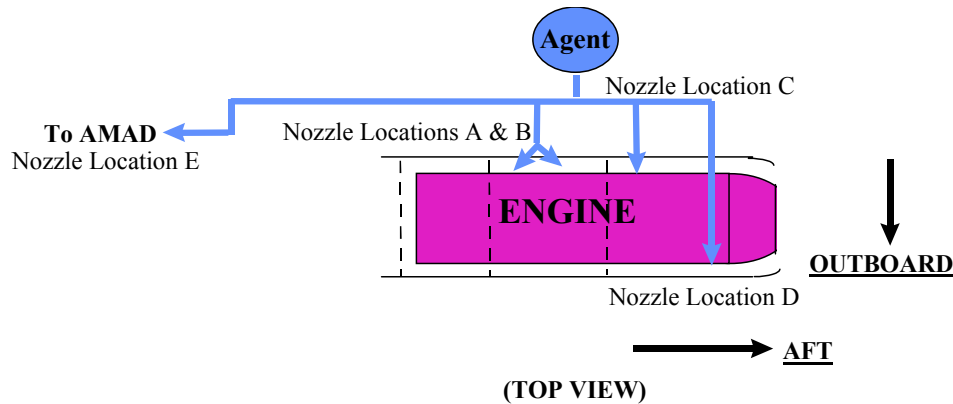


**Figure 10–9. Typical Future Fighter Aircraft Agent Distribution System.**

The general characteristics of the enhanced plumbing highlight the significance of plumbing modifications. Compared with the much simpler legacy aircraft plumbing scheme, which employs a single discharge nozzle, the future aircraft four-nozzle system prepositions the HFC-125 throughout the nacelle. This pre-positioning, in concert with the prevailing nacelle airflows, optimizes agent presence at any fire in the nacelle. The future fighter aircraft distribution system utilizes the same plumbing diameters as the legacy system.<sup>27</sup>

### Fire Protection System Components and Procedures

It was assumed that the procedures for future fighter aircraft fire protection systems are similar to the procedures for the legacy systems as described previously. Table 10-10 displays the components of the future aircraft engine nacelle fire suppression system.<sup>28</sup>

### Fire Suppression System Optimization

The Naval Air Systems Team conducted and participated in several varied halon 1301 replacement programs. Each offered data that gave rise to the opportunity of successfully applying HFC-125 to the in-service fleet as an adequate alternative to halon 1301. The particular on-board retrofit applications being promoted are the fixed halon 1301 fire protection systems protecting the engine nacelles aboard aircraft.

Future fighter aircraft will not have the luxury of accepting any system larger than the halon 1301 system currently aboard earlier models. Future fighter aircraft utilized the same bottle compartment dimensions as their legacy fighter aircraft counterparts, which had only minimal growth opportunity for a new agent cylinder.<sup>22</sup> Consequently, the Navy invested in a system optimization program. This program focused on nacelle airflow analyses and plumbing optimization and proved that enhanced distribution of the less effective chemical could, and did, deliver an HFC-125 system design capable of meeting the performance of the halon 1301 system it was replacing. This was extremely beneficial since original estimates predicted up to 200 % to 300 % system growth required.<sup>11</sup>

Due to the early system optimization, the resulting future fighter aircraft Engine/AMAD/APU fire extinguishing mass system mass only grew by 19 %, and the agent mass only grew by 27 %. Table 10–11 shows a comparison of the fire extinguishing system masses.

**Table 10–10. Future Fighter Aircraft Engine Nacelle Fire Protection System Components.**

Part Number	Description	Units Per Assembly
2-100280-1	Fire Extinguisher Tank (4SQT109) Cartridge, Aircraft (Left Engine Cartridge) (05167) (McDonnell Douglas Corp Spec 74-500054-101) (4SQT109-J1)	1
M25988/1-905	O-Ring (Packing) (81349)	1
33500009	Tank Fire Extinguisher (05167) (McDonnell Douglas Corp Spec 74-500052-111) (4SQT109)	1
M25988/1-906	O-Ring (Packing) (81349)	1
2-100280-3	Cartridge, Aircraft (APU Cartridge) (05167) (McDonnell Douglas Corp Spec 74-500054-103) (4SQT109-J3)	1
M25988/1-905	O-Ring (Packing) (81349)	1
2-100280-5	Squib, Electric (Right Engine Cartridge) (05167) (McDonnell Douglas Corp Spec 74-500054-105) (4SQT109-J2)	1
74A502115-1001	Tube Assembly (76301)	1
74A502116-1003	Tube Assembly (76301)	1
74A330710-2341	Shim (76301)	1
4M36-02020	Washer, Flat (76301)	2
NAS6604-4	Bolt, Shear (80205)	2
AN894J10-8	Adapter, Straight, TU (88044)	1
74A502106-1003	Tube Assembly (76301)	1
74A330710-2339	Shim (76301)	1
74D490106-1001	Dummy Connector, Plug (Shorting Plug) (76301)	3

**Table 10–11. Fighter Aircraft Fire Suppression System Mass Comparison.**

	Halon 1301 System (1 nozzle) <sup>a</sup>		HFC-125 System (4 nozzles) <sup>a</sup>	
	kg	lb	kg	lb
Bottle Mass	4.2	9.3	5.6	12.2
Agent Mass	2.5	5.5	3.2	7.0
Plumbing Mass	4.3	9.5	4.6	10.1
Total Mass	11.0	24.3	13.4	29.3

<sup>a</sup> in addition to the agent outlets in the AMAD and APU bays

### Design Guide Estimation

To show the value of investment in system optimization, estimates were made during this program of the required mass and volume impact and the resulting costs of not utilizing an optimized system. These estimates were made using the referenced report generated as a part of the Halon Replacement Program for Aviation.<sup>11</sup>

The intent of the design guide was to retain an equivalent level of fire fighting performance to the current halon 1301 systems. Like the halon 1301 systems they replace, the new systems incorporating HFC-125 will not extinguish every imaginable fire condition created and if so, it could not be verified via experimentation. Historical data revealed an overall effectiveness of 60 % to 80 % for halon 1301 systems. The HFC-125 design guidance demonstrates a validated 80 % to 100 % effectiveness. Systems designed using HFC-125 will generally require varying degrees of additional quantities per application compared to their halon 1301 counterparts for an identical application, assuming an optimized halon 1301 system was used. Many fielded halon 1301 systems are not optimal in sizing, and the estimate of installing a replacement HFC-125 container has resulted in much smaller size increase impacts than expected.

The design guide presumed optimal mixing. Less efficient distribution systems will require higher masses to achieve the required concentration simultaneously for a half second during certification, with the designer having the option of accepting higher mass requirements or modifying and improving the distribution system.

Table 10–12 shows the future fighter aircraft specific parameters used to estimate the mass of HFC-125 required. The concentration estimate is based upon an air mass flow of 0.4 kg/s (0.9 lb/s) (within the bounds of the equation), and the mass estimate is based upon the actual air mass flow of 0.96 kg/s (2.11 lb/s) as directed by the design guide.

**Table 10–12. Future Fighter Aircraft Specific Parameters.**

Parameter	Value
Airflow	0.96 kg/s (2.11 lb/s)
Fuel Source	JP-8, hydraulic fluid
Maximum air temperature	104.4 °C (220 °F)
Free Volume	1.10 m <sup>3</sup> (38.8 ft <sup>3</sup> )

Estimates of the HFC-125 system concentration, mass, and volume increase are given in Table 10–13. The resulting concentration and mass estimates were 25 % and 2.70 kg (5.96 lb), respectively, which differed somewhat from the Navy-generated results of 18 % and 2.21 kg (4.87 lb), respectively.

**Table 10–13. Estimates of System Parameters for Proposed Future Fighter Aircraft System Description.**

	Concentration	Mass		Volume	
	% by volume	kg	lb	L	in <sup>3</sup>
Legacy Fighter Aircraft (halon 1301) – (1 nozzle) <sup>b</sup>	6	2.5	5.5	3.0	185
Future Fighter Aircraft (HFC-125) - (4 nozzles) <sup>b</sup>	9	3.2	7	4.0	242
Estimated HFC-125- non-optimally distributed (this study)	25	8.4	18	13	800
Estimated HFC-125- non-optimally distributed (Navy study)	18	6.2	14	10	600

<sup>b</sup> in addition to the agent outlets in the AMAD and APU bays

Table 10–14 shows the current and proposed system extinguishant and bottle masses. This is only an (proportional) estimate because the larger bottles would have to be designed by a fire suppression system

manufacturer using factors such as agent density, agent pressure, percent liquid fill, and required container wall thickness.

**Table 10–14. Future Fighter Aircraft Extinguisher Container and Agent Mass.**

	Legacy Fighter Aircraft (Halon 1301) (1 nozzle) <sup>C</sup>		Future Fighter Aircraft (HFC-125) (4 nozzles) <sup>C</sup>		Future Fighter Aircraft Non-Optimally Distributed <sup>D</sup>	
	kg	lb	kg	lb	kg	lb
Bottle Mass	4.2	9.3	5.6	12.2	15.5	34.3
Agent Mass	2.5	5.5	3.2	7.0	8.4	18.4
Plumbing Mass	4.3	9.5	4.6	10.1	6.0	13.3
Total Mass	11.0	24.3	13.2	29.3	29.9	66.0

<sup>C</sup> in addition to the agent outlets in the AMAD and APU bays

<sup>D</sup> Proportionally estimated

As evidenced by the two previous tables, the Navy's investment in distribution system optimization realized a substantial payoff in weight and volume savings.

#### 10.4.4 Rotary-wing Aircraft

##### System Description

For these calculations, it was assumed that future rotary-wing aircraft would utilize a four-nozzle HFC-125 fire suppression system. The location for the future rotary-wing aircraft fire suppression system is the same as in the legacy rotary-wing aircraft fire suppression system, i.e., between the engines. The single bottle provides a dual-shot extinguishing capability.

##### Fire Protection System Components and Procedures

It was assumed that the procedures for actuating the future rotary-wing aircraft fire protection systems are the same as the procedures for the legacy systems, as described previously.

##### HFC-125 Design Guide Estimation

At the time of these calculations, testing was underway to determine the required masses of various halon 1301 alternative fire extinguishing agents for rotary-wing platforms. Thus, the mass of HFC-125 had to be estimated for the current purpose. The following is a description of that process and the resulting design guide.<sup>3</sup>

The intent of the design guide was to retain a level of fire fighting performance equivalent to the current halon 1301 systems. Like the halon 1301 systems they would replace, the new systems incorporating HFC-125 would not extinguish every imaginable fire condition created and if so, it could not be verified via experimentation, since finite (albeit even numerous) repeated successes in tests cannot statistically guarantee 100 % effectiveness in extended field use. Historical data revealed an overall fire suppression effectiveness of 60 % to 80 % for halon 1301 systems. The HFC-125 design guidance provides a validated 80 % to 100 % effectiveness. Systems designed using HFC-125 will generally require

additional masses and volumes of agent, compared to their halon 1301 counterparts for an identical application. Fortunately, many fielded halon 1301 systems were overdesigned, so the replacement HFC-125 containers showed much smaller size increases than expected.

The design guide presumes optimal mixing of the agent within the nacelle. Less efficient distribution systems will require higher masses to achieve the required concentration simultaneously for 0.5 s during certification, with the designer having the option of accepting higher mass requirements or modifying and improving the distribution system.

Table 10–15 shows the future rotary-wing aircraft specific parameters used to estimate the amount of HFC-125 required.

**Table 10–15. Future Rotary-wing Aircraft Specific Parameters.**

Parameter	Value
Air flow	0.5 kg/s to 1.6 kg/s (1.2 lb/s to 3.5 lb/s)
Fuel source	MIL-H-83282, MIL-H-5606, JP-8
Maximum air temperature	52 °C (125 °F)
Free volume	0.5 m <sup>3</sup> (16.1 ft <sup>3</sup> )

The design guide yielded a platform HFC-125 mass estimate of kg 3.6 kg (7.9 lb.). However, the design guide assumes the HFC-125 is optimally distributed. The following analysis was performed to provide another estimate of the required mass required using the ratio of the molecular weights. This estimate assumes that the HFC-125 is not optimally distributed. The resulting platform HFC-125 mass estimate was 7.6 kg (16.8 lb.).

### Analysis of Increase in Total System Mass

The representative rotary-wing platform provided a breakdown of the various fire suppression system component masses, as shown in Table 10-16; the “Other” includes distribution tubing, brackets, wiring, detectors and other miscellaneous components. However, it was unclear whether the provided bottle mass ( $M_{\text{agent}}$ ) (0.8 kg (1.8 lb)) included the squib. A process to determine the mass of the original bottle is described in detail in Reference 3. Within the representative rotary-wing platform, there is minimal room for an increase in the diameter of the fire suppression system cylinder. However, there is room for an increase in the cylinder length. Another process was used to analyze the increase in total fire suppression system mass and is also described in Reference 3. Table 10–16 shows the results of these analyses.

**Table 10–16. Future Rotary-wing Aircraft Analysis of Increase in Total Mass.**

Mass per Platform	Current Halon 1301 Design		Redesigned Halon 1301 (optimally distributed)		Redesigned Halon 1301 (not optimally distributed)		HFC-125 (optimally distributed)		HFC-125 (not optimally distributed)	
	kg	lb	kg	lb	kg	lb	kg	lb	kg	lb
Agent	0.7	1.5	1.1	2.4	3.3	7.2	3.6	7.9	7.6	16.8
Bottle	2.6	5.7	4.0	8.9	11.8	26.0	15.9	35.1	33.4	73.7
Other	4.2	9.3	4.2	9.3	4.2	9.3	4.2	9.3	4.2	9.3
TOTAL	7.5	16.5	9.3	20.6	19.3	42.5	23.7	52.3	45.4	99.8

## 10.5 COSTS OF CURRENT AND REPLACEMENT SYSTEMS

The life cycle cost of a system includes the acquisition, operation, and maintenance over the life of the system. Both the HFC-125 systems and halon 1301 systems are reusable and rechargeable. The pressure vessels must be hydrostatically tested periodically, and the explosive initiators used in the design must be changed periodically due to the limited propellant life. Support equipment and facilities required to service these units add to the life cycle cost. Costs associated with actual system utilization are generally low because of the infrequent need to use the system, although the rate of inadvertent discharge in some older aircraft may be significant. The life cycle cost of a system can be heavily impacted by the potential for increased mass that may result from incorporation of a non-ozone depleting fire extinguishing chemical.<sup>29</sup>

The costs estimated in this effort are those that would be incurred in the research, development, test and evaluation (RDT&E), procurement, and operations and maintenance (O&M) phases of an acquisition. RDT&E costs deal with all costs required to develop the fire suppression technology into a deployable system. Procurement (also called initial or nonrecurring) costs are those associated with the purchase of the fire suppression system (and associated hardware) and suppressant. O&M costs are broad and far-reaching. Included in this category are those costs associated with program management support and life cycle sustainment management.

There are some limitations to these cost estimates:

- The significant cost impact of modifying an aircraft (including its structure) to accommodate fire system changes could not be accurately estimated and was thus not included
- Dimensioned drawings of the aircraft were proprietary. As an alternative, technical orders were used.
- Minimal FOS data existed. The data available were used and adapted.

Prior to performing this cost analysis, the ground rules and assumptions (similar for all three platform assessments) were developed to bound this assessment:

- Minimal FOS data existed. The data available were used and adapted.
- This cost analysis was performed for the existing halon 1301 system and the off-the-shelf-alternative (HFC-125) for both legacy and future cargo platforms and developed for a system with equivalent performance of halon 1301.
- Raw Inflation Indices, dated 2001, from the Office of the Secretary of Defense were used to arrive at then-year (inflated) dollars.
- This cost analysis assumes that each platform will be retrofitted for only one agent.
- The maintenance concept assumed was the contractor logistics support (CLS). The average of CLS costs for analogous platforms was used. This estimate is assumed to be funded out of procurement dollars.
- This cost analysis assumes a similar delivery schedule and number of aircraft to existing fielded aircraft.
- Prime mission equipment (PME) unit costs for the legacy aircraft fire suppression system are based on Technical Orders (TOs) and FEDLOG pricing.

- For the legacy aircraft, no RDT&E costs for the halon 1301 option were included since it was assumed that these were sunk costs.
- HFC-125 is available at the time of retrofit.
- The basic research data pertaining to HFC-125 is complete and available. Such information includes its chemical, thermophysical, thermodynamic, and transport properties. Other key items include: pressure, boiling point, molecular weight, liquid density, vapor pressure, critical temperature.
- The following small- to medium-scale effectiveness experiments have been performed on HFC-125 and the data are complete and available:
  - ISO cup burner
  - Laminar opposed-flow diffusion flame (OFDF)
  - Turbulent spray flame
  - Propane inertion testing
  - Baffle-stabilized pool fire testing
- The following small-scale environmental experiments have been performed on HFC-125 and that the data are complete and available:
  - Measurement of ozone depleting potential (ODP).
  - Measurement of global warming potential (GWP).
  - Measurement of acute toxicity (high-exposure, short-duration).
  - Evaluation of the production of acid gases and other hazardous by-products by small-scale R&D fire testing in a reasonably accurate simulation of the fire challenge or application under consideration.
  - Favorable completion of a typical corrosion test such as those conducted in the evaluation of new agents for aircraft engine fire suppression in accordance with ASTM Standard F1110-90, entitled "Standard Test Method for Sandwich Corrosion Test."
- A full-scale testing of the suppressor in a military simulator has been performed and that the data are complete and available.
- The agent meets the following time and concentration requirements as prescribed by the Air Force certification requirements specified in MIL-E-22285. For engine nacelles and APUs in USAF fixed wing aircraft, a certification test series is conducted using the calculated agent mass requirement as a starting point for discharge measurements using the calibrated concentration measurement equipment to insure the attainment of the required concentration for a prescribed time interval, usually 0.5 seconds. During this test series, adjustments in agent mass and/or distribution parameters are made until the system meets the requirement.
- HFC-125 must leave no damaging residue to harm electronic or other components. For many applications, HFC-125 must fill a space to inert flammable or explosive atmospheres. With no damaging residue, HFC-125 cleanup would be with minimal effort.
- HFC-125 is not electrically conductive.
- According to DuPont, HFC-125 has an indefinite shelf life if the material is stored properly in a sealed container that prevents leakage as well as entering moisture. HFC-125 meets NFPA

2001 specifications for clean agents. These specifications are set to ensure product performance over long storage periods (many years).

Additional details are available in References 1, 2, and 3.

### 10.5.1 Life Cycle Cost Estimate (LCCE) Summary for Legacy Aircraft

The following tables contain the life cycle cost estimate summary for the existing halon 1301 system and the off-the-shelf-alternative (HFC-125) for legacy cargo, fighter, and rotary-wing platforms and developed for a system with equivalent performance of halon 1301.

#### Cargo Aircraft

Table 10–17 shows the Life Cycle Cost Estimate (LCCE) for the legacy cargo aircraft halon 1301 and HFC-125 systems in FY00 constant dollars and then-year dollars by type of funding.

**Table 10–17. Comparison of Halon 1301 and HFC-125 System Life Cycle (FY00 to FY22) Cost Estimates for Legacy Cargo Aircraft (\$ M).**

Description of Effort	Halon 1301 Total	HFC-125 126 kg (280 lb)			HFC-125 40 kg (88 lb)		
		Container Mod	Container and Nozzle Mod	Container and Distribution Sys Mod	Container Mod	Container and Nozzle Mod	Container and Distribution Sys Mod
<b>FY2000 Constant Dollars</b>							
1.0 RDT&E (\$M)	0	0.3	0.3	0.4	0.3	0.3	0.3
2.0 PROCUREMENT	10.3	20.1	21.2	21.8	18.3	19.4	19.9
3.0 O&M	14.7	17.2	17.3	18.5	15.8	15.9	17.0
4.0 MILITARY PERSONNEL	0.2	0.2	0.2	0.2	0.2	0.2	0.2
5.0 MILITARY CONSTRUCTION	0	0	0	0	0	0	0
TOTAL	25.2	37.9	39.1	40.8	34.5	35.7	37.5
TOTAL COST PER AIRCRAFT	0.2	0.3	0.3	0.3	0.3	0.3	0.3
<b>Then Year Dollars</b>							
1.0 RDT&E	0	0.3	0.3	0.4	0.2	0.3	0.3
2.0 PROCUREMENT	11.0	22.2	23.5	24.1	20.2	21.4	22.1
3.0 O&M	18.4	21.5	21.6	23.0	19.8	19.9	21.2
4.0 MILITARY PERSONNEL	0.3	0.3	0.3	0.3	0.3	0.3	0.3
5.0 MILITARY CONSTRUCTION	0	0	0	0	0	0	0
TOTAL	29.7	44.4	45.8	47.8	40.5	41.9	44.0

In terms of FY00 (Fiscal Year 2000) constant dollars, the legacy cargo aircraft halon 1301 fire suppression system cost is estimated to be \$208 k per aircraft over a 23-year life cycle (FY00 to FY22), based on 121 aircraft. This is approximately 0.11 % of the total flyaway aircraft cost of \$183 M. In FY00 constant dollars, the non-optimally distributed HFC-125 system, weighing 126 kg (280 lb) is estimated to range from \$313 k to \$338 k per aircraft. This is approximately 0.17 % to 0.18 % of the total flyaway aircraft cost. The optimally distributed HFC-125 system, weighing 40 kg (88 lb) ranges from \$285 k to \$310 k. This is approximately 0.16 % to 0.17 % of the total flyaway aircraft cost.

### Fighter Aircraft

Table 10–18 shows the LCCE for the legacy fighter aircraft halon 1301 and HFC-125 systems in FY00 constant dollars and then-year dollars by type of funding. In terms of FY00 constant dollars, the legacy fighter aircraft halon 1301 fire suppression system cost is estimated to be \$20.5 k per aircraft over a 29-year life cycle (FY00 to FY28), based on 549 aircraft. This is approximately 0.04 % of the total flyaway aircraft cost of \$51.1 M. In FY00 constant dollars, the non-optimally distributed HFC-125 system, weighing 8.4 kg (18.4 lb) is estimated to be \$32.5 k per aircraft. This is approximately 0.06 % of the total flyaway aircraft cost. The optimally distributed HFC-125 system, weighing 3.2 kg (7.0 lb) is estimated to be \$28.6 k. This is approximately 0.05 % of the total flyaway aircraft cost. Using the conservative value of 60 % system effectiveness, the breakpoint between cost and benefit is \$282 k per aircraft.

**Table 10–18. Comparison of Halon 1301 and HFC-125 System Life Cycle (FY00 to FY28) Cost Estimates for Legacy Fighter Aircraft (\$ M).**

Description of Effort	Halon 1301	HFC-125 (optimally distributed)	HFC-125 (not optimally distributed)
	2.5 kg (5.5 lb)	3.2 kg (7lb)	8.4 kg (18.4 lb)
<b>FY2000 Constant Dollars</b>			
1.0 RDT&E (\$M)	0	2.0	2.0
2.0 PROCUREMENT	8.1	9.5	9.6
3.0 O&M	3.0	4.0	6.1
4.0 MILITARY PERSONNEL	0.14	0.14	0.14
5.0 MILITARY CONSTRUCTION	0	0	0
TOTAL	11.2	15.7	17.8
TOTAL COST PER AIRCRAFT	0.02	0.03	0.03
<b>Then Year Dollars</b>			
1.0 RDT&E	0	2.0	2.0
2.0 PROCUREMENT	9.1	10.9	11.0
3.0 O&M	3.9	5.4	8.0
4.0 MILITARY PERSONNEL	0.2	0.2	0.2
5.0 MILITARY CONSTRUCTION	0	0	0
TOTAL	13.3	18.5	21.3

## Rotary-Wing Aircraft

Table 10–19 shows the LCCE for the legacy rotary-wing aircraft halon 1301 and HFC-125 fire suppression systems in FY03 constant dollars and then-year dollars by type of funding. In terms of FY00 constant dollars, the legacy rotary-wing aircraft non-optimally distributed halon 1301 system, weighing 3.3 kg (7.18 lb) is estimated to be \$30.3 k per aircraft over a 33-year life cycle (FY03 to FY35), based on 1213 aircraft. This is approximately 0.18 % of the total flyaway aircraft cost. The optimally distributed halon 1301 system, weighing 1.1 kg (2.4 lb) is estimated to be \$28.2 k per aircraft. This is approximately 0.17 % of the total flyaway aircraft cost. In FY03 constant dollars, the non-optimally distributed HFC-125 system, weighing 7.6 kg (16.8 lb) is estimated to be \$43.7 k per aircraft. This is approximately 0.26 % of the total flyaway aircraft cost. The optimally distributed HFC-125 system, weighing 3.6 kg (7.9 lb) is estimated to be \$39.5 k per aircraft. This is approximately 0.24 % of the total flyaway aircraft cost. Using the conservative value of 60 % system effectiveness, the breakpoint between cost and benefit is \$306.8 k per aircraft.

**Table 10–19. Comparison of Halon 1301 and HFC-125 System Life Cycle (FY03 to FY35) Cost Estimates for Legacy Rotary-wing Aircraft (\$ M).**

Description of Effort	Halon 1301 (optimally distributed)	Halon 1301 (not optimally distributed)	HFC-125 (optimally distributed)	HFC-125 (not optimally distributed)
	1.1 kg (2.4 lb)	3.3 kg (7.2 lb)	3.6 kg (7.9 lb)	7.6 kg (16.8 lb)
<b>FY2003 Constant Dollars</b>				
1.0 RDT&E (\$M)	0	0	3.2	3.2
2.0 PROCUREMENT	23.7	24.0	30.2	30.4
3.0 O&M	10.3	12.6	14.3	19.2
4.0 MILITARY PERSONNEL	0.19	0.19	0.18	0.18
5.0 MILITARY CONSTRUCTION	0	0	0	0
TOTAL	34.2	36.8	48.0	53.1
TOTAL COST PER AIRCRAFT	0.03	0.03	0.04	0.04
<b>Then Year Dollars</b>				
1.0 RDT&E	0	0	3.3	3.3
2.0 PROCUREMENT	28.3	28.8	37.0	37.3
3.0 O&M	14.1	17.3	19.6	26.4
4.0 MILITARY PERSONNEL	0.32	0.32	0.32	0.32
5.0 MILITARY CONSTRUCTION	0	0	0	0
TOTAL	42.8	46.3	60.2	67.2

### 10.5.2 Life Cycle Cost Estimate (LCCE) Summary for Future Aircraft

The following tables contain the life cycle cost estimate summary for the existing halon 1301 system and the off-the-shelf-alternative (HFC-125) for future cargo, fighter, and rotary-wing platforms and developed for a system with equivalent performance of halon 1301.

## Cargo Aircraft

Table 10–20 shows the LCCE for the future cargo aircraft halon 1301 and HFC-125 systems in FY00 constant dollars and then-year dollars by type of funding. In terms of FY00 constant dollars, the future cargo aircraft halon 1301 fire suppression system cost is estimated to be \$301 k per aircraft over a 32-year life cycle (FY00-31), based on 121 aircraft. This is approximately 0.16 % of the total flyaway aircraft cost of \$183 M. In FY00 constant dollars, the non-optimally distributed HFC-125 system, weighing 125.6 kg (276.8 lb) is estimated to range from \$318 k to \$366 k per aircraft. This is approximately 0.17% to 0.20 % of the total flyaway aircraft cost. The optimally distributed HFC-125 system, weighing 39.9 kg (87.9 lb) ranges from \$288 k to \$336 k. This is approximately 0.16 % to 0.18 % of the total flyaway aircraft cost.

**Table 10–20. Comparison of Halon 1301 and HFC-125 System Life Cycle (FY00 to FY31) Cost Estimates for Future Cargo Aircraft (\$ M).**

Description of Effort	Halon 1301 Total	HFC-125 125.6 kg (276.8 lb)			HFC-125 39.9 kg (87.9 lb)		
		Container Mod	Container and Nozzle Mod	Container and Distribution Sys Mod	Container Mod	Container and Nozzle Mod	Container and Distribution Sys Mod
<b>FY2000 Constant Dollars</b>							
1.0 RDT&E (\$M)	0.56	0.61	0.69	0.75	0.54	0.62	0.68
2.0 PROCUREMENT	18.3	17.8	20.2	22.0	15.9	18.2	20.0
3.0 O&M	17.3	19.8	20.0	21.3	18.1	18.3	19.6
4.0 MILITARY PERSONNEL	0.31	0.31	0.31	0.31	0.31	0.31	0.31
5.0 MILITARY CONSTRUCTION	0	0	0	0	0	0	0
TOTAL	36.5	38.5	41.1	44.3	34.9	37.5	40.6
TOTAL COST PER AIRCRAFT	0.30	0.32	0.34	0.37	0.29	0.31	0.34
<b>Then Year Dollars</b>							
1.0 RDT&E	0.57	0.62	0.70	0.77	0.55	0.63	0.70
2.0 PROCUREMENT	22.3	21.7	24.6	26.8	19.4	22.2	24.4
3.0 O&M	25.7	29.2	29.5	31.3	26.8	27.1	29.0
4.0 MILITARY PERSONNEL	0.54	0.54	0.54	0.54	0.54	0.54	0.54
5.0 MILITARY CONSTRUCTION	0	0	0	0	0	0	0
TOTAL	49.1	52.1	55.3	59.4	47.3	50.5	54.6

## Fighter Aircraft

Table 10–21 shows the LCCE for the future fighter aircraft halon 1301 and HFC-125 systems in FY00 constant dollars and then-year dollars by type of funding. In terms of FY00 constant dollars, the future

fighter aircraft halon 1301 fire suppression system cost is estimated to be \$26.3 k per aircraft over a 33-year life cycle (FY00 to FY32), based on 549 aircraft. This is approximately 0.05 % of the total flyaway aircraft cost of \$51.1M. In FY00 constant dollars, the non-optimally distributed HFC-125 system, weighing 8.4 kg (18.4 lb) is estimated to be \$32.7 k per aircraft. This is approximately 0.06 % of the total flyaway aircraft cost. The optimally distributed HFC-125 system, weighing 3.2 kg (7.0 lb) is estimated to be \$28.7 k. This is approximately 0.05 % of the total flyaway aircraft cost. Using the conservative value of 60 % system effectiveness, the breakpoint between cost and benefit is \$285 k per aircraft.

**Table 10–21. Comparison of Halon 1301 and HFC-125 System Life Cycle (FY00 to FY32) Cost Estimates for Fighter Cargo Aircraft (\$ M).**

	Halon 1301	HFC-125	HFC-125
DESCRIPTION OF EFFORT	2.5 kg (5.5 lb)	3.2 kg (7lb)	8.4 kg (18.4 lb)
<b>FY2000 Constant Dollars</b>			
1.0 RDT&E (\$M)	2.0	2.0	2.0
2.0 PROCUREMENT	9.1	10.2	10.3
3.0 O&M	3.2	3.5	5.5
4.0 MILITARY PERSONNEL	0.16	0.16	0.16
5.0 MILITARY CONSTRUCTION	0	0	0
TOTAL	14.4	15.8	18.0
TOTAL COST PER AIRCRAFT	0.03	0.03	0.03
<b>Then Year Dollars</b>			
1.0 RDT&E	2.0	2.0	2.0
2.0 PROCUREMENT	11.0	12.3	12.5
3.0 O&M	4.5	4.8	7.8
4.0 MILITARY PERSONNEL	0.29	0.29	0.29
5.0 MILITARY CONSTRUCTION	0	0	0
TOTAL	17.8	19.4	22.5

### Rotary-Wing Aircraft

Table 10–22 shows the LCCE for the future rotary-wing aircraft halon 1301 and HFC-125 fire suppression systems in FY03 constant dollars and then-year dollars by type of funding. In terms of FY03 constant dollars, the future rotary-wing aircraft non-optimally distributed halon 1301 system, weighing 3.3 kg (7.2 lb) is estimated to be \$35.9 k per aircraft over a 42-year life cycle of FY03 to FY41, based on 1213 aircraft. This is approximately 0.22 % of the total flyaway aircraft cost. In terms of FY03 constant dollars, the future rotary-wing aircraft optimally distributed halon 1301 system, weighing 1.1 kg (2.4 lb) is estimated to be \$33.7 k per aircraft over a 42-year life cycle of FY03 to FY41, based on 1213 aircraft. This is approximately 0.20 % of the total flyaway aircraft cost. In FY03 constant dollars, the non-optimally distributed HFC-125 system, weighing 7.6 kg (16.8 lb) is estimated to be \$41.4 k per aircraft. This is approximately 0.25 % of the total flyaway aircraft cost. The optimally distributed HFC-125 system, weighing 3.6 kg (7.9 lb) is estimated to be \$37.1 k per aircraft. This is approximately 0.22 % of the total flyaway aircraft cost. Using the conservative value of 60 % system effectiveness, the breakpoint between cost and benefit is \$312.2 k per aircraft.

**Table 10–22. Comparison of Halon 1301 and HFC-125 System Life Cycle (FY03 to FY41)  
Cost Estimates for Future Rotary-wing Aircraft (\$ M).**

	Halon 1301	Halon 1301	HFC-125	HFC-125
DESCRIPTION OF EFFORT	1.1 kg (2.4 lb)	3.3 kg (7.2 lb)	3.6 kg (7.90 lb)	7.6 kg (16.8 lb)
<b>FY2003 Constant Dollars</b>				
1.0 RDT&E (\$M)	3.2	3.2	3.1	3.1
2.0 PROCUREMENT	26.9	27.3	27.2	27.4
3.0 O&M	10.6	12.9	14.5	19.5
4.0 MILITARY PERSONNEL	0.22	0.22	0.22	0.22
5.0 MILITARY CONSTRUCTION	0	0	0	0
TOTAL	40.9	43.6	45.0	50.3
TOTAL COST PER AIRCRAFT	0.03	0.04	0.04	0.04
<b>Then Year Dollars</b>				
1.0 RDT&E	3.2	3.2	3.2	3.2
2.0 PROCUREMENT	35.4	35.9	35.8	36.1
3.0 O&M	16.2	19.8	22.2	29.9
4.0 MILITARY PERSONNEL	0.43	0.43	0.43	0.43
5.0 MILITARY CONSTRUCTION	0	0	0	0
TOTAL	55.2	59.4	61.6	69.6

### 10.5.3 Detailed Cost Element Structure (CES)

This fire suppression system's detailed cost element structure (CES) given in Table 10–23 is based on the DoD 5000.4-M and MIL-HDBK-881 CES. It was customized for each system and approach. Due to space limitations and for clarity, only general information about the various cost elements is presented here. Additional details are available in References 1, 2, and 3.

### 10.5.4 Cost Element Structure Data Development

Cost factors used by government and industry were obtained from the Aeronautical Systems Center (ASC) Cost Library and ESC/FMC. These cost factors were then applied to the subsystem costs (Group A/Group B kits). A Group A Kit is defined as the hardware used to install/mount the fire suppression system while the Group B Kit is actually the fire suppression system itself, including the agent. The following sections are organized according to the Cost Element codes in Table 10–23. When no information was available for a given Element, a cost factor was used (multiplied by the appropriate Group A/Group B kit price) to estimate this element. However, cost factors were not available for every element.

**Table 10–23. Detailed Cost Element Structure.**

Cost Elements	
1.0	RDT&E (3600)
1.1	Concept Exploration
1.2	Prototype Engineering And Manufacturing Development (EMD) Cost Sharing (Fire Suppression System Prototype)
1.2.1	Subsystem
1.2.1.1	Group A Kit (Hardware to install/mount fire suppression system)
1.2.1.2	Group B Kit (Fire suppression system)
1.2.2	Commercial-Off-The-Shelf (COTS)/Government-Off-The Shelf (GOTS) Software – N/A
1.2.3	Development Software – N/A
1.2.4	Integration, Assembly, Test and Checkout
1.3	System/Platform Integration
1.4	System Engineering/Program Management
1.4.1	Systems Engineering
1.4.2	Program Management
1.4.3	Travel
1.5	System Test and Evaluation
1.5.1	Developmental Test and Evaluation (DT&E)
1.5.2	Operational Test and Evaluation (OT&E)
1.6	Data
1.7	Training
1.8	Evolutionary Technology Insertions (ETIs) - N/A
1.8.1	Program Management
1.8.2	Prototype and Test Bed
1.8.3	Market Surveys
1.9	Support Equipment
1.9.1	Common Support Equipment
1.9.2	Peculiar Support Equipment
2.0	PROCUREMENT (3010)
2.1	Prime Mission Product (Fire Suppression System)
2.1.1	Subsystems
2.1.1.1	Group A Kit (Hardware to install/mount fire suppression system)
2.1.1.2	Group B Kit (Fire suppression system)
2.1.2	Non-Recurring Engineering – N/A
2.1.3	Software Integration – N/A
2.1.4	Integration, Assembly, Test and Checkout
2.2	System/Platform Integration and Assembly (Cost of installation)
2.3	Systems Engineering/Program Management
2.3.1	Systems Engineering
2.3.2	Program Management
2.3.3	Logistics Management
2.4	System Test and Evaluation
2.4.1	Operational Test and Evaluation
2.5	Engineering Change Orders (ECOs)
2.6	Initial Cadre Training
2.7	Data
2.8	Operational Fielding/Site Activation
2.9	Depot Setup - N/A
2.10	Support Equipment
2.10.1	Common Support Equipment

<b>Cost Elements</b>	
2.10.2	Peculiar Support Equipment
2.11	Initial Spares and Repair Parts
2.12	Warranty
2.13	Evolutionary Technology Insertions (ETIs) - N/A
2.14	Interim Contractor Support (ICS)
2.15	Flexible Sustainment Support (Maintenance Support)
3.0	OPERATIONS AND MAINTENANCE (3400)
3.1	Program Administration
3.1.1	Program Management Support
3.1.1.1	Miscellaneous Contract Services
3.1.1.2	Government Technical Support
3.1.1.3	Travel
3.1.2	Life Cycle Sustainment Management (LCSM)
3.2	Program Operational Support
3.2.1	Recurring Training
3.2.2	Technical Data Revision
3.2.3	Software Maintenance - N/A
3.2.4	Hardware Maintenance
3.2.4.1	Organic Support
3.2.4.2	Contractor Maintenance
3.2.5	Replenishment Spares
3.2.6	Repair Parts and Materials
3.2.7	Transportation, Packaging, and Handling
3.2.8	Storage
3.2.9	Disposal
3.2.10	Facility Projects/Upgrades/Leases
3.2.11	Operational O&M Impacts of ETIs - N/A
3.2.12	Program Operations
3.2.13	Unit Level Support
3.2.13.1	Recurring Training (Unit Travel/TDY Costs)
3.2.13.2	Operating Consumables
3.2.13.3	Unit Level O&M Impacts of ETIs
3.2.14	Depot Level Support
3.2.15	Contractor Logistics Support (CLS)
4.0	MILITARY PERSONNEL (3500)
5.0	MILITARY CONSTRUCTION – N/A

## **RDT&E (1.0)**

No cost information was available for the concept exploration (1.1).

The prototype EMD cost sharing (1.2) is the hardware and software used to accomplish the primary mission and includes all integration, assembly, test and checkout, as well as all technical and management activities associated with individual hardware/software elements. ASC Avionics Support Cost Element Factors were used to estimate costs for systems engineering/program management, system test and evaluation, data, and training.

The data used to derive these cost factors were extracted from Cost Performance Reports (CPR) and Cost/Schedule Status Report (C/SSR) reports. The other cost factors used in this estimate originated from Electronic Systems Center (ESC/FMC). Data used for these factors encompassed thirty-seven CPR and

C/SSR stored in the Automated Cost Estimating Integrated Tool's (ACE-IT) Automated Cost Data Base (ACDB). The data represent ESC production contract efforts occurring between 1974 and 1992.

Technical orders and FEDLOG pricing were used to capture the cost of the Group A (1.2.1.1) and Group B (1.2.1.2) kits for the fire suppression system. The cost factors are applied to the Group A and Group B Kit costs.

The integration, assembly, test and checkout (1.2.4) includes the effort associated with bending metal, mating surfaces, structures, equipment, parts, and materials required to assemble all equipment, components and subsystems into an operational system. Since specific cost information was not available, a multiplicative cost factor was used to estimate this element, as is common practice when such cost data is not available.

System/platform integration (1.3) includes the efforts associated with integrating/installing systems or subsystems into an existing platform/weapon system. No cost information was available for this cost element.

Systems engineering/program management (1.4) involves all associated elements to be reported, including the overall planning, directing, and controlling of the definition, development, and production of a system or program. Since specific cost information was not available, a cost factor was used to estimate this element.

System test and evaluation (1.5) is the use of prototype, production, or specifically fabricated hardware and/or software to obtain or validate engineering data on the performance of the system during the development phase of the program. It includes detailed planning, conduct of, support for, data reduction, and reports from such testing, and all hardware/software items which are consumed or planned to be consumed in the conduct of such testing as well as all effort associated with the design and production of models, specimens, fixtures, and instrumentation in support of the system level test program. Since specific cost information was not available, a cost factor was used to estimate this element.

Data (1.6) includes the effort required to develop technical and managerial data in support of the program. Since specific cost information was not available, a cost factor was used to estimate this element.

Training (1.7) includes all efforts associated with the design, development, and production of deliverable training equipment as well as the execution of training services. Since specific cost information was not available, a cost factor was used to estimate this element.

Support equipment (1.9) includes the effort required to design, develop and produce system peculiar and common support equipment. Since specific cost information was not available, the cost factors were used to estimate these elements.

## **Procurement (2.0)**

The prime mission product (PMP) (2.1) is the hardware and software used to accomplish the primary mission and includes all integration, assembly, test and checkout, as well as all technical and management activities associated with individual hardware/software elements. Technical Orders (TOs) and FEDLOG pricing were used to capture the cost of the Group A/B Kits for the fire suppression system.

The integration, assembly, test and checkout (2.1.4) includes the effort associated with bending metal, mating surfaces, structures, equipment, parts, and materials required to assemble all equipment, components and subsystems into an operational system. Since specific cost information was not available, a cost factor was used to estimate this element.

System/platform integration and assembly (2.2) includes the efforts associated with integrating/installing systems or subsystems into an existing platform/weapon system. Depending on the alternative, labor was estimated for modifications to the container, nozzles, and the distribution system.

Systems engineering/program management (2.3) includes the effort required for system definition; overall system design; design integrity, cost effectiveness, weight, and balance analyses; intra-system and inter-system compatibility; safety, security, and survivability requirements; human engineering; and performance specifications. Program management includes the effort required for configuration, contract, and data management; cost and schedule management; transportation and packaging management; vendor liaison; value engineering; and quality assurance. Logistics management includes the effort required for reliability, maintainability and logistics support integration. Since specific cost information was not available, a cost factor was used to estimate this element.

System test and evaluation (2.4) includes the effort required for: all detailed test planning, support data consolidation and corresponding reports; hardware items consumed in the conduct of testing; and efforts associated with models, specimens, fixtures and instrumentation. No cost information was available for this cost element.

Engineering change orders (2.5) includes the effort required for anticipated "in scope" contract engineering changes to the prime mission product. No cost information was available for this cost element.

Initial cadre training (2.6) includes the effort required for the design, development, and production of training equipment, course material preparation, and travel costs associated with conducting training for an initial cadre of both operational and depot personnel. Since specific cost information was not available, a cost factor was used to estimate this element.

Data (2.7) includes the effort required to develop technical and managerial data in support of the program. Since specific cost information was not available, a cost factor was used to estimate this element.

Operational fielding/site activation (2.8) includes the real estate, construction, conversion, utilities, and equipment to provide all facilities required to house, service, and launch prime mission equipment at the organizational and intermediate level. Since specific cost information was not available, a cost factor was used to estimate this element.

Common support equipment (2.10.1) involves the acquisition of additional support equipment, over and above existing support equipment inventories, required to support the acquisition of a new system or subsystems. Peculiar equipment (2.10.2) generally involves unique or special purpose vehicles, equipment or tools used to transport and hoist; service, repair, overhaul, assemble and disassemble; test and inspect; and to perform other maintenance on the prime mission product. Since specific cost information was not available, cost factors were used to estimate these elements.

Initial spares and repair parts (2.11) includes the effort required to procure modules, spare components and assemblies used for replacement purposes (building logistical pipeline) to support prime mission product. Since specific cost information was not available, a cost factor was used to estimate this element.

The maintenance concept assumed was the contractor logistics support (CLS). Therefore, there are no costs associated with flexible sustainment support (2.15).

### **Operations and Maintenance (O&M) (3.0)**

Program management support (3.1.1) includes the effort required for configuration, contract and data management, cost and schedule management, transportation and packaging management, vendor liaison, value engineering, and quality assurance. Since specific cost information was not available, a cost factor of 0.05 was used to estimate this element for the halon 1301 system and 0.10 for the HFC-125. The cost factor is varied depending on the maturity of the system; therefore, a higher factor was applied to the HFC-125 system since it is in the earliest stages for this platform.

Hardware maintenance organic support (3.2.4.1) includes civilian labor, material, and overhead costs incurred after deployment. This cost element was estimated by taking the number of flying hours for a typical cargo platform (contained in the Air Force Instruction (AFI) 65-503 Attachment 42-1 for Aircraft Endstrengths) and multiplying by the average civilian hourly pay (contained in AFI 65-503 Attachment A28-1) and the average maintenance staff hour per flying hour.

Replenishment spares include the cost of materials consumed in operation, maintenance, and support of the primary system and associated support at the unit level. Since specific cost information was not available, a cost factor in relation to initial spares and repair parts was used to estimate this element.

The maintenance concept assumed was the CLS. The average of CLS costs (3.2.15) for analogous platforms was used.

The tubing and brackets for the fire suppression system are nonrepairable and condemned at the field level, with a local manufacturing capability. The bottles are repaired (recharged) and condemned at the depot and have limited "O" and "I" level repair.<sup>30</sup>

### **Military Personnel (4.0)**

Military personnel support was estimated by taking the number of military personnel endstrengths (contained in the AFI 65-503 Attachment 42-1 for Aircraft Endstrengths) and multiplying by the average officer and enlisted pay (contained in AFI 65-503 Attachment A19-1) and the percentage of the fire suppression system to the total aircraft cost.

## **10.6 COST SAVINGS**

In a previous study (Reference 31), the historical and projected costs to the U.S. Air Force aircraft fleet due to in-flight fires were determined. By combining the components which comprise the costs of peacetime aircraft losses due to fire, a resulting historical cost (over a 30 year period) of approximately \$9.3 billion was determined, measured in 1995 dollars. The costs of combat aircraft losses due to fire

were estimated to be approximately \$5.9 billion (in 1995 dollars), based primarily on Southeast Asia experience. The costs of utilizing aircraft fire protection were estimated to be approximately \$316 million (in 1995 dollars). Thus, the total historical costs of fire to the U.S. Air Force over the 1966 to 1995 time period was estimated to be \$15.5 billion (in 1995 dollars). The total projected costs of fire to the U.S. Air Force over the 1996 to 2025 time period was estimated to be \$16.0 billion (in 1996 dollars). A net present value of over \$119 million was projected to be the benefit of fire suppression systems over the next 30 years, in terms of the reduction in casualty-related losses due to their presence, even with the costs of the protection systems themselves included.

The cost savings for the life of the legacy and future aircraft were estimated by using the traditional extinguishing success rate for existing engine halon systems, the estimated fire costs per flight hour, and the number of flight hours for the legacy cargo aircraft. Field experience of existing engine halon systems on current aircraft, depending on the platform, shows that the systems have a 60 % to 80 % success rate. This study (Reference 31) postulated that future aircraft losses due to fire incidents were a function of the total number of flight hours (FH) for this period. An historical relationship between fire costs and flight hours was established. The resulting average fire cost per flight hour (in 2000 dollars) was \$63.<sup>31</sup>

Table 10–24 through Table 10–26 show the estimated cost savings determined, while using on-board fire protection for legacy and future aircraft of the three types.

**Table 10–24. Cargo Aircraft Cost Savings Estimation.**

Cost Factors	Legacy Aircraft	Future Aircraft
PAA Quantity Cumulative	121	121
Flying Hours Cumulative	3.24 M	3.60 M
Fire Cost Cumulative	\$204 M	\$226 M
Cost Savings: 60 % effective system	\$122 M	\$136 M
Cost Savings: 80 % effective	\$163 M	\$181 M

**Table 10–25. Fighter Aircraft Cost Savings Estimation.**

Cost Factors	Legacy Aircraft	Future Aircraft
PAA Quantity Cumulative	549	549
Flying Hours Cumulative	4.10 M	4.15 M
Fire Cost Cumulative	\$258 M	\$261 M
Cost Savings: 60 % effective system	\$155 M	\$157 M
Cost Savings: 80 % effective	\$206 M	\$209 M

**Table 10–26. Rotary-wing Aircraft Costs Savings Estimation.**

Cost Factors	Legacy Aircraft	Future Aircraft
PAA Quantity Cumulative	1,213	1,213
Flying Hours Cumulative	9.9 M	10,0 M
Fire Cost Cumulative	\$620 M	\$631 M
Cost Savings: 60 % effective system	\$372 M	\$379 M
Cost Savings: 80 % effective	\$496 M	\$505 M

## 10.7 COST ANALYSIS USING ALTERED FIRE SUPPRESSION PERFORMANCE

Analyses discussed up to this stage in the cost analyses for halon 1301 and HFC-125 for legacy and future platforms have assumed a replacement HFC-125 system with an equivalent level of performance to legacy halon 1301 systems. For the next stage of this analysis, a methodology for legacy and future platforms utilizing systems with performance levels from traditional, fielded halon 1301 systems was developed. This allowed examination of whether there was an optimal performance or success rate that balances the costs of the system size (at that performance level) vs. the savings of the assets preserved at that success rate. Such a methodology could determine, for instance, if only a negligible increase in success rate resulted from doubling the size or cost of the system.

To address the issue of a potential fire suppression system with altered performance, data from the Factor of Safety study performed during Phase III of the Halon Replacement Program for Aviation (HRPA) were used.<sup>11</sup> Phase III was conducted in order to develop system sizing design equations for using HFC-125 as a halon replacement. As a final step in Phase III, the resulting design equations were "qualified" by performing Factor of Safety (FOS) tests. FOS testing provided an estimation of the fire protection effectiveness (as a percentage of fires successfully extinguished) of the amount of HFC-125 predicted by the design equation. Additional testing then determined the fire protection effectiveness percentages at agent capacities above and below the design equation amount. FOS data for the F-22 were used and adapted. These suppression system masses and corresponding effectiveness were correlated to the cargo and fighter aircraft platforms. The resulting systems' costs, costs savings, and net costs were calculated. The relationship between varying the system size and system effectiveness (and therefore costs and savings) was determined. More detailed information regarding these cost analyses are available in References 25, 26, and 27.

### 10.7.1 Factor of Safety Testing

The resulting system sizing design formula from the HRPAs was "qualified" by performing FOS tests under conditions similar to those of actual aircraft applications. The goals of FOS testing were twofold:

- Determine the fire protection effectiveness (expressed as the success rate percentage in extinguishing fires) of the amount of HFC-125 predicted by the design equation for a typical aircraft application.
- Compare the level of fire protection provided by the amount of HFC-125 predicted by the design equation with the level of fire protection offered by an aircraft's current halon 1301 system. This comparison not only provided an estimate of how much HFC-125 is needed for equivalent protection to halon 1301 for the particular aircraft, but also provided a guideline for use in similar aircraft engine nacelles.

The FOS testing and the need to estimate the effectiveness of the quantity of HFC-125 predicted by the design equation were driven by the fact that the bracketing technique used to determine the final successful mass in each test run could not consistently check the repeatability of the results. These FOS tests provided the data necessary to estimate the actual effectiveness of varying quantities of HFC-125. These tests were also performed to see if a suitable universal scale-up factor could be identified to estimate the masses of HFC-125 associated with near 100 % effectiveness, or to estimate masses of HFC-125 having the same effectiveness as current halon systems.

Fire suppression engineers for various military aircraft systems were queried about "typical" operating conditions for their respective aircraft. These operating conditions were then translated into level settings for the parameters used in the testing. Information was gathered on three aircraft system engine nacelles in order to obtain a wide range of possible test conditions. The aircraft chosen were the RAH-66, F-22, V-22, and F-15.

In keeping with the overall test strategy, the dependent variable was the observation of whether or not the fire was extinguished at the given agent amount. It was determined that at least ten shots at each agent amount of interest were required to capture the response of the system with sufficient precision of success rate, as measured by the percentage of fires extinguished.<sup>32</sup>

FOS data for the F-22 were used and adapted for this methodology. This methodology is explained in the next section.

### 10.7.2 System Description

Table 10–27 through Table 10–29 show the resulting system description for the actual cargo, fighter, and rotary-wing aircraft, respectively, selected and used for consideration and replication in the FOS tests.

**Table 10–27. Estimated Cargo Aircraft System Description.**

	Aircraft Engine Nacelle					Auxiliary Power Unit					Total Agent Per Platform	
	Conc.	Mass		Volume		Conc.	Mass		Volume		lb	kg
	% by vol.	lb	kg	in <sup>3</sup>	L	% by vol.	lb	kg	in <sup>3</sup>	L	lb	kg
Current Halon 1301 System	6	21	9.5	630	10	6	2.5	1.1	86	1.4	86	39
Estimated HFC-125-Optimally Distributed	24	21	9.7	810	13	24	2.6	1.2	111	1.8	88	40
Estimated HFC-125-Non-Optimally Distributed	24	67	30	2580	42	24	8	3.6	350	5.8	280	125

**Table 10–28. Estimated Fighter Aircraft System Description.**

	Legacy Fighter Aircraft (Halon 1301) (1 nozzle) <sup>e</sup>		Future Fighter Aircraft (HFC-125) (4 nozzles) <sup>e</sup>	
	kg	lb	kg	lb
Bottle Mass	4.2	9.3	5.6	12.2
Agent Mass	2.5	5.5	3.2	7.0
Plumbing Mass	4.3	9.5	4.6	10.1
Total Mass	11.1	24.4	13.3	29.4

<sup>e</sup> in addition to the agent outlets in the AMAD and APU bays

**Table 10–29. Estimated Rotary-wing Aircraft System Description.**

Mass per Platform	Current Halon 1301 Design		Redesigned Halon 1301 – small		Redesigned Halon 1301 – large		HFC-125 – small		HFC-125 – large	
	kg	lb	kg	lb	kg	lb	kg	lb	kg	lb
Agent	0.7	1.5	1.1	2.4	3.3	7.2	3.6	7.9	7.6	16.8
Bottle	2.6	5.7	4.0	8.9	11.8	26.0	15.9	35.1	33.4	73.7
Other	4.2	9.3	4.2	9.3	4.2	9.3	4.2	9.3	4.2	9.3
TOTAL	7.5	16.5	9.3	20.6	19.3	42.5	23.7	52.3	45.3	99.8

**10.7.3 Altered Fire Suppression Performance**

FOS data for the F-22 (shown in Figure 10–10) were used and adapted for this methodology.

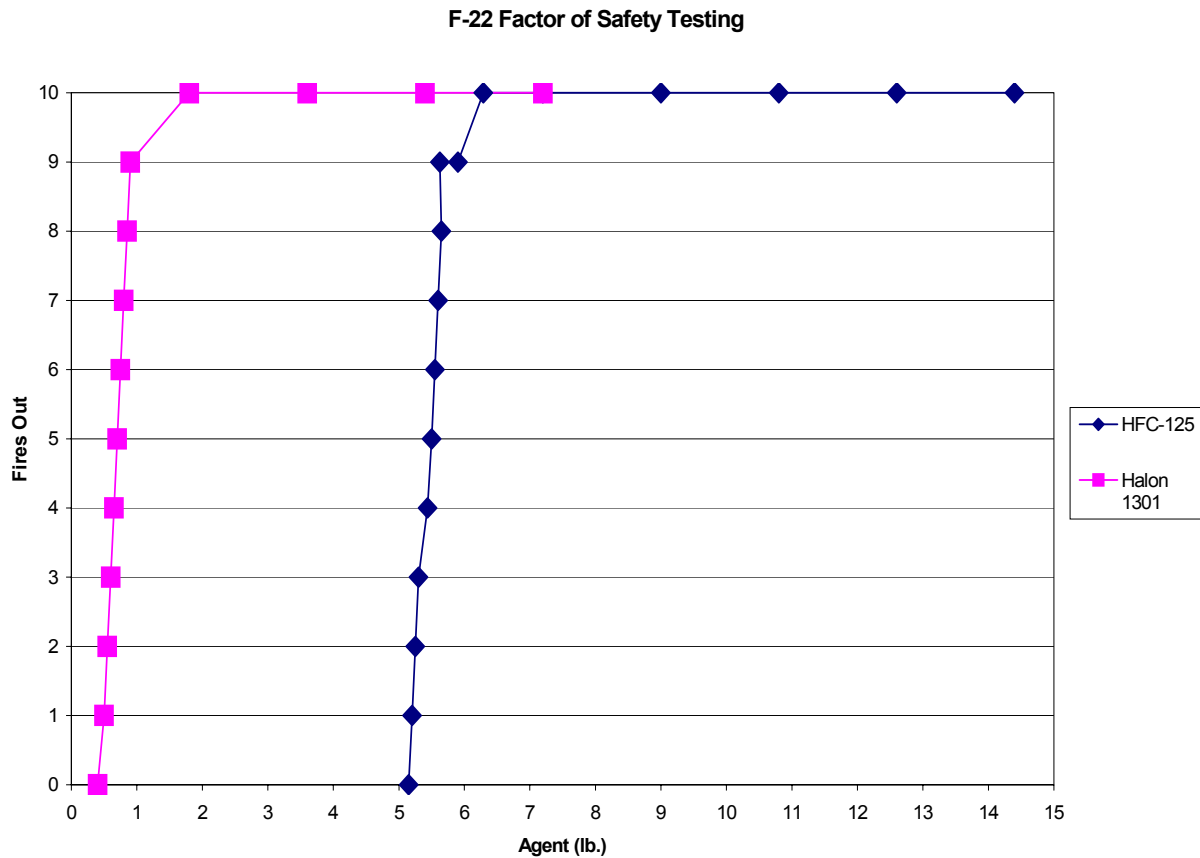


**Figure 10–10. F-22 Factor of Safety Data.**

These data were scaled from the corresponding Design Guide amount to the required amount of HFC-125 for the cargo, fighter, and rotary-wing aircraft, respectively, yielding an altered system description. For example, the 40 % success rate for HFC-125 resulted in an estimated mass of 2.5 kg (5.4 lb). The 90 % success rate for HFC-125 in the F-22 FOS resulted in an estimated mass of 2.6 kg (5.6 lb). The resulting

Design Guide amount was 6.4 lb. Thus, the ratio for 40 % success rate was 5.4/6.3 (or 0.9) of the Design Guide amount, and the 90 % success rate was 5.6/6.3 (or 0.9) of the Design Guide amount. These ratios were applied to the required amount of HFC-125 for the cargo, fighter, and rotary-wing aircraft, respectively. Table 10–30 through Table 10–32 show the resulting altered system descriptions for the cargo, fighter, and rotary-wing aircraft, respectively. These altered fire suppression system masses were used in the cost analysis for varied performance.

**Table 10–30. Cargo Aircraft Altered System Description.**

	Aircraft Engine Nacelle					Auxiliary Power Unit					Total Agent Per Platform	
	Design Conc.	Mass Estimation		Volume Estimation		Design Conc.	Mass Estimation		Volume Estimation			
	% by vol.	kg	lb	L	in <sup>3</sup>	% by vol.	kg	lb	L	in <sup>3</sup>	kg	lb
<b>100 % Laboratory Success Rate</b>												
Current halon 1301 system	6	9.5	21	10	630	6	1.1	2.5	1.4	86	39	86
Estimated HFC-125-optimally distributed	24	9.7	21	13	810	24	1.2	2.6	1.8	110	40	88
Estimated HFC-125- non-optimally distributed	24	30	67	42	2580	24	3.6	8	5.8	350	125	277
<b>90 % Laboratory Success Rate</b>												
Current halon 1301 system	5.4	8.5	19	9	560	5.4	1.0	2.2	1.3	77	35	77
Estimated HFC-125-optimally distributed	21	8.7	19	12	730	21	1.0	2.3	1.6	99	36	79
Estimated HFC-125- non-optimally Distributed	21	27	60	38	2310	21	3.2	7.2	5.2	315	112	248
<b>40 % Laboratory Success Rate</b>												
Current halon 1301 system	5.2	8.2	18	9	540	5.2	1.0	2.2	1.2	74	34	75
Estimated HFC-125-optimally distributed	21	8.4	18	11	700	21	1.0	2.2	1.6	96	34	76
Estimated HFC-125- non-optimally distributed	21	26	58	37	2230	21	3.1	6.9	5.0	300	110	240

**Table 10–31. Fighter Aircraft Altered System Description.**

	Halon 1301		HFC-125 Optimally Distributed		HFC-125 Non-optimally Distributed	
	kg	lb	kg	lb	kg	lb
<b>100% Laboratory Success Rate</b>						
Bottle mass	4.2	9.3	5.6	12.2	15.5	34.3
Agent mass	2.5	5.5	3.2	7	8.4	18.4
Plumbing mass	4.3	9.5	4.6	10.1	6.0	13.3
Total mass	11.1	24.4	13.3	29.4	29.9	65.9
<b>90 % Laboratory Success Rate</b>						
Bottle mass	3.8	8.3	5.0	10.9	13.9	30.7
Agent mass	2.2	4.9	2.8	6.3	7.5	16.5
Plumbing mass	3.9	8.5	4.1	9.1	5.4	11.9
Total mass	9.9	21.8	11.9	26.3	26.7	59
<b>40 % Laboratory Success Rate</b>						
Bottle mass	3.7	8.1	4.8	10.6	13.4	29.6
Agent mass	2.2	4.8	2.7	6.1	7.2	15.9
Plumbing mass	3.7	8.2	4.0	8.8	5.2	11.5
Total mass	9.6	21.1	11.5	25.4	25.9	57.0

**Table 10–32. Rotary-wing Aircraft Altered System Description.**

Mass per Platform	Current Halon 1301 Design		Redesigned Halon 1301-small		Redesigned Halon 1301-large		HFC-125-small		HFC-125-large	
	kg	lb	kg	lb	kg	lb	kg	lb	kg	lb
<b>100% Laboratory Success Rate</b>										
Agent	0.7	1.5	1.1	2.4	3.3	7.2	3.6	7.9	7.6	16.8
Bottle	2.6	5.7	4.0	8.9	11.8	26.0	15.9	35.1	33.4	73.7
Other	4.2	9.3	4.2	9.3	4.2	9.3	4.2	9.3	4.2	9.3
TOTAL	7.5	16.5	9.3	20.6	19.3	42.5	23.7	52.3	45.3	99.8
<b>90 % Laboratory Success Rate</b>										
Agent	0.6	1.3	1.0	2.1	2.9	6.4	3.2	7.1	6.8	15.0
Bottle	2.3	5.1	3.6	7.9	10.6	23.3	14.2	31.4	29.9	65.9
Other	3.8	8.3	3.8	8.3	3.8	8.3	3.8	8.3	3.8	8.3
TOTAL	6.7	14.7	8.3	18.4	17.2	38.0	21.2	46.7	40.5	89.2
<b>40 % Laboratory Success Rate</b>										
Agent	0.6	1.3	0.9	2.1	2.8	6.2	3.1	6.8	6.6	14.5
Bottle	2.2	4.9	3.5	7.7	10.2	22.5	13.7	30.3	28.9	63.7
Other	3.7	8.0	3.7	8.0	3.7	8.0	3.7	8.0	3.7	8.0
TOTAL	6.5	14.2	8.1	17.8	16.7	36.7	20.5	45.2	39.1	86.3

### 10.7.4 Cost Analysis

These altered suppression system masses and corresponding effectiveness were correlated to the cargo, fighter, and rotary-wing aircraft for the cost studies using the methodology in References 1, 2, and 3. The resulting systems costs (which are a function of system size/mass), costs savings (which are a function of extinguishant effectiveness and the resultant aircraft saved), and net costs (cost of the system minus the cost savings) were calculated. The relationship between varying the system size and system effectiveness (and therefore costs and savings) was determined.

#### Cargo Aircraft

Table 10–33 and Table 10–34 show the resulting net costs for the legacy and future cargo aircraft, respectively. “Slope” is the net cost (\$M) divided by the percent system effectiveness, determined from Figure 10–11, Figure 10–12, and Figure 10–13. The negative cost numbers indicate a net cost savings due to the presence of fire protection on board. Larger negative numbers mean a greater cost savings incurred.

**Table 10–33. Legacy Cargo Aircraft Net Costs (\$ M).**

Effectiveness (%)	Halon 1301	HFC-125 – non-optimized (276.8 lb)			HFC-125 – optimized (87.9 lb)		
		Container Mod	Container and Nozzle Mod	Container and Distribution Sys Mod	Container Mod	Container and Nozzle Mod	Container and Distribution Sys Mod
24	-23.9	-11.9	-10.7	-9.1	-14.1	-12.9	-11.3
32	-40.2	-28.2	-27.0	-25.4	-30.4	-29.2	-27.6
54	-85.0	-72.5	-71.3	-69.7	-75.7	-74.5	-72.9
60	-97.0	-84.4	-83.2	-81.4	-87.7	-86.5	-84.8
72	-121.7	-109.2	-108.0	-106.3	-112.3	-111.2	-109.5
80	-137.8	-125.1	-123.9	-122.2	-128.5	-127.3	-125.6
slope	-2.03	-2.02	-2.02	-2.01	-2.04	-2.04	-2.04

**Table 10–34. Future Cargo Aircraft Net Costs (\$ M).**

Effectiveness (%)	Halon 1301	HFC-125 – non-optimized (276.8 lb)			HFC-125 – optimized (87.9 lb)		
		Mod 1	Mod 2	Mod 3	Mod 4	Mod 5	Mod 6
		Container Mod	Container and Nozzle Mod	Container and Distribution Sys Mod	Container Mod	Container and Nozzle Mod	Container and Distribution Sys Mod
24	-18.0	-16.7	-14.1	-11.1	-19.1	-16.5	-13.5
32	-36.1	-34.8	-32.1	-29.2	-37.2	-34.6	-31.6
54	-85.8	-83.9	-81.3	-78.3	-87.3	-84.7	-81.7
60	-99.1	-97.1	-94.4	-91.3	-100.7	-98.1	-95.0
72	-126.4	-124.6	-121.9	-118.9	-128.0	-125.4	-122.4
80	-144.3	-142.3	-139.6	-136.5	-145.9	-143.3	-140.2
slope	-2.25	-2.24	-2.24	-2.23	-2.27	-2.27	-2.26

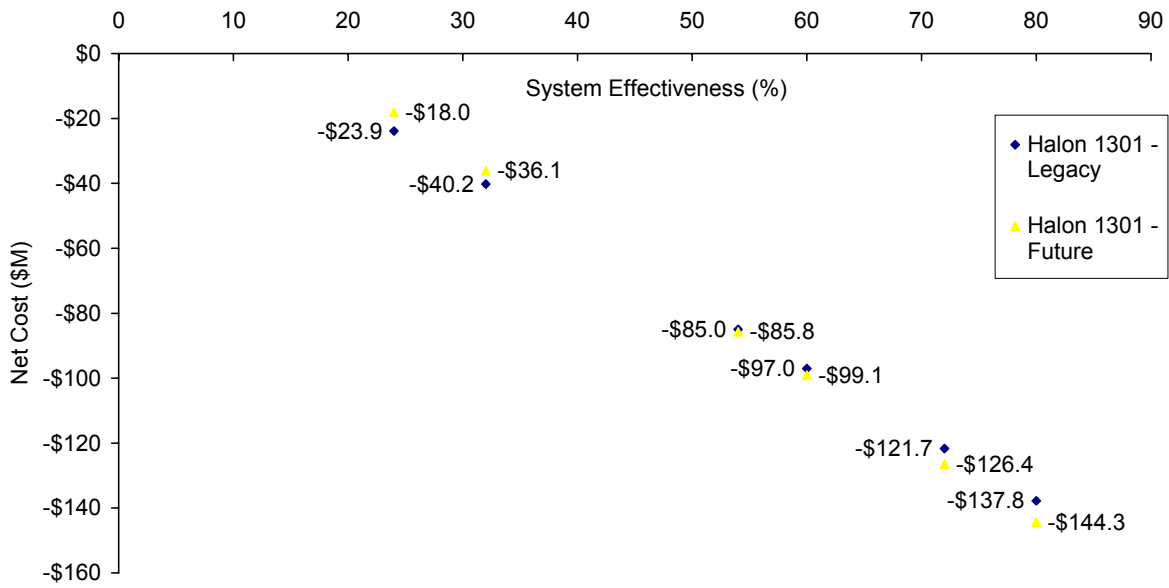


Figure 10–11. Legacy and Future Cargo Aircraft Net Costs vs. System Effectiveness for Halon 1301.

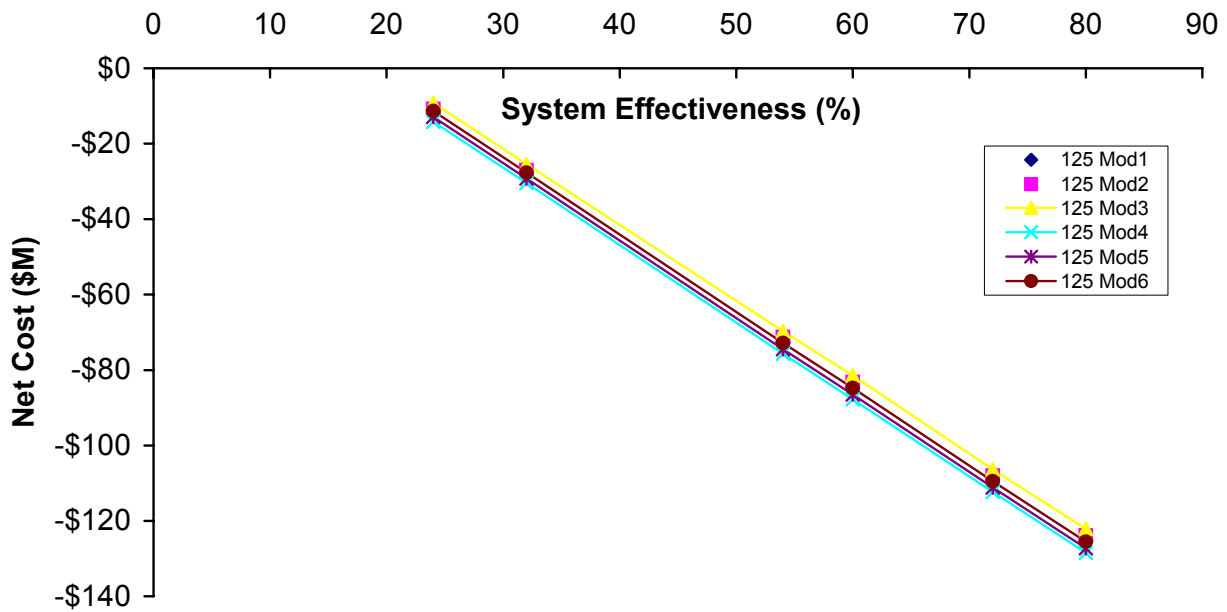


Figure 10–12. Legacy Cargo Aircraft Net Costs vs. System Effectiveness for HFC-125.

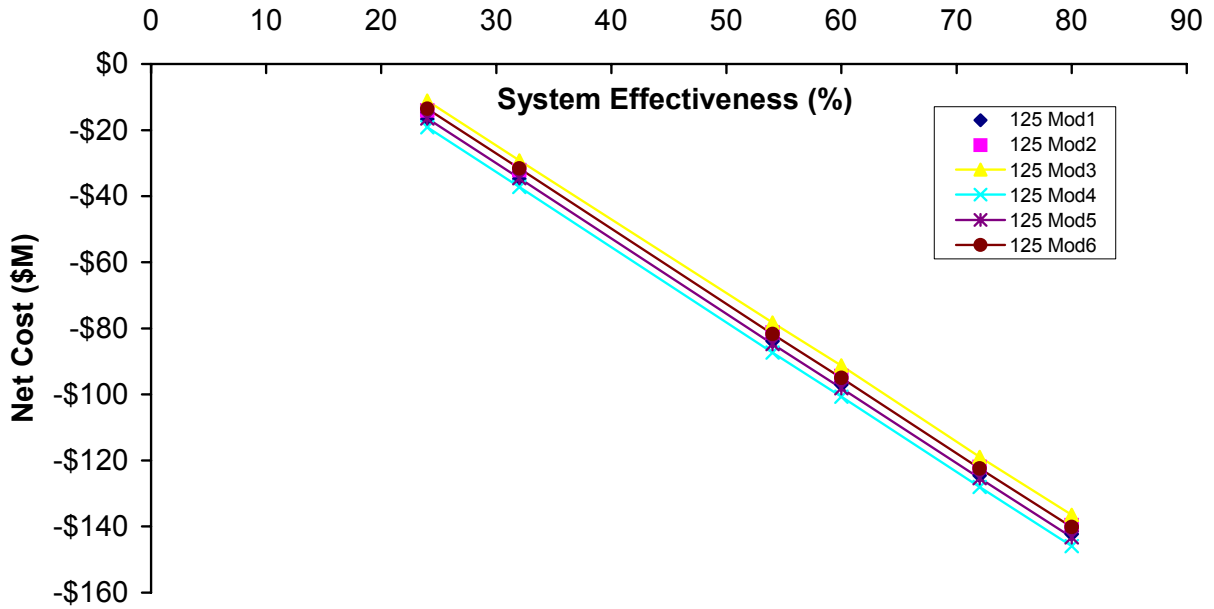


Figure 10–13. Future Cargo Aircraft Net Costs vs. System Effectiveness for HFC-125.

Figure 10–14 shows the legacy and future cargo aircraft cost savings vs. system effectiveness. For cargo aircraft, the net cost change per single percent change in extinguishing of the fire system was approximately -\$2.0 M. These estimates showed that additional investment in optimizing fire suppression system performance pays off in assets (costs) saved.

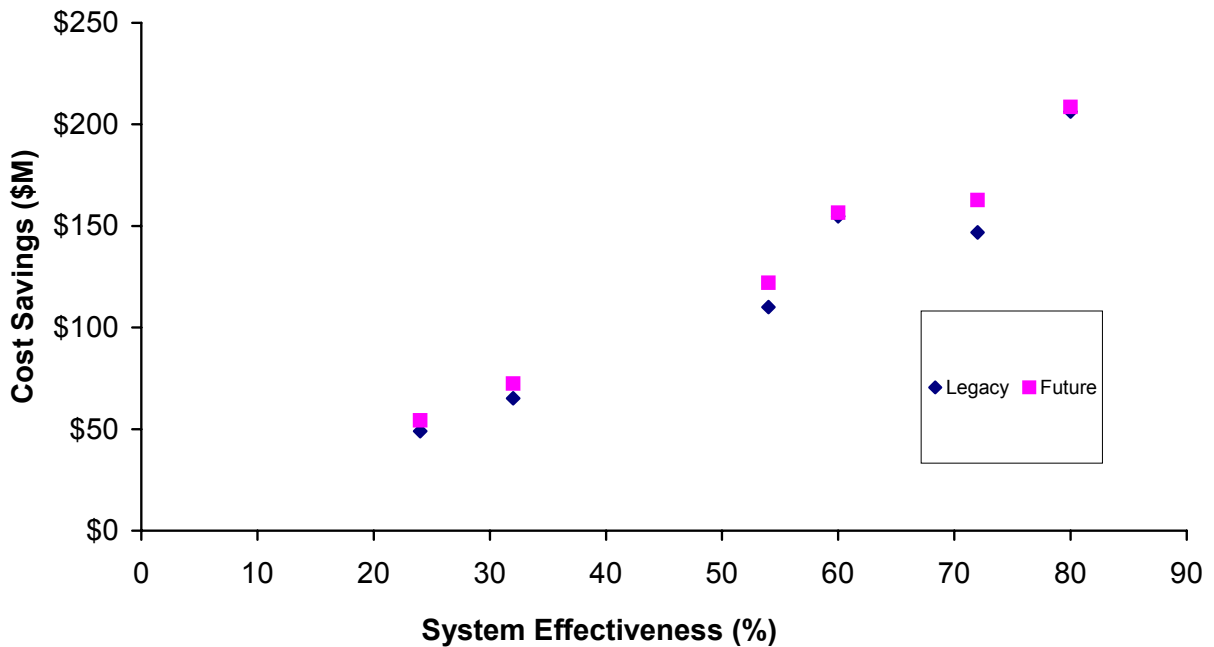


Figure 10–14. Legacy and Future Cargo Aircraft Cost Savings vs. System Effectiveness.

## Fighter Aircraft

Table 10–35 and Table 10–36 show the net costs for the legacy and future fighter aircraft, respectively. Figure 10–15 and Figure 10–16 show the legacy and future fighter aircraft net costs vs. system effectiveness for halon 1301 and HFC-125, respectively. Figure 10–17 shows the legacy and future fighter aircraft cost savings vs. system effectiveness.

**Table 10–35. Legacy Fighter Aircraft Net Costs (\$M).**

Effectiveness (%)	Net Costs		
	Halon 1301 (5.5 lb)	HFC-125 (7 lb)	HFC-125 (18.4 lb)
24	-51	-475	-45
32	-71	-67	-65
54	-128	-124	-122
60	-143	-139	-137
72	-1756	-170	-168
80	-195	-191	-188
slope	-2.57	-2.57	-2.57

**Table 10–36. Future Fighter Aircraft Net Costs (\$M).**

Effectiveness (%)	Net Costs		
	Halon 1301 (5.5 lb)	HFC-125 (7 lb)	HFC-125 (18.4 lb)
24	-48	-47	-45
32	-69	-68	-66
54	-127	-125	-123
60	-142	-141	-138
72	-174	-172	-170
80	-194	-193	-191
slope	-2.60	-2.60	-2.60

For fighter aircraft, the net cost change per single percent change in extinguishing effectiveness of the fire system was approximately -\$2.5 M. These estimates showed that additional investment in optimizing fire suppression system performance pays off in assets (costs) saved.

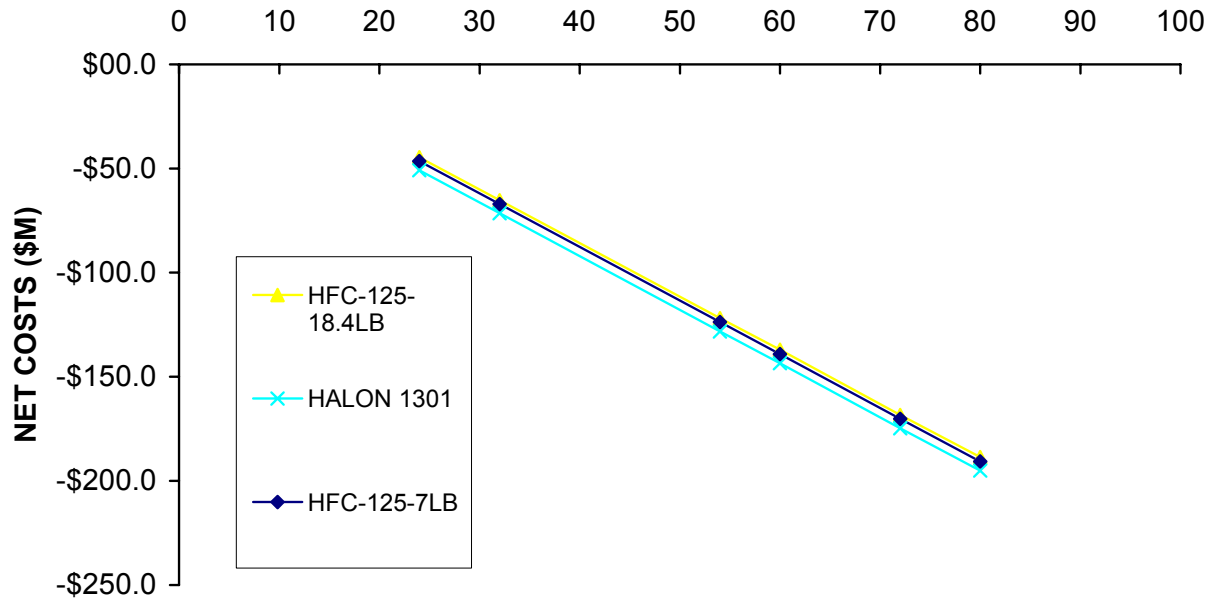


Figure 10-15. Legacy Fighter Aircraft Net costs vs. System Effectiveness.

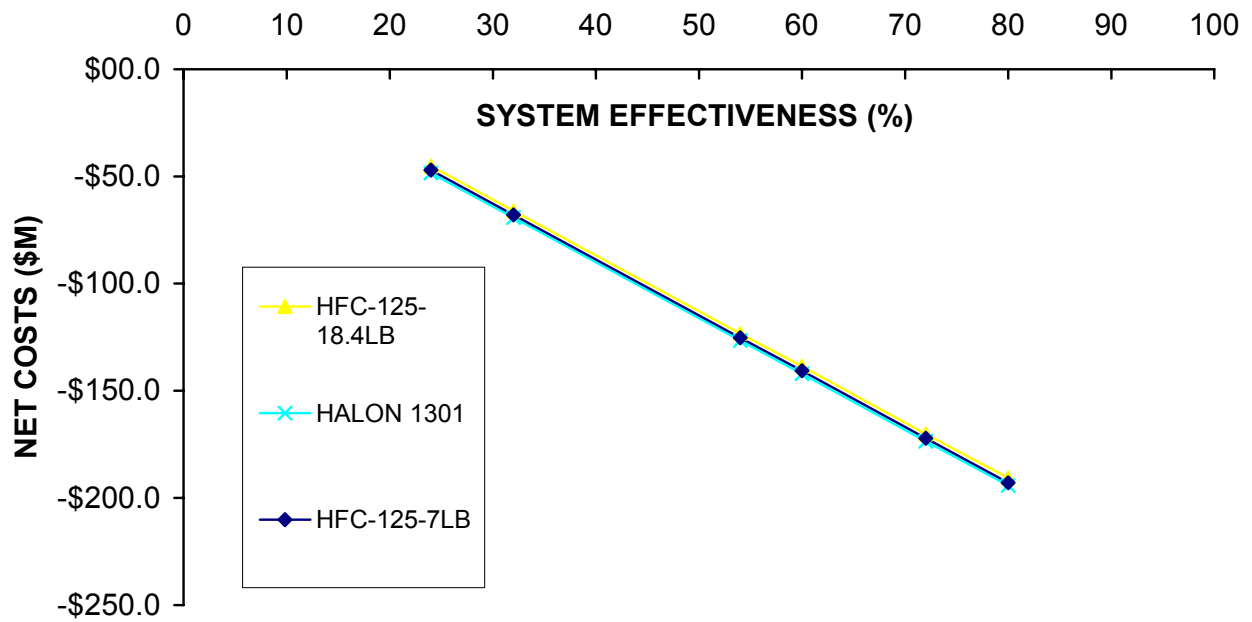
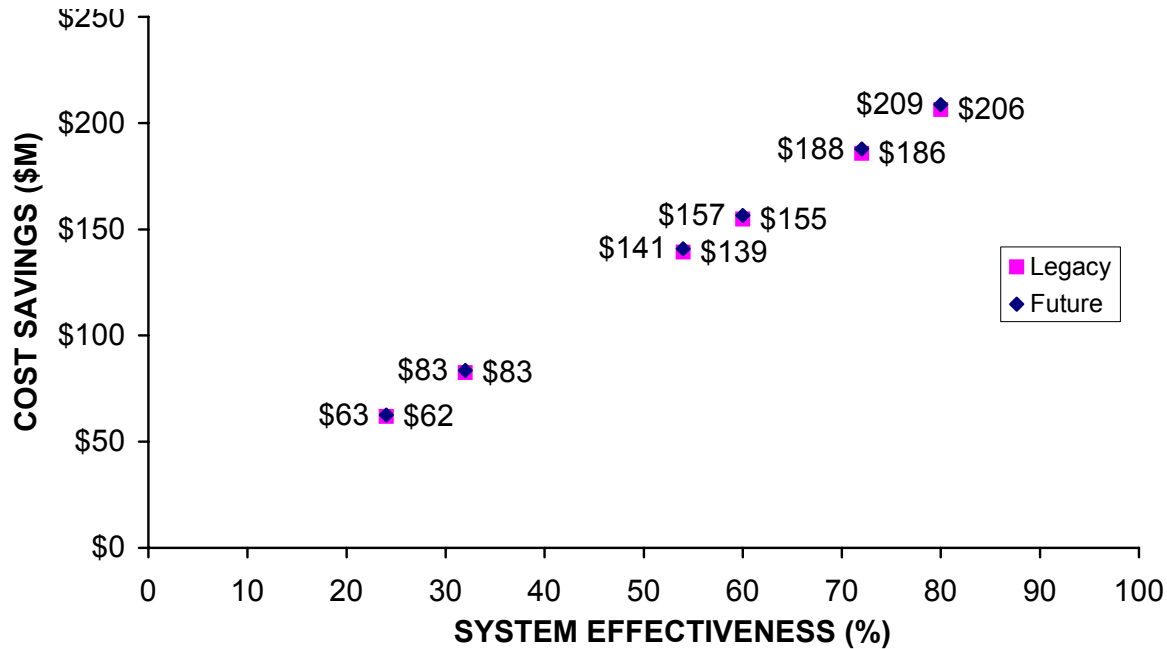


Figure 10-16. Future Fighter Aircraft Net Costs vs. System Effectiveness.



**Figure 10–17. Legacy and Future Fighter Aircraft Cost Savings vs. System Effectiveness.**

### Rotary-Wing Aircraft

Table 10–37 and Table 10–38 show the resulting net costs for the legacy and future rotary-wing aircraft, respectively. Figure 10–18 and Figure 10–19 show the legacy rotary-wing aircraft net costs vs. system effectiveness for halon 1301 and HFC-125, respectively. Figure 10–20 and Figure 10–21 show the future rotary-wing aircraft net costs vs. system effectiveness for halon 1301 and HFC-125, respectively. Figure 10–22 shows the legacy and future rotary-wing aircraft cost savings vs. system effectiveness.

For legacy rotary-wing aircraft, the net cost change per single percent change in extinguishing effectiveness (i.e., 91 % successful vs. 90 % in the field) of the fire system was approximately \$-6.2M. For future rotary-wing aircraft, the net cost change per single percent change in extinguishing effectiveness of the fire system is estimated to be -\$6.3 M. These estimates showed that additional investment in optimizing fire suppression system performance pays off in assets (costs) saved.

**Table 10–37. Legacy Rotary-wing Aircraft Net Costs (\$M).**

Effectiveness (%)	Net Costs			
	Halon 1301		HFC-125	
	1.1 kg (2.4 lb)	3.3 kg (7.2 lb)	3.6 kg (7.9 lb)	7.6 kg (16.8 lb)
24	-115	-113	-102	-97
32	-165	-162	-151	-147
54	-301	-299	-287	-283
60	-338	-335	-324	-319
72	-413	-410	-399	-395
80	-462	-459	-448	-443
slope	-6.19	-6.19	-6.18	-6.17

**Table 10–38. Future Rotary-wing Aircraft Net Costs (\$M).**

Effectiveness %	Net Costs			
	Halon 1301		HFC-125	
	1.1 kg (2.4 lb)	3.3 kg (7.2 lb)	3.6 kg (7.9lb)	7.6 kg (16.8 lb)
24	-111	-109	-107	-103
32	-161	-159	-158	-153
54	-300	-298	-296	-292
60	-338	-335	-334	-328
72	-414	-411	-410	-405
80	-464	-461	-460	-455
Slope	-6.30	-6.30	-6.29	-6.28

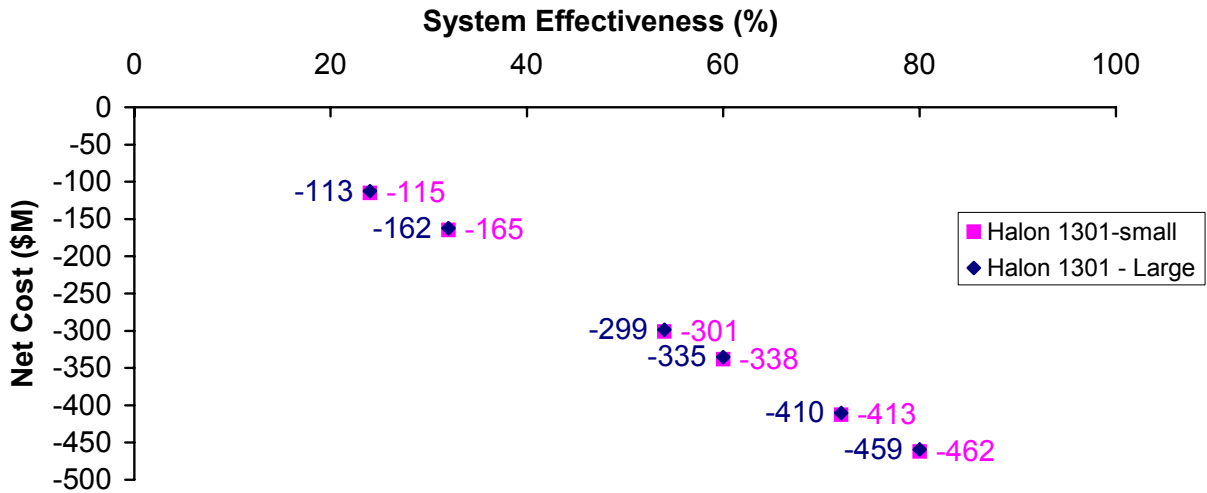


**Figure 10–18. Legacy Rotary-wing Aircraft Net Costs vs. System Effectiveness for Halon 1301.**

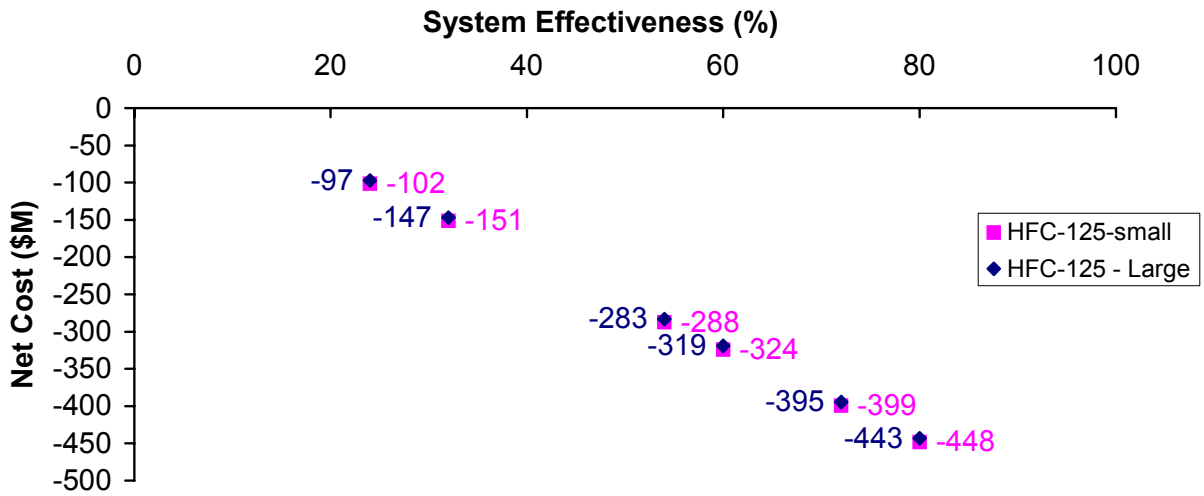


Figure 10–19. Legacy Rotary-Wing Aircraft Net Costs vs. System Effectiveness for HFC-125.

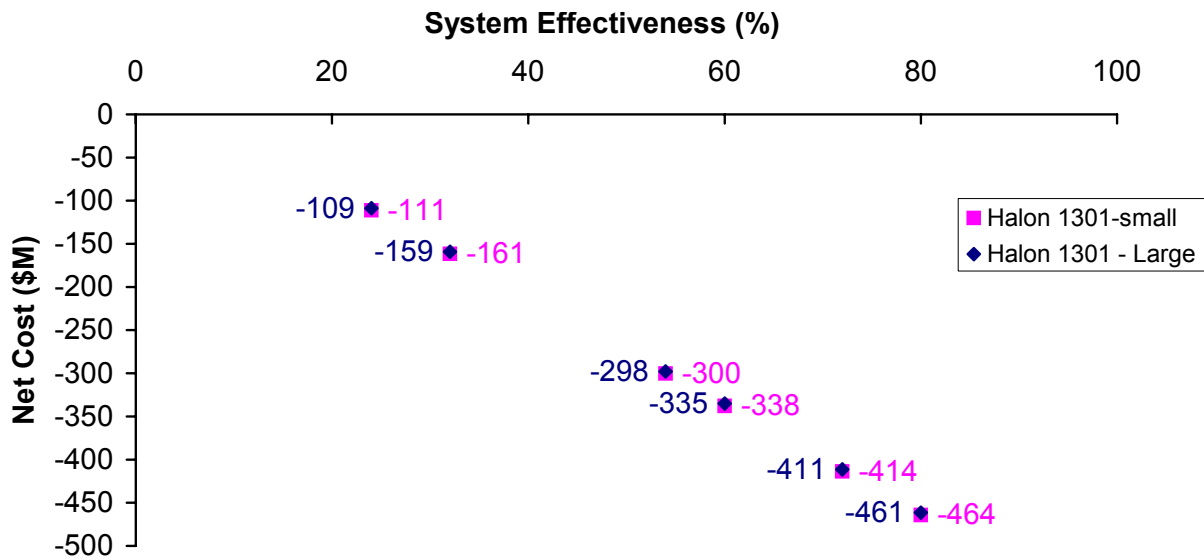


Figure 10–20. Future Rotary-Wing Aircraft Net Costs vs. System Effectiveness for Halon 1301.

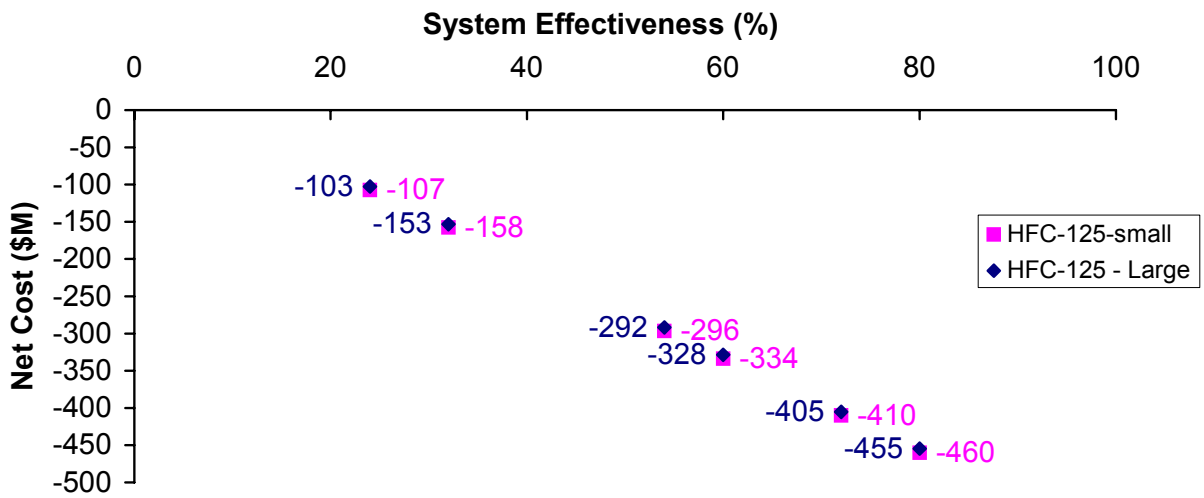


Figure 10–21. Future Rotary-Wing Aircraft Net Costs vs. System Effectiveness for HFC-125.

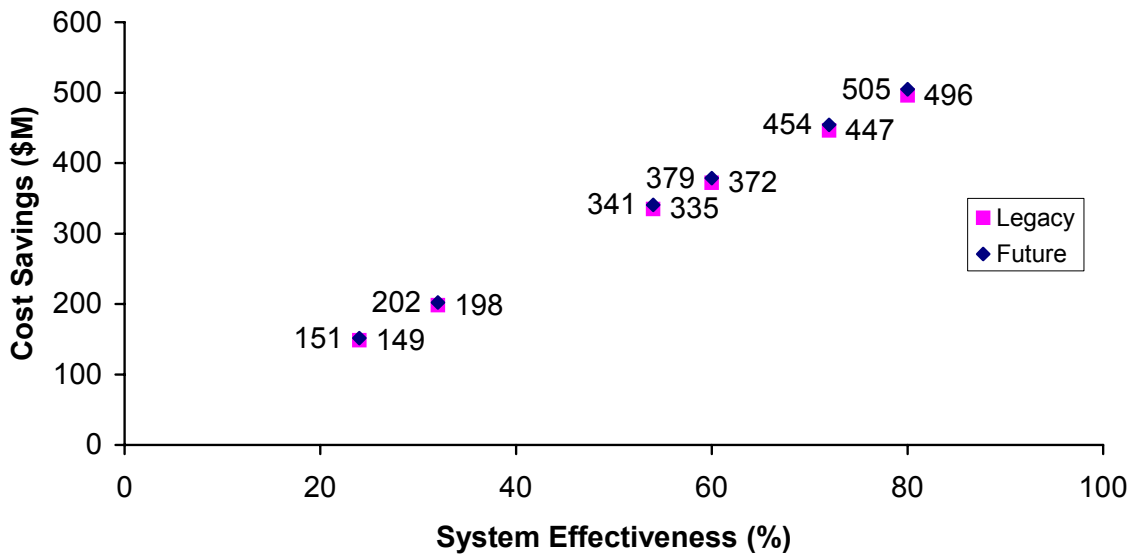


Figure 10–22. Legacy and Future Rotary-Wing Aircraft Cost Savings vs. System Effectiveness.

## 10.8 CONCLUSIONS

The NGP adapted a life cycle cost model to estimate the cost benefits of carrying fire protection systems for engine nacelles and dry bays on board military aircraft and developed a methodology for estimating the total cost of either retrofitting existing aircraft or configuring future aircraft with new systems based on a non-ozone-depleting fire suppressant. The calculations were performed for cargo, fighter, and rotary wing aircraft. The model replacement agent was HFC-125, since some data were available for such systems. These estimates showed that additional investment in optimizing fire suppression system performance pays off in assets saved for all the platforms examined. Specifically:

- It is highly cost effective for aircraft to carry fire protection systems, despite their life cycle costs (about 0.05 % to 0.2 % of the total cost of the aircraft) and the infrequency of their use. This is largely due to the high cost of losing an aircraft. Based on historical data, the return on investment in halon 1301 fire protection systems was estimated to be about 5:1 for cargo aircraft, 15:1 for fighter aircraft, and 12:1 for rotary-wing aircraft.
- It would also have been highly cost effective for HFC-125 systems, of fire suppression effectiveness comparable to these halon 1301 systems, to have been installed on military aircraft. The return on investment would have been at least two-thirds that of the halon 1301 systems.
- For comparable fire suppression effectiveness, the net cost of a system using HFC-125 installed in a future aircraft is approximately the same as the net cost of a conventional halon 1301 system.
- The cost of replacing the halon 1301 system with one of equal effectiveness, using HFC-125, in a legacy cargo aircraft is of the order of \$77 k to \$120 k per aircraft, which amounts to approximately 0.042 % to 0.066 % of the total cost of the aircraft. The estimates for fighter and rotary-wing aircraft are \$8.1 k to \$12.0 k (0.016 % to 0.023 %) and \$9.2 k to \$13.4 k (0.055 % to 0.080 %), respectively.
- Additional investment in a system of fire suppression performance above the historical levels is cost effective. For each 1 % increase in effectiveness (above the historical 60 % to 80 %), there is a net life cycle cost savings of about \$5 k per fighter or rotary-wing aircraft and about \$17 k per cargo aircraft. These estimates would be substantially improved were more extensive experimental data regarding factors of safety developed.

Already, the team overseeing at least one aircraft platform in development has used this methodology for estimating the costs associated with the selection of each alternative fire protection system, for deciding among those alternatives, for selecting the preferable system performance level, and for sizing the capacity of the system. This methodology can be expanded to meet the additional challenges of new aircraft, new fire suppression technologies, and additional applications, such as fuel tank inerting.

## 10.9 REFERENCES

1. Kolleck, M.L., Bennett, M.V., and Mercer, K.L., *Cost Analysis of Fire Suppression Systems for Cargo Aircraft*, SURVIAC TR-00-006, Booz Allen & Hamilton Inc., Dayton, Ohio, (2002).
2. Kolleck, M.L., Bennett, M.V., and Mercer, K.L., *Cost Analysis of Fire Suppression Systems for Fighter Aircraft*, SURVIAC TR-01-005, Booz Allen & Hamilton Inc., Dayton, Ohio, (2002).
3. Kolleck, M.L., Bennett, M.V., and Mercer, K.L., *Cost Analysis of Fire Suppression Systems for Rotary-wing Aircraft*, SURVIAC TR-01-007, Booz Allen & Hamilton Inc., Dayton, Ohio, (2002).
4. Bennett, J.M., "Cost Analysis of Fire Suppression Systems," 2006, in Gann, R.G., Burgess, S.R., Whisner, K.C., and Reneke, P.A., eds., *Papers from 1991-2006 Halon Options Technical Working Conferences (HOTWC)*, CD-ROM, NIST SP 984-4, National Institute of Standards and Technology, Gaithersburg, MD, (2006).
5. Bennett, J.M., and Kolleck, M.L., "Cost Analysis of Fire Suppression Systems," 2002, in Gann, R.G., Burgess, S.R., Whisner, K.C., and Reneke, P.A., eds., *Papers from 1991-2006 Halon Options Technical Working Conferences (HOTWC)*, CD-ROM, NIST SP 984-4, National Institute of Standards and Technology, Gaithersburg, MD, (2006).
6. Bennett, J.M., and Kolleck, M.L., "Cost Analysis of Fire Suppression Systems," 2001, in Gann, R.G., Burgess, S.R., Whisner, K.C., and Reneke, P.A., eds., *Papers from 1991-2006 Halon Options Technical Working Conferences (HOTWC)*, CD-ROM, NIST SP 984-4, National Institute of Standards and Technology, Gaithersburg, MD, (2006).
7. Bennett, M.V., "Relative Benefit Assessment of Fire Protection System Changes," 2000, in Gann, R.G., Burgess, S.R., Whisner, K.C., and Reneke, P.A., eds., *Papers from 1991-2006 Halon Options Technical Working Conferences (HOTWC)*, CD-ROM, NIST SP 984-4, National Institute of Standards and Technology, Gaithersburg, MD, (2006).
8. Bennett, M.V., "Relative Benefit Assessment of Fire Protection System Changes," 1999, in Gann, R.G., Burgess, S.R., Whisner, K.C., and Reneke, P.A., eds., *Papers from 1991-2006 Halon Options Technical Working Conferences (HOTWC)*, CD-ROM, NIST SP 984-4, National Institute of Standards and Technology, Gaithersburg, MD, (2006).
9. Finnerty, A.E., Peregino, P.J., Vande Kieft, L.J., Tucker, J.R., Weiland, D.E., Sheinson, R.S., Gann, R.G., Bennett, M.V., and Wheeler, J.A., *Fires Experienced and Halon 1301 Fire Suppression Systems In Current Weapon Systems*, Report TR-00-007, Survivability/Vulnerability Information Analysis Center (SURVIAC), Wright-Patterson Air Force Base, OH, (2003).
10. Bennett, M.V., *Relative Benefit Assessment of Fire Protection System Changes - Phase I, Task 1.1 – Analysis of Current Configurations*, SURVIAC file number 20945, (August, 1999).
11. Bennett, J.M., and Bennett, M.V., *Aircraft Engine/APU Fire Extinguishing System Design Model (HFC-125)*, AFRL-VA-WP-TR-1999-3068, Wright-Patterson Air Force Base, OH, (1997).
12. Kolleck, M.L., Birghtsen, G.M., Bennett, M.V., and Wheeler, J.A., *Annual Fire Protection Cost Model [1966-1995;1996-2025]*, SURVIAC 97-033, Booz Allen & Hamilton Inc., Dayton, OH, (1997).
13. Bennett, J.M., Caggianelli, G.M., Kolleck, M.L., and Wheeler, J.A., *Halon Replacement Program for Aviation, Aircraft Engine Nacelle Application Phase II – Operational Comparison of Selected Extinguishants*, WL-TR-97-3076, Wright-Patterson Air Force Base, OH, (1997).
14. Vogel, T.J., *C-17A Fire Protection System Evaluation*, Final Report, AFFTC-TR-94-03, Air Force Flight Test Center, Edwards Air Force Base, California, (1994).

15. *Technical Manual, Fault Isolation, Organizational Maintenance, Fire Protection, USAF Series, C-17A, Aircraft*, TO 1C-17A-26-FI-00-1, McDonnell Douglas Corporation, Military Transport Aircraft, 1 June 1995.
16. *Technical Manual, Illustrated Parts Breakdown, Organizational Maintenance, Fire Protection, USAF Series, C-17A, Aircraft*, TO 1C-17A-4-26, McDonnell Douglas Corporation, Military Transport Aircraft, 1 September 1999.
17. F/A-18E/F Interactive Electronic Technical Manuals (IETMs), Public Affairs Office, Naval Air Engineering Station, Lakehurst, NJ, [www.lakehurst.navy.mil](http://www.lakehurst.navy.mil).
18. Sheinson, R.S., and Ash, L., "NAVAIR's Response to NGP Program Element 1a Questions," Public Affairs Office, Naval Air Engineering Station, Lakehurst, NJ, [www.lakehurst.navy.mil](http://www.lakehurst.navy.mil), 1 December, 1998.
19. Leach, W., "Retrofit Opportunities For HFC-125 In Aircraft Engine Nacelles," 1999, in Gann, R.G., Burgess, S.R., Whisner, K.C., and Reneke, P.A., eds., *Papers from 1991-2006 Halon Options Technical Working Conferences (HOTWC)*, CD-ROM, NIST SP 984-4, National Institute of Standards and Technology, Gaithersburg, MD, (2006).
20. A1-F-18AC-NFM-000, Technical Manual, "Fire Detection/Extinguishing Systems", pp. 1-70-1-71.
21. Tedeschi, M., *Fixed-Wing Aircraft Fire Protection, Halon 1301 Fire Suppression Systems Effectivity Analysis*, NAWCADLKE-MISC-05-SR-0146, US Naval Air System Team, Naval Air Warfare Center, 30 September 1994.
22. Bubash, J., U.S. Army Tank Automotive Command, Memorandum for Bennett, J.M., and Steele, J., Wright Laboratory, WPAFB, WL/FIV, October 10, 1995.
23. Haaland, P., *Fire Suppression Options for the RAH-66 Comanche Helicopter*, Huntington Research and Engineering, presentation to the Comanche PM IPT, October 10-13, 2001.
24. MIL-E-22285, Military Specification, Extinguishing System, Fire, Aircraft, High-Rate-Discharge Type, Installation and Test of, April 27, 1960.
25. Tedeschi, M., and Leach, W., *Rotary Aircraft Fire Protection, Halon 1301 Fire Suppression Systems Effectivity Analysis*, NAWCADLKE-MISC-05-SR-0132, Naval Air Warfare Center, May 26, 1994.
26. Electronic communication from Marco Tedeschi, Naval Air Warfare Center to J. Michael Bennett, "F/A-18E/F Engine/AMAD/APU Production and EMD Fire Extinguishing System Information, p.2, February 8, 2001.
27. Leach, W., "Retrofit Opportunity For HFC-125 Aircraft Engine Systems," in *Proceedings of the International Aircraft Fire & Cabin Safety Conference*, CD-ROM, DOT/FAA Report No. DOT/FAA/AR-99/68, National Technical Information Service, Springfield, VA, (1998).
28. (PS)A1-F-18EA-240-300, *Technical Manual, Organizational Maintenance, System Maintenance with Illustrated Parts Breakdown, Fire Extinguisher Tank (4SQT109), Fire Extinguishing System*, Public Affairs Office, Naval Air Engineering Station, Lakehurst, NJ, [www.lakehurst.navy.mil](http://www.lakehurst.navy.mil).
29. Roberts, G., Doria, G., and Breeden, T., "The Impact of Halon Replacement On Aircraft Engine Bay Fire Protection System Design," 1999, in Gann, R.G., Burgess, S.R., Whisner, K.C., and Reneke, P.A., eds., *Papers from 1991-2006 Halon Options Technical Working Conferences (HOTWC)*, CD-ROM, NIST SP 984-4, National Institute of Standards and Technology, Gaithersburg, MD, (2006).
30. Electronic communication from Captain Brian M. Godfrey, ASC/YCLII, to J. Michael Bennett, October 2, 2000.

31. Kolley, M.L., and Bennett, J.M., "Assessing The Cost Impact Of Fire To The U.S. Air Force," in *Proceedings of the International Aircraft Fire & Cabin Safety Conference*, CD-ROM, DOT/FAA Report No. DOT/FAA/AR-99/68, National Technical Information Service, Springfield, VA, (1998).
32. Presentation of Factor of Safety Testing – Aircraft Engine Nacelle, Wright Laboratory, WL/FIVS.



---

---

## Chapter 11: VERIFICATION OF FIRE SUPPRESSION PRINCIPLES

Richard G. Gann, Ph.D.  
National Institute of Standards and  
Technology

J. Michael Bennett, Ph.D.  
Bennetech, LLC

---

---

### TABLE OF CONTENTS

11.1	Context.....	1088
11.2	Complexity of In-flight Fires and Their Suppression.....	1088
11.3	New Understanding of the Fire Suppression Process.....	1090
11.3.1	Overview of Fire Suppression.....	1090
11.3.2	Control of the Air Supply to the Fire.....	1090
11.3.3	Delivery of the Fire Suppressant to the Fire.....	1090
11.3.4	Effectiveness of a Fire Suppressant at Quenching Flames.....	1094
11.4	Evaluation of Candidate Fire Suppressant Technologies.....	1098
11.4.1	Screening Measures.....	1098
11.4.2	Measurements during Fire Tests.....	1100
11.4.3	Life-cycle Cost Assessment.....	1101
11.5	Potential for New, Viable Suppressants.....	1101
11.6	Fire Suppression Principles to be Tested.....	1103
11.7	Methodology for Real-scale Testing and Validation.....	1106
11.7.1	Aircraft Engine Nacelle Test Facility (AENTF) Features and Capabilities.....	1106
11.7.2	Design of Experiments Methodology.....	1112
11.7.3	“Bracketing” Procedure for Testing.....	1115
11.7.4	Experimental Approach, Configuration and Procedure.....	1115
11.8	Results and Analysis.....	1125
11.8.1	Summary of General Data Collected.....	1125
11.8.2	Principle 1.....	1126
11.8.3	Principle 3.....	1127
11.8.4	Principle 5.....	1128
11.8.5	Principle 6.....	1128
11.8.6	Principle 7.....	1129
11.8.7	Extinguishing Mixing Models.....	1130
11.8.8	Principle 4.....	1134
11.8.9	Principle 2.....	1137
11.8.10	Phase III Results.....	1141
11.9	Summary.....	1141
11.10	References.....	1143

## 11.1 CONTEXT

As can be learned from the prior chapters of this book, the participants in the Next Generation Fire Suppression Technology Program accumulated and developed abundant knowledge of the subject. This new knowledge falls into five categories:

- Sources of difficulties of suppression of in-flight fires
- Fire suppressants and the fire suppression process
- Tools for evaluating fire suppressants and fire suppressant systems
- Potential for new fire suppressant chemicals
- Precepts for optimizing a fire suppression system, capitalizing on even a mediocre agent

Much of the understanding of fire suppressants and the fire suppression process was obtained from computations and reduced-scale experiments. This chapter summarizes those findings, including verified prior knowledge, and documents a series of real-scale experiments to verify the most important of the principles developed from those findings.

As stated in its goal, the NGP focused on processes, techniques, and fluids that meet the operational requirements currently satisfied by halon 1301 systems in aircraft. Nonetheless, both the knowledge gained and the principles developed have application to a range of military and civilian installations.

## 11.2 COMPLEXITY OF IN-FLIGHT FIRES AND THEIR SUPPRESSION

Analyses under the TDP (Chapter 2) had revealed the geometric intricacy of engine nacelles and dry bays and the difficulty of suppressing fires in those spaces. The NGP studies confirmed and clarified the implications of the complexity to new suppressant technologies.

Aircraft engine nacelle fires have resulted in the loss of aircraft both in combat and non-combat operations (Chapter 2). The roughly annular interior of an aircraft engine nacelle is bounded by the engine core on the inside and the aerodynamic skin on the outside. To cool the engine and to mitigate the buildup of flammable fuel/air mixtures, air flows through this space, with a typical residence time of the order of tenths of a second. Because of the fluid lines (for fuel, oil, and hydraulic/brake fluids) and other hardware in the annular space, the surfaces are irregular, and the air flow is highly turbulent. The exterior shell of the nacelle is nominally at ambient temperature, which can be as low as -40 °C. The interior of the annulus, the exterior of the engine housing, is somewhat warmer (Chapter 2).

A fire can arise in numerous locations within the nacelle. In a typical peacetime fire scenario, one of the fluid lines leaks and sprays or streams the flammable fluid onto the hot machinery components, which results in a fire. The flaming fluid can also settle in the lower cavities of the engine nacelle, burning as a pool fire. During combat, there is the additional risk of an incoming round rupturing a line and causing the leak or spray.

Upon detection of a fire and the shutdown of the engine, the fire suppressant agent must get from the storage bottle to the nacelle quickly, then fill the entire space with a sufficient concentration of agent for sufficient time duration to quench the flames. This must be accomplished before the air flow flushes the

agent out the nacelle exhaust. Because mass and storage volume are at a premium on any aircraft, the mass of the agent and its hardware must be kept to the minimum to do the job.

The second principal location of aircraft fires is in the dry bays (Chapter 2). In fuselage dry bays, the majority of peacetime fires are due to an equipment failure or failure of the engine or starter. Equipment failures also have caused a large number of fires in wing dry bays. By contrast, combat dry bay fires are usually initiated by a ballistic projectile penetrating the dry bay wall and an adjacent fuel cell. The interiors of dry bays are irregular in shape and highly cluttered. The nature and magnitude of air flow within the dry bay depends critically on the location and extent of breach of the outer wall.

The rapid pressure buildup following an ignition can rupture the dry bay wall. This can result in an explosion as air mixes with the released fuel. Thus, dry bay fires must be suppressed before the pressure reaches levels that threaten the survival of the aircraft, typically within a few tenths of a second.

From examination of fires in both venues, there were findings that guided the search for alternatives to the current halon 1301 systems:

- Efficient and rapid distribution of the suppressant is essential. Halon 1301 accomplishes this with little assistance, because its boiling point ( $T_b$ ) is below even the lowest ambient temperatures, which leads to flashing (Chapter 8). Other suppressants must have similarly low boiling points or be dispersed by other means. Effective dispersion can be affected by improved powder panels (for dry bays) and solid propellant fire extinguishers (Chapter 9). Misting of a high boiling chemical will not necessarily be sufficient, due to the potential for condensation of the droplets on the inside of the cold exterior surface of the aircraft.
- There are significant weight and storage volume penalties for an inefficient or inefficiently distributed agent that affects the relative cost of alternative fire suppressant technologies (Chapter 10).
- Despite the complexity of the flames in actual in-flight fires, there are existing laboratory burners that manifest sufficiently similar properties that they can be used to extract the properties of chemicals that effect fire suppression.

Fuel tank fires during combat are also a major cause of aircraft losses (Chapter 2). However, only two U.S. aircraft, the F-16 and the F-117, use halon 1301 to inert the fuel tanks against ballistically caused explosions. At the time of the NGP, the decision had been taken to vintage the existing halon 1301 systems. Thus, no detailed examination of the dynamics of inerting against this type of fire was performed.

The suppression requirements for fires in military ground vehicle crew compartments are similar to those for in-flight dry bay fires. Most commonly, these vehicle fires are mist explosions or hydraulic spray fires, initiated by hot fragments from ballistic impact. The flames must be quenched within 250 ms to prevent incapacitation of the crew (Chapter 5).

For most other common fires that have historically been controlled using halon 1301, the requirement for rapid suppression is not as stringent. However, the physics and chemistry of the fires is similar.

## 11.3 NEW UNDERSTANDING OF THE FIRE SUPPRESSION PROCESS

### 11.3.1 Overview of Fire Suppression

The quenching of flames can be accomplished by:

- Removing the fuel or separating the fuel from an air supply,
- Reducing the available oxygen supply,
- Reducing the time in which the fuel and oxygen are mixed and available to react,
- Cooling the fuel/air mixture below a temperature that supports sufficiently rapid chemical reaction for flame propagation, or
- Adding a combustion inhibiting chemical at a concentration sufficient to reduce the rate of fuel oxidation below that needed for flame propagation.

Conversely, flame extinguishment will not occur, or be less efficient, if:

- Too little of the flame suppressant reaches the fire zone in a timely manner,
- The flame suppressant passes through the flames too quickly to effect its role,
- The flame suppressant is released so slowly, or disperses so broadly, that the fire is not exposed to an extinguishing concentration.

### 11.3.2 Control of the Air Supply to the Fire

An annular band of intumescent material applied to the inside of an engine nacelle can significantly reduce the flow of air through the nacelle (Chapter 8). The material would be applied to the downstream end of the housing so that the heat from an upstream fire would activate the chemical expansion of the material. This would result in decreasing the mass of fire suppressant chemical needed to effect flame quenching by two processes:

- Decreasing the flow of air through the nacelle, which would increase the residence time of the chemical in the flame zone; giving it longer to work, and
- Allowing the flames to deplete the local oxygen concentration, reducing the flame reaction rate, and allowing a smaller mass of fire suppressant to complete the extinguishment.

A second effect of air supply to the fire results from the inflow of the fire suppressant. The turbulence created can enhance the mixing of air with the vaporizing fuel, enhancing the rate of combustion (Chapter 8). This increased reaction rate and heat release, combined with a marginal or insufficient concentration of fire suppressant, can create an overpressure that could damage the aircraft.

### 11.3.3 Delivery of the Fire Suppressant to the Fire

#### Dispensing from a Storage Bottle

In the absence of extensive distribution piping, the discharge rate of a suppressant fluid from its storage bottle depends on the prevailing internal pressure within the bottle ullage. To ensure the high pressure

needed for rapid discharge of the fluid at low ambient temperatures, a compressed gas is added to the bottle.

The pressure in the ullage of the storage bottle is a function of the fluid vapor pressure (which is exponentially dependent on the bottle temperature), the partial pressure of pressurizing gas in the ullage, and the solubility of the pressurizing gas in the fluid. The computer code PROFISSY predicts the pressure to within 10 % using only the agent mass, the bottle volume, the fill temperature, and either the nitrogen mass needed to pressurize the vessel or the fill pressure of the vessel (Chapter 8).

### **Fluid Flow through Distribution Plumbing**

Upon the opening of the storage bottle, the fluid enters the distribution piping as a two-phase mixture of superheated liquid and vapor. There is significant thermodynamic and thermal non-equilibrium between the phases. Furthermore, due to the large pressure drop in the piping, continuous flashing is anticipated as the fluid travels through the piping, and two-phase critical (choked) flow can occur at various locations. This can severely reduce the discharge rate of the fluid into the engine nacelle or dry bay.

The mass flow of a two-phase fluid through a complex pipe run (with bends, tees, and elbows) depends on the nature of the piping and several thermodynamic and transport properties of both phases: specific heat, thermal expansion coefficient, isothermal compressibility, specific volume, specific entropy, dynamic viscosity, and thermal conductivity. The surface tension of the liquid phase and the saturation temperature are also needed.

The computer code FSP estimates the pressure history and discharge flow from a pipe run of arbitrary design (Chapter 8). The code is also able to replicate the qualitative behavior associated with the release of dissolved gas as the delivery system undergoes rapid depressurization during the discharge of the suppressant agent. The shapes of the calculated pressure histories are similar to experimental curves. The predicted discharge times are accurate to within 15 %. Because of these characteristics, the code appears to be a viable tool for the analysis or design of suppressant delivery systems.

### **Effective Fluid Dispersion**

Coordinated experiments and fluid dynamics modeling added the following knowledge enhancements to the general expectations that (a) clutter retards the flow of suppressant and can reduce the mass available to reach the site of a fire and (b) fires stabilized behind obstructions are the most difficult to extinguish (Chapter 8):

- The mass fraction of suppressant in the air stream is a key determinant of the success of flame extinguishment. Thus, the speed of suppressant injection is more important than the total mass of agent deployed. For chemically active suppressants, the reaction rates are a few orders of magnitude faster than the residence time inside the nacelle. Consequently, if a “wave” of sufficiently high agent concentration reaches all the potential zones of fire for even a fraction of a second, the fire will be extinguished.
- A fire suppression system design based on room temperature test data may well fail to provide adequate fire protection when activated at low temperatures.

- Low temperatures of the agent storage bottle, airflow, and nacelle surfaces can adversely affect agent dispersion performance, especially when the prevailing temperature is below the normal boiling point of the agent. These increase the probability that a gaseous or aerosol suppressant will condense, resulting in liquid pooling at low points in the space. The subsequent evaporation from the pool is likely to be too slow to generate an extinguishing concentration.
- Similarly, high clutter density and low air velocity significantly and synergistically act to reduce the mass of agent convected downstream by increasing the likelihood of agent contact with cold surfaces.
- The transport of liquid droplets downstream is dependent on the droplet size. Droplets larger than 30  $\mu\text{m}$  to 50  $\mu\text{m}$  tend to impinge on clutter surfaces. Smaller droplets entrain into the gas stream and transport around the clutter into the recirculation region behind an obstacle. Droplets with lower boiling points tend to vaporize more readily, resulting in decreased droplet size or even complete evaporation. It is unlikely that droplets will shatter (and produce smaller droplets) upon impact with clutter.
- Electrically charged droplets of agents offer no advantage over neutral droplets, despite the presence of ions in flames.
- Clutter at an elevated temperature, e.g., heated by the engine, can affect the agent effectiveness.
  - A vapor stream can form downstream of the object due to liquid vaporizing off the hot surface.
  - Coating of the obstacle surface with droplets can result in significant surface cooling, which can be advantageous in preventing re-ignition.
- Rapid lateral distribution of the suppressant in an engine nacelle is enhanced by multiple injection ports, as contrasted with the single port that is sufficient for halon 1301. Three well-located ports is a reasonable starting point for suppression system design.
- The time to mix agent into the flame-stabilizing recirculation zone behind *isolated* clutter is proportional to the size of the clutter divided by the velocity past the clutter.
- Interaction between *multiple* clutter objects can reduce or extend the time to mix agents into recirculation zones behind obstructions.
  - A nearby (second) piece of clutter that is the same distance from the agent injection port as a flame-stabilizing piece of clutter *reduces* the mixing rate of agent into the flame stabilization region. The second object pulls the streamlines away from the recirculation zone.
  - A nearby (second) piece of clutter that is behind (downstream of) a flame-stabilizing piece of clutter *increases* the mixing rate of agent into the flame stabilization region. The downstream object pushes the streamlines into the recirculation zone.
  - The magnitude of these effects is related to the drag of the adjacent clutter object. Larger drag coefficients tend to influence the mixing process more strongly.
- Three fire simulation programs (VULCAN, FDS, and FPM) used in the NGP research capture much of the physical knowledge summarized above.
  - Any of the three can help design a fire suppression system in practically any space inside an aircraft. (While their application to spaces in ground vehicle, shipboard or

- buildings was not investigated in this effort, there seems to be no conceptual impediment to such an application.)
- Any of the three can be used to guide the optimization of the design of qualification tests which may be required for acceptance of a fire-suppression system for an aircraft or ground vehicle. Such utility allows the planner of tests to focus on those cases for which these simulations show that flame extinction is marginal, thus reducing the number of tests required to “prove” the system.
  - Each of these software programs incorporates a slightly different set of assumptions, so that using more than one of them may ameliorate unforeseen effects of the peculiar, embedded assumptions in any particular model. Thus, if two or more fire simulation programs agree in the outcome, the tests likely will confirm. If there be disagreement in the predicted outcome from different fire-simulation programs for the same case, then the conditions are approaching the edge of the extinguishment envelope.
  - In NGP full-scale nacelle testing, almost all the predictions of borderline extinguishment outcomes were, in fact, extinguished.
- Improved powder panels, as weight efficient as halon 1301 systems, can provide excellent quenching of ballistically initiated explosions in aircraft dry bays (Chapter 9).
    - Compared to conventional designs, these new panel designs provide greater powder release into the dry bay, better dispersion of the powder to prevent ignition off the shotline, longer powder suspension to prevent fire ignition for a longer time, and greater flexibility of design to effect application-specific objectives. The effectiveness of prototype panels was demonstrated in live fire testing.
    - Front face crack growth, which promotes more and better powder dispersion, can be optimized through the use of particular front face materials, thicknesses, rib designs, attachment methods to the ribs, and even surface scoring.
    - Additional benefit can be obtained by back face improvement and taking advantage of the strong synergism between the rib structure and the front face design.
    - Accidental leakage can be prevented by proper choice of plastics or composites, combined with modern adhesives.
    - While these improvements were demonstrated using  $\text{Al}_2\text{O}_3$ , an inert powder, additional enhancements can be obtained with chemically active powders that are also lighter.
    - There is logical extension of this technology to fire suppression in ground vehicles.
  - A new generation of solid propellant fire extinguishers offers effective fire suppression for both engine nacelles and dry bays (Chapter 9).
    - Effluent temperature reduction of 30 %, thus reducing the potential for thermal damage, was obtained by incorporating the new high nitrogen propellant BTATZ ( $\text{C}_4\text{H}_4\text{N}_{14}$ ) and by the introduction of a coolant to the propellant formulation.
    - Enhanced fire suppression efficiency can be obtained by the introduction of chemically active compounds to the formulation. The incorporation of  $\text{K}_2\text{CO}_3$  into the otherwise inert propellant reduced the mass needed for fire suppression by a factor of 3.

- Hybrid fire extinguishers (HFEs), in which a chemically active suppressant is added to the propellant effluent, offer the potential for even larger gains in fire suppression efficiency.
- Prototype units have shown *system* weight reductions by over a factor of two, with still greater reductions possible by optimizing the findings.
- This technology has been demonstrated effective in the quenching of automotive gasoline tank fires.
- Significant masses of some suppressants can be adsorbed onto inorganic particles, at mass fractions of 0.2 or higher. This might be a delivery option for compounds whose fire suppression efficiency is about a factor of five or more higher than that of halon 1301 and which pose environmental or toxicological threats.

### 11.3.4 Effectiveness of a Fire Suppressant at Quenching Flames

#### Required Agent Residence Time

For an open flame, the criterion for flame extinguishment is that the concentration of suppressant exceeds some minimal value long enough for the chemical kinetics to quench the flame chemistry. (See below.) For occluded flames, there are two distinct flame stabilization conditions: rim-attached and wake-stabilized. In the former, the flame detaches and goes out as soon as the agent arrives. In the latter, the shear layer first becomes unstable, followed by flame extinguishment in the recirculation zone. Time is required for an extinguishing concentration of agent to exist in this recirculation zone. This time depends on the concentration of the agent in the free stream and the time interval over which the agent has been injected into the free stream, i.e., the duration of the suppressant wave.

The minimum volume fraction of  $\text{CF}_3\text{Br}$  for suppression at different injection time intervals, normalized by its value for continuous application, correlates with  $[1 - \exp(-\Delta t/\tau)]^{-1}$ , where  $\Delta t$  is the injection time interval and  $\tau$  characterizes the mixing time behind the obstacle in the flow (Chapter 8). The agent mass needed for suppression can be minimized by injecting the agent for a period near the characteristic mixing time, which scales with the obstacle height divided by the velocity of the flow. The minimum volume fraction of agent required to suppress the wake stabilized flames investigated is similar to the value determined in cup burner tests.

To the extent that a significant fraction of the suppressant mass is in the form of a volatile aerosol, there are additional dwell time and droplet size considerations that determine whether that fraction will take part in the flame extinguishment process (Chapter 4). For a given mass of suppressant, small droplet diameters are to be preferred. Droplets that are too large will not be entrained into the recirculation zone. Smaller droplets may be entrained, but may require extended time within the recirculation zone to evaporate fully. Droplets with diameters below about 30  $\mu\text{m}$  were entrained into laboratory flames and evaporated fully.

Combined with the boiling point requirement for non-loss at cold services, this small droplet requirement for effective evaporation has significant implications for the dispensing of an agent. To make use of the full mass of suppressant stored and released in the bottle, a chemical must be:

- Released as a gas, a condition virtually impossible for a volume-efficient fluid;

- Prone to flashing upon release, requiring a boiling point below the ambient temperature, a condition satisfied for very few fluids; or
- Dispensed as fine droplets, a condition requiring fine nozzles on the distribution piping and a high backing pressure. This will be difficult to achieve a sufficiently high discharge rate.

## Chemistry of Fire Suppression

Building on more than 50 years of flame inhibition research, intensive NGP efforts have generated more detailed understanding of the interaction of inhibiting chemicals with flames and culminated in a unified model of fire suppression. This included effectiveness by both physical and chemical processes. In different ways, each of these affects the rates of the chemical reactions that must proceed at rates sufficient to sustain fuel combustion.

Flame extinguishment without any direct chemical or catalytic activity entails making it harder for the flame-generated enthalpy to maintain the fuel/air “bath” at a temperature high enough for these reactions to continue.

- The sink for this enthalpy is the heat needed to raise the suppressant from the ambient temperature to flame temperature (Chapter 7). For a gaseous agent, this enthalpy is determined by its heat capacity. A high heat capacity typically results from a molecule having a large number of atoms, with the associated large number of excitable vibronic modes. It is also possible that one or more weak chemical bonds can be thermally dissociated. For compounds that reach the flame zone as an aerosol, additional endothermic contributions come from the liquid phase heat capacity and the heat of vaporization.
- Fire suppressants also dilute the fuel/air mixture, slowing the reaction rates. This is small effect in any case, since the magnitude is linear in additive concentration, while the thermal cooling has an exponential effect on reaction rate. For compounds near halon 1301 in flame suppression effectiveness, the effect is negligible.
- For a constant mass of an aerosol, there is a monotonic increase in the flame extinction efficiency with decreasing droplet size. Water aerosols below about 30  $\mu\text{m}$  in diameter were found to be more effective on a mass basis than halon 1301 at extinguishing counterflow diffusion flames. These droplets are small enough to evaporate fully in the flame zone. Modeling studies confirm that this effectiveness is largely due to the high heat of vaporization and the complete evaporation of such small droplets.
- Aerosols delivered to the hot surfaces in the vicinity of a fire can assist in quenching the flames and preventing relight by cooling surfaces. Effectiveness is enhanced by high values of the mass delivered, the droplet diameter, and the droplet velocity.

Efficient chemical extinguishment of flames results from depletion of the H, OH, and O radicals that drive flame propagation (Chapter 3). The process can be simple removal or catalysis of radical combination to less reactive compounds. In either case, the vibronic modes of the suppressant also absorb enthalpy and function, in part, as a thermal suppressant. Typically, for agents that are comparable in flame suppression efficiency (mass basis) to halon 1301, this thermal component is smaller than the chemical component.

Many of the pre-NGP (and some NGP) studies of the effects of additives on flames addressed flame *inhibition*. The additives were added to the flames in small quantities, and decreases in burning velocity, free radical concentrations, etc. were measured. The additive concentrations were generally not increased

to near the point of flame extinguishment, since these flames become unstable, and measurements become difficult. From these studies emerged insights into the chemical and physical processes that degraded the flames. It is recognized that additional processes contribute to the extinguishment of actual fires.

In the simplest chemical process, radical trapping, a suppressant's breakdown products react with the radicals to form stable product species which are relatively inert in the flame. The most prevalent example is that of fluorine atoms. These are generated by pyrolysis or reaction of fluorine-containing suppressants and combine with hydrogen atoms to form HF. The H-F chemical bond is sufficiently strong (570 kJ/mol) that the H atom no longer participates in the flame propagation chemistry.

By contrast, catalytic radical recombination is a chain reaction process. Species formed from the thermal or chemical breakdown of the suppressant molecule initiate a cyclical process. (The typical bond energy between a catalytic scavenger and a flame radical is in the range of 300 kJ/mol to 400 kJ/mol, notably weaker than the H-F bond energy.) The net result is that pairs of reactive radicals combine to form more stable molecules, while the catalytic species is regenerated. In flames, the H, OH, and O radical concentrations in the reaction zone are well above those that correspond to thermal equilibrium. The rapid catalytic process drives the system toward thermal equilibrium (Chapter 3).

Among compounds containing non-metallic elements, catalytic activity has only been determined for the halogen atoms, Br, I, and Cl, and for phosphorus.

- The addition of bromine- (and by analogy, iodine- and chlorine-) containing compounds to flames does decrease the H atom and OH radical populations. This decrease occurs at a slightly lower temperature location in the flame zone than at the location of the peak H atom concentration.
- These families of compounds are more effective at inhibiting laboratory flames when added to the air than when added to the fuel.
- The effectiveness of these compounds is not sensitive to the form of the non-catalytic moiety. However, any included hydrogen acts as fuel, which offsets the apparent flame suppression effectiveness.
- The relative efficiency of these atoms in inhibiting flames is  $\text{Cl} < \text{Br} = \text{I}$ . This reflects the ratio of the forward to reverse rates of the  $\text{HCl} + \text{H} = \text{H}_2 + \text{Cl}$  reaction, which causes Cl to be less effective at flame temperatures.

Extensive research on phosphorus-containing compounds (Chapter 3) showed that:

- Compounds containing a single phosphorus atom are at least as effective as halon 1301 on a molar basis.
- These compounds catalytically decrease the H and O atom and OH radical populations, as do the halogens.
- The effectiveness is independent of the structure of the non-phosphorus moiety, as long as the phosphorus is fully in the gas phase in the flame zone. This requires vaporization or decomposition with sufficient residence time.
- Chemical kinetic modeling of an organophosphonate (DMMP) showed that the active phosphorus-containing species concentrations reached plateaus at levels below those required for flame extinguishment. This indicated that thermal effects also contributed to flame extinguishment.

From a detailed examination of the published literature, compounds containing 21 transition metallic elements demonstrated inhibitory effects in flame systems and/or on engine knock. Of these, five (P, Cr, Pb, Fe, and Mn) have a high potential for flame inhibition and three (Ni, W, and Mo) a medium potential, in the absence of condensation of the active species to form inactive particles.

Iron-containing compounds were studied as examples of highly efficient flame inhibitors (Chapter 3).

- $\text{Fe}(\text{CO})_5$  and ferrocene are 10 times more effective as flame velocity inhibitors as halon 1301.
- The mechanism for the effectiveness of iron-containing compounds primarily results in H atom recombination. A secondary catalytic cycle results in O atom recombination.
- Gas phase transport of the active iron-containing species to the region of high H atom concentration is necessary for efficient inhibition.
- Particle formation near the location of peak H atom concentration can act as a sink for the iron-containing intermediate species and reduce the catalytic effect.
- The volume fraction of inhibitor influences condensation since at low values, it may be below its saturation value.
- The available residence time affects particle growth.
- If the particles are small enough, they can re-evaporate upon passing into the high-temperature region of the flame.
- Thermophoretic forces can be large in the flame and re-distribute particles away from the region of peak H atom concentration.
- Convection and drag forces, combined with the existing flow field in the flame, can prevent particles from reaching the region of peak H atom concentration.
- The flame temperature of the stabilization region of diffusion flames (such as in unwanted fires and the cup burner) is much lower than in premixed or counterflow laboratory diffusion flames, exacerbating the condensation potential.
- Ferrocene was ineffective at suppressing a spray burner flame, presumably due to extensive condensation of the iron-containing species into particles.

This loss of fire suppression potential due to particle formation in some flame systems has been observed for Cr, Pb, Mn, Sn, Co, and Sb, as well (Chapter 3). Were this condensation to occur in practical fires, as was observed for ferrocene, compounds of these metals would likely not demonstrate fire suppression capabilities commensurate with their high flame velocity inhibition efficiency that was observed when added at low concentration to laboratory premixed flames. There are no data to indicate the potential for particle formation for compounds containing Ni, W, and Mo. The vapor pressures of the suggested flame-quenching species (for which data are available) are reasonably high.

Prediction of the potential loss of effectiveness due to condensation is presently difficult. The potential depends upon the local supersaturation ratio in the inhibited flame. Calculation of this ratio depends upon knowing both the detailed kinetic mechanism of inhibition as well as the vapor pressure of all of the intermediate species. Further, the kinetics of the condensation (and potential re-evaporation of particles) will be highly dependent on the flow-field of the particular flame system to be extinguished.

Emerging from these studies is the principle that the effectiveness of a catalytically acting agent can be temperature dependent.

- For a higher temperature (e.g., premixed) flame, the radical pool will be larger, so that a fixed amount of inhibitor will have a smaller relative effect on the radical pool.
- The higher temperature also leads to a smaller difference between the superequilibrium radical concentrations and the equilibrium concentrations, further decreasing the effectiveness of the additive.
- A higher temperature can also lead to a shifting of the equilibrium of the key intermediate species (for example, to the right in the  $\text{HBr} + \text{HX} \cdot \rightleftharpoons \text{H}_2 + \text{BrX}$  reaction), leading to a lower effectiveness.
- A higher flame temperature can decrease the condensation rate (or increase the vapor pressure) of the particles, increasing their effectiveness.

The spatially resolved experiments and chemical kinetic modeling demonstrated that, for effective catalytic flame inhibition, the active species need to be present at the right part of the flame. The active species are usually one or more decomposition products of the agent. Hence, the agent must decompose near the flame (due to high reactivity or a sufficiently low activation energy), so that the proper intermediates for the catalytic cycle are present for a sufficient time to deplete the radical pool. The right place in the flame is where the radicals are most prevalent. An active species will be most effective if it is in high concentration where the peak chain branching reactions (and hence, peak radical volume fractions) are located.

In summary, a unified view of the suppression of flames by chemically active agents is as follows:

Flame propagation results from the fast reactions of key species (H and O atoms, OH radicals) with vaporized fuel molecules. These species exist at concentrations far above those expected from thermal equilibrium at flame temperatures. Chemically active agents decompose in the flame to generate the entities that catalytically reduce the radical concentrations toward equilibrium levels. While this catalytic process slows the flame, it does not necessarily extinguish it. Both chemically active and physically active suppressants increase the heat capacity of the fuel/air mixture, reducing the flame temperature and thus, along with the decreased concentrations of radical reactants, decrease the flame reaction rates below the level needed to sustain combustion. These two effects are synergistic. Thus, if weight limitations allow, the effectiveness of a chemical agent can be enhanced by combination with a high heat capacity chemical.

## 11.4 EVALUATION OF CANDIDATE FIRE SUPPRESSANT TECHNOLOGIES

### 11.4.1 Screening Measures

The NGP anticipated the need to evaluate thousands of chemicals in its search for alternative fluids to halon 1301. While full-scale testing of chemicals is eventually necessary to demonstrate acceptability, it was impractical to use such tests to narrow that large a list of candidates. Moreover, many of the chemicals would need to be custom synthesized and/or would be of unknown toxicity. Thus, a protocol for rapid and inexpensive screening was developed to identify those relatively few agents worthy of further examination. For each property to be screened, the first result from a three-step process was used: literature search for a published value, estimation of the value based on analogous compounds, and performance using the selected screening test.

The screening tests determined to be most critical were for fire suppression effectiveness, volatility, atmospheric impact, and toxicity.

The criterion for fire suppression effectiveness was a cup burner flame extinguishment value below 5 % by volume, comparable to halon 1301 and superior to the HFCs.

- For thermally active compounds, the first step sufficed (Chapter 7). To be efficient at flame extinguishment without any chemical or catalytic activity, a compound needs to have high values of heat of vaporization, liquid phase heat capacity, total heat absorption due to a phase change, and/or heat needed to raise the liquid or gas to combustion temperatures. Such data were available for thousands of compounds, and thousands more could be eliminated by analogy. The NGP approach involved developing a figure of merit for evaluating each of thousands of compounds based on the total enthalpy absorbed by the compound as it was heated from room temperature to flame temperature, represented by 1400 K.
- For chemically active compounds, the cup burner was the main tool (Chapter 6). Many compounds had already been tested, enabling additional appraisals by analogy. Others were acquired in small quantities and approximate flame extinguishment values determined.
- Two other laboratory flame suppression devices were developed to examine specialized aspects. The Dispersed Liquid Agent Fire Suppression Screen (DLASFSS) was used to appraise the differences between a chemical being applied as a gas or a liquid. The Transient Application Recirculating Pool Fire Agent Effectiveness Screen (TARPF) was used to identify differences in effectiveness that might arise from impulsive (rather than steady state) injection of the suppressant, such as from a solid propellant fire extinguisher. Experiments indicated that reignition of flames could occur at hot surface temperatures as low as 400 °C. The knowledge gained from each was used in evaluating chemicals in general, but neither was used as a routine screen (Chapter 6).

Volatility was reflected in a compound's boiling point. For reasons noted above, compounds whose boiling points were above 20 °C were eliminated from further consideration.

- Including compounds with boiling points up to 20 °C was fairly liberal, in that this allowed consideration of compounds that could only achieve an extinguishing concentration at equilibrium. Reaching this concentration by evaporation from a liquid pool is a slow process. Flushing of the chemical from the engine nacelle or reaching a dangerous overpressure in a dry bay would likely precede flame extinguishment unless a large excess of the chemical were dispensed. This would be the case even if the lowest ambient in-flight temperature were -18 °C (Chapter 2) rather than the specified -40 °C.
- If the *surface* temperatures within in-flight engine nacelles were as high as the predicted nacelle interior *air* temperatures (Chapter 2), (about 10 °C to 30 °C), then some of the higher boiling point compounds with boiling points near 20 °C would flash and disperse effectively.
- Meeting the boiling point criterion also discriminated against chemicals indirectly. A chemical that has a high heat capacity and/or a feature that leads to degradation in the troposphere was likely to have a high molecular weight. More massive molecules typically have higher boiling points.

No measurements were made of the molecular properties that determine atmospheric lifetime. A chemical continued under consideration if it had a feature that rendered it tropodegradable, i.e., likely to have a short atmospheric lifetime.

The screening criterion for toxicity was the absence of data indicating that serious effects on people could occur at a concentration lower than that needed to extinguish flames. The focus was on acute toxicity, in particular cardiotoxicity.

- No effective screen was found for the cardiac sensitization of dogs, the standard test. (Dog tests of chemicals, conducted in parallel with the NGP, revealed unexpectedly high toxicity.) In vitro tests are in their infancy, especially for cardiac arrhythmia. The use of octanol/water partition coefficients showed promise as a screen for cardiotoxicity.
- Research was performed to extend and apply a realistic human exposure model (whose input was animal exposure data). This has the potential for more accurate assessment of the hazard from a short exposure to a discharged suppressant.
- Literature values were obtained for some appealing compounds. However, no new compounds survived screening for all four properties. Thus, the NGP performed no animal tests for candidate agents for in-flight fire suppression.

The cost and availability of a compound were not initial screening criteria. However, it was recognized that, for a non-commercial chemical, the difficulty (or non-existence) of a synthetic approach and the cost of the starting materials could prove problematic in obtaining operational quantities of the chemical.

#### 11.4.2 Measurements during Fire Tests

Conventional real-scale testing of fire suppression effectiveness involved little instrumentation. This was typically limited to measurement of the time of fire extinguishment and the concentration of suppressant that lead to extinguishment. The latter was measured with a time constant of the order of 0.5 s. To learn more about the fire extinguishment process and to pave the way for improved qualification testing, the NGP developed additional measurement technology for real-time, *in situ* monitoring of the suppression event.

- Time-resolved measurement of the concentration of a suppressant,  $C_2F_5H$ , in a single location was performed using a Differential Infrared Rapid Agent Concentration Sensor (DIRRACS, Chapter 5). The portable device used modulated light absorption in the 8.5  $\mu\text{m}$  spectral region. The optical path length is 1 cm. The combined standard uncertainty was about 2 % (0.005 volume fraction). Turbulent fluctuations of about 10 ms were clearly resolved. The technique can be extended to other suppressants with discrete infrared absorption.
- Steady state concentrations of  $CF_3I$  were measured using ultraviolet absorption at 270 nm (Chapter 8). The repeatability was  $\pm 15\%$ . The technique can be extended to other suppressants that absorb in the ultraviolet.
- Concentrations of  $O_2$  during live fire testing were measured using a four-location laser absorption apparatus. Data points were obtained every 10 ms, and the optical path was 10 cm. The minimum detection limit was 3000  $\mu\text{L/L}$ .
- Fuel vapor concentrations were obtained using a novel two-laser, infrared absorption probe, with nominal wavelengths of 1.31  $\mu\text{m}$  and 1.71  $\mu\text{m}$ . The limit of detection was about 200 ( $\mu\text{L/L}$ )-m. The unit had not yet been tested at real scale.
- Concentrations of HF, a principal combustion product generated during fire suppression by fluorinated agents, were measured using infrared absorption at 1.31  $\mu\text{m}$ . The measurement duration was 10 ms, with a minimum repetition period of 100 ms. The optical path length was approximately 10 cm.

### 11.4.3 Life-cycle Cost Assessment

The NGP adapted a life cycle cost model to estimate the cost benefits of carrying fire protection systems for engine nacelles and dry bays on board military aircraft, and developed a methodology for estimating the total cost of either retrofitting existing aircraft or configuring future aircraft with new systems based on a non-ozone-depleting fire suppressant (Chapter 10). The calculations were performed for cargo, fighter, and rotary-wing aircraft. The currently installed agent baseline was halon 1301; the modeled replacement agent was HFC-125.

These estimates showed that additional investment in optimizing fire suppression system performance pays off in assets saved. Specifically:

- It is highly cost effective for aircraft to carry fire protection systems, despite their life cycle costs and the infrequency of their use. Based on historical data, the return on investment in halon 1301 fire protection systems (in terms of the cost of aircraft assets saved by their use and their historical extinguishing success rate) was estimated to be over five-fold.
- It would also have been highly cost effective for the larger HFC-125 systems, of fire suppression effectiveness comparable to these halon 1301 systems, to have been installed on military aircraft. The return on investment would have been at least two-thirds that of the halon 1301 systems.
- For comparable fire suppression effectiveness, the net cost of a system using HFC-125 installed in a future aircraft is comparable to the net cost of a conventional halon 1301 system as a ratio of the overall fire protection system cost of ownership to the total aircraft platform cost, although in absolute terms it can differ by many millions of dollars for each aircraft platform of interest, with even higher differences observed for retrofit applications.
- Additional investment in developing systems with superior fire suppression performance (as indicated by higher extinguishing success rates in the field) to systems exhibiting historical levels of performance was observed to be cost effective and beneficial.

The methodologies were fashioned to serve as a stand-alone product, to provide the framework to build modified models for future halon replacements, and to serve as analysis tools to identify key indicators of desirable halon replacement properties to consider in later research on new technologies. Since their formulation, this approach has already been used on some developmental aircraft. This methodology can be expanded to meet the additional challenges of new aircraft, new fire suppression technologies, and additional applications, such as fuel tank inerting.

## 11.5 POTENTIAL FOR NEW, VIABLE SUPPRESSANTS

Over the course of the NGP, virtually the entire world of chemistry was reviewed, screened, and, if warranted, tested against the criteria described earlier (Chapter 7).

No inorganic compounds were identified that met the screening criteria. The findings for specific families of inorganic compounds are as follows:

- Compounds of radioactive elements were toxicological unsuitable.
- Aqueous solutions of some of the salts mentioned below were highly efficient flame suppressants. However, the freezing points of these solutions are above the lower agent storage temperatures for in-flight aircraft.

- Compounds of Group I elements in the periodic table (lithium, sodium, potassium, rubidium, cesium, and francium) are flammable or are solids at room temperature. Alkali metal compounds applied as dry powders or liquid solutions are well known to be extremely effective fire extinguishants. Since these have not already been accepted for use on in-flight aircraft fires, due to corrosion problems, alternative compounds were not screened. In these powders, potassium salts are more effective than the corresponding sodium salts, consistent with the lower decomposition of the former to generate vapor phase potassium atoms.
- The compounds of Group II elements (beryllium, magnesium, calcium, strontium, and barium) are solids or low volatility liquids and have not shown the needed fire suppression effectiveness.
- The compounds of Group III elements (boron, aluminum, gallium, indium, and thallium) showed no promise. Boron compounds are flammable, toxic, or simply carriers of any bonded halogen or Group I atoms. Aluminum in compounds has not shown any catalytic flame suppressant capability. Thallium and indium compounds are toxic. There are no reported fire suppression data for the rare gallium compounds, but they are not expected to be superior to the other Group III compounds.
- In Group IV (carbon, silicon, germanium, tin, and lead), carbon-based compounds are discussed below as organic chemicals. There are no data to suggest that silicon-based and germanium-based compounds offer flame suppression advantages over the similar carbon-based compounds. Compounds of the heavy metals, tin and lead, are environmentally unacceptable.
- Within Group V (nitrogen, phosphorus, arsenic, antimony, and bismuth), arsenic and antimony compounds are too toxic; antimony and bismuth are environmentally unacceptable heavy metals. As discussed earlier, phosphorus compounds are very efficient at fire suppression; however, they are not sufficiently volatile for total flooding, and some are toxic. Inorganic nitrogen compounds did not show sufficient fire suppression effectiveness.
- Of the compounds of Group VI elements (oxygen, sulfur, selenium, tellurium, and polonium), oxygen has no fire suppression function itself, and inorganic oxides are too low in volatility. Sulfur and selenium compounds have not shown good fire suppression efficiency. Selenium compounds are generally toxic, as are the byproducts of sulfur oxidation during suppression. Tellurium and polonium compounds have not been tested, but are unlikely to be more efficient suppressants than sulfur compounds.
- As noted earlier in this chapter and in Chapter 3, compounds of several of the transition metals are far more efficient flame inhibitors than halon 1301. However, these compounds are insufficiently volatile for flooding applications. Ferrocene was not effective at suppressing a spray flame, likely due to condensation of the active iron species into relatively inert particles.
- Compounds containing four of the halogen atoms in Group VII (fluorine, chlorine, bromine, iodine) have been studied extensively. These are discussed further under the organic compounds. Bromine- and iodine-containing compounds are efficient suppressants.
- The noble gases in Group VIII (helium, neon, argon, krypton, and xenon) are inefficient fire suppressants.

Examination of organic compounds was barely more successful (Chapter 7):

- There were no available compounds that did not contain a halogen or phosphorus atom that met all the screening criteria, especially fire suppression efficiency and volatility.  $N(CF_3)_3$

was reported to have a boiling point of  $-10\text{ }^{\circ}\text{C}$  and should have fire suppression efficiency superior to HFC-125. However, since the compound is fully fluorinated and since the compound could give rise to nitrogen oxides (potent ozone depleters) in the stratosphere, there was caution about its environmental acceptability. Attempts to synthesize this compound for further testing were unsuccessful.

- There were organophosphorus compounds with fire suppression efficiencies at least comparable to halon 1301. However, even with extensive fluorination, their volatility was too low, and some reacted in air.
- The replacement of hydrogen atoms with fluorine atoms and fluoroalkyl groups generally decreased the combustibility and increased the volatility of a wide range of organic chemical families. Nonetheless, only  $\text{CF}_3\text{CN}$  and the small fluorocarbons, fluoroamines, and fluoroethers were sufficiently volatile. The atmospheric lifetimes of the fully fluorinated compounds were too long for consideration. The remaining compounds were not comparable to halon 1301, or significantly superior to HFC-125, in fire suppression efficiency.
- Among the remaining halogenated compounds, most attention focused on those containing bromine. Chlorinated organic compounds are less efficient at flame suppression than the analogous compounds containing bromine or iodine atoms. The iodinated compounds are no more effective fire suppressants than the analogous brominated compounds, and there were concerns regarding stability and toxicity.
- Nearly all the brominated compounds tested, or for which literature data were available, showed cup burner flame extinguishment values comparable to halon 1301. The presence of multiple hydrogen atoms tended to offset this efficiency.
- To have a negligible ozone depletion potential, a compound containing bromine (or iodine or chlorine) must have a second feature that leads to rapid decay in the troposphere.
  - Heavily, but not fully, fluorinated bromoalkenes have sufficiently high fire suppression efficiency and short atmospheric lifetimes. However, even the smallest of these were insufficiently volatile.
  - The bromofluoroethers show good fire suppression efficiency. However, unless somewhat protonated, they are insufficiently reactive in the troposphere. Furthermore, their boiling points are too high for effective dispersion.
  - $\text{CF}_2\text{BrCN}$  has a boiling point of  $3\text{ }^{\circ}\text{C}$ , the lowest of any tropodegradable brominated compound. It extinguished cup burner flames at under 4 % by volume. This compound may have promise if the low temperature requirement were relaxed, as suggested by the fire suppression incidence data in Chapter 5. However, a rumor of high toxicity needs to be examined, and the estimation of a modest atmospheric lifetime needs to be confirmed.

## 11.6 FIRE SUPPRESSION PRINCIPLES TO BE TESTED

The knowledge summarized above was, for the most part, obtained from laboratory measurements and calculations. These systems were carefully chosen in the context of the actual applications: in-flight engine nacelle and dry bay fires. Nonetheless, laboratory experiments do not fully replicate three-dimensional flows and transient mixing processes, and the computational models must, of necessity, assume some simplifications of geometry and reactivity to be tractable.

Thus, it was important to know the extent to which the research results will be valid for realistic fires occurring in the configuration and environmental conditions of a full-scale, or “real scale” engine nacelle. Accordingly, the NGP Technical Coordinating Committee and Principal Investigators identified a set of principles to be tested in such a test fixture. The following is a list of those principles, a statement of the importance of each, and the real scale experimental approach used to investigate them.

**Principle 1: Extinguishants with boiling points higher than the local engine nacelle airflow and surface temperatures do not disperse sufficiently in time for engine nacelle fire mitigation, whereas those with boiling points below the prevailing temperature can disperse sufficiently if properly applied.**

Importance: The ability of a fire suppressant to fill an engine nacelle quickly and completely is paramount to minimizing the mass needed for flame extinguishment and minimizing the total mass of the fire suppression system. The boiling point screening criterion, which was based on this principle, led to the rejection of a large number of otherwise promising candidates.

Real-scale Experimental Approach: The fixture temperature was set above or below the boiling point of either of two chemicals. Chemical portions that had not fully vaporized due to local temperatures below the chemical’s boiling point would presumably condense on upstream clutter or pass by the fire zone to some degree in unvaporized state, and hence not contribute to the vapor concentration readings in the local instruments placed around the nacelle. The concentration of the chemical vapor was measured upstream and in the vicinity of potential flame zones. Additional factors varied were the degree of clutter and the air and chemical discharge rates.

**Principle 2: The measured cup burner extinguishing concentration of a candidate extinguishant is an effective predictor of the critical flame suppression concentrations required within the flame recirculation zone of an engine nacelle fire.**

Importance: Virtually all assessments of fire suppression efficiency have been obtained using the cup burner; this is likely to continue. The geometry of the flame and flow field is consistent with exposed flames. In practice, the extinguishing concentration is also dependent on the type of fire and the suppressant residence time in the flame zone. Laboratory experiments and calculations indicate that the flame extinguishment values are the limiting values for extinguishment of pool fires behind obstructions, the most difficult fires to quench.

Real-scale Experimental Approach: For a physically acting and a chemically acting suppressant, the minimum fire zone concentration that caused flame extinguishment was measured. Additional variables included the temperature of the air and extinguisher system, the degree of clutter, the air and chemical discharge rates, and the type of fire (fuel spray and pool).

**Principle 3: Increasing the number of local extinguishant discharge sites increases the dispersion quality in terms of balanced concentration profiles, up to some practical limit.**

Importance: The efficiency of dispersion of a suppressant throughout an engine nacelle or dry bay can be enhanced by the installation of a set of well located and designed agent discharge ports. However, each discharge port, with its associated hardware, increases the mass and complexity of the fire suppression

system. Thus, it is important to know the extent to which there is a benefit from adding additional discharge sites.

**Real-scale Experimental Approach:** A fire suppressant was dispensed into the nacelle test fixture through two contrasting piping designs. The first comprised a single discharge port located far upstream of the fire site. Inside the nacelle, the piping terminated in either two nozzles or two open ends. The other design involved four discharge ports, at four positions spaced angularly around the diameter of the nacelle and at four separate distances downstream, in a helical arrangement to promote balanced flow distribution both radially and axially. The piping through each port again terminated in two open ends or nozzles. Concentration measurements at 12 locations in the nacelle enabled determination of the uniformity of dispersion. Additional variables included the air and chemical discharge rates, the degree of clutter, and the temperature of the test fixture.

**Principle 4: The extinguishant concentration established in the recirculation zone is a function of the injection time and mixing time behind the obstacle (“clutter”) that stabilizes the flame.**

**Importance:** The NGP correlation, developed at laboratory scale, is the potential basis for designing the preferred time profile of discharge of the suppressant. The correlation holds that the relative quantity of extinguishant entrained from the free stream over a bluff body that anchors a flame into the flame’s recirculation zone is a function of the ratio of the free stream velocity over the clutter to the height of the clutter. The agent discharge time also affects the total time the entrained extinguishant resides in the recirculation zone.

**Real-scale Experimental Approach:** The concentration of the agent was measured upstream of and within the recirculation zone. The variable was the size of the upstream obstacle.

**Principle 5: The passage of a suppressant through an engine nacelle is significantly affected by the degree of clutter in the nacelle.**

**Importance:** Prior NGP research efforts had characterized the degree of flow interruption, pressure drop and re-direction through clutter of various idealized configurations, including any condensation of liquid portions of mixed-phase extinguishant flows on the clutter arrays. Most of these studies were performed on idealized, two dimensional clutter representations, and computer models of this behavior were also derived. The complex three-dimensional flows and clutter arrangements in realistic nacelles may challenge these simplified representations.

**Real-scale Experimental Approach:** Measurements of agent concentration were performed at multiple locations in the test fixture. The standard deviation in those measurements, an indicator of the effect of the clutter on suppressant transport, was determined as a function of rib height and agent discharge rate.

**Principle 6: Assuming that a mix of extinguishant vapor and liquid aerosol reach the flame reaction zone, the sufficient vaporization of liquid particles to enhance extinguishment will be dependent upon, among other parameters, the liquid’s residence time in the recirculation zone.**

**Importance:** A significant fraction of the suppressant may be discharged in the liquid state. Droplets that do not evaporate fully before or in the flame zone are essentially wasted. If some mixture of liquid aerosol particles is interspersed with the extinguishant vapor as it enters the recirculation zone of the

flame, the ability of the particles to evaporate and increase the extinguishant vapor loading in the flame to facilitate extinguishment is dependent upon its vaporization characteristics and residence time in the flame. The evaporation rate is based upon the common heat transfer properties known for these extinguishants, and the droplet diameters (or characterization of their distribution).

**Real-scale Experimental Approach:** The agent was discharged either through open ended piping or through nozzles that created a fine spray of droplets. Concentrations of agent vapor were measured at 12 locations in the nacelle to identify the total extinguishant mass required to be discharged to reach a given measured concentration just before and in the recirculation zone. Additional factors varied were the air and chemical discharge rates, the degree of clutter, and the temperature of the test fixture. Increases in the extinguishment mass required to reach a given concentration were interpreted as being due to increased collection of liquid portions of the extinguishant on the clutter upstream and prior to reaching the fire site, or passing through the fire site without sufficient vaporization.

**Principle 7: The suppression effectiveness of a non-catalytic extinguishant in a full-scale engine nacelle is determined by its ability to absorb heat as it enters the flame zone.**

**Importance:** Tests have indicated this is so for a variety of laboratory flames. The degree to which the latent heat can be used to decrease the amount of extinguishant necessary to suppress a fire in a full-scale engine nacelle needs to be verified. Verification under actual engine nacelle conditions will confirm the basis for fire suppression system design equations.

**Real Scale Experimental Approach:** The minimum concentration of suppressant needed to quench both pool fire and a spray fire were determined. Additional factors varied were the overall flow within the nacelle, the discharge rate of the suppressant, and the temperature of the test fixture.

## 11.7 METHODOLOGY FOR REAL-SCALE TESTING AND VALIDATION

### 11.7.1 Aircraft Engine Nacelle Test Facility (AENTF) Features and Capabilities

#### Overall Test Facility

The Aircraft Engine Nacelle Test Facility (AENTF) at Wright-Patterson Air Force Base had been constructed expressly to realistically recreate the environment experienced within a wide range of aircraft engine nacelles, with the capability to conduct repeated, full-scale nacelle fire tests under those conditions. An overall diagram of the facility is shown in Figure 11–1. Figure 11–2 is a photograph of the nacelle section, and Table 11–3 is a cutaway view of the interior.

A primary feature of the facility was the capability to re-create realistic air flow and temperature conditions within the nacelle volume. An atmospheric blower and associated high-pressure bottle farm was used to provide up to 5 kg/s (11.0 lb/s) of air flow, which was more than adequate for the types of aviation platforms currently in operation. An industrial chiller was used to cool the rapidly flowing air. Even with subsequent heating due to insulation limitations between the chiller and the nacelle section, temperatures inside the nacelle of -34 °C (-30 °F) or below were achieved. Alternatively, industrial heaters heated the incoming air as hot as 135 °C (275 °F). A water quench system was used to cool the effluent from the nacelle fire test section and eliminate some of the combustion by-products, with a

scrubber system used to remove the remaining contaminants before the effluent was exhausted to the atmosphere.

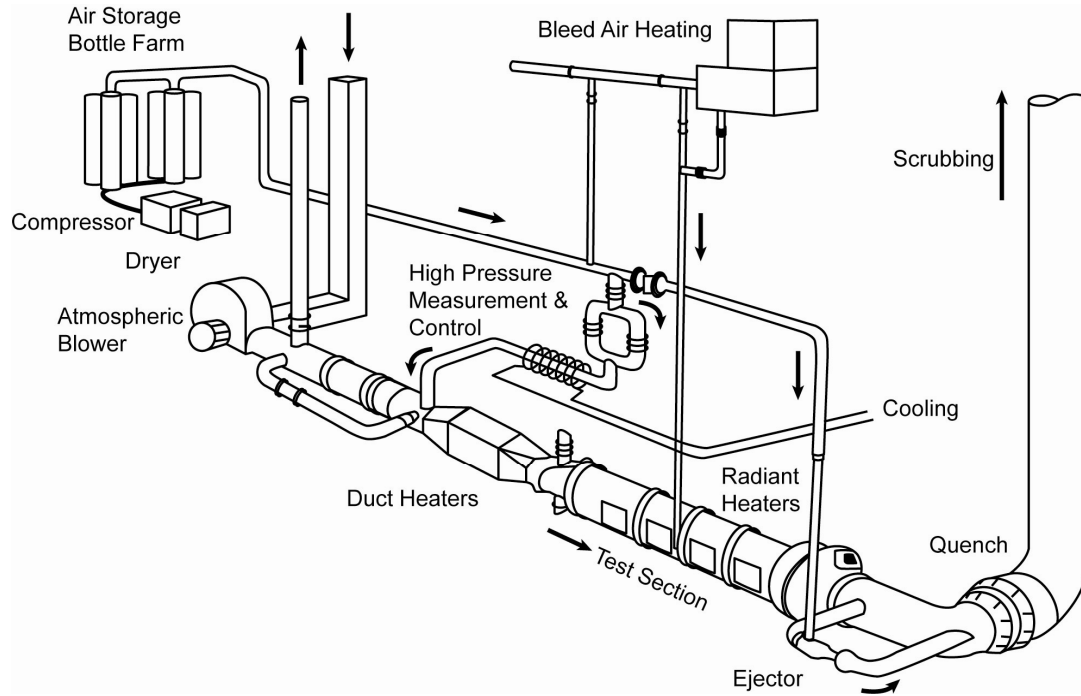
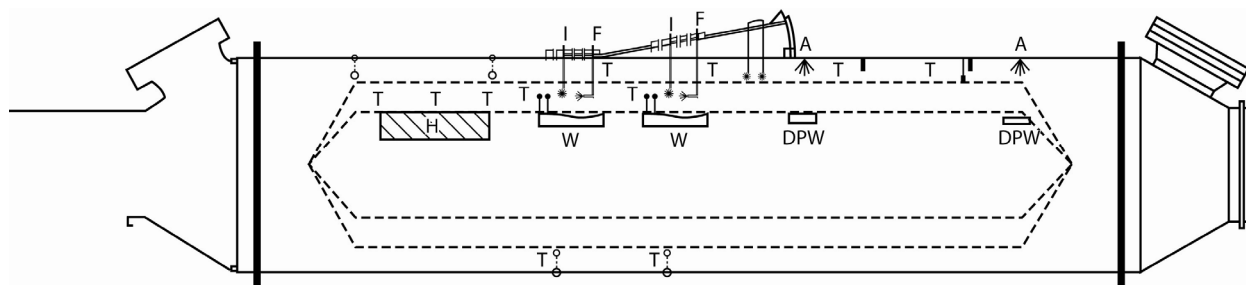


Figure 11-1. AENTF Primary Mechanical Components.



Figure 11-2. Photograph of Universal Test Fixture.



**Figure 11-3. Cutaway View of the Engine Core inside the Nacelle Fixture.** A: Agent Injection Port, F: Fuel Injection Site, I: Igniter, T: Thermocouple site, DPW: Dual Port Window. W: Window.

A remote fuel supply cart was used to supply heated flammable fluids, such as JP-8 jet fuel or an aviation hydraulic fluid, preheating and pressurizing them to their appropriate operating values before introducing them into the nacelle section. A separate extinguisher unit (Figure 11-4) permitted heating or cooling of the fire suppressant. For low temperature tests, the unit was immersed in a dry ice bath, regulated by a heat tape wrap, enabling a container temperature as low as  $-54\text{ }^{\circ}\text{C}$  ( $-65\text{ }^{\circ}\text{F}$ ). A remote control room (Figure 11-5) was used to monitor the internal nacelle air flow, temperature and pressure, as well as fuel and extinguishant conditions, before and during each test. The operation of the fuel release, airflow control, fire and extinguisher initiation, and shutdown procedures were all computer-automated controls.



**Figure 11-4. Vertical Extinguisher Unit Attached to the Nacelle Fixture.**

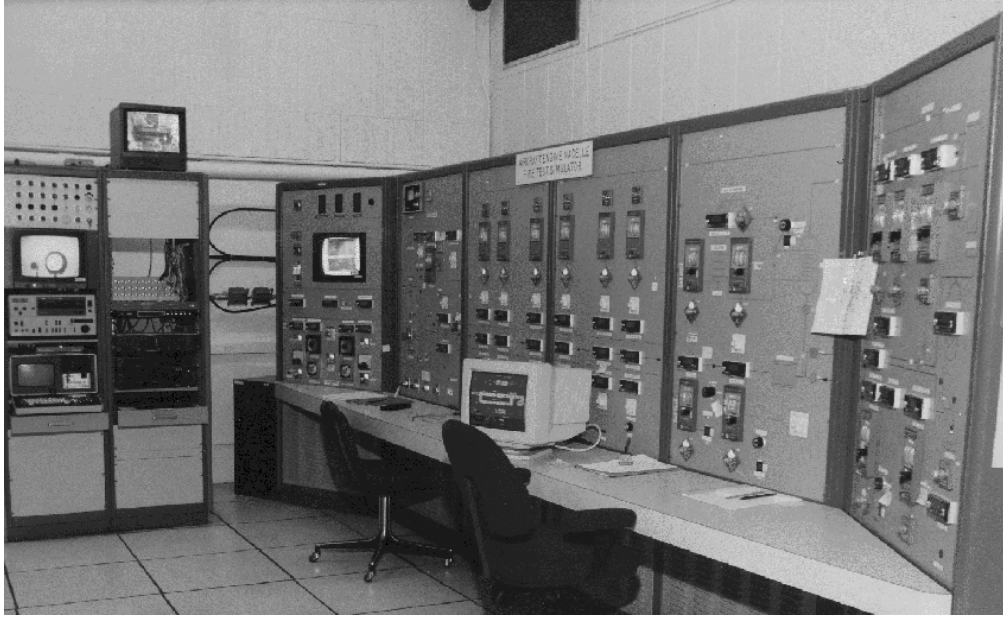


**Figure 11–5.**  
**AENTF Control Room.**

### **“Generic” Real-scale Nacelle Test Fixture**

The test section was a generic (i.e., reconfigurable) engine nacelle previously used in the National Halon Replacement for Aviation Program (conducted from 1992 to 1996)<sup>1</sup>, as well as in more recent halon replacement testing for the U.S. Army. It featured the capability to replicate a variety of engine nacelle configurations and operating conditions. It had withstood thousands of full-scale fire tests under extreme thermal loads, and had shown the capability to retain its structural integrity, even when serving as a pressure vessel during fire tests at elevated pressures, due to the unique sliding graphite joint and clamshell design.

The outer nacelle case was a cylinder 1.22 m (4.0 ft) in diameter, and 5 m (16.25 ft) in length, housing a simulated engine core 3.8 m (12.4 ft) in length serving as the effective test section. Conical flow transition sections, each 0.27 m (10.5 in) deep, were attached at each end. Several internal cylindrical simulated engine core sections had been constructed and used in concert with this fixture. Their diameters were 0.61 m (2.0 ft), 0.76 m (2.5 ft), and 0.91 m (3.0 ft). For this program, only the largest diameter core was used, in order to minimize the free volume of the fixture and thus make efficient use of extinguishant for the considerable number of tests conducted. Rather than changing core diameters and the annular air flow clearance area between the nacelle and engine core, which was 0.15 m (6.0 in.) wide for these experiments, the air flow patterns (including local recirculation) were changed by varying the clutter (rib) height. The outer nacelle had multiple ports for making measurements in the nacelle. There were also ports at two distances downstream to mount fuel nozzles and spark ignitors. These enabled varying the distance between the agent discharge sites and the site of the fire, creating, in effect, a “long nacelle” or a “short nacelle.” The entire nacelle assembly could be rotated to represent top, side, or bottom fire locations.

Two types of fires were used in these tests – spray fires and pool fires. Figure 11–6 is a semi-transparent view of the internal configuration of the test fixture (with airflow moving from right to left in the illustration). Both the spray fires and pool fires could be created in the bottom of the nacelle (each in

their own separate experiments). The pool fire site was 30 cm (1 ft) downstream of the spray fire site. Each flame was stabilized by a variable height rib mounted just upstream of the flame site to act as a flame holder.

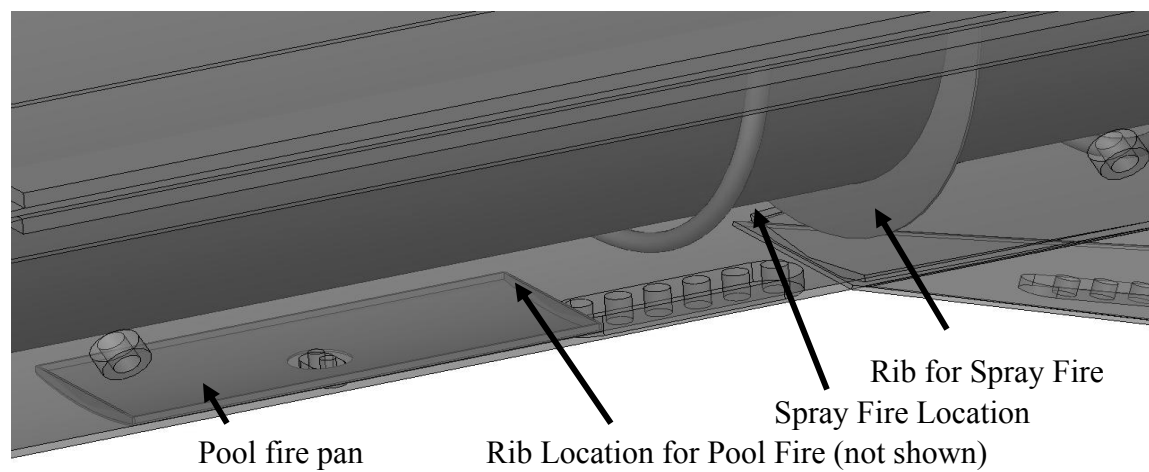


**Figure 11–6. Semi-Transparent View of Components in Fire Section of the Test Fixture.**

Figure 11–7 shows the pool fire pan. Figure 11–8 shows the configuration of components in the fixture interior near the origin of spray fires site, in the upper left quadrant of Figure 11–2.



**Figure 11–7. Pool Fire Pan in Nacelle.**

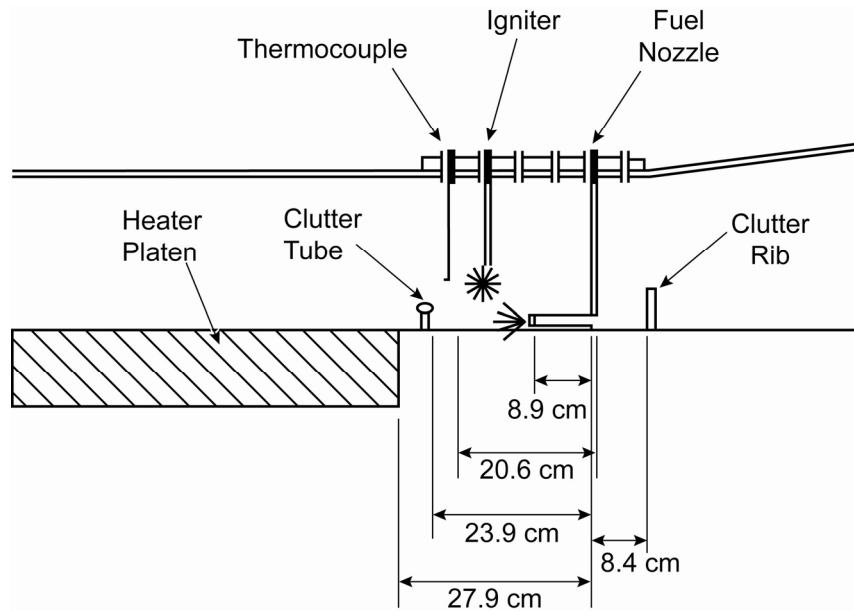


**Figure 11–8. Schematic of Spray Fire Vicinity.**

The agent could be discharged in-line, 90 ° off center, or 180 ° off center from the site of the fire. This enabled evaluating the ability of the extinguishant to wrap around the nacelle volume to remote sites before it was exhausted from the nacelle.

Annular ribs, simulating structural ribs, supports, and nacelle components, could be mounted on the inside of the outer nacelle and on the inner engine core. The rib heights varied from 2.5 cm (1 in.) to 7.6 cm (3 in.). Spaced at 30.5 cm (12 in.), they alternate between the nacelle surface, extending radially inward, and the engine core, extending radially outward (Figure 11–9). These ribs served to block the flow of extinguishant realistically and served as bluff bodies that shielded the base of the fire and create recirculation zones that made fires stable and resistant to blowout. The reddish material at the rib bases is a sealant to prevent air or fuel seeping under the rib connections.

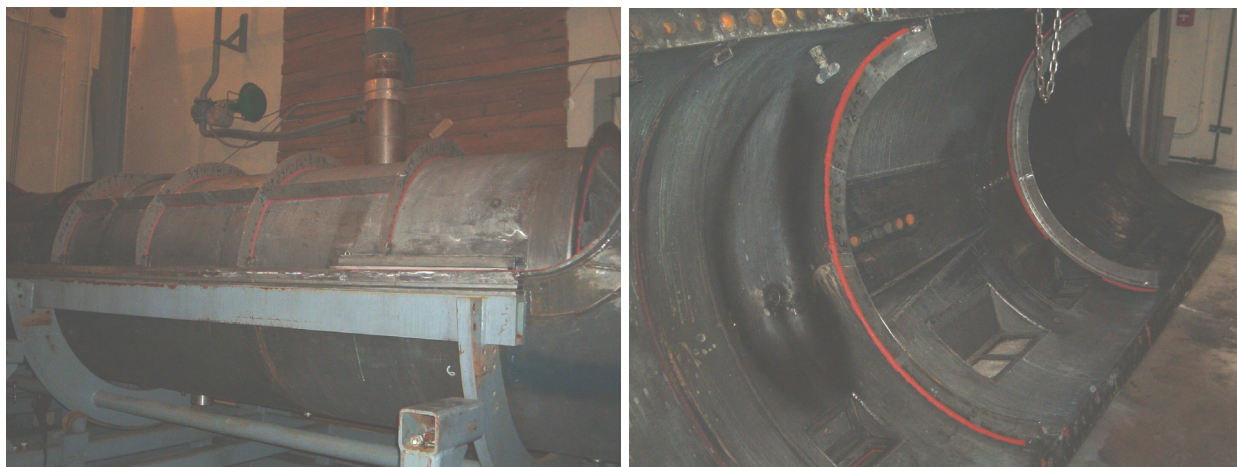


**Figure 11–9. 7.6 cm Ribs Mounted on the Underside of the Nacelle (left) and the Engine Core (right).**

In the flame region, there were also clutter-simulating ribs parallel to the flow. These inhibited the lateral movement of the extinguishant flow around the engine core surface, requiring entrainment over these lengthwise obstructions to enter the recirculation zone of a flame on the other side of the barrier.

A hot surface section, operating at temperature up to 830 °C (1500 °F), extended 120 ° around the engine core, just downstream of the aft fire origin site. It served as a flame re-ignition source after initial extinguishment. This was not used in the current experimental series, since it decreased the repeatability of the test results.

Side view ports for camera recording were installed (a) downstream of the extinguishant inlets, to observe agent flow in the nacelle during discharge, and (b) near the two possible downstream fire locations, to monitor the flame extinguishing process. An additional port was mounted at an angle to the nacelle axis, permitting an upstream view from the downstream extinguisher port region, past both fire sites, to the aft end of the heater platen on the core, near the very end of the engine core. This permitted the monitoring of the entire agent entrainment and extinguishing process, as well as identification of potential re-ignition sites. Figure 11–3 shows the positioning of the video view ports, extinguisher ports, and other relevant features on and inside the nacelle.

### 11.7.2 Design of Experiments Methodology

A review of the seven fire extinguishing principles to be examined under full-scale testing reveals that a large number of physical parameters are involved in their assessment. A basic set of these included the nacelle air flow, air temperature, clutter height, fire type, whether the agent is chemically active or not, agent boiling point, agent discharge rate, nozzle usage, and discharge location. A test series featuring two extreme settings of each of these nine parameters (or “factors”) would entail 512 runs, each with a different combination of the settings. Approximately 20 tests at varying extinguishant masses would need to precede each run to identify the threshold amount needed for extinguishment (as discussed in the next section). This full factorial test matrix of about ten thousand tests was prohibitive.

Fortunately, there existed a statistically valid technique to collect such data with a smaller, specially selected sample of the aforementioned number of different experimental runs, with nearly the same degree of fidelity of the data. It involved a fractional factorial, orthogonal test matrix, developed using a methodology commonly referred to as a statistical Design of Experiments (DOE) approach. The test matrix is termed “fractional factorial” in that it used a small, symmetric sub-set of the full factorial array of tests. (“Symmetric” means that each factor has an equal number of runs represented at each of its extreme settings.) The matrix was “orthogonal” in that it allowed sorting the effect of each individual factor, independent of all the other factors. It also allowed sorting the effect of combinations of individual factors, referred to as “two (or more)-factor interactions.”

This type of matrix is formally structured. Thus, for the test series performed here, there was a row for each test to be run and a column for each factor or group of factors. Each cell in the matrix contained the setting for each factor or group of factors for that given “run” or set of experimental conditions. For a column with a discrete, two-value factor, the setting in a cell would be the high or low value.

The associated mathematical analysis protocol for the test results, formally known as Analysis of Variance (ANOVA), provided the ability to assess quantitatively the influence of each factor and multi-factor interaction on a test result, also referred to as a response variable. ANOVA also allowed for

comparison of the relative contributions of the factors on the response variables and for comparison with the experimental uncertainty. This latter comparison facilitated determining which factors' influences were so small as to be statistically insignificant, permitting its exclusion from further consideration.

The objective of examining the seven selected NGP principles involved determining the influence of specific factors on the agent discharge and flame extinguishment process. Thus, this analysis approach of confirming the mathematical significance or insignificance of each factor, based upon the test results, was a proper technique to analyze the principles themselves. Success required (a) that both the factors and the response variables (or their post-test, mathematically-transformed derivatives), be properly chosen, defined, measured and analyzed to relate correctly to the principles of interest and (b) use of an orthogonal test array.

The ANOVA procedure also permitted the ability to exploit regression analysis and develop formulas to predict, with a estimable high degree of statistical certainty, values of the response variable for intermediate settings of the factors of interest that were not included in the test matrix. This capability permitted the selection of optimal settings of the design factors (such as extinguisher port location, discharge rate, etc.) that resulted in the most desirable response variable value (such as the minimum mass to extinguish the fire).

As might be expected, the ability to quantify the effects of numerous factors and two-factor interactions came with a price. For these streamlined orthogonal test matrices, the relative significance of each of the single factors or multiple-factor interactions could be "confounded" with each other to varying degrees in the post-analysis. By "confounding," it is meant that one cannot decipher the role of each factor in the variance of the test results. Confounded factors could be separated by additional testing.

It is helpful to note that experience with DOX protocols in most fields of interest found that three-level or higher interactions were rarely significant and were reasonably dismissed as significant sources of variance. Moreover, in actual practice, few two-factor interactions have been found to be significant, further reducing the requirement for substantial additional tests to decouple interactions to find and isolate the true significant term. These observations were consistent with the findings of the National Halon Replacement Program for Aviation experimental data, where only a couple of two-factor interactions were found to be consistently significant and worthy of consideration in the design and sizing of fire suppression systems.

The degree of confounding present in an orthogonal array experimental matrix of a particular size and with a set number of primary factors is known as the "resolution" of the matrix.

- A resolution 4 design is a full factorial matrix, and all factors and interactions are unconfounded. As noted earlier, this is not feasible for the current test series.
- In a resolution 3 design, all factors and two-factor interactions are unconfounded. While higher-order interaction terms may be confounded with either, this is most likely insignificant for this application, as noted earlier. This is the most desirable resolution.
- In a resolution 2 design, individual factors are not confounded with two-factor interactions, but groups of two-factor interactions may be confounded with each other, requiring future decoupling either experimentally or by engineering judgment for those found to be significant. A resolution 2 design is commonly used when many factors of interest are

present and test resources are limited, with limited additional work to decouple two-factor interactions if only two or three are assigned to each column.

- In a resolution 1 design, individual factors will be confounded with two-factor interactions. As expected, lower resolution designs permit more primary factors in a smaller experimental matrix.

Thus, a test plan is characterized by the number of tests to be performed, the number of factors, and the number of settings for each of the factors. For example (for two settings for each factor):

- A four run array (denoted L-4) is resolution 4 if two factors are being considered, but only resolution 2 with three factors considered.
- An L-8 array is resolution 4 with up to three factors, and resolution 2 with four factors.
- An L-16 array is resolution 3 with five factors, and resolution 2 with up to eight factors.
- An L-32 array is resolution 3 with up to six factors, and resolution 2 with up to 16 factors.

Increasing the number of experiments and the array is not always the most efficient manner for collecting the desired amount of data within a limited time. Splitting a test plan into two matrices may be superior, especially if the global process can be conceptualized as two or more separate and independent sub-processes. Here, “independent” means that the sub-processes are controlled by different sets of factors. (Some, but not all, factors may be common to these different sets, but the settings for these factors can be different for each matrix.) An important benefit of splitting the test plan is that one can select a different critical response variable for each sub-process matrix.

This splitting was deemed preferable for this test program. For the global process of putting out the fire, the two sub-processes were:

- Discharging the extinguishant in an appropriate quantity and manner uniformly throughout the nacelle in an efficient manner.
- Effecting flame extinguishment at the site of the fire zone.

Not only did these two sub-processes have different factors that control each process (with some in common), but they had different required instrumentation needs, and even differed in their need for the presence of a fire. These unique test setup differences suggested that additional experiment and analysis optimization was possible by indeed segregating each of their associated experiments into independent sub-matrices, each of which required its own special test configurations and required procedures, as well as unique measurements. The large number of factors of interest also provided a favorable exploitation of smaller experimental arrays within the limited test schedule period, particularly when factoring in the need for substantial replication and extinguishant mass test quantity “bracketing” to get final run values of their respective response variables, as will be discussed in the next section.

As will be shown in the following sections, the plan for this series of NGP tests involved two L-16 matrices of resolution 2. In each matrix, up to 28 variations of L-16s with six variables assigned in the eight allowed columns were found to be possible. All resulted in columns with either main factors only or a pair of two-factor interactions, with one excepting column having three two-factor interactions, and two columns being empty. (These two columns could be used for a factor with which no other interactions are assured (if possible), and/or for error columns to assess experimental error in the matrix.)

The selection of the array variation and column assignment for each of the factors was dictated by the preference to place a meaningless interaction or one of a high expectation of insignificance in the column with three two-factor interactions, and if possible place similarly likely insignificant interactions in each of the two-factor interaction pairs, to prevent the need for future decoupling experiments.

### 11.7.3 “Bracketing” Procedure for Testing

The testing to appraise the seven principles was divided into two categories. Examination of Principles 2, 4, and 7 required a fire in the test fixture. Principles 1, 3, 5, and 6 applied only to the effective distribution of the fire suppressant and did not require a fire. For efficient design of the experiments for the first group, it was important to know the minimum mass of fire suppressant that will suppress the fire types that were being considered, and the associated concentrations measured in the fire zone. For the second group, it was still necessary to know the concentrations measured throughout the nacelle when discharging various masses of agent, since the experimental factors might have influenced the outcome differently if the extinguishant concentration were of different levels of magnitude.

Determining the exact mass for flame extinguishment was difficult due to the inherent instability and lack of precise repeatability of fire extinguishing tests. This variation resulted from such phenomena as localized and transient air turbulence and thermal instabilities that could not be realistically controlled precisely by the investigator in full-scale tests. Obtaining a high precision was unlikely and would have required a large number of tests for each ensemble of settings of the factors affecting agent dispersion and fire suppression.

Rather, a modest, statistically designed series of tests was conducted to obtain the mass needed to extinguish the flames at a chosen success rate. This process, evolved in the course of the previous National Halon Replacement Program for Aviation, included tests in which the mass quantities were sequentially varied based on the results of prior tests (to converge on a threshold level) and repeated tests at a set quantity (to determine the repeated success rate at that set value).<sup>i</sup> Using the criterion that a true success had to be repeated four times, a test run would iterate until the lowest successful weight and the highest unsuccessful weight were separated only by the defined acceptable maximum convergence criterion, which was 10 % of the lowest successful weight.<sup>ii</sup> With five successful extinguishment repeats without a failure, this process identified the minimum agent mass for an extinguishing success rate of 86 %. This was consistent with the observed success rate of fielded halon systems for the aircraft under consideration.

### 11.7.4 Experimental Approach, Configuration and Procedure

#### Phase I – Fire Zone Conditions Required for Extinguishment

This set of tests involved a suppressant being added to the nacelle air flow and observing the effect on a downstream fire. The purpose of these tests was to determine how the local fire zone configuration,

---

<sup>i</sup> Earlier bracketing procedures designed to converge on a test mass had relied on the results of a single test to determine the next mass to be tested. Implicit in such a scheme is the assumption that each and every result is perfectly repeatable.

<sup>ii</sup> On fielded aircraft, this convergence criterion must be determined to a high degree of accuracy and precision, due to the severe weight and ultimate cost impacts associated with an inefficient overdesign and the high safety risk associated with an underdesign.

operating conditions, and extinguishant discharge conditions and composition influence the conditions required within the recirculation zone of the fire to result in flame extinguishment. The principles addressed were 1, 2, 4, 6, and 7.

The response variables measured were:

- The peak volumetric extinguishant (vapor) concentration that was reached in the recirculation zone where the flame was present when the minimum mass of extinguishant was discharged from the extinguisher that resulted in flame extinguishment.
- The total mass and moles of extinguishant discharged under those conditions.

The ratio of the number of moles discharged to peak concentration in the fire zone was also used as a measure of the efficiency of the transport of effective fire suppressant.

The experimentally varied factors of interest were:

- A. Air Flow. This affects the extinguishant concentration-time profile, the local residence time, fire characteristics, and the degree of entrainment into the flame's recirculation zone. The two settings were 0.45 kg/s (1.0 lb/s) and 1.36 kg/s (3.0 lb/s). These are within the normal operating range of most aircraft, and were at rates that could be cooled to the required temperatures by the existing chiller.
- B. Fire Type. Two different types of fires, i.e., spray fires and pool fires, presented different entrainment and flame interaction challenges to the incoming stream of suppressant. As stated previously, the nacelle fixture was turned to locate both types of fires in the bottom portion.

The spray fires were created using the high-pressure fuel nozzles used for typical AENTF fire tests. The nozzles discharged JP-8 jet fuel at a rate of 0.4 L/min (6 gal/h) at a pressure of 3 MPa (400 psi). As depicted in Figure 11–8, the sprays were ignited with a spark ignitor and allowed to “pre-burn” for 20 s before initiating the extinguisher.<sup>iii</sup> The fuel nozzle and associated spark ignitor (placed several cm downstream of it) were mounted approximately 2.5 m (8 ft) downstream from the extinguisher discharge port (located at the upstream beginning of the 0.9 m (36 in.) engine core), shielded by an engine core rib, which serves as a bluff body flame holder for the resulting flame.

Since both the pool fire and spray fire could not co-exist at the same location (due to excess fuel from the spray collecting and burning in the pan), the fuel pool pan was shifted 30 cm (1 ft) downstream, and subsequently shielded by the next nacelle rib. The fuel pan was positioned in the bottom of the nacelle (Figure 11–7), as if fuel had leaked and formed a pool there. The pan bottom was beveled to the nacelle curvature. The pan length was 60 cm (27¼ in.) The pan width was limited to 24 cm (9.5 in.), due to (a) the narrowness of the clearance gap between the engine core and the nacelle and (b) the shortness of the flame-stabilizing rib jut in front of it, when using the 2.5 cm (1 in.) rib configuration. The fuel surface in the pan needed to be below the rib tip to permit the rib to function as a bluff body flame stabilizer. The pan was filled with about 2 L (0.5 gal) of fuel, with the fuel surface

---

<sup>iii</sup> It has been found in previous testing with this fixture that pre-burn times longer than this can heat the surrounding structure sufficiently to create additional hot surface ignition sources (complicating the results of the tests) as well as applying repeated severe thermal stresses to the fixture. This 20 s duration assures a well stabilized, repeatable flame.

being about 0.5 cm (1/4 in.) below the pan lip. The fire was ignited by a propane torch and allowed to “pre-burn” for 30 s before discharging the suppressant.

- C. Clutter (rib) Height. The height of the bluff body, represented by the rib upstream of the flame, affected the flame structure and recirculation zone dimensions, as well as the degree of entrainment of extinguishant into the recirculation zone. The heights of ribs further upstream impacted air and extinguishant flow patterns, turbulence, and degree of difficulty (and rate) of extinguishant mixing throughout the nacelle, as well as providing potential surfaces for extinguishant condensation during cold (sub-boiling point) conditions. The rib height settings were 2.5 cm (1 in.) and 7.6 cm (3 in.). These dimensions were representative of those in actual aircraft nacelles. These rib heights stabilized flames while permitting some axial flow and minimizing excessive turbulence. The shallower rib height provided a relatively unimpeded flow of 10 cm (4 in) between the opposing ribs (resulting in a slight serpentine flow path as it slaloms past the alternating ribs). The deeper rib height simulated “deep frame” nacelles, where the entire 15 cm (6 in.) clearance distance was blocked by the sum of the core ribs and nacelle ribs, creating a severely serpentine flow path, with large recirculation zones and stagnant flow areas created behind the ribs.

The ribs were placed on the engine core and interior walls of the nacelle, alternating every 30 cm (1 ft) one foot downstream (thus the ribs on either the core or nacelle exclusively were spaced two feet apart). As mentioned earlier, lengthwise ribs parallel to the core axis were placed on either side of the flame site to simulate components above the core exterior that normally impede the extinguishant from “wrapping” around the core.

- D. Flame Reactivity of the Extinguishant. The efficiency of a flame suppressant should be a function of the degree to which it exceeds its flame cooling capacity by catalyzing the removal of the flame-propagating free radicals. Efficiency may also be enhanced by the shorter residence time required for the catalytic reactions, relative to that required for the slower heat absorption process.  $\text{CF}_3\text{I}$  ( $T_b = -22.5\text{ }^\circ\text{C}$ ,  $-8.5\text{ }^\circ\text{F}$ ) was chosen as the chemically active candidate, and HFC-227ea ( $T_b = -16.3\text{ }^\circ\text{C}$ ,  $-2.7\text{ }^\circ\text{F}$ ) as the non-chemically active candidate, for the following reasons:
- Apparatus temperature limitation. The facility could not reliably cool the air below  $-34.4\text{ }^\circ\text{C}$  ( $-30\text{ }^\circ\text{F}$ ) for the range of flows of interest, requiring extinguishants with  $T_b > -24.4\text{ }^\circ\text{C}$  to meet the “ $-10\text{ }^\circ\text{C}$ ” setting criterion. This requirement eliminated many candidates, including halon 1301, HFC-125 and HFC-134a. The “ $+60\text{ }^\circ\text{C}$ ” setting requires a minimum nacelle temperature of  $37.5\text{ }^\circ\text{C}$  ( $92\text{ }^\circ\text{F}$ ), which is slightly above ambient. This supports creating consistent test conditions, and was a primary reason for selection of the upper temperature criterion.
  - Similarity of agent boiling points. This allowed similar air and storage bottle temperatures in all tests, reducing the potential for any hidden factor variability due to large air temperature differences.
  - History. Both fluids had been examined previously in the AENTF, with prior performance data thus being available to compare with the NGP data of this project. For instance, in the Army Halon Replacement Program, 0.31 kg (0.69 lb) of  $\text{CF}_3\text{I}$  was sufficient for flame suppression in high ambient temperature tests, while 1.56 kg (3.45 lb) was needed for cold ambient air tests. This showed that an increased mass of  $\text{CF}_3\text{I}$  was required at low temperatures (presumably due to inefficient transport and condensation), but that it could extinguish fires with an amount that was practical for

test purposes. Both extinguishants had been examined previously in the TDP and the NGP, providing further reference performance data.

- Availability. Both extinguishants were readily available in the large quantities required for the planned testing.
  - Extinguishant Flow. For a fixed mass of agent, the mass flow affected the peak level and the concentration-time profile of the extinguishant in the nacelle and in the recirculation zone of the flame. The discharge duration also affected whether the extinguishant can reach a flame extinguishing concentration everywhere in the nacelle.
- E. Air Temperature, Relative to the Extinguishant Boiling Point. At issue was the extent to which the two-phase fluid suppressant vaporizes before reaching the flame zone. Only the vapor and very fine droplets could be relied upon to contribute to flame extinguishment. Prior NGP experiments had indicated that flash vaporization only occurred for fluids whose boiling point was below the ambient temperature. Evaporation of the agent liquid was slower and would depend on the agent boiling point, and the temperatures of the nacelle surfaces and the ventilation air. To the extent that the agent remained as a liquid, the charged mass of extinguishant (and the total mass of the storage system) would have to be increased to ensure sufficient vapor for flame suppression.

For these experiments, the suppressants were selected for other properties; the air/bottle temperature was set to examine the boiling point importance.<sup>iv</sup> The two values were 10 °C (18 °F) below the boiling point of the extinguishant tested, and 60 °C (108 °F) above the extinguishant boiling point. (The relative values of these settings were also influenced by facility limitations and other environmental conditions.)

- F. Agent Discharge Rate. This was varied by changing the pressure of the nitrogen in the storage bottle after the extinguishant mass had been set and added.<sup>v</sup> Bottle pressures of 1.4 MPa (200 psi) and 5.4 MPa (800 psi) were used for HFC-227ea, and pressures of 0.95 MPa (140 psi) and 3.8 MPa (560 psi) were used for CF<sub>3</sub>I. The lower CF<sub>3</sub>I pressures provided comparable mass flows for the higher molecular weight compound.

The internal volume of the adjustable capacity extinguisher (Figure 11–4) was set for each test condition to maintain a realistic 50 % liquid fill density. The point of discharge was in the bottom of the nacelle, in line and 2.4 m (8 ft) upstream from the spray fire site, and 2.7 m (9 ft) from the pool fire site. The agent was discharged by means of a fast-response solenoid valve into a short, 2.5 cm (1 in.) ID hose leading into the nacelle. Once in the nacelle, it was discharged in opposing directions through a “T”-section, with each end being 1.3 cm (½ in.) in inner diameter, as shown in the upper component in Figure 11–10. (The lower component is the same “T”-section with nozzles added, for use in Phase II). The opposing discharge orifices were centered between the inner nacelle wall and the engine core, spaced 7.6 cm (3 in.) on center from each of them. They discharged upward and downward in the nacelle to promote “wrapping” around the nacelle and helical transport downstream, as is common with fielded systems.

---

<sup>iv</sup> The extinguishant storage system was kept at the same temperature as the air temperature for each experimental run. This was to simulate ambient conditions in the flight envelope.

<sup>v</sup> The mass flows varied over the discharge time due to pressure drop as the extinguisher evacuated.

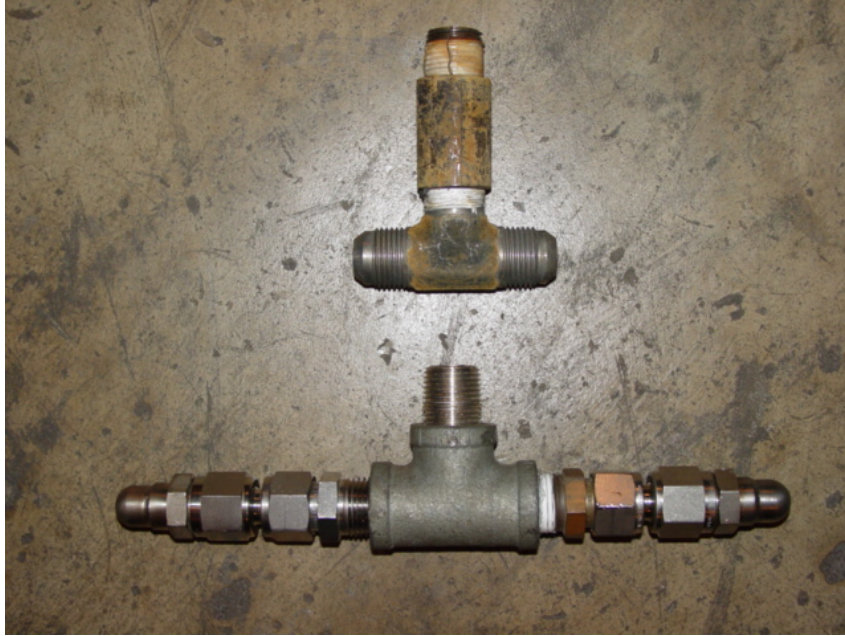


**Figure 11–10.**  
**Discharge “T”**  
**(top), and with**  
**Nozzles Added**  
**for Phase II**  
**(bottom).**

Fire suppressant concentrations were measured using the 12-probe Halonyzer resident at WPAFB. This device functions by siphoning a sample of the atmosphere, heating and vaporizing the air/agent mixture, measuring the density of the mixture, and comparing it to calibrated mixtures of that extinguishant in air.<sup>vi</sup> The response time of the instrument is about 0.2 s or longer.

Since the probes were not tolerant of the corrosive combustion products generated during suppression of a fire, concentration distribution measurements were made following each Phase I test, under identical conditions, but without igniting the fire. The mass flow of agent was the minimum determined to extinguish the fire. It was recognized that this necessary approach led to some unavoidable flow field modification from omitting the thermal effects of the fire.

Since each test involved either a spray fire *or* a pool fire, the 12 Halonyzer 3 probes were deployed in two sets of six. Six probes were associated with the upstream spray fire, and the next six probes with the pool fire downstream of it. This splitting allowed the conduct of multiple tests without the need to move and re-align the probes. Figure 11–11 is a general illustration of the layout of these Halonyzer 3 probes for either of the fire regions (spray or pool).

For each fire type, three probes were placed just above the rib shielding the flame, between the top of the rib and the top of the nacelle, to measure the free stream concentration of extinguishant as it entered the flame region. One of these probes was mounted in line with the fuel nozzle and the presumed base of the flame, and one probe on either side, approximately 10 cm (4 in.) away, to determine the extent of inhomogeneities in the mixture as it flowed past the rib. Three similarly spaced probes sampled the mixture behind the rib downstream, in a region normally immersed in the flame and in the recirculation zone. Again, probes were placed roughly 10 cm on either side to measure lateral inhomogeneities in the concentration within the recirculation zone. Figure 11–12 shows two views of the probe placements.

<sup>vi</sup> This device is typically used with twelve probes placed in a dispersed pattern throughout the nacelle. This serves as an FAA-certified method for verifying a uniform concentration of discharged extinguishant in nacelle systems to confirm the sufficiency of balance of the discharge system (Chapter 2).

Combined, the two triads of probes permitted comparison of agent profiles and peak concentration values, to determine what portion of the free stream flow was entrained by the recirculation zone, and the rate at which it changed the recirculation zone concentration. These results could then be compared to prior (and upgraded) models, which will be discussed in detail in the data analysis sections.

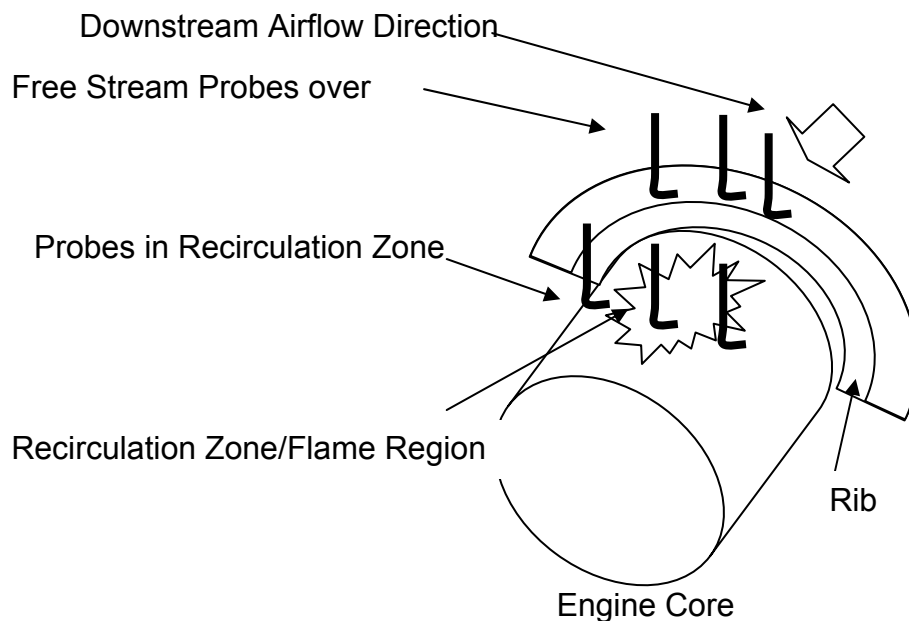


**Figure 11–11. Halonyzer Probe Mounting in Flame Region.**

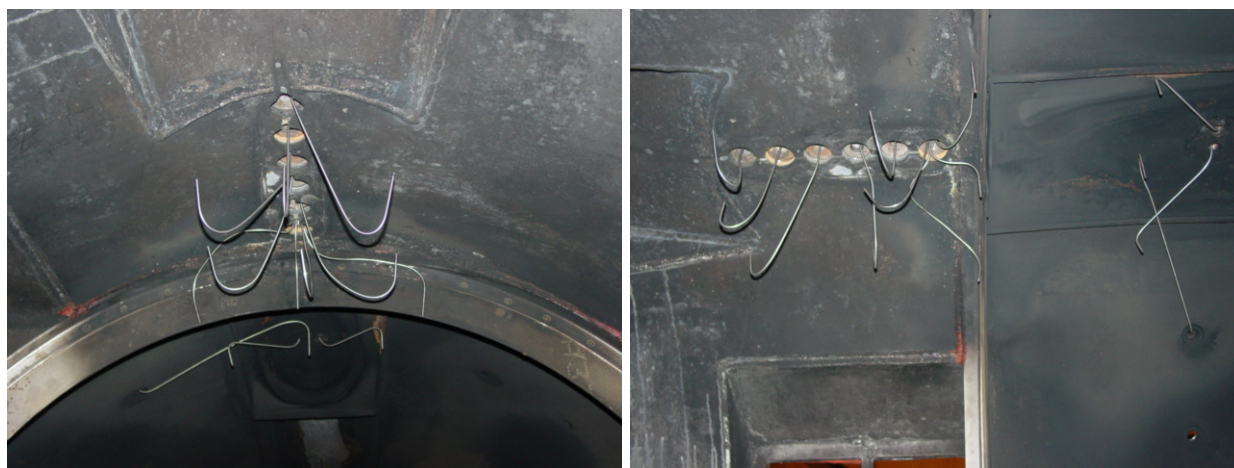


**Figure 11–12. Halonyzer Probes in Nacelle Fixture.**  
(left: downstream view; right: side view)

Table 11–1 shows the L-16 test matrix utilized for Phase I. It includes the aforementioned six factors at two levels (Table 11–2) with “-1” indicating the lower level and “1” indicating the higher level. It was

assumed that the interaction term, “Chemical Reactivity vs. Rib Height,” was one of the least relevant. Therefore, it was chosen as one of the trio of confounded interaction terms.

**Table 11–1. Local Conditions Fire Test (Phase I) Matrix.**

Run #	Factors														
	A	B	EF CD AB	C	BD AC	AD BC	D	E	BF AE	BE AF	F	DF CD			DE CF
1	-1	-1	-1	-1	-1	-1	-1	-1	-1	-1	-1	-1	-1	-1	-1
2	-1	-1	-1	-1	-1	-1	-1	1	1	1	1	1	1	1	1
3	-1	-1	-1	1	1	1	1	-1	-1	-1	-1	1	1	1	1
4	-1	-1	-1	1	1	1	1	1	1	1	1	-1	-1	-1	-1
5	-1	1	1	-1	-1	1	1	-1	-1	1	1	-1	-1	1	1
6	-1	1	1	-1	-1	1	1	1	1	-1	-1	1	1	-1	-1
7	-1	1	1	1	1	-1	-1	-1	-1	1	1	1	1	-1	-1
8	-1	1	1	1	1	-1	-1	1	1	-1	-1	-1	-1	1	1
9	1	-1	1	-1	1	-1	1	-1	1	-1	1	-1	1	-1	1
10	1	-1	1	-1	1	-1	1	1	-1	1	-1	1	-1	1	-1
11	1	-1	1	1	-1	1	-1	-1	1	-1	1	1	-1	1	-1
12	1	-1	1	1	-1	1	-1	1	-1	1	-1	-1	1	-1	1
13	1	1	-1	-1	1	1	-1	-1	1	1	-1	-1	1	1	-1
14	1	1	-1	-1	1	1	-1	1	-1	-1	1	1	-1	-1	1
15	1	1	-1	1	-1	-1	1	-1	1	1	-1	1	-1	-1	1
16	1	1	-1	1	-1	-1	1	1	-1	-1	1	-1	1	1	-1

**Table 11–2. Factors and Values for Phase I Fire Test Matrix.**

Factor	Symbol	Low Value (-1)		High Value (1)	
Air flow	A	0.45 kg/s (1.0 lb/s)		1.36 kg/s (3.0 lb/s)	
Fire type	B	Pool		Spray	
Rib height	C	2.5 cm (1 in.)		7.6 cm (3 in)	
Chemical reactivity	D	No, HFC-227ea		Yes, CF <sub>3</sub> I	
Air temperature, relative to Tb	E	-10 °C, -18 °F		60 °C, 108 °F	
Discharge rate (controlled by storage bottle pressure)	F	HFC-227ea 1.4 MPa (200 psi)	CF <sub>3</sub> I 0.95 MPa (140 psi)	HFC-227ea 5.4 MPa (800 psi)	CF <sub>3</sub> I 3.8 MPa (560 psi)

The test data were analyzed using ANOVA and other established protocols for orthogonal arrays to:

- Determine which factors most influenced the minimum peak concentration required in the fire zone to extinguish the test fires under the range of experimental conditions.
- Assess the efficiency with which the discharged extinguishant resulted in measurable vapor in the fire zone. This was based on the ratio of the moles of extinguishant discharged to the peak concentration measured in the fire zone.
- Verify correlations for predicting the mass of agent entrained into the recirculation zone.

## Phase II – Assessment of Extinguishant Dispersion Optimization

The purpose of these tests was to determine how the nacelle geometry and the discharge/flow conditions determined the speed and uniformity of agent distribution throughout the nacelle volume. This was done for four masses of chemical discharged. There were no fires present. The principles tested were 1, 3, 5, and 6. The response variables were the mean and standard deviation of the extinguishant concentration, measured simultaneously at 12 roughly equally distributed locations throughout the nacelle.

The experimentally varied factors of interest were:

- A. Air Flow. See the discussion under Phase I. The two settings were the same.
- B. Number of Agent Injection Sites. A larger number of well distributed injection sites decreases the distance over which agent must move laterally to fill the full annulus within the nacelle. Thus, it is more likely that a fire will encounter an extinguishing concentration of suppressant.

In these tests, two agent injection arrays were used. The first (low value) was the same as used for Phase I: a single extinguisher discharging into a single port in the bottom of the nacelle, located 2.44 m (8.0 ft) and 2.75 m (9.0 ft) upstream of the spray and pool fire sites, respectively. The second setting used two independent extinguishers, fired simultaneously. The flow from each was directed to two separate ports, for a total of four port locations. The second discharge port from the first extinguisher was added on the side of the nacelle, 1.22 m (4.0 ft) and 1.52 m (5.0 ft) upstream of the spray and pool sites, respectively.

The second extinguisher can be seen behind the left (downstream) end of the test fixture in Figure 11–4. Its first discharge site was on the top of the nacelle, 30 cm (1.0 ft) and 61 cm (2.0 ft) upstream of the spray and pool sites, respectively. Its second discharge site was 61 cm (2.0 ft) and 30 cm (1.0 ft) downstream of the spray and pool sites, respectively, and on the opposing side of the nacelle. Thus, discharge ports were present at the top, bottom and both sides of the nacelle, and at four spaced positions downstream, with each site split into opposing jets once discharged inside the nacelle, for a near optimally mixed (in realistic terms) configuration.

- C. Clutter (rib) Height: See the discussion under Phase I. The settings were the same.
- D. Nozzle Exploitation. Nozzles can be used to break the liquid flow into much smaller droplets of controlled diameter distribution, compared to the sizes emerging from open pipe ends. For a given total mass of fluid, an array of smaller droplets evaporates faster due to its higher total surface area. A corollary to this is that the smaller droplets will be more likely to evaporate fully before they are transported out the exhaust of the nacelle. This would make more gaseous agent available for quenching flames at cold operating temperatures, when

flash vaporization is not possible. The two settings for this factor are shown in Figure 11–10: the presence of nozzles or no nozzles at all.

- E. Air Temperature, Relative to the Extinguishant Boiling Point. See the discussion under Phase I. The settings and the chemicals were the same.
- F. Agent Discharge Rate. HFC-227ea was used. The settings were flows associated with bottle pressures of 800 psi and 200 psi.

For this series of tests, the Halonyzer probes were spread into 12 distributed locations to measure the uniformity of concentration in the nacelle during and after discharge. Each of three downstream segments of the nacelle was split into quadrants, as illustrated in Figure 11–13. Pre-existing ports on the nacelle fixture were used to insert Halonyzer probes to make readings in these 12 quadrants. The axial locations of the planes of these port sites were 0.23 m (0.75 ft), 2.21 m (7.2 ft), and 3.50 m (11.5 ft) from the upstream edge of the engine core, with the far upstream and downstream port planes being the same distance from the front and aft ends of the nacelle, respectively. The middle port plane was slightly upstream of the middle of the nacelle. At each of these axial distances, the four ports existed at the approximate “two o’clock,” “four o’clock,” “eight o’clock,” and “ten o’clock” positions on the nacelle perimeter, comprising four fairly even spaced quadrant positions. Figure 11–14 indicates the port locations.

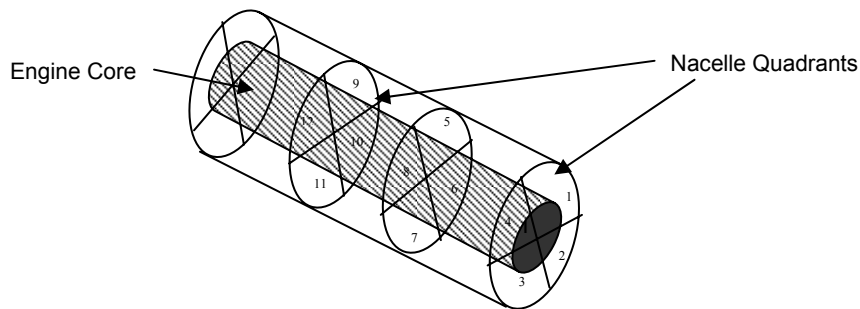


**Figure 11–13. Phase II Nacelle Concentration Measurement Quadrants.**

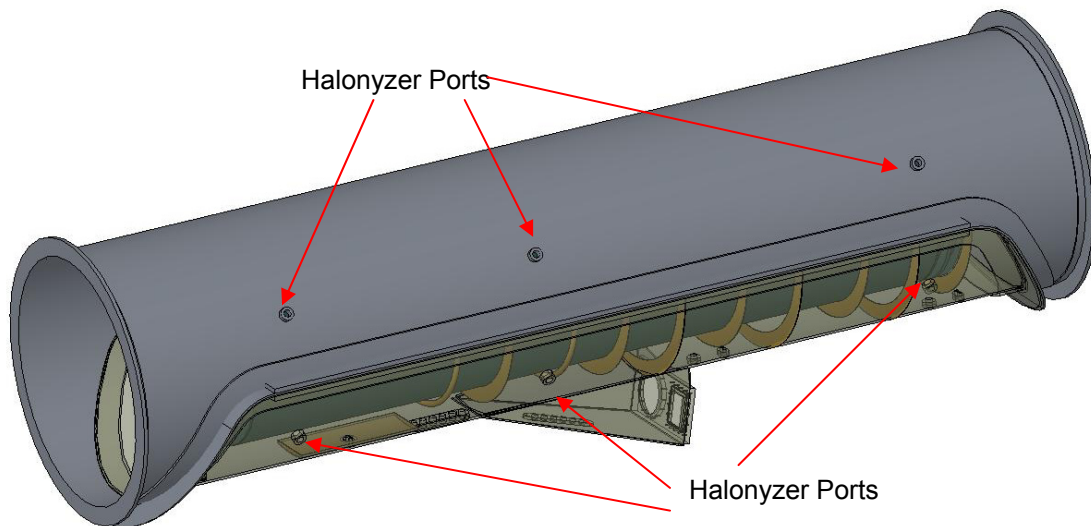


**Figure 11–14. Layout for Multi-Port Discharge.**

The following L-16 test matrix (Table 11–3) was used for Phase II experiments, with six factors at two levels (Table 11–4). It was assumed that the interaction term, “Nozzles vs. Rib Height,” was one of the least relevant. Therefore, it was chosen as one of the trio of confounded interaction terms.

**Table 11–3. Extinguishant Dispersion Optimization (Phase II) Test Matrix.**

Run #	Factors														
	A	B	EF CD AB	C	BD AC	AD BC	D	E	BF AE	BE AF	F	DF CD			DE CF
1	-1	-1	-1	-1	-1	-1	-1	-1	-1	-1	-1	-1	-1	-1	-1
2	-1	-1	-1	-1	-1	-1	-1	1	1	1	1	1	1	1	1
3	-1	-1	-1	1	1	1	1	-1	-1	-1	-1	1	1	1	1
4	-1	-1	-1	1	1	1	1	1	1	1	1	-1	-1	-1	-1
5	-1	1	1	-1	-1	1	1	-1	-1	1	1	-1	-1	1	1
6	-1	1	1	-1	-1	1	1	1	1	-1	-1	1	1	-1	-1
7	-1	1	1	1	1	-1	-1	-1	-1	1	1	1	1	-1	-1
8	-1	1	1	1	1	-1	-1	1	1	-1	-1	-1	-1	1	1
9	1	-1	1	-1	1	-1	1	-1	1	-1	1	-1	1	-1	1
10	1	-1	1	-1	1	-1	1	1	-1	1	-1	1	-1	1	-1
11	1	-1	1	1	-1	1	-1	-1	1	-1	1	1	-1	1	-1
12	1	-1	1	1	-1	1	-1	1	-1	1	-1	-1	1	-1	1
13	1	1	-1	-1	1	1	-1	-1	1	1	-1	-1	1	1	-1
14	1	1	-1	-1	1	1	-1	1	-1	-1	1	1	-1	-1	1
15	1	1	-1	1	-1	-1	1	-1	1	1	-1	1	-1	-1	1
16	1	1	-1	1	-1	-1	1	1	-1	-1	1	-1	1	1	-1

**Table 11–4. Factors and Values for Phase II Agent Distribution Test Matrix.**

Factor	Symbol	Low Value (-1)	High Value (1)
Air flow	A	0.45 kg/s (1.0 lb/s)	1.36 kg/s (3.0 lb/s)
Injection Sites	B	1	4
Rib height	C	2.5 cm (1 in.)	7.6 cm (3 in.)
Nozzles	D	No	Yes
Air temperature, relative to $T_b$	E	-10 °C, -18 °F	60 °C, 108 °F
Agent discharge rate	F	1.4 MPa, 200 psi	5.4 MPa, 800 psi

The test data were analyzed using ANOVA and other established protocols for orthogonal arrays to determine which factors most influenced the average value and standard deviation of the extinguishant concentration measured simultaneously at all 12 Halonyzer probe locations at the time that all 12 probes met or exceeded the same concentration level at its highest value during discharge (as with certification tests), for a given mass of extinguishant.

### Phase III – Additional Fire Extinguishment Tests

As an additional dimension to Principle 2, the test series briefly examined the performance of a brominated fire suppressant other than halon 1301. As mentioned in Chapter 7, 2-bromo-3,3,3-trifluoropropene ( $\text{CF}_3\text{CBr}=\text{CH}_2$ ), BTP, has a boiling point of 34 °C (93 °F) and thus did not meet this screening criterion for effective dispersion at cold in-flight operating conditions. However, it had a cup burner flame extinguishment value of 2.6 % by volume, which is characteristic of brominated compounds. It has a short atmospheric lifetime due to tropospheric attack at the double bond.

It was intended to perform a series of experiments under conditions identical to those under which HFC-227ea had been tested. However, the high boiling point of BTP required conducting experiments at a “cold” air flow and agent storage temperature of 24 °C (75 °F) and a “hot” temperature of 94 °C (200 °F), to maintain the same temperature conditions, relative to boiling point, as with the other agents tested. These notably hotter temperatures significantly increased the flame stability and strength, which required larger amounts of extinguishing agent, and required re-testing HFC-227ea under the same conditions to facilitate comparison.

Experiments with two condition variations, simulating two prior HFC-227ea run conditions (except at higher temperatures), were conducted to determine the threshold of agent mass required to extinguish the fires generated under the conditions cited, using a traditional agent mass “bracketing” method. Due to a limited quantity of agent available, in some cases fewer repeats (relative to the earlier test series) at the same mass level were conducted. The experimental conditions for the two experiment variations were:

Test Condition 1: 1.36 kg/s (3.0 lb/s) air flow, 24 °C (75 °F) agent/air temp (10 °C below boiling point), 5.1 MPa (750 psi) extinguisher pressure, spray fire, with nozzles.

Test Condition 2: 0.45 kg/s (1 lb/s) air flow, 94 °C (200 °F) agent/air temp (60 °C above boiling point), 5.1 MPa (750 psi) extinguisher pressure, pool fire, with nozzles

## 11.8 RESULTS AND ANALYSIS

### 11.8.1 Summary of General Data Collected

The ANOVA analyses can provide a rich assessment of the relative importance of the test factors on the response variables. The following results focus on the specific analyses that cast light on the validity of the principles being tested.

Table 11–5 summarizes the data collected in Phase I, including the minimum mass required for extinguishing in each run and the resultant peak concentration measured in the fire zone (averaged of three repeats). The data from adjacent probes were similar enough to use peak data readings in the analysis. (It did not affect the ANOVA analysis.) Table 11–6 summarizes the Phase II data, including the standard deviation data of the concentrations measured in each of the remote twelve probe locations, for both extreme mass discharge levels of 0.68 kg (1.5 lb) and 5.44 kg (12.0 lb). These aforementioned data were used for all ANOVA and other data analyses, including transformations of these data.

**Table 11–5. Phase I Summary Data.**

Run	Mass (kg, lb)	Peak Concentration, % by volume	Run	Mass (kg, lb)	Peak Concentration, % by volume
1	1.70, 3.75	14.8	9	1.42, 3.13	10.4
2	1.77, 3.90	13.5	10	1.24, 2.73	12.7
3	1.13, 2.50	6.3	11	1.24, 2.73	11.2
4	0.85, 1.88	6.4	12	0.71, 1.56	11.2
5	0.85, 1.88	3.3	13	0.99, 2.19	6.5
6	0.57, 1.25	3.0	14	0.99, 2.19	7.7
7	0.57, 1.25	2.4	15	0.29, 0.63	2.0
8	0.43, 0.94	2.6	16	0.21, 0.47	2.4

**Table 11–6. Phase II Summary Data.**

Run	Concentration Standard Deviation (0.68 kg released), % by volume	Concentration Standard Deviation (5.44 kg released), % by volume	Run	Concentration Standard Deviation (0.68 kg released), % by volume	Concentration Standard Deviation (5.44 kg released), % by volume
1	2.3	10.9	9	1.4	5.0
2	1.5	3.5	10	1.1	3.5
3	1.4	5.9	11	2.9	14.2
4	2.3	9.4	12	2.9	13.6
5	1.0	5.0	13	1.5	9.9
6	1.5	6.5	14	1.5	8.6
7	2.4	12.3	15	1.4	6.6
8	2.5	15.4	16	1.2	7.0

### 11.8.2 Principle 1

*Extinguishants with boiling points higher than the local engine nacelle airflow and surface temperatures do not disperse sufficiently in time for engine nacelle fire mitigation, whereas those with boiling points below the prevailing temperature can disperse sufficiently if properly applied.*

Figure 11–15 plots the ratio of the g-moles of agent injected into the test fixture to the volume percent of agent measured in the fire zone. The data showed that experiments at colder temperatures (below the agent's boiling point) required about a third more moles of agent to achieve a required fire zone concentration compared to hot conditions. This extra amount was assumed lost due to condensation of liquid agent on the upstream nacelle components, or unvaporized after passing through the fire zone, thereby providing no benefit.

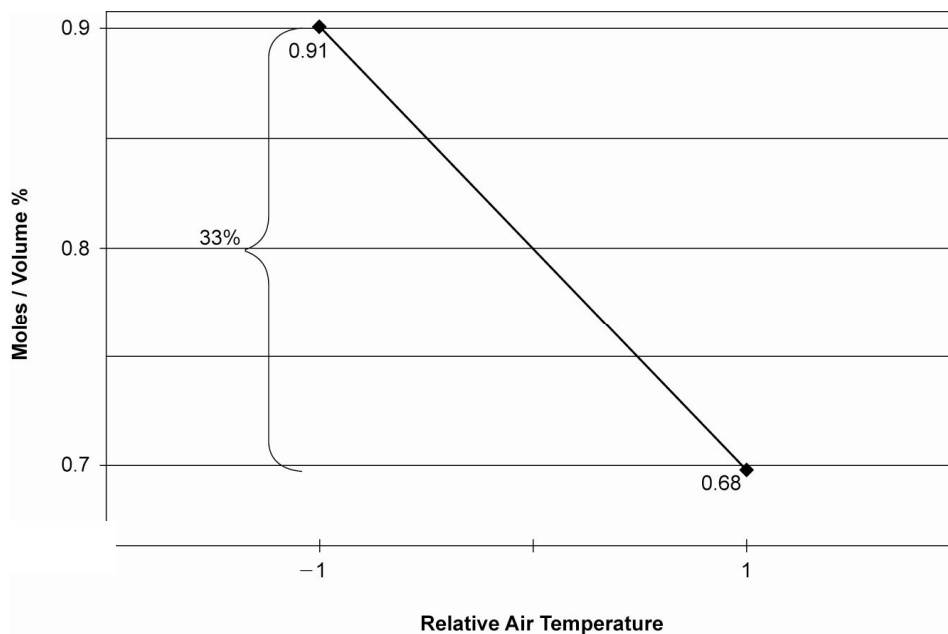


**Figure 11-15.** Variation of Moles of Injected Chemical per Fire Zone Volume Percent with Relative Air Temperature. (“-1” is 10 °C below the agent boiling point; “1” is 60 °C above the agent boiling point.)

### 11.8.3 Principle 3

*Increasing the number of local extinguishant discharge sites increases the dispersion quality in terms of balanced concentration profiles, up to some practical limits.*

It was found that increasing the number of injection sites from one to four (well distributed) reduced the standard deviation of the 12 concentration probes (measured at a time when the lowest of the 12 is at its highest amount, as is used for certification testing) by about 22 % on average (as seen in Figure 11-16), when discharging 0.68 kg (1.5 lb) of agent. It was observed that when discharging 5.4 kg (12 lb), the effect of injection sites was not statistically significant. It may be that discharging excessive quantities of agent may saturate the nacelle, even with only one discharge port, as well as discharge longer and let the nacelle concentration even out, and hence dilute the benefits of distributed discharge.

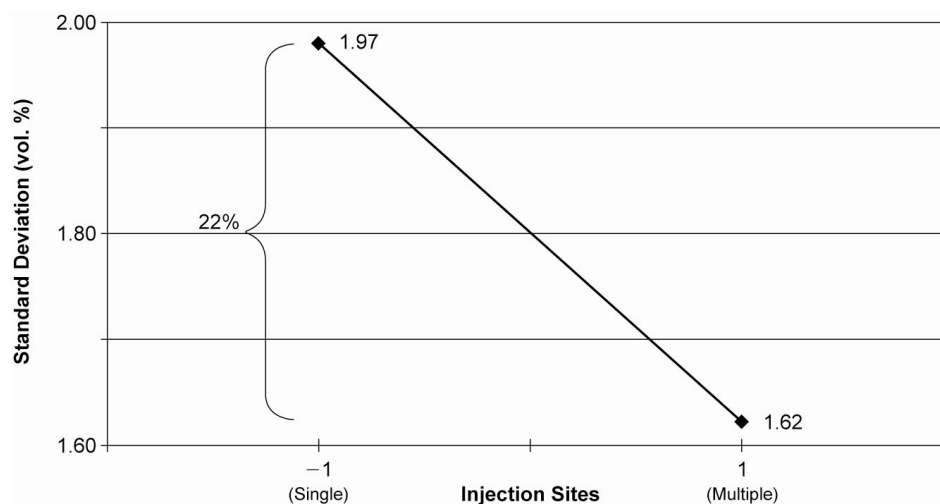


**Figure 11-16.** Variation of Concentration Standard Deviation with Number of Discharge Sites.

### 11.8.4 Principle 5

*The passage of a suppressant through an engine nacelle is significantly affected by the degree of clutter in the nacelle.*

Figure 11–17 shows that the 7.6 cm (3 in.) tall rib heights resulted in a 45 % increase in standard deviation of concentration for the 0.68 kg (1.5 lb) agent discharge, compared to the same discharge with 2.5 cm (1 in.) rib height. The increase was 60 % for the 5.44 kg (12 lb) discharge. Therefore, the height of ribs (and, by analogy, other nacelle obstructions) was demonstrated to play a significant role in the efficient distribution of extinguishing agent in a nacelle.

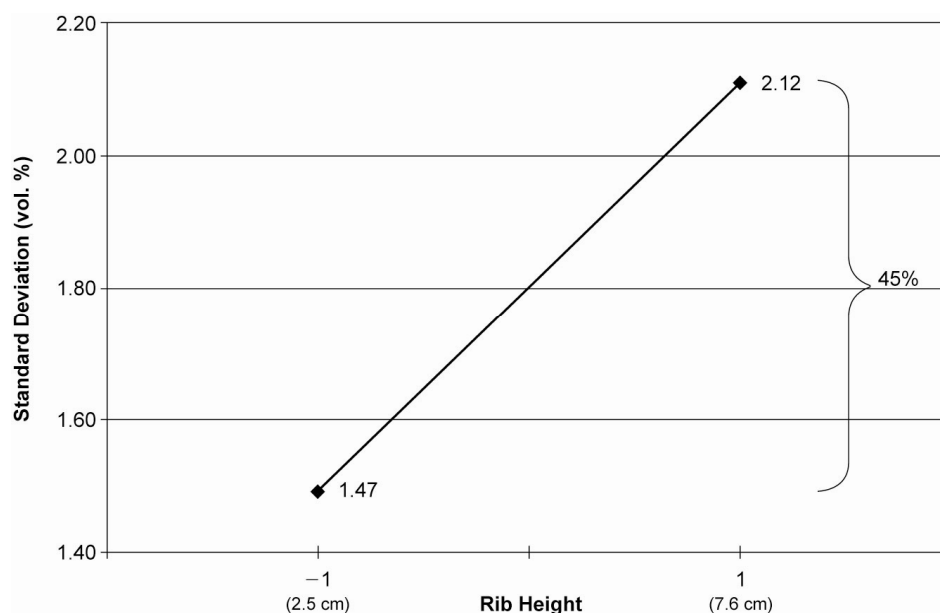


**Figure 11–17.**  
Variation of  
Concentration  
Standard Deviation  
with Rib Height.

### 11.8.5 Principle 6

*Assuming that a mix of extinguishant vapor and liquid aerosol reach the flame reaction zone, the sufficient vaporization of liquid particles to enhance extinguishment will be dependent upon, among other parameters, the liquid's residence time in the recirculation zone.*

This type of full-scale testing was not an ideal means to assess the particle size of liquid aerosols, and the heat transfer aspect was addressed in the next principle. However, the residence time in the recirculation zone was estimated indirectly. Hamins et al.<sup>2</sup> stated that the characteristic entrainment or mixing time is equal to the residence time in the recirculation zone. This “characteristic mixing time” will be defined and estimated in Section 11.8.7. An estimate of the characteristic time has been calculated for each of the 16 sets of conditions represented in the 16 test runs, and the influence of individual parameters on these calculations (using actual agent concentration data) has been evaluated using the ANOVA process. Figure 11–18 is a plot of the g-moles of extinguishant discharged, divided by peak volume fraction of

extinguishant in the fire zone, as a function of this characteristic time,  $\tau$ , for those runs of spray fires under cold conditions having the smallest  $\tau$  values.

These data showed a drop in the required moles of extinguishant as  $\tau$  increases. This finding was consistent with the hypothesis that, if the residence time increased with the increase in the value of  $\tau$ , then increased residence times reflect a reduced amount of moles of agent needed to provide a given fire zone concentration. This, in turn, suggested that during longer residence times in the fire zone, more of the liquid aerosol was indeed vaporizing in the fire zone and contributing to the local concentration, thereby increasing efficiency. This effect diminished with further increases in  $\tau$ , such as under hotter air conditions, presumably because vaporization in the fire zone was nearly complete under less benign conditions.

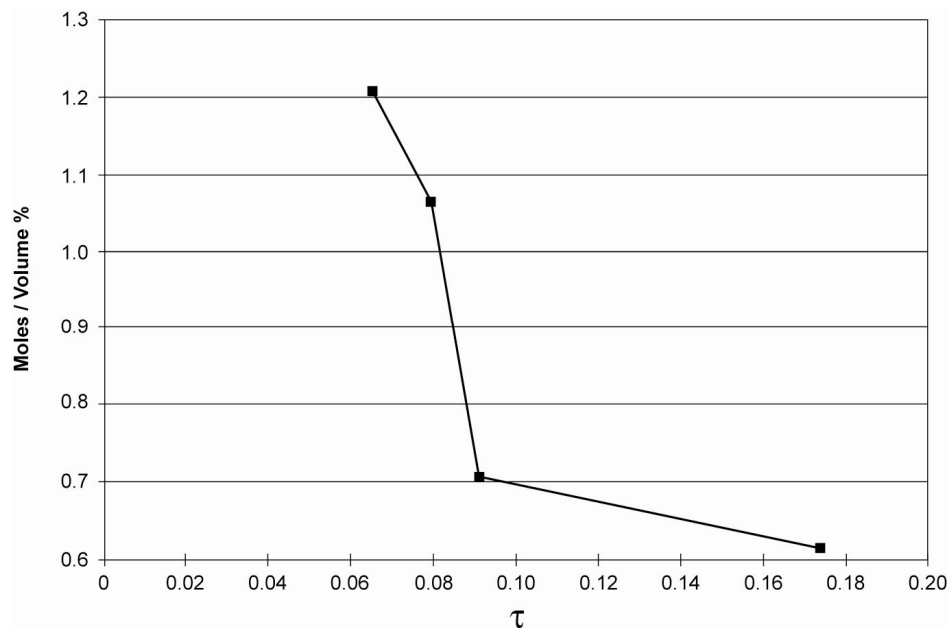


**Figure 11–18.**  
Reduction in  
Moles/Concentration  
with Increasing  $\tau$ ,  
Residence Time.

### 11.8.6 Principle 7

*The suppression effectiveness of a non-catalytic extinguishant in a full-scale engine nacelle is determined by its ability to absorb heat as it enters the flame zone.*

There are three sources of information that collectively indicate support for this principle.

- Figure 11–19 is a plot of required extinguishing concentration as a function of air and agent storage temperature (either above or below the agent's boiling point) for both the catalytic  $\text{CF}_3\text{I}$  and the non-catalytic HFC-227ea. Neither agent exhibited any notable difference in required concentration between the hot and cold conditions, given the experimental uncertainty in the measurements. The lower inflow of agent and air in the “cold” temperature tests resulted in a lower flame temperature and a higher aerosol fraction of the agent. The minimal temperature dependence in this Figure shows that these two factors, and the resulting possible difference in heat extraction, were not important in these tests.

- Other data provide further evidence that HFC-227ea was fully vaporized in the fire zone in these tests. Figure 11–15 shows that HFC-227ea volatility was significantly dependent on the environmental temperature for a non-fire test. Figure 11–19 indicates that the same chemical showed no temperature dependence of volatility in a fire test. In the tests with a fire, all the HFC-227ea was effective. This likely means that the temperature in the fire zone was high enough and the agent residence time was long enough for all of the HFC-227ea to volatilize. Alternatively stated, at even the lower temperature, none of HFC-227ea was surviving as an aerosol through the fire zone.
- In cup burner tests, the suppressant fluids were fully vaporized. For HFC-227ea, the extinguishing values were ca. 7 volume %; for CF<sub>3</sub>I, the value is ca. 3 volume %. The relative effectiveness of the two compounds was about the same as in the engine nacelle experiments. (The consistently higher extinguishing concentrations for the two agents in the nacelle tests likely reflected the effect of clutter and agent residence time in the real-scale tests relative to the open geometry in the cup burner. See the discussion under Principle 5.) Certainly, there was no indication of a significant contribution beyond the thermal effects seen in the cup burner for the HFC-227ea vapor.

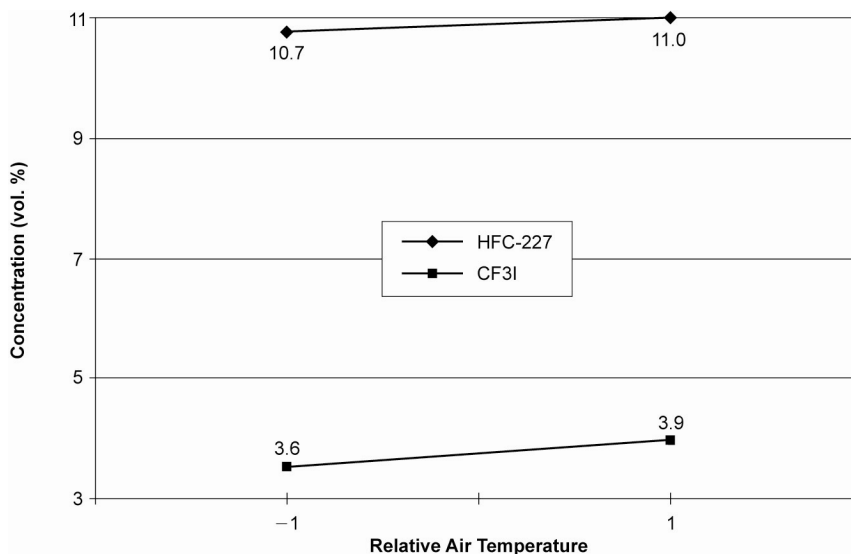


**Figure 11–19.**  
**Effect of Agent Type and Relative Temperature on Extinguishing Concentration.**  
 (“-1” is 10 °C below the agent boiling point; “1” is 60 °C above the agent boiling point.)

### 11.8.7 Extinguishing Mixing Models

#### Basic Mixing Model

Before proceeding to the next principles, several basic concepts related to extinguishing baffle-stabilized fires need to be established:

Longwell et al.<sup>3</sup> developed a model to explain the blow off of pre-mixed flames by treating the air flow recirculation zone created by a bluff body stabilizing a flame as a well-stirred reactor. The key parameter in this model is the characteristic mixing time for reactants to entrain from the free stream into the recirculation zone. Mestre<sup>4</sup> also found that the blow-off velocity was related to the characteristic time for entrainment into the recirculation zone. Bovina<sup>5</sup> found that the characteristic time ( $\tau$ ) is related to a baffle

diameter (assuming it is suspended in a tube and serves to stabilize a flame), divided by the upstream velocity. Winterfeld<sup>6</sup> also found that  $\tau$  was inversely proportional to the upstream velocity for both combusting and non-combusting cases, as well as the geometry of the flame holder. Importantly, he found that  $\tau$  was approximately a factor of two larger for a combustion situation relative to isothermal conditions. Additional details of this prior research can be found in Reference 2.

Hamins et al.<sup>2</sup> extended the model to explain the mixing process of an extinguishing agent discharged upstream into an air flow, resulting in a steady and constant concentration of the agent. A portion of this stream is entrained into the flame's recirculation zone, where it is perfectly and instantaneously mixed with the existing species. The process is characterized by the following governing equation:

$$X_f = X_\infty / (1 - e^{-\Delta t/\tau}) \quad (11-1)$$

where:

$X_f$  is the free stream volume fraction of agent, held for the time  $\Delta t$ ,

$X_\infty$  is the volume fraction of agent needed in the fire zone to accomplish extinguishment, and

$\tau$  is the volume fraction mixing time for the flame holder configuration and conditions of interest.

This expression demonstrates that the free stream volume fraction must be higher than the minimum volume fraction required to extinguish a fire within the recirculation zone unless the time that the agent is applied is significantly longer than the characteristic time. This time condition is met for a cup burner flame (although there is no recirculation zone), but is not met for an agent typically discharged into an aircraft engine nacelle.

Takahashi et al.<sup>7</sup> determined that the coefficient relating  $\tau$  to the ratio of rib height to free stream velocity was 22.79 for the two-dimensional bluff body/rib stabilizing a pool fire in their experiments. Literature values of  $X_\infty$  and  $\tau$  for both baffle-stabilized spray (centered in a stream) and pool fires (with the baffle against the flow chamber floor) for the agents of interest, with their associated references are shown in Table 11-7.

**Table 11-7. Values of  $X_\infty$  and  $\tau$  from Prior Experimentation.**

Fire Type	$X_\infty$ (HFC-227ea, CF <sub>3</sub> I), % by volume	$\tau$ , s
Spray	0.062, 0.032	0.1, 0.04
Pool	0.11, 0.068	0.7, 1.0, 0.04 to 0.4 <sup>7</sup> , 0.1 to 0.2 <sup>8</sup> , 0.1 to 1.0 <sup>9</sup>

Data from Reference 2, except as noted.

### Detailed Mixing Model

Hamins et al.<sup>2</sup> also reported the following differential equation expression for the mixing process behind a bluff body in general:

$$\tau (dX(t)/dt) = X_f(t) - X(t) \quad (11-2)$$

where:

$X_f(t)$  is the free stream volume fraction of agent at time  $t$  (at least at one point on a streamline, preferably just over the top of the bluff body stabilizing the fire),

$X(t)$  is the recirculation zone volume fraction of agent at time  $t$  (along the same streamline), and

$\tau$  is the characteristic mixing time of the recirculation zone.

This more general model permitted consideration of the types of complex realistic concentration profiles associated with Halonyzer “no fire” concentration measurements in real engine nacelles. This model did not require a two-dimensional flow pattern of uniform velocity magnitude and direction. It also obviated the requirement of a simplified bluff body geometry, since measured concentration data in both locations determined an empirical value of  $\tau$ .

Note that if the flow was expected to come from multiple directions, one should determine a volumetric, flow-adjusted, average flow free stream concentration profile external to the recirculation zone. If concentration measurements were made in only one location in the recirculation zone, then one must assume that mixing is uniform and complete there. Otherwise, an average from multiple probe sites in the recirculation zone would be necessary.

Equation (11-2) was functionally similar to that used to determine the extinguishant mass required to totally flood a room to a given volume fraction, accounting for leakage, as prescribed in NFPA 2001.<sup>10</sup> That model simulated mixing and local volume fraction changes of an additive in a fluid (such as air) in a fixed volume. It included an air inflow with an additive of volume fraction,  $X_f$ , (between 0 and 1) in the fluid, and an outflow of the room mixture, maintaining a constant pressure within the volume. In the case of the design equation used in NFPA 2001, the inflow value of  $X_f$  was 1.0, since pure extinguishant was coming out of the tank, resulting in the simplified structure shown in that publication. Although the enclosure volume fraction changes during the discharge, it peaks as the extinguisher completes its discharge. With no further influx, the agent volume fraction remains nominally constant at that value if there were no ventilation forcing flow from the enclosure. If the influx volume fraction were a constant value other than 1.0, then Equation (11-2) simplifies to the structure of Equation (11-1), used in the NGP as the a simplified case of a free stream influx of a constant volume fraction for a set period of time,  $\Delta t$ . For application to an engine nacelle, Equation (11-2) can be adapted to include the introduction of extinguishant and air, assuming that the density of the flow across the recirculation zone remains constant. The characteristic time,  $\tau$ , can be seen to be the ratio of volume of the recirculation zone,  $V_R$ , divided by the volumetric flow,  $V_{in}$ , into the recirculation zone. The recirculation zone volume is a function of the fire type (spray vs. pool) and local geometry.  $V_{in}$  is a function of the free stream volumetric flow and the local bluff body geometry.

Equation (11-2) was used to predict the influence of many operating parameters on the extinguishing concentrations to be required in the free stream and measured under “no fire” conditions. The most common profiles of extinguishant concentration in the free air stream of an engine nacelle were somewhat Gaussian in shape, such as shown above, with a rise, peak and decay. (This neglected fluctuations and even second peaks that occurred due to agent flashing or other surging behavior during discharge, or due to other perturbations to the upstream flow.) Figure 11–20 illustrates realistic notional concentration profiles that might be measured in an engine nacelle in both the free stream, such as over a bluff body, and behind the bluff body in the flame’s recirculation zone, using a Halonyzer device.

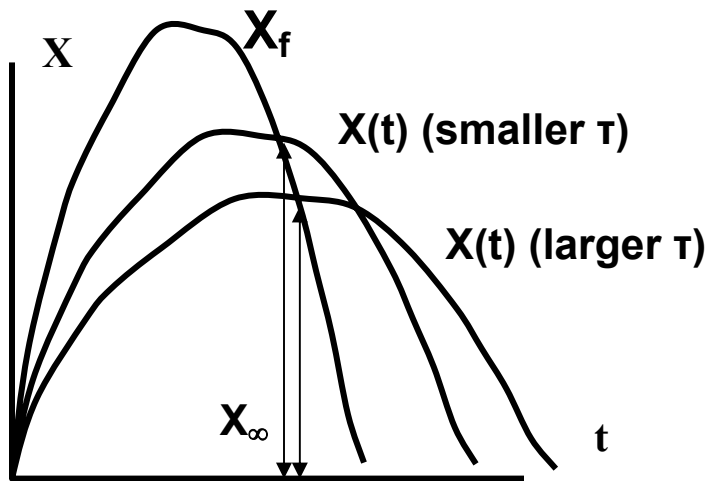


**Figure 11–20. Notional Graphs of Concentration in the Free Stream and Recirculation Zone.**

The agent concentration in the recirculation zone rose and fell more slowly than the free stream concentration. In effect, the recirculation zone volume exhibited a type of mass transfer concentration inertia, taking time to build up a concentration (depending upon the ratio of the volume to the incoming volumetric flow), then taking time to offload the agent as fresh air is entrained. In Equation (11-2), the peak of the agent concentration in the flame's recirculation zone occurred when the free stream concentration decayed to the level already in the recirculation volume, i.e.,  $dX/dt = 0$  when  $X_f = X$ .

The decrease in slope of  $X(t)$  relative to that of  $X_f(t)$  was controlled by the characteristic mixing time,  $\tau$ , which reflected the relative incoming flow in proportion to the recirculation zone volume. As shown in Figure 11–20, as  $\tau$  increased,

- The rise and fall of the agent concentration in the recirculation zone decreased;
- The peak value,  $X_p$ , occurred is at a later time; and
- The peak concentration in the recirculation zone was relatively lower, because the concentration curve for  $X_f(t)$  had decayed further during that extended time before it intersected the peak.

Thus, flame regions with larger characteristic times (due to local geometries and velocities) required a greater excess agent peak in the free stream to reach a desired concentration within the recirculation zone. This feature impacted the interpretation of “no fire” concentration measurements and provided a guide to estimating conditions under actual “fire” conditions, as will be shown later.

Actual values of the characteristic mixing time were estimated for real engine nacelle regions by discretizing the free stream and recirculation zone concentration data collected, and using a discretized form of Equation (11-2), as shown in Equation (11-3).  $t_1$  is any time when a concentration is measured.

$$\tau = (X_f(t_1) - X(t_1)) / (\Delta X / \Delta t) \quad (11-3)$$

This approach can be illustrated using actual Halonyzer concentration data collected in the nacelle simulator in this experimental program. At a point in time,  $t_1$ , the concentrations from both the free stream (just above the rib that stabilizes the flame) and recirculation (behind the rib) probe data traces were selected. This time was during the rising segment of the concentration curves, which was generally the most stable segment for all test conditions.<sup>vii</sup> Figure 11–21 shows 12 Halonyzer traces for a test in which the minimum mass of extinguishant to extinguish the fire was discharged. Three replicate tests were analyzed separately and the results averaged.

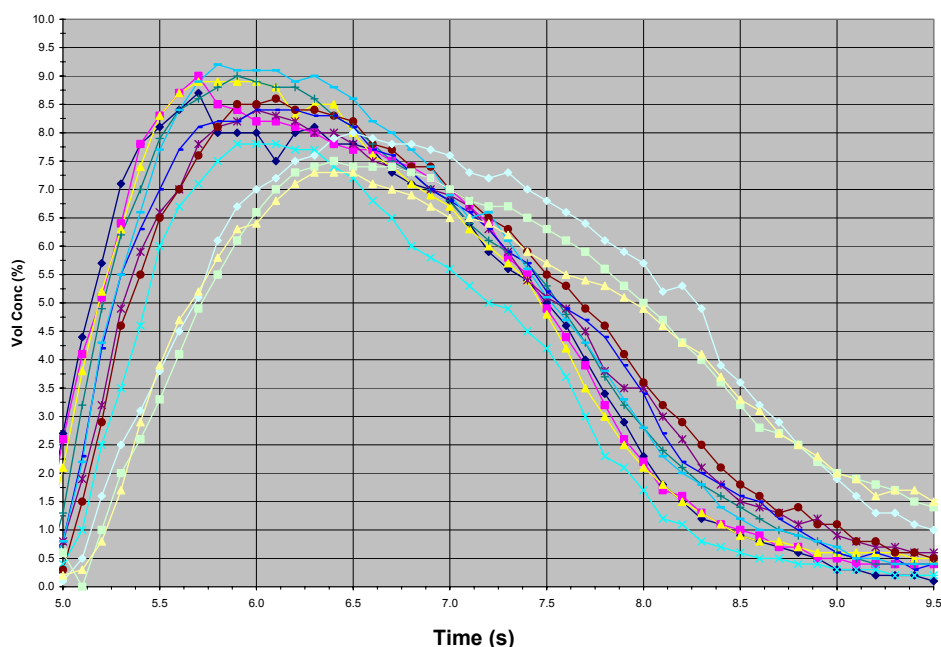


**Figure 11–21. Sample Halonyzer Traces.**

The denominator of Equation (11-3) was calculated from the recirculation zone concentrations 0.1 s before and 0.1 s after the selected point. This gave the shortest data collection interval possible with the Halonyzer on either side of  $t_1$ , a total  $\Delta t$  of 0.2 s. Using this approach for each of the sets of Halonyzer data for each run, the  $\tau$  values for all of the runs were calculated to range from 0.024 s to 0.17 s for the spray fires and 0.25 s to 0.54 s for the pool fires. This range correlates well with that in Table 11–7, thereby suggesting that this approach may have some merit for estimating  $\tau$  values for fire suppression using data from non-fire tests.

#### 11.8.8 Principle 4

*The extinguishant concentration established in the recirculation zone is a function of the mixing time behind the obstacle (“clutter”) that stabilizes the flame.*

Mixing times for the 16 tests in Phase I were calculated using (a) Takahashi’s correlation, with AENTF nacelle velocity measurements by Davis and Disimile<sup>11</sup> and (b) Equation (11-3), with Halonyzer

<sup>vii</sup> Under some conditions, various mixing phenomena resulted in erratic concentration traces in the recirculation zone after the peak was reached. Some traces showed great turbulence, and some have profiles with two peaks.

concentration data measured over the top of the bluff bodies stabilizing the flame and within the flame recirculation zone region. Table 11–8 compares the values of  $\tau$  for both approaches. Since the velocity and rib height approach does not define a proportionality constant, the runs were rank ordered in terms of their value of  $\tau$ , from lowest to highest. (When the proportionality constant of 22.79 was used, then  $\tau$  values of 0.13 to 0.71 were observed, which was consistent with prior literature.) The data were segregated by rib height and fire type, since these two factors largely influenced the test results.

**Table 11–8. Rank Order of  $\tau$  Values in All Test Run Conditions for Both Mixing Models.**

2.5 cm Clutter (Runs 1 to 8)				7.6 cm Clutter (Runs 9 to 16)			
Pool Fires		Spray fires		Pool fires		Spray Fires	
Correlation	Eq. (3)	Correlation	Eq. (3)	Correlation	Eq. (3)	Correlation	Eq. (3)
5	2	7	8	9	14	11	12
2	1	4	4	14	10	16	16
1	6	3	7	13	9	15	15
6	5	8	3	10	13	12	11

The two sets of results did not correlate well. It was hypothesized that the calculated values using only the free stream, steady state velocity and fixed rib height may have deviated from those using actual concentration data for at least two reasons:

- The local velocity was greatly perturbed and changed in a transient manner during the extinguisher discharge period. This was due to the entrainment and mixing into the free stream of a high mass, high momentum flow of extinguishant. Provisions to artificially adjust the air velocity to accommodate and dampen this perturbation, made in some laboratory scale tests, were not practical under these full-scale conditions.
- The velocity-and-rib height approach did not consider that different types of fires created different thermally influenced dimensions of the recirculation zone. These, in turn, resulted in different mixing and concentration dilution rates as well as local velocity changes. To the extent that the different character of the recirculation zones required larger agent mass discharges, there were secondary effects on the mixing rate, as discussed later.

Therefore, it was not surprising to find that the simple correlation, when applied to the complex flow fields associated with real engine nacelle geometries and conditions, did not provide satisfactory prediction of the test results. The veracity of the approach of using Halonyzer concentration curves and Equation (11-3) will be supported further with additional analysis discussed later in this chapter.

It was then of interest to determine what impact the various physical parameters of the nacelle had on the calculated values of  $\tau$ , as determined from the fire test data and concentration measurements, using the ANOVA data analysis technique.

- The calculated values of  $\tau$  for the 7.6 mm (3.0 in.) ribs were nearly double those for the 2.5 cm (1.0 in.) ribs, as seen in Figure 11–22. Thus, the increase in  $\tau$  with rib height (the “L” of L/U) in the correlation was justified, although the magnitude of the effect was not predicted to be so large. This was likely due to the influence of other factors, such as fire type.
- The calculated values of  $\tau$  for the pool fires were nearly four times those for the spray fires, as shown in Figure 11–23. This appeared logical, given that pool fires created larger, less

turbulent recirculation zones than spray fires. However, the Halonyzer data were collected under non-fire conditions. The question then became whether the Halonyzer data somehow retained some influence of fire type in its non-fire data. Larger extinguishing agent masses were required to extinguish the pool fire tests, and the same amounts were used in the Halonyzer tests. These larger masses were injected at higher mass flows. There were several possible hypotheses for this mass effect to increase  $\tau$ , but additional data were needed to appraise them.

- Figure 11–24 shows 50 % larger values of  $\tau$  for colder air and agent temperature. This may have been due to increased agent and air density at constant mass flows, which could have decreased the velocity and volumetric flow. It is also possible that some of the agent may have remained in a liquid state, which reduces the agent's contribution to the velocity and flow, relative to hotter conditions.

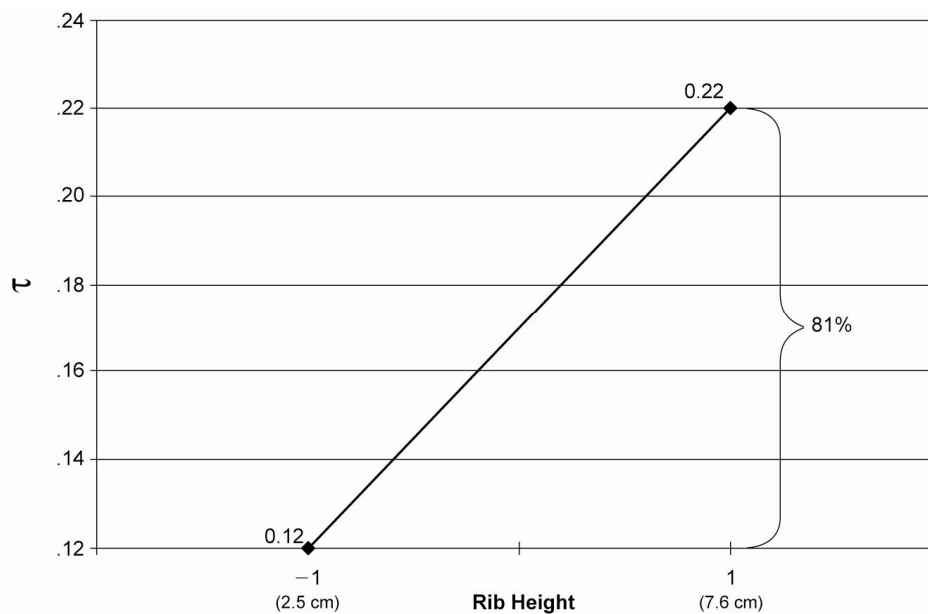


**Figure 11–22.**  
Influence of Flame  
Stabilizing Rib  
Height on Value of  
 $\tau$ .

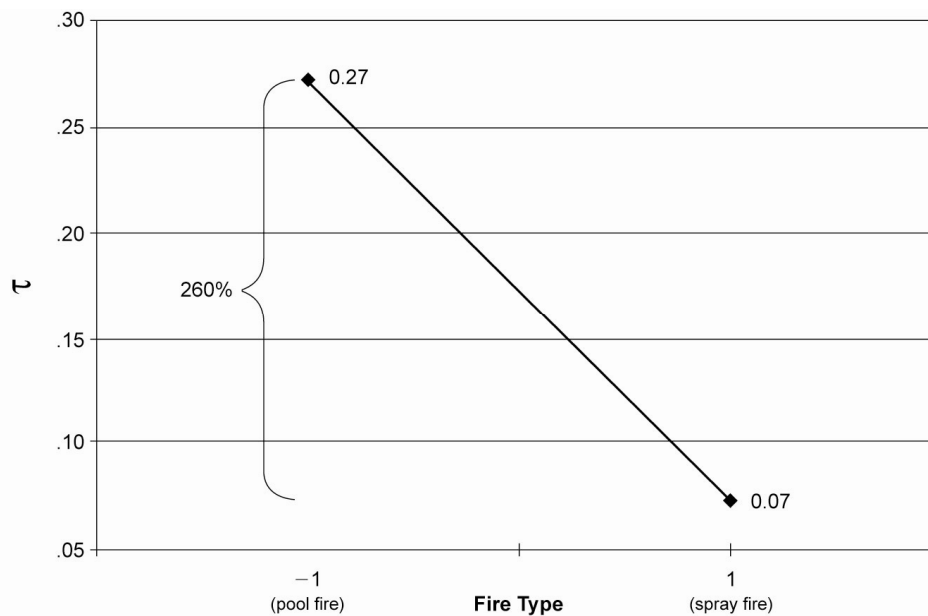


**Figure 11–23.**  
Influence of Fire  
Type on Value of  $\tau$ .

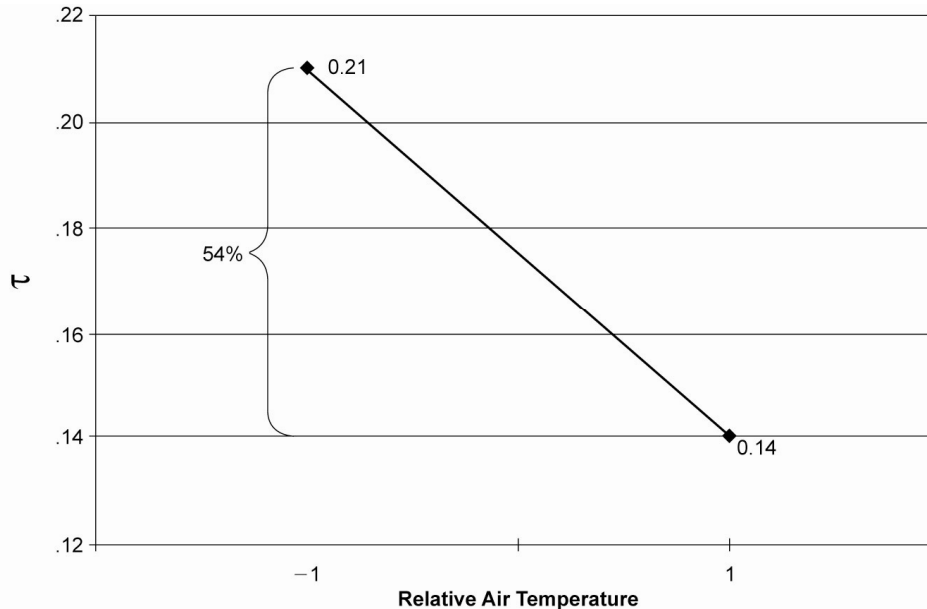


**Figure 11–24.** Influence of Agent and Air Temperature on Value of  $\tau$ . (“-1” is 10 °C below the agent boiling point; “1” is 60 °C above the agent boiling point.)

### 11.8.9 Principle 2

*The measured cup burner extinguishing concentration of a candidate extinguishant is an effective predictor of the critical flame suppression concentrations required within the flame recirculation zone of an engine nacelle fire.*

Table 11–9 is a summary of the Phase I fire extinguishing data. For each of the 16 run conditions, the minimum agent mass for flame extinguishment was determined, with an estimated uncertainty of  $\pm 0.005$  kg (0.01 lb). The minimum agent discharge was then repeated with no fire, to enable making Halonyzer 3 measurements of agent concentration above the rib stabilizing the flame in the region, and where the flame’s recirculation zone had been. For each run, the value used for further analysis was the highest concentration in the recirculation zone. This value was selected because the reaction rate time scale was so much shorter than the residence time scale, that the quenching process was estimated to be immediate. The concentrations in the table were derived from this group of 16 data points.

**Table 11–9. Flame Extinguishment Concentrations. (% by Volume)**

	HFC-227ea	CF <sub>3</sub> I
Minimum and maximum values of the 8 sets of conditions for each agent	6.3, 14.8	2.4, 7.7
Mean value and std. dev. of the 8 sets of conditions for each agent	10.8 $\pm$ 3.1	3.7 $\pm$ 2.1
Mean value (of 4 runs) for spray fire extinguishment	8.9 $\pm$ 2.8	2.5 $\pm$ 0.25
Mean value (of 4 runs) for pool fire extinguishment	12.9 $\pm$ 1.8	5.1 $\pm$ 2.3
Cup burner value	6.2	3.2
Flammability limit	11.0	6.8

The first two rows show a considerable spread in the extinguishing concentrations for both agents. The three mean values correlated with the cup burner values, but were numerically larger, i.e., it generally appeared to require more chemical to quench the real-scale fires.

The results for spray fire and pool fire extinguishment (rows 3 and 4) were not likely to have been in error. They were consistent with the results of Hamins et al.,<sup>2</sup> who obtained 6.2 % and 11 % for HFC-227ea and 3.2 % and 6.8 % for CF<sub>3</sub>I. The differences were within the combined experimental uncertainties.

It was therefore important to determine whether the real-scale fires were more difficult to suppress than small diffusion flames or whether a smaller concentration of extinguishant was actually reaching the fire. Since the flow patterns and thermal conditions were different between the tests with a fire and the equivalent test without a fire, it was beneficial to obtain  $X_{\text{fire}}(t)$ , the extinguishant concentration in the recirculation zone, for the former using data from the latter. The following is a proposed protocol for obtaining an estimate.

Equation (11-4) is a reasonable fit to the rising portion of the time-dependent agent concentration in the recirculation zone area, but with no fire present:

$$X_{nf}(t) = X_{\infty nf} e^{-a_{nf}(t-t_{p_{nf}})^2} \quad (11-4)$$

where:

- $X_{nf}(t)$  is the concentration in the non-fire region at time  $t$ ,
- $X_{\infty nf}$  is the peak concentration measured in the fire zone,
- $a_{nf}$  is an exponential coefficient, and
- $t_{p_{nf}}$  is time corresponding to the peak of the Halonyzer trace in the fire zone (with the beginning of the concentration rise defined as  $t = 0$ ).

The exponent has been raised empirically to the second power. Although it would have been preferable to adjust it based on the data, the limited number of independent boundary conditions required that one of the parameters be fixed.

1. Using an extra intermediate data point prior to the peak on the concentration trace, and measured values of  $X_{\infty nf}$  and  $t_{p_{nf}}$ , calculate  $a_{nf}$ .
2. Assume that the value of  $\tau$  for the “fire” condition is twice that for the equivalent “non-fire” condition, consistent with the findings of Winterfeld.<sup>6</sup> Hamins et al. also published data from which such an assumption could be drawn.<sup>2</sup>
3. Use Equation (11-2), twice, to express  $X_f$  as a function of either  $X_{nf}$  or  $X_{\text{fire}}$ .
4. The free stream concentration  $X_f$  is expected to be roughly the same whether a fire existed or not. Therefore, set the two expressions for  $X_f$  equal to each other. Use the previously calculated value of  $\tau$  for the conditions of interest, and use  $(2 \tau)$  to replace  $\tau$  in the expression using  $X_{\text{fire}}$ . Set the values of  $X_{nf}$ ,  $X_{\text{fire}}$  and  $X_f$  to be equal at  $t = 0$ .
5. Using Equation (11-5), calculate the exponential coefficient for the fire condition.

$$a_{\text{fire}} = (a_{nf} \times t_{p_{nf}}) / (2 \times t_{p_{\text{fire}}}) \quad (11-5)$$

6. Solve the expression  $X_{nf}(0) = X_{fire}(0)$ . The former term can be calculated directly, permitting one to calculate  $X_{\infty fire}$  as an expression of only  $t_{p fire}$ .
7. Apply the boundary condition  $X_f(t_{p fire}) = X_{\infty fire}$ , since the free stream concentration curve crosses the fire zone curve at its peak.
8. Solve the equation for  $t_{p fire}$  using iterative techniques.
9. Using an equation of the form of Equation (11-4), calculate  $X_{\infty fire}$ ,  $a_{fire}$  and  $X_{fire}(t)$  to obtain a theoretical concentration profile under fire conditions.

This somewhat complex approach was used to calculate theoretical peak concentration profiles for two extremely different sets of experimental run conditions, using different extinguishing agents, fire types and air flows, and with widely varying  $\tau$  values, as examples to test the “robustness” of this proposed approach. The calculated peak concentrations expected under fire conditions and threshold agent mass requirements are shown in Table 11–10.

**Table 11–10. Calculated Peak Concentrations under Fire Extinguishment Conditions.**  
(% by Volume)

Run Conditions	$\tau$	$X_{\infty conf}$	$X_{\infty fire}$
Run 13: CF <sub>3</sub> I, pool fire, 7.6 cm rib height, low air flow	0.54	6.3	3.0
Run 11: HFC-227ea, spray fire, 7.6 cm rib height, high air flow	0.17	11	5.8

The peak concentrations in the far right column are very close to the cup burner flame extinguishment values for the two agents, even with all of the approximations and assumptions used in this analysis. These limited results suggested:

- Cup burner values may be widely applicable indicators of peak agent concentrations in the fire zone at flame extinguishment.
- The preceding estimation protocol may be of some utility in estimating threshold flame extinguishing concentrations using only non-fire Halonyzer data. Further experiments and theoretical analysis are needed to establish the reliability of the protocol.

An alternative representation of the agent concentration profile assumed that the nacelle portion upstream of the fire zone was well mixed, as shown in Equation (11-6):

$$X_f(t) = \frac{Q_E}{(Q_E + Q_A)} \left[ 1 - e^{-\frac{(Q_A + Q_E)t}{V_T}} \right] \quad (11-6)$$

where:

- $X_f(t)$  is the free stream concentration just upstream of the fire zone,
- $Q_E$  is the volumetric flow of the extinguisher during discharge,
- $Q_A$  is the volumetric flow of the ventilation air inflow, and
- $V_T$  is the total volume of the nacelle upstream of the fire location.

After the extinguisher flow subsides, the upstream concentration gradually decays, as represented by the following upstream concentration model:

$$X_f(t) = X_{fD} e^{\frac{-Q_d(t-t_D)}{V_T}} \quad (11-7)$$

where  $X_{fD}$  is the free stream concentration at the time ( $t_D$ ) that extinguishant stops flowing (actually the peak concentration). This rendition was not used in the preceding analysis, but warrants further study.

As noted above, this analysis suggested that, for each fire suppressant and fire type, a single concentration in the fire recirculation zone may lead to extinguishment under all engine nacelle operating conditions. Therefore, it was valuable to examine the extent to which the test factors affected the response variable. This ANOVA analysis used the Halonyzer peak concentration reached in the fire zone at the threshold extinguishing mass for each set of run conditions in the experimental series.

- The agent flow, determined by the extinguisher storage pressure, had only a modest influence, as shown in Figure 11–25. A change of a factor of 4 in storage pressure resulted in a 30 % change in the response variable.
- As shown in Figure 11–26, increased clutter (taller rib heights decreased the response variable by about 20 %.
- No other parameters (or “factors”) were shown to have statistically significant influences.

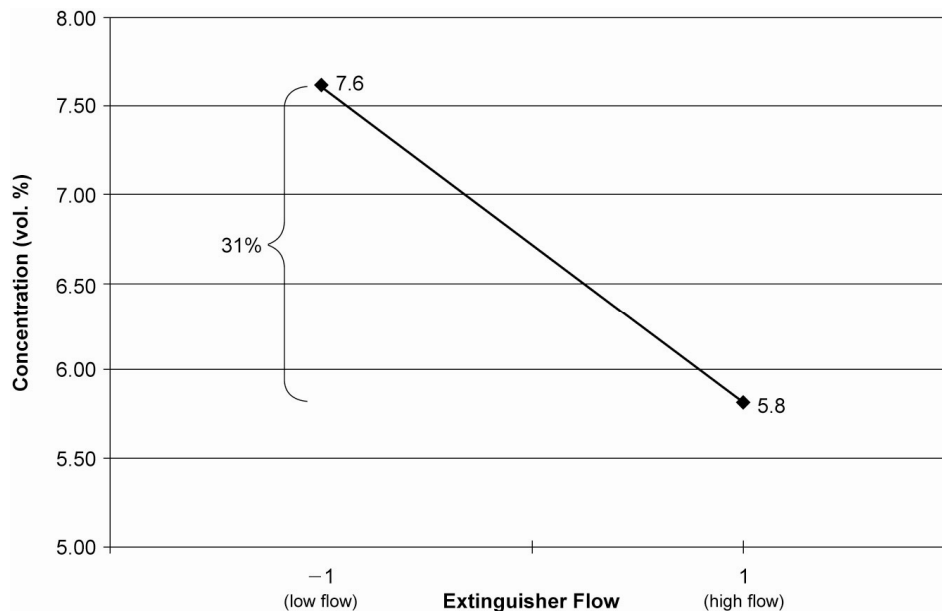


**Figure 11–25.**  
Variability in  
Peak  
Concentration  
Required Due  
to Extinguisher  
Flow.

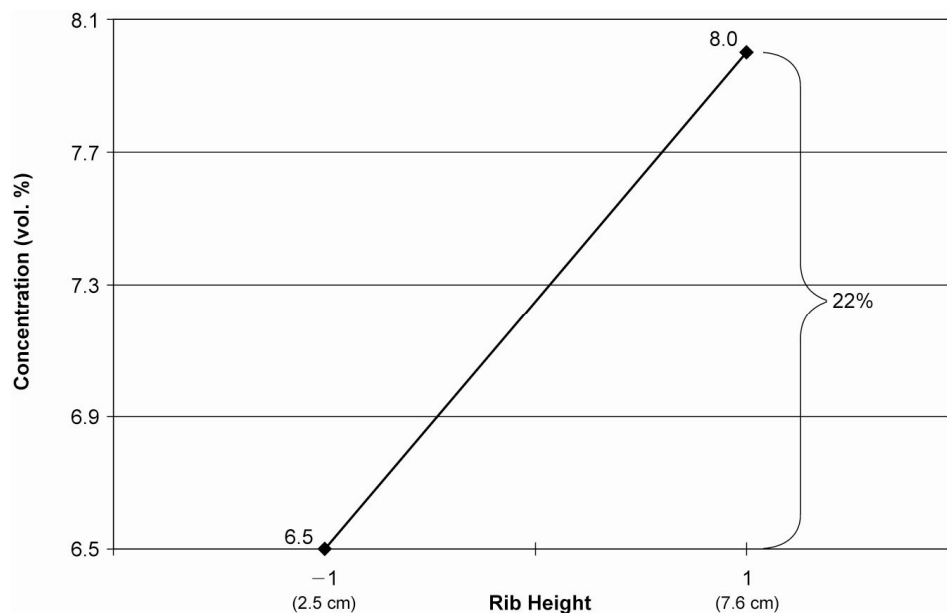


**Figure 11–26.**  
**Variability in Peak**  
**Concentration**  
**Required Due to**  
**Rib Height.**

### 11.8.10 Phase III Results

The results of the Phase III experiments are compiled in Table 11–11. The limited data showed that on a mass basis, BTP was at least as effective at flame suppression as HFC-227ea. This indicated at least some benefit from the presence of the bromine atom. Since BTP extinguished the fires in essentially all the tests, additional testing with lower discharged BTP mass would be needed to (a) ascertain the magnitude of the improvement in efficiency and (b) determine whether the magnitude was comparable to the improvement over HFC-227ea in the cup burner apparatus.

**Table 11–11. Results of Fire Experiments with HFC-227ea and 2-bromo-3,3,3-trifluoropropene.**

Test Conditions	HFC-227ea		2-bromo-3,3,3-trifluoropropene	
	Mass Discharged kg (lb)	Flame Suppressions/Number of Tests	Mass Discharged kg (lb)	Flame Suppressions/Number of Tests
1	1.06 (2.34)	4/5	1.0 (2.2)	1/1
1	0.91 (2.00)	0/4	0.91 (2.0)	3 /4
2	1.24 (2.73)	0/5	1.24 (2.73)	4/4
2			1.06 (2.34)	3/3

## 11.9 SUMMARY

In its 10 years of research, the Department of Defense's Next Generation Fire Suppression Technology Program:

- Developed new understanding of the fire suppression process,

- Established sound tools for screening and evaluating large numbers of alternate fire suppressant fluids,
- Screened tens of thousands of compounds, and
- Developed technology for obtaining the best fire suppression system performance for a given suppressant.

Most of the research was performed using laboratory apparatus. In the process of compiling the copious knowledge that resulted from the research, seven principles were identified that were appraised using a fully complex, real-scale engine nacelle test facility. The following principles were confirmed:

- In general, to deliver an extinguishing concentration of suppressant to a fire, a significantly higher mass of an agent with a boiling point higher than the engine nacelle temperature must be discharged compared to an agent with a boiling point below the prevailing temperature. Should the suppressant be efficiently transported through the nacelle annulus and spend sufficient time in the fire zone, local vaporization may allow full efficiency for a suppressant with a boiling point slightly below the engine nacelle temperature.
- The measured cup burner extinguishing concentration of a candidate extinguishant can be a predictor of the critical flame suppression concentrations required within the flame recirculation zone of an engine nacelle fire.
- When deploying near-minimal masses of agent needed to suppress a fire, increasing the number of extinguishant discharge sites increases the uniformity of suppressant concentration throughout the nacelle. As with all the mixing-related principles, discharging sufficient additional suppressant can result in an extinguishing concentration throughout the nacelle.
- Obstructed pool fires require more agent for flame extinguishment than do spray fires.
- The extinguishant concentration established in the recirculation zone is a function of the free stream concentration, the magnitude of the obstacle (“clutter”) that stabilizes the flame, and the mixing time behind that obstacle.
- The degree of clutter typically present in an engine nacelle can significantly hinder the uniform distribution of a fire suppressant.
- Assuming that a mix of extinguishant vapor and liquid aerosol reach the flame reaction zone, the sufficient vaporization of liquid particles to enhance extinguishment will be dependent upon, among other parameters, the liquid’s residence time in the recirculation zone.
- The suppression effectiveness of a non-catalytic extinguishant in a full-scale engine nacelle is determined by its ability to absorb heat as it enters the flame zone.
- Agent concentrations in the recirculation zone near a fire can be estimated from concentration measurements made under the same nacelle operating conditions, but without the fire.

## 11.10 REFERENCES

1. Bennett, J.M., Caggianelli, G.M., Kolley, M.L., and Wheeler, J.A., *Halon Replacement Program for Aviation, Aircraft Engine Nacelle Application Phase II – Operational Comparison of Selected Extinguishants*, WL-TR-97-3076, Wright-Patterson Air Force Base, OH, 1997.
2. Hamins, A. et al, “Suppression of Engine Nacelle Fires,” in Gann, R.G., ed., *Fire Suppression System Performance of Alternative Agents in Aircraft Engine and Dry Bay Laboratory Simulations*, NIST Special Publication SP 890, National Institute of Standards and Technology, Gaithersburg, MD, vol. 2, pp.1-199, 1995.
3. Longwell, J.P., Frost, E.E., and Weiss, M.A., “Flame Stability in Bluff Body Recirculation Zones,” *Industrial and Engineering Chemistry* **45**, 1629, (1953).
4. Mestre, A., “Etudes des Limites de Stabilité en Relation avec la résistance des Obstacles à l’écoulement,” *Combustion Researches and Reviews*, 6<sup>th</sup> and 7<sup>th</sup> AGARD Meetings, pp. 72-85, Butterworths Scientific, London, 1955.
5. Bovina, T.A., “Studies of Exchange Between Re-Circulation Zone Behind the Flame Holder and Outer Flow,” *Proceedings of the Combustion Institute* **7**, 692-696, (1958).
6. Winterfeld, G., “On Processes of Turbulent Exchange Behind Flame Holders,” *Proceedings of the Combustion Institute* **10**, 1265-1275, (1965).
7. Takahashi, F., Schmoll, W.J., and Strader, E.A., “Effects of Obstruction on Flame Suppression Efficiency,” 1999, in Gann, R.G., Burgess, S.R., Whisner, K.C., and Reneke, P.A., eds., *Papers from 1991-2006 Halon Options Technical Working Conferences (HOTWC)*, CD-ROM, NIST SP 984-4, National Institute of Standards and Technology, Gaithersburg, MD, (2006).
8. Takahashi, Fumiaki, Schmoll, W.J., and Belovich, V.M., “Suppression of Bluff-Body Stabilized Diffusion Flames,” paper AIAA 98-3529, 34<sup>th</sup> AIAA/ASME/SAE/AEE Joint Propulsion Conference, American Institute of Aeronautics and Astronautics, Reston, VA, 1998.
9. Grosshandler, W., Donnelly, M., Charagundla, R., and Presser, C., “Suppressant Performance Evaluation In A Baffle-Stabilized Pool Fire,” 1999, in Gann, R.G., Burgess, S.R., Whisner, K.C., and Reneke, P.A., eds., *Papers from 1991-2006 Halon Options Technical Working Conferences (HOTWC)*, CD-ROM, NIST SP 984-4, National Institute of Standards and Technology, Gaithersburg, MD, (2006).
10. *NFPA 2001, Clean Agent Fire Protection Systems*, NFPA, Quincy, MA, 2004.
11. Davis, J.M., and Disimile, P.J., *Full Scale Generic Annulus Airflow Survey*, Engineering and Scientific Innovations, Inc., Dayton, OH, April 2006.



---

---

## Chapter 12: AFTERWORD

**Richard G. Gann, Ph.D.**  
**National Institute of Standards and  
Technology**

---

---

### TABLE OF CONTENTS

12.1 A View Ahead.....	1145
12.2 References.....	1148

### 12.1 A VIEW AHEAD

The previous 11 chapters comprise an objective account of a focused and sustained research effort to effect a change in the state of fire suppression science and technology. The following few pages are a personal prognosis of the evolution of the context into which that technology will be applied and the changes that I believe will result. The ideas have been shaped by my 35 years in fire safety, attendance at hundreds of science, technology, and engineering conferences, and innumerable discussions with friends, colleagues, and adversaries.

The threat that led to the revisitation of clean fire suppressant chemicals toward the end of the 20<sup>th</sup> century was truly global in expanse. As such, it differed from the motivations for the earlier fire suppression research, e.g., reduced toxicity and greater efficiency. Even though the worldwide losses of life and property mitigated by effective fire protection approach those of global magnitude<sup>1</sup>, fire protection is treated by our societies as a regional issue. Our success at localizing the impact of a fire, the cumulative benefit of millennia of empiricism and science, has moved fire control far down the list of perceived global societal necessities. Fires exist and there are local people who put them out.

We can thus presume that when the next issue affecting fire suppression arises, the outcome will be comparable to what we have experienced over the past three decades. An updated set of cultural values, manifested as societal criteria, will emerge. The fire protection community will be called upon to re-assess the necessity and mode of fire suppression in each application. For those cases where such capability is an integral part of providing safety, continuity of operation, preservation of property, etc., we will develop new criteria for acceptable agents and systems. The fire research community and the fire protection industries will then commence the research and engineering to realize the needed capability within the new bounds. The Next Generation Fire Suppression Technology Program (NGP) has provided extensive knowledge for responding to the current threat and provided a durable basis for responding to future stimuli. This knowledge should ease the transitions to new fire protection systems.

During the decade of the NGP, both research and practical solutions for fire control have come a long way. There are forces, already in motion, that over the next few decades will define the future of how fire safety is delivered. Thus, my prognosis is that, by the end of the 21<sup>st</sup> century:

- Performance-based codes will have replaced the current prescriptive versions. Facility constructors, owners and operators will be required to provide a communally chosen degree of safety. They will have broad flexibility of design and will have to demonstrate that they have achieved the safety objectives.
- Driven by increased international trade, fire standards for product qualification will have been harmonized worldwide, likely within the construct of performance-based codes. Because of the conservative nature of countries and industries, many of these standards will be compromises and thus have the potential to fall short of their purposes.
- People around the world will have accumulated increased possessions and furnishings, as already enjoyed by those in the wealthier countries. As a result, fire loads in dwellings and offices will increase, presenting a larger challenge to building and fire codes.
- The development of fire safety technology, much of it derived from military research investments, will continue to be a (limited) commercially successful undertaking.
- The public will have high expectation for low (*i.e.*, perceived zero) risk. The continued increase in the average age of the population will further increase the demands for safety measures.
- Environmental risk and benefit will receive increased attention.
- Municipal and corporate budgets (*e.g.*, for fire service staff) will continue to be under pressure.
- More sophisticated systems will have become increasingly automated to improve reliability in the face of an insufficient pool of knowledgeable service people.

All of these will drive the development and implementation of installed fire control technologies. By the end of the 21<sup>st</sup> century, I believe that life loss from fires in the United States and the other developed countries will have diminished by an order of magnitude. There will be similar decreases underway in countries with emerging economies. New hardware and materials technologies will have enabled this accomplishment while decreasing the total cost of fire as well.

Success in the delivery of fire safety has generally resulted from the compounded effectiveness of redundant tactics, *e.g.*, fire resistant walls *plus* fire-retardant products. Performance-based codes are intended to reduce cost and improve design flexibility, both of which are easier to provide when including a fire suppression system. I thus expect that automatic fire suppression will become far more widespread than it is today. In particular, by the end of the 21<sup>st</sup> century, I expect we will at least see the following:

- Detectors with multiple sensors, backed by pattern recognition software, should soon provide ever earlier recognition of a fire and rejection of spurious signals from non-fire sources. Smart and early fire detection combined with next generation fire suppression devices will ensure the quenching of most fires at non-hazardous levels and with no complications from nuisance alarms.
- Commercial and public buildings and spaces with contents of high or unique value will be protected with low volume water systems, systems using short atmospheric lifetime fluorinated organic suppressants, or systems based on a new generation of solid propellant fire extinguishers (SPFEs).
- New and renovated residences will have fixed central or localized suppression systems using the above technologies.

- In current dwellings that are still occupied and unrenovated 100 years from now, plug-in units, probably based on SPFEs, will be installed.

To mitigate in-flight fires in aircraft cabins and cargo bays, new very low flammability materials are under exploration in such establishments as the Federal Aviation Administration Technical Center. Use of these materials will reduce the frequency and severity of such fires from their already low levels to virtual non-existence.

Well into the 21<sup>st</sup> century and beyond, aircraft will still be flying on petroleum-derived fuels. (Some workhorse aircraft have extensive lifetimes. For instance, the first 737 flew in 1967<sup>2</sup>, and the first B-52 flew in 1954.<sup>3</sup>) Thus, in-flight fires in engine nacelles, fuel tanks, and (in combat) dry bays will continue to be of concern.

Under the present system performance requirements, NGP research has made fire suppression engineering far easier. Designers can proceed with the implementation of C<sub>2</sub>F<sub>5</sub>H (HFC-125) systems, since it is unlikely that a superior fluid will be discovered for these specialized applications. The volatility requirement (i.e., effectiveness at -40 °C) is restrictive. However, should a risk analysis allow for relaxing this requirement, NGP research has indicated the few potentially productive chemical directions for moderately less volatile fluids (Chapter 7). In general, new knowledge of how to optimize agent delivery, understanding of transport of agents to obstructed fires, and guidance for the time duration of agent release will help reduce weight and storage volume penalties associated with the evolution from halon 1301 (Chapter 8). The advanced total cost and cost/benefit methodology (Chapter 10) is already enabling choices among competing technologies. There is potential for the use of intumescent materials to restrict the air flow through an engine nacelle and improve the efficiency of any fire suppressant.

NGP research has brought new life to the consideration of two existing fire suppression technologies (Chapter 9). For military aircraft, powder panels now offer a cost- and mass-effective alternative to fluid-based systems for dry bays. Additional testing of the improved designs and examination of powders with catalytic fire suppression capability will further add to their economic and operational benefits. Similar advances in solid propellant fire extinguishers make them competitive with fluid-based systems for engine nacelles and with fluids and powder panels for dry bays. The NGP identified families of compounds from which to select chemicals for inclusion within the propellant or for downstream delivery. The hot exhaust removes the volatility constraint and allows the choice of additive to be made on other grounds, such as cost or materials compatibility.

Nonetheless, there are still some substantive gaps in the full knowledge base needed for the design and implementation of aircraft fire suppression systems.

- Screening for cardiotoxicity from an acute exposure to a fire suppressant. The NGP results indicated that effective fluid suppressants will contain bromine, iodine, or phosphorus atoms. The principal effect of concern from inhalation of a brominated or iodinated compound is cardiac arrhythmia. No accurate test has been identified that predicts the outcome of the dog exposure test described in Chapter 6. Moreover, objections have been raised that the dog test itself is not predictive of human reaction to these chemicals. Physiologically based pharmacokinetic (PBPK) modeling now provides a basis for relating environmental exposure to the concentration of agent in the bloodstream. It remains to develop a quantitative relationship between that concentration and actual harm to people, including those people of heightened sensitivity. The movement of the world away from the use of laboratory animals

speaks further for the need of an *in vitro* test or a chemical measurement, such as octanol-water partitioning.

- Predictive capability for fire suppression system performance. Full-scale testing of chemicals and delivery systems in realistic aircraft-like test fixtures is still necessary to demonstrate acceptability. The NGP developed knowledge of the behavior of agent vapors and aerosols in cluttered environments, the effects of timing and mass loading of the incoming air stream, and flame quenching dynamics. The research has shown that CFD models, combined with validating experiments, can lead to accurate prediction of the success or failure of an injected agent in putting out a fire (Chapter 8). However, the in-flight performance of a fire suppression system is strongly influenced by the initial and boundary conditions surrounding the fire and the fire “compartment.” It remains for succeeding engineering to extend the NGP simulation results to achieve assured replication of the performance of the range of suppression system operations for the suite of possible fire and fire suppression events. The results would serve as a design tool and as the basis for simplified system certification.
- Instrumentation for new chemicals. The NGP was successful in developing technology for high speed, real-time, *in situ* monitoring of HFC-125 (Chapter 5). This is the most likely agent to be implemented as a compressed fluid. The NGP also demonstrated that the incorporation of a molecule containing, e.g., bromine, iodine, potassium, or phosphorus atoms, into a solid propellant fire extinguisher (SPFE) led to a highly efficient system. As the use of such additives evolves, quantification methods for the active species will be essential for system design and certification. The lack of an established method for potassium atom concentration measurement has already delayed acceptance of an advanced SPFE system.

Filling these gaps is within the capability of the appropriate technical communities, and I believe this will occur.

## 12.2 REFERENCES

1. Gann, R.G., “A Millennial View of Fire Suppression,” 2000, in Gann, R.G., Burgess, S.R., Whisner, K.C., and Reneke, P.A., eds., Papers from 1991-2006 Halon Options Technical Working Conferences (HOTWC), CD-ROM, NIST SP 984-4, National Institute of Standards and Technology, Gaithersburg, MD, (2006).
2. <http://www.b737.org.uk/history.htm>
3. <http://www.af.mil/factsheets/factsheet.asp?fsID=83>

---

## Appendix A: Acknowledgements

---

The outcome of an effort as extensive as the Next Generation Fire Suppression Technology Program reflects the contributions of a large number of individuals and teams.

During the decade of the NGP, there were hundreds of technical staff involved in the research itself. These scientists, engineers, and technicians are listed as NGP project leaders and Contracting Officer's Representatives (Appendix B) and co-authors of the NGP publications (Appendix C), or are acknowledged in those publications.

Chapter 2 contains original material not available in other NGP reports. The following people and organizations provided assistance and contributions, without which this compilation of information would not have been possible. Ms. Donna Egner, SURVIAC, who was able to unearth every historical report requested from SURVIAC and DTIC; Joe Manchor, NAVAIR Survivability, Naval Air Warfare Center Weapons Division, who provided valuable source information related to vulnerability assessments, live fire testing, and continuing JASPO-sponsored testing activity; Frank Bosworth, Meggitt Safety Systems, Inc., Harlan Hagge, Kidde Aerospace, and Roger Butler, AirScrew Ltd., for their assistance in obtaining authorization to use graphics of fire suppression system components owned by their respective companies; James Jackson, Rolls-Royce Corporation, for his assistance in obtaining authorization to use graphics of a Rolls-Royce turboshaft engine; the Naval Air Systems Command Public Affairs Offices, for their review and public release authorization of source material; and Robert Clodfelter, AFP Associates, Chuck Dorney, USAF, Air Force Materiel Command, Ronald McGregor, USAF, Kirtland Air Force Base, and William Leach, Naval Air Systems Command, for their expert reviews of the material.

The second part of Chapter 11 also contains original material. Several organizations and individuals provided valuable assistance in the complex tests that led to validation of NGP principles. Andy Fultz and Tracy Barnes, Wyle Laboratories, provided leadership of the experimental facility operations and experimental project management; Dr. Peter Disimile and John Davis, ESI Systems, Inc., assisted with the airflow studies and other aspects of the experiments; Dr. Anthony Hamins, National Institute of Standards and Technology (NIST), consulted on fire dynamics and extinguishant mixing; Drs. John Hewson and Gregory Homicz, Sandia National Laboratories, provided numerical analysis of flow and mixing in engine nacelle environments; Bradford Colton, Halotron, Inc., supplied the "second-generation" BTM agent, and Gerry Brabham, Kidde Aerospace, Inc., supplied nozzles for flow and discharge studies.

The members of the NGP Technical Coordinating Committee (listed in Chapter 1) provided perspective and insight during the formulation of the research program, the performance of the 42 research projects, and the interpretation of the results.

There would have been no NGP, but for the initiative of Dr. Donald Dix and Mr. Paul Piscopo of the Office of the Secretary of Defense. In addition, they, along with the members of the Halon Alternatives R&D Steering Group (HASG) provided guidance as the policies within the Department of Defense evolved over the lifetime of the NGP.

With a large program come diverse and often difficult administrative requirements. Frank and Linda Gamboa (Gamboa International Corp.) handled all the expected and unexpected tasks as they arose, freeing the Technical Program Manager to focus on the technical program. In addition, Frank's interactions with staff of various units of the Department of Defense provided guidance on the priorities and realities of research in the public interest. Linda's facilitation of the Halon Options Technical Working Conferences promoted a flow of information into the NGP and effective dissemination of NGP results.

The leadership and committees of the DoD Strategic Environmental Research and Development Program (directed initially by Dr. John Harrison and subsequently by Bradley Smith, with Managers Dr. Jeff Marquese, Dr. Carl Adema, Dr. Robert Holst, and Charles Pellerin) provided valuable oversight, guidance, and advice, as well as the lion's share of the funding.

Several additional people were instrumental in bringing this book to fruition. Ed Mai and Mike Fancher (NIST) re-drew and edited many of the figures from versions photocopied from NGP reports. Sonya Wilson, HeiTech Services, Inc., put the text into final format and compiled the various indexes, no mean feat given the size complexity of the document. Sheila Turner, HeiTech Services, Inc., and Paul Reneke of NIST read the manuscript to check spelling, grammar, and consistency. Ilse Putman, NIST, assisted with the logistics of publication.

The legacy of all these contributors is safer, yet greener, aircraft.

---

## Appendix B: NGP Projects

---

### B.1 SUPPRESSANT SCREENING TESTS

**Dispersed Liquid Agent Fire Suppression Screen;** Principal Investigator: Jiann C. Yang, National Institute of Standards and Technology; 1997-1999.

**Transient-Application-Recirculating-Pool-Fire Agent Effectiveness Screen;** Principal Investigator: William L. Grosshandler, National Institute of Standards and Technology; 1998-2000.

**Toxicological Assessment of Human Health Consequences Associated with Inhalation of Halon Replacement Chemicals;** Principal Investigator: Darol E. Dodd, Air Force Research Laboratory; 1998-1999.

**Agent Compatibility with People, Materials and the Environment;** Principal Investigators: Marc R. Nyden, National Institute of Standards and Technology, and Stephanie R. Skaggs, Universal Technical Services; 1998.

### B.2 NEW FLAME SUPPRESSION CHEMISTRY

**Mechanisms of Ultra-High Efficiency Chemical Suppressants;** Principal Investigators: James W. Fleming, Naval Research Laboratory, and Kevin L. McNesby, Army Research Laboratory; 1997-2000.

**Identification and Proof Testing of New Total Flooding Agents;** Principal Investigator: Robert E. Tapscott, New Mexico Engineering Research Institute; COR: Andrzej W. Miziolek, Army Research Laboratory; 1997.

**Main Group Compounds As Extinguishants;** Principal Investigator: J. Douglas Mather, New Mexico Engineering Research Institute; COR: Ronald S. Sheinson, Naval Research Laboratory; 1998.

**Tropodegradable Bromocarbon Extinguishants;** Principal Investigator: J. Douglas Mather, New Mexico Engineering Research Institute; COR: Ronald S. Sheinson, Naval Research Laboratory; 1998, 2001.

**Flame Inhibition by Phosphorus-containing Compounds;** Principal Investigator: Elizabeth M. Fisher, Cornell University; COR: Andrzej W. Miziolek, Army Research Laboratory; 1997-1998.

**Fluoroalkyl Phosphorous Compounds;** Principal Investigator: J. Douglas Mather, New Mexico Engineering Research Institute; COR: Richard G. Gann, National Institute of Standards and Technology; 2001.

**Super-effective Thermal Suppressants;** Principal Investigator: William M. Pitts, National Institute of Standards and Technology; 1998-1990

**Effective, Non-Toxic Metallic Fire Suppressants;** Principal Investigator: Gregory T. Linteris, National Institute of Standards and Technology; 2001.

**Environmental Impact Of New Chemical Agents For Fire Suppression;** Principal Investigators: Robert E. Huie and Marc R. Nyden, National Institute of Standards and Technology; Andrzej W. Miziolek, Army Research Laboratory; 2000-2001.

**Low Temperature Performance of High Boiling Point Suppressants;** Principal Investigator: Jiann C. Yang, National Institute of Standards and Technology; 2000-2004.

**Alternative Suppressant Chemicals;** Principal Investigator: Richard G. Gann, National Institute of Standards and Technology; 2000-2004.

**Environmentally Acceptable Suppressants;** Principal Investigator: J. Douglas Mather, Chemical Development Systems; Scientific Officer: Richard G. Gann, National Institute of Standards and Technology; 2002-2004.

### **B.3 NEW AND IMPROVED AEROSOL SUPPRESSANTS**

**Suppression Effectiveness of Aerosols and Particles;** Principal Investigator: Ronald S. Sheinson, Naval Research Laboratory; 1998-2001.

**Droplet Interactions with Hot Surfaces;** Principal Investigator: Yudaya Sivathanu, En'Urga, Inc.; COR: William L. Grosshandler, National Institute of Standards and Technology; 1998-1999.

**Technical Support for the Study of Droplet Interactions with Hot Surfaces;** Principal Investigator: Jiann C. Yang, National Institute of Standards and Technology; 1998-1999.

**Powder-Matrix Systems;** Principal Investigator: Gregory T. Linteris, National Institute of Standards and Technology; 1998-2000.

**Electrically Charged Water Mists for Extinguishing Fires;** Principal Investigator: Charles H. Berman, Titan Corp.; COR: Ronald S. Sheinson, Naval Research Laboratory; 1997.

**Development of a Self Atomizing Form of Water;** Principal Investigator: Richard K. Lyon, EER, Inc.; COR: William L. Grosshandler, National Institute of Standards and Technology; 1997.

**Dendritic Polymers as Fire Suppressants;** Principal Investigator: Nora C.B. Tan, ARL; 1998.

### **B.4 IMPROVED SUPPRESSANT DELIVERY**

**Stabilization of Flames;** Principal Investigator: Vincent M. Belovich, Air Force Research Laboratory; 1997-1999.

**Dual Agent Approach to Crew Compartment Explosion Suppression;** Principal Investigator: Douglas Dierdorf, ARA Corp.; COR: Andrzej W. Miziolek, Air Force Research Laboratory; 1998.

**A Method for Extinguishing Engine Nacelle Fires by Use of Intumescent Coatings;** Principal Investigator: Leonard E. Truett, Eglin AFB; 2000.

**Parametric Investigation of Droplet Atomization and Dispersion of Liquid Fire Suppressants;** Principal Investigator: Cary Presser, National Institute of Standards and Technology; 2000-2002.

**Advanced Propellant/Additive Development for Gas Generators;** Principal Investigators: Gary F. Holland, Aerojet, and Russell Reed, Naval Air Weapons Center; COR: Richard G. Gann, National Institute of Standards and Technology; 2000-2003.

**Enhanced Powder Panels;** Principal Investigator: Daniel Cyphers, Skyward, Ltd.; COR: Martin Lentz, Eglin AFB; 2001-2002.

**Fire Suppressant Dynamics in Cluttered Weapons System Compartments;** Principal Investigator: David R. Keyser, INS, Inc.; 2000-2004.

**Guidance For Re-ignition Suppression;** Principal Investigator: Anthony Hamins, National Institute of Standards and Technology; 2003.

**Suppressant Flow through Piping;** Principal Investigator: John Chen, Lehigh University; COR: William L. Grosshandler, National Institute of Standards and Technology; 1998-1999.

**Mechanism of Unwanted Accelerated Burning;** Principal Investigator: Anthony Hamins, National Institute of Standards and Technology; 2001.

## **B.5 VIABILITY OF NEW SUPPRESSANT TECHNOLOGIES**

**Development of Model Fires for Fire Suppression Research;** Principal Investigator: Anthony E. Finnerty, ARL; Associate Investigators: James R. Tucker, Air Force Research Laboratory; Juan Vitali, ARA, Inc.; Ronald S. Sheinson, Naval Research Laboratory; 1997-1998.

**Relative Benefit Assessment of Fire Protection System Changes;** Principal Investigator: J. Michael Bennett, Eglin AFB; 1998-2001.

**Laser-Based Instrumentation for Real-Time, in-situ Measurements of Combustible Gases, Combustion By-products, and Suppressant Concentrations;** Principal Investigator: Kevin L. McNesby, ARL.; 1997-1999.

**Fast Response Species Characterization During Flame Suppression;** Principal Investigator: George W. Mulholland, National Institute of Standards and Technology; 1998-2000.

**Verification of Suppression Principles;** Principal Investigator: J. Michael Bennett, Bennetech, LLC; COR: Martin Lentz, Eglin AFB; 2003-2004.

## **B.6 FUEL TANK INERTION**

**Active Suppression for Fuel Tank Explosions;** Principal Investigator: Leonard E. Truett, Eglin AFB; 1999.



---

## Appendix C: NGP Publications

---

Nearly all of the papers listed below are included on the CD that accompanies this volume. They are also available from the NGP web site: [www.bfrl.nist.gov/866/NGP](http://www.bfrl.nist.gov/866/NGP).

NGP researchers have presented much of their work at the annual Halon Options Technical Working Conferences (HOTWCs). Copies of these papers can be obtained in two ways:

- From NIST: Gann, R.G., Burgess, S.R., Whisner, K.C., and Reneke, P.A., eds., *Papers from 1991-2006 Halon Options Technical Working Conferences (HOTWC)*, CD-ROM, NIST SP 984-4, National Institute of Standards and Technology, Gaithersburg, MD, (2006).
- From the HOTWC web site: [www.bfrl.nist.gov/866/HOTWC](http://www.bfrl.nist.gov/866/HOTWC). Click on “Proceedings,” then ON-LINE,” and then do a subject search on “NGP” (or any other subject, author, or year of interest).

### C.1 GENERAL

Gann, R. G., *FY2004 Annual Report – Next Generation Fire Suppression Technology Program (NGP)*, NIST Technical Note 1466, National Institute of Standards and Technology, Gaithersburg, MD, (2005).

Gann, R. G., “Next Generation Fire Suppression Technology Program: FY2004 Progress,” 2005, in Gann, R.G., Burgess, S.R., Whisner, K.C., and Reneke, P.A., eds., *Papers from 1991-2006 Halon Options Technical Working Conferences (HOTWC)*, CD-ROM, NIST SP 984-4, National Institute of Standards and Technology, Gaithersburg, MD, (2006).

Gann, R. G., *FY2003 Annual Report -- Next Generation Fire Suppression Technology Program (NGP)*, NIST Technical Note 1457, National Institute of Standards and Technology, Gaithersburg, MD, (2004).

Gann, R.G., “Next Generation Fire Suppression Technology Program: FY2002 Progress,” 2003, in Gann, R.G., Burgess, S.R., Whisner, K.C., and Reneke, P.A., eds., *Papers from 1991-2006 Halon Options Technical Working Conferences (HOTWC)*, CD-ROM, NIST SP 984-4, National Institute of Standards and Technology, Gaithersburg, MD, (2006).

Gann, R. G., *FY2002 Annual Report -- Next Generation Fire Suppression Technology Program (NGP)*, NIST Technical Note 1451, National Institute of Standards and Technology, Gaithersburg, MD. (2003).

Gann, R.G., *FY2001 Annual Report -- Next Generation Fire Suppression FY2002 Annual Report -- Next Generation Fire Suppression Technology Program (NGP)*, NIST Technical Note 1445, National Institute of Standards and Technology, Gaithersburg, MD, (2002).

Gann, R.G., *Next Generation Fire Suppression Technology Program: FY2000 Annual Report*, NIST Technical Note 1437, National Institute of Standards and Technology, Gaithersburg, MD, (2001).

Gann, R.G., *Next Generation Fire Suppression Technology Program: FY1999 Annual Report*, NISTIR 6479, National Institute of Standards and Technology, Gaithersburg, MD, (2000).

Gann, R.G., “Next Generation Fire Suppression Technology Program - Technical Highlights,” 1999, in Gann, R.G., Burgess, S.R., Whisner, K.C., and Reneke, P.A., eds., *Papers from 1991-2006 Halon Options Technical Working Conferences (HOTWC)*, CD-ROM, NIST SP 984-4, National Institute of Standards and Technology, Gaithersburg, MD, (2006).

Gann, R.G., "Next Generation Fire Suppression Technology Program (NGP)," *Fire Technology* **34**, 363-371 (1999). Also available as NISTIR 6163, *National Institute of Standards and Technology*, Gaithersburg, MD, (1998).

Finnerty, A.E., Peregino, P.J., Vande Kieft, L.J., Tucker, J.R., Weiland, D.E., Sheinson, R.S., Gann, R.G., Bennett, M.V., and Wheeler, J.A., "Fires Experienced and Halon 1310 Fire Suppression Systems in Current Weapon Systems," Report SURVIAC TR-00-007, Air Force Research Laboratory – Survivability and Safety Branch, Wright-Patterson Air Force Base, OH, (2003). Restricted Distribution.

*Next Generation Fire Suppression Technology Program Strategy (Update)*, Office of the Deputy Undersecretary of Defense (Science and Technology), 2000, available on the NGP web site: [www.bfrl.nist.gov/866/NGP](http://www.bfrl.nist.gov/866/NGP).

*Next-Generation Fire Suppression Technology: Strategy for a National Program*, Office of the Director, Defense Research and Engineering, 1996, available on the NGP web site: [www.bfrl.nist.gov/866/NGP](http://www.bfrl.nist.gov/866/NGP).

## C.2 NEW FLAME SUPPRESSION CHEMISTRY

Linteris, G.T., Rumminger, M.D., and Babushok, V.I., "Catalytic Inhibition of Laminar Flames by Metal Compounds," *Progress in Energy and Combustion Science*, in press, (2007).

Mather, J.D., and Tapscott, R.E., *Environmentally Acceptable Extinguishants*, Final Report, NIST GCR 06-901, National Institute of Standards and Technology, Gaithersburg, MD, 2007.

Linteris, G.T., "NGP Research in Fire Suppression Chemistry," 2006, in Gann, R.G., Burgess, S.R., Whisner, K.C., and Reneke, P.A., eds., *Papers from 1991-2006 Halon Options Technical Working Conferences (HOTWC)*, CD-ROM, NIST Special Publication 984-4, National Institute of Standards and Technology, Gaithersburg, MD, 2006.

Mather, J.D., and Tapscott, R.E., "NGP Search for New Chemicals – Environmentally Acceptable Fire Suppressants," 2006, in Gann, R.G., Burgess, S.R., Whisner, K.C., and Reneke, P.A., eds., *Papers from 1991-2006 Halon Options Technical Working Conferences (HOTWC)*, CD-ROM, NIST Special Publication 984-4, National Institute of Standards and Technology, Gaithersburg, MD, 2006.

Mather, J.D., and Tapscott, R.E., "Environmentally Acceptable Flame Extinguishants," 2005, in Gann, R.G., Burgess, S.R., Whisner, K.C., and Reneke, P.A., eds., *Papers from 1991-2006 Halon Options Technical Working Conferences (HOTWC)*, CD-ROM, NIST Special Publication 984-4, National Institute of Standards and Technology, Gaithersburg, MD, 2006.

Linteris, G.T., Katta, V.R., and Takahashi, F., "Experimental and Numerical Evaluation of Metallic Compounds for Suppressing Cup-burner Flames," *Combustion and Flame* **138**, 78-96 (2004).

Linteris, G., *Limits to Effectiveness of Metal-containing Fire Suppressants, Final Report To the Strategic Environmental Research and Development Program*, NISTIR 7177, National Institute of Standards and Technology, Gaithersburg, MD, 2004.

Mather, J.D., and Tapscott, R.E., "Environmentally Acceptable Flame Extinguishants," 2004, in Gann, R.G., Burgess, S.R., Whisner, K.C., and Reneke, P.A., eds., *Papers from 1991-2006 Halon Options Technical Working Conferences (HOTWC)*, CD-ROM, NIST SP 984-4, National Institute of Standards and Technology, Gaithersburg, MD, (2006).

Donnelly, M.K., Harris, R.H., Yang, J.C., *CF<sub>3</sub>I Stability under Storage*, NIST TN 1452, National Institute of Standards and Technology, Gaithersburg, MD, 2004.

Fleming, J.W., and Williams, B.A., *Mechanisms of Ultra-high Efficiency Chemical Suppressants, Final Report to the Strategic Environmental Research and Development Program*, Naval Research Laboratory, Washington, DC, 2003.

Williams, B.A., and Fleming, J.W., *Influence of Bond Energies on Catalytic Flame Inhibition: Implications for the Search for New Fire Suppressants*, NRL/MR/6180-03-8728, Naval Research Laboratory, Washington DC, 2003.

Shreeve, J.M., Singh, R.P., Tapscott, R.E., and Mather, J.D., *Fluoroalkyl Phosphorus Compounds, Final Report To the Strategic Environmental Research and Development Program*, Report 2003/1/34501, New Mexico Engineering Research Institute, Albuquerque, NM, 2003.

Mather, J.D., and Tapscott, R.E., Shreeve, J.M., and Singh, R.P., "Fluoroalkyl Phosphorus Compounds," 2003, in Gann, R.G., Burgess, S.R., Whisner, K.C., and Reneke, P.A., eds., *Papers from 1991-2006 Halon Options Technical Working Conferences (HOTWC)*, CD-ROM, NIST SP 984-4, National Institute of Standards and Technology, Gaithersburg, MD, (2006).

Mather, J.D., and Tapscott, R.E., "Tropodegradable and other Environmentally Acceptable Flame Extinguishants," 2003, in Gann, R.G., Burgess, S.R., Whisner, K.C., and Reneke, P.A., eds., *Papers from 1991-2006 Halon Options Technical Working Conferences (HOTWC)*, CD-ROM, NIST SP 984-4, National Institute of Standards and Technology, Gaithersburg, MD, (2006).

Rumminger, M.D., Babushok, V.I., and Linteris, G.T., "Temperature Regions of Optimal Chemical Inhibition of Premixed Flames," *Proceedings of the Combustion Institute* **29**, 329-336 (2002).

Williams, B.A., and Fleming, J.W., CF<sub>3</sub>Br and Other Suppressants: Differences in Effects on Flame Structure," *Proceedings of the Combustion Institute* **29**, 345-351 (2002).

Linteris, G.T., Rumminger, M., Babushok, V., Chelliah, H., Lazzarini, T., and Wanigarathne, P., *Effective Non-Toxic Metallic Fire Suppressants, Final Report To the Strategic Environmental Research and Development Program*, National Institute of Standards and Technology, Gaithersburg MD, 2002. Also available as NISTIR 6875, National Institute of Standards and Technology, (2002).

Linteris, G.T., "Extinction of Cup-Burner Diffusion Flames by Catalytic and Inert Inhibitors," *Second NRIFD Symposium - Science, Technology and Standards for Fire Suppression Systems*, pp. 269-282, National Research Institute of Fire and Disaster, Tokyo, Japan, 2002.

Rumminger, M.D., Babushok, V.I., and Linteris, G.T., "Temperature Regions of Optimal Chemical Inhibition of Premixed Flames," *Proceedings of the Combustion Institute* **29**, 329-336, (2002).

Linteris, G.T. and Rumminger, M.D., "Particle Formation in Laminar Flames Inhibited by Metals," *Proceedings of the Western States Section Meeting*, Paper 030, The Combustion Institute, Pittsburgh, PA, 2002.

Linteris, G.T., Knyazev, V.D., and Babushok, V.I., "Inhibition of Premixed Flames by Manganese and Tin Compounds," *Combustion and Flame* **129**, 221, (2002).

Rumminger, M.D., and Linteris, G.T., "The Role of Particles in the Inhibition of Counterflow Diffusion Flames by Iron Pentacarbonyl," *Combustion and Flame* **128**, 145 (2002).

Geiss, K.T., Frazier, J.M., and Dodd, D.E., "Toxicity Screening of Halogenated Aliphatics Using a Novel *In Vitro* Volatile Chemical Exposure System," 2002, in Gann, R.G., Burgess, S.R., Whisner, K.C., and Reneke, P.A., eds., *Papers from 1991-2006 Halon Options Technical Working Conferences (HOTWC)*, CD-ROM, NIST SP 984-4, National Institute of Standards and Technology, Gaithersburg, MD, (2006).

Mather, J.D., and Tapscott, R.E., "Tropodegradable Bromocarbon Extinguishants – Compound Selection and Testing Issues," 2002, in Gann, R.G., Burgess, S.R., Whisner, K.C., and Reneke, P.A., eds., *Papers*

from 1991-2006 Halon Options Technical Working Conferences (HOTWC), CD-ROM, NIST SP 984-4, National Institute of Standards and Technology, Gaithersburg, MD, (2006).

Mather, J.D., and Tapscott, R.E., "Thermodynamics of Metal Agent Fire Extinguishment," 2002, in Gann, R.G., Burgess, S.R., Whisner, K.C., and Reneke, P.A., eds., *Papers from 1991-2006 Halon Options Technical Working Conferences (HOTWC)*, CD-ROM, NIST SP 984-4, National Institute of Standards and Technology, Gaithersburg, MD, (2006).

Tapscott, R.E., Shreeve, J.M., and Mather, J.D., "Fluoroalkyl Phosphorus Fire Extinguishing Agents," 2002, in Gann, R.G., Burgess, S.R., Whisner, K.C., and Reneke, P.A., eds., *Papers from 1991-2006 Halon Options Technical Working Conferences (HOTWC)*, CD-ROM, NIST SP 984-4, National Institute of Standards and Technology, Gaithersburg, MD, (2006).

Huie, R.E., Orkin, V.L., Louis, F., Kozlov, S.N., and Kurylo, M.J., "Effect of Bromine Substitution on the Lifetimes and Ozone Depletion Potentials of Organic Compounds," 2002, in Gann, R.G., Burgess, S.R., Whisner, K.C., and Reneke, P.A., eds., *Papers from 1991-2006 Halon Options Technical Working Conferences (HOTWC)*, CD-ROM, NIST SP 984-4, National Institute of Standards and Technology, Gaithersburg, MD, (2006).

Nogueira, M.F.M., and Fisher, E.M., "Effects of Dimethyl Methylphosphonate on Premixed Methane Flames," *Combustion and Flame* **132**, 352-363 (2002).

Nogueira, M.F.M., *Effects of Dimethyl Methylphosphonate on Premixed Methane Flames*, Ph.D. Thesis, Cornell University, Ithaca, NY, (2001).

Lifke, J., Martinez, A., Tapscott, R.E., and Mather, J.D., *Tropodegradable Bromocarbon Extinguishants, Final Report To the Strategic Environmental Research and Development Program*, Report 99/8/33350, New Mexico Engineering Research Institute, Albuquerque NM, 2001.

Tapscott, R.E., Sheinson, R.S., Babushok, V., Nyden, M.R., Gann, R.G., *Alternative Fire Suppressant Chemicals: A Research Review with Recommendations*, NIST Technical Note 1443, December, 2001.

Williams, B.A., "Sensitivity of Calculated Extinction Strain Rate to Molecular Transport Formulation in Nonpremixed Counterflow Flames," *Combustion and Flame* **124**, 330-333 (2001).

MacDonald, M.A., Gouldin, F.C., and Fisher, E.M., "Temperature Dependence of Phosphorus-based Flame Inhibition," *Combustion and Flame* **125**, 668-683 (2001).

Linteris, G.T., Rumminger, M.D., Babushok, V.I., and Tsang, W., "Flame Inhibition by Ferrocene, and by Blends of Inert and Catalytic Agents," *Proceedings of the Combustion Institute* **28**, 2965-2972 (2000).

Jayaweera, T.M., Fisher, E.M., and Flaming, J.W., "Flame Suppression by Sprays of Aqueous Solutions Containing Phosphorus," *Proceedings of the 2nd Joint Meeting of the U.S. Sections of the Combustion Institute*, Oakland, CA, 2001.

Rumminger, M.D. and Linteris, G.T., "The Role of Particles in Counterflow Diffusion Flames Inhibited by Iron Pentacarbonyl," *Proceedings of the 2nd Joint Meeting of the United States Sections of the Combustion Institute*, Oakland, CA, March 2001.

Linteris, G.T., "Suppression of Cup-Burner Diffusion Flames by Super-Effective Chemical Inhibitors and Inert Compounds," 2001, in Gann, R.G., Burgess, S.R., Whisner, K.C., and Reneke, P.A., eds., *Papers from 1991-2006 Halon Options Technical Working Conferences (HOTWC)*, CD-ROM, NIST SP 984-4, National Institute of Standards and Technology, Gaithersburg, MD, (2006).

Linteris, G. T., Knyazev, V., and Babushok, V., "Premixed Flame Inhibition by Manganese and Tin Compounds," 2001, in Gann, R.G., Burgess, S.R., Whisner, K.C., and Reneke, P.A., eds., *Papers from 1991-2006 Halon Options Technical Working Conferences (HOTWC)*, CD-ROM, NIST SP 984-4, National Institute of Standards and Technology, Gaithersburg, MD, (2006).

Skaggs, R.R., McNesby, K.L., Daniel, R.G., Homan, B., and Miziolek, A.W., "Spectroscopic Studies of Low Pressure Opposed Flow Methane/Air Flames Inhibited By  $\text{Fe}(\text{CO})_5$ ,  $\text{CF}_3\text{Br}$ , or  $\text{N}_2$ ," *Combustion Science and Technology* **162**, 1, (2001).

Williams, B.A. and Fleming, J.W., "Is  $\text{CF}_3\text{Br}$  Representative Of Efficient Fire Suppressants?," *Proceedings of the 2<sup>nd</sup> Joint Meeting of the U.S. Sections of the Combustion Institute*, Oakland CA, paper 221, (2001).

Mather, J. D. and Tapscott, R. E., "Tropodegradable Bromocarbon Extinguishants – II and Fluoroalkyl Phosphorus Compounds- Research Update," 2001, in Gann, R.G., Burgess, S.R., Whisner, K.C., and Reneke, P.A., eds., *Papers from 1991-2006 Halon Options Technical Working Conferences (HOTWC)*, CD-ROM, NIST SP 984-4, National Institute of Standards and Technology, Gaithersburg, MD, (2006).

Linteris, G.T., Rumminger, M.D., and Babushok, V.I., "Premixed Carbon Monoxide-Nitrous Oxide-Hydrogen Flames: Measured and Calculated Burning Velocities with and without  $\text{Fe}(\text{CO})_5$ ," *Combustion and Flame* **122**, 58-75 (2000).

Rumminger, M.D., and Linteris, G.T., "Inhibition of Premixed Carbon Monoxide-Hydrogen-Oxygen-Nitrogen Flames by Iron Pentacarbonyl," *Combustion and Flame* **120**, 451-464 (2000).

Rumminger, M.D. and Linteris, G.T., "The Role of Particles in the Inhibition of Premixed Flames by Iron Pentacarbonyl," *Combustion and Flame* **123**, 82-94 (2000).

Linteris, G.T. and Rumminger, M.D., "Flame Inhibition by Ferrocene, Alone and with  $\text{CO}_2$  and  $\text{CF}_3\text{H}$ ," 2000, in Gann, R.G., Burgess, S.R., Whisner, K.C., and Reneke, P.A., eds., *Papers from 1991-2006 Halon Options Technical Working Conferences (HOTWC)*, CD-ROM, NIST SP 984-4, National Institute of Standards and Technology, Gaithersburg, MD, (2006).

Babushok, V., and Tsang, W., "Inhibitor Rankings for Alkane Combustion," *Combustion and Flame* **123**, 488-506 (2000).

Williams, B.A. and Fleming, J.W., "On the Suitability of  $\text{CF}_3\text{Br}$  as a Benchmark for Replacement Fire Suppressants," 2001, in Gann, R.G., Burgess, S.R., Whisner, K.C., and Reneke, P.A., eds., *Papers from 1991-2006 Halon Options Technical Working Conferences (HOTWC)*, CD-ROM, NIST SP 984-4, National Institute of Standards and Technology, Gaithersburg, MD, (2006).

Brabson, G.D., Garcia, M.M., Heinonen, E.W., Juarez, G., Mather, J.D., and Tapscott, R.E., *Main Group Compounds as Extinguishants*, New Mexico Engineering Research Institute Report No. 98/8/33380, U.S. Department of Defense, Strategic Environmental Research and Development Program, (2001).

Pits, W.M., Yang, J.C., Bryant, R.A., Blevins, L.G., and Huber, M., *Characteristics and Identification of Super-effective Thermal Fire-extinguishing Agents, Final Report to the Strategic Environmental Research and Development Program*, NIST Technical Note 1440, National Institute of Standards and Technology, Gaithersburg, MD, 2001.

Pitts, W.M., Bryant, R.A., and Yang, J.C., "Thermal Agent Extinguishment of Two Types of Diffusion Flames," *Proceedings of the 2<sup>nd</sup> Joint Meeting of the United States Sections of The Combustion Institute*, Oakland, CA, (2001).

Pitts, W.M., Yang, J.C., and Bryant, R.A., "Fuel Effects on the Extinguishment of Laminar Diffusion Flames by Thermal Agents," 2001, in Gann, R.G., Burgess, S.R., Whisner, K.C., and Reneke, P.A., eds., *Papers from 1991-2006 Halon Options Technical Working Conferences (HOTWC)*, CD-ROM, NIST SP 984-4, National Institute of Standards and Technology, Gaithersburg, MD, (2006).

Pitts, W.M., and Blevins, L.G., "An Investigation of Extinguishment by Thermal Agents Using Detailed Chemical Kinetic Modeling of Opposed Jet Diffusion Flames," *Proceedings of the Fifteenth Meeting of the U.S.-Japan Panel on Fire Research and Safety*, NISTIR 6588, pp. 242-249, National Institute of Standards and Technology, Gaithersburg, MD (2000).

Yang, J.C., Bryant, R.A., Huber, M.L., and Pitts, W.M., "Experimental Investigation of Extinguishment of Laminar Diffusion Flames by Thermal Agents," 2000, in Gann, R.G., Burgess, S.R., Whisner, K.C., and Reneke, P.A., eds., *Papers from 1991-2006 Halon Options Technical Working Conferences (HOTWC)*, CD-ROM, NIST SP 984-4, National Institute of Standards and Technology, Gaithersburg, MD, (2006).

Tapscott, R.E., and Mather, J.D., "Tropodegradable Fluorocarbon Replacements for Ozone Depleting and Global Warming Chemicals," *Journal of Fluorine Chemistry* **101**, 209-213 (2000).

McNesby, K.L., "Flame and Temperature Measurement Using Vibrational Spectroscopy," ARL-TR-2378, Army Research Laboratory, Aberdeen MD (2001).

Skaggs, R.R., Daniel, R.G., Miziolek, A.W., McNesby, K.L., Babushok, V.I., Tsang, W., and Smooke, M.D., "Spectroscopic Studies of Inhibited Opposed Flow Propane/Air Flames," ARL-TR-2388, Army Research Laboratory, Aberdeen MD (2001).

McNesby, K.L., "Flame and Temperature Measurement Using Vibrational Spectroscopy," in *Encyclopedia of Spectroscopy and Spectrometry*, Academic Press, London, pp. 548-559 (2000).

Linteris, G.T., Rumminger, M.D., and Babushok, V.I., "Premixed Carbon monoxide-Nitrous Oxide-Hydrogen Flames: Measured and Calculated Burning velocities with and without  $\text{Fe}(\text{CO})_5$ ," *Combustion and Flame* **122**, 58, (2000).

Williams, B.A., L'esperance, D.M., and Fleming, J.W., "Intermediate Species profiles in Low-pressure Methane/oxygen Flames Inhibited by 2-Heptafluoropropane: Comparison of Experimental Data with Kinetic modeling," *Combustion and Flame* **120**, 160, (2000).

Zegers, E.J.P., Williams, B.A., Fisher, E.M., Fleming, J.W., and Sheinson, R.S., "Suppression of Nonpremixed Flames by Fluorinated Ethanes and Propanes," *Combustion and Flame* **121(3)**, 471-487 (2000).

Skaggs, R.R., Daniel, R.G., Miziolek, A.W., McNesby, K.L., Babushok, V.I., Tsang, W., and Smooke, M.D., "Spectroscopic Studies Of Inhibited Opposed Flow Propane/Air Flames," 1999, in Gann, R.G., Burgess, S.R., Whisner, K.C., and Reneke, P.A., eds., *Papers from 1991-2006 Halon Options Technical Working Conferences (HOTWC)*, CD-ROM, NIST SP 984-4, National Institute of Standards and Technology, Gaithersburg, MD, (2006).

Skaggs, R.R., Daniel, R.G., Miziolek, A.W., McNesby, K.L., "Spectroscopic Studies Of Inhibited Opposed Flow Propane/Air Flames," *Proceedings of the 1<sup>st</sup> Joint Meeting of the United States Sections of the Combustion Institute*, pp. 575-578, (1999).

Rumminger, M.D., Reinelt, D., Babushok, V., and Linteris, G.T., "Numerical Study of the Inhibition of Premixed and Diffusion Flames by Iron Pentacarbonyl," *Combustion and Flame* **116**, 207-219 (1999).

Rumminger, M.D., and Linteris, G.T., "The Role of Particles in Flame Inhibition by Iron Pentacarbonyl," 1999, 2005, in Gann, R.G., Burgess, S.R., Whisner, K.C., and Reneke, P.A., eds., *Papers from 1991-2006 Halon Options Technical Working Conferences (HOTWC)*, CD-ROM, NIST SP 984-4, National Institute of Standards and Technology, Gaithersburg, MD, (2006).

Rumminger, M.D., and Linteris, G.T., "Measurements of Particle Formation in Flames Inhibited by Iron Pentacarbonyl," *Proceedings of the 1<sup>st</sup> Joint Meeting of the United States Sections of the Combustion Institute*, Washington, DC, (March, 1999).

Linteris, G.T., and Rumminger, M.D., "Flame Inhibition by Ferrocene, Carbon Dioxide, and Trifluoromethane Blends: Synergistic and Antagonistic Effects," *Proceedings of the 1999 Fall Technical Meeting, Eastern States Section of the Combustion Institute*, (1999).

Rumminger, M.D., and Linteris, G.T., "Numerical Modeling of Counterflow Diffusion Flames Inhibited by Iron Pentacarbonyl," *Proceedings of the Sixth International Symposium on Fire Safety Science*, Poitiers, France, pp. 289-300 (1999).

Davis, M.P., Fleming, J.W., Williams, B.A., and Ladouceur, H.D., "Flow Field Considerations for Counter Flow Burners," *Proceedings of the Fall Technical Meeting of the Eastern States Section of the Combustion Institute*, Raleigh NC, pp. 200-203, (1999).

Fleming, J.W., "Chemical Fire Suppressants: How Can We Replace Halon?" *Proceedings of the Fall Technical Meeting of the Eastern States Section of the Combustion Institute*, Raleigh NC, pp. 16-23 (1999).

Pitts, W.M. and Blevins, L.G., "An Investigation of Extinguishment by Thermal Agents Using Detailed Chemical Modeling of Opposed-Flow Diffusion Flames," 1999, in Gann, R.G., Burgess, S.R., Whisner, K.C., and Reneke, P.A., eds., *Papers from 1991-2006 Halon Options Technical Working Conferences (HOTWC)*, CD-ROM, NIST SP 984-4, National Institute of Standards and Technology, Gaithersburg, MD, (2006).

Pitts, W.M., Yang, J.C., Huber, M.L., and Blevins, L.G., *Characterization and Identification of Super-Effective Thermal Fire Extinguishing Agents - First Annual Report*, NISTIR 6414, National Institute of Standards and Technology, Gaithersburg, MD, (1999).

Tapscott, R.E., and Mather, J.D., "Tropodegradable Fluorocarbon Replacements for Ozone Depleting and Global Warming Chemicals," *Proceedings of the International Conference on Fluorine Chemistry '99*, Tokyo, (1999).

Tapscott, R.E., and Mather, J.D., "Research on Main Group Element Compounds and Tropodegradable Halocarbons as Halon Substitutes," *Proceedings, Fire Suppression and Detection Research Application Symposium*, Orlando, Fire Protection Research Foundation, Quincy, MA, (1999).

MacDonald, M.A., Jayaweera, T.M., Fisher, E.M., and Gouldin, F.C., "Inhibition of Non-Premixed Flames by Phosphorus-containing Compounds," *Combustion and Flame* **116**, 166-176 (1999).

MacDonald, M.A., Jayaweera, T.M., Fisher, E.M., and Gouldin, F.C., "Variation of Chemically Active and Inert Flame-Suppression Effectiveness with Stoichiometric Mixture Fraction," *Proceedings of the Combustion Institute* **27**, 2749-2756 (1998).

Babushok, V.I. and Tsang, W., "Influence of Phosphorus-containing Additives on Methane Flames," *Proceedings of the 1<sup>st</sup> Joint Meeting of the United States Sections of the Combustion Institute*, Washington, DC, pp. 587-590, (1999).

Mather, J.D. and Tapscott, R.E., "Tropodegradable Halocarbons and Main Group Element Compounds," 1999, in Gann, R.G., Burgess, S.R., Whisner, K.C., and Reneke, P.A., eds., *Papers from 1991-2006 Halon Options Technical Working Conferences (HOTWC)*, CD-ROM, NIST SP 984-4, National Institute of Standards and Technology, Gaithersburg, MD, (2006).

Fisher, E.M., Gillette, J.W., Gouldin, F.C., Jayaweera, T.M., and MacDonald, M.A., *Chemical Flame Inhibition by Phosphorus-containing Compounds, Final Report To the Strategic Environmental Research and Development Program*, Cornell University, Ithaca NY, 1999.

L'esperance, D., Williams, B.A., and Fleming, J.W., "Intermediate Species Profiles in Low Pressure Premixed Flames Inhibited by Fluoromethanes," *Combustion and Flame* **117**, 709, (1999).

Fisher, E.M., Gouldin, F.C., Jayaweera, T.M., and MacDonald, M.A., *Flame Inhibition by Phosphorus-containing Compounds, Final Report To the Strategic Environmental Research and Development Program*, Cornell University, Ithaca NY, 1998.

Babushok, V.I., Tsang, W., Linteris, G.T., and Reinelt, D., "Chemical Limits to Flame Inhibition," *Combustion and Flame* **115**, 551-560 (1998).

Rumminger, M.D., Reinelt, D., Babushok, V., and Linteris, G.T., "Inhibition of Flames by Iron Pentacarbonyl," 1998, in Gann, R.G., Burgess, S.R., Whisner, K.C., and Reneke, P.A., eds., *Papers from 1991-2006 Halon Options Technical Working Conferences (HOTWC)*, CD-ROM, NIST SP 984-4, National Institute of Standards and Technology, Gaithersburg, MD, (2006).

Noto, T., Babushok, V.I., Hamins, A., and Tsang, W., "Inhibition Effectiveness of Halogenated Compounds," *Combustion and Flame* **112**, 147-160 (1998).

Skaggs, R.R., Daniel, R.G., Miziolek, A.W., McNesby, K.L., "Spectroscopic Studies of Inhibited Opposed Flow Propane/Air Flames," *Proceedings of the 1998 JANNAF Combustion Meeting*, (1998).

Daniel, R.G., Skaggs, R.R., Homan, B.E., Miziolek, A.W., and McNesby, K.L., "Laser Induced Fluorescence in Inhibited Counterflow Diffusion Flames," *Laser Applications to Chemical and Environmental Analysis*, (1998).

Skaggs, R.R., McNesby, K.L., Daniel, R.G., Homan, B., Lancaster, E., and Miziolek, A.W., "Mechanisms of Fire Suppression by Superagents," Paper No. 1053, *The Pittsburgh Conference*, (1998).

Linteris, G.T., Burgess, D.R., Babushok, V., Zachariah, M., Tsang, W., and Westmoreland, P., "Inhibition of premixed Methane-air Flames by Fluoroethanes and Fluoropropanes," *Combustion and Flame* **113**, 164, (1998).

Tapscott, R.E., Heinonen, E.W., and Mather, J.D., *Identification and Proof Testing of New Total Flooding Agents: Toxicity and Global Environmental Assessment, Final Report To the Strategic Environmental Research and Development Program*, New Mexico Engineering Research Institute Report 97/29/33010, (1998).

Tapscott, R.E., Mather, J.D., Heinonen, E.W., Lifke, J.L., and Moore, T.A., *Identification and Proof Testing of New Total Flooding Agents: Combustion Suppression Chemistry and Cup-burner Testing, Final Report To the Strategic Environmental Research and Development Program*, New Mexico Engineering Research Institute Report 97/6/33010, (1998).

Skaggs, R.R., Daniel, R.G., Miziolek, A.W., and McNesby, K.L., "Spectroscopic Studies Of Inhibited Opposed Flow Propane/Air Flames," *Proceedings of the 1998 JANNAF Combustion Meeting*, (1998).

Fisher, E.M., Williams, B.A., and Fleming, J.W., "Determination of the Strain in Counterflow Diffusion Flames From Flow Conditions," *Proceedings of the Eastern States Section of the Combustion Institute*, pp. 191-194, (1997).

MacDonald, M.A., Jayaweera, T.M., Fisher, E.M., and Gouldin, F.C., "Inhibition of Non-Premixed Flames by Dimethyl Methylphosphonate," *Proceedings of the Central States Section of the Combustion Institute*, (1997).

Jayaweera, T.M., MacDonald, M.A., Fisher, E.M., and Gouldin, F.C., "A Novel Method for Evaluating the Effectiveness of Low Volatility Flame Inhibitors with an Opposed-Jet Burner," *Proceedings of the Eastern States Section of the Combustion Institute*, (1997).

MacDonald, M.A., Jayaweera, T.M., Fisher, E.M., and Gouldin, F.C., "Inhibited Counterflow Non-Premixed Flames with Variable Stoichiometric Mixture Fractions," *Proceedings of the Eastern States Section of the Combustion Institute*, (1997).

Daniel, R.G., McNesby, K.L., Skaggs, R.R., Saguear, P., and Miziolek, A.W., "Spectroscopy of Inhibited Counterflow Diffusion Flames," *Proceedings of the 1997 JANNAF Combustion Meeting*, (1997).

### C.3 SUPPRESSANT SCREENING TESTS

Li, Y., Patten, G., Youn, D., and Wuebbles, D.J., "Potential Impacts of CF<sub>3</sub>I on Ozone as a Replacement for CF<sub>3</sub>Br in Aircraft Applications," *Atmospheric Chemistry and Physics* **6**, 4559-4568, (2006).

Wuebbles, D.J., and Li, Y., "Potential Impacts of CF<sub>3</sub>I on Ozone as a Replacement for CF<sub>3</sub>Br in Aircraft Applications," 2005, in Gann, R.G., Burgess, S.R., Whisner, K.C., and Reneke, P.A., eds., *Papers from 1991-2006 Halon Options Technical Working Conferences (HOTWC)*, CD-ROM, NIST SP 984-4, National Institute of Standards and Technology, Gaithersburg, MD, (2006).

Kozlov, S.N., Orkin, V.I., Huie, R.E., and Kurylo, M.J., "OH Reactivity and UV Spectra of Propane, n-Propyl Bromide, and isopropyl Bromide," *Journal of Physical Chemistry A* **107**, 1333-1338, (2003).

Orkin, V.I., Louis, F., Huie, R.E., and Kurylo, M.J., "Photochemistry of Bromine-Containing Fluorinated Alkenes: Reactivity toward OH and UV Spectra," *Journal of Physical Chemistry A* **106**, 10195-10199, (2002).

Huie, R.E., Orkin, V.L., Louis, F., Kozlov, S.N., and Kurylo, M.J., "Effect of Bromine Substitution on the Lifetimes and Ozone Depletion Potentials of Organic Compounds," 2002, in Gann, R.G., Burgess, S.R., Whisner, K.C., and Reneke, P.A., eds., *Papers from 1991-2006 Halon Options Technical Working Conferences (HOTWC)*, CD-ROM, NIST SP 984-4, National Institute of Standards and Technology, Gaithersburg, MD, (2006).

Vinegar, A., "PBPK Modeling of Canine Inhalation Exposures to Halogenated Hydrocarbons," *Toxicological Sciences* **60**, 20-27 (2001).

Vinegar, A., "Modeling Cardiac Sensitization Potential of Humans Exposed to Halon 1301 or Halon 1211 aboard Aircraft," *Aviation, Space, and Environmental Medicine* **72**, 928-936 (2001).

Yang, J.C., Donnelly, M.K., Prive, N.C., and Grosshandler, W.L., "An Apparatus for Screening Fire Suppression Efficiency of Dispersed Liquid Agents," *Fire Safety Journal* **36**, 55-72 (2001).

Grosshandler, W., Hamins, A., Yang, J., McGrattan, K., and Presser, C., "Transient Application, Recirculating Pool Fire, Agent Effectiveness Screen: Final Report," 2001, in Gann, R.G., Burgess, S.R., Whisner, K.C., and Reneke, P.A., eds., *Papers from 1991-2006 Halon Options Technical Working Conferences (HOTWC)*, CD-ROM, NIST SP 984-4, National Institute of Standards and Technology, Gaithersburg, MD, (2006).

Jomaas, G., Roberts, B.T., DuBois, J., and Torero, J.L., *A Study of the Mechanisms Leading to Re-ignition in a 'Worst Case' Fire Scenario*, Final Report, Cooperative Agreement No. 70NANB8H0043, Department of Fire Protection Engineering, University of Maryland College Park, MD20742-3031 (2000); also NIST GCR 01-806, National Institute of Standards and Technology, Gaithersburg, MD (2001).

Grosshandler, W., Hamins, A., McGrattan, K., and Presser, C., *Transient Application, Recirculating Pool Fire, Agent Effectiveness Screen: Final Report to the Strategic Environmental Research and Development Program*, NISTIR 6733, National Institute of Standards and Technology, Gaithersburg, MD, (2001).

Grosshandler, W.L., Hamins, A., McGrattan, K.B., Charagundla, R., and Presser, C., "Suppression of a Non-Premixed Flame Behind a Step," *Proceedings of the Combustion Institute* **28**, 2957-2964 (2001).

Louis, F., Gonzalez, C., Huie, R. E., and Kurylo, M. J., "An *ab Initio* Study of the Kinetics of the Reactions of Halomethanes with the Hydroxyl Radical. Part 3. Reactivity Trends and Kinetics Parameter Predictions for the Potential Halon Replacements CH<sub>2</sub>FBr, CH<sub>2</sub>Br<sub>2</sub>, CHFClBr, CHCl<sub>2</sub>Br, and CHClBr<sub>2</sub>," *Journal of Physical Chemistry A* **105**, 1599-1604 (2001).

Yang, J.C., Donnelly, M.K., Privé, N., and Grosshandler, W.L., *Dispersed Liquid Agent Fire Suppression Screen, Final Report To the Strategic Environmental Research and Development Program*, National Institute of Standards and Technology, Gaithersburg MD, 2000.

Louis, F., Gonzalez, C., Huie, R. E., and Kurylo, M. J., "An *ab Initio* Study of the Kinetics of the Reactions of Halomethanes with the Hydroxyl Radical. Part 2: A Comparison between Theoretical and Experimental Values of the Kinetic Parameters for 12 Partially Halogenated Substituted Methanes," *Journal of Physical Chemistry A* **104**, 8773-8778 (2000).

Louis, F., Gonzalez, C., Huie, R. E., and Kurylo, M. J., "An *ab initio* Study of the Reaction of Halomethanes with the Hydroxyl Radical. Part 1: CH<sub>2</sub>Br<sub>2</sub>, *Journal of Physical Chemistry A* **104**, 2931-2938 (2000).

Huie, R.E., Louis, F., Gonzalez, C.A., and Kurylo, M.J., "An *Ab initio*-Based Screening Tool for the Atmospheric Lifetimes of Halon Replacements," 2000, in Gann, R.G., Burgess, S.R., Whisner, K.C., and Reneke, P.A., eds., *Papers from 1991-2006 Halon Options Technical Working Conferences (HOTWC)*, CD-ROM, NIST SP 984-4, National Institute of Standards and Technology, Gaithersburg, MD, (2006).

Grosshandler, W.L., Hamins, A., Charagundla, R., and Presser, C., "Suppression Effectiveness Screening for Impulsively Discharged Agents," 2000, in Gann, R.G., Burgess, S.R., Whisner, K.C., and Reneke, P.A., eds., *Papers from 1991-2006 Halon Options Technical Working Conferences (HOTWC)*, CD-ROM, NIST SP 984-4, National Institute of Standards and Technology, Gaithersburg, MD, (2006).

Vinegar, A., Jepson, G.W., Cisneros, M., Rubenstein, R., and Brock, W.J., "Setting Safe Acute Exposure Limits for Halon Replacement Chemicals Using Physiologically Based Pharmacokinetic Modeling," *Inhalation Toxicology* **12**, 751-763 (2000).

Vinegar, A., and Jepson, G., "Toxicological Assessment of Human Health Consequences Associated with Inhalation of Halon Replacement Chemicals; Section I: Physiologically-based Modeling of Halon Replacements for Human Safety Evaluations, Final Report to the Strategic Environmental Research and Development Program, Air Force Research Laboratory, Wright Patterson Air Force Base, OH, (2000).

Dodd, D.E., Jepson, G.W., and Macko, Jr., J.A., "Toxicological Assessment of Human Health Consequences Associated with Inhalation of Halon Replacement Chemicals; Section II: Human Health Safety Evaluation of Halon Replacement Candidates, Final Report to the Strategic Environmental Research and Development Program, Air Force Research Laboratory, Wright Patterson Air Force Base, OH, (2000).

Yang, J.C., Donnelly, M.K., Prive, N.C., and Grosshandler, W.L., *Dispersed Liquid Agent Fire Suppression Screen Apparatus*, NISTIR 6319, National Institute of Standards and Technology, Gaithersburg, MD, (1999).

Orkin, V.L., Villenave, E., Huie, R.E., and Kurylo, M.J., 'Atmospheric Lifetimes and Global Warming Potentials of Hydrofluoroethers: Reactivity Toward OH, UV Spectra, and IR Absorption Cross Sections,' *Journal of Physical Chemistry A* **103**, 9770-9779 (1999).

Yang, J.C., Donnelly, M.K., Prive, N.C., and Grosshandler, W.L., "Fire Suppression Efficiency Screening Using a Counterflow Cylindrical Burner," *Proceedings of the 5<sup>th</sup> ASME/JSME Joint Thermal Engineering Conference*, San Diego, CA, (1999).

Nyden, M.R. and Skaggs, S.R., *Screening Methods for Agent Compatibility with People, Materials and the Environment*, NISTIR 6323, National Institute of Standards and Technology, Gaithersburg MD (1999).

Yang, J.C., Donnelly, M.K., Prive, N.C., and Grosshandler, W.L., "On the Design of an Apparatus for Screening Liquid Fire Suppressants," *Proceedings of the 8<sup>th</sup> International Fire Science and Engineering Conference*, Edinburgh, Scotland, (1999).

Grosshandler, W.L., Charagundla, R., and Presser, C., "Suppressant Performance Evaluation in a Baffle-Stabilized Pool Fire," 1999, in Gann, R.G., Burgess, S.R., Whisner, K.C., and Reneke, P.A., eds., *Papers from 1991-2006 Halon Options Technical Working Conferences (HOTWC)*, CD-ROM, NIST SP 984-4, National Institute of Standards and Technology, Gaithersburg, MD, (2006).

Yang, J.C., Prive, N.C., Donnelly, M.K., and Grosshandler, W.L., "Recent Results from the Dispersed Liquid Agent Fire Suppression Screen," 1999, in Gann, R.G., Burgess, S.R., Whisner, K.C., and Reneke, P.A., eds., *Papers from 1991-2006 Halon Options Technical Working Conferences (HOTWC)*, CD-ROM, NIST SP 984-4, National Institute of Standards and Technology, Gaithersburg, MD, (2006).

Yang, J.C., Donnelly, M.K., Prive, N.C., and Grosshandler, W.L., "An Apparatus for Evaluating Liquid Fire Suppressants," 1998, in Gann, R.G., Burgess, S.R., Whisner, K.C., and Reneke, P.A., eds., *Papers from 1991-2006 Halon Options Technical Working Conferences (HOTWC)*, CD-ROM, NIST SP 984-4, National Institute of Standards and Technology, Gaithersburg, MD, (2006).

Reed, M.D., Fleming, J.W., Williams, B.A., and Sheinson, R.S., "Laboratory Evaluation of Bicarbonate Powders as Fire Suppressants," *Proceedings of the International Conference on Ozone Protection Technologies*, (1997).

Reed, M.D., Williams, B.A., Sheinson, R.S. and Fleming, J.W., "Behavior of Bicarbonate Powders in Counterflow Diffusion Flames," *Proceedings of the Eastern States Section of the Combustion Institute*, (1997).

Grosshandler, W.L., Yang, J.C., and Cleary, T.G., "Screening Methods for New Fire Suppression Technologies," *Proceedings of the 1996 International Conference on Ozone Protection Technologies*, 643-650, (1996).

#### **C.4 NEW AND IMPROVED AEROSOL SUPPRESSANTS**

Chelliah, H.K., "Flame Inhibition/suppression by Water Mist: droplet Size/surface Area. Flame Structure, and Flow Residence Time Effects," *Proceedings of the Combustion Institute* **31**, 2711-2719, (2007).

Fleming, J.W., and Sheinson, R.S., "A Next Generation Fire Suppression Technology Program Summary on the Properties of Aerosols," 2006, in Gann, R.G., Burgess, S.R., Whisner, K.C., and Reneke, P.A., eds., *Papers from 1991-2006 Halon Options Technical Working Conferences (HOTWC)*, CD-ROM, NIST Special Publication 984-4, National Institute of Standards and Technology, Gaithersburg, MD, 2006.

Sheinson, R.S., and Fleming, J.W., *Aerosols, Final Report To the Strategic Environmental Research and Development Program*, Naval Research Laboratory, Washington, DC, 2003.

Chelliah, H.K., Lazzarini, A.K., Wanigarathne, P.C., and Linteris, G.T., "Inhibition of Premixed and Non-premixed Flames with Fine Droplets of Water and Solutions," *Proceedings of the Combustion Institute* **29**, 369-376, (2002).

Fleming, J.W., Williams, B.A., and Sheinson, R.S., "Suppression Effectiveness of Aerosols: The Effect of Size and Flame Type," 2002, in Gann, R.G., Burgess, S.R., Whisner, K.C., and Reneke, P.A., eds., *Papers from 1991-2006 Halon Options Technical Working Conferences (HOTWC)*, CD-ROM, NIST SP 984-4, National Institute of Standards and Technology, Gaithersburg, MD, (2006).

Chelliah, H.K., Lazzarini, A.K., Wanigarathne, P.C., and Linteris, G.T., "Comparison of the Fire Suppression Effectiveness of Sodium Bicarbonate Particles and Fine-water Droplets in Non-premixed and Premixed Flames," 2001, in Gann, R.G., Burgess, S.R., Whisner, K.C., and Reneke, P.A., eds., *Papers from 1991-2006 Halon Options Technical Working Conferences (HOTWC)*, CD-ROM, NIST SP 984-4, National Institute of Standards and Technology, Gaithersburg, MD, (2006).

Lazzarini, A.M., Krauss, R.H., Chelliah, H.K., and Linteris, G.T., "Extinction Conditions of Non-premixed Flames with Fine Droplets of Water and Water-NaOH Solutions," *Proceedings of the Combustion Institute* **28**, 2939-2945 (2001).

Linteris, G.T., and Chelliah, H.K., *Powder-Matrix Systems for Safer Handling and Storage of Suppression Agents (4A/1 Final Report)*, NISTIR 6766, National Institute of Standards and Technology, Gaithersburg, MD (2001).

Zegers, E.J.P., Fuss, P., Fleming, J.W., Williams, B.A., Maranghides, A., and Sheinson, R.S., "Better Use of Water for Fire Suppression," 2001 NRL Review, pp. 102-104 (2001).

Sivathanu, Y., Oke, H.P., Fu, C., Wang, T., Sojka, P.E., *Droplet Interaction with Hot Surfaces, Final Report to the Strategic Environmental Research and Development Program*, En'Urga, Inc, West Lafayette IN, (2000).

Yang, J.C., *Technical Support for the Study of Droplet Interactions with Hot Surfaces, Final Report to the Strategic Environmental Research and Development Program*, National Institute of Standards and Technology, Gaithersburg MD, (2000).

Lyon, R., *Development of a Self-Atomizing Form of Water, Final Report to the Strategic Environmental Research and Development Program*, EER, Inc., NJ, (1998).

Fuss, S.P., Dye, D.J., Williams, B.A., and Fleming, J.W., "Inhibition of Premixed Methane-Air Flames by Submicron Water Mists," 2000, in Gann, R.G., Burgess, S.R., Whisner, K.C., and Reneke, P.A., eds., *Papers from 1991-2006 Halon Options Technical Working Conferences (HOTWC)*, CD-ROM, NIST SP 984-4, National Institute of Standards and Technology, Gaithersburg, MD, (2006).

Zegers, E.J.P., Williams, B.A., Sheinson, R.S., and Fleming, J.W., "Water Mist Suppression of Methane/Air and Propane/Air Counterflow Flames," 2000, in Gann, R.G., Burgess, S.R., Whisner, K.C., and Reneke, P.A., eds., *Papers from 1991-2006 Halon Options Technical Working Conferences (HOTWC)*, CD-ROM, NIST SP 984-4, National Institute of Standards and Technology, Gaithersburg, MD, (2006).

Zegers, E.J.P., Williams, B.A., Sheinson, R.S., and Fleming, J.W., "Dynamics and Suppression Effectiveness of Monodisperse Water Droplets in Non-Premixed Counterflow Flames," *Proceedings of the Combustion Institute* **28**, 2931-2938 (2000).

Lazzarini, A. K., Krauss, R. H., Chelliah, H. K., and Linteris, G. T., "Extinction of Counterflow Diffusion Flames with Fine-Water Droplets," 2000, in Gann, R.G., Burgess, S.R., Whisner, K.C., and Reneke, P.A., eds., *Papers from 1991-2006 Halon Options Technical Working Conferences (HOTWC)*, CD-ROM, NIST SP 984-4, National Institute of Standards and Technology, Gaithersburg, MD, (2006).

Wanigarathne, P.A., Krauss, R. H., Chelliah, H. K., and Davis, R.J., "Fire Suppression by Particulates Containing Metallic Compounds," 2000, in Gann, R.G., Burgess, S.R., Whisner, K.C., and Reneke, P.A., eds., *Papers from 1991-2006 Halon Options Technical Working Conferences (HOTWC)*, CD-ROM, NIST SP 984-4, National Institute of Standards and Technology, Gaithersburg, MD, (2006).

Fuss, S.P., Dye, D.J., Williams, B.A., and Fleming, J.W., "Inhibition of Premixed Methane-Air Flames by Water Mist," *Proceedings of the Fall Technical Meeting of the Eastern States Section of the Combustion Institute*, Raleigh NC, pp. 105-108, (1999).

Zegers, E.J.P., Williams, B.A., Sheinson, R.S., and Fleming, J.W., "Water Mist Suppression of Non-Premixed Counterflow Flames," *Proceedings of the Fall Technical Meeting of the Eastern States Section of the Combustion Institute*, Raleigh NC, pp. 109-112, (1999).

Fu, C., Sojka, P.E., and Sivathanu, Y.R., "Water Mist Impingement onto a Heated Surface," Paper No: AJTE99-6367. *Proceedings of the 5th Joint ASME/JSME Joint Thermal Engineering Conference*, (1999).

Fu, C., Sojka, P.E., and Sivathanu, Y.R., "On the Interaction between Evaporating Sprays and Heated Surfaces," *Proceedings of the 12th Annual Conference on Liquid Atomization and Spray Systems*, Indianapolis, pp. 271-276 (1999).

Oke, H.P., *An Experimental Study of Flame Spread Over PMMA Subject to a Water Mist*, M.S. Thesis, School of Mechanical Engineering, Purdue University, (November, 1999).

Williams, B.A. and Fleming, J.W., "Suppression Mechanisms of Alkali Metal Compounds," 1999, in Gann, R.G., Burgess, S.R., Whisner, K.C., and Reneke, P.A., eds., *Papers from 1991-2006 Halon Options Technical Working Conferences (HOTWC)*, CD-ROM, NIST SP 984-4, National Institute of Standards and Technology, Gaithersburg, MD, (2006).

Tan, N.C.B., DeSchepper, D.C., and Balogh, L., *Dendritic Polymers as Fire Suppressants*, ARL-TR-2071, Army Research Laboratory, Aberdeen, MD, (1999).

Rumminger, M.D., and Linteris, G.T., "Particle Measurements in Fe(CO)<sub>5</sub>-Inhibited Flames," *NIST Annual Conference on Fire Research*, Rockville MD, (1998).

Lentati, A.M. and Chelliah, H.K., "Dynamics of Water Droplets in a Counterflow Field and Their Effect on Flame Extinction," *Combustion and Flame* **115**, 158-179 (1998).

Lyon, R.K., *Development of a Self Atomizing Form of Water, Final Report to the Strategic Environmental Research and Development Program*, (1998).

Berman, C.H., Andersen, Jr., O.P., and Hoenig, S.A., *Electrically Charged Water Mists for Extinguishing Fires, Final Report to the Strategic Environmental Research and Development Program*, (1998).

Fleming, J.W., Reed, M.D., Zegers, E.J.P., Williams, B.A., and Sheinson, R.S., "Extinction Studies of Propane/Air Counterflow Diffusion Flames: The Effectiveness of Aerosols," 1998, in Gann, R.G., Burgess, S.R., Whisner, K.C., and Reneke, P.A., eds., *Papers from 1991-2006 Halon Options Technical Working Conferences (HOTWC)*, CD-ROM, NIST SP 984-4, National Institute of Standards and Technology, Gaithersburg, MD, (2006).

Sivathanu, Y., Oke, H.P., Fu, C., and Sojka, P.E., *Droplet Interaction with Hot Surfaces, Annual Report to the Strategic Environmental Research and Development Program*, (1998).

Yang, J.C., Chien, W., King, M., and Grosshandler, W.L., "A Simple Piezoelectric Droplet Generator," *Experiments in Fluids* **23**, 445, (1997).

Reed, M.D., Fleming, J.W., Williams, B.A., and Sheinson, R.S., "Laboratory Evaluation of Bicarbonate Powders as Fire Suppressants," *Proceedings of the International Conference on Ozone Protection Technologies*, pp. 333-334, Baltimore MD, (1997).

Reed, M.D., Williams, B.A., Sheinson, R.S. and Fleming, J.W., "Behavior of Bicarbonate Powders in Counterflow Diffusion Flames," *Proceedings of the Eastern States Section of the Combustion Institute*, Hartford CT, pp. 83-86 (1997).

## C.5 IMPROVED SUPPRESSANT DELIVERY

Hewson, J.C., and Keyser, D.R., *Suppression of Pool Fires with HFC-125 in a Simulated Engine Nacelle*, Technical Report SAND2007-3442, Sandia National Laboratories, Albuquerque NM, 2007.

Yang, J.C., and Keyser, D.R., "Fluid Dispensing and Dispersion," 2006, in Gann, R.G., Burgess, S.R., Whisner, K.C., and Reneke, P.A., eds., *Papers from 1991-2006 Halon Options Technical Working Conferences (HOTWC)*, CD-ROM, NIST Special Publication 984-4, National Institute of Standards and Technology, Gaithersburg, MD, 2006.

Bein, D., "A Review of the History of Fire Suppression on U.S. DoD Aircraft," 2006, in Gann, R.G., Burgess, S.R., Whisner, K.C., and Reneke, P.A., eds., *Papers from 1991-2006 Halon Options Technical Working Conferences (HOTWC)*, CD-ROM, NIST Special Publication 984-4, National Institute of Standards and Technology, Gaithersburg, MD, 2006.

Grosshandler, W.L., Cyphers, D., and Holland, G., "NGP Advances in Powder Panel and Propellant Technologies," 2006, in Gann, R.G., Burgess, S.R., Whisner, K.C., and Reneke, P.A., eds., *Papers from 1991-2006 Halon Options Technical Working Conferences (HOTWC)*, CD-ROM, NIST Special Publication 984-4, National Institute of Standards and Technology, Gaithersburg, MD, 2006.

Presser, C., and Avedisian, C.T., "Transport of High Boiling-Point Fire Suppressants in a Droplet-Laden Homogeneous Turbulent Flow Past a Heated Cylinder," *Atomization and Sprays*, **16** (6), 627-656, (2006).

Presser, C., Papadopoulos, G., and Widmann, J.F., "PIV Measurements of Water Mist Transport in a Homogeneous Turbulent Flow past an Obstacle," *Fire Safety Journal* **41**, 580-604, (2006).

Yoon, S.S., DesJardin, P.E., Presser, C., Hewson, J.C., and Avedisian, C.T., "Numerical Modeling and Experimental Measurements of Water Spray Impact and Transport over a Cylinder," *International Journal of Multiphase Flow* **32**, 132-157, (2006).

Disimile, P.J., Tucker, J.R., Crowell, B., and Davis, J.M., "The Transport of Water Sprays Past Generic Clutter Elements Found Within Engine Nacelles," *Fire Safety Journal* **40**, 65-78 (2005).

Swanson, L.A., Davis, J.M., and Disimile, P.J., "Vortex Entrainment and Separation using Flow Superposition," *Journal of Visualization* **9(1)**, (2006).

Keyser, D.R., and Hewson, J.C., "Assessment of Fire Suppression Simulations Using Full-scale Engine Nacelle Tests," 2005, in Gann, R.G., Burgess, S.R., Whisner, K.C., and Reneke, P.A., eds., *Papers from 1991-2006 Halon Options Technical Working Conferences (HOTWC)*, CD-ROM, NIST SP 984-4, National Institute of Standards and Technology, Gaithersburg, MD, (2006).

Hewson, J.C., and Keyser, D.R., "Predicting Fire Suppression in an Engine Nacelle," 2004, in Gann, R.G., Burgess, S.R., Whisner, K.C., and Reneke, P.A., eds., *Papers from 1991-2006 Halon Options Technical Working Conferences (HOTWC)*, CD-ROM, NIST SP 984-4, National Institute of Standards and Technology, Gaithersburg, MD, (2006).

Keyser, D.R., and Hewson, J.C., "Fire Suppressant Distribution in an Engine Nacelle," 2004, in Gann, R.G., Burgess, S.R., Whisner, K.C., and Reneke, P.A., eds., *Papers from 1991-2006 Halon Options Technical Working Conferences (HOTWC)*, CD-ROM, NIST SP 984-4, National Institute of Standards and Technology, Gaithersburg, MD, (2006).

Bein, D., "In-flight Suppressant Deployment Temperatures," 2004, in Gann, R.G., Burgess, S.R., Whisner, K.C., and Reneke, P.A., eds., *Papers from 1991-2006 Halon Options Technical Working Conferences (HOTWC)*, CD-ROM, NIST SP 984-4, National Institute of Standards and Technology, Gaithersburg, MD, (2006).

Fleming, J.W., and Yang, J.C., "Modeling Study of the Behavior of Liquid Fire Suppression Agents in a Simulated Engine Nacelle," 2004, in Gann, R.G., Burgess, S.R., Whisner, K.C., and Reneke, P.A., eds., *Papers from 1991-2006 Halon Options Technical Working Conferences (HOTWC)*, CD-ROM, NIST SP 984-4, National Institute of Standards and Technology, Gaithersburg, MD, (2006).

Disimile, P.J., Tucker, J.R., Stern, J., Mehl, L., and Crowell, B.J., "Velocity and Drop Size Distributions Downstream Generic Clutter Elements Found Within Engine Nacelles," 2004, in Gann, R.G., Burgess, S.R., Whisner, K.C., and Reneke, P.A., eds., *Papers from 1991-2006 Halon Options Technical Working Conferences (HOTWC)*, CD-ROM, NIST SP 984-4, National Institute of Standards and Technology, Gaithersburg, MD, (2006).

Yang, J.C., Manzello, S.L., Nyden, M.R., and Connaghan, M.D., "Cold Discharge of  $CF_3I$  in a Simulated Aircraft Engine Nacelle," *Proceedings of the Seventh International Symposium on Fire Safety Science*, International Association for Fire Safety Science, pp. 715-726, (2003).

Hamins, A., McGrattan, K., and Forney, G., *Unwanted Accelerated Burning After Suppressant Delivery*, NIST Special Publication 1004, National Institute of Standards and Technology, Gaithersburg, MD, (2003)

Presser, C., *Parametric Investigation of Droplet Atomization and Dispersion of Liquid Fire Suppressants, Final Report to the Strategic Environmental Research and Development Program*, National Institute of Standards and Technology, Gaithersburg, MD (2003).

Hewson, J.C., Tieszen, S.R., Sundberg, W.D., and DesJardin, P.E., "CFD Modeling of Fire Suppression and Its Role in Optimizing Suppressant Distribution," 2003, in Gann, R.G., Burgess, S.R., Whisner, K.C., and Reneke, P.A., eds., *Papers from 1991-2006 Halon Options Technical Working Conferences (HOTWC)*, CD-ROM, NIST SP 984-4, National Institute of Standards and Technology, Gaithersburg, MD, (2006).

Fallis, S., Reed, R., Weirenga, P., and Holland, G.F., "Advanced Propellant/Additive Development for Fire Suppressing Systems," 2003, in Gann, R.G., Burgess, S.R., Whisner, K.C., and Reneke, P.A., eds., *Papers from 1991-2006 Halon Options Technical Working Conferences (HOTWC)*, CD-ROM, NIST SP 984-4, National Institute of Standards and Technology, Gaithersburg, MD, (2006).

Cyphers, D.C., *Enhanced Powder Panels, Final Report to the Strategic Environmental Research and Development Program*, Skyward, Ltd., Wright-Patterson Air Force Base, OH, 2003.

Yang, J.C., Manzello, S.L., Nyden, M.R., and Connaghan, M.D., "Discharge Of  $CF_3I$  in a Cold Simulated Aircraft Engine Nacelle," 2002, in Gann, R.G., Burgess, S.R., Whisner, K.C., and Reneke, P.A., eds., *Papers from 1991-2006 Halon Options Technical Working Conferences (HOTWC)*, CD-ROM, NIST SP 984-4, National Institute of Standards and Technology, Gaithersburg, MD, (2006).

Cyphers, D.C., Frederick, S.A., and Haas, J.P., "Enhanced Powder Panels," 2002, in Gann, R.G., Burgess, S.R., Whisner, K.C., and Reneke, P.A., eds., *Papers from 1991-2006 Halon Options Technical Working Conferences (HOTWC)*, CD-ROM, NIST SP 984-4, National Institute of Standards and Technology, Gaithersburg, MD, (2006).

Presser, C., Widmann, J., and Papadopoulos, G., "Liquid Agent Transport Around Solid Obstacles," 2002, in Gann, R.G., Burgess, S.R., Whisner, K.C., and Reneke, P.A., eds., *Papers from 1991-2006 Halon Options Technical Working Conferences (HOTWC)*, CD-ROM, NIST SP 984-4, National Institute of Standards and Technology, Gaithersburg, MD, (2006).

DesJardin, P.E., Presser, C., Disimile, P.J., and Tucker, J.R., "A Droplet Impact Model for Agent Transport in Engine Nacelles," 2002, in Gann, R.G., Burgess, S.R., Whisner, K.C., and Reneke, P.A., eds., *Papers from 1991-2006 Halon Options Technical Working Conferences (HOTWC)*, CD-ROM, NIST SP 984-4, National Institute of Standards and Technology, Gaithersburg, MD, (2006).

Hamins, A., "Mechanisms of Unwanted Accelerated Burning," 2002, in Gann, R.G., Burgess, S.R., Whisner, K.C., and Reneke, P.A., eds., *Papers from 1991-2006 Halon Options Technical Working Conferences (HOTWC)*, CD-ROM, NIST SP 984-4, National Institute of Standards and Technology, Gaithersburg, MD, (2006).

Bennett, M.V., "Intumescent "Instant Firewalls" for Low-Cost Fire Protection," 2002, in Gann, R.G., Burgess, S.R., Whisner, K.C., and Reneke, P.A., eds., *Papers from 1991-2006 Halon Options Technical Working Conferences (HOTWC)*, CD-ROM, NIST SP 984-4, National Institute of Standards and Technology, Gaithersburg, MD, (2006).

Fallis, S., Reed, R., McCormick, J.L., and Holland, G.F., "Advanced Propellant/Additive Development for Fire Suppressing Gas Generators: Development + Test," 2002, in Gann, R.G., Burgess, S.R., Whisner, K.C., and Reneke, P.A., eds., *Papers from 1991-2006 Halon Options Technical Working Conferences (HOTWC)*, CD-ROM, NIST SP 984-4, National Institute of Standards and Technology, Gaithersburg, MD, (2006).

Black, A.R., Suo-Anttila, J.M., Disimile, P.J., and Tucker, J.R., *Numerical Predictions and Experimental Results of Air Flow in a Smooth Quarter-scale Nacelle*, 40<sup>th</sup> AIAA Aerospace Sciences Meeting, paper 2002-0856, (2002).

Black, A.R., Suo-Anttila, J.M., Gritzo, L.A., Disimile, P.J., and Tucker, J.R., *Numerical Predictions and Experimental Results of Air Flow in a Smooth Quarter-scale Nacelle*, Report SAND2002-1319, Sandia National Laboratories, Albuquerque, NM (2002).

DesJardin, P.E., Nelsen, J.M., Gritzo, L.A., and Ghee, T.A., *On the Development of a Subgrid Scale Clutter Model*, 40<sup>th</sup> AIAA Aerospace Sciences Meeting, paper 2002-0984, (2002).

Presser, C., Widmann, J.F., DesJardin, P.E., and Gritzo, L.A., *Measurement and Numerical Prediction of Homogeneous Turbulent Flow over a Cylinder: A Baseline for Droplet-laden Flow Studies*, 40th AIAA Aerospace Sciences Meeting, paper 2002-0905, (2002).

Takahashi, F., Schmoll, W.J., Strader, E.A., and Belovich, V.M., "Suppression Behavior of Obstruction-Stabilized Pool Flames," *Combustion Science and Technology* **163**, 107-130, (2001).

Bennett, M.V., *A Method for Extinguishing Engine Nacelle Fires by Use of Intumescent Coatings, Final Report To the Strategic Environmental Research and Development Program*, Booz-Allen & Hamilton, Inc., Dayton, OH, 2001.

Yang, J.C., Nyden, M.R., and Manzello, S.L., "Cold Discharge of CF3I in a Simulated Aircraft Engine Nacelle," 2001, in Gann, R.G., Burgess, S.R., Whisner, K.C., and Reneke, P.A., eds., *Papers from 1991-2006 Halon Options Technical Working Conferences (HOTWC)*, CD-ROM, NIST SP 984-4, National Institute of Standards and Technology, Gaithersburg, MD, (2006).

DesJardin, P.E., Nelsen, J.M., Gritzo, L.A., Lopez, A.R., Suo-Anttila, J.M., Keyser, D.R., Ghee, T.A., and Disimile, P.A., "Towards Subgrid Scale Modeling of Suppressant Flow in Engine Nacelle Clutter," 2001, in Gann, R.G., Burgess, S.R., Whisner, K.C., and Reneke, P.A., eds., *Papers from 1991-2006 Halon Options Technical Working Conferences (HOTWC)*, CD-ROM, NIST SP 984-4, National Institute of Standards and Technology, Gaithersburg, MD, (2006).

Presser, C., Widmann, J.F., DesJardin, P.E., and Gritzo, L.A., "Measurements and Numerical Predictions of Liquid Agent Dispersal Around Solid Obstacles," 2001, in Gann, R.G., Burgess, S.R., Whisner, K.C., and Reneke, P.A., eds., *Papers from 1991-2006 Halon Options Technical Working Conferences (HOTWC)*, CD-ROM, NIST SP 984-4, National Institute of Standards and Technology, Gaithersburg, MD, (2006).

Bennett, M.V., *A Method for Extinguishing Engine Nacelle Fires By Use of Intumescent Coatings, Final Report to the Strategic Environmental Research and Development Program*, Booz-Allen & Hamilton, Dayton, OH, (2001).

Tuzla, K., Palmer, T., Chen, J., Sundaram, R., Yeung, W., *Development of Computer Program for Fire Suppressant Fluid Flow Final Technical Report Volume I -- Main Report (6B1 Suppressant Flow Through Piping Final Report Vol. 1)*, Final Report to the Strategic Environmental Research and Development Program, September, Lehigh university, Bethlehem, PA, (2000)

Tuzla, K., Palmer, T., Chen, J., Sundaram, R., Yeung, W., *Development of Computer Program for Fire Suppressant Fluid Flow Final Technical Report Volume II -- Input Manual for the Program Experimental Data Assessment of the Program (6B1 Suppressant Flow Through Piping Final Report Vol. 2)*, Final

*Report to the Strategic Environmental Research and Development Program*, Lehigh university, Bethlehem, PA, (2000).

Fallis, S.; Reed, R.; McCormick, J. L.; Wilson, K. A.; Holland, G F., "Advanced Propellant/Additive Development for Fire Suppressing Gas Generators: Hybrid Systems," 2001, in Gann, R.G., Burgess, S.R., Whisner, K.C., and Reneke, P.A., eds., *Papers from 1991-2006 Halon Options Technical Working Conferences (HOTWC)*, CD-ROM, NIST SP 984-4, National Institute of Standards and Technology, Gaithersburg, MD, (2006).

Fallis, S.; Reed, R.; Lu, Y.C.; Wierenga, P.H.; Holland, G F., "Advanced Propellant/Additive Development for Fire Suppressing Gas Generators," 2000, in Gann, R.G., Burgess, S.R., Whisner, K.C., and Reneke, P.A., eds., *Papers from 1991-2006 Halon Options Technical Working Conferences (HOTWC)*, CD-ROM, NIST SP 984-4, National Institute of Standards and Technology, Gaithersburg, MD, (2006).

Takahashi, F., Schmoll, W.J., Strader, E., and Belovich, V.M., "Suppression of a Non-premixed Flame Stabilized by a Backward-Facing Step," *Combustion and Flame* **122**, 105-116 (2000).

Takahashi, F., Schmoll, W. J., and Belovich, V. M., "Suppression of Bluff-Body Stabilized Pool Flames," *AIAA 37th Aerospace Sciences Meeting*, Paper No. 99-0327, (1999).

Takahashi, F., Schmoll, W. J., and Belovich, V. M., "Stabilization and Suppression of a Diffusion Flame Behind a Step," *Proceedings of the 1<sup>st</sup> Joint U.S. Sections Meeting of the Combustion Institute*, Washington DC, (1999).

Takahashi, F., Schmoll, W. J., E. A. Strader, and Belovich, V. M., "Effects of Obstruction on Fire Suppression Efficiency," 1999, in Gann, R.G., Burgess, S.R., Whisner, K.C., and Reneke, P.A., eds., *Papers from 1991-2006 Halon Options Technical Working Conferences (HOTWC)*, CD-ROM, NIST SP 984-4, National Institute of Standards and Technology, Gaithersburg, MD, (2006).

Tieszen, S.R. and Lopez, A.R., "Issues in Numerical Simulation of Fire Suppression," 1999, in Gann, R.G., Burgess, S.R., Whisner, K.C., and Reneke, P.A., eds., *Papers from 1991-2006 Halon Options Technical Working Conferences (HOTWC)*, CD-ROM, NIST SP 984-4, National Institute of Standards and Technology, Gaithersburg, MD, (2006).

Takahashi, F., Schmoll, W.J., and Belovich, V.M., "Suppression of Bluff-body Stabilized Flames," Paper AIAA 98-3529, *AIAA/ASME/ASSEE Joint Propulsion Conference*, (1998).

Takahashi, F., Schmoll, W. J., and Belovich, V. M., "Extinction of Bluff-Body Stabilized Diffusion Flames," *Proceedings of the Spring Technical Meeting of the Central States Section of the Combustion Institute*, Paper no. 37, (1998).

Bennett, M.V., "Examining the Feasibility of Extinguishing Engine Nacelle Fires by the Strategic Placement of Intumescent Materials," 2001, in Gann, R.G., Burgess, S.R., Whisner, K.C., and Reneke, P.A., eds., *Papers from 1991-2006 Halon Options Technical Working Conferences (HOTWC)*, CD-ROM, NIST SP 984-4, National Institute of Standards and Technology, Gaithersburg, MD, (2006).

Bennett, M.V., "A Method for Extinguishing Engine Nacelle Fires By Use of Intumescent Coatings," 2000, in Gann, R.G., Burgess, S.R., Whisner, K.C., and Reneke, P.A., eds., *Papers from 1991-2006 Halon Options Technical Working Conferences (HOTWC)*, CD-ROM, NIST SP 984-4, National Institute of Standards and Technology, Gaithersburg, MD, (2006).

## **C.6 VIABILITY OF NEW SUPPRESSION TECHNOLOGIES**

Bennett, J.M., "NGP Life-cycle Cost Analysis of Aircraft Fire Suppression Systems," 2006, in Gann, R.G., Burgess, S.R., Whisner, K.C., and Reneke, P.A., eds., *Papers from 1991-2006 Halon Options*

*Technical Working Conferences (HOTWC)*, CD-ROM, NIST Special Publication 984-4, National Institute of Standards and Technology, Gaithersburg, MD, 2006.

McNesby, K.L., and Johnsson, E.L., Instrumentation for Bench- and Large-scale Test Fixtures,” 2006, in Gann, R.G., Burgess, S.R., Whisner, K.C., and Reneke, P.A., eds., *Papers from 1991-2006 Halon Options Technical Working Conferences (HOTWC)*, CD-ROM, NIST Special Publication 984-4, National Institute of Standards and Technology, Gaithersburg, MD, 2006.

Bennett, J.M., “Verification of NGP Fire Suppression principles,” 2006, in Gann, R.G., Burgess, S.R., Whisner, K.C., and Reneke, P.A., eds., *Papers from 1991-2006 Halon Options Technical Working Conferences (HOTWC)*, CD-ROM, NIST Special Publication 984-4, National Institute of Standards and Technology, Gaithersburg, MD, 2006.

Johnsson, E.L., Mulholland, G.W., Fraser, G.T., Leonov, I.I., and Golubiatnikov, G.Y., *Development of a Fast-response Fire Suppressant Concentration Meter*, NIST Technical Note 1464, National Institute of Standards and Technology, Gaithersburg, MD, (2004).

Johnsson, E.L., Mulholland, G.W., Fraser, G.T., Leonov, I.I., and Golubiatnikov, G.Y., *Description and Usage of a Fast-response Fire Suppressant Concentration Meter*, NIST Technical Note 1463, National Institute of Standards and Technology, Gaithersburg, MD, (2004).

Davis, J.M., and Disimile, P.J., “Effect of Optical Configuration Selection on Phase Doppler Anemometer Fire Suppressant Nozzle Characterizations,” 2004, in Gann, R.G., Burgess, S.R., Whisner, K.C., and Reneke, P.A., eds., *Papers from 1991-2006 Halon Options Technical Working Conferences (HOTWC)*, CD-ROM, NIST SP 984-4, National Institute of Standards and Technology, Gaithersburg, MD, (2006).

Kolleck, M.L., Bennett, M.V., and Mercer, K.L., *Cost Analysis of Aircraft Dry Bay Fire Suppression Systems*, SURVIAC Report, Booz Allen Hamilton, Dayton, OH, (2003). Restricted Distribution.

Kolleck, M.L., Bennett, M.V., and Mercer, K.L., *Cost Analysis of Fire Suppression Systems For Fighter Aircraft*, SURVIAC Report TR-01-005, Booz Allen Hamilton, Dayton, OH, (2002). Restricted Distribution.

Kolleck, M.L., Bennett, M.V., and Mercer, K.L., *Cost Analysis of Fire Suppression Systems For Cargo Aircraft*, SURVIAC Report TR-00-006, Booz Allen Hamilton, Dayton, OH, (2002). Restricted Distribution.

Kolleck, M.L., Bennett, M.V., and Mercer, K.L., *Cost Analysis of Fire Suppression Systems For Rotary-Wing Aircraft*, SURVIAC Report TR-02-007, Booz Allen Hamilton, Dayton, OH, (2002). Restricted Distribution.

Kolleck, M.L., Bennett, M.V., and Mercer, K.L., *Cost Analysis of Fire Suppression Systems Methodology Using Altered Fire Suppression Performance*, SURVIAC Report TR-01-006, Booz Allen Hamilton, Dayton, OH, (2002). Restricted Distribution.

Bennett, J.M., and Kolleck, M.L., “Cost Analysis of Fire Suppression Systems,” 2002, in Gann, R.G., Burgess, S.R., Whisner, K.C., and Reneke, P.A., eds., *Papers from 1991-2006 Halon Options Technical Working Conferences (HOTWC)*, CD-ROM, NIST SP 984-4, National Institute of Standards and Technology, Gaithersburg, MD, (2006).

McNesby, K.L., Miziolek, A.W., and Skaggs, R.R., *Laser-Based Instrumentation for Real-Time, In-Situ Measurements of Combustible Gases, Combustion By-Products, & Suppression Concentrations, Final Report to the Strategic Environmental Research and Development Program*, Army Research Laboratory, Aberdeen MD, 2002.

Bennett, J.M. and Kolleck, M.L., “Cost Analysis of Fire Suppression Systems,” 2001, in Gann, R.G., Burgess, S.R., Whisner, K.C., and Reneke, P.A., eds., *Papers from 1991-2006 Halon Options Technical*

*Working Conferences (HOTWC)*, CD-ROM, NIST SP 984-4, National Institute of Standards and Technology, Gaithersburg, MD, (2006).

Skaggs, R.R., Daniel, R.G., Miziolek, A.W., McNesby, K.L., Herud, C., Bolt, W.R., and Horton, D., *Diode Laser Measurements of HF Concentrations from Heptane/Air Pan Fires Extinguished by FE-36 and FE-36 Plus Ammonium Polyphosphate*, ARL-TR-2143, Army Research Laboratory, Aberdeen, MD, (2000).

McNesby, K.L., Wainner, R.T., Daniel, R.G., Skaggs, R.R., Morris, J.B., Miziolek, A.W., Jackson, W.M., and McLaren, I.A., "Detection and Measurement of Middle Distillate Fuel Vapors Using Tunable Diode Lasers," *Applied Optics* **40**, 840-845 (2001).

McNesby, K.L., Wainner, R.T., Miziolek, A.W., Jackson, W.M., and McLaren, I.A., "High Sensitivity Laser Absorption Measurements of Broad Band Absorbers in the Near Infrared Spectral Region," *Applied Optics* **39**, 5006-5011 (2000).

McNesby, K.L., Miziolek, A.W., and McLaren, I.A., "Rapid High Sensitivity Laser Absorption Measurements of Broad Band Absorbers in the Near Infrared Spectral Region," *Proceedings of 2000 Laser Applications to Chemical and Environmental Analysis Topical Meeting Technical Digest*, Optical Society of America, Washington, DC, pp. 80-83, (2000).

Lancaster, E.D., McNesby, K.L., Daniel, R.G., and Miziolek, A.W., "Spectroscopic Analysis of Fire Suppressants and Refrigerants by Laser-induced Breakdown Spectroscopy," *Applied Optics* **38**, 1476-1480 (1999). Also issued as ARL-TR 2300, Army Research Laboratory, Aberdeen MD (2000).

Bennett, M.V., "Relative Benefit Assessment of Fire Protection System Changes," 1999, in Gann, R.G., Burgess, S.R., Whisner, K.C., and Reneke, P.A., eds., *Papers from 1991-2006 Halon Options Technical Working Conferences (HOTWC)*, CD-ROM, NIST SP 984-4, National Institute of Standards and Technology, Gaithersburg, MD, (2006).

Skaggs, R.R., Daniel, R.G., Miziolek, A.W., McNesby, K.L., Herud, C., Bolt, W.R. and Horton, D., "Diode Laser Measurements of HF Concentrations From Heptane/Air Pan Fires Extinguished by FE-36 And FE-36 Plus Ammonium Polyphosphate," *Proceedings of the International Society for Optical Engineering: Photonics East*, 156f (1999).

McNesby, K.L., Skaggs, R.R., and Miziolek, A.M., *Diode Laser-Based Measurements of Hydrogen Fluoride Gas during Chemical Suppression of Fires*, ARL Technical Report, ARL-TR-1785, Army research Laboratory, Aberdeen, MD, (1999).

McNesby, K.L., Skaggs, R.R., Miziolek, A.W., and McLaren, I.A., "Diode Laser-Based Sensor for Fast Measurement of Binary Gas Mixtures," 1999, in Gann, R.G., Burgess, S.R., Whisner, K.C., and Reneke, P.A., eds., *Papers from 1991-2006 Halon Options Technical Working Conferences (HOTWC)*, CD-ROM, NIST SP 984-4, National Institute of Standards and Technology, Gaithersburg, MD, (2006).

Skaggs, R.R., Daniel, R.G., Miziolek, A.W., McNesby, K.L., Herud, C., Bolt, W.R., and Horton, D., "Diode Laser Measurements of HF Concentrations Produced from Heptane/Air Pan Fires Extinguished By FE-36, FM-200, FE-36 Plus APP, or FM-200 Plus APP," *Applied Spectroscopy*, **53**, 1143-1148 (1999).

Bennett, M.V., "Use of the Department of Defense Operational Requirements-Base Casualty Assessment (ORCA) Software System to Determine Occupant Response to Fire and the Extinguishment Process," *Human Behavior in Fire, Proceedings of the First International Symposium*, Belfast, Northern Ireland, pp. 769-777 (1998).

Williamson, C.K, McNesby, K.L., Daniel, R.G., and Miziolek, A.W., "Laser-Induced Breakdown Spectroscopy for Real-Time Detection of Halon Alternative Agents," *Analytical Chemistry*, **70**, 1186-1191 (1998).

McNesby, K.L., Daniel, R.G., Skaggs, R.R., Miziolek, A.W., and Miser, C.S., "Near-Infrared Tunable Diode Laser Diagnostics in Laboratory and Real-Scale Inhibited Flames," *Proceedings of Laser Applications to Chemical and Environmental Analysis Topical Meeting*, p. 203, (1998).

McNesby, K.L., Skaggs, R.R., and Miziolek, A.M., "Diode Laser-Based Measurements of Hydrogen Fluoride Gas During Chemical Suppression of Fires," *Applied Physics B*, **67**, 443-447 (1998).

McNesby, K.L., Miser, C.S., Lancaster, E., Skaggs, R.R., and Miziolek, A.W., "Laser-Based Measurements of Combustion Species During Firefighting Onboard Military Vessels," Paper No. 943, *The Pittsburgh Conference*, 46f (1998).

McNesby, K.L., Skaggs, R.R., Miziolek, A.W., Clay, M., Hoke, S.H., and Miser, C.S., "Diode Laser-Based Measurements Of Fuels, Oxidizers, and Combustion Products During Fire Suppressant Testing," 1998, in Gann, R.G., Burgess, S.R., Whisner, K.C., and Reneke, P.A., eds., *Papers from 1991-2006 Halon Options Technical Working Conferences (HOTWC)*, CD-ROM, NIST SP 984-4, National Institute of Standards and Technology, Gaithersburg, MD, (2006).

McNesby, K.L., Daniel, R.G., Miziolek, A.W., and Modiano, S.H., "Optical Measurement of Toxic Gases Produced During Firefighting Using Halons," *Applied Spectroscopy* **51**, 678-683, (1997). Also available as ARL Report ARL-TR-1349, Army Research Laboratory, Aberdeen, MD, (1997).

McNesby, K.L., Daniel, R.G., Miziolek, A.W., and Modiano, S.H., "Laboratory and Field Measurements of Hydrogen Fluoride Produced in Inhibited Flames Using Near-Infrared Tunable Diode Laser Spectroscopy," *NIST Annual Conference on Fire Research*, (1996).

## **C.7 IMPROVED FUEL TANK INERTION**

Bennett, M.V., *Review of Technologies for Active Suppression for Fuel Tank Explosions, Final Report to the Strategic Environmental Research and Development Program*, Booz-Allen & Hamilton, Dayton, OH, (2000).

Bennett, M.V., "Review of Technologies for Active Suppression of Fuel Tank Explosions," 2000, in Gann, R.G., Burgess, S.R., Whisner, K.C., and Reneke, P.A., eds., *Papers from 1991-2006 Halon Options Technical Working Conferences (HOTWC)*, CD-ROM, NIST SP 984-4, National Institute of Standards and Technology, Gaithersburg, MD, (2006).

---

## Index

---

<b>Term</b>	<b>Section Location</b>
<b>Aerosol properties</b>	
burning surface	4.2, 4.4, 4.6, 4.7, 9.3
droplet diameter	4.2, 4.3, 4.4, 4.5, 4.6, 4.7, 8.4, 8.7, 11.3, 11.7
particle diameter	3.3, 4.2, 4.3, 4.5, 9.2
<b>Environmental effects</b>	
atmospheric lifetime	1.5, 6.3, 6.5, 6.8, 7.1, 7.2, 7.3, 7.4, 7.5, 10.3, 11.4, 11.6, 11.7, 12.1
global warming	1.5, 2.5, 6.3, 6.5, 7.1, 7.4, 10.3, 10.5
OH rate constant	6.5, 7.3, 7.4
ozone depletion	1.4, 1.5, 2.2, 2.4, 6.3, 6.4, 6.5, 7.1, 7.3, 7.4, 7.5
photolysis	3.3, 3.4, 6.5, 7.1, 7.3, 7.4
<b>Fire suppressants</b>	
aerosols	1.6, 3.3, 4.1, 4.2, 4.3, 4.4, 4.5, 4.6, 4.7, 6.4, 6.5, 7.5
alkali metal	3.3, 3.5, 4.1, 4.5, 4.6, 7.3, 9.2, 9.3
aluminum oxide	2.5, 9.2
bicarbonates	4.2, 4.5

<b>Term</b>	<b>Section Location</b>
2-bromo-3,3,3-trifluoropropene	7.1, 11.8
bromofluoro compounds	7.4, 7.5
CF <sub>3</sub> I	2.3, 2.4, 2.5, 3.2, 3.3, 5.4, 6.7, 7.1, 7.4, 7.5, 8.1, 8.2, 8.3, 8.4, 8.5, 9.3, 11.5, 11.8
CO <sub>2</sub> hydrate	8.2, 9.1, 9.2
complexation (complexes)	2.2, 2.3, 3.3, 4.6, 6.7, 7.4, 11.3, 11.7, 11.8
dendrimers	4.6
dimethyl methylphosphonate (DMMP)	3.4, 3.5, 4.2, 7.4, 11.3
FC-218	2.5, 3.2, 3.3, 5.4, 7.4, 8.3
ferrocene	3.3, 3.4, 9.3, 11.3, 11.5
flame retardants	7.3
halon 1001	1.3, 2.5
halon 1011	2.2, 2.3, 2.5
halon 1202	2.2, 2.3, 2.5
halon 1211	1.3, 1.5, 2.3, 3.2, 6.1, 7.1, 9.2
halon 1301	1.3, 1.4, 1.5, 1.6, 2.2, 2.3, 2.4, 2.5, 3.2, 3.3, 3.4, 3.5, 4.1, 4.5, 4.6, 5.4, 6.1, 6.3, 6.4, 6.5, 7.1, 7.3, 7.4, 7.5, 8.1, 8.3, 8.4, 8.5, 8.7, 9.1, 9.2, 9.3, 10.1, 10.2, 10.3, 10.4, 10.5, 10.7, 10.8, 11.1, 11.2, 11.3, 11.4, 11.5, 11.6, 11.7, 11.8, 12.1
HFC-125	1.5, 2.3, 2.5, 3.1, 3.2, 3.3, 5.4, 5.5, 6.1, 6.2, 6.3, 6.4, 7.1, 7.4, 8.3, 8.4, 8.5, 8.6, 8.7, 9.2, 9.3, 10.2, 10.3, 10.4, 10.5, 10.7, 11.1, 11.5, 11.6, 11.7, 12.1

---

<b>Term</b>	<b>Section Location</b>
HFC-227ea	1.5, 2.5, 3.2, 3.3, 3.5, 3.5, 5.3, 5.4, 6.4, 7.1, 7.4, 8.3, 8.4, 9.3, 11.7, 11.8
hydrofluorocarbons	1.4, 3.2, 3.5, 6.4, 6.5, 6.7, 7.1, 7.4
inorganic chemical families	4.2, 6.3, 7.3, 7.4, 11.3, 11.6
iron pentacarbonyl	3.3, 4.7, 9.3
iron-containing compounds	3.2, 3.6, 9.3, 11.4
main group elements	7.3
metal-containing compounds	3.3, 3.4, 3.5, 7.4
Monnex	9.2
phosphorus-containing compounds	3.2, 3.5, 7.3, 7.4, 11.3
potassium lactate	4.2, 6.4
Purple K	9.2
thermal agents	4.7, 7.4
tropodegradable compounds	7.2, 7.4
water mist	1.5, 4.2, 4.3, 4.5, 4.7, 5.1, 7.1, 8.7, 9.2
water vapor	2.5, 4.5, 4.6, 5.3, 6.4, 6.5, 6.6, 9.2, 9.3

<b>Term</b>	<b>Section Location</b>
Fire suppression principles	1.5
Fire test platforms	
Aerospace Vehicle Survivability Facility	9.2
Aircraft Engine Nacelle Test Facility	11.7
Bradley Fighting Vehicle	5.3
Iron Bird	8.6
Super Cobra	9.2, 9.3
Fire threats	4.2
Flame inhibition processes	
catalytic flame inhibition	7.4, 11.4
condensation	3.3, 3.4, 3.5, 4.2, 4.5, 4.6, 6.4, 7.3, 7.4, 8.3, 8.7, 11.2, 11.3, 11.6, 11.7, 11.8
engine knock	3.3, 3.4, 11.3
flame inhibition	2.5, 3.1, 3.2, 3.4, 3.5, 4.2, 4.5, 4.6, 6.4, 6.5, 11.3
flame structure	3.2, 3.3, 3.4, 3.5, 4.5, 4.6, 6.4, 6.5, 11.7
kinetic mechanism	3.2, 3.3, 3.4, 3.5, 3.6, 4.2, 4.5, 7.4, 11.4
radical recombination	3.2, 3.3, 3.4, 3.5, 4.2, 4.5, 4.6, 7.3, 11.3

<b>Term</b>	<b>Section Location</b>
Flame suppression efficiency	
aerosol properties	4.2, 4.7, 5.1, 5.2
burning velocity	3.2, 3.3, 3.4, 3.5, 4.2, 4.5, 4.6, 7.3, 11.3
catalytic flame inhibition	7.4, 11.4
chemical contribution	3.2, 3.3, 4.5
cup burner	3.2, 3.3, 3.4, 3.5, 4.2, 4.5, 5.2, 6.4, 6.5, 7.3, 7.4, 7.5, 8.6, 8.7, 10.5, 11.3, 11.4, 11.6, 11.7, 11.8, 11.9, 12.1
DLAFSS (dispersed liquid agent fire suppression screen)	4.6, 4.7, 6.4, 6.5, 6.8, 7.4
extinction concentration	3.3, 3.5, 4.5, 6.4
extinction strain rate	3.2, 3.3, 3.4, 3.5, 4.4, 6.4
flame temperature	2.3, 3.3, 3.4, 3.5, 3.6, 4.2, 4.4, 4.5, 4.6, 4.7, 5.2, 7.4, 9.2, 9.3, 11.3, 11.4, 11.8
fluid dispersion	8.2, 8.5
particles	2.3, 3.1, 3.2, 3.3, 3.4, 4.1, 4.2, 4.3, 4.4, 4.5, 4.6, 4.7, 5.1, 5.2, 5.3, 6.4, 7.3, 8.4, 8.7, 9.2, 11.3, 11.4, 11.6, 11.7, 11.8, 12.1
physical contribution	3.3
suppression efficiency	1.3, 1.4, 1.5, 2.5, 3.2, 3.5, 4.2, 4.5, 6.3, 6.4, 6.5, 7.1, 7.3, 7.4, 9.3, 10.1, 10.2, 10.3, 11.3, 11.6, 11.7
surface cooling	4.7, 4.8, 11.3

<b>Term</b>	<b>Section Location</b>
TARPF (transient application, recirculating pool fire apparatus)	5.4, 5.5, 6.4, 6.5, 7.4, 11.4
<b>Flame types</b>	
diffusion flame	1.4, 2.3, 3.1, 3.2, 3.3, 3.4, 3.5, 3.6, 4.2, 4.3, 6.4, 6.5, 7.3, 7.4, 8.5, 8.7, 9.2, 10.5, 11.3, 11.4
non-premixed flame	3.2, 3.3, 3.4, 3.5, 4.4, 4.5, 4.6, 5.2
premixed flame	3.2, 3.3, 3.4, 3.5, 4.2, 4.3, 4.5, 4.6, 4.7, 5.2, 7.4, 8.7, 11.4
<b>Fluid delivery</b>	
clutter	2.3, 2.5, 8.1, 8.4, 8.5, 8.6, 8.7, 9.2, 10.4, 11.3, 11.7, 11.8, 12.1
dispersion	1.5, 2.5, 4.2, 4.5, 4.7, 5.1, 6.4, 7.2, 7.4, 7.5, 8.1, 8.5, 8.4, 8.6, 9.2, 9.3, 10.1, 10.3, 10.4, 11.2, 11.3, 11.6, 11.7, 11.8
pipng	4.3, 8.1, 8.3, 8.4, 8.5, 8.7, 9.2, 11.3, 11.7
recirculation zone	2.2, 2.3, 6.5, 8.4, 8.5, 8.6, 11.3, 11.7, 11.8, 11.9, 12.1
VULCAN	8.5, 8.6, 8.7, 9.2, 11.3
<b>Fuels</b>	
DF-2	5.2, 5.3, 8.5
gasoline	3.3, 5.2, 5.3, 11.3
heptane	3.2, 3.3, 3.4, 4.2, 4.3, 4.5, 5.3, 6.4, 7.4, 7.5, 8.5, 8.7
JP-8	2.3, 2.4, 4.2, 4.6, 4.7, 5.2, 5.3, 6.4, 6.5, 8.5, 8.7, 9.2, 9.3, 10.3, 10.4, 10.5, 11.7

<b>Term</b>	<b>Section Location</b>
methane	1.3, 3.1, 3.2, 3.3, 3.4, 3.5, 4.2, 4.5, 4.6, 5.2, 5.3, 6.4, 7.3
propane	3.2, 3.3, 3.4, 3.5, 4.4, 4.5, 4.6, 5.2, 6.4, 6.5, 7.3, 7.4, 8.7, 9.3
<b>Gas generators</b>	
HFE (hybrid fire extinguisher)	4.7, 7.4, 8.4, 9.1, 9.3, 10.3
pressure exponent	9.3, 10.1
SPFE (solid propellant fire extinguisher)	10.3, 12.1
SPGG (solid propellant gas generator)	3.3, 6.4, 6.5, 8.3, 9.1, 9.2, 9.3, 10.1, 10.2, 10.3
<b>Government agencies and programs</b>	
Aberdeen Proving Ground	5.3
ARL (Army Research Laboratory)	4.6, 5.3, 10.3
Department of Defense	1.1, 1.4, 1.5, 2.1, 2.2, 2.3, 2.4, 2.5, 3.1, 3.2, 6.3, 7.1, 9.3, 10.5, 12.1
FAA (Federal Aviation Administration)	2.2, 2.3, 2.4, 2.5, 3.2, 9.2
JASPO (Joint Aircraft Survivability Program Office)	3.1, 3.2, 9.2

<b>Term</b>	<b>Section Location</b>
NAVAIR (Naval Air Systems Command)	8.6, 8.7, 9.3
NAWC (Naval Air Warfare Center)	9.3
NIST (National Institute of Standards and Technology)	2.4, 2.5, 3.2, 4.2, 4.4, 4.6, 5.4, 6.4, 7.4, 8.3, 8.5, 9.2, 10.3, 11.1, 12.1
NRL (Naval Research Laboratory)	3.2, 4.2, 4.5, 5.2, 7.1
SERDP (Strategic Environmental Research and Development Program)	1.5
TDP (Technology Development Program)	1.4, 1.5, 2.2, 2.3, 2.4, 2.5, 7.1, 7.4, 11.1, 11.7
Wright-Patterson Air Force Base	2.5, 5.4, 8.1, 9.2, 11.7, 12.1
Halon Options Technical Working Conferences (HOTWC)	1.5, 2.3, 6.3, 7.1, 7.3, 10.3, 11.1, 12.1
<b>Life cycle costing</b>	
future aircraft	10.4, 10.7, 11.1, 11.5
legacy aircraft	2.3, 9.2, 10.4, 10.5

<b>Term</b>	<b>Section Location</b>
<b>Life Safety</b>	
arrhythmia	6.4, 6.7, 7.2, 7.4, 11.4, 12.1
cardiac sensitization	2.3, 6.4, 6.7, 7.1, 7.2, 11.4
partition coefficient	6.7, 6.8, 7.5, 11.4
PBPK model	6.7
toxicity	1.3, 1.4, 1.5, 2.3, 2.5, 3.3, 3.4, 4.2, 4.6, 6.1, 6.4, 6.7, 6.8, 7.1, 7.2, 7.3, 7.4, 9.2, 9.3, 10.3, 10.5, 11.4, 11.5, 12.1
<b>Measurement techniques</b>	
DIRRACS (differential infrared rapid agent concentration sensor)	5.4, 5.5, 11.4
Halonyzer	2.5, 5.1, 10.4, 11.7, 11.8, 11.9
LDV (laser Doppler velocimetry)	3.2, 3.3, 4.3, 4.5, 8.5
LIBS (laser induced breakdown spectroscopy)	5.3, 5.4
PDI (phase Doppler interferometry)	4.3, 8.4
PDPA (phase Doppler particle anemometry)	4.5, 4.7

---

<b>Term</b>	<b>Section Location</b>
PIV (particle image velocimetry)	4.3, 8.4
TDLAS (tunable diode laser absorption spectroscopy)	5.2, 5.3
Next Generation Fire Suppression Technology Program	1.1, 2.1, 4.1, 6.1, 12.1
Non-government organizations	
AeroChem Research Laboratories	8.7
Aerojet	9.3
Chemical Development Studies	6.4
Lehigh University	9.2
NMERI (New Mexico Engineering Research Institute)	6.4, 7.1, 7.3, 7.4, 8.7
Sandia National Laboratories	7.4, 8.5
Skyward	9.1, 9.2, 10.3
University of Virginia	3.3, 4.5
Powder panels	9.1, 9.2

<b>Term</b>	<b>Section Location</b>
<b>Protected compartments</b>	
APU	1.4, 2.2, 2.3, 2.4, 2.5, 9.2, 10.3, 10.4, 10.5, 10.7
auxiliary power unit	2.2, 9.2, 10.3, 10.4
cargo compartment	2.2, 2.3
dry bay	1.5, 2.1, 2.2, 2.3, 2.4, 2.5, 3.1, 3.2, 5.1, 5.4, 6.4, 7.1, 7.4, 8.4, 8.5, 9.1, 9.2, 9.3, 10.2, 11.1, 11.2, 11.3, 11.5, 11.6, 11.7, 12.1
engine nacelle	1.5, 2.2, 2.3, 2.4, 2.5, 3.2, 4.7, 6.4, 7.1, 7.3, 7.4, 8.1, 8.2, 8.4, 8.5, 8.6, 8.7, 9.2, 10.2, 10.3, 10.4, 10.5, 10.7, 11.1, 11.3, 11.8, 11.9, 12.1
fuel tank ullage	2.1, 2.2, 2.3, 9.2
<b>Types of fires</b>	
cold soak	2.3, 9.3
incident data	2.3, 2.4, 10.1
pool fires	1.4, 2.3, 4.2, 4.6, 5.3, 8.1, 8.5, 8.6, 8.7, 10.3, 10.4, 11.7, 11.8, 12.1
spray fires	2.3, 5.3, 8.1, 11.3, 11.7, 11.8, 12.1
temperature environment	2.2, 2.3, 4.4, 4.5, 7.4, 9.2
<b>Volatility</b>	
boiling point	2.3, 2.4, 3.2, 3.3, 4.3, 4.7, 6.3, 6.4, 6.5, 6.7, 7.1, 7.2, 7.3, 7.4, 7.5, 8.1, 8.2, 8.3, 8.4, 8.5, 8.6, 9.2, 10.1, 10.3, 10.6, 11.2, 11.3, 11.4, 11.5, 11.6, 11.7, 11.8, 12.1
evaporation rate	3.4, 4.5, 6.4, 6.7, 8.6, 11.7

